CODEN: JASMAN

The Journal of the Acoustical Society of America

ISSN: 0001-4966

Vol. 116, No. 1, July 2004

(Continued)

THE JOURNAL OF THE ACOUSTICAL SOCIETY OF AMERICA VOL. 116, NO. 1, JUlY 2004

CONTENTS—*Continued from preceding page*

(Continued)

THE JOURNAL OF THE ACOUSTICAL SOCIETY OF AMERICA VOL. 116, NO. 1, JULY 2004

CONTENTS—*Continued from preceding page*

(Continued)

THE JOURNAL OF THE ACOUSTICAL SOCIETY OF AMERICA VOL. 116, NO. 1, JUlY 2004

CONTENTS—*Continued from preceding page*

ACOUSTICAL NEWS—USA

Elaine Moran
Acoustical Society of America, Suite 1NO1, 2 Huntington Quadrangle, Melville, NY 11747-4502

Editor's Note: *Readers of this Journal are encouraged to submit news items on awards, appointments, and other activities about themselves or their colleagues. Deadline dates for news items and notices are 2 months prior to publication.*

Reviewers of Manuscripts, 2003

Each year the *Journal* endeavors to publish a list of all the persons who reviewed manuscripts during the preceding year. Such a list is a compendium of names supplied by the Associate Editors. Because our peer review system depends strongly on the continuing anonymity of the reviewers, the *Journal* publishes these names in alphabetical order without identification of the associate editors who provided the names and without identification of the papers they reviewed. The primary reason for the publication of the list is to express the *Journal's* gratitude to its reviewers. Reviewing a paper is often a very time consuming and demanding task, and the anonymity requirement yields no professional recognition to those who generously provide their time to help the Associate Editors decide which papers should be published and to give constructive criticisms to the authors. The *Journal* is justifiably proud of this list, which includes a goodly proportion of all the researchers and eminent authorities in acoustics and related fields. In a compendium of this length, omissions and errors are inevitable. If anyone notices such, please send the corrections and missing names via e-mail or regular mail to either Elaine Moran (asa@aip.org) or Allan Pierce (adp@bu.edu).

Aaron, Arnold
Abbas, Paul
Abdala, Caroline
Abhayapala, Thushara D.
Abraham, Bruce
Achenbach, Jan D.
Ackermann, Hermann
Ahmad, Faiz
Ahmed, F.
Akagi, Masato
Akamatsu, Tomonari
Akay, Adnan
Alam, Kaiser
Alam, Sheikh
Albert, Donald
Albertson, John D.
Alipour, Fariborz
Alku, Paavo
Allemang, Randall J.
Allen, John
Allen, Jont
Altman, Naomi
Ames, Gregory
Angus, James
Antes, Heinz
Arai, Takayuki
Arehart, Kathryn
Arenas, Jorge
Arnold, Walter
Arnott, Pat
Arora, Manish
Arruda, Jose R.
Asano, Futoshi
Ashmead, Dan
Ashmore, Jonathan
Astley, Jeremy
Atal, Bishnu S.
Atchley, Anthony
Atlas, Les
Attenborough, Keith
Au, Whitlow W.L.
Audoin, B.
Auer, Edward T.
Avan, Paul
Bachowaroski, Jo-Anne
Backhaus, Scott
Bacon, Sid P.
Bai, Mingsian
Bailey, Michael
Bailey, Peter
Baillet, Helen
Baken, Ronald
Baker, Richard
Balaban, Evan
Balant, Anne
Balk, Helge
Ballandras, Sylvain
Ballato, Arthur
Bamber, J.
Bangerth, Wolfgang
Barbone, Paul E.
Barnett, David
Barney, Anna
Barron, Michael
Barros, J. L.
Barton, John
Bass, Henry E.
Batliner, Anton
Batra, Romesh C.
Battle, David
Baum, Shari
Baxley, Paul
Beauchamp, James W.
Bech, Soren
Bedard, Alfred
Beddor, Patrice
Bednarik, Michal
Beecher, Michael D.
Begault, Durand
Behrman, Alison
Benesty, Jacob
Benjamin, Kim
Benkí, José
Benoit-Bird, Kelly
Berengier, Michel C.
Berger, Elliott
Berger, John R.
Beristain, Sergio
Berliner, Marilyn
Berman, David Harry
Bernstein, Leslie
Bernstein, Lynne
Berry, Alain
Berryman, James G.
Bhattacharyya, Joydeep
Bhattacharyya, S.K.
Bilgutay, Nihat
Bilsen, F. A.
Bishop, Garner
Bjorno, Leif
Blanc Benon, Philippe
Blauert, Jens
Bliss, Donald
Blodgett, Earl Daniel
Blue, Joseph E.
Bobrovnitskii, Yuri
Boehnke, Susan
Boettcher, Flint A.
Boitnott, Greg
Boone, Marinus M.
Boothroyd, Arthur
Bork, Ingolf
Bosmans, Ivan L.
Boström, Anders
Bottledooren, Dick
Bouchon, Michel
Boulanger, Patrice
Bourne, Neil
Bowles, Ann
Braasch, Jonas
Bradbury, Jack
Bradley, David L.
Bradley, John
Bradlow, Ann
Brambilla, Giovanni
Brancazio, Lawrence
Brandstatt, Peter
Brayman, Andrew
Breebaart, Jeroen
Bremner, Paul
Brick, Haike
Briggs, Kevin
Broadstone, Steve
Bronkhorst, Adelbert
Brown, David
Brown, Lex
Brown, Michael
Bruce, Ian
Brungart, Douglas
Bucaro, Joseph
Buchanan, George
Bucker, Homer P.
Buckingham, Michael J.
Buick, Jim
Bunnell, H. Timothy
Burkhard, Mahlon
Burkhard, Robert
Burnett, Ian S.
Burns, Stephen
Burroughs, Courtney B.
Busch-Vishniac, Ilene
Butler, John L.
Buus, Soren
Buyukdura, Merih
Byrd, Dani
Cable, Peter
Cai, Hongxue
Campbell, Joseph
Campbell, Murray
Campbell, Nick
Campillo, Michael
Candy, James V.
Canlon, Barbara
Cantrell, John
Carcione, J. M.
Carey, William M.
Cariani, Peter
Carin, Lawrence
Carlyon, Robert
Carney, Arlene
Carney, Laurel
Carney, Walter
Carpenter, Steven
Carstensen, Edwin L.
Carter, G. Clifford
Cassereau, Didier
Castaings, Michel
Castellanos, Paul
Cathignol, Dominique
Cattafesta, Louis
Cawley, Peter
Cazzolato, Ben S.
Ceccio, Steven L.
Censor, Dan
Chadwick, Richard
Chahine, Georges
Chambers, David
Chambers, James
Champagne, Benoit
Chan, Philemon
Chancon, Hubert
Chandrasekhar, S.
Chang, Enson
Chang, Eric
Chapman, N. Ross
Chatterjee, Monita
Chazan, Dan
Cheeke, David
Chen, R. L.
Chen, W.
Chen, Weiqiu
Cheney, Margaret
Cheng, Arthur
Cheng, Li
Chertoff, Mark
Cherukuri, Harish
Cheung, Y.K.
Chew, Weng Cho

 0001-4966/2004/116(1)/1/6/$20.00

Cheyne, Stanley
Chiu, Ching-Sang
Chivers, R. C.
Chotiros, Nicholas P.
Christie, Douglas
Christman, Russel
Chu, Dezhang
Chu, Wing T.
Church, Charles
Ciocca, Valter
Clark, Christopher
Clark, William W.
Clarke, Eric
Clay, Clarence
Clements, Mark
Cleveland, Robin
Cohen, Leon
Collins, Leslie
Collins, Michael
Colosi, John
Coltman, John
Commander, Kerry
Conoir, Jean Marc
Cooke, Martin P.
Cooper, Nigel
Corey, John
Cornuelle, Bruce
Corsaro, Robert
Cosgrove, John
Coulevrat, Francois
Covey, Ellen
Cowin, S.
Cox, Ed
Cox, Henry
Cox, Robyn
Cox, Steven
Cox, Trevor
Craik, Alex D.D.
Crawford, John
Cray, Benjamin
Creamer, Denis
Crocker, Malcolm
Crosta, Giovanni F.
Crowther, Court
Cummings, Alan
Cummins, Fred
Cunefare, Kenneth
Cuschieri, Joseph
Cynader, Max
Dabelsteen, Torben
Dacol, Dalcio
Dahl, Peter
Dai, Huanping
Daigle, Gilles
Dalecki, Diane
d'Alessandro, Christophe
Daly, Peter
Dancer, Armand
Darwin, Chris J.
Datta, Subhendu
Dau, Torsten
Davies, Patricia
Davis, A.
Dawson, Steve
de Boer, Egbert
de Cheveigne, Alain
Defrance, Jerome
De Hoop, Adrianus
De Hoop, Martin
Delebarre, Christophe
Del Vescovo, Dionisio
Demany, Laurent
Demma, A.
de Moustier, Christian
de Mul, Fritz F.M.
Denardo, Bruce
Denda, Mitsunori
Deng, Cheri
Dent, Micheal
Depollier, Claude
Derode, Arnaud
Deschamps, Marc
Destrade, Michel
Devaney, Anthony Jude
Devore, Sasha
De Vries, Diemer
Dewhurst, Richard
Dezhang, Chu
Dhar, Sumit
Diebold, G.
Diebold, John
Diehl, Randy
Dillier, Norbert
Dimitriadis, Emilios
Ding, Desheng
DiPerna, Daniel
Dlubac, James
Dockrell, Judy
Doherty, Karen
Don, Manuel
Donaldson, Gail
Dong, W. G.
Donskoy, Dimitri
Dorman, Michael
Dornfeld, D. A.
Dosso, Stan
Dougherty, Robert
Dowling, David R.
Dragonette, Louis R.
Drennan, Ward
Dreschler, Wouter A.
Dreyer, Thomas
Drinkwater, Bruce
Drullman, Rob
D'Spain, Gerald
Dubno, Judy
Dubus, B.
Duda, Richard
Duda, Timothy
Duifhuis, Hendrikus
Duke, Jack
Dunn, Martin L.
Durlach, Nathaniel
Dvorkin, Jack
Dye, Raymond H.
Dziechuch, Matthew
Ebenezer, D. D.
Edelmann, Geoffrey
Edelson, Geoffrey S.
Edwards, Brent
Eggermont, Jos
Ehrenberg, John E.
Eisenburg, Laurie
Eisler, Thomas J.
El Hawary, Ferial
Elko, Gary W.
Elliott, Stephen J.
Ellison, William
Embrechts, Jean-Jacques
Emelianov, Stanislav
Eneroth, Peter
Enflo, B.
Engwall, Olov
Enru, Liu
Envia, Ed
Erdogan, Hakan
Erickson, Robert
Escabi, Monty
Evans, Gary
Evans, Richard
Evans, William
Everbach, Carr
Eversman, Walter
Everstein, Gordon
Every, Arthur
Faber, Alice
Fahey, Paul
Fahnline, John
Fallat, Mark
Farina, Angelo
Fastl, Hugo
Faulkner, Andrew
Fawcett, John
Fay, Richard
Feeney, Patrick
Fehler, Michael
Feit, David
Feke, D.
Fellah, Zine E.
Feng, Albert S.
Feng, Lipleng
Ferguson, Brian G.
Ferguson, Sarah
Ferla, Carlo
Ferri, Aldo A.
Feth, Lawrence L.
Ffowcs Williams, S.
Fidell, Sanford
Finegold, Lawrence
Fink, Mathias
Finlayson, Paul
Finneran, James
Fisher, Julia
Fitch, W.Tecumseh
Flatte, Stanley
Flege, James E.
Fletcher, Neville
Florentine, Mary
Folegot, Thomas
Foote, Kenneth
Ford, John
Forssen, Jens
Forsythe, Stephen
Fowler, Carol
Fowlkes, Jeffrey
Fox, Robert
Fox, Warren
Frampton, Kenneth
Francis, Alexander
Francis, D.
Frankel, Joe
Frankenthal, Shimshon
Franks, John
Franzoni, Linda
Frazer, L.Neil
Frederick, Theunissen
Frederickson, Carl
Freeman, Dennis
Freyman, Richard L.
Friberg, Anders
Friedl, William
Frisk, George V.
Fristrup, Kurt
Frizzell, Leon
Fromm, David M.
Fromme, Paul
Fu, Qian-Jie
Fuks, Iosef
Furumura, Takashi
Furusawa, Masahiko
Gabrielson, Thomas
Gaensler, Tomas
Gales, Mark J.F.
Garces, Milton
Garrelick, Joel M.
Garrett, Steven
Gaskell, Gareth
Gaumond, Charles F.
Gaunaurd, Guillermo
Gauss, Roger
Ge, Maochen
Gehr, Sara
Geller, Robert
Gentner, Tim
Gentry, Roger
Genuit, Klaus
Gerratt, Bruce
Gershman, Alex B.
Gerstoft, Peter
Ghanem, Roger
Ghitza, Oded
Ghose, Kaushik
Ghoshal, Anindya
Gibbs, Barry
Gilbert, Kenneth E.
Gilmore, Richard Grant
Givelberg, Edward
Gjestland, Truls
Gladden, Joseph
Gladwell, Graham
Glasberg, Brian
Glass, James
Glattke, Ted
Glner, G. C.
Godin, Oleg
Goeckel, Hedwin
Goldsworthy, Ray
Gonzalez, Iciar
Goodman, Ralph
Gopinath, Ashok
Gordon, Jonathan
Gorga, Michael
Gotoh, Yoshi
Gough, Colin
Grant, Kenneth W.
Grantham, D. Wesley
Green, Phil
Greenberg, J. Barry
Greenberg, Julie E.
Greenberg, Steven
Greene, Charles
Greening, Michael V.
Greenleaf, James F.
Greenwood, J. A.
Gregersen, Peter
Gridin, Dimitri
Griffiths, Timothy
Grimault, Nicolas
Grose, John H.
Grosh, Karl
Grossberg, Stephen
Gspan, Stefan
Guenther, Frank
Guicking, Dieter

Guillot, Francois
Guion, Susan
Gumerov, Nail A.
Gurevich, Boris
Gusev, Vitaly
Guski, Rainier
Gustaffson, Mats
Haak, Hein
Haisch, Christoph
Hall, Debbie
Hall, Donald E.
Hall, Joseph
Hambric, Steven
Hansen, Colin
Hansen, John
Hansen, Martin
Hansen, Uwe
Hanson, Helen
Hanyga, Andrzej
Hao, Yue
Hari, Riitta
Harris, Frances
Harris, Gerald
Harris, John G.
Harris, Paul
Harrison, Chris
Hart, Roger
Hartmann, William M.
Hasegawa-Johnson, Mark
Hastings, Mardi C.
Hatfield, Julie
Hauser, Marc
Havelock, David I.
Hawks, John
Hay, Alex
Hayek, Sabih
Hazan, Valerie
Hazen, Timothy
He, David
Heckmann, Martin
Hedberg, Claes
Hedlin, Michael
Hefner, Todd
Helffrich, Jerry
Hellgren, John
Hellman, Rhona
Hellweg, Robert
Hertrich, Ingo
Herzel, Hans-Peter
Hess, Cecil
Hess, Peter
Hickey, Craig
Hickling, Robert
Hicks, Michelle
Hill, Nicolas
Hillenbrand, James
Hiller, Robert
Hillion, Pierre
Hinders, Mark K.
Hines, Paul
Hinich, Melvin
Hinkelman, Laura
Hinton, Oliver
Hirschberg, Avraham
Hirsekorn, Sigrun
Hlawatsch, Franz
Hodge, Megan
Hodges, Dewey
Hodgkiss, William
Hodgson, Murray
Hoekje, Peter
Hoffman, Michael W.
Hogden, John
Holland, Charles
Holmes, Wendy
Holt, Lori L.
Holt, R. Glynn
Holzfuss, Joachim
Homm, Anton
Honda, Kiyoshi
Honorvar, Farhang
Hoppe, Ulrich
Hornsby, Benjamin
Horoshenkov, Kirill
Hosten, Bernard
Houser, Dorian
Houtgast, Tammo
Houtsma, Adrianus
Hovem, Jens
Howarth, Thomas
Howe, Bruce
Howe, Michael S.
Howell, Henry
Hsu, David K.
Huang, Dehua
Huang, Lixi
Hugo, Ronald J.
Humes, Larry
Humphrey, V.F.
Humphreys, William
Hurley, Donna C.
Hursky, Paul
Ih, Jeong-Guon
Insana, Michael F.
Irino, Toshio
Ishizuka, Kentaro
Ivakin, Anatoliy
Ivansson, Sven
Iverson, Paul
Iwasa, Kuni
Jackson, Darrell
Jacobs, Laurence J.
Jacobsen, Finn
Jaffe, Jules S.
Jain, Prathiba
James, Willott
Jansson, Erik
Jarzynski, Jacek
Jen, Philip
Jensen, Finn
Jensen, Jorgen Arendt
Jesteadt, Walt
Jesus, Sergio
Joachim, Dale
Johnson, David Linton
Johnson, Joel
Johnson, Keith
Johnson, Marty
Johnston, Pat
Jokisch, Oliver
Jones, Jeffery
Jongman, Allard
Juola, Jim
Kaernbach, Christian
Kahle, Eckhard
Kalveram, Karl
Kamakura, Tomoo
Kanai, H.
Kang, Hang-Goo
Kaplunov, Julius
Kargl, Steven
Kastak, Colleen
Kastak, David
Kastelein, Ronald
Kates, James
Kato, Hiroaki
Katz, Brian F.G.
Katz, Larry
Katz, Richard
Kauffmann, Christiaan
Keefe, Douglas H.
Keltie, Richard
Kennedy, Rodney A.
Kennett, Brian
Kent, Raymond D.
Keolian, Robert
Keppens, Verle
Kergomard, Jean
Ketterling, Jeffrey
Kewley-Port, Diane
Kidd, Gary
Kidd, Gerald
Kiefte, Michael
Kieser, Robert
Kim, Duck
Kim, Yang-Ham
Kingston, John
Kinra, Vikram
Kirby, Raymond
Kirkby, Ole
Kirsteins, Ivars
Kitahara, Michihiro
Klaeboe, Ronny
Klatzky, Rebecca
Kluender, Keith
Kluwick, A.
Knobles, David
Knowles, James K.
Koenig, Laura
Kohlrausch, Armin
Kollmeier, Birger
Konecni, Vladimir
Konrad-Martin, Dawn
Koppl, Christine
Korman, Murray
Kortekaas, Reinier
Kourtiche, Djilali
Krause, Jean
Krefting, Dagmar
Kreimen, Jodi
Kremkau, Frederick
Kripfgans, Oliver
Krishnamurti, T. N.
Krishnaswamy, Sridhar
Kroll, Judith
Kropp, W.
Kros, Crone
Krylov, Victor
Kryter, Karl D.
Kuc, Roman
Kuhl, Patricia
Kumaresan, Ramdas
Kumon, Ronald
Kundu, Tribikram
Kuperman, William A.
Kuttruff, Heinrich
Kuzmenko, A.
Kuznetsov, Andrey
Lafarge, Denis
Lafluer, L. Dwynn
Lai, Peter
Lai, Yi-San
Lam, Y. W.
Lammers, Marc
Langley, Robin
Langton, Christian
Laprie, Yves
Large, Edward
Larsen, Ole
Larson, Gregg
Larson, Vernon D.
Laskey, Robert
Lauchle, Gerald C.
Laugier, Pascal
Launer, Stefan
Lauterborn, Werner
Lavely, Eugene
Lavenex, Pamela Banta
Lawrence, Feth
Lawrie, Jane
Lee, Hua
Lee, Lin-Shan
Lee, Nigel
Lehman, Sean
Leighton, Timothy J.
Leishman, Timothy
Leissa, Arthur W.
Lennartson, R.
Lentz, Jennifer
Lercher, Peter
Letowski, Tomasz
Le'vesque, Daniel
Levine, Harold
Levinson, Stephen E.
Lewicki, Michael
Lewin, Peter
Li Cheng, M.
Li, Xu
Li, Y. K.
Licht, Torben R.
Lim, Raymond
Lindberg, Jan F.
Lindblom, Bjorn
Lingewitch, John
Lipkens, Bart
Lister, Jennifer
Litovsky, Ruth
Liu, Donald
Liu, E.
Liu, Qing
Lizzi, Frederic
Lo, Kam
Lobel, Philip
Lobkis, Oleg
Loepport, Peter
Loizou, Philip
Long, Glenis
Lopatnikov, Sergey
Lopez, Enrique
Lorenzi, Christian
Lotto, Andrew
Lou, G.
Love, Richard
Lovetri, Joe
Lowe, Michael
Lubman, David
Luczkovich, Joseph J.
Lueptow, Richard
Lukashkin, Andrei
Lutfi, Robert
Lutknehoner, Bernd
Lutman, Mark
MacKay, Robert
Macpherson, Ewan

Madigosky, Walter
Madsen, Ernest
Madsen, Peter
Maeda, Shinji
Maev, Roman
Maguer, Alain
Maia, Nuno
Mak, Brian
Makino, Shoji
Makris, Nicholas
Mal, Adjit
Malme, Charles I.
Manasseh, Richard
Mann, David
Mann, J. Adin
Manohar, C. S.
Mansur, Webe Jo
Mapes, Theodore
Marsh, Alan
Marshall, Vincent
Marshall, William J.
Marston, Philip
Martens, William
Martin, Paul A.
Martin, Rainer
Maslov, Konstantin
Mason, Christine
Massaro, Dominic
Mast, T. Douglas
Matveev, K.
Mauermann, Manfred
Max, Michael
May, Bradford
Mayer, Andreas
Maynard, Julian D.
McClatchie, Sam
McCoy, John
McDaniel, J. Gregory
McDonald, Bryant
McDonald, Mark
McDonald, Robert J.
McFadden, Dennis
McFadden, Sandra
McGowan, Richard S.
McKay, Colette
McLaughlin, Stephen
Mechel, F. P.
Meddis, Ray
Meegan, G. Douglas
Mellen, Robert H.
Mellert, Volker
Mellinger, David
Mendel, Jerry
Mercado, Eduardo, III
Meyer, Georg
Meyers, James
Michalopoulou, Zoi-Heleni
Micheyl, Christophe
Migliori, Albert
Mignery, Peter
Mikhalevsky, Peter
Miklos, A.
Milenkovic, Paul
Miles, Ronald
Miller, Charles
Miller, James
Miller, Morton
Mills, David
Milner, Ben
Ming, Ji
Mirkin, Adam
Mobley, Joel
Moeser, Michael
Moffett, Mark
Mohl, Bertl
Molet, Thiery
Moleti, Arturo
Molis, Michelle
Monaghan, Alex I.C.
Monchalin, Jean-Pierre
Mongeau, Luc
Moore, Brian C.J.
Moore, Patrick
Morimoto, Masayuki
Mourjopoulos, John
Mozurkewich, George
Muehleisen, Ralph
Muesch, Hannes
Muir, Thomas
Munhall, Kevin
Munjal, M.L.
Murphy, Peter
Murphy, William
Murray, Bruce
Murray, Iain R.
Murray, Todd
Myrberg, Art
Nadim, Ali
Nagem, Raymond
Naghshineh, K.
Nagle, Daniel T.
Nagreira, Culos
Nagshineh, Koorosh
Naguib, Mark
Nagy, Peter B.
Nardone, Steven
Narins, Peter
Naugolnykh, Konstantin
Nayfeh, Adnan H.
Nearey, Terrance
Nederveen, Cornelius
Nedzelnitsky, Victor
Neely, Stephen
Neff, Donna
Neitzel, Richard
Nelson, Brian S.
Nelson, David
Nelson, Douglas
Nelson, James T.
Nelson, Peggy
Nelson, Philip
Neuhoff, John
Neuman. Arlene C.
Newhall, Bruce K.
Newman, Rochelle
Ng, Larry
Nicholson, Patrick
Nielsen, Peter
Niemiec, Jan
Niezrecki, Christopher
Nightingale, Trevor R.
Nittrouer, Susan
Noble, John
Nolle, A.W.
Nolte, Loren W.
Norris, Andrew
Norris, David
Norton, Guy
Novarini, Jorge
Nowacek, Douglas
Nur, Amos
Nusbaum, Howard
Nuttall, Albert
Nyborg, Wesley
Nystuen, Jeffrey
O'Brien, William
O'Donnell, Matthew
O'Neill, Brian
O'Neill, William
Ochmann, Martin
Oded, Ghitza
Odom, Robert
Oelze, Michael
Oguz, Hassan
Ohde, Ralph
Ohkawa, Keiichi
Ohl, Claude
Ohrstrom, Evy
Okal, Emile
Olson, Elizabeth
Orcutt, John
Orr, Marshall
Orris, Gregory J.
Osler, John
Ostashev, Valdimir
Ostrovsky, Lev
Oud, Mireille
Owren, Michael
Oxenham, Andrew
Padilla, Frederic
Page, John
Pagneux, Vincent
Palmer, Allan
Palmer, Caroline
Palmer, Catherine
Palmer, David
Palmer, Stuart
Pan, Jie
Panneton, Raymond
Papanicolaou, George C.
Pardue, Sally
Parker, David
Parker, Kevin
Parthasarathy, S.
Pasqualini, Donatella
Pastille, Holger
Patterson, James H.
Payton, Karen
Peake, William
Peat, Keith
Pedersen, Michael
Pelorson, Xavier
Percin, Gokham
Percival, Donald
Perkell, Joseph
Pestorius, F. Michael
Petelescu, Andi
Petelescu, Gabriel
Peter, Scheifele
Petropoulos, Peter
Petrovska, Dijana
Pfingst, Bryan
Phillips, Allyn
Phillips, Dennis P.
Picheny, Michael
Picton, Terry
Pierucci, Mauro
Piquette, Jean C.
Piscoya, Rafael
Pisoni, David
Plack, Christopher
Plona, Thomas
Plotkin, Kenneth
Poese, Matt
Polka, Linda
Pols, Louis
Ponton, Curtis
Port, Robert
Porter, Michael
Potel, Catherine
Poterek, Thomas
Potter, John
Potty, Gopu
Poulsen, Torben
Poveda, E. Lopez
Powers, James M.
Prada, Claire
Pratt, R. Gerhard
Preisig, James
Premus, Vincent E.
Pressnitzer, Daniel
Prevrhal, Sven
Prince, Mary
Prosperetti, Andrea
Qu, Jianmin
Rajan, Subrahaniam
Raju, P.K.
Raman, Arvind
Ramasubramanian, V.
Ramm, A. G.
Ramoorthy, S.
Ramsay, Gordon
Rankovic, Christine
Raphael, Lawrence
Rasmussen, Karsten
Raspet, Richard
Ratilal, Purnima
Rauschecker, Josef
Ravicz, Michael
Rayess, Nassif E.
Rebinsky, Douglas A.
Reddy, Anil
Reichmulth Kastak, Colleen
Reid, John M.
Reinath, Michael
Remez, Robert
Ren, Tianying
Renals, Steve
Repp, Bruno
Richards, Roger T.
Richards, Virginia
Richardson, Michael
Ricketts, Todd
Rindel, Jens
Ritcey, James
Roberts, Brian
Robertson, John S.
Robinson, Harold
Rodriguez, Orlando
Rogers, Peter H.
Roitblat, Herbert L.
Rokhlin, Stanislav I.
Romano, Anthony J.
Rose, Joseph L.
Rosen, Stuart
Rosowski, John J.
Rossing, Thomas D.
Rouseff, Daniel
Roux, P.
Roy, Ronald A.
Royer, Daniel
Royston, Thomas J.
Rubenstein, Jay
Rudolphi, Thomas

Ruggero, Mario
Rumerman, Melvyn
Rumsey, Francis
Rupp, Andre
Rutledge, Janet C.
Ryan, James G.
Saari, Peeter
Sabatier, James
Saffran, Jenny
Saijyou, Kenji
Sakagami, Kimihiro
Salt, Alec
Salvi, Richard
Sammelman, Gary
San Emetrio, Jose Luis
Sanghvi, Narendra
Santi, Peter
Santos, J. E.
Sarikaya, Ruhi
Sarkissian, Angie
Sarvazyan, Armen
Sathian, Krish
Sawusch, James R.
Scaif, Ronan
Scalerandi, Marco
Scandrett, Clyde
Scavone, Gary
Scharf, Bert
Schellenberg, Glenn
Schlauch, Robert
Schmeer, Lester W.
Schmidt, Henrik
Schmidt-Nielsen, Astrid
Schmiedt, Richard
Schmitt, Denis
Schneider, Hans G.
Schoenberg, Michael
Schomer, Paul D.
Schreiner, Christoph
Schuhmacher, Andreas
Schulte-Fortkamp, Brigitte
Schultheiss, Peter M.
Schusterman, Ronald
Scott, Nigel
Sehgal, Chandra
Selamet, Ahmet
Sessler, Gerhard
Sethares, William
Seyforth, Robert
Shackleton, Trevor
Shadle, Christine
Shah, Arvind
Shamma, Shihab
Shang, Er-Chang
Shankar, P. Mohana
Shannon, Robert V.
Sharp, Stephen
Shattuck-Hufnagel, Stefanie
Sheft, Stanley
Sheplak, Mark
Shera, Christopher
Shertukde, Hemchandra
Shim, Victor P.W.
Shimizu, Yasushi
Shinn-Cunningham, Barbara
Shockley, Richard
Shore, Susan
Shung, K. Kirk
Shuwen, Pan
Sibul, Leon H.
Sickney, Ginger
Siderius, Martin
Siegel, Jonathan
Simmons, Andrea
Sinha, Bikash
Sinha, Dipen N.
Sinnott, Joan
Skelton, E.A.
Skowronski, Mark
Slaney, Malcolm
Slaton, William
Sloboda, John
Smith, Bruce
Smith, John
Smith, Julius
Smith, Kevin
Smith, L. Scott
Smurzynski, Jacek
Snowdon, Charles
Snyder, Russell
Sock, Rudolph
Soedel, Werner
Sofie, Van Parij
Soize, Christian
Solna, Knut
Solodov, Igor
Solokhin, Nickolay
Sommerfeldt, Scott
Sommers, Michell
Sondhi, Mohan
Song, Hee Chun
Sorokin, Victor
Southall, Brandon
Souza, Pamela
Sperry, Brian
Spicer, Jim
Spiesberger, John
Spisar, Monica
Spoor, Philip
Stanton, Timothy
Stavsky, Yehuda
Steele, Charles
Steinberg, Ben Zion
Stelmachowicz, Pat
Stepanishen, Peter
Stephan, Yann
Stephenson, Mark R.
Stephenson, Uwe
Stevens, Kenneth
Stewart, Robert W.
Stickler, David
Stinson, Michael
Stojanovic, Milica
Stone, Michael
Storey, Brian
Stotts, Steven
Strange, Winifred
Strickland, Elizabeth A.
Strifors, Hans
Strong, William J.
Studebaker, Gerald
Stusnick, Eric
Sugimoto, Nobumasa
Summers, Ian R.
Summers, Van
Sundberg, Johan
Supin, Alexander
Sussman, Joan
Sutherland, Louis
Svensson, Peter
Svirsky, Mario
Swearingen, Michelle
Swift, Gregory W.
Syrdal, Ann
Szabo, Thomas
Takagi, Kenshiro
Takahashi, Daiji
Takeuchi, T.
Talmadge, Carrick
Tang, Dajun
Tang, Shiu-keung
Tanter, Michaël
Tarnow, Viggo
Tatarinov, Alexej
Tattersall, M.
Taylor, Larry
Telschow, Ken
Temkin, Samuel
Tenenbaum, Roberto
Ter Haar, Gail
Teti, Robert
Thiessen, Erik
Thode, Aaron
Thomas, Jeanette
Thompson, David J.
Thompson, Lonny
Thompson, William Forde
Thomson, Dave
Thorne, Peter D.
Thorsos, Eric
Thwaites, Suszanne
Thys, Willy J.
Tichy, Jiri
Timmerman, Nancy
Tindle, Christopher
Ting, Thomas C.T.
Tito, Frank
Tittmann, Bernard
Titze, Ingo
Tognola, Gabriela
Tolstoy, Alexandra
Tomita, Y.
Toole, Floyd
Topaz, Chad M.
Torres, Rendell
Tracey, Brian
Trahey, Gregg E.
Tran van Nhieu, Michel
Tricas, Timothy
Trucco, Angela
Tsikluri, David
Tsingos, Nicolas
Tubis, Arnold
Tun, Pat
Turk, Alice
Turkel, Eli
Turner, Christopher W.
Turner, Joseph
Tyack, Peter
Tyler, Richard
Uberall, Herbert
Uchanski, Rosalie M.
Vainshtein, P.
Valdivia, Nicholas
Valimak, Vesa
Valle, Christine
van de Par, Steven
vanderborck, Gerard
van Walstijn, Maarten
Van Dijk, Pim
Van Kamp, Irene
Van Noorden, Leo
Van Parijs, Sophie
Van Son, Rob
Van Tasell, Dianne
Vanderborck, Gerard
Varadan, Vasundara
Varadan, Vijay
Veidt, Martin
Venkatesan, Murugesan
Venkatsen, M.
Verkeyn, Andy
Versluis, Michel
Vickers, Deborah
Vidmar, Paul
Viemeister, Neal
Viergever, Max A.
Ville, Jean-Michel
Virginia, Mann
Visser, Rene
Vlahopoulos, Nickolas
von Estorff, Otto
Vorobyov, Sergiy
Voronovich, Alex
Vos, Henk
Vos, Joos
Voss, Susan
Waag, Robert C.
Wagner, Randall P.
Wakeland, Ray
Walcott, Charles
Walden, Therese
Walhberg, Magnus
Walker, Bruce
Walsh, Edward
Walsh, Timothy
Wang, Can-Yun
Wang, DeLiang
Wang, Kon-Well
Wang, Lily
Wang, Xiaoqin
Wapenaar, C.P.A.
Ward, Darren B.
Warren, Daniel
Warusfel, Olivier
Watkins, Andrew J.
Watkins, Anthony
Watson, Charles
Waxler, Roger
Wear, Keith
Weaver, John
Weaver, Richard L.
Webb, Jacqueline
Weglein, Arthur
Weiland, Nathan
Weinreich, Gabriel
Weisenberger, Janet
Werby, Michael
Werner, Lynne
Whitaker, Rod
Wickesberg, Robert
Wightman, Fred
Wilen, Lawrence
Willett, Peter
Williams, Earl G.
Williams, Kevin
Williams, Warwick
Wilm, Mickael
Wilson, D. Keith
Wilson, Josh
Winter, Ian
Wirgin, Armand
Withnell, Robert
Witten, Alan

Wojtczak, Magdalena
Wolfe, Joseph
Wolfson, Michael
Woodhouse, James
Woods, William
Worcester, Peter
Wouters, Jan
Wright, Beverly
Wright, Matthew
Wu, Jun-Ru
Wu, K.
Wu, Kuangcheng
Wu, Lei
Wu, Lixie
Wu, Sean
Wu, Tsung-Tsong
Wurmser, Daniel
Xiang, Ning
Xu, Yi
Yamamoto, Tok
Yan, Hong
Yan, Yonghong
Yang, T. C.
Yang, Tsih
Yano, Takashi
Yano, Takero
Ye, Zhen
Yegnanarayana, B.
Yoder, Timothy
Yoshikawa, Shigeru
Yost, W. T.
Yost, William
Young, Jane
Young, Joel
Young, Victor
Zagbeski, James
Zahorian, Stephen
Zakharia, Manell
Zamaneh, Mikhak
Zampolli, Mario
Zatorre, Robert
Zeegers, Jos
Zeng, Fan-Gang
Zeqiri, Bajram
Zhao, Yunxin
Zheng, Yanqing
Zheng, Yibing
Zheng, Z. Charlie
Zhu, Songlin
Ziolkowski, Richard
Zolotoyabko, Emil

USA Meetings Calendar

Listed below is a summary of meetings related to acoustics to be held in the U.S. in the near future. The month/year notation refers to the issue in which a complete meeting announcement appeared.

2004

3–7 Aug. 8th International Conference of Music Perception and Cognition, Evanston, IL [School of Music, Northwestern Univ., Evanston, IL 60201; WWW: www.icmpc.org/conferences.html].

20–24 Sept. ACTIVE 2004-The 2004 International Symposium on Active Control of Sound and Vibration, Williamsburg, VA (INCE Business Office, Iowa State Univ., 212 Marston Hall, IA 50011-2153 Fax: 515 294 3528; E-mail:ibo@ince.org; WWW: inceusa.org).

15–19 Nov. 148th Meeting of the Acoustical Society of America, San Diego, CA [Acoustical Society of America, Suite 1NO1, 2 Huntington Quadrangle, Melville, NY 11747-4502; Tel.: 516-576-2360; Fax: 516-576-2377; Email: asa@aip.org; WWW: http://asa.aip.org].

2005

16–19 May Society of Automotive Engineering Noise & Vibration Conference, Traverse City, MI [Patti Kreh, SAE International, 755 W. Big Beaver Rd., Ste. 1600, Troy, MI 48084, Tel.: 248-273-2474; Email: pkreh@sae.org].

Cumulative Indexes to the Journal of the Acoustical Society of America

Ordering information: Orders must be paid by check or money order in U.S. funds drawn on a U.S. bank or by Mastercard, Visa, or American Express credit cards. Send orders to Circulation and Fulfillment Division, American Institute of Physics, Suite 1NO1, 2 Huntington Quadrangle, Melville, NY 11747-4502; Tel.: 516-576-2270. Non-U.S. orders add $11 per index.

Some indexes are out of print as noted below.

Volumes 1–10, 1929–1938: JASA, and Contemporary Literature, 1937–1939. Classified by subject and indexed by author. 131 pp. Price: ASA members $5; Nonmembers $10.

Volumes 11–20, 1939–1948: JASA, Contemporary Literature and Patents. Classified by subject and indexed by author and inventor. 395 pp. Out of Print.

Volumes 21–30, 1949–1958: JASA, Contemporary Literature and Patents. Classified by subject and indexed by author and inventor. 952 pp. Price: ASA members $20; Nonmembers $75.

Volumes 31–35, 1959–1963: JASA, Contemporary Literature and Patents. Classified by subject and indexed by author and inventor. 1140 pp. Price: ASA members $20; Nonmembers $90.

Volumes 36–44, 1964–1968: JASA and Patents. Classified by subject and indexed by author and inventor. 485 pp. Out of Print.

Volumes 36–44, 1964–1968: Contemporary Literature. Classified by subject and indexed by author. 1060 pp. Out of Print.

Volumes 45–54, 1969–1973: JASA and Patents. Classified by subject and indexed by author and inventor. 540 pp. Price: $20 (paperbound); ASA members $25 (clothbound); Nonmembers $60 (clothbound).

Volumes 55–64, 1974–1978: JASA and Patents. Classified by subject and indexed by author and inventor. 816 pp. Price: $20 (paperbound); ASA members $25 (clothbound); Nonmembers $60 (clothbound).

Volumes 65–74, 1979–1983: JASA and Patents. Classified by subject and indexed by author and inventor. 624 pp. Price: ASA members $25 (paperbound); Nonmembers $75 (clothbound).

Volumes 75–84, 1984–1988: JASA and Patents. Classified by subject and indexed by author and inventor. 625 pp. Price: ASA members $30 (paperbound); Nonmembers $80 (clothbound).

Volumes 85–94, 1989–1993: JASA and Patents. Classified by subject and indexed by author and inventor. 736 pp. Price: ASA members $30 (paperbound); Nonmembers $80 (clothbound).

Volumes 95–104, 1994–1998: JASA and Patents. Classified by subject and indexed by author and inventor. 632 pp. Price: ASA members $40 (paperbound); Nonmembers $90 (clothbound).

BOOK REVIEWS

P. L. Marston
Physics Department, Washington State University, Pullman, Washington 99164

These reviews of books and other forms of information express the opinions of the individual reviewers and are not necessarily endorsed by the Editorial Board of this Journal.

Editorial Policy: *If there is a negative review, the author of the book will be given a chance to respond to the review in this section of the Journal and the reviewer will be allowed to respond to the author's comments. [See "Book Reviews Editor's Note," J. Acoust. Soc. Am.* ***81****, 1651 (May 1987).]*

Handbook of Elastic Properties of Solids, Liquids, and Gases

Moises Levy, Henry E. Bass, Richard R. Stern, editors-in-chief

Academic Press, San Diego, CA, 2001
1959 pp. Price: $1665 (hardcover, 4 volume set),
ISBN: 0-12-445760-6

The word ''Handbook'' in the title of a technical reference book can denote a variety of formats, ranging from a collection of data tables to a series of review articles. The latter is the case for the Handbook of Elastic Properties of Solids, Liquids, and Gases. The four volumes of this Handbook consist of many chapters, written by different authors. The format of the chapters is varied—in some chapters the emphasis is on data and trends in the data, while other chapters include development of background theories. Measurement techniques are described in some detail—Vol. 1 is devoted to measurement techniques for solids, and there are also descriptions of measurement procedures and instrumentation in various chapters of Vols. 2–4. Most of the measurement techniques and the data presented in the Handbook are dynamic, extending over a wide frequency range. Many of the measurement techniques are acoustic or ultrasonic. Attenuation of elastic waves is included by adding an imaginary component, proportional to the attenuation coefficient, to the elastic modulus. A summary of contents is as follows:

Volume 1 (edited by Arthur G. Every and Wolfgang Sachse) consists of six parts, devoted mainly to description of techniques for measuring elastic constants and elastic wave attenuation in isotropic, anisotropic, and composite solid materials. *Part 1* is an *Introductory Chapter* which develops the background theory in elasticity and elastodynamics. Plane wave solutions are developed both for isotropic and anisotropic solids. Both bulk waves and surface waves are considered. *Part 2*, Chaps. 2–6, presents *Bulk Wave Techniques*. Chapter 2 describes pulse superposition techniques for precise measurement of ultrasonic velocity. Chapter 3, describes through-transmission methods for measuring the complex stiffness moduli, C_{ij}, of composite materials. Both air-coupled and water immersion configurations are described. Chapter 4 is on point-source/point-receiver excitation and detection of ultrasound, to determine elastic properties of solids. The Green's function for an infinite anisotropic elastic continuum is developed. The experimental setups described include laser generation/detection of ultrasound, and very high frequency (GHz range) phonon imaging techniques. The title of Chap. 5 is Magnetic Resonance Elastography. This is a recent development, where magnetic resonance imaging (MRI) techniques are used to image propagation of low frequency (100–300 Hz) shear waves, primarily through the human body. MR elastography is a promising technique for detecting malignant tissue. Chapter 6 describes ultrasonic systems based on phase-sensitive-gated interferometry, for precise measurement of signal phase and amplitude over a wide range of frequencies. From this data phase or group velocity and attenuation can be determined. This order elastic constants can be determined from measurements of amplitudes of higher harmonics. *Part 3* is on *Guided Wave Techniques*. These include, in Chap. 7, surface acoustic waves (SAW) both at free surfaces and at interfaces between two elastic media. The SAW's can be generated and detected using both noncontact laser techniques and piezoelectric transducers. The chapter concludes with a discussion of nonlinear SAWs. Chapter 8 describes Acoustic Microscopy of solids (100 MHz to 2 GHz). Application to thin films, and to anisotropic materials are described. Chapter 9 presents a short description of travelling waves in rods and cylindrical shells. The inverse problem of determining elastic parameters from measured dispersion curves is solved using a nonlinear fitting algorithm. Data for filament-wound cylindrical shells is presented. *Part 4* is on *Resonance Methods*. Chapter 10 describes Resonant Ultrasound Spectroscopy (RUS), which is an interesting recent development. In this technique a large number of successive resonances of a (small) sample are measured and the elastic constants tensor is determined from a best fit of calculated to measured resonances. This technique has been used over a temperature range of 1825–0.25 K, and at pressures up to 150 bar. Chapter 11 is on electromagnetic acoustic transducer (EMAT) techniques for exciting and detecting ultrasonic waves in conducting or magnetostrictive solids. Advantages of EMATs are noncontact generation and detection of ultrasound, and generation of various types of ultrasonic waves. However, the efficiency of the transduction mechanism is relatively low. Chapters 12 and 13 are, respectively, on plate resonance modes, and on torsional and flexural vibrations, and resonances, of rods. Determinations of elastic constants of both single crystal and textured polycrystalline materials are considered. *Part 5* presents *Light, Neutron, and X-Ray Scattering Techniques*. Chapter 14 describes how Brillouin light scattering measurements from high frequency (~GHz) bulk phonons can be used to determine elastic constants of single crystals. Chapter 15 describes measurements of surface Brillouin light scattering (SBS), and how this data can be used to determine elastic constants of opaque solids, thin supported films, and superlattices over a wide temperature and pressure range. Chapter 16 is on the Schaefer–Bergmann method for determination of elastic constants of transparent solids, typically single crystals. This technique uses the diffraction pattern produced when ultrasonic waves (~5 to 50 MHz) in the sample interact with a light beam. Inelastic neutron scattering measurements, described in Chap. 17, are used to determine phonon dispersion curves. Chapter 18 describes techniques based on x-ray diffraction and scattering from acoustic phonons. These include thermal diffuse scattering and scattering from externally excited acoustic phonons, such as bulk or surface acoustic waves. *Part 6* deals with *Non-Linearity*. Chapter 19 develops the basic relations for acoustoelasticity of anisotropic elastic solids. Expressions are developed for effective elastic coefficients of solids under high static stresses, and measurement techniques are reviewed. Also included is the acoustoelasticity of surface acoustic waves. Finally, Chap. 20 describes dynamic measurements of elastic moduli at high pressures and temperatures, including anvil cell systems for ultrasonic and Brillouin scattering measurements, for pressures up to 13 GPa and temperatures to 1000 °C.

Volumes 2 and 3 (edited by Moises Levy and Libby Furr) cover the elastic properties of solids. Volume 2 is divided into six parts. *Part 1* is an *Introduction and Theory Section* and begins, in Chap. 1, with a macroscopic description of elastic properties of solids. Chapter 2 provides a short introduction to microscopic theory and prediction of elastic properties of selected elements and oxides. Chapter 3 presents Blackman Diagrams, for a variety of materials, and shows that these diagrams contain many features, including clustering of materials with similar interatomic bonding. Chapter 4 shows how the bulk modulus and Debye temperature of materials, mainly metal oxides, can be estimated from their crystal structure and density. Part 1 concludes with a short but interesting chapter on Einstein's theoretical studies related to elastic constants, and shows Einstein's ability to develop theoretical models which ''are as simple as possible, but not simpler.'' *Part*

 0001-4966/2004/116(1)/15/3/$20.00

2 presents *Elastic Properties of Selected Elements and Compounds*. Chapter 6 gives the elastic properties of solid inert gases, including ^{3}He and ^{4}He. In Chap. 7 monocrystal elastic constants are tabulated for 41 cubic-symmetry and 21 hexagonal-symmetry elements, and calculations of some derived properties (polycrystal elastic constants, Debye temperature) are discussed. This part ends with Chap. 8 on the evaluation of the Gruneisen parameters of cubic elements and compounds (halides, oxides, and covalent compounds). Second and third order elastic constants are also tabulated. *Part 3* is titled *Novel Materials* and starts with Chap. 9 on elastic properties of quasicrystals, mainly precise determinations of anisotropy in AlCuLi quasicrystal samples. Chapter 10 reviews low-dimensional materials, particularly the change in elastic moduli at density-wave phase transitions, and electric field dependence of the moduli. Chapter 11, Fullerenes and Nanotubes, presents properties (elastic moduli, tensile strength) of fullerences and single wall and multiwall nanotubes. Chapter 12—materials with low-*f* anharmonic local modes, and plutonium—reviews elastic properties and thermodynamics (including filled skutterudites). Finally, Chaps. 13 and 14 are devoted to Superconductors, including high T_c, heavy fermion superconductors. *Part 4*, titled *Technological Materials*, is limited to Chap. 15 on crystalline quartz, and Chap. 16 on semiconductors. Quartz is an important component of timing and frequency control devices, and Chap. 15 includes extensive data on elastic moduli (second order and third order), and piezoelectric and dielectric constants. Chapter 16 considers the dependence of elastic moduli, particularly Poisson's ratio, on fractional covalent-ionic character for tetrahedral semiconductors. Included are technologically important semiconductors (Ge, Si). *Part 5* presents data on *Alloys*. A short Chap. 17 reviews monocrystal–polycrystal elastic constants of stainless steels. Extensive data on elastic moduli of iron alloys, including effects of heat treatment, is presented in Chap. 18. The title of Chap. 19 is elastic constants of aluminum alloys. However, the emphasis in this chapter is on elastic moduli of single crystal and polycrystalline aluminum, including texture. Chapter 20 summarizes data on Young's modulus and its temperature dependence for 40 engineering alloys (aluminum, copper, iron, and nickel). Finally, *Part 6* presents the elastic and anelastic properties of *Building Materials*, specifically inorganic glasses (Chap. 21), composite materials (Chap. 22), and concrete (Chap. 23). Chapters 21 and 23 include both data and discussions of relation of the data to structural models of the materials. Chapter 22 emphasizes measurement techniques.

Volume 3 is composed of three parts. *Part 1* is titled *Organic Materials* and includes discussion of elastic properties of crystalline organic molecules (Chap. 1); polymers (Chap. 2); wood and forest products (Chap. 3); and paper (Chap. 4). Properties of organic molecules are of interest to the pharmaceutical industry, and the emphasis in Chap. 1 is on calculation of elastic moduli of single crystals and aggregates for different assumed intermolecular potentials. Chapter 2, on polymers, includes discussion of the frequency dependence of the complex elastic moduli in the glass transition region, additive properties of elastic moduli, and relation to polymer morphology. Chapter 3, in addition to ultrasonic velocity and elastic moduli data, considers wood structure, property variation, and measurement issues. Chapter 4 includes models for elastic properties of paper, sample data on elastic orthotropic properties of several papers, and impact of papermaking processing and environmental conditions on elastic properties. *Part 2—Biological Materials*—describes elastic properties of soft tissue (Chap. 5); elastic properties of food (Chap. 6); elastic properties and measurement techniques of hard tissue (Chap. 7); and ceramics from invertebrate animals (Chap. 8). The soft tissue materials in Chap. 5 include tendon, heart, and muscle. Extensive data on the Young's modulus is presented, and applications to medical diagnostics are discussed. Chapter 6 presents a single theoretical framework for solids, liquids, and viscoelastic materials, followed by an extensive table of elastic properties of foods, including dynamic compressibility, impedance, sound velocity, and complex moduli. Hard tissues, described in a long Chap. 7, are materials, such as bone, which are constituted both of mineral and organic matter. These materials may be anisotropic and also their elastic moduli are density dependent. Tables of sample moduli data are presented, and both static (nanoindentation) and dynamic (ultrasound critical angle reflectometry, acoustic microscopy) measurement techniques are described. The materials described in Chap. 8 are structures such as corals, sponges, and various shells and tubes. *Part 3*, the longest section, relates to *Earth and Marine Sciences*. Chapter 9, on elastic properties of ice, includes elastic moduli data on different phases of nonsaline ice, and static and dynamic data on saline ice. Chapter 10 presents thermoelastic parameters (such as Debye temperature, Gruneisen parameter). Through these parameters acoustic data can be used to determine thermal properties of a solid. The full set of thermoelastic parameters is examined and applied to geophysical materials. Chapter 11 reviews various models for converting monocrystal elastic moduli to effective polycrystal isotropic elastic constants. The title of Chap. 12 is Elastic Properties of Minerals and Planetary Objects. Extensive data is presented on elastic moduli of single crystals of geological minerals. The corresponding polycrystal elastic moduli are calculated and compared with profiles in the Earth of compressional and shear wave velocities, obtained from seismic studies. This is continued in Chap. 13, titled Rock and Earth's Crust, which includes extensive data tables on seismic velocities in the Earth's crust at depths to ~50 km. Also included are data tables on elastic moduli of geological minerals, and a discussion of theoretical models for calculating the elastic properties of rocks from the known elastic properties of their mineral components. Elastic Constants of Porous Ceramics are the topic of Chap. 14, which presents theoretical models for elastic constants of ceramics with different shape pores (spherical, oblate spheroid, prolate spheroid). Theoretical predictions are compared with data for alumina. Finally, Chap. 15, on Elastic Properties of the Earth's Surface, describes sound propagation near the surface of the Earth. The ground surface is modeled as an air-filled poroelastic layer above an elastic substrate. Derivation of the sound field for spherical wave incidence is presented, followed by experimental techniques and comparison with measurements.

Volume 4 (edited by Moises Levy, Dipen Sinha, and Richard Raspet) is divided into two parts. *Part 1* is on *Elastic Properties of Liquids* and *Part 2* is on *Elastic Properties of Gases*. Chapter 1, introduces the Swept-Frequency Acoustic Interferometry technique, where it is applied to the somewhat complicated test geometry required for chemical warfare agents. This chapter includes a tabulation of the sound speed and attenuation for chemical warfare agents and precursor chemicals. Chapter 2 is titled ''The Speed of Sound in Pure and Neptunian Water.'' (For the uninitiated, Neptunian water is seawater limited to a specified range of temperature, pressure and salinity.) This chapter presents the recommended equations for sound speed in water and seawater and a discussion of the measurement methodology. Also included is an exhaustive comparison of the likely accuracy of each reported equation or data set. Chapter 3 presents sound absorption in water and seawater. This is a well-balanced chapter, containing a description of the various basic loss mechanisms including that of chemical relaxation. It introduces some of the laboratory and shipboard techniques, and provides an understanding of the terms in the final tabulated sound absorption equation. Chapters 4 and 5, respectively, provide a description of propagation of first, second, and fourth sound in superfluid helium He3 (a Fermi fluid) and He4 (a Bose–Einstein fluid). Included are interesting discussions of the behavior of these quantum fluids along with the use of acoustic data in evaluating their elastic properties. Chapter 6 addresses propagation of first and second sound in liquid crystals. The emphasis is on theoretical description, but descriptive experimental data is included. Chapter 7 considers speed and attenuation of sound in bubbly liquids. A comprehensive (linear) theoretical analysis is presented, with some discussion of extensions beyond linear response. For one important system (air bubbles in water) sufficient data is provided to demonstrate the accuracy of the formulations. Chapters 8 (acoustic properties in petroliferous liquids, namely hydrocarbons) and 9 (acoustic properties in rocks saturated with petroliferous liquids) present data that is important to commercial oil exploration. The emphasis of both chapters is on tabulating data and providing practical interpolative expressions. In Chap. 9 the *P*- and *S*-wave velocity data are given as functions of temperature and pressure. *Part 2* starts with Chap. 10, which presents a classical theoretical description of sound propagation, absorption, and dispersion in gases. It includes descriptions of relaxation processes, diffusion, and contains sufficient experimental results to demonstrate the principal behaviors. Chapter 11 develops a model in which sound speed is a thermodynamic quantity that can be calculated to high accuracy from knowledge of the Helmholtz free energy surface of the fluid. This reference quantity has only been developed for certain fluids, and often relies on information from precision sound speed measurements. However, once available it is demonstrated that it results in accurate calculated sound speed values over a wide range of conditions, including mixtures. Extensive results are tabulated for argon, nitrogen, air, and water. Chapters 12 and 13 describe resonator devices for sound speed measurements. Chapter 12 describes several resonators for high accuracy determination of thermophysical properties, including

sound speeds with 0.01% accuracy. Thermophysical properties for 24 gases are tabulated. Chapter 13 presents a simpler cylindrical acoustic resonator for inexpensive sound speed measurements on gases and gas mixtures with 0.1% accuracy. Data for ten different gases and for He–Ar mixtures are tabulated. The last three chapters are a separate unit on extraterrestrial materials. Chapter 14 considers the atmospheres of the planets (and one satellite, Titan). Sound speed profiles are presented, measured by instruments on planetary landers. The relevance of this data to transport mechanisms is discussed. Chapter 15 presents sound speed profiles in stars, including the Sun. The profiles are calculated from models for stellar structure or, for the Sun, from helioseismology data. Finally, Chap. 16 gives the properties of condensed matter in white dwarfs and neutron stars. Compared to the interior of our Sun the densities of matter are seven orders of magnitude higher in white dwarfs and 15 orders of magnitude higher in neutron stars. Equations of state for matter at such high densities are described. At these densities the speed of sound, calculated from the equation of state, can approach the speed of light.

As can be seen from the above overview, the Handbook is unique in its inclusion of data, and discussion of models and techniques, for a very wide range of materials. Nevertheless, there are materials with interesting elastic properties which are not included in the above compilation. This statement is not intended as a criticism of the Handbook. Rather, the inevitable omissions are a consequence of the splendid variety of materials and structures provided both by Nature and synthesized in the laboratory.

Missing topics fall into two categories. In the first category are research areas for which reviews are not available elsewhere. Examples of this category are the dynamic, viscoelastic properties of liquids used for lubrication and other tribological applications, and the elastic properties of protein crystals. In the second category are materials whose dynamic elastic properties are already available in review articles published elsewhere. An example of this category are liquids such as water, liquid argon, and liquid metals, in which sound attenuation is due to structural relaxation, and organic liquids, such as carbon bisulfide and benzene, in which sound attenuation is related to molecular relaxation processes.

What recommendations can be made for a second edition of the Handbook? The obvious direction to go is simply to add further chapters on materials for which no comprehensive reviews are available. At the same time it should be clearly stated in the preface that there is some selection in the contents of the Handbook, with emphasis on recent materials developments, data, and measurement techniques. For researchers who need quick access to data a separate set of references should be added, specifically for the materials data available, in table and other formats, in the handbook. Also a chapter could be added summarizing reviews, and other sources of data on elastic properties of materials, available elsewhere in the literature.

The chapters in the handbook are written by authors who are recognized authorities on the chapter topics. The printing, graphics, and page layout are of uniformly high quality. Because chapters are written by different authors, there is some overlap of material. For example, conversion of monocrystal elastic moduli to effective polycrystal elastic constants is described in three different chapters, with no cross-referencing. But such overlap is not frequent, and does not detract from the quality of the handbook. The price of the handbook is too high to recommend it to individual researchers. However, this handbook does belong on the shelves of libraries at universities, research institutes, and libraries maintained by research groups involved in basic and applied studies of materials.

JACEK JARZYNSKI
SFA/Naval Research Laboratory,
Physical Acoustics Branch,
Washington, DC 20375-5320

REVIEWS OF ACOUSTICAL PATENTS

Lloyd Rice
11222 Flatiron Drive, Lafayette, Colorado 80026

The purpose of these acoustical patent reviews is to provide enough information for a Journal reader to decide whether to seek more information from the patent itself. Any opinions expressed here are those of reviewers as individuals and are not legal opinions. Printed copies of United States Patents may be ordered at $3.00 each from the Commissioner of Patents and Trademarks, Washington, DC 20231. Patents are available via the Internet at http://www.uspto.gov.

Reviewers for this issue:

GEORGE L. AUGSPURGER, *Perception, Incorporated, Box 39536, Los Angeles, California 90039*
MARK KAHRS, *Department of Electrical Engineering, University of Pittsburgh, Pittsburgh, Pennsylvania 15261*
HASSAN NAMARVAR, *Department of BioMed Engineering, University of Southern California, Los Angeles, California 90089*
DAVID PREVES, *Starkey Laboratories, 6600 Washington Ave. S., Eden Prairie, Minnesota 55344*
DANIEL R. RAICHEL, *2727 Moore Lane, Fort Collins, Colorado 80526*
CARL J. ROSENBERG, *Acentech Incorporated, 33 Moulton Street, Cambridge, Massachusetts 02138*
WILLIAM THOMPSON, JR., *Pennsylvania State University, University Park, Pennsylvania 16802*
ROBERT C. WAAG, *Univ. of Rochester, Department of Electrical and Computer Engineering, Rochester, New York 14627*

6,678,210

43.20.Rz FREQUENCY DIVISION BEAMFORMING FOR SONAR ARRAYS

Francis D. Rowe, assignor to Rowe–Deines Instruments, Incorporated
13 January 2004 (Class 367/103); filed 28 August 2002

It is proposed to form a set of tilted and dynamically steerable beams from a line array or planar grid array of transducers, either in transmission or reception, by associating a fixed amount of phase shift (or a set of fixed values) with each element of the array in order to produce a tilted beam(s) in a certain direction(s). Then, as frequency is varied while the phase shifts are kept constant, the directions of tilt will, of course, change.—WT

6,694,261

43.30.Gv METHOD FOR IDENTIFICATION OF SHALLOW WATER FLOW HAZARDS USING MARINE SEISMIC DATA

Alan Royce Huffman, assignor to Conoco Incorporated
17 February 2004 (Class 702/1); filed 4 November 1999

A method is discussed for detecting a sedimentary layer which has an abnormally high fluid pressure and thus a very low shear wave velocity, but is overlaid by other relatively impermeable layers. This is accomplished by an analysis of the change in amplitude of seismic waves reflected from such a layer.—WT

6,678,209

43.30.Nb APPARATUS AND METHOD FOR DETECTING SONAR SIGNALS IN A NOISY ENVIRONMENT

Luc Peng, Boynton Beach, and Danny Peng, Deerfield Beach, both of Florida
13 January 2004 (Class 367/95); filed 26 February 2002

A technique for improving the performance of a sonar system in noisy environments consists of dynamically selecting the transmission frequency to match a low ambient noise frequency in the operating band of interest. The system automatically scans the ambient noise across this band, selects a frequency with low ambient noise level, and changes the transmission frequency to that value.—WT

6,690,622

43.30.Sf PORTABLE REMOTE-CONTROLLED FISH LOCATING SYSTEM

Paul A. Eckberg, Sr. and Thomas W. Mobilia III, both of Palatine, Illinois
10 February 2004 (Class 367/173); filed 24 June 2002

A portable remote-controlled fish finding system comprises a radio-controlled toy boat that supports a sonar unit with an attached cable up to 110 ft in length. The assembly can be launched from shore, a dock, or another boat where the display unit is located. One can then search for fish in a region with a circular footprint up to 110 ft in radius without moving.—WT

6,684,160

43.30.Wi MARINE SEISMIC ACQUISITION SYSTEM AND METHOD

Ali Ozbek *et al.*, assignors to WesternGeco
27 January 2004 (Class 702/17); filed in the United Kingdom 20 May 1998

A system for performing a marine seismic survey is described. By sampling the wave field at intervals less than the coherence length of the dominant noise components, the system converts the seismic signal, as measured by a single hydrophone of a towed array, into a noise-reduced version of that same signal.—WT

6,671,228

43.30.Yj SONAR TRACKING ARRAY

Maurice J. Griffin and Ira B. Cohen, assignors to The United States of America as represented by the Secretary of the Navy
30 December 2003 (Class 367/153); filed 6 August 2002

A sonar system is described in which a projector is surrounded by a set of hydrophones (four such in an equispaced, coplanar arrangement are discussed in the preferred embodiment). The assembly is mounted on a rotatable support structure and the output from the receiving array is connected

 0001-4966/2004/116(1)/19/20/$20.00

to control devices that affect the steering direction of the sonar array. The relatively large spacing of the hydrophones is intended to produce a narrow receiving beamwidth. However, there is no discussion of the consequences of the grating lobes that will arise because of this spacing and the frequency range in question.—WT

6,671,229

43.30.Yj TORPEDO SONAR COMPRISING A PLURALITY OF ACOUSTIC TRANSDUCERS

Joerg Schmidt, assignor to L-3 Communications Elac Nautik GmbH
30 December 2003 (Class 367/153); filed in Germany 8 November 2000

In an attempt to reduce the total number of individual transducers required by a torpedo sonar, the following arrangement is proposed. On a hemispherical or paraboloidal shaped torpedo head, the transducers are arranged in four distinct zones as illustrated in the figure. Circular zone **f** at the apex (which may be void of any transducers as sketched) is about 1.5 wavelengths in extent (note that the individual transducers are spaced about one-

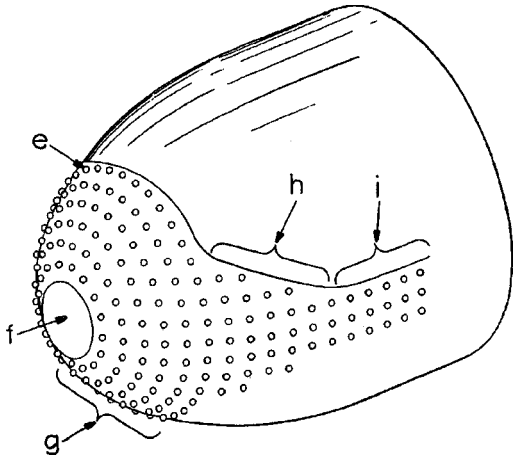

half a wavelength apart). Ring-shaped second zone **g** extends back from the apex about five wavelengths. Transition zone **h** extends to about seven wavelengths from the apex and the fourth zone **i**, of constant height, extends backward at least to the great circle of the torpedo head. The latter two zones exist on both port and starboard sides. The plurality of beams generated by the transducers in these various zones should provide substantial spatial coverage.—WT

6,683,819

43.30.Yj SONAR ARRAY SYSTEM

Michelle K. Estaphan *et al.*, assignors to Raytheon Company
27 January 2004 (Class 367/106); filed 21 January 2003

A towed line array is discussed. Novelty seems to reside in the fact that the array includes both collinearly aligned projectors as well as receivers.—WT

6,690,620

43.30.Yj SONAR TRANSDUCER WITH TUNING PLATE AND TUNING FLUID

Theodore J. Mapes, assignor to The United States of America as represented by the Secretary of the Navy
10 February 2004 (Class 367/152); filed 12 September 2002

By deploying a waveguide consisting of an entrained layer of fluid corralled by a thin plate of metal, plastic, or rubber, between the radiating face of a piston-type transducer and the surrounding acoustic medium, it is proposed to both increase the resistive radiation loading on the radiating face and also adjust the resonant frequency of the transducer because of the attendant modification of the reactive radiation loading. The variable parameters at the designer's disposal include the thickness of the layer of fluid, its characteristic impedance, as well as the density and thickness of the thin plate, which is simply modeled as a mass element.—WT

6,693,849

43.30.Yj PIEZOELECTRIC AUDIO TRANSDUCER

Adolf Eberl *et al.*, all of Kincardine, Ontario, Canada
17 February 2004 (Class 367/160); filed 3 October 2002

A transducer, intended to be used as an underwater receiver, consists of a piezoelectric wafer **16** adhesively attached to a thin membrane **20** with conducting epoxy. The membrane also supports, at opposite edges, a pair of inertial weights (although only one, item **24b**, shows in this cross-sectional view). A damping layer **28**, such as a rubber disk, is attached to the back or under side of the membrane **20**. This assembly is enveloped, top and bottom, by layers **30** of open cell foam which also serve to position the transduction

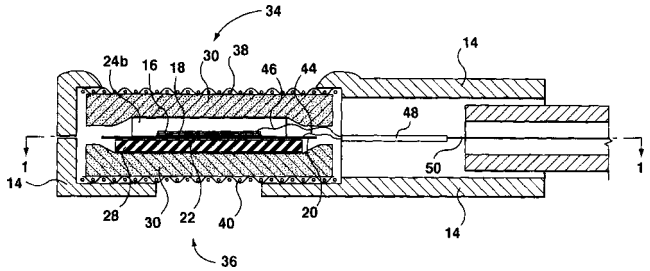

element within the housing **14** and to mechanically isolate it therefrom. Metal screens **38** and **40** extend across top and bottom openings **34** and **36** in the housing. The device may be used as an air microphone but, when submerged in water, the open cell foam readily allows the space surrounding the transduction element to flood, thus equalizing the ambient pressure on both faces of the element. One can only assume that the transduction element has also been waterproofed.—WT

6,689,087

43.35.Ty FLOATING PROBE FOR ULTRASONIC TRANSDUCERS

Dharmendra Pal and Thomas Peterson, assignors to Cybersonics, Incorporated
10 February 2004 (Class 604/22); filed 28 March 2002

This apparatus uses a combination of ultrasonic and subsonic vibrations to perform drilling and coring. These vibrations are generated by a frequency compensation coupler or free mass to produce a hammering action with relatively low axial force required. The device may also incorporate irrigation and aspiration capabilities. A body sensor feedback unit is

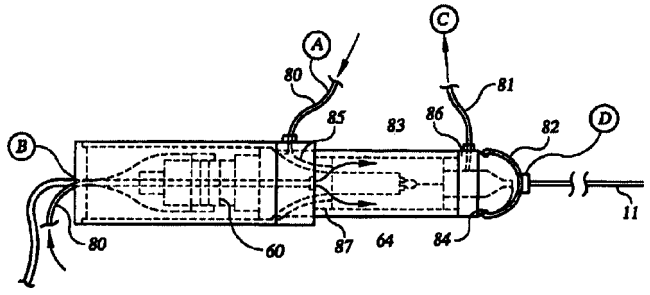

furnished to provide feedback to the operator as to the optimal frequency and power for the generator. The assembly also contains a coolant jacket to keep the drill or coring component at optimum temperature, thus prolonging the life of the instrument.—DRR

6,689,064

43.35.Yb ULTRASOUND CLUTTER FILTER

Richard A. Hager *et al.*, assignors to Koninklijke Philips Electronics N.V.
10 February 2004 (Class 600/454); filed 22 June 2001

This device is directed toward providing a filtering technique that minimizes unwanted clutter signals in the evaluation of blood velocity while maintaining sensitivity to low-velocity blood flow. Such adaptive filtering, rooted in the concepts of linear filtering, involves estimating the signal strength of the blood stream sample and determining the filter order on the basis of a relationship between the signal strength estimate and a signal strength threshold. The filter order is increased and filter coefficients are

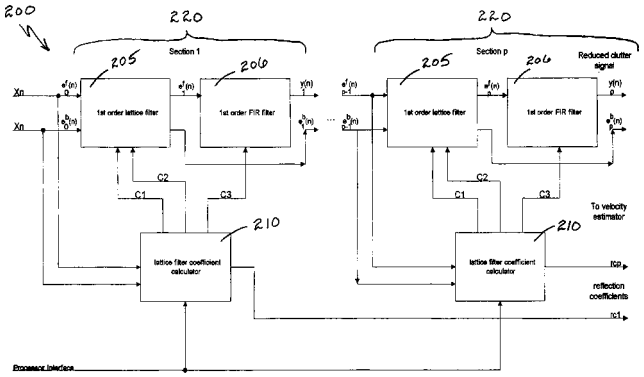

determined based on the input signal and user-definable control inputs. The filter coefficients are chosen so that the filter zeroes correspond to partial correlation coefficients, or are on the unit circle at the frequency of the partial correlation coefficients, or are selected from a preset table of filter coefficients. Dynamic and adaptive modification of the filter order and filter coefficients allow fine-tuning the clutter filter according to a particular application or tissue type.—DRR

6,674,197

43.38.Dv ELECTROMAGNETIC SOUND GENERATOR

Katsuya Iwabuchi *et al.*, assignors to NEC Tokin Iwate, Limited
6 January 2004 (Class 310/81); filed in Japan 1 February 2001

A specific construction is described for an electromagnetic buzzer as shown in the figure. A coil **3** is wound on a core **4** with terminals **6**. This is inside the yoke and spool (**1** and **2**, respectively). As the solenoid pushes

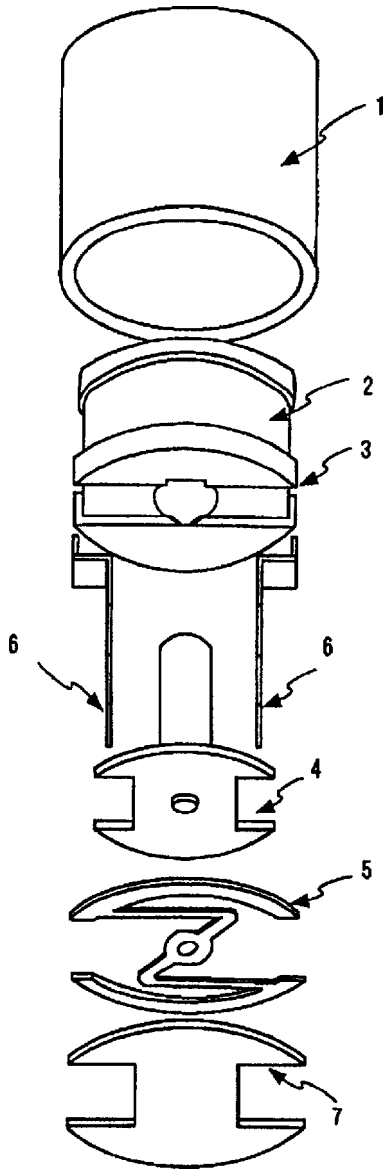

out, it pushes against the round spring **5**, thereby hitting the backplate **7**.—MK

6,671,380

43.38.Fx ACOUSTIC TRANSDUCER WITH SPIRAL-SHAPED PIEZOELECTRIC SHELL

Chung Chang and Hiroshi Hori, assignors to Schlumberger Technology Corporation
30 December 2003 (Class 381/190); filed 26 February 2001

The active element of this transducer is a bender in the shape of a spiral of piezoelectric material. The figures show two orthogonal cross-sectional views of the assembled unit. Item **20** is the spiral piezoelectric shell with outer surface **21** and inner surface **22**, both of which are electroded and the shell is polarized through its thickness. The shell is clamped between steel end plates **51** and **52** via stress bolt **55** but is isolated from them by Teflon plates **53** and **54**. The entire inner space including the spiral cavity is oil filled. The assembly is coated with a rubber housing **78**. The spiral shell is typically 2 cm in diameter, 6 mm high, and the thickness of the spiral shell is 2 mm. The gap between the spiral layers is about 3 mm and the spiral preferably has between 1 and 3 turns. The preferred method of making the spiral shell is to cut it from a solid disk of piezoelectric material

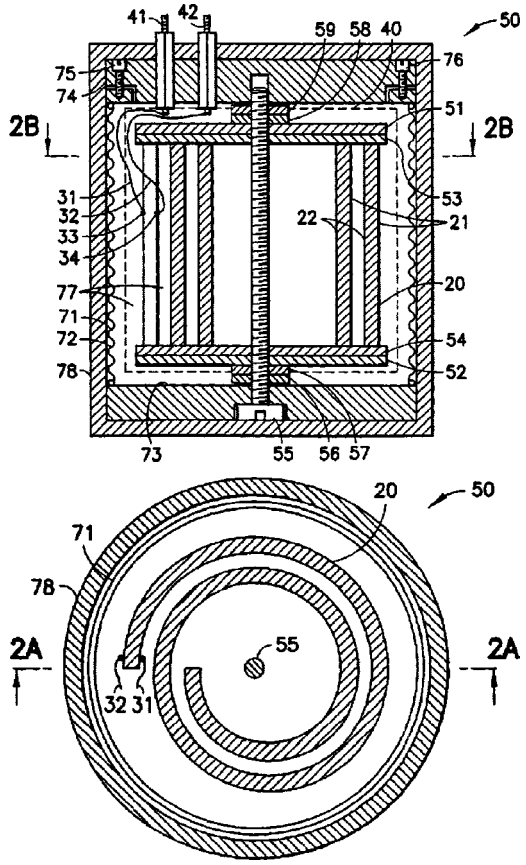

with a diamond-impregnated wire, apply electrodes, and polarize. A second, preferred, bender-type active element is similar to the spiral shell **20** except that an elongated spiral slot is cut parallel to surfaces **21** and **22**. The additional interior faces of the slot are also electroded and the two wall thicknesses of this spiral shell are polarized in such directions that they can be electrically connected in series or parallel. Once the Teflon and steel end plates are applied, this spiral slot becomes an isolated and sealed cavity, so it must be oil filled prior to applying the end plates. Because of the larger surface area associated with either spiral shell, compared to the disk from which it was cut, this device is alleged to have a larger capacitance and, when used with charge amplifiers, a higher sensitivity.—WT

6,668,969

43.38.Ja MANIFOLD FOR A HORN LOUDSPEAKER AND METHOD

John D. Meyer *et al.*, assignors to Meyer Sound Laboratories, Incorporated
30 December 2003 (Class 181/177); filed 11 January 2002

A typical high-frequency compression driver delivers nearly planar waves to a circular horn throat, perhaps 25 to 50 mm in diameter. However, the horn throat of a contemporary line array module is usually a vertical slot. The trick is to couple one to the other while maintaining a constant acoustical path length from the driver to all locations along the slot. Several

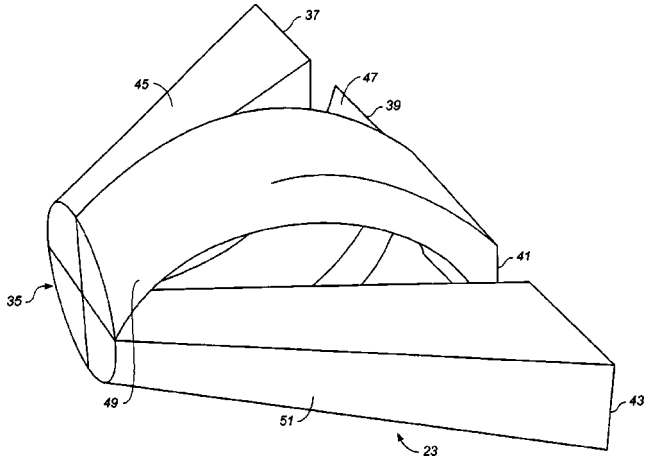

varieties of pretzel bending are already in use and this patent describes yet another. A total of 44 patent claims make sure that every bend in the pretzel is described in full detail.—GLA

6,671,385

43.38.Ja SPEAKER AND MAGNETIC CIRCUIT USED FOR THE SPEAKER

Takashi Suzuki and Satoshi Koura, assignors to Matsushita Electric Industrial Company, Limited
30 December 2003 (Class 381/412); filed 20 August 2002

According to the patent document, this invention ''...aims to provide a compact and light-weight full-range speaker that has a sufficiently high efficiency and can be assembled with ease during its production process.'' The magnetic circuit shown is largely conventional. Voice coil **7** is centered in magnetic gap **A** which is formed between pole piece **1** and pot structure

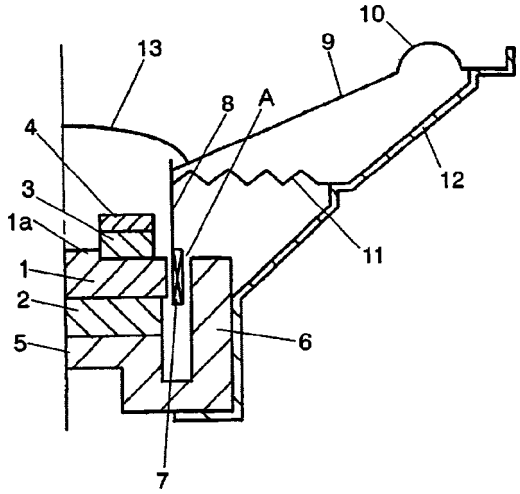

6. Magnetic lines of force are generated by center magnet **2**. In addition, however, a second magnet **3** and top ring **4** are added to repel stray flux, presumably concentrating it in the gap and thus increasing efficiency. Although the patent text makes numerous assertions as statements of fact, no actual test results are shown.—GLA

6,678,381

43.38.Ja ULTRA-DIRECTIONAL SPEAKER

Koji Manabe, assignor to NEC Corporation
13 January 2004 (Class 381/77); field in Japan 25 November 1997

If a directional transducer is driven by an audio-modulated ultrasonic carrier, sound waves can be produced in a defined region of empty space. This technique has received considerable attention over the past 20 years,

but functional results have been mostly disappointing. Most prior art employs amplitude modulation. In a preferred embodiment and several variants, this patent suggests that greater efficiency results if simple frequency modulation is used instead. Almost as an afterthought, the patent body concludes with, ''A plurality of the electro-acoustic transducers may be driven by the single frequency modulator, or by a plurality of the ultrasonic generators and the frequency modulators connected to the electro-acoustic transducers.'' All of the 21 patent claims appear to be restricted to the final 17 words above.—GLA

6,678,384

43.38.Ja SPEAKER STRUCTURE

Hiroshi Kowaki and Hiroyuki Yoshii, assignors to Fujitsu Ten Limited; Timedomain Corporation
13 January 2004 (Class 381/182); filed in Japan 8 June 2000

Two loudspeakers **20** and **30** are mounted back-to-back and rigidly connected by rod **50**. This much is prior art. In this case, however, resilient

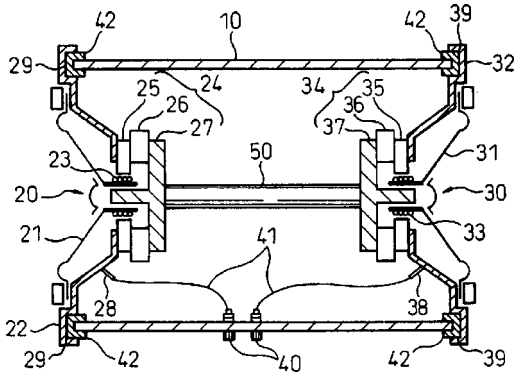

gaskets **42** supply the sole mechanical bridges between the speakers and the cabinet. Thus, ''...the ringing of the cabinet is reduced.''—GLA

6,681,024

43.38.Ja DEVICE INCLUDING A BUILT-IN ELECTROACOUSTIC TRANSDUCER FOR OPTIMUM SPEECH REPRODUCTION

Erich Klein and Heinz Renner, assignors to Koninklijke Philips Electronics N.V.
20 January 2004 (Class 381/389); filed in the European Patent Office 5 August 1997

A small loudspeaker assembly **7** (one of a stereo pair) is recessed into the upper portion of an upholstered chair or automobile seat. The assembly

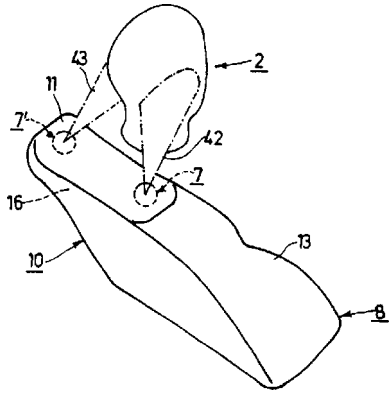

includes a vented back chamber. In this case, however, the vent is sized and damped in such a way as to make lower speech frequencies somewhat directional, and to aim them at the user's ear.—GLA

6,681,026

43.38.Ja RECTANGULAR TRANSDUCER FOR PANEL-FORM LOUDSPEAKER

Tai-Yan Kam, Hsin Chu, Taiwan, Province of China
20 January 2004 (Class 381/412); filed 30 November 2001

The illustration shows a flat, rectangular voice coil assembly **30** that positions the top half of the coil in one magnetic gap and the bottom half in a second gap of opposite polarity. In response to electrical current, forces are

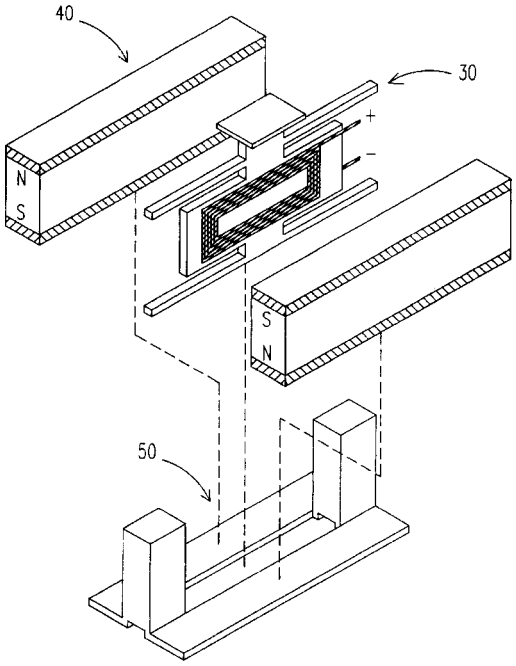

generated in the plane of the coil so that it moves up and down. This is what is described in the patent summary, the preferred embodiment, and the patent claims, but it is not a new idea.—GLA

6,681,027

43.38.Ja MAGNETIC CORE FOR SPEAKER

Yi-Hung Lu, assignor to Zylux Acoustic Corporation
20 January 2004 (Class 381/412); filed in Taiwan, Province of China 12 July 2002

In a conventional moving coil loudspeaker, the magnetic return path adds weight and takes up space. This design has only an annular magnet **1**,

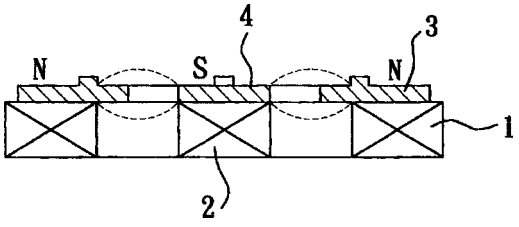

a center magnet **2**, and pole pieces **3** and **4**. The basic concept has been used in planar loudspeakers to energize long, parallel magnetic gaps, but its application to a circular gap is apparently new.—GLA

6,674,870

43.38.Kb ADJUSTABLE SOUND CAPTURING DEVICE (MICTUBZ)

Scott C. Price, assignor to Scott C. Price
6 January 2004 (Class 381/361); filed 24 August 2002

Recording engineers will be happy to learn that they can cut their microphone inventories in half. A single, high-quality, expensive microphone **50** is mounted to dual waveguide **20** fitted with extensible ends **10A**,

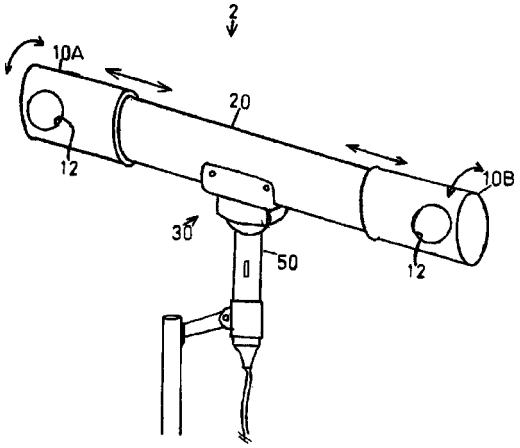

10B. This simple fitting allows the microphone to ''...selectively pick up the sounds of two spaced-apart instruments without also picking up ambient sounds or other noise.''—GLA

6,681,023

43.38.Kb RADIAL PICKUP MICROPHONE ENCLOSURE

Brian Turnbull and Dale Zimmerman, assignors to River Forks Research Corporation
20 January 2004 (Class 381/369); filed 8 September 2000

This patent discloses ''...a microphone system which includes a microphone and a pair of dishes which channel the sound past the microphone.'' If 360° pickup is desired, then the system becomes a familiar radial horn. For more directional pickup, a wedge-shaped portion can be filled with absorptive stuffing **18**. In all cases, however, sound waves are allowed to

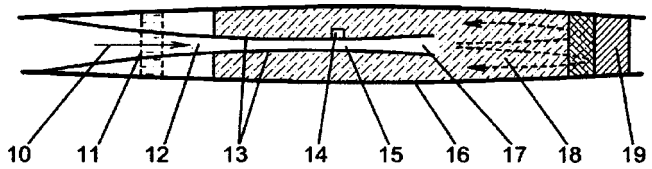

pass microphone **14** without interference. The patent includes test results to back up its assertion that the device functions as the equivalent of one, or as many as six, parabolic microphones. The inventor deserves credit for actually testing his invention, but this reviewer remains unconvinced.—GLA

6,675,511

43.38.Md ACOUSTIC CARD

Benjamin A. Pines, assignor to Apple Corporate Technologies, Incorporated
13 January 2004 (Class 40/124.03); filed 20 April 2001

The world of greeting cards was extended to include sound a long time ago. Typically, a switch is closed when the card is opened and then the audio program begins. The inventor asserts that the switch is too thick and therefore a magnet and reed switch is the solution.—MK

6,680,431

43.38.Md VIOLIN SHOULDER REST

Michael Vanden *et al.*, assignors to Fishman Transducers, Incorporated
20 January 2004 (Class 84/279); filed 16 January 2003

Miking a violin is typically done by placing the transducer near the bridge. This inventor proposes adding a microphone inside the shoulder rest. The issue of shadowing by the jaw is not addressed.—MK

6,680,753

43.38.Md METHOD AND APPARATUS FOR SKIPPING AND REPEATING AUDIO FRAMES

Michael Kahn, assignor to Matsushita Electric Industrial Company, Limited
20 January 2004 (Class 348/512); filed 7 March 2001

Synchronization of compressed audio with video can be an issue due to the differing data rates. This proposed algorithm would compute an amplitude value from an audio frame and compare it against a threshold. If the audio time is less than the video time, then frames must be repeated to bring the time up. Frames that are below the threshold can be considered silent (by this algorithm) and skipped. Likewise, if the audio time is ahead of the video time, then the frames must be skipped.—MK

6,683,241

43.38.Md PSEUDO-LIVE MUSIC AUDIO AND SOUND

James W. Wieder, Ellicott City, Maryland
27 January 2004 (Class 84/609); filed 6 November 2001

The inevitable sameness of audio recording is this author's woe. He proposes breaking a composition into a number of segments (called snippets) that are variably assembled at playback. Valuable details about the time varying process are notably absent. The multitrack playback details (including pointer organization in memory) are certainly not very original.—MK

6,686,531

43.38.Md MUSIC DELIVERY, CONTROL AND INTEGRATION

James D. Pennock and Robin M. Urry, assignors to Harmon International Industries Incorporated
3 February 2004 (Class 84/615); filed 27 December 2001

This patent proposes online delivery of music that is changed at the user's discretion. Essentially, each instrument track is separately recorded at the studio and then mixed down in the user's machine. The instruments can also be pitch shifted or time warped (of course these mechanisms are not discussed or elaborated). Or, various tracks can be omitted entirely, so it can become ''music minus *n*,'' where *n* is the number of missing tracks.—MK

6,687,193

43.38.Md AUDIO REPRODUCTION APPARATUS HAVING AUDIO MODULATION FUNCTION, METHOD USED BY THE APPARATUS, REMIXING APPARATUS USING THE AUDIO REPRODUCTION APPARATUS, AND METHOD USED BY THE REMIXING APPARATUS

Dong-kwan Jung, assignor to Samsung Electronics Company, Limited
3 February 2004 (Class 369/4); filed in the Republic of Korea 21 April 2000

Turntable music (or ''scratching'') is the now ancient technique of hand control of vinyl playback with the fingers controlling the platter motion. Here again (see United States Patent 6,535,462 [reviewed in J. Acoust. Soc. Am. **114**(3), 1205 (2003)]) is another digital version that aims to avoid needles, table inertia, surface noise, and fun.—MK

6,694,126

43.38.Md DIGITAL MEMO RECORDER

Paul S. Van Lente, assignor to Johnson Controls Interiors Technology Corporation
17 February 2004 (Class 455/66.1); filed 11 July 2000

The transition of the car from motor vehicle to home on wheels continues. Here, the office memo recorder has morphed into a car memo recorder for those brilliant inspirations that occur during the rush hour.—MK

6,671,379

43.38.Si EAR MICROPHONE APPARATUS AND METHOD

Guerman G. Nemirovski, assignor to Think-A-Move, Limited
30 December 2003 (Class 381/93); filed 31 July 2001

The ''side tone'' that one hears while speaking is mostly airborne energy. However, this patent argues that physiological processes generate detectable acoustic signals in the ear canal even if the external ear is sealed. This means that an in-the-ear microphone can be used for two-way communication. Ear button **18** contains a receiver **22** and a microphone **20** in close

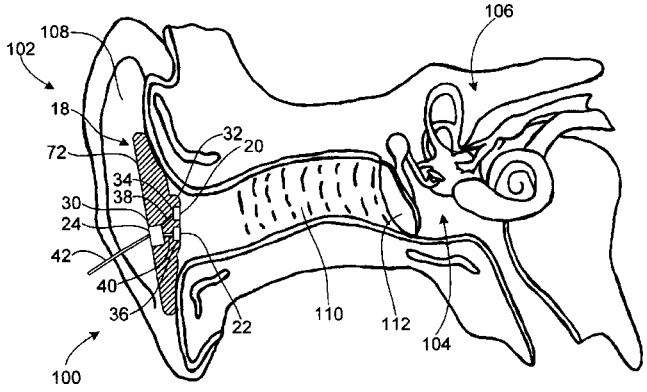

proximity, both facing into the ear canal. Anti-feedback electronic circuitry is included to ''...minimize the delivery of a feedback component to the communications device.'' A second, external microphone can be added if noise-cancelling capability is desired.—GLA

6,674,863

43.38.Tj MICROPHONE-SPEAKER APPARATUS

Takefumi Ura, assignor to Matsushita Electric Industrial Company, Limited
6 January 2004 (Class 381/93); filed in Japan 5 March 2002

In voice amplification systems and loudspeaking telephones, gain is usually limited by the onset of acoustic feedback. Within the past few years, digital signal processing has made it possible to identify and suppress feedback howling in real time. This patent describes an improved method for detecting incipient howling that is said to be less subject to error, especially in the presence of background noise. Unfortunately, the patent is almost

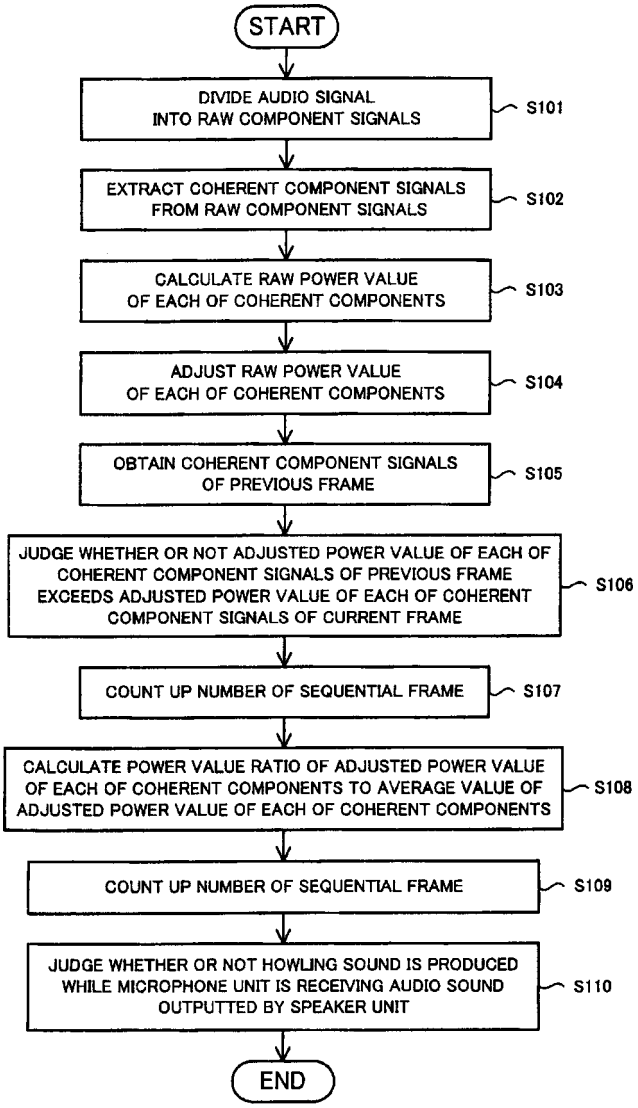

impossible to follow because information is presented in enormously long sentences containing dozens of commas and semicolons. Judging from two straightforward flow charts, however, it appears that comparisons are made between adjusted raw power values rather than absolute threshold values in individual frames.—GLA

6,681,019

43.38.Vk POLARITY DETERMINING CIRCUIT FOR LOUDSPEAKERS, AN AUDIO CIRCUIT HAVING A FUNCTION OF DETERMINING POLARITIES OF LOUDSPEAKERS, AND AN AUDIO CIRCUIT HAVING FUNCTIONS OF DETERMINING POLARITIES OF LOUDSPEAKERS AND SWITCHING THE POLARITIES

Mikio Kitano and Takatsugu Uragami, assignors to Yamaha Corporation; Kabushiki Kaisha Daiichikosho
20 January 2004 (Class 381/59); filed in Japan 22 September 1998

Yamaha has somehow managed to patent a polarity-reversing switch.

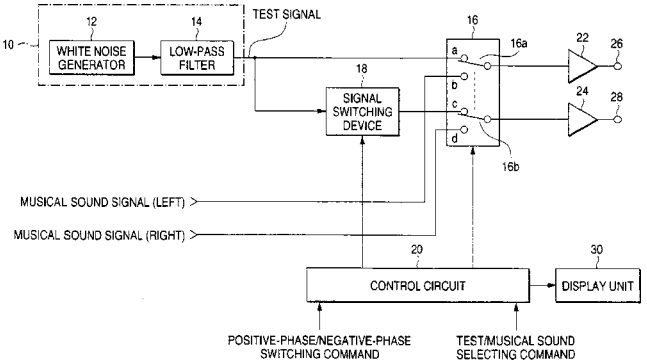

Four embodiments are described.—GLA

6,668,650

43.38.Yn VIBRATION TESTING APPARATUS AND METHOD USING ACOUSTICAL WAVES

François Lafleur *et al.*, assignors to Intellium Technologies Incorporated
30 December 2003 (Class 73/571); filed in Canada 28 June 1999

Production testing of electronic components such as circuit boards may involve subjection to vibration forces at specified frequencies and acceleration levels. In some instances, a push–pull acoustic test chamber may be more efficient than a shaker table. The concept can be carried one step farther by using one set of transducers **35** to supply high-frequency energy

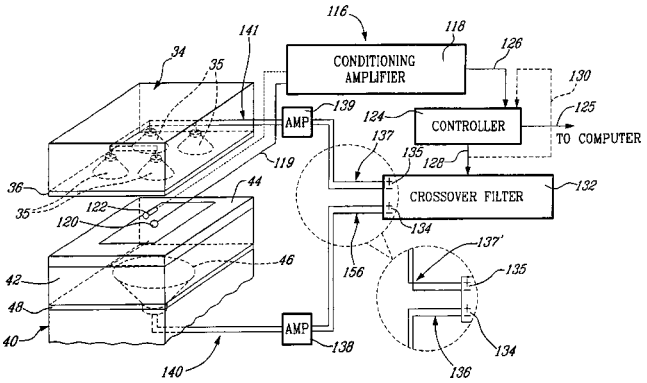

and the opposing transducer **46** to supply low-frequency energy. During actual testing, a sample is brought into place near sensing microphone **122** and the upper assembly is then lowered to seal the two chambers together. To obtain optimum spectral density through the crossover region, the polarity of one of the drive signals can be inverted.—GLA

6,684,700

43.40.Yq STRESS WAVE SENSOR

David B. Board, assignor to Swantech, L.L.C.
3 February 2004 (Class 73/579); filed 11 August 2000

This sensor is specifically designed as a stress wave analysis system. In order to negate the effects of vibration, audible noise, acoustic sources not directly related to friction, and mechanical impact events in operating machinery, it is desired to detect stress waves in a narrow frequency range, such as 35 to 40 kHz. In order to maximize the signal-to-noise ratio of the stress waves relative to the background noise and vibration, the sensor should have a resonance gain of approximately 30 dB at its primary resonant frequency. To enable selective amplification of stress waves, it should provide a total energy content of REI (resonant energy integral) within a specified tolerance band that can be measured using standard test equipment to yield calibration data that is traceable to established standards, and its resonant peak amplitude output should decay to half amplitude within five cycles and be down to no more than 20% of the initial response in the number of cycles that occur during the time interval that corresponds to the corner frequency of a low-pass filter.—DRR

6,682,472

43.50.Gf TINNITUS REHABILITATION DEVICE AND METHOD

Paul Benjamin Davis, assignor to TinniTech Limited
27 January 2004 (Class 600/25); filed in Australia 17 March 1999

This tinnitus rehabilitation method entails intermittent masking of tinnitus through the use of software that spectrally modifies an audio signal according to a predetermined masking algorithm. The intensity of the audio signal at chosen frequencies is tailored to the audiometric configuration of the patient. The algorithm provides intermittent masking of the tinnitus whereby it is completely obscured during peaks of the audio signal while the perception of tinnitus occasionally emerges during troughs.—DRR

6,688,424

43.50.Gf NOISE ABSORBING DEVICE AND DEVICE FOR TAKING AIR INTO ENGINE ROOM OF A CONSTRUCTION MACHINE

Kuniaki Nakada *et al.*, assignor to Komatsu Limited
10 February 2004 (Class 181/224); filed in Japan 24 October 1997

This device carries the dual purpose of providing sound attenuation and increased cooling effect with smaller airflow resistance in the air supply

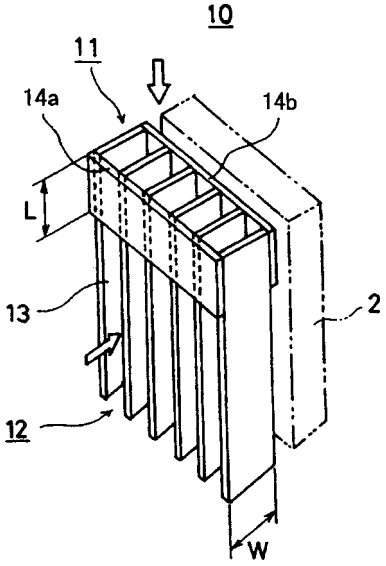

to the engine room of a construction machine. The design incorporates multiple air inlets to receive airflow, a split-type noise absorbing region, and a cellular-type noise absorbing region.—DRR

6,688,425

43.50.Gf INDUCTION SYSTEM WITH LOW PASS FILTER FOR TURBO CHARGER APPLICATIONS

Roderic Cole *et al.*, assignors to Siemens VDO Automotive, Incorporated
10 February 2004 (Class 181/264); filed 9 October 2002

An induction system is equipped with a turbo charger. A flow tube channels air into a longitudinal path past a noise attenuation plate located within the flow tube. The internal surface of the tube is lined with a number of ribs that are spaced apart from one another and are tuned to a desired frequency. The noise attenuation plate contains a number of holes with

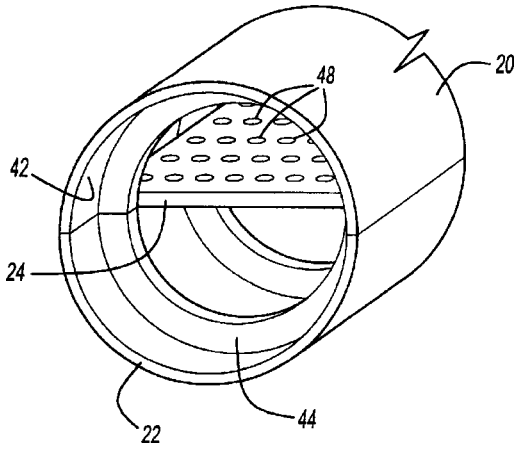

varying diameter and depth (think of them as Helmholtz attenuators). When acoustic energy produced by the turbo charger flows over the plate and the ribs, the change in impedance results in acoustic reflections back toward the turbo charger. The noise attenuation plate and the ribs together function as a low-pass filter in the air flow.—DRR

6,688,841

43.50.Gf WIND ENERGY SYSTEM WITH ADJUSTMENT OF THE SOUND LEVEL

Aloys Wobben, Aurich, Germany
10 February 2004 (Class 415/1); filed in Germany 10 June 1999

Wind power installations are capable of generating noise levels that may not be acceptable to residents who live nearby. This is a system intended to allow a wind energy system to stay within noise emission limits. The rotational speed of the turbine rotor is reduced as soon as maximum set sound level values are reached. The allowable maxima are adjusted according to the wind speed, wind direction, or time of day. Another method involves the physical placement of turbines without a speed reduction capability. The argument is that by strategic placement of turbines within a specific area, they can be arranged so as to impede each other's air flow, thus reducing the maximum rotational speed reached by any one turbine.—DRR

6,686,839

43.50.Qp METHOD AND SYSTEM FOR NOISE NOTIFICATION

Paul Bao-Luo Chou *et al.*, assignors to International Business Machines Corporation
3 February 2004 (Class 340/540); filed 4 April 2001

This conceptual patent was filed to stop office noise, specifically excess yakking. Yes, according to the introduction, ''Much of the noise is created by the workers themselves in the course of their work. However, the noise is not always intentional, nor are they necessarily aware that they are speaking too loudly or making noise in any other way. Noise indicating light systems are known. However, none of these systems directs notification to the person responsible for the noise.'' 1984 has come and gone and yet looms forever on the horizon.—MK

6,594,365

43.55.Br ACOUSTIC SYSTEM IDENTIFICATION USING ACOUSTIC MASKING

Graham P. Eatwell, assignor to Tenneco Automotive Operating Company Incorporated
15 July 2003 (Class 381/73.1); filed 18 November 1998

This patent describes an automatic system for characterizing the acoustic behavior of a room. An initial test pulse is picked up by one or more sensors in the room. The room response as well as noise masking thresholds and perceptual characteristics are then considered in the calculation of a new test pulse. A second response pulse is picked up by the sensor and used to fine tune the knowledge of the acoustic system. It is not clear in the patent what sort of room or other acoustic system is targeted. One stated goal, however, is to be able to reduce the effect of room noises on speech perception within the room.—DLR

6,676,479

43.58.Wc TURKEY CALL

Jeffery A. Zimmerman, Shawano, Wisconsin
13 January 2004 (Class 446/397); filed 9 November 2001

Turkeys are maligned creatures. Ben Franklin respected them and wanted to make them the national bird. Hunting them is tricky; hunters need all the help they can get. In this patent, a striker is used to scrape a slate piece mounted on top of a hollow sound box.—MK

6,679,927

43.58.Wc DOG BONE TOY WITH VARIABLE SOUND EMITTERS

Ned Strongin, assignor to Hands On Toys, Incorporated
20 January 2004 (Class 44/213); filed 18 October 2001

A dog toy shaped like a bone uses a series of tubes with whistles that

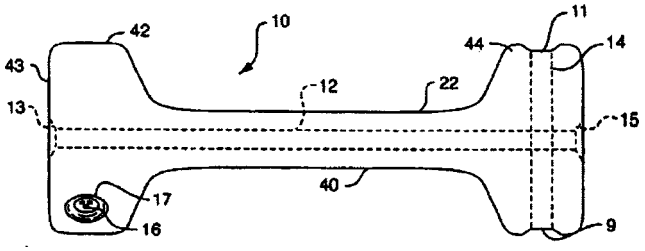

move due to gravity. Dogs might be pleased with the result but the effect on the owner is unclear.—MK

6,690,805

43.60.Bf AUDIO SIGNAL NOISE REDUCTION SYSTEM

Masayuki Tsuji *et al.*, assignors to Mitsubishi Denki Kabushiki Kaisha
10 February 2004 (Class 381/94.1); filed in Japan 17 July 1998

This audio signal noise reduction system is said to be capable of removing pulselike noise in a car radio caused by engine ignition plugs, a power window driving motor, etc. A noise detecting circuit detects the onset

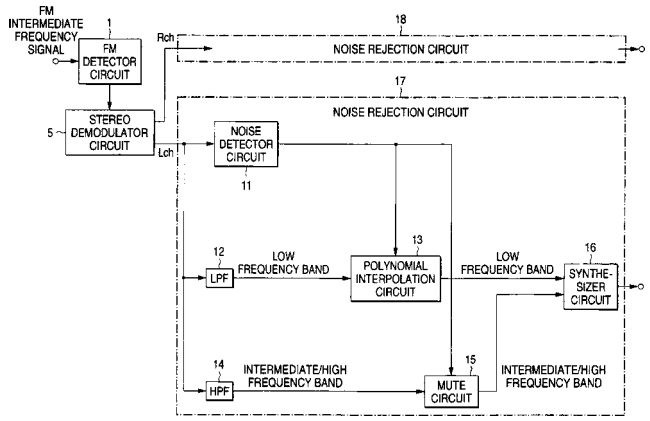

and cessation of the noise period and determines the low-frequency component of the noise. A polynomial interpolating circuit interpolates the noise period of the detected low-frequency component. A muting circuit attenuates the output level at the noise period of the intermediate- and high-frequency components. A signal synthesizing circuit synthesizes the lower-frequency component.—DRR

6,693,107

43.64.Gz PHARMACEUTICAL COMPOSITION USEFUL FOR THE TREATMENT OF TINNITUS AND HEARING LOSS

Shmuel Simon, Ashdod, Israel
17 February 2004 (Class 514/266); filed in Israel 15 July 1999

The patent relates to a pharmaceutical composition which contains an active ingredient sildenafil and related compounds, intended for treatment of tinnitus and hearing loss. The pharmaceutical composition can be prepared for oral administration in the form of a tablet, a pill, a powder, or syrup.—DRR

6,690,265

43.64.Ri INFRASOUND HAZARD-WARNING METHOD AND DEVICE FOR ALERTING NIGHT-MIGRATING BIRDS TO OBSTACLES

Jonathan Tryon Hagstrum, assignor to The United States of America as represented by the Department of the Interior
10 February 2004 (Class 340/384.3); filed 4 December 2001

The device is premised on the assumption that if artificial obstacles or attached devices are made to radiate infrasound at the same frequency as natural topographic features, night-migrating birds will avoid them in the same way as they would avoid colliding with, say, a hillside. The device includes a recorder and loudspeaker affixed to the structure. The recorder provides an infrasonic signal that contains a frequency close to that of a natural topographic feature. In another embodiment, the recorder supplies a signal mimicking the sound of thunder and/or the sound of a lighting strike.—DRR

6,684,063

43.66.Ts INTEGRATED HEARING AID FOR TELECOMMUNICATIONS DEVICES

H. Stephen Berger *et al.*, assignors to Siemens Information & Communication Networks, Incorporated
27 January 2004 (Class 455/90.1); filed 2 May 1997

A hearing aid is integrated with the headset or handset of a wireless communications device such as a cellular telephone. Hearing aid parameters

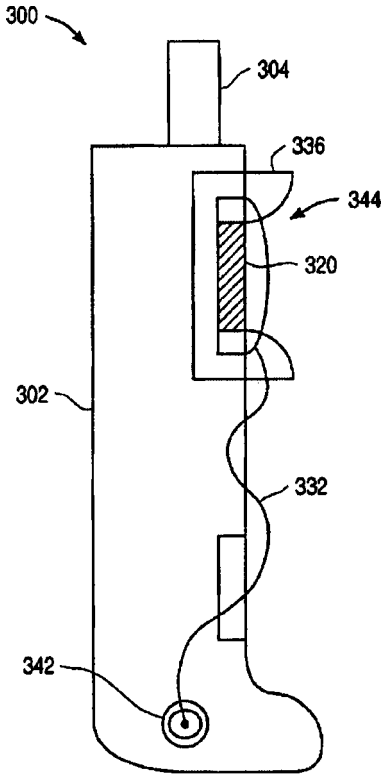

relating to the wearer's hearing loss are programmed into an on-board processor. The design is said to reduce interference signals produced by the cellular device in the hearing aid.—DAP

6,687,377

43.66.Ts METHOD AND APPARATUS FOR DETERMINING IN SITU THE ACOUSTIC SEAL PROVIDED BY AN IN-EAR DEVICE

Jeremie Voix and Frederic Laville, assignors to Sonomax Hearing Healthcare Incorporated
3 February 2004 (Class 381/60); filed 20 December 2000

A probe and reference microphones are used to determine the quality of the acoustic seal provided by an expandable in-ear hearing protector or hearing aid. The probe and reference microphones measure the sound pressure level in the wearer's ear canal and just outside of the ear canal entrance,

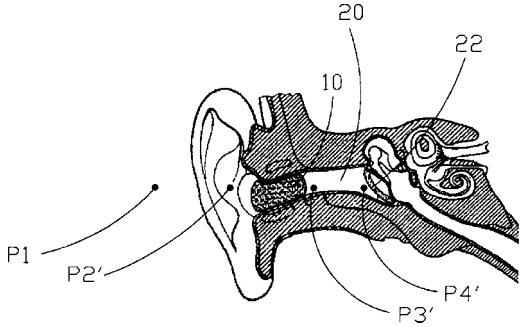

respectively. The difference between the two is the measured insertion loss. The system is used for monitoring attenuation provided during expansion of the in-ear device in the ear canal.—DAP

6,694,034

43.66.Ts TRANSMISSION DETECTION AND SWITCH SYSTEM FOR HEARING IMPROVEMENT APPLICATIONS

Stephen D. Julstrom *et al.*, assignors to Etymotic Research, Incorporated
17 February 2004 (Class 381/315); filed 28 December 2000

A hearing aid system detects the quality of a wireless transmission from a secondary audio source such as a remote microphone or telephone. A switching mechanism automatically selects, via the quality of transmission, either the output of conventional hearing aid microphone and/or the remote

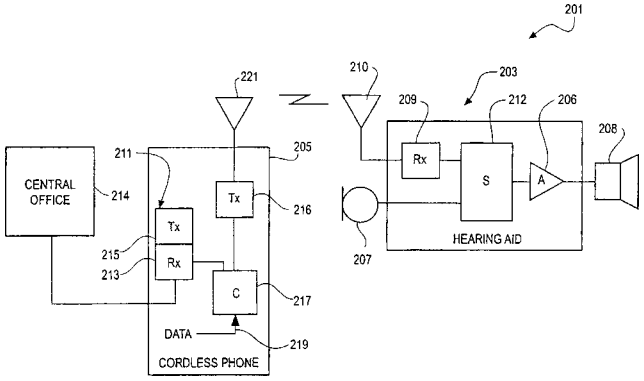

audio source for amplification and delivery to the ear canal of the wearer. Means for analyzing the secondary audio signal quality include exceeding a minimum threshold level.—DAP

6,694,035

43.66.Ts SYSTEM FOR CONVEYING MUSICAL BEAT INFORMATION TO THE HEARING IMPAIRED

Martin Teicher, Waltham and Steven Lowen, Burlington, both of Massachusetts
17 February 2004 (Class 381/326); filed 5 July 2001

The device, intended for those who have severe hearing impairment to the extent that regular hearing aids do not help, conveys musical beat information through a tactile representation so the wearer can follow music on the dance floor. In one embodiment, the system consists of a sound detector for receiving music and provides a signal corresponding to the music to an audio processing unit. The audio processing unit generates one or more electrical outputs to tactile actuators (such as pulsers which can be felt) for

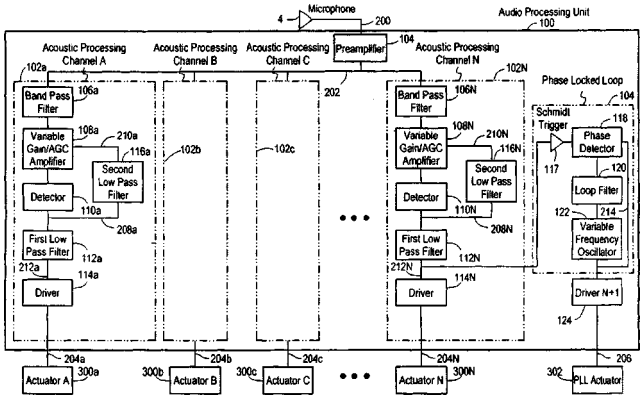

conveying the musical beat information to the user. In another embodiment, the audio processing unit contains one or more electronic filters for selecting audio-frequency bands and relaying signals to the actuators in response to the beat within a particular audio-frequency band.—DRR

6,669,527

43.72.Ar DOLL OR TOY CHARACTER ADAPTED TO RECOGNIZE OR GENERATE WHISPERS

Albert Wai Tai Chan, assignor to Thinking Technology, Incorporated
30 December 2003 (Class 446/175); filed 3 January 2002

Equipping dolls with microphones is easy enough to do. The question is: what can you do with them? Here, the inventor proposes using a whisper detection algorithm (not specified of course) and generating whispers in return (also not detailed).—MK

6,678,647

43.72.Gy PERCEPTUAL CODING OF AUDIO SIGNALS USING CASCADED FILTERBANKS FOR PERFORMING IRRELEVANCY REDUCTION AND REDUNDANCY REDUCTION WITH DIFFERENT SPECTRAL/TEMPORAL RESOLUTION

Bernd Andreas Edler and Christof Faller, assignors to Agere Systems Incorporated
13 January 2004 (Class 704/200.1); filed 2 June 2000

An encoding system for speech and music audio is proposed that provides independent selection of spectral and temporal resolution for the reduction of redundancy and irrelevancy. A first analysis filterbank converts

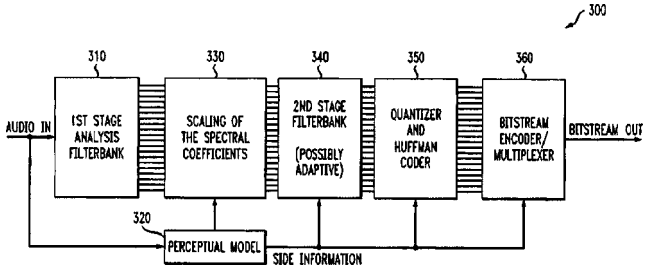

the input samples into a subsampled spectral representation for irrelevancy reduction. A second analysis filterbank performs redundancy reduction using a subband technique and is optionally adaptive to the statistics of its input signal to determine the best spectral and temporal resolutions.—DAP

6,678,653

43.72.Gy APPARATUS AND METHOD FOR CODING AUDIO DATA AT HIGH SPEED USING PRECISION INFORMATION

Mineo Tsushima *et al.*, assignors to Matsushita Electric Industrial Company, Limited
13 January 2004 (Class 704/220); filed in Japan 7 September 1999

A system with relatively less computational overhead is proposed to improve the spectral resolution of audio encoding and the resulting sound

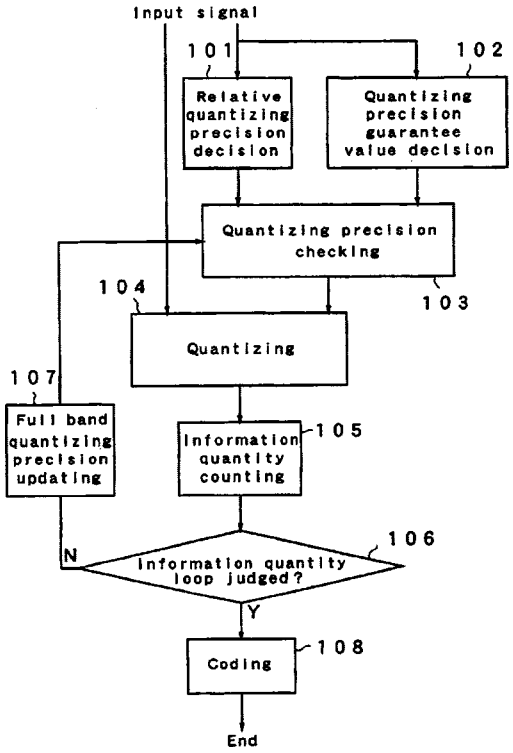

quality. Quantizing precision decisions based on a psychoacoustic model are made to ensure a minimum signal amplitude for each frequency band relative to the noise level.—DAP

6,681,365

43.72.Gy METHOD AND APPARATUS FOR PROVIDING CHANNEL ERROR PROTECTION FOR A SOURCE CODED BIT STREAM

Raghavan Anand *et al.*, assignors to Lucent Technologies Incorporated
20 January 2004 (Class 714/790); filed 6 October 2000

Unequal channel error protection for progressive or partitioned source-coded bit streams is provided by puncturing a channel code. The method

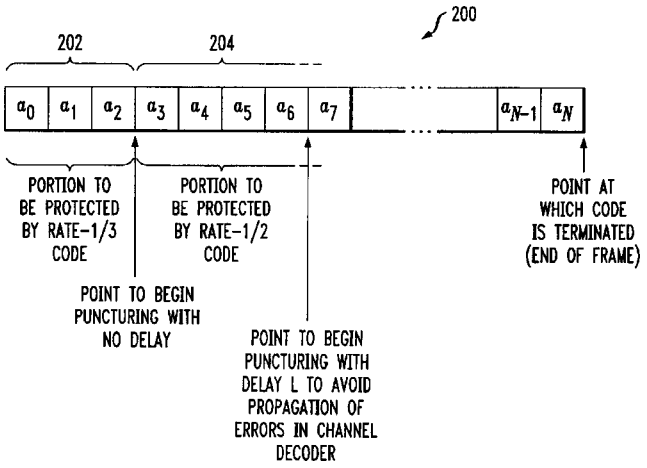

eliminates the need for tail bits to terminate subblocks. The number of bits of delay before puncturing is related to at least the memory of the channel code so that errors are not propagated in the decoder.—DAP

6,591,240

43.72.Ja SPEECH SIGNAL MODIFICATION AND CONCATENATION METHOD BY GRADUALLY CHANGING SPEECH PARAMETERS

Masanobu Abe, assignor to Nippon Telegraph and Telephone Corporation
8 July 2003 (Class 704/278); filed in Japan 26 September 1995

This speech synthesis system includes a method of gradually morphing certain characteristics of the speech of one speaker into those of a second speaker. This is said to be useful, for example, when new material must be interspersed with prerecorded material. The assumption is that such a

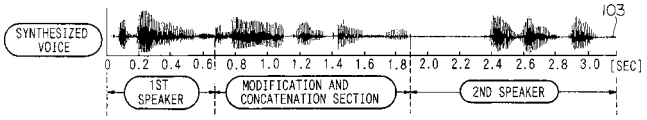

gradual morphing would make the transition less abrupt and jarring. The description deals almost entirely with adjustments of the average pitch range. The idea of changing a man into a woman in this way is considered.—DLR

6,594,631

43.72.Ja METHOD FOR FORMING PHONEME DATA AND VOICE SYNTHESIZING APPARATUS UTILIZING A LINEAR PREDICTIVE CODING DISTORTION

Shisei Cho *et al.*, assignors to Pioneer Corporation
15 July 2003 (Class 704/268); filed in Japan 8 September 1999

The premise here is that speech analysis for purposes of synthesis is reasonably straight forward if you can just separate the pitch signal from the ''phoneme characteristics.'' The approach taken is to analyze a frame of natural speech to obtain LPC coefficients and the corresponding cepstral vector. This cepstral vector is then used to resynthesize the vowel using a range of different source pitches. These vowels are again analyzed and the cepstral vectors are compared with the original, adjusting the pitch for the minimum ''cepstral distortion.'' The synthetic token which produced the minimum error value is taken as representative of the phoneme in question. This procedure is repeated for all like phonemes in the speech sample to construct representative phoneme classes for synthesis.—DLR

6,587,822

43.72.Ne WEB-BASED PLATFORM FOR INTERACTIVE VOICE RESPONSE (IVR)

Michael Kenneth Brown *et al.*, assignors to Lucent Technologies Incorporated
1 July 2003 (Class 704/275); filed 6 October 1998

The system described here would allow Internet (or other network) pages to be accessed remotely using a voice device, such as a cell phone. The pages would be loaded at a server site, perhaps a cell base station or an Internet service provider. The page content would be analyzed and summarized verbally over the phone link. At the same time, a grammar would be created for use by a recognizer in understanding user queries about the page. Such a grammar would, for example, allow DTMF tones as well as voice in querying the page contents. The page analyzer would contain several reference models of possible page content, said to aid in the construction of a grammar for the page. The patent represents an interesting comment on earlier schemes known as ''voice-enabled web'' and ''semantic web,'' which would use XML annotations in the page text to aid in voicing or understanding the page. Very few sites have added such specialized annotations. This patented system would, on the other hand, work with existing page content.—DLR

6,591,236

43.72.Ne METHOD AND SYSTEM FOR DETERMINING AVAILABLE AND ALTERNATIVE SPEECH COMMANDS

James R. Lewis and Kerry Ortega, assignors to International Business Machines Corporation
8 July 2003 (Class 704/251); filed 13 April 1999

The speech recognition system presented here represents what we all hope is a fast-disappearing mode of recognizer operation. Since an arbitrary sentence will rarely fit the recognizer's initial analysis, two actions may be taken. Either the recognizer can adapt to the human or the human can adapt to the recognizer. A sentence in the ''Background of the Invention'' section opines that natural-language-understanding recognizers will not be available anytime soon. This patent addresses the issue by attempting to teach the human more about the recognizer's internal structures, what sentences can be parsed, etc. Do we really need this?—DLR

6,594,632

43.72.Ne METHODS AND APPARATUS FOR HANDS-FREE OPERATION OF A VOICE RECOGNITION SYSTEM

Daniel F. White, assignor to NCR Corporation
15 July 2003 (Class 704/270); filed 2 November 1998

The need being addressed by this patent is completely hands-free operation of a speech recognizer. Clearly, a nonspeech input would be needed to turn on the system. The proposed solution is that one of a variety of other methods would be available for that purpose. These include blowing into the microphone or another physical action such as actuating some type of pressure, motion, or touch sensor. Once such a mechanism is available, it may also be useful in other ways in conjunction with the recognition system.—DLR

6,598,019

43.72.Ne EVALUATION METHOD, APPARATUS, AND RECORDING MEDIUM USING OPTIMUM TEMPLATE PATTERN DETERMINATION METHOD, APPARATUS AND OPTIMUM TEMPLATE PATTERN

Naoyuki Tokuda and Hiroyuki Sasai, assignors to Sunflare Company, Limited
22 July 2003 (Class 704/255); filed 20 June 2000

This speech recognizer uses a set of sentence models referred to as template patterns. Constructed by language experts, each template pattern would provide scores for the words it uses depending on the probable importance of those words in the context. As input speech is processed by the application of various templates, the word scores for each template are accumulated. The template with the highest word score is taken as the correct analysis of the sentence and can be used to correct areas of uncertainty in the analysis.—DLR

6,684,186

43.72.Ne SPEAKER RECOGNITION USING A HIERARCHICAL SPEAKER MODEL TREE

Homayoon S. M. Beigi *et al.*, assignors to International Business Machines Corporation
27 January 2004 (Class 704/246); filed 26 January 1999

A hierarchy-based speaker model is generated from the sample data for each speaker. Each individual model describes the features of the audio signal for the associated speaker. Similar speaker models are grouped together to construct a basis layer. Using that basis layer, a corresponding parent speaker model is created in the higher level of the tree.—HHN

6,687,673

43.72.Ne SPEECH RECOGNITION SYSTEM

Robert James Mann, assignor to International Business Machines Corporation
3 February 2004 (Class 704/244); filed in the United Kingdom 4 September 1999

A method to determine a particular alphabetic character is developed by recognizing a single alphabetic character and a word associated with the single character. The system tries to match the single character with the first character of the word. A matching history is saved in memory.—HHN

6,694,294

43.72.Ne SYSTEM AND METHOD OF MU-LAW OR A-LAW COMPRESSION OF BARK AMPLITUDES FOR SPEECH RECOGNITION

Harinath Garudadri, assignor to Qualcomm Incorporated
17 February 2004 (Class 704/234); filed 31 October 2000

Use of mu-law or A-law compression/expansion of bark amplitudes is said to reduce the detrimental effect of noisy environments on speech recognition. These techniques are preferred to log compression for low-

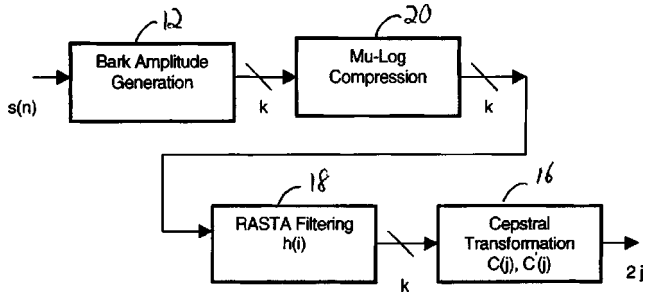

amplitude signals on the bark channels to avoid excessive amplification of noise. The system also includes mu-law expansion of RelAtive SpecTrAl (RASTA) filter outputs.—DAP

6,694,296

43.72.Ne METHOD AND APPARATUS FOR THE RECOGNITION OF SPELLED SPOKEN WORDS

Fileno A. Alleva *et al.*, assignors to Microsoft Corporation
17 February 2004 (Class 704/255); filed 3 November 2000

A dictation language model modifies the output of a speech recognizer based on the most likely recognized letter sequences. A weighting system among the dictation, spelling, and acoustic-model outputs optimizes the performance of the overall system.—HHN

6,664,454

43.75.Ef MUSICAL INSTRUMENT

Mark A. Johnson, Salt Lake City, Utah
16 December 2003 (Class 84/383 R); filed 28 June 2000

The inventor admits that he borrowed the concept of the folded bore from the Renaissance racket and applied it to the dijeridoo. It'll be more compact and will definitely fit in the overhead bin.—MK

6,664,456

43.75.Ef HARMONIC VIBRATION DAMPING DEVICE FOR MUSICAL INSTRUMENTS AND FIREARMS

Philip Momchilovich, Washington, District of Columbia
16 December 2003 (Class 84/400); filed 3 April 2001

This reviewer has always suspected a hidden link between woodwinds and firearms. To quote from the patent abstract ''Resilient material and/or rubber O-rings are placed at various predetermined locations to reduce unwanted sympathetic vibrations on musical instruments and firearms. This improves the performance and sound of musical instruments and makes them easier to play. The resilient material improves shooting accuracy, produces a tighter grouping of firings, and reduces flash, report and recoil of firearms.''—MK

6,681,661

43.75.Gh DETACHABLE AND ADJUSTABLE SOUND AND FEEDBACK CONTROL DEVICE FOR STRINGED MUSICAL INSTRUMENTS HAVING A HOLLOW BODY WITH A SOUND HOLE

Anthony F. Lalonde, San Jose, California
27 January 2004 (Class 81/267); filed 5 March 2002

The inventor proposes an insertable sound-hole cover with adjustable vanes. The main idea is to provide a variable opening for an acoustic guitar. Additionally, it can be used to hang a dessicant in the body for use in humid environments.—MK

6,686,526

43.75.Hi PERCUSSION PRACTICE AID

Leonard E. Ezbicki, Framingham, Massachusetts
3 February 2004 (Class 84/411 R); filed 17 October 2001

To encourage the student to hit the center of the drumhead, an annulus is placed on top of the head as shown in the figure. Various refinements are

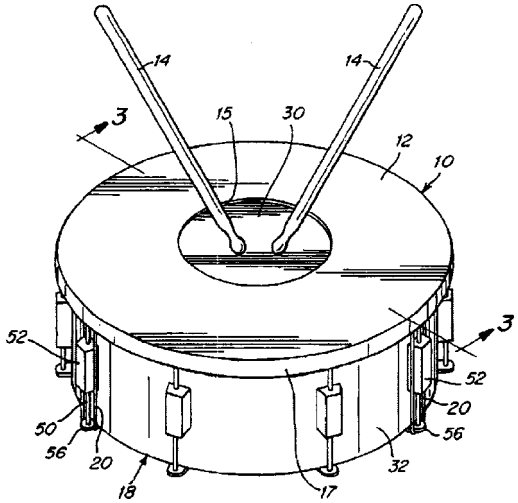

possible and also applicable to cymbals and other percussion instruments.—MK

6,689,944

43.75.Hi DRUM ACOUSTIC WIRE AND DRUM

Yukimasa Okumura, assignor to Yamaha Corporation
10 February 2004 (Class 84/411 R); filed in Japan 12 April 1999

The timbre of the snare drum depends on the vibrating wires located underneath the drum head. These wires are difficult to install and are exceedingly sensitive to environmental sounds (like loud amplified guitars).

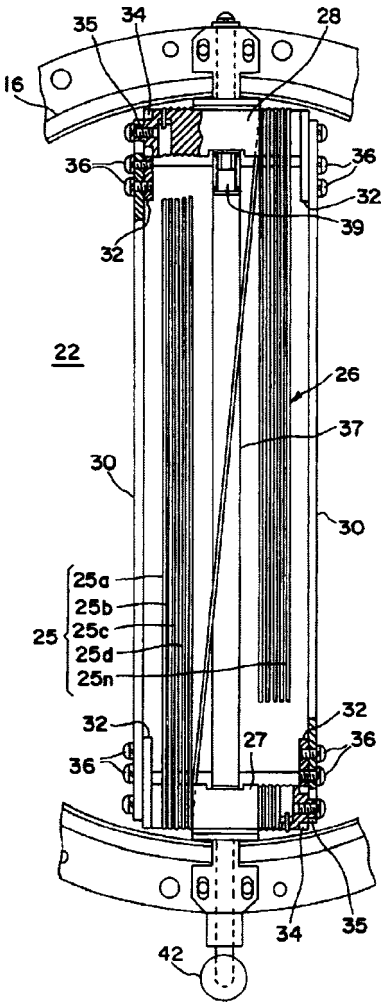

Yamaha proposes using a single long wire as shown stretched between tensioners **27** and **28**.—MK

6,632,988

43.75.Mn DAMPER ADJUSTMENT DEVICE

M. Scott Jones and Maik Jenfeldt, assignors to Steinway Musical Instruments, Incorporated
14 October 2003 (Class 84/216); filed 4 April 2000

Steinway describes a new method of damping grand piano strings. The timing of the underdampers creates the action. And so, as shown in the

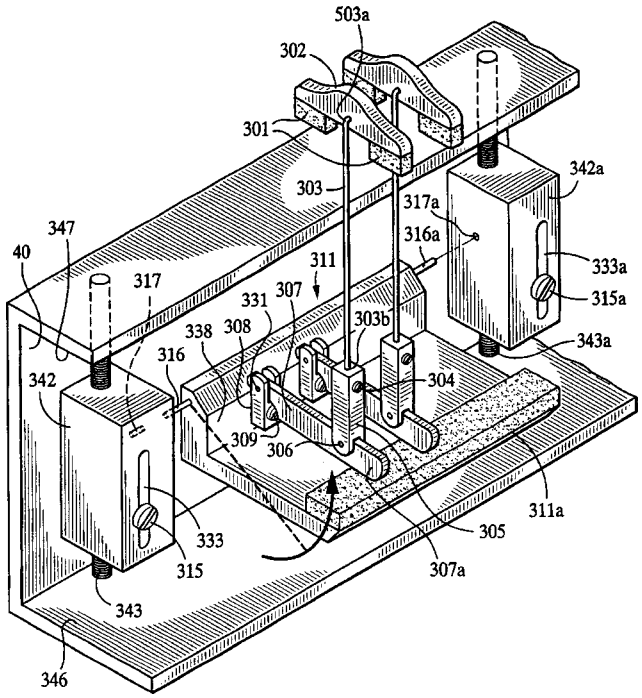

figure, the two adjustment blocks **342** and **342A** control the overall position whereas the individual dampers **301** can be adjusted via the adjustment screw **304**.—MK

6,683,242

43.75.Mn COMPOSITE KEYBOARD MUSICAL INSTRUMENT, SILENT SYSTEM FOR PERFORMANCE WITHOUT ACOUSTIC TONES AND REGULATING BUTTON MECHANISM FOR CHANGING ESCAPE TIMING DEPENDING UPON MODE OF OPERATION

Satoshi Inoue and Kiyoshi Kawamura, assignors to Yamaha Corporation
27 January 2004 (Class 84/719); filed in Japan 1 March 2001

As keyboard players know, the mechanical action of a piano is critical to the feel. Silent pianos are not a contradiction in terms if the action can be

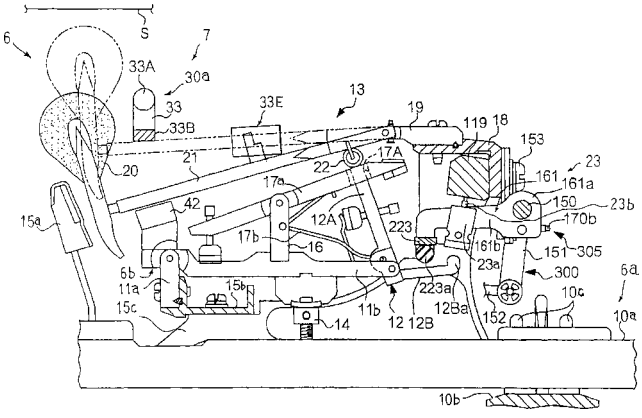

preserved (silence is needed for practice in apartments and other sonically sensitive environments). Accordingly, Yamaha has redesigned the string mechanism as shown. The details are readable for piano mechanics.—MK

6,663,491

43.75.St GAME APPARATUS, STORAGE MEDIUM AND COMPUTER PROGRAM THAT ADJUST TEMPO OF SOUND

Hajime Watabe *et al.*, assignors to Namco Limited
16 December 2003 (Class 463/36); filed in Japan 18 February 2000

Imagine a game where your dance moves are analyzed and the sound track tempo is changed in accordance with your movements. Now add scoring (e.g., how close you are to the system reference) and you'll be ready for the arcade. Specifics about the image processing are left to the reader's imagination—and the dance moves will probably be restricted to large limb movements—subtleties (like isolations) are just too hard.—MK

6,686,529

43.75.St METHOD AND APPARATUS FOR SELECTING HARMONIC COLOR USING HARMONICS, AND METHOD AND APPARATUS FOR CONVERTING SOUND TO COLOR OR COLOR TO SOUND

Gir-Ho Kim, assignor to Harmonicolor System Company, Limited
3 February 2004 (Class 84/464 R); filed 18 February 2002

It's not enough to display the spectrum in color. Instead one can display western harmonic intervals by analyzing the sound with the ubiquitous FFT and then applying peak detection. And these frames can be converted into color. The patent is unfortunately in black and white.—MK

6,664,460

43.75.Wx SYSTEM FOR CUSTOMIZING MUSICAL EFFECTS USING DIGITAL SIGNAL PROCESSING TECHNIQUES

James D. Pennock *et al.*, assignors to Harman International Industries, Incorporated
16 December 2003 (Class 84/662); filed 4 January 2002

Consider an effects box that accepts a signal flow as seen in the figure. An electric guitar input can have various effects applied before simulating

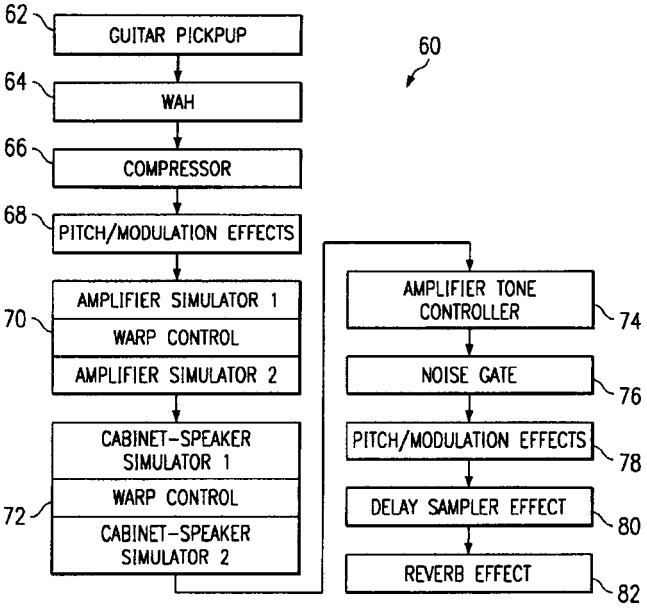

the classic amplifier and speaker sound. Further, as the patent clearly lays out, the coefficients of the filters can be interpolated (or warped) to form a ''new'' sound. Other effects can be added after that as shown.—MK

6,667,433

43.75.Wx FREQUENCY AND PHASE INTERPOLATION IN SINUSOIDAL MODEL-BASED MUSIC AND SPEECH SYNTHESIS

Xiaoshu Qian and Yinong Ding, assignors to Texas Instruments Incorporated
23 December 2003 (Class 84/659); filed 12 December 1997

McAulay and Quatieri proposed using sums of sinusoids to model complete waveforms. This ''MQ'' representation has found great favor in the audio DSP community. However, complex tones will demand a considerable number of sinusoids to be generated in real time. Furthermore, the MQ parameters are typically derived/found through FFT-based methods, leading to frame boundaries. Between these boundaries, the phase of the sinusoid must be interpolated. For real time generation, speed becomes the issue. The authors propose a least squares fit to the data, providing quadratic interpolation.—MK

6,685,638

43.80.Qf ACOUSTIC MONITORING SYSTEM

Terri K. Taylor *et al.*, assignors to Codman & Shurtleff, Incorporated
3 February 2004 (Class 600/437); filed 23 December 2002

The aim of this device is to noninvasively monitor the performance of an implanted adjustable shunt valve without the necessity of using x rays, ultrasound, or telemetry. It is an acoustic monitoring system that verifies the position of the valve under a variable opening pressure. The system is based on the fact that the mechanical motion due to the movement of the valve components produces vibrations that lead to acoustic energy. The system includes a programmer for generating a sequence of commands to adjust the valve mechanism, a means for receiving acoustic signals for analysis, a transmitter to implement the command and adjust the valve, and a sensor for detecting the acoustic signal generated from the valve during execution of the commands.—DRR

6,685,644

43.80.Qf ULTRASOUND DIAGNOSTIC APPARATUS

Yasutsugu Seo *et al.*, assignors to Kabushiki Kaisha Toshiba; Fuji Photo Optical Company, Limited
3 February 2004 (Class 600/447); filed in Japan 24 April 2001

This ultrasonic diagnostic device is equipped with a high-frequency internal probe that can be inserted into a body cavity such as a blood vessel or bile duct. A second, external probe operates at a lower frequency in order to provide guidance to the penetration of the internal probe. The inside of

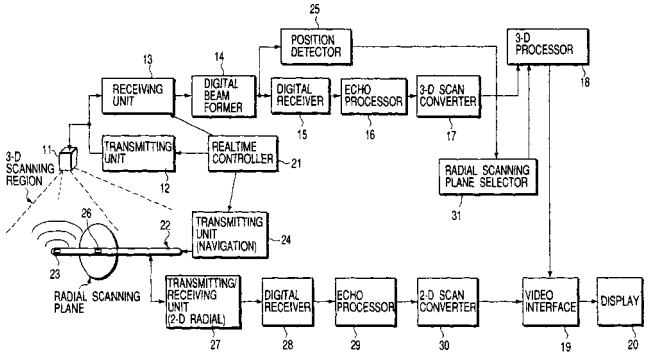

the object under examination is scanned at a high resolution with the internal probe. The external probe scans the object, yielding image data with a broader coverage than that provided by the internal probe. Data from the two probes are synthesized to provide a more complete image of the region of interest. A position detector provides information on the relative position of the two probes.—DRR

6,685,646

43.80.Qf MEASUREMENT OF VOLUMETRIC FLUID FLOW AND ITS VELOCITY PROFILE

Eduardo Ignacio Cespedes *et al.*, assignors to Jomed Incorporated
3 February 2004 (Class 600/454); filed in the European Patent Office 1 November 1996

The purpose of this device is to provide an ultrasonic method for measuring volumetric flow and to map the flow velocity profile in a lumen

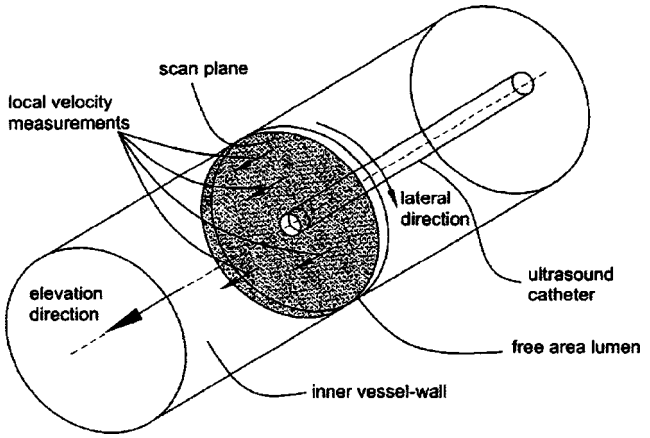

or other body cavity. This is achieved by interrogating the cross-sectional area using several ultrasonic beams. An estimate of the spatial flow is derived from a combination of estimates of axial, lateral, and total flow. The estimation of one or more flow components is acquired through a combination of time-shift and decorrelation analysis of two or more beam signals of the interrogating sound transducer. The accuracy of the estimate is further enhanced by the use of a reference decorrelation curve obtained from experiments or beam theory or both.—DRR

6,689,065

43.80.Qf ULTRASONOGRAPHY

Anne Kirsti Aksnes *et al.*, assignors to Amersham Health AS
10 February 2004 (Class 600/458); filed 4 June 2002

A continuation of United States Patent 6,428,479 [reviewed in J. Acoust. Soc. Am. **113**(2), 694 (2003)], this disclosure relates to the method of diagnosing and characterizing prostate abnormalities through the use of ultrasound contrast-agent-enhanced ultrasonography. More specifically, the method determines the kinetics of the contrast agent in-flow and thus the state of vascularization in the prostate as a means for such diagnosis. Observation of disease-related asymmetries in the spokelike vascular pattern of the prostate is rendered possible.—DRR

6,689,066

43.80.Qf ULTRASONIC PROBE

Masayoshi Omura and Hiroshi Fukuda, assignors to Olympus Corporation
10 February 2004 (Class 600/463); filed 3 December 2002

The special feature of this ultrasonic probe is that its ultrasonic transducer can transmit and receive ultrasound through an acoustic window that is formed of a resin including a mixture of polyamide block and polyether ester block copolymer resin and polyurethane. It is argued that multiple reflections are reduced in the vicinity of the windows. The sheath portion of the probe may also be formed of the same resin.—DRR

6,690,958

43.80.Qf ULTRASOUND-GUIDED NEAR INFRARED SPECTROPHOTOMETER

Stephen D. Walker *et al.*, assignors to Nostix LLC
10 February 2004 (Class 600/323); filed 7 May 2002

Disclosure is made of a device that utilizes near infrared spectrometry and ultrasound in combination to detect subnormal blood oxygenation in a number of medical conditions. The apparatus includes a near infrared spectrophotometer (NIRS) and an ultrasonic transducer that operate in combination to enhance diagnostic measurements. The NIRS measures an analyte, for example, tissue oxygenation, in an optical sample volume. The ultrasound imager is used to accurately position the optical sample volume in biological tissues or vessels. In one embodiment, the diagnostic apparatus includes an optical source, a linear array of ultrasound transducers, and an optical photodetector arranged in the same plane so that the ultrasound sample volume interrogated by the transducers intersects the optical sample volume formed by the optical source and detector.—DRR

6,691,821

43.80.Qf CUSTOMIZABLE SPILT STEM STETHOSCOPE AND A METHOD FOR PROVIDING SAME

Craig D. Oster and Douglas W. Voegeli, assignors to 3M Innovative Properties Company
17 February 2004 (Class 181/131); filed 7 September 2001

Stethoscope users come in all shapes and sizes, so the length of a stethoscope would be the issue here. The present device provides a specialized chest piece that will adapt to a dual lumen binaural, without that binaural having a mold-in connection. This allows binaurals for stethoscopes to be manufactured in a generic fashion at the maximum desirable length on the expectation that they can be cut down to the length the user desires at the time of assembly.—DRR

6,692,440

43.80.Qf ULTRASONIC DIAGNOSTIC APPARATUS

Hiroshi Hashimoto and Shinichi Amemiya, assignors to GE Medical Systems Global Technology Company, LLC
17 February 2004 (Class 600/443); filed in Japan 21 September 2001

A problem has been identified in that the fundamental component of received data for a previous ultrasonic pulse may intrude with considerable intensity into the fundamental component of received data for a current pulse, resulting in the inability to obtain a good harmonic image. This system provides an imaging method for transmitting an ultrasonic pulse into a subject and receiving an echo to generate received data. It acquires

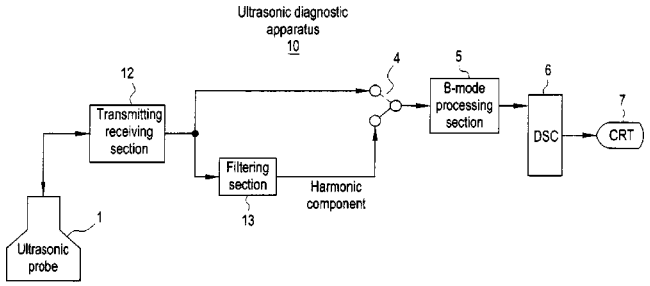

harmonic-mode data using a harmonic component from the received data. The next ultrasonic pulse is transmitted at a sufficiently later time so as to focus on a certain acoustic line. The fundamental component of received data for the previous pulse is prevented from intruding into the fundamental component of received data for the current pulse. Thus, a good harmonic image can be obtained.—DRR

6,682,544

43.80.Sh ULTRASONIC CURVED BLADE

Dominick L. Mastri and Corbett W. Stone, assignors to United States Surgical Corporation
27 January 2004 (Class 606/169); filed 11 September 2002

The patent discloses an ultrasonic instrument consisting of a curved blade and a clamp member designed to perform dissection and coagulation of tissue. The instrument features an elongated body extending from a housing. An ultrasonic transducer within the housing connects to a cutting jaw through a vibration coupler. The cutting jaw has a blade surface curved with respect to the axis of vibration and is configured in such a manner that the

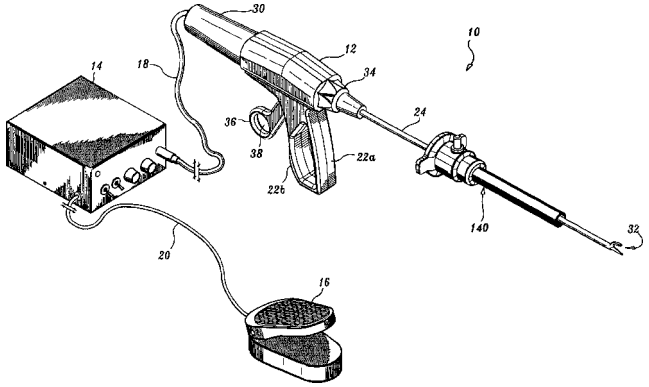

angle between a line tangent to the elongated body varies from 5° to about 45° along the length of the surface. A clamp member with a tissue contact surface is positioned next to the cutting jaw. It is movable from an open position (where the tissue contact surface is spaced from the blade surface) to a clamped position where the tissue contact surface is in close juxtaposed alignment with the blade surface to clamp tissue in between.—DRR

6,685,639

43.80.Sh HIGH INTENSITY FOCUSED ULTRASOUND SYSTEM FOR SCANNING AND CURING TUMOR

Zhilong Wang *et al.*, assignors to Chongqing Hifu
3 February 2004 (Class 600/439); filed in China 25 January 1998

This patent relates to a high-intensity focused ultrasound (HIFU) scanning and treatment system for tumor detection and control. The B-mode ultrasound probe is mounted on the control part of the therapeutic head so that the focal region falls within the image display plane of the B-mode ultrasound scanner. The device also includes a multidimensional digit-controlled motion apparatus, a vacuum degasser apparatus, a therapeutic bed, and a computer. The combined probe/therapeutic head is mounted on the multidimensional motion apparatus, which executes a scanning maneuver outside the body under computer control in order to aim the HIFU beam. As a result of the high intensity, the temperature of the tissues in the focal region instantaneously rises to more than 70 °C and the tissues are affected by the mechanical action of the cavitation, resulting in degeneration and necrosis.—DRR

6,685,656

43.80.Sh ULTRASONIC TREATMENT FOR WOUNDS

Luiz R. Duarte and Roger J. Talish, assignors to Exogen, Incorporated
3 February 2004 (Class 601/2); filed 13 January 1999

Advantage is taken of the fact that both longitudinally propagating ultrasound and shear waves generated by an ultrasound transducer prove effective in healing of wounds. The patent describes a portable device that

includes a transducer possessing an annular shaped operative surface and which is positioned next to the wound so as to effectively emit ultrasound to propagate in the direction of the wound. Reflections of the ultrasound from bone tissue and skin layers propagate toward the wound as longitudinal waves and shear waves are generated by the longitudinal waves. Both of these types of waves promote the healing of the wound. A focusing element focuses the propagation of the ultrasound at a predetermined angle toward the target wound. A housing may be provided to locate the transducer over a portion of the skin near a wound and for indenting the skin to form a cavity. Adjustable straps or other fixtures are provided to position the transducer near a wound.—DRR

6,685,657

43.80.Sh METHODS FOR SELECTIVELY DISSOLVING AND REMOVING MATERIALS USING ULTRA-HIGH FREQUENCY ULTRASOUND

Joie P. Jones, Laguna Beach, California
3 February 2004 (Class 601/2); filed 31 August 2001

This device selectively dissolves and removes unwanted solid or semi-solid materials within a highly localized region through the use of ultra-high-energy ultrasound having a frequency in the range exceeding 50 MHz, for example, up to as high as 1 GHz. The design is based on a piezoelectric transducer that is modified to elevate the amplitude of acoustical waves of a given frequency without an increase in power to the system. The device may be applied to surgical procedures for treatment of atherosclerotic plaque, prostate disorders, cancers, orthopedic and cosmetic surgery, and also to nonsurgical applications in industrial processes in which it is desired to selectively remove materials in highly localized areas.—DRR

6,686,195

43.80.Sh METHOD AND APPARATUS FOR ULTRASONIC LYSIS OF BIOLOGICAL CELLS

Bruno Colin *et al.*, assignors to Biomerieux S.A.
3 February 2004 (Class 435/306.1); filed in France 1 April 1999

Lysis is the process of disintegration or dissolution of biological cells. The apparatus consists of at least one sonotrode **2** designed to generate ultrasound of variable power in a receptacle **4** containing a biological sample **5** of cells to be lysed. The sonotrode directly contacts the receptacle.

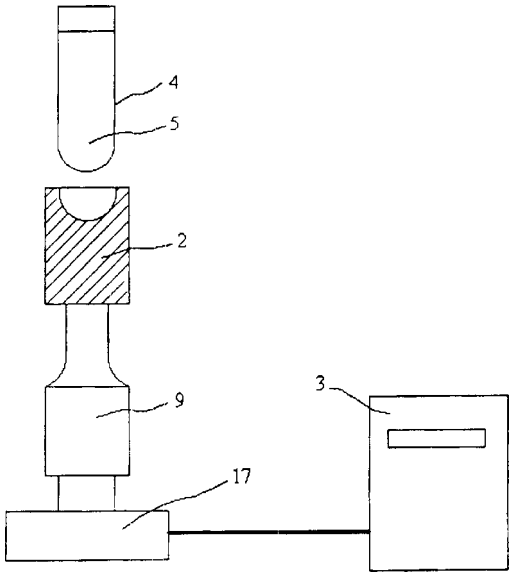

A method is also disclosed for lysing a biological sample by placing the receptacle in direct contact with the sonotrode and activating the sonotrode for long enough to lyse the cells in the sample but preserving the DNA and/or RNA molecules released for subsequent operations, e.g., amplification.—DRR

6,689,067

43.80.Sh METHOD AND APPARATUS FOR ULTRASOUND GUIDANCE OF NEEDLE BIOPSIES

Frank Sauer *et al.*, assignors to Siemens Corporate Research, Incorporated
10 February 2004 (Class 600/464); filed 26 November 2002

This ultrasound scanning system consists of a transducer to provide ultrasound data and a computer to process the information and to position and scale images for display on a monitor. The size of the displayed image would be similar to the actual physical size of the ultrasound target. A semi-silvered mirror redirects the image so that the user perceives the image as if it occupies the actual physical location of the structures pictured in the image. A lamp unit projects into the patient a ray of light that is within the imaging plane projected by the transducer into the patient. Also, a video camera may be utilized to display a guideline that is coplanar with the imaging plane.—DRR

6,692,450

43.80.Sh FOCUSED ULTRASOUND ABLATION DEVICES HAVING SELECTIVELY ACTUATABLE ULTRASOUND EMITTING ELEMENTS AND METHODS OF USING THE SAME

R. Glen Coleman, assignor to Medtronic Xomed, Incorporated
17 February 2004 (Class 601/3); filed 19 January 2000

This disclosure relates to the treatment of anatomical tissue with high intensity focused ultrasound energy, in particular, thermal ablation, whereby lesions of selected sizes and/or configuration are formed in anatomical tissue. The apparatus includes an ultrasound-emitting member containing multiple individual ultrasound elements arranged in an array. These elements may be actuated selectively and independently to emit ultrasound energy and focus the emitted energy.—DRR

6,682,482

43.80.Vj MEDICAL ULTRASONIC IMAGING PULSE TRANSMISSION METHOD

Sriram Krishnan, assignor to Acuson Corporation
27 January 2004 (Class 600/437); filed 30 August 2000

A large amplitude pulse is transmitted from an aperture and smaller amplitude pulses are transmitted from smaller subapertures. The sum of the subapertures is equal to the aperture used for the larger amplitude pulse. This allows pulses of different amplitudes to be produced without varying the power level of individual transducer elements.—RCW

6,682,483

43.80.Vj DEVICE AND METHOD FOR MAPPING AND TRACKING BLOOD FLOW AND DETERMINING PARAMETERS OF BLOOD FLOW

Kenneth Abend and Elsayed H. Attia, assignors to VueSonix Sensors, Incorporated
27 January 2004 (Class 600/437); filed 20 March 2002

Beamformed echoes from a phased array are processed to obtain blood flow data in a volume. Points that produce locally maximum blood velocity signals are identified and tracked. The coordinates of tracked points are used to form a blood-vessel map that can be used to select multiple points of interest for continuous and unattended blood flow monitoring.—RCW

6,682,487

43.80.Vj ULTRASONIC IMAGING ABERRATION CORRECTION USING HARMONIC AND NON-HARMONIC SIGNALS

Bernard J. Savord, assignor to Koninklijke Philips Electronics N.V.
27 January 2004 (Class 600/443); filed 10 September 2002

An image produced from harmonic echoes is used as a reference for comparison with aberration in a nonharmonic image formed at the same frequency and estimates of aberration corrections in the aperture are obtained by backpropagation of image data.—RCW

6,682,488

43.80.Vj ULTRASOUND PROBE WITH PROGRESSIVE ELEMENT SIZING

Kenneth Abend, assignor to Vuesinx Sensors, Incorporated
27 January 2004 (Class 600/453); filed 12 April 2001

This probe employs array elements that are nonuniform in size and spacing for determination of blood flow parameters and for tracking blood

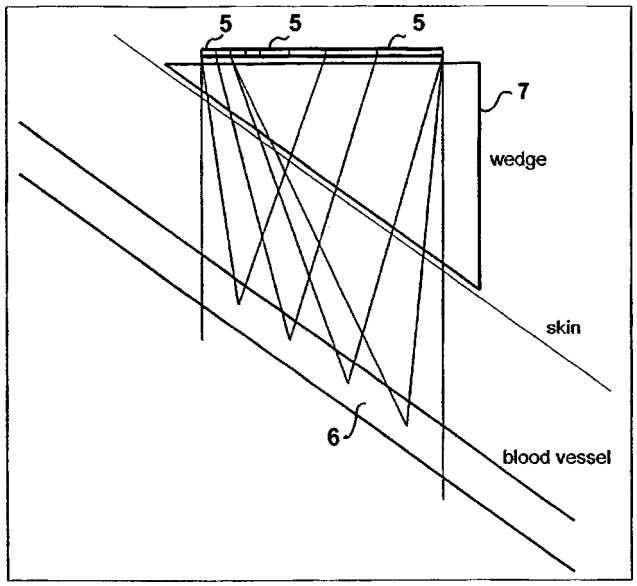

flow as well as for creating a three-dimensional blood flow image with higher resolution than images produced using present systems.—RCW

6,685,642

43.80.Vj SYSTEM AND METHOD FOR BRIGHTENING A CURVE CORRESPONDING TO A SELECTED ULTRASOUND ROI

Rohit Garg *et al.*, assignors to Koninklijke Philips Electronics N.V.
3 February 2004 (Class 600/443); filed 3 October 2002

Stored ultrasonic images are displayed using a graphical user interface that enables a stored image sequence to be modified and replayed. The interface displays time intensity curves in a region of interest. When the curves are displayed, the ones in the selected region of interest are brightened relative to the other curves.—RCW

6,685,643

43.80.Vj METHOD AND DEVICE FOR RECORDING ULTRASONIC IMAGES

Johannes Waldinger *et al.*, assignors to Tomtec Imaging Systems GmbH
3 February 2004 (Class 600/444); filed in Germany 21 August 1998

An ultrasonic probe is displaced or rotated relative to an object. The movement of the probe is progressively detected. Position differences between images are determined for three-dimensional display of image data.—RCW

6,685,645

43.80.Vj BROAD-BEAM IMAGING

Glen McLaughlin and Ting-Lan Ji, assignors to Zonare Medical Systems, Incorporated
3 February 2004 (Class 600/447); filed 1 August 2002

Echo location data are produced by a multidimensional transform that uses phase and magnitude to distinguish between echoes from ultrasound beam components and image an area using a single ultrasound transmission.—RCW

6,685,647

43.80.Vj ACOUSTIC IMAGING SYSTEMS ADAPTABLE FOR USE WITH LOW DRIVE VOLTAGES

Bernard J. Savord and William J. Ossmann, assignors to Koninklijke Philips Electronics N.V.
3 February 2004 (Class 600/459); filed 28 June 2001

The acoustic element in this system includes a so-called dematching layer between the backing and the piezoelectric element. The dematching layer has an acoustic impedance that is greater than that of the piezoelectric

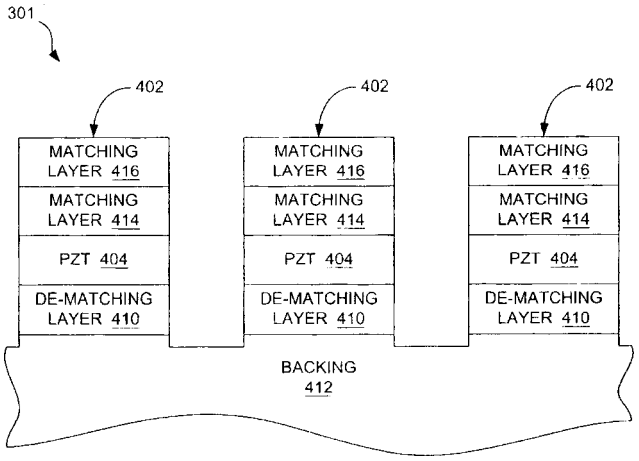

element. The thickness of the piezoelectric element is less than one-half of the center-frequency wavelength produced by the element.—RCW

6,689,061

43.80.Vj ULTRASONIC IMAGING APPARATUS

Kazuyoshi Hayasaka, assignor to GE Medical Systems Global Technology Company, LLC
10 February 2004 (Class 600/437); filed in Japan 30 May 2001

A current image frame and previous image frame are correlated to determine a value that is used to change the acoustic line density, dynamic

range of echo reception, and frame averaging that are employed in the apparatus.—RCW

6,689,063

43.80.Vj METHOD AND APPARATUS FOR ACQUIRING IMAGES BY RECURSIVE ULTRASOUND IMAGES

Jørgen Arendt Jensen and Svetoslav Nikolov, assignors to B-K Medical A/S

10 February 2004 (Class 600/443); filed in Denmark 10 May 1999

For every pulse emission, a new frame is created by parallel implementation of the receive beamformation. Beamformed rf data are added to previously formed rf lines. High frame rate images are produced to enhance blood flow imaging.—RCW

6,692,438

43.80.Vj ULTRASONIC IMAGING SYSTEM AND METHOD FOR DISPLAYING TISSUE PERFUSION AND OTHER PARAMETERS VARYING WITH TIME

Danny M. Skyba *et al.*, assignors to Koninklijke Philips Electronics NV

17 February 2004 (Class 600/440); filed 18 December 2001

An electrocardiographic signal triggers an ultrasonic imaging system to obtain contrast image data that shows tissue perfusion at a predetermined time during each of a number of heart beats. Parametric data for locations in a region of interest such as the myocardium are determined from the temporal contrast data acquired during reperfusion of the tissue in the region. The parameters are mapped using color to display perfusion. Sequences of

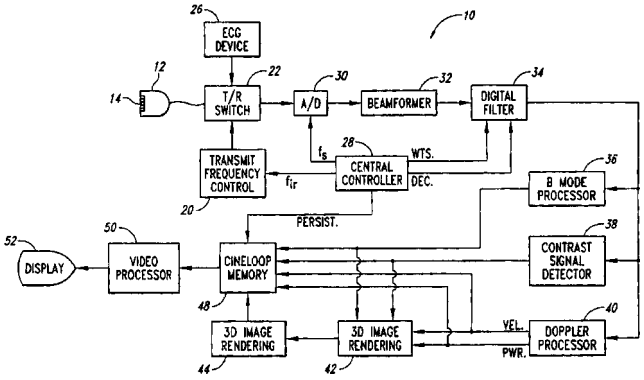

images show both perfusion characteristics and wall motion in the same image.—RCW

6,692,439

43.80.Vj ANGULAR SCATTER IMAGING SYSTEM USING TRANSLATING APERTURES AND METHOD THEREOF

William F. Walker *et al.*, assignors to University of Virginia Patent Foundation; Duke University

17 February 2004 (Class 600/443); filed 3 June 2002

Translating apertures are used to acquire data at a number of angles. For omnidirectional scatterers, the translating apertures ideally yield identical speckle patterns at all angles of interrogation. The result is strong contrast relative to previous angular scattering measurement methods that produce speckle patterns that vary rapidly with interrogation angle. The translating aperture method enables acquisition of data in which variation with angle is mostly due to the intrinsic scattering of the target.—RCW

6,692,441

43.80.Vj SYSTEM FOR IDENTIFYING A VOLUME OF INTEREST IN A VOLUME RENDERED ULTRASOUND IMAGE

McKee D. Poland and Ivan S. Salgo, assignors to Koninklijke Philips Electronics N.V.

17 February 2004 (Class 600/443); filed 12 November 2002

A three-dimensional ultrasonic image is rendered and selected portions of the acoustic data are modified to form a highlighted region that defines an included volume.—RCW

6,692,442

43.80.Vj DEVICE FOR PRODUCING AN ON-LINE IMAGE OF A BODY PART INTO WHICH A CONTRASTING AGENT HAS BEEN INTRODUCED

George Brock-Fisher and Patrick G. Rafter, assignors to Koninklijke Philips Electronics N.V.

17 February 2004 (Class 600/458); filed 13 December 2001

An image of a region that contains a contrast agent is produced. The contrast agent is modified and an image of the region containing the modified contrast agent is produced. From the image data, a processor forms an image that represents the flow of blood or other fluid.—RCW

Separation of compressibility and shear deformation in the elastic energy density (L)

Mark F. Hamilton, Yurii A. Ilinskii, and Evgenia A. Zabolotskaya
Applied Research Laboratories, The University of Texas at Austin, Austin, Texas 78713-8029, and Department of Mechanical Engineering, The University of Texas at Austin, 1 University Station C2200, Austin, Texas 78712-0292

(Received 25 June 2003; accepted for publication 15 March 2004)

A formulation of the elastic energy density for an isotropic medium is presented that permits separation of effects due to compressibility and shear deformation. The motivation is to obtain an expansion of the energy density for soft elastic media in which the elastic constants accounting for shear effects are of comparable order. The expansion is carried out to fourth order to ensure that nonlinear effects in shear waves are taken into account. The result is $\mathcal{E}\simeq\mathcal{E}_0(\rho)+\mu I_2+\frac{1}{3}AI_3+DI_2^2$, where ρ is density, I_2 and I_3 are the second- and third-order Lagrangian strain invariants used by Landau and Lifshitz, μ is the shear modulus, A is one of the third-order elastic constants introduced by Landau and Lifshitz, and D is a new fourth-order elastic constant. For processes involving mainly compressibility $\mathcal{E}\simeq\mathcal{E}_0(\rho)$, and for processes involving mainly shear deformation $\mathcal{E}\simeq\mu I_2+\frac{1}{3}AI_3+DI_2^2$. © *2004 Acoustical Society of America.* [DOI: 10.1121/1.1736652]

PACS numbers: 43.25.Dc, 43.25.Ba [ANN] Pages: 41–44

I. INTRODUCTION

The purpose of this Letter is to develop a fourth-order expansion of the elastic energy density of an isotropic medium that permits separation of effects due to compressibility and shear deformation. The motivation is to identify the terms and corresponding elastic constants that describe nonlinear effects of shear deformation when effects of compressibility are negligible. Such conditions pertain especially to nonlinear shear waves in a liquid-like medium having shear modulus small compared with bulk modulus, such as tissue. For plane shear waves in incompressible media, nonlinearity is absent at third order in the particle displacement, and therefore a fourth-order expansion of the energy density is required.[1,2]

This work is motivated by measurements of elastic constants reported recently by Catheline *et al.*[3] For several soft, tissue-like solids (Agar-gelatin-based phantoms) they report measured values for the second-order (Lamé) constants λ and μ, and for the third-order elastic constants A, B, and C used by Landau and Lifshitz.[4] The values of μ and A are on the order of kPa, whereas the values of λ, B, and C are on the order of GPa, the differences being more than 5 orders of magnitude. Other traditional expansions of the elastic energy density likewise contain elastic constants having vastly differing values for soft solids (see, e.g., Norris[5] for relations between A, B, and C and third-order elastic constants used in expansions introduced by others). This poses difficulties when one attempts to model nonlinear effects associated with shear deformation in soft solids. As shown below, shear effects in soft solids are described to third order entirely by the small constants of order μ and A. However, small errors in measured values of the large constants λ, B, and C easily obscure effects associated with shear deformation. This difficulty is avoided with the alternative expansion introduced here, in which effects of compression and shear are separated.

There are a number of constitutive models for incompressible and slightly compressible media described in the field of finite elasticity. They include the so-called neo-Hookean and Mooney–Rivlin materials; see Ciarlet[6] for discussion of these materials and references to others. However, these models are subject to constraints (e.g., incompressibility) or approximations, and thus lack the generality of classical expansions used below and in acoustics in general, such as those listed by Norris.[5]

The analysis begins by extending to fourth order the third-order expansion of the strain energy density introduced by Landau and Lifshitz. The elastic constants in this expansion are related to those for liquids to facilitate assessment of their magnitudes. At third order the relations obtained by Kostek *et al.*[7] are recovered. Next, the energy density is expressed in terms of an alternative set of invariants that allows separation of effects due to compressibility and shear deformation. A three-term expansion is obtained up to fourth order for pure shear deformation. At this order there are only three independent elastic constants: the shear modulus μ at second order, the coefficient A at third order, and a new constant at fourth order.

II. FOURTH-ORDER EXPANSION OF ELASTIC ENERGY DENSITY

The third-order expansion proposed by Landau and Lifshitz[4] for the elastic energy density of an isotropic elastic solid is expressed in terms of invariants of the Lagrangian strain tensor

$$u_{i'k'}=\frac{1}{2}\left(\frac{\partial u_i}{\partial\tilde{x}_{k'}}+\frac{\partial u_k}{\partial\tilde{x}_{i'}}+\frac{\partial u_l}{\partial\tilde{x}_{i'}}\frac{\partial u_l}{\partial\tilde{x}_{k'}}\right), \tag{1}$$

where u_i is particle displacement, x_i are Eulerian coordinates, $\tilde{x}_{i'}$ are Lagrangian coordinates, and $x_i=\tilde{x}_{i'}+u_i$. The invariants are defined as follows:

$$I_1=\mathrm{tr}\,\mathbf{u}=u_{i'i'}, \quad I_2=\mathrm{tr}\,\mathbf{u}^2=u_{i'k'}u_{k'i'},$$
$$I_3=\mathrm{tr}\,\mathbf{u}^3=u_{i'k'}u_{k'l'}u_{l'i'}. \tag{2}$$

Their expansion of the elastic energy density to cubic order in strain is written[4]

$$\mathcal{E}=\mu I_2+(\tfrac{1}{2}K-\tfrac{1}{3}\mu)I_1^2+\tfrac{1}{3}AI_3+BI_1I_2+\tfrac{1}{3}CI_1^3, \tag{3}$$

where μ is the shear modulus, K the bulk modulus, and A, B, and C are referred to as the third-order elastic constants. The second term in Eq. (3) can also be expressed as $\frac{1}{2}\lambda I_1^2$, where $\lambda=K-\frac{2}{3}\mu$ is a Lamé constant.

At fourth order there are four independent ways to pair up indices such that a scalar is formed from the product $u_{i'j'}u_{k'l'}u_{m'n'}u_{p'q'}$. The most natural choice is the set I_1^4, I_2^2, $I_1^2I_2$, and I_1I_3. An appropriate extension of the Landau–Lifshitz expansion to fourth order is thus[8]

$$\mathcal{E}=\mu I_2+(\tfrac{1}{2}K-\tfrac{1}{3}\mu)I_1^2+\tfrac{1}{3}AI_3+BI_1I_2+\tfrac{1}{3}CI_1^3+EI_1I_3 + FI_1^2I_2+GI_2^2+HI_1^4, \tag{4}$$

where E, F, G, and H are fourth-order elastic constants.

The notation in Eq. (4) resembles that used in Ref. 1 but for one difference. In Eq. (12) of Ref. 1 a fifth term of fourth order was included involving I_4, where $I_4=\mathrm{tr}\,\mathbf{u}^4$. However, only three invariants can be independent, and therefore $I_4=I_4(I_1,I_2,I_3)$. To derive this relation we may use the Caley–Hamilton theorem, which states that a matrix obeys its own characteristic equation. For the Lagrangian strain tensor we thus have

$$-\mathbf{u}^3+I_u\mathbf{u}^2-II_u\mathbf{u}+III_u\mathbf{I}=0, \tag{5}$$

where $\mathbf{I}$ is the identity matrix and[9]

$$I_u=\mathrm{tr}\,\mathbf{u}, \quad II_u=\tfrac{1}{2}[(\mathrm{tr}\,\mathbf{u})^2-\mathrm{tr}\,\mathbf{u}^2], \quad III_u=\det\mathbf{u}, \tag{6}$$

are the principal invariants of $\mathbf{u}$, which are related to Eqs. (2) as follows:[9]

$$I_u=I_1, \quad II_u=\tfrac{1}{2}(I_1^2-I_2), \quad III_u=\tfrac{1}{6}I_1^3-\tfrac{1}{2}I_1I_2+\tfrac{1}{3}I_3. \tag{7}$$

Now, multiply Eq. (5) by $\mathbf{u}$, take the trace of the result, and express the principal invariants in terms of $I_{1,2,3}$ to obtain

$$I_4=\tfrac{1}{6}I_1^4-I_1^2I_2+\tfrac{4}{3}I_1I_3+\tfrac{1}{2}I_2^2, \tag{8}$$

which completes the connection to the notation in Ref. 1. The values of the constants E, F, G, and H in Eq. (4) differ from those introduced in Ref. 1 when $D\neq 0$ in the latter.

III. COMPARISON WITH LIQUIDS

The elastic constants in Eq. (4) are related here to the coefficients used most frequently in the expansion of the equation of state for a liquid. The purpose of this comparison is to assess the magnitudes of the elastic constants for soft solids.

An isentropic liquid may be described by an equation of state $P=P(\rho)$, where P is pressure and ρ is density. When considering acoustical disturbances it is conventional to expand this relation about the equilibrium state $(P,\rho)=(P_0,\rho_0)$. The usual expansion to cubic order is as follows:[10]

$$P=P_0+A_l\left(\frac{\rho-\rho_0}{\rho_0}\right)+\frac{B_l}{2!}\left(\frac{\rho-\rho_0}{\rho_0}\right)^2+\frac{C_l}{3!}\left(\frac{\rho-\rho_0}{\rho_0}\right)^3, \tag{9}$$

where

$$A_l=\rho_0\left(\frac{\partial P}{\partial\rho}\right)_{\rho=\rho_0}, \quad B_l=\rho_0^2\left(\frac{\partial^2P}{\partial\rho^2}\right)_{\rho=\rho_0},$$
$$C_l=\rho_0^3\left(\frac{\partial^3P}{\partial\rho^3}\right)_{\rho=\rho_0}. \tag{10}$$

The partial derivatives are taken with entropy held constant.

To permit comparison with Eq. (4), Eq. (9) is rewritten in terms of the dimensionless specific volume w defined by

$$w=\rho_0/\rho. \tag{11}$$

Equation (9) thus becomes

$$P=P_0+P'(1)(w-1)+\frac{P''(1)}{2!}(w-1)^2 + \frac{P'''(1)}{3!}(w-1)^3, \tag{12}$$

where

$$P'(1)=\left(\frac{\partial P}{\partial w}\right)_{w=1}=-A_l,$$
$$P''(1)=\left(\frac{\partial^2P}{\partial w^2}\right)_{w=1}=B_l+2A_l,$$
$$P'''(1)=\left(\frac{\partial^3P}{\partial w^3}\right)_{w=1}=-(C_l+6B_l+6A_l). \tag{13}$$

The internal energy of the liquid per unit volume is therefore

$$\mathcal{E}_l=-\int_1^w P\,dw=-P_0(w-1)-\frac{P'(1)}{2!}(w-1)^2 - \frac{P''(1)}{3!}(w-1)^3-\frac{P'''(1)}{4!}(w-1)^4. \tag{14}$$

A relation between Eqs. (14) and (4) can be developed by writing[9]

$$w=(1+2I_u+4II_u+8III_u)^{1/2}. \tag{15}$$

Substitution of Eqs. (7) into (15), the latter into (14), and expansion of the result up to fourth order in $\mathbf{u}$, noting that $I_n=O(\mathbf{u}^n)$, yields, after some lengthy algebra

$$\mathcal{E}_l=\frac{A_l}{2}\left[I_1^2+(I_1^3-2I_1I_2)+\left(\frac{7}{12}I_1^4+I_2^2-I_1^2I_2+\frac{8}{3}I_1I_3\right)\right] - \frac{B_l+2A_l}{6}\left[I_1^3+\left(\frac{3}{2}I_1^4-3I_1^2I_2\right)\right]+\frac{C_l+6B_l+6A_l}{24}I_1^4. \tag{16}$$

Comparison of Eqs. (16) and (4) reveals that

$$\mu = 0, \quad K = A_l, \tag{17}$$

$$A = 0, \quad B = -A_l, \quad C = \tfrac{1}{2}(A_l - B_l), \tag{18}$$

$$E = \tfrac{4}{3}A_l, \quad F = \tfrac{1}{2}(B_l - A_l), \quad G = \tfrac{1}{2}A_l,$$

$$H = \tfrac{1}{24}(A_l + C_l). \tag{19}$$

Relations (17) are known from linear theory, relations (18) for the third-order elastic constants were derived previously by Kostek *et al.*,[7] and relations (19) for the fourth-order elastic constants are new.

IV. ALTERNATIVE EXPANSION OF ENERGY DENSITY

Presented here is an alternative expansion of the elastic energy density that permits separation of effects due to compressibility and shear deformation. For incompressible media, the expansion yields the minimum number of terms that describe shear deformation alone. These terms are sufficient for describing shear deformation when the energy stored in compression is comparatively insignificant. Phenomena satisfying this condition include nonlinear shear waves, and nonlinear effects of shear stress on bubble oscillations in liquid-like elastic media such as tissue.

The motivation for the alternative expansion is the enormous disparity between the magnitudes of the elastic constants in Eq. (4) for liquid-like elastic media, characterized by $\mu \ll K$. Measurements reported by Catheline *et al.*[3] for a soft-tissue phantom reveal that among the third-order elastic constants, A is of order μ, while B and C are of order K. Moreover, the reported values of μ and A are less than those of K, B, and C by 5 to 6 orders of magnitude. Because of this enormous difference, and because individual terms in Eq. (4) account for both compressibility and shear deformation, determining the numerical values of the parameters associated with shear deformation alone requires measurement of the large elastic constants to a precision better than one part in 10^5. However, reported measurements of third-order elastic constants are less precise by many orders of magnitude, and no measurements are reported for the fourth-order elastic constants.

Rather than express $\mathcal{E}$ in terms of I_1, I_2, and I_3 as in Eq. (4), we choose instead to express $\mathcal{E}$ in terms of the set of independent invariants III_G, I_2, and I_3, where I_2 and I_3 are defined in Eqs. (2), and III_G is the third principal invariant of the Green deformation tensor

$$G_{i'k'} = \frac{\partial x_l}{\partial \tilde{x}_{i'}} \frac{\partial x_l}{\partial \tilde{x}_{k'}}. \tag{20}$$

The choice of III_G is motivated by the fact that[9] $III_G = \rho_0^2/\rho^2$, which permits the functional relation for the energy density to be written in the form

$$\mathcal{E} = \mathcal{E}(\rho, I_2, I_3). \tag{21}$$

Up to fourth order in $\mathbf{u}$, the strain energy density may thus be expressed as follows:

$$\mathcal{E} = \mathcal{E}_0(\rho) + \mu(\rho) I_2 + \tfrac{1}{3}A(\rho) I_3 + D I_2^2. \tag{22}$$

The first term, $\mathcal{E}_0(\rho)$, depends only on compressibility. If expanded in terms of the invariants I_1, I_2, and I_3 as in Eq. (4), there can be no terms involving I_2 and I_3 alone because $\mu = A = 0$ in that expansion according to Eqs. (17) and (18). We thus identify $\mu(\rho_0)$ and $A(\rho_0)$ in Eq. (22) as the coefficients μ and A of Landau and Lifshitz in Eq. (4) for any elastic medium. However, D in Eq. (22) is not equivalent to G in Eq. (4). For a liquid we must have $\mathcal{E} = \mathcal{E}_0(\rho)$, because $\mathcal{E}$ cannot depend on I_2 and I_3, and therefore $\mu(\rho) = A(\rho) = D = 0$, whereas $G = A_l/2$ from Eq. (19).

For liquid-like elastic media for which $\mu \ll K$, the coefficients μ, A, and D are nonzero but still many orders of magnitude less than the coefficients A_l, B_l, and C_l characterizing liquids. As seen from Eqs. (17)–(19), and noting that $B_l \simeq 5A_l$ for water[10] with C_l somewhat larger but of the same order, μ, A, and D are extremely small compared with *all* other elastic constants in Eq. (4). Therefore, to describe processes involving compressibility in liquid-like media, such as longitudinal wave propagation, one may take $\mathcal{E} \simeq \mathcal{E}_0(\rho)$.

Now, consider shear deformation when the relative portion of energy stored in compression is negligible. Such is normally the case for shear wave propagation, and for shear deformation of soft elastic media such as tissue. In this context (e.g., negligible coupling between shear and compressional waves) we consider the medium to be practically incompressible, such that $\rho \simeq \rho_0$. We thus take $\mu \simeq \mu(\rho_0)$, $A \simeq A(\rho_0)$, $\mathcal{E}_0 \simeq \mathcal{E}_0(\rho_0) = 0$, and rewrite Eq. (22) as

$$\mathcal{E} = \mu I_2 + \tfrac{1}{3}A I_3 + D I_2^2. \tag{23}$$

Up to fourth order there are only three independent elastic constants for incompressible media, μ and A from the expansion of Landau and Lifshitz, with the coefficient D identified as a new elastic constant. The constant A determines the nonlinear shear stress in the vicinity of a pulsating bubble,[11] while D is required to describe nonlinear distortion of shear waves of finite amplitude. Given the values of μ and A, measurement of shear wave distortion is thus a means of determining the fourth-order elastic constant D.

ACKNOWLEDGMENTS

This work was supported by the Internal Research and Development Program at Applied Research Laboratories, The University of Texas at Austin, and by the Office of Naval Research.

[1] E. A. Zabolotskaya, "Sound beams in a nonlinear isotropic solid," Sov. Phys. Acoust. **32**, 296–299 (1986).
[2] S. Catheline, J.-L. Gennisson, M. Tanter, and M. Fink, "Observation of shock transverse waves in elastic media," Phys. Rev. Lett. **91**, 164301-1–164301-4 (2003).
[3] S. Catheline, J.-L. Gennisson, and M. Fink, "Measurement of elastic nonlinearity of soft solid with transient elastography," J. Acoust. Soc. Am. **114**, 3087–3091 (2003).
[4] L. D. Landau and E. M. Lifshitz, *Theory of Elasticity*, 3rd ed. (Pergamon, New York, 1986).
[5] A. N. Norris, "Finite-amplitude waves in solids," in *Nonlinear Acoustics*, edited by M. F. Hamilton and D. T. Blackstock (Academic, San Diego, 1998), Chap. 9, pp. 263–277.
[6] P. G. Ciarlet, *Mathematical Elasticity, Volume I: Three-Dimensional Elasticity* (North-Holland, Amsterdam, 1988), pp. 189–190.
[7] S. Kostek, B. K. Sinha, and A. N. Norris, "Third-order elastic constants for an inviscid fluid," J. Acoust. Soc. Am. **94**, 3014–3017 (1993).

[8] D. R. Bland, *Nonlinear Dynamic Elasticity* (Blaisdell, Waltham, MA, 1969), p. 49.
[9] A. C. Eringen and E. S. Suhubi, *Elastodynamics* (Academic, New York, 1974), Vol. 1.
[10] R. T. Beyer, ''The parameter B/A,'' in *Nonlinear Acoustics*, edited by M. F. Hamilton and D. T. Blackstock (Academic, San Diego, 1998), Chap. 2, pp. 25–39.
[11] S. Y. Emelianov, M. F. Hamilton, Yu. A. Ilinskii, and E. A. Zabolotskaya, ''Nonlinear dynamics of a gas bubble in an incompressible elastic medium,'' J. Acoust. Soc. Am. **115**, 581–588 (2004).

Simple discrimination method between False Acoustic Emission and Acoustic Emission revealed by piezoelectric sensors, in Gran Sasso mountain measurements (L)

Paolo Diodati[a] and Stefano Piazza
Dipartimento di Fisica, Università di Perugia and Istituto Nazionale per la Fisica della Materia Sezione di Perugia, Via Pascoli, 06123 Perugia Italy

(Received 18 June 2003; revised 30 January 2004; accepted 5 April 2004)

Recently it was shown, studying data acquired with *in-situ* measurements on the Gran Sasso mountain (Italy), for about ten years, by means of a high sensitivity transducer coupled to the free-end section of a stainless steel rod fixed by cement in a rock-drill hole 10 m high, about 2500 m above sea level, that Acoustic Emission (AE) can be affected by more than 90% False Acoustic Emission (FAE) of an electromagnetic origin. A very simple method to solve the problem of the discrimination between AE events due to elastic waves, from FAE signals, due to electromagnetic noise, both coming from the same ''reception-point,'' is presented. The reliability of the obtained separation is confirmed also by the reported amplitude and time distribution of AE events, typical of fracture dynamics and those of FAE events, similar to those of noise. [DOI: 10.1121/1.1756895]

PACS numbers: 43.58.Vb, 43.38.Ar [AJZ] Pages: 45–48

Fractures, dislocations, phase transformations, structural movements, friction, and, in general, various processes of deformation and transformation of materials, generate elastic waves detectable at the surface of a body as Acoustic Emission (AE). The expression AE is used for the physical process generating elastic impulsive vibrations, as well as for the technique used to detect these elastic waves on the surface of the body.

Two types of AE exist, usually named burst and continuous.[1] This last definition is misleading (*persistent* is a more adequate word), since continuous AE is made of individual emissions occurring in rapid succession such that the signal level appears sustained and the characterization of single emissions presents an increasing difficulty with the increasing of emission frequency.

AE studies started, first of all with in-situ applications, in the late 1930s.[1] Piezoelectric crystals, working at frequencies from 150 to 10^4 Hz, were mounted in steel tubes inserted in rock-drill holes, with the aim to predict rock bursts and, by triangulation methods, to locate microseism sources in mines. Steel rods, fixed by cement in a rock-drill hole are still used because of the very good acoustic coupling among rock, cement and steel. Hardy *et al.* inserted them in a hole that had been drilled into the rock mass traversing four or more rock layers.[2]

A laboratory study of the AE response of metals and various rocks at ultrasonic frequencies, started with Mason,[3] Kaiser,[4] and Mogi, who, first, using frequencies up to the low MHz range, showed similarities between AE from rocks and the statistical behavior of earthquakes.[5]

AE has increasing applied use for laboratory measurements, and system controls, in many fields, from the traditional and simple applications, until the more sophisticated and modern ones, like as an example, noise elimination from a gravitational wave interferometer[6] as well as for *in-situ* applications, one of which showed a resounding confirmation of the Self-Organized Criticality theory[7] in the middle-scale dimension, between laboratory and geophysical scale, by measurements of AE from volcanic rocks, performed on Stromboli.[8,9]

For AE measurements, capacitive sensors can be used, but piezoelectric crystals, or ceramics, are normally used. Due to the reversible effect (electric signals can generate sensor vibration), the latter can originate signals of False Acoustic Emission (FAE) since an electrical impulsive signal generates an output signal that can be erroneously considered as an AE signal. In other words, elastic vibrations of a piezoelectric sensor can be driven by elastic vibration of the medium in contact with the piezoelectric disk, as well as by changes of the electric polarity of at least one face of the disk.

The existence of this ambiguity has been a well-known problem since the first AE applications.

So, in the AE measures we must identify and then eliminate signals due to the network noise, to an electromagnetic origin and also coming from the ambient mechanical noise. For the laboratory measures these problems have been easily resolved, by means, for example,[1] of spectral analysis and spatial filtering.

For *in-situ* measurements in geological materials, where an increase in pressure, at high or low tension levels, can generate persistent AE,[8] a more wide-band AE must be expected, even though the frequency depends on the structure of the material and the dimension of the fractures. Moreover, especially when metallic wave guide rods must be used, underground sources of em noise, can generate FAE. For these reasons, noise elimination from *in-situ* measurements constitutes a more difficult problem.

The AE waveforms not originating from cracks, that is

[a]Electronic mail: paolo.diodati@fisica.unipg.it

due to origins such as traffic, mechanical, and fretting noise, are distinguishable from crack-related AE because of their lower-frequency content and much longer rise times and durations.

Methods based on the location of the AE source by means of an array of transducers and a triangulation technique are used as well as a pattern recognition technique, depending on the comparison between the characteristic of every single AE signal and a ''pattern'' deduced extracting a number of parameters (arrival times, amplitudes, principal frequency components,...) from a set of sure AE events (an example is the digital discriminator proposed by Sondergeld[10]).

To acquire only AE due to fractures, eliminating that due to manmade or environmental noise, frequency and waveform analyzers are generally also used. A ''blank'' sensor, which is a sensor not coupled to the rock, but electrically connected to the same network of the other sensors coupled to the rock, can be used to identify, and then eliminate, electric noise internal to the network or of atmospheric origin, since their signals are detected at the same time by all sensors.

Therefore, in *in-situ* applications, the authors should specify the used methods to eliminate FAE. On the contrary, it is not clear in the literature how Sondergeld first wrote[10] whether authors have omitted and omit or unknowingly included and include such noise sources in their data.

Sondergeld's observation and his recommendation to specify if and how data of AE had been separate from noise, are still sometimes disregarded.

Recent papers report data as AE, when more than 90% are surely FAE, as we could verify (see, for example, Refs. 11 and 12).

In a recent paper, the Working Group for estimating the primary state of stress in a rock mass using the AE technique says that ''Electromagnetic noise can be reduced (*not eliminated, Authors' note*) by grounding and shielding electrical components and by using coaxial-shielded cable for transmission lines. Mechanical vibration occurs predominantly in the low-frequency range and low-frequency em noise can be eliminated by using a low-frequency cutoff analog filter.'' [13]

Hardy wrote, ''Unfortunately the background noise was quite high and it was determined that at least five borehole probes would be needed for sources location.'' [14]

In these communications the authors emphasize that em noise can be *reduced* and not eliminated.

Bearing this in mind, when metallic bars must be coupled to piezoelectric sensors, when burst and persistent AE could be present and when it is necessary to answer only the question if AE is, or is not here, how can we identify and then eliminate electromagnetic noise due, in addition, to the other remembered origins, to underground currents? For these particular conditions, we used the simplest and cheapest method, valid for both types of AE, up to the highest frequencies.

In this paper we describe this method that should be used to make a new AE sensor, made up of two piezoelectric sensors electrically but not acoustically connected, only one of them to be coupled to the body whose AE must be studied.

Initially, for the first AE studies, which were related to *in-situ* applications and started in the 1940s to predict rock bursts in mines, there was great hope to obtain such predictions, but the high economic price and the number of false alarms, were discouraging.[1]

In these applications the main problem is the high attenuation of AE energy in geologic materials. To partially overcome this disadvantage, working at a frequency above 100 KHz, the most common solution is to couple the transducer to mechanical waveguides, for example, a steel rod fixed into the ground, characterized by a relatively low attenuation value. In the frequency range 100 KHz–300 KHz the attenuation values for iron and steel range from 0.1 to 1 dB/ft, while for intact rock the attenuation increases from 2 up to 700 dB/ft and even more for fractured rock masses. On the volcano Stromboli and on the volcanic island Lipari, we observed a drastic decrease in amplitude and number of detected signals using sensors coupled directly to the rock.

Difficulties in rock mass monitoring have been described since the first AE applications. Hardy *et al.* wrote about the use of mechanical waveguides and acoustic antennas in geological AE studies.[13]

In an AE measurement *in-situ*, also in the frequency range 100 KHz–1 MHz, the main source of noise is of an electromagnetic origin.[10] The simplest method to discriminate AE bursts from bursts due to electromagnetic noise is to use two sensors: the first (T) coupled to the bar inserted in the ground and the second (T_{blank}) set free in air and used as a blank. An elastic wave generated in the ground cannot travel up to T_{blank} through the air, being, in general, of too low an intensity, while electromagnetic bursts are revealed by both the sensors. Our measurements on the Gran Sasso Mountain[11] showed that this method is not reliable, if the two sensors are connected to the same electrical network. In this way we can only recognize the electromagnetic noise generated in the electric network. Noise due to the inserted bar and underground currents, arrives to T, but not to T_{blank}. In this way the FAE arriving to T is erroneously considered as true AE.

Sondergeld proposed a noise discriminator[10] made of two circuits: a principal circuit to classify as an AE event every signal above a set frequency and exceeding a preset voltage level for a minimum number of cycles; an additional circuit to discriminate coherent noise, in general of an electromagnetic origin, not recognized by the first circuit. An even revealed by two of the used sensors within a time interval of 40 ns must be classified obviously as noise and not recorded.

We suggest a very simple discrimination method that can be used even if AE is revealed only on a single point, or on such a small sample that time coincidence becomes inapplicable.

It is sufficient to connect the metallic case of T_{blank} electrically, but not acoustically, to the bar to which T is coupled. To do this we used an electric cable with a cross section of 20 mm^2, more than 2 m long and composed of about 100 very thin wires. So the cable acts as an excellent electrical connection between T and T_{blank} and, at the same time, as an optimal soundproofing material. The sensitive part of T_{blank} was set free, so being able to reveal only electrical signals

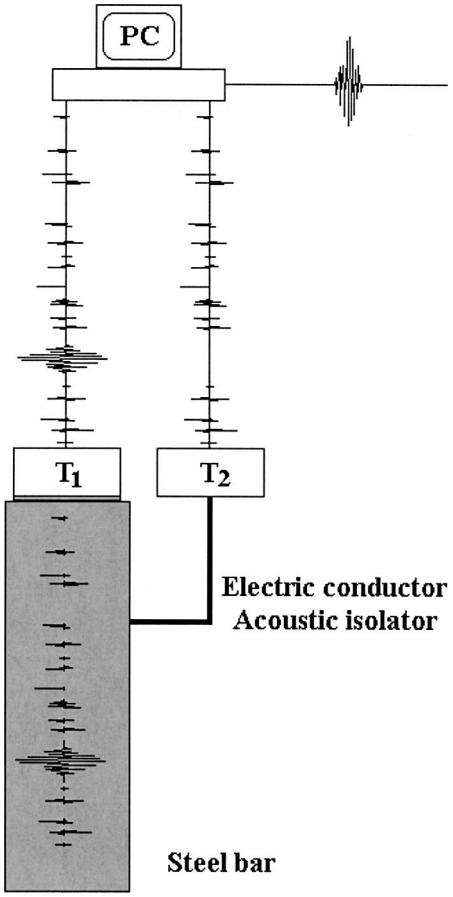

FIG. 1. Experimental setup. T_1, piezoelectric sensor, is acoustically coupled to the bar, while T_2, a second piezoelectric and soundproof element, is electrically connected to the bar. So T_1 reveals either acoustic and electric signals coming from the bar, while T_2 reveals only electric noise. The acquisition program in the Personal Computer (PC) recognizes and excludes noise signals revealed by both sensors. At the end, only true AE events are recorded.

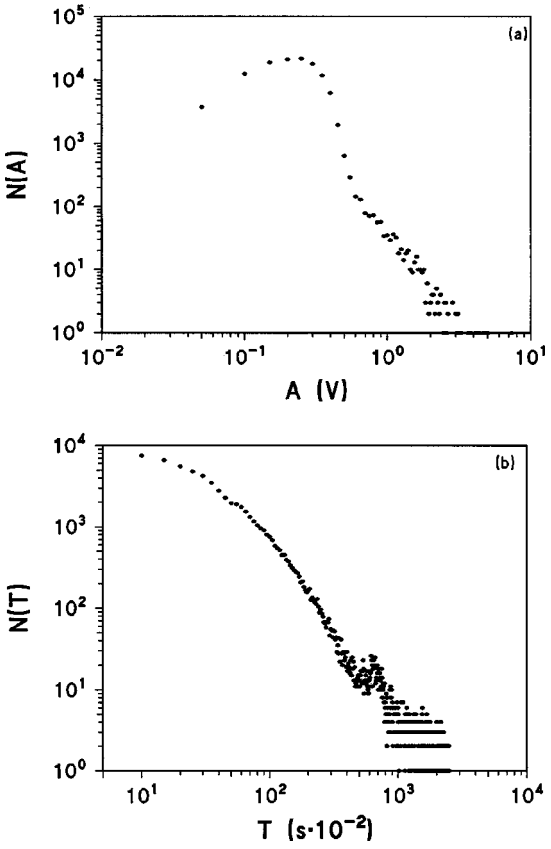

FIG. 2. Statistical distribution in amplitude (a) and time (b) of FAE events.

coming from the bar, acoustic pulses being totally deadened by even a few centimeters of cable. On the contrary, *T* reveal either AE and FAE (Fig. 1). So the FAE signals can be subtracted from the events revealed by *T*. Obviously, em atmospheric noise, as well as noise related to the electric network, are detected by *T* and T_{blank}, so being eliminated as FAE. In laboratory tests, acoustic pulses were generated with variable intensity at one end of a bar about 3 m long. A sensor (*T*) was acoustically coupled to the opposite end of the bar and T_{blank} was electrically connected to the bar. It was possible to verify that elastic waves cannot arrive through the cable to T_{blank}, while *T* reveals signals up to the amplifier overload level. Obviously, electric bursts were detected by both sensors.

We use this elementary system also *in-situ*, measuring AE in geological structures. It is necessary to use a discrimination technique between AE and FAE when FAE signals have or could have comparable or greater amplitude with respect to AE signals, while it is not when, as for laboratory applications and for particular *in-situ* measurements of AE, as we performed on volcano Stromboli,[8] only rare events of FAE exist, with respect to the number of true events of AE. On the contrary we showed that FAE of electromagnetic origin detected in the tunnel of the underground National Laboratory of the Gran Sasso mountain, Italy, is correlated with manmade noise and, in addition, in the open, at about 2500 m above sea level, a systematic increase in number, and intensity of FAE events exists, starting from sunset up to about midnight, FAE being about 99% of all the detected signals.[11]

The evidence of this dramatic, but unquestionable, conclusion is refused if the reversible piezoelectric effect is undervalued and if unsuitable methods for discrimination are used.

On Gran Sasso, using the discrimination method described above, rare events of AE and even more rare periods of high AE, are usually observable mostly in the summer.[11] Subtle but convincing evidence that FAE and AE, as discriminated experimentally, have really different physical origins, is given by their temporal and amplitude distributions. Figure 2 shows our first results for FAE, showing the typical amplitude and time distributions of the noise. In Fig. 2 and in Fig. 3(a) is the maximum amplitude of the AE signals measured by a peak detector, $N(A)$ is the number of events with maximum amplitude between A and $A+0.1$ V, and $N(T)$ is the distribution function of the time interval between two successive AE events.

Finally, we report a single period of enhanced AE activity about two hours long, composed of events registered by *T* but not T_{blank}. Figure 3 shows the statistical distribution of these AE events. In Fig. 3(a), the line represents a power law $N(A) \propto A^{-\beta}$, with $\beta = 4.5$. In Fig. 3(b) the line represents a power law $N(T) \propto T^{-\gamma}$, with $\gamma = 2.1$.

We obtained similar power law distributions on

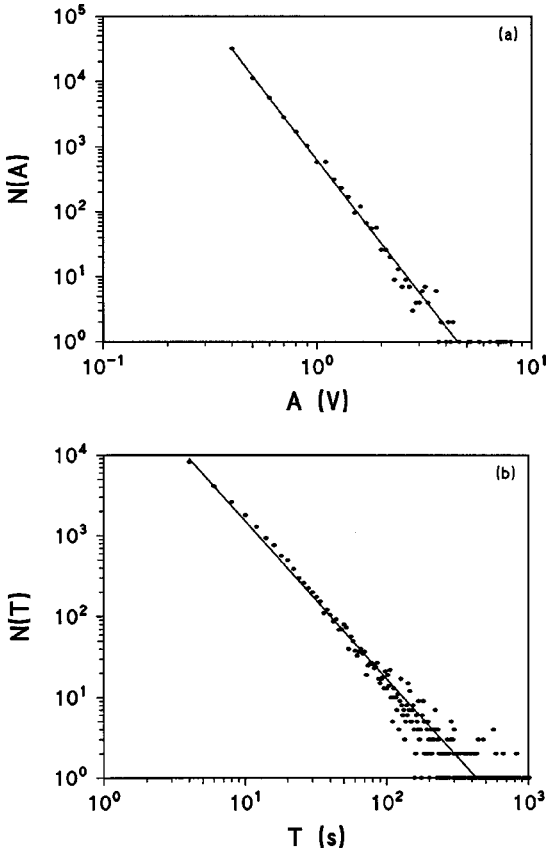

FIG. 3. Statistical distribution in amplitude (a) and time (b) of AE events.

Stromboli,[8] though with different exponents ($\beta = 2.0$ and $\gamma = 1.2$), the exponent values being related to the stress state of the microfracturing material.

In conclusion, we have reported here a very elementary discrimination technique between FAE and AE and a fine mathematical confirmation of the obtained separation.

To our knowledge, this method, even though so simple, sure, and economic, has never been presented or used.

[1] For a general review, see E. Lord, Jr., "Acoustic emission," in *Physical Acoustics*, edited by X. Mason and X. Thurstone (Academic, New York, 1975), Vol. XI, pp. 289–353; "Acoustic Emission, an up to date," 1981 Vol. XV, p. 295.
[2] H. R. Hardy *et al.*, World Meeting on Acoustic Emission, Charlotte, North Carolina, 20–22 March, 1989.
[3] W. P. Mason, H. J. McSkimin, and W. Shockley, Phys. Rev. **73**, 1213 (1948).
[4] J. Kaiser, Arch. Eisenhuettenwes. **24**, 43–45 (1953).
[5] K. Mogi, Bull. Earthquake Res. Inst., Univ. Tokyo **40**, 125 and 831 (1962) and **46**, 1103 (1968).
[6] S. Braccini *et al.*, "Monitoring the acoustic emission of the blades of the mirror suspension for a gravitational wave interferometer," Phys. Lett. A **301**, 389–397 (2002).
[7] P. Bak, *How Nature Works. The Science of Self-Organized Criticality* (Copernicus, New York, 1996).
[8] P. Diodati, F. Marchesoni, and S. Piazza, "Acoustic emission at Stromboli: an example of self-organized criticality," Phys. Rev. Lett. **67**, 2239–2243 (1991).
[9] P. Diodati, P. Bak, and F. Marchesoni, "Acoustic emission at the Stromboli volcano: scaling laws and seismic activity," Earth Planet. Sci. Lett. **182**, 253–258 (2000).
[10] C. H. Sondergeld, "Effective noise discriminator for use in acoustic emission studies," Rev. Sci. Instrum. **51**, 1342–1344 (1980).
[11] P. Diodati, S. Piazza, A. Del Sole, and L. Masciovecchio, "Daily and annual electromagnetic noise variation and acoustic emission revealed on the Gran Sasso mountain," Earth Planet. Sci. Lett. **184**, 719–724 (2001).
[12] G. Paparo *et al.*, "Acoustic Emission as a diagnostic tool in geophysics," Ann. Geophys. **45**, 401–416 (2002).
[13] Working Group, "Suggested method for *in-situ* stress measurements from a rock core using the AE technique," *Proceedings of the 5th International Workshop on the Application of Geophysics in Rock Engineering*, Toronto, Canada, 2002, p. 63.
[14] H. R. Hardy, Jr., *Proceedings of the 1st Conference on Acoustic Emission/Microseismic Activity in Geologic Structures and Materials*, edited by H. R. Hardy, Jr. and F. W. Leighton, Trans. Tech. Publ. Clausthal, Germany, 1977, p. 357.

The role of high-CF fibers in speech perception: Comments on Horwitz *et al.* (2002) (L)

Elizabeth A. Strickland[a)]
Department of Audiology and Speech Sciences, Purdue University, 500 Oval Drive, West Lafayette, Indiana 47907

Neal F. Viemeister
Department of Psychology, University of Minnesota, 75 East River Road, Minneapolis, Minnesota 55455

Dianne J. Van Tasell
Department of Communication Disorders, University of Minnesota, Minneapolis, Minnesota 55455

Jill E. Preminger
University of Louisville School of Medicine, Program in Audiology, Myers Hall, Louisville, Kentucky 40292

(Received 18 August 2003; revised 8 April 2004; accepted 9 April 2004)

In a recent paper, Horwitz *et al.* [J. Acoust. Soc. Am. **111**, 409–416 (2002)] concluded that listeners with high-frequency hearing impairment show a decrement in the perception of low-frequency speech sounds that is due to loss of information normally carried by auditory-nerve fibers with high characteristic frequencies (CFs). However, in their own study and in other studies, highpass-filtered noise did not degrade the perception of lowpass-filtered speech in listeners with normal hearing. An alternate conclusion proposed by Strickland *et al.* [J. Acoust. Soc. Am. **95**, 497–501 (1994)] is that information conveyed by high-CF fibers is not necessary for speech perception. To reconcile these opposite conclusions, we suggest that the hearing-impaired listeners tested by Horwitz *et al.* may not have had normal hearing even in the low frequencies, and that the conclusion from Strickland *et al.* remains correct: high-CF fibers are not necessary for normal speech perception. © *2004 Acoustical Society of America.* [DOI: 10.1121/1.1756614]

PACS numbers: 43.71.Es, 43.71.An [PFA] Pages: 49–50

Horwitz *et al.* (2002) examined the role of high-frequency information (above 2 kHz) in the perception of speech by normal-hearing listeners and listeners with high-frequency hearing loss. They concluded that their results were consistent with the hypothesis that high-frequency fibers encode useful low-frequency speech information. This contradicts the conclusion from our similar study (Strickland *et al.*, 1994), that fibers with characteristic frequencies (CFs) above the speech range are not necessary for speech perception in quiet or in noise. In this letter we attempt to address the issues raised by Horwitz *et al.* and further justify our conclusion about this important issue.

Horwitz *et al.* (2002) compared the recognition of consonant–vowel and vowel–consonant syllables by normal-hearing listeners and listeners with high-frequency hearing loss. Performance was measured in quiet and in three levels of speech-shaped noise. Listeners with high-frequency hearing loss had speech recognition scores that were significantly lower than those of normal-hearing listeners in all conditions. Because pure-tone thresholds were the same for both groups in the speech-shaped noise, Horwitz *et al.* (2002) concluded that their performance was not determined by audibility alone, and set out to examine what else might be a limitation on performance for the hearing-impaired listeners. One possibility is that normal-hearing listeners are able to use high-CF nerve fibers to code low-frequency speech information, and the hearing-impaired listeners are not. A second possibility, which the authors note but essentially ignore, is that the hearing-impaired listeners may not have had normal speech processing even at low frequencies. This would undermine the implicit assumption that the hearing-impaired listeners were like normal-hearing listeners except for unusable high-CF fibers. Supporting this possibility is the fact that the hearing-impaired listeners had low-frequency thresholds in quiet that were on average 9 dB higher than those for normal-hearing listeners.

One way to differentiate between these two possibilities is to measure the effects of highpass noise on speech recognition, because this should decrease the contribution of information from high-CF fibers. In the Horwitz *et al.* (2002) study, an additional condition was included for the normal-hearing listeners in which highpass noise was presented in addition to the speech-shaped noise, for all three levels. The highpass noise was set at 59 dB SPL, the highest level which did not elevate thresholds from 0.5 to 2.0 kHz. Syllable recognition scores did not change appreciably with the addition of the highpass noise. The authors hypothesized that this level of noise may not have been enough to degrade speech information in high-CF fibers. Indeed, the spectrum level of the noise would have been only approximately 21 dB. The authors conclude that this technique cannot be used to determine the role of high-CF fibers in coding low-frequency information, because levels high enough to disrupt the coding in the high-CF fibers would also cause downward spread of masking.

[a)]Electronic mail: estrick@purdue.edu

A similar study (Strickland *et al.,* 1994) used highpass noise sufficiently intense (55 dB spectrum level) to disrupt activity in high-CF fibers. Our study measured the identification of iterated vowels and recognition of spondees by normal-hearing listeners. As in the Horwitz *et al.* study, performance was measured in quiet and in several levels of speech-shaped noise, with and without highpass noise. The addition of the highpass noise had an effect only on spondee recognition, and only at the two lowest signal-to-noise ratios. Error analysis and the measurement of thresholds for pure tones at and below the highpass noise cutoff frequency showed that this might be attributable to downward spread of masking from the highpass noise. This hypothesis was supported by data showing an almost identical decrement in performance when the stimuli were lowpass filtered to simulate the effects of downward spread of masking. A similar result was found by Van Tasell and Turner (1984). They found that for normal hearing listeners, the addition of highpass noise at a spectrum level of 35 dB decreased the percentage of CVCs correctly identified. The error analysis revealed that the decrease was mainly in place cues, which could be disrupted by downward spread of masking from the highpass noise (although this was not the interpretation suggested by the authors). Thus, both Strickland *et al.* (1994) and Van Tasell and Turner (1984) provide data showing that highpass noise does not disrupt the perception of these types of stimuli, beyond what might be expected from audibility limitations due to downward spread of masking.

A second piece of evidence that might distinguish between the two possibilities could be the pattern of errors. In the Horwitz *et al.* (2002) study, an error analysis did not reveal any particular pattern for the errors. This is contrary to what might be expected both from physiological and behavioral results. Physiological results have shown that the low-frequency information carried by high-CF fibers is the envelope and low-frequency periodicity, particularly first formant cues (Kiang and Moxon, 1974; Young and Sachs, 1979; Sinex and Geisler, 1983). This is supported by behavioral data from a listener with low-frequency hearing loss from Van Tasell and Turner (1984). In their study, an analysis of the decrement in the identification of lowpass filtered speech with the addition of highpass noise suggested that the main features coded by the high-CF fibers were voicing and nasality cues. Voicing may be partially carried by envelope cues. The nasality cue depends on a low (near 300 Hz) intense first formant. Thus these results are consistent with what might be expected from the physiological data. The fact that the listeners in the Horwitz *et al.* (2002) study show more global deficits would seem, if anything, to favor the hypothesis of a deficit in the low-CF fibers.

In summary, the results of Horwitz *et al.* (2002) suggest that listeners with high-frequency hearing loss may have more difficulty processing low-frequency information than might be expected from their low-frequency quiet thresholds. Their results do not, however, differentiate between the hypothesis that it is specifically the lack of information from high-CF fibers that causes the drop in performance and the hypothesis that the hearing-impaired listeners may not have normal auditory processing even at low frequencies. It is in fact quite interesting that the hearing-impaired listeners had significantly higher low-frequency thresholds in quiet than the normal-hearing listeners, an effect also found in another similar (unpublished) study of listeners with high-frequency hearing loss (Kim and Turner, 1988). It may indicate that damage to high-frequency areas does affect low-frequency processing. It could also mean that the low-frequency areas are damaged too. The results of Horwitz *et al.* therefore do not contradict our earlier conclusion that high-CF fibers are not necessary for normal speech perception.

Horwitz, A. R., Dubno, J. R., and Ahlstrom, J. B. (**2002**). ''Recognition of low-pass filtered consonants in noise with normal and impaired high-frequency hearing,'' J. Acoust. Soc. Am. **111**, 409–416.

Kiang, N. Y.-S. and Moxon, E. C. (**1974**). ''Tails of tuning curves of auditory nerve fibers,'' J. Acoust. Soc. Am. **55**, 620–630.

Kim, M. and Turner, C. W. (**1988**). ''Low-pass speech recognition in high-frequency hearing-impaired subjects,'' ASHA **30**, 193.

Sinex, D. G. and Geisler, C. D. (**1983**). ''Response of auditory-nerve fibers to consonant-vowel syllables,'' J. Acoust. Soc. Am. **73**, 602–615.

Strickland, E. A., Viemeister, N. F., Van Tasell, D. J., and Preminger, J. E. (**1994**). ''Is useful speech information carried by fibers with high characteristic frequencies?,'' J. Acoust. Soc. Am. **95**, 497–501.

Van Tasell, D. J. and Turner, C. W. (**1984**). ''Speech recognition in a special case of low-frequency hearing loss,'' J. Acoust. Soc. Am. **75**, 1207–1212.

Young, E. D. and Sachs, M. B. (**1979**). ''Representation of steady-state vowels in the temporal aspects of the discharge patterns of populations of auditory-nerve fibers,'' J. Acoust. Soc. Am. **66**, 1381–1403.

The Laplace transform to describe bounded inhomogeneous waves

Nico F. Declercq[a] and Joris Degrieck
Soete Laboratory, Department of Mechanical Construction and Production, Faculty of Engineering, Ghent University, Sint Pietersnieuwstraat 41, 9000 Gent, Belgium

Oswald Leroy
Interdisciplinary Research Center, KULeuven Campus Kortrijk, E. Sabbelaan 53, 8500 Kortrijk, Belgium

(Received 23 February 2004; accepted for publication 11 April 2004)

The inhomogeneous waves theory deals with plane waves having complex valued wave vectors and with their superposition to form bounded beams. Since infinite inhomogeneous plane waves cannot be formed experimentally, verifications of the theory have to be performed using bounded inhomogeneous waves. In this paper we clarify how a bounded inhomogeneous wave is described as a superposition of inhomogeneous waves. This is done by applying the Laplace transform. The paper also shows from a theoretical point of view why bounded inhomogeneous waves behave like infinite inhomogeneous waves in numerous experiments. © *2004 Acoustical Society of America.*
[DOI: 10.1121/1.1756672]

PACS numbers: 43.20.Bi, 43.20.El, 43.35.Pt [ADP] Pages: 51–60

I. INTRODUCTION

From the moment infinite inhomogeneous waves have made their entry in the 1980's, they have been used in the study of the propagation and the scattering of sound. They gained sympathy because of their ability to describe—often better than pure infinite homogeneous plane waves—critical phenomena like the generation of Leaky Rayleigh waves. An extensive survey on the properties of infinite inhomogeneous plane waves can be found in the literature.[1–4] While infinite inhomogeneous plane waves are often studied in the context of their superposition to form bounded beams,[5–7] perhaps even more interesting is the theoretical and experimental study of individual inhomogeneous waves. A lot of experiments are reported that confirm theoretical predictions of the behavior of inhomogeneous waves while interacting with interfaces.[2,8–11] The interesting part of these confirmations is the fact that infinite inhomogeneous waves can only be approached experimentally within a limited spatial interval, depending on the apparatus that is used experimentally.[8] The overall experimentally generated wave is in fact a bounded inhomogeneous wave, being a chopped and smoothened version of the theoretical infinite inhomogeneous wave. The importance of bounded inhomogeneous waves, as compared with bounded Gaussian beams, is the fact that they contain the inhomogeneity features of inhomogeneous waves (i.e., the exponential decay of the amplitude along the wave front) and are hence capable of stimulating more efficiently critical phenomena such as leaky Rayleigh waves or leaky Lamb waves than Gaussian beams. Furthermore, this resemblance with infinite inhomogeneous waves is the reason why at incidence angles that correspond to the stimulation of critical phenomena, a strong beam shift occurs[2,8–11] to the reflected beam as the principle effect, which is different from the Schoch effect (the creation of two reflected lobes with a null zone in between) that occurs if Gaussian beams are used. In what follows, we investigate bounded inhomogeneous waves in terms of infinite inhomogeneous plane waves, using a numerical technique that has never been applied before in such a context, namely the Laplace transform. In fact, as far as we know, no reports exist at all where bounded inhomogeneous waves are described in terms of infinite inhomogeneous plane waves.

Whenever the expression ''profile'' is used in this text, it refers to the normalized particle displacement amplitude profile. Further below, we will consider the oblique incidence of a bounded inhomogeneous wave at an interface (X',$Z'=0$); see Fig. 1. The profile of this bounded beam can be compared with the profile of the reflected beam if one considers the amplitude distribution along an axis X (see Fig. 1) that coincides with the wave front and for theoretical simplicity has the same origin as the fixed (X',Z') coordinate system. The latter enables us to compare for example possible shifts of the reflected profile along the X-axis with respect to the incident profile.

II. INFINITE INHOMOGENEOUS PLANE WAVES IN A NUTSHELL

For the reader who is not familiar with the theory of infinite inhomogeneous waves, a first glimpse is offered in this section. Anyone who needs to get to know more about this theory is invited to read Refs. 1, 3–4, 6–7.

If a ''plane wave solution'' having an amplitude A, polarization $\mathbf{P}$, wave vector $\mathbf{k}$ and angular frequency ω,

$$A\mathbf{P}\exp(i\mathbf{k}\cdot\mathbf{r}-i\omega t) \tag{1}$$

is entered into the wave equation for viscoelastic media, then it can be shown that the dispersion relation must hold:

$$\mathbf{k}\cdot\mathbf{k}=\left(\frac{\omega}{v}+i\alpha_0\right)^2=\frac{\omega^2}{(\tilde{v})^2}, \tag{2}$$

[a]Electronic mail: NicoF.Declercq@ugent.be

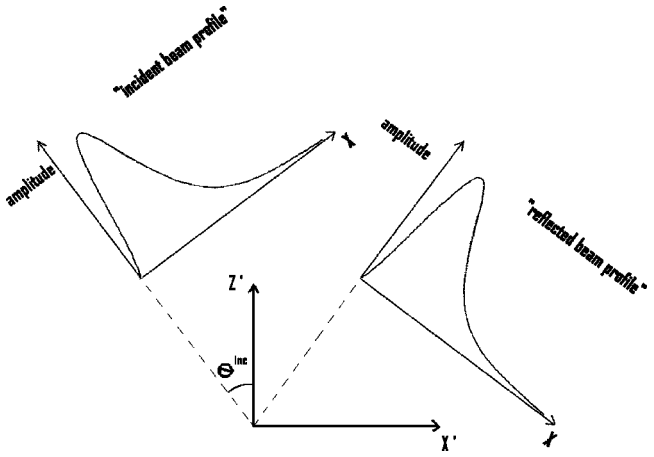

FIG. 1. Schematic of the different coordinate systems. The reflection interface coincides with the X'-axis. The incident beam profile is described along a rotated X'-axis, denoted by X, perpendicular to the propagation direction. The reflected beam profile is also described along a rotated X'-axis, denoted by the same symbol X. Hence, it is possible to compare the profile of the incident beam with that of the reflected beam in a diagram where the amplitude is depicted as a function of the ''common'' X axis. For convenience, we suppose that the X-axis for both incident and reflected beams has the same origin as the (X',Z') coordinate system.

in which ν is the phase velocity of traditional infinite homogeneous harmonic plane waves, $\tilde{\nu}$ is often called ''the complex wave velocity'' and α_0 is the intrinsic damping coefficient. Therefore in general the wave vector $\mathbf{k}$ can be complex valued, whence

$$\mathbf{k}=\mathbf{k}_1+i\mathbf{k}_2; \quad \mathbf{k}_1,\mathbf{k}_2\in\Re^3 \tag{3}$$

and

$$\mathbf{k}_2=\boldsymbol{\alpha}+\boldsymbol{\beta}, \text{ with } \boldsymbol{\beta}\perp\mathbf{k}_1 \text{ and } \boldsymbol{\alpha}\parallel\mathbf{k}_1. \tag{4}$$

The vector $\mathbf{k}_1$ is called the propagation wave vector. The vector $\boldsymbol{\beta}$ is called the inhomogeneity vector while $\boldsymbol{\alpha}$ is called the damping vector. In many publications the opposite sign for $\boldsymbol{\beta}$ in (4) can be found, but it is more convenient in this outline to use a positive sign. In order to prevent confusion with other papers, we will describe physical problems in terms of the imaginary part of the wave vector, i.e., k_2, therefore the sign convention of $\boldsymbol{\beta}$ will have no influence on these discussions. If (3) and (4) are entered in (2), one finds

$$\mathbf{k}_1\cdot\mathbf{k}_2=k_1\alpha=\frac{\omega}{\nu}\alpha_0 \tag{5}$$

and

$$(k_1)^2-(\alpha)^2-(\beta)^2=\left(\frac{\omega}{\nu}\right)^2-(\alpha_0)^2. \tag{6}$$

Relations (5) and (6) are called the dispersion equations. Due to (5), the damping vector can only exist if there is intrinsic visco-elastic damping in the media. Furthermore, its value depends not only on the intrinsic damping α_0, but also on the inhomogeneity vector $\boldsymbol{\beta}$. Typical waves (1) are depicted in Figs. 2–4. In the context of what follows, it must be stressed that waves like (1) have a wave front that extends to infinity, i.e., such waves are not bounded in space.

The term infinite inhomogeneous plane waves in the current paper stands for ''plane waves'' (1) having a complex valued wave vector and a real valued frequency. The polarization will be complex too, but this fact has no influence on the amplitude distribution in space, and is not highlighted here.

Whenever an infinite inhomogeneous plane wave interacts with a plane interface between two media, continuity of the component of $\mathbf{k}$ along the interface is required. This is called the generalized Snell–Descartes law.

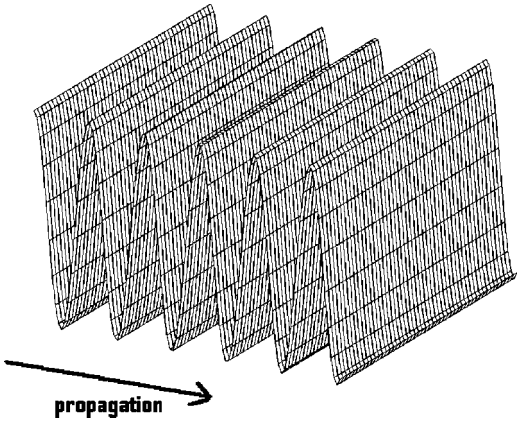

FIG. 2. An infinite pure plane wave (undamped). The amplitude along the wave front remains constant, as well as the amplitude along the propagation direction.

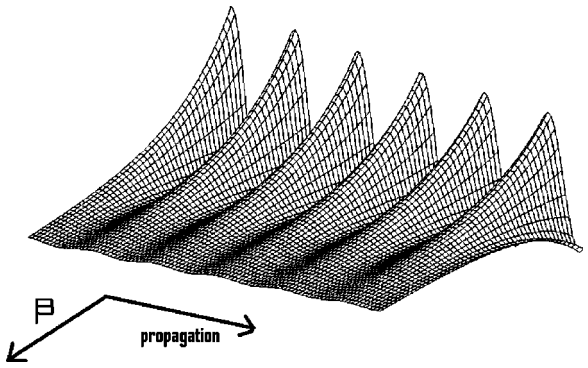

FIG. 3. An infinite inhomogeneous wave (undamped). The amplitude along the wave front decays exponentially down the inhomogeneity vector β [according to its definition in (4)]. The amplitude remains constant along the propagation direction.

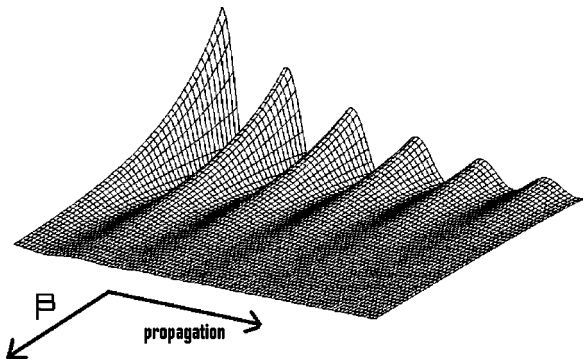

FIG. 4. The same as in Fig. 3, except that there is now damping, therefore the amplitude also decays exponentially along the propagation direction.

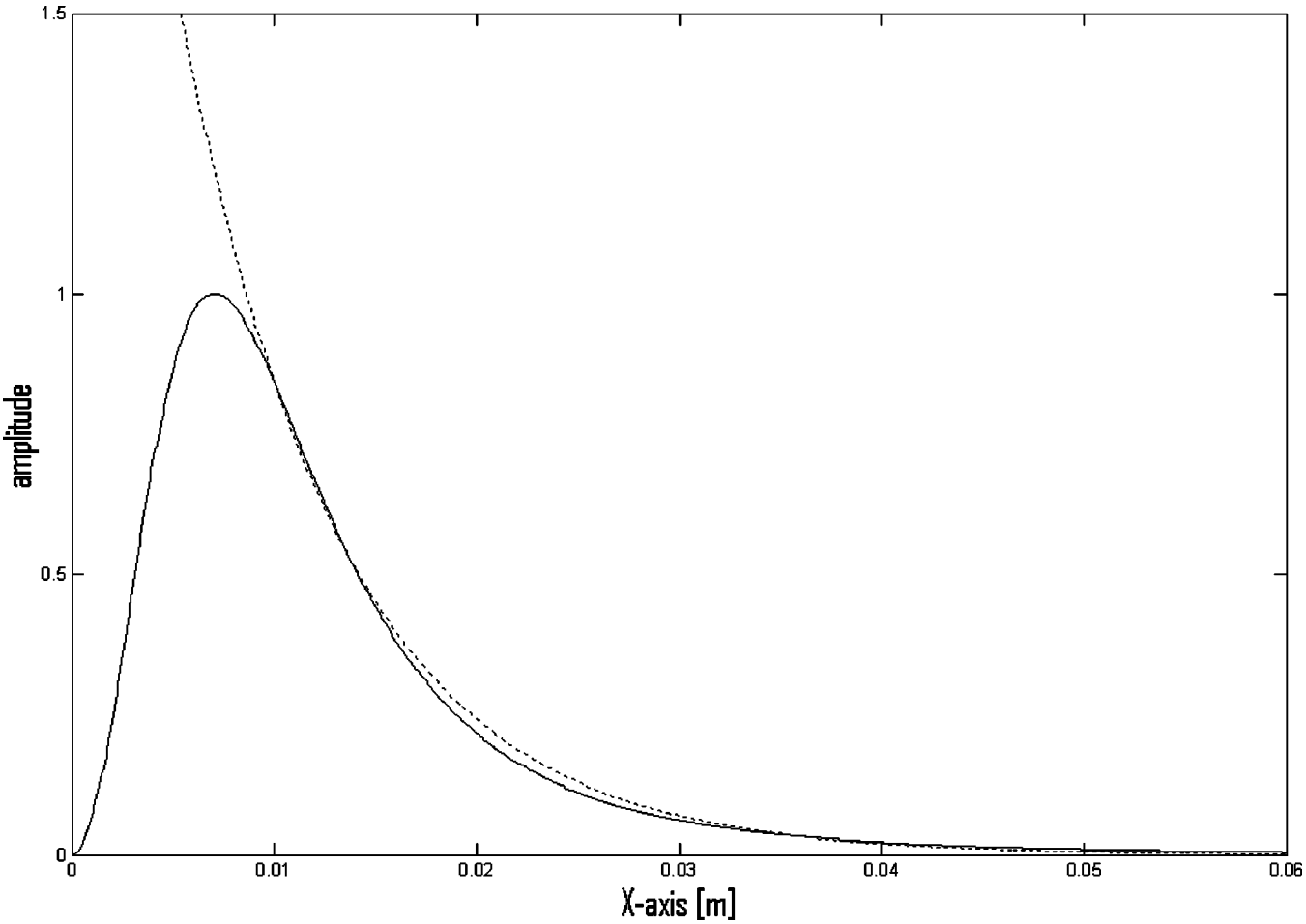

FIG. 5. Solid line: the exact profile (11). Dotted line: the profile of an infinite inhomogeneous wave having an inhomogeneity 125/m.

III. CLASSICAL BOUNDED BEAM FORMATION IN TERMS OF THE FOURIER THEORY

As this method is so widely known, we limit the discourse to a short description in words. In the Fourier theory, a bounded beam profile in X-space (consider Fig. 1) is transformed into $k_{1,x}$-space by means of the discrete Fourier transform. The amplitudes that correspond to each $k_{1,x}$ value are then attributed to a plane wave having a wave vector component $k_{1,x}$ and another component $k_{1,z}$ that is found as a function of $k_{1,x}$ and the dispersion relation for pure plane waves, i.e. (6) for $\alpha=\beta=0$. Physically this means that the bounded beam whose profile is considered in the discrete Fourier transform, is built up by means of infinite plane waves all traveling in different directions and having amplitudes determined by that discrete Fourier transform. The beauty of this approach is of course that practically all kinds of beam profiles can be approximated by means of this method. However, from a theoretical point of view, the method is strictly only valid for beams that propagate in infinite space or at most perpendicular to any boundary. That is because integration is performed from $X=-\infty$ to $X=+\infty$ which is strictly only possible if space is uninterrupted in this interval. Therefore, if the oblique incidence is considered, the method is strictly wrong. Nevertheless, many authors apply the method even for oblique incidence. Furthermore, if large oblique incidence is considered for a narrow beam, there is yet another difficulty which is again a consequence of the fact that the method is strictly only valid for normal incidence, and that is that ''incident'' infinite plane waves must be considered that are actually ''coming from the continuing media.'' This is of course a contradictive situation which is not present in the inhomogeneous waves decomposition of bounded beams (see below). Yet another important problem that arises if the Fourier method is applied is the fact that no inhomogeneous waves are present in the bounded beam under consideration. This may lead to wrong numerical simulations especially whenever complicated surfaces (for example corrugated surfaces) are considered.[12–15] The reason is that inhomogeneous waves interact at interfaces differently from pure plane waves. This fact is very important because if one simulates a bounded inhomogeneous wave by means of the Fourier method, the resulting bounded beam may simulate reality incorrectly, especially in cases where rough surfaces are considered.[12–15] That is the reason why this paper focuses on the description of bounded inhomogeneous waves in terms of infinite inhomogeneous plane waves.

IV. CLASSICAL GAUSSIAN BOUNDED BEAM FORMATION IN TERMS OF INFINITE INHOMOGENEOUS WAVES

The previous section suggests that it is not recommended to decompose a bounded inhomogeneous wave into

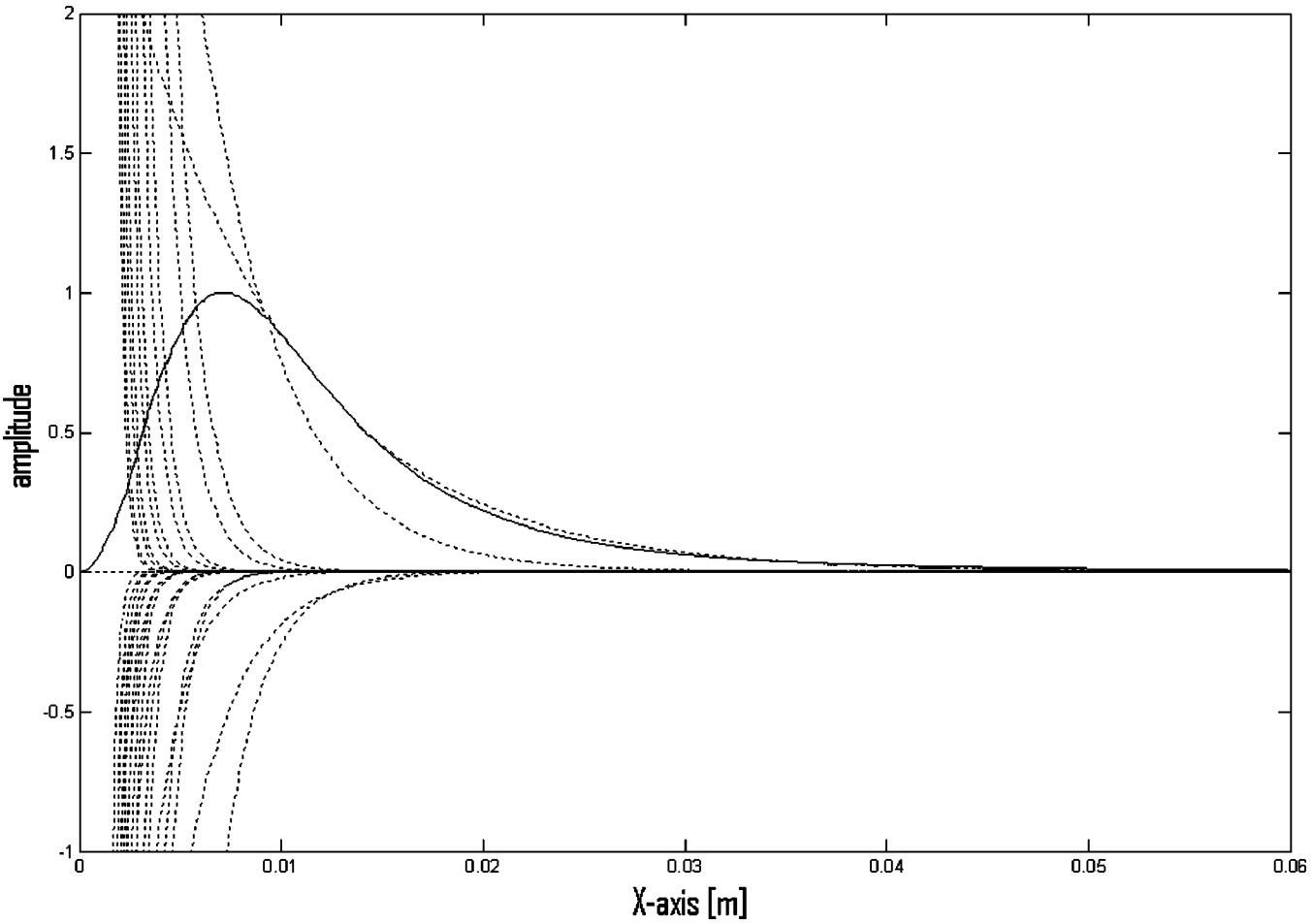

FIG. 6. Solid line: the exact profile (11). Dotted lines: the profiles of the infinite inhomogeneous waves that form the exact profile as in (13).

plane waves (Fourier method) because ''contradictions'' might occur and more importantly because the nature of plane waves is so different from that of (infinite) inhomogeneous (plane) waves that it is possible to perform the wrong simulations especially if the interaction is concerned with complicated interfaces such as periodically corrugated surfaces.[12–15] Therefore it is necessary to focus on the decomposition of bounded beams by means of a superposition of infinite inhomogeneous plane waves. Several years ago Leroy *et al.*[5–7] proposed such a method. The method consists of the formation of a bounded beam as a superposition of infinite inhomogeneous plane waves all propagating in the same direction, but having different amplitudes and inhomogeneities. Let us consider a beam with profile $f(x)$ which has to be decomposed as a superposition of inhomogeneous waves; then, if the sign convention (4) is adopted, one has[5]

$$f(x)=\sum_{n=0}^{N} A_n \exp(-\beta_n x). \tag{7}$$

Furthermore, one performs a coordinate transformation $x=p\ln y$ with $p\in\Re_0^+$ and $y\in(0,+\infty)$, whence, if $\beta_n=-n/p$,

$$\sum_{n=0}^{N} A_n y^n = f(p\ln y); \tag{8}$$

on the other hand, one applies a decomposition into Laguerre polynomials[5] $L_n(y)$, such that

$$\sum_{n=0}^{N} B_n L_n(y) = f(p\ln y), \tag{9}$$

with

$$B_n=\int_0^{+\infty} \exp(-y) f(p\ln y) L_n(y)\,dy; \tag{10}$$

then the coefficients A_n in (7)–(8) are searched as a linear combination of B_i for $1\leqslant i\leqslant N$. The drawback of this method is that (10) can only be found numerically, while the mentioned linear combination is not found straightforwardly but as an optimization procedure. The procedure is found to be best suited if Gaussian profiles are considered and is hence only applied for Gaussian beams or beam profiles that can be approximated by means of a small number of superposed Gaussian beams.[5–7] Therefore, in what follows, we bring to light an analytical method that is valid for the kind of bounded beams $f(x)$ that is important in this report and is called ''bounded inhomogeneous waves.''

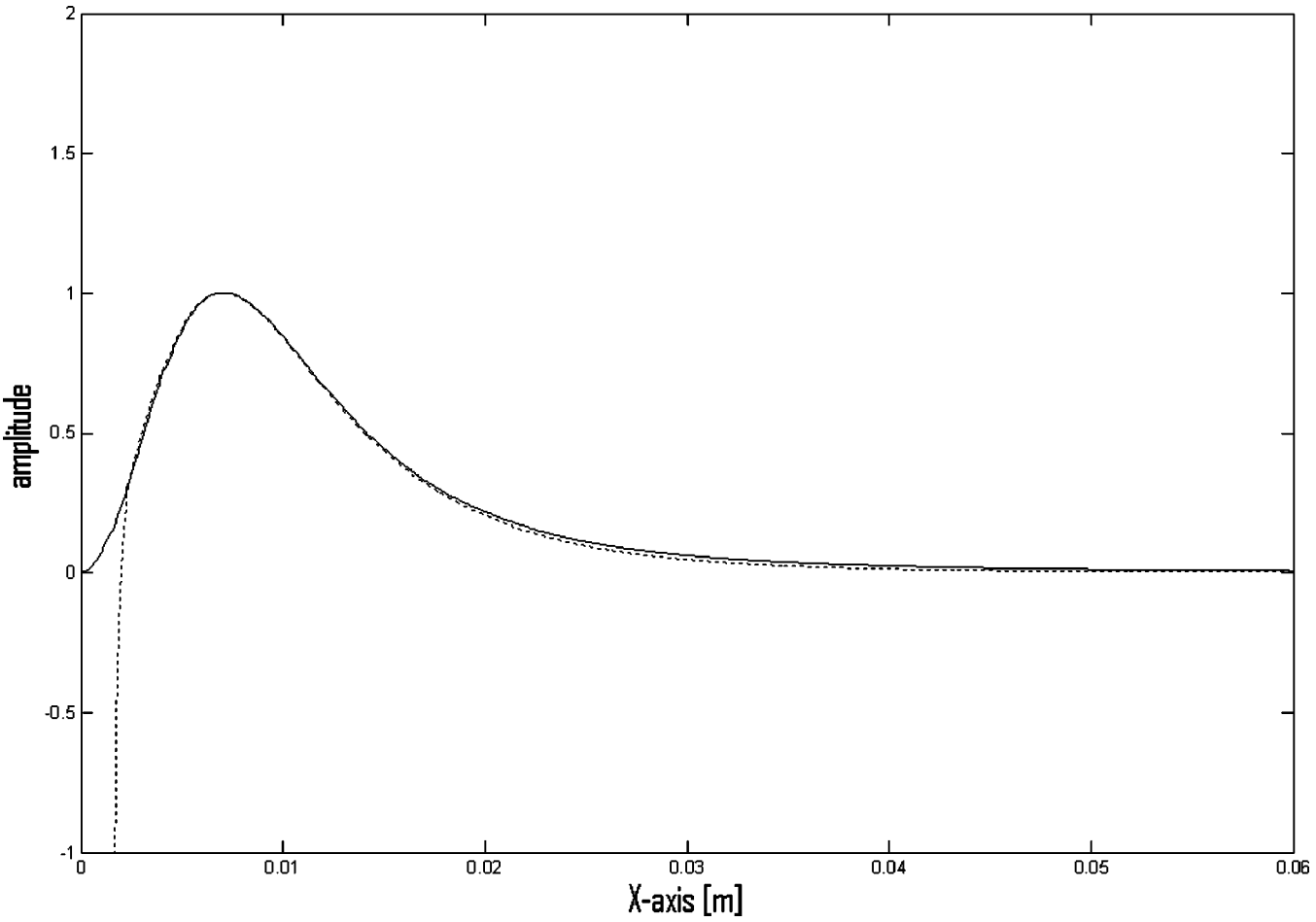

FIG. 7. Solid line: the exact profile (11). Dotted line: the summation of the inhomogeneous waves as in (13).

V. THE DESCRIPTION OF BOUNDED INHOMOGENEOUS WAVES BY MEANS OF THE LAPLACE TRANSFORM

A bounded inhomogeneous wave looks like an infinite inhomogeneous wave except for the important fact that it is chopped as a small interval in x-space. Hence it does not extend to infinity and is bounded in space. The main feature of such a bounded inhomogeneous wave is that it is exponentially shaped inside the beam and that its amplitude drops at the borders. Hence, depending on the method that is used to generate such waves, the shape at the borders may differ a bit, but the exponential feature remains unchanged. There are therefore many mathematical functions possible that describe the profile of a bounded beam. We have chosen a function for which an analytical solution exists for the amplitudes A_n in (7).

The profile of a bounded inhomogeneous wave, representing an exponentially decaying infinite inhomogeneous wave and traveling perpendicular to the x-axis, can sufficiently be described in the x-interval $[0,+\infty]$ by the analytical expression

$$f(x)=\frac{27W^4x^2}{4(x^2+W^2)^3} \tag{11}$$

in which W is a parameter that is proportional to the ''width'' of the beam profile. $f(x)$ reaches its maximum at

$$x_m=\frac{\sqrt{2}}{2}W. \tag{12}$$

Now, it would be possible to apply the numerical optimization technique of the previous section. However, it is here more convenient to apply an analytical approach. The first reason is that a numerical optimization procedure is far from natural and is in fact a fitting procedure. The expression ''give me enough parameters and I will fit you an elephant'' is perhaps most suitable to understanding the artificial character of any fitting procedure. The second reason is that it is known from experiments that bounded inhomogeneous waves behave like infinite inhomogeneous waves, therefore there must be a physical and an inherent analytical relation between the two kinds of waves.

Therefore we decompose $f(x)$ into decaying infinite inhomogeneous waves and we let the interval of the inhomogeneities β_n mathematically tend to infinity, while decreasing the distance between the successive inhomogeneities; hence

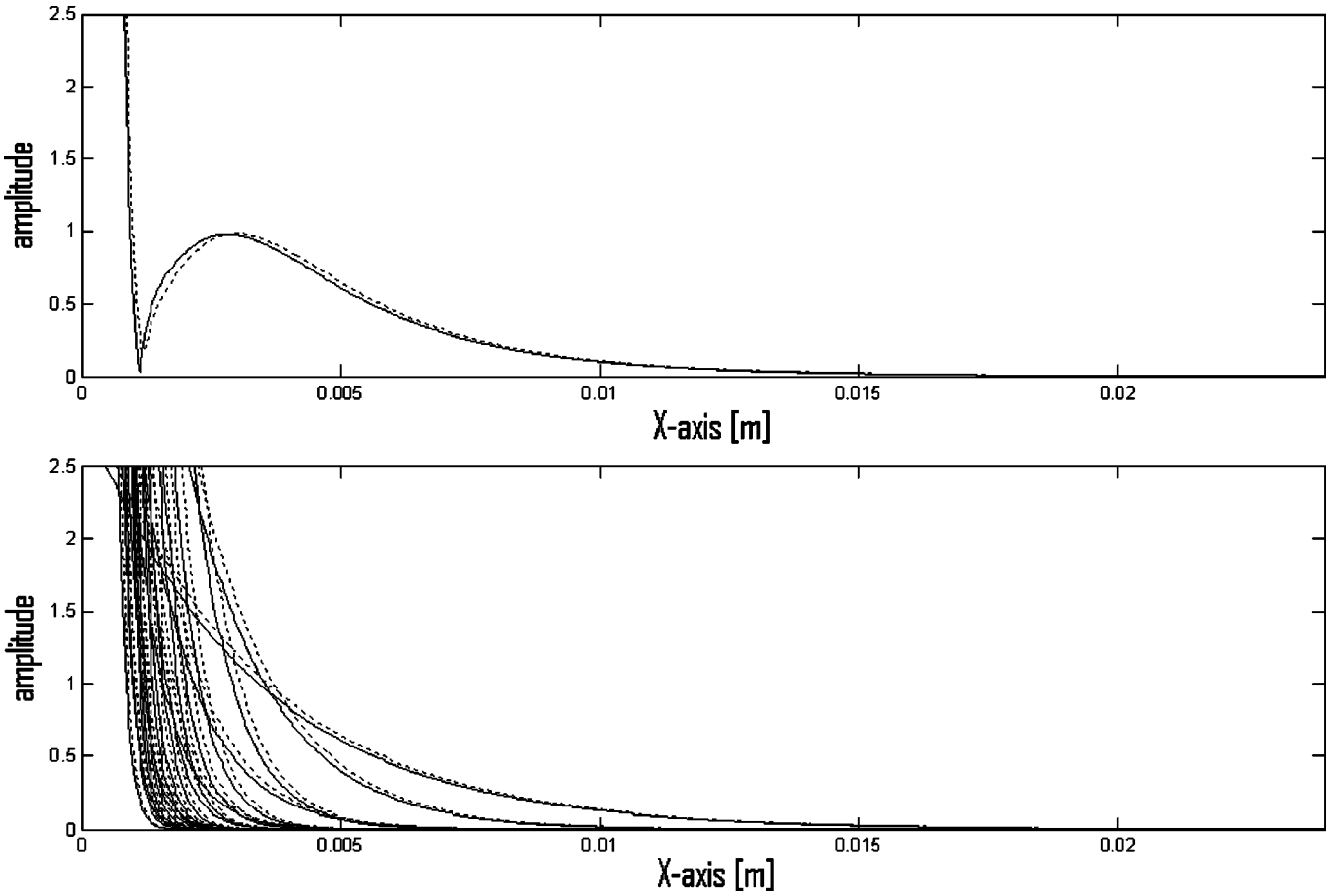

FIG. 8. Solid line: absolute value of the amplitude of the incident bounded inhomogeneous beam profile (top) and its infinite inhomogeneous waves building blocks (bottom). Dotted line: absolute value of the amplitude of the reflected bounded inhomogeneous beam profile (top) and its reflected infinite inhomogeneous waves building blocks (bottom). Inhomogeneity: 311.56/m. Angle of incidence: 30° (not in the vicinity of the Rayleigh angle).

$$f(x)=\sum_{n=0}^{N} B(-\beta_n)\exp(-\beta_n x)$$

$$\cong \int_0^{+\infty} e^{-\beta x}A(\beta)d\beta, \quad \text{with}$$

$$B(-\beta_n)=A(\beta_n)\Delta\beta_n . \tag{13}$$

The integral in (13) can be interpreted as the Laplace transform L of $A(\beta)$, therefore the unknown coefficients $A(\beta)$ can be obtained applying the inverse Laplace transform L^{-1} of the profile (11), thus releasing the problem of impractical numerical optimization procedures as they occur in the previous section. From textbooks containing tables of Laplace transforms, an analytical expression can be extracted,

$$A(\beta)=L^{-1}(f(x))$$

$$=\frac{37W}{32}[(1+W^2\beta^2)\sin(W\beta)-W\beta\cos(W\beta)]. \tag{14}$$

This is an oscillating function with increasing amplitude as a function of β, involving very high amplitudes attributed to very rapidly decreasing inhomogeneous waves. Therefore, high β values will only contribute to the amplitude near the origin, since their amplitude becomes negligible at larger distances. Still, in practice, we shall have to chop the integral retaining a finite integration interval from $\beta=0$ to a chosen $\beta=\beta_{\max}$, whence the recovered bounded inhomogeneous wave profile will deviate considerably near $x=0$. The two reasons for this chop process are ''numerical ease'' and the requirement that $\mathbf{k}_1$ and $\mathbf{k}_2$ must be real, then considering (5) and (6) necessitates

$$\alpha \leqslant \alpha_0 \tag{15}$$

and

$$\beta^2 \leqslant \omega^2/\nu^2-(\alpha_0)^2. \tag{16}$$

The second step is the re-discretization of the chopped integral in order to keep a finite number of infinite inhomogeneous waves forming the profile.

We therefore now examine the properties of the discrete and chopped summation of infinite inhomogeneous waves [see (13)] representing the bounded inhomogeneous wave as described in (11).

$$f(x)=\sum_{\beta=0}^{\beta_{\max}} A(\beta)\exp(-\beta)\Delta\beta. \tag{17}$$

It is always necessary to choose one value for W or, respectively, for β and then optimize the value of β, respectively, W in order to have the best agreement between the bounded inhomogeneous wave and the infinite inhomogeneous wave under consideration. As an example we consider the case

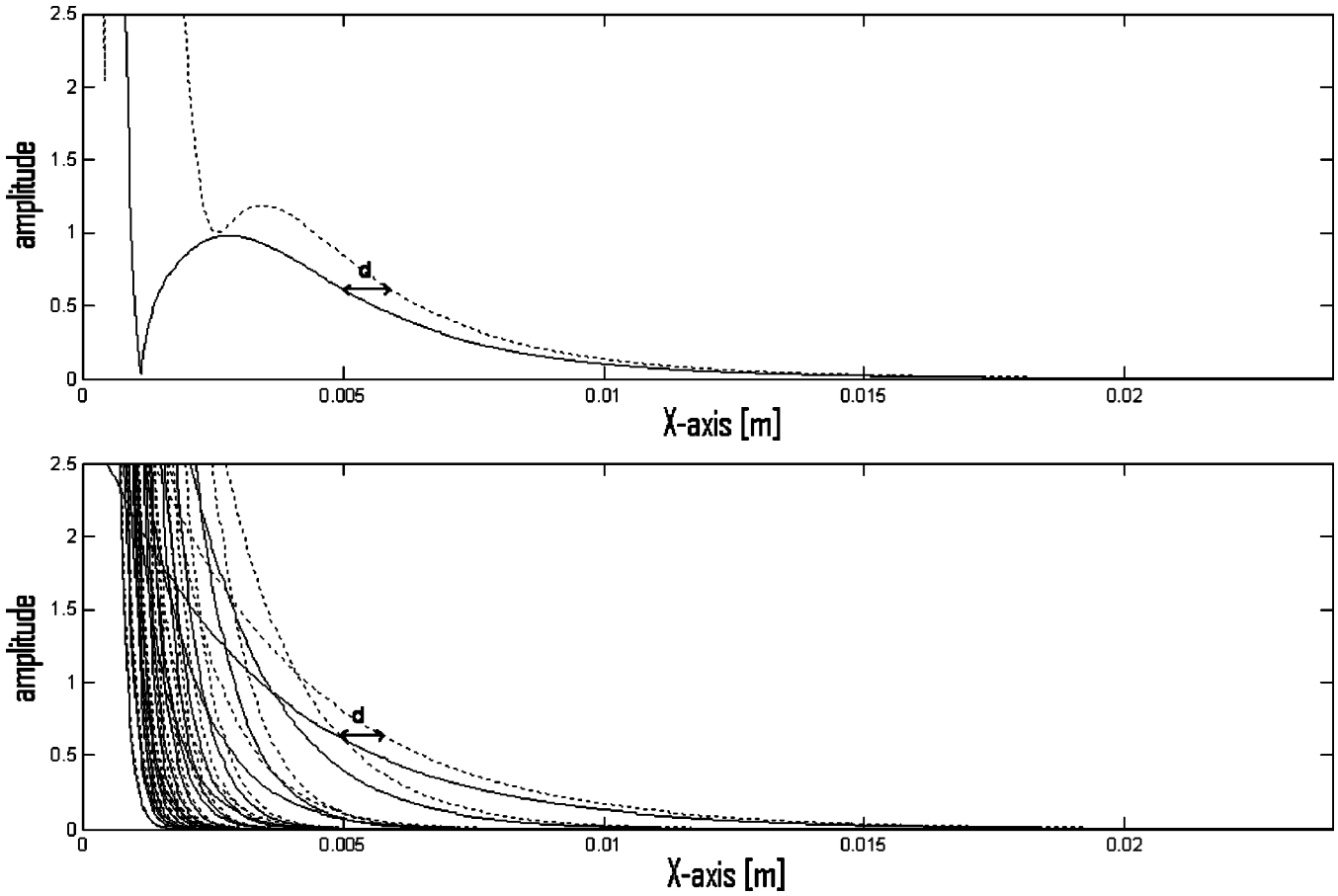

FIG. 9. Solid line: absolute value of the amplitude of the incident bounded inhomogeneous beam profile (top) and its infinite inhomogeneous waves building blocks (bottom). Dotted line: absolute value of the amplitude of the reflected bounded inhomogeneous beam profile (top) and its reflected infinite inhomogeneous waves building blocks (bottom). Inhomogeneity: 311.56/m. Angle of incidence: 42° (in the neighborhood of the Rayleigh angle). It is seen that both the infinite and the bounded inhomogeneous wave are displaced by a distance *d*.

$W=0.01$ m. It is seen from Fig. 5 that the upper part of profile (11) can almost perfectly be approximated using one single inhomogeneous wave, having in this case an inhomogeneity $\beta=125/m$. This is as expected, since the profile (11) was made to locally represent an infinite inhomogeneous wave. If we need to approximate the complete profile (11), additional infinite inhomogeneous plane waves will be involved. In order to explain the behavior of a bounded inhomogeneous wave in the experiments cited above, we need to investigate the influence of the additional infinite inhomogeneous waves in the upper part of the bounded profile (11).

In Fig. 6, we have added each of the N terms in the summation (17) for $N=31$ and for $\beta_{\max}=3750/m$. The upper exponential is again the one for $\beta=125/m$. It is clear that this infinite inhomogeneous plane wave still dominates the upper part, i.e., for higher x values, of the bounded inhomogeneous wave (11). All other inhomogeneous waves dominate in the lower parts, i.e., for x values near zero, of the profile. That can explain why a bounded inhomogeneous wave in experiments behaves almost exactly (if the part of the beam near $X=0$ is not considered) as if it was an infinite inhomogeneous wave.

Next, in Fig. 7, all 31 inhomogeneous waves are summed to form the dashed line which is an approximation of the exact bounded inhomogeneous wave (solid line). A considerable deviation occurs near the origin, as explained above.

VI. THE SCATTERING OF BOUNDED INHOMOGENEOUS WAVES

A. Theoretical development

We will now examine, by means of a numerical example, how a bounded inhomogeneous wave behaves during scattering at an interface between a liquid and an isotropic solid. We therefore highlight each individual incident infinite inhomogeneous wave and describe how it interacts with the interface.

Taking into account the generalized Snell–Descartes law (i.e., $k_x=k_x^{\text{inc}}$), we denote the potential for the incoming wave by

$$\varphi^{\text{inc}}=\exp i(k_x^{\text{inc}}x+k_z^{\text{inc}}z), \tag{18}$$

for the reflected wave by

$$\varphi^{r}=R\exp i(k_x^{\text{inc}}x+k_z^{r}z), \tag{19}$$

for the transmitted longitudinal wave by

$$\varphi^{t}=T_d\exp i(k_x^{\text{inc}}x+k_z^{td}z), \tag{20}$$

and for the transmitted shear wave by

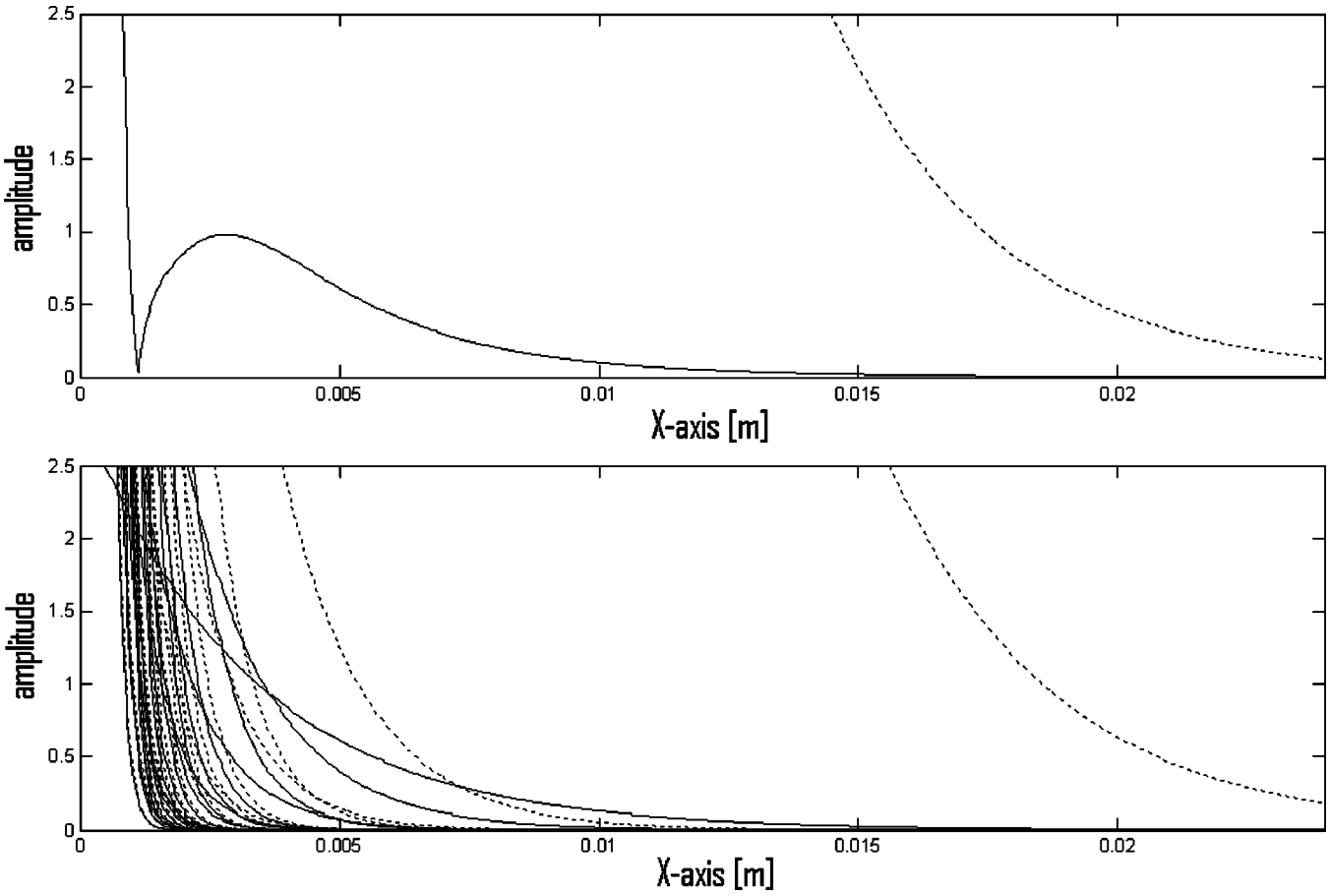

FIG. 10. Solid line: absolute value of the amplitude of the incident bounded inhomogeneous beam profile (top) and its infinite inhomogeneous waves building blocks (bottom). Dotted line: absolute value of the amplitude of the reflected bounded inhomogeneous beam profile (top) and its reflected infinite inhomogeneous waves building blocks (bottom). Inhomogeneity: 311.56/m. Angle of incidence: 44.045° (exactly the Rayleigh angle).

$$\boldsymbol{\psi}^t = T_s \exp i(k_x^{\text{inc}} x + k_z^{ts} z)\mathbf{e}_y \tag{21}$$

where R is the reflection coefficient, T_d is the transmission coefficient for longitudinal waves and T_s is the transmission coefficient for shear waves. All wave vectors involved in (18)–(21) are supposed to be complex valued; cf. (3). Again we note that the sign of β is opposite to the one in Ref. 5, however, this is no problem because all the physics in the current paper is expressed in terms of $\mathbf{k}_1$ and $\mathbf{k}_2$ immediately. Taking into account (13), and taking into account the dispersion relation for inhomogeneous waves (2), we have

$$\begin{bmatrix} k_x^{\text{inc}} \\ k_z^{\text{inc}} \end{bmatrix} = \begin{bmatrix} \cos\theta^{\text{inc}} & \sin\theta^{\text{inc}} \\ -\sin\theta^{\text{inc}} & \cos\theta^{\text{inc}} \end{bmatrix} \begin{bmatrix} i\beta^{\text{inc}} \\ \sqrt{(\omega/\nu + i\alpha_0)^2 - (\beta^{\text{inc}})^2} \end{bmatrix} \tag{22}$$

and

$$k_z^r = \sqrt{(\omega/\nu + i\alpha_0)^2 - (k_x^{\text{inc}})^2}, \tag{23}$$

$$k_z^{td} = \sqrt{(\omega/\nu_d + i\alpha_{0d})^2 - (k_x^{\text{inc}})^2}, \tag{24}$$

$$k_z^{ts} = \sqrt{(\omega/\nu_s + i\alpha_{0s})^2 - (k_x^{\text{inc}})^2}. \tag{25}$$

In (22)–(25), ν is the wave velocity in the liquid, and ν_d and ν_s are the longitudinal, respectively, shear wave velocities in the solid.

The intrinsic damping coefficients in the liquid for longitudinal waves, respectively, in the solid for longitudinal and shear homogeneous plane waves are denoted by α_0, α_{0d}, and α_{0s}. For simplicity, we will suppose that there is no damping involved in our calculations.

We then develop the continuity conditions along the interface for normal displacements,

$$u_z^{\text{liquid}} = u_z^{\text{solid}}, \tag{26}$$

and for normal stress,

$$T_{p3}^{\text{liquid}} = T_{p3}^{\text{solid}}, \tag{27}$$

with

$$\mathbf{u}^{\text{liquid}} = \boldsymbol{\nabla}(\varphi^{\text{inc}} + \varphi^r), \tag{28}$$

$$\mathbf{u}^{\text{solid}} = \boldsymbol{\nabla}(\varphi^t) + \boldsymbol{\nabla} \times \boldsymbol{\psi}^t, \tag{29}$$

and

$$T_{pj}^q = \delta_{pj} \tilde{\lambda}^q \varepsilon_{rr}^q + 2\tilde{\mu}^q \varepsilon_{pj}^q, \tag{30}$$

in which we have used the Einstein double suffix notation convention, $q=1$ for the liquid and $q=2$ for the solid, and

$$\tilde{\lambda}^q = \lambda^q + i\omega\lambda'^q = \rho(\tilde{\nu}_d)^2, \tag{31}$$

$$\tilde{\mu}^q = \mu^q + i\omega\mu'^q = \rho\frac{(\tilde{\nu}_s)^2 - (\tilde{\nu}_d)^2}{2}, \tag{32}$$

$$\varepsilon_{kl}^{q}=\frac{1}{2}[\partial_l u_k^q+\partial_k u_l^q]. \tag{33}$$

The Lamé constants are denoted by λ and μ, while the viscoelastic damping coefficients are given by λ' and μ'. The definition of the "complex velocity $\tilde{\nu}$" is found in (2), for the appropriate choice of shear or longitudinal wave material properties.

By applying the continuity conditions (26) and (27), we obtain

$$\begin{bmatrix} RD \\ T_D \\ T_S \end{bmatrix} = \begin{bmatrix} k_z^r & -k_z^{td} & -k_x^{\mathrm{inc}} \\ 0 & -2k_z^{td}k_x^{\mathrm{inc}} & \left(\dfrac{\omega}{\nu_s}+i\alpha_{0s}\right)^2-2(k_x^{\mathrm{inc}})^2 \\ -\tilde{\lambda}^1\left(\dfrac{\omega}{\nu}+i\alpha_0\right)^2 & \tilde{\lambda}^2\left(\dfrac{\omega}{\nu_d}+i\alpha_{0d}\right)^2+2\tilde{\mu}^2(k_z^{td})^2 & 2\tilde{\mu}^2k_z^{ts}k_x^{\mathrm{inc}} \end{bmatrix}^{-1} \begin{bmatrix} -k_z^{\mathrm{inc}} \\ \tilde{\lambda}^1\left(\dfrac{\omega}{\nu}+i\alpha_0\right)^2 \end{bmatrix}. \tag{34}$$

Remember that in order to obtain (34), we have incorporated the dispersion relation for inhomogeneous waves. Solving (34) requires proper choices of the signs of the z components of the wave vector. The latter can be found in the literature[6] and is outlined in terms of $\mathbf{k}_1$ and $\mathbf{k}_2$, i.e., independent of the choice of the sign of β in (4), as follows. The bulk critical angle for transmitted waves of type c ($c=s$ for shear, $c=d$ for longitudinal) is given by

$$\theta^c=\arcsin\frac{\nu}{\nu_c}. \tag{35}$$

Whenever $\theta^{\mathrm{inc}}<\theta^c$, $\mathbf{k}_1$, for that particular transmitted mode must point into the solid, which corresponds to the classical Sommerfeld conditions. Whenever $\theta^{\mathrm{inc}}\geqslant\theta^c$, $\mathbf{k}_2$, for that particular transmitted mode must point into the solid. For the reflected wave, it is always so that $\mathbf{k}_1$ must point into the liquid.

B. Numerical results

We consider a water/brass interface with $\nu=1480$ m/s, $\nu_d=4840$ m/s, $\nu_s=2270$ m/s, $\rho_l=1000$ kg/m^3, $\rho_s=8100$ kg/m^3.

ρ_l, respectively, ρ_s are the densities of the liquid and the solid and are needed for the determination of the Lamé constants when applying the dispersion relation for inhomogeneous waves (2).

We know from calculations of the reflection coefficient by means of (34), involving inhomogeneous waves, that for 5 MHz, a Rayleigh wave is stimulated when $\theta^{\mathrm{inc}}=44.045°$ and $\beta^{\mathrm{inc}}=311.56$/m, corresponding to the so called Rayleigh pole.

We thus consider a bounded inhomogeneous wave, having a Rayleigh wave stimulating inhomogeneity, i.e., $\beta=311.56/\mathrm{m}\Leftrightarrow W=0.004$ m. We calculate the reflected profiles for different angles of incidence. All calculations are performed for $\beta_{\max}=6231.2$ and for 21 inhomogeneous waves with equidistant inhomogeneity coefficients $\beta\in[0,\beta_{\max}]$. In Fig. 8, the angle of incidence θ^{inc} is 30°. This angle is far less than the Rayleigh angle. We notice that each infinite inhomogeneous wave by which the bounded inhomogeneous wave is built up, is shifted very little and so is the bounded inhomogeneous wave. In Fig. 9, the angle of incidence $\theta^{\mathrm{inc}}=42°$, which is in the vicinity of the Rayleigh angle. We notice that the bounded inhomogeneous wave is shifted along the x-axis, by the same amount as its infinite inhomogeneous counterpart. At last, in Fig. 10 we have taken the exact Rayleigh angle of incidence $\theta^{\mathrm{inc}}=44.045°$. We observe that both the bounded inhomogeneous wave and its infinite counterpart are shifted by almost the same distance along the interface. We must stress, however, that Figs. 5–10 cannot be used to check energy conservation, but solely to check displacement. The reason for that is the fact that the bounded inhomogeneous wave is written as a finite sum over a finite inhomogeneity interval. This causes deviations near $x=0$, therefore energy conservation cannot be checked. It is impossible to use the exact integral expression (13) without encountering numerical problems, otherwise such calculations would undoubtedly better involve the conservation of energy and hence limit the calculated intensities of the dotted line near $x=0$ in Fig. 10.

In contrast to bounded Gaussian beams, a bounded inhomogeneous wave does not cause a null zone or other peculiarities due to the Schoch effect. Hence nondestructive testing of materials using bounded inhomogeneous waves is quite different from the use of other types of bounded beams.

VII. CONCLUSIONS

We have presented the Laplace transform as a tool for analytically determining the unknown coefficients in the infinite inhomogeneous plane wave decomposition of a bounded inhomogeneous wave. We have also shown that it is understood from a theoretical point of view why in experiments bounded inhomogeneous waves behave almost as if they were infinitely extended. As an example, we have exposed how a bounded inhomogeneous wave is deformed after interaction with a water/brass interface and have verified that it is shifted in space by the same amount as its infinite inhomogeneous counterpart. This shift which is not really accompanied by a deformation is typical for bounded as well as for infinite inhomogeneous waves and differs much from strong deformations such as the well known Schoch effect for Gaussian beams.

ACKNOWLEDGMENTS

The authors are indebted to ''The Flemish Institute for the Encouragement of the Scientific and Technological Research in Industry (I.W.T.)'' for research support and to acknowledge the constructive suggestions and comments of the reviewers.

[1] B. Poirée, ''Plane evanescent waves in ideal liquids and elastic solids,'' J. Acoust. **2**, 205–216 (1989).
[2] M. Deschamps, ''The plane heterogeneous wave and its applications in linear acoustics,'' J. Acoust. **4**, 269–305 (1991).
[3] B. Poirée, ''Complex harmonic waves,'' *Physical Acoustics*, edited by O. Leroy and M. A. Breazeale (Plenum, New York, 1991), pp. 99–117.
[4] G. Quentin, A. Derem, and B. Poirée, ''The formalism of evanescent plane waves and its importance in the study of the generalized Rayleigh wave,'' J. Acoust. **3**, 321–336 (1990).
[5] J. M. Claeys and O. Leroy, ''Reflection and transmission of bounded sound beams on half spaces and through plates,'' J. Acoust. Soc. Am. **72**, 585–590 (1982).
[6] K. Van Den Abeele and O. Leroy, ''Complex harmonic wave scattering as the framework for investigation of bounded beam reflection and transmission at plane interfaces and its importance in the study of vibrational modes,'' J. Acoust. Soc. Am. **93**, 308–323 (1993).
[7] K. Van Den Abeele and O. Leroy, ''On the influence of frequency and width of an ultrasonic bounded beam in the investigation of materials: Study in terms of heterogeneous plane waves,'' J. Acoust. Soc. Am. **93**, 2688–2699 (1993).
[8] M. Deschamps and B. Hosten, ''The generation of bulk heterogeneous waves in a non-absorbing liquid,'' Acustica **68**, 92–95 (1989).
[9] W. Huang, R. Briers, S. I. Rokhlin, and O. Leroy, ''Experimental study of inhomogeneous wave reflection from a solid-air periodically rough boundary using leaky Rayleigh waves,'' J. Acoust. Soc. Am. **96**, 363–369 (1994).
[10] M. Deschamps, ''Reflection and refraction of the evanescent plane wave on plane interfaces,'' J. Acoust. Soc. Am. **96**, 2841–2848 (1994).
[11] R. Briers, O. Leroy, O. Poncelet, and M. Deschamps, ''Experimental verification of the calculated diffraction field generated by inhomogeneous waves obliquely incident on a periodically rough liquid-solid boundary,'' J. Acoust. Soc. Am. **106**, 682–687 (1999).
[12] N. F. Declercq, J. Degrieck, R. Briers, and O. Leroy, ''Theoretical verification of the backward displacement of waves reflected from an interface having superimposed periodicity,'' Appl. Phys. Lett. **82**, 2533–2534 (2003).
[13] N. F. Declercq, J. Degrieck, R. Briers, and O. Leroy, ''A theoretical treatment of the backward beam displacement on periodically corrugated surfaces and its relation to leaky Scholte–Stoneley waves,'' submitted elsewhere.
[14] N. F. Declercq, J. Degrieck, R. Briers, and O. Leroy, ''A theoretical elucidation for the experimentally observed backward displacement of waves reflected from an interface having superimposed periodicity,'' J. Acoust. Soc. Am. **112**, 2414 (2002).
[15] A. A. Teklu and M. A. Breazeale, ''Backward displacement of ultrasonic waves reflected from a corrugated interface,'' J. Acoust. Soc. Am. **113**, 2283–2284 (2003).

Ultrasonic wave propagation in human cancellous bone: Application of Biot theory

Z. E. A. Fellah[a] and J. Y. Chapelon
National Institute of Health and Medical Research (INSERM U556), 151 cours Albert Thomas, 69424 Lyon Cedex 03, France

S. Berger and W. Lauriks
Laboratorium voor Akoestiek en Thermische Fysica, Katholieke Universiteit Leuven, Celestijnenlaan 200 D, B-3001 Heverlee, Belgium

C. Depollier
Laboratoire d'Acoustique de l'Université du Maine, UMR-CNRS 6613, Université du Maine, Avenue Olivier Messiaen 72085 Le Mans Cedex 09, France

(Received 22 March 2003; revised 24 March 2003; accepted 31 March 2004)

Ultrasonic wave propagation in human cancellous bone is considered. Reflection and transmission coefficients are derived for a slab of cancellous bone having an elastic frame using Biot's theory modified by the model of Johnson *et al.* [J. Fluid Mech. **176**, 379–402 (1987)] for viscous exchange between fluid and structure. Numerical simulations of transmitted waves in the time domain are worked out by varying the modified Biot parameters. The variation is applied to the governing parameters and is about 20%. From this study, we can gain an insight into the sensitivity of each physical parameter used in this theory. Some parameters play an important role in slow-wave wave form, such as the viscous characteristic length Λ and pore fluid bulk modulus K_f. However, other parameters play an important role in the fast-wave wave form, such as solid density ρ_s and shear modulus N. We also note from these simulations that some parameters such as porosity ϕ, tortuosity α_∞, thickness, solid bulk modulus K_s, and skeletal compressibility frame K_b, play an important role simultaneously in both fast and slow wave forms compared to other parameters which act on the wave form of just one of the two waves. The sensitivity of the modified Biot parameters with respect to the transmitted wave depends strongly on the coupling between the solid and fluid phases of the cancellous bone. Experimental results for slow and fast waves transmitted through human cancellous bone samples are given and compared with theoretical predictions. [DOI: 10.1121/1.1755239]

PACS numbers: 43.20.Bi, 43.20.Hq, 43.20.Jr, 43.80.Cs [ANN] Pages: 61–73

I. INTRODUCTION

Bone occurs in two forms: as a dense solid (compact bone) and as a porous network of connecting rods or plates (cancellous bone). The most obvious difference between these two types of bone is their relative density, or volume fraction of solids. Bone with a volume fraction of solids below 70% is classified as cancellous, and over 70% is compact. Cancellous bone is a dual-component material of high porosity. The calcified bone itself forms the matrix and fatty marrow is located in the pores. The calcified matrix builds up along stress lines and forms a three-dimensional pattern typical of the site in the skeleton.

Osteoporosis is a disease caused by biochemical and hormonal changes, affecting the equilibrium between the resorption and deposition of new bony tissue. It leads to modification of the structure (porosity and thickness of trabeculae) and composition (mineral density) of this material. There has been much discussion on changes in trabecular pattern due to osteoporosis, but general indications are that the trabeculae grow thinner, possibly disappearing, and are therefore more widely spaced.[1] Early clinical detection of this pathology via ultrasonic characterization would be of fundamental interest.

The mechanical behavior of cellular materials can be modeled by idealizing the observed structure,[2] characterizing the cell wall properties, and analyzing the mechanisms by which cells deform. Cancellous bone has a cellular structure and develops four types of structure. At low relative densities, it is made up of a network of rod-like elements which form open cells. At higher densities it is made up of a network of plate-like elements forming closed cells. Under asymmetric loading conditions, bone develops an asymmetric geometry. But when loading is largely uniaxial, as in some parts of the vertebrae for example, the structure can develop cylindrical symmetry. Gibson[2] shows that there are four resulting structures then: open and closed celled asymmetric, and open and closed celled columnar. Each of these structures can be modeled using an open or closed cubic or hexagonal array of beam or plate-like elements. The geometries chosen for the models[2] are all simple and highly idealized, and so geometric properties, such as anisotropy in asymmetric cancellous bone, are poorly modeled.

Ultrasound can be used to characterize the elastic prop-

[a]Electronic mail: fellah@lyon.inserm.fr

erties of both cortical and cancellous bone. Fry and Barger[3] considered both types of bone when investigating the human skull while Ashman *et al.*[4,5] used ultrasound to measure the elastic properties of cancellous bone.

One particular ultrasonic technique involves the frequency dependence of ultrasonic attenuation in cancellous bone.[6] This method is often referred to as broadband ultrasonic attenuation (BUA) and measures the frequency dependence of ultrasonic attenuation over a range from 200 kHz to 1 MHz. The assumption is made that attenuation $a(f)$ is a linear function of frequency $a(f)=(\mathrm{BUA})f+K$, with K a constant. The term BUA is the gradient in dB/MHz, evaluated by linear regression. Langton[6] found that the BUA value of the spectrum was significantly lower in older women with osteoporotic fractures compared with young normals, a finding confirmed by later studies. Despite the fact that this technique, based on a linear relationship of the attenuation, does not have any physical basis, it is widely accepted that the BUA gradient is relevant to the study of osteoporosis. Bone condition is also assessed using the speed of sound (SOS) at the frequencies used for BUA. The measurement is based on simply evaluating the difference in transient time over the distance between the transducers with and without the bone in place. Hence it is a group velocity. To determine the bone condition of a patient, measurements of BUA and SOS are compared with those values expected in a young normal range. Of the two parameters, BUA is a better detector than SOS of changes in bone tissue, and has become the principal index in quantitative ultrasonography.

Since trabecular bone is an inhomogeneous porous medium, the interaction between ultrasound and bone will be highly complex. Modeling ultrasonic propagation through trabecular tissue has been considered using porous media theories, such as Biot's theory.[7,8]

The Biot theory is an established way of predicting ultrasonic propagation in an inhomogeneous material and was originally applied to fluid saturated porous rocks for geophysical testing. The Biot model treats both individual and coupled behavior of the frame and pore fluid. Energy loss is considered to be caused by the viscosity of the pore fluid as it moves relative to the frame. The model predicts that sound velocity and attenuation in a two phase media will depend on frequency, the elastic properties of the constituting materials, porosity, permeability, tortuosity, and effective stress. This method should allow us to relate the physical parameters of our phantom to ultrasonic velocity and attenuation.

Applications of Biot's theory to trabecular bone have enjoyed varying degrees of success.[9–15] The theory predicts two compressional waves: a fast wave, where the fluid (blood and marrow) and solid (calcified tissue) move in phase, and a slow wave where fluid and solid move out of phase. Fast and slow waves were identified independently in bovine trabecular bone in the late 1990s by Hosokawa and Otani.[14,15]

In 1987, a substantial contribution was made by Johnson *et al.*[16] with their theory of dynamic fluid flow (i.e., as a function of frequency) in porous media, introducing the concept of dynamic tortuosity and permeability and viscous characteristic length. Originally, the research was mainly oriented on geophysical and petroleum industry applications. The Johnson *et al.* model was used for different kinds of porous materials.[11,16–21]

One important assumption of the Biot theory is that the wavelength must be large compared with the dimensions of a macroscopic elementary volume. This volume has well-defined properties, such as porosity, permeability, and elastic moduli, which are representative of the medium. Scattering effects are thus neglected. However when the sizes or features of the trabecular bone are close to the wavelength, scattering effects must be taken into account.[22–24] This alternative method of predicting ultrasonic propagation in a porous material will consider that the inhomogeneous medium scatters the incident field, the total field being the sum of all contributions from the scattering matrix. The phantom can be modeled by considering the scattering to be either single or multiple depending on the geometry of the scatterers and the properties of the constituent materials.

The purpose of this article is to calculate analytically the reflection and transmission coefficients in the frequency domain using the Biot model modified by Johnson *et al.*[16] Numerical simulations of transmitted waves in the time domain are worked out by means of a variation in the parameters of a porous medium. The variation is applied to the governing parameters and is 20%; the sensitivity of each parameter is studied. Experimental results for fast and slow waves transmitted through samples of human cancellous bone are given and finally, a comparison with theoretical predictions is made.

II. MODEL

The equations of motion for the frame and fluid are given by the Euler equations applied to Lagrangian density. To take into account the effects due to relative motion between solid and fluid, a drag force derived from the dissipation function $D=b/2\|\partial\mathbf{u}/\partial t-\partial\mathbf{U}/\partial t\|^2$ is introduced. Here $\mathbf{u}$ and $\mathbf{U}$ are the displacements of the solid and fluid phases. When the fluid flow $\mathbf{u}-\mathbf{U}$ relative to the solid is of the Poiseuille type, b is a constant (drag coefficient) related to fluid viscosity η and the permeability of the porous material k_0, $b=\eta\phi^2/k_0$. This assumption restricts the validity of the model to the low frequency range ($f<\eta\pi/4\rho_0 d^2$ where d is the diameter of the pore). In this case, the equations of motion can be written in the following form:

$$\tilde{\rho}_{11}\frac{\partial^2\mathbf{u}}{\partial t^2}+\tilde{\rho}_{12}\frac{\partial^2\mathbf{U}}{\partial t^2}=P\boldsymbol{\nabla}\cdot(\boldsymbol{\nabla}\cdot\mathbf{u})+Q\boldsymbol{\nabla}(\boldsymbol{\nabla}\cdot\mathbf{U})-N\boldsymbol{\nabla}\wedge(\boldsymbol{\nabla}\wedge\mathbf{u}), \tag{1}$$

$$\tilde{\rho}_{12}\frac{\partial^2\mathbf{u}}{\partial t^2}+\tilde{\rho}_{22}\frac{\partial^2\mathbf{U}}{\partial t^2}=Q\boldsymbol{\nabla}(\boldsymbol{\nabla}\cdot\mathbf{u})+R\boldsymbol{\nabla}(\boldsymbol{\nabla}\cdot\mathbf{U}). \tag{2}$$

In these equations, P, Q, and R are generalized elastic constants which are related, via gedanken experiments, to other, measurable quantities, namely ϕ (porosity), K_f (bulk modulus of the pore fluid), K_s (bulk modulus of the elastic solid) and K_b (bulk modulus of the porous skeletal frame). N is the shear modulus of the composite as well as that of the skeletal

frame. The equations which explicitly relate P, Q, and R to ϕ, K_f, K_s, K_b, and N are given by

$$P=\frac{(1-\phi)\left(1-\phi-\frac{K_b}{K_s}\right)K_s+\phi\frac{K_s}{K_f}K_b}{1-\phi-\frac{K_b}{K_s}+\phi\frac{K_s}{K_f}}+\frac{4}{3}N,$$

$$Q=\frac{\left(1-\phi-\frac{K_b}{K_s}\right)\phi K_s}{1-\phi-\frac{K_b}{K_s}+\phi\frac{K_s}{K_f}},\quad R=\frac{\phi^2K_s}{1-\phi-\frac{K_b}{K_s}+\phi\frac{K_s}{K_f}}.$$

The Biot coefficients, $\tilde{\rho}_{mn}=\rho_{mn}+(-)^{m+n}b/j\omega$ where $\omega=2\pi f$ is the angular frequency of motion and ρ_{mn} are the "mass coefficients" which are related to the densities of solid (ρ_s) and fluid (ρ_f) phases by $\rho_{11}+\rho_{12}=(1-\phi)\rho_s$ and $\rho_{12}+\rho_{22}=\phi\rho_f$. The coefficient ρ_{12} represents the mass coupling parameter between the fluid and solid phases and is always negative $\rho_{12}=-\phi\rho_f(\alpha-1)$, α being the tortuosity of the medium. If the dynamic tortuosity $\alpha(\omega)$ is defined by $\alpha(\omega)=\alpha-jb\phi/\omega\rho_f$, mass and viscous couplings appear in the same function, and $\tilde{\rho}_{mn}=\rho_{mn}$ when $\alpha(\omega)$ is used in place of α.

A. The modified Biot theory

To extend his theory to a high-frequency range, Biot[7,8] multiplied the drag coefficient b by a frequency correction factor which represents deviation from Poiseuille friction as frequency increases. This correction is in fact a modification in fluid density through the tortuosity factor α. Fluid density is hence renormalized by the viscous exchange between fluid and structure. Unfortunately, in the case of materials with noncylindrical pores the Biot correction factor is generally not valid.[16]

The correction factor is given by the dynamic tortuosity $\alpha(\omega)$ in the following form: $\rho_f\rightarrow\rho_f\alpha(\omega)$. Its theoretical expression is

$$\alpha(\omega)=\alpha_\infty\left(1+\frac{\eta\phi}{j\omega\alpha_\infty\rho_fk_0}\sqrt{1+j\frac{4\alpha_\infty^2k_0^2\rho_f\omega}{\eta\Lambda^2\phi^2}}\right),\qquad(3)$$

where α_∞ is the tortuosity, and Λ the viscous characteristic length.[16] The function $\alpha(\omega)$ expresses the viscous exchanges between the fluid and the structure which plays an important role in damping the acoustic wave in porous material.

The parts of the fluid affected by this exchange can be estimated by the ratio of a microscopic characteristic length of the medium, for example pore sizes, to the viscous skin depth thickness $\delta=(2\eta/\omega\rho_0)^{1/2}$. This domain corresponds to the region of the fluid in which velocity distribution is disturbed by the frictional forces at the interface between the fluid and the frame. With this modification, the coefficients of the equations of motion are now frequency-dependent.

At high frequencies, viscous skin thickness is very thin. The viscous effects, which are concentrated in a small volume near the surface of the frame $\delta/r\ll1$, can be neglected. The fluid then behaves almost like a perfect fluid (without viscosity). The high frequency approximation of the $\alpha(\omega)$ function is given by[16]

$$\alpha(\omega)=\alpha_\infty\left(1+\frac{2}{\Lambda}\left(\frac{\eta}{j\omega\rho_f}\right)^{1/2}\right).\qquad(4)$$

When $\alpha(\omega)$ is used instead of α in Eqs. (1) and (2), the equations of motion (1) and (2) will be written as[25]

$$\tilde{\rho}_{11}(\omega)\frac{\partial^2\mathbf{u}}{\partial t^2}+\tilde{\rho}_{12}(\omega)\frac{\partial^2\mathbf{U}}{\partial t^2}=P\boldsymbol{\nabla}\cdot(\boldsymbol{\nabla}\cdot\mathbf{u})+Q\boldsymbol{\nabla}(\boldsymbol{\nabla}\cdot\mathbf{U})-N\boldsymbol{\nabla}\wedge(\boldsymbol{\nabla}\wedge\mathbf{u}),\qquad(5)$$

$$\tilde{\rho}_{12}(\omega)\frac{\partial^2\mathbf{u}}{\partial t^2}+\tilde{\rho}_{22}(\omega)\frac{\partial^2\mathbf{U}}{\partial t^2}=Q\boldsymbol{\nabla}(\boldsymbol{\nabla}\cdot\mathbf{u})+R\boldsymbol{\nabla}(\boldsymbol{\nabla}\cdot\mathbf{U}),\qquad(6)$$

where the frequency coefficients $\tilde{\rho}_{11}(\omega)$, $\tilde{\rho}_{12}(\omega)$, and $\tilde{\rho}_{22}(\omega)$ are given by

$$\tilde{\rho}_{11}(\omega)=\rho_{11}+\frac{2\phi\alpha_\infty}{\Lambda}\left(\frac{\rho_f\eta}{j\omega}\right)^{1/2},$$

$$\tilde{\rho}_{12}(\omega)=\rho_{12}-\frac{2\phi\alpha_\infty}{\Lambda}\left(\frac{\rho_f\eta}{j\omega}\right)^{1/2},$$

$$\tilde{\rho}_{22}(\omega)=\rho_{22}+\frac{2\phi\alpha_\infty}{\Lambda}\left(\frac{\rho_f\eta}{j\omega}\right)^{1/2}.$$

B. Longitudinal waves

As in the case of an elastic solid, the wave equations of dilatational and rotational waves can be obtained using scalar and vector displacement potentials, respectively. Two scalar potentials for the frame and the fluid, $\widetilde{\Phi_s}$ and $\widetilde{\Phi_f}$, are defined for compressional waves giving

$$\mathbf{u}=\boldsymbol{\nabla}\widetilde{\Phi_s},\quad \mathbf{U}=\boldsymbol{\nabla}\widetilde{\Phi_f}.$$

Equations (5) and (6) become, in the frequency domain,

$$\Delta\begin{pmatrix}\Phi_s\\ \Phi_f\end{pmatrix}=M\begin{pmatrix}\Phi_s\\ \Phi_f\end{pmatrix},\qquad(7)$$

where Δ is the Laplacian, Φ_s and Φ_f are the Fourier transforms of $\widetilde{\Phi_s}$ and $\widetilde{\Phi_f}$, we note $\Phi_s(\omega)$ the Fourier transform of $\widetilde{\Phi_s}(t)$ defined by

$$\Phi_s(\omega)=\mathcal{L}[\widetilde{\Phi_s}(t)]=\int_{-\infty}^{\infty}\exp(-j\omega t)\widetilde{\Phi_s}(t)dt,\qquad(8)$$

the matrix M is given by

$$M=\begin{pmatrix} -(R'\rho_{11}-Q'\rho_{12})\omega^2+A(j\omega)^{3/2}(R'+Q') & -(R'\rho_{12}-Q'\rho_{22})\omega^2-A(j\omega)^{3/2}(R'+Q') \\ -(P'\rho_{12}-Q'\rho_{11})\omega^2-A(j\omega)^{3/2}(P'+Q') & -(P'\rho_{22}-Q'\rho_{12})\omega^2+A(j\omega)^{3/2}(P'+Q'), \end{pmatrix} \tag{9}$$

with

$$A=2\frac{\phi\alpha_\infty}{\Lambda}\sqrt{\eta\rho_f}, \quad \text{and} \quad \begin{pmatrix} R' & -Q' \\ -Q' & P' \end{pmatrix}=\begin{pmatrix} P & Q \\ Q & R \end{pmatrix}^{-1}. \tag{10}$$

Coefficients R', P', and Q' are given by

$$R'=\frac{R}{PR-Q^2}, \quad Q'=\frac{Q}{PR-Q^2}, \quad P'=\frac{P}{PR-Q^2}.$$

The result of solving this system of equations is that there are two distinct longitudinal modes which are called fast and slow. The system (7) can be written on a basis of fast and slow waves Φ_1 and Φ_2, respectively, by

$$\Delta\begin{pmatrix}\Phi_1\\ \Phi_2\end{pmatrix}=\begin{pmatrix}\lambda_1(\omega) & 0\\ 0 & \lambda_2(\omega)\end{pmatrix}\begin{pmatrix}\Phi_1\\ \Phi_2\end{pmatrix}, \tag{11}$$

where $\lambda_1(\omega)$ and $\lambda_1(\omega)$ are frequency coefficients given the eigenvalues of the system (7). Their expressions are

$$\lambda_1=\frac{\mathrm{tr}(M)-\sqrt{\mathrm{tr}^2(M)-4\det(M)}}{2},$$

$$\lambda_2=\frac{\mathrm{tr}(M)+\sqrt{\mathrm{tr}^2(M)-4\det(M)}}{2},$$

where $\mathrm{tr}(M)$ and $\det(M)$ are the trace and determinant of the matrix M, respectively,

$$\mathrm{tr}(M)=-(R'\rho_{11}+P'\rho_{22}-2Q'\rho_{12})\omega^2+A(P'+R'+2Q')(j\omega)^{3/2},$$

$$\det(M)=(P'R'-Q'^2)[(\rho_{11}\rho_{22}-\rho_{12}^2)\omega^4+A(\rho_{11}+\rho_{22}-2\rho_{12})(j\omega)^{7/2}].$$

The eigenvalues $\lambda_1(\omega)$ and $\lambda_2(\omega)$ are the squared complex wave numbers of the two compressional waves and are given by

$$\lambda_1(\omega)=\tfrac{1}{2}(-\tau_1\omega^2+\tau_2(j\omega)^{3/2}-\sqrt{(\tau_1^2-4\tau_3)\omega^4+2(\tau_1\tau_2-2\tau_4)(j\omega)^{7/2}+\tau_2^2(j\omega)^3}),$$

$$\lambda_2(\omega)=\tfrac{1}{2}(-\tau_1\omega^2+\tau_2(j\omega)^{3/2}+\sqrt{(\tau_1^2-4\tau_3)\omega^4+2(\tau_1\tau_2-2\tau_4)(j\omega)^{7/2}+\tau_2^2(j\omega)^3}),$$

which can be written in this frequency domain

$$\lambda_1(\omega)=-\frac{1}{2}(\tau_1-\sqrt{\tau_1^2-4\tau_3})\omega^2+\frac{1}{2}\left(\tau_2-\frac{\tau_1\tau_2-2\tau_4}{\sqrt{\tau_1^2-4\tau_3}}\right)\times(j\omega)^{3/2}-\frac{1}{4}\left(\frac{\tau_2^2}{\sqrt{\tau_1^2-4\tau_3}}-\frac{(\tau_1\tau_2-2\tau_4)^2}{2(\tau_1^2-4\tau_3)^{3/2}}\right)j\omega,$$

$$\lambda_2(\omega)=-\frac{1}{2}(\tau_1+\sqrt{\tau_1^2-4\tau_3})\omega^2+\frac{1}{2}\left(\tau_2+\frac{\tau_1\tau_2-2\tau_4}{\sqrt{\tau_1^2-4\tau_3}}\right)\times(j\omega)^{3/2}+\frac{1}{4}\left(\frac{\tau_2^2}{\sqrt{\tau_1^2-4\tau_3}}-\frac{(\tau_1\tau_2-2\tau_4)^2}{2(\tau_1^2-4\tau_3)^{3/2}}\right)j\omega,$$

with

$$\tau_1=R'\rho_{11}+P'\rho_{22}-2Q'\rho_{12},$$

$$\tau_2=A(P'+R'+2Q'),$$

$$\tau_3=(P'R'-Q'^2)(\rho_{11}\rho_{22}-\rho_{12}^2),$$

$$\tau_4=A(P'R'-Q'^2)(\rho_{11}+\rho_{22}-2\rho_{12}).$$

For wave propagation along the x axis, the solutions for Eq. (7) are given by

$$\Phi_1(x,\omega)=\overline{\Phi}_1(\omega)e^{-x\sqrt{\lambda_1(\omega)}}+\overline{\Phi}_1'(\omega)e^{x\sqrt{\lambda_1(\omega)}}, \tag{12}$$

$$\Phi_2(x,\omega)=\overline{\Phi}_2(\omega)e^{-x\sqrt{\lambda_2(\omega)}}+\overline{\Phi}_2'(\omega)e^{x\sqrt{\lambda_2(\omega)}}, \tag{13}$$

the functions $\overline{\Phi}_1(\omega)$, $\overline{\Phi}_1'(\omega)$, $\overline{\Phi}_2(\omega)$, and $\overline{\Phi}_2'(\omega)$ can be determined by the boundary conditions at the porous medium interfaces.

The eigenvectors $(1,\mathfrak{I}_1(\omega))$, et $(1,\mathfrak{I}_2(\omega))$ associated with the eigenvalues $\lambda_1(\omega)$ and $\lambda_2(\omega)$ link the fluid and solid potentials Φ_s and Φ_f, respectively, to the fast and slow waves Φ_1 and Φ_2 through the following relation:

$$\begin{pmatrix}\Phi_s\\ \Phi_f\end{pmatrix}=\begin{pmatrix}1 & 1\\ \mathfrak{I}_1(\omega) & \mathfrak{I}_2(\omega)\end{pmatrix}\begin{pmatrix}\Phi_1\\ \Phi_2\end{pmatrix}, \tag{14}$$

the eigenvectors $\mathfrak{I}_1(\omega)$ and $\mathfrak{I}_2(\omega)$ are given by

$$\mathfrak{I}_1(\omega)=\frac{(2\tau_5-\tau_1)\omega^2+(\tau_2-2\tau_6)(j\omega)^{3/2}-\sqrt{(\tau_1^2-4\tau_3)\omega^4+2(\tau_1\tau_2-2\tau_4)(j\omega)^{7/2}+\tau_2^2(j\omega)^3}}{2(-\tau_7\omega^2-\tau_6(j\omega)^{3/2})}, \tag{15}$$

$$\mathfrak{I}_2(\omega)=\frac{(2\tau_5-\tau_1)\omega^2+(\tau_2-2\tau_6)(j\omega)^{3/2}+\sqrt{(\tau_1^2-4\tau_3)\omega^4+2(\tau_1\tau_2-2\tau_4)(j\omega)^{7/2}+\tau_2^2(j\omega)^3}}{2(-\tau_7\omega^2-\tau_6(j\omega)^{3/2})},$$

where

$$\tau_5=(R'\rho_{11}-Q'\rho_{12}),\quad \tau_6=A(R'+Q'),$$

$$\tau_7=(R'\rho_{12}-Q'\rho_{22}).$$

$\mathfrak{I}_1(\omega)$ and $\mathfrak{I}_2(\omega)$ can be written as

$$\mathfrak{I}_1(\omega)=\frac{\tau_1-2\tau_5-\sqrt{\tau_1^2-4\tau_3}}{2\tau_7}+\frac{1}{4\tau_7^2\sqrt{j\omega}}\times\left[\left(\tau_2-2\tau_6-\frac{\tau_1\tau_2-2\tau_4}{\sqrt{\tau_1^2-4\tau_3}}\right)2\tau_7+(\tau_1-2\tau_5-\sqrt{\tau_1^2-4\tau_3})2\tau_6\right],$$

$$\mathfrak{I}_2(\omega)=\frac{\tau_1-2\tau_5-\sqrt{\tau_1^2-4\tau_3}}{2\tau_7}+\frac{1}{4\tau_7^2\sqrt{j\omega}}\times\left[\left(\tau_2-2\tau_6+\frac{\tau_1\tau_2-2\tau_4}{\sqrt{\tau_1^2-4\tau_3}}\right)2\tau_7+(\tau_1-2\tau_5-\sqrt{\tau_1^2-4\tau_3})2\tau_6\right],$$

Reflection and transmission coefficients can be derived using Eqs. (12) and (13), the expressions of fast and slow waves and the boundary conditions. Section III is devoted to this objective.

III. REFLECTION AND TRANSMISSION COEFFICIENTS

When a sound wave in the fluid impinges upon a porous medium at normal incidence, part of it is reflected back into the fluid, part is transmitted into the porous medium as a fast wave, and part is transmitted as a slow wave. For non-normal angles of incidence, part of it is also transmitted as a shear wave. In this paper we consider only the reflection and transmission at normal incidence. The amplitudes of these reflected and transmitted waves are determined by the relevant boundary conditions.

In this section some notation is introduced. The problem geometry is shown in Fig. 1. A homogeneous porous material occupies the region $0\leqslant x\leqslant L$. This medium is assumed to be isotropic and to have an elastic frame. A short sound pulse

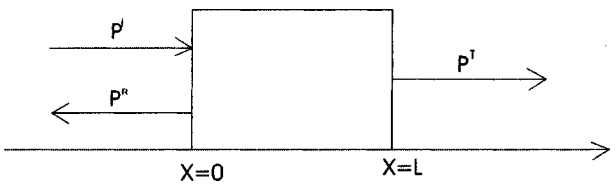

FIG. 1. Problem geometry.

impinges normally on the medium from the left. It generates solid and fluid displacements **u** and **U**, respectively, inside the porous medium, which satisfies the propagation equations (5) and (6).

If the incident sound wave is launched in region $x\leqslant 0$, then the expression of the pressure field in the region to the left of the material is the sum of the incident and reflected fields,

$$p_1(x,t)=p^i\left(t-\frac{x}{c_0}\right)+p^r\left(t+\frac{x}{c_0}\right),\quad x<0, \tag{16}$$

here $p_1(x,t)$ is the field in region $x<0$, p^i and p^r denoting the incident and reflected waves, respectively. In addition, a transmitted field is produced in the region at the right of the material. This has the form

$$p_3(x,t)=p^t\left(t-\frac{(x-L)}{c_0}\right),\quad x>L \tag{17}$$

[$p_3(x,t)$ is the field in region $x>L$ and p^t is the transmitted field].

The incident and scattered fields are related by the scattering operators (i.e., reflection and transmission operators) for the material. These are integral operators represented by

$$p^r(x,t)=\int_0^t\tilde{\mathcal{R}}(\tau)p^i\left(t-\tau+\frac{x}{c_0}\right)d\tau=\tilde{\mathcal{R}}(t)*p^i(t)*\delta\left(t+\frac{x}{c_0}\right), \tag{18}$$

$$p^t(x,t)=\int_0^t\tilde{\mathcal{T}}(\tau)p^i\left(t-\tau-\frac{(x-L)}{c_0}\right)d\tau=\tilde{\mathcal{T}}(t)*p^i(t)*\delta\left(t-\frac{(x-L)}{c_0}\right), \tag{19}$$

where the asterisk denotes the time convolution operation. In Eqs. (18) and (19) the functions $\tilde{\mathcal{R}}$ and $\tilde{\mathcal{T}}$ are the reflection and transmission kernels, respectively, for incidence from the left. Note that the lower limit of integration in Eqs. (18) and (19) is given as 0, which is equivalent to assuming that the incident wave front first impinges on the material at $t=0$.

The scattering operators given in Eqs. (18) and (19) are independent of the incident field used in scattering experiment and depend only on the properties of the materials. In the region $x\leqslant 0$, the field $p_1(x,t)$ is given by

$$p_1(x,t)=\left[\delta\left(t-\frac{x}{c_0}\right)+\tilde{\mathcal{R}}(t)*\delta\left(t+\frac{x}{c_0}\right)\right]*p^i(t). \tag{20}$$

Equations (5) and (6) are solved using the Fourier transform method, taking the boundary conditions into account. The Fourier transform of the field outside the materials is given by

$$P_1(x,\omega)=\left[\exp\left(-j\omega\frac{x}{c_0}\right)+\mathcal{R}(\omega)\exp\left(j\omega\frac{x}{c_0}\right)\right]\varphi(\omega),\quad x\leqslant 0, \tag{21}$$

$$P_3(x,\omega)=\mathcal{T}(\omega)\exp\left(-j\omega\frac{(x-L)}{c_0}\right)\varphi(\omega),\quad x\geqslant L. \tag{22}$$

Here $P_1(x,\omega)$ and $P_3(x,\omega)$ are, respectively, the Fourier transform for the field left and right of the material, $\varphi(\omega)$ denotes the Fourier transform of the incident field $p^i(t)$, and finally $\mathcal{R}(\omega)$ and $\mathcal{T}(\omega)$ are Fourier transforms of the reflection and transmission kernels, respectively.

Using the appropriate boundary conditions at the interfaces $x=0$ and $x=L$ (Appendix A), we obtain the expressions of the reflection and transmission coefficients,

$$\mathcal{R}(\omega)=\frac{(j\omega\rho_f c_0 F_4(\omega))^2+1-(j\omega F_3(\omega))^2}{(j\omega F_3(\omega)-1)^2-(j\omega\rho_f c_0 F_4(\omega))^2}, \tag{23}$$

$$\mathcal{T}(\omega)=\frac{j\omega 2\rho_f c_0 F_4(\omega)}{(j\omega\rho_f c_0 F_4(\omega))^2-(j\omega F_3(\omega)-1)^2}, \tag{24}$$

where

$$F_i(\omega)=(1+\phi(\mathfrak{I}_i(\omega)-1))\sqrt{\lambda_i(\omega)}\times\frac{\Psi_i(\omega)}{\sinh(l\sqrt{\lambda_i(\omega)})}\frac{2}{\Psi(\omega)},\quad i=1,2. \tag{25}$$

$$F_3(\omega)=\rho_f c_0(F_1(\omega)\cosh(l\sqrt{\lambda_1(\omega)})+F_2(\omega)\cosh(l\sqrt{\lambda_2(\omega)})),$$

$$F_4(\omega)=F_1(\omega)+F_2(\omega). \tag{26}$$

The coefficients $\Psi_1(\omega)$, $\Psi_2(\omega)$, and $\Psi_3(\omega)$ are given by

$$\begin{aligned}\Psi 1(\omega)&=\phi Z2(\omega)-(1-\phi)Z4(\omega),\\ \Psi_2(\omega)&=(1-\phi)Z_3(\omega)-\phi Z_1(\omega),\\ \Psi(\omega)&=2(Z_1(\omega)Z_4(\omega)-Z_2(\omega)Z_3(\omega)),\end{aligned} \tag{27}$$

and the coefficients $Z_1(\omega)$, $Z_2(\omega)$, $Z_3(\omega)$, and $Z_4(\omega)$ are given by

$$\begin{aligned}Z_1(\omega)&=(P+Q\mathfrak{I}_1(\omega))\lambda_1(\omega),\\ Z_2(\omega)&=(P+Q\mathfrak{I}_2(\omega))\lambda_2(\omega),\\ Z_3(\omega)&=(Q+R\mathfrak{I}_1(\omega))\lambda_1(\omega),\\ Z_4(\omega)&=(Q+R\mathfrak{I}_2(\omega))\lambda_2(\omega).\end{aligned} \tag{28}$$

Figure 2 shows a simulation of the transmission coefficient for a bone sample M1 with the following characteristics: thickness 0.7 cm, porosity $\phi=0.83$, tortuosity $\alpha_\infty=1.05$, viscous characteristic length $\Lambda=5$ μm, solid density $\rho_s=1960\,\mathrm{kg\,m^{-3}}$, bulk modulus of the pore fluid $K_f=2.28$ GPa, bulk modulus of the elastic solid $K_s=20$ GPa, bulk modulus of the bone skeletal frame $K_b=3.3$ GPa, shear modulus of the frame $N=2.6$ GPa, fluid viscosity $\eta=10^{-3}\,\mathrm{kg\,m\,s^{-1}}$, fluid density $\rho_f=1000\,\mathrm{kg\,m^{-3}}$.

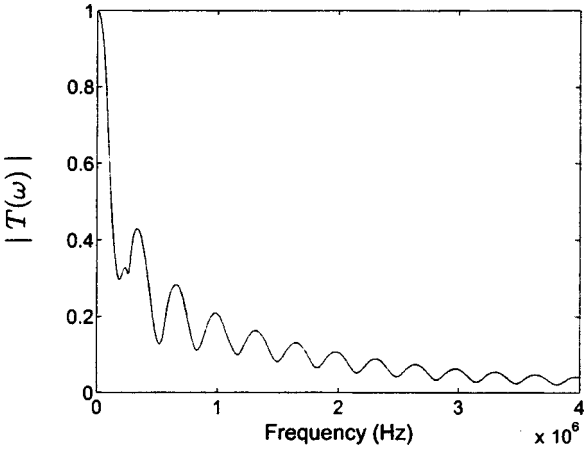

FIG. 2. Numerical simulation of the transmission coefficient in frequency domain.

The pressure field in region $(x\geqslant L)$ is given by relation (19) and the scattering operator $\tilde{T}(t)$ is calculated by inverse Fourier transform of the transmission coefficient $\mathcal{T}(\omega)$ [Eq. (24)]. Analytical calculus of the transmission operator $\tilde{T}(t)$ in the time domain is difficult because of the complexity of the transmission coefficient expression in the frequency domain $\mathcal{T}(\omega)$. However, because of the transient nature of the signals,[18,19] it is interesting to compare the domain data. The scattering operator $\tilde{T}(t)$ is then calculated numerically from $\mathcal{T}(\omega)$ and its convolution with the incident signal gives us the transmitted signal in the time domain. Figure 3 shows the incident signal (pulse wave form traveling in water), and Fig. 4 shows its spectrum.

IV. SENSITIVITY OF THE MODIFIED BIOT PARAMETERS

In this section, numerical simulations of transmitted waves are run by varying the parameters of a cancellous bone described acoustically using the modified Biot's theory. The variation is applied to the governing parameters and is 20%. A first numerical simulation is done. The numerical values chosen for the physical parameters are those taken from sample M1. The result of the simulation is a signal shown in Fig. 5. The amplitude is represented by an arbitrary

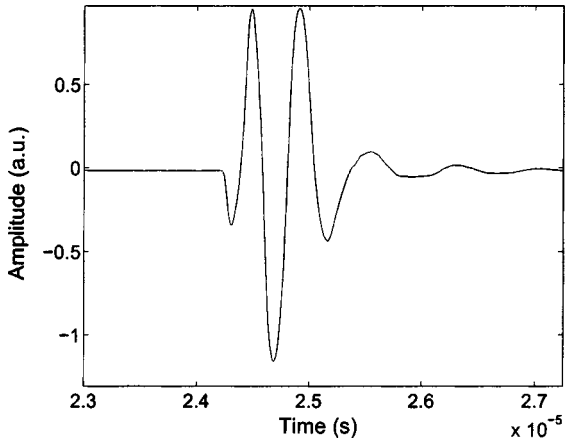

FIG. 3. Incident signal.

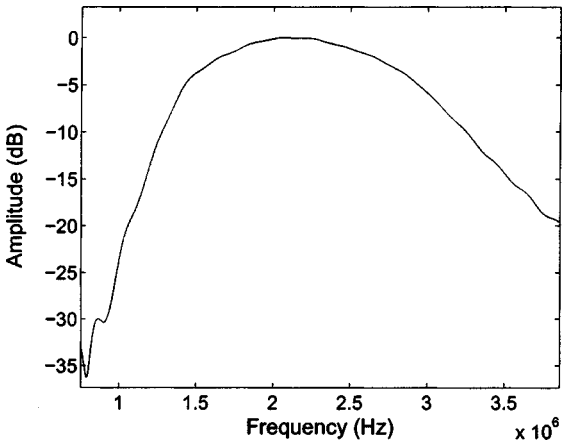

FIG. 4. Spectrum of the incident signal.

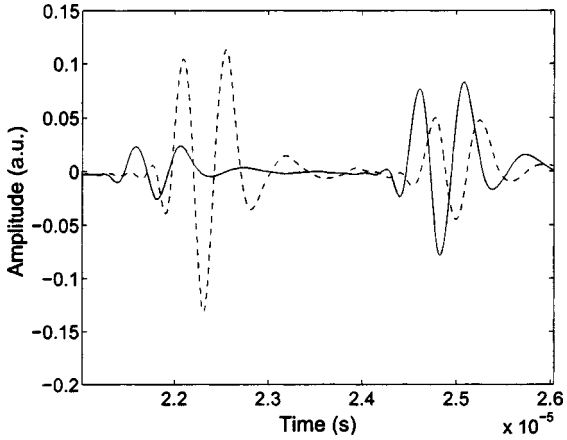

FIG. 6. Comparison between simulated transmitted signals corresponding to $\phi=0.83$ (solid line) and $\phi=0.66$ (dashed line).

unit and the point number represented in the abscissa is proportional to time. In Fig. 5, the two signals correspond to the fast and slow compressional waves, respectively. Their speeds are 3890 and 1450 $\mathrm{m\,s^{-1}}$, respectively.

One important parameter which appears in theories of sound propagation in porous materials is porosity. Porosity is the relative fraction, by volume, of the fluid contained within the material. Unlike other parameters included in the description of various different phenomena occurring in the acoustical propagation of porous media at high frequencies, such as tortuosity and viscous characteristic length, or at low frequencies, such as flow resistivity or permeability, porosity is a key parameter that plays an important role in propagation at all frequencies.

Figure 6 shows the results obtained after decreasing porosity by 20% of its initial value. The first signal (solid line) corresponds to the simulated transmitted signal for $\phi=0.83$ and the second one (dashed line) to $\phi=0.66$. The values of the other parameters have been kept constant. The reader can see the sensitivity of porosity in transmitted mode for a 20% change. An important change occurs at the amplitudes of the two waves (fast and slow). By decreasing porosity, amplitude of the fast wave increases by 300% of its initial value, while the amplitude of the slow wave decreases by 33%. This result can be predicted by the fact that when porosity decreases, the solid proportion in the porous material increases and the coupling between both phases of the porous medium favors solid phase more than fluid phase propagation. The speeds of the two waves also changed. Both fast and slow wave velocities decreased. The speed of the fast wave decreased from 3890 to 3050 $\mathrm{m\,s^{-1}}$ and the speed of the slow wave from 1450 to 1400 $\mathrm{m\,s^{-1}}$.

When the thickness decreases by 20% of its initial value, the transmitted signal changes also. Figure 7 shows the comparison between two transmitted signals with two different thickness values. The first one (solid line) corresponds to a thickness of 0.7 cm and the second one (dashed line) to a thickness of 0.56 cm. It can be seen that the arrival time of the slow wave has not changed compared with the arrival time of the fast wave which has changed considerably. The speed of the slow wave is very close to the speed of the acoustic wave in water, and changing the thickness of the medium does not have a major effect on the arrival time of the slow wave. However the speed of the fast wave is higher than the speed of the water and reducing the thickness of the porous medium delays the fast wave arrival time. We also note that the amplitude of the slow wave is less attenuated when the thickness decreases while a very small change appears for the amplitude of the fast wave. The increase in amplitude of the slow wave is 73% of its initial value. The

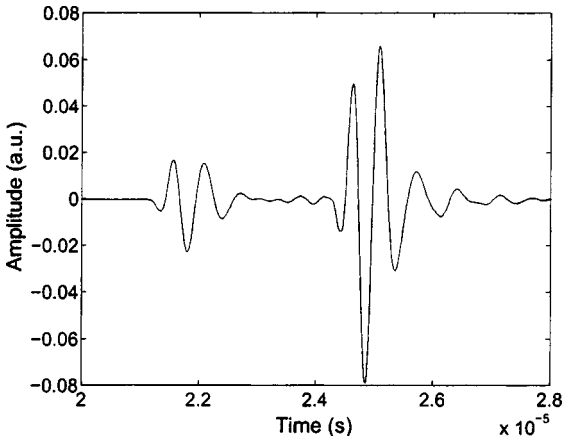

FIG. 5. Simulated transmitted signal for sample M1.

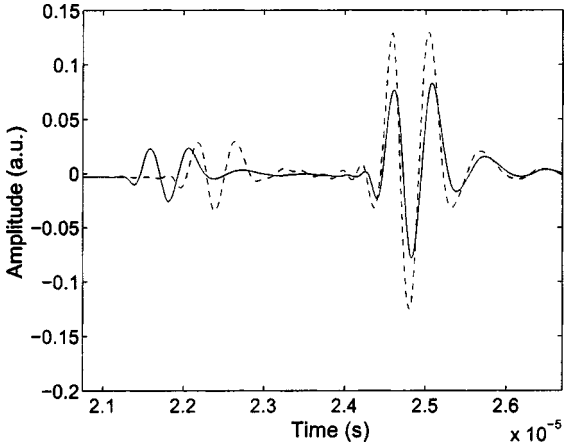

FIG. 7. Comparison between simulated transmitted signals corresponding to $L=0.7$ cm (solid line) and $L=0.56$ cm (dashed line).

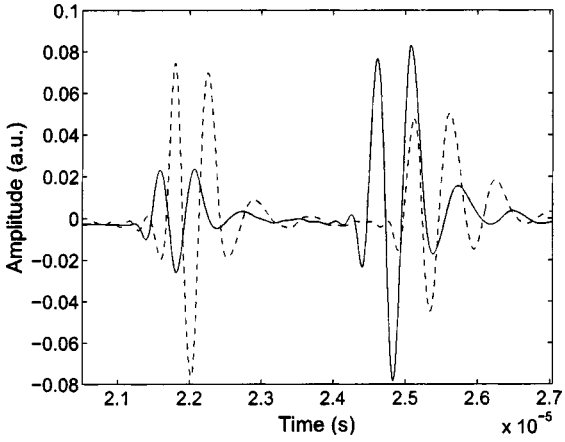

FIG. 8. Comparison between simulated transmitted signals corresponding to $\alpha_\infty = 1.05$ (solid line) and $\alpha_\infty = 1.26$ (dashed line).

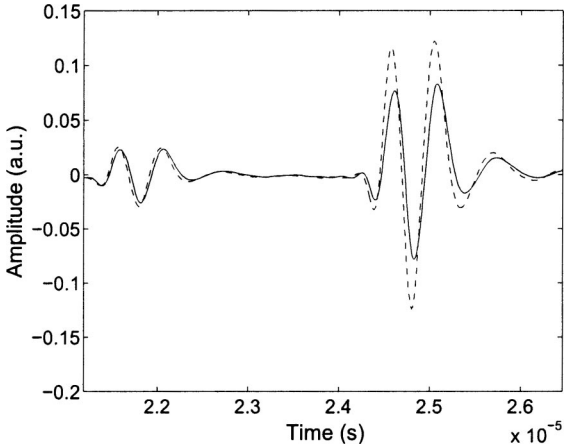

FIG. 9. Comparison between simulated transmitted signals corresponding to $\Lambda = 5$ μm (solid line) and $\alpha_\infty = 6$ μm (dashed line).

strength of the slow wave is less affected by conversion losses caused by impedance mismatch than by propagation losses due to viscous attenuation. In contrast, the strength of the fast wave is more affected by conversion losses caused by the larger impedance mismatch than by propagation losses due to viscous attenuation.

Another important parameter in describing ultrasonic propagation in a porous medium is the tortuosity α_∞. This geometrical parameter is used in describing inertial interactions between fluid and structure in porous material at a high frequency range. The tortuosity expresses the sinuosity and change in diameter of the pores. For cylindrical pores at an angle ϑ to the direction of propagation, $\alpha_\infty = 1/\cos^2 \vartheta$, tortuosity can be evaluated by electrical measurement,[17] or by using a superfluid ^{4}He as the pore fluid.[16] It can also be evaluated using acoustical techniques such as the ultrasonic measurement of transmitted waves.[19] Figure 8 shows the comparison between two simulated transmitted signals, the first (solid line) corresponding to a tortuosity of $\alpha_\infty = 1.05$ and the second one (dashed line) to a tortuosity of $\alpha_\infty = 1.26$. From the two signals, the reader can see that tortuosity plays an important part in propagation. By increasing the value of tortuosity, the speeds of both fast and slow waves have decreased. The speed of the fast wave has decreased from 3890 to 3500 m s^{-1} and the speed of the slow wave from 1450 to 1308 m s^{-1}. However, when the amplitude of the slow wave is attenuated (by 64% of its initial amplitude), the fast wave is amplified (by 295% of its initial value). On increasing tortuosity, the inertial couplings between fluid and structure also increase, and thus the slow wave is much attenuated. This is observed in the case of air-saturated porous materials such as plastic foams.[19,20]

Figure 9 shows the sensitivity of viscous characteristic length Λ introduced by Johnson *et al.*[16] to describe viscous exchanges between fluid and structure. The signal plotted as a solid line corresponds to $\Lambda = 5$ μm and the dashed line transmitted signal to $\Lambda = 6$ μm. From the two signals, it can be seen that the effect of Λ is, in fact, only observed at the amplitude of the slow wave, its amplitude increasing by 66% of its initial value. The amplitude of the fast wave remains practically unchanged. No significant change occurs at the speeds or arrival times of the two waves. Generally, more resistant porous media (with low permeability), have lower viscous characteristic lengths. This length (linked to viscous exchange) gives an idea of the radius of narrow pores in the medium which are preferred points of viscous exchange.[16] This length appears in the second term in the asymptotic expression of dynamic tortuosity at high frequencies [Eq. (4)], and as the numerical simulation shows, Λ plays a less important role in transmission than does tortuosity α_∞, which appears at the first order in Eq. (4).

Figure 10 shows a comparison between two simulated transmitted signals for two different solid density values ρ_s. The first one (solid line) corresponds to $\rho_s = 1960$ kg/m^3 and the second one (dashed line) to $\rho_s = 1568$ kg/m^3. The slow wave remains unchanged (amplitude and speed), while fast wave velocity changes. As solid density decreases, fast wave velocity increases, its value changing from 3890 to 4200 m s^{-1}.

Figure 11 shows a comparison between simulated transmitted signals corresponding to a pore fluid bulk modulus of $K_f = 2.28$ GPa (solid line) and $K_f = 1.82$ GPa (dashed line). The simulation shows that on decreasing the value of the pore fluid bulk modulus, slow wave velocity decreases (from 1450 to 1190 m s^{-1}) and is much attenuated (20% of its initial amplitude). No major changes were observed in fast

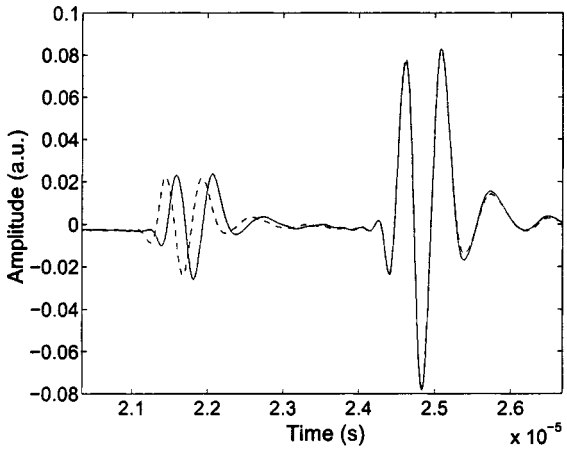

FIG. 10. Comparison between simulated transmitted signals corresponding to $\rho_s = 1960$ kg/m^3 (solid line) and $\rho_s = 1568$ kg/m^3 (dashed line).

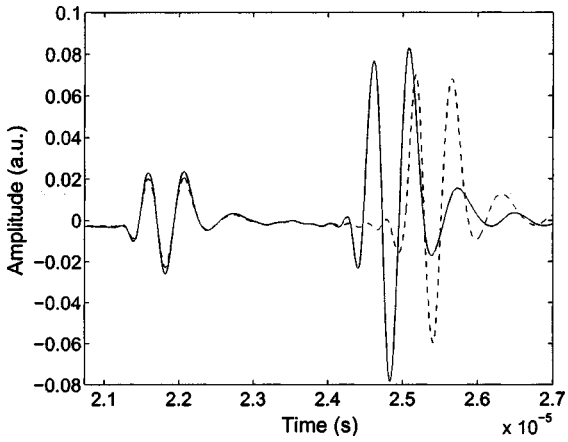

FIG. 11. Comparison between simulated transmitted signals corresponding to $K_f = 2.28$ GPa (solid line) and $K_f = 1.82$ GPa (dashed line).

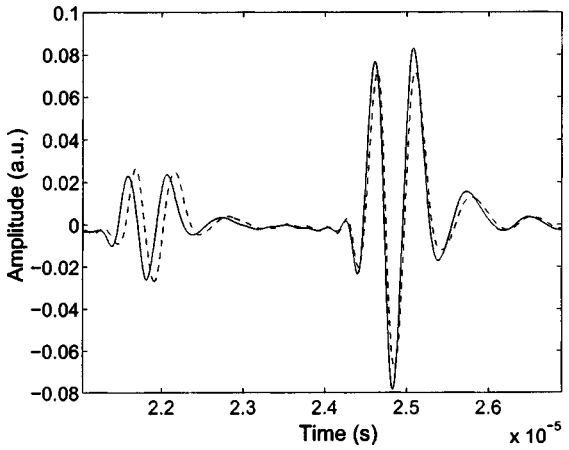

FIG. 13. Comparison between simulated transmitted signals corresponding to $K_b = 3.3$ GPa (solid line) and $K_b = 2.64$ GPa (dashed line).

wave velocity. Fast wave amplitude decreased by 1.2% of its initial value. We can conclude that the fluid bulk modulus K_f plays an important role essentially for the slow wave.

Along similar lines, Fig. 12 shows the effect of the solid bulk modulus K_s by comparing simulated transmitted waves. The solid curve shows a transmitted signal for $K_s = 20$ GPa and the dashed line curve for $K_s = 16$ GPa. On decreasing the value of K_s, fast wave velocity is unchanged while its amplitude falls by 1.1% of its initial value. However the slow wave is amplified by 1.1% and its speed increases (from 1450 to 1460 m s^{-1}). In this case it can be seen that solid bulk modulus sensitivity is not very important for a 20% change in both fast and slow waves.

Figure 13 shows the sensitivity of the skeletal compressibility frame K_b of the porous medium. The transmitted signal shown by the solid line corresponds to $K_b = 3.3$ GPa and that of the dashed line to $K_b = 2.64$ GPa. By decreasing the value of K_b, slow wave amplitude is much attenuated (1.05% of its initial value) and its speed is lower (from 1450 to 1445 m s^{-1}). Fast wave amplitude is increased (1.2% of its initial value) while its velocity has fallen from 3890 to 3707 m s^{-1}. The sensitivity of parameter K_b is not negligible for fast and slow wave amplitudes and speeds.

Finally, Fig. 14 shows the comparison between two simulated transmitted signals corresponding to two shear modulus values of frame N. The first signal (solid line) corresponds to a shear modulus of $N = 2.6$ GPa and the second signal (dashed line) to $N = 2.08$ GPa. In this case slow wave amplitude has fallen by 2.5% of its initial value while its velocity is unchanged. For the fast wave, only the speed has changed, falling from 3890 to 3690 m s^{-1}.

From this study, we can gain an insight into the sensitivity of each physical parameter used in this theory. Some parameters play an important role in slow-wave wave form, such as the viscous characteristic length Λ and pore fluid bulk modulus K_f. However, other parameters play an important role in the fast-wave wave form, such as solid density ρ_s and shear modulus N.

We also note from these simulations that some parameters such as porosity ϕ, tortuosity α_∞, thickness, solid bulk modulus K_s, and skeletal compressibility frame K_b, play an important role simultaneously in both fast and slow wave forms compared to other parameters which act on the wave form of just one of the two waves. The sensitivity of the modified Biot parameters with respect to the transmitted wave depends strongly on the coupling between the solid and

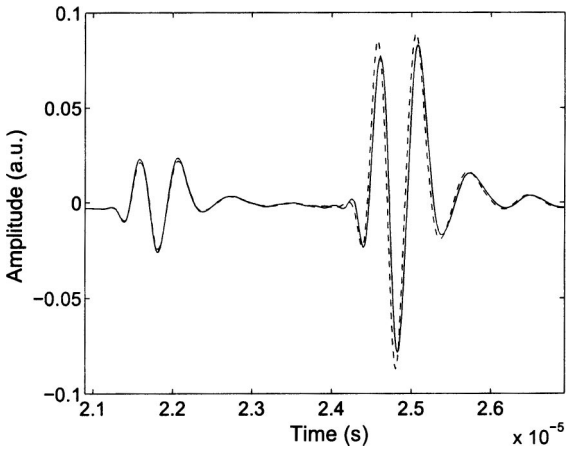

FIG. 12. Comparison between simulated transmitted signals corresponding to $K_s = 20$ GPa (solid line) and $K_s = 16$ GPa (dashed line).

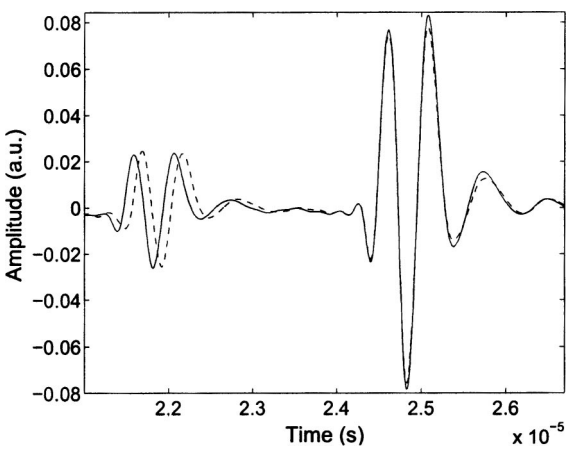

FIG. 14. Comparison between simulated transmitted signals corresponding to $N = 2.6$ GPa (solid line) and $N = 2.08$ GPa (dashed line).

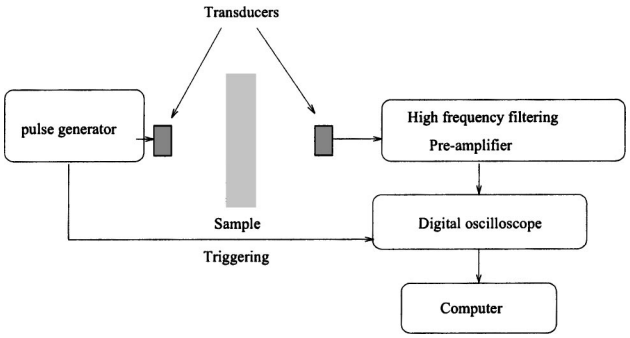

FIG. 15. Experimental setup for ultrasonic measurements.

fluid phases of the porous material and thus on the other parameters which were kept constant during this study.

V. ULTRASONIC MEASUREMENTS

As an application of this model, some numerical simulations are compared with experimental results. Experiments are performed in water using two broadband Panametrics A 306S piezoelectric transducers with a central frequency of 2.25 MHz in water. 400 V pulses are provided by a 5058PR Panametrics pulser/receiver. The signals received are amplified to 90 dB and filtered above 10 MHz to avoid high frequency noise (energy is totally filtered by the sample in this upper frequency domain). Electronic interference is removed by 1000 acquisition averages. The experimental setup is shown in Fig. 15. The parallel-faced cubic samples were machined from human cancellous bone in femoral heads. The liquid in the pore space (blood and marrow) is removed from the bone sample and substituted by water. The transmitting transducer insonifies the sample at normal incidence with a short (in time domain) pulse. When the pulse hits the front surface of the sample, part is reflected, part is transmitted as a fast wave, and a part is transmitted as a slow wave. When any of these components, traveling at different speeds, hit the second surface, a similar effect takes place: part is transmitted into the fluid, part is reflected as a fast or slow wave. Sample characteristics are measured using standard methods[11,16,17,19,25–27] (Appendix B) and given in Table I. The fluid (water) characteristics are: bulk modulus $K_f = 2.28\,\mathrm{GPa}$, density $\rho_f = 1000\,\mathrm{kg\,m^{-3}}$, viscosity $\eta = 10^{-3}\,\mathrm{kg\,m\,s^{-1}}$. The incident experimental signal generated by the transducer is shown in Fig. 3 and its spectrum in Fig. 4.

TABLE I. Biot's model parameters of cancellous bone.

Biot's model parameters of cancellous bone	M1	M2	M3
Thickness L (cm)	0.7	0.5	0.38
Density ρ_s (kg/m^3)	1960	1960	1960
Porosity ϕ	0.83	0.77	0.88
Tortuosity α_∞	1.05	1.01	1.02
Viscous characteristic length Λ (μm)	5	2.7	5
Bulk modulus of the elastic solid Ks (GPa)	20	20	26
Bulk modulus of bone skeletal frame Kb (GPa)	3.3	4	1.3
Shear modulus of the frame N (GPa)	2.6	1.7	0.35

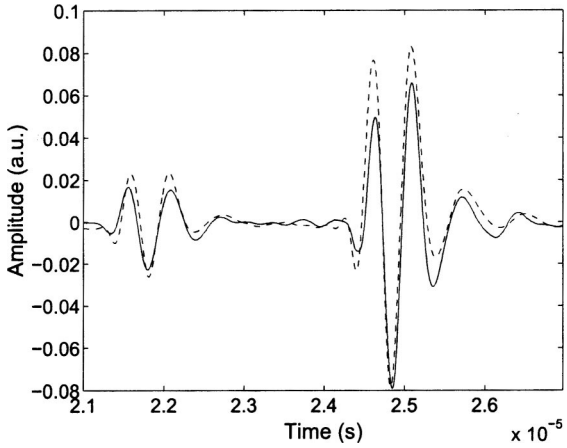

FIG. 16. Comparison between experimental transmitted signal (solid line) and simulated transmitted signal (dashed line) for bone sample M1.

Figures 16, 17, and 18 show the comparison between experimental transmitted signals (solid line) and simulated signals (dashed line) for bone samples M1, M2, and M3, respectively. The experimental transmitted wave forms are traveling through the cancellous bone in the same direction as the trabecular alignment (x direction). For some situations, fast and slow waves are superimposed, depending on the coupling between the two porous medium phases, so that this is due to the modified Biot's parameters for cancellous bone, which as mentioned in Sec. IV, play an important role in the arrival time of the two waves.

The experimental data and theoretical prediction are seen to match closely, which allowed us to conclude that the modified Biot theory using the Johnson *et al.* model is quite suitable for describing the propagation of ultrasonic wave in cancellous bone.

VI. CONCLUSION

In this paper, analytical calculus of the reflection and transmission coefficient of a slab of cancellous bone with an elastic frame is established. This calculus is based on Biot's theory modified by the Johnson *et al.* model to describe the viscous interaction between fluid and structure. Numerical simulations of transmitted waves in the time domain were

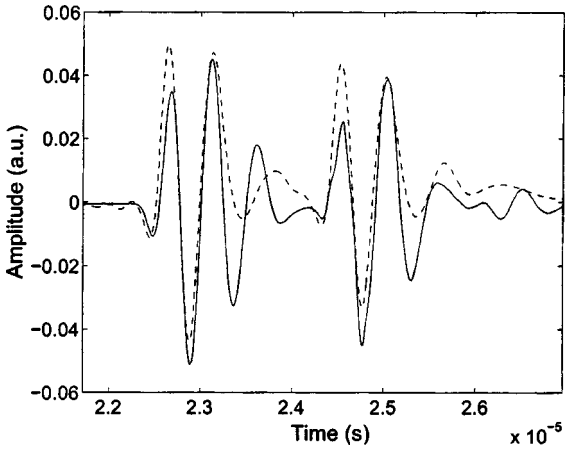

FIG. 17. Comparison between experimental transmitted signal (solid line) and simulated transmitted signal (dashed line) for bone sample M2.

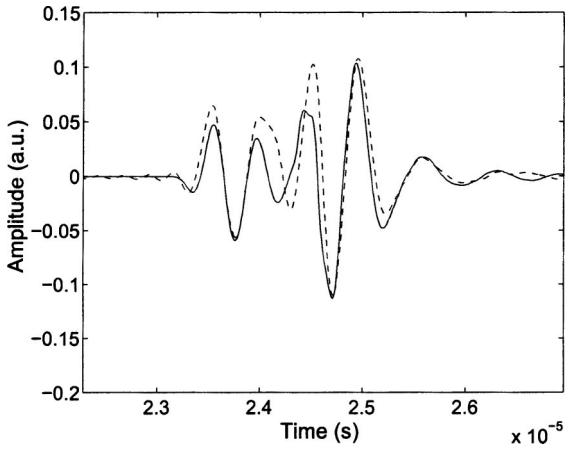

FIG. 18. Comparison between experimental transmitted signal (solid line) and simulated transmitted signal (dashed line) for bone sample M3.

run by varying the parameters of a porous medium. The variation applied to the governing parameters was 20% and the sensitivity of each parameter was studied, showing the importance of the values of these parameters in fast and slow wave arrival times (speeds) and attenuation, respectively. Experimental validation of this model using waves transmitted through samples of human cancellous bone was performed and found to produce excellent agreement between theory and experiment. To make progress in this area, future projects will compare experimental data at oblique incidence with theoretical predictions by taking the shear wave in the medium into account. One future hope is to solve the inverse problem and return to the physical parameters of the medium from reflected and transmitted experimental data.

APPENDIX A: CALCULUS OF THE REFLECTION AND TRANSMISSION COEFFICIENTS

Let σ_{ij}^s and σ_{ij}^f be the frame and fluid stress tensors, respectively, and $\epsilon_{ij}=\frac{1}{2}(u_{ij}+u_{ji})$ the frame strain tensor. The stress–strain equations in the porous medium[28] are given by

$$\sigma_{ij}^s=[(P-2N)\nabla\mathbf{u}+Q\nabla\mathbf{U}]\delta_{ij}+N(u_{ij}+u_{ji}), \tag{A1}$$

$$\sigma_{ij}^f=-\phi p_f\delta_{ij}=(R\nabla\mathbf{U}+Q\nabla\mathbf{u})\delta_{ij}. \tag{A2}$$

p_f is the pressure of the fluid. It is assumed that the pressure field and the normal stress in the porous medium are continuous at the boundary[29] of the material, at $x=0$,

$$\sigma^f(0^+,\omega)=-\phi P_1(0^-,\omega),$$
$$\sigma^s(0^+,\omega)=-(1-\phi)P_1(0^-,\omega), \tag{A3}$$

and, at $x=L$,

$$\sigma^f(L^-,\omega)=-\phi P_3(L^+,\omega),$$
$$\sigma^s(L^-,\omega)=-(1-\phi)P_3(L^+,\omega), \tag{A4}$$

σ^f and σ^s are the solid and fluid normal stresses, respectively, inside the porous medium. The expression of σ^s is given by [Eq. (A1)]

$$\sigma^s=(P-2N)\boldsymbol{\nabla}\cdot\mathbf{u}+Q\boldsymbol{\nabla}\cdot\mathbf{U}+2N\frac{\partial u}{\partial x}. \tag{A5}$$

For longitudinal waves, the relation (A5) will be given by

$$\sigma^s(x,\omega)=(P-2N)\frac{\partial^2\Phi_s}{\partial x^2}+Q\frac{\partial^2\Phi_f}{\partial x^2}+2N\frac{\partial^2\Phi_s}{\partial x^2}. \tag{A6}$$

Using relations (12)–(14),

$$\begin{aligned}\sigma^s(x,\omega)=&Z_1(\omega)(\overline{\Phi}_1(\omega)+\overline{\Phi}_1'(\omega))\cosh(x\sqrt{\lambda_1(\omega)})\\&+Z_2(\omega)(\overline{\Phi}_2(\omega)+\overline{\Phi}_2'(\omega))\cosh(x\sqrt{\lambda_2(\omega)})\\&+Z_1(\omega)(\overline{\Phi}_1(\omega)-\overline{\Phi}_1'(\omega))\sinh(x\sqrt{\lambda_1(\omega)})\\&+Z_2(\omega)(\overline{\Phi}_2(\omega)-\overline{\Phi}_2'(\omega))\sinh(x\sqrt{\lambda_2(\omega)}),\end{aligned} \tag{A7}$$

where the coefficients $Z_1(\omega)$ and $Z_2(\omega)$ are given by Eq. (28).

The stress–strain relation in the fluid is [Eq. (A2)]

$$\sigma^f=R\boldsymbol{\nabla}\cdot\mathbf{U}+Q\boldsymbol{\nabla}\cdot\mathbf{u}, \tag{A8}$$

for propagation along the x axis

$$\sigma^f(x,\omega)=R\frac{\partial^2\Phi_f}{\partial x^2}+Q\frac{\partial^2\Phi_s}{\partial x^2}, \tag{A9}$$

using relation (14), we obtain

$$\begin{aligned}\sigma^f(x,\omega)=&(\mathfrak{I}_1(\omega)R+Q)\frac{\partial^2\Phi_1(\omega)}{\partial x^2}\\&+(\mathfrak{I}_2(\omega)R+Q)\frac{\partial^2\Phi_2(\omega)}{\partial x^2},\end{aligned} \tag{A10}$$

and, with relations (12) and (13)

$$\begin{aligned}\sigma^f(x,\omega)=&Z_3(\omega)(\overline{\Phi}_1(\omega)+\overline{\Phi}_1'(\omega))\cosh(x\sqrt{\lambda_1(\omega)})\\&+Z_4(\omega)(\overline{\Phi}_2(\omega)+\overline{\Phi}_2'(\omega))\cosh(x\sqrt{\lambda_2(\omega)})\\&+Z_3(\omega)(\overline{\Phi}_1(\omega)-\overline{\Phi}_1'(\omega))\sinh(x\sqrt{\lambda_1(\omega)})\\&+Z_4(\omega)(\overline{\Phi}_2(\omega)-\overline{\Phi}_2'(\omega))\sinh(x\sqrt{\lambda_2(\omega)}),\end{aligned} \tag{A11}$$

where the coefficients $Z_3(\omega)$ and $Z_4(\omega)$ are given by Eq. (28).

Using the boundary conditions (A3) and (A4), it is easy to calculate the expressions of $\overline{\Phi}_1(\omega)$, $\overline{\Phi}_1'(\omega)$, $\overline{\Phi}_2(\omega)$, and $\overline{\Phi}_2'(\omega)$,

$$\begin{aligned}\overline{\Phi}_1(\omega)=\varphi(\omega)\frac{\Psi_1(\omega)}{\Psi(\omega)}\Bigg[&(1+\mathcal{R}(\omega))\left(1+\frac{\cosh(l\sqrt{\lambda_1(\omega)})}{\sinh(l\sqrt{\lambda_1(\omega)})}\right)\\&-\frac{\mathcal{T}(\omega)}{\sinh(l\sqrt{\lambda_1(\omega)})}\Bigg],\end{aligned} \tag{A12}$$

$$\begin{aligned}\overline{\Phi}_1'(\omega)=\varphi(\omega)\frac{\Psi_1(\omega)}{\Psi(\omega)}\Bigg[&(1+\mathcal{R}(\omega))\left(1-\frac{\cosh(l\sqrt{\lambda_1(\omega)})}{\sinh(l\sqrt{\lambda_1(\omega)})}\right)\\&+\frac{\mathcal{T}(\omega)}{\sinh(l\sqrt{\lambda_1(\omega)})}\Bigg],\end{aligned} \tag{A13}$$

$$\overline{\Phi}_2(\omega)=P(\omega)\frac{\Psi_2(\omega)}{\Psi(\omega)}\left[(1+\mathcal{R}(\omega))\left(1+\frac{\cosh(l\sqrt{\lambda_2(\omega)})}{\sinh(l\sqrt{\lambda_2(\omega)})}\right)-\frac{\mathcal{T}(\omega)}{\sinh(l\sqrt{\lambda_2(\omega)})}\right], \tag{A14}$$

$$\overline{\Phi}_2'(\omega)=\varphi(\omega)\frac{\Psi_2(\omega)}{\Psi(\omega)}\left[(1+\mathcal{R}(\omega))\left(1-\frac{\cosh(l\sqrt{\lambda_2(\omega)})}{\sinh(l\sqrt{\lambda_2(\omega)})}\right)+\frac{\mathcal{T}(\omega)}{\sinh(l\sqrt{\lambda_2(\omega)})}\right], \tag{A15}$$

where the coefficients $\Psi_1(\omega)$, $\Psi_2(\omega)$, and $\Psi(\omega)$ are given by Eq. (27).

To derive the reflection and transmission coefficients, the boundary conditions of flow velocity at the $x=0$ and $x=L$ interfaces are required. The equation of flow continuity at $x=0$ is written as

$$V_1(0^-,\omega)=(1-\phi)V_s(0^+,\omega)+\phi V_f(0^+,\omega), \tag{A16}$$

where V_1 is the acoustic velocity field in the region (1) ($x\leqslant 0$), V_s and V_f are the solid and fluid acoustic fields, respectively, inside the porous medium. The flow continuity equation at $x=L$ is written as

$$V_3(L^-,\omega)=(1-\phi)V_s(L^-,\omega)+\phi V_f(L^-,\omega), \tag{A17}$$

here V_3 is the acoustic velocity field in region (3) ($x\geqslant L$).

The Euler equation is written in region (1) ($x\leqslant 0$),

$$\rho_f j\omega V_1(x,\omega)=-\frac{P_1(x,\omega)}{\partial x}. \tag{A18}$$

Using Eqs. (21) and (A18), we obtain the expression of the velocity field in region (1),

$$V_1(x,\omega)=\frac{1}{\rho_f c_0}(e^{-(x/c_0)j\omega}-\mathcal{R}(\omega)e^{(x/c_0)j\omega})\varphi(\omega) \quad \text{at } x=0,$$

$$V_1(0,\omega)=\frac{1}{\rho_f c_0}(1-\mathcal{R}(\omega))\varphi(\omega). \tag{A19}$$

In the same way, at $x=L$, the Euler equation gives in region (3) ($x\geqslant L$),

$$\rho_f j\omega V_3(x,\omega)=-\frac{P_3(x,\omega)}{\partial x}. \tag{A20}$$

Using Eqs. (22) and (A20), we obtain the expression of the velocity field in region (3),

$$V_3(x,\omega)=\mathcal{T}(\omega)\frac{\varphi(\omega)}{\rho_f c_0}\exp\left(-\frac{x-l}{c_0}j\omega\right) \quad \text{at } x=L,$$

we have

$$V_3(L,\omega)=\mathcal{T}(\omega)\frac{\varphi(\omega)}{\rho_f c_0}. \tag{A21}$$

The expression of the solid velocity field inside the porous material is given by

$$V_s(x,\omega)=j\omega\left(\frac{\partial\Phi_s(\omega)}{\partial x}\right). \tag{A22}$$

From Eq. (14), we have the following relation:

$$\Phi_s(\omega)=\Phi_1(\omega)+\Phi_2(\omega).$$

Using Eqs. (12) and (13), we obtain the following relation of the solid velocity field inside the porous medium:

$$\begin{aligned}V_s(x,\omega)=&j\omega\sqrt{\lambda_1(\omega)}((\overline{\Phi}_1(\omega)+\overline{\Phi}_1'(\omega))\sinh(x\sqrt{\lambda_1(\omega)})+(\overline{\Phi}_1'(\omega)-\overline{\Phi}_1(\omega))\cosh(x\sqrt{\lambda_1(\omega)}))+j\omega\sqrt{\lambda_2(\omega)}\\&\times((\overline{\Phi}_2(\omega)+\overline{\Phi}_2'(\omega))\sinh(x\sqrt{\lambda_2(\omega)})+(\overline{\Phi}_2'(\omega)-\overline{\Phi}_2(\omega))\cosh(x\sqrt{\lambda_2(\omega)})).\end{aligned} \tag{A23}$$

In the same way, expression of the fluid velocity field inside the porous material is given by

$$V_f(x,\omega)=j\omega\left(\frac{\partial\Phi_f(\omega)}{\partial x}\right), \tag{A24}$$

and, from Eq. (14),

$$\Phi_f(\omega)=(\mathfrak{I}_1(\omega)\Phi_1(\omega)+\mathfrak{I}_2(\omega)\Phi_2(\omega)). \tag{A25}$$

Using Eqs. (A24) and (A25), we obtain the expression of the fluid velocity field inside the porous medium

$$\begin{aligned}V_f(x,\omega)=&j\omega\mathfrak{I}_1(\omega)\sqrt{\lambda_1(\omega)}((\overline{\Phi}_1(\omega))+\overline{\Phi}_1'(\omega))\sinh(x\sqrt{\lambda_1(\omega)})+(\overline{\Phi}_1'(\omega)-\overline{\Phi}_1(\omega))\cosh(x\sqrt{\lambda_1(\omega)}))\\&+j\omega\mathfrak{I}_2(\omega)\sqrt{\lambda_2(\omega)}((\overline{\Phi}_2(\omega)+\overline{\Phi}_2'(\omega))\sinh(x\sqrt{\lambda_2(\omega)})+(\overline{\Phi}_2'(\omega)-\overline{\Phi}_2(\omega))\cosh(x\sqrt{\lambda_2(\omega)})).\end{aligned} \tag{A26}$$

Using the boundary conditions (A16) and (A17) and the expressions of V_s, V_f, V_1, and V_3 [Eqs. (A23), (A26), (A19), and (A21), respectively], we obtain the equations given the reflection and transmission coefficients

$$\mathcal{R}(\omega)(j\omega F_3(\omega)-1)=\rho_f c_0 j\omega F_4(\omega)\mathcal{T}(\omega)-j\omega F_3(\omega)-1, \tag{A27}$$

$$\mathcal{T}(\omega)(j\omega F_3(\omega)-1)=\rho_f c_0 j\omega F_4(\omega)(1+\mathcal{R}(\omega))), \tag{A28}$$

where the coefficients F_i $i=1,...,4$ are given by Eqs. (25) and (26).

Solving Eqs. (A27) and (A28) gives the reflection and transmission coefficient given [Eqs. (23) and (24)].

APPENDIX B: DETERMINATION OF THE MODIFIED BIOT PARAMETERS

To characterize the bone sample, the water in the pore space is drained and replaced by air. Due to the tremendous difference in density between the frame and air, partial decoupling of the Biot waves occurs.[11,17] The slow wave propa-

gates in the fluid and the fluid particles do not have enough mass to generate a motion in a heavy solid frame. The fast wave travels in the solid frame and some air particles move along with the frame. The velocity of the fast wave approximates the velocity in the frame as measured in vacuum and is given by $v^2=(K_b+4/3N)/((1-\phi)\rho_s)$. Measuring the pulse transit time in a sample whose pores are filled with air results in a value of $K_b+4/3N$. The shear modulus N can be evaluated independently using the velocity of the shear wave, which can be generated and detected in air-saturated bone by an adapted contact transducers (Panametrics V 151). The porosity can be determined in different ways. The simplest method[11] to measure ϕ is to measure the change in height of a water column in a recipient when the sample is immersed and all the air is drained from the pores. The porosity can be measured using the reflection of ultrasound by air-saturated bone.[27] If all the pores are interconnected and if no closed cells are present, the density of the frame material can be determined from the apparent density of the porous bone. The tortuosity can be determined by different methods[16,17,19,26,27] mentioned in the previous section. The viscous characteristic length Λ can be determined easily from transmitted[19] or reflected waves[27] by air-saturated porous bone.

[1] A. M. Parfitt, ''Trabecular bone architecture in the pathogenesis and prevention of fracture,'' Am. J. Med. **82**, 68–72 (1987).
[2] L. J. Gibson, ''The mechanical behavior of cancellous bone,'' J. Biomech. **18**, 317–328 (1985).
[3] F. J. Fry and J. E. Barger, ''Acoustical properties of the humain skull,'' J. Acoust. Soc. Am. **63**, 1576–1590 (1978).
[4] R. B. Ashman, J. D. Corin, and C. H. Turner, ''Elastic properties of cancellous bone: Measurement by an ultrasonic technique,'' J. Biomech. **10**, 979–989 (1987).
[5] R. B. Ashman and J. Y. Rho, ''Elastic modulus of trabecular bone material,'' J. Biomech. **21**, 177–181 (1988).
[6] C. M. Langton, S. B. Palmer, and R. W. Porter, ''The measurement of broadband ultrasonic attenuation in cancellous bone,'' Eng. In. Med. **13**, 89–91 (1984).
[7] M. A. Biot, ''The theory of propagation of elastic waves in fluid-saturated porous solid. I. Low frequency range,'' J. Acoust. Soc. Am. **28**, 168–178 (1956).
[8] M. A. Biot, ''The theory of propagation of elastic waves in fluid-saturated porous solid. I. Higher frequency range,'' J. Acoust. Soc. Am. **28**, 179–191 (1956).
[9] R. Lakes, H. S. Yoon, and J. L. Katz, ''Slow compressional wave propagation in wet humain and bovine cortical bone,'' Science **220**, 513–515 (1983).
[10] J. L. Wilson, ''Ultrasonic wave propagation in cancellous bone and cortical bone: Prediction of some experimental results by Biot's theory,'' J. Acoust. Soc. Am. **91**, 1106–1112 (1992).
[11] W. Lauriks, J. Thoen, I. Van Asbroeck, G. Lowet, and G. Vanderperre, ''Propagation of ultrasonic pulses through trabecular bone,'' J. Phys. Colloq. (Paris) **4**, 1255–1258 (1994).
[12] M. L. Mckelvie and S. B. Palmer, ''The interaction of ultrasound with cancellous bone,'' Phys. Med. Biol. **36**, 1331–1340 (1991).
[13] T. J. Haire and C. M. Langton, ''Biot theory: A review of its application on ultrasound propagation through cancellous bone,'' Bone (N.Y.) **24**, 291–295 (1999).
[14] A. Hosokawa and T. Otani, ''Ultrasonic wave propagation in bovine cancellous bone,'' J. Acoust. Soc. Am. **101**, 558–562 (1997).
[15] A. Hosokawa and T. Otani, ''Acoustic anisotropy in bovine cancellous bone,'' J. Acoust. Soc. Am. **103**, 2718–2722 (1998).
[16] D. L. Johnson, J. Koplik, and R. Dashen, ''Theory of dynamic permeability and tortuosity in fluid-saturated porous media,'' J. Fluid Mech. **176**, 379–402 (1987).
[17] J. F. Allard, *Propagation of Sound in Porous Media: Modeling Sound Absorbing Materials* (Chapman and Hall, London, 1993).
[18] Z. E. A. Fellah and C. Depollier, ''Transient acoustic wave propagation in rigid porous media: A time-domain approach,'' J. Acoust. Soc. Am. **107**, 683–688 (2000).
[19] Z. E. A. Fellah, M. Fellah, W. Lauriks, and C. Depollier, ''Direct and inverse scattering of transient acoustic waves by a slab of rigid porous material,'' J. Acoust. Soc. Am. **113**, 61–73 (2003).
[20] P. Leclaire, L. Kelders, W. Lauriks, C. Glorieux, and J. Thoen, ''Determination of the viscous characteristic length in air-filled porous materials by ultrasonic attenuation measurements,'' J. Acoust. Soc. Am. **99**, 1944–1948 (1996).
[21] J. M. Carcione, ''Wave fields in real media: Wave propagation in anisotropic, anelastic and porous media,'' in *Handbook of Geophysical Exploration*, edited by K. Helbig and S. Treitel (Pergamon, An Imprint of Elseiver Science, 2001).
[22] K. A. Wear, ''Frequency dependence of ultrasonic backscatter from human trabecular bone: Theory and experiment,'' J. Acoust. Soc. Am. **106**, 3659–3664 (1999).
[23] S. Chaffai, V. Roberjot, F. Peyrin, G. Berger, and P. Laugier, ''Frequency dependence of ultrasonic backscattering in cancellous bone: Autocorrelation model and experimental results,'' J. Acoust. Soc. Am. **108**, 2403–2411 (2000).
[24] F. Luppe, J. M. Conoir, and H. Franklin, ''Scattering by a fluid cylinder in a porous medium: Application to trabecular bone,'' J. Acoust. Soc. Am. **111**, 2573–2582 (2002).
[25] D. L. Johnson, T. J. Plona, and H. Kojima, ''Probing porous media with first and second sound. II. Acoustic properties of water-saturated porous media,'' J. Appl. Phys. **76**, 115–125 (1994).
[26] Z. E. A. Fellah, S. Berger, W. Lauriks, C. Depollier, C. Aristegui, and J. Y. Chapelon, ''Measuring the porosity and tortuosity of porous materials via reflected waves at oblique incidence,'' J. Acoust. Soc. Am. **113**, 2424–2433 (2003).
[27] Z. E. A. Fellah, C. Depollier, S. Berger, W. Lauriks, P. Trompette, and J. Y. Chapelon, ''Determination of transport parameters in air-saturated porous materials via reflected ultrasonic waves,'' J. Acoust. Soc. Am. **114**, 2561–2569 (2003).
[28] C. Depollier, J. F. Allard, and W. Lauriks, ''Biot theory and stress-strain equations in porous sound-absorbing materials,'' J. Acoust. Soc. Am. **84**, 2277–2279 (1988).
[29] K. Wu, Q. Xue, and L. Adler, ''Reflection and transmission of elastic waves from a fluid-saturated porous solid boundary,'' J. Acoust. Soc. Am. **87**, 2349–2358 (1990).

Analysis and design of conical concentric tube resonators

T. Kar and M. L. Munjal[a)]
Facility for Research in Technical Acoustics, Department of Mechanical Engineering, Indian Institute of Science, Bangalore—560 012, India

(Received 22 November 2003; revised 10 April 2004; accepted 29 April 2004)

The concept of perforate impedance and its exploitation for acoustic attenuation through several elements including concentric tube resonators, is common in practice. Variable cross-sectional area ducts are often used for better performance at lower frequencies (like in horns), whereas concentric tube resonators are often used to provide attenuation at relatively higher frequencies. A combination of the two leads to conical concentric-tube resonators. Using a one-dimensional control volume approach, a mathematical model is presented that accounts for waves in an incompressible mean flow in the center tube, wave propagation in the cavity, and an acoustic coupling between the two due to the impedance of the perforate. The matrizant model results have been validated for self consistency. In the sections dealing with discussion and parametric study, the effect of the moving medium has been neglected so as to bring out clearly the physical effect of the variable area ducts. A few notable effects have been found that include an effective length shorter than the geometric length for an inhomogeneous duct. Some useful features like the absence of pass bands are noticed in the transmission loss spectrum. Finally, results of a parametric study are presented for use by the noise control engineers. © *2004 Acoustical Society of America.* [DOI: 10.1121/1.1763953]

PACS numbers: 43.20.Bi, 43.20.Hq, 43.20.Mv [DKW] Pages: 74–83

I. INTRODUCTION

In the design of acoustic mufflers, it is a usual practice to exploit the acoustic impedance offered by perforated tubular components inside annular cavities for better acoustic attenuation. A low frequency resonator is characterized by a large volume cavity. In contrast, a concentric-tube configuration means a relatively higher frequency resonator.[1] The two may be combined into a variable area concentric tube resonator. A variable area duct has been the subject of analysis ever since the effect of area discontinuity. Eisenberg and Kao[2] analyzed propagation of sound through a variable area duct by assuming a steady compressible flow and making use of the linear perturbation theory. Although the mass continuity equation for a moving medium was derived accurately, in the equation of dynamical equilibrium the term relating to gradient of the mean flow velocity was not considered. Nevertheless they came out with a generalized analytical solution for any flow condition, which would be misleading for a higher Mach number fluid flow with such assumed linearization.

Alfredson[3] predicted the behavior of sound propagation in a circular duct of continuously varying area. This was in essence a segmentation of the duct into a number of parallel subsections of plain uniform tubes with discontinuity at the end of each subsection that would generate higher order modes, including more than one radial mode.

Miles[4] then followed with a modest segmentation model for developing the acoustic transmission matrix of a variable area duct or nozzle carrying a compressible subsonic flow. He assumed a constant mean flow for each individual segments whereas the area variation in that region was approximated by an exponential relation to take advantage of the constant coefficients attached to the state vectors later described by Munjal.[5]

Gupta, Easwaran, and Munjal[6] analyzed numerically the plane-wave propagation in nonuniform ducts with compressible subsonic mean flow by means of a segmentation approach, and derived a simplified transfer matrix for individual segments and consequently for the tube. They compared their result with the analytical, experimental, and computational results published elsewhere in the literature.

The elementary nonuniform duct used as a flow metering device, the Herschel–Venturi tube, involves wave propagation and attenuation and was analyzed by Selamet and Easwaran.[7] Selamet *et al.*[8] investigated the acoustic performance of such venturi tubes for a plane-wave propagation with a stationary medium, and showed that the analytical predictions compare well with experimental observations.

But the solution becomes more complex with a wave equation with variable coefficients, that would result from an exact analysis of nonuniform ducts. A genuine attempt was made by Dokumaci[9] to make use of the matrix calculus theory, better known as matrizant approach,[10] to solve the coupled governing equations. His analysis included the relatively higher Mach number (the case of compressible flow). He presented approximate analytical solutions based upon certain assumptions.

Thus, in the published literature, variable area ducts and uniform area concentric-tube resonators (CTR) have been analyzed. However, the authors are not aware of any worthwhile attempts at the acoustic analysis of any generalized variable area concentric tube resonators, as shown in Fig. 1. Meanwhile the conical concentric-tube Resonators (CCTR) that fall under the same league of variable area concentric tube resonators (see Figs. 2(a) and (b) and 3), form the sub-

a)Author to whom correspondence should be addressed; electronic mail: munjal@mecheng.iisc.ernet.in

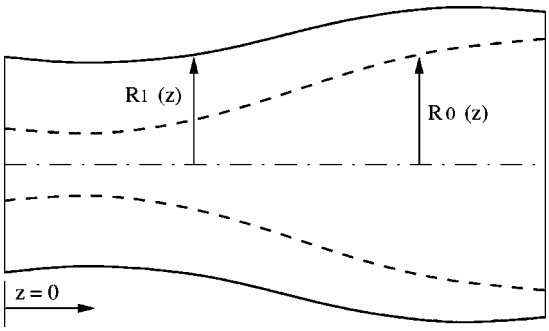

FIG. 1. Line diagram for a variable area concentric tube resonator.

ject matter of the present paper. Incidentally, the cross-sectional area of the annular cavity is made nonzero, at any point along the axis, in order to avoid numerical instability.

II. GOVERNING EQUATIONS

Assumptions made in the formulation of the governing equations of motion for the CCTR are the same as made by Sullivan.[11] These are as follows:

1. Spatial variations of acoustic pressure and thence density across the wave fronts in both the inner tube and annular cavity are negligible.

2. Amplitudes of pressure and density perturbation in both the tube and cavity are negligible compared to their mean values.

3. For an incompressible moving medium, axial gradients of the mean flow are negligible for a uniform tube.

4. The annular cavity contains stationary medium.

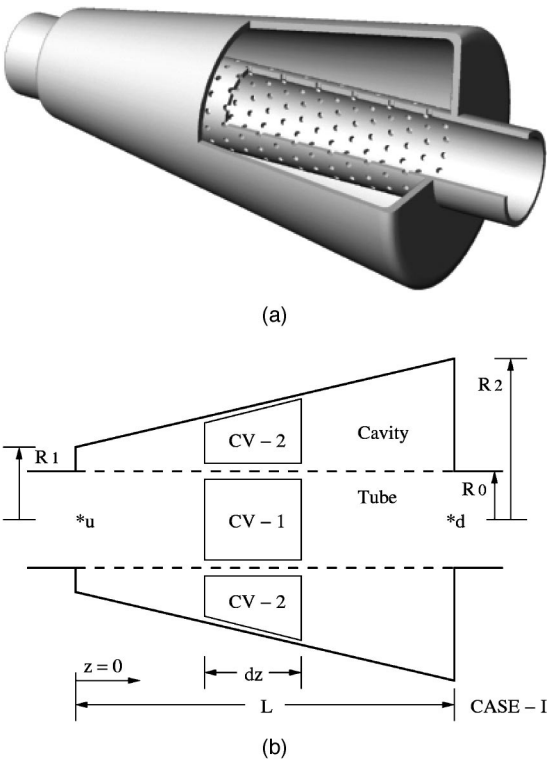

FIG. 2. A muffler configuration with uniform inner tube and conical cavity. (a) Line diagram and (b) A 3D solid model of Case I. showing the cross-sectional isometric view. The downstream and the upstream ends are shown by $*d$ and $*u$, respectively.

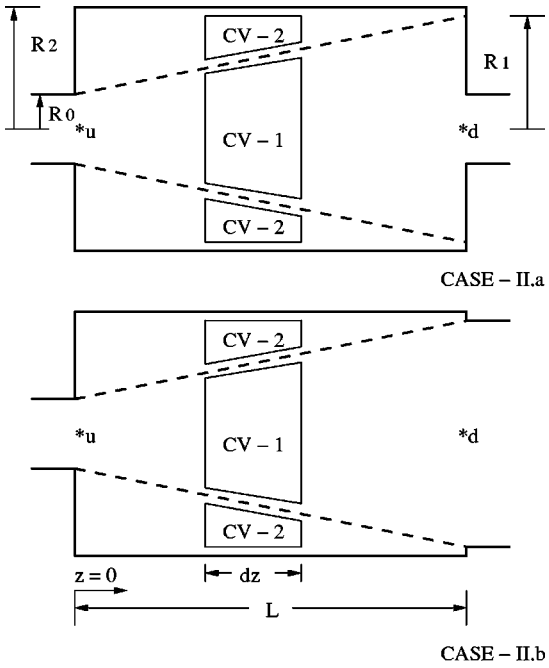

FIG. 3. Muffler configurations with conical tube, conical cavity, and uniform shell. Line diagrams of configurations, Case II.a and Case II.b

5. Temperature variation and viscous effect of the medium are negligible.

6. Perforation along the entire length of the tube is uniform.

7. Wall thickness of the inner (perforated) tube is negligible as compared to the radius.

Consider two coaxial control volumes of length dz as shown in Fig. 2(a). The central conical tube has radius $R_1(z)$ whereas the truncated conical annular cavity has radius $R_2(z)$, with constant gradient in each case.

A. Conservation of mass

Let ρ_0 be the time-mean component of the density for both the inner tube and the annular cavity, and $\rho_1(z,t)$ and $\rho_2(z,t)$, be the density perturbations averaged over the cross-sectional areas S_1 and S_2, respectively. The mean flow velocities in the tube and cavity are $U_1(z)$ and $U_2(z)$, with $u_1(z,t)$ and $u_2(z,t)$ being the corresponding velocity perturbations. It may be noted that $S_1(z)=\pi R_1^2(z)$ and $S_2(z)=\pi[R_2^2(z)-R_1^2(z)]$ vary only with respect to z. Then, the linearized form of the continuity equation for control volume 1 is given by

$$\frac{\partial \rho_1}{\partial t}+U_1\frac{\partial \rho_1}{\partial z}+\rho_0\frac{\partial u_1}{\partial z}+u_1\rho_0\frac{dS_1(z)}{S_1(z)dz}+\frac{2\pi R_1(z)u^*\rho_0}{S_1(z)}=0 \tag{1}$$

and that for the control volume 2 may be written as

$$\frac{\partial \rho_2}{\partial t}+U_2\frac{\partial \rho_2}{\partial z}+\rho_0\frac{\partial u_2}{\partial z}+u_2\rho_0\frac{dS_2(z)}{S_2(z)dz}-\frac{2\pi R_1(z)u^*\rho_0}{S_2(z)}=0, \tag{2}$$

where u^* is the radial particle velocity at the interface ($r=R_1$), reckoned to be positive for the radially outward direction (from 1 to 2).

B. Conservation of momentum

The conservation of momentum equations for dynamical equilibrium for the control volumes are based on the assumption that there is no momentum transfer across the interface between the control volumes. The condition of such a dynamically passive interface holds good for the grazing flow assumption. A generalized momentum equation becomes

$$\rho_0\left[\frac{\partial u_i}{\partial t}+U_i\frac{\partial u_i}{\partial z}\right]+\frac{\partial p_i}{\partial z}-(\rho_0 u_i+\rho_i U_i)\frac{U_i dS_i(z)}{S_i(z)dz}=0,$$

$$i=1 \quad \text{and} \quad 2. \tag{3}$$

The indicial notation i represents the tube and the cavity for the numerical values of 1 and 2, respectively. Variables p_1 and p_2 are respective space average pressure perturbations over areas S_1 and S_2. The fluctuating radial particle velocity through perforations u^* as mentioned in Eqs. (1) and (2) is a function of the pressure difference across the perforations. Thus

$$u^*=\frac{p_1(z)-p_2(z)}{\rho_0 a_0 \zeta}, \tag{4}$$

where ζ is the nondimensional specific acoustic impedance of the perforate and a_0 is the speed of sound. Assuming an isentropic process in both the control volumes, the pressure and density perturbations are related by

$$p_i=\rho_i a_0^2; \quad i=1,2. \tag{5}$$

III. SOLUTION

For steady state simple harmonic motion

$$\left.\begin{aligned} p_i(z,t)&=p_i(z)e^{j\omega t}\\ u_i(z,t)&=u_i(z)e^{j\omega t}\\ u^*(z,t)&=u^*(z)e^{j\omega t}\end{aligned}\right\} \quad i=1,2. \tag{6}$$

Eliminating ρ_1 and ρ_2 from the continuity and momentum equations using the isentropicity relationship of Eq. (5), and expressing radial velocity as in Eq. (4) with the assumption of a stationary medium in the cavity, Eqs. (1) and (2) become

$$\frac{U_1}{a_0^2}\frac{dp_1}{dz}+\left[\frac{j\omega}{a_0^2}+\frac{2\rho_0}{R_1(\rho_0 a_0\zeta)}\right]p_1-\frac{2\rho_0}{R_1(\rho_0 a_0\zeta)}p_2+$$

$$+\rho_0\frac{dS_1}{S_1 dz}u_1+\rho_0\frac{du_1}{dz}=0, \tag{7}$$

$$\left[\frac{j\omega}{a_0^2}+\frac{2\pi R_1\rho_0}{S_2(\rho_0 a_0\zeta)}\right]p_2-\frac{2\pi R_1\rho_0}{S_2(\rho_0 a_0\zeta)}p_1+\rho_0\frac{dS_2}{S_2 dz}u_2+\rho_0\frac{du_2}{dz}$$

$$=0. \tag{8}$$

The resistance and inertance parts of the perforate impedance at the interface, $\zeta=\Re+j\Im$, are given by[12,13]

$$\Re=[0.00734(1+72.23M)]/\sigma;$$

$$\Im=[k_0(t_h+0.85d_h)]/\sigma,$$

where σ is the porosity of the perforate interface, t_h is thickness of the perforated tube, and d_h is the hole diameter, respectively.

Mean flow inside any control volume causes the coupling of the velocity and pressure derivatives as in Eq. (7). Equations (7) and (8) are further rearranged to single out one of them, and thus come up with a form of an algebraic equation in space state variables, where two state vectors get coupled by the characteristic matrix of the system. Thus

$$\frac{du_1}{dz}=\mathbf{A}_1 p_1+\mathbf{B}_1 p_2+\mathbf{C}_1 u_1+\mathbf{D}_1\frac{dp_1}{dz}, \tag{9}$$

$$\frac{du_2}{dz}=\mathbf{A}_2 p_1+\mathbf{B}_2 p_2+\mathbf{C}_2 u_2, \tag{10}$$

where

$$\mathbf{A}_1=-\left[\frac{j\omega}{\rho_0 a_0^2}+\mathbf{B}_1\right]; \quad \mathbf{B}_1=\frac{2}{R_1(\rho_0 a_0\zeta)},$$

$$\mathbf{C}_1=-\frac{dS_1}{S_1 dz}; \quad \mathbf{D}_1=-\frac{U_1}{a_0^2\rho_0},$$

$$\mathbf{A}_2=\frac{2\pi R_1}{S_2(\rho_0 a_0\zeta)}; \quad \mathbf{B}_2=-\left[\frac{j\omega}{\rho_0 a_0^2}+\mathbf{A}_2\right];$$

$$\mathbf{C}_2=-\frac{dS_2}{S_2 dz}.$$

Similarly, making use of isentropicity condition in the conservation of momentum equation for any generalized ith duct one gets

$$\frac{dp_i}{dz}-\frac{U_i^2}{S_i a_0^2}\frac{dS_i}{dz}p_i+\left[j\omega\rho_0-\frac{\rho_0 U_i}{S_i}\frac{dS_i}{dz}\right]u_i+\rho_0 U_i\frac{du_i}{dz}=0. \tag{11}$$

This may be rearranged to single out the pressure derivative

$$\frac{dp_i}{dz}=\mathbf{E}_i p_i+\mathbf{F}_i u_i+\mathbf{G}_i\frac{du_i}{dz}, \quad i=1,2, \tag{12}$$

where the coefficients $\mathbf{E}_i$, $\mathbf{F}_i$, and $\mathbf{G}_i$ are given by

$$\mathbf{E}_i=\frac{U_i^2}{S_i a_0^2}\frac{dS_i}{dz}, \tag{13}$$

$$\mathbf{F}_i=\left[-j\omega\rho_0+\frac{\rho_0 U_i}{S_i}\frac{dS_i}{dz}\right], \tag{14}$$

$$\mathbf{G}_i=-\rho_0 U_i. \tag{15}$$

Substituting Eq. (12) in Eq. (9) for $i=1$, and Eq. (10) back into Eq. (12) for $i=2$, one can separate out the pressure and velocity derivatives. This leads to the desired space state vectors as follows:

$$\frac{dp_i}{dz}=a(i,1)p_1+a(i,2)p_2+a(i,3)u_1+a(i,4)u_2,$$

$$i=1,2, \tag{16}$$

$$\frac{du_i}{dz} = a(k,1)p_1 + a(k,2)p_2 + a(k,3)u_1 + a(k,4)u_2,$$

$$k = i + 2. \tag{17}$$

The column vector $\{\mathbf{Y}\}$ consists of the state variables p_1, p_2, u_1, and u_2, which may be altered for dimensional uniformity among the elements. Thus

$$\{\mathbf{Y}\} = [p_1 \;\; p_2 \;\; (\rho_0 a_0)u_1 \;\; (\rho_0 a_0)u_2]^T, \tag{18}$$

where $\rho_0 a_0$ is the characteristic impedance of the medium.

Considering vector $\{\mathbf{Y}\}$ as a dependent entity and a function of axial coordinate z, Eqs. (16) and (17) may be rearranged as a set of a first-order homogeneous differential equations

$$\{\mathbf{Y}'\} = [\mathbf{\Omega}]\{\mathbf{Y}\}, \tag{19}$$

where

$$\mathbf{Y}_i' = \frac{d\mathbf{Y}_i}{dz}$$

and

$$\mathbf{\Omega}_{ik} = a_{ik}, \quad i,k = 1,4.$$

The constituent elements of the system matrix $[\mathbf{\Omega}]$ are explicit functions of coefficients $\mathbf{A}_1$, $\mathbf{A}_2$, $\mathbf{B}_1$, $\mathbf{B}_2$, $\mathbf{C}_1$, $\mathbf{C}_2$, $\mathbf{D}_1$, $\mathbf{E}_i$, $\mathbf{F}_i$, $\mathbf{G}_i$. $(i = 1,2)$ and the characteristic impedance of air $\rho_0 a_0$

$$[\mathbf{\Omega}] = \begin{bmatrix} \dfrac{\mathbf{E}_1 + \mathbf{A}_1\mathbf{G}_1}{1 - \mathbf{D}_1\mathbf{G}_1} & \dfrac{\mathbf{B}_1\mathbf{G}_1}{1 - \mathbf{D}_1\mathbf{G}_1} & \dfrac{\mathbf{F}_1 + \mathbf{C}_1\mathbf{G}_1}{(1 - \mathbf{D}_1\mathbf{G}_1)\rho_0 a_0} & 0 \\ 0 & 0 & 0 & \dfrac{\mathbf{F}_2}{\rho_0 a_0} \\ \dfrac{(\mathbf{A}_1 + \mathbf{D}_1\mathbf{E}_1)\rho_0 a_0}{1 - \mathbf{D}_1\mathbf{G}_1} & \dfrac{\mathbf{B}\rho_0 a_0}{1 - \mathbf{D}_1\mathbf{G}_1} & \dfrac{\mathbf{C}_1 + \mathbf{D}_1\mathbf{F}_1}{1 - \mathbf{D}_1\mathbf{G}_1} & 0 \\ \mathbf{A}_2 & \mathbf{B}_2 & 0 & \mathbf{C}_2 \end{bmatrix}. \tag{20}$$

$$1 - \mathbf{D}_i\mathbf{G}_i = 1 - M_i^2, \tag{21}$$

where $M_i = (U_i/a_0)$ is the flow Mach number in the ith duct.

Making use of the structure of the state vector $\{\mathbf{Y}\}$, it may be noted that elements of the odd numbered rows of the system matrix $[\mathbf{\Omega}]$ reflect the physical attributes of the tube and the even ones those of the annular cavity. In a generalized system matrix, elements associated with either of the ducts turn out to be similar. But application of specific conditions on certain ducts would modify the corresponding coefficients and hence the related elements of the system matrix.

So elements $\mathbf{\Omega}_{ij}$, associated with the cavity turn out to be similar to the corresponding ones of the inner tube with the exception of the effect of the no flow condition ensured by the assumed grazing flow in the inner duct. This makes some coefficients either vanish or reduce to certain physical anticipations when pushed to the limits. Thus a stationary medium in the cavity lets the coefficients $\mathbf{D}_2$, $\mathbf{E}_2$, and $\mathbf{G}_2$ vanish and the coefficient $\mathbf{F}_2$ reduces to its primitive inertial term or a pure inertive impedance. This explains implicitly that the sole resistance offered by the system comes from the perforate impedance.

In general, simultaneous coupled equations are solved by decoupling and reducing the number of equations at the cost of increasing the order of the mutated equations. For example, the basic equations of mass continuity and momentum balance result in a second-order wave equation and thence a second-order Helmholtz equation. The adopted matrizant approach, a semianalytical method which offers the convenience to solve a set of coupled first-order equations without mutating them to half the number of decoupled second-ordered equations. When the elements of the system matrix are functions of a variable z then the matrix is bound to have the elements $\mathbf{\Omega}_{ij}$, which are continuous functions of any real variable. This applies equally to any other complex variable. In either case, possible singularities should be avoided. Then the solution of the first order differential Eq. (19) would be within the limits and will have the form[9,10]

$$\{\mathbf{Y}\}_{z=L} = \mathbf{e}^{\int_0^L [\mathbf{\Omega}]dz}\{\mathbf{Y}\}_{z=0} \tag{22}$$

or

$$\{\mathbf{Y}\}_{z=0} = \mathbf{e}^{[\mathbf{\Gamma}]}\{\mathbf{Y}\}_{z=L}, \tag{23}$$

where $\{\mathbf{Y}\}_{z=0}$ and $\{\mathbf{Y}\}_{z=L}$ are the upstream and downstream state vectors, respectively, related to the concerned boundaries and

$$[\mathbf{\Gamma}] = -\int_0^L [\mathbf{\Omega}]dz.$$

Coefficients of this matrix (System matrix) are given in the Appendix. $\mathbf{e}^{[\mathbf{\Gamma}]}$ the transfer matrix, can be represented by the Maclaurin's series

$$\mathbf{e}^{[\mathbf{\Gamma}]} = [\mathbf{I}_N] + \sum_{n=1}^{\infty} \frac{[\mathbf{\Gamma}]^n}{n!}, \tag{24}$$

where $[\mathbf{I}_N]$ is the fourth-order identity matrix.

The matrix $[\mathbf{\Gamma}]$ and hence the corresponding forward transfer matrix $[\mathbf{e}^{\lambda}]$ is diagonalized using the modal matrix $[\mathbf{\Psi}]$ and the latent roots (eigen values). They are given as

$$[\mathbf{\Gamma}]=[\mathbf{\Psi}][\lambda][\mathbf{\Psi}]^{-1}, \quad \mathbf{e}^{[\mathbf{\Gamma}]}=[\mathbf{\Psi}][\mathbf{e}^{\lambda}][\mathbf{\Psi}]^{-1}, \tag{25}$$

$$[\mathbf{e}^{\lambda}]_{ik}=\begin{cases}\mathbf{e}^{\lambda_i} & \text{if } i=k\\ 0 & \text{if } i\neq k,\end{cases} \tag{26}$$

where λ_i is the ith latent root.

Equations (25) transform one vector to another that contains space state variables at boundaries of both the tube and the cavity. Thus a set of four simultaneous linear algebraic equations are obtained upon which two boundary conditions of the muffler configuration are applied to get the final 2×2 transfer matrix that relates the downstream vector at the exit to the upstream vector at the flow entrance.

A. Case I: Uniform inner tube, conical cavity

Figure 2 shows a muffler configuration comprising a perforated uniform tube interacting with a conical cavity. Thus the area of cross-section S_1 remains constant whereas S_2 varies with z. The variable outer radius $r(z)$ of the cavity is given by

$$\begin{aligned} &r(z)=R_1+\phi z; \quad \phi=\frac{(R_2-R_1)}{L},\\ &S_1=\pi R_0^2; \quad S_2=C_1z^2+C_2z+C_3, \end{aligned} \tag{27}$$

where the coefficients are

$$\left.\begin{aligned} C_1&=\pi\phi^2\\ C_2&=2\pi R_1\phi\\ C_3&=\pi(R_1^2-R_0^2)\end{aligned}\right\}, \tag{28}$$

and ϕ is the gradient of radius $r(z)$.

The cavity is assumed to have a stationary medium. Employing other geometrical attributes in Eqs. (A1) to (A13) and then substituting the derived matrix $[\mathbf{\Gamma}]$ back into either of Eqs. (24) or (25), a 4×4 transfer matrix is obtained. The normal particle velocity is zero at both the axial boundaries of the cavity. Thus the boundary conditions are

$$u_2=0\begin{cases}z=0\\ z=L.\end{cases} \tag{29}$$

Applying the boundary conditions of Eq. (29) in the 4×4 transfer matrix $[\mathbf{e}^{\Gamma}]$, a four pole parameter forward transmission matrix $[\mathbf{T}]$ is derived.[5]

$$\begin{bmatrix} p_1(0)\\ \rho_0a_0u_1(0)\end{bmatrix}=\begin{bmatrix} T_{11} & T_{12}\\ T_{21} & T_{22}\end{bmatrix}\begin{bmatrix} p_1(L)\\ \rho_0a_0u_1(L)\end{bmatrix}. \tag{30}$$

Transmission loss (TL) can be calculated from the absolute sum of the four pole parameters.

$$\mathrm{TL}=20\log_{10}\left[\frac{1}{2}\left(\frac{S_d}{S_u}\right)^{0.5}\left(\frac{1+M_u}{1+M_d}\right)|T_{11}+T_{12}+T_{21}+T_{22}|\right], \tag{31}$$

whereas S_d and S_u are the cross-sectional areas, and M_d and M_u are the flow mach numbers of the outlet and the inlet tubes, respectively.

B. Case II: Conical inner tube, conical cavity, uniform shell

In another configuration, the tube is made conical keeping the shell radius (outermost radial dimension of the cavity) constant, in order to incorporate geometrical nonuniformities in both the control volumes as shown in Fig. 3. The mathematical modeling for both the subconfigurations in Fig. 3 are the same but an additional sudden contraction in case of the former leads to different TL expressions. The coaxial cylindrical cavity has a constant outer radius R_2 whereas the variable cavity-tube interface radius $r(z)$, varies linearly from R_0 at $z=0$ to R_1 at $z=L$, and is given by

$$r(z)=R_0+\theta z; \quad \theta=\frac{(R_1-R_0)}{L}. \tag{32}$$

With the variation of $r(z)$, the effective cross-sectional areas of wave propagation in the tube and the cavity are given by

$$S_1(z)=\pi r(z)^2,$$

$$S_2(z)=\pi\{R_2^2-r(z)^2\}.$$

On applying Eq. (32), $S_1(z)$ and $S_2(z)$ take quadratic forms of the independent variable z

$$S_1(z)=C_{11}z^2+C_{12}z+C_{13},$$

$$S_2(z)=C_{21}z^2+C_{22}z+C_{23},$$

where the coefficients are

$$\left.\begin{aligned} C_{11}&=\pi\theta^2\\ C_{12}&=2\pi R_0\theta\\ C_{13}&=\pi R_0^2\end{aligned}\right\} \tag{33}$$

and the corresponding coefficients for the annular cavity can be written as

$$C_{21}=-C_{11}; \quad C_{22}=-C_{12}; \quad C_{23}=\pi(R_2^2-R_0^2). \tag{34}$$

The mean flow parameter can be simplified in order to get rid of the complex structure of the constituent elements in the resulting system matrix $[\mathbf{\Omega}]$ in Eq. (20). For a moving medium in an inhomogeneous duct the flow velocity becomes a function of axial coordinate z that leads to more complex interlacing functions in the system matrix, even for a steady incompressible flow. Recognizing that the convective effect of the meanflow on wave propagation is only marginal, it is set equal to its spatial mean. Averaging it out on the basis of the average cross-sectional area

$$\hat{U}_0=\frac{U_0S_{1(z=0)}}{\dfrac{1}{L}\displaystyle\int_0^L S\,dz}, \tag{35}$$

where $\hat{U}_0$ denotes the average mean flow of the variable duct and S_1 the cross-sectional area at the inlet tube.

Later conditions evolved for this configuration are applied in Eqs. (A1) to (A13) to get the first hand 4×4 transfer matrix. Using boundary conditions similar to Case I as explained in Eq. (29) gives the final transmission matrix and thence the TL.

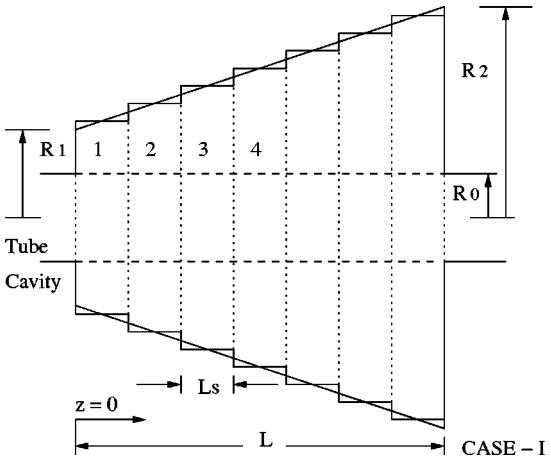

FIG. 4. Line diagram for a stepped conical concentric tube resonator for Case I.

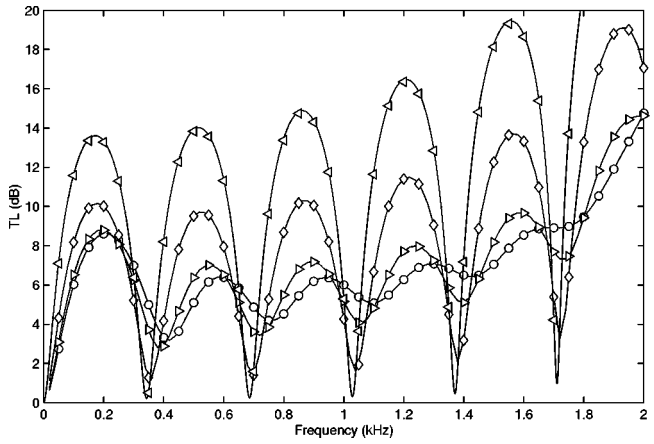

FIG. 5. Effect on TL with variation of R_1 for Case I: ○-○-○, 25 mm; ▷-▷-▷, 30 mm; ◇-◇-◇, 45 mm, and ◁-◁-◁, 75 mm.

IV. STEPPED CTR APPROACH

A powerful evidence of this theoretical approach for authenticity is provided by comparing the upshots with those of another approximate but entrenched mathematical model. Here the established theory of stepped concentric-tube resonator (CTR) corroborates the present approach. In the version of stepped concentric-tube resonator, each of the variable area ducts is segmented to a finite number of short ducts with uniform radius as shown in Fig. 4. The number of segments is dependent upon the extent of inhomogeneity and on the desired accuracy. Individual segments may be specified to be of equal length for convenience, particularly for a duct with a radius of uniform gradient. State vectors between each segmental ends are related by a first hand transfer matrix of a simple CTR, $[\mathbf{Ta}_n]$ for any such nth segment. Thus for the nth segment

$$\{\mathbf{Y}\}^n_{z=(n-1)Ls}=[\mathbf{Ta}_n]\{\mathbf{Y}\}^n_{z=nLs}, \tag{36}$$

where the state vector at the left-hand side denotes the upstream end of the nth segment that links the corresponding one at the downstream end by means of the transfer matrix of the tubular segment $[\mathbf{Ta}_n]$, given by Eq. (3.117) of Ref. 5.

The discontinuity between two consecutive segments is effectively treated by incorporating a sudden area change at the interface, using a respective forward transmission matrix $[\mathbf{Tb}_n]$, a diagonal matrix that links to the interface of the nth, and $(n+1)$th segments. It may be given as

$$\{\mathbf{Y}\}^n_{z=nLs}=[\mathbf{Tb}_n]\{\mathbf{Y}\}^{n+1}_{z=nLs}, \tag{37}$$

where, for stationary medium,

$$[\mathbf{Tb}_n]_{kk}=\begin{cases}1 & \text{if } k=1,2\\ \delta_{ni} & \text{if } k=i+2 \ \ (i\text{th duct})\end{cases}. \tag{38}$$

In Eq. (38), δ_{ni} is the ratio of the effective cross-sectional area of the $(n+1)$th to the nth segment of the ith duct. Use of Eqs. (37) and (38) in Eq. (36) yields

$$\{\mathbf{Y}\}^n_{z=(n-1)Ls}=[\mathbf{Tc}_n]\{\mathbf{Y}\}^{n+1}_{z=(n)Ls} \tag{39}$$

where

$$[\mathbf{Tc}_n]=[\mathbf{Ta}_n][\mathbf{Tb}_n].$$

Sequential multiplication of these matrices generates a 4×4 transfer matrix $[\mathbf{TF}]$, for an acoustic element sliced into "N" hypothetical steps or segments:

$$[\mathbf{TF}]=\left[\prod_{i=1}^{n-1}[\mathbf{Tc}_i]\right][\mathbf{Ta}_N]. \tag{40}$$

Applying appropriate boundary conditions to the above transfer matrix $[\mathbf{TF}]$, a 2×2 four pole parametric relationship is established between the upstream and downstream ends. Finally, TL is evaluated as in Eq. (31).

V. DISCUSSION

The governing equations above and the subsequent analysis takes an incompressible mean flow into account. However, results are computed and discussed here for the case of stationary medium in order to bring out the physical effect of variable area ducts and CCTR's. All numerical computations were performed for sonic speed of 340 m/s and a fixed set of dimensions of the resonator unless mentioned explicitly for specific cases. For the configuration of Case I, as in Fig. 2, the dimensions R_0, R_1, and R_2 are fixed at 25, 30, and 75 mm, respectively, whereas all the computations are performed on a length L of 50 cm. Corresponding dimensions for Case II of Fig. 3, are the same as those of Case I, with the exception of R_1, that is taken nearly equal to the value of R_2 to avoid the singularity due to the zero cross-sectional area (i.e., if $R_2=75$ mm $R_1=74.9$ mm). The perforated tube thickness t_h and hole diameter d_h have the default option values of 1 and 3 mm, respectively, and the porosity is kept at 0.06 (6%). While evaluating the four-pole parameters of a muffler with a variable area duct, in order to enhance numerical stability, the entire muffler is segmented into several short segments (steps) keeping the nonuniform profile intact for each of these segments, unlike the stepped CTR approach (where each step is assumed to have a uniform cross-sectional area).

A. Effect of the duct geometry

For Case I, R_0 and R_2 are kept invariant, while varying R_1 in steps, in order to incorporate areawise inhomogeneity in the cavity for analyzing the wave propagation and its ef-

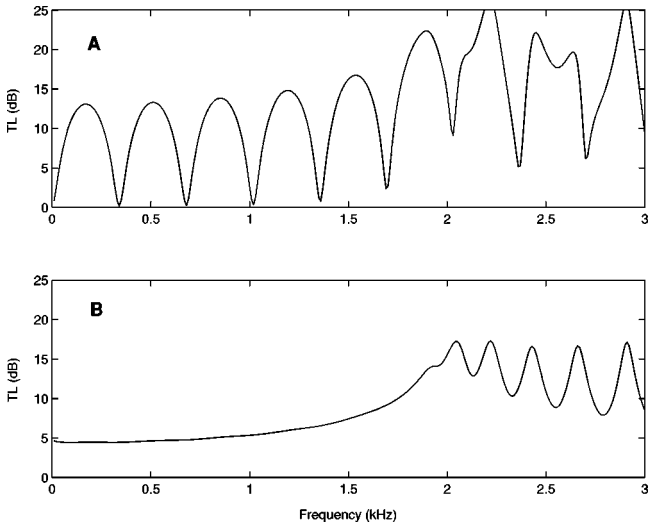

FIG. 6. Comparison of results between A—Case II.a and B-Case II.b.

fect on the TL. The result is plotted in Fig. 5 for a set of four different values of R_1 spanning over the limits. It is noticed that the peaks of TL spectrum have come down with a reduction in R_1. But significantly, at the same time troughs have gone up, resulting in a flatter curve, which is desirable from the design point of view. Incidentally, a similar effect was noticed by Selamet *et al.*[8] while analyzing acoustic attenuation with flow loss for venturi tubes. Both the outcomes have the same genesis. In view of the fact that the entire wave front of the cavity does not reflect with the same phase value, the probability of both resonance and antiresonance has gone down due to the nonuniformity of the cross section. For the limiting case of $R_1 \simeq R_0$ (when $R_1 = R_0$, it generates a singularity effect), the trough has gone up by about 3 dB at the lower frequencies to 8 dB at higher frequencies, when compared to an equivalent simple concentric tube resonator, which is in fact the other limiting case of $R_1 \cong R_2$.

The TL spectrum for the two subconfigurations of Case II (Fig. 3) are shown in Fig. 6, where the dimensions of the inlet and outlet tubes set the essential difference between the configurations. In the case of the configuration of Case II.b, a flat and enhanced response similar to the sudden expansion is observed for a near limiting case of $R_1 \simeq R_2$ at the lower frequencies. In view of the fact that the wave at lower frequencies finds the perforated screen apparently transparent, the outcome looks logical. Absence of pass bands is encouraging, although peaks and troughs set in at relatively higher frequencies. In contrast the configuration of Fig. 3(a) (Case II.a) acts more like an expansion chamber particularly at lower frequencies due to the incorporation of sudden contraction at the downstream end, and thereby curtails the advantage of a variable area duct.

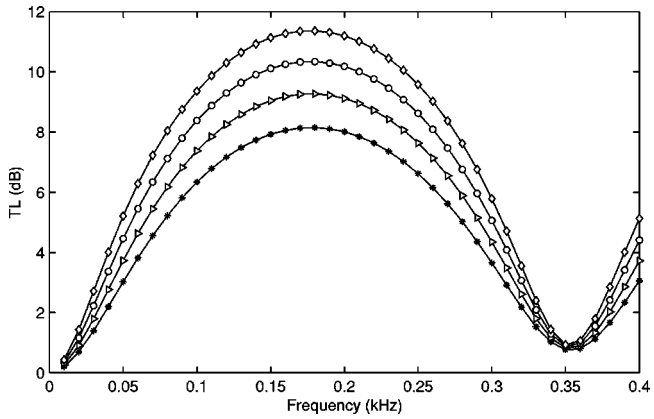

FIG. 7. Different sets of R_2 and R_1 with constant overall length L, radius of the perforated tube R_0 and area ratio R_a, produce equal effective length (Case I). ◇-◇-◇, 80-50; ○-○-○, 75-47.42; ▷-▷-▷, 70-44.87; *-*-*, 65-42.35; mm-mm.

B. Effective length

The position of the first trough shifts along the frequency coordinate as seen in Fig. 5, for a conical concentric tube resonator of Case I, when compared to the corresponding simple concentric-tube resonator of equal length. Further drifting is noticed with an increased gradient of the outer radius of cavity, suggesting a reduced effective length of the resonator. The corresponding effective length of the fundamental trough in TL spectrum is calculated according to the Helmholtz resonance frequency, i.e., $k_0 L_{\text{eff}} = \pi$, or

$$L_{\text{eff}} = \frac{a_0}{2 f_r},$$

where f_r is the corresponding resonant frequency.

Effective length is predominantly independent of the tapering as long as the slope remains constant, but keeps a covalent relationship with R_a, the ratio of annular cross-sectional areas A_0 and A_l at the ends of the cavity for a constant L and R_0. The area ratio R_a for Case I is given by

$$R_a = \frac{R_2^2 - R_0^2}{R_1^2 - R_0^2}.$$

Different sets of radial dimensions of R_1 and R_2 of the cavity manifest the same resonance frequency, resulting in equal effective lengths for a constant value of $R_a (= 3.08)$ as shown in Fig. 7. The alteration of effective length with the ratio R_a, shows the existence of a phenomenological relationship between L_c, the ratio of effective length to the geometric length of the cavity, and the area ratio. For a fixed geometric length of the cavity, different values of L_c are obtained for different values of R_a, and the result is plotted in Fig. 8. An empirical relationship is brought forth connecting the two variables

$$y = \begin{cases} 1 - 1.7\times 10^{-2} x + 8\times 10^{-4} x^2 - 1.4\times 10^{-5} x^3; & x \leqslant 20 \\ 0.91 - 3\times 10^{-3} x + 3.9\times 10^{-5} x^2 - 1.8\times 10^{-7} x^3; & x > 20 \end{cases}, \tag{41}$$

where variables x and y denote R_a and L_c, respectively.

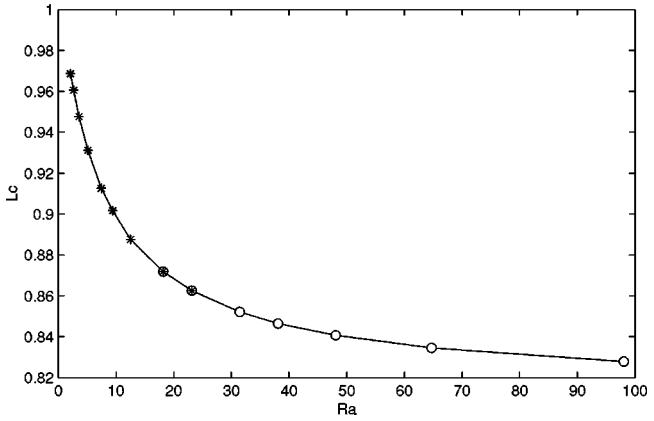

FIG. 8. Effect of the end cross-sectional area ratio of cavity on the effective length as given by Eq. (41). ∗-∗-∗, $R_a \leqslant 20$ and ○-○-○, $R_a > 20$.

C. Conical CTR vis-a-vis stepped CTR

Validity of the predictions from the exact matrizant approach for the CCTR is verified by comparing them with those from the stepped CTR (Fig. 4) described earlier and the results are shown in Figs. 9 to 11. In all these figures, abscissa is limited to 3 kHz, which is a little above the cutoff frequency of 2763 Hz for a maximum radius of 150 mm. As the number of steps increases the results converge better as shown in Figs. 9 and 10, for Case I (Fig. 2) and Case II.b (Fig. 3), respectively. Incidentally, the stepped equivalent of the configuration of Case II.b (Fig. 3) has not been included in this paper.

The TL spectrum for a CCTR of Case II.a is compared with an equivalent simple concentric tube resonator (here it is a CTR with all dimensions the same, except the perforated tube diameter, that is equal to the minimum of the conical perforated tube of the corresponding CCTR Case II.a) and the result is plotted in Fig. 11. For the simple CTR, the peaks and troughs remain up to about 2 kHz, but vanish at higher frequencies. At lower frequencies the acoustic wave ''sees'' no perforate screen between the ducts, that is, the interface is more or less acoustically transparent and therefore both the configurations behave like simple expansion chambers.

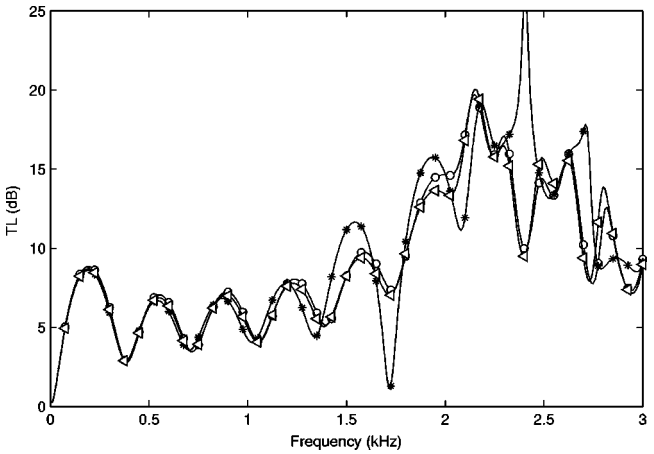

FIG. 9. For Case I: Comparison between the exact theoretical analysis and approximate stepped simple CTR analysis for stationary medium. ○-○-○, exact analysis; ∗-∗-∗, 5, and ◁-◁-◁, 10 steps.

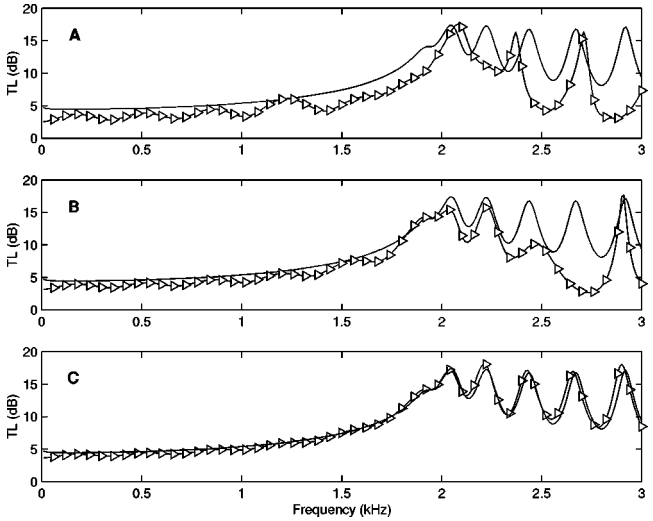

FIG. 10. For Case II.b, comparison between exact —, theoretical analysis and ▷-▷-▷, approximate stepped simple CTR analysis. Convergence with A-4, B-6, and C-10 segments.

D. Effect of segmented cavity

Transmission loss spectrum for the multichamber cavity CCTR of equal segments (Fig. 12) is similar to the corresponding partitioned CTR and the result is shown in Fig. 13. But one may not ensure a broadband TL by just introducing unequal partitions along the length of the CCTR like in the plain CTR. Figure 14 shows the possible configurations due to a single partition, where the segments are separated by a narrow uniform tube of length L_t. The corresponding TL spectrum of Fig. 15 predicts an unequal performance for the different configurations, although each of them is individually symmetric for a stationary medium. Configuration ''A'' promises an enhanced broadband TL with no significant peaks and troughs, that ensures an attenuation of at least 10 dB for frequencies beyond 0.37 kHz. The configurations ''B'' and ''C'' fail in this regard, whereas the final configuration ''D'' predicts a moderate broadband TL. Here it may be noted that an important implication of antilogarithmic addition is that a TL curve with raised troughs yields higher overall value of TL than the one with strong peaks and troughs.

VI. CONCLUSION

Starting with a mathematical model based on the control volume approach with the assumption of the plane wave

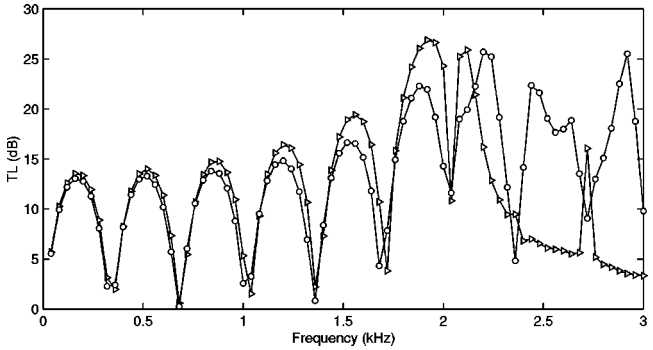

FIG. 11. Comparison between the configurations, ○-○-○, Case II.a and ▷-▷-▷, Equivalent simple concentric-tube resonator.

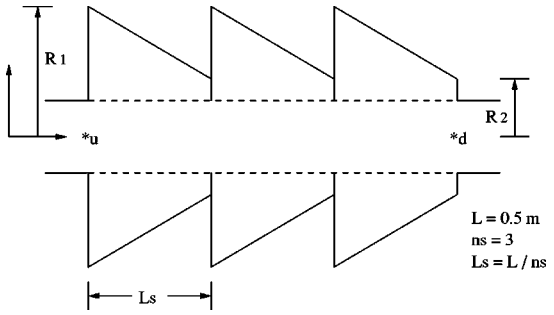

FIG. 12. Configuration for a three-chamber cavity CCTR, (Case I) of equal segments.

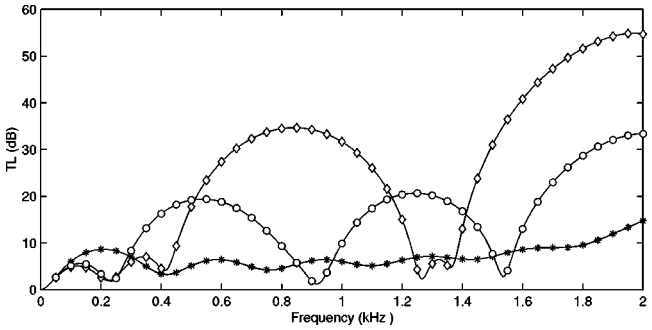

FIG. 13. Effect of partitioning on the transmission loss spectrum of the segmented CCTR of equal segments of Fig. 12. ∗-∗-∗, Single-chamber cavity; ○-○-○, two-chamber cavity and ◇-◇-◇, and three-chamber cavity.

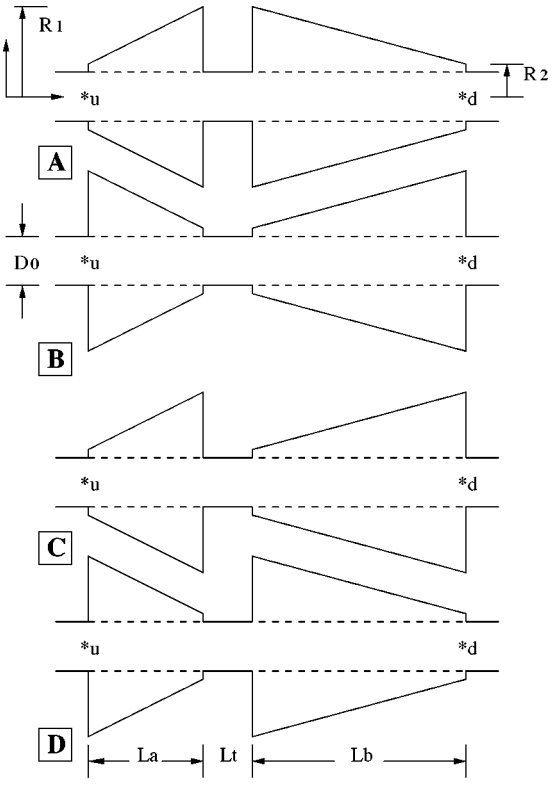

FIG. 14. Various possible configurations of unequal segments.

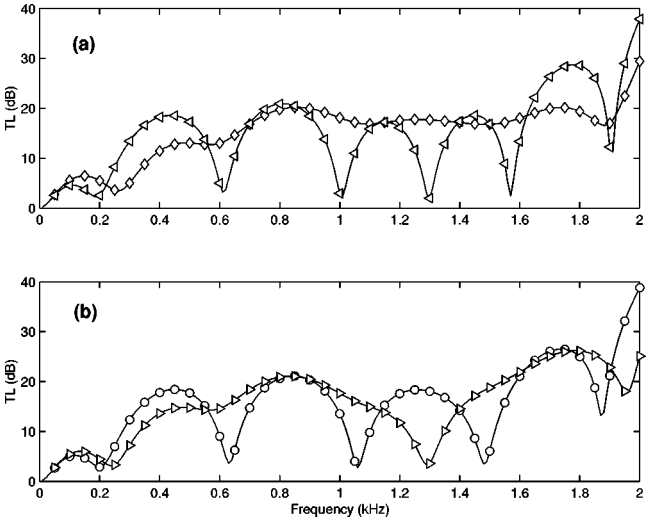

FIG. 15. (a) and (b) TL spectrum for configurations of unequal segments of Fig. 14. ◇-◇-◇, (A); ◁-◁-◁, (B); ○-○-○, (C), and ▷-▷-▷, (D).

propagation in nonuniform concentric tube resonators, the matrizant approach is made use of in this paper to solve a set of simultaneous first order differential equations. The model is checked for self consistency, and has been validated against the stepped CTR approach. The parametric studies have produced a few notable effects. One of them is the reduced effective length for a conical concentric tube resonator that makes the troughs (and peaks) to drift apart. Absence of passbands over a considerable frequency range is vital for a designer; raising of troughs is more important than higher peaks in a TL spectrum because of the implication of the antilogarithmic addition. So, the reduced cavity volume is no more disadvantageous as the troughs have been raised considerably. While the analysis takes into account an incompressible mean flow, the parametric study has been limited to stationary medium in order to elucidate acoustics of variable area ducts.

ACKNOWLEDGMENTS

The authors would like to place on record their appreciation of the financial sponsorship of the Facility for Research in Technical Acoustics (FRITA) by the Department of Science and Technology of the Government of India.

APPENDIX: GENERALIZED COEFFICIENTS OF THE SYSTEM MATRIX

The square matrix $[\Gamma]$ associated with the transfer matrix of Eq. (23) has generalized elements α_{ij} for any arbitrary concentric tube resonator (CTR) configuration, provided no singularity is encountered there during analytical modeling. Such singularities are mostly because of the extrapolation of the model into its limits. One such singularity arises when an area of the wave propagating duct at any instance becomes zero. This has to be avoided as shown in Figs. 2 and 3. Neglecting the M_i^3 and higher-order terms, the matrix elements are given by

$$\alpha_{11} = \gamma_1 \left[jk_0 L M_1 + \int_0^L \frac{M_1^2 S_1'}{S_1} dz \right] - \alpha_{12}, \tag{A1}$$

$$\alpha_{12} = -2\gamma_1 \int_0^L \frac{M_1}{\zeta r(z)} dz, \tag{A2}$$

$$\alpha_{13} = \gamma_1 \left[-jk_0 L + 2 \int_0^L \frac{M_1 S_1'}{S_1} dz \right], \tag{A3}$$

$$\alpha_{21} = -2\pi\gamma_2 \int_0^L \frac{M_2 r(z)}{\zeta S_2(z)} dz, \tag{A4}$$

$$\alpha_{22} = \gamma_2 \left[jk_0 L M_2 + \int_0^L \frac{M_2^2 S_2'}{S_2} dz \right] - \alpha_{21}, \tag{A5}$$

$$\alpha_{24} = \gamma_2 \left[-jk_0 L + 2 \int_0^L \frac{M_2 S_2'}{S_2} dz \right], \tag{A6}$$

$$\alpha_{31} = -jk_0 L \gamma_1 - \alpha_{32}, \tag{A7}$$

$$\alpha_{32} = 2\gamma_1 \int_0^L \frac{dz}{\zeta r(z)}, \tag{A8}$$

$$\alpha_{33} = \gamma_1 \left[jk_0 L M_1 - \int_0^L \frac{M_1^2 S_1'}{S_1} dz - \log_e \frac{S_{1(L)}}{S_{1(0)}} \right], \tag{A9}$$

$$\alpha_{41} = 2\pi\gamma_2 \int_0^L \frac{r(z)}{\zeta S_2(z)} dz, \tag{A10}$$

$$\alpha_{42} = -jk_0 L \gamma_2 - \alpha_{41}, \tag{A11}$$

$$\alpha_{44} = \gamma_2 \left[jk_0 L M_2 - \int_0^L \frac{M_2^2 S_2'}{S_2} dz - \log_e \frac{S_{2(L)}}{S_{2(0)}} \right], \tag{A12}$$

where $r(z)$ is the radius of tube. Matrix coefficients α_{14}, α_{23}, α_{34}, and α_{43} are equal to zero, and

$$\gamma_i = \frac{1}{1 - M_i^2}; \quad i = 1,2. \tag{A13}$$

The above generalization is equally applicable for the cross flow CTRs as well, assuming that the flow velocities and hence the Mach numbers are not constant, but some functions of variable z. Though γ_i in Eq. (A13) depends on z, it is assumed invariant on the basis of an averaged out mean flow velocity for simplification as mentioned earlier in Eq. (35).

[1] J. W. Sullivan and M. J. Crocker, "Analysis of concentric tube resonators having unpartitioned cavities," J. Acoust. Soc. Am. **64**(1), 207–215 (1978).
[2] N. A. Eisenberg and T. W. Kao, "Propagation of sound through variable area duct with a steady compressible flow," J. Acoust. Soc. Am. **49**(1), 169–175 (1972).
[3] R. J. Alfredson, "The propagation of sound in a circular duct of continuously varying cross-sectional area," J. Sound Vib. **23**(4), 433–442 (1972).
[4] J. H. Miles, "Acoustic transmission matrix of a variable area duct or nozzle carrying a compressible subsonic flow," J. Acoust. Soc. Am. **69**(6), 1577–1586 (1981).
[5] M. L. Munjal, *Acoustics of Ducts and Mufflers* (Wiley, New York, 1987).
[6] V. H. Gupta, V. Easwaran, and M. L. Munjal, "A modified segmentation approach for analyzing plane wave propagation in non-uniform ducts with mean flow," J. Sound Vib. **182**(5), 697–707 (1995).
[7] A. Selamet and V. Easwaran, "Wave propagation and attenuation in Herschel–Venturi tubes," J. Acoust. Soc. Am. **101**(2), 936–942 (1997).
[8] A. Selamet, N. S. Dickey, Y. Kim, and J. M. Novak, "Venturi tubes: acoustic attenuation with flow loss considerations," J. Vibr. Acoust. **120**, 607–613 (1998).
[9] E. Dokumaci, "On the transmission of sound in a nonuniform duct carrying a subsonic compressible flow," J. Sound Vib. **210**(3), 391–401 (1998).
[10] R. A. Frazer, W. J. Duncan, and A. R. Collar, *Elementary matrices and Some Applications to Dynamics and Differential Equations* (Cambridge University, Cambridge, England, 1952).
[11] J. W. Sullivan, "A method for modeling perforated tube muffler components. I. Theory," J. Acoust. Soc. Am. **66**(3), 772–778 (1979).
[12] T. H. Melling, "The acoustic impedance of perforates at medium and high sound level," J. Sound Vib. **29**(1), 1–65 (1973).
[13] K. N. Rao and M. L. Munjal, "Experimental evaluation of impedance of perforates with grazing flow," J. Sound Vib. **108**(2), 283–295 (1986).

Effectiveness of acoustic power dissipation in lossy layers

Daniel Razansky[a)]
Department of Biomedical Engineering, Technion—Israel Institute of Technology, Haifa 32000, Israel

Pinchas D. Einziger
Department of Electrical Engineering, Technion—Israel Institute of Technology, Haifa 32000, Israel

Dan R. Adam
Department of Biomedical Engineering, Technion—Israel Institute of Technology, Haifa 32000, Israel

(Received 24 November 2003; revised 5 April 2004; accepted 11 April 2004)

The effect of losses in the dissipative object becomes crucial when maximal power absorption of the incident wave is of top priority. In order to assess the phenomenon of acoustic power absorption in finite size dissipative medium, a prototype model of linear pressure waves absorption in dissipative layer is considered. The conditions, parameters and bounds for the optimal (maximal) incident power absorption within the layer have been found analytically and explicitly versus its normalized thickness. These conditions are presented in terms of the basic wave propagation parameters, namely sound velocity and attenuation constant. It is shown that, for thin layers (in terms of acoustic wavelength), the upper bound on the absorptivity tends to the value of 50%, when prescribed resonant dispersion/absorption conditions, characterized by the so-called Kramers–Kronig relations, are met within the layer. For sufficiently thick layers absorption of close to 100% of the incident wave power can be achieved, when specific optimal values are selected for the corresponding real and imaginary parts of dissipative layer wave number. The model may serve as a canonical prototype problem for engineered dissipative materials design and optimization of the sound/ultrasound absorption in lossy targets, e.g., biological tissues. © *2004 Acoustical Society of America.* [DOI: 10.1121/1.1756671]

PACS numbers: 43.20.El, 43.35.Bf, 43.80.Sh, 43.55.Ev. [JGM] Pages: 84–89

I. INTRODUCTION

Transmission and reflection of plane longitudinal pressure waves in a stratified nondissipative fluid or gaseous media is a well-known phenomenon, e.g., Refs. 1–4. The principle of resonant layered structures is also widely used in electromagnetics and optics, e.g., Fabry–Perot interferometers and filters,[5] though the losses in the layers have usually much less consideration. The effect of losses in the dissipative object becomes crucial when maximal absorption of the incident wave power is of top priority, e.g., when designing optimal acoustic or elastic wave absorbers,[6,7] noise insulators,[8] or optimizing hyperthermia-based ultrasonic treatments.[9,10]

Various effects of acoustic wave transmission through finite-thickness layers were considered by many authors. Some of the related studies are discussed below. Various configurations of acoustic waves interaction with layered media are described by Brekhovskikh,[1,2] where no special attention is drawn to lossy media. Gramotnev and coworkers[11–13] investigated an anomalous absorption of acoustic and electromagnetic waves by ultra-thin layers of complex media (viscous fluids in the case of acoustic waves). Their studies have an impact on the interaction of longitudinal and shear elastic waves with dissipative fluid surface. Prosperetti[14] and others[15,16] studied extensively linear and nonlinear effects of bubbly liquid layers on the propagation of acoustic waves. It was found that, when gas bubbles are added to the liquid (even lossless liquid), the mixture may give a substantial rise to absorptivity and/or reflectivity of the medium by changing its basic wave propagation parameters, namely, acoustic velocity and dissipation constant. Recently, the optimization of ultrasonic power absorption has become of increased interest due to an extensive research in the area of therapeutic ultrasound, where several studies propose the use of free microbubbles[10] or ultrasound contrast agents[17] for the improvement of biological media absorptivity, again, by actually synthesizing the medium inside the region of interest in terms of its acoustic velocity and dissipation constant.

The main intention here was to obtain a closed-form results and analytical bounds for a general optimal dissipative layer in terms of the mentioned above basic linear wave propagation parameters, independently of the specific nature of the dissipative medium. Herein, the focus is on the basic prototype model of linear plane acoustic wave absorption in a dissipative finite thickness layer. The optimal dissipative layer parameters (maximal incident power absorption, optimal acoustic velocity and dissipation constant) are found analytically via closed-form explicit expressions and expressed versus layer thickness (normalized to the wavelength of the incident acoustic wave). Finally, the asymptotic bounds on layer absorptivity are derived in the limits of thick and thin layers.

II. FORMULATION

A three layers simplified model is considered. This model is used herein for the absorptivity optimization proce-

a)Electronic mail: danir@tx.technion.ac.il

 0001-4966/2004/116(1)/84/6/$20.00

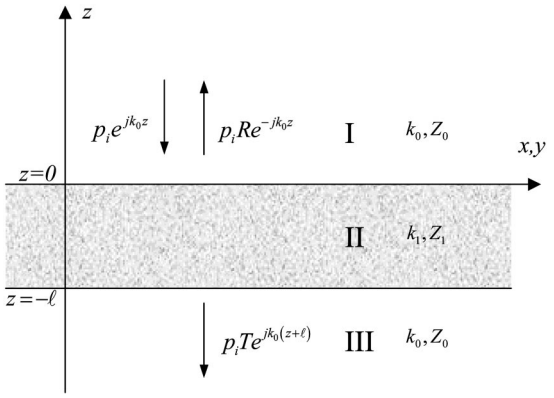

FIG. 1. Physical configuration of linear pressure wave impingement upon the dissipative layer.

dure outlined below. It consists of a spatially-infinite dissipative acoustic layer (Fig. 1) of thickness l characterized by complex specific acoustic impedance $Z_1=\sqrt{\rho_1/K_1}$ and the corresponding complex acoustic wave number $k_1=\omega\sqrt{\rho_1 K_1}$, where ρ_1 and K_1 are the medium density and its complex compressibility, respectively, while it is assumed that $\Im\{k_1\}\leqslant 0$ and $\Im\{Z_1\}\geqslant 0$. The dissipative layer is surrounded by nondissipative media with appropriate constants $Z_0=\sqrt{\rho_0/K_0}$ and $k_0=\omega\sqrt{\rho_0 K_0}$. An incident plane longitudinal acoustic wave, having a pressure amplitude of p_i and harmonic time dependence $e^{j\omega t}$, propagates in the $-z$ direction through layer I and impinges normally upon a boundary between layer I and layer II.

For the above stated problem, the fraction of incident power absorbed in the dissipative layer, namely, the absorption efficiency, is given as

$$\eta_{\text{abs}}=1-|R|^2-|T|^2, \tag{1}$$

where R and T denote global layer reflection and transmission coefficients, respectively, as depicted in Fig. 1. The solution procedures for obtaining these coefficients are well known[1–3,5] and the resulting expressions, for the present purposes, are

$$R=\frac{\frac{1-Z}{1+Z}(1-e^{-j2\delta Z})}{1-\left(\frac{1-Z}{1+Z}\right)^2 e^{-j2\delta Z}} \tag{2}$$

and

$$T=\frac{\left[1-\left(\frac{1-Z}{1+Z}\right)^2\right]e^{-j\delta Z}}{1-\left(\frac{1-Z}{1+Z}\right)^2 e^{-j2\delta Z}}, \tag{3}$$

where $Z=u-jv$ and δ, denoting the normalized complex impedance ratio and the normalized layer thickness, are given via

$$Z=Z_0/Z_1=k_1\rho_0/(k_0\rho_1)=u-jv \tag{4}$$

and

$$\delta=k_0 l\rho_1/\rho_0, \tag{5}$$

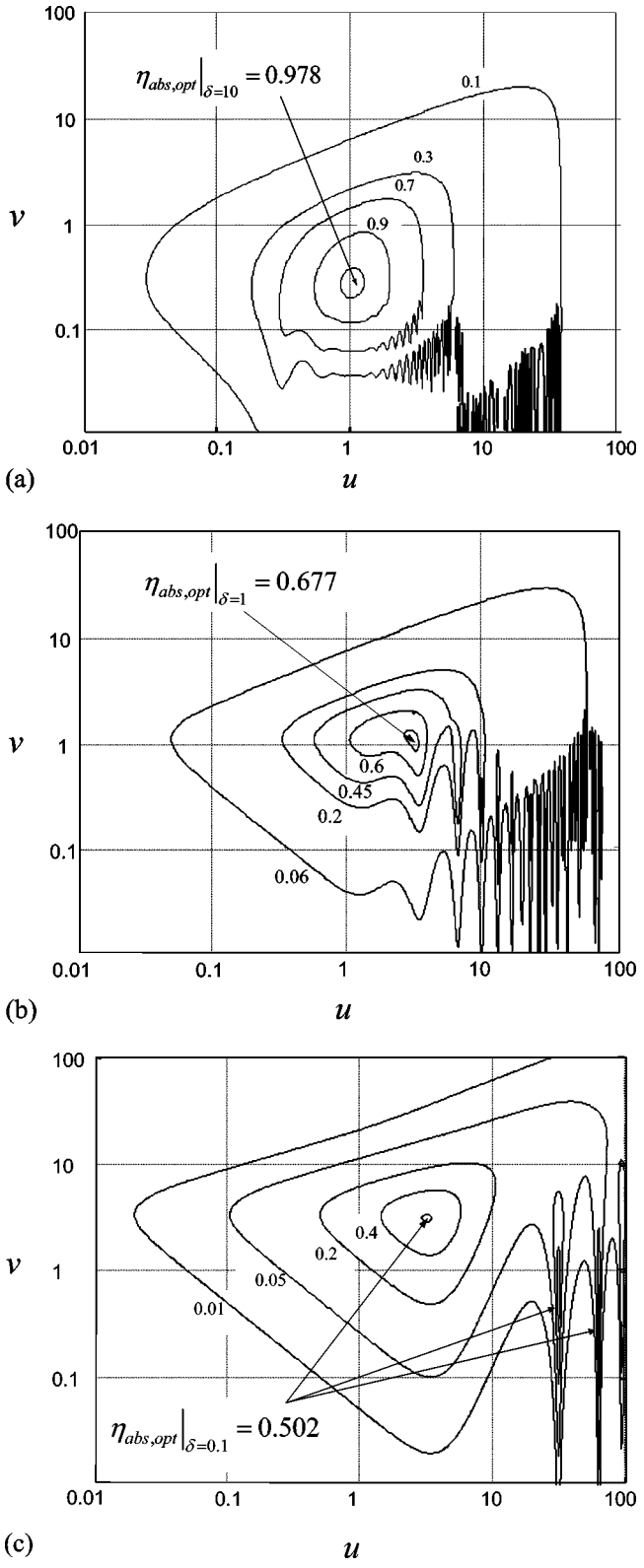

FIG. 2. Equaefficiency contours of η_{abs} in the $u-v$ plane, calculated via (1)–(5), for three different values of δ: (a) $\delta=10$; (b) $\delta=1$; (c) $\delta=0.1$.

respectively.

Note that the speed of sound c_1 in the dissipative layer is now determined (for low losses), via (4), by $\Re\{k_1\}=\omega/c_1=k_0 u\rho_1/\rho_0$, whereas $\Im\{k_1\}=-k_0 v\rho_1/\rho_0$ is the attenuation coefficient of the layer, directly related to the penetration depth $\Delta_1=-1/\Im\{k_1\}$. Thus, when the wave penetration ratio l/Δ_1, given via

$$l/\Delta_1 = -\Im\{k_1 l\} = v\,\delta, \tag{6}$$

is sufficiently large, the dissipative layer behavior approaches that of a semi-infinite layer.

III. OPTIMIZATION PROCEDURE

It should be noted that when Z is pure real (i.e., $v=0$), for any u and δ, the power of the incident wave will not be absorbed in the intermediate layer (layer II), since it becomes nondissipative, namely $\eta_{\text{abs}}=0$. On the other hand, for $v \to \infty$ the incident acoustic wave will be totally reflected at $z=0$ boundary, since $|Z_1| \to \infty$, thus, again, $\eta_{\text{abs}}=0$. Between these two extreme cases one may expect that, for any given u and δ, there exists at least one optimal value $v_{\max}$, which maximizes the power absorption efficiency η_{abs}. In a more general way, two-dimensional optimization must be performed on η_{abs} in terms of both u and v, i.e., finding the maximal values of η_{abs} for any given δ. In other words, one seeks for $\eta_{\text{abs,opt}}$, u_{opt}, and v_{opt}, depending on δ. The existence of the predicted maximal efficiencies can be readily verified via Fig. 2, where the two-dimensional equaefficiency contours of η_{abs} in the $u-v$ plane are calculated via (1)–(5) for three different values of δ.

While precise optima values could be obtained via the contour maps, as depicted in Fig. 2, an efficient analytical optimization scheme can be facilitated by expressing η_{abs} in terms of two independent complex variables, namely, $Z=u-jv$ and its complex conjugate $Z^*=u+jv$, leading to

$$\eta_{\text{abs}} = 1 - \frac{\sin(\delta Z)\sin(\delta Z^*) + \dfrac{4ZZ^*}{(1-Z^2)(1-Z^{*2})}}{\left[\dfrac{1+Z^2}{1-Z^2}\sin(\delta Z) - j\,\dfrac{2Z}{1-Z^2}\cos(\delta Z)\right]\left[\dfrac{1+Z^{*2}}{1-Z^{*2}}\sin(\delta Z^*) - j\,\dfrac{2Z^*}{1-Z^{*2}}\cos(\delta Z^*)\right]}. \tag{7}$$

The extremum values of $\eta_{\text{abs}}=\eta_{\text{abs,opt}}$ are obtained at the set of points $Z=Z_{\text{opt}}$ and $Z^*=Z^*_{\text{opt}}$, which are solutions of

$$\partial\eta_{\text{abs}}/\partial Z = 0, \quad \partial\eta_{abs}/\partial Z^* = 0. \tag{8}$$

Due to symmetry of (7) with respect to Z and Z^*, it can be readily verified that $(Z_{\text{opt}})^* = Z^*_{\text{opt}}$ and $(\partial\eta_{\text{abs}}/\partial Z)^* = \partial\eta_{\text{abs}}/\partial Z^*$. Hence, Eq. (8) can equivalently be represented, at $Z=Z_{\text{opt}}$, as

$$\Re\{d\,\eta_{\text{abs}}/dZ\} = 0, \quad \Im\{d\,\eta_{\text{abs}}/dZ\} = 0, \tag{9}$$

where $Z^*_{\text{opt}}=(Z_{\text{opt}})^*$ is taken as a parameter. Taking the derivative $d\,\eta_{\text{abs}}/dZ=0$ at $Z=Z_{\text{opt}}$, via (7), i.e.,

$$\left[j2\sin(\delta Z_{\text{opt}})\sin(\delta Z^*_{\text{opt}}) - \frac{4\,\delta Z_{\text{opt}} Z^*_{\text{opt}}}{1-Z^{*2}_{\text{opt}}}\right] \times \left[\frac{1+Z^2_{\text{opt}}}{1-Z^2_{\text{opt}}}\cos(\delta Z_{\text{opt}}) + j\,\frac{2Z_{\text{opt}}}{1-Z^2_{\text{opt}}}\sin(\delta Z_{\text{opt}})\right] + \frac{4Z^*_{opt}}{1-Z^{*2}_{opt}}\sin(\delta Z_{\text{opt}}) - j\,\delta 2 Z_{\text{opt}}\sin(\delta Z^*_{\text{opt}}) = 0, \tag{10}$$

leads to an implicit representation of Z_{opt} dependence on the normalized layer thickness δ.

IV. EXTREME CASES

A. Thick layer approximation: $\delta \gg 1$

For obtaining maximal power absorption efficiency in case of a thick dissipative layer it would be reasonable to set the real part of Z close to unity, i.e., $Z \to 1-jv$, in order to obtain minimal wave reflection at $z=0$. Then, the imaginary part v must be set to the values that will cause most of the wave to be attenuated while passing through the layer. Thus, v must meet a compromise—it should be large enough in order to absorb the great majority of incident wave in the dissipative layer, however, it must be also much less than unity otherwise the absolute value of the total reflection coefficient at $z=0$ will be affected. One would expect that, given these conditions, the maximal absorption efficiency would be close to unity, i.e., $\eta_{\text{abs,opt}} \approx 1$ ($\delta \gg 1$). Indeed, this intuition is justified via Fig. 2(a), where the contours of power absorption efficiency are depicted for a relatively thick layer ($\delta=10$). The numerical evaluation of Eq. (7) readily shows that maximal efficiency of $\eta_{\text{abs,opt}}|_{\delta=10} = 0.978$ is obtained for $u_{\text{opt}}=1.026$ and $v_{\text{opt}}=0.256$.

For large values of u and small values of v an oscillatory behavior of η_{abs} can be observed. This is due to the fact that, in this region, the exponential terms in Eq. (7), which are proportional to v, approach the unit value, while the arguments of the sinusoidal functions are large (proportionally to u). Thus, it may be expected that the whole expression would be very sensitive to changes in u.

Motivated by the above discussion, one should seek for solution of the form $Z_{\text{opt}}=1+\epsilon_{\text{opt}}$, where $|\epsilon_{\text{opt}}| \ll 1$ is a solution of (10). Accounting for the leading terms of the highest exponential and algebraic growth [i.e., the terms in the first square brackets in (10)], one obtains $\epsilon_{\text{opt}} = -jv_{\text{opt}}$ and an implicit thick layer approximation for (10), i.e.,

$$v_{\text{opt}} e^{2v_{\text{opt}}\delta} \sim 4\,\delta. \tag{11}$$

Upon converting (11) into the following iterative expression:

$$v^{(p)}_{\text{opt}} \sim \frac{\ln(4\,\delta/v^{(p-1)}_{\text{opt}})}{2\,\delta}, \tag{12}$$

the solution of (11) can be expressed, after two iterations, as

$$v_{\mathrm{opt}}^{(0)}=1, \quad v_{\mathrm{opt}}^{(1)}=\frac{\ln(4\delta)}{2\delta}, \quad v_{\mathrm{opt}}^{(2)}=\frac{\ln[8\delta^2/\ln(4\delta)]}{2\delta}. \quad (13)$$

Hence, the optimal impedance ratio Z_{opt} and the optimal power absorption efficiency $\eta_{\mathrm{abs,opt}}$ take the asymptotic forms

$$Z_{\mathrm{opt}}\sim 1-j\ln[8\delta^2/\ln(4\delta)]/2\delta \quad (14)$$

and

$$\eta_{\mathrm{abs,opt}}\sim 1-v_{\mathrm{opt}}^2/4-e^{-2\delta v_{\mathrm{opt}}}=1-\{\ln^2[8\delta^2/\ln(4\delta)] + \ln(16\delta^2)\}/16\delta^2\sim 1, \quad (15)$$

respectively.

B. Thin layer approximation: $\delta\ll 1$

The behavior of power absorption efficiency for the cases of thin dissipative layers is much more intriguing. In this limit, one may expect that the attenuation coefficient must be large enough to produce high absorptivity, however, not too large otherwise large reflectivity will arise at $z=0$. Obviously, the limit $\delta\ll 1$ in conjunction with finite $|Z|$ (i.e., $\delta|Z|\to 0$) is of no interest since in this limit $R\to 0$ [Eq. (2)] and $T\to 1$ [Eq. (3)], leading to $\eta_{\mathrm{abs}}\to 0$ [Eq. (1)]. Hence, to obtain higher efficiency, the normalized impedance has to be large (i.e., $|Z|\gg 1$), so as to provide finite $\delta|Z|$. In the subsequent analysis it will be shown that the efficiency in this case can be enhanced up to $\eta_{\mathrm{abs,opt}}=1/2$.

An analytic optimization procedure can be repeated, similar to that performed for the thick layer's approximation. The thin layer limit renders, via (10), $\sin(\delta Z)\to 0$ and $\cos(\delta Z)\to 1$. Maintaining terms up to $O(|\sin(\delta Z)|^2)$ and $O(\sin(\delta Z)/Z)$ results in the thin layer approximation for Eq. (10), i.e.,

$$\delta Z_{\mathrm{opt}}[\sin(\delta Z_{\mathrm{opt}}^*)-j2\cos(\delta Z_{\mathrm{opt}})/Z_{\mathrm{opt}}^*]+\sin(\delta Z_{\mathrm{opt}}) \times[\sin(\delta Z_{\mathrm{opt}}^*)\cos(\delta Z_{\mathrm{opt}})-j2/Z_{\mathrm{opt}}^*]\sim 0. \quad (16)$$

The solution of (16) for both square brackets, associated with the leading orders, discussed above, is readily given by the following quadratic equation:

$$\delta Z_{\mathrm{opt},m}-\pi m\sim -j2/Z_{\mathrm{opt},m}, \quad (17)$$

leading to

$$Z_{\mathrm{opt},m}\sim\frac{\pi m}{2\delta}[1+\sqrt{1-j8\delta/(\pi m)^2}]. \quad (18)$$

Note that the second root of (17) was ignored since the associated Z_{opt} corresponds to an active media, i.e., $\Im\{Z_{\mathrm{opt}}\}=v_{\mathrm{opt}}>0$. The asymptotic limit $Z\gg 1$ in (18) can be satisfied if and only if $\delta\ll 1$, revealing that optimal light medium ($Z\gg 1$) solution in (18) is restricted to thin layers. The substitution of $m=0$ provides the following approximation for the zeroth-order mode of the optimal impedance ratio:

$$Z_{\mathrm{opt},m}|_{m=0}\sim(1-j)/\sqrt{\delta}. \quad (19)$$

For either $\delta\ll 1$ or $m\gg 1$ one obtains

$$Z_{\mathrm{opt},m}|_{m\neq 0}\sim\pi m/\delta-j2/\pi m. \quad (20)$$

For thin layers, all modes (all values of m) provide the same asymptotic value of the optimal power absorption efficiency, namely,

$$\eta_{\mathrm{abs,opt}}\sim 1/2. \quad (21)$$

C. Intermediate range

The optimization procedure for the normalized impedance ratio $Z_{\mathrm{opt}}=u_{\mathrm{opt}}-jv_{\mathrm{opt}}$ and the resultant optimal power absorption efficiency η_{opt} as well as the wave penetration ratio $v_{\mathrm{opt}}\delta$ in (7) and (6), respectively, can be carried out numerically via (10), recovering various limiting cases, as discussed above and depicted in Fig. 3. The exact solutions of (10), i.e., u_{opt} and v_{opt}, are shown in Fig. 3(a), whereas its substitutions into (7) and (6), namely $\eta_{\mathrm{abs,opt}}$ and $l/\Delta_{1,\mathrm{opt}}$, are depicted in Figs. 3(b) and 3(c), respectively.

The basic classification of power absorption mechanism is readily obtained via Fig. 3(c). While the thin layer limit, supporting the lossy modes of index $m=0,1,2,...$, extends approximately over $0\leqslant v\delta\leqslant 1$, the thick layer limit, in the complementary range $1<v\delta<\infty$, supports a consecutive continuation of the $m=1$ mode only. It should be noted, though, that the pressure distribution within the layer for the $m=1$ mode in the range $0\leqslant v\delta\leqslant 1$ is basically that of a standing wave (half period) field, whereas its continuation in the range $1<v\delta<\infty$ decays exponentially. In applications like ultrasonic hyperthermia of living tissue (e.g., ablation of cancerous tissue) it is important to know the actual distribution of wave intensity as it passes through the dissipative object since it directly affects the level of local energy absorption of the wave and, consequently, the local temperature rise within the layer. Considering the $1<v\delta<\infty$ range for $m=1$ mode in Fig. 3(c): the power distribution uniformity within the layer is determined in terms of wave penetration depth defined by Eq. (6). It can be readily evaluated numerically using Eqs. (4)–(7) that the penetration depth $\Delta_{1,\mathrm{opt}}$ of the optimal absorbing layer becomes less than its actual thickness l for approx. $\delta>1$. The ratio $l/\Delta_{1,\mathrm{opt}}$, however, grows relatively slowly with δ, following the logarithmic dependence of (13), thus, allowing for the optimal penetration depth to be of the order of the layer thickness, over a wide range of thicknesses. It should also be noted that thicker layers $\delta\gg 1$ support higher order modes $m\gg 1$, which, however, extend over finite δ range and eventually terminate.

For a zeroth-order mode ($m=0$), the real part of the normalized impedance ratio becomes almost equal to its imaginary part (in absolute values), i.e., $u_{\mathrm{opt}}\approx v_{\mathrm{opt}}$. This is the case when the phase between the applied pressure and the velocity of the particles in the medium reaches the 90° value. For linear pressure waves, this kind of anomalous behavior is usually related with an anomalous dispersion/absorption, well described by the so-called Kramers–Kronig relations.[18,19] It usually occurs when real part of the medium complex compressibility becomes zero or very small comparatively to its imaginary part (equivalently to the negligible real part of the complex permittivity in electrodynamics[18]). In this case, a composition of an optimal thin dissipative layer is set by the dispersive relations, consequently, having resonant properties with resonance fre-

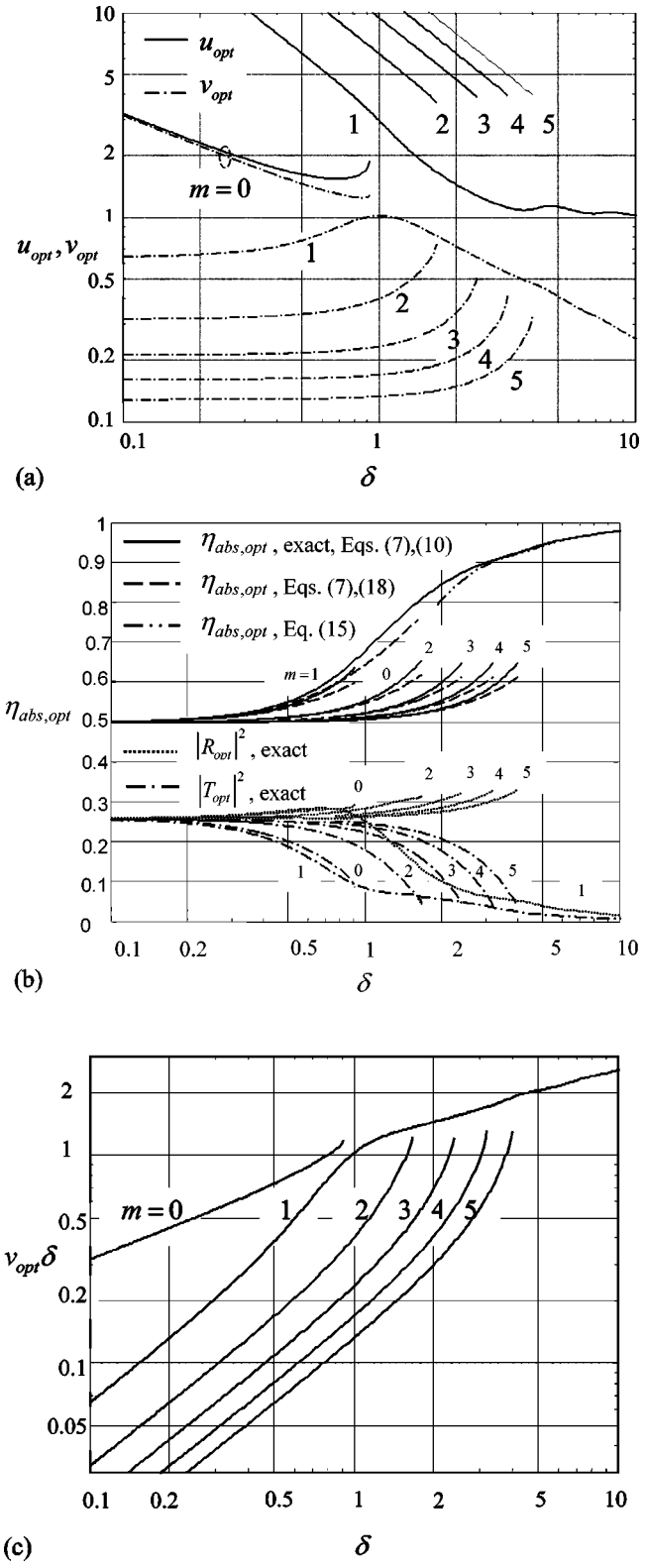

FIG. 3. Optimal power absorption efficiency $\eta_{\mathrm{abs,opt}}$, normalized impedance ratio $Z_{\mathrm{opt}}=u_{\mathrm{opt}}-jv_{\mathrm{opt}}$, and wave penetration ratio $v_{\mathrm{opt}}\delta$, depicted in (a), (b), and (c), respectively, vs normalized thickness δ for first five lossy modes ($m=0,1,...,5$).

quency (frequencies). Thus, in order to reach the upper bound on power absorption efficiency by applying the optimal absorption conditions in the thin dissipative layer (resulting in $u_{\mathrm{opt}}\approx v_{\mathrm{opt}}$), the ensonifying frequency must be close to this/these resonance frequency/frequencies. To obtain this kind of resonant behavior in a relatively low frequency range (KHz or MHZ range) resonant elements can be added to the layer. Good examples are porous media, bubbly liquid layers[15] or media containing ultrasound contrast agents.[17]

The substitution of the approximations for u_{opt} and v_{opt} in (18)–(20) into (7) results in approximated values of power absorption efficiency, which agree very well with the exact numerically evaluated results, as depicted in Fig. 3(b). Both $|R_{\mathrm{opt}}|^2$ and $|T_{\mathrm{opt}}|^2$, the constituents of $\eta_{\mathrm{abs,opt}}$, are also depicted in Fig. 3(b) for reference. One notes that the $m=1$ mode establishes an upper bound (global maxima) for all the other modes. It coincides, however, with the other modes as the values of $\eta_{\mathrm{abs,opt}}\rightarrow 1/2$ and $|R_{\mathrm{opt}}|^2\rightarrow|T_{\mathrm{opt}}|^2\rightarrow 1/4$ are reached as $\delta\rightarrow 0$.

Finally, to provide some assessment of the applicability of the derived estimates, one may consider a simple case of the linear $f=10\,\mathrm{KHz}$ pressure wave, propagating in water with $c_0=1500\,\mathrm{m/s}$ and $\rho_0=1000\,\mathrm{kg/m^3}$, which impinges normally upon the dissipative layer of air at STP, having $c_1=330\,\mathrm{m/s}$ and $\rho_1=1.2\,\mathrm{kg/m^3}$. For instance, one may look for the thickness l of this layer, providing the optimal power absorption efficiency for the dominant mode $m=1$. Given these values and utilizing definitions and results of Eqs. (4), (5), and (20) it is readily obtained that $u=\rho_0 c_0/\rho_1 c_1=3787.9$, $\delta=\pi m/u=8.294\times 10^{-4}$, and, consequently, $l=16.5\,\mathrm{mm}$. It should be emphasized that the obtained optimum value of l is extremely sensitive to changes in u, as expected for a lossy mode with very small δ at the optimum. Furthermore, while the value of u is approximately constant for an air layer in water, the value of v is determined via attenuation coefficient $\alpha_1=-\Im\{k_1\}$ of air at $f=10\,\mathrm{KHz}$, which is taken as approximately[19] $\alpha_1=0.01\,[\mathrm{Neper/m}]$, thus, $v=\alpha_1\rho_0/k_0\rho_1\approx 0.2$. Substitution of the obtained values into (1)–(5) renders $\eta_{\mathrm{abs}}=0.3638$. Note that the required optimal value of v must be slightly different, i.e., $v_{\mathrm{opt}}=2/\pi m=0.64$, for which the optimal value of $\eta_{\mathrm{abs}}=0.5$ is reached. For comparison, the intensity of the same pressure wave, propagating in air, is attenuated by 0.033% only every 16.5 mm.

V. CONCLUSIONS

The phenomenon of acoustic power absorption in a finite size dissipative medium is analyzed utilizing an elementary prototype model of plane longitudinal acoustic wave impingement upon the dissipative finite-thickness layer, surrounded by semi-infinite nondissipative media. It is found that, for sufficiently thick layers (in terms of its thickness normalized to wavelength), the absorption of close to 100% of the incident wave power can be achieved provided that specific optimal values are selected for the real and the imaginary parts of the wave number of the dissipative layer. These values are found analytically and explicitly depending on the normalized thickness of the layer. It was also found that, as the thickness of the optimal absorbing layer becomes greater, the ratio between layer thickness and wave penetration depth, at the optimum, also grows. For a very thick optimal layer, with absorption close to 100%, most of the

power is absorbed in the vicinity of its boundary. Another observation, important for the modeling of realistic media, can be made regarding the optimal results for a thick layer. The acoustic velocity in homogeneous media can be usually considered as approximately constant over wide range of frequencies, i.e., u is also constant. This rule is also true for many macroscopically quasihomogeneous media like living tissues. On the contrary, the normalized attenuation constant v is usually frequency dependent. For instance, the attenuation in living tissues grows,[19] approximately, with f^n $(1.1 < n < 2)$, where f is the frequency of insonation, thus, v, since it is normalized to $k_0 \sim f$, is expected to slowly grow with the frequency. Naturally, if u is set to unity, the selection of frequency becomes important since it directly determines the value of v and, consequently, the value of the power absorption efficiency.

For thin layers, the upper bound (maximum) on power absorption efficiency tends to the value of 50% as layer thickness becomes smaller. This maximum occurs for infinite number of possible optimal layers (lossy modes), whereas all modes, except for the zeroth-order one, are supported by slightly dissipative layers. The important observation acutally means that even very thin contrast layers are able to absorb up to 50% of the incident energy, provided that specific physical parameters of the layer and its surroundings are established. Due to this kind of resonant absorption, it is hypothesized that, in some special cases, the commonly used definitions in ultrasonic safety assessments, based on bulk attenuation constants[19], may fail in their ability to predict an enhanced local power deposition in thin layers (small sites) of biological tissue. The zeroth-order lossy mode occurs for highly losses provided almost equal optimal (absolute) values of real and imaginary parts of the layer wave number. For linear pressure waves, the latter kind of wave propagation usually corresponds to an anomalous absorption or an anomalous dispersion propagation regime, which is well described by the so-called Kramers–Kronig relations. This behavior, resulting in an almost zero real part of complex compressibility of the dissipative layer (equivalently to zero real part of complex permittivity in electrodynamics), may occur when the dissipative medium has resonant properties (and, consequently, resonance frequency/frequencies). In this case, the ensonifying frequency must normally be close to this/these resonant frequency/frequencies in order to cause $\Re\{k_1\} \approx |\Im\{k_1\}|$ within the dissipative layer. Naturally, as the wavelength of pressure waves approaches the dimensions of the molecular structure of matter, the anomalous absorption occurs. However, in order for the wavelength to reach these values, the frequency of insonation must be on the order of GHz for liquids and solids and on the order of MHz for gases. Nevertheless, when the medium is porous or a gaseous bubbles are inserted into it, e.g., ultrasound contrast agents, the resonance frequencies of the matter can be even within the KHz range, providing drastic improvement in absorption efficiency.

[1] L. M. Brekhovskikh, *Waves in Layered Media*, 2nd ed., translated from the Russian by R. T. Beyer (Academic, New York, 1980).
[2] L. M. Brekhovskikh and O. A. Godin, *Acoustics of Layered Media I: Plane and Quasi-plane waves* (Springer-Verlag, Berlin, 1990).
[3] J. Lekner, ''An upper bound on acoustic reflectivity, and the Rayleigh approximation,'' J. Acoust. Soc. Am. **86**, 2359–2362 (1989).
[4] M. Rousseau, ''Floquet wave properties in a periodically layered medium,'' J. Acoust. Soc. Am. **86**, 2369–2376 (1989).
[5] M. Born and E. Wolf, *Principles of Optics: Electromagnetic Theory of Propagation, Interference and Diffraction of Light*, 7th ed. (Cambridge University Press, Cambridge, 1999).
[6] F.-C. Lee and W.-H. Chen, ''Acoustic transmission analysis of multi-layer absorbers,'' J. Sound Vib. **248**, 621–634 (2001).
[7] V. V. Tyutekin, ''Simulation and synthesis of elastic wave absorbers at the boundary of a rigid body: Incidence of longitudinal waves,'' Acoust. Phys. **47**, 461–467 (2001).
[8] K. V. Horoshenkov, K. Sakagami, and M. Morimoto, ''On the dissipation of acoustic energy in a thin, infinite, poroelastic plate,'' Acustica **88**, 500–506 (2002).
[9] W. L. Lin, C. T. Liauh, J. Y. Yen, Y. Y. Chen, and M. J. Shieh, ''Treatable domain and optimal frequency for brain tumors during ultrasound hyperthermia,'' Int. J. Radiat. Oncol., Biol., Phys. **46**, 239–247 (2000).
[10] S. D. Sokka, R. King, and K. Hynynen, ''MRI-guided gas bubble enhanced ultrasound heating in *in-vivo* rabbit thigh,'' Phys. Med. Biol. **48**, 223–241 (2003).
[11] D. K. Gramotnev and J. A. Ross, ''Anomalous absorption of electromagnetic waves in a layered structure with complex permittivities,'' Opt. Commun. **162**, 280–290 (1999).
[12] D. K. Gramotnev and M. L. Mather, ''Anomalous absorption of bulk shear acoustic waves by an ultra-thin layer of a non-Newtonian fluid,'' J. Acoust. Soc. Am. **106**, 2552–2559 (1999).
[13] L. A. Chernozatonskii, D. K. Gramotnev, and M. L. Vyukov, ''Anomalous absorption of longitudinal acoustic waves by a thin layer of viscous fluid,'' Phys. Lett. A **164**, 126–132 (1992).
[14] S. Karpov, A. Prosperetti, and L. Ostrovsky, ''Nonlinear wave interactions in bubble layers,'' J. Acoust. Soc. Am. **113**, 1304–1316 (2003).
[15] H. Medwin, ''Counting bubbles acoustically,'' Ultrasonics **15**, 7–13 (1977).
[16] M. J. Miksis and L. Ting, ''Effects of bubbly layers on wave propagation,'' J. Acoust. Soc. Am. **86**, 2349–2358 (1989).
[17] S. Fujishiro *et al.*, ''Increased heating efficiency of hyperthermia using an ultrasound contrast agent: A phantom study,'' Int. J. Hyperthermia **14**, 495–502 (1998).
[18] J. D. Jackson, *Classical Electrodynamics*, 3rd ed. (Wiley, New York, 1999), pp. 309–316.
[19] B. A. J. Angelsen, *Ultrasound Imaging* (Emantec AS, Trondheim, Norway, 2000), pp. 4.31–4.123.

Determining the pulse-echo electromechanical characteristic of a transducer using flat plates and point targets

Thomas L. Szabo[a)]
Department of Aerospace and Mechanical Engineering, Boston University, Boston, Massachusetts 02115

Başak Ülker Karbeyaz[b)]
Department of Electrical Engineering and Computer Science, Northeastern University, Boston, Massachusetts 02115

Robin O. Cleveland[c)]
Department of Aerospace and Mechanical Engineering, Boston University, Boston, Massachusetts 02115

Eric L. Miller[d)]
Department of Electrical Engineering and Computer Science, Northeastern University, Boston, Massachusetts 02115

(Received 17 July 2003; accepted for publication 12 April 2004)

A common technique to determine the electromechanical response of a spherically focusing transducer is to use a reference pulse echo from a flat plate in the focal plane of the transducer. We show that when the pressure focusing gain of the transducer is much greater than unity, the focal plane reflection is a valid approximation of the desired electromechanical response. An alternative calibration target is a point scatterer and we show theoretically and experimentally that this waveform is the double time differential of the flat-plate response. The use of calibration to describe general scatterers through a Born approximation (Jensen, J. A. (**1991**), J. Acoust. Soc. Am. **89**, 182–190) is discussed. © *2004 Acoustical Society of America.* [DOI: 10.1121/1.1756893]

PACS numbers: 43.20.Fn, 43.20.Rz, 43.20.Bi, 43.35.Bf [SFW] Pages: 90–96

I. INTRODUCTION

In pulse-echo ultrasound imaging, a single transducer is used to both transmit an acoustic pulse and receive acoustic echoes. An electromechanical transfer function is associated with the transducer for both the transmit process (converting the electrical excitation into an acoustic disturbance) and the receive process (converting the acoustic disturbance into an electrical signal). To characterize the emitted and received acoustic pulse and to accomplish transducer calibration, the electromechanical response of the transducer must be determined.

The common practice to calibrate a transducer is to place a large flat plate either on the beam axis in the extreme near-field or farfield of a nonfocusing transducer or in the focal plane of a focusing transducer (Carpenter and Stepanishen, 1984; Chen *et al.*, 1997; Machado and Foster, 1998). A waveform measured under these conditions, can, in principle, be used to aid in the removal or compensation of transducer response and field effects on the measurement of tissue properties (Carpenter and Stepanishen, 1984; Chen *et al.*, 1997; Machado and Foster, 1998; Thijssen, 2000).

In this paper we provide a framework for calibration which consistently integrates much of the previous literature in this area (Hunt *et al.*, 1983; Carpenter and Stepanishen, 1984; Madsen *et al.*, 1984; Jensen, 1991; Bridal *et al.*, 1996; Chen *et al.*, 1997). We examine in detail the case of a spherically focused transducer and prove that the electromechanical response can also be measured by the use of a point target as well as a plate reflector. We show both theoretically and experimentally that the scattered signal from a plate and point target are related by double differentiation in time. We present a simple physical model that results in an accurate simulation of the backscattered field from arbitrary shaped weak scatterers. In particular, we bring to attention a possible misinterpretation of data taken from a flat-plate when applied to scattering from a point target. This clarification is of importance for the time domain scattering theory of Jensen (1991), which is based on the impulse response of a point scatterer.

II. THEORY AND BACKGROUND

In this section we discuss the theory of scattering of sound and the relation between the electromechanical impulse response of a transducer and the measured backscattered signal from specific obstacles. We consider the case of the received signal for a monostatic pulse-echo configuration, although it is straightforward to generalize our results to bistatic geometries.

Following the notation in Jensen (1991), a model for the scattering process that has a simple physical interpretation as well as a straightforward implementation that can be summarized by the following equation:

$$v_0(t) = v_i(t) *_t e_T(t) *_t h_T(\mathbf{r},t) *_t s(\mathbf{r},t) *_t h_R(\mathbf{r},t) *_t e_R(t), \tag{1}$$

where $v_i(t)$ is the excitation voltage, $e_T(t)$ is the electromechanical response that is the ratio of the derivative of the

[a)]Electronic mail: tlszabo@bu.edu
[b)]Electronic mail: bulker@ece.neu.edu
[c)]Electronic mail: robinc@bu.edu
[d)]Electronic mail: elmiller@ece.neu.edu

 0001-4966/2004/116(1)/90/7/$20.00

normal particle velocity with respect to time relative to the transmit voltage, $h_T(\mathbf{r},t)$ is the transmit spatial impulse response, $h_R(\mathbf{r},t)$ is the receive spatial impulse response of the transducer located at position vector $\mathbf{r}$, $s(\mathbf{r},t)$ is a scattering term located at $\mathbf{r}$ that accounts for perturbations or inhomogeneities in the medium that give rise to the scattered signal, $v_0(t)$ is the output voltage from the transducer, $e_R(t)$ is the receive voltage to force electromechanical response, and $*_t$ is convolution with respect to time.

We define the round-trip pulse-echo electromechanical impulse response of the transducer, $e_{\text{pe}}(t)$ as

$$e_{\text{pe}}(t)=v_i(t)*_t e_T(t)*_t e_R(t). \tag{2}$$

For the case where $v_i(t)$ is a very short electrical impulse (e.g., less than about 1/10th of the characteristic period of the transducer), e_{pe} will be proportional to $e_T*_t e_R$ that is the true electromechanical impulse response of the transducer. Equation (1) can now be written as

$$v_0(t)=e_{\text{pe}}(t)*_t h_T(\mathbf{r},t)*_t s(\mathbf{r},t)*_t h_R(\mathbf{r},t), \tag{3}$$

where the remaining terms account for propagation and scattering. If one assumes that the absorption of the medium (e.g., deionized and degassed water in the low megahertz frequencies) is negligible, then analytical expressions exist for h_T and h_R for a spherically focused transducer (Arditi *et al.*, 1981; Hunt *et al.*, 1983). The scattering term $s(\mathbf{r},t)$ depends on the target.

In this paper we will discuss scattering from three different obstacles: a flat plate, a point target, and an arbitrary shaped weak scatterer. The first two cases will be presented for calibration and the third for imaging applications that require such calibration.

A. Scattering from a flat plate

In this section, we discuss the conditions under which the focal plane reflection from a flat plate is a valid approximation of the electromechanical impulse response.

When the flat plate is an ideal acoustic mirror placed at a distance from the transmitter, z, perpendicular to the beam axis, the receiver can be considered as the mirror image of the transmitter. Hence in pulse-echo imaging of an acoustic mirror, the problem is the same as that of two identical transducers separated by a distance $2z$, as shown by Rhyne (1977) for a nonfocusing transducer, and by Chen *et al.* (1994) for both nonfocusing and focusing transducers.

Rhyne (1977) derived a time domain expression for the reflection from a flat plate and called it the ''radiation coupling'' function. This result is the same as the problem of finding diffraction loss, D_F, between two identical transducers at a distance $2z$ (Seki *et al.*, 1956; Rogers and van Buren, 1974). In both cases, this loss represents the reduction in amplitude and change in phase when only a portion of a transmitted beam is intercepted by a receiving transducer.

For a focusing aperture, Chen *et al.* (1994) showed that for the mirror placed in the focal plane, the diffraction loss in the frequency domain is equal to

$$D_F(z=2F,f)=-\{1-\exp(jG_p)[J_0(G_p)-jJ_1(G_p)]\}, \tag{4a}$$

where the pressure focal gain is

$$G_p=\frac{\pi f a^2}{c_0 F}, \tag{4b}$$

in which f is frequency, c_0 is the speed of sound in water, a is the aperture radius, and F is the focal length. Chen *et al.* (1997) found that this expression has only a weak dependency of frequency. If the argument parameter G_p is large, an asymptotic expression for Bessel functions of large arguments [Eq. (9.2.1) of Abramowitz and Stegun, 1964], can be used to approximate Eq. (4a) by

$$\begin{aligned} D_F(z=2F,f)&\approx-\left\{1-\sqrt{\frac{2}{\pi G_p}}\exp\left(\frac{j\pi}{4}\right)\right\}\\ &=-\left\{1-\frac{1}{\sqrt{\pi G_p}}-\frac{j}{\sqrt{\pi G_p}}\right\}. \end{aligned} \tag{5}$$

When $G_p\geqslant 16$ the error of either the real or imaginary part of Eq. (5) compared to Eq. (4a) is less than 0.042. Because the terms involving the square root are small, the main contribution is from the real part of Eq. (5). Both Eqs. (4a) and (5) vary extremely slowly with frequency over a transducer bandwidth (e.g., 90% fractional bandwidth), so to a good approximation, the frequency can be set equal to transducer center frequency, $f=f_c$. Physically the result of this small loss can be interpreted in terms of ray theory as a cone of energy focused onto a plate and reflected back, almost but not quite perfectly, along the same cone to the aperture of the transducer.

To use the transfer function defined in Eq. (5) in Eq. (2), we must account for propagation delays to and from the plate and for the case where the plate is not an ideal reflector. Then we can carry out an inverse Fourier transform to obtain the time domain response. Given that a nonideal mirror has a plane wave pressure reflection coefficient,

$$R_F=\frac{Z_2-Z_1}{Z_2+Z_1}, \tag{6}$$

where Z_2 is the specific acoustic impedance of the reflector and Z_1, the characteristic impedance of the fluid, then the three rightmost terms of Eq. (3) correspond to the following inverse Fourier transform:

$$\begin{aligned} h_T(\mathbf{r},t)*_t s(\mathbf{r},t)*_t h_R(\mathbf{r},t)&=\text{Real}\{\Im^{-1}[D_F(\mathbf{r},f_c)\\ &\quad\times R_F\exp(-j2\pi f(2F)/c_0)]\}\\ &=R_F[\sqrt{1/(\pi G_p)}-1]\delta(t-t_{2F}). \end{aligned} \tag{7}$$

From Eq. (7) we can see that the acoustic propagation and scattering from a plate at the focus of a transducer [that is, $h_T(\mathbf{r},t)*_t s(\mathbf{r},t)*_t h_R(\mathbf{r},t)$] is a scaled impulse delayed in time by $t_{2F}=2F/c_0$. Under these conditions, the output voltage is an amplitude scaled delayed replica of the system response e_{pe},

$$v_0(t)\approx R_F[\sqrt{1/(\pi G_p)}-1]e_{\text{pe}}(t-2F/c_0). \tag{8}$$

The round trip reference signal e_{pe} can be determined from the measured output voltage signal, $v_0(t)$, and the scaling constant from Eq. (8).

B. Scattering from a point target

Often it is necessary to determine scattering from an ideal point scatterer (explained below) rather than a flat plate. As an example, determining the spatial impulse response (h_T and h_R) experimentally requires the use of a point scatterer. Moreover, randomly positioned point scatterers form the basis of simulation models for speckle and phantom-like objects that can be created from organized patterns of point scatterers with assigned weighting (Jensen and Munk, 1997). In this section, we show how the reflection from a point scatterer can be determined from a flat-plate response.

The starting point for a model of an ideal point scatterer is that of a *rigid* (incompressible) sphere with a diameter much smaller than a wavelength, density $\rho \gg \rho_0$, and compressibility $\kappa \ll \kappa_0$, where $c=1/\sqrt{\rho\kappa}$ and $c_0=1/\sqrt{\rho_0\kappa_0}$. The scattering for this sphere known to be proportional to $-k^2$ (Morse and Ingard, 1986), where $k=\omega/c_0$, and a geometrical factor *A*. Since the inverse Fourier transform theory of $j\omega$ is $\partial/\partial t$, $-k^2$ corresponds to the transform $(1/c_0^2)\partial^2/\partial t^2$. For this type of target at the origin,

$$s(\mathbf{r},t)=\frac{A}{c_0^2}\frac{\partial^2}{\partial t^2}*_t\delta(t-|\mathbf{r}|/c_0), \tag{9a}$$

where *A* is a time-independent quantity that is given by (Eq. 8.2.19, Morse and Ingard, 1986)

$$A=\frac{a^3}{3}\left(1-\frac{3}{2}\cos\theta\right), \tag{9b}$$

where a is the radius of the scatterer and θ is the scattering angle. The $1/|\mathbf{r}|$ dependence has been absorbed into the receive factor h_R (Hunt *et al.* 1983). For direct backscatter, $\theta=\pi$ and *A* has the value

$$A=\frac{5a^3}{6}. \tag{9c}$$

Real transducers have a finite aperture and collect signals over a range of angles, however, for $160<\theta<200$, which is appropriate for most ultrasound imaging scenarios, the variation in *A* over the surface of the transducer is less than 5% and the use of Eq. (9c) is appropriate. If this target is placed at the focal point, then each of the spatial impulse responses in Eq. (1) reduces to an impulse function centered on $|\mathbf{r}|/c_0$ (Hunt *et al.*, 1983),

$$h_T(\mathbf{r},t)=h_R(\mathbf{r},t)=l\,\delta(t-|\mathbf{r}|/c_0), \tag{10a}$$

where [Arditi *et al.*, 1981 Eq. (7)]

$$l=F\left[1-\left(1-\frac{a^2}{F^2}\right)^{1/2}\right]. \tag{10b}$$

Putting these results into Eq. (1) for a small spherical target at the focal point, we find

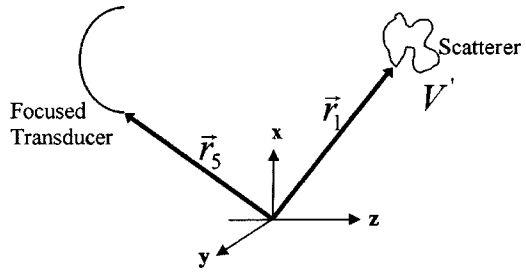

FIG. 1. Schematic showing the transducer/scatterer arrangement and the theoretical and experimental coordinate systems.

$$v_0(t)=\frac{Al^2}{c_0^2}\frac{\partial^2 e_{\text{pe}}(t-2|\mathbf{r}|/c_0)}{\partial t^2}, \tag{10c}$$

therefore, the reflected signal from a point target will have the same shape as the doubly differentiated reference waveform, $e_{\text{pe}}(t)$, with the respect to time.

Although we derived this in terms of a rigid sphere target, we note that other targets smaller than a wavelength have a similar functional dependency in the backscattered direction ($\theta=\pi$) toward the transducer at distances greater than a few wavelengths (Rayleigh, 1872; Pierce, 1989). In particular, Nassiri and Hill (1986) have shown that backscatter from a disk is similar to that of a sphere, differing only in the constant *A*. Both the sub-wavelength sphere and disk are practical realizations of an ideal point target as viewed at moderate to large distances. Because of the practical difficulties involved in realizing a point target, it may be difficult to determine the constant *A*. An alternative approach to calibration described by Hunt *et al.* (1983) is to redefine the electromechanical response based on a point target. Their electromechanical response would be the equivalent of e_{pe} convolved with *s* for a point target from Eq. (1) and would include a double differentiation with time. However, if *A* is not known, it is not possible to apply the calibration to the problem of quantitative imaging.

C. Scattering from arbitrary shaped weak scatterers: Born approximation

In the previous two sections we showed that the electromechanical impulse response of a transducer can be measured using either a plate or a point target. Once this reference signal is known, it can be applied to simulate the backscattered field from arbitrary shaped targets through the Born approximation (Jensen, 1991).

Jensen's time domain formulation of the Born approximation provides a computationally compact and useful method for simulating the backscattered field from arbitrary shaped weak scatterers for an inhomogeneous medium. Equation (44) of Jensen (1991) can be rearranged according to Eq. (1):

$$v_0(\mathbf{r}_5,t)=e_{\text{pe}}(t)*_t\left[s(\mathbf{r}_1)*_r\frac{\partial^2 H_{\text{pe}}(\mathbf{r}_1,\mathbf{r}_5,t)}{\partial t^2}\right], \tag{11}$$

in which $\mathbf{r}_5$ is the vector to a characteristic position of the transducer and $\mathbf{r}_1$ represents a vector to a point within the scatterer (Fig. 1) and, as defined by Jensen (1991),

$$H_{\mathrm{pe}}(\mathbf{r}_1,\mathbf{r}_5,t)=h(\mathbf{r}_1,\mathbf{r}_5,t)*_t\ h(\mathbf{r}_5,\mathbf{r}_1,t) \tag{12}$$

is equivalent to $h_T*_t h_R$ in our Eq. (1). More explicitly, Eq. (11) is

$$\begin{aligned} v_0(\mathbf{r}_5,t)&=e_{\mathrm{pe}}(t)*_t\left[\int_{V'}\left[\frac{\Delta\rho(\mathbf{r}_1)}{\rho_0}\right.\right.\\ &\quad\left.\left.-\frac{2\Delta c(\mathbf{r}_1)}{c_0}\right]\frac{1}{c_0^2}\frac{\partial^2 H_{\mathrm{pe}}(\mathbf{r}_1,\mathbf{r}_5,t)}{\partial t^2}\,d^3_{\mathbf{r}_1}\right]\\ &=\frac{1}{c_0^2}\frac{\partial^2 e_{\mathrm{pe}}(t)}{\partial t^2}*_t\left[\int_{V'}\left[\frac{\Delta\rho(\mathbf{r}_1)}{\rho_0}\right.\right.\\ &\quad\left.\left.-\frac{2\Delta c(\mathbf{r}_1)}{c_0}\right]H_{\mathrm{pe}}(\mathbf{r}_1,\mathbf{r}_5,t)\,d^3_{\mathbf{r}_1}\right], \end{aligned} \tag{13}$$

where $\Delta\rho$ and Δc are the perturbations in density and sound speed with respect to the background and V' is the scattering region.

In the case of a point scatterer, Eq. (13) reduces to

$$\begin{aligned} v_0(\mathbf{r}_5,t)&=\left[\frac{\Delta\rho(\mathbf{r}_1)}{\rho_0}-\frac{2\Delta c(\mathbf{r}_1)}{c_0}\right]\frac{1}{c_0^2}\\ &\quad\times\frac{\partial^2 e_{\mathrm{pe}}(t)}{\partial t^2}*_t h(\mathbf{r}_1,\mathbf{r}_5,t)*_t h(\mathbf{r}_5,\mathbf{r}_1,t), \end{aligned} \tag{14}$$

which is consistent with Jensen's Eq. (50). Specifically, in the case of a *point scatterer* placed at the focal point, Eq. (14) reduces to the form of Eq. (10c). This observation reveals a potential area of confusion with respect to the results in Jensen (1991) in which Eq. (14) is taken to be the response to a *flat plate* at the focal plane. More correctly, as indicated by the results in the previous two sections of this paper, this flat-plate response is obtained by removing the double time derivative.

In this work the overall outcome of the Born approximation derived by Jensen (1991) is unchanged. However, we have used the twice time derivative of the plate response in our simulations. The method of finding $e_{\mathrm{pe}}(t)$ described in Secs. II A and II B can be applied directly to the more general case of scattering through the Born approximation, as given by Eq. (13).

III. EXPERIMENTS

We carried out experiments to verify the fact that the scattered signal from a plate and a small scatterer are related by double differentiation in time. We used a spherically focused ultrasonic transducer, 3.5 MHz, 50.8 mm focal length, 12.8 mm radius (Model V380, Panametrics, Waltham, MA). This strongly focusing transducer (F number 2 and $G_p=24$) was placed in a water tank (0.8 m×0.8 m×1.5 m) that was filled with deionized degassed water at approximately 21 °C. The transducer was operated in a pulse-echo mode using a pulse receiver (UA 5052, Panametrics, Waltham, MA). The pulser–receiver excited the transducer with a short excitation signal that approximated a delta function and the received echo was acquired on digital scope (LC 334a, LeCroy, Chestnut Ridge, NY) and transferred to a personal computer for later analysis. We investigated the reflections from two targets. The first was a 12.5 mm thick flat acrylic plate acoustic mirror. The second point like target was the cleaved end of an optical fiber 110 microns in diameter.

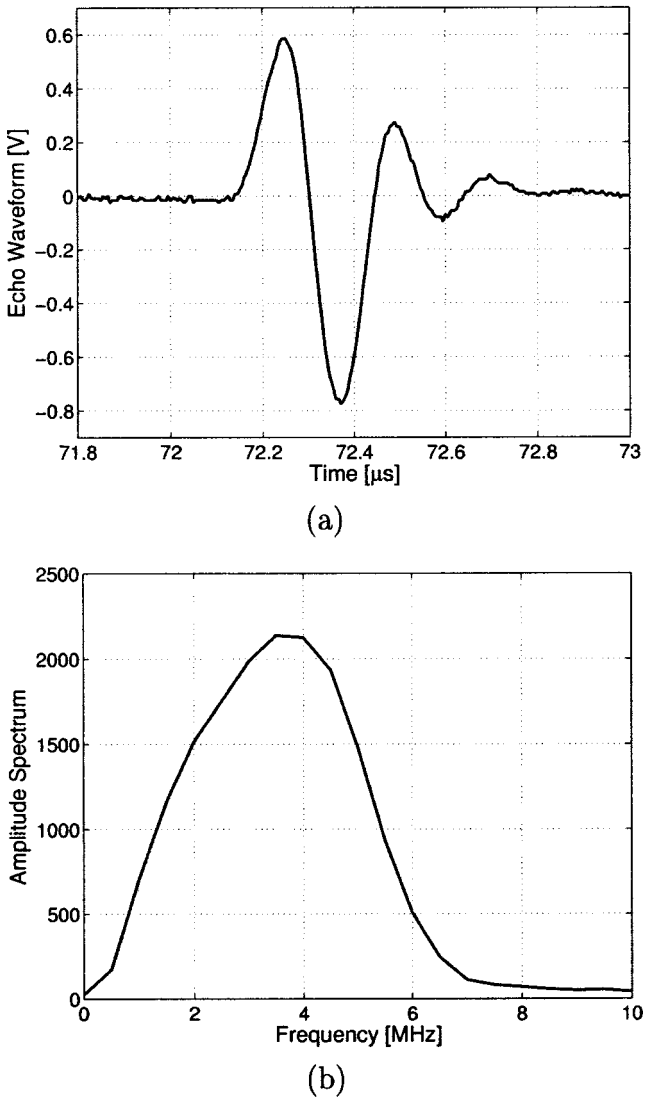

FIG. 2. (a) Reference pulse-echo from a large thick acrylic plate placed in the geometric focal plane of a 3.5 MHz spherically focused transducer. (b) Amplitude spectrum of pulse echo.

Figure 2(a) shows the reflected pulse measured from the front surface of the acrylic plate, $v_0(t)$. This is the scaled pulse-echo impulse response, $e_{\mathrm{pe}}(t)$, according to Eq. (7). Here $G_p=24$, so the diffraction correction factor is 0.885 and the reflection coefficient at the water–acrylic interface is $R_F=0.348$. Figure 3 compares three normalized waveforms: (1) the signal measured from the plate; (2) the signal measured from the optical fiber; and (3) the doubly differentiated e_{pe} waveform obtained from Eq. (8) (note that this equation gives a sign inversion). We see that carrying out the double differentiation is crucial to obtaining good agreement between predictions based on the impulse response of the transducer (e_{pe}) and the received signal from a point scatterer. Without this operation neither the leading negative half-cycle

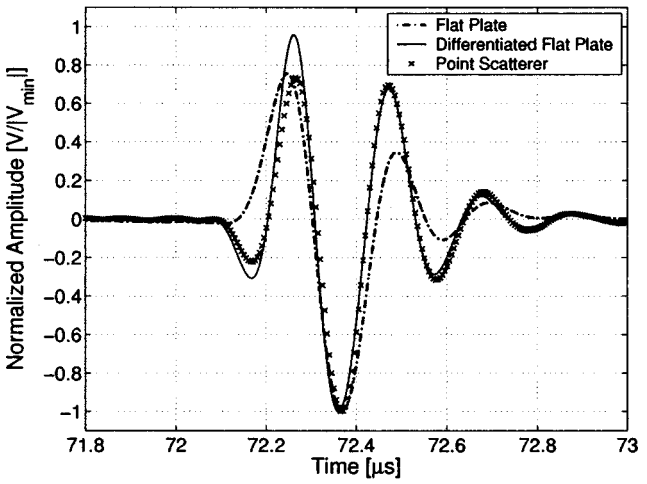

FIG. 3. A comparison of the flat-plate pulse echo [Fig. 2(a), normalized and filtered], differentiated flat-plate pulse echo [Fig. 2(a), normalized and doubly differentiated with respect to time] and a pulse echo from the tip of an optical fiber placed at the geometric spherical focal point of a 3.5 MHz transducer.

nor the details of the ringdown are captured correctly. This result shows that the time–domain calibration function that is determined from a flat plate can be used to predict the waveform from a point scatterer at the focus.

Once this reference signal is known, it can be applied to simulate the free diffraction field of the transducer or backscattering from other scattering targets. We used Eq. (1) with the point scatterer characteristic, Eq. (8), and the round trip spatial impulse response (Arditi *et al.*, 1981) with a 2 GHz sampling frequency in time, to simulate the echoes scattered from a small point-like target. To confirm our predictions, the optical fiber was mechanically scanned through the tank and echo waveforms recorded at each location. Figure 4 shows the measured and predicted contour maps of the amplitude envelope of the scattered fields for the case where the fiber was placed in the focal plane and translated perpendicular to the acoustic beam axis. Figure 5 is a similar scan but at an axial distance of 53.8 mm (about 3 mm or 10 wavelengths behind the focus). In both cases, there is a close agreement between the measured and predicted scattered field. The slight differences are attributable to imperfections in both the transducer as an ideal piston source, as determined by extensive hydrophone measurements, and the cleaved optical fiber as an isolated ideal point target. The source transducer was found to have a mildly distorted, asymmetric transmitted field when compared to simulations based on an ideal uniformly weighted piston source. Pulse-echo simulations based on the point target waveform at the focal point gave slightly better agreement with measurements than those shown here; however, we believe this result to be a consequence of the imperfect realization of an ideal spherical scatterer by the cleaved optical fiber that had its own unique response characteristic, as shown in Fig. 3. These comparisons confirm that the plate-derived calibration waveform can be used to predict the response of a scatterer anywhere in the field of the transducer.

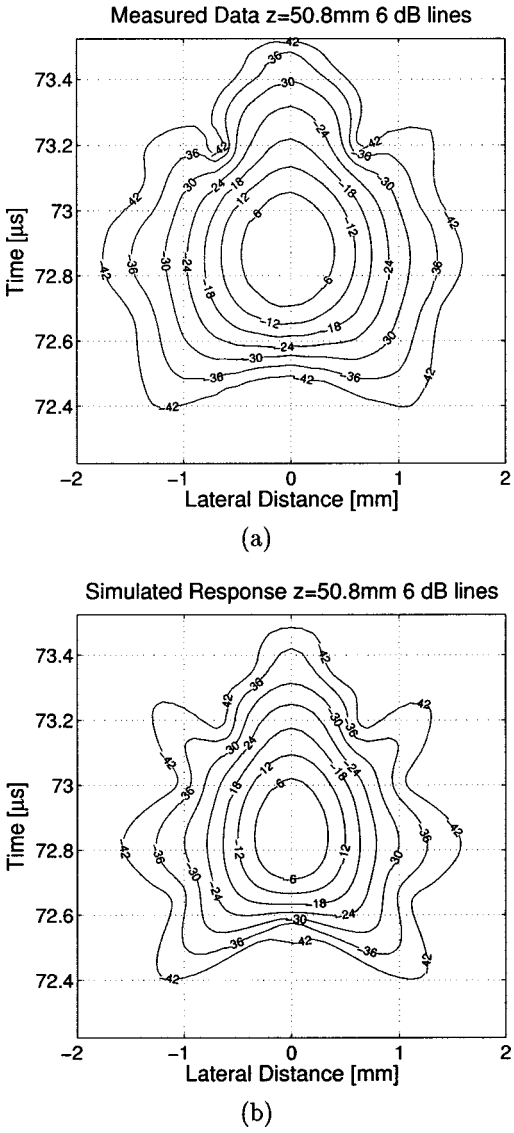

FIG. 4. (a) Amplitude envelope of the pulse-echo field of a 3.5 MHz transducer as measured by scanning an optical probe laterally at an axial distance equal to the focal length. (b) Amplitude envelope of the simulated pulse-echo field using Eq. (10c) and a differentiated signal from Fig. 3.

IV. CONCLUSION

We have shown, both theoretically and experimentally, that the pulse-echo impulse response of a spherically focused transducer can be measured using either a flat plate or a point scatterer. The reflected waveforms in each case are not identical but are rather related by an operation of double differentiation. Because of the difficulty of determining the precise geometry of practical realizations of sub-wavelength point targets and, consequently, the calibration constant A, a reflection from a flat-plate is recommended for a determination of the reference pulse. For values of focal gain greater than or equal to 16, the error in the approximation [Eq. (5)], is less than five percent.

The formulation in Eq. (1) and the relation between the flat-plate and point target echoes can be used to resolve differences among various calibration methods in the literature (Hunt *et al.*, 1983; Carpenter and Stepanishen, 1984; Madsen *et al.*, 1984; Jensen, 1991; Bridal *et al.*, 1996; Chen *et al.*,

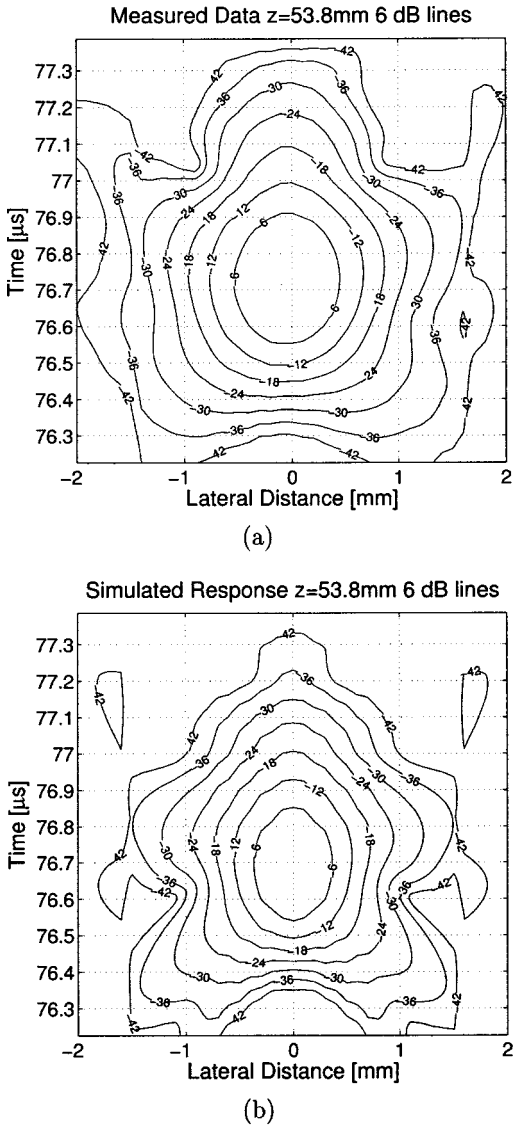

FIG. 5. (a) Amplitude envelope of the pulse-echo field of 3.5 MHz transducer as measured by scanning an optical probe laterally at an axial distance $z=53.8$ mm. (b) Amplitude envelope of the simulated pulse-echo field using Eq. (10c) and differentiated signal from Fig. 3.

1997) each of which can be used self-consistently but may be in conflict with other methods. For example, Hunt *et al.*, (1983) obtained a reference waveform from a point scatterer but their formulation for the scatterer does not include the double differentiation of Eq. (10c). Their waveform is used consistently to simulate speckle as a summation of random point scatterers.

The time domain Born approximation of Jensen (1991) in Eq. (13) includes the double differentiation and shows that the echo signal from an inhomogeneous medium can be obtained by convolving the point-scattered waveform with the medium properties, in agreement with Eqs. (1) and (9a). If one wishes to use the signal measured from a flat plate for this Born model, it is necessary to differentiate the reference signal twice with respect to time first. The wording in Jensen (1991) could be misinterpreted to mean that the flat-plate signal was already differentiated.

In summary, the commonly used reference waveform from a flat-plate target in the focal plane of a strongly focusing transducer ($G_p \geqslant 16$) is appropriate to determine $e_{\mathrm{pe}}(t)$ without distortion. This reference signal is useful for transducer calibration and diffraction correction (Sigelmann and Reid, 1973; Reid, 1974; Chen *et al.*, 1997; Machado and Foster, 1998). However, the waveform must be used with care for other scattering targets.

ACKNOWLEDGMENTS

This work was supported in part by CenSSIS (the Center for Subsurface Sensing and Imaging Systems), under the Engineering Research Centers Program of the National Science Foundation (Award No. EEC-9986821). The authors are grateful for technical assistance provided by Yuan Jing in setting up the experiments.

Abramowitz, M., and Stegun, I. A. (**1964**). *Handbook of Mathematical Functions* (Dover, New York), Chap. 9.

Arditi, M., Foster, S. F., and Hunt, J. W. (**1981**). "Transient fields of concave annular arrays," Ultrason. Imaging **3**, 37–61.

Bridal, S. L., Wallace, K. D., Trousil, R. L., Wickline, S. A., and Miller, J. G. (**1996**). "Frequency dependence of acoustic backscatter from 5 to 65 MHz ($0.06<ka<4.0$) of polystyrene beads in agarose," J. Acoust. Soc. Am. **100**, 1841–1848.

Carpenter, R. N., and Stepanishen, P. R. (**1984**). "An improvement in the range resolution of ultrasonic pulse echo systems by deconvolution," J. Acoust. Soc. Am. **75**, 1084–1091.

Chen, X., Phillips, D., Schwarz, K. Q., Mottley, J. G., and Parker, K. J. (**1997**). "The measurement of backscatter coefficient from a broadband pulse-echo system: a new formulation," IEEE Trans. Ultrason. Ferroelectr. Freq. Control **44**, 515–525.

Chen, X., Schwarz, K. Q., and Parker, K. J. (**1994**). "Acoustic coupling from a focused transducer to a flat plate and back to the transducer," J. Acoust. Soc. Am. **95**, 3049–3054.

Hunt, J. W., Arditi, M., and Foster, F. S. (**1983**). "Ultrasound transducers for pulse-echo medical imaging," IEEE Trans. Biomed. Eng. **BME-30**, 453–481.

Jensen, J. A. (**1991**). "A model for the propagation and scattering of ultrasound in tissue," J. Acoust. Soc. Am. **89**, 182–190.

Jensen, J. A., and Munk, P. (**1997**). "Computer phantoms for simulating ultrasound B-mode and cfm images," *23rd Acoustical Imaging Symposium*, Boston, MA, 13–16 April.

Madsen, E. L., Insana, M. F., and Zagzebski, J. A. (**1984**). "Method of data reduction for accurate determination of acoustic backscatter coefficients," J. Acoust. Soc. Am. **76**, 913–923.

Machado, J. C., and Foster, F. S. (**1998**). "Experimental validation of a diffraction correction model for high frequency measurement of ultrasound backscatter coefficients," *IEEE Ultrasonics Symposium Proceedings*, pp. 1869–1872.

Morse, P. M., and Ingard, K. U. (**1986**). *Theoretical Acoustics* (Princeton University Press, Princeton, NJ), Chap. 8.

Nassiri, D. K., and Hill, C. R. (**1986**). "The use of angular acoustic scattering measurements to estimate structural parameters of human and animal tissues," J. Acoust. Soc. Am. **79**, 2048–2054.

Pierce, A. D., *Acoustics*, (Acoustical Society of America, Woodbury, NY, 1989), Chap. 9.

Rayleigh, J. W. S. (**1872**). "Investigation of the disturbance produced by a spherical obstacle on the waves of sound," Proc. London Math. Soc. **4**, 253–283.

Reid, J. M. (**1974**). "Self-reciprocity calibration of echo-ranging transducers," J. Acoust. Soc. Am. **55**, 862–868.

Rhyne, T. L. (**1977**). "Radiation coupling of a disk to a plane and back or a disk to disk: An exact solution," J. Acoust. Soc. Am. **61**, 318–324.

Rogers, P. H., and Van Buren, A. L. (**1974**). "An exact expression for the Lommel diffraction correction integral," J. Acoust. Soc. Am. **55**, 724–728.

Seki, H., Granato, A., and Truell, R. (**1956**). ''Diffraction effects in the ultrasonic field of a piston source and their importance in the accurate measurement of attenuation,'' J. Acoust. Soc. Am. **28**, 230–238.
Sigelmann, R. A., and Reid, J. M. (**1973**). ''Analysis and measurement of ultrasonic backscattering from an ensemble of scatterers excited by sine-wave bursts,'' J. Acoust. Soc. Am. **53**, 1351–1355.
Thijssen, J. M. (**2000**). ''Spectroscopy and image texture analysis,'' Ultrasound Med. Biol. **26**, S41–S44.

Spectral estimation for characterization of acoustic aberration

Trond Varslot
Department of Mathematical Sciences, Norwegian University of Science and Technology, 7491 Trondheim, Norway

Bjørn Angelsen
Department of Circulation and Imaging, Norwegian University of Science and Technology, 7489 Trondheim, Norway

Robert C. Waag
Department of Electrical and Computer Engineering and Department of Radiology, University of Rochester, Rochester, New York 14627

(Received 30 October 2003; revised 5 March 2004; accepted 24 April 2004)

Spectral estimation based on acoustic backscatter from a motionless stochastic medium is described for characterization of aberration in ultrasonic imaging. The underlying assumptions for the estimation are: The correlation length of the medium is short compared to the length of the transmitted acoustic pulse, an isoplanatic region of sufficient size exists around the focal point, and the backscatter can be modeled as an ergodic stochastic process. The motivation for this work is ultrasonic imaging with aberration correction. Measurements were performed using a two-dimensional array system with 80×80 transducer elements and an element pitch of 0.6 mm. The *f* number for the measurements was 1.2 and the center frequency was 3.0 MHz with a 53% bandwidth. Relative phase of aberration was extracted from estimated cross spectra using a robust least-mean-square-error method based on an orthogonal expansion of the phase differences of neighboring wave forms as a function of frequency. Estimates of cross-spectrum phase from measurements of random scattering through a tissue-mimicking aberrator have confidence bands approximately ±5° wide. Both phase and magnitude are in good agreement with a reference characterization obtained from a point scatterer.
[DOI: 10.1121/1.1760799]

PACS numbers: 43.20.Fn, 43.80.Vj, 43.60.Cg [TDM] Pages: 97–108

I. INTRODUCTION

An ultrasound image is a map of reflected sound intensity from different spatial locations. By focusing the transmitted sound pulse at a specific location, the intensity of the transmitted field is highest around the focal point. The reflected intensity then largely originates from this region. A limitation is therefore imposed on the image resolution by the size of the focal zone. The smallest obtainable size is limited by diffraction.

In medical ultrasonic imaging, the transmitted pulse typically travels through the body wall before arriving at the intended focal point. The body wall consists of a heterogeneous configuration of muscular, fatty, and connective tissue. The result of propagation through a medium with variable speed of sound is degradation of the initial geometric focus beam by widening the focal zone. The transmitted pulse is then said to be *aberrated*. Experimental studies of abdominal wall[1,2] and breast[3–5] as well as simulations[6,7] indicate that this aberration can significantly reduce the image resolution. The need to consider aberration in ultrasonic imaging is also shown in experimental studies that illustrate image degradation caused by aberration and image improvement resulting from aberration correction.[8,9]

Several different approaches have been suggested to counter the aberration. These are mostly based on either the time-reversal mirror[10] or a time-delay model for the aberration.[11,12] The need for a strong point scatterer in the time-reversal mirror limits its applicability in clinical applications. Furthermore, a time-delay screen may not be adequate for describing the aberration. This model does not describe the distortion of the pulse shape observed in medical ultrasound.[13] Moving the screen away from the transducer surface has been suggested as a way to characterize the pulse-shape distortion and amplitude fluctuation introduced by interference between different parts of the pulse,[14] but this too is an oversimplification that may not model aberration satisfactorily.

This paper uses an aberration model called a *generalized screen* by Angelsen[15] and a *filter bank* by Lin and Waag.[16] Using the time-reversal argument, the generalized screen will correspond to an ideal aberration correction filter. This motivates the quest for the screen from an aberration correction perspective. For scattering from a spatially stationary random distribution of scatterers, the generalized screen may be estimated from the cross spectra of the measured signal at the transducer.

The aim of this paper is to determine the generalized screen using a set of scattering measurements from a motionless random medium with very short correlation length compared to the wavelength. Relatively independent measurement samples are obtained by focusing at different locations within the random medium for which the aberration is essentially the same. This limits the possible focal points to a

region in which essentially the same aberration path exists between the transmit–receive aperture and the focal point.

The paper is organized in the following way. After a brief review of the classical spectral estimation in Sec. II A, a characterization of the aberration using the cross spectrum of backscatter measurements is given in Sec. II B. In Sec. II C, a least-mean-square-error method for extracting the relative phase of the aberration from the spectral estimates is described. Implementation issues, signal processing, and metrics to evaluate the estimates are discussed in Sec. III. The experimental configuration and the measurement procedure are described in Sec. IV, and estimation[3] of aberration as frequency domain magnitude and phase are presented in Sec. V. Discussion and concluding remarks are given in Secs. VI and VII, respectively.

II. THEORY

A. Spectral estimation

The subject of spectral estimation, is thoroughly described in literature[17–20] and, therefore, only important relations needed here are given for the convenience of the reader and for the introduction of notation.

The cross covariance between two stationary second-order stochastic processes $X(t)$ and $Y(t)$ with zero mean is defined as

$$R_{XY}(s)=E[X(0)\overline{Y(s)}],$$

where $E[\cdot]$ is the expectation operator. The corresponding cross spectrum $P_{XY}(\omega)$ is the Fourier transform of the covariance function.

Suppose the stochastic processes $X(t)$ and $Y(t)$ are ergodic, and the function $k(t)$ is a window function that satisfies the appropriate conditions.[21] Let $\lambda_M(t)=k(t/M)$, where M is a positive scaling parameter. An asymptotically unbiased, consistent estimator of $P_{XY}(\omega)$ is given by

$$P_{XY}^{(N)}(\omega)=\frac{1}{2\pi}\sum_{t=-(N-1)}^{N-1}\lambda_M(t)R_{XY}^{(N)}(t)e^{i\omega t},$$

where

$$R_{XY}^{(N)}(s)=\frac{1}{N}\sum_{t=0}^{N-|s|}X(t)\overline{Y(t+s)}.$$

This is known as the Blackman–Tukey estimator for the cross spectrum, with window function λ_M. The implementation of this estimator will be based on the cross periodogram of the processes, and therefore computed efficiently using the fast Fourier transform (FFT).[22]

The magnitude $r(\omega)$ and the phase $\theta(\omega)$ of the cross spectrum can now be estimated as

$$\hat{\theta}(\omega)=\arg[P_{XY}^{(N)}(\omega)],\quad \hat{r}(\omega)=|P_{XY}^{(N)}(\omega)|.$$

Letting $I=\int|k(t)|^2dt$, approximate expressions for the variance of these estimators are given by

$$\mathrm{Var}[\hat{\theta}(\omega)]\approx\frac{IM}{2N}\left(\frac{1}{|w_{XY}(\omega)|^2}-1\right) \tag{1}$$

$$\mathrm{Var}[\hat{r}(\omega)]\approx\frac{IM}{2N}|P_{XY}(\omega)|^2\left(\frac{1}{|w_{XY}(\omega)|^2}+1\right), \tag{2}$$

respectively, where

$$w_{XY}(\omega)=P_{XY}(\omega)/\sqrt{P_X(\omega)P_Y(\omega)}$$

is the coherence between the processes $X(t)$ and $Y(t)$. The variance is assumed to be small for these approximations to be valid.[23]

B. Characterization of aberration

Let $p_0(\omega)$ be the temporal Fourier transform of a point source located at the position r_0. Assuming linear wave propagation in a homogeneous nonabsorbing medium, the received signal at a position r on the transducer is

$$p_{r_0}^{(h)}(r,\omega)=p_0(\omega)\frac{e^{-i\omega|r-r_0|/c}}{4\pi|r-r_0|}$$

in the temporal-frequency domain. In this expression, c is the speed of sound. A superscript (h) is used to indicate quantities resulting from propagation through a homogeneous medium. Let $p_{r_0}(r,\omega)$ denote the temporal Fourier transform of the signal received from the same point source in the heterogeneous medium. If the wave propagation in the heterogeneous medium is linear, the relation between $p_{r_0}^{(h)}(r,\omega)$ and $p_{r_0}(r,\omega)$ may be described by a unique function $s_{r_0}(r,\omega)$ as

$$p_{r_0}(r,\omega)=s_{r_0}(r,\omega)p_{r_0}^{(h)}(r,\omega).$$

Using Huygens' principle, the temporal Fourier transform of the corresponding signal received from a general scatterer distribution $\sigma(r_0,\omega)$ is

$$p^{(h)}(r,\omega)=\int p_{r_0}^{(h)}(r,\omega)d\sigma(r_0,\omega)$$

and

$$p(r,\omega)=\int p_{r_0}(r,\omega)d\sigma(r_0,\omega),$$

where the integration in each expression is over the spatial support of σ. For a given r_f, let Ω be the largest neighborhood of r_f in which $s_{r_0}(r,\omega)$ may be assumed constant as a function of r_0. If $p_{r_0}(r,\omega)$ is zero outside Ω, then the approximation

$$p(r,\omega)=s_{r_f}(r,\omega)p^{(h)}(r,\omega)$$

is valid. In this case, the function s_{r_f} is called the *generalized screen*, and Ω is denoted the *isoplanatic region*. Using a polar form for the complex function s_{r_f} and omitting the subscript r_f, the screen is

$$s(r,\omega)=A(r,\omega)e^{i\theta(r,\omega)},$$

where A and θ are real-valued functions, denoted the *magnitude of aberration*, and the *phase of aberration*, respectively. If $A(r,\omega)=a(r)$ and $\theta(r,\omega)=\omega\tau(r)/c$, this description is the commonly used time delay and amplitude screen.

The scatterer distribution is assumed to have a correlation length very short compared to the wavelength of the

transmitted pulse so for all practical purposes the distribution is δ-correlated. Pointlike reflectors distributed according to a spatial Poisson point process is an example. Let r_k be the coordinate of a particular transducer element k. Under this assumption, the received signal is a sample function of an approximate Gaussian stochastic process with zero mean for each r_k when the average number of point scatterers per unit area is large.[24] If, in addition, the received signal is a stationary process, a complete characterization of $p(r_k,\omega)$ is given by the corresponding cross-power spectrum.

The cross spectrum between the received signal at elements k and l is

$$\begin{aligned} P_{kl}(\omega) &= E[p(r_k,\omega)\overline{p(r_l,\omega)}] \\ &= A(r_l,\omega)A(r_k,\omega)e^{-i[\theta(r_k,\omega)-\theta(r_l,\omega)]}P_{kl}^{(h)}(\omega), \end{aligned} \tag{3}$$

where $P_{kl}^{(h)}(\omega)$ is the cross spectrum of the received signal without aberration. The cross spectrum, thus, contains information about the phase and amplitude of the aberration.

Let now $p_0(r,\omega)$ be the temporal Fourier transform of the transmit waveform used when imaging through a homogeneous medium. The time-reversal argument states that an optimal aberration correction for focusing at r_f may be achieved by replacing $p_0(r,\omega)$ with an aberration corrected pulse $\overline{s(r,\omega)}p_0(r,\omega)$, *i.e.*, filtering the transmit pulse using a filter with transfer function equal to the complex conjugate of $s(r,\omega)$. Similarly, aberration correction for the receive pulse $p(r,\omega)$ is obtained by the same filter. Thus, the generalized screen corresponds to an aberration correction filter.[16]

C. Relative phase

1. Relative phase

The angle of the cross spectrum is a relative phase difference between the all pairs of transducer elements. Ideally, the relative phase across the transducer could be found by integration of these phase differences. In the presence of estimation error, however, errors accumulate and straightforward integration is unsatisfactory. Here, an estimate for the relative phase is found as a least-mean-square-error fit to the phase defined by the phase differences.

Let $\phi_i(\omega)$ be the relative phase at transducer element i. Following Liu and Waag,[13] $\phi_i(\omega)$ may be expressed as

$$\begin{aligned} \phi_{i+1}(\omega)-\phi_i(\omega) &= \theta_j(\omega), \\ \phi_{i+M+1}(\omega)-\phi_i(\omega) &= \theta_{j+1}(\omega), \\ \phi_{i+M}(\omega)-\phi_i(\omega) &= \theta_{j+2}(\omega), \\ \phi_{i+M}(\omega)-\phi_{i+1}(\omega) &= \theta_{j+3}(\omega), \end{aligned} \tag{4}$$

where θ_k is the phase of the appropriate cross spectrum. In matrix notation with the conventions in Fig. 1, Eq. (4) can be written

$$A\phi(\omega)=\theta(\omega). \tag{5}$$

For an $m\times n$ element transducer, A is a $L\times mn$ matrix, with $L=4mn-3(m+n)+2$. As the rank of A is $mn-1$, this equation is solved by means of Moore–Penrose inverse $A^{\dagger}$ of A.

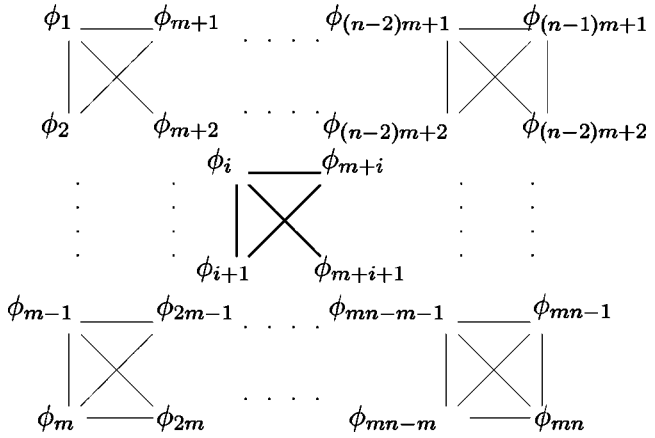

FIG. 1. Relative phase over a two-dimensional aperture containing $m\times n$ elements. The figure gives the mapping of the relative phase ϕ_k at a particular grid point to element k in a vector ϕ. With the exception of the right and bottom edges, all available phase differences are included by repeating the same basic cell pattern. The result is therefore a matrix formulation of the relative phase retrieval problem, in which the matrix is almost banded.

If $A=U\Sigma V^H$ is a singular value decomposition of A, then the Moore–Penrose inverse of A can be expressed

$$A^{\dagger}=V\Sigma^{+}U^H,$$

where the diagonal matrix Σ^{+} is defined

$$\Sigma_{ij}^{+}=\begin{cases} 1/\Sigma_{ij}, & \Sigma_{ij}\neq 0 \\ 0, & \Sigma_{ij}=0. \end{cases}$$

2. Information across frequencies

The procedure described thus far produces a unique solution of the relative phase retrieval problem based on the phase of the cross spectra, in the least-mean-square-error sense. However, as the estimate is formed for each frequency separately, the estimate does not include frequency-to-frequency information. This may introduce undesired jumps in the relative phase estimate as a function of frequency.

Consider now the phase estimated in a frequency band (a,b). Let $\{\psi_k(\omega)\}_{k=0}^{\infty}$ be a basis for $L^2(a,b)$. In this basis, the relative phase may be written as

$$\phi(\omega)=\sum_{k=0}^{\infty}\langle\phi,\psi_k\rangle\psi_k(\omega).$$

Equation (5), therefore, becomes

$$\sum_{k=1}^{\infty}A\langle\phi,\psi_k\rangle\psi_k(\omega)=\theta(\omega),$$

where the matrix A is the same as in Eq. (5), and

$$\langle\phi,\psi_k\rangle=[\langle\phi_1,\psi_k\rangle,\langle\phi_1,\psi_k\rangle,\ldots\langle\phi_{MN},\psi_k\rangle]^T.$$

Taking the inner product with ψ_n, the resulting equation

$$A\langle\phi,\psi_n\rangle=\langle\theta,\psi_n\rangle,$$

is the same as Eq. (5), but for each coefficient instead of for each frequency. Using a reduced set of appropriately smooth basis functions, therefore, preserves the smoothness across frequencies.

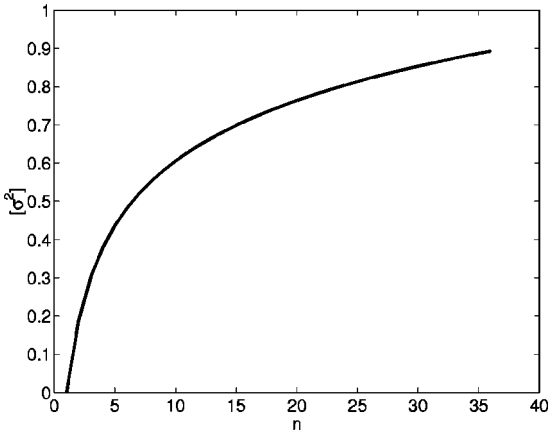

FIG. 2. A bound for the variance for the estimated relative phase. The estimate is based on relative phase differences with additive white noise of variance σ^2.

This procedure is seen to be equivalent to obtaining the least-mean-square-error solution for each frequency separately, and then projecting this onto the same reduced set of basis functions. However, from a computational point of view, doing the projection first is advantageous, because this greatly reduces the number of unknowns. It may also be of interest to use a different number of coefficients, or even a different set of basis functions, for different parts of the transducer. In this case, the equivalence between projection before and after finding the least-mean-square-error solution disappears.

3. Stability

Since the stability of the relative phase retrieval algorithm based on coefficients in the orthogonal expansion is the same as the stability of Eq. (5), only the latter is treated here.

Let $\hat{\theta}(\omega)=\theta(\omega)+\epsilon(\omega)$, where $\epsilon(\omega)$ is a zero-mean random vector representing additive noise. Assuming $\epsilon(\omega)$ has the covariance matrix

$$C_\epsilon(\omega)=E[\epsilon\epsilon^H],$$

the estimate is $\hat{\phi}(\omega)=\phi(\omega)+\nu(\omega)$ in which $\nu(\omega)$ is a zero-mean random vector representing the noise. The covariance matrix of the estimation noise is

$$C_\nu(\omega)=E[\nu\nu^H]=A^\dagger C(\omega)(A^\dagger)^H,$$

where $A^\dagger=V\Sigma^+U^H$. Let the noise ϵ be white with variance σ^2. Then, $C(\omega)=\sigma^2 I$, and

$$C_\nu(\omega)=\sigma^2 V|\Sigma^+|^2V^H.$$

Consider an aperture with $m=n$, *i.e.*, a transducer with n^2 transducer elements. The maximum value of any element on the diagonal of $C_\nu(\omega)$ is a bound for the variance of the error in the estimated relative phase. As can be readily seen from Fig. 2, the error in the cross spectrum phase estimate is not be significantly amplified when retrieving the relative phase. However, the relative phase estimation noise is no longer white, as the covariance matrix $C_\nu(\omega)$ is not diagonal. Error in the phase estimates can, therefore, have long-range effects on the estimate of the relative phase.

III. METHOD

A. Correlation

Because the effective diameter of the beam used in this study is comparable to the separation between focuses, the effective scattering volumes overlapped. Hence, different measurements in each data set were correlated. This correlation was estimated using the autocorrelation between two measurements for each transducer element. The average of this autocorrelation is a measure of the correlation between the data sets.

Let $X_k(t)$ and $X_n(t)$ be two stochastic variables representing two different measurements from the same transducer element. If the processes $X_k(t)$ and $X_n(t)$ are ergodic and have zero mean, the correlation between the two measurements may be estimated as

$$\hat{C}(s)=\frac{\Sigma_{j=1}^N X_k(t_j)\overline{X_n(t_j-s)}}{\sqrt{\Sigma_{j=1}^N|X_k(t_j)|^2\Sigma_{j=1}^N|X_n(t_j)|^2}},$$

where the realizations of the measurements are sampled at points $\{t_j\}_{j=1}^N$. Now, $\hat{C}(0)$ is an estimate for the correlation between the two measurements.

B. Window selection

The choice of window function λ for the Blackman–Tukey estimator is not obvious. A rule of thumb used here is that the window function should not significantly distort the central part of the covariance function. This in turn implies restricting the bandwidth of the window to be less than the bandwidth of the spectrum to be estimated.

The spectrum to be estimated is smooth and continuous and does not contain spectral lines. Blurring of spectral lines is, thus, not an issue. Since the correlation length of the random scatterers is assumed to be very short, a natural conclusion is that the correlation length of the received signal should be about the same as the pulse length. This is based on the independence of scattering from nonoverlapping regions in the random medium.

To be considered also is the implementation of the Blackman–Tukey estimator. Using a window function that is rectangular in the frequency domain gives the Daniell estimator,[22] also known as a smoothed periodogram. This is implemented most efficiently using one FFT and a relatively short sliding average. A Parzen window[21] is most efficiently implemented using three FFTs; one to compute the periodogram, and two to perform the convolution with the frequency domain representation of the window function.

The Parzen window is used in this study due to its sharp cutoff of the covariance function beyond the correlation length. However, if efficiency is an issue, a window with a narrow support in the frequency domain, like the Daniell estimator, would be preferable.

C. Construction of basis functions

An ''optimal'' set of basis functions for representing the true phase of aberration could be constructed by performing a singular-value decomposition of a matrix containing the true aberration over the aperture as a function of frequency.

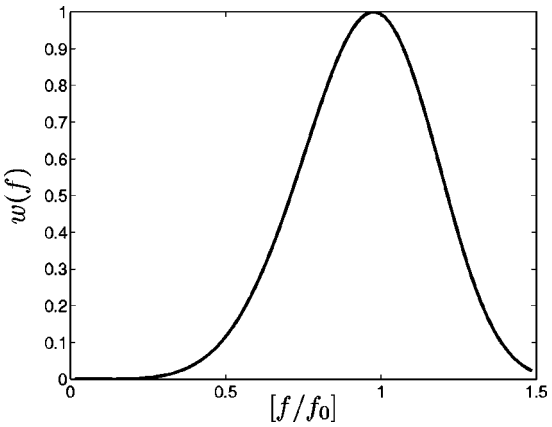

FIG. 3. Weightfunction for the inner product which was used to construct the orthogonal basis functions.

Here, optimal is taken to mean that only a few significant coefficients are needed to give a good representation. This basis, however, would be dependent on the particular aberration, and thus not necessarily be optimal for a different aberration. To handle the variations in aberration found in ultrasonic imaging, a basis independent of the particular aberration is desired.

Not much is known about the frequency dependence of aberration found in ultrasound imaging, but physical reasoning suggests that the aberration should be smooth. The basis functions should, therefore, also be smooth. Furthermore, most of the phase aberration is accounted for by a time delay. Since this is represented by a linear function of frequency, and a constant phase is unimportant in this context, $\psi(f)=f$ is chosen as the first basis function.

Also, the phase estimates are most reliable close to the center frequency f_0. This is due to a much higher signal-to-noise ratio close to f_0 than further away. A weighted inner product that emphasizes this region when defining orthogonality of the basis functions is, therefore, employed. The following inner product, which uses a weightfunction to accentuate a band slightly narrower than the bandwidth of the transmit pulse was found to give good results.

$$\langle u,v\rangle = \int_0^{3f_0/2} w(f)u(f)\overline{v(f)}df,$$

$$w(f) = f^5 \exp(-[2/5+f/f_0])^6.$$

The weightfunction $w(f)$ is plotted in Fig. 3.

An orthogonal set of n polynomials is constructed from this inner product using the Gram–Schmidt algorithm on the set of functions $\{f,f^2,f^3\ldots f^{n-1},1\}$ in that order. By construction, the basis functions are smooth, and the first coefficient in the orthogonal expansion using this basis corresponds directly to a physical time delay. Other coefficients correspond to higher-order polynomial corrections to the time delay. The higher-order correction terms, thus, give an indication of the need to consider phase variations beyond a time delay.

D. Inactive transducer elements

The transducer is known to have some bad elements, *i.e.*, elements that do not behave the way they should. These have a different bandpass or sensitivity than the rest of the transducer elements in the array. Since additive noise in the measurements can have long-range effects on the algorithm for finding the relative phase, bad elements are identified and removed from the processing.

The bad elements were identified during calibration of the two-dimensional array system. Measurements from these elements were replaced by substituting the average of eight neighboring transducer elements.

To deal with remaining outliers in the dataset, a robust implementation of the relative phase retrieval was used.[25] The procedure was as follows.

(1) An initial least-mean-square-error estimate for the relative phase was calculated from

$$\phi^{(0)}(\omega) = A^{\dagger}\theta(\omega).$$

(2) A weight matrix W^0 was calculated using

$$\mu = \mu(\omega) = \frac{1}{L}\|A\phi(\omega) - \theta(\omega)\|_1$$

$$(W^0)_{i,j} = \delta_{ij}\exp(-|\phi^{(0)}(\omega)_i - \theta(\omega)_i|^2/4\mu^2).$$

(3) A new least-mean-square-error estimate $\phi^{(1)}(\omega)$ was obtained from the inner product

$$\langle x,y\rangle_{W^0} = y^H W^0 x.$$

(Assuming outliers do not corrupt the initial estimate too badly, this estimate is less influenced by outliers than the first one.)

(4) Steps 2 and 3 were repeated three times to get the final estimate $\phi^{(3)}(\omega)$, which is taken to be the relative phase over the transducer.

The stability of this algorithm is difficult to examine exactly due to its nonlinear nature. However, as long as the dataset does not contain too many outliers, the estimator behaves approximately in a linear fashion. Moreover, in the application of the algorithm, the estimate did not seem to change much from the second to the third iteration, indicating convergence for the measurements presented here.

E. Validation of estimates

Accuracy of the spectral estimates can be validated by constructing confidence intervals at each frequency for the phase and amplitude of the spectral estimates. However, the motivation for the estimation is to perform aberration correction. Therefore, of greater interest is to compare the characterization based on the cross-spectral estimates to an ideal aberration correction filter.

A reference characterization was obtained as follows. The random scatterer distribution was replaced by a pointlike reflector that was the rounded tip of a rod. The reflector was in turn placed at each of the focal positions of the random scattering measurements in order to get samples of the aberrated point scattering at each location. From these signals, a reference spectrum was created. Care was taken to apply the

TABLE I. Important quantities for this study.

Transmit pulse	
Frequency	3 MHz
Pulse length	1.5 μs
Bandwidth	53%
Aberrator (MAB)	
Arrival time fluctuations	65 ns
Arrival time corr. length	8.2 mm
Energy level fluctuations	2.7 dB
Energy level corr. length	2.7 mm
Aberrator (SAB)	
Arrival time fluctuations	65.3 ns
Arrival time corr. length	5.4 mm
Energy level fluctuations	3.1 dB
Energy level corr. length	1.5 mm
Measurements	
Focal zone radius	0.45 mm
Sample range	3.00 mm
Sampling frequency	20 MHz
Focal range	~55 mm
f number	~1.2

same spectral smoothing as introduced by the window in the spectral estimation, thus ensuring the minimum bandwidth for the two spectra was the same.

The point source scattering process is deterministic. Thus, the only stochastic element in obtaining the reference characterization is measurement error. For the current setup, this is negligible for the purpose of this study. The reference may therefore be viewed as a deterministic quantity. Also, a low variation in the reference spectrum from focal point to focal point indicates that the isoplanatic hypothesis is valid.

From the reference spectrum, a reference for the relative phase of aberration and magnitude of aberration was constructed by the same method as for the estimated spectrum

$$s_{\mathrm{ref}}(r,\omega)=A_{\mathrm{ref}}(r)e^{i\theta_{\mathrm{ref}}(r,\omega)}.$$

The quantity s_{ref} is the generalized screen for focusing at r_f, but weighted by a system response as seen in Eq. (3). For a point reflector, however, the system response is merely the square of the amplitude of the transmit pulse, and hence the same across the aperture. Therefore, s_{ref} corresponds, as shown in simulations,[6] to an ideal aberration correction filter. Agreement between the estimated aberration characterization and this reference, thus, implies aberration correction properties for the estimated characterization.

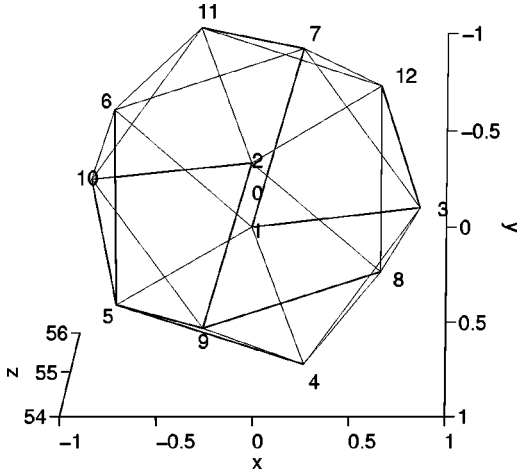

FIG. 4. Labeling of the vertices of the icosahedron used for focusing.

In order to quantify the difference between the relative phase and the reference, a root-mean-square-difference (RMSD) was calculated after subtracting the mean difference. This allows the relative phase estimate to differ from the reference by an unimportant arbitrary constant phase factor.

For the estimated magnitude of aberration to be comparable to the reference, the power should be the same in both. Both the reference and the estimate were, therefore, normalized. The difference was then measured using the L^2 norm.

IV. MEASUREMENTS

The measurements used in this study were performed using a 80×80 element two-dimensional transducer array with 0.6 mm pitch, center frequency 3 MHz, and a sampling

TABLE II. Correlation between different measurements. These are values for the correlation $\hat{C}(0)$ between the measurement labeled $k=0$ and different measurements n in the same dataset. The presented values were calculated as an average over a 20×20 neighborhood of the center transducer element. Mean values for the correlation in the 0.50 mm, 1.00 mm, and 0.79 mm case are 0.31, 0.03, and 0.00, respectively.

n	$\hat{C}(0)$ ($r=0.5$ mm) (MAB)	$\hat{C}(0)$ ($r=1.0$ mm) (MAB)	$\hat{C}(0)$ ($r=0.79$ mm) (SAB)
1	0.31	0.07	0.24
2	0.19	0.10	0.16
3	0.03	−0.22	0.12
4	0.38	−0.08	−0.09
5	0.35	0.12	−0.20
6	0.04	−0.00	−0.02
7	0.39	0.06	−0.04
8	0.48	0.23	−0.01
9	0.44	−0.09	0.07
10	0.31	−0.02	−0.01
11	0.23	0.06	0.09
12	0.52	0.18	0.19

rate 20 MHz. The relevant *f* number was approximately 1.2. The length of the transmitted pulse was approximately 1.5 μs, with a 53% bandwidth.

From the transducer array was emitted an ultrasound pulse wavefront that focused at a spatial location corresponding to a vertex or the center of an icosahedron of radius *r*. The scattering region was a tissue-mimicking phantom. The correlation length of this scattering region is known to be short relative to the wavelength. Hence, the scatterers were assumed to be δ-correlated. To obtain the reference characterization of the aberration, the sequence of measurements were repeated after replacing the scattering phantom by the rounded tip of a rod with a diameter of 0.82 mm.

A dataset consisted of 13 measurements, one for each of the 12 vertices and one for the center of the icosahedron, or a set of 75 measurements. In the set of 75 measurements, the focus was placed at the center and the 12 vertices of an inner icosahedron, the 20 vertices of an enclosing dodecahedron, the 12 vertices of an outer icosahedron, and the midpoints of the 30 circular arcs that connect adjacent vertices of the outer icosahedron. The polyhedra had a common center and were configured with each vertex of the dodecahedron located along a ray from the origin through the center of one of the faces of the icosahedra while each vertex of the icosahedra was located along a ray from the origin through the center of one of the faces of the dodecahedron. The icosahedra were spatially oriented so one axis that passed through two vertices and the common center was normal to the plane of the transducer array at its center. From the common center, the distance to the vertices of the inner icosahedron, dodecahedron, and outer icosahedron were 0.79, 1.50, and 1.50 mm, respectively.

Aberration mimicking the distortion produced by an abdominal wall was introduced by placing a specially designed phantom[26] between the transducer and the scattering region. The phantom was either a *medium aberrator* (MAB) or a *strong aberrator* (SAB). For these phantoms, the isoplanatic patch is known to be large enough to contain all focal positions used in the study. Table I summarizes relevant measurement information.

The 13 measurements in a dataset were numbered from 0 to 12. The labeling reflected the corresponding icosahedron vertices in Fig. 4.

The effective radius of the focal zone at a relative amplitude of $1/\sqrt{e}$ was 0.45 mm. An 80 sample interval that corresponds to a range of 3.00 mm at the 20 MHz sampling rate of the two-dimensional array system was used in the processing.

A total of 22 transducer elements were identified as bad during the calibration process. These were effectively removed from the datasets as described in Sec. III D. This was done prior to any other processing.

V. RESULTS

The average correlations between measurement 0 and each of the measurements 1 to 12 in the datasets are listed in Table II for icosahedra with three different radii. The correlation in the data set with 0.50 mm radius icosahedron is clearly higher than that of the dataset with the same aberrator and 1.00 mm focal point separation. Moreover, measurements from focal points with 1.00 mm separation are relatively uncorrelated. Averaging *n* spectral estimates from different measurements in this dataset will, therefore, reduce the estimate variance by a factor of close to *n*. Measurements on the dataset with 0.79 mm focal point separation are also sufficiently uncorrelated for this to be the case. The true variance reduction when averaging *n* spectral estimates from the dataset with 0.50 mm separation is expected to be much less than *n* due to the significantly higher correlation. Only the results from estimating spectra using measurements in the dataset with 0.79 mm focal point separation are presented in detail.

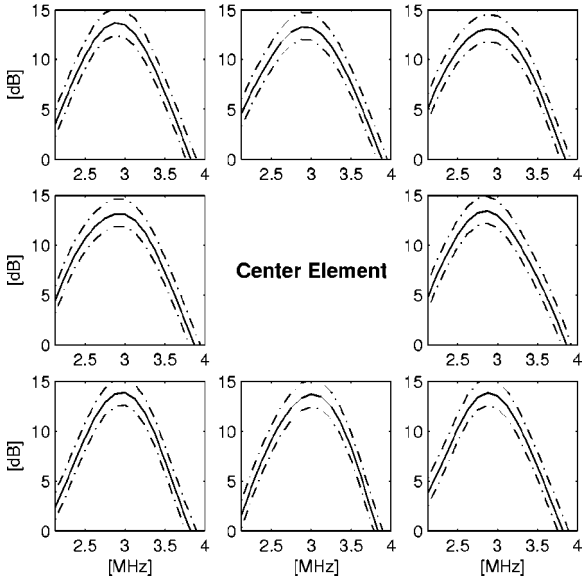

FIG. 5. Magnitude of estimated cross spectrum for the backscatter received at eight transducer elements surrounding the center element. The dash–dot line corresponds to a 95% confidence interval.

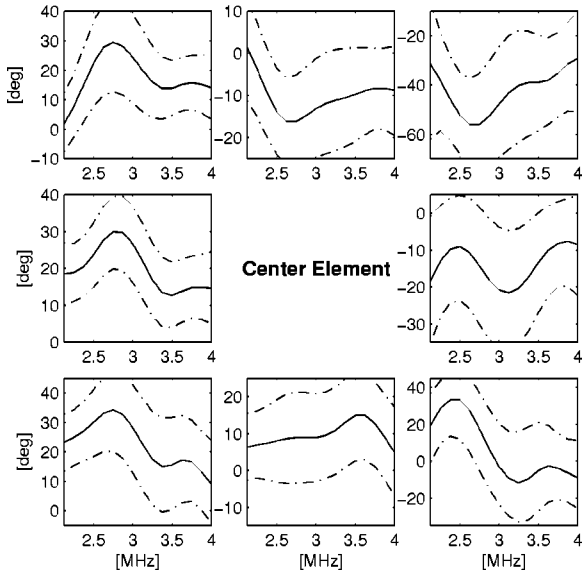

FIG. 6. Phase of the estimated cross spectra between the center transducer element and each of the surrounding eight elements. The dash–dot line corresponds to a 95% confidence interval.

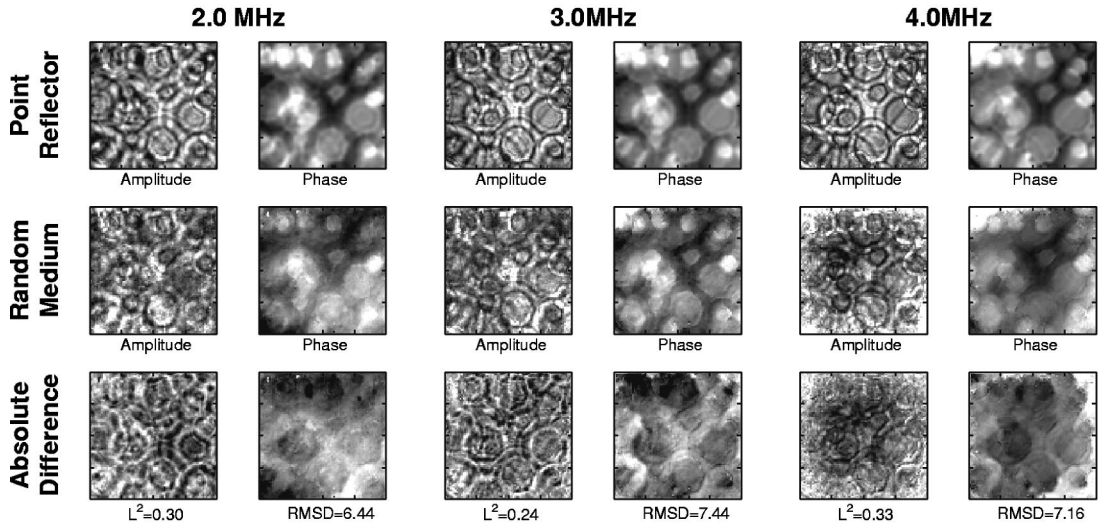

FIG. 7. Magnitude and relative phase of aberration recovered from the estimated cross spectra. The magnitude has been adjusted by a constant factor to compensate for the energy difference between point-reflector data and stochastic data. The RMSD is expressed in units of degrees.

A Parzen window was employed in the Blackman–Tukey estimator. The measurement sampling frequency of 20 MHz and a pulse length of 1.5 μs for the transmitted pulse indicate that the scaling factor M should be chosen such that the window does not distort the covariance function significantly for lags less than 30 samples. The value of M was, thus, chosen to be 50 for the Parzen window.

Figure 5 shows the estimated power spectrum for eight transducer elements surrounding the center element. The 95% confidence intervals are approximately ± 2 dB wide for this estimate. A normalization was chosen such that the corresponding autocorrelation functions are 1 for zero lag. The square root of this quantity is an estimate for the magnitude of aberration.

The phase of the estimated cross spectrum between the center element and each of its eight neighbors is plotted in Fig. 6. In this case, the 95% confidence intervals are about $\pm 15°$ wide. These phases are the relative phase differences from which the relative phase across the transducer is to be recovered.

A comparison between the estimate and the point source reference for the amplitude and the phase of aberration is presented in Fig. 7. Recovery of the relative phase was performed for each frequency separately, thus not utilizing the spectral smoothness inherent in the spectral phase estimate. The reference magnitude obtained from the point reflector has been normalized to account for the energy difference in the scattering from point reflector and stochastic medium.

In order to preserve the smoothness of the phase, the orthogonal expansion technique discussed in Sec. II C 2 and the basis functions discussed in Sec. III C were used. The resulting first six coefficients of this expansion are shown in Fig. 8. Visual inspection reveals that all of these six coefficients exhibit reasonable spatial structure for the reference. The coefficients for the estimate, however, only display obviously similar spatial structure in the first coefficient, and to a lesser extent in the second coefficient. The lack of spatial structure in the estimated coefficients beyond the first two indicate that they consist mainly of noise, although there is

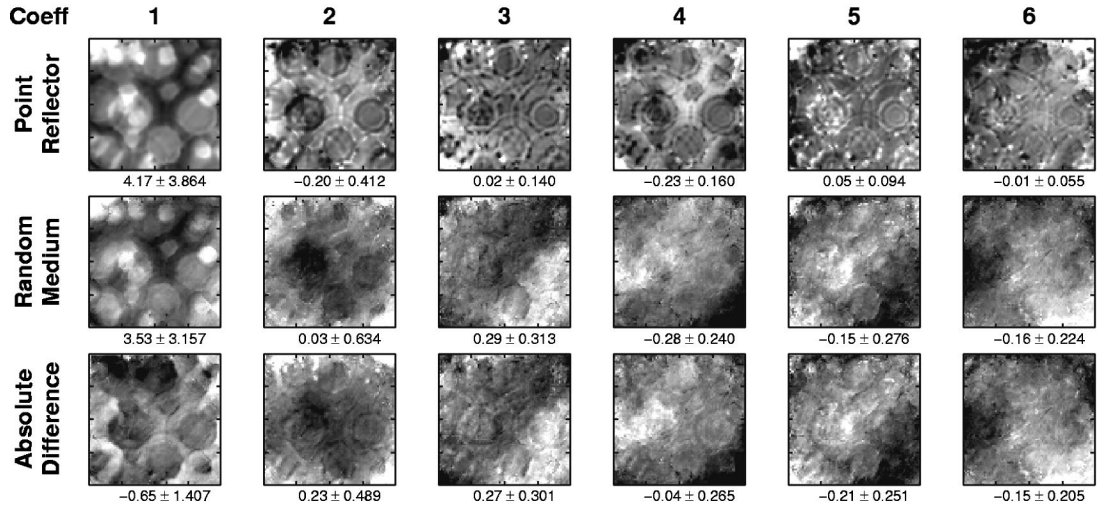

FIG. 8. Coefficients in an orthogonal expansion of the relative phase. Mean value and standard deviation are indicated below each panel.

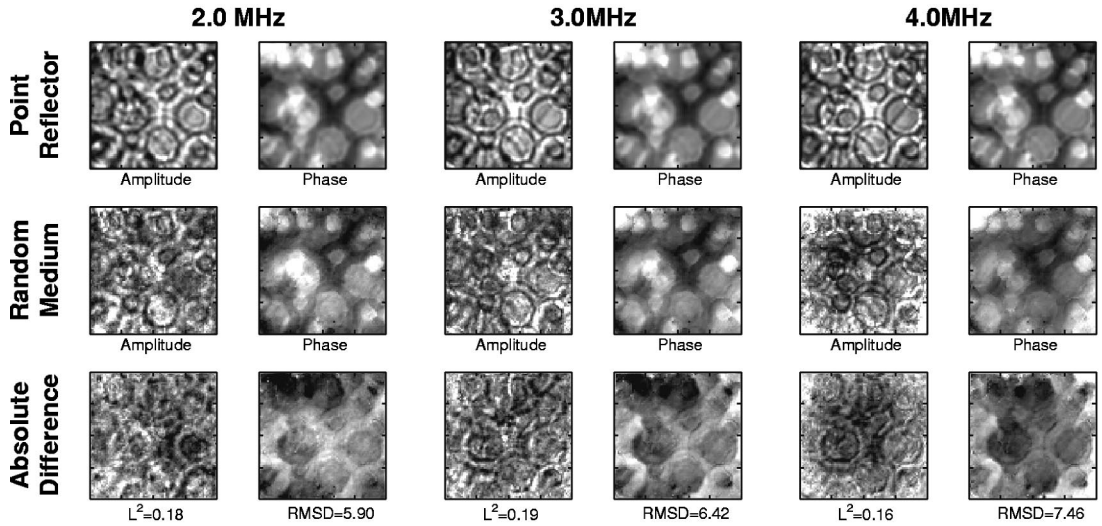

FIG. 9. Magnitude and relative phase of aberration. The phase has been recovered from the estimated cross spectra using an orthogonal expansion. The magnitude determined from the point reflector has been adjusted by multiplicative constant for each frequency separately. The RMSD is expressed in units of degrees.

still a vague structure similar to that of the reference in higher coefficients as well.

In Fig. 9, the relative phase has been reconstructed using the first two coefficients in the orthogonal expansion of the phase. The magnitude of aberration has been adjusted for each frequency separately to account for some of the difference in system response between point reflector and stochastic medium.

In light of the confidence bands for the amplitude and phase estimates in Figs. 5 and 6, the dataset was augmented to contain 75 measurements with focal points distributed as described in Sec. IV. The estimated power spectrum and cross-spectral phase for this dataset are plotted in Figs. 10 and 11. In this case, confidence bands for the power spectra are about 1 dB wide, while confidence bands for the cross spectral phase are about $\pm 5°$. The associated coefficients and final aberration characterization is plotted in Figs. 12 and 13, respectively.

VI. DISCUSSION

The data in Table II show that 0.50 mm focal point separation is not enough to obtain an independent set of measurements for this experimental configuration. Using a 0.79 mm or 1.00 mm radius icosahedron to place the focal points, however, does appear to give independent samples. This is in agreement with the predicted size of the focal region in Sec. IV. The conclusion is also supported by the fact that no significant improvement was observed when combining the 0.50 mm and the 1.00 mm datasets to get an aggregate estimate. This demonstrates the necessity of separating the focal points for different measurements to get statistically independent samples.

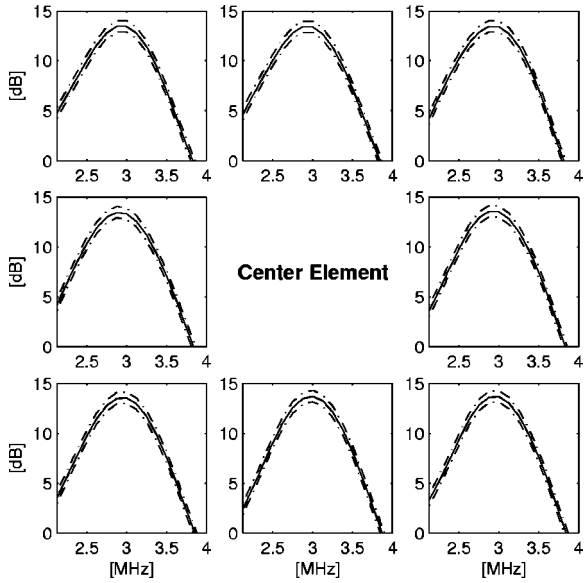

FIG. 10. Magnitude of estimated cross spectrum for the backscatter based on 75 measurements, with corresponding 95% confidence interval.

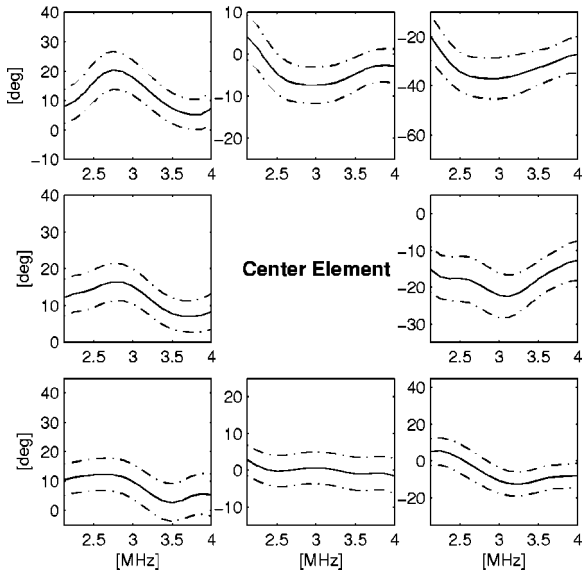

FIG. 11. Phase of the estimated cross spectra based on 75 measurements, with corresponding 95% confidence interval.

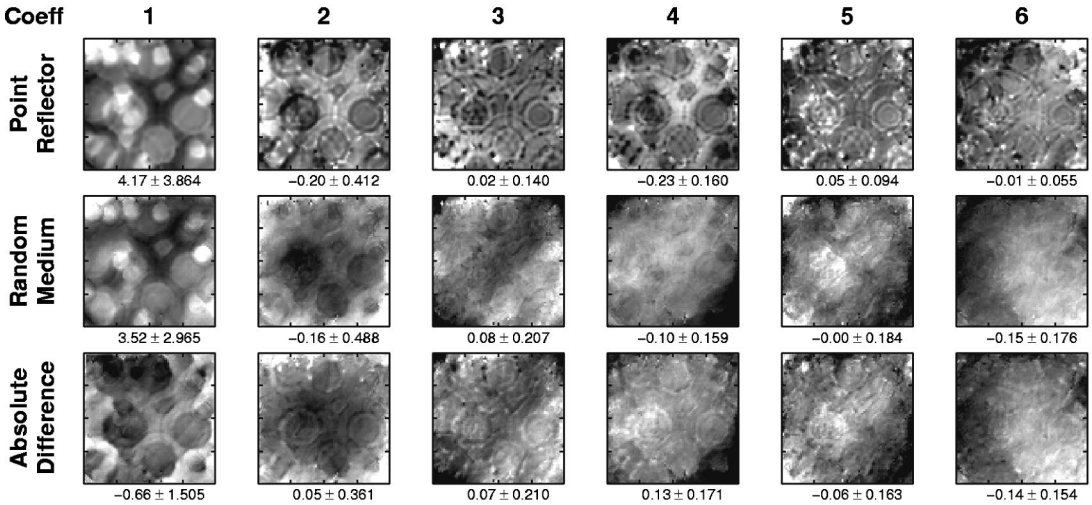

FIG. 12. Coefficients in an orthogonal expansion of the relative phase based on 75 measurements. Mean value and standard deviation are indicated below each panel.

The confidence bands are appreciable for both the estimated cross-spectrum phase and amplitude when using a dataset of 13 measurements. The estimation variance could be reduced by choosing a smaller parameter M, but at the expense of increased estimation bias and blurring of the spectral estimate. Increasing the sample length would also seemingly reduce the variance. However, the stationarity assumption about the received scattering can only be expected to hold locally, *i.e.*, within the depth of field. Furthermore, increasing the sample length would lead to a significant overlap of the scattering regions in the depth direction, thus increasing the correlation between the samples. A better solution to reduce the estimation variance is, therefore, to increase the number of measurements in the dataset. Indeed, using an augmented dataset consisting of 75 measurements gives significantly improved spectral estimates as shown in Figs. 10 and 11. In the situation of interest, however, the possibility of increasing the number of measurements is fundamentally limited by the size of the isoplanatic region. When moving out of the isoplanatic region, the phase and amplitude of aberration will gradually change. Averaging measurements outside this region will, therefore, give a blurred estimate.

Despite the wide confidence bands for the spectral estimates in Figs. 5 and 6, the magnitude and relative phase of aberration obtained from the estimated spectra have the same spatial structure observed in the reference solution as seen in Fig. 7. The similarity is quantified by the L^2 norm and RMSD given in Fig. 7.

Projecting the relative phase onto the first two basis functions improves the phase retrieval as shown clearly by comparison of Figs. 7 and 9. However, the data in Fig. 8 also show that the spectral estimates obtained from 13 measurements is not good enough to warrant looking for more than two coefficients in this expansion, *i.e.*, classical time delay with a second-order correction term. For 75 measurements, the estimates are improved as seen in Figs. 10–13. However, the higher-order correction coefficients still contain limited

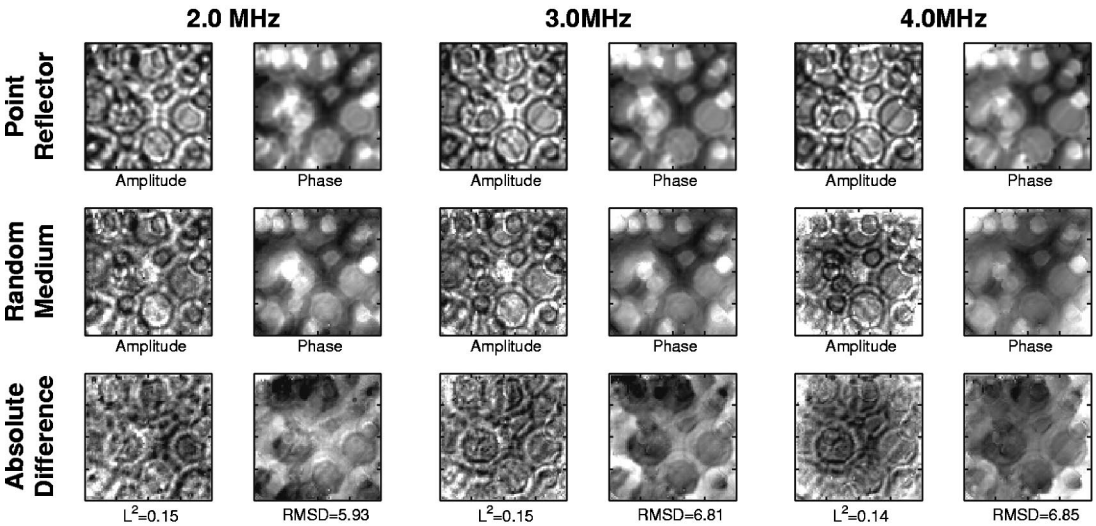

FIG. 13. Magnitude and relative phase of aberration based on 75 measurements. The phase has been recovered from the estimated cross spectra using an orthogonal expansion. The magnitude determined from the point reflector has been adjusted by multiplicative constant for each frequency separately. The RMSD is expressed in units of degrees.

information. (See Fig. 12.) This indicates that a classical time delay is a good approximation to the frequency-dependent phase in the measurements reported here.

For the case with 13 measurements, the RMSD for the relative phase is approximately one-half of the size of the width of the confidence bands. (See Figs. 6 and 7.) Approximately four relative phase estimates were used to obtain the least-mean-square-error estimate of the phase at each point. A reduction of the error by a factor of 2 is therefore optimal, and indicates that the error in each of the relative phase estimates is independent.

For the case with 75 measurements, the error is not reduced significantly compared to the width of the confidence bands. The quantitative measure of improvement is in fact not as good as one would expect when going from 13 to 75 measurements. (See Figs. 10–13.) The reason is that the aberration from the random scatterers is smoothed out. The difference between the reference and the estimate clearly shows that the main contribution to the deviation is around the edges of spatial structures, a clear sign of blurring. This is a deviation that grows as more measurements from a larger region are used, as the isoplanatic assumption is gradually invalidated. The same trend is visible for the amplitude estimates. A simple spatial blur of the reference amplitude or phase, *e.g.*, averaging over a 3 by 3 neighborhood of each point, reduces the difference between the reference and the estimate. This also supports the conclusion that a spatial blurring is taking place.

A major part of the RMSD is, due to the spatial blurring, contributed around the edges of spatial structures in the phase estimate. (See Figs. 7 and 13.) Another reason for the estimate to differ from the reference is that the system response is different for scattering from the random medium and scattering from the point reflector. According to Eq. (3), the relative phase reconstructed from phase differences from the cross spectrum will also contain the phase of the system function $P^{(h)}$. The same is true for the magnitude. A better estimate would therefore be obtained if the system response could be identified and removed.

The choice of window function and orthogonal basis functions here is not based on an optimality criterion. Indeed, such an optimality criterion would be difficult to construct so as to be valid for a wide range of aberration cases. An alternate choice will, therefore, certainly result in different performance. The choices based on a plausibility rationale are still reasonable, and serve to illustrate features that the window function and basis functions should possess. As such, they are also good for demonstrating characterization of aberration by means of this technique. Also, the presented basis functions were able to describe the true aberration with almost as few significant coefficients as a basis obtained using a singularvalue decomposition of the aberration. It should, therefore, not be a bad choice.

An important issue with the spectral estimation is that the coherence in the received signals is low ($\sim$0.6) for the aberrated signal. It can be shown that, assuming the aberration is well described by a screen model, the coherence is determined by the aberration on transmit, and not on receive.[15] Therefore, if a limited correction of the aberration is be obtained, the coherence will also improve, resulting in better conditions for the spectral estimation. An iterative approach would, therefore, seem natural. It is, however, not clear that an iterated estimate would in fact result in an improved estimate for the situation studied here. The problem is that the scatterers will remain the same, and therefore the measurements will be correlated from one iteration to the next. The way this affects the convergence of the iterated estimate is not obvious.

VII. CONCLUSION

The confidence bands for the presented estimates are appreciable for both the cross-spectrum phase and amplitude when using a dataset of 13 measurements. Despite the wide confidence bands, a good estimate of the time-delay and, to a certain extent, a *second-order correction* has been obtained using the processing and data described here. The magnitude estimate also resolves most of the structure observed in the reference solution, and is in agreement with the reference.

In order to utilize fully the method presented, and use higher-order corrections, an increase in the quality of the phase difference estimate is required. A different choice of window function is worth investigating, in order to improve these estimates. However, the best way to improve the estimates is most likely to increase the number of measurements. When doing this, care must be taken not to exceed the isoplanatic region.

Using an augmented dataset consisting of 75 measurements yielded a significant improvement in the spectral estimates. The visual impression of the retrieved magnitude and phase of aberration is also improved. It is, however, difficult to quantify this improvement, as spatial blurring of the estimate seems to dominate the difference between the estimate and the reference. This deviation from the reference will only become more of a problem when the region of measurements is expanded further.

The presented characterization of the aberration is, nevertheless, well suited for the construction of a filter for the purpose of aberration correction.

ACKNOWLEDGMENT

The authors thank Dr. Daniel B. Phillips and Wayne Pilkington for collection of the data used in the processing. Dr. Jeffrey P. Astheimer in the United States and Professor Harald Krogstad at NTNU are thanked for useful discussions. Support for this work was provided by The Research Council of Norway, NIH grants CA74050 and HL50855, and the University of Rochester Diagnostic Ultrasound Research Laboratory Industrial Associates Program.

[1] U. Haberkorn, G. Layer, V. Rudat, I. Zuna, A. Lorenz, and G. van Kaick, ''Ultrasound image properties influenced by abdominal wall thickness and composition,'' J. Clin. Ultrasound **21**, 423–429 (1993).

[2] L. Hinkelman, D.-L. Liu, L. A. Metlay, and R. C. Waag, ''Measurements of ultrasonic pulse arrival time and energy level variations produced by propagation through abdominal wall,'' J. Acoust. Soc. Am. **95**, 530–541 (1994).

[3] G. E. Trahey, P. D. Freiburger, L. F. Nock, and D. C. Sullivan, ''In-vivo measurements of ultrasonic beam distortion in the breast,'' Ultrason. Imaging **13**, 71–90 (1991).

[4] P. D. Freiburger, D. Sullivan, B. H. LeBlanc, and G. E. Trahey, ''Two-dimensional ultrasonic beam distortion in the breast: in-vivo measurements and effects,'' Ultrason. Imaging **14**, 398–414 (1992).
[5] Q. Zhu and B. D. Steinberg, ''Wavefront amplitude distribution in the female breast,'' J. Acoust. Soc. Am. **96**, 1–9 (1994).
[6] S. E. Måsøy, T. F. Johansen, and B. Angelsen, ''Correction of ultrasonic wave aberration with a time delay and amplitude filter,'' J. Acoust. Soc. Am. **113**, 2009–2020 (2003).
[7] M. Tabei, T. D. Mast, and R. C. Waag, ''Simulation of ultrasonic focus aberration and correction through human tissue,'' J. Acoust. Soc. Am. **113**, 1166–1176 (2003).
[8] D.-L. Liu and R. C. Waag, ''Estimation and correction of ultrasonic wavefront distortion using pulse-echo data received in a two-dimensional aperture,'' IEEE Trans. Ultrason. Ferroelectr. Freq. Control **45**, 473–490 (1998).
[9] K. W. Rigby, C. L. Chalek, B. H. Haider, R. S. Lewandowski, M. O'Donnell, L. S. Smith, and D. G. Wildes, ''Improved in vivo abdominal image quality using real-time estimation and correction of wavefront arrival time errors,'' *2000 IEEE Ultrasonics Symposium Proceedings* (IEEE, New York, 2000), Cat. No. 00CH37121, Vol. II, pp. 1645–1653.
[10] M. Fink, ''Time reversal of ultrasonic fields—Part I: Basic principles,'' IEEE Trans. Ultrason. Ferroelectr. Freq. Control **39**, 555–567 (1992).
[11] M. O'Donnell and S. W. Flax, ''Phase-aberration correction using signals from point reflectors and diffuse scatterers: Measurements,'' IEEE Trans. Ultrason. Ferroelectr. Freq. Control **35**, 768–774 (1988).
[12] G. C. Ng, S. S. Worrell, P. D. Freiburger, and G. E. Trahey, ''A comparative evaluation of several algorithms for phase aberration correction,'' IEEE Trans. Ultrason. Ferroelectr. Freq. Control **41**, 631–643 (1994).
[13] D.-L. Liu and R. C. Waag, ''Time-shift compensation of ultrasonic pulse focus degradation using least-mean-square-error estimates of arrival time,'' J. Acoust. Soc. Am. **95**, 542–555 (1994).
[14] D.-L. Liu and R. C. Waag, ''Correction of ultrasound wavefront distortion using backpropagation and a reference waveform method for time-shift compensation,'' J. Acoust. Soc. Am. **96**, 649–659 (1994).
[15] B. A. Angelsen, *Ultrasound Imaging. Waves, Signals, and Signal Processing* (Emantec, Trondheim, Norway, 2000), Vol. 2, http://www.ultrasoundbook.com.
[16] F. Lin and R. C. Waag, ''Estimation and compensation of ultrasonic wavefront distortion using a blind system identification method,'' IEEE Trans. Ultrason. Ferroelectr. Freq. Control **49**, 739–755 (2002).
[17] G. M. Jenkins and D. G. Watts, *Spectral Analysis and its Applications* (Holden-Day, San Francisco, 1968).
[18] S. Kay and S. Marple, ''Spectrum analysis—A modern perspective,'' Proc. IEEE **69**, 1380–1419 (1981).
[19] M. B. Priestley, *Spectral Analysis and Time Series* (Academic, London, 1981).
[20] P. Stoica and R. Moses, *Introduction to Spectral Analysis* (Prentice–Hall, New Jersey, 1997).
[21] M. B. Priestley, *Spectral Analysis and Time Series* (Academic, London, 1981), Chap. 6.
[22] P. Stoica and R. Moses, *Introduction to Spectral Analysis* (Prentice–Hall, New Jersey, 1997), Chap. 2.
[23] M. B. Priestley, *Spectral Analysis and Time Series* (Academic, London, 1981), Chap. 9.
[24] D. L. Snyder, *Random Point Processes* (Wiley, New York, 1975).
[25] J. S. Simonoff, *Smoothing Methods in Statistics* (Springer, New York, 1996).
[26] J. C. Lacefield, W. C. Pilkington, and R. C. Waag, ''Distributed aberrators for emulation of ultrasonic pulse distortion by abdominal wall,'' Acoust. Res. Lett. Online **3**, 47–52 (2002).

Ultrasonic attenuation due to grain boundary scattering in copper and copper-aluminum[a)]

X.-G. Zhang, W. A. Simpson, Jr., and J. M. Vitek
Oak Ridge National Laboratory, Oak Ridge, Tennessee 37831-6164

D. J. Barnard, L. J. Tweed, and J. Foley
Ames Laboratory and Iowa State University, Ames, Iowa 50011

(Received 8 January 2004; revised 18 March 2004; accepted 23 March 2004)

Ultrasonic attenuation in copper and copper-aluminum samples is measured as a function of frequency and average grain size. At low frequencies the attenuation scales quadratically with the frequency and linearly with average grain size. In addition, there is a large difference in attenuation between powder metallurgy samples and cast-and-wrought samples, although their qualitative behaviors are similar both in terms of frequency dependence and grain size dependence. Such difference and the discrepancy with the existing theory may point to mechanisms of scattering by grain boundaries that are not included in the current theoretical model. © *2004 Acoustical Society of America.* [DOI: 10.1121/1.1744752]

PACS numbers: 43.20.Hq [RR] Pages: 109–116

I. INTRODUCTION

The study of wave propagation and scattering in an inhomogeneous medium dates back to the beginning of modern science.[1] The approach of using a homogeneous effective medium as the starting point and treating the inhomogeneity as a perturbation was also established well over a century ago.[2] Today's researchers are more interested in nonlinear phenomena, and the basic concepts within the linear regime, such as the effect of attenuation due to the imperfections of the medium, are well-understood and rarely questioned. The theoretical model for acoustic attenuation due to grain boundary scattering, first proposed by Lifshitz and Parkhomovskii[3] and embraced by almost all subsequent works,[4–6] is based on the effective medium consideration and treats each crystalline grain as an independent scatterer within an average effective medium. This model produces the expected Rayleigh scattering solution in the low frequency regime. The Green's function formulation by Stanke and Kino,[5] extending the theoretical consideration to all frequencies, appeared to have completed the theoretical development and placed the understanding on a solid theoretical framework. Although the mean-field approach of Stanke–Kino model is far from rigorous, it has been the most complete theoretical description of grain boundary scattering so far and is accepted as the ''standard'' theoretical model.

There are few experimental measurements of ultrasonic attenuation in single phase polycrystalline materials[7,8] with sufficient accuracy that can be used to examine on a quantitative basis the Stanke–Kino model, whose detailed numerical prediction for a given material can be evaluated easily. Particularly notable is the measurement by Stanke[8] of pure copper samples. We believe that the agreement between this measurement and the predictions of the Stanke–Kino model is at best qualitative. Although the experimental data are bracketed by the theory curves corresponding to the average grain sizes within $\pm 20\%$ of the measured average grain size, we note that for the single sample with a fixed average grain size, the measured curve overshoots the theory at low frequencies and undershoots it at high frequencies. This turns out to be a rather consistent feature for all of the cast-and-wrought (CW) samples we measured in our experiment. At the lowest frequency of Stanke's measurement, the 20% difference in the average grain size would translate into more than 70% disagreement in the value of the attenuation coefficient.

There are a number of difficulties associated with experimental measurements of acoustic attenuation in solids. First, most materials contain a significant density or population of scattering centers such as voids and precipitates, which contribute a large fourth-power scattering term, and impurities at the boundaries which might weaken the intergrain correlation. Second, materials that are free of these defects usually have large grain sizes which cause too much attenuation for reliable measurements. Third, there are a number of sources of attenuation that can scale quadratically with frequency, such as absorption and dislocation contributions, thus making the actual grain boundary contribution difficult to identify. It has been our experience in the past, as well as that of many of our colleagues, that the measured attenuation coefficients for pure cast-and-wrought (CW) samples with attenuation at a level of a fraction of 1 Nepers/cm can vary by as much as a factor of 2 between different samples with the same microstructures, and sometimes even with the same samples measured with different techniques. Thus a 70% difference between theory and measurement as discussed above has been generally accepted as ''good agreement.'' Such variability of the measurements points to the need to refine both the measurement approaches and sample preparation methods.

There are also a number of physical issues yet unresolved related to the attenuation due to grain boundary scattering. We have seen large variations of attenuation between samples with similar average grain sizes. As we will present later in this paper, these differences seem to suggest that the grain size distribution and/or impurities along grain boundaries can impact attenuation. For an ensemble of Rayleigh scatterers, on the other hand, Gubernatis *et al.*[9] proved that only the mean size of the scatterers, not the details of their size distribution, is of importance for determining the attenuation. Furthermore, the model of Stanke and Kino clearly establishes that the two point correlation function $\langle \Delta(\mathbf{r})\Delta(\mathbf{r}')\rangle$, where Δ are the fluctuations of the elastic tensor at points $\mathbf{r}$ and $\mathbf{r}'$, respectively, determines the attenuation within the second-order perturbation theory, and that impurities along grain boundaries should have no impact on attenuation as long as their volume fraction is negligible. The resolution of these issues will significantly impact our understanding of acoustic propagation and attenuation in solids, and the scattering theory in general.

II. CHOICE OF A MODEL SYSTEM AND SAMPLE PREPARATION

A large body of literature exists on attenuation measurements of materials with porosity such as composite materials or ceramics. There have been very few measurements on relatively clean and well-characterized systems, in which the grain boundaries make up the microstructure that dominates the contribution to attenuation. It has been difficult to isolate and quantify the effects of grain boundaries from past experiments. Therefore the careful choice of a model system is essential for a quantitative examination of the attenuation model. The essential requirements for the model system are as follows: (1) It needs to be relatively clean of impurities, voids, second phases and other uncontrolled microstructures. (2) It can be easily made with a reasonably uniform grain structure. (3) It has a high crystalline anisotropy so that grain boundary scattering will be more pronounced compared to other sources of attenuation. Another factor that may need to be taken into account in choosing a model system for experiments is that the theoretical models can be simplified greatly if the underlying lattice of the material has the cubic symmetry. Thus measurements in cubic systems will help facilitate future theoretical development and comparison with theory.

Given these requirements, one would then expect pure copper, which can be produced easily, to be an excellent candidate material. Pure copper has in fact been used in one of the previous studies of attenuation.[8] Unfortunately, conventional methods of preparing high-purity copper (casting, powder metallurgy, etc.) also tend to produce large grains, and this leads to high attenuation which makes accurate measurements difficult. Two different techniques can be applied to produce copper samples with desired small grain size. Both techniques are used in our experiment and are described below.

The first approach was to use a copper-rich solid solution that contains a small amount of aluminum (nominally 0.5 and 2 at% aluminum) rather than high-purity copper. These samples were prepared by the powder metallurgy (PM) method. It is expected that these rather dilute solutions will have minimal effect on the single-crystal anisotropy. Reasonably fine-grained samples were produced, even with the lowest percentage of aluminum. The powders were produced using high pressure gas atomization (HPGA) at Ames Laboratory. The Ames Laboratory method has been shown to minimize oxide formation on the surface of the powder during atomization.[10] Two of the samples were produced with 2 at% Al (samples PM1 and PM2). Three other samples were produced with 0.5 at% Al (samples PM3, PM4, and PM5). For samples PM3, PM4, and PM5, the original batch of powders was sieved to obtain initial powder size ranges of 0–25 (PM3), 25–53 (PM4), and 53–76 μm (PM5). Each powder size range was consolidated in a polymer bag using cold isostatic pressing (CIP) at 20 Ksi. The CIP sample was then placed in a copper can and hot isostatic pressed (HIP) at 44.5 Ksi and 900 °C.

A second model system was produced by equal channel angular extrusion (ECAE)[11,12] and annealing of wrought materials. High purity ($>$99.99%) OFHC polycrystalline copper was used as the bulk material in this study. In order to obtain a uniform recrystallized microstructure with controllable grain size after a static recrystallization anneal, it was necessary to introduce a high degree of plastic deformation into the material prior to static recrystallization. This was accomplished by using the ECAE technique. With this technique, significant cold deformation was applied without any appreciable alteration of the large sample cross-section. This is in contrast to more conventional cold rolling processes where the sample size is reduced during deformation and extensive cold deformation would result in a large reduction of cross-section as well. Bars of approximately 22×22 mm in cross-section were taken from 38.1-mm-thick plate stock. The copper bars were passed through an ECAE die with a 90° angle and were rotated 90° between passes following the so-called B route.[12] Four total passes were used to ensure that the deformed microstructure was uniform across the cross-section. The estimated total true strain[13] after four ECAE passes is over 4.0, corresponding to an equivalent reduction in area during cold rolling of approximately 98%. It has been shown[13] that after four passes followed by static annealing for one hour at various temperatures, it is possible to obtain grain sizes ranging from 4 to 52 μm, depending upon the annealing temperature. This allowed for a broader range of grain sizes to be examined in the present study compared to conventional cold rolling and annealing. The greater range of achievable grain sizes can be attributed directly to the large amount of plastic strain introduced after four ECAE passes, and the corresponding lower onset temperature for recrystallization following such extensive cold deformation.[12] Moreover, the degree of crystallographic texture is low and the recrystallized grain structure can be considered random after the ECAE plus static annealing processing. We found that the pure copper samples produced by ECAE and annealing have generally good isotropy [anisotropy parameter $\eta=2C_{44}/(C_{11}-C_{12})-1$ was less than 0.02 for all samples]. This addresses one of the concerns with wrought or extruded samples, namely the texture of the grain

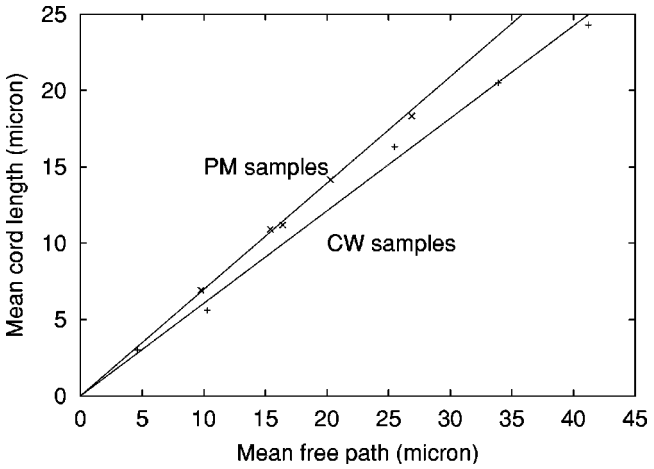

FIG. 1. Linear regression between the mean-free-path and the mean-cord-length for powder metallurgy (PM) samples (crosses) and cast-and-wrought (CW) samples (pluses). The slopes of the fitted lines are 0.7 (PM samples) and 0.6 (CW samples), compared to the ratio of 0.5 for the Poisson distribution of the grains.

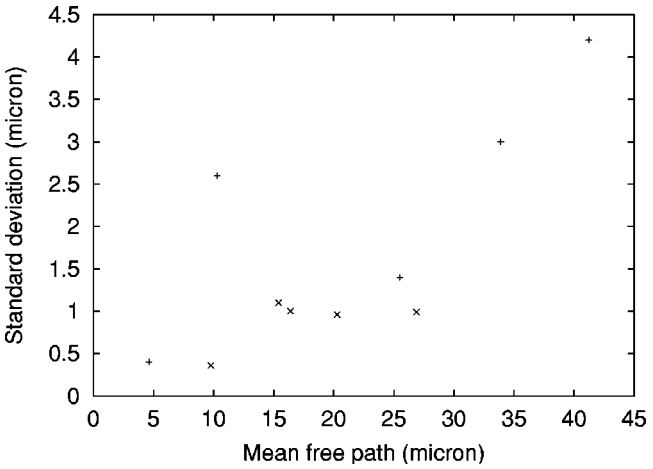

FIG. 2. Standard deviations in the mean-free-path measurements for powder metallurgy (PM) samples (crosses) and cast-and-wrought (CW) samples (pluses).

distribution that can significantly affect attenuation measurements.

Blocks approximately 25 mm thick were cut from the bars and the acoustic measurements were made on the polished cross-sections after the bars were cold deformed and recrystallized. Six samples were produced with the ECAE technique. One of the CW samples showed signatures of a texture in acoustic measurements (beam direction in the sample not perpendicular to the surface at normal incidence) and was not included in the study. All of the PM and CW samples had diameters of at least 2.5 cm, and thicknesses varied from 0.6 to 2.5 cm. All samples had opposing parallel faces polished to a mirror like finish for the attenuation measurements.

To quantitatively determine the average grain size, we analyzed the micrographs of the grain structure of the specimen employing the techniques by Margetan *et al.*[14] From the micrographs we measured the normalized line segment density $\rho(r)$, defined such that $\rho(r)dr$ is the probability that a randomly drawn line on the photo will intersect any grain at two points that are separated by a distance of r. Two metrics of the grain size can be obtained directly from this measurement. They are the mean cord length, defined as

$$l = \int_0^\infty \rho(r) r dr, \tag{1}$$

and the mean free path,

$$d = \frac{1}{l} \int_0^\infty \rho(r) r^2 dr. \tag{2}$$

For Poisson distribution of grain size,[5] $\rho(r) = \exp(-r/l)/l$, and $l/d = 0.5$. In Fig. 1 we show the correlation between the mean-free-path and the mean-cord-length for all samples. There is a significant difference in the slope of the distribution for the PM samples (slope of 0.7) and the CW samples (slope of 0.6). Both are quite different from the ratio of 0.5 between the mean-cord-length and the mean-free-path for the Poisson distribution of grains. The difference in the slopes indicates that the grain size distributions are different in the two types of samples. This is further confirmed by plotting the standard deviation of the mean-free-path as a function of the mean-free-path, as shown in Fig. 2. We see that the CW samples have a much wider distributions of the grain size than the PM samples.

One concern with the ECAE samples with the small average grain size is whether the annealing has completely removed the strain and anisotropy introduced during deformation. During the PM processing, the samples underwent only a fraction of the deformation experienced by the CW samples during ECAE. One would expect significantly more twin boundaries in the CW samples if annealing did not bring these samples close to thermodynamic equilibrium. Figure 3 plots the measured mean-free-path with and without the twin boundaries counted for all the samples. It is remarkable that all of the PM and the CW samples fall on a single line. This gives us indication that the CW samples are well annealed, and the distribution of the grains is essentially random.

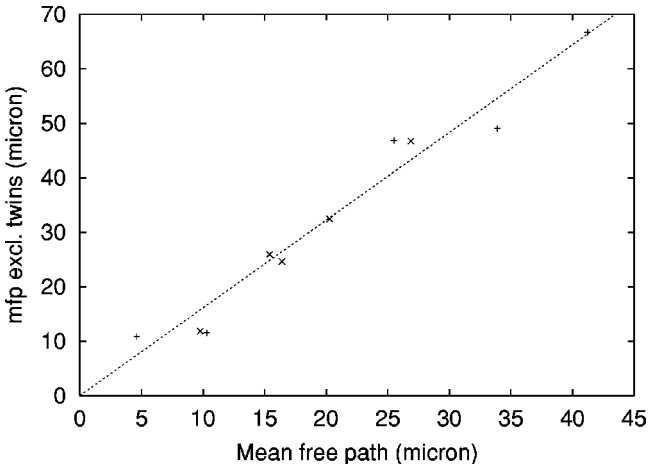

FIG. 3. Linear regression between the mean-free-paths with and without the twin boundaries counted. The slope of the line is 1.6, meaning that approximately 38% of the boundaries are twins boundaries. Crosses are PM samples and pluses are CW samples.

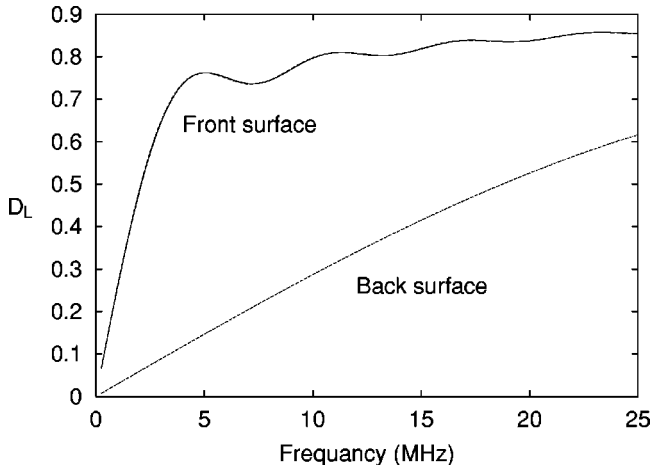

FIG. 4. Diffraction corrections for the front and the back surface signals. Both lines are two indistinguishable curves, one using the approximation of Eq. (4) and one with numerical integration.

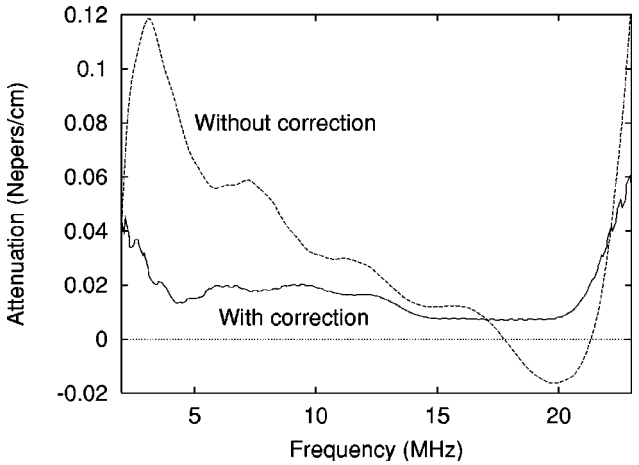

FIG. 5. Attenuation of the Si_3N_4 sample with and without the correction term from the fused quartz calibration measurement.

III. ATTENUATION MEASUREMENT APPROACH

For frequencies up to 30 MHz, measurements were made in immersion using a 20-MHz transducer. A single pulse signal was generated and the reflected signals off the front and back surfaces of the sample were recorded. The acquired data were deconvolved to remove the transducer and amplifier responses, then corrected for the appropriate acoustic impedance mismatches and diffraction.

The common approach for diffraction correction is to use the expression derived by Rogers and Van Buren[15] for a homogeneous medium, which gives the factor due to diffraction as

$$D_L = 1 - \exp(-i2\pi/s)[J_0(2\pi/s) + iJ_1(2\pi/s)], \qquad (3)$$

where J_0 and J_1 are the Bessel functions and $s = 2\pi z/ka^2$ with k being the wavenumber, a being the radius of the transducer, and z being the distance from the transducer. Equation (3) is an approximation that is accurate whenever $ka \gg 1$ or $z \gg a$. In order to apply this diffraction correction to the water-sample system which contains two different media, we define the effective acoustic path length as the distance measured in terms of the wavelength, normalized to the wavelength in water. Thus, the parameter s in the diffraction correction is defined as $s = 2\pi\bar{z}/ka^2$ where

$$\bar{z} = z_{\text{water}} + z_{\text{sample}} \frac{\lambda_{\text{water}}}{\lambda_{\text{sample}}}, \qquad (4)$$

and the subscripts indicate the distance of travel z and the wavelength λ in water or in the sample. Obviously this substitution is only approximately valid. In order to estimate the error caused by this approximation, we numerically integrated the diffraction field of our experimental setup with a transducer of radius 1.5875 mm (the radius of the actual transducer used in the measurements) and a typical copper sample. We compared diffraction corrections to both the front and back surface signals with those obtained by Eqs. (3) and (4). The results are shown in Fig. 4. Both curves plotted are actually two results, the numerical integral and the results from Eqs. (3) and (4). In each case, both results are indistinguishable from each other for all frequencies. This gives us confidence that Eqs. (3) and (4) give accurate diffraction corrections for our measurements.

Although these corrections are usually considered sufficient for attenuation measurements, we found that the resulting data still had poor reproducibility, especially at lower frequencies. Possible remaining sources of error are inaccurate calibration of the attenuator settings, nonuniform frequency response of the attenuator, and the nonlinearities of the electrical circuit and/or the transducer. These errors do not depend on the sample, and are difficult to correct individually. Thus we used a fused quartz sample as a calibration measurement to extract a correction term. Fused quartz has very little attenuation within the frequency range of our measurement. After accounting for impedance and diffraction corrections, the remaining difference between the front and back surface signals for the quartz sample was used as the calibration curve which gives an estimate of the additional correction term. This correction term was verified on another low attenuation sample, Si_3N_4. The particular sample used was very fine-grained and fully dense, and the attenuation in the frequency range between 5 and 20 MHz was well below the sensitivity of our apparatus. The measured attenuation of the Si_3Ni_4 sample with and without using the calibration curve is plotted in Fig. 5, where the essentially flat result after the correction indicates the noise floor of the measurements. It is evident that the correction term is significant. After the correction, the remaining error in the attenuation coefficient is less than 0.02 Nepers/cm in the frequency range between 5 and 20 MHz. This is an acceptable level of error since for most of our copper samples within the frequency range of our measurement, the attenuation coefficient is between 0.1 and 1 Nepers/cm. There is a small remaining error evident in Fig. 5 that appears to be a constant shift in the attenuation curve. The source of this error is not clear and it is sample dependent. It is only significant for samples with very small attenuation coefficients. For each sample we simply subtracted a constant from the attenuation curve so that it extrapolates to the origin. For PM samples this constant is about 0.005 Nepers/cm and for the CW samples it is close to 0.04 Nepers/cm. The application of this calibration proce-

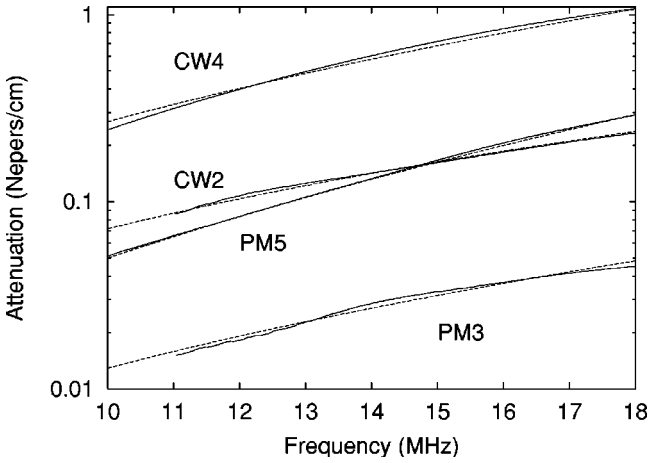

FIG. 6. Attenuation as a function of frequency for samples PM3, PM5, CW2, and CW4 (solid lines). The polynomial fits (dashed lines) to the curves are $1.2\times10^{-4}f^2+9\times10^{-8}f^4$ for PM3, $7.1\times10^{-4}f^2+7.0\times10^{-8}f^4$ for CW2, $3.2\times10^{-4}f^2+1.8\times10^{-6}f^4$ for PM5, and $2.4\times10^{-3}f^2+2.8\times10^{-6}f^4$ for CW4.

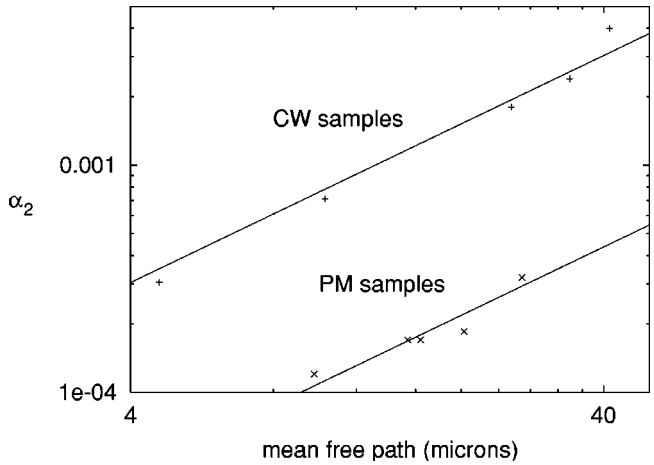

FIG. 7. The coefficient of the quadratic frequency term, α_2, as a function of mean-free-path. Fitted lines have a slope of 1 corresponding to linear scaling with the mean-free-path.

dure yielded much greater reproducibility for all our attenuation measurements.

IV. RESULTS

The attenuation coefficient, α, is defined as the exponent of the decaying amplitude of the acoustic wave,

$$A(x)=A_0\exp(-\alpha x). \tag{5}$$

The measurement of α was performed for two groups of copper and copper aluminum samples, the CW samples which were all pure copper, and the PM samples which contained a small amount of aluminum additions, as described in the earlier section.

Dependence of the attenuation coefficient α as a function of frequency is plotted for four of the samples, PM3, PM5, CW2, and CW4, in Fig. 6 for the low frequency range. Two of the samples, PM3 and CW2, have similar mean-free-paths, (see Table I), and the other two, PM5 and CW4, have similar mean-free-paths. For the sample with the largest grain size, $d=33.9$ μm, the frequency at which $2\pi d/\lambda=1$ is 23 MHz. For the range of frequency in the measurements, the ratio $2\pi d/\lambda$ ranges from about 0.07 to just below 1 for all the samples. The order of magnitude difference in attenuation between the PM samples (PM3 and PM5) and the corresponding CW samples (CW2 and CW4) with the same average grain size is striking. It is also clear from the polynomial fits that all four curves are dominated by quadratic frequency terms. This figure demonstrates two points. First, the leading frequency term in the low frequency regime is quadratic, not quartic as predicted by the Stanke–Kino model. Second, the dramatic difference in attenuation between PM and CW samples with the same average grain size suggests that grain size distribution is also important in determining the attenuation coefficient.

TABLE I. Measured mean-free-path (MFP) and mean-cord-length (MCL) of the powder metallurgy (PM) copper-aluminum samples and the cast-and-wrought (CW) pure copper samples.

Samples	PM1	PM2	PM3	PM4	PM5
MFP (μ)	15.4±1.1	16.4±1.0	9.77±0.36	20.3±1.0	26.9±1.0
MCL (μ)	10.9±0.8	11.2±0.5	6.92±0.26	14.2±0.8	18.3±0.9
Density	8.778	8.778	8.896	8.906	8.899
Samples	CW1	CW2	CW3	CW4	CW5
MFP (μ)	4.6±0.4	10.3±2.6	25.5±1.4	33.9±3	41.2±4.2
MCL (μ)	3.0±0.2	5.6±1.8	16.3±0.6	20.5±1.6	24.3±2.5
Density	8.939	8.940	8.935	8.950	8.942

The analysis of the scaling of attenuation with the average grain size is less straightforward. If both the quadratic and the quartic frequency terms are due to grain boundary scattering, they should scale differently with the average grain size. From dimensionality considerations, the quadratic frequency term should scale linearly with the grain size, while the quartic term should scale with the cubic power of the grain size. At low frequencies we can express the attenuation coefficient in a general form,

$$\alpha=\alpha_2 f^2+\alpha_4 f^4, \tag{6}$$

where f is the frequency and α_2 and α_4 are scaling coefficients. In Fig. 7 we plot α_2 for all the samples. The linear scaling with the mean-free-path is clearly evident. We also note that the striking difference between PM and CW samples exhibited in Fig. 6 exists generally between all PM and CW samples and their quadratic frequency terms differ by nearly a factor of 7 for the same value of mean-free-path. The close correlation between α_2 and the grain size strongly suggests that the quadratic frequency term arises from grain boundary scattering.

In contrast to the order of magnitude difference in the quadratic frequency terms between the CW and PM samples, the quartic frequency coefficients, α_4, are much closer between the two types of samples. The quartic frequency term is known to contain contributions from impurity and defect scattering. The most likely source of the fourth order term, beside grain boundary scattering, is scattering by voids. The volume fraction of voids, F_v, can be estimated from the density measurements. We also need to estimate the average diameter of the voids. For this we assume the Zener limit,

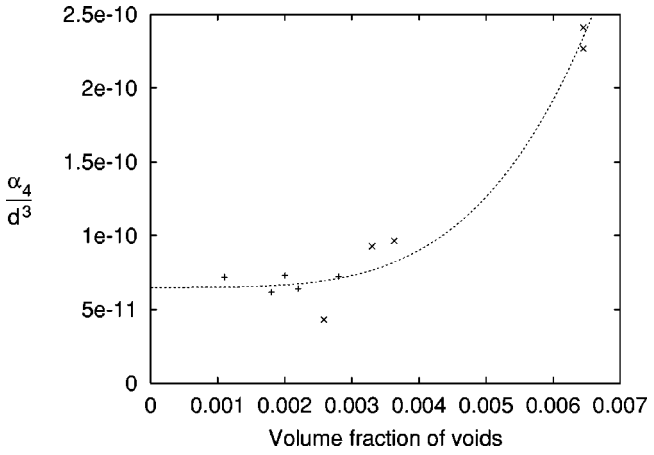

FIG. 8. The coefficient of the fourth order frequency term as a function of the volume fraction of voids.

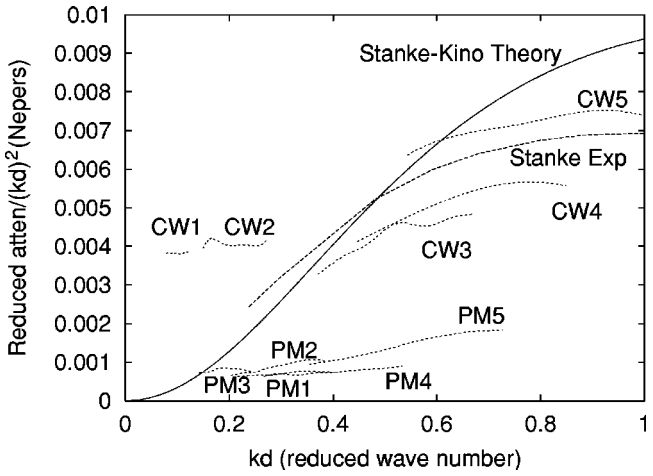

FIG. 9. Attenuation of the copper and copper-aluminum samples as a function of reduced wave number. The mean-free-path of the samples are used to scale all quantities to dimensionless units. The y axis plots the (reduced) attenuation divided by the square of the reduced wave number, thus a nonzero intercept in the y axis is proportional to the coefficient of the quadratic frequency term.

which gives the diameter of voids d_v in terms of the average grain size (here we use the mean-free-path d) and the volume fraction,

$$d_v \propto F_v d. \tag{7}$$

The scattering cross section of an average void is proportional to $k^4 d_v^6$ in the Rayleigh limit. Under these assumptions, the attenuation contribution from voids should be proportional to

$$\frac{F_v}{d_v^3} k^4 d_v^6 = k^4 F_v^4 d^3. \tag{8}$$

Thus we can fit the fourth order frequency coefficient, α_4, to the form

$$\frac{\alpha_4}{d^3} = c_1 + c_2 F_v^4, \tag{9}$$

where c_1 and c_2 are constants. In Fig. 8 we plot α_4/d^3 as a function of F_v, and the fit using Eq. (9). The strong correlation between α_4 and the volume fraction of voids seems to suggest that a large portion of the fourth order frequency term is due to scattering by voids.

The theoretical model by Stanke and Kino[5] predicts that the dimensionless attenuation αd, where d is the effective mean-free-path due to the grain boundary scattering, is a unique function of the reduced wave number kd. Thus, when the dimensionless attenuation αd is plotted against the reduced wave number kd, all data for samples with different average grain sizes should fall onto a single curve. The results plotted in Fig. 9 contain measurements between 10 and 20 MHz for all samples. The data are plotted on a linear scale in order to make the differences between the curves easier to see. We further scaled the y axis by $1/(kd)^2$ (where d is the mean-free-path) to amplify any possible differences between theory and measurements, and between different measurements. In the curves for the PM samples, the estimated contribution to the fourth order term due to scattering by voids according to the F_v^4 term in Eq. (9) has been removed. Including the void contribution would introduce more scatter in the data but would not change the position of the curves significantly. In all of our samples, twin boundaries are included when counting the grain boundaries, consistent with the common practice in attenuation measurements.[8] Plotted in the same figure is the prediction by the Stanke–Kino model (solid curve) which is a universal curve for all grain sizes and frequencies. First we notice that there is considerable difference in attenuation between different samples. The measured curves fall into two groups. The powder metallurgy samples consistently exhibit considerably lower attenuation than cast-and-wrought samples for the same or similar grain sizes. Within the same group, the attenuation shows remarkable reproducibility across different samples. The scaled curves for the PM samples and for the CW samples each fall within a narrow band with a weak dependence on the frequency (or the reduced wave number). It is evident that all curves would have significant nonzero intercepts at $kd=0$, indicating nonzero coefficients of the quadratic frequency term because of the factor of $1/(kd)^2$ in the y axis.

At the low frequency end, the Stanke–Kino model predicts as much as an order of magnitude smaller attenuation than the measured results for the CW samples, while at higher frequencies, the theory is higher than all of the samples, and up to an order of magnitude larger than the results for the PM samples. The measured results for pure copper by Stanke[8] are also plotted (dashed curve). Stanke's data are within the range of our measured results for the CW samples. Although Stanke presented his measurement as the confirmation of the theory, the significant differences between the theory and Stanke's measurements may not be explained by the uncertainty in the grain size measurement since his data were based on the same sample for all frequencies and the disagreement is opposite in sign at high and low frequencies. In view of our measurements at lower frequencies/smaller grain sizes, it is clear that there is in fact no agreement between theory and experiment. The dramatically smaller attenuation for the PM samples is more puzzling, and is completely unexplained by any existing model for attenuation.

V. DISCUSSION

The measured attenuation for the copper and copper-aluminum samples clearly contains a nonzero quadratic frequency term. The scaling of our results with the grain size and the consistency of the data across different samples provide strong evidence that the measured attenuation is indeed due to grain boundary scattering. Let us consider some alternative possible sources that might be proposed to explain the quadratic frequency dependence at low frequencies.

A. Thermoelastic attenuation

In addition to grain boundary scattering, there are several other causes of ultrasonic attenuation in a solid. Many absorption processes contribute to attenuation that scales quadratically with frequency. However, these processes typically do not depend on the grain size. Our results have a consistent dependence on the grain size, as evident from the convergence of the curves from different samples plotted in dimensionless units after scaling with the grain size. This kind of grain size dependence automatically rules out any absorption process that does not involve grain boundaries.

We discuss here in some detail the thermoelastic effect. The attenuation due to the thermoelastic effect can be expressed in the form[16]

$$\alpha_{\text{thermo}} = \frac{1}{2v\tau}\frac{\Delta M}{M}\frac{\omega^2\tau^2}{1+\omega^2\tau^2}, \tag{10}$$

where v is the sound velocity, τ is the relaxation time of an elastic after-effect, M is the unrelaxed modulus, ΔM is the change in M after relaxation, and $\omega = 2\pi f$ is the angular frequency of the sound wave. Using the data provided in Ref. 16 for copper, the direction that shows the largest attenuation due to the thermoelastic effect is the [100] direction. Using $v\tau = 2.63\times10^{-6}$ cm, $\omega\tau = 3.81\times10^{-4}$ at the frequency of $f = 10$ MHz, and $\Delta M/M = 2.43\times10^{-2}$, we obtain $\alpha_{\text{thermo}} = 6.7\times10^{-4}$ Nepers/cm. This is orders of magnitude smaller than the measured attenuation of our samples and should have no impact on the analysis of grain boundary scattering in our samples.

B. Dislocation damping

Attenuation due to dislocation damping also scales quadratically with the frequency at very low frequencies.[16] However, the frequency dependence of dislocation damping is characterized by resonances. There is evidence[17] that the lowest resonance for pure copper is well below the frequency range of 10–20 MHz used in our measurement. In fact, Alers and Thompson[17] showed that for a well-annealed unirradiated pure copper sample, attenuation due to dislocation damping decreases monotonically above 10 MHz, and that the average dislocation loop length is about 1 to 3 μm. All of our samples are reasonably well-annealed, and the smallest average grain size of our samples is well above the range of 1 to 3 μm. Thus the maximum of the attenuation due to dislocation damping is likely to be below 10 MHz for all of our samples. This would rule out the possibility of dislocation damping as a source of the quadratic frequency term in attenuation.

In the unlikely event that a very high dislocation density causes the effective loop length to be reduced several fold, which would move the resonance frequency higher, attenuation due to dislocation damping would be greatly reduced since it scales with the fourth power of the loop length. In addition, the consistency in the data from different samples also indicates that dislocation damping is not important, since the variation in the dislocation density between samples with different annealing histories is likely to be large but it is clearly not reflected in the attenuation data.

C. Grain size distribution

Our measurement of the grain size distribution shows that both PM and CW samples deviate significantly from the Poisson distribution assumed by the Stanke–Kino model. There is also a significant difference between the PM and the CW samples. Naturally, one would suspect grain size distribution as a possible explanation for the difference between theory and experiment. Although we suspect that the difference between the PM and CW samples is likely caused by the difference in grain size distribution, we do not believe the grain size distribution can explain the disagreement between theory and measurement for the following reasons. First, grain size distribution, and even the possibility of a texture, should not qualitatively change the frequency dependence of grain boundary scattering, unless strong long range correlations between the grains exist, which is highly unlikely, especially in the PM samples which exhibit the largest disagreement with the theory. Second, the CW samples appear to have a grain distribution closer to the Poisson distribution; the slope for the CW samples is 0.6 in Fig. 1 compared to 0.7 for the PM samples and 0.5 for the ideal Poisson distribution. Yet the attenuation for the CW samples is higher than that predicted by Stanke–Kino model at low frequencies and lower at high frequencies. There is no such cross-over behavior between the CW samples and the PM samples. Thus, as long as we assume the Stanke–Kino solution to be the correct result for the Poisson distribution, we cannot obtain a consistent picture of the dependence of attenuation on grain size distribution.

We emphasize again that the attenuation in the PM samples is almost an order of magnitude smaller than the prediction of the theory. If there are other sources that contribute significantly to the attenuation, the disagreement between experiment and theory after subtracting such contributions would be even larger than what we measured. Therefore we believe that the difference between the theory and the experiment is genuine and calls for further investigation.

VI. CONCLUSIONS

For single phase polycrystalline materials of near-theoretical density (i.e., containing few independent scatterers), the attenuation behavior in the long-wavelength regime was shown to scale quadratically with frequency and linearly with the average grain size, rather than as the fourth power of the frequency and cubic power of the grain size, as expected when the scatterers are independent. The presence of voids

or other independent scatterers introduces such a fourth-power frequency term, but at sufficiently low frequencies the losses will approach a quadratic asymptotic limit. In addition, the absolute magnitude of the quadratic coefficient was shown to vary with the type of the sample, varying by close to an order of magnitude from a PM sample to a cast-and-wrought sample with the same average grain size.

ACKNOWLEDGMENTS

The authors thank helpful discussions with James Rose and Bruce Thompson at Ames Laboratory, and Sean Agnew at University of Virginia. The ECAE samples (before annealing) were provided by Thomas Lillo at INEEL. This work was supported by the Office of Basic Energy Sciences Division of Materials Sciences of the U.S. Department of Energy. Oak Ridge National Laboratory is operated by UT-Battelle, LLC, for the U.S. Department of Energy under Contract No. DE-AC05-00OR22725.

[1] C. Huygens, *Traité de la Lumière* (completed in 1678, published in Leyden in 1690); see Max Born and Emil Wolf, *Principles of Optics*, 5th ed. (Pergamon, New York, 1975), p. xxii.
[2] Lord Rayleigh, ''On the Influence of Obstacles arranged in Rectangular Order upon the Properties of a Medium,'' Philos. Mag. Ser. **5**(34), 481–502 (1892).
[3] I. M. Lifshitz and G. D. Parkhomovskii, ''On the theory of the propagation of supersonic waves in polycrystals,'' Z. Exsperim. Theor. Fiz. **20**, 175 (1950).
[4] F. C. Karal, Jr. and J. B. Keller, ''Elastic, electromagnetic, and other waves in a random medium,'' J. Math. Phys. **5**, 537–547 (1964).
[5] F. E. Stanke and G. S. Kino, ''A unified theory for elastic wave propagation in polycrystalline materials,'' J. Acoust. Soc. Am. **75**, 665–681 (1984).
[6] J. E. Gubernatis and A. A. Maradudin, ''Elastic wave propagation through polycrystals,'' Rev. Prog. Quant. Nondestr. Eval. **4B**, 901–907 (1985).
[7] E. P. Papadakis, *Physical Acoustics Principles and Methods*, Vol. IVB, edited by W. P. Mason and R. N. Thurston, p. 269 (Academic, New York, 1968).
[8] F. E. Stanke, ''Inversion of attenuation measurements in terms of a parameterized autocorrelation function,'' in *NDE of Microstructure for Process Control*, edited by H. N. G. Wadley (ASM, Metals Park, OH, 1985), pp. 55–60.
[9] J. E. Gubernatis and E. Domany, ''Effects of Microstructure on the Speed and Attenuation of Elastic Waves: Some Results for Porous Materials,'' *Reviews of Progress in Quantitative NDE*, edited by D. O. Thompson and D. E. Chimenti (Plenum, New York, 1984), Vol. 3B, pp. 1129–1135.
[10] I. E. Anderson and J. C. Foley, ''Determining the role of surfaces and interfaces in the powder metallurgy processing of aluminum alloy powders,'' Surf. Interface Anal. **31**(7), 599–608 (2001).
[11] V. M. Segal, ''Materials Processing by Simple Shear,'' Mater. Sci. Eng., A **197**, 157–164 (1995).
[12] S. Ferrasse, V. M. Segal, K. T. Hartwig, and R. E. Goforth, ''Microstructure and Properties of Copper and Aluminum Alloy 3003 Heavily Worked by Equal Channel Angular Extrusion,'' Metall. Mater. Trans. A **28A**, 1047–1057 (1997).
[13] J. E. Flinn, D. P. Field, G. E. Korth, T. M. Lillo, and J. Macheret, ''The Flow Stress Behavior of OFHC Polycrystalline Copper,'' Acta Mater. **49**, 2065–2074 (2001).
[14] F. J. Margetan, R. B. Thompson, I. Yalda-Mooshabad, and Y. K. Han, ''Detectability of Small Flaws in Advanced Engine Alloys,'' U.S. Air Force Technical Report, Center for NDE, Iowa State University, Ames, Iowa (1993).
[15] P. H. Rogers and A. L. Van Buren, ''An exact expression for the Lommel diffraction correction integral,'' J. Acoust. Soc. Am. **55**, 724–728 (1974).
[16] R. Truell, C. Elbaum, and B. B. Chick, *Ultrasonic Methods in Solid State Physics* (Academic, New York, 1969).
[17] G. A. Alers and D. O. Thompson, ''Dislocation contribution to the modulus and damping in copper at megacycle frequencies,'' J. Appl. Phys. **32**, 283 (1961).

Quantitative analysis of the vibration modes in a finite set of coupled spheres

Anne-Christine Hladky-Hennion and Arnaud Devos
IEMN Department ISEN, 41 Boulevard Vauban, 59046 Lille, France

Michel de Billy
LED, Université Paris 7, Case courrier 7087, 2 Place Jussieu, 75251 Paris Cedex 05, France

(Received 12 June 2003; accepted for publication 26 April 2004)

This paper deals with the propagation of waves along a one-dimensional chain made up of welded spheres. First, a theoretical analysis allows the vibration modes of the chain to be quantitatively described. It has been validated by a comparison between numerical results, using the finite element method and experimental results, restricted to sets of two or three coupled spheres. It is numerically and experimentally verified that the peaks associated with the Rayleigh modes broaden out as the mode number increases and that the passband structure is strongly influenced by the characteristics of the welding between the cells of the periodic structure. The interest of such an approach is then illustrated by the examination of an inverse problem, in which the analytical model is used to deduce the characteristics of the welding. © *2004 Acoustical Society of America.*
[DOI: 10.1121/1.1763598]

PACS numbers: 43.20.Ks [RLW] Pages: 117–124

I. INTRODUCTION

The propagation of waves through aggregates and layered structures has been thoroughly studied in the recent past. The motivation of such studies is a description of natural phenomena such as the propagation of seismic shocks[1] or artificial effects such as the existence of elastic waves in superlattices[2,3] or in one[4] and two-dimensional composite materials or multilayer media.[5–7] To go forward in the comprehension of vibration phenomena related to aggregates and layered structures, the study of linear chains of spheres has been proposed. This simplified model has revealed the existence of allowed and forbidden frequency bands.[8–13] Recently, we have proposed a qualitative interpretation of the chain vibrations with the help of an analogy with phonons of solid-state physics.[9] In this paper, a model is developed to describe quantitatively the frequency bands, in writing the dispersion relations. The model is validated both by the measurement of the vibration modes[14] of a set of spheres and by a full calculation using the finite element method. One of the main interests of the model is that a coupling factor is introduced in the equations, directly related to the mechanical coupling between spheres. Therefore, it is possible to use the model to solve the inverse problem on periodic sets of welded spheres: With the help of the experimental measurement of the set vibration frequencies, one can give quantitative information on the mechanical bind between spheres.

In this paper, the theoretical formulation is presented, first in the case of an infinite chain of identical spheres, and second in the particular case of a finite chain. Then, the experimental setup is presented. Experimental results on various sets of spheres are compared with theoretical results, allowing the inverse problem to be solved.

II. THEORETICAL APPROACH

The vibration modes of the single sphere have previously been presented in detail in the general case.[15–17] In the case of a single sphere submitted to a compressional acoustic excitation, three types of vibration modes exist.[9] The first is the Rayleigh modes $R(n>1,1)$ which are caused by the circumnavigations of standing waves so that a phase matching condition is satisfied. In that case, the surface of the sphere is moving, whereas the center does not move.

In this paper, one distinguishes the odd Rayleigh modes $R(2n+1,1)$, in which the displacements of two points diametrically opposed are in phase, and the even Rayleigh modes $R(2n,1)$, in which the displacements of two points diametrically opposed are out of phase. The second is the whispering gallery modes $[WG(n>0,\ell=2,3,4...)]$, for which, theoretically, the surface of the sphere does not move whereas a vibration is observed in the heart of the sphere. And finally, at a higher frequency, there is the breathing mode, which corresponds to a radial vibration of the sphere.

We will focus our attention on the vibrations of a system composed of identical spheres regularly spaced. As we shall see, most of the collective modes of the whole structure come from the individual vibrations of one sphere.

The first part of this section is devoted to the case of an infinite chain of identical spheres, with particular equations of the dispersion curves. Then, the vibration modes of a finite chain of identical spheres are presented as a particular case of the vibration modes of the infinite chain with specific boundary conditions. It gives us a way of finding the vibration modes of a finite chain of identical spheres, with the help of the dispersion curve of the infinite chain only, it means with the mesh of only one sphere with specific boundary conditions.

A. Case of an infinite chain of identical spheres

Consider an infinite chain of identical spheres of radius a, regularly spaced at a distance d. The welding between spheres is described in Fig. 1. Due to the periodicity of the system, the wave number k is introduced for designating the

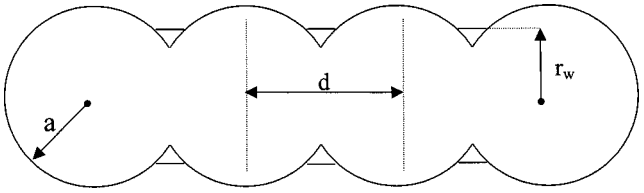

FIG. 1. Definition of the characteristic distances for a chain of welded spheres (a, r_w, and d).

vibration modes. Furthermore, one knows that k should belong to the first Brillouin zone,[18–20] which is given by $[-\pi/d, \pi/d]$. For each k value, a vibration frequency ω exists that leads to a dispersion curve $\omega(k)$. One can notice that for $k=0$, all spheres are vibrating in phase, whereas for $k=\pi/d$ two adjacent spheres are out of phase.

Four kinds of collective vibrations would result from the association of spheres in a linear chain. First, each sphere can be seen as a rigid ''atom'' which can be translated with respect to its neighbors. The dispersion relationship is:[18,19]

$$\omega(k)=(4K/m)^{1/2}\sin kd/2, \tag{1}$$

where K designates the coupling constant and m is the mass of an individual sphere. These modes are low-frequency (LF) due to the nature of the displacement of the whole sphere around its equilibrium position. If the sphere was perfectly stiff, these modes would be the only permitted modes. In solid-state physics, these vibrations are designated as phonons belonging to the *acoustical branch*.

A second kind of collective vibration appears since each sphere is elastic and able to vibrate. Each sphere vibration generates a collective mode associated with a dispersion curve. Depending on the nature of this vibration, we distinguish three kinds of such collective modes (R, WG, and breathing modes). In solid-state physics, similar phenomena have been observed in molecular crystals, such as C_{60} compounds.[21] Thus, these branches may be designated as *intramolecular vibrations* due to their origin. For each sphere mode n, the corresponding collective mode is defined by the value of the vibration amplitude of the sphere s (designated in the following by u_s) in the mode n.

Considering first the odd Rayleigh modes, we derive the dispersion curves describing the chain as composed of coupled pendulums. Considering the dynamics of a one-dimensional chain made up of spheres equally spaced along a line and harmonically coupled with their neighbors, the vibration amplitude of the sphere s satisfies the equation (for small oscillations):

$$m\ddot{u}_s-K_n(u_{s+1}-u_s)+K_n(u_s-u_{s-1})+m\omega_{0,n}^2u_s=0, \tag{2}$$

where $\omega_{0,n}(=2\pi f_{0,n})$ designates the resonance frequency of the mode for a single sphere and K_n measures the coupling between neighbors spheres for the mode n. When a sphere is vibrating in an odd Rayleigh mode, it acts on its neighbors as if the sphere was displaced in one direction: The displacements of two points diametrically opposed on the sphere surface are in phase. This is the reason why Eq. (2) is written as a dynamical equation for displacement of a sphere with K_n as the force constant. The last term contains the energy of the sphere vibration. Assuming that the spheres oscillate in harmonic movement with the same frequency, we have for sphere s:

$$u_s(x,t)=A_s(x)\cos\omega t. \tag{3}$$

Inserting Eq. (3) into Eq. (2) and eliminating the temporal factor, we get

$$\omega_n^2(k)=\omega_{0,n}^2[1+(4K_n/m\omega_{0,n}^2)\sin^2(kd/2)]. \tag{4}$$

The angular frequency varies between the extreme values $\omega_{0,n}$ and $\sqrt{\omega_{0,n}^2+4K_n/m}$ which correspond, respectively, to $kd=0$ and $kd=\pi$. For $k=\pi/d$, all spheres are vibrating out of phase and, due to the surface motion, need more energy than for the $k=0$ mode in which one retrieves the isolated sphere frequency.

In the case of even Rayleigh modes, because the motions of two points diametrically opposed are in that case out of phase, the signs of u_{s+1} and of u_{s-1} have to be changed in Eq. (2). The equation for the corresponding branch can thus be written as

$$\omega_n^2(k)=\omega_{0,n}^2[1+(4K_n/m\omega_{0,n}^2)\cos^2(kd/2)]. \tag{5}$$

The angular frequency varies between the extreme values $\omega_{0,n}$ and $\sqrt{\omega_{0,n}^2+4K_n/m}$ which correspond, respectively, to $kd=\pi$ and $kd=0$. One should notice that the lowest frequency mode is the mode with $kd=\pi$. For such a wave number, neighboring spheres are moving out of phase which consumes far less energy than for $k=0$ due to the nature of the surface displacement. Thus, the minimum on the branch appears at $k=0$ for odd modes, whereas it appears at $k=\pi/d$ for even modes. The situation is reversed between odd and even cases. This remark provides us with another way to derive Eq. (5). In fact, it acts as if the energy of a mode with a wave number k in an odd branch corresponded to a mode with $\pi/d-k$ in an even branch. By introducing this variable change in Eq. (4) one obtains Eq. (5).

Finally, in the case of WG modes, the displacement is located inside the sphere. Only weak coupling exists between spheres, leading to a flat dispersion curve.

The propagation of plane acoustic waves in an infinite and periodic structure is studied with the help of the finite element method, using only the mesh of one unit cell, thanks to Bloch–Floquet relations.[22] Due to the symmetry of the structure, an axisymmetrical model is used, that only requires bidimensional elements. The unit cell is meshed and divided into elements connected by nodes. In this study, isoparametric elements are used, with a quadratic interpolation along the sides of the element. The calculation provides dispersion curves from which results of physical interest can be easily extracted: Identification of propagation modes, cutoff frequencies, passbands, and stop bands.[22,23] Figure 2 presents the first branches of the dispersion curve of an infinite chain of steel spheres, the diameter of which is equal to 10 mm. The welding between spheres is characterized by $r_w=1.46\,\text{mm}\pm0.02\,\text{mm}$. The parameters which appear in Eqs. (1), (4), and (5) ($\omega_{0,n}$ and K_n/m) are fitted with the help of the numerical frequencies at $k=0$ and $k=\pi/d$. The corresponding curves are drawn in Fig. 2. It shows that the equations fit well the dispersion curves, obtained using the finite

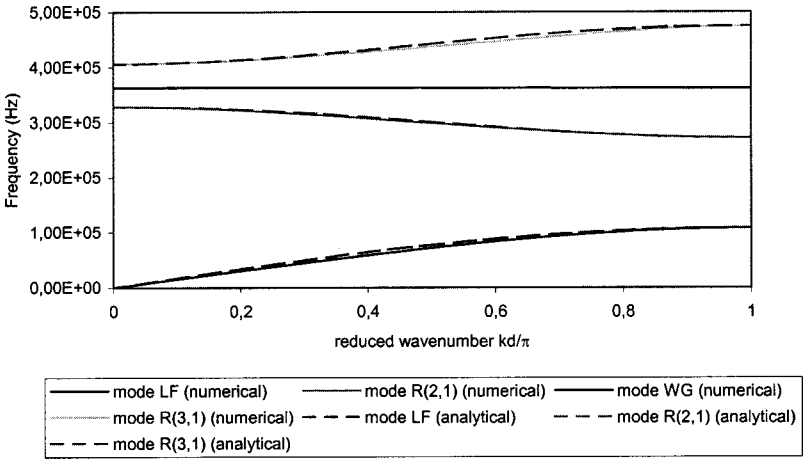

FIG. 2. First branches of the dispersion curves of an infinite chain of steel spheres in the first Brillouin zone, with reduced scale. Full line: Numerical results, dashed line: Analytical results.

element method. The calculation confirms that the frequency of the single sphere is always the lowest value of the branch.

B. Case of a finite chain of identical spheres

A finite chain can be considered as a particular case of an infinite chain by applying appropriate boundary conditions at the two extremities. Considering N particles with both ends free, which simulates experimental conditions, then the appropriate boundary conditions require

$$du(x=0)/dx=0 \quad \text{and} \quad du(x=Nd)/dx=0. \tag{6}$$

If the displacement is written as

$$u(x)=C(x)\cos\omega t=(A\sin kx+B\cos kx)\cos\omega t, \tag{7}$$

then relation (6) implies $A=0$ and $\sin(kNd)=0$. It gives discrete values for k, which depends on the considered mode (even or odd).

(a) For odd modes, $u(0)=u(d)$ at the frequency of the single sphere. Thus, the corresponding value of k is 0 and the other values are $k=s\pi/Nd$, with $s=1...N-1$.

(b) For even modes, $u(0)=-u(d)$ at the frequency of the single sphere. Thus, the corresponding value of k is N and the other values are $k=s\pi/Nd$, with $s=N-1...1$.

As previously stated, one can notice that the quantification for an odd branch could be deduced from the even case using the variable change $k->\pi/d-k$.

For a finite chain of N spheres, N discrete frequencies are obtained for each branch. Thanks to the quantification of the wave number k, one can deduce the vibration modes of a finite chain of N spheres, using the previous dispersion curves (Fig. 2). The mesh of only one sphere is enough.

The vibration modes in the particular case of a set of two identical spheres are shown by marks in Fig. 3. For the LF and R(3,1) branches, the quantification gives $k=0$ and $k=\pi/2d$, whereas for the R(2,1) branch, the quantification gives $k=\pi/2d$ and $k=\pi/d$. To confirm this point, two spheres have been meshed, using 541 isoparametric elements and 1222 solid nodes. The vibration modes are calculated using a modal analysis[22] and the corresponding displacement fields are drawn (Fig. 4). The set of two spheres is supposed to have both ends free. In Fig. 4, one can notice the small element between the two spheres, that models the weld.

The lowest frequency of the R(2,1) mode (271 kHz) corresponds to $k=\pi/d$ (frequency of the single sphere, the two extremities of the one sphere are out of phase) [Fig. 4(a)], whereas the other R(2,1) mode (298 kHz) corresponds to $k=\pi/2d$ (phase of $\pi/2$ between the two extremities of one sphere) [Fig. 4(b)].

The lowest frequency of the R(3,1) mode (405 kHz) corresponds to $k=0$ (frequency of the single sphere, the two extremities of the one sphere are in phase) [Fig. 4(c)],

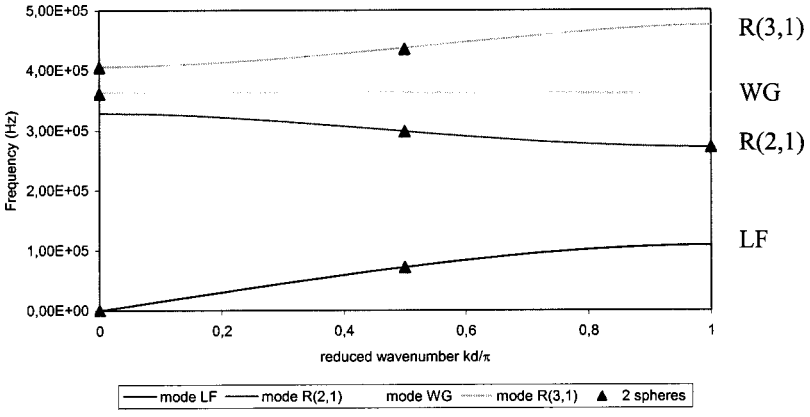

FIG. 3. Numerical results (marks) on a set of two welded spheres, positioned on the dispersion curves of the infinite chain of welded spheres.

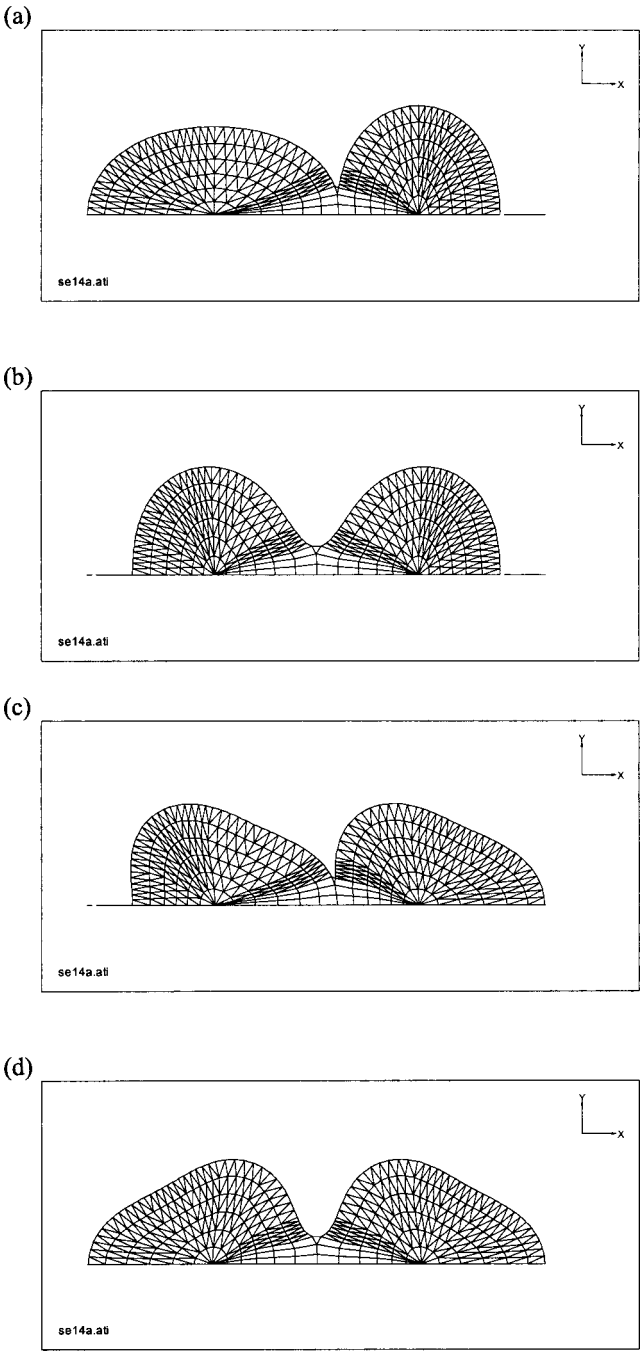

FIG. 4. Vibrations modes of two welded spheres. (a) R(2,1) mode and $kd=\pi$, (b) R(2,1) mode and $kd=\pi/2$, (c) R(3,1) mode and $kd=0$, and (d) R(3,1) mode and $kd=\pi/2$.

whereas the other R(3,1) mode (435 kHz) corresponds to $k=\pi/2d$ (phase of $\pi/2$ between the two extremities of one sphere) [Fig. 4(d)].

For the WG modes, the branch is flat: The two frequencies are identical. Since the frequencies are degenerated, the displacement field is a linear combination of the displacement fields obtained at various k values. Therefore, the numerical value is arbitrarily placed at $k=0$ (Fig. 3).

Figure 5 presents the results obtained on a set of three spheres, with identical welding between the spheres. Numerical results are obtained using the dispersion curve (one sphere meshed) and the corresponding quantification for three spheres.

III. EXPERIMENTS

A. Experimental conditions

1. Experimental setup

The experimental setup used for the measurement has been previously described.[14] It includes a pair of broadband transmitters longitudinally polarized and driven by short ultrasonic pulses. The amplitude of the detected signal is so small that it is necessary to average it over 500 signals to improve the signal-to-noise ratio. A frequency analysis of the time domain response of the periodic medium is realized via a fast Fourier transform algorithm. The sample is submitted to an axial force F_0, the value of which does not alter the position of the resonance in the frequency spectra.

2. Description of the samples

The main study of this work is concerned with N (=2 or 3) steel spheres of 10 mm in diameter and coupled with a spot welding process, using a high value of current going through the contact points between the spheres. Material properties are $C_1=5931$ m/s, $C_t=3225$ m/s, and $\rho=7900$ kg/m^3. As there is no shrinking of the matter, a circular roll around the welding area appears, its dimensions vary with the performances of the setup (Fig. 1). By varying the conditions of the welding process (the intensity of the current, the applied pressure on the electrodes, or the transit time of the current), it is possible to modify the parameters of the weld. The welding, or the coupling between the spheres, is characterized by the distance r_w that is measured by optical process. r_w is the only parameter used to describe the welding, assuming mass conservation. The use of very well cali-

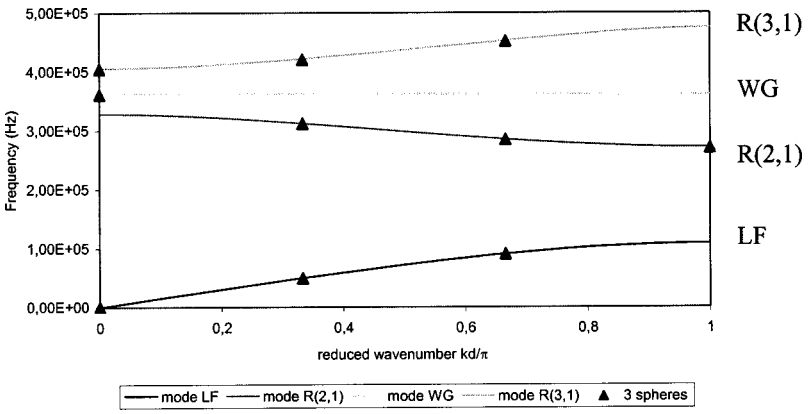

FIG. 5. Numerical results (marks) on a set of three welded spheres, positioned on the dispersion curves of the infinite chain of welded spheres.

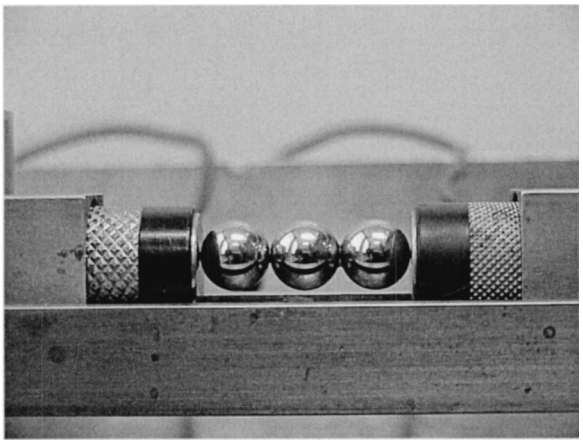

FIG. 6. Picture of a set of three welded spheres.

brated spheres is essential to get good experimental observations. Experiments have shown that aspherical structures imply a splitting of the modes. The nominal diameter of the spheres used for the investigated specimen is 10.00 mm and the tolerance (maximum allowable deviation from the basic diameter) is 10 μm. The error of the asphericity, difference between the largest and the smallest diameter on a single ball, is 0.25 μm and the rugosity is about 0.04 μm. Moreover, the alignment has to be carefully done. Figure 6 gives a picture of a sample with three welded spheres clamped between the emitter and the receiver. Several couples of spheres have been built and the characteristic measured distance r_w of each set is given in the second column of Table I.

B. Experimental results on a finite set of spheres

In this section, experimental results are presented and compared with numerical results. They are concerned with a one-dimensional finite set made up of two or three spherical cells. The frequency spectra of the transmitted signal are analyzed. The position of the main peaks and the frequency difference between these peaks are compared with the numerical calculations. The influence of the coupling on the frequency response is more specifically investigated. The results allow the coupling between adjacent spheres to be characterized. The study is limited to Rayleigh modes.

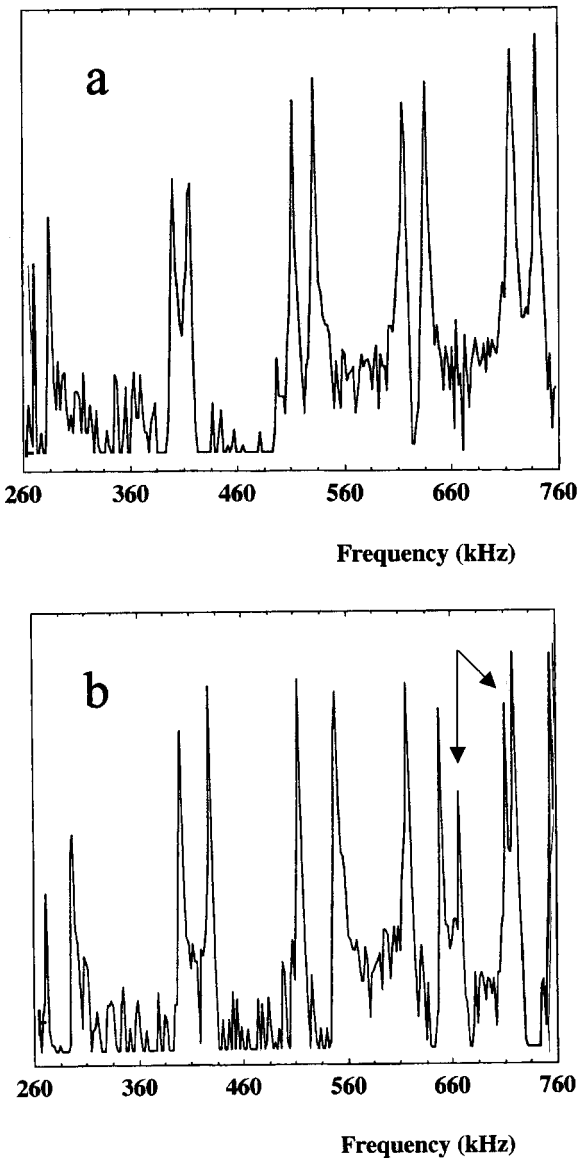

FIG. 7. Examples of frequency spectra obtained with a specimen made up of two welded spheres: (a) sample S1 and (b) sample S9.

1. Case of two welded spheres

Two examples of a frequency spectrum are given in Figs. 7(a) and (b), for samples S1 and S9: The S1 sample

TABLE I. Comparison between the experimental and the numerical values of Δf (in kHz) for different welded samples made up of two steel spheres of 10 mm in diameter. The percentage characterizes the difference between the two determinations.

Sample	$r_w \pm$ 0.02 mm	Mode R(2,1)			Mode R(3,1)			Mode R(5,1)		
		Exp.	Num.	%	Exp.	Num.	%	Exp.	Num.	%
S1	0.74	14	13.9	0.7	16	17.1	6.8	22	22.1	0.4
S2	0.97	18	17.9	0.6	22	21.6	2.7	26	26.8	3.0
S3	1.00	18	18.4	2.2	22	22.2	1.0	26	27.2	4.6
S4	1.06	20	19.5	2.5	23	23.3	1.3	27	28.4	5.1
S5	1.12	20	20.5	2.5	22	24.4	10.9	28	29.4	5.0
S6	1.20	22	21.9	0.4	26	25.8	0.7	30	30.5	1.6
S7	1.25	22	22.7	3.2	26	26.7	2.7	30	31.1	3.6
S8	1.32	24	23.9	0.4	28	27.9	0.3	32	31.9	0.3
S9	1.40	26	25.3	2.7	30	29.3	2.3	32	32.6	1.8
S10	1.46	26	26.2	0.7	30	30.3	1.0	32	32.9	2.8

Note: Exp.=Experimental value and Num.=numerical value.

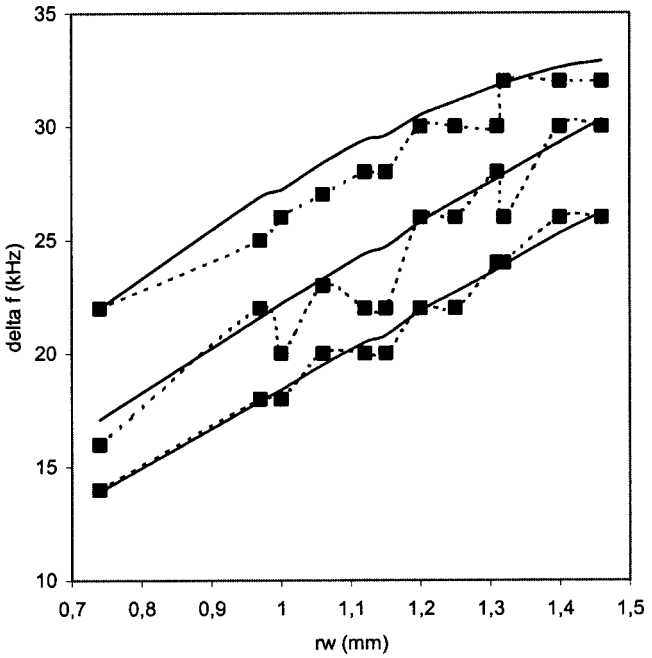

FIG. 8. Experimental and numerical variations of Δf versus r_w for the R(2,1), R(3,1), and R(5,1) Rayleigh modes. Full line: Numerical results, marks: Experimental results.

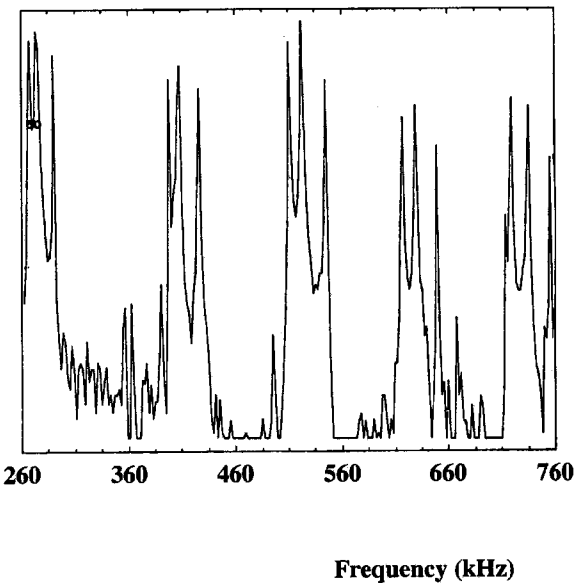

FIG. 9. Experimental spectrum of a finite set made up of three welded steel spheres.

presents a weak contact, with a low value of r_w, whereas the S9 sample presents a strong contact, with a high value of r_w. The values of r_w are measured within an error $\pm$ of 0.02 mm. The most important feature of these experimental data is the splitting observed for each normal mode of the Rayleigh series R(n,1): Two main peaks are observed. The lower peak of each multiplet appears at the same frequency value whatever the welding conditions and corresponds exactly to the resonance observed with a single sphere of the same material and diameter, as mentioned in Sec. II B and in Ref. 9. As the contact increases between the spheres, the two peaks are more separated. Both peaks shown by an arrow in Fig. 7 could correspond to WG modes that appear only for strong contact. As expected, no splitting is observed for these modes.

Table I presents a comparison between the experimental and the numerical values of Δf (in kHz), the frequency difference between the two peaks of the Rayleigh modes, for different welded samples. The R(4,1) mode is not presented because, numerically, it is mixed with the breathing mode. The frequency resolution of the experimental setup is 2 kHz. There is a very good agreement between numerical and experimental results (less than 5% in major cases), for a weak as well as for a strong coupling between the spheres. The slight discrepancy observed between the two determinations is attributed to the changes of material properties in the welding area during the welding process. Even if it is difficult to investigate the influence of the r_w distance on the splitting of the modes, Table I allows one to notice that the splitting is increasing as the contact is increasing.

To see the influence of the contact on the splitting effect, Fig. 8 presents the variations of Δf of the three Rayleigh modes (R(2,1), R(3,1), and R(5,1)) as a function of r_w. It shows an approximately linear dependence of Δf with r_w. Moreover, Δf increases with the order of the mode. In the numerical calculation, experimental values are used to describe the modelized structure, thus, due to the error on the measurement, numerical curves are not perfectly smooth. Nevertheless, thanks to Fig. 8, one can use the predicting model to solve the inverse problem: The characteristic distance of a set of two welded spheres (r_w) can be deduced using the frequency difference between the two peaks of the R(2,1), R(3,1), and R(5,1) Rayleigh modes.

2. Case of three welded spheres

Two samples made up of three welded spheres have been built with the previous procedure and have also been investigated. From measurements, it was observed that the characteristic distance of the two welds is the same. Figure 9

TABLE II. Comparison between the experimental and the numerical values of Δf (in kHz) for different welded samples made up of three steel spheres of 10 mm in diameter. The percentage characterizes the difference between the two determinations.

Sample	$r_w \pm$ 0.02 mm	Mode R(2,1)			Mode R(3,1)			Mode R(5,1)		
		Exp.	Num.	%	Exp.	Num.	%	Exp.	Num.	%
S′1	1.00	9	9.4	4.4	12	11.5	4.1	16	16.5	3.1
		19	19.4	2.1	22	23.4	1.8	22	22.1	0.4
S′2	0.80	8	7.6	5.0	10	9.4	6.0	12	13.2	10.0
		16	15.7	4.3	18	19.2	6.6	20	20.8	4.0

Note: Exp.=Experimental value and Num.=numerical value.

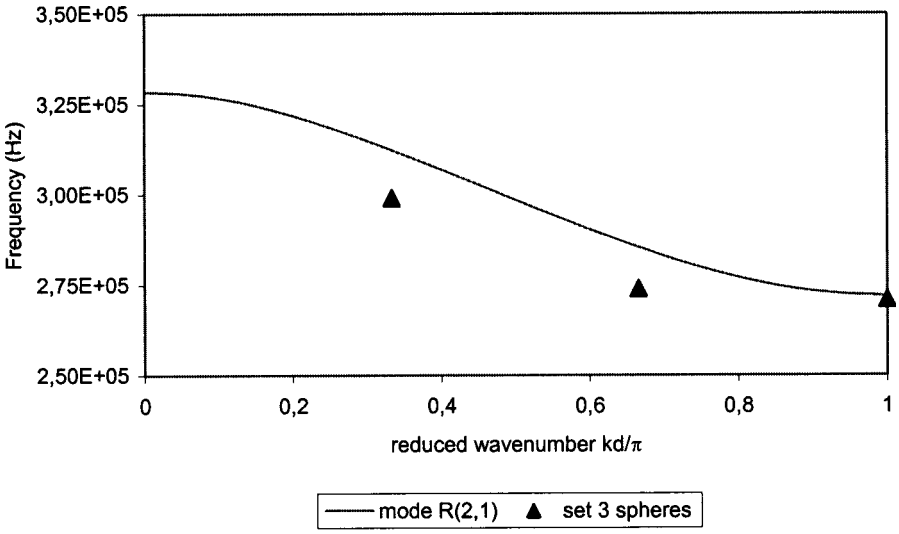

FIG. 10. Experimental results (marks) on a set of three welded spheres with mixed couplings (weld and stick), positioned on the dispersion curves of the infinite chain of welded spheres.

presents a frequency spectrum observed with the second sample. As expected, each Rayleigh mode shows multiplets, made of three distinct resonance frequencies (or peaks). The lowest frequency of each multiplet corresponds to the one observed with a single sphere. Table II presents a comparison between the experimental and the numerical values of Δf (in kHz), the frequency difference between the peaks of the Rayleigh modes, for the two samples. The agreement between numerical and experimental results is good, better than 5%. As expected in the previous analysis in Sec. II B (Fig. 5), the differences between the frequencies of a given branch are not constant.

One may wonder about the extension of this work to a more complicated case. One interesting case could be a set of spheres with a mixed coupling between the spheres. First experimental results show that the detected frequencies are strongly affected by such a change in the coupling. Figure 10 presents the experimental frequencies of a mixed set of three spheres (coupled by a weld and a stick), compared with the previous dispersion curve of the infinite chain, for the R(2,1) mode. The experimental results are no longer superimposed on the dispersion curve of the infinite chain, since our theoretical description does not take into account the different contacts between spheres. In the future, we will try to improve that point in order to solve more realistic problems, like a default in a set.

IV. CONCLUSION

In this paper, the propagation of short acoustic pulses in a chain made of welded spheres has been numerically and experimentally studied. First, it was shown that, for a finite chain of N spheres, we obtain N discrete frequencies for each branch. From a numerical point of view, the vibrations modes of a finite chain can be deduced from the dispersion curves of an infinite chain with specific boundary conditions, it means with the mesh of only one sphere, thanks to a quantification of the wave number. Then, considering a variable weld between the spheres, results of a finite chain have shown that, for a given mode, as the contact is stronger between the spheres, the frequency range of the N discrete frequencies is wider. Parametric study shows that one can use the predicting model to solve the inverse problem, it means to deduce the characteristic of the weld between the spheres using the discrete frequencies. The latest experiments led us to extend the physical model with a view to studying the effect of irregularities in a set of spheres.

[1] F. A. Dahlen and J. Tromp, *Theoretical Global and Seismology* (Princeton University Press, Princeton, New Jersey, 1998).
[2] E. H. El Boudouti and B. Djafari-Rouhani, ''Acoustic waves in finite superlattices,'' Phys. Rev. B **49**, 4586–4592 (1994).
[3] E. H. El Boudouti, B. Djafari-Rouhani, E. M. Khourdifi, and L. Dobrzynski, ''Surface and interface elastic waves in superlattices: Transverse localized and resonant modes,'' Phys. Rev. B **48**, 10987–10997 (1993).
[4] M. S. Kushwaha, P. Halevi, L. Dobrzynski, and B. Djafari-Rouhani, ''Acoustic band structure of periodic elastic composites,'' Phys. Rev. Lett. **71**, 2022–2025 (1993).
[5] F. R. Montero de Espinosa, E. Jiménez, and M. Torres, ''Ultrasonic band gap in a periodic two-dimensional composite,'' Phys. Rev. Lett. **80**, 1208–1211 (1998).
[6] A. Safaeinili and D. Chimenti, ''Floquet analysis of guided waves in periodically layered composites,'' J. Acoust. Soc. Am. **98**, 2336–2342 (1995).
[7] R. James, S. M. Woodley, C. M. Dyer, and V. F. Humphrey, ''Sonic bands, band gaps, and defect states in layered structures-Theory and experiment,'' J. Acoust. Soc. Am. **97**, 2041–2047 (1995).
[8] J. A. Turner, M. E. Chambers, and R. L. Weaver, ''Ultrasonic band gaps in aggregates of sintered aluminum beads,'' Acustica **84**, 628–631 (1998).
[9] A. C. Hladky-Hennion, F. Cohen Ténoudji, A. Devos, and M. de Billy, ''On the existence of subresonance generated in a one-dimensional chain of identical spheres,'' J. Acoust. Soc. Am. **112**, 850–855 (2002).
[10] S. Parmley, T. Zobrist, T. Clough, A. Perez-Miller, M. Makela, and R. Yu, ''Phononic band structure in a mass chain,'' Appl. Phys. Lett. **67**, 777–779 (1995).
[11] W. M. Robertson and J. F. Rudy III, ''Measurement of acoustic stop bands in two-dimensional periodic scattering arrays,'' J. Acoust. Soc. Am. **104**, 694–699 (1998).
[12] V. F. Humphrey and C. M. Dyer, ''Experimental observation of sonic bands, band gaps, and defect passbands in layered structures,'' *Proceedings of the 1995 World Congress on Ultrasonics* (Berlin, Germany 1995), pp. 105–108.
[13] J. C. Couchman, F. H. Chang, Bill G. W. Yee, and J. R. Bell, ''Resonance splitting in ultrasonic spectroscopy,'' IEEE Trans. Sonics Ultrason. **25**, 293–300 (1978).
[14] M. de Billy, ''Experimental study of sound propagation in a chain of spherical beads,'' J. Acoust. Soc. Am. **108**, 1486–1495 (2000).
[15] P. H. Morse and H. Feshback, *Methods of Theoretical Physics* (McGraw–Hill, New York, 1953).

[16] B. A. Auld, *Acoustic Fields and Waves in Solids* (Wiley, New York, 1973), Vol. II.
[17] H. Lamb, ''On the vibrations of an elastic sphere,'' Proc. London Math. Soc. **13**, 189–212 (1882).
[18] R. A. Smith, *Wave Mechanics of Crystalline Solids* (Chapman and Hall, London, 1963).
[19] C. Kittel, *Introduction to Solid State Physics* (Wiley, New York, 1996).
[20] L. Brillouin, *Wave Propagation in Periodic Structures* (Dover, New York, New York, 1953).
[21] O. Gunnarsson, ''Superconductivity in fullerides,'' Rev. Mod. Phys. **69**, 575–606 (1997).
[22] *ATILA Finite Element Code for Piezoelectric and Magnetostrictive Transducer Modeling*, Version 5.2.1, User's Manual (ISEN, Acoustics Laboratory, Lille, France, 2002).
[23] P. Langlet, A. C. Hladky-Hennion, and J. N. Decarpigny, ''Analysis of the propagation of plane acoustic waves in passive periodic materials using the finite element method,'' J. Acoust. Soc. Am. **98**, 2792–2800 (1995).

On the feasibility of elastic wave visualization within polymeric solids using magnetic resonance elastography

Anthony J. Romano,[a] Joseph A. Bucaro, and Brian H. Houston
Naval Research Laboratory, Washington, DC 20375

Jennifer L. Kugel, Phillip J. Rossman, Roger C. Grimm, and Richard L. Ehman
Mayo Clinic and Foundation, Rochester, Minnesota, 55905

(Received 27 October 2003; revised 17 March 2004; accepted 22 March 2004)

In this paper, the feasibility of extending previously described magnetic resonance elastography (MRE) dynamic displacement (and associated elasticity) measurement techniques, currently used successfully in tissue, to solid materials which have much higher shear rigidity and much lower nuclear spin densities, is considered. Based on these considerations, the MRE technique is modified in a straightforward manner and used to directly visualize shear wave displacements within two polymeric materials, one of which is relatively stiff. © *2004 Acoustical Society of America.*
[DOI: 10.1121/1.1738841]

PACS numbers: 43.20.Ye, 43.58−e [YHB] Pages: 125–132

I. INTRODUCTION

The development of a noninvasive method which could provide the ability to directly visualize elastic wave propagation within nontransparent solid materials would be of great benefit in the areas of structural vibration analysis, nondestructive evaluation (NDE), and material science in general. Not only would such a measurement method enable the researcher to analyze displacements and boundary conditions occurring on the surfaces of inclusions or interfaces, but it would also permit the evaluation of the elastic parameters of such materials using either local wavelength estimation, dispersion relations, or inversion algorithms.

In the biomedical field, ultrasound as well as magnetic resonance imaging techniques have been implemented in an attempt to visualize internal elastic displacements as well as to quantitatively characterize tissue, and these latter methods have been called magnetic resonance elastography (MRE).

Pioneering work in the area of ultrasound elasticity imaging has been accomplished using either a quasistatic stress approach,[1–5] or a dynamic approach.[6–12] Quasistatic stress methods compare ultrasound images of the structure taken before and after a compression is applied, thereby revealing a strain distribution. Dynamic methods, on the other hand, utilize Doppler ultrasonography to observe interior displacements arising from a dynamically applied mechanical stress. Although these methods have demonstrated a certain degree of success in the visualization of interior vibration and structure, they are still limited by poor resolution in the off-axial directions inherent to this modality.[13] Additionally, only a single displacement component can be determined from a single measurement.

Quasistatic magnetic resonance (MR) methods have been introduced[14–17] which utilize stimulated echo sequences to compare images of the structure before and after a compression is applied, portraying a strain distribution. Dynamic MR methods have also been introduced and can be further separated into either ''non-steady-state''[18–22] or ''steady-state''[23,24] acquisitions. When the object under investigation is excited by a dynamically applied stress (generally harmonic motion), the first approach measures the elastic displacements as the wave progresses through the object in a time-dependent fashion before steady-state conditions have been obtained, while the second approach measures the resultant elastic displacement distribution only after steady-state conditions have been obtained. Both of these approaches have demonstrated the ability to visualize dynamic elastic wave propagation within biological materials or biologically mimicking phantoms.

In this paper, we have chosen to utilize the non-steady-state, dynamic MR method in our investigation of the feasibility of elastic wave visualization within polymeric solids for several reasons. First, in contrast to ultrasonic methods, we wish to be able to noninvasively measure all three displacement components throughout volume of the medium under investigation during the same experimental situation. Second, although absolute elastic moduli can be obtained using quasistatic MR methods given a knowledge of the boundary conditions, boundary conditions generally cannot be accurately known except for the most simple of situations, which rarely physically exist. Additionally, the dependence of wave velocity on frequency portrays dispersive behavior of materials which is a characteristic we wish to analyze; therefore, a dynamic approach is required. Third, by measuring time-dependent wave progression instead of attaining steady-state conditions, we avoid having to invoke directional filtering to alleviate nodes caused by standing wave patterns within the material.

Since soft, biological tissues, are composed primarily of water, there is an abundance of ^{1}H proton nuclear spins. Therefore, it is reasonable to refer to this measurement method in soft tissue as ''high spin density'' MRE. In this paper, we investigate the application of this technique to solid-like, nontissue materials such as nonferromagnetic composites, plastics, and polymers. These materials are important in many applications, and, as mentioned above, the

[a]Electronic mail: romano@pa.nrl.navy.mil

ability to visualize, quantitatively, internal dynamic displacements as well as to determine subsequent elastic parameter maps through displacement dispersion images or inversion of the equations of elasticity would represent an important advance in material analysis techniques. In addition, there are solid-like biological materials such as bone, cartilage, and tendon, for which such a capability would be of great benefit (for a recent demonstration of dynamic MRE in cartilage, see Ref. 25). All of these materials can be characterized as having modest or low nuclear spin densities relative to water, and it is correspondingly reasonable to refer to this method as ''low spin density'' MRE. These low spin density materials provide proportionately lower net MRE-related signal amplitudes (therefore decreasing SNR). In addition, there are other complicating issues, such as those caused by relatively short T_2 (transverse) relaxation times, higher sound speeds, as well as susceptibility effects in heterogeneous media.

In Sec. II, we give a brief explanation of the background and theoretical development involved in high spin density MRE, and include some recent developments. In Sec. III, we discuss the challenges posed by low spin density materials. In Sec. IV, we present the modifications we have made and the associated MRE results we have obtained in silicone rubber and a voided polymer material.

II. BACKGROUND OF DYNAMIC MRE AS APPLIED TO TISSUE

The MRE technique developed by the Mayo Clinic[18] permits a direct visualization of elastic waves in soft tissue subject to dynamic excitation. The method utilizes a standard MRI apparatus (in this case, a 1.5-T General Electric Medical Systems Signa) which has been appropriately augmented.

As discussed in Ref. 18, in the presence of a magnetic-field gradient, the motion of nuclear spins causes a phase shift, φ, in an NMR signal given by

$$\phi = \gamma \int_0^{\tau} \mathbf{G}_r(t) \cdot \mathbf{r}(t) dt, \tag{1}$$

where γ is the gyromagnetic ratio characteristic of the nuclei, τ is the duration of the gradients after excitation, $\mathbf{G}_r(t)$ is a temporal function of the magnetic gradient superimposed on the static magnetic field, $\mathbf{B}_0$, and $\mathbf{r}(t)$ describes the position of the nuclear spins as a function of time.

Defining the position vector as follows:

$$\mathbf{r}(t) = \mathbf{r}_0 + \boldsymbol{\xi}(r_0, t), \tag{2}$$

where $\mathbf{r}_0$ is the mean position of the nuclear spin, and $\boldsymbol{\xi}(r_0, t)$ is the displacement of the spin about its mean position, then for specific time profiles of the magnetic gradient, a relation between the phase shift and displacement amplitude can be obtained through the use of Eq. (1). For the acoustic case in which the nuclear spins undergo simple harmonic motion about their mean position, $\mathbf{r}_0$

$$\boldsymbol{\xi}(\mathbf{r}_0, \theta) = \boldsymbol{\xi}_0 \cos(\mathbf{k} \cdot \mathbf{r}_0 - \omega t + \theta), \tag{3}$$

where $\mathbf{k}$ is the wave vector, θ is an initial phase offset, ω is the angular frequency of the mechanical excitation, and $\boldsymbol{\xi}_0$ is the displacement amplitude. If the time duration, τ, and the magnetic gradient time profile are chosen such that $\int_0^{\tau} \mathbf{G}_r(t) dt = 0$, then the observed phase shift in the NMR signal is given by

$$\phi(\mathbf{r}_0, \theta) = \gamma \int_0^{\tau = NT < TE} \mathbf{G}_r(t) \cdot \boldsymbol{\xi}_0 \cos(\mathbf{k} \cdot \mathbf{r}_0 - \omega t + \theta) dt$$

$$= \frac{2\gamma NT(\mathbf{G} \cdot \boldsymbol{\xi}_0)}{\pi} \sin(\mathbf{k} \cdot \mathbf{r}_0 + \theta), \tag{4}$$

where N is the number of gradient cycles, T is the period of the mechanical excitation, TE is the time at which the NMR signal is received, and $\omega = 2\pi/T$. Equation (4) indicates that the observed phase shift in the NMR signal obtained under these conditions is proportional to the scalar product of the displacement amplitude vector and the gradient vector, and to N. In practice, the phase offset values (θ) are chosen such that one obtains a sufficient number of equally spaced samples over the excitation wave form to determine the displacement amplitude using a temporal Fourier transform. Experiments to assess the sensitivity of this wave-imaging method at low amplitudes of mechanical excitation in tissue-like materials have demonstrated that displacements less than 100 nanometers can be readily observed.[18]

Since its inception, MRE has been used quite successfully in tissue and tissue phantom materials to produce high-quality, quantitative displacement images.[18,19] One example of this is shown in Fig. 1, in part taken from Ref. 18, in which two shear wave transducers are exciting a tissue phantom. The upper image is the standard MRI image and the bottom is the MRE image of the acoustic displacements. In addition, a number of successful efforts to obtain material parameter maps through inversion of the displacements have also been reported.[26–29]

III. TECHNICAL ISSUES WITH MRE IN SOLID MATERIALS

As one attempts to apply the MRE technique and the associated postprocessing inversion algorithms to nontissue materials of the type we have indicated, difficulties arise which are related in particular to three material parameter differences which these materials exhibit compared to those of tissue. These are the nuclear spin density (ρ_s), the spin relaxation time (T_2), and the elastic modulus (μ). The issues that arise from the first two of these are the same well-known issues associated with attempting to carry out magnetic resonance imaging (MRI) in these solid-like materials.[30] The issues resulting from the elastic modulus parameter are peculiar to MRE and the imaging of elastic waves. Values for all three parameters are shown in Table I for four elastic materials which together span the types of materials of interest here compared to those parameters for tissue.

Consider first the nuclear spin density parameter, ρ_s, where the value for tissue has been normalized to 1. As can be seen, this parameter is considerably lower for the nontissue materials ranging from 0.2 down to 10^{-3} compared to biological tissues which are, for the most part, water, having an abundance of ^{1}H proton nuclear spins. The lower nuclear spin densities result in proportionately lower measured magnetic phase signals [see Eq. (1)], and examination of Eq. (4)

FIG. 1. (a) MR image of a uniform tissue-simulating gel phantom measuring 0.2 m transversely. (b) Shear wave image for two source excitation at 500 Hz obtained using Eq. (4) and gradient echo. Note that displacement is out of plane.

shows that the minimum observable acoustic signal amplitude, ξ_0, for MRE will also be proportionately increased by this reduction in the nuclear spin densities.

The second important parameter is the transverse spin–spin relaxation time[31] called T_2. This time is a measure of the lifetime of the externally produced (by an rf pulse) transverse magnetization oscillations at the Larmor frequency (called the Zeeman effect), which are subsequently spatially encoded through the use of magnetic field gradients. This relaxation time is important because the encoding-related signal processing following the short excitation pulse must be carried out within the time period T_2 for both MRI and MRE. Also, short relaxation times and their associated frequency broadening can lead to a loss in the spatial resolution of the images. As can be seen in Table I, T_2 is 100 ms for tissue. This relatively long relaxation time is a consequence of the relatively benign internuclear environment in liquids. However, solid materials exhibit relatively large dipolar spin interactions which lead to a much faster dephasing of the transverse spins and much shorter T_2 relaxation times. This is evident in Table I, where the times in the materials of interest here are from 1 to almost 3 orders of magnitude shorter than those in tissue. In addition to the incoherent decay leading to T_2, spatial inhomogeneity in the magnetic field can add to the decay rate, and the resultant relaxation time is labeled T_2^*. The later decay effect can be mitigated by appropriate pulse sequencing.

The third parameter, the shear wave speed, is important for MRE techniques. In tissue materials, the shear speed is on the order of 5 m/s. A typical spatial field of view for MRE is on the order of 0.2 m or so. Most applications for MRE require that there be at least one acoustic wavelength in the field of view, and often times many more. In tissue, taking several (say 3) wavelengths across the aperture as the criterion leads to a lower acoustic frequency limit of 70 Hz, at which frequency the period, T, is 14 ms. As a result, most MRE-related studies in tissue have been carried out at relatively low frequencies (100 to 500 Hz). For the stiffer materials of interest here (see the shear speeds listed in Table I), this constraint leads to the need to use higher acoustic frequencies. For example, in the case of polyvinyl-chloride which is the stiffest material listed, the lowest usable frequency would be on the order of 15 kHz. The need to go to higher frequencies leads to problems on two fronts. First, as can be seen in Eq. (4), the signal strength is proportional to the elastic wave period T and thus falls off linearly with frequency. Second, at high frequencies elastic damping effects could become significant.

With reference to the parameters in Table I, the more serious challenges associated with the extension of MRE to the nonbiological materials is the loss of signal to noise expected from both the drop in nuclear spin densities and the increase in elastic wave speeds, the latter entering through the wave period T in Eq. (4). If we normalize the S/N to 1 for the tissue case and otherwise take electronic system parameters to be identical, the expected S/N for the other materials would 50×10^{-3}, 4.5×10^{-4}, and 4.5×10^{-6} for the silicone, voided polymer, and the two hard plastics, respectively. Assuming that the noise is white, improved S/N could be achieved by averaging a number of data realizations. Since the S/N of a typical MRI signal depends on the square root of the number of averages, we would need to have 400, 5×10^{6}, and 5×10^{10} averages for the silicone, voided polymer, and the two hard plastics, respectively. Considering that

TABLE I. Comparison of relative proton spin densities (ρ_s), T_2 relaxation times, and typical shear wave velocities (c_s) for biological tissue, silicone rubber, a voided polymer, *cis*-polybatadiene, and PVC, respectively. (Taken in part from Ref. 33).

Material	Tissue	Silicone rubber	Voided polymer	*cis*-polybutadiene	Polyvinyl chloride
Normalized ρ_s	1	0.2	10^{-2}	10^{-3}	10^{-3}
T_2	100 ms	12.3 ms	16 ms	290 μs	442 μs
c_s	4.5 m/s	18 m/s	80–120 m/s	$\sim10^3$ m/s	$>10^3$ m/s

a typical pulse repetition time (*TR*) might be on the order of several tens of milliseconds in tissue, that there are two polarizations required in a typical measurement, and that we determine the temporal data at a minimum of four equally spaced time samples (phase offsets), then a single beam of data would take 0.24 s to acquire. To arrive at an S/N equal to that for tissue then would require averaging times of 96 s, 13.9 days, and 380.5 years for the silicone, voided polymer, and the hard plastics, respectively. While such realizations are feasible for the silicone and possible (yet perhaps impractical) for the voided polymer, clearly more sophisticated approaches will be required in the application of MRE to the harder polymer cases.

Before leaving this section, it should be pointed out that an additional complication results for solid materials which are heterogeneous, examples of which are voided polymer systems of the type referred to in Table I. Magnetic field strengths can vary spatially in heterogeneous materials, resulting in unintended spatial smearing of the Larmor frequencies with a concomitant loss in spatial resolution. In addition, the inhomogeneities can lead to signal loss.

IV. EXTENSION TO LOW SPIN DENSITY MATERIALS AND EXPERIMENTAL RESULTS IN POLYMERIC SOLIDS

With this as background, experiments were undertaken in an attempt to apply MRE techniques to silicone rubber and to a voided polymer material. As can be seen in Table I, of the materials listed, silicone should present the least challenge in attempting to extend MRE from biological tissue to solid materials. First, the nuclear spin density is one-fifth that of tissue, and this decrease, while representing a significant drop in signal level, was addressed by implementing suitable averaging techniques. Second, while the spin relaxation time is much shorter than that of tissue (by a factor of 8), it is still a factor of 30 longer than that for plastics. In addition to providing the first demonstrations of MRE in solid materials, successful experimental studies in silicone rubber and a voided polymer serve to validate our understanding of the technical limiting factors which would be important for future attempts at applying MRE to the more problematic solid materials.

The experiments were conducted at the Mayo Clinic using a modified version of the MRE method previously described in detail.[18,19] In order to partially compensate for the expected order of magnitude drop in signal level related to the lower spin density of silicone compared to water (see Table I), four averaging scans were implemented to increase S/N. Since the T_2 and T_2^* of the silicone sample are 12.3 and 2 ms, respectively, a spin–echo sequence[30] with a minimum echo time (8–16 ms) was implemented to maximize the available signal. Additionally, the center Larmor frequency of the silicone sample was found to be 453 Hz lower than water. Taking into account the higher silicone elastic modulus compared to tissue requires the use of higher acoustic frequencies. In this regard, a frequency of about 500 Hz would produce several acoustic wavelengths across the field of view. Accordingly, the cw transducer displacements were made to cover the band 400 to 700 Hz. Figure 2 shows the pulse sequence design and the motion sensitizing gradient used at a frequency of 400 Hz.

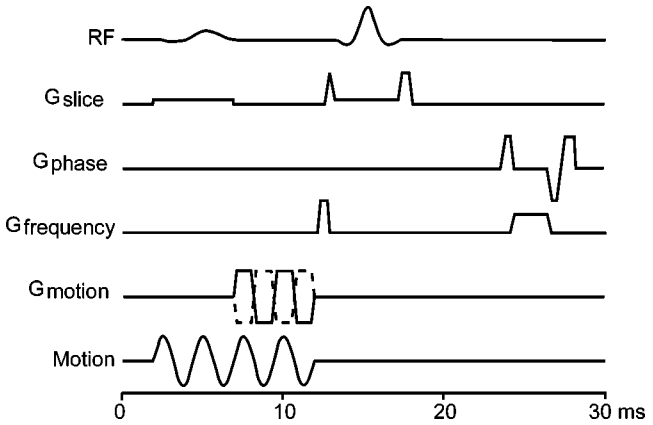

FIG. 2. The spin–echo MRE pulse sequence shown here exhibits two 400-Hz gradient pairs used to sensitize to the shear motion. In these experiments the motion-sensitizing gradients are applied along the slice direction. For each phase encoding step, two samples are acquired. The second sample is acquired with gradients of inverted amplitude. From these two samples a phase difference image is generated. After the phase difference image is acquired, the phase of the applied motion (θ) is modified to demonstrate wave progression.

As shown in Fig. 3, an electromechanical transducer was used to apply sinusoidal shear motion in a tangential direction (reference arrows in Fig. 3) to the flat surface of a solid silicone cylinder 0.083 m in diameter and 0.07 m long. Motion-sensitizing gradients were applied in the direction of transducer motion, and quantitative MRE images of the dynamic displacement were obtained in the silicone rubber in a plane perpendicular to the transducer displacement direction, over 256×256 pixels within a field of view of 0.20×0.20 m. With a *TR* of 500 ms ($T_1=685$ ms), four averages (NEX), and eight phase offsets, the measurements took on the order of 34 min per frequency.

Shown in Fig. 4 are two images obtained in the silicone rubber cylinder which are analogous to those shown in Fig. 1 for the tissue phantom. As in the latter case, the upper image is the standard MRI image while the lower image is the MRE

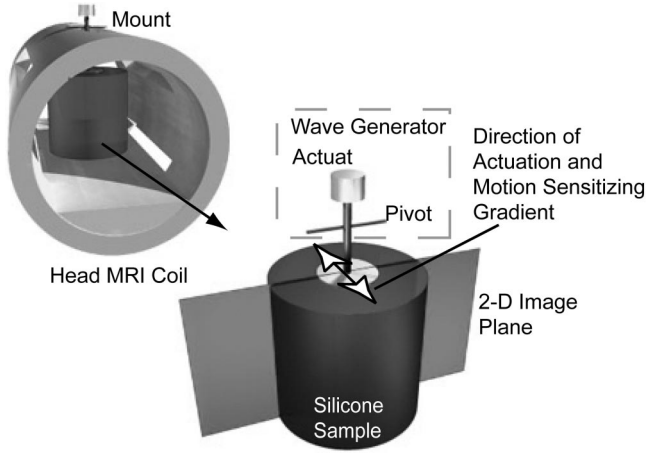

FIG. 3. Experimental setup for measuring shear waves in the silicone sample. Pivot of actuator coil is attached to head MRI coil directly over the object. Direction of actuation and motion-sensitizing gradient is out of the page as indicated by arrows.

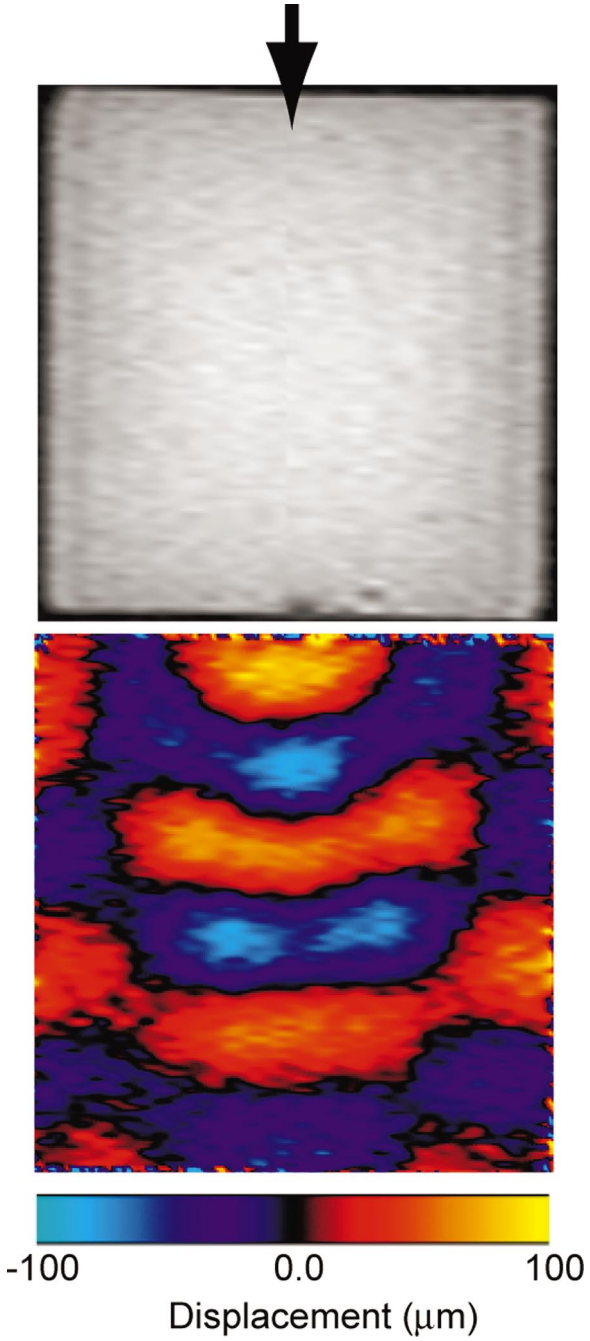

FIG. 4. (a) MR image of the silicone sample. (b) Shear wave image for single source excitation at 700 Hz obtained using Eq. (4) and spin–echo. Arrow indicates location of actuator and displacement is out of plane.

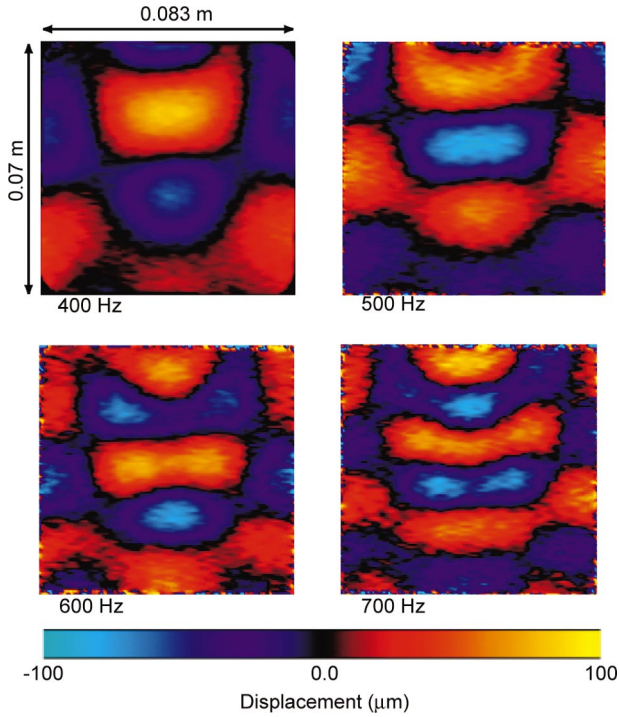

FIG. 5. Shear wave images measured in the silicone at (a) 400 Hz; (b) 500 Hz; (c) 600 Hz; and (d) 700 Hz, with observable wavelengths of 0.045, 0.036, 0.03, and 0.0257 m, respectively. Note decreasing SNR with increasing frequency. Displacement is out of plane.

generated acoustic displacement image carried out at 700 Hz.

Shown in Fig. 5 are the MRE displacement images for the four frequencies 400, 500, 600, and 700 Hz, with observable wavelengths of 0.045, 0.036, 0.03, and 0.0257 m, respectively. With respect to these frequencies and resultant wavelengths, it can be seen that the silicone is nondispersive in this frequency regime with a shear wave velocity of approximately 18 m/s as indicated in Table I. As can be seen, the quality of all the displacement images is good. We estimate the S/N at each of these frequencies to be 20, 16, 13, and 11 dB, respectively. These estimates were computed in the following manner. The phase represented by Eq. (4) was determined for eight equally spaced offsets (i.e. $\theta=0$, $\pi/4$, $\pi/2$, $3\pi/4$, π, $5\pi/4$, $3\pi/2$, and $7\pi/4$) over the period of the monochromatic excitation. A temporal Fourier transform of the displacements was performed at each pixel, and the magnitudes of the individual harmonics were separately averaged over all pixels contained within the sample. For an eight-point DFT, the actual monochromatic signal amplitude will appear in bins 2 and 8, while bins 1, 3, 4, 5, 6, and 7 contain components of what we will label as noise. A comparison of these relative amplitudes yields our estimate of signal to noise. As can be seen in Eq. (4), the signal level is proportional to the frequency-dependent product $NT\xi$. In our experiments, the number of gradient cycles, N, was two except for 700 Hz where it was increased to three, and ξ fell approximately as the square of the frequency due to the transducer transfer function. It should be noted that although the higher harmonics of the displacements have been used as a measure of nonlinearity[32] in some situations, an analysis of the individual harmonics in these experiments indicated no such nonlinear behavior, and the measured levels of these harmonics were fairly constant across the frequency band of interrogation. Taking all this into account, we would expect an S/N drop of 11 dB going from 400 to 700 Hz, which is close to what we observed.

Next, we attempt to visualize shear wave propagation in a voided polymer sample. As can be seen from Table I, the signal loss due to the reduced spin density is now a factor of 100 less than that of tissue. Since the T_2 of this sample is on the order of the silicone sample (16 vs 12.3 ms), the spin–echo sequence was once again utilized with an echo time of 10 ms. Additionally, the center Larmor frequency of the voided polymer sample was found to be 430 Hz lower than

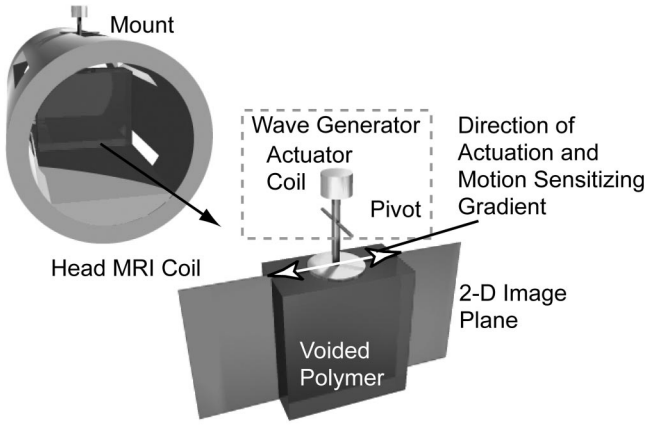

FIG. 6. Experimental setup for measuring shear waves in the voided polymer sample. Pivot of actuator coil is attached to head MRI coil directly over the object. Direction of actuation and motion-sensitizing gradient is in the plane of the page as indicated by arrows.

water. As mentioned above, a further complicating factor is the increased shear wave velocity, which for a measurement comparable to that for silicone, would require frequencies in the kHz range. As shown in Fig. 6, the voided polymer had a rectangular shape with dimensions 0.17×0.236 m, and a thickness of 0.05 m. In this case, the sinusoidal shear motion and the motion-sensitizing gradients were applied in a left to right direction, as indicated by the arrows in Fig. 6, over 256×256 pixels, within a field of view of 0.48×0.48 m. With a *TR* of 1 s ($T_1=2$ s), five averages (NEX), and four phase offsets, the measurements took on the order of 43 min per frequency. Shown in Fig. 7 are the MRE displacement images for the four frequencies 800, 900, 1100, and 1200 Hz, with observable wavelengths of 0.09, 0.1, 0.11, and 0.09 m, respectively. With respect to these frequencies and resultant wavelengths, it can be seen that the voided polymer is dispersive in this frequency regime, with velocities ranging from approximately 80 m/s at 800 Hz to 120 m/s at 1200 Hz, as indicated in Table I. As can be observed, the quality of the displacement images is rather poor, which is to be expected in light of the two orders of magnitude drop in spin density and the increased temporal frequencies required due to the shear wave velocity. In light of the discussion at the end of Sec. III dealing with the averaging time required for equivalent SNR in tissue, we see that the SNR in this experimental case should be approximately 40 dB lower than in the silicone case, which is close to observation. In spite of this poor SNR, however, it is remarkable that shear waves are clearly identifiable in Fig. 7.

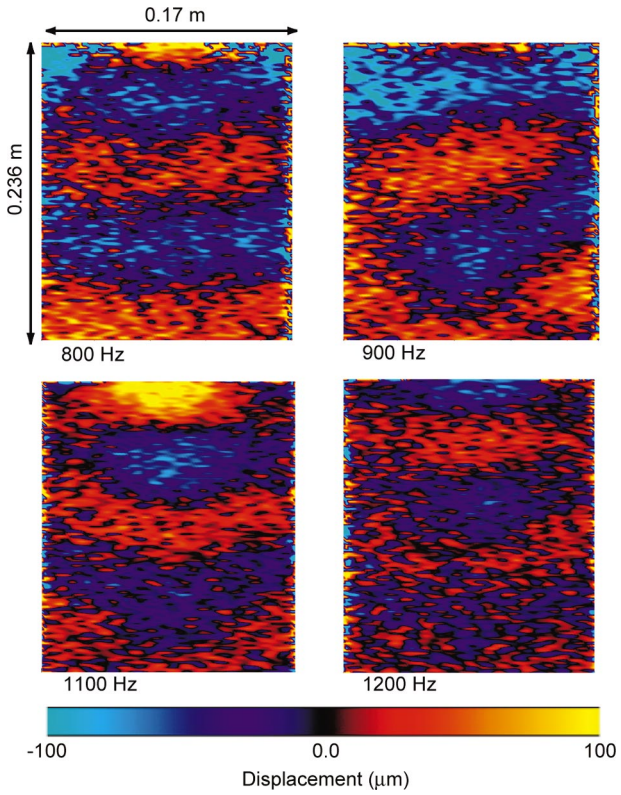

FIG. 7. Shear wave images measured in the voided polymer at (a) 800 Hz; (b) 900 Hz; (c) 1100 Hz; and (d) 1200 Hz, with observable wavelengths of 0.09, 0.1, 0.11, and 0.09 m, respectively. Displacement is in plane.

Next, an inversion algorithm was applied to the silicone displacement data which extracts the complex shear modulus/density, μ/ρ, throughout the material. We used the inversion algorithm described by Romano *et al.*,[3] namely

$$(\mu/\rho)_m=-\int \omega^2 u_3 v_3 \mathrm{d}\Omega_m \Big/ \int u_3\left(\frac{\partial^2 v_3}{\partial x_1^2}+\frac{\partial^2 v_3}{\partial x_2^2}\right)\mathrm{d}\Omega_m . \tag{5}$$

Here, u_3 is the complex out-of-plane shear displacement, v_3 is an arbitrary, smooth virtual function, the subscript m is a local incremental volume element, and 1 and 2 are the two directions perpendicular to the shear displacement. Representing the real and imaginary parts of $(\mu/\rho)_m$ as m_r and m_i, respectively, the shear wave velocity c_s can be determined from the expression

$$c_s=\sqrt{\frac{2(m_r^2+m_i^2)}{mr+\sqrt{m_r^2+m_i^2}}}. \tag{6}$$

A representative example of the result of such an inversion for the 400-Hz displacement data in the midplane of the silicon cylinder is shown in Fig. 8. Here, we display the shear wave speed computed using Eqs. (5) and (6). The average value indicated is 18 m/s, which is in the range expected for this parameter in silicone rubbers. With a knowledge of the density of the sample (1019.65 kg/m^3), the shear modulus was estimated to be on the order of 330 kPa. The nonuniformity seen in the shear wave map in Fig. 8 is due to artifacts associated with nodal lines that can be seen in the displacement images of Fig. 5, for which the low displacement levels become problematic for the inversion algorithm [see Eq. (5)]. Application of this approach to the voided polymer displacement data yields inconclusive results due primarily to the poor SNR of the measurements.

V. DISCUSSION

The successful imaging using MRE of elastic waves in silicone rubber with sufficient S/N to allow elastic parameter inversions is significant. However, applying MRE to materi-

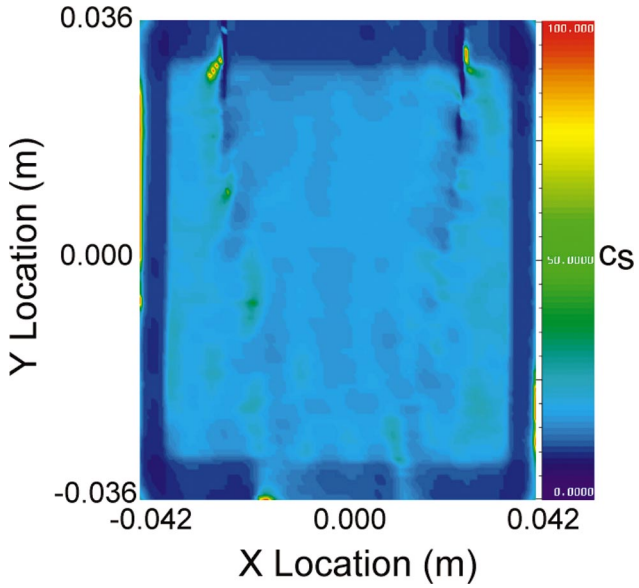

FIG. 8. Shear wave velocity estimation within silicone obtained using Eqs. (5) and (6) at 400 Hz. Average value is on the order of 18 m/s.

als having even lower nuclear spin densities, shorter spin relaxation times, and longer elastic wavelengths will require further innovations.

The S/N problem associated with very low spin densities could be addressed by considering a number of modifications including optimizing voxel size, increasing averaging and decreasing bandwidth, increasing magnetic field strength [which enters through **G** in Eq. (4)]. While the very short T_2 relaxation times characteristic of plastic materials would appear to be a formidable issue, MRI images have already been successfully generated in both polyvinyl chloride and *cis*-polybutadiene using a new spatial encoding technique named SPRITE.[33] Other techniques that mitigate the effect of very short spin relaxation times in MRI images include spin-locking,[34] multipulse coherent averaging,[35] and optimizing rf pulse trains to produce dipolar line narrowing.[36] All of these techniques could be adapted for the MRE case in order to overcome the short T_2 times in the plastic materials.

The results for MRE shown here are encouraging, and current research is focusing on the extension to other solid materials by considering some of the techniques discussed above.

ACKNOWLEDGMENT

This work was supported in part by the Office of Naval Research and the National Institute of Health Grants CA91959 and EB001981.

[1] J. Ophir, I. Cespedes, H. Ponnekanti, Y. Yazdi, and X. Li, "Elastography: A quantitative method for imaging the elasticity of biological tissues," Ultrason. Imaging **13**, 111–134 (1991).
[2] I. Cespedes, J. Ophir, H. Ponnekanti, and N. Maklad, "Elastography: Elasticity imaging using ultrasound with application to muscle and breast *in vivo*," Ultrason. Imaging **15**, 73–88 (1993).
[3] M. O'Donnel, A. R. Skovoroda, B. M. Shapo, and S. Y. Emellanov, "Internal displacement and strain imaging using ultrasonic speckle tracking," IEEE Trans. Ultrason. Ferroelectr. Freq. Control **41**, 314–325 (1994).
[4] B. S. Garra, E. I. Cespedes, J. Ophir, S. R. Spratt, R. A. Zuurbier, C. M. Magnant, and M. F. Pennanen, "Elastography of breast lesions: Initial clinical results," Radiology **202**(1), 79–86 (1997).
[5] F. Kallel and M. Bertrand, "Tissue elasticity reconstruction using linear perturbation method," IEEE Trans. Med. Imaging **15**, 299–313 (1996).
[6] L. Gao, K. J. Parker, and S. K. Alam, "Sonoelasticity imaging: Theory and experimental verification," J. Acoust. Soc. Am. **97**, 3875–3885 (1995).
[7] S. R. Huang and D. J. Roach, "Sonoelasticity imaging: Results in *in vitro* tissue specimens," Radiology **181**, 237–239 (1991).
[8] F. J. Lee, J. P. Bronson, R. M. Lerner, K. J. Parker, S. T. Huang, and D. J. Roach, "Sonoelasticity imaging: Results in *in vitro* tissue specimens," Radiology **181**, 237–239 (1991).
[9] R. M. Lerner, S. R. Huang, and K. J. Parker, "Sonoelasticity images derived from ultrasound signals in mechanically vibrated tissues," Ultrasound Med. Biol. **16**, 231–239 (1990).
[10] K. J. Parker, S. R. Huang, R. A. Musulin, and R. M. Lerner, "Tissue response to mechanical vibrations for sonoelasticity imaging," Ultrasound Med. Biol. **16**(3), 241–246 (1990).
[11] K. Parker and R. Lerner, "Sonoelasticity of organs: Shear waves ring a bell," J. Ultrasound Med. **11**, 387–392 (1992).
[12] D. J. Rubens, M. A. Hadley, S. K. Alam, L. Gao, R. D. Mayer, and K. J. Parker, "Sonoelasticity imaging of prostate cancer: *In vitro* results," Radiology **195**, 379–383 (1995).
[13] J. B. Weaver, E. E. W. Van Houten, M. I. Miga, F. E. Kennedy, and K. D. Paulsen, "Magnetic resonance elastography using 3D gradient echo measurements of steady-state motion," Med. Phys. **28**(8), 1620–1628 (2001).
[14] T. L. Chenvert, S. Y. Emelianov, and A. R. Skovoroda, "Elasticity reconstructive imaging using static displacement and strain estimations," Proceedings of the International Society of Magnetic Resonance in Medicine, Vol. 461 (1997).
[15] T. L. Chenevert, A. R. Skovoroda, M. O'Donnel, and S. Y. Emelianov, "Elasticity reconstruction via stimulated echo MRI," Magn. Reson. Med. **39**(3), 482–490 (1998).
[16] D. B. Plewes, J. Bishop, A. Samani, and J. Sciarretta, "Visualization and quantification of breast cancer biomechanical properties with magnetic resonance elastography," Phys. Med. Biol. **45**, 1591–1610 (2000).
[17] D. D. Steele, T. L. Chenevert, A. R. Skovoroda, and S. Y. Emelianov, "Three-dimensional static displacement, stimulated echo NMR elasticity imaging," Phys. Med. Biol. **45**, 1663–1648 (2000).
[18] R. Muthupillai, P. J. Rossman, D. J. Lomas, J. F. Greenleaf, S. J. Riederer, and R. L. Ehman, "Magnetic resonance elastography by direct visualization of propagating acoustic strain waves," Science **269**, 1854–1857 (1995).
[19] R. Muthupillai, P. J. Rossman, D. J. Lomas, J. F. Greenleaf, S. J. Riederer, and R. L. Ehman, "Magnetic resonance imaging of transverse acoustic strain waves," Magn. Reson. Med. **36**, 266–274 (1996).
[20] J. Bishop, G. Poole, M. Leitch, and D. B. PLewes, "Magnetic resonance imaging of shear wave propagation in excised tissue," J. Magn. Reson Imaging **8**(6), 1257–1265 (1998).
[21] A. Manduca, V. Dutt, D. T. Borup, R. Muthupillai, R. L. Ehman, and J. F. Greenleaf, "Reconstruction of elasticity and attenuation maps in shear wave imaging: An inverse approach," Lecture Notes in Computer Science: Medical Image Computing and Computer-Assisted Intervention-MICCAI'98, Vol. 1496, pp. 606–613 (1998).
[22] M. Suga, K. Minato, T. Matsuda, O. Oshiro, K. Chihara, M. Ohta, S. Tsutsumi, M. Lomori, T. Takahashi, J. Okamoto, and O. Takizawa, "Measurement and evaluation of local tissues elastic modulus using MR elastography," Med. Imaging Technol. **18**(6), 769–775 (2000).
[23] R. Sinkus, J. Lorenzen, D. Schrader, M. Lorenzen, M. Dargatz, and D. Holz, "High resolution tensor MR elastography for breast tumor detection," Phys. Med. Biol. **45**, 1649–1664 (2000).
[24] E. E. W. Van Houten, J. B. Weaver, M. I. Miga, F. E. Kennedy, and K. D. Paulsen, "Elasticity reconstruction from experimental MR displacement data: Initial experience with an overlapping subzone finite element inversion process," Med. Phys. **27**, 101–107 (2000).
[25] O. Lopez, P. J. Rossman, and R. L. Ehman, "Dynamic MR Elastography of Cartilage," Proc. Intl. Soc. Mag. Reson. Med. 11 (2003).
[26] A. Manduca, T. E. Oliphant, M. A. Dresner, J. L. Mahowald, S. A. Kruse, E. Amromin, J. P. Felmlee, J. F. Greenleaf, and R. L. Ehman, "Magnetic resonance elastography: Non-invasive mapping of tissue elasticity," Med. Image Anal **5**, 237–254 (2001).
[27] A. J. Romano, J. A. Bucaro, R. L. Ehman, and J. J. Shirron, "Evaluation

of a material parameter extraction algorithm using MRI-based displacement measurements,'' IEEE Trans. Ultrason. Ferroelectr. Freq. Control **47**, 1575–1581 (2000).
[28] A. J. Romano, P. J. Rossman, R. C. Grimm, J. A. Bucaro, and R. L. Ehman, ''Recent developments in the determination of elastic moduli from MRE displacement measurements,'' Proc. Int. Soc. Mag. Reson. Med. **10**, 2603 (2002).
[29] A. J. Romano, P. J. Rossman, R. C. Grimm, J. A. Bucaro, and R. L. Ehman, ''Broad-spectrum beam magnetic resonance elastography,'' Proc. Int. Soc. Mag. Reson. Med. **11**, 1803 (2003).
[30] See, for example, P. T. Callaghan, *Principles of Nuclear Magnetic Resonance Microscopy* (Clarendon, Oxford, UK, 1991), pp. 308–318.
[31] E. M. Haacke, R. W. Brown, M. R. Thompson, and R. Venkatesan, *Magnetic Resonance Imaging: Physical Principles and Sequence of Design* (Wiley, New York, 1999), Vol. 1, pp. 118–124.
[32] R. Sinkus, S. Weiss, E. Wiggert, J. Lorenzen, M. Dargatz, and C. Kuhl, ''Non-linear elastic tissue properties of the breast measured by MR-elastography—Initial *in-vitro* and *in-vivo* results,'' Proc. Intl. Soc. Mag. Reson. Med. **10**, (2002).
[33] C. B. Kennedy, B. J. Balcom, and I. V. Mastikhin, ''Three-dimensional magnetic resonance imaging of rigid polymeric materials using single-point ramped imaging with T_1 enhancement (SPRITE),'' Can. J. Chem. **76**, 1753–1765 (1998).
[34] E. Rommel, and R. Kimmich, ''Slice excitation and localization NMR spectroscopy on the basis of spin locking,'' J. Magn. Reson. (1969-1992) **83**, 299–308 (1989).
[35] G. C. Chingas, J. B. Miller, and A. N. Garroway, ''NMR images of solids,'' J. Magn. Reson. (1969-1992) **66**, 530–535 (1986).
[36] D. G. Cory and W. S. Veeman, ''Applications of line narrowing to H-1 NMR imaging of solids,'' J. Magn. Reson. (1969-1992) **84**, 392–397 (1989).

Transient modeling of Lamb waves generated in viscoelastic materials by surface bonded piezoelectric transducers

Laurent Duquenne, Emmanuel Moulin,[a] Jamal Assaad, and Sébastien Grondel
IEMN, UMR CNRS 8520, OAE Department, Université de Valenciennes et du Hainaut Cambrésis, le Mont Houy, 59313-Valenciennes Cedex 9, France

(Received 24 July 2003; revised 10 April 2004; accepted 19 April 2004)

In order to help optimize health monitoring systems based on Lamb wave propagation, a hybrid finite element–normal mode expansion modeling technique has been developed. This technique allows one to predict the Lamb waves generated in a structure as a function of the transducer parameters (size, location, material, etc.). The present paper shows how this hybrid modeling, initially valid for nonlossy materials and harmonic excitation, can be extended to lossy (viscoelastic) materials and transient excitation. For this purpose, simplifying assumptions have been proposed and validity conditions have been established and verified. Moreover, numerical results concerning Lamb wave generation have been successfully compared to experimental ones. As a result, the method has proved to be pertinent and practically unrestrictive. © *2004 Acoustical Society of America.* [DOI: 10.1121/1.1760109]

PACS numbers: 43.20.Ks, 43.35.Mr, 43.40.Le [ANN] Pages: 133–141

I. INTRODUCTION

Advantages of composite materials in aerospace applications (low density along with very good mechanical properties) are well known. But since they are subject to a hostile environment and are very sensitive to impacts, costly scheduled inspections are required. The concept of sensitive materials (or integrated health monitoring) using Lamb waves appears to be a potentially promising method to reduce maintenance costs. Various studies concerning the use of piezoelectric transducers generating and receiving Lamb waves have shown the feasibility of this technique in various practical cases such as riveted aluminum plates,[1] composite wingbox structures,[2] and radomes.[3] These studies have demonstrated the capability of Lamb waves to interact with defects in the propagation medium. To achieve better performances and allow better interpretation of the received signals, determination and optimization of the contribution of each Lamb mode in the generated waveforms is an important issue.

The normal mode expansion technique[4] appears to be suitable for solving this problem. This method makes it possible to determine the contribution of each mode as a function of the applied surface and/or volume excitations. Applications of normal mode expansion have been successfully performed for various kinds of transduction such as solid[5,6] and liquid[7] wedge transducers, Hertzian contact transducers,[8] laser-generated Lamb waves,[9] and surface-mounted interdigital transducers (IDT).[10] In all of these cases, some assumptions are made which allow analytical calculation of the excitation applied to the plate. However, in the case of integrated transducers with arbitrary dimensions, such preliminary analytical prediction of the excitation terms appears to be very difficult. Therefore a hybrid finite element–normal mode expansion modeling technique has been developed.[11] This technique has allowed us to take into account the actual excitation profile provided by surface-bonded or bulk-embedded piezoelectric elements. Then, the method has been extended and validated for the case of surface multi-element transducers[12,13] and initial preliminary results have been presented for the case of transient excitation.[14,15] Continuation of this work and additional results of the transient application will be given in this paper.

Application of the normal mode theory requires the knowledge of acoustic fields and wavenumbers of propagative modes. A great amount of theoretical work has been performed in this domain, both with nonlossy[16,17] and lossy (viscoelastic) materials.[18] In the case of lossy materials, experimental determination of attenuation constants is a necessary preliminary step. Suitable techniques have been developed for the case of thin[19–21] plate-shaped structures such as considered in the present work.

In the theoretical derivations of normal mode expansion, Auld[4] deals with real wavenumbers only. This allows us to use simple orthogonality properties of the Lamb modes. In this way, neither the nonpropagative (evanescent) modes nor the case of viscoelastic materials can be considered. In order to introduce attenuation effects in the modeling, a simplifying, though reasonable, assumption will be proposed. As a consequence, under certain conditions, the hybrid finite element–normal mode expansion technique can be easily adapted to viscoelastic materials.

After a brief overview of Lamb waves and the normal mode expansion method, the symplifying assumptions allowing the application of the hybrid finite element–normal mode expansion technique to viscoelastic materials and transient excitation will be presented in Sec. II. Then in Sec. III, the technique will be partially validated by comparing its results to purely numerical finite element computations. In addition, validity conditions of the approximations will be established and discussed. Finally, Sec. IV will be focused on experi-

[a]Electronic mail: emmanuel.moulin@univ-valenciennes.fr

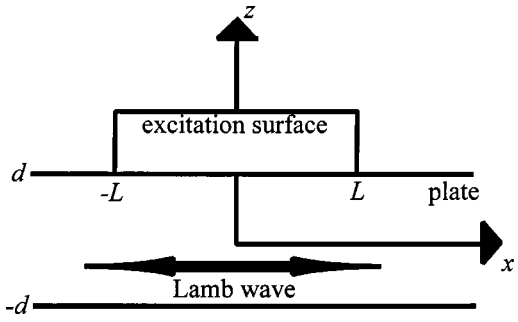

FIG. 1. Description of the Lamb wave generation configuration.

mental validation of the accuracy and the prediction capabilities of the proposed technique.

II. MODEL DESCRIPTION AND ASSUMPTIONS

A. Lamb waves characteristics

The excitation of a piezoelectric element bonded on a plate of thickness $2d$ (Fig. 1) generates guided acoustic waves known as Lamb waves. This type of propagation is dispersive and, at a given frequency-thickness product, a finite number of propagative modes exists. Displacement field for the nth Lamb mode propagating along the x direction can be expressed as follows:

$$u_i^n(x,z,f)=U_i^n(z,f)e^{-jk_n(f)x}, \tag{1}$$

where $U_i^n(z,f)$ is the amplitude of the displacement u_i^n along the i direction (where i denotes either x, y or z), and $k_n(f)$ is the wavenumber according to the x direction at the frequency f. Values of $U_i^n(z,f)$ and $k_n(f)$ can be obtained by substituting Eq. (1) into the following wave equation:

$$\rho\frac{\partial^2 u_i}{\partial t^2}=C_{ijkl}\frac{\partial^2 u_k}{\partial x_j\partial x_l}+\eta_{ijkl}\frac{\partial^3 u_k}{\partial x_j\partial x_l\partial t}, \tag{2}$$

where u_i is the global displacement field in the i direction. In the case of a viscoelastic material, the stiffness tensor can be formulated in a complex form:[22]

$$\overline{C_{ijkl}}=C_{ijkl}+2j\pi f\eta_{ijkl}. \tag{3}$$

If the material is purely elastic, the stiffness tensor $\overline{C_{ijkl}}$ is real (viscosity constants η_{ijkl} are zero) and then propagative Lamb waves have real wavenumbers. For viscoelastic materials, every Lamb wave has a complex wavenumber. In this case, the real and imaginary parts represent the propagation and the damping, respectively.

I. A. Viktorov,[16] A. H. Nayfeh,[17] and other authors[18] have derived solutions allowing us to predict the Lamb mode wavenumbers and the modal displacement and stress fields, in the case of elastic as well as viscoelastic materials. Such solutions will be exploited in the present work.

B. The problem of Lamb wave generation

According to the normal modes theory,[4] the acoustic field $(\mathbf{u},\mathbf{T})$ at a given position x_0 can be expressed as a linear combination of the eigenmode acoustic fields $(\mathbf{u}^n,\mathbf{T}^n)$:

$$\mathbf{u}(x_0,z,f)=\sum_n A_n(x_0,f)\mathbf{u}^n(z,f), \tag{4a}$$

$$\mathbf{T}(x_0,z,f)=\sum_n A_n(x_0,f)\mathbf{T}^n(z,f), \tag{4b}$$

where $\mathbf{u}$ is the displacement field vector and $\mathbf{T}$ is the stress tensor. The amplitude A_n of the nth mode depends on the excitation applied to the plate. In the case of lossless materials, A_n can be derived by using the complex reciprocity relation and the eigenmode orthogonality condition.[4] Assuming that only surface tractions are applied to the plate (no volume force), the following equation is obtained:

$$\frac{\partial A_n}{\partial x}+jk_nA_n=\frac{f_S^n}{4P_{nn}}, \tag{5}$$

with

$$f_S^n(x)=\{2j\pi f\mathbf{u}^{n*}(d)\cdot\mathbf{T}_S^+(x)-2j\pi f\mathbf{u}^{n*}(-d)\cdot\mathbf{T}_S^-(x)\}\cdot\mathbf{z}, \tag{6}$$

$$P_{nn}=\frac{1}{4}\int_{-d}^{d}(-2j\pi f\mathbf{u}^{n*}\cdot\mathbf{T}^n-2j\pi f\mathbf{u}^n\cdot\mathbf{T}^{n*})\cdot\mathbf{x}\,dz, \tag{7}$$

where f_S^n is called the surface forcing function, $\mathbf{u}^n$ is the displacement field associated to the nth mode, d is the plate half-thickness, $\mathbf{T}_S^+$ and $\mathbf{T}_S^-$ are the tractions applied to the upper and lower surfaces respectively, $\mathbf{x}$ and $\mathbf{z}$ are the unit vectors along the propagation and thickness directions, and P_{nn} is the average power flow density associated to the nth mode. The star (*) denotes complex conjugation.

Integration of Eq. (5) yields

$$A_n=\frac{e^{-jk_nx_0}}{4P_{nn}}\int_{-L}^{L}f_S^n(\eta)e^{jk_n\eta}\,d\eta. \tag{8}$$

In the case of a localized excitation, at the upper surface, in the area $-L\leqslant x\leqslant L$ (Fig. 1), $\mathbf{T}_S^-=0$ and $\mathbf{T}_S^+$ is equal to the applied stress components $(\sigma_{xz},\sigma_{zz})$ at the plate surface. The integral in Eq. (8) can then be reformulated as

$$\int_{-L}^{L}f_S^n(\eta)e^{jk_n\eta}\,d\eta=[2j\pi fu_x^{n*}(d)I_{xz}(k_n)+2j\pi fu_z^{n*}(d)I_{zz}(k_n)], \tag{9}$$

with

$$I_{xz}(k_n)=\int_{-L}^{L}\sigma_{xz}(x,d)e^{jk_nx}\,dx \tag{10}$$

and

$$I_{zz}(k_n)=\int_{-L}^{L}\sigma_{zz}(x,d)e^{jk_nx}\,dx. \tag{11}$$

In simple cases, the surface forcing function f_S^n can be explicitly determined or approximated. As an example Ditri *et al.*[5] used a parabolic pressure distribution to model the effect of a wedge transducer. X. Jia[7] has modified the surface forcing function to take into account the impedance mis-

match at the liquid and solid interface of a liquid wedge transducer.

In the case of an integrated transducer, the surface forcing function is not straightforward. To compute the "actual" localized stress field provided by the transducer's presence and its interactions with the plate, the finite element method can be used. Then the surface forcing function can be determined using Eq. (6). Finally, using the normal mode expansion method, the amplitude associated to each mode can be computed [Eq. (8)]. Full details of this modeling technique have been given in Ref. 11 and will not be reminded here.

C. Application to viscoelastic materials

Normal mode formulation as presented in the previous section is theoretically not applicable to solutions with complex wavenumbers.[4]

In the case of lossless materials, the lack of solution for inhomogeneous modes (imaginary wavenumbers) is not a problem, since only long range propagation is of interest. Coping with propagating solutions only (real wavenumbers) is then convenient. However, in the case of viscoelastic materials, as said above, every wavenumber is complex and application of normal mode expansion is not straightforward.

Therefore, in this section, a simplifying assumption will be proposed in the case of a moderate attenuation. Indeed it will be assumed that the effects of attenuation on the local Lamb wave generation process is negligible. On the other hand, the effects on propagation will be taken into account.

This approximation can be partially justified by considering the formulation introduced by Nunez *et al.*[6] The displacement field is reformulated so that the terms depending on the thickness direction z are separated from the terms depending on the propagation direction x [Eqs. 12(a) and 12(b)]. By substituting Eqs. (8) and (9) into Eq. (4), the following expressions are obtained:

$$u_x(x_0,z,f)=\sum_n [H^n_{xx}(z,f)I_{xz}(k_n) + H^n_{xz}(z,f)I_{zz}(k_n)]e^{-jk_nx_0}, \tag{12a}$$

$$u_z(x_0,z,f)=\sum_n [H^n_{zx}(z,f)I_{xz}(k_n) + H^n_{zz}(z,f)I_{zz}(k_n)]e^{-jk_nx_0}, \tag{12b}$$

with

$$H^n_{xx}(z,f)=\frac{2j\pi f u^n_x(z,f)u^{n*}_x(d,f)}{4P_{nn}(f)}, \tag{13}$$

$$H^n_{xz}(z,f)=\frac{2j\pi f u^n_x(z,f)u^{n*}_z(d,f)}{4P_{nn}(f)}, \tag{14}$$

$$H^n_{zx}(z,f)=\frac{2j\pi f u^n_z(z,f)u^{n*}_x(d,f)}{4P_{nn}(f)}, \tag{15}$$

and

$$H^n_{zz}(z,f)=\frac{2j\pi f u^n_z(z,f)u^{n*}_z(d,f)}{4P_{nn}(f)}, \tag{16}$$

where u_z and u_x are also called normal and tangential displacements, respectively.

For a given n, the terms H^n_{ij} allow estimation of the favorable and unfavorable frequencies for the generation of the nth mode.

Grounds of the above-mentioned assumption on attenuation come from the following considerations. First, every term involved in the expressions of H^n_{xx}, H^n_{xz}, H^n_{zx}, and H^n_{zz} of Eqs. (12a) and (12b) is dependent on the thickness dimension z only. Second, terms I^n_{zz} and I^n_{xz} consist in integrations along the transducer width $2L$. In most practical cases, both the plate thickness and the transducer width can be considered very small compared to the propagation distance x_0. Thus if attenuation is sufficiently weak, its influence on the computed values of I^n_{zz}, I^n_{xz}, H^n_{xx}, H^n_{xz}, H^n_{zx}, and H^n_{zz} can be neglected. In other words, terms associated to the local Lamb wave generation phenomenon will be computed merely using the traditional normal mode expansion technique [Eqs. (9)–(16)], neglecting attenuation effects.

On the other hand, attenuation over the propagation, from $x=0$ to $x=x_0$, has to be taken into account since its effect is cumulative all along the non-negligible distance x_0. Thus attenuation will be introduced in the modeling only by computing the propagation function $e^{-jk_nx_0}$ [Eqs. (12a) and (12b)] with a complex wavenumber k_n.

In this manner, the normal mode expansion method as described by Eqs. (12a) and (12b) can be applied to viscoelastic materials. We will see in the numerical validation (Sec. III D) the limit of this approximation.

D. Application to transient excitation

In the particular problem addressed in this paper, the transducer will be considered to be relatively broadband compared to the applied electrical excitation waveform. This may appear to be a nonstandard assumption when referring to traditional nondestructive testing methods, to which the very opposite is often a rule. However, in integrated health monitoring applications using Lamb waves, the situation is different. First, since relative mode selectivity is required, it is often more judicious to use narrow-band, though time-limited, driving signals rather than short pulses. Typically, time-windowed sinusoid waveforms are used. Second, resonance of a thin piezoelectric element firmly coupled to a host material is significantly damped and, hence, its frequency behavior is accordingly smoothed. Hence, the frequency dependence of the surface traction can be assumed to be imposed essentially by the spectrum of the excitation signal.[14,15] Validity of this simplifying assumption will be verified in Sec. IV A.

Consequently, after a single finite element computation at the central frequency, the obtained surface traction profile created by the transducer is weighted, relative to the excitation spectrum, over the whole bandwidth.

Since they are independent of the excitation, the other terms (k_n and H^n_{ij}) required for the application of Eqs. (12a) and (12b) can be computed at each frequency once and for all for a given material.

Then the frequency-dependent displacement fields along

the i direction can be obtained and, by applying an inverse Fourier transform, the predicted time signal at the plate surface and at a chosen distance x_0 from the source transducer is obtained as follows:

$$u_{i,}(x_0,z,t)=\sqrt{2\pi}\sum_n \int_{f_1}^{f_2} A_n(x_0,f)u_i^n(z,f)e^{2j\pi ft}\,df, \tag{17}$$

where f_1 and f_2 are the lower and upper limits of the bandwidth, respectively.

A major particularity of the technique is that the contribution of each mode in the global response can be easily isolated.[14] In addition, since the transient behavior is extrapolated from a unique finite element computation at a single frequency, computation time is dramatically reduced compared to a purely time-marching finite element solution. Indeed, considering that the determination of the modal acoustic fields and phase velocities (calculated once and for all) do not contribute to the effective computation time, the calculation is approximately 75% to 95% faster when using the hybrid method.

Application to a transient excitation of the transducer with a nonviscoelastic host material (aluminum plate) has been experimentally validated in a previous work.[15] In the next section, the model will be applied to the case of a viscoelastic plate.

III. NUMERICAL VALIDATION

A. Examples description

The cases studied to validate the assumptions consist in two glass fiber reinforced plastic (GFRP) composite plates with 1- and 6-mm thickness, respectively. The x axis is chosen to be the fiber direction. The complex stiffness tensor[23] used for both the analytical method and the FEM analysis is given in the Appendix.

For the numerical validation, a mere homogeneous pressure of 10 000 Pa has been considered along a 4-mm-wide area on the plate surface. This allowed us to apply the normal mode expansion technique independently of the finite element modeling. Results of a transient, purely finite element, computation using the ATILA[24,25] code have then been compared to the analytical results.

The applied excitation signal is a five-cycle sinusoidal pressure with central frequency 300 kHz, windowed by a Hanning window. In the case of the 1-mm-thick plate (fd $=0.3$ MHz mm), mainly two nondispersive modes (A_0 and S_0) are to be expected, whereas in the 6-mm-thickness case (fd$=1.2$ MHz mm), a more complex signal consisting of several higher order modes could be obtained.

B. Computation and results

The dispersion [Fig. 2(a)] and attenuation curves [Figs. 2(b) and (c) for the 1- and 6-mm plates, respectively] have been computed. These curves allow us to estimate the significance of mode attenuation beforehand. For example, it can be seen that the A_0 mode is, globally speaking, more attenuated than S_0 in the 1-mm plate.

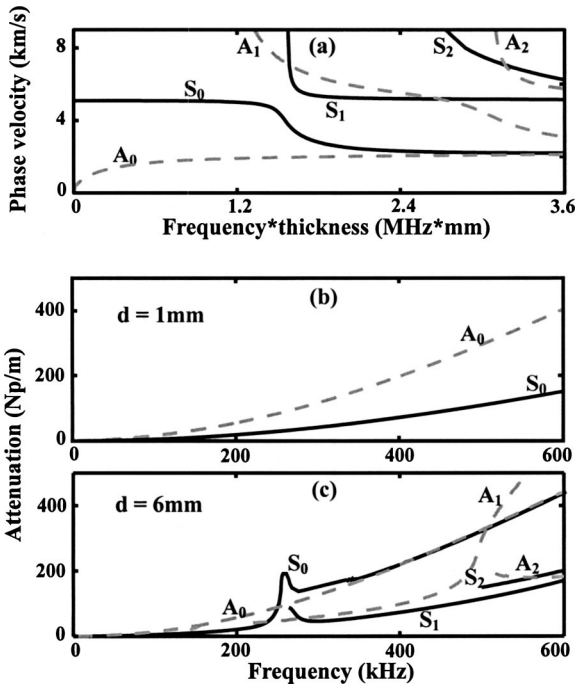

FIG. 2. Dispersion curves (a) and attenuation curves for 1-mm-thick (b) and 6-mm-thick (c) plates.

First, the analytical normal mode expansion method presented in detail in Sec. II has been applied to the 1-mm plate. The normal and tangential surface displacements have been computed, using Eq. (17), for the 1-mm plate excited at 300 kHz. The corresponding results are displayed in Figs. 3(a) and 4(a), respectively. Additionally, a time-marching finite element computation for the same simulated case has been performed. Results are shown in Figs. 3(b) and 4(b). The successful quantitative comparison observed (Figs. 3 and 4) allows us to validate the application of the analytical method in the case of a viscoelastic material, at least provided the attenuation is sufficiently weak. This particular point will be discussed later.

It can be remarked that the normal surface displacement (Fig. 3) is globally more important than the tangential one (Fig. 4). A low-amplitude wavepacket, arriving around 0.02

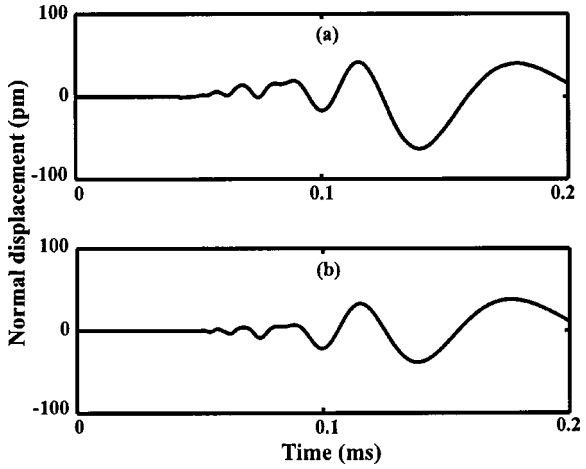

FIG. 3. Predicted normal surface displacements for the 1-mm-thick plate for a central frequency 300 kHz: (a) analytical method and (b) FEM.

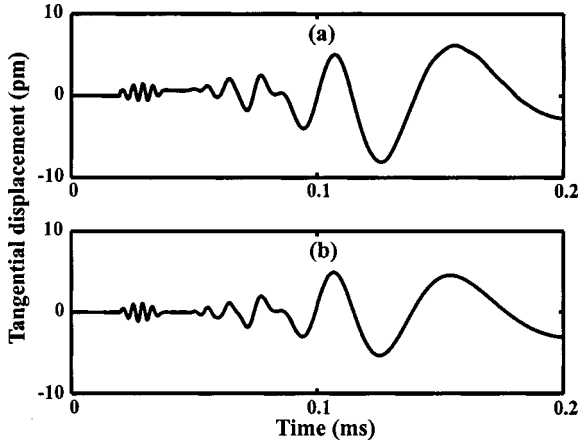

FIG. 4. Predicted tangential surface displacements for the 1-mm-thick plate for a central frequency 300 kHz: (a) analytical method and (b) FEM.

ms and with a frequency close to the central excitation frequency, is visible in the tangential displacement curve. This wavepacket can be identified as the S_0 mode. The next, time-scattered, wavepacket is the A_0 mode contribution. Its apparent frequency range corresponds to the lower part of the excitation bandwidth.

The case of the 6-mm plate allows validation of the assumption in more challenging conditions (more Lamb modes and higher mode attenuations). Similarly, surface displacements predicted using the analytical method and the FEM are presented in Figs. 5(a) and (b), respectively. Only the tangential displacement is shown, since similar conclusions can be drawn from the normal component. Here again, comparison between analytical and finite element predictions appears very successful. As in the previous case, the low-frequency wavepacket arriving after 0.05 ms corresponds to the A_0 contribution. The first wavepacket, around the central frequency, is a superposition of S_0, S_1, and A_1 contributions. Additional oscillations visible on the analytical predictions [Fig. 5(a)] have been identified as the S_1 mode at a frequency of 270 kHz. Clearly this S_1 contribution is somehow overestimated, since it does not appear in the FEM result [Fig. 5(b)]. Interpretation of this slight discrepancy will be discussed in the next section.

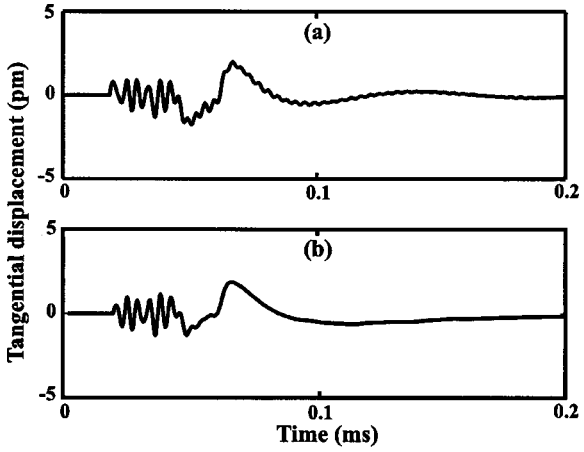

FIG. 5. Predicted tangential surface displacements for the 6-mm-thick plate for a central frequency 300 kHz: (a) analytical method and (b) FEM.

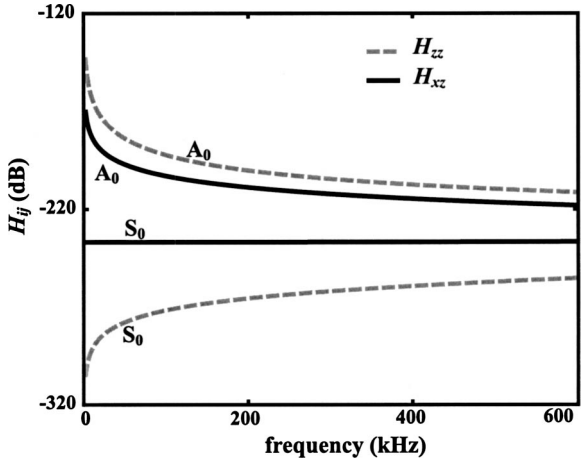

FIG. 6. Comparison of terms H^n_{xz} (solid line) and H^n_{zz} (dashed line) for the case of the 1-mm-thick plate.

C. Interpretation and discussion

Focus on functions H^n_{ij} of Eq. (12) gives an insight into the interpretation and justification of the computed waveforms (Figs. 3–5). Additionally, as will be seen, it will contribute to precising the validity conditions of the attenuation assumption presented in Sec. II C.

Terms H^n_{xz} and H^n_{zz} have been computed and represented as a function of frequency (Fig. 6) for the case of the 1-mm-thick plate. According to the computed values of H^n_{xz} and H^n_{zz}, the A_0 mode is more easily excitable than the S_0 mode in the considered frequency range. Thus, contribution of A_0 in the global waveform is expected to be dominant. However, since attenuation of A_0 is smaller at the lower limit of the excitation bandwidth [Fig. 2(b)] than at the central frequency, it is not surprising that low-frequency A_0 components are most significant in the computed waveforms (Figs. 3 and 4). Moreover, at low frequency, the normal displacement associated to the A_0 mode is much higher than the tangential displacement. Since the difference between A_0 and S_0 modes is more significant for H^n_{zz} than for H^n_{xz}, the A_0 contribution in Fig. 3 is consequently so dominant that the S_0 wavepacket is completely masked.

D. Comments on the approximation

Actually, in the context of Lamb wave propagation, the effective influence of attenuation is strongly dependent on the value of the frequency-plate thickness product. For a given attenuation value, it is well known indeed that, in the low frequency region, Lamb wave dispersion behavior is very similar to the attenuation-free case.[26] As the frequency is increased, some sort of interaction between modes occurs, which results in connections between ''plateauing'' regions of the phase velocity dispersion curves.[27,28] These mode coupling effects lead to significant differences between the phase velocities and mode shapes (through-thickness displacement and stress) computed with and without attenuation. In that case, attenuation is likely to have a significant influence on the local mode generation process and the approximation of Sec. II C is no longer valid.

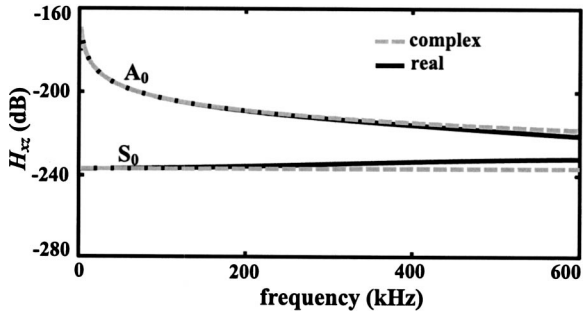

FIG. 7. Comparison of terms H_{xz}^n computed in the attenuation-free case (solid line) and the attenuated case (dashed line) for the case of the 1-mm-thick plate.

These considerations suggest a way of checking the validity of the approximation before performing the normal mode computation. Technically, the phase velocity curves as well as every component of the through-thickness displacement and stress fields computed both in the attenuated and attenuation-free cases should be compared. For frequency regions where all the curves match, the assumption could be reasonably supposed valid. Reciprocally, for frequency regions where differences are observed, the suggested approximation would be theoretically unfounded. However, performing comparisons for all of these terms would be a rather tedious process and it thus appears more judicious to consider grouped terms such as H_{xz}^n.

Values of H_{xz}^n for the attenuated and the attenuation-free cases have then been represented in Fig. 7 for the 1-mm plate. In the considered frequency range, only negligible differences can be observed. This implies that the approximation on attenuation discussed above should be perfectly applicable in this case. This is consistent indeed with the fact that curves in Figs. 3(a) and (b) as well as Figs. 4(a) and (b), respectively, look very much alike.

On the other hand, in the 6-mm case, comparison between H_{xz}^n computed with and without attenuation (Figs. 8(a) and b) shows that application of the same approximation should be looked at more carefully. For instance, significant differences between solid and dashed curves are clear for the S_1 mode around 270 kHz, and the A_0, A_1, and S_1 modes above 400 kHz. Accordingly, the approximated treatment of

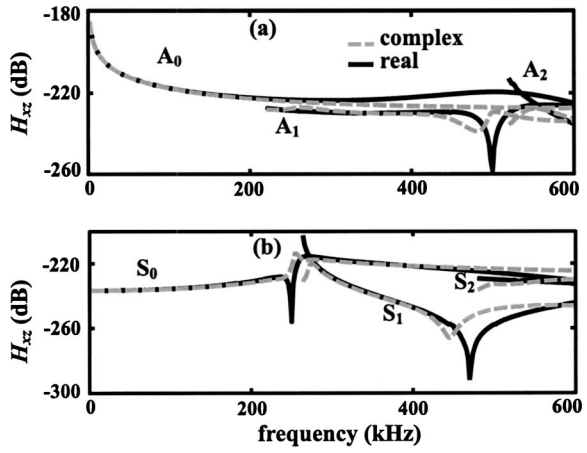

FIG. 8. Same as Fig. 7 but for the 6-mm-thick plate.

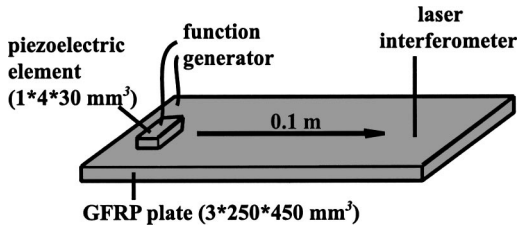

FIG. 9. Experimental setup.

the attenuation for these modes at these frequencies should lead to erroneous results. Computation results shown in Fig. 5 constitute an enlightening illustration of this point. The global waveform shape is correctly predicted by the approximated technique [Fig. 5(a)]. This can be justified by the negligible difference between solid and dashed curves of Fig. 8 at the central excitation frequency (300 kHz). However, the fact that the contribution of S_1 at 270 kHz is slightly overestimated can now be understood by the above-mentioned differences in H_{xz}^n values. Besides, it can be noted that, for lower frequencies (0–200 kHz), the situation is similar to the previous case and then the approximation is applicable undoubtedly.

Hence, differences between the values of H_{xz}^n computed with and without attenuation have been proven to be a suitable quantitative indicator of the limit of the approximation. Moreover, the comparison between Figs. 8 and 2(c) shows that, for a given frequency, the divergence between both computations of H_{xz}^n is related to a strong attenuation of the considered mode. This means that whenever the approximation on attenuation is not applicable for a given Lamb mode, then long-range propagation is practically unachievable. In a context of structural, full scale, health monitoring, the considered mode will thus be meaningless and its contribution to the received signal is likely to be negligible. Consequently, in a practical point of view, the simplifying assumption seems to have relatively little restriction.

IV. TEST CASE AND EXPERIMENTAL VALIDATION

A. Experimental conditions

Figure 9 shows the setup used for the experimental validation. The piezoelectric transducer used as the emitter had the following dimensions: 1 mm thickness, 4 mm width, and 30 mm length. This transducer has been bonded to the surface of a 3-mm-thick GFRP plate, at a distance of 0.1 m from the plate edge. The measurement point was chosen to be 0.1 m away from it. This allowed us to separate direct propagated waves from parasitic reflected wavepackets.

More precisely, the plate is made of a composite material consisting of short, randomly oriented glass fibers embedded in a polyester matrix. This material is commonly used in transportation industry. The elastic properties have been measured elsewhere[29] and only the attenuation constants are not precisely known. Experimental estimation of these constants will be presented in the next section.

A heterodyne optical interferometer has been used to experimentally validate the modeling method. Response of such an interferometer is a voltage signal proportional to the

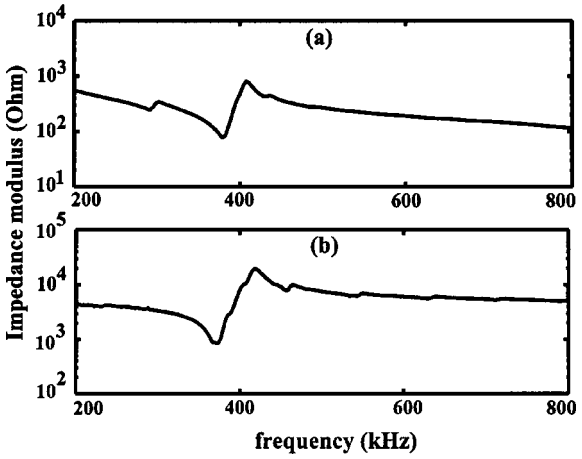

FIG. 10. Modulus of the measured electrical impedance of the piezoelectric transducers (a) integrated transducer. (b) Free transducer in vacuum.

normal surface displacement. Since the precise value of the proportionality factor is difficult to know, measured voltages will be normalized with respect to their maximum values.

The electrical impedance of the bonded piezoelectric transducer has been measured using a HP4194A network analyzer [Fig. 10a]. It has been compared to the impedance of a free transducer vibrating in vacuum [Fig. 10b]. The width resonance has been identified around the frequency 400 kHz. As can be seen, integration of the transducer brings a reduction of the impedance amplitude at the resonance but no dramatic modification of the resonance frequency. An additional resonance exists around 300 kHz but it is weaker than the main width resonance.

In order to test the applicability of the assumption presented in Sec. II D (transient application), the surface stress profile created by the presence of the transducer has been computed using the FEM and is presented in Fig. 11. Results obtained for different frequencies outside the resonance domains show indeed that the applied stress is only slightly dependent on frequency.

B. Estimation of attenuation

Attenuation associated to the material used in this study appeared to be non-negligible. Therefore attenuation constants will be taken into account in the modeling by following the approximation described in Sec. II C. Since the full complex part of the elastic tensor was not available for this material, the necessary parameters have first been experimentally estimated.

The experimental setup (Fig. 9) has been used with a liquid-coupled mobile wedge-transducer as the receiver instead of the interferometer. This transducer can easily be moved along the propagation direction and thus allows measurements at different distances. Moreover, Lamb modes can be selectively received by adjusting the incidence angle between the plate surface and the transducer axis.

Figure 12 shows results of the A_0 attenuation measurement. The excitation signal used in this case was a five-cycle sinusoid with a central frequency 50 kHz. The amplitude of the A_0 wavepacket has been measured at different locations, separated by a spatial step of 5 mm. The experimental attenuation value thus corresponds to the slope of the obtained curve and has been estimated using a least-square technique.

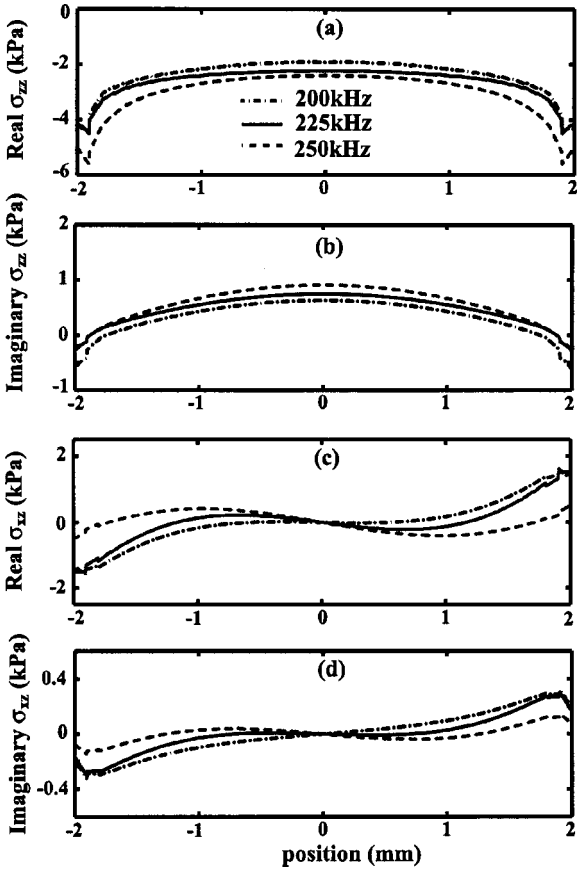

FIG. 11. Surface stress applied to the plate by the bonded transducer. (a) Real part of σ_{zz}. (b) Imaginary part of σ_{zz}. (c) Real part of σ_{xz}. (d) Imaginary part of σ_{xz}.

Results obtained from different measurements have allowed estimation of the attenuation constants (complex part of the elastic tensor) by seeking the weakest difference between the measured and computed attenuation, with the use of the Nelder-Mead method pre-programmed in Matlab. Attenuation values thus obtained are presented in the Appendix.

For the excitation frequencies considered in the follow-

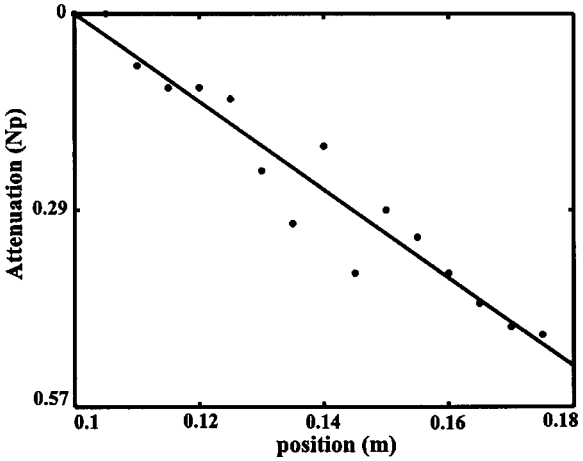

FIG. 12. Measurement results of A_0 attenuation (stars) and corresponding sample regression line (solid line).

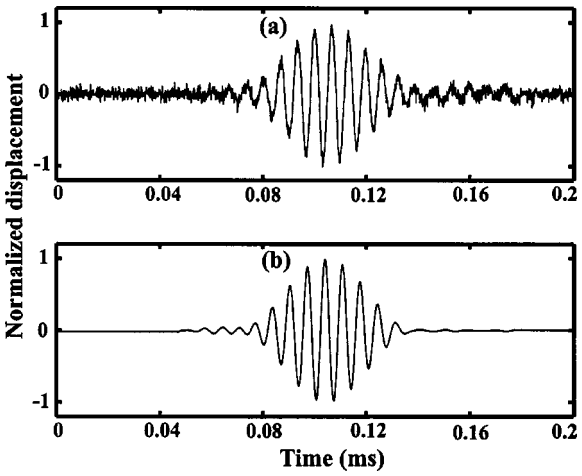

FIG. 13. Normal surface displacements for a central frequency 150 kHz. (a) Measured displacement. (b) Predicted displacement.

ing section (150 and 300 kHz, respectively), these attenuation values have appeared to be compatible with the conditions established in Sec. III D. This allowed the use of the approximation described in Sec. II C.

C. Experimental results and comparisons

First, the emitting transducer has been excited by a ten-cycle Hanning-windowed sinusoidal driving signal with central frequency 150 kHz. Figure 13(a) shows the normal displacement measured using the interferometer at the distance 0.1 m away from the source. Comparison to the theoretical normal displacement computed using the hybrid finite element–normal mode method [Fig. 13(b)] appears to be very successful. In particular, the neat predicted prevalence of the A_0 wavepacket is confirmed by the experimental measurement. In this case, the S_0 mode contribution is buried in noise.

A second example is presented in Fig. 14. The emitter driving signal is a five-cycle cosine-windowed sinusoid with 300 kHz central frequency. This case is of particular interest, since the transducer exhibits a slight resonance around 300 kHz and the bandwidth of the excitation signal is broader than in the previous case. Thus conditions required for the transient application of the hybrid method (Sec. II D) are not strictly enforced.

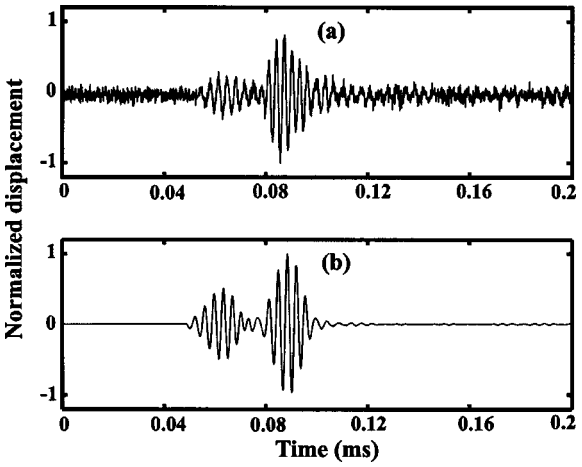

FIG. 14. Normal surface displacements for a central frequency 300 kHz. (a) Measured displacement. (b) Predicted displacement.

However, even in this case, the predicted signal [Fig. 14(b)] appears to be very close to the experimental one [Fig. 14(a)] in terms of both waveform shapes and relative mode amplitudes. These results tend to demonstrate to which extent the transient hybrid method is robust to the proposed simplifying assumptions. Indeed the method remains accurate, provided the transducer resonances inside the excitation bandwidth remain moderate.

V. CONCLUSION

In this paper, extension of the hybrid finite element–normal mode expansion technique to the case of transient excitation and lossy materials has been presented. The necessary simplifying assumptions have been detailed and validity criteria have been presented and discussed. These assumptions have thus appeared to be pertinent and only very slightly restricting for health monitoring applications. As a result, Lamb waves generated by a thin piezoelectric transducer bonded on the surface of a viscoelastic composite plate and excited with a transient driving signal can be predicted in a very efficient way. Compared to a time-marching, purely finite element modeling, computation time is hugely decreased and, since it is a semi-analytical model, parametric studies and understanding of wave generation mechanisms should be made easier.

Future work should concentrate on further investigations and validations of the method. Then it could be used to design the transducer characteristics so that damage detection potential is made optimal. Additionally, taking into account the behavior and response of an integrated Lamb wave receiver will be an important step towards the complete modeling of an integrated health monitoring system based on Lamb waves.

APPENDIX: MATERIAL PROPERTIES

The material used in Sec. III consists of glass fiber reinforced epoxy where the x-axis is chosen to be the fiber direction. The stiffness values are (in GPa) $\overline{C_{11}}=52+2.5j$, $\overline{C_{13}}=5.8+0.2j$, $\overline{C_{33}}=20+0.7j$, and $\overline{C_{55}}=10+0.3j$. The complex part is given for the frequency 400 kHz. Values for other frequency can be obtained using Eq. (3).

The material used in Sec. IV consists of short randomly oriented glass fibers integrated into a polyester matrix. Estimated values of stiffness matrix are (complex part at 400 kHz) $\overline{C_{11}}=21.3+3.2j$, $\overline{C_{13}}=6.5+0.5j$, $\overline{C_{33}}=16.2+0.4j$, and $\overline{C_{55}}=4.3+0.3j$.

[1] S. Grondel, C. Delebarre, J. Assaad, J. P. Dupuis, and L. Reithler, "Fatigue crack monitoring of riveted aluminum strap joints by Lamb wave analysis and acoustic emission measurement technique," NDT & E Int. **35**(3), 137–146 (2002).

[2] S. Grondel, "Contribution à l'optimisation du contrôle santé intégré par ondes de Lamb. Application à la surveillance de structures aéronautiques"; "Contribution to the optimization of integrated health monitoring based on Lamb waves. Application to aeronautic structures." PhD. thesis, Report 0034, Université de Valenciennes et du Hainaut Cambrésis, France, December 2000.

[3] N. Bourasseau, E. Moulin, C. Delebarre, and P. Bonniau, ''Radome health monitoring with Lamb waves: experimental approach,'' NDT & E Int. **33**(6), 393–400 (2000).
[4] B. A. Auld, *Acoustical fields and waves in solids*, 2nd ed. (Krieger, Malabar, FL, 1990), Vol. 2.
[5] J. J. Ditri and J. L. Rose, ''Excitation of guided waves in generally anisotropic layers using finite sources,'' Trans. ASME **61**, 330–338 (1994).
[6] I. Núnez, R. K. Ing, C. Negreira, and M. Fink, ''Transfer and Green functions based on modal analysis for Lamb waves generation,'' J. Acoust. Soc. Am. **107**, 2370–2378 (2000).
[7] X. Jia, ''Modal analysis of Lamb wave generation in elastic plates by liquid wedge transducers,'' J. Acoust. Soc. Am. **101**, 834–842 (1997).
[8] F. L. Degertekin and J. L. Rose, ''Lamb wave excitation by Hertzian contacts with application in NDE,'' IEEE Trans. Ultrason. Ferroelectr. Freq. Control **44**, 769–778 (1997).
[9] J. C. Cheng and S. Y. Zhang, ''Quantitative theory for laser-generated Lamb waves in orthotropic thin plates,'' Appl. Phys. Lett. **74**(14), 2087–2089 (1999).
[10] J. Jin, S. T. Quek, and Q. Wang, ''Analytical solution of excitation of Lamb waves in plates by interdigital transducers,'' Proc. R. Soc. London, Ser. A **459**, 1117–1134 (2003).
[11] E. Moulin, J. Assaad, C. Delebarre, and D. Osmont, ''Modeling of Lamb waves generated by integrated transducers in composites plates using a coupled finite element-normal modes expansion method,'' J. Acoust. Soc. Am. **107**, 87–94 (2000).
[12] E. Moulin, J. Assaad, C. Delebarre, S. Grondel, and D. Balageas, ''Modeling of integrated Lamb waves generation systems using a coupled finite element-normal modes expansion method,'' Ultrasonics **38**, 522–536 (2000).
[13] S. Grondel, C. Paget, C. Delebarre, J. Assaad, and K. Levin, ''Design of optimal configuration for generating A_0 Lamb mode in a composite plate using piezoceramic transducers,'' J. Acoust. Soc. Am. **112**, 84–90 (2002).
[14] L. Duquenne, E. Moulin, J. Assaad, and C. Delebarre, ''Transient modeling of Lamb Lamb waves generation by surface bonded piezoelectric transducers,'' in Proceedings of the Asset Workshop, Presqu'île de Giens, France (2002).
[15] L. Duquenne, E. Moulin, J. Assaad, and C. Delebarre, ''Transient modeling of waves emitted by intergrated transducers using a hybrid finite element-normal mode expansion technique,'' 144th meeting of the ASA, Fiesta Americana Grand Coral Beach, Mexico (2002).
[16] I. A. Viktorov, *Rayleigh and Lamb Waves* (Plenum, New York, 1967).
[17] A. H. Nayfeh, ''The general problem of elastic wave propagation in multilayered anisotropic media,'' J. Acoust. Soc. Am. **89**, 1521–1531 (1991).
[18] M. J. S. Lowe, ''Matrix techniques for modeling ultrasonic waves in multilayered media,'' IEEE Trans. Ultrason. Ferroelectr. Freq. Control **42**, 525–541 (1995).
[19] B. Hosten, ''Reflection and transmission of acoustic plane waves on an immersed orthotropic and viscoelastic solid layer,'' J. Acoust. Soc. Am. **89**, 2745–2752 (1991).
[20] M. Deschamps and B. Hosten, ''The effect of viscoelasticity on the reflection and transmission of ultrasonic waves by an orthotropic plate,'' J. Acoust. Soc. Am. **91**, 2007–2015 (1992).
[21] A. Bonnin, R. Huchon, and M. Deschamps, ''Ultrasonic waves propagation in absorbing thin plates: Application to paper characterization,'' Ultrasonics **37**(8), 555–563 (2000).
[22] J. L. Rose, *Ultrasonic Waves in Solid Media* (Cambridge U.P., Cambridge, 1999).
[23] M. Castaings and B. Hosten, ''Propagation d'ondes de Lamb dans les plaques composites stratifiées constituées de matériaux anisotropes et viscoélastiques''; ''Lamb wave propagation in anisotropic and viscoelastic laminated composite plates,'' in Proceedings of the French Congress of Acoustics (CFA), Lausanne, Switzerland (2000).
[24] J. Assaad, M. Ravez, and C. Bruneel, ''Application of the finite-element method for modeling backed transducers,'' J. Acoust. Soc. Am. **100**, 3098–3103 (1996).
[25] E. Moulin, J. Assaad, C. Delebarre, H. Kaczmarek, and D. Balageas, ''Piezoelectric transducer embedded in composite plate: Application to Lamb wave generation,'' J. Appl. Phys. **82**, 2049–2055 (1997).
[26] C. W. Chan and P. Cawley, ''Lamb waves in highly attenuative plastic plates,'' J. Acoust. Soc. Am. **104**, 874–881 (1998).
[27] A. Bernard, M. J. S. Lowe, and M. Deschamps, ''Guided waves energy velocity in absorbing and nonabsorbing plates,'' J. Acoust. Soc. Am. **110**, 186–196 (2001).
[28] M. Castaings and B. Hosten, ''Guided waves propagating in sandwich structures made of anisotropic, viscoelastic, composite materials,'' J. Acoust. Soc. Am. **113**, 2622–2634 (2003).
[29] T. Monnier, ''Ondes de Lamb dans les milieux stratifiés. Application à la surveillance in situ et en temps réel de l'endommagement de structures composites''; ''Lamb waves in laminated media. Applications to in-situ and on-line monitoring of composite structures,'' PhD. thesis, Université de Lyon, France, 2001.

Time domain holography: Forward projection of simulated and measured sound pressure fields

Ombeline de La Rochefoucauld, Manuel Melon, and Alexandre Garcia[a)]
Laboratoire d'acoustique, Conservatoire National des Arts et Métiers, 292 rue Saint Martin, 75141 Paris cedex 3, France

(Received 12 July 2002; revised 17 April 2004; accepted 26 April 2004)

In this article, the fundamental principles of forward projecting time domain acoustic pressure fields are summarized. Four different numerical approaches are presented and compared both with simulated and measured signals. The approaches differ in their definition domain: Frequency/time and space/wave vector domains. The simulated source is a planar baffled piston excited with a Gaussian pulsed velocity. The pressure radiated by two different real sources has been measured: The first source is made up of two baffled loudspeakers (a Gaussian white noise can be radiated by a third loudspeaker). The second one is a baffled aluminum plate excited by a short impact at its center. The influence of parameters such as the sound source radius, the array size, the number of microphones and the propagation distance is studied. Finally, results concerning the optimization of the sampling of the sound field are presented. © *2004 Acoustical Society of America.*
[DOI: 10.1121/1.1763600]

PACS numbers: 43.20.Px, 43.60.Pt, 43.60.Sx [EGW] Pages: 142–153

I. INTRODUCTION

Nearfield Acoustical Holography (NAH)[1–3] has proven to be useful for the study of the radiation of harmonic sound fields. This technique enables the reconstruction of sound fields when the measurement is done close to the source in order to take into account evanescent waves.[4]

However, when dealing with non-stationary sources like engines throttling up, the sound field must be measured simultaneously with a microphone array. Therefore, a large number of microphones and an appropriate data acquisition system are needed to carry out the measurements of the time domain signals.

A method of forward projecting time dependent pressure fields has been developed by Forbes *et al.*[5] and has been applied to the field radiated by an underwater ultrasonic planar transducer:[6] The transient signals obtained from a fiber-optic pressure sensor are projected and their comparison with direct measurements is fairly good. Hansen[7,8] presents the formulation and the computation schemes, in the time domain, of planar near field measurement for acoustic and electromagnetic fields in order to calculate the far-field pattern.

In this article, four time domain methods to forward project time dependent pressure fields are described and compared. The theoretical pressure field radiated by a baffled planar piston is used to study the influence of various parameters such as the array size, the number of microphones and the propagation distance on these methods. The pressure field is forward propagated and then compared to the direct calculation. Results obtained with the various algorithms are satisfactory in their own validity domains, which depend on the propagation distance, the signal shape and the microphone number. The last section contains experimental results obtained with two baffled loudspeakers and a baffled aluminum plate. Using the more efficient algorithm, measurements are forward propagated and compared to the direct measurement.

II. TRANSIENT RADIATION FROM A BAFFLED PLANAR PISTON

As the transient radiation of a circular piston in an infinite rigid planar baffle is well described in the literature[9–12] only a brief summary will be presented here. The geometry utilized here is described in Fig. 1. The planar piston of radius a is centered at the origin O of the Cartesian coordinates and the planar baffle lays on the plane $z=0$. The velocity potential $\Phi(\mathbf{r},t)$ in the half-space $z\geqslant 0$ is given by the following equation:

$$\Phi(\mathbf{r},t)=v(t)*h(\mathbf{r},t), \tag{1}$$

where the asterisk $(*)$ denotes convolution. The function $h(\mathbf{r},t)$ is the spatial impulse response of the planar piston and $v(t)$ is the velocity of the piston. The parameters $R_{\min}$ and $R_{\max}$ are, respectively, the minimum and the maximum distance to the edge of the piston from the point of coordinates (x,y,z) in the half space $z\geqslant 0$. They are given by the following relations:

$$R_{\min}=\sqrt{z^2+(r_1-a)^2}, \quad R_{\max}=\sqrt{z^2+(r_1+a)^2}, \tag{2}$$

where $r_1=\sqrt{x^2+y^2}$.

The impulse response of the piston in the different regions of the half space is summarized in Table I, where the sound velocity in air is denoted by c. The pressure $p(\mathbf{r},t)$ is given by:

$$p(\mathbf{r},t)=\rho_0\frac{\partial\Phi(\mathbf{r},t)}{\partial t}=\rho_0 h(\mathbf{r},t)*\frac{\partial v(t)}{\partial t}, \tag{3}$$

where ρ_0 is the density of air. The transient pressure radiated by a piston, resulting from a Gaussian shape velocity, has been calculated using Eq. (3). The Gaussian pulsed velocity

a)Electronic mail: garcia@cnam.fr

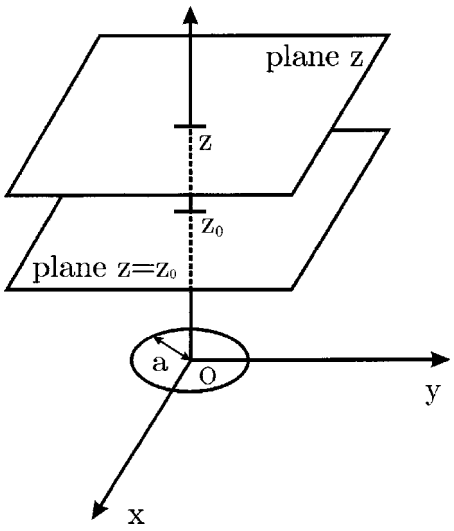

FIG. 1. Geometry of interest.

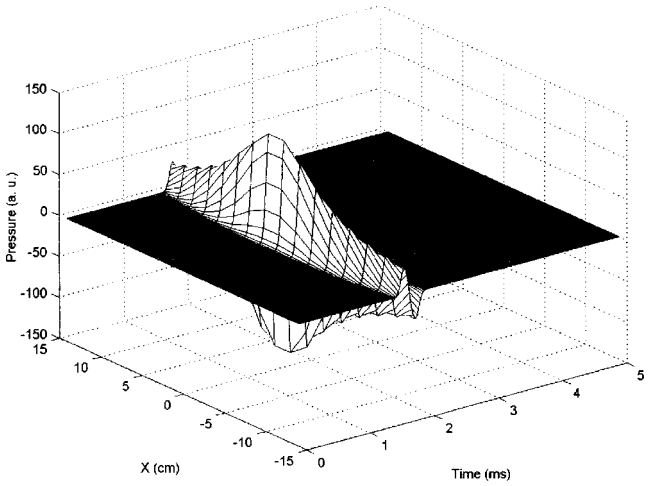

FIG. 2. Simulated pressure field radiated by a baffled planar piston in the plane $z=8$ cm as a function of radial position x and time t.

has the following form: Full width at half maximum of 120 μs ($\Gamma=120$ μs), maximum amplitude normalized to one. The piston diameter is 8 cm. The pressure field which is shown in Fig. 2 as function of radial position x and time t on the plane $z=8$ cm, exhibits several interesting characteristics. As the velocity distribution is normalized, the pressure amplitude is expressed in arbitrary units. For $r_1>a$, the pressure field is emitted by the piston edge, whereas, for $r_1<a$, the sound field results from the contribution of the plane wave radiated by the piston and the edge wave. This particular shape of sound field (superposition of a plane and an edge wave) is an interesting way to test the algorithms of forward projecting time dependent pressure fields. These algorithms are based on methods described in the next section.

III. FORWARD PROJECTION OF PLANAR SOUND FIELDS

The pressure field $p(\mathbf{r}_0,t)$ on the hologram plane $z=z_0$ is known. The forward projection problem is defined as being the reconstruction of the pressure field $p(\mathbf{r},t)$ on the plane z with $z>z_0$ (Fig. 1). In this section, different methods,[7,8] i.e., with or without Fourier Transforms, of forward projecting planar sound fields are summarized. Their numerical implementations will be compared in an other section.

The first method is based on the integral formulation written in the time and space domains. The pressure field $p(\mathbf{r},t)$ is given by the three dimensional integral

TABLE I. Values of the impulse response of the planar circular piston in the different regions of the half-space.

	$r_1>a$	$r_1\leqslant a$
$ct<z$	0	0
$z<ct<R_{\min}$	0	c
$R_{\min}<ct<R_{\max}$	$\frac{c}{\pi}\cos^{-1}\left[\frac{(ct)^2-z^2+r_1^2-a^2}{2r_1\sqrt{(ct)^2-z^2}}\right]$	$\frac{c}{\pi}\cos^{-1}\left[\frac{(ct)^2-z^2+r_1^2-a^2}{2r_1\sqrt{(ct)^2-z^2}}\right]$
$ct>R_{\max}$	0	0

$$p(\mathbf{r},t)=\int_{-\infty}^{\infty}dt_0\int\int_{-\infty}^{\infty}dS_0\left(G(\mathbf{r},t;\mathbf{r}_0,t_0)\frac{\partial p(\mathbf{r}_0,t_0)}{\partial n}-p(\mathbf{r}_0,t_0)\frac{\partial G(\mathbf{r},t;\mathbf{r}_0,t_0)}{\partial n}\right), \tag{4}$$

with the following initial conditions

$$\begin{cases}\left.\dfrac{\partial p(\mathbf{r}_0,t_0)}{\partial t_0}\right|_{t_0=0}=0\\ p(\mathbf{r}_0,t_0)|_{t_0=0}=0\end{cases}\quad\text{and Sommerfeld condition to infinity.}$$

The Green's function associated with the problem and satisfying the Dirichlet condition [$G(\mathbf{r},t;\mathbf{r}_0,t_0)=0$ for $z_0=0$], has the form

$$G(\mathbf{r},t;\mathbf{r}_0,t_0)=\frac{\delta\left(\frac{R}{c}-\tau\right)}{4\pi R}-\frac{\delta\left(\frac{R'}{c}-\tau\right)}{4\pi R'}, \tag{5}$$

where

$$R=|\mathbf{r}-\mathbf{r}_0|=\sqrt{(x-x_0)^2+(y-y_0)^2+(z-z_0)^2},$$

$$R'=|\mathbf{r}-\mathbf{r}_0'|=\sqrt{(x-x_0)^2+(y-y_0)^2+(z+z_0)^2},$$

and

$$\tau=t-t_0.$$

The Dirichlet condition permits to rewrite Eq. (4) using Eq. (5) as follows:

$$p(\mathbf{r},t)=\int_{-\infty}^{\infty}dt_0\int\int_{-\infty}^{\infty}p(\mathbf{r}_0,t_0)\frac{\partial G(\mathbf{r},t;\mathbf{r}_0,t_0)}{\partial z_0}dS_0. \tag{6}$$

For $z_0=0$, $z=d$ and $t_0=0$, the pressure field $p(\mathbf{r},t)$ becomes

$$p(\mathbf{r},t)=\frac{d}{2\pi}\int\int_{-\infty}^{\infty}\left(\frac{1}{R^3}p\left(\mathbf{r}_0,t-\frac{R}{c}\right)+\frac{1}{cR^2}\frac{\partial p\left(\mathbf{r}_0,t-\frac{R}{c}\right)}{\partial t}\right)dS_0. \quad (7)$$

The pressure $p(\mathbf{r},t)$ is computed from the pressure field on the z_0 plane and its time derivative. It can be calculated separately for each position on the z plane. This method is called TSD (time–space domains).

The time Fourier Transform of the pressure field $p(\mathbf{r}_0,t)$ is defined by

$$P(\mathbf{r}_0,\omega)=\int_{-\infty}^{\infty}p(\mathbf{r}_0,t)e^{j\omega t}dt, \quad (8)$$

while inverse time Fourier Transform is given by

$$p(\mathbf{r}_0,t)=\frac{1}{2\pi}\int_{-\infty}^{\infty}P(\mathbf{r}_0,\omega)e^{-j\omega t}d\omega. \quad (9)$$

Then, by taking the time Fourier Transform of Eq. (6), the second formulation is obtained, defined in the frequency/space domains (FSD1):

$$P(\mathbf{r},\omega)=\int\int_{-\infty}^{\infty}P(\mathbf{r}_0,\omega)\frac{d}{2\pi R^3}(1-jkR)e^{jkR}dS_0, \quad (10)$$

or, equivalently,

$$P(\mathbf{r},\omega)=P(\mathbf{r}_0,\omega)**G_2(x,y,d,\omega), \quad (11)$$

where the double asterisk $(**)$ denotes the two-dimensional convolution in the plane (xOy). The function $G_2(x,y,d,\omega)$ is given by

$$G_2(x,y,d,\omega)=\frac{d}{2\pi(x^2+y^2+d^2)^{3/2}}\times(1-jk\sqrt{x^2+y^2+d^2})e^{jk\sqrt{x^2+y^2+d^2}}. \quad (12)$$

The pressure $p(\mathbf{r},t)$ is then recovered by inverse time Fourier Transforms.

The third method is also defined in the frequency/space domains (FSD2). It is obtained by taking the spatial Fourier Transform of Eq. (11). The pressure field $P(k_x,k_y,z,\omega)$ is then given by

$$P(k_x,k_y,z,\omega)=P(k_x,k_y,z_0,\omega)\cdot G_3(k_x,k_y,d,\omega), \quad (13)$$

where $G_3(k_x,k_y,d,\omega)$ is the spatial Fourier Transform of $G_2(x,y,d,\omega)$

$$G_3(k_x,k_y,d,\omega)=\int\int_{-\infty}^{\infty}G_2(x,y,d,\omega)e^{-j(k_xx+k_yy)}dxdy, \quad (14)$$

or equivalently,

$$G_3(k_x,k_y,d,\omega)=e^{jd\sqrt{k^2-k_x^2-k_y^2}}. \quad (15)$$

The third method uses Eqs. (13) and (14), where the Green's function is defined in the frequency/space domains, whereas the use of Eqs. (13) and (15) corresponds to the fourth method, expressed in the frequency/k-space domains (FKD).

The pressure field $p(x,y,z,t)$ is then simply recovered by taking the spatial and time inverse Fourier Transforms of $P(k_x,k_y,z,\omega)$

$$p(x,y,z,t)=\frac{1}{8\pi^3}\int\int\int_{-\infty}^{\infty}p(k_x,k_y,z,\omega)\times e^{j(k_xx+k_yy)}e^{-j\omega t}dk_xdk_yd\omega. \quad (16)$$

IV. NUMERICAL IMPLEMENTATION

The four methods presented in the previous section are numerically implemented in the MATLAB® environment. The computation requires the discretization of both pressure sound field and functions involved in the processing.

The first assumption is that the pressure field is finite in the space domain $\{|x|,|y|\}<L/2$ (L, width of the square array of microphones) and in the time domain ($0<t<t_{\max}$) and the energy is negligible outside the previous domains.

The second one is that the wavefield must be sampled by discrete values without significant loss of information. This assumption is fulfilled when the Nyquist criterion is respected both in space and time domains.

The discrete pressure fields are sampled using a time-two-dimensional (2D) space grid given by

$$x_l=-L/2+l\Delta_L,\quad y_m=-L/2+m\Delta_L,\quad t_n=n\Delta_t, \quad (17)$$

with integers l, $m=0,1,...,M-1$ and $n=0,1,...,N-1$. The spacing between the time points, Δ_t, is equal to $t_{\max}/(N-1)$ while the spacing between the spatial points, Δ_L, is equal to $L/(M-1)$.

The forward projection methods presented in the previous section can be rewritten using finite and discrete operations. The TSD given by Eq. (7) becomes

$$p(x_p,y_q,t_n)=\frac{d}{2\pi}\sum_{l,m=0}^{M-1}\left(\frac{1}{R^3}p\left(x_l,y_m,t_n-\frac{R}{c}\right)+\frac{1}{cR^2}\times\frac{p\left(x_l,y_m,t_n-\frac{R}{c}+\Delta_t\right)-p\left(x_l,y_m,t_n-\frac{R}{c}\right)}{\Delta_t}\right)\Delta_L^2, \quad (18)$$

where $R=\sqrt{(x_p-x_l)^2+(y_q-y_m)^2+d^2}$. The coordinates (x_p,y_q) are chosen from the grid (x_l,y_m). The term R/c is rounded to the nearest value of the discrete time scale.

The other methods require the calculation of direct and inverse Discrete Fourier Transforms (DFT and IDFT) both in time-frequency (index t) and space-wave vector (index 2D) domains. Then Eq. (11) required for the FSD1 method can be rewritten as follows

TABLE II. Summary of the four different forward projection methods.

$p(x,y,z_0,t)\rightarrow \mathrm{DFT}_t \rightarrow P(x,y,z_0,\omega)\rightarrow \mathrm{DFT}_{2D}\rightarrow$		$P(k_x,k_y,z_0,\omega)$
TSD	FSD1	FSD2 and FKD
$\Downarrow$ Eq. (18)	$\Downarrow$ Eq. (19)	$\Downarrow$ Eqs. (20)–(22)
$p(x,y,z,t)\leftarrow \mathrm{IDFT}_t \leftarrow P(x,y,z,\omega)\leftarrow \mathrm{IDFT}_{2D}\leftarrow$		$P(k_x,k_y,z,\omega)$

$$p(x_p,y_q,z,t_n) = \mathrm{IDFT}_t[P(x_l,y_m,z_0,\omega_\nu)**G_2(x_l,y_m,d,\omega_\nu)], \quad (19)$$

where $\omega_\nu = 2\pi(\nu - N/2)/t_{\max}$ and $\nu = 0,1,...,N-1$.

The third (FSD2) and fourth (FKD) methods are expressed by Eq. (13), which becomes:

$$P(k_\lambda,k_\mu,z,\omega_\nu) = P(k_\lambda,k_\mu,z_0,\omega_\nu)\cdot G_3(k_\lambda,k_\mu,d,\omega_\nu). \quad (20)$$

FSD2 and FKD can be achieved using two different implementations of the Green's function $G_2(x_l,y_m,d,\omega_\nu)$, i.e., the discrete formulations of Eqs. (14) and (15), respectively, given by

$$G_3(k_\lambda,k_\mu,d,\omega_\nu) = \mathrm{DFT}_{2D}(G_2(x_l,y_m,d,\omega_\nu)), \quad (21)$$

and

$$G_3(k_\lambda,k_\mu,d,\omega_\nu) = \exp\left(jd\sqrt{\frac{\omega_\nu^2}{c^2} - k_\lambda^2 - k_\mu^2}\right). \quad (22)$$

As the result of FSD1 is defined on a $[(2M-1)\times(2M-1)]$ grid and the convolution theorem[2,13] is used to obtain methods FSD2 and FKD, the pressure is then characterized on a $(M\times M)$ grid. To calculate correctly Eq. (20), the domain must be extended over a $[(2M-1)\times(2M-1)]$ spatial domain by zero-padding.

Table II summarizes the four different methods, useful to compute the pressure field on the z plane from the pressure on the z_0 plane.

V. COMPARISON OF THE DIFFERENT PROJECTION METHODS

Even if those methods are mathematically equivalent, results obtained in the same condition of simulation are different. In this section the four methods of forward projecting pressure fields are compared. The sound source used in the computation is the ideal baffled planar piston described in the first section. Table I and Eqs. (1)–(3) are used to calculate the pressure field as a function of time and along x and y directions. The relative accuracy of the numerical processes described in the previous section is estimated with normalized indicators. The root mean square (RMS) difference between the forward projected field $p(l,m,n)$ and the reference field $p_r(l,m,n)$ (simulated or measured) is evaluated using the following equation over the dimensions x and y:

$$E_{\mathrm{RMS}} = \sqrt{\frac{\sum_{l,m=0}^{M-1}\left(\sqrt{\sum_{n=0}^{N-1}p^2(l,m,n)} - \sqrt{\sum_{n=0}^{N-1}p_r^2(l,m,n)}\right)^2}{\sum_{l,m=0}^{M-1}\sqrt{\sum_{n=0}^{N-1}p_r^2(l,m,n)}}}. \quad (23)$$

Another error parameter (E_{axis}) is used, evaluated at the nearest point from the axis of the sound source ($l=M/2$, $m=M/2$). It compares the time variations of both pressure fields:

$$E_{\mathrm{axis}} = \sqrt{\frac{\sum_{n=0}^{N-1}(p(M/2,M/2,n) - p_r(M/2,M/2,n))^2}{\sum_{n=0}^{N-1}p_r^2(M/2,M/2,n)}}. \quad (24)$$

In these simulations, the baffled planar piston is excited by a Gaussian pulsed velocity (amplitude normalized to one) with two different widths at half maximum: $\Gamma = 120$ and 710 μs. These widths have been chosen in order to avoid frequency aliasing (the maximum cut-off frequency at -6 dB is 5700 Hz).

The influence of various parameters (the distance between microphones Δ_L, the propagation distance and the number of microphones) is investigated on the four propagation methods. For each simulation, the distance z_0 from the source to the hologram plane is fixed at 2 cm. This value of z_0 allows us to achieve a minimum resolvable propagation distance of 1 cm with a signal to noise ratio of 55 dB.[1,3] Algorithms have been checked with a null propagation distance which gives error rates around 10^{-14}%.

A. Influence of the distance between microphones

Three conditions, which ensure that the signal is entirely and correctly described by the microphone array, are to be taken into account. They depend on parameters such as the source radius, the distance between microphones and the waveband of the signal. They ensure an appropriate grid size which optimizes the signal acquisition.[14,15]

First of all, the square microphone array used in this study must be larger than the source to measure the majority of the field. Considering that with an array twice as large as the source the results are accurate, this first condition can be written as $L/2 > 2a$ (where a is the source radius and L the array width): The pressure is negligible on the array edges. During simulations, this criterion is easily checked.

The second condition is linked to the spacing of microphones: Δ_L must be sufficiently small, so that the shortest wavelength of the signal ($\lambda_{\min}$) is described by at least two points of the array ($\Delta_L \leqslant \lambda_{\min}/2$). Furthermore, having an array larger than or equal to the largest signal wavelength is more adapted ($L \geqslant \lambda_{\max} = c/f_{\min}$). Otherwise, frequencies below $c/2L$ are considered as plane waves because of the wavevector sampling. This condition can be rewritten using the distance Δ_L as $\Delta_L \geqslant \lambda_{\max}/31$, since the grid is composed of 32×32 microphones ($L = 31\Delta_L$).[15]

The various conditions are summarized as follows:

$$\frac{4a}{31} \leqslant \Delta_L \quad \text{and} \quad \frac{\lambda_{\max}}{31} \leqslant \Delta_L \leqslant \frac{\lambda_{\min}}{2}. \quad (25)$$

These relations define a theoretical domain for Δ_L. Theoretically, working inside this domain guarantees the best results. The previous conditions [Eq. (25)] are required to respect the Nyquist sampling rate and to ensure appropriate anti-aliasing sampling of all frequencies. The limits depend on the signal center frequency as well as the sound source size.

TABLE III. Conditions of Δ_L/a from Eq. (25) depending on the Gaussian profile and the piston radius.

Γ (μs)	a (cm)	f_{cent} (Hz)	f_{min} (Hz)	f_{max} (Hz)	$L/2>2a$	$L\geqslant\lambda_{max}$	$\Delta_L\leqslant\lambda_{min}/2$
120	2.5	3000	960	5725	$0.13\leqslant\frac{\Delta_L}{a}$	$0.46\leqslant\frac{\Delta_L}{a}$	$\frac{\Delta_L}{a}\leqslant 1.19$
120	4	2800	900	5327	$0.13\leqslant\frac{\Delta_L}{a}$	$0.31\leqslant\frac{\Delta_L}{a}$	$\frac{\Delta_L}{a}\leqslant 0.80$
710	2.5	600	196	1020	$0.13\leqslant\frac{\Delta_L}{a}$	$2.25\leqslant\frac{\Delta_L}{a}$	$\frac{\Delta_L}{a}\leqslant 6.71$
710	4	600	196	1020	$0.13\leqslant\frac{\Delta_L}{a}$	$1.41\leqslant\frac{\Delta_L}{a}$	$\frac{\Delta_L}{a}\leqslant 4.19$

The pressure radiated by a planar piston was propagated over the same distance but for different values of the parameter Δ_L. Those simulations allowed us to compare the domain of Δ_L where the error was minimum to the one obtained theoretically from Eq. (25) and find the most important conditions to respect during experiments, depending on the propagation method used.

The following simulation conditions were used: The source radius a was 2.5 or 4 cm, $\Gamma=120$ and 710 μs, the spacing between microphones varied from 0.25 to 4.5 cm. The hologram plane was placed at 2 cm from the source and the propagation distances were 2 and 15.41 cm. The grid was composed of $(32\times32\times256)$ points. The maximum frequency studied was given by the selected temporal step ($\Delta t=1/2f_{max}$). In these simulations, f_{max} was equal to 25 600 Hz. For each configuration ($\Gamma=120$ and 710 μs and $a=2.5$ or 4 cm), the various theoretical domains of the distance between microphones Δ_L, according to the conditions to check (Table III), were compared to those found during simulations.

Figure 3 represents the evolution of the global error (E_{RMS}) according to the dimensionless parameter Δ_L/a, for the four algorithms and the following conditions: $\Gamma=120$ μs, $a=2.5$ cm. The upper curve describes results obtained for $d=2$ cm ($d/\lambda_{mean}=0.18$, where λ_{mean} is the wavelength calculated from the frequency at the maximum of the spectrum) whereas for the lower one, the distance is equal to 15.41 cm ($d/\lambda_{mean}=1.4$).

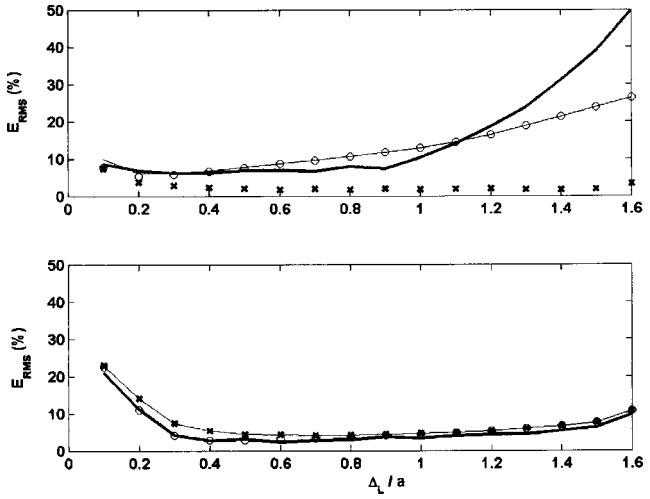

FIG. 3. Evolution of the global error E_{RMS} as a function of the dimensionless parameter Δ_L/a for the four algorithms ($\Gamma=120$ μs and $a=2.5$ cm): Upper curve $d=2$ cm ($d/\lambda_{mean}=0.18$) and lower curve $d=15.41$ cm ($d/\lambda_{mean}=1.4$). $\times\times\times$: FKD, thin line: FSD1, $\bigcirc\bigcirc\bigcirc$: FSD2, thick line: TSD.

For the small propagation distance, error rates obtained with the four methods differ: TSD gives satisfactory results for small Δ_L/a ($E_{RMS}<10\%$ for $\Delta_L/a\leqslant1.0$). Then the error presents a sharp increase (from 10% to 60% as Δ_L/a goes from 1 to 1.7). Methods FSD1 and FSD2 give equivalent results: The two curves are superposed. The error increases slowly from 6% to 29% as Δ_L/a varies from 0.2 to 1.7. The FKD method gives the smallest errors and shows a domain where the error is minimum from 0.5 to 1.5 ($E_{RMS}<2\%$). For the bigger propagation distance, results obtained with the four methods are similar. The four curves present the same validity domain (with $E_{RMS}<6\%$) from 0.4 to 1.3. This domain is close to the theoretical variation field of Δ_L/a which, for $\Gamma=120$ μs and $a=2.5$ cm extends from 0.46 to 1.20. The difference between the methods due to the propagation distance are explained in the next section.

As FKD seems to be the most appropriate method for the two propagation distances, this one is used to compare the theoretical domains given by Eq. (25) to those obtained during simulation and then determine the most important conditions of Eq. (25). The evolution of the global error resulting from the FKD method, as a function of the dimensionless parameter Δ_L/a is plotted (Fig. 4) for four different configurations ($\Gamma=120$ μs and $a=2.5$ or 4 cm; $\Gamma=710$ μs and $a=2.5$ or 4 cm). The propagation distance is 2 cm for the 4 curves. The parameter Δ_L/a, as shown in Eq. (25) strongly depends on the signal waveband (velocity and radius of the piston). For the same velocity profile, if the source radius differs, the two curves are close but not superposed. Indeed, for a fixed velocity distribution and a bigger source, Δ_L/a is smaller. A validity domain with an error less than 3% is observed for each configuration.

Table IV summarizes the different simulation and theoretical domains of Δ_L/a. This table shows that the validity domains determined during simulations are in agreement with the theoretical ones for $\Gamma=120$ μs ($E_{RMS}<2\%$ over the theoretical domain of Δ_L/a) but differ for $\Gamma=710$ μs ($E_{RMS}>5\%$ over the theoretical domain). For $\Gamma=710$ μs, it appears that as soon as $\Delta_L/a>4/31=0.13$ and even for $\Delta_L/a<\lambda_{max}/31a$ good results are obtained during simulations. In Fig. 4, it is clearly notice that the error rates are very

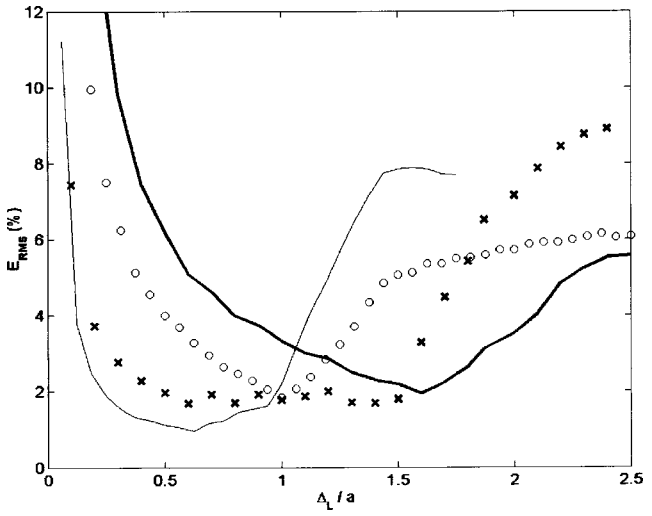

FIG. 4. Evolution of the global error E_{RMS} as a function of the dimensionless parameter Δ_L/a for four different configurations. $\times\times\times$: $\Gamma=120$ μs and $a=2.5$ cm ($d/\lambda_{\mathrm{mean}}=0.18$); thin line: $\Gamma=120$ μs and $a=4$ cm ($d/\lambda_{\mathrm{mean}}=0.16$); thick line: $\Gamma=710$ μs and $a=2.5$ cm ($d/\lambda_{\mathrm{mean}}=0.035$); $\bigcirc\bigcirc\bigcirc$: $\Gamma=710$ μs and $a=4$ cm ($d/\lambda_{\mathrm{mean}}=0.035$).

high for Δ_L/a smaller than 0.13. This domain strongly depends on parameters such as the signal waveband, i.e., the velocity and the radius of the piston. The differences between theoretical and simulation results (particularly when the array is small) are explained by the characteristics of the pressure field radiated by the planar piston. When the array is small, the piston is considered as infinite and the microphones measure principally the plane wave. Propagating plane waves does not pose major problems with the four different programs. So, even if the array is smaller than the source, the error rates are weak. Although the signal can not be perfectly described by the array, the results are satisfactory.

As a conclusion of this section, it is necessary to find a compromise between the source radius, the spacing of microphones and the number of microphones in order to cover the source with an adapted grid. Finally, it is important to follow two main conditions: The Nyquist condition has to be verified and the array has to cover grandly the sound source ($L/2>2a$). Then, for a 32×32 microphone grid, the validity domain is defined as follows: $0.13<\Delta_L/a<\lambda_{\mathrm{min}}/2a$.

B. Propagation distance

The preceding analysis defines the appropriate conditions for the spacing of microphones and the source radius. Using these parameters, the influence of the propagation distance is studied.

Veronesi[2] presents the conditions relative to the sampling of the Green's function for stationary signals. The authors demonstrate that, for small propagation distances ($d/\lambda<0.5$), the graph representing the evolution of the Green's function $G_2(x,y,\omega)$, at a given frequency, according to y is very narrow. On the contrary, for the same distance and frequency, the function $G_3(k_x,k_y,\omega)$ varies slowly according to k_y. Thus, for a small distance, it is worth sampling the Green's function directly in the k-space domain (FKD). The problem which arises with a signal defined by only a few points, is the inevitable loss of information. When large propagation distances are concerned, it is better to sample $G_2(x,y,\omega)$ and then calculate its Fourier Transform, rather than sample directly $G_3(k_x,k_y,\omega)$, which is an oscillating signal over a very short period.

An attempt was made to find these conclusions during the study of non stationary sources. The pressure field radiated by a planar piston was propagated over different distances with the four methods. Results were compared to the calculated field at this new distance. This work was carried out under the following conditions: A source radius of 2.5 cm, a hologram plane placed at 2 cm from the source, a propagation distance which varied from 2 to 50 cm by steps of $\Delta_z=0.67$ cm. The array width was equal to 62 cm ($\Delta_L/a=0.8$). From Fig. 4, this parameter was appropriate for $d=2$ cm and for both $\Gamma=120$ μs ($E_{\mathrm{RMS}}=1.7\%$) and $\Gamma=710$ μs ($E_{\mathrm{RMS}}=4\%$). The sampling frequency was equal to 51 200 Hz, the spacing between time points was $\Delta_t=1/51\,200$ s. The step chosen for the propagation distance was proportional to the product of the temporal step by the sound velocity: $\Delta_z=c\,\Delta_t=c/51\,200=0.0067$ m.

Figure 5 represents the evolution of the global error (E_{RMS}) for the four various algorithms as a function of the dimensionless parameter $d/\lambda_{\mathrm{mean}}$, where λ_{mean} is the wavelength calculated from the frequency of the spectrum maximum. The 120 μs Gaussian velocity is used for this graph ($\lambda_{\mathrm{mean}}=11.4$ cm). It is noticed that TSD, FSD1 and FSD2 behave in the same way; the three curves are close. There is

TABLE IV. Comparison between theoretical and simulation results as a function of the Gaussian profile and the piston radius.

Γ (μs)	a (cm)	$\Delta_L/a_{\mathrm{theoretical}}$	$\Delta_L/a_{\mathrm{simulation}}$
120	2.5	$0.46\leqslant\frac{\Delta_L}{a}\leqslant1.20$	$0.5\leqslant\frac{\Delta_L}{a}\leqslant1.5$
120	4	$0.31\leqslant\frac{\Delta_L}{a}\leqslant0.80$	$0.24\leqslant\frac{\Delta_L}{a}\leqslant0.98$
710	2.5	$2.25\leqslant\frac{\Delta_L}{a}\leqslant6.71$	$1.1\leqslant\frac{\Delta_L}{a}\leqslant1.85$
710	4	$1.41\leqslant\frac{\Delta_L}{a}\leqslant4.20$	$0.68\leqslant\frac{\Delta_L}{a}\leqslant1.2$

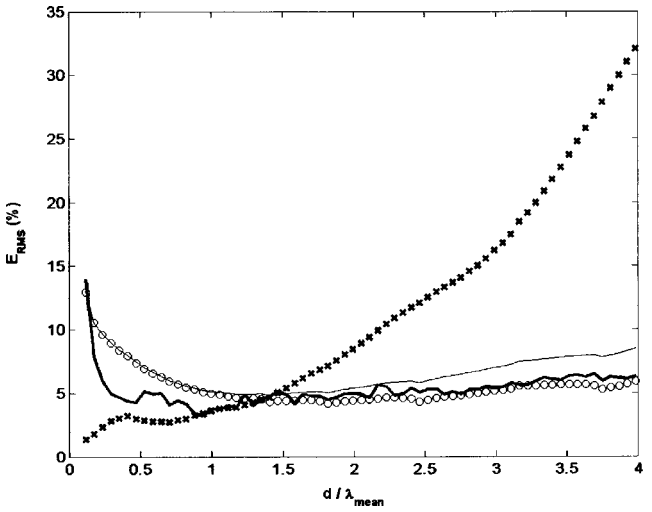

FIG. 5. Evolution of the global error E_{RMS} as a function of dimensionless parameter $d/\lambda_{\mathrm{mean}}$ for $\Gamma=120$ μs ($\Delta_L/a=0.8$). $\times\times\times$: FKD; thin line: FSD1; $\circ\circ\circ$: FSD2; thick line: TSD.

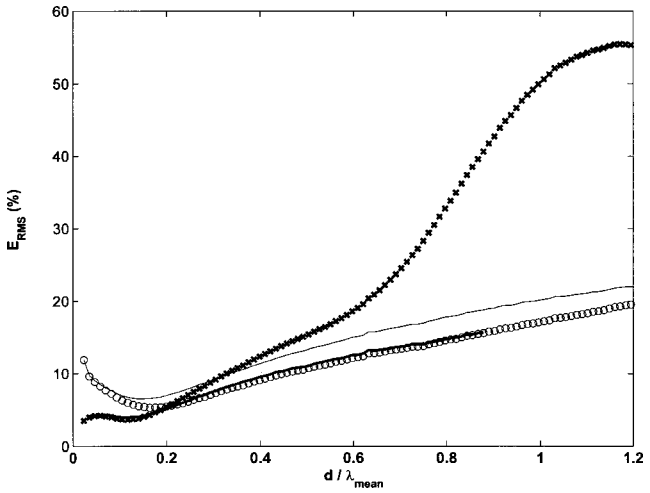

FIG. 6. Evolution of the global error E_{RMS} as a function of dimensionless parameter $d/\lambda_{\mathrm{mean}}$ for $\Gamma=710$ μs ($\Delta_L/a=0.8$). $\times\times\times$: FKD; thin line: FSD1; $\circ\circ\circ$: FSD2; thick line: TSD.

a decrease of the error, from 14% to 5% as $d/\lambda_{\mathrm{mean}}$ decreases from 0.1 to 1.2. And then for $d/\lambda_{\mathrm{mean}}$ varying from 1.2 to 4, the error increases very slowly. With FKD, the error extends from 1 to 32% in a quasi-linear way. The four curves cross at $d/\lambda_{\mathrm{mean}}=1.4$. For large distances ($d/\lambda_{\mathrm{mean}}>1.4$), it is better to use TSD, FSD1 and FSD2. FKD appears more suitable for shorter distances ($E_{\mathrm{RMS}}=2\%$ for $d/\lambda_{\mathrm{mean}}=0.12$). However, the other methods also give good results for the same distance ($E_{\mathrm{RMS}}=11\%$). This remark is also illustrated by Fig. 3. The upper curve corresponds at $d/\lambda_{\mathrm{mean}}=0.18$. FKD appears more appropriate than the others whereas for the lower curve, $d/\lambda_{\mathrm{mean}}=1.4$ and similar results are obtained with the four algorithms. For $\Gamma=120$ μs, the distance at which the curves cross is clearly identifiable. This is not the case for the much broader velocity distribution ($\Gamma=710$ μs, $\lambda_{\mathrm{mean}}=57$ cm) for which, over small distances ($d/\lambda_{\mathrm{mean}}<0.25$), the four curves are close (Fig. 6). For a dimensionless parameter $d/\lambda_{\mathrm{mean}}$ up to 0.35, the differences between the algorithms grow wider. Again, TSD, FSD1 and FSD2 follow the same evolution: There is a decrease (from 10% to 5% as $d/\lambda_{\mathrm{mean}}$ goes from 0.035 to 0.16) followed by an increase (from 5% for $d/\lambda_{\mathrm{mean}}=0.16$ to 20% for $d/\lambda_{\mathrm{mean}}=1.2$), whereas FKD presents a very sharp increase (from 4% for $d/\lambda_{\mathrm{mean}}=0.035$ to 55% for $d/\lambda_{\mathrm{mean}}=1.2$). The curves cross at 0.25.

Figures 5 and 6 enable us to verify Veronesi's conclusions[2] in the case of nonstationary sources. For small propagation distances ($d/\lambda_{\mathrm{mean}}\leqslant 0.5$), it is worth sampling the *k*-space Green's function, i.e., use the FKD method and for larger distances, better results are obtained by sampling the Green's function directly in the space domain and then calculating its Fourier Transform, i.e., FSD1 or FSD2. The TSD method, which does not use Fourier Transform, seems to be equivalent to FSD1 and FSD2.

C. Number of microphones

In this section, the influence of the grid size, i.e., the number of microphones was studied under the following simulation conditions. The array was $L=64$ cm wide and the source had a 2.5 cm radius. The hologram plane was placed at 2 cm from the source and the propagation distances were 2 and 15.41 cm. Time was defined on 256 points. The number n of microphones on the array width was $n=8$, 16, 32, 64 and the spatial grid was, respectively (8×8), (16×16), (32×32), and (64×64). The spacing between microphones, Δ_L, was linked to the array width and the number of microphones, $\Delta_L=L/(n-1)$. For the chosen configurations, the parameter Δ_L/a was equal, respectively, to 3.66, 1.71, 0.83, and 0.41 as the microphone number increased.

Figure 7 shows the evolution of the global error as a function of the spatial grid (upper curve: $\Gamma=120$ μs, $d/\lambda_{\mathrm{mean}}=0.18$, lower curve: $\Gamma=120$ μs, $d/\lambda_{\mathrm{mean}}=1.4$) in a logarithmic scale. The error obtained with TSD is very high with a small array (8×8). Therefore, the space resolution is not accurate enough to estimate the delay (t_n-R/c). This generates high error rate, but it decreases for a (64×64) grid. Note that timewaves are very short for this kind of excitation, thus their Fourier Transforms are larger and can be

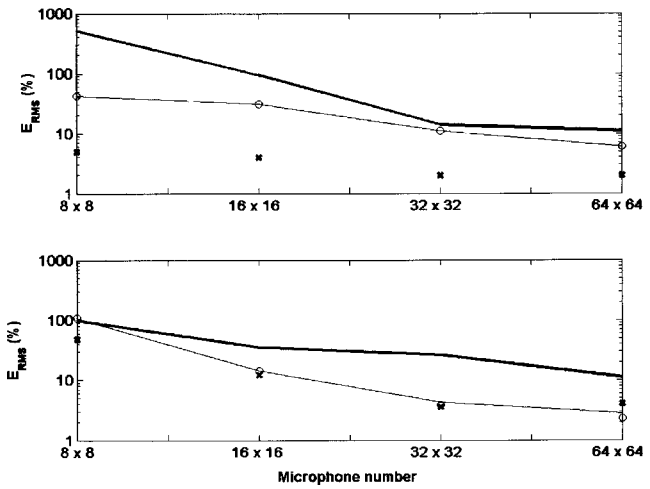

FIG. 7. Evolution of the global error E_{RMS} as a function of the microphone number of the array (log scale): Upper curve $d/\lambda_{\mathrm{mean}}=0.18$ and lower curve $d/\lambda_{\mathrm{mean}}=1.4$. $\times\times\times$: FKD; thin line: FSD1; $\circ\circ\circ$: FSD2; thick line: TSD.

sampled with a better accuracy. This explains the lower error rates obtained with the three other methods. Curves for FSD1 and FSD2 are superposed as those two methods are theoretically equivalent. The error is very high for a small grid (8×8) and decreases regularly more the grid increases. As the convolution of two rectangular windows [$G_2(x,y,d,\omega)$ and $P(x,y,z,\omega)$ in this study] produced a triangular one, the result of the convolution product (obtained with FSD1 and FSD2) was shifted from the piston center ($x=0$). The error, due to this gap, was accentuated when the grid was small. The error algorithm compared the pressures point by point so it was very sensitive to small differences. The FKD method yields good results even for a small grid. Increasing the number of microphones does not change the error significantly but greatly extends the calculation time. Again, this figure illustrates that for a higher d/λ_{mean} results obtained with the four methods are similar whereas best results were obtained with the FKD method for $d/\lambda_{\text{mean}}=0.18$.

As a conclusion, the FKD method works properly even with a few microphones. It is an argument for choosing this method during measurement study, where only a small array is available. The high error rates for the array composed of 8×8 microphones can be explained by the value of the corresponding ratio Δ_L/a. The Nyquist condition is not verified anymore. Therefore, for $d/\lambda_{\text{mean}}=0.18$, with the FKD method, the accuracy of the results is good even if this condition is not respected. The FKD method is more adapted to the experimental conditions.

D. Computing time

The computing time is a significant criterion to take into account during the comparison of the four methods. This parameter depends on the number of microphones but also on the method. It is measured on a PC (550 MHz, 256MB RAM) under MATLAB® environment. It represents the time necessary for the calculation of the forward propagating pressure field, over a ($32\times32\times256$) grid. With TSD, the time necessary to calculate the propagated pressure on only one unspecified grid point is 5 s and to calculate the field propagated over the whole grid is 46 minutes. This algorithm necessitates a long computing time and gives the same results as FSD1 and FSD2. The advantage of TSD is that the pressure in the time domain can be determined on any point on the plane *z*.

The FKD method, directly implementing the Green's function in the *k*-space domain, is the quickest one: It takes 16 s. The FSD2 method needs slightly more time (22 s) than FKD. This result is expected because this algorithm uses one more Fourier Transform than FKD. The FSD1 method, using the convolution, is time consuming, 62 s. This result is also expected because it is known that the convolution function is slower than the discrete Fourier Transform.

E. Simulation conclusions

The behavior of the four different methods with parameters such as the spacing between microphones, the source radius, the propagation distance, the number of microphones and also the computation time has been studied.

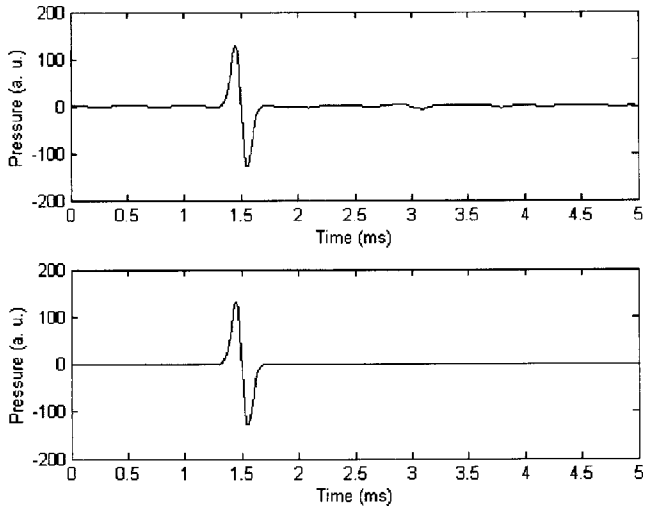

FIG. 8. Upper plot: Forward projected pressure of a distance of 6 cm from the simulated one on plane $z=2$ cm as a function of time at (0.94, 0.94, and 8 cm). Lower plot represents the measured pressure on plane $z=8$ cm, at the same point, as a function of time.

The first part of this work was to check the three theoretical conditions presented Eq. (25) with simulations using four different algorithms. The forward propagation of the pressure field radiated by a planar piston gives good results in a domain of the distance between microphones defined by Eq. (25). The limits depend on the source radius and the center frequency of the signal. It appears that the main condition to follow is the Nyquist theorem. The use of one of the four algorithms depends on the parameters of the experiment: for a dimensionless parameter d/λ_{mean} less than 0.5, more accurate results are obtained with the FKD method whereas for a higher parameter, the use of one of the three other methods is more adapted. These conclusions fit in well with results obtained with stationary sources.[1,2] With methods FSD1, FSD2, and TSD, an accurate sample in the space domain and an array which covers grandly the source surface are important parameters. The FKD method which is defined in the *k*-space and frequency domains gives low error rates even with a small array and is less time consuming than the others. The TSD method gives similar results than the ones obtained with FSD1 or FSD2 but needs a longer processing time. This method is useful to determine the pressure field in the time domain on any point of the grid.

Figure 8 illustrates the good results obtained using the FKD method: The pressure field simulated on the plane $z=2$ cm is 6 cm forward propagated. The upper graph shows the propagated pressure as a function of time at the point (0.94, 0.94, and 8 cm) while the graph below represents the direct calculated pressure on plane $z=8$ cm as a function of time at the same point. Figure 9 represents the propagated pressure as a function of radial position *x* and time *t*. This figure can be compared to Fig. 2. The error rates obtained are as follows: $E_{\text{axis}}=7\%$ and $E_{\text{RMS}}=4\%$. The comparison of the two fields being point by point, the error criterion is highly demanding. So even if the two figures seem similar,

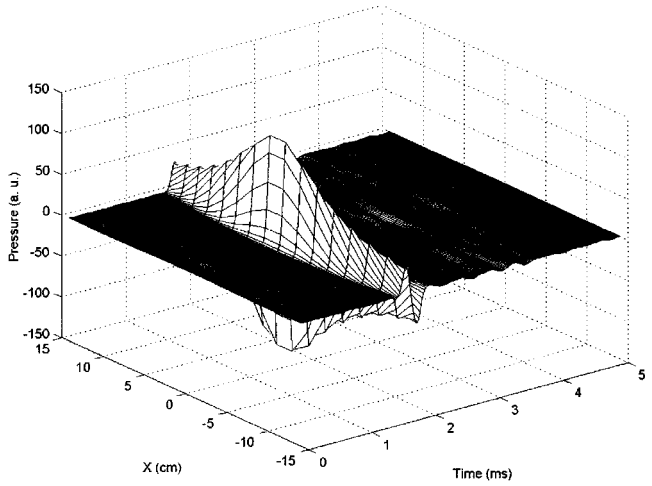

FIG. 9. Forward projection pressure field on the plane $z=8$ cm from the measured one on the plane $z=2$ cm, as a function of radial position x and time t.

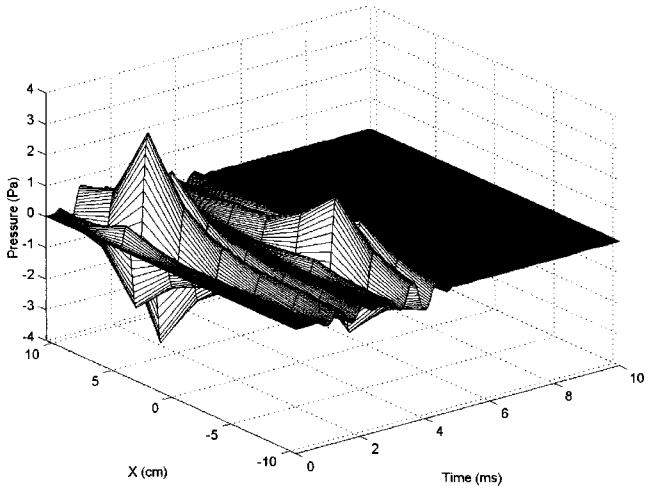

FIG. 11. Pressure field (Pa), measured on $z=1.3$ cm, radiated by the two loudspeakers, as a function of time and x, in $y=-4.5$ cm.

every small delay in time or difference in amplitude increase the rate.

VI. EXPERIMENTAL RESULTS

Experimental results with the pressure radiated first by two loudspeakers and then by an aluminum blaffled plate are presented in the next section.

A. Propagation of the pressure field radiated by two loudspeakers

The sound source was made up of loudspeakers mounted in a large planar baffle as shown on Fig. 10. The lower ones were driven by independent electrical signals while the third one could be used to radiate a Gaussian white noise. Measurements of the timewaves were performed by using a square planar array composed of sixteen Sennheiser electret microphones (4×4) equally spaced every 3 cm. The microphones were calibrated in amplitude and phase for frequencies below 1200 Hz. A two-axis robot allowed the displacement of the microphone array, parallel to the baffle, covering the sound source. The first microphone of the array was moved 1.5 cm to the right and 10.5 cm to the top of the center of the baffle. The pressure was defined on a (8×8 ×512) matrix. The triggering of the recording was set on the electrical transient signal. The electrical signals from the sixteen microphones were amplified and digitally stored on an Hewlett Packard HPE1432 acquisition card and then passed to a computer running HP VEE. The signal processing of the measured temporal signals was done using MATLAB®.

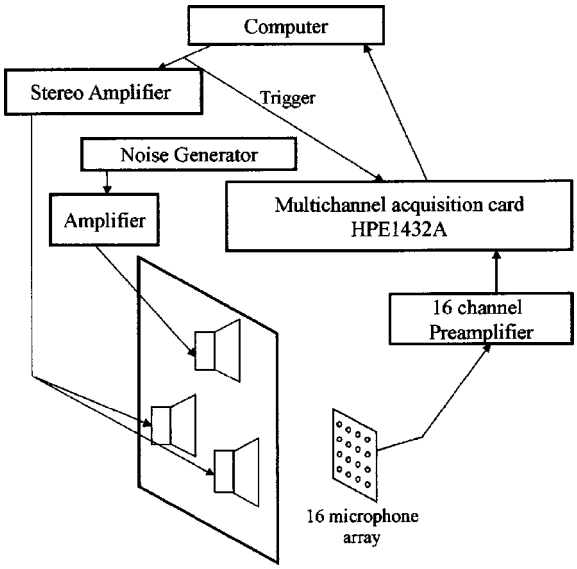

FIG. 10. Experimental setup.

Measurements of the pressure radiated by the two baffled loudspeakers were performed on several hologram planes: $z=1.3$, 2.3, 3.4, 4.4, 6.5, and 11.5 cm. The signal studied in this part was composed of bursts of two periods of a sinewave, sampled at 51.2 kHz send to each loudspeaker (center frequency: 1161 Hz, low and high cut-off frequencies at −6 dB: 900 and 1670 Hz). The second channel was 2.5 ms shifted from the first one. This time was long enough to avoid temporal overlap. The two loudspeakers were similar, with a radius of 1.2 cm. The distance between the two centers was 9 cm.

Concerning the sampling conditions given by Eq. (25), the Nyquist criterion was verified ($\Delta_L=3$ cm$<\lambda_{\min}/2=10$ cm) whereas the two other conditions were not fulfilled: $\lambda_{\max}=38$ cm$>L=21$ cm and $L>2\times s$, where s was the largest dimension of the sound source. Here, $s=11.4$ cm was equal to the sum of a diameter and the distance between the two loudspeakers. Although, these conditions were not completely verified, the results were satisfactory.

The measured pressure field at a distance of 1.3 cm from the source, is represented Fig. 11 as a function of time and the radial coordinate, x, for $y=-4.5$ cm. This figure illustrates the time dependence of the pressure field.

In order to compare these measurements with pressure fields extrapolated with the propagation algorithms, the error analysis presented earlier is used: The global error (E_{RMS}) and the on axis error in front of each loudspeaker: E_{axis1} (bottom right loudspeaker) and E_{axis2} (bottom left loudspeaker). The pressure field measured on plane $z=1.3$ cm

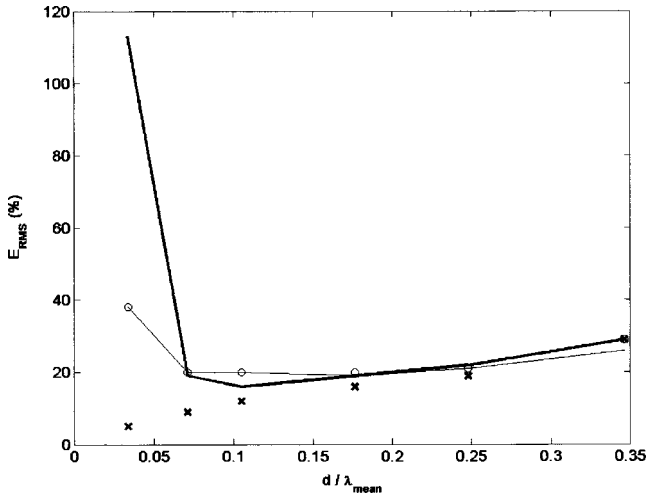

FIG. 12. Evolution of the global error (E_{RMS}) as a function of the dimensionless parameter $d/\lambda_{\mathrm{mean}}$ for the four algorithms. ×××: FKD; thin line: FSD1; ○○○: FSD2; thick line: TSD.

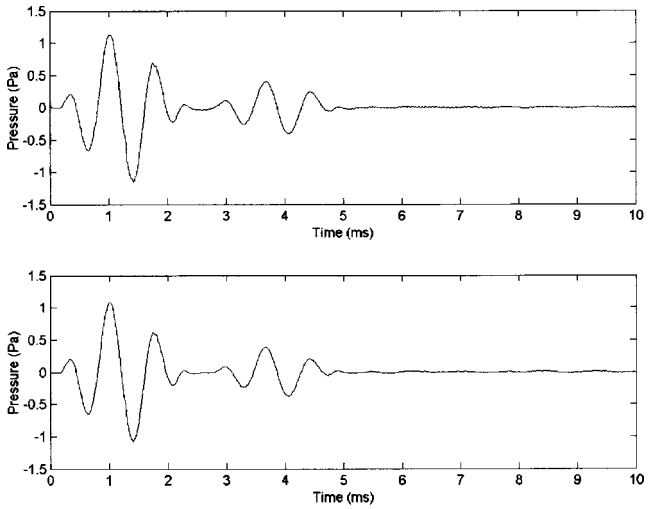

FIG. 13. Upper plot: Forward projected pressure as a function of time at (4.5, −4.5, and 4.4 cm), calculated from the measured pressure on plane $z = 1.3$ cm. Lower plot: Measured pressure as a function of time at (4.5, −4.5, and 4.4 cm) radiated by two baffled loudspeakers.

was forward propagated to the various planes ($d = 1$, 2.1, 3.1, 5.2, and 10.2 cm) with the four algorithms and then compared to direct measurements on the corresponding planes. Figure 12 represents the evolution of the global error (E_{RMS}) according to the propagation distance for the four algorithms. With FKD, the global error increases regularly with the distance, from 5% for $d/\lambda_{\mathrm{mean}} = 0.034$ to 29% for $d/\lambda_{\mathrm{mean}} = 0.35$. The signal is well extrapolated. For $d/\lambda_{\mathrm{mean}} = 0.034$, high error rates are observed for TSD ($E_{\mathrm{RMS}} = 113\%$), FSD1 ($E_{\mathrm{RMS}} = 38\%$) and FSD2 ($E_{\mathrm{RMS}} = 38\%$). For higher values (from 0.07 to 0.35), results with those three methods are similar: the error is quasi-linear, between 20% and 29%. TSD is not adapted for very small $d/\lambda_{\mathrm{mean}}$. Up to 0.2 ($d/\lambda_{\mathrm{mean}} > 0.2$), the four algorithms are similar: Regular increase of the error as $d/\lambda_{\mathrm{mean}}$ increases. The four curves cross at $d/\lambda_{\mathrm{mean}} = 0.25$. Those results are similar to the simulation ones: For small propagation distance better results are obtained with the FKD method. For larger distances, measurements should be done beyond 11.5 cm ($d/\lambda_{\mathrm{mean}} > 0.35$) to confirm the simulation conclusions, i.e., best results with FSD1, FSD2 or TSD methods. Under these experimental conditions, FKD is the most appropriate method to propagate the pressure field. This one is well adapted to small propagation distances (maximum of $d/\lambda_{\mathrm{mean}} = 0.35$ during the experiment) and to the array size (8×8).

Given those conclusions, the FKD method is used to forward propagate the measured signals. The upper graph (Fig. 13) shows the forward projected pressure field of a 3.1 cm propagation distance, from the measured pressure on plane $z = 1.3$ cm, as a function of time, at the point (4.5, −4.5, and 4.4 cm). The lower graph represents the measured pressure at the same point as a function of time. The comparison of those two curves gives an axis error (E_{axis1}) equal to 9%. Considering that no windowing or filtering functions was applied to the measured data, the agreement between the two curves is quite good.

Measurements with additional white noise have also been performed. The same frequency, 1161 Hz was sent respectively to each loudspeaker. The first signal was 2.5 ms time shifted from the second one. The signal-to-noise ratio, measured on the axis of the loudspeaker in the bottom on the right, was 22 dB on plane $z = 1.3$ cm. Because of the position of the third loudspeaker which generated noise, the error was calculated in front of the one placed in the bottom on the right. Results are illustrated Fig. 14. The upper graph represents the forward projected pressure field of a 2.1 cm propagation distance, from the measured pressure on plane $z = 1.3$ cm as a function of time, at the point (4.5, −4.5, and 3.4 cm). Lower graph represents the measured pressure at the same point as a function of time. The axis error (E_{axis1}) is equal to 46%. The first signal which corresponds to the sinewaves send to the loudspeaker on the bottom on the right has enough amplitude so that it is well recognizable. The second one, which is radiated from the second loudspeaker, is mixed with noise and then is not discernible.

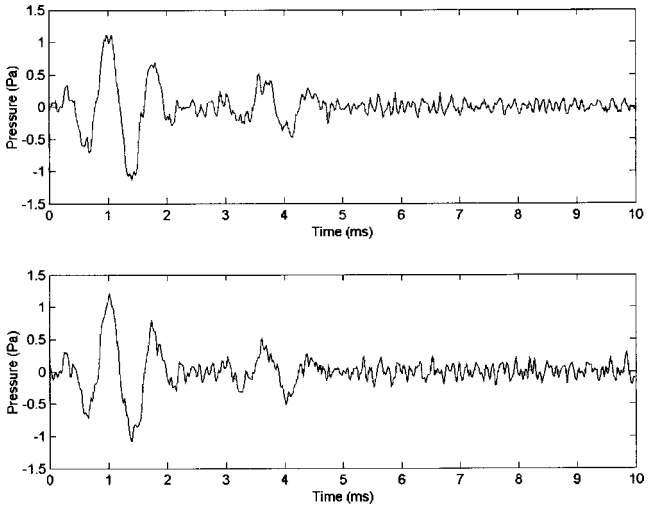

FIG. 14. Upper plot: Forward projected pressure of a distance of 2.1 cm from the measured one on plane $z = 1.3$ cm as a function of time at (4.5, −4.5, and 3.4 cm). Lower plot represents the measured pressure on plane $z = 3.4$ cm, at the same point as a function of time.

From this first set of measurements, even if Eq. (25) was not fulfilled, the pressure field (noisy or not) could be propagated with accuracy.

B. Propagation of the pressure field radiated by a baffled plate

The algorithms were applied to the pressure radiated by a more complex source: An aluminum baffled plate ($60\times40\times0.6$ cm) which vibrated under the effect of an impact at its center. The pressure radiated by the plate was measured over a (28×20) grid of microphones covering the source by moving the 4×4 microphone array 35 times. The plate's characteristics were: Mass, 4 kg; Young modulus $0.74\cdot10^{11}$ Pa; coincidence frequency, 2000 Hz. The center frequency of the measured pressure spectrum radiated by the plate was equal to 2500 Hz, giving a bending wavelength equal to 15 cm. This value was larger than the microphone spacing (3 cm). The measurement surface was 81 cm$\times$57 cm. This surface was not twice as large as the sound source in order to keep a microphone number consistent with reasonable calculation times. The first microphone was initially placed on a corner of the measurement surface. For each position of the array, the mean of 20 measurements was calculated.

The measurement setup was similar to the one drawn on Fig. 10, with an aluminum baffled plate as a sound source. Furthermore, an amplified pulse generator was used to drive an electomagnet which iron core was connected to a semispheric impact head. This device was used to apply a short impact at the center of the plate. An accelerometer placed near the impact point was used to trigger the multiple acquisitions. The reproducibility of the impact has been achieved by time averaging 25 signals.

Concerning the sampling conditions given by Eq. (25), the Nyquist criterion ($\Delta_L=3$ cm$<\lambda_{\text{mean}}/2=6.8$ cm) and the second condition ($\lambda_{\text{mean}}=13.6$ cm$<L=81$ cm) were verified. The third one was not fulfilled ($L=81$ cm$>2s=120$ cm, where s was the largest dimension of the plate, $s=60$ cm).

The measured pressure field is plotted in Fig. 15 as function of radial position x and time t. The global error (E_{RMS}) and the error at the center of the plate (E_{cent}) were used to compare the accuracy of the different algorithms (as usual: Forward propagated signals versus measured signals). As for the previous results, the errors increased with the distance. Results obtained with methods FSD1 and FSD2 were similar. The FKD method appeared to be more adapted to forward propagate the pressure field even for $d/\lambda_{\text{mean}}=1.02$ (FKD: $E_{\text{RMS}}=15\%$ and FSD2: $E_{\text{RMS}}=17\%$).

Given those results, FKD was used to forward propagate the measured signals. The upper graph in Fig. 16 shows the forward projected pressure field of a 6 cm propagation distance, from the measured pressure on plane $z=1$ cm, as a function of time, on plane $z=7$ cm. The lower graph represents the measured pressure at the same point as a function of time. This high error rate ($E_{\text{cent}}=24\%$) is explained by the principle of the error algorithm which compares point by point the two fields (the measured and the calculated ones). Small differences, like time shifts between the two fields, highly increase the error rate.

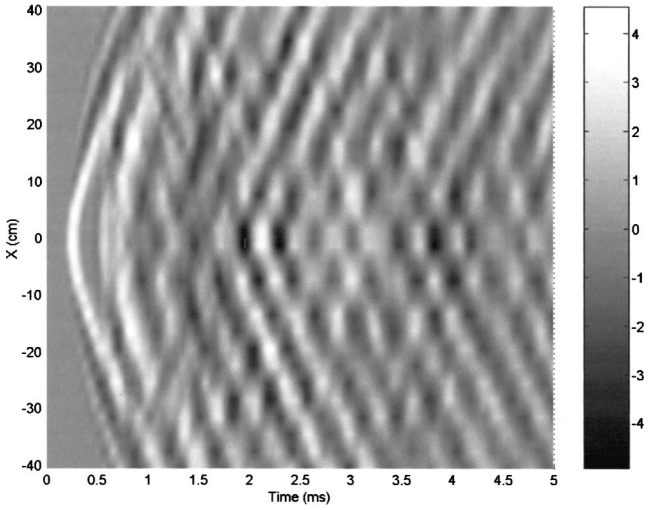

FIG. 15. Measured pressure field on the plane $z=1$ cm as function of radial position x and time t.

The four algorithms have been tested on measured signals. Given the small propagation distance used here, results have shown good agreement between the forward projected and measured pressure fields for the two experimental configurations using FKD method.

VII. CONCLUSION

Four different methods concerning the propagation of the acoustical pressure fields are implemented and compared. In the first part, the theoretical pressure field radiated by a planar piston is simulated and then forward propagated with the four algorithms. The influence on those methods of parameters such as the sound source, the distance between microphones, the number of microphones and the propagation distance is studied.

As expected, the results are good, in the validity domain defined by Eq. (25) even if the array size is only slightly larger than that of the source. The limits of this domain de-

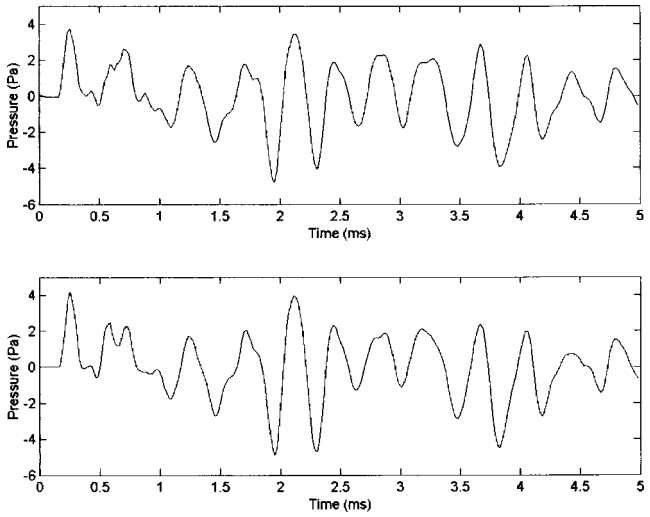

FIG. 16. Upper plot: Forward projected pressure of a distance of 6 cm from the measured pressure on plane $z=1$ cm as a function of time at the plate center. Lower plot represents the measured pressure on plane $z=7$ cm, at the same point, as a function of time.

pend on the characteristics of the source: Its size and frequency range. For small propagation distances ($d/\lambda_{mean} < 0.5$), using the method implementing the Green's function directly in the *k*-space domain (FKD) gives better results. And for a larger propagation distance, it is better to consider the algorithm which calculates the Green's function in the space domain and then computes its Fourier Transform (FSD2). This conclusion is similar to the one obtained with stationary sources.[1,2] A method which directly implements the algorithm in the time domain is also tested. This one requires a long computing time and does not allow better accuracy than the others (FSD1 and FSD2).

In the second part, measurements of the pressure field radiated by loudspeakers and by an aluminum baffled plate are performed. First of all, the simulation conclusions are checked against the measured pressure. The agreement between direct measurements and the results after forward propagation is fairly good. The algorithm shows good robustness even in a noisy environment.

Backward propagation of acoustic fields can also be achieved with this method. Regularization techniques (L-curve, Generalized Cross Validation), already successfully tested on stationary acoustic sources[16–18] must be used to minimize amplification of the noise mixed with evanescent waves. Different methods of filtering are tested, such as Tikhonov and Veronesi filters, on the measured pressure field radiated by two loudspeakers[19] and by a plate.[20] These results will be summarized in a further article.[21] Other methods are under study in our laboratory, such as wavelet[22] for the noise filtering of the pressure data field and Radon Transform[7,8] for the propagation of the pressure field.

The encouraging results obtained by both simulations and measurements make it possible to consider various industrial applications for those algorithms such as the localization of the noise generated by different parts of a car engine or the localization of aerodynamic sources and vortices from measurements realized outside the jet.

[1] J. D. Maynard, E. G. Williams, and Y. Lee, "Nearfield acoustic holography: I theory of generalized holography and the development of NAH," J. Acoust. Soc. Am. **78**(4), 1395–1413 (1985).

[2] W. A. Veronesi and J. D. Maynard, "Nearfield acoustic holography (NAH) II. holographic reconstruction algorithms and computer implementation," J. Acoust. Soc. Am. **81**(5), 1307–1322 (1987).

[3] E. G. Williams, *Fourier Acoustics, Sound Radiation and Nearfield Acoustical Holography* (Academic, San Diego, 1999).

[4] E. G. Williams and J. D. Maynard, "Holographic imaging without the wavelength resolution limit," Phys. Rev. Lett. **45**, 554–557 (1980).

[5] M. Forbes, S. Letcher, and P. Stepanishen, "A wave-vector, time-domain method of forward projecting time-dependent pressure fields," J. Acoust. Soc. Am. **90**(5), 2782–2792 (1991).

[6] G. T. Clement, R. Liu, S. V. Letcher, and P. R. Stepanishen, "Forward projection of transient signals obtained from a fiber optic pressure sensor," J. Acoust. Soc. Am. **104**(3), 1266–1273 (1998).

[7] T. B. Hansen and A. D. Yaghjian, "Planar near-field scanning in the time domain, part 1: Formulation," IEEE Trans. Antennas Propag. **42**(9), 1280–1291 (1994).

[8] T. B. Hansen and A. D. Yaghjian, "Planar near-field scanning in the time domain, part 2: Sampling theorems and computation schemes," IEEE Trans. Antennas Propag. **42**(9), 1292–1300 (1994).

[9] J. W. Miles, "Transient loading of a baffled piston," J. Acoust. Soc. Am. **25**(2), 200–203 (1953).

[10] P. R. Stepanishen, "Transient radiation from pistons in an infinite planar baffle," J. Acoust. Soc. Am. **49**(5), 1629–1638 (1971).

[11] G. R. Harris, "Review of transient field theory for a baffled planar piston," J. Acoust. Soc. Am. **70**(1), 10–20 (1981).

[12] G. R. Harris, "Transient field of a baffled planar piston having an arbitrary vibration amplitude distribution," J. Acoust. Soc. Am. **70**(1), 186–204 (1981).

[13] M. Kleiner, H. Gustafsson, and J. Backman, "Measurement of directional scattering coefficients using near-field acoustic holography and spatial transformation of sound fields," J. Audio Eng. Soc. **45**(5), 331–346 (1997).

[14] S. M. Dumbacher, D. L. Brown, J. R. Blough, and J. R. Bono, "Practical aspects of making NAH measurements," *Noise and Vibration Conference, Traverse City, Michigan*, 1999, May 17–20.

[15] A. Ross, G. Ostiguy, and M. Amram, "New signal processing developments for low cost near-field acoustical holography systems," Noise Control Eng. J. **47**(1), 28–44 (1999).

[16] E. G. Williams, "Regularization methods for near-field acoustical holography," J. Acoust. Soc. Am. **110**(4), 1976–1988 (2001).

[17] J.-Y. Der Mathéossian, "Problème inverse régularisé pour l'holographie acoustique de champ proche: Applications en milieu perturbé (regularized inverse problems for nearfield acoustic holography: Application to disturbed pressure fields)," Ph.D. Thesis, Université de Paris VII, 1994.

[18] A. Schuhmacher, J. Hald, K. B. Rasmussen, and P. C. Hansen, "Sound source reconstruction using inverse boundary element calculations," J. Acoust. Soc. Am. **113**(1), 114–127 (2003).

[19] O. de La Rochefoucauld, M. Melon, and A. Garcia, "Time domain acoustic holography: Influence of filtering on localisation of non stationary source," in *the Proceedings of the 17 International Congress on Acoustics*, Rome, Italy, 2001, September 2–7.

[20] O. de La Rochefoucauld, M. Melon, and A. Garcia, "Etude du rayonnement transitoire d'une plaque par holographie acoustique de champ proche (study of the transient radiation of a plate by nearfield acoustical holography)," *Proceeding of the 6th French Conference on Acoustics*, Lille, France, 2002, April 8–11.

[21] M. Melon, O. de La Rochefoucauld, and A. Garcia, "Time domain holography: Backward projection of planar sound pressure fields," J. Acoust. Soc. Am. (to be submitted).

[22] Y. Y. Kim, J.-C. Hong, and N.-Y. Lee, "Frequency response function estimation via a robust wavelet de-noising method," J. Sound Vib. **244**(4), 635–649 (2001).

Mindlin plate theory for damage detection: Source solutions

L. R. F. Rose[a] and C. H. Wang
Platform Sciences Laboratory, Defence Science and Technology Organisation, Melbourne 3001, Australia

(Received 22 April 2003; accepted for publication 22 March 2004)

A consideration of the relevant length scales and time scales suggests that Mindlin plate theory provides a judicious model for damage detection. A systematic investigation of this theory is presented that emphasizes its mixed vector-scalar character and analogies with 3D elasticity. These analogies lead to the use of Helmholtz potentials, and to compact statements of the reciprocal theorem and the representation theorem. The plate response for a point moment is derived using a direct source specification, rather than an indirect specification through boundary conditions. Solutions are presented for combinations of such point moments (doublets) that represent, respectively, a center of bending, a center of twist and a center of inplane twist. The flexural response due to finite sources, such as piezoelectric actuators, can be modeled by distributions of centers of bending. Detailed results are presented for a circular, and for a narrow rectangular actuator. The far-field radiation pattern for an array of equally spaced actuators parallel to a straight boundary is derived. The solutions presented for the point moment and the point force constitute the components of a dyadic Green's function which is required, along with its spatial derivatives, for a representation of plate-wave scattering by flexural inhomogeneities. © *2004 Acoustical Society of America.* [DOI: 10.1121/1.1739482]

PACS numbers: 43.20.Rz, 43.35.Cg, 43.40.Dx [ANN] Pages: 154–171

I. INTRODUCTION

The present work is motivated by the prospect of *in situ* structural health monitoring (SHM) for plate-like structural components.[1–3] An effective implementation of *in situ* SHM must eventually combine two aspects that have traditionally been pursued separately, *viz.* damage detection and damage assessment. Possible approaches and options for *in situ* damage detection, as opposed to the more conventional non destructive inspection techniques, is a topic attracting considerable research interest, particularly for the detection of barely visible impact damage in composite laminates.[3–6] To achieve a fully integrated SHM system, the detection process must provide a quantitative characterization that can be used for damage assessment. For the purposes of damage assessment, the primary effect of a delamination is to change the local value of the bending stiffness and of the transverse-shear stiffness. A theoretical model for predicting the residual strength of a composite laminate containing a flexural inhomogeneity has only recently been developed.[7] The primary objective in the present work is to provide a theoretical framework suitable for *in situ* characterization of flexural inhomogeneities due to delamination in composite laminates. The theory is equally applicable for other types of laminar defects, such as corrosion thinning, that can be modeled as flexural inhomogeneities.

The underlying strategy is to characterize the scattering of plate waves by flexural inhomogeneities within the framework of Mindlin plate theory,[8] and using the Born approximation for scattering.[9,10] It is envisaged that the plate has built-in (or surface mounted) actuators and sensors that generate the primary wave and detect the scattered wave.[5,6] The rationale for using the Mindlin and Born approximations is briefly as follows. Mindlin plate theory is known to be exceptionally accurate down to wavelengths comparable with the plate thickness h, whereas classical plate theory is of acceptable accuracy only for wavelengths greater than, say, $20h$. Thus, Mindlin plate theory offers the prospect of much better resolution of damage size, relative to classical plate theory, while retaining a tractable analysis of wave scattering, whereas an analysis using the exact 3D-elasticity equations would be quite intractable. The Born approximation is appropriate for weak inhomogeneities, which however is the case of greatest practical interest, for example with barely visible impact damage, or with early detection of damage generally.

The reconstruction of a flexural inhomogeneity from scattered-wave data is an inverse problem. Because a plate is a two-dimensional object, a tomographic reconstruction would appear to be an attractive prospect. This approach has recently been explored experimentally by Hinders *et al.*,[11,12] who also provide a comprehensive bibliography. They found the conventional tomographic reconstruction algorithm to be unforgiving and intractable. However, the present work may provide an appropriate theoretical framework for a more successful tomographic reconstruction. In this respect, it is encouraging to note that a 1D version of the present theory, based on Timoshenko beam theory, has been found to give quite reasonable agreement with experimental observations of scattering from delaminations in a quasi-1D configuration.[13]

Although Mindlin's equations were first derived 50 years ago, and have since appeared in several text books,[14,15] there has not been a systematic investigation of the fundamental source solutions, or of scattering by inhomogeneities, except for a recent analytical solution of scattering by a circular inhomogeneity.[16] This paper focuses on source solu-

[a]Electronic mail: francis.rose@dsto.defence.gov.au

 0001-4966/2004/116(1)/154/18/$20.00

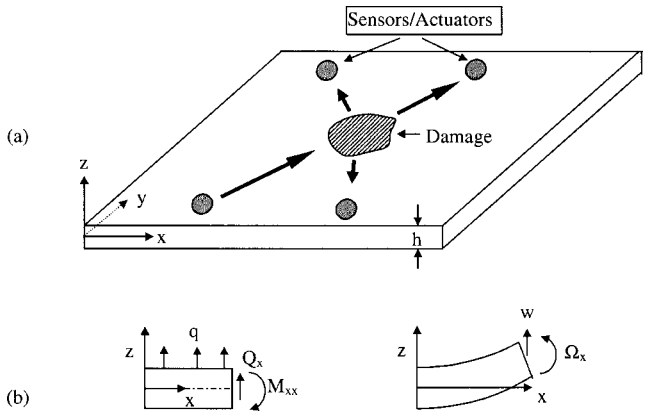

FIG. 1. Coordinate axes and sign conventions for Mindlin plate theory. (a) A plate with built-in actuators and sensors for detection of delamination damage. (b) Sign conventions for positive bending moment M_{xx}, shear force Q_x, rotation Ω_x, and deflection w.

tions and is organized as follows. Section II presents Mindlin's equations in a manner that highlights their mixed vector and scalar character, and hence the analogies and differences with elasticity theory.[17–19] Section III presents detailed calculations for a point moment and higher-order combinations (doublets) that are required for characterizing both the waves generated by actuators and the scattered waves from inhomogeneities. Section IV provides finite-source results, and Sec. V examines the influence of a straight boundary on the radiation pattern from a center of bending, which represents an appropriate point-source representation for a circular piezoelectric patch actuator[6] or for laser-generated plate waves.[20,21] Finally, Sec. VI presents a discussion of the results, including a brief comparison with previous related work. The scattering of plate waves by flexural inhomogeneities is discussed in a companion paper,[22] hereafter referred to as Part II.

II. MINDLIN PLATE THEORY

A. Governing equations

There are four key steps in deriving Mindlin's plate-theory equations,[8] as follows.

1. Equilibrium equations

$$M_{\beta\alpha,\beta}-Q_\alpha+m_\alpha=0, \tag{1a}$$

$$Q_{\alpha,\alpha}+q=0, \tag{1b}$$

or, in vector notation,

$$\nabla\cdot\mathbf{M}-\mathbf{Q}+\mathbf{m}=0, \tag{2a}$$

$$\nabla\cdot\mathbf{Q}+q=0, \tag{2b}$$

where $\mathbf{M}\equiv M_{\alpha\beta}$ denotes the tensor of bending moments; $\mathbf{Q}\equiv Q_\alpha$ is the shear force; $\mathbf{m}\equiv m_\alpha$ is the area density of external bending moment; and q is the area density of external vertical force. The coordinate axes and sign conventions are shown in Fig. 1. Equations (1a) and (1b), or equivalently (2a) and (2b), are derived from the equilibrium equations of elasticity theory by integrating across the plate thickness, and they constitute three equations for five unknowns, the plate-theory "forces": $M_{\alpha\beta}$, Q_α, noting that $M_{\alpha\beta}$ is symmetric ($M_{\alpha\beta}=M_{\beta\alpha}$) and that Greek subscripts stand for x or y, as is conventional in 2D elasticity. The source densities $\mathbf{m}$ and q, which play the role of body-force terms, are assumed to be prescribed. Equations of motion are derived from these equilibrium equations by including appropriate inertia forces as part of the body-force terms, in accordance with d'Alembert's principle.

2. Kinematic assumption

$$u_\alpha(x,y,z,t)=-z\Omega_\alpha(x,y,t), \tag{3a}$$

$$u_z(x,y,z,t)=w(x,y,t). \tag{3b}$$

Equations (3a) and (3b) express the 3D elastic displacement $\mathbf{u}$ in terms of the plate-theory "displacements," *viz.* the components of the rotation $\mathbf{\Omega}$ $(=\Omega_\alpha)$, and the deflection w.

3. Force-displacement relations

The stress-strain and strain-displacement relations of 3D elasticity lead to the following relations between plate-theory forces and displacements, on using the standard definitions for $\mathbf{M}$ and $\mathbf{Q}$[14,15] and the kinematic assumption (3a) and (3b):

$$M_{\alpha\beta}=-D\left\{\nu\nabla\cdot\mathbf{\Omega}\delta_{\alpha\beta}+\frac{1-\nu}{2}(\Omega_{\alpha,\beta}+\Omega_{\beta,\alpha})\right\}, \tag{4a}$$

$$\mathbf{Q}=\bar{\mu}h(\nabla w-\mathbf{\Omega}), \tag{4b}$$

where $D=E'I=E'h^3/12$ denotes the plate bending stiffness, E' is the plane-strain Young's modulus $E'=E/(1-\nu^2)$, ν is the in-plane Poisson ratio, and $\bar{\mu}$ is the effective transverse-shear modulus. The correct value of $\bar{\mu}$ has been the subject of considerable debate and controversy. It is only necessary to note here that $\bar{\mu}$ is an *undetermined parameter* within the framework of Mindlin plate theory: it is only restricted to have the same dimensions as a shear modulus. Furthermore, Eqs. (4a) and (4b) apply equally for a transversely isotropic plate, with the axis of transverse isotropy normal to the plate surface, and the subsequent equations, which were originally derived for an isotropic plate,[8] can therefore also be used for a quasi-isotropic composite laminate,[23] with an appropriate choice for $\bar{\mu}$. This choice is further discussed in Sec. V.

4. Mindlin plate equations

Substituting (4a) and (4b) into (1a) and (1b) or (2a) and (2b), and including rotary inertia and transverse inertia terms, one obtains the following equations of motion for a homogeneous plate, with ρ denoting the mass density per unit volume:

$$D\left\{\nabla\nabla\cdot\mathbf{\Omega}-\frac{1-\nu}{2}\nabla\times\nabla\times\mathbf{\Omega}\right\}+\bar{\mu}h(\nabla w-\mathbf{\Omega})-\rho I\ddot{\Omega}=\mathbf{m}, \tag{5a}$$

$$\bar{\mu}h\nabla\cdot(\nabla w-\mathbf{\Omega})-\rho h\ddot{w}=-q \tag{5b}$$

where $\ddot{\Omega}\equiv\partial^2\mathbf{\Omega}/\partial t^2$ and t denotes time. In Eq. (5a), $\mathbf{\Omega}=(\Omega_x,\Omega_y,0)$ for the purposes of evaluating $\nabla\times\mathbf{\Omega}$, or equivalently, use is made of the vector identity $\nabla\times\nabla\times\mathbf{\Omega}=\nabla(\nabla\cdot\mathbf{\Omega})-\nabla^2\mathbf{\Omega}$. These constitute three equations for three unknowns (the plate-theory displacements $\mathbf{\Omega}$, w), the

source terms $\mathbf{m}$, q being prescribed. Equations (5a) and (5b) were first derived by Mindlin,[8] but they are presented here in vector notation to highlight analogies and differences with the equations of 3D elasticity theory, as discussed next.

B. Comparison with 3D elasticity

Equations (5a) and (5b) may be usefully compared with the Lamé equations of 3D elasticity,[17–19]

$$(\lambda+2\mu)\nabla\nabla\cdot\mathbf{u}+\mu\nabla\times\nabla\times\mathbf{u}-\rho\ddot{\mathbf{u}}=-\mathbf{f}, \tag{6}$$

where $\mathbf{u}$ denotes the elastic displacement, λ, μ denote the Lamé parameters, ρ is the mass density, and $\mathbf{f}$ is the (prescribed) body force per unit volume. There are three points worth noting in this comparison.

1. Potentials

The vector character of (5a) and (5b) suggests the use of potentials, in accordance with the familiar Helmholtz representation used in elasticity. Accordingly, let

$$\mathbf{\Omega}=\nabla\varphi+\nabla\times(\hat{z}\psi) \tag{7}$$

where $\hat{z}$ denotes the unit vector in the z-direction, and $\varphi(x,y,t)$, $\psi(x,y,t)$ are potentials analogous to those representing respectively dilatational and shear motions in 2D elasticity.[17] Substituting (7) into (5a) and (5b), one can separate the irrotational and the divergence-free components of the plate rotation $\mathbf{\Omega}$ as follows,

$$\begin{bmatrix}(D\nabla^2-\overline{\mu}h-\rho I\partial_t^2)\nabla^2 & \overline{\mu}h\nabla^2\\ -\nabla^2 & \nabla^2-(\rho/\overline{\mu})\partial_t^2\end{bmatrix}\begin{bmatrix}\varphi\\ w\end{bmatrix}=\begin{bmatrix}\nabla\cdot\mathbf{m}\\ -\dfrac{q}{\overline{\mu}h}\end{bmatrix}, \tag{8a}$$

$$\left[\frac{1}{2}D(1-\nu)\nabla^2-\overline{\mu}h-\rho I\partial_t^2\right]\nabla^2\psi=-\hat{z}\cdot\nabla\times\mathbf{m}, \tag{8b}$$

where $\partial_t\equiv\partial/\partial t$ and $\mathbf{m}=(m_x,m_y,0)$. It can be seen that while the equations governing φ and ψ are thereby decoupled, one is left with coupled equations for the two scalar functions φ and w, unlike the case in 3D elasticity. Nevertheless, Eqs. (8a) and (8b) will still be more convenient to use for determining source solutions (Sec. III) than the original Eqs. (5a) and (5b).

2. Reciprocal theorem

Although the rotation $\mathbf{\Omega}$ is not strictly speaking a displacement, being nondimensional whereas a displacement would have dimensions of Length, it is useful to regard the combination

$$\mathbf{u}\equiv u_i=(-\mathbf{\Omega}_x,-\mathbf{\Omega}_y,w) \tag{9a}$$

as defining a 3D vector of plate-theory displacement, analogous to the elastic displacement $\mathbf{u}$ of 3D elasticity. In the same spirit, one can define a 3D vector of plate-theory traction $\mathbf{T}$ acting at a point $\mathbf{x}=(x,y)$ on a curve C with (outward) normal $\mathbf{n}$ by

$$\mathbf{T}\equiv T_i=(M_{\alpha x}n_\alpha,M_{\alpha y}n_\alpha,Q_\alpha n_\alpha) \tag{9b}$$

and a body-force vector $\mathbf{f}$ by

$$\mathbf{f}\equiv f_i=(m_x,m_y,q). \tag{9c}$$

The statement of the reciprocal theorem for Mindlin plate theory then assumes exactly the same form as the well-known Betti reciprocal theorem in elasticity.[17–19] Specifically, for any two solutions of Eqs. (5a) and (5b), distinguished by subscripts 1 and 2, respectively, and pertaining to a given plate of area S bounded by a curve C,

$$\iint_S(\mathbf{f}_1-\overline{\rho}\ddot{\mathbf{u}}_1)\cdot\mathbf{u}_2\,d^2x+\int_C\mathbf{T}_1\cdot\mathbf{u}_2\,ds=\iint_S(\mathbf{f}_2-\overline{\rho}\ddot{\mathbf{u}}_2)\cdot\mathbf{u}_1 d^2x+\int_C\mathbf{T}_2\cdot\mathbf{u}_1\,ds, \tag{10}$$

where $\overline{\rho}=\rho I$ for the first two components and $\overline{\rho}=\rho h$ for the third component of displacement.

3. Green's function

The reciprocal theorem in turn provides the basis for a representation theorem by choosing one of the solutions in Eq. (10) to be a Green's function, i.e., a fundamental solution of Eqs. (5a) and (5b) corresponding to a source term specified by delta functions in x and t. Such representation theorems are fundamental in all linear field theories,[17,24] but do not appear to have previously been developed for Mindlin plate theory. We shall not attempt to derive here the most general form of representation theorem, but focus instead on a restricted formulation which, however, covers most applications encountered in practice. Accordingly, consider the case where the boundary conditions on C are independent of time t, and consider the Fourier transform over time of all the plate-theory variables, using a circumflex to denote this Fourier transform,

$$\hat{u}(\mathbf{x},\omega)=\int_{-\infty}^{\infty}u(\mathbf{x},t)e^{i\omega t}\,dt. \tag{11}$$

Convolution integrals over time then turn into products of the respective Fourier transformed variables.

Let $\hat{g}_{ij}(\mathbf{x}|\boldsymbol{\xi})$ denote a dynamic Green's function representing the ith component of the displacement vector u_i [referring to Eq. (9a)] at location $\mathbf{x}$ due to the jth component of force acting at an arbitrary point $\mathbf{x}=\boldsymbol{\xi}$ within S. This Green's function corresponds to the solution of (5a) and (5b) when the relevant component of body-force f_i in (9c) is specified by

$$f_j=\delta(\mathbf{x}-\boldsymbol{\xi}), \tag{12}$$

where $\delta(\mathbf{x})$ denotes the Dirac delta function. Then, using $\hat{g}_{ij}$ as the displacement field $\mathbf{u}_1$ in Eq. (10), and dropping the subscript 2 for the second displacement field, one obtains, with minor rearrangement, the following representation theorem,

$$\hat{u}_j(\boldsymbol{\xi})=\iint_S\hat{f}_i(\mathbf{x})\hat{g}_{ij}(\mathbf{x}|\boldsymbol{\xi})dS+\int_C[\hat{T}_i(\mathbf{x})\hat{g}_{ij}(\mathbf{x}|\boldsymbol{\xi})-\hat{T}_{ij}^g(\mathbf{x})\hat{u}_i(\mathbf{x})]ds, \tag{13}$$

where $\hat{T}^g_{ij}(\mathbf{x})$ denotes the traction vector (9b) at $\mathbf{x}$ associated with the displacement field $\hat{g}_{ij}(\mathbf{x}|\boldsymbol{\xi})$ and the summation convention is used over subscripts i, j. This representation can be further simplified for the case of homogeneous boundary conditions which is often encountered in practice. In that case, $\hat{g}_{ij}$ can be shown to exhibit spatial reciprocity, i.e., $\hat{g}_{ij}(\mathbf{x}|\boldsymbol{\xi})=\hat{g}_{ij}(\boldsymbol{\xi}|\mathbf{x})$, and one of the two terms in the boundary integral vanishes. This simplification occurs for the case of a clamped plate (zero displacement) and a free plate (zero traction), which are both of practical interest.

In the present work, we shall only require the Green's function for (*i*) an infinite plate, in which case the only relevant boundary condition is the Sommerfeld radiation condition, requiring that the solution $\hat{g}_{ij}(\mathbf{x}|\boldsymbol{\xi})$ should represent an outgoing wave at infinity, and (*ii*) a semi-infinite plate with a straight boundary, discussed in Sec. IV.

C. Plane-wave results

Before proceeding to derive source solutions, it will prove convenient to summarize here certain key results for plane waves that will be required subsequently in Secs. III and IV. In particular, the results in Eqs. (19)–(26) do not appear to have been recorded previously, whereas Eqs. (14)–(18) are known results,[8,14,15] but are included here for completeness and for later use.

1. Frequency equation

The homogeneous form of the equations of motion (8a),

$$\begin{bmatrix} (D\nabla^2-\overline{\mu}h-\rho I\partial_t^2)\nabla^2 & \overline{\mu}h\nabla^2 \\ -\nabla^2 & \nabla^2-(\rho/\overline{\mu})\partial_t^2 \end{bmatrix}\begin{bmatrix}\varphi\\ w\end{bmatrix}=\begin{bmatrix}0\\0\end{bmatrix}, \tag{14a}$$

admits plane-wave solutions of the form

$$\varphi=\Phi(k,\omega)e^{i(kx-\omega t)},\quad w=W(k,\omega)e^{i(kx-\omega t)}, \tag{14b}$$

provided that k and ω satisfy the following *Timoshenko-Mindlin frequency equation*, which corresponds to a vanishing determinant when (14b) is substituted into the matrix operator (14a),

$$\Delta(k,\omega)\equiv k^4-2Bk^2\omega^2+C(\omega)\omega^4=0, \tag{15a}$$

$$B=\frac{1}{2}\left(\frac{\rho I}{D}+\frac{\rho}{\overline{\mu}}\right),\quad C(\omega)=\frac{\rho I}{D}\frac{\rho}{\overline{\mu}}-\frac{\rho h}{D}\frac{1}{\omega^2}. \tag{15b}$$

If the frequency ω is regarded as being prescribed, Eq. (15a) represents a bi-quadratic equation for the wave number k. The pertinent roots k_1, k_2 representing either traveling or evanescent waves in the direction of increasing x are given as follows,

$$k_{1,2}^2=\omega^2(B\pm\sqrt{B^2-C(\omega)}), \tag{15c}$$

$$k_1=\sqrt{k_1^2}, \tag{15d}$$

$$k_2=\begin{cases} i\sqrt{|k_2^2|}, & \omega<\omega_c, \\ \sqrt{k_2^2}, & \omega\geqslant\omega_c, \end{cases} \tag{15e}$$

where the cutoff frequency ω_c for the second root occurs when $C(\omega)=0$, i.e.,

$$\omega_c=\sqrt{\frac{\overline{\mu}h}{\rho I}}. \tag{15f}$$

The ratio of amplitudes in (14b) is given by

$$\gamma(k,\omega)\equiv\frac{\Phi(k,\omega)}{W(k,\omega)}=1-\frac{\rho}{\overline{\mu}}\frac{\omega^2}{k^2} \tag{15g}$$

with $k=k_1$ or k_2, for the first and second branches, respectively.

The frequency equation for the ψ-potential is readily derived from Eq. (8b) in the form

$$k^2-2\frac{\rho I\omega^2-\overline{\mu}h}{D(1-\nu)}=0. \tag{16}$$

The pertinent root corresponding to traveling or evanescent waves in the direction of increasing x is given by

$$k_3=\begin{cases} i\sqrt{2\dfrac{\overline{\mu}h-\rho I\omega^2}{D(1-\nu)}}, & \omega<\omega_c, \\ \sqrt{2\dfrac{\rho I\omega^2-\overline{\mu}h}{D(1-\nu)}}, & \omega\geqslant\omega_c, \end{cases} \tag{16c}$$

where the cutoff frequency ω_c is again given by (15f).

2. Phase and group velocity

The phase velocity $c=\omega/k$ for each of the three branches is readily obtained from Eqs. (15) and (16) as follows,

$$c_1(\omega)=1/h_1(\omega), \tag{17a}$$

$$c_2(\omega)=H(\omega-\omega_c)/h_2(\omega), \tag{17b}$$

$$c_3(\omega)=H(\omega-\omega_c)/h_3(\omega), \tag{17c}$$

where H denotes the Heaviside step function, and

$$h_1(\omega)=\sqrt{B+\sqrt{B^2-C(\omega)}}, \tag{17d}$$

$$h_2(\omega)=\sqrt{B-\sqrt{B^2-C(\omega)}}, \tag{17e}$$

$$h_3(\omega)=\sqrt{2\frac{\rho I-\overline{\mu}h/\omega^2}{D(1-\nu)}}. \tag{17f}$$

The group velocity $c_g=d\omega/dk$ for each of the three branches is given by

$$c_{gi}(\omega)=[h_i(\omega)+\omega h_i'(\omega)]^{-1},\quad i=1,2,3, \tag{18a}$$

where h_i is given by (17d), (17e), and (17f), $h'=dh/d\omega$, and the Heaviside functions in (17b) and (17c) apply for $i=2$, 3. An alternative expression may be obtained from (15a):

$$c_g=-\frac{\partial\Delta/\partial k}{\partial\Delta/\partial\omega}. \tag{18b}$$

3. Energy transport

It is known from general theoretical considerations that the group velocity c_g represents the *speed of energy transport* c_e, but it is nevertheless valuable as a cross check to derive an expression for c_e directly from the relation[17]

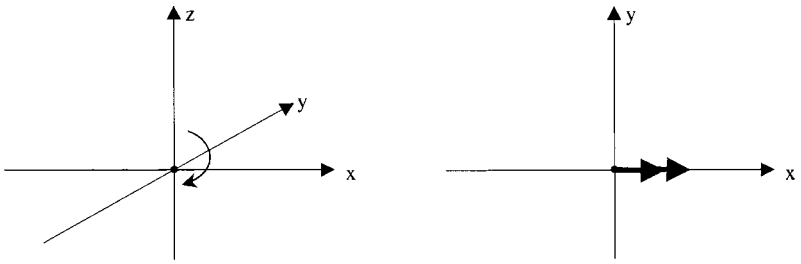

FIG. 2. Diagrammatic representation of a point moment. (a) The conventional representation indicating the sense of rotation in the x-z plane. (b) An alternative representation highlighting the analogy with an in-plane body force in 2D elasticity.

$$\langle \mathcal{P} \rangle = c_e \langle \mathcal{E} \rangle, \tag{19}$$

where $\langle\ \rangle$ is used to denote the time average over a cycle, $\mathcal{P}$ denotes the power flux (per unit length along the wave front, i.e., along the y-axis for plane waves of the form (14b)), $\mathcal{E}$ denotes the total energy density (per unit length), which is the sum of the kinetic energy and strain-energy densities, and c_e denotes the speed of energy transport, which is defined by the relation (19).

For the *first branch* corresponding to the root k_1 in Eq. (15), the eigenfunctions of Eq. (14a) are given by

$$w = We^{i(k_1 x - \omega t)} \tag{20a}$$

$$\varphi = \gamma_1 We^{i(k_1 x - \omega t)}, \tag{20b}$$

$$\gamma_1 = 1 - \frac{\rho}{\bar{\mu}} \left(\frac{\omega}{k_1} \right)^2. \tag{20c}$$

The *power flux* is given by

$$\mathcal{P} = M_{xx} \dot{\Omega}_x - Q_x \dot{w} \tag{21a}$$

so that, using the force-displacement relations (4a) and (4b),

$$\langle \mathcal{P} \rangle = \tfrac{1}{2} W^2 k_1 \omega [D \gamma_1^2 k_1^2 + \bar{\mu} h (1 - \gamma_1)]. \tag{21b}$$

Using the general principle that the energy in a vibrating system is half potential and half kinetic, we have

$$\mathcal{E} = \rho I \dot{\Omega}_x^2 + \rho h \dot{w}^2, \tag{22a}$$

$$\langle \mathcal{E} \rangle = \tfrac{1}{2} W^2 \omega^2 [\rho I \gamma_1^2 k_1^2 + \rho h], \tag{22b}$$

and hence

$$c_e = \frac{k_1}{\omega} \frac{D \gamma_1^2 k_1^2 + \bar{\mu} h (1 - \gamma_1)}{\rho I \gamma_1^2 k_1^2 + \rho h}. \tag{23}$$

Although it is not immediately apparent, it can be verified that this expression gives the same numerical value as (18a) for c_g, for $i = 1$, thereby providing a useful check on both equations.

These results are readily modified to apply for the *second branch*. Consider a plane wave specified by

$$w = We^{i(k_2 x - \omega t)}, \tag{24a}$$

$$\varphi = \gamma_2 We^{i(k_2 x - \omega t)}, \tag{24b}$$

$$\gamma_2 = 1 - \frac{\rho}{\bar{\mu}} \left(\frac{\omega}{k_2} \right)^2, \quad \omega > \omega_c. \tag{24c}$$

The power flux, energy density, and speed of energy transport are obtained from Eqs. (21)–(23) simply by replacing k_1 and γ_1 by k_2 and γ_2, noting the restriction that propagating waves only occur above the cutoff frequency ($\omega > \omega_c$). Thus, for the second branch,

$$c_e = \frac{k_2}{\omega} \frac{D \gamma_2^2 k_2^2 + \bar{\mu} h (1 - \gamma_2)}{\rho I \gamma_2^2 k_2^2 + \rho h}, \quad \omega > \omega_c, \tag{25}$$

which can also be shown to agree with (18a) for $i = 2$.

The corresponding results for the *third branch* may be summarized as follows. For a plane wave specified by

$$\psi = \Psi e^{i(k_3 x - \omega t)}, \tag{26a}$$

$$\mathcal{P} = M_{xy} \dot{\Omega}_y, \tag{26b}$$

$$\langle \mathcal{P} \rangle = \frac{D(1 - \nu)}{4} k_3^3 \omega \Psi^2, \tag{26c}$$

$$\langle \mathcal{E} \rangle = \tfrac{1}{2} \rho I k_3^2 \omega^2 \Psi^2, \tag{26d}$$

$$c_e = \frac{D(1 - \nu)}{2 \rho I} \frac{k_3}{\omega}. \tag{26e}$$

It can again be verified that Eq. (26e) agrees with the group velocity given by Eq. (18a) for $i = 3$.

III. POINT-SOURCE RESULTS

The objective in this section is to derive analytical solutions for the fundamental plate-theory sources [the point moment and the (vertical) point force], as well as for higher-order point sources (doublets) that can be constructed from those two. The solution procedure is outlined for the case of a point moment, which is considered first, and only the key results are noted for the other cases. The key features of interest are (*i*) the radiation patterns and (*ii*) the partition of energy between the three modes.

In terms of the notation introduced earlier for plate-theory displacements and forces [Eqs. (9a) and (9c)], the solution derived below in Sec. III A provides the components $\hat{g}_{i1}$ of the dynamic Green's function $\hat{g}_{ij}$ of Eq. (13). The full set of components of $\hat{g}_{ij}$ is listed in the Appendix for future reference.

A. Point moment

1. Source solution

The source specification

$$m_x = \delta(\mathbf{x}) \delta(t), \tag{27a}$$

$$m_y = q = 0 \tag{27b}$$

in Eqs. (5a) and (5b), or equivalently in Eqs. (8a) and (8b) in terms of potentials, defines a *point moment of unit strength*, acting at the origin, in the x-z plane, as indicated in Fig. 2(a).

The essence of the solution procedure is to use integral transforms over time t and over spatial coordinates x, y, to reduce Eqs. (8a) and (8b) to algebraic equations that are readily solved. This yields an explicit algebraic expression for the doubly transformed unknown, from which all the required solutions can be recovered by performing the inverse transforms. Applying a Fourier transform over t to Eqs. (8a) and (8b), using the notation introduced earlier in Eq. (11), leads to

$$\begin{bmatrix} (D\nabla^2-\overline{\mu}h+\rho I\omega^2)\nabla^2 & \overline{\mu}h\nabla^2 \\ -\nabla^2 & \nabla^2+(\rho/\overline{\mu})\omega^2 \end{bmatrix}\begin{bmatrix} \hat{\varphi} \\ \hat{w} \end{bmatrix} = \begin{bmatrix} \delta'(x)\,\delta(y) \\ 0 \end{bmatrix}, \tag{28a}$$

$$\left[D\frac{1-\nu}{2}\nabla^2-\overline{\mu}h+\rho I\omega^2\right]\nabla^2\hat{\psi}=\delta(x)\,\delta'(y). \tag{28b}$$

At this stage, it is possible to proceed by applying a double Fourier transform over x, y. However, a more effective approach is to introduce auxiliary functions which are selected to be such that the source term, and hence the auxiliary functions, are radially symmetric. Accordingly, let

$$\hat{\varphi}=\frac{\partial\hat{u}}{\partial x}, \quad \hat{w}=\frac{\partial\hat{v}}{\partial x}, \tag{29a}$$

$$\hat{\psi}=-\frac{\partial\hat{\chi}}{\partial y}, \tag{29b}$$

so that Eqs. (28a) and (28b) lead to

$$\begin{bmatrix} (D\nabla^2-\overline{\mu}h+\rho I\omega^2)\nabla^2 & \overline{\mu}h\nabla^2 \\ -\nabla^2 & \nabla^2+(\rho/\overline{\mu})\omega^2 \end{bmatrix}\begin{bmatrix} \hat{u} \\ \hat{v} \end{bmatrix} = \begin{bmatrix} \dfrac{\delta(r)}{2\pi r} \\ 0 \end{bmatrix}, \tag{30a}$$

$$\left[D\frac{1-\nu}{2}\nabla^2-\overline{\mu}h+\rho I\omega^2\right]\nabla^2\hat{\chi}=-\frac{\delta(r)}{2\pi r}, \tag{30b}$$

where we have used[25]

$$\delta(x)\,\delta(y)\equiv\delta(\mathbf{x})=\frac{\delta(r)}{2\pi r}. \tag{30c}$$

It can be seen that the auxiliary functions u, v, χ depend only on the radial distance r, and not on the angle θ, relative to polar coordinates r, θ [Fig. 2(b)]. Equations (30a) and (30b) can now be solved by applying a Hankel transform of order zero.[17,24] Using the corresponding capital letter to denote a doubly transformed variable, as follows,

$$V(k,\omega)=\mathcal{H}_0\{\hat{v}(r,\omega)\}=\int_0^\infty\hat{v}(r,\omega)J_0(kr)r\,dr \tag{31}$$

with the conventional notation for the Bessel function J_0, and using also the relation[24]

$$\mathcal{H}_0\{\nabla^2\hat{v}\}=-k^2\mathcal{H}_0\{\hat{v}\}, \tag{31c}$$

one obtains from Eq. (30a)

$$U(k,\omega)=\gamma(k,\omega)V(k,\omega), \tag{32a}$$

$$V(k,\omega)=\frac{1}{2\pi D\Delta(k,\omega)}, \tag{32b}$$

where γ and Δ are the functions previously defined by (15g) and (15a) in connection with plane-wave solutions. In particular, it is recalled that

$$\Delta(k,\omega)=(k^2-k_1^2)(k^2-k_2^2), \tag{32c}$$

where $k_{1,2}^2$ are given by (15c). The inverse Hankel transform can now be evaluated by contour integration, as follows,[24]

$$\hat{v}(r,\omega)=\int_0^\infty V(k,\omega)J_0(kr)k\,dk \tag{33a}$$

$$=\frac{1}{2}\int_{-\infty+i\varepsilon}^{\infty}V(k,\omega)H_0^{(1)}(kr)k\,dk \tag{33b}$$

$$=\frac{i}{4D}\frac{H_0^{(1)}(k_1r)-H_0^{(1)}(k_2r)}{k_1^2-k_2^2}. \tag{33c}$$

There are three points worth noting in this derivation.

(i) Extending the range of integration to $(-\infty+i\varepsilon,\infty)$ and replacing J_0 by the Hankel function $H_0^{(1)}$ relies on $V(k,\omega)$ being even in k.

(ii) The advantage of this replacement is that $H_0^{(1)}(z)$ is analytic and decays exponentially for $\mathrm{Im}(z)>0$, as indicated by its asymptotic expansion for $|z|\to\infty$,[26]

$$H_0^{(1)}(z)\sim\sqrt{\frac{2}{\pi z}}e^{i(z-\pi/4)}, \quad |z|\to\infty, \tag{34}$$

so that the integral in (33b) can be evaluated by residues on closing the contour in the upper half-plane. The notation $(-\infty+i\varepsilon,\infty)$ is meant to indicate that the integration path lies above the real axis for $\mathrm{Re}(k)<0$ and below the real axis for $\mathrm{Re}(k)>0$.[24]

(iii) The inverse (33c) consists of two terms that involve the same functional form, but with k_1 replaced by k_2. This feature stems from the factorization of the frequency equation shown in (32c) and it will also apply to all the results derived in this section.

Having obtained $\hat{v}(r,\omega)$, the remaining step is to perform an inverse Fourier transform over frequency ω to recover the time-domain form $w(r,t)$. This last inversion must generally be performed numerically,[15] as further discussed in Sec. VI. However, $\hat{v}(r,\omega)$ can be used directly for deriving the radiation patterns and the radiated energy as a function of frequency, recalling that $\hat{v}(r,\omega)$ can be interpreted as the steady-state response for a source term with a harmonic time dependence $e^{-i\omega t}$.[9,15] Consequently, in this section and the next, the solutions for both point sources and finite sources will be presented as the Fourier transforms over time.

To complete the solution for the point moment, it is now necessary to return to Eq. (29a) to derive the displacement $\hat{w}$ and the potential $\hat{\varphi}$. This gives

$$\hat{w}(\mathbf{x},\omega)=-\frac{i}{4D}\frac{k_1H_1^{(1)}(k_1r)-k_2H_1^{(1)}(k_2r)}{k_1^2-k_2^2}\cos\theta, \tag{35a}$$

where the Hankel function of order one, $H_1^{(1)}$, arises from using the recurrence relation,

$$\frac{dH_0^{(1)}(z)}{dz} = -H_1^{(1)}(z). \tag{35b}$$

The corresponding $\hat{\varphi}$ is given by

$$\hat{\varphi}(\mathbf{x},\omega) = -\frac{i}{4D}\frac{\gamma_1 k_1 H_1^{(1)}(k_1 r) - \gamma_2 k_2 H_1^{(1)}(k_2 r)}{k_1^2 - k_2^2}\cos\theta, \tag{36a}$$

in accordance with the relation (15g). This potential contributes only to the irrotational component of the vector field $\mathbf{\Omega}$. According to Eq. (7), that component is given by

$$\hat{\Omega}_r(\mathbf{x},\omega) = -\frac{i}{4D}\frac{k_1\gamma_1 G(k_1 r) - k_2\gamma_2 G(k_2 r)}{k_1^2 - k_2^2}\cos\theta, \tag{36b}$$

$$G(kr) \equiv \frac{d}{dr}H_1^{(1)}(kr) = k\left[H_0^{(1)}(kr) - \frac{1}{kr}H_1^{(1)}(kr)\right], \tag{36c}$$

$$\hat{\Omega}_\theta(\mathbf{x},\omega) = \frac{i}{4D}\frac{k_1\gamma_1 H_1^{(1)}(k_1 r) - k_2\gamma_2 H_1^{(1)}(k_2 r)}{k_1^2 - k_2^2}\frac{\sin\theta}{r}. \tag{36d}$$

The solenoidal component of $\mathbf{\Omega}$ is obtained by solving Eq. (30b) for the auxiliary function $\hat{\chi}(r,\omega)$, using the same procedure as outlined above, then substituting in Eqs. (29b) and (7). This leads to

$$\hat{\psi}(\mathbf{x},\omega) = -\frac{i}{2D(1-\nu)}\frac{H_1^{(1)}(k_3 r)}{k_3}\sin\theta \tag{37a}$$

$$\hat{\Omega}_r(\mathbf{x},\omega) = -\frac{i}{2D(1-\nu)}\frac{H_1^{(1)}(k_3 r)}{k_3}\frac{\cos\theta}{r}, \tag{37b}$$

$$\hat{\Omega}_\theta(\mathbf{x},\omega) = \frac{i}{2D(1-\nu)}\left[H_0^{(1)}(k_3 r) - \frac{1}{k_3 r}H_1^{(1)} \times (k_3 r)\right]\sin\theta. \tag{37c}$$

This completes the solution for the plate displacements corresponding to a point moment of unit strength. The Cartesian components of Ω, and of the deflection w derived from the relations (14b) and (15g), constitute the Cartesian components of $\hat{g}_{i1}$. The full set of components $\hat{g}_{ij}$ is listed in the Appendix for convenience.

2. Radiation pattern and partition of energy

The radiation patterns and the partition of radiated energy between the three modes can now be determined from Eqs. (35)–(37). There are two points worth noting in presenting these results.

(i) The only terms that contribute to the radiated energy are those whose amplitude decays with distance as $r^{-1/2}$. Thus, $\hat{\Omega}_r$ in (37b) and $\hat{\Omega}_\theta$ in (36d) would not contribute to the radiated energy.

(ii) Because the displacement field for a point moment is not radially symmetric, it is not immediately obvious that the radiated energy can be derived from the plane-wave relations between wave amplitude and power flux that were derived in Sec. II C 4.

The correct expression for the power flux in the radial direction is given by

$$P_r(r,\theta) = M_{rr}\dot{\Omega}_r + M_{r\theta}\dot{\Omega}_\theta - Q_r\dot{w}. \tag{38a}$$

For waves corresponding to the *first mode*, the first and the third terms on the right-hand side of (38a) are taken into account in the plane-wave expression (21a), but the second term is not. However, it can be verified from Eqs. (36) and (37) and from the constitutive relation[27]

$$M_{r\theta} = -D\frac{1-\nu}{2}\left\{\frac{1}{r}\left(\frac{\partial\Omega_r}{\partial\theta} - \Omega_\theta\right) + \frac{\partial\Omega_\theta}{\partial r}\right\} \tag{38b}$$

that the product $M_{r\theta}\dot{\Omega}_\theta$ only contains terms that decay faster than r^{-1}, and hence that product does not contribute to the radiated energy. Thus, the plane-wave relations (21b) and (26c) can indeed be used to determine the radiated power flux in terms of the amplitude of the deflection w [given by (35a) and (35b) for modes 1 and 2] and the amplitude of the ψ-potential [given by (37a)] for mode 3.

The time-averaged radiated energy $\langle\mathcal{R}\rangle$ for each of these three modes is determined by integrating the power flux over $0 \leqslant \theta < 2\pi$, i.e., $\langle\mathcal{R}\rangle = (1/T)\int_0^{2\pi}\int_0^T P_r r\, dt\, d\theta$, where T is the period, which leads to

$$\langle\mathcal{R}\rangle_1 = \frac{\gamma_1^2 k_1^2 D + (1-\gamma_1)\overline{\mu h}}{16D^2(k_1^2 - k_2^2)^2}k_1^2\omega, \tag{39a}$$

$$\langle\mathcal{R}\rangle_2 = \frac{\gamma_2^2 k_2^2 D + (1-\gamma_2)\overline{\mu h}}{16D^2(k_1^2 - k_2^2)^2}k_2^2\omega, \quad \omega > \omega_c, \tag{39b}$$

$$\langle\mathcal{R}\rangle_3 = \frac{\omega}{8D(1-\nu)}, \quad \omega > \omega_c. \tag{39c}$$

The variation of $\langle\mathcal{R}\rangle_1$ with frequency, and of the ratios $\langle\mathcal{R}\rangle_2/\langle\mathcal{R}\rangle_1$, $\langle\mathcal{R}\rangle_3/\langle\mathcal{R}\rangle_1$, is shown in Fig. 3 for $\nu = \frac{1}{3}$. The normalized energy plotted in Fig. 3 depends only on the Poisson ratio ν (in addition to frequency). It can be seen that the radiated energy in the second mode is quite comparable with that in the first mode for $\omega > \omega_c$, whereas the third mode makes a relatively small contribution. It is also noted that the radiated energy in modes 2 and 3 exhibits a step discontinuity at $\omega = \omega_c$ in the present case.

The radiation pattern for the deflection w and the radial rotation Ω_r is $\cos\theta$ for all three modes, and it is $\sin\theta$ for Ω_θ, as can be seen from Eqs. (35)–(37). This is unlike the case of a point force in elasticity where the dilatational (irrotational) and shear (solenoidal) waves have different radiation patterns. Nevertheless, the radiation patterns for the point moment, and for the other point sources discussed below, can assist with damage identification from observations of scattered waves.[22]

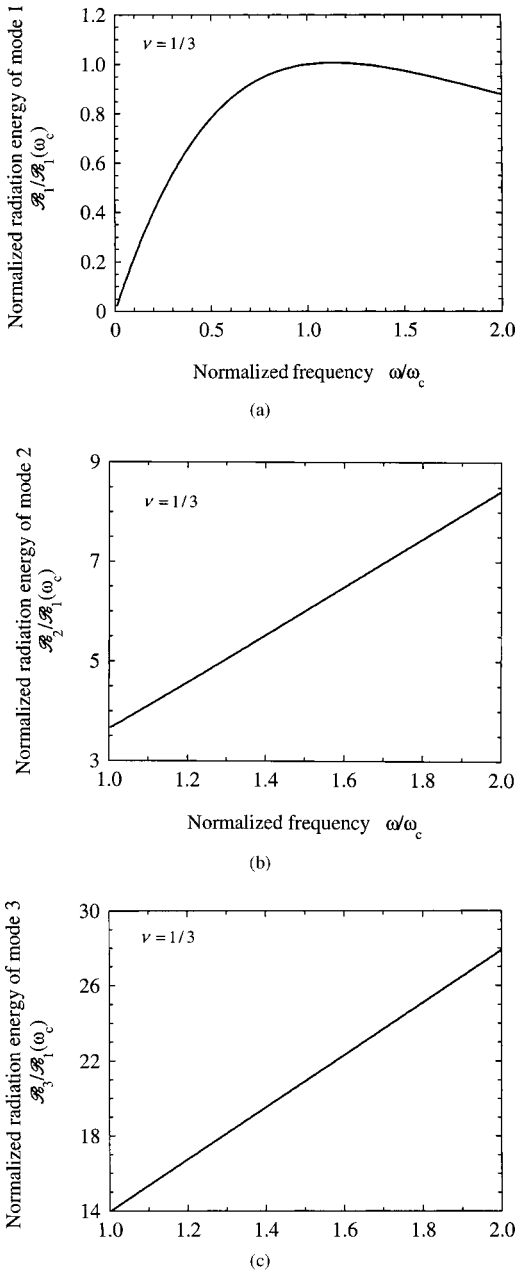

FIG. 3. Normalized radiated energy between the three modes of Mindlin plate theory for a point moment. (a) Radiated energy versus frequency for the first mode; (b), (c) ratio of radiated energy in the second and third modes relative to the first.

3. Diagrammatic representation

Before proceeding to construct higher-order point singularities, it will prove convenient to introduce here an alternative to the conventional representation shown in Fig. 2(a) for a point moment, acting at the origin, where the curved arrow lying in the x-z plane serves to indicate the sense of rotation. This corresponds to the source specification in Eqs. (27a) and (27b). Because we are considering a 2D configuration, it is possible to unambiguously identify this point moment by an arrow in the direction of the x axis, as shown in Fig. 2(b). This alternative representation highlights the analogy between the point moment and the (in-plane) point force in 2D elasticity, a double arrowhead being used to distinguish a point moment from a point force. A moment doublet can then be represented as in Fig. 4(a), which is clearer than the conventional representation in Fig. 2(a) would be, and this advantage increases as one considers more complex combinations such as that in Fig. 4(b), which corresponds to a center of bending.

B. Center of bending

The displacement field for the moment doublet shown in Fig. 4(a) can be constructed from the solution for the point moment in Fig. 2(b) by the usual process for constructing a dipole field from that of a monopole,[9,19,28] *viz.* by differentiating with respect to a coordinate axis. The appropriate source specification for Fig. 4(a) is given by

$$m_x = -\delta'(x)\,\delta(y)\,\delta(t), \tag{40a}$$

$$m_y = 0, \quad q = 0 \tag{40b}$$

instead of (27a) and (27b). The corresponding displacements can therefore be obtained from the radially symmetric auxiliary functions u, v, χ introduced in Eqs. (29a) and (29b), as follows:

$$\hat{\varphi}_{md} = -\frac{\partial^2 \hat{u}}{\partial x^2}, \quad \hat{w}_{md} = -\frac{\partial^2 \hat{v}}{\partial x^2}, \tag{41a}$$

$$\hat{\psi}_{md} = \frac{\partial^2 \hat{\chi}}{\partial x\,\partial y}. \tag{41b}$$

Although detailed expressions for the various field variables can be readily derived from Eqs. (41a) and (41b), they are omitted here for brevity. Of greater interest in the present context is the combination of two orthogonal moment doublets shown in Fig. 4(b). Following the procedure indicated above, it is readily verified that the source term is now given by

$$\nabla \cdot \mathbf{m} = -\nabla^2 \delta(\mathbf{x})\,\delta(t), \tag{42a}$$

$$\hat{\mathbf{z}} \cdot \nabla \times \mathbf{m} = 0, \quad q = 0, \tag{42b}$$

and the corresponding displacement field by

$$\hat{\varphi}_b = -\nabla^2 \hat{u}, \quad \hat{w}_b = -\nabla^2 \hat{v}, \tag{43a}$$

$$\hat{\psi}_b = 0. \tag{43b}$$

It can be seen that the displacement field is purely radial and irrotational. This combination of axial doublets can aptly be named a *center of bending*. It constitutes the analog for plate bending theory of a center of dilatation in elasticity.[17–19]

Because of the radial symmetry, there is no need to introduce auxiliary functions in this case. Equation (8a) leads directly to

$$\begin{bmatrix} \nabla^2 - \dfrac{\overline{\mu}h}{D} + \dfrac{\rho I \omega^2}{D} & \dfrac{\overline{\mu}h}{D} \\ -\nabla^2 & \nabla^2 + \dfrac{\rho}{\overline{\mu}}\omega^2 \end{bmatrix} \begin{bmatrix} \hat{\varphi}_b \\ \hat{w}_b \end{bmatrix} = \begin{bmatrix} -\dfrac{\delta(r)}{2\pi r D} \\ 0 \end{bmatrix}, \tag{44a}$$

which can be solved to obtain

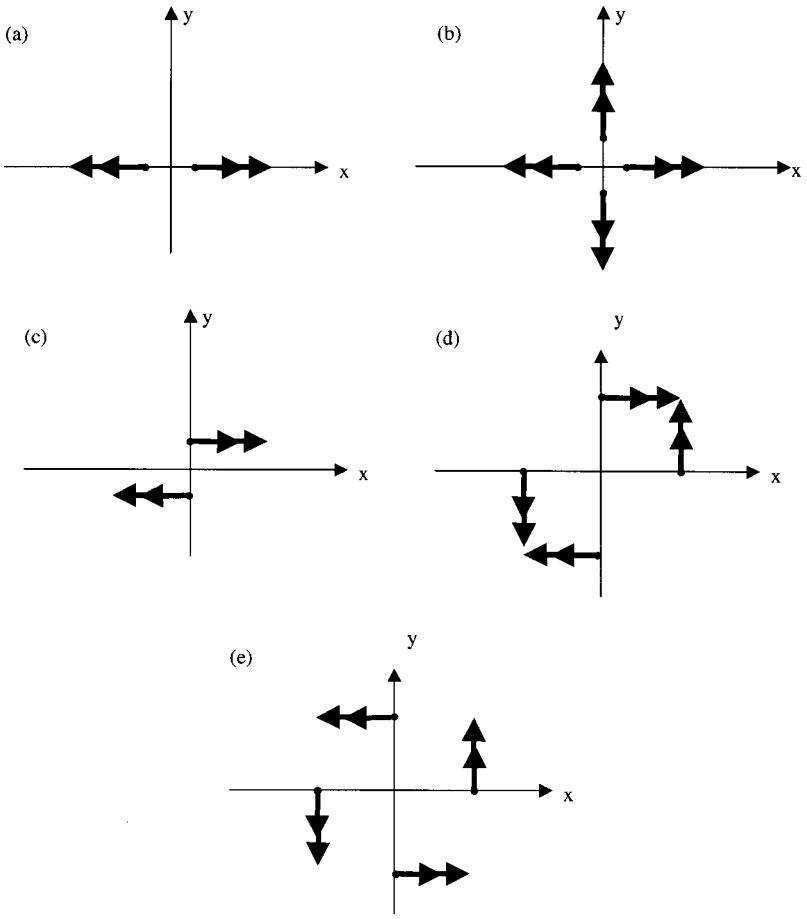

FIG. 4. Moment doublets. (a) An axial moment doublet; (b) combination of two orthogonal moment doublets, equivalent to a center of bending; (c) a transverse moment doublet; (d) combination of two orthogonal transverse-doublets, equivalent to a center of twist; and (e) combination equivalent to a center of in-plane twist.

$$\hat{w}_b(r,\omega)=\frac{i}{4D}\,\frac{k_1^2H_0^{(1)}(k_1r)-k_2^2H_0^{(1)}(k_2r)}{k_1^2-k_2^2}, \tag{44b}$$

$$\hat{\varphi}_b(r,\omega)=\frac{i}{4D}\,\frac{\gamma_1k_1^2H_0^{(1)}(k_1r)-\gamma_2k_2^2H_0^{(1)}(k_2r)}{k_1^2-k_2^2}. \tag{44c}$$

Expressions for the rotation, bending moments, and shear force are readily derived from these results and Eqs. (4) and (7). In particular it is readily seen that the radiation pattern for w and Ω_r is isotropic, and that $\Omega_\theta=M_{r\theta}=Q_\theta=0$. It is worth recording the result for $\nabla\cdot\mathbf{\Omega}$, the trace of the curvature tensor, because a small circular piezoelectric sensor in effect responds to this quantity (as further discussed in Sec. VI):

$$\nabla\cdot\hat{\Omega}(r,\omega)=\nabla^2\hat{\varphi}(r,\omega)$$

$$=-\frac{i}{4D}\,\frac{\gamma_1k_1^4H_0^{(1)}(k_1r)-\gamma_2k_2^4H_0^{(1)}(k_2r)}{k_1^2-k_2^2}. \tag{44d}$$

The time-averaged radiated energy for a *center of bending of unit strength* is given by

$$\langle\mathcal{R}\rangle=\frac{D\gamma^2k^2+(1-\gamma)\overline{\mu}h}{8D^2(k_1^2-k_2^2)^2}k^4\omega, \tag{45}$$

with k, γ taken to be k_1, γ_1 for mode 1, and k_2, γ_2 for mode 2. The variation of radiated energy with frequency is shown in Fig. 5.

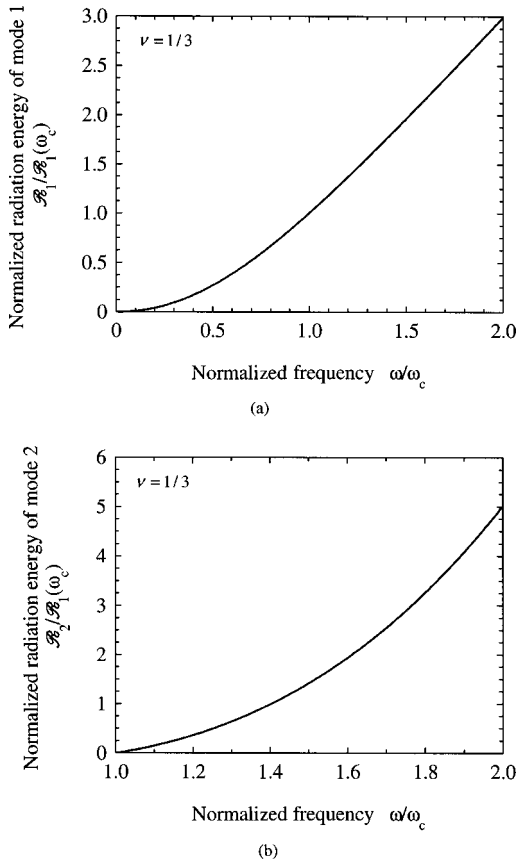

FIG. 5. Normalized radiated energy for a center of bending. (a) Radiated energy versus frequency for the first mode; (b) ratio of radiated energy in the second mode relative to the first.

C. Center of twist

The moment doublet in Fig. 4(a) is an axial doublet. It is also possible to define a transverse doublet, as in Fig. 4(c), for which the source specification is given by

$$\nabla\cdot\mathbf{m}=-\delta'(x)\,\delta'(y)\,\delta(t),$$
$$\hat{\mathbf{z}}\cdot\nabla\times\mathbf{m}=\delta(x)\,\delta''(y)\,\delta(t), \tag{46}$$
$$q=0.$$

Here again, combinations of such doublets are of greater interest in practice than individual doublets. In particular, the combination shown in Fig. 4(d) can be named a *center of twist*. It is the analog for plate bending theory of a center of shear in elasticity,[28] which is also known as a double couple in seismology.[19] The appropriate source specification for a center of twist of *unit strength* is

$$\nabla\cdot\mathbf{m}=-2\,\delta'(x)\,\delta'(y)\,\delta(t),$$
$$\hat{\mathbf{z}}\cdot\nabla\times\mathbf{m}=[\,\delta(x)\,\delta''(y)-\delta''(x)\,\delta(y)\,]\,\delta(t), \tag{47}$$
$$q=0.$$

Solving Eqs. (8a) and (8b) as before we now obtain

$$\hat{w}(\mathbf{x},\omega)=\frac{i}{4D}\,\frac{k_1G(k_1r)-k_2G(k_2r)}{k_1^2-k_2^2}\sin 2\theta$$
$$\hat{\varphi}(\mathbf{x},\omega)=\frac{i}{4D}\,\frac{k_1\gamma_1G(k_1r)-k_2\gamma_2G(k_2r)}{k_1^2-k_2^2}\sin 2\theta, \tag{48}$$
$$\hat{\psi}(\mathbf{x},\omega)=-\frac{i}{2D(1-\nu)}\left[H_0^{(1)}(k_3r)\cos 2\theta-2\,\frac{H_1^{(1)}(k_3r)}{k_3r}\cos^2\theta\right],$$

where the function G is given by Eq. (36c). The radiation pattern for w and Ω_r is $\sin 2\theta$, while that for Ω_θ is $\cos 2\theta$. The time-averaged radiated energy for a center of twist of unit strength is given by

$$\langle\mathcal{R}\rangle_{1,2}=\frac{D\gamma^2k^2+(1-\gamma)\overline{\mu h}}{16D^2(k_1^2-k_2^2)^2}k^4\omega \tag{49a}$$

for the first two modes (k, $\gamma=k_1$, γ_1 for mode 1, $=k_2$, γ_2 for mode 2), and for mode 3

$$\langle\mathcal{R}\rangle_3=\frac{k_3^2\omega}{8D(1-\nu)}. \tag{49b}$$

It can be seen that the radiated energy in the first two modes is nearly the same as that for center of bending, except that the magnitude differs by a factor of 2. The variation of radiated energy with frequency in the third mode is shown in Fig. 6.

It is also of interest to consider briefly an alternative combination of transverse doublets, shown in Fig. 4(e), which can be termed as a *center of in-plane twist*. The source specification in this case reduces to

$$\nabla\cdot\mathbf{m}=0,$$

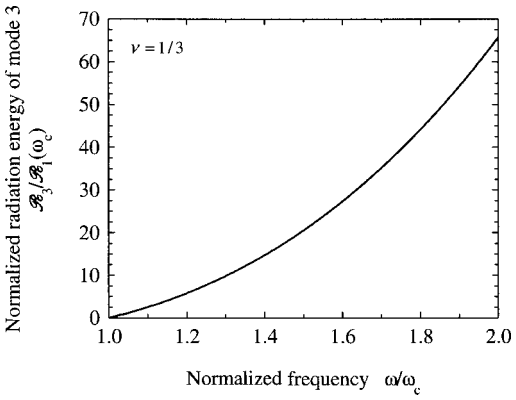

FIG. 6. Ratio of radiated energy in the third mode relative to the first for a center of twist.

$$\hat{z}\cdot\nabla\times\mathbf{m}=\nabla^2\delta(\mathbf{x})\,\delta(t), \tag{50}$$
$$q=0.$$

i.e., the only nonvanishing contribution is generated by the ψ-potential in Eq. (8b), which results in a purely solenoidal field:

$$w=0,\quad \Omega_r=0,$$
$$\hat{\Omega}_\theta=-\frac{i}{2D(1-\nu)}k_3H_1^{(1)}(k_3r). \tag{51}$$

This corresponds to the anti-plane, or SH, deformation mode for a plate.[17]

D. Point force and force doublet

The case of a downward pointing force of unit strength appears to be the only one of the fundamental point sources that has been previously studied for Mindlin plate theory,[29,30] albeit by quite a different approach from that used here. In keeping with the present notation, consider a vertical point force specified by

$$\mathbf{m}=0,$$
$$q=\delta(\mathbf{x})\,\delta(t). \tag{52a}$$

The pertinent deflection and rotation are given by

$$\hat{w}(\mathbf{x},\omega)=\frac{i}{4D}\left(\frac{H_0^{(1)}(k_1r)}{(k_1^2-k_2^2)\gamma_1}-\frac{H_0^{(1)}(k_2r)}{(k_1^2-k_2^2)\gamma_1}\right), \tag{52b}$$
$$\hat{\phi}(\mathbf{x},\omega)=\frac{i}{4D}\,\frac{H_0^{(1)}(k_1r)-H_0^{(1)}(k_2r)}{k_1^2-k_2^2}, \tag{52c}$$
$$\Omega_r(\mathbf{x},\omega)=-\frac{i}{4D}\,\frac{k_1H_1^{(1)}(k_1r)-k_2H_1^{(1)}(k_2r)}{k_1^2-k_2^2}, \tag{52d}$$
$$\Omega_\theta(\mathbf{x},\omega)=0. \tag{52e}$$

Equations (52b), (52d), and (52e) provide the components of $\hat{g}_{i3}$ in the representation theorem (13).

The important point worth noting here is that *the field for a vertical force doublet does not coincide with that for a point moment*, within the framework of Mindlin plate theory, contrary to what might be expected intuitively, and contrary

to what would be the case in classical plate theory. This difference is apparent already from the source specification (52a) for the point force, since $\hat{z}\cdot\nabla\times\mathbf{m}=0$ for that case, and therefore also for the force doublet whose specification is obtained as $-\partial/\partial x$ of (52a). Thus, for both the vertical force, and the force doublet, $\psi=0$, i.e., the generated displacement field is irrotational, unlike the case of a point moment. It is noted, however, that the radiation patterns for w and $\mathbf{\Omega}$ for the force doublet are the same as those for a point moment, and those patterns only involve the first two modes.

IV. FINITE-SOURCE RESULTS

The flexural response due to a source of finite size can now be obtained from the point-source solutions of Sec. III by integrating over the source region. In the general case, this integral would require numerical evaluation, but it can be anticipated that for localized sources, or for scattering from localized defects, useful analytical approximations can be derived that are analogous to the multipole expansions, or to far-field (radiation zone) approximations, that are used in acoustics[9] and in several other contexts.[19,31] Accordingly, in this section, two special cases of practical interest for which analytical results can be derived in a convenient form are considered first. Then, a general formula for the far-field approximation of the radiation from an arbitrary source is derived, that reduces the problem to that of evaluating the 2D Fourier transform of the source density.

A. Circular-patch actuator

Consider a source specified by a surface traction

$$\sigma_{zr}(r,\theta,z=h/2,t)=p(t)\,\delta(r-a), \tag{53a}$$

as shown in Fig. 7(a), using conventional notation for the relevant component of the stress tensor, σ_{zr}, to denote a radially directed surface traction on the top face ($z=h/2$) of a plate. This specification may be used to characterize (*i*) a surface-mounted piezoelectric circular-patch actuator[3,6] or (*ii*) laser-generated ultrasound.[20,21] The adequacy of this characterization is discussed further in Sec. VI. An equivalent plate-theory specification for this source involves two contributions, both applied at the plate's mid-plane $z=0$, *viz.* (*i*) radially directed membrane forces [Fig. 7(b)], specified by a 2D body-force density

$$f_r=p(t)\,\delta(r-a),\quad f_\theta=0, \tag{53b}$$

and (*ii*) radially directed bending moments [Fig. 7(c)], uniformly distributed along a ring of radius a,

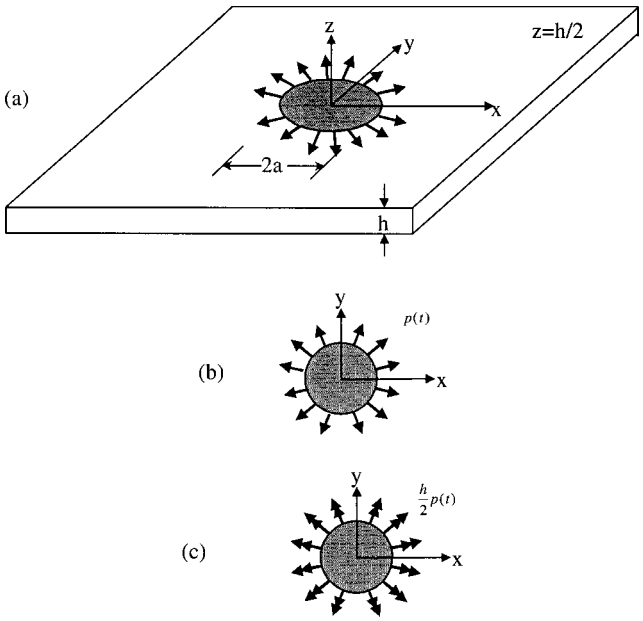

FIG. 7. Source specification for a surface-mounted circular patch actuator. (a) Ring of surface traction on $z=h/2$. (b) and (c) Plate-theory equivalent source, comprising radially directed membrane forces (b), and bending moment (c), uniformly distributed over a ring of radius $r=a$ in the mid-plane $z=0$.

$$m_r=\frac{h}{2}p(t)\,\delta(r-a),\quad m_{r\theta}=0. \tag{53c}$$

The response to the membrane forces (53b) will involve only in-plane displacements and will not be considered further in the present work. (However, in-plane deformations will be generated for the configuration shown in Fig. 1, and will be discussed in future work.) The focus here is on the flexural response due to the bending moments (53c).

It is readily verified from (53c) that the appropriate source specification for Eqs. (8a) and (8b) has only one nonzero term,

$$\begin{aligned}&\boldsymbol{\nabla}\cdot\mathbf{m}=-\frac{h}{2}p(t)\nabla^2H(r-a),\\ &\hat{\mathbf{z}}\cdot\boldsymbol{\nabla}\times\mathbf{m}=0,\quad q=0,\end{aligned} \tag{54}$$

where H denotes the Heaviside step function. It follows from Eqs. (54) and (8b) that $\psi=0$, i.e., the flexural response is irrotational. The source term in (54) being radially symmetric, the solution can be obtained directly, as in the case of a center of bending (Sec. III B), as follows

$$\hat{w}(r,\omega)=\frac{i\pi h\hat{p}(\omega)}{4D}\,\frac{k_1aJ_1(k_1a)H_0^{(1)}(k_1r)-k_2aJ_2(k_2a)H_0^{(1)}(k_2r)}{k_1^2-k_2^2}, \tag{55a}$$

$$\hat{\Omega}_r(r,\omega)=-\frac{i\pi h\hat{p}(\omega)}{4D}\,\frac{\gamma_1k_1^2aJ_1(k_1a)H_1^{(1)}(k_1r)-\gamma_2k_2^2aJ_1(k_2a)H_1^{(1)}(k_2r)}{k_1^2-k_2^2}, \tag{55b}$$

$$\hat{\Omega}_\theta(r,\omega)=0, \tag{55c}$$

$$\nabla\cdot\mathbf{\Omega}(r,\omega)=-\frac{i\pi h\hat{p}(\omega)}{4D}\,\frac{\gamma_1 k_1^3 aJ_1(k_1a)H_0^{(1)}(k_1r)-\gamma_2 k_2^3 aJ_2(k_2a)H_0^{(1)}(k_2r)}{k_1^2-k_2^2}. \tag{55d}$$

Equations (55a)–(55e) constitute a compact *exact solution for the flexural response due to a circular patch actuator* in the frequency domain. The time-domain response is obtained by an inverse Fourier transform, as further discussed in Sec. VI. However, in practice, the frequency-domain solution is often directly useful for deriving radiation patterns, as discussed in Sec. III, and for deriving asymptotic approximations, as discussed next.

There are three length-scales inherent in Eqs. (55), *viz.* the source radius a, the distance r, and the wave length $\lambda \equiv 2\pi/k$, where $k=k_1$ for mode 1 and k_2 for mode 2. Various asymptotic approximations can be derived corresponding to various combinations of limiting values for the ratios between these three lengths.[9,31] The two cases of greatest interest in the present context correspond to (*i*) the *multipole expansion* for $ka\ll 1$, and (*ii*) the *far-field (or radiation zone) approximation* for $kr\gg 1$, $ka\cdot a/r\ll 1$. There are two important results worth noting here, because they provide useful approximations for cases where an exact solution is not available.

First a multipole expansion in the present case can be obtained by using the series representation for the Bessel function $J_1(z)$,[26] which also constitutes an asymptotic expansion for $z=0$. Retaining only the first term in this expansion leads to

$$\hat{w}(r,\omega)\approx\frac{ih\hat{p}(\omega)\pi a^2}{8D}\,\frac{k_1^2H_0^{(1)}(k_1r)-k_2^2H_0^{(1)}(k_2r)}{k_1^2-k_2^2}. \tag{56}$$

Comparing this result with Eq. (44b) it can be seen that *the first term of the multipole expansion for a circular patch actuator corresponds to a center of bending of strength* $h/2\hat{p}(\omega)\pi a^2$, i.e., to the product of the moment arm $h/2$, the force amplitude $\hat{p}(\omega)$, and the source area πa^2. This result provides a convenient approximation for surface-mounted or embedded piezoelectric actuators of any other shape, provided that the moment arm, the force amplitude, and the area of the actuator are known. The important point is that the source specification (53c) for a circular-patch actuator as a ring of bending moments, as in Fig. 7(c), is equivalent to a source specification as a uniform distribution of centers of bending [of strength $(h/2)p(t)$] over a circular region of radius a, as can be seen by comparing Eq. (54a) with Eq. (42a). This equivalence has been previously noted for the case of laser-generated ultrasound.[20]

Second, the far-field approximation can be obtained by using the asymptotic expansion (34) for $H_0^{(1)}(kr)$. This leads to

$$g(k_1r;ka)=kaJ_1(ka)\sqrt{\frac{2}{\pi kr}}\,e^{i(kr-\pi/2)},\quad kr\gg 1, \tag{57}$$

in Eq. (55e). This result can be recovered from a more general form of the far-field approximation that applies for localized sources of arbitrary shape, as further discussed in Sec. IV C below.

B. Narrow rectangular patch actuator

Consider next a rectangular actuator of length $2a$ and width $2b$, with $b\ll a$, as shown in Fig. 8(a).[5,32,33] In accordance with the discussion in Sec. IV A, we focus here on the flexural response, for which the source specification is a uniform distribution of centers of bending over the region $|x|\leqslant a$, $|y|\leqslant b$. For $kb\ll 1$, this specification can be further simplified to a uniform distribution along the line segment $|x|\leqslant a$, $y=0$, with the specification

$$\nabla\cdot\mathbf{m}=-hbp(t)\nabla^2[H(a^2-x^2)\,\delta(y)],\qquad \hat{\mathbf{z}}\cdot\nabla\times\mathbf{m}=0,\quad q=0. \tag{58}$$

The solution of Eqs. (8a) and (8b) is now given by

$$\hat{w}(r,\theta;\omega)=\frac{ihb\hat{p}(\omega)}{4D}\,\frac{k_1^2g(\theta,k_1;a)-k_2^2g(\theta,k_2;a)}{k_1^2-k_2^2}, \tag{59a}$$

$$\hat{\varphi}(r,\theta;\omega)=\frac{ihb\hat{p}(\omega)}{4D}\,\frac{k_1^2\gamma_1g(\theta,k_1;a)-k_2^2\gamma_2g(\theta,k_2;a)}{k_1^2-k_2^2}, \tag{59b}$$

$$g(\theta,k;a)=\int_{-a}^{a}H_0^{(1)}(k\sqrt{r^2-2\xi r\cos\theta+\xi^2})\,d\xi, \tag{59c}$$

and $\hat{\psi}=0$. The multipole expansion for this case illustrates the procedure that can be used for an arbitrary source region,

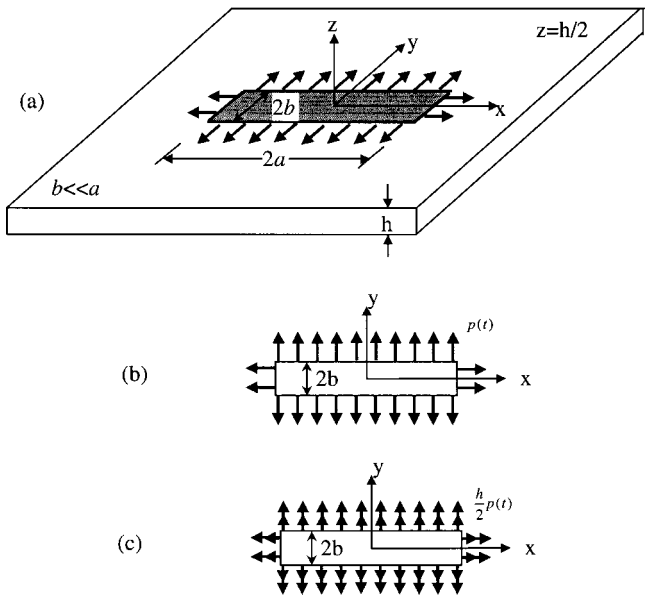

FIG. 8. Source specification for a surface-mounted narrow rectangular patch actuator.

which relies on the addition theorem for the Hankel function,[26,31]

$$H_0^{(1)}(k\sqrt{r^2-2\xi r\cos\theta+\xi^2})=J_0(k\xi)H_0^{(1)}(kr)+2\sum_{n=1}^{\infty}J_n(k\xi)H_n^{(1)}\times(kr)\cos n\theta. \tag{60}$$

Substituting (60) into (59c) yields the expansion

$$g(\theta,k;a)=\sum_{n=0}^{\infty}A_n(ka)H_n^{(1)}(kr)\cos n\theta, \tag{61a}$$

$$A_0(ka)=2\int_0^a J_0(k\xi)d\xi=2aJ_0(ka)+\pi a[J_1(ka)\mathbf{H}_0(ka)-J_0(ka)\mathbf{H}_1(ka)], \tag{61b}$$

where $\mathbf{H}_n$ denote Struve functions.[26] Because of the symmetry of the source distribution about the origin in the present case (as in the case of the circular patch), all moments A_n of odd order vanish (i.e., $A_1=A_3=\cdots=0$). Retaining only the first term in the multipole expansion (61a) and the first term in the expansion of $A_0(ka)$ for $ka\ll 1$ leads to

$$\hat{w}(r,\omega)\approx\frac{ihab\hat{p}(\omega)}{2D}\,\frac{k_1^2H_0^{(1)}(k_1r)-k_2^2H_0^{(1)}(k_2r)}{k_1^2-k_2^2}, \tag{62}$$

i.e., this first term corresponds to a center of bending of strength equal to $(h/2)\hat{p}(\omega)$ multiplied by the actuator area $4ab$, in accordance with the result stated in Sec. IV B.

C. Far-field approximation

Consider a source consisting of a distribution of centers of bending specified by

$$\nabla\cdot\mathbf{m}=-\nabla^2\sigma(\mathbf{x},t),\qquad \hat{\mathbf{z}}\cdot\nabla\times\mathbf{m}=0,\quad q=0, \tag{63}$$

where the source density $\sigma(\mathbf{x},t)$ is localized to a region of area A such as that shown as the shaded region in Fig. 1(a). The corresponding displacement can be obtained from Eqs. (44b) and (44c) in the following form:

$$\hat{w}(r,\theta;\omega)=\frac{i}{2D}\,\frac{k_1^2g(k_1;A)-k_2^2g(k_2;A)}{k_1^2-k_2^2}, \tag{64a}$$

$$g(k;A)=\int\int_A\hat{\sigma}(\boldsymbol{\xi},\omega)H_0^{(1)}(k|\mathbf{x}-\boldsymbol{\xi}|)d^2\boldsymbol{\xi}. \tag{64b}$$

The far-field approximation is obtained by (*i*) replacing $H_0^{(1)}$ in (64b) by its asymptotic form (34), and (*ii*) using $|\mathbf{x}-\boldsymbol{\xi}|\approx|\mathbf{x}|-|\boldsymbol{\xi}|\cos\phi$ in the exponential, where ϕ denotes the angle between $\mathbf{x}$ and $\boldsymbol{\xi}$, and $|\mathbf{x}-\boldsymbol{\xi}|\approx|\mathbf{x}|=r$ for the radial decay. This leads to, noting $|\boldsymbol{\xi}|\cos\phi=\mathbf{k}\cdot\boldsymbol{\xi}$,

$$g(k;A)=\sqrt{\frac{2}{\pi kr}}\,e^{i(kr-\pi/4)}\int_{-\infty}^{\infty}\int\hat{\sigma}(\boldsymbol{\xi},\omega)e^{-i\mathbf{k}\cdot\boldsymbol{\xi}}d^2\boldsymbol{\xi}, \tag{64c}$$

where $\mathbf{k}=k\hat{\mathbf{x}}$, ($\hat{\mathbf{x}}=\mathbf{x}/|\mathbf{x}|$) and the range of integration has been extended to infinity taking into account that the source term $\hat{\sigma}(\boldsymbol{\xi},\omega)$ vanishes outside the source area A. The integral in (64c) can be recognized as the 2D Fourier transform over the spatial variables of the time-transformed source density. Thus, determining the far-field approximation for $\hat{w}(\mathbf{x},\omega)$ in (64a) is reduced to evaluating this 2D spatial Fourier transform. For cases where the source density $\hat{\sigma}(\mathbf{x},\omega)$ depends only on the radial distance r, this 2D Fourier transform reduces to a Hankel transform[17]

$$\int_{-\infty}^{\infty}\int\hat{\sigma}(\boldsymbol{\xi},\omega)e^{-i\mathbf{k}\cdot\boldsymbol{\xi}}d^2\boldsymbol{\xi}=2\pi\int_0^{\infty}\hat{\sigma}(r,\omega)J_0(kr)r\,dr. \tag{64d}$$

Using (64d) and the source specification (54), one can readily verify the far-field approximation (57) derived earlier for the circular-patch actuator.

For the case of the narrow rectangular patch actuator specified by (58), Eq. (64c) leads to the following far-field approximation:

$$\hat{w}(r,\theta;\omega)=\frac{ihab\hat{p}(\omega)}{2D}\,\frac{k_1^2g(\theta,k_1;a)-k_2^2g(\theta,k_2;a)}{k_1^2-k_2^2}, \tag{65a}$$

$$\nabla\cdot\boldsymbol{\Omega}(r,\theta;\omega)=-\frac{ihab\hat{p}(\omega)}{2D}\times\frac{\gamma_1k_1^4g(\theta,k_1;a)-\gamma_2k_2^4g(\theta,k_2;a)}{k_1^2-k_2^2}, \tag{65b}$$

$$g(\theta,k;a)=\sqrt{\frac{2}{\pi kr}}\,e^{i(kr-\pi/4)}\frac{\sin(ka\cos\theta)}{ka\cos\theta}. \tag{65c}$$

The procedure illustrated above for a distribution of centers of bending can equally be applied to derive the far-field approximation for the other types of point source discussed in Sec. III.

V. SOURCES NEAR A BOUNDARY

The configurations that are being investigated experimentally for structural health monitoring (SHM) often involve actuators and sensors located close to a boundary,[3,6] as indicated in Fig. 1(a). Accordingly, the objective in this section is to derive the displacements, and in particular the radiation pattern, for an array for N equally spaced actuators along the straight boundary of a semi-infinite plate, as shown in Fig. 9.

Consider first the case of a single circular-patch actuator of radius a, centered at $x=0$, $y=b$, subjected to the boundary conditions

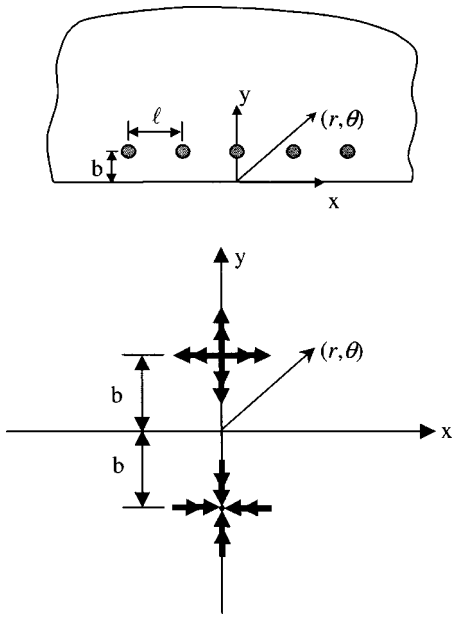

FIG. 9. Configuration for an array of equally spaced actuators/sensors. (a) Semi-infinite plate, simply supported along $y=0$. (b) Representation of a single actuator/sensor as a center of bending and an image source in an infinite plate.

$$M_{yy}=\Omega_y=w=0, \quad -\infty<x<\infty, \quad y=0, \tag{66}$$

corresponding to a simply supported boundary $y=0$. This boundary condition can be implemented experimentally for fundamental studies.[34] The exact solution for this case can be obtained by the method of images.[9,31] Thus, the displacement field for an actuator specified by Eq. (54) may be written down directly from Eqs. (55a)–(55e), allowing for a translation of the origin to $(0,b)$ and $(0,-b)$, as follows:

$$\hat{w}(r,\theta,\omega)=\frac{i\pi h\hat{p}(\omega)}{4D}\,\frac{g(k_1)-g(k_2)}{k_1^2-k_2^2}, \tag{67a}$$

$$\nabla\cdot\mathbf{\Omega}(r,\theta,\omega)=-\frac{i\pi h\hat{p}(\omega)}{4D}\,\frac{k_1^2\gamma_1 g(k_1)-k_2^2\gamma_2 g(k_2)}{k_1^2-k_2^2}, \tag{67b}$$

$$g(k)=kaJ_1(ka)[H_0^{(1)}(k\sqrt{r^2-2br\sin\theta+b^2})-H_0^{(1)} \times(k\sqrt{r^2+2br\sin\theta+b^2})]. \tag{67c}$$

This configuration contains four length-scales, *viz.* the edge distance b, in addition to the three considered before in Sec. IV, the radius a, the range, r, and the wavelength λ $(=2\pi/k)$. There is therefore a wider range of possible asymptotic regimes that can be identified, depending on the ratios of these four lengths. In the SHM context, it would appear reasonable to assume $ka\ll 1$. Then, the actuator can be represented approximately by a center of bending, of strength $(h/2)\hat{p}(\omega)\pi a^2$ (Sec. IV A), located at $x=0$, $y=b$, with the image source, of negative strength $-(h/2)\hat{p}(\omega)\pi a^2$, located at $(0,-b)$ in an infinite plate, as indicated in Fig. 9(b). Using the addition theorem (60) in (67c), one obtains the following multipole expansion:

$$\hat{w}(r,\theta,\omega)=\frac{i\pi a^2 h\hat{p}(\omega)}{8D}\,\frac{g(k_1)-g(k_2)}{k_1^2-k_2^2}, \tag{68a}$$

$$\nabla\cdot\mathbf{\Omega}(r,\theta,\omega)=\frac{i\pi a^2 h\hat{p}(\omega)}{8D}\,\frac{k_1^2\gamma_1 g(k_1)-k_2^2\gamma_2 g(k_2)}{k_1^2-k_2^2}, \tag{68b}$$

$$g(k)=4\sum_{n=0}^{\infty} J_{2n+1}(kb)H_{2n+1}^{(1)}(kr)\sin((2n+1)\theta). \tag{68c}$$

The radiation pattern can be obtained from Eq. (68) by using the asymptotic expansion of $H_{2n+1}^{(1)}(kr)$ for $kr\gg 1$ or, more directly, by using the far-field approximation (64c). This leads to $g(k)$ in (68c) being given by

$$g_1(k)=-2i\sqrt{\frac{2}{\pi kr}}\,e^{i(kr-\pi/4)}\sin(kb\sin\theta), \quad kr\gg 1. \tag{68d}$$

It can be seen that proximity to a boundary alters the radiation pattern dramatically, relative to the isotropic radiation pattern for a center of bending in an infinite plate. Furthermore, the pattern given by (68d) varies with kb, and is therefore different for each of the two modes, since $k_1 b\neq k_2 b$.

By virtue of the reciprocal theorem (13), *the response of a circular piezoelectric sensor* (near a boundary) to a (mode 1 or mode 2) plane wave incident at an angle θ (to the boundary) has the same angular dependence as the radiation pattern given by Eqs. (68b) and (68d) for $\nabla\cdot\mathbf{\Omega}$, in the limit $ka\ll 1$, when the piezoelectric element can be modeled as a center of bending, as for the case of an actuator.

Returning now to the array of N equally spaced actuators [Fig. 9(a)], by virtue of the Fourier-transform character of the far-field approximation in Eq. (64c), the radiation pattern for the array excited simultaneously and in-phase is obtained as the product of (i) the single actuator pattern and (ii) a function characteristic of the array (i.e., depending only on the number N and the spacing ℓ).[31] Thus, for an array of N equally spaced actuators as in Fig. 9(a), $g_1(k)$ is replaced by

$$g_N(k)=g_1(k)\,\frac{\sin(Nk\ell\cos\theta)}{\sin(k\ell\cos\theta)}, \quad kr\gg 1. \tag{68e}$$

The far-field approximation for $\hat{\omega}$ and $\nabla\cdot\mathbf{\Omega}$ is obtained by using g_N as an approximation for the function g in (68a) and (68b).

The image-source approach can also be used for sources corresponding to arbitrary distributions of any of the point sources discussed in Sec. III, but it is restricted to the boundary condition (66). For a clamped or a free boundary, the relevant boundary conditions cannot be satisfied by the image construction alone. For the case of a center of bending, for example, additional terms would be required that would result in a nonzero ψ-potential. These more complicated boundary conditions will be studied in future work.

VI. DISCUSSION

Figure 1 illustrates schematically a possible configuration of actuators and sensors for *in situ* damage detection.[3,6]

An important objective of theoretical modeling is to provide a rigorous, yet tractable, characterization of sources and of wave scattering by inhomogeneities, to assist with the design and interpretation of experiments. Mindlin plate theory provides an attractive approach for that purpose. The aim in this section is to provide a perspective on the range of applicability, as well as the limitations, of the results derived in this paper, as indicated by the subheadings. Significant complications for theoretical modeling arise from (*i*) the infinite number of plate-wave modes within the exact 3D elasticity formulation,[17,18] and (*ii*) the dispersive nature of these modes. Mindlin plate theory provides an excellent representation of the lowest antisymmetric Rayleigh–Lamb mode, which, it will be argued below, should prove adequate for characterizing wave scattering from flexural inhomogeneities.

A. Frequency range

A useful guide in selecting an appropriate theoretical model is to examine the relevant length scales and time scales. Typical plate thicknesses used in aircraft construction are in the range of 2–5 mm; maximum allowable delamination sizes are in the range 10–20 mm in diameter; and in-plane plate (or panel) dimensions are in the range of 200–500 mm or greater. The frequency range envisaged in the present work would typically be around 0.5–1 MHz,[11,12,32] corresponding to frequencies of $0.3\omega_c - \omega_c$, where ω_c denotes the cutoff frequency of the second antisymmetric mode (according to either the exact Rayleigh–Lamb theory or to Mindlin plate theory, which can be adjusted to reproduce exactly that cutoff frequency, as further discussed in Sec. VI E below). The wavelength of the first flexural mode in this frequency range would be typically 5–10 mm, i.e., greater than, but comparable with, the plate thickness; less than the expected in-plane dimensions of delamination damage; and much smaller than the plate's in-plane dimensions. Thus, in terms of nondimensional parameters: $kh \sim 1$, $kd \gtrsim 1$, $kr \gg 1$, where k denotes the wave number, h the plate thickness, d the damage size, and r the distance from an actuator to a defect, or from a defect to a sensor.

The first of these, $kh \sim 1$, indicates that classical plate theory would be grossly inadequate,[14] unlike the case for plate vibration modes, where the relevant natural frequencies that are considered in practice are $\leqslant 10$ kHz and classical plate theory is perfectly adequate. On the other hand, for $\omega < \omega_c$, only the lowest of the antisymmetric modes has a real wavenumber (i.e., is a propagating mode), so that the exact 3D theory of the plate waves is not required. It is pertinent to note here that although Lamb's paper appeared almost a century ago,[17,18] there has not been an exact solution for the reflection of plane waves from a straight free boundary in a semi-infinite plate, which could be regarded as the simplest wave scattering problem for plates.[18] Kane[35] has provided a solution to this problem within Mindlin plate theory. Thus, a refined plate theory would appear to be the best theoretical approach for characterization of actuators and of scattering by inhomogeneities when $kh \sim 1$.

The third ratio, $kr \gg 1$, indicates that the far-field approximation of Sec. IV C should be adequate in the present context, for both actuators and for the scattered wave from an inhomogeneity, since the latter can be regarded as the radiation from a distribution of induced sources, as further discussed in Part II.[22]

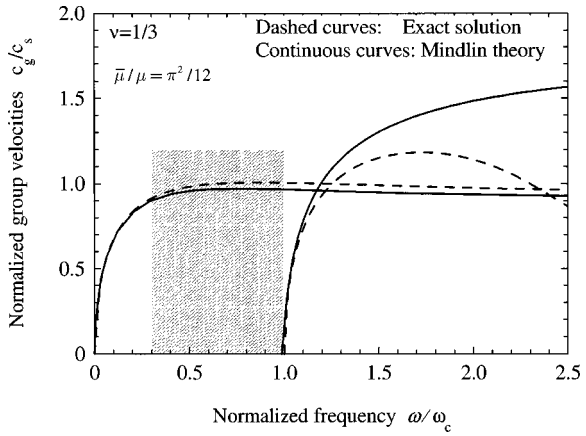

FIG. 10. Group velocity for modes 1 and 2 of Mindlin plate theory. The shaded region indicates the frequency range for use of Mindlin plate theory which is proposed in the present work.

The second ratio, $kd \gtrsim 1$, indicates that there is a reasonable prospect of achieving some limited resolution of spatial variations within the damage zone. Evidently, better resolution could be achieved for larger delaminations, or by using shorter wavelengths, but a plate theory cannot be expected to be applicable for wavelengths less than the plate thickness ($kh \gg 1$).

Figure 10 indicates the frequency range envisaged in the present work for applicability of Mindlin plate theory. It is worth emphasizing that this frequency range is eminently suitable for a quantitative reconstruction of defects that can be modeled as flexural inhomogeneities.[22] By contrast, conventional NDE techniques typically use frequencies around, or above, 10 MHz, which provides greater detection sensitivity, but at the cost of being unable to develop tractable theoretical models for inverse scattering and quantitative reconstruction algorithms.

B. Time-domain response

An important time-scale is the travel time of a pulse across the width of a panel. For panel dimensions of around 500 mm, this travel time T is typically of the order of 100 μs. The focus in the present work is on the transient response of a damaged plate for times $t \leqslant T$, i.e., before the occurrence of multiple reflections from the plate boundaries. Although it is always possible, in principle, to represent the transient response of a plate in terms of its normal modes of vibration, this is not a practically useful approach for $t \leqslant T$, because the series converges very slowly. A more efficient approach in this time range is to model the plate as being infinite, or semi-infinite, as has been done in the present work. The sum over the natural frequencies of vibration is then replaced by an integral over frequency, representing the inverse Fourier transform of various frequency-domain solutions that have been presented above in Secs. III–V.

This inverse Fourier transform cannot be evaluated analytically in terms of known functions for Mindlin plate

theory.[18,29] However, it is possible to derive analytically asymptotic approximations that not only provide useful physical insights, but that can also assist with the efficient numerical evaluation of the inverse transforms using the fast Fourier transform (FFT) algorithm.[15] These approximations are based on the stationary phase approximation.[17–19,24] Two difficulties are encountered in applying the stationary phase approximation to the results in Secs. III–V. These are attributable to (*i*) the presence of a maximum in the group-velocity curve for mode 1, at $\omega=\omega_m\approx 0.75\omega_c$, and (*ii*) a branch point for $k_1(\omega)$ at $\omega=0$. These difficulties, however, also lead to distinctive features of the time-domain response, as has been noted previously for waves in a circular cylindrical rod,[36] and waves in layered media.[37] According to DeVault and Curtis,[36] the group-velocity maximum should lead to an *Airy phase* at the head of the pulse. The amplitude of this *Airy phase* decays as $r_0^{-5/6}$ with increasing distance (corresponding to the product of a geometrical decay factor $r_0^{-1/2}$ for a nondispersive 2D wave, and a further decay of $r_0^{-1/3}$ for the contribution from a maximum in the c_g curve). By contrast, the contributions corresponding to first-order stationary points can be shown to decay as r^{-1}, so that the *Airy phase* should dominate in the far-field. However, preliminary computational studies using the FFT method have not shown clear evidence of this expected feature. Instead, a band limited pulse with center frequency in the range betweem ω_m and ω_c (and negligible frequency content below ω_m) appears to propagate like a nondispersive wave packet, as a first approximation.

At the other end, the branch point at $\omega=0$ gives a characteristic appearance to the tail of the pulse. In that limit, k_1 and k_2 in Eq. (15c) reduce to the expressions which would be obtained using classical plate theory, *viz.*

$$k_1(\omega\to 0)\approx\left(\frac{\rho h}{D}\right)^{1/4}\sqrt{\omega}, \tag{69a}$$

$$k_2(\omega\to 0)\approx i\left(\frac{\rho h}{D}\right)^{1/4}\sqrt{\omega}. \tag{69b}$$

The far-field approximation for the various solutions derived in Secs. III–V can then be obtained in terms of the Fresnel integral.[18,24] This latter feature in particular can be used to assist with the numerical inversion, because the last oscillation should occur at a predictable time, for a given distance from the source. Examples of numerical inversions and analytic approximations will be presented elsewhere.

C. Source modeling

The possibility of having well-characterized and controllable actuators and sensors is an important feature for a successful implementation of SHM. The actuator/sensor characterization that has been most widely used in the context of smart material and structures represents an approximation that ignores the structural response and impact of the piezoelectric element. In that case, the time dependence $p(t)$ in the source specification (53a) for a circular patch actuator is taken to be directly proportional to the applied voltage $V(t)$. More correctly, however, one should allow for a structure-dependent transfer function, $\hat{T}(\omega)$, so that

$$\hat{p}(\omega)=\hat{T}(\omega)\hat{V}(\omega).$$

This transfer function is not trivial to determine theoretically, and may need to be characterized experimentally or computationally.[32,38] However, the frequency-domain solutions presented in Secs. IV and V continue to apply, regardless of the intricacies of the transfer function $\hat{T}(\omega)$.

D. Shear parameter

The correct choice of the ratio $\overline{\mu}/\mu$ of the effective shear modulus to the bulk shear modulus has been a topic of considerable discussion and controversy, even for the case of an isotropic plate.[39] The two main points to note here are, first, this ratio is *undetermined* within the framework of Mindlin plate theory: it can be chosen to suit the specific requirements of any particular context. Second, the various choices do not generally differ greatly in numerical value. This was noted already by Mindlin[8] who discussed two possible choices, dictated by ensuring that (*i*) $c_1(\omega\to\infty)\to c_R$, the speed of Rayleigh surface waves, which is the correct limiting value according to 3D elasticity theory, or (*ii*) $\omega_c=\pi c_T/h$, again in agreement with 3D elasticity, where $c_T=\sqrt{\mu/\rho}$ denotes the transverse wave velocity.[17] The latter choice would appear to be the more plausible, on the grounds that a plate theory cannot be expected to be accurate in the limit $\omega\to\infty$, but the former choice leads in fact to (slightly) better agreement with the exact dispersion curve. Thus, given the key importance in the present context of the shaded frequency range in Fig. 10, the recommended choice for $\overline{\mu}/\mu$ is $\pi^2/12$.

As noted in Sec. I, the governing equations (5a) and (5b), while derived originally for an isotropic plate, apply equally for a transversely isotropic plate, representative of a quasi-isotropic composite laminate, provided that the bulk shear modulus in the ratio $\overline{\mu}/\mu$ is chosen to be the transverse shear modulus, conventionally denoted by $G_{zx}(=G_{zy})$.[23,40]

VII. CONCLUSION

A consideration of the relevant length-scales and time scales for a structural health monitoring system using built-in actuators and sensors, as illustrated in Fig. 1, suggests that Mindlin plate theory provides an eminently suitable model for characterizing the flexural response. Accordingly, the aim of this work has been to present a systematic development of this theory, comparable to what is available for 3D elasticity.[17–19] Although Mindlin's equations were first derived 50 years ago, and are well known, there does not appear to have been a systematic development that includes a representation theorem and the associated Green's function corresponding to the response to a point moment and a point force. Particular combinations of these point sources, most notably the center of bending defined in Sec. III, provide a convenient theoretical approach for characterizing actuators and sensors, as well as for characterizing the scattering due to flexural inhomogeneities, which is considered in Part II.[22]

The present paper has focused on characterizing sources of plate waves, noting in particular that the far-field response reduces to evaluating a 2D Fourier transform of the source density. The influence of proximity to a boundary on the radiation pattern has been studied for the case of a simply supported boundary. It is hoped that this theoretical framework will prove useful in guiding the design and interpretation of experimental investigations aimed at developing systems for *in situ* structural health monitoring.

APPENDIX: GREEN'S FUNCTION FOR MINDLIN PLATE THEORY

The components of the time-harmonic Green's function $\hat{g}_{ij}$ in the representation theorem, Eq. (13), are listed here for convenient reference, using the notation introduced in Sec. II B, i.e., $\hat{g}_{ij}$ denotes the ith component of the plate-theory "displacement" $\hat{u}_i \equiv (-\hat{\Omega}_x, -\hat{\Omega}_y, \hat{w})$ due to the jth component of "body force" $f_i \equiv (m_x, m_y, q)$. A matrix representation is

$$\begin{Bmatrix} -\hat{\Omega}_x \\ -\hat{\Omega}_y \\ \hat{w} \end{Bmatrix} = \begin{bmatrix} \hat{g}_{11} & \hat{g}_{12} & \hat{g}_{13} \\ \hat{g}_{21} & \hat{g}_{22} & \hat{g}_{23} \\ \hat{g}_{31} & \hat{g}_{32} & \hat{g}_{33} \end{bmatrix} \begin{Bmatrix} \hat{m}_x \\ \hat{m}_y \\ \hat{q} \end{Bmatrix}, \tag{A1}$$

where

$$\hat{g}_{11} = -\frac{i}{4D(k_1^2 - k_2^2)} \frac{\partial^2}{\partial x^2} [\gamma_1 H_0^{(1)}(k_1 r) - \gamma_2 H_0^{(1)}(k_2 r)] - \frac{1}{2D(1-\nu^2)k_3^2} \frac{\partial^2 H_0^{(1)}(k_3 r)}{\partial y^2}, \tag{A2}$$

$$\hat{g}_{21} = -\frac{i}{4D(k_1^2 - k_2^2)} \frac{\partial^2}{\partial x \partial y} [\gamma_1 H_0^{(1)}(k_1 r) - \gamma_2 H_0^{(1)}(k_2 r)] + \frac{1}{2D(1-\nu^2)k_3^2} \frac{\partial^2 H_0^{(1)}(k_3 r)}{\partial x \partial y}, \tag{A3}$$

$$\hat{g}_{31} = \frac{i}{4D(k_1^2 - k_2^2)} \frac{\partial}{\partial x} [H_0^{(1)}(k_1 r) - H_0^{(1)}(k_2 r)], \tag{A4}$$

$$\hat{g}_{12} = \hat{g}_{21}, \tag{A5}$$

$$\hat{g}_{22} = -\frac{i}{4D(k_1^2 - k_2^2)} \frac{\partial^2}{\partial y^2} [\gamma_1 H_0^{(1)}(k_1 r) - \gamma_2 H_0^{(1)}(k_2 r)] - \frac{1}{2D(1-\nu^2)k_3^2} \frac{\partial^2 H_0^{(1)}(k_3 r)}{\partial x^2}, \tag{A6}$$

$$\hat{g}_{32} = \frac{i}{4D(k_1^2 - k_2^2)} \frac{\partial}{\partial y} [H_0^{(1)}(k_1 r) - H_0^{(1)}(k_2 r)], \tag{A7}$$

$$\hat{g}_{13} = -\hat{g}_{31}, \tag{A8}$$

$$\hat{g}_{23} = -\hat{g}_{32}, \tag{A9}$$

$$\hat{g}_{33} = \frac{i}{4D(k_1^2 - k_2^2)} \left[\frac{H_0^{(1)}(k_1 r)}{\gamma_1} - \frac{H_0^{(1)}(k_2 r)}{\gamma_2} \right]. \tag{A10}$$

It is also of interest to record here the coefficients G_{ijn} that occur in the far-field expansion of $\hat{g}_{ij}$, as defined by

$$\hat{g}_{ij}(\mathbf{x}|0;\omega) \approx \sum_{n=1}^{3} G_{ijn} \sqrt{\frac{2}{\pi k_n r}} e^{i(k_n r - \pi/4)}, \quad k_n r \gg 1, \tag{A11}$$

where $n = 1, 2, 3$ identifies the contribution from each of the three wave modes in Mindlin plate theory:

$$G_{\alpha\beta n} = \frac{i}{4D} \frac{\gamma_n k_n^2}{k_1^2 - k_2^2} \frac{\partial r}{\partial x_\alpha} \frac{\partial r}{\partial x_\beta}, \quad \alpha, \beta = 1,2, \quad n = 1,2, \tag{A12}$$

$$G_{113} = \frac{i}{2D(1-\nu)} \left(\frac{\partial r}{\partial y} \right)^2, \tag{A13}$$

$$G_{223} = \frac{i}{2D(1-\nu)} \left(\frac{\partial r}{\partial x} \right)^2, \tag{A14}$$

$$G_{123} = G_{213} = \frac{i}{2D(1-\nu)} \frac{\partial r}{\partial x} \frac{\partial r}{\partial y}, \tag{A15}$$

$$G_{3\alpha n} = -\frac{i}{4D} \frac{k_n}{k_1^2 - k_2^2} \frac{\partial r}{\partial x_\alpha}, \quad n = 1,2, \tag{A16}$$

$$G_{\alpha 3n} = -\frac{1}{4\overline{\mu}h} \frac{\gamma_n k_n}{k_1^2 - k_2^2} \left(k_n^2 + \frac{\overline{\mu}h}{D} - \frac{\rho I}{D} \omega^2 \right) \frac{\partial r}{\partial x_\alpha}, \quad n = 1,2, \tag{A17}$$

$$G_{33n} = \frac{i}{4\overline{\mu}h} \frac{1}{k_1^2 - k_2^2} \left(k_n^2 + \frac{\overline{\mu}h}{D} - \frac{\rho I}{D} \omega^2 \right), \quad n = 1,2. \tag{A18}$$

[1] C. Boller, "Fundamentals on damage monitoring," in *Smart Structures and Materials: Implications for Military Aircraft of New Generation*, AGARD SMP Lecture Series, LS-205 (1996).

[2] G. Bartelds, "Aircraft structural health monitoring, prospects for smart solutions from a European viewpoint," J. Intell. Mater. Syst. Struct. **9**, 906–910 (1998).

[3] C. S. Wang, F. Wu, and F.-K. Chang, "Structural health monitoring from fiber-reinforced composites to steel-reinforced concrete," Smart Mater. Struct. **10**, 548–552 (2001).

[4] T. N. Kudra, A. J. Lockyer, and C. B. van Way, "Structural health monitoring of aircraft components," in *Smart Structures and Materials: Implications for Military Aircraft of New Generation*, AGARD SMP Lecture Series, LS-205 (1996).

[5] S. H. Diaz Valdes and C. Soutis, "Health monitoring of composites using Lamb waves generated by piezoelectric devices," Plast. Rubber Compos. **29**, 475–481 (2000).

[6] M. Lemistre and D. Balageas, "Structural health monitoring system based on diffracted Lamb wave analysis by multiresolution processing," Smart Mater. Struct. **10**, 504–511 (2001).

[7] C. Pickthall and L. R. F. Rose, "A damage-zone model for the residual strength of composite laminates under combined compression and bending," DSTO Research Report (in press, 2003).

[8] R. D. Mindlin, "Influence of rotatory inertia and shear on flexural motions of isotropic, elastic plates," J. Appl. Mech. **18**, 31–38 (1951).

[9] P. M. Morse and K. U. Ingard, *Theoretical Acoustics* (Princeton U.P., Princeton, NJ, 1968), Chap. 9.

[10] J. E. Gubernatis, E. Domany, J. A. Krumhansl, and M. Huberman, "The Born approximation in the theory of the scattering of elastic waves by flaws," J. Appl. Phys. **48**, 2812–2819 (1977).

[11] J. C. P. McKeon and M. K. Hinders, "Parallel projection and crosshole Lamb wave contact scanning tomography," J. Acoust. Soc. Am. **106**, 2568–2577 (1999).

[12] E. V. Malyarenko and M. K. Hinders, ''Fan beam and double crosshole Lamb wave tomography for mapping flaws in aging aircraft structures,'' J. Acoust. Soc. Am. **108**, 1631–1639 (2000).
[13] C. H. Wang and L. R. F. Rose, ''Wave reflection and transmission in beams containing delamination and inhomogeneity,'' J. Sound Vib. **264**, 851–872 (2003).
[14] Y.-Y. Yu, *Vibrations of Elastic Plates* (Springer, New York, 1995).
[15] J. F. Doyle, *Wave Propagation in Structures*, 2nd ed. (Springer, New York, 1997).
[16] C. Vemula and A. N. Norris, ''Flexural wave propagation and scattering on thin plates using Mindlin theory,'' Wave Motion **26**, 1–12 (1997).
[17] J. D. Achenbach, *Wave Propagation in Elastic Solids* (North-Holland, Amsterdam, 1973), Chaps. 3, 4, and 6.
[18] J. Miklowitz, *The Theory of Elastic Waves and Waveguides* (North-Holland, Amsterdam, 1978), Chaps. 1–4 and 7.
[19] K. Aki and P. G. Richards, *Quantitative Seismology, Vol. 1* (Freeman, San Francisco, 1980), Chaps. 2, 3, and 6.
[20] L. R. F. Rose, ''Point-source representation for laser-generated ultrasound,'' J. Acoust. Soc. Am. **75**, 723–732 (1984).
[21] J. B. Spicer, ''Laser Ultrasonics in Finite Structures: Comprehensive Modelling with Supporting Experiments,'' Ph.D thesis, Johns Hopkins University, Maryland, 1991.
[22] L. R. F. Rose and C. H. Wang, ''Mindlin plate theory for damage detection II. Scattering by flexural inhomogeneities,'' to be submitted for publication in J. Acoust. Soc. Am. (2003).
[23] B. D. Aggarwal and L. J. Broutman, *Analysis and Performance of Fibre Composites*, 2nd ed. (Wiley, New York, 1980).
[24] L. B. Felsen and N. Marcuwitz, *Radiation and Scattering of Waves* (Prentice–Hall, Englewood Cliffs, NJ, 1973), Chap. 4.
[25] I. M. Gelfand and G. E. Shilov, *Generalized Functions* (Academic New York, 1964), Vol. 1.
[26] M. Abramowitz and I. A. Stegun, *Handbook of Mathematical Functions* (Dover, New York, 1965), Chap. 9.
[27] R. D. Mindlin and H. Deresiewicz, ''Thickness-shear and flexural vibrations of circular disc,'' J. Appl. Phys. **25**, 120–123 (1954).
[28] L. R. F. Rose, ''The mechanics of transformation toughening,'' Proc. R. Soc. London, Ser. A **412**, 169–197 (1987).
[29] J. Miklowitz, ''Flexural stress waves in an infinite elastic plate due to a suddenly applied concentrated transverse load,'' J. Appl. Mech. **27**, 681–689 (1960).
[30] A. Kalnins, ''On fundamental solutions and Green's functions in the theory of elastic plates,'' J. Appl. Mech. **33**, 31–38 (1966).
[31] L. J. Eyges, *The Classical Electromagnetic Field* (Addison–Wesley, Reading, MA, 1972), Chaps. 13 and 15.
[32] M. Viedt, T. Liu, and S. Kitipornchai, ''Flexural waves transmitted by rectangular piezoceramic transducers,'' Smart Mater. Struct. **10**, 681–688 (2001).
[33] S. H. Diaz Valdes and C. Soutis, ''Real-time non-destructive evaluation of fibre composite laminates using low-frequency Lamb waves,'' J. Acoust. Soc. Am. **111**, 2026–2033 (2002).
[34] J. J. Tracy and G. C. Pardoen, ''Effect of delamination on the natural frequencies of composite laminates,'' J. Compos. Mater. **23**, 1200–1215 (1989).
[35] T. R. Kane, ''Reflection of flexual waves at the edge of a plate,'' J. Appl. Mech. **21**, 213–220 (1954).
[36] G. P. DeVault and C. W. Curtis, ''Elastic cylinder with free lateral surfaces and mixed time-dependent end conditions,'' J. Acoust. Soc. Am. **34**, 421–432 (1962).
[37] L. M. Brekhovskikh, *Waves in Layered Media*, 2nd ed. (Academic, San Diego, 1980).
[38] E. Moulin, J. Assaad, C. Delebarre, H. Kaczmarek, and D. Balageas, ''Piezoelectric transducer embedded in a composite laminate: application to Lamb wave generation,'' J. Appl. Phys. **82**, 2049–2055 (1997).
[39] N. G. Stephen, ''On the variation of Timoshenko's shear coefficient with frequency,'' J. Appl. Mech. **45**, 695–697 (1978).
[40] C. T. Sun and T. M. Tan, ''Wave propagation in a graphite/epoxy laminate,'' J. Aeronautical Sci. **32**, 269–284 (1984).

A partial field decomposition algorithm and its examples for near-field acoustic holography

Kyoung-Uk Nam and Yang-Hann Kim[a)]
Center for Noise and Vibration Control (NOVIC), Department of Mechanical Engineering, Korea Advanced Institute of Science and Technology (KAIST), Science Town, Daejeon, 305-701, Korea

(Received 22 May 2003; revised 12 February 2004; accepted 12 April 2004)

In this paper we introduce a practical algorithm that can accurately implement partial field decomposition for near-field acoustic holography (NAH). Unlike other methods, the algorithm does not require sensors near sources because it uses calculations rather than measured signals in order to decompose a holography image into the images of individual sources. Therefore it makes holography measurement easier than other methods. The algorithm is composed of five steps: measurement of pressure on a hologram plane, estimation of pressure on a source plane, selection of maximum pressure, estimation of the sound field from one source, and estimation of the remaining sound field. In this paper we also report two experiments that verify and demonstrate the algorithm. In one experiment six speakers are operated independently. The other is a vortex shedding experiment. Their results show that the decomposition method is useful for identifying hidden sources and estimating the power of individual sources. © *2004 Acoustical Society of America.* [DOI: 10.1121/1.1756896]

PACS numbers: 43.20.Rq, 43.60.Cg, 43.60.Sx [SPW] Pages: 172–185

I. INTRODUCTION

The objective of this paper is to introduce a practical algorithm for a partial field decomposition method[1] of near-field acoustic holography.[2,3]

Acoustic holography images convey spatial distributions of acoustic pressure, vector plots of intensity, and other acoustic variables. The images can be obtained, not only on a measurement plane but also on any plane of interest. Especially, the image on a source plane is often useful for identifying source characteristics. Figure 1 shows two examples of holography results. Figure 1(a) can be regarded as what can be produced by a monopole. However, it is difficult to interpret Fig. 1(b). In fact, the image of Fig. 1(b) is what is obtained by summing three independent sources (Fig. 2). As shown in Fig. 2, it is our aim to decompose the composite sound image into those from the individual sources.

There have been many attempts to achieve this objective.[4–9] These methods are based on virtual[10] or partial coherence,[11–13] which requires the placement of reference microphones near the sources. That is because those methods use signals obtained by the reference microphones to decompose individual sources, which essentially introduces practical difficulties. One is that prior information on source positions is required before NAH can be applied. It negates one of NAH's valuable properties: It can successfully mimic the spatial characteristics of sound sources. It is also noteworthy that it is often difficult to place reference microphones near the sources, even if the source positions are known.

A decomposition method[1] that does not require sensors near the sources was recently proposed. The proposed method makes holography measurement easier than other methods because the reference microphones need not be placed near the sources. In spite of this practical advantage, the algorithm of the proposed method was not well addressed: Reference 1 only conveys the theory and basic concepts. In addition, the method's performance, for example, its accuracy, was not verified by experiments.

In this paper we introduce the method's algorithm derived from spectral matrices (instead of the vector notation used in Ref. 1) and also report on two results that were obtained experimentally. The first was a controlled experiment in which six speakers were used to mimic the independent or incoherent sources. In the other, more realistic experiment, it was attempted to separate two sets of vortex shedding noise: noises due to drag and lift forces.

II. PROBLEM DEFINITION

In this section we introduce basic equations for the partial field decomposition, referring to Ref. 13. In the following expressions, small letters represent scalar quantities and capital letters express vectors or matrices. All the variables are functions of frequency.

A. Noise rejection in a single-input/single-output system with output noise

Before introducing the general idea of partial field decomposition, let us consider a single-input/single-output sys-

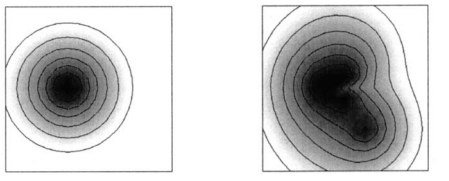

(a) easy to interpret (b) difficult to interpret

FIG. 1. Two examples of holography results, which are pressure distributions at a selected frequency on source planes.

a)Electronic mail: yanghannkim@kaist.ac.kr

 0001-4966/2004/116(1)/172/14/$20.00

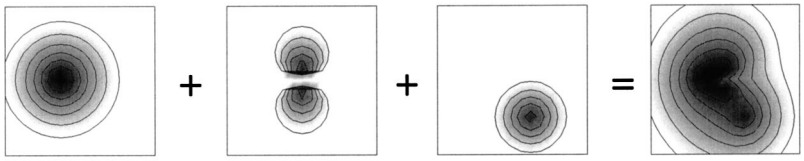

FIG. 2. Three independent sources of constituting Fig. 1(b).

tem with output noise, as shown in Fig. 3(a). The x and y are an input and an output. The $\hat{y}$ and n are measured output and noise. The noise is assumed to be incoherent to the input.

Let w be a signal coherent to the input. That is,

$$w = cx. \tag{1}$$

Then the true output spectrum s_{yy} can be expressed as[13]

$$s_{yy} = \hat{\gamma}_{wy}^2 \hat{s}_{yy} = |\hat{s}_{wy}|^2 / s_{ww}, \tag{2}$$

where the $\hat{\gamma}_{wy}^2$ is the coherence function between the w and $\hat{y}$, the $\hat{s}_{yy}$ is a measured output autospectrum, the s_{ww} is the autospectrum of the w, and the $\hat{s}_{wy}$ is the cross-spectrum between the w and $\hat{y}$. Equation (2) means that a true output spectrum can be calculated from a distorted output if a signal coherent to an input is given.[13] This relation can be readily extended to a two-input/single-output system [Fig. 3(b)].

B. Contribution analysis for a two-input/single-output system

Let us consider a two-input/single-output system, as shown in Fig. 3(b). The x_1 and x_2 are two inputs, the y_1 and y_2 are outputs due to the x_1 and x_2, and the y is a total output. The two inputs are assumed to be incoherent, considering the circumstance that those are generated by different causes. The total output spectrum s_{yy} can be readily written as[13]

$$s_{yy} = s_{y1y1} + s_{y2y2}, \tag{3}$$

where the s_{ylyl} is the autospectrum of the y_l, in other words, the contribution of the lth input to the total output spectrum. In this case, $l = 1, 2$.

Because the inputs are incoherent to each other, the output due to one input can be regarded as noise to the other input. If a signal w_l coherent to the lth input is given, the lth contribution s_{ylyl} can be calculated by[13]

$$s_{ylyl} = \gamma_{wly}^2 s_{yy} = |s_{wly}|^2 / s_{wlwl}, \tag{4}$$

like Eq. (2), where the γ_{wly}^2 is the coherence function between the w_l and y, the s_{wlwl} is the autospectrum of the w_l, and the s_{wly} is the cross-spectrum between the w_l and y. Equation (4) essentially expresses what can be applied to a multiple-input/single-output system.[13] Next, this result is extended to acoustic holography, which has many outputs.

C. Partial field decomposition in near-field acoustic holography

Let N be the number of measurement points on a hologram plane and p_{Hn} be pressure at the nth point. Let M be the number of prediction points on a source plane and p_{Sm} be pressure at the mth point. For mathematical convenience, let us define two row vectors as

$$P_H = [p_{H1} \ \cdots \ p_{HN}] \quad \text{and} \quad P_S = [p_{S1} \ \cdots \ p_{SM}]. \tag{5}$$

These two vectors have the relation of

$$P_S = P_H T, \tag{6}$$

where the T is a matrix of propagating pressure from the hologram to the source plane.[2,3] The spectral matrices on the hologram and source planes can be defined as

$$S_{HH} = E[P_H^* P_H] \quad \text{and} \quad S_{SS} = E[P_S^* P_S], \tag{7}$$

where the E and $*$ represent expectation and conjugate transpose. Equation (6) rewrites Eq. (7) as

$$S_{SS} = T^* S_{HH} T. \tag{8}$$

Let us assume that the number of sources is L and they are incoherent. Then the spectral matrix S_{SS} on the source plane is expressed as

$$S_{SS} = \sum_{l=1}^{L} S_{SlSl}, \tag{9}$$

which is the matrix version of Eq. (3). The S_{SlSl} expresses how much the lth source contributes to the total spectral matrix S_{SS}. In Appendix A we explain the mathematical definition of the S_{SlSl}. If w_l is a signal coherent to the lth source, the S_{SlSl} can be rewritten as

$$S_{SlSl} = S_{wlS}^* S_{wlS} / s_{wlwl}, \tag{10}$$

where

$$S_{wlS} = E[w_l^* P_S], \tag{11}$$

which is the matrix form of Eq. (4). The S_{wlS} is the row vector representing the cross-spectral matrix between the w_l

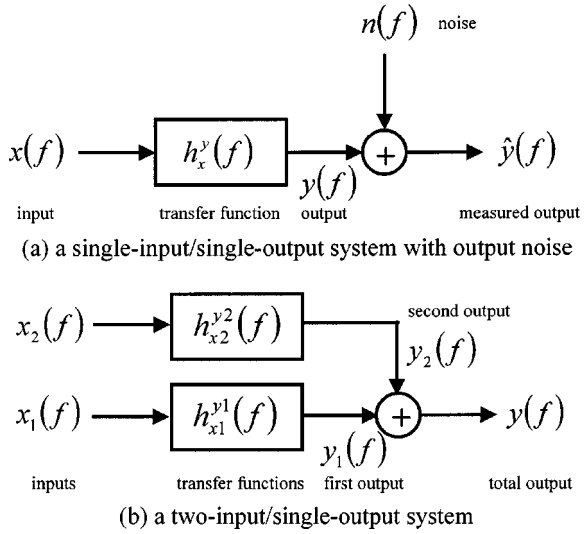

FIG. 3. Two simple systems for the problem definition of partial field decomposition.

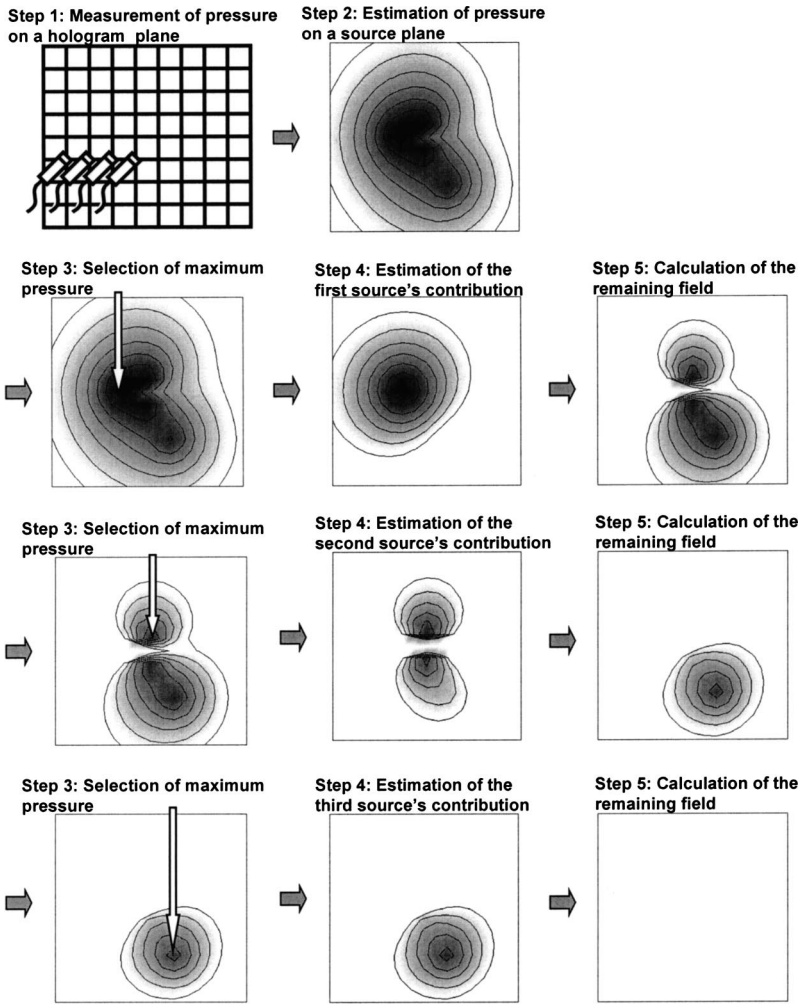

FIG. 4. An illustration of the decomposition algorithm. This figure illustrates the procedure that separates the sound field in Fig. 1(b). The images of step 4 show the estimated contributions of individual sources.

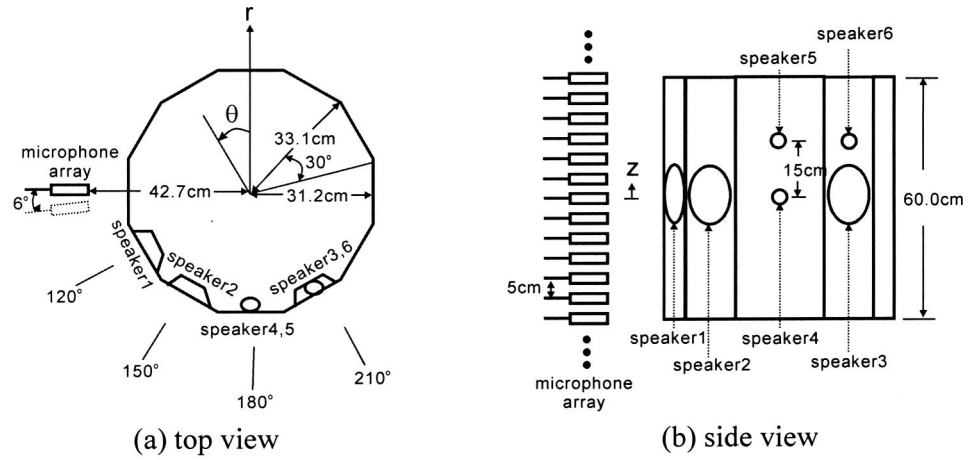

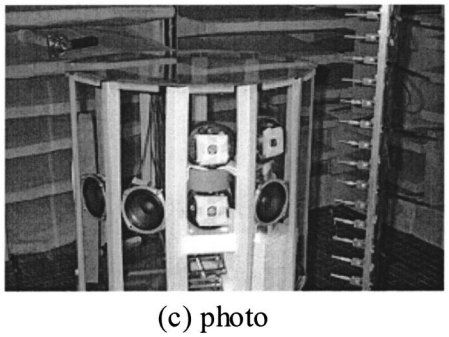

FIG. 5. Setup of the speaker experiment.

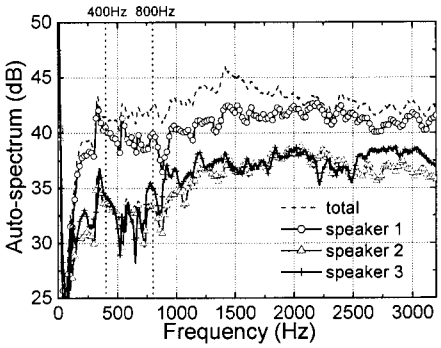

(a) the auto-spectra of speaker 1, 2, 3

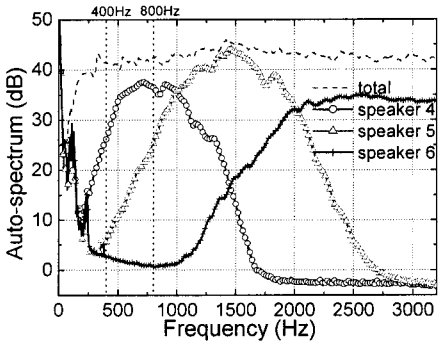

(b) the auto-spectra of speaker 4, 5, 6

	speaker1	2	3	4	5	6
400Hz	41dB	33	34	26	5	2
800Hz	40dB	33	35	37	25	0

(c) the auto-spectra of speakers at 400 and 800Hz

FIG. 6. Autospectra at one reference microphone in the speaker experiment. Decomposition results will be displayed at 400 and 800 Hz.

and pressure on the source plane. In Appendix B we prove Eq. (10).

This result confirms that one needs signals coherent to individual sources to separate incoherent sources. Conventional methods[4–9] have obtained such coherent signals by placing sensors near sources.

III. DECOMPOSITION ALGORITHM

It is well known that NAH can get a signal coherent to a source signature. Using this rather straightforward idea, Ref. 1 developed a theory, which can effectively separate source shapes. The method assumes that the sound fields from individual sources hardly overlap on the source plane. That is, the method regards maximum pressure on a source plane as a signal coherent to one source. This is essentially equivalent to the idea of placing sensors near the sources. Figure 4 illustrates the details of the procedure that separates the individual noise sources in Fig. 1(b).

The first step measures the hologram spectral matrix S_{HH} [Eq. (7)]. The measurement can be done simultaneously, or by other well established methods.[4,5,14,15] Let $\hat{S}_{HH}$ be the measured spectral matrix. It is noteworthy that the spectral

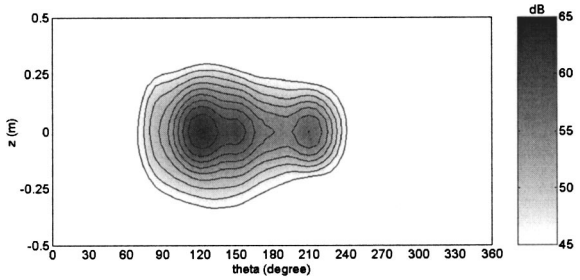

(a) the auto-spectra of pressure at 400Hz on the source plane

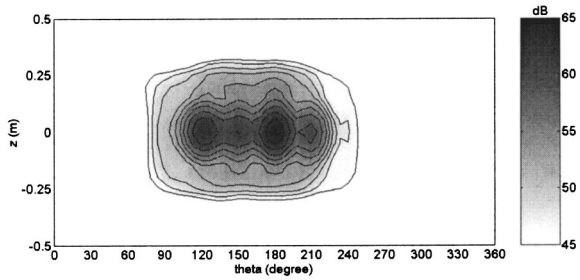

(b) the auto-spectra of pressure at 800Hz on the source plane

FIG. 7. Contour plot of the autospectra on the source plane in the speaker experiment.

matrix requires a heavy calculation because of its large size. In order to reduce the calculation time, let us consider a reduced matrix $\hat{\Gamma}_H$, which is defined as

$$\hat{S}_{HH}=\hat{\Gamma}_H^*\hat{\Gamma}_H. \tag{12}$$

The decomposition of Eq. (12) is possible because $\hat{S}_{HH}$ is Hermitian and semipositive definite.[16] The $\hat{\Gamma}_H$ is a $K\times N$ matrix, where K is the rank of $\hat{S}_{HH}$. The $\hat{\Gamma}_H$ is not unique. It can be obtained by singular value decomposition,[14] LU decomposition,[14] or in other ways.

Second, the spectral matrix S_{SS} on the source plane is estimated. Denoting $\hat{S}_{SS}$ as its estimator [Eq. (8)], then it can be written as

$$\hat{S}_{SS}=T^*\hat{S}_{HH}T=T^*\hat{\Gamma}_H^*\hat{\Gamma}_H T=\hat{\Gamma}_S^*\hat{\Gamma}_S, \tag{13}$$

where

$$\hat{\Gamma}_S=\hat{\Gamma}_H T. \tag{14}$$

It is noteworthy that the autospectrum at the mth point, the mth diagonal term of $\hat{S}_{SS}$, can be expressed as $\hat{\Gamma}_{S,m}^*\hat{\Gamma}_{S,m}$, where $\hat{\Gamma}_{S,m}$ is the mth column of $\hat{\Gamma}_S$. The mth row of $\hat{S}_{SS}$ is expressed as $\hat{\Gamma}_{S,m}^*\hat{\Gamma}_S$. The first and second steps essentially construct the data for acoustic holography.

The third step searches the autospectra on the source plane for maximum pressure. Let the autospectrum $\hat{\Gamma}_{S,m'}^*\hat{\Gamma}_{S,m'}$ at the m'th point be the maximum.

Then, step 4 estimates the contribution of the first source to the spectral matrix by using Eq. (10). By the assumption that maximum pressure is coherent to one source, the s_{wlwl} in Eq. (10) is $\hat{\Gamma}_{S,m'}^*\hat{\Gamma}_{S,m'}$. The S_{wlS} in Eq. (10) is $\hat{\Gamma}_{S,m'}^*\hat{\Gamma}_S$. Therefore the estimator $\hat{S}_{S1S1}$ can be written as

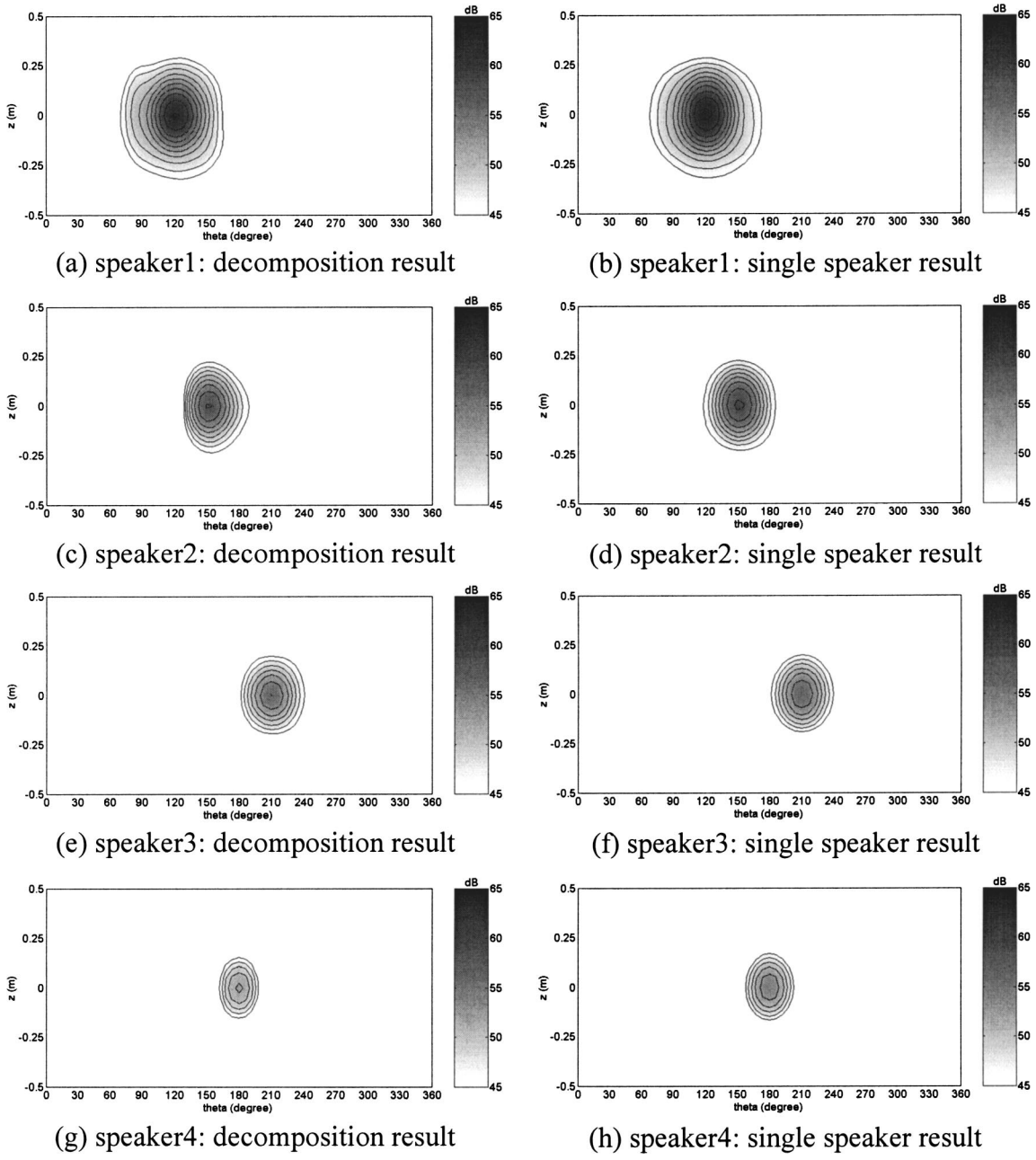

FIG. 8. Decomposition results at 400 Hz in the speaker experiment. The left column shows the decomposition results when all the speakers were operated and the right one exhibits the holography results when only single speaker was operated.

$$\hat{S}_{S1S1}=(\hat{\Gamma}^*_{S,m},\hat{\Gamma}_S)^*(\hat{\Gamma}^*_{S,m},\hat{\Gamma}_S)/\hat{\Gamma}^*_{S,m},\hat{\Gamma}_{S,m'}=\hat{\Gamma}^*_{S1},\hat{\Gamma}_{S1}, \tag{15}$$

where

$$\hat{\Gamma}_{S1}=\hat{\Gamma}^*_{S,m},\hat{\Gamma}_S/\sqrt{\hat{\Gamma}^*_{S,m},\hat{\Gamma}_{S,m'}}. \tag{16}$$

Next (step 5) is to estimate the remaining spectral matrix $S_{SS\cdot 1}$, which is the sum of all the source contributions except for the first source. Equations (9), (13), (15), and (16) lead the estimator $\hat{S}_{SS\cdot 1}$ to be expressed as

$$\hat{S}_{SS\cdot 1}=\hat{S}_{SS}-\hat{S}_{S1S1}=\hat{\Gamma}^*_S\hat{\Gamma}_S-\hat{\Gamma}^*_{S1}\hat{\Gamma}_{S1}=\hat{\Gamma}^*_{S\cdot 1}\hat{\Gamma}_{S\cdot 1}, \tag{17}$$

where

$$\hat{\Gamma}_{S\cdot 1}=\left(I-\frac{\hat{\Gamma}_{S,m'}\hat{\Gamma}^*_{S,m'}}{\hat{\Gamma}^*_{S,m},\hat{\Gamma}_{S,m'}}\right)\hat{\Gamma}_S, \tag{18}$$

because

$$\hat{\Gamma}^*_S\left(I-\frac{\hat{\Gamma}_{S,m'}\hat{\Gamma}^*_{S,m'}}{\hat{\Gamma}^*_{S,m},\hat{\Gamma}_{S,m'}}\right)^*\left(I-\frac{\hat{\Gamma}_{S,m'}\hat{\Gamma}^*_{S,m'}}{\hat{\Gamma}^*_{S,m},\hat{\Gamma}_{S,m'}}\right)\hat{\Gamma}_S$$
$$=\hat{\Gamma}^*_S\left(I-\frac{\hat{\Gamma}_{S,m'}\hat{\Gamma}^*_{S,m'}}{\hat{\Gamma}^*_{S,m},\hat{\Gamma}_{S,m'}}\right)\hat{\Gamma}_S=\hat{\Gamma}^*_S\hat{\Gamma}_S-\hat{\Gamma}^*_{S1}\hat{\Gamma}_{S1}. \tag{19}$$

This fifth step basically follows a partial coherence procedure.[11–13]

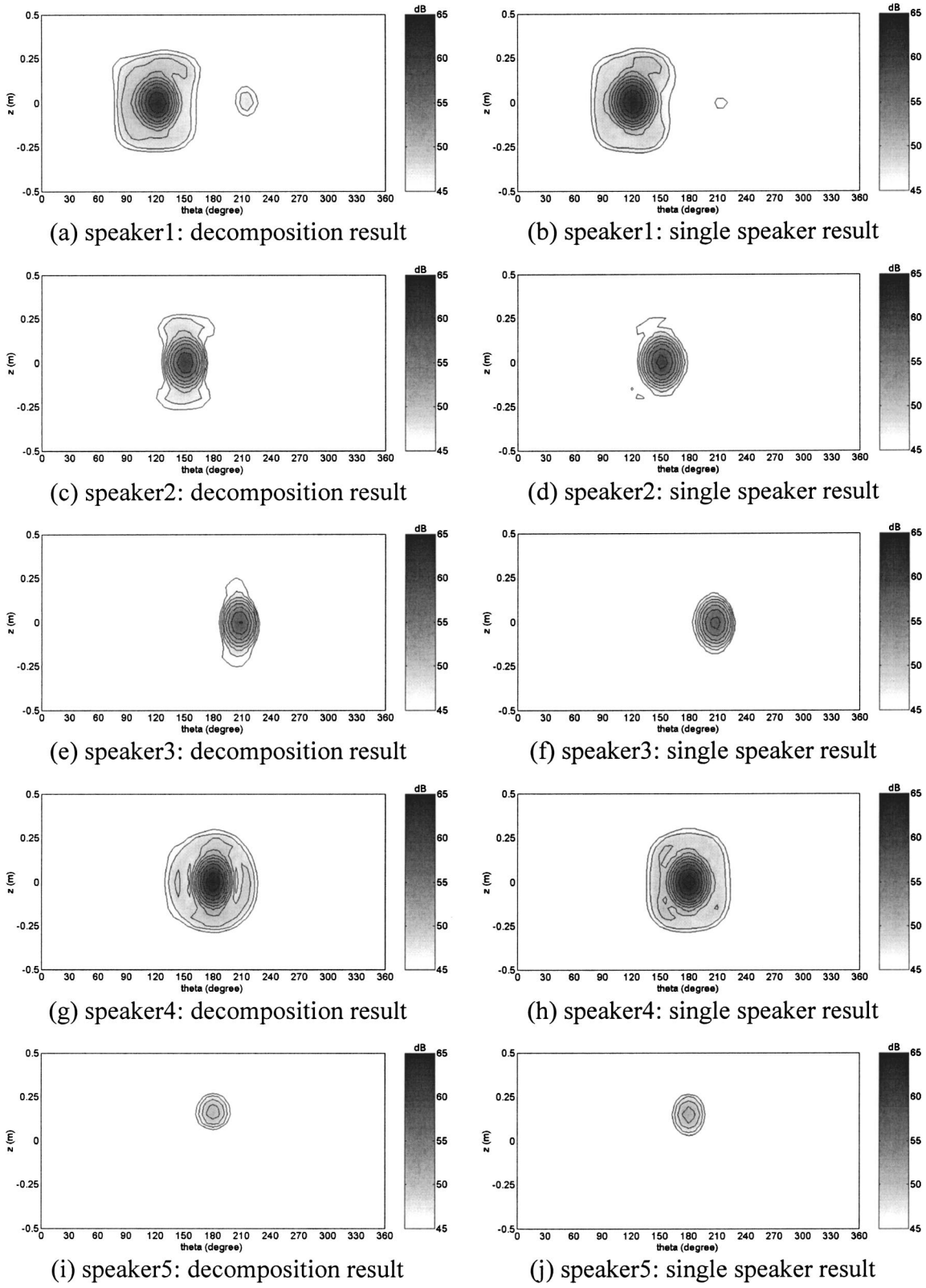

FIG. 9. Decomposition results at 800 Hz in the speaker experiment. The left column shows the decomposition results when all the speakers were operated and the right one exhibits the holography results when only single speaker was operated.

One has to repetitively apply steps 3–5 to the remaining spectral matrix $\hat{S}_{SS\cdot 1}$ to estimate the contributions of other sources. The maximum number of repetitions is the rank K of the $\hat{S}_{HH}$ because the remaining spectral matrix is zero after the Kth repetition.

The results of Fig. 4 are a little distorted in comparison with Fig. 2. That is because individual sound fields are partially overlapped. The spatial overlap makes the pressure at the maximum point not perfectly induced by one source. Therefore the quality of the proposed method depends on

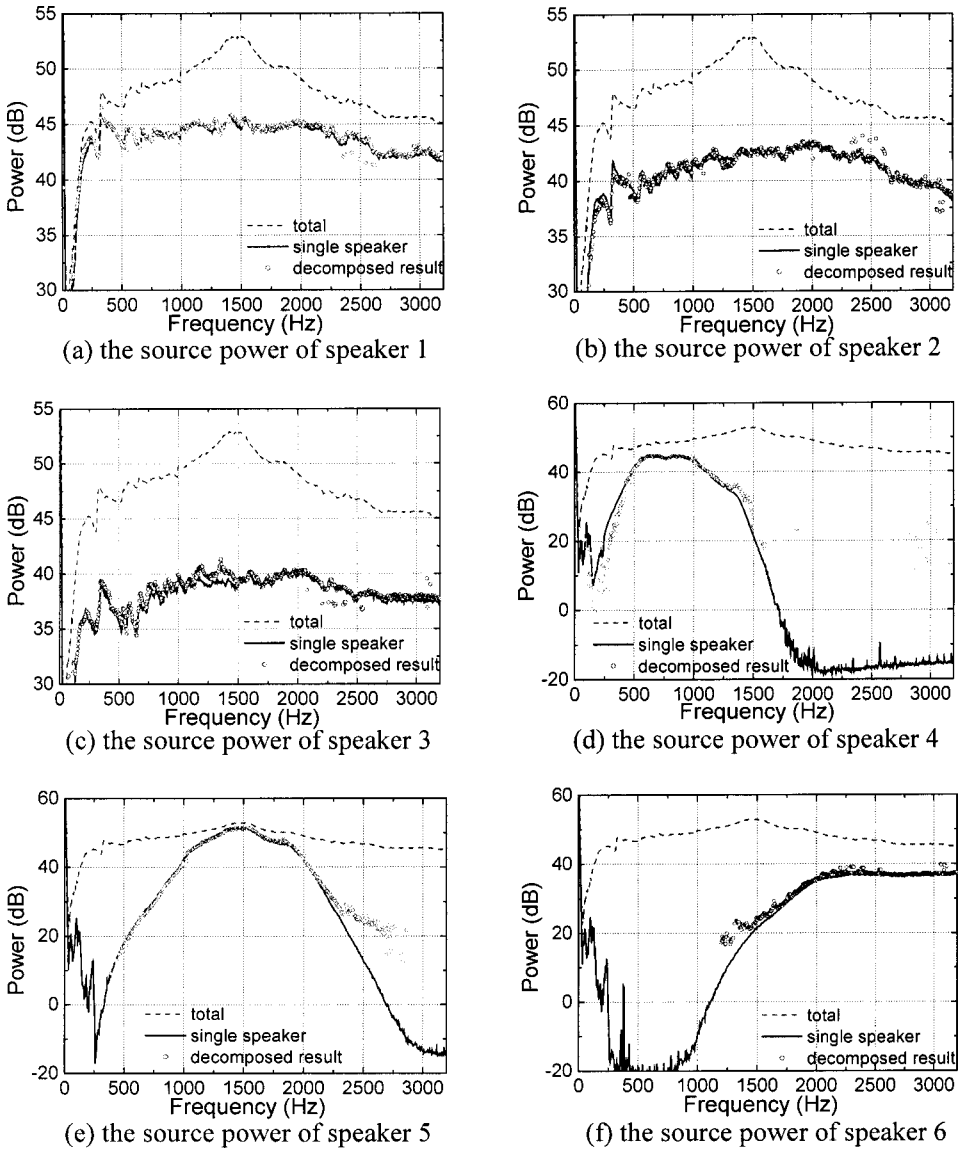

FIG. 10. Decomposition results of the source power in the speaker experiment.

how strongly the sound fields, generated by individual sources, overlap one another. In Appendix C we introduce some examples of the decomposition error due to the spatial overlap.

In the next two sections we present results from two experiments that demonstrate, as well as verify, the algorithm.

IV. SIX-SPEAKER EXPERIMENT

Figure 5 illustrates the experimental setup with six sound sources. Speakers 1, 2, 3 are loud speakers of 4 in. diameters and speakers 4, 5, 6 are horn drivers. The speakers were fixed on the wall of an acryl box of 0.5 cm thickness. Six function generators independently operated the speakers. A cylindrical holography was performed. The radii of the hologram and source planes were 42.7 and 33.1 cm. The measurement spacings in the θ and z direction were 6° and 5 cm. The numbers of measurement points in the θ and z direction were 60 and 24. For the construction of the hologram spectral matrix $\hat{S}_{HH}$ [Eq. (7)], a 24-microphone array scanned the hologram points step-by-step in the θ-direction. Six reference microphones were used and located about 1 m away from the source plane. In Appendix D we provide details on some issues related to this step-by-step scanning method.

The maximum frequency and frequency resolution were 3200 and 4 Hz, respectively. For the spectra calculation, a Hanning window was used and the time data overlapped by 50%. The average number was 40. For the estimation of pressure on the source plane, the spatial window minimizing errors[17] and the wave number filter proposed by Veronesi and Maynard[18] were used. Zeros were added outside the measurement area so that the number of data including the zeros in the z direction was 64.

For the comparison of the decomposition results, the data from each single speaker were also measured. Figure 6 shows the autospectra of pressure at one reference microphone. Speakers 1, 2, and 3 generated nearly white noise while speakers 4, 5, and 6 generated bandlimited noise. Their main bands were 500–1000, 1000–2000, and 2000–3200 Hz.

Figure 7 shows the autospectra of the pressure at 400 and 800 Hz on the source plane. As shown in Fig. 6, the

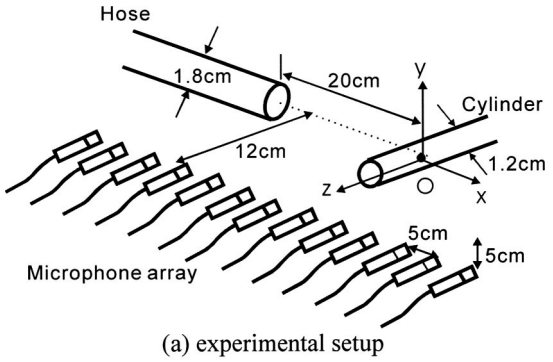

(a) experimental setup

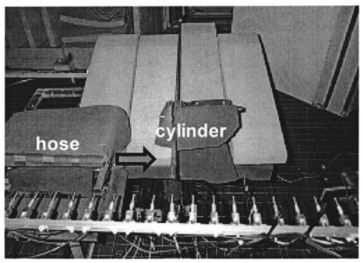

(b) photo

FIG. 11. Setup of the vortex shedding experiment.

noise was mainly generated by speakers 1, 2, 3, and 4 at 400 Hz and by speakers 1, 2, 3, 4, and 5 at 800 Hz. However, all the sources are not clearly seen in Fig. 7.

Figure 8 shows the decomposition results at 400 Hz. The left column shows the decomposition results and the right one exhibits the holography results of the single speaker experiments. The decomposition results clearly demonstrate that the sound fields from speakers 1–4 were well decomposed. The result from the speaker 2 is a little distorted near the peak point of speaker 1 (Appendix C). Because the number of reference microphones is six, the rank of the spectral matrix is also six.[4] Therefore the number of the estimated contributions is six. At 400 Hz, however, the fifth and sixth contributions were so small that they were not seen in the color range of Fig. 8. Figure 9 shows the decomposition results at 800 Hz. The hidden source, speaker 5, is also seen. The distortions of the shapes at 800 Hz are smaller than those at 400 Hz because the spatial overlap is smaller at the higher frequency.

Figure 10 shows the decomposition results of the source power. The results from speakers 1, 2, and 3 were very similar to the single speaker results at almost all the frequencies. The results from speakers 4, 5, and 6 were also very similar to the single speaker results in their main bands. However, the results had large errors at the frequencies with low-power levels, as discussed in Appendix C. Especially, speakers 4, 5, and 6 at the frequency bands of very low levels, for example, 1500–3200 Hz of Fig. 10(d), were rarely observed.

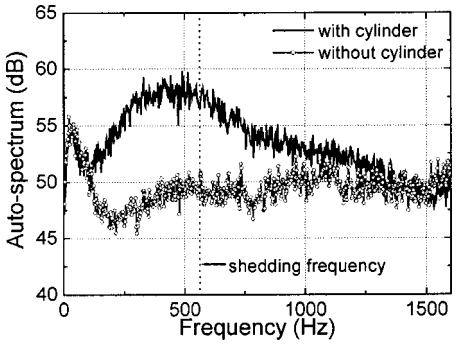

FIG. 12. Autospectra at (0, 15 cm) on the hologram plane in the vortex shedding experiment.

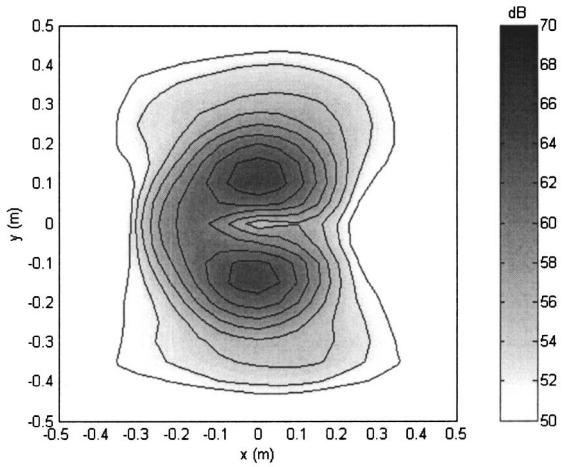

(a) the auto-spectra of pressure at 500Hz on the source plane

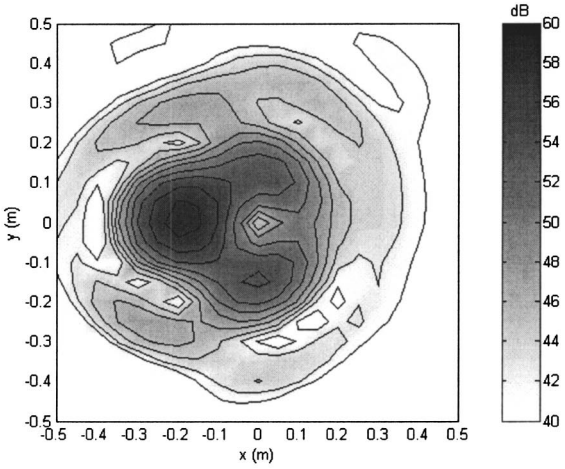

(b) the auto-spectra of pressure at 1000Hz on the source plane

FIG. 13. Contour plot of autospectra on the source plane in the vortex shedding experiment.

V. VORTEX SHEDDING EXPERIMENT

Figure 11 shows the experimental setup that generates a vortex shedding. Compressed air was injected into a circular cylinder from a hose. The positions of the hose end and cylinder were (−20 cm, 0) and (0,0) in the x-y plane. The diameters of the hose and cylinder were 1.8 and 1.2 cm. The mean velocity of the flow was 33.8 m/s at the origin where the flow meets the cylinder. Planar holography was used to visualize the sound field. The distance between the hologram and source plane was 12 cm. The measurement spacing was 5 cm. The number of measurement points was 24×24. A

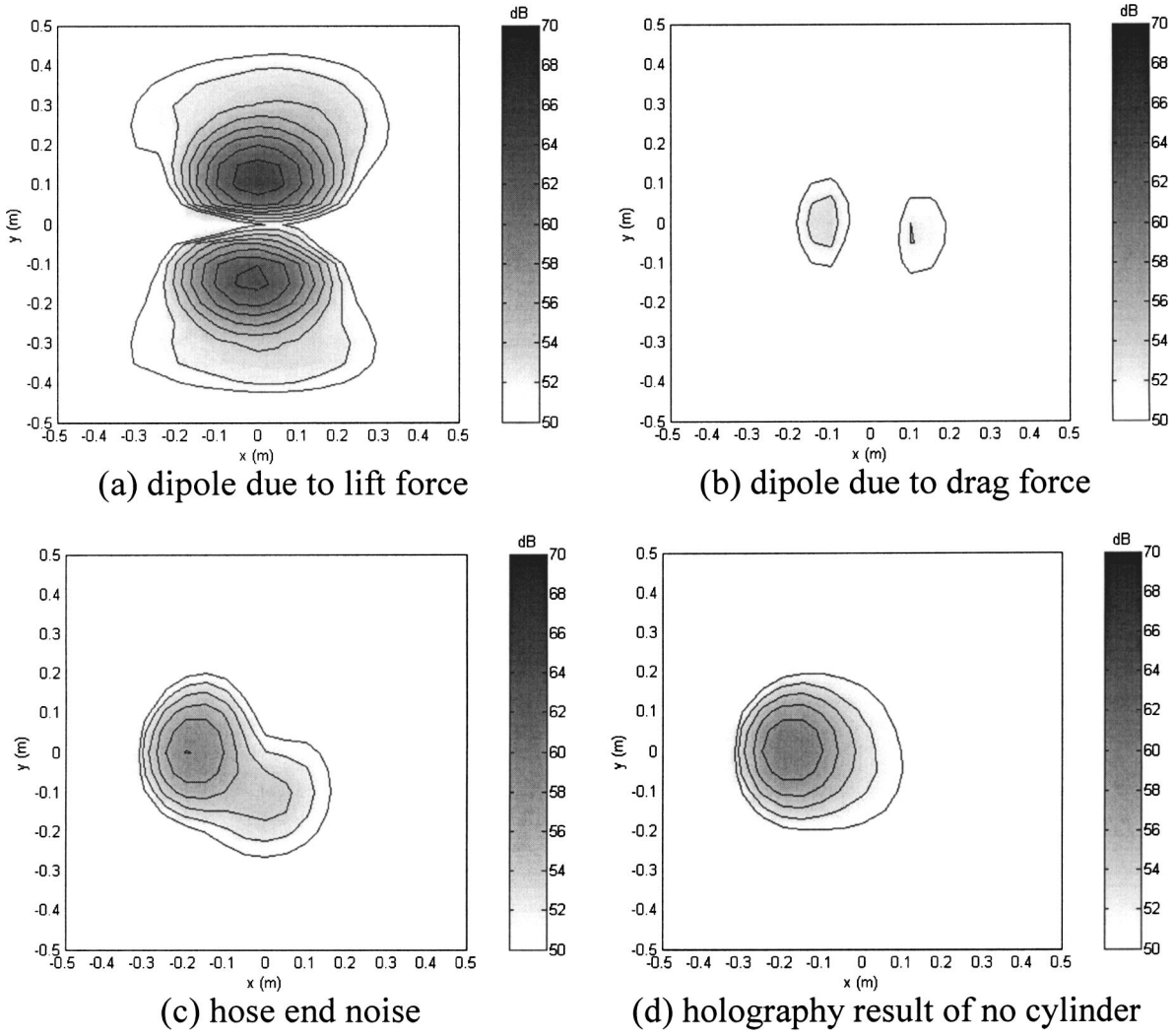

FIG. 14. Decomposition results at 500 Hz in the vortex shedding experiment.

24-microphone array scanned the hologram points in the y direction. Five reference microphones were used and placed about 50 cm away from the source plane.

The maximum frequency and frequency resolution were 1600 and 2 Hz, respectively. Other specifications for the spectrum and propagation calculation were the same as in the speaker experiment.

It is noteworthy that not only the cylinder but also the hose end generated noise. To observe only the hose end noise, the sound field when the cylinder was absent was also measured. Figure 12 shows the autospectrum at (0, 15 cm) on the hologram plane. There was nearly white noise when the cylinder was absent and bandlimited noise close to a shedding frequency (562 Hz) when the cylinder was in place.

Figure 13 shows the autospectra of the pressure at 500 and 1000 Hz on the source plane. The two dipoles (lift and drag direction) and the hose end noise are not clearly separated.

Figure 14 shows the decomposition results at 500 Hz. The dipoles due to the lift and the drag forces are shown. The hose-end noise is also shown [Fig. 14(c)]. However, its shape is a little distorted in comparison with the result when the cylinder was absent [Fig. 14(d)]. This is an error due to the spatial overlap (Appendix C). Figure 15 shows the decomposition results at 1000 Hz. The results show the dipoles and the hose-end noise more clearly than those at 500 Hz. That is because the spatial overlap becomes smaller as the frequency becomes higher.

Figure 16 shows the decomposition results of the source power. The hose end result is nearly equal to that without the cylinder at frequencies higher than 300 Hz. The dipole due to the lift has the bandlimited noise close to the shedding frequency. The dipole due to the drag shows that its power is centered round $2\times$ the shedding frequency. The dipole due to the drag at frequencies lower than 500 Hz is hardly noticeable.

VI. CONCLUSIONS

In this paper we introduced a practical algorithm that successfully implements partial field decomposition for nearfield acoustic holography. The algorithm includes five steps: the measurement of pressure on a hologram plane, the estimation of pressure on a source plane, the selection of maximum pressure, the estimation of the sound field from one source, and the estimation of the remaining sound field. In

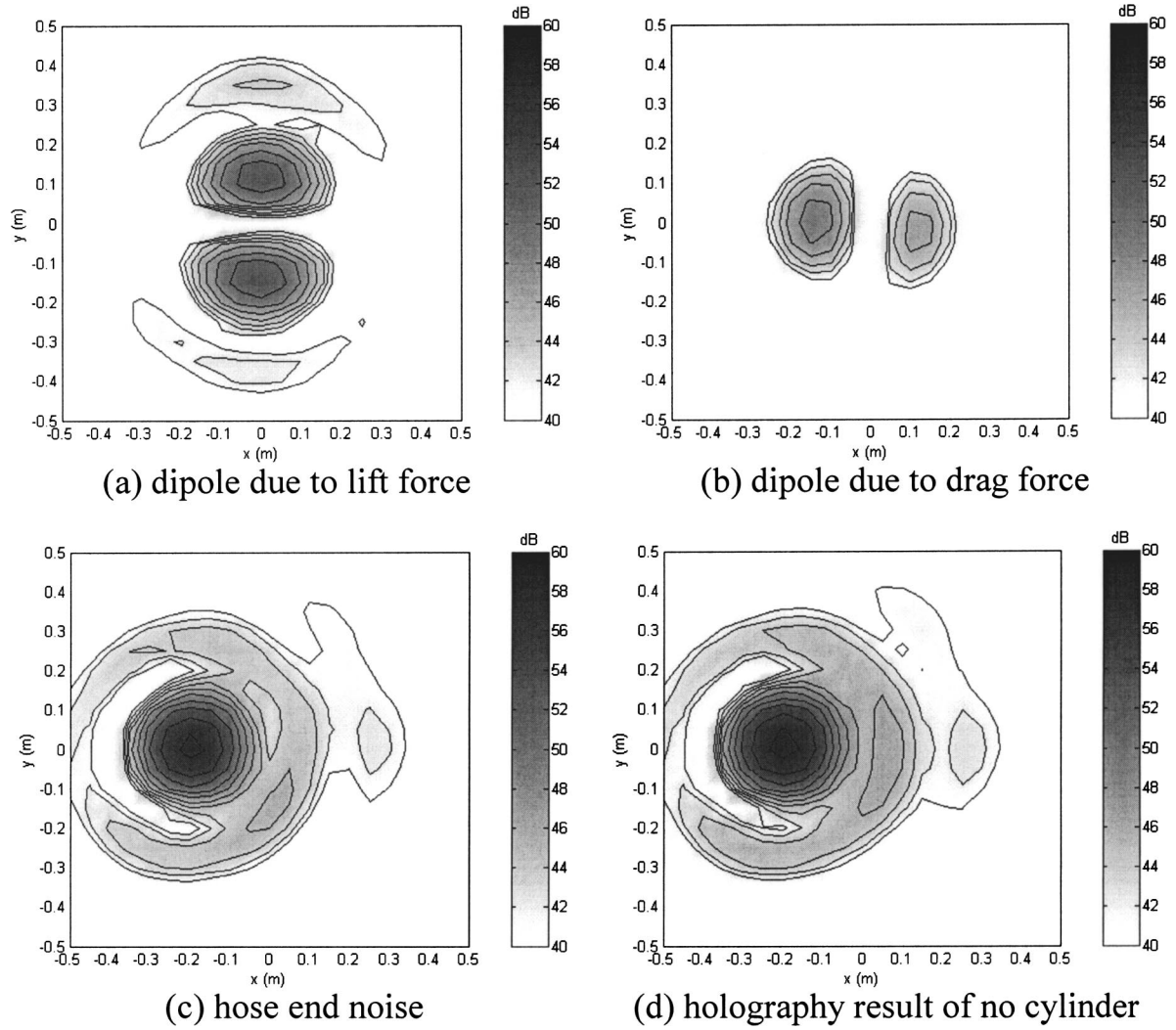

FIG. 15. Decomposition results at 1000 Hz in the vortex shedding experiment.

this paper we also reported two experiments that verify the algorithm and certainly demonstrate how it is useful. The experimental results showed that it is useful for identifying hidden sources and estimating the power of individual sources.

ACKNOWLEDGMENTS

This study was partly supported by the NRL (National Research Laboratory) project of KISTEP (Korea Institute of Science & Technology Evaluation and Planning), the BK21 (Brain Korea 21) project initiated by the Ministry of Education & Human Resources & Development of Korea, and the Hyundai Motor Company & Kia Motor Corporation.

APPENDIX A: MATHEMATICAL DEFINITION OF S_{SISI} IN EQ. (9)

Let h_{xl}^{Sm} be the transfer function between the lth source input x_l and the pressure at the mth point on the source plane. Let us define a row vector as

$$H_{xl}^{S}=[h_{xl}^{S1} \ \cdots \ h_{xl}^{SM}]. \tag{A1}$$

If the inputs are incoherent and s_{xlxl} is the autospectrum of x_l, the spectral matrix S_{SS} in Eq. (7) can be expressed as[11]

$$S_{SS}=\begin{bmatrix} H_{xl}^{S} \\ \vdots \\ H_{xL}^{S} \end{bmatrix}^{*}\begin{bmatrix} S_{xlxl} & & \\ & \ddots & \\ & & S_{xLxL} \end{bmatrix}\begin{bmatrix} H_{xl}^{S} \\ \vdots \\ H_{xL}^{S} \end{bmatrix}$$

$$=\sum_{l=1}^{L} s_{xlxl}H_{xl}^{S*}H_{xl}^{S}. \tag{A2}$$

Therefore S_{SlSl} in Eq. (9) is $s_{xlxl}H_{xl}^{S*}H_{xl}^{S}$.

APPENDIX B: PROOF OF EQ. (10)

Let w_l be coherent to the lth source input x_l as

$$w_l=c_l x_l. \tag{B1}$$

Let s_{xlSm} be the cross-spectrum between the x_l and p_{Sm}, and s_{wlSm} be the cross-spectrum between the w_l and p_{Sm}. Then the S_{wlS} in Eq. (11) can be rewritten as

$$S_{wlS}=[s_{wlS1} \ \cdots \ s_{wlSM}]=c_l^{*}[s_{xlS1} \ \cdots \ s_{xlSM}]. \tag{B2}$$

Because the inputs are incoherent, the h_{xl}^{Sm} in Appendix A is expressed as[13]

$$h_{xl}^{Sm}=s_{xlSm}/s_{xlxl}. \tag{B3}$$

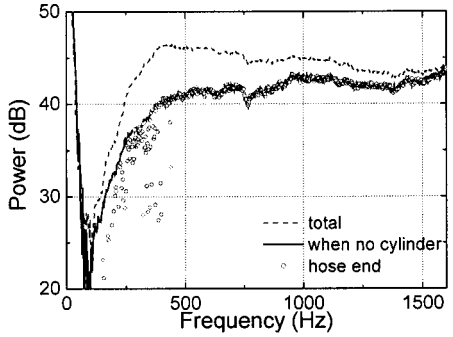

(a) the source power of hose end noise

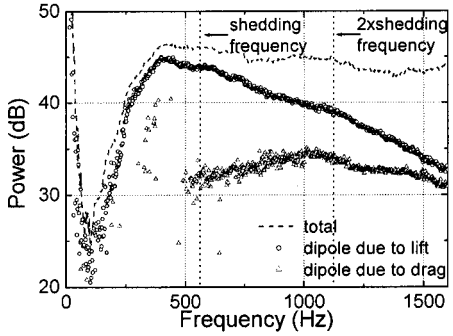

(b) the source power of dipoles

FIG. 16. Decomposition results of source power in the vortex shedding experiment.

Therefore Eqs. (A1) and (B1)–(B3) derive Eq. (10) as

$$
\begin{aligned}
S_{wlS}^{*}S_{wlS}/s_{wlwl} &= c_l^{*}[s_{xlS1} \ \cdots \ s_{xlSM}]^{*} \\
&\quad \times c_l[s_{xlS1} \ \cdots \ s_{xlSM}]/|c_l|^2 s_{xlxl} \\
&= s_{xlxl}[s_{xlS1}/s_{xlxl} \ \cdots \ s_{xlSM}/s_{xlxl}]^{*} \\
&\quad \times [s_{xlS1}/s_{xlxl} \ \cdots \ s_{xlSM}/s_{xlxl}] \\
&= s_{xlxl}[h_{xl}^{S1} \ \cdots \ h_{xl}^{SM}]^{*}[h_{xl}^{S1} \ \cdots \ h_{xl}^{SM}] \\
&= s_{xlxl}H_{xl}^{S*}H_{xl}^{S} = S_{SlSl}. \qquad \text{(B4)}
\end{aligned}
$$

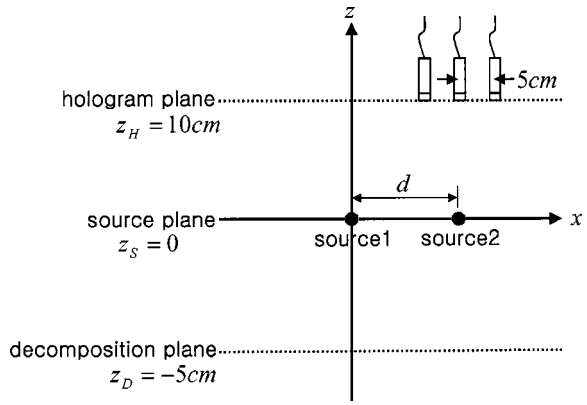

FIG. 17. Specifications for the numerical examples of a decomposition error. Variables are source types (monopole or dipole), distance d between the two sources, and source strength (or peak level).

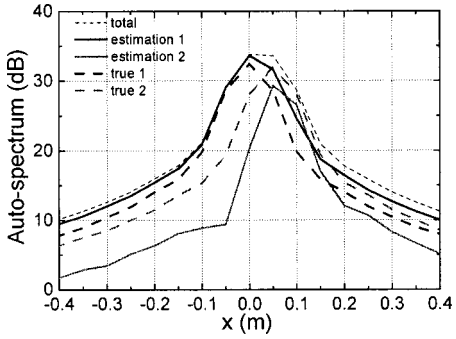

FIG. 18. Decomposition result of two monopoles, $d=5$ cm, and the same peak level (total: the autospectrum of pressure on the source plane, estimation 1: the first estimated contribution, estimation 2: the second estimated contribution, true 1: the true contribution of the first source, true 2: the true contribution of the second source).

APPENDIX C: SOME EXAMPES OF DECOMPOSITION ERROR

In this appendix we illustrate some numerical examples of decomposition errors. Spatial overlap generates a decomposition error. However, it is difficult to know how much is the spatial overlap or decomposition error. That is because the spatial overlap is directly related to the spatial distributions of individual sources, which is the objective of the decomposition. Therefore some numerical examples of this appendix cannot provide perfect guidelines on the spatial overlap. However, the examples will be helpful for the judgment of decomposition results because they have some common symptoms and features.

In this appendix we focuse on the behavior at peak points because the contribution of one source is more distorted at the peak points of other sources. Let us consider a two-input/single-output system (Sec. II B). Let $\hat{s}_{y1y1}$ and $\hat{s}_{y2y2}$ be the estimators of the true s_{y1y1} and s_{y2y2} [Eq. (4)]. If the $\hat{s}_{y1y1}$ is $s_{y1y1}+\epsilon$, then the $\hat{s}_{y2y2}$ is $s_{y1y1}-\epsilon$ because their sum is equal to the total output spectrum. That is, the two estimators have the same absolute errors. If $\hat{s}_{y1y1} \ll \hat{s}_{y2y2}$, however, the $\hat{s}_{y1y1}$ has a large relative error and the $\hat{s}_{y2y2}$ has a small relative error. Therefore the contribution of one source has a large error at the peak points of other sources.

Figure 17 shows the specifications of the numerical simulations on two incoherent sources. The hologram (z_H) and source planes (z_S) were located at 10 cm and 0. The measurement spacing was 5 cm and the number of measurement points was 32×32. The frequency was 343 Hz. Zeros were added so that the number of data including the zeros was 64×64. The spatial window minimizing errors[17] and the wave number filter proposed by Veronesi and Maynard[18] were used. For the decomposition, this simulation used the maximum pressure on the plane located at $z_D=-5$ cm instead of the source plane. The plane at the back of the source plane is often more useful than the source plane.[1] The variables are the source type (monopole or dipole), the distance ($d=5,10,15$ cm) between the sources, and the source strength (or peak level difference: 6, 0, −6 dB).

Figure 18 is the result of two monopoles, $d=5$ cm, and the same peak level. The symptom is the steep decrease of the second contribution near the peak point of the first con-

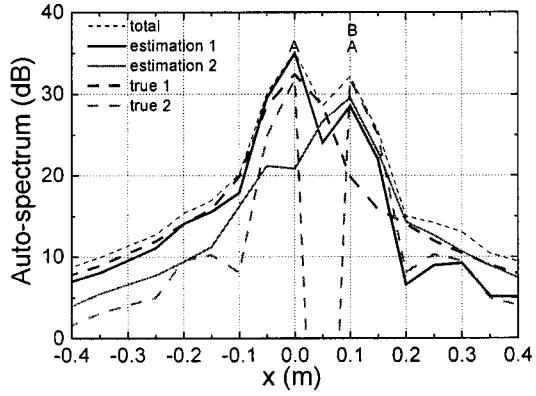

(a) d = 5cm, the same peak level

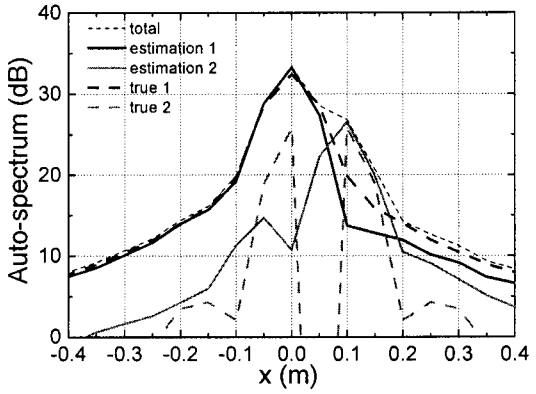

(b) d = 5cm, dipole peak = monopole peak – 6dB

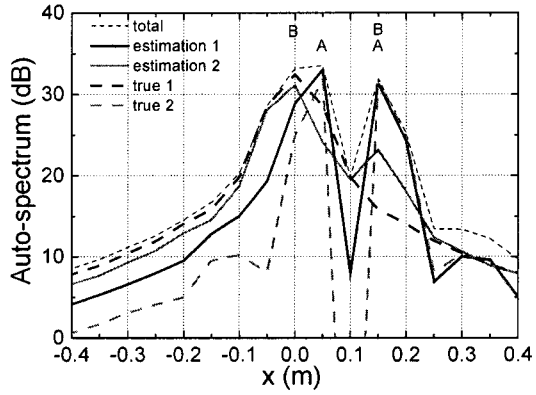

(c) d = 10cm, the same peak level

FIG. 19. Decomposition results of a monopole and a dipole (total: the autospectrum of pressure on the source plane, estimation 1: the first estimated contribution, estimation 2: the second estimated contribution, true 1: the true contribution of the first source, true 2: the true contribution of the second source, A and B: the peak points of the first and second contributions).

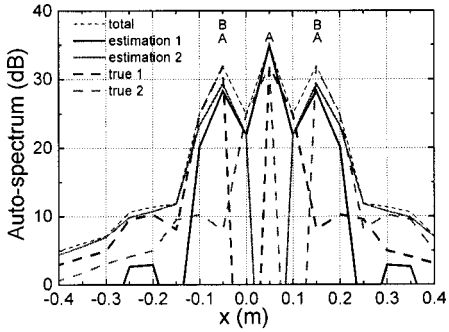

(a) d = 10cm, the same peak level

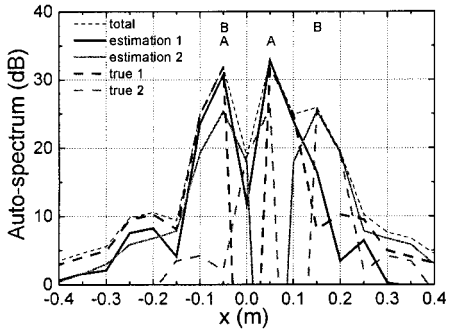

(b) d = 10cm, peak difference = 6dB

FIG. 20. Decomposition results of two dipoles (total: the auto-spectrum of pressure on the source plane, estimation 1: the first estimated contribution, estimation 2: the second estimated contribution, true 1: the true contribution of the first source, true 2: the true contribution of the second source, A and B: the peak points of the first and second contributions).

tribution. The first and second are over- and underestimated, respectively. When there are two monopoles, the results of other distances and peak levels showed the same phenomena as Fig. 18, or were well decomposed.

Figure 19 shows the results with a monopole and a dipole. Figure 19(a) is the result of $d=5$ cm and the same peak level. The symptom is that the peak point (B) of the second is also the peak point (A) of the first. All the contributions were largely distorted. Figure 19(b) shows the result when the dipole peak is 6 dB less than the monopole peak and $d=5$ cm. The symptom is the steep decrease of the first near the peak point of the second. Only the second contribution has a large error. Figure 19(c) is the result of $d=10$ cm and the same peak level. One of the peak points (B) of the second is also the peak point (A) of the first, but the other is not. The second is largely distorted only near the coinciding peak point. The results of other distances and peak levels were similar to those in Fig. 19, or were well decomposed.

Figure 20 shows the results when there are two dipoles. Fig. 20(a) is the result of $d=10$ cm and the same peak level. All the peak points (B) of the second are also those of the first. All the contributions had large errors. This is the same phenomenon as Fig. 3(a). Figure 20(b) is the result when the peak level difference is 6 dB, and is the same as Fig. 19(c). The results of other distances and peak levels were the same as in Fig. 20, or well decomposed.

From the above observation, Table I summarizes the common symptoms and features of the decomposition errors.

APPENDIX D: CONSIDERATION FOR A STEP-BY-STEP SCANNING METHOD

A measurement problem always includes ''how to measure'' and ''how to check the accuracy.'' The ''how to measure'' of the step-by-step scanning method[4,5] is related to the number and positions of reference microphones. The ''how to check the accuracy'' is related to the evaluation method of the error in the real measurement.

It is well known that the number of reference microphones has to be more than that of incoherent sources.[4] This implies that one has to use as many reference microphones as

TABLE I. Common symptoms and features of decomposition error.

Symptom	Feature	Example
The second contribution steeply decreases near the peak point of the first contribution.	The first contribution is overestimated and the second contribution is underestimated.	Fig. 18
The first contribution steeply decreases near the peak point of the second contribution.	Only the second contribution has a large error.	Fig. 19(b)
All the peak points of the second contribution coincide with those of the first contribution.	All the contributions have large errors.	Figs. 19(a), 20(a)
Some peak points of the second contribution coincide with those of the first contribution.	The second contribution has a large error only near the coinciding peak points.	Figs. 19(c), 20(b)

possible if the number of sources is unknown. From this viewpoint, the six-speaker and vortex shedding experiments used as many reference microphones as possible. This strategy can be inefficient if the number of sources is small, but does not decrease the accuracy. The singular value decomposition of the spectral matrix may be useful for identifying the number of sources.[19]

If there are enough reference microphones, the step-by-step scanning method does not depend on their positions. Therefore the reference microphones can be farfield like the six-speaker and vortex shedding experiments if the signal-to-noise ratio is high enough. At times, it has been proposed that reference microphones be placed near the sources. That is because the reference microphones are often used for the partial field decomposition as well as the construction of the hologram spectral matrix. If the objective of the step-by-step scanning is only the construction of the hologram spectral matrix, it is not necessary to place the reference microphones near the sources.

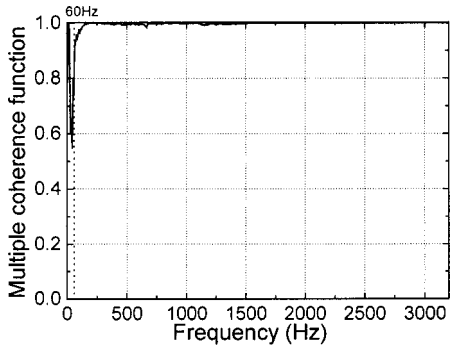

(a) 6-speaker experiment

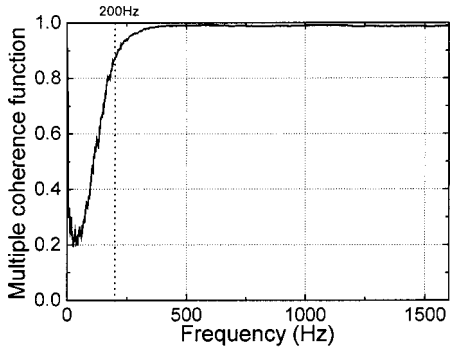

(b) vortex shedding experiment

FIG. 21. Spatially averaged multiple coherence functions of the main text experiments.

For the error evaluation, let us define an error derived from a matrix norm[16] as

$$\epsilon_{HH}=\sum_{m=1}^{N}\sum_{n=1}^{N}|s_{HmHn}-\hat{s}_{HmHn}|\Big/\sum_{m=1}^{N}\sum_{n=1}^{N}|s_{HmHn}|, \tag{D1}$$

where the s_{HmHn} and $\hat{s}_{HmHn}$ are the (m,n)th element of the true and measured hologram spectral matrix (S_{HH} and $\hat{S}_{HH}$). However, all the elements of the true cannot be obtained. As an alternative, let us define a modified error as

$$\epsilon'_{HH}=\sum_{n=1}^{N}|s_{HnHn}-\hat{s}_{HnHn}|\Big/\sum_{n=1}^{N}s_{HnHn}. \tag{D2}$$

The modified error can be calculated when there is no noise because the true autospectra can be measured by step-by-step scanning. Because the $\hat{s}_{HnHn}$ is the coherent output spectrum of s_{HnHn} with respect to the reference signals, the $\hat{s}_{HnHn}$ is always less than the s_{HnHn}.[13] Therefore Eq. (D2) can be rewritten as

$$\epsilon'_{HH}=1-\gamma^2_{H:R}, \tag{D3}$$

where

$$\epsilon'_{HH}=\sum_{n=1}^{N}\hat{s}_{HnHn}\Big/\sum_{n=1}^{N}s_{HnHn}. \tag{D4}$$

As the $\gamma^2_{H:R}$ approaches 1, the error becomes smaller. We call the $\gamma^2_{H:R}$ a spatially averaged multiple coherence function. It is the expansion of a multiple coherence function.[11,13] Figure 21 shows its values in the speaker and vortex shedding experiments. If the criterion is 0.8 (about 1 dB error), the speaker and vortex shedding experiments are reliable at frequencies higher than 60 and 200 Hz, respectively.

[1] K.-U. Nam and Y.-H. Kim, "Visualization of multiple incoherent sources by the backward prediction of near-field acoustic holography," J. Acoust. Soc. Am. **109**, 1808–1816 (2001).

[2] E. G. Williams, J. D. Maynard, and E. Skudrzyk, "Sound source reconstruction using a microphone array," J. Acoust. Soc. Am. **68**, 340–344 (1980).

[3] E. G. Williams and J. D. Maynard, "Holographic imaging without the wavelength resolution limit," Phys. Rev. Lett. **45**, 554–557 (1980).

[4] J. Hald, "STSF—A unique technique for scan-based near-field acoustic

holography without restrictions on coherence,'' B&K Technical Review No. 1, 1989.
[5] K. B. Ginn and J. Hald, ''STSF—Practical instrumentation and applications,'' B&K Technical Review No. 2, 1989.
[6] D. Hallman and J. S. Bolton, ''Multi-reference near-field acoustical holography,'' in Proceedings of Inter-Noise '92, 1992 International congress on noise control engineering, Held in Toronto, Canada on 1992 July, edited by Gilles A. Daigle and Michael R. Stinson, International Institute of Noise Control Engineering, 1992, pp. 1165–1170.
[7] H.-S. Kwon and J. S. Bolton, ''Partial field decomposition in nearfield acoustical holography by the use of singular value decomposition and partial coherence procedures,'' in Proceedings of Noise-Con '98, the 1998 national conference on noise control engineering, Held in Ypsilanti, Michigan on 1998 April, edited by J. Stuart Bolton and Luc Mongeau, The Institute of Noise Control Engineering of the USA, 1998, pp. 649–654.
[8] R. J. Ruhala and C. B. Burroughs, ''Separation of leading edge, trailing edge, and sidewall noise sources from rolling tires,'' in Proceedings of Noise-Con'98, the 1998 national conference on noise control engineering, Held in Ypsilanti, Michigan on 1998 April, edited by J. Stuart Bolton and Luc Mongeau, The Institute of Noise Control Engineering of the USA, 1998, pp. 109–114.
[9] M. A. Tomlinson, ''Partial source discrimination in near field acoustic holography,'' Appl. Acoust. **57**, 243–261 (1999).
[10] S. M. Price and R. J. Bernhard, ''Virtual coherence: A digital signal processing techniques for incoherent source identification,'' in Proceedings of IMAC IV, the 4th International Modal Analysis Conference, Held in Los Angeles, California on 1986, February, Society for experimental mechanics, 1986, pp. 1256–1262.
[11] G. M. Jenkins and D. G. Watts, *Spectral Analysis and its Applications* (Holden-Day, San Francisco, 1968), pp. 458–513.
[12] C. J. Dodds and J. D. Robson, ''Partial coherence in multivariate random process,'' J. Sound Vib. **42**, 243–249 (1975).
[13] J. S. Bendat and A. G. Piersol, *Random Data: Analysis and Measurement Procedures*, 2nd ed. (Wiley, New York, 1986), pp. 164–251.
[14] H.-S. Kwon and Y.-H. Kim, ''Moving frame technique for planar acoustic holography,'' J. Acoust. Soc. Am. **103**, 1734–1741 (1998).
[15] S.-H. Park and Y.-H. Kim, ''An improved moving frame acoustic holography for coherent band-limited noise,'' J. Acoust. Soc. Am. **104**, 3179–3189 (1998).
[16] P. Lancaster and M. Tismenetsky, *The Theory of Matrices with Application*, 2nd ed. (Academic, New York, 1985), pp. 71–440.
[17] H.-S. Kwon and Y.-H. Kim, ''Minimization of bias error due to windows in planar acoustic holography using a minimum error window,'' J. Acoust. Soc. Am. **98**, 2104–2111 (1995).
[18] W. A. Veronesi and J. D. Maynard, ''Nearfield acoustic holography (NAH): 2 Holographic reconstruction algorithms and computer implementation,'' J. Acoust. Soc. Am. **81**, 1307–1322 (1987).
[19] M. S. Kompella, P. Davies, R. J. Bernhard, and D. A. Ufford, ''A technique to determine the number of incoherent sources contributing to the response of a system,'' Mech. Syst. Signal Process. **8**, 363–380 (1994).

Acoustic nonlinearity of liquid containing encapsulated microbubbles

Jian Ma, Jinfei Yu, Zheng Fan, Zhemin Zhu,[a] Xiufen Gong, and Gonghuan Du
State Key Laboratory of Modern Acoustics & Institute of Acoustics, Nanjing University, Nanjing 210093, People's Republic of China

(Received 24 September 2003; revised 2 April 2004; accepted 18 April 2004)

Recently, a high value nonlinear parameter of liquid containing contrast agents (encapsulated microbubbles) has been reported by some measurements, however an effective way to study it theoretically has not been found so far. In this paper, an approach, based on the concept of the equivalent nonlinear parameter is presented to estimate the nonlinear property of such media. The liquid containing encapsulated microbubbles is treated as a homogenous liquid with a equivalent nonlinear parameter. An experimental approximate linear relationship for attenuation and nonlinear parameter with bubble volume is confirmed from our calculation. It is also found that when a microbubble is encapsulated by a shell, the nonlinear oscillation of the bubble is restrained; the second and higher harmonics are generated not so effectively compared to a free bubble. Naturally this causes the nonlinear parameter of such a liquid to decrease greatly. Favorable agreement between the theory and Wu *et al.*'s experiments shows this approach could effectively estimate the nonlinearity of encapsulated bubbly liquid. Finally, some applicable limitations for this approach are also mentioned. [DOI: 10.1121/1.1760792]

PACS numbers: 43.25.Ba, 43.25.Yw [MFH] Pages: 186–193

I. INTRODUCTION

An emerging field in medical ultrasound diagnosis is harmonic imaging using ultrasound contrast agents. The majority of such agents are microbubbles, encapsulated by a shell (encapsulated bubbles) to provide stabilization against diffusion caused by surface tension. Because of the introduction of the shell, the bubble's oscillation is restrained by the shell, which causes it to behave differently as compared to free bubbles,[1–6] e.g., the resonant frequency of encapsulated bubbles increases due to the shell rigidity. De Jong *et al.*[1–3] developed a detailed theoretical description of the behavior of encapsulated bubbles, which was validated by extensive experimental results.[4,5] In 1995 Church[6] derived a well-founded Rayleigh–Plesset-like equation to describe the oscillation of encapsulated bubbles. By solving this equation he demonstrated the changes occurring to properties like scattering, attenuation, and sound speed in liquid containing encapsulated bubbles. Hoff[7] developed Church's approach further, to model bubbles encapsulated by a polymer shell. By fitting calculated attenuation spectra to measured spectra, he estimated values for two shell parameters: shell elasticity and viscosity.

The study of the nonlinear characteristics of ultrasound contrast agents forms an important research field; recently, the nonlinear parameter B/A describing the nonlinear property of media has been investigated in such different fields as ultrasound diagnosis and second harmonic imaging.[8–12] It is well known that, at frequencies close to their resonant frequency, microbubbles oscillate vigorously in an external ultrasonic field. These oscillating microbubbles behave as secondary sources for ultrasound. Due to the nonlinear nature of the oscillation higher harmonics, particularly the second harmonic component, become significant. Consequently, the nonlinearity of the host media is enhanced dramatically due to the presence of microbubbles. This advantage has been widely exploited in second harmonic imaging techniques. For instance, the image contrast related to the second harmonic image of blood flow in the color Doppler mode is greatly strengthened by using contrast agents because the second harmonic signals associated with the motion of vascular walls are small. Thus the acoustic nonlinear parameter B/A is an important parameter that could be used to define the nonlinearity of the media, and may emerge as a new parameter for characterization in ultrasonic biomedicine.[18] As we find in the literature, the study of the nonlinearity parameter B/A of liquid containing contrast agents has attracted much attention recently. Gong *et al.* reported B/A values of liquids containing contrast agents.[8] Later Wu *et al.* measured attenuation of the fundamental harmonic to determine the resonant frequency of contrast agents, and measured the second harmonic to obtain the B/A values of two contrast agents (Albunex® and Levovist®) in a saline solution.[10] Zhang and Gong *et al.* investigated the nonlinearity parameter of sonicated contrast agents sonicated dextrose albumin.[18]

To our knowledge, most of these works are experiment based. Although the nonlinear oscillation of individual encapsulated bubbles is well understood,[6] a suitable theory to estimate the macroscopic nonlinearity parameter of liquid containing contrast agents is, we believe, still to be proposed. In this article we present a theoretical approach to estimate the nonlinear property of the liquid containing encapsulated microbubbles. Combining the wave equation for bubbly liquid and the dynamic equation for encapsulated bubbles and using the perturbation method, equations for fundamental

[a]Electronic mail: zhudu@nju.edu.cn

 0001-4966/2004/116(1)/186/8/$20.00

and second harmonic are obtained. We then employ the concept of effective nonlinear parameter, treating liquid containing encapsulated bubbles as a homogeneous medium with an effective nonlinear parameter $(B/A)_e$. In this way, a formula to estimate the equivalent acoustic nonlinearity parameter $(B/A)_e$ of such media is achieved. Since our intention is to quantitatively match the experimental data, a comparison is made between our theoretical calculation and Wu's experimental results for contrast agents Albunex®. Favorable agreement shows the efficiency of our approach. The relations of $(B/A)_e$ to attenuation and bubble concentration are also discussed subsequently. To see the influence of the encapsulating shell on the nonlinearity of bubbles, we made another comparison for the $(B/A)_e$ of liquid containing encapsulated bubbles to that of free bubbles. Compared to free bubbles, for the encapsulated bubbles, both attenuation of fundamental harmonic and the nonlinear parameter underwent a large decrease in magnitude. We present possible interpretations and finally, we comment upon some applicable limitations to this approach and ways to improve them.

II. THEORY

A. Wave equation for bubbly liquid

First, for clarity, all the variables definitions through this paper are listed in the Appendix. Employing an equivalent medium approach,[20] we begin our analysis from the wave equation for bubbly liquid. For mathematical simplicity, we neglect the viscosity, thermal conduction and the nonlinearity parameter of the pure water, since their effects are small. Therefore, the bubbly liquid can be viewed as an equivalent continuous medium and the wave equation could be expressed as[20]

$$\frac{1}{c_0^2}\frac{\partial^2 p}{\partial t^2}-\frac{\partial^2 p}{\partial x^2}=\rho_0\frac{\partial^2 \beta}{\partial t^2}. \tag{1}$$

The bubbly liquid is described in an average sense and p is defined as average pressure. ρ_0, c_0 are the density and speed of sound for the pure water, respectively. β is bubble volume fraction. For simplicity, we first assume that all encapsulated bubbles have identical radius, and later we will introduce the bubble radius distribution of a real contrast agent Albunex®. In an identical radius case, $\beta=NV=N(V_0+V')$, where N is bubble number density per unit volume, and V, V_0, and V' are the instantaneous volume, equilibrium volume, and volume variation of an individual bubble respectively. Then the wave equation (1) for bubbly liquid goes to

$$\frac{1}{c_0^2}\frac{\partial^2 p}{\partial t^2}-\frac{\partial^2 p}{\partial x^2}=\rho_0 N\frac{\partial^2 V'}{\partial t^2}. \tag{2}$$

We follow the procedure of the perturbation approach and let

$$p=p_1+p_2+\cdots \quad V'=V_1'+V_2'+\cdots, \tag{3}$$

where p_1, V_1' and p_2, V_2' are the first-order terms and the second-order terms, respectively. Substituting Eq. (3) into Eq. (2) and neglecting the higher order terms, we obtain

$$\frac{1}{c_0^2}\frac{\partial^2 p_1}{\partial t^2}-\frac{\partial^2 p_1}{\partial x^2}=\rho_0 N\frac{\partial^2 V_1'}{\partial t^2}, \tag{4}$$

$$\frac{1}{c_0^2}\frac{\partial^2 p_2}{\partial t^2}-\frac{\partial^2 p_2}{\partial x^2}=\rho_0 N\frac{\partial^2 V_2'}{\partial t^2}. \tag{5}$$

B. Dynamic equation for encapsulated bubble

To solve Eqs. (4) and (5), another equation describing individual bubble oscillation in the ultrasound field of the mixture is required. For the free bubble case, this is provided by the well known Rayleigh–Plesset equation, which has been investigated in detail for a long time. However, in the encapsulated bubble case, several models of Rayleigh–Plesset-like equations describing oscillation of the encapsulated bubble have been proposed. Due to the different properties of contrast agents, particularly the different encapsulated layer influence, these models are quite different from each other. For example, Frinking and de Jong presented a phenomenological mode for contrast agents Quantison;[1] Church derived a nonlinear theoretical model for contrast agents Albunex®.[6] A suitable choice of these models according to different contrast agents is important for our approach to properly estimate its nonlinearity, because the nonlinearity of the media containing contrast agents is derived from the nonlinear oscillation behavior of the individual contrast agent. In this paper, we use Church's model for the encapsulated bubbles, since it has been shown that this model could effectively describe the acoustic behavior of the contrast agents Albunex®. This contrast agent was also used in Wu *et al.*'s measurement, which will be compared later to validate our theory. The Rayleigh–Plesset-like equation derived by Church could be expressed as a form of linear order terms with added second order terms[6]

$$\ddot{x}[1+(1+\alpha_n)x]+\frac{3}{2}\left(1+\frac{\alpha_n}{3}\right)\dot{x}^2+(\delta_d-\delta_{dn}x)\dot{x}+\omega_0^2 x - \omega_{0n}^2 x^2=p(\rho_s R_{01}^2\alpha)^{-1}, \tag{6}$$

where the coefficients of the linear terms are

$$\delta_d=\beta_{\mathrm{vis},L,S}+\beta_{\mathrm{th}}+\beta_{\mathrm{ac}},$$

$$\beta_{\mathrm{vis},L,S}=2\left[\frac{V_s\mu_s+R_{01}^3\mu_L}{R_{02}^3}\right](\rho_s R_{01}^2\alpha)^{-1},$$

$$\beta_{\mathrm{th}}=2\mu_{\mathrm{th}}(\rho_s R_{01}^2\alpha)^{-1},$$

$$\beta_{\mathrm{ac}}=\frac{\omega}{2}\left(\frac{\omega R_{02}}{c}\right)\left[1+\left(\frac{\omega R_{02}}{c}\right)^2\right]^{-1},$$

$$\alpha=\left[1+\left(\frac{\rho_l-\rho_s}{\rho_s}\right)\frac{R_{01}}{R_{02}}\right],$$

$$\omega_0^2=(\rho_s R_{01}^2\alpha)^{-1}\left\{3\kappa P_0-\frac{2\sigma_1}{R_{01}}-\frac{2\sigma_2 R_{01}^3}{R_{02}^4}+4\frac{V_s G_s}{R_{02}^3}\left[1+Z\left(1+\frac{3R_{01}^3}{R_{02}^3}\right)\right]\right\}.$$

The coefficients of the nonlinear terms are

$$\alpha_n=\left(\frac{\rho_l-\rho_s}{\rho s}\right)\frac{V_s R_{01}}{\alpha R_{02}^4},$$

$$\delta_{dn}=\delta_d\left(1+\frac{3R_{01}^3}{R_{02}^3}\right)-\frac{12R_{01}\mu_l}{\rho_s R_{02}^3\alpha},$$

$$Z=\left(\frac{2\sigma_1}{R_{01}}+\frac{2\sigma_2}{R_{02}}\right)\left(\frac{R_{02}^3}{V_s}\right)(4G_s)^{-1},$$

$$Vs=R_{02}^3-R_{01}^3,$$

$$\omega_{0n}^2=(\rho_s R_{01}^2\alpha)^{-1}\left\{\frac{3\kappa(3\kappa+1)}{2}P_0-\frac{2\sigma_1}{R_{01}}-\frac{2\sigma_2 R_{01}^3(R_{01}^3-Vs)}{R_{02}^7}+4\frac{V_s G_s}{R_{02}^3}\left[\left(1+\frac{3R_{01}^3}{R_{02}^3}\right)+Z\left(1+\frac{9R_{01}^6}{R_{02}^6}\right)\right]\right\}.$$

In his article ρ_l, ρ_s are the densities of the liquid and the shell, respectively, R_{01} is the radius of the gas-filled cavity, and R_{02} is the radius of the bubble with shell layer. κ is the polytropic exponent. x is the radius variation compared to the R_{01}. G_s is the modulus of rigidity. μ_l, μ_s are the viscosities in the liquid and layer, respectively, assuming that the dilatational viscosity is negligible. σ_1, σ_2 are the interfacial tension. V_s is the volume of the shell layer. It could be seen that this equation is also a nonlinear equation and has a form similar to the Rayleigh–Plesset equation for free bubbles. We transfer Eq. (6) using volume fluctuation of the bubble as a variable, into a consistent form, as follows:

$$\ddot{V}'+\omega_0^2V'-\frac{\omega_{0n}^2}{3V_0}(V')^2+\frac{1}{V_0}\left(\frac{m}{3}V'\ddot{V}'-\frac{n}{3}\dot{V}'V'+\frac{m}{6}(\dot{V}')^2\right)+\delta_d\dot{V}'=-\epsilon p, \tag{7}$$

with

$$m=\alpha_n-1,\quad n=\delta_{dn}+2\delta_d,\quad \epsilon=\frac{4\pi R_{01}}{\rho_s\alpha}.$$

Special attention must be paid to the definition of p in Eq. (7). It is defined as the pressure at the position occupied by the bubble, if the bubble was absent. It was realized by Foldy,[19] and Commander and Prosperetti[20] that in a dilute mixture, this quantity coincides with the average pressure defined in Eq. (2). In this limit, the bubbles do not interact with each other's field, but with the average field.

C. Nonlinear wave equation for encapsulated bubbly liquid

Equation (7) could also be approximately solved through perturbation approach

$$p=p_1+p_2+\cdots\quad V'=V_1'+V_2'+\cdots.$$

This yields

$$\ddot{V}_1'+\omega_0^2V_1'+\delta_d\dot{V}_1'=-\epsilon p_1, \tag{8}$$

$$\ddot{V}_2'+\omega_0^2V_2'+\delta_d\dot{V}_2'-\frac{\omega_{0n}^2}{3V_0}(V_1')^2+\frac{1}{V_0}\left[\frac{m}{3}V_1'\ddot{V}_1'-\frac{n}{3}\dot{V}_1'V_1'+\frac{m}{6}(\dot{V}_1)^2\right]=-\epsilon p_2. \tag{9}$$

Solving these two equations we get

$$\ddot{V}_1'=\frac{-\epsilon p_1}{\left(1-\frac{1}{z^2}+\frac{1}{jQ}\right)}, \tag{10}$$

$$\ddot{V}_2'=\frac{-\epsilon p_2}{\left(1-\frac{1}{4z^2}+\frac{1}{2jQ}\right)}+\frac{\left(\frac{m\omega^2}{2V_0}+\frac{(\omega_{0n}^2+\omega_0^2)}{3V_0}+\frac{\omega n}{3V_0}j\right)V_1'^2}{\left(1-\frac{1}{4z^2}+\frac{1}{2jQ}\right)}, \tag{11}$$

where

$$Q=\frac{\omega}{\delta_d}\quad z=\frac{\omega}{\omega_0}.$$

From Eq. (11), we can see that the second-order term of volume variation V_2' is contributed by both the second-order term of pressure p_2 and the first-order term of volume variation $V_1'^2$. Substituting Eqs. (10), (11) into Eqs. (4), (5), we obtain wave equations for p_1, p_2, respectively, as follows:

$$\frac{\partial^2 p_1}{\partial x^2}-\frac{1}{c_0^2}\frac{\partial^2 p_1}{\partial t^2}=\frac{\rho_0 p_1 N\epsilon}{\left(1-\frac{1}{z^2}+j\frac{1}{Q}\right)}, \tag{12}$$

$$\frac{\partial^2 p_2}{\partial x^2}-\frac{1}{c_0^2}\frac{\partial^2 p_2}{\partial t^2}=\frac{\rho_0 p_2 N\epsilon}{\left(1-\frac{1}{4z^2}+j\frac{1}{2Q}\right)}-\rho_0 p_1^2 ND. \tag{13}$$

Here

$$D=\frac{\left[\frac{m}{2V_0}\omega^2+\frac{\omega n}{3V_0}j+\frac{1}{3V_0}(\omega_0^2+\omega_{0n}^2)\right]\epsilon^2}{\left(1-\frac{1}{4z^2}-j\frac{1}{2Q}\right)\left(1-\frac{1}{z^2}-j\frac{1}{Q}\right)^2\omega^4}.$$

D. Fundamental harmonic

To solve Eq. (12), we let

$$p_1=p_{1A}\cdot\exp[j(\omega t-\overline{k_1}x)]\quad \overline{k_1^2}=A_1-jB_1,$$

$$A_1 = k_0^2 - \frac{\rho_0 N\epsilon\left(1-\frac{1}{z^2}\right)}{\left(1-\frac{1}{z^2}\right)^2+\frac{1}{Q^2}} \quad B_1 = \frac{\rho_0 N\epsilon}{\left[\left(1-\frac{1}{z^2}\right)^2+\frac{1}{Q^2}\right]Q}.$$

Here $k_0=\omega/c_0$, $\overline{k_1}=k_1-j\alpha_1$, $k_1=\omega/c_1$ and c_1, α_1 are the sound velocity and attenuation coefficient of the fundamental harmonic, respectively. In pure liquid, we can make the approximation of $\overline{k_1^2}\approx k_1^2-j2\alpha_1 k_1$ to simplify the calculation for α_1, since the condition $\alpha_1 \ll k_1$ is always satisfied. However, this approximation cannot be adopted for the liquid containing microbubbles, because both the theoretical[15] and experimental[9] results show that the attenuation in such media is much stronger than that in pure liquid and is comparable with the wave number k_1. So when we neglect the loss due to viscosity of water, the attenuation coefficient and the wave number caused only by the presence of microbubbles can be expressed, respectively, as

$$\alpha_1 = \frac{1}{\sqrt{2}}\left\{\sqrt{k_0^4+\frac{(\rho_0 N\epsilon)^2-2k_0^2\rho_0 N\epsilon\left(1-\frac{1}{z^2}\right)}{\left(1-\frac{1}{z^2}\right)^2+\frac{1}{Q^2}}} - \left[k_0^2-\frac{\rho_0 N\epsilon\left(1-\frac{1}{z^2}\right)}{\left(1-\frac{1}{z^2}\right)^2+\frac{1}{Q^2}}\right]\right\}^{1/2},$$
$$k_1 = \frac{B_1}{2\alpha_1}. \tag{14}$$

We can clearly see that the presence of microbubbles changes the attenuation coefficient of the fundamental harmonic. Rather than being linearly proportional to frequency as in pure liquid, the attenuation coefficient of the bubbly medium displays a resonance characteristic with respect to the frequency. For liquid containing uniform microbubbles, the resonant frequency of the attenuation coefficient is simply determined by the radius of the bubble. However, for practical contrast agents, which have a different size distribution, the resonance frequency depends mainly on the size distribution of the given contrast agents.[16,17]

E. Second harmonic

Equation (13) is an inhomogeneous differential equation. We can see that the nonlinear characteristic bubble oscillation enhances the second harmonic field. Considering that at the resonant frequency $2k_1\approx k_2$, it can be solved with the boundary condition $x=0$, $p_2=0$ as

$$p_2 = \frac{\rho_0 ND}{(4\overline{k_1^2}-\overline{k_2^2})}p_{1A}^2[\exp(-2\alpha_1 x) - \exp(-\alpha_2 x)]\exp j(2\omega t - k_2 x), \tag{15}$$

Here

$$\alpha_2 = \sqrt{(\sqrt{A_2^2+B_2^2}-A_2)/2} \quad k_2 = \frac{B_2}{2\alpha_2},$$

$$A_2 = \frac{4\omega^2}{c_0^2} - \frac{\rho_0 N\epsilon\left(1-\frac{1}{4z^2}\right)}{\left(1-\frac{1}{4z^2}\right)^2+\frac{1}{4Q^2}},$$

$$B_2 = \frac{\rho_0 N\epsilon}{2Q\left[\left(1-\frac{1}{4z^2}\right)^2+\frac{1}{4Q^2}\right]}.$$

F. Equivalent acoustic nonlinearity parameter $(B/A)_e$

Besides being the basic parameter of fluid, B/A could also be used to quantify the distortion process of the acoustic wave. For pure liquid medium, through the propagation, the ultrasonic wave distorts and part of the acoustic energy of fundamental harmonic is transferred to its harmonics.[14] Thus, the amplitude of second harmonic in propagation would be greatly influenced by the B/A for this medium, which follows the relationship as[14]

$$p_2 = \frac{\omega(B/A+2)[\exp(-2\alpha_1 x)-\exp(-\alpha_2 x)]}{4\rho_0 c_0^3(2\alpha_1-\alpha_2)}p_{1A}^2 \times \exp j(2\omega t - k_2 x). \tag{16}$$

Here x is the distance through propagation away from the source. Conversely, B/A for pure medium could be obtained by measuring the second harmonic. This approach proposed by Cobb is well known as the finite amplitude method and has been widely used by many researchers.[14,18] With this principle in mind, comparing Eqs. (15) and (16), we find that these two analytical expressions for the second harmonic are very similar in formulation. This gives us an idea of resorting to the concept of equivalent nonlinear parameter $(B/A)_e$ to estimate the nonlinear property of the liquid containing microbubbles. That is, we treat the second harmonic field of bubbly liquid as a pure liquid with equivalent nonlinear parameter $(B/A)_e$, expressed as

$$(B/A)_e = \left|\frac{4\rho_0^2 ND c_0^3(2\alpha_1-\alpha_2)}{(4\overline{k_1^2}-\overline{k_2^2})\omega}-2\right|. \tag{17}$$

We should emphasize here, Eq. (17) is just the nonlinearity parameter caused by the presence of microbubbles in liquid, while the nonlinearity caused by pure liquid is neglected at the beginning of our analysis. One way to include these may be by resorting to Apfel's mixture law for nonlinearity parameter.[11] However, it is widely validated from experiments that the nonlinearity caused by host liquid is much smaller than that due to microbubbles so it can safely be neglected.[9,10,12]

III. NUMERICAL CALCULATIONS

In order to evaluate the validity of this approach, we make numerical calculations using the contrast agents

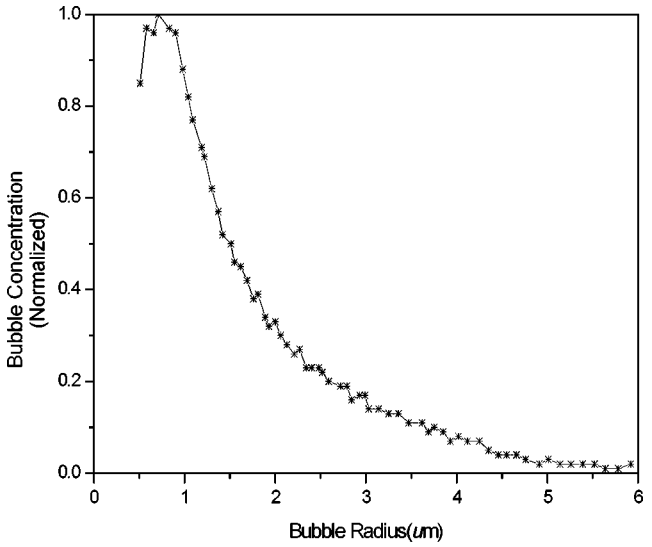

FIG. 1. The complete bubble size distribution used in our calculation given by Church (Ref. 6).

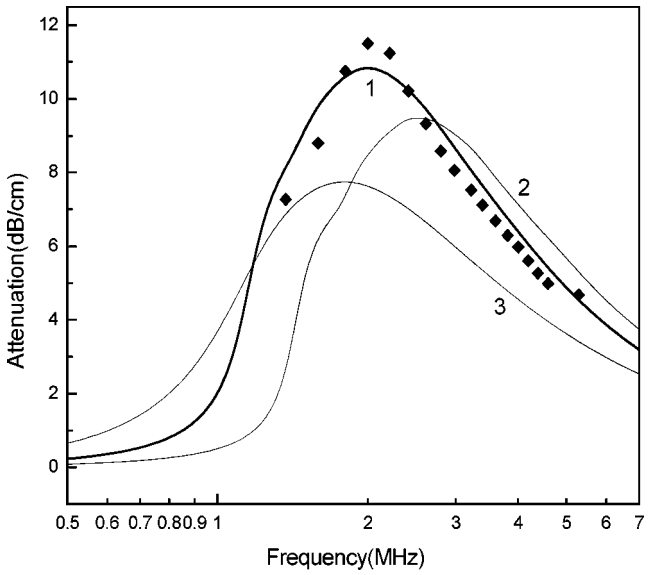

FIG. 2. Attenuation coefficient of fundamental harmonic vs frequency f in liquid containing encapsulated bubbles. Black diamond dots are measured values by Wu *et al.* (Ref. 10). Curve 1 is theory calculation for the case: bubble's shell rigidity $G_s = 55.6$ MPa, bubble's shell viscosity $\mu_s = 2.2$ Pa s; Curve 2 is theory calculation for the case: $G_s = 88.8$ MPa, $\mu_s = 2.2$ Pa s; Curve 3 is theory calculation for the case: $G_s = 55.6$ MPa, $\mu_s = 8$ Pa s.

Albunex® as an example and compare with Wu's experimental results.[10] The size distribution of microbubbles has a strong influence on the ultrasonic characteristics of suspensions. Hence it is necessary to make our calculation with the real distribution of Albunex® rather than assuming an identical radius of microbubbles. Then the β in Eq. (1) should be substituted by $\beta = \int_R V(R)n(R)dR$, where $n(R)$ is the bubble size distribution of contrast agents. Following analysis, the procedure is exactly the same as the identical bubbles and it is unnecessary to repeat it again here. The distribution of Albunex®, which we used in our calculation, is shown in Fig. 1 by Church.[6] This curve gives the complete Albunex® size distribution. The mean radius and concentration of the original distribution is 1.7 μm and 1.29×10^9 bubbles/cm^3, respectively.[6] Besides the size distribution of bubbles, two shell parameters, shell rigidity G_s, and shell viscosity μ_s also have significant influence on bubble behavior and for the contrast agents Albunex® G_s and μ_s values span a wide range.[6] Since Wu *et al.* haven't given the parameters of Albunex® used in their experiment, it makes our comparison difficult. To get these two shell parameters used in his experiment, we follow the Hoff[7] and Marsh's[13] approaches. This involves adjusting these two shell parameters in such a way as to minimize the square of the difference between the theoretical curves and the corresponding experimental values for attenuation measured by Wu (shown in Fig. 2). In this way, the two shell parameters could be estimated to be 55.6 MPa and 2.2 Pa s, respectively, which nearly match the values obtained by Marsh[13] for Albunex®. The other parameters used are listed as follows: $\rho_l = 1000$ kg/m^3, $\rho_s = 1300$ kg/m^3, $\mu_l = 0.001$ Pa s, $\sigma_1 = 0.04$ N/m, $\sigma_2 = 0.005$ N/m, and $c_0 = 1500$ m/s. The pressure amplitude is 22 kPa which is the value Wu *et al.* used in their experiment.

Figure 2 shows the frequency dependence of the attenuation coefficient for the fundamental harmonic. Curve 1 is our theoretical calculation to fit the experimental data (black dots) measured by Wu *et al.* To demonstrate the influence of shell parameters, we also choose $G_s = 88.8$ MPa, $\mu_s = 8$ Pa s in our numerical calculations as done by Church.[7] The fact that the attenuation coefficient peaks at the resonant frequency hints that it is a resonance phenomenon as we suggested before. Also it is clear that both G_s and μ_s have great influence on attenuation. Curve 2 is the curve for a case with the same shell viscosity as for Curve 1 but with different shell rigidity. Comparing them, we see that the position of the maximum in attenuation shifts to a higher frequency due to increasing shell rigidity. This is well explained by Church: the increase of shell rigidity makes the bubble exhibit greater stiffness. Also, the attenuation decreases as the rigidity of the shell increases. Curve 3 is obtained for another case with the same shell rigidity as for Curve 1, but with a different shell viscosity μ_s. Comparing Curves 1 and 3, we see that the attenuation produced by the encapsulated bubbles decreases with increasing shell viscosity. The reason is that when the bubble is encapsulated by a shell, it needs to overcome the effect of the viscosity of the shell, in addition to other lossy mechanisms encountered by the free bubble. In other words, the presence of the shell restrains the nonlinear oscillation of the bubble and causes the resonance mechanism of individual bubbles to weaken.

IV. COMPARISONS

A. Comparison between theory and Wu's experiments

The comparisons between our theory and Wu's experiments for the attenuation of fundamental harmonic α_1 and effective nonlinear parameter $(B/A)_e$ of Albunex® are listed in Table I. In the first column, v is the concentration of Albunex®. It is the volume of undiluted Albunex® divided by the volume of Isoton solution. The data in parentheses are measured by Marsh.[13] It is found that our calculated values match the experimental results quite well. Both the theoreti-

TABLE I. Comparison between our calculation and Wu's measurements.

v(μL/mL)[a]	Calculated α_1 (dB/cm)	Measured α_1 (dB/cm)	Calculated $(B/A)_e$[c]	Measured B/A[d]
0.32	15	13(15)[b]	399	15
0.65	29.7	26(25)[b]	798	640
0.97	44.5	38(45)[b]	1197	1083
1.29	59.3	60(68)[b]	1595	1523
1.61	74.1	75(77)[b]	1991	2172

[a]The concentration of contrast agents Albunex®.
[b]The values in parentheses are results measured by Marsh *et al.* (Ref. 13).
[c]$(B/A)_e$ is effective nonlinear parameter by our calculation [Eq. (17)].
[d]B/A is measured nonlinear parameter by Wu *et al.* (Ref. 10).

cal calculation and measured data show that the presence of encapsulated microbubbles greatly increases the nonlinear parameter of the liquid: for pure water the B/A is 5 while B/A for most soft issues is a value of around 10. This phenomenon gives contrast agents a wide application in second harmonic imaging as we mentioned above. A second observation is that from the calculations of attenuation and equivalent $(B/A)_e$, we find that both these values are nearly proportional to the bubble concentration, and this is also strongly substantiated by measured results.[10] The reason is that in linear area, the attenuation is due to the energy loss caused by bubble scattering. Since the bubble concentration used here in both our calculation and Wu *et al.*'s measurements is low, the interaction among bubbles is very small, and each bubble could be considered as an independent scatterer. Thus attenuation exhibits a linear relation with bubble concentration. But as the increase of concentration, the interaction among bubbles will become prominent. Then, the attenuation of the first harmonic may not always follow a linear relationship with the bubble concentration and therefore our approach may need some modifications to describe this complex interaction process. The effective nonlinear parameter is greatly influenced by α_1, as we can see from Eq. (17), and thus it also exhibits a similar characteristic. We should also mention here there is quite a mismatch between the nonlinear parameter obtained from theory and the measured data, in the lowest concentration case, although the attenuation values agree well in the same region. We admit that we are at the moment, unable to explain this and neither can we find in Wu *et al.*'s paper any comment in this regard. A further check is needed to conclusively determine whether this deviation is caused by the influence of apparatus or if there are some other physical mechanisms behind it. However, considering the influence of environment and stability of the contrast agent, we believe our approach can effectively estimate the nonlinear parameter of the liquid containing contrast agent.

B. Comparison between encapsulated bubbly liquid and free bubbly liquid

In order to estimate the effect of the shell, we also make comparisons between free bubbly liquid and encapsulated bubbly liquid (with shell parameter $\mu_s = 2.2\,\mathrm{Pa\,s}$, $G_s = 55.6\,\mathrm{MPa}$) as shown in Table II. When the Rayleigh–Plesset equation for free bubble oscillation is employed to substitute Eq. (6), Eqs. (14) and (17) could also be used to calculate the attenuation coefficient of fundamental harmonic α_1, and $(B/A)_e$ for the free bubbly liquid. These values match Wu and Zhu's measured data well[9] (in parentheses). But obviously, our approach overestimates both these values, especially the nonlinear parameter. The agreement is not so good as the comparison with Wu *et al.*'s experiment, and possible reasons will be given in Sec. V. The calculations here for both free and encapsulated microbubbles assumed that all the microbubbles have an equivalent spherical radius of 3.3 μm, which corresponds to the situation in Wu and Zhu's experiment.[9] Compared to free bubbly liquid, obviously both the attenuation coefficient and the $(B/A)_e$ of the encapsulated bubbly liquid decrease greatly. This is due to the fact that the encapsulated shell brings in the shell viscosity, restraining the bubble's oscillation, thus causing a reduction in the attenuation of first harmonic. For $(B/A)_e$ as we discussed before, the strong nonlinearity of bubbly liquid is due to the nonlinear oscillation of the bubble. The second harmonic and high harmonics are generated by bubble oscillation. Naturally, the restraining of the bubble oscillation will reduce the generation of the harmonics, thereby reducing the

TABLE II. Comparison of the calculated attenuation coefficient α_1 and effective nonlinear parameter $(B/A)_e$ between liquid containing encapsulated bubbles and free bubbles.

Bubble type	Bubble radius r (μm)	Resonance frequency f_0 (MHz)	Bubble volume fraction β	Calculated α_1 (NP/m)	Calculated $(B/A)_e$
Free bubble	3.3	0.98	8×10^{-3}	7.4×10^4 (7×10^4)[a]	4.88×10^5 (2×10^5)[a]
Encapsulated bubble	3.3	2.60	8×10^{-3}	3.94×10^4	3.92×10^4

[a]The values in parentheses are experimental data measured by Wu and Zhu (Ref. 9).

nonlinearity of the medium containing the encapsulated microbubbles. We should also mention that both the calculated and experimental results above were obtained when the fundamental frequency of the external sound field was near the resonant frequency of the encapsulated bubbly liquid.

V. CONCLUSION AND DISCUSSION

In this paper, an approach to estimate the acoustic nonlinearity of the liquid containing encapsulated microbubbles is presented. The nonlinear wave equation for such a liquid is derived and a concept of equivalent nonlinear parameter $(B/A)_e$ is proposed to estimate the nonlinear property of liquid containing contrast agents. Results show that such encapsulated bubbly liquid is a highly nonlinear and highly attenuative medium. Theoretical analysis reveals that the high nonlinearity of such liquid is due to the nonlinear nature of bubble oscillation. The second harmonic and high harmonics are generated by the bubble's nonlinear oscillation. In turn, they drive subsequent bubbles. The interaction between microbubbles and the external field makes the acoustic field in this liquid bear high nonlinearity. An almost linear relationship of attenuation and nonlinear parameter with bubble concentration is confirmed by our theory, which has been observed from experiments. Possible reasons for such phenomena are given. A comparison for liquid containing encapsulated bubbles and free bubbles is also presented in this paper. To a great extent decrease of both attenuation and nonlinear parameter has been found for the encapsulated bubble case. Since the bubble nonlinear oscillation is restrained by the introduction of shell viscosity and rigidity, both the attenuation and the transformed energy to high harmonics decrease and that leads to reduction of the nonlinearity. Favorable agreement between our numerical calculations for a contrast agent Albunex® and Wu *et al.*'s experiments, shows our approach could have a good estimation for the liquid containing contrast agents.

Although good agreement with measurement is obtained, some comments still need to be given here for factors that influence the efficiency of our approach. The very important one is the bubble concentration. In this paper, the bubble concentration for both our theory and Wu *et al.*'s experiment is low, which could be treated as a dilute mixture. At this level of concentration, the bubbles only interact with mean acoustic field without high-order scattering. That is, the field scattered from a bubble may interact with one or more new bubbles in the distribution, but a portion of that scattered field may not be scattered back to any previous bubble. Recently, many investigations have been carried on to study the interactions among bubbles. Kargl's study of including high-order scattering between bubbles to modify the equivalent medium approach highly captivates our interest. One of his main conclusions is that the clear demarcation of transition from bubble volume fractions β composed from noninteracting bubbles to bubble volume fraction where high-order multiple scattering become important occurs near $\beta = 10^{-4}$. In this paper, both our theory and Wu *et al.*'s measurement are processed in the bubble volume fraction, mostly $\beta = 10^{-6}$, so the influence of high-order interaction is negligible. When $\beta > 10^{-4}$, it could be inferred from Kargl's paper that the acoustic field behaves somewhat different from here. That may explain why the agreement is not so good to estimate the nonlinear parameter of Wu and Zhu's experiment for free bubbly liquid as we see above. Our approach is a bit of an overestimate of the nonlinear parameter compared to the experiment. Certainly, there may be some influences coming from the bubbles' instability, bubble size distribution, etc. But a more reliable interpretation may be that the bubble volume fraction $\beta = 8 \times 10^{-3}$ used in their experiment is very high, which is far beyond the limit fraction. So at this level of fraction, the interaction between bubbles is strong, and the high-order scattering is needed to modify our approach. Certainly, this is our continued interest in the future.

ACKNOWLEDGMENTS

This work is supported by NSF of China (Grant No. 10274032) and (Grant No. 10074033). The author wishes to thank Prahbu Rajagopal at the Department of Mechanical Engineering, Imperial College, London, U.K. for his review of this work, which has surely contributed to improve the grammatical content.

APPENDIX

Variables definitions

c_0	speed of sound of pure liquid
c	speed of sound of liquid containing microbubbles
ρ_0	density of pure liquid
ρ_s	density of shell layer
p_1	first-order sound pressure
p_2	second-order sound pressure
V	bubble instantaneous volume
V_0	bubble equilibrium volume
V'	bubble volume variation
V_1'	first-order bubble volume variation
V_2'	second-order bubble volume variation
R_{01}	equilibrium inner radius of encapsulated bubble
R_{02}	equilibrium outer radius of encapsulated bubble
ω_0	resonance angular frequency of encapsulated bubbles
ω	angular frequency
α_1	attenuation coefficient of fundamental harmonic
k_1	wave number of fundamental harmonic
B/A	nonlinear parameter
$(B/A)_e$	effective nonlinear parameter
G_s	shell rigidity of encapsulated bubble
μ_s	shell viscosity of encapsulated bubble
μ_l	viscosity of pure liquid
σ_1	inner interfacial tension of encapsulated bubble
σ_2	outer interfacial tension of encapsulated bubble
v	concentration of Albunex®
β	bubble volume fraction
N	number density of encapsulated bubble
$n(R)$	bubble size distribution

[1] P. J. A. Frinking and N. de Jong, "Acoustic modeling of shell-encapsulated gas bubbles," Ultrasound Med. Biol. **24**, 523–533 (1998).
[2] N. de Jong, L. Hoff, T. Skotland, and N. Bom, "Absorption and scatter of

encapsulated gas filled microspheres: theoretical considerations and some measurements,'' Ultrasonics **30**, 95–103 (1992).
[3] N. de Jong, R. Cornet, and C. T. Lancee, ''High harmonics of vibration gas-filled microspheres. Part one: simulations,'' Ultrasonics **32**, 447–453 (1994).
[4] N. de Jong, R. Cornet, and C. T. Lancee, ''High harmonics of vibration gas-filled microspheres. Part one: measurments,'' Ultrasonics **32**, 455–459 (1994).
[5] N. de Jong, F. J. T. Cate, C. T. Lance, J. R. T. C. Roelandt, and N. Bom, ''Principles and recent developments in ultrasound contrast agents,'' Ultrasonics **29**, 324–330 (1991).
[6] C. C. Church, ''The effects of an elastic solid surface layer on the radial pulsation of gas bubbles,'' J. Acoust. Soc. Am. **97**, 1510–1521 (1995).
[7] L. Hoff, ''Acoustic characterization of contrast agents for medical ultrasound imaging,'' Dissertation of Norweigian University of Science and Technology, Norway, 2000.
[8] X. F. Gong, S. G. Ye, and D. Zhang, ''Measurement of nonlinearity parameter of contrast agents,'' Proceedings of 14th ISNA 1996, p. 475.
[9] J. R. Wu and Z. M. Zhu, ''Measurements of effective nonlinearity parameter B/A of water containing trapped cylindrical bubbles,'' J. Acoust. Soc. Am. **89**, 2634–2639 (1991).
[10] J. R. Wu and J. Tong, ''Measurements of the nonlinearity parameters B/A of contrast agents,'' Ultrasound Med. Biol. **24**, 153–159 (1997).
[11] R. E. Apfel, ''The effective nonlinearity parameter for immisible liquid mixture,'' J. Acoust. Soc. Am. **74**, 1866 (1983).
[12] X. F. Gong, Z. M. Zhu, T. Shi, and J. Huang, ''Determination of the acoustics nonlinearity parameter in biological media using FAIS and ITD methods,'' J. Acoust. Soc. Am. **86**, 1–5 (1989).
[13] J. N. Marsh and C. S. Hall, ''Broadband through-transmission signal loss measurements Albunex® suspensions at concentrations approaching *vivo* does,'' J. Acoust. Soc. Am. **101**, 1155–1161 (1997).
[14] W. N. Cobb, ''Finite amplitude method for the determination of the acoustics parameter B/A,'' J. Acoust. Soc. Am. **73**, 1525–1531 (1983).
[15] J. R. Wu, Z. M. Zhu, and G. H. Du, ''Nonlinear behavior of a liquid containing uniform bubbles: comparison between theory and experiments,'' Ultrasound Med. Biol. **21**, 545–552 (1995).
[16] F. S. Henyey, ''Correction to Foldy's effective medium theory for propagation in bubble clouds and other collections of very small scatters,'' J. Acoust. Soc. Am. **105**, 2149–2154 (1999).
[17] S. G. Kargl, ''Effective medium approach to linear acoustics in bubbly liquid,'' J. Acoust. Soc. Am. **111**, 168–173 (2002).
[18] D. Zhang, X. F. Gong, J. H. Liu, L. Z. Shao, X. R. Li, and Q. L. Zhang, ''The experiment investigation of ultrasonic properties for a sonicated contrast agents and its application in biomedicine,'' Ultrasound Med. Biol. **26**, 374–351 (2000).
[19] L. L. Foldy, ''The multiple scattering of waves,'' Phys. Rev. **67**, 107–119 (1945).
[20] K. W. Commander and A. Prosperitti, ''Linear pressure waves in bubbly liquids: Comparison between theory and experiments,'' J. Acoust. Soc. Am. **85**, 732–746 (1989).

Numerical simulation of two-dimensional nonlinear standing acoustic waves

Christian Vanhille[a)]
ESCET, Universidad Rey Juan Carlos, Tulipán, s/n. 28933 Móstoles, Madrid, Spain

Cleofé Campos-Pozuelo[b)]
Instituto de Acústica, CSIC, Serrano, 144. 28006 Madrid, Spain

(Received 31 October 2003; revised 12 March 2004; accepted 18 April 2004)

In this paper the behavior of strongly nonlinear waves in two-dimensional resonators filled with thermoviscous fluid is studied. For this purpose a set of differential equations, written in Lagrangian coordinates, is proposed and a time-domain numerical scheme is developed for solving them. Full nonlinear equations are derived from the conservation laws and state equation by assuming an irrotational fluid. Auxiliary conditions are written by considering a rigid-walled cavity, excitation at some points of the boundary, and rest at the outset. Finite differences are applied in the space and time domains, and lead to an implicit scheme. The numerical model solves the problem in terms of displacement vector field. The pressure field is then obtained from the displacement values. The algorithm allows us to analyze the evolution of the behavior of complex standing waves. The nonlinear characteristics of standing waves, well known in one-dimensional chambers, are now apparent in two-dimensional resonators by means of this new computational model. Some numerical experiments are carried out, a validation of the model is achieved, and results are given at a complex mode for which plane wave approximation is not appropriate. Several aspects of the nonlinear pressure field inside two-dimensional resonators are presented, such as harmonic distortion and nonlinear attenuation effects. In particular the quasi-standing character of such waves is detected and described. The effect of redistribution of rms pressure inside a two-dimensional cavity is commented. [DOI: 10.1121/1.1760798]

PACS numbers: 43.25.Gf [MFH] Pages: 194–200

I. INTRODUCTION

Nonlinear standing acoustic waves in one-dimensional (1-D) resonators have been extensively studied in the last few years.[1–5] In this paper two-dimensional (2-D) resonators are analyzed. The interest is to obtain some knowledge closer to the practical needs.[6,7] In the framework of industrial applications of power ultrasound, 1-D reactors are not sufficiently close to the practical reality. Actually, reactors of big dimensions in relation to the ultrasonic field wavelength and working at high modes are needed. The prediction of the evolution of nonlinear pressure distribution and the harmonic components distribution inside a 2-D ultrasonic resonator possibly helps the designing of such resonators in industrial processes. As far as we know, the knowledge of strongly nonlinear waves inside such resonators is not very extended. Few theoretical or experimental literature exist. References 8, 9 deal with experimental analysis and perturbation models of complex modes in three-dimensional cavities. The model in Ref. 8 is analytical, and the one in Ref. 9 is based on the finite-element method. Other work[10] deals with 2-D cavities in which a plane wave mode is established.

In the present paper the objective is to analyze how some of the well-known characteristics of 1-D nonlinear standing waves are apparent inside a 2-D resonator. The full nonlinear 2-D equation is solved in the time domain. Nonlinear effects are particularly analyzed at a high mode of a 2-D resonator, for which transversal dimension has to be taken into account. For this purpose, a set of differential equations and auxiliary conditions is proposed in Sec. II. Equations are written in Lagrangian coordinates and no limits are considered for the acoustic Mach number value, except the isentropic character of the state equation.[11–13,4] Irrotational fluid and a rigid-walled resonator are assumed. The fluid is at rest at the outset. Time-dependent mechanical excitation of the fluid is supposed at the boundary. A numerical model is developed for solving the equations in Sec. III. Finite differences in space and time are considered to construct the implicit numerical scheme.[14] The evolution of both the displacement and pressure fields is obtained. In Sec. IV some numerical experiments are carried out and allow us to validate the model and to observe the behavior of these 2-D waves. We have chosen the third mode of a cavity that requires a real 2-D model. Harmonic distortion, nonlinear attenuation effects, and rms pressure redistribution are especially described and commented. The global results of this work are defined in Sec. V.

II. PHYSICAL PROBLEM AND MATHEMATICAL MODEL

In this section the acoustical problem is described and its governing differential equations and auxiliary conditions are given. A 2-D rectangular cavity of dimension $L_x \times L_y$ is modeled. An irrotational thermoviscous Newtonian fluid is con-

a)Electronic mail: c.vanhille@escet.urjc.es
b)Electronic mail: ccampos@ia.cetef.csic.es

sidered to fill the rigid-walled resonator (domain $\Omega \subset \mathbb{R}^2$). The fluid is absolutely at rest at the outset (null displacement and velocity). The excitation is realized by means of a source placed anywhere on the boundary. The study is carried out during N_p periods, i.e., the domain $\mathrm{T}=[0,t_{\max}] \subset \mathbb{R}^+$. We work in Lagrangian coordinates because it allows us to derive the differential equation without limit about the nonlinear degree, as opposed to the Eulerian case. The vector of displacement $\mathbf{u}$ is considered to be the dependent variable, in time (t) and 2-D (x, y) spaces. Its components are u_x and u_y. The limitations about the isentropic character of the system are the same as in the 1-D case.[4] Null normal displacement conditions are applied at the boundaries, except where the source is placed.

The conservation laws (mass and momentum[15]), together with the assumption of Newtonian and irrotational fluid ($\boldsymbol{\nabla} \times \mathbf{u} = \mathbf{0}$), and state equation (by considering an ideal gas) lead to the following set of equations, written in Lagrangian coordinates:

$$\frac{\rho_0 - \rho}{\rho} = \boldsymbol{\nabla} \cdot \mathbf{u}, \tag{1}$$

$$\rho_0 \frac{\partial^2 \mathbf{u}}{\partial t^2} = -\boldsymbol{\nabla} p + \mu \overline{\nabla}^2 \frac{\partial \mathbf{u}}{\partial t} + \left(\mu_B + \frac{1}{3}\mu \right) \left(\boldsymbol{\nabla} \left(\boldsymbol{\nabla} \cdot \frac{\partial \mathbf{u}}{\partial t} \right) \right), \tag{2}$$

$$\frac{p}{p_0} = \left(\frac{\rho}{\rho_0} \right)^{\gamma}, \tag{3}$$

where ρ_0 is the ambient density, ρ is the density, p is the acoustic pressure, μ is the shear viscosity, μ_B is the bulk viscosity, $p_0 = \rho_0 c_0^2 / \gamma$ is the ambient pressure, c_0 is the small amplitude value of the sound speed, and γ is the specific heat ratio. The combination of these equations leads to the considered vectorial wave equation:

$$\left\{ \begin{array}{c} \rho_0 \dfrac{\partial^2 \mathbf{u}}{\partial t^2} = \gamma p_0 \dfrac{\boldsymbol{\nabla}(\boldsymbol{\nabla} \cdot \mathbf{u})}{(1 + \boldsymbol{\nabla} \cdot \mathbf{u})^{\gamma+1}} + \mu \overline{\nabla}^2 \dfrac{\partial \mathbf{u}}{\partial t} + \left(\mu_B + \dfrac{1}{3}\mu \right) \left(\boldsymbol{\nabla} \left(\boldsymbol{\nabla} \cdot \dfrac{\partial \mathbf{u}}{\partial t} \right) \right) \\ \boldsymbol{\nabla} \times \mathbf{u} = \mathbf{0} \end{array} \right\}, \quad (x,y,t) \in \Omega \cup \mathrm{T}. \tag{4}$$

Equations corresponding to u_x and u_y are coupled by using the irrotational condition and by the nonlinear terms in the wave equation.

In the model developed in this paper we are able to consider acoustic problems for which excitation is applied to $\mathbf{u}$ anywhere at the boundary in the x and/or y directions. However, here, for simplicity, the presentation of the mathematical model, numerical method, and examples only deals with excitation at some points of the side $x=0$ (this set of excitation points is represented by $\{x=0, y \in \Theta_{0y}\}$) applied in the x direction (to the u_x component). The boundary conditions are written by considering rigid walls and the irrotational character of the fluid at the boundary. Any time, function $f(t)$ at the source is assumed:

$$\left\{ \begin{array}{l} u_x = f(t) \forall y \in \Theta_{0y} \ \text{ or } \ u_x = 0 \forall y \notin \Theta_{0y} \\ \dfrac{\partial u_y}{\partial x} = 0, \end{array} \right. \quad (x=0),$$

$$\left\{ \begin{array}{l} u_x = 0 \\ \dfrac{\partial u_y}{\partial x} = 0 \end{array} \right. \quad (x=L_x),$$

$$\left\{ \begin{array}{l} u_y = 0 \\ \dfrac{\partial u_x}{\partial y} = 0 \end{array} \right. \quad (y=0), \qquad \left\{ \begin{array}{l} u_y = 0 \\ \dfrac{\partial u_x}{\partial y} = 0 \end{array} \right. \quad (y=L_y). \tag{5}$$

The initial conditions are written by assuming absolute rest of the fluid at the outset:

$$\mathbf{u} = \mathbf{0}(t=0), \quad \forall (x,y) \in \Omega,$$

$$\frac{\partial \mathbf{u}}{\partial t} = \mathbf{0}(t=0), \quad \forall (x,y) \in \Omega / \text{if } \ x=0: \ y \notin \Theta_{0y}. \tag{6}$$

The acoustic pressure p is deduced from the mass conservation [Eq. (1)] and state equation [Eq. (3)] as a function of the displacement vector. This leads to the following formula:

$$p(x,y,t) = p_0 (1 + \boldsymbol{\nabla} \cdot \mathbf{u}(x,y,t))^{-\gamma} - p_0, \quad (x,y,t) \in \Omega \cup \mathrm{T}. \tag{7}$$

III. NUMERICAL METHOD

In this section the numerical model developed to solve the problem presented in Sec. II is described. The problem is solved in the time domain. This important feature of the model allows us to consider any time function as excitation at the boundaries (harmonic, Gaussian pulse, rectangular pulse,...), to obtain the whole signal (all the harmonic components) by only one computation, and to model the transient phase. Finite differences in time and space are used to develop the model.

Three dimensionless independent variables are considered: $X = x/L_x$, $Y = y/L_y$, and $T = \omega t$, where ω is the angular frequency. Their domains are, respectively, [0,1], [0,1], and $[0, 2\pi N_p]$. These variables are introduced into Eqs. (4)–(7). The dimensionless space domain Ω' is discretized by means of a 2-D grid, with steps h_x and h_y. N_x and N_y are the number of grid points in the X direction and Y direction. The dimensionless time domain T' is discretized by using the step τ, N_t is the number of time points. $\mathbf{u}_{m_x, m_y, n}$

$=\binom{u_{x\ m_x,m_y,n}}{u_{y\ m_x,m_y,n}}$ is the value of the dependent variable at the point $((m_x-1)h_x,(m_y-1)h_y,(n-1)\tau)$ of the grid, where m_x, m_y, and n indicate, respectively, the number of the considered grid point in the *X*, *Y*, and *T* direction. The discrete domain of m_x, m_y, and n is, respectively, 1 to N_x, 1 to N_y, and 1 to N_t. The $O(h_x^2,h_y^2,\tau^2)$ finite differences, $O(h_x,h_y)$ in the nonlinear term, are applied to the system, Eqs. (4)–(6), with dimensionless independent variables. This leads to an implicit scheme for which a set of algebraic equations has to be solved at each time step. A couple of difference equations, one for u_x and one for u_y, are defined at each point of the grid. In this system the nonlinear term is included onto the right-hand side vector. A solver for linear systems can then be used, for which the $2\times N_x\times N_y$ unknowns are related by $2\times N_x\times N_y$ equations. The solution gives the value of u_x and u_y at every point of the 2-D grid at the running time step *n*. The right-hand side vector depends on the solution obtained at the previous time steps. After setting

$$A_1=\frac{\left(\mu_B+\frac{4}{3}\mu\right)\tau}{2L_x^2h_x^2\rho_0\omega},\quad A_2=\frac{\left(\mu_B+\frac{4}{3}\mu\right)\tau}{2L_y^2h_y^2\rho_0\omega},$$

$$D_1=\frac{\gamma p_0\tau^2}{L_x^2h_x^2\rho_0\omega^2},\quad D_2=\frac{\gamma p_0\tau^2}{L_y^2h_y^2\rho_0\omega^2},$$

$$D_1'=\frac{\gamma p_0\tau^2}{L_xL_yh_xh_y\rho_0\omega^2},\quad N_1=\frac{1}{L_xh_x},\quad \text{and}\quad N_2=\frac{1}{L_yh_y},$$

the set of algebraic equations, obtained from Eqs. (4), (5) with dimensionless independent variables, is defined by the following formulas:

$$\begin{cases} m_x=1 \\ \forall m_y\in[1,N_y]/y\in\Theta_{0y}, \end{cases}\quad u_{x\ m_x,m_y,n}=f((n-1)\tau)$$

$$\text{or}\quad \begin{cases} m_x=1 \\ \forall m_y\in[1,N_y]/y\notin\Theta_{0y}, \end{cases}\quad u_{x\ m_x,m_y,n}=0 \tag{8a}$$

$$\begin{cases} \forall m_x\in[2,N_x-1] \\ m_y=1 \end{cases},\quad u_{x\ m_x,m_y+1,n}-u_{x\ m_x,m_y,n}=0, \tag{8b}$$

$$\begin{cases} \forall m_x\in[2,N_x-1] \\ \forall m_y\in[2,N_y-1], \end{cases}\quad -A_2u_{x\ m_x,m_y-1,n}-A_1u_{x\ m_x-1,m_y,n}+(1+2A_1+2A_2)u_{x\ m_x,m_y,n}-A_1u_{x\ m_x+1,m_y,n}-A_2u_{x\ m_x,m_y+1,n}$$
$$=2u_{x\ m_x,m_y,n-1}-u_{x\ m_x,m_y,n-2}+D_1(u_{x\ m_x-1,m_y,n-1}-2u_{x\ m_x,m_y,n-1}+u_{x\ m_x+1,m_y,n-1})$$
$$+D_2(u_{x\ m_x,m_y-1,n-1}-2u_{x\ m_x,m_y,n-1}+u_{x\ m_x,m_y+1,n-1})+A_1(-u_{x\ m_x+1,m_y,n-2}+2u_{x\ m_x,m_y,n-2}-u_{x\ m_x-1,m_y,n-2})$$
$$+A_2(-u_{x\ m_x,m_y+1,n-2}+2u_{x\ m_x,m_y,n-2}-u_{x\ m_x,m_y-1,n-2})+[1+N_1(u_{x\ m_x,m_y,n-1}-u_{x\ m_x-1,m_y,n-1})$$
$$+N_2(u_{y\ m_x,m_y,n-1}-u_{y\ m_x,m_y-1,n-1})]^{-\gamma-1}, \tag{8c}$$

$$\begin{cases} \forall m_x\in[2,N_x-1] \\ m_y=N_y \end{cases},\quad u_{x\ m_x,m_y,n}-u_{x\ m_x,m_y-1,n}=0, \tag{8d}$$

$$\begin{cases} m_x=N_x \\ \forall m_y\in[1,N_y], \end{cases}\quad u_{x\ m_x,m_y,n}=0, \tag{8e}$$

$$\begin{cases} m_y=1 \\ \forall m_x\in[1,N_x], \end{cases}\quad u_{y\ m_x,m_y,n}=0 \tag{8f}$$

$$\begin{cases} \forall m_y\in[2,N_y-1] \\ m_x=1 \end{cases},\quad u_{y\ m_x+1,m_y,n}-u_{y\ m_x,m_y,n}=0 \tag{8g}$$

$$\begin{cases} \forall m_y\in[2,N_y-1] \\ \forall m_x\in[2,N_x-1], \end{cases}\quad -A_2u_{y\ m_x,m_y-1,n}-A_1u_{y\ m_x-1,m_y,n}+(1+2A_1+2A_2)u_{y\ m_x,m_y,n}-A_1u_{y\ m_x+1,m_y,n}-A_2u_{y\ m_x,m_y+1,n}$$
$$=2u_{y\ m_x,m_y,n-1}-u_{y\ m_x,m_y,n-2}+D_1'(u_{x\ m_x,m_y,n-1}-u_{x\ m_x-1,m_y,n-1}-u_{x\ m_x,m_y-1,n-1}+u_{x\ m_x-1,m_y-1,n-1})$$
$$+D_2(u_{y\ m_x,m_y-1,n-1}-2u_{y\ m_x,m_y,n-1}+u_{y\ m_x,m_y+1,n-1})+A_1(-u_{y\ m_x+1,m_y,n-2}+2u_{y\ m_x,m_y,n-2}-u_{y\ m_x-1,m_y,n-2})$$
$$+A_2(-u_{y\ m_x,m_y+1,n-2}+2u_{y\ m_x,m_y,n-2}-u_{y\ m_x,m_y-1,n-2})+[1+N_1(u_{x\ m_x,m_y,n-1}-u_{x\ m_x-1,m_y,n-1})$$
$$+N_2(u_{y\ m_x,m_y,n-1}-u_{y\ m_x,m_y-1,n-1})]^{-\gamma-1}, \tag{8h}$$

$$\begin{cases} \forall m_y \in [2, N_y - 1] \\ m_x = N_x \end{cases}, \quad u_{y\ m_x, m_y, n} - u_{y\ m_x - 1, m_y, n} = 0, \tag{8i}$$

$$\begin{cases} m_y = N_y \\ \forall m_x \in [1, N_x] \end{cases}, \quad u_{y\ m_x, m_y, n} = 0. \tag{8j}$$

D_1' arises from the coupling between the u_x and u_y equations, carried out by the introduction of $\nabla \times \mathbf{u} = \mathbf{0}$ into the dynamical term of the u_y equation. N_1 and N_2 come from the application of the nonlinear term of Eq. (4), which also acts like a coupling between both equations. The formation of the matrix system has to be carried out carefully to facilitate the solving process. The same sequence is applied to the equations of the matrix and to the unknown values: a loop over m_y inside a loop over m_x for the u_x equations, and a loop over m_x inside a loop over m_y for the u_y equations. The acoustic field is known at $n=1$ and $n=2$ by applying the difference equations obtained from the initial conditions, Eq. (6), with dimensionless independent variables:

$$u_{x\ m_x, m_y, 1} = 0 \quad \begin{cases} \forall m_x \in [1, N_x] \\ \forall m_y \in [1, N_y] \end{cases}, \quad u_{x\ m_x, m_y, 2} = 0 \quad \begin{cases} \forall m_x \in [2, N_x] \\ \forall m_y \in [1, N_y] \end{cases},$$

$$\begin{cases} u_{x\ m_x, m_y, 2} = f(\tau) \quad \begin{cases} m_x = 1 \\ \forall m_y \in [1, N_y] / y \in \Theta_{0y} \end{cases} \\ \text{or} \\ u_{x\ m_x, m_y, 2} = 0 \begin{cases} m_x = 1 \\ \forall m_y \in [1, N_y] / y \notin \Theta_{0y} \end{cases} \end{cases}, \quad u_{y\ m_x, m_y, 1} = 0 \quad \begin{cases} \forall m_y \in [1, N_y] \\ \forall m_x \in [1, N_x] \end{cases},$$

$$u_{y\ m_x, m_y, 2} = 0 \begin{cases} \forall m_y \in [1, N_y] \\ \forall m_x \in [1, N_x] \end{cases}. \tag{9}$$

Thus the first time iteration is $n=3$. The pressure values on the 2-D grid are evaluated from the displacement values, via Eq. (7) with dimensionless independent variables, by means of a $O(h_x, h_y)$ finite difference scheme. After the N_t steps the whole behavior of the wave is known, from the rest at the outset up to the steady state.

IV. NUMERICAL EXPERIMENTS AND RESULTS

In this section the method described above is applied to resonators for which the fluid medium is considered to be air. The parameters of the fluid are the following: $c_0 = 340$ m/s, $\gamma = 1.4$, $\rho_0 = 1.29$ kg/m^3. The excitation is applied to the component u_x of the displacement vector (in the X direction). In order to include the wall friction we use the *ad-hoc* dissipation parameter defined by

$$\alpha = \alpha_{\text{bulk}} + \alpha_{\text{wall}}, \tag{10}$$

where $\alpha_{\text{bulk}} = \omega^2 \nu b / 2c_0^3$, $\alpha_{\text{wall}} = 2^{-3/2} (\omega \mu / \rho_0 c_0^2)^{1/2} [1 + (\gamma - 1)/\text{Pr}^{1/2}][(2L_x + 2L_y)/L_x L_y]$, ν is the kinematic shear viscosity, $b = \mu_B / \mu + 4/3 + \kappa / \mu (1/c_v - 1/c_p)$ is the viscosity number, c_v is the specific heat at constant volume, c_p is the specific heat at constant pressure, κ is the thermal conductivity, and $\text{Pr} = \mu c_p / \kappa$ is the Prandtl number.[13] The two spatial grid steps are considered to be equal: $h_x = h_y = h$. By using several relations between the spatial grid steps and the time step, it has been experimentally proved that the numerical method described in Sec. III is conditionally stable. However, it has also been noted that the same relation as the one given in Ref. 4 can be used to obtain a stable scheme. This relation is used here:

$$\tau = \frac{-\nu b \omega}{2c_0^2} + \sqrt{\left(\frac{\nu b \omega}{2c_0^2}\right)^2 + (\pi h)^2}. \tag{11}$$

It has also been empirically noted that the pressure level reached inside the resonator depends on the dimension of the source and where it is placed.

In order to validate the numerical model a narrow tube in which a plane wave [mode (1,0)] is established is first considered. This simple case is also simulated by a previously developed and validated 1-D numerical model,[4] and results are compared. After validation a more complex mode (1,1) is analyzed.

A narrow tube of dimensions $L_x = \lambda/2$, $L_y = 2 \times 10^{-3}$ m is first considered and excited at the constant frequency f

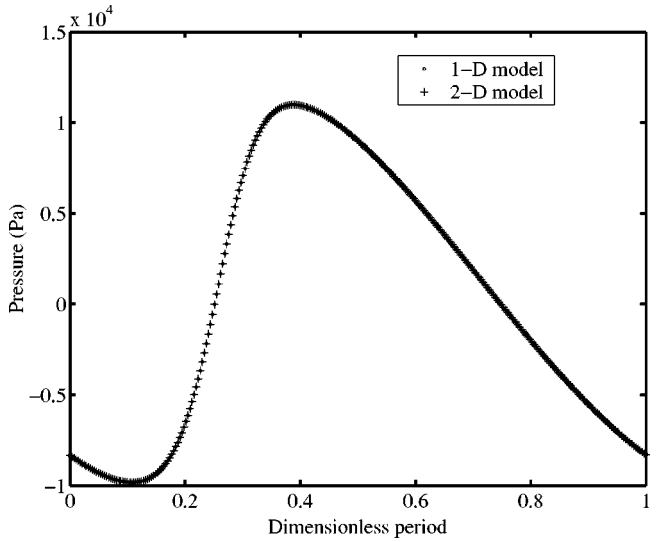

FIG. 1. Plane pressure waveform at $X=1$. 2-D and 1-D models. $f = 20$ kHz, $u_0 = 10$ μm.

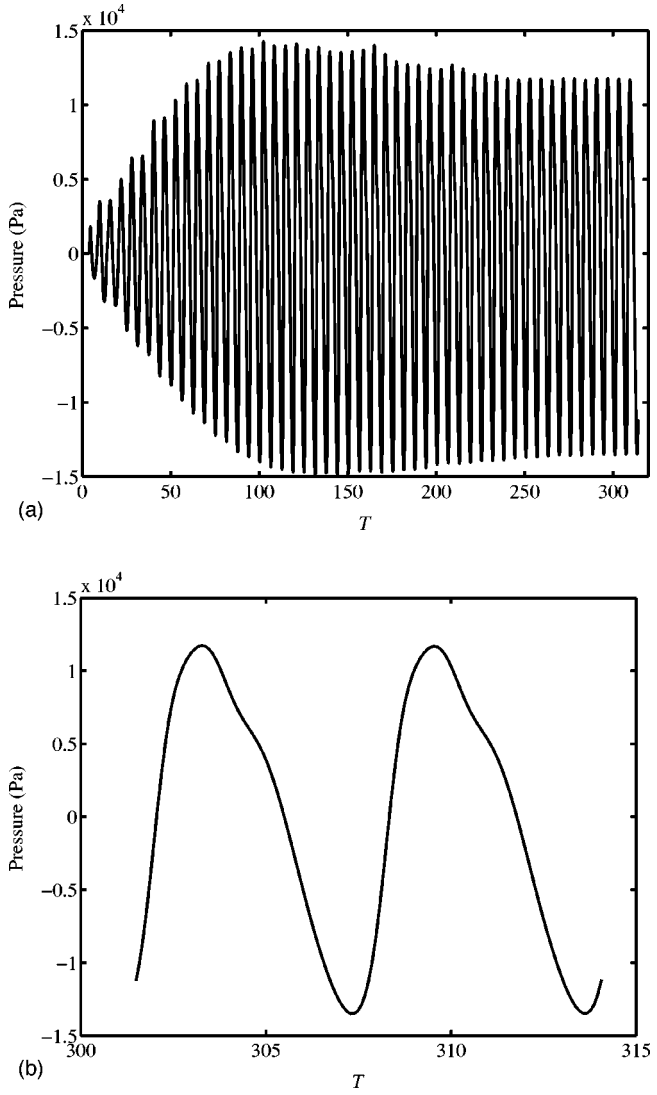

FIG. 2. Rectangular resonator. Pressure waveform at $(X=1, Y=0)$ from the rest to the steady state (a), during the two last periods (b). $f=20$ kHz, $u_0=140$ μm.

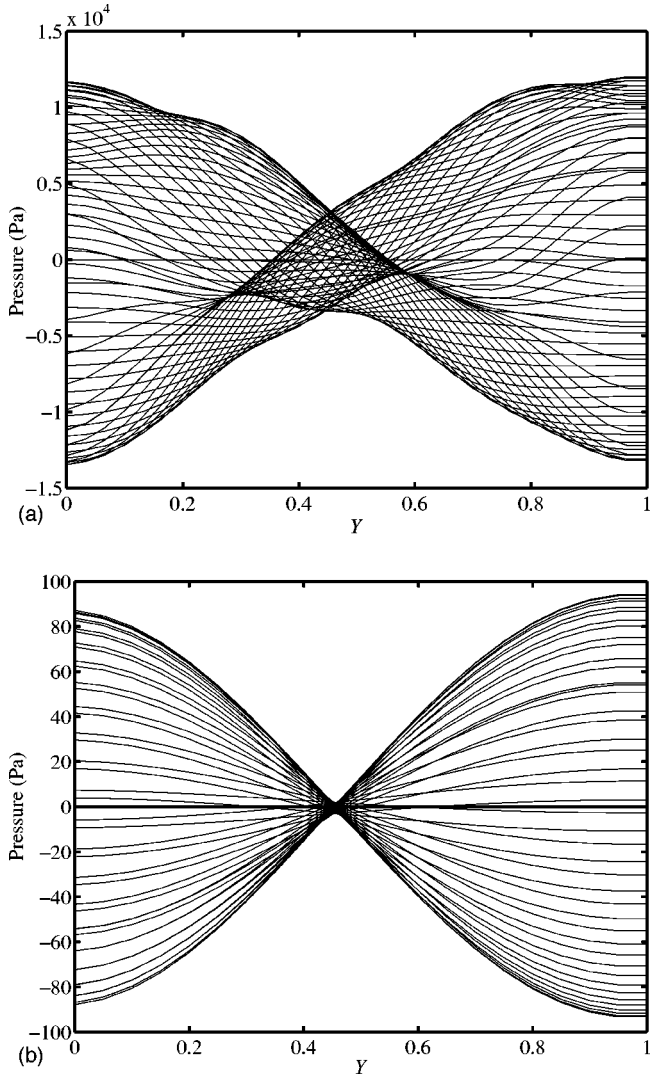

FIG. 3. Rectangular resonator. Evolution of the pressure distribution during a cycle of the steady state along the wall at $X=1$. $f=20$ kHz, $u_0=140$ μm (a); $u_0=1$ μm (b).

$=20$ kHz, where λ is the wavelength. It has to be noted that this tube is still considerably wider than the boundary layer thickness (of the order of 1.7×10^{-5} m). The piston fills the entire wall side $X=0$; it harmonically oscillates in the X direction with constant shape and generates a plane wave: $f(n)=u_0\sin((n-1)\tau)$, $\forall Y\in[0,1]$, $X=0$, where u_0 is the excitation amplitude. In this example $u_0=10$ μm and the attenuation parameter value is $\alpha=4.12$ m^{-1}. The 2-D model is compared to the 1-D model of Ref. 4. Figure 1 shows the pressure waveform during one period of the steady state at $X=1$ (the middle point of the side $X=1$ of the 2-D resonator). The agreement validates the new 2-D model.

We now consider a cavity for which $L_x=L_y=12\times10^{-3}$ m and study its third (1,1) mode, excited at the constant frequency $f=20$ kHz. The attenuation parameter value is $\alpha=2.5$ m^{-1}. A small constant shape piston situated at the side $X=0$ between $Y=0.033$ ($y=0.4\times10^{-3}$ m) and $Y=0.066$ ($y=0.8\times10^{-3}$ m) is excited harmonically, and oscillates in the X direction:

$$u_x=0,\quad u_y=0,\quad \forall Y\in[0,0.033],\quad X=0,$$
$$u_x=u_0\sin((n-1)\tau),\quad u_y=0,$$
$$\forall Y\in[0.033,0.066],\quad X=0,\qquad (12)$$
$$u_x=0,\quad u_y=0,\quad \forall Y\in]0.066,1],\quad X=0.$$

The small size of the piston in relation to L_y generates a wave absolutely different from a plane wave. Figures 2–5 present results for $u_0=140$ μm. Figure 2 shows the pressure waveform at the point $(X=1,Y=0)$. The evolution of the wave from the rest to the steady state can be observed [Fig. 2(a)], as well as its distortion during the two last periods [Fig. 2(b)]. The amplitude of the wave initially increases and then decreases to a steady-state value. The small size of the piston in relation to the large 2-D domain implies that before the steady state is reached, a lot of constructive or destructive (depending on the instant and place) interferences occurs, which make the reflection pattern complex. Figure 3(a) shows the evolution of the nonlinear pressure distribution during a cycle of the steady state along the wall at $X=1$. This nonlinear distribution, obtained by using $u_0=140$ μm in the model, is compared to the linear case [Fig. 3(b)] for

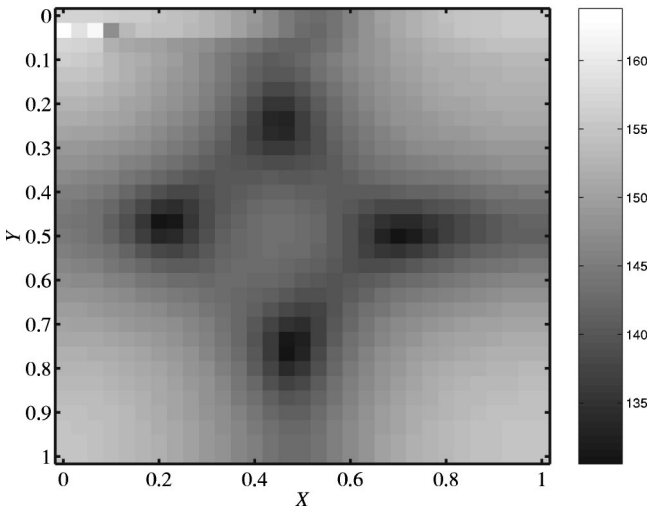

FIG. 4. Rectangular resonator. The rms pressure distribution. $f=20$ kHz, $u_0=140$ μm.

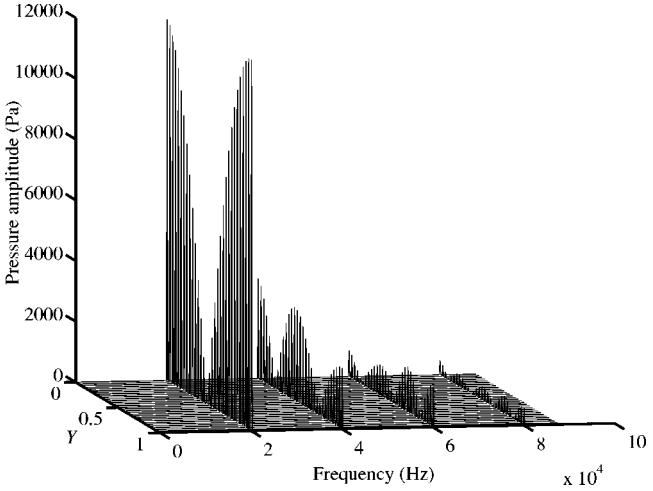

FIG. 5. Rectangular resonator. Harmonic decomposition along the wall at $X=1$. $f=20$ kHz, $u_0=140$ μm.

which the small amplitude $u_0=1$ μm has been employed in the model. The node on the wall at $X=1$, present in the linear case, is absent from the nonlinear field. The nodes are moving during a cycle, and the profile of the spatial distribution of the wave is very different from the one of the linear case: distortion is observed. The four opposite poles present in the distribution of the linear field inside the resonator become deformed in the nonlinear configuration, as well as the shapes of the distribution. These characteristics imply an important effect: the redistribution of pressure inside the resonator. Such an effect can be appreciated in Fig. 4, which shows the rms pressure distribution inside the resonator. This nonlinear pressure is redistributed inside the cavity in such a way that no node exists (the minimal value reached is 67.35 Pa): this is a quasistanding wave. In industrial applications, this behavior is fundamental to correctly predict the level pressure in cavities. It has to be noted that the pressure field at the left-upper corner presents large gradient values due to the small size of the piston situated in this corner. The harmonic decomposition obtained by fast Fourier transform along the wall at $X=1$ is represented in Fig. 5. The generation of these high-frequency components (harmonic distortion) implies nonlinear attenuation. In the 2-D domain, at the nodes of the odd harmonics, the maximal values of the even harmonics appear, and *vice versa*. This fact is the reason for which the nodes, present in the linear wave, do not exist anymore in the nonlinear wave when several harmonic components are present. This also implies that the bigger the harmonic distortion, the more homogeneous the distribution of pressure inside the resonator.

V. CONCLUSIONS

Numerical simulations of two-dimensional high-power ultrasonic standing waves inside resonators are carried out. The study is achieved by means of the derivation of the mathematical model and the development of the time–domain numerical scheme. Lagrangian coordinates and irrotational fluid are assumed in the model. The full nonlinear two-dimensional wave equation is solved. The fluid inside the rigid-walled cavity, at rest at the outset, is excited by means of the time-dependent movement of some points at the boundary. An implicit scheme is constructed by applying finite differences in time and space domains. The evolution of the displacement vector and pressure fields is obtained. The nonlinear characteristics of standing waves are now apparent in two-dimensional resonators via use of the model. Complex modes, for which one-dimensional models are not appropriate, can be analyzed. Results allow the description of several aspects of these waves, such as its quasistanding character. Harmonic distortion, nonlinear attenuation effects, and rms pressure redistribution are presented.

ACKNOWLEDGMENTS

This work has been developed within the frame of the Projects MCYT (Spanish Ministry of Science and Technology) No. DPI2002-03409 and URJC (Rey Juan Carlos University) No. PIPR-2003-46.

[1] C. C. Lawrenson, B. Lipkens, T. S. Lucas, D. K. Perkins, and T. W. Van Doren, ''Measurements of macrosonic standing waves in oscillating closed cavities,'' J. Acoust. Soc. Am. **104**, 623–636 (1998).
[2] Y. A. Ilinskii, B. Lipkens, T. S. Lucas, T. W. Van Doren, and E. A. Zabolotskaya, ''Nonlinear standing waves in an acoustical resonator,'' J. Acoust. Soc. Am. **104**, 2664–2674 (1998).
[3] C. P. Lee and T. G. Wang, ''Nonlinear resonance and viscous dissipation in an acoustic chamber,'' J. Acoust. Soc. Am. **92**, 2195–2206 (1992).
[4] C. Vanhille and C. Campos-Pozuelo, ''Numerical model for nonlinear standing waves and weak shocks in thermoviscous fluids,'' J. Acoust. Soc. Am. **109**, 2660–2667 (2001).
[5] C. Young-Doo and K. Yang-Hann, ''Numerical analysis for nonlinear resonant oscillations of gas in axisymmetric closed tubes,'' J. Acoust. Soc. Am. **108**, 2765–2774 (2000).
[6] T. J. Mason, ''Large scale sonochemical processing: aspiration and actuality,'' Ultrason. Sonochem. **7**, 145–149 (2000).
[7] O. V. Abramov, *High-Intensity Ultrasound: Theory and Industrial Applications* (Gordon and Breach, London, UK, 1998).
[8] A. B. Coppens and J. V. Sanders, ''Finite-amplitude standing waves within real cavities,'' J. Acoust. Soc. Am. **58**, 1133–1140 (1975).
[9] C. Campos-Pozuelo, L. Elvira-Segura, and B. Dubus, ''Numerical andexperimental analysis of second order effects and loss mechanisms in axi-

symmetrical cavities,'' sent to J. Acoust. Soc. Am. **115**, 1973–1981 (2004).
[10] T. Yano, ''Turbulent acoustic streaming excited by resonant gas oscillation with periodic shock waves in a closed tube,'' J. Acoust. Soc. Am. **106**, L7–L12 (1999).
[11] R. T. Beyer, *Nonlinear Acoustics in Fluids*, Benchmark Papers in Acoustics Series (Van Nostrand Reinhold, New York, 1984).
[12] *Nonlinear Acoustics*, edited by M. F. Hamilton and D. T. Blackstock (Academic, New York, 1998).
[13] A. D. Pierce, *Acoustics* (Acoustical Society of America, New York, 1989).
[14] L. Lapidus and G. F. Pinder, *Numerical Solution of Partial Differential Equations in Science and Engineering* (Wiley-Interscience, New York, 1999).
[15] S. Temkin, *Elements of Acoustics* (Wiley, New York, 1981).

Acoustic radiation force on a compressible cylinder in a standing wave

Wei Wei, David B. Thiessen, and Philip L. Marston[a)]
Department of Physics, Washington State University, Pullman, Washington 99164-2814

(Received 14 January 2004; revised 1 April 2004; accepted 2 April 2004)

The radiation force-per-length on an infinitely long circular cylinder in an acoustic plane standing wave is expressed in terms of partial-wave scattering coefficients for the corresponding traveling wave scattering problem. This information allows a dimensionless radiation force function to be expressed using coefficients available from two-dimensional scattering theory. Four examples are given for fluid circular cylinders: A hot gas column (used to approximate a small flame), a compressible liquid bridge in a Plateau tank, a liquid bridge in air, and a cylindrical bubble of air in water. A long-wavelength approximation for the force is also examined which is analogous to one for the radiation force on compressible spheres [K. Yosioka and Y. Kawasima, Acustica **5**, 167–173 (1955)]. A long-wavelength approximation is also known for the monopole and dipole scattering coefficients of a compressible elliptical cylinder and the radiation force is also examined for that situation. Some of the results for the radiation force are relevant to the acoustic stabilization of liquid cylindrical bridges in reduced gravity. © *2004 Acoustical Society of America.*
[DOI: 10.1121/1.1753291]

PACS numbers: 43.25.Qp, 43.35.Ty [MFH] Pages: 201–208

I. INTRODUCTION

Yosioka and Kawasima[1] and Gorkov[2] derived a long-wavelength approximation for the radiation force on spherical drops in a standing wave. That approximation has been helpful for estimating the conditions for the acoustical trapping of drops in host liquids[3,4] and there have been several investigations of the acoustical manipulation of drops. Gorkov's effective-potential method[2] has been used to predict radiation forces on spheres in typical acoustic resonators[5,6] and there have been several extensions of expressions for the radiation force on spheres.[7,8] The radiation force on small[9,10] and large[10,11] spherical (or nearly spherical) bubbles in acoustic standing waves has also been investigated.

The acoustic radiation force on cylindrical objects has received significantly less attention. Much of that research has been concerned with the radiation force on solid, circular cylinders with the symmetry axis perpendicular to the propagation direction of a traveling acoustic wave.[12,13] Wu *et al.*[14] gave a long-wavelength approximation for the radiation force on a rigid circular cylinder for the situation where the cylinder's axis is constrained to be parallel to the equiamplitude surfaces of a plane standing wave. Our purpose in the present paper is to analyze and discuss the radiation force on a two-dimensional fluid cylinder in a plane standing wave. The cylinder's axis is assumed to be constrained in the direction considered by Wu *et al.* The radiation force-per-length is calculated as a function of the wavenumber–radius product for the incident acoustic wave for a few examples including the following: a liquid cylinder surrounded by a host liquid (relevant to experiments on acoustic stabilization and vibration of liquid columns in a host liquid[15,16]), a liquid cylinder in air,[17] a hot column of gas in air, and a cylindrical bubble of air in water. The results are compared with a long-wavelength approximation analogous to the long-wavelength approximation given by Yosioka and Kawasima[1] and by Gorkov[2] for spherical objects. The usual approximation is made in which the inner and outer fluids are taken to be inviscid. For the case of a sphere in a plane standing wave, Doinikov[7] predicts that when the thickness of the viscous boundary layer (which oscillates at the acoustic frequency) is small in comparison to the radius of the sphere, the viscous corrections are small. This conclusion is supported by measurements of the radiation force on small spherical particles in a liquid host.[18] The predictions of Doinikov appear to be consistent with a negligible radial variation of the time-averaged pressure in the vicinity of sufficiently-thin oscillating viscous boundary layers. It is plausible that the viscous corrections to the radiation force in the case of circular cylinders in a standing wave are also small when the oscillating boundary layers are sufficiently thin. These viscous corrections are outside the scope of the present paper.

The calculation given here is for a two-dimensional acoustic field so that any corrections to the radiation force associated with the ends of the cylinders are neglected. The radiation force per unit length on a cylinder in a standing wave is expressed using dimensionless coefficients in the partial-wave series for the corresponding *traveling wave* far-field scattering problem. Though the explicit coefficients are given only for the case of a fluid cylinder surrounded by a host fluid, the relevant coefficients are available for solid circular cylinders[12] and solid cylindrical shells[13] so that the series result given here in Eq. (19) could be easily generalized to these cases.

Readers familiar with the effects of surface tension might conceivably wonder about the value of considering the acoustic radiation force on a circular liquid cylinder or on a circular cylindrical bubble. The reason is that ordinarily a

a)Electronic mail: marston@wsu.edu

capillary instability studied by Rayleigh[19] and by Plateau[20] causes long liquid columns[16,17,21] and bubbles[22] to break up. At least in the case of liquid columns (often in the form of capillary bridges) there are now several methods for suppressing the Rayleigh–Plateau instability. Some of these stabilization methods are based on the application of acoustic radiation pressure[16,17] while others involve the application of electrostatic stresses.[23] Some of the examples described here are relevant to understanding the conditions for the transverse equilibrium in the case of acoustic stabilization or the oscillation of liquid bridges.[15–17] The spatial distribution of the acoustic radiation pressure on a liquid bridge can cause the column to deform from a circular shape.[15,17] In the absence of significant weight or buoyancy the equilibrium shape is a balance between radiation and capillary stresses[17,24] as previously noted for nearly spherical drops.[25,26] Typically, a liquid bridge in air in a standing wave takes on a slightly elliptical profile. This deformation is not considered here. While the analysis of that deformation is outside the scope of the present paper, in Sec. IV we examine certain aspects of the generalization to elliptical cylinders.

II. GENERAL EXPRESSION FOR RADIATION FORCE ON A CYLINDER

A. Incident and scattered wave for a traveling wave along the *z*-axis

Assume the cylinder is axisymmetric, and the outer fluid medium has density ρ_o and sound speed c_o. The adiabatic compressibility is related to the sound speed and density by $\beta_o = 1/\rho_o c_o^2$. A plane wave traveling along the z-axis can be expressed as the complex pressure $P_i = P_{i0} e^{-i\omega t}$, where the time-independent factor is[27]

$$P_{i0} = P_a e^{ik_o z} = P_a \sum_{n=0}^{\infty} \epsilon_n i^n J_n(k_o r)\cos(n\theta), \tag{1}$$

where $k_o = \omega/c_o$, J_n denotes the cylindrical Bessel function of order n, $\epsilon_n = 2 - \delta_{0n}$, and δ_{0n} is the Kronecker delta. The scattered wave field, $P_s = P_{s0} e^{-i\omega t}$, must look like an outgoing wave when $r \to \infty$; therefore its time-independent part can be expanded as a sum of cylindrical Hankel functions in the form[27]

$$P_{s0} = P_a \sum_{n=0}^{\infty} \epsilon_n i^n a_n H_n^{(1)}(k_o r)\cos(n\theta), \tag{2}$$

where the dimensionless scattering coefficients a_n for each partial wave can be determined from the boundary condition at the surface of the cylinder. At a large distance from the cylinder, the following asymptotic approximation is used:

$$i^n H_n^{(1)}(k_o r) \to \sqrt{\frac{2}{\pi k_o r}} e^{i(k_o r - \pi/4)}. \tag{3}$$

The complex velocity potential is related to the complex pressure by $\Phi = P/i\omega\rho_o$, so that in the total velocity potential, $\Phi = \Phi_0 e^{-i\omega t}$, the time-independent factor far from the cylinder is

$$\lim_{k_o r \to \infty} \Phi_0 = \Phi_{i0} + \lim_{k_o r \to \infty} \Phi_{s0} = \Phi_{i0} + \frac{f(\theta)}{\sqrt{k_o r}} e^{ik_o r}, \tag{4}$$

where $\Phi_{i0} = P_{i0}/(i\omega\rho_o)$, and $f(\theta)$ and the coefficients a_n can be determined from the boundary conditions at the surface of the cylinder. In Sec. II C, a similar expression is used to express scattering by a cylinder in a standing wave.

B. Evaluation of radiation force

The calculation here is based on the Brillouin acoustic radiation stress tensor $\mathbf{S}_T$ utilizing an Eulerian description of the fluid motion.[28] Pointed brackets $\langle\ \rangle$ are used for the temporal average at constant Eulerian coordinates. The time varying description of the acoustic wavefield is based entirely on a linear analysis in which the acoustic particle velocity is denoted by $\mathbf{u}$ and the acoustic pressure by p. The Brillouin stress tensor may be written as[10,25,28–30]

$$\mathbf{S}_T = (\langle K\rangle - \langle V\rangle)\mathbf{I} - \rho_o\langle \mathbf{uu}\rangle, \tag{5}$$

where $\mathbf{I}$ is the unit tensor, $\langle K\rangle = (\rho_o/2)\langle u^2\rangle$ is the local average of the acoustic kinetic energy density (in the linear acoustic approximation), and $\langle V\rangle = \langle p^2\rangle/(2\rho_o c_o^2)$ is the local average of the acoustic potential energy density in the same level of approximation. The acoustic particle velocity and pressure are related to the velocity potential ϕ by

$$\mathbf{u} = \nabla\phi, \tag{6}$$

$$p = -\rho_o \frac{\partial\phi}{\partial t}, \tag{7}$$

where ϕ and p are related to the corresponding complex quantities by $\phi = \mathrm{Re}(\Phi) = \mathrm{Re}(\Phi_0 e^{-i\omega t})$ and $p = \mathrm{Re}(P)$. Since the outer fluid is assumed to be free of dissipation, the radiation force is given by the following integral over a closed surface A that contains the object of interest:

$$\mathbf{F} = \oint_A \mathbf{S}_T \cdot d\mathbf{A}, \tag{8}$$

where the area differential $d\mathbf{A}$ is directed away from the object. The radiation force on spherical objects[8,10] has been given by the evaluation of Eq. (8) and the long-wavelength approximation of Yosioka and Kawasima has been derived in this way (see, e.g., Ref. 31). As explained below, the integral in Eq. (8) may be expressed using a far-field integration. Examples where this method has been used previously include Refs. 2, 10, and 32.

When $\nabla \cdot \mathbf{S}_T$ is integrated over the volume between the surface of this cylindrical object S_o and a circular cylindrical surface at a large radius S_r, this volume integral vanishes since $\nabla \cdot \mathbf{S}_T = 0$. Therefore, by Gauss' divergence theorem,

$$\mathbf{F} = \oint_{S_o} \mathbf{S}_T \cdot d\mathbf{A}$$

$$= \oint_{S_r} \mathbf{S}_T \cdot d\mathbf{A}$$

$$= -\oint_{S_r} \rho_o \langle \mathbf{uu} \rangle \cdot d\mathbf{A} + \oint_{S_r} \left\{ \frac{\rho_o}{2} \langle |\mathbf{u}|^2 \rangle - \frac{1}{2\rho_o c_o^2} \langle p^2 \rangle \right\} d\mathbf{A}, \tag{9}$$

where in the integration over S_r the area differential $d\mathbf{A}$ is directed away from the object. Contributions from the ends of the closed surface are not shown in Eq. (9) since they vanish and $d\mathbf{A} = L r d\theta \hat{\mathbf{e}}_\mathbf{r}$, where L is the length of the volume considered and $\hat{\mathbf{e}}_\mathbf{r}$ is a radial unit vector. The integration over S_r at radius r gives the force on the object in terms of far-field properties. The net force will only have the z component due to the symmetry, so

$$F_z = \mathbf{F} \cdot \hat{\mathbf{e}}_\mathbf{z}$$

$$= -\oint_{S_r} \rho_o \hat{\mathbf{e}}_\mathbf{z} \cdot \langle \mathbf{uu} \rangle \cdot d\mathbf{A} + \oint_{S_r} \left\{ \frac{\rho_o}{2} \langle |\mathbf{u}|^2 \rangle - \frac{1}{2\rho_o c_o^2} \langle p^2 \rangle \right\} d\mathbf{A} \cdot \hat{\mathbf{e}}_\mathbf{z}. \tag{10}$$

The time average of the products in the above equation may be expressed as one-half of the real part of the product of the first corresponding complex quantity with the complex conjugate of the second corresponding complex quantity. The force per unit length in terms of the complex velocity potential at very large distance r becomes

$$F_z/L = -2\rho_o r \int_{\theta=0}^{\theta=\pi} \frac{1}{2} \mathrm{Re}\left(\frac{\partial \Phi_0}{\partial r} \frac{\partial \Phi_0^*}{\partial z} \right) d\theta$$

$$+ \rho_o r \int_{\theta=0}^{\theta=\pi} \frac{1}{2} \mathrm{Re}(|\boldsymbol{\nabla} \boldsymbol{\Phi}_0| |\boldsymbol{\nabla} \boldsymbol{\Phi}_0^*|) \cos\theta \, d\theta$$

$$- \frac{r\rho_o}{c_o^2} \int_{\theta=0}^{\theta=\pi} \frac{1}{2} \mathrm{Re}[(-i\omega\Phi_0)(-i\omega\Phi_0^*)] \cos\theta \, d\theta. \tag{11}$$

Substituting Eq. (4) into Eq. (11) gives

$$F_z/L = -\rho_o k_o \int_{\theta=0}^{\theta=\pi} |f(\theta)|^2 \cos\theta \, d\theta$$

$$- \rho_o r \int_{\theta=0}^{\theta=\pi} \mathrm{Re}\left(\frac{\partial \Phi_{i0}}{\partial r} \frac{\partial \Phi_{i0}^*}{\partial z} \right) d\theta$$

$$- \frac{\rho_o r}{2} \int_{\theta=0}^{\theta=\pi} (k_o^2 |\Phi_{i0}|^2 - |\boldsymbol{\nabla} \Phi_{i0}|^2) \cos\theta \, d\theta$$

$$- \rho_o r k_o^2 \int_{\theta=0}^{\theta=\pi} \mathrm{Re}\left(\Phi_{i0}^* \frac{f(\theta) e^{ik_o r}}{\sqrt{k_o r}} \right) \cos\theta \, d\theta$$

$$+ \rho_o r k_o \int_{\theta=0}^{\theta=\pi} \mathrm{Im}\left(\frac{\partial \Phi_{i0}^*}{\partial z} \frac{f(\theta) e^{ik_o r}}{\sqrt{k_o r}} \right) d\theta. \tag{12}$$

The acoustic radiation force should vanish if there is no scatterer such that $f(\theta) = 0$. Therefore the sum of the second and third terms in Eq. (12) vanishes. The force can be expressed as

$$F_z/L = -\rho_o k_o \int_{\theta=0}^{\theta=\pi} |f(\theta)|^2 \cos\theta \, d\theta$$

$$- \rho_o r k_o^2 \int_{\theta=0}^{\theta=\pi} \mathrm{Re}\left(\Phi_{i0}^* \frac{f(\theta) e^{ik_o r}}{\sqrt{k_o r}} \right) \cos\theta \, d\theta$$

$$+ \rho_o r k_o \int_{\theta=0}^{\theta=\pi} \mathrm{Im}\left(\frac{\partial \Phi_{i0}^*}{\partial z} \frac{f(\theta) e^{ik_o r}}{\sqrt{k_o r}} \right) d\theta. \tag{13}$$

This expression gives the radiation force which is entirely determined by the scattered field at a large radius r.

C. Radiation force on a general cylinder in a standing wave

Now consider a cylinder with radius R in a planar standing wave field. The cylinder's axis is parallel to the standing wave nodal planes. Let $z = 0$ be the center of the cylinder, and $z = -h$ be the nearest pressure antinode. The time-independent factor of such a plane standing wave can be described as two counter-propagating plane waves:

$$\tilde{P}_{i0} = P_a \cos[k_o(z+h)]$$

$$= P_a \frac{e^{ik_o(z+h)} + e^{-ik_o(z+h)}}{2}$$

$$= P_a \sum_{n=0}^{\infty} \frac{e^{ik_o h} + (-1)^n e^{-ik_o h}}{2} \epsilon_n i^n J_n(k_o r) \cos(n\theta). \tag{14}$$

The time-independent factor of the corresponding scattered wave field is given as

$$\tilde{P}_{s0} = P_a \sum_{n=0}^{\infty} \frac{e^{ik_o h} + (-1)^n e^{-ik_o h}}{2}$$

$$\times \epsilon_n i^n a_n H_n^{(1)}(k_o r) \cos(n\theta). \tag{15}$$

At a large distance from the cylinder, the time-independent part of the total velocity potential approaches the form

$$\lim_{k_o r \to \infty} \tilde{\Phi}_0 = \tilde{\Phi}_{i0} + \tilde{\Phi}_{s0} = \tilde{\Phi}_{i0} + \frac{\tilde{f}(\theta)}{\sqrt{k_o r}} e^{ik_o r},$$

where

$$\tilde{\Phi}_{i0} = \frac{P_a \cos[k_o(z+h)]}{i\omega\rho_o}, \tag{16}$$

$$\tilde{f}(\theta) = \frac{P_a e^{-i\pi/4}}{i\omega\rho_o\sqrt{2\pi}} \sum_{n=0}^{\infty} [e^{ik_o h} + (-1)^n e^{-ik_o h}] \epsilon_n a_n \cos(n\theta). \tag{17}$$

In Eq. (17) the a_n are the partial wave coefficients for the corresponding traveling wave scattering problem considered in Sec. II A. Substituting Eq. (16) and Eq. (17) into Eq. (13),

the radiation force per unit length on a cylinder in a standing wave becomes

$$F_z/L = \frac{R}{4} P_a^2 \beta_o \sin(2k_o h) Y_{\mathrm{st}}, \tag{18}$$

and Y_{st} is the dimensionless radiation force function given in terms of the scattering coefficients as

$$Y_{\mathrm{st}} = \frac{8}{k_o R} \sum_{n=0}^{\infty} (-1)^n \left(a_n^{(R)} a_{n+1}^{(I)} - a_{n+1}^{(R)} a_n^{(I)} - \frac{\epsilon_n}{2} a_n^{(I)} \right), \tag{19}$$

where the superscript (R) and (I) denote the real and imaginary part, respectively.

The result given by Eq. (19) involves the partial-wave scattering coefficients of the corresponding traveling wave scattering situation. It can be used to calculate the radiation force on a cylinder, either rigid or compressible, in a standing wave.

Note that F_z is directed toward a velocity antinode if $Y_{\mathrm{st}} > 0$ and is directed toward a pressure antinode if $Y_{\mathrm{st}} < 0$. The radiation force vanishes if the cylinder is centered on either a pressure antinode $(h = 0)$ or on a velocity antinode $(k_o h = \pm \pi/2)$. The magnitude of the radiation force is maximum when the cylinder is at the intermediate location $(k_o h = \pm \pi/4)$.

D. Radiation force on a compressible cylinder in a standing wave

For a compressible fluid cylinder, the scattering coefficients determined from the boundary conditions at the cylinder surface are found to be[27]

$$a_n = \frac{(\rho_o c_o/\rho_i c_i) J_n(k_o R) J_n'(k_i R) - J_n(k_i R) J_n'(k_o R)}{J_n(k_i R) H_n^{(1)\prime}(k_o R) - (\rho_o c_o/\rho_i c_i) J_n'(k_i R) H_n^{(1)}(k_o R)}, \tag{20}$$

where ρ_i and c_i are the density and sound speed of the inner fluid which has an adiabatic compressibility $\beta_i = 1/\rho_i c_i^2$ and $k_i = \omega/c_i$. In addition to the assumption of loss-less fluids (so that viscous and thermal dissipation is neglected), the common assumption is made that interfacial tension has a negligible direct effect on the dynamics of the cylinder at the acoustic frequency of interest. The radiation force function Y_{st} can be found by substituting this into Eq. (19).

For $k_o R \ll 1$ and $k_i R \ll 1$, it is usually sufficient to consider only the monopole and dipole scattering terms which can be approximated as follows:

$$a_0^{(R)} = 0,$$

$$a_0^{(I)} = \frac{\pi (k_o R)^2}{4} \left(\frac{\beta_i}{\beta_o} - 1 \right),$$

$$a_1^{(R)} = 0,$$

$$a_1^{(I)} = \frac{\pi (k_o R)^2}{4} \left(\frac{1 - \rho_o/\rho_i}{1 + \rho_o/\rho_i} \right). \tag{21}$$

Then the long-wavelength approximation for the radiation force function on a compressible cylinder is found to be

$$Y_{\mathrm{st}} = \pi k_o R [f_1 + f_2], \tag{22}$$

where f_1 and f_2 are, respectively,

$$f_1 = 1 - \frac{\beta_i}{\beta_o},$$

$$f_2 = 2 \left(\frac{\rho_i/\rho_o - 1}{\rho_i/\rho_o + 1} \right). \tag{23}$$

The notation f_1 and f_2 was selected to be analogous to the notation introduced by Gorkov[2] for the radiation force problem for spheres. Inspection of Eq. (21) shows that f_1 and f_2 are proportional to the low frequency approximations of the monopole and dipole partial-wave amplitudes, respectively. In the case of an incompressible cylinder, $f_1 = 1$ and the force predicted by Eqs. (18) and (22) reduces to the upper part of Eq. (24) of Ref. 14. [There appears to be an error of transcription in the lower part of Eq. (24).] Notice that f_2 differs from the corresponding term for spheres.[2]

III. NUMERICAL CALCULATIONS OF Y_{st}

A. Compressible cylinder example: Diffusion flames

Small diffusion flames of natural gas in air in an ultrasonic standing wave were observed to be attracted to the pressure antinode adjacent to the flame.[33] It is relevant to the interpretation of those observations to determine the sign of Y_{st} for the analogous situation of a hot gas cylinder surrounded by air at room temperature. If the radius R of the cylinder is identified with the outer radius of the widest visible portion of the flame, the observations correspond to $R \approx 2$ mm and $k_o R \approx 1.1$ since the frequency was 29.8 kHz. Since $k_o R$ is not very large, the temperature and density variations within the flame are averaged so that the acoustical scattering by the flame is approximated as that of an inert cylinder of gas having a uniform density and sound speed ρ_i and c_i. This approximation neglects any direct effect of the acoustic pressure oscillations on the rate of combustion and it neglects small changes in the shape of the flame induced by the ultrasound. The estimated cylinder properties are $\rho_i/\rho_o = 0.2$ and $c_i/c_o = 2.163$. These correspond to an approximate flame temperature of 1500 K which is near the low end of the range expected from experimental and computational studies (see, e.g., Ref. 34).

Figure 1 compares the calculated results from Eq. (22) with the complete series, Eqs. (19) and (20). It can be seen from the graph that for small $k_o R$, Y_{st} is negative. The flame cylinder in the standing wave is predicted to be attracted to pressure antinodes, which agrees with what is reported in the experiment. Also note at very small $k_o R$, Eq. (22) works well. An inspection of Eq. (21) indicates that when $k_o R$ is small, the scattering is dominated by the dipole term for the situation under consideration and in Eq. (22), the magnitude of f_2 greatly exceeds that of f_1. This is also the case when Gorkov's approximations[2] for f_1 and f_2 in the spherical case are used. Consequently, the prediction that small flames are attracted to pressure antinodes of the standing wave is insensitive to the details of approximating ρ_i and c_i and appears to be insensitive to the flame shape.

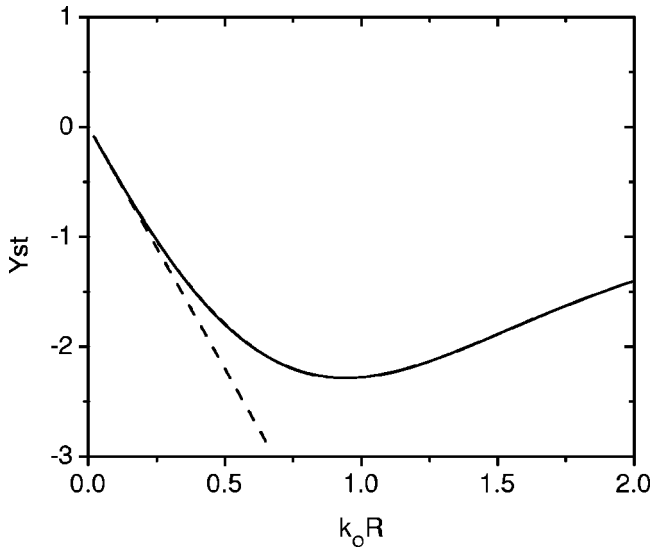

FIG. 1. The radiation force function Y_{st} as a function of k_oR for a hot gas cylinder in air with $\rho_i/\rho_o=0.2$ and $\beta_i/\beta_o=1.07$. The solid curve is given by Eq. (19) with $n_{max}=40$ and Eq. (20). The dashed line shows the long-wavelength approximation, Eq. (22).

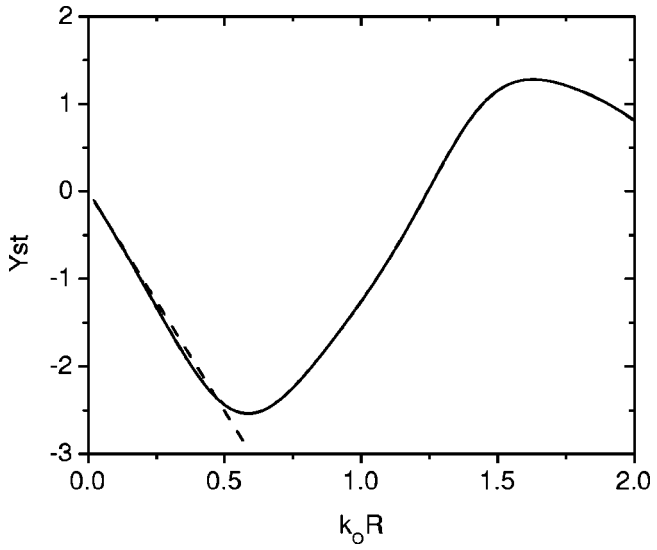

FIG. 2. The radiation force function Y_{st} as a function of k_oR for a liquid bridge in a Plateau tank with $\rho_i/\rho_o=1$ and $\beta_i/\beta_o=2.6$. The solid curve is given by Eq. (19) with $n_{max}=40$ and Eq. (20). The dashed line shows the long-wavelength approximation, Eq. (22).

It is instructive to note that the direction of the radiation force on a hot region of gas is opposite that recently predicted and observed for *dense* regions of gas.[35] The observations in Ref. 35 show that small dense clouds of gas surrounded by air are attracted to *velocity* antinodes of ultrasonic standing waves. In that case f_2 in a spherical or cylindrical model of the cloud is positive.

B. Compressible cylinder example: Liquid bridge in a Plateau tank

When investigating the dynamics of liquid bridges a common practice is to eliminate the effects of buoyancy by placing the liquid bridge in an immiscible host liquid having the same density as the bridge liquid. This configuration is commonly referred to as a Plateau tank.[15,16,20] Taking $\rho_i=\rho_o$ gives $f_2=0$ so that (unlike the aforementioned flame example) the dipole scattering is negligible at low frequencies. It was reported that Plateau tank bridges in a standing wave were attracted to pressure antinodes of the standing wave.[15,16] In both of these observations the bath liquid was water and the bridge liquid was a PDMS-TBE mixture reported to have $\beta_i/\beta_o=2.6$ (giving $c_i/c_o=0.62$). In the experiments k_oR was 0.66 in Ref. 15 and 1.09 in Ref. 16. Figure 2 shows Y_{st} as a function of k_oR and the approximation from Eq. (22). The cylindrical bridge is predicted to be attracted to pressure antinodes over the relevant range of k_oR. In one of the experiments the attraction of the bridge liquid to the pressure antinode was used to suppress the Rayleigh–Plateau instability.[16]

C. Liquid bridge in air and the rigid limit

Cylindrical liquid bridges in air have been deployed for short intervals in the simulated weightlessness of parabolic flights of NASA's KC-135 aircraft.[17,23,24] When weightless liquid bridges are subjected to ultrasonic standing waves in air, it has been reported that the bridges are attracted to velocity antinodes of the standing wave.[17,24] The typical observation was for $k_oR=0.84$. For the purpose of investigating the k_oR dependence of Y_{st}, Eq. (19) was evaluated for a circular cylindrical bridge of water in air. For water bridges in air, the density ratio ρ_i/ρ_o is 800, and the sound speed ratio c_i/c_o is 4.48. The radiation force function from Eq. (19) and the long-wavelength approximation are plotted in Fig. 3. At small k_oR, they agree with each other and the bridge is predicted to be attracted to velocity antinodes over a wide range of k_oR. This is analogous to the attraction of drops of water in air to velocity antinodes.[5,36,37]

Since the liquid is usually about 1000 times denser than air and the acoustic impedances of liquid and air are mis-

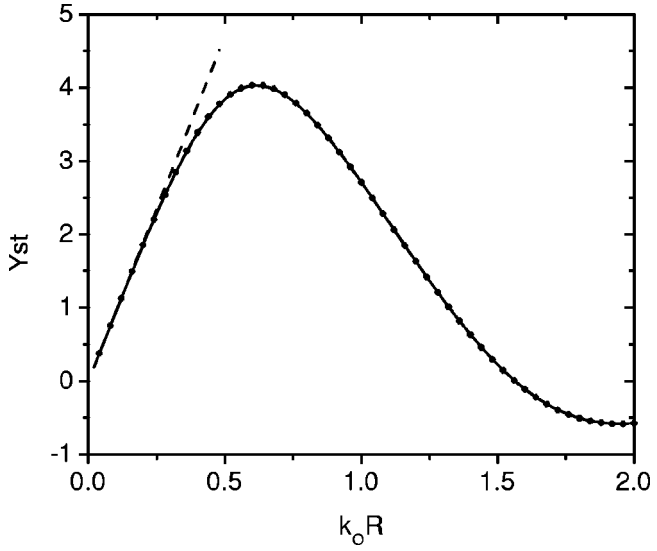

FIG. 3. The radiation force function Y_{st} as a function of k_oR for a bridge of water in air in a standing wave. The solid curve shows the result for $\rho_i/\rho_o=800$ and $\beta_i/\beta_o=6.2\times10^{-5}$, given by Eq. (19) with $n_{max}=40$ and Eq. (20). The dashed line corresponds to the long-wavelength approximation, Eq. (22). The dotted curve is for a fixed rigid cylinder given by Eq. (19) with $n_{max}=40$ and Eq. (20).

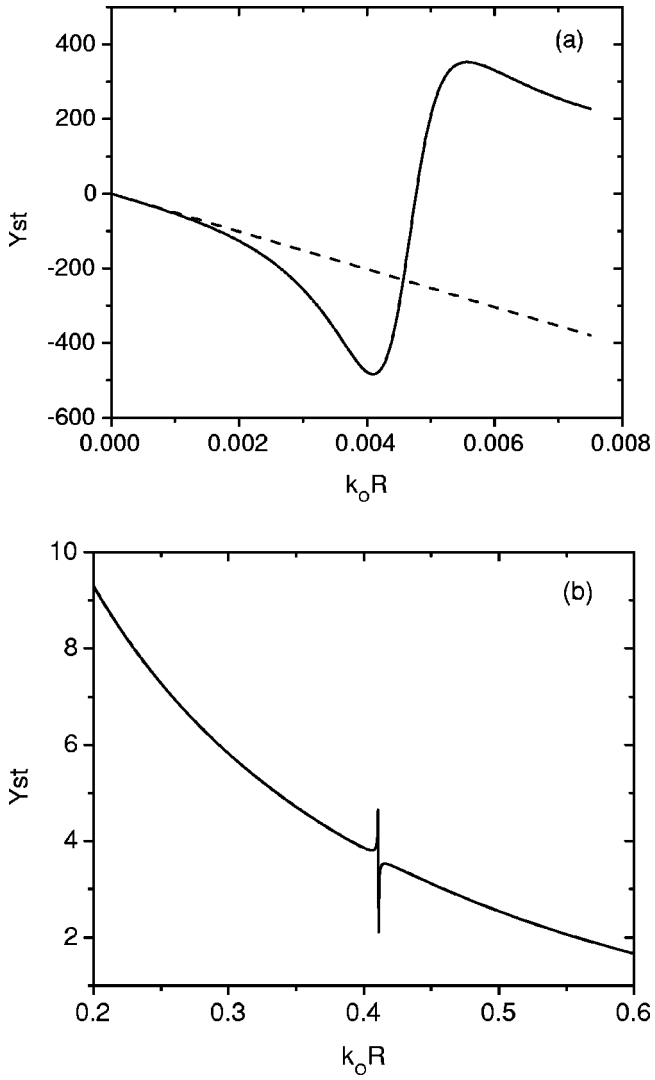

FIG. 4. The radiation force function Y_{st} as a function of k_oR for a cylindrical bubble of air in water with $\rho_i/\rho_o=1.25\times10^{-3}$ and $\beta_i/\beta_o=1.61\times10^4$, in a standing wave: (a) for the region of k_oR which contains a monopole resonance, the solid curve is given by Eq. (19) with $n_{max}=40$ and Eq. (20) and the dashed line corresponds to the long-wavelength approximation, Eq. (22); (b) the prediction of Eq. (19) for a region where k_oR is larger and an internal mode is evident.

matched, in the k_oR region of interest liquid cylinders in air may be approximated as perfectly rigid. Therefore, the limiting value of the scattering coefficients becomes

$$a_n(k_oR)=-\frac{J_n'(k_oR)}{H_n^{(1)\prime}(k_oR)}. \tag{24}$$

Using these limiting values of scattering coefficients for perfectly rigid cylinder gives the radiation force function shown by the points in Fig. 3. It is evident that liquid bridges in air can be modeled as perfectly rigid cylinders and that the force is insensitive to the specific values of ρ_i and c_i for the liquid.

D. Cylindrical bubble of air in water

The case of a cylindrical bubble of air in water is an example of a situation where it is necessary for k_oR to be very small for Eq. (22) to be applicable. This case is modeled by taking $\rho_i/\rho_o=1/800$ and $c_i/c_o=1/4.48$. Figure 4(a) shows the predictions of Eq. (19) (solid curve) and Eq. (22) (dashed curve). It is evident that when k_oR is very small cylindrical bubbles are predicted to be attracted to pressure antinodes, as is also the case for small spherical bubbles.[9,10] Notice also that Y_{st} is relatively large in magnitude but that it vanishes and reverses sign when $k_oR\approx0.0048$. Associated with this reversal is a large deviation from the approximation in Eq. (22). The reversal is caused by a radial resonance of the bubble and the quasi-static monopole response approximated by f_1 in Eq. (23) breaks down. This resonance is similar to the monopole resonance of spherical bubbles[9,10] except that in the cylindrical case the compressibility of the water must be included in the analysis of the mode frequency. The mode frequency is given by the implicit root of[38,39]

$$k_oR=\{-2\gamma_gP_g/[\rho_o\ln(\gamma k_oR/2)]\}^{1/2}/c_o, \tag{25}$$

where γ_g is the polytropic exponent of the gas, P_g is the hydrostatic pressure in the gas, and $\gamma=1.781\cdots=\exp(0.5772\ldots)$ where $0.5772\ldots$ is Euler's constant. For the present case of a cylindrical air bubble in water at atmospheric pressure, the solution of Eq. (25) gives $k_oR=0.0048$. Both Eqs. (20) and (25) neglect the effects of surface tension on the dynamics of the bubble that can be important when R is very small. The attraction of large spherical bubbles to velocity antinodes has been demonstrated and the force has been inferred from the equilibrium position.[11]

An evaluation of the series for Y_{st}, Eq. (19), over a larger region of k_oR is shown in Fig. 4(b). The prominent feature visible near $k_oR=0.41$ is the consequence of an internal dipole resonance of the bubble which affects the scattering pattern of the bubble. This resonance condition may be approximated by finding the lowest two-dimensional mode of an air-filled cylinder having rigid walls. The *internal* velocity potential is proportional to $J_n(k_ir)\cos(n\theta)$ where θ is the polar angle. The approximation that the radial component of velocity vanishes at $r=R$ gives the condition $k_iR=X$ where X is a root of $J_n'(X)=0$. The lowest mode has $n=1$ and $X=1.841\ldots$. It follows that $k_oR=(c_i/c_o)X\approx0.411$. An analogous internal mode is predicted to exist for spherical bubbles of air in water where the associated value of k_oR is estimated to be $k_oR\approx0.47$ where R becomes the radius of the spherical bubble.[40]

IV. GENERALIZATION TO ELLIPTICAL CYLINDERS

Consider now the evaluation of F_z/L for an infinitely-long elliptical cylinder in a standing wave where either the major axis or the minor axis of the cylinder lies on the z axis of the incident wave described by Eq. (14). This situation is illustrated in Fig. 5 for the case where the minor axis is along the z-axis and the semi-minor axis is denoted by a and the semi-major axis is denoted by b. The scattered wave in the corresponding case of an incident traveling wave is given by Eq. (2) where the scattering coefficients a_n now depend on the aspect ratio b/a of the ellipse. This representation of the scattered wave for this type of cylinder has been previously noted[41] and is consistent with a Fourier series for the angular dependence of the scattering. The symmetry of the elliptical cylinder is such that the expansion in Eq. (17) describes the

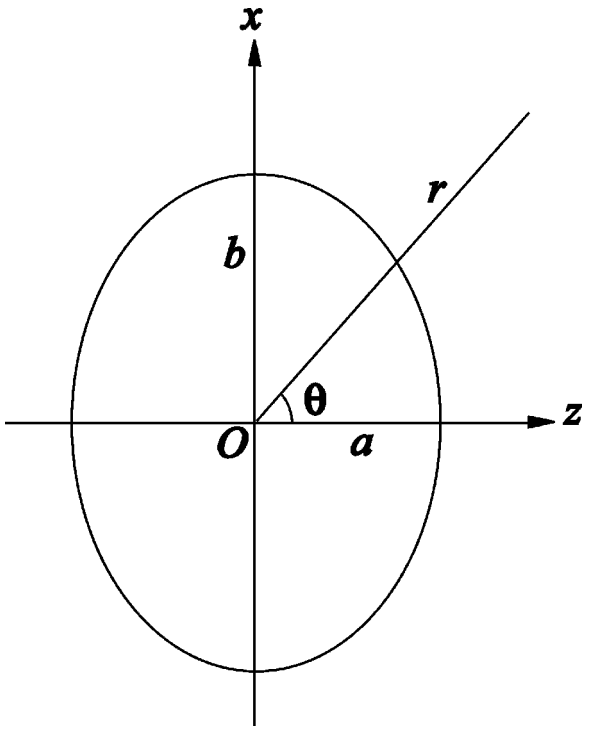

FIG. 5. Elliptical cylinder geometry. The incident standing wave is described by Eq. (15). The angle θ is the scattering angle with an incident traveling wave described by Eq. (1).

angular dependence of far-field scattering when the incident wave becomes a standing wave. It is convenient to take $R=(ab)^{1/2}$ so that R is the radius of a circle having the same area as the ellipse. It follows that Eqs. (18) and (19) give F_z/L in terms of the scattering coefficients of the elliptical cylinder. In the case of a fluid elliptical cylinder, an exact expression for the a_n which replaces Eq. (20) appears to be unavailable. That is because the exact solution for the scattering is ordinarily expressed in a basis that uses Mathieu functions.[24]

Rayleigh[42] and Twersky[43] derived a low-frequency approximation for the two-dimensional scattering by a fluid elliptical cylinder in a traveling wave. That result [Eqs. (3) and (75) of Ref. 43] for the geometry shown in Fig. 5 is identical to Eq. (21) with $a_1^{(I)}$ replaced by

$$a_1^{(I)}=\frac{\pi k_o^2 ab}{4}\,\frac{1-\rho_o/\rho_i}{D}, \tag{26}$$

$$D=2\{1+[(\rho_o/\rho_i)-1]Q_a\}, \tag{27}$$

where (following the notation of Twersky) $Q_a=1/(1+a/b)$. In the case of a circular cylinder, $a=b=R$ and $Q_a=1/2$ so that Eq. (26) reduces to Eq. (21). Rayleigh[42] and Twersky[43] predict that in the low-frequency limit, the approximation of the monopole term a_0 depends on the area of the ellipse but not on b/a.

The long-wavelength approximation for the radiation force function is given by Eq. (22) with f_2 in Eq. (23) replaced by

$$f_2=2(\rho_i/\rho_o-1)/D, \tag{28}$$

where D is given by Eq. (27). Consider the case of an elliptical cylinder of liquid in air where $f_2\approx 2$ in the limit of a circular cylinder. Let $\varepsilon=[(b/a)-1]$ denote a dimensionless deviation from a circular shape. When ε is small, it follows from Eqs. (27) and (28) that $f_2\approx 2[1+(\varepsilon/2)]$. Liquid bridges in air deployed close to a velocity antinode of the standing wave are deformed with the orientation shown in Fig. 5[17] so that $b>a$ and $\varepsilon>0$. Consequently, the radiation force is predicted to increase as a consequence of the deformation when ε is small. Since the radiation force contributes to the stabilization of the bridge in response to transverse perturbations that displace the bridge from the velocity antinode of the standing wave, it is noteworthy that the deformation of the bridge is predicted to enhance the restoring force when $k_oR\ll 1$. It is not presently known, however, if this prediction remains valid for the experimental conditions which typically have[17,24] $k_oR=0.84$.

V. CONCLUDING REMARKS

Though the analysis of the present paper is restricted to the case of the radiation force-per-length on infinitely long cylinders, the results are relevant to understanding the force on finite cylinders when the length-to-diameter ratio is sufficiently large that end corrections may be neglected. The radiation force function for plane standing waves $Y_{\rm st}$ is given in Eq. (19) in terms of the dimensionless scattering coefficients a_n from the corresponding situation for scattering by traveling waves in Eq. (2). The coefficients are given by Eq. (20) for a fluid circular cylinder. In the long-wavelength limit, the coefficients are approximated by Eq. (21) and the force function is approximated by Eqs. (22) and (23). This limiting case is analogous to the approximation by Yosioka and Kawasima[1] for the force on small spherical drops. The results of the series expansion for $Y_{\rm st}$ are illustrated in Figs. 1–4 (along with predictions of the long-wavelength approximation) for the following situations: a cylindrical column of hot gas (used as an acoustic approximation of a flame), a compressible liquid bridge in a Plateau tank, a liquid bridge in air, and a cylindrical bubble of air in water. Cylinders are predicted to be attracted to pressure antinodes when $Y_{\rm st}$ is negative and to velocity antinodes when $Y_{\rm st}$ is positive.

Section IV concerns the generalization to the case of cylinders having an elliptical profile with the orientation shown in Fig. 5 relative to the z axis of the standing wave. In that case, a low-frequency approximation for the scattering coefficients a_0 and a_1 is known for a fluid cylinder from the work of Rayleigh[42] and Twersky.[43] In Eq. (22) the dipole term f_2 is predicted to depend on the ratio b/a of the elliptical profile though the monopole term f_1 has the same value as that of a circular cylinder having the same area as the ellipse.

Instead of evaluating the integral in Eq. (9) on a surface having a large radius, an alternative approach is to evaluate the integral on the surface of the circular cylinder. For confirmation, that surface integral was evaluated for a circular column having the same parameters as the fluid circular cylinder considered in Fig. 1 with the result that the prediction for $Y_{\rm st}$ was numerically equivalent to the prediction of Eq. (19) plotted in Fig. 1. This comparison supports the deriva-

tion of Eq. (19) given here. In the near-field method the expression for the force had a more complicated form than the series given here in Eq. (19).

ACKNOWLEDGMENT

This research was supported by NASA.

[1] K. Yosioka and K. Kawasima, ''Acoustic radiation pressure on a compressible sphere,'' Acustica **5**, 167–173 (1955).
[2] L. P. Gorkov, ''On the forces acting on a small particle in an acoustical field in an ideal fluid,'' Sov. Phys. Dokl. **6**, 773–775 (1962).
[3] L. A. Crum, ''Acoustic force on a liquid droplet in an acoustic stationary wave,'' J. Acoust. Soc. Am. **50**, 157–163 (1971).
[4] R. E. Apfel, ''Technique for measuring the adiabatic compressibility, density, and sound speed of submicroliter liquid samples,'' J. Acoust. Soc. Am. **59**, 339–343 (1976).
[5] M. Barmatz and P. Collas, ''Acoustic radiation potential on a sphere in plane, cylindrical, and spherical standing wave fields,'' J. Acoust. Soc. Am. **77**, 928–945 (1985).
[6] G. Whitworth and W. T. Coakley, ''Particle column formation in a stationary ultrasonic-field,'' J. Acoust. Soc. Am. **91**, 79–85 (1992).
[7] A. A. Doinikov, ''Acoustic radiation force on a spherical particle in a viscous heat-conducting fluid. III. Force on a liquid drop,'' J. Acoust. Soc. Am. **101**, 731–740 (1997).
[8] X. C. Chen and R. E. Apfel, ''Radiation force on a spherical object in an axisymmetric wave field and its application to the calibration of high-frequency transducers,'' J. Acoust. Soc. Am. **99**, 713–724 (1996).
[9] A. Eller, ''Force on a bubble in a standing acoustic wave,'' J. Acoust. Soc. Am. **43**, 170–171 (1968).
[10] C. P. Lee and T. G. Wang, ''Acoustic radiation force on a bubble,'' J. Acoust. Soc. Am. **93**, 1637–1640 (1993).
[11] T. J. Asaki and P. L. Marston, ''Acoustic radiation force on a bubble driven above resonance,'' J. Acoust. Soc. Am. **96**, 3096–3099 (1994).
[12] T. Hasegawa, K. Saka, N. Inoue, and K. Matsuzawa, ''Acoustic radiation force experienced by a solid cylinder in a plane progressive sound field,'' J. Acoust. Soc. Am. **83**, 1770–1775 (1988).
[13] T. Hasegawa, Y. Hino, A. Annou, H. Noda, M. Kato, and N. Inoue, ''Acoustic radiation pressure acting on spherical and cylindrical shells,'' J. Acoust. Soc. Am. **93**, 154–161 (1993).
[14] J. Wu, G. Du, S. Work, and S. Warshaw, ''Acoustic radiation pressure on a rigid cylinder: An analytical theory and experiments,'' J. Acoust. Soc. Am. **87**, 581–586 (1990).
[15] S. F. Morse, D. B. Thiessen, and P. L. Marston, ''Capillary bridge modes driven with modulated ultrasonic radiation pressure,'' Phys. Fluids **8**, 3–5 (1996).
[16] M. J. Marr-Lyon, D. B. Thiessen, and P. L. Marston, ''Stabilization of a cylindrical capillary bridge far beyond the Rayleigh–Plateau limit using acoustic radiation pressure and active feedback,'' J. Fluid Mech. **351**, 345–357 (1997).
[17] M. J. Marr-Lyon, D. B. Thiessen, and P. L. Marston, ''Passive stabilization of capillary bridges in air with acoustic radiation pressure,'' Phys. Rev. Lett. **86**, 2293–2296 (2001). [An erratum that $\langle K\rangle-\langle V\rangle$ should read as $\langle V\rangle-\langle K\rangle$ has been published in Phys. Rev. Lett. **87**, 209901 (2001).]
[18] K. Yasuda and T. Kamakura, ''Acoustic radiation force on micrometer-size particles,'' Appl. Phys. Lett. **71**, 1771–1773 (1997).
[19] Lord Rayleigh, ''On the instability of jets,'' Proc. London Math. Soc. **10**, 4–13 (1879).
[20] J. Plateau, Statique Experimentale et Theorique des Liquides Soumis aux Seules Forces Moleculaires (Gauthier-Villars, Paris, 1873).
[21] T. R. Powers, D. Zhang, R. E. Goldstein, and H. A. Stone, ''Propagation of a topological transition: The Rayleigh instability,'' Phys. Fluids **10**, 1052–1057 (1998).
[22] M. S. Longuet-Higgins, ''Bubble noise spectra,'' J. Acoust. Soc. Am. **87**, 652–661 (1990).
[23] D. B. Thiessen, M. J. Marr-Lyon, and P. L. Marston, ''Active electrostatic stabilization of liquid bridges in low gravity,'' J. Fluid Mech. **457**, 285–294 (2002).
[24] M. J. Marr-Lyon ''Stabilization of capillary bridges far beyond the Rayleigh–Plateau limit with acoustic radiation pressure or electrostatic stresses,'' Ph.D. dissertation, Washington State University, Pullman, WA, 2000.
[25] P. L. Marston, ''Shape oscillation and static deformation of drops and bubbles driven by modulated radiation stresses-theory,'' J. Acoust. Soc. Am. **67**, 15–26 (1980).
[26] P. L. Marston, S. E. LoPorto, and G. L. Pullen, ''Quadrupole projection of the radiation pressure on a compressible sphere,'' J. Acoust. Soc. Am. **69**, 1499–1501 (1981); Y. Tian, R. G. Holt, and R. E. Apfel, ''Deformation and location of an acoustically levitated liquid drop,'' *ibid.* **93**, 3096–3104 (1993).
[27] P. M. Morse and K. U. Ingard, *Theoretical Acoustics* (McGraw-Hill, New York, 1968), pp. 401, 402, 464.
[28] L. Brillouin, *Tensors in Mechanics and Elasticity* (Academic, New York, 1964).
[29] C. P. Lee and T. G. Wang, ''Acoustic radiation pressure,'' J. Acoust. Soc. Am. **94**, 1099–1109 (1993).
[30] K. Beissner, ''The acoustic radiation force in lossless fluids in Eulerian and Lagrangian coordinates,'' J. Acoust. Soc. Am. **103**, 2321–2332 (1998).
[31] P. L. Marston, S. G. Goosby, D. S. Langley, and S. E. LoPorto-Arione, ''Resonances, radiation pressure, and optical scattering phenomena of drops and bubbles,'' Proceedings of the 2nd International Colloquium on Drops and Bubbles, Jet Prop. Lab., Pub. 82-7, Pasadena, CA, 1982, pp. 166–174.
[32] R. Lofstedt and S. Putterman, ''Theory of long wavelength acoustic radiation pressure,'' J. Acoust. Soc. Am. **90**, 2027–2033 (1991).
[33] D. B. Thiessen, M. J. Marr-Lyon, W. Wei, and P. L. Marston, ''Radiation pressure of standing waves on liquid columns and small diffusion flames,'' J. Acoust. Soc. Am. **112**, 2240(A) (2002).
[34] C. S. McEnally, U. O. Koylu, L. D. Pfefferle, and D. E. Rosner, ''Soot volume fraction and temperature measurements in laminar nonpremixed flames using thermocouples,'' Combust. Flame **109**, 701–720 (1997).
[35] R. Tuckermann, B. Neidhart, E. G. Lierke, and S. Bauerecker, ''Trapping of heavy gases in stationary ultrasonic fields,'' Chem. Phys. Lett. **363**, 349–354 (2002).
[36] E. H. Trinh, ''Compact acoustic levitation device for studies in fluid dynamics and material science in the laboratory and microgravity,'' Rev. Sci. Instrum. **56**, 2059–2065 (1985).
[37] G. Kaduchak, D. N. Sinha, and D. C. Lizon, ''Novel cylindrical, air-coupled acoustic levitation/concentration devices,'' Rev. Sci. Instrum. **73**, 1332–1336 (2002).
[38] D. E. Weston, ''Acoustic interaction effects in arrays of small spheres,'' J. Acoust. Soc. Am. **39**, 316–322 (1966).
[39] D. L. Miller, ''A cylindrical-bubble model for the response of plant-tissue gas bodies to ultrasound,'' J. Acoust. Soc. Am. **65**, 1313–1321 (1979).
[40] K. A. Sage, J. George, and H. Uberall, ''Multipole resonances in sound scattering from gas bubbles in a liquid,'' J. Acoust. Soc. Am. **65**, 1413–1422 (1979).
[41] S. Baskar, V. V. Varadan, and V. K. Varadan, ''Thin shell theories and acoustic wave scattering by infinitely long cylindrical shells of arbitrary cross section,'' J. Acoust. Soc. Am. **75**, 1673–1679 (1984).
[42] Lord Rayleigh, ''On the incidence of aerial and electric waves upon small obstacles in the form of ellipsoids or elliptic cylinders, and on the passage of electric waves through a circular aperture in a conducting screen,'' Philos. Mag. **44**, 28–52 (1897).
[43] V. Twersky, ''Acoustic bulk parameters of random volume distributions of small scatterers,'' J. Acoust. Soc. Am. **36**, 1314–1329 (1964).

Nonlinear tube waves in permeable formations: Difference frequency generation

Yaroslav Tserkovnyak
Harvard University, Lyman Laboratory of Physics, Cambridge, Massachusetts 02138

David Linton Johnson[a)]
Schlumberger-Doll Research, Old Quarry Road, Ridgefield, Connecticut 06877-4108

(Received 2 April 2004; accepted for publication 2 April 2004)

We extend earlier work on nonlinear tube wave propagation in permeable formations to study, analytically and numerically, the generation and propagation of a difference frequency, $\Delta\omega=\omega_1-\omega_2$, due to an initial pulse consisting of carrier frequencies ω_1 and ω_2. Tube waves in permeable formations have very significant linear dispersion/attenuation, which is specifically addressed here. We find that the difference frequency is predicted to be rather easily measurable with existing techniques and could yield useful information about formation nonlinear properties. © *2004 Acoustical Society of America.* [DOI: 10.1121/1.1753293]

PACS numbers: 43.25.Ts [MFH]

Pages: 209–216

I. INTRODUCTION

A tube wave is an acoustic normal mode in which the energy is confined to the vicinity of a fluid-filled cylinder within an elastic solid. From a practical point of view it is generally the dominant signal that appears in a typical borehole-logging measurement, and thus it is important in a variety of contexts in the search for hydrocarbon sources.

One of these contexts lies in the fact that the tube wave may couple to fluid flow within the rock formation if the latter is permeable. The linearized tube wave propagation in this regime has been extensively studied both theoretically and experimentally (Winkler *et al.*, 1989) (see also Pampuri *et al.*, 1998 and references therein). In the present article, we use a model of the tube wave of Liu and Johnson (1997). According to the model, the fluid in the borehole is separated from the porous formation by an elastic membrane (mudcake) of finite thickness. As a tube wave propagates, the membrane flexes in and out of the pores, thus forcing the fluid to flow through the formation. This leads to the coupling between the tube wave and the acoustic slow wave in the formation, which in turn leads to attenuation and dispersion of the tube waves. In formations of moderate to large permeability, this mechanism is the largest known source of attenuation/dispersion of the tube wave and is the reason why it is specifically considered in the present article.

Quite apart from this effect it is also known that sedimentary rocks have very large coefficients of nonlinearity and so Johnson *et al.* (1994) developed a theory for nonlinear tube waves neglecting the effects of the permeable formation. Later, Johnson (1999) combined this theory with the linearized theory of Liu and Johnson (1997) to describe a situation when the two effects are simultaneously present. As a numerical demonstration of the theory, Johnson (1999) considered the propagation of a narrow-banded (long duration) pulse consisting of a single carrier frequency. He showed that for realistic system parameters, the main signal (the fundamental) quickly decays, but before completely disappearing it generates a second harmonic and a low-frequency band (the ''self-demodulated'' pulse), both of which are due to the nonlinearity of the problem. The second harmonic decays even faster than the carrier, with the result that the self-demodulated pulse eventually dominates the entire signal at large enough distances.

Because the second harmonic decays so fast, often it is advantageous to determine nonlinear characteristics by using pulses that consist of two different carrier frequencies, ω_1 and ω_2. In addition to the second harmonics (above), nonlinear effects lead to the generation of a signal centered around the difference frequency, $\Delta\omega=\omega_1-\omega_2$. This component may be reasonably energetic while at the same time it is not attenuated as much as either second harmonic, or even as much as either carrier frequency. Thus, in this article we are motivated to consider the propagation of two narrow-banded pulses whose frequency separation $\Delta\omega$ is, say, 10% of the central frequency. Moreover, because $\Delta\omega$ is not that different from $\omega_{1,2}$, it is often possible to measure its amplitude with the same acoustic transducers as for the fundamental. In general, the nonlinear generation of a sum or difference frequency from two distinct initial frequencies is often referred to as ''three-wave mixing.''

The organization of the article is as follows. First, in the next section we review the theory and derive analytical results for the nonlinear propagation of a pulse consisting of two different frequencies. We derive an approximation for the propagation of the entire signal and we find an analytical form for the energy of the band with frequency $\Delta\omega$. In Sec. III we report the results of numerical calculations for a few different parameter sets and we show good agreement between our analytical and our numerical results. We make a brief summary of our work in Sec. IV.

[a)]Electronic mail: johnson10@slb.com

II. THEORY

The dispersion and attenuation of the linear tube wave propagation has been studied in Liu and Johnson (1997). To simplify our discussion we use an approximate form of the dispersion relation from Johnson (1999):

$$k_z(\omega)=\omega[S_\infty+\tilde{\Theta}(\omega)], \tag{1}$$

where k_z is the wave vector along the z direction (the tube axis), ω is the angular frequency of the wave, S_∞ is the slowness at infinite frequency, and $\tilde{\Theta}$ is given by

$$\tilde{\Theta}(\omega)=\frac{\rho_f}{S_\infty b[W_{\rm mc}+W_p(\omega)]}. \tag{2}$$

Here, ρ_f is the density of the borehole fluid, b is the borehole radius, $W_{\rm mc}$ is the mudcake membrane stiffness defined in Liu and Johnson (1997), and W_p characterizes permeability effects. W_p depends on the borehole fluid viscosity, η, formation permeability, κ, and the diffusivity of the slow wave,

$$C_D=\frac{\kappa K_f^*}{\eta\phi}, \tag{3}$$

through the equation

$$W_p(\omega)=-\frac{\eta C_D k_{S1}H_0^{(1)}(k_{S1}b)}{\kappa H_1^{(1)}(k_{S1}b)}. \tag{4}$$

Here, $k_{S1}=\sqrt{\iota\omega/C_D}$ is the wave vector of the slow-compressional wave and $H_{0,1}^{(1)}$ are Hankel functions.

Tube waves in nonlinear hyperelastic and impermeable formations have been studied in Johnson *et al.* (1994). In Johnson (1999) the effects of linear attenuation/dispersion and nonlinearity have been combined to obtain an approximate equation of motion for tube wave propagation in a realistic borehole. In the retarded time frame $\tau=t-S_\infty z$ this equation is

$$\frac{\partial p(z,\tau)}{\partial z}+\frac{\partial F(z,\tau)}{\partial\tau}-\frac{\beta S_\infty^3}{2\rho_f}\frac{\partial p^2(z,\tau)}{\partial\tau}=0, \tag{5}$$

where p is the pressure, and β is a dimensionless parameter defined in Johnson (1999). The function $F(z,\tau)$ is most simply related to the acoustic pressure in the Fourier transform domain:

$$\tilde{F}(z,\omega)=\tilde{\Theta}(\omega)\tilde{p}(z,\omega). \tag{6}$$

After performing the Fourier transform of Eq. (5), one obtains

$$\left(\frac{\partial}{\partial z}-\iota q(\omega)\right)\tilde{p}(z,\omega)+\frac{\iota\omega\beta S_\infty^3}{2\rho_f}\tilde{p}^2(z,\omega)=0, \tag{7}$$

where

$$q(\omega)=\omega\tilde{\Theta}(\omega) \tag{8}$$

is the reduced wave number. In Eq. (7), $\tilde{p}^2(z,\omega)$ is the Fourier transform of the square of $p(z,\tau)$ (*not* the square of the Fourier transform).

In Johnson (1999), Eq. (7) has been used to study the generation of the second harmonic as well as that of a low-frequency self-demodulated signal in a situation in which initially the pressure is a narrow band/long duration pulse centered on the frequency, ω_1. In the present article we consider a situation when two narrow-banded pulses are initially present. As discussed in the Introduction, for practical relevance we will take the difference in the pulse frequencies $\Delta\omega$ to be 10% of the central frequency ω'. The initial signal is given by

$$p(z=0,\tau)=E_1(\tau)\sin[\omega_1\tau+\phi_1]+E_2(\tau)\sin[\omega_2\tau+\phi_2]. \tag{9}$$

Here, $E_i(\tau)$ are the envelope functions, $\omega_1\equiv\omega'+\Delta\omega/2$, and $\omega_2\equiv\omega'-\Delta\omega/2$. For the numerical demonstration of the next section, we take the same envelope functions as in Johnson (1999):

$$E_1(\tau)=E_2(\tau)=\tfrac{1}{2}P_0\exp[-(\tau/T_W)^{10}]. \tag{10}$$

By setting $\omega_1=\omega_2$ and $\phi_1=\phi_2$ in Eq. (9), one recovers the pulse considered in Johnson (1999). In all three parameter sets used for the numerical calculations in the present article (see Table I), we take $\Delta\omega/\omega'=0.1$ and $\omega'\times T_W=125\pi$ so that initially the different signals we consider all "look" the same.

There are two characteristic distances relevant to the problem: the decay length of the linearized theory, $Z_{\rm att}=1/\gamma(\omega')$, where

$$\gamma(\omega)=\omega\Im[\tilde{\Theta}(\omega)], \tag{11}$$

and the distance over which a shock front would develop, in the absence of attenuation. The latter is found in Hamilton and Blackstock (1998) to be

$$Z_{\rm shock}=\frac{\rho_f}{\beta S_\infty^3\omega' P_0}. \tag{12}$$

The Gol'dberg number,

$$\Gamma=Z_{\rm att}/Z_{\rm shock}, \tag{13}$$

measures the importance of nonlinear effects relative to the linear. In the three parameter sets (Table I), the amplitude P_0 is chosen so that $\Gamma=0.21$, i.e., the nonlinear effects are significant, but overall pulse propagation is dominated by linear dispersion/attenuation.

For $\Gamma\ll 1$, the nonlinear effects can be ignored to a first approximation. Because, by assumption, the signal consists of two narrow-band pulses, one has the usual result of linear acoustics:

$$\begin{aligned}p'(z,\tau)=&E_1(\tau-\Delta S_{g1}z)e^{-\gamma_1 z}\sin[\omega_1(\tau-\Delta S_{p1}z)+\phi_1]\\&+E_2(\tau-\Delta S_{g2}z)e^{-\gamma_2 z}\\&\times\sin[\omega_2(\tau-\Delta S_{p2}z)+\phi_2],\end{aligned} \tag{14}$$

where ΔS_p and ΔS_g are the additional phase and group slownesses, respectively, relative to S_∞:

$$\begin{aligned}\Delta S_p(\omega)&=\Re[\tilde{\Theta}(\omega)],\\ \Delta S_g(\omega)&=\frac{\rm d}{{\rm d}\omega}\Re[\omega\tilde{\Theta}(\omega)].\end{aligned} \tag{15}$$

Throughout this paper, the subscripts 1 and 2 correspond to frequencies ω_1 and ω_2, respectively. The physical meaning

of Eq. (14) is transparent: The pulse envelope propagates with the group velocity and attenuates while each peak and trough travels with the phase velocity. If the envelope is broad enough, the relevant attenuation/dispersion quantities should be evaluated at the central frequency of each pulse.

If the Gol'dberg number Γ is small compared to unity but is not completely negligible, Eq. (14) still gives a reasonable approximation for the propagation of the original pulses but, because of the quadratic nonlinearity in Eq. (7), new frequency components will be generated that are centered around $\omega=2\omega_1$, $2\omega_2$, 0 as well as those centered around $\omega_1-\omega_2$ and $\omega_1+\omega_2$. Apart from a direct numerical solution of Eq. (7), which we present in Sec. III (below), one can develop a perturbation theory thereof:

$$p(z,\tau)=p'(z,\tau)+p_0(z,\tau)+p_\Delta(z,\tau)+p_{2\omega_1}(z,\tau)+p_{2\omega_2}(z,\tau)+p_{\omega_1+\omega_2}(z,\tau)+\cdots. \tag{16}$$

Here, p_0 refers to the self-demodulated signal, p_Δ refers to the signal whose bandwidth is centered around $\Delta=\omega_1-\omega_2$, etc. By the substitution of Eqs. (14) and (16) into Eq. (7), one can derive an approximate equation for the evolution of these nonlinearly generated components, even in the presence of significant linear dispersion and attenuation.

In this manner the generation of the second harmonic and of the self-demodulated signal has been studied in Johnson (1999). In the present article we focus on the component centered around the frequency $\Delta\omega=\omega_1-\omega_2$. (The analytical expressions we derive for this mode can easily be generalized to the $\omega=\omega_1+\omega_2$ case by redefining $\omega_2\rightarrow-\omega_2$.) We obtain ($\Delta\phi\equiv\phi_1-\phi_2$),

$$p_\Delta(z,\tau)=E_1(\tau-\Delta S_{g1}z)E_2(\tau-\Delta S_{g2}z)\frac{\Delta\omega\beta S_\infty^3}{2\rho_f}\times\Re\left[\mathrm{e}^{-\iota(\Delta\omega\tau+\Delta\phi)}\frac{\mathrm{e}^{\iota(q_1-q_2^*)z}-\mathrm{e}^{\iota q(\Delta\omega)z}}{q(\Delta\omega)-q_1+q_2^*}\right]. \tag{17}$$

One is reminded that this equation is valid only for narrow-banded pulses ($\Delta\omega\times T_W\gg1$) and small nonlinear effects ($\Gamma<1$).

Next, we consider the energy of the carrier ($\omega\approx\omega'$) band, $\mathcal{E}'(z)$, as well as that of the band centered on the difference frequency $\omega\approx\Delta\omega$, $\mathcal{E}_\Delta(z)$. We define them by

$$\mathcal{E}'(z)\equiv\int_{\omega'/2}^{3\omega'/2}|\tilde{p}(z,\omega)|^2\,\mathrm{d}\omega, \tag{18}$$

$$\mathcal{E}_\Delta(z)\equiv\int_{\Delta\omega/2}^{3\Delta\omega/2}|\tilde{p}(z,\omega)|^2\,\mathrm{d}\omega. \tag{19}$$

We refer to Eqs. (18) and (19) as the energy in the ω' and the $\Delta\omega$ bands, respectively. Using Parseval's theorem and Eqs. (14) and (17), one gets

TABLE I. Values of input parameters for the calculation of tube wave characteristics.

Sample		A	B	C	
Input parameters	ϕ	0.30	0.30	0.30	
	η	0.01	0.01	0.01	Poise
	K_f^*	2.25	2.25	2.25	GPa
	b	0.1	0.1	0.1	m
	ρ_f	1000.	1000.	1000.	kg/m^3
	S_∞	667.	667.	667.	μs/m
	β	50.5	50.5	50.5	
	W_{mc}	250.	250.	100.	GPa/m
	κ	2.	0.2	0.2	μm^2
	$\omega'/2\pi$	10^2	10^4	10^4	Hz
	$\Delta\omega/2\pi$	10	10^3	10^3	Hz
	T_W	625.	6.25	6.25	ms
	P_0	81.	80.	92.	kPa
Calculated quantities	C	15	1.5	1.5	m^2/s
	Z_{att}	278	2.8	2.4	m
	Z_{shock}	1323	13.4	11.6	m
	$\Gamma=Z_{\mathrm{att}}/Z_{\mathrm{shock}}$	0.21	0.21	0.21	
	$\Delta S_p(\omega')$	55.9	6.8	6.9	μs/m
	$\Delta S_g(\omega')$	52.7	3.5	3.5	μs/m

$$\mathcal{E}'(z)/\pi\approx\int_{-\infty}^{+\infty}|\tilde{p}'(z,\omega)|^2\,\mathrm{d}\omega=\mathrm{e}^{-2\gamma_1 z}\int_{-\infty}^{+\infty}E_1^2(\tau)\mathrm{d}\tau+\mathrm{e}^{-2\gamma_2 z}\int_{-\infty}^{+\infty}E_2^2(\tau)\mathrm{d}\tau \tag{20}$$

and

$$\mathcal{E}_\Delta(z)/\pi\approx\int_{-\infty}^{+\infty}|\tilde{p}_\Delta(z,\omega)|^2\,\mathrm{d}\omega=\left(\frac{\Delta\omega\beta S_\infty^3}{2\rho_f}\right)^2\left|\frac{\mathrm{e}^{\iota(q_1-q_2^*)z}-\mathrm{e}^{\iota q(\Delta\omega)z}}{q(\Delta\omega)-q_1+q_2^*}\right|^2\times\int_{-\infty}^{+\infty}E_1^2(\tau-\Delta S_{g1}z)E_2^2(\tau-\Delta S_{g2}z)\mathrm{d}\tau. \tag{21}$$

In the special case that the two envelope functions are identical, $E_1(\tau)\equiv E_2(\tau)$, one can derive a simple analytic result for the nonlinearly generated signals centered around $\Delta\omega$ as well as the self-demodulated signal centered around $\omega=0$. For this, we rewrite the input signal (9) in the form

$$p(z=0,\tau)=E'(\tau)\sin[\omega'\tau+\phi'], \tag{22}$$

where $\phi'\equiv(\phi_1+\phi_2)/2$ and

$$E'(\tau)=2E_1(\tau)\cos[(\Delta\omega/2)\tau+\Delta\phi/2]. \tag{23}$$

$E'(\tau)$ is now viewed as a narrow-banded envelope function for the ω' mode (assuming that $\Delta\omega\ll\omega'$). As before, the total signal can be approximated by

$$p(z,\tau)\approx p_{[\mathrm{slow}]}(z,\tau)+p'(z,\tau), \tag{24}$$

where $p_{[\mathrm{slow}]}(z,\tau)\equiv p_0(z,\tau)+p_\Delta(z,\tau)$ now includes both the self-demodulated component as well as the components

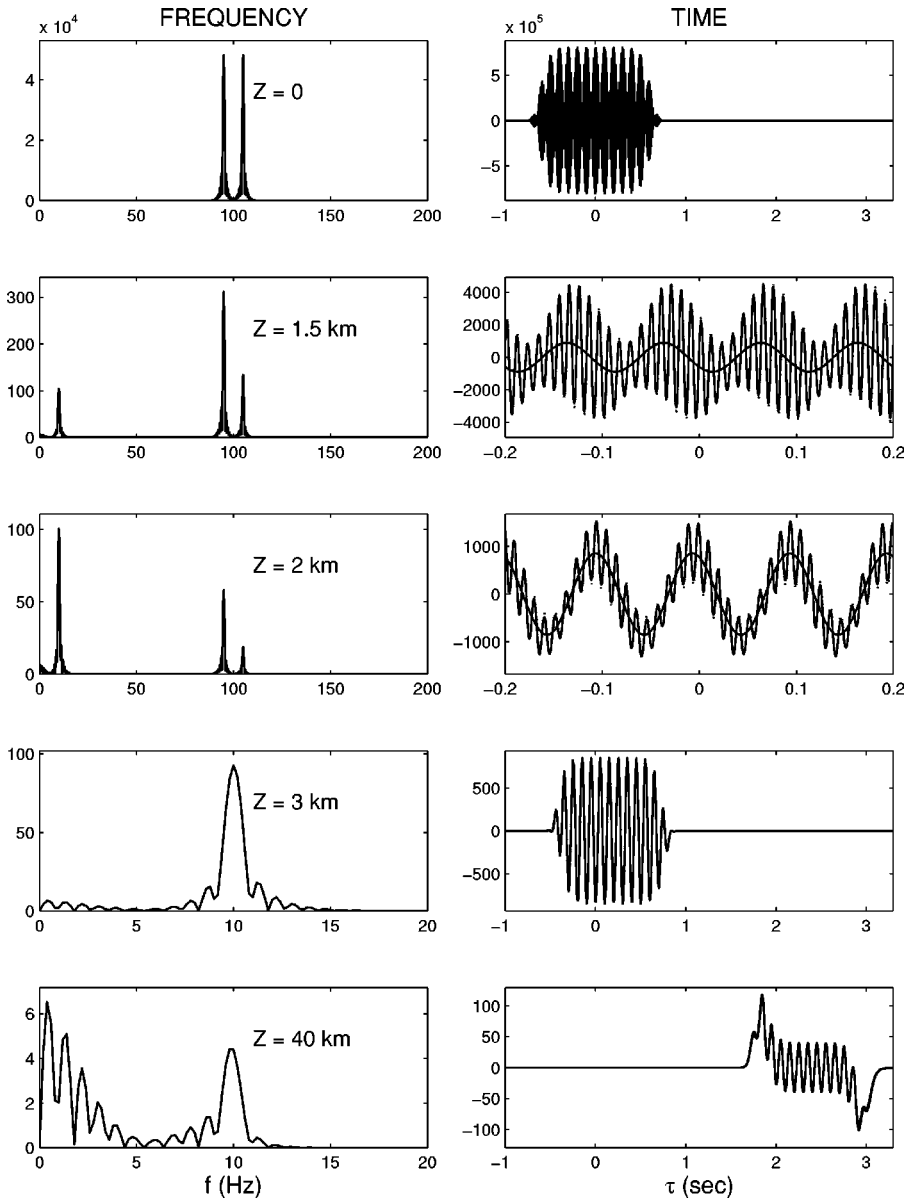

FIG. 1. The calculated pulse evolution using parameter set A, from Table I. The right column is the signal in the time domain, the left is the frequency spectrum. Also shown as a solid line on the right is the analytical expression for the low-frequency pulse, Eq. (25), toward which the pulse evolves. Similarly, the analytical expression for the total signal, Eq. (24), is shown as a dotted line: It essentially overlies the numerically calculated signal. Notice the various changes of scale.

centered around $\Delta\omega$. Within the context of the foregoing approximations it is given by

$$p_{[\mathrm{slow}]}(z,\tau)=\frac{\beta S_\infty^3}{4\rho_f}\int_{-\infty}^{+\infty}\frac{-\imath\omega\tilde{E}'^2(\omega)}{\imath\omega\Delta S_g'-2\gamma'-\imath q(\omega)}\times[\mathrm{e}^{(\imath\omega\Delta S_g'-2\gamma')z}-\mathrm{e}^{\imath q(\omega)z}]\mathrm{e}^{-\imath\omega\tau}\,\mathrm{d}\omega. \quad (25)$$

The primed quantities $\Delta S_g'$ and γ' are evaluated at the frequency ω'.

III. NUMERICAL RESULTS

For the numerical calculations, we consider three parameter sets, {A, B, C}, which are listed in Table I. These parameters are identical to those considered in Johnson (1999), where the relevance of these parameters to realistic borehole properties is discussed. There is one change in that in this article we take T_W to be five times larger. This is done in order to make the bandwidths of the pulses so narrow that the $\Delta\omega$ mode clearly separates from the rest of the low-frequency signal.

In order to solve the equation of motion (7) we use the same Lax–Wendroff algorithm as in Johnson (1999) and the initial pulse (9) with envelope functions (10) and phases $\phi_1=\phi_2=0$. Figures 1, 2, and 3 show several snapshots of the pulse profile in both time and frequency domains for three parameter sets (Table I) A, B, and C, respectively. Cases B and C have similar initial pulses, but differ somewhat in their dispersion relations, as can be seen from the corresponding parameter sets in Table I. Sample A has a center frequency two orders of magnitude lower than samples B and C, and as a consequence, the relevant modes have much longer attenuation length Z_{att}.

It is pedagogically useful to first examine Fig. 3 in detail. Considering the left column of plots, one can trace an intuitively clear sequence of events: Initially, the signal is given by two narrow-band pulses separated by 10% frequency difference $\Delta\omega$ (first row of plots). In the time do-

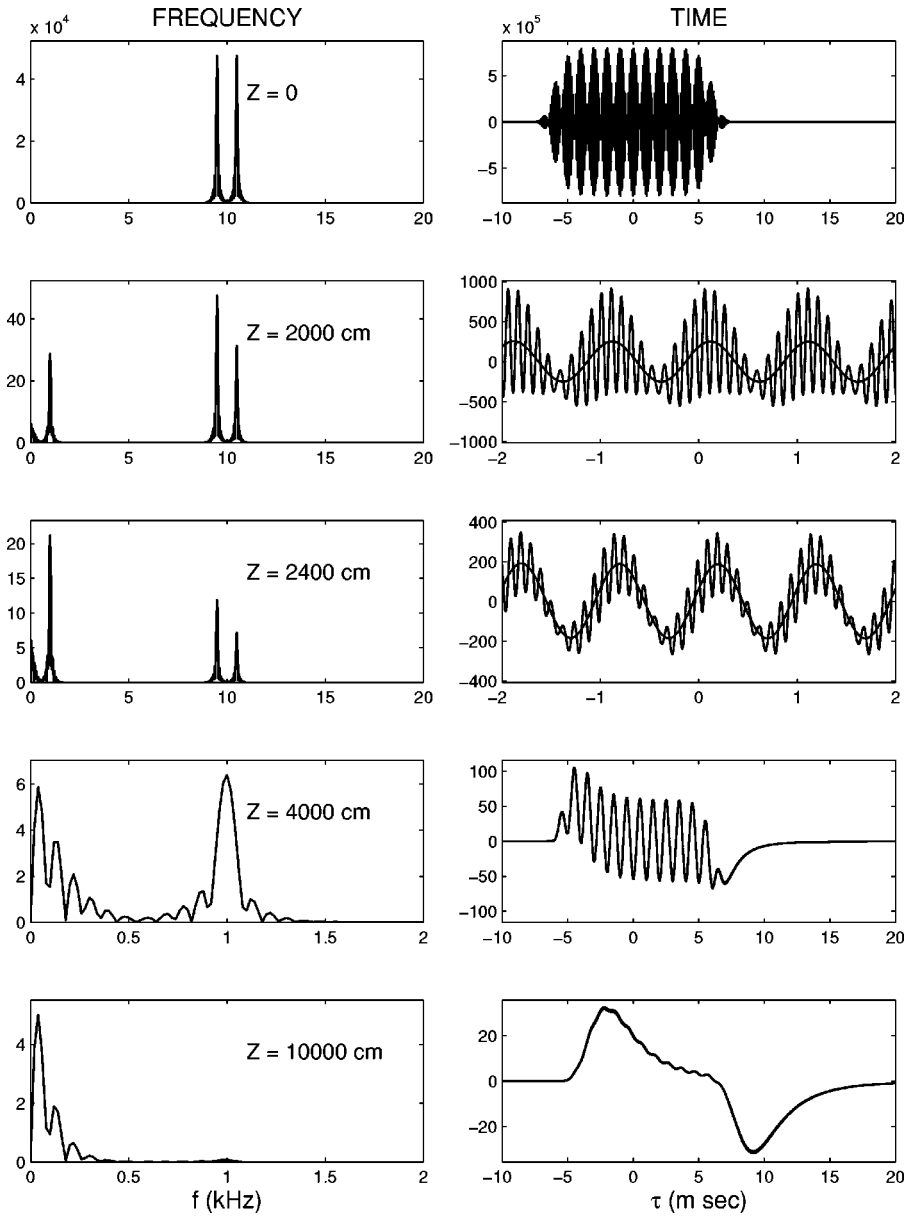

FIG. 2. Calculated pulse evolution using parameter set B, from Table I. The same conventions as Fig. 1.

main, on the right, one can see the beat frequency of the two carriers. As this signal propagates through the borehole and gradually attenuates, modes centered at $\omega \approx \Delta\omega$ are being generated (second row). They soon start to dominate the general shape of the pulse because they attenuate less than does the carrier (third row). We have expanded the time scale in the plots on the right so as to emphasize this effect. Concomitantly, modes centered on the band $\omega \approx 0$ start to appear and give a significant "background" for the $\Delta\omega$ signal (fourth row). Here, we have returned to the original time scale so one can see the relationship of this pulse to the original. In the end, all higher-frequency components decay and the completely self-demodulated signal $\omega \approx 0$ contains most of the energy (fifth row). This final signal is qualitatively similar to those described in Johnson (1999); the main difference in the present article is the presence of the difference frequency components. Generally speaking, these components attain a peak value larger than those of the $\omega \approx 0$ band and they decay somewhat faster. Although Eq. (24) is also plotted, it is indistinguishable from the results of the full numerical calculation. For a large enough distance $p(z,\tau)$ evolves to $p_{[\mathrm{slow}]}(z,\tau)$, Eq. (25), as is indicated in the plot.

Qualitatively Fig. 1 and Fig. 2 look similar to Fig. 3. But in the case of sample A, because of the smaller attenuation, the $\Delta\omega$ component does not demodulate completely, even after propagating a distance of $\sim$40 km.

Next, for each of the three cases, A, B, and C, we calculate the energy of the $\omega=\omega'$ band directly using Eq. (18) and also using Eq. (20). Similarly, we calculate the energy of the $\omega=\Delta\omega$ band using Eq. (19) as well as Eq. (21). The results are plotted in Figs. 4, 5 and 6. The intersections of the solid and dashed curves in Figs. 4, 5, and 6 indicate the crossover region, where the $\omega=\Delta\omega$ band starts dominating over the carrier band $\omega=\omega'$, as can be seen in Figs. 1, 2, and 3, respectively. Figure 5 is analogous to Fig. 6 of Johnson, 1999, which shows the energy of the second harmonic and of the dc band (i.e., that centered on $\omega=0$) for an almost monochromatic initial pulse and the same system parameters. As can be intuitively expected, the $\Delta\omega$ band is intermediate in both the maximal energy it gains and in the distance it propa-

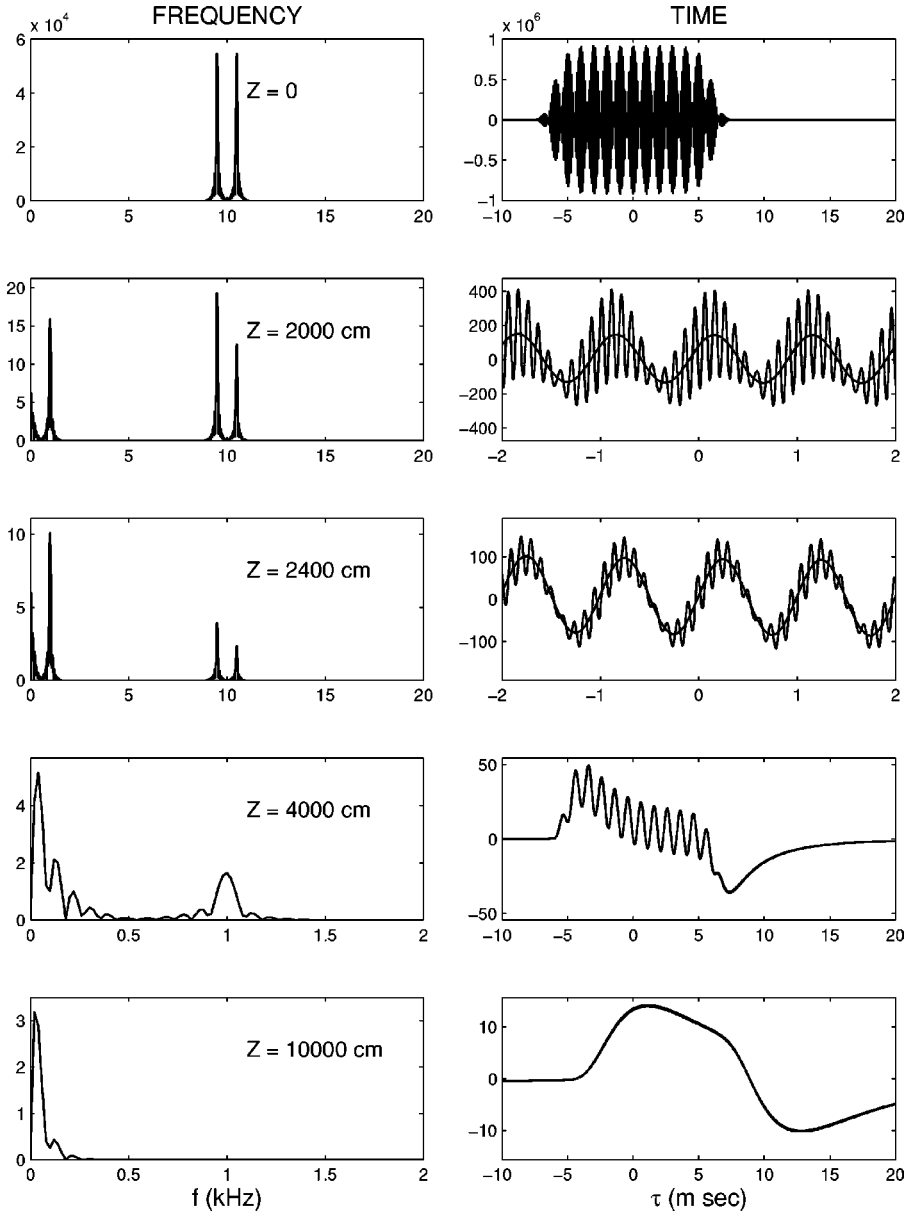

FIG. 3. Calculated pulse evolution using parameter set C, from Table I. The same conventions as Fig. 1.

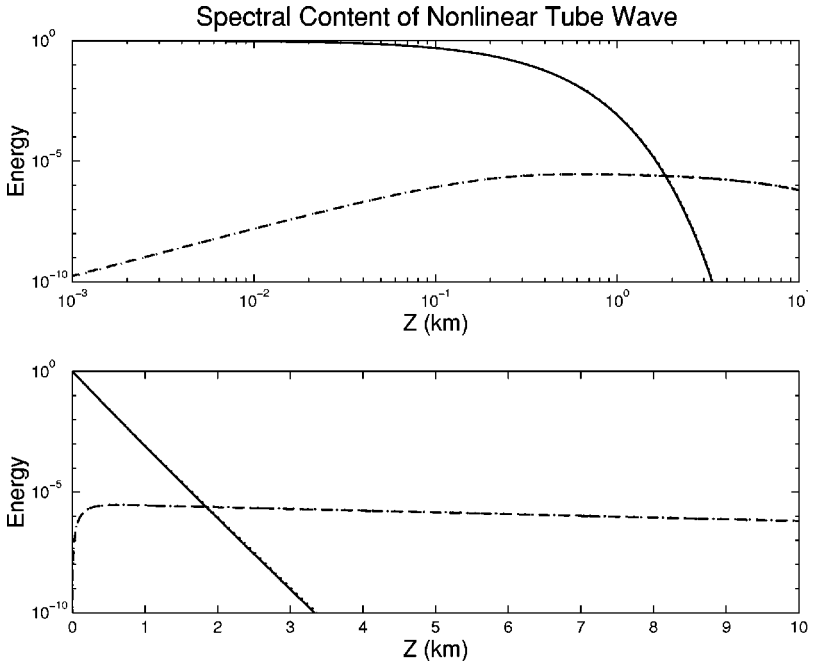

FIG. 4. Numerically calculated values of the energy $\mathcal{E}'(z)$ (solid line) and $\mathcal{E}_\Delta(z)$ (dashed line) defined by Eqs. (18) and (19) for the waveforms of Fig. 1, sample A. Each curve has been normalized by the value of $\mathcal{E}'(z=0)$. The data are shown in both log–log and semilog plots, in order to emphasize the short and long distance behavior, respectively. The dotted lines show the analytical expressions, Eqs. (20) and (21); the fact that they are almost indistinguishable from the numerically calculated curves is precisely the point.

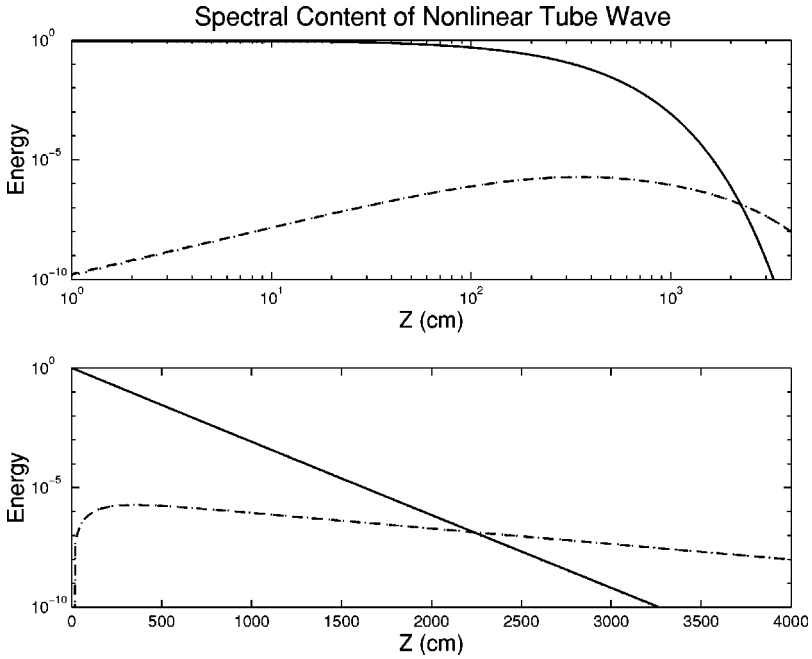

FIG. 5. Numerically calculated values of the energy $\mathcal{E}'(z)$ and $\mathcal{E}_\Delta(z)$ for the waveforms of Fig. 2, sample B. The same conventions as Fig. 4.

gates, as compared to either the dc band or the higher harmonics. The $\Delta\omega$ component does not reach energies as high as do the second harmonics, but it propagates much further, still carrying a significant fraction of energy; it is $\sim$55 dB down from the initial carrier energy, $\mathcal{E}'(z=0)$, in our examples. On the other hand, while the dc signal persists longer than the $\Delta\omega$ modes, it is never as energetic and it would be more difficult to measure, even in principle.

One might well ask whether the difference energy, $\mathcal{E}_\Delta(z)$ Eq. (19), is sensitive to the dispersion in the modes or if it has more or less the same dependence on distance as that expected for, e.g., a viscous fluid, for which there is little dispersion. In Eq. (21) the z dependence in the integral is negligible so the question is whether the scaled energy,

$$\mathcal{E}_\Delta^{\text{scale}}(z) \overset{\text{def}}{=} \left| \frac{e^{\iota(q_1 - q_2^*)z} - e^{\iota q(\Delta\omega)z}}{q(\Delta\omega) - q_1 + q_2^*} \right|^2, \tag{26}$$

is the same as if there were no dispersion at all. This latter assumption is equivalent to the substitution $q_{1,2} \to i\gamma(\omega')$ and $q(\Delta\omega) \to i\gamma(\Delta\omega)$, which leads to the approximation

$$\mathcal{E}_\Delta^{\text{scale}}(z) \overset{?}{=} \left| \frac{e^{-2\gamma(\omega')z} - e^{-\gamma(\Delta\omega)z}}{\gamma(\Delta\omega) - 2\gamma(\omega')} \right|^2. \tag{27}$$

Equations (26) and (27) appear nearly identical when plotted on the scale of Figs. 4, 5, or 6. This is because even though the modes are dispersive one has $\Re[q_1 - q_2] \approx \Re[q(\Delta\omega)]$. Of course, in order to use an approximation such as Eq. (27)

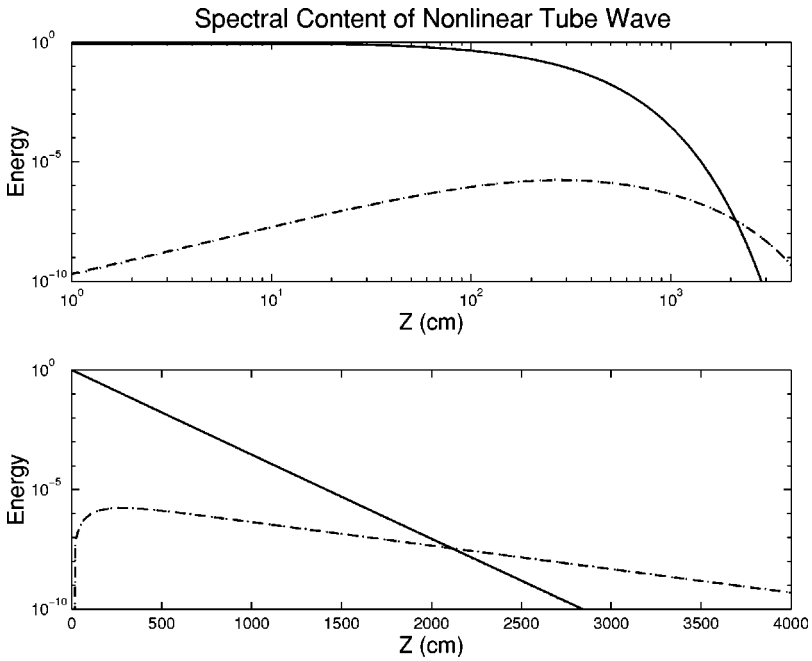

FIG. 6. Numerically calculated values of the energy $\mathcal{E}'(z)$ and $\mathcal{E}_\Delta(z)$ for the waveforms of Fig. 3, sample C. The same conventions as Fig. 4.

it is *not* true that the attenuation may be further approximated by that of an equivalent viscous fluid, for which $\gamma(\omega) \propto \omega^2$. The location of the peak in the function $\mathcal{E}_\Delta(z)$ is determined mostly by the attenuation $\gamma(\omega')$, whereas the rate of fall-off is determined by $\gamma(\Delta\omega)$. There is no way that an equivalent viscous fluid can fit both of these conditions because the frequency dependence of the attenuation of a tube wave is very different from that of a quadratic cf. Fig. 1 of Johnson (1999); the specific attenuation of a viscous fluid is given by $1/Q \propto \omega$.

IV. CONCLUSIONS

We have used the theory of Johnson (1999) of tube wave propagation in permeable formations to describe the nonlinear interaction of two narrow-banded pulses. The theory incorporates both nonlinear effects and a realistic model for dispersion/attenuation of tube waves. We have extended this previous work on the propagation of a single narrow-banded pulse to describe the generation and propagation of the $\omega = \Delta\omega$ band when two different carrier frequencies are present in the initial pulse. The difference frequency so-generated generally has a peak energy larger than that of the demodulated signal and it decays slowly, albeit faster, than does the demodulated signal. In terms of quantifying nonlinear effects via three-wave mixing measurements, the difference frequency seems best suited to this task.

We have derived analytical results for the self-demodulated component, the $\Delta\omega$ band, and the total signal in the regime of weak nonlinearity and they are in excellent agreement with an accurate numerical calculation using three different parameter sets. Specifically, we have studied the spectral content of the signal and demonstrated that the $\Delta\omega$ band can have a potential application because of its long attenuation length and its relatively high energy content. Also, if $\Delta\omega/\omega' \sim 0.1$, as we consider here, there is a practical bonus as the same transducers used for the generation of the carrier signal can, presumably, be used for the detection of the $\Delta\omega$ band.

ACKNOWLEDGMENTS

This work was supported in part by NSF Grant No. DMR 99-81283. We are grateful for several suggestions from M. A. Hamilton.

Hamilton, M. F., and Blackstock, D. T. (**1998**). *Nonlinear Acoustics* (Academic, New York).

Johnson, D. L. (**1999**). ''Nonlinear pulse propagation in arbitrary dispersive media: Tube waves in permeable formations,'' J. Acoust. Soc. Am. **105**, 3087–3096.

Johnson, D. L., Kostek, S., and Norris, A. N. (**1994**). ''Nonlinear tube waves,'' J. Acoust. Soc. Am. **96**, 1829–1843.

Liu, H.-L., and Johnson, D. L. (**1997**). ''Effects of an elastic membrane on tube waves in permeable formations,'' J. Acoust. Soc. Am. **97**, 3322–3329.

Pampuri, F., Rovellini, M., Brie, A., and Fukusima, T. (**1998**). ''Effective evaluation of fluid mobility from Stoneley waves using full Biot model inversion: Two case histories,'' in SPE Annual Technical Conference and Exhibition, Paper 49132, New Orleans (SPE, Richardson, TX).

Winkler, K. W., Liu, H.-L., and Johnson, D. L. (**1989**). ''Permeability and borehole Stoneley waves: Comparison between experiment and theory,'' Geophysics **54**, 66–75.

Levitation force induced by pressure radiation in gas squeeze films

Adi Minikes[a] and Izhak Bucher[b]
Dynamics Laboratory, Faculty of Mechanical Engineering, Israel Institute of Technology, Technion, Haifa 32000, Israel

Shimon Haber[c]
Faculty of Mechanical Engineering, Israel Institute of Technology, Technion, Haifa 32000, Israel

(Received 24 July 2003; revised 7 February 2004; accepted 19 April 2004)

An analytical and numerical study on the levitation force induced by pressure radiation in gas squeeze films is investigated. The levitation phenomenon is known to occur when a planar object is placed at close proximity to a vibrating piston. The existing analytical approaches are based on either conventional acoustic radiation, where the fluid is assumed inviscid or on a variant of the Reynolds equation that incorporates viscous effects. Alas, these solutions are often in poor agreement with accurate numerical results and, at best, describe appropriately cases that include a limited range of object weights and vibration frequencies. In this work, two cases are addressed: the flow induced by vibrations perpendicular to a flat surface and that by flexural wave propagation parallel to the surface. For the first case, numerical and second-order analytical perturbation solutions are obtained and compared, proving them to be in good agreement. In addition, a novel, analytical expression for the levitation force is also suggested that proves to be valid for a wider physical range of squeeze numbers and vibration amplitudes. For the second and more complex case (recently used in noncontacting transportation systems where the driving surface exhibited flexural traveling waves), the skin-friction force exerted on the flat surface is derived analytically based on a first-order perturbation solution, and the levitation force is analyzed numerically. Some insights on the physical behavior are then highlighted and discussed.
[DOI: 10.1121/1.1760110]

PACS numbers: 43.25.Uv, 43.25.Op [MFH] Pages: 217–226

I. INTRODUCTION

The near field acoustic levitation phenomenon, where planar objects are being levitated when brought close to a vibrating piston, has been carried out by several studies in the past (e.g., Refs. 1–6). More recently, the acoustic levitation effect was applied in noncontacting linear transportation systems[7–10] where a combination of normal and lateral motions was observed. Such a combination is of fundamental importance if the transportation of objects without any direct contact with the driving surface is desired.

Normal levitation occurs when a planar target is placed in the path of an unbounded acoustic beam, the time average pressure (often referred to as the Langevin radiation pressure) exerted on the target, creates a levitation force which is related to variation in acoustic impedance with time. The levitated planar object acts as a reflector and the closer the object approaches the radiating source the larger the levitation force becomes. This is different from the conventional acoustic levitation of small objects (such as drops), where the levitation takes place near the nodes of standing pressure waves that are formed between a radiating source and a reflector.

Hashimoto *et al.*[1] provided a simplified mathematical formulation by which the levitation force based on the acoustic radiation theory presented by Chu *et al.*[2] was calculated for a one-dimensional field. Nomura *et al.*[4] numerically analyzed a two-dimensional axisymmetric pressure field, solving the continuity and momentum equations for adiabatic conditions. The disagreement between the numerical results[4] and the analytical solution[1] was attributed to energy leakages in the peripheries of the levitated object, not accounted for by the one-dimensional model.

A different approach for obtaining the pressure field was suggested by Langlois[11] who performed an order of magnitude analysis of the continuity, momentum, and energy equations to derive the nonlinear, incompressible, and isothermal Reynolds equations for the fluid layer (squeeze film) between two normal vibrating surfaces. Langlois[11] was not concerned with radiation pressure since he dealt with an incompressible medium. Salbu,[5] however, studied experimentally a compressible squeeze film and solved analytically the Reynolds equation using mass conservation across the boundaries. Such a solution introduces a discontinuity of the pressure field at the boundaries and, therefore, is limited to cases where a relatively large amount of energy is introduced into the medium, i.e., for large squeeze numbers (this will be explained in detail in the next section).

Lateral motion accompanied with normal levitation[7–10] occurs when the oscillatory motion between two surfaces, creates traveling waves. Such a lateral motion is the result of

[a]Electronic mail: minikes@technion.ac.il
[b]Author to whom correspondence should be addressed. Electronic mail: bucher@technion.ac.il
[c]Electronic mail: mersh01@tx.technion.ac.il

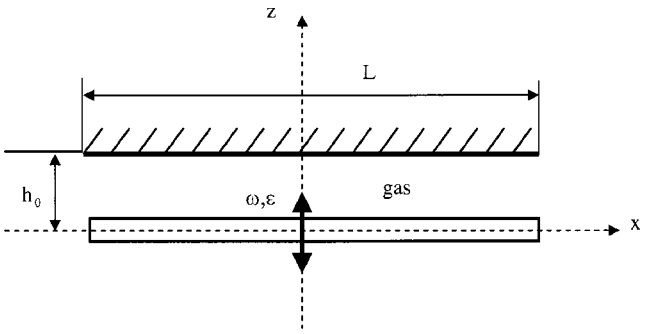

FIG. 1. Schematic layout of the problem.

wall shear stresses and the nonuniform lateral pressure gradients. Since the shear forces are related to the viscosity of the medium, acoustic theories for inviscid fluids must be accompanied with the theory of acoustic streaming.

In the present paper, we begin with a brief discussion of the Reynolds equation, examine previous solutions, and discuss their restrictions. Next, we study an analytical solution for the radiation pressure generated by the normal vibration of a flat piston. A perturbation approach is used, in combination with the mass conservation equation. Finally, we investigate the case which incorporates a driving surface that includes flexural traveling waves. A first-order perturbation scheme is used to obtain the shear stresses force exerted on the surface, whereas for the levitation force a numerically study is performed.

II. STATEMENT OF THE PROBLEM

Consider the case illustrated in Fig. 1 where a flat surface is placed at a mean distance h_0 from a flat plane of width (L) and of a much larger length. The driving surface oscillates at a frequency ω and amplitude $\varepsilon h_0(\varepsilon<1)$. The vibrating surface squeezes the compressible fluid that occupies the clearance between the planes, generating a time average pressure higher than the surrounding. This load-carrying phenomenon arises from the fact that the viscous flow is not instantaneously squeezed out from the clearance giving rise to a cushioning effect.

The nondimensional Reynolds number could be estimated by $\mathrm{Re}=\rho\omega h_0^2/\mu$. For typical values (in M.K.S. units) of the physical parameters in this problem density $\rho \approx O(1)$, $\omega\approx O(10^4)$, $h_0\approx O(10^{-5})$, and viscosity $\mu \approx O(10^{-5})$, the Reynolds number is of order $\mathrm{Re} \approx O(10^{-1})$, suggesting that the fluid inertia is negligible in comparison to viscous forces.

The fluid velocity normal to the surfaces is of the order of $h_0\varepsilon\omega$ and the fluid velocity tangent to the surface is of order $L\omega\varepsilon$. Hence, since $L\gg h_0$, the normal velocity is negligibly small compared with the gas velocity in the lateral direction. Performing an order of magnitude analysis, the differential momentum equation reveals that the pressure gradient in the normal direction is of order h_0/L, which is much smaller than that in the lateral direction (order unity) and, as a consequence, the pressure gradient in the normal direction can be neglected.

We further assume that the squeezed film is isothermal. The latter is a reasonable assumption since the gas film is very thin and of low heat capacity when compared with that of the bearing surfaces. The characteristic time of temperature variations across the squeezed film is approximately given by $t\approx h_0^2/\alpha\approx O(10^{-5}[\mathrm{s}])$ where α is the thermal diffusivity of the gas. This characteristic time is an order of magnitude shorter than that of the periodic oscillation time $1/\omega=O(10^{-4}[\mathrm{s}])$. Therefore the temperature field is nearly uniform across the squeezed film during each time cycle. Moreover, if the bounding surfaces are of uniform temperature, the whole fluid occupying the space between the plates is isothermal.

Integrating the continuity equation across the film thickness and substituting the velocity profile into the momentum equation results in the governing one-dimensional, time-dependent Reynolds equation for laminar, Newtonian, isothermal, and compressible thin film flow:[12]

$$\frac{\partial}{\partial X}\left(H^3P\frac{\partial P}{\partial X}\right)=\sigma\frac{\partial}{\partial T}(PH), \tag{1}$$

where

$$P=\frac{p}{p_a},\quad H=\frac{h}{h_0},\quad X=\frac{x}{L},\quad T=\omega t,\quad \sigma=\frac{12\omega\mu L^2}{p_a h_0^2}.$$

Here, P_a is the ambient pressure, P, H, X, and T are the dimensionless pressure, mean clearance, lateral coordinate, and time, respectively, and σ stands for the squeeze number.

III. FLAT DRIVING SURFACE

Assume that the clearance between the surfaces illustrated in Fig. 1 varies with time according to

$$H(T)=1+\varepsilon\cos(T). \tag{2}$$

Langlois[11] solved Eq. (1) assuming that the pressure field can be expanded as a regular perturbation series in ε:

$$P(X,T)=1+\varepsilon\Pi(X,T)+O(\varepsilon^2). \tag{3}$$

Substituting Eqs. (2) and (3) into Eq. (1) and neglecting terms of order higher than ε^2 results in a linear, inhomogeneous diffusion equation of the form

$$\frac{\partial\Pi}{\partial T}=\frac{1}{\sigma}\frac{\partial^2\Pi}{\partial X^2}+\sin(T)+O(\varepsilon^2). \tag{4}$$

Subjected to ambient pressure ($P=1$) at the initial and boundary conditions,

$$\text{I.C.:}\quad \Pi(X,T=0)=0,\quad \text{B.C.:}\quad \Pi(X=\pm 0.5,T)=0,$$

a steady-state solution of Eq. (4) that oscillates with the excitation frequency is

$$\Pi(X,T)=\Pi_1(X)\cos(T)+\Pi_2(X)\sin(T). \tag{5}$$

Substituting Eq. (5) solution into Eq. (4) and collecting similar terms yields

$$\left(\sigma\Pi_2-\frac{\partial^2\Pi_1}{\partial X^2}\right)\cos(T)=\left(\sigma\Pi_1+\frac{\partial^2\Pi_2}{\partial X^2}+\sigma\right)\sin(T). \tag{6}$$

Since the foregoing equation should hold for all values of T, both sides must vanish identically and Π_1 and Π_2 vanish at $X=\pm 0.5$. Thus, Π_1 and Π_2 are determined by a pair of

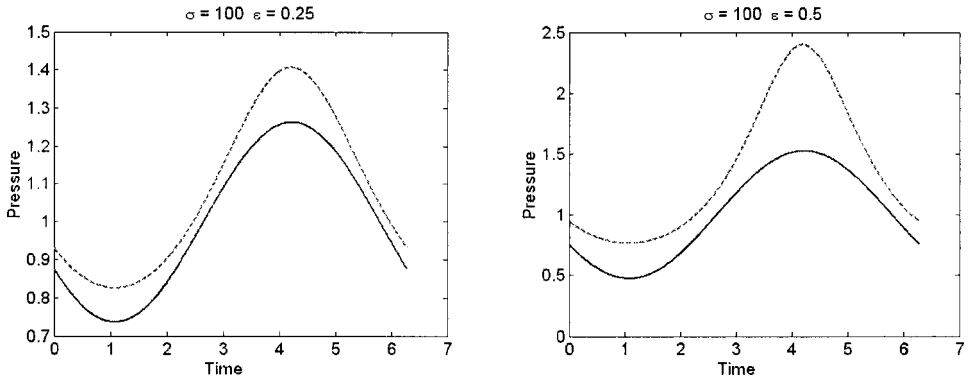

FIG. 2. Pressure change during one time period at the center of the plate; Eq. (6) and the numerical solution are shown by solid and dashed lines, respectively. (a) $\sigma=100$, $\varepsilon=0.25$ and (b) $\sigma=100$, $\varepsilon=0.5$.

coupled differential equations whose solution is[11]

$$\Pi_1(X)=\frac{2}{\cosh(\beta)+\cos(\beta)}\left[\cosh\left(\frac{\beta}{2}\right)\cos\left(\frac{\beta}{2}\right)\cosh(\beta X)\times\cos(\beta X)+\sinh\left(\frac{\beta}{2}\right)\sin\left(\frac{\beta}{2}\right)\times\sinh(\beta X)\sin(\beta X)\right]-1, \tag{7a}$$

$$\Pi_2(X)=\frac{2}{\cosh(\beta)+\cos(\beta)}\left[\sinh\left(\frac{\beta}{2}\right)\sin\left(\frac{\beta}{2}\right)\cosh(\beta X)\times\cos(\beta X)-\cosh\left(\frac{\beta}{2}\right)\cos\left(\frac{\beta}{2}\right)\sinh(\beta X)\sin(\beta X)\right], \tag{7b}$$

where $\beta=\sqrt{\sigma/2}$.

A comparison between this solution [Eq. (5)] and a numerical solution of the Reynolds equation [Eq. (1)] is plotted in Fig. 2. It shows how the pressure at the center of the wall varies over a single time period for two different values of ε. Equation (1) was solved numerically by means of a second-order central-finite differences in space and adaptive time integration.[10] The plots reveal that the solutions are in phase. However, while the numerically calculated average pressure is greater than unity, the analytically approximated one equals exactly to unity (i.e., equals to the ambient pressure). As expected, the numerical solution suggests that the squeeze film levitation phenomenon is related to nonlinear effects associated with higher-order terms of the perturbation solution. The pressure oscillations, obtained numerically, which are not pure cosine functions, also suggest that the solution consists of higher harmonics of the excitation frequency. The differences between the numerical and the analytical solutions decrease as the vibration amplitude (ε) is decreased. Obviously, in the presence of small vibration amplitudes, less energy is delivered into the system and the squeeze effect barely takes place.

Instead of finding the pressure distribution in time and space we could search for a weaker solution by integrating the governing equation with respect to time and space. Salbu[5] utilized this methodology investigating the case of a flat driving surface oscillating in the normal direction. He showed that gaseous squeezed films behave as if they were incompressible at the boundaries and solely compressible in the interior. The size of the interior region increases from zero to the full wall width as σ increases. The interior region behaves like a spring (the pressure in phase with the vibration displacement) and the exterior region behaves like a damper (the pressure becomes proportional to the vibration velocity). Such behavior of a phase shift in the pressure along the film is associated with the energy leakage at the boundaries. Figure 3 shows numerical results of the pressure distribution along the wall as it varies over a time period.

The contours in Fig. 3 represent isobars in the film. The curvature of contours illustrates the phase shift in pressure along the wall. Observing the pressure gradients along the wall indicates that the gas flow takes place mostly near the boundaries, alternating between inward and outward directions. Comparing the two figures 3(a) and 3(b) confirms that the interior region increases with the increase of the squeeze

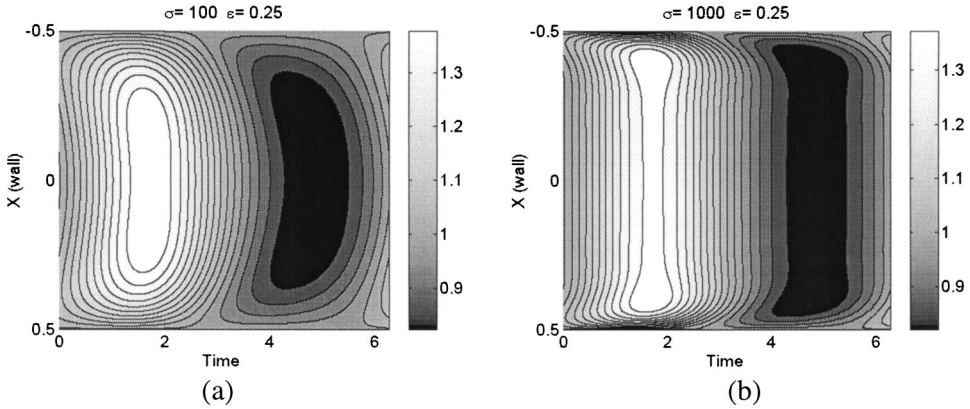

FIG. 3. Numerical results of the pressure distribution along the wall as it varies over a time period for two different squeeze numbers: (a) $\sigma=100$, $\varepsilon=0.25$ and (b) $\sigma=1000$, $\varepsilon=0.25$.

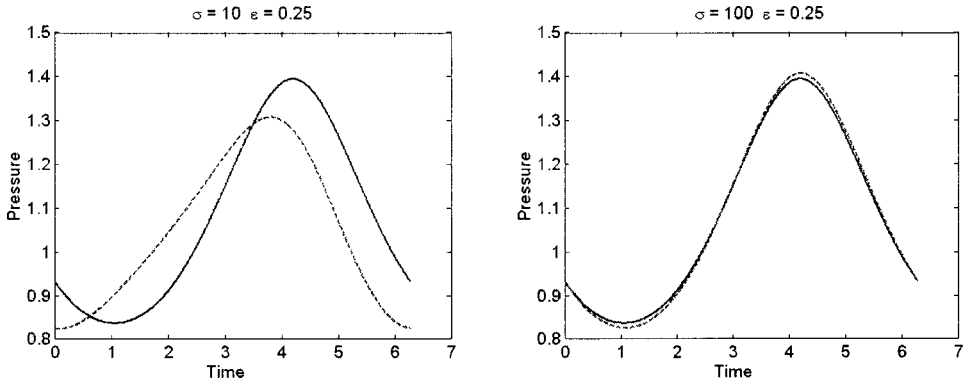

FIG. 4. Change of pressure at the center of the wall during a single time period as obtained by Eq. (12) (solid curves) and numerically (dashed curves): (a) $\sigma=10$, $\varepsilon=0.25$ and (b) $\sigma=100$, $\varepsilon=0.25$.

number and the phase shift in the pressure begins at a closer region to the boundaries.

At high squeeze numbers, virtually no flow occurs at the peripheries of the wall, and the system mimics that of a piston in a closed channel. In such a case and under the isothermal condition assumption, mass conservation yields $PH=C=\text{const}$ [the term $\sigma\partial(PH)/\partial T$ must remain bounded when $\sigma\to\infty$]. This assumption violates the boundary conditions since it introduces a discontinuity in the pressure field. Under this assumption, integrating both sides of Eq. (1) over a time period yields[5]

$$\int_0^{2\pi}\frac{\partial}{\partial X}\left(H^3P\frac{\partial P}{\partial X}\right)dT=\sigma\int_0^{2\pi}\frac{\partial}{\partial T}(PH)\,dT=0. \tag{8}$$

Further integrating with respect to X (from X to $X=0$) reduces the equation to

$$\left[\int_0^{2\pi}H^3P\frac{\partial P}{\partial X}dT\right]_x=\left[\int_0^{2\pi}H^3P\frac{\partial P}{\partial X}dT\right]_{x=0}=\text{const}. \tag{9}$$

Thus, Eq. (9) holds for all values of X. Owing to system's symmetry, the pressure gradient at the center of the wall satisfies the condition $\partial P/\partial X=0$ and, thereby, the constant in Eq. (9) must vanish. Integrating Eq. (9) once again with respect to X (from X to $X=\frac{1}{2}$) yields

$$\left[\int_0^{2\pi}H^3P^2\,dT\right]_x=\left[\int_0^{2\pi}H^3P^2\,dT\right]_{x=1/2}=\text{const}. \tag{10}$$

Since practically no flow takes place at the peripheries of the wall, the assumption of nonleakage of energy permits us to utilize a pressure release boundary condition ($P=1$), and the constant on the rhs of Eq. (10) becomes

$$\text{const}=\int_0^{2\pi}H^3\,dT=\int_0^{2\pi}[1+\varepsilon\cos(T)]^3dT=\pi(2+3\varepsilon^2). \tag{11}$$

Since $PH=C$, where C is determined from Eq. (10) by solving $C^2\int_0^{2\pi}H\,dT=\pi(2+3\varepsilon^2)$, the pressure possesses the form

$$P=\frac{C}{H}=\frac{(1+\frac{3}{2}\varepsilon^2)^{1/2}}{1+\varepsilon\cos(T)}. \tag{12}$$

This mass conservation solution obtained by Salbu[5] is not only independent of the squeeze number σ but also does not incorporate the pressure distribution along the wall. Therefore it would be suitable for cases with large squeeze numbers. An example for realizing the values of such high squeeze numbers is, for instance, the squeeze number for standard atmospheric air under vibration frequency $\omega=4\pi\times10^4$ (rad/s) with a mean clearance $h_0=50\,(\mu\text{m})$ and a bearing width $L=0.1\,(\text{m})$ which results in $\sigma=1000$.

A comparison between this analytical solution [Eq. (12)] and a numerical solution of the governing equation is plotted in Fig. 4, where the change of pressure with time at the center of the wall (at steady state) for two different squeeze numbers is presented. Figure 4 suggests that Salbu's analytical solution for the pressure at the center of the wall, where relative large squeeze numbers exist, correlates well with our numerical solutions. However, examination of the numerical results of the maximum pressure distribution along the wall for different squeeze numbers (as illustrated in Fig. 5) clearly demonstrates that the assumption $PH=\text{const}$ is valid only for high squeeze numbers where the pressure distribution becomes nearly uniform. Under a vibration amplitude of $\varepsilon=0.25$, the maximum pressure value obtained by Eq. (12) is $P=1.395$. This value is plotted in Fig. 5 together with the numerical results.

The estimation of the pressure distribution in Eq. (12) could be enhanced by edge corrections that would satisfy the boundary conditions. Equation (12) assumes uniform pressure distribution along the wall, independent of the squeeze number. On the other hand, the first-order perturbation solu-

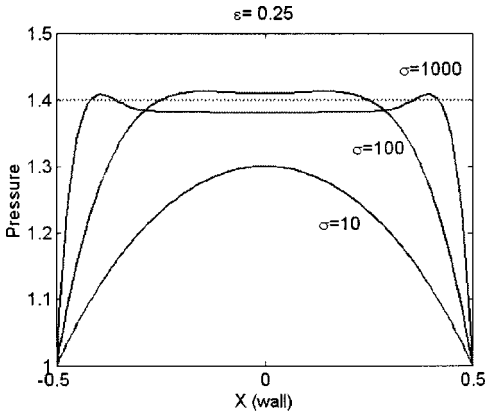

FIG. 5. Numerical results obtained by Eq. (1) for the maximum pressure distribution along the wall for various squeeze numbers (solid curves), and the maximum pressure obtained by Eq. (12) (dotted curve). Here $H(T)=1+0.25\cos(T)$.

tion, Eq. (5), offers an adequate approximation for the relative pressure distribution along the wall at a given moment in time. Consequently, we suggest correcting the conservation mass solution in the following manner:

$$P=1+\left(\frac{(1+\frac{3}{2}\varepsilon^2)^{1/2}}{1+\varepsilon\cos(T)}-1\right)\underset{x}{\mathrm{MAX}}\{\Pi(X,T)\}. \tag{13}$$

The operator MAX means that one should take the largest enveloped shape within the time period. The enveloped shape is, obviously, not time independent but, while time differences may be significant, the value of Eq. (12) is negligibly affected. In order to find this enveloped shape one must find the time $T_{\max}$ where the pressure amplitude is maximal. It appears that for squeeze numbers greater than 20 the two solutions are in phase, therefore allowing us to find the time $T_{\max}$ by solving

$$\frac{\partial}{\partial T}P(T)=\frac{\partial}{\partial T}\left(\frac{(1+\frac{3}{2}\varepsilon^2)^{1/2}}{1+\varepsilon\cos(T)}\right)=0\Rightarrow T_{\max}=\pi. \tag{14}$$

Substituting $T_{\max}=\pi$ into Eq. (5) yields the maximum enveloped shape and consequently the rectified mass conservation solution possesses the form

$$P=1+\left(\frac{(1+\frac{3}{2}\varepsilon^2)^{1/2}}{1+\varepsilon\cos(T)}-1\right)\left(1-2\,\frac{\cosh(\beta/2)\cos(\beta/2)\cosh(\beta X)\cos(\beta X)+\sinh(\beta/2)\sin(\beta/2)\sinh(\beta X)\sin(\beta X)}{\cosh(\beta)+\cos(\beta)}\right). \tag{15}$$

Our proposed correction allows solving analytically the levitation force for a larger range of squeeze numbers than was initially offered by Eq. (12). The dimensionless time averaged levitation force (W) per unit depth at steady state can be expressed by

$$W=\frac{1}{2\pi}\int_0^{2\pi}\int_{-1/2}^{1/2}(P-1)\,dX\,dT, \tag{16}$$

where W is normalized by p_aL.

Figure 6 confirms the agreement between the levitated forces obtained by Eq. (16) and the numerical solution over a large range of the squeeze number. In essence, we have obtained a good agreement between the two solutions for relatively small squeeze numbers in the range where Eq. (12) does not hold. Furthermore, the corrected solution [Eq. (15)] holds for relatively large amplitudes (ε) while the second-order perturbation solution does not (as will be shown next).

So far, we have shown that the first order perturbation solution cannot predict the levitation force. A second-order solution, accounting for nonlinear effects, may be more successful. Assume that the deviation from the ambient pressure is expanded up to order ε^2 terms as follows,

$$P(X,T)=1+\varepsilon\Pi_A(X,T)+\varepsilon^2\Pi_B(X,T)+O(\varepsilon^2). \tag{17}$$

Substituting Eq. (17) together with $H(T)=1+\varepsilon\cos(T)$ into Eq. (1) gives

$$\sigma\frac{\partial\Pi_A}{\partial T}=\frac{\partial^2\Pi_A}{\partial X^2}+\sigma\sin(T)+O(\varepsilon^2), \tag{18a}$$

$$\sigma\frac{\partial\Pi_B}{\partial T}=\frac{\partial^2\Pi_B}{\partial X^2}+G(\Pi_A)+O(\varepsilon^3), \tag{18b}$$

with

$$\text{I.C.:}\quad \Pi_{A,B}(X,T=0)=0,\quad \text{B.C.:}\quad \Pi_{A,B}(X=\pm 0.5,T)=0,$$

where the forcing term of Eq. (18b) possesses the simplified form

$$G(\Pi_A)=\frac{1}{\sigma}\left(\frac{\partial\Pi_A}{\partial X}\right)^2+\frac{\partial\Pi_A}{\partial T}[\Pi_A+2\cos(T)]-\frac{3}{2}\sin(2T). \tag{19}$$

Substituting the first-order perturbation solution Eq. (5) into Eq. (19) results in an expression of the following form:

$$G(\Pi_A)=G_1(X)\cos(2T)+G_2(X)\sin(2T)+A(X), \tag{20}$$

where $G_1(X)$, $G_2(X)$ and $A(X)$ are known functions of X.

A steady-state harmonic solution based on Eq. (20) is

$$\Pi_B(X,T)=\Pi_3(X)\cos(2T)+\Pi_4(X)\sin(2T)+\Pi_5(X). \tag{21}$$

Substituting this solution into Eq. (18b) and performing harmonic balancing results in

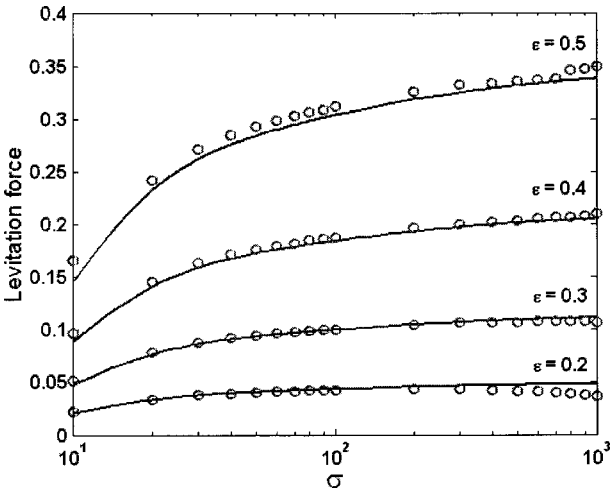

FIG. 6. Time averaged levitation force versus squeeze number (σ) for different vibration amplitudes (ε). Solid curves—Eq. (16). Circles—numerical solution.

$$\left(2\sigma\Pi_4-\frac{\partial^2\Pi_3}{\partial X^2}+\sigma G_1(X)\right)\cos(2T)$$
$$=\left(2\sigma\Pi_3+\frac{\partial^2\Pi_4}{\partial X^2}+\sigma G_2(X)\right)\sin(2T)$$
$$+\left(\frac{\partial^2\Pi_5}{\partial X^2}+A(X)\right). \tag{22}$$

Integrating over a time period, the lhs and the first term on the rhs vanish. The second term on the rhs is not a function of time and, therefore, must vanish identically:

$$\frac{\partial^2\Pi_5}{\partial X^2}+A(X)=0, \quad \text{B.C.:} \quad \Pi_5(X=\pm 0.5,T)=0. \tag{23}$$

A solution of Eq. (23) would eventually provide the difference between the time-averaged pressure in the squeeze film and the ambient pressure. The solution for $\Pi_5(X)$ is given by

$$\Pi_5(X)=\frac{1}{4\cos(\beta)+4\cosh(\beta)}\left[5\cosh(\beta)+5\cos(\beta)\right.$$
$$-\cosh(2\beta X)-\cos(2\beta X)-4\cos\left(\beta X-\frac{\beta}{2}\right)$$
$$\times\cosh\left(\beta X+\frac{\beta}{2}\right)-4\cos\left(\beta X+\frac{\beta}{2}\right)$$
$$\left.\times\cosh\left(\beta X-\frac{\beta}{2}\right)\right]. \tag{24}$$

Utilizing Eq. (16), the time-averaged levitation force per unit depth is

$$W=\frac{1}{2\pi}\int_0^{2\pi}\int_{-1/2}^{1/2}(P-1)dX\,dT=\int_{-1/2}^{1/2}\varepsilon^2\Pi_5(X)dX, \tag{25}$$

$$W=\frac{5\varepsilon^2}{4\beta}\left[\frac{\beta\cos(\beta)+\beta\cosh(\beta)-\sinh(\beta)-\sin(\beta)}{\cos(\beta)+\cosh(\beta)}\right].$$

Figure 7 compares between the time-averaged levitation forces obtained by Eq. (25) and that of the rectified mass conservation solution [Eq. (16)]. It shows that for vibration amplitudes, up to about one-third of the mean gap, the second-order perturbation solution and the corrected mass solution are in good agreement. As expected, with the increase of the vibration amplitude (ε), the agreement deteriorates since third-order terms are no longer negligible and the differences can reach up to 12% for $\varepsilon=0.5$.

IV. TRAVELING WAVE VIBRATIONS

Let us now consider a more complex case illustrated in Fig. 8 where a kinematical flexural traveling wave is brought closely to a wall of width (L) and its (y direction) length is much larger than its width. The traveling wave propagates in the positive x direction with uniform amplitude along the y direction (which is much larger than L), oscillating at frequency (ω), possessing an amplitude (ε) and wavelength (λ).

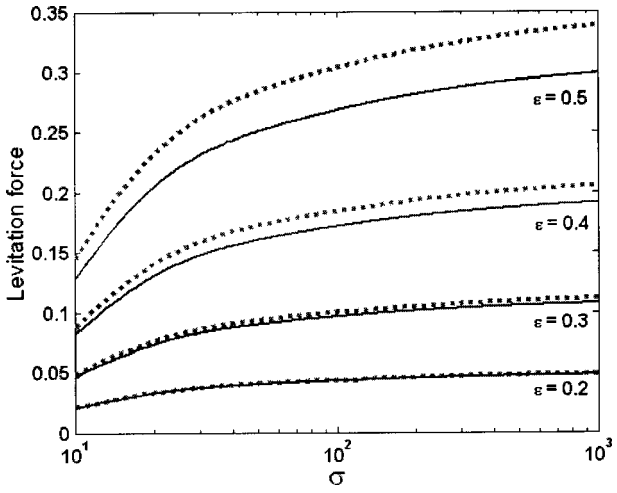

FIG. 7. Time averaged levitation force versus squeeze number (σ) for different vibration amplitudes (ε). Solid curve—Eq. (25). Dotted curves—Eq. (16) with Eq. (15).

The sound field generated by the traveling wave produces two forces acting on the wall surface: the acoustic radiation force acting in the normal direction and the shear force acting in the tangential direction. The viscous shear force results from the gradients in the acoustic streaming velocity at the viscous boundary layer adjacent to the wall surface. This case is of fundamental importance in analyzing noncontacting transportation mechanisms. It is worth distinguishing between the boundary conditions created by a moving wavy surface and a surface experiencing flexural traveling wave. While in the first case, a material point propagates laterally with the surface, in the latter, a material point vibrates in a direction perpendicular to the wave propagation. Consequently, in the case of flexural traveling waves, lateral velocity of the fluid along the wall is a direct result of pressure gradients only. In this case, the clearance between surfaces can be described by

$$H(X,T)=1+\varepsilon\cos(T-kX), \tag{26}$$

where $k=2\pi L/\lambda$ denotes the dimensionless wave number.

A first-order solution is obtained in a similar fashion to that shown in the previous section, namely, assuming that the pressure possesses a regular expansion in ε $P(X,T)=1$

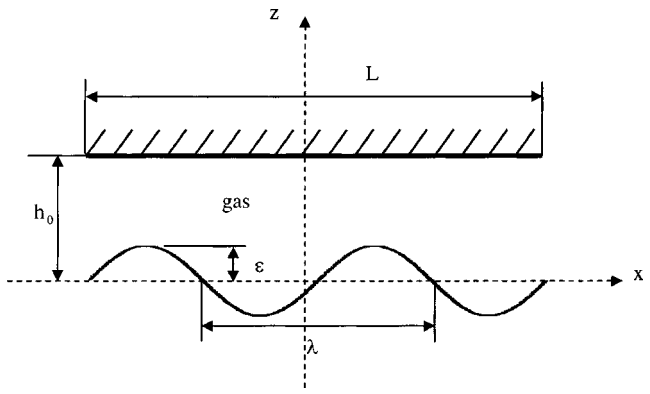

FIG. 8. Schematic layout of the problem.

$+\varepsilon\Pi(X,T)+O(\varepsilon^2)$. The resulting differential equation for the first-order perturbation function Π is a linear, inhomogeneous diffusion equation of the form

$$\frac{\partial \Pi}{\partial T}=\frac{1}{\sigma}\frac{\partial^2 \Pi}{\partial X^2}+\sin(T-kX)+O(\varepsilon^2) \tag{27}$$

subjected to the following initial and boundary conditions,

$$\text{I.C.:}\quad \Pi(X,T=0)=0,\quad \text{B.C.:}\quad \Pi(X=\pm 0.5,T)=0.$$

Again we assume that a steady-state solution of Eq. (27) varies harmonically in time, oscillating with the excitation frequency:

$$\Pi(X,T)=\Pi_1(X)\cos(T)+\Pi_2(X)\sin(T). \tag{28}$$

Substituting Eq. (28) into Eq. (27) and collecting similar terms in time yields

$$\left(\sigma\Pi_2-\frac{\partial^2\Pi_1}{\partial X^2}+\sigma\cos(kX)\right)\cos(T)$$

$$=\left(\sigma\Pi_1+\frac{\partial^2\Pi_2}{\partial X^2}+\sigma\sin(kX)\right)\sin(T). \tag{29}$$

Since Eq. (29) is valid for all values of T, the terms in the (large) parenthesis must vanish identically. Similarly, the boundary conditions are that both Π_1 and Π_2 vanish at $X=\pm 0.5$. Thus, Π_1 and Π_2 are determined by the following pair of coupled differential equations

$$\frac{\partial^2\Pi_1}{\partial X^2}-\sigma\Pi_2-\sigma\sin(kx)=0, \tag{30a}$$

$$\frac{\partial^2\Pi_2}{\partial X^2}+\sigma\Pi_1+\sigma\cos(kx)=0, \tag{30b}$$

and boundary conditions

$$\text{B.C.:}\quad \Pi_1(X=\pm 0.5,T)=\Pi_2(X=\pm 0.5,T)=0.$$

Equations (30a) and (30b) can be combined into a single second-order equation of the complex variable $\Phi=(\Pi_1-i\Pi_2)$ with boundary conditions $\Phi(X=\pm 0.5,T)=0$. The solution of Φ possesses the general form

$$\Phi=\frac{2\beta^2}{i2\beta^2+k^2}\left(\frac{\sin(k/2)\sin(\beta X-i\beta X)}{\sin((\beta-i\beta)/2)}-\sin(kX)\right.$$
$$\left.+\frac{i\cos(k/2)\cos(\beta X-i\beta X)}{\cos([\beta-i\beta]/2)}-i\cos(kX)\right), \tag{31}$$

where here, as before, $\beta=\sqrt{\sigma/2}$ and $i=\sqrt{-1}$.

Equation (31) degenerates into Eqs. (7a) and (7b) when setting the wavelength to infinity ($k\to 0$) and thus serves as a generalization of the results in Ref. 11. The first-order perturbation solution in Eq. (31) is valid for incompressible fluids and for low squeeze numbers (as compressibility effects are negligible). This solution may be rewritten in the form

$$\Pi_1(X)=\Phi_1\sin(\beta X)\cosh(\beta X)+\Phi_2\cos(\beta X)\sinh(\beta X)$$
$$+\Phi_3\cos(\beta X)\cosh(\beta X)$$
$$+\Phi_4\sin(\beta X)\sinh(\beta X)+\Phi_5\cos(kX)$$
$$+\Phi_6\sin(kX), \tag{32a}$$

$$\Pi_2(X)=-\Phi_2\sin(\beta X)\cosh(\beta X)+\Phi_1\cos(\beta X)$$
$$\times\sinh(\beta X)+\Phi_4\cos(\beta X)\cosh(\beta X)$$
$$-\Phi_3\sin(\beta X)\sinh(\beta X)-\Phi_6\cos(kX)$$
$$+\Phi_5\sin(kX), \tag{32b}$$

where

$$\Phi_1=\frac{2\beta^2}{\Delta_1}\left[k^2\sin\left(\frac{\beta}{2}\right)\cosh\left(\frac{\beta}{2}\right)\right.$$
$$\left.+2\beta^2\cos\left(\frac{\beta}{2}\right)\sinh\left(\frac{\beta}{2}\right)\right]\sin\left(\frac{k}{2}\right),$$

$$\Phi_2=\frac{2\beta^2}{\Delta_1}\left[k^2\cos\left(\frac{\beta}{2}\right)\sinh\left(\frac{\beta}{2}\right)\right.$$
$$\left.-2\beta^2\sin\left(\frac{\beta}{2}\right)\cosh\left(\frac{\beta}{2}\right)\right]\sin\left(\frac{k}{2}\right),$$

$$\Phi_3=\frac{2\beta^2}{\Delta_2}\left[2\beta^2\cos\left(\frac{\beta}{2}\right)\cosh\left(\frac{\beta}{2}\right)\right.$$
$$\left.+k^2\sin\left(\frac{\beta}{2}\right)\sinh\left(\frac{\beta}{2}\right)\right]\cos\left(\frac{k}{2}\right),$$

$$\Phi_4=\frac{2\beta^2}{\Delta_2}\left[2\beta^2\sin\left(\frac{\beta}{2}\right)\sinh\left(\frac{\beta}{2}\right)\right.$$
$$\left.-k^2\cos\left(\frac{\beta}{2}\right)\cosh\left(\frac{\beta}{2}\right)\right]\cos\left(\frac{k}{2}\right),$$

$$\Phi_5=-\frac{4\beta^4}{4\beta^4+k^4},\quad \Phi_6=-\frac{2\beta^2k^2}{4\beta^4+k^4},$$

$$\Delta_1=(4\beta^4+k^4)\left[\cosh\left(\frac{\beta}{2}\right)^2-\cos\left(\frac{\beta}{2}\right)^2\right],$$

$$\Delta_2=(4\beta^4+k^4)\left[\cosh\left(\frac{\beta}{2}\right)^2+\cos\left(\frac{\beta}{2}\right)^2-1\right].$$

Figures 9(a) and 9(b) compares an example of pressure distribution along the wall over one time period obtained by the first-order solution in Eq. (32) and a numerical solution of Eq. (1). The inclination angle of the contours in Figs. 9(a) and 9(b) are formed as a result of the wave propagation. This inclination angle will decrease with the increase of the wavelength (increase of the propagation velocity of the wave) until it reaches the field described in Fig. 3(a). The plots in Figs. 9(a) and 9(b) are for a flexural wave, traveling from $X=-0.5$ to $X=0.5$. It is clearly seen that the absolute pressure values increase along the wall in the direction of the traveling wave, therefore introducing a moment on the wall. Furthermore, while the nominal values of the pressure field in Fig. 9(b) are slightly higher than those shown in Fig. 9(a), due to the pressure radiation, the pressure gradients along the wall are comparable, suggesting that the first-order solution may offer a good approximation for the pressure distribution along the wall. The shear stresses experienced in the flow are proportional to the lateral pressure gradients. Hence we seek to obtain an approximated analytical expression for the shear

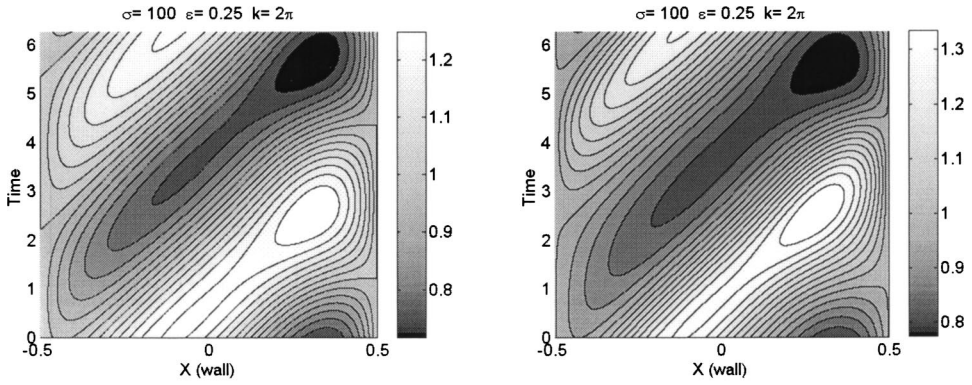

FIG. 9. Pressure distribution along the wall over one time period for $\sigma=100$, $\varepsilon=0.25$, $k=2\pi$. (a) First-order solution Eq. (32). (b) Numerical solution of Eq. (1).

stress exerted on the wall, based on the pressure first-order solution.

Solving the momentum equation in the X direction, assuming that the inertia terms can be neglected and that the velocity adheres to the walls, yields

$$v_x=\frac{z}{2\mu}\frac{\partial p}{\partial x}(z-h). \tag{33}$$

The shear stress on the wall becomes

$$\tau_{zx}|_{z=h}=\mu\left.\frac{\partial v_x}{\partial z}\right|_{z=h}=\frac{h}{2}\frac{\partial p}{\partial x} \tag{34}$$

and the dimensionless time averaged shear force per unit depth exerted on the wall at steady state is

$$F=-\frac{1}{2\pi}\int_0^{2\pi}\int_0^1 H\frac{\partial P}{\partial X}dX\,dT. \tag{35}$$

Here, F is normalized by $h_0p_a/2$.

Substituting Eq. (3) together with Eqs. (5) and (32) into Eq. (35) derives the first-order solution for the time average shear force on the wall (F) as a function of wave number, squeeze number, and vibration amplitude:

$$F=\frac{-\varepsilon^2}{16\beta^4+4k^4}\left\{\left[C_1\sin\left(\frac{\beta}{2}\right)\sinh\left(\frac{\beta}{2}\right)+C_2\cos\left(\frac{\beta}{2}\right)\times\cosh\left(\frac{\beta}{2}\right)\right]\sin\left(\frac{k}{2}\right)+\left[C_3\cos\left(\frac{\beta}{2}\right)\sinh\left(\frac{\beta}{2}\right)+C_4\sin\left(\frac{\beta}{2}\right)\cosh\left(\frac{\beta}{2}\right)\right]\cos\left(\frac{k}{2}\right)+C_5\right\}, \tag{36}$$

where

$$C_1=(8\beta^3k+4\beta k^3)\Phi_1+(8\beta^3k-4\beta k^3)\Phi_2-16\beta^4\Phi_3-8\beta^2k^2\Phi_4,$$

$$C_2=(4\beta k^3-8\beta^3k)\Phi_1+(8\beta^3k+4\beta k^3)\Phi_2-8\beta^2k^2\Phi_3+16\beta^4\Phi_4,$$

$$C_3=8\beta^2k^2\Phi_1+16\beta^4\Phi_2+(4\beta k^3-8\beta^3k)\Phi_3-(8\beta^3k+4\beta k^3)\Phi_4,$$

$$C_4=16\beta^4\Phi_1-8\beta^2k^2\Phi_2+(8\beta^3k+4\beta k^3)\Phi_3+(4\beta k^3-8\beta^3k)\Phi_4,$$

$$C_5=2k^5\Phi_6+8k\beta^4\Phi_5.$$

Comparison between the time-averaged shear force obtained analytically with Eq. (36) and the one obtained numerically by solving Eq. (1) is presented in Fig. 10. The plot shows an agreement between the solutions for different vibration amplitudes (ε) as a function of the wave number (k) for squeeze number $\sigma=100$. The results confirm that for cases where the vibration amplitudes do not exceed about one-third of the mean clearance ($\varepsilon=0.3$), the first-order perturbation solution provides a good approximation for the time-averaged shear force.

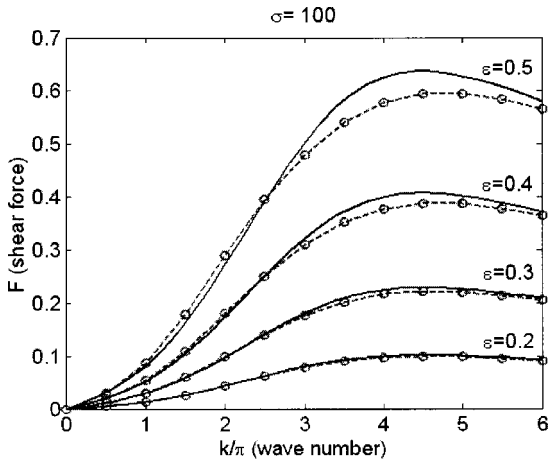

FIG. 10. Time averaged shear force exerted on the wall as function of the wave number for different vibration amplitudes, obtained analytically (solid curves) and numerically (circles). Here $\sigma=100$.

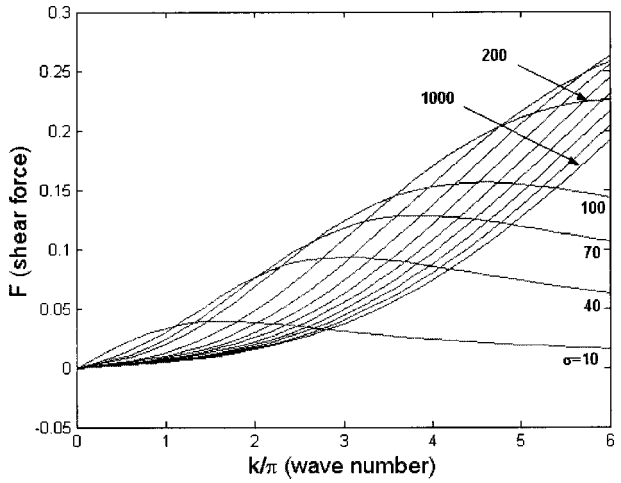

FIG. 11. Shear force exerted on the wall as a function of the wave number (k) for different values of squeeze numbers (σ), obtained by Eq. (36) provided $H(X,T)=1+0.25\cos(T-kX)$.

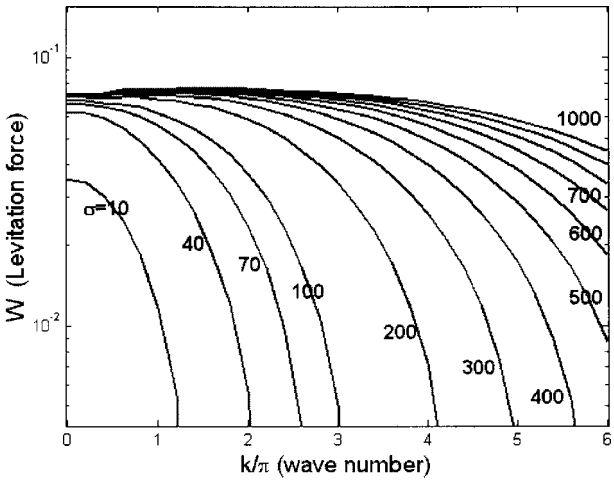

FIG. 12. Numerical results of the change of levitation force (W) with the increase of the wave number (k) for different values of squeeze numbers (σ) with $H(X,T)=1+0.25\cos(T-kX)$.

Figure 11 depicts the dependence of time-averaged shear force on the wave number, for various values of squeeze numbers and for wave amplitude $\varepsilon=0.25$. It manifests that each curve pertaining to a particular squeeze number possesses a maximum that shifts up and to the right with an associated increase of the squeeze number. That a maximum value must exist can be explained by examining the behavior at two extreme cases. When the wave number is zero, the pressure along the wall is symmetric with respect to the surface center and, consequently, no net shear force is exerted. On the other hand, when the wave number approaches infinity, the velocity of the propagating wave approaches to zero and the driving surface is nearly symmetric (with respect to the center), once again no net shear force is being generated.

Trying to enhance our solution by adding a second-order perturbation requires tedious manipulations of very long analytical expressions in trying to solve Eq. (23) for $\Pi_5(X)$. Consequently, this approach loses its appeal as a vehicle for gaining a better understanding of the governing parameters. Alternatively, we may apply the mass conservation method in a manner similar to that of the former case, resulting in

$$P=\frac{C}{H}=\frac{(1+\frac{3}{2}\varepsilon^2)^{1/2}}{1+\varepsilon\cosh(T-kX)}. \tag{37}$$

Although this solution depends explicitly on X and the wave number, the mean levitation force over a time period depends only on (ε), since the term kX is merely a phase shift. Therefore, Eq. (37) can only account for the case of traveling waves for extremely large values of σ(over 5000).

A numerical study was performed for the levitation force introduced by pressure radiation. Figure 12 presents the change of levitation force with wave number for different values of squeeze numbers and for a wave amplitude $\varepsilon=0.25$. It clearly shows that as the wave number increases (or the wave length decreases), the levitation force decreases. This is reasonable since while some regions experience compression others experience expansion, thus reducing the effective squeeze area.

The last two figures suggest that one may encounter difficulties when attempting to optimize the working parameters that would yield a maximum shear force together with a maximum levitation force. It appears that the maximum shear force on the wall occurs at wave numbers larger than those able to sustain significant levitation force for a given squeeze number.

V. CONCLUSIONS

The pressure field between a wall and a near-vibrating surface was investigated in order to obtain expressions for the pressure radiation and the shear forces acting on the wall. A novel and concise analytical expression for the time-averaged levitation force was developed and was shown to be more suitable over a wider range of squeeze numbers and vibration amplitudes than that obtained by a second-order perturbation solution. In the presence of flexural traveling waves, a first-order perturbation solution for the time-averaged shear force exerted on the wall was derived, proving to be suitable in cases where the wave amplitude does not exceed one-third of the mean clearance. Analysis of the shear-force reveals a maximum value, which depends on the wave number and the squeeze number. For this maximum shear force, at a given squeeze number, the levitation force becomes insignificant, hence, one is forced to use an intermediate operational range for simultaneous levitation and transportation. Numerical results show that the larger the wave number, the more energy is required (large squeeze numbers) for sustaining significant levitation force. In search for an analytical solution, the levitated object was considered as a rigid clamped wall in order to avoid the coupling of the object's dynamical equations with the Reynolds equation. In practice, for flat driving surfaces, according to experimental and numerical results,[4,6] this assumption holds as the vibration amplitudes of the levitated object are two orders of magnitude smaller than those of the driving surface. However, in the presence of flexural traveling waves, this assumption may not be valid since alternating moments, induced by the film, may cause the levitated object to tilt harmonically

around an average attack angle while propagating.[10] Still, we believe that the presented analysis clarifies the physical mechanisms underling the levitation phenomena in the presence of traveling waves.

[1] Y. Hashimoto, Y. Koike, and S. Ueha, ''Near-field acoustic levitation of planar specimens using flexural vibration,'' J. Acoust. Soc. Am. **100**, 2057–2061 (1996).

[2] B. T. Chu and R. E. Apfel, ''Acoustic radiation pressure produced by beam of sound,'' J. Acoust. Soc. Am. **72**, 1673–1687 (1982).

[3] C. P. Lee and T. G. Wang, ''Acoustic radiation pressure,'' J. Acoust. Soc. Am. **94**, 1099–1109 (1993).

[4] H. Nomura, T. Kamakura, and K. Matsuda, ''Theoretical and experimental examination of near-field acoustic levitation,'' J. Acoust. Soc. Am. **111**, 1578–1583 (2002).

[5] E. O. J. Salbu, ''Compressible squeeze films and squeeze bearings,'' J. Basic Eng. **86**, 355–366 (1964).

[6] A. Minikes and I. Bucher, ''Coupled dynamics of a squeeze-film levitated mass and a vibrating piezoelectric disc—numerical analysis and experimental study,'' J. Sound Vib. **263**(2), 241–268 (2003).

[7] Y. Hashimoto, Y. Koike, and S. Ueha, ''Transporting objects without contact using flexural travelling waves,'' J. Acoust. Soc. Am. **103**, 3230–3233 (1998).

[8] S. Ueha, Y. Hashimoto, and Y. Koike, ''Non-contacting transportation using near-field acoustic levitation,'' Ultrasonics **38**, 26–32 (2000).

[9] J. Hu, G. Li, H. L. W. Chan, and C. L. Choy, ''A standing wave-type nonconctact linear ultrasonic motor,'' IEEE Trans. Ultrason. Ferroelectr. Freq. Control **48**(3), 699–708 (2001).

[10] A. Minikes and I. Bucher, ''Noncontacting lateral transportation using gas squeeze film generated by flexural traveling waves-Numerical analysis,'' J. Acoust. Soc. Am. **113**, 2464–2473 (2003).

[11] W. E. Langlois, ''Isothermal squeeze films,'' Q. Appl. Math. **XX**(2), 131–150 (1962).

[12] W. A. Gross, *Gas Film Lubrication* (Wiley, New York, 1962).

Travel-time sensitivity kernels in ocean acoustic tomography

E. K. Skarsoulis[a)]
Institute of Applied and Computational Mathematics, Foundation for Research and Technology Hellas, P.O. Box 1527, 711 10 Heraklion, Crete, Greece

B. D. Cornuelle
Scripps Institution of Oceanography, University of California, San Diego, 9500 Gilman Drive, La Jolla, California 92093-0230

(Received 22 December 2003; revised 29 March 2004; accepted 29 March 2004)

Wave-theoretic ocean acoustic propagation modeling is combined with the peak arrival approach for tomographic travel-time observables to derive the sensitivity kernel of travel times with respect to sound-speed variations. This is the Born–Fréchet kernel relating the three-dimensional spatial distribution of sound-speed variations with the induced travel-time variations. The derivation is based on the first Born approximation of the Green's function. The application of the travel-time sensitivity kernel to an ocean acoustic waveguide gives a picture close to the ray-theoretic one in the case of high frequencies. However, in the low-frequency case, of interest in ocean acoustic tomography, for example, there are significant deviations. Low-frequency travel times are sensitive to sound-speed changes in Fresnel-zone-scale areas surrounding the eigenrays, but not on the eigenrays themselves, where the sensitivity is zero. Further, there are areas of positive sensitivity, where, e.g., a sound-speed increase results in an increase of arrival times, i.e., a further delay of arrivals, in contrast with the common expectation. These findings are confirmed by forward acoustic predictions from a coupled-mode code.
[DOI: 10.1121/1.1753292]

PACS numbers: 43.30.Pc, 43.30.Bp [AIT] Pages: 227–238

I. INTRODUCTION

Ocean acoustic tomography was introduced by Munk and Wunsch[1,2] as a remote-sensing technique for large-scale monitoring of the ocean interior using low-frequency sound. Measuring the travel/arrival times of pulsed acoustic signals propagating from a source to a distant receiver through the water mass over a multitude of different paths, and exploiting the knowledge about how travel times are affected by the sound-speed (temperature) distribution in the water, the latter can be obtained by inversion.

Ray-theoretic modeling has been the most common approach in ocean acoustic tomography, so arrival times are modeled as travel times along eigenrays connecting the source and receiver (ray arrivals).[3,4] Their variations are associated with variations of the sound speed along the geometric ray paths, forming the basis of the corresponding inversion scheme (ray tomography). Geometric ray theory is simple to apply and also provides a kernel with which to invert from travel time perturbation to ocean perturbation. Nevertheless, it is a high-frequency asymptotic approximation and suffers from limitations in low-frequency applications.[5] Although the underlying acoustic propagation is linear, geometric ray paths are solutions of the nonlinear eikonal equation, and can be chaotic at long ranges in realistic mediums, which makes them hard to produce and difficult to interpret.[6] Acousticians have long recognized that the infinitely thin geometric ray paths are a limiting case, and the true ray sampling is spread over a region comparable to the Fresnel zone.[7] In an attempt to improve ray-theoretic predictions, Bowlin[8] gave wave-theoretic formulas for ray tube widths, based on single scattering theory. As an alternative to ray-theoretic modeling of travel times, wave-theoretic approaches have been proposed, such as the modal arrival[9,10] and the peak arrival approach.[11,12]

The present work applies wave-theoretic modeling to obtain the three-dimensional (3-D) sensitivity kernel of travel-time observables for finite-frequency transmissions in ocean acoustic tomography. The travel-time sensitivity kernel (TSK) is the Born–Fréchet kernel of the linear (first-order) integral representation of travel-time variations in terms of the spatial distribution of sound-speed variation.[13,14] It represents the 3-D spatial distribution of sensitivity of arrival times to sound-speed variations. In the ray approximation this distribution degenerates into a weakly varying sensitivity along the eigenray corresponding to a particular arrival. This means that ray arrival times are sensitive to medium changes only along the geometric ray paths connecting the source and receiver. The wave-theoretic results approach this approximation only in the high-frequency case, whereas for lower frequencies the ray-theoretic model may be an oversimplification.

In seismic tomography the application of 3-D full-wave theory for travel-time modeling of finite-frequency seismic waves has changed the ray-theoretic picture[15,16] by revealing that low-frequency travel times are sensitive to sound-speed changes in areas surrounding the eigenrays, but not at all to changes taking place on the eigenrays: the wave-theoretic travel-time sensitivity kernels for seismic travel times attain their maximum at a distance from the eigenrays, within the

a)Electronic mail: eskars@iacm.forth.gr

first Fresnel zone, whereas the sensitivity is zero on the eigenrays themselves. Due to their shape, resembling that of a hollow banana, these kernels are often called banana-doughnut kernels in the seismic literature. Furthermore, there are areas of positive sensitivity where a sound-speed increase slows down (rather than advances) the seismic wave. A distribution-theoretic analysis of the sensitivity kernel in seimic tomography[17] revealed that the unperturbed eigenrays are contained in the support of the kernel even though its finite-bandwidth regularization may show a vanishing contribution on the eigenrays in odd dimensions; in this context the medium perturbations should be viewed as test functions on which the kernel acts.

The results from seismic wave propagation motivated the present study of travel-time sensitivity kernels for ocean acoustic propagation, in connection with ocean acoustic tomography. Even though there are significant differences in the definition and processing of travel-time observables in seismic[18] and ocean acoustic tomography,[2,11] the results obtained here exhibit similarities to those reported in the seismic literature, the more striking ones being the zero sensitivity on the eigenrays and the emergence of areas of positive sensitivity at the boundary of the first Fresnel zone about the eigenrays. Instances of positive sensitivity have been reported before in numerical/forward studies of modal travel times in range-independent ocean environments.[19] These findings suggest that, especially in the low-frequency case, geometric ray modeling may lead to interpretation errors and its replacement by full-wave modeling has to be considered.

If the ocean perturbations (or models of ocean perturbations, in the case of tomographic inversions) are smooth, then the structure in the kernel averages out and the difference from ray theory will be small. However, for smaller-scale sound-speed structures such as the seasonal thermocline, or model parametrizations based on sharp-edged elements such as layers or boxes, the differences will be significant. For example, in a layered inverse model the ray sensitivity will be large or zero depending on whether the ray touches a particular layer; the forward model can therefore change as the ray path evolves with changing sound speed structure, complicating the inverse. In these cases the wave-theoretic kernel can reduce the difficulties or nonlinearities associated with these models; a smoother kernel should reduce nonlinearities in models with vertical or horizontal scales comparable to Fresnel zone scales.

The contents of this work are organized as follows. In Sec. II we deal with the Green's function for ocean acoustic propagation and its perturbations in the Born approximation. In Sec. III the problem of travel-time modeling in ocean acoustic tomography is addressed. Using the notion of peak arrivals and the Born approximation, an expression is derived for the three-dimensional travel-time sensitivity kernel of finite-frequency tomographic transmissions. In Sec. IV we present some numerical results for the travel-time sensitivity kernel based on normal-mode propagation modeling. Finally, Sec. V contains a discussion of results and main conclusions from this work. An explanation for the regimes of zero, positive, and negative travel-time sensitivity in free space is given in Appendix A. Further, an expression for the (one-dimensional) vertical sensitivity of peak arrival times is derived in Appendix B.

II. THE GREEN'S FUNCTION

The Green's function $G(\mathbf{r}|\mathbf{r}_s)$ of an ocean acoustic waveguide describes the acoustic field of a harmonic point source of unit strength and satisfies the following inhomogeneous Helmholtz equation:

$$\left[\nabla^2+\frac{\omega^2}{c^2(\mathbf{r})}\right]G(\mathbf{r}|\mathbf{r}_s)=-\delta(\mathbf{r}-\mathbf{r}_s), \tag{1}$$

where $\mathbf{r}$ is the space vector, ω the circular frequency of the source, and $\mathbf{r}_s$ its location, $c(\mathbf{r})$ the sound-speed distribution, and δ the Dirac δ function. The equation above is supplemented by boundary and interface conditions according to which G vanishes at the sea surface whereas pressure and normal velocity are continuous across interfaces, as well as by a radiation condition according to which the field decays away from the source and describes an outgoing wave.[20,21]

If $S(\mathbf{r})$ is a arbitrary source distribution the induced acoustic field $P(\mathbf{r})$ satisfying the inhomogeneous Helmholtz equation,

$$\left[\nabla^2+\frac{\omega^2}{c^2(\mathbf{r})}\right]P(\mathbf{r})=S(\mathbf{r}), \tag{2}$$

and the boundary/interface/radiation conditions mentioned above, can be represented through the Green's function by the integral[22]

$$P(\mathbf{r})=-\int\int\int_V G(\mathbf{r}|\mathbf{r}')S(\mathbf{r}')dV(\mathbf{r}'), \tag{3}$$

i.e., it is a superposition of the acoustic fields of point sources distributed over the support of $S(\mathbf{r})$.

A. Born approximation

A perturbation of the sound-speed distribution in Eq. (1) by Δc will cause a perturbation in the Green's function by ΔG. The perturbed Green's function $G+\Delta G$ will satisfy the equation

$$\left[\nabla^2+\frac{\omega^2}{[c(\mathbf{r})+\Delta c(\mathbf{r})]^2}\right][G(\mathbf{r}|\mathbf{r}_s)+\Delta G(\mathbf{r}|\mathbf{r}_s)] =-\delta(\mathbf{r}-\mathbf{r}_s). \tag{4}$$

By subtracting Eq. (4) from Eq. (1) and adding the term $\omega^2\Delta G/c^2$ to both sides, the following equation is obtained:

$$\left[\nabla^2+\frac{\omega^2}{c^2(\mathbf{r})}\right]\Delta G(\mathbf{r}|\mathbf{r}_s)=-\left[\frac{\omega^2}{[c(\mathbf{r})+\Delta c(\mathbf{r})]^2}-\frac{\omega^2}{c^2(\mathbf{r})}\right] \times[G(\mathbf{r}|\mathbf{r}_s)+\Delta G(\mathbf{r}|\mathbf{r}_s)]. \tag{5}$$

The perturbation ΔG satisfies the same boundary/interface/radiation conditions as the unperturbed Green's function. In this connection, the integral representation (3) can be used by considering the right-hand side of Eq. (5), as a function of $\mathbf{r}$, to be the source term

$$\Delta G(\mathbf{r}|\mathbf{r}_s)=\int\int\int_V G(\mathbf{r}|\mathbf{r}')\left[\frac{\omega^2}{[c(\mathbf{r}')+\Delta c(\mathbf{r}')]^2}-\frac{\omega^2}{c^2(\mathbf{r}')}\right][G(\mathbf{r}'|\mathbf{r}_s)+\Delta G(\mathbf{r}'|\mathbf{r}_s)]dV(\mathbf{r}'). \tag{6}$$

By retaining terms of first order, the following approximation for the perturbation of the Green's function is obtained:

$$\Delta G(\mathbf{r}|\mathbf{r}_s)=-2\omega^2\int\int\int_V G(\mathbf{r}'|\mathbf{r}_s)G(\mathbf{r}|\mathbf{r}')\times\frac{\Delta c(\mathbf{r}')}{c^3(\mathbf{r}')}dV(\mathbf{r}'). \tag{7}$$

This is called the first Born approximation.[23] It is also called the single- or weak-scattering approximation, or wave-field linearization and is widely used in connection with scattering problems.[24] It is a linear relation between the perturbation in the sound-speed distribution and the induced perturbation in the Green's function.

The Green's function above is defined in the frequency domain—the circular frequency ω enters the Helmholtz equation as a parameter. Further, the Green's function depends on the sound-speed distribution that also enters the Helmholtz equation. In order to explicitly describe these dependencies, G is written in the following as $G(\mathbf{r}|\mathbf{r}_s;\omega;c)$.

III. TRAVEL-TIME MODELING

In ocean acoustic tomography the acoustic field of an impulsive (broadband) point source is recorded at a distant receiver in the time domain. This can be expressed through the inverse Fourier transform in terms of the source signal $P_s(\omega)$ in the frequency domain and the frequency–domain Green's function evaluated at the receiver's location $\mathbf{r}=\mathbf{r}_r$,

$$p_r(t;c)=\frac{1}{2\pi}\int_{-\infty}^{\infty}G(\mathbf{r}_r|\mathbf{r}_s;\omega;c)P_s(\omega)e^{j\omega t}d\omega. \tag{8}$$

Due to multipath propagation, the pressure magnitude at the receiver in the time domain $a(t;c)=|p_r(t;c)|$ consists, in general, of a number of peaks, the acoustic arrivals, whose shape and temporal locations (arrival times) τ_i, $i=1,2...,I$, are dependent on the sound-speed distribution within the water column. The function $a(t;c)$ is called the arrival pattern. For most ocean tomography experiments to date, small-scale sound speed variability makes the magnitudes of each peak rapidly variable in time, while the corresponding arrival times τ_i are stable and reliable characteristics of the arrival pattern. Arrival times thus constitute the basic set of observables in most ocean tomography experiments and their perturbations are used for the retrieval of the underlying sound-speed perturbations.

This is a simplified, yet sufficient, description of the modeling problem in ocean acoustic tomography, neglecting signal processing issues of importance for the experimental implementation,[1,2,25] but not essential for modeling purposes. In practice, it is the autocorrelation of the emitted signal that is impulsive, not the signal itself, and the arrival pattern results from the cross-correlation of the received signal with a replica of the emitted signal (matched filter);[26–28] equivalent expressions to those presented here hold for the corresponding correlated quantities in the time-lag domain.[11]

For the wave-theoretic modeling of arrival times the notion of peak arrivals[11,12] is used. Peak arrivals are defined as the significant local maxima of the arrival pattern. The peak-arrival times are the time instants τ_i, $i=1,2,...,I$, corresponding to these maxima,

$$\dot{a}(\tau_i;c)=0, \tag{9}$$

where the overdot denotes differentiation with respect to time. Expressing the complex pressure p_r in terms of its real and imaginary parts $p_r(t;c)=v(t;c)+jw(t;c)$, the definition above can be alternatively expressed as

$$v(\tau_i;c)\dot{v}(\tau_i;c)+w(\tau_i;c)\dot{w}(\tau_i;c)=0. \tag{10}$$

The definition of peak arrivals has its origin in the procedure followed in experimental practice for obtaining arrivals and arrival times and allows for any kind of modeling approach, either geometric or wave-theoretic. Since the arrival pattern depends on the sound-speed distribution, the peak-arrival times do so as well, i.e., $\tau_i=\tau_i(c)$.

A perturbation Δc of the sound-speed distribution will cause a variation ΔG in the Green's function, expressed to the first order by Eq. (7), which, in turn, will cause a variation Δp_r in the acoustic pressure at the receiver in the time domain,

$$\Delta p_r(t;c;\Delta c)=\frac{1}{2\pi}\int_{-\infty}^{\infty}\Delta G(\mathbf{r}_r|\mathbf{r}_s;\omega;c;\Delta c)\times P_s(\omega)e^{j\omega t}d\omega. \tag{11}$$

The pressure perturbation will produce a perturbation of the arrival pattern and finally a perturbation $\Delta\tau_i$ of the peak arrival times. According to their definition (9), the perturbed peak arrival times will satisfy the equation

$$\dot{a}(\tau_i+\Delta\tau_i;c+\Delta c)=0. \tag{12}$$

Using a first-order Taylor expansion with respect to time about τ_i, the equation above can be written in the form

$$\dot{a}(\tau_i;c+\Delta c)+\ddot{a}(\tau_i;c+\Delta c)\Delta\tau_i=0. \tag{13}$$

Expressing the pressure perturbation Δp_r in terms of its real and imaginary parts, $\Delta p_r(t;c;\Delta c)=\Delta v(t;c;\Delta c)+j\Delta w(t;c;\Delta c)$, and taking into account the relations $a(t;c)=\sqrt{v^2+w^2}$ and $a(t;c+\Delta c)=\sqrt{(v+\Delta v)^2+(w+\Delta w)^2}$, as well as Eq. (10), holding at the unperturbed arrival time τ_i, the following expression can be derived from (13) for the perturbation of the peak arrival time,

$$\Delta\tau_i=-\frac{\dot{v}_i\Delta v_i+v_i\Delta\dot{v}_i+\dot{w}_i\Delta w_i+w_i\Delta\dot{w}_i}{\dot{v}_i^2+v_i\ddot{v}_i+\dot{w}_i^2+w_i\ddot{w}_i}. \tag{14}$$

The index i denotes that all quantities on the right-hand side of Eq. (14) are evaluated at the background (unperturbed) arrival time τ_i, i.e., for a particular peak they have fixed values.

A. Travel-time sensitivity kernel

Equation (14) relates the arrival-time perturbation $\Delta\tau_i$ with the perturbation Δp_r of the acoustic pressure at the receiver in the time domain. The latter is related to the perturbation ΔG of the Green's function through Eq. (11). Finally, ΔG is related to the perturbation Δc in the sound-speed distribution through the first Born approximation (7). By combining these, an integral relation can be derived, expressing the arrival-time perturbation $\Delta\tau_i$ in terms of the underlying sound-speed variation Δc,

$$\Delta\tau_i = \int\int\int_V \Delta c(\mathbf{r}') K_i(\mathbf{r}'|\mathbf{r}_s;\mathbf{r}_r;c)\, dV(\mathbf{r}'), \tag{15}$$

where $K_i(\mathbf{r}'|\mathbf{r}_s;\mathbf{r}_r;c)$ is the sensitivity kernel for the ith peak arrival and is given by

$$\begin{aligned} K_i(\mathbf{r}'|\mathbf{r}_s;\mathbf{r}_r;c) = \Re\Bigg\{ & \frac{1}{2\pi}\int_{-\infty}^{\infty} \frac{\dot v_i + j v_i \omega}{b_i} \\ & \times Q(\mathbf{r}'|\mathbf{r}_s;\mathbf{r}_r;\omega;c) e^{j\omega\tau_i}\, d\omega \Bigg\} \\ & + \Im\Bigg\{ \frac{1}{2\pi}\int_{-\infty}^{\infty} \frac{\dot w_i + j w_i \omega}{b_i} Q(\mathbf{r}'|\mathbf{r}_s;\mathbf{r}_r;\omega;c) \\ & \times e^{j\omega\tau_i}\, d\omega \Bigg\}, \end{aligned} \tag{16}$$

where $\Re$ and $\Im$ denote real and imaginary parts, respectively, $b_i = \dot v_i^2 + v_i \ddot v_i + \dot w_i^2 + w_i \ddot w_i$ is one-half the second time derivative of the squared arrival pattern $a^2 = v^2 + w^2$ at the background peak arrival time, and

$$\begin{aligned} Q(\mathbf{r}'|\mathbf{r}_s;\mathbf{r}_r;\omega;c) = & G(\mathbf{r}'|\mathbf{r}_s;\omega;c) G(\mathbf{r}_r|\mathbf{r}';\omega;c) \\ & \times \frac{2\omega^2 P_s(\omega)}{c^3(\mathbf{r}')}. \end{aligned} \tag{17}$$

The linear operator $\int\int\int (K_i \cdot) dV$, Eq. (15), resulting from the first Born approximation, is the Fréchet derivative of the travel time τ_i with respect to the sound-speed distribution.[29] In this connection, the travel-time sensitivity kernel K_i is a Born–Fréchet kernel relating sound-speed and travel-time perturbations.[13,14] By rearranging terms, the kernel $K_i(\mathbf{r}'|\mathbf{r}_s;\mathbf{r}_r;c)$ can be alternatively written as follows:

$$\begin{aligned} K_i(\mathbf{r}'|\mathbf{r}_s;\mathbf{r}_r;c) = \Re\Bigg\{ & \frac{v_i - j w_i}{2\pi b_i}\int_{-\infty}^{\infty} j\omega Q(\mathbf{r}'|\mathbf{r}_s;\mathbf{r}_r;\omega;c) \\ & \times e^{j\omega\tau_i}\, d\omega + \frac{\dot v_i - j\dot w_i}{2\pi b_i} \\ & \times \int_{-\infty}^{\infty} Q(\mathbf{r}'|\mathbf{r}_s;\mathbf{r}_r;\omega;c) e^{j\omega\tau_i}\, d\omega \Bigg\}. \end{aligned} \tag{18}$$

On the basis of Eq. (15), the kernel $K_i(\mathbf{r}'|\mathbf{r}_s;\mathbf{r}_r;c)$ gives a quantitative description of the sensitivity of the peak arrival time τ_i to sound-speed changes at any (three-dimensional) location $\mathbf{r}'$ within the acoustic waveguide. A positive value for K_i at a particular location indicates that a sound-speed increase at that location will cause an increase in travel time. A negative value, on the other hand, indicates that a sound-speed increase will cause a decrease in travel time. Finally, a zero indicates that a change in sound speed will have no effect on the travel time.

B. Normal-mode representation

In the case of a horizontally stratified (range-independent) background environment, normal-mode theory can be used to represent the background Green's function G, which is axisymmetric about the vertical axis through the source. A three-dimensional cylindrical coordinate system (r,z,ϕ) is used with its origin at the sea surface and the source located on the vertical z axis (positive downward) at depth $z=z_s$. The background sound speed will be a function of depth only: $c=c(z)$. If the source is harmonic, with unit strength, circular frequency ω and time dependence $e^{j\omega t}$, the farfield expression for the Green's function at (r,z) can be expressed in the form[20,21]

$$G(r,z|z_s;\omega;c) = \frac{e^{-j\pi/4}}{\rho\sqrt{8\pi}} \sum_{n=1}^{M} \frac{u_n(z_s)u_n(z)}{\sqrt{k_n r}} e^{-jk_n r}, \tag{19}$$

where ρ is the water density and k_n and u_n, $n=1,...,M$, are the real eigenvalues and the corresponding eigenfunctions (propagating modes) of the vertical Sturm–Liouville problem:

$$\frac{d^2 u_n(z)}{dz^2} + \frac{\omega^2}{c^2(z)} u_n(z) = k_n^2 u_n(z), \tag{20}$$

supplemented by the conditions that $u_n = 0$ at the sea surface $(z=0)$, u_n and $\rho^{-1}\, du_n/dz$ are continuous across the interfaces, and u_n and du_n/dz are vanishing as $z\to\infty$. By substituting (19) into (17), the quantity Q can be expressed as follows:

$$\begin{aligned} & Q(r,z,\phi|z_s;R,z_r;\omega;c) \\ & = \frac{\omega^2 P_s(\omega) e^{-j\pi/2}}{4\pi\rho^2 c^3(z)} \sum_{m=1}^{M} \frac{u_m(z_s)u_m(z)}{\sqrt{k_m r}} e^{-jk_m r} \\ & \quad \times \sum_{n=1}^{M} \frac{u_n(z)u_n(z_r)}{\sqrt{k_n \sqrt{r^2+R^2-2rR\cos\phi}}} \\ & \quad \times e^{-jk_n\sqrt{r^2+R^2-2rR\cos\phi}}, \end{aligned} \tag{21}$$

where z_s and z_r are the source and receiver depths, respectively, and R is the horizontal distance between the source and receiver. The expression (21) can be used for the calculation of the kernel K_i at any location (r,z,ϕ).

IV. NUMERICAL RESULTS

In this section we present numerical results for the travel-time sensitivity kernel, assuming three-dimensional (3-D) perturbations of a horizontally stratified background environment. In this connection, the normal-mode representations can be applied. The water depth is 2500 m. The background sound-speed profile in the water is assumed to be

linear, with 1503 m/s at the sea surface and 1547 m/s at the bottom. Both the source and receiver are placed at 150 m depth with horizontal distance 52 km. This configuration is motivated by the Thetis[30] tomography experiment that took place in the Gulf of Lions (western Mediterranean sea) in winter 1991–92. An absorbing bottom[11,31] is assumed, filtering out the bottom-interacting part of the acoustic energy. The upward refracting sound speed profile also reduces the influence of the relatively shallow bottom.

Figure 1 shows ray-theoretic results for the example configuration. In particular, the ray intensity, launch angle, and turning depth versus arrival time, as well as the geometry of the corresponding eigenrays are shown in this figure from top to bottom.[32] There are 15 non-bottom-interacting eigenrays spanning the upper 1100 m of the water column. All of them are subject to surface reflections, due to the upward refracting sound-speed profile. The eigenray -3 is the steepest one and has the earliest arrival time. The eigenrays ± 4 are slightly shallower and arrive about 30 ms later, with identical arrival times, forming the central arrival of a ray group (triplet). The eigenray $+5$ corresponds to the late arrival of the first triplet. Later arrivals are due to gradually shallower eigenrays. The shallowest ray, with a lower turning depth just above 150 m is ± 10, corresponding to the last arrival.

The top of Fig. 2 shows the wave-theoretic prediction for the arrival pattern, assuming that the emitted signal is a Gaussian pulse with central frequency 400 Hz and bandwidth 60 Hz (3-dB bandwidth). The broadband calculation in the frequency domain was carried out with a normal-mode code at 191 frequencies, from 305 to 495 Hz with frequency step 1 Hz, and a standard FFT was applied to obtain time-domain results. The first five arrivals in Fig. 2 can be directly associated with individual ray arrivals in Fig. 1, whereas the last peak corresponds to the group of the six latest ray arrivals. In the lower panels of Fig. 2, the travel-time sensitivity kernel (TSK) is presented for the first three arrivals (peaks 1, 2, and 3). In particular, a section of the 3-D TSK is shown in the vertical plane through the source/receiver—the TSK has mirror symmetry about this plane. The Green's function underlying the TSK calculations was evaluated at 191 frequencies, as above, with a spatial resolution of 5 m in depth and 260 m in range. A moving average window, 100 m in the vertical and 520 m in the horizontal, was applied to the graphical presentation in order to suppress short-scale oscillations due to mode interference.

Peaks 1 and 3 correspond to eigenrays -3 and $+5$, respectively (cf. Fig. 1), which are also shown in Fig. 2 (dashed lines). The TSK reproduces the eigenray geometry and also provides quantitative information about the sensitivity of the travel times to sound-speed changes anywhere in the medium. The maximum sensitivity is near the eigenray paths where the TSK takes negative values. This means that a sound-speed decrease along the eigenray will result in a travel-time increase, as expected. The oscillatory behavior of the TSK away from the eigenrays is associated with Fresnel-zone behavior and is expected to cancel out in the integral (15), provided that the sound-speed perturbation is a smooth function of $\mathbf{r}$; in the limit $\omega \to \infty$, the wave-theoretic travel-time sensitivity kernel converges to the ray-theoretic one.[33] Close to the deep turning points, it is observed that the negative sensitivity maximum is not at the core of the high-sensitivity area, i.e., not along the eigenray, but at a distance from it. This spread sensitivity will become more pronounced in the next example where the frequency is reduced. Peak 2 corresponds to two symmetric eigenrays (± 4). The geometry of the two eigenrays is well reproduced by the TSK of peak 2. While the eigenrays are well separated in the upper 600 m layer, there is overlapping close to the turning points. The TSK of an arrival peak made up of two different ray paths is not generally useful for inversion, since in a realistic ocean environment ray intensities will vary, and one or the other of the two peaks may dominate at any time. A vertical array of hydrophones at the receiver could separate the two rays by time-delay beamforming for the different angles, but that is beyond the scope of this work.

The top panel in Fig. 3 presents the arrival pattern of a lower-frequency Gaussian pulse: The central frequency is now 100 Hz while the bandwidth is the same as before (60 Hz). The first 3 peaks marked in the arrival pattern correspond to the first triplet in Figs. 1 and 2. The TSK for each of these three peaks are shown in the lower panels of Fig. 3, along with the corresponding eigenrays (dashed lines). The more striking change from the previous 400-Hz case is that the domain of lower sensitivity of peaks 1 and 3 along the eigenrays has increased drastically in length and width, and in fact, it has become a domain of insensitivity along the eigenray. On the other hand, the (negative) maximum of the

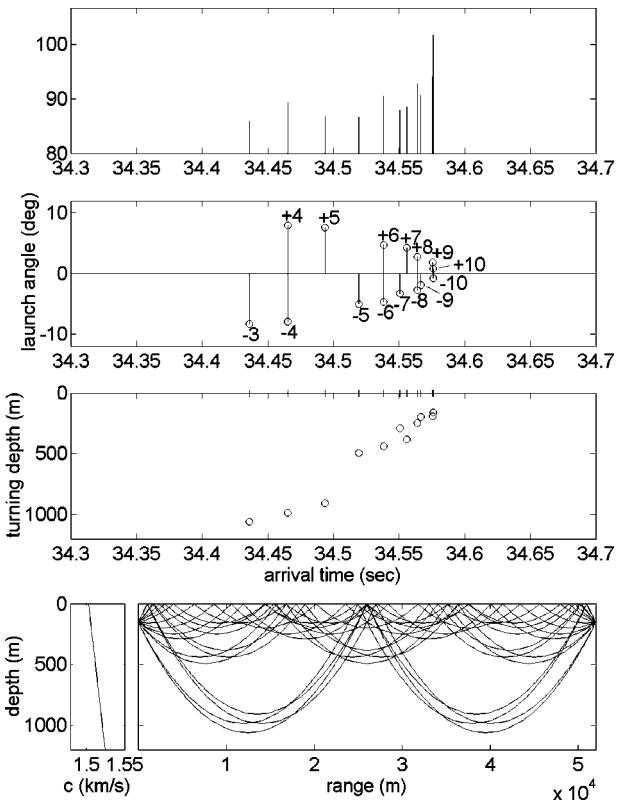

FIG. 1. Ray-theoretic results for a linear sound-speed profile (bottom left), for source/receiver depth 150 m and distance 52 km. The graphs show (from top to bottom) the eigenray intensities, launch angles, turning depths versus arrival time, and the eigenray geometry.

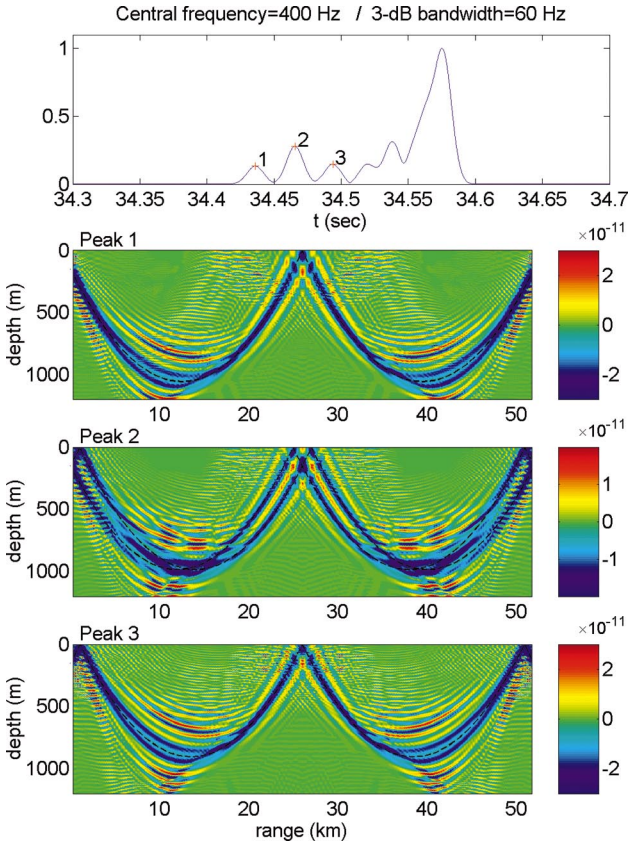

FIG. 2. Top panel: Wave-theoretic arrival pattern of a Gaussian pulse of central frequency 400 Hz and bandwidth 60 Hz. Lower panels: 2-D vertical cross-section of the 3-D travel-time sensitivity kernel ($s^2\,m^{-4}$) for peaks 1, 2, and 3 (marked in the top panel) and the corresponding eigenrays (dashed lines).

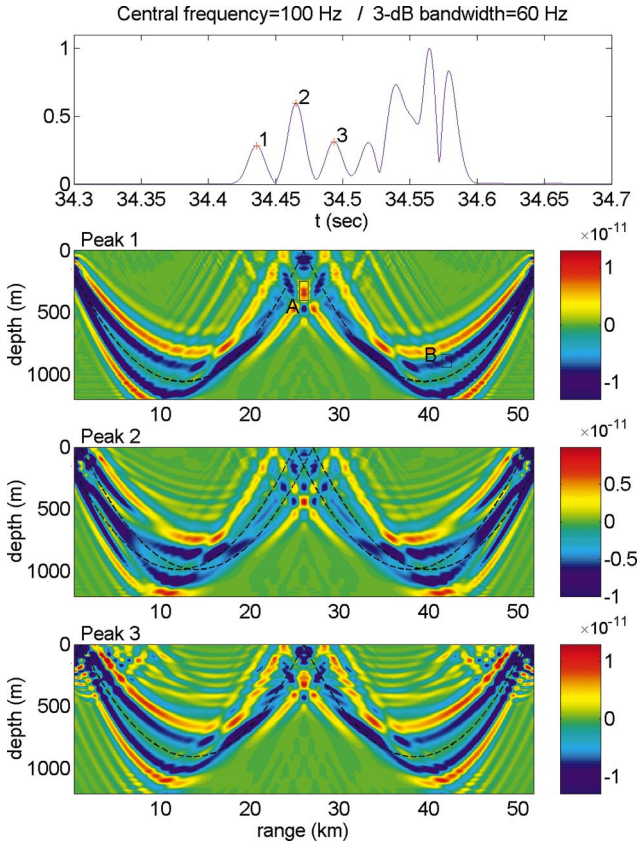

FIG. 3. Top panel: Wave-theoretic arrival pattern of a Gaussian pulse of central frequency 100 Hz and bandwidth 60 Hz. Lower panels: 2-D vertical cross-section of the 3-D travel-time sensitivity kernel ($s^2\,m^{-4}$) for peaks 1, 2 and 3 (marked in the top panel) and corresponding eigenrays (dashed lines). The boxes A and B denote areas where isolated (axisymmetric) sound-speed perturbations are applied for verification purposes.

travel-time sensitivity is attained in an annulus surrounding the eigenray with variable diameter reaching 280 m. Further, there are areas of positive sensitivity, where a sound-speed increase will slow down the acoustic wave.

The broadening of the high-sensitivity domain for lower frequencies can be explained in terms of Fresnel zone behavior, and in this sense it was expected, e.g., in the context of the ray-tube approach. However, the domain of low (vanishing) sensitivity in the middle (along the eigenray) was not, and it was a surprise for the seismic tomography community, where it was first encountered.[15] The picture is more complex in the case of peak 2 due to the overlapping of the two contributing eigenrays. The two boxes marked on the TSK of peak 1 in Fig. 3 denote the locations of test perturbations for verification purposes and will be addressed shortly.

Figure 4 shows a cross-section of the 100-Hz TSK for the first three peaks at ranges 10, 18, and 26 km. The color scales in this figure are relative to the local maxima and are, in general, different from those of Fig. 3. Since the source/receiver configuration is symmetric, the results for 10 km also apply for the range of 42 km. Similarly, the results for 18 km also apply for the range of 34 km. At the range of 10 (42) km, the cross-section shows that the negative sensitivity annulus close to its broadest position has a horizontal extent of about 400 m and a vertical extent of about 280 m. In the center of the annulus, where the eigenrays pass (positions denoted by asterisks), the sensitivity is zero. At the range of 18 (34) km, the TSK collapses in the vertical while preserving its horizontal extent. Finally, at the source–receiver midrange (26 km), where reflection takes place for peaks 1 and 3 complicated patterns, occur with strong positive and negative sensitivities.

An explanation of the generating mechanism for the regimes of negative/positive/zero travel-time sensitivity in free space is given in Appendix A, in terms of acoustic scattering taking place in the vicinity of an eigenray. The scattered field may cause advancement or the further delay to an acoustic arrival, or have no effect at all, depending on its phase and arrival time at the receiver. The latter are directly associated with the location of the scatterer, thus defining positive, negative, and zero sensitivity regimes. The sensitivity is zero on the eigenray, whereas the negative sensitivity maximum is attained at a distance from the eigenray. The negative-sensitivity core is contained within the first Fresnel zone (of radius R_F) and is followed by a positive-sensitivity regime at the boundary of the first Fresnel zone. Thus, the characteristic radius for the positive-sensitivity regime is the Fresnel radius R_F, whereas for the negative-sensitivity core it is $R_F/\sqrt{2}$.

Assuming propagation in free space, the Fresnel radius[34,35] as a function of distance r from the source is given by

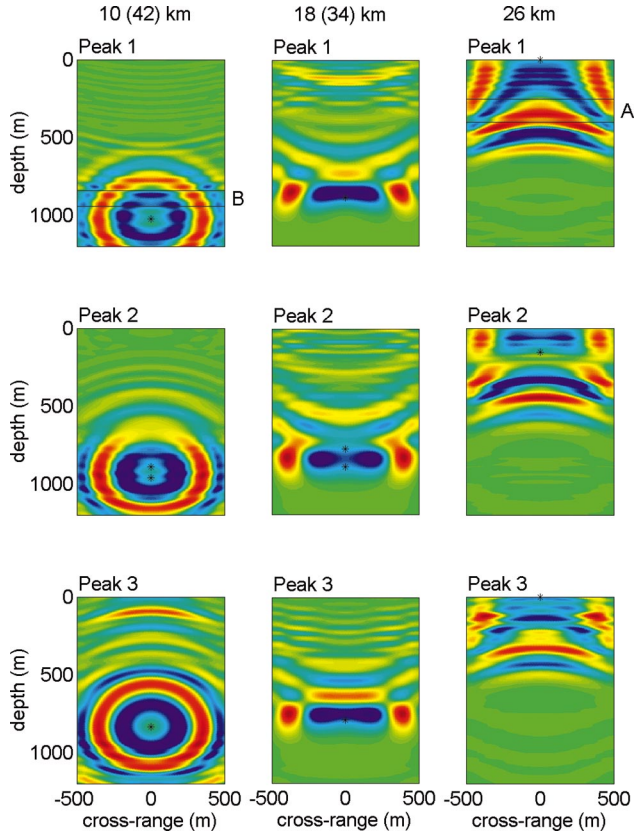

FIG. 4. Longitudinal cross-sections of the 100-Hz travel-time sensitivity kernel for peaks 1, 2, and 3 (marked in the top panel of Fig. 3) at ranges 10, 18, and 26 km. The asterisks denote the locations of corresponding eigenrays. Due to symmetry, the sections at the first two ranges are also valid for the ranges 42 and 34 km, respectively (in parentheses). The layers A and B denote the areas where isolated (axisymmetric) sound-speed perturbations are applied for verification purposes.

$$R_F(r) = \sqrt{\frac{r(R-r)c}{fR}}, \tag{22}$$

where R is the source–receiver distance, f is the frequency of propagation, and c is the sound speed. Taking $R = 52\,000$ m, $c = 1500$ m/s, and $f = 100$ Hz, the Fresnel radius at the ranges of 10, 18, and 26 km is 348, 420, and 441 m, respectively. The horizontal (cross-range) extent of the high-sensitivity regimes in Fig. 4 are in agreement with these estimates. For example, at the range of 10 km, the horizontal distance of the positive-sensitivity area from the corresponding eigenray for peak 3 at is about 350 m, whereas the outer horizontal semiaxis of the negative-sensitivity core is about 250 m. The presence of stratification causes significant deformations of the TSK structure in the vertical, from deviations from the circular symmetry to full collapse of the negative-sensitivity regime.

A test of the observed positive/negative travel-time sensitivity in the 100-Hz case was carried out to check the TSK calculations. For this purpose sound-speed perturbations in two areas, A and B, of positive and negative sensitivity, respectively, were introduced and the effects on peak 1 were calculated using a coupled-mode code. The areas A and B are identified in Figs. 3 and 4 and their location/dimensions are given in Table I. The perturbations are axisymmetric with respect to the z axis, such that the domains A and B are not limited in the azimuthal, as shown in Fig. 4. In each perturbed realization the sound speed was raised by 4 m/s at the mid-depth of the perturbation area, linearly decreasing toward the unperturbed values at the upper and lower limits of the area. In this connection, the propagation is divided into three range-independent subdomains. One from the source to the starting range of the perturbation area, one covering the perturbation area, and one from its end range to the receiver.

TABLE I. Geometry of perturbation areas.

	Horizontal		Vertical	
	Start range (km)	End range (km)	Top depth (m)	Bottom depth (m)
A	25.5	26.5	250	400
B	41.5	42.5	840	940

The results from the forward calculations are shown in Fig. 5. The top panel shows the unperturbed state of peak 1, focusing in the area about its maximum (marked by an asterisk in the top panel and by a vertical dashed line in the panels below). The perturbation in case A has resulted in a delay of peak 1 that is compatible with the positive values of the TSK in area A; cf. Figs. 3 and 4. The perturbation in case B where the negative TSK values dominate has the opposite effect of causing an advancement of peak 1. Note that both areas A and B lie well off the eigenray associated with peak 1. The effect in case A is stronger than in case B. This is attributed to the different azimuthal extent of the high sensitivity areas in the two cases, as shown in Fig. 4. Thus, the forward calculations verify the TSK behavior observed in the previous figures. It is noted that the sound-speed perturbations in both cases A and B reduce the amplitude of peak 1.[36]

Figure 6 shows the TSK for the last peak of the arrival

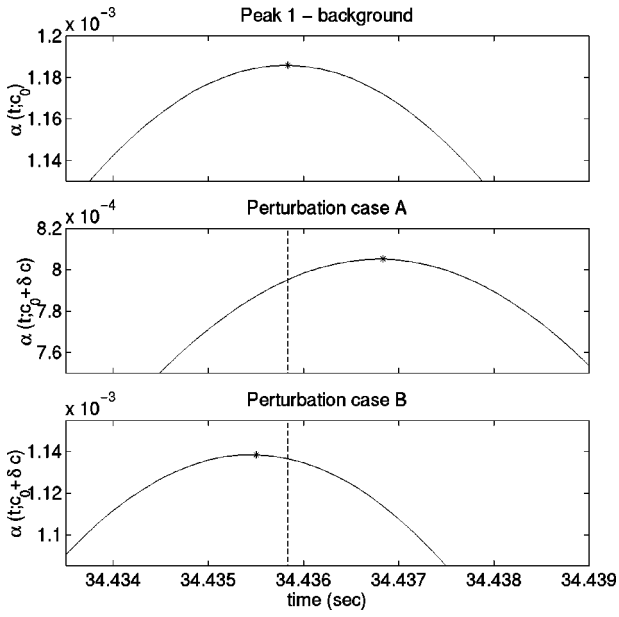

FIG. 5. Coupled-mode results for medium perturbations in the 100-Hz case for the first arrival. Top panel: Unperturbed (background) state—this is a detailed view of peak 1 (Fig. 3 top panel). Lower panels: Forward predictions of peak 1 for sound-speed perturbations in the areas A and B. The asterisk denotes the peak maximum. The vertical dashed line denotes the background peak arrival time.

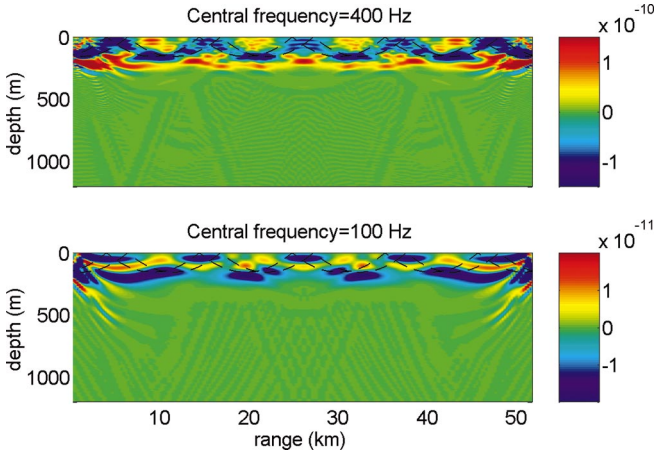

FIG. 6. The 2-D vertical cross-section of the 3-D travel-time sensitivity kernels ($s^2\,m^{-4}$) for the last peak in the 400- and 100-Hz cases—the emitted signal is a Gaussian pulse of bandwidth 60 Hz.

patterns of Figs. 2 and 3 for the two cases of central frequencies 400 and 100 Hz. In the ray-theoretic results the last arrival is ± 10 with deep turning depth just above 150 m. In this connection, a smaller moving average window, 40 m in the vertical and 260 m in the horizontal, was applied for the presentation in Fig. 6. The ten turning points of ray arrival ± 10 can be recognized in the geometry of the negative TSK areas in Fig. 6, especially in the 400-Hz case; the ray arrival ± 10 is associated with two symmetric eigenrays also shown in Fig. 6 (dashed lines). Still there are structural differences in the TSK patterns as the frequency changes. This suggests that the influence coefficients will be different for different frequency characteristics of the emitted signal (pulse shape, central frequency, bandwidth). The frequency effects on the influence coefficients of late arrivals have been studied in a previous work.[37]

Figure 7 shows the range-average travel-time sensitivity kernel, i.e., the vertical sensitivity, for peaks 1, 2, and 3 in the 100- and 400-Hz cases. The solid lines represent the wave-theoretic kernels (after the application of a 100-m moving average window), whereas the dashed lines are the ones calculated from ray theory. The wave-theoretic vertical sensitivity kernel was obtained from perturbation analysis of the range-independent problem, as discussed in an earlier paper,[11] rather than by integrating the 3-D TSK. The range-independent perturbation analysis is presented in Appendix B. From Fig. 7, it is seen that the oscillations of the full-wave sensitivity persist in the range average, even with vertical smoothing, and it is clear that the sharp edge of the geometric kernel at the lower turning depth is blurred. At 400 Hz (upper panel), the smoothing is not severe, but at 100 Hz (lower panel), the turning point sensitivity is spread by about 200 m, which is significant for internal wave perturbations or practical inverse models.

V. DISCUSSION AND CONCLUSIONS

According to geometric ray theory, travel times are only sensitive to sound-speed changes on the corresponding eigenrays connecting the source and receiver. In ray tomography travel times are considered as integral measures of the

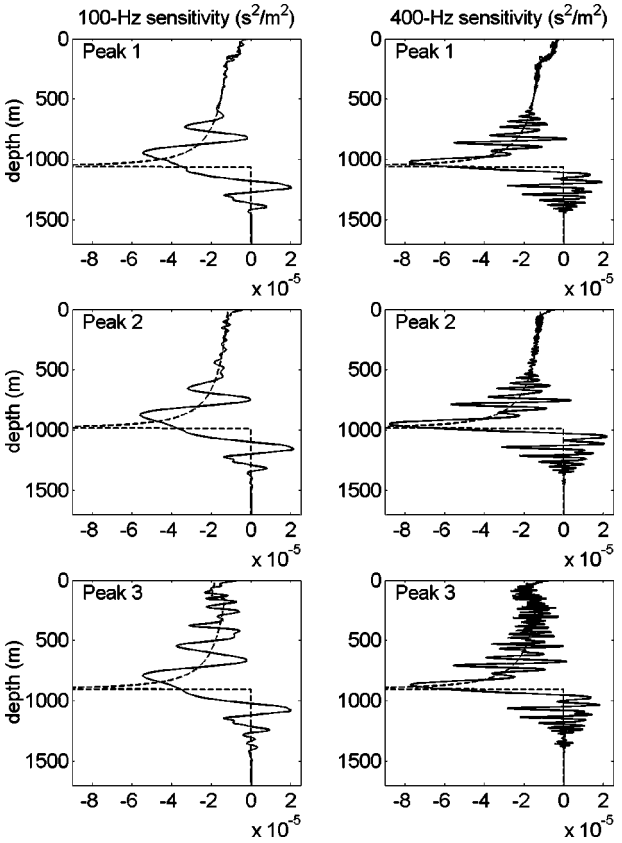

FIG. 7. Vertical travel-time sensitivity functions of peaks 1, 2, and 3 in the 100- and 400-Hz cases—the emitted signal is a Gaussian pulse of bandwidth 60 Hz. The solid lines denote wave-theoretic results whereas the dashed lines represent predictions from ray theory.

reciprocal sound-speed (slowness) along the geometric eigenrays, and ray inversion methods infer sound-speed perturbations from their effects on these line integrals. Nevertheless, ray theory is a high-frequency asymptotic approximation, and a question arises if the geometric sensitivity kernel remains valid for the low frequencies used in ocean acoustic tomography experiments.

To address this question a wave-theoretic modeling approach for acoustic propagation, allowing for the treatment of finite-frequency effects, was combined here with a general modeling approach for travel-time observables, the peak arrival approach, that reflects the procedure followed in experimental practice for obtaining arrivals and arrival times. In this way a general wave-theoretic expression for the 3-D travel-time sensitivity kernel was obtained, which reveals in a quantitative manner the effect that sound-speed perturbations and their spatial distribution have on finite-frequency travel times.

In the case of higher frequencies, the wave-theoretic calculations result in a picture of the travel-time sensitivity that is close to the ray picture. The sensitivity kernel is concentrated around the corresponding eigenrays and decays away from them forming an oscillating Fresnel pattern. In the asymptotic high-frequency limit the integral contribution of the kernel is coming from the first Fresnel zone around the eigenray, as can be obtained by applying the stationary-phase approach to the cross-ray integral, reproducing the ray-theoretic sensitivity.[16,33]

In the low-frequency case, the wave-theoretic results exhibit significant deviations from ray theory: Low-frequency travel times of early arrivals, corresponding to steep rays, are sensitive to sound-speed changes in areas surrounding the eigenrays, but not on the eigenrays themselves. The sensitivity kernels for these arrivals attain their negative maxima at a distance from the eigenrays whereas the sensitivity is zero on the eigenrays. Still, in a distribution-theoretic context,[17] the eigenrays belong to the support of the senstivity kernel, in the sense that the result of the kernel acting on any finite-support perturbation of the medium about the eigenray will be non-zero in general. Further, there are areas of positive sensitivity, where, e.g., a sound-speed increase results in an increase of arrival times, i.e., a further delay of arrivals. An explanation for the travel-time sensitivity behavior in free space is given in Appendix A. The presense of horizontal stratification suppresses/deforms the TSK structure in the vertical, giving rise to elliptical rather than circular sensitivity patterns about the eigenrays.

Low-frequency travel times exhibit sensitivity to sound-speed changes at distances 100 m or more beyond the turning depth of the corresponding ray. This sensitivity is also present in the range average, where the wave-theoretic vertical sensitivity kernel oscillates around the ray sensitivity, even exhibiting regions of positive sensitivity that cannot be explained by ray theory. In this connection, the use of path-integral methods based on ray theory for evaluating the effects of features, such as internal waves, on travel times may be inaccurate for low acoustic frequencies and high-vertical-mode ocean features. The spreading of the sensitivity past the turning point is due to diffraction, which is partially responsible for the increased vertical spread of time fronts in long-range ocean transmission experiments.[38,39]

In seismic transmission tomography, the behavior of travel-time sensitivity kernels of compressional and shear waves has been the objective of a number of papers[13–16] based on the assumption of known source characteristics in the space/time/frequency domains. In seismic transmission tomography, however, the excitation of the medium is due to earthquakes, and the characterization of natural earth-quakes as seismic sources is associated with ambiguities which in turn affect the travel-time sensitivity kernel.[17] This problem does not arise in ocean acoustic tomography, due to the fact that the sources are controlled and their spatial, temporal and frequency characteristics are known.

Travel-time sensitivity kernels offer a method to study the effect of 3-D spatial scales of sound-speed variations on finite-frequency travel-time observables. This is particularly important for the study of ocean propagation in range-dependent media, such as internal-wave fields. In this connection, the sensitivity kernels have been used for the study of wavefront healing,[40] a diffraction phenomenon that affects travel times when the scale of the 3-D variations in the wave speed is comparable with the characteristic wavelength.

The background state for the numerical results presented in the previous section was taken to be range independent. Nevertheless, the present derivation and the expressions for the travel-time sensitivity kernel are general and can apply to range-dependent background environments as well. This could provide a wave-theoretic tool to study finite-frequency travel-time effects of ray and "wave" chaos[41]—an interesting area for future work. A further area of interest would be the study of the TSK behavior for very long range propagation in order to see how the TSK structure is affected by the broadening of the Fresnel zones; the Fresnel radius is proportional to $\sqrt{R}$ and should become very large for propagation over megameter ranges.

The present derivation for the travel-time sensitivity kernel was based on the first Born (weak scattering) approximation. This approximation is known to be reliable in the case of small perturbations. Other methods such as the Rytov approximation provide a better representation of the transmitted (or forward scattered) part of the wave field.[42] The use of the Born approximation in this work is justified by the fact that it is applied for obtaining an expression for the Fréchet derivative of travel times with respect to sound-speed perturbations, and in this connection infinitesimally small perturbations can be assumed.

APPENDIX A: TRAVEL-TIME SENSITIVITY IN FREE SPACE

In this appendix an explanation is given for the zero/negative/positive sensitivity of finite-frequency travel times to sound-speed perturbations in free space. Let a point source (of circular frequency ω) and a receiver at fixed locations $\mathbf{r}_s$ and $\mathbf{r}_r$, respectively, in an unbounded medium with constant background sound speed c. The corresponding Green's function at the location of the receiver has the form[21]

$$G_s(\omega)=\frac{e^{-ikR}}{4\pi R}=\frac{e^{-i\omega T}}{4\pi R}, \tag{A1}$$

where $R=|\mathbf{r}_s-\mathbf{r}_r|$ is the source–receiver distance, $k=\omega/c$ and $T=R/c$.

A scatterer (a volume dV of sound-speed change Δc) at distance R_1 from the source and R_2 from the receiver will cause a perturbation to the Green's function, which, according to the first Born approximation (7), will be

$$\Delta G_{sr}(\omega)=-\frac{2dV\Delta c}{(4\pi)^2R_1R_2c^3}\omega^2e^{-ik(R_1+R_2)}$$

$$=-\frac{2dV\Delta c}{(4\pi)^2R_1R_2c^3}\omega^2e^{-i\omega(T_1+T_2)}, \tag{A2}$$

where $T_1=R_1/c$ and $T_2=R_2/c$.

The background pressure at the receiver in the time domain is given by the inverse Fourier transform (8), which by substitution of (A1) becomes

$$p_r(t)=\frac{p_s(t-T)}{4\pi R}=\frac{\tilde{p}_s(t-T)e^{i\omega_0(t-T)}}{4\pi R}, \tag{A3}$$

where $p_s(t)$ is the pressure at the source in the time domain, and ω_0 is the central circular frequency of the source; an overtilde denotes demodulated quantities.

The perturbation of the pressure at the receiver in the time domain can be obtained by substituting the expression (A2) into Eq. (11),

$$\Delta p_r(t) = -\frac{2dV\Delta c}{(4\pi)^2 R_1 R_2 c^3}\frac{1}{2\pi}\int_{-\infty}^{\infty}\omega^2 e^{-i\omega(T_1+T_2)} \times P_s(\omega)e^{i\omega t}\,d\omega = \frac{2dV\Delta c}{(4\pi)^2 R_1 R_2 c^3} p_s''(t-T_1-T_2). \tag{A4}$$

Thus, the time–domain pressure anomaly due to the scatterer is proportional to the second time derivative of the background pressure at the receiver, centered about the time instant T_1+T_2 instead of T. The pressure $p_s(t-T_1-T_2)$ can be written in terms of the demodulated source pressure,

$$p_s(t-T_1-T_2) = \tilde{p}_s(t-T_1-T_2)e^{i\omega_0(t-T_1-T_2)}. \tag{A5}$$

Accordingly, its first and second derivatives can be written as follows:

$$p_s'(t-T_1-T_2) = e^{i\omega_0(t-T_1-T_2)}[i\omega_0\tilde{p}_s(t-T_1-T_2) + \tilde{p}_s'(t-T_1-T_2)], \tag{A6}$$

$$p_s''(t-T_1-T_2) = e^{i\omega_0(t-T_1-T_2)}[-\omega_0^2\tilde{p}_s(t-T_1-T_2) + i2\omega_0\tilde{p}_s'(t-T_1-T_2) + \tilde{p}_s''(t-T_1-T_2)]. \tag{A7}$$

Thus, by combining Eqs. (A3) and (A4) and using demodulated quantities, the perturbed pressure at the receiver in the time domain can be written in the form

$$\begin{aligned} p_r(t)+\Delta p_r(t) &= \frac{p_s(t-T)}{4\pi R} + \frac{2dV\Delta c}{(4\pi)^2 R_1 R_2 c^3} p_s''(t-T_1-T_2) \\ &= \frac{\tilde{p}_s(t-T)e^{i\omega_0(t-T)}}{4\pi R} + \frac{2dV\Delta c}{(4\pi)^2 R_1 R_2 c^3} e^{i\omega_0(t-T_1-T_2)} \\ &\quad \times[-\omega_0^2\tilde{p}_s(t-T_1-T_2) + i2\omega_0\tilde{p}_s'(t-T_1-T_2) \\ &\quad + \tilde{p}_s''(t-T_1-T_2)] \\ &= e^{i\omega_0(t-T)}\left\{\frac{\tilde{p}_s(t-T)}{4\pi R} + \frac{2dV\Delta c}{(4\pi)^2 R_1 R_2 c^3}\right. \\ &\quad \times e^{i\omega_0(T-T_1-T_2)}[-\omega_0^2\tilde{p}_s(t-T_1-T_2) \\ &\quad \left. + i2\omega_0\tilde{p}_s'(t-T_1-T_2) + \tilde{p}_s''(t-T_1-T_2)]\right\}. \end{aligned} \tag{A8}$$

The squared amplitude of the perturbed pressure, i.e., the squared arrival pattern, will be

$$\begin{aligned} A(t) = a^2(t) &= |p_r(t)+\Delta p_r(t)|^2 \\ &= \left[\frac{\tilde{p}_s(t-T)}{4\pi R} - \frac{2dV\Delta c}{(4\pi)^2 R_1 R_2 c^3}\cos(\omega_0\tau) \right. \\ &\quad \times(\omega_0^2\tilde{p}_s(t-T_1-T_2) - \tilde{p}_s''(t-T_1-T_2)) \\ &\quad - \frac{2dV\Delta c}{(4\pi)^2 R_1 R_2 c^3}\sin(\omega_0\tau)2\omega_0\tilde{p}_s'(t-T_1-T_2) \\ &\quad + \left[\frac{2dV\Delta c}{(4\pi)^2 R_1 R_2 c^3}\cos(\omega_0\tau)2\omega_0\tilde{p}_s'(t-T_1-T_2) \right. \\ &\quad - \frac{2dV\Delta c}{(4\pi)^2 R_1 R_2 c^3}\sin(\omega_0\tau)(\omega_0^2\tilde{p}_s(t-T_1-T_2) \\ &\quad \left.\left. - \tilde{p}_s''(t-T_1-T_2))\right]^2, \end{aligned} \tag{A9}$$

where $\tau = T-T_1-T_2$ is the differential travel time between the straight line from the source to the receiver and the line passing through the scatterer ($\tau \leqslant 0$). By retaining first-order terms with respect to Δc, the following expression can be obtained for $A(t)$:

$$\begin{aligned} A(t) &= \frac{\tilde{p}_s^2(t-T)}{(4\pi R)^2} - 2\frac{\tilde{p}_s(t-T)}{4\pi R}\frac{2dV\Delta c}{(4\pi)^2 R_1 R_2 c^3}\cos(\omega_0\tau) \\ &\quad \times[\omega_0^2\tilde{p}_s(t-T_1-T_2) - \tilde{p}_s''(t-T_1-T_2)] \\ &\quad - 2\frac{\tilde{p}_s(t-T)}{4\pi R}\frac{2dV\Delta c}{(4\pi)^2 R_1 R_2 c^3} \\ &\quad \times\sin(\omega_0\tau)2\omega_0\tilde{p}_s'(t-T_1-T_2). \end{aligned} \tag{A10}$$

The first term on the right-hand side is the unperturbed squared arrival pattern whereas the other two terms represent the perturbation of the squared arrival pattern due to the scatterer.

In the following, a number of cases is considered depending on the value of $\omega_0\tau$, i.e., on the position of the scatterer, sheding light to the travel-time sensitivity behavior. Assuming $\tilde{p}_s$ to be a real-valued pulse (a spike) with its maximum at zero, then $\tilde{p}_s''$ will have a negative maximum at zero whereas $\tilde{p}_s'$ will be a decreasing antisymmetric function about zero.

(a) $\tau=0$: In this case the scatterer lies on the straight line from the source to the receiver and the third term in (A10) vanishes due to the effect of $\sin(\omega_0\tau)$. Since $T = T_1+T_2$, the expression for $A(t)$ becomes

$$A(t) = \frac{\tilde{p}_s^2(t-T)}{(4\pi R)^2} - 2\frac{\tilde{p}_s(t-T)}{4\pi R}\frac{2dV\Delta c}{(4\pi)^2 R_1 R_2 c^3}[\omega_0^2\tilde{p}_s(t-T) - \tilde{p}_s''(t-T)]. \tag{A11}$$

Since the functions $\tilde{p}_s$ and $\tilde{p}_s''$ have their positive/negative maximum at zero, the perturbed squared arrival pattern in this case will have its maximum at $t=T$. The bracketed term in the vicinity of $t=T$ is positive. Accordingly, a sound-speed increase ($\Delta c>0$) will reduce the arrival amplitude whereas a sound-speed decrease ($\Delta c<0$) will cause amplification. The arrival time will remain unaffected (*zero sensitivity*).

(b) $0>\omega_0\tau>-\pi/2$: In this case the scatterer lies slightly off the straight line connecting the source and the receiver and both scattering terms in (A10) are active and centered at $T_1+T_2>T$, i.e., at the right flank of the unperturbed arrival. In the case of a positive sound-speed perturbation ($\Delta c>0$) the second term in (A10)

will be negative whereas the factor of $\tilde{p}_s'$ in the third term will be positive, since $\sin(\omega_0 t)<0$. This means that the positive forms $\tilde{p}_s$ and $-\tilde{p}_s''$ (centered at $T_1+T_2>T$) are subtracted from the unperturbed arrival (centered at T), whereas the decreasing from $\tilde{p}_s'$ is added. This will cause the arrival maximum to move to the left, i.e., to smaller time values. In the case of a negative sound-speed perturbation ($\Delta c<0$) the opposite operations will cause a shift at the arrival maximum to larger arrival times (*negative sensitivity*).

(c) $\omega_0\tau=-\pi/2$: In this case the scatterer lies further off the straight line connecting the source and the receiver, and now only the second scattering term in (A10) will be active. As in the previous case this case is characterized by negative sensitivity too.

(d) $-\pi/2>\omega_0\tau>-\pi$: The term $\cos(\omega_0\tau)$ now attains negative values, starting from zero ($\omega_0\tau=-\pi/2$) and going to -1 ($\omega_0\tau=-\pi$). For $\omega_0\tau=-\pi/2$ (the previous case) the second scattering term in (A10) dominates and gives negative sensitivity, whereas for $\omega_0\tau=-\pi$ it is the first scattering term that dominates, giving positive sensitivity, as described below. Thus, there should be a value for $\omega_0\tau$ in the open interval $(-\pi, -\pi/2)$ where zero sensitivity is attained. This value will depend on the characteristics of the emitted signal $\tilde{p}_s$.

(e) $\omega_0\tau=-\pi$: In this case it is the first scattering term that dominates in (A10)—the second scattering term disappears since $\sin(-\pi)=0$. The expression for $A(t)$ becomes

$$A(t)=\frac{\tilde{p}_s^2(t-T)}{(4\pi R)^2}+2\frac{\tilde{p}_s(t-T)}{4\pi R}\frac{2dV\Delta c}{(4\pi)^2R_1R_2c^3}\times[\omega_0^2\tilde{p}_s(t-T_1-T_2)-\tilde{p}_s''(t-T_1-T_2)]. \quad \text{(A12)}$$

A positive sound-speed perturbation ($\Delta c>0$) will cause the positive forms $\tilde{p}_s$ and $-\tilde{p}_s''$ centered at $T_1+T_2>T$, i.e., at the right flank of the unperturbed arrival to be added to it, thus moving the arrival maximum to the right, i.e., to larger time values. A negative sound-speed perturbation ($\Delta c<0$) will cause the positive forms to be subtracted from the unperturbed arrival, thus moving the arrival maximum to the left, i.e., to smaller time values (*positive sensitivity*).

The condition $\omega_0\tau=-\pi$ defines the Fresnel radius R_F, i.e., the radius of the first Fresnel zone.[34,35] Thus, the outer boundary of the first Fresnel zone is a surface of positive travel-time sensitivity. The negative-sensitivity core has an outer radius larger than (but close to) $R_F/\sqrt{2}$ and smaller than R_F, the precise value depending on the characteristics of the emitted signal.

APPENDIX B: VERTICAL SENSITIVITY OF PEAK ARRIVAL TIMES

A wave-theoretic expression for the vertical sensitivity kernel of peak arrival times is derived in the following by assuming range independence for both the background environment $c(z)$ and the sound-speed perturbation $\Delta c(z)$. Since the medium preserves its horizontal stratification the Green's function in the perturbed case can be represented by the normal-mode expansion (19) with perturbed eigenvalues $k_n+\Delta k_n$ and eigenfunctions $u_n+\Delta k_n$, $n=1,...,M$. By applying perturbation theory to the vertical eigenvalue problem (20), the following perturbation relations can be derived for the eigenvalues and eigenfunctions:[11,43]

$$\Delta k_n=-\frac{\rho\omega^2}{k_n}\int_0^h\frac{\Delta c(z')}{c^3(z')}u_n^2(z')dz' \quad \text{(B1)}$$

and

$$\Delta u_n(z)=-2\rho\omega^2\int_0^h\frac{\Delta c(z')}{c^3(z')}\times\sum_{\substack{m=1\\m\neq n}}^{M}\frac{u_n(z')u_m(z')u_m(z)}{k_n^2-k_m^2}dz', \quad \text{(B2)}$$

where h is the water depth. Taking a first-order perturbation of the normal-mode representation (19), with respect to eigenvalues and eigenfunctions, and substituting the relations (B1) and (B2), the perturbation of the Green's function in the range independent case can be related to the underlying sound-speed perturbations as follows:

$$\Delta G=-\int_0^h\sum_{n=1}^{M}\left[\sum_{\substack{m=1\\m\neq n}}^{M}\frac{U_{nm}u_n(z')u_m(z')}{k_n^2-k_m^2}+\frac{1}{k_n}\left(\frac{1}{2k_n}+jR\right)\times U_{nn}u_n^2(z')\right]\frac{e^{-jk_nR}}{\sqrt{k_n}}\,\omega^2\frac{e^{-j\pi/4}}{\sqrt{2\pi R}}\frac{\Delta c(z')}{c^3(z')}dz', \quad \text{(B3)}$$

where $U_{nm}=u_n(z_s)u_m(z_r)+u_n(z_r)u_m(z_s)$ for $n\neq m$ and $U_{nn}=-u_n(z_s)u_n(z_r)/2$. By substituting the expression above into the Fourier transform (11), the corresponding perturbation of the pressure at the receiver in the time domain can be obtained. By combining this with the relation (14) the perturbation of the peak arrival time $\Delta\tau_i$ can be written in the form

$$\Delta\tau_i=\int_0^h S_i(z')\Delta c(z')dz' \quad \text{(B4)}$$

where

$$S_i(z')=\Re\left\{\frac{1}{2\pi b_i}\int_{-\infty}^{\infty}[j\omega(v_i-jw_i)+(\dot{v}_i-j\dot{w}_i)]L(z';\omega)e^{j\omega\tau_i}d\omega\right\} \quad \text{(B5)}$$

and

$$L(z';\omega)=\frac{\omega^2P_s(\omega)e^{-j\pi/4}}{c^3(z')\sqrt{2\pi R}}\times\sum_{n=1}^{M}\left[\sum_{\substack{m=1\\m\neq n}}^{M}\frac{U_{nm}u_n(z')u_m(z')}{k_n^2-k_m^2}+\frac{1}{k_n}\left(\frac{1}{2k_n}+jR\right)U_{nn}u_n^2(z')\right]\frac{e^{-jk_nR}}{\sqrt{k_n}}. \quad \text{(B6)}$$

The quantity $S_i(z')$ is the vertical sensitivity kernel of the peak arrival time τ_i with respect to depth. This is equivalent to integrating the 3-D travel-time sensitivity kernel K_i over range and azimuth.

ACKNOWLEDGMENTS

The authors would like to thank Maarten de Hoop for valuable remarks, as well as the anonymous reviewers for their comments and suggestions. The second author would like to acknowledge ONR support, on contract N00014-01-1-0768 and N00014-03-1-0182

[1] W. H. Munk and C. Wunsch, ''Ocean acoustic tomography: A scheme for large scale monitoring,'' Deep-Sea Res. **26A**, 123–161 (1979).
[2] W. H. Munk, P. F. Worcester, and C. Wunsch, *Ocean Acoustic Tomography* (Cambridge University Press, New York, 1995).
[3] The Ocean Tomography Group, ''A demonstration of ocean acoustic tomography,'' Nature (London) **299**, 121–125 (1982).
[4] B. M. Howe, P. F. Worcester, and R. C. Spindel, ''Ocean acoustic tomography: Mesoscale velocity,'' J. Geophys. Res. **92**, 3785–3805 (1987).
[5] L. Brekhovskikh and Y. Lysanov, *Fundamentals of Ocean Acoustics* (Springer-Verlag, New York, 1982).
[6] F. Tappert and X. Tang, ''Ray chaos and eigenrays,'' J. Acoust. Soc. Am. **99**, 185–195 (1996).
[7] M. B. Porter and H. P. Bucker, ''Gaussian beam tracing for computing ocean acoustic fields,'' J. Acoust. Soc. Am. **82**, 1349–1359 (1987).
[8] J. B. Bowlin, ''Generating eigenray tubes from two solutions of the wave equation,'' J. Acoust. Soc. Am. **89**, 2663–2669 (1991).
[9] W. H. Munk and C. Wunsch, ''Ocean acoustic tomography: Rays and modes,'' Rev. Geophys. Space Phys. **21**, 777–793 (1983).
[10] E. C. Shang, ''Ocean acoustic tomography based on adiabatic mode theory,'' J. Acoust. Soc. Am. **85**, 1531–1537 (1989).
[11] G. A. Athanassoulis and E. K. Skarsoulis, ''Arrival-time perturbations of broadband tomographic signals due to sound-speed disturbances. A wave-theoretic approach,'' J. Acoust. Soc. Am. **97**, 3575–3588 (1995).
[12] E. K. Skarsoulis, G. A. Athanassoulis, and U. Send, ''Ocean acoustic tomography based on peak arrivals,'' J. Acoust. Soc. Am. **100**, 797–813 (1996).
[13] F. A. Dahlen, S.-H. Hung, and G. Nolet, ''Fréchet kernels for finite-frequency traveltimes—I. Theory,'' Geophys. J. Int. **141**, 157–174 (2000).
[14] S.-H. Hung, F. A. Dahlen, and G. Nolet, ''Fréchet kernels for finite-frequency traveltimes—II. Examples,'' Geophys. J. Int. **141**, 175–203 (2000).
[15] H. Marquering, G. Nolet, and F. A. Dahlen, ''Three-dimensional sensitivity kernels for finite-frequency travel times: the banana-doughnut paradox,'' Geophys. J. Int. **137**, 805–815 (1999).
[16] H. Marquering, F. A. Dahlen, and G. Nolet, ''Three-dimensional waveform sensitivity kernels,'' Geophys. J. Int. **132**, 521–534 (1998).
[17] M. V. de Hoop and R. D. van der Hilst, ''On sensitivity kernels for wave equation tomography,'' Colorado School of Mines, Center for Wave Phenomena, Research Report CWP-433P (2002).
[18] Y. Luo and G. T. Schuster, ''Wave equation traveltime tomography,'' Geophysics **56**, 645–653 (1991).
[19] E. C. Shang and Y. Y. Wang, ''On the possibility of monitoring El Nino by using modal ocean acoustic tomography,'' J. Acoust. Soc. Am. **91**, 136–140 (1992).
[20] C. A. Boyles, *Acoustic Waveguides. Applications to Oceanic Science* (Wiley, New York, 1984).
[21] F. B. Jensen, W. A. Kuperman, M. B. Porter, and H. Schmidt, *Computational Ocean Acoustics* (American Institute of Physics, Woodbury, NY, 1994).
[22] P. M. Morse and H. Feshbach, *Methods of Theoretical Physics* (McGraw-Hill, New York, 1953).
[23] M. Born, ''Quantum mechanics of impact processes,'' Z. Phys. **38**, 803–827 (1926).
[24] J. R. Taylor, *Scattering Theory* (Wiley, New York, 1972).
[25] J. L. Spiesberger, ''Gyre-scale acoustic tomography: Biases, iterated inversions, and numerical methods,'' J. Geophys. Res. **90**, 869–876 (1985).
[26] P. J. Sutton, P. F. Worcester, G. Masters, B. D. Cornuelle, and J. F. Lynch, ''Ocean mixed layers and acoustic pulse propagation in the Greenland Sea,'' J. Acoust. Soc. Am. **94**, 1517–1526 (1993).
[27] R. C. Spindel, ''An underwater acoustic pulse compression system,'' IEEE Trans. Acoust., Speech, Signal Process. **ASSP-27**, 723–738 (1979).
[28] K. Metzger, Jr., ''Signal processing equipment and techniques for use in measuring ocean acoustic multipath structures,'' Ph.D. thesis, University of Michigan, Ann Arbor, MI, 1983.
[29] P. Blanchard and E. Brüning, *Variational Methods in Mathematical Physics* (Springer-Verlag, New York, 1992).
[30] The THETIS Group, ''Open-ocean deep convection explored in the Mediterranean,'' EOS Trans. Am. Geophys. Union **75**, 217–221 (1994).
[31] S. E. Dosso and N. R. Chapman, ''Measurement and modelling of downslope acoustic propagation loss over a continental slope,'' J. Acoust. Soc. Am. **81**, 258–268 (1987).
[32] The notation $\pm n$ is used as a ray identifier, where $\pm$ is the sign of grazing angle of the eigenray at the source ($+$ for upward, $-$ for downward), and n is the number of turning points (upper and lower) of the eigenray.
[33] J. Tong, F. A. Dahlen, G. Nolet, and H. Marquering, ''Diffraction effects upon finite-frequency travel times: A simple 2-d example,'' Geophys. Res. Lett. **25**, 1983–1986 (1998).
[34] A. D. Pierce, *Acoustics. An Introduction to its Physical Principles and Applications* (ASA/AIP, New York, 1989).
[35] J. Pearce and D. Mittleman, ''Defining the Fresnel zone for broadband radiation,'' Phys. Rev. **66**, 056602/1-4 (2002).
[36] F. A. Dahlen and A. M. Baig, ''Fréchet kernels for body wave amplitudes,'' Geophys. J. Int. **150**, 440–466 (2002).
[37] E. K. Skarsoulis and G. A. Athanassoulis, ''Second-order perturbations of peak-arrival times due to sound-speed variations,'' J. Acoust. Soc. Am. **104**, 3313–3325 (1998).
[38] B. D. Dushaw, B. M. Howe, J. A. Mercer, and R. C. Spindel, ''Multimegameter-range acoustic data obtained by bottom-mounted hydrophone arrays for measurement of ocean temperature,'' IEEE J. Ocean. Eng. **24**, 202–214 (1999).
[39] J. A. Colosi, E. K. Scheer, S. M. Flatte, B. D. Cornuelle, M. A. Dzieciuch, W. H. Munk, P. F. Worcester, B. M. Howe, J. A. Mercer, R. C. Spindel, K. Metzger, T. G. Birdsall, and A. B. Baggeroer, ''Comparisons of measured and predicted acoustic fluctuations for a 3250-km propagation experiment in the eastern North Pacific Ocean,'' J. Acoust. Soc. Am. **105**, 3202–3218 (1999).
[40] S.-H. Hung, F. A. Dahlen, and G. Nolet, ''Wavefront healing: a banana-doughnut perspective,'' Geophys. J. Int. **146**, 289–312 (2001).
[41] F. Tappert, ''Theory of explosive beam spreading due to ray chaos,'' J. Acoust. Soc. Am. **114**, 2775–2781 (2003).
[42] W. B. Beydoun and A. Tarantola, ''First Born and Rytov approximations: Modeling and inversion conditions in a canonical example,'' J. Acoust. Soc. Am. **83**, 1045–1055 (1988).
[43] L. D. Landau and E. M. Lifshitz, *Quantum Mechanics: Nonrelativistic Theory* (Pergamon, Oxford, 1977).

On the acoustic diffraction by the edges of benthic shells

Timothy K. Stanton[a] and Dezhang Chu
Department of Applied Ocean Physics and Engineering, Woods Hole Oceanographic Institution, Woods Hole, Massachusetts 02543-1053

(Received 15 September 2003; revised 7 January 2004; accepted 14 January 2004)

Recent laboratory measurements of acoustic backscattering by individual benthic shells have isolated the edge-diffracted echo from echoes due to the surface of the main body of the shell. The data indicate that the echo near broadside incidence is generally the strongest for all orientations and is due principally to the surface of the main body. At angles well away from broadside, the echo levels are lower and are due primarily to the diffraction from the edge of the shell. The decrease in echo levels from broadside incidence to well off broadside is shown to be reasonably consistent with the decrease in acoustic backscattering from normal incidence to well off normal incidence by a shell-covered seafloor. The results suggest the importance of the edge of the shell in off-normal-incidence backscattering by a shell-covered seafloor. Furthermore, when considering bistatic diffraction by edges, there are implications that the edge of the shell (lying on the seafloor) can cause significant scattering in many directions, including at subcritical angles. © *2004 Acoustical Society of America.* [DOI: 10.1121/1.1675813]

PACS numbers: 43.30.Sf, 43.30.Hw [KGF] Pages: 239–244

I. INTRODUCTION

There is significant evidence that benthic shells, when occurring in sufficiently large numbers, can dominate acoustic backscattering by the seafloor, especially at angles of incidence away from normal (Jackson *et al.*, 1986; Stanic *et al.*, 1989; Fenstermacher *et al.*, 2001; Stanton, 2000; Williams *et al.*, 2001). A major limiting factor in the analyses of these data has been the lack of understanding of the fundamental scattering process of the shells. The shape of the shells is complex and it is impossible to formulate exact analytical models. Stanton *et al.* (2000) have recently shown that the scattering by one class of benthic shells, periwinkles, whose shape is rounded (low aspect ratio), has significant contributions from the front interface, the interface exposed from the opercular opening for certain orientations, and Lamb circumferential waves for other orientations.

In this paper, measurements of the backscattering by empty bivalve and sand dollar shells in free space (i.e., away from boundaries) are presented. In contrast to the periwinkles studied in Stanton *et al.* (2000), these shells have an oblate shape (high aspect ratio) with distinct edges around the perimeter of the bodies. Applying a pulse-compression technique to the broadband echoes, the diffraction by the edges are resolved over a wide range of orientation angles. The results are compared with the scattering by a machined aluminum disk of similar dimensions, which provides additional insight into the scattering process. The results are also compared with previously published scattering measurements from two cases involving a shell-covered seafloor. The significance of the edge in the scattering process is discussed both with respect to backscattering by a shell-covered seafloor and penetration of acoustic energy into the seafloor.

[a]Electronic mail: tstanton@whoi.edu

II. EXPERIMENT

The experiment involved insonifying individual bivalve shells (one-half shell at a time), sand dollar shells, and machined circular metal disks with a broadband acoustic signal in a laboratory tank. The shells were empty. Both backscattering and forward scattering were measured. Since the analysis below involves just backscattering from one scatterer per category listed above, experimental data presented cover only relavent information.

A. Targets

The bivalve was collected off of Florida as part of the SAX99 experiment (Thorsos *et al.*, 2001) and the sand dollar was collected near Humboldt Bay, CA. The disk was machined out of aluminum, which has a similar density and sound speed as that of the shells. All objects were of comparable size (Table I) so that comparisons of the scattering characteristics could be made (Fig. 1). The three objects represent, in essence, a progression of shapes of increasing complexity. The machined disk, used as a control target, is flat and circular. The sand dollar is generally circular, mostly flat on one side, and rounded on the other side. The one-half bivalve shell has an edge in a somewhat elliptical pattern with an open surface that is concave. The surface and edge of the sand dollar are generally smooth while these features of the bivalve are corrugated.

B. Experimental setup

The acoustic scattering measurements were conducted in a flume tank filled with fresh water in Fall 2002 (Fig. 2). The tank was 23 m long, with a square cross section 1.2 m on a side. The targets and acoustic transducers were placed in the center of the cross section of the tank. A pair of closely spaced transducers was used, one as transmitter and the other as receiver, to emit and receive a broadband chirp (linear frequency modulated) signal over the frequency range 40–95

TABLE I. Dimensions of targets. The terms ''horizontal'' and ''vertical'' refer to cross dimensions of the objects in the deployed position (Fig. 2), thus the vertical dimension is measured along a line parallel to the tethers shown in Fig. 1 and the horizontal dimension is along a perpendicular line. The upper camber gives an indication of the curvature of the shells. With the flat side of the sand dollar or concave side of the bivalve on a flat surface, the upper camber is the largest distance or deviation measured between the surface and the opposite side of the shell. Since the disk is flat, this measurement corresponds to its thickness of 0.19 cm. The aluminum is an alloy (#6061), received a T6 heat treatment, and contained 97.92% aluminum.

Target	Species or material	ID no	Horizontal dimension (cm)	Vertical dimension (cm)	Upper camber (cm)
disk	Aluminum	AL02-4	8.0	8.0	0.19
sand dollar	*Dendraster excentricus*	HSU02-02	7.25	6.7	1.1
bivalve	*Dinocardium robustum vanhyningi*	SAX99-C-08	7.0	6.9	2.9

kHz. The received signal was digitized with a digital oscilloscope and stored onto a personal computer for postprocessing. The target was rotated with a computer-controlled stepper motor in 1° increments between pings, so that scattering could be measured over a 360° range of orientations. Care was taken so that multi-path echoes from all surfaces of the narrow tank did not interfere with the echoes of interest. Once the echoes were temporally compressed through cross correlating the echoes with the calibration signal, the multipath signals were resolved and eliminated in the analysis. Because of the finite dimensions of the transducers, the two-transducer setup deviated from true backscatter. The center-to-center separation between the transducers was 0.33 m and the target-transducer separation was 3.0 m, resulting in a 6.3° deviation from true backscatter. Details of the pulse compression signal processing, electronics, measurement procedure, and calibration are given in Chu and Stanton (1998), Stanton *et al.* (1998, 2000), and Reeder *et al.* (in press).

III. RESULTS

The backscattering by all three objects was strongly directional (Figs. 3–6). This dependence is consistent with the fact that $kD \gg 1$, where k $(=2\pi/\lambda$, where λ is the acoustic wavelength) is the acoustic wavenumber and D is a characteristic outer dimension, such as length, width, or diameter. The scattering is shown to be strongest near broadside incidence with the exception of the convex aspect of the bivalve. The scattering pattern is especially strong and directional near broadside incidence for the flat surfaces since, in these cases, the echoes from a flat interface tend to add constructively and dominate the scattering.

Well away from broadside, diffraction from edges becomes important. This is best illustrated through use of the temporally compressed signal (Figs. 4–6). In the color contour plots of scattered pressure versus orientation, the edge diffracted waves produce a nearly sinusoidal pattern, which is especially apparent in the data concerning the disk and, to some extent from the sand dollar. The patterns from the machined metallic disk and sand dollar show multiple orders of diffraction, due to multiple circumnavigations around the surfaces of the targets. The first-order return is from a direct arrival from the leading or trailing edge. The second-order return is from diffraction by one edge (leading or trailing), traveling along the surface of the target, then diffraction by the other edge. (Similarly, higher order returns appear at times corresponding to higher-order circumnavigations.

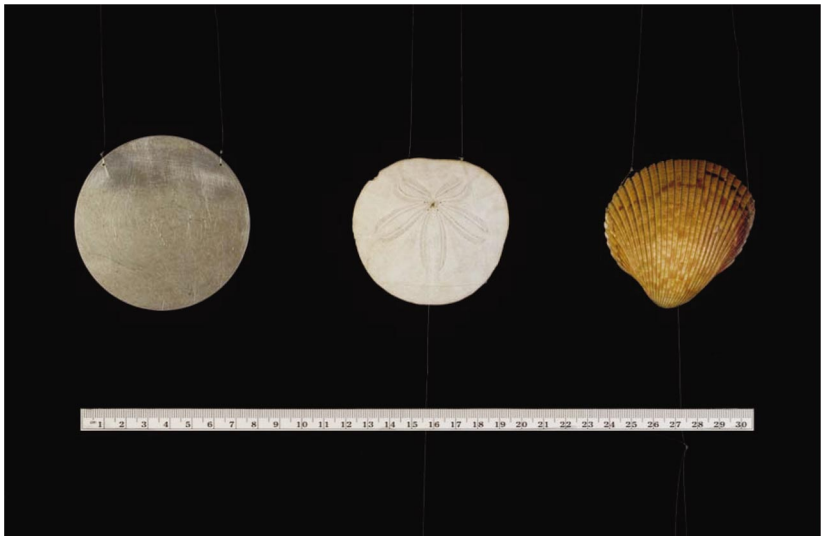

FIG. 1. Photo of targets used in acoustic scattering measurements. Left: aluminum disk, middle: sand dollar, and right: bivalve. Centimeter ruler in photo for scale. The thin lines perpendicular to the ruler are the tethers used to suspend and rotate the targets.

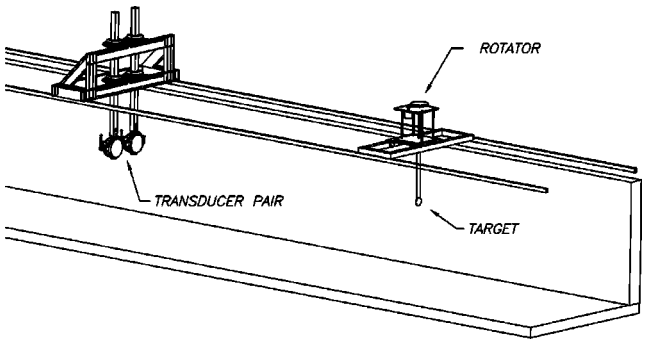

FIG. 2. Sketch of backscattering measurement. Thickness of tethers exaggerated for purpose of illustration.

Travel times along the surface are associated with waves of supersonic speeds, at least for the disk.

There is a striking resemblance between the pattern of first-order edge-diffracted waves from the sanddollar and metallic disk. In addition to the similar near-sinusoidal patterns, both show consistent strength across much of the range of orientation away from broadside incidence. There are important differences between the patterns as well—for example, near broadside, the main lobe of the scatter pattern of the sand dollar is asymetrical about the plane of the body since one side is nearly flat and the other side is rounded.

The scatter pattern from the bivalve is more complex than those of the other targets. Since the radius of curvature of the shell is smaller than that of the other targets and the shell subtends such a large range of angles, the main lobe of the scatter pattern is much broader than those of the other targets. In fact, most of the pattern is from either the scattering from the convex surface (e.g., 110° to 250°) or concave surface [e.g., −70°(290°) to 50°]. Over a small span of orientations (e.g., 50° to 110° and 250° to 290°) where the surface scattering is not dominating, there are features that correspond to edge diffraction.

The physics of the scattering by these elastic objects is complex and a detailed description of the various scattering mechanisms associated with the scattering is beyond the scope of this work. The reader is referred to the experimental studies of the scattering by elastic disks presented in Hefner (2000) and Hefner and Marston (2001, 2002). In those studies, the pattern of scattering by the edges was observed. Also, other effects, involving excitation of Lamb waves, were observed and described in those studies. The series of echoes near 20° and 160° in Figs. 4 and 5 of this work are consistent with such excitation. For analytical and numerical descriptions of scattering by impenetrable curved or bounded edges, as well as more experimental results, the reader is referred to the works of Lyamshev (1999), Kristensson and Waterman (1982), Norton *et al.* (1993), Medwin (1981), Jebsen and Medwin (1982), and Svensson *et al.* (1999).

IV. IMPLICATIONS FOR SCATTERING BY SHELL-COVERED SEAFLOOR

Because of the significant observed diffraction by the edge of the shells, there are implications of the importance of the diffraction by the edge of the shells both in applications of backscattering as well as penetration of the acoustic energy into the seafloor.

A. Backscattering

The results show that the diffraction by the edge in the backscattering direction for oblique orientations is generally about 10–30 dB below the level of the backscattering from the shell for near-broadside orientations where the shell surface dominates the scattering. In order to understand the importance of this level in the context of acoustic scattering by a shell-covered seafloor, data from the seafloor are required. There are limited scientific data available to date for this particular type of scattering.

In one study involving the bivalve used in this analysis, a number of known shells were laid on the seafloor and the backscattering was measured at 40 kHz and at a fixed grazing angle of 16°. This experiment, known by the name SAX99, was conducted in the Gulf of Mexico in 1999 and is described, in part, in Thorsos *et al.* (2001) and Williams *et al.* (2001). The bivalve used in the measurements described herein was 1 of the 81 large shells (all approximately 6 cm in diameter) used in the SAX99 experiment. In one of the (SAX99) measurements involving just the large shells, the bivalves were laid out on the seafloor in a random spacing with a number density of about $20/m^2$, all with the concave side in the upward direction. The measured area scattering strength (or, equivalently, target strength of a square meter of seafloor) as defined in Urick (1983) was −27 dB. The target strength of the bivalve in this study at an orientation of 74° (concave aspect, Fig. 3), which corresponds to the 16° grazing angle, is about −42.5 dB. Although this value corresponds to the 70-kHz frequency component, a

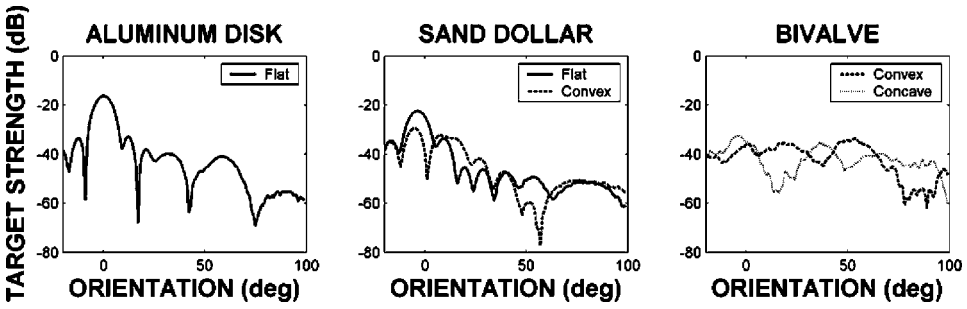

FIG. 3. Target strength derived from 70–kHz component of echo versus orientation for each target. Since the spectral component of the signal is inherently narrow-band, various scattering highlights are not temporally resolved in this plot. The orientation is relative to broadside incidence (0°) for each surface of each target, thus the angles in this plot may not directly correspond with the angles given in Figs. 4–6 where broadside occurs at 0°, 180°, and 360°.

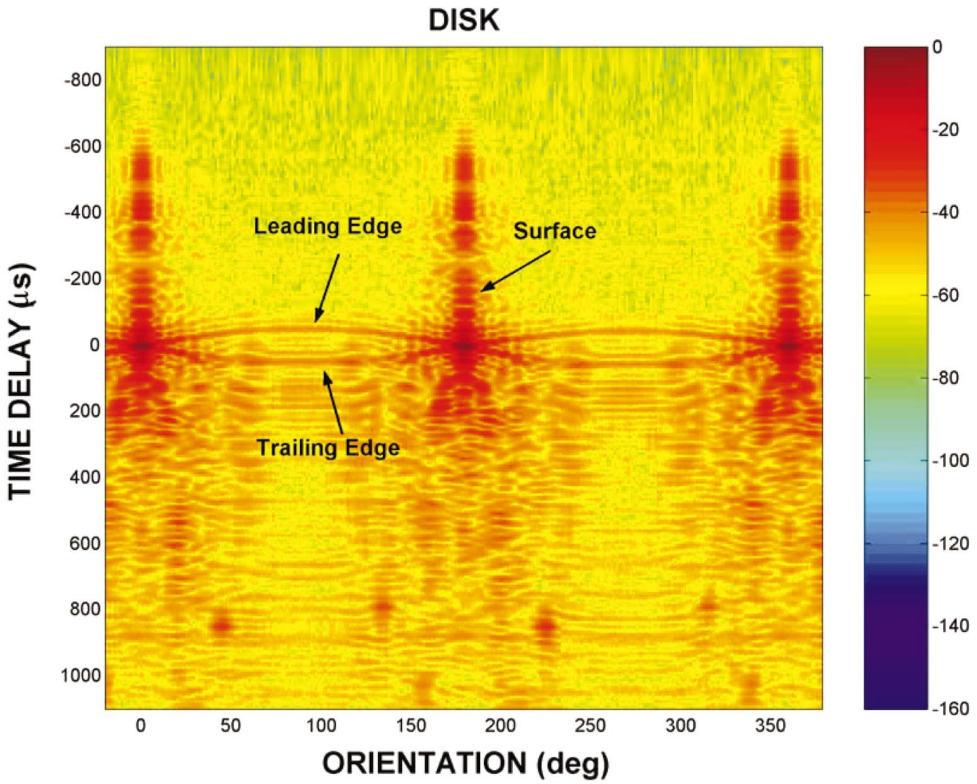

FIG. 4. Color contour image of temporally compressed echo versus orientation for aluminum disk. Various echoes from the target are resolved, including diffracted echoes from leading and trailing edges of the target and echo from surface. Range resolution of this signal is approximately 2 cm. The color scale is in dB relative to the maximum value. Apparent echoes from the surface at orientations near 0°, 180°, and 360° arriving at negative time delays are actually processing sidelobes from the large 0-time-delay echoes.

similar range of values was observed at 50 kHz (not shown) and presumably it would be similar at 40 kHz as well (the 40 kHz component is at the edge of the band and is not included in this analysis). Using Eqs. (2) and (4) from Stanton (2000), the area scattering strength (same definition as above) from an aggregation of randomly distributed targets lying on a planar low-reflective substrate is approximately $S_A = TS + 10 \log n$, where n is the numerical density. From this equa-

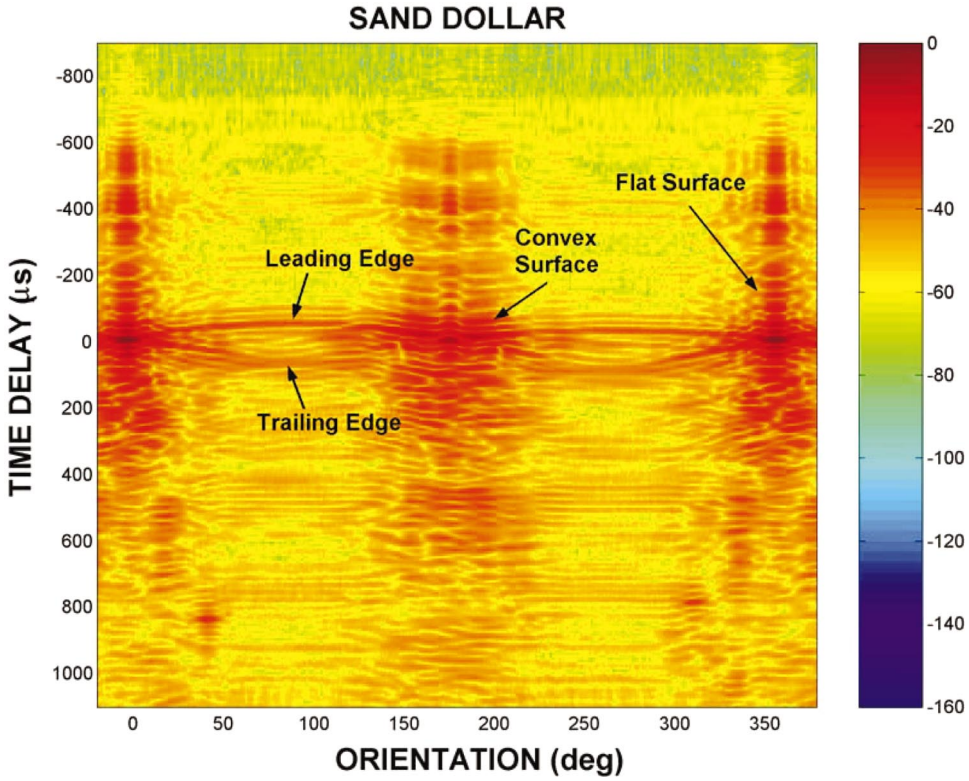

FIG. 5. Color contour image of temporally compressed echo versus orientation for the sand dollar. See caption to Fig. 4 for more details.

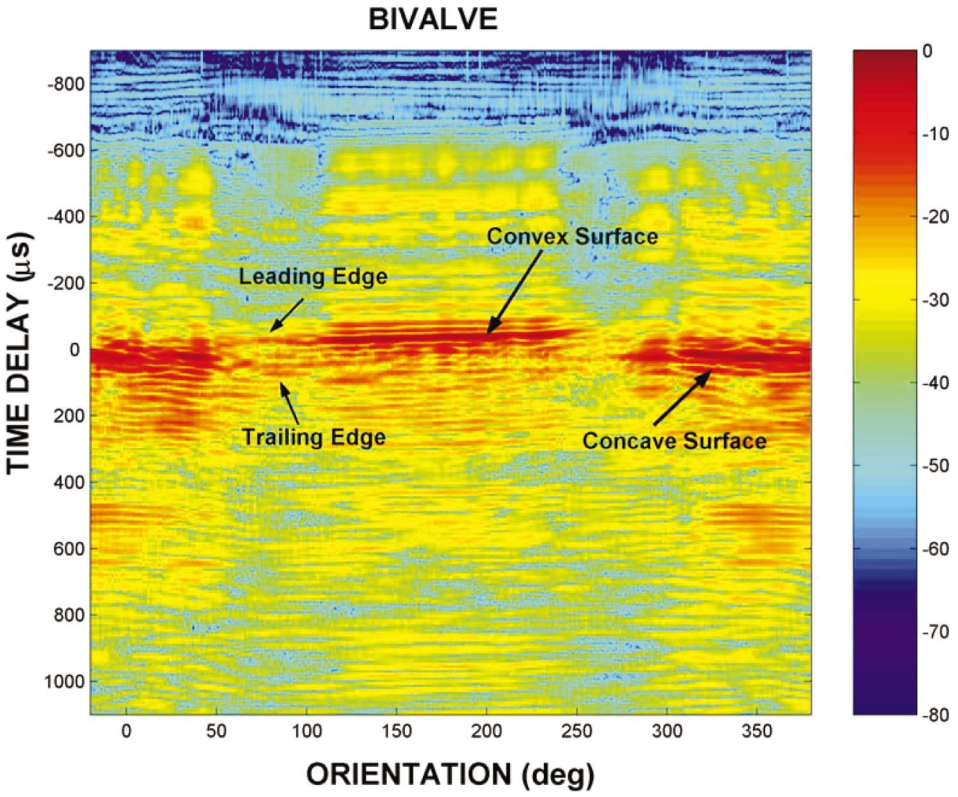

FIG. 6. Color contour image of temporally compressed echo versus orientation for bivalve. See caption to Fig. 4 for more details.

tion, and assuming all targets have the same target strength of −42.5 dB, the area scattering strength is predicted at approximately −29.5 dB. This predicted value is about 2.5 dB lower than the observed value in the SAX99 experiments. Of course, the model had approximations, and, very importantly, the target-to-target variability and effects due to the seafloor substrate (such as its roughness and the edge-seafloor ray path) were not taken into account. For example, the scattering strength by the seafloor without the shells was −31 dB. Assuming that the echoes from the shells and seafloor add incoherently and that the shells shadowed only a small fraction of the seafloor, then the combination of scattering by the seafloor and shells would be approximately 27.2 dB, which is essentially the same as the observed value of the shell-covered seafloor. Accounting for the shell-seafloor ray path can further enhance the contribution from the shells—an effect predicted by Williams *et al.* (2001) in the case of marbles. Although these are crude estimates, the backscattering value of the individual shell provides a plausible explanation for the increase in scattering by the seafloor when shells are present. As shown in Fig. 6, this region of shallow grazing angles (16°) corresponds to the angles (near 74°) at which the edge of the shell is contributing significantly to the scattering. Thus, it is important to account for the edge of the shell when making scattering predictions at angles well off normal incidence.

In another study, Jackson *et al.* (1986) presented results of measurements of backscattering as a function of grazing angle for a shell-covered seafloor over the range 20–50 kHz. The seafloor was nearly completely covered with a thick, dense layer of live mussels and cockles (both types are bivalves) (Darrell Jackson, personal communication, 1998). The grazing angles ranged from 90° (normal incidence) down to about 10°. The data show that the backscattering by a shell-covered seafloor at angles well away from normal incidence is about 20 dB below the levels at normal incidence. This amount of decrease is essentially the same as for the convex case of the bivalve at the corresponding orientation of 80° in Fig. 3 and 100° in Fig. 6 (only the convex side of the live mussels and cockles are ''seen'' by the acoustic system). The comparison is not definitive since the shells in the Jackson *et al.* (1986) paper were not documented. Also, it is conceivable that the shells in their study were oriented such that there were significant contributions to the scattering from the surface of the shells. Nonetheless, since the edge-diffracted echoes are significant at these angles, the comparison shows that it is possible that the diffraction by the edges alone could dominate the backscattered echo at angles well off normal incidence.

B. Bottom penetration

The demonstration of the importance of the edge diffracted wave in the backscatter direction also has significance for the bistatic geometry. It has been demonstrated both theoretically and experimentally that edges can diffract an acoustic wave into directions other than the forward direction. For example, in the work of Bremhorst (1978) and Medwin (1981), it is shown that the diffracted wave due to a semi-infinite plate is in the range −15 to −25 dB below the level of the incidence wave for the case where the source is near the plate and for diffraction angles 90° past the forward diffraction angle [i.e., curve $\theta = 270°$ of Fig. 5 in Medwin (1981)]. For the seafloor problem, this angle would correspond to a shallow grazing incidence angle and near-vertical penetration of the diffracted wave. Although the edges of that

study were straight and impenetrable, it is reasonable to expect a similar effect for the curved and penetrable edges of the benthic shell, even when lying on a penetrable surface such as the seafloor.

If the edges of the shell diffract energy into directions different than that of the incident field, then a shell lying on the seafloor will diffract sound into the seafloor, which is also penetrable acoustically. A bed of randomly located, randomly oriented shells can scatter sound diffusely into the seafloor. It is known that for grazing angles below a certain value (i.e., the critical angle), sound will not penetrate a flat homogeneous seafloor. However, the presence of shells with edges can cause the sound to scatter into the seafloor at these angles due to diffraction by the edges. Because of this effect, objects within the seafloor could possibly be detected acoustically at subcritical angles when shells are present that could not have otherwise been detected.

V. SUMMARY AND CONCLUSIONS

Measurements have been made in which the free-field acoustic diffraction by the edge of individual benthic shells has been isolated from echoes from the shell surface. The diffracted echoes are shown to be of a strong enough level to be potentially significant in applications of acoustic scattering by a shell-covered seafloor. For backscattering applications, the ratio of the (free-field) edge-diffracted echo at oblique angles of incidence to the surface-scattered echo at broadside incidence is shown in one case to be comparable to the corresponding ratio (involving shallow grazing angles and normal incidence) for a shell-covered seafloor. These results imply that there may be conditions under which the edge of the shells can dominate the backscattering by a shell-covered seafloor for angles off of normal incidence. Another implication from these results is that the edge may cause significant penetration of acoustic energy into the seafloor, even at angles below the critical angle. This has importance in detecting targets that are below the water/bottom interface.

Although the results of this study are strongly suggestive in the applications to a shell-covered seafloor, verification is required such as through experimentation and simulation. Very importantly, the influence of the water/bottom interface on the edge-diffracted echo needs to be explored.

ACKNOWLEDGMENTS

This research was supported by the U.S. Office of Naval Research (Grant No. N00014-02-1-0095) and the Woods Hole Oceanographic Institution (WHOI), Woods Hole, MA. The authors are grateful to Craig Johnson of WHOI for constructing the mechanical mounts for the measurements, Shirley Barkley (WHOI) for preparing the manuscript to this paper, and Tom Kleindinst (WHOI) for taking the photograph for Fig. 1.

Bremhorst, J. H. (**1978**). ''Impulse wave diffraction by wedges and plates,'' M.S. thesis, Naval Postgraduate School, December.

Chu, D., and Stanton, T. K. (**1998**). ''Application of pulse compression techniques to broadband acoustic scattering by live individual zooplankton,'' J. Acoust. Soc. Am. **104**, 39–55.

Fenstermacher, L. E., Crawford, G. B., Borgeld, J. C., Britt, T., George, D. A., Klein, M. A., Driscoll, N. W., and Mayer, L. A. (**2001**). ''Enhanced acoustic reflectivity due to high abundance of sand dollars, *Dendraster excentricus*,'' Marine Georesources Geotechnol. **19**, 135–145.

Hefner, B. T. (**2000**). ''Acoustic backscattering enhancements for circular elastic plates and acrylic targets, the application of acoustic holography to the study of scattering from planar elastic objects, and other research on the radiation of sound,'' Ph.D. thesis, Washington State University.

Hefner, B. T., and Marston, P. L. (**2001**). ''Backscattering enhancements associated with the excitation of symmetric Lamb waves on a circular plate: direct and holographic observations,'' ARLO **2**, 55–60.

Hefner, B. T., and Marston, P. L. (**2002**). ''Backscattering enhancements associated with antisymmetric Lamb waves confined to the edge of a circular plate: direct and holographic observations,'' ARLO **3**, 101–106.

Jackson, D. R., Baird, A. M., Crisp, J. J., and Thompson, P. A. G. (**1986**). ''High-frequency bottom backscatter measurements in shallow water,'' J. Acoust. Soc. Am. **80**, 1188–1199.

Jebsen, G. M., and Medwin, H. (**1982**). ''On the failure of the Kirchhoff assumption in backscatter,'' J. Acoust. Soc. Am. **72**, 1607–1611.

Kristensson, G., and Waterman, P. C. (**1982**). ''The *T* matrix for acoustic and electromagnetic scattering by circular disks,'' J. Acoust. Soc. Am. **72**, 1612–1625.

Lyamshev, L. M. (**1999**). ''Nonspecular reflection, resonance scattering and radiation of sound by plates and shells in water,'' Acoust. Phys. **45**, 693–716.

Medwin, H. (**1981**). ''Shadowing by finite noise barriers,'' J. Acoust. Soc. Am. **69**, 1060–1064.

Norton, G. V., Novarini, J. C., and Keiffer, R. S. (**1993**). ''An evaluation of the Kirchhoff approximation in predicting the axial impulse response of hard and soft disks,'' J. Acoust. Soc. Am. **93**, 3049–3056.

Reeder, D. B., Jech, J. M., and Stanton, T. K. (**in press**). ''Broadband acoustic backscatter and high-resolution morphology of fish: Measurement and modeling,'' J. Acoust. Soc. Am.

Stanic, S., Briggs, K. B., Fleischer, P., Sawyer, W. B., and Ray, R. I. (**1989**). ''High-frequency acoustic backscattering from a coarse shell ocean bottom,'' J. Acoust. Soc. Am. **85**, 125–136.

Stanton, T. K. (**2000**). ''On acoustic scattering by a shell-covered seafloor,'' J. Acoust. Soc. Am. **108**, 551–555.

Stanton, T. K., Chu, D., Wiebe, P. H., Martin, L., and Eastwood, R. L. (**1998**). ''Sound scattering by several zooplankton groups. I. Experimental determination of dominant scattering mechanisms,'' J. Acoust. Soc. Am. **103**, 225–235.

Stanton, T. K., Chu, D., Wiebe, P. H., Eastwood, R. L., and Warren, J. D. (**2000**). ''Acoustic scattering by benthic and planktonic shelled animals,'' J. Acoust. Soc. Am. **108**, 535–550.

Svensson, U. P., Fred, R. I., and Vanderkooy, J. (**1999**). ''An analytic secondary source model of edge diffraction impulse responses,'' J. Acoust. Soc. Am. **106**, 2331–2344.

Thorsos, E. I., Williams, K. L., Chotiros, N. P., Christoff, J. T., Commander, K. W., Greenlaw, C. F., Holliday, D. V., Jackson, D. R., Lopes, J. L., McGehee, D. E., Piper, J. E., Richardson, M. D., and Tang, D. (**2001**). ''An overview of SAX99: Acoustic measurements,'' IEEE J. Ocean. Eng. **26**, 4–25.

Urick, R. J. (**1983**). *Principles of Underwater Sound* (McGraw–Hill, New York).

Williams, K. L., Richardson, M. D., Briggs, K. B., and Jackson, D. R. (**2001**). ''Scattering of high-frequency energy from discrete scatterers on the seafloor: Glass spheres and shells,'' Proc. Inst. Acoust. **23**, 369–374.

Tracking sperm whale (*Physeter macrocephalus*) dive profiles using a towed passive acoustic array[a)]

Aaron Thode[b)]
Marine Physical Laboratory, Scripps Institution of Oceanography, San Diego, California 92093-0205

(Received 1 March 2004; revised 13 April 2004; accepted 15 April 2004)

A passive acoustic method is presented for tracking sperm whale dive profiles, using two or three hydrophones deployed as either a vertical or large-aperture towed array. The relative arrival times between the direct and surface-reflected acoustic paths are used to obtain the ranges and depths of animals with respect to the array, provided that the hydrophone depths are independently measured. Besides reducing the number of hydrophones required, exploiting surface reflections simplifies automation of the data processing. Experimental results are shown from 2002 and 2003 cruises in the Gulf of Mexico for two different towed array deployments. The 2002 deployment consisted of two short-aperture towed arrays separated by 170 m, while the 2003 deployment placed an autonomous acoustic recorder in tandem with a short-aperture towed array, and used ship noise to time-align the acoustic data. The resulting dive profiles were independently checked using single-hydrophone localizations, whenever multipath reflections from the ocean bottom could be exploited to effectively create a large-aperture vertical array. This technique may have applications for basic research and for real-time mitigation for seismic airgun surveys. © *2004 Acoustical Society of America.* [DOI: 10.1121/1.1758972]

PACS numbers: 43.30.Sf, 43.80.Ka [WWA] Pages: 245–253

I. INTRODUCTION

Sperm whales (*Physeter macrocephalus*) were the first large cetaceans to be associated with a distinctive underwater sound, particularly a 6–10-ms impulsive sound described as a click.[1–4] Decades of additional research have revealed that sperm whales are among the most acoustically active cetaceans. Over the course of a typical dive, which can last longer than 45 min, an individual animal can produce thousands of clicks.[5–10] A considerable body of knowledge has accumulated about these sounds, including statistics on their time-frequency characteristics,[5] repetition rates,[9] possible correlations between animal size and click structure,[11,12] and the identification of regional differences between acoustic repertoires.[13–15]

The rich acoustic lives of sperm whales have made passive acoustic monitoring a fundamental tool for researching their behavior, as well as for designing mitigation protocols to protect them from potentially harmful anthropogenic activities. One standard configuration involves deploying two towed hydrophones behind a monitoring vessel, with the hydrophones separated by a few meters. By measuring the relative arrival times of impulsive sounds on the hydrophones, the animal's bearing relative to the monitoring vessel can be determined, subject to a left–right ambiguity. Small aperture towed-array systems have proven successful in mapping sperm whale population distributions,[16–18] and automated detection bearing estimation software has been developed for public use.[19,20] There are circumstances, however, when more precise estimates of an animal's position are desirable. These situations include mitigation monitoring, when it is important to establish whether an animal is in an ''exclusion zone,'' or to determine what sound characteristics an animal is being exposed to. For deep-diving animals such as sperm whales, depth may have to be solved simultaneously with range, to avoid inaccurate range estimates. While some proposed techniques use signal amplitude to estimate range,[21] this approach is problematic for sperm whales, whose sound source levels, even from a single individual, are highly variable.[22,23] Furthermore, evidence is accumulating that sperm whale sounds are highly directional,[23–25] and so the received signal amplitude of a sperm whale sound may vary with an animal's orientation relative to the hydrophone, as well as range. Therefore a single small-aperture array configuration is generally insufficient for range and depth tracking.

If additional hydrophones are deployed, separated by large baselines, the position of a whale within the volume in the vicinity of the deployment can be tracked by measuring the relative arrival times of all direct-path signals across the hydrophones. Both bottom-mounted[26] and portable configurations[27–30] of this type exist. Deploying such a distributed system to observe a mobile group of animals can be logistically difficult. For example, sperm whales typically move at horizontal speeds of up to 3 knots (1.5 m/s) relative to local currents in the Gulf of Mexico and other regions.[31]

Multipath reflections of underwater biological sounds can be used to reduce the number of physical hydrophones required to acquire a position.[32,33] The surface-reflected path, or surface ''ghost'' of a click, has been used to track sperm whales from a vertical array,[34] as well as a horizontal array when a depth-recording tag has been attached to an animal.[35]

[a)]Section II of this work was briefly presented in ''Passive three-dimensional tracking of sperm whales using two towed arrays during the 2001 SWAMP cruise,'' by A.M. Thode, David K Mellinger, and Anthony Martinez, at Cancun, Mexico, 144th ASA Conference, December 2002. However, the data in this work have never been presented.

[b)]Electronic mail: thode@mpl.ucsd.edu

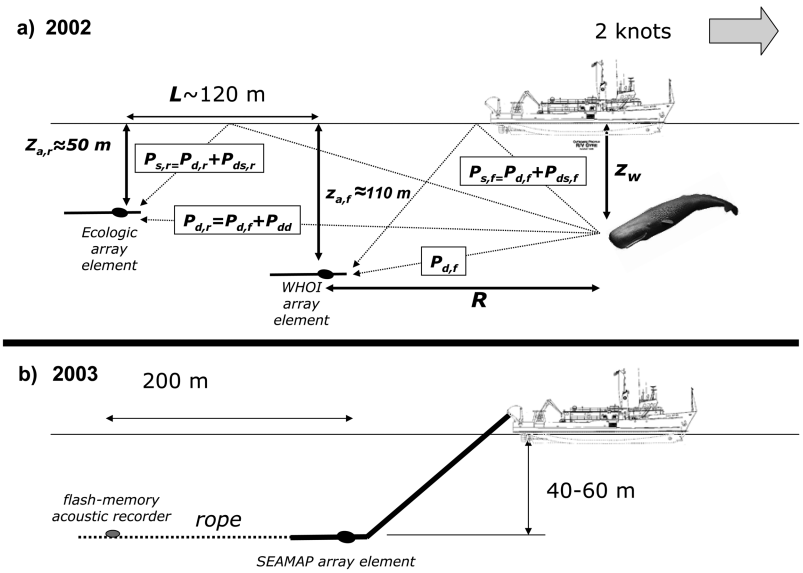

FIG. 1. Deployment geometries of towed passive acoustic range-depth tracking system, illustrating acoustic propagation paths used in the tracking: (a) 2002 configuration, consisting of two short-aperture towed arrays, with the forward (f) array deployed to a depth of around 110 m, and the rear (r) array to a depth of about 50 m. Tow cables are not shown for clarity. (b) 2003 configuration. An autonomous acoustic recorder is attached to a 5/8 in polypropylene rope, the end of which is attached to a towed acoustic array manufactured by SEAMAP, Inc. Only a single element of the short-aperture arrays is displayed for clarity.

Bottom-reflected paths have also been used to obtain dive profiles of sperm whales using a single hydrophone;[25] however, bottom-arrivals are often not available, are difficult to detect with automated software whenever they are present, and are difficult to associate with a particular direct arrival whenever more than one animal is acoustically active.

This paper presents a two-hydrophone tracking technique for obtaining low-resolution dive tracks of multiple animals simultaneously, provided that the hydrophone depths are measured independently. Such techniques are already being explored theoretically.[36] The hydrophones can be deployed as either a vertical array or a wide-aperture towed array, but all experimental work to date has been performed on a towed configuration. By exploiting surface-reflected sounds, a virtual planar array can be created that can track animals out to 1 km horizontal range, for hydrophone separations on the order of 200 m. The surface-reflections have been observed even when the ocean surface is agitated.

The computations required by the method lend themselves to automation, and have been tested on two separate sperm whale research cruises in the Gulf of Mexico in 2002 and 2003, as part of a larger research consortium called the Sperm Whale Seismic Study (SWSS), supported jointly by the Minerals Management Service (MMS), the Industry Research Funders Coalition (a coalition of oil and gas and geophysical survey companies), the Office of Naval Research (ONR), and the National Science Foundation (NSF).

In this paper, Sec. II discusses the basic tracking concept, including assumptions and limitations, while Sec. III details the practical implementation of the method, including deployment geometries and automated signal processing techniques. Finally, Sec. IV presents the results from two different towed array deployments in 2002 and 2003.

II. THEORY

A. Notation

The basic tracking geometry is illustrated in Fig. 1 for two possible towed configurations. Two hydrophones, labeled ''forward'' and ''rear,'' are deployed at respective depths $z_{a,f}$ and $z_{a,r}$. A whale at horizontal range R_f from the forward hydrophone and depth z_w makes an impulsive sound that travels a distance (slant range) $P_{d,f}$ before being recorded by the forward hydrophone as a ''direct'' path. A ''surface-reflected'' path $P_{s,f}$ also exists, arriving at a time $t_{ds,f}=P_{ds,f}/c$ after the direct path arrival, where $P_{ds,f}=(P_{s,f}-P_{d,f})$ is the path-length difference, and c is the effective speed of sound in water. It is assumed here that c is constant with depth, so that all sound propagation paths can be represented by straight lines. Even in the Gulf of Mexico, where the sound speed is a strong function of depth, a previous analysis[25] found that at ranges less than 1 km, ray refraction effects could be neglected, a conclusion shared by other work.[37]

The sound also travels a distance $P_{d,r}=(P_{d,f}+P_{dd})$ before being recorded on the rear hydrophone, where P_{dd} is the path difference between the direct arrivals on both hydrophones. An additional surface-reflected path arrives at the rear hydrophone at a time $t_{ds,r}$ after the direct arrival. The times $t_{ds,f}$, $t_{ds,r}$, and $t_{dd}=P_{dd}/c$ are the measurable quantities from the hydrophone data, as illustrated in Fig. 2. Thus a relationship between these times and the whale's range and depth is required.

B. Derivation of tracking formulas

For each hydrophone the slant range $P_{d,i}$ and surface-reflected path length $P_{s,i}$ can be expressed as

$$P_{d,i}=\sqrt{R_i^2+(z_w-z_{a,i})^2},$$
$$P_{s,i}=\sqrt{R_i^2+(z_w+z_{a,i})^2}, \tag{1}$$

where the subscript i represents either the forward (f) or rear (r) hydrophone. Squaring the two expressions, then subtracting from each other yields

$$4z_{a,i}z_w=P_{s,i}^2-P_{d,i}^2=c^2t_{ds,i}(2t_{d,i}+t_{ds,i}). \tag{2}$$

Dividing Eq. (2) for the forward phone by the equation for the rear phone and substituting for $t_{d,r}$ yields

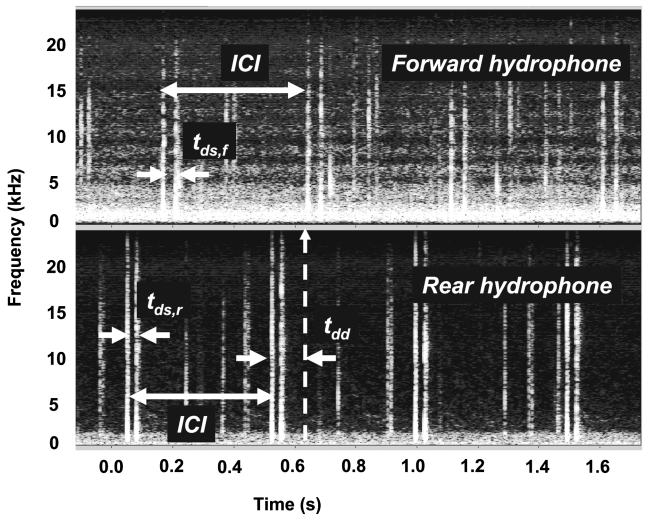

FIG. 2. A spectrogram display illustrating the measurements required for range-depth tracking, taken from data collected during 2002 (48 kHz sample rate, 1024 pt. FFT samples, 75% overlap). The top spectrogram display shows data from the forward hydrophone, and the bottom display shows a simultaneous recording from the rear hydrophone. Three pieces of information can be obtained from each click an individual makes: the differences between the arrival times of the direct and surface-reflected paths on the forward ($t_{ds,f}$) and rear ($t_{ds,r}$) hydrophones, and the arrival time difference between the direct arrivals on both hydrophones (t_{dd}). Also shown is the inter-click interval (ICI), which is used to identify the same whale on both hydrophones.

$$\frac{z_{a,f}}{z_{a,r}} = \frac{t_{ds,f}(2t_{d,f}+t_{ds,f})}{t_{ds,r}(2t_{d,f}+2t_{dd}+t_{ds,r})}. \tag{3}$$

The left-hand side of Eq. (3) is the ratio between the two hydrophone depths. Therefore, if the hydrophone depths are independently measured, the slant range $P_{d,f}$ can be determined:

$$P_{d,f} = c\,\frac{t_{ds,f}-(t_{ds,r}+2t_{dd})S}{2(S-1)},$$
$$S = (t_{ds,r}z_{a,f}/t_{ds,f}z_{a,r}). \tag{4}$$

The whale depth and range can then be obtained from Eqs. (2) and (1), respectively. Note that if ray refraction effects are negligible, knowledge of the horizontal separation L between the two hydrophones is not required to obtain a range-depth dive profile. However, to obtain a full three-dimensional fix, including azimuth, the horizontal separation must be estimated. Equations (1)–(4) are equally valid for a wide-aperture vertical array deployment.

The "stability factor" S in Eq. (4) determines the stability of Eq. (4); the closer S is to one, the more precise the measurements of $P_{ds,i}$ and the array depths need to be to obtain a precise answer. A binomial expansion of Eq. (1), assuming $R_i \gg z_{a,i}+z_w$, produces $ct_{ds,i} \approx R_i+(z_w+z_{a,i})^2/2R_i - R_i-(z_w-z_{a,i})^2/2R_i = 2z_wz_{a,i}/R_i$, which reduces the stability factor in Eq. (4) to $S \approx R_f/R_r$. Therefore at large ranges S tends to be greater than one if the animal is behind the towed array, less than one if the animal is ahead of the array, and close to one when the animal is broadside of the hydrophones, i.e., when t_{dd} is nearly zero. At large ranges the stability factor can be physically interpreted as a crude measure of whale azimuth.

Equation (4) thus indicates that the tracking procedure is least accurate whenever the hydrophones are shallow and the animal is nearly equidistant from both hydrophones, with horizontal ranges greater than roughly five times the mean hydrophone depths. By contrast, the procedure is most stable whenever the animals are directly ahead or behind the towing vessel, the hydrophones are relatively deep, and the animal range is less than a few hydrophone depths. However, at close ranges some locations slightly forward or aft of broadside may still yield unstable tracks, depending on the relative hydrophone depths.

Occasionally faint bottom-reflected paths can be detected in the acoustic data. If the water depth is known, this additional arrival time information can yield a range and depth from a single hydrophone,[25] providing an independent check of the procedure presented here.

III. EXPERIMENTAL SETUP

This section discusses the practicalities of deploying a towed array configuration sufficient for tracking animals out to 1–2 km horizontal range, as well as the signal-processing techniques required to automatically extract estimates of P_{dd}, $t_{ds,f}$, and $t_{ds,r}$ in Fig. 2.

A. Array deployments

In order to use Eq. (4) effectively, a practical towed array deployment needs the following characteristics:

(1) Two hydrophones spaced at least 200 m apart permit stable tracking of animals up to a range of 1–2 km. Ideally, one of the locations contains a level short-aperture towed array, to estimate whale azimuth along with the dive profile.
(2) Two hydrophones placed at least 30 m deep to obtain relatively large values of P_{ds}. Consequently arrays should be towed at 3 knots (about 1.5 m/s) or less, unless the hydrophone cable can be attached to a dive wing.
(3) Hydrophone depths recorded accurately and continuously. The deeper the array, the less precise the measurement needs to be, but an accuracy of at least 1 m is recommended.

Two deployment geometries meeting these criteria were tested during separate SWSS research cruises in the Gulf of Mexico during 2002 and 2003.

1. 2002 deployment

On 5 September 2002, a feasibility test was conducted in the Gulf of Mexico off the R/V *Gyre*, owned by Texas A&M University. The data were collected during weather conditions that were too rough to permit other activities associated with the SWSS project.

Two arrays were deployed simultaneously off the port and starboard sides of the stern, as illustrated in Fig. 1(a). The port array, which consisted of three elements spaced over 3 m, was built by the Woods Hole Oceanographic Institution (WHOI). A dive wing was used to keep the hydro-

phones at depths greater than 100 m, while maintaining a 20-m horizontal separation between the forward hydrophone and ship stern. A calibrated pressure transducer was attached to the top of the dive wing, and a LED display permitted notes to be taken of the transducer depth over time. Unfortunately, this sensor failed during the experiment, so the WHOI array depth had to be estimated, based on earlier measurements, as a function of ship speed through the water.

The starboard array, a two-element oil-filled array built by Ecologic Inc., was deployed approximately 300 m behind the stern. This created a horizontal separation of 170 m between the forward (WHOI) and rear (Ecologic) hydrophone. A Suunto Vyper dive computer was attached to the head of the array, which logged the array hydrophone depth every 10 s. Typical recorded depths for this configuration were between 40 and 60 m. For this array data from only one array element were available.

The acoustic data from both arrays were sampled at 48 kHz and recorded simultaneously to hard disk and tape for later analysis. Unfortunately, while bottom-reflected paths could be identified in the acoustic record, the number of whales present made assignment of a particular bottom echo to a particular direct arrival difficult.

2. 2003 deployment and data preprocessing

During May and June of 2003 the deployment illustrated in Fig. 1(b) was attempted from the R/V *Ewing*, operated by the Lamont-Doherty Earth Observatory for the National Science Foundation (NSF). Instead of deploying two separate array cables, a single array, manufactured by SEAMAP Inc., was deployed roughly 300 m behind the stern. The array had four hydrophones unevenly spaced over a span of 50 m, each of which sampled at 48 kHz. Depth data were measured by a pressure transducer embedded in the array, which were converted into a data string that could be sampled over a serial port by a laptop. During the times to be discussed here, the array depth varied between 37 and 50 m.

An autonomous flash-memory acoustic recorder,[38] built by Bill Burgess of Greeneridge Sciences Inc., was taped to 261 m of a 16-mm ($\frac{5}{8}$ in.) polypropylene rope. A 7-kg shackle that served as an end anchor was tied to one rope end, while the other was attached to the end of the array. The recorder had a pressure transducer to log a time-stamped depth, which varied between 42 and 62 m over the results presented here. It also had 1 Gbyte of flash memory, sufficient to record at 8.192 kHz for nearly 17 h. In order to retrieve the data the entire assembly had to be retrieved from the water.

The acoustic data on the recorder was time-aligned with the data of the leading array element by cross-correlating the ship engine noise recorded on both hydrophones. First, both time series were interpolated and decimated to produce two time series sampled at 8 kHz. Next, a digital high-pass filter was applied to both time series to emphasize frequencies above 500 Hz. Although ship noise was present at lower frequencies, flow noise on the autonomous recorder dominated the lower frequency bands, decorrelating the data. As the hydrophone depths and the length of the rope between the recorder and array were already known, the time lag expected from the cross-correlation between a hydrophone on the SEAMAP array and the autonomous recorder could be estimated, and the acoustic data were subsequently time-aligned. The autonomous recorder clock drift relative to the most forward array element was not linear, but experienced sudden clock jumps about once an hour, which seemed to correspond to large changes in ship course and speed. These jumps were corrected before further analysis.

Neither the rope deployment nor the attachment of the autonomous recorder to the rope was very sophisticated. As a result, flow noise was extensive, and the hydrophone physically fluttered in the current, resulting in the acoustic data from the autonomous recorder being clipped between 50 to 600 times per second. Fortunately, since sperm whale sounds are impulsive, the subsequent signal processing could still extract useful information.

3. General tracking procedure

The basic tracking procedure for both deployments was similar. The experiments were conducted in the evening, while other sperm whale research activities were suspended, and the passive acoustic monitoring team had full control of the vessel. The acoustic operator tried to maneuver the vessel so that a group of animals was forward and to one side of the vessel. The ship speed through the water was then reduced to a minimum possible speed that still permitted steerage—typically around 2 knots (1 m/s). The ship maintained a steady heading as the vessel gradually overtook and passed a set of animals, who moved horizontally at speeds of about 2–3 knots (1–1.5 m/s), relative to the current. The distance of the vessel from the animals was adjusted so that surface reflections were visible on the spectrogram monitoring display (e.g., Fig. 2). After a complete pass, the vessel increased speed, turned away from the group, circled around, and attempted another pass. Attempts were made to avoid approaching the animals too closely, but as the subsequent tracking results show, the ship did pass over an animal at depth.

B. Signal processing and estimate extraction

An advantage of using surface-reflected paths for tracking animals, besides reducing the number required hydrophones, is that it simplifies the signal processing. In this section the methods for extracting estimates for $t_{ds,f}$, $t_{ds,r}$, and t_{dd} are presented, assuming that any needed preprocessing, such as time-synchronization, has already been performed on the forward and rear time-series.

The first step in tracking a group of animals is to analyze the acoustic data using a pulse detection program, such as Ishmael,[39] that outputs a set of times at which the spectral power over a certain bandwidth exceeds a threshold value. For the higher-bandwidth towed array this detection bandwidth was set between 4 and 15 kHz, while for the autonomous recorder the detection bandwidth was set between 2 and 3 kHz, which still provided sub-millisecond time resolution. The set of possible click detections for a given hydrophone is designated t_{pulse}, and t^i_{pulse} is the ith detection of that set.

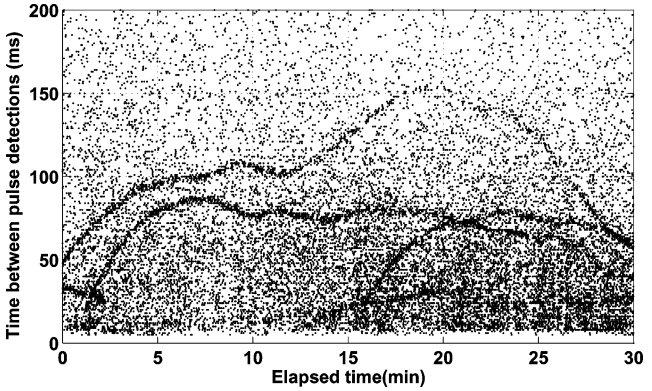

FIG. 3. Demonstration of how individual whales can be separately identified on a single hydrophone by estimating t_{ds}, using data beginning at 5 September 2002, 22:15 CDT, on the forward hydrophone element. Because different whales generally have different t_{ds} values at a particular moment, up to four whales can be identified simultaneously from a single time series.

The next step involves distinguishing a set of direct arrivals from one individual from surface reflections and direct arrivals from other animals. There are two ways to do this. If the forward hydrophone location actually contains two hydrophones separated by a few meters, as was the case in 2003, then the direct arrivals from different animals can be isolated by plotting the estimated bearing of detected pulses versus time. Bearings from surface reflections can be distinguished from those of direct arrivals because the apparent arrival angles of the surface reflections vary greatly over a short period of time (a high variance in estimated array bearing), while the bearings from direct paths have little variance over a short time period.

If data are available from only a single hydrophone at the rear location, as was the case in 2002 with the Ecologic array, then the direct arrivals can still be identified by plotting the time difference between sequential detections, $t_{pulse}^{i+1} - t_{pulse}^{i}$, as a function of time (Fig. 3). The most likely pulse to arrive after a true direct arrival is the associated surface reflection, unless a direct arrival from a different individual arrives first. As the time separation $t_{ds,f}$ is generally less than 50 ms, the likelihood of a direct arrival from another individual falling within this interval is relatively small, as long as four animals or less are present. Plotting the time differences is thus a crude way of estimating $t_{ds,f}$ from a single hydrophone. Since no two whales generally share the same $t_{ds,f}$ value at a given moment, multiple animals can often be separated within a single time series.

Once the direct arrivals are identified, a more precise estimate of $t_{ds,f}$ often can be obtained using cepstral analysis,[35,40,41] a coherent deconvolution technique that works well if the surface-reflected signal can be modeled as a broadband-filtered version of the direct arrival. During the mild summer conditions in the Gulf of Mexico, the ocean surface was smooth enough that these conditions were usually met for the forward and rear hydrophone data, as illustrated in Figs. 4(a) and 4(b), respectively, using 2003 data.

The time delay between front and rear hydrophones, t_{dd}, is then obtained by exploiting the fact that the interval between subsequent clicks by the same animal, or the "interclick interval" (ICI), must be the same at both hydrophone

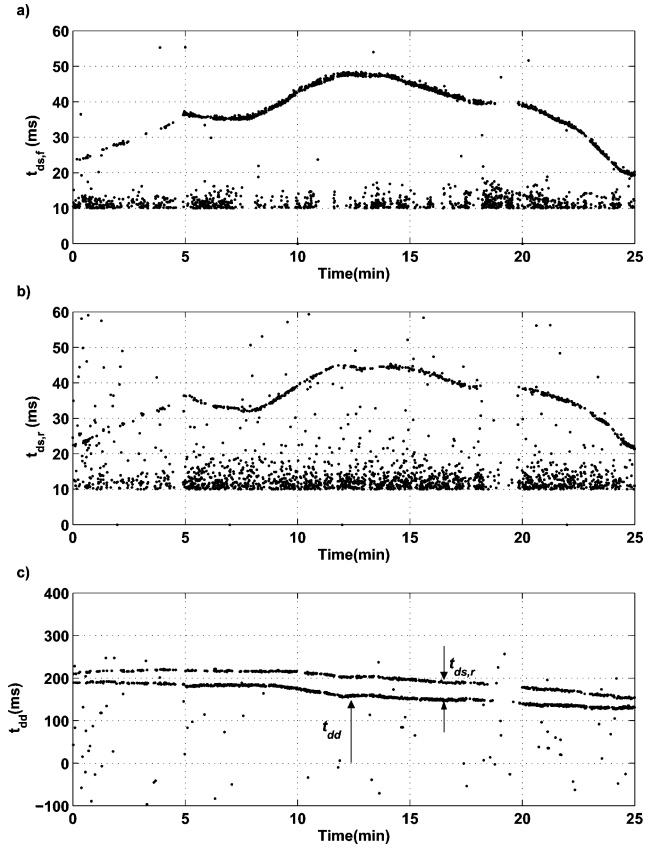

FIG. 4. Example of automated estimates of (a) $t_{ds,f}$ (b) $t_{ds,r}$ and (c) t_{dd}, using data from 19 June 2003, starting at 00:20 CDT. Cepstral analysis was used to estimate (a) and (b), while a "rhythm analysis" that compared sets of nine ICI sequences between hydrophones was used to derive (c). Note the presence of an additional "ghost" curve in (c), which represents the arrival time difference between the surface reflection on the rear phone and the direct arrival on the forward phone. Thus the difference between the two curves provides an alternate means for computing $t_{ds,r}$.

locations (see Fig. 2). A routine can be written where the N ICIs following a given direct-path arrival at the forward location are compared with a set of candidate pulses at the rear location. All candidate pulses lie within a time L/c of the original direct-path arrival at the forward location. For each candidate pulse, the routine checks whether N additional pulses are present at the rear location during future times required by the ICIs, to within a 1 ms tolerance. The candidate pulse that shares the most ICIs is selected as the corresponding direct arrival for the rear hydrophone location. This software "rhythm analysis" technique, illustrated in Fig. 4(c), has been extensively used in automated marine mammal monitoring at various Naval Test ranges,[42,43] where it is informally called a "scanning sieve."

An interesting side effect of the rhythm analysis is that the surface reflection associated with the rear hydrophone often emerges as a secondary choice in the output [Fig. 4(c)]. In other words, the analysis often identifies the arrival time difference between the surface reflection on the rear hydrophone location and the direct arrival on the forward hydrophone. From the definition of t_{dd} it is apparent that the surface-reflected "ghost" t_{dd} is always more positive than the actual t_{dd}. The time difference between the two curves thus provides an alternate means of computing $t_{ds,r}$. This

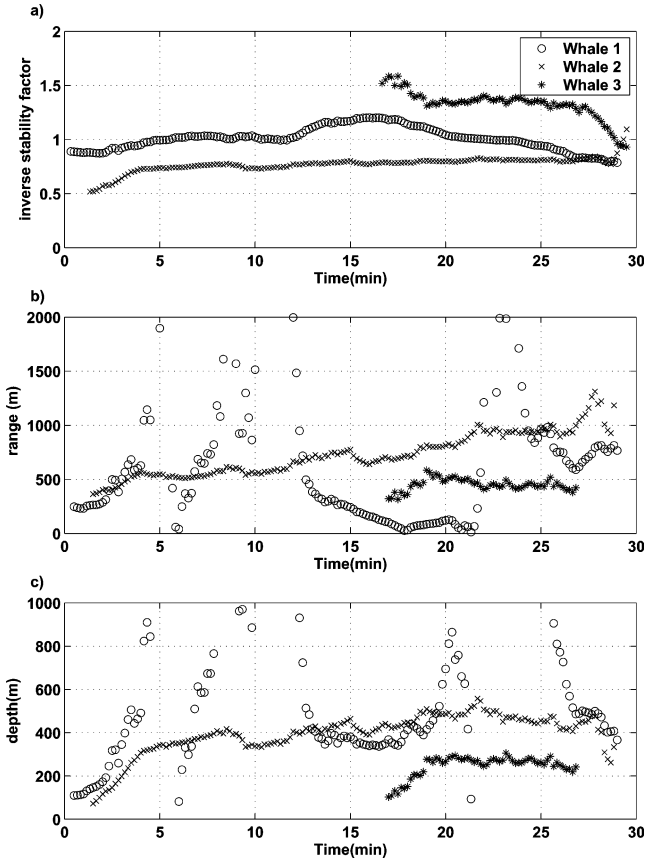

FIG. 5. Range-depth track estimate of three whales, using data beginning at 5 September 2002, 22:15 CDT, covering the same time period as Fig. 3. For each whale track the inverse stability factor ($1/S$) of Eq. (4) is shown in (a), the horizontal ranges from the forward hydrophone are shown in (b), and the whale depths are shown in (c). Note the instability of the track estimate whenever $S \sim 1$. The animals seem to be diving to depths between 300 and 500 m.

technique was useful in the 2003 experiment, when clipping and flow noise on the autonomous recorder often precluded cepstral analysis and other coherent techniques [the time period shown in Fig. 4(b) being an exception].

Once a display like Fig. 4 is obtained, a final step involves tracing the curves for the three time quantities, interpolating the samples into evenly spaced time samples, then inserting the values into Eqs. (1)–(4). Although this tracing process can be automated,[35] the results presented here were obtained by manually selecting the tracks using a graphical user interface.

IV. RESULTS

A. 2002 configuration

In 2002 4 h of data were collected on 5 September to test the tracking procedure. Figure 5 shows the 30-min period during that experiment, beginning at 22:15 CDT, when three whales were clearly identified using the single-hydrophone method discussed in Sec. III B, and illustrated in Fig. 3. During this period the ship made two port turns of 45 and 30 degrees at 2 and 8 min, respectively. The ship's course paralleled the whales', because the relative bearings changed only gradually with time, except during the ship turns. Figure 5 plots the inverse stability factor $1/S$, the horizontal range from the forward hydrophone R_f, and the depth for each whale. The inverse stability factor is shown so that an animal forward of the vessel displays a larger positive value on the graph.

The track for whale 1 illustrates how the procedure becomes inaccurate whenever the stability factor wanders close to 1. Initially whale 1 was on the port side of the vessel, slightly aft of the array. After the ship made its first port turn, the apparent position of whale 1 shifted broadside to the array, so that $1/S$ became one, t_{dd} became close to zero, and tracking became unstable. After the second port turn the towed array shifted again at 11 min, the apparent position of the whale shifted forward of the array, the inverse stability factor increased to 1.25 at 15 min, and stable depths and ranges were reacquired. Whale 1 passed in front of the vessel at 18 min, and eventually the ship passed the whale. At 21 min the whale became broadside to the array again, $1/S$ falls past one, and the track was lost.

By contrast whale 2 always remained roughly aft of the array, while whale 3 was forward of the array for most of the sequence. Thus the inversion results for these animals always remained stable. Initial descents and presumed foraging depths between 200 and 400 m can be observed for both whales. When stable depth estimates are available for whale 1, they are comparable to the whale 2 depth of roughly 400 m.

Unfortunately, independent checks of the dive profiles derived here were not possible. Bottom-reflected arrivals, although present, were fleeting and could not be matched with their corresponding direct arrivals with confidence, due to the number of animals present. None of the animals were tagged at this time, but some indirect comparisons can be made with time/depth data from animals tagged during the same cruise.[44] The estimated initial descent rates of whales 2 and 3 are 1.6 and 1.22 m/s, respectively. The estimated depths at the end of the initial descents of whales 2 and 3 in Fig. 5 were 390 and 270 m, respectively, and maximum estimated depths attained by all three animals were 490, 500, and 280 m, respectively.

A tag deployed on an animal from the same group the following morning (JD 249a) measured two complete dive cycles, with mean descent rates of 1.17 ± 0.17 m/s, close to the average rate of 1.15 ± 0.14 m/s estimated from whales tagged in the Gulf of Mexico and the Mediterranean.[45] The initial steep descents ended at depths of 508 and 528 m, but during presumed foraging the whale reached maximum depths of 650 and 690 m. The results from 64 dives from all 13 animals tagged during the 2002 cruise had initial descent depths ranging between 400 and 800 m, with the mode at 500 m, and maximum dive depths ranging between 475 and 850 m, with a peak clustered between 600 and 700 m.[46] The estimated descent rates roughly correspond to those derived from all tag data, as well as from whale 249a only. However, the initial and maximum dive depths estimated from the passive acoustic measurements for whales 1 and 2 are on the extreme lower end of the 2002 tag dive depth distributions, and 100 m shallower than the maximum dive depths of whale 249a. The depths of whale 3 are nearly 200 m shallower than those of whales 1 and 2, and thus are incompat-

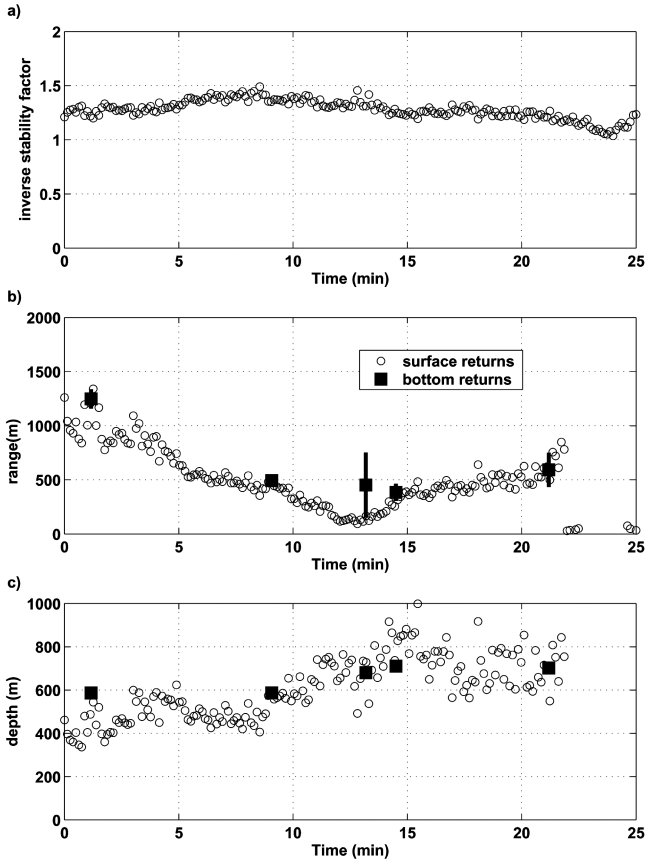

FIG. 6. Track of whale using autonomous recorder data starting at 19 June 2003, 00:20 CDT. (a) Inverse stability factor; (b) range from forward hydrophone; and (c) depth. The black squares mark independent localization estimates opportunistically obtained by exploiting bottom-reflected acoustic paths. Black bars on squares represent one standard deviation of the estimates derived from bottom arrivals over a 20-s interval.

ible with any of the tag dive profiles. It is impossible to tell, from the 2002 data, whether these depth discrepancies are due to incorrect estimates of the towed array depths, or reflect actual differences in diving behavior when animals are in close proximity to the ship. Additional measurements with simultaneous independent location estimates were a high priority for 2003.

B. 2003 configuration

From the evening of 18 June through the early morning of 19 June 2003, the autonomous recorder configuration shown in Fig. 1(b) was used to collect additional data to test the procedure. One particularly clear set of time measurements was available between 00:20 and 00:45 CDT, and is displayed in Fig. 4. The dive profile derived from Fig. 4 is shown in Fig. 6. The inverse stability factor plot in Fig. 6(a) indicates that the animal remained forward of the rear hydrophone location, although the close proximity of the animal precludes a simple interpretation of the stability factor. The majority of the animal's depths vary between 400 and 800 m—deeper than depths estimated in 2002. The plot of horizontal range from the forward hydrophone indicates that the array passed directly over the animal approximately 12 to 15 min into the sequence.

Sets of bottom-reflected arrivals were recorded on the array several times during this sequence, and by manual observation of spectrogram displays they could be matched to the corresponding direct-path arrivals, since only two animals were acoustically active during this time. Occasional estimates of the whale position could then be made using only a single hydrophone,[25] by measuring sets of bottom arrivals over a 20-s interval. The array depth estimated from this procedure matched the measured depth of the SEAMAP array to within a few meters. The mean and standard deviations of the positions obtained from each set of bottom arrivals are marked as black squares and vertical lines in Figs. 6(b) and 6(c). They overlap the positions estimated by the two-hydrophone method to within the standard deviation.

V. CONCLUSION

A two-hydrophone passive acoustic method for tracking sperm whale dive profiles has been presented, for the particular configuration of a wide-aperture towed array. By taking advantage of surface-reflected paths, which occur over 90% of the time when the array is less than 2 km range from the animal, this approach simplifies the signal processing required to extract the relative arrival time information needed for tracking. The algorithm has been tested using data collected during 2002 and 2003 in the Gulf of Mexico, and in 2003 the results were independently checked using additional information provided by bottom-reflected paths. While the focus of the work has been on sperm whales, any impulsive biological sound could be tracked using the same principles discussed here,[47] provided that the directivity of the signals is not so great that surface multipath arrival amplitudes are reduced below background noise levels. Given the broadband nature of most biological pulses, and the size of most deep-diving marine mammals, it seems reasonable that some portion of the lower end of the pulse's acoustic spectrum would be nearly omnidirectional. Low source signal amplitudes and surface roughness are currently expected to be the limiting restrictions on the approach discussed here, especially for any vertical or towed array deployment deeper than 100 m.

To date all configurations tested have used two to three towed hydrophones spaced less than 300 m apart, restricting the usable horizontal tracking range of less than 2 km. Other configurations are possible, including a vertical array, and even towed array configurations of greater aperture. However, at some range beyond 1 km the approximation of a uniform water-column sound speed becomes increasingly inaccurate and ray refraction effects would have to be explicitly incorporated into the procedure. Another uncertainty about the procedure is under what weather conditions the surface roughness would increase to the point where coherent-processing techniques, such as cepstral analysis, could no longer be applied to surface-reflected signals, and less-precise incoherent methods, such as the "rhythm analysis" presented in Sec. III B, would have to be employed instead. While a more quantitative error analysis for this technique is desirable, preliminary modeling by the author and modeling work by other researchers (e.g., Ref. 37) has suggested that "measurement errors" in terms of imprecise es-

timation of relative time-of-arrivals dominate ''model-based errors'' arising from neglecting ray-refraction effects, for the tracking ranges and depths discussed in this paper.

A final question concerning this procedure is how closely an observational vessel can approach a group of animals without provoking deviations in their natural dive behavior. This issue is of concern to any cetacean research experiment that attempts to measure possible responses of marine mammals to various types of anthropogenic noise. It is hoped that further development of this method can help provide insight into what ''stand-off'' distances should be observed in open-ocean marine mammal research.

ACKNOWLEDGMENTS

The author thanks Bill Burgess of Greeneridge Sciences Inc., Tim Pinnington and Craig Douglas of SEAMAP, Inc., Jonathan Gordon of Ecologic, Inc., Anthony Martinez of SE Fisheries Science Center, and Mark Johnson, Patrick Miller, and Alessandro Bocconcelli of Woods Hole Oceanographic Institution (WHOI) for providing the opportunity to use their passive acoustic equipment for this work. Mark Johnson in particular was very generous with technical advice and assistance during the 2003 SWSS D-tag cruise. Patrick Miller also provided paper preprints and dive profiles from the 2002 D-tag data to compare with the 2002 results presented here. Jonathan Gordon, Jonathan Vallarta, Peter Tyack, and Kimberly Hiland provided useful comments and encouragement for the research. Acoustic observers that helped log and monitor the data included Natascha Aguilar de Soto, Matt Grund, Valeria Teloni, Sarah Tsoflias, and Sue Rocca. Dave Mellinger modified his software Ishmael to meet some specialized needs, while Matt Howard of Texas A&M University and John Diebold of Lamont-Doherty Earth Observatory provided data on the water depth beneath the R/V *Gyre* in 2002 and the R/V *Ewing* in 2003. The deck crews of both the R/V *Gyre*, R/V *Ewing*, and *Kondor* were always good-natured, even at odd hours, and in particular the author thanks Marc and Mike of Pacific Geophysical Services, who provided the rope and autonomous recorder attachment in 2003. This work was supported by the U.S. Minerals Management Service, under Cooperative Agreement 1435-01-02-CA-85186. Ann Jochens and Doug Biggs of Texas A&M University helped arrange this support, and have been supportive of this research since its inception.

[1] W. A. Watkins, ''Acoustics and the behavior of sperm whales,'' in *Animal Sonar Systems*, edited by R.-G. Busnel and J. F. Fish (Plenum, New York, 1980), pp. 283–290.
[2] W. A. Watkins, ''Acoustic behaviors of sperm whales,'' Oceanus **20**, 50–58 (1977).
[3] L. V. Worthington and W. E. Schevill, ''Underwater sounds heard from sperm whales,'' Nature (London) **180**, 291 (1957).
[4] J. H. Backus and W. E. Schevill, ''Physeter clicks,'' in *Whales, Dolphins, and Porpoises*, edited by K. S. Norris (Berkeley U.P., Berkeley, 1966), pp. 510–527.
[5] J. C. Goold and S. E. Jones, ''Time and frequency-domain characteristics of sperm whale clicks,'' J. Acoust. Soc. Am. **98**, 1279–1291 (1995).
[6] J. Gordon, ''The acoustic world of sperm whales,'' Eur. Res. Cetaceans **9**, 29–33 (1995).
[7] J. C. Gordon. ''The behaviour and ecology of sperm whales off Sri Lanka,'' Ph.D. thesis, University of Cambridge, Cambridge, UK, 1987.
[8] P. T. Madsen, R. Payne, N. U. Kristiansen, M. Wahlberg, I. Kerr, and B. Møhl, ''Sperm whale sound production studied with ultrasound time/depth-recording tags,'' J. Exp. Biol. **205**, 1899–1906 (2002).
[9] H. Whitehead and L. Weilgart, ''Click rates from sperm whales,'' J. Acoust. Soc. Am. **87**, 1798–1806 (1990).
[10] L. Douglas. ''Click counting: An acoustic censusing method for estimating sperm whale abundance,'' Masters thesis, University of Otago, Dunedin, New Zealand, 2000.
[11] J. C. Goold, ''Signal processing techniques for acoustic measurement of sperm whale body lengths,'' J. Acoust. Soc. Am. **100**, 3431–3441 (1996).
[12] J. C. D. Gordon, ''Evaluation of a method for determining the length of sperm whales (*Physeter catodon*) from their vocalizations,'' J. Zool. **224**, 301–314 (1991).
[13] G. Pavan, T. J. Hayward, J. F. Borsani, M. Priano, M. Manghi, C. Fossati, and J. Gordon, ''Time patterns of sperm whale codas recorded in the Mediterranean sea 1985–1996,'' J. Acoust. Soc. Am. **107**, 3487–3495 (2000).
[14] L. Weilgart and H. Whitehead, ''Group-specific dialects and geographical variation in coda repertoire in South Pacific sperm whales,'' Behav. Ecol. Sociobiol. **40**, 277–285 (1997).
[15] H. Whitehead, M. Dillon, S. Dufault, L. Weilgart, and J. Wright, ''Non-geographically based population structure of south Pacific sperm whales: Dialects, fluke-markings and genetics,'' J. Anim. Ecol. **67**, 253–262 (1998).
[16] J. Barlow and B. L. Taylor, ''Preliminary abundance of sperm whales in the northeastern temperate pacific estimated from a combined visual and acoustic survey,'' Int. Whal. Comm. Report SC/50/CAWS 20 (1998).
[17] A. Gannier, V. Drouot, and J. C. Goold, ''Distribution and relative abundance of sperm whales in the Mediterranean sea,'' Mar. Ecol.: Prog. Ser. **243**, 281–293 (2002).
[18] R. Leaper, O. Chappell, and J. Gordon, ''The development of practical techniques for surveying sperm whale populations acoustically,'' Rept. Int. Whal. Commn. **42**, 549–560 (1992).
[19] D. Gillespie and R. Leaper, ''Detection of sperm whales (*Physeter macrocephalus*) clicks, and discrimination of individual vocalisations,'' Res. Cetaceans **10**, 87–91 (1997).
[20] D. Gillespie, ''An acoustic survey for sperm whales in the southern ocean sanctuary conducted from the rsv aurora australis,'' Rep. Int. Whal. Commn. **47**, 897–907 (1997).
[21] D. H. Cato, ''Simple methods of estimating source levels and locations of marine animal sounds,'' J. Acoust. Soc. Am. **104**, 1667–1678 (1998).
[22] V. Teloni, W. Zimmer, C. Fossati, M. Manghi, G. Pavan, and M. Priano, ''Variability of temporal and spectral click characteristics of sperm whales (*Physeter macrocephalus*),'' in *14th Ann. Conf. European Cetacean Society*, Cork, Ireland, 2000.
[23] B. Møhl, M. Wahlberg, P. T. Madsen, L. A. Miller, and A. Surlykke, ''Sperm whale clicks: Directionality and source level revisited,'' J. Acoust. Soc. Am. **107**, 638–648 (2000).
[24] B. Møhl, M. Wahlberg, P. T. Madsen, A. Heerfordt, and A. Lund, ''The monopulsed nature of sperm whale clicks,'' J. Acoust. Soc. Am. **114**, 1143–1154 (2003).
[25] A. Thode, D. K. Mellinger, S. Stienessen, A. Martinez, and K. Mullin, ''Depth-dependent acoustic features of diving sperm whales (*Physeter macrocephalus*) in the Gulf of Mexico,'' J. Acoust. Soc. Am. **112**, 308–321 (2002).
[26] J. Ward, M. Fitzpatrick, N. DiMarzio, D. Moretti, and R. Morrissey, ''New algorithms for open ocean marine mammal monitoring,'' in *OCEANS 2000 MTS/IEEE Conference and Exhibition. Conference Proceedings (Cat. No. 00CH37158)* (IEEE, Piscataway, NJ, 2000), pp. 1749–1752.
[27] W. A. Watkins and W. E. Schevill, ''Sound source location by arrival times on a non-rigid three-dimensional hydrophone array,'' Deep-Sea Res. **19**, 691–706 (1972).
[28] B. Møhl, M. Wahlberg, and A. Heerfordt, ''A large-aperture array of non-linked receivers for acoustic positioning of biological sound sources,'' J. Acoust. Soc. Am. **109**, 434–437 (2001).
[29] D. E. McGehee, ''1997 sperm whale abundance and population structure cruise leg II sonobuoy project, final report,'' Tracor Applied Sciences Report T-97-56-0002-U (1997).
[30] S. A. Hayes, D. K. Mellinger, D. A. Croll, D. P. Costa, and J. F. Borsani, ''An inexpensive passive acoustic system for recording and localizing wild animal sounds,'' J. Acoust. Soc. Am. **107**, 3552–3555 (2000).
[31] M. Wahlberg, ''The acoustic behaviour of diving sperm whales observed with a hydrophone array,'' J. Exp. Mar. Biol. Ecol. **281**, 53–62 (2002).
[32] R. Aubauer, M. O. Lammers, and W. W. L. Au, ''One-hydrophone method

of estimating distance and depth of phonating dolphins in shallow water,'' J. Acoust. Soc. Am. **107**, 2744–2749 (2000).
[33] P. A. Lepper, K. Kaschner, P. R. Connelly, and A. D. Goodson, ''Development of a simplified ray path model for estimating the range and depth of vocalising marine animals,'' in *Proc. Inst. Acoust.* (St. Albans, 1997), pp. 227–234.
[34] W. Whitney, ''Observations of sperm whale sounds from great depths,'' Marine Physical Laboratory, Scripps Institute Oceanography Report MPL-U-11/68 (1968).
[35] W. M. X. Zimmer, M. P. Johnson, A. D'Amico, and P. L. Tyack, ''Combining data from a multisensor tag and passive sonar to determine the diving behavior of a sperm whale (*Physeter macrocephalus*),'' IEEE J. Ocean. Eng. **28**, 13–28 (2003).
[36] E. K. Skarsoulis, A. Frantzis, and M. Kalogerakis, ''Passive localization of pulsed sound sources with a 2-hydrophone array,'' in *Seventh European Conference on Underwater Acoustics* (Delft, The Netherlands, 2004).
[37] M. Wahlberg, B. Møhl, and P. T. Madsen, ''Estimating source position accuracy of a large-aperture hydrophone array for bioacoustics,'' J. Acoust. Soc. Am. **109**, 397–406 (2001).
[38] W. C. Burgess, ''The bioacoustic probe: A general-purpose acoustic recording tag,'' J. Acoust. Soc. Am. **108**, 2583 (2000) (abstract).
[39] D. K. Mellinger, ''Tshmael 1.0 user's guide,'' NOAA/PMEL Tech. Mem. Report PMEL-120 (2002).
[40] G. Q. Wu, ''Estimation of range and depth of a submerged moving object by using noise cepstrum,'' J. Sound Vib. **245**, 835–843 (2001).
[41] A. V. Oppenheim and R. W. Schafer. *Discrete-time Signal Processing* (Prentice Hall, Englewood Cliffs, NJ, 1989).
[42] J. Hu and H. Vincent, ''A real-time multi-hydrophone data association algorithm for marine mammal transient signals,'' Naval Undersea Warfare Center Report NUWCDIVNPT TM-01-107 (2001).
[43] J. Ward, ''Sperm whale bioacoustic characterization at the tongue of the ocean, Bahamas (u),'' Naval Undersea Warfare Center Report NUWCDI-VNPT TM-01-106 (2001).
[44] M. Johnson and P. L. Tyack, ''A digital acoustic recording tag for measuring the response of wild marine mammals to sound,'' IEEE J. Ocean. Eng. **28**, 3–13 (2003).
[45] P. J. O. Miller, M. P. Johnson, P. L. Tyack, and E. A. Terray, ''Swimming gaits, passive drag, and buoyancy of diving sperm whales (*Physeter macrocephalus*),'' J. Exp. Biol. (in press) (2004).
[46] P. J. Miller, Personal communication, 2004.
[47] S. K. Hooker and H. Whitehead, ''Click characteristics of northern bottlenose whales (*Hyperoodon ampullatus*),'' Marine Mammal Sci. **18**, 69–80 (2002).

Experimental verification of an interpolation algorithm for improved estimates of animal position

Chad Schell and Jules S. Jaffe[a)]
Marine Physical Laboratory, Scripps Institution of Oceanography, U.C.S.D., La Jolla, California 92093-0238

(Received 25 October 2002; revised 30 March 2003; accepted 12 April 2004)

This article presents experimental verification of an interpolation algorithm that was previously proposed in Jaffe [J. Acoust. Soc. Am. **105**, 3168–3175 (1999)]. The goal of the algorithm is to improve estimates of both target position and target strength by minimizing a least-squares residual between noise-corrupted target measurement data and the output of a model of the sonar's amplitude response to a target at a set of known locations. Although this positional estimator was shown to be a maximum likelihood estimator, in principle, experimental verification was desired because of interest in understanding its true performance. Here, the accuracy of the algorithm is investigated by analyzing the correspondence between a target's true position and the algorithm's estimate. True target position was measured by precise translation of a small test target (bead) or from the analysis of images of fish from a coregistered optical imaging system. Results with the stationary spherical test bead in a high signal-to-noise environment indicate that a large increase in resolution is possible, while results with commercial aquarium fish indicate a smaller increase is obtainable. However, in both experiments the algorithm provides improved estimates of target position over those obtained by simply accepting the angular positions of the sonar beam with maximum output as target position. In addition, increased accuracy in target strength estimation is possible by considering the effects of the sonar beam patterns relative to the interpolated position. A benefit of the algorithm is that it can be applied "*ex post facto*" to existing data sets from commercial multibeam sonar systems when only the beam intensities have been stored after suitable calibration.
 [DOI: 10.1121/1.1756894]

PACS numbers: 43.30.Sf, 43.30.Vh [RAS] Pages: 254–261

I. INTRODUCTION

Although the traditional use of acoustics in both fisheries and zooplankton ecology has primarily involved counting animals, the technical capabilities of the most modern generation of underwater sonars provides opportunities for observing the behavior of underwater animals *in situ*. Because of the difficulties in observing animals in an underwater environment, oceanic ecologists have largely used inferential techniques in the field and lab experiments to study animal behavior. For example, laboratory studies of zooplankton have shown that the animals can display a wide variety of behaviors under different circumstances, but judging what role these behaviors may play in an animal's survival is difficult without adequate data from the field.

In the case of zooplankton, lab observations of behavior (Yen, 1988) have revealed a varied and important repertoire of behavior. A classic study on krill (Price, 1989) in a large seawater tank indicated how their turning behavior was related to a patch of food and how it increased their residence time in that patch. However, there is little direct evidence available to confirm the occurrence and frequency of these same behaviors in the wild, and this information is necessary to explain what role these behaviors play as animals attempts to forage, mate, and evade predators. Unfortunately, the traditional methods of observation such as net tows and acoustic echo counting do not provide this information (Wiebe and Benfield, 2003). Modern sonars can provide observations of animal behavior if the locations of the animals are know accurately. Target-tracking techniques can then be used to infer animal trajectories.

The use of target tracking in fisheries acoustics came about largely with the deployment of dual and split-beam systems, and commercial acoustical systems manufacturers are now providing tracking software with their instruments. However, the definition of target tracking in fisheries acoustics generally refers more to the data association aspects of grouping echoes into single tracks based on their 3D position than to improvements in the actual position and velocity estimates of the tracked target. The reason for this emphasis is that the goal of the tracking is to increase the accuracy of animal counts and animal size estimates as they pass though the beam. This emphasis can be seen in the target-tracking literature of fisheries acoustics. Ehrenberg and Torkelson (1996) list the advantages of tracking in split-beam fisheries studies as better estimation of target strength by averaging over multiple echoes generated by the same individual; the ability to distinguish upstream-swimming fish from downstream-swimming fish or drifting debris; and improved ability to detect multiple tracks that would appear as a single track on an echogram (hand counting of tracks on echograms was a common method used before the advent of tracking software).

Enzenhofer *et al.* (1998) conducted an experiment using

a)Electronic mail: jules@mpl.ucsd.edu

simultaneous acoustic and video data on the Frasier River in British Columbia, Canada to test the effectiveness of the tracking software provided by Hydroacoustics Technology Inc. (HTI), a sonar manufacturer. The experiment focused only on the tracking software's ability to successfully enumerate the number of targets that passed though the beam. It was found that the software was effective at fish passage rates of less than 2000 fish/hour, an adequate level for fish passage rates on most salmon streams. It was also noted that the tracking software was susceptible to grossly inflated counts when a single target remained in the field of view for extended periods of time. The effect of this milling behavior is not surprising as the software is not designed to deal with such occurrences, but rather to be used in situations where the fish are actively migrating along stream. In a survey paper of split-beam studies on 14 rivers in Europe and North America written by Ransom *et al.* (1998), they explicitly state the requirement that fish be actively migrating past sample sites and not milling around or engaging in variable behavior. Xie (2000) presents a range-based echo association technique as an improved replacement for the algorithm in the HTI tracking software. The algorithm again focuses only on data association issues, and is again designed for migrating fish not milling about.

Other areas of research outside of salmonid populations have also used split-beam target tracking. In these studies, the emphasis has been more on behavioral observations than on counting of animals. The swimming speed and tilt angle distributions of herring were studied by Huse and Ona (1996). Tilt angles were determined with still photography, and swimming speeds were determined from acoustic tracks provided by a split beam sonar. Torgersen and Kaartvedt (2001) studied the swimming velocities of pearlside (*Maurolicus muelleri*) and lantern fish (*Benthosema glaciale*). Although the exact method of velocity calculations was not provided in the previous two studies, it seems that the tracking algorithms used were again for grouping echoes rather than improving velocity estimates (personal communication, E. Ona, 2003).

Tracking animals in order to assess their orientation has also been applied to zooplankton. In a discussion of the use of acoustics to estimate the abundance of Antarctic krill (Hewitt and Demer, 2000), the need for accurate modeling of krill target strength is stressed to avoid biases in the abundance estimates. Accurate modeling of krill target strength requires accurate estimation of their orientation (Traykovski *et al.*, 1998), (McGehee *et al.*, 1998). Knowledge of *in situ* animal swimming trajectories can provide additional information to help constrain the possible animal orientations.

The latest development in the fisheries acoustics field is the increasing use of multibeam sonar systems. These systems have the advantages of relatively high resolution and large observation volumes. It is natural and interesting to ask whether these systems can be used to track individuals and thus be used to infer behavior. The technical requirements for this task can be somewhat stringent. Coherent and unambiguous tracking of animals necessitates high frame rates, and excellent spatial localization. Factors such as platform stability and the ability to differentiate animal motions from the mean flow of water are also important. The actual requirements in terms of frame rates and spatial localization for a specific application will naturally depend upon the density and size of animals and their swimming speeds. For the most part, the instrument designer would like to achieve wide volume coverage at high resolution and fast frame rates, goals that are not necessarily in conflict. However, practical and economic issues given a certain amount of financial reserves, hardware, and acquisition software necessitate the traditional set of engineering trade-offs.

Most of the commercially available multibeam systems have been designed for use in geological studies such as seafloor mapping, with their software designed to remove returns from the middle of the water column. However, these systems are now being adapted for use in biological applications. The systems tend to have multiple beams that are narrow in one direction but wide in the other, such as the Reson SeaBat 6012, which operates at 455 kHz and has 60 beams that are each 1.5 by 15 deg. This system has been used to observe the behavior of schools of herring in response to killer whales (Nottestad and Axelsen, 1999) and Atlantic puffins (Axelsen *et al.*, 2001).

The advantages of using multibeam systems for side-looking sonar surveys of fish biomass in shallow waters are presented by Gerlotto *et al.* (2000). The advantages include better ability to differentiate multipath returns, large volume coverage, and the ability to observe fish behaviors such as vessel avoidance reactions. Soria *et al.* (1996) discuss the observation of vessel avoidance behaviors using multibeam sonars and the biasing effects of these behaviors on biomass estimates using other techniques. Simrad, another commercial sonar provider, has recently developed the SM2000 for use as a midwater multibeam sonar. It operates at 200 kHz and provides up to 128 beams sweeping a total of either a 120- or 150-deg arc, and is capable of being coupled with a second head to provide the same coverage in both directions.

Software for handling the massive amount of data generated by this sonar is being developed in a joint venture between Kongsberg–Simrad–Mesotech, the herring fishing industry, the Canadian Department of Fisheries and Oceans, and researchers from the University of New Brunswick's Ocean Mapping Group and the University of New Hampshire's Center for Coastal and Ocean Mapping (Mayer *et al.*, 2002). The software includes features for the real-time extraction and 3D display of target locations with future goals of providing target tracking for behavior quantification.

Several multibeam systems have emerged in recent years whose goal is precisely that of measuring animal behavior *in situ*. One example is a three-dimensional multibeam sonar system that has been used to observe the behavioral responses of riverine salmonids at the entrance of a hydroelectric dam on the Columbia River (Johnson and Moursund, 2000). Here, a set of Simrad SM2000 systems was used in order to judge animal position in three dimensions. Tracks were extracted through manual selection by data technicians using software tools that provided a visual user interface to the data. Additional tools and sensors were used to correct the data for movement of the transducers and provide 3D fish positions. Instantaneous velocities and aver-

age positions and speeds were calculated for each target.

Another example is the multibeam sonar systems developed by Jaffe and co-workers: FishTV (Jaffe *et al.*, 1995) and FishTVjr (a 1.6-MHz version of the same system). FishTV was deployed over several field systems in a fjord in British Columbia (Jaffe *et al.*, 1999a, De Robertis *et al.*, 2000). A recent publication highlights the information obtained from analysis of the three-dimensional trajectories of hundreds of thousands of organisms (De Robertis *et al.*, 2003).

In the course of these investigations it became clear that an algorithm which was capable of interpolating animal's azimuthal position to a fraction of a beamwidth would allow a more realistic portrayal of animal trajectories. The problem was the spatial quantization of the system's native 2-deg beamwidths was too coarse compared to the animals' behavior, resulting in relatively large errors in measuring both the animals' trajectories and velocities. An interpolation algorithm for target position was proposed in order to achieve this goal (Jaffe, 1999a) where it was shown that the estimate of animal position is a maximum likelihood estimator under sufficiently high signal-to-noise ratio (SNR). For a range of animal reflectivity this SNR is achieved under normal operating conditions. Phase-coherent methods were not used in the forward model because changes in animal position between transmitter pulses within a single frame ($8\times8\times512$) would result in a target response that is not phase coherent. One advantage of the method is that it can be simply applied to the output data of other existing multibeam echosounder systems, as it only requires a list of reflectivity versus beam number which is a typical output of such systems.

This paper presents experimental verification of the algorithm via lab studies. Two laboratory experiments were conducted, one involving the use of a stationary target observed at a series of known locations, and the second involving live aquarium fish that were simultaneously imaged with a multibeam sonar system and a stereo camera system. The experiments were conducted to verify the use of the algorithm on field data, where the improved angular resolution is helpful in permitting accurate animal trajectories and velocities to be obtained in order to study their behavior.

II. METHODS

A. Instrument description

Although the FishTV system has been described previously (Jaffe *et al.*, 1995), we include a brief description here. The system was devised for the study of macro zooplankton (*euphausiids*) and as such uses a frequency of 445 kHz. It consists of eight transmitters and eight receivers, all of which are unshaded rectangular elements with a 2-deg by 20-deg main lobe beam pattern. With reference to Fig. 1, it can be seen that the transmitters are arranged in a spiral fashion, as each is rotated by 2 deg relative to the previous one. The receivers are constructed similarly; however, they are oriented differently by rotating them by 90 deg (about the range axis).

The system is operated by transmitting on each of the transmitting transducers in sequence with all of the receivers

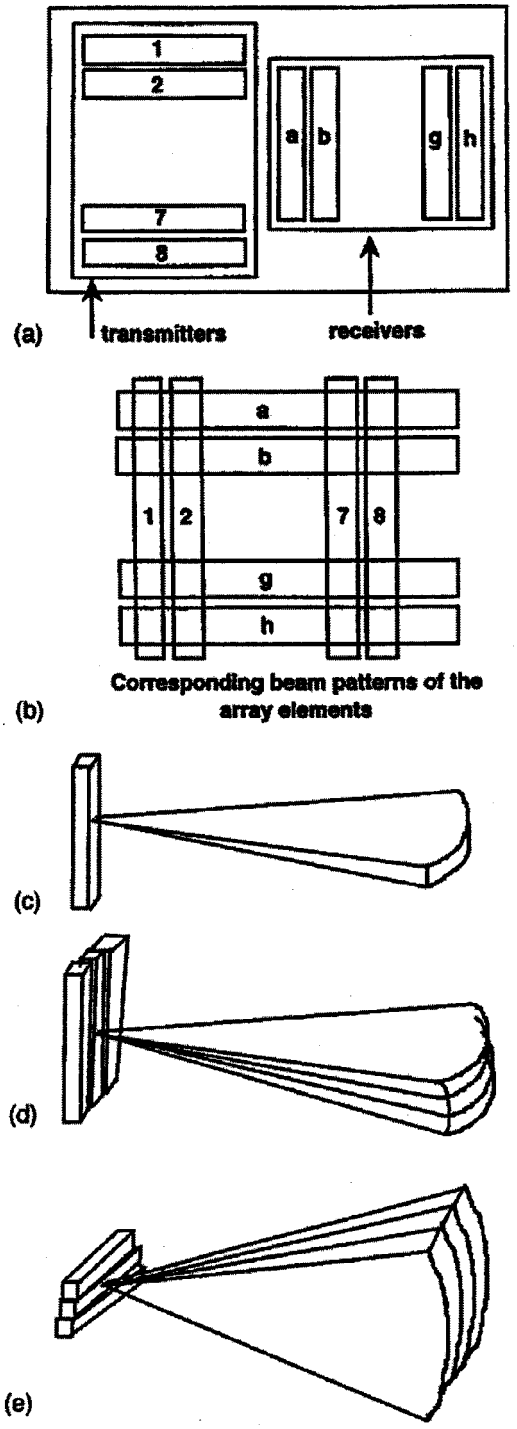

FIG. 1. Diagram of FishTV's transducer layout and beam pattern.

listening to each transmission. It thus takes eight successive transmissions to collect a frame (each transmission is delayed by the approximate round-trip travel time of the sound). The system thereby creates a set of 64 (8×8) 2-deg by 2-deg beams over its 16-deg by 16-deg field of view. The geometry of such system is a ''hard-wired'' version of a Mills Cross (Urich, 1983). System temporal bandwidth is approximately 25 kHz and in the experiments presented here a 25-cycle, 445-kHz sinusoidal pulse was used as the transmit waveform. Extensive tests have indicated that the system provides a range resolution of approximately 1 cm over its field of view, as measured by the jitter in the maximum peak

of the received waveform from a stable target. Frame rates as high as 4 Hz are possible. In a typical application, an expanding wedge at a start range of 3.5 m and an ending range of 7.34 m records the reflections of individuals in a volume of 9.14 m^3. This is a result of digitizing the complex demodulated waveforms (16 A→D channels) at 100 kHz with 16-bit dynamic range for 512 range bins.

B. Algorithm

The specific algorithm is as follows. For a given frame of data, the target is first localized in range by searching for an above-threshold amplitude response in each of FishTV's 64 beams after processing each beam with a matched filter (matched to the transmitted waveform) to reject out of band noise. The matched filter cross correlates a stored version of the transmitted waveform with the time-varying recording. A target's uninterpolated position is defined as the range (time sample) corresponding to the peak output of this matched filter, and the elevation and bearing angles of the beam that contained the peak. The interpolation algorithm only affects the elevation and bearing estimates, so the output target range, R, will not change after interpolation.

Let the vector $\mathbf{a}(R,\beta,\epsilon)$ represent the amplitude response of FishTV to a target of unit amplitude at range R, bearing β, and elevation ϵ. $\mathbf{a}(R,\beta,\epsilon)$ is a 64-element vector containing the stacked amplitude responses from each of FishTV's 64 beams. Define the noisy measured target response vector $\mathbf{m}=\alpha\mathbf{a}(R,\beta,\epsilon)+\sigma$, where α is the target amplitude and σ is the measurement noise vector, whose elements are assumed to be mutually independent zero-mean white Gaussian distributed with diagonal covariance matrix $V=\mathrm{diag}[\sigma]$.

Now, using a forward model of FishTV's amplitude response to a point target of unit amplitude at range R, bearing β, and elevation ϵ, details of which are presented in Jaffe (1999a), compute the set of modeled amplitude response vectors $\tilde{\mathbf{a}}(R,\beta,\epsilon)$ over the set of possible interpolated bearing and elevation angles, β_λ and ϵ_λ, given by

$$\beta_\lambda,\epsilon_\lambda=\{-8+16\cdot[k/(8\lambda-1)]\},\quad k=0,1,2,...,(8\lambda-1), \tag{1}$$

where λ is the interpolation factor, an input to the algorithm representing the desired increase in angular resolution. For example, with $\lambda=4$, the set of $\{\beta,\epsilon\}$ values is $[\{-8.0,-8.0\},\{-8.0,-7.5\},...,\{7.5,\ 8.0\},\{8.0,\ 8.0\}]$. This has increased the angular resolution of the system from 2 to 0.5 deg.

The forward model uses the exact geometric placement of the transducers (including parallax as illustrated in Fig. 1) in order to compute the three-dimensional pattern of sound intensity in the field of view of the system, assuming that the targets are in the far field. The 64 beam patterns are thus the result of spatially multiplying each of the beam patterns for the eight transmitters and eight receivers. The targets themselves are modeled as point reflectors. The output of the system is therefore the impulse response (in intensity or amplitude) to a target at a given range and bearing. Attenuation and spherical spreading are also included in the model. Extensive calibrations of the system were performed in order to compute estimates of target strengths of animals observed with the system (Jaffe *et al.*, 1998).

The interpolated range is defined as the measured range R, and the interpolated bearing and elevation angles are defined as β_m and ϵ_m, respectively, corresponding to the best match between the measurement and the forward model in a least-squares sense. Specifically, β_m and ϵ_m are the interpolated angles that minimize the error given by

$$\mathrm{Err}(\beta,\epsilon)=(\mathbf{m}-\alpha'\tilde{\mathbf{a}}(R,\beta,\epsilon)\cdot(\mathbf{m}-\alpha'\tilde{\mathbf{a}}(R,\beta,\epsilon)),\quad \text{where: } \beta\in\beta_\lambda,\epsilon\in\epsilon_\lambda. \tag{2}$$

Here, α' is an amplitude scaling factor defined as $\max[\mathbf{m}]/\max[\tilde{\mathbf{a}}(R,\beta,\epsilon)]$. $\max[x]$ represents the largest element of the vector x. Note that in Eq. (2) we are assuming that all elements of FishTV's measurement noise vector are mutually independent and of equal amplitude. If this were not the case, the error in Eq. (2) should be scaled by the inverse of the noise matrix V. No measurements of the FishTV's noise correlation matrix have been made, although doing so might further improve the accuracy of the algorithm.

Once the interpolated position has been determined, the amplitude of the target is refined in order to provide a better estimate of target strength. That is, one compensated for the spatial transmit pattern of both the transmitters and the spatial sensitivity of the receivers. The improved amplitude estimate is calculated as

$$\alpha_m=\frac{\mathbf{m}\cdot\tilde{\mathbf{a}}(R,\beta_m,\epsilon_m)}{\tilde{\mathbf{a}}(R,\beta_m,\epsilon_m)\cdot\tilde{\mathbf{a}}(R,\beta_m,\epsilon_m)}. \tag{3}$$

Note that the 1D search for the best amplitude fit originally presented in Jaffe (1999a) has been replaced by Eq. (3). Equation (3) can be seen as a least-squares solution to the overdetermined system of equations $\mathbf{m}=\alpha_m\tilde{\mathbf{a}}(R,\beta_m,\epsilon_m)$, which consists of 64 measurements for $\mathbf{m}$ and $\tilde{\mathbf{a}}(R,\beta_m,\epsilon_m)$ and one unknown, α_m. The solution is $\alpha_m=(\tilde{\mathbf{a}}(R,\beta_m,\epsilon_m)^T\tilde{\mathbf{a}}(R,\beta_m,\epsilon_m))^{-1}(\tilde{\mathbf{a}}(R,\beta_m,\epsilon_m))^T\mathbf{m}$ (Strang, 1980). Equation (3) could be used as a more accurate replacement for α' in the search for interpolated position, but experiments showed that there was little difference between results using either scaling factor, so the less computationally expensive α' expressed earlier was used.

C. Experiments

1. Bead

In order to validate the effectiveness of the algorithm, a series of calibration tests using FishTV was performed. These tests were conducted in a cylindrical tank measuring 4 m in diameter and 2 m deep. The first experiment, specifically designed to test the effectiveness of the interpolation algorithm, consisted of moving a 2-mm-diameter glass bead across FishTV's field of view at a distance of 3.83 m. The bead was translated in 2.52-mm steps using a micrometer, and 25 frames were recorded at each position after the bead had been allowed to settle. This was repeated across the length of the micrometer, a distance of 0.69 m.

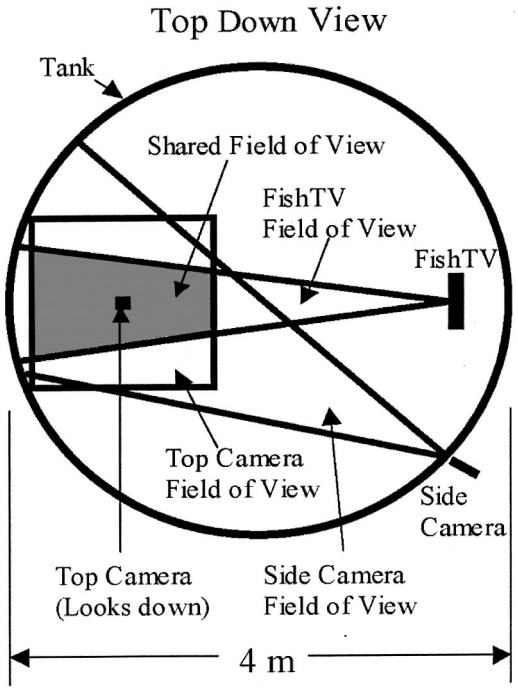

FIG. 2. Top-down view of the experimental setup for the combined sonar and video fish tracking tests. Tank dimensions are 4 m (diameter) by 2 m (height).

2. Fish

The second set of experiments was conducted as part of a larger experiment involving the development of tracking algorithms for the study of animals using sonar. The goal here was to test the result of applying the algorithm when applied to live, free-swimming targets. A number of fish (common pet store goldfish, *Carassius auratus*, approximately 2.5 cm in length, and an unknown species of Australian rainbow fish, *Melanotaenia sp.*, approximately 8 cm in length) were placed in the tank, and their movements were recorded simultaneously using FishTV and a pair of video cameras. A top-down diagram of the experimental setup, showing the fields of view of FishTV and the two cameras, is presented in Fig. 4. One camera was placed above the tank looking down, and the second camera was placed beside the tank at midwater level, looking into the only available porthole that would provide a view of FishTV's observation volume. The two video cameras were used as a stereo camera system to provide an independent corroboration of the target positions reported by FishTV.

The stereo camera system was calibrated by placing a grid of targets spaced 1 in. apart at known locations inside the cameras' overlapping fields of view. The $x-y$ pixel coordinates of each point on the grid in the image from each camera were recorded, and a look-up table mapping pixel coordinate pairings to 3D tank position was generated. This calibration resulted in a system that could provide 3D position to an accuracy of ± 2.5 cm in the horizontal and vertical directions. Time synchronization between the cameras and the sonar was accomplished by projecting a digital readout of FishTV's frame count into the field of view of each camera. The third camera frame after an update of the FishTV frame counter was taken as the matching frame. At the FishTV

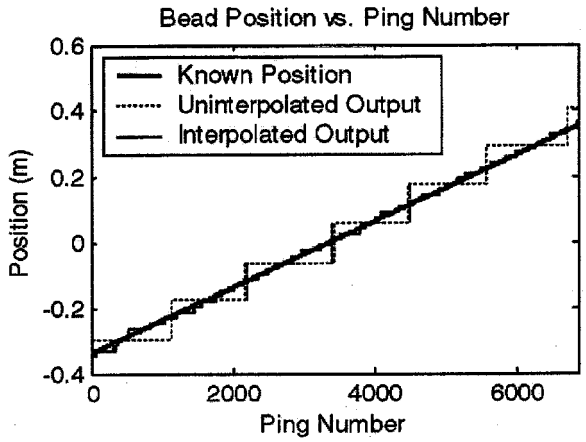

FIG. 3. Interpolated position estimation results for the 2-mm glass bead experiments. The bead was translated in 2.52-mm steps and recorded for 25 pings at each position. The interpolator's improvement over the coarse physical beams of the uninterpolated output is clearly visible.

operational settings used in this experiment, the total time required to collect a frame of FishTV data was 181 ms. As the cameras operated at 29.97 Hz, selecting the third frame placed the camera data point at approximately the middle time period of the FishTV frame.

III. RESULTS

A. Bead

The data were then processed using the interpolation algorithm for various interpolation factors λ as described above. The results for $\lambda=8$ (representing an 8-times increase in angular resolution) are presented in Figs. 3 and 4. Figure 3 presents the improved positional information, on a ping-to-ping basis, provided by the interpolation algorithm. Figure 4 presents the average estimated target strength for the 25 frames recorded at each target position, and demonstrates the improved estimated target strength calculation as the target moves between beams. The improvement in root-mean-squared (rms) position error along the axis of translation was from 3.48 cm for the uninterpolated position to 0.79 cm for the interpolated position. Higher interpolation factors produced better fits, but at a diminishing rate of return and a cost

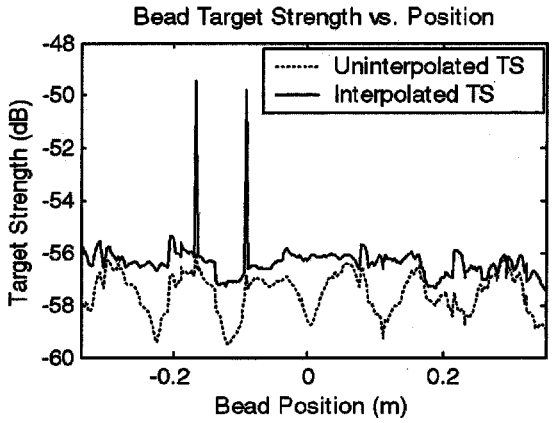

FIG. 4. The target strength results from the same bead experiment shown in Fig. 1. The dips in target strength as the bead travels from one physical beam to the next are reduced.

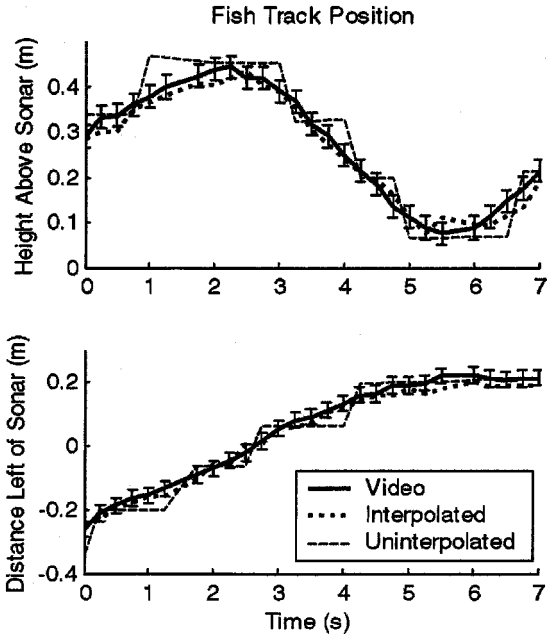

FIG. 5. Plot of a goldfish track representing the improved position estimates provided by interpolation of the elevation (top) and bearing (bottom) angles of FishTV. The output of the stereo camera system, with 2.5-cm error bars, is shown as a reference of the true target position.

of substantially increased processing time. For example, an interpolation factor of $\lambda=16$, which requires four times the processing time of $\lambda=8$, resulted in an rms position error of 0.65 cm.

The estimated target strengths shown in Fig. 4 are not calibrated against a known signal source, but are internally consistent. It is believed that the two spikes in the interpolated output of target strength are caused by small ''holes'' in the array's field of view due to the fact that the beams do not actually lie exactly on 2-deg beam spacings. The standard deviation of the average target strength across all positions was 0.798 dB for the uninterpolated results, and 0.712 dB for the interpolated results. Removing the two outlying points from the interpolated results provides a target strength standard deviation of 0.417 dB.

B. Fish

A total of 31 separate fish tracks was extracted from the sonar and video data, and the interpolation algorithm was applied to the sonar data with an interpolation factor of $\lambda=8$. Using the positions extracted from the video systems as the baseline ''true'' track, the position errors for both the uninterpolated and interpolated sonar positions were computed. An example track of a goldfish as it swims though the shared field of view of both systems is shown in Fig. 5. The positions are reported in a coordinate system centered on the sonar's location. Only two axes of motion, are presented, as the third axis represents FishTV's range measurement, which is not affected by the interpolation algorithm. Figure 6 presents the error between the FishTV measurements, both uninterpolated and interpolated, and the measurements of the video system for the track shown in Fig. 5. The errors for each interpolated axis are graphed individually, as well as the total position error for both axes, defined as

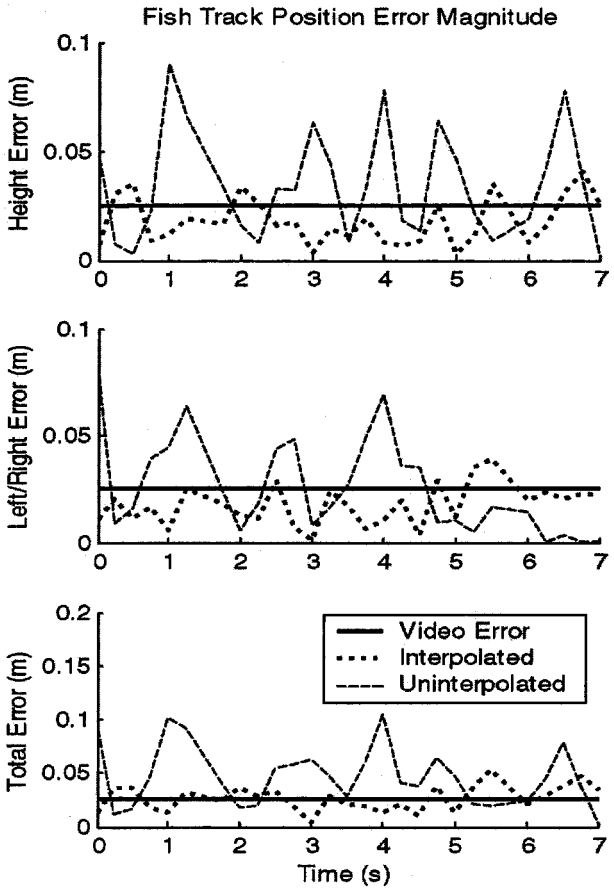

FIG. 6. Plot of the position error magnitudes of the interpolated and uninterpolated FishTV output relative to the position reported by the stereo camera system for the goldfish track of Fig. 5. The horizontal lines in the plots show the ± 2.5-cm uncertainty in the video estimated positions.

$$\text{Total error}=\sqrt{(\text{height error})^2+(\text{left/right error})^2}. \quad (4)$$

The rms position error along both interpolated axes and the total rms position error for the 31 tracks is presented in Fig. 7 as a function of track number. The numerical values for the total rms errors for all tracks combined are presented in Table I.

IV. DISCUSSION

As can be seen from the results of the two experiments, the algorithm works quite well, especially on the small bead, which most closely resembles the point target on which the model is based. As stated above, an interpolation factor of 8 was achieved which results in an angular resolution of 0.25 deg. A higher interpolation factor yielded only a marginal improvement in localization accuracy with much more computational burden. The likely cause of this limitation was the noise in the recorded waveform, assumed to be due primarily to the preamplifiers of the system. Since the model used assumes a point scatterer, and the bead conforms very closely to this model, it seems reasonable that the algorithm achieves a large increase in the localization capability for the bead in high signal-to-noise case tested here.

In the case of the fish, the algorithm works somewhat worse. This is likely due, in part, to the fact that the fish is a ''distributed target.'' The residual was approximately ± 2.5

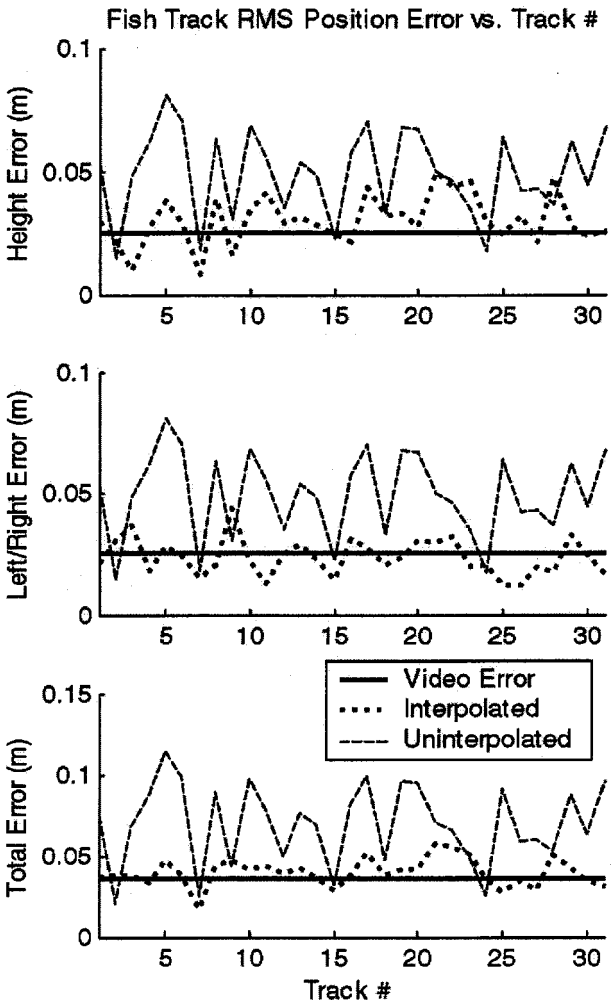

FIG. 7. Plot of the total track rms position error of the interpolated and uninterpolated FishTV output relative to the position reported by the stereo camera system for all 31 fish tracks as a function of track number. The horizontal lines in the plots show the ±2.5-cm uncertainty in the video estimated positions.

cm, about the size of the fish. It is not surprising that our capability to localize the animals is on the order of their size. Another factor in evaluating the accuracy of the algorithm in the case of the fish is that the positional data from the video system are not as accurate as those from the micrometer in the bead experiment. As indicated above, the positional accuracy from the video was also ±2.5 cm, so the residual was approximately the same magnitude. Interestingly, inspection of the records revealed that many of the estimated locations were within the body of the animal. The results indicate that the interpolator does reduce the error in the positional estimate of the fishes' locations.

Another problem encountered but not shown in these results is that the effectiveness of the algorithm was reduced for targets close to the edge of the sonar array. This is due to the fact that the sidelobes of the target response are important information in localizing the target, but as the target gets closer to the edge of the array, a portion of the sidelobes is not recorded, so the information is not available. This was hinted at in Jaffe (1999a) but not fully explored.

TABLE I. Total fish track position errors (referenced to video position).

	Interpolated position	Uninterpolated position
rms height error (m)	0.0329	0.0512
rms left/right error (m)	0.0238	0.0512
rms total error (m)	0.0406	0.0725

An interesting question concerns the general utility of the algorithm for arbitrary targets. Although our results here assumed that the target was in the far field of the instrument, it is natural to ask what the effects of a large target might be when the sonar is not in the far field of the animal. This will nominally happen when the animal is larger than a beamwidth (assuming that the animal is in the far field of the sonar). In this case, one cannot be sure that the algorithm can be applied, and it seems prudent to form a more complicated model of the animal or its anatomical features (such as a swim bladder) and use it with a model of the sonar system in order to validate the use of the approach, as taken here. These models might lead to better results in estimating the positions of the animals to an accuracy that would be less than their size.

Currently, the algorithm has been used to process FishTV data recorded in the field for purposes of studying the behavior of *Euphasia pacifica* (Jaffe *et al.*, 1999b, De Robertis, 2000, 2003). In this case the animals' sizes are at most one-eighth of a beamwidth (at the closest ranges), which lends confidence to the applicability of the point reflector assumption.

Note that in this article we have only considered the application of these ''interpolation'' techniques to recorded intensity or amplitude data. The use of phase-coherent localization methods has not been considered. These coherent techniques will likely provide better estimates of animal positions in high-SNR environments than the type of incoherent technique considered here. Since the primary motivation for this study was to validate a previously proposed algorithm (Jaffe, 1999a), and the sonar system considered here cannot use phase-coherent methods (in one of the directions), the results here concern only the use of this interpolation algorithm on intensity data. The general question of optimal target localization as a general function of SNR has not been considered across a broad range of methodologies, and there remain many interesting and open questions in this regard.

Finally, we note that the algorithm was applied to the data *ex post facto*. This points out one of the greatest strengths of this approach, that it can be applied to existing systems and existing data sets, not just to newly created systems. So, for example, the Simrad SM2000 system, in its most commonly used recording mode, stores just the intensity of the reflected sound as a function of beam number (above some threshold) with no data about phase. This algorithm could be applied, in a straightforward way, to these data. Perhaps through the use of this method more information can be obtained from existing systems and existing data sets, extending the scientific usefulness of these systems and data, and allowing more work to be done without the added expense of completely new systems and experiments.

ACKNOWLEDGMENTS

This material is based upon work supported under a National Science Foundation Graduate Fellowship. The authors thank their colleague, Dr. Jeff Krolik, for helpful discussions.

Axelsen, B. E., Anker-Nilssen, T., Fossum, P., Kvamme, C., and Nottestad, L. (**2001**). ''Pretty patterns but a simple strategy: Predator–prey interactions between juvenile herring and Atlantic puffins observed with multibeam sonar,'' Can. J. Zool. **79**, 1586–1596.

De Robertis, A., Jaffe, J. S., and Ohman, M. D. (**2000**). ''Size-dependent visual predation risk and the timing of vertical migration in zooplankton,'' Limnol. Oceanogr. **45**(N8), 1838–1844.

De Robertis, A., Schell, C., and Jaffe, J. S. (**2003**). ''Acoustic observations of the swimming behavior of the euphausiid *Euphausia pacifica Hansen*,'' ICES J. Mar. Sci. **60**, 885–898.

Ehrenberg, J. E., and Torkelson, T. C. (**1996**). ''Application of dual-beam and split-beam target tracking in fisheries acoustics,'' ICES J. Mar. Sci. **53**, 329–334.

Enzenhofer, H. J., Olsen, N., and Mulligan, T. J. (**1998**). ''Fixed-location riverine hydroacoustics as a method of enumerating migrating adult Pacific salmon: Comparison of split-beam acoustics vs visual counting,'' Aquat. Living Resour. **11**(2), 61–74.

Gerlotto, F., Georgakarakos, S., and Eriksen, P. K. (**2000**). ''The application of multibeam sonar technology for quantitative estimates of fish density in shallow water acoustic surveys,'' Aquatic Living Resources **13**(5), 385–393.

Hewitt, R. P. and Demer, D. A. (**2000**). ''The use of acoustic sampling to estimate the dispersion and abundance of euphausiids, with an emphasis on Antarctic krill, Euphausia superba,'' Fisheries Research. **47**(2-3), 215–229.

Huse, I., and Ona, E. (**1996**). ''Tilt angle distribution and swimming speed of overwintering Norwegian spring spawning herring,'' ICES J. Mar. Sci. **53**, 863–873.

Jaffe, J. S. (**1999a**). ''Target localization for a three-dimensional multibeam sonar imaging system,'' J. Acoust. Soc. Am. **105**, 3168–3175.

Jaffe, J. S., De Robertis, A., and Ohman, M. D. (**1999b**). ''Sonar estimates of daytime activity levels of *Euphausia pacifica* in Saanich Inlet,'' Can. J. Fish. Aquat. Sci. **56**, 2000–2010.

Jaffe, J. S., Ohman, M. D., and DeRobertis, A. (**1998**). ''OASIS in the sea: Measurement of the acoustic reflectivity of zooplankton with concurrent optical imaging,'' Deep-Sea Res. **45**, 1239–1253.

Jaffe, J. S., Reuss, E., McGehee, D., and Chandran, G. (**1995**). ''FTV, a sonar for tracking macrozooplankton in 3-dimensions,'' Deep-Sea Res. **42**, 1495–1512.

Johnson, R. L., and Moursund, R. A. (**2000**). ''Evaluation of juvenile salmon behavior at Bonneville Dam, Columbia River, using a multibeam technique,'' Aquatic Living Resources **13**, 313–318.

Mayer, L., Li, Y., and Melvin, G. (**2002**). ''3D visualization for pelagic fisheries research and assessment,'' ICES J. Mar. Sci. **59**, 216–225.

McGehee, D. E., O'Driscoll, R. L., and Traykovski, L. V. M. (**1998**). ''Effects of orientation on acoustic scattering from Antarctic krill at 120 kHz.'' Deep-Sea Research Part II-Topical Studies in Oceanography. **45**(7), 1273–1294.

Nottestad, L., and Axelsen, B. E. (**1999**). ''Herring schooling manoeuvres in response to killer whale attacks,'' Can. J. Zool. **77**, 1540–1546.

Price, H. J. (**1989**). ''Swimming behavior of krill in response to algal patches: a mesocosm study.'' Limology and Oceanography, **34**, 649–659.

Ransom, B. H., Johnston, S. V., and Steig, T. W. (**1998**). ''Review on monitoring adult salmonid (*Oncorhynchus* and *Salmo spp.*) escapement using fixed-location split-beam hydroacoustics,'' Fisheries Research (Amsterdam) **35**, 33–42.

Soria, M., Freon, P., and Gerlotto, F. (**1996**). ''Analysis of vessel influence on spatial behavior of fish schools using a multibeam sonar and consequences for biomass estimates by echo-sounder,'' ICES J. Mar. Sci. **53**, 453–458.

Strang, G. S. (**1980**). *Linear Algebra and Its Applications* (Academic, Orlando).

Torgersen, T., and Kaartvedt, S. (**2001**). ''*In situ* swimming behaviour of individual mesopelagic fish studied by split-beam echo target tracking,'' ICES J. Mar. Sci. **58**, 346–354.

Traykovski, L. V. M., Stanton, T. K., Wiebe, P. H., and Lynch, J. F. (**1998**). ''Model-based covariance mean variance clasification techniques - algorithm development and application to the acoustic classification of zooplankton,'' IEEE Journal of Oceanic Engineering, **23**(4), 344–364.

Urich, R. J. (**1983**). *Principles of Underwater Sound*, 3rd ed. (McGraw-Hill Company, New York).

Wiebe, P. H., and Benfield, M. C. (**2003**). ''From the Hensen net towards 4-D biological oceanography,'' Prog. Oceanogr. **56**, 7–136.

Xie, Y. (**2000**). ''A range-dependent echo-association algorithm and its application in split-beam sonar tracking of migratory salmon in the Fraser River watershed,'' IEEE J. Ocean. Eng. **25**, 387–398.

Yen, J. (**1988**). ''Directionality and swimming speeds in predator-prey and male-female interactions of *Euchaeta rimana*, a subtropical marine copepod,'' Bull. Mar. Sci. **43**(3), 175–193.

Blind deconvolution in ocean waveguides using artificial time reversal[a)]

Karim G. Sabra and David R. Dowling[b)]
Department of Mechanical Engineering, University of Michigan, Ann Arbor, Michigan 48109-2133

(Received 11 April 2003; revised 19 March 2004; accepted 25 March 2004)

Sound that travels through the ocean from a source to a receiver is commonly distorted by multipath acoustic propagation. The severity and details of this distortion are determined by the sound channel's characteristics, which may not be known. However, recovery or reconstruction of undistorted signals from recordings made in unknown complex multipath environments—a process commonly referred to as blind deconvolution—is advantageous in many applications of underwater acoustics. This paper presents a simple and robust means to achieve blind deconvolution in unknown sound channels with an array of receiving transducers. The technique, artificial time reversal (ATR), can be effective when there is a linear relationship between frequency and the phase of the low-order propagating modes of the sound channel. Broadband simulations of ATR in a generic shallow ocean sound channel show that the maximum correlation between the original signal and the reconstructed signal may approach 100% for signal pulses having a 258 Hz bandwidth and a 500 Hz center frequency. Application of ATR to ocean sound-propagation measurements produces original-to-reconstructed signal correlations from 80% to 95%. Possible extensions and improvements of ATR are discussed. [DOI: 10.1121/1.1751151]

PACS numbers: 43.30.Wi, 43.60.Pt, 43.30.Bp. [EJS] Pages: 262–271

I. INTRODUCTION

A passive array that receives a signal from a remote source will record the combined characteristics of the source signal and the environment. In applications of acoustic (and electromagnetic) remote sensing and communication, it is often desirable to separate the source signal from environmental factors to detect, locate, or identify the signal source. When the environment is complicated, the original signal may be distorted and spread in time after propagation from the source to the array. Reconstructing an unknown signal from remote measurements made in an unknown and potentially complicated wave-propagation environment is a remote sensing problem commonly referred to as blind deconvolution. In general, blind deconvolution is not a well-posed problem because the array-recorded information is insufficient to determine both the source signal and the propagation characteristics (i.e., the Green's function) of the environment. However, blind deconvolution schemes may be successful under constrained circumstances. This paper presents a blind deconvolution technique applicable to sound sources in underwater sound channels. The results presented here are potentially important for remote sound source detection, localization, and identification, and may be readily extended to electromagnetic, structural acoustic, or seismic remote sensing and/or communication in guided-wave environments.

The recorded signal at each element of a passive receiving array is the convolution of the broadcast source(s) signal(s) with the Green's function(s) of the environment. For multiple sources, the blind deconvolution problem consists of estimating simultaneously the unknown source signal(s) and the unknown Green's function(s) of the environment based on the passive-array recorded data alone (Tohyama *et al.*, 1998). Blind deconvolution problems have been studied by many investigators (Mansour *et al.*, 2000) and several algorithms have been proposed notably based on polynomial algebra (Rietsch, 1997), on minimum entropy (Wiggins, 1978; Cabrelli, 1984), on high-order statistics of the recorded data in the frequency (Capdevielle *et al.*, 1995) or time (Hansen *et al.*, 2000) domains, and on adaptive techniques (Gürelli *et al.*, 1995; Sibul *et al.*, 2002) for different source signal types. These algorithms have been applied in a variety of fields such as room acoustics (Benesty, 2000), tomographic problems in geoacoustics (Ernst and Herman, 2000), and underwater acoustics.

Several blind deconvolution techniques for underwater acoustics have been reported in recent years. The virtual receiver algorithm uses a strategically located guide source, to recover the initial source signal in multipath shallow water environments (Siderius *et al.*, 1997). Information criteria (Xinhua *et al.*, 2001), adaptive super-exponential methods (Weber and Bohme, 2002), high-order statistics (Broadhead and Pflug, 2000a,b), time-frequency analysis (Martins *et al.*, 2002), and multiple convolutions (Smith, 2003) have also been used to achieve blind deconvolution in multipath underwater sound channels.

To be successful, blind deconvolution methods usually rely, directly or indirectly, on assumptions or measurements of the propagation physics in the underwater sound channel of interest. For instance, the guide source signal used in the virtual receiver algorithm provides information about multi-

[a)]Portions of this research were presented at the 145th ASA meeting in Nashville, TN.
[b)]Author to whom all correspondence should be addressed; electronic mail: drd@engin.umich.edu

path propagation effects. Other algorithms rely on the choice of an efficient cost function for the selected environments (Weber and Bohme, 2002), or depend on finding strong arrival paths (Martins *et al.*, 2002). Unfortunately, such paths will only exist when the environment's Green's function is sufficiently ''sparse'' (Broadhead and Pflug, 2000a,b). Wavelet and statistical analyses have been carried out to gain knowledge of the Green's function characteristics in shallow water environment to improve blind deconvolution algorithm efficiency (Morgan *et al.*, 2001; Chapin *et al.*, 2001).

The blind deconvolution technique presented here, artificial time reversal (ATR), differs from the prior techniques in that it does not require specific signal types, auxiliary measurements, computational optimizations, strong independent signal paths, or statistical synthesis. Instead, ATR is based on stable features of the low-order acoustic normal modes common to most (if not all) underwater sound channels, and on a receiving array with sufficient transducer density and aperture. In particular, ATR relies on the phase velocity of the low-order propagating modes being independent of frequency, and on the receiving array having sufficient spatial diversity to capture signal information throughout the bandwidth of interest. In many underwater remote-sensing and communication scenarios, these requirements are likely to be met. In addition, this paper also emphasizes blind deconvolution when only a single source is present.

Artificial time reversal is formally described in Sec. II, but can be verbally summarized in four steps. First, the passive array recordings are Fourier analyzed and normalized. These normalized signal spectra include the source signal phase. Second, the signal phase is removed from the normalized recorded spectra to yield a broadband estimate of the Green's function of the environment. Next, this estimated Green's function is complex conjugated and multiplied with the original signal spectra to produce an estimate of the original signal spectrum via artificial back propagation (i.e., artificial time reversal). The final step is merely an inverse Fourier transform that brings the estimated signal into the time domain. Thus, ATR involves little signal processing effort and takes advantage of the inherent robustness of the time-reversal process in the ocean (Kuperman *et al.*, 1998; Hodgkiss *et al.*, 1999). Furthermore, the recorded-data normalization step renders ATR equivalent to array-element-averaged inverse filtering with the estimated Green's function, so ATR may also embody some of the superior side lobe suppression and signal reconstruction performance of inverse filtering techniques. The ATR simulations presented here for broadband pulses centered on 500 Hz in a shallow ocean sound channel suggest that original-source-signal to ATR-estimated-source-signal correlations approaching 100% are possible. When ATR is applied to high signal-to-noise ratio shallow water sound measurements in a comparable frequency range, the maximum original-estimated signal correlation is generally near or above 90%.

The remainder of this paper is divided into four sections. Section II presents the mathematical formulation of ATR. In Sec. III, ATR is illustrated with broadband simulations of shallow ocean sound propagation. The influence of the source depth and source-array range on ATR's performance is reported. Section IV presents the performance of ATR with underwater sound measurements made as part of unique experimental studies of acoustic time reversal in the ocean (Kuperman *et al.*, 1998; Hodgkiss *et al.*, 1999; Kim *et al.*, 2001). Section V summarizes this research effort and presents the conclusions drawn from it.

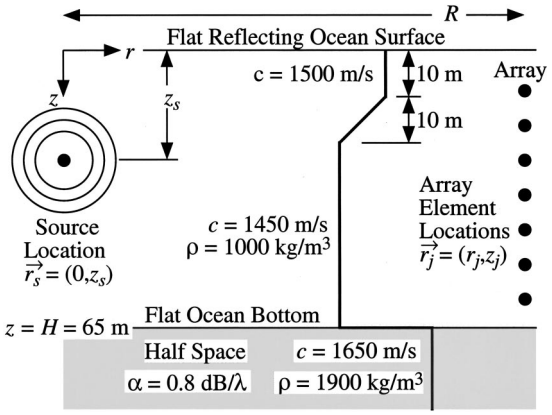

FIG. 1. Computational sound channel used to simulate the performance of artificial time reversal. The bottom is modeled on the properties of sand; hard but lossy.

II. FORMULATION OF ARTIFICIAL TIME REVERSAL

This section presents the formal development of ATR as a means for blind deconvolution of the signal from a lone source in an unknown sound channel. As depicted in Fig. 1, consider a point source located at $\mathbf{r}_s$ that emits a signal $S(t)$ having Fourier transform $\tilde{S}(\omega)$:

$$\tilde{S}(\omega) = \frac{1}{2\pi}\int_{-\infty}^{+\infty} S(t)e^{i\omega t}dt = |\tilde{S}(\omega)|e^{i\theta_s(\omega)}, \tag{1}$$

where t=time, ω=temporal radian frequency, and $\theta_s(\omega)$ is the signal's phase as a function of frequency. Although Fig. 1 depicts a shallow ocean sound channel, the following development should be general enough to include deep-water sound channels as well. The emitted sound travels through the ocean sound channel where it is recorded as $P_j(t)$ by an array of N receiving transducers located at $\mathbf{r}_j$. Here the recording interval is presumed to be longer than the multipath time spread of the sound channel. The Fourier transform of $P_j(t)$ will be

$$\tilde{P}_j(\omega) = G(\mathbf{r}_j, \mathbf{r}_s, \omega)\tilde{S}(\omega), \tag{2}$$

where $G(\mathbf{r}_j, \mathbf{r}_s, \omega)$ is the sound channel's Green's function between the source location $\mathbf{r}_s$ and the receiving transducer locations $\mathbf{r}_j$, at the frequency ω. The goal of the signal processing technique is to recover $S(t)$ from the recordings $P_j(t)$ without explicit knowledge of $G(\mathbf{r}_j, \mathbf{r}_s, \omega)$.

The ATR deconvolution technique involves constructing a surrogate for $G(\mathbf{r}_j, \mathbf{r}_s, \omega)$ from $\tilde{P}_j(\omega)$, and using this artificial Green's function to reconstruct $S(t)$ to within an unknown time shift. First, a normalized data vector, $D_j(\omega)$, is formed from the measured signal spectra $\tilde{P}_j(\omega)$:

$$D_j(\omega)=\frac{\tilde{P}_j(\omega)}{\sqrt{\Sigma_{j=1}^{N}|\tilde{P}_j(\omega)|^2}}=\frac{G(\mathbf{r}_j,\mathbf{r}_s,\omega)e^{i\theta_s(\omega)}}{\sqrt{\Sigma_{j=1}^{N}|G(\mathbf{r}_j,\mathbf{r}_s,\omega)|^2}}, \quad (3)$$

where the second equality follows from Eq. (2). The normalization introduced in Eq. (3) is a nonlinear operation and therefore may be sensitive to recorded noise when the sum of Green's functions has deep fades. The normalization in Eq. (3) can also be interpreted as a pre-emphasis filter for the measured data. However, for a well-populated vertical array in an ocean sound channel (the main focus of this paper), the normalization in Eq. (3) is nearly flat in frequency and introduces no phase shift, thus limiting its importance as a pre-emphasis filter.

Although Eq. (3) shows that $|\tilde{S}(\omega)|$ can be removed from $\tilde{P}_j(\omega)$, the signal phase $\theta_s(\omega)$ remains part of $D_j(\omega)$ at this point. The crux of ATR involves removing the signal phase from Eq. (3) using a phase correction factor that replaces $\theta_s(\omega)$ with an artificial phase having desired properties. One possible class of phase correction factors, $\exp\{-i\alpha(\omega)\}$, can be constructed using a weighted sum of the normalized recordings:

$$\alpha(\omega)=\arg\left\{\sum_{j=1}^{N} W_j D_j(\omega)\right\}$$
$$=\arg\left\{\sum_{j=1}^{N} W_j G(\mathbf{r}_j,\mathbf{r}_s,\omega)\right\}+\theta_s(\omega), \quad (4)$$

where the W_j are the transducer weights; other possible phase correction factors for Eq. (3) are not considered here. The product of the phase-correction factor and the normalized data vector produces a rotated normalized data vector $\hat{D}_j(\omega)$ that does not contain $\theta_s(\omega)$,

$$\hat{D}_j(\omega)=D_j(\omega)\exp\{-i\alpha(\omega)\}=\frac{G(\mathbf{r}_j,\mathbf{r}_s,\omega)}{\sqrt{\Sigma_{j=1}^{N}|G(\mathbf{r}_j,\mathbf{r}_s,\omega)|^2}}$$
$$\times\exp\left\{-i\arg\left\{\sum_{j=1}^{N} W_j G(\mathbf{r}_j,\mathbf{r}_s,\omega)\right\}\right\}. \quad (5)$$

Here, $\hat{D}_j(\omega)$ can be an acceptable surrogate for $G(\mathbf{r}_j,\mathbf{r}_s,\omega)$ if the weights, W_j, can be chosen so that the extra phase in Eq. (5), $\Gamma(\omega)$, is linearly dependent on frequency, i.e.,

$$\Gamma(\omega)\equiv\arg\left\{\sum_{j=1}^{N} W_j G(\mathbf{r}_j,\mathbf{r}_s,\omega)\right\}=a+b\omega, \quad (6)$$

where a and b are real constants. Suitable choices for the W_j's will be discussed before the end of this section.

An estimate of the original signal spectrum, $\tilde{S}_{\mathrm{BP}}(\omega)$, can now be constructed from the surrogate Green's function, $\hat{D}_j(\omega)$, via artificial backpropagation (equivalent to time reversal),

$$\tilde{S}_{\mathrm{BP}}(\omega)=\sum_{j=1}^{N}\hat{D}_j^*(\omega)\tilde{P}_j(\omega), \quad (7)$$

where an asterisk denotes a complex conjugate. Alternatively, the original signal spectrum can be estimated by inverse filtering each receiver channel and averaging across array elements to suppress the potentially negative influences of dividing by $\hat{D}_j(\omega)$ when it is small,

$$\tilde{S}_{\mathrm{IF}}(\omega)=\frac{1}{N}\sum_{j=1}^{N}\frac{\tilde{P}_j(\omega)}{\hat{D}_j(\omega)}. \quad (8)$$

Although backpropagation and inverse filtering are not equivalent in general, they can be shown to be the same for the present situation. First, substitute for $\hat{D}_j(\omega)$ in Eq. (8) using Eqs. (5) and (6),

$$\tilde{S}_{\mathrm{IF}}(\omega)=\frac{1}{N}\sum_{j=1}^{N}\tilde{P}_j(\omega)\frac{\sqrt{\Sigma_{l=1}^{N}|G(\mathbf{r}_l,\mathbf{r}_s,\omega)|^2}}{G(\mathbf{r}_j,\mathbf{r}_s,\omega)}$$
$$\times\exp\{+i\Gamma(\omega)\}. \quad (9)$$

Now use Eq. (2) for $\tilde{P}_j(\omega)$ and cancel the common numerator and denominator factor of $G(\mathbf{r}_j,\mathbf{r}_s,\omega)$ to find:

$$\tilde{S}_{\mathrm{IF}}(\omega)=\frac{1}{N}\sum_{j=1}^{N}\tilde{S}(\omega)\sqrt{\Sigma_{l=1}^{N}|G(\mathbf{r}_l,\mathbf{r}_s,\omega)|^2}$$
$$\times\exp\{+i\Gamma(\omega)\}. \quad (10)$$

Here, the summand does not depend on summation index j, so the sum reduces to a product of N and the summand leaving

$$\tilde{S}_{\mathrm{IF}}(\omega)=\tilde{S}(\omega)\sqrt{\Sigma_{l=1}^{N}|G(\mathbf{r}_l,\mathbf{r}_s,\omega)|^2}\exp\{+i\Gamma(\omega)\}$$
$$=\tilde{S}(\omega)\frac{\Sigma_{l=1}^{N}|G(\mathbf{r}_l,\mathbf{r}_s,\omega)|^2}{\sqrt{\Sigma_{l=1}^{N}|G(\mathbf{r}_l,\mathbf{r}_s,\omega)|^2}}\exp\{+i\Gamma(\omega)\}, \quad (11)$$

where the second equality follows from multiplying and dividing by the square-root of the summed Green's functions. Now put $\tilde{S}(\omega)$ back inside the numerator summation and write $|G|^2$ as the product GG^*:

$$\tilde{S}_{\mathrm{IF}}(\omega)=\frac{\Sigma_{l=1}^{N}\tilde{S}(\omega)G(\mathbf{r}_l,\mathbf{r}_s,\omega)G^*(\mathbf{r}_l,\mathbf{r}_s,\omega)}{\sqrt{\Sigma_{l=1}^{N}|G(\mathbf{r}_l,\mathbf{r}_s,\omega)|^2}}$$
$$\times\exp\{+i\Gamma(\omega)\}. \quad (12)$$

The first two factors under the summation are $\tilde{P}_l(\omega)$ from Eq. (2), and the remaining ones are $\hat{D}_l^*(\omega)$ from Eqs. (5) and (6), thus

$$\tilde{S}_{\mathrm{IF}}(\omega)=\sum_{l=1}^{N}\tilde{P}_l(\omega)\hat{D}_l^*(\omega)=\tilde{S}_{\mathrm{BP}}(\omega), \quad (13)$$

where the final equality follows from Eq. (7) and completes the proof of the equivalence between inverse filtering and backpropagation in this situation. Here, the normalization of $\hat{D}_j(\omega)$, which provides some equalization between different frequencies, is the key to this equivalence.

ATR differs from true backpropagation or time reversal because it produces the reconstructed signal at the receiving array, not at the remote source location. ATR differs from common implementations of inverse filtering in that neither $G(\mathbf{r}_j,\mathbf{r}_s,\omega)$ nor $\tilde{S}(\omega)$ are known ahead of time, nor are ei-

ther measured separately. However, the fact that the two approaches are equivalent for ATR means that it should incorporate, at least in part, the optimal spatial-temporal matched filtering of time reversal (Kuperman *et al.*, 1998), and the superior side lobe suppression and signal reconstruction properties of inverse filtering (Tanter *et al.*, 2000, 2001; Aubry *et al.*, 2001; Cazzalotto *et al.*, 2001).

An inverse Fourier transform of the first equality in Eq. (11) produces the final ATR-estimated signal, $S_e(t)$, in the time domain,

$$S_e(t)=\int_{-\infty}^{+\infty}\tilde{S}(\omega)\exp\{-i\omega t+i\Gamma(\omega)\}\times\sqrt{\sum_{j=1}^{N}|G(\mathbf{r}_j,\mathbf{r}_s,\omega)|^2}d\omega. \tag{14}$$

When the sum over $G(\mathbf{r}_j,\mathbf{r}_s,\omega)$ defines an all-pass filter, or equivalently, its Fourier transform has a single sharp peak in the time domain—a common occurrence for multiple-element spatially dispersed arrays operating in the ocean (Kuperman *et al.*, 1998; Rouseff *et al.*, 2001)—and the final equality in Eq. (6) holds, then

$$S_e(t)\propto S(t-b). \tag{15}$$

The preceding presentation of ATR is incomplete without a means for determining the weights used in Eqs. (4)–(6). The goal here is to use the W_j to extract a phase from the sum of Green's functions that is independent or—at worst—linearly dependent on frequency. This is the point at which the propagation physics of ocean sound channels are exploited for ATR blind deconvolution. In a range-independent ocean sound channel with depth dependent density $\rho(z)$ and sound speed $c(z)$, the Green's function can be represented as a sum over propagating modes (see Jensen *et al.*, 1994):

$$G(\mathbf{r}_j,\mathbf{r}_s,\omega)=\frac{e^{i\pi/4}}{\rho(z_s)\sqrt{8\pi}}\sum_m\frac{\Psi_m(z_s)\Psi_m(z_j)}{\sqrt{k_m(\omega)r_j}}e^{ik_m(\omega)r_j}, \tag{16}$$

where for simplicity the cylindrical coordinates (r,θ,z) used in Eq. (16) are centered on the source so that $\mathbf{r}_s=(0,0,z_s)$ and $\mathbf{r}_j=(r_j,\theta_j,z_j)$. The ATR array-weighting strategies determined here may be readily extended to mildly range-dependent environments through the adiabatic normal mode version of Eq. (16) (see Jensen *et al.*, 1994). Here, the $\Psi_m(z)$ are the mode functions, $k_m(\omega)$ is the horizontal wave number of the mth mode, and it has been assumed that $k_m r_j\gg 1$. The mode functions are orthogonal through the water column depth H (Jensen *et al.*, 1994), so that

$$\int_{z=0}^{z=H}\frac{\Psi_m(z)\Psi_n(z)}{\rho(z)}dz=\delta_{mn}\approx\sum_{j=1}^{N}\frac{\Psi_m(z_j)\Psi_n(z_j)}{\rho(z_j)}\Delta z_j. \tag{17}$$

The approximate equality holds when the set of vertical sample points z_j and their vertical spacings Δz_j are sufficient to distinguish between the various mode shapes. A similar approximate equality holds for sample points arrayed horizontally at different ranges r_j, (Bogart and Yang, 1994; Tantum and Nolte, 2000):

$$\delta_{mn}\approx\frac{1}{N}\sum_{j=1}^{N}\exp\{i(k_m-k_n)r_j\}. \tag{18}$$

Thus, Eqs. (16)–(18) suggest that weightings, W_j, based on mode shapes and/or mode wave numbers can be used to extract the phase of individual modes or groups of modes. For example, with a vertical receiving array located a distance $r=R$ from the source, setting $W_j=e^{-i\pi/4}\Psi_l(z_j)/\rho(z_j)$ produces

$$\Gamma(\omega)\equiv\arg\left\{\sum_{j=1}^{N}W_jG(\mathbf{r}_j,\mathbf{r}_s,\omega)\right\}\approx\arg\left\{\frac{\Psi_l(z_s)}{\rho(z_s)\sqrt{8\pi k_l R}}e^{ik_lR}\right\}=+\mathrm{Re}\{k_l\}R \tag{19}$$

when $G(\mathbf{r}_j,\mathbf{r}_s,\omega)$ is drawn from Eq. (16). If the cutoff frequency of the lth mode is well below the frequencies of interest, the phase speed c_l of the lth mode is independent of the frequency and the extra phase of the ATR process, $\Gamma(\omega)=\mathrm{Re}\{k_l\}R=\omega R/c_l$, will increase linearly with increasing frequency for a fixed source to receiver geometry. For a horizontal array at a depth z_a, a similarly motivated extension of these array-weighting ideas leads to $W_j=\exp\{-i(\mathrm{Re}\{k_l\}\Delta r_j+\pi/4)\}$ where Δr_j is the range spacing from the jth array element to the center of the array. The extra phase for this horizontal array weighting is

$$\Gamma(\omega)\approx\arg\left\{\frac{\Psi_l(z_s)\Psi_l(z_a)}{\rho(z_s)\sqrt{8\pi k_l R}}e^{ik_lR}\right\}=+\mathrm{Re}\{k_l\}R, \tag{20}$$

where R is the distance from the source to the center of the array. For endfire horizontal arrays, the Δr_j will be the linear distances between elements along the array. For off-endfire array orientations, the Δr_j need to account for the azimuthal angle of the source-array geometry.

Overall, when mode shape and/or mode wave number information is available, the W_j are readily selected for either vertical or horizontal arrays. In fact, there is little ATR performance difference between weightings based on exact mode shapes or estimated mode shapes. Low-order mode shape estimates can be drawn from sound channel characteristics (Shang, 1984; Kinsler *et al.*, 2000; Kim *et al.*, 2001) or array measurements (Buck *et al.*, 1997; Hursky *et al.*, 2001; Neilsen and Westwood, 2002). Successful ATR weightings for tilted arrays are likely to be composite versions of the vertical- and horizontal-array schemes presented here.

The expressions above for the transducer weightings and the form of Eq. (6) are similar to those for a deconvolution scheme based on simple mode filtering. However, mode filtering suppresses signal energy not transmitted on the selected mode, while ATR uses the signal energy in every propagating mode and merely relies on mode filtering to obtain the extra phase, $\Gamma(\omega)$. Thus, if the signal energy is spread over many propagating modes and noise is present, ATR may provide a signal-to-noise advantage over simple mode filtering. Moreover, ATR can be applied with reasonable success even when the channel's mode shapes are unknown.

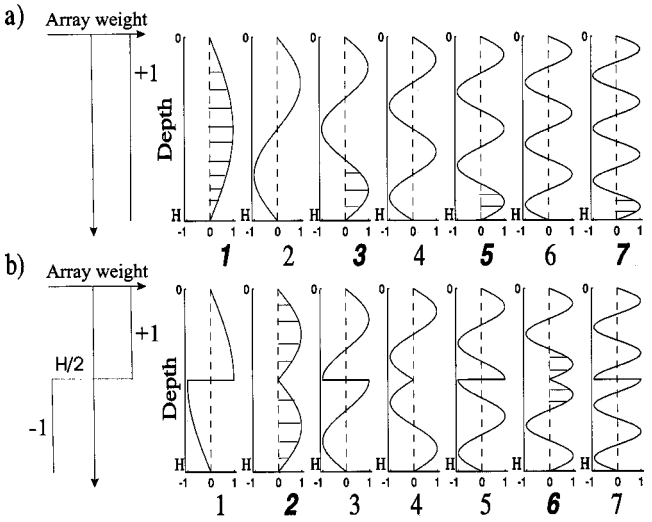

FIG. 2. Notional mode selection diagrams for ATR array weighting schemes (a) binary-1 ($W_j=+1$), and (b) binary-2 ($W_j=+1$ in the upper half of the sound channel and $W_j=-1$ in the lower half of the sound channel). The curves shown are $W_j\Psi_m(z_j)$ where m is the mode number that is listed below each subplot. The mode shapes are typical for an isospeed sound channel when the modes are far from being cutoff. The horizontal lines mark mode lobes that survive the summation after weighting. The modes with bold numbers contribute to the extra ATR phase.

When modal shape and wave number information is not available and cannot be estimated, reasonable ATR deconvolution results can still be obtained from simple binary (± 1) weighting schemes. For example, in an isospeed sound channel, a simple uniform weighting, $W_j=+1$ (referred to as "binary-1" in this paper), and a well-populated vertical array tend to select the phase of the odd-numbered modes because

$$\sum_{j=1}^{N} \Psi_{2m}(z_j) \approx 0 \tag{21}$$

when m is a positive integer. Similarly, if $W_j=+1$ for the upper half of the array and $W_j=-1$ for the lower half of the array (referred to as "binary-2" in this paper), the phase of the second, sixth, tenth, etc., modes will tend to be emphasized provided the modes are symmetric or anti-symmetric about mid water column depth. Figure 2 illustrates the effects of binary weighting on common mode shapes. Row (a) shows the results of multiplying binary-1 weighting with the first 7 mode shapes. Row (b) shows binary-2 (a weight vector with a value of $+1$ for the upper half and -1 for the lower half of the water column) multiplied with the same mode shapes. The horizontal marks indicate the portions of each mode that persist after summation across the array aperture, and thereby contribute to the extra phase $\Gamma(\omega)$. The mode index for each mode that has some persistent portion is printed in bold. As mode number increases, the persistent contributions that survive the binary-1 and binary-2 weightings become progressively smaller. Thus, the binary-1 and binary-2 weightings lead to extra phase values drawn primarily from the first and second propagating modes, respectively.

These binary weighting schemes have the advantage of simplicity but their performance is below that of mode-shape-based weightings. This occurs because the binary weighting schemes incorporate the propagation properties of multiple modes, and the binary-weighted extra phase becomes indistinct at ranges and depths where these modes destructively interfere. For example, if two modes are included by the ATR weighting, modes l and q, and these modes are excited by the source, then regions of low ATR performance are likely to be separated by the modal cycling distance, $2\pi/|k_l-k_q|$.

Additional binary weightings, $W_j=\pm 1$, that follow the anticipated lobe patterns of other low-order propagating modes are possible and can be easily pursued. In Sec. III, results from weighting schemes based on the shapes of the first two propagating modes of the water-column calculated at the center frequency of the signal (referred to as mode-1 and mode-2 weightings), and from the binary-1 and binary-2 weighting schemes will be presented.

III. SIMULATIONS OF ARTIFICIAL TIME REVERSAL

The intent of the material in this section is to illustrate the potential strengths and limitations of ATR without having to contend with the complications and uncertainties inherent in measured data. Thus, the results presented here almost certainly represent the upper performance limit of the ATR technique. The primary performance metric considered in this and in the next section is the temporal maximum of the correlation between the broadcast signal, $S(t)$, and the ATR reconstructed signal, $S_e(t)$,

$$C_{\max}=\max_t\left(\frac{\int_{-\infty}^{+\infty}\tilde{S}_e(\omega)\tilde{S}(\omega)e^{-i\omega t}d\omega}{\sqrt{\int_{-\infty}^{+\infty}|\tilde{S}_e(\omega)|^2d\omega}\sqrt{\int_{-\infty}^{+\infty}|\tilde{S}(\omega)|^2d\omega}}\right), \tag{22}$$

where Eqs. (1) and (14) define $\tilde{S}(\omega)$ and $\tilde{S}_e(\omega)$, respectively. Tests of ATR with experimental data are presented in Sec. IV.

The shallow ocean simulations of ATR were performed using the KRAKEN normal mode code (Porter and Reiss, 1984) and the range-independent sound channel depicted in Fig. 1 at source-array ranges from 1 to 20 km and for source depths from the channel surface to its bottom. The source broadcast signal was a Gaussian-windowed sine pulse having a center frequency of 500 Hz and a 99%-signal energy bandwidth of 258 Hz. The receiving array, centered in the sound channel, is linear and vertical. It has 21 elements spaced 3 m apart. Pulse propagation was simulated by Fourier synthesis of 527 single-frequency propagation calculations at frequencies from 244 to 756 Hz.

Figure 3 illustrates the broadcast signal and a sample received signal as functions of time. For this figure, the source is at a depth of 27 m, the receiver is at a depth of 36.7 m, and the source-array range is 6 km. The time scales are equal for each part of Fig. 3, but the time origins have been shifted so that the pulses line up. As might be expected, the received signal is spread in time by the multipath propagation to a duration twenty or more times longer than the original pulse. The third trace in Fig. 3 is the temporal signal that a time-reversing array would produce at the source location in this sound channel under these conditions. The peak correlation between a time reversed version of the original sig-

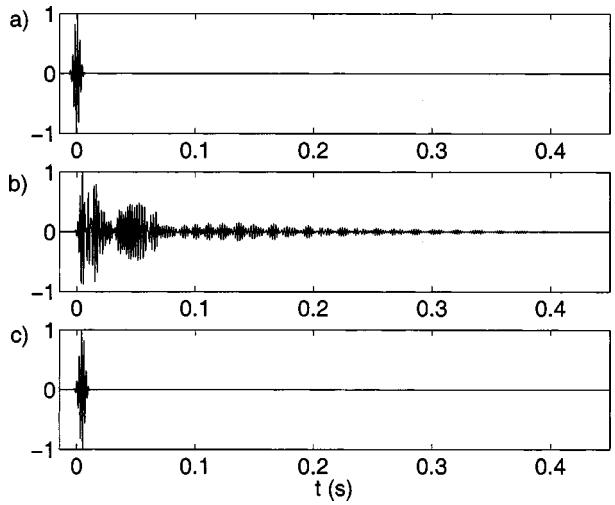

FIG. 3. (a) The signal broadcast by the source. (b) A sample received signal at a range of 6 km and a depth of 36.7 m when the source is at a depth of 27 m. (c) Signal produced at the source location by a time reversing array in this sound channel.

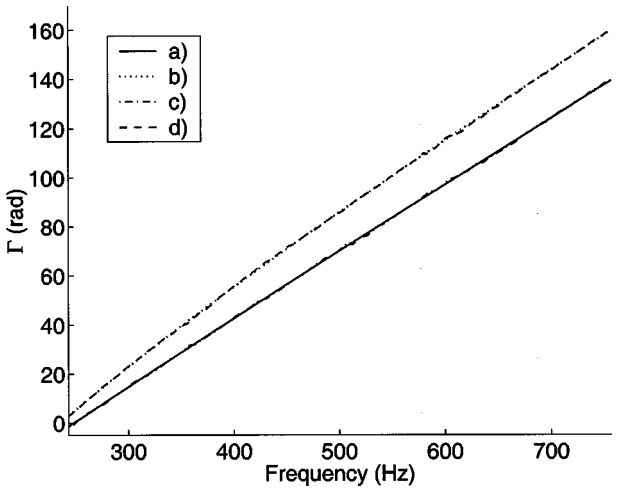

FIG. 5. ATR extra phase, Γ [see Eq. (6)], as a function of frequency for the four weighting schemes of Fig. 3: (a) mode-1, (b) mode-2, (c) binary-1, and (d) binary-2. The mode-1 and binary-1 results lie on top of each other, as do the mode-2 and binary-2 results. In all cases, Γ is almost perfectly linear.

nal and this signal produced by the time-reversing array is $C_{\max}=99\%$. The goal of ATR is to reconstruct the original signal with similarly high fidelity, based only on the signals recorded at the receiving array, without the requisite back-propagation step of the usual time reversal process.

Sample ATR reconstructed signals are shown in Fig. 4 for the source-array range and source depth of Fig. 3. The upper two signals in Fig. 4 have maximum correlations of 99% and 98%, and correspond to mode-1 and mode-2 weighting schemes, respectively, using mode shapes calculated at 500 Hz (the center frequency of the signal) for the entire signal bandwidth (244–756 Hz). The lower two signals in Fig. 4 have maximum correlations of 91% and 95%, and correspond to the binary-1 and binary-2 weighting schemes, respectively. For comparison, the peak correlation of the original signal with the sample received signal shown in Fig. 3(b) is 45%. Although the correlation numbers for the mode based weighting schemes are superior, the binary scheme results are respectable and suggest that ATR will remain useful even when mode-based array weighting is not possible.

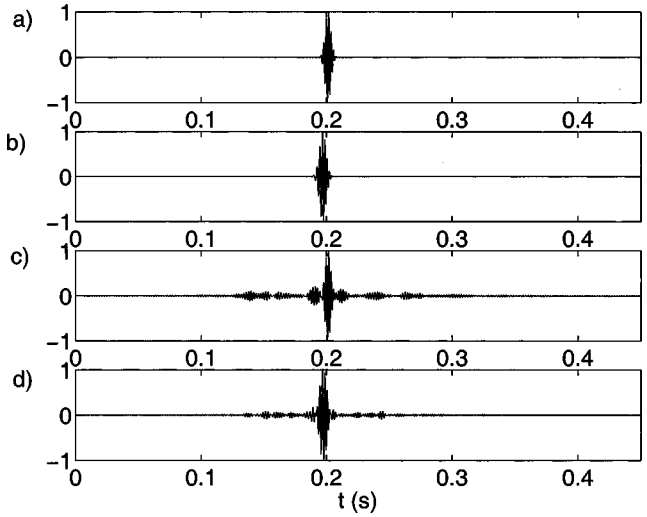

FIG. 4. ATR reconstructed signals when the array weighting is: (a) mode-1 ($C_{\max}=99\%$), (b) mode-2 ($C_{\max}=98\%$), (c) binary-1 ($C_{\max}=91\%$), and (d) binary-2 ($C_{\max}=95\%$).

The successful signal reconstructions shown in Fig. 4 occur when the various weighting schemes successfully extract a linearly marching extra phase, $\Gamma(\omega)$, from the recorded signals. For these simulations, this extra phase can be readily determined and is displayed in Fig. 5. Although four curves are plotted, the extra phase for the mode-1 and binary-1 weightings are nearly identical, as are the extra phases of the mode-2 and binary-2 weightings. In all cases, $\Gamma(\omega)$ is an almost perfectly linear function of frequency from 250 to 750 Hz. The small deviations between the pairs of extra phase curves lead to the differences in the reconstructed signals shown in Fig. 4.

The results shown in Figs. 3–5 correspond to one source-array range and one source depth. Figures 6 and 7 illustrate how $C_{\max}$ behaves through the depth of the sound channel at a fixed range, and at ranges from 1 to 20 km for a fixed source depth. First consider the results in Fig. 6 where $C_{\max}$, at a fixed source-array range of 6 km, is displayed versus source depth for the four different array weightings used in Fig. 4; mode-1 (a), mode-2 (b), binary-1 (c) and, binary-2 (d). The source depth, $z_s=27$ m, used for Fig. 4 is indicated by a dashed line. Figure 6 shows that mode-1 weighting allows ATR signal reconstructions to be nearly perfect when source is in the lower three quarters of the sound channel (below the thermocline). When the source is in the upper quarter of the sound channel, lower $C_{\max}$ values occur because the first mode is only weakly excited by shallow sources. Similarly, mode-2 weighting is successful for source depths that excite the second mode with the additional caveat that ATR with mode-2 weighting struggles when the source depth coincides with the node of the second mode ($z_s\approx 40$ m in Fig. 6). Although both binary weightings achieve $C_{\max}$ values above 90% over a range of source depths, their performance is generally below that of the modal weightings, with binary-1 being slightly better than binary-2 overall. The main purpose for showing binary-

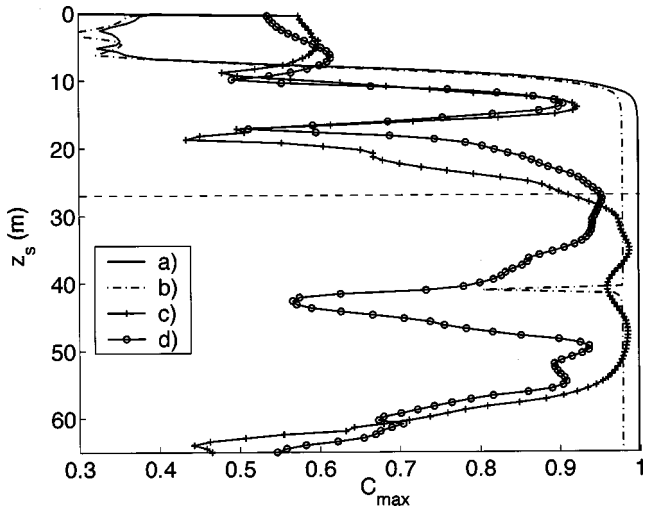

FIG. 6. Maximum correlation of the ATR reconstructed signal with the original source signal, $C_{\max}$, vs source depth z_s at a source-array range of 6 km for the four ATR weighting schemes of Fig. 3: (a) mode-1, (b) mode-2, (c) binary-1, and (d) binary-2. Although the modal weighting schemes are generally superior, both binary weights produce regions where $C_{\max}$ is well above 90%. The dashed line indicates the source depth, $z_s = 27$ m, used to generate the results in Fig. 4.

weighting ATR performance is to illustrate that the ATR technique may still work well with imperfect array weighting.

Sometimes the weighting changes necessary to lift ATR performance are small. For example, at a source-array range of 2.3 km and source depth of 27 m, $C_{\max}$ increases to 93% from 82% with binary-2 weighting when the location of the sign change is lowered by two array elements and W_j is set to zero for the shallowest four array elements lying above the thermocline. These modifications allow the binary-2 weighting scheme to better match the second mode's shape and thereby reject the phase of all but the second mode.

The performance of ATR at source array ranges from 1 to 20 km at a fixed source depth of 27 m is shown in Fig. 7

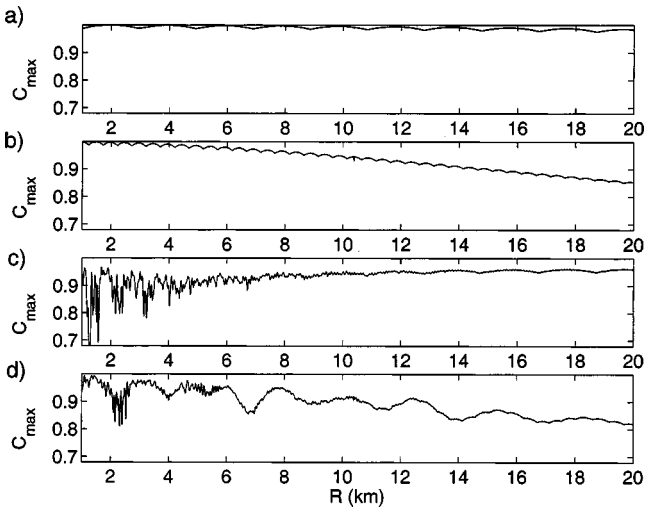

FIG. 7. Maximum correlation of the ATR reconstructed signal with the original source signal, $C_{\max}$, vs source-array range R for a source depth of 27 m for the four ATR weighting schemes of Fig. 3: (a) mode-1, (b) mode-2, (c) binary-1, and (d) binary-2. The modal weighting schemes are generally superior at short ranges.

for the four array weightings used in Fig. 4; mode-1 (a), mode-2 (b), binary-1 (c) and, binary-2 (d). Here, both modal weightings successfully produce $C_{\max}$ values well above 95%, with only minor variations. The gradual decay of the correlation $C_{\max}$ at longer ranges can likely be attributed to several factors. First, the presence of bottom absorption prevents the propagating modes from being precisely orthogonal so any mode-based weighting scheme will be imperfect. Second, modal dispersion of the chosen mode over the bandwidth of the simulated signal may cause problems when the signal energy arrives at the array via many modes. And third, variations in the chosen mode shape over the signal bandwidth were not taken into account during ATR deconvolution.

In Fig. 7, the two binary weightings are successful at most ranges with binary-1 and binary-2 following the trends shown by mode-1 and mode-2 weightings, respectively. However, both binary weightings show erratic performance at short ranges (less than 3 km) since the imperfect binary-array weighting unintentionally includes the contributions of higher modes in $\Gamma(\omega)$. However, higher modes attenuate faster than the lower modes so that at longer ranges (i.e., 10 km in Fig. 7) the modal weightings and their counterpart binary weightings arrive at almost the same results.

IV. APPLICATION OF ATR TO MEASURED SIGNALS

This section describes the performance of ATR with high signal-to-noise ratio ocean sound channel measurements made in the Mediterranean Sea in 1997 at source-array ranges of 3.75–20 km in a sound channel of average depth of 123 m [Kuperman *et al.*, 1998; Hodgkiss *et al.*, 1999; Kim *et al.*, 2001]. These data sets were recorded during active time reversal experiments, and were provided for the present ATR study by Dr. W. A. Kuperman and Dr. H. C. Song of the Marine Physical Laboratory of the Scripps Institution of Oceanography. The mildly range-dependent sound channel and the experimental hardware are described in the above-mentioned references. The signal pulse sent to the source transducer was a 50 ms-gated sinusoidal pulse at 445 Hz. The actual source broadcast was modified by the frequency-response characteristics of the source transducer which was typically located below the mild thermocline of the sound channel. The receiving array was nearly vertical and centered within the sound channel. It spanned 77 m of the water column with 23 hydrophones having a nominal vertical spacing of 3.33 m. The received signals were bandpass filtered (445 Hz center frequency, 53 Hz, 3 dB down bandwidth) and then recorded in the frequency range from 350 to 550 Hz.

Two features of the experiment have some impact on the ATR test results presented here. The actual source broadcast signal was not recorded, so an experimental source broadcast signal, $S_{\text{expt.}}(t)$, was synthesized by filtering an ideal 50 ms 445 Hz sinusoidal pulse with the same bandpass filter used with receiving array, and then truncating the signal spectrum so that it was nonzero only in the 350–550 Hz frequency range. At the receiver end of the experiment, the frequency responses, $E_j(\omega)$, of the receiving transducers may also play a role in ATR performance because variations in $E_j(\omega)$ be-

TABLE I. Peak ATR correlation percentages using experimental measurements.

Range (km)	Mode-1	Mode-2	Binary-1	Binary-2	Time reversal
3.75	88.5	92	80	93	80
15	95	93	94	95	93
20	91	93	93	91	91

tween transducers cannot be distinguished from variations in $G(\mathbf{r}_j,\mathbf{r}_s,\omega)$. When $E_j(\omega)$ is included in the ATR formulation, Eqs. (6) and (14) become

$$\Gamma_{\text{expt.}}(\omega)\equiv\arg\left\{\sum_{j=1}^{N} W_j G(\mathbf{r}_j,\mathbf{r}_s,\omega)E_j(\omega)\right\}, \tag{23}$$

$$S_{e,\text{expt.}}(t)=\int_{-\infty}^{+\infty}\tilde{S}(\omega)\exp\{-i\omega t+i\Gamma_{\text{expt.}}(\omega)\}\times\sqrt{\sum_{j=1}^{N}|G(\mathbf{r}_j,\mathbf{r}_s,\omega)E_j(\omega)|^2}\,d\omega. \tag{24}$$

When the $E_j(\omega)$ are not identical but known, a correction can be introduced into the weights W_j before the ATR signal processing to prevent $E_j(\omega)$ from influencing Γ. For the 1997 experiments the receiving transducers were identical model transducers with an almost flat frequency response in the signal bandwidth, so the $E_j(\omega)$ were presumed identical in the analysis presented here.

The main results of the experimental tests of ATR are provided in Table I, which lists the $C_{\max}$ values for the four weighting schemes illustrated in Fig. 4 and for the signal that time reversal produces at the source location. Due to the presence of the thermocline, the effective depth of the waveguide was set to $D_e=91$ m (Kim *et al.*, 2001). The mode-1 and mode-2 array weightings were estimated using the simple approximate mode shape $\Psi_m(z)=\sin(m\pi z/D_e)$, for $m=1$, 2, respectively. Similarly for binary-2 weighting, the weights W_j were set to zero for the shallowest four array elements above the thermocline with the sign change occurring after the 12th element, in order to better match the second mode's shape. The tabulated $C_{\max}$ values are drawn from three experimental source-array configurations: $z_s=47$ m at a range of 3.75 km, $z_s=85$ m at a range of 15 km, and $z_s=81$ m at a range of 20 km. The experimental time reversal results were spatially interpolated using an average of the recorded time traces from the two transducers nearest to the source depth. This interpolated signal was correlated with the estimated source signal to determine $C_{\max}$.

The tabulated ATR values are all generally above 90% even though the receiving array did not fully span the water column and the source broadcast signal used in this analysis is merely an estimate of the actual source broadcast signal. An interesting feature of the values in Table I is the fact that the ATR correlation values are equal to or slightly greater than those obtained from genuine time reversal. This probably occurs because the genuine time reversal signals undergo more absorption losses and are more sensitive to environmental dynamics than ATR signals because genuine time reversal requires forward and backward propagation while ATR requires only the forward step. Additionally, the amplitude normalization in Eq. (3) may also contribute to the mildly superior performance of ATR.

Sample signals representing the highest and lowest correlations at the shortest experimental source-array range, 3.75 km, are shown in Fig. 8. The synthesized source-broadcast signal, $S_{\text{expt.}}(t)$, is shown for reference in Fig. 8(a). The recorded signal at the 12th array element is shown in Fig. 8(b). The experimentally measured time-reversed signal, shown in Fig. 8(c), provides reasonable pulse reconstruction ($C_{\max}=80\%$) at this source depth and source-array range. The ATR deconvolved signals corresponding to mode-2 and binary-1 weightings are provided in Figs. 8(d) and (e), respectively. For this source-array configuration, the deconvolved ATR signal using the approximate mode-2 weighting performs better ($C_{\max}=93\%$) than binary-1 weighting ($C_{\max}=80\%$). The main visual difference between the reconstructed signals is the lower temporal side lobe levels that occur at the higher correlation values. Here, the performance

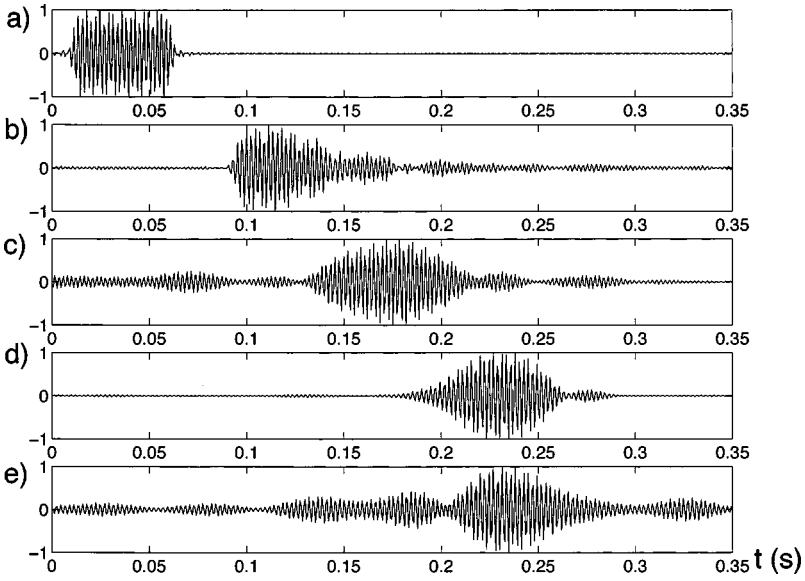

FIG. 8. Comparison of signals from the ocean measurements for a source-array range of 3.75 km: (a) synthesized source broadcast signal, (b) signal recorded near the middle of the receiving array at a depth of 65 m, (c) measured time-reversed signal at the initial source location ($C_{\max}=80\%$), (d) ATR deconvolved signal using the approximate mode-2 array weighting ($C_{\max}=93\%$), and (e) ATR deconvolved signal using binary-1 array weighting ($C_{\max}=80\%$).

of binary-1 weighting is likely suppressed by the unintended contribution of higher-order modes to the extra ATR phase, $\Gamma(\omega)$. This contention is supported by the fact that the performance of binary-1 weighting improves at the longer ranges (see Table I) where higher-order modes have been attenuated.

V. SUMMARY AND CONCLUSIONS

This paper has presented a new technique for blind deconvolution of a broadband point-source signal from the propagation characteristics of an unknown oceanic waveguide. The technique, artificial time reversal or ATR, requires a passive receiving array and is based on the invariance of the phase speed of the low order propagating modes of the sound channel with respect to changes in acoustic frequency. The technique was illustrated via broadband computer simulations of acoustic propagation in a shallow ocean sound channel between a point source and a water-column-spanning vertical array. In addition, the technique was tested with high signal-to-noise ratio ocean propagation measurements.

The research presented here leads to two conclusions. First, ATR appears to be a robust and viable technique for deconvolution of an unknown signal from an unknown remote source in an unknown ocean waveguide. When accurate mode shape information is available and the mode selected for ATR weighting is excited by the source, original-to-reconstructed signal correlations approaching 100% are possible. Even when mode shape information is not used and a simple binary array-weighting scheme is adopted, original-to-reconstructed signal correlations of 95% have been produced with ATR from measured array data. Moreover, based on both its formulation and performance, ATR appears to combine, at least partially, the simplicity and robustness of time reversal with the precision of inverse filtering. Thus, like time reversal, ATR may be relatively insensitive to low-Mach-number source motion (Sabra and Dowling, 2004). In addition, implementation of ATR for a vertical array is computationally simple; it does not require propagation calculations or any optimization searches through a parameter space. Of course, extensions and improvements of the version of ATR presented here may require some additional computational effort.

Second, ATR has few inherent limitations at high signal-to-noise ratio when there is sufficient spatial diversity of the receiving array and the source excites the sound channel's low order modes (e.g., the source does not lie too close to either the ocean surface or bottom). Thus, ATR may lead to improvements in correlation-based signal-detection and source-identification signal processing schemes. It may even be applicable to underwater acoustic communication for pulse compression and suppression of intersymbol interference. For the future, investigation of the technique's performance in noisy environments and comparison of its capabilities to mode filtering appear to be important.

In addition, we speculate that ATR may be relatively easy to improve or extend. Coherently averaging the output of different weighting schemes might enhance the accuracy of ATR reconstructed signals by suppressing temporal side lobes and noise. A singular value decomposition of the array measurements may make ATR possible with multiple sources. Use of acoustic-ray-based array weightings in place of modal-based weightings may allow ATR to be successful at higher frequencies.

There may also be other potential applications for ATR in acoustic, electromagnetic, seismic, or even structural waveguides. For example, it may be possible to estimate the source-array range when the signal is long compared to the reverberation time of the waveguide and ATR is successful with two (or more) different mode weightings. The ATR-determined time origin, b in Eq. (15), is proportional to the source-array range and inversely proportional to the phase speed of the mode used for array weighting. Thus, the source-array range R might be estimated from $R = |\Delta b_{l,m}/(c_l^{-1} - c_m^{-1})|$, where $\Delta b_{l,m}$ is the time shift between ATR outputs calculated from mode-l and mode-m weightings, and c_l and c_m are the mode-l and mode-m phase speeds. Other ranging schemes may be possible as well, and changes in ATR reconstructed signals might also be used to monitor time-varying environments.

ACKNOWLEDGMENTS

The authors are indebted to Dr. Heechun C. Song and Dr. William A. Kuperman for their generosity and patience in providing and assisting with the use of their ocean acoustic measurements. In addition, D.R.D. wishes to thank Dr. George B. Smith for sharing his insights on this topic through several constructive and interesting discussions. This research was sponsored by the Ocean Acoustics Program of the Office of Naval Research under Grant No. N00014-96-1-0040.

Aubry, J.-F., Tanter, M., Gerber, J., Thomas, J.-L., and Fink, M. (**2001**). ''Optimal focusing by spatio-temporal inverse filter. I. Basic principles,'' J. Acoust. Soc. Am. **110**, 48–58.

Benesty, J. (**2000**). ''Adaptive eigenvalue decomposition algorithm for passive acoustic source localization,'' J. Acoust. Soc. Am. **107**, 384–391.

Bogart, C. W., and Yang, T. C. (**1994**). ''Source localization with horizontal arrays in shallow water: Spatial sampling and effective aperture,'' J. Acoust. Soc. Am. **96**, 1677–1686.

Broadhead, M. K., and Pflug, L. A. (**2000a**). ''Performance of some sparseness criterion blind deconvolution methods in the presence of noise,'' J. Acoust. Soc. Am. **107**, 885–893.

Broadhead, M. K., and Pflug, L. A. (**2000b**). ''Use of higher order statistics in source signature estimation,'' J. Acoust. Soc. Am. **107**, 2576–2585.

Buck, J. R., Preisig, J. C., Johnson, M., and Catipovic, J. (**1997**). ''Single-mode excitation in the shallow-water acoustic channel using feedback control,'' IEEE J. Ocean. Eng. **22**, 281–291.

Cabrelli, C. A. (**1984**). ''Minimum entropy deconvolution and simplicity: A noniterative algorithm,'' Geophysics **50**, 394–413.

Capdevielle, V., Serviere, C., and Lacoume, J. L. (**1995**). ''Blind separation of wide-band sources in the frequency domain,'' in *ICASSP-95 Proceedings* (IEEE, New York), Vol. 3, pp. 2080–2083.

Cazzolato, B. S., Nelson, P., Joseph, P., and Brind, R. J. (**2001**). ''Numerical simulation of optimal deconvolution in a shallow water environment,'' J. Acoust. Soc. Am. **110**, 170–185.

Chapin, S. R., Ioup, J. W., Ioup, G. E., and Smith, G. B. (**2001**). ''Statistical analysis of Green's functions in a shallow ocean environment,'' J. Acoust. Soc. Am. **109**, 2295.

Ernst, F. E., and Herman, G. C. (**2000**). ''Tomography of dispersive media,'' J. Acoust. Soc. Am. **108**, 105–116.

Gürelli, M. I., and Nikais, C. L. (**1995**). ''EVAM: An eigenvector-based algorithm for multichannel blind deconvolution of input colored signals,'' IEEE Trans. Signal Process. **43**, 134–149.

Hansen, L. K., Larsen, J., and Kolenda, T. (**2000**). ''On independent component analysis for multimedia signals,'' in *Multimedia Image and Video Processing* (CRC Press, New York), Chap. 7, pp. 175–199.

Hodgkiss, W. S., Song, H. C., Kuperman, W. A., Akal, T., Ferla, C., and Jackson, D. R. (**1999**). ''Long-range and variable focus phase-conjugation experiment is shallow water,'' J. Acoust. Soc. Am. **105**, 1597–1604.

Hursky, P., Hodgkiss, W. S., and Kuperman, W. A. (**2001**). ''Matched field source localization with data derived modes,'' J. Acoust. Soc. Am. **109**, 1355–1366.

Jensen, F. B., Kuperman, W. A., Porter, M. B., and Schmidt, H. (**1994**). *Computational Ocean Acoustics* (AIP Press, New York).

Kim, S., Edelmann, G. F., Kuperman, W. A., Hodgkiss, W. S., Song, H. C., and Akal, T. (**2001**). ''Spatial resolution of time-reversal arrays in shallow water,'' J. Acoust. Soc. Am. **110**, 820–829.

Kinsler, L. E., Fry, A. R., Coppens, A. B., and Sanders, J. V. (**2000**). *Fundamentals of Acoustics*, 4th ed. (Wiley, New York), pp. 261–266.

Kuperman, W. A., Hodgkiss, W. S., Song, H. C., Akal, T., Ferla, C., and Jackson, D. R. (**1998**). ''Phase-conjugation in the ocean: Experimental demonstration of an acoustic time reversal mirror,'' J. Acoust. Soc. Am. **103**, 25–40.

Mansour, A., Barros, A. K., and Ohnishi, N. (**2000**). ''Blind separation of sources: methods, assumptions and applications,'' IEICE Trans. Fundam. **8**, 1498–1512.

Martins, N., Jesus, S., Gervaise, C., and Quinquis A. (**2002**). ''A time-frequency approach to blind deconvolution in multipath underwater channels,'' in *Proceedings ICASS2002* (IEEE, New York), pp. 1225–1228.

Morgan, A. M., Ioup, J. W., Ioup, G. E., and Smith, G. B. (**2001**). ''Wavelet analysis of Green's functions in a shallow ocean environment,'' J. Acoust. Soc. Am. **109**, 2297.

Neilsen, T. B., and Westwood, E. K. (**2002**). ''Extraction of acoustic normal mode depth functions using vertical line array data,'' J. Acoust. Soc. Am. **111**, 748–756.

Porter, M., and Reiss, E. L. (**1984**). ''A numerical method for ocean-acoustic normal modes,'' J. Acoust. Soc. Am. **76**, 244–252.

Rietsch, E. (**1997**). ''Euclid and the art of wavelet estimation. I. Basic algorithm for noise free data,'' Geophysics **62**, 1931–1938.

Rouseff, D., Jackson, D. R., Fox, W. L. J., Jones, C. D., Ritcey, J. A., and Dowling, D. R. (**2001**). ''Underwater acoustic communication by passive phase conjugation: Theory and experimental results,'' IEEE J. Ocean. Eng. **26**, 821–831.

Sabra, K. G., and Dowling, D. R. (**2004**). ''Broadband performance of a time reversing array with a moving source,'' J. Acoust. Soc. Am. **115**, 2807–2817.

Shang, E. C. (**1984**). ''Source depth estimation in waveguides,'' J. Acoust. Soc. Am. **77**, 1413–1418.

Sibul, L. H., Roan, M. J., and Erling, J. (**2002**). ''Deconvolution and signal extraction in geophysics and acoustics,'' J. Acoust. Soc. Am. **112**, 2389.

Siderius, M., Jackson, D. R., Rouseff, D., and Porter, R. (**1997**). ''Multipath compensation in shallow water environments using a virtual receiver,'' J. Acoust. Soc. Am. **102**, 3439–3449.

Smith, G. B. (**2003**). ''Multipath compression by multiple convolutions,'' J. Acoust. Soc. Am. **113**, 2213.

Tanter, M., Aubry, J.-F., Gerber, J., Thomas, J.-L., and Fink, M. (**2001**). ''Optimal focusing by spatio-temporal inverse filter. I. Basic principles,'' J. Acoust. Soc. Am. **110**, 37–47.

Tanter, M., Thomas, J.-L., and Fink, M. (**2000**). ''Time reversal and the inverse filter,'' J. Acoust. Soc. Am. **108**, 223–234.

Tantum, S. L., and Nolte, L. W. (**2000**). ''On array design for matched-field processing,'' J. Acoust. Soc. Am. **107**, 2101–2111.

Tohyama, M., Tsunehiko, K., and Koike, T. (**1998**). *Fundamentals of Acoustic Signal Processing* (Academic, New York), pp. 274–314.

Weber, R., and Bohme, J. F. (**2002**). ''Adaptive super-exponential methods for blind multichannel equalization,'' in *Sensor Array and Multichannel Signal Processing Workshop* (IEEE, New York), pp. 585–589.

Wiggins, R. A. (**1978**). ''Minimum entropy deconvolution,'' Geoexploration **16**, 21–35.

Xinhua, Z., Anqing, Z., Jianping, F., and Shaoquing, Y. (**2001**) ''Study on blind separation of underwater acoustic signals,'' in *Proceedings ICSP2000* (IEEE, New York), pp. 1802–1805.

On the acoustic vaporization of micrometer-sized droplets

Oliver D. Kripfgans[a)]
Applied Physics Program, University of Michigan, Ann Arbor, Michigan 48109-1120

Mario L. Fabiilli, Paul L. Carson, and J. Brian Fowlkes
Department of Radiology, University of Michigan, Ann Arbor, Michigan 48109-0553

(Received 8 November 2002; revised 22 January 2004; accepted 5 April 2004)

This paper examines the vaporization of individual dodecafluoropentane droplets by the application of single ultrasonic tone bursts. High speed video microscopy was used to monitor droplets in a flow tube, while a focused, single element transducer operating at 3, 4, or 10 MHz was aimed at the intersection of the acoustical and optical beams. A highly dilute droplet emulsion was injected, and individual droplets were positioned in the two foci. Phase transitions of droplets were produced by rarefactional pressures as low as 4 MPa at 3 MHz using single, 3.25 μs tone bursts. During acoustic irradiation, droplets showed dipole-type oscillations along the acoustic axis (average amplitude 1.3 μm, independent of droplet diameter which ranged from 5 to 27 μm). The onset of vaporization was monitored as either spot-like, within the droplet, or homogeneous, throughout the droplet's imaged cross section. Spot-like centers of nucleation were observed solely along the axis lying parallel to the direction of oscillation and centered on the droplet. Smaller droplets required more acoustic intensity for vaporization than larger droplets, which is consistent with other experiments on emulsions. © *2004 Acoustical Society of America.* [DOI: 10.1121/1.1755236]

PACS numbers: 43.35.Bf, 43.35.Ty, 43.28.Kt, 43.35.Ei [AJZ] Pages: 272–281

I. INTRODUCTION

It has been observed in the past that micrometer sized droplets of perfluorocarbon liquids in emulsions can be vaporized into gas bubbles by the application of tone bursts in the frequency and power range of diagnostic ultrasound.[1–3] This phenomenon is here referred to as acoustic droplet vaporization (ADV). More recently Giesecke and Hynynen[4] reported the acoustic vaporization of droplet emulsions by the application of low amplitude and high duty cycle bursts. These emulsions can be produced with up to 97% of the particles being smaller than 10 μm in diameter and an average diameter of 3 μm.[5] After filtering, such particles are transpulmonary thereby remaining in the blood stream as they are circulated through the body. Exposure to ultrasound creates larger than 6 μm gas bubbles that become trapped in the vasculature. Depending on the dilution of the emulsion, the effects of ADV *in vivo* can, for example, be used for tissue occlusion or for the creation of point targets.[5]

This paper will show the experimental results of the vaporization of single, albumin-stabilized droplets as they are exposed to single, acoustic tone bursts.

Possible mechanisms for ADV will be hypothesized and discussed using experimental results as well as findings from the literature. These include: (a) hydrodynamic cavitation which could potentially nucleate the superheated droplet; and (b) droplet deformation which could lead to shell rupturing or a nonuniform Laplace pressure on the sphere.

There are several scenarios in which hydrodynamic cavitation might occur. First of all, it is known from ship propellers that the motion of a body in water will cause cavitation on that body.[6] For venturi liners, this damage has been found to be proportional to the flow velocity.[7] Observations have shown that phase changes occur when, for example, a sphere touching a wall is pulled away,[8] or in small water tunnel experiments, using flow past lead specimen[9] at 14–23 $\mathrm{m\,s^{-1}}$. The former case could occur during the collision of two droplets or when a droplet interacts with a wall; whereas the latter one is possible for just a single droplet without contact to any surface.

One of the classic acoustic experiments involving droplets is acoustic levitation.[10–12] Twenty to sixty kilohertz are usually used to levitate drops of millimeter diameter. Shi and Apfel,[13] for example, levitated a 1.18 mm radius water drop in air at 28 kHz and up to 3 kPa sound pressure. This corresponds to a ka value of 0.14. During the experiment they observed shape oscillations with aspect ratios of up to 2. Similar experiments were performed by Su and Feng.[14] They reported translational oscillations of levitated drops as a result of the shape oscillation, and counteraction of gravitational force and radiation pressure. For millimeter-sized water drops (22 kHz driving frequency), shape oscillations of 100–200 Hz were observed and even slower translational oscillations. Observations reported in this paper are based on experiments with similar ka values. Droplets in the 10 μm range will be exposed to ultrasonic waves in the MHz range. Even though levitation experiments are performed under continuous wave conditions, one can expect a droplet–wave interaction which includes droplet translation and deformation.

II. MATERIALS AND METHODS

More than 2000 high speed photography images were analyzed, where the data in this paper represent 32 individual droplets. Each droplet was measured for its diameter, the

a)Electronic mail: oliver.kripfgans@umich.edu

 0001-4966/2004/116(1)/272/10/$20.00

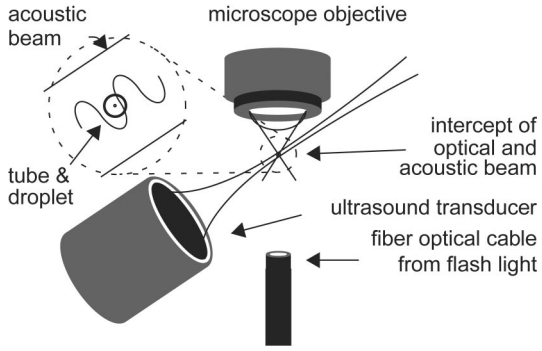

FIG. 1. The ultrasound transducer (3.5 MHz) has an aperture of 25.4 mm and a lateral focal beam diameter of 0.96 mm. The polyethylene flow tube has a 200 μm inner diameter and 50 μm wall thickness. The inset (not to scale) shows the geometric arrangement, including a 3.5 MHz two cycle tone burst.

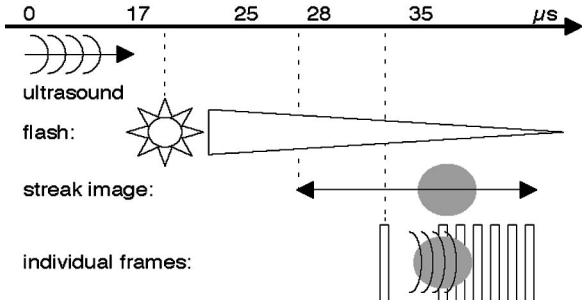

FIG. 2. Timing diagram of the transmitted ultrasound burst, light pulse, acquired streak image, and individual frames. The launch of the acoustic tone burst is time zero. It triggers the flash/strobe light with a 17 μs delay, 3.3 μs before the tone burst arrives at the focus. Eight microseconds later, at 25 μs, the streak image starts recording for 10 μs and at 28 μs the first full frame picture is taken. The remaining six images are taken at various time points to investigate either the translation or the vaporization process.

acoustic pressure necessary to vaporize it, and any optically observable action when exposed to ultrasound.

A. High speed video setup

An Imacon 468 high speed video system (DRS Technologies, DRS Hadland, Inc., Cupertino, CA) was used to optically image the process of ADV. Full-frame pictures of 576×385 pixels were taken with an exposure time of 100–200 ns. In streak mode, the vertical center line of an image was captured at 57.6 MHz (17.4 ns per streak line). Since ADV occurs at a micron scale, an optical microscope (JenaVAL, Carl Zeiss Jena GmbH, Jena, Germany) was connected to the video system. Micrometer-sized droplets were monitored full frame at 0.1 μs temporal and 0.46 μm spatial resolution. The light of a 2.5 kW argon flash lamp was guided into the optical path, facing the 100× objective of the microscope (see Fig. 1). An estimate for the potential of the light as a heat source will be addressed in Sec. VI.

The acoustic exposure occurred in a small tank (26 ×9×10 cm) with degassed water. A polyethylene tube (200 μm i.d., 50 μm wall thickness) was mounted 5 cm from the far end of the tank just below the water surface. Two single-element, 2.54 cm aperture, 3.81 cm focus transducers, with center frequencies of 3.5 and 10 MHz, were used. Transmit bandwidth and focal diameter were 41% and 90% as well as 0.96 and 0.34 mm, respectively. For a given experiment one of the transducers would be mounted on a three-dimensional micro-positioner and aimed at the intersection of the tube and the optical beam (see Fig. 1). The calibrated ultrasound transducer was driven by a rf gated amplifier (model 350, Matec, Northboro, MA) and controlled by a multipurpose function generator (HP3314, Agilent, Palo Alto, CA). Three frequencies were used in the experiments: 3, 4, and 10 MHz. The burst length was selected for a constant time duration, i.e., 10, 13, and 33 cycles, respectively. rf signals were monitored using an oscilloscope (9310L, LeCroy Corp., Chestnut Ridge, NY). The transducers were calibrated for transmitted acoustic pressure using a membrane hydrophone (Reference Shock Wave Hydrophone™, Sonic Industries, Hatboro, PA).

Droplet emulsions were made from 75 vol % saline-albumin solution (5 mg mL^{-1}) and 25 vol % dodecafluoropentane (DDFP, C_5F_{12}, CAS #678-26-2). The mixture was sealed in a 3 mL auto sampler glass vial and shaken for 30 s at 5000 cpm (MSD Wig-L-Bug, Crescent Dental Mfg. Co., Elgin, IL). A highly concentrated droplet emulsion with 9.5 $\times 10^9$ droplets per mL resulted. This emulsion was diluted (1:10 000 in saline) and small volumes of it were injected into the flow tube.

For each picture taken, an individual droplet was positioned on the center line of the screen of the video system. This center line coincided with the acoustic and optical foci. As seen in Fig. 2, at time zero the function generator produces a 3.33 μs tone burst, which was converted into an acoustic wave by the single element transducer and propagated through the water to the flow tube. The argon flash lamp was triggered at 17 μs, when the camera's gain control could be used to adjust its optical sensitivity to the decaying ambient background light. The persistence of the light flash was long enough to record a 10 μs streak image and 7 individually spaced full frame images. The first image was taken before the sound wave reached the tube. Subsequent frames were either placed back-to-back in order to monitor the process of ADV or were separated by several hundred nanoseconds to monitor the droplet during the insonification before ADV started. Each droplet was exposed to a series of acoustic tone bursts of increasing acoustic power. For each power level a set of seven full frames and one streak image was acquired and saved. The acoustic pressure was increased until the droplet vaporized.

MATLAB™ scripts (MathWorks Inc., Natick, MA) were written to read the image files from the camera and analyze them for droplet size and position. The droplet's top and bottom edge was manually selected in the streak image for analysis for dipole and possible shape oscillation. The white line in Fig. 3 shows the top and bottom trace on the boundary

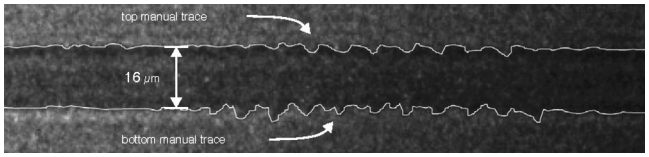

FIG. 3. Traced streak line of a 16-μm-diam droplet. One can see the onset of oscillation at the bottom trace, before onset occurs in the top trace and the eventual dipole motion is established.

of a droplet. The terms dipole and shape oscillation are used for a translational oscillation of the droplet's center of mass and for an oscillation of the droplet's diameter, respectively. Only streak images were used to measure the action of the droplets in the acoustic field (for 3 and 4 MHz). Full-frame images were solely used to monitor the onset and spatial progress of nucleation (for 3, 4, and 10 MHz) as well as any large scale geometric changes of the droplet, if any.

B. Laser vibrometer setup

It is possible that the flow tube which hosts the droplets is moving in the wave field, yielding the impression that the droplet itself moves with respect to its host fluid *in* the tube. Tube stability was not verified in the original high speed video setup. Therefore, a laser vibrometer (OFV 3001S and OVD-04/06, PolyTech PI, Inc., Auburn, MA) was used to measure the possible translation of the flow tube in the acoustic field. Limited by the bandwidth of the vibrometer, a range of 1.1–2.1 MHz was scanned. An acoustic field of maximum pressure of 10 MPa peak-to-peak was used. The raw data were corrected for the filter response of the laser vibrometer, the Doppler angle, and the ultrasound transducer transfer function.

III. THEORETICAL DESCRIPTION

A. Sound field

It was expected that acoustic field inside the flow tube, adjacent microscope objective, is relatively complex (see Fig. 1). Due to the very short focal length of the objective, the tube was in direct contact with the microscope. To calculate the acoustic field, the objective is modeled as a rigid planar wall and the tube is described as an infinite hollow cylinder in the field of a planar wave with boundary conditions on its surface. Modeling the interior of a hollow cylinder is based on the solution of a solid cylinder[15] with an iteration of boundary conditions for a second cylinder on the inside. An incident planar wave is formulated in cylindrical coordinates. Interior fields were modeled with Bessel functions of the first kind, while the scattered fields were described using Hankel functions. The first boundary condition is continuity of pressure on the outer surface of the hollow cylinder. Two equations are derived for each boundary. One equation is the continuity of pressure, at the outer surface, and at the inner surface of the hollow cylinder. The second set of equations on the first boundary is derived for the continuation of normal velocity on the boundary, which is proportional to the gradient of the pressure. This is only valid in linear acoustics, i.e., when the density of the host medium is not a function of the instantaneous pressure. The number of terms in all computations was selected to satisfy a criterion given by Bohren and Huffman,[16] here 20 orders in Bessel functions. The radial step size was typically $2\pi/(100k)$, where k is the wave number. A mirror source was introduced to complete the model for the flow tube being placed next to a rigid wall. The following parameters used were: for water and tube wall: speed of sound 1489 and 2500 $\mathrm{m\,s^{-1}}$, mass density 1000 and 970 $\mathrm{kg\,m^{-3}}$; incident sound pressure amplitude 3.5 MPa, outer and inner tube diameter 208.5 and 152 μm. The simulation is used to estimate the magnitude of interference inside the tube. For the computed spatial pressure distributions the absolute value of the complex valued solution is plotted in order to get the temporal peak pressure.

B. Droplet oscillations

First order models were used to compute the amplitude of oscillation of droplets in an acoustic field. It is assumed that the sole effect of the ''encapsulating'' albumin is prevention of coalescence. Therefore the droplet appears acoustically as a nonrigid sphere. Such a model and its solutions[15] are given in Eq. (1), which describes the total pressure outside a sphere ($r \geqslant a$). The Bessel (j_m) and Hankel (h_m) functions on the right-hand side of Eq. (1) represent the incident and scattered wave, respectively. Legendre polynomials are abbreviated with P_m. The amplitude of the incident wave is A, i is the imaginary unit, and θ is the in plane angle. The droplet radius is denoted by a; mass densities of water and droplet are $\rho = 1000$ and $\rho_e = 1660\,\mathrm{kg\,m^{-3}}$, respectively. Speed of sound of water and inside the droplet are $c = 1489$ and $c_e = 471\,\mathrm{m\,s^{-1}}$, respectively.

$$
\begin{aligned}
p_\omega(r,\theta) &= A\sum_{m=0}^{\infty}(2m+1)i^m P_m(\cos\theta) \\
&\quad \times\cdots\left(j_m(kr) - \tfrac{1}{2}(1+R_m)h_m(kr)\right), \\
R_m &= \frac{h_m'^{*}(ka) + i\beta_m h_m^{*}(ka)}{h_m'(ka) + i\beta_m h_m(ka)}, \\
\beta_m &= i\frac{\rho c}{\rho_e c_e}\frac{j_m'(k_e a)}{j_m(k_e a)},
\end{aligned}
\tag{1}
$$

$$
\begin{aligned}
\mathbf{F} &= \int d\mathbf{F} = \oint_A p_\omega(r,\theta)\,d\mathbf{A} \\
&= \oint_A p_\omega(r,\theta)\begin{bmatrix}\sin\theta\cos\phi\\ \sin\theta\sin\phi\\ \cos\theta\end{bmatrix} a^2\sin\theta\,d\theta\,d\phi, \\
m\ddot{\xi} &= -V\nabla p_i + F_{\mathrm{sc}}, \\
\tfrac{4}{3}\pi a^3\rho\ddot{\xi} &= \left(\frac{3}{2}\frac{\rho_e-\rho}{\rho_e+\tfrac{1}{2}\rho}-1\right)\tfrac{4}{3}\pi a^3\nabla p_i - F_{\mathrm{sc}}.
\end{aligned}
\tag{2}
$$

In this linear approach the droplet's displacement can be computed from the integrated force on the sphere, which is derived from the pressure at the droplet's surface. Newton's second law can be used to estimate the associated motion of the droplet. Furthermore, both the inertia of the moving droplet and that of the displaced water has to be taken into consideration.[17] Equation (2) relates the acceleration of the droplet with the pressure gradient of the incident pressure wave and the force of the scattered field on the droplet's surface. Furthermore, the inertia of the mass of the displaced water is added in the second part of Eq. (2). Here m is the mass of the droplet, ξ is the location of center of mass of the droplet, V is its volume, p_i is the incident acoustic field, and F_{sc} is the force exerted on the droplet by the scattered wave, i.e., the second part of the pressure equation in Eq. (1).

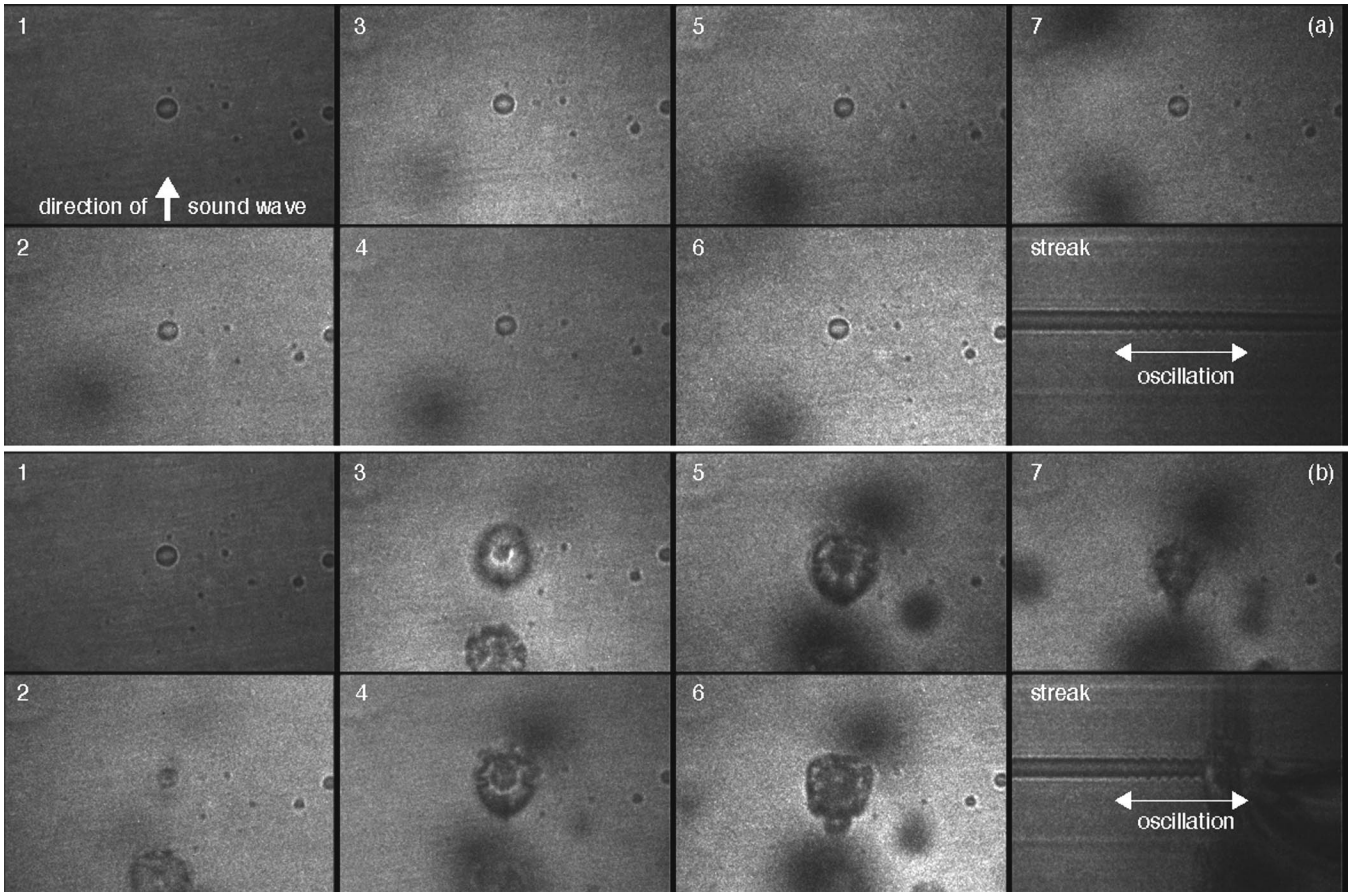

FIG. 4. Acoustic vaporization of an 18-μm-diam droplet. Two sequences are shown. (a) Images 1–7 are full frame pictures of the droplet in the flow tube. The eighth frame is a streak image. The acoustic pressure in the first sequence is not sufficient to vaporize the droplet. In the center of the streak image one can see a translatory motion of the droplet (arrows) for the duration of the 10 cycle, 3 MHz tone burst (magnified image in Fig. 5). (b) Increasing the acoustic pressure to 6.5 MPa peak–peak (which is $P=2.6$ MPa) leads to the vaporization of the droplet after 8 cycles.

Double integration in time, assuming an oscillatory motion at ω, yields the displacement amplitude.

C. Droplet shape oscillation

A theoretical model which allows shape changes[12] was used to evaluate the change in aspect ratio of a droplet in an acoustic field. The acoustic radiation pressure on a droplet as well as the field inside a droplet of fixed shape is computed. Given those, the droplet shape is allowed to change in order to minimize the overall energy of the system. This process is iterated for shape change and subsequently for increasing sound pressures. Equation (3) is an order of magnitude estimate for the coupling of drop shape oscillation and translation.[18] β_l is defined by Eq. (3); U is the droplet's velocity, σ is the interfacial tension, l is the mode of oscillation; a, ρ, and ρ_e were defined earlier. For the cases $\beta_l a/U$: $\gg 1$, $=1$, and $\ll 1$, the drop is isolated, the relative motion between the two phases cannot be neglected, and the droplet does not perform shape oscillations, respectively,

$$\frac{\beta_l a}{U} = \sqrt{\frac{\sigma l(l+1)(l-1)(l+2)}{a^3(\rho l+\rho_e(l+1))}}\frac{a}{U}. \tag{3}$$

IV. EXPERIMENTAL RESULTS

A. Droplet dipole type oscillations

Single, sinusoidal tone bursts of 3 and 4 MHz at P_- up to 4 and 7 MPa, respectively, were sufficient to phase transition individual droplets. High speed video images are shown in Figs. 4–6. The streak image of the droplet in Fig. 4 shows a translational, dipole-type motion with the same frequency and duration as the transmitted 3 MHz acoustic tone burst (see zoomed version in Fig. 5 and manual traced streak in Fig. 3). No motion can be seen in the streak image of Fig. 6, where a droplet is exposed to a 10 MHz sound field.

Measurements were performed on droplets in the size range from 5 to 27 μm diameter. All droplet sizes are larger than the mean size of the emulsion because of the spatial resolution of the microscope used. At the acoustic pressure threshold (i.e., where the droplets vaporize), average displacements of 2.7 ± 0.4 μm and 2.5 ± 0.4 μm at 3 and 4 MHz, respectively, were measured. These displacements were not adjusted for any possible out of plane oscillation of the droplets due to the 45° angle between the ultrasound transducer and microscope objective (see Fig. 1). The measured peak to peak displacement was found to be independent of the droplet's size and the frequency used (see Fig. 7).

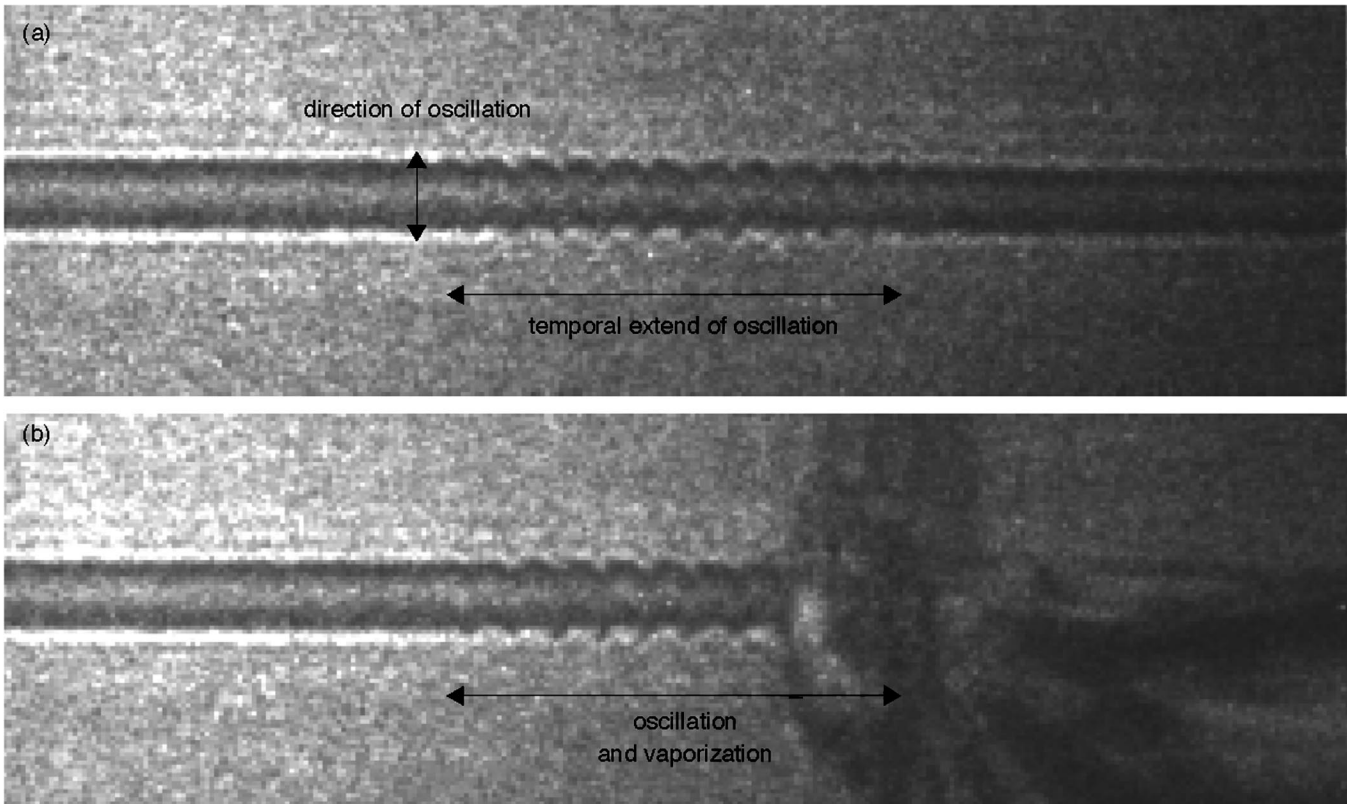

FIG. 5. Zoomed and brightness/contrast enhanced streak images from Fig. 4. Not the dipole (translatory) motion of the droplet.

The average velocity v at which the droplet is oscillating results directly from the oscillation amplitude x and the insonification frequency f as $v=2\times f$. For 3 MHz and 2.7 μm, v is equal to 16.2 ± 2.3 m s^{-1}, the 4 MHz data yields 20 ± 3.1 m s^{-1} for the same displacement. The velocity values are also not corrected for any possible motion out of the image plane. Due to the image quantization of 0.46 μm per pixel, plus image noise, an error of approximately 20% must be expected.

Figure 8(a) shows the dependence of the oscillation amplitude on the sound pressure. For seven droplets the oscillation amplitude has been analyzed as a function of sound pressure. That pressure was normalized to the power needed for vaporization for each droplet since the droplets were of varying size. All seven droplets follow the same relationship between oscillation and power. Moreover, Fig. 8(b) displays that all droplets will follow that path until the amplitude of oscillation reaches a certain value, upon which ADV occurs. Figures 7(a), 8(b), and 11 show the same data points of a three-dimensional data set. For each measured droplet there is a droplet resting diameter (d), the pressure necessary to vaporize it (p), and the amplitude of oscillation (x) when exposed to that pressure. Above-mentioned Figs. 7(a), 8(b), and 11 show the three combinations $x(d)$, $x(p)$, and $p(d)$, respectively.

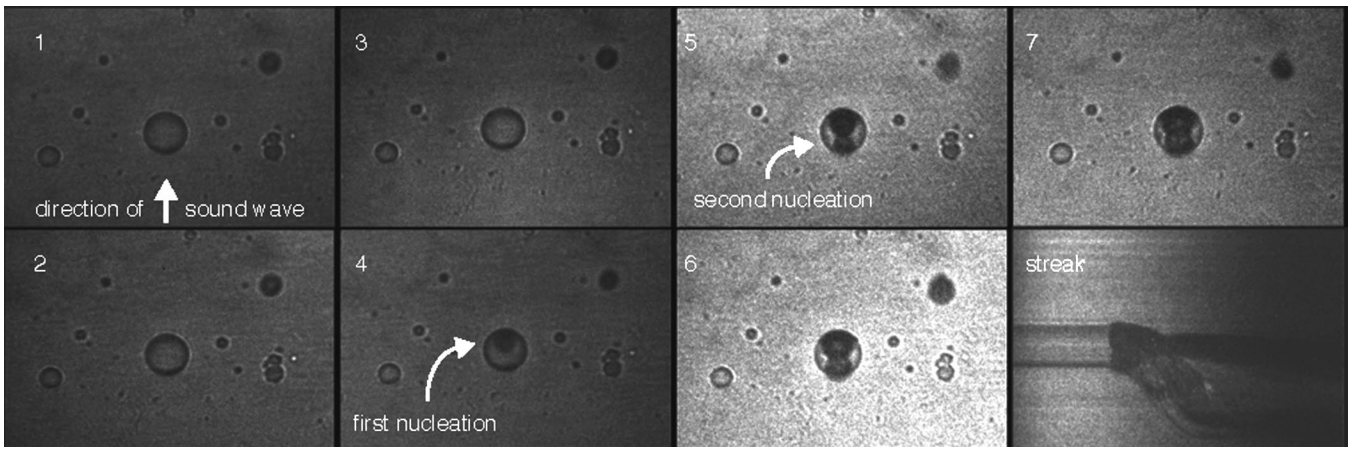

FIG. 6. Frame 4 of the sequence shows the first nucleation point of the droplet's vaporization, and frame 5 shows another nucleation site. The frames were placed back to back with 100 ns duration. A 10 MHz and 33 cycle tone burst at 9 MPa was used, with a 45-μm-diam droplet.

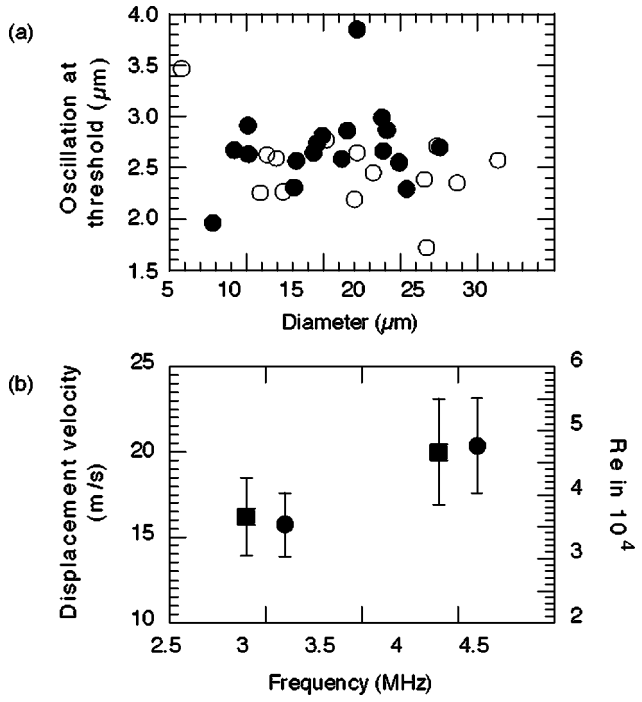

FIG. 7. Droplets of various diameters were analyzed for the magnitude of dipole oscillation at the threshold of vaporization. (a) The peak to peak amplitude was found to be ~2.6 μm, independent of the droplet's size. (b) The average displacement amplitude at a given frequency was used to compute the average velocity (circles) at which the droplet was assumed to be moving relative to the host fluid. Additionally, the corresponding Reynolds number was computed (squares). The error bars are based on the single standard deviation of the displacement amplitude.

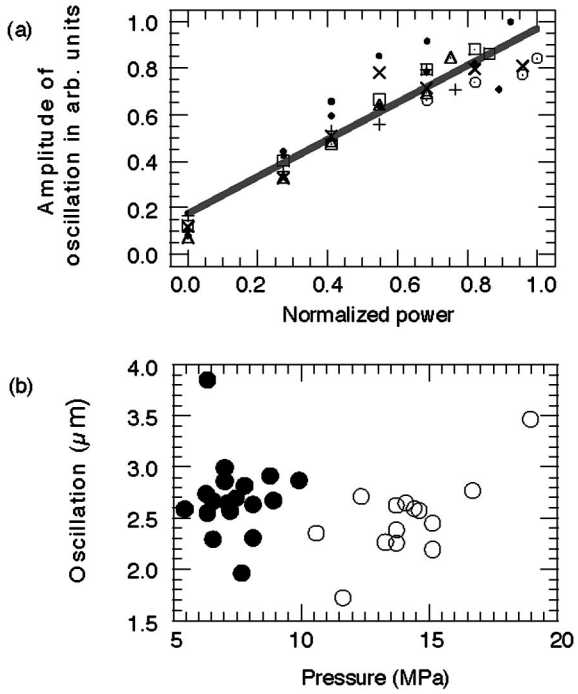

FIG. 8. (a) Amplitude of oscillation of individual droplets as a function of normalized acoustic power. Shown are the results for seven droplets. A linear fit yields $y=0.17+0.80x$ with $R^2=0.87$, i.e., the amplitude of oscillation increases linearly with applied power. (b) Amplitude of oscillation at threshold for ADV as a function of applied pressure. The data points represent distinct droplets of various diameters.

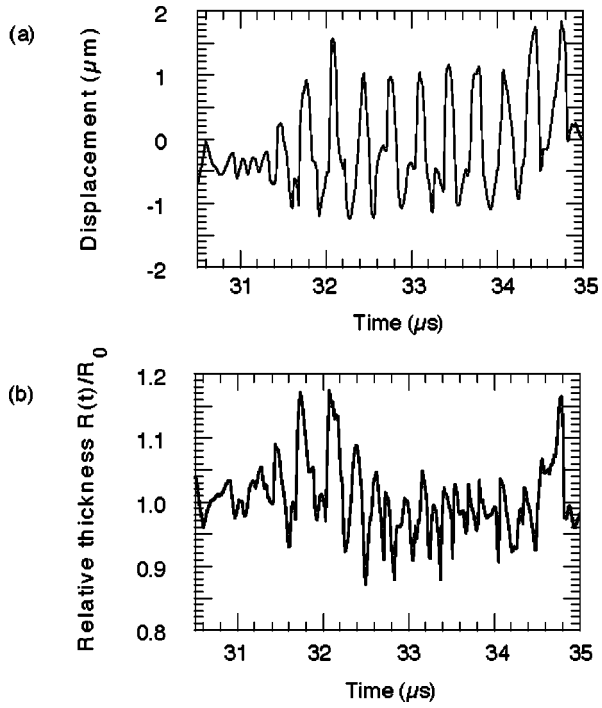

FIG. 9. Dipole (displacement) and thickness oscillation of a 16-μm-diam droplet. The spectral amplitude of the displacement is 40 dB above the noise and 13 dB above the image resolution. The thickness oscillation (i.e., the axial width in the streak image) is 7 dB above the noise and of the same order as the image resolution. However, in general, it has been observed that the initial thickness oscillation does show a spectral response at 3 MHz.

B. Aspect ratio

In terms of a potential variation in the aspect ratio of the droplets, an oscillation of the droplet radius on the order of 0.85–1.15 radii was observed [see Fig. 9(b)]. This magnitude of oscillation is not very large compared to the beforementioned optical resolution of 0.46 μm per image pixel. Streak line traces were transformed into frequency space in order to extract the amount of oscillation at the frequency of the transmitted acoustic wave. Spectral amplitudes were then compared to pixel resolution and noise floor of the spectrum.

Equation (4) was used to evaluate the predicted error in the aspect ratio estimate, which is based on two assumptions: (1) conservation of volume ($V_1=V_2$) and (2) equal deformation in the two dimensions (y and z), which cannot be seen in the streak image,

$$V_1=V_2,\quad \tfrac{4}{3}\pi R_0^3=\tfrac{4}{3}\pi x y^2,\quad \Lambda=\frac{y}{x},$$
$$\delta\Lambda=\sum_{s\in\{R_0,x\}}\left|\frac{\partial}{\partial s}\left(\frac{R_0}{x}\right)^{3/2}\right|\Delta s=\frac{3\Delta R}{R_0}. \tag{4}$$

For Eq. (4), R and x are the initial and "streak" radii, respectively; ΔR and Δx are the experimental errors and they are of the same order. Therefore the error for the aspect ratio (Λ) is 18%, which is of the same order as the magnitude of the thickness vibration.

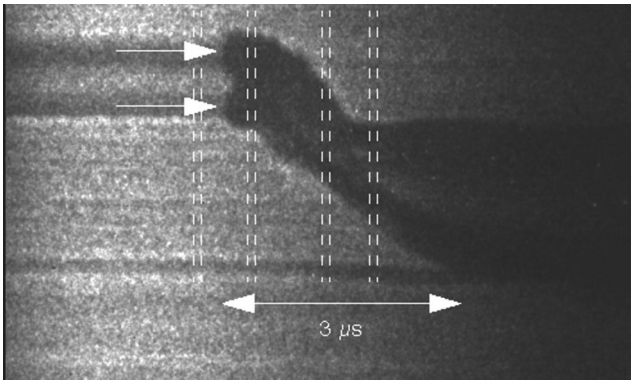

FIG. 10. The streak image shows that the nucleation is starting at the proximal and distal positions on the central axis of the droplet (see arrows). The vertical lines are the beginning and end of exposure of single full frame images. As in Fig. 3, the time axis is from the left to the right.

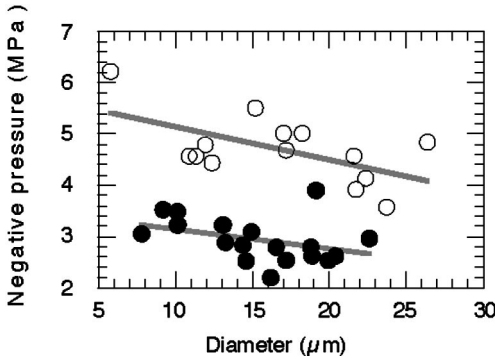

FIG. 11. The pressure threshold for ADV was evaluated as a function of droplet diameter. In general smaller droplets required higher pressures for vaporization. (fit parameters: $P=3.5-0.038\,d$ ($R^2=0.14$) for 3 MHz (closed circles) and $P=5.8-0.065\,d$ ($R^2=0.35$) for 4 MHz (open circles).

C. Nucleation site

The onset of vaporization was monitored as either spot-like and subsequently expanding centers of nucleation inside the droplet, or as homogeneous throughout the droplet's imaged cross section. The latter is possibly due to the limited temporal resolution of the full frame two-dimensional images of the camera system. Spot-like centers of nucleation were observed solely along the axis parallel to the direction of oscillation and centered on the droplet along the direction of dipole-type motion of the droplet. This axis is essentially the same as the direction of the propagating acoustic wave (see Fig. 6). The positions where the nucleation occurs will be referred to as proximal and distal with respect to the incident sound wave, where proximal is toward the incident sound wave and distal is away from it. Typically a second nucleation site was observed. Its location was diametrically opposed to the first site which conforms with the change in direction of motion, i.e., with the oscillatory movement of the droplet as seen in the streak image in Fig. 3. The experiments of Figs. 6 and 10 were performed at an acoustic center frequency of 10 MHz. Each full frame image covers 0.1 μs, which is the same as one cycle of the acoustic wave. If there are motion induced nucleations based on a preferred direction, then those should be occurring in the same full frame image or at least in the following frame. Figures 6 and 10 show that the gas nuclei complete the phase transition within the droplet on a time scale from several hundred nanoseconds to 3 μs. The same dual nucleation site of phase transition was also observed for insonification at center frequencies of 3 and 4 MHz, even though the effect was not well visualized. This was assumed because of the increase in exposure time for each frame from 100 to 200 ns.

D. Acoustic threshold

Observing ADV of droplets with diameters ranging from 7 to 22 μm yielded acoustic peak-to-peak pressure thresholds at 3 MHz of 3.9 to 2.2 MPa, respectively. It has been observed that smaller droplets require more acoustic energy for vaporization than larger droplets (see Fig. 11) This functional dependence of the ADV pressure threshold on droplet size is consistent with earlier experiments where the pressure threshold for vaporization of filtered and unfiltered emulsions was measured [see Fig. 12 and Kripfgans *et al.* (2000) for materials and methods]. Earlier free field experiments on emulsions over a wider frequency range showed a decrease in threshold for ADV with increasing frequency, which is contradictory to the current experiments. However, this contradiction and the higher thresholds for ADV may be caused by the rather complex acoustic field resulting from the presence of the flow tube and its location just beneath the microscope objective. This should not affect the dependence of the pressure needed for ADV on the droplet's size. More on this follows in the numerical results below.

E. Potential motion of the flow tube

Laser interferometry yielded an average tube displacement amplitude of 0.24 μm. This is on the order of the error in the displacement measurement from the streak camera and approximately one order of magnitude smaller than the droplet translatory motion. The tube displacement could be correlated in delay time as well as burst length with the transmitted 20 cycle acoustic tone burst.

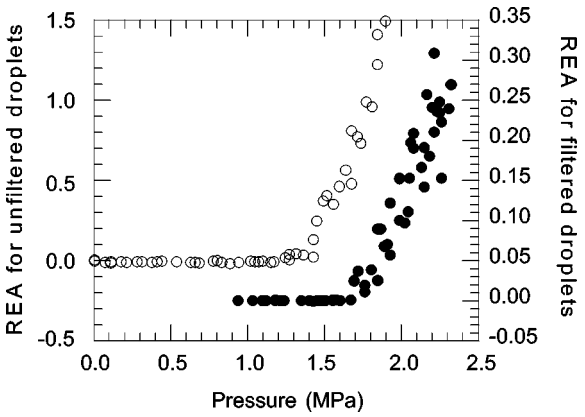

FIG. 12. The pressure threshold for ADV was measured for unfiltered (open circles) and for 8 μm filtered droplets (closed circles). Filtering increased the threshold from 1.4 to 1.7 MPa P.

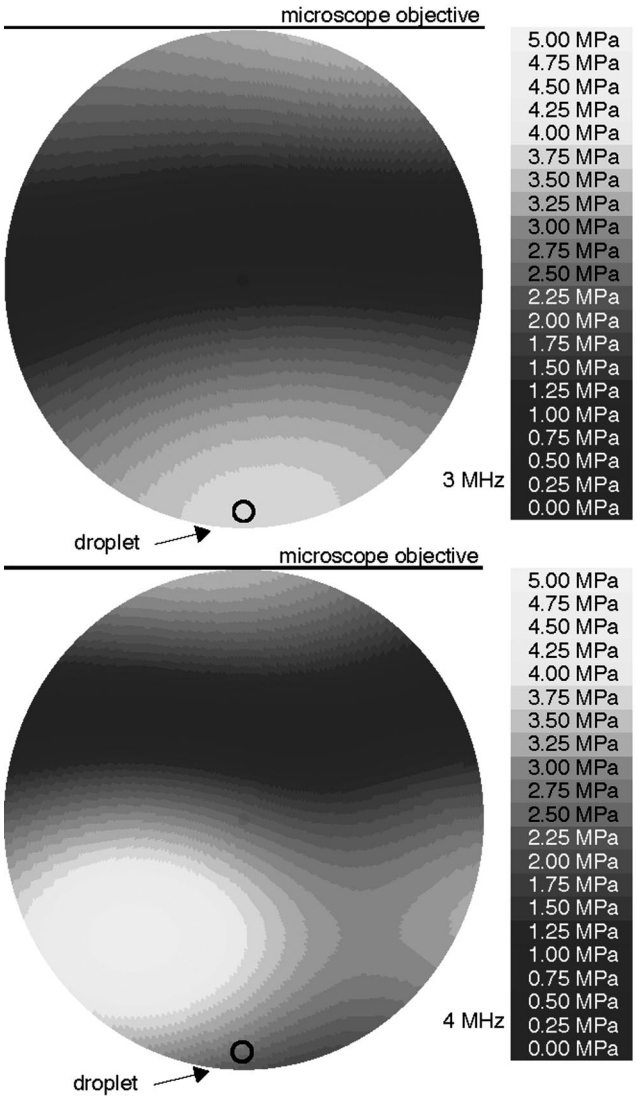

FIG. 13. Envelope of acoustic field inside a 152-μm-i.d. cylinder (50 μm wall thickness). At 3 MHz, the water and solid wavelength are 500 and 833 μm, respectively. Top 3 MHz, bottom 4 MHz. Note that the range of acoustic field at the droplet location (small black circle on top of image) is small (3.3–3.7 MPa) for the case of 4 MHz compared to the 3 MHz case (4.5–4.8 MPa). A nonlinear gamma function has been used for the amplitude to gray scale conversion.

V. NUMERICAL RESULTS

A. Field simulation

Sound fields were computed for 3 and 4 MHz. The goal of the simulation was to derive the pressure amplitude distribution inside the flow tube for various frequencies and to show how unpredictable the acoustic field is due to the interference of tube and microscope objective. The small hollow black circle in Fig. 13 has been added to the bottom of the graphs to illustrate where the droplet would be located. The simulated area is the inside of the flow tube. The acoustic field at the droplet location is smaller (2.5 MPa) for the case of 4 MHz and larger in the 3 MHz case (3.7 MPa). This could explain the apparent discrepancy in frequency dependence for ADV in this experimental arrangement compared to that seen previously.[3,5] Therefore, the actual pressure amplitudes that the droplets experienced were not the free field values obtained by the transducer calibration.

B. Droplet oscillation

A droplet with 8.5 μm radius was simulated to be exposed to a 3 MHz and 6.7 MPa peak-to-peak sound field. Bessel and other functions [see Eq. (1)] were included to order 1. An oscillatory force along the central axis with an amplitude of 0.1 mN results. Subsequently Eqs. (1) and (2) yield a displacement amplitude of 0.128 μm. This is one order of magnitude smaller than the approximately 1.3 μm displacement observed in the experiment.

Earlier measurements on the potential motion of the flow tube were presented indicating that the motion was small compared to that of the droplets. In addition, data already presented can be analyzed in a slightly different way to further argue for the motion of the droplet rather than the tube. Figure 8(a) shows how the observed oscillation increases with acoustic power for any given droplet. Figure 7(a) shows that all droplets oscillate with a maximum amplitude of $\sim$1.3 μm before they are vaporized. Figures 11 and 12 show that smaller droplets require more acoustic energy to vaporize and moreover they also require more energy to oscillate $\sim$1.3 μm [Fig. 7(a)]. However if the droplets oscillated rigidly with the tube, an increase in power should increase the oscillatory motion regardless of the observed droplet and its size. This is not the case as shown in Fig. 8(b) since it is the amplitude of the droplet oscillation, not the amplitude of the acoustic field, that predicts the threshold for ADV. It is therefore concluded that the observed droplets are moving and acoustic scattering as well as hydrodynamic flow lead to a constant amplitude of oscillation which is assumed to be the cause for ADV itself and discussed in the following.

C. Droplet shape oscillation

Shape oscillation amplitudes were computed in addition to translational motion. It has been seen that the diameter of the droplet changes while exposed to the acoustic wave (see Figs. 3 and 9). The experimental deformations were on the order of 15%. The following parameters were used for the simulation: $ka=0.108$, 8.5 μm spherical droplet radius, and a DDFP/saline interfacial tension $33.8\times10^{-3}\,\mathrm{N\,m^{-1}}$ (as measured in our lab). A droplet of that size and acoustic excitation of 1, 2, 5, 10, and 20 MPa (assuming a free field which is likely not the case here) should deform the droplet by 0.56%, 1.1%, 2.8%, 6.0%, and 13.8%, respectively. Slightly higher aspect ratios were observed, even though those values were of the same order as the noise. The thickness oscillation as seen in Fig. 9 is maximum at the beginning and at the end of the acoustic burst. This is where the droplet's center of mass motion, with respect to the surrounding fluid, accelerates and decelerates. A droplet as given before, with a translational velocity of $16.2\,\mathrm{m\,s^{-1}}$ and first-order shape oscillation ($l=2$), yields a coupling of 0.23 (see Sec. III C.). However, while the droplet is in transition from rest to steady state oscillation, the ratio as given in Eq. (3) is closer to unity, *allowing* the droplet to perform shape oscillations (Fig. 14).

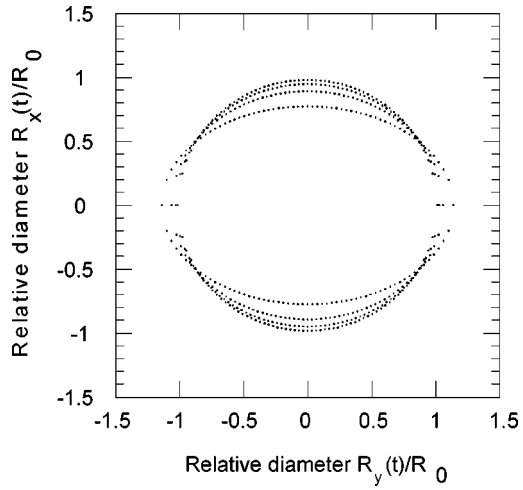

FIG. 14. Simulated droplet deformation using a droplet levitation theory (Ref. 12). The normalized droplet shape is plotted for acoustic pressure amplitudes of 2, 5, 10, and 20 MPa.

VI. DISCUSSION

The apparent oscillations in the streak images (3 and 4 MHz cases) and the derived droplet motion were compared to theoretical models as given in the literature. These models do not account for the complex geometry of the acoustic field or for its highly nonlinear character due to the large sound pressures used. However, these models could provide some understanding of the motion of the droplet in the acoustic field and help build a hypothetical basis for the nucleation. The same holds for the field simulation. However, it is assumed that including focusing and/or nonlinearities will also show that a free field pressure calibration cannot predict the *in situ* pressure. Therefore the result of the pressure threshold for ADV at 3 MHz being smaller than at 4 MHz may not contradict our earlier findings.[3,5] In fact the ratio of the simulated pressure values for 3 to 4 MHz is 1.33. A previously measured frequency dependence of ADV[5] yielded a ratio of 3 to 4 MHz of 1.24, which is close when taking the shortcomings of the model into account.

Dowson and Taylor report nucleation events in the lubrication fluid between a spherical cap sliding in close contact over a plane surface as well as between a sphere separating perpendicularly from a wall.[19] An object separating from a surface is assumed to cause a similar situation as when an object moves through a liquid. Hydrodynamic cavitation and its subsequent shock wave on the object's surface might trigger the vaporization of the DDFP inside the droplet. The location of the cavitation with respect to the relative motion of the fluid is similar to that in our experiments, e.g., the case of the first nucleation as seen in Fig. 6.

The dynamics of flow past a sphere can be easily found in fluid dynamics textbooks.[20] For a Reynolds number of $\mathrm{Re}_{cr} \sim 5 \times 10^5$, a sudden dip in the drag coefficient occurs due to the transition of the boundary layer to turbulence. In super cavitation,[21] cavitation is used to reduce drag. A linear velocity of 50 $\mathrm{m\,s^{-1}}$ is required to induce super cavitation on torpedoes. For ADV the speed for the possible oscillation is 15–20 $\mathrm{m\,s^{-1}}$, and cavitation induced this way would occur first at the direction of motion. Another example of flow induced cavitation has been reported on concrete tunnels. A so-called "threshold" velocity of 30 $\mathrm{m\,s^{-1}}$ was necessary to initiate cavitation.[22] A comparison with the above-noted examples should be done with caution, since the exact mechanism for ADV has not been established.

The heating of the droplet due to the radiation from the 2.5 kW light source and possible focusing of the light inside the droplet were estimated. Two cases were evaluated: (1) An evenly distributed light intensity yields a temperature rise of 0.008 °C which lasts for milliseconds, and (2) focusing the light intercepted by the droplet into 2.5% of the droplet's diameter yields a temperature rise to more than 200 °C, which lasts for approximately 50 μs (refer to chapter 15 in Kittel and Kroemer[23] for details on the heat conduction equation). A more precise estimate is beyond this paper because (a) focusing through the curved walls of the droplet (refractive index 1.24, water 1.33), is best described by what is known as a caustic pattern, where the focus is distributed along a epicycloid and (b) the reflection and transmission coefficients vary largely by the angle of the incident light beam.

However, one might argue that the light is not the cause for the vaporization because droplets do not vaporize (a) if the acoustic pressure is too low and (b) focusing of the incident light beam occurs along the axis of the incident light beam, which should appear in the center of the droplet in the images taken, since the axis of the light beam is perpendicular to the image plane (see Fig. 1).

It is assumed that ADV is either (a) the result of the superposition of dipole radiation and the incident field itself leading to acoustic cavitation or (b) hydrodynamic cavitation with a separation of the boundary layer and coupling of the external flow field to the interior of the droplet, causing an internal circulation.

VII. SUMMARY

The vaporization of single droplets has been observed. Experiments revealed translational motion of droplets in the acoustic field with an average 2.6 μm peak to peak displacement (independent of droplet size), at which point vaporization occurred. The theoretical model of a rigid sphere predicts a translation of 0.33 μm peak to peak. Furthermore it has been observed that droplets deform when exposed to ultrasound. A theoretical prediction of up to 15% deformation was confirmed through the experiment. The process of vaporization has been observed with full frame images as well as in streak mode. The nucleation starts at the proximal and distal positions on the central axis of motion. From the droplet displacement amplitude an average droplet speed of 15 to 20 $\mathrm{m\,s^{-1}}$ was computed. The acoustic pressure threshold for ADV was found to be inversely related to the droplet size.

ACKNOWLEDGMENTS

We would like to thank Dr. C. L. Marcelo for use of her microscope. Furthermore we thank Professor K. Grosh and T. Nawar for their great support with their laser vibrometer. Dr. C. P. Lee is acknowledged for letting us use his software

to simulate the action of a droplet in the acoustic field. Supported in part by PHS Grant No. R01HL54201 and U.S. Army Grant No. DAMD17-00-1-0344.

[1] R. E. Apfel, ''The superheated drop detector,'' Nucl. Instrum. Methods Phys. Res. A **162**, 603–608 (1979).
[2] R. E. Apfel, ''Activatable infusable dispersions containing drops of a superheated liquid for methods of therapy and diagnosis,'' US patent 5,840,276 (1998).
[3] O. D. Kripfgans, J. B. Fowlkes, D. L. Miller, O. P. Eldevik, and P. L. Carson, ''Acoustic droplet vaporization for therapeutic and diagnostic applications,'' Ultrasound Med. Biol. **26**, 1177–1189 (2000).
[4] T. Giesecke and K. Hynynen, ''Ultrasound-mediated cavitation thresholds of liquid perfluorocarbon droplets *in vitro*,'' Ultrasound Med. Biol. **29**, 1359–1365 (2003).
[5] O. D. Kripfgans, J. B. Fowlkes, M. Woydt, P. O. Eldevik, and P. L. Carson, ''*In vivo* droplet vaporization for occlusion therapy and phase aberration corrections,'' IEEE Trans. Ultrason. Ferroelectr. Freq. Control **49**, 726–738 (2002).
[6] M. Strasberg, ''Propeller cavitation noise after 35 years of study,'' ASME Symposium on Noise and Fluids Engineering, 1997, pp. 89–99.
[7] D. H. Trevena, ''Cavitation and the generation of tension in liquids,'' J. Phys. D **17**, 2139–2164 (1984).
[8] H. K. Christenson and P. M. Claesson, ''Direct measurements of the force between hydrophobic surfaces in water,'' Adv. Colloid Interface Sci. **91**, 391–436 (2001).
[9] K. K. Shal'nev, I. I. Varga, and D. Sebestyen, ''Investigation of the scale effects of cavitation erosion,'' Philos. Trans. R. Soc. London, Ser. A **260**, 256–266 (1966).
[10] Y. R. Tian, R. G. Holt, and R. E. Apfel, ''Deformation and location of an acoustically levitated liquid-drop,'' J. Acoust. Soc. Am. **93**, 3096–3104 (1993).
[11] Z. C. Feng and Y. H. Su, ''Numerical simulations of the translational and shape oscillations of a liquid drop in an acoustic field,'' Phys. Fluids **9**, 519–529 (1997).
[12] C. P. Lee, A. V. Anilkumar, and T. G. Wang, ''Static shape and instability of an acoustic levitated liquid drop,'' Phys. Fluids A **3**, 2497–2516 (1991).
[13] W. T. Shi and R. E. Apfel, ''Deformation and position of acoustically levitated liquid drop,'' J. Acoust. Soc. Am. **99**, 1977–1984 (1996).
[14] Y.-H. Su and Z. C. Feng, ''Numerical simulation of the dynamics of acoustically levitated drops,'' J. Acoust. Soc. Am. **99**, 2799–2810 (1996).
[15] P. M. Morse and K. U. Ingard, *Theoretical Acoustics* (Princeton University Press, Princeton, NJ, 1986), pp. 418–441.
[16] C. F. Bohren and D. R. Huffman, *Absorption and Scattering of Light by Small Particles* (Wiley, New York, 1983), p. 477.
[17] A. D. Pierce, *Acoustics—An Introduction to its Physical Principles and Applications* (Acoustical Society of America, New York, 1991), pp. 434–435.
[18] O. A. Basaran, T. C. Scott, and C. H. Byers, ''Drop oscillations in liquid-liquid systems,'' AIChE J. **35**, 1263–1270 (1989).
[19] D. Dowson and C. M. Taylor, ''Cavitation in bearings,'' Annu. Rev. Fluid Mech. **11**, 35–66 (1979).
[20] P. K. Kundu, *Fluid Mechanics* (Academic, San Diego, 1990), p. 638.
[21] S. Ashley, ''Warpdrive underwater,'' Sci. Am. **284**, 70–79 (2001).
[22] M. J. Kenn, ''Cavitation and cavitation damage in concrete structures,'' Proceedings of the Sixth International Convention on Erosion by Liquid and Solid Impact., 1983, paper 12, pp. 1–6.
[23] C. Kittel and H. Kroemer, *Thermal Physics*, 2nd ed. (Freeman, San Francisco, 1980).

Using finite element method for the determination of elastic moduli by resonant ultrasound spectroscopy

Jiri Plesek,[a] Radek Kolman, and Michal Landa
Institute of Thermomechanics, Academy of Sciences of the Czech Republic, Dolejskova 5, 182 00 Prague, Czech Republic

(Received 11 February 2004; accepted for publication 19 April 2004)

Resonant ultrasound spectroscopy is a recent experimental/numerical method for the determination of moduli of elastic materials. Generally, all 21 elastic components of the elastic tensor can be determined by the numerical procedure based on the knowledge of a mechanical spectrum of a specimen. This involves the solution of a demanding inverse problem. Presently, Levenberg–Marquardt's (LM) algorithm with the Ritz method for the solution of eigenfrequencies is usually applied. The LM method is based on the modified Newton–Raphson procedure, where all the eigenfrequencies and eigenvectors must be known for the computation of relevant gradients. Finite element method offers an analogous but more general optimization. The tested specimen, for instance, can be made of a composite material consisting of several layers with different material properties; the form of the specimen can be of a more complex shape, etc. In the present work, the elastic moduli are optimized by the fixed point iteration method, which requires only the lowest few eigenfrequencies to be known. The proposed algorithm is verified by test examples and suitable convergence criteria are established.
[DOI: 10.1121/1.1760800]

PACS numbers: 43.35.Cg, 43.40.At, 43.20.Ks [YHB] Pages: 282–287

I. INTRODUCTION

The resonant ultrasound spectroscopy[1–3] (RUS) method was developed for the determination of elastic moduli of generally anisotropic materials, especially those of single crystals, In the RUS technology, complex amplitudes of the forced harmonic vibration and natural frequencies are identified for a particular specimen. Provided a sufficient number of frequencies were accurately measured and given mass density, dimensions, the shape of the specimen and the type of material symmetry, all elastic moduli can be determined in a single experiment. Recently, the application of RUS has also been extended to attenuation measurements,[4] nondestructive testing[5] behavior evaluation of heterogeneous media[6] (rocks, etc.).

The RUS method is not entirely an experimental method since it poses a difficult inverse problem of resolving the elastic constants from a resonance spectrum. The formulation of the inverse problem is as follows. Find the elastic moduli so that the computed eigenfrequencies corresponding to these moduli are as close as to the measured spectrum as possible. This identification process is schematically shown in Fig. 1.

Resonance frequencies are calculated from a mathematical model of the free vibration of an elastic body with stress free boundaries. Frazer *et al.*[7] presented an analytical solution of the free vibration for a sphere made of isotropic homogeneous material and proposed a graphical method to deduce the elastic properties of this sphere specimen. A pioneering numerical algorithm based on the Rayleigh–Ritz method using trigonometric functions for cubic specimens was proposed by Holland.[8] Its convergence was later improved introducing Legendre's polynomials by Demarest.[9] Ohno[10] extended the Demarest's solution to a parallelepiped rectangle with orthorhombic symmetry. Visscher *et al.*[11] proposed a simple computational scheme for the free vibration of a specimen with anisotropic properties using base functions in the form $x^l y^m z^n$. This algorithm is known as the *xyz algorithm* and the method is applicable, even for various irregular-shaped bodies composed of anisotropic media. A modified algorithm (known as *xyzr*) for laminated spheres and cylinders was presented by Yoneda.[12]

Using the Ritz method for the solution of the governing eigenproblem is limited to specimens of simple shapes as blocks, spheres, cylinders, etc. Instead, the finite element method (FEM) can be employed. FEM is quite general and easy to apply. It allows the determination of eigenfrequencies for an arbitrary shape of the specimen made of heterogeneous, anisotropic materials. As pointed out below, however, its use necessitates a significant modification of the standard optimization procedures.

The inverse problem in question is essentially a multidimensional fit, which represents nonlinear optimization in the sense of the least square method. Various approaches have already been studied in geophysics. The most popular optimizing procedure is the Levenberg–Marquardt method (LM), based on the modified Newton method and the steepest descent algorithm. It was adopted for parallelepiped orthorhombic crystals using Visscher's *xyz* algorithm in the RPR code[13] designed by Migliori *et al.*[14]

The LM method demands the gradient and Hessian of the error function to be evaluated at each iteration step. The knowledge of all eigenfrequencies and eigenvectors of the discretized system is thus necessary. Of course, this poses no

[a]Corresponding author. Electronic mail: plesek@it.cas.cz

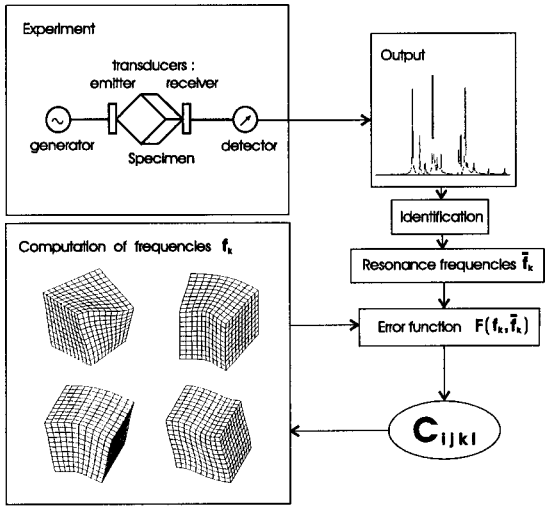

FIG. 1. Schematic depiction of the resonant ultrasound spectroscopy.

problem for the combination of the Ritz and LM methods but is definitely prohibitive in regard to FEM. Therefore, a different optimization algorithm, which requires only the lowest few eigenfrequencies to be known, must be introduced. It turns out that the fixed point iteration method (FPI) is capable to carry out the task efficiently. Details about its convergence and numerical stability can be found, e.g., in the textbook by Lambert.[15]

In this paper, a procedure for the solution of the inverse problem, combining FEM and FPI, is derived, tested, and compared with the Ritz and LM method. In Sec. II, the definition of the error function and an estimate of the relative error of measurement are proposed and the basis of the Levenberg–Marquardt method is recalled. In Sec. III, the fixed point iteration method and the algorithm for the identification of the elastic moduli using FEM and FPI are presented. The paper concludes with examples in Secs. IV and V. These examples test the solution of the forward problem, the inverse problem, and a problem with real experimental inputs. The convergence of both optimization methods is studied and suitable convergence criteria are set.

II. INVERSE PROBLEM AS A TUNING PROCESS

A criterion for the converged solution can be proposed in the form

$$F(f_k,\bar{f}_k)=\sum_{k=1}^{N} w_k\left(\frac{\bar{f}_k-f_k}{\bar{f}_k}\right)^2. \tag{1}$$

The error function F is the quadratic deviation between the computed and measured frequencies f_k and $\bar{f}_k$. Weighting factors $w_k \in [0,1]$ allow us to suppress the influence of poorly excited vibration modes. N denotes the number of measured frequencies, which must be greater than or equal to the number of independent material moduli M.

Theoretically, the minimum of F is zero. In practice, this can never be achieved. Frequencies $\bar{f}_k$ are scattered by experimental errors so that their distribution does probably not correspond to any theoretical spectrum defined by material constants. Therefore, Eq. (1) indirectly points to the error of measurement. An estimate of the relative error $\varepsilon(\bar{f})$ can be deduced from the true minimum $F_{\min}>0$ attained by the error function as

$$\varepsilon(\bar{f})=\sqrt{F_{\min}/N}. \tag{2}$$

Denote by $\mathbf{c}$ a vector of all independent elastic moduli,

$$\mathbf{c}=[C_{11},C_{12},\ldots,C_{66}]^T, \tag{3}$$

whose number is M. C_{ij} are the components of the elastic matrix $\mathbf{C}$. The ith entry of the vector $\mathbf{c}$ will also be written as c_i.

The eigenfrequencies f_k depend on $\mathbf{c}$ and, through them, also F is a function of $\mathbf{c}$. Finding the minimum of the error function $F(\mathbf{c})$ is equivalent to meeting the condition

$$\operatorname{grad} F(\mathbf{c})=\mathbf{0}. \tag{4}$$

A modern version of solution algorithms relies on the procedure proposed by Visscher *et al.*[11] and Migliori *et al.*[14] This algorithm uses the Levenberg–Marquardt method,[16–18] mentioned in the Introduction.

The LM method requires the knowledge of the first and second partial derivatives of the error function with respect to all independent moduli c_i. These derivatives can be computed from eigenvalues and eigenvectors of the Hessian of F. Such a computation is simple with the Ritz method only because the matrices of the system have small order. By contrast, the discretized system obtained by FEM leads to a large number of the degrees of freedom and calculation of all frequencies is not possible. Therefore, it is necessary to modify the algorithm so that only the lowest few frequencies are required in the optimization process and Eq. (4) is directly not used. The latter condition can be met by employing the FPI method.

III. FIXED POINT ITERATION SCHEME

A. FEM formulation

Suppose that an initial estimate of material properties is given. Then it is possible to assemble the stiffness and mass matrices $\mathbf{K}$, $\mathbf{M}$ and solve the generalized eigenvalue problem for the spatial discretization due to FEM as

$$\mathbf{K}\mathbf{v}_i=\lambda_i\mathbf{M}\mathbf{v}_i, \tag{5}$$

where $\lambda_i=(2\pi f_i)^2$. We have the spectral decomposition of the stiffness matrix $\mathbf{K}$ in the form

$$\mathbf{K}=\mathbf{V}\mathbf{\Lambda}\mathbf{V}^T, \tag{6}$$

where $\mathbf{V}=[\mathbf{v}_1,\mathbf{v}_2,\ldots,\mathbf{v}_N]$ is the modal matrix and $\mathbf{\Lambda}$ is the diagonal spectral matrix that stores the eigenvalues.

An intuitive idea underlying FPI is as follows. The stiffness matrix $\mathbf{K}$ can be improved by inserting matrix $\bar{\mathbf{\Lambda}}$ in place of the original spectral matrix $\mathbf{\Lambda}$. Components of $\bar{\mathbf{\Lambda}}$ are defined as the eigenvalues calculated from experimental data $\bar{f}_k$. Since the eigenvectors are determined quite reasonably, even for the initial guess (provided that this guess is not far from the true solution), it can be expected that the matrix

$$\tilde{\mathbf{K}}=\mathbf{V}\bar{\mathbf{\Lambda}}\mathbf{V}^T \tag{7}$$

is closer to reality and it can be used as a new approximation. This process can be repeated in iterative cycles, until the searched parameters will stabilize. On exit, the computed eigenfrequencies f_k should tend to the measured values $\overline{f_k}$.

A definition of a matrix by its spectral decomposition is inconvenient in FEM, thus, the outlined process must be adapted. The elastic operator **C** in the relationship

$$\mathbf{K}=\int_V \mathbf{B}^T\mathbf{C}\mathbf{B}\,\mathrm{d}V, \tag{8}$$

B being the strain-displacement matrix, can be expressed as a linear combination of the base matrices $\mathbf{P}_i$ as

$$\mathbf{C}=\sum_{i=1}^{M} c_i\mathbf{P}_i\,. \tag{9}$$

A base matrix $\mathbf{P}_i$ is the zero matrix except of two unit entries placed symmetrically at the appropriate positions corresponding to the c_i coefficient. Then the stiffness matrix takes the form

$$\mathbf{K}=\sum_{i=1}^{M} c_i\mathbf{R}_i\,, \tag{10}$$

where

$$\mathbf{R}_i=\int_V \mathbf{B}^T\mathbf{P}_i\mathbf{B}\,\mathrm{d}V. \tag{11}$$

Denote

$$\mathbf{S}_i=\mathbf{V}^T\mathbf{R}_i\mathbf{V}, \tag{12}$$

and from Eq. (7) we get

$$\mathbf{V}^T\tilde{\mathbf{K}}\mathbf{V}=\sum_{i=1}^{M} c_i\mathbf{S}_i=\overline{\mathbf{\Lambda}}. \tag{13}$$

In the latter equation, Eq. (13), the unknowns are the independent elastic moduli c_i. The matrices $\mathbf{S}_i$ and $\overline{\mathbf{\Lambda}}$ are symmetric, therefore, it is sufficient to compare the upper triangles in the matrix Eq. (13), which leads to the system of linear algebraic equations,

$$\mathbf{A}\mathbf{c}=\overline{\mathbf{b}}. \tag{14}$$

Matrix **A** is of the type $[L\times M]$ with $L=(N+1)N/2$ and $\overline{\mathbf{b}}$ is the upper triangle of matrix $\overline{\mathbf{\Lambda}}$ cast in the column format. Since $L>M\leqslant 21$, the system, Eq. (14), is overdetermined and must be solved by the least squares method.

Finally, the desired iteration scheme can be proposed as

$$\mathbf{A}^{(j)}\mathbf{c}^{(j+1)}=\overline{\mathbf{b}}, \tag{15}$$

which serves as a basis for the FPI approach.

B. FPI implementation

Numerical implementation of the algorithm is based on Eq. (15). The mass matrix **M** and stiffness matrices $\mathbf{K}^{(j)}$ are assembled for the estimation of the vector of independent elastic moduli $\mathbf{c}^{(j)}$. The generalized eigenvalue problem, Eq. (5), is then solved and the error function $F^{(j)}$ evaluated. This procedure is repeated until the process has been terminated by convergence criteria.

The iterative process is stopped if the value $F^{(j)}$ is less than or equal to a critical value F_{error} or if the iteration counter reaches $I_{\max}$ or the evolution of the error function F increases with respect to the previous value. The tolerance F_{error} can be determined from the described error analysis of measurements and number $I_{\max}$ is suitably chosen as, e.g., $I_{\max}=10$.

If the termination conditions are false, the process continues and a new estimate of the vector **c** is calculated from the least square problem, Eq. (15). Doing this, matrices $\mathbf{R}_i$ should be computed before iterations commence, whereas the modal matrices $\mathbf{V}^{(j)}$ must be updated at each iteration cycle.

The complete optimization process is summarized in Sec. III C as it was implemented in the finite element code PMD.[19]

The elastic matrix **C** must be positive definite, which should be continuously verified during iterations. To this end, the generalized Cholesky decomposition[20] serves as a good tool. We can write

$$\mathbf{C}=\mathbf{Z}^T\mathbf{Q}\mathbf{Z}, \tag{16}$$

where **Z** is the upper triangle matrix with positive diagonal components, and **Q** is the diagonal matrix. The matrix **C** is positive definite if the diagonal components of matrix **Q** are equal ones.[20] If the elastic matrix **C** is not positive definite, it is necessary to enter a new guess c_i, and the entire process must start from the very beginning.

The resulting system of linear algebraic equations, Eq. (15), is overdetermined and, consequently, the least squares solution $\mathbf{c}^{(j+1)}$ can be found in the form[20]

$$\mathbf{c}^{(j+1)}=\mathbf{W}^T\mathbf{\Sigma}^{-1}\mathbf{U}\overline{\mathbf{b}}, \tag{17}$$

where matrices **U**, $\mathbf{\Sigma}$, and **W** are determined by the singular value decomposition (SVD),

$$\mathbf{A}=\mathbf{U}\mathbf{\Sigma}\mathbf{W}^T, \tag{18}$$

where **U** is an orthogonal matrix of the type $[L\times M]$, **W** is also orthogonal $[M\times M]$, and $\mathbf{\Sigma}$ is the diagonal matrix $[M\times M]$. The singular value decomposition consists of two steps.[20] In the first step, the matrix is reduced to Householder's bidiagonal form and in the second step, it is diagonalized by the QR procedure with shifts.[18]

In practice, it is necessary to treat the situations when some frequencies $\overline{f_m}$ bear unreliable information due to poor excitation of their corresponding modes. Such frequencies had better be omitted in the deviation assessment. The algorithm using FPI needs to be adapted only so that the modal matrix **V** is assembled from eigenvectors $\mathbf{v}_k$, $k\neq m$, for the relevant eigenvalues λ_k.

C. Algorithm for determination of elastic moduli by FPI and FEM

(1) Input dimensions, orientation of the specimen, mesh density, and the type of material symmetry. Set the

TABLE I. Measured spectrum in MHz.

k	$\overline{f_k}$ (MHz)	w_k	k	$\overline{f_k}$ (MHz)	w_k	k	$\overline{f_k}$ (MHz)	w_k
1	0.390 168	1	19	1.020 336	1	37	[a]	0
2	0.482 360	1	20	1.024 863	1	38	[a]	0
3	0.521 220	1	21	[a]	0	39	1.303 665	1
4	0.640 609	1	22	1.033 888	1	40	1.308 766	1
5	0.664 684	1	23	1.046 764	1	41	1.313 157	1
6	0.683 808	1	24	1.069 304	1	42	1.335 314	1
7	0.712 148	1	25	1.077 958	1	43	1.342 817	1
8	0.723 915	1	26	[a]	0	44	[a]	0
9	0.741 532	1	27	1.086 059	1	45	[a]	0
10	0.803 335	1	28	1.104 869	1	46	1.402 282	1
11	0.809 689	1	29	1.115 959	1	47	[a]	0
12	0.825 370	1	30	1.125 377	1	48	1.419 437	1
13	0.831 488	1	31	1.145 332	1	49	[a]	0
14	0.854 720	1	32	1.163 642	1	50	1.438 375	1
15	0.906 646	1	33	1.168 694	1	51	1.464 062	1
16	0.964 361	1	34	1.205 361	1	52	1.483 602	1
17	[a]	0	35	1.256 418	1	53	1.497 083	1
18	1.004 111	1	36	1.274 547	1			

[a]Frequency was omitted because of poor excitation.

TABLE II. Eigenfrequencies in MHz computed by the Ritz method.

k	$P=8$	$P=9$	$P=10$	$P=11$	$P=12$	Round-off
1	0.389 244	0.389 244	0.389 154	0.389 154	0.389 141	0.389 000
2	0.483 680	0.483 680	0.483 641	0.483 641	0.483 637	0.484 000
3	0.523 585	0.523 585	0.523 541	0.523 541	0.523 538	0.524 000
4	0.643 511	0.643 221	0.643 221	0.643 214	0.643 214	0.643 000
5	0.669 073	0.669 073	0.669 073	0.669 073	0.669 073	0.669 000
6	0.684 467	0.684 467	0.684 101	0.684 101	0.684 066	0.684 000
7	0.714 981	0.714 654	0.714 654	0.714 639	0.714 639	0.715 000
8	0.725 569	0.723 969	0.723 969	0.723 729	0.723 729	0.724 000
9	0.742 797	0.742 797	0.742 704	0.742 704	0.742 694	0.743 000
10	0.805 857	0.805 857	0.805 803	0.805 803	0.805 787	0.806 000
11	0.813 913	0.813 858	0.813 858	0.813 844	0.813 844	0.814 000
12	0.830 211	0.829 406	0.829 406	0.829 294	0.829 294	0.829 000
13	0.832 004	0.831 333	0.831 333	0.831 237	0.831 237	0.831 000
14	0.859 629	0.856 984	0.856 984	0.856 504	0.856 504	0.857 000
15	0.912 617	0.912 615	0.912 615	0.912 614	0.912 614	0.913 000
16	0.968 886	0.968 886	0.968 261	0.968 261	0.968 242	0.968 000
17	1.000 742	1.000 742	1.000 643	1.000 643	1.000 636	1.001 000
18	1.008 309	1.008 309	1.007 362	1.007 362	1.007 289	1.007 000
19	1.025 102	1.024 199	1.024 199	1.023 977	1.023 977	1.024 000
20	1.028 357	1.028 101	1.026 957	1.026 957	1.026 657	1.027 000

number of independent elastic moduli M and assemble matrices $\mathbf{P}_i$, $i=1,2,...,M$.

(2) Input experimental spectrum $\overline{f_k}$, $k=1,2,...,N$ and weighting coefficients w_k. Compute $\overline{\lambda_k}=4\pi^2\overline{f_k^2}$. Assemble $\overline{\mathbf{b}}$ array.

(3) $\mathbf{R}_i=\int_V \mathbf{B}^T\mathbf{P}_i\mathbf{B}\,dV$, $\mathbf{M}=\int_V \rho\mathbf{N}^T\mathbf{N}\,dV$.

(4) Choose $\mathbf{c}^{(0)}$, check on positive definiteness of $\mathbf{C}^{(0)}$, set $j=0$.

(5) $\mathbf{K}^{(j)}=\int_V \mathbf{B}^T\mathbf{C}^{(j)}\mathbf{B}\,dV$.

(6) Solve $(\mathbf{K}^{(j)}-\lambda_k^{(j)}\mathbf{M})\mathbf{v}_k^{(j)})=\mathbf{0}$, for $k=1,2,...,N$.

(7) Evaluate error function $F^{(j)}=\Sigma_{k=1}^{N} w_k(\overline{f_k}-f_k^{(j)})^2/\overline{f_k^2}$.

(8) If $F^{(j)}<F_{\text{error}}$ or $j=I_{\max}$, exit with $\mathbf{C}=\mathbf{C}^{(j)}$.

(9) If $F^{(j)}>F^{(j-1)}$, exit with $\mathbf{C}=\mathbf{C}^{(j-1)}$.

(10) $\mathbf{S}_i^{(j)}=\mathbf{V}^{T(j)}\mathbf{R}_i\mathbf{V}^{(j)}$. Assemble $\mathbf{A}^{(j)}$.

(11) Solve $\mathbf{A}^{(j)}\mathbf{c}^{(j+1)}=\overline{\mathbf{b}}$, using SVD decomposition.

(12) Assemble $\mathbf{C}^{(j+1)}$ from $\mathbf{c}^{(j+1)}$.

(13) If $\mathbf{C}^{(j+1)}$ is not positive definite, goto **4**.

(14) Set $j=j+1$ and goto **5**.

IV. EXPERIMENT

The specimen had the rectangular block form with dimensions $2.333\times2.889\times3.914$ mm made of glass. Material's elastic moduli $\overline{C_{11}}=82.0407$, $\overline{C_{12}}=23.5666$, and $\overline{C_{44}}=29.2371$ in GPa were identified by the pulse method.[21] The maximum error of the measurement was estimated to 1.3% and, therefore, the ranges of the elastic moduli were $C_{11}\in(80.97;83.11)$, $C_{12}\in(23.26;23.87)$, and $C_{44}\in(28.86;29.62)$. Glass is an isotropic material; thus, $C_{44}=(C_{11}-C_{12})/2$. For simulation purposes, the moduli C_{11},

TABLE III. Eigenfrequencies in MHz computed by FEM.

k	$3\times3\times3$	$4\times4\times4$	$5\times5\times5$	$10\times10\times10$	$20\times20\times20$	Round-off
1	0.390 611	0.389 687	0.389 389	0.389 158	0.389 140	0.389 000
2	0.487 940	0.485 102	0.484 267	0.483 680	0.483 639	0.484 000
3	0.527 863	0.525 014	0.524 170	0.523 580	0.523 540	0.524 000
4	0.647 059	0.644 579	0.643 800	0.643 253	0.643 216	0.643 000
5	0.669 740	0.669 289	0.669 162	0.669 079	0.669 074	0.669 000
6	0.687 810	0.685 490	0.684 713	0.684 109	0.684 061	0.684 000
7	0.722 411	0.717 346	0.715 799	0.714 716	0.714 642	0.715 000
8	0.730 344	0.726 157	0.724 803	0.723 784	0.723 705	0.724 000
9	0.749 471	0.745 040	0.743 704	0.742 760	0.742 695	0.743 000
10	0.811 122	0.807 611	0.806 573	0.805 840	0.805 789	0.806 000
11	0.817 682	0.815 081	0.814 360	0.813 875	0.813 843	0.814 000
12	0.834 703	0.831 324	0.830 186	0.829 346	0.829 286	0.829 000
13	0.836 651	0.833 077	0.832 024	0.831 275	0.831 221	0.831 000
14	0.865 381	0.859 937	0.858 027	0.856 580	0.856 469	0.857 000
15	0.913 770	0.912 987	0.912 768	0.912 624	0.912 615	0.913 000
16	0.978 851	0.972 900	0.970 339	0.968 386	0.968 248	0.968 000
17	1.018 740	1.006 890	1.003 210	1.000 800	1.000 640	1.001 000
18	1.019 980	1.011 220	1.008 960	1.007 390	1.007 280	1.007 000
19	1.037 060	1.029 990	1.026 770	1.024 160	1.023 970	1.024 000
20	1.039 050	1.031 070	1.028 600	1.026 770	1.026 630	1.027 000

TABLE IV. Solution of the inverse problem by the LM method.

Iteration	C_{11}[a]	C_{12}[a]	C_{44}[a]	F	$\|\text{grad } F\|$
0	90.00	30.00	35.00	6.7799e-2	1.190 394
1	87.80	32.00	30.40	3.2468e-3	0.217 299
2	83.10	25.30	29.30	1.0238e-4	0.029 736
3	82.20	23.70	29.20	2.0488e-6	0.001 255
4	82.23	23.74	29.22	1.9478e-6	0.000 001
Stopped by $\|\text{grad } F\| < 0.001$					
Exact values	82.04	23.57	29.24		

[a]Values in GPa.

TABLE V. Solution of the inverse problem by the FPI method.

Iteration	C_{11}[a]	C_{12}[a]	C_{44}[a]	F
0	90.00	30.00	35.00	6.7722e-2
1	83.14	26.33	29.68	8.9392e-4
2	82.80	24.58	29.26	1.4888e-5
3	82.46	24.03	29.22	2.4827e-6
4	82.26	23.79	29.22	2.1680e-6
5	82.18	23.70	29.22	2.1991e-6
Stopped by F increase				
Exact values	82.04	23.57	29.24	

[a]Values in GPa.

C_{12}, and C_{44} were understood as independent, that is, cubic behavior was assumed. Mass density $\rho = 2459.9$ kg/m^3 was determined by weighing in the water.

The eigenfrequencies $\overline{f}_k$ of the specimen (Table I) were determined by the RUS method with the absolute error 105 Hz. Hence, the relative error is 10^{-4} and the minimum value of the error function $F(\mathbf{c})$, corresponding to this precision, cannot be less than 5×10^{-7}. Weighting factors w_k for poorly excited frequencies were set to zero.

V. EXAMPLES

A. Forward problem

In the first instance, it is necessary to verify the solution of the forward problem (calculation of eigenfrequencies). Moduli $\overline{C}_{11}$, $\overline{C}_{12}$, and $\overline{C}_{44}$ were used as the input data for the analysis of the forward problem. Numerical computations were executed by programs RPR[13] (Ritz method) and PMD[19] (subspace iteration method).

Convergence of the Ritz method by increasing polynomial degree P is shown in Table II. The degree $P=10$ is satisfactory to the stabilization of the fourth digit. There is no point in further increasing the polynomial degree since the truncation error 10^{-5} corresponding to $P=10$ is already smaller by the order of magnitude than that of the measured spectrum.

The assessment of FEM results can be made in a similar fashion. Its convergence upon mesh refinement is shown in Table III. 20-node isoparametric finite elements were used for the discretization of the specimen. The division 10 corresponds to the solution accuracy 10^{-5}.

The last columns in Table II and Table III show the round-off values that are identical for both the methods. Hence, it is guaranteed that if the eigenfrequencies are computed either by the Ritz method with the polynomial degree $P=10$ or FEM with the mesh density $10\times10\times10$, the solutions of the forward problem will be identical up to three digits at least. At the same time, the frequency error simulated in the ''round-off'' column is exactly known and has the value 10^{-4}. Roughly the same error is expected in a typical measurement.

B. Inverse problem

Testing the inverse problem, it is favorable to use the truncated frequencies as the input data both for LM and FPI methods. The input error 10^{-4} is known reliably from the previous analysis, therefore, the solution of the forward problem will not be influenced by the selection of a solution procedure (FEM and Ritz methods possess identical and more than sufficient accuracy 10^{-5}). Furthermore, the correct solution is known as the originally entered moduli $\overline{C}_{11}$, $\overline{C}_{12}$, and $\overline{C}_{44}$. The initial values $C_{11}=90$, $C_{12}=30$, and $C_{44}=35$ GPa were set on the input to the iteration process.

The course of convergence of LM and FPI methods follows from Tables IV and V. The error function F was minimized to the value 2×10^{-6} in both cases, which was in a good agreement with its estimated true minimum 5×10^{-7}. Both procedures were stopped after four iterations. The LM method due to $F<0.001$, and in FPI the error function reached its numerical minimum. Convergence rates are compared in Fig. 2.

C. Solution of a real problem

This time, the measured frequencies in Table I were used as input data. The results of the optimization by both methods are listed in Table VI. A comparison of the computed elastic moduli with the values determined independently by the pulse method, $\overline{C}_{11}=82.04$, $\overline{C}_{12}=23.57$, and $\overline{C}_{44}=29.24$ in GPa gives an idea of the accuracy of RUS. Since the elastic moduli differ by less than 1.3%, both approaches are virtually equivalent. The LM method yields almost identical results as the FPI method.

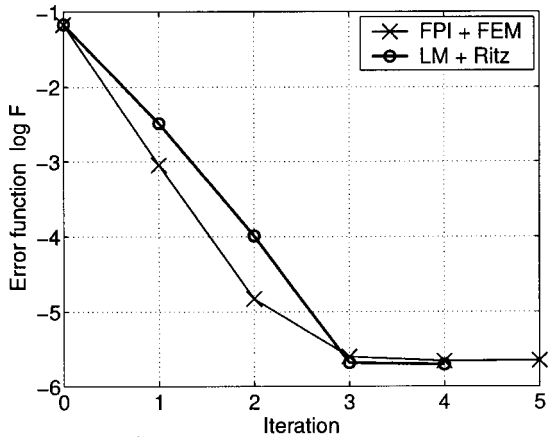

FIG. 2. Convergence of the fixed point iteration method and the Levenberg–Marquardt method.

TABLE VI. RUS results.

Method	C_{11}[a]	C_{12}[a]	C_{44}[a]	$F\times10^4$	G[b]	I[c]	Stopped by
LM	81.25	23.25	29.13	3.1634	1e-6	8	$G<0.001$
FPI	81.08	23.24	29.21	2.5344	⋯	10	$I_{\max}=10$
Pulse	82.04	23.57	29.24				

[a]Values in GPa.
[b]$G=\|\text{grad } F\|$.
[c]I is the number of iterations.

VI. CONCLUSIONS

The resonant ultrasound spectroscopy proved to be a reliable and efficient tool for the identification of material elastic moduli. A single measurement is sufficient to determine all independent coefficients. Moreover, its accuracy is comparable with the well-established pulse method, in which the elastic moduli are identified by the measurement of the speed of acoustic waves.

The finite element method in connection with the fixed point iteration procedure represents an alternative to the Levenberg–Marquardt optimization. On the one hand, the FEM solution is substantially more expensive—it takes about fifteen minutes on the present-day computers—whereas the program RPR that uses the LM method runs only a few seconds. On the other hand, it is an indisputable fact that FEM is more general and widely available in commercial codes. The described algorithm can be readily implemented in the form of a post-processor or batch commands.

Apart from the test examples described in this paper, other problems were solved. The elastic moduli of cubic materials with different anisotropy factors were determined by RUS whose results compared well to the independent data obtained by the pulse method. The tested materials were the monocrystals of silicon, copper and CuAlNi alloy. The temperature dependence of the elastic moduli for a single crystal CuAlNi in the ranges of temperature from −100 °C to 25 °C was also successfully measured by the RUS/FEM technology.

ACKNOWLEDGMENTS

The authors thank Dr. Migliori of NL Los Alamos for providing the program RPR. This work was supported by the grant projects of GACR No. 106/01/0396, and No. 101/03/0331 in the framework of Research Project No. AVOZ2076919. Portions of this work were presented in ''Determination of Elastic Moduli by the Resonant Ultrasound Spectroscopy Method'' (in Czech), Engineering Mechanics 2003, Svratka, Czech Republic, May 2003, and ''Modification of the Levenberg-Marquardt Method of the RUS Method for Using in FEM'' (in Czech), Structure Computations by Finite Element Method 2003, Brno, Czech Republic, November 2003.

[1] J. Maynard, ''Resonant ultrasound spectroscopy,'' Phys. Today **49**, 26–31 (1996).
[2] A. Migliori and J. L. Sarrao, *Resonant Ultrasound Spectroscopy: Applications to Physics, Materials Measurements, and Non-Destructive Evaluation* (Wiley, New York, 1997).
[3] R. G. Leisure and F. A. Willis, ''Resonant ultrasound spectroscopy,'' J. Phys. Condens. Matter **9**, 6001–6029 (1997).
[4] L. Ostrovsky, A. Lebedev, A. Matveyev, A. Potapov, A. Sutin, I. Soustova, and P. Johnson, ''Application of three-dimensional resonant acoustic spectroscopy method to rock and building materials,'' J. Acoust. Soc. Am. **110**, 1770–1777 (2001).
[5] J. J. Schwarz and G. W. Rhodes, ''Resonance inspection for quality control,'' in *Rev. Progr. QNDE 15*, edited by D. O. Thompson and D. E. Chimenti (Plenum, New York, 1996), p. 2265.
[6] M. Scalerandi, P. P. Delsanto, V. Agostini, K. Van Den Abeele, and P. A. Johnson, ''Local interaction simulation approach to modeling nonclassical, nonlinear elastic behavior in solids'' J. Acoust. Soc. Am. **113**, 3049–3059 (2003).
[7] D. B. Frazer and R. C. LeCraw, ''Novel method of measuring elastic and anelastic properties of solids,'' Rev. Sci. Instrum. **35**, 1113–1115 (1964).
[8] R. Holland, ''Resonant properties of piezoelectric ceramic rectangular parellelepipeds,'' J. Acoust. Soc. Am. **43**, 988–997 (1968).
[9] H. H. Demarest, ''Cube resonance method to determine the elastic constants of solids,'' J. Acoust. Soc. Am. **49**, 768–775 (1971).
[10] I. Ohno, ''Free vibration of a rectangular parallelepiped crystal and its application to determination of elastic constants of orthorhombic crystals,'' J. Phys. Earth **24**, 355–379 (1976).
[11] W. M. Visscher, A. Migliori, T. M. Bell, and R. A. Reinert, ''On the normal modes of free vibration of inhomogeneous and anisotropic elastic objects,'' J. Acoust. Soc. Am. **90**, 2154–2162 (1991).
[12] A. Yoneda, ''The *xyz* algorithm specialized for eigenvibration problem of bored and laminated objects,'' J. Sound Vib. **236**, 431–441 (2000).
[13] A. Migliori, M. Lei, and R. Schwarz, Program RPR, Version 2.02, 1998.
[14] A. Migliori, J. L. Sarrao, W. M. Visscher, T. M. Bell, M. Lei, Z. Fisk, and R. G. Leisure, ''Resonant ultrasound spectroscopic techniques for measurement of the elastic moduli of solids,'' Physica B **183**, 1–24 (1993).
[15] J. D. Lambert, *Numerical Methods for Ordinary Differential Systems* (Wiley, Chichester, 1993), Chap. 1, pp. 12–13.
[16] K. Levenberg, ''A method for the solution of certain nonlinear problems in least squares,'' Proc. Soc. Exp. Stress Anal. **2**, 164–168 (1944).
[17] D. W. Marquardt, ''An algorithm for least squares of nonlinear parameters,'' J. Soc. Ind. Appl. Math. **11**, 431–441 (1963).
[18] W. H. Press, B. P. Flannery, S. A. Teukolsky, and W. T. Vetterling, *Numerical Recipes* (Cambridge University Press, Cambridge, 1986), Chap. 15, pp. 675–683.
[19] PMD, FEM program, Vamet s.r.o., version f77.7, 2002.
[20] D. S. Watkins, *Fundamentals of Matrix Computation* (Wiley, New York, 1991).
[21] E. P. Papadakis, ''The measurement of ultrasonic velocity, The measurement of ultrasonic attenuation,'' Phys. Acoust. **19**, 1113–1115 (1990).

Sensorless control of a thermoacoustic refrigerator[a)]

Tony L. Shearer[b)] and Heath F. Hofmann[c)]
Penn State, Department of Electrical Engineering, University Park, Pennsylvania 16802

Robert W. M. Smith[d)] and Steven L. Garrett[e)]
Penn State, Applied Research Laboratory, State College, Pennsylvania 16804-0030

(Received 10 September 2003; revised 2 April 2004; accepted 5 April 2004)

A method for commanding the frequency of the signal that drives an electrodynamic sound source to maintain the coupled thermoacoustic resonator at its resonance frequency is described. The method uses only the current and voltage applied to the source terminals to select the operating frequency, thereby eliminating the need for pressure and displacement sensors used in previous phase-locked-loop frequency tracking systems. An equivalent circuit model of the coupled electro-mechanical system is used to extract piston position and pressure from the measured input current and voltage waveforms. Parameters of the electro-mechanical model can be obtained from a least-squares fit of the model using measured current, voltage, position, and force over the frequency range of interest. Parameters thus obtained are in good agreement with individual physical measurements of those same parameters. Results are presented for the implementation of this controller in a large thermoacoustic chiller. © *2004 Acoustical Society of America.*
[DOI: 10.1121/1.1756612]

PACS numbers: 43.35.Ud, 43.38.Dv, 43.20.Ye, 43.58.Wc [RR] Pages: 288–293

I. INTRODUCTION

The optimum operating frequency of electrically-driven thermoacoustic refrigerators is known to change with the temperature and/or heat loads imposed by their heat exchangers and with changes in the power delivered to the driver. Since the development of the earliest thermoacoustic refrigerators, phase-locked-loops have been used to command the drive frequency to be equal to the acoustic resonance frequency of the thermoacoustic resonator by eliminating the phase difference between the velocity of the driver's piston and the pressure at the piston face. Typically,[1] the piston's velocity is determined by an attached accelerometer and the acoustic pressure at the piston face is measured with a microphone. Recently, Li *et al.*[2] described a frequency control system which relied on direct computation of electroacoustic conversion efficiency, again using sensors.

Although these strategies have been employed successfully in the laboratory and in field experiments,[3] the commercialization of thermoacoustic technology requires that the cost of these systems be reduced and their reliability be increased. The pressure and vibration sensors add cost and breakage of their leads or gas leaks through sensor feedthroughs required to bring their signals out of the pressure vessel provide significant potential failure mechanisms. The sensing of piston position, based on electrical current and voltage measurements at the input terminals of a linear motor, has already been documented for Stirling Cycle refrigerators,[4] but the frequency control of thermoacoustic refrigerators also requires the determination of the relative phase between the piston motion and the pressure at the piston face or, equivalently, the force exerted by the piston.

We present a means for accomplishing this goal of ''sensorless control'' by using a model of the coupled electromechanical system that will produce the required pressure and velocity information from the electrical current and voltage waveforms of the electrical power delivered to the driver.[5] The parameters required for the model can be determined by physical measurements or by a least-squares fit to the model using measured current, voltage, position, and force over the frequency range of interest. We show that both methods of parameter determination are in good agreement. A method is described for implementing the sensorless control strategy using a microcontroller to extract the relative phase of the pressure and velocity and integrate the error signal to correct the drive frequency and track the acoustic resonance in real time. Data is presented for the performance of such a system controlling a large thermoacoustic refrigerator that is producing several kilowatts of useful cooling power with electrical power provided by a custom-built, 26 kW-rated full-bridge inverter.

II. THE THERMOACOUSTIC SYSTEM AND SELECTION OF OPERATING POINT

The sensorless control system was developed for a standing-wave based thermoacoustic air-conditioner, called TRITON (for 3-tons of refrigeration or equivalently a 10-kW cooling capacity capable unit).[6] In TRITON, acoustic power

[a)]Portions of this work are contained in the Master's of Science thesis of T. L. Shearer, ''Thermoacoustic refrigeration using a linear actuator without pressure and displacement transducers,'' The Pennsylvania State University, Department of Electrical Engineering, May 2002, Applied Research Laboratory Technical Report No. TR 02-002. A presentation based on this manuscript was delivered at the 145th Meeting of the Acoustical Society of America, in Nashville, TN, on 30 April 2003 [J. Acoust. Soc. Am. **113**(4), 2268 (2003)].

[b)]Present address: Northrop Grumman Corporation, Electronic Systems, 7301 Sykesville Road—MS 8955, Sykesville, Maryland 21784-5101. Electronic mail: tony.shearer@ngc.com
[c)]Electronic mail: hofmann@ee.psu.edu
[d)]Electronic mail: rws100@psu.edu
[e)]Electronic mail: sxg185@psu.edu

is delivered at one of the two pressure antinodes of a double Helmholtz resonator. The unit operates with a mixture of helium and argon at 3 MPa nominally at 62.9 Hz. For the measurements described here, only two heat exchangers were available, so the unit was operated with a single 19-inch diameter stack rather than with two stacks and two pairs of heat exchangers, with each set normally placed in each of the end bulbs near the pressure antinodes. The acoustic source is a moving magnet linear motor[7] which couples the mechanical work to the resonator via a metal bellows, and to which a supplemental mechanical spring has been added, such that the *in-vacuo* mechanical resonance of the motor and the acoustic resonance frequency are matched at the nominal operating point. While the moving-magnet linear motor is capable of producing 10-kW, excursion limits of the springs and bellows associated with material high cycle fatigue limit the maximum output of the acoustic source to 5-kW.

As the temperature and cooling load changes, the drive frequency should be changed to maintain optimum efficiency. As noted earlier, it is possible to directly track the maximum efficiency, if the acoustic input power to the system can be measured.[2] A disadvantage of such an approach is that it requires the location of an optimal value, without *a priori* knowledge of the value of the optimum, or the direction of increasing efficiency with changing frequency. As such, a system must ''hunt'' for the optimum efficiency, subject to a tolerance threshold. In contrast, the identification of the acoustic resonance of the system, and tracking with a phase-locked loop, is fairly straightforward and has been done many times in the past with sensors.[1,3]

A lumped parameter model of the acoustic system, developed by one of the authors[8] indicates that, for this system, driving the system to track the acoustical resonance frequency provides very nearly the optimum achievable electroacoustic conversion efficiency. For example, in the model the electroacoustic conversion efficiency at the nominal operating point is 85.8%. For an acoustic system detuned such that the acoustic resonance occurs at 58.9 Hz, rather than 62.9 Hz, the maximum electroacoustic conversion efficiency is 76.5%, occurring at 58.7 Hz. The optimum occurs 0.18 Hz from the acoustic resonance frequency. Operating at the acoustic resonance, instead of the frequency of optimum efficiency, results in an electroacoustic conversion efficiency of 75.8%, just 0.7% from optimum efficiency. Analagous results occur for a system with an acoustic resonance 4 Hz above the nominal operating point. Similar experience in terms of efficiency are also observed by Smith[9] and Tejani.[10] This 8 Hz frequency range is substantially larger than that observed to be needed for a practical operating range, as suggested by the data presented later in the section on experimental results.

It should be noted that, while the acoustic resonance was chosen as the operating point for this work, it is also possible, since the acoustic pressure and piston velocity and their relative phase at the source are extracted from the measured voltage and current, to directly control for parameters such as maximum efficiency, maximum power or a given value of acoustic impedance, should this prove useful for other systems. For these cases, further refinement in the electro-mechanical models, beyond that developed below, may be useful and justified.

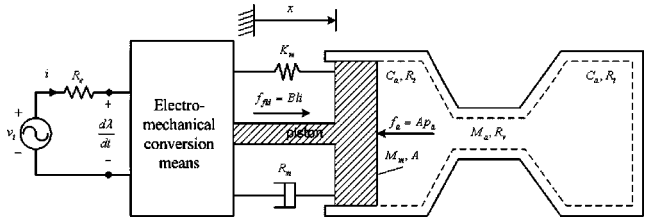

FIG. 1. Physical model of a singly excited electromechanical system coupled to an acoustic resonator by a piston of area A.

III. MODELING AND EQUIVALENT CIRCUIT REPRESENTATION

A model that captures the pertinent electrical and mechanical dynamics of the thermoacoustic refrigerator provides the basis for the sensorless control strategy. The physical model for such a thermoacoustic system is shown in Fig. 1. As the proposed sensorless controller requires only electrical and mechanical dynamics, these will be discussed in detail in the following.

A. Electrical dynamics

The dynamics of the linear electrodynamic machine[11] can be expressed as

$$v_t = iR_e + \frac{d\lambda(x,i)}{dt}, \tag{1}$$

where v_t is the voltage excitation at the terminals of the machine, i is the stator current, R_e represents electrical losses associated with the stator winding current, and λ is the flux linkage. It should be noted that current-dependent losses in the iron core of the machine due to magnetic hysteresis and eddy currents have been lumped into R_e. For a given core material, hysteresis losses typically vary linearly with frequency while eddy current losses usually vary with frequency squared.[12] Also, the winding will experience frequency-dependent conduction losses due to the skin and proximity effects. These losses may be treated explicitly in the model by making R_e frequency-dependent.

The flux linkage of the machine can be expressed as the sum of the flux linkage due to the self inductance of the windings $L_e(i)$, here assumed to be a function of the current, and the permanent magnet flux-linkage λ_{pm}:

$$\lambda(x,i) = L_e(i)i + \lambda_{\mathrm{pm}}(x), \tag{2}$$

where it is assumed that the inductance of the machine is independent of position (i.e., there are no ''reluctance'' forces in the machine). The position-dependent component of magnetic stored co-energy W'_{fld} associated with the winding can be expressed as[12]

$$W'_{\mathrm{fld}}(x,i) = \int \lambda(x,i)di = \int L_e(i)i di + \int \lambda_{\mathrm{pm}}(x)di$$

$$= \int L_e(i)i di + \lambda_{\mathrm{pm}}(x)i. \tag{3}$$

Hence, the interaction force f_{fld} between the permanent magnet field and the stator magnetomotive force (mmf) is given by

$$f_{\text{fld}}=\frac{\partial W'_{\text{fld}}(x,i)}{\partial x}=\frac{\partial \lambda_{\text{pm}}(x)}{\partial x}i. \tag{4}$$

The change in permanent magnet flux linkage with respect to displacement is often assumed to be constant and in conventional loudspeaker applications[13] is referred to as the Bl product:

$$Bl=\left(\frac{\partial \lambda_{\text{pm}}(x)}{\partial x}\right). \tag{5}$$

B. Mechanical dynamics

The mechanical dynamics of the driver, bellows, and spring configuration can be modeled accurately with the traditional mass, spring, and damper system. The spring constant is K_m (compliance may be used, $C_m=1/K_m$). The actuator moving mass is M_m. The mechanical damping is represented by a dashpot with damping constant R_m. The mechanical and acoustical dynamics are coupled by an actuating piston (bellows with effective piston area A) that is exposed to the acoustical normal force f_a. The result is an acoustical pressure p_a in the resonator at the piston. The velocity $v_m=dx/dt$, with which the piston moves, corresponds to a volume velocity $u_a=Av_m=A\,dx/dt$ in the acoustical chamber. The forces related to the spring, mass, damper, and external acoustic action are

$$f_s=K_m(x-x_0), \tag{6}$$

$$f_m=M_m\frac{d^2x}{dt^2}, \tag{7}$$

$$f_d=R_m\frac{dx}{dt}, \tag{8}$$

$$f_a=Ap_a, \tag{9}$$

where x_0 is the equilibrium value of x with the spring unstretched. The spring is assumed to be linear and will be operated around the equilibrium point of $x_0=0$. The mechanical dynamics can now be represented as the sum of the forces,

$$f_{\text{fld}}=Bli=M_m\frac{d^2x}{dt^2}+R_m\frac{dx}{dt}+K_mx+Ap_a. \tag{10}$$

IV. IMPLEMENTATION

A. State estimation

If the complex resonator pressure and the actuator displacement are known, a PLL (Phase-Locked Loop) controller can be used to track the acoustical resonance frequency. In this paper we propose a sensorless control approach where the actuator displacement and the resonator pressure phase angles are accurately estimated from knowledge of the voltage and current at the terminals of the machine.[14] Others have inferred an actuator position from direct measurements of the linear machine's terminal voltage and current.[4,15]

TABLE I. A comparison of electro-mechanical model parameters extracted by a least squares fit to sensors and values obtained by other means

Parameter	Measured By Other Techniques[a]	Least Squares Extracted Value		Units
		Mag	Phase (Deg)	
R_e (DC)	0.774	0.5183	19.4	Ω
R_e (65.3 Hz)	0.956	1.112		Ω
L_0	39.83	43.0		mH
Bl	101.2	102.1	0.304	N/A
M_m	19.78	21.54		Kg
K_m	3.33	3.467		MN/m
R_m	56.28	45.56		N s/m
L_2	⋯	1.13e−6	11.8	V s/A^3
L_4	⋯	7.73e−7	−9.08	V s/A^5

[a]Reference 17.

In order to obtain an accurate estimation of displacement and pressure, it was determined that nonlinear aspects of the system, such as magnetic saturation, must be considered. The flux–linkage relationship can incorporate magnetic saturation effects due to current by making the winding inductance an even polynomial function of current, as follows:[16]

$$L_e(i)=L_0+L_2i^2+L_4i^4. \tag{11}$$

It was also determined that the frequency dependence of the winding resistance must be taken into account. This was done by making R_e a linear function of frequency as follows:

$$R_e(\omega)=R_0+R_1\omega. \tag{12}$$

With some manipulation of the preceding equations, the actuator displacement can therefore be estimated through the following expression:

$$\hat{x}=\frac{1}{Bl}\left\{\int[v_t-R_e(\omega)i]dt-L_e(i)i\right\}. \tag{13}$$

Once displacement is known, using (13), pressure can be estimated through the following differential equation:

$$\hat{p}_a=\frac{1}{A}\left(Bli-M_m\frac{d^2\hat{x}}{dt^2}-R_m\frac{d\hat{x}}{dt}-K_m\hat{x}\right). \tag{14}$$

The parameters in (13) and (14) are found using a least-squares curve-fitting technique with phasor values of v_t, i, x, p_a, and excitation frequency ω over the expected operating frequency range.[8] Acoustic pressure was measured with an Endevco model 8530B 500-psi piezo-resistive pressure sensor. Displacement was measured with a Shavitz model HR500 LVDT sensor and ATA 2001 signal conditioner operating with a 10-kHz excitation. Compensation for the measured phase lag associated with the filter characteristics of the LVDT signal conditioning electronics (on the order of 4 degrees) was provided for operation near 60 Hz. Measurement of magnitude and phase was performed with an HP 4192A impedance analyzer operating in gain-phase mode, for all 4 signals. In all cases, the measured displacement served as the reference phase. Table I shows the values of the parameters extracted by the least squares technique, com-

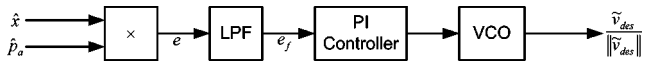

FIG. 2. Tracking the acoustical resonance frequency with a Phase-Locked Loop (PLL) controller.

pared with values obtained by direct measurements as described by Heake.[17] In some cases the parameter extractions resulted in parameters which had complex components, pointing to some possibility for further refinement in the model represented in Eqs. (13) and (14).

The above estimation technique requires knowledge of only parameters in the electrical and mechanical systems, and not the acoustic system. This is advantageous, as the electrical and mechanical models are commonly used and better understood. Using the experimentally-determined parameters in the state estimation of (13) and (14) is a robust approach, since the parameters in these models are relatively constant with changes in excitation amplitude, temperature, and frequency for this system (within the typical operating region). Other approaches to estimated pressure and displacement may require knowledge of the acoustical parameters. In this case, temperature effects would need to be modeled, thus increasing the complexity of the acoustical model, and possibly the controller.

B. Voltage frequency control

To excite the acoustical resonance of the system, the frequency of the commanded terminal voltage v_t applied to the linear machine must be the same as the acoustical resonance frequency. In this section we describe the techniques used to track the acoustical resonance frequency and thereby determine the appropriate frequency of $\tilde{V}_{\text{des}}$. To enforce operation at the acoustical resonance frequency, a PLL (Phase-Locked Loop) controller is used to force the resonator pressure and the actuator displacement into a quadrature phase relationship.[3,18] This controller only provides the frequency, as the amplitude of the voltage-controlled oscillator (VCO) output is normalized. The magnitude of the desired terminal voltage $\|\tilde{v}_{\text{des}}\|$ is dependent on the load temperature and not the operating frequency. Figure 2 shows how the estimated displacement $\hat{x}$ and the estimated pressure $\hat{p}_a$ are used to drive the frequency of the voltage excitation to the acoustical resonance frequency.

C. Voltage amplitude control

The PLL was used to track the optimal frequency. Another control loop is needed to control the amplitude of the voltage excitation. The desired amplitude of the input voltage to the machine is determined by the thermal load temperature. The control loop consists of a commanded load temperature $\tilde{T}_l$ as the input, a temperature transducer providing the actual load temperature T_l, and a Proportional–Integral (PI) controller to drive the steady-state error between the desired and actual temperature to zero.[19] A PI control loop was chosen due to its computational simplicity over other methods. The addition of derivative control (PID) was seen as not being necessary, as there is no perceived need for this controller to have a high bandwidth. Figure 3 shows a diagram of this control loop. It should be noted that the PI constants are negative, as an increase in the terminal voltage magnitude would result in a decrease in load temperature.

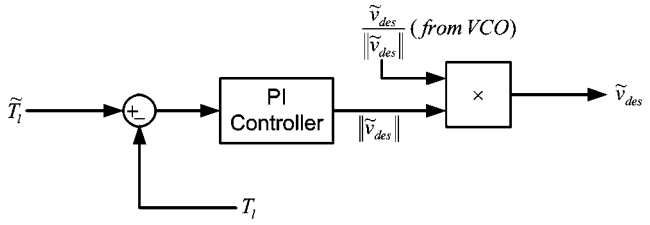

FIG. 3. Commanded voltage amplitude control loop.

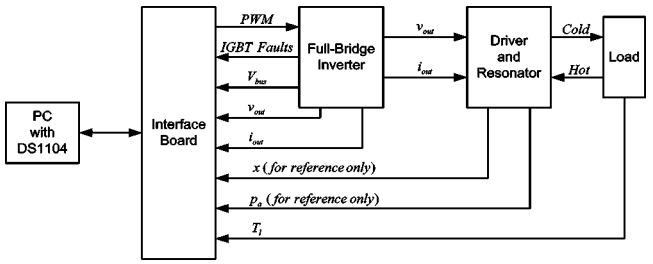

FIG. 4. Diagram of the experimental setup.

D. Experimental results

The sensorless control algorithms are developed in Matlab's Simulink. The algorithms are then compiled by Matlab's Real-Time Workshop and then implemented on a dSPACE® DS1104 controller card. A 26 kW full-bridge inverter was designed and built to drive the 5-kW acoustic source. Figure 4 gives an overview of the experimental setup.

For all the comparisons shown, the estimated pressure and displacement were computed using only the real components of the extracted parameters, given in Table I, to facilitate direct numerical computations to be performed on the real-time voltage and current waveforms. Figure 5 shows a comparison of the estimation of actuator displacement, with simultaneously measured values, taken during the process of

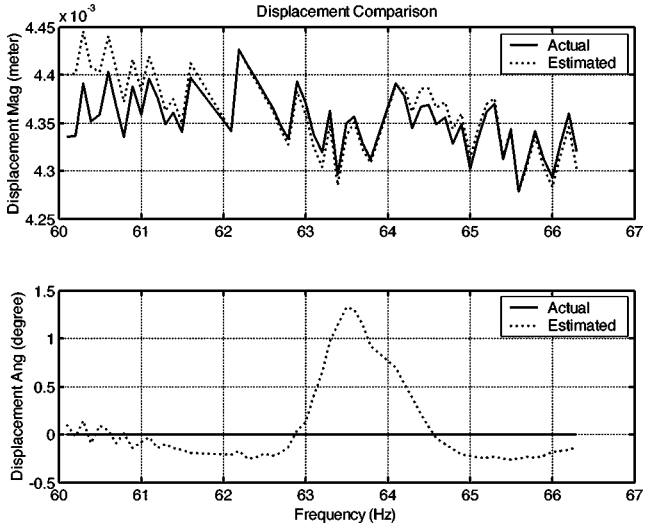

FIG. 5. A comparison between the actual and estimated displacement magnitude and phase.

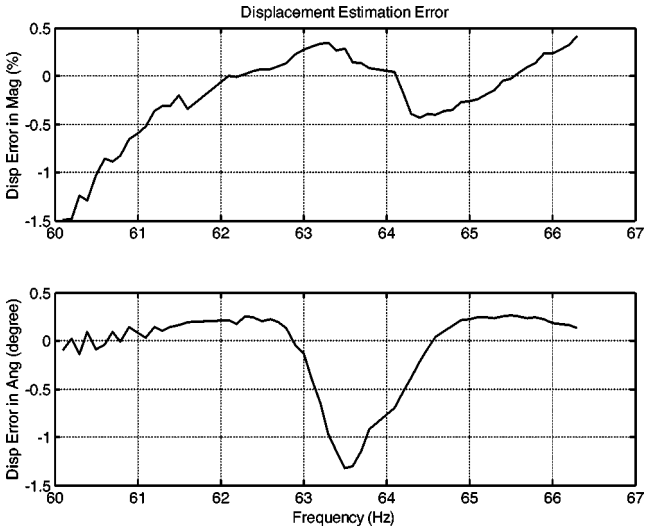

FIG. 6. The residual error in the estimation of displacement magnitude and phase.

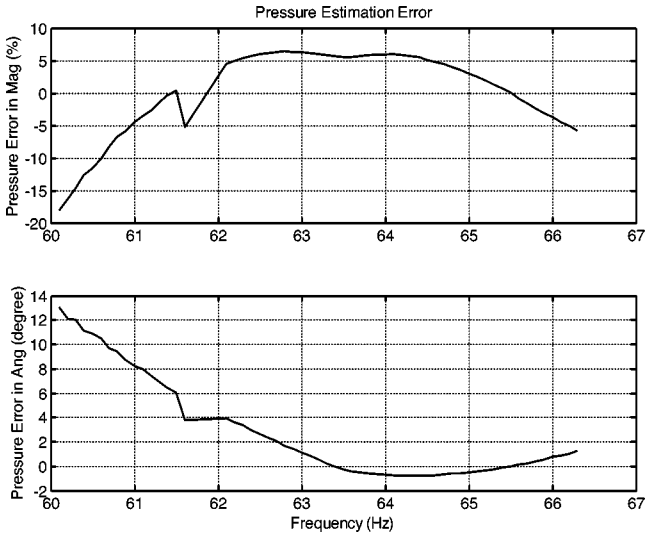

FIG. 8. The residual error in the estimation of pressure magnitude and phase.

parameter evaluation. Figure 6 provides the error in the displacement estimation. Similar plots are given for the pressure estimation in Fig. 7 and the pressure estimation error in Fig 8. Measured position served as the reference phase (i.e., it is defined to be zero degrees at all frequencies). It should be noted in Figs. 5 and 6 that with regard to displacement, and the results in Figs. 7 and 8 regarding pressure, that differences between the estimated and measured values represent in some cases compromises with regard to complexity in the model and a particular choice of real time implementation of the equations, as well as differences between actual and measured values inherent in the reference sensors, which is probably of the order of 1% in magnitude, and perhaps 1 degree in phase. Improved agreement could be achieved with an attendant increase in complexity in the model and/or the implementation. Agreement between the two is, however, very good and was found to be perfectly adequate for tracking the acoustic resonance.

With the control system performing the resonance tracking function based upon the position and pressure estimations, the cold side heat exchanger of the thermoacoustic refrigerator was permitted to vary from 45 °F to 73 °F, while the hot side heat exchanger was held at 90 °F, on two separate days. The acoustic power delivered was 3 kW. The observed acoustic resonance of the system changed by approximately 1 Hz, as shown in the range of the horizontal axis of Fig. 9. The vertical axis in this figure represents the phase angle between measured piston pressure and measured piston velocity, where a 0 degree phase shift would correspond to the acoustic resonance.[20] One may observe that the acoustic resonance was maintained to within four degrees in the phase relationship between displacement and pressure over the full range of cold temperature tested. One can estimate, based upon the data in Fig. 6 that, near resonance, the resonance frequency error as a function of phase error is about 0.01 Hz per degree of phase between pressure and velocity. The sen-

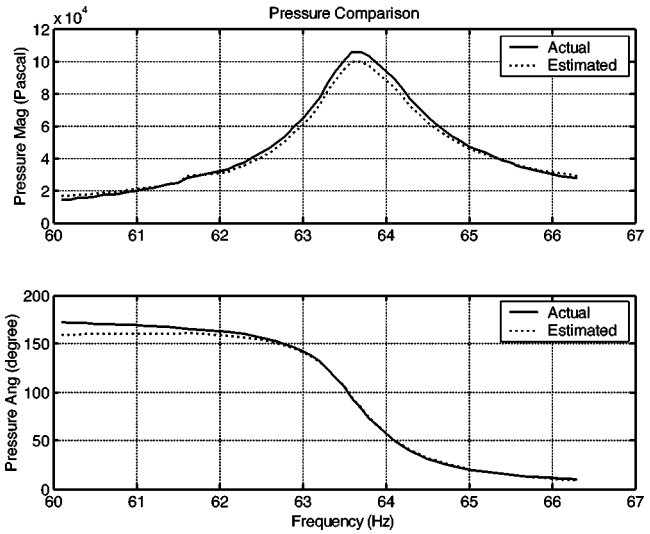

FIG. 7. A comparison between the actual and estimated pressure magnitude and phase.

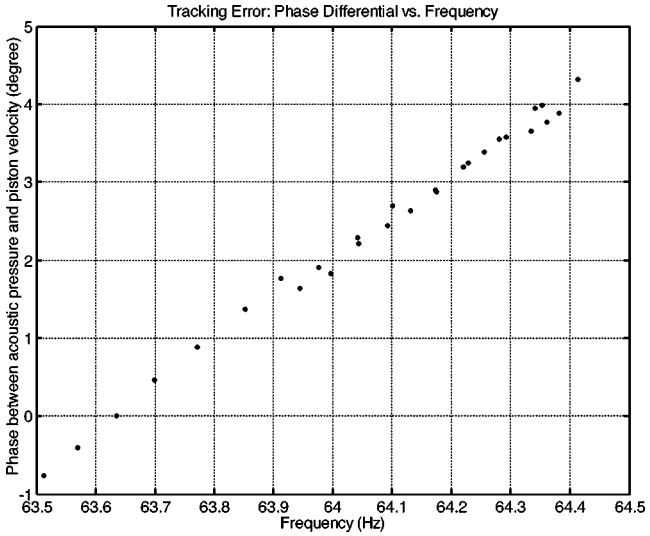

FIG. 9. The phase between the measured acoustic pressure and piston velocity as a function of operating frequency, observed during tracking of the acoustic resonance by the sensorless control system as cold-side varied from 45 °F to 75 °F.

sorless control resulted in reaching optimum electroacoustic conversion efficiency to within the measurement capabilities of the sensor-obtained displacement and pressure values. The driver excitation in this case was provided by the custom-designed power inverter instead of linear amplifiers, which were used in obtaining the values in Figs. 5–8. This provides further evidence that the method is robust even when the voltage excitation is only approximately sinusoidal, as is the case with conventional power inverters. For the latter, it is necessary to provide identical filters to both the current and voltage signals, to reject high frequency content in the voltage signal and ensure that the current and voltage signals experience the same phase delay.

V. CONCLUSION

This work has presented the development and implementation of a sensorless control scheme for a thermoacoustic refrigeration system. The proposed sensorless scheme is implemented in a real-time motor drive system, and is shown through experimentation to be accurate in estimating the actuator displacement and resonator pressure. A method for establishing system parameters from empirical data was developed and implemented. In order to optimize future sensorless control designs, other nonlinear effects should probably be taken into account for these types of moving magnet linear machines.

ACKNOWLEDGMENTS

This material is based upon work supported by the Office of Naval Research through the Naval Sea Systems Command under Contract No. N00039-D-0042, Delivery Order No. 0111. The authors also thank the Pennsylvania State University Applied Research Laboratory for additional support of this effort.

[1] T. Hofler, ''Accurate acoustic power measurements with a high-intensity driver,'' J. Acoust. Soc. Am. **83**, 777–786 (1988).
[2] Y. Li, B. L. Minner, G. T.-C. Chiu, L. Mongeau, and J. E. Braun, ''Adaptive tuning of an electrodynamically driven thermoacoustic cooler,'' J. Acoust. Soc. Am. **111**, 1251–1258 (2002).
[3] S. L. Garrett, J. A. Adeff, and T. J. Hofler, ''Thermoacoustic refrigerator for space applications,'' J. Thermophys. Heat Transfer **7**, 595–599 (1993).
[4] R. W. Redlich, ''Method and apparatus for measuring piston position in a free piston compressor,'' U.S. Patent No. 5,342,176, 30 August 1994.
[5] T. L. Shearer, R. W. M. Smith, and H. F. Hofmann, ''Sensorless control of an harmonically driven linear reciprocating electrodynamic machine,'' U.S. Patent Application No. 10/706,550, filed 12 November 2003.
[6] R. A. Johnson, S. L. Garrett, and R. M. Keolian, ''Thermoacoustic cooling for surface combatants,'' Naval Eng. J. **112**, 335–345 (2000).
[7] G. A. Yarr and J. A. Corey ''Linear electrodynamic machine'' U.S. Patent No. 5,389,844, 14 February 1995, describes the basic permanent-magnet motor configuration. The C-10C Linear-Motor Alternator used for the design was manufactured by CFIC Inc./Resonant Power Group, 302 Tenth Street, Troy, NY 12180.
[8] T. L. Shearer, ''Thermoacoustic refrigeration using a linear actuator without pressure and displacement transducers'' Master's thesis, the Pennsylvania State University, and PSU/Applied Research Lab Technical Report No. TR02-002, May 2002.
[9] R. W. Smith, ''High efficiency two kilowatt acoustic source for a thermoacoustic refrigerator,'' Master's thesis, Penn State Department of Engineering Science and Mechanics, and PSU/Applied Research Lab Technical Report No. TR01-001, December 2000.
[10] M. E. H., Tijani, ''Loudspeaker-driven thermo-acoustic refrigeration,'' Ph.D. dissertation, Technische Universiteit Eindhoven, 2001.
[11] I. Boldea and S. A. Nasar, ''Linear electric actuators and generators,'' IEEE Trans. Energy Convers. **14**, 712 (1999).
[12] A. E. Fitzgerald, C. Kingsley, Jr., and S. D. Umans, *Electric Machinery*, 5th ed. (McGraw-Hill, New York, 1990).
[13] F. V. Hunt, *Electroacoustics: The Analysis of Transduction, and its Historical Background* (Acoustical Society of America, 1984); ISBN 0-88318-401-X.
[14] F. M. Callier and C. A. Desoer, *Linear System Theory* (Springer-Verlag, Berlin, 1991).
[15] M. R. Bai and H. Wu, ''Robust control of a sensorless bass-enhanced moving-coil loudspeaker system,'' J. Acoust. Soc. Am. **105**, 3283–3289 (1999).
[16] H. Polinder, J. G. Slootweg, M. F. Hoeijmakers, and J. C. Compter, ''Modeling of a linear PM Machine including magnetic saturation and end effects: maximum force-to-current ratio,'' IEEE Trans. Ind. Appl. **39**, 1681–1688 (2003).
[17] J. F. Heake, ''Characterization of a 10-kilowatt linear motor/alternator for use in a thermoacoustic refrigerator,'' Master's thesis, Penn State Graduate Program in Acoustics, and PSU/Applied Research Lab. Technical Report No. TR02-003, December 2001.
[18] R. B. Byrnes, Jr., ''Electronics for autonomous measurement and control of a thermoacoustic refrigerator in a space environment,'' Master's thesis, Naval Postgraduate School, DTIC Report No. AD B141-388, December 1989.
[19] B. C. Kuo, *Automatic Control Systems*, 8th ed. (Wiley, New York, 2003).
[20] L. A. Kinsler, A. R. Frey, A. B. Coppens, and J. V. Sanders, *Fundamentals of Acoustics*, 4th ed. (Wiley, New York, 2000).

Calculated effects of pressure-driven temperature oscillations on heat exchangers in thermoacoustic devices with and without a stack

Ray Scott Wakeland and Robert M. Keolian[a)]
The Pennsylvania State University, Graduate Program in Acoustics and Applied Research Laboratory, P.O. Box 30, State College, Pennsylvania 16804-0030

(Received 29 July 2003; accepted for publication 5 April 2004)

A Lagrangian computational method is used to explore the performance of heat exchangers in conditions of oscillating flow and oscillating pressure relevant to thermoacoustic devices. Pressure oscillations cause temperature oscillations within the working gas. Depending on phase, these ''pressure-driven temperature oscillations'' can enhance or degrade heat transfer within the exchangers of a thermoacoustic device. © *2004 Acoustical Society of America.*
[DOI: 10.1121/1.1755238]

PACS numbers: 43.35.Ud, 44.27.+g, 07.20.Pe [RR] Pages: 294–302

I. INTRODUCTION

This paper reports the results of a simple computational model for studying the combined effects of oscillating flow and oscillating pressure on the performance of heat exchangers in thermoacoustic devices. Originally motivated by our work on an unusual type of thermoacoustic device having neither stack nor regenerator, the model predicts effects that may be of considerable importance for heat exchangers in all types of thermoacoustic devices.

In a previous paper,[1] the authors developed a semianalytical model to examine the feasibility of ''no-stack'' thermoacoustic devices, consisting of two heat exchangers separated by a small gap and placed in a standing wave of high amplitude (>15% of mean pressure). The semianalytical model involves many assumptions, the most important being that the heat exchangers make perfect thermal contact with the oscillating gas, i.e., that the exchangers have an effectiveness of 100%. At the time that the model was developed, it was presumed that the imperfect performance of real heat exchangers would invariably degrade performance, but the magnitude of the effect was unknown. The present computational method was developed to explore the effects of imperfect heat exchangers on the efficiency of no-stack devices. The conclusions are somewhat startling: reducing heat exchanger effectiveness (from 100%) can actually *increase* the amount of heat pumped by a no-stack refrigerator. The effect comes about because of an interaction in the gas within an exchanger between temperature changes caused by thermal conduction and temperature changes caused by pressure oscillations. It is likely that this same mechanism has considerable influence on the performance of the heat exchangers in the more common sorts of thermoacoustic devices.

The computational model uses a time constant to characterize the degree of thermal contact between a Lagrangian parcel of gas and the exchanger. By removing pressure oscillations from the computation, it is possible to determine how effective each simulated exchanger would be in a simple oscillating flow, without externally imposed pressure oscillations. We have recently measured the effectiveness of parallel-plate heat exchangers in such oscillating flow,[2] so that it is now possible to match the relaxation parameter used in the model to the physical dimensions of real exchangers operating with laminar flows. The results support the validity of the one-dimensional model, and indicate that even heat exchangers that have very high effectiveness in pure oscillating flow are still subject to a large effect from pressure-driven temperature oscillations.

Because the oscillating-flow apparatus used for the measurements is incapable of imposing pressure oscillations, those measurements do not test experimentally the hypotheses of the present work. It is possible, however, to infer some experimental support for the idea from measurements on a working thermoacoustic refrigerator that have been described in a paper by Mozurkewich;[3] this evidence is presented in Sec. V.

Some potentially important physical phenomena are not included at all in the present model. Experiments carried out by Stephan Turneaure, a post-doctoral researcher working in this same laboratory, have already demonstrated one inadequacy in the method described in this paper. Turneaure's no-stack prime mover would reach onset and maintain oscillation at amplitudes such that no single parcel entered both exchangers. This outcome is not predicted by the model in this paper. The explanation of sustained, low-amplitude oscillations involves the thermal interactions *between* parcels, and this requires a calculation that tracks all of the parcels simultaneously as they oscillate. The computer programs used to generate the results of the present paper calculate the path of each parcel separately. This is a much simpler programming task, and we believe it is adequate to lend credence to the assertion that without inclusion of the contribution of pressure oscillations, any model of heat exchanger performance in thermoacoustic devices is incomplete.

II. THE COMPUTATIONAL MODEL

In a no-stack device, heat transfer and work consumption or production are carried out primarily by the volume of

a)Electronic mail: keolian@psu.edu

 0001-4966/2004/116(1)/294/9/$20.00

gas that enters both hot and cold heat exchangers. This volume of gas, the ''working gas,'' can be conceptually broken into thin transverse slices (''parcels''). If the heat exchangers are perfect, then all parcels perform equally, since all undergo identical, complete temperature changes upon entering either exchanger. To relax the assumption of heat-exchanger ideality, it is necessary to consider the parcels separately, since each spends a different amount of time in each of the two exchangers. Thus, an additional goal of the present calculation is to access the performance of parcels near the edges of the working gas, which spend a large fraction of the cycle in one exchanger but very little in the other.

The present model is as simple as possible. It is a one-dimensional model for parallel-plate heat exchangers. Individual parcels are taken to be lumped elements that undergo ordinary conductive thermal relaxation toward the exchanger temperature during periods when they are within an exchanger. The relaxation time is taken to be a constant, independent of velocity or position within the exchanger. Since the heat exchangers are imperfect, pressure oscillations cause temperature changes even in the gas that is within an exchanger. The oscillation period is partitioned into 1000 time steps. Within each small time step a thermal relaxation term is added to the temperature change that the gas *would have undergone* had it been adiabatic. Each parcel is treated independently. Thermal conduction between the parcels is neglected.

In a two-dimensional view, each parcel (slice) would be further divided along the transverse direction into many smaller units, called ''elements'' in the following discussion. The one-dimensional parcel approximation lumps the thermal decays of the various elements that make up a parcel into a single relaxation time, averaging over the faster decays of elements closer to a plate and the slower decays of those that are further away (viewing heat flow within the exchanger as the linear superposition of independent heat flows from each element). Effectively, we are using the average temperature of the elements of a parcel as the one-dimensional temperature of the model, assuming that the average over those elements is adequately described by a single exponential decay time.

Note that for laminar flow this averaging procedure is unaffected by the spatial distortion of the parcel into parabolic or other profiles because the distance from each element of the parcel to a plate remains the same. This holds as long as enough of the elements of the parcel are sufficiently far from the ends of the exchanger that end effects on the heat flow from an element to the exchanger can be neglected—a distance on the order of the gap between the plates, which is independent of velocity and should not be confused with the thermal or hydrodynamic entry lengths used in Eulerian heat exchange calculations. We therefore expect this one-dimensional approach to be an adequate approximation even when the flow is two-dimensional. The one-dimensional temperature T used in the model then becomes a label for the average of the temperatures of the fluid elements of a parcel of fluid that is a planar slice when it is between the exchangers and that distorts into another shape within the exchangers. The Lagrangian position of the parcel used in the model is the average position of its elements. The shape distortion may increase the thermal coupling between the parcels, which is neglected in the model, by bringing them into more intimate contact with each other. But since in the end we are interested in the total work and total heat transfer summed over all the parcels, this interparcel transfer of heat is assumed to be unimportant. Thus, we expect the model to be most reliable for parallel-plate heat exchangers that are long compared to the gap between the plates, and for parcel displacements into the exchangers that are larger than the gap but smaller than the plate length. Our use of a single relaxation time implicitly assumes that the thermal conductivity of the gas is constant.

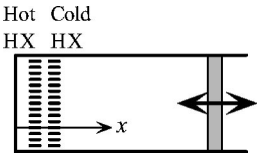

FIG. 1. Locations of the hot and cold heat exchangers.

With some care, it may be possible to adapt the results of the model to exchangers that have turbulent flow between the plates, shortening the average relaxation time because turbulent mixing brings elements into better overall thermal contact with the plates, but keeping in mind that our measurements were made using exchangers for which the flow was laminar (see Ref. 4, p. 150 for details).

In the FORTRAN program written to carry out the calculations, we use the following procedure: the extent of the working gas is determined; the working gas is divided into small parcels, each with its own displacement amplitude as well as its own mean position; the steady-state starting temperature for each parcel is determined by iterating until the cycle begins and ends at the same temperature; the heat and work are calculated for each individual parcel; and the total heat and work are calculated by adding up the contributions of all the working parcels. The equations are summarized in Sec. III. The complete FORTRAN code, along with detailed documentation, can be found in Ref. 4.

Other assumptions in the model are as follows.

(1) The model emulates the conditions in a cylinder of gas driven by a piston at a frequency that is well below the lowest acoustic resonance of the gas in the enclosure, so that, at each instant, the pressure is the same everywhere within the cylinder. This is the situation in a no-stack device [see Figs. 1, 2(a), and 7(a) of Ref. 1].

(2) The piston oscillates sinusoidally, and the gas acts as a gas spring undergoing uniform ''strain amplitude'' S, so that, for the gas parcel at mean position x_0 from the closed end of the cylinder,

$$x(x_0,t)=x_0+x_0 S \sin \omega t. \tag{1}$$

(3) The cylinder contains two heat exchangers, one hot and one cold, as shown in Fig. 1. As the gas is pushed back and forth, it contacts the two heat exchangers, which cause parcels of gas to change temperature, and therefore volume. A major assumption of the model used here is that the volume of the working gas is such a small fraction of the total

volume of the cylinder that these temperature-induced volume fluctuations have negligible effect on the pressure in the cylinder. As the pressure in the cylinder varies in time, the location $x(t)$ of the parcel that has equilibrium position x_0 varies, so that the instantaneous pressure and position of the parcel are related by the adiabatic gas law according to

$$p(t)=p_0\left(\frac{x}{x_0}\right)^{-\gamma}=p_0(1+S\sin\omega t)^{-\gamma}, \tag{2}$$

where p_0 is the quiescent pressure and γ is the ratio of specific heats, c_p/c_v. This assumption is equivalent to a common thermoacoustics approximation that the heat exchangers operate in a pure standing wave, with negligible traveling-wave component. This approximation is used in Ref. 1 as well. The main consequence for the computation is that it is not possible to calculate work input or output at the piston. Instead, work must be calculated from the difference in the magnitudes of the input and output heats.

III. METHOD OF CALCULATION

There are three types of regions: between the heat exchangers, within the exchangers, and beyond the exchangers. Regions between and beyond the exchangers are adiabatic. The regions where the gas is within the exchangers are the ones that require numerical time stepping. The rate of thermal relaxation is given by a time constant τ, such that

$$\Delta T_{\text{relaxation}}=-(T-T_{\text{hx}})\frac{\Delta t}{\tau}, \tag{3}$$

where Δt is the time step and T_{hx} is the heat exchanger temperature. For an adiabatic, ideal gas,[5] $pV=mRT$ and $pV^{\gamma}=p_0V_0^{\gamma}$, so that

$$\frac{\Delta T_{\text{adiabat}}}{T}=\frac{\gamma-1}{\gamma}\frac{\Delta p}{p}. \tag{4}$$

Thus, the model of heat exchange propounded here is summarized by

$$\Delta T=\Delta T_{\text{adiabat}}+\Delta T_{\text{relaxation}} \tag{5}$$

$$=\left[\frac{\gamma-1}{\gamma}\frac{T\tau}{p}\frac{dp}{dt}-(T-T_{\text{hx}})\right]\frac{\Delta t}{\tau}. \tag{6}$$

Volume changes are calculated from the ideal gas law,

$$\frac{dV}{V}=\frac{dT}{T}-\frac{dp}{p}. \tag{7}$$

Separate heats from the cold exchanger and the hot exchanger (Q_{cold} and Q_{hot}) are calculated using

$$dQ=-C_p(T-T_{\text{hx}})\frac{dt}{\tau}, \tag{8}$$

where $C_p=mR\gamma/(\gamma-1)$, with m being the mass of the gas in the parcel. The net work produced by the cycle is $W_{\text{net}}=Q_{\text{hot}}+Q_{\text{cold}}$.

We can estimate the relation between τ and the parameters of a parallel-plate heat exchanger with a simple "RC" thermal model. The gas filled gap between the plates is $2y_0$. The characteristic distance that heat can diffuse in $1/\pi$ of an acoustic period is called the thermal penetration depth $\delta_\kappa=\sqrt{k_0/\rho_m c_p \pi f}$, where f is frequency, k_0 is the thermal conductivity, ρ_m is the mean density, and c_p is the isobaric specific heat of the gas. If the wetted area of a parallel-plate exchanger is A and the film thickness is δ_κ for $\delta_\kappa<y_0$, then the thermal "capacitance" of the gas in the exchanger is $\rho_m c_p y_0 A$ and the "resistance" is $\delta_\kappa/k_0 A$, their product giving a time constant τ such that

$$\tau f\simeq\frac{1}{\pi}\frac{y_0}{\delta_\kappa} \tag{9}$$

for large values of τf or y_0/δ_κ. For small values of y_0/δ_κ we may expect that the thermal capacitance is given by the same expression, but that the length in the resistance might have an upper limit of approximately $y_0/2$, so that the resistance becomes $y_0/2k_0A$, resulting in

$$\tau f\simeq\frac{1}{2\pi}\frac{y_0^2}{\delta_\kappa^2} \tag{10}$$

for small values of τf or y_0/δ_κ.

IV. RESULTS

A. No-stack refrigerator

In the following, we use the parameters from our previous semianalytical model of an optimized no-stack refrigerator as inputs to the present time-stepping model. In that semianalytical model, these parameters resulted in model performance of $\dot{Q}_{\text{inviscid}}=1190\,\text{W}$, $\eta_{\text{II}_{\text{inviscid}}}=60.6\%$, and $\eta_{\text{II}_{\text{net}}}=38.0\%$ at $P_A/p_m=26.0\%$, where η_{II} is the second-law efficiency, which compares the coefficient of performance of the refrigerator to that of a Carnot refrigerator, and the subscripts "net" and "inviscid" indicate whether or not viscous losses are included in the calculation. As applied to the present time-stepping model, the relevant values, adapted from Tables I and III of Ref. 1, are: $p_0=2.07\,\text{MPa}$, $\gamma=1.667$, $f=320\,\text{Hz}$, $T_{\text{hot}}=303.1\,\text{K}$, $T_{\text{cold}}=276.9\,\text{K}$, $x_{\text{hot}}=0.012\,97\,\text{m}$, $x_{\text{cold}}=0.016\,12\,\text{m}$, $x_0=0.014\,55\,\text{m}$, $A_{\text{fr}}=0.0095\,\text{m}^2$, and $S=0.1487$, where x_{hot} and x_{cold} are the locations of the inside edges of the heat exchangers, T_{hot} and T_{cold} are the exchanger temperatures, A_{fr} is the cross-sectional area of the device, and S is the strain amplitude of Eq. (1). For these parameters,[6] the present time-stepping model produces the results in Fig. 2.

Figures 2(a) and (b) are the temperature-versus-position plot (Tx diagram) and the pV diagram for the centered parcel, the parcel that has an equilibrium position halfway between the inner edges of the exchangers. The heavy gray lines in the Tx diagram represent the temperatures and locations of the heat exchangers. Markers highlight the places where the parcel enters and exits the exchangers, and the points of maximum and minimum excursion. The asterisk marker shows the equilibrium position of the parcel in the x direction, while in the T direction it shows the start and end of the iterated cycle, where the matching condition on temperature must be met. For refrigerators, the parcel goes around these closed paths in a counterclockwise direction.

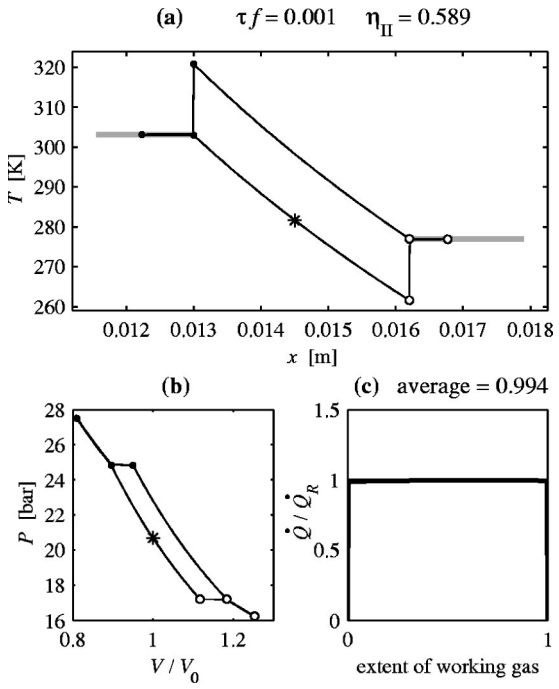

FIG. 2. Center-parcel results for the no-stack refrigerator with $\tau f = 0.001$. This is the smallest possible value of τf for the number of time steps used, so effectively $\tau f \simeq 0$.

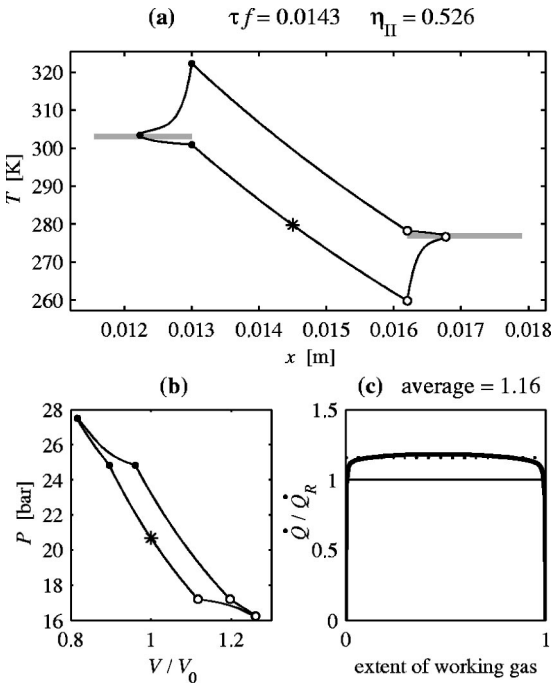

FIG. 3. Center-parcel results for the no-stack refrigerator with $\tau f = 0.0143$.

Figure 2(c) summarizes the results for the entire extent of the working fluid. The time-averaged rate of heat removal from the cold exchanger $\dot{Q}$ calculated by the time-stepping model is divided by the reference value $\dot{Q}_R = 1190\,\mathrm{W}$, the inviscid performance of the idealized refrigerator from the semianalytical model at this amplitude. In this simulation, the working gas is partitioned into 100 parcels. The results for each of the 100 parcels are plotted from left to right along the abscissa, with the left-most parcel of the working gas at 0 and the right-most parcel at 1. For each parcel, the heavy curve shows the magnitude of the rate at which heat would have been removed from the cold exchanger had every parcel performed equally with this parcel. This normalization makes it easy to compare the performance of each parcel to the *average* performance of the entire working volume, which is shown by a dotted horizontal line. [This line is obscured in plots with $\tau f \simeq 0$, since each parcel performs nearly identically, but is visible in part (c) of the other figures.] There is also a light-weight line at $\dot{Q}/\dot{Q}_R = 1$. The result for the time-stepped computation is not identical to that from the semianalytical model because the models are not identical—there is no linearization of the oscillating pressure in the time-stepped model, and there are small numerical errors. However, the average heat transfer result [printed above part (c)] agrees with the semianalytical model to 0.6%, and the inviscid second-law efficiency $\eta_{\mathrm{II}_{\mathrm{inviscid}}}$ [printed above part (a) simply as η_{II}, since this is an inviscid computation] agrees to 3%.

Figure 3 shows the result of slightly reducing the degree of thermal contact of the exchangers by increasing the normalized time constant to $\tau f = 0.0143$. In the Tx diagram of Fig. 3(a), we can follow the temperature of the gas as it decays toward the exchanger temperatures. Because the thermal contact is still excellent, near the extremes of displacement the temperature comes to the temperature of the exchanger. Then, as the gas moves back out of, say, the hotter exchanger, the declining pressure reduces the temperature of the gas, and the imperfect exchanger cannot hold the gas to its temperature. The gas exits this exchanger *colder* than it left the ideal exchanger; the rate of heat transport has been increased.

It is not so for all parcels. For any but perfect exchangers, the parcels at the edge of the working gas must transport zero heat, since they spend zero time in one exchanger or the other. Figure 3(c) shows the performance of the parcels near the edges falling off toward zero. For this excellent thermal contact, however, the great majority of parcels perform better than they did with ideal exchangers, with the net result that 16% more heat is removed from the cold exchanger. This is one of the primary results of this paper.

There is a cost to the enhancement. The second-law inviscid efficiency $\eta_{\mathrm{II}_{\mathrm{inviscid}}}$ has dropped 11%. This is also seen in the ''opening up'' of the pV diagram in Fig. 3(b). The enclosed area represents the amount of work done per cycle. In contrast to the corresponding diagram in Fig. 2(b), net work is being done even while the parcel is within the exchangers.

Similar results are shown for increasing τf in Figs. 4–6. Figure 4 shows the results for $\tau f = 0.0455$, the value at which $\dot{Q}$ reaches its maximum value, 33% higher than the value obtained for ideal exchangers, with an inviscid efficiency that is 77% of that for the ideal exchangers.

The value $\tau f = 0.136$ in Fig. 5 is interesting because the average heat pumping is the same as for ideal exchangers. The inviscid efficiency is down by almost 28% from its peak value. These are *inviscid* efficiencies, however. Presumably there is some cost in exchanger viscous loss and minor loss

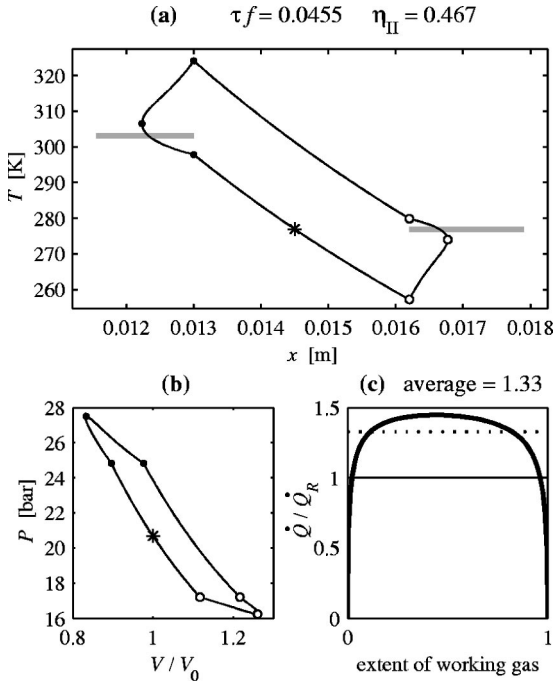

FIG. 4. Center-parcel results for the no-stack refrigerator with $\tau f = 0.0455$, which maximizes the average value of $\dot{Q}$.

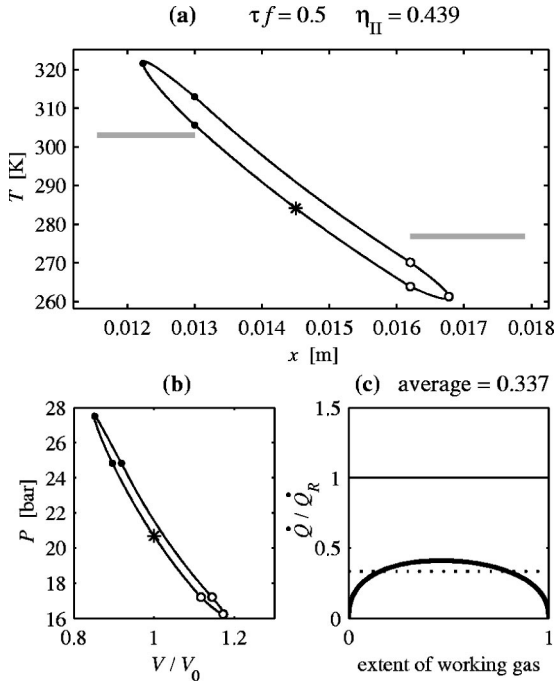

FIG. 6. Center-parcel results for the no-stack refrigerator with $\tau f = 0.5$.

to an exchanger that has nearly perfect thermal contact, so it is not immediately apparent which configuration would have the best *net* efficiency.

Comparing Fig. 4(c) to Fig. 5(c), the performance of off-center parcels has fallen faster than that of the centered parcel as τf has increased from 0.0455 to 0.136.

Finally, Fig. 6 shows the results for poor thermal contact, with $\tau f = 0.5$. The parcel path in xT space has begun to collapse toward the curve that results from adiabatic compression and expansion.

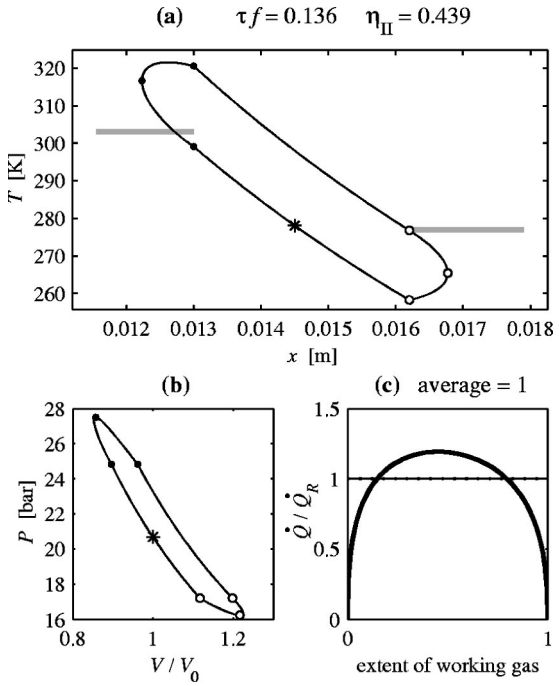

FIG. 5. Center-parcel results for the no-stack refrigerator with $\tau f = 0.136$.

B. Adjacent exchangers with no pressure oscillations: Correlation of τf with y_0/δ_κ

In our FORTRAN code, we provide for the possibility ''turning off'' the pressure oscillations (and the associated temperature oscillations) while leaving the displacement oscillations the same. This produces a simulation similar to the situation used to make the heat exchanger measurements in Ref. 2. Essentially, that experiment consisted of placing two parallel-plate heat exchangers, at different temperatures, close together, forcing air back and forth between them, and measuring the rate of heat transfer from the hot to the cold heat exchanger. By matching the measured effectiveness of the real heat exchangers to the effectiveness that is calculated using the present method, we can match values of τf from the model to values of the physical parameter y_0/δ_κ. ''Effectiveness'' is the ratio of the actual rate of heat transfer to the maximum possible heat transfer for a given temperature difference and heat capacity flow rate, and it is quite useful for analyzing heat exchangers in oscillating flow, as shown in Ref. 2.

For this comparison, we may set the parameters to any convenient values, provided that the exchangers are long enough. We then calculate $\dot{Q}$ divided by the value of $\dot{Q}$ obtained for $\tau f \simeq 0$, giving the combined effectiveness of the two-exchanger system. Figure 7 shows zero-pressure-amplitude results for $\tau f = 0.216$, which produces a combined, total effectiveness for the two-exchanger system of $[\epsilon_T]_{hx} = 70\%$. In the measurements,[2] this same effectiveness was observed for heat transfer between two adjacent parallel-plate heat exchangers for $y_0/\delta_\kappa = 1.0$. By running this heat-exchanger-measurement simulation at many different values of τf, the correspondence between τf and y_0/δ_κ can be mapped, as shown in Fig. 8. The values denoted by the + signs are based measurements of effectiveness which we

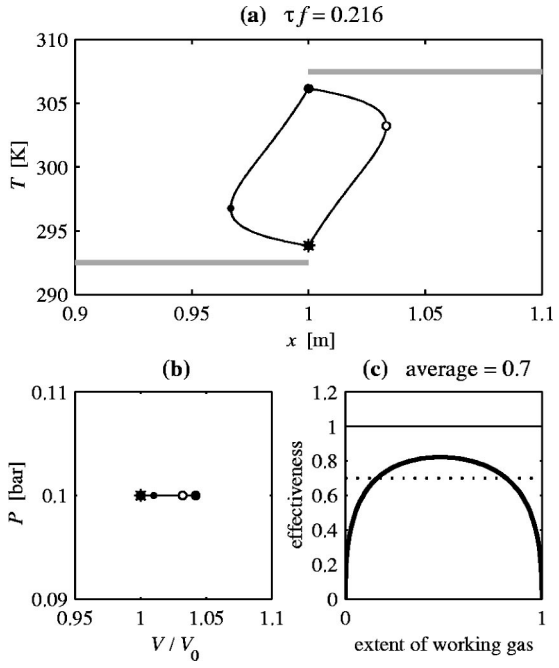

FIG. 7. Computational model of adjacent exchangers with no pressure oscillations for $\tau f = 0.216$. For this case, with no gap between the exchangers and no pressure oscillations, the average value $\dot{Q}/\dot{Q}_R$ corresponds to the total *effectiveness* $[\epsilon_T]_{\mathrm{hx}}$ measured in Ref. 2. The parcel follows a counterclockwise path in the *Tx* diagram.

judge to be somewhat less reliable than the others.[4] For large y_0/δ_κ, the correspondence is $\tau f = (1/3.487) y_0/\delta_\kappa$, indicated by the diagonal line. The constant 1/3.487 is smaller by 10% than the value $1/\pi$ that was predicted by the simple relaxation model, Eq. (9). At small τf there is a suggestion of a transition to the behavior described by Eq. (10), which is shown by the dashed curve. We see then that the one-dimensional model, together with rather crude estimates of the time constants, does a good job of reproducing the effectiveness results of the experiment performed without pressure oscillations. This bolsters our confidence that we can draw reasonable conclusions from the model predictions of situations that include pressure oscillations, particularly if we use the measurements to correct the correspondence between the plate spacings and the time constants.

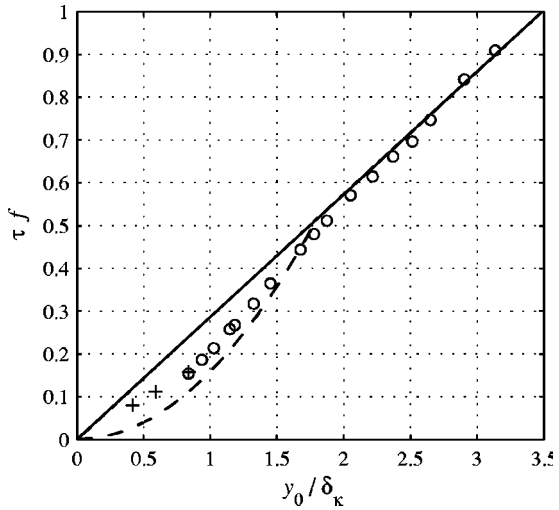

FIG. 8. Correspondence between y_0/δ_κ and τf, determined by matching the overall effectiveness $[\epsilon_T]_{\mathrm{hx}}$ measured for y_0/δ_κ and computed for τf. The values denoted by the + signs are based on less reliable measurements of effectiveness. The straight diagonal fit line is $\tau f = 0.90(y_0/\pi\delta_\kappa)$, a 10% correction on Eq. (9), which was used to estimate τf for large y_0/δ_κ. The dashed curve is Eq. (10), $\tau f = y_0^2/2\pi\delta_\kappa^2$, which was expected to approximate τf for small y_0/δ_κ.

For the values of τf shown in the figures, $\tau f = 0.0143$, 0.0455, 0.136, 0.216, and 0.500, the effectivenesses are $[\epsilon_T]_{\mathrm{hx}} = 0.999$, 0.981, 0.848, 0.700, and 0.379, respectively, with values of plate spacing $y_0/\delta_\kappa = 0.07$, 0.25, 0.76, 1.0, and 1.85 obtained by interpolating the data of Fig. 8. The correspondences for the smallest of these, $y_0/\delta_\kappa = 0.07$ and 0.25, are relatively uncertain.

What is striking about the results is just how sensitive the no-stack device is to small changes in effectiveness. For $\tau f = 0.0143$, the effectiveness *without* pressure oscillations is 99.9%, with a regenerator-like $y_0/\delta_\kappa \simeq 0.07$, yet this level of τf produces effects that are clearly visible in Fig. 3, and causes a 16% increase in total heat transport. The value $\tau f = 0.0455$, which maximizes heat transport in the no-stack refrigerator, has an effectiveness of 98.1% without pressure oscillations, corresponding to $y_0/\delta_\kappa \simeq 0.25$. The value $\tau f = 0.136$, which gives $\dot{Q}/\dot{Q}_R = 1$ in the no-stack refrigerator in Fig. 5(c), corresponds to $y_0/\delta_\kappa = 0.76$. This is not much greater than the value $y_0/\delta_\kappa = 0.63$ used in the calculation of overall efficiency in the semianalytical model of Ref. 1. In that paper, we assumed that $y_0/\delta_\kappa = 0.63$ would give "excellent thermal contact" in the heat exchangers, and it *does* in the absence of pressure oscillations, with $[\epsilon_T]_{\mathrm{hx}} = 90.4\%$, but the influence of the large pressure oscillations required in the no-stack refrigerator makes this a *minimum* value of effectiveness for high efficiency in that type of device.

When we first saw the result that decreasing the effectiveness of the exchangers in a no-stack refrigerator could increase heat pumping, we imagined that this might provide an opportunity to increase *net efficiency*, since looser exchangers would have lower viscous and minor losses. With the abstract quantity τf now connected to physical dimensions, though, it becomes apparent that the loosest of these "looser" exchangers is about what was already used in our previous modeling, so the hoped-for improvement is unrealizable. The value $y_0/\delta_\kappa = 0.63$ used in Ref. 1 corresponds to $\tau f = 0.104$. In the time-stepping model, this produces a heat-pumping enhancement of 15% but drops the inviscid efficiency by 27%. Substituting the time-stepping results into the semianalytical model of Ref. 1 drops the overall coefficient of performance relative to Carnot from $\eta_{\mathrm{II}_{\mathrm{net}}} = 38\%$ to 32%. In other words, the previous model was overly optimistic, assuming nearly perfect heat transfer with a spacing of $y_0/\delta_\kappa = 0.63$, which turns out actually to be fairly "loose" in the context of such a large pressure amplitude.

C. No-stack engines

The results for no-stack engines are equally interesting, but also somewhat disheartening. The no-stack refrigerator of the previous section can be converted into an engine by increasing the temperature difference between the exchangers. For this example, the temperature difference is increased

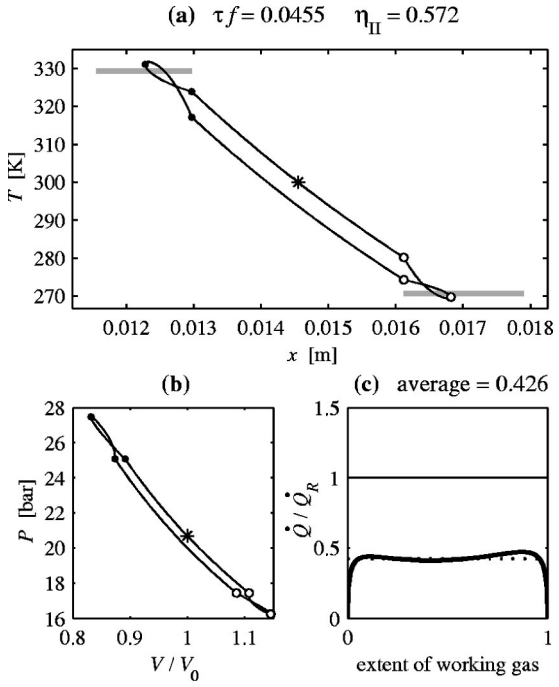

FIG. 9. Center-parcel results for no-stack engine with $\tau f = 0.0455$. Note that, in contrast to similar diagrams for refrigerators, the paths in Figs. 9(a) and (b) go clockwise, and $\dot{Q}$ and $\dot{Q}_R$ are taken at the hot heat exchanger.

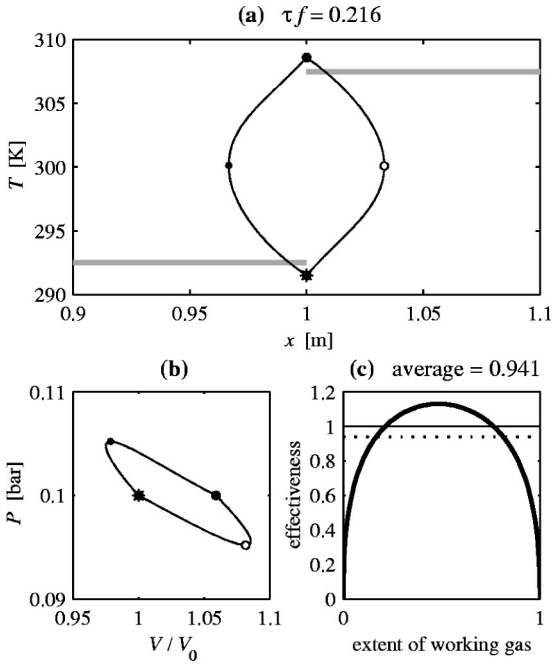

FIG. 10. The heat exchanger on the left corresponds to the hot heat exchanger in a stack-based refrigerator, here operated at an amplitude of 5% of mean pressure. The heat exchanger on the right corresponds to the hot end of the stack. The parcel follows a counterclockwise path in the Tx and pV diagrams.

until the heat input is $\dot{Q}_R = 1.18\,\mathrm{kW}$ for $\tau f = 0.001$. The value of τf is then increased to 0.0455, producing Fig. 9. This is the same value of τf as for the refrigerator in Fig. 4, but the effect is even more dramatic on the engine than on the refrigerator—the heat input, and the corresponding work output, are cut by more than half. Interestingly, $\eta_{\mathrm{II}_{\mathrm{inviscid}}}$ drops only 8%. When τf is reduced to 0.136 (not shown), the heat input is reduced to 13% of the original.

D. Heat exchangers in stack-based devices

With the FORTRAN program we can also illuminate the possible influence of pressure-driven temperature oscillations on the performance of heat exchangers in ordinary thermoacoustic devices. In Figs. 10 and 11, conditions have been selected so that when the pressure oscillations are "turned on," this same gas stroke generates a pressure amplitude that is 5% of the mean pressure, typical of stack-based devices.

Recall that Fig. 7 shows the selection of $\tau f = 0.216$, with $[\epsilon_T]_{\mathrm{hx}} = 70\%$, and corresponding to $y_0/\delta_\kappa = 1.0$, without pressure oscillations. Figure 10 shows the same gas motion, but with 5% pressure oscillations. The pressure increases as the gas moves *to the left*. Thus, the heat exchanger on the left, at 292.5 K, represents the ambient (exhaust) exchanger in a stack-based refrigerator, and the hotter exchanger on the right represents the hot end of the stack. The pressure oscillations cause fluctuations in temperature that raise the rate of heat removal from the stack to $0.941\,\dot{Q}_R$, an increase of 35%. Values of τf greater than 0.188 (corresponding to $y_0/\delta_\kappa = 0.95$) result in heat transfer exceeding what would be achieved with an ideal exchanger, peaking at an effectiveness value of 1.15 for $\tau f = 0.077$ (or $y_0/\delta_\kappa = 0.5$). We see from the pV diagram that work is required to achieve this enhancement.

In Fig. 11, the temperatures are reversed, but the pressure still increases as the gas moves to the left. This situation is similar to that of a hot (input) exchanger in a stack-based *engine*, with the colder exchanger on the right now repre-

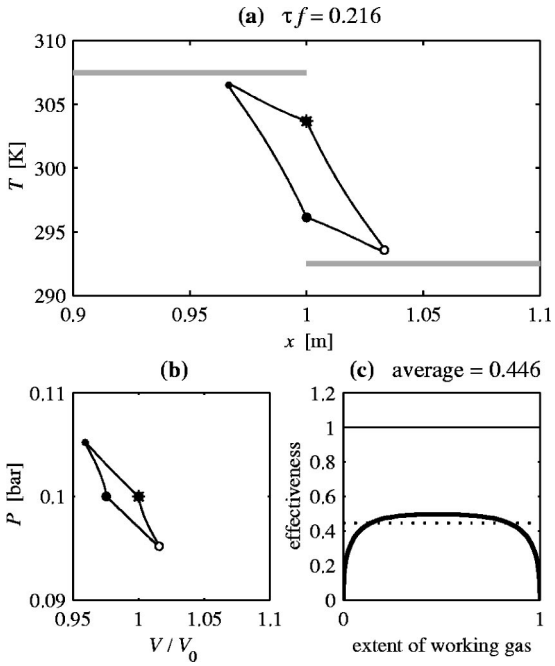

FIG. 11. The heat exchanger on the left corresponds to the hot heat exchanger in a stack-based engine, here operated at an amplitude of 5% of mean pressure. The heat exchanger on the right corresponds to the hot end of the stack. The parcel follows a clockwise path in the Tx and pV diagrams.

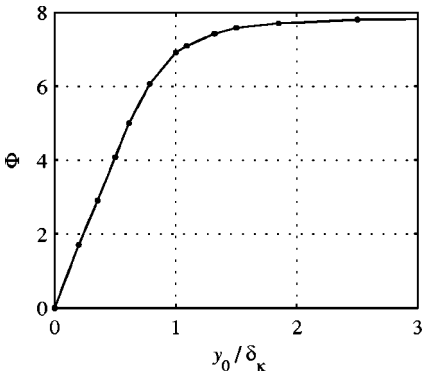

FIG. 12. Function Φ used in Eq. (11) to describe the amount of enhancement (or degradation) expected in a standing-wave thermoacoustic refrigerator (or engine).

senting the hot end of the stack. The gas now enters the hotter region while the pressure increases, and in this case the rate of heat transport *drops* by 35% compared with the same situation in the absence of the 5% pressure oscillation.

In the refrigerator-like situation, as the gas enters the left exchanger (which represents the ambient exchanger of the refrigerator), the increasing pressure tends to keep the gas temperature farther above the exchanger temperature in the period of time just after the gas enters the exchanger, thus increasing the average gas-to-exchanger temperature difference during this crucial part of the cycle. In the engine-like situation, increasing pressure tends to drive the temperature of the gas quickly toward the (left) exchanger temperature, decreasing the average temperature difference.

The amount of heat-transfer enhancement for stack-based refrigerators is about the same magnitude as the degradation for stack-based engines. The enhancement of heat transfer (either plus or minus) caused by pressure oscillations depends on both oscillation amplitude and τf. For a given value of τf, the amount of enhancement grows linearly with amplitude. That is, if $[\epsilon_T]_{\mathrm{hx}}$ is the effectiveness in the absence of pressure oscillations, then apparent effectiveness $[\epsilon_T]_{\mathrm{apparent}}$ in the presence of pressure oscillations is

$$[\epsilon_T]_{\mathrm{apparent}} = [\epsilon_T]_{\mathrm{hx}} \left(1 \pm \Phi \frac{p_A}{p_0} \right), \tag{11}$$

where p_A is the pressure amplitude and Φ is a function that depends on y_0/δ_κ, plotted in Fig. 12. The function Φ grows linearly for small y_0/δ_κ, eventually approaching a constant value of about 8. The values of y_0/δ_κ plotted in Fig. 12 are determined from τf using the correspondence plotted in Fig. 8. Note that Eq. (11) assumes that the stack and heat exchanger have the same value of y_0/δ_κ, which will often not be the case in an actual device.

In all of the above-mentioned examples, the exchangers are long enough that none of the working gas ever goes *beyond* either exchanger. The degree of influence of the pressure oscillations is smaller for exchangers shorter than the peak-to-peak gas displacement, since the gas spends less time interacting with the exchangers.

V. EVIDENCE IN SUPPORT OF THE MODEL

Mozurkewich has recently carried out measurements of heat transfer between a thermoacoustic stack and a tube heat exchanger within a thermoacoustic refrigerator.[3] The test heat exchanger was the one nearer the velocity node, the ''hot heat exchanger'' in a standing-wave refrigerator, which exhausts heat from the stack. Mozurkewich measured the amount of exhaust heat, the temperature T_{hhx} of the heat exchanger, and the temperature T_H of the stack material at the end of the stack adjacent to the exchangers. One of his interesting observations was of significant heat transfer when $T_H - T_{hhx}$ was *zero*. In Mozurkewich's experiments, this ''heat flow at zero temperature difference'' grew linearly with amplitude, as in his Fig. 2. (In this standing-wave type of device, displacement amplitude and pressure amplitude increase together.) By adjusting the temperature of the heat exchanger at the opposite end of the stack, he could bring the heat transfer to zero by forcing the temperature of the stack to be many degrees *below* that of the exchanger to which it was exhausting heat.

Clearly, a heat transfer model where $\dot{Q}$ is proportional to the temperature difference between the exchanger and the end of a stack or regenerator cannot account for this type of phenomenon, even when calibrated against oscillating-flow heat transfer experiments like the ones in Ref. 2, that do not include pressure oscillations. Further study may reveal some simple way to add pressure-amplitude-dependent terms to this type of model, along the lines of Eq. (11), but it may be necessary to incorporate a calculational model such as the one used here into the design software. David Gedeon's Sage software[7] uses a method that accounts for time-dependent temperature differences between gas and heat exchanger. It is not a time-stepping method, however, but rather a ''globally implicit'' method.[8] It would be quite instructive to compare the results of Sage modeling to those of the simple model presented here.

Of course, measurements are necessary to validate the ideas put forward in this paper. Such experiments would require a device similar to an alpha Stirling engine. For purposes of unambiguous analysis and interpretation, however, it would be better if this apparatus did not have a regenerator, but simply two heat exchangers, as in a no-stack refrigerator.

VI. CONCLUSIONS

The main purpose of this paper is to convey our conviction that pressure-driven temperature oscillations play an important role in the performance of heat exchangers in thermoacoustic devices. This means that the heat exchanger measurements and analysis of Ref. 2 are less definitive than they might appear.

The original motivation for this study was to examine the consequences for the no-stack model. The full implications were not exposed until the recent analysis of the heat exchanger measurements. The conclusions are rather negative for no-stack devices, suggesting that *extremely* effective heat exchangers would be required for efficient operation of

a no-stack refrigerator, and that the idea of a high-power no-stack engine may be unrealistic.

Regardless of the future of no-stack devices, the undertaking has been valuable because of the important implications for conventional thermoacoustic devices. It appears that the exchangers in standing-wave refrigerators probably receive a substantial boost in performance from the effects of pressure-driven temperature oscillations, and vice versa for standing-wave engines. The implications for regenerator-based devices have yet to be worked out.

The simple one-dimensional thermal relaxation model used here seems to work well even though this is a two-dimensional laminar flow. With further refinement of the time history of heat transfer from a parcel to the exchanger plates, the calculation should become nearly exact. We find that it is sometimes clearer to take a Lagrangian point of view in the time domain rather than to take the traditional Eulerian point of view in the spatial domain with its focus on hydrodynamic and thermal entry lengths.

ACKNOWLEDGMENTS

This work was supported by the Office of Naval Research, the Penn State Applied Research Laboratory, and the Pennsylvania Space Grant Consortium.

[1] R. S. Wakeland and R. M. Keolian, "Thermoacoustics with idealized heat exchangers and no stack," J. Acoust. Soc. Am. **111**, 2654–2664 (2002).

[2] R. S. Wakeland and R. M. Keolian, "Effectiveness of parallel-plate heat exchangers in thermoacoustic devices," J. Acoust. Soc. Am. (to be published).

[3] G. Mozurkewich, "Heat transfer from transverse tubes adjacent to a thermoacoustic stack," J. Acoust. Soc. Am. **110**, 841–847 (2001).

[4] R. S. Wakeland, "Heat exchangers in oscillating flow, with application to thermoacoustic devices that have neither stack nor regenerator," Ph.D. thesis, The Pennsylvania State University, 2003.

[5] In the version of the ideal gas law used here, m is the mass of the gas and R is the gas constant. The gas constant is defined such that $mR=nR$, where n is the number of moles in the parcel and R is the universal gas constant.

[6] Because p varies nonlinearly with x in the present model, we have used the displacement amplitude to match the two models.

[7] D. Gedeon, "Sage: Stirling-cycle model class reference guide," Gedeon Associates, 16922 South Canaan Rd., Athens, OH 45701 (1999).

[8] D. Gedeon, "A globally-implicit Stirling cycle simulation," in *Proceedings of the 21st IECEC* (American Chemical Society, Washington, DC, 1986), pp. 550–554.

The system-on-chip design of a silicon micromachined condenser microphone array

Mingsian R. Bai[a] and Shihwei Huang
Department of Mechanical Engineering, National Chiao-Tung University, 1001 Ta-Hsueh Road, Hsin-Chu 300, Taiwan, Republic of China

(Received 29 August 2003; revised 25 March 2004; accepted 30 March 2004)

A miniature condenser microphone array that combines array signal processing and micro-electro-mechanical systems (MEMS) technologies is presented. A linear dynamic model and a quasistatic analysis are presented. The array configuration serves two purposes: enhancement of the signal-to-noise ratio (SNR) and the directivity of sensor. A least-squares beamforming design based on the template resulting from the Multiple Signals Classification algorithm is proposed to achieve a directive beam pattern. To minimize the parasitic effects on the MEMS device, a system-on-chip design composed of a microphone module, a dc bias circuit, an impedance matching circuit, and array beamforming filters is proposed in the paper. The performance of the proposed design is evaluated in terms of the frequency response, SNR improvement, and directional response through numerical simulations and experiments. © *2004 Acoustical Society of America.*
[DOI: 10.1121/1.1753295]

PACS numbers: 43.38.Bs, 43.38.Gy, 43.38.Hz, 43.38.Kb [AJZ] Pages: 303–312

I. INTRODUCTION

3C (computer, communication, and consumer) industry has recently emerged as one of the most rapidly growing industries of modern days. Commercial products such as notebook computers, personal data assistants, mobile phones, and MP3 players are currently making their way into people's lives. Miniaturization has been known to be one of the chief concerns of 3C products. This is particularly true for microphones that are important components of 3C products. A condenser microphone based on micro-electro-mechanical systems (MEMS) technology offers a potential solution in achieving ultimate miniaturization for 3C products. Silicon microphones have received a great deal of research interest for years and an excellent review can be found in Ref. 1. However, there remain technical issues that need to be resolved before we find widespread use of such device. Although conventional capacitive microphones have higher sensitivity than piezoresistive microphones, sensitivity is still a crucial consideration in micromachined capacitive microphones. This sensitivity problem pertinent to silicon microphones is due partly to the built-in stress in the diaphragm resulting from the MEMS fabrication process, and partly to the parasitic capacitance in electrical connections. This problem is further worsened by the self-noise in the chip, which may overwhelm the exceedingly weak signal generated by the device. Hence, the signal-to-noise ratio (SNR) has always been one of the major design factors in MEMS microphones.

To address this issue of low sensitivity, a system-on-chip (SoC) design of the microphone that integrates the sensor structure, a dc bias circuit, an impedance buffer, and array beamforming filters in one chip is presented in this paper. The purpose of this paper is threefold. The first purpose is to show how electroacoustic transducers, array signal processing, and MEMS technology can be applied in a multidisciplinary design problem. The second purpose is to improve SNR through integration into arrays. The third purpose is to improve directionality through integration into arrays. However, for the last purpose, it shall be shown that it can be achieved above moderately high frequency due to the physical constraint of array size. In the single chip design, parasitic effects are reduced due to elimination of interconnections between modules. Apart from the SoC design, a microphone array configuration is also proposed in this study to further enhance the SNR of the device. One benefit of using such array configuration is that the SNR (in terms of power) increases by the number of elements in the array.[2] Furthermore, the microphone array serves as a spatial filter to focus only on the source and reject unwanted noise at the other directions, making the array an attractive solution for hands-free communications. In order to achieve a highly directive beam pattern, a constant beamwidth array based on the template from the Multiple Signals Classification (MUSIC)[3] algorithm is designed using the least-squares method. For simplicity, the resulting filters are realized by analog circuits. The MEMS fabrication is well suited for such multichannel array SoC design.

In this paper, the properties of the condenser microphone and array filters are investigated. Electro-acoustical analogy is employed to establish a linear dynamic model of the silicon microphone, while a quasistatic analysis based on the finite difference method is conducted to find the collapse condition. Some previous research on this aspect should be mentioned. Hohm and Kühnel[4,5] applied an analytical approach to calculate the nonlinear deflection of the diaphragm of a silicon microphone. Bergqvist[6] suggested a more complex model based on the finite elements method (FEM). Pedersen[1] examined the effects of the perforation in the back plate on microphone stability and performance by using the

[a]Author to whom all correspondence should be addressed; electronic mail: msbai@mail.nctu.edu.tw

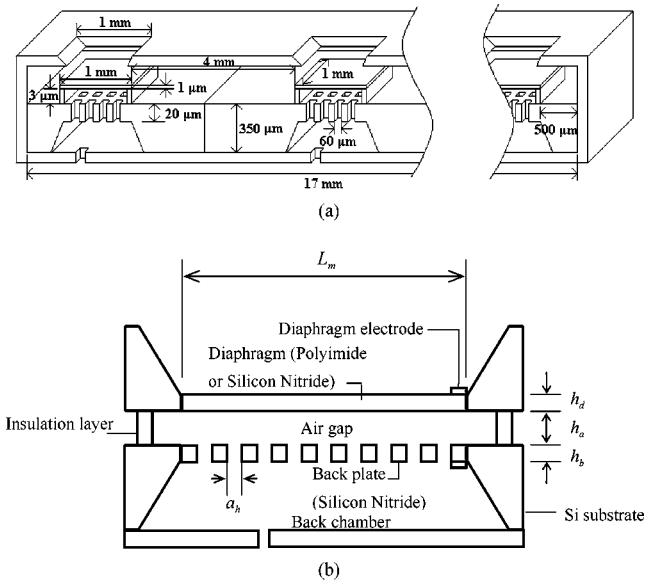

FIG. 1. A schematic diagram of the microphone array. (a) The microphone array with four MEMS condenser microphones. (b) Cross section of a condenser microphone with a perforated backplate.

finite differences method (FDM). Similar to the work by Pedersen and other researchers,[4–6] electro-acoustical analogy[7–9] is exploited in this paper to account for the complex coupling among the acoustical, mechanical, and electrical domains. The collapse condition of the microphone is determined from a quasistatic analysis of the nonlinear system. On the basis of the linear dynamic model, performance analysis was carried out to justify the proposed MEMS microphone array. As for the MEMS microphone arrays, two references are relevant to the present study. Chowdhury *et al.* presented a 3×3 MEMS capacitive microphone array.[10] In their design, beamforming was accomplished by the simple delay-sum method. However, there was an error in the analysis of directional response, and no experimental results are presented. Another work by Arnold *et al.* developed a 16-element MEMS piezoresistive microphone array for wind tunnel studies.[11] The fast Fourier transform is used for frequency-domain beamforming. However, instead of being fabricated on one chip, the microphones are mounted on a printed circuit board. Thus, the performance of such design was found comparable to conventional microphone arrays.

II. DESIGN OF MEMS CONDENSER MICROPHONE ARRAY

Consider a four-channel MEMS microphone array shown in Fig. 1(a). Four condenser microphones are fabricated with equal spacing on a straight line. In this section, the quasistatic and the linear dynamic models and the array beamforming design will be presented.

A. Quasistatic analysis and linear dynamic analysis

We begin with a single channel condenser microphone with a square diaphragm and a perforated backplate, as shown in Fig. 1(b). In the metallization process, Cr and Au are deposited using evaporation as the adhesion layer and the electrode layer, respectively. The metallization layer can be released by a lift-off process. The metallization scheme should play a role in the diaphragm stress and the parasitic capacitance. Like traditional condenser microphones, a dc bias voltage source is needed in our MEMS microphone. To predict the large deflection of the diaphragm resulting from an excessive dc bias, a quasistatic analysis in Ref. 1 is reviewed.

Assume that the backplate is rigid and the deflection is small so that the linear model applies. For simplicity, nonlinear stiffening that may affect the prediction of the electrostatic collapse point is not considered in the following presentation. The equation of motion for the diaphragm is given as[12]

$$C_{11}\frac{\partial^4 w_d}{\partial x^4}+2(C_{12}+2C_{44})\frac{\partial^4 w_d}{\partial x^2\partial y^2}+C_{11}\frac{\partial^4 w_d}{\partial y^4}=\frac{12}{h_d^3}\left[p_{\mathrm{sp}}+p_{\mathrm{el}}+\sigma_d h_d\left(\frac{\partial^2 w_d}{\partial x^2}+\frac{\partial^2 w_d}{\partial y^2}\right)\right], \tag{1}$$

where h_d is the plate thickness, σ_d is the built-in stress, and $w_d(x,y)$ is the deflection. $C_{11}=C_{22}$, $C_{12}=C_{21}$, and C_{44} are material constants of the plate. For isotropic materials, the forgoing material constants are given by

$$C_{11}=\frac{E}{1-\upsilon^2},\quad C_{12}=\frac{E\upsilon}{1-\upsilon^2},\quad C_{44}=\frac{E}{2(1+\upsilon)}, \tag{2}$$

where E and υ are the Young's modulus and Poisson's ratio, respectively. In Eq. (1), p_{sp} is the sound pressure, p_{el} represents the electrostatic force per unit area due to the dc bias between the diaphragm and the backplate and is given by

$$p_{\mathrm{el}}(x,y)=K_{\mathrm{holes}}\frac{\epsilon_d\epsilon_0}{2(h_d+\epsilon_d(h_a-w_d))}V_{ba}^2, \tag{3}$$

ϵ_d is the relative permittivity of the diaphragm material, ϵ_0 is the vacuum permittivity, h_a is the distance of air gap, and V_{ba} is the dc bias voltage. The constant K_{holes} accounts for the effect when the backplate is perforated.[1] Although in a practical setting the diaphragm is fixed by a tapered and somewhat asymmetric junction, it is assumed for convenience that the diaphragm is clamped at the edge, i.e.,

$$w_d(x,y)=\frac{\partial w_d(x,y)}{\partial x}=0,\quad w_d(x,y)=\frac{\partial w_d(x,y)}{\partial y}=0$$

on the boundary. An iterative quasistatic analysis based on the FDM is carried out for the partial differential equations in Eq. (1). The large deflection of diaphragm and the collapse condition of the microphone is found from this analysis. The details of the procedure can be found in Ref. 1.

Next, electro-acoustical analogy[1,8,9] is adopted for predicting the linear dynamic behavior of the MEMS condenser microphone. The equivalent circuits of the microphone are shown in Fig. 2, wherein the acoustical, mechanical, and electrical domains are coupled through ideal transformers.

In the acoustical subsystem of Fig. 2(b), the radiation impedance is approximated by the analogous circuits[8] in Fig. 2(c), where $R_{A1}=0.441\rho_0 c/L_m^2$, $C_{A1}=5.94L_m^3/\rho_0 c^2\pi\sqrt{\pi}$, $R_{A2}=\rho_0 c/L_m^2$, $M_{A1}=8\rho_0/3\pi\sqrt{\pi}L_m$, ρ_0 is the density of air,

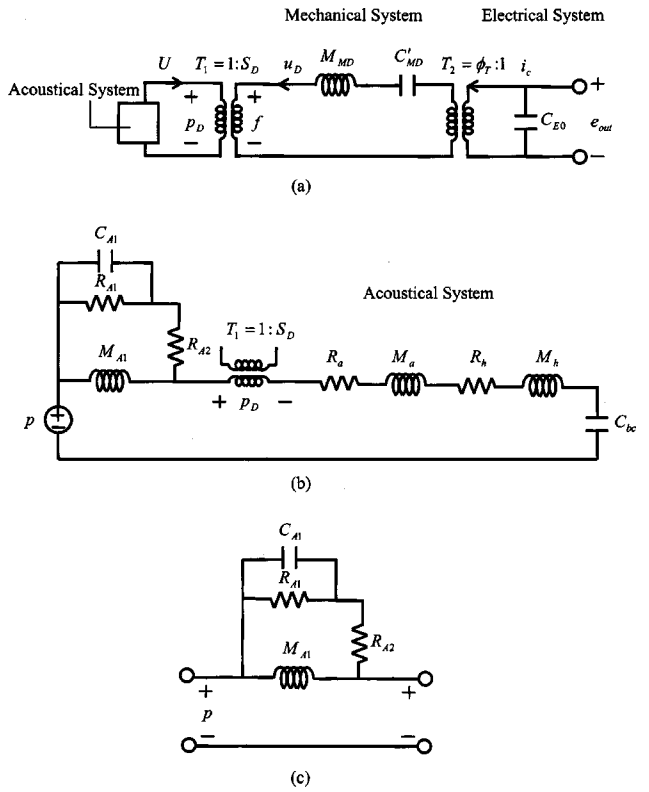

FIG. 2. The equivalent circuit based on electro-acoustical analogy of the condenser microphone. (a) Complete system composed of three coupled subsystems: the acoustical system, mechanical system, and electrical system. (b) Detailed circuit representation of the acoustical subsystem. (c) Circuit representation of the radiation impedances.

c is the sound speed in air, and L_m is the width of the square diaphragm. Similar to the approach taken by Skvor,[13] the effect of the air gap is modeled as equivalent resistance and mass elements in the acoustical domain: $R_a = (1.22\eta\pi b^2/h_a^3 L_m^2)B$ and $M_a = (0.102\rho_0\pi b^2/h_a L_m^2)B$, where $\eta = 1.86\times 10^{-5}$ N s/m^2 at 20 °C is the dynamic viscosity of air, h_a is the distance of the air gap, and B is defined as

$$B = \frac{1}{4}\ln\left(\frac{0.16b^2}{a_h^2}\right) - \frac{3}{8} + \frac{a_h^2}{0.16b^2} - \frac{a_h^4}{0.204b^4}, \tag{4}$$

where a_h is one-half of the width of the acoustical hole. The acoustical holes are modeled by an acoustical resistor $R_h = 12\eta h_b/b^2 L_m^2$ and mass $M_h = 24\rho_0 h_b a_h^2/5b^2 L_m^2$, where h_b is the thickness of the backplate. The acoustical compliance of the backchamber is $C_{\rm bc} = V_{\rm bc}/\rho_0 c^2$, where $V_{\rm bc}$ is the effective volume. A transformer T_1 with turn ratio 1: S_D (the area of diaphragm) accounts for the coupling of the acoustical system and mechanical system.

In the mechanical subsystem, the flexural rigidity of the diaphragm is predominantly due to the built-in stress acquired during MEMS fabrication. That renders the compliance of the diaphragm[5] $C_{MD} = 32/\pi^6\sigma_d h_d L_m^2$, where σ_d is the built-in stress and h_d is the thickness of the diaphragm. The mechanical mass of the diaphragm is given as $M_{MD} = \rho_d h_d L_m^2$, with ρ_d being the density of the diaphragm material. The mechanical-electrical coupling factor $\phi_T = C_{E0}/C_{EM}$, where C_{E0} is the capacitance due to the dc bias and is given by $C_{E0} = K_{\rm holes}\epsilon_b\epsilon_d\epsilon_0 L_m^2/(h_a\epsilon_b\epsilon_d + h_b\epsilon_d + h_d\epsilon_b)$, and $C_{EM} = (h_a - w_d)/V_{ba}$. Hence, the impedance matrix for the condenser microphone can be written as

$$\mathbf{Z}_{\rm mic} = \begin{bmatrix} Z_E & \dfrac{1}{j\omega C_{EM}} \\ \dfrac{1}{j\omega C_{EM}} & Z_M \end{bmatrix}, \tag{5}$$

where Z_E and Z_M are the equivalent electrical impedance and mechanical impedance, respectively. Note that this matrix is symmetric, as expected for a reciprocal electro-static transducer.

B. Constant beamwidth design based on the MUSIC template

Assume that M microphones are uniformly distributed with interelement spacing d. One benefit of using arrays is the improvement of SNR that can be assessed by the *array white noise gain* (WNG) defined as the increase of the SNR between one sensor and the output of the entire array[2]

$$G = \frac{\rm SNR_{array}}{\rm SNR_{sensor}}.$$

The array inputs ($\mathbf{x}$) and the output (y) are given, respectively, by

$$\mathbf{x} = s(t)\mathbf{a} + \mathbf{n},$$

$$y = \mathbf{w}^H\mathbf{x} = s(t)\mathbf{w}^H\mathbf{a} + \mathbf{w}^H\mathbf{n},$$

where $s(t)$ is the source signal, $\mathbf{a} = [1\ \exp[j\omega_c(d\sin\theta/c)]\cdots\exp[j\omega_c(M-1)d\sin\theta]/c]^T$ is called the "manifold vector" associated with the look angle (with respect to the normal) and the center frequency ω_c, $\mathbf{n}$ is the noise vector (assumed to be wide-sense stationary uncorrelated white noise with equal power σ_n^2), and $\mathbf{w}$ is the array coefficient vector. Hence,

$${\rm SNR_{array}} = \frac{E\{|s(t)\mathbf{w}^H\mathbf{a}|^2\}}{E\{|\mathbf{w}^H\mathbf{n}|^2\}} = \frac{E\{|s(t)|^2\}\mathbf{w}^H\mathbf{a}\mathbf{a}^H\mathbf{w}}{\sigma_n^2\mathbf{w}^H\mathbf{w}}.$$

Recognizing that

$$\frac{E\{|s(t)|^2\}}{\sigma_n^2} = {\rm SNR_{sensor}},$$

we end up with

$$G = \frac{\mathbf{w}^H\mathbf{a}\mathbf{a}^H\mathbf{w}}{\mathbf{w}^H\mathbf{w}}.$$

For example, the array WNG of a benchmark delay-sum array can be calculated by setting $\mathbf{w} = \mathbf{a}/M$:

$$G = \frac{(1/M^2)\mathbf{a}^H\mathbf{a}\mathbf{a}^H\mathbf{a}}{(1/M^2)\mathbf{a}^H\mathbf{a}} = \mathbf{a}^H\mathbf{a} = M.$$

The physical ground to result in this desirable feature is that uncorrelated noises tend to add or cancel with equal probability, while signals add in phase among the array channels.

Our goal is to design a narrow beam throughout a wide range of frequency. Pattern inversion by Fast Fourier Trans-

form (FFT) would not work well in this case because the aperture size of the four-element MEMS microphone array is just too small to produce any meaningful directivity. The spectral leakage of the truncation effect resulting from the small aperture simply destroys the directivity.

To achieve high directivity, a beamforming design based on MUSIC[3] template is adopted. In the MUSIC algorithm, the beam pattern is given as

$$S_{MU}(\theta)=\frac{1}{\mathbf{a}^H\mathbf{P_N}\mathbf{a}}, \tag{6}$$

where the angle θ and the manifold vector $\mathbf{a}$ are as defined previously, the projection matrix $\mathbf{P}_N=\Sigma_{m=J+1}^{M}\mathbf{u}_m\mathbf{u}_m^H$, J is the number of sources, and $\mathbf{u}_m$ is the mth eigenvector of the signal correlation matrix.

The beam pattern produced by the MUSIC is known to be highly directional. However, the MUSIC is mainly intended for finding direction of arrival and it requires intensive computation in the correlation matrix and eigendecomposition. Instead of direct implementation, we adopted a practical approach that utilizes the beam pattern resulting from MUSIC as a design template. That is, we seek the array filters to yield a narrow beam throughout a wide frequency range, as close as possible to that generated by the MUSIC template. To this end, a MUSIC template is generated using Eq. (6) with a source located at 0°, at frequency ω_c, e.g., one-half of the sampling frequency f_s. This template with identical subtending angle applies to all frequencies, hence the name ''constant beamwidth.'' The vector of the MUSIC template denoted as $\mathbf{s}_T=[S_{MU}(\theta_1)\cdots S_{MU}(\theta_{Q_d})]^T$ is created by uniformly sampling at Q_d discrete angles ($-90°\leqslant\theta_1\leqslant\cdots\leqslant\theta_{Q_d}\leqslant 90°$) the MUSIC beam pattern in Eq. (6). Next, P_w equally spaced discrete frequencies, $f_r(l)=(f_s/P_w)l$ ($1\leqslant l\leqslant P_w$, are selected within the Nyquist frequency. Let the filter gain at the mth element and the lth frequency be $w_m(l)$. The array pattern at the lth frequency can be written as

$$P_T(l,\theta)=\sum_{m=1}^{M} w_m^*(l)\exp\left(j2\pi f_r(l)\frac{(m-1)d\sin\theta}{c}\right). \tag{7}$$

The symbol * denotes complex conjugate. Since we wish to match an array pattern to the MUSIC template, i.e., $P_T(l,\theta)\approx S_{MU}(\theta)$, the model matching problem for a specific angle can be written as

$$\left[1\ \exp\left(j2\pi f_r(l)\frac{d\sin\theta}{c}\right)\ \cdots\ \exp\left(j2\pi f_r(l)\frac{(M-1)d\sin\theta}{c}\right)\right]\begin{bmatrix} w_1^*(l)\\ w_2^*(l)\\ \vdots\\ w_M^*(l)\end{bmatrix}=S_{MU}(\theta). \tag{8}$$

Assembling all angles, $\theta_1,\ldots,\theta_{Q_d}$ of Eq. (8) leads to the following matrix equation:

$$\begin{bmatrix} 1 & \exp\left(j2\pi f_r(l)\frac{d\sin\theta_1}{c}\right) & \cdots & \exp\left(j2\pi f_r(l)\frac{(M-1)d\sin\theta_1}{c}\right)\\ 1 & \exp\left(j2\pi f_r(l)\frac{d\sin\theta_2}{c}\right) & \cdots & \exp\left(j2\pi f_r(l)\frac{(M-1)d\sin\theta_2}{c}\right)\\ \vdots & \vdots & \ddots & \vdots\\ 1 & \exp\left(j2\pi f_r(l)\frac{d\sin\theta_{Q_d}}{c}\right) & \cdots & \exp\left(j2\pi f_r(l)\frac{(M-1)d\sin\theta_{Q_d}}{c}\right)\end{bmatrix}\begin{bmatrix} w_1^*(l)\\ w_2^*(l)\\ \vdots\\ w_M^*(l)\end{bmatrix}=\begin{bmatrix} S_{MU}(\theta_1)\\ S_{MU}(\theta_2)\\ \vdots\\ S_{MU}(\theta_{Q_d})\end{bmatrix}. \tag{9}$$

Let the array gain vector $\mathbf{w}(l)=[w_1^*(l)\cdots w_M^*(l)]^T$, $\mathbf{s}_T=[S_{MU}(\theta_1)S_{MU}(\theta_2)\ldots S_{MU}(\theta_{Q_d})]^T$, and

$$\mathbf{\Phi}(l)=\begin{bmatrix} 1 & \exp\left(j2\pi f_r(l)\frac{d\sin\theta_1}{c}\right) & \cdots & \exp\left(j2\pi f_r(l)\frac{(M-1)d\sin\theta_1}{c}\right)\\ 1 & \exp\left(j2\pi f_r(l)\frac{d\sin\theta_2}{c}\right) & \cdots & \exp\left(j2\pi f_r(l)\frac{(M-1)d\sin\theta_2}{c}\right)\\ \vdots & \vdots & \ddots & \vdots\\ 1 & \exp\left(j2\pi f_r(l)\frac{d\sin\theta_M}{c}\right) & \cdots & \exp\left(j2\pi f_r(l)\frac{(M-1)d\sin\theta_M}{c}\right)\end{bmatrix}. \tag{10}$$

The optimization problem can be written as a model matching problem

$$\min_{\mathbf{w}(k)}=\|\mathbf{s}_T-\mathbf{\Phi}(l)\mathbf{w}(l)\|_2, \tag{11}$$

where we choose the two norm $\|\cdot\|_2$ as the measure of match. In general, $\mathbf{\Phi}(l)$ is not square and $Q_d>M$. This ''overdetermined'' problem has the least-squares solution, $\mathbf{w}_{\mathrm{LS}}(l)=(\mathbf{\Phi}^H\mathbf{\Phi})^{-1}\mathbf{\Phi}^H\mathbf{s}_T$. Direct calculation of this pseudoinverse

often yields impractical solutions because $\mathbf{\Phi}(l)$ usually has very small singular values. Alternatively, Tikhonov regularization[14] is employed to solve this problem,

$$\mathbf{w}_{\mathrm{LS}}(l)=(\mathbf{\Phi}^H\mathbf{\Phi}+\beta\mathbf{I})^{-1}\mathbf{\Phi}^H\mathbf{s}_T. \tag{12}$$

By varying the parameter β, we can control the degree of regularization. Repeating the same procedure for P_w frequencies, the frequency response samples of the mth channel $w_m^*(l)$ can be obtained. To ensure real impulse responses, the following symmetry of frequency response must be applied

$$\begin{aligned} &H_m(0)=w_m^*(1),\\ &H_m(l)=w_m^*(l), \quad l=1,2,...,P_w,\\ &H_m(l)=w_m(l), \quad l=(P_w+1),(P_w+2),\ldots,(2P_w-1). \end{aligned} \tag{13}$$

The impulse response for each channel is then calculated with the aid of inverse FFT,

$$\begin{aligned} &h_m(k)=\frac{1}{2P_w}\sum_{l=0}^{2P_w-1}H_m(l)e^{j(\pi/P_w)lk},\\ &k=0,1,...,(2P_w-1). \end{aligned} \tag{14}$$

The resulting $h_m(k)$ is generally noncausal and circular shift is required to obtain a causal impulse response $h'_m(k)$.

Since we wished to simplify the array design on the chip, we chose simple implementation using analog filters. The frequency responses of the FIR filters $h'_m(k)$ are calculated

$$H'_m(l)=\sum_{k=0}^{2P_w-1}h'_m(k)e^{-j(\pi/P_w)lk}, \quad l=0,1,...,(2P_w-1). \tag{15}$$

The transfer functions of the analog filters are fitted with the MATLAB[15] command *invfreqs*. The resulting analog filters of array beamforming are realized by using active filter techniques such as the biquad circuits.[16]

C. Discussion of self-noise

The self-noise, or background noise, is defined as the *rms* output signal of the microphone in the absence of acoustical excitation. An in-depth comparison of the background noise in piezoresistive, eletret condenser, and ceramic microphones can be found in the paper by Zuckerwar *et al.*[17] Their analysis identified four types of background sources:

(1) mechanical Johnson noise due to the Brownian motion of air molecules impinging on the diaphragm, as represented by a damping resistor R_A, and $1/f$ (inversely proportional to frequency) noise generated by motion of the diaphragm;
(2) thermal channel noise generated in the FET channel;
(3) gate shot noise generated in the FET;
(4) electrical Johnson noise generated in the drain resistor R_d.

An equivalent circuit analysis in their work led to the following expression of the power spectral density of background noise in terms of the above-mentioned sources:

TABLE I. The parameters assumed in the FDM procedure for the quasistatic analysis of the MEMS condenser microphone.

Diaphragm material	Silicon nitride
Diaphragm length (L_m)	1 mm
Diaphragm thickness (h_d)	1 μm
Air gap distance (h_a)	3 μm
Acoustical holes number (N_m)	100
Acoustical holes side length (a_d)	60 μm
Vacuum permittivity (e_0)	8.85×10^{-12} F/m
Dielectric constant of the diaphragm (e_d)	7
Young's modulus (E)	300 GPa
Built-in stress (σ_d)	50 MPa
Poisson's ratio (υ)	0.2
Bias voltage (V_{ba})	50 V
Pressure loading (P_{sp})	5 Pa

$$J=\frac{S^2(4kTR_A+A_m^2/f)}{(1-\omega^2/\omega_0^2)^2+(\omega/\omega_0Q)^2}+\left[\frac{4(0.65)kT}{g_m}+\frac{2qI_G}{(\omega C_{t0})^2}\right](g_mR_d)^2+4kTR_d. \tag{16}$$

In Eq. (16), S is the diaphragm area, k is the Boltzmann constant, T is the absolute temperature, f and ω are frequencies in Hz and rad/s, respectively, ω_0 and Q are the resonance and quality factor of the diaphragm, A_m^2 is the $1/f$ coefficient, g_m is the FET transconductance, C_{t0} is the diaphragm-backplate capacitance, q is the electronic charge, and I_G is the gate leakage current. As revealed in Eq. (16), the gate shot noise introduces a $1/\omega^2$ component. At frequencies well below the resonance, the membrane damping (Brownian) component behaves as a Johnson noise source, which dominates over the channel and drain resistor components.

An important finding in their work is a formula obtained by linear regression that correlates the $1/f$ noise coefficient (b_1) with the diaphragm damping resistor R_A.

$$\log(b_1)=-24.1+1.89\log(R_A). \tag{17}$$

This empirical relationship applies to any diaphragm-based microphone, independent of detection technology. Because the diaphragm damping resistance increases inversely with diaphragm diameter, one may expect a significant $1/f$ component in MEMS microphones. As a caveat, the SNR of a microphone with overly damped diaphragm can be quite poor at low frequencies due to the associated $1/f$ noise.

III. NUMERICAL AND EXPERIMENTAL INVESTIGATIONS

A. Quasistatic analysis

Following the aforementioned iterative procedure of FDM, the quasistatic analysis was carried out to predict the collapse condition. Table I shows the parameters assumed in this simulation. The diaphragm material was assumed to be silicon nitride. The FDM calculation was based on a mesh with 25×25 grid points, covering a quarter of the diaphragm. The built-in stress=50 MPa and the Young's modulus=300 GPa is assumed for a 1 mm square diaphragm made of sili-

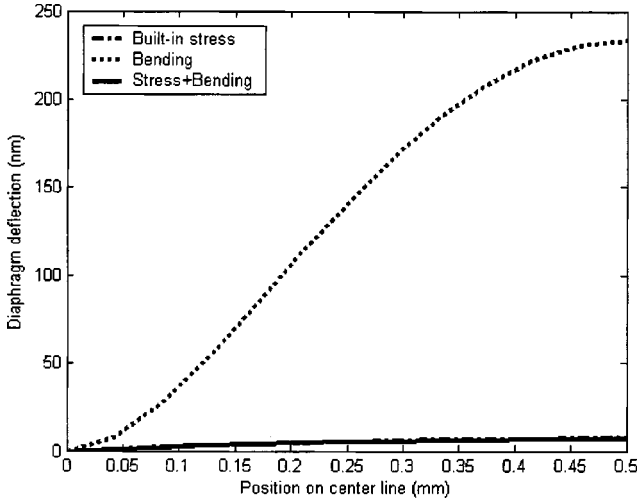

FIG. 3. The deflection profiles calculated by the FDM for three different conditions: bending effect only, built-in stress only, and "stress+bending." The diaphragm material was assumed to be silicon nitride. The built-in stress=50 MPa, the Young's modulus=300 GPa, and the diaphragm is subject to a uniform load of 5 Pa.

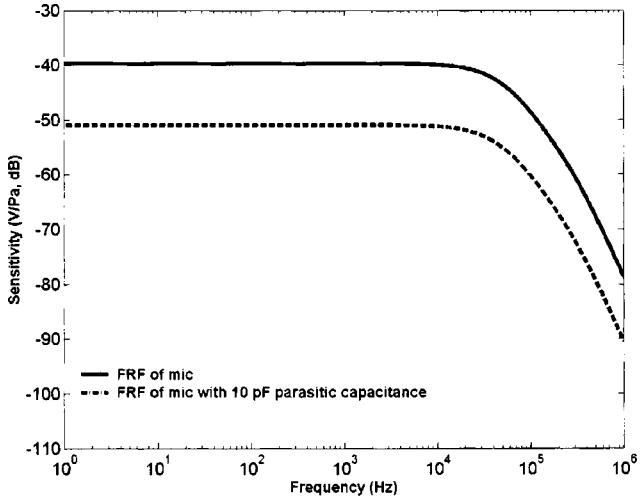

FIG. 4. The frequency response of the MEMS condenser microphone simulated by using the PSPICE. The effects of parasitic capacitance on sensitivity are also indicated in the same plot. In the simulation, 10 pF parasitic capacitance is assumed.

con nitride.[18] The calculated deflection profiles for three different conditions including "bending effect only," "built-in stress only," and "stress+bending" are shown in Fig. 3. The results indicate that the effect due to built-in stress is the dominant factor in overall diaphragm stiffness (about two orders higher than the bending effect). If only the built-in stress is considered, the maximum deflection at the center of the diaphragm reaches 7 nm, which is of the same order as the value 3.3 nm predicted by a parallel plate/linear spring model with the spring constant deduced from $C_{MD}=32/\pi^6\sigma_d h_d L_m^2$. Using this FDM model, the critical bias voltage near collapse was found to be 84 V for the present setting. For stability of the device, a conservative value, 60% of the previously calculated critical voltage, or 50 V, was thus selected to be the dc bias. The maximum static deflection of the diaphragm corresponding to such dc bias voltage attained 0.32 μm. Since the predicted deflection is far less than the nominal air gap (3 μm), the condenser microphone should be rather safe during operation without the risk of collapse.

TABLE II. The parameters assumed in the linear dynamic analysis of the MEMS condenser microphone.

Diaphragm material	Silicon nitride
Diaphragm length (L_m)	1 mm
Diaphragm thickness (h_d)	1 μm
Diaphragm density (ρ_d)	3440 kg/m^3
Backplate thickness (h_b)	20 μm
Air gap distance (h_a)	3 μm
Air density (ρ_0)	1.3 kg/m^3
Sound speed (c)	343 m/s
Dynamic viscosity of air (η)	1.86×10^{-5} N s/m^2
Acoustical holes number (N_m)	100
Acoustical holes side length (a_d)	60 μm
Vacuum permittivity (e_0)	8.85×10^{-12} F/m
Dielectric constant of the diaphragm (e_d)	2
Dielectric constant of the back plate (e_b)	2
Young's modulus (E)	300 GPa
Built-in stress (σ_d)	50 MPa
Poisson's ratio (υ)	0.2
Bias voltage (V_{ba})	50 V
Pressure loading (P_{sp})	5 Pa

B. Simulation of linear dynamic model and preamplifier circuits

The linear dynamic model is simulated with the aid of the PSPICE.[19] Table II summarizes the parameters assumed in this simulation. For simplicity, the linear analysis considers only the dynamic response, but not the dc deflection of the diaphragm caused by the bias voltage. The partial pull-down may change the effective compliance, increasing it or decreasing it depending on the proximity to snap-down. Increasing (decreasing) the compliance reduces the bandwidth (responsivity). Figure 4 shows the simulated frequency response between the incident sound pressure and the open-circuit output voltage of the microphone with a 1 mm$\times$1 mm

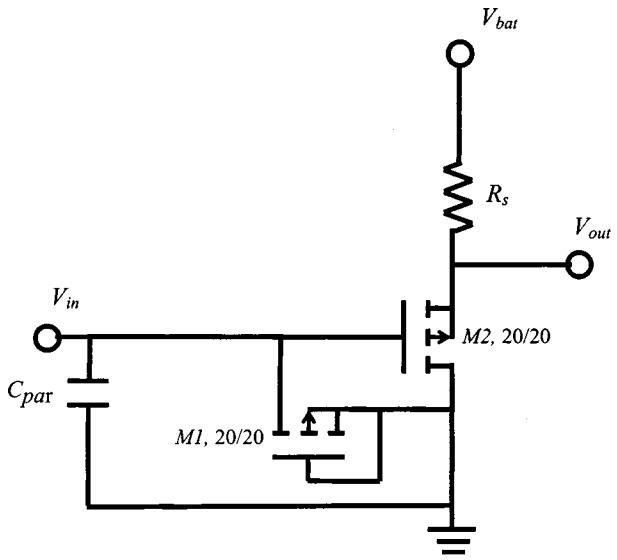

FIG. 5. The PMOS source-follower preamplifier. Two PMOS transistors of 20 μm/20 μm are selected to implement the amplifier.

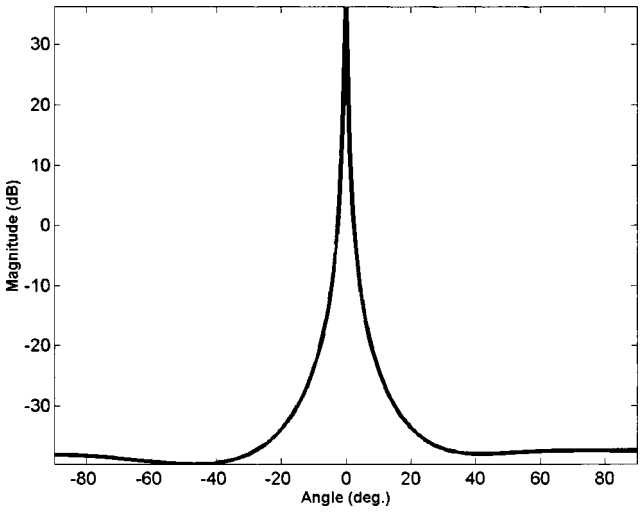

FIG. 6. A template obtained using MUSIC algorithm for $Q_d=181$, $P_w=256$. The beam pattern of this template exhibits a sharp peak at 0° with beamwidth approximately 10° for 40 dB attenuation.

square diaphragm. The 3 dB cut-off frequency occurs at 42.7 kHz. The frequency response is relatively flat throughout the band 0–42 kHz. The predicted open-circuit sensitivity was approximately −39.7 dB V/Pa, or 10.35 mV/Pa. The obtained sensitivity of MEMS microphone is comparable to conventional 1/4 in. condenser microphones.

The preamplifier shown in Fig. 5 is needed because of the relatively large output impedance of the condenser microphone. This buffering preamplifier utilizes the PMOS transistor as the bias element, owing to its high impedance characteristic. The optimum SNR is achieved by having much higher input impedance than the sensor impedance. After the preamplifier, the signal should be robust and can be taken off chip if necessary. However, on-chip integration of the buffering preamplifier is still important to reduce parasitics. Figure 4 also plots the microphone frequency response if the parasitic capacitance $C_{\text{par}}=10\,\text{pF}$ is present. The loss of sensitivity is frequency dependent. The sensitivity of MEMS

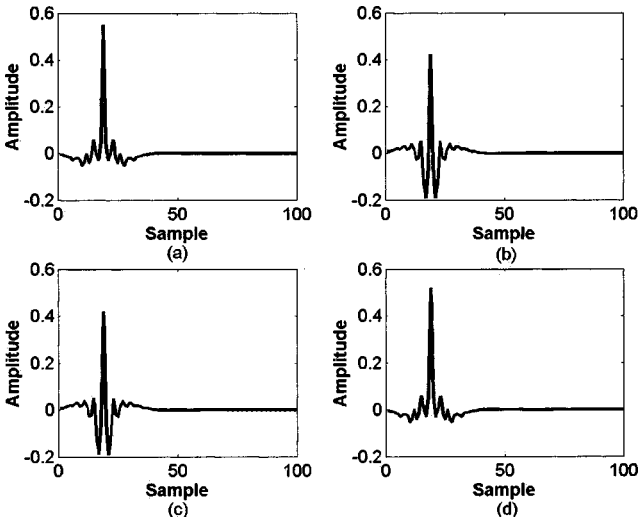

FIG. 7. The calculated impulse responses of the array FIR filters after the circular shift. (a) Channel one. (b) Channel two. (c) Channel three. (d) Channel four.

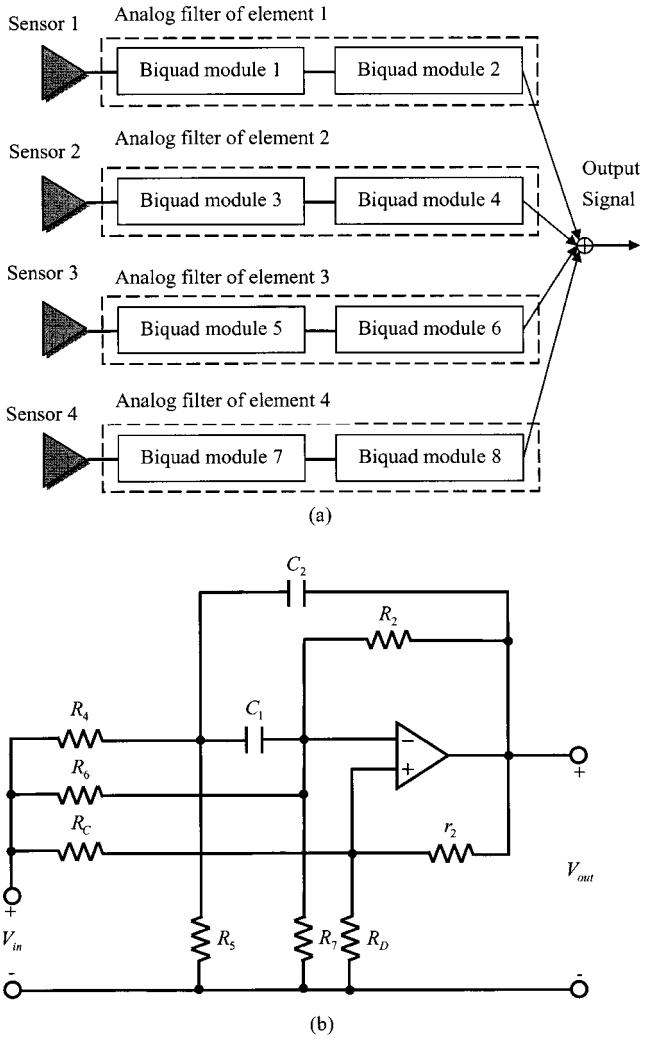

FIG. 8. Analog implementation of the array filters. (a) Four channel microphone array implemented by the biquad modules. (b) Detailed biquad circuit.

microphones is significantly reduced by 10 dB up to the cutoff frequency due to the parasitic capacitance. As evident from this result, the SoC design is crucial for MEMS microphones to yield sufficient sensitivity.

C. Constant beamwidth design based on the MUSIC template

In this section, the constant beamwidth design based on the MUSIC template is presented. The array contains four microphones in a line, with interelement spacing 5 mm. A MUSIC template is constructed using Eq. (6) for $Q_d=181$ discrete angles and $P_w=256$ discrete frequencies. The beam pattern of the resulting template is shown in Fig. 6. This is the MUSIC spectrum plotted in the angle space, and not the conventional Fourier spectrum. This template exhibits a sharp peak at 0° with beamwidth approximately 10° for 40 dB attenuation. After obtaining the frequency response of the microphone array, the impulse response, or the FIR filter coefficients, are calculated using inverse FFT. Circular shift is applied to obtain causal FIR filters. The resulting impulse responses of the array FIR filters are shown in Fig. 7. The MATLAB function *invfreqs* is used to find the continuous time

TABLE III. The parameters used in the analog biquad circuits of the array filters.

	Module 1	Module 2	Module 3	Module 4
R_2	$2.65\times10^3\ \Omega$	$3.64\times10^3\ \Omega$	$1.75\times10^3\ \Omega$	$5.60\times10^3\ \Omega$
R_4	$8.31\times10^2\ \Omega$	$7.68\times10^3\ \Omega$	$7.89\times10^2\ \Omega$	$1.07\times10^4\ \Omega$
R_5	Infinite	$3.44\times10^3\ \Omega$	Infinite	$3.18\times10^3\ \Omega$
R_6	Infinite	$4.34\times10^3\ \Omega$	Infinite	$2.83\times10^4\ \Omega$
R_7	$7.87\times10^2\ \Omega$	$2.22\times10^4\ \Omega$	$2.75\times10^2\ \Omega$	$1.74\times10^4\ \Omega$
R_C	$6.82\times10^3\ \Omega$	$2.39\times10^3\ \Omega$	$9.75\times10^3\ \Omega$	$5.25\times10^3\ \Omega$
R_D	$1.17\times10^3\ \Omega$	$1.72\times10^3\ \Omega$	$1.11\times10^3\ \Omega$	$1.24\times10^3\ \Omega$
r_2	$10.0\times10^3\ \Omega$	$10.0\times10^3\ \Omega$	$10.0\times10^3\ \Omega$	$10.0\times10^3\ \Omega$
C_1	0.01 μF	0.01 μF	0.01 μF	0.01 μF
C_2	0.01 μF	0.01 μF	0.01 μF	0.01 μF
	Module 5	Module 6	Module 7	Module 8
R_2	$2.26\times10^3\ \Omega$	$5.52\times10^3\ \Omega$	$1.64\times10^3\ \Omega$	$3.82\times10^3\ \Omega$
R_4	$7.88\times10^2\ \Omega$	$8.59\times10^3\ \Omega$	$8.15\times10^2\ \Omega$	$1.32\times10^4\ \Omega$
R_5	Infinite	$3.42\times10^3\ \Omega$	Infinite	$2.78\times10^3\ \Omega$
R_6	Infinite	$2.19\times10^4\ \Omega$	Infinite	$7.71\times10^3\ \Omega$
R_7	$4.26\times10^2\ \Omega$	$1.99\times10^4\ \Omega$	$2.76\times10^2\ \Omega$	$7.18\times10^4\ \Omega$
R_C	$6.83\times10^3\ \Omega$	$4.20\times10^3\ \Omega$	$1.63\times10^4\ \Omega$	$4.15\times10^3\ \Omega$
R_D	$1.17\times10^3\ \Omega$	$1.31\times10^3\ \Omega$	$1.07\times10^3\ \Omega$	$1.32\times10^3\ \Omega$
r_2	$10.0\times10^3\ \Omega$	$10.0\times10^3\ \Omega$	$10.0\times10^3\ \Omega$	$10.0\times10^3\ \Omega$
C_1	0.01 μF	0.01 μF	0.01 μF	0.01 μF
C_2	0.01 μF	0.01 μF	0.01 μF	0.01 μF

transfer functions of the array filters, applicable to the frequency range 0–8 kHz. Next, these array filters are implemented by using analog biquad circuits. Since each analog transfer function is of order four, two biquad circuits shown in Fig. 8 are cascaded to realize the array filter. The parameters of the biquad circuits are shown in Table III. The frequency responses obtained using the simulation and the experiment, respectively, are compared in Fig. 9. The equivalent filter weights at four frequencies are shown in Table IV. The magnitude and phase responses are in good agreement. It is worth noting that the 180° phase inversion at 6 kHz for elements 2 and 3 results in the increased directivity.

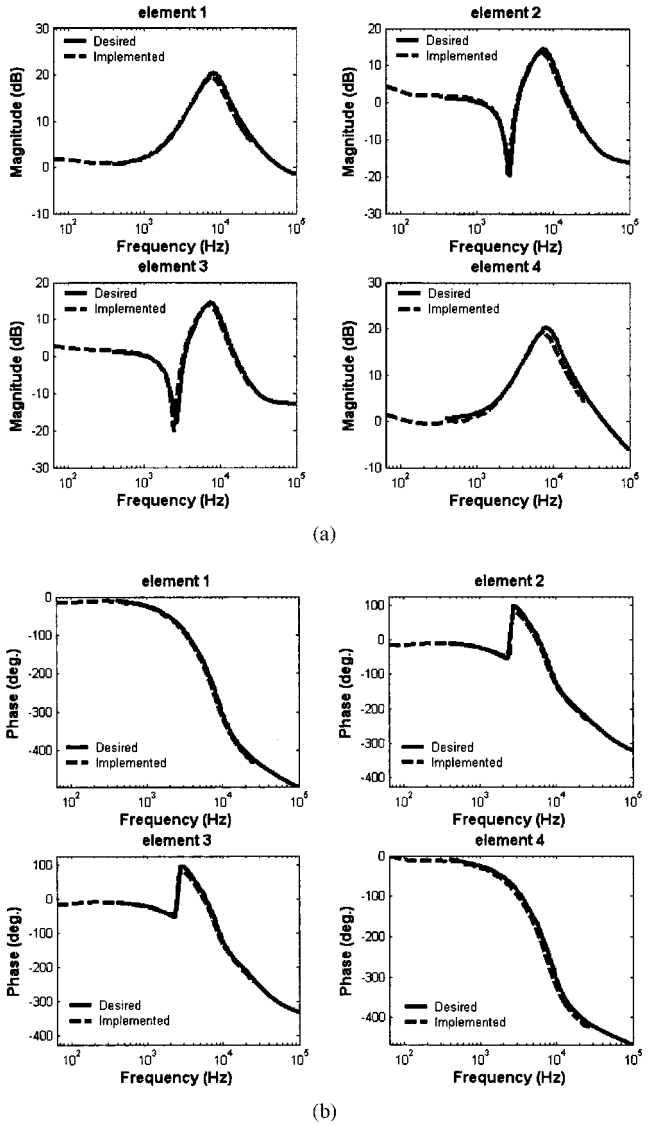

FIG. 9. Comparison of the frequency responses of the analog array filters obtained using the simulation and the experiment, respectively. (a) Magnitude response. (b) Phase response.

D. Experimental investigation

In order to verify the proposed array microphone system, experiments were carried out using a commercial product of silicon condenser microphone, SP0103NC3-2 of EMKAY. This omni-directional microphone has the frequency range of 100 Hz–10 kHz and sensitivity of −42 dB V/Pa at 1 kHz. With the same configuration as in the simulation, a linear array comprising four elements of such microphones with 5 mm interelement spacing was constructed, as shown in Fig. 10. The previously designed array filters for these four microphone elements were realized by using operational amplifier circuit. Using this experimental arrangement, tests were conducted inside an anechoic chamber to evaluate the SNR as well as the directivity for various microphone configurations.

First experiment compares the SNRs of one single microphone and the four-element array. In each case, the SNR is calculated by subtracting the power of the sensor output when the microphones are exposed to a white noise input band-limited to 20 kHz, from the power of the sensor output when the source is switched off. Hence, the noise would be the combination of the electronic self-noise and the background noise inside the anechoic chamber. The thus measured SNRs were found to be 24.1 and 35.5 dB for the single microphone and the array microphone, respectively. The SNR was improved by 11.4 dB, which was not far from the theoretical prediction, 12 dB. This experimental result suggests that array configuration is capable of enhancing SNR, as compared to one sensor element. However, the broadband measurement does not assess the performance at 6 kHz.

A second experiment compares the measured directional responses of the silicon microphones for three cases. The results are shown in Fig. 11. The first case labeled in Fig. 11(a) as ''one microphone'' refers to the measured directivity of a single microphone. The second case labeled in Fig. 11(b) as ''four microphones'' refers to the measured directivity produced by the direct sum of four microphone outputs. The third case labeled in Fig. 11(c) as ''four microphones with filters'' refers to the measured directivity produced by

TABLE IV. The equivalent filter weights and directivity indices at four frequencies.

Frequency (Hz)	Element	Weights: Magnitude (dB)	Weights: Phase (degree)	Directivity index (dB): Delay Sum	Directivity index (dB): MUSIC
	1	0.678 36	−15.87		
500	2	1.586	−13.619	0.004	0.004
	3	1.352	−13.576		
	4	0.475 28	−15.285		
	1	2.498 5	−27.868		
1000	2	0.602 49	−24.254	0.015	0.016
	3	0.360 99	−24.558		
	4	1.260 2	−31.171		
	1	5.659 4	−52.9		
2000	2	−4.723 8	−44.433	0.060	0.087
	3	−5.925 4	−43.677		
	4	4.780 6	−58.882		
	1	17.578	−194.06		
6000	2	12.482	−14.345	0.533	1.997
	3	12.652	−14.392		
	4	17.859	−202.77		

filtering the four microphone outputs with the aforementioned analog filter circuits. Comparison of the experimental results of cases 1 and 2 reveals that only minor improvement on directivity is obtained if the array outputs are directly summed. However, significant improvement on directivity is observed by comparing cases 1 and 3 if the array outputs are preprocessed by the previously designed constant beamwidth array filters. Specifically, at the frequency 6 kHz, deep notches appear at the end-fire direction and the 10 dB beamwidth reaches approximately $\pm 60°$ when the four microphone outputs are filtered with the aforementioned analog filter circuits. This is also revealed in the measured directivity indices at four frequencies in Table IV: 0.533 dB for the delay-sum array versus 1.997 for the MUSIC array at 6 kHz.

IV. CONCLUSIONS AND FUTURE PERSPECTIVES

The present work represents a multidisciplinary effort that combines the knowledge in electroacoustic transducers, array signal processing, and MEMS technology. The original contribution of this paper can be summarized as follows. First, by taking advantage of MEMS process, we have ac-

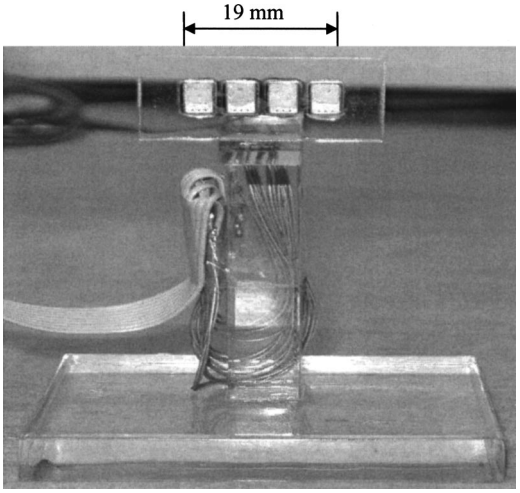

FIG. 10. Experimental arrangement of the four-element MEMS microphone array.

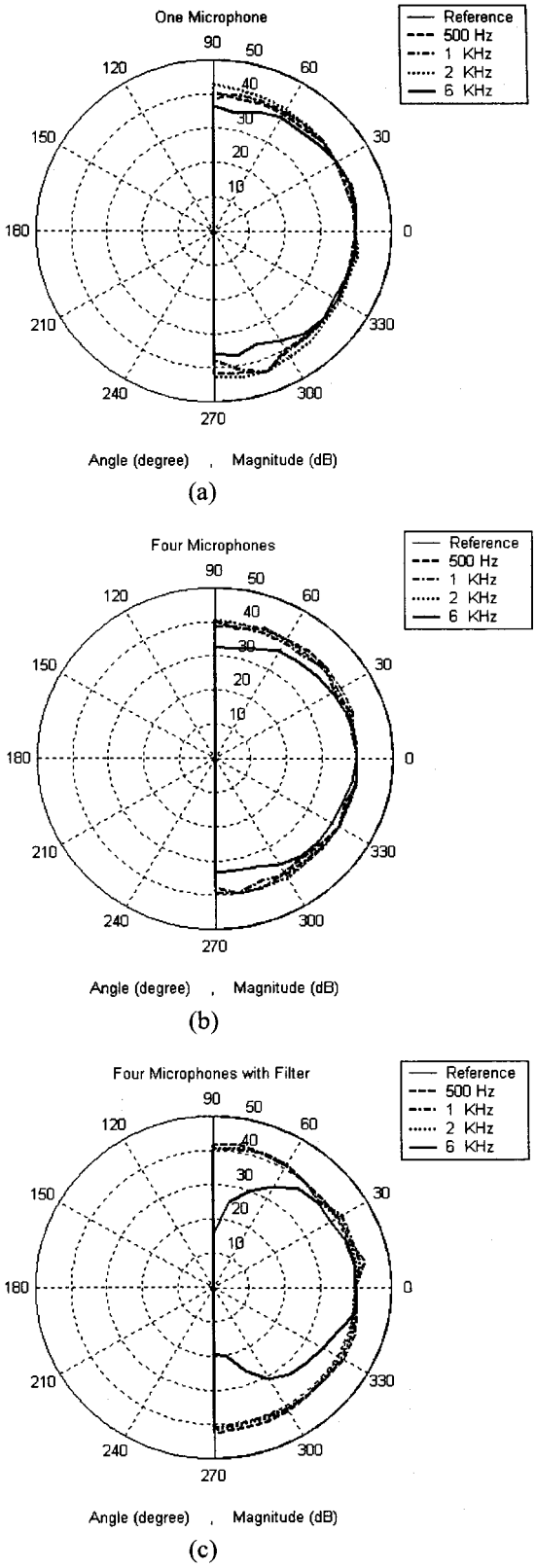

FIG. 11. Comparison of the measured directional responses of the silicon microphones. (a) The measured directivity of a single microphone. (b) The measured directivity produced by the direct sum of four microphone outputs. (c) The measured directivity produced by filtering the four microphone outputs with the analog filter circuits.

complished a system design which attempts to integrate a microphone array and the associated circuit on one chip. This differs from common approaches of microphone arrays that are predominantly based on single channel conventional microphones. Second, a beamforming technique more sophisticated than simple delay-sum method was developed in this study to improve the SNR and directionality. A least-squares model match procedure is proposed in the synthesis of the array filters to modify a DOA algorithm into a practical beamforming method. Third, in addition to the array beamforming design, the proposed idea was actually implemented and verified through experiments. The array filters are based on analog implementation that avoids the complexity of digital implementation.

Apart from the work accomplished in this study, certain limitations concerning the proposed system should be mentioned. Although the SNR is improved using the array configuration, little directivity is seen in the results of the array for frequencies below 5 kHz, which is the range for human speech. To further enhance the array directivity, a number of solutions are planned for the future research. The array configuration adopted in the present study is the so-called ''dimensional array.''[20] Directivity of such arrays is frequency-dependent and proportional to the aperture size of the array. Under the physical constraint of the small aperture of the present MEMS microphone, instead of the present analog implementation, high directivity can possibly be attained by using direct digital implementation of the beamforming algorithms. Yet, another possibility is using the so-called differential array.[20] In contrast to the dimensional arrays, the directivity of differential arrays is independent of frequency and aperture size. However, the price to pay using this approach is that its frequency response has ω^n (ω: frequency, n: element number -1) dependence. This is a characteristic with differential arrays—higher directivity but lower array WNG, and hence lower dynamic range. This suggests that equalization is required to boost the gain at the low frequencies, while suppressing the noise amplification at the high frequencies. This could be quite challenging for a MEMS device since the SNR is generally a crucial problem at low frequencies due to the previously mentioned $1/f$ noise component. The issue of whether both attributes—SNR improvement and good directivity in terms of array configurations—can be best compromised will be addressed in future research.

ACKNOWLEDGMENTS

The work was supported by the Nation Science Council in Taiwan, Republic of China, under Project No. NSC 91-2212-E009-032. The authors also wish to thank Knowles Electronics, Inc. for free samples of the MEMS microphones.

[1] M. Pedersen, ''A polymer condenser microphone realized on silicon containing preprocessed integrated circuits,'' Ph.D. dissertation, University of Twente, The Netherlands, 1997.
[2] H. L. Van Trees, *Optimal Array Processing* (Wiley, New York, 2002).
[3] R. O. Schmidt, ''Multiple emitter location and signal parameter estimation,'' IEEE Trans. Antennas Propag. **AP-34**, 276–280 (1986).
[4] D. Hohm and G. Hess, ''A subminiature condenser microphone with silicon nitride membrane and silicon back plate,'' J. Acoust. Soc. Am. **85**, 476–480 (1989).
[5] W. Kühnel and G. Hess, ''A silicon condenser microphone with structured back plate and silicon nitride membrane,'' Sens. Actuators, A **30**, 251–258 (1992).
[6] J. Bergqvist, ''Finite element modeling and characterization of a silicon condenser microphone with a highly perforated back plate,'' Sens. Actuators, A **39**, 191–200 (1993).
[7] H. F. Olson, *Acoustical Engineering* (Van Nostrand, Princeton, NJ, 1957).
[8] L. L. Beranek, *Acoustics* (McGraw–Hill, New York, 1954).
[9] M. Pedersen, W. Olthuis, and P. Bergveld, ''High-performance condenser microphone with fully integrated CMOS amplifier and DC-DC voltage converter,'' J. Microelectromech. Syst. **7**, 387–394 (1998).
[10] S. Chowdhury, M. Ahmadi, G. A. Jullien, and W. C. Miller, ''A MEMS Implementation of an Acoustical Sensor Array,'' Proceedings of the IEEE International Symposium on Circuits and Systems (ISCAS 2001), Sydney, Australia, 2 May, 2001, pp. 273–276.
[11] D. P. Arnold, T. Nishida, L. N. Cattafesta, and M. Sheplak, ''A directional acoustic array using silicon micromachined piezoresistive microphones,'' J. Acoust. Soc. Am. **113**, 289–298 (2003).
[12] S. P. Timoshenko and S. Woinowsky-Krieger, *Theory of Plates and Shells* (McGraw–Hill, New York, 1959).
[13] Z. Skvor, ''On the acoustical resistance due to viscous losses in the air gap of electrostatic transducers,'' Acoustica **19**, 295–299 (1968).
[14] A. Schuhmacher, J. Hald, K. B. Rasmussen, and P. C. Hansen, ''Sound source reconstruction using inverse boundary element calculations,'' J. Acoust. Soc. Am. **113**, 114–127 (2003).
[15] A. Grace, A. J. Laub, J. N. Little, and C. M. Thompson, *Matlab Control System Toolbox* (The Math Works, Natick, MA, 1999).
[16] W. K. Chen, *Passive and Active Filters: Theory and Implementations* (Wiley, New York, 1986).
[17] A. J. Zuckerwar, T. R. Kuhn, and R. M. Serbyn, ''Background noise in piezoresistive, electret condenser, and ceramic microphones,'' J. Acoust. Soc. Am. **113**, 3179–3187 (2003).
[18] M. Madou, *Fundamentals of Microfabrication* (CRC Press, New York, 1997).
[19] *OrCad, PSPICE, Mixed A/D Circuit Simulator* (Cadence Design Systems, San Jose, CA, 2002).
[20] G. M. Sessler and J. H. West, ''Directional Transducers,'' IEEE Trans. Audio Electroacoust. **AU-19**, 19–23 (1971).

A theoretical study for the propagation of rolling noise over a porous road pavement

Wai Keung Lui and Kai Ming Li[a)]
Department of Mechanical Engineering, The Hong Kong Polytechnic University, Hung Hom, Hong Kong

(Received 10 April 2003; revised 18 February 2004; accepted 29 March 2004)

A simplified model based on the study of sound diffracted by a sphere is proposed for investigating the propagation of noise in a hornlike geometry between porous road surfaces and rolling tires. The simplified model is verified by comparing its predictions with the published numerical and experimental results of studies on the horn amplification of sound over a road pavement. In a parametric study, a point monopole source is assumed to be localized on the surface of a tire. In the frequency range of interest, a porous road pavement can effectively reduce the level of amplified sound due to the horn effect. It has been shown that an increase in the thickness and porosity of a porous layer, or the use of a double layer of porous road pavement, attenuates the horn amplification of sound. However, a decrease in the flow resistivity of a porous road pavement does little to reduce the horn amplification of sound. It has also been demonstrated that the horn effect over a porous road pavement is less dependent on the angular position of the source on the surface of tires. [DOI: 10.1121/1.1751153]

PACS numbers: 43.50.Lj [DKW] Pages: 313–322

I. INTRODUCTION

The mechanisms of the generation of rolling noise caused by the interaction between a tire and the surface of a road[1–4] have received considerable attention over the past few decades. The noise comes from the vibrations of tires, the deflections from the surface of the tires, and the resulting displacement of air in the gap between the tire and the road.[4] In this case, the propagation of noise is thus confined to a small area enveloped by the surface of the road and the tire belt, forming a hornlike geometry. This hornlike configuration leads to a substantial amplification of the sound that is radiated. Schaaf and Ronneberger[5] demonstrated this effect experimentally, and theoretically identified this so-called ''horn effect'' by a simple image source model. The phenomenon of the horn effect amplification was also confirmed experimentally by Iwao *et al.*[1]

Kropp *et al.*[6] suggested a theoretical model based on multipole synthesis.[7] The model can provide a reasonable prediction of noise levels at mid and high frequencies for a tire placed on a hard surface. However, it overestimates the horn amplification effect at low frequencies. Since the Kropp model is a two-dimensional one, the model can only be valid for estimating the amplification of sound when the receiver is located in the plane of a tire. Although a three-dimensional (3D) model of a tire can, by virtue of the boundary element method (BEM),[8,9] be used for this purpose, the BEM can be a time-consuming tool for predicting the horn effect for practical geometries. Moreover, the BEM cannot be used in a parametric study of the influence of porous ground on the horn amplification. In the meanwhile, researchers have endeavored to develop three-dimensional (3D) analytical models based on the modal decomposition of the sound pressure[10] and on the asymptotic theories[11] for modeling the horn effect. However, these models either do not consider the effect of impedance ground or are somewhat inadequate in light of the recent advances in predicting the propagation of sound outdoors.[12–14] It is also worth pointing out that the two asymptotic models presented by Kuo *et al.*,[11] a ray theory for high frequencies and a compact body scattering model for low frequencies, were found to be accurate on a typical tire at frequencies of above 3 kHz and below 300 Hz, respectively. However, at the frequencies of practical interest (approximately 500–2500 Hz), it is not possible for the asymptotic models to provide satisfactory predictions.

In view of the intrinsic limitations of the existing numerical methods and analytical models for predicting the horn amplification, and the increase in interest in using porous pavement,[15–17] especially double-layer porous pavement,[18,19] to reduce tire/road noise, it is thus desirable to offer a simplified theoretical model to allow highway designers to carry out a parametric study when selecting appropriate materials for porous road pavement. The purpose of this paper is to explore a simplified theoretical model to account for the amplification of noise due to the propagation of sound in the tire/road gap over a porous road pavement. The theoretical model is centered on a recent analytical formulation to study the sound diffracted by a sphere above an impedance ground.[20,21] In Sec. II, we explain and justify the choice of our analytical model, as there are many other numerical models[6,8,11] devoted to the study of the acoustic interaction between tires and road. Section III gives numerical predictions based on our analytical formulation. These numerical results are compared with the published experimental data and theoretical predictions based on other computationally intensive schemes. A parametric study of the influence of porous ground on the horn effect is discussed in Sec. IV. Finally, in Sec. V, we offer some concluding remarks.

[a)]Author to whom correspondence should be addressed; Electronic mail: mmkmli@polyu.edu.hk

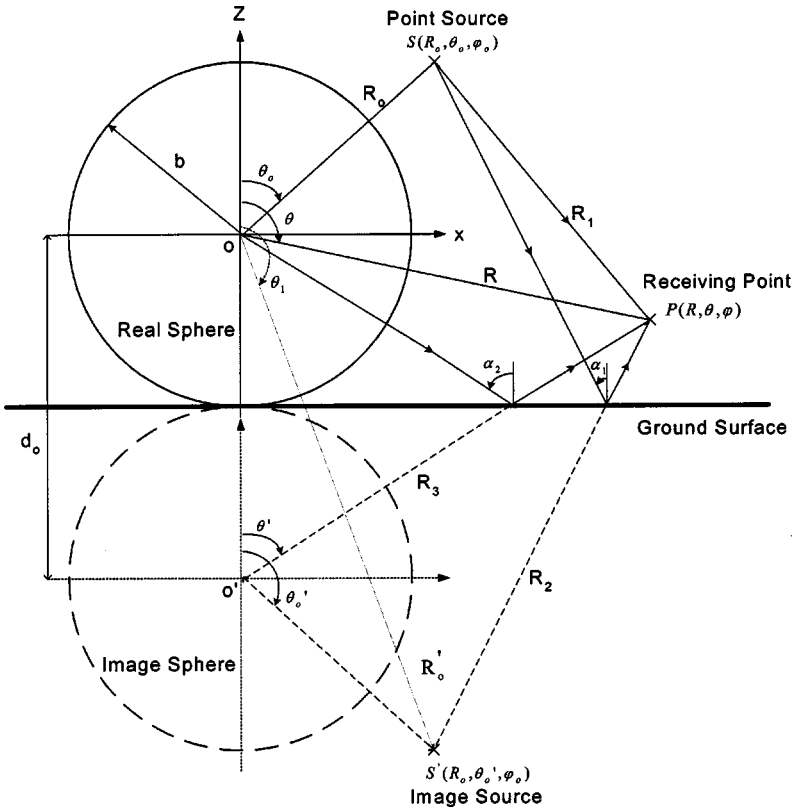

FIG. 1. Geometrical configuration of a sphere on flat ground irradiated by a point source.

II. THEORETICAL FORMULATION

A. Justifications for the use of a simple theoretical model

The dependence of the horn effect on different geometrical parameters such as the radius of the curvature of the tire shoulders, the load, the width of the tire, and the geometrical configurations of the source/receiver have been investigated through experiments, the formulation of exact boundary element (BEM)[8] and other asymptotic theories.[11] The experimental measurements showed that the effect of the horn amplification accounted for about 10–20 dB, with the maximum amplification occurring at the plane of the tire. In view of the fact that the amplification of sound reaches a maximum at the plane of the tire, as shown by the published experimental results,[6,8,11] we hypothesize that the horn effect induced by the semi-closed space formed between the curved surface of a sphere and the ground surface is similar to that created by the hornlike geometry formed between the tire belt and the surface of the road. Although this hypothesis may at first appear questionable, we will validate it through detailed comparisons of the numerical predictions using the published experimental data described in Sec. III.

B. Review of sound diffracted by a sphere above an extended reaction ground

When an object is subject to radiation from a point source located at $\mathbf{x}_s$, the total sound field at point $\mathbf{x}$ is governed by the Helmholtz equation, expressed in terms of a scalar velocity potential, ϕ, as follows:

$$\nabla^2\phi + k_o^2\phi = -\delta(\mathbf{x}-\mathbf{x}_s), \tag{1}$$

where $k_o = \omega/c$ is the wave number, ω is the angular frequency of the source, and c is the sound speed in air. For a sphere resting on a ground surface, the total sound field at the receiver is contributed by the direct waves, by scattered waves from the sphere, and by waves disseminating from the image source and the image sphere, as shown in Fig. 1. The origin is taken as the center of the sphere. In this situation, the acoustical properties of the porous medium are crucial in determining the sound field produced due to the combination of direct and boundary-reflected sound waves. In our earlier study,[20,21] we developed a numerical scheme to compute the diffraction of sound by a sphere located above an impedance ground. The scheme was based on the expansion of the wave field in terms of a series of associated Legendre functions. Here, we extend the solution to model the corresponding sound field above an extended reaction ground. In particular, the road pavement is modeled as either a single or double porous layer above a hard-backed layer. In fact, Bérengier *et al.*[16] used a hard-back layer model to study the acoustical characteristics and propagation effects of porous road pavements.

The effect of a single or double porous layer above a hard-backed layer on the radiation from a point source can be modeled by an approximate analytical solution developed by Li *et al.*[14] for the reflection of a spherical wave. By introducing an effective admittance, β_g, the sound field contributed from the point source above a hard-backed layer surface can be approximated by

$$\phi_T^i = \frac{e^{ik_o R_1}}{4\pi R_1} + Q_1 \frac{e^{ik_o R_2}}{4\pi R_2}, \tag{2}$$

where

$$Q_1 = V + (1-V)F(\varpi), \tag{3a}$$

$$V = \frac{\cos\alpha_1 - \beta_g}{\cos\alpha_1 + \beta_g}, \tag{3b}$$

$$F(\varpi) = 1 + i\sqrt{\pi}\varpi e^{-\varpi^2}\,\mathrm{erfc}(-i\varpi), \tag{3c}$$

$$\varpi = +\sqrt{\frac{1}{2} ik_o R_2}(\cos\alpha_1 + \beta_g). \tag{3d}$$

For a single porous layer above a hard-backed layer, the effective admittance is

$$\beta_g = -im_1\sqrt{n_1^2 - \sin^2\alpha_1}\,\tan(k_o l_1\sqrt{n_1^2 - \sin^2\alpha_1}), \tag{4}$$

and for a double layer with a hard backing, the effective admittance can be determined according to

$$\beta_g = -im_1\sqrt{n_1^2 - \sin^2\alpha_1}\left\{\frac{\tan(k_o l_1\sqrt{n_1^2 - \sin^2\alpha_1}) + \overline{g_1}\tan(k_o l_2\sqrt{n_2^2 - \sin^2\alpha_1})}{1 - \overline{g_1}\tan(k_o l_1\sqrt{n_1^2 - \sin^2\alpha_1})\tan(k_o l_2\sqrt{n_2^2 - \sin^2\alpha_1})}\right\}, \tag{5}$$

where

$$\overline{g_1} = \frac{m_2\sqrt{n_2^2 - \sin^2\alpha_1}}{m_1\sqrt{n_1^2 - \sin^2\alpha_1}}, \tag{6a}$$

$$n_j = k_j/k_o \quad \text{and} \quad m_j = \rho_o/\rho_j \quad \text{with} \quad j = 1,2. \tag{6b}$$

Here, ρ_o is the density of air, g_1 is a dimensionless ratio characterizing the change of media properties from the first layer to the second, R_2 is the distance between the image source and the field point, α_1 is the angle of incidence of the reflected wave, and l_1 and l_2 are the thickness of the first and second layers, respectively. According to the phenomenological model for porous pavement proposed by Bérengier *et al.*,[16] the complex wave number and characteristic impedance can be written as

$$k = k_o q F_\mu^{1/2}[\gamma - (\gamma-1)/F_\theta]^{1/2}, \tag{7}$$

$$Z_c = (\rho_o c q/\Omega)F_\mu^{1/2}[\gamma - (\gamma-1)/F_\theta]^{-1/2}. \tag{8}$$

The functions

$$F_\mu = 1 + if_\mu/f \tag{9}$$

and

$$F_\theta = 1 + if_\theta/f \tag{10}$$

are related to the viscous and thermal dependencies, which are given respectively by

$$f_\mu = \Omega R_s/(2\pi\rho_o q^2), \tag{11}$$

$$f_\theta = R_s/(2\pi\rho_o N_{\mathrm{pr}}). \tag{12}$$

In the above equations, γ is the specific heat ratio, N_{pr} is the Prandtl number, R_s is the airflow resistivity of the porous structure, Ω is the porosity of the air-filled connected pores, and q^2 is the tortuosity. These last three parameters can be independently determined, directly or indirectly, which makes this simple model for porous road pavements attractive. In addition, the density ratio m_1, the index of refraction n_1, and the normalized surface impedance $Z = Z_c/\rho_o c$ are related according to the following relationship:

$$\frac{1}{Z} = m_1 n_1. \tag{13}$$

Hence, by using Eqs. (4)–(13), we can determine the effective admittance for a given frequency and other physical parameters.

Since the scattered waves from the sphere above a ground surface are spherically spreading waves, the total scattering sound field due to the presence of a hard-backed porous ground can be calculated by[20,21]

$$\phi_T^s = \phi^s + Q_2\phi_r^s, \tag{14}$$

where ϕ^s is the scattered sound field from a real sphere in free space and ϕ_r^s is the scattered sound field from the image sphere. The spherical wave reflection coefficient Q_2 for a scattered wave reflection on an impedance ground can be obtained in a similar formulation as Eq. (3a). In fact, Q_2 can be computed by replacing α_1 and R_2 in Eqs. (3)–(6) with α_2 and R_3, respectively, where R_3 is the distance of separation between the center of the image sphere and the field point, and α_2 is the angle of incidence of the scattered wave on the porous layer. The total sound field above a hard-backed porous layer can now be represented in a real spherical coordinates system, which consists of four components: direct source, scattered waves from the real sphere, image source, and scattered waves from the image sphere, as follows:[20,21]

$$\phi^T = \phi^i + Q_1\phi_r^i + \phi^s + Q_2\phi_r^s$$

$$= \sum_{n=0}^{\infty}\sum_{m=0}^{n} a_{mn}h_n^{(1)}(k_oR_o)j_n(k_oR)P_n^m(\cos\theta)P_n^m(\cos\theta_o)\cos m(\varphi-\varphi_o) + Q_1\sum_{n=0}^{\infty}\sum_{m=0}^{n} a_{mn}h_n^{(1)}(k_oR_0')j_n(k_oR)$$

$$\times P_n^m(\cos\theta)P_n^m(\cos\theta_1)\cos m(\varphi-\varphi_o) + \sum_{n=0}^{\infty}\sum_{m=0}^{n} b_{mn}h_n^{(1)}(k_oR_o)h_n^{(1)}(k_oR)P_n^m(\cos\theta)P_n^m(\cos\theta_o)\cos m(\varphi-\varphi_o)$$

$$+ Q_2\sum_{q=0}^{\infty}\sum_{m=0}^{q}(-1)^{m+q}b_{mq}h_q^{(1)}(k_oR_o)P_q^m(\cos\theta_o)\sum_{n=m}^{\infty} A_{mn}^{mq}(k_od_o)j_n(k_oR)P_n^m(\cos\theta)\cos m(\varphi-\varphi_o), \quad (15)$$

where

$$a_{mn} = \frac{i(n-m)!(2n+1)(2-\delta_{m0})k_o}{4\pi(n+m)!}, \quad (16)$$

and δ_{m0} is a Kronecker delta function that vanishes if $m \neq 0$. The translation coefficient $A_{mn}^{mq}(k_od_o)$ is given in Refs. 20 and 21. The unknown scattering coefficient b_{mn} can be determined by imposing the rigid boundary condition on the surface of the sphere if it is regarded as acoustically hard. As a result, we can get a set of coupled linear complex equations for solving b_{mn} in a matrix form, as follows:

$$\mathbf{XB} = \mathbf{D}. \quad (17)$$

The diagonal elements of **X** are

$$X_{mn} = h_n^{(1)}(k_oR_o)P_n^m(\cos\theta_o) + Q_2T_n(-1)^{m+n}h_n^{(1)} \times (k_oR_o)P_n^m(\cos\theta_o)A_{mn}^{mn}(k_od_o), \quad (18a)$$

the off-diagonal elements of **X** are

$$X_{nq} = Q_2T_n(-1)^{m+q}h_q^{(1)}(k_oR_o)P_q^m(\cos\theta_o)A_{mn}^{mq}(k_od_o), \quad (18b)$$

and the elements of the vector **D** are

$$D_n = -a_{mn}T_n[h_n^{(1)}(k_oR_o)P_n^m(\cos\theta_o) + Q_1h_n^{(1)}(k_oR_o') \times P_n^m(\cos\theta_1)], \quad (18c)$$

with

$$T_n = \frac{j_n'(k_ob)}{h_n'(k_ob)}. \quad (18d)$$

The system of complex equations in Eq. (17) can be truncated to an order of N; that is, the number of sums from n or $q=0$ to N, depending on the degree of accuracy required. The complex matrix **X** has an order of $(N+1-m)\times(N+1-m)$, and the complex vectors **B** and **D** have dimensions of $(N+1-m)$ for each m, where m ranges from 0 to N. The details of the numerical techniques, which can be found elsewhere,[20,21] are not repeated in this paper for brevity.

III. COMPARISONS WITH PUBLISHED RESULTS

According to the hypothesis stated in Sec. II above, the tire belt can be replaced by a sphere for predicting the horn effect of a tire/road interaction. In order to apply this simplified model to investigate the influence of porous ground, it is important to validate the hypothesis. There are published experimental results and BEM calculations for the interaction of a tire with hard ground. In this section, these published results are compared with the predictions computed by the simplified model.

Based on the experimental configuration described in Ref. 8, the following geometrical configuration is used (unless stated otherwise) for all of the numerical calculations throughout this section. The sphere, which has a diameter of 0.64 m, is placed on the ground, and a point source is located 2.57 m from the center of the sphere and 0.72 m above the surface of the ground. In the graphs, the amplification due to the horn effect is plotted against the frequency. Throughout this section, amplification is defined as the difference in sound levels with and without the presence of the sphere. Equation (15) is used in the computations, with Q_1 and Q_2 set to 1 in the case of hard ground. For all of the simulations in this section, the receiver is located on the ground at a distance d from the contact point and at an offset distance o from the center of the sphere (see Fig. 2). The computed results are plotted for comparison with the published experimental results.

Figure 3, which is extracted from Fig. 11 of Ref. 8, shows the experimental measurements for a cylinder and an unloaded tire for different distances d from the contact point. In the same figure, we also show the theoretical predictions for the amplification of sound, calculated by assuming a hard sphere rested on a hard ground for the same geometrical configurations. In these measurements and numerical predic-

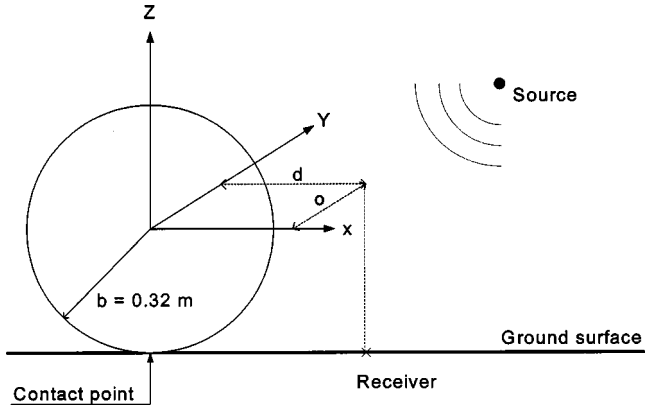

FIG. 2. A rigid sphere on flat ground to simulate the horn effect. The receiver is located on the ground at a distance d from the contact point (the center of the sphere) and at an offset distance o from the contact point.

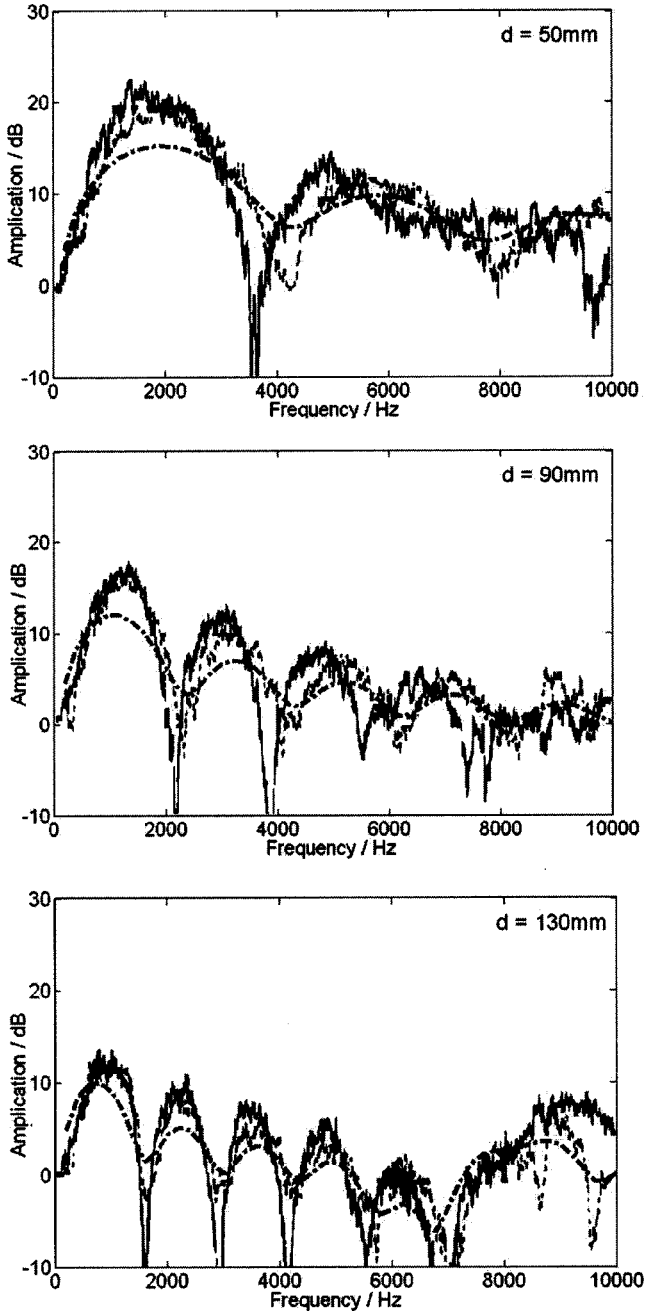

FIG. 3. Comparison of sound amplification by a rigid sphere simulation model to the experimental measurements of cylinder/tire (Fig. 11 in Ref. 8) on a hard ground for different distances *d*. The receiver is located at the centerline of the scatter. The solid line and dotted line represent the experimental results of a cylinder and tire, respectively. The dash-dotted line represents the result predicted by the simulation model.

tions, the receiver was located at the centerline, $o=0$, of the respective scatter. It can be seen from Fig. 3 that, according to our model, the predicted dips are shallower than those shown in the experimental measurements for the cylinder and the tire. According to Graf *et al.* with respect to the BEM results shown in Fig. 12 of Ref. 8, the effect of the rounded shoulders of the tire can broaden the dips of the acoustic interferences, reduce the maximum amplification, and shift the dips to higher frequencies. This can be confirmed in our numerical predictions because a sphere has a much larger radius curvature of the round edges than an unloaded tire.

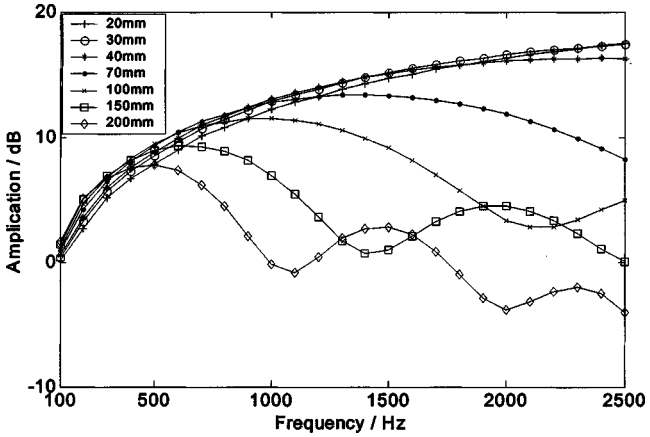

FIG. 4. Dependence of sound amplification on *d* by a rigid sphere simulation model (compared to Fig. 4 in Ref. 8).

Not surprisingly, the predicted amplification spectra are in closer agreement with the measured results of an unloaded tire than with the corresponding results of a cylinder. This is understandable, because the hypothesis of using a sphere to replace a tire belt is used in our numerical simulations.

The dependence of the amplification on *d* is plotted in Fig. 4. It is obvious that at low frequencies the amplification is independent of *d*. The amplifications give almost no differences for sufficiently small values of *d* (less than 40 mm). Our theoretical predictions show good qualitative agreement with the trends shown in the experimental observations found in Ref. 8; see their Fig. 4. In Fig. 5 of this paper, the results of the simulation of different *d* at various offset distances *o* of the receiver away from the center of the sphere are shown for comparison with the experimental measurements obtained from Fig. 16 in Ref. 8. Our theoretical model is consistent with this in predicting the general trend of the amplification due to the horn effect: it decreases as the offset distance increases. We note that, as shown in Figs. 4 and 5, the interference minima are less distinct in the predicted results according to the numerical model presented in this paper. This is due to the corner effect of the sphere.

The ability of the proposed simulation model to describe the amplification of sound by a smooth tire is compared with the ray theory developed by Kuo *et al.*,[11] as shown in Fig. 6. The numerical results predicted by the ray theory and the measurements given in Fig. 6 are extracted from Fig. 5 of Ref. 11. The locations of the microphone and receiver are given in Fig. 6, where *d* is the distance of the source from the contact patch, *L* is the distance of the receiver from the contact patch, and ø is the angle made by the receiver with the ground (see Figs. 2 and 5 of Ref. 11). It is of interest to point out that our proposed simulation model seems to give closer agreement with the experimental data than the ray model. However, as in our previous observations, the interference dips predicted by our simulation model are consistently shallower than those obtained by the ray model and measurements.

It is worth noting that use of a sphere to represent a tire has somewhat limited the quantitative accuracy of the numerical model proposed in Sec. II. Indeed, it can be seen from Fig. 3 that the BEM results of a cylinder and the ex-

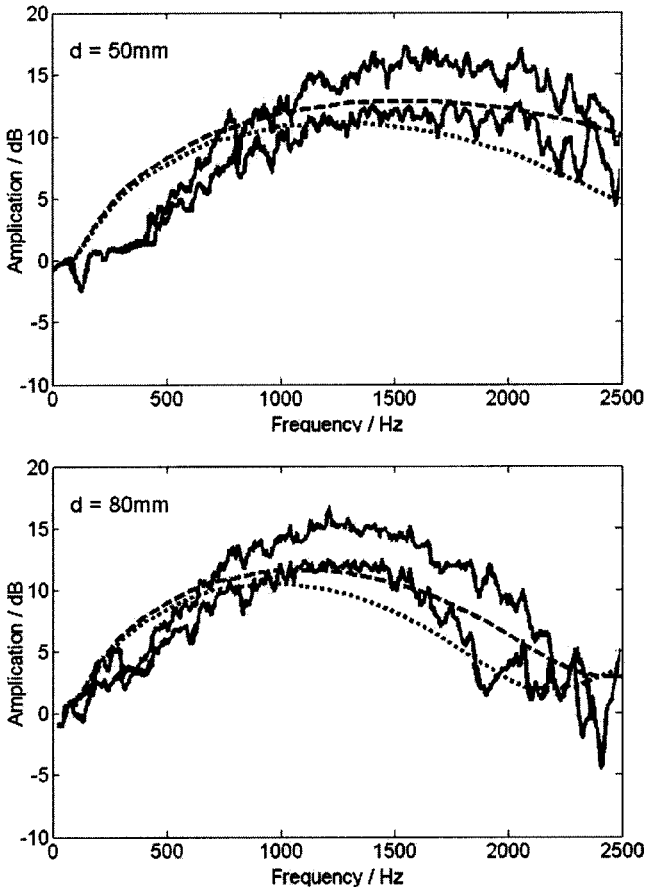

FIG. 5. Comparison of sound amplification by a rigid sphere simulation model to the experiments for a cylinder (Fig. 16 in Ref. 8) on a hard ground for different offset distances o from the centerline of the scatter. The solid lines represent the experimental results of a cylinder. The dashed line and dotted line represent the simulation results of an offset distance 5 and 8 cm, respectively.

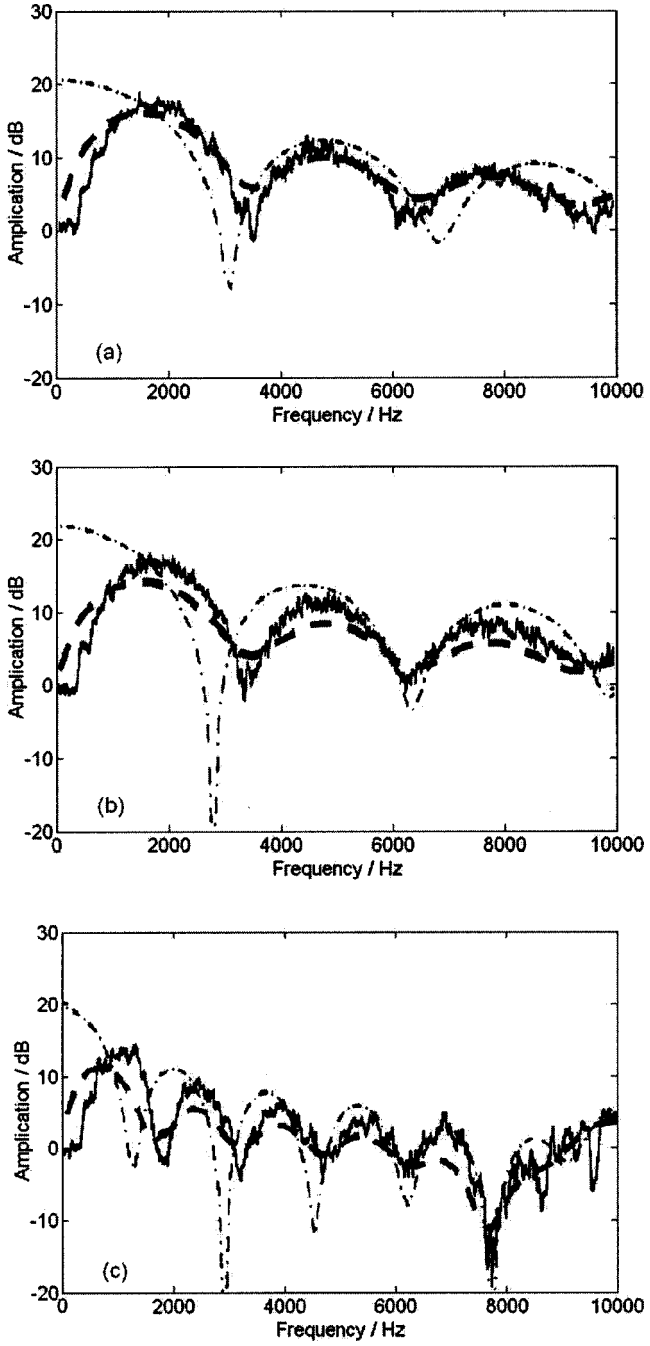

FIG. 6. Comparison of sound amplification by a rigid sphere simulation model with smooth tire measurement and ray theory given in Fig. 5 of Ref. 11. The solid line and dash-dotted line represent results from smooth tire measurement and ray theory, respectively. The dashed line represents the simulation result. (a) $d=60$ mm, $(L,\phi)=(2.67\text{ m},15°)$; (b) $d=60$ mm, $(L,\phi)=(1.92\text{ m},2.4°)$; (c) $d=120$ mm, $(L,\phi)=(2.67\text{ m},15°)$.

perimental data of a tire are different from our predicted results by an order of 5 dB. However, we stress that an objective of our present study is to exploit the acoustic characteristic of porous road pavement for reducing the amplification of sound due to the horn effect. As our model has proved to be accurate in predicting the general trend of the amplification spectra at a much reduced computational time especially at high frequencies, we shall use it in a parametric study of porous road pavement, as detailed in Sec. IV. This detailed study can lay a foundation to optimize the design of porous road pavements for reducing noise caused by the interaction between tire and road.

Next, we verify the validity of Li's approximate analytical model[14] for the propagation of sound above a hard-backed layer of porous ground, as follows. Bérengier's published results (Fig. 7 of Ref. 16) are compared with the numerical predictions according to the approximate model for porous ground (see Fig. 7). The geometrical configurations and other details of the porous pavement can be found in Ref. 16. We can confirm that Li's prediction results are consistent with Bérengier's numerical results. Hence, our proposed sound propagation model for a spherical wave propagated above a porous road pavement can be confidently adopted to study the horn effect above a porous road pavement.

Finally, we end this section by comparing our predictions with those calculated by a 2D-BEM model for a rigid cylinder on porous ground. The predicted results of the 2D-BEM model are taken from Fig. 2 of Ref. 10. Figure 8 shows the geometrical locations of a point source and receiver of the simulation. In this numerical example and other simulations shown in Sec. IV, unless otherwise stated, the sound source is assumed to be localized at a single point on the

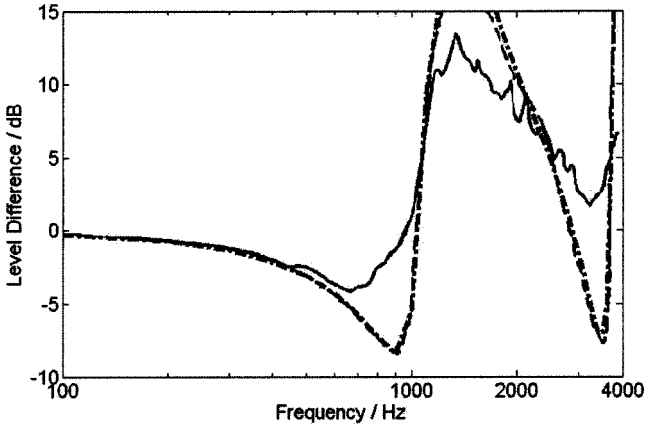

FIG. 7. Reproduction of Bérengier's results (Fig. 7 in Ref. 16) of level differences obtained above a porous asphalt using Li's approximate analytical model for sound propagation above a finite hard-backed layer of porous ground.[14] Solid line: measurement results by Bérengier; dashed line: results predicted by Bérengier; dash-dotted line: results predicted by Li.[14]

surface of a sphere with a radius of 0.3 m and situated at an angle of $\psi = 5°$ measured from the vertical axis. The receiver is located at a horizontal distance of 1 m from the contact point of the sphere and situated at a height of 0.3 m above the porous pavement. The acoustical structural parameters of the porous layer are $R_s = 20\ \mathrm{kN\,s\,m^{-4}}$, $\Omega = 15\%$, $q^2 = 3.5$, and $l_1 = 0.04$ m. It is shown in Fig. 9 that our model gives comparable spectra as that computed by the 2D-BEM model. Again, the difference in the amplification factor is of an order of about 5 dB. This observation is consistent with the earlier simulation results for hard ground, shown in Fig. 3. It is worth pointing out that the discrepancies between the predictions made by our model and the 2D-BEM model for porous ground are less than that for hard ground. The differences in magnitude are less than 3 dB in the frequency range between 800 Hz to 4000 Hz in the case of the amplification of sound over porous ground.

IV. A PARAMETRIC STUDY OF POROUS ROAD PAVEMENT ON THE HORN EFFECT

Section III presents a set of comprehensive numerical comparisons with published experimental data and theoretical predictions of horn amplification above the surface of the ground. It is reassuring to find that the numerical results of our simulation model can give a reasonable agreement with the general trend of the published experimental data and the-

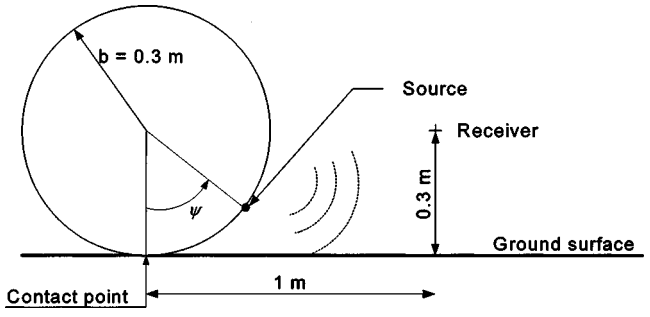

FIG. 8. Localized sound source located on the surface of the sphere at an angle ψ measured from the vertical axis.

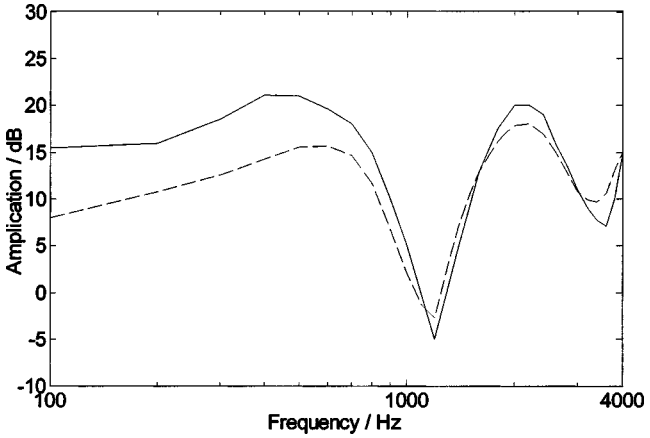

FIG. 9. Comparison of the amplification of sound by a rigid sphere simulation model to a 2D-BEM model for a rigid cylinder on porous ground. The acoustical structural parameters of the porous layer are $R_s = 20\,000\ \mathrm{N\,s\,m^{-4}}$, $\Omega = 15\%$, $q^2 = 3.5$, and $l_1 = 0.04$ m. (Solid line: 2D-BEM model; dotted line: rigid sphere simulation model.)

oretical predictions based on other numerical schemes. We can now use our prediction model to explore the effect of sound propagation due to a point source located in the gaps between the tire and a porous road pavement. The road pavement has either a single layer or double layers. The influence of porous road pavement on the horn effect can be investigated by using Eq. (15). The phenomenological model as described in Eqs. (7)–(12) can be employed to determine the effective admittance of the porous layer by using Eq. (13). The horn effect considered in this section is the difference in sound pressure level due to a localized sound source on the surface of the tire with and without porous ground. The source/receiver configurations of the following examples are given in Fig. 8.

In Fig. 10, we show the influence of the thickness of a porous layer on the reduction in the horn amplification of sound radiating from tires. In these simulations, the acoustical structural parameters of the porous layer are $R_s = 20\ \mathrm{kN\,s\,m^{-4}}$, $\Omega = 15\%$, $q^2 = 3.5$, with the thickness of the porous layer varying from 0.0 m (hard ground) to 0.04 m at

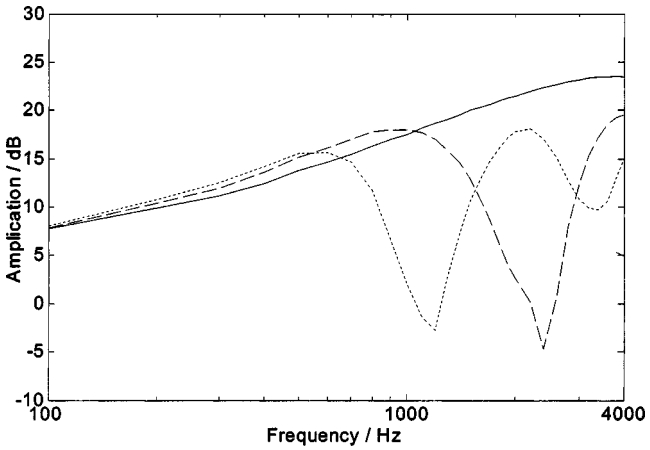

FIG. 10. Influence of the thickness of a porous road pavement on the horn effect. The acoustical structural parameters of the porous layer: $R_s = 20\,000\ \mathrm{N\,s\,m^{-4}}$, $\Omega = 5\%$, and $q^2 = 3.5$. (Solid line: hard ground; dashed line: $l_1 = 0.02$ m; dotted line: $l_1 = 0.04$ m.)

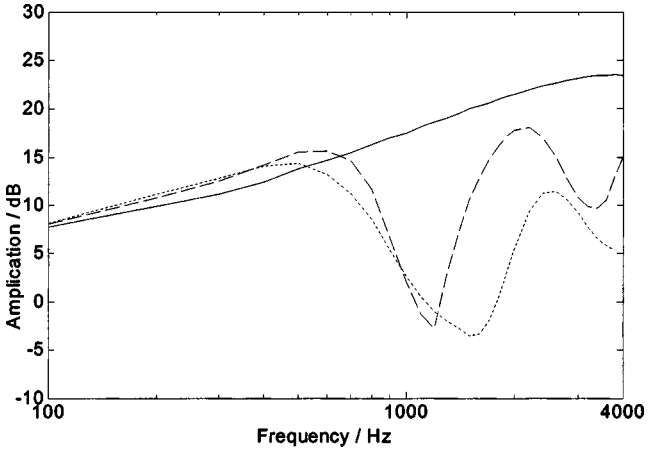

FIG. 11. Influence of the porosity of a porous road pavement on the horn effect. The acoustical structural parameters of the porous layer: $R_s = 20\,000\ \mathrm{N\,s\,m^{-4}}$, $q^2 = 3.5$, and $l_1 = 0.04$ m. (Solid line: hard ground; dashed line: $\Omega = 15\%$; dotted line: $\Omega = 30\%$.)

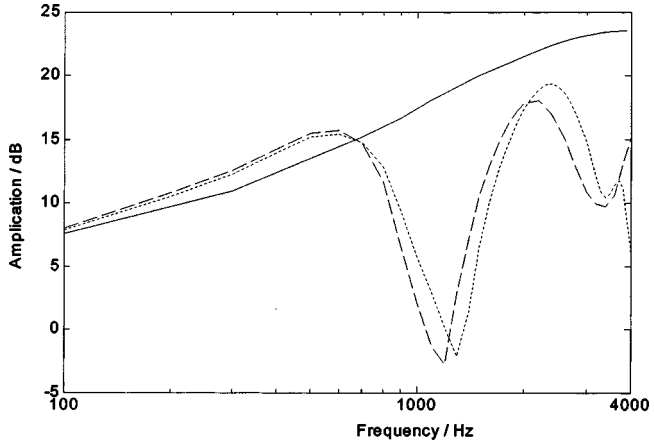

FIG. 12. Influence of the flow resistivity of a porous road pavement on the horn effect. The acoustical structural parameters of the porous layer: $\Omega = 15\%$, $q^2 = 3.5$, and $l_1 = 0.04$ m. (Solid line: hard ground; dashed line: $R_s = 20\,000\ \mathrm{N\,s\,m^{-4}}$; dotted line: $R_s = 5000\ \mathrm{N\,s\,m^{-4}}$.)

a step of 0.02 m. A porous road pavement can effectively suppress the amplification of sound due to the horn effect by creating interference minima in the amplification spectrum. The interference ''dips'' shift to higher frequencies when the thickness of the porous layer is reduced. Obviously, the overall effectiveness of the porous road pavement in reducing noise will decrease as the thickness of the layer decreases. For instance, there is only one interference dip in the dominant frequency range of the noise of a rolling tire, i.e., 500 to 4000 Hz, at a layer thickness of 0.02 m.

Figure 11 presents another important piece of information for investigating the material properties of a porous layer on the horn effect. It shows the effect of the porosity of a porous layer on the horn amplification of sound. In this example, the acoustical structural parameters of the porous layer are chosen to be $R_s = 20\ \mathrm{kN\,s\,m^{-4}}$, $q^2 = 3.5$, and $l_1 = 0.04$ m. The respective porosity with $\Omega = 0\%$ (for a hard ground), 15%, and 25% are shown in the same figure for ease of comparison. As expected, a higher porosity can provide a better attenuation of the horn effect by reducing the magnitude of the sound amplification. The finding is consistent with the conclusion drawn in Ref. 15. With regard to the flow resistivity of a porous layer, the change in its value does not do much to alter the sound spectrum, as evidenced in Fig. 12. Nevertheless, some noticeable changes can still be observed at frequencies higher than 3500 Hz.

Recent studies[17–19] have identified that a double layer of porous road pavement can better reduce the road traffic noise. Its application in road construction has received attention in recent years. Hence, the influence of a double layer of porous road pavement on the horn amplification of sound is worth exploring in the present study. For practical significance and numerical convenience, two different types of double-layer porous road pavement are investigated. The first type has a coarse porous surface and the second type has a fine porous surface. Both types of double-layer porous road pavement are currently used in the Netherlands[18] and are selected for the current study. Figures 13 and 14 illustrate the comparison of a double layer of porous road pavement with that of a single layer of road pavement. The spectra of sound amplification above a hard ground are also given in the figures for the purpose of comparison.

In Fig. 13, the acoustical structural parameters of the coarse top layer are given by $R_s = 6000\ \mathrm{N\,s\,m^{-4}}$, $\Omega = 20\%$, $q^2 = 3.5$, and $l_1 = 0.025$ m. For the bottom layer, $R_s = 1500\ \mathrm{N\,s\,m^{-4}}$, $\Omega = 20\%$, $q^2 = 4$, and $l_2 = 0.045$ m are used in Fig. 13. On the other hand, the predicted amplification factors for the porous road pavement with a fine top layer are shown in Fig. 14. The respective acoustical structural parameters of the top and bottom layers are given as follows. For the top layer, $R_s = 24\,000\ \mathrm{N\,s\,m^{-4}}$, $\Omega = 20\%$, $q^2 = 2.5$, and $l_1 = 0.015$ m, and, for the bottom layer, $R_s = 1500\ \mathrm{N\,s\,m^{-4}}$, $\Omega = 25\%$, $q^2 = 4$, and $l_1 = 0.055$ m.

It is not surprising to see that a double layer of porous road pavement can provide better attenuation of the horn amplification by creating more interference dips in the frequency range of interest. The first dip shifts to the lower frequency region in the case of a double layer of porous road pavement.

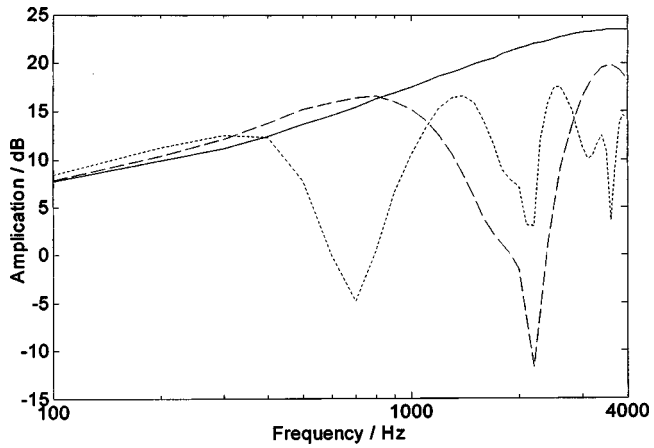

FIG. 13. Reduction in the horn effect due to a double layer of porous road pavement—the top layer is a coarse porous surface. (Solid line: hard ground; dashed line: a coarse top layer with $R_s = 6000\ \mathrm{N\,s\,m^{-4}}$, $\Omega = 20\%$, $q^2 = 3.5$, and $l_1 = 0.025$ m; dotted line: double layers—a coarse top layer and a bottom layer with $R_s = 1500\ \mathrm{N\,s\,m^{-4}}$, $\Omega = 25\%$, $q^2 = 4$, and $l_2 = 0.045$ m.)

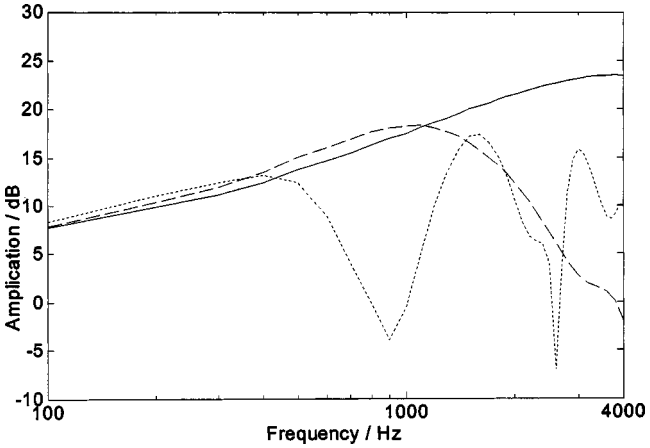

FIG. 14. Reduction in the horn effect due to a double layer of porous road pavement—the top layer is a fine porous surface. (Solid line: hard ground; dashed line: a fine top layer with $R_s = 24\,000$ N s m^{-4}, $\Omega = 20\%$, $q^2 = 2.5$ and $l_1 = 0.015$ m; dotted line: double layers—a fine top layer and a bottom layer with $R_s = 1500$ N s m^{-4}, $\Omega = 25\%$, $q^2 = 4$, and $l_2 = 0.055$ m.)

The dependence of the horn effect on the angular position of the source on the surface of the sphere is presented in Fig. 15. It shows that the amplification factor is rather insensitive to changes in the angular position of the source. There is a slight tendency for the interference dips to shift to lower frequencies when the angular position of the source increases.

Finally, a general remark can be drawn by studying Figs. 10–15: the acoustical properties of a porous layer and the angular position of the source on the surface of a tire do not have a noticeable influence on the horn effect at the low frequency region below 300 Hz.

V. CONCLUSIONS

This paper has contributed a theoretical model to study the amplification of noise due to the propagation of sound confined to a gap between the tire and the road over a porous road pavement. The simplified model can give good predictions of the general trend of amplification spectra compared to the published numerical and experimental results for the studies of the horn effect above hard and porous types of ground. The principal aim of this simplified model is to provide a parametric study of the acoustical parameters of porous road pavements on the horn effect. In the study, the source of the noise is assumed to be a monopole point source localized on the surface of the tire. It has been shown that a porous road pavement can effectively reduce the level of sound amplification resulting from the horn geometry of the tire/road in the frequency range of interest. A decrease in the thickness of the porous layer leads to an increase in the sound amplification of the horn effect. An increase in porosity or the use of a double layer of porous road pavement can enhance the attenuation of sound and create more interference dips in the amplification spectrum. The interference dips shift to lower frequencies when porosity increases or when a double layer of porous road pavement is used. However, changes in the flow resistivity of a porous road pavement do not seem to have a significant effect on horn amplification. As shown in the predictions, the variations in the angular position of the source on the tire surface have no significant effect on the horn amplification of sound.

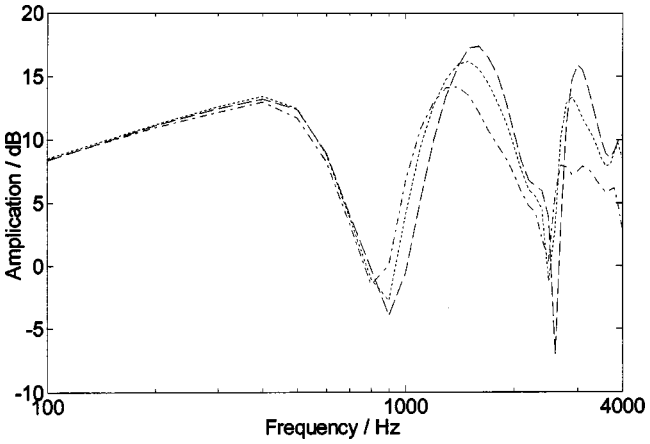

FIG. 15. Dependence of the horn effect on the angular position of the source on the surface of the tire. A fine double layer of porous road pavement is used for the simulation. (Dashed line: source at $\psi = 5°$; dotted line: source at $\psi = 10°$; dash-dotted line: source at $\psi = 15°$.)

ACKNOWLEDGMENTS

The research described in this paper was financed jointly by the Innovation and Technology Commission of the Hong Kong Special Administrative Region and the Mass Transit Railway Corporation Limited, through the award of a grant from the Innovation and Technology Fund under the category of the University-Industry Collaboration Program (Project No. UIM/39). The project was supported in part by the Research Grants Council of the Hong Kong Special Administrative Region (Project No. 8-Q334). The authors gratefully acknowledge the technical and administrative support given by the Hong Kong Polytechnic University.

[1] K. Iwao and I. Yamazaki, "A study on the mechanism of tire/road noise," JSAE Rev. **17**, 139–144 (1996).
[2] J. Perisse, "A study of radial vibrations of a rolling tire for tire-road noise characterization," Mech. Syst. Signal Process. **16**, 1043–1058 (2002).
[3] K. Larsson, S. Barrelet, and W. Kropp, "The modeling of the dynamic behaviour of tire tread blocks," Appl. Acoust. **63**, 659–677 (2002).
[4] M. Heckl, "Tire noise generation," Wear **13**, 157–170 (1986).
[5] K. Schaaf and D. Ronneberger, "Noise radiation from rolling tires—sound amplification by the horn effect," *Inter-Noise* **82**, San Francisco, CA, pp. 131–134.
[6] W. Kropp, F.-X. Becot, and S. Barrelet, "On the sound radiation from tyres," Acta Acust. **86**, 769–779 (2000).
[7] M. Ochmann, "The source simulation technique for acoustic radiation problems," Acustica **81**, 512–526 (1995).
[8] R. A. G. Graf, C.-Y. Kuo, A. P. Dowling, and W. R. Graham, "On the horn effect of a tire/road interface, Part I: experiment and computation," J. Sound Vib. **256**, 417–431 (2002).
[9] A. Fadavi, D. Duhamel, P. Klein, and F. Anfosso-Ledee, "Tire/road noise: 3D model for horn effect," Inter-noise 2000, Nice, France, 2000.
[10] F. Anfosso-Ledee, P. Klein, A. Fadavi, and D. Duhamel, "Tire/road noise: comparison of 2D and 3D models for horn effect," *Inter-Noise 2000*, Nice, France, 2000.
[11] C.-Y. Kuo, R. A. G. Graf, A. P. Dowling, and W. R. Graham, "On the horn effect of a tire/road interface, Part II: asymptotic theories," J. Sound Vib. **256**, 433–445 (2002).
[12] K. Attenborough, "Review of ground effects on outdoor sound propagation from continuous broadband sources," Appl. Acoust. **24**, 289–319 (1988).
[13] T. F. W. Embleton, "Tutorial on sound propagation outdoors," J. Acoust. Soc. Am. **100**, 31–48 (1996).

[14] K. M. Li, T. W. Fuller, and K. Attenborough, ''Sound propagation from a point source over extended-reaction ground,'' J. Acoust. Soc. Am. **104**, 679–685 (1998).
[15] S. Iwai, Y. Miura, H. Koike, and G. Levy, ''Influence of porous asphalt pavement characteristics on the horn amplification of tire/road contact noise,'' *Inter-Noise 94*, Yokohama, Japan, 1994.
[16] M. C. Bérengier, M. R. Stinson, G. A. Daigle, and J. F. Hamet, ''Porous road pavements: Acoustical characterization and propagation effects,'' J. Acoust. Soc. Am. **101**, 155–162 (1997).
[17] T. Iwase, ''Measurements of basic acoustical properties of the porous pavement and their applications to the estimation of road traffic noise reduction,'' J. Acoust. Soc. Jpn. **20**(1), 63–74 (1999).
[18] A. Kuijpers and G. Van Blokland, ''Modeling and optimization of two-layer porous asphalt roads,'' *Inter-Noise 2000*, Nice, France, 2000.
[19] T. Iwase, ''Acoustic properties of porous pavement with double layers and its reduction effects for road traffic noise,'' *Inter-Noise 2000*, Nice, France, 2000.
[20] K. M. Li, W. K. Lui, and G. H. Frommer, ''The diffraction of sound by an impedance sphere in the vicinity of a ground surface,'' J. Acoust. Soc. Am. **115**, 42–56 (2004).
[21] K. M. Li, W. K. Lui, and G. H. Frommer, ''The scattering of sound by a hard sphere above an impedance ground,'' Acta Acust. **90**, 251–262 (2004)

Annoyance with aircraft noise in local recreational areas, contingent on changes in exposure and other context variables[a)]

Norun Hjertager Krog[b)] and Bo Engdahl[c)]
Norwegian Institute of Public Health, Division of Environmental Medicine, P.O. Box 4404 Nydalen, NO-0403 Oslo, Norway

(Received 26 April 2002; revised 12 March 2004; accepted 5 April 2004)

Few socioacoustic studies have examined the effect of noise on outdoor recreationists. The areas studied have been mountain and wilderness areas that people typically travel for a distance to visit. In this article we examine the reactions to aircraft noise in local recreational areas experiencing either decreased (1930 survey respondents), or increased noise exposure (1001 survey respondents). Field studies were conducted before and after the relocation the main airport of Norway in 1998 in one area near each airport. The relationship between individual noise exposure (L_{Aeq} for the aircraft events, percentage of time aircraft were audible, and L_{Asel}) for the aircraft events. The analyses included the ''situation'' in which data were collected (before or after the relocation), and variables describing the recreational context. A strong effect of the ''situation'' was found in both cases, but the size of the effect was influenced by the choice of exposure variable in one of the study areas. Other context variables were also influencing annoyance. The effect of the situation (before/after a change in exposure) on the dose–response relationship may be influenced by the initial noise levels, the amount of change, and the time elapsed since the change at the time of the second survey. Further research should investigate the significance of these variables. © *2004 Acoustical Society of America.* [DOI: 10.1121/1.1756162]

PACS numbers: 43.50.Lj, 43.50.Qp [DKW] Pages: 323–333

I. INTRODUCTION

During the last few years growing attention has been given to adverse effects of noise on outdoor recreationists (International Recreational Noise Symposium, 1998; FICAN Symposium on the Preservation of Natural Quiet, 1999). Still, however, relatively few studies are conducted in this area of research. Some of the studies focus solely on describing the soundscapes of natural areas, without any description of how the soundscapes are perceived by visitors (e.g., Krause, 1999; Downing *et al.*, 1999). Other studies are social surveys without acoustical measurements of noise exposure (Cessford, 1998; McDonald *et al.*, 1995). A few studies have combined noise measurements with social surveys, and established dose–response relationships (Anderson *et al.*, 1993; Fidell *et al.*, 1996; Fleming *et al.*, 1998; Miller *et al.*, 1999; Krog *et al.*, 2000). Dose–response studies have also been conducted, where the exposure is described exclusively by nonacoustical variables (Tarrant *et al.*, 1995; Sutton 1999). Kariel (1990) and McDonald *et al.* (1995) compare recreationists' attitudes toward different sound sources, but the main noise source of concern has been different kinds of aircraft activity. Reactions to scenic flights (Anderson *et al.*, 1993; Sutton, 1999), but also the impact of military training activity (Elias, 1998; Miller *et al.*, 1999; Krog *et al.*, 2000) have been examined. In the study by Fidell *et al.* (1996) study areas were selected to cover different kinds of aircraft overflights, but the most frequently observed type was commercial overflights. The kinds of areas that have been studied are typically areas that people travel for a distance to visit. The studies referred to that connect aircraft noise exposure to visitors' response, are from national parks and wildernesses in the US (Anderson *et al.*, 1993; Fidell *et al.*, 1996; Fleming *et al.*, 1998; Miller *et al.*, 1999) and mountain areas in New Zealand (Sutton, 1999) and Norway (Krog *et al.*, 2000).

Different methods and parameters are used in the studies that combine noise exposure and survey data in dose–response analyses. The results are not directly comparable. The authors themselves (Anderson *et al.*, 1993; Fidell *et al.*, 1996; Krog *et al.*, 2000) state that one should be cautious in generalizing the results to other recreational settings. Several aspects of importance might be different from area to area and from situation to situation. In this article we examine the modifying effects of contextual variables on reactions to aircraft noise in local outdoor recreational areas.

The need to incorporate contextual variables in the predictions of reactions to noise in recreational settings is indicated by the results from studies by Kariel (1990) and Tarrant *et al.* (1995). Anderson *et al.* (1993) control for some contextual variables in the analyses of reactions to noise in National Parks, and Staples (1998) criticizes Fidell *et al.* (1996; 1998) for not incorporating contextual variables in their analysis, among other things with reference to the results of Anderson *et al.*. Dose–response relationships are used not only to describe an environmental situation, but also to predict the effect of changes in exposure. Anderson *et al.* (1993) present their dose–response curves together with

[a)]Portions of this work were presented at the Internoise 2001 Congress, The Hague, The Netherlands.
[b)]Electronic mail: norun.krog@fhi.no
[c)]Current affiliation: BREKKE & STRAND akustikk as, Hovfaret 17, 0275 Oslo, Norway.

schemes for calculating what proportions of visitors would be annoyed under various other conditions than those studied. Reactions to changed noise levels are proposed to be predictable on the basis of the results. However, both the study by Anderson *et al.* and the other studies referred to are undertaken in the context of a stable state situation. With growing recognition of the importance of the contextual aspects of reactions to noise, this common assumption regarding the use of dose–response curves has been criticized, that estimates on the grounds of a stable state situation could be used in the prediction of effects of change (Flindell and Porter, 2000; Guski, 2000). Especially, an abrupt change in noise levels may cause people to ''overreact,'' compared to the reaction that is predicted on the basis of established dose–response relationships (Horonjeff and Robert, 1997; Fields *et al.*, 2000). An abrupt change is defined as a change occurring over a short time period, it may occur from one day to another or over a few days or weeks (Horonjeff and Robert, 1997).

Recently, Fidell and Pearsons (2003) studied residents' reactions to imagined prospective increases in number and level of street traffic and aircraft noise exposure. The studied population was only exposed to modest levels of road traffic noise and minor levels of aircraft noise at the time of the study. The results showed larger increases in annoyance prevalence rates than what was predicted on the grounds of existing dose–response curves based on steady-state situations. The findings are, however, not based on real, experienced changes in exposure. The findings may result from the respondents inability to imagine the prospective changes correctly. On the other hand, results from some studies of real altered noise load in residential areas indicate that the context of change itself is a variable influencing reactions to noise (e.g., Langdon and Griffiths, 1982; Brown *et al.*, 1985; Fidell *et al.*, 2002). However, reviews of the literature do not unequivocally support this finding (Fields, 1993; Horonjeff and Robert, 1997). Horonjeff and Robert (1997) find a greater change in annoyance than expected following an abrupt change in noise exposure in most of the reviewed road traffic data, but only little or no effect of the change itself in data from airports. The studies conducted at airports were, however, few. Both Horonjeff and Robert (1997) and Fields *et al.* (2000) point to difficulties in conducting studies suited for detecting an abrupt change effect at airports. They recommend that more studies are conducted regarding effects of changes in aircraft noise levels. None of the studies reviewed examine reactions to changed noise exposure in outdoor recreational areas. The studied populations (Horonjeff and Robert, 1997; Fields *et al.*, 2000) were exposed to the noise dose on a daily basis, which differs from recreational settings. Whether or not the ''overreaction'' effect occurs outside a daily exposure context cannot be inferred from these studies.

The study presented in this article is part of a larger study containing both a field and laboratory experiment (Aasvang and Engdahl, in press), field surveys with a simultaneous collection of acoustical data (presented here), and telephone surveys. In this article we examine both the effect of a decrease and an increase in noise exposure on the reactions to noise in outdoor recreational areas that are situated in the local environment of the users. Field studies were conducted both before and after the relocation of the main airport of Norway on the 8th of October, 1998. The old airport, Fornebu, was situated close to the center of the capitol, Oslo. The new airport, Gardermoen, is located in a rural district, about 50 km north of Oslo. Whereas the old airport was totally closed down, the new airport was an existing airport that was expanded. The potential significance of change itself as a context affecting the experience of noise logically depends on the degree of former experience with the particular outdoor recreational area among the visitors, and their awareness of the change itself. In outdoor recreational areas with a large proportion of regular visitors from the local community, the frame of reference of past experience and the knowledge of change might potentially influence the visitors' perception of noise in the after situation. We hypothesized that the visitors would tend to be less annoyed following the decrease in noise exposure at the old airport, than the results from before the change (t_1) would indicate. Likewise, we hypothesized that the increased noise exposure at the new main airport would be followed by a stronger annoyance response than predicted by the results from t_1. Further, it was hypothesized that the degree of annoyance in the recreational areas depends on characteristics of the recreational situation: reasons for participation in outdoor recreation, the duration of the visit, and whether the area is the recreationist's primary recreational area or not.

II. MATERIALS AND METHODS

A. Site selection

The outdoor recreational areas selected for the study were Bygdøy near the old main airport, and Romeriksåsen near the new main airport. The areas were selected because of their location relative to the airports, and because they were much used by the local communities. Bygdøy is an area of about 2.6 km^2, containing both a popular beach and a small forest. Romeriksåsen is a larger forest area of about 7600 km^2. There are several small lakes in the area, and a network of forest roads and paths. There are also some private and public cabins.

A comparison between results from before and after the change in each area was the main issue of the study, not a comparison between the areas. Therefore, it was not regarded important that the areas were totally comparable in all aspects. The main point was that they were areas experiencing opposite changes in aircraft noise exposure.

B. Procedure

Noise measurements with a simultaneous collection of survey data were carried out at one site at Bygdøy and three different sites in Romeriksåsen. The questionnaire was tested in the field prior to the data collection. Field studies at Bygdøy were conducted during six weekend days in the period from the 18th of April to the 10th of May, 1998 (t_1), and again during seven weekend days in the period from the 17th of April to the 2nd of May, 1999 (t_2). The first field study in Romeriksåsen was carried out during five weekend

days from the 5th to the 26th of September, 1998 (t_1), and the second during ten weekend days in the period from the 21st of August to the 26th of September, 1999 (t_2). The response rates at Bygdøy were 62% (t_1) and 52% (t_2), respectively. In Romeriksåsen, 88% answered the questionnaire at t_1, and 77% at t_2. Data were obtained from 965 respondents each study year at Bygdøy. In Romeriksåsen we obtained data from 296 respondents before the change, and 705 after the change.[1] Valid cases for each analysis are those who had answered all the questions included in the particular analysis.

The survey data were collected at the trail close to a parking lot, or at parking lots. All hikers aged 18 or older were asked to fill in a questionnaire about today's visit while on their way out of the area. An inclusion criterion was further that the respondents should have stayed in the area for at least 15 minutes.

To avoid influencing the answers to the questions about the experience of aircraft in the area, the study was presented as a general study about outdoor recreational areas in the region. The respondents were, however, informed about the purpose to study the effects of changed aircraft noise exposure after the questions were answered. Only people who had not participated in the study before the change were allowed to participate in the second survey. Otherwise the conditions for answering the questionnaire would not be equal, since the participants of the first survey would already be familiar with the study and its purpose.

C. Acoustic measurements

Acoustic data were collected at one location for each interview site, which is three different locations in Romeriksåsen and one at Bygdøy. The locations were chosen to be representative to the walking area in terms of aircraft sound levels and background sound levels and were hidden from the respondents. To obtain exposure data for the whole visit for all participants, sound recordings started each day at least one and a half hours before the collection of the survey data, and ended when the last questionnaire was handed in.

Sounds were recorded onto the hard disk of a stationary Pentium PC or a laptop with a high-quality sound card through a Brüel&Kjær 4190-type microphone connected to a Norsonic 336 front-end. A second low-noise channel was added to the recordings obtained in the low-noise areas. This channel consisted of a 1 in. low-noise condenser microphone (Brüel&Kjær 4179), preamplifier (Brüel&Kjær 2660), and power-supply (Brüel&Kjær 5935). In addition to an ordinary 3 1/2 in. windscreen, the low-noise microphone was protected by an outer 20 in. windscreen consisting of semicircular ribs covered with tightly fitting Spandex fabric (Anderson *et al.*, 1993). A custom-made program was developed in Delphi so that an observer easily could mark the start of a new event and afterward make the appropriate categorization. The program automatically stored each sound event on different files in a windows linear PCM wave format. A-weighted sound exposure levels were calculated for each sound event with filters according to IEC/CD 1672 by a code written in Matlab.

The observer was responsible for categorizing sound sources as either aircraft, human or natural. The aircraft category was further specified into civilian jet, military jet, propeller, or helicopter. The human category was specified into vehicle or voice sounds. Even though questionnaires were filled out at a spot close to a parking lot, sounds from vehicles were seldom in the area of hiking and were not a major part of the acoustic data collected. The major sources to the natural sound were wind in the trees and singing birds. Aircraft sound was dominated by sound from jet aircraft in both areas. There was also occasional traffic with smaller aircraft and helicopters.

The respondents indicated the time when they arrived in the area (hour and minute), whereas the field staff recorded the time when the questionnaire was handed in. The field workers used watches calibrated to the time on the PC used for the sound recordings. Individual sound exposure doses were calculated by combining the sound exposure levels from each aircraft sound event with the time of visit of each respondent.

The acoustic measurements are described in detail elsewhere (Engdahl, 2001).

D. Analyses

The data were analyzed using SPSS 11.0 for Windows. An initial analysis was done to evaluate how representative the samples were compared to the area populations,[2] and to evaluate the comparability of the subsamples of each area. Pearsons Chi-Square was used in these comparisons.

Separate contextual dose–response analyses were conducted for the two areas. Each analysis included data from both t_1 and t_2. Multivariate linear regression was chosen for the analyses of the relationship between noise exposure, contextual variables, and noise annoyance. Linear regression has the advantage over logistic regression analysis that the information contained in the total measurement scale is kept. Because the dependent variable was a category scale, and not a continuous variable, the suitability of linear models was tested by comparing the results to the results of multivariate monotonic regression models. The program GOLDMineR from SPSS was used in these analyses. The monotonic regression models did mostly not prove significantly better, nor give a different result than the linear regression models. The improvement in explained variance was in no cases more than a few percent. Since the linear regression analysis does also have the advantage of offering standardized coefficients, which facilitates the direct comparison of effect sizes, the linear models are presented.

E. Variables

Gender was used to evaluate how representative the samples were compared to the area populations. This was the only variable that was collected to describe the visitors who refused to participate in the study, since it was the only demographic variable that could easily and accurately be observed without asking questions. To estimate the population distribution of male and female visitors, the numbers of men and women refusing to participate were added to the num-

bers of men and women participating. This was done for each subsample separately. Further, the variables ''gender,'' ''age,'' ''educational level,'' ''duration of the visit,'' and ''noise sensitivity'' were used in the evaluation of the comparability of the subsamples. Noise sensitivity was measured by one question in the study. The respondents were asked to evaluate how easily they were disturbed by noise on a ten-point scale, where 1 was ''gets hardly disturbed'' and 10 indicated ''gets very easily disturbed.''

Three different noise dose parameters were included in separate analyses, to test whether the choice of dose parameter influenced the results of the contextual analysis. The dose variables were A-weighted equivalent aircraft sound levels (''$L_{\mathrm{Aeq,air}}$''), A-weighted cumulative sound exposure level for aircraft (''$L_{\mathrm{Asel,air}}$''), and percentage of time aircraft were audible. The percentage of time that aircraft were audible was based on the recordings of an observer. The parameters $L_{\mathrm{Aeq,air}}$ and percentage of time that aircraft were audible were also used in the study by Anderson *et al.* (1993). $L_{\mathrm{Aeq,air}}$ was chosen for the main analysis, because it is a commonly used acoustic parameter. The parameter has the advantage that it does not increase with increasing time spent in the area, as does $L_{\mathrm{Asel,air}}$. As time spent in the area might be a contextual variable indicating different kinds of use of the recreational area, the authors wanted to test the ''duration of the visit'' as a separate variable, not only as a component of the noise dose parameter. The ''duration of the visit'' was measured in minutes.

The response measure that was used was ''aircraft noise annoyance'' during the present visit to the area, measured on a four-category scale: ''not annoyed,'' ''slightly annoyed,'' ''rather annoyed,'' or ''very annoyed.'' The scale was chosen to make the results comparable to the results of a telephone survey that was included in the same research project. Since telephone interviews put restrictions on the number of categories that can be presented per question, a four-category scale was used instead of the more commonly used five-category annoyance scale (Anderson *et al.*, 1993; Fleming *et al.*, 1998; Miller *et al.*, 1999).

Whether the studies from before and after the airport change showed different responses to the *same* exposure levels, that is whether there was an ''abrupt change effect,'' was tested by including a ''situation'' variable. The ''situation'' variable was a dichotomous variable indicating in which situation, before or after the airport change, the response was given.

Two additive indices were constructed, describing reasons for participation in outdoor recreation related to experiential qualities of natural areas.[3] The questionnaire contained parallel sets of questions about reasons for today's visit to the particular area, and questions about reasons for visiting outdoor recreational areas in general. Reasons for participation in outdoor recreation in general were chosen as mediator variables, because it was assumed that the expectations of experiences at today's visit to the particular area might be adjusted to the conditions in the area, and thus less suited to predict noise annoyance. Reasons for participation in outdoor recreation in general were, on the other hand, assumed to express underlying values, or needs, that the conditions in the areas might or might not meet. The variables composing the indices were adopted from Vaagbø (1993). The respondents were asked to indicate whether a series of possible reasons for participation were ''very important,'' ''rather important,'' or ''not very important'' to them. The variables were coded so that a higher score meant higher importance. Since a relationship between the evaluation of the aesthetic qualities of landscapes and exposure to noise has been demonstrated in the laboratory (Mace *et al.*, 1999), separate indices were formed measuring the importance of the visual nature experience and the acoustic nature experience. The index ''reasons for participation: the visual nature experience'' was composed of the variables ''how important is the experience of birds and animals, flowers and trees'' and ''how important is the experience of the greatness of the creation.'' The index ''reasons for participation: the acoustic nature experience/mental relaxation'' combined the variables ''how important is the experience of silence and peace of nature,'' ''how important is it to get away from noise and pollution,'' and ''how important is it to get away from hustle and bustle.'' To improve the interpretability of the index scores, the scores were transformed to standard deviation units.

If the area was the visitor's ''primary recreational area'' or not was based on answers to a question about what area was most frequently used for the purpose of outdoor recreational activities. The response categories were ''this area,'' ''another area,'' or ''not sure.'' In the analyses the category ''not sure'' was combined with ''another area.''

TABLE I. Sample characteristics, Bygdøy and Romeriksåsen, t_1 and t_2. Percent.

		Bygdøy		Romeriksåsen	
		t_1	t_2	t_1	t_2
Gender	Male (%)	43	43	51	51
	Female (%)	57	57	49	49
	Valid *n*	930	929	280	674
	Missing	35	36	16	31
Age	18–39 (%)	49	48	36	43
	40–66 (%)	39	42	55	48
	67+ (%)	11	10	8	9
	Valid *n*	937	941	289	675
	Missing	28	24	7	30
Educational Level	Primary school (%)	2	1	4	5
	High school (%)	15	12	30	27
	College/university (%)	83	87	65	68
	Valid *n*	937	944	289	682
	Missing	28	21	7	23

III. RESULTS

A. Sample characteristics and comparability between same area subsamples

The population gender distribution at Bygdøy was 43% men and 57% women both years, and 51% men and 49% women both years in Romeriksåsen. A comparison with Table I shows that the gender distributions in the samples

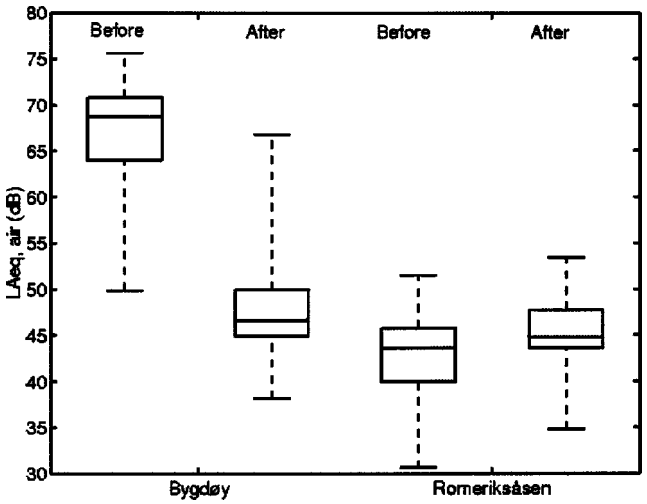

FIG. 1. The distribution of the respondents' individual aircraft noise exposure on the visit before and after the change in both study areas. The boxes mark the 25th, the 50th (the median), and the 75th percentiles, while the dotted-and-dash lines show the total range of the data.

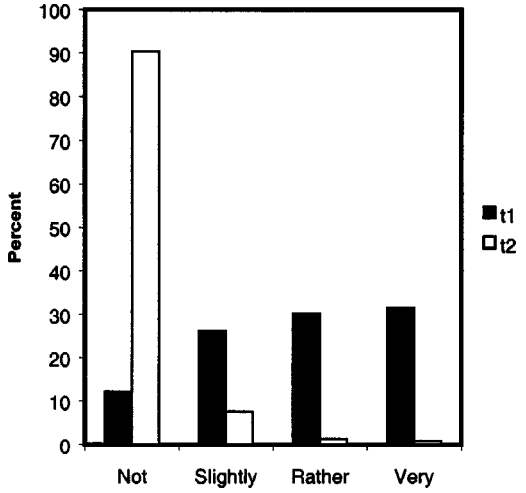

FIG. 2. Proportions annoyed by aircraft noise at Bygdøy, t_1 ($n=945$) and t_2 ($n=935$).

were close to the gender distribution of all observed visitors during the respective field studies.

Table I contains the composition of the samples regarding gender, age, and educational level. The relatively small numbers of missing cases indicate that the real composition of the samples cannot be very different from the distribution of the valid data. There were no significant differences between the same area samples, except a small difference in educational level between the two Bygdøy samples (Pearsons Chi-Square$=7.447$, 2 df, $p<0.05$).

There was no difference in the mean duration of the respondents' visits to the area between the two Bygdøy subsamples. Regarding Romeriksåsen, the mean duration of visits was slightly higher at t_2 than at t_1, 136 vs 122 min ($t=-3.034$, df 999, $p<0.01$).

In both areas there was a minor difference in mean noise sensitivity between the t_1 and t_2 samples. At Bygdøy the t_1 sample was on the average slightly less noise sensitive than the t_2 sample (mean t_1:4.49, mean t_2:4.91, $t=-4.012$, df 1869, $p<0.001$). In Romeriksåsen it was the opposite (mean t_1:4.43, mean t_2:4.02, $t=2.704$, df 493, $p<0.01$). The differences in mean noise sensitivity may indicate a slight but systematic change in the composition of the visitor populations of the two areas regarding this characteristic. But overall, the differences between the subsamples of each area were small. The subsamples were assessed to be sufficiently equal to test the hypothesis about the effect of the situation on the dose–response relationship.

B. Exposure and annoyance at t_1 and t_2

Before proceeding to the results of the multivariate linear regression models of the relationship between exposure, response, and mediator variables, we present the distribution of the individual recreationists' noise exposure, and the distribution of annoyance responses for each subsample. The percentages choosing each annoyance response in five-decibel noise groups are also presented for each area sample. Figure 1 shows the distribution of individual A-weighted equivalent aircraft sound exposure levels ($L_{\mathrm{Aeq,air}}$) for each of the four subsamples. Although there was overlap at the extreme ends, there was a marked change in the bulk of the respondents' exposures measured in $L_{\mathrm{Aeq,air}}$ from t_1 to t_2 in the data from Bygdøy. The median exposure was 69 dB A at t_1 and 47 dB A at t_2. The median exposure measured in $L_{\mathrm{Asel,air}}$ was 101 dB A at t_1 and 77 dB A at t_2. The median percentage of time aircraft were audible was 29% at t_1 and 15% at t_2.

In Romeriksåsen the median exposure measured in $L_{\mathrm{Aeq,air}}$ was only slightly higher at t_2 than at t_1, 45 vs 44 dB A, and there was substantial overlap in the individual exposures between the two survey years. The median exposure measured in $L_{\mathrm{Asel,air}}$ was 75 dB A at t_1 and 79 dB A at t_2. The increase in the median percentage of time the aircraft were audible was, however, more marked, and equivalent to the decrease at Bygdøy. The median percentage of time the aircraft were audible was 12% at t_1 and 26% at t_2.

The distributions of answers to the question about annoyance with aircraft noise at t_1 and t_2 are shown in Figs. 2 and 3. At Bygdøy (Fig. 2) there was a large decrease in

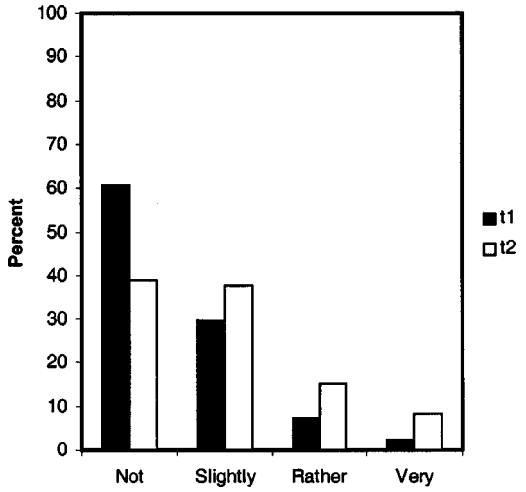

FIG. 3. Proportions annoyed by aircraft noise in Romeriksåsen, t_1 ($n=292$) and t_2 ($n=691$).

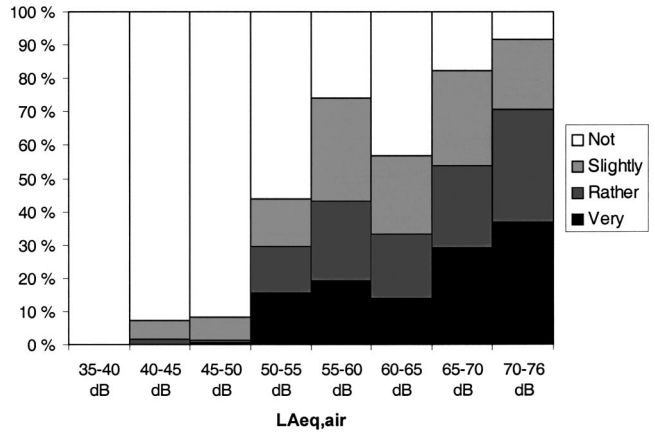

FIG. 4. Percentage choosing each annoyance response in 5-decibel noise groups. Bygdøy t_1 and t_2.

annoyance from t_1 to t_2. Relative to the change at Bygdøy there was a smaller increase in the proportions rather or very annoyed in Romeriksåsen (Fig. 3). The majority of the respondents were not or only slightly annoyed both before and after the change.

The relationship between noise exposure and response in each area sample, without regard of the context variables, is illustrated in Figs. 4 and 5. The figures indicate that the reactions to aircraft noise was not equal in the two area samples.

C. Analyses of dose–response relationships, contingent on context variables

Table II (Bygdøy) and Table III (Romeriksåsen) present the results of the multivariate linear regression analyses of the relationship between individual noise dose and annoyance, controlled for context variables. The standardized betas are the parameters that are used in commenting the effects of the variables, since these are directly comparable across the different measurement units. The other parameters are given for the sake of the reader who might want to check on the statistics.

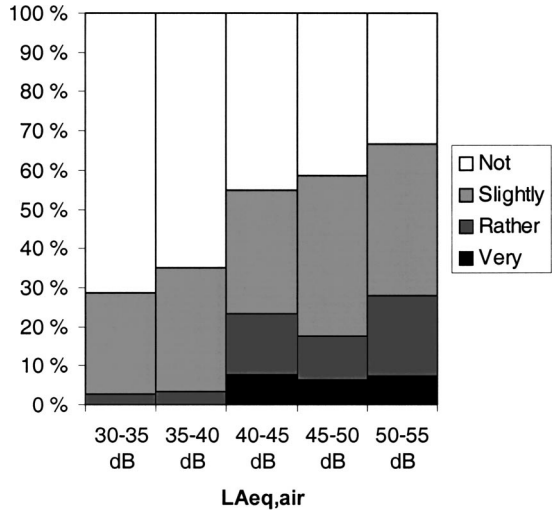

FIG. 5. Percentage choosing each annoyance response in 5-decibel noise groups. Romeriksåsen t_1 and t_2.

1. Results from Bygdøy, at the old airport

The results (Table II) show that given the same individual noise exposure, the visitors to Bygdøy tended to be less annoyed after the change than before the change. The sizes of the standardized betas indicate that the situation variable was more influential than the noise exposure itself, measured in $L_{\mathrm{Aeq,air}}$ for the individual visits to the area. The context variables ''duration of the visit,'' ''reasons for participation: the acoustic nature experience/mental relaxation,'' and ''reasons for participation: the visual nature experience'' did also significantly influence annoyance. People who had stayed in the area for a while tended to be more annoyed than people on shorter visits. People for whom the acoustical or visual nature experience were important reasons for visiting natural areas tended to be more annoyed by aircraft noise than those for whom these were less important reasons. The results indicate that the effects of these other context variables were smaller than the effect of $L_{\mathrm{Aeq,air}}$. If the area was the visitor's primary recreational area or not, did not influence annoyance at Bygdøy. The model explained 55% of the variance in the data.

Additional analyses were done, to test whether the use of other dose metrics would change the results. The variables tested were percentage of time aircraft were audible and $L_{\mathrm{Asel,air}}$. The substitution of the dose parameter $L_{\mathrm{Aeq,air}}$ for percentage of time the aircraft were audible did not change the result that the situation was the variable that was indicated to be the most influential in the model. The effect of the situation was estimated to be about the same as in the model with $L_{\mathrm{Aeq,air}}$ (beta$=-0.694$, $p<0.001$). Although there was a significant relationship between the response measure and percentage of time the aircraft were audible, the size of the beta (beta$=0.060$, $p<0.01$) indicates that this dose parameter did not predict annoyance as well as $L_{\mathrm{Aeq,air}}$. The effects of the other variables were not substantially changed.

The second additional analysis indicates that the effect of $L_{\mathrm{Asel,air}}$ was larger (beta$=0.157$, $p<0.001$) than the effect of $L_{\mathrm{Aeq,air}}$. On the other hand, as one would expect, the effect of the duration of the visit was diminished, and no longer significant (beta$=0.033$, $p=0.069$). Otherwise the replacement of the dose parameter $L_{\mathrm{Aeq,air}}$ with $L_{\mathrm{Asel,air}}$ did not change the overall results. The ''situation'' was still estimated to be the most influential variable in the model, although the size of the effect was somewhat smaller in this analysis (beta$=-0.597$). The percent of the variance explained by the model was the same for the two additional analyses as for the first.

2. Results from Romeriksåsen, at the new airport

In Romeriksåsen the visitors tended to be more annoyed after the change than before the change, at the same exposure levels (Table III). As for Bygdøy, the sizes of the betas indicate that the situation was the variable most strongly affecting the level of predicted annoyance at given noise levels. In addition to the variables ''reasons for participation: the acoustic nature experience/mental relaxation'' and ''duration of the visit,'' there was a significant positive effect of the area

TABLE II. Aircraft noise annoyance dependent on exposure and context variables, Bygdøy t_1 and t_2. Multivariate linear regression analysis ($n=1733$,*$-p<0.05$**$-p<0.01$***$-p<0.001$).

Bygdøy ($R^2=0.547$)	Unit[a]	Unst. B[b]	SE[c]	Beta[d]		t
Constant		3.406	0.257			13.26
Situation	0—before/ 1—after	−1.476	0.065	−0.646	***	−22.82
$L_{\mathrm{Aeq,air}}$	dB A	0.011	0.003	0.102	***	3.59
Reasons for participation: the visual nature experience	SD[e]	0.043	0.021	0.038	*	2.05
Reasons for participation: the acoustic nature experience/mental relaxation	SD	0.063	0.021	0.054	**	2.95
Duration of the visit	minutes	0.002	0.000	0.061	***	3.75
Primary recreational area	0—no/1—yes	0.003	0.040	0.001		0.07

[a]Variable unit.
[b]Unstandardized beta.
[c]Standard error of the unstandardized beta.
[d]Standardized beta.
[e]Standard deviation units.

being the visitor's primary recreational area. The variable ''reasons for participation: the visual nature experience'' was not significantly influencing annoyance in Romeriksåsen. The model explained eight percent of the variance in the data.

The results of additional analysis suggest that percentage of time aircraft were audible was a better predictor of annoyance in Romeriksåsen than $L_{\mathrm{Aeq,air}}$ (beta=0.161, $p<0.001$). In this analysis the percentage of time the aircraft were audible was estimated to have the largest effect in the model. The estimated effect of the situation was substantially reduced (beta=0.126, $p<0.001$), and indicated to be about the same size (slightly smaller) as the effect of the context variable ''reasons for participation: the acoustic nature experience/mental relaxation'' (beta=0.134, $p<0.001$). The effects of the other variables were not substantially altered by the change of dose parameter. This model explained nine percent of the variance in the data.

In accordance with the results from Bygdøy, the effect of $L_{\mathrm{Asel,air}}$ was estimated to be somewhat larger (beta=0.120, $p<0.001$) than the effect of $L_{\mathrm{Aeq,air}}$. Also, the effect of the duration of the visit was diminished, and no longer significant (beta=0.048, $p=0.195$). But unlike the results from Bygdøy, the percentage of time the aircraft were audible, not $L_{\mathrm{Asel,air}}$, was the dose parameter that was estimated to have the largest effect on annoyance in Romeriksåsen. Although the estimated effect size was somewhat smaller, the situation variable was still indicated to have the largest effect on annoyance in this analysis (beta=0.171, $p<0.001$). In other respects the results were not substantially altered by changing the dose parameter to $L_{\mathrm{Asel,air}}$. Eight percent of the variance in the data were explained by this model.

In all three analyses the relative importance of the variables were estimated to be different in Romeriksåsen than at Bygdøy. However, the relative sizes of the betas should be interpreted with care. Basing the test on the standard errors of the beta values, only the estimated effects of the ''primary recreational area'' variable were significantly different between the two samples ($p<0.05$) in the analysis with $L_{\mathrm{Aeq,air}}$ as the dose parameter. The most significant differences between the areas were found in the analysis that included percent of time the aircraft were audible. The effect of percent of time the aircraft were audible was significantly larger ($p<0.05$) than the effect of the same variable in the results

TABLE III. Aircraft noise annoyance dependent on exposure and context variables, Romeriksåsen t_1 and t_2. Multivariate linear regression analysis ($n=898$,*$-p<0.05$**$-p<0.01$***$-p<0.001$).

Romeriksåsen ($R^2=0.081$)	Unit[a]	Unst. B[b]	SE[c]	Beta[d]		t
Constant		−0.007	0.346			−0.02
Situation	0—before/ 1—after	0.398	0.068	0.201	***	5.88
$L_{\mathrm{Aeq,air}}$	dB A	0.019	0.008	0.080	*	2.34
Reasons for participation: the visual nature experience	SD[e]	−0.020	0.033	−0.021		−0.59
Reasons for participation: the acoustic nature experience/mental relaxation	SD	0.115	0.032	0.130	***	3.62
Duration of the visit	minutes	0.001	0.000	0.091	**	2.80
Primary recreational area	0—no/1—yes	0.181	0.064	0.091	**	2.81

[a]Variable unit.
[b]Unstandardized beta.
[c]Standard error of the unstandardized beta.
[d]Standardized beta.
[e]Standard deviation units.

from Bygdøy, where this variable was estimated to have the smallest effect of the dose parameters. In addition significant differences were found between the betas of the variables ''reasons for participation: the acoustic nature experience/mental relaxation'' and ''primary recreational area'' ($p < 0.05$). There were no significant differences between the two samples in the analysis that included $L_{\mathrm{Asel,air}}$. The difference between the betas of the situation variable was not tested, since the variable represents a different frame of reference in the two areas. At Bygdøy the variable represents the contextual effect of a decrease in noise levels, while the context is an increase in noise levels in Romeriksåsen.

IV DISCUSSION

A. Summary of results

The contextual model was tested with three different noise parameters. $L_{\mathrm{Acq,air}}$ was chosen for the first analyses. The results showed a strong effect of the situation of change itself, beyond that was expected on the grounds of the actual changes in noise exposure levels. The situation was in both recreational areas the variable that was estimated to have the largest effect on annoyance. The analyses of the data from both areas pointed to a mediating effect of the following context variables; ''Reasons for participation: the acoustic nature experience/mental relaxation,'' and the duration of the visit. The results from Bygdøy included in addition a significant small effect of the variable ''reasons for participation: the visual nature experience.'' The results from Romeriksåsen included a significant effect of the area being the primary recreational area. The relative importance of the variables in the model was indicated to be different in the two datasets. Most of the betas were, however, not significantly different between the two samples.

The overall results were not essentially altered by changing the dose parameter of the model except that using percentage of time the aircraft were audible as dose parameter substantially reduced the effect of the situation in Romeriksåsen. The effect of percentage of time the aircraft were audible was significantly larger in Romeriksåsen than at Bygdøy.

B. Noise annoyance and exposure in the two study areas

There was a difference in reactions to the same noise levels in the two areas (Figs. 4 and 5). This may be due to intrinsic area differences in expectations to sound and silence, the different level and range of the exposure, and a different effect of the change. Bygdøy is a smaller forest area near the city, while Romeriksåsen is a vast forest area in a rural area. The additional regression analysis also showed that percentage of time the aircraft were audible corresponded better to the annoyance in Romeriksåsen than $L_{\mathrm{Aeq,air}}$. The range of individual exposure may be an indicator of the frame of reference of the experienced visitors, which may influence expectations as well as the experience at today's visit. The range of individual noise exposure was considerably narrower in Romeriksåsen than at Bygdøy, measured in $L_{\mathrm{Aeq,air}}$, and at the lower end of the total exposure range found in the study areas. The percentage of time the aircraft were audible described the change in exposure better, but this may also indicate that at lower exposure levels, in this kind of area, it is not so much the level as the intrusion just by hearing aircraft that counts.

It is difficult to directly compare the results with the results from other studies, because there are several differences both in the kind of areas studied, the kind of use, duration of the visits, in annoyance scales, mediator variables used, and in analyses and presentation. The descriptive data in Figs. 4 and 5 enable, however, the reader with access to other data materials to do an approximate comparison on his own.

C. The effect of the situation

Although there was overlap in aircraft noise exposure at t_1 and t_2 in both areas, there had been a marked shift in median exposure, especially at Bygdøy. A too high correlation between aircraft noise exposure and the situation could mean that the results were not reliable because of covariance. The highest correlations were between $L_{\mathrm{Aeq,air}}/L_{\mathrm{Asel,air}}$ and the situation variable at Bygdøy (-0.81, Spearman's rho, in both cases). The other correlations between the situation and the exposure variables were of the order of 0.68 (Spearman's rho) and below. To find out if the highest correlations caused the results to be unstable, we conducted separate multivariate linear regression analyses where the variables $L_{\mathrm{Aeq,air}}$ and the situation were added one at a time, in different order. The result was the same independent of which variable was added to the model first, which indicates that the results are reliable.

The subsamples of each area are shown to be comparable regarding several background characteristics, which indicates that the effect of the situation was not due to differences in the composition of the subsamples. The slight difference in noise sensitivity between the subsamples of each area is not a likely explanation of the effect of the situation. If anything, it may have led to a weaker effect of the situation, because the sample was slightly more noise sensitive at t_2 in the area where the noise exposure had decreased, and the opposite in the area where the noise exposure had increased.

The results indicate that the relative strength of the exposure and the situation variables may depend on the specific exposure measure that is used. The results suggest that different dose parameters might be better suited in different noise situations. The shift in exposure in Romeriksåsen was not so much in levels ($L_{\mathrm{Aeq,air}}$, $L_{\mathrm{Asel,air}}$) as in the percentage of time the aircraft were audible. This indicates that some of the effect expressed by the situation variable in the analysis with $L_{\mathrm{Aeq,air}}/L_{\mathrm{Asel,air}}$ actually was the effect of changed noise exposure in terms of percentage of time the aircraft were audible. But although the effect of the situation was diminished when the noise exposure was more adequately described, a significant effect of the variable was still found.

The effect of the situation was indicated to be largest in the area where the most dramatic change in noise exposure took place. However, one should be cautious in directly comparing the effects, since the situation variable represents a

different kind of change in the two areas. Presumably, the effect depends on prior exposure and on the amount of change. The effect size of the situation may also depend on the direction of change, as well as on different expectations to sound quality in different kinds of recreational areas. There are differences between the study areas regarding more than one of these dimensions, and our material cannot be used to decide what factors influence the size of the effect.

The effect of the situation logically presupposes that many of the visitors have experienced the area in both noise situations, or that the change is well known among new visitors. An abrupt change in noise exposure levels may influence reactions to noise less in areas that people travel for a distance to visit, and that are visited more infrequently by the same visitors than in frequently used local recreational areas.

An additional factor that must be taken into consideration is the time span between the relocation of the main airport and the time of the second studies. Fields *et al.* (2000) suggest that this factor should be taken into account in future studies, together with the amount of change. In both areas the second study was conducted during the first similar season as the first study, that is 6 to 7 months after the change at Bygdøy and 10 to 11 months after in Romeriksåsen. The effect of the change as a positive or negative happening influencing the reaction to noise in the areas may decay over time. None of the studies reviewed by Horonjeff and Robert (1997) were conducted more than a year after a change. A decay of the effect of the change was not demonstrated in these studies. In his meta-analysis Fields (1993) found mixed evidence regarding ''relatively long-term'' (long-term was not defined) adaptation to an increase in noise levels in the residential setting. Fidell *et al.* (2002) report an exaggerated response to aircraft noise in nearby residential areas, compared to well-known dosage–response relationships, 21 months after the opening of a new runway at an established airport. The process of adapting to a new noise exposure level may be different in a recreational than a residential area, and research is needed on adaptation to noise in recreational areas that have a large proportion of regular users. The results should not be generalized to a substantial different time span after the change than what has been studied.

D. The effect of other context variables

The significance of reasons for participating in outdoor recreation in general for annoyance with aircraft noise during the visit was demonstrated by the effect of the index variable ''reasons for participation: the acoustic nature experience/mental relaxation.'' The importance of natural quiet as a reason for visiting the natural areas was also found to be an important mediator variable in the Anderson *et al.* (1993) study from the national parks in the US. The acoustic aspect of the nature experience and mental relaxation have been shown by other authors (Vaagbø, 1993; Driver *et al.*, 1987) to be central reasons why people participate in outdoor recreational activities, and to be more important than the visual aspects of the nature experience. Anderson *et al.* (1993) initially tested the variable ''importance of reasons for visiting: viewing natural scenery'' as a candidate for mediator variable in their dose–response analyses, but no important effect of the variable was found, and it was not included in their dose–response models. The results from this study and the study by Anderson *et al.* (1993) are similar in this respect, although the variables in this study describe reasons for the participation in outdoor activities in general, while the study by Anderson *et al.* used variables describing the special reasons for the present visit to the study area. Mace *et al.* (1999) demonstrate in the laboratory that exposure to helicopter noise influences the evaluation of the aesthetic quality of natural landscapes, but the results of this study as well as Anderson's study do not indicate that special expectations to the visual nature experience influence reactions to noise.

The result that people on visits of longer duration tended to be more annoyed than people on shorter visits may be explained by the fact that people on longer visits have been exposed to more aircraft events than people on a short visit. On the other hand, visits of different duration may also have different recreational meaning to the visitors that influences the tolerance for noise on the visit. Both explanations are possible on the grounds of the results. The significant effect of the duration of the visit disappeared when $L_{\mathrm{Asel,air}}$ was used to describe exposure, but this is attributable to the fact that duration is incorporated in $L_{\mathrm{Asel,air}}$. One cannot conclude from this result that the duration of the visit did not also have another meaning than being an indicator of different exposure. Of the same reason one cannot conclude that $L_{\mathrm{Asel,air}}$ was a better predictor of annoyance than $L_{\mathrm{Aeq,air}}$, although the effect size was indicated to be larger.

In a study of effects of noise from military jets (Krog *et al.*, 2000), people who spent a longer time on the visit were found to be more disturbed by noise from military jets than people who finished their hike in a shorter time. This was so, even though the number of overflights experienced was the same, which means that a longer duration of the visit actually meant lower exposure relative to the time spent in the area. The result illustrates the point that duration may be an indication of different expectations and different meaning content of the visits. The duration of the visit was not included in the dose–response models developed by Anderson *et al.* (1993) or Sutton (1999). But in the study by Anderson *et al.* it was included indirectly, since a main feature of the two different area types was the duration of the visit. A consistent difference in accordance with our findings was found between overlooks (five minutes or less to walk) and short hike areas (twenty minutes to an hour to walk), people being more annoyed at the same exposure levels at the short hike sites. In the study of Fidell *et al.* (1996), the duration of the visit was only tested as an alternative indication of noise exposure, and not as a mediator variable.

Differences in the direction of change, and the availability of alternative areas of similar qualities, are possible reasons why an effect of the primary recreational area variable was only found in the data from Romeriksåsen.

V. CONCLUDING REMARKS

The results show that to estimate the effects of aircraft noise in outdoor recreational areas, it is not sufficient just to calculate the relationship between noise exposure and a re-

action measure, without adjusting for context specific variables. The results indicate that neither the effect of an increase nor a decrease in noise levels in local outdoor recreational areas would be very well estimated on the grounds of data from before the change only. An ''overreaction'' to the changes, represented by the effect of the situation variable, was found in both datasets. The size of the effect was influenced by the choice of noise dose parameter, however. The same parameter was not equally suited to describe the noise exposure in both study areas. The results point to the importance of carefully selecting the dose parameter that best corresponds to annoyance and to the character of the change in exposure in future studies. Further studies should examine under what conditions an ''overreaction'' effect of change is to be expected. The significance of the initial noise levels, as well as the size and the direction of change for this abrupt change effect should be investigated. Studies of the duration of the effect of change are also needed, that is, how long it takes for the effect to cease. The effect of change logically depends on some prior experience of the area, or knowledge of the change. The results presented concern local outdoor recreational areas, with many regular users. Studies should be conducted in areas with varying proportions of experienced and new visitors to examine what levels of experience and/or knowledge of a change are necessary for the effect to occur.

ACKNOWLEDGMENTS

We would like to thank Eyolf Osmundsen for initiating the study and Kristian Tambs for his contributions to the planning of the study. We thank the members of the reference group of the study for useful discussions in the early phases: Birgitta Berglund, Idar Granøien, Ronny Klæboe, and Kåre Liasjø. The content of this article is, however, the responsibility of the authors alone. We would also like to express our gratitude to the recreationists who participated in the study, and the field staff who conscientiously collected the data. Finally, we would like to thank the anonymous reviewers for valuable suggesttions in their reviews of this article. The study was supported by The Research Council of Norway and the Norwegian Air Traffic and Airport Management.

[1]The number of interviews was deliberately restricted at t_1 to secure that a sufficient number of new respondents would be available for the second survey. Although Romeriksåsen is visited by many people, there are also many entrances to the area, which means that fewer visitors were passing the interviewing sites each survey day than at Bygdøy. The same caution was not necessary at Bygdøy.

[2]The totality of visitors who were passing the survey sites during data collection.

[3]Initially, a model also including the reasons for participation ''spending time with family and friends'' and ''keep fit'' was tested. These variables were excluded from the model since they did not contribute significantly to the prediction of annoyance in either of the recreational areas, and they are also recreational motives that are not exclusively connected to natural areas.

Aasvang, G. M., and Engdahl, B. ''Subjective responses to aircraft noise in an outdoor recreational setting: a combined field and laboratory study,'' J. Sound Vib. (**in press**).

Anderson, G. S., Horonjeff, R. D., Menge, C. W., Miller, N. P., Robert, W. E., Rossano, C., Sanchez, G., Baumgartner, R. M., and McDonald, C. (**1993**). ''Dose–response relationships derived from data collected at Grand Canyon, Haleakala and Hawaii Volcanoes National Parks,'' HMMH Report No. 290940.14; NPOA Report No. 93–6, National Park Service, Denver, CO.

Brown, A. L., Hall, A., and Kyle-Little, J. (**1985**). ''Response to a reduction in traffic noise exposure,'' J. Sound Vib. **98**, 235–246.

Cessford, G. (**1998**). ''Visitor satisfactions, impact perceptions, and attitudes toward management options on the Milford Track,'' Report No. 87, Department of Conservation, Wellington, New Zealand.

Downing, M., Hobbs, C., and Stusnick, E. (**1999**). ''Measurement of the natural soundscapes in south Florida national parks,'' in *FICAN Symposium on the Preservation of Natural Quiet. 138th Meeting of the Acoustical Society of America. November 3, 1999*. Available online at ⟨http://www.fican.org/download/downing.pdf⟩.

Driver, B. L., Nash, R., and Haas, G. (**1987**). ''Wilderness benefits: A state-of-knowledge review,'' in *Proceedings, National Wilderness Research Conference: Issues, State of Knowledge, Future Directions*, USDA Forest Service General Technical Report INT-220, Fort Collins, CO, pp. 294–319.

Elias, B. (**1998**). ''Strategies for mitigating aircraft noise impacts on outdoor recreationists,'' in *Noise Effects '98 Congress Proceedings*, Sydney—Australia, Vol. 2, pp. 497–502.

Engdahl, B. (**2001**). ''Flystøy i rekreasjonsområdet på Bygdøy og Romeriksåsen. Analyse av lydopptak i forbindelse med en feltundersøkelse om effekt av flystøy i rekreasjons- og friluftsområder'' (''Aircraft noise in the outdoor recreational areas at Bygdøy and in Romeriksåsen. Analysis of sound recordings from field studies of effects of aircraft noise in recreational areas''), Rapport 2001:2, Folkehelsa, Oslo, Norway.

FICAN Symposium on the Preservation of Natural Quiet. 138th Meeting of the Acoustical Society of America November 3 1999 (**1999**). Proceedings available online at ⟨http://www.fican.org/pages/sympos.html⟩.

Fidell, S., Gramann, J., Knopf, R., and Pearsons, K. (**1998**). Response to ''Comments on 'Effects of aircraft overflights on wilderness recreationists''' [J. Acoust. Soc. Am. **104**, 1726 (1998)],'' J. Acoust. Soc. Am. **104**, 1729–1732.

Fidell, S., and Pearsons, K. (**2003**). ''Sensitivity to prospective transportation noise exposure,'' Noise Control Eng. J. **51**, 106–113.

Fidell, S., Silvati, L., and Haboly, E. (**2002**). ''Social survey of community response to a step change in aircraft noise exposure,'' J. Acoust. Soc. Am. **111**, 200–209.

Fidell, S., Silvati, L., Howe, R., Pearsons, K. S., Tabachnick, B., Knopf, R. C., Gramann, J., and Buchanan, T. (**1996**). ''Effects of aircraft overflights on wilderness recreationists,'' J. Acoust. Soc. Am. **100**, 2909–2918.

Fields, J. M. (**1993**). ''Effect of personal and situational variables on noise annoyance in residential areas,'' J. Acoust. Soc. Am. **93**, 2753–2763.

Fields, J. M., Ehrlich, G. E., and Zador, P. (**2000**). ''Theory and design tools for studies of reactions to abrupt changes in noise exposure,'' NASA Contractor Report No. CR-2000-210280, NASA Langley Research Center, Hampton, VA.

Fleming, G. G., Roof, C. J., Rapoza, A. S., Read, D. R., Webster, J. C., Liebman, P. C., Valihura, P. J., Lewis, K. C., Schomer, P. D., Plante, J. A., and Draper, J. A. (**1998**). ''Development of Noise Dose/Visitor Response Relationships for the National Parks Overflight Rule: Bryce Canyon National Park Study,'' FAA-AEE-98-01/DOT-VNTSC-FAA-98-6, U.S. Department of Transportation, Federal Aviation Administration.

Flindell, I., and Porter, N. (**2000**). ''The implications of context-based assessment for noise management,'' in *Proceedings Internoise 2000*, Nice, France.

Guski, R. (**2000**). ''Aspects contributing to global annoyance judgments in field interviews,'' in *Proceedings Internoise 2000*, Nice, France.

Horonjeff, R. D., and Robert, W. E. (**1997**). ''Attitudinal responses to changes in noise exposure in residential communities,'' NASA Contractor Report No. 97-205813, NASA Langley Research Center, Hampton, VA.

International Recreational Noise Symposium. (**1999**). ''Effects on man and on the environment. Queenstown, New Zealand, 1999.'' Proc. Noise Control Eng. J. **47**, 78–162.

Kariel, H. G. (**1990**). ''Factors affecting response to noise in outdoor recreational environments,'' Can. Geogr. Geogr. Can. **34**, 142–149.

Krause, B. (**1999**). ''Loss of natural soundscapes within the Americas,'' in *FICAN Symposium on the Preservation of Natural Quiet.* 138th Meeting of the Acoustical Society of America, 3 November, 1999. Available online at ⟨http://www.fican.org/download/krause.pdf⟩.

Krog, N. H., Aasvang, G. M., Osmundsen E., and Engdahl, B. (**2000**). ''Ef-

fects of noise from military jets on hikers in a recreational area'' in *Proceedings Internoise 2000*, Nice, France.
Langdon, F. J., and Griffiths, I. D. (**1982**). ''Subjective effects of traffic noise exposure, II: Comparisons of noise indices, response scales, and the effects of changes in noise levels,'' J. Sound Vib. **83**, 171–180.
Mace, B. L., Bell, P. A., and Loomis, R. J. (**1999**). ''Aesthetic, affective, and cognitive effects of noise on natural landscape assessment,'' Soc. Natur. Resour. **12**, 225–242.
McDonald, C. D., Baumgarten, R. M., and Iachan, R. (**1995**). ''Aircraft management studies: National Park Service Visitors Survey,'' HMMH Report No. 290940.12; NPOA Report No. 94-2, National Park Service, U.S. Department of the Interior.
Miller, N. P., Anderson, G. S., Horonjeff, R. D., and Thompson, R. H. (**1999**). ''Mitigating the effects of military aircraft overflights on recreational users of parks,'' AFRL-HE-WP-TR-2000-0034, Lexington, MA, Harris, Miller, Miller and Hanson, Inc.
Staples, S. L. (**1998**). ''Comment on 'Effects of aircraft overflights on wilderness recreationists' [J. Acoust. Soc. Am. **100**, 2909–2918 (1996)],'' J. Acoust. Soc. Am. **104**, 1726–1728.
Sutton, S. T. (**1999**). ''Aircraft noise impacts: A case study in the glacier region of the west coast of New Zealand,'' Noise Control Eng. J. **47**, 87–90.
Tarrant, M. A., Haas, G. E., and Manfredo, M. J. (**1995**). ''Factors affecting visitor evaluations of aircraft overflights of wilderness areas,'' Soc. Natur. Resour. **8**, 351–360.
Vaagbø, O. (**1993**). ''Den norske turkulturen: friluftslivets år 1993,'' (''The Norwegian tradition of outdoor life: the year of outdoor life 1993'') (FRIFO).

Noise annoyance from stationary sources: Relationships with exposure metric day–evening–night level (DENL) and their confidence intervals

Henk M. E. Miedema[a] and Henk Vos
TNO Inro, Department Environment and Health, P.O. Box 6041, 2600 JA Delft, The Netherlands

(Received 1 July 2003; revised 24 March 2004; accepted 30 March 2004)

Relationships between exposure to noise [metric: day–evening–night levels (DENL)] from stationary sources (shunting yards, a seasonal industry, and other industries) and annoyance are presented. Curves are presented for expected annoyance score, the percentage ''highly annoyed'' (%HA, cutoff at 72 on a scale from 0 to 100), the percentage ''annoyed'' (%A, cutoff at 50 on a scale from 0 to 100), and the percentage ''(at least) a little annoyed'' (%LA, cutoff at 28 on a scale from 0 to 100). The estimates of the parameters of the relations are based on the data from a field study ($N=1875$) at 11 locations (2 shunting yards, 1 seasonal industry, 8 other industries) in the Netherlands. With the same (yearly) DENL, the seasonal industry causes less annoyance than the other industries, while the other industries cause less annoyance than the shunting yards. It appears that annoyance caused by vibrations from shunting yards and annoyance caused by noise from through trains are (partly) responsible for the relatively high annoyance from shunting yards. The relatively low annoyance from the seasonal industry presumably is related to the presence of a relatively quiet period. Results for the two shunting yards and the seasonal industry are based on fewer data than the other industrial sources, and are indicative. The same patterns of influence of age and noise sensitivity that are generally found are also found in this study. For comparison, results regarding transportation sources are also given, including previously unpublished results for expected annoyance. [DOI: 10.1121/1.1755241]

PACS numbers: 43.50.Sr, 43.50.Qp [DKW] Pages: 334–343

I. INTRODUCTION

The growing transportation network with increasing traffic intensities is an important cause of noise annoyance. Having relationships that show which annoyance level is associated with a given noise exposure level is an important basis for policy aiming at the reduction of annoyance caused by transportation noise. Miedema and Oudshoorn (2001) presented relationships between the noise exposure metrics day–night level (DNL) and day–evening–night level (DENL), and noise annoyance for aircraft, road traffic, and railways. The working group of the European Commission on health effects of environmental noise recommends in its position paper these relationships for the estimation of noise annoyance on the basis of the noise exposure of dwellings (EU/DG Env WG2, 2002). Such relationships have not been established for industrial noise, presumably because this noise is less widespread than transportation noise and because industrial noise is heterogeneous due to the different types of industrial activities that cause noise.

The few noise annoyance studies that included study areas with (nonimpulsive) industrial sources, notably Finke *et al.* (1980; also see Rohrmann *et al.*, 1980); Groeneveld and Gerretsen, 1984; and Guski *et al.*, (1989), also investigated other sources (transportation, workshops, shooting ranges, sporting areas) and have a limited number of cases in the surroundings of factories. Moreover, the three studies used methods of noise exposure or annoyance assessment that make their results difficult to compare. Consequently, these studies do not provide a suitable basis for establishing exposure-response relationships for industrial noise. For two specific types of stationary sources, namely sources with predominantly impulsive noise and wind turbines, more is known.

For impulsive noise (shooting as well as other) a relatively large scale international study has been conducted (Groeneveld and De Jong, 1985) while for fire arms results are reviewed by Vos (1995; also see Buchta and Vos, 1998), and for wind turbines exposure-response curves have been presented by Pedersen and Persson-Waye (2003; also see Wolsink and Sprengers, 1993).

Locally industrial noise causes considerable annoyance, and having relationships for these sources that predict the noise annoyance on the basis of the exposure would help in dealing with this noise. Therefore a study has been conducted to establish relationships between noise exposure metric DENL and noise annoyance for industrial sources with predominantly nonimpulsive noise (and for shunting yards) in such a way that they are comparable to the relationships for transportation noise in the above-mentioned publication. The study consists of a social survey in the surroundings of nine industrial locations and two shunting yards, the assessment of the noise exposure of the respondents, and exposure–response analyses. In the analyses, attention is given to the differences between types of sources as a potential cause of variation in annoyance at the same exposure in terms of DENL. The uncertainty regarding the

[a]Electronic mail: hme.miedema@inro.tno.nl

TABLE I. Overview of the noise sources, comments regarding the dominant industrial or shunting noise, and the presence of other types of noise sources.

Location	Dominant source(s)	Comments	Other sources
Emmen	DSM (chemical), Twaron (fibers), Wellman (fibers)	All three plants are producing 24 h per day	Railway.
Wormerveer	Meneba (flour products)	In harvesting period, there are ships with running diesel generators. Alarm bell when malfunctioning.	Boats. Provincial road and arterial road. Aircraft noise.
Breda	CSM (sugar)	Beets harvesting season lasts about 90 days per year. Peak levels during unloading of beets.	Transportation center, during daytime peak levels possible
Foxhol	Avebe (potato products)	Peak levels from stream outlet, malfunctioning, or transportation. Production time 24 h per day.	Highway at 500 m. Railway at 250 m.
Martenshoek	Kappa Graphic Board (carton products), SCA (paper products), Armstrong (ceiling cover plates)	Carton factory: Peak levels when malfunction, or from stream mufflers.	Railway.
Leerdam	Glass factory	Peak levels of glass sounds are well shielded at the immission points.	Provincial road and a sports complex
Delft	DSM Gist (food ingredients and pharmaceutical bulk active ingredients)	Peak levels during starting and stopping of production (air and steam release)	Provincial road. Tramway. Busy railway.
IJmond	Corus (metal products)	In 2000 during the start-up of a new plant, there were high peak levels. Also peak levels due to shunting.	Boats. Highway at 200 m.
Sluiskill	Hydro Agri (ammonium products), De Schroef (shipyard)	Ammonium factory: during stopping or starting of process peak levels. Shipyard: 2 weeks per 3 months peak levels (hammering)	Two provincial roads. Boats.
Venlo	Shunting Yard of Netherlands' Railways (NS)	Much difference between winter (diesel generators and heating) and summer.	Busy arterial road. Railway through traffic.
Nijmegen	Shunting Yard of Netherlands' Railways (NS)		Busy arterial road. Railway through traffic.

relationships is characterized by the 95% confidence intervals of the relationships.

II. NOISE METRICS AND ANNOYANCE MEASURES

The DENL is used as the descriptor of the noise exposure. It is defined in terms of the L_{Aeq}'s (''average'' levels) during daytime, evening, and night-time, and applies a 5 dB penalty to noise in the evening and a 10 dB penalty to noise in the night. The definition is as follows:

$$\mathrm{DENL} = 10\ \lg[(12/24)\times 10^{\mathrm{LD}/10} + (4/24)\times 10^{(\mathrm{LE}+5)/10} + (8/24)\times 10^{(\mathrm{LN}+10)/10}]. \quad (1)$$

Here LD, LE, and LN are the *A*-weighted long term L_{Aeq} as defined in ISO 1996-2 (2002) for the day (7–19 h), evening (19–23 h), and night (23–7 h) determined over the year at the most exposed facade. DENL is the new uniform noise metric for noise mapping in the European Union (EU/DG Env., 2002).

In this study, a noise annoyance question with eleven categories is used. Annoyance responses are translated into a scale from 0 to 100. The translation is based on the assumption that the annoyance categories divide the range from 0 to 100 in equally spaced intervals. The general rule that gives the position of a category boundary on a scale from 0 to 100 is: $\mathrm{score}_{\mathrm{boundary}\ i} = 100i/m$. Here i is the rank number of the category boundary, starting with 0 for the lower boundary of the lowest annoyance category, and m is the number of categories. In this study with eleven categories the boundary scores are 0, 9, 18 ,..., 82, 91, 100.

The distribution of the annoyance scores at a given noise exposure level can be summarized in various ways. Often a cutoff point is chosen on the scale from 0 to 100 and the percentage of the responses exceeding the cutoff is reported. If the cut-off is 72 on a scale from 0 to 100, then the result is

TABLE II. The distribution of the respondents over the noise classes, and the average age and the percentage of females in the sample at each location.

Location	Mean age	%female	Distribution of respondents over DENL classes						Total N
			<40	41–45	46–50	51–55	56–60	>60	
Emmen	55.7	42.9		3	70	70	18		161
Wormerveer	53.2	63.2		5	88	21			114
Breda	42.3	45.1			57	87	38		182
Foxhol	47.1	58.4	5	27	44	46	3		125
Martenshoek	48.3	57.0	6	4	76	120	28	1	235
Leerdam	49.6	61.1	4	20	95	48	13		180
Delft	48.4	56.0		1	67	106	73	1	248
IJmond	51.4	56.4			66	85	5		156
Sluiskil	50.7	56.5		21	100	132	28		262
Venlo	52.1	46.4	21	5	46	10	2		84
Nijmegen	48.9	58.6	26	11	54	26	11		128
Total	49.5	54.9	62	78	763	751	219	2	1875

called the percentage ''highly annoyed'' persons (%HA), with a cutoff at 50 it is called the percentage ''annoyed'' (%A), and with a cutoff at 28 the percentage ''(at least) a little annoyed'' (%LA). An alternative to the percentage measures is the expected annoyance score, EA.

III. LOCATION SELECTION AND NOISE EXPOSURE

Locations with one or a few dominant noise sources were selected for which noise data were available and with sufficient dwellings in the DENL range 45–65 dB (with N preferably >300). Table I gives an overview of the industrial noise sources, and the presence of other types of noise sources. All industrial sources are factories, i.e., not smaller workshops. The noise data for the selected nine industrial locations and the two shunting yards were assessed by various acoustical engineering companies. They were collected and updated by one of these companies, DGMR Raadgevende Ingenieurs bv. The emission data were updated on the basis of contacts with the other acoustical companies, the factories concerned, and the local authorities involved in noise permission procedures. From the emissions and the additional required input data, immission levels (L_{Aeq}) during operation of a source were calculated for the residential areas, using the Netherlands' standard calculation method for industrial noise (Brackenhoff *et al.*, 1981). The average operation times within the periods distinguished by DENL, i.e., 7–19 h, 19–23 h, and 23–7 h, were assessed for each noise source on the basis of information from the factories concerned, and used to calculate DENL from the L_{Aeq}'s during operation time.

IV. SAMPLE AND QUESTIONNAIRE

The target for the sample was circa 180 respondents at each industrial location, and circa 200 respondents at both shunting yards. For the two shunting yards, data of 137 respondents were available from a previous study (De Jong and Vos, 2000), so that for these two locations only 134 and 129 extra interviews, respectively, were needed. On the basis of the contours available at the start of the study for DENL =45, 50, 55, 60, and 65 dB, six strata were distinguished for drawing a stratified sample with, in principle, a uniform distribution of the respondents over the strata. When there were too little dwellings in a (high) noise class, this was compensated by selecting extra dwellings in an adjacent zone. If this was not possible, extra respondents were selected from other locations. Due to limitations regarding the actual number of dwellings in the noise strata and differences between the provisional contours used for drawing the sample and the later updated calculated exposures, the resulting distribution of the respondents over the strata is far from uniform. Table II gives an overview of the distribution of the respondents over the noise classes (updated noise levels), and the average age and percentage females in the sample at each location.

The interviews were held by telephone in April and May, 2001. 1875 interviews were successfully completed. The nonresponse rate, defined as (100×) the number of successfully completed interviews divided by the number of successfully completed interviews plus refusals, was 65.5%. It took about 10 min to complete an interview. The questionnaire addressed the following subjects: dwelling and surroundings; noise annoyance from various sources; noise annoyance from specific activities of the industry/shunting yard or from specific characteristics of the noises; changes in exposure; visibility of industry/shunting yard; annoyance from odor, vibration, concern about safety; demographical characteristics; relation with or use of the source; noise sensitivity. The wording of the annoyance question was chosen to be equal to the wording used in a large aircraft noise annoyance study conducted in the Netherlands, which unfortunately meant that it did not exactly fit the recommendations by Fields *et al.* (2001). The wording of the noise annoyance question was as follows: If you are thinking of the past year, to which extent do you find the noise of ... (industrial area/shunting yard) annoying or not annoying? (0=not at all annoying ,..., 10=very much annoying). Categories in between the extremes were unlabeled. If the source was not heard, this could also be indicated. A respondent who not heard the source was assumed not to be annoyed by the source. The annoyance then was scored in the lowest category.

V. EXPOSURE–RESPONSE MODEL

The same exposure–response model as used by Miedema and Oudshoorn (2001) is used here. We refer to that publication for a more detailed description.

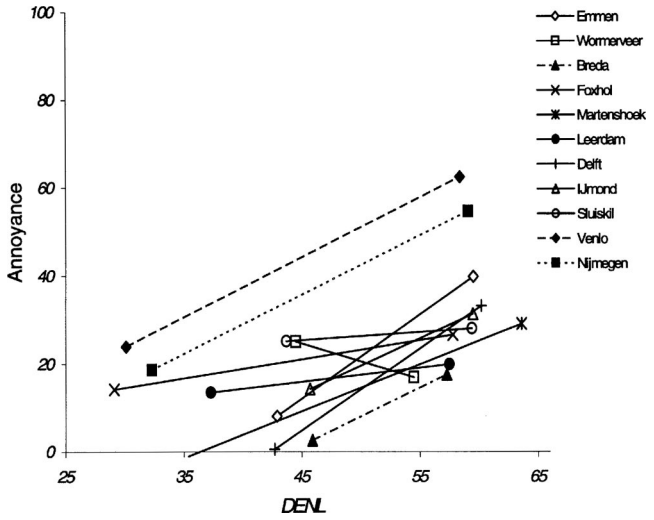

FIG. 1. Simple linear relationships between DENL and annoyance for the individual locations. Symbols are used for labeling purposes only and are no data points.

The noise annoyance on a scale from 0 to 100 of individual i at location j is denoted by A^*_{ij}. Instead of observing the individual noise annoyance A^*_{ij} precisely, it is only known for an individual in which interval on the scale from 0 to 100 A^*_{ij} comes. The locations of the boundaries in this study are 0, 9, 18 ,..., 82, 91, 100. Instead of modeling A*, we model the related latent random variable A, which is assumed to be normally distributed at a given noise exposure level and can have values outside the range 0–100. The correspondence between A and A^* is as follows: A^* equals A if $A \in [0,100]$, $A^*=0$ when $A<0$, and $A^*=100$ when $A>100$.

A_{ij} is modeled as a linear combination of the noise exposure DENL and other predictor variables. Including random location and individual effects, the model is as follows:

$$A_{ij}=\beta_0+\beta_1\mathrm{DENL}_{ij}+\beta_2X_{2ij}+\cdots+\beta_NX_{Nij}+u_{0j}+\epsilon_{ij}, \quad (2)$$

where u_{0j} is a random location factor, normally distributed with zero mean and variance σ_0^2, and ϵ_{ij} is a normally distributed random individual ''error'' term with mean zero and variance σ_1^2. The variables $X_{2ij}\cdots X_{Nij}$ are predictor variables, such as type of dwelling or noise sensitivity, depending on the particular analysis. The two random variables u_{0j} and ϵ_{ij} are assumed to be independent so that the total variance $\sigma^2=\sigma_0^2+\sigma_1^2$. According to this model the relation between, on the one hand, DENL and the other predictor variables and, on the other hand, annoyance can have a different ''intercept'' at each location. The average intercept is equal to β_0. The total random component in the model is equal to $u_{0j}+\epsilon_{ij}$. This means that the observations within one location are not independent.

Without a location effect the model becomes

$$A_{ij}=\beta_0+\beta_1\mathrm{DENL}_{ij}+\beta_2X_{2ij}+\cdots+\beta_NX_{Nij}+\epsilon_{ij}. \quad (3)$$

The random location factor has been omitted so that now all random variation is represented by the normally distributed ϵ_{ij} with zero mean and variance σ^2. In the next section it will be investigated whether the model with the random location factor is needed, or the simpler model without this factor can be used.

TABLE III. Comparison of model with and model without location effect, i.e., Eqs. (2) and (3), respectively. In addition to σ_0^2, σ_1^2 and β_0, the β's of the predictors are given. When a variable does not have a statistically significant contribution to the model ($p<0.05$), it is printed in italic. The measure of model fit is $-2\times$LogLikelihood: smaller means a better fit. For technical purposes *Age* was divided by 100, as indicated.

	Model with location effect	Model without location effect
Model fit	5574.6	5601.8
σ_0^2	*76.91*	...
σ_1^2	1743.86	1922.91
β_0	−113.27	−136.57
DENL	*0.64*	*0.78*
Shunt	40.35	49.88
Season	−50.53	−34.72
$Age/100$	245	282
$(Age/100)^2$	−268	−301
Own	8.93	11.60
Work	8.01	8.97
Sensi	*−61.41*	*−29.64*
Sensi×DENL	2.56	*1.94*

Dependent variable:

Annoyance	0–100	11-point scale for annoyance of industry or shunting

Predictor variables:

DENL	29–64	Noise exposure
Shunt	0–1	0=no shunting yard; 1=shunting yard
Season	0–1	0=no seasonal industry; 1=seasonal industry
Age	16–92	Age of respondent in years
Own	0–1	0=rented dwelling; 1=own dwelling
Work	0–1	0=not employed at noise source; 1=employed at noise source
Sensi	0–100	11-point scale for noise sensitivity of respondent

The parameters of the models are estimated by (a multilevel version of) grouped regression. As a measure of the fit of a model, $-2\times$LogLikelihood is given (lower value means better fit). For each model, the estimates of the β's are given.

For calculating the expected observed annoyance as a function of DENL and possibly additional predictors, it is important to note that the estimated latent annoyance distribution is nonzero also outside the interval [0,100], while the observed annoyance scores are restricted to that interval. More specifically, the latent annoyance has a normal distribution such that the corresponding distribution censored on the interval [0,100] describes the observed annoyance [see introduction of this section and Eq. (1)]. Consequently, not the mean of the normal latent annoyance distribution, but the mean of the corresponding censored normal distribution is an estimate of the expected observed annoyance:

$$\mathrm{EA}=100\times\Phi(-\delta_U)+(\Phi(\delta_U)-\Phi(\delta_L))\times[\delta+\sigma\times(\phi(\delta_L)-\phi(\delta_U))/(\Phi(\delta_U)-\Phi(\delta_L))], \quad (4)$$

where $\delta=\beta_0+\beta_1\mathrm{DENL}+\beta_2X_2+\cdots+\beta_NX_N$, $\delta_U=(100-\delta)/\sigma$, $\delta_L=-\delta/\sigma$, Φ is the cumulative standard normal distribution, and ϕ the standard normal density function.

With the estimates of the parameters, the expected observed annoyance score can be calculated by inserting these

TABLE IV. Basic model (model 1), with stepwise addition of extra independent variables. For each model, in addition to β_0, the estimates of the β's of the predictors [see Eq. (3)] are given. When a contribution is not statistically significant ($p<0.05$), it is printed in italic. The measure of model fit is $-2\times$LogLikelihood. For technical reasons *Age* and *Sensi* are divided by 100, as indicated ($N=1725$).

	Model 1	Model 2	Model 3	Model 4	Model 5	Model 6	Model 7	Model 8
Model fit	5604.8	5440.4	5142.8	5124.1	5037.0	4922.9	4885.5	4869.1
β_0	−88.44	−123.13	−125.71	−128.05	−80.42	−80.91	−78.13	−76.73
DENL	1.75	2.43	*0.78*	*1.00*	*−0.03*	*0.07*	*0.01*	*−0.13*
Shunt		43.36	46.80	48.58	46.36	41.68	29.83	34.05
Season		−29.47	−33.81	−33.09	−26.47	−22.92	−25.27	−26.09
Age/100			232	219	220	172	172	183
$(Age/100)^2$			−255	−244	−238	−188	−186	−194
Own			12.46	7.07	7.12	6.66	6.20	6.15
Work			8.31	8.41	7.44	6.49	6.38	6.12
Sensi/100			*−0.76*	*−2.14*	*−119.19*	*−119.27*	*−116.9*	*−115.93*
(*Sensi*/100)×DENL			*1.40*	*1.44*	3.58	3.40	3.31	3.25
Flat				−14.67	−11.90	−11.22	−9.58	−10.74
LivRoom					9.14	7.02	5.64	5.47
Bedroom					11.34	9.65	9.49	8.84
Fear						0.42	0.36	0.31
Vib							0.36	0.33
Odor								0.16

Dependent variable:		
Annoyance	0–100	11-point scale for annoyance of industry or shunting
Predictor variables:		
DENL	45–64	Noise exposure
Shunt	0–1	0=no shunting yard; 1=shunting yard
Season	0–1	0=no seasonal industry; 1=seasonal industry
Age	16–92	age of respondent in years
Own	0–1	0=rented dwelling; 1=owned dwelling
Work	0–1	0=not employed at noise source; 1=employed at noise source
Sensi	0–100	11-point scale for noise sensitivity
Flat	0–1	0=other; 1=flat
Liv.Room	0–1	0=noise source not visible from living room; 1=visible
Bedroom	0–1	0=noise source not visible from bedroom; 1=visible
Fear	0–100	11-point scale for fear of industry or shunting
Vib	0–100	11-point scale for annoyance from vibration from industry or shunting
Odor	0–100	11-point scale for annoyance from odor from industry or shunting

estimates and the levels of the predictor variables in the above-presented equation.

Instead of computing the curves for expected annoyance (EA), the curve for the annoyance response above a cutoff point C can be used. They are given by

$$P_C = 100\times(1-\Phi((\mathrm{C}-[\beta_0+\beta_1\mathrm{DENL}+\beta_2X_2+\cdots+\beta_NX_N])/\sigma)), \quad (5)$$

where P_C is the estimated percentage of persons with an annoyance score (scale 0–100) above cutoff point C. The %HA at a given DENL is obtained by substituting the values of the predictor variables and estimates of the parameters in the above equation, and by substituting 72 for C. When 50 is substituted for C then the estimate of %A is obtained, and substituting 28 gives %LA. Exposure–response relationships computed with the above formulas will be presented in Sec. VIII.

VI. DIFFERENCE BETWEEN SOURCES

In order to explore possible systematic, meaningful differences between relationships for different sources, Fig. 1 gives for each location the observed annoyance score as a linear function of DENL. The figure indicates that the noise annoyance in the surroundings of the two shunting yards is higher than the annoyance found at the same DENL at other locations. At the location where most activities are restricted to one season, the annoyance is lowest. For this reason, in the following analyses we distinguish three types of sources (shunting yards, seasonal industry, and other industries) and investigate in more detail whether the noise annoyance differs significantly between these locations.

In order to investigate whether there is a significant random location effect, in addition to a systematic effect of the source type, models with and without a random location effect were fitted and compared. In these analyses noise annoyance is the dependent variable. In addition to DENL and dummy variables for type of source, predictor variables that

TABLE V. Estimates of parameters for DENL-annoyance model, their standard errors and the covariance matrix of the parameter estimates. For comparison the similar results for transportation noise from Miedema and Oudshoorn (2001) have been added, including the covariances that were not presented earlier.

Stationary Sources (1751 observations, 1 study)						
Parameter	Estimate	s.e.	Covariances of parameter estimates			
σ^2	2054.43	130.43	β_0	DENL	*Shunt*	*Season*
β_0	−126.52	19.28	372.04			
DENL	2.49	0.37	−7.204	0.1405		
Shunt	40.74	3.96	−10.63	0.158	15.72	
Season	−29.97	4.80	12.39	−0.271	1.32	23.06

Parameter	Estimate	s.e.	Covariances of parameter estimates	
Aircraft (27081 observations, 19 studies)				
σ_0^2	77.64	25.83		
σ_1^2	1187.11	20.13	β_0	DENL
β_0	−91.42	3.30	10.88	
DENL	2.17	0.04	−0.105	0.0017
Road traffic (19172 observations, 26 studies)				
σ_0^2	150.54	42.99		
σ_1^2	1150.71	18.66	β_0	DENL
β_0	−106.97	3.91	15.30	
DENL	2.22	0.05	−0.146	0.0023
Railway (7632 observations, 8 studies)				
σ_0^2	53.86	28.55		
σ_1^2	1078.73	47.21	β_0	DENL
β_0	−110.09	6.33	40.04	
DENL	2.10	0.08	−0.478	0.071

might explain the difference in annoyance between locations were added. The results are presented in Table III, with the lower part the explanation of the variables in the analyses. Table III shows that the fit is a little lower when no random location effect is included, but the difference is small. Furthermore, the pattern of the weights of the variables is the same in both analyses, and the random location effect is not significant. Therefore, the simpler models without random location effect are used in the further analyses. Eight models with different predictors will be discussed. In model 1 DENL is the only predictor, in model 2 the source type dummies are added, and in the models 3–8 additional predictors are included.

VII. THE INFLUENCE OF DENL AND OTHER FACTORS ON ANNOYANCE

A simple model with DENL as the only predictor (model 1) is extended in a stepwise manner (models 2–8). The estimates of the parameters of the models can be found in Table IV, and are discussed in the following.

Model 1. This is the simplest model, with DENL as the only predictor. The effect of this predictor on annoyance is statistically significant, which means that DENL explains a part of the annoyance of stationary sources.

Model 2. Inclusion of source type (shunting yard, seasonal industry, or other) strongly improves the model fit. All variables included in this model are statistically significant. The coefficients of source type-dummies reflect what also can be seen in Fig. 1, namely that shunting yards are more annoying than the industrial sources, and that the seasonal industry causes relatively little annoyance.

Model 3. Inclusion of, among others, the variable *Age* substantially improves the model fit. In addition to *Age*, the square of *Age* was included, because previous research (Miedema and Vos, 1999) showed that annoyance has an inverse U-shaped relation with age. The same relationship with age is found here. At a given DENL, the annoyance is maximal for persons of approximately 46 years of age. The estimates of the age where annoyance is maximal range from 44.8 in model 4 to 47.1 in model 8. The maximum is computed by equating the derivative of the curvilinear effect of age to zero and then solving for age. That is, the maximum is $-100\times$(b_age/2$\times$b_age2), where b_age is the coefficient for *Age* and b_age2 is the coefficient for *Age*^{2}. Noise sensitivity is included together with its interaction with DENL, because previous research (Miedema and Vos, 2003) showed that the difference in annoyance between sensitive and nonsensitive respondents increases with the exposure level. This is also found here, but only after *LivRoom* and *Bedroom* are included in model 5. The effect of *Sensi* can be written as follows: b_lsensi$\times$(DENL-λ), where $\lambda = b\_\text{sensi}/b\_\text{lsensi}$, and b_sensi and b_lsensi are the coefficients of *Sensi*/100 and its product with DENL, respectively. The λ is interpreted as the annoyance threshold of DENL. It has a value of ~35 dB. Its estimate varies between 33.3 dB in model 5 and 35.7 dB in model 8.

Model 4. Inclusion of dwelling type in the model shows that the annoyance in flats is lower than in other dwellings.

Model 5. Whether the source was visible from the living

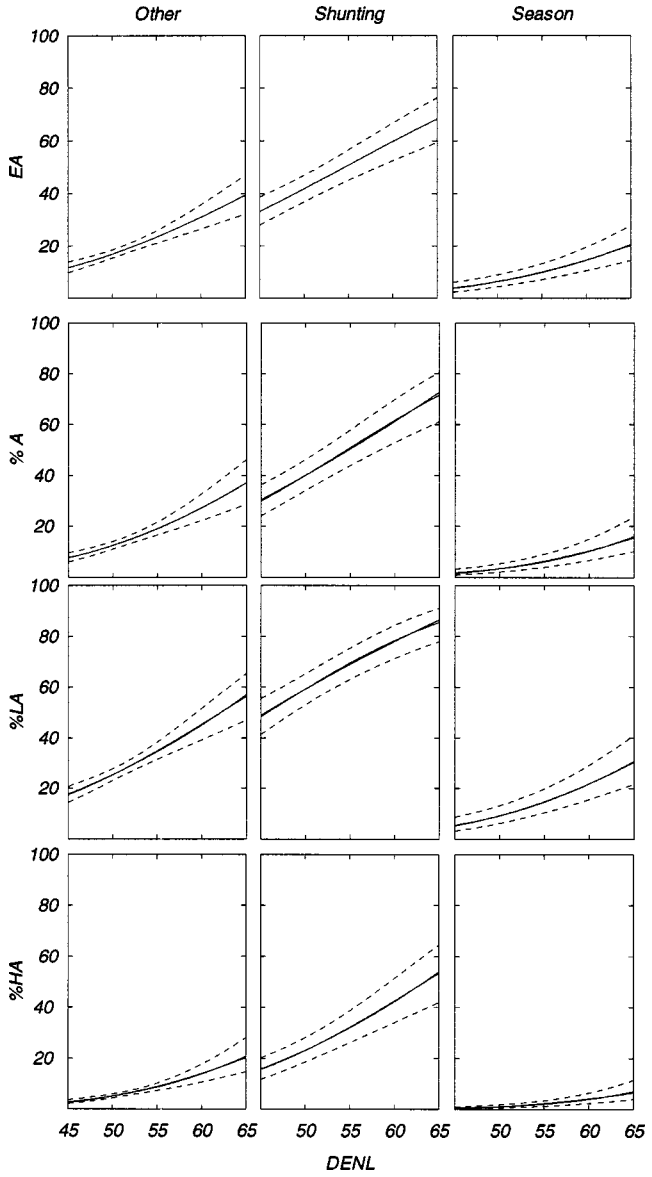

FIG. 2. The expected annoyance score (EA), and the percentages "(at least) a little annoyed" (%LA), annoyed (%A), and highly annoyed (%HA) as a function of DENL, for the shunting yards, the seasonal industry, and the other industry. Both the model curves and their polynomial approximation, which nearly coincide, are given. The broken lines are the 95% confidence intervals.

room, and from the bedroom (indicating the position of the rooms with respect to the source) contribute to the annoyance. The following analyses show that the effect of visibility of the source from the bedroom decreases less than the effect of visibility of the source from the living room, when fear, annoyance by vibration, and annoyance by odor are included in the model. This finding suggests that visibility from the living room is an indication of living close to the source, while the effect of visibility from the bedroom possibly is an indication of a higher exposure level while resting or sleeping.

Model 6. Inclusion of *Fear* is expected to have a large effect on annoyance, because fear is a component of annoyance. The large effect is found.

Model 7. Inclusion of *Vib* reduces the effect of the dummy *Shunt*, while there is no influence on the effect of *Season*. This means that the extra noise annoyance of shunting yards is partly caused by the annoyance due to vibrations.

Model 8. The effect of *Odor* is about half the size of the effects of *Fear* or *Vib*. The inclusion of *Odor* in the model has no effect on pattern of influences from the other variables.

VIII. EXPOSURE–RESPONSE RELATIONSHIPS

The previous analyses used data from noise calculations and a social survey that were carried out in the scope of a new field study. To establish exposure–response relationships, 26 cases from an earlier study (see Sec. IV) with DENL$\geqslant$45 dB were added. With the combined data set the analyses for model 2 from Table IV were repeated. Results are given in Table V, together with earlier results for transportation noise. The corresponding curves for stationary sources are given in Fig. 2. With the parameter estimates and their covariances in Table V, the curves for EA, %LA, %A, %HA and their confidence intervals can be calculated for stationary and transportation sources.

Because calculating annoyance values with Eqs. (4) and (5), which involve the cumulative normal distribution, using the parameter estimates in Table V, may be somewhat tedious in practice, accurate polynomial approximations are given in the following. Although earlier we used cubic functions to approximate the annoyance curves for transportation noise (see Table VI), here quadratic functions are sufficient to get very close approximations (see Fig. 2). The following polynomials for stationary sources were fitted for the DENL range 35–65 dB:

$$\begin{aligned}
&\text{Other:} && \mathrm{EA} = 17.247 - 1.172\ \mathrm{DENL} + 0.023\,32\ \mathrm{DENL}^2,\\
&\text{Shunting:} && \mathrm{EA} = -25.051 + 0.972\ \mathrm{DENL} + 0.007\,308\ \mathrm{DENL}^2,\\
&\text{Seasonal:} && \mathrm{EA} = 25.476 - 1.390\ \mathrm{DENL} + 0.020\,17\ \mathrm{DENL}^2,
\end{aligned} \tag{6}$$

$$\begin{aligned}
&\text{Other:} && \%\mathrm{LA} = 11.477 - 1.130\ \mathrm{DENL} + 0.028\,15\ \mathrm{DENL}^2,\\
&\text{Shunting:} && \%\mathrm{LA} = -69.963 + 3.171\ \mathrm{DENL} - 0.0176\ \mathrm{DENL}^2,\\
&\text{Seasonal:} && \%\mathrm{LA} = 39.156 - 2.146\ \mathrm{DENL} + 0.030\,96\ \mathrm{DENL}^2,
\end{aligned} \tag{7}$$

$$\begin{aligned}
&\text{Other:} && \%\mathrm{A} = 36.854 - 2.121\ \mathrm{DENL} + 0.032\,70\ \mathrm{DENL}^2,\\
&\text{Shunting:} && \%\mathrm{A} = -27.629 + 0.722\ \mathrm{DENL} + 0.012\,65\ \mathrm{DENL}^2,
\end{aligned} \tag{8}$$

TABLE VI. The coefficients of the polynomial approximations with the form $y=ax+bx^2+cx^3$ are given for three sources (air, road, rail) and four annoyance measures y (EA,%LA,%A,%HA), with x the noise exposure. The approximations are taken from Miedema and Oudshoorn (2001), except the polynomials for EA which were not presented earlier.

Measure		Aircraft	Road traffic	Railway
			$x=$DENL-32	
EA	a	1.120	0.537	0.234
	b	$1.439E-2$	$2.307E-2$	$2.068E-2$
	c	$-8.786E-5$	$-9.154E-5$	$-5.045E-6$
			$x=$DENL-32	
%LA	a	1.738	0.669	0.167
	b	$3.410E-2$	$5.509E-2$	$4.871E-2$
	c	$-6.158E-4$	$-6.235E-4$	$-3.229E-4$
			$x=$DENL-37	
%A	a	1.221	0.535	0.213
	b	$1.777E-2$	$2.110E-2$	$9.482E-3$
	c	$8.588E-6$	$1.795E-4$	$4.538E-4$
			$x=$DENL-42	
%HA	a	0.294	0.512	0.170
	b	$3.932E-2$	$-1.436E-2$	$-7.851E-3$
	c	$-9.199E-5$	$9.868E-4$	$7.239E-4$

$$\begin{aligned}
&\text{Seasonal:} && \%\text{A} = 32.137 - 1.635\ \text{DENL} \\
&&& + 0.021\,24\ \text{DENL}^2, \\
&\text{Other:} && \%\text{HA} = 36.307 - 1.886\ \text{DENL} \\
&&& + 0.025\,23\ \text{DENL}^2, \\
&\text{Shunting:} && \%\text{HA} = 16.980 - 1.367\ \text{DENL} \\
&&& + 0.029\,80\ \text{DENL}^2, \qquad (9) \\
&\text{Seasonal:} && \%\text{HA} = 18.123 - 0.887\ \text{DENL} \\
&&& + 0.010\,91\ \text{DENL}^2.
\end{aligned}$$

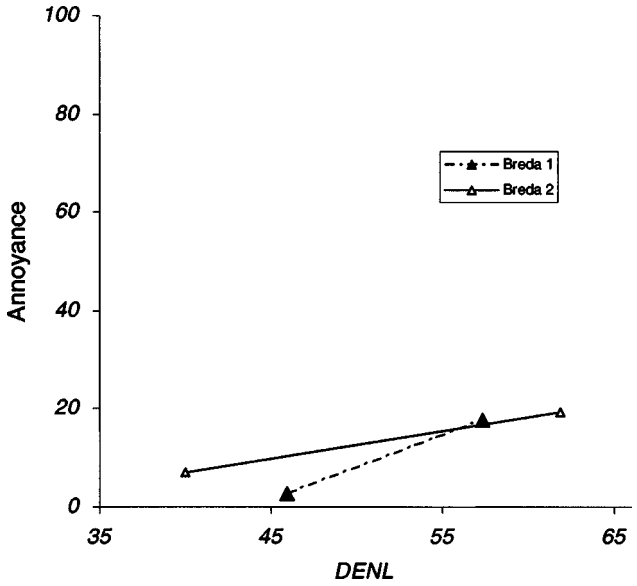

FIG. 3. Simple linear relationships between DENL and annoyance for the first and the second round for seasonal industries, location Breda. Symbols are used for labeling purposes only and are no data points.

For comparison, similar polynomial approximations for transportation noise from Miedema and Oudshoorn (2001) are given in Table VI. These polynomials, which on the basis of earlier results were forced through zero at 32 dB (EA,%LA), 37 dB (%A), and 42 dB (%HA), respectively, are based on model curves fitted to data in the DNL range 45–75 dB.

IX. EFFECT OF NOISE FROM THROUGH TRAINS ON ANNOYANCE FROM SHUNTING YARDS

The results in the preceding sections indicate that, with the same DENL, shunting yards cause more annoyance than industrial sources. One cause of this higher annoyance appears to be the vibrations from the shunting yards.

TABLE VII. Basis model (model 1), with stepwise addition of extra determinants. When a contribution is not statistically significant ($p<0.05$) it is printed in italic. The model fit is $-2\times$LogLikelihood: smaller means a better fit. ($N=354$). For technical reasons *Age* and *Sensi* are divided by 100, as indicated. Noise levels are ⩾45 dB.

	Model No.							
	1	2	3	4	5	6	7	8
Model fit	718.8	716.4	693.2	688.3	678.6	662.0	649.5	646.1
β_0	−178.59	−189.79	*−199.4*	*−197.80*	*−28.94*	*−9.89*	*−12.82*	*12.36*
DENL	3.06	3.19	*2.15*	*2.39*	*−0.73*	*−0.87*	*−1.15*	*−1.20*
*Round*2		*8.62*	*8.36*	*8.07*	*4.47*	*2.63*	*1.23*	*−0.42*
Age/100			*129*	*120*	*87*	*37*	*1*	*−4*
(*Age*/100)^2			*−120*	*−115*	*−78*	*−30*	*7*	*20*
Own			*12.88*	*5.98*	*4.24*	*−0.02*	*1.77*	*2.18*
Work			*−5.78*	*−6.12*	*−7.53*	*−5.56*	*−9.17*	*−9.20*
Sensi/100			*−41.68*	*−41.78*	*−265.01*	*−242.68*	*−205.48*	*−205.53*
(*Sensi*/100)*DENL			*1.76*	*1.73*	5.97	*5.29*	*4.42*	*4.43*
Flat				−15.16	−14.90	*−12.94*	*−12.72*	*−12.94*
Liv.Room					*6.56*	*6.91*	*5.85*	*4.43*
Bedroom					*10.30*	*8.50*	*7.03*	*5.22*
Fear						0.52	0.42	0.34
Vib							0.48	0.47
Odor								*0.18*

To investigate whether the higher annoyance from shunting yards is also due to noise from through trains, which was not included in DENL, further analyses are carried out. Analyses with the annoyance from through trains as one of the predictors indicate that this annoyance contributes substantially to the reported annoyance from shunting yards. Therefore, the noise exposure from the through trains also was assessed, and DENL for the total noise (shunting and through trains) was calculated. The analyses as reported in Table IV are repeated with this total DENL. Then the difference between shunting yards and industrial sources decreases a little, but still is substantial. The coefficient of *Shunt* decreases from 43 in Table IV for model 2, to 29 with the similar model but with total DENL. However, the model fit decreases slightly. Thus, the total DENL is not a better predictor of the noise annoyance from shunting yards than the DENL specifically for shunting yards.

Another possible explanation of the high annoyance from shunting yard noise is the impulse character of some noises at shunting yards. Analyses with the annoyance from impulse sounds as one of the predictors indicate that this annoyance contributes to the overall noise annoyance, but does not reduce the coefficient of *Shunt*. It appears that also at the industrial locations impulses are heard even though the noise was predominantly not impulse noise, and that both at the shunting and industrial locations these impulses contribute to the overall noise annoyance.

X. EFFECT OF PERIOD OF INTERVIEWING ON ANNOYANCE FROM THE SEASONAL INDUSTRY

The results for the seasonal industry indicate that, with the same yearly DENL, the annoyance is lower when the noise activities are concentrated in a limited period. To investigate whether this outcome depends on the time period in which the interviews are conducted, the social survey was repeated at the location with the seasonal industry. In the second round the interviews were conducted in autumn (of 2002), from 4 to 12 November, when the sugar plant was in full operation, instead of the spring (of 2001), in April and May, in the relatively quiet period. The sample design and questionnaire were similar as in the first round. In the second round 200 interviews were successfully completed (same person first round: 37; other person: 121; not known: 42). The nonresponse rate was 65%. The average age is 42 and 48% is female. Figure 3 gives for both rounds the observed annoyance score as a linear function of DENL. The analyses for the models in Table IV were repeated for the data from the two rounds at the seasonal industry location, with the change that the type of sources dummies (*Shunt* and *Season*) were replaced by dummy *Round*2 with value 0 for round one and value 1 for round two. The results are shown in Table VII. The effect of *Round*2 on annoyance is small, and in none of the models it is significant. The difference between the seasonal industry and the other industries found in the first round is between -23 and -34 (coefficient of *Season* in Table V), while in the second round the annoyance was only between 0 and 9 higher (not significant; coefficient of $Round2$ in Table VII). This indicates that the lower annoyance found for the seasonal industry cannot be explained by the period of interviewing in the first round (Fig. 3).

XI. CONCLUSION AND DISCUSSION

A model of the distribution of noise annoyance with the mean varying as a function of the noise exposure has been presented for industrial sources and shunting yards. DENL was used as the noise descriptor. Because the entire annoyance distribution has been modeled, any annoyance measure that summarizes this distribution can be calculated from the model. Polynomial approximations are given for the relationships between DENL and EA (expected annoyance score), %LA (—at least—a little annoyed), %A (annoyed), and %HA (highly annoyed). With the same (yearly) DENL, the seasonal industry causes less annoyance than the other industries, while the other industries cause less annoyance than the shunting yards. It appears that annoyance caused by vibrations from shunting yards and annoyance caused by noise from through trains are (partly) responsible for the relatively high annoyance from shunting yards. The relatively low annoyance from the seasonal industry presumably is related to the presence of a relatively quiet period. The same patterns of influence of age and noise sensitivity that are generally found, are also found in this study.

The data set on which these relationships are based is much smaller than the data set from which earlier similar relationships were derived for transportation noise (also presented here). In particular, the results based on data concerning two shunting yards and the results based on data concerning a single seasonal industry are indicative. But also the results concerning noise annoyance from the other industrial sources need further confirmation in other, preferably international studies.

ACKNOWLEDGMENTS

This work and its publication was made possible by financial support of the Netherlands' Ministry of Environment, and the Norwegian Pollution Control Authority.

Brackenhoff, H. E. A., Buis, P. M., and von Meier, A. (**1981**). ''Handleiding meten en rekenen industrielawaai (Guide for measuring and calculating industrial noise),'' Den Haag, Ministry of Environment ICG-Report No. IL-HR-13-01.

Buchta, E., and Vos, J. (**1998**). ''A field survey on the annoyance caused by sounds from large firearms and road traffic,'' J. Acoust. Soc. Am. **140**, 2890–2902.

de Jong, R. G., and Vos, H. (**1999**). ''Hinder door milieuverontreiniging in Nederland 1998. Verslag van deelstudies naar rangeerterreinen, militaire en kleine burgerluchtvaart (Annoyance by environmental pollution in the Netherlands, 1998. Report of studies about shunting yards, military and small aviation),'' Leiden, TNO-PG. Report No. PG/VGZ/99.042.

EU/DG Env WG2. (**2002**). ''Position paper on dose response relationships between transportation noise and annoyance,'' Brussels, EU/DG Environment.

EU/DG Env. (**2002**). ''Directive 2002/49/EC of the European Parliament and of the Council,'' Brussels, EU/DG Environment.

Fields, J. M., de Jong, R. G., Gjestland, T., Flindell, I. H., Job, R. F. S., Kurra, S., Lercher, P., Vallet, M., Yano, T., Guski, R., Felscher-Suhr, U., and Schuemer, R. (**2001**). ''Standardized noise reaction questions for community noise surveys: Research and a recommendation,'' J. Sound Vib. **242**, 641–679.

Finke, H. O., Guski, R., and Rohrmann, B. (**1980**). ''Betroffenheit einer Stadt durch Lärm: Bericht über eine interdisziplinäre Untersuchung'' (Noise Impact on a Town: Report of an Interdisciplinary Investigation), Berlin, Umweltbundesamt.

Groeneveld, Y., and de Jong, R. G. (**1985**). ''C.E.C. Joint research project 'Effects of impulse noise on human beings' (field study),'' Leiden, NIPG-TNO Report No. 85008.

Groeneveld, Y., and Gerretsen, E. (**1984**). ''Karakterisering en beoordeling van industrielawaai—samenvattend rapport'' (Characterization and evaluation of industrial noise—summary report), Den Haag, Ministery of Environment. ICG-report No. IL-HR-09-02.

Guski, R., Probst, W., Neuschwinger, B., Schlebusch, P., Van den Brulle, P., and Gerlinger, H. (**1989**). ''Störwirkungen von Sportgeräuschen im Vergleich zu Störwirkungen von Gewerbe- und Arbeitsgeräuschen'' (Disturbances due to sports noise in comparison with disturbances due to noise from small industries and workshops. An interdisciplinary field study about leisure time noise or workshop noise in residential areas), Bochum, Ruhr-Universität Bochum Forschungsbericht 105 01317/02.

ISO 1996-2 (**2002**). ''Acoustics—Description, measurement and assessment of environmental noise—Part 2: Determination of environmental noise levels,'' ISO/CD 1996-2, Geneva, International Standards Organization.

Miedema, H. M. E., and Oudshoorn, C. G. M. (**2001**). ''Annoyance from transportation noise: Relationships with exposure metrics DNL and DENL and their confidence intervals,'' Environ. Health Perspect. **109**, 409–416.

Miedema, H. M. E., and Vos, H. (**2003**). ''Noise sensitivity and reactions to noise and other environmental conditions,'' J. Acoust. Soc. Am. **113**, 1492–1504.

Miedema, H. M. E., and Vos, H. (**1999**). ''Demographic and attitudinal factors that modify annoyance from transportation noise,'' J. Acoust. Soc. Am. **105**, 3336–3344.

Pedersen, E., and Persson-Waye, K. (**2003**). ''Wind Turbine Noise: Dose-response relationship,'' Proceedings of the Eighth International Congress on the Biological Effects of Noise, ICBEN 2003, Rotterdam, The Netherlands.

Rohrmann, B., Finke, H. O., and Guski, R. (**1980**). ''Analysis of reactions to different environmental noise sources in residential areas (an urban noise study),'' Proceedings of the Third International Congress on the Biological Effects of Noise ICBEN, Rockville, MD, ASHA Report No. 10, pp. 548–555.

Vos, J. (**1995**). ''A review of research on the annoyance caused by impulse sounds produced by small firearms,'' Proceedings of Internoise '95. Newport Beach, CA, Vol. 2, pp. 875–878.

Wolsink, M., and Sprengers, M. (**1993**). ''Windturbine noise: A new environmental threat?,'' Proceedings of the Sixth International Congress on the Biological Effects of Noise, ICBEN, Nice, France, Vol. 2, pp. 235–238.

Behavioral criterion quantifying the effects of circumferential air gaps on porous materials in the standing wave tube

Dominic Pilon and Raymond Panneton[a)]
GAUS, Department of Mechanical Engineering, Université de Sherbrooke, Sherbrooke (QC) J1K 2R1, Canada

Franck Sgard
LASH-DGCB URA CNRS 1652, ENTPE, 2 Maurice Audin, 69518 Vaulx-en-Velin Cedex, France

(Received 5 October 2003; revised 2 April 2004; accepted 9 April 2004)

The influence of mounting conditions on the measurement of the absorption coefficient in the standing wave tube (swt) is investigated. In a previous paper [D. Pilon, R. Panneton, and F. Sgard, J. Acoust. Soc. Am. **114**, 1980–1987 (2003)], a behavioral criterion was developed to access the effect of a circumferential edge constraint on elastic foams. Similarly, the effect of circumferential air gaps on porous materials is studied here. The objective is to identify the materials, in terms of a ratio based on their physical properties, for which it is possible to measure the theoretical absorption coefficient when mounted inside the swt with a circumferential air gap. The difference between the measured and theoretical absorption coefficient is evaluated for a wide range of materials with various sample sizes. These errors are then sorted in terms of the chosen ratio. It is shown that for certain values of the ratio, the theoretical absorption coefficient can be efficiently measured using the swt. Through the use of this acousto-visco-inertial criterion, an experimenter can determine which absorption is going to be measured: the theoretical absorption or one that will be influenced by the circumferential air gaps.
[DOI: 10.1121/1.1756611]

PACS numbers: 43.55.Ev, 43.20.Mv, 43.20.Jr [LLT] Pages: 344–356

I. INTRODUCTION

The objective of sound absorption measurements in the standing wave tube (swt) is to obtain the normal incidence theoretical absorption coefficient (α_{th}) of the tested sample. α_{th} refers here to the absorption of a material with laterally infinite dimensions, as shown in Fig. 1(a). However, one of the main uncertainties regarding the accuracy of those measurements may arise from the potentially poor fit between the sample and tube diameters: the sample's diameter can either be smaller or larger than the swt inner diameter. This can lead to various mounting conditions inside the tube, as pointed out in Fig. 1(b). In the event that both diameters are the same and that the axial motion of the sample is not constrained, the measured absorption α_m will yield the theoretical absorption α_{th}. In reality, this mounting condition, known as the sliding condition, is hardly likely to be encountered compared to the other ones.

A larger sample diameter can induce sufficiently high friction forces, between the sample circumference and the tube wall, to nearly constrain the sample's edge from axial motion. This condition, referred to as the bonded condition, can greatly affect the vibro-acoustic behavior of the sample. A behavioral criterion was developed by the authors to quantify the effect of the edge constraint on elastic foams.[1] This criterion can identify, *a priori*, the foams for which the edge constraint will have an effect on the acoustical measurements in the swt. Through the use of this elasto-acoustic criterion, an experimenter can make an educated guess as to which absorption will be measured with the tube: the theoretical absorption α_{th} or one that is affected by either the edge constraint or the sample's dimension.

The case that is of particular interest to the present research is when the sample's diameter is smaller than the swt inner diameter; a circumferential air gap is then created between the two. This situation becomes an experimental reality when considering, for example, rigid metallic foams (aluminum, copper, iron, nickel,...) that need to be made smaller than the inner diameter of the swt to avoid difficulties in mounting them.[2] The presence of such air gaps can greatly modify the vibro-acoustic behavior of materials as acoustical

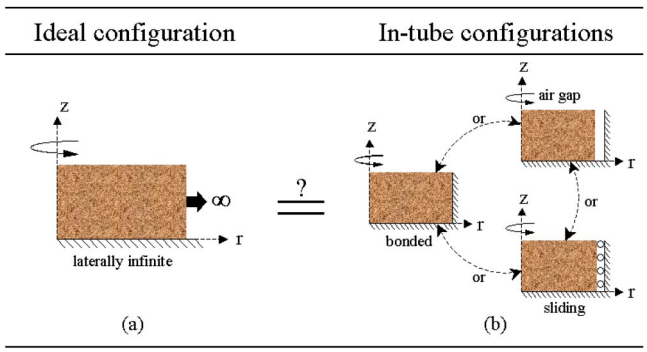

FIG. 1. Various types of lateral conditions on a disk-shaped porous sample. (a) Ideal or theoretical configuration: sample with infinite radial dimension. (b) In-tube configurations: the bonded, the free (with a circumferential air gap), and the sliding conditions. Under normal acoustic excitations, the in-tube sliding condition is equivalent to the radial infinite condition; however, in reality, this condition is hardly likely to happen.

[a)]Corresponding author Raymond Panneton; electronic mail: Raymond.Panneton@USherbrooke.ca

leakage may occur. It is therefore reasonable to assume that the swt measurements will not always lead to α_{th} when air gaps are present. Hence, two distinct questions arise from this situation. First, do the circumferential air gaps inevitably impact on the swt measurements for all porous materials? Second, how far from the theoretical absorption will the measured absorption be? Our main objective in this paper is to answer these questions.

The sample's sensitivity to air gaps is an experimental reality that has been known for some time. Early work by Schwartz and Gohmann[3] showed that important variations in the absorption coefficient could be observed due to the presence of lateral air gaps. The influence of air gaps was also studied in part by Allard and Delage.[4] They showed that the impedance of a highly resistive polyurethane foam was sensitive to the thickness of the air gaps. Cummings[5] carried out an experimental and analytical study of air gaps and found that their effects on the impedance increased as the frequency decreased and the flow resistivity increased. Through numerical modeling, Johansen *et al.*[6] observed similar effects as they concluded that it was mostly the real part of the impedance that was influenced by the air gaps. Dauchez[7] came to similar conclusions when he observed that swt measurements were quite sensitive to this particular mounting condition. The main conclusion of the combined previous works is that the principal effect of air gaps is to decrease the real part of the surface impedance and, ultimately, decrease the measured absorption coefficient α_m. This is a direct consequence of the acoustical leakage that occurs in the air gap.

Most of the previous researches were carried out to study the direct influence of circumferential air gaps on acoustical measurements. No information was given in order to identify which materials would be affected by this mounting condition. Furthermore, the latter have only been conducted on a small number of materials, usually two or three. It is therefore difficult to make a general assessment of the effects of that condition on the vibro-acoustic behavior of other materials, i.e., which ones will be affected and which will not. This is where the present research aims at bringing new developments.

By studying the air gap and porous material as a whole, one has a system that can be considered as a double porosity media. While studying these types of problems, Olny and Boutin[8] concluded that the phenomena involved were much more complicated than previously thought. They noticed that the presence of macroperforations, or in our case air gaps, could sometimes induce pressure diffusion phenomena in the porous material. These phenomena can actually increase the imaginary part of the surface impedance in such a way that the absorption coefficient will also increase. It is therefore wrong to assume that the effect of an air gap will automatically result in the reduction of the absorption. This was also verified by Atalla *et al.*[9] who studied the absorption of macroperforated porous materials. The double porosity theory, which is summarized in Sec. V, is applied to the air gap problem so as to better understand the effects of this mounting condition on various porous materials.

As stated previously, our main objective in this paper is to devise a method that allows for an efficient identification of the porous materials for which α_{th} can be measured using the swt—in the case where the sample is mounted with a circumferential air gap in the tube. This method must be relatively easy to carry out at any point during the characterization process. As a result, a simple ratio of the material properties is chosen as the identification tool. A secondary objective is to quantify the difference between α_m and α_{th} when the latter cannot be measured using the tube. This is achieved through the evaluation of the global error committed between α_m and α_{th}—which is noted as $\Sigma\Delta_\alpha$. Furthermore, in view of drawing general conclusions on the effect of the air gaps, the investigation is performed on a large number of porous materials (elastic foams, fibrous materials, and rigid metallic foams) and sample configurations.

This paper is structured as follows. In the first section, α_{th} and α_m are briefly introduced to set the bases of the forthcoming analysis. In the second section, the error estimation depicting the effect of the circumferential air gaps is presented. In the third section, the properties and dimensions of the studied porous materials are given. Finally, the development of the acousto-visco-inertial behavioral criterion is detailed and discussed.

II. EXPRESSION OF α_{th} AND α_m

To identify how the sound absorption coefficient measured with the swt (α_m) compares with the expected theoretical absorption coefficient (α_{th}) of a material, both coefficients need first to be defined.

Following Biot's theory,[10,11] three waves may propagate simultaneously in an air-saturated open-cell poroelastic material; two compressional waves and one shear wave. If the material is assumed to be of infinite lateral extent and excited by a normally incident acoustical plane wave, no shear wave propagates. Under these circumstances, the normal-incidence sound absorption coefficient of the poroelastic material is written as

$$\alpha_{\text{th}} = 1 - |R_x|^2, \tag{1}$$

with R_x, the complex reflection coefficient, given by

$$R_x = \frac{Z_n - \rho_0 c_0}{Z_n + \rho_0 c_0}, \tag{2}$$

where ρ_0 and c_0 are the ambient density and velocity of sound in the air, and Z_n is the normal-incidence surface impedance of the poroelastic material. The expression of Z_n is detailed in the Appendix.

Since it is difficult to master correctly the boundary conditions applied on a porous sample in the experimental setup of the swt, numerical simulations of the swt are used to evaluate the ''measured'' absorption α_m with a circumferential air gap. The simulations use high-order axisymmetric finite elements[12] based on the mixed Biot (u-p) poroelastic formulation.[13] The boundary and coupling conditions to be applied on the mixed Biot (u-p) and acoustical formulations are detailed by Debergue *et al.*[14] The general method used to evaluate the absorption coefficient from the numerical results is presented elsewhere.[9,15]

III. ERROR ESTIMATION

In this study, the computed solution of interest for the analysis is the sound absorption coefficient. Since the absorption is a global indicator and a frequency-dependent variable, the difference, or error, between α_m and α_{th} is characterized by the sum ($\Sigma\Delta_\alpha$) of the area between α_m and α_{th} from 0 to the cutoff frequency of the tube.

Depending on the effect of the air gap (an increase or a decrease in the absorption), the error can either be positive or negative. As the effect of the air gap diminishes, the area between the two curves, and therefore the error $\Sigma\Delta_\alpha$ will tend to zero. Inversely, if the air gap has a great effect on the measurement of the absorption coefficient, $\Sigma\Delta_\alpha$ will be important (either positive or negative). To normalize this error, it is divided by $\Sigma\alpha_{\text{th}}$, which is the total area under the theoretical absorption curve α_{th}.

IV. SAMPLE SIZE AND MATERIAL PROPERTIES

The measurements in a swt are usually performed over three different frequency ranges: high (up to 6900 Hz), medium (up to 3100 Hz), and low (up to 2000 Hz). They correspond to three different tube diameters that are 29, 64, and 99 mm, respectively.

To represent a wide variety of experimental configurations, each material sample is modelled with the three different tube diameters and with four different thicknesses (10, 25, 50, and 100 mm). Furthermore, the effects of three different air gap thicknesses (0.5, 1, and 2 mm) are studied for each tube diameter; nine sample radii are therefore used (12.5, 13.5, 14, 30, 31, 31.5, 47.5, 48.5, and 49 mm). A total of 36 sample sizes are studied for each material. The evaluation of α_{th} and α_m is carried out over 45 different open-cell porous materials (elastic foams, fibrous materials, and rigid metallic foams). Hence, 1620 finite element simulations are carried out to evaluate α_m and 180 analytical results are computed for the evaluation of α_{th}. Consequently, a total of 1800 numerical simulations are accomplished to reach the objectives of this work.

The range of values for the properties of the 45 porous materials are presented in Table I. The mechanical properties (E, ν, and η) of the materials were evaluated using the method described by Langlois *et al.*[16] The flow resistivity (σ), the porosity (ϕ), and the bulk density (ρ_1) are measured using nonacoustical methods,[17,18] whereas the tortuosity (α_∞) and the viscous and thermal lengths (Λ and Λ') are measured using both acoustical[19] and ultrasound[20,21] methods. The acoustical method is used in the high-frequency range, i.e., over the decoupling frequency,[22] to make sure that the elastic effects do not influence the measurements.

V. THE PERMEABILITY RATIO

Before presenting the expression of the permeability ratio, a short review of the theoretical background is done. First, the visco-inertial effects in single and double porosity media are recalled and the expressions of the static visco-inertial permeability of the micro- and macroporous networks are given. The physical interpretation of the permeability ratio is then detailed.

A. Visco-inertial effects and permeability expressions

The presence of macro-perforations, or air gaps, has significant effects on both the visco-inertial and thermal dissipations in a porous material. In the present study, our attention is focused on the visco-inertial phenomena, as they are most relevant to the study of pressure diffusion effects.[8] In the following, the main results regarding visco-inertial effects for single and double porosity media are recalled. In both cases, a homogeneous equivalent fluid medium is considered to simplify the study of the underlying physical phenomena.

1. Single porosity media

From a macroscopic point of view, the general behavior of the viscous flow in a porous material is governed by the dynamic, or generalized, Darcy's law.[23] Considering the one-dimensional problem, the generalized Darcy's law is written as

$$v_z = -\frac{\Pi(\omega)}{\eta}\frac{\partial p_z}{\partial z}, \tag{3}$$

where v_z and $\partial p_z/\partial z$ are the macroscopic mean velocity and pressure gradient of air, respectively, η is the dynamic viscosity of air, and $\Pi(\omega)$ is the Darcy visco-inertial dynamic permeability.

Figure 2 presents the low- and high-frequency asymptotic behaviors of the modulus of $\Pi(\omega)$. As it can be seen, the visco-inertial permeability exhibits two distinct flow regimes, the viscous and inertial flows, which are determined by the viscous characteristic frequency ω_v:

$$\omega_v = \frac{\eta\phi}{\rho_o\alpha_\infty\Pi^s}, \tag{4}$$

where α_∞ and Π^s are the tortuosity and the Darcy static visco-inertial permeability of the porous material, respectively. Below ω_v, the viscous forces are predominant and the flow regime is dissipative. $\Pi(\omega<\omega_v)$ is constant and its value, as a first approximation, is equal to Π^s. For a typical porous material, the expression of the static visco-inertial permeability Π^s is

$$\Pi^s = \frac{\eta}{\sigma}, \tag{5}$$

where σ is the static airflow resistivity of the porous material. Beyond ω_v, the viscous forces become small compared to the inertial ones. The flow regime is therefore propagative and the dynamic behavior is driven by the inertial forces.

2. Double porosity media

The various visco-inertial effects in double porosity media are summarized in the following. To simplify the explanation of the underlying physical phenomena, an approach using the visco-inertial permeability contrast is used. Although intuitive, the accuracy of this approach is limited to porous materials having a relatively low tortuosity ($\alpha_\infty < 3$), as the latter can influence the various visco-inertial properties of a material, like ω_v and $\Pi(\omega)$. The choice of the permeability contrast approach is based on the necessity to

develop a practical criterion that needs to be relatively easy to evaluate throughout the characterization process. Nevertheless, the results presented here are valid for most typical porous materials ($\alpha_\infty < 3$). For a more rigorous presentation of the theory of wave propagation in double porosity media, the reader can refer to the work of Olny and Boutin.[8]

Three scales are needed to describe the structure of a double porosity media: macroscopic (the wavelength in the material), mesoscopic (the macro-perforations), and microscopic (the micropores).[8] In other words, a double porosity material essentially consists of a typical porous material to which large holes, or macroperforations, are added. This is illustrated in Fig. 3. For such a material, two porous networks can be identified: a micro- and a macroporous network. The microporous network consists of the porous material itself, without the macroperforations. On the other hand, the macroporous network consists of the large holes, which are parallel to the direction of propagation (z), placed in an impervious solid instead of the porous material.

The static visco-inertial permeability of the double porosity material, Π^s_{dp}, is given by

$$\Pi^s_{\mathrm{dp}} = (1-\phi_m)\Pi^s + \Pi^s_m, \tag{6}$$

where ϕ_m is the porosity associated to the macroporous network and Π^s and Π^s_m are the static visco-inertial permeability of the micro- and macroporous networks, respectively. For the configuration presented in Fig. 3, the expression of ϕ_m is

$$\phi_m = \frac{\pi b^2}{a^2}, \tag{7}$$

where b is the radius of the macroperforations and a is the side of the square lattice. The expression of Π^s is given by Eq. (5) whereas the expression of Π^s_m is given by the static visco-inertial permeability of a cylinder (where $\alpha_\infty = 1$):

$$\Pi^s_m = \frac{\phi_m b^2}{8}. \tag{8}$$

Figure 4 shows the low and high-frequency asymptotic behaviors of the modulii of the dynamic visco-inertial permeabilities $\Pi(\omega)$ and $\Pi_m(\omega)$. Regarding the dynamic behavior of the flow, the same comments as mentioned before for single porosity media can be made for both the micro- and macroporous networks. There is a viscous and an inertial flow in both porous networks. The viscous characteristic frequency for the micro-porous network ω_v is given by Eq. (4). The viscous characteristic frequency of the macroporous network ω_{vm} is written as

$$\omega_{vm} = \frac{8\eta}{\rho_0 b^2}. \tag{9}$$

As it can be seen in Fig. 4, above ω_v, Π^s and Π^s_m are the same. Therefore, past this frequency, the macroperforations (or air gaps in our case) will have no effect on the behavior of the material. Below ω_v, the dynamic behavior of the double porosity material can be very different depending if a low or high permeability contrast exists.

TABLE I. Range of values for the properties of the 45 porous materials.

Properties		Range of values	Units
Name	Symbol		
Young's modulus	E	1000–4 400 000	N/m^2
Bulk density	ρ_1	9–396	kg/m^3
Poisson's ratio	ν	0–0.46	
Loss factor	η	0–0.88	
Static airflow resistivity	σ	2000–465 000	Ns/m^4
Porosity	ϕ	0.7–0.995	
Tortuosity	α_∞	1–2.57	
Viscous length	Λ	14–322	μm
Thermal length	Λ'	48–524	μm

In the low permeability contrast situation, the flow dynamics is governed by the generalized Darcy's law, just as in a single porosity medium. The difference lies in the properties of $\Pi_{\mathrm{dp}}(\omega)$. In the middle-frequency range, from ω_{vm} to ω_v, the flow is simultaneously viscous in the micropores and inertial in the macropores. The behavior of the double porosity medium is then influenced by both porous networks. In the low-frequency range ($\omega < \omega_{vm}$), the flow is essentially viscous. Since the wavelength in the macropores is large compared to the one in the micropores, the flow behavior is mostly governed by the flow in the macropores. Hence, when ω tends toward 0, $\Pi_{\mathrm{dp}}(\omega)$ tends toward Π^s_m. Therefore, generally speaking, in the low permeability contrast situation, the absorption of a double porosity material is globally inferior to the absorption of the same porous material without the macroperforations. This is a direct consequence of the acoustical leakage that occurs in the latter.

In the high permeability contrast situation, a new dissipation effect that does not exist in simple porosity media is induced: the pressure diffusion effect. This pressure diffusion phenomenon occurs around the frequency ω_d, the characteristic frequency of pressure diffusion effects, which is defined as

$$\omega_d = \frac{(1-\phi_m)P_0\Pi^s}{\phi\eta D^s}, \tag{10}$$

where P_0 is the ambient pressure, ϕ the porosity of the po-

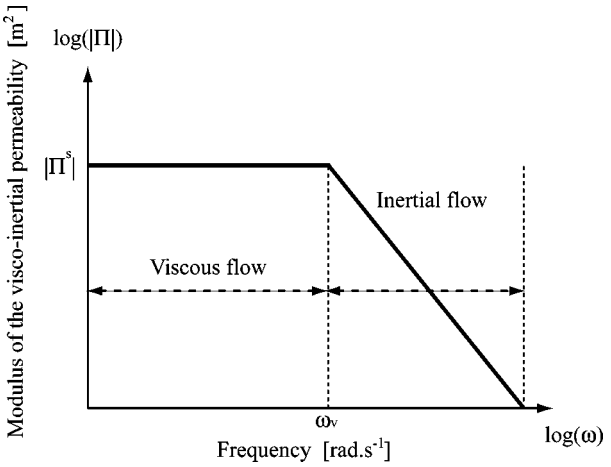

FIG. 2. Asymptotic behavior of the visco-inertial permeability in a single porosity media.

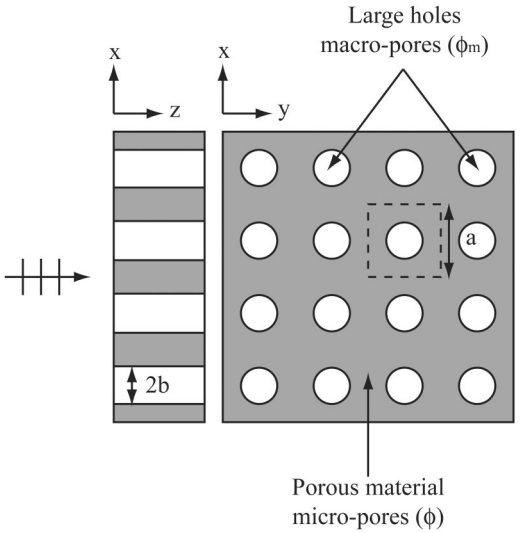

FIG. 3. An example of a double porosity media. A typical porous material with macroperforations (large holes).

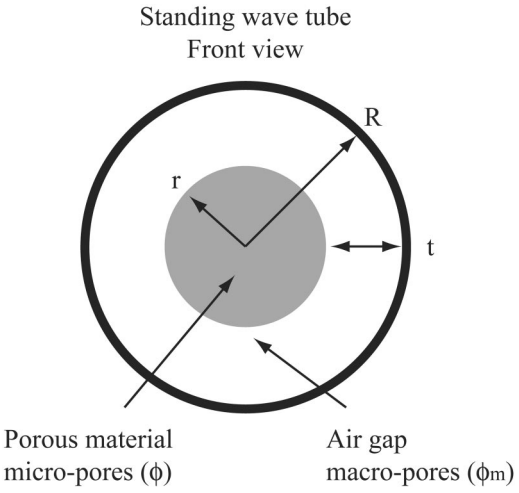

FIG. 5. In-tube configuration of the material sample with the circumferential air gap.

rous material without the macroperforations, and D^s is the static diffusion permeability. This last parameter is analog to the static thermal permeability of Lafarge *et al.*[24] Its expression is given elsewhere.[8] At low frequency ($0<\omega<\omega_d$), the dynamic behavior of the flow is viscoinertial and is driven mainly by the macropores. Here again, when ω tends toward 0, $\Pi_{\mathrm{dp}}(\omega)$ tends toward Π_m^s. In the middle-frequency range ($\omega_d<\omega<\omega_v$), the micropores do not participate in the macroscopic behavior of double porosity material. The dynamic behavior of the flow is inertial and is dictated by the macropores. The most interesting behavior is, of course, obtained around ω_d. Because of the dissipative nature of the flow in the micropores and the fact that the size of the wavelength in this network is similar to the characteristic dimension of the macroperforations, a pressure diffusion phenomenon takes place.[8] This induces a new dissipation effect, which leads to an increase in the absorption on a wide frequency range centered around ω_d. Therefore, in the high permeability contrast, the absorption of a double porosity material is globally superior compared to the absorption of the same porous material without the macroperforations.

3. The macro- and microporous networks in the swt setup

The theory of double porosity media is now applied to the problem of a material sample mounted inside the swt with an air gap. The expressions of Π^s and Π_m^s are defined here for this particular configuration. Figure 5 shows a porous material sample mounted inside the tube with an air gap. R is the inner radius of the tube, r the radius of the material sample, and t is the thickness of the air gap.

The micro- and macroporous networks are represented by the porous material and the air gap, respectively. In the present study, the macro-porous network is considered as an equivalent cylinder having the same surface area as the air

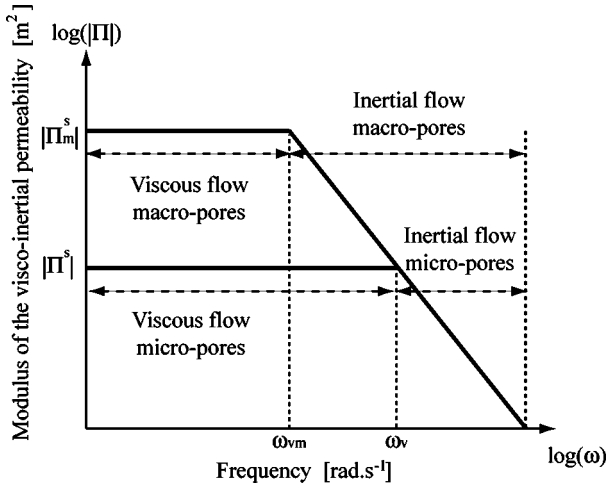

FIG. 4. Asymptotic behavior of the dynamic visco-inertial permeabilities of both the micro- and macroporous networks in a double porosity media.

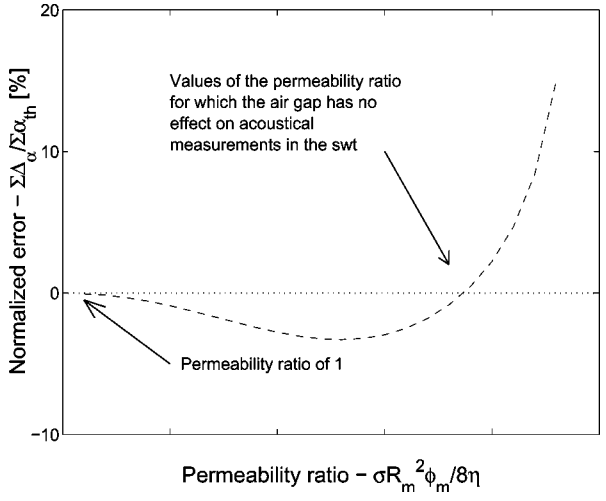

FIG. 6. Expected typical evolution of the normalized error as a function of the permeability ratio for various porous materials in a given sample configuration inside the swt.

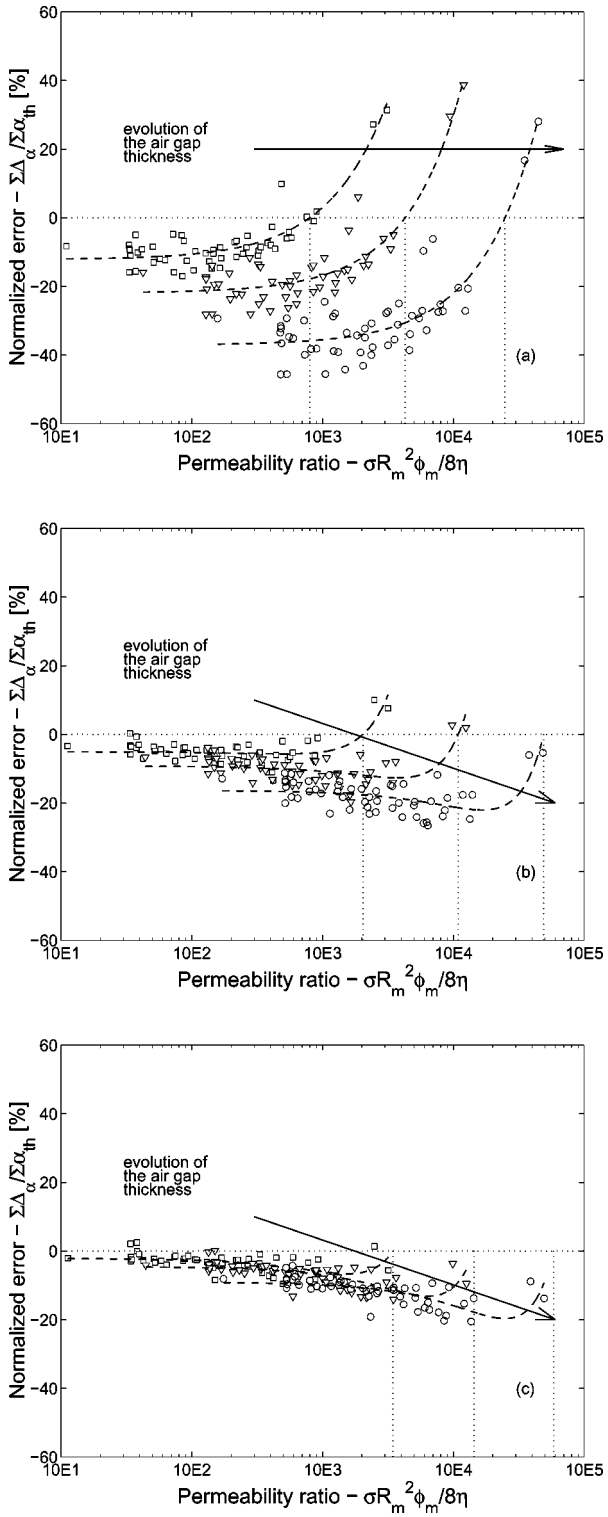

FIG. 7. Evolution of the normalized error $\Sigma\Delta_\alpha/\Sigma\alpha_{\text{th}}$ as a function of the permeability ratio $\sigma R_m^2\phi_m/8\eta$ for the three air gap thicknesses (□: 0.5 mm, ▽: 1 mm, and ○: 2 mm) and a 10 mm sample thickness. Tube diameters of (a) 29 mm, (b) 64 mm, and (c) 99 mm.

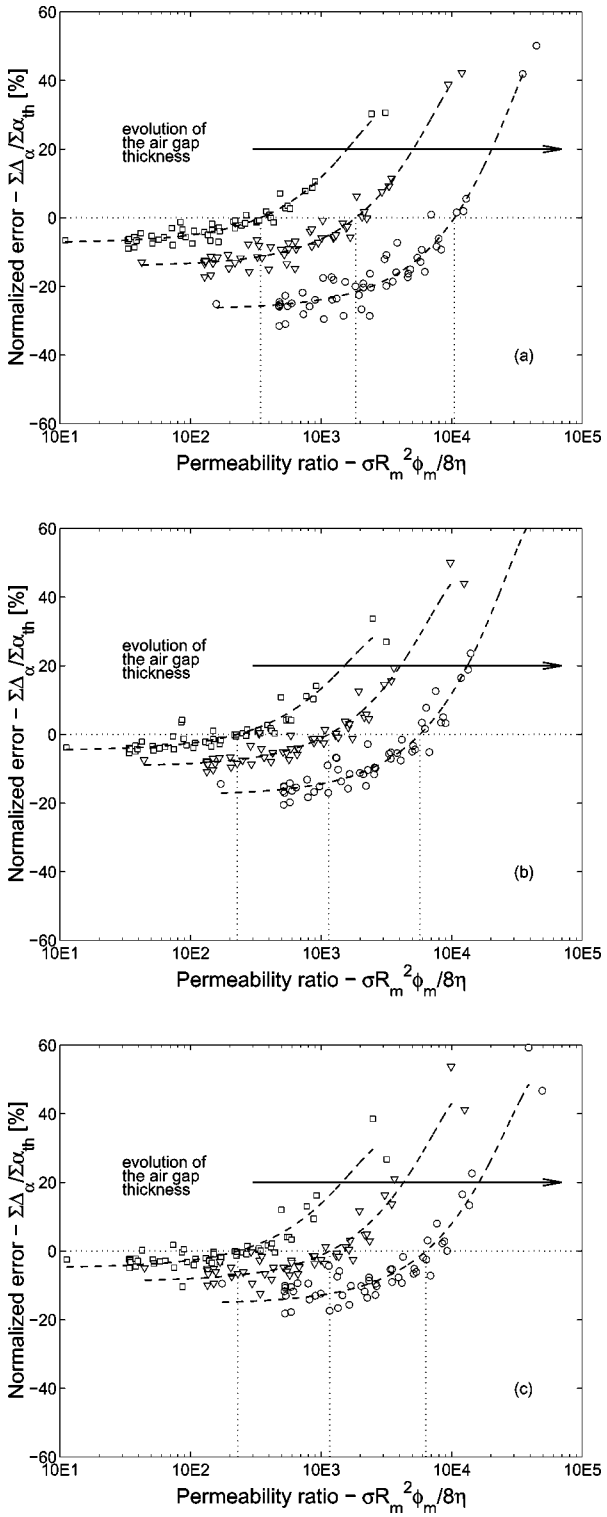

FIG. 8. Evolution of the normalized error $\Sigma\Delta_\alpha/\Sigma\alpha_{\text{th}}$ as a function of the permeability ratio $\sigma R_m^2\phi_m/8\eta$ for the three air gap thickness (□: 0.5 mm, ▽: 1 mm, and ○: 2 mm) and a 25 mm sample thickness. Tube diameters of (a) 29 mm, (b) 64 mm, and (c) 99 mm.

gap; hence, its tortuosity is equal to one ($\alpha_\infty=1$). The resulting porosity of the macro-porous network, ϕ_m, is defined as follows:

$$\phi_m=\frac{R^2-r^2}{R^2}=\frac{R_m^2}{R^2}, \tag{11}$$

with R_m, the radius of the equivalent cylinder:

$$\left.\begin{array}{c}\pi R_m^2=\pi R^2-\pi r^2\\ r=R-t\end{array}\right\}\Rightarrow R_m=\sqrt{2Rt-t^2}. \tag{12}$$

The expressions of Π^s and Π_m^s can now be defined as

TABLE II. Polynomial equations and validity range for a 10 mm sample thickness.

Setup		$f(x)=ax^2+bx+c$					
		Polynomial coefficients			Range		$f(x_0)=0$
$2R$ (mm)	t (mm)	a	b	c	$[x_{\min}$	$x_{\max}]$	x_0
29	0.5	−2.3689e−7	1.5413e−2	−12.1538	[11	3100]	798
29	1	8.9449e−9	5.0860e−3	−21.8994	[43	11 950]	4274
29	2	−8.6213e−10	1.5161e−3	−37.0652	[158	44 500]	24 798
64	0.5	2.4620e−6	−2.5243e−3	−5.0639	[12	3150]	2035
64	1	2.4720e−7	−1.8471e−3	−9.2123	[45	12 400]	10 893
64	2	2.0835e−8	−6.9054e−4	−16.3343	[171	48 200]	49 107[a]
99	0.5	1.8439e−6	−5.7393e−3	2.1625	[12	3170]	3452[a]
99	1	2.0738e−7	−2.6709e−3	−4.5518	[45	12 550]	14 403[a]
99	2	1.7318e−8	−8.5802e−4	−9.0767	[175	49 300]	58 503[a]

[a]Extrapolated values.

$$\Pi^s=\frac{\eta}{\sigma},$$

$$\Pi^s_m=\frac{\phi_m R_m^2}{8}. \tag{13}$$

B. Interpretation of the permeability ratio

As pointed out earlier, the devised criterion needs to be relatively easy to evaluate throughout the characterization process. Hence, the ratio used to sort out the different errors is the ratio of Π^s_m to Π^s. This dimensionless parameter represents the permeability contrast and takes into account the various visco-inertial effects in the air gap–porous material system:

$$\frac{\Pi^s_m}{\Pi^s}=\frac{\sigma\phi_m R_m^2}{8\eta}. \tag{14}$$

Since Π^s_m cannot be inferior to Π^s, the ratio is always superior or equal to 1. A low value of the ratio points to a low permeability contrast between the air gap and the porous material. As described previously, in this situation the error committed on the measurement of the absorption is negative as acoustical leakage occurs. Furthermore, in the particular situation where the ratio is equal to 1 the error between α_m and α_{th} is equal to zero, i.e., the acoustical measurements in the swt are not influenced by the air gap. But this situation hardly ever occurs for typical porous materials. As for high values of the ratio, the error committed is positive since the permeability contrast is high (pressure diffusion effects occur in the system).

For a given sample configuration in the tube (a fixed R, r, t, and sample thickness), as the flow resistivity of the tested materials increases, the permeability ratio also increases. Hence, the permeability contrast evolves from low to high and the error from negative to positive. Therefore, in a given range of values of the permeability ratio, other than near 1, the error must necessarily be equal or close to zero as it goes from a negative value to a positive one. This phenomenon can be observed in Fig. 6, where the expected typical evolution of the normalized error as a function of the permeability ratio is presented. As it can be seen, the normalized error is close to 0 for a permeability ratio of 1 and for a higher range of the permeability ratio. This higher range of the ratio is what the present research aims at identifying, i.e., identifying the configurations and the materials for which the air gap has no effects on the measurement of the absorption.

VI. RESULTS AND DISCUSSION

In the following, the various errors for the different sample configurations are sorted according to the permeability ratio. Hence, the various ranges of values of the ratio for which no error is committed between α_m and α_{th} are identi-

TABLE III. Polynomial equations and validity range for a 25 mm sample thickness.

Setup		$f(x)=ax^2+bx+c$					
		Polynomial coefficients			Range		$f(x_0)=0$
$2R$ (mm)	t (mm)	a	b	c	$[x_{\min}$	$x_{\max}]$	x_0
29	0.5	−3.0743e−6	2.2095e−2	−7.2422	[11	3100]	344
29	1	−2.8415e−7	8.1592e−3	−14.0722	[43	11 950]	1843
29	2	−2.3850e−8	2.7860e−3	−26.6358	[158	44 500]	10 505
64	0.5	−3.2064e−6	2.1182e−2	−4.6649	[12	3150]	228
64	1	−3.1581e−7	8.5105e−3	−9.3273	[45	12 400]	1145
64	2	−3.1993e−8	3.2763e−3	−17.6841	[171	48 200]	5717
99	0.5	−3.2408e−6	2.1920e−2	−4.8747	[12	3170]	230
99	1	−2.7011e−7	7.8975e−3	−8.8592	[45	12 550]	1168
99	2	−2.3960e−8	2.5760e−3	−15.3910	[175	49 300]	6350

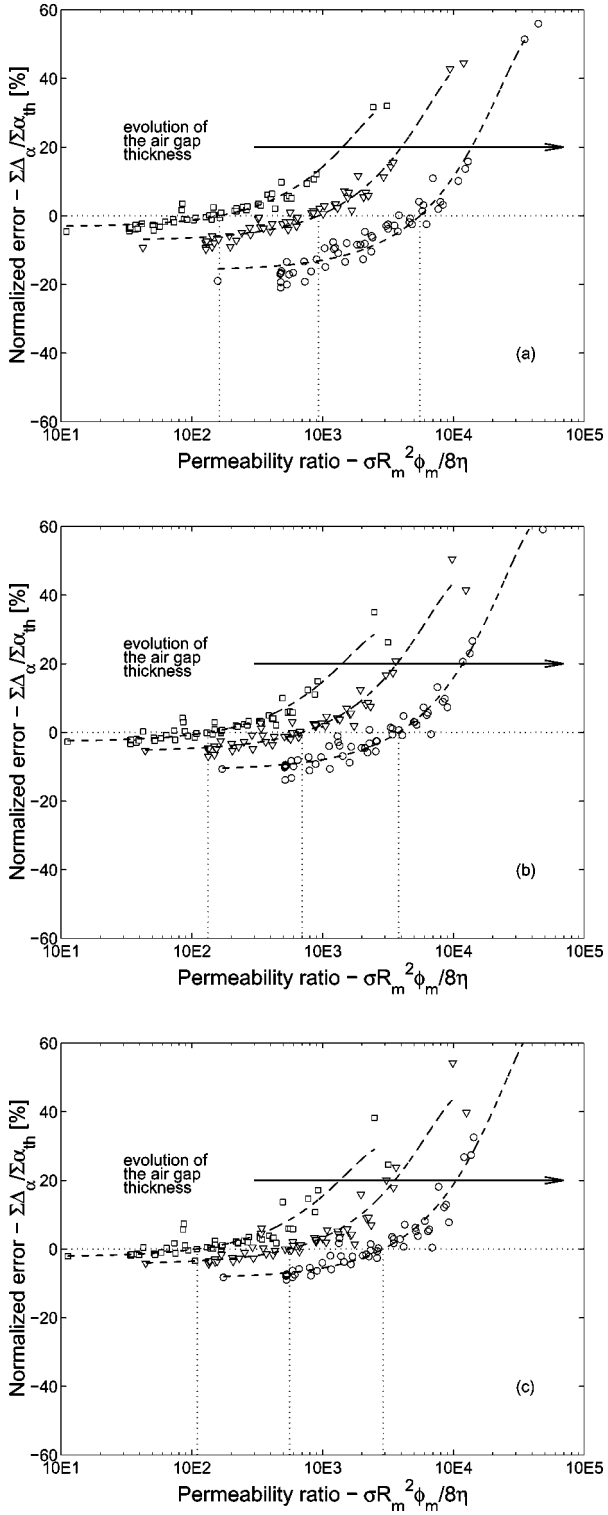

FIG. 9. Evolution of the normalized error $\Sigma\Delta_\alpha/\Sigma\alpha_{\mathrm{th}}$ as a function of the permeability ratio $\sigma R_m^2\phi_m/8\eta$ for the three air gap thickness (□: 0.5 mm, ▽: 1 mm, and ○: 2 mm) and a 50 mm sample thickness. Tube diameters of (a) 29 mm, (b) 64 mm, and (c) 99 mm.

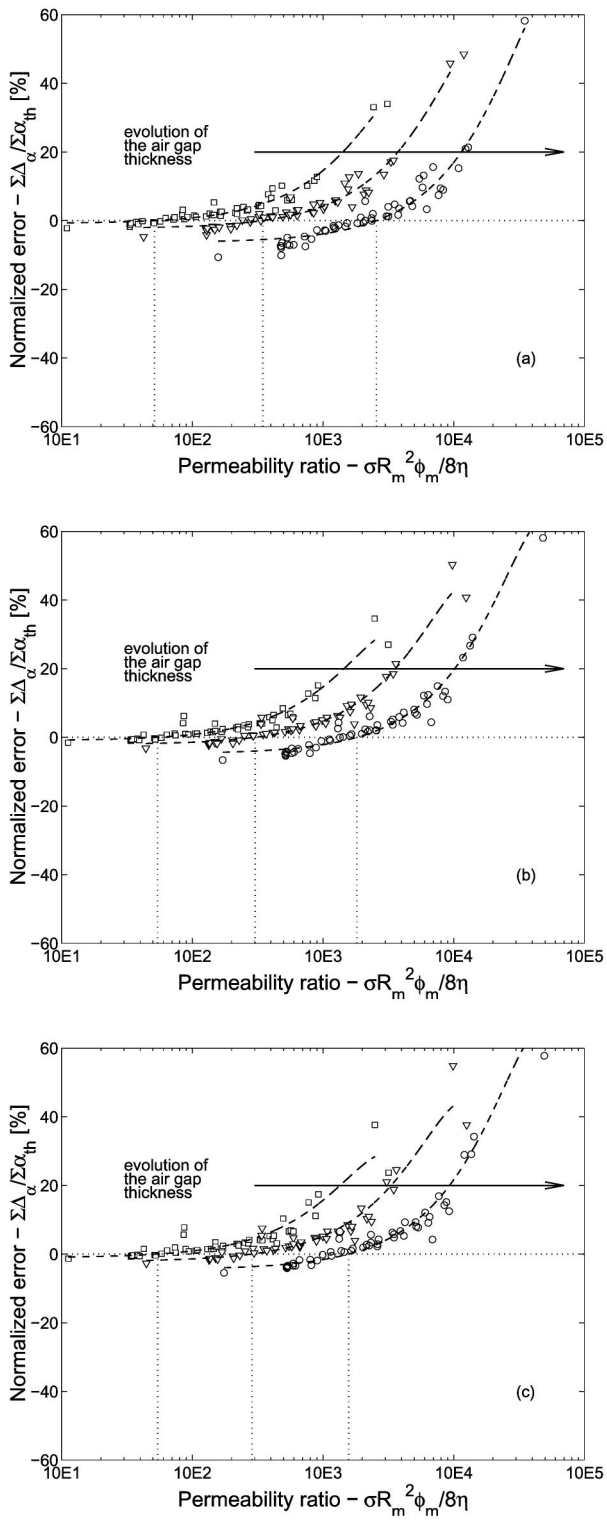

FIG. 10. Evolution of the normalized error $\Sigma\Delta_\alpha/\Sigma\alpha_{\mathrm{th}}$ as a function of the permeability ratio $\sigma R_m^2\phi_m/8\eta$ for the three air gap thickness (□: 0.5 mm, ▽: 1 mm, and ○: 2 mm) and a 100 mm sample thickness. Tube diameters of (a) 29 mm, (b) 64 mm, and (c) 99 mm.

fied. An analysis of the results obtained for a 10, 25, 50, and a 100 mm sample thickness is done. The acousto-visco-inertial criterion is then presented as a function of the inner tube radii and of the sample thicknesses.

A. Sample thickness of 10, 25, 50, and 100 mm

1. 10 mm sample thickness

Figures 7(a)–7(c) present the normalized errors $(\Sigma\Delta_\alpha/\Sigma\alpha_{\mathrm{th}})$ as a function of the permeability ratio for the different material samples having a 10 mm thickness. In the different figures, the squares represent the errors obtained

TABLE IV. Polynomial equations and validity range for a 50 mm sample thickness.

Setup		$f(x)=ax^2+bx+c$					
		Polynomial coefficients			Range		$f(x_0)=0$
$2R$ (mm)	t (mm)	a	b	c	$[x_{min}$	$x_{max}]$	x_0
29	0.5	−2.7949e−6	2.0328e−2	−3.2444	[11	3100]	163
29	1	−3.0600e−7	8.0236e−3	−7.2009	[43	11 950]	930
29	2	−3.2852e−8	3.0689e−3	−15.9901	[158	44 500]	5539
64	0.5	−3.3123e−6	2.0802e−2	−2.7099	[12	3150]	133
64	1	−3.1895e−7	8.0846e−3	−5.4833	[45	12 400]	697
64	2	−2.9756e−8	2.9798e−3	−10.9147	[171	48 200]	3808
99	0.5	−3.4738e−6	2.1214e−2	−2.2905	[12	3170]	110
99	1	−3.1585e−7	7.9756e−3	−4.3647	[45	12 550]	600
99	2	−3.0100e−8	3.0403e−3	−8.5751	[175	49 300]	2904

with a 0.5 mm air gap, the triangles with a 1 mm air gap, and the circles with a 2 mm air gap. Figure 7(a) is for a 29 mm tube diameter, Fig. 7(b) for a 64 mm tube diameter, and Fig. 7(c) for a 99 mm tube diameter. The dashed lines have been obtained using a curve fitting procedure (a polynomial function of degree 2). They show the average tendency curves of the errors committed for a particular sample setup. The polynomial coefficients of the different curves and the validity range of the polynomial functions are presented in Table II.

Generally speaking, in all three graphs in Fig. 7, it can be seen that the presence of an air gap usually leads to a global decrease in the absorption. Only the materials with an extremely high flow resistivity, which yields a very high permeability contrast, show pressure diffusion effects (i.e., an absorption increase). This is related to the thickness of the samples; though existing, the pressure diffusion phenomena are not efficient in thin samples. This will be confirmed later when analyzing the results obtained for thicker samples. The vertical dotted lines in the different figures point out the values of the permeability ratio for which the error is equal to zero $[f(x_0)=0]$. These values are also listed in Table II. The extrapolated values of x_0 in Table II were given only as an indication, as no tested materials in the particular sample setups had a permeability ratio high enough to actually have no error. Furthermore, the expected behavior presented in Fig. 6 is clearly apparent here. Figures 7(b) and 7(c) exhibit the expected behavior close to a permeability ratio of 1. As for Fig. 7(a), it clearly depicts the transition between a negative and a positive error.

2. 25 mm sample thicknesses

Figures 8(a)–8(c) present the normalized errors $(\Sigma\Delta_\alpha/\Sigma\alpha_{th})$ as a function of the permeability ratio for the different material samples having a 25 mm thickness. The data is presented in the exact same manner as in Fig. 7. The polynomial coefficients of the tendency curves and the validity range of the polynomial functions are presented in Table III. The vertical dotted lines in the different figures point out the values of the permeability ratio for which the error is equal to zero $[f(x_0)=0]$. These values are also listed in Table III.

The transition between a positive and a negative error is apparent in all three figures. This is a direct result of the greater sample thickness that yields more efficient pressure diffusion phenomena. The latter increases the absorption, hence providing a more apparent transition between negative and positive errors. Also, a tendency can be identified regarding the effect of the air gap thickness: the larger the air gap, the more important the error. This result was expected and is verified for the three tube diameters.

TABLE V. Polynomial equations and validity range for a 100 mm sample thickness.

Setup		$f(x)=ax^2+bx+c$					
		Polynomial coefficients			Range		$f(x_0)=0$
$2R$ (mm)	t (mm)	a	b	c	$[x_{min}$	$x_{max}]$	x_0
29	0.5	−1.7986e−6	1.7249e−2	−0.8804	[11	3100]	51
29	1	−1.9590e−7	6.6873e−3	−2.2963	[43	11 950]	347
29	2	−2.1851e−8	2.5509e−3	−6.3996	[158	44 500]	2565
64	0.5	−2.6060e−6	1.8257e−2	−0.9827	[12	3150]	54
64	1	−2.6735e−7	7.1464e−3	−2.1405	[45	12 400]	303
64	2	−2.6460e−8	2.7047e−3	−4.8281	[171	48 200]	1817
99	0.5	−3.3120e−6	2.0060e−2	−1.0819	[12	3170]	54
99	1	−3.1986e−7	7.7387e−3	−2.1914	[45	12 550]	287
99	2	−2.9887e−8	2.9102e−3	−4.4965	[175	49 300]	1570

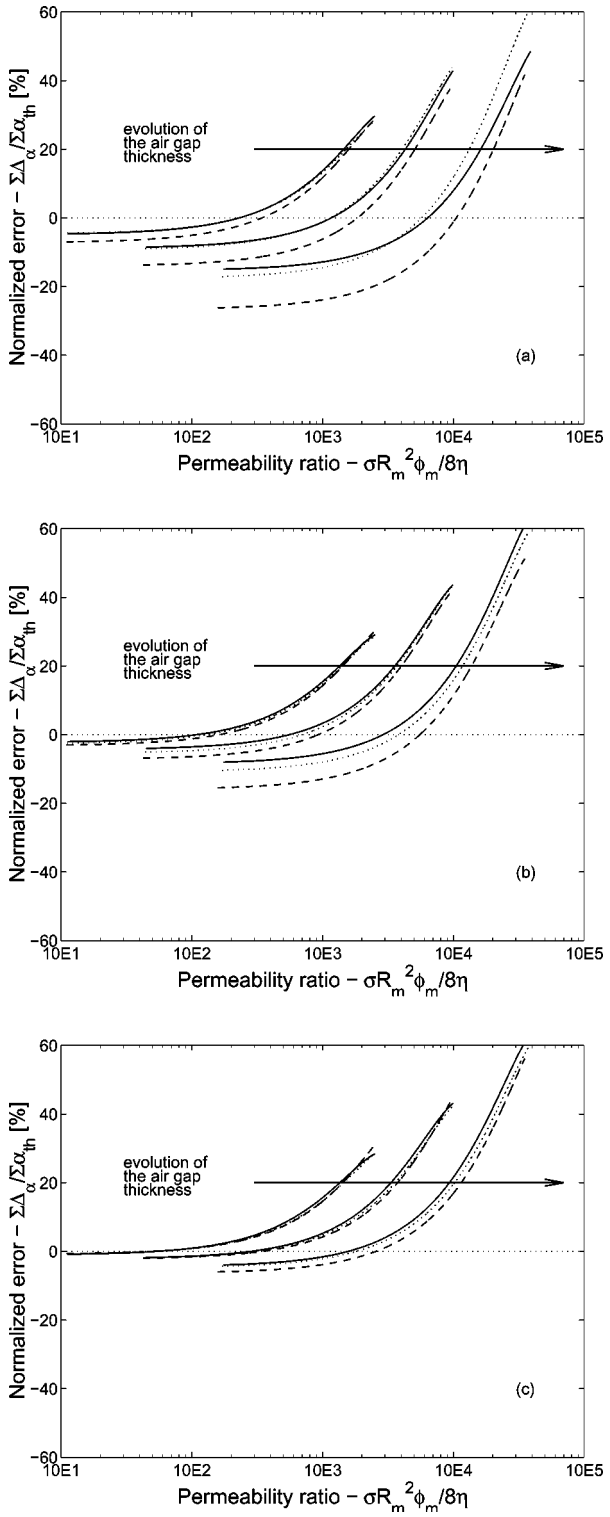

FIG. 11. Evolution of the normalized error $\Sigma\Delta_\alpha/\Sigma\alpha_{\mathrm{th}}$ as a function of the permeability ratio $\sigma R_m^2\phi_m/8\eta$ for the three air gap thickness (0.5, 1, and 2 mm) and three tube diameters; — — —, 29 mm; ⋯, 64 mm; —, 99 mm. Sample thickness of (a) 25 mm, (b) 50 mm, and (c) 100 mm.

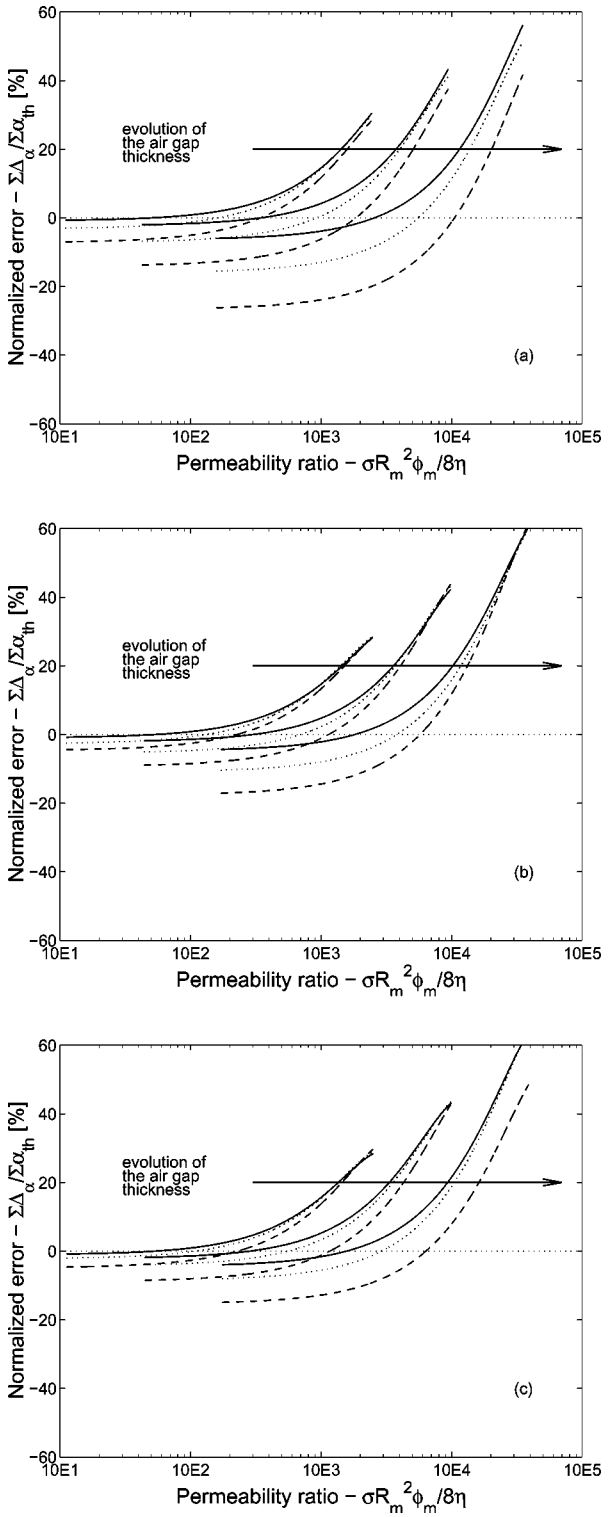

FIG. 12. Evolution of the normalized error $\Sigma\Delta_\alpha/\Sigma\alpha_{\mathrm{th}}$ as a function of the permeability ratio $\sigma R_m^2\phi_m/8\eta$ for the three air gap thickness (0.5, 1, and 2 mm) and three sample thickness; — — —, 25 mm; ⋯, 50 mm; —, 100 mm. Tube diameters of (a) 29 mm, (b) 64 mm, and (c) 99 mm.

3. 50 mm sample thickness

Figures 9(a)–9(c) present the normalized errors ($\Sigma\Delta_\alpha/\Sigma\alpha_{\mathrm{th}}$) as a function of the permeability ratio for the different material samples having a 50 mm thickness. The data is presented in the exact same manner as in Fig. 7. The polynomial coefficients of the tendency curves and the validity range of the polynomial functions are presented in Table IV. The vertical dotted lines in the different figures point out the values of the permeability ratio for which the error is equal to zero [$f(x_0)=0$]. These values are also listed in Table IV.

It is clear that as the permeability ratio increases, the

error goes from negative to positive, just as explained previously. Also, the tendency regarding the effect of the air gap thickness on the amplitude of the errors is confirmed: smaller air gaps yield smaller errors.

4. 100 mm sample thickness

Figures 10(a)–10(c) present the normalized errors ($\Sigma\Delta_\alpha/\Sigma\alpha_{\text{th}}$) as a function of the permeability ratio for the different material samples having a 100 mm thickness. The data is presented in the exact same manner as in Fig. 7. The polynomial coefficients of the tendency curves and the validity range of the polynomial functions are presented in Table V. The vertical dotted lines in the different figures point out the values of the permeability ratio for which the error is equal to zero [$f(x_0)=0$]. These values are also listed in Table V.

Generally speaking, in all three graphs in Fig. 10, it can be seen that the presence of an air gap usually leads to a global increase in the absorption. Only the materials with a low flow resistivity, which yields a low permeability contrast, show a decrease in the absorption. As previously explained, this is due to the fact that the samples are very thick. Hence, the pressure diffusion phenomena are very efficient, which almost always leads to an increase in the absorption.

B. All the data as a function of the sample thicknesses and tube diameter

Figures 11(a)–11(c) present all of the data for a 25, 50, and 100 mm sample thickness, respectively. The data for a sample thickness of 10 mm are not presented here since the various curves would be hard to read if all placed in the same figure. The squares, triangles, and circles depicting the errors in the previous figures are also omitted here so as to simplify the reading of the various curves. In each figures, the set of curves most to the left are for a 0.5 mm air gap, the ones in the middle are for a 1 mm air gap, and the ones to the right are for a 2 mm air gap. Also, the dashed lines are for a 29 mm swt diameter, the dotted lines are for a 63 mm tube diameter, and the continuous lines are for a 99 mm tube diameter.

Presenting the data in this way allows the user to make a ''visual interpolation'' when identifying the error committed for a tube diameter that is not specifically studied here. A general observation can be made regarding the effect of the sample thickness: the thicker the sample, the more the error made on the absorption measurement tends to be positive. As explained previously, this is related to the sample thickness: the thicker is the sample is, the more efficient the pressure diffusion phenomena.

Figures 12(a)–12(c) present all of the data for a 25, 50, and 100 mm sample thickness, respectively. The data for the 10 mm thickness is also omitted here. In each figure, all of the data for one swt diameter is presented. Hence, Fig. 12(a) presents the data computed for the 29 mm tube diameter on all the three sample thicknesses. In each figure, the set of curves most to the left are for a 0.5 mm air gap, the ones in the middle are for a 1 mm air gap, and the ones to the right are for a 2 mm air gap. Also, the dashed lines are for a 25 mm sample thickness, the dotted lines are for a 50 mm sample thickness, and the continuous lines are for a 99 mm sample thickness. Presenting the data in this way allows the user to make a ''visual interpolation'' when identifying the error committed for a sample thickness that is not specifically studied here.

TABLE VI. Properties of material samples A and B.

Material	H (m)	R (m)	t (m)	σ (Ns/m^4)	$\sigma R_m^2\phi_m/8\eta$	$\Sigma\Delta_\alpha/\Sigma\alpha_{\text{th}}$ (%)
A	0.1	0.0145	0.0005	13 748	92	0.7
B	0.1	0.0145	0.0005	135 000	900	13

C. How to use the criterion and the figures

In the following, a short explanation on how to use the criterion and the various figures is carried out. Two examples, using material A and B, are given. The properties of the material samples are presented in Table VI. The normalized errors in Table VI are computed using the proper polynomial function.

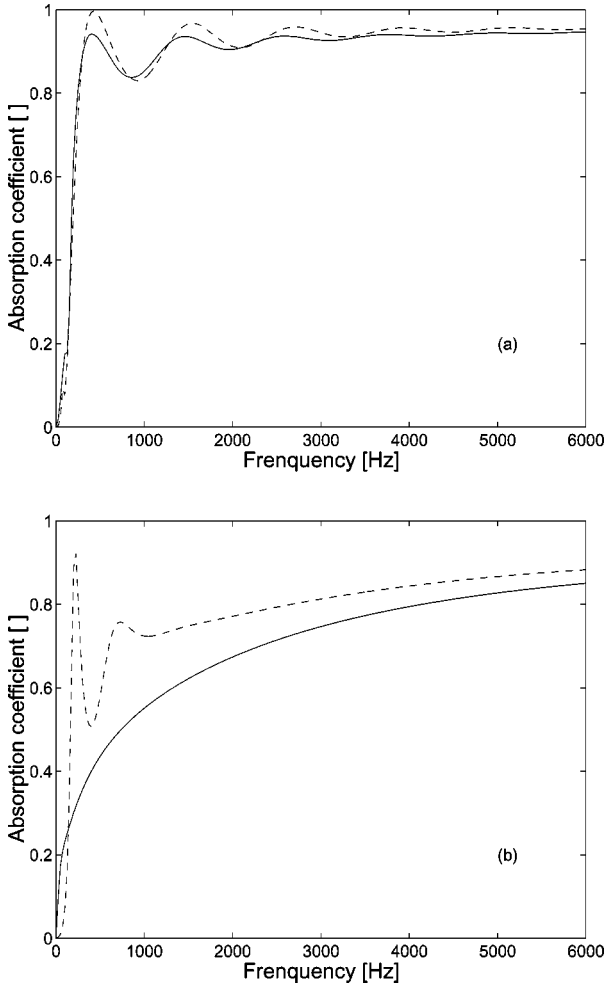

FIG. 13. Absorption coefficient as a function of the frequency in the 29 mm diameter swt for a 100 mm sample thickness. — — —, α_m (absorption with a 0.5 mm air gap); —, α_{th} (theoretical absorption). (a) material A and (b) material B.

Once the material samples have been cut to fit in the swt, the experimenter needs to evaluate the samples' properties. For example, each sample is 100 mm thick and has been cut to fit in the 29 mm diameter tube with a 0.5 mm air gap. Knowing that the static airflow resistivity of materials A and B are 13 748 Ns/m^4 and 135 000 Ns/m^4, respectively, the experimenter can evaluate the various parameters (R_m, ϕ_m, Π_m^s, Π^s, and the ratio) using Eqs. (11)–(14). The corresponding errors are obtained using the curve on the far left (0.5 mm air gap) in Fig. 10(a) (29 mm tube diameter and 100 mm sample thickness). The errors can also be computed using the first polynomial equation in Table V. For this sample configuration, the global error on the measured absorption coefficient is about 0.7% and 13% for material A and B, respectively. These values give a general idea of the effect of the air gap on the material behavior. Hence, α_m should be about the same as α_{th} for material A and globally superior to α_{th} for material B. This can be seen in Figs. 13(a) and 13(b) where α_m and α_{th} are plotted for the two materials and the previously described mounting conditions.

VII. CONCLUSION

The objective of this paper was to develop a practical method to identify the porous materials that are affected by the presence of a circumferential air gap. To achieve this objective, an acousto-visco-inertial criterion was developed. The criterion relies on the evaluation of a simple ratio, a function of easily measured properties of the material sample. The chosen ratio, $\sigma R_m^2 \phi_m / 8\eta$, expresses the permeability contrast between the macroporous (air gap) and microporous (porous material) networks. It takes into account the various visco-inertial effects that take place within the air gap–porous material system. The method consists in evaluating the ratio for a given material sample and experimental setup and to use Figs. 7–12 (or Tables II–V) to see what the error on the measured absorption coefficient will be. It is seen that for certain values of the ratio, the error or difference between the measured absorption α_m and the theoretical absorption α_{th} is close to zero. In that situation, the circumferential air gap as no effect on the vibro-acoustic behavior of the sample. The use of the different figures is valid for a wide range of porous materials (elastic foams, fibrous materials, rigid metallic foams,...) as long as their properties are within the prescribed range of values of Table I (especially the tortuosity that needs to be inferior to 3). Through the use of this acousto-visco-inertial criterion, an experimenter can make an educated guess as to which absorption will be measured with the tube: the theoretical absorption α_{th} or one that is affected by the air gap.

ACKNOWLEDGMENTS

The authors wish to thank N.S.E.R.C. Canada, F.Q.R.N.T. Quebec and C.Q.R.D.A. Quebec for their financial support. This study was also supported in part by the ''IMPACT'' research project of the Rhône–Alpes Region in France.

APPENDIX A: ANALYTICAL EXPRESSION OF Z_n

In making the assumption that the poroelastic material has infinite lateral dimensions and that it is excited by a normally incident plane wave, one can thus neglect the effect of the shear wave in the material. Hence, the normal surface impedance only depends on the two compressional waves and is defined as[25]

$$Z_n = -j \frac{(Z_1^s Z_2^f \mu_2 - Z_2^s Z_1^f \mu_1)}{D}, \tag{A1}$$

where D is

$$D = (1-\phi+\phi\mu_2)[Z_1^s - (1-\phi)Z_1^f \mu_1]\tan(\delta_2 l) + (1-\phi+\phi\mu_1)[Z_2^f \mu_2 (1-\phi) - Z_2^s]\tan(\delta_1 l), \tag{A2}$$

with

$$\left.\begin{aligned} \mu_i &= \frac{\tilde{P}\delta_i^2 - \omega^2 \tilde{\rho}_{11}}{\omega^2 \tilde{\rho}_{12} - \tilde{Q}\delta_i^2} \\ Z_i^f &= (\tilde{R} + \tilde{Q}/\mu_i)\frac{\delta_i}{\phi\omega} \\ Z_i^s &= (\tilde{P} + \tilde{Q}\mu_i)\frac{\delta_i}{\omega} \end{aligned}\right\}, \quad \forall, \quad i = 1,2, \tag{A3}$$

and

$$\delta_1^2 = \frac{\omega^2}{2(\tilde{P}\tilde{R} - \tilde{Q}^2)}[\tilde{P}\tilde{\rho}_{22} + \tilde{R}\tilde{\rho}_{11} - 2\tilde{Q}\tilde{\rho}_{12} - \sqrt{\Delta}], \tag{A4}$$

$$\delta_2^2 = \frac{\omega^2}{2(\tilde{P}\tilde{R} - \tilde{Q}^2)}[\tilde{P}\tilde{\rho}_{22} + \tilde{R}\tilde{\rho}_{11} - 2\tilde{Q}\tilde{\rho}_{12} + \sqrt{\Delta}], \tag{A5}$$

$$\Delta = (\tilde{P}\tilde{\rho}_{22} + \tilde{R}\tilde{\rho}_{11} - 2\tilde{Q}\tilde{\rho}_{12})^2 - 4(\tilde{P}\tilde{R} - \tilde{Q}^2)(\tilde{\rho}_{11}\tilde{\rho}_{22} - \tilde{\rho}_{12}^2). \tag{A6}$$

In the previous equations, ϕ is the porosity of the material, μ_1 and μ_2 are the ratios of the velocity of the air over the velocity of the frame for the given compressional wave. They indicate the phase of the material in which the waves mainly propagate. Z_1^s and Z_2^s are characteristic impedances related to the propagation of the compressional waves in the frame, and Z_1^f and Z_2^f are related to their propagation in the air. δ_1 and δ_2 are the complex wave numbers. $\tilde{P}, \tilde{Q}, \tilde{R}$ and $\tilde{\rho}_{11}, \tilde{\rho}_{12}, \tilde{\rho}_{22}$ are, respectively, Biot's complex elastic coefficients and complex effective densities. The expressions of these parameters are detailed elsewhere.[25]

[1] D. Pilon, R. Panneton, and F. Sgard, ''Behavioral criterion quantifying the edge-constrained effects on foams in the standing wave tube,'' J. Acoust. Soc. Am. **114**, 1980–1987 (2003).
[2] T. J. Lu, A. Hess, and M. F. Ashby, ''Sound absorption in metalic foams,'' J. Appl. Phys. **85**, 7528–7539 (1999).
[3] M. Schwartz and E. J. Gohmann, ''Influence of surface coatings on impedance and absorption of urethane foams,'' J. Acoust. Soc. Am. **34**, 502–512 (1962).
[4] J.-F. Allard and P. Delage, ''Free field measurements of absorption coefficients on square panels of absorbing materials,'' J. Sound Vib. **101**, 161–170 (1985).

[5] A. Cummings, ''Impedance tube measurements on porous media: the effects of air-gaps around the sample,'' J. Sound Vib. **151**, 63–75 (1991).
[6] T. F. Johansen, J.-F. Allard, and B. Brouard, ''Finite element method for predicting the acoustical properties of porous samples,'' Acta Acoustica **3**, 487–491 (1995).
[7] N. Dauchez, ''Etude vibroacoustique des matériaux poreux par éléments finis,'' Ph.D. thesis, INSA, Lyon, France, 1999.
[8] X. Olny and C. Boutin, ''Acoustic wave propagation in double porosity media,'' J. Acoust. Soc. Am. **114**, 73–89 (2003).
[9] N. Atalla, F. Sgard, R. Panneton, and X. Olny, ''Acoustic absorption of macro-perforated porous materials,'' J. Sound Vib. **243**, 659–678 (2001).
[10] M. A. Biot, ''Theory of propagation of elastic waves in a fluid-saturated porous solid. I. Low-frequency range,'' J. Acoust. Soc. Am. **28**, 168–178 (1956).
[11] M. A. Biot, ''Theory of propagation of elastic waves in a fluid-saturated porous solid. II. Higher frequency range,'' J. Acoust. Soc. Am. **28**, 179–191 (1956).
[12] D. Pilon, R. Panneton, and F. Sgard, ''Convergence of *N*th order Biot poroelastic finite elements,'' Proceedings of the 9th International Conference on Sound and Vibration, Orlando, 8–11 July 2002.
[13] N. Atalla, R. Panneton, and P. Debergue, ''A mixed displacement-pressure formulation for poroelastic materials,'' J. Acoust. Soc. Am. **104**, 1444–1452 (1998).
[14] P. Debergue, R. Panneton, and N. Atalla, ''Boundary conditions for the weak formulation of the mixed (*u*,*p*) poroelasticity problem,'' J. Acoust. Soc. Am. **106**, 2383–2390 (1999).
[15] R. Panneton and N. Atalla, ''An efficient finite element scheme for solving the three-dimensional poroelasticity problem in acoustics,'' J. Acoust. Soc. Am. **101**, 3287–3298 (1997).
[16] C. Langlois, R. Panneton, and N. Atalla, ''Polynomial relations for quasi-static mechanical characterization of isotropic poroelastic materials,'' J. Acoust. Soc. Am. **110**, 3032–3040 (2001).
[17] M. R. Stinson and G. A. Daigle, ''Electronic system for the measurement of flow resistance,'' J. Acoust. Soc. Am. **83**, 2422–2428 (1988).
[18] Y. Champoux, M. R. Stinson, and G. A. Daigle, ''Air-based system for the measurement of the porosity,'' J. Acoust. Soc. Am. **89**, 910–916 (1990).
[19] R. Panneton, Y. Atalla, D. Blanchet, and M. Bloor, ''Validation of the inverse method of acoustic material characterization,'' SAE Noise and Vibration Conference and Exhibition, Grand Traverse, MI, May 2003.
[20] J.-F. Allard, B. Castagnède, M. Henry, and W. Lauriks, ''Evaluation of tortuosity in acoustic porous materials saturated by air,'' Rev. Sci. Instrum. **65**, 754–755 (1994).
[21] P. Leclaire, L. Kelders, W. Lauriks, M. Melon, N. R. Brown, and B. Castagnede, ''Determination of the viscous and thermal characteristic lengths of plastic foams by ultrasonic measurements in helium and air,'' J. Appl. Phys. **80**, 2009–2012 (1996).
[22] O. C. Zwikker and C. W. Kosten, *Sound-Absorbing Materials* (Elsevier, Amsterdam, 1949).
[23] J. L. Auriault, L. Borne, and R. Chambon, ''Dynamics of porous saturated media checking of the generalized law of Darcy,'' J. Acoust. Soc. Am. **77**, 1641–1650 (1985).
[24] D. Lafarge, P. Lemarinier, J.-F. Allard, and V. Tarnow, ''Dynamics compressibility of air in porous structures at audible frequencies,'' J. Acoust. Soc. Am. **104**, 1995–2006 (1997).
[25] J.-F. Allard, *Propagation of Sound in Porous Media. Modeling Sound Absorbing Materials* (Elsevier, New York, 1993).

Objective evaluation of chamber-music halls in Europe and Japan[a)]

Takayuki Hidaka[b)] and Noriko Nishihara
Takenaka R & D Institute, 1-5-1, Otsuka, Inzai, Chiba 270-1395, Japan

(Received 27 December 2002; accepted for publication 26 January 2004)

The room acoustical parameters reverberation time, RT; early decay time, EDT; clarity, C_{80}; time gravity, T_g; bass ratio, BR; strength, G; initial time delay gap, ITDG; interaural cross-correlation coefficient, $IACC_E$, the where binaural quality index BQI equals $[1\text{-}IACC_{E3}]$; and stage support, ST1 were measured in 18 major chamber-music halls in Austria, Germany, the Netherlands, Czech Republic, Switzerland, and Japan, employing procedures in accordance with ISO 3382 (1997). In combination with the architectural data, the intrinsic objective parameters for the acoustics of chamber-music halls and their variation range were examined. The results of these studies reveal four pertinent orthogonal parameters: RT, G, ITDG, BQI. General design guidelines for a chamber-music hall are presented. © *2004 Acoustical Society of America.*
[DOI: 10.1121/1.1760112]

PACS numbers: 43.55.Fw, 43.55.Gx, 43.55.Hy [MK] Pages: 357–372

I. INTRODUCTION

For symphony halls and opera houses, the results of measurements of current room acoustical parameters have been reported in the literature (Beranek, 1996, 2003a, 2003b; Hidaka and Beranek, 2000). There are only limited numbers of similar studies on chamber-music halls (Barron, 1993; Meyer, 1978a, 1978b). There is no assurance whether existing data or design guidelines for large symphony halls are also suitable for smaller-sized spaces. Therefore, it seems important to assemble acoustical data for them and to survey their architectural features. In this paper, nine highly reputed chamber halls of traditional design in Europe and nine of contemporary design in Japan are compared and studied. This paper also discusses various qualities peculiar to chamber-music halls.

II. THE SURVEYED HALLS

A. Styles and features

The halls that were studied, that are regularly used for chamber music in each city and are regarded as important venues for music lovers, are listed in Table I. European halls can be classified as those of traditional style, and Japanese halls as those of modern construction and materials. That is, all of the traditional halls have walls and ceilings made of heavy materials, like those of existing symphony halls, but the majority of the modern halls have interiors that are constructed from gypsum board, usual or reinforced, supported by light-gauge steel backing, mounted on sound-insulating concrete walls. For the traditional halls the ceilings and upper side walls are built from plaster with baroque ornamentation, which is highly sound reflective and diffusive over a reasonably wide frequency range.

1. Amsterdam, Kleinersaal Concertgebouw (abbreviated AC)

This chamber-music hall is located in the Concertgebouw in Amsterdam (Fig. 1). It is oval in plan, with a single balcony that overhangs the rear end of the hall. The interior surfaces are mainly of plaster. Deep decorations on the side walls contribute to sound diffusion. The ceiling has a modestly concave (upward) plain surface, from which a large chandelier hangs. Door niches on all sides of the main floor (a total of ten) are covered by thick curtains, which apparently help solve the sound focusing and uneven distribution normally caused by an oval shape. There are only a small number of oval-shaped halls in Europe, like those investigated and reported here. Chairs in this hall have lighter upholstering than those used in the adjacent Grossersaal.

2. Berlin, Kleinersaal Konzerthaus, BK (Fasold et al., 1987)

This chamber-music hall is located inside the Konzerthaus, Berlin (Fig. 2). It is shoebox shaped, with one surrounding, nonoverlapping balcony. Mortar is used for all the interior surfaces, decorated with splendid paintings. The left sidewall looking toward the stage at the main-floor level is alternately curtains and rigid wall. The hall has many diffusing elements, such as chandeliers and decorations. Because the sound reflector over the stage is movable, this is the only element in this study that is not integrated with the architecture. Apparently, this hall is used to some extent for multiple purposes. Judging from the details of the stage enclosure, it would seem that there are insufficient reflections of the performers' sounds to the audience area. The light upholstering of the chairs in BK is almost the same as that in the adjacent Grossersaal.

3. Prague, Martine Hall, PM

The Martine Hall has the smallest seat count, 201, among those investigated, and the row-to-row seat spacing is

[a)]Presented at the 17th ICA, Rome in 2001.
[b)]Electronic mail: hidaka.takayuki@takenaka.co.jp

TABLE I. Chamber halls for which objective measurements are available. Listing is alphabetical. The subscripts "L," "M," and "3" mean, respectively, that the octave band average is for 125 and 250 Hz, 500 and 1000 Hz, and 500, 1000, and 2000 Hz. All data were measured by the Takenaka R. & D. Institute.

Halls		V m^3	N	V/S_A m	$RT_{M,occ}$ s	$EDT_{M,unocc}$ s	$BR_{occ.}$ –	$C_{80,3\,B,unocc}$ dB	$T_{g3\,B,unocc}$ ms	$G_{L,unocc}$ dB	$G_{M,unocc}$ dB	1-$IACC_{E3}$ (80 ms)	ITDG ms
AC	Amsterdam, Kleinersaal in Concertgebouw	2190	478	9.4	1.25	1.49	1.21	1.5	101	13.7	12.9	0.69	17.0
BK	Berlin, Kleinersaal in Konzerthaus	2150	440	9.0	1.08	1.32	1.24	2.0	89	12.2	10.9	0.67	12.0
KH	Kanagawa, Higashitotsuka Hall	3576	482	8.6	1.20	1.21	0.90	1.9	86	5.4	8.7	0.67	18.5
KM	Kirishima, Miyama Conceru	8475	770	15.8	1.84	1.80	1.12	−0.1	130	8.2	8.3	0.75	25.5
PM	Prague, Martine Hall	2410	201	18.4	1.76	2.19	1.12	−1.9	150	12.7	12.6	0.68	15.5
SG	Salzburg, Grossersaal in Mozarteum	4940	844	11.5	1.66	2.06	1.07	−1.6	147	9.9	9.6	0.69	19.5
SW	Salzburg, Wiennersaal in Mozarteum	1070	209	8.4	1.11	1.33	1.09	1.7	93	14.9	14.3	0.77	15.0
TC	Tokyo, Casals Hall	6060	511	17.8	1.67	1.79	1.00	−1.3	137	7.6	9.4	0.71	16.5
TD	Tokyo, Dai-ichi Seimei Hall	6800	767	13.3	1.66	1.83	1.09	−0.1	126	9.8	10.8	0.71	24.0
TH	Tokyo, Hamarikyu Asahi Hall	5800	552	14.7	1.67	1.82	0.93	0.0	122	7.1	8.7	0.71	14.0
TI	Tokyo, Ishibashi memorial Hall	5450	662	14.9	1.70	1.84	1.10	−0.8	139	9.2	10.8	0.75	19.5
TM	Tokyo, Mitaka Arts Center	5500	625	13.3	1.73	2.26	1.01	−2.2	164	9.0	11.1	0.75	16.5
TS	Tokyo, Sumida Small Sized Hall	1460	252	9.7	0.93	1.08	1.03	2.8	77	8.1	10.6	0.74	8.5
TT	Tokyo, Tsuda Hall	4500	490	12.5	1.33	1.42	0.90	0.8	110	7.6	10.7	0.71	17.0
VB	Vienna, Brahmssaal	3390	604	10.0	1.63	2.37	1.16	−2.8	174	12.8	13.6	0.77	10.0
VM	Vienna, Mozartsaal in Konzerthaus[a]	3920	716	9.1	1.49	1.79	1.14	−0.2	127	11.6	10.8	0.70	20.5
VS	Vienna, Schubertsaal in Konzerthaus[a]	2800	336	15.6	1.98	2.54	1.14	−3.3	186	14.7	13.6	0.77	11.5
ZT	Zurich, Kleinersaal in Tonhall	3234	610	9.3	1.58	2.11	1.18	−1.8	149	14.1	13.2	0.70	13.5

[a]Measured before recent acoustic renovation.

1.05 m, far larger than in the rest of the halls (Fig. 3). The simple rectangular shape with flat floor and no balcony is reminiscent of a ballroom. Glass windows on the side walls are on the outside of 1-m-deep niches, which form large-scale sound-diffusing elements. The walls, niches, and the ceiling are nearly plane and are finished with painted plaster. A large pipe organ is located at the rear of the stage. There are no sound-absorbing materials in the room.

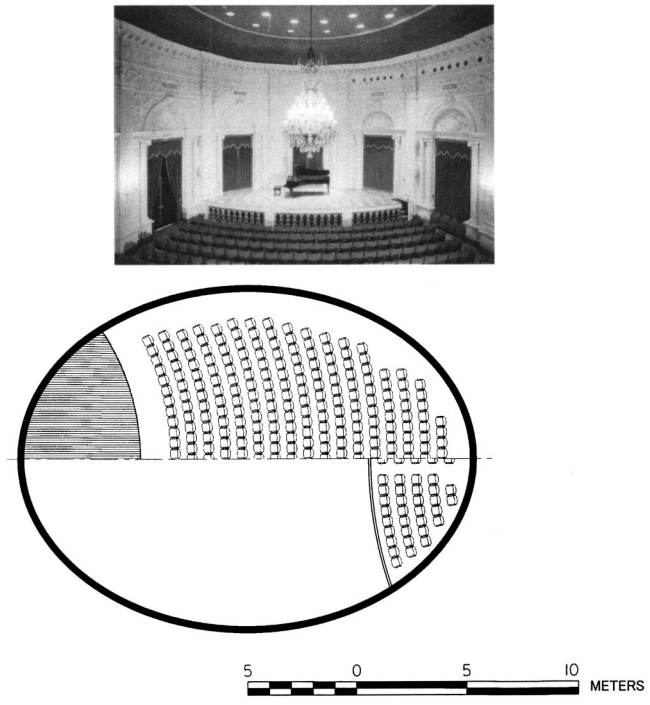

FIG. 1. Amsterdam, Kleinersaal Concertgebouw, AC, plan and photo.

4. Salzburg, Grossersaal Mozarteum, SG

This hall has the largest seating capacity, 844, of those investigated (Fig. 4). It may be described as an architecturally reduced version of traditional European shoebox symphony halls, e.g., the Grosser Musikvereinssaal of Vienna. There is one balcony and the pipe organ is fully embedded in the rear wall of the stage. The ceiling and upper walls are joined by a concave curvature. The side walls of the main floor and the rear wall of the stage are finished with thin wood, while the ceiling and side walls above the balcony are

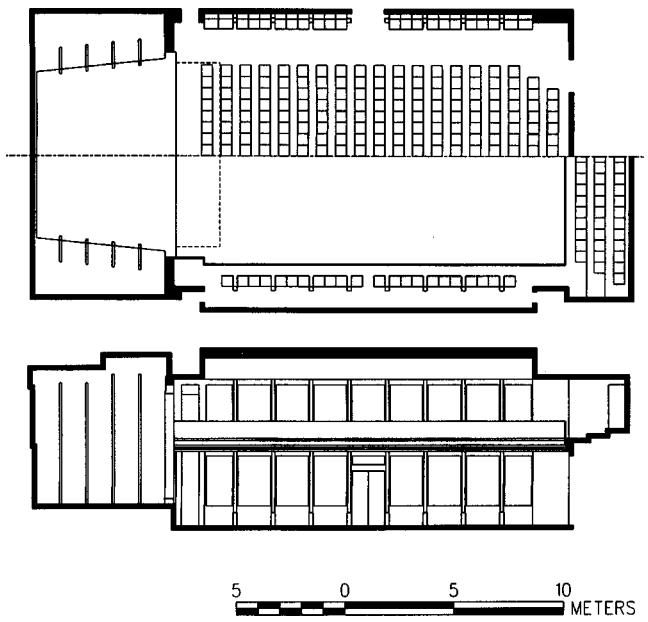

FIG. 2. Berlin, Kleinersaal Konzerthaus, BK, plan and section.

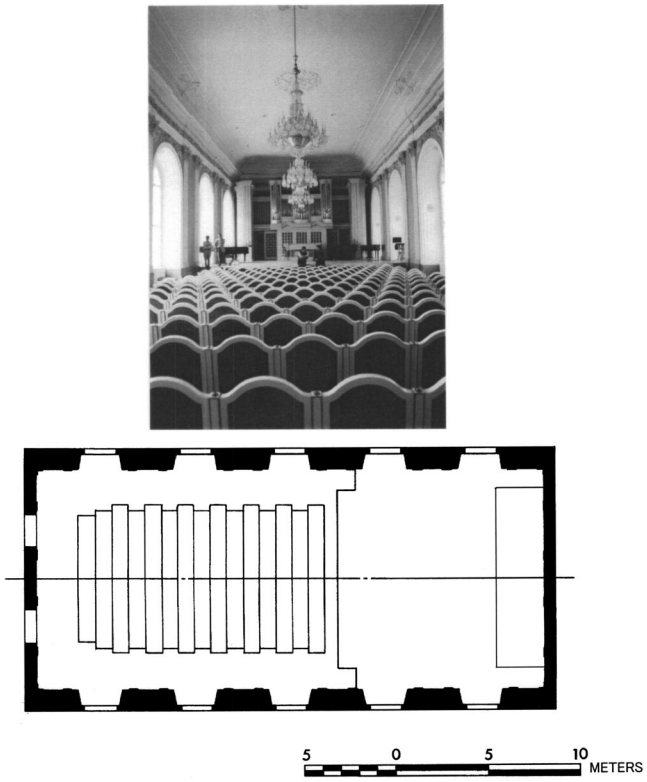

FIG. 3. Prague, Martine Hall, PM, plan and photo.

finished with thick plaster. Sound-diffusing elements of classical design abound. The doors are located at niches, which also function as large-scale diffusers. Curtains are drawn over the rear wall of both the first and second levels to eliminate reflections.

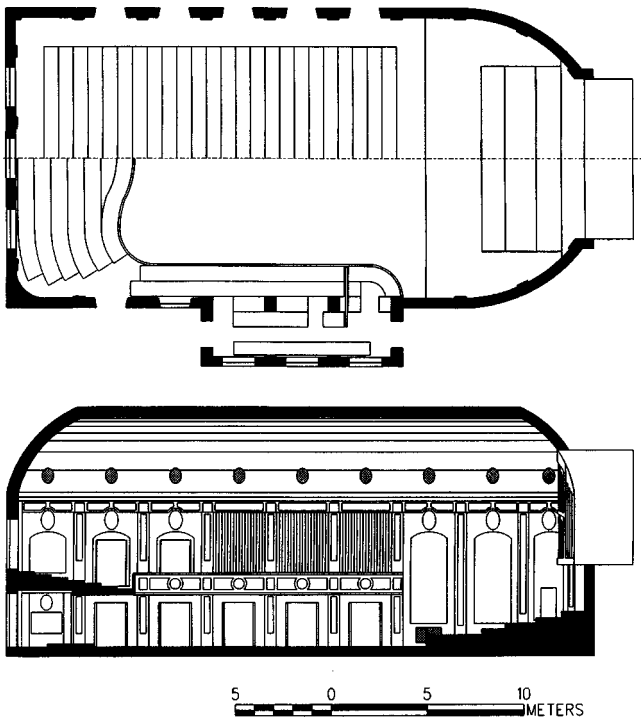

FIG. 4. Salzburg, Grossersaal Mozarteum, SG, plan and section.

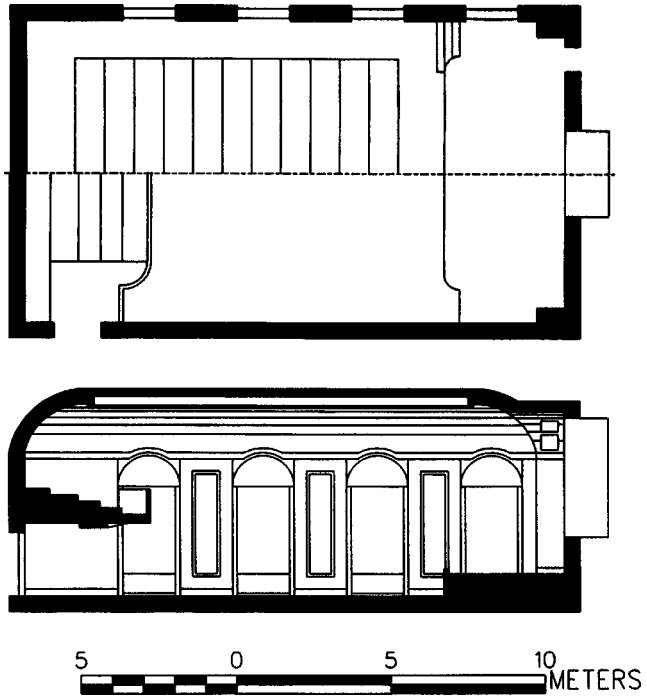

FIG. 5. Salzburg, Wienersaal Mozarteum, SW, plan and section.

5. Salzburg, Wienersaal Mozarteum, SW

SW and SG (above) are adjacent in the same building. This hall has the smallest room volume, 1070 m^3, among those investigated (Fig. 5) and seats only 209 persons. A small pipe organ is recessed in the rear end of the stage. There is also a front balcony. Plaster side walls and ceiling have a relatively large area of plane surface, so that there are not many sound-diffusing elements. The stage side wall is finished with thick wood. Windows are located on the right side of the stage, with curtains installed. The rear wall of the first floor is finished with reflective wood panels.

6. Vienna, Brahmssaal, VB

This typical shoebox-shaped hall is located in the same building as the famous Grosser Musikvereinsaal (Fig. 6). Ap-

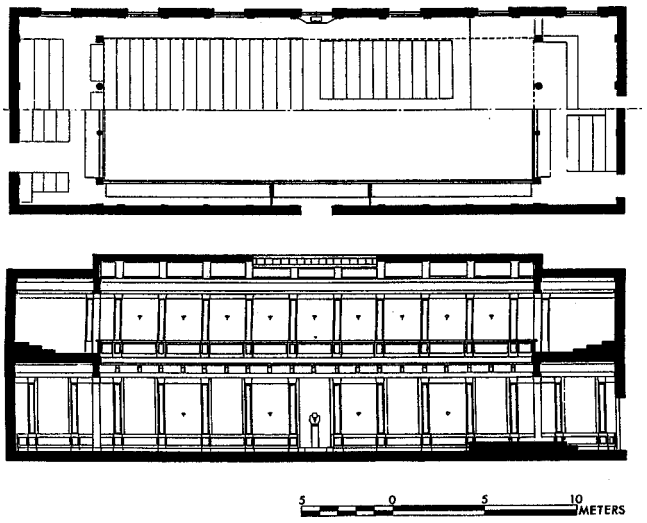

FIG. 6. Vienna, Brahmssaal, VB, plan and section.

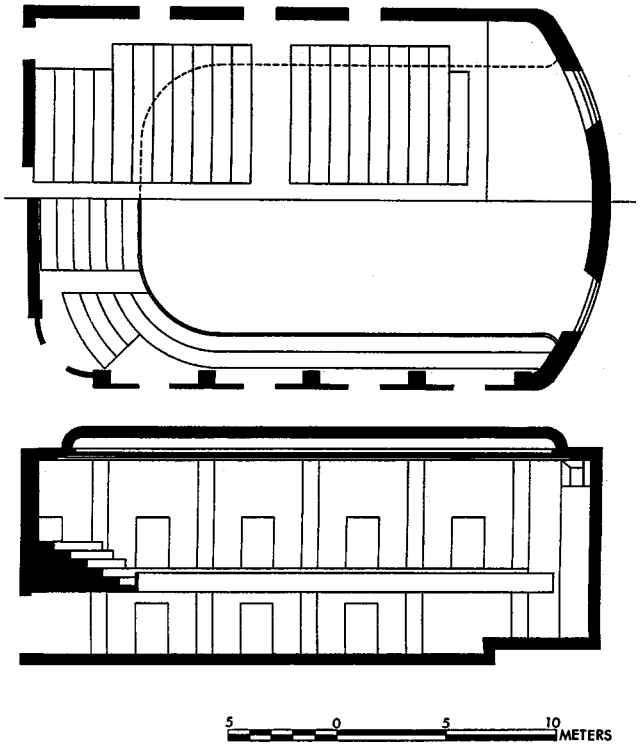

FIG. 7. Vienna, Mozartsaal, VM, plan and section.

proximately 75% of the ceiling is shaped like a ship's bottom (convex downward) with a slope of 10 deg, part of which (about 10%) is made of glass for ambient lighting. A single balcony surrounds the entire periphery of the hall, but 59 seats immediately above the stage are completely out of sight line to the stage. Plaster is the main finish material, almost the same as that for the Grossersaal. Fine Viennese decorations are used at various parts of the surfaces. Curtains are hung only at some parts of the side wall at the right of the stage, probably to eliminate flutter echo. The lower part of the side walls' wainscot is very thin wooden paneling. The chairs are very lightly upholstered, and are almost the same as those in the Grossersaal. The interior finish was refurbished in 1993.

7. Vienna, Mozartsaal, VM

This shoebox hall with a single balcony is located in the Konzerthaus in Vienna (Fig. 7). A small pipe organ is installed in the recess at the rear of the stage. Plaster side walls are plain and almost free of surface irregularities both above and below the balcony. Cyclical pilasters are arranged on the upper side walls. The type of chair is light with its seat back lightly upholstered. The only sound-diffusing elements are at the corners.

8. Vienna, Schubertsaal, VS

This similarly shaped hall is also in the Konzerthaus building (Fig. 8). Among those investigated, the reverberation time of VS is longest, 2.76 s, at 500 Hz, unoccupied. Bending in the decay curves was observed, presumed to be caused by the concave ceiling of 3-m depth. The walls of the seating area and the stage enclosure are finished with thick

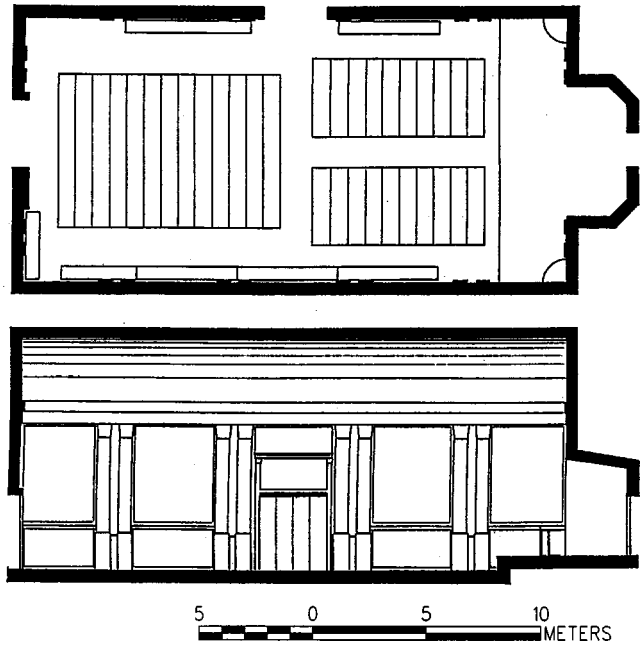

FIG. 8. Vienna, Schubertsaal, VS, plan and section.

wood. The upper part of the wall and the ceiling are finished with plaster. There is a distinct recessed space, 2.7 m in depth and 5.5 m in width, at the rear of the stage.

9. Zurich, Kleinersaal Tonhalle, ZT

This rectangular-shaped chamber hall is located in the Tonhalle (Fig. 9). A single balcony, with a seating capacity of 181, is found at the rear of the hall. The side walls and ceiling are joined by curved sections. The lower four side walls are finished with relatively thin wood panels, and the upper side walls and the ceiling are finished with thick plaster. Detailed deep decorations cover those surfaces to provide good sound diffusion. The chairs on the main floor, except just under the balcony, are very lightly upholstered. Those

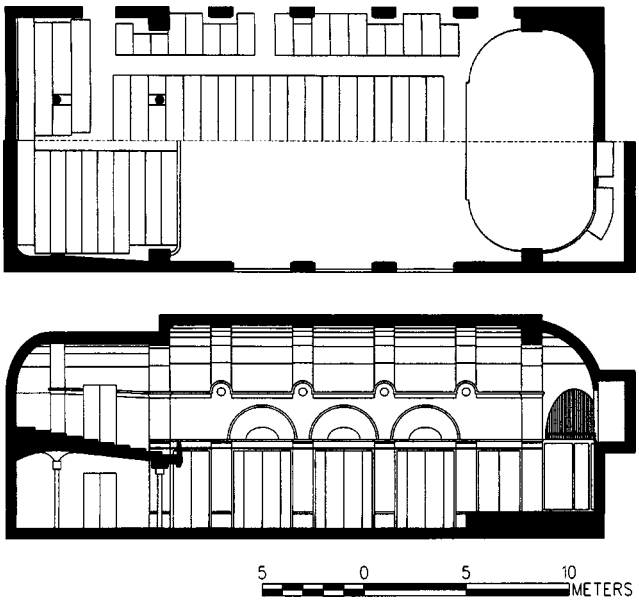

FIG. 9. Zurich, Kleinersaal Tonhalle, ZT, plan and section.

under and on the balcony have no upholstery. A big window is situated on the left side of the stage, covered with curtains, making the hall asymmetrical. There are a few balcony seats just above the rear of the stage.

10. Kanagawa, Higashitotsuka Chamber Hall, KH (Hidaka et al., 2001)

The KH auditorium, seating 482, is fan-shaped with no balcony. For chamber music it has a movable stage enclosure. Small-scale ceramic tiles are on the lower parts of the side walls, and larger scale diffusive elements are on the upper parts. The ceiling is finished with metal panels. The hall is multipurpose when the stage enclosure is removed. (Designed by Takenaka Corp., completed in 1992).

11. Kirishima, Miyama Conseru, KM (Ando, 1997)

The main floor of this single-balcony hall is somewhat rectangular, with side walls that bulge outward, while the upper part is more complex and said to resemble a tree leaf. The side walls tilt inward and are surrounded by irregularly spaced vertical corrugated ribs made of concrete. The ceiling is finished with flat gypsum boards. This hall, seating 770, has a volume, 8475 m^3, which is much larger than the other halls investigated. No sound-absorbing materials are used. (Designed by Fumihiko Maki, completed in 1995).

12. Tokyo, Casals Hall, TC (ASA, 2003)

Classical shoebox shape, seating 511, with one balcony. The interior finish is mainly fiber-reinforced gypsum boards or artificial wood, 40 mm in thickness. Curtain-like mortar walls for sound diffusion are used for first-floor side walls. Porous materials and curtains are installed, respectively, at a periphery part of the ceiling and the rear wall. A pipe organ was installed in 1997. (Designed by Arata Isozaki, completed in 1987).

13. Tokyo, Dai-ichi Seimei Hall, TD (ASA, 2003; Beranek, 2003b)

Oval hall, seating 767, with one balcony. To solve the acoustic problems caused by this shape, the rear wall of the main floor is asymmetrically covered by QRD panels, the wells of some of which are filled with porous materials. Small-scale diffusion elements are also provided to the surfaces of the side walls under the balcony. From an acoustical viewpoint, the oval concave surface is comprised of polygonal lines produced by flat panels, made of reinforced gypsum board, and their direction is adjusted to minimize sound concentration (focusing). (Designed by Takenaka Corp., completed in 2001).

14. Tokyo, Hamarikyu-Asahi Hall, TH (Beranek, 1996; Beranek 2003b)

Shoebox-shaped with one balcony. Walls and ceiling are finished by gypsum boards supported by reinforced backing. The three sides of the audience below the balcony are covered by small-scale diffusing shapes made of calcium silicate with urethane coating. No sound-absorbing materials are used for adjustment of reverberation. However, balancing of the high frequencies relative to middle frequencies was accomplished by installing felt, 8 mm in thickness, covered by thin impermeable film in the niches in the side walls above the balcony. (Designed by Takenaka Corp., completed in 1992).

15. Tokyo, Ishibashi Memorial Hall, TI (Talaske et al., 1982)

Although an almost rectangular parallelepiped in plan, the hall has a downward-sloping ceiling, with its edge lines diminishing in height from the stage to the rear of the hall. A pipe organ is located at rear of the stage. The hall has no balcony and no small-scale diffusion. The front parts of the side walls are made of concrete shaped like a Japanese folding screen, while the rear parts are finished with mortar. The rear wall is covered by a porous sound-absorbing material. The ceiling, finished with calcium silicate boards, is substantially smooth. (Completed in 1974).

16. Tokyo, Mitaka Art Center, TM (ASA, 2003)

The Mitaka Art Center is also a typical shoebox hall with one balcony, but the ceiling is shaped like a moderate-stepped truncated pyramid, with the ceiling level higher by 3.6 m at the center. The side walls on three sides of the main floor under the balcony have small-scale diffusion design same as Tokyo Opera City Concert Hall (Hidaka *et al.*, 2000), while the upper walls are made of concrete and above the balcony have large-scale irregularities. The ceiling is finished with reinforced gypsum boards. A small amount of glass wool, 25 mm in thickness, for reverberation time adjustment is installed along the upper ceiling edges and is not visible from the seating area. (Designed by Takahiko Yanagisawa, completed in 1995).

17. Tokyo, Sumida Triphony Small Sized Hall, TS (ASA, 2003)

Rectangular hall with no balcony. Very thin curtains are installed on the side walls for some sound-quality adjustment. The rear wall is made absorptive by porous panels, while the walls and ceiling are formed with gypsum board plus thin veneer with little diffusion. (Completed in 1997).

18. Tokyo, Tsuda Hall, TT (ASA, 2003)

The plan shape is an ordinary rectangle. However, the unusual feature of the hall is its longitudinal cross section: it has an angular-shaped ceiling, in which the height gradually decreases from the center to both sides. Fine diffusing elements made of stone are distributed at the lower part of the side walls, while gypsum boards cover the ceiling and the upper side wall. This sidewall gradually waves in cross section. At the ceiling near the corners and the rear wall some sound-absorbing treatment is utilized. (Designed by Fumihiko Maki, completed in 1988).

B. Shape and scale

Table II compares architectural features of the halls surveyed. For 15 out of 18 halls, the shoebox or a small deformation of it is found, i.e., their plans are rectangular. The

TABLE II. Architectural features of surveyed 18 halls. "H," "M," "L," and "VL," respectively, corresponds to heavily, medium, lightly, and very lightly upholstering (Beranek and Hidaka, 1998).

Halls	Plan shape	Ceiling height H (m)	Mainfloor width W (m)	Mainfloor length L (m)	Aspect ratio L/W	Balcony	Curtain	Chair	Distance of seating row (mm)	Width of chair (mm)
AC	Oval	9.5	15[a]	20.3[a]	···	Front	Door's niches at periphery	L	760	480
BK	Rectangle	8.0	12.5	21.0	1.7	Front+sides	Window's niches, left side	L	880	520
PM	Rectangle	8.7	12.0	25.1	2.1	···	···	M/H	1050	570
SG	Rectangle	12.0	14.8	29.2	2.0	Front+sides	Door's niche, rear and both sides	L	760	510
SW	Rectangle	6.4	9.8	17.4	1.8	Front	Window's niches, left side	L	950	570
VB	Rectangle	10.5[a]	10.3	32.8	3.2	Four sides	Window's niches, left side	L/VL	790	520
VM	Rectangle	10.0	16.2	25.5	1.6	Front+sides	Window's niches, left side	L	900	570
VS	Rectangle	10.4[a]	11.4	24.0	2.1	···	···	L	790	640
ZT	Rectangle	10.0	12.0	28.2	2.4	Front	Window's niches, right side	L/VL	910	480
KH	Fan+rectangle	8.0	19.8	29.7	1.5	···	···	H	1100	620
KM	Fan+rectangle[b]	13.5	18.0	32.5	–	Front+sides	···	M		
TC	Rectangle	11.6	13.6	21.5	1.6	Front+sides	Rear wall	M		
TD	Oval	12.0	20.0	29.5	–	Front+sides	···	M	972	525
TH	Rectangle	12.6[a]	13.5	24.3	1.8	Front+sides	···	M	950	525
TI	Moderate fan shape	12.8[a]	13.5	26.4	2.0	···	···	M		
TM	Rectangle	15.5[a]	14.6	20.0	1.4	Front	···	L	950	500
TS	Rectangle	7.0	9.8	22.9	2.3	···	Both side walls (÷50%)	M	950	500
TT	Fan+rectangle	13.1[a]	15.0	23.2	1.5	···	···	M		

[a]Maximum value
[b]Main floor

aspect ratio, length over width, ranges from 1.4 to 3.2, with the VB's value at the extremely high end (3.2). Halls with other shapes include oval-shaped AC and TD, and KM, whose above-balcony shape alone is irregular. The seating capacities of the halls range from 201 to 844, while the volumes range from 1070 to 8475 m^3. Both numbers spread broadly, but are not in direct proportion to each other. The volumes per seating capacities, V/N, range from 4.6 to 12.0 m^3, with a 2.6-times difference between the smallest and the largest. However, for traditional type halls (Figs. 1–9, with PM and VS excluded as explained later) the V/N variation is smaller, 4.6 to 5.9 m^3.

C. Interior finishes

The upholstering of the chairs in the traditional (European) halls, other than PM, is from light, L, to very light, VL (Beranek and Hidaka, 1998). It is interesting to note that of those halls, other than PM and VS, curtains are present, which presumably were added to adjust the reverberation time. In all cases they cover niches, behind which doors or windows are located, so that there is an air layer behind them. The reverberant absorption coefficients of curtains as measured by the author are shown in Fig. 10. It is seen that the curtain absorbs effectively above 250 Hz when the air layer depth is over 200 mm. Another interesting fact is that 5 of the 7 halls utilize curtains only on one side wall (usually that of the stage), so the sound field in them is not symmetrical. The use of absorbing materials over the rear wall, which is often found in modern multipurpose halls, was present in only one European hall, SG.

The upholstering of chairs in modern halls differs in variety, ranging from light, L, to high, H, but 7 out of 9 halls have medium-upholstered ones, M (Table II). The room volumes per seat in modern halls are distributed over a wider range from 5.8 to 11.9 m^3 (Table I). Consequently, absorption materials like mineral wool or perforated board are often used to adjust the reverberation times downward, and highly absorptive finishing is applied at the rear wall in many of them (TC, TD, TI, TS, and TT) to reduce echoes. In addition, at Tokyo Hamarikyu, an absorbing material specially designed to blend the subjective timbre at upper frequencies was applied to part of the sidewalls above the balcony (Fig. 11).

III. MEASUREMENT PROCEDURES

The measurements were executed without audience and with no instruments, musicians' chairs, or music stands on

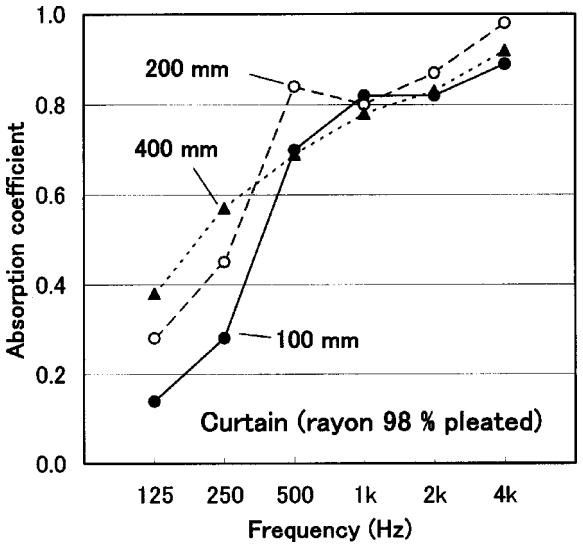

FIG. 10. Measurement result of reverberant absorption coefficient of a singly pleated thick curtain for RT control as a function of air layer depth (mm) in front of the rigid wall. The surface mass density of the tested curtain is 350 $g \cdot m^{-2}$.

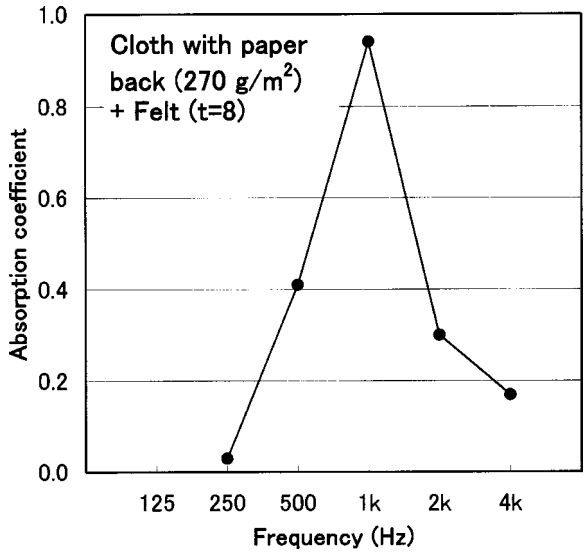

FIG. 11. Measurement result of reverberant absorption coefficient of a specially designed absorbing material in order to soften glare reflection at 1000 Hz, which was installed at upper side wall in part at Tokyo Hamarikyu Hall (Beranek, 1996). [Surface cloth with paper back: 270 $g \cdot m^{-2}$ + felt: $t = 8$ mm].

the stage (sometimes a piano was at the corner of the stage). The general outline for the measurement procedure is in accordance with that of ISO 3382 (1997). A calibrated dodecahedral loudspeaker (Fostex UP-120, each side of the array is 21.5 cm) radiated a revised time-stretched impulse, repeated from five to ten times for each seat, and recorded on a two-channel DAT tape recorder (Sony, TCD-D10 Pro). Multiple measurements for each location were made so that subsequently in the laboratory, the S/N ratio was improved by synchronous summation method and later processing. Further details about the measurement can be found in Hidaka and Beranek (2000).

Up to three on-stage source positions using an omnidirectional loudspeaker with height above the stage of 1.5 m were selected depending on the time available for the measurements, as shown in Fig. 12, where *S*0, 1.5 to 3 m from the stage edge on the center line, was used in every hall. SL and SR, arranged at the left and right side of *S*0, are set at an intermediate point between *S*0 and either side wall. The number of receiving points in the audience areas, at a height equal to 1.1 to 1.2 m, were distributed uniformly at 6 to 20 seats corresponding to the seating capacity of each, and selected at the left side of the hall, looking at the stage, whenever the halls were symmetrical. The receivers were placed at the position of a seated listener's ear. The binaural measurements were made with tiny microphones (Sony, ECM-77) taped to the outer ear canals of seated persons with DAT tape recorders held in their laps. The numbers of monaural and binaural measurements were almost the same.

IV. FINDINGS FROM THE OBJECTIVE MEASUREMENTS

The correlation matrix for the objective measures is shown in Table III. Coefficients shown in bold type mean that the corresponding two variables correlate with each

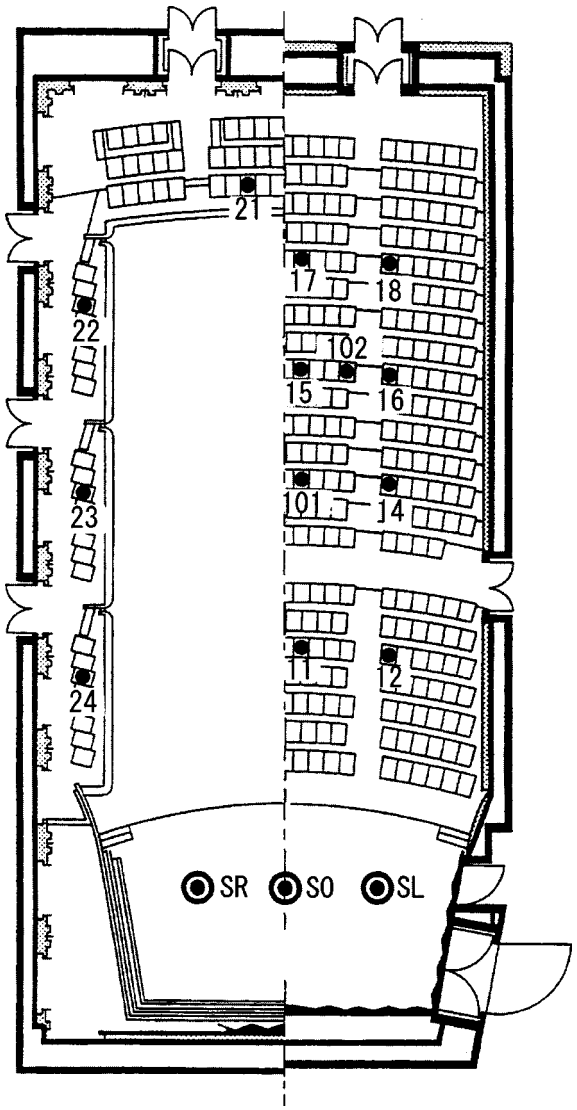

FIG. 12. Definition of receiver locations and source position in the Tokyo Hamarikyu Hall (Beranek, 1996). These locations and position were used typically in all halls studied.

other within the significance level of 1%. It indicates that the independent parameters are RT_M, G_L (or G_M) $IACC_{E3}$, ITDG. A similar correlation matrix is also found in symphony halls (Hidaka *et al.*, 2000) and opera houses (Hidaka and Beranek, 2000). The suffix "L," "M," and "3" associated with the octave-band measured quantities indicate the average over 125/250-Hz, 500/1000-Hz, and 500/1000/2000-Hz bands, respectively. The occupied values were transformed from measured unoccupied values using the empirical method reported by Hidaka *et al.* (2001).

A. Reverberation time, RT

The room volume per person on average is 6.4 m^3 for the traditional halls and 9.1 m^3 for the modern halls; thus, the volumes of the latter are about 40% larger. The reason for the size differences comes from two facts: the seats are closer together in the European halls (except for PM), and modern architects prefer medium-upholstered chairs for greater comfort, which absorb more sound. Consequently, many of the modern halls have greater room volume or V/S_A so as to

TABLE III. Correlation coefficients (r) among objective acoustical factors and architectural parameters calculated from the results of measurements in 18 chamber halls listed in Table I. The subscript "L," "M," and "3" mean, respectively, that the octave band average is for 125 and 250 Hz, 500 and 1000 Hz, and 500, 1000, and 2000 Hz. The occupied values were transformed from measured unoccupied values using the empirical method reported by Hidaka *et al.* (2001). The coefficients with significance level $p \leqslant 1\%$ are in bold type.

	RT_M unocc	RT_M occ	EDT_M unocc	$C_{80,3\,B}$ unocc	$C_{80,3\,B}$ occ	$T_{g3\,B}$ unocc	G_L unocc	G_M unocc	$IACC_{E3}$ unocc	BR occ	ITDG	Width	V	N
$RT_{M,unocc}$	⋯													
$RT_{M,occ}$	**0.92**	⋯												
$EDT_{M,unocc}$	**0.98**	**0.88**	⋯											
$C_{80,3\,B,unocc}$	**−0.96**	**−0.88**	**−0.98**	⋯										
$C_{80,3\,B,occ}$	**−0.90**	**−0.94**	**−0.91**	**0.95**	⋯									
$T_{g3\,B,unocc}$	**0.97**	**0.88**	**0.99**	**−0.99**	**−0.93**	⋯								
$G_{L,unocc}$	0.29	0.04	0.36	−0.28	−0.09	0.30	⋯							
$G_{M,unocc}$	0.21	−0.05	0.31	−0.26	−0.08	0.29	**0.89**	⋯						
$IACC_{E3,unocc}$	−0.30	−0.22	−0.26	0.25	0.20	−0.33	−0.19	−0.35	⋯					
BR_{occ}	0.24	0.06	0.26	−0.17	−0.02	0.20	**0.80**	0.55	−0.04	⋯				
ITDG	0.12	0.33	−0.02	0.02	−0.10	−0.02	−0.33	−0.49	0.18	−0.11	⋯			
Width	−0.01	0.18	−0.13	0.13	0.03	−0.14	−0.55	**−0.64**	0.40	−0.32	**0.83**	⋯		
V	0.39	**0.62**	0.26	−0.29	−0.44	0.30	−0.58	**−0.67**	−0.06	−0.30	**0.72**	**0.66**	⋯	
N	0.40	0.43	0.28	−0.29	−0.28	0.30	−0.30	−0.46	0.09	0.02	**0.65**	**0.61**	**0.75**	⋯

achieve more favorable frequency characteristics for RT. Here, S_A means the acoustical audience area which is defined by the area over which the audience sits plus the edge corrections.

Let us take from Beranek (2003b) the equation $RT_{M,occ} = K \cdot V/S_A$, where $K = 0.161/[\alpha_A + (S_R \cdot \alpha_R/S_A)]$ and the suffix "R" means residual area (all other surfaces except the acoustical audience area). We see in Fig. 13 a plot of $RT_{M,occ}$ vs V/S_A for the two groups of halls, "Europe" and "Japan." It is seen that a line $K = 0.144$ approximately fits the European halls and a line $K = 0.120$ approximately fits the Japanese halls. In both cases, the reverberation times level off at about $RT_{M,occ} = 1.8$ s. The different K values indicate that the audience absorption and the residual absorption are larger in the Japanese halls. Parenthetically, $K = 0.144$ was found as the average for large concert halls (Beranek 2003b). The leveling off at $RT_{M,occ} = 1.8$ s indicates that in some halls the reverberation is optimum for classical symphony, whereas the recommended value for chamber music is 1.6 s, which is the median for most of the halls.

Figure 14 illustrates the frequency characteristics of occupied RTs of traditional and modern halls, and Fig. 15 compares the same set of RTs normalized to the values at 500 Hz. The median values of RT_{occ} at 500 Hz in both categories are almost the same, 1.66 and 1.64 s. Figure 16 shows that the

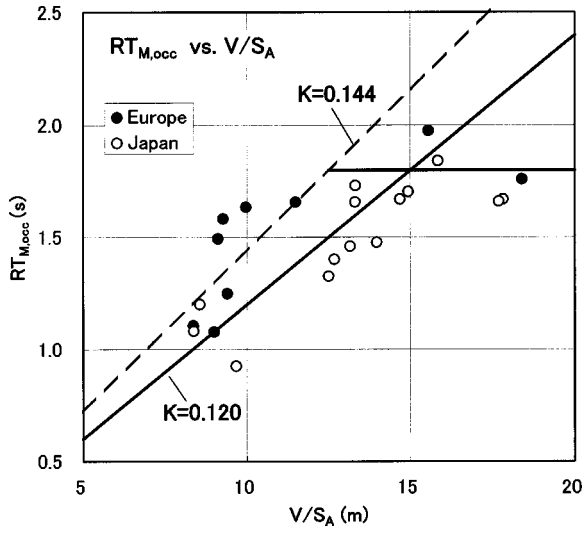

FIG. 13. Plot of the reverberation times for occupied chamber halls versus the volume divided by the acoustical area of the audience. The text discusses how the RTs (occupied) were derived from the RTs (unoccupied) where they were not directly measured. The simplified Sabine equation is $RT = K \cdot V/S_A$. The value of K for chamber halls is 0.13 to 0.14, and the RT converged to around 1.8 s. Four Japanese halls were added.

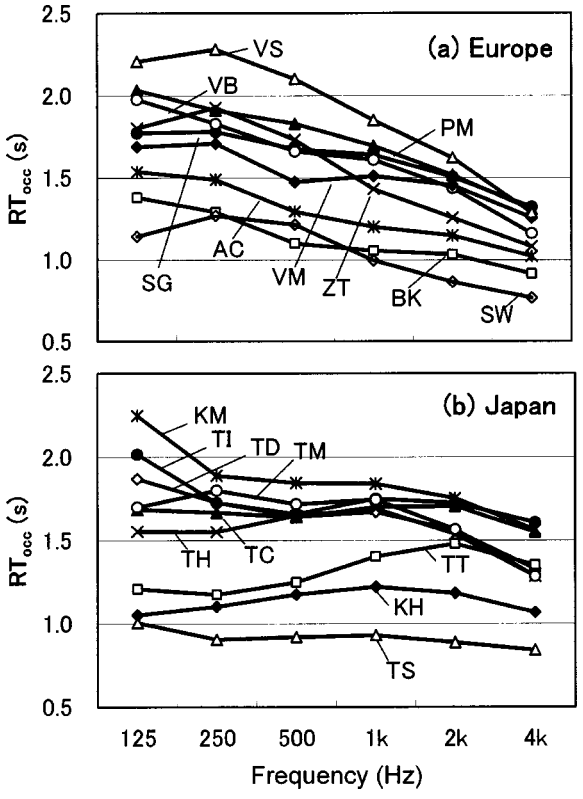

FIG. 14. Frequency characteristics of the reverberation times under occupied condition with audience in 18 chamber halls determined from those measured under unoccupied condition. Empirical equation by Hidaka and Beranek (2001) was in use.

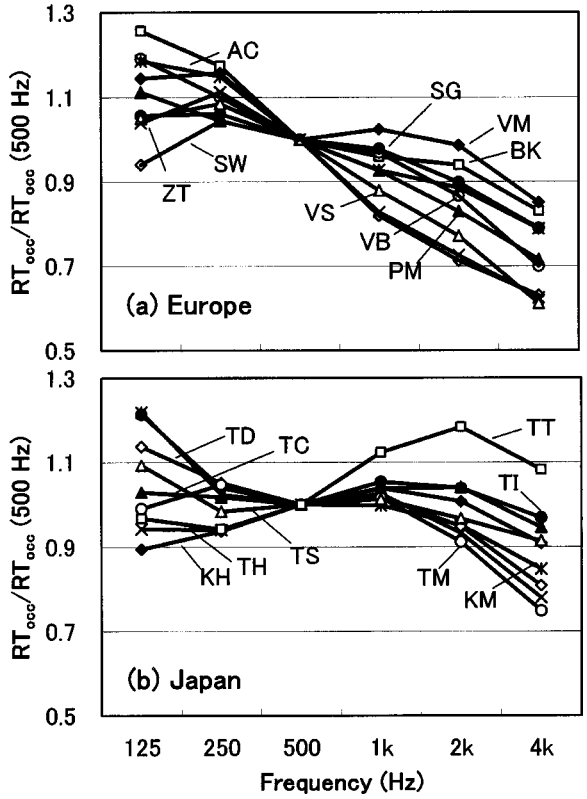

FIG. 15. Same set of RTs in Fig. 14 normalized to the value at 500 Hz.

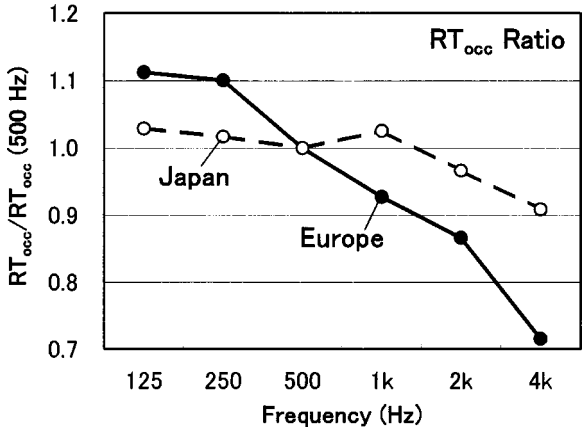

FIG. 16. Median values of the normalized RTs shown in Fig. 15 for European and Japanese halls.

median values of RT_{occ} for each category have similar frequency characteristics—that is to say, in traditional halls RT_{occ} falls nearly linearly from 250 to 4000 Hz, while for modern halls the median values are almost flat, except at 4 kHz. The 2000- and 4000 difference between the two categories is mainly attributed to the absorption by curtains regardless of the differences in the seat upholstering.

Table IV compares the residual absorption coefficient α_R (before installation of the chairs) measured in two typical traditional halls, Hubertussaal in Munich (every interior surface made of thick plaster) and Sala Lluis Millet in Barcelona (same as Hubertussaal but the floor is stone), and in two modern halls in Japan (KH and TH). The traditional halls have smaller residual absorption values for every frequency band similar to most large concert halls (Beranek and Hidaka, 1998). This means that the extra absorption at low frequencies will reduce the RTs in the Japanese halls, even with audience.

B. Early decay time, EDT, and clarity factor, C_{80}

EDT and C_{80} are variables that are very highly correlated, which is also true for symphony halls (Hidaka *et al.*, 2000) and opera houses (Hidaka and Beranek, 2000). Only when early reflections are sparse in number do these parameters not correlate with each other. The regression equation between EDT and C_{80} for unoccupied and occupied conditions can be written by: $C_{80,3,unocc} = -4.4 \times EDT_{M,unocc} + 7.6$ ($r = -0.98$) and $C_{80,3,occ} = -3.7 \times EDT_{M,unocc} + 7.7$ ($r = -0.91$), respectively, where the empirical equation (Hidaka *et al.*, 2001) was used to obtain the occupied values of $C_{80,3}$ as shown in Fig. 17.

From Fig. 17, C_{80}'s (occupied) may be classified into two groups: (0.2 ± 1.6) and (3.4 ± 0.4) dB. The former coincides with the optimal range for Mozart music, that is (0 ± 1.5) dB, which was proposed by Reichardt and his group (1975). The latter includes a smaller hall (SW), multipurpose halls (KH, TS, and BK), and a hall with relatively large amount of absorption (AC). Obviously, every hall exceeds the lower limit of -1.5 dB, indicating that the chamber halls are deader than symphony halls whose C_{80} ranges from (-2.0 ± 1.6) dB for highly reputed ones (Beranek, 1996, Table 12.1).

TABLE IV. Values of residual absorption coefficient measured before installation of seats: Hubertussaal, Munich ($V = 2682$ m^3, $S_A = 1382$ m^2), Sala Lluis Millet, Barcelona ($V = 739$ m^3, $S_A = 528$ m^2), two modern halls in Tokyo, KH and TH, and average for symphony halls with thin materials which is classified as Group A by Beranek and Hidaka (1998, Table II). The first two placed in old castle or building are considered as traditional European chamber halls. All the data were taken before installing chairs.

	Frequency (Hz)					
	125	250	500	1000	2000	4000
Munich, Hubertussaal	0.12	0.10	0.07	0.06	0.06	0.04
Barcelona, Sala L Millet	0.07	0.07	0.07	0.06	0.06	0.06
Kanagawa, Higashitotsuka Hall	0.17	0.14	0.11	0.08	0.08	0.07
Tokyo, Hamarikyu Asahi Hall	0.16	0.14	0.11	0.10	0.09	0.07
Average for symphony halls with thin materials	0.16	0.13	0.10	0.09	0.08	0.08

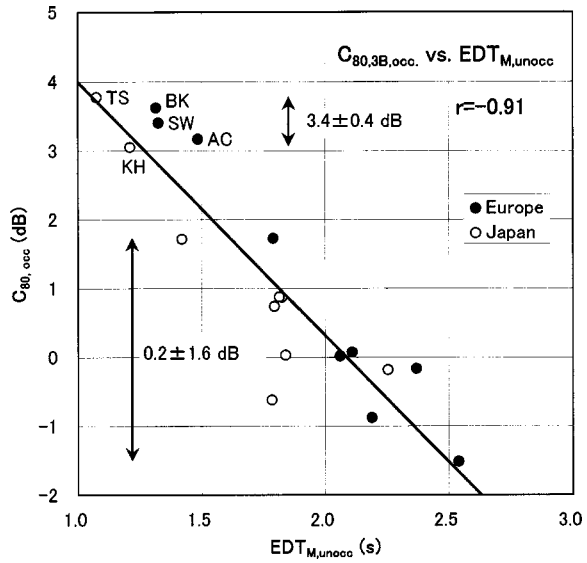

FIG. 17. Plot of the clarity factor $C_{80,3}$ (occupied) versus the early decay time EDT_M (unoccupied). The occupied C_{80}'s were converted from unoccupied C_{80}'s by the direct measurement by similar empirical equation. Two categories (3.4 ± 0.4) and (0.2 ± 1.6) dB are derived regarding the clarity factor and most of the regular chamber halls belong to the latter range.

For the traditional (European) halls surveyed, the difference in the measured physical parameters between the unoccupied and occupied conditions is remarkable. In a smaller space, the number of the early reflections in the first 50 to 80 ms after the arrival of the direct sound is much greater than that in large symphonic halls; therefore, the fraction of the early reflections that arrives at a listener's position traveling over an absorptive seating area is higher in a chamber hall. Thus, it is more difficult for a listener to estimate the sound quality with audience when his/her prior auditory experience in the chamber hall is only without audience.

The median value of the frequency characteristics of $C_{80,occ}$ for the two categories of halls is shown in Fig. 18. We might speculate that a 1-dB difference at 500 Hz and 4 kHz is significant because it has been shown that for music with fairly fast moving passages the subjective difference limen for C_{80} is 0.44 ± 0.07 (Cox *et al.*, 1993). These data indicate

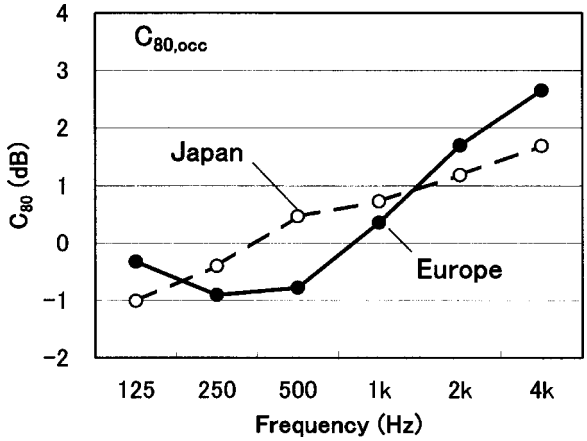

FIG. 18. Median values of the C_{80}'s for 18 chamber halls in two categories, Europe and Japan. Empirical equation by Hidaka and Beranek (2001) was used, which transforms unoccupied value measured in each hall to the occupied value.

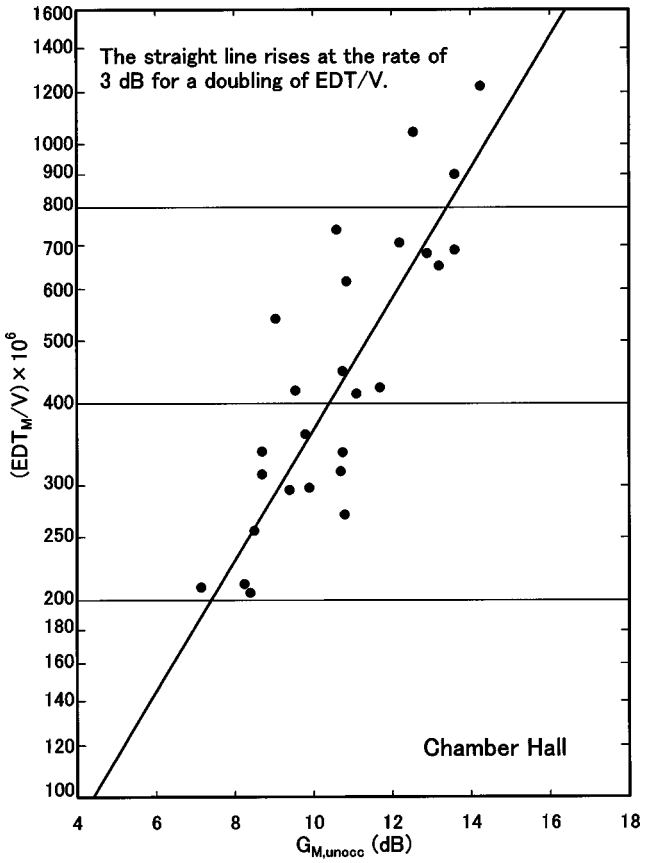

FIG. 19. The early decay time EDT_M divided by the volume V is plotted against the strength factor G_M, both quantities for unoccupied houses with the source at S_0. The measurements were the average of the positions throughout the audience areas.

that the traditional halls should sound more reverberant at 500 Hz and less so at 4 kHz.

C. Time gravity, T_g

Time gravity, T_g, is another parameter correlating with the temporal quality of the sound field. Taking account of the fact that C_{80} has a problem in the use of time window with sudden cutoff at $t=80$ ms (Hidaka *et al.*, 2000), and the result that T_g has been suggested as the best indicator of the sound quality in small spaces (Fürjes *et al.*, 2000), T_g was included in this analysis. However, EDT, C_{80}, and T_g are not independent of each other for chamber halls as shown in Table III.

D. Strength factor, G

As shown in Fig. 19, $G_{M,unocc}$ of chamber halls is proportional to log(EDT/V), similar to the case of concert halls (Beranek, 1996, 2003b) and opera houses (Hidaka and Beranek, 2000). From Table III, G_M (average of 500, 1000 bands) correlates highly with G_L (average of 125, 250 bands) ($r=0.89$). However, the values of G as a function of frequency are quite different between the traditional and modern chamber-music halls. On average, G_L and G_M of the traditional chamber-music halls are, respectively, about 5 dB (see Fig. 20) and 3 dB larger than they are in the modern chamber-music halls.

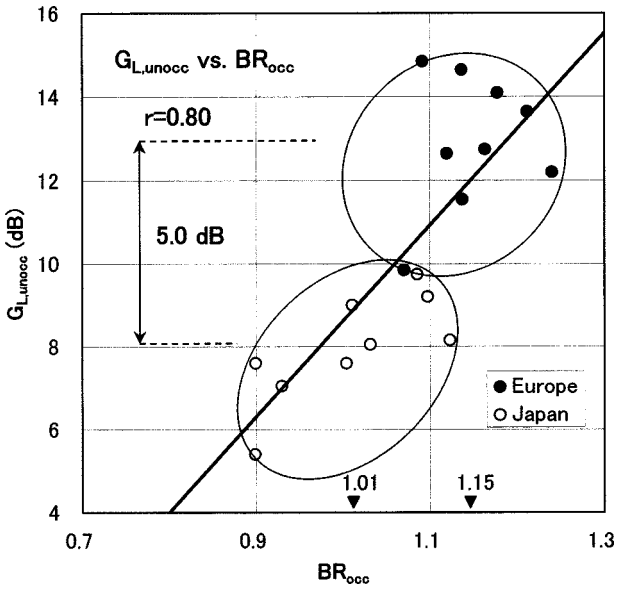

FIG. 20. Plot of the strength factor G_L (unoccupied) versus the bass ratio BR (occupied). These two parameters highly correlate with each other in total ($r=0.80$), and traditional and modern halls distribute separately. Two groups differs 5 dB in average, which came from the intrinsic difference in the surface interior materials, i.e., mortar/plaster plus brick or board materials with furring, even though they are stiff and heavy.

1. Further comments

In Fig. 21, the measured differences in the median values of G for all the chamber-music halls are compared with the theoretical differences computed by $10\cdot\log(\mathrm{EDT}/V)$, which assumes a completely diffuse sound field, and where EDT and V are the median values for the halls. It may be expected that the diffusivity in chamber halls is better than in symphony halls on the whole, because the smaller the room volume the higher the density of early reflections (see Fig. 22, for example). If one could count on this fact, one would expect the difference in the two indices, measured G and computed $10\cdot\log(\mathrm{EDT}/V)$, to coincide, approximately. However, less sound is absorbed in traditional halls in the lower two frequency bands. Unfortunately, EDT at 63 Hz

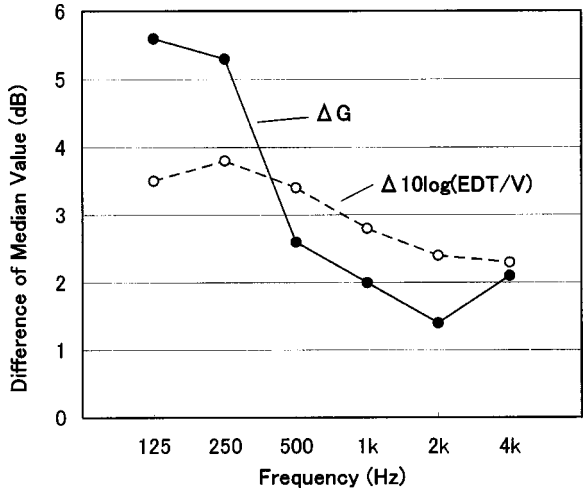

FIG. 21. Difference in two indices, G and $10\cdot\log(\mathrm{EDT}/V)$, for traditional and modern halls.

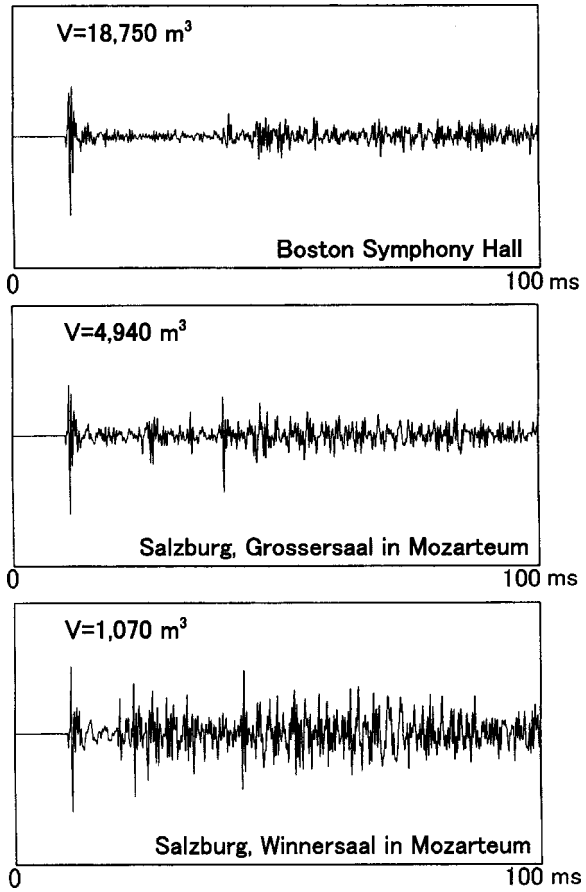

FIG. 22. Reflectograms at receiver position 101 on the main floor and source at $S0$ (Fig. 12). These diagrams were the impulse responses proceeded by bandpass filtering of three octave bands whose lower and upper cutoff frequencies are 354 and 2828 Hz, respectively, which are similar to the sum of three 1/1-octave band filters with midfrequencies 500/1000/2000 Hz. Three typical shoebox halls with different volume were chosen: Boston Symphony Hall ($V=18\,750$ m^3), Grossersaal (4940 m^3), and Wienersaal (1070 m^3) in Mozarteum, Salzburg.

was not measured in every hall, but for the data available, a similar or more striking tendency was observed.

Obviously, this result indicates that other factors irrelevant to room volume or residual absorption coefficient should exist. Perhaps the most probable is ''reradiation'' of sound by the stage floor, judging from our listening experience and several interviews with halls' management. Believing that this is true, throughout the acoustical measurements in this report, the sound source was supported by a tripod standing on the stage floor so that reradiation would also be included in the measured results. The reverse result in Fig. 21 at mid to high frequencies may be associated with the use of curtains in the traditional halls (see Table II).

It is known that reradiation is an effect more important at low frequencies (Cremer, 1984). As a typical example, for VB and BK, whose EDT/V are almost the same, their G values at 63 Hz were 18.4 and 13.0 dB, respectively, i.e., a 5.4-dB difference. In the Vienna hall, VB, pine was in use for the stage floor so that the floor is fairly flexible and also it was mounted so as to vibrate the floor easily. On the other hand, in the Berlin hall, BK, Eiche (oak) was used for the stage floor, which was the stiffest and thickest among the traditional halls surveyed. This observation may be evidence

as to why the stage floor effect should be presumed to be one of the important factors for the G (63-Hz) discrepancy. This objective observation has also been confirmed by a series of listening experiences at these two halls over a period of a few months by one of the authors. The author was convinced that reradiation or enhancement of bass tones by the stage floor via the endpins of cello and contrabass (double bass) in the Vienna hall, VB, was very significant. Subjectively, the loudness in the low tones was much greater than that indicated by the objective measure G.

It is noted that the lowest six tones of the cello, C_2 (65 Hz) to F_2 (87 Hz), are contained in the octave band with midfrequency of 63 Hz, and the lowest six tones of the contrabass are contained in the 31.5-Hz band. Schubert's piano quintet ''Trout'' is one of the preferable pieces for allowing one to identify the stage floor effect. In this composition, proper unison and ensemble by the combination of cello, contrabass, and piano occur in various places. One knows that for baroque music the bass strings are important in terms of continuo. The author also listened in the Berlin hall to a cello sonata played by a modern cello with its endpin taken off, and in that case the subjective loudness of the cello was greatly diminished. In a chamber-music hall, proper stage floor design is obviously important because the distance between the audience and the stage is usually short.

For every hall, except for Vienna VS, the RT decay curves were fairly straight, i.e., no bending, a sign that there was no diffusion anomaly (see Sec. II A 8).

E. Bass ratio, BR

The bass ratio, BR, equals the sum of the RTs in the 125- and 250-Hz bands divided by the sum in the 500- and 1000-Hz bands. The bass ratios for the occupied condition range from 1.07 to 1.24 for traditional halls and from 0.90 to 1.12 for modern halls (median values are 1.15 and 1.01 as seen in Fig. 20), respectively, which are narrower ranges than that of concert halls, 0.92 to 1.45, in spite of the wider range of V/N. The BR correlates well with G_L ($r=0.8$) for this set of halls. Bradley and Soulodre (1995) find in laboratory judgment tests that unless G_L does correlate well with the BR, only the G_L (mainly at 125 Hz) is of significance.

F. The binaural quality index, BQI=[1-IACC$_{E3}$], where IACC is the interaural cross-correlation coefficient, "E" means determination over 80 ms, and 3 means the average in the three octave bands from 500 to 2000 Hz

The binaural quality index, BQI=[1-IACC$_E$], is also an independent variable for chamber halls but the variation range is extremely narrow, 0.67 to 0.77. This range is the same as the subjective difference limen by Cox *et al.* (1993), namely it can be said that every chamber hall researched has similar binaural quality, provided the other acoustical attributes just discussed have reasonable values. This situation is quite different from that for symphony halls or opera houses, where the variation range in BQI is larger, 0.39 to 0.72. In a small hall, the ITDGs are almost always smaller than 20 ms so that there is time for a multitude of early

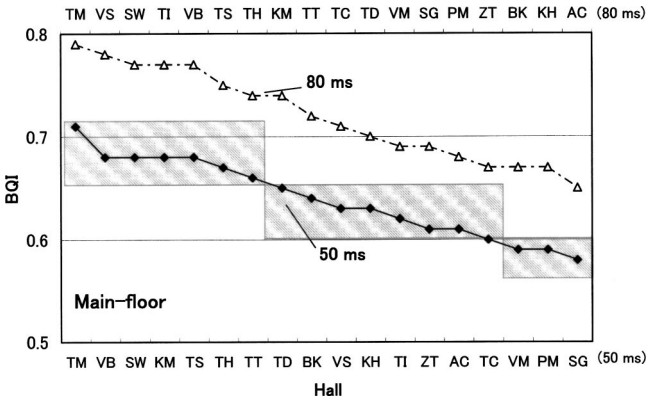

FIG. 23. Plot of binaural quality index, BQI=[1-IACC$_{E3}$], against the names of halls (not rank ordered). The upper integration limits were 50 and 80 ms for two curves. These values are the average only over the seats on the main floors. Source at position $S0$.

lateral reflections before the first 80 ms (Fig. 22). This is the reason [1-IACC$_{E(80\,ms)}$] is approximately the same among chamber halls.

After Kuhl (1978), spatial impression is a subjective attribute that is detected for the orchestra music and only for its ''*f*'' or ''*ff*'' passages. Accordingly, it is not rigorous to assume that [1-IACC$_E$] is a measure for the spatial impression for chamber halls. Nevertheless, binaural hearing plays an important role for chamber-music listening. One has the power of concentration with binaural hearing, which means that with a performing group, one can focus and concentrate on a particular instrument and focus less on the reverberation. Given that BQI indicates binaural quality for concert halls and opera houses equall well (Beranek, 2003a), some modification is suggested.

One tentative idea is to separate them using BQI$_{50}$, where only the information within the first 50 ms is used. As shown in Fig. 23, the change to 50 ms for chamber-music halls gives an upper limit to BQI$_{50}$ of about 0.70, which approaches that of BQI$_{80}$ as the upper limit for large symphonic halls (Beranek, 2003b). Unfortunately, no subjective judgments of acoustical quality exist for the halls in this study, so it is not possible to relate measured BQI$_{50}$'s to subjective rank orderings. For Fig. 23, BQI$_{50}$ was averaged only over the seats on the main floors, because not every hall has a balcony, and the balcony seating arrangements are not similar.

There are several possible features that imply using a lower integration period for chamber halls: (a) audiences for chamber-music value light, clear, and transparent tone color, that is to say, in baroque music, the detail is important and no portion of the sound should mask another (Beranek, 1996, 2003b); (b) the time it takes for a musical sound to rise to its steady state, in the case of delicate instruments like harpsichord, ancient instruments, guitar, and so on, is shorter than that of instruments for orchestral music (Reichardt and Kussev, 1973); (c) psychological experiments on subjective transparency have indicated the efficacy of C_{20} over C_{80} in a small space (Fürjes *et al.*, 2000); and (d) Beranek and Schultz (1965) explained running liveness of music introducing ''reverberant-to-early-sound ratio,'' where the 50 ms is

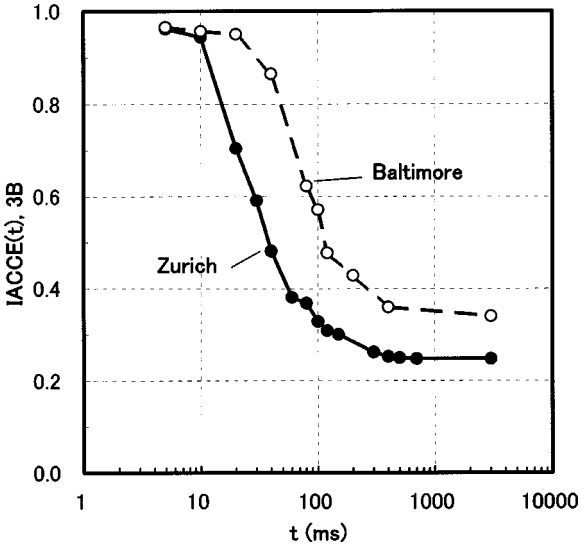

FIG. 24. Plot of $IACC_{E(t),3}$ as a function of the upper integration limit, *t*. ●: Kleinersaal Tonhalle in Zurich, ZT ($V=3234\ m^3$); ○: Meyerhoff Symphony Hall in Baltimore, BL ($21\,524\ m^3$). Source at *S*0 and receiver position 101 (Fig. 12).

the boundary value between the two energies. Perceived balance and fullness of tone correlates with the frequency curve of this parameter.

Figure 24 compares $IACC_{E(t),3}$ at the center seat for an unoccupied chamber hall (TK) and a symphony hall (Baltimore, Meyerhoff Symphony Hall). It shows that the time that separates the early and late reflections in a chamber hall exists in the range around 50 ms, where the *x*-axis value corresponds to the upper integration limit "*t*" of $IACC_{E(t)}$. Similar results were obtained for other halls.

BQI_{50} is almost the same whether the hall is occupied or unoccupied. The measured values under occupied and unoccupied conditions, respectively, at all the seats are 0.63/0.63 (KH), 0.61/0.63 (TD), 0.66/0.63 (TH), and 0.63/0.67 (TM), that is to say, the difference is 0.04 at maximum. For the chamber halls surveyed, BQI_{50} and BQI_{80} are not strongly correlated, $r=0.64$, and BQI_{50}'s are also independent of the ITDGs, $r=0.19$. This means that BQI, i.e., IACC, and ITDG are independent.

The ellipsoids in Fig. 25 show the set of reflecting points of the image room's wall with mirror image source, from which the reflected sound arrives at the receiver (shown by white circle) with the time delay 80 ms (upper) and 50 ms (lower) after the direct sound arrival, respectively. Both are uniquely determined when the source and the receiving positions are given. Two typical halls were chosen: Vienna Musikverinssaal ($15\,000\ m^3$, $RT_M=2$ s) and TH ($5800\ m^3$; $RT_M=1.7$ s). Seeing these, it can be estimated that the total number of image sources, that is, early reflections contained in the 50-ms ellipsoid for chamber halls, is almost equal to that in the 80 ms for symphony halls. This may be another argument for the use of 50 ms in BQI for chamber-music halls.

G. Initial time delay gap, ITDG

The intimacy parameter, ITDG (Beranek, 1996, 2003b) was also shown for the chamber halls in Table I. It is deter-

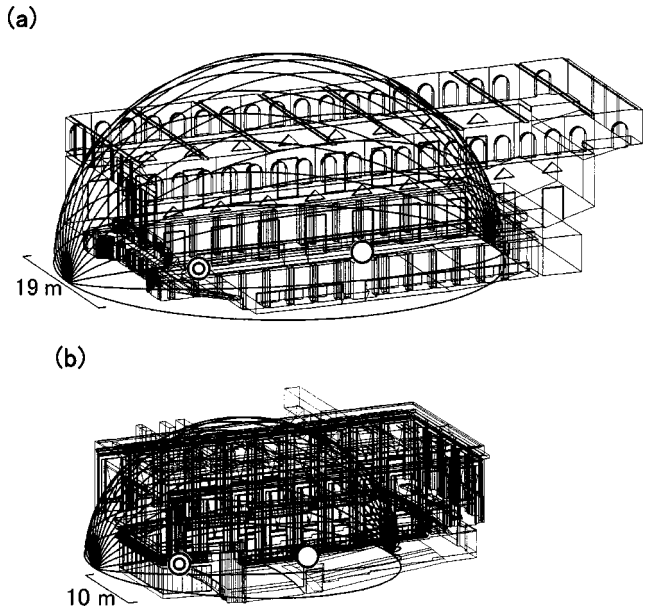

FIG. 25. The upper-half ellipsoids show the region of reflecting points of the image rooms with mirror image source, from which the reflected sound arrives at the receiver with 80- and 50-ms delay after the direct sound arrival. Two typical halls are chosen: (a) Vienna Musikverinssaal ($V=15\,000\ m^3$, hall width=19 m) and (b) Tokyo, Hamarikyu Hall ($5800\ m^3$, 10 m). Source (⊙) at *S*0 and receiver position (○) at 101 (Fig. 12).

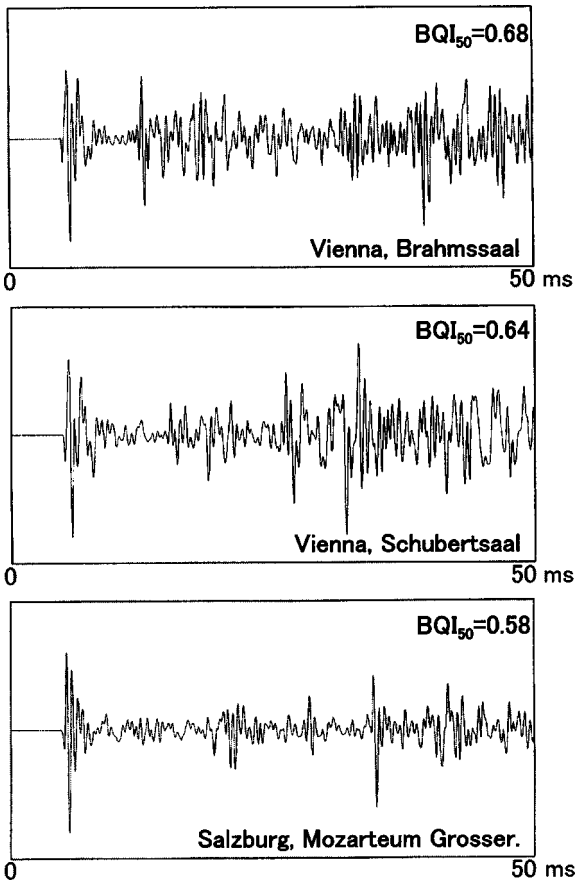

FIG. 26. Reflectograms at typical receiving positions, where the average $BQI_{50}=[1\text{-}IACC_{E(50ms),3}]$ value is high (0.68), median (0.64), and low (0.58) in the range of Fig. 23. These diagrams are the impulse responses processed by bandpass filtering of three octave bands (500/1000/2000) width whose lower and upper cutoff frequencies are 354 and 2828 Hz, respectively.

TABLE V. List of architectural stage parameters and stage support ST1 of 18 halls surveyed. The subscript "4B" means the average of 250 to 2000-Hz octave bands.

Halls	Stage area (m^2)	Stage volume (m^3)	Stage–ceiling height (m)	Stage depth (m)	Stage–floor height (mm)	Pipe organ	$ST1_{4B}$ (dB)
AC	40	339	8.5	5.3	1020	···	−10.0
BK	75	525	7.0	6.0	1000	···	−10.5
PM	101	798	7.9	8.6	800	y	−7.7
SG	92	1049	11.4	8.0	600	y	−8.3
SW	37	207	5.6	4.0	750	y	−5.1
VB	82	820	10.0	8.0	450	···	−6.2
VM	60	555	9.3	4.8	750	y	−11.6
VS	49	470	9.6	6.5	600	···	−6.4
ZT	51	469	9.2	6.2	800	···	−4.4
KH	47	348	7.4	6.5	600	···	···
KM	104	1352	13.0	9.0	750	···	−12.8
TC	150	1650	11.0	11.3	600	y	−12.5
TD	104	1196	11.5	7.2	750	···	−12.8
TH	73	861	11.8	7.0	750	···	−9.8
TI	100	1280	12.8	10.3	900	···	−12.8
TM	111	1388	12.5	7.6	800	···	−9.7
TS	43	275	6.4	5.3	600	···	−4.8
TT	95	874	9.2	7.5	750	···	−8.3

mined by the first reflection after arrival of the direct sound, and usually has a value in the range of 9 to 26 ms, when measured near the center of the main floor (see P-101 in Fig. 12). It is believed that the subjective term "intimacy" is observed provided the first reflection is immediately followed by a series of other reflections before the 50-ms point. As might be expected, the ITDG correlates highly with hall width, W ($r=0.83$), because the first reflection arrives from a side wall in every chamber hall surveyed.

H. Reflectogram

Figure 26 shows monaural reflectograms at typical receiving positions in three halls, where the average BQI_{50} value is high (0.68), median (0.64), and low (0.58), as given in Fig. 23. These diagrams are the impulse responses processed by a bandpass filter equal in width to that spanned by 3 octave bands (lower and upper cutoff frequencies of 354 and 2828 Hz) (Hidaka and Nishihara, 2002). This figure indicates that the BQI of a hall can almost be determined by visual inspection of the temporal density of reflections within the initial 50 ms.

I. Surface diffusivity index, SDI

Similar to every successful symphony hall having an abundance of surface irregularities, sound-energy diffusion by both large- and fine-scale irregularities is important in chamber halls, also (Barron, 1993; Beranek, 1996, 2003a). Currently, there is no means to physically measure the degree of surface irregularity, but the relevant method, called the surface diffusivity index SDI, after Haan and Fricke (1993), is applied. This method scales the surface irregularity from 0 to 1.0 by visual inspection. They categorized the degree of irregularities of the ceiling and side walls (end walls are neglected) into three levels of diffusivity: high, medium, and low, and assigned a numerical rating: 1, 0.5, and 0, respectively. Then, the SDI is given as a weighted average of the diffusivity of each surface area. The results for European halls are distributed over a broad range, i.e., 1.0 (VB); 0.88 (SG); 0.84 (BK, VM, ZT); 0.72 (AC, PM); 0.63 (SW); 0.53 (VS).

J. Support, ST1

The support factor ST1 is a measure of the degree to which a lone musician's sound is reflected by surfaces around the stage back to him (Gade, 1989). To the audience in a symphony hall, this factor is no measure of the acoustical quality (Beranek, 2003b), but it is important to the players on stage. In Table V, ST1 and dimensional factors around the stages of the halls: stage area; stage volume; stage–ceiling height; stage depth; and stage–floor height are listed. The stage areas of traditional chamber halls range from 37 to 101 m^2 (median: 60 m^2) and the stage depth 4 to 8.6 m (median: 6.2 m). This stage space is generally more compact than that of the modern chamber halls with the median of the stage areas equal to 95 m^2 and the stage depths equal to 7.5 m. It is not known whether ST1 corresponds to ease of ensemble, but obviously there are stronger reflections to players when the stage is smaller, thereby increasing ST1. Every dimensional parameter in Table V correlates to some extent with ST1, but the stage volume correlates most with ST1 ($r=0.71$), as shown in Fig. 27. The existence of a pipe organ showed no correlation with ST1.

V. SEVERAL INTERVIEWS OF MUSICIANS AND QUESTIONNAIRE RESULTS

A survey of the relative subjective acoustical qualities of the chamber halls in this paper was not possible. Some comments from world-class artists are given here.

(i) R. Honeck (Concertmaster of Wiener Philharmoniker): "The reverberation in VB under unoccupied

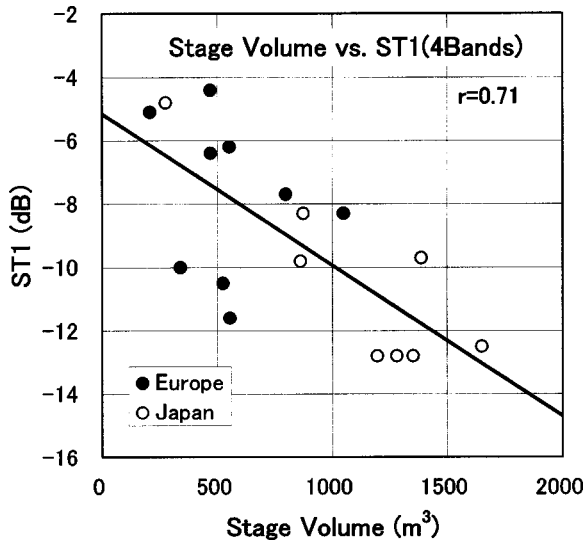

FIG. 27. Plot of stage support ST1 versus volume of the stage space, where 4 bands mean the average over 250-, 500-, 1000-, and 2000-Hz bands. High correlation ($r=0.71$) is obtained.

condition (2.3 s) is too long to ensure good ensemble. RT under occupied condition (1.6 s) is very much to be preferred.''

(ii) T. Yasunaga (Concertmaster of Berliner Philharmonisches Orchester): ''The acoustic condition of TH is just right and makes it easy for us to maintain ensemble. The sound of the violins is just right, but this hall would be better if the contrabasses were a bit louder.''

(iii) J. Sterker (Cellist): ''The RT of TM (1.7 s at mid frequencies) is just right. Diffusing elements such as chandeliers in a concert hall are very important, because they add patina to the sound.''

(iv) Prague Piano Trio: ''The side walls of the stage enclosure should not be parallel to each other but splayed outward somewhat toward the audience. If splayed, a cellist feels that his sound is being projected toward the audience effectively. A splayed angle of less than 15 degrees is insufficient for every instrument to contribute its share to the ensemble.''

(v) H. Iwaki (Conductor): ''The reverberation time of TH (1.7 s) is good, but I prefer more strength in the higher tones of the violin. Sound reflection from the stage enclosure is excellent for ensemble.''

As a partial reference, questionnaire test results can be shown for five Japanese halls: TH, TM, TT, TD, and one other chamber hall, Tokyo Bunka-Kaikan Small Hall (TB) ($N=649$ seats, RT$=1.4$ s). After the full concerts, on average ten subjects consisting of professional musicians, recording engineers, and concert-goers, were asked for rating scales of the subjective reverberance assigned the numbers 1 to 5: *Too long* (5); *Somewhat long* (4); *Just right* (3); *Somewhat short* (2); *Too short* (1). They were well experienced in taking this kind of test, and no singular results were observed in their replies. Then, the averaged scale values of the three halls (TD, TH, TM) with RT ranging from 1.6 to 1.7 s were included in the category ''Just right,'' (2.8, 3.0, 3.4), while those of the two halls (TT, TB) with RT less than 1.5 s were in the category ''Somewhat short,'' (2.2, 2.3).

These comments and findings support the conclusion that when $N=500$ to 600 seats, which is the upper limit of adequate seating capacity for a string quartet performance (Meyer, 1978a), the RT should be 1.5 to 1.7 s. For the famous halls in England similar values are found, i.e., the Wigmore Hall seats 544 and has an RT_M of 1.5 s, and Maltings Concert Hall seats 824 and has an RT_M equal to 1.6 s (Barron, 1993).

VI. CONCLUSIONS

Based on the measurement at 18 chamber halls in Europe and Japan in the unoccupied condition, four independent objective acoustical parameters were studied: reverberation time at midfrequencies RT_M (occupied); strength of sound throughout the hall at low frequencies G_L (unoccupied); binaural quality index BQI$=[1\text{-IACC}_{E3}]$ (unoccupied); and intimacy ITDG (determined from reflectograms).

(1) The reverberation times at midfrequencies with full occupancy in highly rated European halls range from 1.1 to 1.8 s. If the smaller-sized ($N<339$ seats) and the multipurpose halls are excluded, the RT ranges from 1.5 to 1.7 s for 9 out of 11 halls (Table I). If the seating numbers are between 500 and 600, musicians stated that halls with RTs of 1.5 to 1.7 s are optimum. Although highly correlated with RT and EDT, the (unoccupied) hall-averaged clarity factor, $C_{80,3}$, should lie between (0.2 ± 1.6) dB throughout the audience areas with the on-stage main source position (Fig. 17). Time gravity shows very high correlation with $C_{80,3}$, and has independent meaning (Table III).

(2) For traditional European chamber-music halls, the range for (unoccupied) hall-averaged sound strength G_M with the omnidirectional source at the main position on stage is 10 to 14 dB, and G_L is 10 to 15 dB (Figs. 19 and 20). In modern halls, G_M and G_L are less by 3 and 5 dB, respectively, on average, which are caused by the absorption of the gypsum board used for the interior materials even when the gypsum is loaded to make it more massive and rigid. In the halls of this study, the parameters G_M and G_L were highly correlated, $r=0.89$. It also appears that reradiation from flexible stage floors might have an important role in reinforcing low tones.

(3) Excellent chamber halls (either unoccupied or occupied) should have hall-averaged binaural quality indexes (integrated over 80 ms) that exceed 0.68 (Table I). If the BQIs are integrated over 50 ms and averaged only over the main-floor seatings, the value of $BQI_{50}=[1\text{-IACC}_{E(50\text{ ms}),3}]$ should exceed 0.58.

(4) The initial-time-delay gap, ITDG, measured at locations near the center of the main floor, should be 20 ms or less (Table I). The side walls must be shaped to provide an adequate number of lateral reflections to the main floor.

(5) The bass ratio, BR (occupied), which is the ratio of summed reverberation times in the 125/250-Hz bands to those in the 500/1000-Hz bands, is not an independent

parameter for chamber halls, because BR correlates highly with G_L (Table III). For European halls, BR varies from 1.07 to 1.24.

(6) One can closely judge the BQI of a chamber hall by visual inspection of reflectograms in the time range between the arrival of the direct sound and 50 ms thereafter. In that time period, there should exist a substantial number of early reflections. (see Fig. 26.)

(7) Finally, a chamber hall must have large-scale diffusion and fine-scale diffusion to give the sound ''patina'' (Barron, 1993; Beranek, 1996). Thus, both large- and small-scale irregularities should be designed on the walls, balcony fronts, and ceiling from everywhere early sound is reflected. If Haan and Fricke's (1993) visual inspection scheme is utilized, the sound-diffusion index, SDI, must exceed 0.80 for a hall to reach the top ranks.

In this study, the frequency characteristics of RT, C_{80}, and G between traditional and modern categories showed significant differences, which probably contribute to the tone color in frequency domain to some extent as suggested by Beranek (1996). Future study is necessary to determine how significant the observed differences in the three parameters are subjectively, although they are certainly important for practical design purposes.

ACKNOWLEDGMENTS

The authors wish to express their sincere gratitude to Leo L. Beranek for his invaluable suggestions. Thanks are due T. Okano of Takenaka R&D Institute for his assistance in the analysis of data and for providing the drawings of several of the European halls, and Josef Novak of Prague for his effort in arranging for the measurement in part of the halls.

Acoustic Society of America (ASA) (**2003**). *Halls for Music Performance: Another Two Decades of Experience*, (Acoust. Soc. Amer., Melville, New York), 1982–2002.

Ando, Y., and Noson, D. (**1997**). *Music and Concert Hall Acoustics* (Academic, New York), pp. 11–12.

Barron, M. (**1993**). *Auditorium Acoustics and Architectural Design* (E and FN Spon and Chapman & Hall, London), Chap. 6.

Beranek, L. L., and Schultz, T. J. (**1965**). ''Some recent experiences in the design and testing of concert halls with suspended panel arrays,'' Acustica **15**, 307–316.

Beranek, L. L., and Hidaka, T. (**1998**). ''Sound absorption in concert halls by seats, occupied and unoccupied, and by the hall's interior surfaces,'' J. Acoust. Soc. Am. **104**, 3169–3177.

Beranek, L. L. (**1996**). *Concert and Opera Hall: How They Sound* (Acoust. Soc. Amer., Melville, New York)

Beranek, L. L. (**2003a**). ''Subjective rank-orderings and acoustical measurements for 58 concert halls,'' Acta Acust. (Beijing) **89**, 494–508.

Beranek, L. L. (**2003b**). *Concert Halls and Opera Houses: Music, Acoustics and Architecture* (Springer, New York).

Bradley, J., and Soulodre, G. (**1995**). ''Objective measures of listeners envelopment,'' J. Acoust. Soc. Am. **98**, 2590–2597.

Cox, T. J., Davies, W. J., and Lam, Y. W. (**1993**). ''The sensitivity of listeners to early sound field changes in auditoria,'' Acustica **79**, 27–41.

Cremer, L. (**1984**). *The Physics of the Violin* (The MIT Press, Cambridge, MA), Chap. 14.5.

Fasold, W., Sonntag, E., and Winkler, H. (**1987**). *Bau-und Raumakustik* (VEB für Bauwesen, Berlin), pp. 317–319.

Fürjes, A. T., Arato-Borsi, E., and Augusztinovicz, F. (**2000**). ''Evaluation and design of small rooms,'' Buil. Acoust. **7(4)**, 277–296.

Gade, A. C. (**1989**). ''Investigations of musicians' room acoustic conditions in concert halls,'' Acustica **69**, 193–203, 249–262.

Haan, C. H., and Fricke, F. R. (**1993**). ''Surface diffusivity as a measure of acoustic quality of concert halls,'' Proceedings of the Conference of the Australian and New Zealand Architectural Science Association, Sidney, 81–90.

Hidaka, T., and Beranek, L. L. (**2000**). ''Objective and subjective evaluations of 23 opera houses in Europe, Japan, and the Americas,'' J. Acoust. Soc. Am. **107**, 368–383.

Hidaka, T., Beranek, L. L., Masuda, S., Nishihara, N., and Okano, T. (**2000**). ''Acoustical design of the Tokyo Opera City (TOC) Concert Hall, Japan,'' J. Acoust. Soc. Am. **107**, 340–354.

Hidaka, T., Nishihara, N., and Beranek, L. L. (**2001**). ''Relation of acoustical parameters with and without audiences in concert halls and a simple method for simulating occupied state,'' J. Acoust. Soc. Am. **109**, 1028–1042.

Hidaka, T., and Nishihara, N. (**2002**). ''On the physical parameter of texture,'' Paper RBA-01-002-IP, Proceedings of Forum Acusticum, Sevilla.

ISO 3382 (**1997**). ''Acoustics—measurement of the reverberation time of rooms with reference to other acoustical parameters.''

Kuhl, W. (**1978**). ''Raumlichkeit als Komponente des Raumeindrucks (Spacial impression as a measure of total room impression),'' Acustica **40**, 167–181.

Meyer, J. (**1978a**). *Acoustics and the Performance of Music* (Das Musikinstrument, Frankfurt/Main), Chap. 6.

Meyer, J. (**1978b**). ''Raumakustik und Orchesterklang in den Konzertsälen Joseph Haydns (Room acoustics and orchestral sound in the concert halls of Joseph Haydn),'' Acustica **41**, 145–162.

Reichardt, W., and Kussev, A. (**1973**). ''Ein- und Ausschwingvorgang von Musikinstrumenten und integrierte Hüllkurven ganzer Instrumentengruppen eines Orchesters (Building-up transients and decaying-out transients of musical instruments and integrated envelope curves of complete instrument groups of an orchestra),'' Z. Electr. Inform.-u. Energietechnik, Leipzig **3**, S. 73–88.

Reichardt, W., Abdel, Alim O., and Schmidt, W. (**1975**). ''Definition und Messgrundlage eines objektiven Masses zur Ermittlung der Grenze zwischen brauchbarer und unbrauchbarer Derchsichtigkeit bet Musikdarbietung (Definition and basis of making an objective evaluation to distinguish between useful and useless clarity defining musical performances),'' Acustica **32**, 126–137.

Talaske, R. H., Wetherill, E. A., and Cavanaugh, W. J. (**1982**). *Halls for Music Performance* (American Institute of Physics, Woodburg, NY).

Blind deconvolution of audio-frequency signals using the self-deconvolving data restoration algorithm

James N. Caron[a)]
Research Support Instruments, 4325-B Forbes Boulevard, Lanham, Maryland 20901

(Received 19 June 2003; revised 18 March 2004; accepted 29 March 2004)

A signal processing algorithm has been developed in which a filter function is extracted from degraded data through mathematical operations. The filter function can be used to restore much of the degraded content of the data through use of a deconvolution process. The operation can be performed without prior knowledge of the detection system, a technique known as blind deconvolution. The extraction process, designated self-deconvolving data reconstruction algorithm, is applied here to audio-frequency signals showing significant qualitative improvement. Degradation arising from the process of electronic recording and reproduction is significantly reduced. © *2004 Acoustical Society of America.* [DOI: 10.1121/1.1751152]

PACS numbers: 43.60.Ac, 43.60.Dh [EJS] Pages: 373–378

I. INTRODUCTION

The self-deconvolving data restoration algorithm, or SeDDaRA,[1–3] enables efficient restoration and enhancement of degraded data by identification of an impulse function. The effect of the impulse function can be removed from the data using a deconvolution process. In this study, the process is applied to empirical audio-frequency signals that were degraded by electronic reproduction. This action imposes an undetermined frequency response upon the signals. The algorithm compares this frequency response to that of a non-degraded, or ''reference'' signal and derives a filter function. The filter function can then be used to restore the signal, and others produced by the same system, using a deconvolution process.

Signal processing[4,5] using blind deconvolution is an active field of study for a broad spectrum of applications.[6–11] Blind deconvolution is required in situations where the impulse function cannot be accurately measured or modeled. Blind deconvolution techniques can be classified as iterative or noniterative. For real-time applications, noniterative techniques are more desirable, but often have limited applicability. Iterative techniques can be more effective, but are more computationally intensive.[1]

The SeDDaRA process is a noniterative technique, and has proven to be quite robust in a broad spectrum of applications. Application requires little user input and is computer efficient, in contrast to iterative techniques. The process compares the magnitude of the data in Fourier space to the same quality of a specified reference data set. A filter function is derived from the comparison and used as a transfer function for restoring the original data.

In this study, the technique is applied to acoustic signals as verification that the technique can be applied to audio-frequency signals. An acoustic signal is produced by a conventional computer speaker, and simultaneously recorded by the computer microphone. This action imposes an unknown frequency response upon the signal. With SeDDaRA, much of the degraded frequency response can be restored. This is demonstrated by the significant qualitative improvement in both the signals and their frequency distributions.

II. THEORY

The following summarizes the theoretical development of the blind deconvolution process. A more complete description can be found in the references.[1]

A. Deconvolution

The goal of data restoration is to remove degradation from a signal that, with an ideal detection system, would not be present. Once the form of the degradation is known, a class of deconvolution processes,[12–15] such as non-negative least squares and the Wiener filter, can be used to remove the defect as best as possible. A mathematical representation of the degraded data $g(t)$ is

$$g(t)=f(t)*d(t)+w(t), \tag{1}$$

where $d(t)$ is the impulse function, $f(t)$ is the truth or non-degraded data, $w(t)$ is a noise term, and the asterisk denotes the convolution. The objective is to find the best estimate of $f(t)$ from $g(t)$ when $d(t)$ and $w(t)$ are unknown. This relationship is simplified by transferring Eq. (1) into frequency space via application of a Fourier transform, yielding

$$G(\nu)=F(\nu)D(\nu)+W(\nu), \tag{2}$$

where ν is the coordinate in frequency space, and transformed functions are represented by capital letters.

For known $d(t)$, a deconvolution process can be applied to $g(t)$ to approximate $f(t)$. A pseudoinverse filter, an approximation of the Wiener filter, is employed here. The deconvolution is produced from

$$F(\nu)\approx\frac{G(\nu)D^*(\nu)}{|D(\nu)|^2+C_2}, \tag{3}$$

where the parameter C_2 prevents amplification of noise and can be chosen by trial and error.

a)Electronic mail: caron@researchsupport.com

B. Blind deconvolution

For unknown $d(t)$, the transfer function $D(\nu)$ is derived from $G(\nu)$ for use in a deconvolution algorithm. To this end, the degradation is assumed invariant, $D(\nu)$ is assumed real and has the form

$$D(u)=[K_G\mathcal{S}\{|G(\nu)-W(\nu)|\}]^{\alpha(\nu)}, \tag{4}$$

where $\alpha(\nu)$ is a tuning parameter and K_G is a real, positive scalar chosen to ensure

$$|D(\nu)|\leqslant 1. \tag{5}$$

Application of the smoothing filter, usually a median filter, $\mathcal{S}\{...\}$ assumes that $D(\nu)$ is a slowly varying function.

Equation (5) demonstrates the difference between the application of SeDDaRA on sounds and images. For images, it is usually sufficient to assume that the degradation only occurs as a result of reduction of specific frequencies. Thus, the criteria for images states that $0\leqslant|D(\nu)|\leqslant 1$. In acoustic settings, the possibility of amplification cannot be ruled out.

Equation (4) is subject to the conditions that the smoothing filter $\mathcal{S}\{...\}$ is separable, and $F(\nu)$ and $W(\nu)$ are uncorrelated. Equation (4) states that application of a smoothing filter and power law to the power spectrum of the reference data, when chosen correctly, will produce the impulse function. Although stated as an equality, in practice this is an approximation stemming from separability condition. For simplicity, the noise term $W(\nu)$ will be assumed negligible.

Since $D(\nu)$ is assumed real, Eq. (2) can be restated as

$$D(\nu)=\frac{\mathcal{S}\{|G(\nu)|\}}{\mathcal{S}\{|F(\nu)|\}}, \tag{6}$$

where the smoothing operator has been applied. Since $D(\nu)$ is a slowly varying function, it can be removed from the influence of the smoothing operator.

Equation (6) is substituted into Eq. (4),

$$\frac{\mathcal{S}\{|G(\nu)|\}}{\mathcal{S}\{|F(\nu)|\}}\approx\frac{K_G\mathcal{S}\{|G(\nu)|\}}{K_{F'}\mathcal{S}\{|F'(\nu)|\}}\approx[K_G\mathcal{S}\{|G(\nu)|\}]^{\alpha(\nu)}. \tag{7}$$

Since the truth data $F(\nu)$ are unknown, we have replaced them with a data set $F'(\nu)$ that contains the desired characteristic frequency spectrum, where $K_{F'}$ is another scaling parameter. With the smoothing filter, the replacement data set needs to satisfy

$$K_{F'}\mathcal{S}\{|F'(\nu)|\}\approx K_F\mathcal{S}\{|F(\nu)|\}. \tag{8}$$

Preferably, this function would be a theoretical model of the anticipated result. However, since modeling a detection system is often complicated, using a fair representation of the truth data can be more efficient.

The function $|F'(\nu)|$ is the key to the success of the process. It is a representation of the frequencies that one expects to achieve. With the presence of the smoothing filter, this function need only be similar to the spectrum of the actual truth $|F(\nu)|$. For example, a good quality recording of a man's voice may be used to restore a degraded recording of another man's voice. In practice, finding a suitable $|F'(\nu)|$ is not a difficult task.

Solving for $\alpha(\nu)$ produces

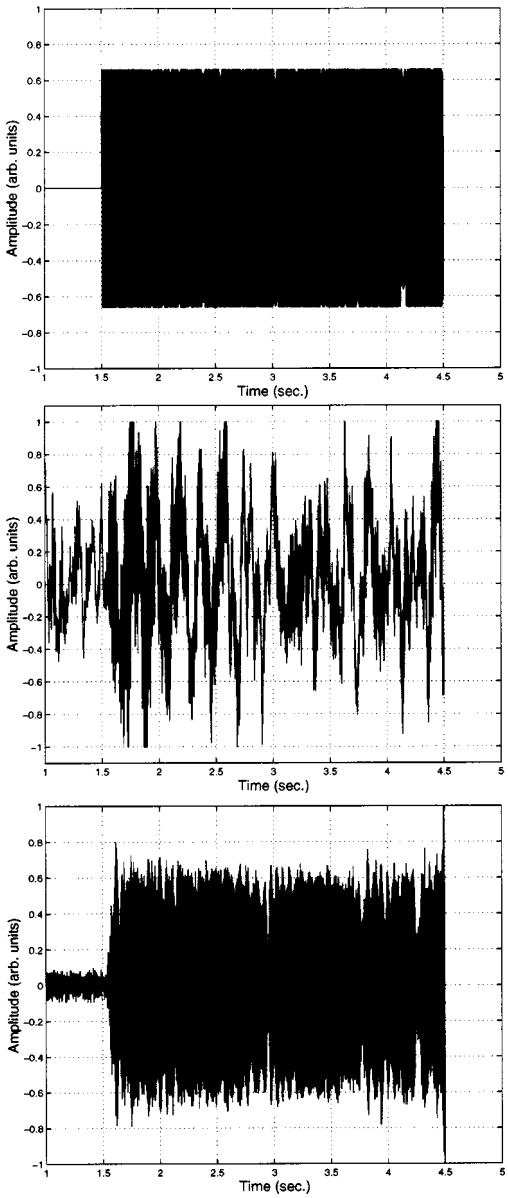

FIG. 1. Top: A synthetic wave form was generated that sweeps the frequency range from 100 to 2000 Hz with an equal amplitude of $A=0.66$. Center: The sound wave after it has been played through the computer audio speaker and recorded on the computer microphone. A significant amount of distortion can be seen. Bottom: The wave form after processing with SeDDaRA. Although noise has been amplified, the low-frequency component has been removed and the amplitude for most frequencies has been regained.

$$\alpha(\nu)\approx\frac{\ln[K_G\mathcal{S}|G(\nu)|]-\ln[K_{F'}\mathcal{S}\{|F'(\nu)|\}]}{\ln[K_G\mathcal{S}|G(\nu)|]}. \tag{9}$$

In this relation, K_G and $K_{F'}$ must be determined such that $|D(\nu)|\leqslant 1$. This condition is satisfied if we set $K_G=1/\max[\mathcal{S}\{|G(\nu)|\}]$ and $K_{F'}=1/\max[\mathcal{S}\{|F'(\nu)|\}]$.

It follows that

$$D(\nu)=\{K_G\mathcal{S}\{|G(\nu)|\}\}^{\alpha(\nu)}, \tag{10}$$

where $\alpha(\nu)$ is given by Eq. (9).

Substitution of Eq. (9) into Eq. (10) produces an approximation of Eq. (6), providing a more concise result.

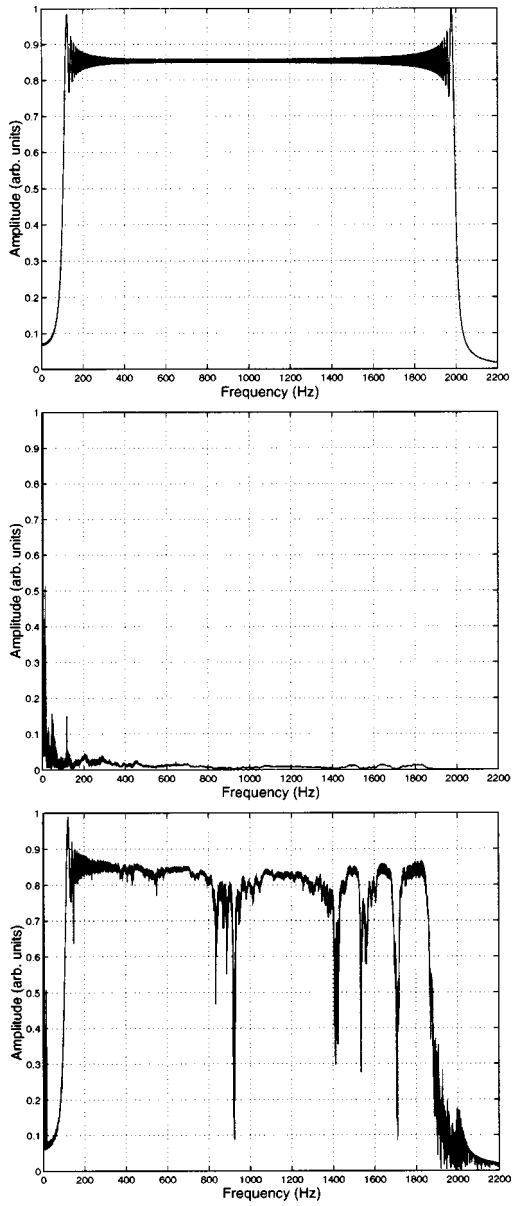

FIG. 2. Top: Frequency of the synthetic wave form sweeping the frequency range from 100 to 2000 Hz. Center: The frequency spectrum of the sound wave after it has been played through the computer audio speaker and recorded on the computer microphone. Bottom: The frequency spectrum of the wave form after processing with the SeDDaRA technique. Although some signal loss is apparent, the spectrum closely matches that of the original signal.

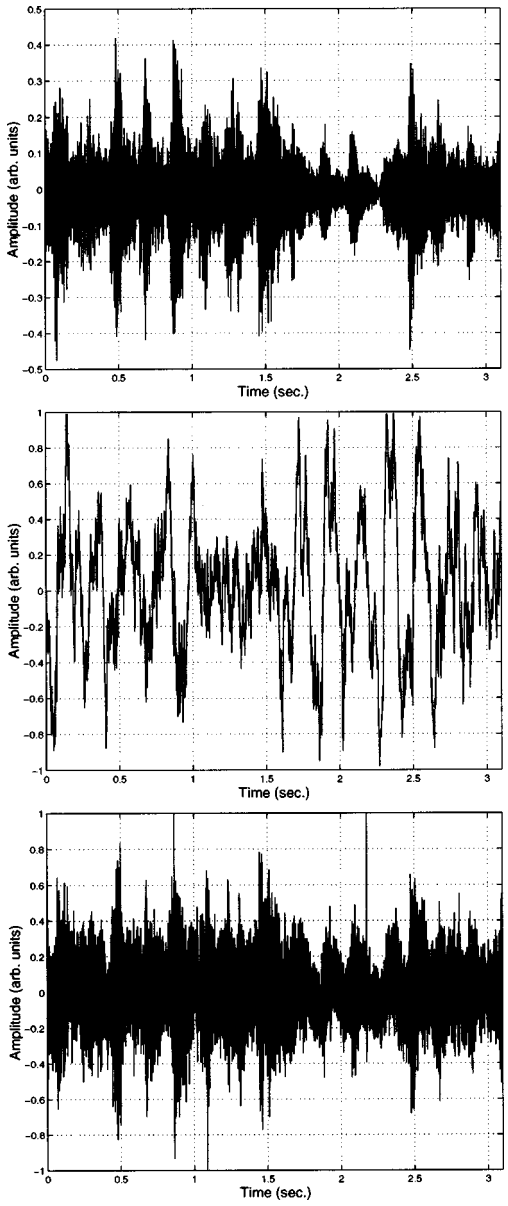

FIG. 3. Top: The original segment of the sound clip. Center: The sound wave after it has been played through the computer audio speaker and recorded on the computer microphone. A significant amount of distortion can be seen. Bottom: The wave form after processing with the SeDDaRA technique.

SeDDaRA is applicable when the degradation is invariant, as it estimates the impulse function from the entirety of the data. In cases where the degradation is not uniform across the data set, some restoration is still possible. However, this may produce nonphysical artifacts. The algorithm has also been applied successfully to signals that contain significant noise. A formal study on the influence of noise has not yet been conducted.

III. EMPIRICAL APPLICATION

A. Deconvolution with known nondegraded signal

The application of SeDDaRA to sound was first verified by restoring a degraded sound wave using the nondegraded sound wave for the reference data. The synthetic sound wave, sweeping the frequency range from 100 to 2000 Hz for a period of 3 s, is displayed in Fig. 1 (top). The wave is sinusoidal in shape, but due to space constrictions, the wave form appears as a block in the graph. This sound wave was played out to the computer's audio speakers and simultaneously recorded on the computer microphone, Fig. 1 (center), located several inches away. A degraded and unknown frequency response is forced onto the sound wave by both the audio speakers and microphone. The recorded sound wave was processed with SeDDaRA using the synthetic wave form as the reference wave.

The synthetic, recorded, and processed wave forms are shown in Fig. 1. The recorded wave form has a considerable low-frequency component that could be attributed to air cur-

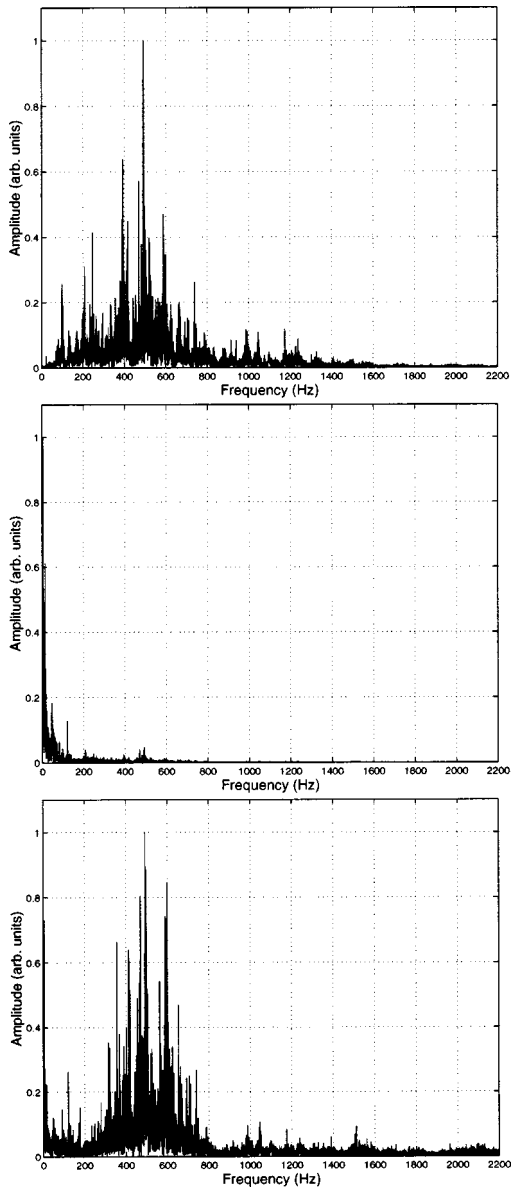

FIG. 4. Top: Frequency spectrum of the music segment. Center: The frequency spectrum of the sound wave after it has been played through the computer audio speaker and recorded on the computer microphone. Bottom: The frequency spectrum of the wave form after it was processed using the SeDDaRA technique.

rents near the microphone. The processed wave form shows obvious amplification of noise, but removes the low-frequency components and restores the amplitude levels to approximately the original values.

The frequency distributions are displayed in Fig. 2. The low-frequency component dominates the sound wave as evident in the frequency spectrum of the recorded sound wave, Fig. 2 (center). The restoration, however, closely resembles the original spectrum. The highest frequencies (greater than 19 kHz) appear diminished. Some loss may have resulted from the signal being clipped at high amplitudes during the sampling process.

B. Deconvolution with derived impulse function

The utility of the previous experiment is that it provides a function that allows for the restoration of any sound wave

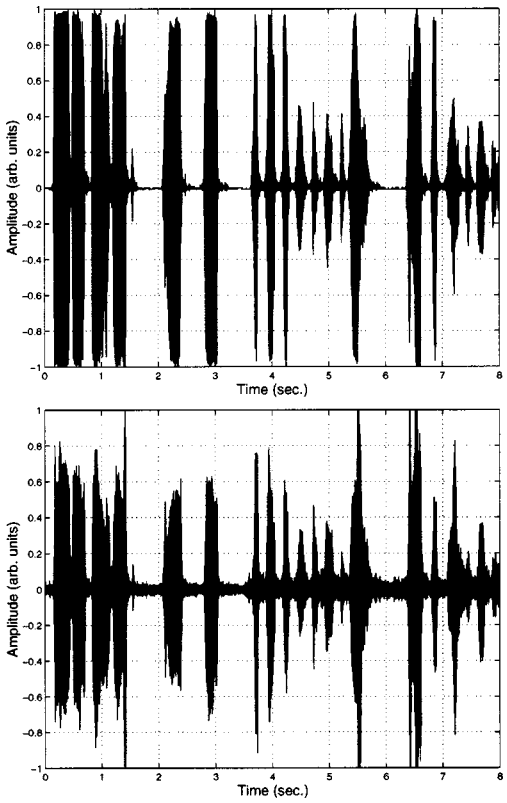

FIG. 5. Top: Sound clip from a speech by John F. Kennedy. Bottom: Restoration of the Clip using SeDDaRA.

that traverses the same path as the sound wave tested above. In a broader sense, a correction function can be measured for any system where a signal with a known frequency function can be generated.

Another sound wave, a segment of a digital recording of a bassoon quartet,[16] was played through the system. The recorded wave was restored using the $\alpha(\nu)$ from Sec. III A. The function $D(\nu)$ was calculated by following the procedure of Sec. III A.

The results of the experiment are shown in Fig. 3. The sound wave is clearly degraded by the playback and recording operation. As shown, application of the pseudoinverse filter with a derived $D(\nu)$ restores the sound wave. The frequency distributions are shown in Fig. 4.

C. Deconvolution with unknown impulse function

The method was then applied to an audio recording with undefined frequency degradation. A potential application of this technique is to restore audio information that was not recorded under optimum settings. To test this application and blind deconvolution in general, SeDDaRA was applied to a sound clip from a speech by President John F. Kennedy.[17] The reference data was a voice of a man recorded recently with significantly better sound quality. Ideally, one would restore a degraded recording of a certain person's voice but using a good quality recording of that person's voice as the reference data, if available. This would best preserve the frequency qualities of the person's voice.

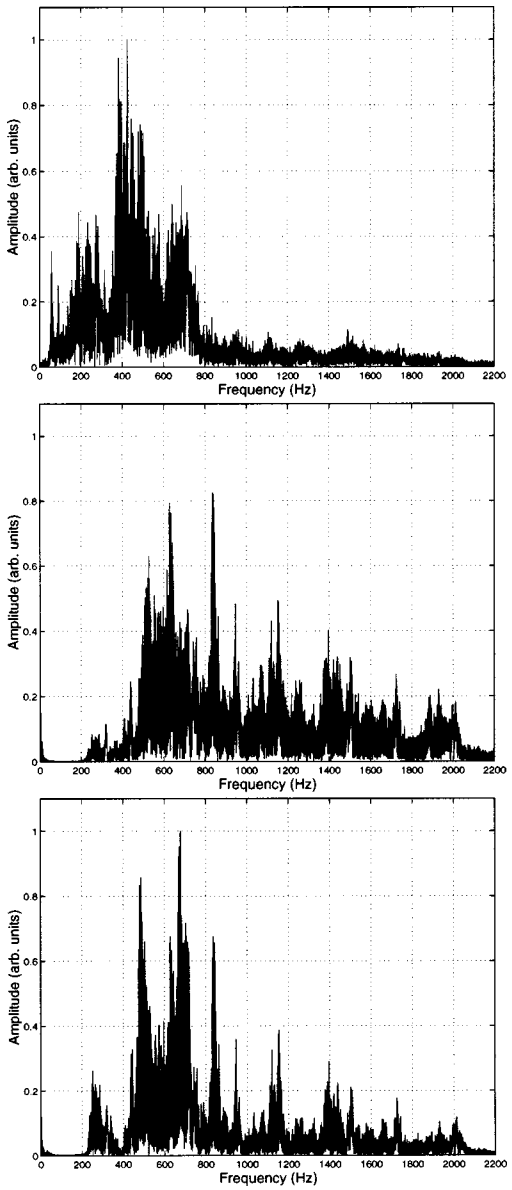

FIG. 6. Top: Reference frequency spectrum of a man's voice. Center: The frequency spectrum of the sound wave taken from a speech by JFK. Bottom: The frequency spectrum of the restored signal.

The original and restored recordings are shown in Fig. 5. The frequency distributions of the reference data, the original recording, and the restored version are shown in Fig. 6.

From Fig. 6, the reference data (top) has an increased response in the 0–500 Hz range and decreased response for frequencies above 800 Hz. After processing, the 200–500 Hz region has been comparatively amplified while frequencies above 800 Hz have been attenuated. These qualities are evident in the restored wave form Fig. 5 (bottom) producing a perceptively better reproduction of the voice. However, the reference wave form does have diminished response near 600 Hz, which may suggest the reference sound wave was not as good an approximation as needed.

As with any blind deconvolution method, some model of the transfer function or nondegraded signal must be estimated to perform the operation. For SeDDaRA, the reference signal shapes the frequency response of the restored wave form. Thus, the more attention given to the choice of reference signal, the better the restoration will be.

IV. CONCLUSION

A blind deconvolution process has been presented that compares the frequency response of a degraded audio-frequency signal to a good-quality signal with the desired frequency response. A transfer function is derived from the two signals and used to restore the degraded signal. The qualitative experiments presented here verify that the algorithm can be applied to acoustic wave forms to restore the frequency characteristics of the signal. The success of the restoration is dependent on the choice of an appropriate reference signal.

The SeDDaRA process has several unique characteristics that are not found in current signal processing algorithms. At the core of the process, this method extracts a reasonably good approximation for the degradation of a signal in a comparatively short amount of time, provided the degradation is invariant across the data set. This algorithm is easy to implement, and can be inserted into existing signal processing packages without much difficulty. As demonstrated, the method works well on a wide variety of signal types, including images, and acoustic wave forms. This is accomplished without direct information about the type or extent of aberration.

Potential commercial applications include research-quality signal processing, restoration of degraded or nonoptimum audio signals, and potentially real-time processing of digital signals, such as those in cell phones. SeDDaRA may also find application in recording studios and home sound systems to counteract effects created by room acoustics, and enhance the quality of the reproduction.

[1] J. N. Caron, N. M. Namazi, and C. J. Rollins, "Noniterative blind data restoration by use of an extracted filter function," Appl. Opt. **41**, 6884–6889 (2002).
[2] J. N. Caron, N. M. Namazi, R. L. Lucke, C. J. Rollins, and P. R. Lynn, Jr., "Blind data restoration with an extracted filter function," Opt. Lett. **26**, 1164–1166 (2001).
[3] J. N. Caron, U.S. Patent pending, anticipated acceptance date: August, 2004.
[4] J. G. Proakis and D. G. Manolakis, *Introduction to Signal Processing* (Macmillan, New York, 1988).
[5] *Signal Processing Methods for Audio, Images, and Telecommunications*, edited by P. M. Clarkson and H. Stark (Academic, San Diego, 1995).
[6] G. R. Ayers and J. C. Dainty, "Iterative blind deconvolution method and its applications," Opt. Lett. **13**, 547–549 (1988).
[7] J.-Y. Lee and A. K. Nandi, "Extraction of impacting signals using blind deconvolution," J. Sound Vib. **232**, 945–962 (2000).
[8] A. K. Nandi, D. Mämpel, and B. Roscher, "Blind deconvolution of ultrasonic signals in nondestructive testing applications," IEEE Trans. Signal Process. **45**, 1382–1390 (1997).
[9] S. Barraza-Felix and B. R. Frieden, "Regularization of the image division approach to blind deconvolution," Appl. Opt. **38**, 2232–2239 (1999).
[10] K. Torkkola, "Blind separation for audio signals—are we there yet," Proceedings of the First International Workshop on Independent Component Analysis and Blind Signal Separation, Aussois, France, 1999, p. 239–244.
[11] M. Joho, H. Mathis, and G. S. Moschytz, "An FFT-based algorithm for multichannel blind deconvolution," IEEE International Symposium on Circuits and Systems, Orlando, FL, 1999, p. III-203–206.
[12] N. Wiener, *The Extrapolation, Interpolation, and Smoothing of Stationary Time Series with Engineering Applications* (Wiley, New York, 1949).
[13] C. W. Helstrom, "Image restoration by the method of least-squares," J. Opt. Soc. Am. **57**, 297–303 (1967).

[14] D. Slepian, ''Linear least-squares filtering of distorted images,'' J. Opt. Soc. Am. **57**, 918 (1998).
[15] O. Kirkeby, P. A. Nelson, H. Hamada, and F. Orduna-Bustamante, ''Fast deconvolution of multichannels using regularization,'' IEEE Trans. Speech Audio Process. **6**, 189 (1998).
[16] *United Sounds of Bassoon*, Milan Turkovi, Daniele Damiano, Clelia Goldings, and Richard Galler, performers, KOCH International GmbH (1994).
[17] From the Inaugural Address by President John F. Kennedy Washington, D.C., 20 January, 1961. Source: John Fitzgerald Kennedy Library, Columbia Point, Boston, MA.

Phenomenological detectors for crack echo families in elastic solids

Daniel E. Asraf and Mats G. Gustafsson[a)]
Signals and Systems Group, Department of Engineering Science, Uppsala University, Box 528, 751 20 Uppsala, Sweden

(Received 17 March 2003; revised 31 March 2004; accepted 19 April 2004)

The potential performance of low-complexity phenomenological detectors for crack echo families in elastic solids is evaluated. Ultrasonic echoes from a strip-like crack residing in an isotropic elastic solid with coarse microstructure are considered and the achieved detector performance is compared to the theoretical upper bounds (constrained only by the underlying physics) obtained by means of a recently presented physics-based optimal detector. A phenomenological signal model for the scattering process is formulated based on the time-domain impulse-response method and used to derive detectors of low numerical complexity which are dependent on a small number of parameters. The proposed detectors are compared in terms of receiver operating characteristic curves, which are computed by means of Monte Carlo simulations for the case of a strip-like crack with uncertain angular orientation. The minimum probability of error criterion is used to optimize the detector parameters for the simulation study and shown to be useful even for small training data sets. These results show that the proposed detectors have close to optimal performance in particular for the case of high signal-to-noise ratios.
[DOI: 10.1121/1.1760108]

PACS numbers: 43.60.Cg, 43.35.Zc, 43.40.Le, 81.70.Cv [EJS] Pages: 379–388

I. INTRODUCTION

In this paper we consider the problem of detecting crack echoes in elastic solids with coarse microstructures using phenomenological detectors of low complexity. By phenomenological modeling, we mean modeling which is qualitative, i.e., which does not rely on an underlying detailed physical model but which is based on a combination of observed measurements and physical qualitative reasoning.

Crack detection is a common problem in ultrasonic nondestructive evaluation (NDE) of materials, in which an acoustic pulse is transmitted into a test specimen and the echoes from inhomogeneities in the material are analyzed in order to determine the presence of defects. Detectors that are high performing, robust, and of low computational and parametric (few free parameters) complexity are of practical importance in many industrial NDE applications such as power plant and aircraft inspection. Here, we show that detectors with these properties can be designed by formulating a simple but still fairly accurate phenomenological parametric model of the defect echoes.

Due to the variability of the shape, position, and orientation of a crack defect, the resulting backscattered echoes will exhibit various wave forms. Therefore, each crack echo may be considered to be a member of a signal family. In this paper three detectors for crack echo signal families are derived. Each detector imposes different assumptions of the statistical properties of the model parameters.

Three main results are reported. The first is the phenomenological signal model for the crack echoes, which is based on the time-domain impulse-response method.[1,2] Due to the generality of this modeling approach it can also be applied to other types of defects. The second main result is the application of the phenomenological model to obtain a practically useful expression for the detection statistic by treating the unknown and random model parameters within a Bayesian framework. The third main result consists of a qualitative performance comparison between the proposed detectors, in terms of receiver operating characteristic (ROC) curves, for the particular problem of detecting a strip-like crack with unknown angular orientation. These ROC curves are also compared to ROC upper bounds (constrained only by the underlying laws of physics) for detecting a crack under the stated conditions.

A well-known method to detect defects in elastic solids is split-spectrum processing[3,4] (SSP). This approach relies on qualitative physical reasoning about interference phenomena in grainy materials instead of explicit parametric mathematical models. Due to the nonlinear features of the SSP technique and the limited theoretical foundations of SSP, extensive experience is required in optimizing the detector-dependent parameters, and it is nontrivial how to obtain and then confirm significant improvements. In a recent work by Demirli and Saniie,[5,6] an explicit mathematical model was used which is similar to the ones presented here; however, the problem considered was not detection but estimation of parameters in ultrasonic echo models.

In another quite recent approach, explicit mathematical models of echoes and clutter were used to derive detectors.[7–10] The present work may be regarded as filling the gap between the work in Refs. 8 and 9, which focused on optimal detection of single echoes, and the work in Refs. 7 and 10, which considered optimal detection of echo families. The detectors studied in this work are also designed for tran-

a)Electronic mail: mg@signal.uu.se

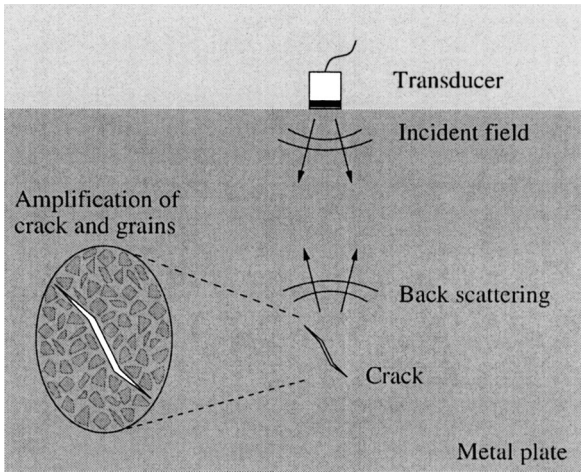

FIG. 1. Sketch of the geometry for the pulse–echo crack detection problem. The material crystallites are illustrated in the inserted amplification of the crack.

sient families but they do not rely on detailed physical modeling as in Ref. 10, and they are based on several well-founded phenomenological signal models other than those in Ref. 7. Furthermore, the presented study offers the first known quantitative comparison of phenomenological detectors for crack echo families with the physically constrained upper bounds obtained using optimal detection in combination with numerical physical modeling. This gives important insights about the loss of performance associated with replacing exact numerical physical modeling by phenomenological signal models for crack echo detection.

The remainder of this paper is organized as follows. In Sec. II, the problem of detecting a family of strip-like cracks residing in an elastic solid with a coarse microstructure is introduced and a phenomenological model for the crack scattering mechanism is presented. In Sec. III, three detectors based on the phenomenological model are derived for different assumptions of the statistical properties of the model parameters. The minimum probability of error optimization of the detector parameters is briefly presented in Sec. IV. Section V presents the signal generating models and the problem scenario used in the Monte Carlo simulations, followed by the detector parameter optimization and a comparative study of the detection performance in terms of ROC curves. Finally, Sec. VI contains a short summary and a discussion about future work.

II. PHENOMENOLOGICAL MODELING OF CRACK ECHO FAMILIES

The problem under consideration is to detect a crack residing in an isotropic elastic material with a coarse microstructure by means of an ultrasonic pulse–echo system. A sketch of the experimental scenario is shown in Fig. 1.

The transducer is assumed to generate a transient compressional wave pulse with a normal angle of incidence with respect to the elastic solid. This field is scattered by inhomogeneities in the solid and received by the same transducer, which converts the backscattered wave field into an electric signal denoted $y(t)$. Assume that the inspection of the test specimen is conducted within some specific depth interval d_0 to d_1, and let $t=0$ be the time when the ultrasonic pulse was transmitted. Then, the depth interval will correspond to the time interval $t_0=2d_0/c$ to $t_1=2d_1/c$, where c is the longitudinal sound speed in the elastic solid. The measured signal from a test specimen containing a crack is modeled as

$$y(t)=s(t;\Omega)+v(t), \quad t\in[t_0,t_1], \tag{1}$$

where $v(t)$ is the clutter noise signal generated by the backscattered field from the grains in the solid, and $s(t;\Omega)$ is the signal generated by the backscattered field from the crack. The parameter Ω is representing the underlying physical parameters for the crack such as position, shape, and angular orientation, etc.

By adopting the impulse-response method proposed by Lhemery and Raillon,[1,2] the crack echo signal can be expressed as

$$s(t;\Omega)=\beta(t)*h_{\text{crack}}(t;\Omega), \tag{2}$$

where $\beta(t)$ is the transducer reference signal and h_{crack} is the impulse response of the crack. Deriving accurate approximations of the crack impulse response is quite involved;[11,12] instead, we postulate a phenomenological representation of the crack impulse response as

$$h_{\text{crack}}(t;\Omega)=h_1(t;\Omega)+h_2(t;\Omega)+h_3(t;\Omega)+\cdots+h_M(t;\Omega), \tag{3}$$

where h_1 and h_2 are the near-tip and far-tip impulse responses, respectively. The remaining terms in Eq. (3) models the impulse responses for the mode-converted contributions in the crack echo,[13,14] and M is a positive integer representing the total number of terms/components in the overall impulse response. The rationale for the model is that the echo return from a crack, exited by a pulse, consists of a few main echoes (direct echoes) followed by a series/tail of pulses due to ''ringing'' of the crack. The ringing is due to mode conversions of the acoustic pulse, the echoes in the tail rapidly decrease in amplitude until they can no longer be separated from the clutter noise.

By combining Eqs. (2) and (3), the crack echo signal can be expressed as

$$s(t;\Omega)=\sum_{m=1}^{M}\beta(t)*h_m(t;\Omega). \tag{4}$$

Due to the bandpass character of the transducer reference signal, β, each term in Eq. (4) will also be bandpass and can thereby be represented by an amplitude modulated sinusoid[15]

$$\beta(t)*h_m(t;\Omega)\approx\begin{cases}A_m a_m(t-\tau_m)\sin(\omega_m(t-\tau_m)+\phi_m), \\ \qquad t\in[\tau_m,\tau_m+T_a] \\ 0, \quad \text{otherwise.}\end{cases} \tag{5}$$

Here, A_m is the amplitude, τ_m is the arrival time, $f_m=\omega_m/2\pi$ is the carrier frequency, ϕ_m is the phase angle, and a_m is the envelope. The phenomenological crack scattering model is obtained by using Eq. (5) in Eq. (4), yielding

$$
\begin{aligned}
s(t;\Omega) &\approx s(t;\theta_1,\ldots,\theta_M,a_1,\ldots,a_M) \\
&= \sum_{m=1}^{M} x[t;\theta_m,a_m(t)], \\
\theta_m &= [A_m \quad \omega_m \quad \tau_m \quad \phi_m],
\end{aligned}
\tag{6}
$$

where $x[t;\theta_m,a_m(t)]$ is given by Eq. (5).

Since crack defects can have different properties, the underlying physical parameters, Ω, will have a statistical variability. The crack echoes may then be interpreted as belonging to a transient family parametrized by Ω. Thus, the signal model parameters, $\theta_1,\ldots,\theta_M$, and the envelopes, $a_1(t),\ldots,a_M(t)$, which are all governed by the physical parameters, can therefore be modeled as stochastic.

In Sec. V C, a specific crack defect is considered and echoes are presented, which have been computed both with an advanced numerical model[13,14,10] and the simple phenomenological model in (6) with a suitable set of parameter values. From this comparison it is apparent that the agreement between the echoes computed by means of the advanced numerical model and the simple phenomenological model are very good. Thus, this result shows the potential of modeling realistic crack echoes by means of (6).

III. DETECTORS FOR CRACK ECHO FAMILIES

The objective of a crack detector is to determine the presence or absence of a crack when presented a sampled version of the measured signal $\overline{y}=[y(t_0),y(t_0+T_s),\ldots,y(t_0+(N-1)T_s)]^T$. Here, T_s is the sampling interval and N is the number of samples, chosen so that $N=\lfloor (t_1-t_0)/T_s \rfloor$. This problem can be cast as the composite hypothesis test

$$
\begin{aligned}
H_0&: \quad \overline{Y}=\overline{V}, \\
H_1&: \quad \overline{Y}=\overline{s}(\theta_1,\ldots,\theta_M,a_1,\ldots,a_M)+\overline{V},
\end{aligned}
\tag{7}
$$

where $\overline{Y}$ is a stochastic vector with realizations denoted by $\overline{y}$, $\overline{s}$ is the crack echo to be detected, and $\overline{V}$ is a stochastic vector representing the clutter noise. Since the clutter noise from materials with a coarse microstructure, like stainless steel and copper, may be accurately modeled as a zero mean colored Gaussian process,[16–19] it is relevant to assume that $\overline{V}\sim\mathcal{N}(0,\Sigma_V)$, where $\mathcal{N}$ denotes a Gaussian distribution and Σ_V the covariance matrix.

A detector based on the likelihood ratio detection statistic is attractive as it is optimal in the Neyman–Pearson (NP) and Bayes sense.[20] The likelihood ratio for the hypothesis problem in Eq. (7) can be expressed as

$$
L(\overline{y}) = E_{\theta_1,\ldots,\theta_M,a_1,\ldots,a_M}\{L(\overline{y}|\,\theta_1,\ldots,\theta_M,a_1,\ldots,a_M)\},
\tag{8}
$$

where $E_{\theta_1,\ldots,\theta_M,a_1,\ldots,a_M}\{\cdot\}$ denotes the expectation, with respect to the model parameters and the envelopes, of the conditional likelihood ratio[20]

$$
\begin{aligned}
&L(\overline{y}|\,\theta_1,\ldots,\theta_M,a_1,\ldots,a_M) \\
&\quad = \exp\{\overline{s}(\theta_1,\ldots,\theta_M,a_1,\ldots,a_M)\Sigma_V^{-1}\overline{y} \\
&\qquad -\tfrac{1}{2}\overline{s}^T(\theta_1,\ldots,\theta_M,a_1,\ldots,a_M)\Sigma_V^{-1} \\
&\qquad \times\overline{s}(\theta_1,\ldots,\theta_M,a_1,\ldots,a_M)\}.
\end{aligned}
\tag{9}
$$

It is generally mathematically intractable to analytically solve the expectation in Eq. (8) for arbitrary signal models and model parameter pdfs. Thus, in order to obtain a simple detection statistic of low computational complexity, the following assumptions will be imposed.

(i) The number of pulses M are assumed to be fixed and the stochastic parameters of the pulses are assumed to be statistically independent.

(ii) The carrier frequencies are assumed to be equal and deterministic but unknown for all M pulses and will be denoted $f_c=\omega_c/2\pi$.

(iii) The discrete time envelopes for all M pulses are assumed to be known and equal and denoted $\overline{a}=[a(1),\ldots,a(N_a)]^T$, where N_a is the number of samples of the envelope. However, the amplitudes A_m are assumed to be different.

(iv) The arrival times $\tau_1,\ldots,\tau_M$ are assumed to be realizations from independent identically distributed stochastic variables with a uniform distribution on the observation interval $[t_0,t_1]$. In the discrete time representation this corresponds to a uniform probability mass function on $[1,N-N_a]$.

(v) The pulse durations are assumed to be short relative the acquisition time, i.e., $N_a \ll N$.

Based on these assumptions, the expression in Eq. (8) is reduced to[21]

$$
L(\overline{y}) = \frac{1}{(N-N_a)^M}\left[\sum_{n=1}^{N-N_a} E_{A,\phi}\{L_{\omega_c}(\overline{y}_n^{n+N_a}|A,\phi)\}\right]^M.
\tag{10}
$$

Here, $L_{\omega_c}(\overline{y}_n^{n+N_a}|A,\phi)$ is the conditional likelihood ratio for a single pulse with the known arrival time n, amplitude A, and phase ϕ. Moreover, $\overline{y}_n^{n+N_a}$ denotes the subvector of $\overline{y}$ from sample n to $n+N_a$. The conditional likelihood ratio is given by[20]

$$
L_{\omega_c}(\overline{y}_n^{n+N_a}|A,\phi) = \exp\{\overline{x}^T\widetilde{\Sigma}_V^{-1}\overline{y}_n^{n+N_a} - \tfrac{1}{2}\overline{x}^T\widetilde{\Sigma}_V^{-1}\overline{x}\},
\tag{11}
$$

where $\widetilde{\Sigma}_V$ is the covariance matrix (of size $N_a\times N_a$) of the noise $\overline{V}$, and the elements of the vector $\overline{x}$ are given by

$$
\begin{aligned}
x(n;A,\phi,\omega_c) &= Aa(n)\sin(\omega_c(n-1)T_s+\phi), \\
& \qquad n=1,\ldots,N_a.
\end{aligned}
\tag{12}
$$

The assumptions listed above are not based on any detailed analysis of the model parameters' statistical properties, but rather imposed to obtain a mathematically tractable problem. Clearly, the position, orientation, and size of a crack will affect the arrival times as well as the waveforms of the pulses via the intricate relationship between the underlying physical parameters and the parameters in Eq. (5). Due to the

lack of knowledge concerning this intricate relationship and the statistical properties of a potential crack's physical parameters, the assumptions listed above are intentionally conservative in the sense that they are ignorant concerning the pulse's arrival times and dependence. By refining these assumptions to agree more with the underlying physical reality, the detector will yield higher performance but become significantly more complex. In the following subsections three approaches to solve $E_{A,\phi}\{L_{\omega_c}(\overline{y}_n^{n+N_a}|A,\phi)\}$ in (10) are pursued based on different assumptions of the statistical properties of the model parameters A and ϕ.

A. The matched-filter detector

The matched-filter detector is constructed for signals where the amplitude A and the phase ϕ in Eq. (12) are considered to be fixed. This approach thereby ignores that the signal model parameters for the M pulses in Eq. (6) can vary, and is the complete opposite of having an ignorant prior. Hence, $E_{A,\phi}\{L_{\omega_c}(\overline{y}_n^{n+N_a}|A,\phi)\}$ in Eq. (10) becomes

$$L_\lambda(\overline{y}_n^{n+N_a}) = \exp\{\overline{h}^T(\lambda)\overline{y}_n^{n+N_a} - \tfrac{1}{2}\overline{x}(\lambda)^T\widetilde{\Sigma}_V^{-1}\overline{x}(\lambda)\}, \quad (13)$$

where

$$\overline{h}(\lambda) = \widetilde{\Sigma}_V^{-1}\overline{x}(\lambda), \quad (14)$$

is the matched filter, $\lambda = [A\ \omega_c\ \phi]$, and $\overline{s}$ is defined in Eq. (12). Note that the likelihood ratio detection statistic in Eq. (13) is dependent on A, ϕ, and ω_c, collected in the variable $\lambda = [A\ \omega_c\ \phi]$.

B. The noncoherent detector

The noncoherent detector is an extension of the matched-filter detector in the sense that the phase angle, ϕ, of the pulse in Eq. (12) is allowed to vary by considering it to be a uniformly distributed random variable, i.e., $\phi \sim U[0,2\pi]$. However, the amplitude A is still considered to be fixed. Under the additional assumption of narrow-band signals, the unconditional likelihood ratio, $E_{A,\phi}\{L_{\omega_c}(\overline{y}_n^{n+N_a}|A,\phi)\}$ in (10), is reduced to[20]

$$L_\lambda(\overline{y}_n^{n+N_a}) = \exp\left\{-\frac{A^2}{4}\overline{a}^T\widetilde{\Sigma}_V^{-1}\overline{a}\right\} \times I_0\left(\sqrt{(\overline{h}_s^T(\lambda)\overline{y}_n^{n+N_a})^2 + (\overline{h}_c^T(\lambda)\overline{y}_n^{n+N_a})^2}\right). \quad (15)$$

Here, $\lambda = [A\ \omega_c]$ are the parameters upon which the detection statistic is dependent, and $I_0(\cdot)$ is the modified Bessel function of order zero. Moreover, by first introducing the vectors

$$z_s(n;\lambda) = Aa(n)\sin(\omega_c(n-1)T_s), \quad n = 1,...,N_a, \quad (16)$$

and

$$z_c(n;\lambda) = Aa(n)\cos(\omega_c(n-1)T_s), \quad n = 1,...,N_a, \quad (17)$$

we can define

$$\overline{h}_c(\lambda) = \widetilde{\Sigma}_V^{-1}\overline{z}_c(\lambda) \quad \text{and} \quad \overline{h}_s(\lambda) = \widetilde{\Sigma}_V^{-1}\overline{z}_s(\lambda), \quad (18)$$

which are commonly called the in-phase and quadrature filters, respectively.

C. The wideband quadrature matched-filter detector

The wideband quadrature matched filter extends the matched-filter approach even further by allowing both the amplitude and phase of the pulse in Eq. (12) to vary. As in the case for the noncoherent statistic, the phase angle is considered to be a uniformly distributed random variable $\phi \sim U[0,2\pi]$. The amplitude, however, is assumed to be a Rayleigh-distributed random variable, i.e., $A \sim R(\sigma_A^2)$, where σ_A is a parameter defining the Rayleigh distribution denoted R. Under these assumptions the unconditional likelihood ratio, $E_{A,\phi}\{L_{\omega_c}(\overline{y}_n^{n+N_a}|A,\phi)\}$ in Eq. (10), can be derived analytically. The derivation is straightforward but still included in the Appendix for completeness and because no complete derivation has been found in the literature. The derivation results in the unconditional likelihood ratio in the form

$$L_\lambda(\overline{y}_n^{n+K}) = \frac{|\widetilde{\Sigma}_V|^{1/2}}{|\widetilde{\Sigma}_V + \Sigma_s(\lambda)|^{1/2}} \exp\left\{ \frac{\sigma_A^2(1-q_{11}(\lambda))}{2} \times [\overline{h}_s^T([1\ \ \omega_c])\overline{y}_n^{n+k}]^2 + \frac{\sigma_A^2(1-q_{22}(\lambda))}{2} \times [\overline{h}_c^T([1\ \ \omega_c])\overline{y}_n^{n+k}]^2 - \frac{\sigma_A^2(q_{12}(\lambda)+q_{21}(\lambda))}{2} \times [\overline{h}_s^T([1\ \ \omega_c])\overline{y}_n^{n+k}][\overline{h}_c^T([1\ \ \omega_c])\overline{y}_n^{n+k}] \right\}. \quad (19)$$

Here, $\lambda = [\sigma_A\ \omega_c]$ represents the parameters on which the detector statistic is dependent, Σ_s is the covariance matrix of the crack echo signal family, and $q_{ij}(\lambda)$, $i, j = 1, 2$, are elements in the 2×2 matrix $Q(\lambda)$ given by Eq. (A9). The vectors $\overline{h}_s$ and $\overline{h}_c$ are defined in Eq. (18).

The classical detector[22,23] for the problem of detecting an amplitude-modulated sinusoid, where the phase is a uniform random variable and the amplitude is a Rayleigh random variable, is commonly called *quadrature matched filter*. In the derivation of the classical *quadrature matched filter* the 2×2 matrix Q in Eq. (A9) is approximated to be diagonal.[22,23] This is based on the assumption of narrow-band signals[22,23] and thus not satisfied for wideband transient pulses, i.e., when the envelope $\overline{a} = [a(1),...,a(N_a)]^T$ in Eq. (12) is of short time duration. Since no approximations are employed in the derivation of Eq. (19), a detector based on the statistic in Eq. (19) is optimal also for wideband signals, i.e., when the envelope $\overline{a}$ has short time duration.

IV. DETECTOR PARAMETER OPTIMIZATION

The previous section presented three different approaches to compute an approximation of the likelihood ratio detection statistic. Hence, a detector for the hypothesis problem in Eq. (7) can thus be described by the decision rule

$$\delta_\lambda(\overline{y}) = \begin{cases} 0 & \text{if } L_\lambda(\overline{y}) < \gamma, \\ 1 & \text{if } L_\lambda(\overline{y}) \geqslant \gamma, \end{cases} \quad (20)$$

where γ is a user-defined threshold and λ represents the parameters in Eqs. (13), (15), or (19). Thus, the decision rule in

Eq. (20), and thereby the detection performance, is dependent on these parameters.

In order to find the parameter values which optimize the detection performance, the minimum probability of error, denoted P_E, is used as the optimization criterion.[20] Hence, the parameter optimization problem can be expressed as

$$\lambda^* = \arg\min_{\lambda}\{P_E(\delta_\lambda)\}. \tag{21}$$

The probability of error is defined by[20]

$$P_E(\delta_\lambda) = \pi_1(1 - P_D(\delta_\lambda)) + \pi_0 P_F(\delta_\lambda), \tag{22}$$

where P_D is the detection probability, P_F is the false-alarm probability, and π_0 and π_1 are the *a priori* probabilities for H_0 and H_1, respectively. The benefit of this strategy, with regard to obtaining detectors of low computational complexity, is that the optimization problem is only solved once based on a representative training data set. As described in more detail below, an exhaustive search is performed to find the best combination of parameter values for each detector. Since the detectors are phenomenological, we do not use any *a priori* physical knowledge to guide the parameter search.

V. DETECTION PERFORMANCE SIMULATION

In order to evaluate the performance of a decision rule based on the three detection statistics presented in Eqs. (13), (15), and (19), a simulation study was conducted. The advantage of basing the performance assessment on simulated signals is that the detectors presented herein can be compared with the detection upper bounds for the particular scenario being simulated. These upper bounds are computed by means of a physical model-based filter-bank detector,[10] which is optimal in the NP and Bayes sense and requires complete knowledge of the underlying physical parameters and their statistical properties.

The transducer reference signal, used in the simulations below, is presented in Sec. A, followed by a brief description of the clutter model and the host material parameters in Sec. B. In Sec. C, the crack echo model is briefly presented, together with the specific parameter settings used to generate the simulated crack echo signals. Finally, in Sec. D, the proposed detectors parameters are optimized based on Eq. (21) and the detection performance is compared by means of receiver operating characteristics (ROCs).

A. The transducer

The transducer reference signal, which is used to obtain both the crack echo and the clutter noise signal, represents both the electro-acoustic and acousto-electrical transductions as well as the electrical excitation of the transducer. The transducer is modeled here as unfocused and circular with radius 5 mm. The reference signal, in the frequency domain, is taken to be[13,14]

$$\tilde{\beta}(\omega) = \begin{cases} \sin^2\left(\pi \dfrac{|\omega| - \omega_1}{\omega_2 - \omega_1}\right), & \omega_1 \leq |\omega| \leq \omega_2, \\ 0, \quad \text{otherwise}, \end{cases} \tag{23}$$

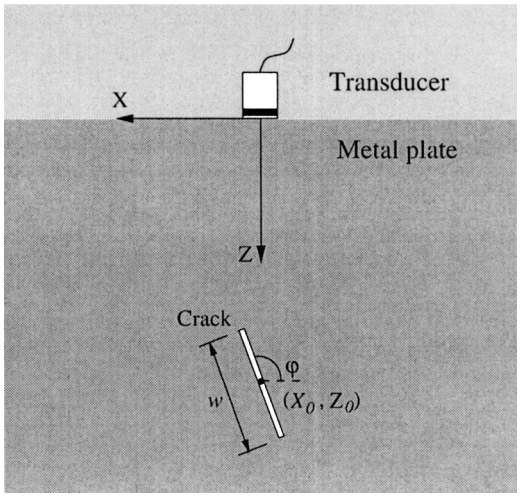

FIG. 2. The geometry of the strip-like crack model showing the parameters specifying the crack's width w, center location $[X_0, Z_0]$, and angular orientation φ with respect to the X axis.

where the lower bound $\omega_1 = 2\pi f_1$ and the upper bound $\omega_2 = 2\pi f_2$ are defined by the frequencies $f_1 = 1.32$ MHz and $f_2 = 6.68$ MHz. Hence, the center frequency of the probe is $f_\beta = \omega_\beta / 2\pi = 4$ MHz and the -3-dB bandwidth is 2.68 MHz, yielding a relative bandwidth of 67%.

The transducer reference signal in the time domain is obtained by the inverse Fourier transform, i.e., $\beta(t) = \mathcal{F}^{-1}\{\tilde{\beta}(\omega)\}$. Furthermore, since $\tilde{\beta}(\omega)$ is bandpass its time-domain signal can be described by[15]

$$\beta(t) = a_\beta(t)\sin(\omega_\beta t + \phi_\beta), \tag{24}$$

where the envelope is

$$a_\beta(t) = \sqrt{\beta(t)^2 + H\{\beta(t)\}^2}, \tag{25}$$

and $H\{\cdot\}$ denotes the Hilbert transform.

B. Host material and clutter noise model

The host material is modeled as an isotropic stainless steel, with the stiffness matrix elements[18] $C_{11} = C_{22} = C_{33} = 280.2$ GPa, $C_{12} = C_{21} = C_{13} = C_{31} = C_{23} = C_{32} = 114.0$ GPa, $C_{44} = C_{55} = C_{66} = 82.6$ GPa, and all other elements equal to zero. The density of the specimen is $\rho = 8420$ kg/m^3, the sound velocity is $c = 5800$ m/s, and the material attenuation coefficient $\alpha = 1.1$ dB/cm.

The clutter noise signals are generated with a model derived in Ref. 10, which is based on a statistical approach where the backscattered echo from the material's microstructural crystals are superimposed. The microcrystals are modeled as spherical grains having Gaussian-distributed radii with mean[18] $\mu_g = 52\,\mu$m and standard deviation[18] $\sigma_g = 10\,\mu$m (the negative part of the distribution is neglected). The density of the grains is taken to be 100 000 grains per cubic centimeter.

C. Crack echo simulation

The crack echoes used in the simulation are computed by a modification[10] of a numerical code, developed by Mattsson, Niklasson, and Eriksson,[13,14] which is based on Auld's

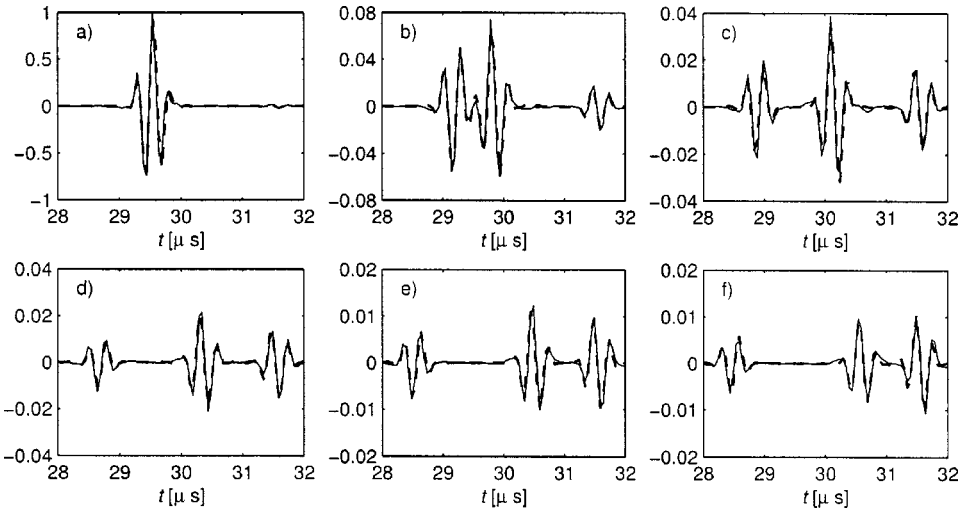

FIG. 3. Pulse–echo signals for a crack with the different angular orientations φ=0° (a); 18° (b); 36° (c); 54° (d); 72° (e); and 90° (f). The crack echoes are computed with the physical model-based numerical package (Refs. 13, 14, 10) (solid) and the phenomenological model (dashed) in (6) with the parameters listed in Table I.

electromechanical reciprocity relation.[24] In this code the crack is modeled as open and strip-like, with an infinite length in the Y direction. The physical parameters, Ω, specifying a crack is thus the width w, location $[X_0, Z_0]$, and angular orientation φ with respect to the X direction; see Fig. 2.

In this simulation study the crack's width is $w=6$ mm, with its center position at $X_0=0$ mm and $Z_0=85$ mm; see Fig. 2. Furthermore, the crack's angular orientation is taken to be random and described by the pdf[10]

$$p_\Theta(\theta)=\begin{cases}\dfrac{1}{C}\exp\left\{-\dfrac{(\theta-\mu_\theta)^2}{2\sigma_\theta^2}\right\}, & \text{if } 0°\leqslant\theta\leqslant 90°,\\ 0, \text{ elsewhere,}\end{cases} \tag{26}$$

where $C=\int_0^{90} e^{-([(\theta-\mu_\theta)^2]/2\sigma_\theta^2)}d\theta$, $\mu_\theta=45°$, and $\sigma_\theta^2=20°$. Thus, this yields that cracks with the orientation $\varphi=45°$ are most likely to occur.

Figure 3 presents a few members of the crack echo family for the scenario described above. The crack echoes are normalized with the maximum amplitude $\max_{\Omega,n}\{s(n;\Omega)\}$ and computed in the time window $t=[28,32]$ μs using the sampling frequency $F_s=20$ MHz, resulting in $N=80$ samples. Also presented, for the case of comparison, are the crack echoes represented by the model in Eq. (6), where the number of pulses M are taken to be 3, each pulse with an envelope equal to the envelope of the transducer reference signal in Eq. (25). This envelope is also used as $\bar{a}$ in Eqs. (13), (15), and (19), for the detector simulations below. The model parameters for the crack echoes at the different angles are presented in Table I.

D. Quantitative simulation results

In the simulations below, Monte Carlo simulated time series of the measured signal $\bar{y}$ under H_0 and H_1, respectively, were generated using the time window and the sampling frequency mentioned above. Similar to Ref. 10, the clutter realizations were scaled in relation to the normalized crack echoes to model different signal-to-noise-ratio (SNR) scenarios (i.e., different detection difficulties). The SNR values used were 1, 0.5, and 0.1, where the SNR is defined as the energy deflection[20]

$$\text{SNR}=\frac{(E_1\{\|\bar{Y}\|^2\}-E_0\{\|\bar{Y}\|^2\})^2}{\text{var}_0\{\|\bar{Y}\|^2\}}. \tag{27}$$

Here, $\|\cdot\|$ denotes the Euclidean norm, $\text{var}_0\{\cdot\}$ denotes the variance operator under H_0, whereas $E_0\{\cdot\}$ and $E_1\{\cdot\}$ are the expectation operators under H_0 and H_1, respectively.

The covariance matrix, $\tilde{\Sigma}_V$, in Eqs. (13), (15), and (19) was estimated according to

$$\tilde{\hat{\Sigma}}_V=\frac{1}{K-1}\sum_{k=1}^{K}\bar{v}_k\bar{v}_k^T, \tag{28}$$

TABLE I. Parameter values for the phenomenological signal model in (6) when modeling echoes from a strip-like crack with the angular orientation $\varphi\in\{0°,18°,36°,54°,72°,90°\}$.

φ	0°	18°	36°	54°	72°	90°
A_1	1	0.06	0.02	0.011	0.008	0.007
A_2	–	0.07	0.04	0.022	0.012	0.01
A_3	0.02	0.02	0.02	0.017	0.011	0.011
τ_1 [μs]	28.7	28.4	28.1	27.9	27.7	27.7
τ_2 [μs]	–	29.0	29.3	29.5	29.7	29.8
τ_3 [μs]	30.7	30.7	30.7	30.7	30.7	30.7
ϕ_1 [rad]	π	0.5π	0.5π	0.6π	0.5π	0.5π
ϕ_2 [rad]	–	1.5π	1.6π	1.5π	1.5π	1.5π
ϕ_3 [rad]	1.7π	1.7π	1.7π	1.7π	1.6π	1.5π
$f_c=\omega_c/2\pi$ [MHz]	3.5	3.5	3.5	3.5	3.5	3.5

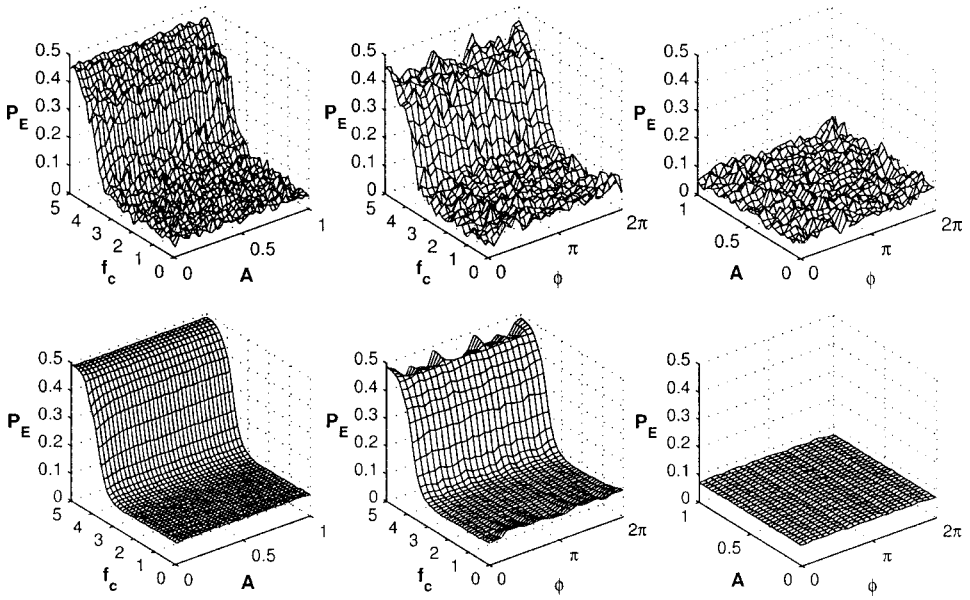

FIG. 4. Probability of error versus the matched-filter detector parameters A, $f_c=\omega_c/2\pi$, and ϕ based on 20 000 and 100 realizations from H_0 and H_1, respectively (upper row), and 20 000 realizations from both H_0 and H_1 (lower row).

where $\overline{v}$ is a clutter noise vector of length N_a and the number of realizations $K=20\,000$.

1. Optimal detector parameters

The detector parameters, λ, in Eqs. (13), (15), and (19) were determined by using the minimum probability of error in Eq. (21) as an optimization criterion. In Figs. 4–6, the minimum probability of error, P_E, is plotted versus the various parameters in λ for the matched filter, the noncoherent, and the wideband quadrature matched-filter detector, respectively. These figures present P_E computed for two cases, where the first case is based on 20 000 realizations from both H_0 and H_1 (lower part of the figures) and the second case is based on 20 000 realizations from H_0 and only 100 realizations from H_1 (upper part of the figures). The plots corresponding to 20 000 realizations from both H_0 and H_1 show that the optimization problem is relatively easy and that detectors are insensitive to the choice of both the amplitude, A, and phase ϕ. The choice of center frequency is more crucial, but any value in the interval $f_c\in[0,3]$ MHz yields similar performance. Since, in a practical situation the amount of training data from H_1 is often limited, the parameter optimization has to be made with much fewer realizations than 20 000. The plots corresponding to 100 realizations from H_1 indicate that it is feasible to obtain satisfactory parameters by

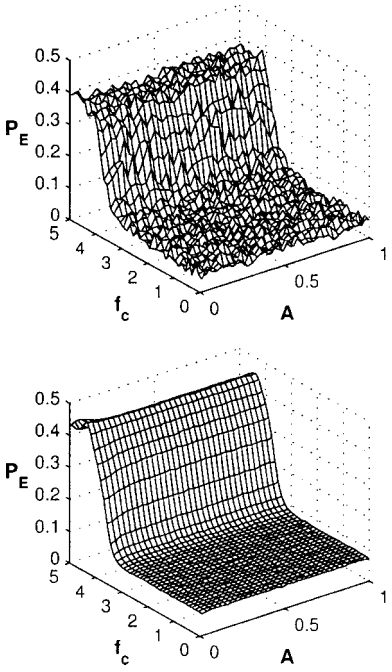

FIG. 5. Probability of error versus the noncoherent detector parameters A and $f_c=\omega_c/2\pi$ based on 20 000 and 100 realizations from H_0 and H_1, respectively (upper), and 20 000 realizations from both H_0 and H_1 (lower).

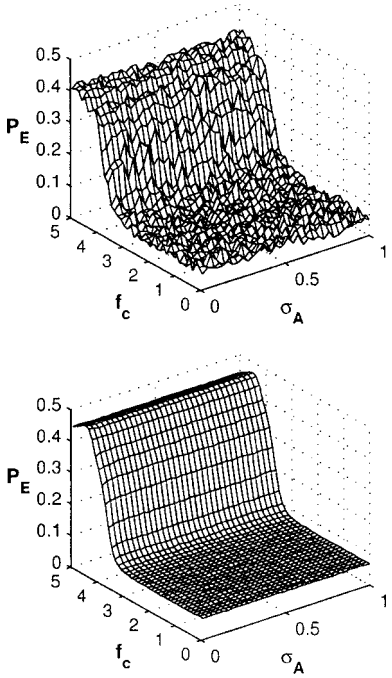

FIG. 6. Probability of error versus the wideband quadrature matched-filter detector parameters σ_A and $f_c=\omega_c/2\pi$ based on 20 000 and 100 realizations from H_0 and H_1, respectively (upper), and 20 000 realizations from both H_0 and H_1 (lower).

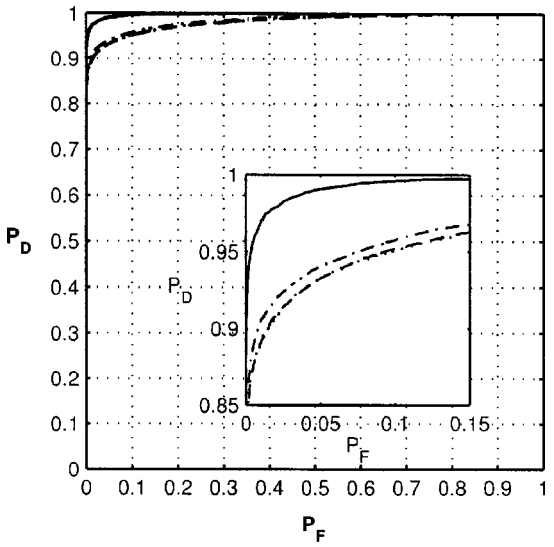

FIG. 7. ROCs for the physical model-based detector (solid), the matched-filter detector (dotted), the noncoherent detector (dashed), and the wideband quadrature matched filter (dash-dotted) with SNR=1. Note that the dotted line coincides with the dashed.

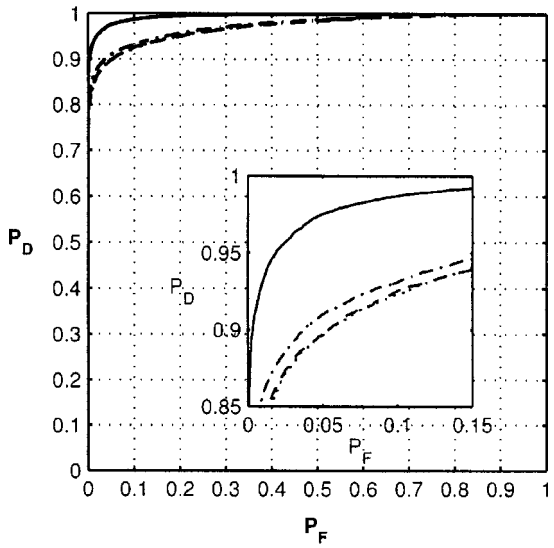

FIG. 8. ROCs for the physical model-based detector (solid), the matched-filter detector (dotted), the noncoherent detector (dashed), and the wideband quadrature matched filter (dash-dotted) with SNR=0.5.

means of, e.g., a global optimization technique, which may avoid the local minima that occur due to the randomness in the estimates of P_E.

2. ROC comparison

The detection performance comparison is quantified in terms of receiver operating characteristic (ROC) curves, where the probability of detection, P_D, is displayed versus the probability of false alarm, P_F. The parameters for the three detectors, i.e., λ in Eqs. (13), (15), and (19), were chosen based on the probability of error simulation above. All three detectors used a center frequency of $f_c=3$ MHz. The amplitude parameter in the noncoherent and the matched-filter detector was set to $A=0.5$, and the phase parameter in the matched-filter detector was $\phi=0$. The Rayleigh parameter for the amplitude distribution in the wideband quadrature matched-filter detector was set to $\sigma_A=0.1$. These parameter settings ensure that the detectors, on average, will have the lowest possible probability of error.

ROC curves for the SNRs 1, 0.5, and 0.1 were computed based on 20 000 realizations from each hypothesis, and are presented in Figs. 7–9, respectively. Also presented in the figures are the ROCs for the physical model-based optimal detector;[10] these ROCs represent the upper performance bounds for the considered problem.

The ROCs for all SNRs show that the wideband quadrature matched filter is slightly better than the matched filter and the noncoherent detector. This is probably because it is designed to detect a larger family of signals including variations in both amplitude and phase. Another possible reason could be that the crack echoes to be detected do not fully satisfy the conditions for narrow-band signals.[22]

Overall, the ROCs for the proposed detectors show a noticeable performance degradation compared to the physical model-based optimal detector. The least performance difference occurs for SNR≈1. The phenomenological model in Eq. (6), with the right choice of parameters, can represent the crack echoes relatively well (see Fig. 3). Therefore, this performance degradation is most likely due to the various assumptions concerning the statistical properties of the model parameters. However, in many practical situations it is difficult to obtain all the *a priori* knowledge that is required to design the physical model-based optimal detector.[10] In such situations the optimal performance bounds, presented in Figs. 7–9, are not even achievable. Then, the three detectors proposed here can serve as simple alternatives.

VI. CONCLUSIONS

The problem of detecting ultrasonic crack echoes in elastic solids with coarse microstructures using low-complexity phenomenological detectors has been considered. This approach, although reliant on an explicit phenomenological (mathematical) crack echo model, does not require an

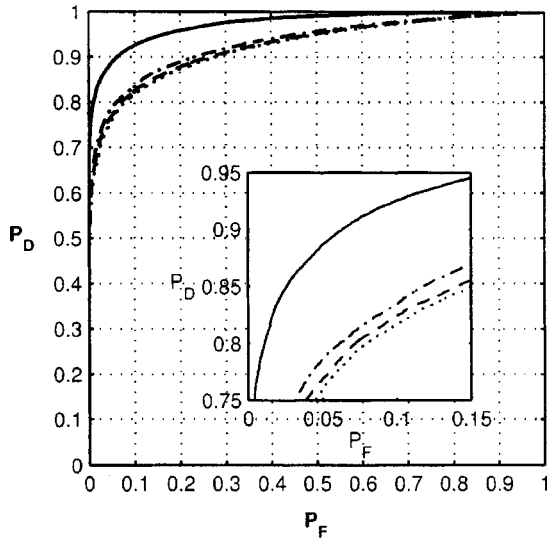

FIG. 9. ROCs for the physical model-based detector (solid), the matched-filter detector (dotted), the noncoherent detector (dashed), and the wideband quadrature matched filter (dash-dotted) with SNR=0.1.

underlying physical model. Instead, a representative set of defect echoes and noise signals is required. Although more examples need to be carried out to be able to offer more reliable guidelines, our results indicate that for a standard crack echo detection problem, it seems sufficient to have on the order of 100 crack echo examples and on the order of 20 000 noise signal observations to be able to design practical, useful detectors. Therefore, the proposed detector design methodology has the potential of being applicable also to other types of defects and to a broad range of detection problems where physical models of the echo responses are unavailable. Another appealing feature of these phenomenological detectors is the explicit signal modeling and explicit assumptions concerning the statistical properties of the model parameters made. This feature makes it straightforward to give criticism and suggest improvements to any suggested phenomenological detector.

A quantitative study of the detection performance of the proposed detectors in terms of ROCs was made by means of Monte Carlo simulations for the case of strip-like cracks with unknown angular orientations. Also presented were the detection upper bounds in terms of ROC curves for the scenario being simulated. These results show that the performance of the proposed detectors was close to optimal for SNR$\approx$1. The ROC study also showed that the wideband quadrature matched-filter detector, which is valid for wideband signals and has the most ignorant prior for the model parameters, is slightly better than the matched filter and the noncoherent detectors.

The Monte Carlo simulations were also used to compute the minimum probability of error versus the various detector parameters. These results show that the detection performance is mainly dependent on the parameter specifying the center frequency of the crack echo pulses. Moreover, the feasibility of the minimum probability of error as an optimization criterion using few defect echoes was shown by computing the minimum probability of error versus the detector parameters based on 100 and 20 000 realizations from the H_1 and H_0 hypotheses, respectively.

The general approach presented in this work may be developed in many directions. An important direction for future work would be to validate the detectors on real data containing echoes from a variety of defects. Another interesting direction is to improve the detection performance by introducing *a priori* knowledge concerning the underlying physical scenario. This means a less ignorant prior for the model parameters, although it comes with the disadvantages of both decreasing the robustness and increasing the complexity of the detectors. Moreover, robustness issues for the proposed detectors should be investigated further by studying the detection performance for different types of defects.

APPENDIX: DERIVATION OF THE WIDEBAND QUADRATURE MATCHED FILTER

The derivation of the detection statistic presented here is included for completeness but also since no appropriate reference for the final expression has been found. The closest reference for the problem studied here is the classical detector[22,23] commonly called *quadrature matched filter*. This detector has been, and still is, widely used in radar, sonar, and communication systems.

Consider a signal, $x(n)$, consisting of a sinusoid modulated by the envelope $Aa(n)$, where the amplitude is $A \sim R(\sigma_A^2)$ and the phase angle of the sinusoid is $\phi \sim U[-\pi,\pi]$. Thus

$$\begin{aligned} x(n) &= Aa(n)\sin(\omega_c(n-1)+\phi) \\ &= \alpha_1 a(n)\sin(\omega_c(n-1)) + \alpha_2 a(n)\cos(\omega_c(n-1)), \\ & n=1,...,N_a, \end{aligned} \tag{A1}$$

where $\alpha_1 = A\cos(\phi)$ and $\alpha_2 = A\sin(\phi)$. The stochastic variables α_1 and α_2 can straightforwardly be shown to be independent, identically distributed zero-mean Gaussian with the variance σ_A, i.e., $\alpha_i \sim N(0,\sigma_A^2)$, $i=[1,2]$. Hence, the signal in Eq. (A1) is zero-mean Gaussian with 2 degrees of freedom. A vector representation of the signal is

$$\overline{x} = \mathcal{S}\begin{pmatrix} \alpha_1 \\ \alpha_2 \end{pmatrix}, \tag{A2}$$

where

$$\mathcal{S} = \begin{pmatrix} 0 & a(1) \\ \vdots & \vdots \\ a(n)\sin(\omega_c n) & a(n)\cos(\omega_c n) \\ \vdots & \vdots \\ a(N_a)\sin(\omega_c N_a) & a(N_a)\cos(\omega_c N_a) \end{pmatrix}. \tag{A3}$$

This straightforwardly yields the signal covariance matrix

$$\Sigma_x = E\{\overline{xx^T}\} = \sigma_A \mathcal{S}\mathcal{S}^T. \tag{A4}$$

The likelihood ratio for a zero-mean Gaussian signal, with covariance Σ_x, corrupted by zero-mean colored Gaussian noise, with covariance matrix $\tilde{\Sigma}_V$, is[20]

$$L(\overline{y}) = \frac{|\tilde{\Sigma}_V|^{1/2}}{|\tilde{\Sigma}_V+\Sigma_x|^{1/2}} \exp\left\{\frac{1}{2}\overline{y}^T\tilde{\Sigma}_V^{-1}\Sigma_x(\tilde{\Sigma}_V+\Sigma_x)^{-1}\overline{y}\right\}. \tag{A5}$$

By using Eq. (A4) in Eq. (A5), the logarithm of the likelihood ratio becomes

$$\Lambda(\overline{y}) = \frac{\sigma_A^2}{2}\overline{y}^T\tilde{\Sigma}_V^{-1}\mathcal{S}\mathcal{S}^T(\tilde{\Sigma}_V+\sigma_A^2\mathcal{S}\mathcal{S}^T)^{-1}\overline{y} + G, \tag{A6}$$

where $G = (1/2)\ln\{|\tilde{\Sigma}_V|/|\tilde{\Sigma}_V+\Sigma_x|\}$. Employing the matrix inversion lemma[22]

$$(\mathcal{A}+\mathcal{B}\mathcal{C}\mathcal{D})^{-1} = \mathcal{A}^{-1} - \mathcal{A}^{-1}\mathcal{B}(\mathcal{D}\mathcal{A}^{-1}\mathcal{B}+\mathcal{C}^{-1})^{-1}\mathcal{D}\mathcal{A}^{-1}, \tag{A7}$$

and letting $\mathcal{A} = \tilde{\Sigma}_V$, $\mathcal{B} = \sigma_A\mathcal{S}$, $\mathcal{D} = \sigma_A\mathcal{S}^T$, and $\mathcal{C} = I_{2\times 2}$, where $I_{2\times 2}$ represents a 2×2 identity matrix, we obtain

$$\begin{aligned} \Lambda(\overline{y}) &= \frac{\sigma_A^2}{2}\overline{y}^T\tilde{\Sigma}_V^{-1}\mathcal{S}\mathcal{S}^T[\tilde{\Sigma}_V^{-1} - \tilde{\Sigma}_V^{-1}\sigma_A^2 \\ &\quad \times \mathcal{S}(\sigma_A^2\mathcal{S}^T\tilde{\Sigma}_V^{-1}\mathcal{S}+I_{2\times 2})^{-1}\mathcal{S}^T\tilde{\Sigma}_V^{-1}]\overline{y} + G \\ &= \frac{\sigma_A^2}{2}\overline{y}^T HH^T\overline{y} - \frac{\sigma_A^2}{2}\overline{y}^T HQH^T\overline{y} + G. \end{aligned} \tag{A8}$$

Here, $H=\tilde{\Sigma}_V^{-1}\mathcal{S}=[\bar{h}_s\ \bar{h}_c]$ is an $N_a\times 2$ filter containing the in-phase and quadrature filters, also defined for the noncoherent detector in Eq. (18), and

$$Q=\sigma_A^2\mathcal{S}^T\tilde{\Sigma}_V^{-1}\mathcal{S}(\sigma_A^2\mathcal{S}^T\tilde{\Sigma}_V^{-1}\mathcal{S}+I_{2\times 2})^{-1}=\begin{pmatrix} q_{11} & q_{12} \\ q_{21} & q_{22}\end{pmatrix}. \tag{A9}$$

Finally, by expressing Eq. (A5) in terms of the in-phase and quadrature filters and the Q matrix elements in Eq. (A9), we obtain a numerically efficient formulation of the likelihood ratio

$$L(\bar{y})=\frac{|\tilde{\Sigma}_V|^{1/2}}{|\tilde{\Sigma}_V+\Sigma_x|^{1/2}}\times\exp\left\{\frac{\sigma_A^2}{2}[(1-q_{11})(\bar{h}_s^T\bar{y})^2 + (1-q_{22})(\bar{h}_c^T\bar{y})^2-(q_{12}+q_{21})(\bar{h}_s^T\bar{y})(\bar{h}_c^T\bar{y})]\right\}. \tag{A10}$$

In the derivation of the classical *quadrature matched filter*, the 2×2 matrix Q in (A9) is approximated to be diagonal[22,23]. This is based on an assumption[22,23] equivalent to the narrow-band approximation,[20] which is not satisfied for wideband transient signals, i.e., when the envelope, $\bar{a}=[a(1),\ldots,a(N_a)]^T$ in Eq. (A1), is of short time duration. Since no approximations are employed in the derivations above, a detector based on the statistic in Eq. (A10) is optimal also for wideband signals, i.e., when the envelope $\bar{a}$ has short time duration.

[1] A. Lhémery and R. Raillon, "Impulse-response method to predict echo responses from targets of complex geometry. II. Computer implementation and experimental validation," J. Acoust. Soc. Am. **95**(4), 1790–1800 (1994).

[2] A. Lhémery and R. Raillon, "Impulse-response method to predict echo responses from targets of complex geometry. III. Application to nondestructive testing," J. Acoust. Soc. Am. **95**(4), 1801–1808 (1994).

[3] V. Newhouse, N. Bilgutay, J. Saniie, and E. Furgason, "Flaw-to-grain echo enhancement by split-spectrum processing," Ultrasonics **20**, 59–68 (1982).

[4] N. Bilgutay, U. Bencharit, R. Murthy, and J. Saniie, "Analysis of a nonlinear diverse clutter suppression algorithm," Ultrasonics **28**, 90–96 (1990).

[5] R. Demirli and J. Saniie, "Model-based estimation of ultrasonic echoes. I. Analysis and algorithms," IEEE Trans. Ultrason. Ferroelectr. Freq. Control **48**(3), 787–802 (2001).

[6] R. Demirli and J. Saniie, "Model-based estimation of ultrasonic echoes. II. Nondestructive evaluation applications," IEEE Trans. Ultrason. Ferroelectr. Freq. Control **48**(3), 803–811 (2001).

[7] M. G. Gustafsson, "Detection of spatio-temporal ultrasonic transient families using filter banks and neural nets," in *Proceedings of the 8th International Conference on Artificial Neural Networks, ICANN98* (Springer, Berlin, 1998), pp. 227–232.

[8] M. G. Gustafsson and T. Stepinski, "Studies of split spectrum processing, optimal detection and maximum likelihood amplitude estimation using a simple clutter model," Ultrasonics **35**, 31–52 (1997).

[9] M. G. Gustafsson, "Nonlinear split spectrum processing using optimal detection," IEEE Trans. Ultrason. Ferroelectr. Freq. Control **43**, 109–124 (1996).

[10] D. E. Asraf and M. G. Gustafsson, "Optimal detection of crack echo families in elastic solids," J. Acoust. Soc. Am. **113**(5), 2732–2741 (2003).

[11] A. Lhémery, "Impulse-response method to predict echo responses from targets of complex geometry. I. Theory," J. Acoust. Soc. Am. **90**(5), 2799–2807 (1991).

[12] A. Lhémery, "Impulse-response method to predict echo responses from defects in solids. I. Theory," J. Acoust. Soc. Am. **98**(4), 2197–2208 (1995).

[13] J. Mattsson, A. Niklasson, and A. Eriksson, "3D ultrasonic crack detection in anisotropic materials," Res. Nondestruct. Eval. **9**, 59–79 (1997).

[14] A. Eriksson, J. Mattsson, and A. Niklasson, "Modeling of ultrasonic crack detection in anisotropic materials," NDT & E Int. **33**, 441–451 (2000).

[15] J. Proakis, *Digital Communications* (McGraw-Hill, New York, 1989).

[16] J. Abbott and F. Thurstone, "Acoustic speckle: Theory and experiment analysis," Ultrason. Imaging **1**(3), 303–324 (1979).

[17] J. Goodman, "Some fundamental properties of speckle," J. Opt. Soc. Am. **66**(11), 1145–1150 (1976).

[18] R. Thompson and T. Gray, "A model relating ultrasonic scattering measurements through liquid–solid interfaces to unbounded medium scattering amplitudes," J. Acoust. Soc. Am. **74**(4), 1279–1290 (1983).

[19] K. Donohue, "Maximum likelihood estimation of A-scan amplitudes for coherent targets in media of unresolvable scatterers," IEEE Trans. Ultrason. Ferroelectr. Freq. Control **39**(3), 422–431 (1992).

[20] H. Poor, *An Introduction to Signal Detection and Estimation* (Springer, New York, 1994).

[21] D. E. Asraf and M. G. Gustafsson, "Optimal detection of crack echo families in elastic solids,"J. Acoust. Soc. Am. **113**(5), 2732–2741 (2003).

[22] S. Kay, *Fundamentals of Statistical Signal Processing: Detection Theory* (Prentice Hall, Englewood Cliffs, NJ, 1993).

[23] H. V. Trees, *Detection, Estimation, and Modulation Theory, Part I* (Wiley, New York, 1968).

[24] B. Auld, "General electromechanical reciprocity relations applied to the calculation of elastic wave scattering coefficients," Wave Motion **1**(1), 3–10 (1979).

Accurate analysis of multitone signals using a DFT

John C. Burgess[a)]
Department of Mechanical Engineering, University of Hawaii, 2540 Dole Street, Honolulu, Hawaii

(Received 29 October 2001; revised 8 January 2004; accepted 9 January 2004)

Optimum data windows make it possible to determine accurately the amplitude, phase, and frequency of one or more tones (sinusoidal components) in a signal. Procedures presented in this paper can be applied to noisy signals, signals having moderate nonstationarity, and tones close in frequency. They are relevant to many areas of acoustics where sounds are quasistationary. Among these are acoustic probes transmitted through media and natural sounds, such as animal vocalization, speech, and music. The paper includes criteria for multitone FFT block design and an example of application to sound transmission in the atmosphere. © *2004 Acoustical Society of America.*
[DOI: 10.1121/1.1687421]

PACS numbers: 43.60.Hj, 43.60.Wy, 43.72.Ar, 43.75.Yy [JCB] Pages: 389–395

I. INTRODUCTION

Discrete Fourier transform (DFT) methods are often used to identify the frequencies and amplitudes of tones (sinusoidal components) in signals, usually by using the more computationally efficient fast Fourier transform (FFT).

Using a DFT with a finite-length sequence (data record) taken from a time series can introduce a major computational problem. The data record truncates the true signal at the record ends. The sequence analyzed is not the original (true) signal, but a periodic repetition of the data record.

Except in the rare case where the periodically extended data record and the true time series are identical, a data record does not accurately represent the true signal. Energy from a truncated true tone is spread over the entire digital spectrum. Normally, *all* discrete Fourier coefficients (DFC) are nonzero, and no individual DFC accurately represents the true signal. This spreading of the spectrum is known as ''leakage.'' The computational problem is to recover true values from the DFT of a data record.[1,2]

Optimum data windows are close approximations to Chebyshev windows.[3] They have three important characteristics.

(i) Their spectra have the narrowest main lobes possible using a specified number of nonzero Fourier coefficients.
(ii) All side lobes are lower than a prescribed maximum.
(iii) They can be expressed as a Fourier series having only a few nonzero coefficients.

Figure 1 shows an example. The opt71 window can be a useful compromise between main lobe width S and noise levels experienced in practice, since there is little advantage in using an optimum window with side lobe levels much below noise levels.

In practical applications, a DFT is often applied to physical multitone signals that are not quite periodic. Examples include speech, music, animal vocalizations, and acoustic probes of any medium, such as the atmosphere and the ocean. Little seems to be known about the accuracy with which the DFT can be applied to such signals and the limits on their application. The procedures described in this paper are intended to shed light on these subjects.

This paper presents some advances over earlier single-tone signal analysis.[1,2] Section II introduces nomenclature with a brief review of single-tone signal analysis. Section III shows how single-tone signal analysis can be applied to quasiperiodic and noisy signals. Section IV extends application to multiple-tone signals, and includes an FFT block design procedure with examples. Section V demonstrates application to an experiment concerning sound transmission through a turbulent atmosphere. The paper includes some discussion of limitations, restrictions, and errors.

II. BASIC EQUATIONS; NOMENCLATURE

A time-discrete signal with multiple tones and additive noise can be described by

$$x(n)=\sum_{l=0}^{L-1} A_l \cos(\phi_l n-\alpha_l)+\mathcal{N}(n), \tag{1}$$

where n is an integer time index defined by $t_n=n\,\Delta t$, the sampling interval is $\Delta t=1/f_s$, f_s is the sampling rate, ϕ is an angle in the z plane proportional to signal frequency, α is an arbitrary lagging phase angle, $\mathcal{N}$ represents noise, and there are L tones.

A time-discrete data window of length N can be represented by

$$b(n)=\sum_{i=0}^{M-1} B_i \cos\frac{2\pi i n}{N}, \quad 0\leqslant n\leqslant N-1, \tag{2}$$

where the B_i are the usual ''one-sided'' Fourier coefficients, and there are M prescribed coefficients (all the rest are zero). A windowed data record becomes the product $\tilde{x}(n)=x(n)b(n)$, where $\tilde{\mathbf{X}}$ and $\mathbf{B}$ are the corresponding complex spectra.

By using optimum windows,[3] multiple tones in a signal can be separated and treated individually. How to treat single tones thus provides the basis for treating multitone signals.

[a)]Electronic mail: jcb@hawaii.edu

A. Single tone; open window

The "open" window is a "do-nothing" window, $b(n)=1.0$, $0\leqslant n\leqslant N-1$, 0.0 otherwise. [This and the usual "rectangular" descriptor are misleading, since the DFT periodically extends the window, in effect making $b(n)=1.0$ for all time.]

The frequency-continuous linear spectrum of a data record of length N for a single tone is given by its z transform on the unit circle,

$$\tilde{\mathbf{X}}=\frac{A}{2}e^{-j\alpha}e^{j[(\phi-\theta)(N-1)/2]}\sin\frac{(\phi-\theta)N}{2}\Big/\sin\frac{(\phi-\theta)}{2}\ (direct)$$
$$+\frac{A}{2}e^{j\alpha}e^{j[(\phi+\theta)(N-1)/2]}\sin\frac{(\phi+\theta)N}{2}\Big/\sin\frac{(\phi+\theta)}{2}\ (image), \tag{3}$$

where θ is a continuous variable proportional to frequency, $-\pi\leqslant\theta\leqslant\pi$, and values $\theta=\pm\pi$ correspond to Nyquist frequencies $f_{\mathrm{Ny}}=\pm f_s/2$.

While the linear spectrum of the true signal consists of two delta functions in the Nyquist range, one each at $\theta=\pm\phi$, the linear spectrum of the data record consists of two functions that result from convolution of the true spectrum and the spectrum of the data window. These two functions can be called[1] the *direct* contribution [top half of Eq. (3)] and *image* contribution [bottom half of Eq. (3)] to the linear spectrum, with maximum values of the z transform at $\theta=\pm\phi$. The linear spectrum thus consists of the complex sum over the entire spectrum of these two contributions. The analysis problem would be simple if the two could be separated. But there seems to be no way to do so. The only available procedure is to minimize the effect of one on the other. Optimum data windows provide the means to do this.

The z transform is a two-sided approach to spectra, while the traditional Fourier series approach is one-sided. The z-transform approach emphasizes the frequency-continuous nature of the linear spectrum, while the Fourier series approach misleadingly implies the opposite. The z-transform approach makes it clear that the spectrum is defined between the DFC, and that, in the absence of aliasing, it can be interpolated from the DFC to any desired degree of accuracy. There is a minor disadvantage. The DFT equations based on the z-transform have a scaling factor, $1/N$, in the inverse transformation. The often-used DFT equations derived from the Fourier series have the same scaling factor in the direct transformation. The equations in this paper are based on the z-transform approach,[2] which have a factor N where earlier equations[1] do not.

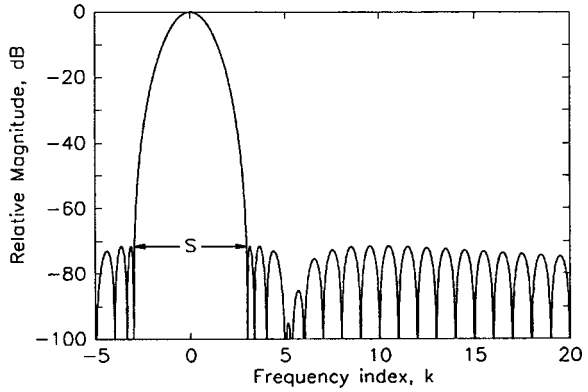

FIG. 1. Spectrum ($20\log_{10}|\mathbf{B}|$) of opt71 optimum data window (Ref. 3). Main lobe width $S=5.907$ k; all side lobes are below -71 dB.

A two-sided DFT of length N can be obtained by sampling the z transform at the discrete frequencies given by

$$\theta(k)=2\pi k/N,\quad -N/2\leqslant k<N/2, \tag{4}$$

where k is an integer frequency index, and values $k=\pm N/2$ correspond to $\pm f_{\mathrm{Ny}}$.

The inverse problem of estimating amplitude, frequency, and phase for tonal components becomes mathematically tractable if the complete linear spectrum can be approximated by either its direct or image contribution. The direct contribution is preferable because its useful values are where they are natural, in the positive frequency range.

In developing a form for a discrete spectrum, it is convenient to represent ϕ by a frequency index[1] m,

$$\phi=2\pi\frac{m}{N}=2\pi\frac{p+q}{N}, \tag{5}$$

where $m=p+q$, $p=integer\ part\ of\ m$, and $q=fractional\ part\ of\ m$, $0.0\leqslant q<1.0$.

Accurate estimates of true signal amplitude, phase, and frequency require only the two *principal* **DFC**,[1,2] at $k=p$ and $k=p+1$.

Estimating q is the key. Combining Eqs. (3), (4), and (5), the DFT for the direct contribution becomes

$$\tilde{\mathbf{X}}_k=\frac{A}{2}e^{-j\alpha}e^{j\pi(m-k)[(N-1)/N]}$$
$$\times\sin\pi(m-k)/\sin\frac{\pi(m-k)}{N}. \tag{6}$$

The ratio of the two principal DFC for the direct contribution is defined as

$$R=|\tilde{\mathbf{X}}_p|/|\tilde{\mathbf{X}}_{p+1}|. \tag{7}$$

Sample sizes used with a DFT are normally large enough to allow replacing $\sin(\pi(m-k)/N)$ by its argument. Noting that $m-k\Rightarrow q$, Eqs. (6) and (7) can be combined to find a simple (open-window) approximation, $q=1/(1+R)$.

TABLE I. Polynomial coefficients a_{ji} for one-sided two-coefficient windows ($M=2, J=4$).

j	$i=0$	$i=1$
0	-2	$-R$
1	$2R+1$	R
2	$R+2$	$R+2$
3	$-R-1$	$-R-1$

B. Single-tone, multicoefficient window

With a multicoefficient window [Eq. (2)], the kth DFC of the direct contribution becomes

$$\tilde{\mathbf{X}}_k=\frac{A}{4}e^{-j\alpha}\sum_{i=0}^{M-1}B_i\Bigg\{e^{j\pi(m-k-i)[(N-1)/N]}\times\sin\pi(m-k-i)/\sin\frac{\pi(m-k-i)}{N}+e^{j\pi(m-k+i)[(N-1)/N]}\times\sin\pi(m-k+i)/\sin\frac{\pi(m-k+i)}{N}\Bigg\}. \tag{8}$$

From Eq. (7),

$$R=\left|\frac{q}{1-q}\sum_{i=0}^{M-1}\frac{B_i}{q^2-i^2}\Bigg/\sum_{i=0}^{M-1}\frac{B_i}{(q-1)^2-i^2}\right|. \tag{9}$$

Equation (9) can be written as a polynomial in q,

$$\sum_{j=0}^{J-1}\sum_{i=0}^{M-1}a_{ji}B_iq^j=0. \tag{10}$$

Only one root of Eq. (10) will be in the range $0.0\leqslant q<1.0$ when an optimum window is used. Optimum window coefficients B_i are available,[3] and coefficients a_{ji} are given in Tables I, II, and III.

Using $e^{\pm ji\pi}=(-1)^i$, the identities for $\sin\pi(q\pm i)$, and assuming large N, Eq. (8) at $k=p$ becomes

$$\tilde{X}_pe^{j\tilde{\phi}_p}\simeq A\frac{Nq\sin\pi q}{2\pi}e^{j(-\alpha+\pi q[(N-1)/N])}\sum_{i=0}^{M-1}B_i\frac{1}{q^2-i^2}. \tag{11}$$

Equation (11) provides the following accurate approximations for large-N single-tone amplitude and phase for any window,

TABLE II. Polynomial coefficients a_{ji} for one-sided three-coefficient windows ($M=3, J=6$).

j	$i=0$	$i=1$	$i=2$
0	12	$6R$	0
1	$-12R-4$	$-5R$	$4R$
2	$-8R-15$	$-8R-12$	$-8R-3$
3	$7R+5$	$6R+4$	$3R+1$
4	$2R+3$	$2R+3$	$2R+3$
5	$-R-1$	$-R-1$	$-R-1$

TABLE III. Polynomial coefficients a_{ji} for one-sided four-coefficient windows ($M=4, J=8$).

j	$i=0$	$i=1$	$i=2$	$i=3$
0	-144	$-72R$	0	0
1	$144R+36$	$54R$	$-48R$	$-18R$
2	$108R+196$	$107R+144$	$92R+36$	$27R+16$
3	$-88R-49$	$-69R-36$	$-24R-9$	$11R-4$
4	$-39R-56$	$-38R-52$	$-35R-40$	$-30R-20$
5	$17R+14$	$16R+13$	$13R+10$	$8R+5$
6	$3R+4$	$3R+4$	$3R+4$	$3R+4$
7	$-R-1$	$-R-1$	$-R-1$	$-R-1$

$$A\simeq\frac{2\pi\tilde{X}_p}{Nq\sin\pi q}\frac{1}{\sum_{i=0}^{M-1}B_i\frac{1}{(q^2-i^2)}}, \tag{12}$$

$$\alpha\simeq-\tilde{\phi}_p+\pi q\frac{N-1}{N}\simeq-\tilde{\phi}_p+\pi q. \tag{13}$$

An accurate approximation for the single-tone frequency is

$$f\simeq\frac{p+q}{N}f_s. \tag{14}$$

Table IV has an error summary for large-N, clean, single-tone signals with various optimum windows.

III. MODERATE NONSTATIONARITY AND NOISE[4]

When used with nonstationary signals, a discrete Fourier transform can only approximate the true spectrum of the underlying signal. This section provides some insight into the magnitudes of errors to be expected in estimating the amplitude and frequency of a single tone, pure and in the presence of noise, stationary and nonstationary.

Short-time Fourier analysis (STFT) has been discussed primarily with respect to speech signal analysis and synthesis.[5–7] In this section we concentrate on a different aspect, the recovery of approximate values for amplitude, frequency, and phase of tonal components in an original signal that has become quasistationary and corrupted by noise.

STFT methods inherently require short DFT block lengths and the use of data windows. While one purpose of window use is to emphasize data in the central part of the DFT block,[7] the aspect emphasized here is the reduction of side lobe effects using optimum windows.

For signals with or without noise, there are several conflicting criteria that contribute to errors.

TABLE IV. Optimum window maximum errors.

Window	A%	$\alpha°$	f/f_s%
opt43	0.750	0.168	0.081
opt59	0.118	0.033	0.016
opt71	0.031	0.010	0.005
opt80	0.012	0.004	0.002
opt90	0.004	0.002	0.001
opt98	0.000	0.000	0.000

(i) Long data records are required for an accurate analysis of periodic components in stationary signals.
(ii) Short data records are required for an analysis of quasiperiodic components in nonstationary signals.
(iii) Accuracy using optimum windows decreases with decreasing DFT block size.
(iv) Accuracy increases with increasing side lobe depression, but computation time and complexity also increase.

The procedure is illustrated by computer simulation. Nonstationarity is introduced by modulating the frequency of a tone. The numerical values used are similar to those found in an experimental investigation (Sec. V).

A. Simulation signal

The simulation signal is

$$x(n)=A\cos\phi(n)=A\cos(2\pi nf-\alpha), \tag{15}$$

where $\phi(n)$ is the signal phase [not ϕ, Eq. (5)]. The instantaneous frequency is defined as $f_{\text{inst}}(n)\triangleq(1/2\pi)\times(d\phi(n)/dn)$. For simplicity, signal amplitude A is taken constant.

For a modulated tone, $\phi(n)$ can be expressed as

$$\phi(n)=\phi_d(n)+2\pi nf_c\,, \tag{16}$$

where

$$\phi_d(n)=\phi_{d0}\cos 2\pi nf_{\text{mod}}, \tag{17}$$

is the modulation phase, f_c represents the tone frequency (''carrier,'' in modulation terminology), ϕ_{d0} is the modulation phase amplitude, and f_{mod} is the modulation frequency. The subscript d is used to emphasize that $\phi_d(n)$ is a phase *differential* relative to $2\pi nf_c$.

Equations (16) and (17) represent a ''clean'' signal, without noise. While noise can be introduced in several ways, the way chosen here is to add it to the phase, resulting in

$$\phi_{\text{noisy}}(n)=\phi(n)(1+\mathcal{N}(n)). \tag{18}$$

$\mathcal{N}(n)$ is taken as a white Gaussian noise with a relatively high level, resulting in a 10 dB signal to noise ratio (SNR). In the simulation, a clean signal is represented by $\mathcal{N}(n)=0$, and a stationary signal by $\phi_{d0}=0$.

The true normalized instantaneous frequency is

$$f_{\text{norm}}(n)=\frac{f_{\text{inst}}(n)}{f_s}=-\frac{\phi_{d0}f_{\text{mod}}}{f_s}\sin 2\pi nf_{\text{mod}}+\frac{f_c}{f_s}. \tag{19}$$

The amplitude of main lobe frequency shifting in a DFT is

$$\frac{\Delta k_{\text{shift}}}{N}=\frac{\phi_{d0}f_{\text{mod}}}{f_s}. \tag{20}$$

Numerical values used for the simulation are $\phi_{d0}=1.0$, $f_{\text{mod}}=50$ Hz, $f_c=500$ Hz, and $f_s=2$ kHz. The high modulation frequency is intended to represent possible rapid changes in atmospheric conditions affecting sound propagation (Sec. V).

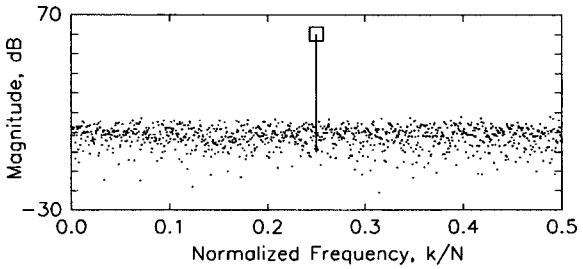

FIG. 2. Spectrum of pure and noisy tone, 10-dB SNR, $N=2048$.

B. Simulation procedure

While optimum window coefficients[3] are intended for use with large DFT block sizes, they can be used, with decreased accuracy, with small block sizes. When used with quasiperiodic signals, optimum windows have the valuable feature of shortening the effective length of the block by emphasizing data in the block's center.

The shortest usable DFT block size for the opt71 window is $N=8$ (Sec. IV). While this value is marginal for quasiperiodic frequency variation, the larger values of N used increasingly account for it.

Four long data records were generated, for single clean and noisy tones, pure and modulated. Short data records ranging in length $8\leqslant N\leqslant 32$ were taken from the long data records with sequential starting values incremented by $n=1$. This high degree of overlap makes it possible to follow error development as the modulated signal progresses. The values shown are averages over 2000 sequential, overlapped blocks.

C. Results of simulation with a pure tone

Figure 2 shows the large-block magnitude spectrum of the pure tone with noise. Figures 3 and 4 show errors with small, increasing DFT block size for the tone with and without noise.

D. Results of simulation with a modulated tone

Figure 5 shows the large-block spectrum of a modulated signal. Modulation appears as side bands around the pure

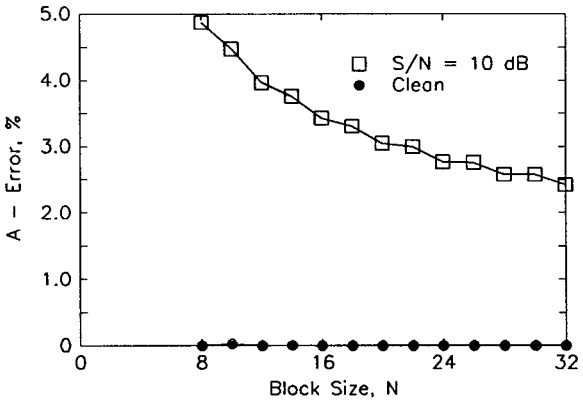

FIG. 3. Amplitude error versus block size—pure tone.

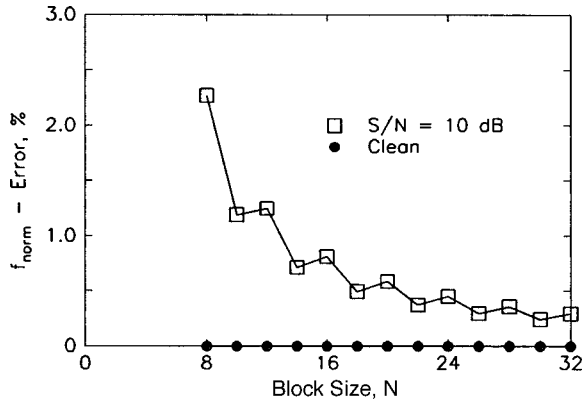

FIG. 4. Frequency error versus block size—pure tone.

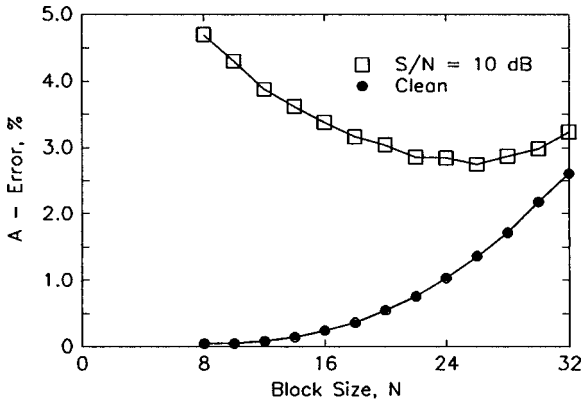

FIG. 6. Amplitude error versus block size—modulated signal.

tone. Figures 6 and 7 show that a ''best'' choice of small block size N depends on both the amount of nonstationarity and the amount of noise.

Figure 8 shows how an approximate value can track a true value. It implies that the procedure can have a practical value.

IV. MULTITONE SIGNAL ANALYSIS[8]

Accurate values for amplitude, phase, and frequency can be estimated for each tone in a signal with multiple tones, provided their amplitudes do not vary substantially and their frequencies are separated adequately, as specified in this section.

Three interacting variables must be chosen in the design of a data acquisition procedure.

(i) The minimum DFT block size, $N_{\min}$, is set by the tone frequencies and the optimum window main lobe width.
(ii) The minimum sampling rate, $(f_s)_{\min}$, is set by $N_{\min}$.
(iii) The time length Δt of the DFT block depends on both N and f_s. It can be reduced by increasing f_s. It can be reduced trivially by shortening N, but this requires using a window with a narrower main lobe (and higher side lobes!). This is a judgment call that depends on a combination of the noise level and the amount of signal nonstationarity.

The following equations show the required minimum values of N and f_s for multitone and single-tone signals: i is the tone index $0 \leqslant i < L$, L is the number of tones, a_i and b_i represent values of $\Delta k_i = k_i - k_{i-1}$, and $\Delta f_i = f_i - f_{i-1}$. The variables are illustrated in Fig. 9 for a stationary three-tone signal. The values used for Fig. 9 are summarized in Table V.

The minimum required tone separation is shown in Fig. 10. While the two main lobes can overlap, they must not overlap either principal DFC. Figure 10 shows that a usable value for the minimum separation of tones from each other and from their image contributions near zero and the Nyquist frequency is

$$\Delta k_{\min} = \frac{S}{2} + 1 + 2\Delta k_{\text{shift}}, \tag{21}$$

where $\Delta k_{\text{shift}} = 0$ for a stationary signal, and can be set using Eq. (20) (or equivalent) for a quasiperiodic signal. The minimum time-discrete tone separation,

$$b_{\min} = \Delta k_{\min}, \tag{22}$$

must be associated with $\Delta f_{\min}$. The minimum ratios $\Delta k/\Delta f$ for the tones are set by Eq. (22) and are equal,

$$\frac{a_0}{f_0} = \frac{b_i}{\Delta f_i} = \frac{N}{f_s} = \frac{b_{\min}}{\Delta f_{\min}}, \tag{23}$$

and the corresponding tone separations are

$$a_0 = \frac{b_{\min}}{\Delta f_{\min}} f_0, \tag{24}$$

$$b_i = \frac{b_{\min}}{\Delta f_{\min}} \Delta f_i. \tag{25}$$

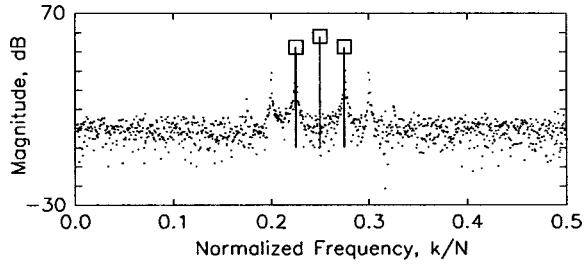

FIG. 5. Spectrum of noisy, modulated tone, 10-dB SNR: $N = 2048$.

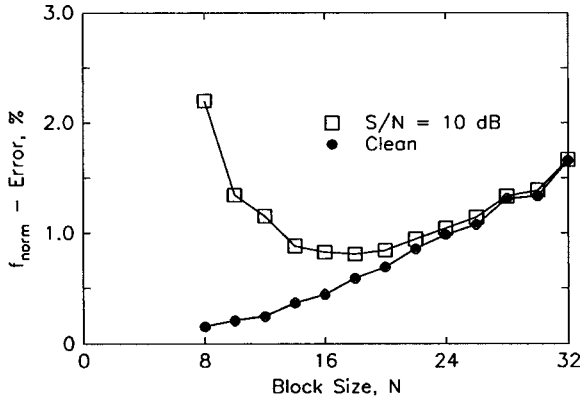

FIG. 7. Frequency error versus block size—modulated signal.

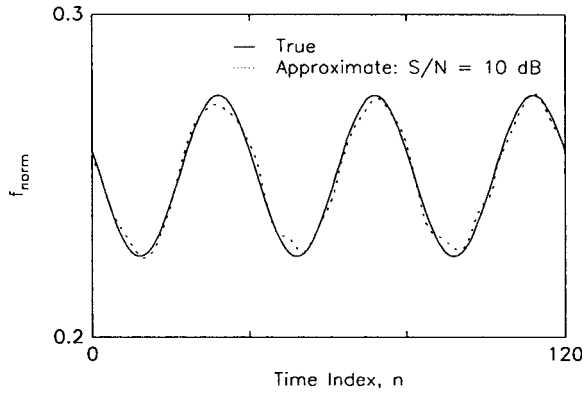

FIG. 8. True and approximate frequency versus time, noisy modulated signal, opt71 window, $N=16$.

At the lowest and highest tone frequencies, the minimum separation from zero and the Nyquist frequencies is

$$a_{\min}=\Delta k_{\min}/2. \tag{26}$$

The minimum value of N is the sum of the separations,

$$N_{\min}=2\left\{a_0+\sum_{i=1}^{L-1} b_i+\Delta k_{\min}/2\right\}, \tag{27}$$

and the minimum sampling rate is

$$(f_s)_{\min}=\frac{N_{\min}}{a_0}f_0. \tag{28}$$

Equations (27) and (28) provide minimum values. The practical problem is to select a combination that meets both the FFT (or DFT) block size and data acquisition restrictions. One procedure is to calculate the minimum block size, select the next larger practical block size, then select the next higher practical sampling rate.

As an example, consider two beating tones ($\Delta f=0.5$ Hz), $f_0=60$ Hz, $f_1=60.5$ Hz, with an opt71 window. The smallest FFT block size is $N=961\Rightarrow 1024$, $(f_s)_{\min}=122$ Hz, and $\Delta t=8.4$ s. A 2 kHz sampling rate reduces Δt to 0.51 s.

Note the following.

(i) Minimum separations for some signals may require iteration, since the requirements set by Eqs. (22) and (26) must always be met.

(ii) $(f_s)_{\min}$ must be greater than twice $f_{\max}$ to provide for minimum overlap of the direct and image main lobes corresponding to $f_{\max}$.

(iii) Increasing block size automatically increases the separation between tones and their images.

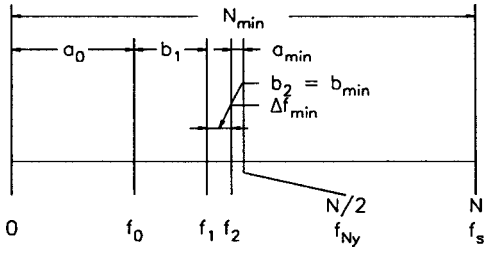

FIG. 9. Data record design relationships for a three-tone signal.

TABLE V. Data record design example, three tones with opt71 window.

i k	f_i Hz	Δf_i Hz	a_0 k	b_i k	$a_{\min}$ k	$N_{\min}$ k	$(f_s)_{\min}$ Hz
0	500		19.770				
1	800	300		11.862			
2	900	100		3.954			
	Ny				1.977		
	f_s					75.126	1900

The procedure can provide useful results with noisy and quasistationary signals, although accuracy will be reduced. When noise is present, using an optimum window with many coefficients may be beneficial, since a window smooths noise.

V. AN APPLICATION TO SOUND TRANSMISSION THROUGH THE ATMOSPHERE[9]

Data described in this section were acquired during a study of sound transmission through a turbulent atmosphere conducted by the National Research Council of Canada under the direction of Dr. David I. Havelock during the summer of 1993.[10] One objective was to measure the time-dependent amplitude and phase of the received signal.

The source was located about 30 cm above ground level and projected a single tone at 500 Hz. The receiver was one of an array of microphones located on the ground surface at a distance of about 700 m from the source. Data acquisition equipment was housed in a small trailer located about 350 m from the receiving microphone. Power was supplied by a portable generator. The sampling rate was 8 kHz.

While the received signal varied from clearly audible to inaudible, it was audible most of the time. Figure 11 shows a part of the spectrum of a typical received signal while it was audible. In addition to the expected signal centered on 500 Hz, the spectrum shows a sequence of disturbing peaks (''glitches'') at approximately 120 Hz intervals. These glitches were caused by an electrical irregularity in the portable power generating equipment. They governed selection of window and block size, since analysis for the signal at 500 Hz required principal DFC not affected by the glitches. With

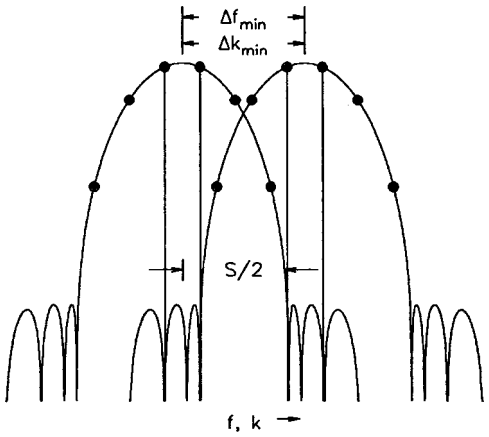

FIG. 10. Overlap of two opt71 main lobes showing minimum required separation of the principal DFC.

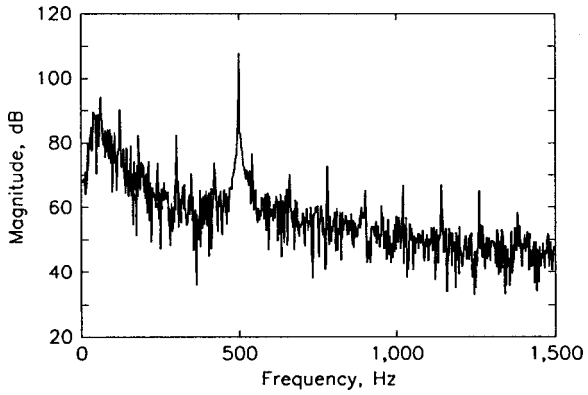

FIG. 11. Measured spectrum averaged over a 4 s interval.

the glitch at 540 Hz closest in frequency to the 500 Hz signal frequency, an opt71 window required a FFT block size $N=1024$.

FFT bocks were incremented by a small step size, and sequential principal DFC were taken from the glitch-free interval around the signal frequency. Figures 12 and 13 show examples of the received signal over short and long time intervals.

With an opt71 data window, the time length of a FFT block $N=1024$ is $T=0.128$ s. Figures 8, 12, and on-site personal observation validate a quasistationary assumption over many 0.128 s time intervals.

VI. CONCLUSIONS

(i) The procedures presented in this paper, based on optimum data windows, can provide accurate estimates of the amplitude, phase, and frequency of stationary single-tone and multitone signals, with and without noise. They can provide useful estimates of equivalent quasistationary signals.

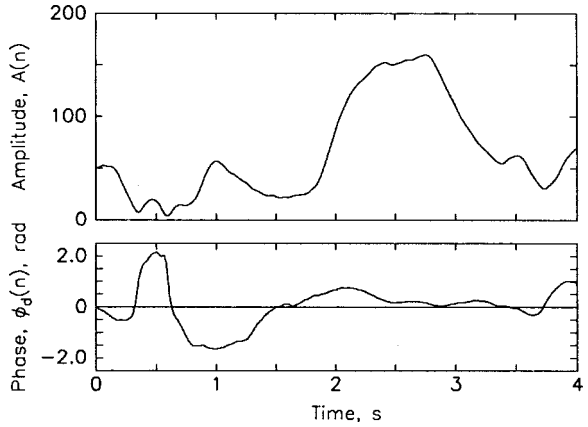

FIG. 12. Measured signal amplitude and modulation phase versus time over a 4 s interval.

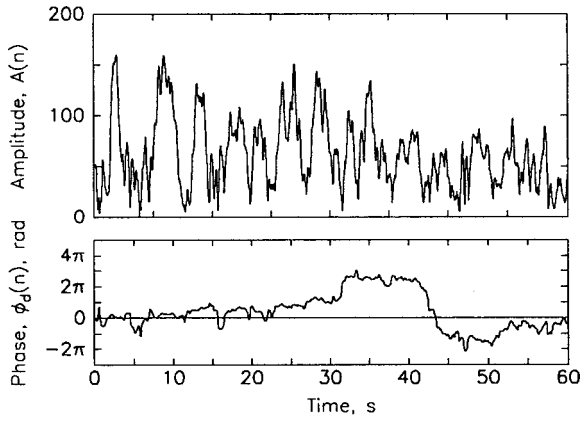

FIG. 13. Measured signal amplitude and modulation phase versus time over a 60 s interval.

(ii) With quasi-stationary signals, the block size for minimum error depends on the degree of nonstationarity and the amount of noise.

(iii) A simple procedure is presented for designing data acquisition parameters for multitone signals.

ACKNOWLEDGMENTS

The author is indebted to Dr. David I. Havelock for providing the data used in Sec. V and for many fruitful discussions. The author particularly appreciates the support of and the intellectual climate provided by the Acoustics and Signal Processing Group at the National Research Council of Canada. The author is grateful to the Acoustical Society of America for providing the opportunity at various meetings from 1977 to 1996 to present early versions of this work.

[1] J. C. Burgess, "On digital spectral analysis of periodic signals," J. Acoust. Soc. Am. **58**, 556–567 (1975).
[2] J. C. Burgess, "Practical considerations in signal processing," in *Encyclopedia of Acoustics*, edited by M. Crocker (Wiley, New York, 1997), Vol. 3, Chap. 101, pp. 1261–1279.
[3] J. C. Burgess, "Optimum approximations to dolph-chebyshev data windows," IEEE Trans. Signal Process. **40**, 2592–2594 (1992).
[4] J. C. Burgess, "Short-time fourier transform (STFT): Error estimation with non-stationary signals," J. Acoust. Soc. Am. **100**, 2637 (1996) (abstract).
[5] J. Allen, "Short term spectral analysis, synthesis, and modification by discrete Fourier transform," IEEE Trans. Acoust., Speech, Signal Process. **ASSP-25**, 235–238 (1977).
[6] L. Rabiner and J. Allen, "On the implementation of a short-time spectral analysis method for system identification," IEEE Trans. Acoust., Speech, Signal Process. **ASSP-28**, 68–78 (1980).
[7] A. Oppenheim and R. Schafer, *Discrete-Time Signal Processing* (Prentice–Hall, Englewood Cliffs, NJ, 1989).
[8] J. C. Burgess, "Accurate spectral estimation of multiple sinusoids using an FFT," J. Acoust. Soc. Am. **85**, S23 (1989) (abstract).
[9] J. C. Burgess and D. Havelock, "Estimation of the time-varying phase (instantaneous frequency) in atmospheric sound propagation," J. Acoust. Soc. Am. **95**, 2838 (1994) (abstract).
[10] D. Havelock, X. Di, G. Daigle, and M. Stinson, "Spacial coherence of a sound field in a refractive shadow: Comparison of simulation and experiment," J. Acoust. Soc. Am. **98**, 2289–2302 (1995).

Regularization method for the application of K-space data extrapolation to near-field acoustical holography

Kenji Saijyou[a)]
Fifth Research Center, Technical R & D Institute, Japan Defense Agency, 3-13-1 Nagase, Yokosuka, 239-0826, Japan

(Received 5 March 2003; revised 25 March 2004; accepted 12 April 2004)

A regularization method for applying the K-space data extrapolation method to near-field acoustical holography (NAH) is proposed. The influence of the finiteness of measurement aperture is a serious impediment to the NAH reconstruction of structural vibration when the size of the measurement aperture is smaller than that of the structure. The K-space data extrapolation method has been proposed to reduce the influence of this finiteness. An appropriate regularization method is necessary to apply the K-space data extrapolation method if the measured pressure is contaminated by noise. Some regularization methods for NAH have been proposed. However, it is difficult to determine an appropriate K-space filter if the finiteness of the measurement aperture becomes an issue. An estimation method of appropriate regularization filter for applying the K-space data extrapolation method is proposed to solve this difficulty. The effectiveness of this method is demonstrated by simulations. The simulation results confirm that (1) an appropriate regularization filter may be constructed to realize spatial wave number characteristics similar to that of ideal full aperture and (2) the reconstruction error is sufficiently suppressed by the proposed method. [DOI: 10.1121/1.1756897]

PACS numbers: 43.60.Sx, 43.60.Pt, 43.40.Rj, 43.20.Ye [EJS] Pages: 396–404

I. INTRODUCTION

Near-field acoustical holography (NAH) is a very powerful tool for structural acoustics.[1,2] NAH enable us to reconstruct the structural vibration without a limitation on spatial resolution.[2] NAH has been extended to the cylindrical geometry,[3] axisymmetric bodies,[4] and an arbitrary geometry.[5–7] Therefore, NAH has been widely applied to analyze the structural acoustics in laboratories.[8–13]

The reconstruction of the pressure and normal velocity based on NAH from the pressure measured near a vibrating object is a linear, ill-posed inverse problem due to the existence of strongly decaying, evanescent waves. The regularization method, which converts an ill-posed problem into a well-posed one by imposing the smoothness constraint, generates a solution to the linear problem in an automated way. Therefore, regularization is regarded as an important technique for the implementation of NAH. Some regularization methods have been proposed,[7,14–21] and an appropriate regularization method of NAH for which the size of measurement aperture is sufficiently larger than that of the vibrating object has been proposed by Williams.[22]

However, if the size of the measurement aperture is less than that of the vibrating object, the wave number-space (abbreviated as ''K-space,'' hereafter) spectrum of the measured pressure and the resulting reconstruction are contaminated by a ''finite aperture effect.'' The restriction of the measurement aperture corresponds to the convolution of the K-space representation of the pressure on the measurement plane and that of the window function which expresses the finite aperture. This convolution causes a leakage of the low-wave number component of the pressure into the high-wave number region. Regularization filters, which have been proposed,[7,14–22] depend on the K-space representation of the measured pressure. Therefore, each cutoff wave number of the regularization filter estimated by these methods is higher than that of the appropriate regularization filter, and the spurious high-wave number components are amplified.

The K-space data extrapolation method[23] has been proposed to reduce the influence of the finite aperture effect. An appropriate K-space filter is necessary to apply this method because K-space data extrapolation is based on the concept of the ''error norm reduction method''.[24] That is, a band limitation of the pressure on the measurement plane is necessary to reduce the error norm. In laboratories, such K-space filter can be estimated because the influence of the measurement noise is negligibly small.[23] However, it is difficult to determine such K-space filter when the measurement noise has to be considered.

To overcome this circumstance, an estimation method of an appropriate regularization filter for K-space data extrapolation is proposed in this paper. This method is based on the fact that the K-space spectrum of the pressure measured on a finite aperture is converged toward that of the pressure on the measurement plane by the K-space data extrapolation method with an appropriate band-limitation filter. The improved Tikhonov regularization filter with the modified generalized cross-validation (GCV) method is applied as the band-limitation filter for the K-space data extrapolation method.

Recently, excellent papers were published about K-space data extrapolation, written by Williams.[25,26] In his method, the determination method of regularization parameter is based on the discrepancy principle attributed to Morozov

a)Electronic mail: saijyou@jda-trdi.go.jp

(MDP). The MDP method provides a simple method to find the regularization parameter when the variance of the noise is known. However, it is difficult to obtain the variance of the noise in field measurement. Therefore, high-wave number components of the pressure are averaged to estimate the noise variance in his method. But, the number of components for averaging has to be predetermined. Moreover, the detailed explanation of the convergence of the extrapolation process is not described in his paper.

In this paper, the modified GCV method is applied for determination of the regularization parameter without predetermined parameter, because the modified GCV method does not require *a priori* knowledge of the noise variance. Therefore, the proposed method seems to be more relevant to find the regularization parameter in field measurement. And, we describe the convergence of the extrapolation process in detail.

The effectiveness of the proposed method is confirmed by simulation. The influence of the finite aperture effect is examined and the algorithm of the proposed method is presented in Sec. II. Results of simulations are shown in Sec. III. The reliability of the proposed method is summarized in Sec. IV.

II. THE ALGORITHM OF THE REGULARIZATION PROCEDURE FOR K-SPACE DATA EXTRAPOLATION METHOD

A. The influence of the finite aperture effect

In the NAH reconstruction process, the appropriate regularization parameter for the improved Tikhonov regularization filter (abbreviated as "Tikhonov filter," hereafter) is determined by the modified GCV method from the pressure measured on a sufficiently large aperture.[22] In this case, an appropriate regularization parameter can be estimated from the K-space spectrum of the measured pressure. On the other hand, if the size of a measurement aperture is less than that of the vibrating object, zero padding should be applied to prevent the wraparound error.[1,13] However, the discontinuity at the measurement aperture edges contaminates the K-space spectrum of the pressure on the measurement plane. The influence of this discontinuity due to the finiteness of measurement aperture is called "finite aperture effect."

Now, let us explain the influence of the finite aperture effect below. The coordinate system $\mathbf{r}=(\xi_1,\xi_2,\xi_3)$ is shown in Fig. 1. Here, the finite aperture is set as S_W on the S_m plane. The zero-padded pressure $p_{\text{zero}}(\mathbf{r}_m)$ is expressed as

$$\begin{aligned} p_{\text{zero}}(\mathbf{r}_m) &= W(\mathbf{r}_m)[p(\mathbf{r}_m)+n(\mathbf{r}_m)] = p(r_m)+n(\mathbf{r}_m) \\ &\quad +[W(\mathbf{r}_m)-1][p(\mathbf{r}_m)+n(\mathbf{r}_m)] \\ &= p_{\text{true}}(\mathbf{r}_m)+p_{\text{error}}(\mathbf{r}_m), \end{aligned} \tag{1}$$

$$p_{\text{true}}(\mathbf{r}_m)=p(\mathbf{r}_m)+n(\mathbf{r}_m), \tag{2}$$

$$p_{\text{error}}(\mathbf{r}_m)=[W(\mathbf{r}_m)-1]p_{\text{true}}(\mathbf{r}_m), \tag{3}$$

$$W(\mathbf{r}_m)=\begin{cases} 1 & \mathbf{r}_m \in S_W \\ 0 & \mathbf{r}_m \notin S_W \end{cases}, \tag{4}$$

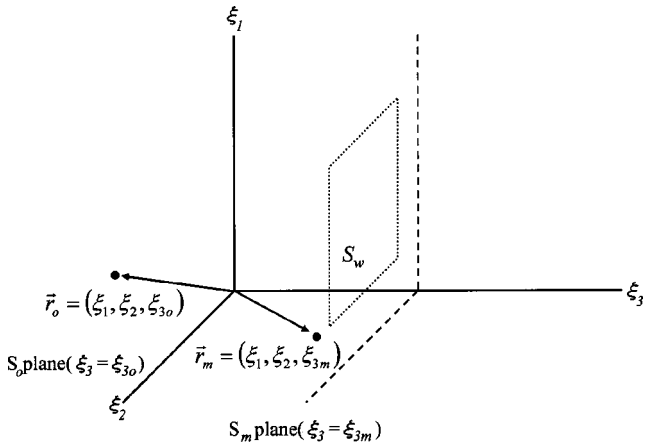

FIG. 1. The general coordinate system applied to the data extrapolation method.

where $\mathbf{r}_m=(\xi_1,\xi_2,\xi_{3m})$ vector represents a point on the S_m plane, W is the real-space window which corresponds to the finite aperture, $p_{\text{true}}(\mathbf{r}_m)$ the pressure on the measurement plane, $p_{\text{error}}(\mathbf{r}_m)$ the error pressure, $p(\mathbf{r}_m)$ the pressure without noise, and $n(\mathbf{r}_m)$ the noise, respectively. The zero-padded pressure $p_{\text{zero}}(\mathbf{r}_m)$ is only obtained at first, and the data extrapolation is realized by reducing the error pressure while conserving the true pressure $p_{\text{true}}(\mathbf{r}_m)$.[23]

To examine the influence of the real-space window W, let us set the window to be

$$W_{\text{rect}}(\mathbf{r}_m)=\text{rect}\left(\frac{|2\xi_1|}{L_m}\right)\text{rect}\left(\frac{|2\xi_2|}{L_m}\right), \tag{5}$$

$$\text{rect}(x)=\begin{cases} 1 & x\leqslant 1 \\ 0 & x>1 \end{cases}, \tag{6}$$

where L_m is the width of measurement aperture. Then, the K-space spectrum of the zero-padded pressure [Eq. (1)] is

$$\begin{aligned} \mathcal{F}[p_{\text{zero}}(\mathbf{r}_m)] &= \mathcal{F}[W_{\text{rect}}(\mathbf{r}_m)\{p(\mathbf{r}_m)+n(\mathbf{r}_m)\}] \\ &= \left[\left(\frac{4L_m}{\pi}\right)^2 \text{sinc}(L_m k_{\xi 1})\text{sinc}(L_m k_{\xi 2})\right] \\ &\quad *[P(k_{\xi 1},k_{\xi 2},\xi_{3m})+N(k_{\xi 1},k_{\xi 2},\xi_{3m})], \end{aligned} \tag{7}$$

where $\mathcal{F}$ means two-dimensional Fourier transform, $P=\mathcal{F}[p]$, and $N=\mathcal{F}[n]$, respectively. Also, the asterisk indicates the convolution, and sinc is the sinc function. This convolution spreads out the low-wave number component of the pressure on the measurement plane over the high-wave number region. Therefore, an appropriate regularization parameter cannot be estimated by the modified GCV method from the zero-padded pressure in a direct manner. This leakage of the low-wave number component to the high wave number region occurs even if any window function (Hanning, Tukey, etc.) is applied, and the influence of the window function is expressed by substituting the window function into Eq. (7).

B. Estimation method of an appropriate regularization parameter for data extrapolation

In this section, the concept of the estimation method of an appropriate regularization parameter of Tikhonov filter for K-space data extrapolation is explained. The coordinate system is shown in Fig. 1.

An appropriate regularization parameter of Tikhonov filter for the K-space data extrapolation method, α_{full}, can be determined by the modified GCV method from the pressure measured on sufficiently large aperture. Here, the appropriate regularization filter effectively eliminates the noise components without changing the pressure $p(\mathbf{r}_m)$; therefore, the cutoff wave number of this filter is higher than the highest wave number of the pressure $p(\mathbf{r}_m)$.[22]

However, as mentioned above, a regularization parameter of Tikhonov filter cannot be directly estimated from zero-padded pressure when the size of the measurement aperture is less than that of the vibrating object. Therefore, the regularization parameter for Tikhonov filter $\alpha_{\mathrm{e},0}$ is set provisionally. Then, the K-space data extrapolation method is applied with the Tikhonov filter to the zero-padded pressure. And, the regularization parameter $\alpha_{\mathrm{e},1}$ is estimated by the modified GCV method from the extrapolated pressure. If the estimated regularization parameter $\alpha_{\mathrm{e},1}$ equals $\alpha_{\mathrm{e},0}$, the $\alpha_{\mathrm{e},1}$ becomes α_{full}. The proposed method is based on this relationship, details of which are explained as follows:

First, we explain the case that $\alpha_{\mathrm{e},0} > \alpha_{\mathrm{full}}$. The K-space spectrum of the zero-padded pressure is expressed as

$$\mathcal{F}[p_{\mathrm{zero}}(\mathbf{r}_m)] = \mathcal{F}[p_{\mathrm{true}}(\mathbf{r}_m)] + \mathcal{F}[p_{\mathrm{error}}(\mathbf{r}_m)]. \tag{8}$$

Here, the Tikhonov filter[22]

$$F^{\alpha,1} = \frac{|\lambda_{k_{\xi_1},k_{\xi_2}}|^2}{|\lambda_{k_{\xi_1},k_{\xi_2}}|^2 + \alpha[\alpha/(\alpha + |\lambda_{k_{\xi_1},k_{\xi_2}}|^2)]^2}, \tag{9}$$

is applied as the band-limitation filter for K-space data extrapolation method, where

$$\lambda_{k_{\xi_1},k_{\xi_2}} = \frac{\rho c k}{i\sqrt{k_{\xi_1}^2 + k_{\xi_2}^2 - k^2}} e^{\sqrt{k_{\xi_1}^2 + k_{\xi_2}^2 - k^2}(\xi_{3m} - \xi_{3o})}, \tag{10}$$

and ρ is the density of medium (air, water, etc.). The K-space spectrum of the zero-padded pressure, which is applied to the Tikhonov filter, is expressed as

$$F^{\alpha_{\mathrm{e},0},1}\mathcal{F}[p_{\mathrm{zero}}(\mathbf{r}_m)] = F^{\alpha_{\mathrm{e},0},1}\mathcal{F}[p_{\mathrm{true}}(\mathbf{r}_m)] + F^{\alpha_{\mathrm{e},0},1}\mathcal{F}[p_{\mathrm{error}}(\mathbf{r}_m)]. \tag{11}$$

In the K-space data extrapolation method,[23] the bandlimited pressure is corrected according to the measured pressure. For convenience, the vector $\mathbf{r}_m$ is omitted after the expressions because all calculations are done in the measurement plane. The corrected pressure is expressed as

$$\begin{aligned} p_{\mathrm{correct},\alpha_{\mathrm{e},0},1} &= p_{\mathrm{zero}} + [1-W]\mathcal{F}^{-1}\{F^{\alpha_{\mathrm{e},0},1}\mathcal{F}[p_{\mathrm{zero}}]\} \\ &= p_{\mathrm{true}} + p_{\mathrm{error}} + [1-W]\mathcal{F}^{-1}\{F^{\alpha_{\mathrm{e},0},1}\mathcal{F}[p_{\mathrm{true}}]\} \\ &\quad + [1-W]\mathcal{F}^{-1}\{F^{\alpha_{\mathrm{e},0},1}\mathcal{F}[p_{\mathrm{error}}]\} \\ &= p_{\mathrm{true}} + p_{\mathrm{error}} + p_{\mathrm{t},\alpha_{\mathrm{e},0},1} + p_{\mathrm{e},\alpha_{\mathrm{e},0},1}, \end{aligned} \tag{12}$$

where

$$p_{\mathrm{t},\alpha_{\mathrm{e},0},1} = [1-W]\mathcal{F}^{-1}\{F^{\alpha_{\mathrm{e},0},1}\mathcal{F}[p_{\mathrm{true}}]\} \tag{13}$$

$$p_{\mathrm{e},\alpha_{\mathrm{e},0},1} = [1-W]\mathcal{F}^{-1}\{F^{\alpha_{\mathrm{e},0},1}\mathcal{F}[p_{\mathrm{error}}]\}, \tag{14}$$

and $\mathcal{F}^{-1}$ is the two-dimensional inverse Fourier transform. The K-space representation of the corrected pressure $p_{\mathrm{correct},\alpha_{\mathrm{e},0},1}$ is expressed as

$$\mathcal{F}[p_{\mathrm{correct},\alpha_{\mathrm{e},0},1}] = \mathcal{F}[p_{\mathrm{true}}] + \mathcal{F}[p_{\mathrm{error}}] + \mathcal{F}[p_{\mathrm{t},\alpha_{\mathrm{e},0},1}] + \mathcal{F}[p_{\mathrm{e},\alpha_{\mathrm{e},0},1}]. \tag{15}$$

If the Tikhonov filter is applied to the corrected pressure $p_{\mathrm{correct},\alpha_{\mathrm{e},0},1}$, we have

$$F^{\alpha_{\mathrm{e},0},1}\mathcal{F}[p_{\mathrm{correct},\alpha_{\mathrm{e},0},1}] = F^{\alpha_{\mathrm{e},0},1}\mathcal{F}[p_{\mathrm{true}}] + F^{\alpha_{\mathrm{e},0},1}\mathcal{F}[p_{\mathrm{error}}] + F^{\alpha_{\mathrm{e},0},1}\mathcal{F}[p_{\mathrm{t},\alpha_{\mathrm{e},0},1}] + F^{\alpha_{\mathrm{e},0},1}\mathcal{F}[p_{\mathrm{e},\alpha_{\mathrm{e},0},1}]. \tag{16}$$

The bandlimited pressure is corrected by the measured pressure again. The corrected pressure is expressed as

$$\begin{aligned} p_{\mathrm{correct},\alpha_{\mathrm{e},0},2} &= p_{\mathrm{zero}} + [1-W]\mathcal{F}^{-1}\{F^{\alpha_{\mathrm{e},0},1}\mathcal{F}[p_{\mathrm{correct},\alpha_{\mathrm{e},0},1}]\} \\ &= p_{\mathrm{true}} + p_{\mathrm{error}} + [1-W]\mathcal{F}^{-1}\{F^{\alpha_{\mathrm{e},0},1}\mathcal{F}[p_{\mathrm{true}}]\} \\ &\quad + [1-W]\mathcal{F}^{-1}\{F^{\alpha_{\mathrm{e},0},1}\mathcal{F}[p_{\mathrm{error}}]\} \\ &\quad + [1-W]\mathcal{F}^{-1}\{F^{\alpha_{\mathrm{e},0},1}\mathcal{F}[p_{\mathrm{t},\alpha_{\mathrm{e},0},1}]\} \\ &\quad + [1-W]\mathcal{F}^{-1}\{F^{\alpha_{\mathrm{e},0},1}\mathcal{F}[p_{\mathrm{e},\alpha_{\mathrm{e},0},1}]\} \\ &= p_{\mathrm{true}} + p_{\mathrm{error}} + p_{\mathrm{t},\alpha_{\mathrm{e},0},1} + p_{\mathrm{e},\alpha_{\mathrm{e},0},1} + p_{\mathrm{t},\alpha_{\mathrm{e},0},2} \\ &\quad + p_{\mathrm{e},\alpha_{\mathrm{e},0},2}, \end{aligned} \tag{17}$$

where

$$p_{\mathrm{t},\alpha_{\mathrm{e},0},2} = [1-W]\mathcal{F}^{-1}\{F^{\alpha_{\mathrm{e},0},1}\mathcal{F}[p_{\mathrm{t},\alpha_{\mathrm{e},0},1}]\} \tag{18}$$

$$p_{\mathrm{e},\alpha_{\mathrm{e},0},2} = [1-W]\mathcal{F}^{-1}\{F^{\alpha_{\mathrm{e},0},1}\mathcal{F}[p_{\mathrm{e},\alpha_{\mathrm{e},0},2}]\}. \tag{19}$$

After l times iterations of this process, the corrected pressure $p_{\mathrm{correct},\alpha_{\mathrm{e},0},l}$ is expressed as

$$\begin{aligned} p_{\mathrm{correct},\alpha_{\mathrm{e},0},l} &= p_{\mathrm{true}} + p_{\mathrm{error}} + \sum_{b=1}^{l} (p_{\mathrm{t},\alpha_{\mathrm{e},0},b} + p_{\mathrm{e},\alpha_{\mathrm{e},0},b}) \\ &= p_{\mathrm{true}} + p_{\mathrm{remain},\alpha_{\mathrm{e},0},l}, \end{aligned} \tag{20}$$

where

$$p_{\mathrm{remain},\alpha_{\mathrm{e},0},l} = p_{\mathrm{error}} + \sum_{b=1}^{l} (p_{\mathrm{t},\alpha_{\mathrm{e},0},b} + p_{\mathrm{e},\alpha_{\mathrm{e},0},b}), \tag{21}$$

is the error pressure after l times iteration of the K-space data extrapolation process,[23] and

$$p_{\mathrm{correct},\alpha_{\mathrm{e},0},\infty}=\lim_{l\to\infty}p_{\mathrm{correct},\alpha_{\mathrm{e},0},l}=p_{\mathrm{true}}+p_{\mathrm{error}}+\lim_{l\to\infty}\sum_{b=1}^{l}(p_{\mathrm{t},\alpha_{\mathrm{e},0},b}+p_{\mathrm{e},\alpha_{\mathrm{e},0},b})=p_{\mathrm{true}}+p_{\mathrm{remain},\alpha_{\mathrm{e},0},\infty}. \tag{22}$$

Here

$$\lim_{a\to\infty}\|p_{\mathrm{t},\alpha_{\mathrm{e},0},a}\|=0, \tag{23}$$

$$\lim_{a\to\infty}\|p_{\mathrm{e},\alpha_{\mathrm{e},0},a}\|=0, \tag{24}$$

because the norms of $p_{\mathrm{t},\alpha_{\mathrm{e},0},a}$ and $p_{\mathrm{e},\alpha_{\mathrm{e},0},a}$ are reduced in real and K-spaces in the iteration process of the K-space data extrapolation process.[23] However

$$\|p_{\mathrm{remain},\alpha_{\mathrm{e},0},\infty}\|=\|p_{\mathrm{error}}+\lim_{l\to\infty}\sum_{b=1}^{l}(p_{\mathrm{t},\alpha_{\mathrm{e},0},\mathrm{b}}+p_{\mathrm{e},\alpha_{\mathrm{e},0},\mathrm{b}})\|\neq 0, \tag{25}$$

because the K-space spectrum $\mathcal{F}[p_{\mathrm{true}}]$ is modified by the Tikhonov filter and the term $p_{\mathrm{error}}=[W-1]p_{\mathrm{true}}$ cannot be eliminated. In the estimation process of the regularization parameter by the modified GCV method, the influence of the high-wave number component of the pressure spectrum is dominant.[22] This error pressure term include a spurious high-wave number component. Therefore, the regularization parameter $\alpha_{\mathrm{e},1}$, which is estimated by the modified GCV method from the extrapolated pressure $p_{\mathrm{correct},\alpha_{\mathrm{e},0},\infty}$, is smaller than the appropriate regularization parameter. In this way, if $\alpha_{\mathrm{e},0}$ is larger than α_{full}, then $\alpha_{\mathrm{e},1}$ is smaller than α_{full}.

Next, we examine the case where $\alpha_{\mathrm{e},0}<\alpha_{\mathrm{full}}$. In this case, the cutoff wave number of the Tikhonov filter $k_{\mathrm{cut},\alpha_{\mathrm{e},0}}$ is higher than the appropriate value. Therefore, the K-space spectrum of the pressure p is hardly modified in the extrapolated process. On the contrary, the noise component above the cutoff wave number $k_{\mathrm{cut},\alpha_{\mathrm{e},0}}$ is reduced, because the noise components are evenly distributed in K-space. Therefore, the cutoff wave number $k_{\mathrm{cut},\alpha_{\mathrm{e},1}}$, which is estimated by the modified GCV method from the extrapolated pressure, is smaller than $k_{\mathrm{cut},\alpha_{\mathrm{e},0}}$, and the corresponding regularization parameter $\alpha_{\mathrm{e},1}$ is larger than $\alpha_{\mathrm{e},0}$.

Finally, we examine the case where $\alpha_{\mathrm{e},0}=\alpha_{\mathrm{full}}$. In this case, as mentioned above, the appropriate regularization filter is applied; therefore, the pressure on the measurement plane p_{true} is hardly modified by the Tikhonov filter. On the contrary, the error pressure term p_{error} is modified by the band-limitation filter. Therefore, the corrected pressure $p_{\mathrm{correct},\alpha_{\mathrm{e},0},1}$ is expressed as

$$\begin{aligned}p_{\mathrm{correct},\alpha_{\mathrm{e},0},1}&=p_{\mathrm{zero}}+[1-W]\mathcal{F}^{-1}\{F^{\alpha_{\mathrm{e},0},1}\mathcal{F}[p_{\mathrm{zero}}]\}\\&=[p_{\mathrm{true}}+p_{\mathrm{error}}]+[1-W]\mathcal{F}^{-1}\{F^{\alpha_{\mathrm{e},0},1}\mathcal{F}[p_{\mathrm{true}}+p_{\mathrm{error}}]\}\\&\approx p_{\mathrm{true}}+[W-1]p_{\mathrm{true}}+[1-W]p_{\mathrm{true}}+p_{\mathrm{e},\alpha_{\mathrm{e},1},1}\\&=p_{\mathrm{true}}+p_{\mathrm{e},\alpha_{\mathrm{Tik}},1}.\end{aligned} \tag{26}$$

where

$$\mathcal{F}^{-1}\{F^{\alpha_{\mathrm{e},0},1}\mathcal{F}[p_{\mathrm{true}}]\}\approx p_{\mathrm{true}}. \tag{27}$$

After l times iteration of this process, the corrected pressure $p_{\mathrm{correct},\alpha_{\mathrm{e},0},l}$ is expressed as

$$p_{\mathrm{correct},\alpha_{\mathrm{e},0},l}\approx p_{\mathrm{true}}+p_{\mathrm{e},\alpha_{\mathrm{e},0},l}, \tag{28}$$

and

$$p_{\mathrm{correct},\alpha_{\mathrm{e},0},\infty}=\lim_{l\to\infty}p_{\mathrm{correct},\alpha_{\mathrm{e},0},l}=\lim_{l\to\infty}(p_{\mathrm{true}}+p_{\mathrm{e},\alpha_{\mathrm{e},0},l})=p_{\mathrm{true}} \tag{29}$$

[cf. Eq. (24)]. Of course, p_{true} contains noise components which are reduced by the regularization process. Therefore, Eq. (29) is not strictly accurate. However, noise components, which are filtered out by the regularization filter, are practically negligible when $\alpha_{\mathrm{e},0}=\alpha_{\mathrm{full}}$, because the amplitude of the $\mathcal{F}[p]$ is sufficiently larger than that of $\mathcal{F}[n]$ in the passband of regularization filter, and the noise component outside the passband of the regularization filter is removed in the NAH reconstruction process. Therefore, the spurious high wave number component is diminished by the K-space data extrapolation method, and the appropriate regularization parameter $\alpha_{\mathrm{e},1}$ is estimated from the extrapolated pressure $p_{\mathrm{correct},\alpha_{\mathrm{e},0},\infty}$.

The above-mentioned discussion is summarized as follows.

(1) When the regularization parameter for bandlimiting filter $\alpha_{\mathrm{e},0}$ is larger than α_{full}, the estimated parameter $\alpha_{\mathrm{e},1}$ is smaller than α_{full};
(2) When the regularization parameter $\alpha_{\mathrm{e},0}$ is smaller than α_{full}, the estimated parameter $\alpha_{\mathrm{e},1}$ is larger than α_{full}; and
(3) When the regularization parameter $\alpha_{\mathrm{e},0}$ equals α_{full}, the estimated parameter $\alpha_{\mathrm{e},1}$ equals α_{full}.

In other words

$$\alpha_{\mathrm{e,i}}\begin{cases}<\alpha_{\mathrm{e,i-1}},\\=\alpha_{\mathrm{e,i-1}},\\>\alpha_{\mathrm{e,i-1}},\end{cases}\ \text{when}\ \begin{cases}\alpha_{\mathrm{full}}<\alpha_{\mathrm{e,i-1}},\\\alpha_{\mathrm{full}}=\alpha_{\mathrm{e,i-1}},\\\alpha_{\mathrm{full}}>\alpha_{\mathrm{e,i-1}}.\end{cases} \tag{30}$$

The algorithm of the estimation method of the regularization parameter, which is based on Eq. (30), is shown in Fig. 2. A brief explanation is as follows.

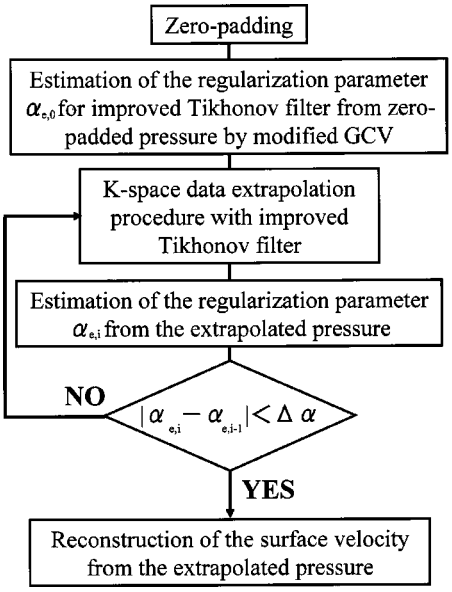

FIG. 2. Procedure to estimate the appropriate regularization parameter.

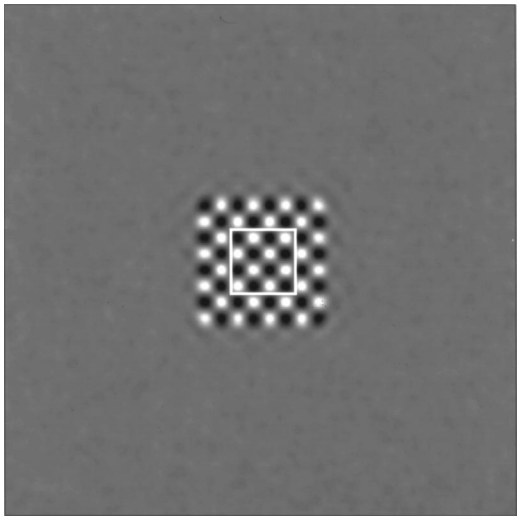

FIG. 3. Velocity reconstruction from full-aperture pressure for (9,9) simply supported plate mode (aperture size is 5.12×5.12 m, plate size is 1.28×1.28 m, SNR=10 dB, frequency is 6 kHz). The white square expresses the small aperture.

Step 1. The measurement aperture size is virtually enlarged by zero padding.

Step 2. Initial regularization parameter $\alpha_{e,0}$ is estimated by modified GCV method from the zero-padded pressure. And, the band-limitation filter for the K-space data extrapolation method is set as $F^{\alpha_{e,0},1}$.

Step 3. The K-space data extrapolation method is applied with the Tikhonov filter to the zero-padded pressure. If the following relationship

$$\Delta p_l = \int_{S_m} |p_l - p_{l-1}| W ds < \Delta p, \tag{31}$$

is satisfied, the data extrapolation process is finished. Here, l is the iteration number of data extrapolation process, p_l the extrapolated pressure, Δp the threshold, and the threshold is set as $\Delta p = \Delta p_1 \times 10^{-4}$.[23,27]

Step 4. The regularization parameter $\alpha_{e,i}$ is estimated by modified GCV method from the pressure obtained by step 3. Here, i is the iteration number of step 3 to step 5.

Step 5. If $|\alpha_{e,i} - \alpha_{e,i-1}| < \Delta\alpha$, then go to step 6. Otherwise, the band-limitation filter for the K-space data extrapolation method is set as $F^{\alpha_{e,q},1}$. Then, go to step 3. In this study, $\Delta\alpha = \alpha_{e,0} \times 10^{-4}$.

Step 6. The $\alpha_{e,i}$, which satisfies $|\alpha_{e,i} - \alpha_{e,i-1}| < \Delta\alpha$, is determined as the regulaization parameter for the K-space data extrapolation method. As a result, the pressure extrapolated by the Tikhonov filter $F^{\alpha_{e,i},1}$ is used to reconstruct the normal velocity or pressure of the structure by NAH.

III. SIMULATIONS

In this section, we examine simulations of the planar geometry example to confirm the effectiveness of the proposed regularization method. The vibrating source is given as a mode (eight half-wavelength in x- and y directions) of a simply supported squired plate. The medium is water. The squire plate (1.28×1.28 m) is baffled. The measurement hologram plane is 2 cm away from the plate and is a square with a width of 5.12 m (full aperture). On the other hand, the measurement aperture is a square with a width of 0.64 m (small aperture). The same mode is used to generate the pressure fields from 4 to 9 kHz in 1-kHz steps. Noise was added to the full aperture hologram to generate an SNR of 10 dB; here, we define the SNR as

$$\mathrm{SNR} = 10 \log_{10} \left(\frac{\|pW\|}{\|nW\|} \right). \tag{32}$$

The surface velocity reconstructed from the pressure measured on the full aperture (abbreviated as ''full aperture pressure,'' hereafter) is shown in Fig. 3, where the frequency is 6 kHz. In this paper, a real-space window at the end of the hologram aperture is not applied because the size of the full aperture is sufficiently larger than that of the vibrating object, and the pressure drops by 30 dB at the edges in a hologram [22]. The error of the reconstructed surface velocity is defined as follows:

$$E = \frac{\|\{v_{\mathrm{true}}(\mathbf{r}_o) - v_{\mathrm{reconst}}(\mathbf{r}_o)\} W_o(\mathbf{r}_o)\|}{\|v_{\mathrm{true}}(\mathbf{r}_o) W_o(\mathbf{r}_o)\|}, \tag{33}$$

$$W_o(\mathbf{r}_o) = W_o(\xi_1, \xi_2, \xi_{3o}) = W(\xi_1, \xi_2, \xi_{3m}), \tag{34}$$

where $v_{\mathrm{true}}(\mathbf{r}_o)$ is the surface velocity which is initially set, and $v_{\mathrm{reconst}}(\mathbf{r}_o)$ is the surface velocity reconstructed. The error reconstructed from the full-aperture pressure of SNR=10 dB is 27%.

First, let us examine the influence of the finite aperture effect to the estimation result of the regularization filter. Here, the amplitude of the K-space spectrum spec$[p](k_m)$ is defined as follows:

$$\mathrm{spec}[p](k_m)=\frac{\int_{-\infty}^{\infty}dk_x\int_{-\infty}^{\infty}dk_y|\mathcal{F}[p]|\left[\mathrm{rect}\left(\frac{\sqrt{k_x^2+k_y^2}}{k_m+\Delta k}\right)-\mathrm{rect}\left(\frac{\sqrt{k_x^2+k_y^2}}{k_m-\Delta k}\right)\right]}{\int_{-\infty}^{\infty}dk_x\int_{-\infty}^{\infty}dk_y\left[\mathrm{rect}\left(\frac{\sqrt{k_x^2+k_y^2}}{k_m+\Delta k}\right)-\mathrm{rect}\left(\frac{\sqrt{k_x^2+k_y^2}}{k_m-\Delta k}\right)\right]}, \tag{35}$$

where $\Delta k=2\pi/L$ and L is the width of full aperture (in this paper, $L=5.12$ m). Figure 4(a) shows the K-space spectrum of the full-aperture pressure and that of reconstructed surface velocity from the full-aperture pressure. The frequency is 6 kHz. The radius of the radiation circle is $k_{\mathrm{rad}}=8\pi$ (rad/m) ($k_{\mathrm{rad}}=2\pi f/c$, where f is the frequency and c is the sound velocity), and the peak of the full aperture pressure spectrum exists near the radiation circle. Figure 4(b) shows the difference between the spectrum of the full-aperture pressure and that of the small-aperture pressure (abbreviated as ''restricted pressure,'' hereafter). Clearly this difference is very large. According to the discussion of Sec. II B, the difference outside the radiation circle ($k>8\pi$) has serious influence on the estimation of regularization parameter, and the spectrum of the restricted pressure is distributed wider than that of the spectrum of the full-aperture pressure. Therefore, the regularization parameter estimated from the restricted pressure by modified GCV method is smaller than that from the full-aperture pressure.

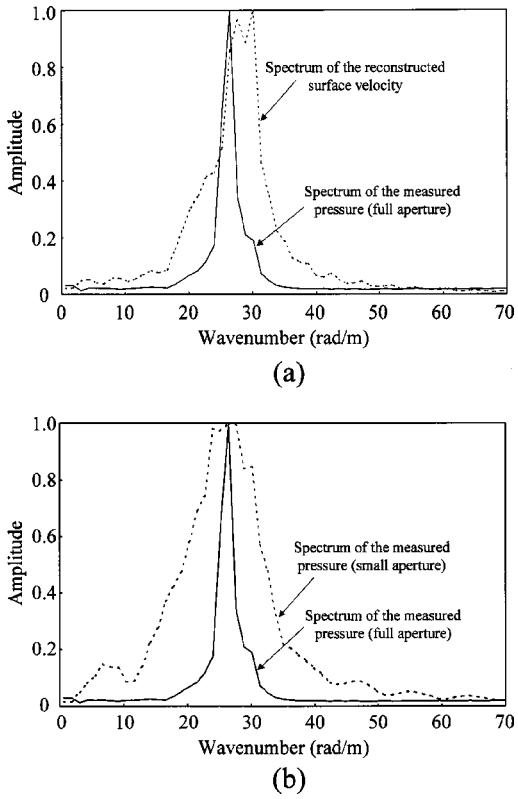

FIG. 4. K-space spectrum of the reconstructed surface velocity and measured pressure. The frequency is 6 kHz. These spectra are normalized by the maximum values, respectively. (a) The solid line shows the spectrum of measured pressure on the full aperture. The dotted line indicates the spectrum of reconstructed surface velocity from the full-aperture pressure. (b) The solid and the dotted lines mean the spectrum of measured pressure on the full aperture and that on the small aperture.

Now, the relationship between the regularization parameter of the Tikhonov filter and the spectrum of the extrapolated pressure is examined. Figure 5 shows the K-space spectrum of the pressure on the measurement plane, which is normalized by the highest wave number component. The frequency is 6 kHz. The dotted line is the spectrum of the full-aperture pressure (SNR=10 dB). The solid line with circles is the spectrum of the extrapolated pressure from the restricted pressure, where the regularization parameter $\alpha_{\mathrm{e},0}$ is 0.01. The regularization parameter is too small, and the cutoff wave number is $k_{\mathrm{cut},\alpha_{\mathrm{e},0}}=81.73$ (rad/m). Therefore, most of the spurious high-wave number component cannot be removed. However, high-wave number component of noise is reduced, and the estimated regularization parameter [$\alpha_{\mathrm{e},1}=0.0611$, $k_{\mathrm{cut},\alpha_{\mathrm{e},1}}=58.2$ (rad/m)] is larger than $\alpha_{\mathrm{e},0}$.

The solid line with triangles is the spectrum of the extrapolated pressure [$\alpha_{\mathrm{e},0}=100$, $k_{\mathrm{cut},\alpha_{\mathrm{e},0}}=25.8$ (rad/m)]. In this case, the cutoff wave number of the Tikhonov filter is too small; therefore, K-space spectrum $\mathrm{spec}[p_{\mathrm{true}}](k_m)$ is modified by the Tikhonov filter, and the term $p_{\mathrm{remain},\alpha_{\mathrm{e},0},\infty}$ remains after the K-space data extrapolation process. This term includes spurious high-wave number component, and the estimated regularization parameter [$\alpha_{\mathrm{e},1}=0.3367$, $k_{\mathrm{cut},\alpha_{\mathrm{e},1}}=41.5$ (rad/m)] is smaller than $\alpha_{\mathrm{e},0}$.

The solid line with rectangles is the spectrum of the extrapolated pressure. The regularization parameter $\alpha_{\mathrm{e},0}$ is

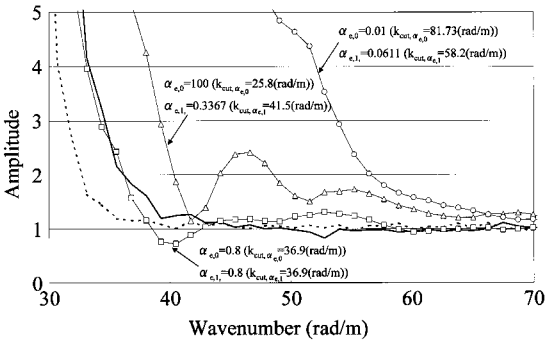

FIG. 5. K-space spectrum of the pressure on the measurement plane. The frequency is 6 kHz. These spectra are normalized by the highest wave number component. The dotted line is the spectrum of the full-aperture pressure (SNR=10 dB). The solid line with circles is the spectrum of the extrapolated pressure from the restricted pressure. The regularization parameter for the band-limitation filter $\alpha_{\mathrm{e},0}$ is 0.01 [$k_{\mathrm{cut},\alpha_{\mathrm{e},0}}=36.9$ (rad/m)]. The solid line with triangles means the spectrum of the extrapolated pressure [$\alpha_{\mathrm{e},0}=100$, $k_{\mathrm{cut},\alpha_{\mathrm{e},0}}=25.8$ (rad/m)]. The solid line with rectangles indicates the spectrum of the extrapolated pressure [$\alpha_{\mathrm{e},0}=0.8$, $k_{\mathrm{cut},\alpha_{\mathrm{e},0}}=36.9$ (rad/m)]. The bold line is the spectrum of the full-aperture pressure (SNR=20 dB).

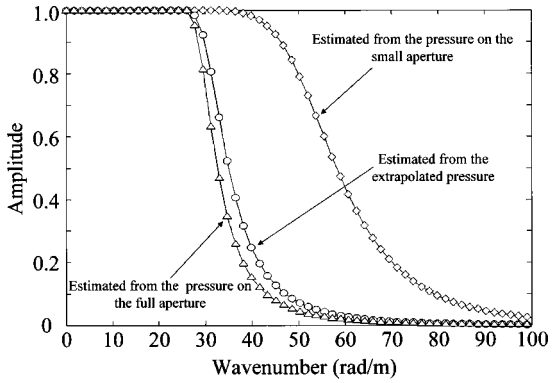

FIG. 6. The filter shapes for the modified Tikhonov regularization filter. The frequency is 6 kHz and SNR=10 dB. The solid line with triangles is the regularization filter estimated by modified GCV method from the full-aperture pressure. The solid line with circles is the filter estimated by the proposed method from the restricted pressure. The solid line with diamonds is the filter estimated by modified GCV method from the restricted pressure.

0.8 [$k_{\mathrm{cut},\alpha_{\mathrm{e},0}}=36.9\,(\mathrm{rad/m})$], which is estimated by the proposed method. This spectrum is different from that of the full-aperture pressure with SNR=10 dB, because the SNR of the restricted pressure, which is obtained by Eq. (32), is 20 dB. The bold line is the spectrum of the full-aperture pressure (SNR=20 dB). A good agreement between the spectrum of the extrapolated pressure ($\alpha_{\mathrm{e},1}=0.8$) and that of the full-aperture pressure (SNR=20 dB) suggests that the proposed method enables us to estimate an appropriate regularization parameter of the band-limitation filter for the K-space data extrapolation method. As a result, the propriety of Eq. (30) is exhibited.

Figure 6 shows the regularization filter. The filter estimated by modified GCV method from the full-aperture pressure is plotted by the solid line with triangles. The cutoff wave number is small compared with the others. The solid line with circles is the filter estimated by the proposed method from the restricted pressure. The cutoff wave number is slightly larger than that of the filter estimated from the full-aperture pressure because the SNR inside the small aperture is larger than that of the full-aperture pressure. This filter suppresses the amplification of the high-wave number noise component, and the reconstruction error is reduced. The solid line with diamonds is the filter estimated by modified GCV method from the restricted pressure. The cutoff wave number is about two times as large as that of the appropriate filter; therefore, the spurious component and noise in the high-wave number region are amplified and the reconstructed result is seriously contaminated.

The relationship between the cutoff wave number and the error of the reconstructed velocity is shown in Fig. 7. The vertical broken lines (6, 7, 8, and 9 kHz) mean the radii of the radiation circles. The reason why the reconstruction error from the full-aperture pressure is larger than that from the extrapolated pressure is the SNR of the pressure. The SNR of the full-aperture pressure is 10 dB. However, the SNR of the extrapolated pressure is 20 dB because the SNR of the restricted pressure is 20 dB. As a result, the reconstruction error from the extrapolated pressure is smaller than that from the full-aperture pressure.

The top row in Fig. 7 shows the reconstruction error of the case where the frequency is below coincidence ($1500\sqrt{2}/0.32\approx6629$ Hz). The reconstruction errors and estimated cutoff wave numbers from the full-aperture pressure (dotted lines and rectangles) show that the modified GCV method is quite good at finding the minimum in the curve for the Tikhonov filter. The reconstruction errors from the extrapolated pressures (solid lines) and the cutoff wave numbers estimated from the proposed method (circles) show that the proposed method provides good results. The reconstruction errors at the cutoff wave numbers that are estimated from the restricted pressure (diamonds) by the modified GCV method are relatively small. However, the cutoff wave numbers estimated from the proposed method are smaller than that estimated by the modified GCV method. Therefore, the influence of the noise to the reconstruction result by the proposed method is smaller than that by the modified GCV method.

The middle row in Fig. 7 is the reconstruction error of the case where the frequency is close to coincidence. The reconstruction errors and estimated cutoff wave numbers from the full-aperture pressure show that the modified GCV method provides good results. The cutoff wave numbers that are estimated from the proposed method are relatively small compared with the appropriate cutoff wave numbers. However, in this critical situation, the reconstruction errors at the estimated cutoff wave numbers are relatively small. On the contrary, the cutoff wave numbers estimated from the restricted pressures by the modified GCV method are too large, and the reconstructed results are seriously contaminated. As the result, the reconstruction errors are very large.

The bottom row in Fig. 7 is the reconstruction error of the case where the frequency is above coincidence. The modified GCV method can find the appropriate cutoff wave numbers from the full-aperture pressure. The proposed method can also estimate the appropriate cutoff wave numbers. On the contrary, the cutoff wave numbers estimated from the restricted pressures by the modified GCV method are too large, and the reconstruction error of the modified GCV method is two times as large as that of the proposed method.

As a result, if the size of the measurement aperture is sufficiently large, an appropriate cutoff wave number can be estimated by modified GCV method in the frequency region below the coincidence frequency to that above the coincidence. However, if the size of the measurement aperture is less than that of the vibrating object, the K-space data extrapolation method is recommended to apply the restricted pressure. But, the cutoff wave number of the band-limitation filter, which is estimated from the restricted pressure by the modified GCV method, is always higher than the appropriate cutoff wave number. This tendency is remarkable in the frequency region near and above coincidence frequency. Therefore, the reconstruction error becomes large in such frequency region.

On the contrary, the proposed method enables us to estimate the appropriate cutoff wave number from the restricted pressure except for that in the frequency region near the coincidence. In this critical frequency region (near coin-

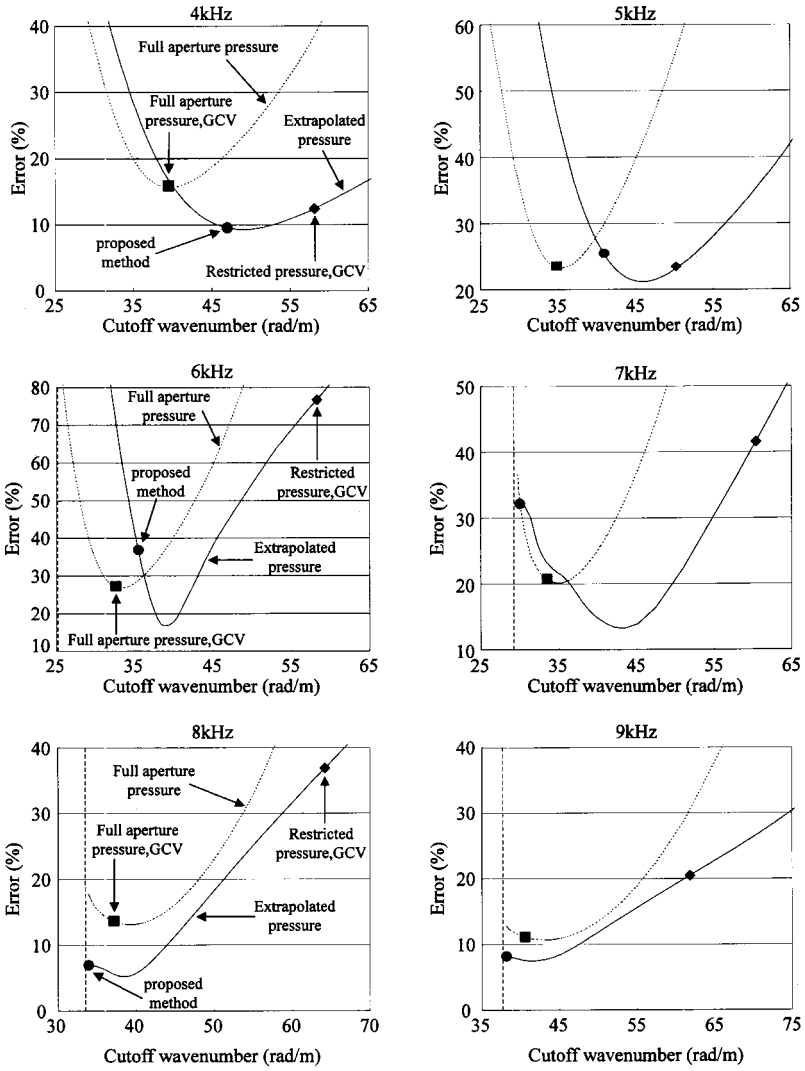

FIG. 7. The relationships between cutoff wave numbers and reconstruction errors. The solid lines are the reconstruction error from the extrapolated pressure and the dotted lines indicate the reconstruction error from the full-aperture pressure. The vertical broken lines mean the radius of the radiation circle. The rectangles are the estimated cutoff wave numbers by the modified GCV method from the full-aperture pressure. The circles and the diamonds are the cutoff wave numbers estimated by the proposed method and the modified GCV method from the restricted pressure, respectively.

cidence frequency), the reconstruction error of the proposed method becomes small.

IV. CONCLUSIONS

A new estimation method of the regularization filter for the K-space data extrapolation method has been presented. The K-space spectrum of the pressure measured on the small aperture is affected by the finite aperture effect, and the appropriate regularization filter cannot be estimated directly. To overcome this situation, the K-space data extrapolation method is modified using the Tikhonov filter. In this proposed method, the regularization parameter of the band-limitation filter for the K-space data extrapolation method is automatically estimated from the restricted pressure by modified GCV method.

The effectiveness of the proposed method is confirmed by the simulation. For the comparison, the regularization parameter is estimated from the restricted pressure by the modified GCV method. The estimated cutoff wave number by the modified GCV method is appropriate but higher than that by the proposed method below the coincidence frequency. Therefore, the influence of the noise to the resulting reconstruction by this modified GCV method is relatively large. Moreover, at the frequency region above the coincidence, the estimated cutoff wave number is much higher than the appropriate cutoff wave number, particularly near the coincidence frequency. Therefore, the reconstructed results are seriously contaminated, and the error is very large. On the contrary, the cutoff wave number of the Tikhonov filter can be adequately determined from the restricted pressure by the proposed method, except in a critical frequency region close to the coincidence. Also, even if the frequency is close to the coincidence, the reconstruction error is relatively suppressed by the proposed method.

As a result, the availability of the proposed method is confirmed. This method may thus be recommended to promote a more quantitative analysis based on NAH for actual large-scale structure.

ACKNOWLEDGMENTS

The author would like to thank Professor Shigeru Yoshikawa of Kyushu University for valuable discussions and comments on this paper. The author also would like to thank Dr. Earl G. Williams at Naval Research Laboratory for helpful suggestions.

[1] J. D. Maynard, E. G. Williams, and Y. Lee, ''Near-field acoustic holography. I. Theory of generalized holography and the development of NAH,'' J. Acoust. Soc. Am. **78**, 1395–1413 (1985).
[2] E. G. Williams and J. D. Maynard, ''Holographic imaging without the wavelength resolution limit,'' Phys. Rev. Lett. **45**, 554–557 (1980).
[3] E. G. Williams, H. D. Dardy, and K. B. Washburn, ''Generalized near-field acoustic holography for cylindrical geometry: Theory and experiments,'' J. Acoust. Soc. Am. **81**, 389–406 (1987).
[4] G. V. Borgiotti, A. Sarkissian, E. G. Williams, and L. Schuetz, ''Conformal generalized near-field acoustic holography for axisymmetric geometries,'' J. Acoust. Soc. Am. **88**, 199–209 (1990).
[5] W. A. Veronesi and J. D. Maynard, ''Digital holographic reconstruction of sources with arbitrary shaped surfaces,'' J. Acoust. Soc. Am. **85**, 588–598 (1989).
[6] M. R. Bai, ''Application of BEM (boundary element method)-based acoustic holography to radiation analysis of sound sources with arbitrary shaped geometries,'' J. Acoust. Soc. Am. **92**, 533–549 (1992).
[7] B.-K. Kim and J.-G. Ih, ''On the reconstruction of the vibro-acoustic field over the surface enclosing an interior space using the boundary element method,'' J. Acoust. Soc. Am. **100**, 3003–3016 (1996).
[8] S. Yoshikawa, ''Fluid–structure coupling by the entrained fluid in submerged concentric double-shell vibration,'' J. Acoust. Soc. Jpn. (E) **14**, 99–110 (1993).
[9] S. Yoshikawa, E. G. Williams, and K. B. Washburn, ''Vibration of two concentric submerged cylindrical shells coupled by the entrained fluid,'' J. Acoust. Soc. Am. **95**, 3273–3286 (1994).
[10] E. G. Williams, B. H. Houston, and J. A. Bucaro, ''Experimental investigation of the wave propagation on a point-driven, submerged capped cylinder using K-space analysis,'' J. Acoust. Soc. Am. **87**, 513–522 (1990).
[11] K. Saijyou, M. Ueda, and S. Yoshikawa, ''Application of generalized near-field acoustical holography to scattering problems,'' Jpn. J. Appl. Phys., Part 1 **33**, 3170–3175 (1994).
[12] C. B. Burroughs, ''Application of near-field acoustical holography in the research of mechanisms of acoustic radiation,'' Proceedings Inter-noise 2001, 2129–2133 (2001).
[13] E. G. Williams, *Fourier Acoustics: Sound Radiation and Nearfield Acoustical Holography* (Academic, London, UK, 1999).
[14] P. C. Hansen, *Rank-Deficient and Discrete Ill-Posed Problems* (SIAM, Philadelphia, PA, 1998).
[15] P. A. Nelson and S. H. Yoon, ''Estimation of acoustic source strength by inverse methods. I. Conditioning of the inverse problem,'' J. Sound Vib. **233**, 643–668 (2000).
[16] S. H. Yoon and P. A. Nelson, ''Estimation of acoustic source strength by inverse methods. II. Experimental investigation of methods for choosing regularization parameters,'' J. Sound Vib. **233**, 669–705 (2000).
[17] B.-K. Kim and J.-G. Ih, ''Design of an optimal wave-vector filter for enhancing the resolution of reconstructed source field by NAH,'' J. Acoust. Soc. Am. **107**, 3289–3297 (2000).
[18] F. Augusztionvicz, ''Reconstruction of source strength distribution by inversing the boundary element method,'' in *Boundary Elements in Acoustics, Advances and Applications*, edited by O. von Estoff (WIT, Southampton, UK, 2000).
[19] P. A. Nelson, ''Some inverse problems in acoustics,'' in Proceedings of the 6th International Congress on Sound and Vibration, Copenhagen, Denmark, July 1999, pp. 7–32.
[20] A. Kirsch, *An Introduction to the Mathematical Theory of Inverse Problem* (Springer, New York, 1996).
[21] A. P. Schuhmacher and P. C. Hansen, ''Sound source reconstruction using inverse BEM,'' Proceedings of Inter-noise 2001, 2109–2114 (2001).
[22] E. G. Williams, ''Regularization method for near-field acoustic holography,'' J. Acoust. Soc. Am. **110**, 1976–1988 (2001).
[23] K. Saijyou and S. Yoshikawa, ''Reduction methods of the reconstruction error for large-scale implementation of near-field acoustical holography,'' J. Acoust. Soc. Am. **110**, 2007–2023 (2001).
[24] R. W. Gerchberg, ''Super-resolution through error energy reduction,'' Opt. Acta **21**, 709–720 (1974).
[25] E. G. Williams, ''Continuation of acoustic near-fields,'' J. Acoust. Soc. Am. **113**, 1273–1281 (2003).
[26] E. G. Williams and B. H. Houston, ''Fast Fourier transform and singular value decomposition formulation for patch near-field acoustical holography,'' J. Acoust. Soc. Am. **114**, 1322–1333 (2004).
[27] K. Saijyou, ''Regularization method of patch near-field acoustical holography for planar geometry,'' Proceedings Inter-noise 2003, 2195–2202 (2003).

Time–frequency analysis of auditory-nerve-fiber and basilar-membrane click responses reveal glide irregularities and non-characteristic-frequency skirts

Tai Lin
Eaton-Peabody Laboratory of Auditory Physiology, Department of Otolaryngology, Massachusetts Eye and Ear Infirmary, 243 Charles St., Boston, Massachusetts 02114

John J. Guinan, Jr.[a)]
Eaton-Peabody Laboratory of Auditory Physiology, Department of Otolaryngology, Massachusetts Eye and Ear Infirmary, 243 Charles St., Boston, Massachusetts 02114, Department of Otology and Laryngology, Harvard Medical School, Boston, Massachusetts 02115, and Speech and Hearing Biosciences and Technology Program, Harvard–MIT Division of Health Sciences and Technology, Massachusetts Institute of Technology, Cambridge, Massachusetts 02139

(Received 20 January 2004; revised 25 March 2004; accepted 30 March 2004)

Although many properties of click responses can be accounted for by a single, frequency-dispersive traveling wave exciting a single, characteristic-frequency (CF) resonance, some properties, such as waxing and waning cannot. Joint time–frequency distributions (TFDs) were used to help understand click responses of cat single auditory-nerve (AN) fibers (CFs$<$4 kHz) and published measurements of chinchilla basilar-membrane (BM) motion. For CFs$>$800 Hz, the peak energy of the response decreased in latency and frequency as the level increased, as expected. However, at high levels the trend reversed for AN, but not BM, responses. Normalized TFDs, which show the frequency with the peak energy at each response time, revealed glides, as previously reported. Classical theory predicts smooth, upward glides. Instead, at low CFs there were downward glides, and at other CFs glides had substantial irregularities. Finally, click skirts, defined as the longest-latency part of click responses, sometimes showed deviations from CF for above-threshold sound levels. Most of these phenomena are not explained by a single, frequency-dispersive traveling wave exciting a single CF resonance, but they can be accounted for by the interaction of two (or more) excitation drives with different latencies and frequency contents. © *2004 Acoustical Society of America.*
[DOI: 10.1121/1.1753294]

PACS numbers: 43.64.Kc; 43.64.Pg; 43.64.Nf [BCM] Pages: 405–416

I. INTRODUCTION

Studying the cochlea using clicks is advantageous because click stimuli provide an impulse of energy and then allow the cochlea to vibrate on its own, thereby revealing its natural resonant frequencies. Classic studies of auditory-nerve-fibers and basilar-membrane motion showed click responses that were dominated by ringing at the local characteristic frequency (CF) (e.g., Kiang *et al.*, 1965; Robles *et al.*, 1976). More recently, Lin and Guinan (2000) studied click responses of single auditory-nerve fibers and found a variety of response features which, according to classical cochlear theory, are anomalies, such as waxing and waning, or reversals of phase across sound levels. These complex click responses were interpreted as being due to the interaction of multiple excitation drives, perhaps due to multiple resonances present at a single cochlear location (Lin and Guinan, 2000). To gain further insight into these phenomena, we have done joint time–frequency analyses of both our auditory-nerve data and of published basilar-membrane responses to clicks.

A recently-described feature of click responses is the change in instantaneous frequency, or "glide," at the onset of the response (de Boer and Nuttall, 1997; Recio *et al.* 1998; Carney *et al.* 1999; Recio and Rhode, 2000; Lin and Guinan, 2000; Shera, 2001a; see also Møller and Nilsson, 1979). For CFs greater than ~1.5 kHz, the response glides up in frequency whereas for CFs less than ~0.75 kHz the response glides down in frequency (Carney *et al.*, 1999). Although the origin of glides has seemed mysterious, Shera (2001a) has shown that their basic properties can be explained by the frequency-dispersive properties of the traveling wave, at least for CFs$>$1–2 kHz, i.e., energy in a click pulse delivered at the stapes moves apically in the traveling wave such that at each cochlear place lower-frequency energy arrives before higher-frequency energy thereby causing an upward glide. For typical cochlear models having a single CF resonance at each place, the resulting glide begins at a low frequency and smoothly approaches CF (de Boer and Nuttall, 1997; Shera, 2001a). On the other hand, if there are multiple resonances at each cochlear place, as suggested by Lin and Guinan (2000), lower-frequency resonances might be excited before higher-frequency resonances and the resulting response might not show a smooth glide in the frequency content with time. A time–frequency analysis of cochlear responses should reveal any such features.

[a)]Author to whom correspondence should be addressed at Eaton-Peabody Laboratory, Massachusetts Eye and Ear Infirmary, 243 Charles St., Boston, Massachusetts 02114. Electronic mail: jjg@epl.meei.harvard.edu

Lin and Guinan (2000) hypothesized that the multiple excitation drives evident at a single cochlear location are associated with different vibration patterns of the cochlear partition, i.e., are due to different vibrational ''modes.'' An alternate hypothesis is that some drives are due to cochlear internal reflections, i.e., from coherent reflection at the traveling wave peak producing a backward wave which is reflected at the stapes (Shera 2001c). With this hypothesis, a deep wane in the click response is due to an almost complete cancellation of the decaying original wave by an out-of-phase reflected wave. For an excitation drive produced by this mechanism, the associated ''resonance'' would be due to global cochlear properties instead of local cochlear properties. Nonetheless, viewed at a particular cochlear place, drives from a reflected-wave would be expected to have about the same tuning properties as the original waves at that place, i.e., both would have their main energy at CF. In contrast, if wanes are due to beating of two excitation drives of different frequencies, we would expect to find energy at two frequencies. The time–frequency analysis of the responses may reveal which of these hypotheses is correct.

A feature of the click responses revealed by time–frequency analysis is the frequency of the decaying part of the response, which we call the click response ''skirt.'' With the view that clicks may excite multiple local cochlear resonances, the frequency of the click skirt would be dominated by the local resonance that lasts the longest, i.e., has the highest quality factor (Q). This may not be the CF resonance. Thus, an examination of the click-response skirt frequency may provide additional information about cochlear resonances.

II. METHODS

A. Time–frequency analysis methods

In analyzing the energy content in a time-varying waveform, there is an inherent trade between time resolution and frequency resolution. Analysis methods have been developed that produce better resolution in both time and frequency than the standard short-term Fourier (STF) spectrograms, but at the expense of introducing ''cross terms'' which show energy at time–frequency locations where there is no energy (Qian and Chen 1999). Since these other methods all had disadvantages,[1] and so that all of the data would be processed in the same way, we have used only short-term Fourier spectrograms.

Short-term Fourier spectrograms were implemented principally in Matlab. The analysis frequencies were made to be closely spaced by using at least 1024 time points, by padding the response time-waveforms with zeros, if necessary. Data were selected in time by applying a fixed duration sliding window, and to avoid spectral splatter, a Blackman (cosine) envelope was applied over 1/4 of the points at the beginning and end of the window.

Response time–frequency patterns were also visualized using the Hilbert-transform analytic method which shows the ''instantaneous frequency'' and ''envelope'' of the response versus time (Oppenheim and Schafer, 1989). This method is very sensitive to the instantaneous signal/noise ratio so that initial band-limiting filtering of the data is often done (e.g., de Boer and Nuttall, 1997, bandpass filtered their basilar-membrane data from 6–20 kHz). Since it was not clear that high-pass filtering was appropriate, and the filter needed to be adjusted for the frequency range of the data being considered, we minimized noise and produced a smoothed result by (1) calculating the required time derivatives of response phase from the differences between points 1/2 CF period apart, and (2) averaging the resulting points over 1/2 CF periods. This is approximately equivalent to low-pass filtering with a cutoff frequency of 2 CF.

In the literature on glides, response frequency versus time is the focus of interest, without regard to response amplitude. Thus, with the Hilbert-transform method, instantaneous frequency versus time is usually plotted without showing the envelope amplitude. A comparable ''normalized spectrogram'' (nSTFS) display was obtained by, at each time point, normalizing the frequency spectrum by the highest amplitude frequency at that time. When plotting superimposed data from many cases, the spectrogram information was further reduced to just the amplitude and frequency of the peak energy versus time. To exclude spurious spectrogram peaks before the response onset or after the response has decayed into the noise, we applied a signal/noise criteria. To be included in a peak-energy plot, the energy in the highest-amplitude spectrogram frequency at a given time had to be above a ''signal criterion.'' For each spectrogram, the criterion was a small increment over the amplitude of the highest-amplitude frequency from the time before the click response started. The increment was the same for all auditory-nerve fibers and the same for all levels at each basilar membrane place.

For Figs. 3–4, the spectrograms used an analysis duration of four periods for CFs$>$0.3 kHz and three periods for CFs$<$0.3 kHz. From the resulting spectrograms we obtained peak-energy versus time plots (the peak-energy frequencies are shown later in Fig. 6) and from these we determined the time and frequency of the peak-energy point at each level [for Figs. 5(a), 5(b)]. In these plots, we subtracted a ''conduction time'' latency which, for the BM data, was the time to the onset of ossicular motion, and for the ANF data, was 1 ms after the acoustic click (to allow for acoustic and nerve conduction time).

The peak-energy frequency versus time plots were further analyzed to determine skirt frequencies. Although the signal/noise criteria described above was used, the peak-energy plots showed substantial wiggles and the last point (the potential ''skirt frequency'') could sometimes be an aberrant one. To minimize such problems, to determine the ''skirt frequency'' we averaged the peak-energy versus time over a long time bin. To adjust the bin duration for each case, we made the bin duration equal to the latency of the peak amplitude at the lowest sound level [i.e., the latency of the lowest point on each curve in Fig. 5(a)]. Thus, the ''skirt frequency'' is the average peak-energy frequency over such a time bin terminated by the energy falling below the criterion (i.e., at the ends of the glide trajectories in Fig. 6).

Some basic properties of short-term Fourier Spectrograms and the Hilbert-transform ''instantaneous frequency''

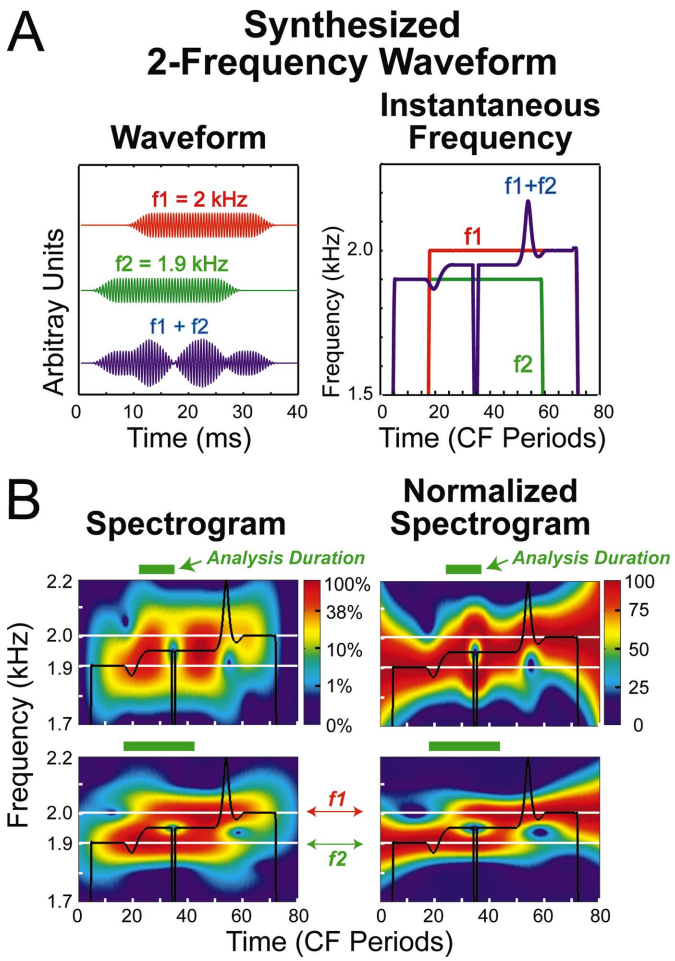

FIG. 1. Analysis of a waveform consisting of two frequencies (f_1,f_2) which produce beating when added [f_1+f_2 in panel (a), left]. Panel (a) right, shows the Hilbert-transform instantaneous frequency of these waveforms. Note that where the waveforms overlap, the instantaneous frequency does not correspond to the frequency of either tone burst. Panel (b): short-term Fourier spectrograms (STFSs, left) and normalized STFSs (nSTFSs, right) of the synthesized wave f_1+f_2. In (b), the upper plots use a shorter analysis duration than the lower plots. Note that the two frequencies are resolved in the lower plots but not in the upper plots.

are illustrated in Fig. 1 which shows the analysis of a synthesized wave containing two frequencies. For the spectrograms, shorter analysis durations track changes in time better [Fig. 1(b), top], while longer durations separate two frequency components better [Fig. 1(b), bottom]. In contrast, the Hilbert-transform method does not trade accuracy in time vs accuracy in frequency but shows the ''instantaneous frequency'' of a waveform with the implicit assumption that a single frequency describes the response at any given time. The Hilbert-transform method is accurate (i.e., produces a result similar to the peak of the short-term Fourier transform) when one frequency is dominant, but not when there are two or more frequency components with almost-equal amplitudes (e.g., at times of 25–50 periods in Fig. 1).

B. Multiple resonances vs multiple reflections

Figure 2 shows time–frequency analysis applied to a linear cochlear model implemented without and with reflections [variations of the Zweig (1991) model without/with roughness and backward traveling waves—Shera, 2001c]. The reflectionless model shows a simple upward gliding response [Fig. 2(a)]. The with-reflections model shows waxing and waning due to the interference between initial and reflected waves [Fig. 2(b)]. In the example of Fig. 2(b) we have chosen a model frequency in which the reflection is out-of-phase with the decaying original wave so that a wane (cancellation) is produced.

It is useful to contrast the time–frequency patterns in Figs. 1 and 2(b). Both show interference wanes but of different origins (two waves of different frequency vs. two wave bursts of similar frequency but different phases). With a short analysis duration, spectrograms of both show a punctate change at the wane. However, with a longer analysis duration, separate frequency components are revealed in the 2-frequency case (Fig. 1), but not in the reflection case (Fig. 2). Thus, by adjusting the analysis duration, we hoped to distinguish between these two possible origins of waxing and waning.

C. Data sources

We used auditory-nerve data from cats (Lin and Guinan, 2000) and basilar-membrane data from chinchillas (from Recio *et al.*, 1998: Fig. 3 (CF 10.0 kHz), Fig. 4 (CF 9.0 kHz); from Recio and Rhode, 2000: Fig. 2 (CF 14.5 kHz), Fig. 3 (CF 5.5 kHz), Fig. 10(c) (CF unknown); and from Recio and Rhode, 2000: click data obtained from the place of Fig. 11 (CF 10.7 kHz). To avoid the effects of dc drifts, basilar-membrane displacement was differentiated to produce velocity. From the auditory-nerve spike times we calculated recovered-probability peristimulus-time (PST) histograms with a recovery time of 3 ms (Gray, 1967) and formed compound PST (cPST) histograms by adding a rarefaction-click PST histogram with positive values and the corresponding condensation-click PST histogram with negative values. The recovered-probability calculation reduced the signal-to-noise ratio. Taking this into account, we only used data from PSTs with at least 1000 clicks. All cats were anesthetized with Dial in urethane following a protocol approved by the Animal Care Committee of the Massachusetts Eye and Ear Infirmary.

III. RESULTS

Examples of short-term Fourier spectrograms and Hilbert-transform instantaneous frequency are illustrated for two basilar-membrane (BM) places (Fig. 3) and three auditory-nerve (AN) fibers (Fig. 4). To conserve space, each case shows at most four sound levels, although the original data sets have many more levels. At each sound level (i.e., each row in the figures), the left column shows the time waveform of the response, the second column shows the corresponding short-term Fourier spectrogram, and the third and fourth columns show corresponding normalized spectrograms with short and long spectrogram analysis durations (in an attempt to get both good time resolution and good frequency resolution). Instantaneous frequency from the Hilbert transform method is superimposed (black line) on all three spectrograms. A white line shows the characteristic frequency (also listed in kHz in the upper left panel) from the

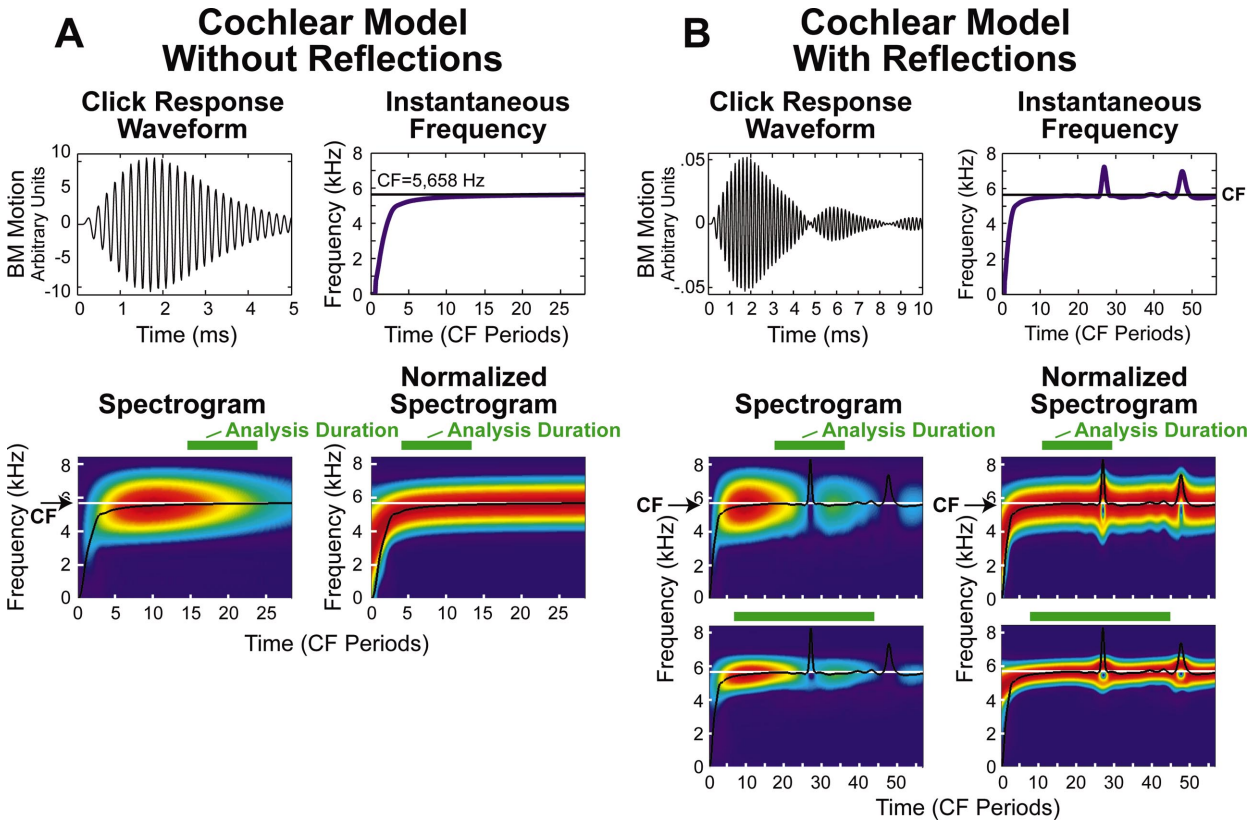

FIG. 2. Time–frequency analysis of impulse responses of cochlear models without (a) and with (b) cochlear reflections (from Shera, in preparation, also see Shera 2001c). In each panel, the top-left plot shows the time waveform of the click response, and the top-right plot shows the corresponding Hilbert-transform instantaneous frequency. At the bottom are STFSs and nSTFSs as in Fig. 1.

tuning curve for AN fibers, or from the original papers for BM places. The normalized spectrograms display the result at every time, even at times before the response has started or after the response has decayed away, so that the data at the beginning and end of these plots is often dominated by noise. To indicate that the signal/noise ratio is poor, while allowing the underlying data to still be seen, graying has been applied in the normalized spectrograms.[2]

The data shown in Figs. 3–4 were chosen to be representative of the range of features seen in a data pool of 6 basilar membrane places and 42 auditory-nerve fibers with suitable click-response level functions. Only auditory-nerve fibers with CFs$<$3.5 kHz were considered because those with higher CFs do not have adequate synchrony.

A. Un-normalized spectrograms: Maximum energy

The un-normalized spectrograms typically consisted of one or two peaks of energy that changed in latency and frequency as a function of sound level (Figs. 3–4). The latency and frequency of the largest magnitude component are shown as a function of stimulus level in Figs. 5(a), 5(b). At low and moderate sound levels, the point of peak energy decreased in both frequency and latency as the level increased, for all basilar-membrane places and for auditory-nerve fibers with CFs above about 1 kHz [Figs. 5(a), 5(b)]. At the highest levels, these trends continued for basilar-membrane places, but for auditory-nerve fibers the peak energy often shifted to latencies and frequencies closer to those seen at low levels [Figs. 5(a), 5(b)]. An examination of individual auditory-nerve responses showed that these peak-energy shifts at high levels appeared to be associated with reductions, reversals, and/or splitting, of the early peaks of the click responses such as those described by Lin and Guinan (2000). In contrast, for auditory-nerve fibers with CFs below 0.8 kHz, there was relatively little change in the peak-energy frequency with increases in sound level, but most latencies decreased at moderate click levels and increased at the highest levels [Figs. 5(a), 5(b), bottom].

B. Normalized spectrograms: Glides

The frequency content of click responses changed systematically with time after the click. The changes can be seen in the un-normalized spectrograms, and more clearly in the normalized spectrograms (Figs. 3–4). To show the trends from many cases, the frequency of peak energy versus time from the normalized spectrograms is plotted in Fig. 6, with the data divided into CF regions. Plots similar to those in Fig. 6 can be made using the Hilbert-transform ''instantaneous frequency,'' but these are more adversely affected by regions with low signal/noise.

For CFs greater than about 0.8 kHz, the frequency content of the responses typically increased with time after onset, i.e., the responses show upward ''glides'' (Figs. 3, 4, 6). For auditory-nerve fibers with CFs below about 0.8 kHz, and particularly those with CFs below 0.4 kHz, the frequency content tended to decrease gradually with time, although in a

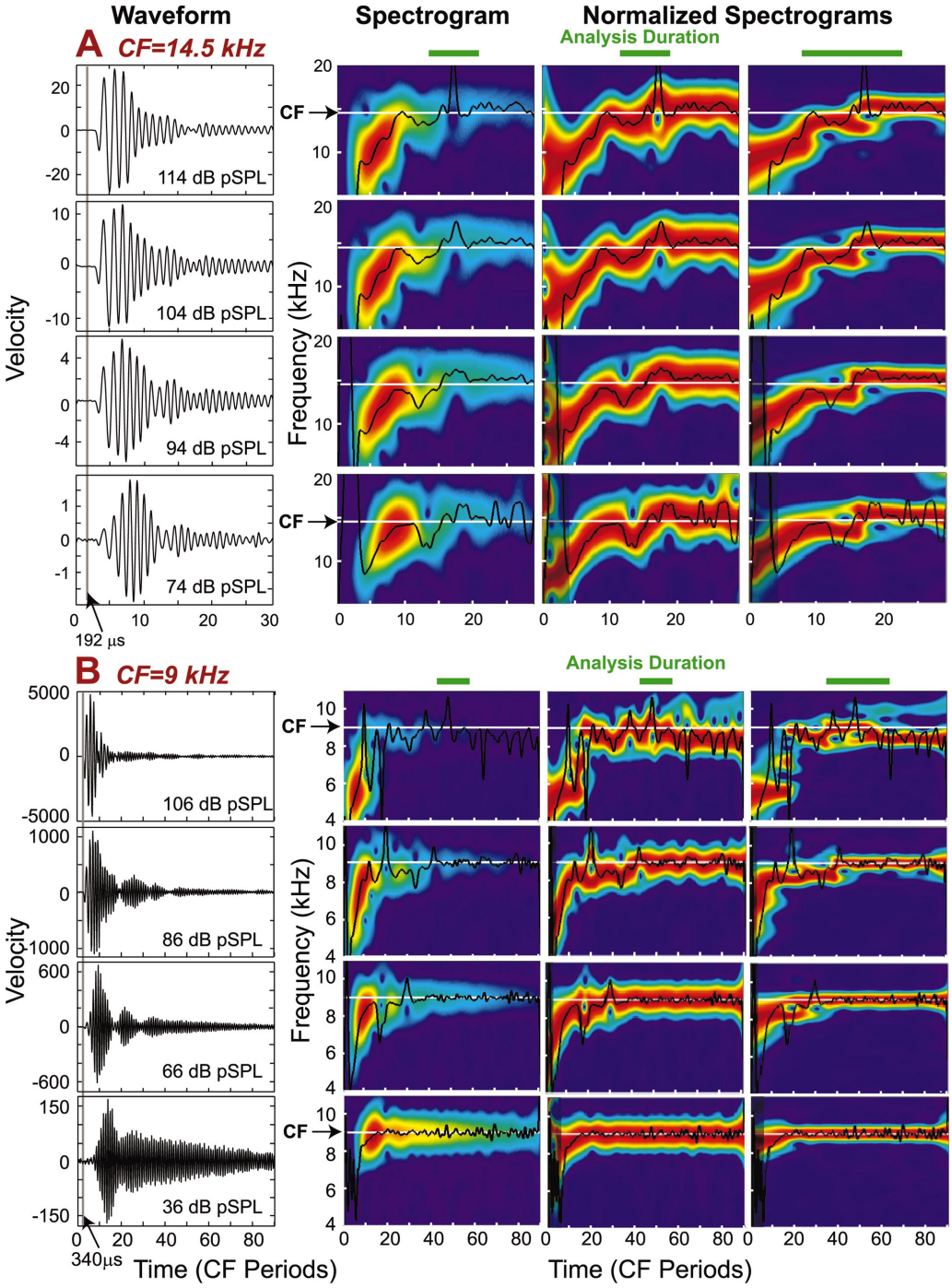

FIG. 3. Time–frequency analysis of click responses from two basilar-membrane places. (a) Characteristic frequency (CF) = 14.5 kHz (data from Recio and Rhode, 2000). (b) CF = 9 kHz (data from Recio *et al.*, 1998). Each row shows data from one sound level [indicated at left in dB peak-equivalent SPL (pSPL)]. The left column shows the response waveform, the second column shows the corresponding short-term Fourier Spectrogram for an analysis duration shown above the column, the third column shows a normalized spectrogram (at each time point the frequency spectrum was divided by its largest amplitude) for the same analysis duration, and the fourth column shows a normalized spectrogram for an analysis duration twice as long. In the spectrograms, the abscissa is time (in periods of CF), the ordinate is frequency (in kHz) with a white line at CF, and the spectral energy level is coded by color as shown in Fig. 1(b) left for spectrograms and Fig. 1(b) right for normalized spectrograms. The black line is the instantaneous frequency calculated by the Hilbert-transform method. Gray areas indicate times when the signal/noise ratio is low. The different durations in (a) vs (b) reflect the available data. Note that (b) shows many glide irregularities despite using a many-period analysis duration.

few cases there was an abrupt jump down in frequency content [e.g., Fig. 4(c)]. Upward glides were first described in preparations with high CFs (de Boer and Nuttall, 1997; Recio *et al.*, 1998; Recio and Rhode, 2000) and later it was discovered that for CFs greater than ~1.5 kHz glides go up, and for CFs less than ~0.8 kHz glides go down (Carney *et al.* 1999). The data shown here extend to higher sound levels than previous data, and for AN fibers with CFs <1.5 kHz, reveal a tendency at the highest levels for the glides to be closer to CF at short latencies (not illustrated).

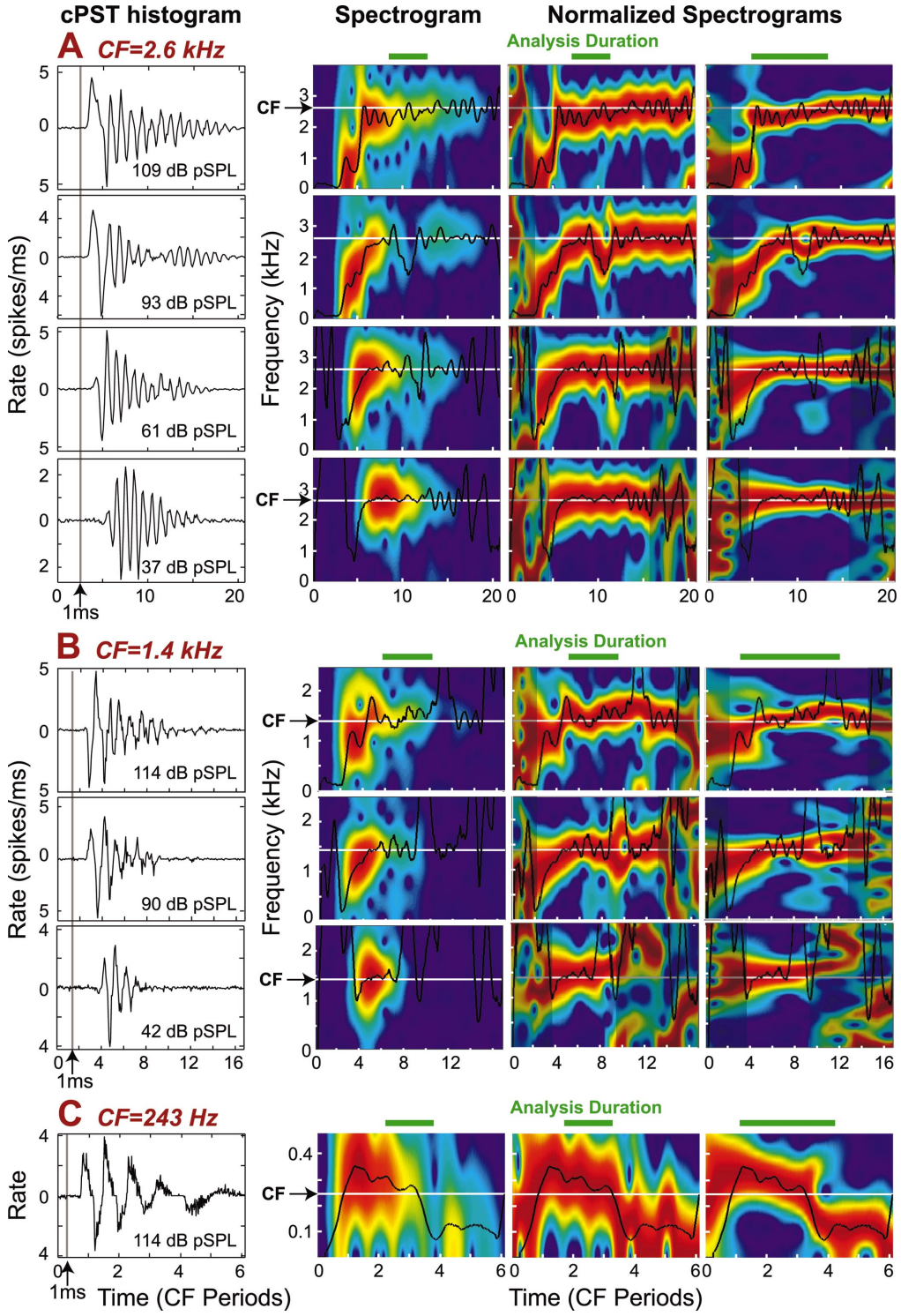

FIG. 4. Time–frequency analysis of click responses from three auditory-nerve fibers. CFs shown orange at the upper-left of each panel. Layout as in Fig. 3. Data from Lin and Guinan (2000). The durations shown reflect the maximum duration with useful information.

C. Glide irregularities

Although the overall properties of the click-responses were similar to previous descriptions of glides, close observation reveals consistent deviations from smooth glides in frequency. These ''glide irregularities'' are apparent in the spectrograms, the normalized spectrograms, and the instantaneous frequency plots, from both auditory-nerve and basilar-membrane data. Compare the predicted smooth frequency change of Fig. 2(a) with the data in Figs. 3, 4, 6 (but in Figs. 3–4 ignore the shaded areas at the beginning and end of the responses where the signal/noise ratios are poor). Glide irregularities can be seen at every basilar membrane place and in almost every auditory-nerve fiber (in every fiber with a CF$>$0.8 kHz). Although while looking at any single plot, one can question whether a particular bend in the gliding response is due to noise, in many cases similar patterns

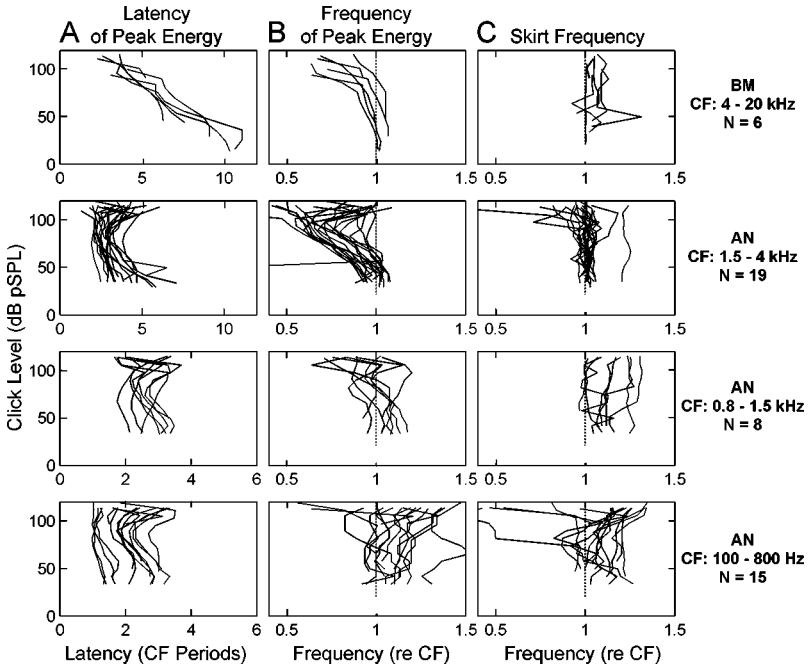

FIG. 5. Properties of individual basilar membrane (BM) places or auditory-nerve (AN) fibers in CF groups. (a),(b): The latency (a) and frequency (b) of the point of peak energy as a function of click level. (c) The skirt frequency as a function of click level. In (a) latency is shown in CF periods with the time origin at the onset of ossicular motion for the BM data, and at 1 ms after the acoustic click (to allow for nerve conduction time) for the ANF data. "N" at the right is the number of BM places or AN fibers.

of irregularities occur across multiple levels [e.g., at ~15 periods in Fig. 3(a)] which is not consistent with the irregularities being produced by noise. This is particularly apparent in the original data sets which contain more sound levels than are shown in Figs. 3–4.

We attempted to quantify glide irregularities but did not find a satisfactory method. We tried both human observers (the two authors counted glide irregularities in each response and obtained about a 60% concordance), and computational methods such as looking for maxima and minima in the ratio of the second derivative to the first derivative of the peak frequency versus time (this, of course, picked out irregularities, but the number of irregularities obtained continued to slowly increase as the criterion was lowered so no satisfactory criterion was obtained). Despite the fact that the various methods found different numbers of irregularities, these methods consistently showed similar patterns of the irregularities across frequency and level. The number of glide irregularities per response decreased at very-low frequencies and for low sound levels. It seems likely that at least part of the decrease in the number of irregularities at low levels is due to the reduced duration over which the S/N of the response is adequate for analysis at low click levels. Glide irregularities at longer latencies tended to have the same latency across a wide range of levels [e.g., Fig. 3(a), at ~15 periods] and to occur at the times of response wanes. When there was waxing and waning and the S/N was good, there was normally a glide irregularity at each wane.

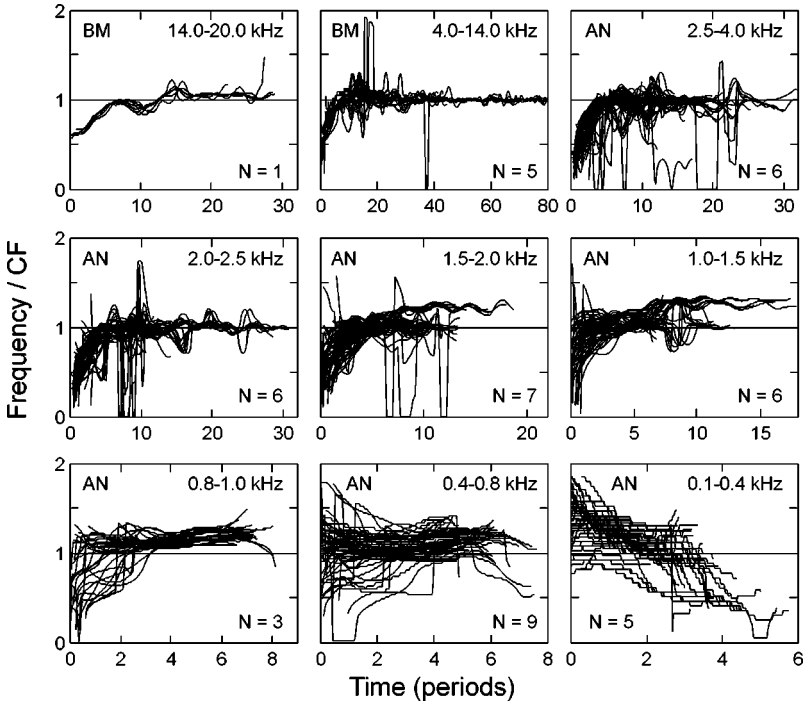

FIG. 6. Glides in different CF ranges. Each panel shows the frequency of peak energy from the normalized spectrograms, versus time, for all available sound levels from BM places or AN fibers with CFs in the range listed in the panel. "N" is the number of places or fibers (each of which has data at many levels). The time origin is as in Fig. 5.

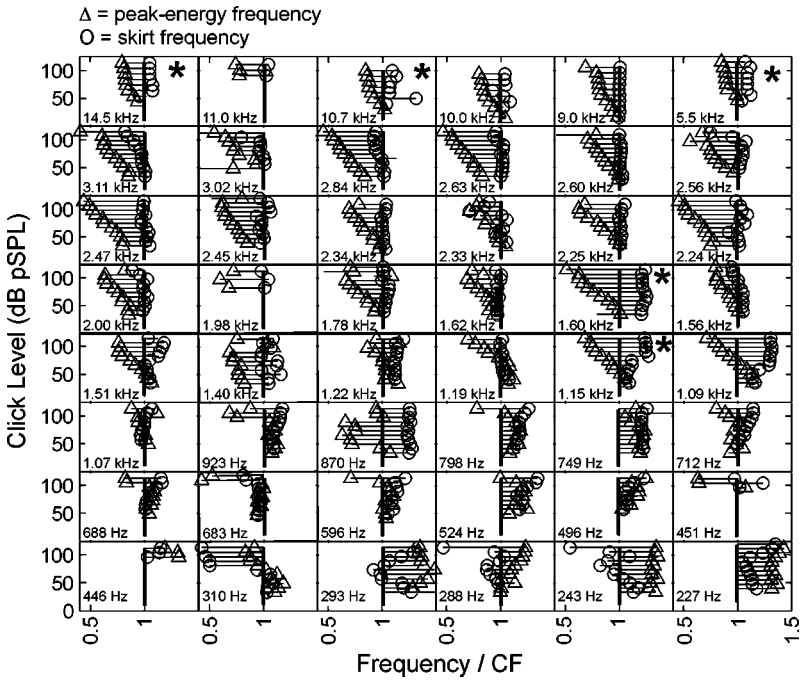

FIG. 7. ''Tree plots'' showing that sometimes the skirt frequency (O) is not at CF. Each panel shows the data as a function of sound level from one fiber or basilar-membrane place; all data used in this paper are included. The CF from the tuning curve or the BM paper is shown by a vertical line, and is listed in each panel. An alternate CF can be obtained from the frequency of the peak energy (Δ) at the lowest sound level. Horizontal lines show the approximate extent of glide frequency excursions at that click level (obtained from averages of the glide frequency over time bins equal to the low-level latency—see Sec. II). Asterisks indicate cases with clear non-CF skirt frequencies. For the BM place with the CF listed at 11.0 kHz, the original CF was not available and CF was taken to be the lowest-level skirt frequency.

As outlined in the Introduction, two potential sources for the waxing and waning of click responses are the beating of responses from multiple resonators and interference between the decaying response and an echo. In an attempt to distinguish between the multiple-resonances-beating hypothesis versus the echo-interference hypothesis, we examined the frequency content at glide irregularities. All short-latency and most long-latency irregularities showed jumps in frequency content at an irregularity [e.g., Fig. 3(a), right column]. However, some long-latency irregularities had little change in frequency content across the irregularity [Fig. 4(a), 93 dB SPL].

D. Click response skirts

One surprising feature of the responses revealed by the time-vs-frequency patterns of Fig. 6 is that the frequency in the declining part of the response (the ''skirt'') was not always at CF. This feature can also be seen in the normalized-spectrogram plots of Figs. 3–4. The skirt frequency as a function of level, for several CF ranges, is shown in Fig. 5(c). This figure reveals that there is a tendency for the skirt frequency to be above CF.

Although such a result might be obtained if the wrong frequency was picked for CF, the data indicate that in most cases, this explanation is not correct. For instance, for the basilar membrane data shown in Fig. 3(a), the energy of the response at the lowest level was at or below the frequency designated by the investigators as CF. Thus, the skirt frequencies at higher levels are not higher than CF because CF was incorrectly chosen to be too low a frequency.

To see how often a skirt frequency different from CF might be attributed to errors in determining CF, for each ANF or BM place, we plotted CF, the skirt frequency and the peak-energy frequency as a function of click level (Fig. 7). These plots show some cases where the peak-energy frequency at the lowest sound level is not at ''CF,'' and suggest that redefining CF to be the frequency with the peak energy at the lowest sound level would make the higher-level skirt frequencies be at CF. However, Fig. 7 also shows many cases where ''CF'' was determined correctly by this criterion, and the skirt frequency at higher sound levels is not at CF (e.g., at the asterisks in Fig. 7).

IV. DISCUSSION

A. Overall glide shapes

Many aspects of the glide shapes revealed by time–frequency analysis agree with the hypothesis that the click response is produced by traveling-wave dispersion causing the low-frequency energy to arrive earlier than the high-frequency energy (Shera, 2001a). At all sound levels, click responses from the basilar membrane, and at low and moderate sound levels, click responses from auditory nerve fibers with CFs$>\sim$1 kHz showed (1) upward sweeping glides with shapes that changed relatively little with sound level (in agreement with de Boer and Nuttall, 1997; Carney *et al.*, 1999), and (2) the frequency and latency of the peak energy decreased as sound level increased. The decrease in frequency of click responses as sound level is increased is consistent with the well-known half-octave shift of the tone response maximum as the sound level is increased (Shera, 2001a).

In contrast to this well-understood behavior of click responses, ANF responses to high-level clicks showed anomalous increases in latency and frequency of the maximum energy point [Figs. 5(a), 5(b)]. These anomalous changes were due to changes in the earliest peak(s) of ANF responses at high sound levels, changes that were not seen in the BM data. It is possible that these differences between ANF and BM responses are due to differences in CF regions and/or species differences. However, it seems most likely that the differences at high sound levels are due to differences in the

mechanical response patterns of the basilar membrane versus the IHC stereocilia. The short-latency, high-level ANF click responses appear to have a cancellation of peaks and peak splitting. Lin and Guinan (2000) found that short-latency, high-level click responses appeared to be due to interference of two short-latency excitatory drives with different decay rates. The present data suggest that these two excitatory drives are seen in ANF, but not BM, click responses. All in all, these data suggest that ANF responses are shaped by interference between a drive from a frequency-dispersive traveling wave acting on the CF resonance, and an additional excitation drive.

Another aspect of the click responses that does not fit with normal traveling-wave frequency dispersion is the downward frequency sweep of glides at very low CFs (Fig. 6, lower right). Several response features of auditory nerve fibers in this frequency region provide clues to the origin of these downward glides. In this frequency region, auditory-nerve fibers have tuning curves with multiple lobes (Liberman and Kiang, 1978), and group delays of tone responses change abruptly at the seams of the lobes (Pfeiffer and Molnar, 1970; Kiang 1984; van der Heijden and Joris, 2003). Such response properties strongly suggest that these low-CF auditory-nerve fibers receive two (or more) excitation drives with different latencies and different frequency content (Lin and Guinan, 2000). Some click responses from this frequency region show time–frequency patterns in which there is a higher-frequency response region followed by a rapid change to a lower-frequency response region [e.g., Fig. 4(c)]. The more gradual downward glides seen in other low-CF fibers (Fig. 6, bottom right) may be attributed to a more gradual transition between two such time–frequency response regions. Thus, it is likely that downward glides in low-CF fibers are due to sequential dominance of the response by excitation drives with different latencies and different frequency content.

B. Glide irregularities

Although simple traveling-wave frequency dispersion produces glides that sweep upward smoothly [e.g., Fig. 2(b)], the time–frequency analyses of click responses provides strong evidence that actual cochlear glides are punctuated by multiple irregularities. Except for some fibers with very low CFs, both auditory-nerve fibers and basilar-membrane measurements had consistent nonsmooth glides. Previous reports on glides show many irregularities in the instantaneous frequency measures of the glides, however, these reports did not note these as glide irregularities, perhaps because with the Hilbert transform method apparent irregularities are often attributable to noise or methodological considerations (de Boer and Nuttall, 1997; Carney *et al.* 1999; Shera, 2001a). A well-documented demonstration of a long-latency glide irregularity is given by Recio *et al.* (1998).

The widespread occurrence of glide irregularities is not consistent with the hypothesis that a single cochlear pressure wave with a smoothly upward-gliding frequency content excites a single resonance at the local CF. In the Introduction we suggested two hypotheses as explanations of these glide irregularities: (1) glide irregularities are due to the sequential dominance of different local cochlear resonances, or (2) glide irregularities are due to drives from cochlear internal reflections (Shera, 2000c).

First, we consider glide irregularities that occur early in the responses, within the first few cycles of the response before the glide frequency reaches CF [e.g., at 5 periods in Fig. 4(a)]. These early glide irregularities are too early to be accounted for by cochlear reflections, and they often show big jumps in the frequency content. Thus it appears likely they are due to the sequential dominance of multiple cochlear resonances (hypothesis 1). These early glide irregularities are most prominent in ANF responses, and often (particularly for fibers with CFs 1–3.5 kHz) occur at the transitions between the click-response initial peak(s) (in which low frequencies predominate) and the later peaks (in which near-CF frequencies predominate) [Figs. 4(a), 4(b)]. This pattern fits with the hypothesis that the initial peaks are produced by excitation drives associated with tuning-curve tails, and the later peaks are produced by excitation drives associated with the tuning-curve tips (Shoonhoven *et al.*, 1994; also see Lin and Goldstein, 1995; Lin and Guinan, 2000). Thus, early glide irregularities appear to be due to the transition from responses dominated by a tail excitation drive to responses dominated by a tip excitation drive, even though cat ANFs with CFs 1–3.5 kHz usually do not show tails that are separated from the tuning-curve tips.

Many of the longer-latency glide irregularities show jumps in frequency content and therefore are likely to be due to the sequential dominance of multiple cochlear resonances. Striking demonstrations of energy at two frequencies are cases where the dominant frequency changes before versus after the irregularity [e.g., Fig. 3(a) at $\sim$15 periods; also see Recio *et al.*, 1998]. However, some long-latency glide irregularities do not show a jump in frequency content [e.g., Fig. 4(b) at $\sim$11 periods] and thus may be attributable to an interaction of the initial traveling wave with a wave due to cochlear internal reflections (although the interaction of two resonances that are very close in frequency is also possible). Another consideration is that many long-latency glide irregularities are associated with response wanes. To produce a wane (a reduction of the response amplitude), the phases of the initial and reflected waves must be within 60 degrees of phase opposition. However, the relative phases of these waves are distributed over 360 degrees (Shera, 2003), so reflections would produce a wane only in 1/3 of cochlear locations. These factors argue that the great majority of the long-latency glide irregularities are not due to cochlear internal reflections. All in all, it appears that most glide irregularities are due to the sequential dominance of multiple cochlear resonances, although is not possible to rule out internal reflections as being the source of some.

C. Click skirts

Compared to the initial part of the click response which shows a half-octave shift, energy in the click-response skirt was usually concentrated near CF at all sound levels. This relative consistency of the skirt frequency is consistent with the conclusion that local cochlear resonances do not change substantially with sound level (Shera, 2001b). Nonetheless,

there were cases in which the skirt frequency was not at CF and this difference does not appear attributable to the incorrect assignment of CF [e.g., Figs. 3(a), 7]. We feel that the present data are conclusive in showing that such cases exist, but are not adequate to show how prevalent this phenomena is. An experimental study specifically addressing this issue is needed to determine the prevalence.

One possible origin of click skirt frequencies that are not at CF is that they are due to click-synchronization of spontaneous cochlear vibrations analogous to synchronized spontaneous otoacoustic emissions. This may explain some of the data from chinchillas, because trauma can produce SOAEs in chinchillas (e.g., Clark *et al.*, 1984) and such trauma may have been produced during the preparation for basilar-membrane recording. However, it seems unlikely that this mechanism will account for most of the cases in which click skirts are not at CF because SOAEs are induced by trauma with a low success rate (only 2 of 28 traumatized chinchilla ears developed SOAEs; Clark *et al.*, 1984) and the published BM data came from preparations with minimal damage. Furthermore, the authors of these papers did not report the presence of SOAEs in these animals. The cat data seem even less likely to be explained by a phenomena corresponding to synchronized SOAEs because the cochlea was intact in the cat experiments and SOAEs are uncommon in cats (no study has reported the presence of SOAEs in cats, and in our own experience in hundreds of cats, we only found an SOAE only in one case—although we seldom looked closely for SOAEs).

One hypothesis to consider is that non-CF skirt frequencies are due to changes in the CF resonance produced by the action of a simple, time-invariant, instantaneous nonlinearity. If the click skirt was produced by such a resonance, then as the response decayed to a low enough level, the frequency would become the same as that of a low-level click response, i.e., it would be at CF. However, in at least some cases when a skirt frequency was determined to be different from CF, the amplitude of the response had become less than the peak amplitude for the lowest click level, a level which showed a CF response [e.g., the skirt at 64 dB for the case in Fig. 3(a) and the top-left panel in Fig. 7; also see Fig. 2 in Recio and Rhode, 2000]. Thus, a simple, time-invariant, instantaneous nonlinearity cannot be the cause of the non-CF click skirt frequencies, at least not in all cases.

The production of such non-CF click skirts appears to require the skirt frequency to be influenced by stimulation history. Non-CF skirt frequencies might be due to a single CF resonance with the CF temporarily changed by the high-amplitude click, or they might be due to there being more than one resonance near CF with the partition of energy between these resonances being dependent on stimulation history. Since the waxing and waning of response amplitudes during the decaying part of the click response suggests the beating of responses at two close frequencies, we favor the explanation that there are multiple near-CF resonances and that CF is due to one of these while a non-CF click skirt is due to another. The idea that there are two near-CF resonances is not new. The model by Zweig (1991) had two resonances that were near CF but not identical. A definitive sorting out of the various hypotheses for the production of non-CF click skirt frequencies must await further experimentation.

D. The origin of the multiple drives/resonances

The properties of downward glides, glide irregularities, and click skirts all point to these phenomena originating from the interactions of two (or more) excitation drives with different resonant frequencies and time courses. What do these two excitation drives correspond to physically? Recent data show that the various parts of the organ of Corti do not all vibrate in phase and suggest that multiple vibrational resonant frequencies exist at each cochlear location (Richter and Dallos, 2003; Fridberger *et al.*, 2002; Karavitaki and Mountain, 2002). Furthermore, explorations of the effects of outer hair cell motility on organ of Corti vibration patterns demonstrate that the vibration of the reticular lamina may move opposite in phase to the basilar membrane (Scherer *et al.*, 2003). These observations do not tell us the origin of the excitation drives that produce the phenomena studied here, but they indicate that the multiple excitation drives are likely to originate in multiple vibrational modes within the cochlear partition, each with its own resonant frequency. They also tell us that models intended to provide an accurate picture of cochlear mechanics will have to take multiple vibrational modes into account and will be both aided, and constrained, by the results in this paper.

Considering current models of cochlear mechanics, we believe that the model that provides the most useful framework for understanding the phenomena presented here is the multi-compartment model of Hubbard and coworkers (2002). In this model, there are two propagated cochlear waves that have different velocities: one associated with transverse-mode (TrM) and one with organ-of-Corti-mode (OCM) cochlear vibrations. It seems natural to associate these two waves with the two drives that interact to produce many of the phenomena shown in the present paper. Also, in this model the OCM mode is much more apparent in the motion of the reticular lamina than the BM due to differences in the effective stiffnesses of these structures. Presumably, this would make the OCM mode more apparent in the motion of IHC stereocilia and ANF firing patterns than in BM motion, and may explain why interactions and cancellations of the two waves are seen much more in ANF responses than in BM responses.

The two waves of this model travel along the basilar membrane at different rates so they could produce excitation drives with different latencies. To account for the downward glides at very low CFs, they would have to have different frequency contents with the first-arriving wave having a *higher* frequency content than the second-arriving wave. To account for the short-latency glide irregularities at moderate sound levels in auditory-nerve fibers with CFs$>\sim$1.5 kHz, the first-arriving wave would need a *lower* frequency content than the second-arriving wave. If the same two waves produce both phenomena, this implies a reversal at around 1 kHz either in which wave arrives first, or in the relative frequency content of the two waves. A reversal of some kind

at about 1 kHz is supported by the reversal of glide direction (Fig. 6) and the reversal of the tuning-curve side which has the tail (Kiang *et al.*, 1977).

Whether the Hubbard *et al.* (2002) model, when adequately explored, has the necessary properties to account for the results presented here remains to be demonstrated. However, some model like that of Hubbard and coworkers (2002) appears to be required to account for the data. Although one can imagine a ''classic'' cochlear model based on a single, but very complex, transverse impedance of the cochlear partition that is formally equivalent to a model with two traveling waves, the complexity of such a model and the difficulty of gaining insight from it would make a two-traveling wave model much preferred. Finally, our recent finding that medial efferents inhibit the earliest peak of ANF click responses, a finding that cannot be accounted for by the classic transverse traveling wave (e.g., the earliest peak of the BM click response appears to be not affected by active processes in outer hair cells—Recio *et al.*, 1998) strongly points to there being two traveling waves along the organ of Corti (Guinan *et al.*, 2004).

V. CONCLUSIONS

(1) A time–frequency analysis shows that many properties of click responses, such as upward glides, can be accounted for by a single, frequency-dispersive traveling wave exciting a single CF resonance.

(2) In contrast, many response properties cannot be explained in this way, such as (a) in ANF responses to high-level clicks, the peak energy becomes higher in frequency than at lower levels, (b) for low CF fibers, glides go downward, (c) glide irregularities are found both early (after the first few peaks) and late (after tens of response cycles) in click responses, and (d) click response skirt frequencies are not always at CF. Most, or all, of these phenomena appear to require the interactions of two (or more) excitation drives with different latencies and different frequency contents. In particular, for very low CF fibers, downward glides appear to be due to the high-frequency mode arriving before the low-frequency mode.

(3) A model with multiple cochlear resonances and traveling waves with different velocities, such as that of Hubbard and co-workers (2002), appears to be required to account for the data.

ACKNOWLEDGMENTS

We thank Dr. Alberto Recio, Dr. Bill Rhode, and Dr. Mario Ruggero for providing us with basilar-membrane data, and Dr. Christopher Shera for results from his model. We thank Dr. John Rosowski and Dr. Christopher Shera for comments on the manuscript. Supported by Grants No. 5 RO1 DC 00235 and No. P30 DC05209 from the National Institute of Deafness and Other Communication Disorders.

[1]In the hope that their advantages would outweigh their disadvantages, we tried two time–frequency analysis methods, Wigner-Ville and Garbor spectrograms, in addition to STF analysis (see Qian and Chen 1999). The Wigner-Ville spectrogram was not useful because of its many artifactual ''cross terms.'' The Garbor spectrogram gave good results (better time–frequency resolution than short-term Fourier spectrograms) when the data were sampled at an optimum time resolution. However, when the data were over sampled (e.g., basilar-membrane data sampled at 4 μ s from Recio *et al.*, 1998), the frequency resolution of the Garbor spectrogram was inadequate because the available software limited the analysis to 128 frequencies (there is only one commercial implementation of the Garbor spectrogram, in National Instruments LabVIEW). Our use of short-term Fourier spectrograms produced some loss of resolution compared to optimum use of the Garbor spectrogram, but this loss was generally small and did not appear to obscure any significant feature of the responses.

[2]The grayed areas correspond, approximately, to times at which the signal energy was below the ''signal criterion'' (see Sec. II). At these times, the Hilbert transform method often shows large rapid excursions in instantaneous frequency because noise dominates the response. Note that graying was not applied in the un-normalized spectrograms because these do not accentuate regions with little energy.

Carney, L. H., McDuffy, M. J., and Shekhter, I. (**1999**). ''Frequency glides in the impulse responses of auditory-nerve fibers,'' J. Acoust. Soc. Am. **105**, 2384–2391.

Clark, W. W., Kim, D. O., Zurek, P. M., and Bohne, B. A. (**1984**). ''Spontaneous otoacoustic emissions in chinchilla ear canals: correlation with histology and suppression by external tones,'' Hear. Res. **16**, 229–314.

de Boer, E., and Nuttall, A. L. (**1997**). ''The mechanical waveform of the basilar membrane. I. Frequency modulations (''glides'') in impulse responses and cross-correlation functions,'' J. Acoust. Soc. Am. **101**, 3583–3592.

Fridberger, A., Boutet De Monvel, J., and Ulfendahl, M. (**2002**). ''Internal shearing within the hearing organ evoked by basilar membrane motion,'' J. Neurosci. **22**, 9850–9857.

Gray, P. R. (**1967**). ''Conditional probability analyses of the spike activity of single neurons,'' Biophys. J. **7**, 759–777.

Guinan, J. J., Lin, T., and Cheng, H. (**2004**). ''Medial-efferent stimulation can inhibit the earliest peak of click responses from cat single auditory-nerve fibers.'' Abstract 1001, 27th Midwinter Meeting of the Association for Research in Otolaryngology.

Hubbard, A. E., Chen, F., and Mountain, D. C. (**2002**). Astract 898, 25th Midwinter Meeting of the Association for Research in Otolaryngology.

Karavitaki, K. D., and Mountain, D. C. (**2002**). ''Three-Dimensional Reconstruction of Electrically-Evoked Motions in the Gerbil Cochlea.'' Abstract 180, 25th Midwinter Meeting of the Association for Research in Otolaryngology.

Kiang, N. Y. S., (**1984**). ''Peripheral neural processing of auditory information,'' *Handbook of Physiology, Section 1: The Nervous System*, Am. Physiological Soc., Bethesda, MD, Vol. 3 (Sensory Processes), pp. 639–674.

Kiang, N. Y. S., Liberman, M. C., and Baer, T. (**1977**). ''Tuning curves of auditory-nerve fibers,'' J. Acoust. Soc. Am. **61**, S27(A).

Kiang, N. Y. S., Watanabe, T., Thomas, E. C. and Clark, L. F., (**1965**). *Discharge patterns of single fibers in the cat's auditory nerve* (MIT Press, Cambridge MA).

Liberman, M. C., and Kiang, N. Y. S. (**1978**). ''Acoustic trauma in cats. Cochlear pathology and auditory-nerve activity,'' Acta Otolaryngolo. **358**, 1–63.

Lin, T., and Goldstein, J. L. (**1995**). ''Quantifying 2-factor phase relations in non-linear responses from low characteristic-frequency auditory-nerve fibers,'' Hear. Res. **90**, 126–138.

Lin, T., and Guinan, Jr., J. J. (**2000**). ''Auditory-nerve-fiber responses to high-level clicks: Interference patterns indicate that excitation is due to the combination of multiple drives,'' J. Acoust. Soc. Am. **107**, 2615–2630.

Møller, A. R., and Nilsson, H. G. (**1979**). ''Inner ear impulse response and basilar membrane modeling,'' Acustica **41**, 258–262.

Oppenheim, A. V. and Schafer, R. W. (**1989**). *Discrete-Time Signal Processing* (Prentice–Hall, Englewood Cliffs, NJ).

Pfeiffer, R. R., and Molnar, C. E. (**1970**). ''Cochlear nerve fiber discharge patterns: Relationship to the cochlear microphonic,'' Science **167**, 1614–1616.

Qian, S., and Chen, D. (**1999**). ''Joint time–frequency Analysis,'' IEEE Signal Process. Mag. **16**, 52–67.

Recio, A., Rich, N. C., Narayan, S. S., and Ruggero, M. A. (**1998**). ''Basilar-membrane responses to clicks at the base of the chinchilla cochlea,'' J. Acoust. Soc. Am. **103**, 1972–1989.

Recio, A., and Rhode, W. S. (**2000**). ''Basilar membrane responses to broadband stimuli,'' J. Acoust. Soc. Am. **108**, 2281–2298.

Robles, L., Rhode, W. S., and Geisler, C. D. (**1976**). ''Transient response of the basilar membrane measured in squirrel monkeys using the Mössbauer effect,'' J. Acoust. Soc. Am. **59**, 926–939.

Richter, C. P. and Dallos, P. (**2003**). Micromechanics in the Gerbil Hemicochlea, in *The Biophysics of the Cochlea: Molecules to Models*, edited by A. W. Gummer *et al.* (World Scientific, Singapore), pp. 278–284.

Scherer, M. P., Nowotny, M., Dalhoff, E., Zenner, H. P., and Gummer, A. W. (**2003**). High-frequency vibration of the organ of Corti *in vitro*, in *The Biophysics of the Cochlea: Molecules to Models*, edited by A. W. Gummer (World Scientific, Singapore), pp. 271–277.

Shera, C. A. (**2001a**). ''Frequency glides in click responses of the basilar membrane and auditory nerve: Their scaling behavior and origin in traveling-wave dispersion,'' J. Acoust. Soc. Am. **109**, 2023–2034.

Shera, C. A. (**2001b**). ''Intensity-invariance of fine time structure in basilar-membrane click responses: implications for cochlear mechanics,'' J. Acoust. Soc. Am. **110**, 332–348.

Shera, C. A. (**2001c**). ''The effect of reflection emissions on impulse responses of the basilar membrane and the auditory nerve,'' Astract 815, 24th Midwinter Meeting of the Association for Research in Otolaryngology.

Shera, C. A. (**2003**). ''Mammalian spontaneous otoacoustic emissions are amplitude-stabilized cochlear standing waves,'' J. Acoust. Soc. Am. **114**, 244–262.

Schoonhoven, R., Keijzer, J., Versnel, H., and Prijs, V. F. (**1994**). ''A dual filter model describing single-fiber responses to clicks in the normal and noise-damaged cochlea,'' J. Acoust. Soc. Am. **95**, 2104–2121.

van der Heijden, M., and Joris, P. X. (**2003**). ''Cochlear phase and amplitude retrieved from the auditory nerve at arbitrary frequencies,'' J. Neurosci. **23**, 9194–9198.

Zweig, G. (**1991**). ''Finding the impedance of the organ of Corti,'' J. Acoust. Soc. Am. **89**, 1229–1254.

Prediction of the characteristics of two types of pressure waves in the cochlea: Theoretical considerations

Masayoshi Andoh and Hiroshi Wada[a)]
Department of Bioengineering and Robotics, Tohoku University, Sendai 980-8579, Japan

(Received 25 June 2003; revised 19 April 2004; accepted 26 April 2004)

The aim of this study was to predict the characteristics of two types of cochlear pressure waves, so-called fast and slow waves. A two-dimensional finite-element model of the organ of Corti (OC), including fluid–structure interaction with the surrounding lymph fluid, was constructed. The geometry of the OC at the basal turn was determined from morphological measurements of others in the gerbil hemicochlea. As far as mechanical properties of the materials within the OC are concerned, previously determined mechanical properties of portions within the OC were adopted, and unknown mechanical features were determined from the published measurements of static stiffness. Time advance of the fluid–structure scheme was achieved by a staggered approach. Using the model, the magnitude and phase of the fast and slow waves were predicted so as to fit the numerically obtained pressure distribution in the scala tympani with what is known about intracochlear pressure measurement. When the predicted pressure waves were applied to the model, the numerical result of the velocity of the basilar membrane showed good agreement with the experimentally obtained velocity of the basilar membrane documented by others. Thus, the predicted pressure waves appeared to be reliable. Moreover, it was found that the fluid–structure interaction considerably influences the dynamic behavior of the OC at frequencies near the characteristic frequency. [DOI: 10.1121/1.1763599]

PACS numbers: 43.64.Bt, 43.64.Kc [BLM] Pages: 417–425

I. INTRODUCTION

When a fluid pressure fluctuation is induced by vibration of the stapes, two types of pressure waves occur in the cochlea. Lighthill (1981) theoretically characterized these pressure waves. One is a fast wave which is a compressional wave caused by the stapes vibration. It is uniformly distributed over the cross-section of each scala, i.e., the scala vestibuli (SV), the scala media (SM) and the scala tympani (ST), respectively, and propagates at the velocity of sound. As each scala is divided by Reissner's membrane or the basilar membrane (BM), the magnitude and/or phase difference of the fast wave between the scalae is possibly caused by the stiffness and damping of the membrane. The other is a slow wave which results from a fluid flow according to the interaction between the BM and the lymph fluid, i.e., it follows a traveling wave on the BM. The slow wave exists in the vicinity of the BM and has equal magnitude with opposite phases at either side of the BM (Lighthill, 1981). Olson (1999) found a notch in the frequency response of the intracochlear pressure, and explained that this notch was caused by the destructive interaction between two modes of pressure waves. As the organ of Corti (OC) is driven by these pressure waves, it is important to understand their frequency characteristics. However, there have been no reports on empirical observations of these waves, because of the difficulty of measuring them independently. Therefore, numerical analysis would seem to be useful for clarifying their frequency characteristics.

As the OC is immersed in lymph fluid, the interaction between the OC and the lymph fluid must be taken into account when the dynamic behavior of the OC and fluid pressure distribution are numerically analyzed. However, the complex structure of the OC and the large difference in material properties between the fluid and the structure of the OC complicate modeling of the lymph–OC interaction. Prior attempts to construct a cochlear model including the microstructure within the OC (Kolston and Ashmore, 1996) have been inconclusive, because only the lymph fluid in the SV was considered.

In the present study, finite-element models of the OC and the lymph fluid surrounding the OC are constructed to predict the frequency characteristics of the two types of pressure waves. The fluid–structure interaction between the model of the OC and those of the lymph fluid is considered by means of a staggered approach. Using these models, first, unknown Young's moduli of individual portions within the OC model are determined based on the static stiffness measurement of the OC (Naidu and Mountain, 1998). The frequency characteristics of the fast and slow waves are then predicted so as to fit the numerically obtained distribution of the intracochlear pressure with the experimentally obtained one (Olson, 2001).

II. MODEL

A. Geometry

The amplitude of the BM vibration in the gerbil cochlea is approximately 5 nm when a pure tone of 80 dB SPL is applied to the ear canal (Ren, 2002). Due to this tiny vibration amplitude and the longitudinally extending structure of the OC, it is assumed that the cross section of the OC main-

a)Electronic mail: wada@cc.mech.tohoku.ac.jp

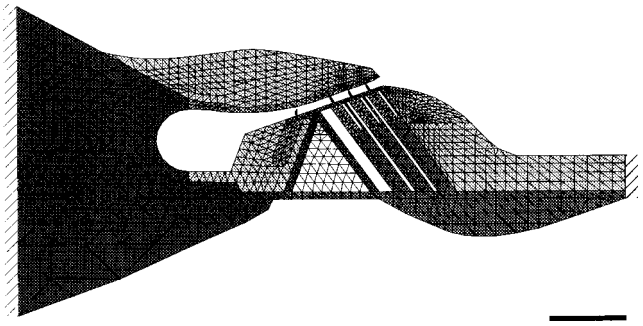

FIG. 1. Model of the organ of Corti discretized with finite elements. The number of nodes is 1274 and the number of elements is 2139. Each shade of gray in the model indicates the portion which has the same mechanical property. Scale bar represents 50 μm.

tains its plane surface when external force is applied. The two-dimensional OC model was therefore constructed under the plane strain condition. The OC at the basal turn of the gerbil cochlea, located 2.5–3.0 mm from the base, is modeled as shown in Fig. 1. The characteristic frequency (CF) of the OC at this location is approximately 16 kHz. Right and left boundaries of the OC model were fixed. Table I indicates geometric parameters of the OC model which are determined based on measurement in the hemicochlea of the gerbil (Edge *et al.*, 1998). Meshing is done at a subcellular level using a triangular element, by which the number of nodes and elements are 1274 and 2139, respectively. The fluid within the Corti tunnel is treated as an elastic body without shear stiffness. Although there is no element in the sub-tectorial space, the viscous force is considered analytically on the assumption that Couette flow occurs in this space. The effect of the mass of the fluid in the sub-tectorial space is assumed to be negligible, because the volume of this space is inconsiderable in comparison with that of the SV.

To simulate the behavior of the lymph fluid and its interaction with the OC, models of the lymph fluid in the SV and the ST are constructed as shown in Figs. 2(a) and (b), respectively. As Reissner's membrane is extremely compliant, it is considered to have little influence on the dynamic behavior of the lymph fluid. Reissner's membrane was, therefore, omitted and the SM was considered to be a part of the SV. The dark area of each model corresponds to the OC. As the lymph fluid in the scalae is assumed to move not only in the radial and transversal directions but also in the longitudinal direction, three-dimensional fluid models were, therefore, constructed. The dynamic behavior of the local section of the OC, which extends in the longitudinal direction, was

TABLE I. Geometric parameters of the OC model. BM, TM, IPC, OPC, and RL are abbreviations for basilar membrane, tectorial membrane, inner pillar cell, outer pillar cell, and reticular lamina, respectively. RL/BM angle indicates an angle between the RL and BM (after Edge *et al.*, 1998).

BM width	170 μm
BM maximum thickness	35 μm
TM width	130 μm
TM maximum thickness	40 μm
OPC height	70 μm
IPC height	55 μm
RL/BM angle	20°

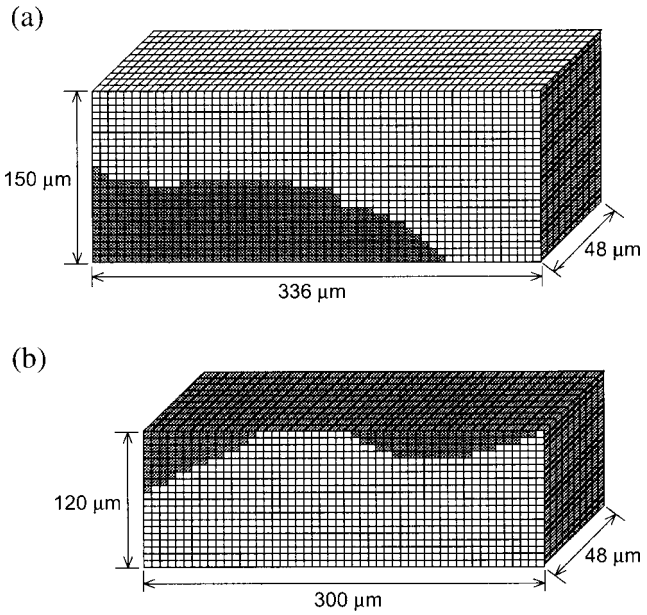

FIG. 2. Models of the lymph fluid. (a) Scala vestibuli. (b) Scala tympani. Dark area in each model corresponds to the OC.

simulated in this study, and thus longitudinal widths of both fluid models were determined to be 48 μm, which is less than one-fourth of the wavelength of the traveling wave (Ren, 2002). In consideration of the modiolus and the cochlear wall, the left and right boundaries of these models are fixed. The boundary of the SV model at 150 μm from the BM and that of the ST model at 120 μm from the BM are also fixed because it is assumed that the lymph fluid does not move across those boundaries. A grid with intervals of 6 μm makes it possible to evaluate the pressure distribution around the OC in the scalae. As a result, the SV model and the ST model have 11 200 and 8000 cubic elements, respectively.

B. Mechanical properties

Young's moduli of individual portions in the model are based on measurements *in vitro* and *in situ*. Young's modulus assigned to the model is 3.0×10^4 N/m^2 at the tectorial membrane (TM) (Steele *et al.*, 2000), 1.0×10^4 N/m^2 at the outer hair cells (OHCs) (Ulfendahl and Chen, 1998), 1.0×10^7 N/m^2 at the phalanxes (Laffon and Angelini, 1996), and 1.0×10^9 N/m^2 at the pillar cells (Tolomeo and Holley, 1997). Young's moduli of the inner hair cell (IHC) and Deiters' cells are assumed to be the same as those of the OHCs and the phalanxes, respectively. Young's moduli of Kimura's membrane and the reticular lamina (RL) are assumed to be 1.0×10^6 N/m^2 and 1.0×10^9 N/m^2, respectively, because these structures would be stiff enough to support adjacent structures. Young's modulus for the osseous spiral lamina is assumed to be 2×10^{10} N/m^3, which is the same value as that of the cortical bone (Ashman *et al.*, 1984), because both of them are composed of bony material. Young's modulus of the stereocilia and its stiffness relative to the tip displacement are assumed to be 1.0×10^7 N/m^2 (Zetes and Steele, 1997) and 2.5×10^{-3} N/m (Langer *et al.*, 2001), respectively.

Although Young's moduli of the BM and Hensen's cell would have a profound effect on the dynamic behavior of the

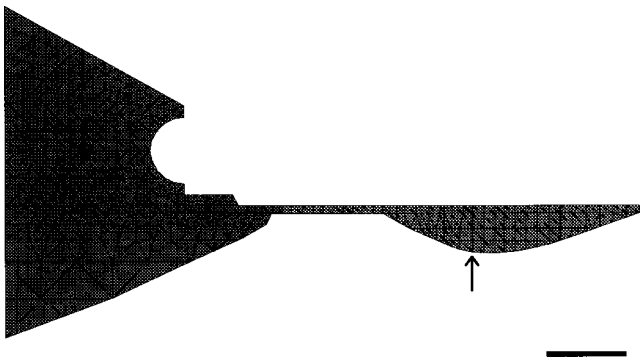

FIG. 3. Model of the BM. This model is a reduced representation of the OC model shown in Fig. 1. Using this model, the stiffness of the BM is calculated to determine the Young's modulus of the BM. The arrow indicates the point where the force is applied and the stiffness is evaluated.

OC, those of the gerbil have not been reported. To determine Young's moduli of these portions, the stiffness of the OC obtained by numerical analysis is compared with that of the gerbil measured by Naidu and Mountain (1998). According to their experiment, the stiffness of the OC is 2–4 N/m at a point beneath the OHCs when the OC at the basal turn is statically deflected. If the cells are removed from the BM, the stiffness of the BM is assumed to be 1.3–2.6 N/m at a point beneath the OHCs. Using the BM model shown in Fig. 3, which is a reduced representation of the OC model, Young's modulus of the BM is determined to be 1.0×10^7 N/m^2. Using the OC model shown in Fig. 1, Young's modulus of Hensen's cells is then determined to be 5.0×10^3 N/m^2.

The Poisson's ratio of soft cells and the TM, which is composed of an extracellular matrix, is assumed to be 0.49 because these portions are nearly incompressible, whereas those of hard cells and the osseous spiral lamina are assumed to be 0.3 because this value is commonly used in structure analysis.

To guide the eye, the OC model shown in Fig. 1 is colored with shades of gray, a different shade being used for each portion having the same mechanical properties. For the lymph fluid models shown in Figs. 2(a) and (b), mechanical properties are assumed to be the same as those of water. Table II shows all mechanical properties of the models.

TABLE II. Mechanical properties assigned to the OC and fluid models.

	Young's modulus (N/m^2)	Poisson's ratio
BM	1.0×10^7	0.3
Deiters' cell	1.0×10^7	0.3
Hensen's cell	5.0×10^3	0.49
Inner hair cell	1.0×10^4	0.49
Kimura's membrane	1.0×10^6	0.3
Osseous spiral lamina	2.0×10^{10}	0.3
OHC	1.0×10^4	0.49
Phalanx	1.0×10^7	0.3
Pillar cell	1.0×10^9	0.3
RL	1.0×10^9	0.3
Stereocilia	1.0×10^7	0.3
TM	3.0×10^4	0.49

The density and viscosity of the lymph fluid are 1.0×10^3 kg/m^3 and 1.0×10^{-3} Pa·s, respectively, which are equal to those of water.

C. Formulation

In the OC model, it is assumed that the cross section of the OC maintains its plane surface when external force is applied to the OC. Therefore, the model of the OC is formulated under the plane strain condition. The equation of the motion of the structure by the finite-element process is represented by the following matrix differential equation:

$$[\mathrm{M}]\frac{\partial^2\mathbf{u}_\mathrm{s}}{\partial t^2}+[\mathrm{C}]\frac{\partial\mathbf{u}_\mathrm{s}}{\partial t}+[\mathrm{K}]\mathbf{u}_\mathrm{s}=\mathbf{f}, \tag{1}$$

where [M], [C], and [K] are the mass, damping, and stiffness matrices, respectively, $\mathbf{u}_\mathrm{s}$ is the structural displacement vector, $\mathbf{f}$ is the force vector, and t is the time. The damping matrix [C] is derived from the linear combination of mass and stiffness matrices, i.e.,

$$[\mathrm{C}]=\alpha[\mathrm{M}]+\beta[\mathrm{K}], \tag{2}$$

where α and β are Rayleigh damping parameters. In the Newmark-β method (Newmark, 1959), the displacement vector at the end of a time interval can be expressed in terms of the displacement, velocity and acceleration vectors at the beginning of the interval as follows:

$$\left([\mathrm{K}]+\frac{2}{\delta t}[\mathrm{C}]+\frac{4}{(\delta t)^2}[\mathrm{M}]\right)\mathbf{u}_\mathrm{s}^{n+1}$$
$$=\mathbf{f}^{n+1}+[\mathrm{M}]\left(\frac{\partial^2\mathbf{u}_\mathrm{s}^n}{\partial t^2}+\frac{4}{\delta t}\frac{\partial\mathbf{u}_\mathrm{s}^n}{\partial t}+\frac{4}{(\delta t)^2}\mathbf{u}_\mathrm{s}^n\right)$$
$$+[\mathrm{C}]\left(\frac{\partial\mathbf{u}_\mathrm{s}^n}{\partial t}+\frac{2}{\delta t}\mathbf{u}_\mathrm{s}^n\right), \tag{3}$$

where δt is the time interval and n is the time step. The velocity and acceleration vectors at the end of a time interval can be expressed in terms of the velocity and acceleration vectors at the beginning of the time interval and the displacement vector at the end of the time interval by the relations

$$\frac{\partial\mathbf{u}_\mathrm{s}^{n+1}}{\partial t}=-\frac{\partial\mathbf{u}_\mathrm{s}^n}{\partial t}+\frac{2}{\delta t}(\mathbf{u}_\mathrm{s}^{n+1}-\mathbf{u}_\mathrm{s}^n), \tag{4}$$

$$\frac{\partial^2\mathbf{u}_\mathrm{s}^{n+1}}{\partial t^2}=-\frac{\partial^2\mathbf{u}_\mathrm{s}^n}{\partial t^2}-\frac{4}{\delta t}\frac{\partial\mathbf{u}_\mathrm{s}^n}{\partial t}+\frac{4}{(\delta t)^2}(\mathbf{u}_\mathrm{s}^{n+1}-\mathbf{u}_\mathrm{s}^n). \tag{5}$$

Using Eqs. (3)–(5), values of the vectors at time step $n+1$ can be obtained from the previously determined values of the vectors and the known value of the force vector.

Regarding the lymph fluid, the Reynolds number (Re) of fluid flow is defined as

$$\mathrm{Re}=\frac{\rho\mathrm{UL}}{\mu}, \tag{6}$$

where U is the approximate maximum fluid velocity in the vicinity of the BM, L is the length of the BM, ρ is the density of water (1×10^3 kg/m^3), and μ is the viscosity of water (1×10^{-3} Pa·s). As characteristic values are U=1 mm/s estimated from experimental data (Olson, 2001) and L=170 μm, Re becomes 0.17. In this range of Reynolds number, an incompressible and viscous flow can be assumed, and thus

an incompressible Navier–Stokes equation is used to analyze the dynamic behavior of the lymph fluid. The incompressible Navier–Stokes equation is as follows:

$$\frac{\partial \mathbf{v}_f}{\partial t} + (\mathbf{v}_f \cdot \nabla)\mathbf{v}_f + \frac{1}{\rho}\nabla p_{OC} - v\Delta \mathbf{v}_f = 0, \tag{7}$$

where $\mathbf{v}_f$ is the fluid velocity vector, p_{OC} is the fluid pressure caused by the OC motion, v is the kinetic viscosity of the fluid, t is the time, and the gradient operator ∇ and the Laplacian operator Δ are defined in the following form

$$\nabla = \left(\frac{\partial}{\partial x}, \frac{\partial}{\partial y}, \frac{\partial}{\partial z}\right), \quad \Delta = \frac{\partial^2}{\partial x^2} + \frac{\partial^2}{\partial y^2} + \frac{\partial^2}{\partial z^2}. \tag{8}$$

Using a Marker-and-Cell (MAC) method (Harlow and Welch, 1965), the fluid is decomposed into rectangular parallelepiped cells and the pressure is discretized at the center of the cell. Discretizing the diffusion term and convection term explicitly and the pressure term implicitly in Eq. (7), the discrete Navier–Stokes equation is derived as follows:

$$\frac{\mathbf{v}_f^{n+1} - \mathbf{v}_f^n}{\delta t} + (\mathbf{v}_f^n \cdot \nabla)\mathbf{v}_f^n + \frac{1}{\rho}\nabla p_{OC}^{n+1} - v\Delta \mathbf{v}_f^n = 0, \tag{9}$$

where δt is the time interval and n is the time step. Rewriting Eq. (9) leads to

$$\mathbf{v}_f^{n+1} = \mathbf{v}_f^n - \delta t\left\{(\mathbf{v}_f^n \cdot \nabla)\mathbf{v}_f^n + \frac{1}{\rho}\nabla p_{OC}^{n+1} - v\Delta \mathbf{v}_f^n\right\}. \tag{10}$$

Considering the divergence of Eq. (10) leads to

$$\nabla \cdot \mathbf{v}_f^{n+1} = \nabla \cdot \mathbf{v}_f^n - \delta t \nabla \cdot \left\{(\mathbf{v}_f^n \cdot \nabla)\mathbf{v}_f^n + \frac{1}{\rho}\nabla p_{OC}^{n+1} - v\Delta \mathbf{v}_f^n\right\}. \tag{11}$$

Following the continuity equation of fluid, $\nabla \cdot \mathbf{v}_f^{n+1} = 0$. By contrast, to reduce numerical error, the first term of the right side $\nabla \cdot \mathbf{v}_f^n$ is allowed to remain. As a consequence, Eq. (11) becomes

$$\Delta p_{OC}^{n+1} = \rho\left[\frac{1}{\delta t}\nabla \cdot \mathbf{v}_f^n - \nabla \cdot \{(\mathbf{v}_f^n \cdot \nabla)\mathbf{v}_f^n - v\Delta \mathbf{v}_f^n\}\right]. \tag{12}$$

Substituting the known value of fluid velocity vector $\mathbf{v}_f^n$ into Eq. (12), p_{OC}^{n+1} can be obtained, and then $\mathbf{v}_f^{n+1}$ is obtainable from Eq. (10).

In this study, as a structural model (OC) and a fluid model (lymph fluid) are constructed separately, the fluid–structure interaction between the model of the OC and that of the lymph fluid is considered by applying a staggered approach. As shown in Fig. 4, the procedure for coupling the fluid and structure equations is as follows: In time step $n = 1$, by multiplying the initial pressure p_{INT}^1, which is a summation of the fast and slow waves, with the area of the fluid–structure (F-S) interface of the OC model, the force vector $\mathbf{f}^1$ over the F-S interface of the OC model is obtained. Applying the force vector $\mathbf{f}^1$ to Eq. (3), the displacement vector $\mathbf{u}_s^1$ can be obtained, and then substituting it into Eq. (4), the velocity vector $\partial \mathbf{u}_s^1/\partial t$ is obtainable. Assuming $\partial \mathbf{u}_s^1/\partial t = \mathbf{v}_f^0$ at the F-S interface, the fluid pressure p_{OC}^1 caused by the OC motion is

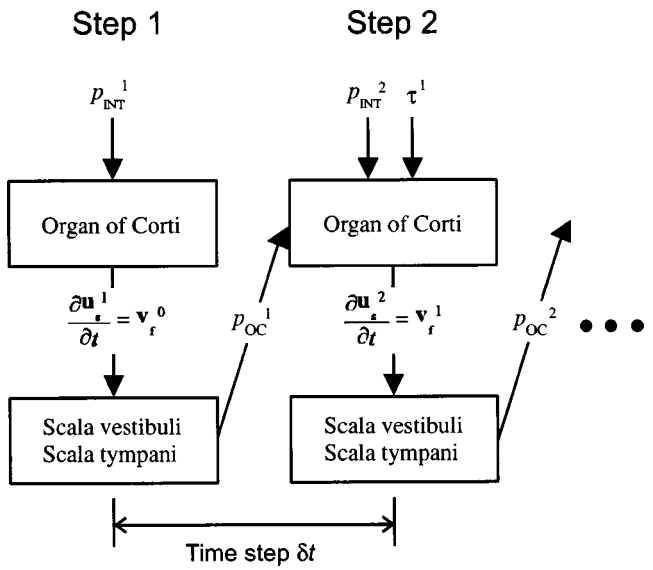

FIG. 4. Scheme of the fluid–structure interaction using the staggered approach. In time Step 1, initial pressure p_{INT}^1 caused by the fast and slow waves is applied to the equations of the OC [Eqs. (3) and (4)] and the velocity of the OC $\partial \mathbf{u}_s^1/\partial t$ is obtained. Then, applying this velocity $\partial \mathbf{u}_s^1/\partial t$ to the equation of the lymph fluid [Eq. (12)] as a fluid velocity $\mathbf{v}_f^0$ over a fluid–structure interface, the fluid pressure p_{OC}^1 in each scala caused by the movement of the OC is obtained at the same time step. In Step 2, this obtained fluid pressure p_{OC}^1, the initial pressure p_{INT}^2 in time Step 2 and shear stress $\boldsymbol{\tau}^1$ exerted on the TM and RL are applied to the equation of the OC. By repeating the above procedure, the time history of the movement of the OC and that of the pressure distribution in each scala are obtained.

obtainable by Eq. (12). In time step $n = 2$, assuming Couette flow in the sub-tectorial space, the shear stress vector $\boldsymbol{\tau}^1$ exerted on the TM and the RL is given by

$$\boldsymbol{\tau}^1 = \mu \frac{\mathbf{v}_{RELATIVE}^1}{2h}, \tag{13}$$

where $\mathbf{v}_{RELATIVE}^1$ is the relative velocity vector between the TM and RL, h is the clearance between the TM and the RL. Multiplying the shear stress vector $\boldsymbol{\tau}^1$ in the sub-tectorial space by areas of the TM and RL, and multiplying the previously obtained fluid pressure p_{OC}^1 and the initial pressure p_{INT}^2 in time step $n = 2$ by the area of the F-S interface, the force vector $\mathbf{f}^2$ in time step $n = 2$ is obtained. This obtained force vector $\mathbf{f}^2$ is applied to Eq. (3). By repeating the above procedure, the time history of the movement of the OC and that of the pressure distribution in each scala are obtained. In this study, the passive cochlea is assumed. Therefore, the force generated by the OHC motility is not taken into account. As mentioned in the Introduction, when numerical calculations are carried out, it is assumed that the fast wave is uniform over the cross-sections of both scalae, and the slow wave is applied to the F-S interface of the OC model and has equal magnitude with opposite phases at either side of the BM.

Numerical calculations are performed on a COMPAQ DS-20E using a 64-bit floating point number representation. Calculation is executed for four cycles for each sinusoidal frequency and took 2 hours.

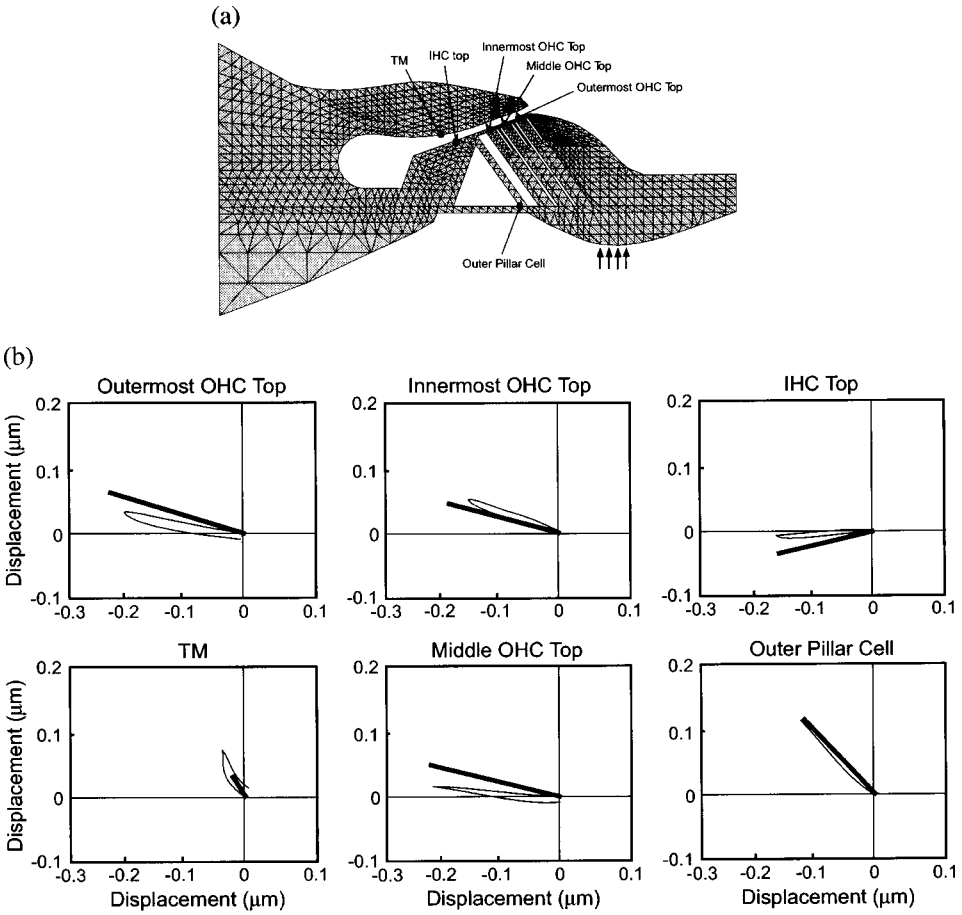

FIG. 5. Trajectories of cochlear structures. (a) Points of measurement when a sinusoidal force of 2.0 Hz and 1.0×10^{-6} N is applied to the bottom of the BM (arrows), such force being similar to the experiment using the hemicochlea. (b) Trajectories of each point within the OC. The horizontal axis is parallel to the BM, and the vertical axis is perpendicular to the BM. Thin lines are the experimental results (Hu *et al.*, 1999) and thick lines are the numerical results.

III. VALIDATION OF THE MODEL: STATIC DISPLACEMENT

When a sinusoidal force of 2.0 Hz and 1.0×10^{-6} N is applied to the bottom of the BM, the amplitude and angle of the each point within the OC model is calculated. This stimulation is equivalent to that of the hemicochlea experiment (Hu *et al.*, 1999), i.e., the application of oscillatory force via a glass paddle. Experimentally obtained trajectories of each measurement point [points in Fig. 5(a)] and those of numerical results are shown by thin and thick lines in Fig. 5(b), respectively.

A comparison between numerical and experimental results reveals that the numerically obtained amplitude and angle at the innermost OHC and outer pillar cell are nearly the same as those obtained by the experiment. However, angles of the outermost OHC top, middle OHC top, and IHC top differ from the experimental values by 7.5° at the outermost OHC top, 10.2° at the middle OHC top, and 11.1° at the IHC top. These discrepancies would result because the angle between the RL and the BM of the model is different from that in the hemicochlea. From the above-mentioned comparison, it is confirmed that the mechanical properties of the model are appropriate.

IV. PREDICTION OF THE CHARACTERISTICS OF THE FAST AND SLOW WAVES

The procedure for predicting the frequency characteristics of the fast and slow waves, which are initial pressures applied to the OC model, is as follows: First, the frequency characteristics of the fast wave in the SV ($P_{\text{fast-SV}}$) are estimated by an analytical method. Second, taking account of the experimentally obtained fluid pressure in the ST (Olson, 2001), the frequency characteristics of the fast wave in the

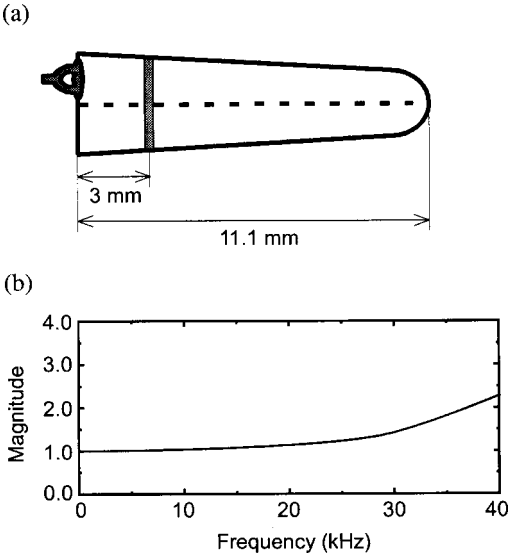

FIG. 6. Frequency response of the fast wave at 3 mm from the base in the gerbil cochlea. (a) Schema of the cochlea and the site where the model is constructed. The total length of the gerbil cochlea is 11.1 mm and the OC at 3 mm from the base (shaded area) is modeled. (b) Magnitude of the fast wave as a function of frequency which is derived from Eq. (14). Magnitude is relative to the sound pressure at the base.

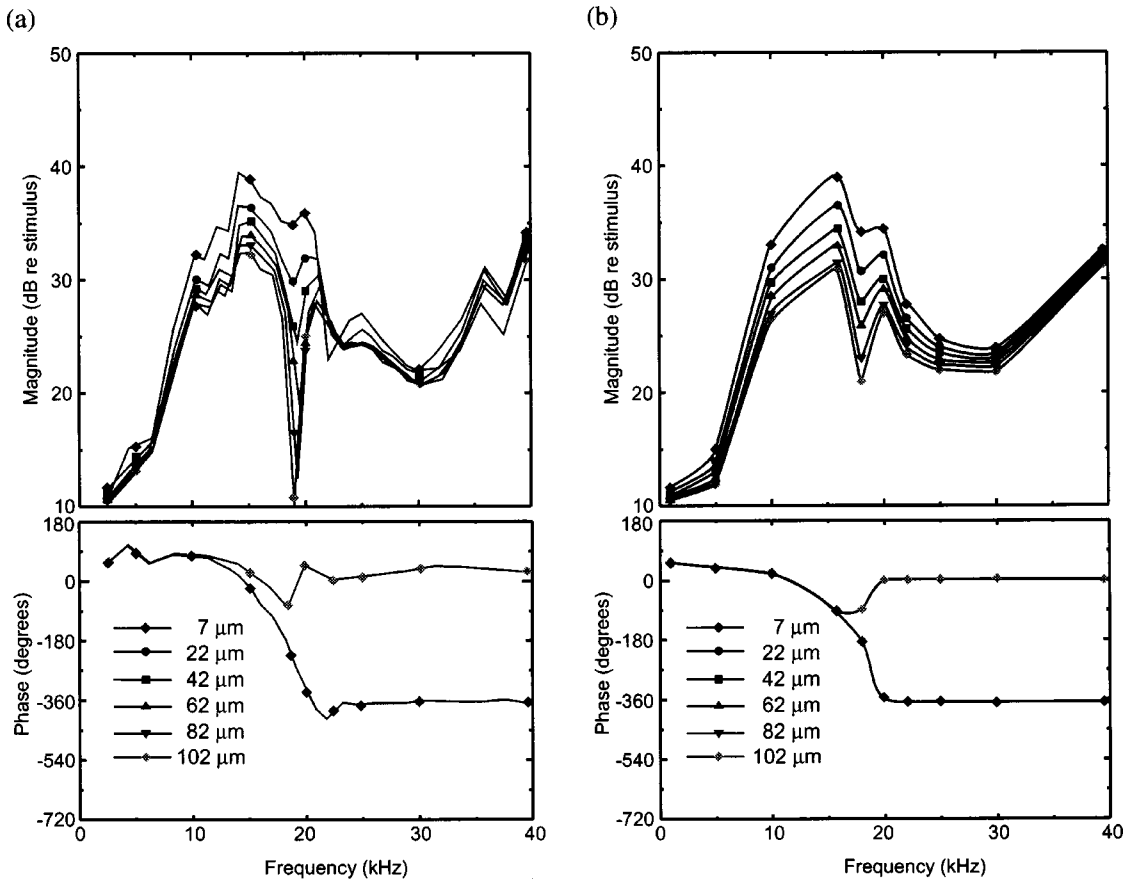

FIG. 7. Magnitude and phase of the fluid pressure in the ST versus frequency when a pure tone of 80 dB SPL is applied to the ear canal. The key indicates the distance from the BM. (a) Experimental data from the basal turn where the CF is about 16 kHz [Olson's Figs. 7(c) and (d) 2001]. (b) Numerical results. Magnitude is relative to the stimulus level in the ear canal. Phase is relative to the pressure near the stapes.

ST ($P_{fast\text{-}ST}$) are estimated. Finally, by comparing these experimental data with the numerical results, the frequency characteristics of the slow wave (P_{slow}) are estimated.

When it is assumed that the cochlea is a tapered closed tube, i.e., the cross-sectional area of the cochlea becomes smaller towards the apex, the magnitude of the fast wave $f(x)$ can be described as follows (Lighthill, 1981):

$$f(x)=f(0)\{J_0[\omega c_0^{-1}(L-x)]\}/\{J_0(\omega c_0^{-1}L)\}, \qquad (14)$$

where $f(0)$ is the magnitude of the fast wave at the base, L is a length of the cochlea, x is the distance from the base, J_0 is the first zero of the Bessel function, ω is the angular frequency, and c_0 is the velocity of sound in water. In this study, the length of the cochlea L is set to be 11.1 mm (Müller, 1996). Figure 6(a) is a schema of the gerbil cochlea indicating the location for which the model is constructed, and Fig. 6(b) shows the magnitude of $f(x)$ relative to $f(0)$ as a function of frequency in the gerbil cochlea at $x=3$ mm. The magnitude of the fast wave increases with increasing frequency and quarter-wavelength resonance occurs at 48 kHz. The frequency characteristics of $P_{fast\text{-}SV}$ are estimated as follows:

(1) The fluid pressure in the vicinity of the stapes is estimated to be 105 dB SPL when the sound stimulus of 80 dB SPL is applied to the ear canal due to the gain of 25 dB in the middle ear. Therefore, it is estimated that the magnitude of $P_{fast\text{-}SV}$ is 105 dB SPL at 1 kHz and increases gradually with increasing frequency and reaches 112 dB SPL at 40 kHz in accordance with Eq. (14).

(2) The phase difference of $P_{fast\text{-}SV}$ relative to the pressure near the stapes is zero for the entire frequency range because the footplate of the stapes is connected to the basal end of the SV and a fast wave propagates at the velocity of sound.

Figure 7(a) shows the experimental data on the fluid pressure in the ST in the basal turn of the gerbil cochlea when a pure tone of 80 dB SPL is applied to the ear canal (Olson, 2001). In that experiment, advancing and retracting the pressure sensor to and from the BM while keeping it perpendicular to the BM, the fluid pressures in the ST were measured at intervals of approximately 20 μm. The base point of the distance from the BM was determined by touching the BM with the sensor. The post-mortem data were changed very little from the pre-mortem one at 80 dB SPL in that experiment, so the pre-mortem data are comparable to our numerical results obtained from the model in which the force generated by the OHC motility is not included. Taking these experimental data into account, the frequency characteristics of $P_{fast\text{-}ST}$ are estimated as follows and as shown in Fig. 7(b):

(3) In the experimental data, the difference of the magnitude of the fluid pressure between nearest-neighbor mea-

suring points for a certain frequency becomes small with increasing distance from the BM, except for frequencies close to the CF of 16 kHz. Because P_{slow} exists in the vicinity of the BM in contrast to $P_{fast\text{-}ST}$ which is uniform in the ST, this behavior implies that the magnitude of P_{slow} does not have a significant effect on the pressure at points far from the BM, i.e., $P_{fast\text{-}ST}$ is dominant. Therefore, from the experimental data at 120 μm from the BM, it is estimated that the magnitude of $P_{fast\text{-}ST}$ is 90 dB SPL at 1 kHz, 93 dB SPL at 5 kHz, 102 dB SPL at 30 kHz, and 111 dB SPL at 40 kHz. The magnitudes of $P_{fast\text{-}ST}$ between 5 and 30 kHz are estimated using linear interpolation.

(4) The phase difference of $P_{fast\text{-}ST}$ relative to the pressure near the stapes is estimated based on the experimental data at 102 μm from the BM, i.e., 60° below 10 kHz and 0° above 16 kHz. This phase advance below 10 kHz can be explained as being due to the damping of the OC (Olson, 2001). The OC is between the SV and ST, and the damping of the OC causes the phase advance of $P_{fast\text{-}ST}$ relative to $P_{fast\text{-}SV}$.

On the other hand, as P_{slow} is regarded as being fluid pressure propagation caused by the fluid flux in the vicinity of the BM, the frequency responses of P_{slow} are similar to those of the traveling wave on the BM. It is widely accepted that the magnitude of the traveling wave increases with increasing frequency up to the CF, and then decays sharply. Therefore, the frequency characteristics of P_{slow} are assumed to be as follows:

(5) The phase delay of the traveling wave is assumed to originate at 1 kHz. And then, following the experimentally obtained phase difference of the fluid pressure at 7 μm from the BM, where P_{slow} is dominant, it is estimated that the phase difference of P_{slow} is $-180°$ at 18 kHz, resulting in destructive interference with $P_{fast\text{-}ST}$ which is observed as a pressure notch in the experimental data. Above 25 kHz, the phase of P_{slow} cannot be estimated because the fast wave dominates the pressure distribution in the cochlea, so that it is considered to be a constant $-360°$ according to the experimental data. Therefore, the phase differences of P_{slow} over the entire frequency range are estimated as shown in Fig. 8(b) using cubic interpolation.

(6) Applying the magnitude and phase of $P_{fast\text{-}SV}$ and $P_{fast\text{-}ST}$ and the phase of P_{slow} to the model, the magnitude of P_{slow} is estimated so as to fit the pressure distribution in the ST obtained by our numerical analysis with that of the experimental data. The stapes vibration at the base of the cochlea generates $P_{fast\text{-}SV}$. At the same time, the BM is vibrated by the stapes vibration via lymph fluid, resulting in a traveling wave on the BM, i.e., P_{slow}. Therefore, the magnitudes of $P_{fast\text{-}SV}$ and P_{slow} are assumed to be the same at the base (Lighthill, 1981). The magnitude of the traveling wave is known to increase as a function of frequency till the stimulus frequency reaches the CF; however, its increase is quite small well below the CF (Ren and Nuttall, 2001). Therefore, at 1 kHz, it is assumed that the magnitude of P_{slow} at 3 mm from the base is the same as that at the base, because 1 kHz is substantially small relative to the CF (16 kHz). $P_{fast\text{-}SV}$ is nearly the same over the entire length of the cochlea except around the quarter-wavelength resonance (48 kHz). As a consequence, at 1 kHz and 3 mm from the base where the model is constructed, it is assumed that the magnitude of P_{slow} has the same value as that of $P_{fast\text{-}SV}$. The magnitude of P_{slow} gradually increases with increasing frequency and reaches a maximum of 125 dB SPL at the CF. The magnitude of P_{slow} is followed by 122 dB SPL at 18 kHz and 110 dB SPL at 22 kHz. Above 25 kHz, the magnitude of P_{slow} is calculated to be 70 dB SPL, a limit beyond which the pressure in the ST at 7 μm from the BM changes more than 1 dB.

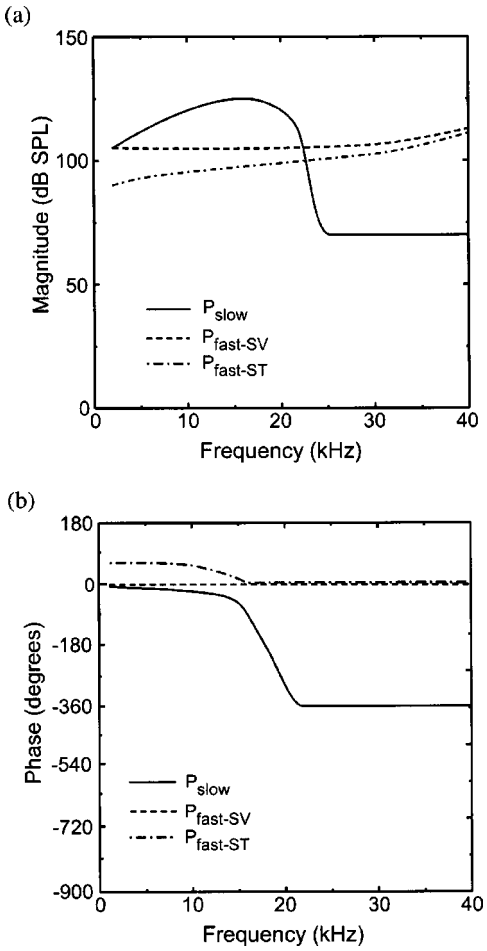

FIG. 8. Numerically obtained frequency characteristics of the slow wave, the fast waves in the SV and the ST when the magnitude and phase of the fluid pressure in the ST are shown in Fig. 7(b). The slow wave is applied to the F-S interface of the OC model and the fast waves are applied to the fluid models uniformly. (a) Magnitude. (b) Phase. Above 25 kHz, the magnitude of P_{slow} is calculated to be 70 dB SPL, a limit beyond which the pressure in the ST at 7 μm from the BM changes more than 1 dB, and the phase of P_{slow} is considered to be a constant $-360°$.

Figure 7(b) shows the numerically obtained pressure distribution in the ST when these predicted pressure waves, which are shown in Figs. 8(a) and (b), are applied to the model. The pressure peak at 16 kHz, the pressure notch at 18 kHz, the pressure increase from 30 kHz, and the phase of pressure relative to the pressure near the stapes are consistent with those of the experimental data. However, the depth and sharpness of the pressure notch at 18 kHz are different. The reason for this discrepancy might be the difference between the boundary condition in the model of the ST and the actual situation in the real cochlea at 120 μm from the BM. Con-

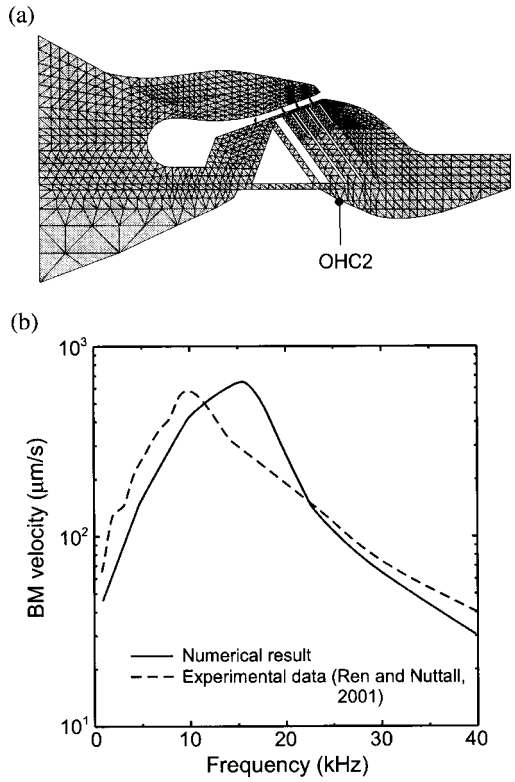

FIG. 9. Velocities of the basilar membrane when a pure tone of 80 dB SPL is applied to the ear canal. (a) Velocity measurement point on the BM. OHC2 is the abbreviation for the OHC of the second row. (b) Numerically obtained velocity of the BM and the experimental one (Ren and Nuttall, 2001) at the position which is indicated in (a). The CF of the model and best frequency of the experiment are 16 and 10 kHz, respectively.

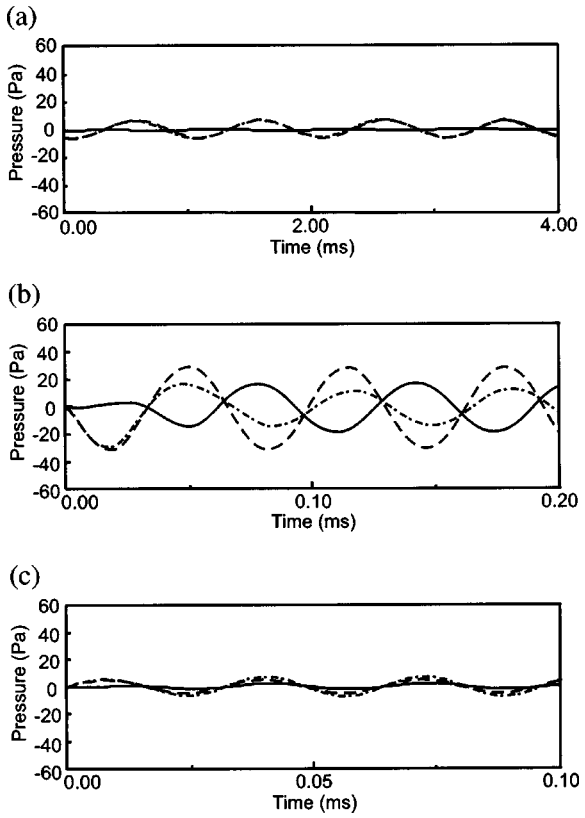

FIG. 10. Time courses of the pressure in the ST at 7 μm from the BM when pressure waves determined in Sec. IV are applied to the model. Three types of pressures are shown in each graph, i.e., the initial pressure which is a summation of the fast and slow waves (dashed line), the pressure caused by the vibration of the OC (solid line), and the resulting pressures including the fluid–structure interaction (dot–dashed line). (a) f=1 kHz. (b) f=16 kHz. (c) f=30 kHz.

sequently, it can be said that the magnitude and phase of the fast and slow waves are appropriately predicted for the most part.

V. VELOCITY OF THE BM AS A FUNCTION OF FREQUENCY

To confirm the validity of the model, the velocity of the BM obtained by the model is compared with that of the experimental data. Using a laser interferometer microscope, Ren and Nuttall (2001) measured the velocity the BM at the basal turn of the gerbil cochlea as a function of frequency. As the force generated by the OHC motility is not included in the model, the post-mortem BM velocity in their study is compared with the numerically obtained velocity of the BM. The best frequency, where the BM velocity takes a maximum, at the location of the measurement is approximately 10 kHz, although the CF of the model is 16 kHz. The distance between the location for the CF of 10 kHz and that of 16 kHz is approximately 7% of the entire length of the BM (Müller, 1996). Moreover, Allen and Sondhi (1979) calculated the frequency response of the velocity of the BM vibration at different locations along the BM, and showed nearly the same shapes of the frequency response at locations corresponding to the CF of 10 and 20 kHz. For these reasons, a comparison between the experimental data and the numerical result is acceptable.

The velocity of the BM is analyzed at the radial position of the second row of OHCs indicated in Fig. 9(a), where the laser beam is focused on the BM in the experiment. Figure 9(b) shows a comparison between the numerically obtained velocity of the BM and experimental one as a function of frequency. Although the frequency where the BM velocity has a maximum value is different, namely, 16 kHz in the model and 10 kHz in the measurement, the shape of the numerical result is similar to that of the experimental data. Therefore, the predicted pressure waves appear to be somewhat reliable. Moreover, it is found that although a pressure notch occurs at 18 kHz as shown in Fig. 7(b), there is no drastic change in the frequency response of the BM vibration.

VI. EFFECT OF THE FLUID–STRUCUTRE INTERACTION

To confirm the effect of the fluid–structure interaction in the model, the time courses of each pressure at 7 μm from the BM in the ST are depicted. In Fig. 10, the dashed line indicates the initial pressure which is a summation of the fast and slow waves, the solid line indicates the pressure caused by the vibration of the OC and the dot-dashed line indicates the resulting pressure including the F-S interaction, i.e., a summation of the two above-mentioned pressures.

At 16 kHz, which is the CF of the model, the pressure caused by the OC vibration is comparable to the initial pressure in magnitude (approximately 40%), and their phases are

opposite. Therefore, the resulting pressure is significantly influenced by the pressure caused by the OC vibration. On the other hand, at 1 and 30 kHz, which are well below or above the CF, the resulting pressure is nearly the same as the initial pressure because the pressure caused by the OC vibration is small relative to the initial pressure. The above-mentioned considerations ensure that the fluid–structure interaction considerably influences the response of the model at frequencies close to the CF. Moreover, by employing time course representation of the pressure in the ST, it is found that pressure fluctuation in the ST reaches a steady state within one cycle at 16 kHz. This is clearly shown in Fig. 10(b).

VII. CONCLUSIONS

A fluid–structure interaction model of the OC is constructed by coupling the two-dimensional OC model and three-dimensional fluid models, and unknown mechanical properties of the model are validated with the experimental results of trajectories within the OC in the hemicochlea. By comparison between numerical results and those of intracochlear pressure measurement, the magnitude and phase of the fast and slow waves are predicted. The frequency response of the BM is then simulated. Conclusions are as follows:

(1) When a pure tone of 80 dB SPL is applied to the ear canal, the magnitude of the fast wave in the SV, which is 105 dB SPL at 1 kHz, increases with increasing frequency and reaches 112 dB SPL at 40 kHz. The phase of the fast wave in the SV is 0° for the entire frequency range. The magnitude of the fast wave in the ST also increases with increasing frequency, but the magnitude in the ST is somewhat lower than that in the SV, i.e., 90 dB SPL at 1 kHz and 111 dB SPL at 40 kHz. The phase of the fast wave in the ST is 60° in the low frequency range and becomes 0° above the CF. The magnitude of the slow wave is the same as that of the fast wave in the SV at 1 kHz (105 dB SPL), and increases gradually with increasing frequency until it reaches a maximum of 125 dB SPL at the CF. It then falls sharply to 70 dB SPL. The phase of the slow wave starts at 0° and is significantly delayed near the CF and becomes −360° above the CF.

(2) It is found that although a pressure notch, which is caused by destructive interference between the fast wave and the slow wave in the ST, occurs in the ST pressure in the vicinity of the BM at 18 kHz, there is no drastic change in the frequency response of the BM vibration.

(3) The F-S interaction considerably influences the response of the OC at frequencies close to the CF.

(4) The pressure fluctuation in the ST seems to reach a steady state within one cycle.

ACKNOWLEDGMENTS

The authors thank Elizabeth S. Olson and Claus-Peter Richter for their comments which were useful in improving the model. This work was supported by a grant from the Human Frontier Science Program, by a Health and Labor Science Research Grant from the Ministry of Health, Labor and Welfare of Japan, by Grant-in-Aid for Scientific Research (B) (2) 13557142 and Grant-in-Aid for Scientific Research on Priority Areas 15086202 from the Ministry of Education, Culture, Sports, Science and Technology of Japan, and by the 21st Century COE Program Special Research Grant of the ''Future Medical Engineering Based on Bionanotechnology.''

Allen, J. B., and Sondhi, M. M. (**1979**). ''Cochlear Macromechanics Time Domain Solutions,'' J. Acoust. Soc. Am. **66**, 123–132.

Ashman, R. B., Cowin, S. C., Van Buskirk, W. C., and Rice, J. C. (**1984**). ''A continuous wave technique for the measurement of the elastic properties of cortical bone,'' J. Biomech. **17**, 349–361.

Edge, R. M., Evans, B. N., Pearce, M., Richter, C.-P., Hu, X., and Dallos, P. (**1998**). ''Morphology of the unfixed cochlea,'' Hear. Res. **124**, 1–16.

Harlow, F. H., and Welch, J. E. (**1965**). ''Numerical calculation of time-dependent viscous incompressible flow of fluid with free surface,'' Phys. Fluids **8**, 2182–2189.

Hu, X., Evans, B. N., and Dallos, P. (**1999**). ''Direct visualization of organ of Corti kinematics in a hemicochlea,'' J. Neurophysiol. **82**, 2798–2807.

Kolston, P. J., and Ashmore, J. F. (**1996**). ''Finite element micromechanical modeling of the cochlea in three dimensions,'' J. Acoust. Soc. Am. **99**, 455–467.

Laffon, E., and Angelini, E. (**1996**). ''On the Deiters cell contribution to the micromechanics of the organ of Corti,'' Hear. Res. **99**, 106–109.

Langer, M. G., Fink, S., Koitschev, A., Rexhausen, U., Hober, J. K. H., and Ruppersberg, J. P. (**2001**). ''Lateral mechanical coupling of stereocilia in cochlear hair bundles,'' Biophys. J. **80**, 2608–2621.

Lighthill, J. (**1981**). ''Energy flow in the cochlea,'' J. Fluid Mech. **106**, 149–213.

Müller, M. (**1996**). ''The cochlear place-frequency map of the adult and developing mongolian gerbil,'' Hear. Res. **94**, 148–156.

Naidu, R. C., and Mountain, D. C. (**1998**). ''Measurements of the stiffness map challenge a basic tenet of cochlear theories,'' Hear. Res. **124**, 124–131.

Newmark, N. M. (**1959**). ''A method of computation for structural dynamics,'' J. Eng. Mech. Div. **85**, 67–94.

Olson, E. S. (**1999**). ''Direct measurement of intra-cochlear pressure waves,'' Nature (London) **402**, 526–529.

Olson, E. S. (**2001**). ''Intracochlear pressure measurements related to cochlear tuning,'' J. Acoust. Soc. Am. **110**, 349–367.

Ren, T. (**2002**). ''Longitudinal pattern of basilar membrane vibration in the sensitive cochlea,'' Proc. Natl. Acad. Sci. U.S.A. **99**, 17101–17106.

Ren, T., and Nuttall, A. L. (**2001**). ''Basilar membrane vibration in the basal turn of the sensitive gerbil cochlea,'' Hear. Res. **151**, 48–60.

Steele, C. R., Baker, G., Tolomeo, J., and Zetes, D. (**2000**). ''Cochlear Mechanics,'' in *The Biomedical Engineering Handbook*, 2nd ed., edited by J. D. Bronzino (CRC Press, Boca Raton, FL), pp. 1–12.

Tolomeo, J. A., and Holley, M. C. (**1997**). ''Mechanics of microtubule bundles in pillar cells from the inner ear,'' Biophys. J. **73**, 2241–2247.

Ulfendahl, M., and Chen, E. (**1998**). ''Axial and transverse stiffness measures of cochlear outer hair cells suggest a common mechanical basis,'' Pfluegers Arch. **436**, 9–15.

Zetes, D. E., and Steele, C. R. (**1997**). ''Fluid–structure interaction of the stereocilia bundle in relation to mechanotransduction,'' J. Acoust. Soc. Am. **101**, 3593–3601.

A biophysical model of an inner hair cell[a)]

David G. Zeddies[b)]
Northwestern University Institute for Neuroscience and Hugh Knowles Center, Frances Searle Building, Northwestern University, Evanston, Illinois 60208-3550

Jonathan H. Siegel[c)]
Northwestern University Institute for Neuroscience, Communication Sciences and Disorders, Audiology and Hearing Sciences, Frances Searle Building, Northwestern University, Evanston, Illinois 60208-3550

(Received 2 July 2003; accepted for publication 5 April 2004)

Whole-cell patch-clamp recordings on isolated inner hair cells (IHCs) of guinea pig cochleae have revealed the presence of voltage-gated potassium channels. A biophysical model of an IHC is presented that indicates activation of slow voltage-gated potassium channels may lead to receptor potentials whose dc component decreases during the stimulus, and membrane potential hyperpolarizes when the stimulus is turned off. Both the decreasing dc and the hyperpolarization are, respectively, consistent with rapid adaptation and suppression of spontaneous rate in the auditory nerve. Receptor potentials recorded *in vivo* do not show these features, and when a nonspecific leak is included in the model to simulate microelectrode impalement, the model's receptor potentials become similar to those *in vivo*. The nonspecific leak creates an electrical shunt that masks slow channel activity and allows the cell to depolarize. Both the decreasing dc and the hyperpolarization are sensitive to the resting potential. Because the reported resting potentials *in vivo* and *in vitro* differ greatly, the model is used to investigate homeostatic mechanisms responsible for the resting potential. It is found that the voltage-gated potassium channels have the greatest influence on the resting potential, but that the standing transducer current may be sufficient to eliminate the decreasing dc and after-stimulus hyperpolarization. [DOI: 10.1121/1.1755237]

PACS numbers: 43.64.Bt, 43.64.Ld, 43.64.Wn [WPS] Pages: 426–441

I. INTRODUCTION

Receptor potentials recorded in guinea pig inner hair cells (IHCs) *in vivo* have a constant dc component throughout the response (Russell and Sellick, 1983; Cody and Russell, 1987) and show little, if any, evidence of voltage-gated ion channel activity (Russell and Sellick, 1983; Dallos, 1984). On the other hand, whole-cell patch-clamp recordings on isolated guinea pig IHCs clearly show voltage-gated ion channel activity (Kros and Crawford, 1990; Kros *et al.*, 1998; Raybould *et al.*, 2001). Kros and Crawford (1990) characterized two distinct populations of voltage-gated K^+ channels: one with extremely fast gating kinetics ($\tau<1$ ms) and the other with somewhat slower kinetics (2 ms$<\tau<$10 ms). Here, we create a biophysical model of an IHC, based primarily on Kros and Crawford's (1990) data, and show that the gating of the slower K^+ channels may cause the dc component of the receptor potential to decrease during the stimulus and the membrane potential to become hyperpolarized following the stimulus. Because the receptor potential drives the synapse, the decreasing dc and the hyperpolarization following the stimulus may contribute to the well-known auditory nerve phenomena adaptation and after-stimulus suppression of the spontaneous rate (see, e.g., Kiang *et al.*, 1965).

If the activity of the slow K^+ channels does contribute to auditory nerve phenomena then we must explain why ion channel activity is not evident in the receptor potentials recorded *in vivo*. To do so, we include a leak in the model to simulate the microelectrode impalement that occurs in the *in vivo* studies. We find that the leak appears to account for the differences, but we also find that multiple mechanisms may be operating. The most obvious is that the leak obscures the activity of the voltage-gated channels (i.e., shunting), but a less obvious mechanism is that the leak allows the cell to depolarize to a potential where the voltage-gated channels are activated and no longer affect the receptor potential in the same manner. Indeed, we find that the decreasing dc and after-stimulus hyperpolarization are very sensitive to the starting potential of the cell and therefore the resting potential could determine whether or not they occur.

Although the resting potential could be of great importance to the development of the receptor potentials, the actual resting potential of IHCs is not known. *In vivo* measurements place the IHC resting potential in the range of −30 to −40 mV (e.g., Cody and Russell, 1987; Dallos, 1985), whereas the resting potentials of guinea pig IHCs determined *in vitro* in patch-clamp experiments are closer to −60 mV (Kros and Crawford, 1990; Gitter and Zenner, 1990; and Dulon *et al.*, 1995). All of these experiments perturb mechanisms directly responsible for the resting potential. *In vitro*

[a)]Portions of this work were presented in "A physiologically based model of the inner hair cell," Midwinter Meeting of the Association for Research in Otolaryngology, St. Petersburg Beach, FL, February 1995, and "Influence of the basolateral membrane on the development of receptor potentials in a simulated inner hair cell," Midwinter Meeting of the Association for research in Otolaryngology, St. Petersburg Beach, FL, February 1996.

[b)]Current address: Center for Comparative and Evolutionary Biology of Hearing, University of Maryland, College Park, MD 20742.
[c)]Electronic mail: j-siegel@northwestern.edu

TABLE I. Electrochemical properties of cochlear fluids.

	V	K^+	Na^+	Cl^-
Endolymph (SM)	85 mV	160 mM	1 mM	130 mM
Perilymph (ST)	0	4	150	125
Intracellular	···	130	5	40

experiments remove the IHC from its native environment and the isolation process may damage transducer channels in the stereocilia. The isolated cells are kept in a bath of high $[Na^+]$ which does not reflect the *in vivo* state where the apical end of the cell is exposed to high $[K^+]$ and an electrical potential. Therefore the standing transducer current of an isolated IHC is expected to be quite different than it is *in vivo*; the magnitude is likely to be diminished and if the transducer channels are open they carry a much larger Na^+ current than they would *in vivo*. The whole-cell patch-clamp method itself can also affect the resting potential. The pipette filling solution diffuses into the cell and artificially sets the intracellular ionic concentrations (Marty and Neher, 1983). While the *in vivo* experiments are less likely to impair the transducer or disturb the cell's normal ionic environment, using sharp microelectrodes introduces a leak in the basolateral membrane that can depolarize the cell and run down the ionic gradients.

What is the likely resting potential *in vivo*? Owing to the nonlinear nature of the cellular components (transducer, voltage-gated channels, and Na^+/K^+ pumps) the effects of measuring the potential with microelectrodes cannot simply be subtracted out. For this reason a nonlinear biophysical model that can keep track of relevant currents and ionic concentrations was created to explore the interactions between mechanisms that influence the resting potential of the IHC.

II. METHODS

A. *In vivo* environment of IHCs

To model the IHC we must take into account its peculiar ionic environment (see Slepecky, 1996 for review). *In vivo*, the basolateral membrane of the cell is bathed in the cerebrospinal-like fluid (low $[K^+]$ and high $[Na^+]$), perilymph, that fills scala tympani. The apical end of the cell is exposed to the intracellular-like (high $[K^+]$ and low $[Na^+]$) endolymph of scala media. In addition to the ionic concentration differences there is also an electrical potential difference such that endolymph is about +85 mV relative to perilymph. This electrical potential is known as the endocochlear potential (EP). A number of studies have been conducted in efforts to measure the magnitude of the EP and to determine the ionic concentrations of mammalian endolymph and perilymph. The compiled results (Salt and Konishi, 1986) are listed in Table I.

Although the intracellular ionic concentrations in mammalian hair cells are not well established, there is some experimental evidence available for the K^+ gradient. Anniko, Lim, and Wroblewski (1984) report that the cytoplasmic K^+/Na^+ is 20:1 in IHCs that have been shock frozen and measured by x-ray microanalysis.

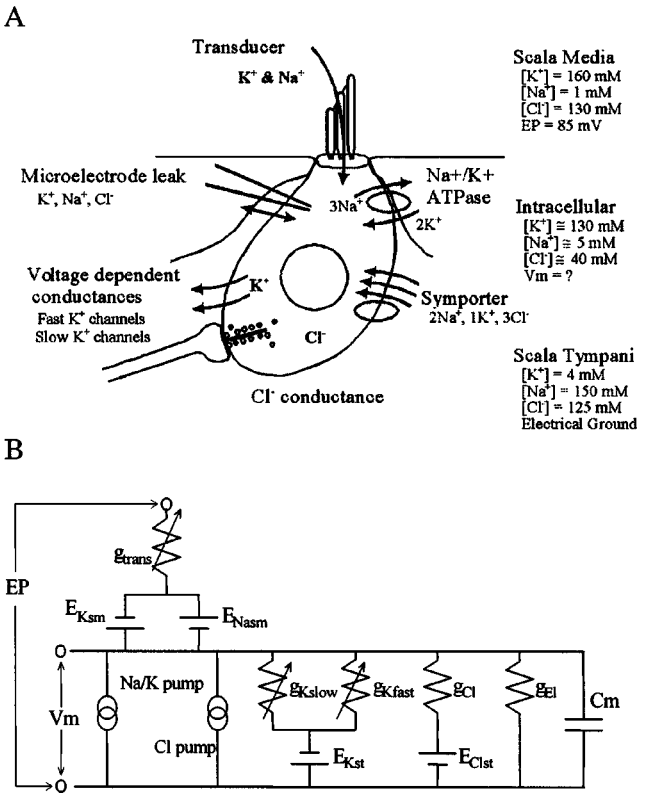

FIG. 1. (a) Cartoon version of the components of the model. (b) Schematic diagram illustrating the basic components of the model. g_{Trans}: conductance of the transducer, EP: endocochlear potential, g_{Leak}: Nonspecific leak conductance, V_m: hair cell membrane potential, g_{KFast}: fast voltage-gated K^+ channels, E_{TSM}: driving force for transducer, g_{KSlo}: slow voltage-gated K^+ channels, E_{KST}: potassium Nernst potential, g_{El}: Electrode leak conductance, C_m: Membrane capacitance.

B. Components of the model

Figure 1 shows the components of the model in cartoon form [Fig. 1(a)] and in circuit diagram form [Fig. 1(b)]. In the model, the endolymph and perilymph electrochemical properties remain constant while the intracellular components are allowed to vary. The starting Nernst potentials calculated with respect to scala media are $E_{\mathrm{Nasm}}=-43$ and $E_{\mathrm{Ksm}}=5$ mV, while the Nernst potentials with respect to scala tympani are $E_{\mathrm{Nast}}=91$, $E_{\mathrm{Kst}}=-93$, and $E_{\mathrm{Clst}}=-30$ mV. The model is designed to simulate an IHC at body temperature (37 °C).

C. Structure of the model

Kros and Crawford (1990) measured the capacitance of isolated guinea pig IHCs to be 9.6 ± 2 pF; we will use 10 pF in the model. By assuming a constant EP, the apical membrane capacitance due to the transducer can be combined with the basolateral membrane (e.g., Mountain and Hubbard, 1996) so that the capacitance used in the model is equal to the capacitance measured in an isolated cell. The cell membrane potential is proportional to the amount of charge on the cell's capacitance, and when current flows into or out of the cell the membrane potential changes. If the net current is known, the change in the membrane potential for a single time step can be calculated from,

$$\Delta V_m = I_{\text{net}} / C_m^* \delta t, \tag{1}$$

where ΔV_m is the change in the membrane potential, I_{net} is the net current, C_m is the membrane capacitance, and δt is the time step.

I_{net} itself changes as a function of V_m (see the following), which means that Eq. (1) is nonlinear and cannot be solved analytically. To determine V_m we use the simple numerical integration technique known as Euler's method. Initial conditions are chosen (including an initial V_m) and from these conditions an initial I_{net} is calculated (as described in the following). ΔV_m is then calculated for one time step and V_m incremented by ΔV_m (i.e., $V_m = V_m + \Delta V_m$). A new I_{net} is then calculated and the process is iterated for a specified length of time. Variables that change as a function of voltage or due to current flow (for example, the conductance of the voltage-gated channels, the current from the pumps, and Nernst potentials) are updated after each time step and V_m is tracked as the model develops in time. The time step used was 0.01 ms for simulated receptor potentials and 0.04 ms for longer simulations investigating homeostatic mechanisms. The model was implemented in the BASIC programming language on a Pentium 1 computer.

D. Defining driving forces, convention, and writing current equations

1. Basolateral membrane currents

The driving force for each ionic species (K^+, Na^+, and Cl^-) across the basolateral membrane is the difference between the membrane potential (V_m) and the Nernst potential for that ion calculated with respect to scala tympani concentrations (E_{Kst}, E_{Nast}, and E_{Clst}). Scala tympani is electrical ground, and in keeping with convention, we define positive current as cations leaving the cell. Thus, current across the basolateral membrane for an ion, X, can be written as $I_{\text{Xblm}} = g_x(V_m - E_x)$, in which $(V_m - E_x)$ is the driving force for the ion and g_x is the conductance to that ion.

2. Transducer currents

To calculate currents through the transducer, the EP must be included in the driving force and the Nernst potentials for K^+ and Na^+ (E_{Ksm} and E_{Nasm}) calculated with respect to scala media concentrations. Note that the transducer channels are cation selective (Corey and Hudspeth, 1979) so no chloride component is considered. The nominal current through the transducer for the cation, X, is written as $I_{\text{Xtr}} = g_{\text{tr}}(V_{\text{m}} - EP - E_{\text{Xsm}})$, where $(V_{\text{m}} - EP - E_{\text{Xsm}})$ is the driving force and g_{tr} is the transducer conductance. Na^+ accounts for only a small portion of the available cations in endolymph and presumably makes up only a small part of the transducer current (Ohmori, 1985). For this reason, we calculate the current carried by either K^+ or Na^+ to be equal to the nominal current multiplied by the fraction of the total that the ionic species represents,

$$I_{\text{Ktr}} = \frac{[K_{\text{sm}}]}{[K_{\text{sm}}] + [Na_{\text{sm}}]} g_{\text{tr}}(V_m - EP - E_{\text{Ksm}}), \tag{2}$$

$$I_{\text{Natr}} = \frac{[Na_{\text{sm}}]}{[K_{\text{sm}}] + [Na_{\text{sm}}]} g_{\text{tr}}(V_m - EP - E_{\text{Nasm}}). \tag{3}$$

E. Calculating I_{net} and net current for each ionic species

To calculate the membrane potential, V_m, we only need the net current through the cell, I_{net}, but to update intracellular ionic concentrations we keep track of each ionic species separately. The net current through the cell, I_{net}, is the sum of the current through the transducer and the current across the basolateral membrane, $I_{\text{net}} = I_{\text{tr}} + I_{\text{Blm}}$. The current through the transducer is the sum of the K^+ and Na^+ currents that flow through the transducer, $I_{\text{tr}} = I_{\text{K tr}} + I_{\text{Na tr}}$. The current across the basolateral membrane, I_{Blm}, is more complicated because channel, pump, transport, and electrode currents must be taken into account. The currents arising from each are calculated as described in the following sections and summed to give the current totals for each ion species [Eqs. (4)–(6)]. For example; the total K^+ current across the basolateral membrane, I_{KBlm}, is equal to the sum of the K^+ currents that flow through both the fast and slow voltage-gated K^+ channels plus the K^+ component of the Na/K-ATPase pumps, the K^+ component of the transporter, and (optionally) the K^+ current that flows as a result of electrode impalement [Eq. (4)]. Na^+ is similar to K^+. We have included a small permeability to Na^+ through the voltage-gated K^+ channels (see the following) so that I_{NaBlm}, includes a contribution from the voltage-gated K^+ channels [Eq. (5)]. The Cl^- current across the basolateral membrane, I_{ClBlm}, is the sum of a static conductance to Cl^-, the Cl^- component of the transporter current, and (optionally) Cl^- current that flows due to electrode impalement [Eq. (6)],

$$I_{\text{KBlm}} = I_{\text{Kfast}} + I_{\text{Kslow}} + I_{\text{K pump}} + I_{\text{K transporter}} + I_{\text{K electrode}}, \tag{4}$$

$$I_{\text{NaBlm}} = I_{\text{Nafast}} + I_{\text{Naslow}} + I_{\text{Na pump}} + I_{\text{Na transporter}} + I_{\text{Na electrode}}, \tag{5}$$

$$I_{\text{ClBlm}} = I_{\text{Clstatic}} + I_{\text{Cl transporter}} + I_{\text{Cl electrode}}. \tag{6}$$

The net current across the basolateral membrane is $I_{\text{Blm}} = I_{\text{KBlm}} + I_{\text{NaBlm}} + I_{\text{ClBlm}}$, and, again, the overall net current across the cell membrane is $I_{\text{net}} = I_{\text{Blm}} + I_{\text{tr}}$.

F. Transducer conductance

1. Maximum and resting transducer conductance

The expected maximum transducer conductance is about 13 nS (see Kros, 1996). The percentage of transducer channels that are opened at rest determines the transducer conductance at rest. Using a water-jet stimulator, Kros *et al.* (1992) found that in neonatal mouse cochleae about 8% of transducer channels were open at rest in OHCs and that an IHC had nearly 0% open. Other studies find a higher percentage of transducer channels opened at rest. *In vitro* studies in lower vertebrates, using a glass probe, report a resting transducer conductance of 10%–25% of the maximum (Ohmori, 1984; Crawford *et al.*, 1989). In mammalian IHCs *in vivo*, the ratio of depolarization to hyperpolarization ranges from

about 8:1 (Dallos and Cheatham, 1989) to 3:1 (Russel and Sellick, 1983). Assuming the resistance of the basolateral membrane is linear, the depolarization to hyperpolarization ratio suggests that between 12.5% and 33% (i.e., 1/8 and 1/3) of the transducer channels are open at rest. If voltage-gated channels were to open during depolarization then the ratios obtained would be an overestimate of the percentage of transducer channels open at rest. This occurs because opening voltage-gated K^+ channels limits depolarization resulting in a smaller depolarization to hyperpolarization ratio. Therefore, the 12.5%–33% values are likely to be overestimates because they do not include the effects of voltage-gated K^+ channels. The presence of the electrode in the cell may also bias the transducer *in vivo*, and as Kros *et al.* (1992) suggest, the higher values obtained from the glass probes that require direct contact may bias the transducer. Here we will test a range of values, but the default resting transducer conductance will be set to 0.5 nS (about 4% of 13 nS).

2. Transducer stimulation

Much of the use of the model will be concerned with homeostatic issues and will use a static resting transducer conductance, but to simulate receptor potentials the transducer conductance can be varied. The second-order Boltzmann function shown in Eq. (7), fit by Kros *et al.* (1993), gives the percentage of channels open, P_o, as a function of the voltage, V, applied to their water-jet stimultor,

$$P_o = (1 + K_2(1 + K_1)^{-1}, \tag{7}$$

where

$$K_1 = \exp^{(1.2*(0.91-V))}, \quad K_2 = \exp^{(0.43*(1.75-V))}.$$

To simulate receptor potentials in response to tone bursts, we calculate P_o as the voltage to the water-jet stimulator, V, is varied sinusoidally. To get the conductance of the transducer, P_o is multiplied by a maximum transducer conductance $G_{\mathrm{Tr\,max}}$. $G_{\mathrm{Tr\,max}}$ was chosen to be 7.5 nS for the experiments simulating receptor potentials, one half of the theoretical maximum.

G. Basolateral membrane: Conductances and currents

1. Voltage dependence of K^+ channel conductance

Kros and Crawford's (1990) patch-clamp experiments on isolated guinea pig IHCs characterized two pharmacologically distinct potassium currents. The larger current exhibited very fast kinetics while the smaller current was somewhat slower. Both currents were active over a voltage range of about −65 to −20 mV. Activation curves for the fast and slow channels were obtained by digitizing the data points in figures from tail current experiments (Figs. 8 and 10 of Kros and Crawford, 1990) using Autocad (Autodesk) with a SummaSketch tablet. These figures are the instantaneous current that flows after a voltage step from different holding potentials to a consistent command potential (−47 mV for fast channels and −46 mV for slow channels). The driving force is therefore constant and can be divided out to yield the channel conductance at various membrane potentials. Our assumption of ohmic instantaneous current–voltage relationships for the two conductances appears to be justified; over the range of membrane potentials in which the model operates the current–voltage (I–V) curves for the two K^+ currents is approximately linear (Figs. 7 and 9 of Kros and Crawford, 1990). Equations (8) and (9) are the sigmoidal functions fit to the digitized data for the fast and slow K^+ channels, respectively,

$$g_{\mathrm{fast}}(V_m) = 0.0215 \Big/ \left[1 + \exp\left(-\frac{V_m + 41}{9.5}\right)\right], \tag{8}$$

$$g_{\mathrm{slow}}(V_m) = 0.0125 \Big/ \left[1 + \exp\left(-\frac{V_m + 45}{8}\right)\right], \tag{9}$$

where $g_{\mathrm{fast}}(V_m)$ is the conductance, in μS, due to the fast channels, $g_{\mathrm{slow}}(V_m)$ is the conductance, in μS, due to the slow channels, and V_m is the membrane potential. The resulting voltage dependent K^+ currents are written as $I_{\mathrm{Kfast}} = g_{\mathrm{fast}}(V_m)*(V_m - E_{\mathrm{Kst}})$ and $I_{\mathrm{Kslow}} = g_{\mathrm{slow}}(V_m)*(V_m - E_{\mathrm{Kst}})$.

The fast potassium channels may be BK channels which are both voltage dependent and calcium dependent (Appenrodt and Kros, 1997; Kirkwood and Kros, 1997; Kros *et al.*, 1998; Raybould *et al.*, 2001). Kros and Crawford (1990) did not find the overall currents to be dependent upon external calcium, and while Raybould *et al.* (2001) did find that the overall currents decreased in nominally calcium-free media when strong intracellular calcium buffering (10 mM BAPTA) was present they also found that there was no reduction when a lower buffer strength was used (0.5 mM EGTA). Most of the interesting behavior evident in this model can be traced back to the activation of the slow K^+ channels, which are not calcium dependent, and the calcium dependence of the fast channels is not well characterized, so extracellular calcium and calcium dependence are not considered in this model.

2. Activation kinetics of K^+ channels

Kros and Crawford (1990) fit the onset of the fast and slow K^+ currents with an equation that describes the kinetics of a channel with two closed states and one open state [their Eq. (2)]. By substituting $g_{\mathrm{fast}}(V_m)*V_m$ and $g_{\mathrm{slow}}(V_m)*V_m$ for the current, I, we have modified their equation to calculate the conductance of the channels as a function of time and voltage. The conductance of fast K^+ channels as a function of time and voltage is shown in Eq. (10). The equation for the slow channels is identical in form (not shown),

$$g_{\mathrm{fast}}(t, V_m) = g_{\mathrm{fast}}(V_m)_\infty - \frac{g_{\mathrm{fast}}(V_m)_\infty - g_{\mathrm{fast}}(V_m)_{t-\partial t}}{\tau_{\mathrm{fast}_1} - \tau_{\mathrm{fast}_2}} \times (\tau_{\mathrm{fast}_1} \exp^{-t/\tau_{\mathrm{fast}_1}} - \tau_2 \exp^{-t/\tau_{\mathrm{fast}_2}}), \tag{10}$$

where $g_{\mathrm{fast}}(t, V_m)$ is the conductance of the fast K^+ channels as a function of time and voltage, $g_{\mathrm{fast}}(V_m)_\infty$ is the conductance of the fast K^+ channels at time infinity, and $g_{\mathrm{fast}}(V_m)_{t-\delta t}$ is the conductance of the fast channels at the prior time step. $g_{\mathrm{fast}}(V_m)_\infty$ is simply the voltage dependence of the fast K^+ channels as calculated in Eq. (8). In Eq. (10), the fast and slow channels each have two time constants

associated them. Kros and Crawford (1990) calculated the time constants for the channels (their Fig. 12) and we fit their data points with sigmoidal functions (or a constant) to be used in the model. (Their data points were digitized using AUTOCAD as was done to obtain the voltage dependence, above.) The equations describing the time constants for the channels are as follows:

$$\tau_{\text{fast}_1} = 0.11 + 0.233/(1 + \exp^{(V_m + 33)/7}), \tag{11a}$$

$$\tau_{\text{fast}_2} = 0.1, \tag{11b}$$

$$\tau_{\text{slow}_1} = 1.1 + 8.9/(1 + \exp^{(V_m + 25)/7}), \tag{11c}$$

$$\tau_{\text{slow}_2} = 0.1 + 0.233/(1 + \exp^{(V_m + 49)/9}). \tag{11d}$$

The channel kinetics are used when simulating receptor potentials, but to reduce computational overhead when investigating homeostatic mechanisms, a reduced form of the model is used. In the reduced model only the voltage dependence of the channels is considered (i.e., Eqs. (8) and (9)], making the channel gating instantaneous.

3. K^+ channel permeability to Na^+

Kros (1989) found that the combined reversal potential of the channels is depolarized 10 mV with respect to the K^+ Nernst potential. If Na^+ entry is responsible for the depolarization, then a permeability ratio, P_{Na^+}/P_{K^+}, of 0.0186 is obtained (Kros, 1989). We also found that the whole-cell currents in guinea pig reversed at about 9 mV more depolarized that the K^+ Nernst potential giving a P_{Na^+}/P_{K^+} of 0.0169, and that in gerbil IHCs the P_{Na^+}/P_{K^+} may be much larger (Zeddies, 2001). In the model we will use a slightly more conservative ratio of 0.01 to calculate the Na^+ currents that flow through the voltage-gated K^+ channels. These Na^+ currents are written as $I_{\text{Nafast}} = g_{\text{fast}}(V_m)0.01(V_m - E_{\text{Na}})$ and $I_{\text{Naslow}} = g_{\text{slow}}(V_m)0.01(V_m - E_{\text{Na}})$.

4. Na/K-ATPase pump currents

Maintenance of the K^+ and Na^+ gradients generally requires active pumping of ions. (Na^+,K^+)-ATPase is an enzyme that concentrates potassium inside the cell and extrudes sodium using the energy of ATP (Skou, 1992). This enzyme constitutes the sodium/potassium pumps and operates in an electrogenic manner ($3\ Na^+$ ions are pumped out for every $2\ K^+$ ions pumped into the cell). The pumping activity is regulated by the concentrations of Na^+ and K^+ and is voltage dependent (as demanded by the thermodynamics of the electrogenic current). Our model of an IHC includes a model of the sodium/potassium pumps that was developed by Lemieux *et al.* (1990) and Chapman *et al.* (1983) for cardiac cells. It is used here calibrated for goldfish saccular hair cells (see Appendix A). The output of the sodium/potassium pump model is the electrogenic current, I_{pump}, so for incorporation into our model: $I_{\text{Na pump}} = 3I_{\text{pump}}$, and $I_{\text{K pump}} = 2I_{\text{pump}}$.

5. Chloride, leak, and transporter currents

Chloride's equilibrium potential in goldfish hair cells appears to be depolarized with respect to the resting potential, suggesting that Cl^- is actively accumulated in the cell (Mroz *et al.*, 1993a). In mammalian hair cells the estimated chloride Nernst potential, -30 mV (see above), also suggests that Cl^- is actively brought in. No data are yet available for hair cell Cl^- transporters, but the squid giant axon has a transporter in which $3\ Cl^-$ ions are brought into the cell along with $2\ Na^+$ and $1\ K^+$ using the energy of the Na^+ gradient (Russell, 1983; Altamirano and Russell, 1987). This stoichiometry is used in our model to provide a mechanism for concentrating Cl^- inside the cell. A Na^+ conductance of 7 pS was chosen for this transporter (see Appendix B), and the currents are written as follows: $I_{\text{Na transporter}} = g_{\text{Na transporter}}(V_m - E_{\text{Na}})$, $I_{\text{K transporter}} = \frac{1}{2}I_{\text{Na transporter}}$, and $I_{\text{Cl transporter}} = \frac{3}{2}I_{\text{Na transporter}}$. No static (leak) conductances to K^+ or Na^+ are incorporated, but a static Cl^- conductance of 100 pS is included (see Appendix B); the passive chloride current is $I_{\text{Cl}} = g_{\text{Cl}}(V_m - E_{\text{Cl}})$.

6. Leak due to microelectrode impalement

In vivo recordings are made using sharp microelectrodes. This recording technique requires the electrode to penetrate the cell's membrane and as a result introduces an additional conductance for each ion (i.e., a nonspecific leak). The additional conductance due to high impedance microelectrodes has been estimated to range from 2 to 50 nS (Pongracz *et al.*, 1991; Stefani and Steinbach, 1969; Spruston and Johnston, 1992). In the model, an optional conductance, $g_{\text{electrode}}$ (additional conductance of cell membrane *not* conductance of electrode), is included to simulate microelectrode impalement. The currents through this conductance are written as $I_{\text{K electrode}} = g_{\text{electrode}}(V_m - E_{\text{K}})$, $I_{\text{Na electrode}} = g_{\text{electrode}}(V_m - E_{\text{Na}})$, and $I_{\text{Cl electrode}} = g_{\text{electrode}}(V_m - \text{E}_{\text{Cl}})$.

III. RESULTS

A. Simulated receptor potentials

1. Simulated receptor potentials have features that are consistent with auditory nerve phenomena

Receptor potentials can be simulated by sinusoidally varying the voltage, V, in the Boltzmann function that relates the voltage applied to the water-jet stimulator to the percentage of open transducer channels [Kros *et al.* (1993), see Methods]. Figure 2, *bottom*, shows the resulting transducer conductance as a function of time for a 700 Hz sinusoid of 5 V amplitude (i.e., 5 V sinusoid applied to the water jet at 700 Hz). Note that the peak conductance during each cycle is the same magnitude.

As the transducer conductance changes, the amount of current flowing into the cell changes, and therefore the membrane potential of the cell changes. Figure 2, *top*, shows the simulated receptor potential produced by the model IHC in response to the 5 V, 700 Hz stimulus. Unlike receptor potentials recorded *in vivo*, the dc component in the simulated receptor potentials is not constant during the stimulus, but is greatest at the beginning of the stimulus and then decreases toward a steady state (Fig. 2, *filled arrowhead*). Considering that the receptor potential drives the synapse, this "sag" would be expected to produce the highest firing rates in the nerve at the beginning of the stimulus and lower rates there-

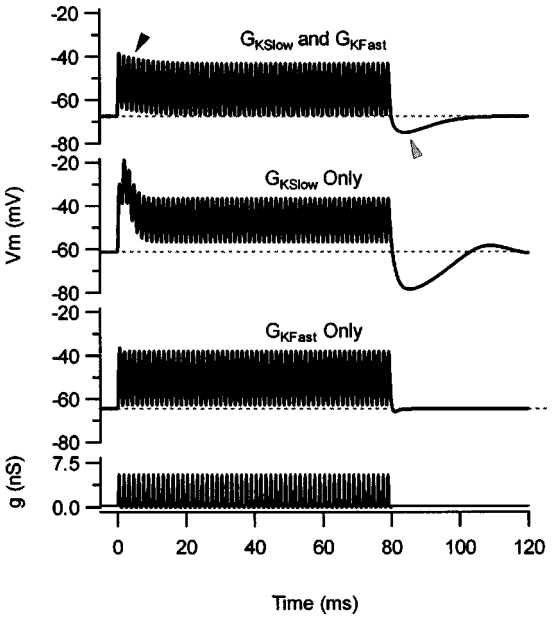

FIG. 2. Simulated receptor potentials produced in response to a 700 Hz, 5 V sinusoidal deflection of the transducer (see the text). The transducer conductance, *bottom*, has a constant peak amplitude, but the receptor potential, *top*, shows a decrease in peak amplitude (*filled arrowhead*) and a hyperpolarization following the stimulus (*gray arrowhead*). These features are exaggerated when the fast K^+ channels are removed (G_{KSlow} *Only*) and nearly absent when the slow K^+ channels are removed (G_{KFast} *Only*).

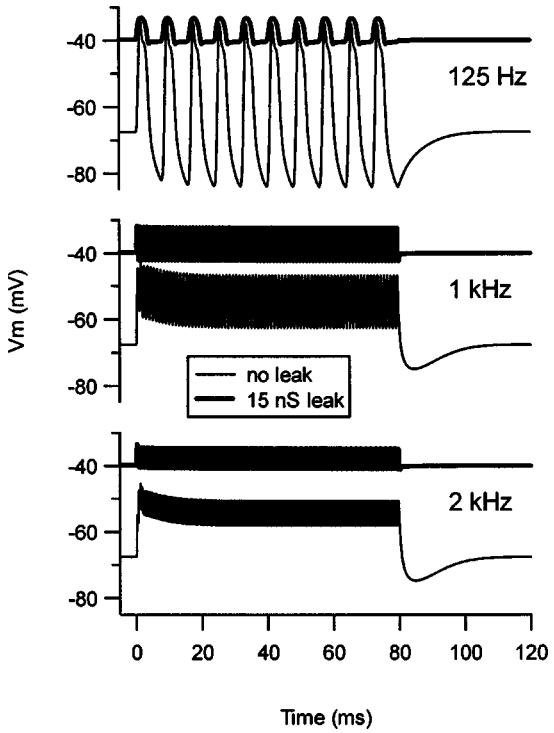

FIG. 3. Including a nonspecific leak, to simulate microelectrode impalement, depolarizes the cell and attenuates the "sag" and after-stimulus hyperpolarization. Each panel shows normal simulated receptor potentials and receptor potentials with a 15 nS nonspecific leak plotted on the same ordinate. *Top*, *middle*, and *bottom* panels are 125 Hz, 1 kHz, and 2 kHz, respectively.

after. Another feature of the simulated receptor potentials that differs from the *in vivo* recordings is the hyperpolarization (relative to the resting potential) that occurs when the stimulus is turned off (Fig. 2, *open arrowhead*). Hyperpolarization would be expected to decrease synaptic activity below the resting rate. The sag in the receptor potentials is consistent with auditory nerve adaptation and the after-stimulus hyperpolarization is consistent with the suppression of spontaneous rate that follows a stimulus (e.g., Kiang *et al.*, 1965).

The sag and the after-stimulus-hyperpolarization appear to be due to the activity of the slow K^+ channels. When the slow K^+ channels are removed (Fig. 2, G_{KFast} Only) the two features are essentially absent, but when only the slow channels are present (Fig. 2, G_{KSlow} Only) those features are exaggerated. The explanation is quite simple. It takes time for the slow channels to open during the stimulus, and as they open they contribute a hyperpolarizing current that brings the membrane potential back toward the resting potential. The after-stimulus-hyperpolarization is similarly explained. The slow channels are opened during the stimulus, and it takes time for the channels to close following the stimulus. Because the channels remain open after the stimulus, a hyperpolarizing current is present until the channels close. The fast K^+ channels also contribute a hyperpolarizing current and produce similar effects in the receptor potentials, but on a faster time scale that is not as readily observable. The fast channels also appear to dampen the effects of the slow channels.

2. Electrode leak and depolarization reduce the sag and after stimulus hyperpolarization

If activation of the slow channels can affect the receptor potentials, why are the sag and after-stimulus-hyperpolarization not evident in the *in vivo* recordings? To find out if the leak introduced by microelectrode impalement in the *in vivo* recordings can explain the difference, we simulated impalement by adding a nonspecific (permeable to K^+, Na^+, and Cl^-) leak conductance to the model. Figure 3 shows that when a 15 nS nonspecific leak is present, the simulated receptor potentials look much more like those recorded *in vivo*; neither the sag nor the after-stimulus hyperpolarization are present and the starting potential is close to the resting potential reported *in vivo*. (Note that for each frequency in Fig. 3 the simulated receptor potentials with and without the leak are plotted on the same ordinate.)

The presence of the nonspecific leak due to microelectrode impalement may be sufficient to explain the differences between the simulated receptor potentials and the receptor potentials recorded *in vivo*, but we cannot conclude that the sag and after-stimulus hyperpolarization are actually present in real IHC receptor potentials. Figure 4 shows that the sag and after-stimulus hyperpolarization are very sensitive to the initial potential of the cell. In Fig. 4 an electrical pedestal current is injected into the cell to depolarize the starting potential (the pedestal current is turned on before the stimulus is delivered and remains on during the time shown). It is clear that when the larger pedestal currents are injected (e.g., 500 and 1000 pA) and the starting potential is depolarized

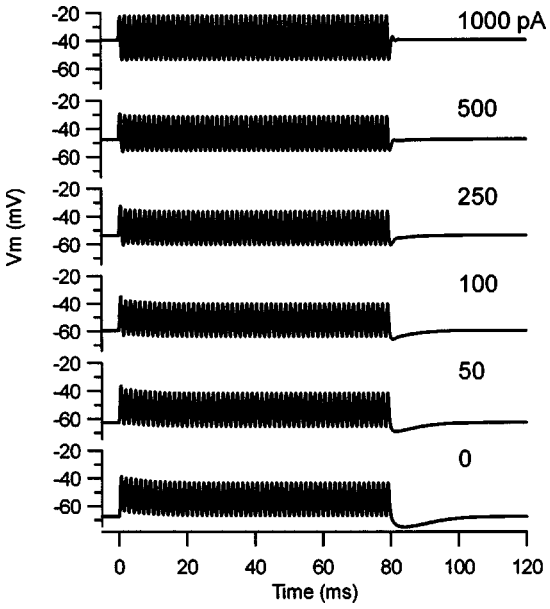

FIG. 4. Depolarization alone attenuates the "sag" and after-stimulus hyperpolarization. Pedestal currents of 0, 50, 100, 250, 500, and 1000 pA are used to depolarize the starting potential. The pedestal current is turned on before the stimulus is presented and remains on throughout the time period shown. Stimulus frequency is 700 Hz and the amplitude is 5 V.

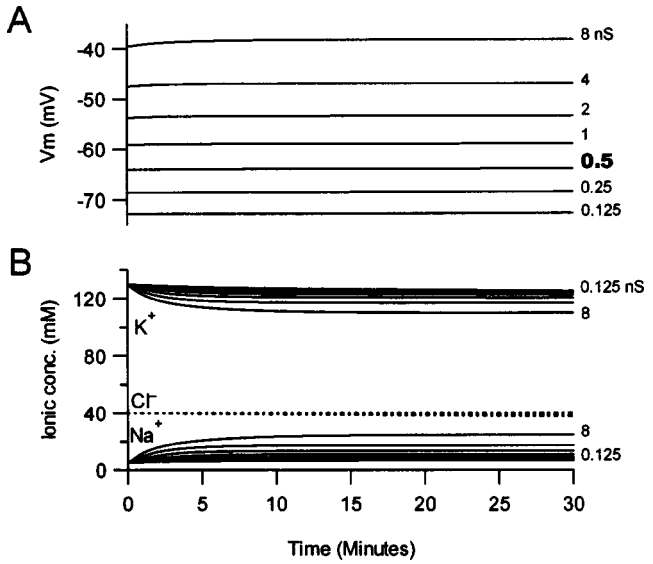

FIG. 5. Simulations with g_{trans} ranging from 0.125 to 8 nS. All simulations start with the default values and differ only in g_{trans}. (a) The membrane potential over time. (b) Intracellular ionic concentrations: $[\text{Na}]_i$ (*solid line*), $[\text{K}]_i$ (*dashed line*), and $[\text{Cl}]_i$ (*dotted line*). Increasing the g_{trans} results in higher $[\text{Na}]_i$ and lower $[\text{K}]_i$; a rundown in ionic gradients.

into the range reported *in vivo* and that the sag and after-stimulus hyperpolarization are eliminated. But, it can also be seen in Fig. 4 that even when 50 and 100 pA currents are injected and the starting potential is still about -60 mV the sag and after-stimulus hyperpolarization are noticeably attenuated.

The amount of slow K^+ channel activation during the stimulus determines how much sag and after-stimulus hyperpolarization occur. Because the resting potential of the cell determines the percentage of the voltage-gated channels that are activated before the stimulus, the resting potential is of critical importance when considering how the voltage-gated channels shape the development of receptor potentials. We should note, however, that any other parameters that affect the activation state of the slow K^+ channels could also influence the development of the receptor potentials. As noted earlier, the fast K^+ channels appear to be BK channels, which are activated by calcium as well as voltage. Increases in the intracellular calcium concentration, for example, because of activation of apically located P2X receptors (see Raybould *et al.*, 2001), would activate the fast K^+ channels leading to a hyperpolarized resting potential and a decrease in the membrane impedance. The hyperpolarized resting potential may increase the sag and after-stimulus hyperpolarization but the decreased impedance would decrease them because of shunting. The model could be useful in exploring such interactions.

B. Homeostasis

Because the resting potential may be important but its true value is not known, the following uses the biophysical model to explore mechanisms affecting the resting potential. The lengths of time simulated are generally much longer than those used to simulate receptor potentials, so to decrease the computational overhead a reduced form of the model is used. In the reduced model, the voltage-dependence of the K^+ channels is retained but not the gating kinetics (the channels gate instantaneously) and a static transducer conductance is used.

1. Factors that determine the resting potential

To provide both operational tests and to shed light on the mechanisms responsible for the resting potential, we explore three of the major parameters: the resting transducer conductance, the sodium/potassium pump density, and the initial intracellular ionic concentrations. In each of the simulations, the membrane potential is unconstrained and all parameters, except the one being varied, are set to their default values (resting transducer conductance: $g_{\text{trans}}=0.5$ nS, (Na^+,K^+)-ATPase pump density: 800 pumps/μm^2, and initial intracellular ionic concentrations: $[\text{K}^+]_i=130$ mM, $[\text{Na}^+]_i=5$ mM, and $[\text{Cl}^-]_i=40$ mM). A description of these and the other parameters can be found in Sec. II.

a. The resting transducer conductance. Figure 5 shows the membrane potential and intracellular ionic concentrations during 30 min of simulation with different resting transducer conductances, g_{trans}, ranging from 0.125 to 8 nS. As an operational test of the model, it is observed that the membrane potential is stable during the simulations and that the ionic concentrations appear to achieve a steady state. Figure 5(a) shows that each doubling of the resting transducer conductance results in a steady-state depolarization of the membrane potential of about 5 to 10 mV. In the default condition, $g_{\text{trans}}=0.5$ nS (4% of maximum), the steady state resting potential is -64 mV. When the resting g_{trans} is 8 nS (61.5% of maximum) the steady state resting potential is -39 mV, and when the resting g_{tr} is 0.125 nS ($\sim$1% of maximum) the resting potential is -73 mV. It is clear that a wide range of resting potentials can be achieved by changing the resting

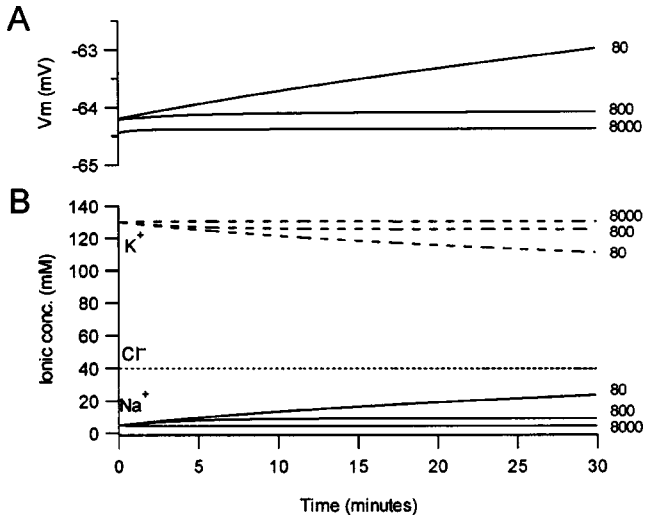

FIG. 6. Simulations with different (Na^+,K^+)-ATPase pump densities of 80, 800, and 8000 pumps per μm^2. All simulations start with the default values and differ only in the pump density. (a) The membrane potential over time. (b) Intracellular ionic concentrations: $[Na]_i$ (*solid line*), $[K]_i$ (*dashed line*), and $[Cl]_i$ (*dotted line*).

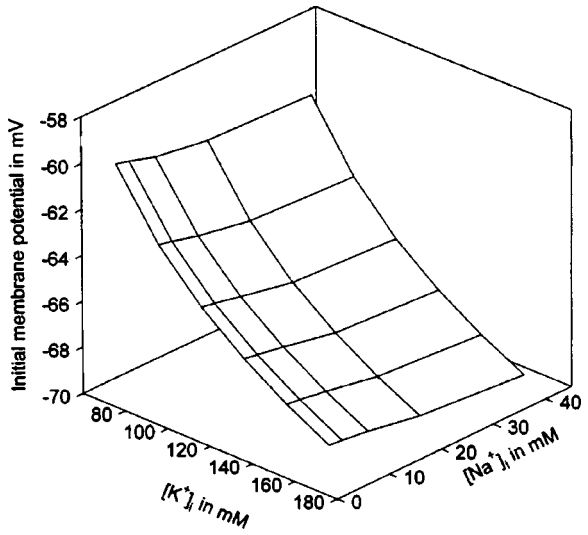

FIG. 7. The membrane potential at the beginning of the simulation (*vertical axis*) is plotted as a function of the $[K]_I$ (*bottom left axis*) and $[Na]_I$ (*bottom right axis*). It is observed that altering $[K]_i$ results in a larger membrane potential change than altering $[Na]_i$; but even large changes in $[K]_i$ do not change the membrane potential by much.

transducer conductance. It is important, however, to note that the depolarization induced by the transducer current is partly counteracted by increased outward K^+ current through the voltage-gated K^+ channels. This negative feedback from the voltage-gated K^+ channels is strong because the maximum conductance of the channels is approximately 43 nS, about three times larger than the maximum transducer conductance. And, it is only when ~61.5% of the transducer channels open that the resting potential begins to approach the resting potential measured *in vivo*.

It has been recognized that, *in vivo*, the charge carrier for the transducer current and the current through the voltage-gated channels is primarily K^+. As a result, it is commonly believed that no compensatory ion pumping is required after the cell has been stimulated (Johnstone and Sellick, 1972; Dallos, 1973; Ashmore and Meech, 1986; Wangemann and Schacht, 1996). Because we included a 1% conductance to Na^+ in the voltage-gated K^+ channels (see Sec. II), depolarizing the membrane potential also increases the basolateral Na^+ conductance and results in a larger inward Na^+ current. Therefore, even though the current through the transducer is carried primarily by K^+, it is a depolarizing current that activates more K^+ channels and thus causes an increase in the inward Na^+ current. Because in the steady state, the net (inward) current through the transducer must equal the net outward basolateral current, the increased inward Na^+ current must be accompanied by greater K^+ outflow across the basolateral membrane than inflow through the transducer. Consequently, simulations that have a large resting transducer conductance also have somewhat ''run down'' gradients [increased intracellular Na^+ and decreased intracellular K^+; Fig. 5(b)].

b. Sodium/potassium pumps. Figure 6(a) shows that running simulations with pump densities of 80, 800, and 8000 pump enzymes/μm^2 results in little difference in the membrane potential. However, the simulations with 800 and 8000 (Na^+,K^+)-ATPase enzymes/μm^2 appear to reach a steady state, while the trace with 80 enzymes/μm^2 is still changing at the end of the simulation. Figure 6(b) shows the corresponding ionic concentrations changing over time.

Figure 6(b) helps to illustrate the operation of the pumps and the mechanism of reaction by the cell. All three runs start from the same initial conditions and differ only in pump density (the small difference in the membrane potential at the start of the simulation is due to the electrogenic nature of the pumps). With pump densities of 80 and 800 pumps per μm^2 $[Na^+]_i$ increases and $[K^+]_i$ decreases. From the starting conditions the passive inward Na^+ current is greater than the Na^+ current developed by the pumps, which leads to an increase in $[Na^+]_i$, a depolarization of the membrane potential, and a corresponding increase in the pump current. So, in the case with 800 pumps per μm^2, after a modest shift in the $[Na^+]_i$ and $[K^+]_i$ (and very little change in membrane potential) the simulation approaches steady state. The simulation with 80 pumps per μm^2 does not reach steady state in 30 min of simulation because the pump current is insufficient to compensate for the inward Na^+ current. With 80 pumps per μm^2 the membrane continues to depolarize, which activates more voltage-dependent K^+ channels and further increases the inward Na^+ current. The default pump density of 800 per μm^2 seems to be a reasonable value for these cells while the low value of 80 per μm^2 appears to be too small. The higher pump density of 8000 pumps/μm^2 illustrates another aspect of the pumps. A tenfold increase in pump density does not significantly change the resting potential or intracellular ionic concentrations, the pumps initially pump out more Na^+ than enters, which decreases the $[Na^+]_i$ and inhibits the pumps.

c. The effect of intracellular ionic concentrations on the resting potential. It can be seen in Fig. 7 that changing $[Na^+]_i$ has little effect on the initial membrane potential.

Because the conductance to Na^+ is small, changing $[Na^+]_i$ from 2.5 to 40 mM only changes the membrane potential by about 1 mV. The larger conductance to K^+ through the voltage-gated K^+ channels means that $[K^+]_i$ will have a much stronger influence on membrane potential. This is borne out in Fig. 7 where it is shown that decreasing $[K^+]_i$ depolarizes the membrane. However, fairly large changes in concentration of about 10 mM result in relatively small changes in the membrane potential (around 2 mV). Figure 7 illustrates that, according to this model, the ionic concentrations of the pipette fluid in patch-clamp experiments could differ considerably from the true concentrations in IHCs and have only a small effect on the resting potential.

2. Simulating microelectrode impalement

As mentioned in Sec. I, the zero-current potential of isolated IHCs *in vitro* is about −60 mV, whereas the resting potential found *in vivo* is about −30 to −40 mV. Our previous simulations, with default conditions, give an *in vivo* resting potential of −64 mV [Figs. 5(a) and 6(a)], a value that corresponds well with the *in vitro* experiments. Pointing out that it is possible that the discrepancy arises due to attenuated transducer currents *in vitro*, Kros and Crawford (1990) argue that the transducer current is not sufficient to account for the difference but that the added conductance due to microelectrode impalement is the likely culprit. Figure 6 is consistent with Kros and Crawford's (1990) suggestion; it takes about 61.5% maximum activation of the transducer to get the resting potential in the range reported in the *in vivo* experiments. We now investigate the effect of introducing a nonspecific conductance into the modeled cell's basolateral membrane to simulate microelectrode impalement.

Figure 8 shows the response of the model cell to an abrupt introduction of a 10 nS nonspecific leak. The simulation is 120 s in length and the default conditions are used, except that g_{trans} is set to zero to make interpretation easier. In Fig. 8(a) the membrane potential starts near −93 mV (close to the Nernst potential for K^+ relative to scala tympani), then upon introduction of the leak jumps to about −40 mV, shows a brief hyperpolarization, then begins to depolarize toward steady state. Figure 8(b) shows the K^+ (dashed line), Na^+ (solid line), Cl^- (dotted line) and the net current crossing the basolateral membrane (note that net current is plotted on a different scale; right axis). Just after the introduction of the leak, the net current is positive indicating net positive charge leaving the cell. The net loss of positive charges from the cell is reflected in Fig. 8(a) as the brief hyperpolarization in the membrane potential. In this interval the outward K^+ current is larger than the inward Na^+ and outward Cl^- combined. After about 10 s the net current becomes negative and the cell begins to depolarize. The hyperpolarization is curious because in a recording from a real cell it might be interpreted as the membrane ''sealing'' around the electrode, but in the model we can be sure that there is no sealing.

To explain the brief hyperpolarization that follows the introduction of the nonspecific leak, Fig. 8(c) plots the Nernst potential for each ion. Before the introduction of the nonspecific leak, $[K^+]_i$ is high (130 mM), $[Cl^-]_i$ is moderate (40 mM), and $[Na^+]_i$ is low (5 mM). When the leak is introduced, the ionic gradients run down, and as can be seen in Fig. 8(c) the Nernst potential for Na^+ initially changes faster than the Nernst potential for K^+ or Cl^- (the initial slope is steeper for Na^+). The Na^+ and K^+ currents are comparable in magnitude ($I_{\text{Kblm}}=1.4\,\text{nA}$, $I_{\text{Nablm}}=1.3\,\text{nA}$), but they cause disproportionate changes in their respective Nernst potentials. In the model the volume of the cell is fixed, so the ionic concentrations change linearly with respect to current while the Nernst potentials change logarithmically. For example a current that produced a 10 mM decrease in $[K^+]_i$ and a 10 mM increase in $[Na^+]_i$ would change E_{Kst} from −93 to −91 mV, but the change in E_{Nast} would be more dramatic, from 91 to 61 mV. The quickly decreasing Na^+ Nernst potential means that the driving force for Na^+ entry is also decreasing quickly, while the driving force for K^+ outflow remains relatively high. In other words, the initial rate of decrease in the outward K^+ current is less than the rate of decrease for the inward Na^+ current; resulting in a net loss of intracellular cations. The situation reverses when the $[K^+]_i$ is low. As can be seen when the membrane potential begins to depolarize, the net current becomes negative and the slope of E_{Kst} is steeper than E_{Nast}. To confirm this interpretation we ran simulations in which the Nernst potentials were not allowed to change. In those simulations the membrane potential remained constant after the introduction of the nonspecific leak (data not shown).

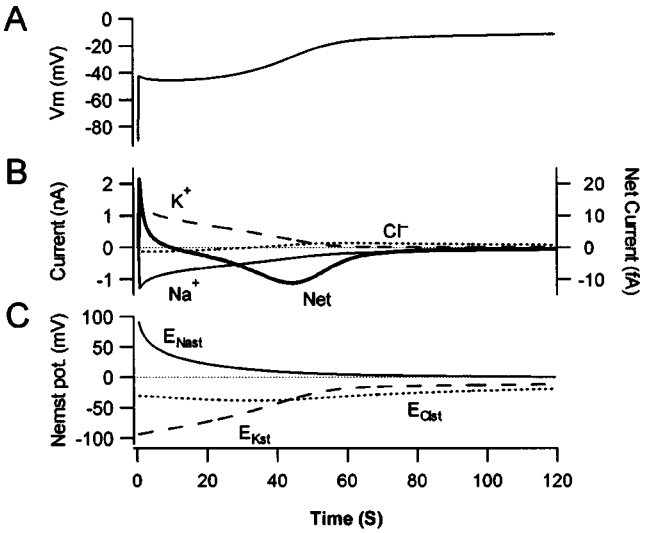

FIG. 8. Shear (120 s) simulations of microelectode impalement showing the response to a 10 nS nonspecific leak in the basolateral membrane that is introduced at time=0. All parameters are set to their default values, except $g_{\text{trans}}=0$. (a) The membrane potential over time. Note that initial membrane potential is close to the Nernst potential for K^+ because g_{trans} is 0. The potential jumps to about −40 mV when the leak is introduced, briefly hyperpolarizes, then depolarizes to a steady value. (b) The ionic currents Na^+ (*solid line*), K^+ (*dashed line*), and Cl^+ (*dotted line*), and the net current (*dark solid line*). Note that the net current is plotted on a different scale (*right axis*). (c) Nernst potential for the ions Na^+ (*solid line*), K^+ (*dashed line*), and Cl^+ (*dotted line*).

Figure 9 shows 30 min simulations following the introduction of nonspecific leaks of 1, 3, and 10 nS. The simulations start from the default values (including $g_{\text{trans}}=0.5\,\text{nS}$), which produce a −64 mV resting potential and 2.5 nS total

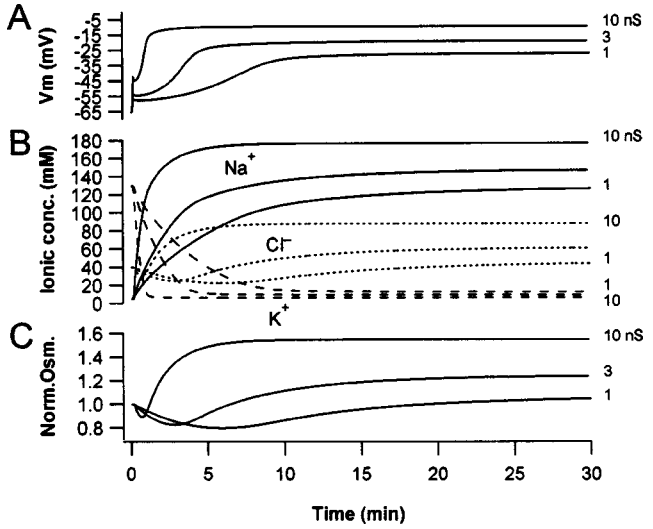

FIG. 9. Longer (30 min) simulations of microelectrode impalement showing the response to a 1, 3, and 10 nS nonspecific leak in the basolateral membrane that is introduced at time=0. All parameters are set to their default values, including $g_{trans}=0.5$ nS. (a) The membrane potential over time. From the resting potential of −64 mV, the potential jumps to more depolarized potential when the leak is introduced, briefly hyperpolarizes, then depolarizes to a steady value. (b) Intracellular ionic concentrations: $[Na]_i$ (*solid line*), $[K]_i$ (*dashed line*), and $[Cl]_i$ (*dotted line*) change rapidly after the nonspecific leak is introduced. (c) The normalized osmolarity. Values less than 1 indicate a net loss of intracellular ions, values greater than 1 indicate a net gain of ions.

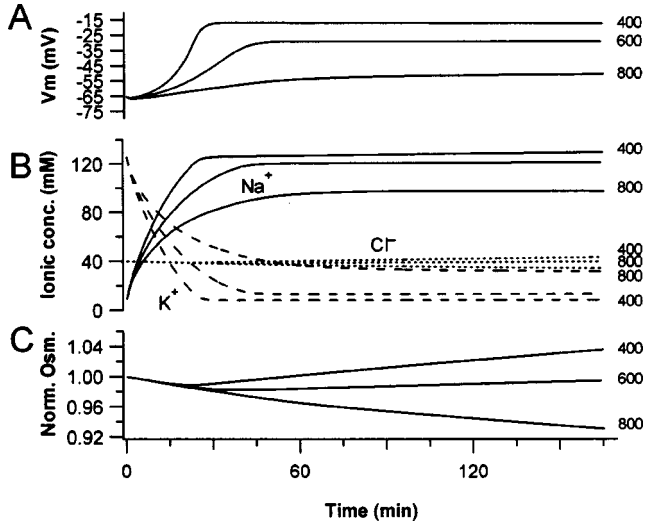

FIG. 10. Simulations of a cell *in vitro* with different (Na^+,K^+)-ATPase pump densities of 400, 600, and 800 pumps per μm^2. To simulate *in vitro* conditions, the ionic concentrations of scala media were set to the scala tympani values and the endocochlear potential was set to 0. All other parameters were set to their default values, including $g_{trans}=0.5$ nS. (a) The membrane potential over time. (b) Intracellular ionic concentrations: $[Na]_i$ (*solid line*), $[K]_i$ (*dashed line*), and $[Cl]_i$ (*dotted line*) change rapidly after the nonspecfic leak is introduced. (c) The normalized osmolarity, where values less than 1 indicate a net loss of intracellular ions, values greater than 1 indicate a net gain of ions. Note that in the case with 800 pumps per μm^2 the cell sustains a net loss of ions although the ionic gradients for Na^+ and K^+ have run down.

cell conductance. In all cases the membrane potential jumps to a depolarized potential that is followed by a brief hyperpolarization and then begins to depolarize toward a steady potential [Fig. 9(a)]. Upon introduction of the nonspecific leak the total cell conductance jumps to 7, 13, and 28 nS, respectively, for the 1, 3, and 10 nS leak (including the nonspecific leak) then continues to increase to a steady value of 30, 35, and 44 nS. These values correspond well with the IHCs in Dallos' (1985) study reporting a mean resting potential of −42 mV and input conductance of 34 nS. Figure 9(b) shows the intracellular ionic concentrations and indicates that after the leak is introduced the ionic concentrations run down rapidly. Even with the small 1 nS leak the intracellular cationic concentrations change rapidly: K^+ drops to 12 mM while Na^+ rises to 126 mM in 30 min, with the steepest changes occurring shortly after the leak is introduced. With the larger leak of 10 nS, intracellular K^+ drops to about 6 mM, Na^+ rises to as much as 177 mM, and Cl^- increases to 88 mM. The intracellular concentration of Na^+ becomes more concentrated than the extracellular fluid because, although not specifically included in the calculations, impermeant anions are implied to ensure bulk solution electroneutrality.

Figure 9(c) plots the ratio of the total number of intracellular ions to the starting number of intracellular ions. Initially the ratio decreases because more ions are leaving than entering, but the trend reverses when the membrane potential becomes depolarized with respect to the Cl^- Nernst potential (about −30 mV). At more positive potentials the total number of intracellular ions increases because Cl^- ions are driven into the cell and are accompanied by Na^+ ions. A real cell would first shrink then swell as water leaves and later enters to maintain the osmotic balance between intracellular and extracellular fluids. In the case of the 10 nS nonspecific leak the final ratio is about 1.5 times the original amount, which could be expected to result in observable swelling. It should be noted that charge balance has been maintained; K^+ decreases from the initial value by 124 mM, while Na^+ increases by 172 mM and Cl^- increases by 48 mM (Cl^- increasing is equivalent to positive charges leaving).

3. Simulating in vitro conditions

To simulate the *in vitro* situation, the ionic composition of scala media is set to the values of scala tympani and the endocochlear potential is set to zero. Figure 10 shows 165 min simuluations of the *in vitro* conditions using the default value for g_{trans} and the initial intracellular ionic concentrations, but including different runs for pump densities of 400, 600, and 800 (default) pumps/μm^2. In general, the membrane potential depolarizes [Fig. 10(a)] and the ionic concentrations change rapidly [Fig. 10(b)]; both, in a manner qualitatively similar to the simulations of microelectrode impalement (Fig. 9). The time course is somewhat slower (note the time scale difference between Figs. 10 and 9), but the explanation for the *in vitro* behavior is nearly the same as for microelectrode impalements. In the model the transducer is conductive only to K^+ and Na^+, acting as a cation-specific leak across the basolateral membrane. The transducer allows Na^+ to enter and K^+ to leave, which runs down the ionic gradients and depolarizes the cell.

In these simulations the Cl^- conductance remains constant, but Cl^- still plays an important role. Cl^- enters the cell when the membrane potential becomes depolarized with

respect to the Nernst potential for Cl^-. As in the case when simulating microelectrode impalement (Fig. 9), when Cl^- enters the cell there is a net accumulation of intracellular ions. Accumulation is evident in simulations with 400 and 600 pumps/μm^2 [Fig. 10(c)]. With 800 pumps/μm^2 the pumps are able to keep the membrane potential below the Cl^- Nernst potential and there is a net loss of ions. In the case with 800 pumps/μm^2, the cell may appear to shrink even though the ionic gradients for Na^+ and K^+ are completely run down.

The sodium/potassium pump capacity is an important parameter in determining how well hair cells survive in isolation, but other parameters are equally important. Increasing the transducer conductance increases the load placed on the pumps and as a result, cells with larger transducer currents would be in greater danger of losing volume regulation. In simulating *in vitro* conditions, we chose to use the default value for g_{trans} even though the conductance of the transducer should be about three times smaller *in vitro* (see Kros, 1996). This was done partially for consistency, but also because it is not clear what the *in vitro* conductance should be. If the transducer channels are damaged during the dissection, it was thought that cutting the tip-links would cause them to close (e.g., Assad *et al.*, 1991), but it has recently been suggested that such damage may cause the channels to open (Meyer *et al.*, 1998).

4. Steady state: Implications for Na^+ currents and membrane potential

Steady state provides the constraint that the passive Na^+ influx and the active Na^+ efflux (extruded by the sodium/potassium pumps) must be equal when the cell is at rest. The Na^+ current that the pumps develop depends on the intracellular Na^+ concentration but the current is also influenced by the membrane potential. More current is produced when $[Na^+]_i$ is high and the cell is depolarized. For example, if $[Na^+]_i$ is 5 mM and the membrane potential is -60 mV, then about 1 pA of Na^+ current is developed by the (Na^+,K^+)-ATPase pump enzymes. When $[Na^+]_i$ is 15 mM and the membrane potential is zero the pumps' Na^+ efflux rises to 18 pA (Fig. 11). In steady state the sum of all routes of Na^+ entry must not exceed the extrusion rate at a given $[Na^+]_i$ and membrane potential. Here we are concerned with Na^+ entry through the voltage-gated potassium channels, but any other routes of entry would be added to this influx. For example, the apical transducer and the Cl^- cotransporter contribute to Na^+ entry, and other cotransporters (not included in the model) such as sodium/calcium exchanges and sodium/proton exchanges could represent significant sources of Na^+. The magnitude of Na^+ entry through cotransporters is not known but in the case of *p*H regulation extruding Na^+ brought in by the sodium/proton exchanger may require a large portion of the (Na^+,K^+)-ATPase pump capacity (Ronan and Mroz, 1996).

In the model we have included a permeability ratio of 0.01 to calculate the Na^+ current entering through the voltage-gated K^+ channels. Because these channels are sensitive to the membrane potential, the Na^+ current through the channels will also be a function of the potential. The more depolarized the membrane potential, the larger the Na^+ current and the greater the demand on the sodium/potassium pumps. In the model, less than 2 pA of Na^+ current flows through the K^+ channels when the membrane potential is -70 mV, but at -40 mV, with more K^+ channels open, 24 pA flows. The Na^+ influx at -40 mV can be greater than the pump capacity at that potential. Does this place an upper limit on the resting potential?

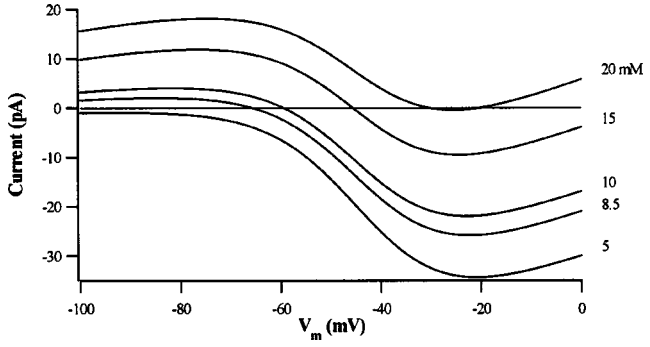

FIG. 11. Net Na^+ current across the basolateral membrane as a function of membrane potential. A positive current is defined as net Na^+ efflux, therefore a negative current occurs when the Na^+ entry exceeds the Na^+ extrusion rate. In the case when $[Na]_i$ is 5 mM there is a net inward flux over the entire membrane potential range indicating that 5 mM $[Na]_i$ cannot be sustained. All of the other $[Na]_i$ cross zero where the active and passive fluxes balance. For $[Na]_i = 8.5$, 10, 15, and 20 mM the zero current occurs at -65, -60, -46, and -31 mV, respectively.

The model is particularly useful for investigating the interactions between the components regulating $[Na^+]_i$. As mentioned, increasing $[Na^+]_i$ and depolarizing the cell stimulates the pumps and increases Na^+ efflux. Increasing $[Na^+]_i$ and depolarizing the cell also decreases the driving force for Na^+ entry, but at the same time depolarization increases Na^+ conductance by opening more K^+ channels. Figure 11 shows the net Na^+ current that flows across the basolateral membrane as a function of voltage and $[Na^+]_i$. Calculations for Fig. 11 include a 7 pS Na^+ conductance for the Cl^- cotransporter (see Appendix) but do not include Na^+ entry through the transducer. For each curve, $[Na^+]_i$ was fixed at the value indicated by the parameter on the curve. Net Na^+ current was then calculated for membrane potentials ranging from -100 to 0 mV. Negative net current is produced when Na^+ entry exceeds Na^+ extrusion. This is equivalent to an experiment in which both voltage and concentration are clamped.

Three distinct regions can be found in Fig. 11 for intermediate values of $[Na^+]_i$. At membrane potentials more hyperpolarized than -65 mV the net current is minimally affected by membrane potential but is strongly dependent upon $[Na^+]_i$. In this region the voltage-gated K^+ channels are closed, so there is little passive Na^+ influx. The slope of the curves is positive due to activation of the pumps and reduction of the driving force for Na^+ influx. Between -65 and -25 mV the K^+ channels activate, producing a voltage-dependent Na^+ influx that results in steep negative slopes for all curves. The negative slopes indicate that it is increasingly difficult for the pumps to handle the added Na^+ influx at any particular $[Na^+]_i$-voltage combination. This is because the

K^+ channels have steeper voltage dependence in this region than the pumps. In the last region, more depolarized than -25 mV, the K^+ channels are fully activated and the inherent properties of the pumps and the driving force are again dominant. Increasing $[Na^+]_i$ stimulates the pumps and depolarizing the cell reduces the driving force for passive entry of Na^+, shifting the balance in the direction of net efflux. In general, the fact that the curves are almost vertically shifted versions of one another is because the pumps are more strongly regulated by $[Na^+]_i$ than by membrane potential over the entire range.

Figure 11 indicates that Na^+ entry is greater than efflux for all values of membrane potential when $[Na^+]_i$ is 5 mM. If the cell were unconstrained, these initial conditions would result in a rise in intracellular Na^+, a slight depolarization, and increased activation of the pumps until the net current was zero at a new Na^+ concentration and membrane potential. For $[Na^+]_i$ equal to 8.5, 10, 15, and 20 mM the net current is zero at potentials of -65, -60, -46, and -31 mV, respectively. With $[Na^+]_i$ greater than 20 mM there is a net efflux at all values of the membrane potential. In unconstrained cells with greater than 20 mM $[Na^+]_i$ the Na^+ would be pumped out to establish a lower internal concentration near 20 mM and -30 mV. From this account, which does not include all routes of Na^+ entry, it appears that the sodium/potassium pumps could maintain the cell at the resting potentials reported *in vivo*, but at elevated internal sodium concentrations (>15 mM) and using a significant portion of the pumping capacity. At 15 mM $[Na^+]_I$ the pumps are activated 50% (compared to saturation at 150 mM $[Na^+]_I$), while at 8.5 mM they are activated 11%–15% over the voltage range which is much more inline with the 10%–15% resting activation expected of the pumps in muscle cells (Skou, 1992).

IV. DISCUSSION

A. Simulated receptor potentials

When receptor potentials were simulated using the model it was found that the dc component is not constant throughout the stimulus, but is largest at the beginning of the stimulus and then decays toward a smaller value. We also found that the membrane potential in the simulated receptor potentials hyperpolarizes with respect to the resting potential when the stimulus is turned off. Noting that the cell's potential drives the synapse, both the sagging dc and the after-stimulus hyperpolarization are consistent with phenomena in the auditory nerve. The sagging dc could contribute to firing rate adaptation and the after-stimulus hyperpolarization could contribute to the after-stimulus suppression of the spontaneous rate. We found that both the sag in the dc component and the after-stimulus hyperpolarization resulted from slow K^+ channel activity. Because the time constant of activation for the slow K^+ channels is 2–10 ms (speeding up with depolarization; Kros and Crawford, 1990), the sag in the receptor potential due to slow channel activation occurs with nearly the same time constant. Rapid adapation occurs in the first 1–10 ms of the stimulus (Ruggero, 1992), therefore if activation of the slow channels contributes to adaptation in the nerve it would contribute to rapid adaptation.

A number of different mechanisms may underlie rapid adaptation. Rapid adaptation is nonlinear with respect to stimulus intensity (Kiang, 1984; Westerman and Smith, 1984; Yates *et al.*, 1985) and appears to involve a complicated interaction of refractoriness, discharge history effects, and additional adaptive mechanisms (Lutkenhoner and Smith, 1986). There is now evidence for a depleteable, readily releasable pool of vesicles in IHCs (Moser and Beutner, 2000), post-synaptic desensitization of neurotransmitter receptors (Raman *et al.*, 1994), and calcium dynamics at the synapse (Sumner *et al.*, 2003) all contributing to adaptation. We cannot, at this point, conclude that the voltage-gated ion channels in IHCs contribute to adaptation as well. To begin with, the simulated receptor potentials that have a sagging dc component and an after-stimulus hyperpolarization must be reconciled with *in vivo* recordings that have neither sags nor after-stimulus hyperpolarizations. To do so, we included a nonspecific leak in the model to simulate the microelectrode impalement that occurs *in vivo*, and found that the leak eliminates the sag and the after-stimulus hyperpolarization. The leak's ability to eliminate the sag and after-stimulus hyperpolarization appears to result from multiple mechanisms. The leak creates an electrical shunt that may mask the activity of the voltage-gated ion channels, but the leak also allows the cell to become depolarized. When the cell is depolarized the channels are partly activated and therefore activate little further during the stimulus and deactivate little after the stimulus. We found that depolarization alone was sufficient to eliminate the sag and the after-stimulus hyperpolarization, and that both features were sensitive to the starting potential of the cell. In fact, even when the starting membrane potential was depolarized by only 6–9 mV using 50 and 100 pA pedestal currents, respectively, the sag and after-stimulus hyperpolarization were noticeably attenuated. There may be experimental evidence to support the sensitivity to the resting potential. Although they chose not to comment on these features, when Dallos and Cheatham (1990) injectected a -2 nA current into a guinea pig IHC *in vivo*, the receptor potential does appear to have a sag in the dc and possibly an after-stimulus hyperpolarization (their Fig. 1). The sensitivity to the starting potential points out the importance of the resting potential and that parameters such as the bias of the transducer may significantly affect the development of the receptor potentials.

B. Homeostasis

1. Factors that influence the resting potential

The resting potential is most influenced by the activation characteristics of the voltage-gated K^+ channels. The K^+ channels have the largest conductance and provide strong negative feedback to counter depolarizing currents. The transducer can produce sufficient current to keep the cell depolarized, but to depolarize the cell to the potential range that is reported *in vivo* requires the transducer to be biased on more than any study suggests. The bias and/or the maximum

conductance of the transducer, however, could be sufficient to eliminate the sag and after-stimulus hyperpolarization seen in the simulated receptor potentials.

2. Resting potential and homeostasis

By considering ionic homeostasis, the model provides another way to think about constraints on the resting potential. The sodium/potassium pumps represent the only method of extruding Na^+ against its gradient and consequently the steady-state influx of Na^+ must be limited to less than the maximum active transport rate.

While the sodium/potassium pump capacity for IHCs has not been measured, it is clear that IHCs do not stain well for (Na^+,K^+)-ATPase (Kuijpers and Bonting, 1969; Mees, 1983; Kerr *et al.*, 1982; Anniko *et al.*, 1984), and the (Na^+,K^+)-ATPase activity in outer hair cells is meager (Sunose *et al.*, 1992). The model used for the sodium/potassium pumps is based on cardiac cells (Lemieux *et al.*, 1990; Chapman *et al.*, 1983) and the pump density is calibrated to data for the goldfish saccular hair cells (Mroz *et al.*, 1993a; Mroz *et al.*, 1993b). In goldfish endolymph the Na^+ concentration is about 53 mM (Naito *et al.*, 1965, as cited by Matsuura *et al.*, 1971) which is substantially higher than the 1 mM found in mammalian endolymph (e.g., Salt and Konishi, 1986). For this reason goldfish hair cells are likely to contend with greater Na^+ influx than mammalian hair cells and calibrating the capacity of the IHC sodium/potassium pump using goldfish data is expected to be an overestimate. Yet, upon inclusion of a minimal Na^+ conductance through the voltage-gated K^+ channels ($P_{Na}/P_K = 0.01$) it was found that as the membrane potential depolarized and the K^+ conductance increased, the inward Na^+ current could be larger than the active efflux capacity of the pumps. As a result, the more depolarized the resting potential the higher the intracellular Na^+ concentration. Maintaining the expected low intracellular $[Na^+]$ at moderate pump capacity requires a hyperpolarized resting potential of about -65 mV to maintain 8.5 mM $[Na^+]_I$ at $<15\%$ pump capacity. In the model, simulations with resting potentials in the range of -30 to -45 mV that are reported for *in vivo* studies with sharp microelectrodes have higher intracellular $[Na^+]$ of >15 mM and the pumps must operate near 50% of maximum capacity.

3. Implications for isolated hair cells and noise-induced hearing loss

A consequence of including a small Na^+ conductance through the voltage-dependent basolateral K^+ channels is that current flowing through the transducer places a metabolic load on the IHC. Even if endolymph contained only K^+ ions, the current through the transducer is depolarizing, it increases the number of basolateral K^+ channels that are open, which increases the Na^+ current that enters the cell through the basolateral K^+ channels. Steady state requires that the net current through the transducer equals the net basolateral current. Therefore, the outward K^+ current through the basolateral K^+ channels must be greater than the K^+ current through the transduction channels by exactly the inward Na^+ current through the basolateral K^+ channels. This leads to an increase in $[Na^+]$ and a decrease in $[K^+]$ inside the cell (a rundown of gradients). Indeed, any depolarizing current that is activated by depolarization would lead to a decrease in the K^+ gradient—for example, calcium entry to drive synaptic transmission (not included in the model).

The least metabolic load and largest ionic gradients occur when the resting transducer conductance is zero. The model predicts that a cell with a nonfunctional transducer would have larger ionic gradients and a more hyperpolarized resting potential than an *in vivo* cell with a standing transducer current. While this means that isolated hair cells with blocked transducers should be healthy, it points out a dilemma for studying hair cells *in vitro*, as noted by Mroz *et al.* (1993a), their low calcium bath improved the yield of isolated goldfish saccular hair cells but rendered the cells unusable for studying transduction.

Simulating *in vitro* conditions with a functional transducer resulted in run down of ionic gradients and an elevation in the membrane potential. Sodium loading of isolated hair cells is a recognized problem (Corey and Hudspeth, 1979; Mroz *et al.*, 1993a; Mroz *et al.*, 1993b; Sunose *et al.*, 1992) and isolated outer hair cells have been observed to have high intracellular sodium (Ikeda *et al.*, 1994). The $[Na^+]_i$ of isolated outer hair cells in a standard NaCl solution has been measured to be about 100 mM (Ikeda *et al.*, 1994), which is comparable to the Na^+ accumulation seen in Fig. 10(b). Both inner and outer hair cells in the isolated cochlea have been observed to accumulate Na^+, and the rate of accumulation could be reduced by blocking transduction (Liu, 1996).

Metabolic exhaustion has been postulated as a cause of noise induced hearing loss but a mechanism has not been forthcoming (Bohne, 1976; Borg *et al.*, 1995). Long exposure (greater than 1 h) to moderate intensity sound (between 90 and 115 dB SPL) results in damage to sensory cells stereotyped by cell swelling and degradation of mitochondria (Spoendlin, 1976). Because endolymph contains primarily K^+ and is at a positive potential, the current that flows through the transducer had been thought to exact little, or no, metabolic cost (Johnstone and Sellick, 1972; Dallos, 1973; Wangemann and Schacht, 1996). However, as explained earlier, if a minimal Na^+ conductance through the voltage-gated K^+ channels is included then the transducer current is no longer metabolically neutral. Cells responding to intense sounds would require greater amounts of ATP to remove the influx of Na^+. The ultimate cause of cell death due to noise is almost certainly more complicated, but Na^+ entry and the consequent run-down of ionic gradients may be a primary event that puts the cell at risk.

ACKNOWLEDGMENTS

The authors wish to thank Dr. Peter Dallos and Dr. Nelson Spruston for their helpful comments. This work was supported by NSF Grant No. BNS-9114245, NIH Grant No. R01 DC02021, and Northwestern University.

APPENDIX A: SODIUM/POTASSIUM PUMPS

While no studies to date have characterized the (Na^+,K^+)-ATPase pump for mammalian inner hair cells, Mroz *et al.* (1993b) have determined the pump's capacity for goldfish hair cells. Their study found that under resting conditions the sodium current developed by the pumps was 5 mM per min and that the maximum sodium current produced by the pumps was 10 mM per min. For a typical goldfish hair cell with 1.3 pL volume, a resting sodium current of 10 pA and a maximum sodium current of 21 pA are calculated. Assuming a cycle time for the enzyme of 0.01 s, Mroz *et al.* (1993b) estimated the presence of 430 000 pumps for a goldfish hair cell (7.5 μm diameter and 30 μm long); a density of 600 pumps per μm^2 of cell surface. Mammalian hair cells do not stain well for (Na^+,K^+)-ATPase (Kuijpers and Bonting, 1969; Mees, 1983; Kerr *et al.*, 1982; Anniko *et al.*, 1984) and the ouabain sensitive current in outer hair cells is very small (Sunose *et al.*, 1992). Because the Na^+ concentration in goldfish endolymph is higher than in mammalian endolymph, the transducer current in goldfish should have a greater Na^+ component than in mammals. For this reason, basing the IHC sodium/potassium pump capacity on goldfish hair cell data is likely to overestimate the true IHC pump capacity.

The sodium/potassium pump has been modeled as a six-step sequential reaction as described for cardiac cells by Lemieux *et al.* (1990) and Chapman *et al.* (1983). This voltage-dependent and concentration-dependent model of the pumps assumes time-independent operation (instantaneous reaction to changing parameters) and calculates the electrogenic current. For use in our model the sodium and potassium current developed by the pump must be calculated from the electrogenic current. The Na^+ current is simply three times the electrogenic current and the K^+ current is two times the electrogenic current.

To establish if this pump model is a suitable description of goldfish hair cell (Na^+,K^+)-ATPase, Fig. 12 shows the Na^+ currents developed for a cell with the known parameters cited by Mroz *et al.* (1993a, 1993b). The unidirectional rate coefficients and most of the physiological parameters used by Chapman *et al.* (1983) and Lemieux *et al.* (1990) for cardiac cells are used here without modification. Pump density, as calculated by Mroz *et al.* (1993b), is 600 pumps per μm^2 in the dashed traces and is 800 per μm^2 in the solid line traces [Chapman *et al.* (1983) employed 753 pumps per μm^2 and Lemieux *et al.* (1990) 722 pumps per μm^2]. Extracellular K^+ and Na^+ concentrations are 3.74 and 114.75 mM, respectively. These concentrations are averages of the four different control media used by Mroz *et al.* (1993b, media contents listed in 1993a). Because Mroz *et al.* (1993b) were calculating the mole percentage of intracellular K^+ and Na^+ with respect to cellular phosphorus (about 100 mM; Mroz *et al.*, 1993a), estimates of intracellular K^+ and Na^+ concentrations were obtained. Under resting conditions the intracellular concentrations were 130 and 15 mM for K^+ and Na^+, respectively. The maximum pumping rate was determined when intracellular K^+ was 15 mM and intracellular Na^+ had risen to about 110 mM. The Mroz *et al.* (1993a) experiments were performed at 37 °C.

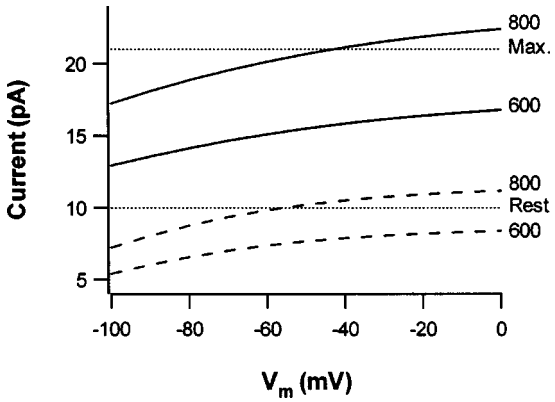

FIG. 12. Calibrating the pumps for goldfish hair cells. The Na^+ current developed by the modeled (Na^+,K^+)-ATPase is plotted as a function of the membrane potential using parameters that are appropriate for goldfish hair cells. The Na^+ pump currents shown are for a pump density of 600 and 800 pumps per μm^2. Rest and Max indicate the resting and maximum Na^+ current determined by Mroz *et al.* (1993b), 10 and 21 pA, respectively. The solid traces show the maximum Na^+ current of the pumps when $[Na]_i = 130$ mM and $[K]_i = 15$ mM. The dashed traces show the "resting" pump current when $[Na]_i = 15$ mM and $[K]_i = 130$ mM. It is observed that 800 pumps per μm^2 gives reasonable values under resting and maximum conditions.

The curves in Fig. 12 represent the Na^+ current developed by the modeled pump under resting and maximal conditions. The dashed curves represent the pump current under resting intracellular concentrations ($[K^+]_i = 130$ mM and $[Na^+]_i = 15$ mM), while the solid curves represent the pump's output for a sodium-loaded cell ($[K^+]_i = 15$ mM and $[Na^+]_i = 110$ mM). Because the expected Na^+ current at rest is 10 pA and the maximum expected Na^+ current is 21 pA (horizontal dotted lines), it is seen that insufficient current is developed at a pump density of 600 pumps per μm^2 in each situation with these parameters.

In order to calculate pump density, Mroz *et al.* (1993b) assumed a pump cycle time of 0.01 s. The aggregate cycle time for goldfish hair cell pumps is not well known. Because the 0.01 s is an estimate, the pump density of 600 per μm^2 is also an estimate. Using a density of 800 pumps per μm^2 (Fig. 12) gives a better correspondence between the model and the capacity of the goldfish hair cells. For this reason 800 pumps per μm^2 will be used as the default value for pump density.

Figure 11 shows the modeled pump's output as a function of membrane potential with a density of 800 pumps per μm^2 and fluid and cell parameters suitable for mammalian IHCs. Extracellular K^+ and Na^+ are 4 and 150 mM, respectively, while intracellular K^+ is equal to 130 mM. Because the intracellular Na^+ concentration is not well established it is useful to consider the pump's operation with different $[Na^+]_i$. Four curves are produced using the intracellular Na^+ concentrations 5, 8.5, 10, and 15 mM. Figure 11 shows that the current developed by the pumps is sensitive to changes in intracellular Na^+ concentration over this range and that consequently the resting Na^+ current will depend heavily on the Na^+ inside the cell. In contrast, the dependence on membrane potential over the likely resting potential range -80 to -20 mV is less pronounced.

Comparing the Na^+ pump currents under the candidate Na^+ resting concentrations to the current produced in a satu-

rating condition of 150 mM $[Na^+]_i$ gives the percentage of maximum pump capacity at rest. If the estimate of the intracellular Na^+ concentration of 5 mM is correct and the model of the pumps is representative, then the pumps are operating at only 3% capacity. However when $[Na^+]_i$ is 15 mM, the resting capacity over the voltage range −100 to 0 mV is 41%–50%, which leaves little reserve for active cells. The expected capacity at rest (for muscle cells) is between 10% and 15% (Skou, 1992). When the intracellular Na^+ concentration is 8.5 mM the pumps are activated to between 11% and 15% over the voltage range (with $[Na^+]_i = 10$ mM activation is 17%–22%).

APPENDIX B: CHLORIDE PUMP, CL⁻ CONDUCTANCE, AND LEAK CONDUCTANCE FOR NA⁺

From the development of the sodium/potassium pumps we have estimates of how much Na^+ current flows across the basolateral membrane under resting conditions (Fig. 11). Because the active extrusion of Na^+ by the sodium/potassium pumps is the only way for sodium to leave the cell, steady-state requirements constrain the passive influx of Na^+ to be equal to the efflux.

The estimate for the Cl^- Nernst potential (E_{Clst}) of −30 mV (see Sec. II) and the assumption that the resting potential is hyperpolarized with respect to −30 mV, requires that the model incorporate an active chloride transporter to concentrate Cl^- inside the cell. The squid giant axon has such a carrier in which 3 Cl^- ions are transported into the cell along with 2 Na^+ and 1 K^+ using the energy of the Na^+ gradient (Russell, 1983; Altamirano and Russell, 1987). In these studies it was found that when the squid axon was voltage clamped to −60 mV, Cl^- was brought into the cell so that the Nernst potential for Cl^- settled at about −40 mV.

No data are available to give an indication of transport capacity of the $Na^+/K^+/Cl^-$ current in hair cells, but it is noted that the steady-state Na^+ influx through the Cl^- transporter must be less than the Na^+ efflux generated by the (Na^+,K^+)-ATPase pumps. If the $Na^+/K^+/Cl^-$ current is maximized, by setting the Na^+ influx equal to the Na^+ current generated by the (Na^+,K^+)-ATPase pumps, then no other Na^+ entry would be tolerable. Conversely, setting the $Na^+/K^+/Cl^-$ cotransport capacity very low makes the effects of this current on resting potential difficult to ascertain in simulations. For these reasons the Na^+ current due to transport carriers will be arbitrarily designated as 1 pA at −50 mV. A 1 pA Na^+ current with the assumptions of $E_{Nast} = 91$ mV and a membrane potential of −50 mV gives a Na^+ conductance for the Cl^- transporter of 7 pS.

For use in the model the $Na^+/K^+/Cl^-$ cotransporter is treated very simplistically. The Na^+ conductance is set to 7 pS, the K^+ current is then calculated as one half of the Na^+ current and the Cl^- current is three halves of the Na^+ current. Isolated hair cells are relatively impermeant to Cl^- ions (Ashmore and Meech, 1986; Sunose *et al.*, 1992). Gitter *et al.* (1986), however, found voltage-gated Cl^- channels in membrane patches pulled from an OHC. Because the biophysical model requires a Cl^- conductance and little information is known, it will be considered static (not voltage dependent) with a magnitude of 100 pS. While there are no direct data to support the chosen value of 100 pS for Cl^- conductance, it is observed that the requirement of a small conductance combined with a low driving force (about 30 mV) means that Cl^- should play only a minor role in setting the IHC resting potential.

Because Na^+ has such a high driving force for entry into the cell, a small conductance would give rise to large current. The 7 pS value chosen for the Na^+ conductance in $Na^+/K^+/Cl^-$ transporter is set to a maximal size that does not impose unwarranted restrictions on Na^+ entry at other sites. While it does represent a maximal value, 7 pS is on the order of a single channel. For this reason no other ''leak'' conductance for Na^+ is incorporated into the model.

Altamirano, A. A., and Russell, J. M. (**1987**). ''Coupled Na/K/Cl efflux. 'Reverse' unidirectional fluxes in squid giant axons,'' J. Gen. Physiol. **89**, 669–686.

Anniko, M., Lim, D., and Wroblewski, R. (**1984**). ''Elemental composition of individual cells and tissues in the cochlea,'' Acta Oto-Laryngol. **98**, 439–453.

Appenrodt, P., and Kros, C. J. (**1997**). ''Single-channel recordings of large-conductance Ca^{2+} activated K^+ channels,'' J. Physiol. (London) **507**, 147P.

Ashmore, J. F., and Meech, R. W. (**1986**). ''Ionic basis of membrane potential in outer hair cells of guinea pig cochlea,'' Nature (London) **322**, 368–371.

Assad, J. A., Shepard, G. M., and Corey, D. P. (**1991**). ''Tip-link integrity and mechanical transduction in vertebrate hair cells,'' Neuron **7**, 985–994.

Bohne, B. A. (**1976**). ''Mechanisms of noise damage in the inner ear,'' in *Effects of Noise on Hearing*, edited by D. Henderson, R. P. Hamernik, and D. S. M. J. H. Dosanjh (Raven, New York), pp. 41–68.

Borg, E., Canlon, B., and Engstrom, B. (**1995**). ''Noise-induced hearing loss. Literature review and experiments in rabbits. Morphological and electrophysiological features, exposure parameters and temporal factors, variability and interactions,'' Scand. Audiol. Suppl. **40**, 1–147.

Chapman, J. B., Johnson, E. A., and Kootsey, J. M. (**1983**). ''Electrical and biochemical properties of an enzyme model of the sodium pump.'' J. Membr. Biol. **74**, 139–153.

Cody, A. R., and Russell, I. J. (**1987**). ''The response of hair cells in the basal turn of the guinea-pig cochlea to tones,'' J. Physiol. (London) **383**, 551–569.

Corey, D. P., and Hudspeth, A. J. (**1979**). ''Ionic basis of the receptor potential in a vertebrate hair cell,'' Nature (London) **281**, 675–677.

Crawford, A. C., Evans, M. G., and Fettiplace, R. (**1989**). ''Activation and adaptation of transducer currents in turtle hair cells,'' J. Physiol. (London) **419**, 405–434.

Dallos, P. (**1973**). *The Auditory Periphery: Biophysics and Physiology* (Academic, New York).

Dallos, P. (**1984**). ''Some electrical circuit properties of the organ of Corti. II. Analysis including reactive elements,'' Hear. Res. **14**, 281–291.

Dallos, P. (**1985**). ''Membrane potential and response changes in mammalian cochlear hair cells during intracellular recording,'' J. Neurosci. **5**, 1609–1615.

Dallos, P., and Cheatham, M. A. (**1989**). ''Cochlear nonlinearities reflected in inner hair cell responses,'' in *Cochlear Mechanisms: Structure, Function, and Models*, edited by J. P. Wilson and D. T. Kemp (Plenum, New York), pp. 197–204.

Dallos, P., and Cheatham, M. A. (**1990**). ''Effects of electrical polarization on inner hair cell receptor potentials,'' J. Acoust. Soc. Am. **87**, 1636–1647.

Dulon, D., Sugasawa, M., Blanchet, C., and Erostegui, C. (**1995**). ''Direct measurements of Ca(2+)-activated K^+ currents in inner hair cells of the guinea-pig cochlea using photolabile Ca^{2+} chelators,'' Pfluegers Arch. **430**, 365–373.

Gitter, A. H., Zenner, H. P., and Fromter, E. (**1986**). ''Membrane potential and ion channels in isolated outer hair cells of guinea pig cochlea,'' ORL J. Otorhinolaryngol. Relat. Spec. **48**, 68–75.

Gitter, A. H., and Zenner, H. P. (**1990**). ''The cell potential of isolated inner hair cells *in vitro*,'' Hear. Res. **45**, 87–93.

Ikeda, K., Sunose, H., and Takasaka, T. (**1994**). ''Ion transport mechanisms in the outer hair cell of the mammalian cochlea,'' Prog. Neurobiol. (Oxford) **42**, 703–717.
Johnstone, B. M., and Sellick, P. M. (**1972**). ''The peripheral auditory apparatus,'' Q. Rev. Biophys. **5**, 1–57.
Kerr, T. P., Ross, M. D., and Ernst, S. A. (**1982**). ''Cellular localization of Na^+, K^+-ATPase in the mammalian cochlear duct: Significance for cochlear fluid balance,'' Am. J. Otolaryngol. **3**, 332–338.
Kiang, N. Y. S. (**1984**). ''Peripheral neural processing of auditory information,'' in *Handbook of Physiology*, edited by I. Darian-Smith (American Physiology Society, Bethesda), Sec. I. (The Nervous System), Vol. III (Sensory Processes, Part 2), pp. 639–694.
Kiang, N. Y. S., Watanabe, T., Thomas, C., and Clark, L. F. (**1965**). *Discharge Patterns of Single Fibers in the Cat's Auditory Nerve* (MIT, Cambridge).
Kirkwood, N. K., and Kros, C. J. (**1997**). ''Rapid photorelease of calcium augments the fast potassium conductance of guinea-pig inner hair cells,'' J. Physiol. (London) **504**, 127P.
Kros, C. J. (**1989**). ''Membrane properties of inner hair cells isolated from the guinea-pig cochlea,'' Ph.D. thesis, University of Cambridge, Cambridge, England.
Kros, C. J. (**1996**). ''Physiology of mammalian cochlear hair cells,'' in *The Cochlea*, edited by P. Dallos, A. N. Popper, and R. R. Fay (Springer, New York), pp. 318–385.
Kros, C. J., and Crawford, A. C. (**1990**). ''Potassium currents in inner hair cells isolated from the guinea-pig cochlea,'' J. Physiol. (London) **421**, 263–291.
Kros, C. J., Ruppersberg, J. P., and Rusch, A. (**1998**). ''Expression of a potassium current in inner hair cells during development of hearing in mice,'' Nature (London) **394**, 281–284.
Kros, C. J., Rusch, A., Lennan, G. W. T., and Richardson, G. P. (**1993**). ''Voltage dependence of transducer currents in outer hair cells of neonatal mice,'' in *Biophysics of Hair Cell Sensory Systems*, edited by H. Duifhuis, J. W. Horst, P. v. Dijk, and S. M. v. Netten (World Scientific, Singapore), pp. 141–150.
Kros, C. J., Rusch, A., and Richardson, G. P. (**1992**). ''Mechano-electrical transducer currents in hair cells of the cultured neonatal mouse cochlea,'' Proc. R. Soc. London, Ser. B **249**, 185–193.
Kuijpers, W., and Bonting, S. L. (**1969**). ''Studies on (Na^+-K^+)-activated ATPase. XXIV. Localization and properties of ATPase in the inner ear of the guinea pig,'' Biochim. Biophys. Acta **173**, 477–485.
Lemieux, D. R., Roberge, F. A., and Savard, P. (**1990**). ''A model study of the contribution of active Na-K transport to membrane repolarization in cardiac cells,'' J. Theor. Biol. **142**, 1–34.
Liu, T. C. (**1996**). ''Measurement of intracellular ionic concentrations in the isolated organ of corti using fluorescent probes,'' Ph.D. thesis, Northwestern University, Evanston, IL.
Lutkenhoner, B., and Smith, R. L. (**1986**). ''Rapid adaptation of auditory-nerve fibers: Fine structure at high stimulus intensities,'' Hear. Res. **24**, 289–294.
Marty, A., and Neher, E. (**1983**). ''Tight-seal whole-cell recording,'' in *Single-Channel Recording*, edited by B. Sakmann and E. Neher (Plenum, New York), pp. 107–121.
Matsuura, S., Ikeda, K., and Furukawa, T. (**1971**). ''Effects of Na^+, K^+, and ouabain on microphonic potentials of the goldfish inner ear,'' Japanese J. Physiol. **21**, 563–578.
Mees, K. (**1983**). ''Ultrastructural localization of K^+-dependent, ouabain-sensitive NPPase (Na-K-ATPase) in the guinea pig inner ear,'' Acta Oto-Laryngol. **95**, 277–289.
Meyer, J., Furness, D. N., Zenner, H. P., Hackney, C. M., and Gummer, A. W. (**1998**). ''Evidence for opening of hair-cell transduction channels after tip-link loss,'' J. Neurosci. **18**, 6748–6746.
Moser, T., and Beutner, D. (**2000**). ''Kinetics of exocytosis and endocytosis at the cochlear inner hair cell afferent synapse of the mouse,'' Proc. Natl. Acad. Sci. USA **97**, 883–888.
Mountain, D. C., and Hubbard, A. E. (**1996**). ''Physiology of mammalian cochlear hair cells,'' in *Auditory Computation*, edited by H. L. Hawkins, T. A. McMullen, A. N. Popper, and R. R. Fay (Springer, New York), pp. 121–156.
Mroz, E. A., Nissim, K. R., and Lechene, C. (**1993a**). ''Electron-probe analysis of isolated goldfish hair cells: Implications for preparing healthy cells,'' Hear. Res. **70**, 9–21.
Mroz, E. A., Nissim, K. R., and Lechene, C. (**1993b**). ''Rapid resting ion fluxes in goldfish hair cells are balanced by (Na^+,K^+)-ATPase,'' Hear. Res. **70**, 22–30.
Naito, T., Uyematsu, H., Nakamura, T., Horii, T., and Miyazaki, T. (**1965**). ''Studies on inorganic ions of inner ear fluids,'' Japanese J. Otol. **68**, 1628 (in Japanese).
Ohmori, H. (**1984**). ''Mechanoelectrical transducer has discrete conductances in the chick vestibular hair cell,'' Proc. Natl. Acad. Sci. USA **81**, 1888–1891.
Ohmori, H. (**1985**). ''Mechano-electrical transduction currents in isolated vestibular hair cells of the chick,'' J. Physiol. (London) **359**, 189–217.
Pongracz, F., Firestein, S., and Shepherd, G. M. (**1991**). ''Electrotonic structure of olfactory sensory neurons analyzed by intracellular and whole cell patch techniques,'' J. Neurophysiol. **65**, 747–758.
Raman, I. M., Zhang, S., and Trussell, L. O. (**1994**). ''Pathway-specific variants of AMPA receptors and their contribution to neuronal signaling,'' J. Neurosci. **14**, 4998–5010.
Raybould, N. P., Jagger, D. J., and Housley, G. D. (**2001**). ''Positional analysis of guinea pig inner hair cell membrane conductances: Implications for regulation of the membrane filter,'' J. Assoc. Res. Otolaryngol. **2**, 362–376.
Ronan, D., and Mroz, E. A. (**1996**). ''Stability of solute composition in a simple hair-cell model,'' Abst. Assoc. Res. Otolaryngol. **19**, 134.
Ruggero, M. A. (**1992**). ''Physiology and coding of sound in the auditory nerve [review],'' in *The Mammalian Auditory Pathway: Neurophysiology*, edited by A. N. Popper and R. R. Fay (Springer, New York), pp. 34–93.
Russell, I. J., and Sellick, P. M. (**1983a**). ''Low-frequency characteristics of intracellularly recorded receptor potentials in guinea-pig cochlear hair cells,'' J. Physiol. (London) **338**, 179–206.
Russell, J. M. (**1983b**). ''Cation-coupled chloride influx in squid axon. Role of potassium and stoichiometry of the transport process,'' J. Gen. Physiol. **81**, 909–925.
Salt, A. N., and Konishi, T. (**1986**). ''The cochlear fluids: Perylimph and endolymph,'' in *Neurobiology of Hearing: The Cochlea*, edited by R. A. Altschuler, D. W. Hoffman, and R. P. Bobbin (Raven, New York), pp. 108–122.
Skou, J. C. (**1992**). ''The Na,K-ATPase,'' News in Physiological Sci. **7**, 95–100.
Slepecky, N. (**1996**). ''Structure of the Mammalian Cochlea,'' in *The Cochlea*, edited by P. Dallos, A. N. Popper, and R. R. Fay (Springer, New York), pp. 44–129.
Spoendlin, H. (**1976**). ''Anatomical changes following various noise exposures,'' in *Effects of Noise on Hearing*, edited by D. Henderson, R. P. Hamernik, and D. S. M. J. H. Dosanjh (Raven, New York), pp. 69–90.
Spruston, N., and Johnston, D. (**1992**). ''Perforated patch-clamp analysis of the passive membrane properties of three classes of hippocampal neurons,'' J. Neurophysiol. **67**, 508–529.
Stefani, E., and Steinbach, A. B. (**1969**). ''Resting potential and electrical properties of frog slow muscle fibers. Effect of different external solutions,'' J. Physiol. (London) **203**, 383–401.
Sumner, C. J., Lopez-Poveda, E. A., O'Mard, L. P., and Meddis, R. (**2003**). ''Adaptation in a revised inner-hair cell model,'' J. Acoust. Soc. Am. **113**, 893–901.
Sunose, H., Ikeda, K., Saito, Y., Nishiyama, A., and Takasaka, T. (**1992**). ''Membrane potential measurement in isolated outer hair cells of the guinea pig cochlea using conventional microelectrodes,'' Hear. Res. **62**, 237–244.
Wangemann, P., and Schacht, J. (**1996**). ''Homeostatic mechanisms in the cochlea,'' in *The Cochlea*, edited by P. Dallos, A. N. Popper, and R. R. Fay (Springer, New York), pp. 130–185.
Westerman, L. A., and Smith, R. L. (**1984**). ''Rapid and short-term adaptation in auditory nerve responses,'' Hear. Res. **15**, 249–260.
Yates, G. K., Robertson, D., and Johnstone, B. M. (**1985**). ''Very rapid adaptation in the guinea pig auditory nerve,'' Hear. Res. **17**, 1–12.
Zeddies, D. G. (**2001**). ''An Investigation of the influence of voltage-gated ion channels on the receptor potential of inner hair cells,'' Ph.D. thesis, Northwestern University, Evanston, IL.

Periodogram based tests for distortion product otoacoustic emissions

Peter F. Craigmile[a)]
Department of Statistics, 404 Cockins Hall, 1958 Neil Avenue, The Ohio State University, Columbus, Ohio 43210

Wayne M. King
Department of Speech and Hearing Sciences, 1070 Carmack Road, The Ohio State University, Columbus, Ohio 43210

(Received 3 February 2004; revised 21 April 2004; accepted 23 April 2004)

Distortion product otoacoustic emissions (DPOAEs) are an important nonbehavioral measure of cochlear function, which provides a close analogue of the behavioral pure-tone audiogram. DPOAEs are sinusoidal distortion products (DPs) produced by nonlinearities in the healthy cochlea. Detection of DPs is accomplished in the Fourier domain with a periodogram based test. The test compares the power in the DP periodogram bin to a noise estimate derived from a certain number of the surrounding bins. Statistical properties of this test to date have only been examined by constructing receiver operator characteristics curves derived from DPOAE measurements in normal and hearing impaired individuals. In this paper the null distribution of this order-statistic based test is explicitly derived, and via simulations intended to mimic the nonwhite features of real-ear noise measurements, the power of the test is demonstrated. These simulations demonstrate that a local F test is more powerful than this DPOAE test, with critical values that are easier to calculate. Although the power of both tests increase with an increasing number of bins, the improvement is negligible at around four bins. Since the power of both tests decrease at lower DP frequencies, it is not recommended to use a large number of bins.
[DOI: 10.1121/1.1760793]

PACS numbers: 43.64.Jb, 43.60.Cg, 43.60.Ac [BLM] Pages: 442–451

I. INTRODUCTION

Nonbehavioral audiologic measures play a critical role in the assessment of the auditory system and the diagnosis of auditory dysfunction. In many patient populations, reliable behavioral data may be difficult or impossible to obtain. These populations include: infants and young children, persons with cognitive impairment, and persons with functional hearing loss. Recent years have witnessed a dramatic increase in the interest in nonbehavioral audiologic testing, primarily driven by the recognized need to implement comprehensive infant screening. The impetus for comprehensive infant screening is in turn motivated by an increasing body of research demonstrating the long-term deleterious effects of undiagnosed and unremediated hearing loss on language and cognitive development.[1,2] The importance of diagnosing hearing loss in these critical populations mandate that reliable nonbehavioral measures of hearing sensitivity are available to health care professionals. These measurements need to be minimally invasive and must be accomplished quickly, accurately, and in less than ideal testing conditions.

Distortion product otoacoustic emissions (DPOAEs) are a nonbehavioral audiologic measure, that exploits the inherent nonlinearity of the normal cochlea and has the potential to provide frequency-specific information about cochlear outer haircell integrity. It is well established the healthy cochlea will produce emissions in response to acoustic stimulation, while a damaged cochlea will not. DPOAEs are observed when two tones f_1 and f_2 are transmitted into the ear. In ears with normal nonlinear cochlear function, a number of different intermodulation distortion products (DPs) are generated by an interaction of the traveling wave patterns of f_1 and f_2 on the basilar membrane. These distortion products travel back out through the middle ear into the external ear canal, where they can be recorded by a sensitive microphone placed near the tympanic membrane. While in principle many DPs of the form $kf_1 \pm mf_2$, $k, m \in \mathbb{Z}$ are observable, the most robust in humans is the so-called cubic DP $2f_1 - f_2$.[3] Otoacoustic emissions can also be observed using broadband stimuli such as clicks, but DPOAEs have the additional advantage of potentially providing a more frequency-specific measure of cochlear integrity. This frequency specificity in principle more closely resembles the pure-tone behavioral audiogram, which is considered the audiologic gold standard in the assessment of peripheral hearing sensitivity.

However, in spite of abundant physiological and psychoacoustic evidence from experimental animals and human subjects that DPOAEs are clinically relevant, there remain serious issues concerning their interpretability.[4] Some of these issues involve imprecise knowledge of DPOAE generation mechanisms, while others emanate from still unresolved statistical issues in the performance of estimators used to extract the putative DP from the surrounding noise.[5] As with any estimator, explicit knowledge of its distribution is critical for any inference based on the resulting estimates.

a)Electronic mail: pfc@stat.ohio-state.edu

Recognition of the importance of this fact is beginning to build awareness in the audiologic community that the robustness of a DPOAE measurement algorithm is possibly the most important factor in terms of clinical application.[6] Unfortunately the issue of statistical signal processing in DPOAE detection and estimation has largely been neglected in the literature. There have been extensive studies of the effects of many variables on DPOAEs including such factors as maturational effects,[7] time of day,[8] gender[8] and age.[9] Additionally, there have been numerous studies on the effect of systematic variations in stimulus-related parameters. These include: intensity differences in the evoking tones[10] and the frequency separation of the evoking tones[11] among others. These studies all constitute important attempts to give hearing-health care professionals a qualitative and quantitative understanding of the significant sources of variance observed in DPOAEs. It must also be stressed that the test statistic used to test for a ''signal'' is itself a nontrivial source of variance that should be systematically addressed.

In this paper the statistical properties of a common test for DPOAE detection are investigated both analytically and via Monte Carlo experiments. This test is based on the spectral estimator called the periodogram which is proportional to the modulus squared of a discrete Fourier transform of the data [see Eq. (2) for a mathematical definition]. DPOAE data are analyzed in the Fourier domain typically using a periodogram based test in which the periodogram bin corresponding to the DP frequency is identified and the power measured. A noise estimate is derived by measuring the power in a number of adjacent periodogram bins and comparing the ratio of the power in the DP bin to the maximum mean power in the specified number of bins above and below the frequency of interest. The actual number of bins used in the noise estimate can vary, but a common number is three bins above and three below the DP frequency.[12] The DP is then considered detected if the ratio of DP power to noise power exceeds a criterion level. Commonly used clinical levels range from 3 to 12 dB.[13–15] It should be noted that these signal to noise measures are in general independent of the recorded expressed sound pressure level (SPL). However, it is common to take the level of the noise power in dB SPL into account during testing. For example, data acquisition may continue until the noise floor reaches some criterion level in dB SPL before testing is terminated, and the DP is either detected or the test is deemed a negative result. Further, it is not uncommon to report the level of the DP in dB SPL, although the fundamental statistical test is based on the power in the DP bin measured relative to some noise floor.

There is some justification for using the DPOAE/noise ratio measurement based on its superior ability to separate normal and impaired ears when compared against just looking at the DPOAE amplitude. The ratio of power at the DP frequency to the noise power was found to be a more sensitive measure for the discrimination of normal and impaired ears than DPOAE amplitude.[16]

The criterion level and the number of bins used in the noise estimate is a clinic specific decision and is often made without the benefit of an explicit statistical basis. The statistical significance of the levels has primarily been arrived at through the examination of receiver operating characteristic curves on DPOAE measurements in large samples of normal-hearing people.[12,17] A consistent conclusion to emerge from these studies is that the detectability of DPOAEs in normal-hearing subjects is extremely difficult at f_2 frequencies below 1 kHz and improves with increasing f_2. One of the putative reasons for the diminished detection of DPOAEs below 1 kHz is the increasing power encountered in the noise bins.[12] The important work of these large scale studies of human DPOAE measurements and their predictability for behavioral audiogram prediction is hampered by the lack of explicit derivations of the properties of the DP/noise test statistic. In this paper, the theoretical distribution of the DP/noise test statistic is explicitly worked out under the null hypothesis (see Ref. 12 for cumulative distributions based on samples of individuals from various populations). Further, the size and power of the test is categorized using both actual and simulated data. Special interest is paid to the analysis of the performance of the test under the assumption of nuisance frequencies (f_1 and f_2) and in the presence of a nonwhite noise error process. The frequency dependence of the test performance in realistic noise models is characterized. The effect of changing the number of bins that is used in the test statistic is investigated (Ref. 5 showed by a simulation study that the test performed better in terms of detection power as the number of bin increases). The DPOAE is also compared to a local *F* test that is inspired by a hypothesis test that is commonly used in the statistics literature.

The statistical model for DPOAE data and hypotheses of interest are stated in Sec. II. A brief review of spectral analysis is provided in Sec. III, and in Sec. IV a standard test for periodicity from the DPOAE literature is analyzed. The local *F* test and its statistical properties are introduced and examined in Sec. V. Real-ear measurements accomplished under realistic DPOAE testing conditions are analyzed in Sec. VI, and under these conditions Monte Carlo simulations are carried out to estimate the size and power of the tests. Some conclusion are made in Sec. VII.

II. TESTING FOR PERIODICITIES IN THE PRESENCE OF BACKGROUND NOISE

Let L be some positive integer. For a sampling interval of Δ, the model for the data $\{X_t : t \in \mathbb{Z}\}$ is

$$X_t = \sum_{l=1}^{L} A_l \cos(2\pi f_l t\Delta + \phi_l) + \eta_t . \tag{1}$$

Presuppose that the frequencies $\{f_l\}$ are fixed and known with unknown amplitudes $\{A_l\}$. There is substantial interest in the case when some of the amplitudes may be large in magnitude. The phases $\{\phi_l\}$ are assumed to be independent random variables, uniform on the range $(-\pi,\pi]$, which are independent of a mean zero stationary Gaussian error process $\{\eta_t : t \in \mathbb{Z}\}$. Suppose the Gaussian error process has a purely continuous bounded spectral density function (SDF) $S(\cdot)$. The hypotheses of interest are

$$H_0 : A_L = 0 \quad \text{versus} \quad H_1 : A_L \neq 0.$$

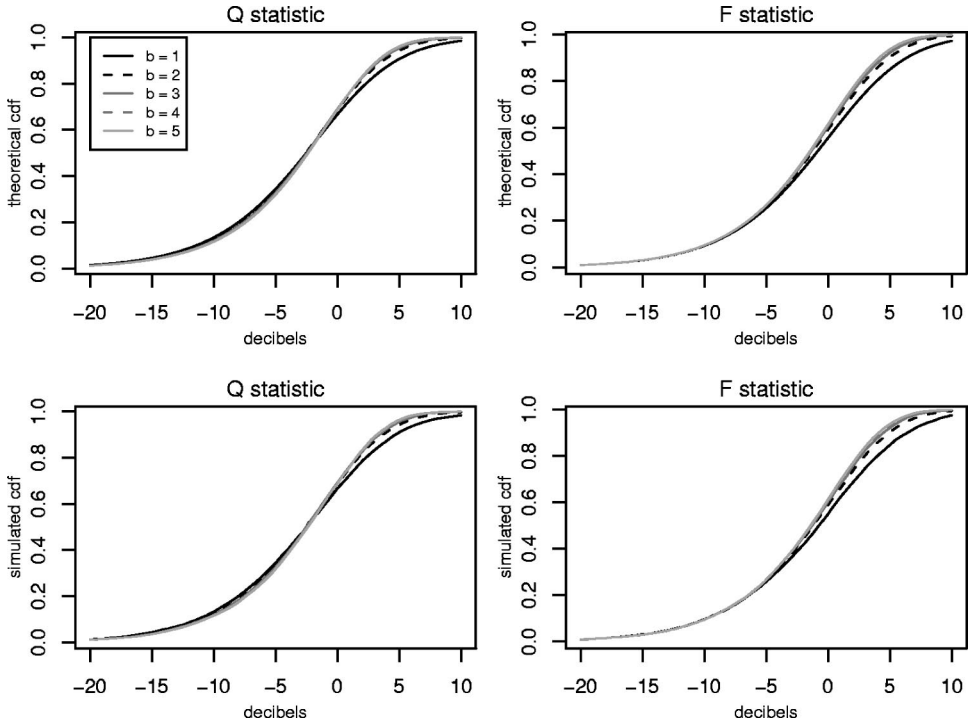

FIG. 1. The top panels display the theoretic cdf of the Q_b and F_b statistics, for various bin sizes b. The bottom panels display the estimated cdf of the same test statistics, calculated using a simulation of 10 000 Gaussian white noise processes of length $N=64$. The maximum pointwise standard error for each estimated cdf is 0.005.

As highlighted in Sec. I, in the simplest case, $L=3$ and $f_3=2f_1-f_2$ for DPOAE detection. In Sec. II the periodogram is defined. This estimator of the SDF is used to calculate the test statistics used in this paper.

III. STATISTICAL PROPERTIES OF THE PERIODOGRAM

The purpose of this section is to provide a brief review of the spectral analysis of time series using the periodogram (for more details see, e.g., Refs. 18–21). Suppose a finite realization, $\{X_t: t=0,1,...,N-1\}$, of the process in Eq. (1) is observed. Letting $\zeta_{(n)}=1/(2\Delta)$ denote the Nyquist frequency, the periodogram is defined as

$$\hat{S}^{(p)}(\zeta)=\frac{\Delta}{N}\left|\sum_{t=1}^{N} X_t e^{-i2\pi ft\Delta}\right|^2, \quad \text{for } |f|\leqslant\zeta_{(n)}. \tag{2}$$

For a given length of time series N, define the set of Fourier frequencies to be $\{\zeta_k=k/(N\Delta)\colon\ k=1,...,m\}$, where $m=\lfloor N/2\rfloor$. Interest is in the statistical properties of the periodogram ordinates $\{\hat{S}^{(p)}(\zeta_k)\colon\ k=1,...,m\}$, when the set of Fourier frequencies is kept constant, but as more than N data points are collected. To express the amount of new data collected (i.e., the data is not zero padded), let N' denote the length of the new time series. As N' (the embedding sample size) increases, more information about the SDF $S(\cdot)$ is obtained.

When there are no periodicities in Eq. (1), i.e., $A_l=0$ for all $l=1,...,L$, the following well known result holds (see Ref. 22, Theorem 8.4.4 for a proof of this result).

Proposition III.1. *Let ζ_k, $\zeta_{k'}$ be frequencies satisfying $0<\zeta_k<\zeta_{k'}<\zeta_{(n)}$. Then $\hat{S}^{(p)}(\zeta_j)$ tends in distribution to a chi squared random variable with 2 degrees of freedom, multiplied by $S(\zeta_k)/2$ as $N'\to\infty$, and $\hat{S}^{(p)}(\zeta_j)$ and $\hat{S}^{(p)}(\zeta_k)$ are asymptotically independent.*

These results continue to hold in the presence of periodicities, that is, these results hold under model (1) as long as: (i) the periodicities occur at the Fourier frequencies and (ii) no periodocity occurs in the regions $[\zeta-1/(N\Delta),\zeta+1/(N\Delta)]$ and $[\zeta'-1/(N\Delta),\zeta'+1/(N\Delta)]$.

The above proposition also demonstrates that $\text{var}(\hat{S}^{(p)}(\zeta_k))=S^2(\zeta_k)$, and hence that the periodogram is not a consistent estimate of the underlying SDF. Consistent estimates are obtained by either smoothing the periodogram estimates (Ref. 21, Chap. 6) or by averaging multitaper spectral estimates (Refs. 23 and 21, Chap. 7).

In practice the data $\{X_t\}$ are often tapered (e.g., using a Hamming window) before calculating the periodogram. Under certain regularity conditions (Ref. 19, Sec. 5.2), these so called direct spectral estimates have the same asymptotic statistical properties as the periodogram. In small samples, however, the correlation between closely spaced frequencies in a direct spectral estimate can be larger than with the periodogram estimates. This may have implications for the statistical tests presented in this paper (see Sec. VII for further comments on tapering).

IV. A STANDARD TEST FOR PERIODICITY

The standard periodogram based test used in the DPOAE literature[12] is now described. Let ζ_k denote the Fourier frequency which is closest to f_L. Define $Y_{L,b}=\Sigma_{j=1}^{b}\hat{S}^{(p)}(\zeta_{k-j})/b$ to be the average of the b spectral bins to the left (i.e., lower in frequency) of the frequency of interest and let $Y_{R,b}=\Sigma_{j=1}^{b}\hat{S}^{(p)}(\zeta_{k+j})/b$ be the average of the b to the right (i.e., higher in frequency). For example, for $b=3$, a sampling interval of $\Delta=1/50\,000$ and time series of length $N=8192$; this corresponds to a frequency range of 18.3 Hz to the left and right of ζ_k. Let $\text{dB}(x)=10\log_{10}x$ denote the decibel function. For some threshold λ, this

TABLE I. For different bin sizes, b, the size of the DPOAE test associated with commonly used critical values.

	Critical value (dB SPL)			
b	3	6	9	12
1	0.167 13	0.067 13	0.022 49	0.006 65
2	0.130 11	0.035 09	0.006 05	0.000 71
3	0.119 39	0.026 00	0.002 89	0.000 17
4	0.114 99	0.021 97	0.001 80	0.000 06
5	0.112 94	0.019 77	0.001 29	0.000 03

"DPOAE test" is based on rejecting H_0 if the periodogram evaluated at the Fourier frequency of interest ζ_k is larger than the maximum of $\mathrm{dB}(Y_{L,b})$ and $\mathrm{dB}(Y_{R,b})$ by λ dB or more, that is, reject H_0 if $\mathrm{dB}(\hat{S}^{(p)}(\zeta_k)) > \max\{\mathrm{dB}(Y_{L,b}),\mathrm{dB}(Y_{R,b})\}+\lambda$. Equivalently, letting

$$Q_b=\frac{\hat{S}^{(p)}(\zeta_k)}{\max\{Y_{L,b},Y_{R,b}\}},$$

H_0 is rejected if Q_b is larger than $10^{(\lambda/10)}$. The size of this test is now investigated by deriving the distribution of Q_b under the null hypothesis (closed form expressions for $b=1,...,5$ are provided in the Corollary that follows). The proofs of these results are given in the Appendix.

Theorem IV.1. *Consider data following Eq. (1). Let f_l be Fourier frequencies with $f_l \notin [\zeta_{k-b},\zeta_{k+b}]$ for $l \neq k$. Suppose $\{\eta_t\}$ is a stationary process with a summable autocovariance sequence, and that the SDF of the process $S(\cdot)$ is locally constant around ζ_k. Then under H_0 (i.e., $A_L=0$), the test statistic Q_b has the following asymptotic cumulative distribution function (cdf)*:

$$P(Q_b \leqslant q)=\frac{1}{[\Gamma(b)]^2 2^{2b-1}}\int_0^\infty y^{b-1}e^{-y/2}[1-e^{-qy/(2b)}] \times\left[\int_0^y v^{b-1}e^{-v/2}dv\right]dy.$$

Corollary IV.2. *Suppose the same conditions as stated in Theorem IV.1. Under H_0, for $b=1,...,5$*

$$P(Q_1 \leqslant q)=1-\frac{2}{(2+q)(1+q)},$$

$$P(Q_2 \leqslant q)=1-32\frac{3q+8}{(4+q)^3(2+q)^2},$$

$$P(Q_3 \leqslant q)=1-1458\left(\frac{10q^2+75q+144}{(6+q)^5(q+3)^3}\right),$$

$$P(Q_4 \leqslant q)=1-131\,072 \times\left(\frac{35q^3+504q^2+2464q+4096}{(8+q)^7(q+4)^4}\right),$$

$$P(Q_5 \leqslant q)=1-19\,531\,250 \times\left(\frac{126q^4+2940q^3+26100q^2+104625q+160000}{(10+q)^9(q+5)^5}\right).$$

A plot of the cdf for bin sizes, $b=1,...,5$, is shown in the top left panel of Fig. 1. To verify this distribution in practice the following small Monte Carlo study was considered. 10 000 Gaussian white noise processes of length $N=64$ were simulated, and for each process the test statistics Q_b, for $b=1,...,5$, were calculated at the 20th Fourier frequency ζ_{20}. The bottom left panel of Fig. 1 displays the empirical cdf estimated using these test statistics for each value of b and demonstrates that it matches exactly with the theory [the maximum standard error of each estimate of the cdf was calculated to be 0.005, using a standard binomial proportion calculation (e.g., Ref. 24)]. Table I shows the size of the test, H_0: $A_L=0$, corresponding to the commonly used critical values of 3, 6, 9, and 12 dB SPL. The size of the test based on these critical values decreases as b increases. Table II displays the critical values as for a 5% test. Reference 6, p. 188, notes that "an amplitude of 6 dB SPL above the noise floor will allow for a 5% probability of falsely detecting an emission." Based on the theory presented here, this is an overestimation of the probability for $b \geqslant 2$. (The probability of false detection is 3.5% for $b=2$, 2.6% for $b=3$, 2.2% for $b=4$, and 2.0% for $b=5$.)

Remember that the results in this section are asymptotic, that is, they hold for large sample sizes. To verify these results for fixed sample sizes, the size and power of the test shall be determined under various simulations intended to mimic nonwhite experimental conditions in Sec. VI. These results are independent of the sampling interval Δ.

V. THE LOCAL *F* TEST FOR PERIODICITY

A common periodogram based test in the statistical literature for a single periodicity in the presence of white noise is the F test. In this section the local F test is examined, a refinement which has the potential to perform well in nonwhite backgrounds, and in the presence of nuisance periodicities.

First consider the standard F test (for further details see Sec. 11.2.4 of Ref. 25). Suppose first the simpler model of Eq. (1) with $L=1$, i.e.,

$$X_t=A_1\cos(2\pi f_1 t\Delta+\phi_1)+\eta_t.$$

Also assume that the error sequence $\{\eta_t\}$ is Gaussian white noise. The hypotheses of the test are H_0: $A_1=0$ versus H_1: not H_0. Let ζ_k $(k=1,...,m-1)$ be the Fourier frequency closest to the periodicity f_1. The test statistic is

$$F=\frac{\hat{S}^{(p)}(\zeta_k)}{\Sigma_{j\neq k}\hat{S}^{(p)}(\zeta_j)/(m-1)}.$$

Using Proposition III.1 it can be argued that the numerator and denominator are asymptotically independent chi squared random variables. Thus, under H_0 the test statistic F has an asymptotic F distribution with 2 and $2(m-1)$ degrees of freedom. Now consider a local F test inspired in part by ideas discussed in Ref. 26. A significant frequency component in a neighborhood of b bins of a Fourier frequency ζ_k is tested. The hypotheses are H_0: $A_1 \neq 0$ versus H_1: not H_0. The local F test statistic is

$$F_b = \frac{\hat{S}^{(p)}(\zeta_k)}{(\Sigma_{j=k-b}^{k-1}\hat{S}^{(p)}(\zeta_j)+\Sigma_{j=k+1}^{k+b}\hat{S}^{(p)}(\zeta_j))/(2b)}.$$

Now suppose that model (1) is true, and consider the same set of assumptions as in Theorem IV.1, that is, assume $\{\eta_t\}$ is a Gaussian process with SDF which is locally constant in the frequency band $[\zeta_{k-b},\zeta_{k+b}]$, and that f_l are Fourier frequencies with $f_l \notin [\zeta_{k-b},\zeta_{k+b}]$ for $l \neq k$. Under H_0, and for sufficiently long time series, it can be argued that F_b has asymptotically an F distribution with 2 and $4b$ degrees of freedom because the model is equivalent to a white noise process with one periodic component locally in a neighborhood of ζ_k. A plot of the empirical cdf for bin sizes, $b=1,...,5$, is shown in the top right hand panel of Fig. 1. The bottom right panel shows the empirical cdf of F_b using the same Monte Carlo study as was used to estimate the cdf for the Q_b statistic in Sec. IV. For each bin size, b, note the slight differences between the shape of cdf of the Q_b statistic and the cdf of the F_b statistic. There is a simple closed form expression for the critical value of the local F test. For a bin size, b, the critical value for a test of size α is $2b(1-\alpha^{1/(2b)})/\alpha^{1/(2b)}$. Table III tabulates these values for a test of size $\alpha=0.05$.

VI. MONTE CARLO SIMULATIONS

In this section the size and power properties of the DPOAE test (i.e., using the Q_b statistic) and local F test (i.e., using the F_b statistic) are examined via simulation. This study begins by investigating some candidate models for the background noise that will be used in the simulations. These background models are not intended to be representative of the entire population of those individuals with healthy hearing, or all experimental conditions. Instead these series are sufficiently nonwhite to demonstrate how the tests perform in more realistic situations than could be highlighted using simulations based on white noise. For studies of the DPOAE test on samples of individuals consult the references provided in Sec. 1.

A. A candidate model for background noise

Candidate noise models were constructed by collecting 100 acquisitions of length 8192 at a sample rate of 50 kHz in the absence of stimulation (with f_1 and f_2) in three human subjects with normal, clear external auditory canals. An Etymotic Research ER10B+research microphone with an ER10B preamplifier providing +40 dB of gain were used in all the acquisitions. After confirmation of no significant spontaneous otoacoustic emissions in the data, each of the 100 samples were temporally averaged. A trimming percentage of 20% was used to produce a robust estimate of the average. This resulted in a three time series of length 8192 and an acquisition time of 16.38 s. Figure 2 shows periodograms for the three subjects. The spectra of subject 1 is clearly different from the other two subjects, but regardless there is strong evidence that these three time series are not white noise. Using standard time series techniques (e.g., Ref. 27) each background process $\{\eta_t\}$ was modeled using an ARMA (4,2) process with model order chosen via the Akaike information model selection criteria. Figure 2 demonstrates the fit of these models, by overlaying the parametric SDF estimates (as denoted by the solid black line) over the periodograms for the three subjects. For reference, the model for the first subject is

$$\eta_t - 0.8720\eta_{t-1} - 0.5618\eta_{t-2} - 0.1412\eta_{t-3} + 0.5768\eta_{t-4} = Z_t - 1.1057Z_{t-1} + 0.6048Z_{t-2}, \quad (3)$$

where $\{Z_t\}$ is an independent sequence of $N(0,3.675\times10^{-4})$ random variables. The model for the second subject (which is similar to the model for the third subject) is

$$\eta_t - 1.8595\eta_{t-1} + 1.0678\eta_{t-2} - 0.1989\eta_{t-3} - 0.0075\eta_{t-4} = Z_t - 1.6517Z_{t-1} + 0.0796Z_{t-2}, \quad (4)$$

where $\{Z_t\}$ is an independent sequence of $N(0,2.294\times10^{-8})$ random variables.

In the simulations that follow model (1) is used with $L=3$. It is well established that the $2f_1-f_2$ DP in humans increases in amplitude as the ratio of f_2/f_1 increases from 1.0 to 1.2 and then generally begins to decrease in amplitude as f_2/f_1 becomes larger than 1.2. As is common in practice, f_1 and f_3 are defined in terms of f_2 which is assumed to lie at a Fourier frequency. Then f_1 is the Fourier frequency closest to $f_2/1.2$, and f_3 denotes the Fourier frequency closest to the DP, $2f_1-f_2=(2/3)f_2$. The phases $\{\phi_l : l=1,...,3\}$ are assumed to be a set of independent uniform random variables on the interval $(-\pi,\pi]$. The sampling interval is $\Delta=1/50\,000$ s, and $N=8192$. The amplitudes A_1 and A_3 are allowed to vary, but A_2 is fixed so that it is 10 dB less that A_1. (In this paper no attempt is made to model the different generating processes that may be present for different values of A_1). The size and power of the DPOAE and local F test are investigated for different values of f_2, and different bin sizes b simulating the background noise using either the ARMA models (3) or (4).

B. The size of the DPOAE and local *F* tests

For a given bin size b, the size of the DPOAE test is

$$P(\text{reject } H_0 | H_0 \text{ true}) = P(Q_b > q_b | A_3 = 0),$$

where q_b is the value which corresponds to an asymptotic size of 0.05 (Corollary IV.2). To verify the theory for a fixed sample size of $N=8192$ the size of the test was estimated

TABLE II. For different bin sizes b the critical values of the DPOAE test for a 5% test.

b	1	2	3	4	5
Critical value (dB SPL)	6.852 32	5.284 74	4.862 26	4.682 35	4.589 25

TABLE III. For different bin sizes b the critical values of the local F test for a 5% test.

b	1	2	3	4	5
Critical value (dB SPL)	6.944 27	4.458 97	3.885 29	3.633 72	3.492 83

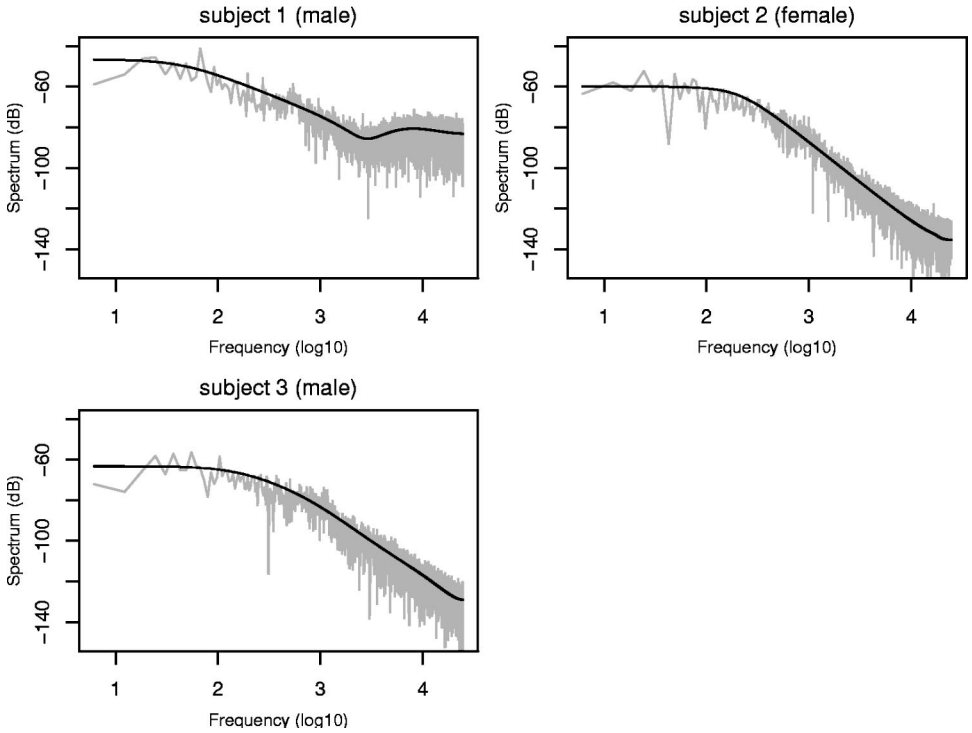

FIG. 2. Plots of the periodograms of the three individuals. The solid black lines denote the parametric SDF calculated using the ARMA(4,2) time series model that was estimated for each subject.

based on Monte Carlo simulations. For $A_1 = 65\,\text{dB}$, $A_2 = 55\,\text{dB}$, and $A_3 = -\infty\,\text{dB}$ (i.e., assuming no distortion product), f_2 was set equal to the be Fourier frequency closest to 500 Hz. A realization of $\{X_t\}$ was then simulated from the model, and the test of hypothesis was carried out based on the DPOAE test statistic Q_b for $b = 1,...,5$. To estimate the size of the test, this procedure was repeated 1000 times and the proportion of times that the hypothesis test was rejected was calculated. The top left panel of Fig. 3 displays the estimated sizes of the test for different values of f_2 (on the $\log_{10}$ scale) and b, using the background ARMA model of subject 1 [Eq. (3)]. The bottom left panel of the same figure plot the estimated size of the same test for simulations based on subject 2 [Eq. (4)]. Because of the interest in the community on low frequency otoacoustic emissions more frequencies in the range [500,1500] were investigated, compared with the range [2000,5000]. Based on a standard binomial calculation, the maximum pointwise standard error for these estimates is 0.008, and hence these results demonstrate good agreement between the theory and the simulations. The size of the test is higher than the nominal value of 0.05 between 2 and 4 kHz using the simulations based on the subject 2

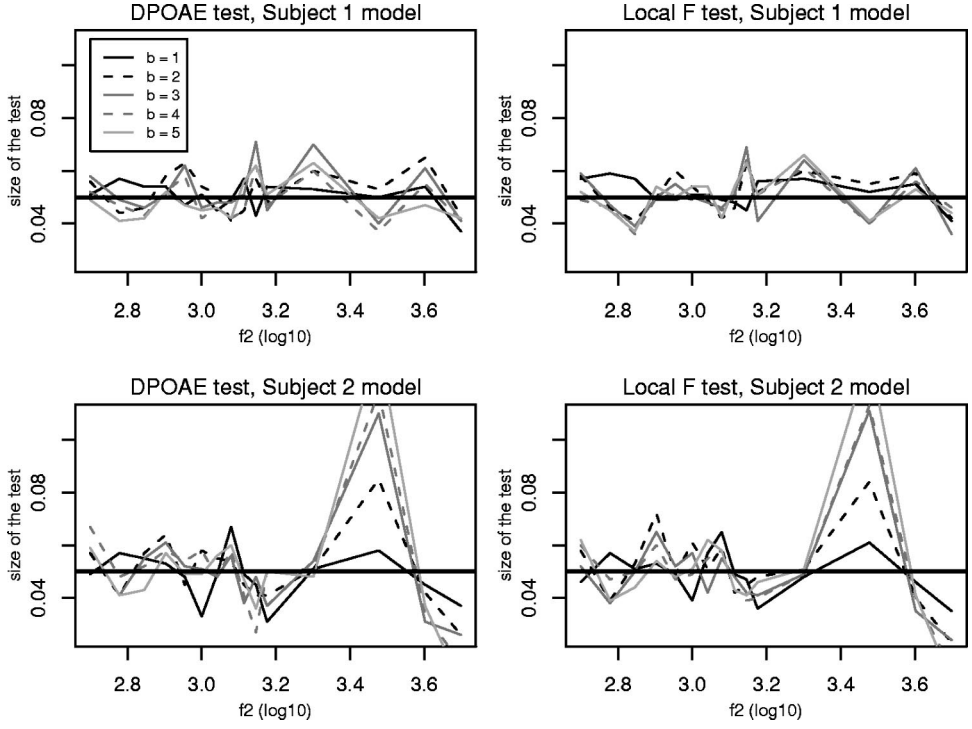

FIG. 3. Plots of the estimated size of the DPOAE test (left panels) and local F test (right panels) for different values of the frequency f_2 and bin sizes b based on either the subject 1 ARMA model (top panels) or the subject 2 ARMA model (bottom panels). In each case, the estimate at each frequency is based on a simulation of 1000 time series. The maximum pointwise standard error of each estimate is 0.008.

model. One reason for this discrepancy may be leakage. It is well known (e.g., Ref. 21, Sec. 6.3) that due to sidelobe behavior, the periodogram estimate can be affected by neighboring frequency bands at frequencies where the true SDF is lowest. This was indeed the case for the subject 2 model. Periodograms of the simulations produced under this model demonstrated leakage due to the nonwhite background process and the frequencies f_1 and f_2. The DPOAE test rejected the null hypothesis slightly more often that is assumed by the theory in the frequency range of 2–4 kHz. Periodograms of the simulations produced under the subject 1 model were significantly less subject to leakage due to the different shape of the SDF.

The size of the local F test is $P(\text{reject}\, H_0 | H_0 \text{ true}) = P(F_b > c_b | A_3 = 0)$, where c_b is the value so that this test has theoretical size 0.05 (Table III). For the same realizations and bin sizes as for the DPOAE test the size of the local F test was estimated by simulation. The results are shown in the right hand panels of Fig. 3 (the top panel for the subject 1 model and the bottom panel for the subject 2 model). Again there is good agreement with the theory in Sec. V for most frequencies. As for the DPOAE test, there was a discrepancy in the size of the test under the subject 2 background model between 2 and 4 kHz.

C. The power of the tests under fixed alternatives

The power of the DPOAE test is defined as

$$P(\text{reject } H_0 | H_0 \text{ is false}) = P(Q_b > q_b | A_3 = a),$$

where a denotes the amplitude of the DP. The power curve of this test was estimated by calculating the power for a range of amplitudes from 0 to A, where A was chosen differently for each underlying background process model. For the subject 1 background model $A = -58$ dB and for the subject 2 model $A = -35$ dB. For each model and each value of a the proportion of times the test rejected H_0 was calculated for $b = 1,...,5$ (based on 1000 replicates). This Monte Carlo experiment was repeated for different values of f_2. The power of the local F test is

$$P(\text{reject } H_0 | H_0 \text{ false}) = P(F_b > c_b | A_3 = a)$$

for some DP amplitude a, and was estimated for $b = 1,...,5$ using the same realizations as for the DPOAE test. The maximum standard error for estimate is 0.016, again calculated using a binomial proportion calculation.

Figure 4 shows plots of the estimated power curves for values of f_2 of 500, 700, and 900 Hz, based on the subject 1 background model (the corresponding power curves for the simulations based on the subject 2 model has a similar shape, but different scale). In this plot, the DPOAE test is shown on the left and the local F test is shown on the right. The different line styles denote the different bin sizes b. Clearly both tests are more powerful with more bins. For both tests the power curves for $b = 2,...,5$ are fairly close together. As expected each test is more powerful for higher frequencies. This is because under the nonwhite noise models used in these simulations, the background SDF is lower at larger frequencies, and thus the test is better able to detect the DP at lower amplitudes.

As a summary measure of how well the tests performed the area under the power curve (AUC) was calculated, which is defined as

$$\text{AUC}_b(f_2) = \int_0^A P(\text{reject } H_0 | A_3 = a)\, da,$$

and was approximated using

$$\sum_{k=0}^{K-1} w_k \hat{P}(\text{reject } H_0 | A_3 = v_k),$$

where $\hat{P}$ denotes the estimated probability from the simulations, and $\{w_k : k = 0,...,K-1\}$, $\{v_k : k = 0,...,K-1\}$ denote the weights and abscissa, respectively, of a Gaussian quadrature rule (see for example Ref. 28, Sec. 5.3). Based on some pilot studies to gauge accuracy of the quadrature rule, $K = 200$ was chosen.

Figure 5 summarizes the estimated relative area under the curve for the two tests at various values of f_2 (on the $\log_{10}$ scale) and $b = 1,...,5$ using simulations based on the subject 1 model (in the top panels) and the subject 2 model (in the bottom panels). Since the area under the power curve is largest for the local F test with $b = 5$, the left hand panel plots the ratio of the areas under the curve for the DPOAE at each frequency and bin size, relative to the area under the curve for the local F test with bin size, $b = 5$. The right hand panel displays the ratio of the areas for the local F test for each frequency and bin size relative to the local F test with bin size, $b = 5$. Smaller values of the ratios of the areas under the curve denote frequencies for which it is harder to detect DPs. These plots confirm the commonly held notion that detection of DPs is harder at lower frequencies. The results also demonstrate that both tests perform slightly better for larger values of b, but that the improvement in the power is not substantial for five bins compared to four bins. The local F test performs better than the DPOAE test, especially for lower frequencies. In terms of the statistical theory these conclusions are related to the choice of noise estimator (the denominators of the test statistics Q_b and F_b; the numerators are the same for both tests). The decreased power at lower frequencies can be attributed in part to higher noise estimates due to the shape of the underlying SDF. The higher power for the local F test compared to the DPOAE test is because the order statistic for the DPOAE test (the maximum of two averages) is a less efficient estimator (i.e., has larger standard deviation) than the single average that is the noise estimate for the local F test. Similarly, increasing b leads to a more efficient noise estimator, but since the standard deviation of each estimator is proportional to $(2b)^{-1/2}$ the gain in efficiency is less substantial as b increases.

VII. CONCLUSIONS

In this paper the cumulative distribution function for the most widely used test of periodicity used in DPOAE testing has been explicitly derived. Using simulations intended to mimic nonwhite backgrounds and the presence of nuisance frequencies, this test has been compared to a local F test. It has been shown that the two tests have similar size properties, but because of the difference in efficiency of the two

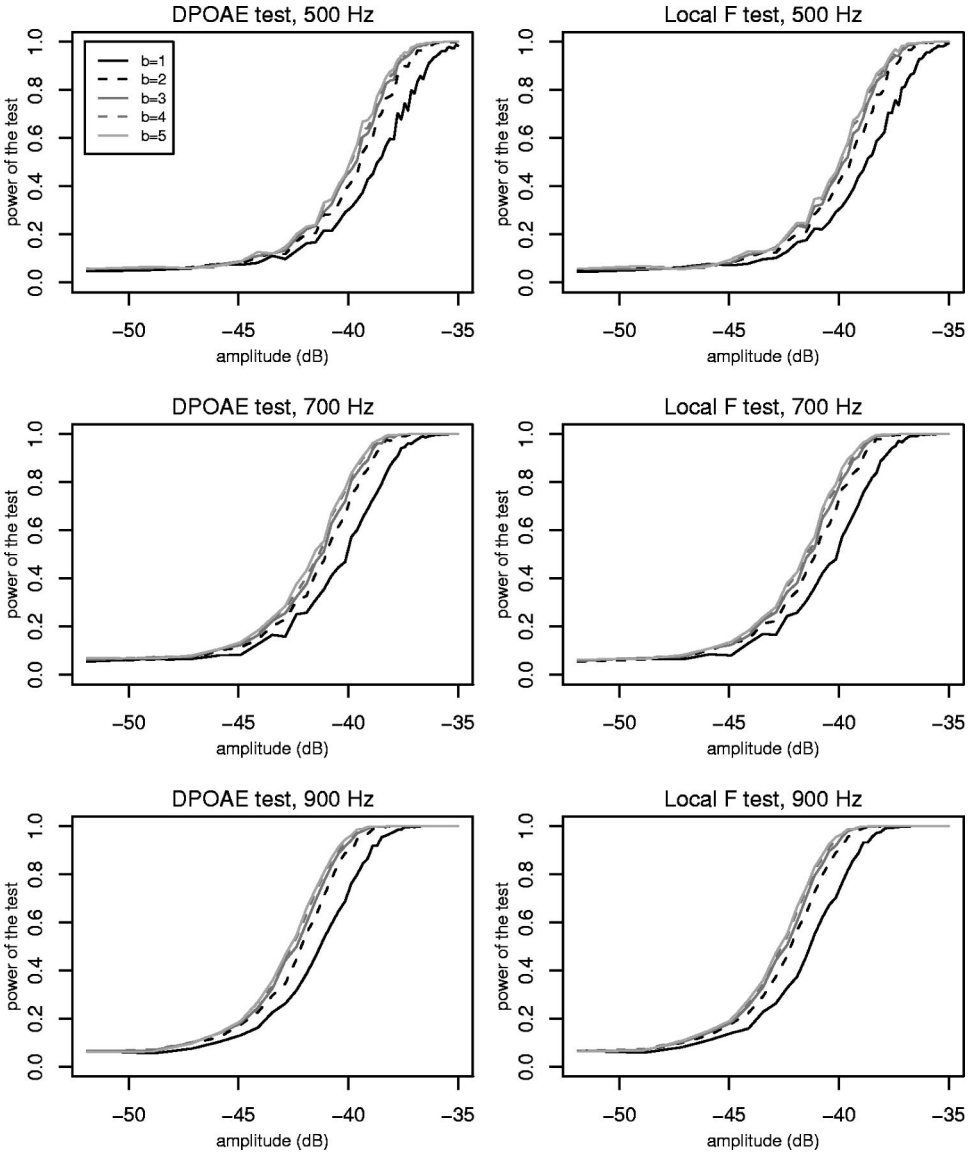

FIG. 4. Estimated power of the DPOAE test (left) and local F test (right) at different amplitudes of the DP for different frequencies f_2 under the model based on the subject 1 data. The different line types denote the different bin sizes ($b=1,...,5$). In each case, the estimate at each frequency and amplitude is based on a simulation of 1000 time series. The maximum pointwise standard error of each estimate is 0.016.

noise estimates used in each test statistic, the local F test is slightly more powerful than the DPOAE test, especially for lower frequencies. Under two experimental situations (using models based on the subject 1 and subject 2 data, respectively), and regardless of anatomical–physical considerations, it has been demonstrated that both tests lose the statistical power to detect the DP at lower frequencies, and that both tests gain power as the numbers of bins increase. This finding is in agreement with the commonly held notion in the audiologic community that increasing the number of adjacent bins used in the estimate increases the power of the test by reducing the variability of the noise floor estimate.[6] These simulations showed that the gain in power for more bins above four bins was not substantial. There is some advantage to keeping b small, especially for low DP frequencies when the frequencies f_1, f_2 and the DP are close together. For all bin sizes, the critical value of the local F test is easier to calculate than the corresponding critical value of the DPOAE test (since the rational expressions in Corollary IV.2 need to be inverted).

All the simulations and theory in this paper are based on the fact that the periodicities to test for along with the nuisance periodicities are Fourier frequencies; i.e., each frequency can be written as $\zeta_k = k/(N\Delta)$ for some $k = 1,...,\lfloor N/2 \rfloor$. The performance of these tests will degrade when the frequencies do not line up with Fourier frequencies, and indeed if the nuisance frequencies are not Fourier frequencies, it is possible that the null distributional assumptions of the DPOAE and local F test statistics are significantly affected. A focus of current research is to investigate this and its possible relation to the phenomenon of DPOAE fine structure.[29,30] DPOAE fine structure refers to quasiperiodic DPOAE amplitude minima and maxima observed in normal hearing people and animals as a function of frequency. The extant theory for the basis of DPOAE fine structure attributes these minima and maxima to interactions between the DP generated at the site of the f_1 and f_2 interaction on the basilar membrane (BM) and a delayed DP component generated by an initially apically moving wave, which proceeds to its characteristic place on the BM and then reflects back. The constructive and destructive interaction of these ''early'' and ''late'' DP components is presumed to be the cause of these quasiperiodic DP amplitude minima and maxima. Currently, there is no discussion of the statistical

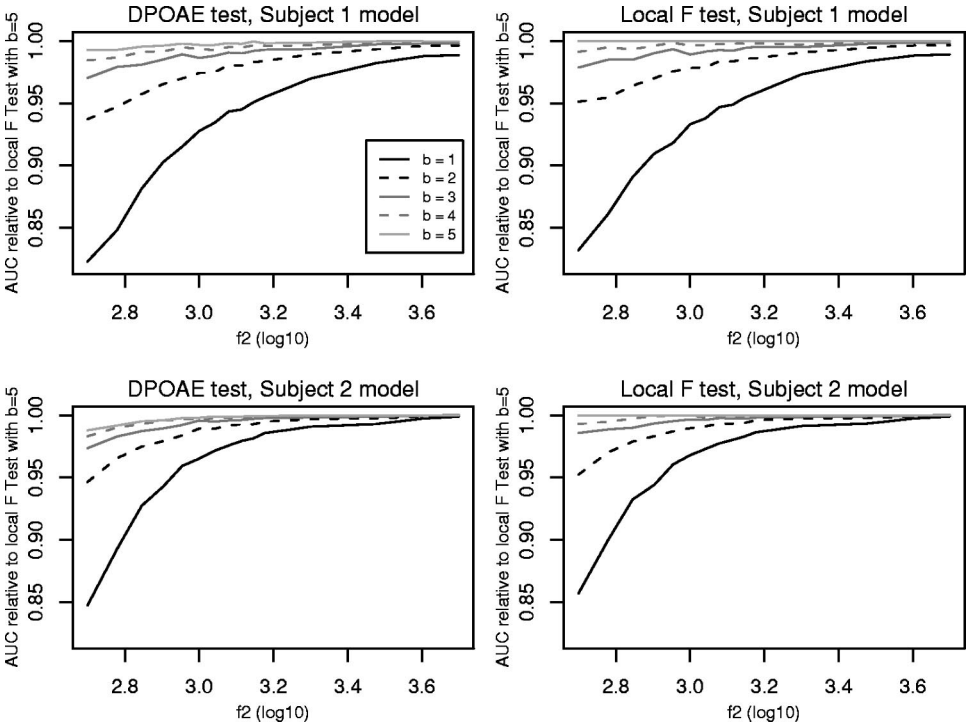

FIG. 5. A comparison of the area under the power curve (AUC) for different values of the frequency f_2, and bin size b, based on Monte Carlo simulations under two different spectral models (subject 1 in the top panels and subject 2 in the bottom panels). The left panels displays the AUC for the DPOAE test relative to the area under the power curve for the local F test with a bin size of $b=5$ (corresponding to the largest AUC for the experimental conditions observed). The right panels displays the relative AUC for the local F test relative to the local F test with $b=5$.

properties of the periodogram estimator at non-Fourier frequencies and its possible contribution to DPOAE fine structure. It should not be suggested that the inherent properties of the estimator are solely responsible for the appearance of DPOAE fine structure, but rather that it is a potentially nontrivial source of variance that warrants investigation.

The analysis of the data in this paper is also based on the assumption that the time series models are stationary Gaussian processes. No evidence of nonstationarities in the data have been observed so far. It is possible to introduce nonstationarities resulting from subject motion, e.g., by swallowing or coughing. A subject of further study is to investigate data with such problems in the future. The Gaussianity assumption also seems a good fit for the data presented in this paper. For long time series, the asymptotic distribution of the periodogram ordinates is unaffected by the non-Gaussianity of data, and thus the theory is still the same (subject to certain finiteness of higher order moments of the process—see, e.g., Ref. 19).

Note that there are many other spectral estimates or tests of periodicity that could have been investigated in this paper. One of the advantages of the periodogram over tapered spectral estimates is the asymptotic independence of the ordinates—this may not be the case for other spectral estimates. Regarding other tests of periodicity, there have been problems using standard tests based on ordinary or general least squares estimates for regression models of periodicities. When nuisance frequencies have been observed at 65 and 55 dB, respectively, these tests perform poorly in detecting the DP. Decreasing the amplitudes in practice may remedy this problem. There is also interest in looking at Thomson's F test for periodicity, which is based on multitaper spectral estimation.[21,23] This test has been shown to perform well in nonwhite backgrounds, and may be adjusted to work in the situation when nuisance periodicities are observed.[21,31]

This paper used time averaging acquisition methods for DP data. A related acquisition method is to collect data in two buffers. At the DP frequency, the grand mean of the spectral estimates in the two buffers is used as the estimate of the signal and the difference of the two buffers are the estimate of the noise. In this way averaging adjacent periodogram bins is no longer a concern. The authors are also investigating spectral averaging methods.

ACKNOWLEDGMENTS

The authors thank Dr. Donald B. Percival for his thoughtful comments which improved this paper. The comments of two anonymous referees and the Associate Editor are also greatly appreciated.

APPENDIX: PROOFS

Proof of IV.1. To make the theory work, assume that as the embedding length of the time series, N', gets large, the Fourier frequencies converge to some fixed frequencies bounded away from zero and the Nyquist frequency. Then by Proposition III.1, $\hat{S}^{(p)}(\zeta_k)$ has a chi squared distribution with 2 degrees of freedom (df) multiplied by $S(\zeta_k)/2$, for large N', which is independent of

$$Y_{L,b}=\frac{1}{b}\sum_{j=1}^{b}\hat{S}^{(p)}(\zeta_{k-j})=_d\frac{1}{b}\sum_{j=1}^{b}\frac{R_j}{2}S(\zeta_{k-j}),$$

where $=_d$ means "is equal in distribution to" and $\{R_1,\ldots,R_b\}$ is a set of independent chi squared random variables (RVs) with 2 df. Under the assumption that $S(\cdot)$ is locally constant around ζ_k, from the independence of the set of RVs, $\{R_j: j=1,\ldots,b\}$ it follows that $Y_{L,b}$ has a chi squared distribution with $2b$ df, multiplied by $S(\zeta_k)/2b$. By similar arguments $Y_{L,b}$ is equal in distribution to $Y_{R,b}$, and $Y_{L,b}$ is

independent of $Y_{R,b}$. To simplify the distributional form of the Q_b statistic, let U be a chi squared RV with 2 df, and let V_L and V_R be chi squared RVs with $2b$ df. Assume U, V_L, and V_R are mutually independent. Then

$$Q_b = {}_d \frac{(U/2)S(\zeta_k)}{\max\{(V_L/(2b))S(\zeta_k),(V_R/(2b))S(\zeta_k)\}} = \frac{bU}{\max\{V_L,V_R\}}.$$

The cdf of $W=\max\{V_L,V_R\}$ is given by $F_W(w)=P([V_L \leqslant w]\cap[V_R \leqslant w])=F_{V_L}(w)^2$, since V_L and V_R have the same distribution. Using a standard result for ratios of independent RVs

$$P(Q_b \leqslant q)=P(bU/W \leqslant q)=P(U/W \leqslant q/b) = \int_0^\infty F_U(qy/b)dF_W(y) = 2\int_0^\infty F_U(qy/b)F_{V_L}(y)\zeta_{V_L}(y)dy.$$

Now

$$F_U(qy/b)=\int_0^{qy/b}\zeta_U(x)dx = \int_0^{qy/b} e^{-x/2}/2dx = 1-e^{-qy/(2b)},$$

and since $\zeta_{V_L}(v)=v^{b-1}e^{-v/2}/(\Gamma(b)2^b)$

$$P(Q_b \leqslant q)=2\int_0^\infty [1-e^{-qy/(2b)}] \times\left[\int_0^y v^{b-1}e^{-v/2}/(\Gamma(b)2^b)dv\right] \times[y^{b-1}e^{-y/2}/(\Gamma(b)2^b)]dy = \frac{1}{[\Gamma(b)]^2 2^{2b-1}}\int_0^\infty y^{b-1}e^{-y/2}[1-e^{-qy/(2b)}] \times\left[\int_0^y v^{b-1}e^{-v/2}dv\right]dy.$$

Proof of IV.2. The corollary follows using standard results for gamma integrals.

[1] C. Yoshinaga-Itano, A. Sedey, and D. Coulter, "Language of early- and later-identified children with hearing loss," Pediatrics **102**, 1161–1171 (1998).

[2] A. Diefendorf, "Detection and assessment of hearing loss in infants and children," in *Handbook of Clinical Audiology*, 5th ed., edited by J. Katz (Lippincott Williams and Wilkins, Baltimore, 2002), pp. 469–480.

[3] J. Hall, *Handbook of Otoacoustic Emissions* (Singular, San Diego, CA, 2000).

[4] F. Harris and R. Probst, "Otoacoustic emissions and audiometric outcomes," in *Otoacoustic Emissions*, edited by M. Robinette and T. Glattke (Thieme, New York, 1997), pp. 151–180.

[5] D. Brass and D. Kemp, "Quantitative assessment of methods for the detection of otoacoustic emissions," Ear Hear. **15**, 378–389 (1994).

[6] B. Kimberly, D. Brown, and J. Allen, "Distortion product emissions and sensorineural hearing loss," in *Otoacoustic Emissions*, edited by M. Robinette and T. Glattke (Thieme, New York, 1997), pp. 181–204.

[7] B. Prieve, T. Fitzgerald, and L. Schulte, "Basic characteristics of click-evoked otoacoustic emissions in infants and children," J. Acoust. Soc. Am. **102**, 2860 (1997).

[8] A. Cacace, W. McClelland, J. Weiner, and D. McFarland, "Individual differences and reliability of the $2f_1-f_2$ distortion product: Effects of time-of-day, stimulus variable, and gender," J. Speech Hear. Res. **39**, 1138 (1996).

[9] L. Stover and S. Norton, "The effects of aging on otoacoustic emissions," J. Acoust. Soc. Am. **94**, 2670 (1993).

[10] R. Hauser and R. Probst, "The influence of systematic primary-tone level variation l_2-l_1 on the acoustic distortion product emission $2f_1-f_2$ in normal human cars," J. Acoust. Soc. Am. **89**, 280 (1991).

[11] S. A. Gaskill and A. M. Brown, "The behavior of the acoustic distortion product, $2f_1-f_2$, from the human ear and its relation to auditory-sensitivity," J. Acoust. Soc. Am. **88**, 821–839 (1990).

[12] M. Gorga, S. Neeley, K. Bergman, B. Beauchaine, J. Kaminski, and W. Jesteadt, "Otoacoustic emissions from normal-hearing and hearing-impaired subjects: Distortion product responses," J. Acoust. Soc. Am. **93**, 2050–2060 (1993).

[13] B. L. Lonsbury-Martin and G. Martin, "Clinical applications of otoacoustic emissions," Ear Hear. **11**, 83–109 (1990).

[14] J. Smurzynski, "Longitudinal measurements of distortion-product and click-evoked otoacoustic emissions of preterm infants," Ear Hear. **15**, 210–223 (1994).

[15] G. Popelka, R. Karzon, and E. Arjmand, "Growth of the $2f_1-f_2$ distortion product otoacoustic for low-level stimuli in human neonates," Ear Hear. **16**, 159–165 (1995).

[16] M. Gorga, S. Neely, B. Ohlrich, B. Hoover, J. Redner, and J. Peters, "From laboratory to clinic: A large scale study of distortion product otoacoustic emissions in ears with normal hearing and ears with hearing loss," Ear Hear. **18**, 440–455 (1997).

[17] M. Gorga, L. Stover, and S. Neeley, "The use of cumulative distributions to determine critical values and levels of confidence for clinical distortion product otoacoustic emission measurements," J. Acoust. Soc. Am. **100**, 968–977 (1996).

[18] P. Bloomfield, *Fourier Analysis Of Time Series: An Introduction* (Wiley, New York, 1976).

[19] D. Brillinger, *Time Series: Data Analysis and Theory* (Holt, New York, 1981).

[20] M. B. Priestley, *Spectral Analysis and Time Series*, Vol. 1, Univariate Series (Academic, London, 1981).

[21] D. Percival and A. Walden, *Spectral Analysis for Physical Applications* (Cambridge University Press, Cambridge, 1993).

[22] T. W. Anderson, *The Statistical Analysis of Time Series*, Classics ed. (Wiley-Interscience, New York, 1994).

[23] D. Thomson, "Spectrum estimation and harmonic analysis," Proc. IEEE **70**, 1055–1096 (1982).

[24] M. Henderson and M. C. Meyer, "Exploring the confidence interval for a binomial parameter in a first course in statistical computing," Am. Stat. **55**, 337–344 (2001).

[25] D. Percival, "Spectral analysis of univariate and bivariate time series," in *Methods of Experimental Physics*, edited by J. L. Stanford and S. B. Vardeman (Academic, New York, 1994), pp. 313–348.

[26] A. Almasri, "Testing for periodicity and trend in long-memory processes," Ph.D. thesis, Lund University, (Lund, Sweden 2003).

[27] P. J. Brockwell and R. A. Davis, *Introduction to Time Series and Forecasting* (Springer, New York, 1996), ISBN 0-387-9471.

[28] R. A. Thisted, *Elements of Statistical Computing* (Chapman and Hall, London, 1988).

[29] H. Ning-je and R. Schmiedt, "Effects of aging on the fine structure of the $2f_1-f_2$ acoustic distortion product," J. Acoust. Soc. Am. **99**, 1002 (1996).

[30] C. Talmadge and A. Tubis, "Modeling otoacoustic emission and hearing threshold fine structures," J. Acoust. Soc. Am. **104**, 1517 (1998).

[31] D. G. T. Denison, A. T. Walden, A. Balogh, and R. J. Forsyth, "Multitaper testing of spectral lines and the detection of the solar rotation frequency and its harmonics," Appl. Stat. **48**, 427 (1999).

Effects of cochlear-implant pulse rate and inter-channel timing on channel interactions and thresholds

John C. Middlebrooks[a)]
Kresge Hearing Research Institute, Department of Otorhinolaryngology, University of Michigan Medical School, 1301 E. Ann St., Ann Arbor, Michigan 48109-0506

(Received 9 February 2004; revised 14 April 2004; accepted 22 April 2004)

Interactions among the multiple channels of a cochlear prosthesis limit the number of channels of information that can be transmitted to the brain. This study explored the influence on channel interactions of electrical pulse rates and temporal offsets between channels. Anesthetized guinea pigs were implanted with 2-channel scala-tympani electrode arrays, and spike activity was recorded from the auditory cortex. Channel interactions were quantified as the reduction of the threshold for pulse-train stimulation of the apical channel by sub-threshold stimulation of the basal channel. Pulse rates were 254 or 4069 pulses per second (pps) per channel. Maximum threshold reductions averaged 9.6 dB when channels were stimulated simultaneously. Among nonsimultaneous conditions, threshold reductions at the 254-pps rate were entirely eliminated by a 1966-μs inter-channel offset. When offsets were only 41 to 123 μs, however, maximum threshold shifts averaged 3.1 dB, which was comparable to the dynamic ranges of cortical neurons in this experimental preparation. Threshold reductions at 4069 pps averaged up to 1.3 dB greater than at 254 pps, which raises some concern in regard to high-pulse-rate speech processors. Thresholds for various paired-pulse stimuli, pulse rates, and pulse-train durations were measured to test possible mechanisms of temporal integration. © *2004 Acoustical Society of America.*
[DOI: 10.1121/1.1760795]

PACS numbers: 43.64.Me, 43.64.Qh, 43.66.Ts [WPS] Pages: 452–468

I. INTRODUCTION

Multi-channel cochlear implants provide users with substantially better speech recognition than do single-channel implants (e.g., Gantz *et al.*, 1988; Cohen *et al.*, 1993; Fishman *et al.*, 1997). Nevertheless, the number of channels of information delivered to the brain by a multi-channel implant typically falls short of the number of physical electrodes present in the device. For instance, users show little or no improvement in speech recognition when the number of activated implant channels is increased beyond about 4 to 7 channels in quiet (Fishman *et al.*, 1997; Friesen *et al.*, 2001) or beyond 7 to 10 in noise (Friesen *et al.*, 2001). In contrast, normal-hearing listeners continue to show improving speech recognition in quiet or in noise as the number of channels is increased to 20 channels in an acoustic vocoder simulation of a cochlear-implant speech processor (Friesen *et al.*, 2001). The difference between normal listeners and implant users almost certainly is due in part to partial loss of auditory nerve fibers in the implant users. Another likely factor, however, is the overlap in the neuronal populations activated by nearby cochlear electrodes, leading to channel interaction.

One possible cause of overlapping activation of neural populations is the summation of electrical fields presented simultaneously through nearby electrodes. That summation can be minimized by presenting electrical stimuli as trains of electrical pulses with pulses interleaved in time, such that pulses are never presented simultaneously (e.g., Eddington *et al.*, 1978; Wilson *et al.*, 1988). Nonsimultaneous pulsatile stimulation strategies in common clinical use include Continuous Interleaved Sampling (CIS; Wilson *et al.*, 1991), Spectral Peak (SPEAK; Seligman and McDermott, 1995), and Advanced Combined Encoding (ACE; Vandali *et al.*, 2000). Alternatively, some strategies interleave pulses such that 2 (Paired Pulsatile Sampler) or 4 (Quadruple Pulsatile Sampler) pulses are presented simultaneously from distant segments of the cochlea, but pulses on nearby electrodes are nonsimultaneous (Loizou *et al.*, 2003). Pulsatile strategies avoid the direct summation of cochlear electrical fields that would arise from simultaneous stimulation of nearby electrodes. Nevertheless, psychophysical results with implant users demonstrate appreciable interaction among implant channels stimulated with interleaved pulse trains. These interactions include influences on pitch judgments (Townshend *et al.*, 1987; McDermott and McKay, 1994; McKay and McDermott, 1996), shifts in thresholds or loudness judgments (Shannon, 1983; McKay *et al.*, 2001), and masking of temporal modulation (Richardson *et al.*, 1998; Chatterjee, 2003). In a recent physiological study, we measured thresholds for activation of the auditory cortex in response to single 80 μs/phase (μs/ph) pulses presented through each of two cochlear electrodes (Bierer and Middlebrooks, 2004). We found that a pulse on one electrode influenced the threshold on another electrode even when the onsets of the pulses were separated by as much as 640 μs. Those psychophysical and physiological results motivate a further detailed examination of the impact of inter-pulse timing on interactions among cochlear-implant channels.

Recent developments in cochlear-implant stimulation strategies have favored higher rates of electrical pulses,

a)Electronic mail: jmidd@umich.edu

 0001-4966/2004/116(1)/452/17/$20.00

along with necessarily shorter phase durations; indeed, the maximum rates seem limited only by technological factors. Anticipated advantages of higher pulse rates include more detailed sampling of speech temporal waveforms (e.g., Wilson, 1997) and auditory nerve firing patterns that more closely resemble the patterns normally evoked by sounds (e.g., Wilson *et al.*, 1997; Rubinstein *et al.*, 1999; Litvak *et al.*, 2003). Little attention has been given to any possible impact of increased pulse rates on channel interactions. For instance, higher pulse rates require that pulses on adjacent cochlear electrodes be closer together in time. One concern is that reduced inter-pulse intervals might increase channel interactions, thereby decreasing the effective number of channels of information from a cochlear implant to the brain.

The present study examined in an animal model the influence of pulse rate and inter-pulse timing on channel interactions. Anesthetized guinea pigs were implanted with two-electrode scala tympani electrode arrays, and responses to monopolar cochlear electrical stimulation were measured at the level of the auditory cortex. The auditory cortex was selected as the recording site because of the notion that information must reach the auditory cortex in some form in order to contribute to perception and behavior. That notion is supported by the large body of clinical results in humans and experimental results in animals showing that cortical lesions can lead to sensory deficits. The guinea pig was selected as the experimental animal because of its readily accessible cochlea, because of the existing behavioral studies using cochlear-implant stimulation in that species (e.g., Miller *et al.*, 1995), and because the physical dimensions of the cortical tonotopic representation of the cochlea in the guinea-pig make it conducive to study with available multi-site recording probes (e.g., Arenberg *et al.*, 2000).

Channel interactions were quantified as the amount by which a sub-threshold pulse train on one channel lowered the threshold for cortical activation by a pulse train on a second channel. The shift in the threshold of one channel by stimulation of another channel indicates the degree to which the two channels fail to act independently. Large threshold shifts would indicate that one channel might mask temporal modulation on another channel and would imply that transmission of spectral contrast (coded as differential activation of nearby cochlear stimulation sites) would be degraded.

The most important result was that threshold shifts were significantly greater for 4069-pulse-per-second (pps) trains than for 254 pps trains. Also, threshold shifts were minimized at particular values of inter-channel temporal offsets. The threshold shifts measured during interleaved stimulation of two electrodes amounted to substantial fractions of the dynamic ranges of cortical neurons under conditions of electrical cochlear stimulation. The mechanism of the pulse-rate effect was explored by studying the effects on cortical thresholds of single-channel pulse rates and inter-pulse times. Those results indicated that the threshold for cochlear stimulation leading to cortical activity in this experimental preparation was determined largely by cochlear stimuli integrated over the initial ~1 ms of electrical pulse trains.

II. METHODS

A. Animals

Data were obtained from 13 pigmented guinea pigs of either sex, each weighing 500 to 1000 g. Data for Experiment I were obtained from 7 of the animals, and data for Experiment II were obtained from one of those 7 animals plus the other 6 animals. Each animal was given an injection of atropine sulfate to suppress secretions (0.1 mg/kg, i.m.), then anesthesia was induced with a combination of ketamine (40 mg/kg, i.m.) and xylazine (10 mg/kg, i.m.). Additional i.m. doses of a 9:1 mixture of ketamine and xylazine (typically, 9 mg of ketamine and 1 mg of xylazine) were given as needed to maintain an areflexive state. Animal preparation typically occupied ~3 h followed by 10–14 h of data collection. All animal procedures were approved by the University of Michigan Committee on Use and Care of Animals.

B. Cochlear electrical stimulation

Cochlear stimuli were presented through a ''ball and helix'' intra-scalar electrode array (Miller *et al.*, 1995). The electrode array was fabricated from two insulated platinum–iridium wires that passed through a 0.25-mm-outside-diameter tube. The tip of one wire was melted in a flame to form a ball, ~0.45 mm in diameter. The other wire was stripped of insulation, then bent back and wrapped around the tube to form a dense helix, ~0.4 mm in diameter and ~0.8 mm in length along the longitudinal axis of the electrode array. The distance between the nearest points of the ball and helix was ~0.75 mm, and the center-to-center distance was ~1.4 mm. The ball-and-helix electrode array was inserted into the scala tympani of the left cochlea through a small cochleostomy and was advanced so that the ball lay about half-way around the basal turn of the cochlea. The ball formed the more apical electrode and the helix the more basal electrode. A further advance of the electrode array was prevented by the tapering dimensions of the scala tympani—that is, at its farthest insertion the ball electrode appeared to span the minimum diameter of the scala tympani. Based on the Greenwood map of characteristic frequency onto cochlear place for the guinea pig (Greenwood, 1990), we estimate that the apical and basal electrodes would have been centered at cochlear sites representing frequencies about a half octave apart, with the apical and basal electrodes at approximately the 17- and 25-kHz cochlear places, respectively. Each electrode was stimulated as a monopolar active electrode with the return electrode consisting of a wire in a neck muscle.

Previous studies from this laboratory (Bierer and Middlebrooks, 2002; 2004) have used a 6-channel animal version of the Nucleus 22 banded electrode array (Cochlear, Englewood, CO). That array had 6 cylindrical electrodes on a 0.4-mm-diameter carrier; the electrodes were 0.4 mm in diameter, 0.3 mm in length, and separated by 0.75 mm center-to-center. The electrode array used in the present study, therefore, had a slightly larger apical-most electrode than did the Nucleus device, and the helix was similar in size and shape to the cylinders on the Nucleus device. The carrier between the ball and helix was slightly narrower (0.25-mm

diameter compare to 0.4 mm on the Nucleus device), and the separation between the ball and helix was about twice as large as the separation between adjacent electrodes in the Nucleus device.

At the time of implantation of the electrode array, the left cochlea was deafened by intra-scalar infusion of neomycin sulfate, which is toxic to cochlear hair cells (e.g., Nuttall *et al.*, 1977). Perilymph was withdrawn from the basal turn, and replaced with a 10% solution of neomycin sulfate. After ~2 min, fluid was withdrawn again and replaced with neomycin. In our experience with other guinea pigs (unpublished), that procedure reliably resulted in a >80-dB elevation of thresholds for the cochlear compound action potential within ~5 min (i.e., the threshold for the compound action potential became too high to measure). The right cochlea was ablated using a carbide burr to eliminate cortical responses to the animal's breathing sounds and other acoustic input.

Experiments were controlled by an Intel-based personal computer interfaced through System 3 hardware from Tucker-Davis Technologies (TDT). Electrical current pulses were generated by a custom optically isolated multi-channel current source controlled by two channels of an 8-channel digital-analog converter (TDT RV8). The current source was capacitatively coupled to the electrodes with an output time constant of 3000 μs. Electrical cross-talk between channels was attenuated by >50 dB. All pulse durations were multiples of 20.45 μs but are reported rounded to integer μs for convenience in presentation. Apical or basal ''channels'' refer to the current paths originating in the RV8 and passing through the current source to the apical (ball) electrode or basal (helix) electrode, respectively. Figure 1(a) shows schematically the electrical waveforms that were used. The rise time of the pulses was ~5 μs. A slight electrical overshoot compensated for the noninstantaneous rise time such that the integral of current over time was within 2% of that expected for a perfect rectangular pulse. The charge-balanced ''biphasic'' waveform was used for Experiment I and, except when indicated otherwise, Experiment II. The duration of each phase of the biphasic pulse was fixed at 20 μs for Experiment I and was varied as an experimental parameter in Experiment II. A few conditions in Experiment II used a monophasic ''cathodic'' pulse or a ''delayed phase'' biphasic pulse. In the delayed phase pulse, each phase duration was 20 μs and the onset of the anodic phase followed the onset of the cathodic phase by 123 μs (i.e., there was an inter-phase gap of 103 μs).

In Experiment I, stimuli consisted of 200-ms trains of pulses at rates of 254 or 4069 pps per channel. The slower rate was chosen to be close to the 250-pps rate that is used in clinical processors that employ the SPEAK speech processing strategy (Seligman and McDermott, 1995). The faster rate was chosen to be near the high end of the range of pulse rates that are available in present-day clinical processors (e.g., Loizou *et al.*, 2003; Vandali *et al.*, 2000; Holden *et al.*, 2002); the precise rates were determined by practical constraints of the stimulating and recording hardware. In Experiment II, pulse rates and train durations varied among conditions, as indicated in Sec. IV. In all cases, pulse trains were repeated at a rate of 1 per second.

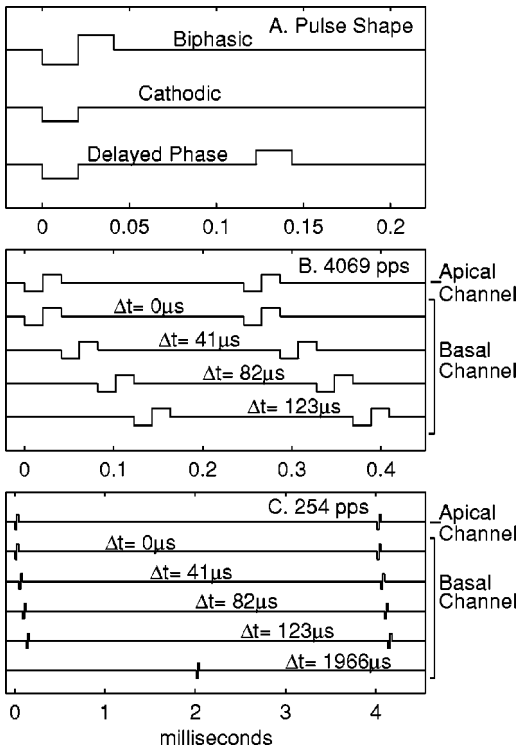

FIG. 1. Single pulse shapes and pulse patterns. Note the differing time scales on the 3 panels. (a) Pulse shapes. Each biphasic and ''delayed-phase'' pulse consisted of a cathodic (i.e., negative-going) phase and an anodic phase. Each cathodic pulse had only a single pulse. (b) Temporal offsets at the 4069-pulse-per-second (pps) per channel pulse rate. The top trace shows the electrical signal delivered to the apical electrode. The 4 lower traces show the signal on the basal electrode at 4 temporal offsets. (c) The same as (b), for the 254-pps per channel pulse rate.

Stimuli in Experiment I consisted of simultaneous or interleaved pulse trains on apical and basal channels. As indicated in Fig. 1(b), between-channel offsets are given as the time from the onset of the cathodic phase on the apical channel to the onset of the cathodic phase on the basal channel; negative offsets (not illustrated) indicate that the basal-channel pulse preceded the apical pulse. At the 4069-pps pulse rate [Fig. 1(b), nonsimultaneous offsets were ±41, 82, and 123 μs; a 0-μs, simultaneous, condition also was tested. The 123-μs offset was half the period of the 4069-pps pulse rate (i.e., the maximum inter-pulse delay possible at that pulse rate). The same offsets were tested at the 254 pps pulse rate [Fig. 1(c)], plus offsets of ±1966 μs, which were half the period of the 254-pps rate.

Stimulus sets consisted of blocks of trials. In Experiment I, pulse rates varied among blocks, and between-channel timing and stimulus current levels varied among trials within blocks. In Experiment II, phase durations varied among blocks, and pulse rates, train durations, and current levels varied among trials within blocks. In both experiments, current levels were varied in 1-dB steps. Within a block, stimuli varied in a pseudorandom order until each stimulus condition had been tested once, then all the stimuli were repeated in a different pseudorandom order. Each stimulus condition was repeated 12–20 times.

C. Cortical recording and spike sorting

Auditory cortical spike activity was recorded simultaneously from 16 sites using multi-channel silicon-substrate recording probes (Drake *et al.*, 1988; Najafi *et al.*, 1985). The probes had 16 recording sites located at 100-μm intervals along a single shank; the shank was 15 μm thick and tapered in width from 100 to 15 μm along the segment containing the recording sites. The recording probe was inserted into active layers of the primary auditory cortex on the right hemisphere, approximately parallel to the cortical surface and oriented from caudo-medial to rostro-lateral. That orientation is approximately parallel to the axis of decreasing characteristic frequency in the cortical tonotopic representation of frequency (Hellweg *et al.*, 1977; Redies *et al.*, 1989; Arenberg *et al.*, 2000; Wallace *et al.*, 2000). In a previous study that used similar recording procedures with acoustical stimulation, the recording probes typically spanned 2–3 octaves of the cortical tonotopic representation (Arenberg *et al.*, 2000). The probe was positioned and left in the same place throughout all the data collection in each animal. Neural waveforms were recorded using a 16-channel TDT RA16 system, which consisted of parallel headstages, amplifiers, 24-bit digitizers, and digital signal processors. Waveforms were digitized at a sample rate of 24 kHz, low-pass filtered, re-sampled at 12 kHz, and then stored on computer disk.

Electrical artifact from the cochlear stimulus could be recorded at the cortical recording probe. This was not a problem for Experiment II, since pulse trains were no longer than 7 ms in duration, which was shorter than the ~10-ms neural conduction delay from cochlear activation, through the ascending auditory pathway, to cortical response. In Experiment I, however, the 200-ms pulse trains overlapped the cortical responses. Two measures were employed that effectively eliminated the electrical artifact. A comb filter programmed into the recording path of the TDT digital signal processor introduced spectral nulls at integer multiples of 4069 Hz, exactly corresponding to the spectral components of the 4069-pps pulse train. That filter entirely eliminated the artifact from the 4069-pps pulse train except for periods of <1 ms at pulse-train onset and offset (as the filter charged and discharged). Those brief periods of artifact were eliminated later during spike sorting. During 254-pps pulse trains, a sample-and-hold function programmed into the signal processor clamped the recorded waveform for ~160 μs encompassing each 20-μs/phase pulse. That amounted to a loss of data during ~4% of each period of the 254-pps stimulus.

Stimulus-evoked spikes recorded with the multi-channel probes were very similar to spikes recorded with conventional metal microelectrodes and, as is common to studies using metal microelectrodes, such spikes were assumed to be extracellularly recorded action potentials. The simultaneous recordings from multiple sites permitted a ''denoising'' procedure that attenuated signals that were correlated among recording channels (Bierer and Anderson, 1999). Such signals included far-field slow-wave potentials and any electrical artifact that remained from the sample-and-hold procedure. Spikes were extracted from the stored neural waveforms using the following off-line spike-sorting procedure. First, the denoised waveforms were interpolated to 48-kHz time resolution using Fourier interpolation. Second, a range of peak-to-trough times was selected (typically 150 to 350 μs), and the distribution of peak-to-trough amplitudes of spikes fitting those time criteria was displayed. Based on visual inspection of that distribution, a range of amplitudes was selected that isolated a single unit or, more often, included a small number of unresolved units. Finally, the entire set of waveforms was processed to isolate spikes that fit specified ranges of peak-to-trough times and amplitudes. Spikes times were stored with 20-μs precision. Figure 2(a) shows a set of four waveforms recorded during one stimulus presentation; spikes selected during the sorting procedure are indicated with plus signs drawn above the waveforms. Typi-

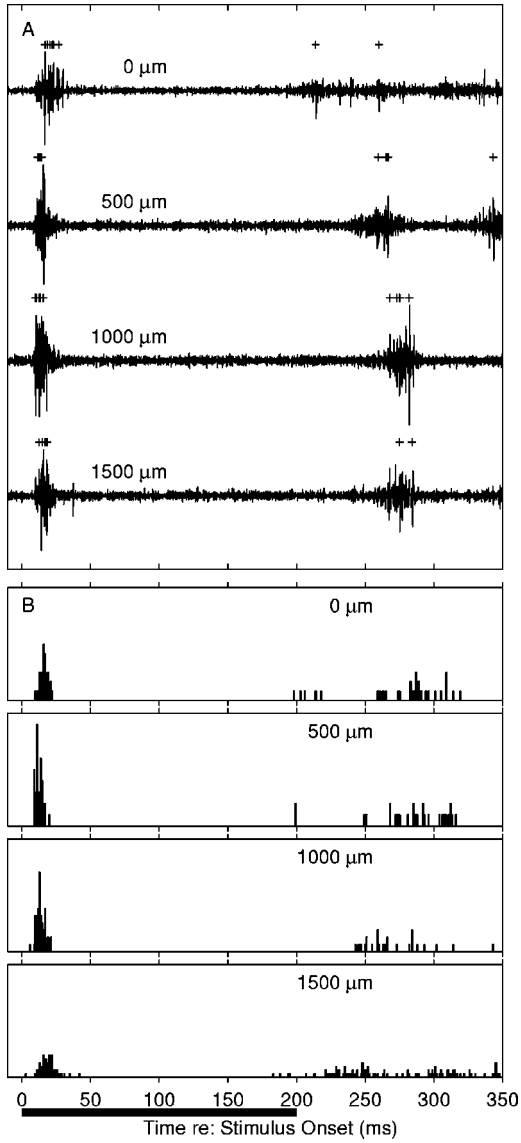

FIG. 2. (a) Recorded waveforms. These voltage traces were recorded simultaneously at 4 cortical sites in response to a single stimulus presentation. The traces were filtered and denoised as described in the text. Plus signs above each trace indicate the times of spikes that were selected by the spike-sorting procedure. Locations of recording sites are given as displacements (0 to 1500 μm) from the most caudo-medial site. (b) Post-stimulus-time histograms. Responses were measured simultaneously at the same 4 recording sites represented in Fig. 2(a). Histograms were compiled over 12 stimulus repetitions. The stimulus was a 4096-pps pulse train, 200 ms in duration.

cally, multi-unit activity was recorded on most of the 16 recording sites, with well-isolated single units on 0 to 2 sites. It was not necessary for the purposes of this experiment to isolate single units, and the dependence of thresholds on stimulus conditions was observed to be essentially identical for multi-unit recordings and for the few single units that were recorded. Nevertheless, in the case of multi-unit recording, increased spike counts associated with increased stimulus levels could have resulted from recruitment of more active cortical neurons as well as from increased probability of firing from a constant ensemble of neurons.

D. Data analysis

Cortical neurons typically responded to electrical-pulse-train stimulation of the cochlea with a brief burst of spikes beginning $\sim$10 ms after pulse-train onset, followed by a period of inactivity typically lasting $>$100 ms, sometimes followed by low-probability temporally-scattered spikes throughout the remainder of the pulse train and extending past the offset of the train. Figure 2(b) shows examples of post-stimulus-time histograms of spikes recorded simultaneously at four cortical sites. Because only the onset responses were reliably locked to the stimuli, we restricted subsequent analysis to spike counts recorded during the period from 5–50 ms after stimulus onset.

Cortical thresholds to cochlear electrical stimulation were determined by computer recognition of spike activity across all 16 recording channels. An artificial-neural network procedure was used to distinguish single trials in which a stimulus was present from identical trials in which there was no stimulus. The neural network was configured as a probabilistic neural network, using the Neural Network Toolbox from the Mathworks (Natick, MA); the network is a form of template matcher. The input to the network consisted of 16-element response vectors, corresponding to the number of spikes recorded on each of the 16 channels on each trial. The network was trained and tested using a one-out procedure as follows. Given responses to N trials at a particular stimulus level and N no-stimulus trials, the network was exposed to $2N$-1 response vectors and trained with feedback to indicate whether each response came from a stimulus or no-stimulus trial. Then the response from the remaining one trial was classified by the network. The procedure was repeated to classify the responses on each of the trials. The results were tabulated as the percentage of ''stimulus'' classifications on stimulus trials and of ''no-stimulus'' classification on no-stimulus trials. Those percentages were expressed as a detection index (d'; Green and Swets, 1966); perfect performance was recorded as $d'=3.29$, which corresponds to $\sim$99% correct. For each stimulus condition, d' was plotted as a function of the stimulus current level, which was varied in 1-dB steps. The stimulus level corresponding to $d'=1$ was estimated using linear interpolation and was taken as the threshold for that stimulus condition.

III. EXPERIMENT I: CHANNEL INTERACTION

In a human cochlear-implant user, stimulation of one channel might interact with another stimulated channel by altering the second channel's threshold or dynamic range, by altering the aggregate pitch, or by masking temporal modulation. In the present physiological study, channel interaction was quantified as the amount by which sub-threshold stimulation of the basal channel changed the threshold for stimulation of the apical channel. It was anticipated that channel interactions would be greatest when pulses on the two channels were presented simultaneously, permitting summation of electrical current fields, and that interactions would be reduced in conditions in which pulse trains on the two channels were interleaved in time. Among interleaved conditions, it was an open question whether interactions would vary according to the amount of temporal offset between channels. That is, would there be a benefit to minimizing or maximizing the delay between the pulses of two interleaved pulse trains? Another question of particular interest was whether the pulse rates would have any impact on channel interactions.

A. Stimuli and procedure

In each experiment, an on-line display of neural waveforms was used to estimate cortical thresholds for stimulation of the apical and basal channels alone. Then, basal-channel stimuli were presented at various levels in 1-dB steps from $\geqslant$7 dB below to at least 1 dB above the estimated threshold, and the apical-channel levels were varied in 1-dB steps across ranges that encompassed the cortical thresholds in the presence of the basal-channel stimulus. Off-line, basal-channel thresholds (Θ_{basal}) were computed as described in Sec. II D, and basal-channel current levels are expressed relative to those computed thresholds. All reported results were obtained at basal-channel levels $>$1 dB below Θ_{basal}.

B. Results

Consistent with our previous studies (Bierer and Middlebrooks, 2002; Bierer and Middlebrooks, 2004), monopolar cochlear stimuli produced widespread activation of the auditory cortex. Figure 3 shows an example from one animal in the form of rate-versus-level functions [Figs. 3(a) and 3(b)] and spatial tuning curves [Figs. 3(c) and 3(d)]; left and right columns of panels show the results of stimulation of the apical and basal channels, respectively. The rate-versus-level functions show that neurons tended to reach saturated firing levels across the range of current levels that was tested. Dynamic ranges for individual recording sites, eliciting responses from near threshold to saturation, were around 2–3 dB. Firing rates for each recording site were normalized by computing the mean firing rate for each combination of apical- and basal-channel current level. For each recording site, the 95% percentile of the distribution of mean rates was taken as the maximum, and all rates were expressed as percentages of that value. Contour lines in Figs. 3(c) and 3(d) represent normalized mean spike rates at each of the 16 recording sites. The vertical axis plots cortical location from caudo-medial (top of the figures) to rostro-lateral (bottom), and the horizontal axis represents the stimulus level. Apical-channel stimulation over a range of $<$3 dB activated all the recorded sites to $>$25% of their maximum rates. The response to basal-channel stimulation was only slightly more

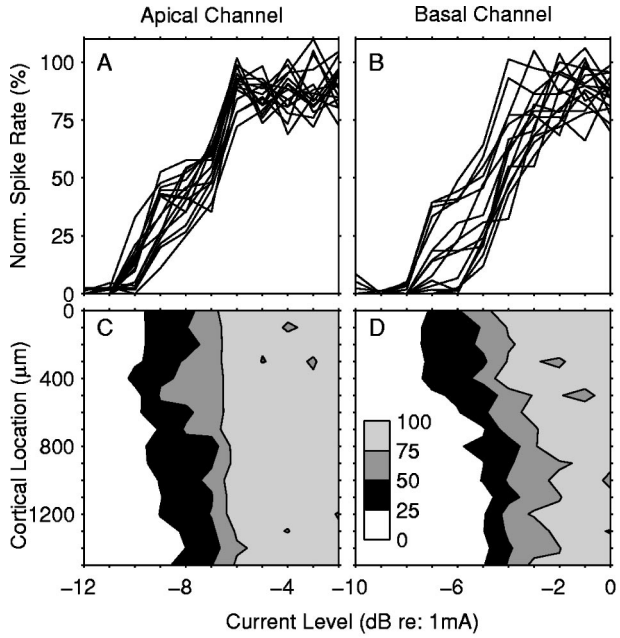

FIG. 3. Rate-versus-level functions and spatial tuning curves resulting from stimulation of apical and basal channels in one animal. Left and right columns of panels represent apical- and basal-channel stimulation, respectively. (a) and (b) Rate-versus-level functions: Each line represents the normalized spike rates recorded at one of 16 recording sites. (c) and (d): Spatial tuning curves: The vertical axis plots the location of the cortical recording site. Location coordinates increase from caudo-medial to rostro-lateral, which is the direction of decreasing characteristic frequency in the cortical tonotopic map. The horizontal axes plot stimulus current levels. The contours indicate current levels at which units at each recording site responded at 25, 50, and 75% of their maximum firing rate. See the text for a normalization procedure.

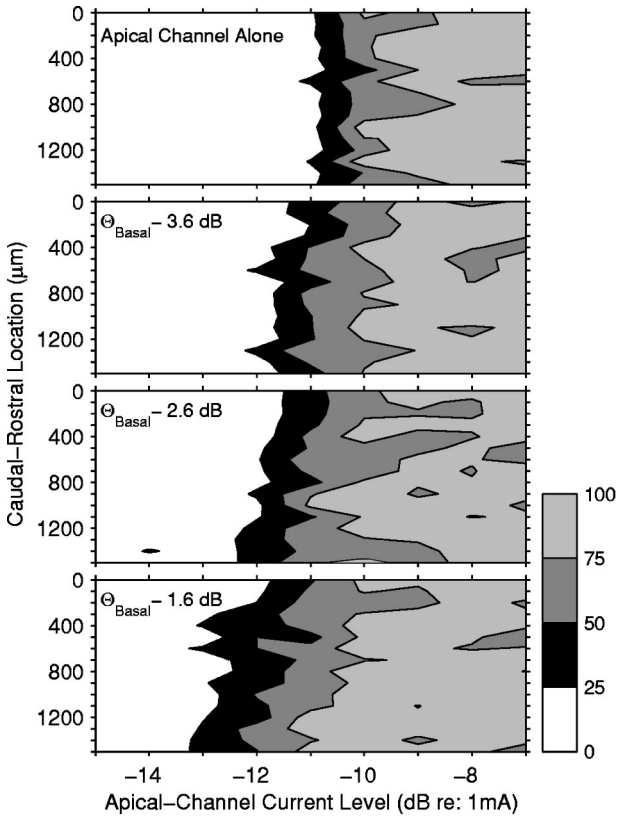

FIG. 4. Spatial tuning curves demonstrating threshold shifts resulting from sub-threshold stimulation of the basal channel. Each panel shows the normalized firing rates of units as a function of current levels on the apical channel. The 4 panels show responses obtained when the apical channel was stimulated alone (top) or when the basal channel was stimulated at one of 3 sub-threshold levels, as indicated. The pulse rate was 4069-pps and the temporal offset in the 3 lower panels was 123 μs. Θ_{basal}: threshold for stimulation of the basal channel alone. The meaning of the vertical and horizontal axes and the normalization procedure is the same as in Fig. 3.

restricted. In all animals, stimulus levels only a few dB above threshold activated largely overlapping cortical populations; presumably this indicates an overlap of activated cochlear-nerve populations.

In all cases in which basal-channel stimulation had appreciable effect on the threshold for apical-channel stimulation, the effect was to lower the threshold. Figure 4 shows spatial tuning curves measured in one animal for the apical-channel stimulus alone and for 3 levels of the basal-channel stimulus. The horizontal axis plots the current level on the apical channel. In these illustrated examples, the 4069-pps pulse trains were interleaved with a temporal offset of 123 μs. The presence of a stimulus on the basal channel at 3.6 dB below the basal-channel threshold lowered the apical-channel threshold by $\sim$1 dB, and the threshold reduction increased to $\sim$2 dB at a basal-channel level 1.6 dB below the basal-channel threshold. In this example, the threshold reduction appeared greater at the more rostral cortical sites, but that effect varied among animals.

Figure 5 quantifies the threshold reductions represented in Fig. 4. The 4 curves represent thresholds measured in the presence of basal-channel stimuli at 4 levels. Each curve plots the d' for the detection of the presence of an apical-channel stimulus as a function of the apical-channel current level. With increasing apical-channel current levels, the accuracy of detection increased from around $d'=0$ (random-chance level performance) to $d'=3.29$ (perfect detection of the apical stimulus). The arrows indicate the thresholds, which are the interpolated current levels at which $d'=1$. The presence of a basal-channel stimulus of increasing level displaced the curves progressively to lower apical-channel levels.

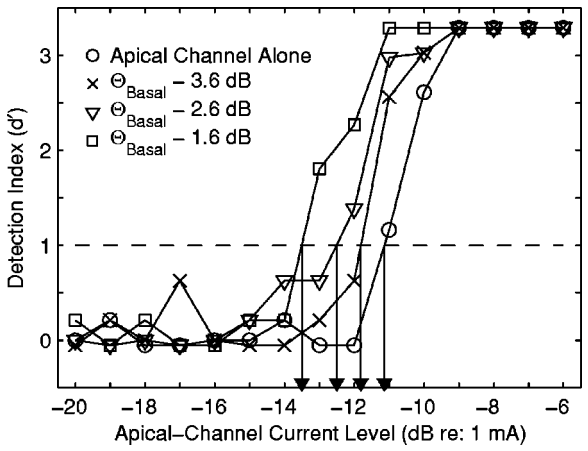

FIG. 5. Estimation of thresholds. Each data point plots the detection index (d') for detecting the presence of a stimulus on the apical channel. The 4 curves represent conditions of apical channel alone or in the presence of one of 3 sub-threshold levels on the basal channel. The data are from the same case as represented in Fig. 4. The point at which each curve crossed $d'=1$ was taken as the threshold for that condition.

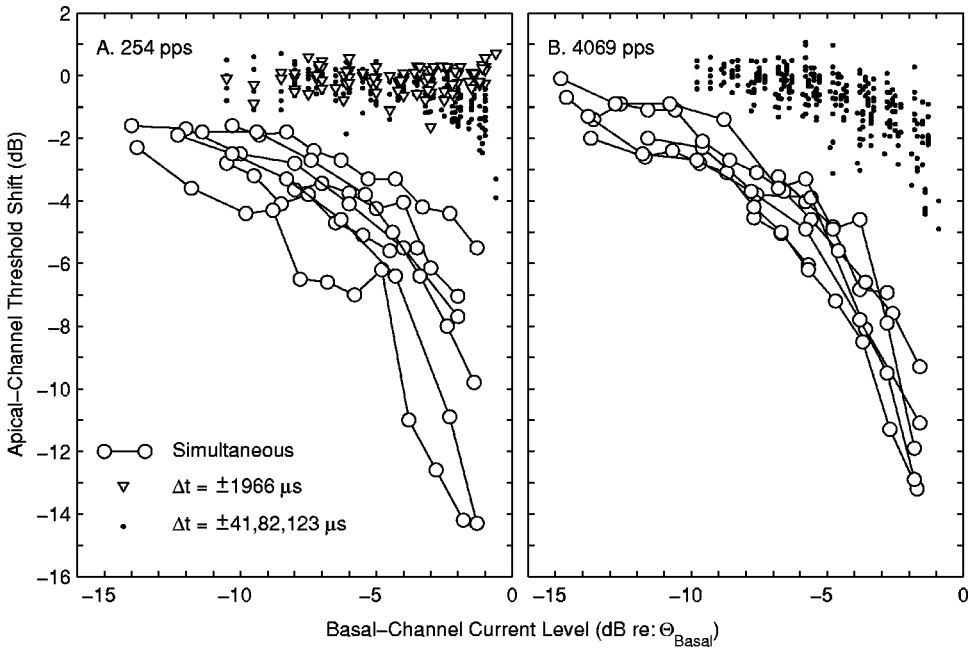

FIG. 6. Shifts in apical-channel thresholds resulting from the presentation of sub-threshold currents on the basal channel. Open circles and curves represent the condition of simultaneous stimulation of apical and basal channels, one curve per animal. Open triangles represent the condition of temporal offset of $\pm 1966\,\mu$s (left panel only), and small filled circles represent temporal offsets of ± 41, 82, and 123 μs. Panels (a) and (b) represent conditions of pulse rates at 254 and 4069 pps, respectively.

Shifts in the apical-channel threshold resulting from basal-channel stimulation are summarized in Fig. 6. The vertical axis plots the threshold for stimulation of the apical channel in the presence of the basal-channel stimulus relative to the threshold for the apical-channel stimulus presented alone. Left and right panels indicate 254- and 4069-pps conditions, respectively. Threshold shifts generally increased with increasing basal-channel current level (plotted on the horizontal axis). It is readily apparent that threshold shifts were greater in the simultaneous condition (open circles connected by lines) than in any of the interleaved conditions (triangles and small filled circles). In the simultaneous condition, there was no significant difference between the threshold shifts compared between 254- and 4069-pps conditions ($p > 0.10$; 2-way ANOVA, factors of pulse rate and basal-channel level).

The most likely explanation for the threshold shifts in the simultaneous condition is that cochlear neurons are activated by the sum of currents passed through the apical and basal electrodes. In a condition in which cochlear electrical fields are spatially restricted and/or electrodes are widely separated in the cochlea, that summation would involve a rather complicated vector summation. In the present experiment, however, the two monopolar electrodes were fairly close together and the two individual electrical fields showed substantial overlap, as suggested by the cortical spatial tuning curves in Fig. 3. For that reason, the effective currents resulting from simultaneous stimulation of both channels could be approximated well by simple addition of the currents. In Fig. 7, the contour lines represent the sums of currents passing through the apical and basal channels (vertical and horizontal axes, respectively); currents from the two channels were expressed in μA, added together, then plotted as dB *re*: 1 mA. Contours are drawn in 1-dB steps, and their values can be read from the points at which they contact the horizontal or vertical axis. The open circles represent the cortical thresholds for apical stimulation in the presence of simultaneous basal-channel stimulation. In the left panel [Fig. 7(a)], the thresholds for apical- and basal-channel stimulation alone were -5.6 and -5.2 dB (*re*: 1 mA; indicated by the arrows pointing to the axes), and the plotted threshold curve closely follows the contour indicating a summed current of -5 dB. In the right panel [Fig. 7(b)], the apical and basal thresholds were somewhat more different from each other (-4.3 and -2.2 dB, respectively), and the plotted threshold curve shifts gradually from near the

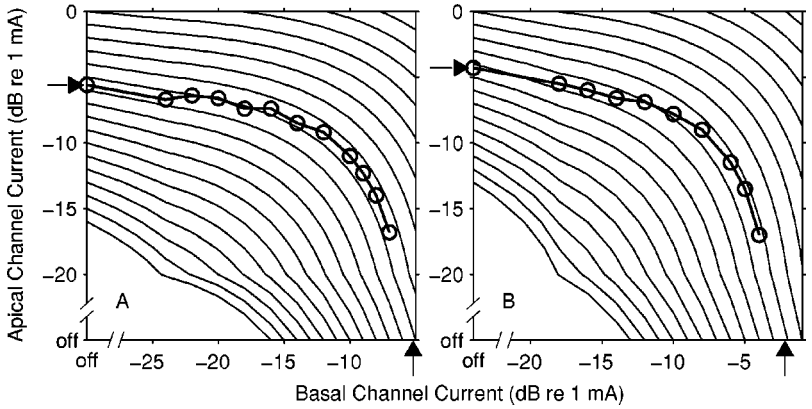

FIG. 7. Sums of currents presented through apical and basal channels in the simultaneous condition. The currents on both electrodes were expressed in μA, added together, then expressed as dB *re*: 1 mA. Heavy lines with open circles indicate the threshold apical-channel levels in the presence of various basal-channel levels. Arrows on the axes represent thresholds for the stimulation apical channel (vertical axis) or basal channel (horizontal axis) alone. Left and right panels represent animals in which thresholds for apical and basal channels alone were nearly equal (left panel) or differed by 2.1 dB (right panel).

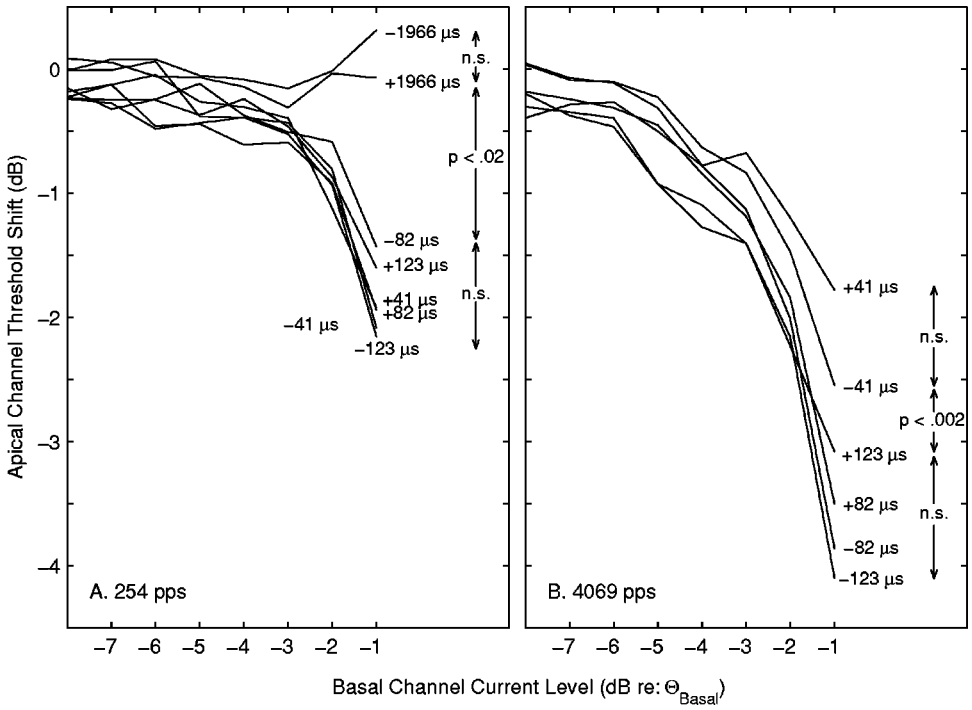

FIG. 8. Mean threshold shifts in nonsimultaneous conditions. Each curve represents mean data from one temporal offset condition. Error bars are omitted for clarity, but the standard error of the mean averaged 0.31 dB. The statistical comparisons are based on 2-way ANOVA (factors of basal-channel level and temporal offset); n.s. indicates $p>0.05$. Panels (a) and (b) show data from conditions of 254 pps and 4069 pps.

-4-dB contour to near the -2-dB contour. In all 6 animals in which the simultaneous condition was tested, and at pulse rates of both 254 and 4069 pps, thresholds for combined stimulation tracked within 1 dB of the values predicted based on simple summation of apical- and basal-channel currents. Variation within that 1-dB range reflects the 1-dB resolution with which current levels were tested and a small amount of variance in the physiological measurements and estimates of thresholds.

Figure 8 summarizes on an expanded scale the threshold shifts measured in the nonsimultaneous conditions. For this plot and for the following statistics, linear interpolation was used within the data from each animal to estimate the threshold shifts at integer values of the basal-channel current; the original data were collected in 1-dB steps but not necessarily at integer values. Each curve in Fig. 8 represents the mean threshold shifts computed at integer basal-channel levels across 6 or 7 animals based on data interpolated in this way. Several features of the plots are noteworthy. *First*, in the 254-pps condition (left panel), the threshold shifts measured for temporal offsets of $\pm 1966\ \mu$s were substantially less than for any of the shorter offsets. Indeed, the threshold shifts in the ± 1966-μs condition showed no significant dependence on basal-channel level ($p>0.1$). Among all of the shorter nonzero offsets in the 254-pps condition (i.e., ± 41 to $\pm 123\ \mu$s), there was no systematic dependence of threshold shift on temporal offset ($p>0.05$). *Second*, in the 4069-pps condition (right panel), the shortest temporal offsets ($\pm 41\ \mu$s) produced significantly smaller threshold shifts than did the longer offsets (± 82 and $\pm 123\ \mu$s; $p<0.002$). There was no significant difference among the threshold shifts measured for the ± 82 and $\pm 123\ \mu$s offsets ($p>0.1$). *Third*, at no temporal offset nor at either pulse rate was there a statistically significant difference in threshold shifts between conditions of the apical-channel leading (positive offsets) or apical-channel trailing (negative offsets) ($p>0.1$). *Finally*, threshold shifts measured in the 4069-pps condition tended to be greater than those measured in the 254-pps condition. An inspection of Fig. 8 suggests that differences in threshold shifts between the two pulse-rate conditions might be substantial for the ± 82- and ± 123-μs temporal offsets and smaller for the ± 41-μs offsets.

Figure 9 compares the threshold shifts measured at the two pulse rates. Each symbol represents threshold shifts measured at one basal-channel level relative to the basal-channel threshold. The apical-channel threshold shifts for the 254- and 4069-pps conditions are plotted on the horizontal and vertical axes, respectively. Each symbol type represents

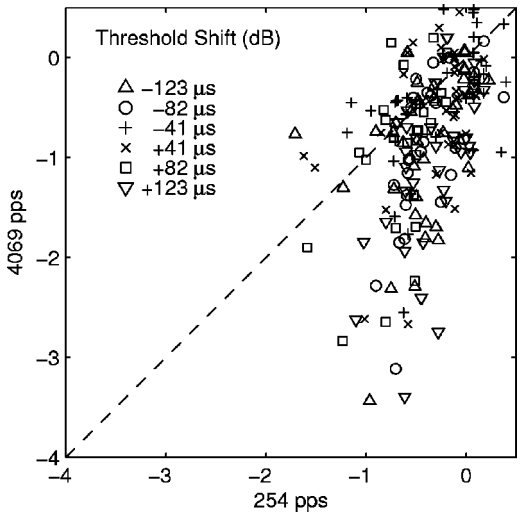

FIG. 9. A comparison of threshold shifts at 4069-pps (vertical axis) and 254-pps (horizontal axis) pulse rates. Shifts in the threshold for apical-channel stimulation are given in dB. Symbols lying below the dashed line indicate greater threshold shifts at the 4069-pps rate.

the indicated temporal offset. Comparing threshold shifts at the two pulse rates across basal-channel levels from 1 to 2 dB below threshold and across temporal offsets of ± 41, ± 82, and ± 123 μs, the shifts were greater in the 4069-pps condition by a mean of 1.13 dB ($p<0.0001$); the mean difference was 0.68 dB ($p<0.0001$) when averaging across basal-channel levels from 1 to 6 dB below threshold. The difference in threshold shifts between the two pulse rates was greater at the longer temporal offsets (± 82 and ± 123 μs) than at offsets of ± 41 μs. For basal-channel levels 1 to 2 dB below threshold, the difference in threshold shifts measured at the two pulse rates was 1.31 dB ($p<0.0001$) for offsets of ± 82 and ± 123 μs compared to 0.94 dB ($p<0.0001$) for offsets of ± 41 μs; across basal-channel levels 1 to 6 dB below threshold, the threshold shifts were 0.78 dB greater ($p<0.0001$) at the 4069-pps rate for the longer temporal offsets compared to 0.47 dB ($p<0.0001$) at the shorter offsets.

The thresholds measured for apical- and basal-channel stimulation *alone* consistently were lower at the 4069-pps pulse rate than at 254 pps. Averaged across all 7 animals in which channel interactions were studied and across both the apical and basal channels, the threshold was 3.2 dB lower at the 4069-pps rate ($p<0.0001$). The dependence of single-channel thresholds on the pulse rate suggested a possible explanation for the differences in threshold shifts observed between 254- and 4069-pps pulse rates. That explanation was explored further in Experiment II.

IV. EXPERIMENT II: TEMPORAL FACTORS INFLUENCING SINGLE-CHANNEL THRESHOLDS

The use of two fairly closely separated monopolar cochlear electrodes in this study resulted in a substantial overlap of activated neural populations, as illustrated in Fig. 3 and as considered in regard to summation of simultaneous current fields (Fig. 7). That observation indicates that the study of responses to pairs of electrical pulses delivered through a single electrode might be an efficient way to examine factors that influence interactions between pulses on two electrodes. Experiment II tested the effects on cortical threshold of single-channel pulse rate, of the duration of a high-rate pulse train, and of the delays between two pulses. Apical and basal channels each were stimulated alone in separate trials.

Figure 10 shows the threshold measured in the auditory cortex as a function of the pulse rate of a train of 20-μs/ph biphasic pulses. These data were measured using a pulse-train duration of 7 ms, but separate control measurements of thresholds for 254- and 4069-pps rates showed that thresholds were identical between train durations of 7 and 200 ms. The top panel [Fig. 10(a)] shows data from one channel in one animal. In this example, thresholds were constant between 250 and 500 pps and began decreasing markedly at rates of 1000 pps and higher. The lower panel [Fig. 10(b)] shows data from one or two channels in each of 5 animals (a total of 7 channels); in that panel, thresholds are expressed relative to the highest threshold measured on each channel. The curves all show a similar form: a negligible slope below 1000 pps, a ''knee'' at 1000 pps, and a negative slope at higher rates. Results from the two channels were qualitatively and quantitatively similar and, therefore, have been combined for statistical purposes. The decrease of threshold with increasing pulse rate was significant for rates at and above 1000 pps (ANOVA, $p<0.0001$) and showed no significant trend for low rates up to 1000 pps ($p>0.1$).

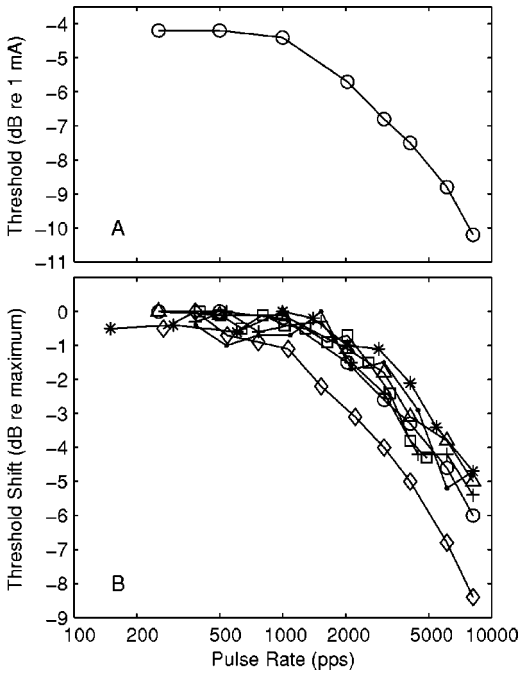

FIG. 10. Thresholds for 7-ms trains of 20-μs/phase pulses at various pulse rates. (a) Data from one animal expressed as dB relative to 1 mA. (b) Data from 1 or 2 channels in each of 5 animals (a total of 7 channels) expressed as dB relative to the highest threshold for each condition.

We tested whether the observed characteristics of pulse-rate sensitivity (i.e., no dependence on rates <1000 pps; decreasing thresholds for rates $\geqslant 1000$ pps) were properties only of brief phase durations. Figure 11 shows the dependence of thresholds on pulse rate for pulses of phase durations from 20 to 164 μs/ph; these data all are from one channel in one animal. In the top panel [Fig. 11(a)], thresholds showed an overall decrease associated with increasing phase durations. That decrease in threshold (quantified below) is anticipated from the increase in charge transferred by longer-duration phases. The lower panel [Fig. 11(b)] shows data from all phase durations expressed relative to the maximum threshold for each phase duration. The curves are similar in form, showing slopes that are essentially zero below 1000 pps and considerably steeper above 1000 pps. That is, the basic characteristics of pulse-rate sensitivity, with a marked increase in slope for rates >1000 pps, are common to all phase durations, at least from 20 to 164 μs.

The dependence of threshold on phase duration, as seen in Fig. 11(a), was tested for a total of 5 channels in 4 animals. The threshold current levels decreased with increases in phase durations from 41 to 164 μs/ph at a rate of 6.7 dB per doubling of the phase duration ($r^2=0.94$). The decrease in threshold between phase durations of 20 to 41 μs/ph was greater: 9.4 dB/doubling ($r^2=0.99$). A simple doubling of transferred charge would predict threshold decreases of ~ 6 dB. A possible explanation for the observed larger-than-

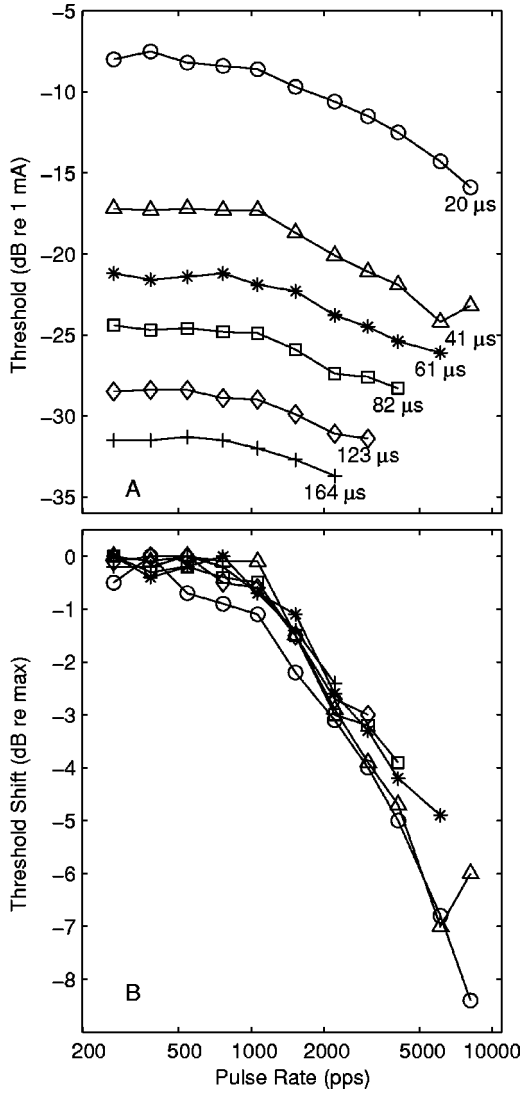

FIG. 11. Thresholds for pulses of various phase durations as a function of pulse rate. All the data are from one animal. In panel (a), thresholds are given in dB *re*: 1 mA. In panel (b), thresholds are in dB relative to the highest threshold for each condition.

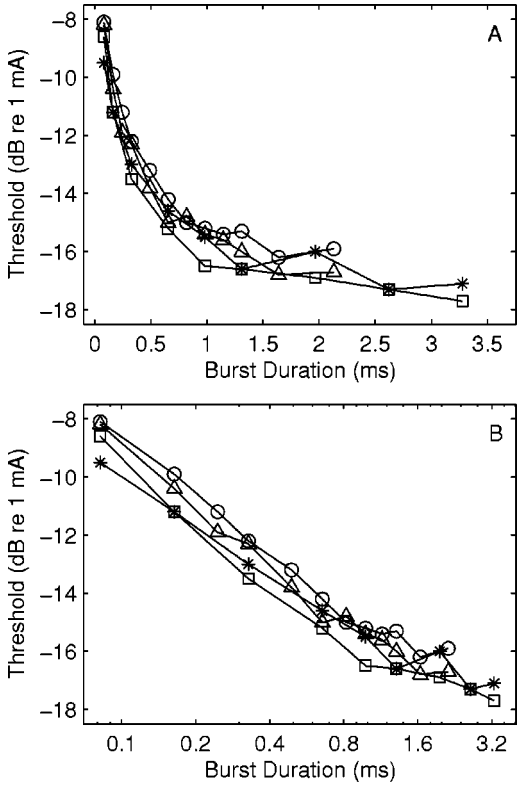

FIG. 12. Threshold for pulse bursts of various durations. Phase durations were constant at 20 μs/phase, and the pulse rate was constant at 12200 pps. Panels (a) and (b) show data on linear and logarithmic duration axes, respectively.

6-dB threshold decreases is discussed in Sec. V B.

One possible explanation for the absence of a pulse-rate effect on threshold at rates below $\sim$1000 pps is that the threshold for the burst of cortical spikes measured at stimulus onset is determined by the integrated cochlear stimuli delivered within the first $\sim$1 ms of the pulse train. At rates $<$1000 pps, the second pulse of the train would fall outside that 1-ms window and, thus, further decreases in rate would have no effect on threshold. That hypothesis was tested by measuring cortical thresholds of 12200-pps pulse trains that varied in train duration (or, equivalently, in the number of pulses from 1 to 26 or 1 to 40); phase durations were fixed at 20 μs/ph. Data from 2 channels in 2 animals are shown in Fig. 12 on linear (top panel) and logarithmic time scales, respectively. For burst durations $<$1 ms, threshold current levels decreased at a rate of $\sim$2 dB per doubling of the burst duration (median: 2.08 dB/doubling, range: 1.68 to 2.16 for durations $<=$0.98 ms). The slope flattened considerably at longer durations (median: 0.80 dB/doubling, range: 0.59 to 1.30 dB/doubling for durations of 1.15 to 3.2 ms). The results largely supported the hypothesis that cortical thresholds in this experimental protocol are dominated by electrical charge integrated over the first $\sim$1 ms of pulse trains.

Integration of currents in the cochlea presumably is influenced not only by the number of pulses falling within a particular ($\sim$1-ms) window but by the intervals between pulses within that window. We measured the time constant for the summation of two pulses separated by various intervals; pairs of pulses were presented from a single monopolar channel. Figure 13 shows the data from 6 channels studied in 3 animals. Three pulse shapes were studied: cathodic (monophasic), biphasic, and delayed phase. The pulse shapes are illustrated in Fig. 1(a); in all cases, phase durations were 20 μs/ph. The dependence of cortical thresholds on inter-pulse intervals varied considerably among stimulus pulse shapes. For inter-pulse intervals $<=$460 μs, the data for the monophasic pulse pairs [Fig. 13(a)] approximated a single exponential (after Cartee *et al.*, 2000) with median time constant for a summation of 352 μs, ranging from 236 to 394 after excluding one outlier. The dashed line in Fig. 13(a) plots a single exponential with a time constant of 352 μs; the vertical position is arbitrary. Intervals greater than 460 μs were excluded from the computation of time constants because the variance among channels and animals increased at longer intervals; in some cases, thresholds continued to increase, whereas curves flattened or turned negative in other cases.

The dependence of cortical threshold on the inter-pulse interval was considerably weaker in the case of biphasic

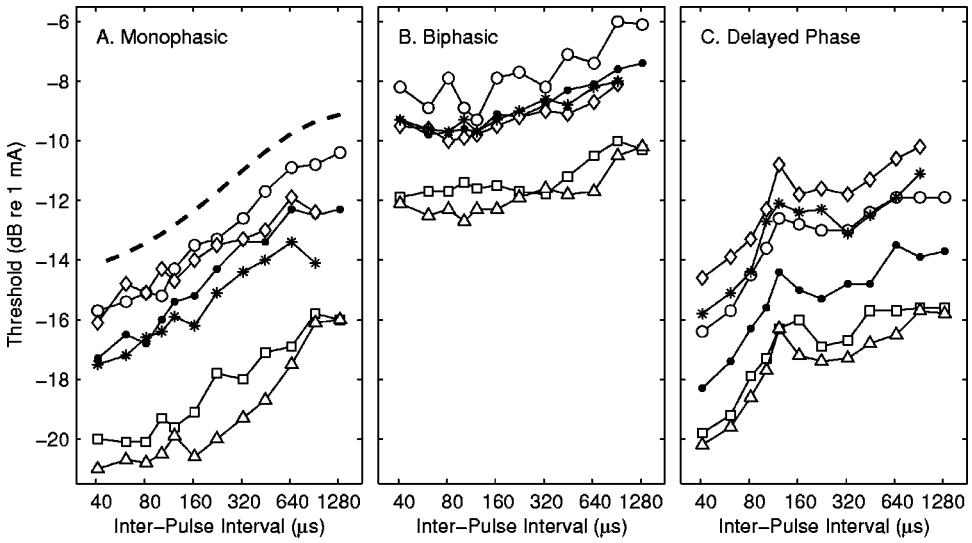

FIG. 13. Sensitivity to inter-pulse intervals. Two-pulse stimuli were presented with various intervals between the two pulses. The phase duration was fixed at 20 μs/phase. Various symbols represent data from 2 channels in each of 3 animals. The assignment of symbols to channels is the same in all panels. The dashed line in panel (a) represents a single exponential function with time constant $=352$ μs.

pulses [Fig. 13(b)]. Thresholds were constant or decreased slightly across increasing intervals from 41 to 123 μs. Across a range of intervals from 123 to 460 μs, thresholds increased with a median time constant of 659 μs, ranging from 456–1061 μs. Overall, thresholds for the biphasic pulses were $\sim$6 dB higher than for the monophasic pulses; thresholds for single pulses were 4.3 to 9.0 dB higher for biphasic than for monophasic cathodic pulse; median $=5.5$ dB, $N=6$ channels in 3 animals). One possible explanation for that overall threshold difference was that depolarization of cochlear neurons by the cathodic phase of the biphasic pulse might have been partially cancelled by the immediately following anodic phase. We tested that hypothesis by measuring thresholds for pulse shapes in which the anodic phase was delayed by 123 μs [Fig. 13(c)]. The plots of the threshold vs inter-pulse interval showed local peaks at an inter-pulse interval of 123 μs. At that interval, the cathodic phase of the second pulse coincided exactly with the anodic phase of the first pulse, thereby canceling the second cathodic phase. Aside from that interval, however, the delayed-pulse data resembled the monophasic data fairly closely, again showing an overall threshold $\sim$6 dB lower than that measured for the biphasic pulses (thresholds for delayed-phase waveforms were 2.1 to 6.3 dB lower than for biphasic pulses, median 5.4 dB; 6 channels, in 3 animals).

V. DISCUSSION

The present results demonstrate several temporal factors of electrical pulse trains delivered through one or two channels that influence thresholds measured in the auditory cortex. *First*, channel interactions, as quantified by the reduction of the threshold for one channel by stimulation of another channel, were substantially greater for the simultaneous stimulation of two channels than for nonsimultaneous stimulation. This rather unsurprising result could be explained quantitatively by a simple summation of current fields in the simultaneous condition. *Second*, among nonsimultaneous conditions, threshold shifts at the lower pulse rate (254 pps) were essentially eliminated by introduction of between-channel temporal offsets of 1996 μs. At the higher rate (4069 pps), threshold shifts were minimized by presenting the second biphasic pulse immediately after the first (i.e., temporal offset of 41 μs from the onset of the first biphasic pulse to the onset of the second). Aside from those two conditions, there was no significant difference in channel interactions among other tested temporal offsets at each pulse rate. *Third*, channel interactions in nonsimultaneous conditions were greater at the higher pulse rate than at the lower rate. That result has important consequences for design of high-pulse-rate speech processors. *Fourth*, in single-channel conditions, cortical thresholds were essentially insensitive to changes in pulse rate for rates below 1000 pps and shifted systematically to lower current levels with increases in rates above 1000 pps. *Finally*, studies of paired pulses with varying inter-pulse intervals and of high-rate bursts of varying duration support the hypothesis that, at least in this experimental preparation, the threshold measured in the auditory cortex is determined largely by integration of cochlear stimuli within the first $\sim$1 ms of stimulation.

The threshold shifts measured in the interleaved conditions might seem unimportant compared to the much larger shifts measured in simultaneous conditions. Nevertheless, a threshold shift of only a few dB is a large fraction of the entire dynamic range of cortical neurons under conditions of electrical cochlear stimulation. For example, the rate-level functions of cortical neurons shown in Fig. 2 are typical in that they rise from threshold to saturation in only 2–3 dB, and, in the data shown in Fig. 5, stimulus detection by ensembles of cortical neurons improved from near-chance levels to perfect detection across a stimulus range of only 3–4 dB. Most dynamic ranges for monopolar stimulation were $<$6 dB in a previous study that used cortical recording and analysis procedures similar to those in the present work (Middlebrooks and Bierer, 2002). Dynamic ranges can vary from around 2 to 20 dB in human cochlear-implant users (e.g., Busby *et al.*, 1994; Nelson *et al.*, 1996; Kreft *et al.*, 2004). For those reasons, one would expect threshold shifts of a few dB due to channel interactions to be of practical significance to implant users. To the degree that a stimulus on one electrode modulates the sensitivity to the stimulation of nearby electrodes, responses on those electrodes will in-

crease in correlation. As the correlation among electrodes increases, the amount of unique information that is transmitted through each electrode will decrease. The present study assessed channel interactions only in conditions in which one of the channels (i.e., the basal channel) was stimulated at more than 1 dB below its own threshold. Extrapolation to suprathreshold levels suggests that an interleaved pulse train on one channel would have potent effects on the transmission of information through nearby channels.

In evaluating the present results in the context of the existing literature, one finds more pertinent human and animal psychophysical studies than animal physiological studies. Of course, it is desirable to attempt to relate animal physiology to human perception, but one must use some caution in making direct comparisons. Conclusions reached in the present study must be confirmed or refuted in studies with human subjects. In any comparison of an animal physiological study with human psychophysics, one must be concerned about the effects of anesthesia and about interspecies differences. Regarding ketamine/xylazine anesthesia, we have found previously in guinea pigs that psychophysical detection thresholds and thresholds for neural spike activity in the pig auditory cortex show a similar dependence on the phase duration of single electrical pulses (Miller *et al.*, 2001). Also, two previous studies have compared the electrically evoked middle latency response (EMLR) in guinea pigs in the presence and absence of ketamine/xylazine anesthesia; ''electrically evoked'' indicates an electrical stimulation of the cochlea with a round-window electrode (Crowther *et al.*, 1989) or an intra-scalar electrode (Miller *et al.*, 2001). The EMLR is thought to originate from neurons within the midbrain and cortex (Kaga *et al.*, 1980; McGee *et al.*, 1991; 1992). Comparisons of the EMLR recorded in awake and anesthetized conditions indicate clear differences in waveform morphology and latency but, pertinent to the present study, no consistent differences in thresholds. Regarding the use of guinea pigs, differences in the geometry of human and guinea-pig cochleas might result in differences in channel interactions. Nevertheless, available comparisons of humans and guinea pigs show general agreement on the effects of stimulus phase durations on thresholds for electrically evoked auditory brainstem responses (Miller *et al.*, 1995) and of phase durations and electrode configurations on psychophysical thresholds (Miller *et al.*, 1999).

Aside from general concerns about inter-species comparisons and the effects of anesthesia, there are three specific *caveats* that should be raised in regard to the present study. *First*, we recorded from neurons at only 16 cortical sites in each animal. We attempted to position the recording probe at an optimal location relative to the cortical tonotopic representation, but we cannot be sure that the probe sampled the neurons having the lowest thresholds. In contrast, a psychophysical threshold might reflect the activity of the most sensitive neurons in the entire brain. Moreover, the degree to which activity in the primary auditory cortex influences threshold judgments in psychophysical tasks is not known. *Second*, our measure of threshold was rather conservative, requiring a reliable stimulus-locked response from neurons at one or more recording sites. Again, we do not know the size of the activated neural population or the magnitude or synchrony of neural firing that is required for detection by a human subject. *Finally*, under the present experimental conditions, cortical neurons gave a strong response at stimulus onset, presumably responding to the first wave of activity from the cochlea and ascending pathway. That onset response was followed by a period of inactivity, >100 ms in duration, probably reflecting intra-cortical inhibitory processes (e.g., Brugge *et al.*, 1969; Wang *et al.*, 2002; Wehr and Zador, 2003). Psychophysical studies in humans and animals suggest that temporal integration underlying detection can take place over hundreds milliseconds (reviewed by Viemeister and Wakefield, 1991); such integration might involve statistical integration of information (Green and Swets, 1966) or ''multiple looks'' (Viemeister and Wakefield, 1991). In contrast, the thresholds in the present study, as in most other physiological studies, were determined entirely by onset responses.

A. Simultaneous versus interleaved pulse trains

It has long been appreciated that interactions among cochlear electrodes are greatest under conditions in which electrical fields from two or more electrodes can summate, i.e., when currents are delivered simultaneously in equal polarity on nearby electrodes (e.g., Eddington *et al.*, 1978; Shannon, 1983; White *et al.*, 1984; Wilson *et al.*, 1988). In an early study in human subjects, for instance, a subthreshold pulse train on one channel reduced by $\sim$10 dB the threshold for the detection of a pulse train on a nearby channel, and that 10-dB reduction was eliminated by interleaving the pulse trains in time (Eddington *et al.*, 1978). Threshold reductions and loudness summation of that magnitude in conditions of simultaneous stimulation have been reported in a physiological study of the cat inferior colliculus (White *et al.*, 1984) and in other psychophysical studies of cochlear-implant users (Shannon, 1983; White *et al.*, 1984; Favre and Pelizzone, 1993; Boëx *et al.*, 2003; deBalthasar *et al.*, 2003). In the present study, thresholds were in all conditions lower when pulses on two channels were presented simultaneously than when they were interleaved in time. The shifts in threshold in the simultaneous condition could be accounted for quantitatively by the simple addition of current fields. That computation was possible in this study because the two monopolar stimulating electrodes were nearby and generated largely overlapping current fields. An estimation of the vector sum of current fields presumably would have been more complex if the electrodes had been farther apart in the cochlea or if current fields had been more restricted. We have shown previously that summation between single pulses on each of two electrodes is reduced considerably when a bipolar or tripolar electrode configuration is used (Bierer and Middlebrooks, 2004).

In most previous studies, the introduction of a temporal offset of some hundreds of microseconds between pulses on pairs of electrodes reduced threshold shifts (or reduced loudness summation) to negligible levels. For instance, Eddington and colleagues reported that the introduction of a 500-μs temporal offset entirely eliminated a $\sim$10 dB threshold shift in human subjects (Eddington *et al.*, 1978). Similarly, Favre

and Pellizzone (1993) reported that subthreshold perturbation pulse trains produced threshold shifts of <1 dB when temporal offsets were 500 to 2500 μs. In our previous study, a single subthreshold pulse could produce a slight *elevation* of the threshold for a pulse that followed by 2000 μs (Bierer and Middlebrooks, 2004). We speculated that that effect was due to induction of a partial refractory state by the leading subthreshold pulse. In the present study, which used 200-ms trains of pulses, temporal offsets of 2000 μs effectively eliminated channel interaction in the form of threshold shifts measured at the level of the auditory cortex.

Reports of effects of temporal offsets shorter than $\sim$1000 μs have varied among studies. McKay and colleagues (1995) reported that loudness summation in human subjects decreased as temporal offsets were increased from a range of 620–920 μs to 2000 μs, but McKay and McDermott (1998) found essentially no difference in loudness summation between temporal offsets of 400 and 800 μs. Indeed, temporal offset is not a parameter in the comprehensive loudness model by McKay and colleagues (2001; 2003). Contrary to other reports, deBalthasar and colleagues (2003) found slight threshold *increases* in human subjects when a sub-threshold ''perturbation'' pulse train was added with a delay of 100 to 200 μs. In our previous study of guinea-pig auditory cortex (Bierer and Middlebrooks, 2004), threshold shifts generally decreased as temporal offsets between single pulses increased from 160 to 640 μs. In the present study, all temporal offsets in the range of $\pm$41 to 123 μs produced comparable threshold shifts at the 254-pps pulse rate. At the 4069-pps rate, shifts were somewhat smaller at the $\pm$41 μs offsets than at $\pm$82 or 123 μs. The most striking finding regarding the brief temporal offsets was that threshold shifts generally were greater at the higher pulse rate. Possible mechanisms of threshold shifts at brief temporal offsets will be considered in the next section.

B. Cochlear determinants of cortical thresholds

Thresholds measured at the level of the auditory cortex represent the cumulative effects from multiple levels of the auditory pathway, from cochlea to cortex. Presumably, at least some interactions between channels reflect lateral excitatory and inhibitory effects within the ascending auditory pathway (as considered in Bierer and Middlebrooks, 2004). Those effects were not explored parametrically in the present study, however, in which cochlear stimuli were presented at a fixed inter-electrode distance. Inasmuch as the two intracochlear electrodes appeared to produce a considerable overlap of electrical fields and that the temporal effects of interest are on a sub-millisecond scale, we choose to focus this discussion on electrode interactions and temporal integration that are likely to have occurred in the cochlea. Also, because of the large overlap of electrical fields and the similar thresholds for the two intracochlear electrodes, one can in most cases regard interleaved pulse trains on two electrodes as similar to pulse trains at a doubled rate on a single electrode.

Most of the conditions in the present experiments used biphasic pulses in which a 20-μs cathodic phase was followed immediately by a 20-μs anodic phase (i.e., zero interphase gap). Previous studies using monophasic pulses have demonstrated that cathodic pulses generally activate the cochlea at lower threshold than do anodic pulses (van den Honert and Stypulkowski, 1987; Miller *et al.*, 1998; 1999). One can think of the cathodic phase of our biphasic pulses as depolarizing neural membranes and initiating activation and inactivation of voltage-sensitive sodium channels; the time constant for sodium-channel activation at mammalian body temperature is <20 μs and the time constant for inactivation is roughly an order of magnitude longer (Schwartz and Eikhof, 1987; also see Rubinstein *et al.*, 2001). The following anodic phase would act to cancel any residual depolarizing charge on the membrane. In a study using biphasic pulses that contained a variable-duration gap between cathodic and anodic phases, van den Honert and Mortimer (1979) showed that a following hyperpolarizing pulse could abolish an action potential initiated by a near-threshold leading depolarizing pulse if the hyperpolarizing pulse fell within a ''vulnerable period'' lasting as long as 100 μs. That study was done in a *Xenopus* sciatic nerve, presumably at room temperature. One would expect the vulnerable period to be shorter at mammalian body temperature because the kinetics of sodium currents tend to be faster at higher temperatures (Schwartz and Eikhof, 1987). In the present experiment, the anodic phase followed the onset of the cathodic phase by only 20 μs, so the anodic phase almost certainly acted to reduce the depolarizing effect of the cathodic phase, resulting in an elevated threshold.

The hypothesis that thresholds would be elevated in conditions of biphasic pulses with brief phase durations is supported by three observations regarding the effects of waveform shape on threshold (i.e., Fig. 13). *First*, thresholds shifted to lower current levels at a rate of 9.4 dB/doubling as phase durations were lengthened from 20 to 41 μs/ph and at a rate of 6.7 dB/doubling as phase durations were lengthened from 41 to 164 μs. All of those threshold decreases are greater than the $\sim$6-dB decrease that is expected from a simple doubling of charge per phase. The present measurements support the view that lengthening a brief cathodic phase not only increased the amount of charge transferred during the cathodic phase but also delayed the repolarizing effect of the following anodic phase. That effect would have been greatest for doubling of the briefest pulse, from 20 to 41 μs/ph. In our previous study of auditory cortical responses to single biphasic electrical pulses delivered to the cochlea, thresholds decreased at a rate of 6.0 dB/doubling for increases in phase duration from 40 to 200 μs and 3.9 dB/doubling for increases from 200 to 1000 μs (Bierer and Middlebrooks, 2002). At the longer phase durations, ''leaky integrator'' properties of the cochlea presumably dominated the threshold. Parkins and Colombo (1987) measured a threshold decrease of 6.3 dB in the squirrel-monkey auditory nerve as phase durations were doubled from 50 to100 μs/ph and decreasing rates of threshold decrease for longer phase durations. Generally, psychophysical results have shown threshold decreases of 6.2 dB/doubling or less (Miller *et al.*, 1995; Pfingst *et al.*, 1995; Smith and Finley, 1997; Zeng *et al.*, 1998; Chatterjee *et al.*, 2000; Miller *et al.*, 2001). *Second*, the threshold for 20-μs/phase biphasic pulses was $\sim$6 dB higher than for a monophasic cathodic pulse of equal

phase duration, supporting the notion that the efficacy of the leading cathodic phase was reduced by the subsequent anodic phase. *Finally*, that ~6-dB threshold elevation was essentially eliminated by the introduction of a 103-μs inter-phase gap, thus moving the anodic phase out of the ''vulnerable period'' for action potential initiation. The effect of the inter-phase gap decreased with increasing phase duration, essentially disappearing for phase durations >60 μs/phase (data not shown). Shepherd and Javel (1999) reported that a gap of 60 μs imposed between two 60-μs phases produced a 2.5-dB threshold reduction compared to the same biphasic stimulus with no gap in a study of cat auditory nerve responses to stimulation with an intra-scalar electrode. McKay and Henshall (2003) tested the effect of inter-phase gaps on loudness judgments by human subjects. Thresholds in that study were reduced by increasing inter-phase gaps from 8.4 to 100 μs, and the effect of the inter-phase gap was greater for phase durations of 26 μs than for 52-μs phase durations.

The integration of cochlear excitation across multiple pulses (either from one or two electrodes) presumably represents the cumulative effects of some combination of residual membrane depolarization and sodium activation. Cartee and colleagues (2000) measured the time constant for the summation of cochlear activation, using pseudo-monophasic stimulation through electrodes in the meatus and recording from auditory nerve fibers. They obtained a time constant of ~150 μs for summation between pairs of pulses. The summation time constant recorded in the present study using monophasic pulses was ~350 μs. The difference in time constants between the two studies might reflect the meatal site of stimulation in the study by Cartee and colleagues compared to the intra-scalar stimulus site. The Cartee group reported a summation time constant of 504 μs for intra-scalar stimulation based on their analysis of data reported by Dynes (1996). The 2000-μs temporal offset tested here with 254-pps pulse trains is substantially longer than any of these time constants, thus explaining the observed lack of channel interactions for that offset. Conversely, all of the brief temporal offsets that we tested ($\pm$41 to 123 μs) were less than any of the reported time constants, thus permitting temporal integration within the cochlea.

In Experiment II of the present study, thresholds were relatively constant as a function of pulse rates <1000 pps, then shifted to lower current levels at a rate of ~2 dB/doubling for rates >1000 pps. At pulse rates of <1000 pps, the interval between successive pulses is 1 ms or greater, several times longer than reported time constants for cochlear summation. At higher pulse rates, inter-pulse intervals are shorter, permitting integration within the cochlea of two or more pulses. The test of thresholds for pulse-trains of increasing duration suggest that, at least in the present experimental system, cochlear electrical pulses are integrated over only the first ~1 ms of a pulse train. If a threshold is crossed in that time window, auditory nerve fibers are activated, and activity is propagated up the ascending auditory pathway. If sufficient synchronous activity reaches the auditory cortex, cortical neurons respond with action potentials followed by a period of intra-cortical inhibition.

Psychophysical results from monkeys and humans demonstrate thresholds that shift to lower current levels with increasing pulse rates at rates of 2–3 dB/doubling beginning at rates as low as 100–300 pps (Shannon, 1985; Pfingst and Morris, 1993; McKay and McDermott, 1998; Kreft *et al.*, 2004). A sensitivity of thresholds to pulse rates around 100 or 300 pps implies that listeners are integrating across inter-pulse intervals of 10 or 3.3 ms, respectively. That would be difficult to explain at the level of the cochlea, given the sub-millisecond time constants that have been measured (i.e., Dynes, 1996; Cartee *et al.*, 2000). It is more likely that the rate sensitivity observed in psychophysical studies represents some sort of long-time-constant temporal integration (reviewed by Viemeister and Wakefield, 1991) or ''multiple-look'' mechanism (Viemeister and Wakefield, 1991) that is at work in perception but not evident in our anesthetized physiological preparation.

Channel interactions consistently were greater at the 4069-pps pulse rate than at the 254-pps rate. In light of the effect of pulse rates on single-channel thresholds, one can interpret the increase in channel interaction at the higher rate as similar to the greater effect of doubling a higher pulse rate on one channel. Doubling the 250-pps rate had little or no effect on a single-channel threshold, and interleaving pulses on a second channel at 254 pps had a relatively small effect. In contrast, doubling the 4000-pps rate produced a threshold reduction of ~3 dB, and interleaving sub-threshold pulses on a second electrode at 4069 pps produced a threshold shift of a few dB, depending on the relative current levels on the two channels. Somewhat more mechanistically, one can think of a pulse on one channel as producing a partial depolarization of cochlear neural membranes. A pulse on a second channel occurring within a summation time constant would add further depolarization. At the 4096-pps rate, a succession of pulses on both channels would add steady increments of depolarization, eventually leading to an action potential. At the 254-pps rate, in contrast, a pair of pulses on two channels would permit some accumulation of depolarization, but the membrane potential would return to near the resting state by the time of the next stimulus period, nearly 4 ms later.

At the 4096-pps pulse rate, temporal offsets of $\pm$41 μs produced significantly less channel interaction than did offsets of $\pm$82 and 123 μs; at an offset of 41 μs, the pulse on the lagging channel immediately followed the pulse on the leading channel. A tentative explanation is that the anodic phase of the leading pulse largely cancelled the cathodic phase of the lagging pulse, thereby reducing the influence of the lagging pulse. It remains to be explained, however, why the 254-pps condition did not also show reduced channel interaction for the $\pm$41-μs temporal offsets relative to the other offsets at that pulse rate.

C. Considerations for speech processor design

When speech is processed through a cochlear prosthesis, spectral contrast in the speech signal is translated to contrast within the distribution of currents sent to the various intra-cochlear electrodes. Ideally, the contrast in the electrode ac-

tivation would produce differential activation of neural populations in the cochlea and in the central auditory pathway. If activity in one electrode facilitates the response to nearby electrodes, however, the spectral contrast that is signaled to the auditory system will be degraded. The most obvious result in the present study was that channel interactions were greatest when nearby channels are stimulated simultaneously. The problem of channel interactions during simultaneous stimulation is well known, and already is a key consideration in speech-processor design. Wilson and colleagues (1988; 1991) were the first to compare speech processing strategies between conditions of continuous, simultaneous stimulation (i.e., the early Compressed Analog strategy) and conditions in which stimuli were discrete pulses interleaved in time (the Continuous Interleaved Sampling strategy). In those studies, speech comprehension was substantially better when stimuli on multiple channels were interleaved in time.

The channel interaction that was observed in the simultaneous condition in the present study was so great that it is difficult to see how spectral contrasts ever could be transmitted by a speech strategy that employs simultaneous stimulation. Although the early Compressed Analog strategy generally has been shown to be inferior to pulsatile strategies (Wilson *et al.*, 1991), many implant users show satisfactory speech comprehension using a newer simultaneous analog strategy, Simultaneous Analog Stimulation (SAS; Zimmerman-Phillips and Murad, 1999). Indeed, some users prefer SAS over pulsatile strategies (Battmer *et al.*, 1999; Osberger and Fisher, 1999). The reason for the success of contemporary simultaneous strategies probably has to do with the design of the implanted electrode arrays. Most modern devices are designed to position the electrode array adjacent to the modiolar wall of the scala tympani, close to auditory neurons, thereby restricting the spatial spread of stimulating current fields. In contrast, the electrode array that was used in the present animal studies was not tailored to the guinea-pig cochlea, and the spread of electrical currents was demonstrably large, with considerable overlap between fields produced by the two electrodes.

Parenthetically, the electrode array used in the present study in guinea pigs was comparable in physical dimensions to the apical end of the Nucleus 22 device (Cochlear, Ltd.), which has been used successfully in the much-larger human cochlea, albeit with pulsatile, nonsimultaneous stimulation strategies (e.g., Skinner *et al.*, 1994). Of course, cochlear implants for humans generally have many more electrodes than the 2-channel device used in the present study and greater separations of activated electrodes are possible. For instance, Cohen and colleagues (2003) used psychophysical and electrophysiological methods to measure spread-of-activation profiles for monopolar electrode configurations in human subjects. Half widths of those profiles measured at half widths ranged from roughly 2 to 3.5 mm, indicating spatial specificity on a larger scale than the ~1.4-mm electrode separation that was used in the present study.

Our previous study showed that the spread of activation was more restricted, and channel interactions reduced, when we tested more restricted electrode configurations, such as bipolar and tripolar (Bierer and Middlebrooks, 2004). Also, that study showed that channel interactions diminish with increased separation between electrodes in a multi-electrode device. For those reasons, the present demonstrations of channel interactions must be regarded as the worst-case condition. Channel interactions presumably could be reduced by several physical changes, including use of a more-closely fitting electrode array, increased inter-electrode separation, and use of electrode configurations producing more restricted electrical fields. In addition to those physical factors, however, the present results reveal temporal factors that do and do not influence channel interactions.

The present results demonstrate that threshold shifts due to channel interactions, as assessed in this cortical-recording preparation, are entirely eliminated when a temporal offset as long as ~2 ms can be introduced between pulses on adjacent electrodes. Such long offsets are feasible when pulse rates are low (i.e., ~250 pps) and the inter-pulse interval on each electrode extends to some milliseconds. Most present-day speech processors operate at faster pulse rates, however, and the trend is toward even faster rates. For instance, the rates commonly used clinically in the ACE strategy range from 500 to 2400 pps per channel (Holden *et al.*, 2002), and rates of 5000 pps per channel have been considered (Rubinstein and Hong, 2003). At a pulse rate of 2400 pps, even if we consider the pulses on only one electrode and its two closest neighbors, that gives an inter-pulse interval on each channel of only 417 μs. That interval must be shared by three channels, yielding temporal offsets between channels of no longer than 139 μs. That maximum offset is less than any of the available estimates of the time constant for cochlear summation (504 μs: Dynes, 1996; ~150 μs: Cartee *et al.*, 2000; ~350 μs: the present results).

We observed similar threshold shifts for all temporal offsets from ± 41 to 123 μs at the 254-pps rate and similar shifts from ± 82 to 123 μs at the 4069-pps rate. That result does not inspire much hope for benefits from fine-grain manipulation of temporal offsets within the period of a fast pulse rate. At the 4069-pps rate, we observed that threshold shifts were significantly reduced when the temporal offset was ± 41 μs. It remains to be seen whether that finding is common among other species (particularly to humans), among other implanted electrode arrays, and among other measures of channel interaction. If it is, one might advocate minimizing the temporal offset between signals on adjacent electrodes.

Probably the observation of greatest practical importance in the present study is that threshold shifts due to channel interactions are appreciably greater at a pulse rate of 4096-pps than at 254-pps. There have been several good reasons given why higher pulse rates might improve speech comprehension with cochlear prostheses. These reasons include more detailed sampling of temporal waveforms (e.g., Wilson, 1997) and less pulse-by-pulse synchrony of auditory nerve fibers (i.e., increased ''stochasticity;'' Rubinstein and Hong, 2003). Nevertheless, increases in rates beyond ~1000–1400 pps have not yielded the consistent improvements in speech comprehension that one might have anticipated (e.g., Loizou *et al.*, 2000; Vandali *et al.*, 2000; Holden *et al.*, 2002). The increase in channel interactions seen in the

present study might account in part for those disappointing results. As pulse rates increase, one must be concerned that channel interactions will increase, thereby leading to a decrease in the effective number of channels of information from the cochlear implant to the brain and concomitant degradation in speech recognition. The present results suggest that any evaluation of new high-rate speech processor designs should be accompanied by detailed human psychophysical measurements of channel interactions.

ACKNOWLEDGMENTS

I thank Dr. Ian Harrington, Dr. Ewan Macpherson, Dr. Bryan Pfingst, Dr. Russell Snyder, and Dr. Chris Stecker for their helpful comments on an early version of the manuscript. Matthew Charous and Ryan Park participated in data collection, and Zekiye Onsan helped in production of the manuscript and illustrations. The research was supported by NIH Grants No. RO1 DC 04312 and No. P30 DC05188.

Arenberg, J. G., Furukawa, S., and Middlebrooks, J. C. (**2000**). ''Auditory cortical images of tones and noise bands,'' J. Assoc. Res. Otol. **1**, 183–194.

Battmer, R., Zilberman, Y., Haake, P., and Lenarz, T. (**1999**). ''Simultaneous Analog Stimulation (SAS)—Continuous Interleaved Sampler (CIS) pilot comparison study in Europe,'' Ann. Otol. Rhinol. Laryngol. Suppl. **177**, 69–73.

Bierer, J. A., and Middlebrooks, J. C. (**2002**). ''Auditory cortical images of cochlear-implant stimuli: Dependence on electrode configuration,'' J. Neurophysiol. **87**, 478–492.

Bierer, J. A., and Middlebrooks, J. C. (**2004**). ''Cortical responses to cochlear implant stimulation: Channel interactions,'' J. Assoc. Res. Otolaryngol. **5**, 32–48.

Bierer, S. M., and Anderson, D. J. (**1999**). ''Multi-channel spike detection and sorting using an array processing technique,'' Neurocomputing **26–27**, 947–956.

Boex, C., De Balthasar, C., Kos, M.-I., and Pelizzone, M. (**2003**). ''Electrical field interactions in different cochlear implant systems,'' J. Acoust. Soc. Am. **114**, 2049–2057.

Brugge, J. F., Dubrovsky, N. A., Aitkin, L. M., and Anderson, D. J. (**1969**). ''Sensitivity of single neurons in auditory cortex of cat to binaural tonal stimulation: Effects of varying interaural time and intensity,'' J. Neurophysiol. **32**, 1005–1024.

Busby, P. A., Whitford, L. A., Blamey, P. J., Richardson, L. M., and Clark, G. M. (**1994**). ''Pitch perception for different modes of stimulation using the Cochlear multiple-electrode prosthesis,'' J. Acoust. Soc. Am. **95**, 2658–2669.

Cartee, L. A., van den Honert, C., Finley, C. C., and Miller, R. L. (**2000**). ''Evaluation of a model of the cochlear neural membrane. I. Physiological measurement of membrane characteristics in response to intrameatal electrical stimulation,'' Hear. Res. **146**, 143–152.

Chatterjee, M. (**2003**). ''Modulation masking in cochlear implant listeners: envelope versus tonotopic components,'' J. Acoust. Soc. Am. **113**, 2042–2053.

Chatterjee, M., Fu, Q. J., and Shannon, R. V. (**2000**). ''Effects of phase duration and electrode separation on loudness growth in cochlear implant listeners,'' J. Acoust. Soc. Am. **107**, 1637–1644.

Cohen, L. T., Richardon, L. M., Saunders, E., and Cowan, R. S. C. (**2003**). ''Spatial spread of neural excitation in cochlear implant recipients: comparison of improved ECAP method and psychophysical forward masking,'' Hear. Res. **179**, 72–87.

Cohen, N. L., Waltzman, S. B., and Fisher, S. G. (**1993**). ''A prospective, randomized study of cochlear implants,'' N. Engl. J. Med. **328**, 233–237.

Crowther, J. A., Cannon, S. C., Miller, J. M., Jyung, R. W., and Kileny, P. (**1989**). ''Anesthesia effects on the electrically evoked middle latency response in guinea pigs,'' Otolaryngol.-Head Neck Surg. **101**, 51–55.

De Balthasar, C., Boex, C., Cosendai, G., Valentini, G., Sigrist, A., and Pelizzone, M. (**2003**). ''Channel interactions with high-rate biphasic electrical stimulation in cochlear implant subjects,'' Hear. Res. **182**, 77–87.

Drake, K. L., Wise, K. D., Farraye, J., Anderson, D. J., and Bement, S. L. (**1988**). ''Performance of planar multisite microprobes in recording extracellular single-unit intracortical activity,'' IEEE Trans. Biomed. Eng. **BME-35**, 719–732.

Dynes, S. B. C. (**1996**). ''Discharge characteristics of auditory nerve fibers for pulsatile electrical stimuli,'' Dissertation, Massachusetts Institute of Technology.

Eddington, D. K., Dobelle, W. H., Brackmann, D. E., Mladejovsky, M. G., and Parkin, J. L. (**1978**). ''Auditory prostheses research with multiple channel intracochlear stimulation in man,'' Ann. Otol. Rhinol. Laryngol. **87**, 1–39.

Favre, E., and Pelizzone, M. (**1993**). ''Channel interactions in patients using the Ineraid multichannel cochlear implant,'' Hear. Res. **66**, 150–156.

Fishman, K. E., Shannon, R. V., and Slattery, W. H. (**1997**). ''Speech recognition as a function of the number of electrodes used in the SPEAK cochlear implant speech processor,'' J. Speech Lang. Hear. Res. **40**, 1201–1215.

Friesen, L. M., Shannon, R. V., Baskent, D., and Wang, X. (**2001**). ''Speech recognition in noise as a function of the number of spectral channels: Comparison of acoustic hearing and cochlear implants,'' J. Acoust. Soc. Am. **110**, 1150–1163.

Gantz, B. J., Tyler, R. S., Knutson, J. F., Woodworth, G., Abbas, P., McCabe, B. F., Hinrichs, J., Tye-Murray, N., Lansing, C., Kuk, F., and Brown, C. (**1988**). ''Evaluation of five different cochlear implant designs: audiologic assessment and predictors of performance,'' Laryngoscope **98**, 1100–1106.

Green, D. M., and Swets, J. A. (**1966**). *Signal Detection Theory and Psychophysics* (Wiley, New York).

Greenwood, D. D. (**1990**). ''A cochlear frequency-position function for several species—29 years later,'' J. Acoust. Soc. Am. **87**, 2592–2605.

Hellweg, F. C., Koch, R., and Vollrath, M. (**1977**). ''Representation of the cochlea in the neocortex of guinea pigs,'' Exp. Brain Res. **29**, 467–479.

Holden, L. K., Skinner, M. W., Holden, T. A., and Demorest, M. E. (**2002**). ''Effects of stimulation rate with the Nucleus 24 ACE speech coding strategy,'' Ear Hear. **23**, 463–476.

Kaga, K., Hink, R. F., Shinoda, Y., and Suzuki, J. (**1980**). ''Evidence for a primary cortical origon of a middle latency auditory evoked potential in cats,'' Electroencephalogr. Clin. Neurophysiol. **50**, 254–266.

Kreft, H. A., Donaldson, G. S., and Nelson, D. A. (**2004**). ''Effects of pulse rate on threshold and dynamic range in Clarion cochlear-implant users,'' J. Acoust. Soc. Am. **115**, 1885–1888.

Litvak, L. M., Smith, Z. M., Delgutte, B., and Eddington, D. K. (**2003**). ''Desynchronization of electrically evoked auditory-nerve activity by high-frequency pulse trains of long duration,'' J. Acoust. Soc. Am. **114**, 2066–2078.

Loizou, P. C., Poroy, O., and Dorman, M. (**2000**). ''The effect of parametric variations of cochlear implant processors on speech understanding,'' J. Acoust. Soc. Am. **108**, 790–802.

Loizou, P. C., Stickney, G., Mishra, L., and Assman, P. (**2003**). ''Comparison of speech processing strategies used in the Clarion implant processor,'' Ear Hear. **24**, 12–19.

McDermott, H. J., and McKay, C. M. (**1994**). ''Pitch ranking with nonsimultaneous dual-electrode electrical stimulation of the cochlea,'' J. Acoust. Soc. Am. **96**, 155–162.

McGee, T., Kraus, N., Littman, T., and Nicol, T. (**1992**). ''Contributions of medial geniculate body subdivisions to the middle latency response,'' Hear. Res. **61**, 147–154.

McGee, T. J., Krause, N., Comperatore, C., and Nicol, T. (**1991**). ''Subcortical and cortical components of the MLR generating system,'' Brain Res. **544**, 211–220.

McKay, C. M., and Henshall, K. R. (**2003**). ''The perceptual effects of interphase gap duration in cochlear implant stimulation,'' Hear. Res. **181**, 94–99.

McKay, C. M., Henshall, K. R., Farrell, R. J., and McDermott, H. J. (**2003**). ''A practical method of predicting the loudness of complex electrical stimuli,'' J. Acoust. Soc. Am. **113**, 2054–2063.

McKay, C. M., and McDermott, H. J. (**1998**). ''Loudness perception with pulsatile electrical stimulation: The effect of interpulse intervals,'' J. Acoust. Soc. Am. **104**, 1061–1074.

McKay, C. M., and McDermott, H. J. (**1996**). ''The perception of temporal patterns for electrical stimulation presented at one or two intracochlear sites,'' J. Acoust. Soc. Am. **100**, 1081–1092.

McKay, C. M., McDermott, H. J., and Clark, G. M. (**1995**). ''Loudness summation for two channels of stimulation in cochlear implants: Effects of

spatial and temporal separation,'' Ann. Otol. Rhinol. Laryngol. **104**, 230–233.
McKay, C. M., Remine, M. D., and McDermott, H. J. (**2001**). ''Loudness summation for pulsatile electrical stimulation of the cochlea: Effects of rate, electrode separation, level, and mode of stimulation,'' J. Acoust. Soc. Am. **110**, 1514–1524.
Middlebrooks, J. C., and Bierer, J. A. (**2002**). ''Auditory cortical images of cochlear-implant stimuli: Coding of stimulus channel and current level,'' J. Neurophysiol. **87**, 493–507.
Miller, A. L., Arenberg, J. G., Middlebrooks, J. C., and Pfingst, B. E. (**2001**). ''Cochlear implant thresholds: comparison of middle latency responses with psychophysical and cortical-spike-activity thresholds,'' Hear. Res. **152**, 55–66.
Miller, A. L., Smith, D. W., and Pfingst, B. E. (**1999**). ''Across-species comparisons of psychophysical detection thresholds for electrical stimulation of the cochlea: II. Strength-duration functions for single, biphasic pulses,'' Hear. Res. **135**, 47–55.
Miller, C. A., Abbas, P. J., Rubinstein, J. T., Robinson, B. K., Matsuoka, A. J., and Woodworth, G. (**1998**). ''Electrically evoked compound action potentials of guinea pig and cat: Responses to monopolar, monophasic stimulation,'' Hear. Res. **119**, 142–154.
Miller, C. A., Abbas, P. J., Robinson, B. K., Rubinstein, J. T., and Matsuoka, A. J. (**1999**). ''Electrically evoked single-fiber action potentials from cat: Responses to monopolar, monophasic stimulation,'' Hear. Res. **130**, 197–218.
Miller, C. A., Woodruff, K. E., and Pfingst, B. E. (**1995**). ''Functional responses from guinea pigs with cochlear implants. I. Electrophysiological and psychophysical measures,'' Hear. Res. **92**, 85–99.
Najafi, K., Wise, K. D., and Mochizuki, T. (**1985**). ''A high-yield IC-compatible multichannel recording array,'' IEEE Trans. Electron Devices **32**, 1206–1211.
Nelson, D. A., Schmitz, J. L., Donaldson, G. S., and Viemeister, N. F. (**1996**). ''Intensity discrimination as a function of stimulus level with electric stimulation,'' J. Acoust. Soc. Am. **100**, 2393–2414.
Nuttall, A. L., Marques, D. M., and Lawrence, M. (**1977**). ''Effects of perilymphatic perfusion with neomycin on the cochlear microphonic potential in the guinea pig,'' Acta Oto-Laryngol. **83**, 393–400.
Osberger, M., and Fisher, L. (**1999**). ''SAS-CIS preference study in postlingually deafened adults implanted with the CLARION cochlear implant,'' Ann. Otol. Rhinol. Laryngol. Suppl. **177**, 74–79.
Parkins, C. W., and Colombo, J. (**1987**). ''Auditory-nerve single-neuron thresholds to electrical stimulation from scala tympani electrodes,'' Hear. Res. **31**, 267–286.
Pfingst, B. E., and Morris, D. J. (**1993**). ''Stimulus features affecting psychophysical detection thresholds for electrical stimulation of the cochlea. II. Frequency and interpulse interval,'' J. Acoust. Soc. Am. **94**, 1287–1294.
Pfingst, B. E., Morris, D. J., and Miller, A. L. (**1995**). ''Effects of electrode configuration on threshold functions for electrical stimulation of the cochlea,'' Hear. Res. **85**, 76–84.
Redies, H., Sieben, U., and Creutzfeldt, O. D. (**1989**). ''Functional subdivisions in the auditory cortex of the guinea pig,'' J. Comput. Neurosci. **282**, 473–488.
Richardson, L. M., Busby, P. A., and Clark, G. C. (**1998**). ''Modulation detection interference in cochlear implant subjects,'' J. Acoust. Soc. Am. **104**, 442–452.
Rubinstein, J. T., and Hong, R. (**2003**). ''Signal coding in cochlear implants: Exploiting stochastic effects of electrical stimulation,'' Ann. Otol. Rhinol. Laryngol. **112**, 14–19.
Rubinstein, J. T., Miller, C. A., Mino, H., and Abbas, P. J. (**2001**). ''Analysis of monophasic and biphasic electrical stimulation nerve,'' IEEE Trans. Biomed. Eng. **48**, 1065–1070.
Rubinstein, J. T., Wilson, B. S., Finley, C. C., and Abbas, P. J. (**1999**). ''Pseudospontaneous activity: stochastic independence of auditory nerve fibers with electrical stimulation,'' Hear. Res. **127**, 108–118.
Schwartz, J. R., and Eikhof, G. (**1987**). ''Na currents and action potentials in rat myelinated nerve fibres at 20 and 37 °C,'' Pfluegers Arch. Gesamte Physiol. Menschen Tiere **409**, 569–577.
Seligman, P., and McDermott, H. (**1995**). ''Architecture of the spectra 22 speech processor,'' Ann. Otol. Rhinol. Laryngol. **104** (Suppl 166), 172–175.
Shannon, R. V. (**1983**). ''Multichannel electrical stimulation of the auditory nerve in man. II. Channel interaction,'' Hear. Res. **12**, 1–16.
Shannon, R. V. (**1985**). ''Threshold and loudness functions for pulsatile stimulation of cochlear implants,'' Hear. Res. **18**, 135–143.
Shepherd, R., and Javel, E. (**1999**). ''Electrical stimulation of the auditory nerve: II. Effect of stimulus waveshape on single fibre response properties,'' Hear. Res. **130**, 171–188.
Skinner, M. W., Clark, G. M., Whitford, L. A., Seligman, P. M., Staller, S. J., Shipp, D. B., Shallop, J. K., Everingham, C., Menapace, C. M., Arndt, P. L., Antogenelli, T., Brimacombe, J. A., Pijl, S., Daniels, P., George, C. R., McDermott, H. J., Beiter, A. L. (**1994**). ''Evaluation of a new spectral peak coding strategy for the Nucleus 22 channel cochlear implant system,'' Am. J. Otol. **15** (Suppl 2), 15–27.
Smith, D. W., and Finley, C. C. (**1997**). ''Effects of electrode configuration on psychophysical strength-duration functions for single biphasic electrical stimuli in cats,'' J. Acoust. Soc. Am. **102**, 2228–2237.
Townshend, B., Cotter, N., Van Compernolle, D., and White, R. L. (**1987**). ''Pitch perception by cochlear implant subjects,'' J. Acoust. Soc. Am. **82**, 106–115.
van den Honert, C., and Mortimer, J. T. (**1979**). ''The response of the myelinated nerve fiber to short duration biphasic stimulating currents,'' Ann. Biomed. Eng. **7**, 117–25.
van den Honert, C., and Stypulkowski, P. H. (**1987**). ''Single fiber mapping of spatial excitation patterns in the electrically stimulated auditory nerve,'' Hear. Res. **29**, 195–206.
Vandali, A. E., Whitford, L. A., Plant, K. L., and Clark, G. M. (**2000**). ''Speech perception as a function of electrical stimulation rate: Using the Nucleus 24 cochlear implant system,'' Ear Hear. **21**, 608–624.
Viemeister, N. F., and Wakefield, G. H. (**1991**). ''Temporal integration and multiple looks,'' J. Acoust. Soc. Am. **90**, 858–865.
Wallace, M. N., Rutkowski, R. G., and Palmer, A. R. (**2000**). ''Identification and localization of auditory areas in guinea pig cortex,'' Exp. Brain Res. **132**, 445–456.
Wang, J., McFadden, S., Caspary, D., and Salvi, R. (**2002**). ''Gamma-aminobutyric acid circuits shape response properties of auditory cortex neurons,'' Brain Res. **944**, 219–231.
Wehr, M., and Zador, A. M. (**2003**). ''Balanced inhibition underlies tuning and sharpens spike timing in auditory cortex,'' Nature (London) **426**, 442–446.
White, M. W., Merzenich, M. M., and Gardi, J. N. (**1984**). ''Multichannel cochlear implants,'' Arch. Otolaryngol. **110**, 493–501.
Wilson, B. S. (**1997**). ''The future of cochlear implants,'' Br. J. Audiol. **31**, 205–225.
Wilson, B. S., Finley, C. C., Lawson, D. T., and Wolford, R. D. (**1988**). ''Speech processors for cochlear prostheses,'' Proc. IEEE **76**, 1143–1154.
Wilson, B. S., Finley, C. C., Lawson, D. T., Wolford, R. D., Eddington, D. K., and Rabinowitz, W. M. (**1991**). ''Better speech recognition with cochlear implants,'' Nature (London) **352**, 236–238.
Wilson, B. S., Finley, C. C., Lawson, D. T., and Zerbi, M. (**1997**). ''Temporal representation with cochlear implants,'' Am. J. Otol. **18** (Suppl 6), S30–34.
Zeng, F.-G., Galvin, III, J. J., and Zhang, C. (**1998**). ''Encoding loudness by electric stimulation of the auditory nerve,'' NeuroReport **9**, 1845–1848.
Zimmerman-Phillips, S., and Murad, C. (**1999**). ''Programming features of the CLARION multi-strategy cochlear implant,'' Ann. Otol. Rhinol. Laryngol. Suppl. **177**, 17–21.

Age reduces response latency of mouse inferior colliculus neurons to AM sounds

Henry Simon
International Center for Hearing & Speech Research, National Technical Institute for the Deaf, Rochester Institute of Technology, Rochester, New York 14623

Robert D. Frisina[a)]
Department of Surgery, Otolaryngology Division, Departments of Neurobiology & Anatomy and Biomedical Engineering, University of Rochester School of Medicine and Dentistry, Rochester, New York 14642-8629, and International Center for Hearing & Speech Research, National Technical Institute for the Deaf, Rochester Institute of Technology, Rochester, New York 14623

Joseph P. Walton
Department of Surgery, Otolaryngology Division, Department of Neurobiology and Anatomy, University of Rochester School of Medicine and Dentistry, Rochester, New York 14642-8629

(Received 9 December 2003; revised 14 April 2004; accepted 23 April 2004)

Age and stimulus rise time (RT) effects on response latency were investigated for inferior colliculus (IC) neurons in young-adult and old CBA mice. Single-unit responses were recorded to unmodulated and sinusoidal amplitude modulated (SAM) broadband noise carriers, presented at 35 to 80 dB SPL. Data from 63 young-adult and 76 old phasic units were analyzed to identify the time interval between stimulus onset and driven-response onset (latency). When controlling for stimulus sound level and AM frequency, significant age-related changes in latency were identified. Absolute latency decreased with age at all stimulus AM frequencies, significantly so for equivalent rise times (RT)$\leqslant$12.5 ms. The linear correlation of latency with AM stimulus RT was significant for both young-adult and old units, and increased significantly with age. It is likely that both the decrease in absolute latency and the increase in latency/RT correlation with age are consistent with a reduction of inhibitory drive with age in the IC. These latency changes will result in age-related timing variations in brainstem responses to stimulus onsets, and therefore affect the encoding of complex sounds. © *2004 Acoustical Society of America.* [DOI: 10.1121/1.1760796]

PACS numbers: 43.64.Qh, 43.64.Ri [WPS] Pages: 469–477

I. INTRODUCTION

Speech comprehension difficulties reported by aged listeners with mild-to-moderate peripheral hearing impairment has motivated research efforts to identify age-related changes in more central processes affecting speech comprehension (Takahashi and Bacon, 1992; Gordon-Salant and Fitzgibbons, 1993; Frisina and Walton, 2001; Frisina *et al.*, 2001; Snell and Frisina, 2000). Listeners employ both spectral, or place, and temporal cues (Rosen, 1992) in speech processing. The relative importance of temporal cues is supported by the demonstration of good speech recognition in the absence of spectral cues (Shannon *et al.*, 1995) as well as by the capability of single channel cochlear implants to restore spoken language comprehension (Cohen *et al.*, 1993). Additionally, although some consonants are not fully represented by a temporal code, replacing single phonemes in speech with noise does not substantially reduce comprehension (Sachs, 1984; Warren, 1970). Moller (1999) presented evidence supporting the position that a temporal code is more important for conveying speech information than place codes. In aged listeners, including those with good absolute sensitivity, degraded temporal processing, such as elevated gap detection thresholds, has been directly linked to speech identification difficulties (Fitzgibbons and Gordon-Salant, 1996; Snell, 1997; Frisina *et al.*, 2001; Snell and Frisina, 2000).

Speech temporal cues include fine structural variations (voicing pulses), the result of abrupt changes in stimulus carrier frequency, and variation in the stimulus envelope occurring over multiple carrier cycles, or amplitude modulation (AM). Vowels may be modeled by periodic, sinusoidal amplitude modulated (SAM) stimuli. When AM cues were modified in a phoneme identification task, the performance of aged listeners dropped relative to that of young listeners (Souza and Kitch 2001). It is interesting to note that signal-processing techniques employed in several types of hearing aids, such as wide-dynamic range compression, significantly alter the AM envelope of the stimulus introduced into the ear canal (Souza, 2000).

Both auditory nerve (AN) and primary auditory cortex (AI) response latencies are known to systematically vary with temporal onset characteristics of the stimulus envelope. In cat, both AN and AI first spike response latency to cosine-squared rise function tones were reported by Heil and Irvine (1996; 1997) to be invariant inverse functions of stimulus maximum acceleration of peak pressure (APP_{max}). For tone stimuli with linear envelopes, Heil (1997) has shown that AI first spike timing is an invariant inverse function of stimulus rate of change, or velocity, of peak pressure (VPP). More recently, Heil and Neubauer (2001) have presented data sup-

a)Electronic mail: rdf@q.ent.rochester.edu

porting the conclusion that auditory nerve (AN) fiber first spike latency is a function of the integral of sound pressure over time, possibly a reflection of inner hair cell/AN fiber mechanisms. Neural temporal processing in AI can change during behavior, even when mean firing rates are unchanged (DeCharms and Merzenich, 1996). Population coding theory suggests that stimulus information is conveyed by the relative timing and activity level across multiple neuronal elements in an array (Langner and Schreiner 1988; Covey 2000; Eggermont, 2001).

IC response latency is influenced by a number of auditory stimulus onset characteristics and peripheral auditory processes, as summarized above, as well as by excitatory and inhibitory processes within the auditory midbrain (Covey and Casseday, 1999), all of which could be differentially affected by aging. IC latency can be influenced by the nature, length and location of ascending pathways, some of which are relatively direct from the cochlear nucleus, others of which involve synaptic processing delays at the levels of the superior olivary complex and nuclei of the lateral lemniscus (e.g., Frisina *et al.*, 1989; 1998; Frisina and Walton, 2001). Single neuron latency has been shown to decrease when inhibitory neurotransmitters in the IC are blocked (Park and Pollak, 1993). Age-related loss of inhibitory neurotransmitters and alteration in synaptic neurochemistry have been documented in the IC of aged rats (Caspary *et al.*, 1990; 1995; 1999; Helfert, 1999), offering evidence that the balance of excitation and inhibition processes are disrupted at advanced age. Furthermore, changes in the interplay between excitation and inhibition have been implicated in age-related alteration of temporal processing (Walton *et al.*, 1998; 2002; Finlayson 2002). Given the extensive afferent innervation from IC to thalamus (LeBeau *et al.*, 1996; Covey and Casseday, 1999) and ultimately to AI, the onset timing of AI neuronal discharges strongly reflect those of IC neurons. Lastly, IC unit response latencies can be influenced by descending (efferent) projections originating from the auditory cortex, via the medial geniculate body and the external and dorsal cortex divisions of the IC.

Walton *et al.* (2002) reported age-related differences in the level of IC driven-spike activity and the relationships of driven-spike activity for best-AM frequency (BMF) and unmodulated stimuli. In the present report, the effects of age on the relationships between AM frequency (effective rise time) and IC latency were characterized to investigate age-related differences in IC temporal processing of a stimulus onset features. To allow detailed comparisons of results between studies, identical SAM broadband noise stimuli and, to the extent possible, the same IC units, were utilized in both investigations.

II. METHODS

A. Experimental procedures: Subjects and surgery

The procedures and data set here were those of Walton *et al.* (2002). Young-adult (2- to 4-months-old) and old (24- to 28-months-old) CBA/CaJ mice were obtained from the National Institute of Aging and Jackson Lab mouse colonies and kept in an isolated, noise-controlled vivarium on a 12-h light:dark cycle. Food and water were provided ad lib. Prior to each experiment, animals were lightly anesthetized with Metofane ®, Pittman-Moore and the external auditory meatus was examined down to the tympanic membrane for blockage. Only animals found to have clear external canals were used. Animals were prepared under aseptic conditions according to the guidelines for recovery surgery approved by the University of Rochester's Committee on Animal Resources. Prior to surgery, mice were deeply anesthetized with Avertin (20 mg/g); the skull was shaved, and the cranium was exposed by reflecting the scalp musculature. Subsequently, a 2% solution of lidocaine was applied locally. The area was cleaned and dried, and a small, threaded metal tube was attached to the skull surface using cyanoacrylate adhesive and dental acrylic. A sharpened tungsten wire served as the indifferent electrode and was implanted in the skull and secured with dental acrylic. Using stereotaxic coordinates, a small (0.5 mm) hole was made in the skull over the IC and then filled with bone wax, after which the animal was allowed to fully recover and then was returned to its cage.

On the experimental day, the animal was mildly tranquilized (Taractan 5-12 μ g/g) and placed in a plastic restraint attached to a custom-built stereotaxic frame. Typically, old mice were administered one-third to one-half the dose required for young-adult animals. The frame was located in the middle of a heated ($27-30\,^{\circ}\mathrm{C}$), double-walled, sound-attenuated room (IAC), lined with sound-absorbing foam (Sonex). The head was fixed to the frame by bolting the threaded tube to a rigid bar attached to the stereotaxic frame. Care was taken to ensure that the animal was as comfortable as possible to avoid undue distress and body movement.

B. Stimuli

Stimuli were generated using a digital signal-processing platform (Tucker-Davis Technologies AP2) running on a Pentium PC. Broadband noise was digitally generated (2–60 kHz), amplified, and fed to a high-frequency leaf tweeter (Panasonic THD 100) located on the horizontal plane 30° contralateral to the recording site. Sound calibration was performed by sampling the noise using a calibrated 1/4 in. condenser microphone (Bruel and Kjaer model 4135) placed at the location of the pinna and connected to a measuring amplifier (Bruel and Kjaer model 2610). The output of the measuring amplifier was fed to an A/D converter, and, via inverse-fast Fourier transform (FFT) signal processing, a speaker's transfer function was equalized to within ± 2 dB from 2 to 60 kHz. Noise bursts and AM stimuli were synthesized on-line. SAM noise bursts were synthesized by multiplying a wideband noise carrier by asine-wave modulator with $m=1$, thereby producing 100% amplitude-modulated noise. SAM stimuli were 100 ms in duration with rise/fall times that followed the SAM envelope. The modulation frequency (MF) was varied from 10 to 800 Hz. Unmodulated stimuli were also 100 ms in duration with 1-ms, linear rise/fall times. Unmodulated and 10 Hz SAM stimuli are illustrated in Fig. 1. Stimuli were presented 50 times at a rate of 4/s, typically at 65 dB SPL. Intensity was varied between 35 and 80 dB SPL as required for a strong unit response.

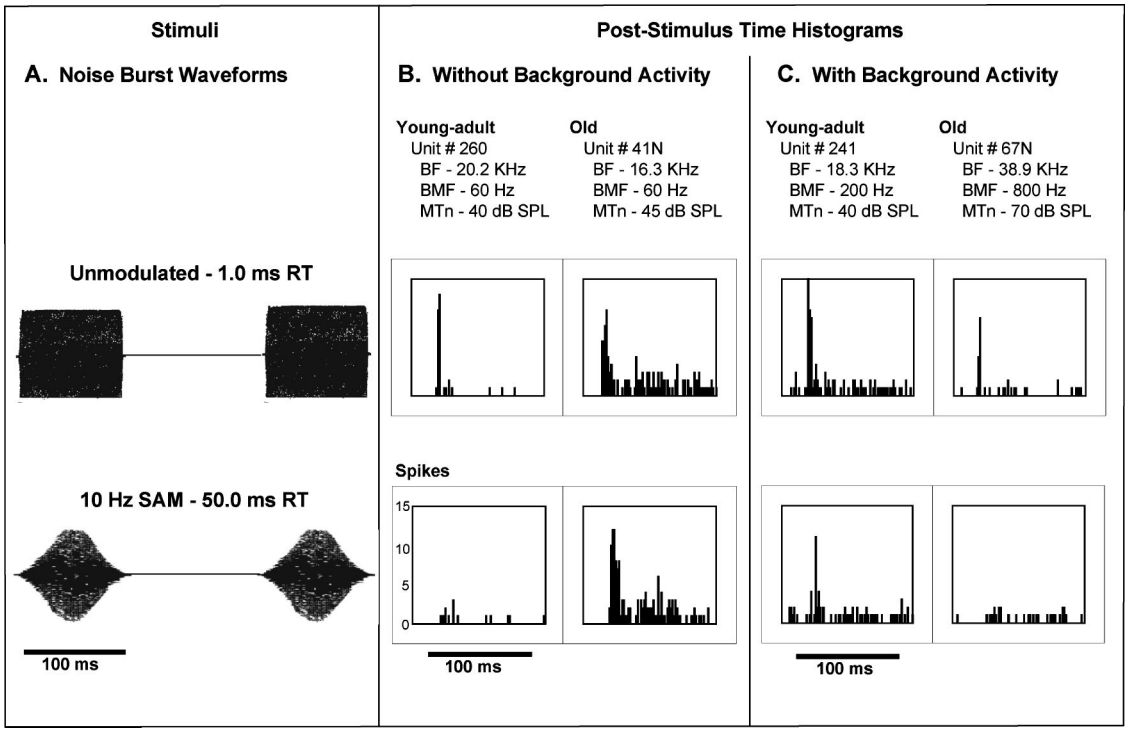

FIG. 1. PSTH representations of typical unit responses from young-adult and old animals are displayed for short and long RT stimuli. Unit number, BF, BMF and MTn are listed. The solid bar beneath the abscissa denotes stimulus timing and duration. (a) Two of fifty noise burst waveforms from unmodulated (top panel) and 10 Hz SAM (bottom panel) stimulus presentations with 1 ms, linear and 50 ms, sine wave, RTs, respectively. (b) Typical PSTHs with response latencies of 12.5 and 15.5 ms for the young-adult unit and 7.0 and 13.5 ms for the old unit to the 1 ms (top panels) and 50 ms (bottom panels) RT stimuli, respectively. Units show no background spike activity prior to stimulus onset. (c) Examples of clear (top panels) and potentially ambiguous (bottom panels) latency results in the presence of background spike activity. Young-adult unit latency was assessed as 13.0 ms for the 1 ms RT stimulus. With the 50 ms RT stimulus however, the relatively modest response at a latency of 17.5 ms was identified as the driven response onset as opposed to the stronger response at a latency of 20.5 ms. Old unit latency was assessed as 12.5 ms for the 1 ms RT stimulus. Some ambiguity exists regarding the 30.5 ms latency assessed for the 50 ms RT stimulus. Bin width: 1 ms.

C. Measurement protocol

After a single-unit was isolated, the following experimental protocol was followed: (*1*) the audio-visual determination of BF and minimum noise threshold (MTn); (*2*) measurement of BF and noise rate-intensity functions; and (*3*) presentation of AM series. The BMF, defined as the MF which resulted in the largest total spike count, was determined from modulation transfer functions of spike activity in response to SAM noise carriers with MFs from 10 to 800 Hz, specifically 10, 20, 40, 60, 80, 100, 200 400, and 800 Hz. The intensity of the noise carriers never exceeded 80 dB SPL. MTn, defined as the lowest intensity at which an increase in activity above the background rate was just noticeable, was determined using the unmodulated noise stimulus.

D. Data analysis

Evoked spikes were time-stamped (10 μs accuracy) and available for display on-line in PSTH form. Automated analysis programs which have been routinely used in our other studies (Frisina *et al.*, 1996; Lesser *et al.*, 1990) were used off-line to obtain rate measures from SAM response files. To measure latency, a new automated program was used to analyze each unit's spike response during 50, 110 ms time intervals, each starting 10 ms prior to stimulus onset, to determine both the level of background activity and the point in time when spike activity exceeded the background activity by a user specified multiple. If no discharge occurred during the initial 15 ms of recording (i.e., background activity was zero), then latency was identified as the difference between the beginning of the first 0.5 ms bin containing one or more spikes and stimulus onset.

A visual inspection of the unit PSTHs revealed no obvious increase in spike activity within 5.0 ms of stimulus onset. Consequently, the first 15 ms of recorded spike count was used to assess background activity. For the determination of background activity, the algorithm summed spikes in 0.5 ms bins and identified the maximum number of spikes per bin during the initial 15 ms of recorded data. The beginning of the first, subsequent, 0.5 ms bin in which spike count exceeded this maximum level by more than 1.5 times, was identified as the onset response. Latency was set equal to the time interval between this point and stimulus onset. Approximately 3% of all latency measurements exceeded 30.0 ms. The PSTH associated with each of these latency measurements was visually examined to judge the accuracy of the calculated value. The bin width and the amount by which spike count must exceed background activity, or zero, in order to be identified as a driven response, were user specified. A 0.5 ms bin width was selected to permit resolution of 0.5 ms latency differences. The one spike criteria for identifying a driven response when no background activity was present during the initial 15 ms of recording reduced the probability of the misidentification of a background spike as a driven

response to $<3.3\%$ since no background activity occurred during the previous 30, 0.5 ms, intervals. In the presence of background spike activity, the 1.5 times criteria insured that a driven response was at least 50% greater than the maximum background activity in any 0.5 ms interval. With one or two background spikes, this criterion dictated a 100% increase over the background activity level.

Latency at stimulus MFs from 0 to 800 Hz was measured for 63 young-adult and 76 old units from 11 and 13 animals, respectively, and analyzed in three young-adult and three old unit sample groups based on stimulus intensity, namely: **Group 1**—all intensity levels (63 young-adult and 76 old units); **Group 2**—a subset of Group 1 at 65 dB SPL (60 young-adult and 34 old units), and **Group 3**—a subset of Group 2 composed of 27 young-adult and old units selected to provide equal sensation level (SL) distributions. The unit pairs were analyzed so as to confirm that the age effects observed for Groups 1 and 2, were statistically significant when *both the absolute and relative* sound level were controlled for. For all three analysis groups, SLs ranged from 10–45 dB. BF, BMF and MTn distributions for each sample group were also evaluated. Stimulus RT values used in the analysis were 1.0 ms for unmodulated stimuli and a linear approximation of 1/2 MF for SAM stimuli. Note that, for modulated stimuli at a fixed SPL, RT was inversely proportional to the maximum VPP (VPP_{max}) and that VPP_{max} occurred at the stimulus onset (Heil 1997). For the unmodulated stimulus, VPP was constant.

Throughout this report, mean differences were evaluated by use of the *t*-test, while median differences were evaluated by use of the Mann-Whitney *U*-test. All statistically significant results indicate a $p<0.05$ for the relevant test. Mann-Whitney *U*-test Z absolute values $\geqslant 1.96$ are considered significant at the 0.05 level using a two-tailed test.

E. Histological verification of unit locations

In addition to close inspection of specific response types according to area, horseradish peroxidase (HRP) microinjections were used to estimate locations of recording sites within the IC. HRP (10% Sigma type XII in 0.5 M KCl, 0.05 M *Tris* buffer, *p*H 7.3) was iontophoretically injected (electrode positive) using 1.5 μA constant DC for 15–20 min, into the center of the area of the IC in which recordings were made (Meininger *et al.*, 1986; Walton *et al.*, 1997, 1998). Animals were returned to their cage and perfusedtranscardially 24 h later with heparinized saline and fixed with glutaraldehyde/paraformaldehyde. Three serial sets of coronal sections were cut at 60 μm. Two sets were processed with tetramethylbenzidine(TMB), and one was counterstained with safranin-O. The third set was reacted with diaminobenzidine (DAB) and counterstained with cresyl violet. The total diameters of the injection sites were 500–990 μm in diameter, the dense-core centers were more restricted, and were confined to the central nucleus of the IC. These procedures were similar to our previous reports of structure-function HRP mapping studies in the IC of unanesthetized mammals (Frisina *et al.*, 1989, 1997, 1998).

III. RESULTS

A. Representative stimuli and PSTH responses

Clearly identified stimulus driven onset responses, as illustrated by the PSTHs shown in the top and bottom panels of Fig. 1(b), and the top panel of Fig. 1(c), were typical of all units measured, regardless of the pre-stimulus background activity level. PSTHs were recorded for each unit in response to unmodulated and SAM noise burst stimuli. Two of the fifty noise bursts comprising stimulus presentation for the unmodulated and 10 Hz MF SAM stimulus are shown schematically in Fig. 1(a). The unmodulated stimulus [Fig. 1(a), top panel] had a 1.0 ms, linear RT while the SAM stimuli RTs followed the SAM envelope, resulting in sine-wave shaped RTs from 50 ms at a MF of 10 Hz [Fig. 1(a), bottom panel] to 0.625 ms at a MF of 800 Hz. 96% of the 1402 PSTHs analyzed yielded driven onset response latencies from 5.0 to 30.0 ms and were included in subsequent data analyses. Latency values calculated from the remaining 41 PSTHs (12 young-adult, 29 old) ranged from 30.5 to 190 ms.

B. Sample group characteristics

1. Group 1. All stimulus intensities

MTn, BF and BMF were measured for 63 young-adult and 76 old phasic IC units from 11 and 13 animals, respectively (Table I). Young-adult median MTn was significantly less than old (35.0 and 52.0 dB SPL, respectively). Young-adult and old BF distributions were similar with medians of 20.4 and 18.7 kHz, respectively. The median BMF of both groups was 80 Hz, although median SPL and SL were significantly different. Young-adult median SPL was 5.0 dB less while median SL was 10.0 dB greater than those of old units.

2. Group 2. 65 dB SPL

In the young-adult and old sample groups of units stimulated at 65 dB SPL (60 and 34 units, respectively), median MTns were significantly different (35 and 40 dB SPL, respectively), median BFs were significantly different (20.2 and 15.1 kHz, respectively), median BMFs were identical (80 Hz) and, median SLs were significantly different (30 dB and 25 dB, respectively). Approximately 99% of young-adult and 98% of old latencies measured for units in these sample groups were $\leqslant 30.0$ ms.

3. Group 3. 65 dB SPL, equal SL

Twenty seven pairs of young-adult and old units stimulated at 65 dB SPL with equal MTn, and therefore equal SL, were identified. In the sample groups containing these units: SL values ranged from 10 to 45 dB; median BFs were similar (18.3 and 16.1 kHz, respectively); median BMFs were significantly different (100 and 80 Hz, respectively). 98.5% of young-adult and 100% of old latencies measured for units in these sample groups were $\leqslant 30.0$ ms.

C. Sample group comparisons

Since most young-adult units were stimulated at 65 dB SPL (60 out of 63), absolute stimulus intensity differences were minimal between Group 1 (the all stimulus-intensity

TABLE I. Sample group characteristics.

	Sample groups					
	1. All stimulus intensities		65 dB SPL			
			2. All SL		3. Equal SL	
	Young	Old	Young	Old	Young	Old
Animals	11	13	10	8	8	6
Units	63	76	60	34	27	27
Unit characteristics, median						
MTn (dB SPL)	35	52	35	40	40	40
BF (kHz)	20.4	18.7	20.2	15.1	18.3	16.1
BMF (Hz)	80	80	80	80	100	80
Stimulus Level, median						
SPL (dB)	65	70	65	65	65	65
SL (dB)	30	20	30	25	25	25
Latency, median (ms)						
Unmodulated stimulus, 1 ms RT	10.5	9.5	10.5	8.5	11.5	8.5
10 Hz MF stimulus, 50 ms RT	14.0	17.0	14.0	14.0	16.5	14.0

sample), and Group 2 (the 65 dB SPL sample), young-adult unit groups. When the old sample group was limited to units stimulated at 65 dB SPL (Group 2), most group parameters changed significantly from the all stimulus intensity group (Group 1), namely: the sample size decreased from 76 to 34; median MTn declined from 52 to 40 dB SPL; median BF decreased from 18.7 to 15.1 kHz; median SPL declined from 70 dB, and; median SL increased from 20 to 25 dB. Median latencies in response to 50.0 and 1.0 ms RT stimuli dropped 3.0 and 1.0 ms, respectively [see Figs. 2(a), 2(b)].

The situation was reversed in moving from sample groups stimulated at 65 dB SPL (Group 2) to those stimulated at 65 dB SPL and of equal SL (Group 3), and therefore, equal MTn. Minimal changes in group parameters occurred between old sample groups while a number of young-adult characteristics changed significantly, namely the sample size dropped from 60 to 27; the median MTn increased from 35 to 40 dB SPL; and the median SL decreased from 30 to 25 dB. Median response latency to 50.0 and 1.0 ms RT stimuli increased by 2.5 and 1.0 ms, respectively [see Figs. 2(b), 2(c).]

D. Sample group latencies

Median latencies were plotted as a function of stimulus RT in Fig. 2 for each of the six sample groups analyzed. In almost all cases, median latency increased with RT, or more precisely, with decreasing VPP_{max}. For all stimulus intensity sample groups [Fig. 2(a)], old unit latencies were significantly less than those of a young-adult at short RTs (1.25, 2.5, 5.0, and 6.25 ms), and considerably greater at 50.0 ms RT. 65 dB SPL stimulus intensity sample groups [Fig. 2(b)] exhibited similar median latencies at long RT and a significant, age-related, decrease in median latency at RTs $\leqslant$12.5 ms. When 65 dB SPL, equal SL stimulus intensity sample group latencies were compared [Fig. 2(c)], the age-related decrease in median latency at longer RTs was more pronounced, and differences at RTs $\leqslant$12.5 ms remained sig-

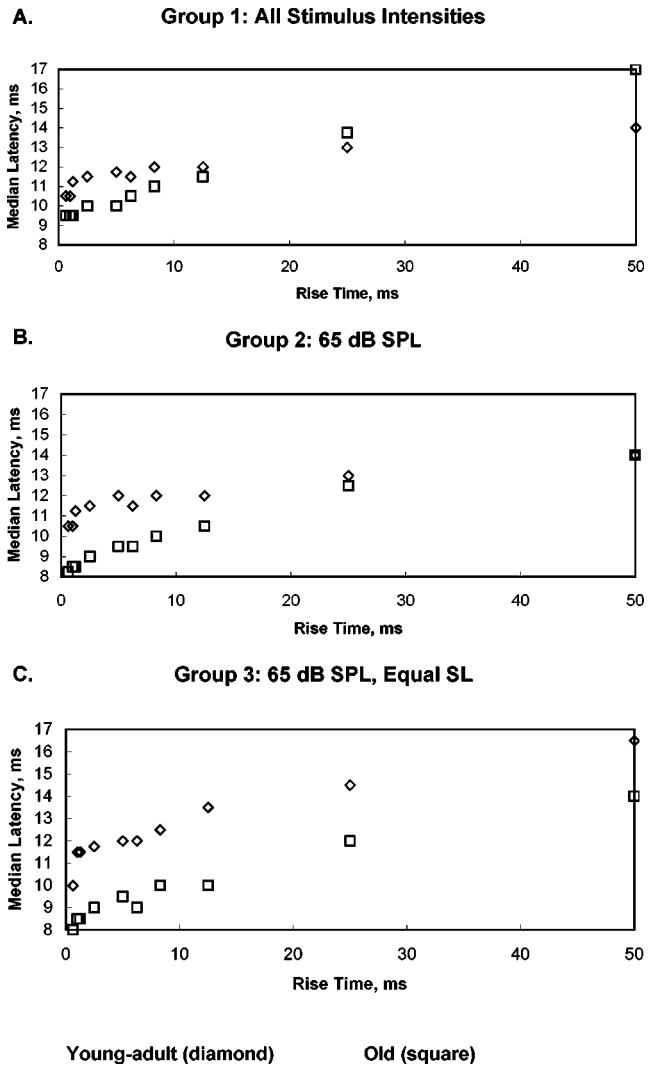

FIG. 2. Plots showing the relationship between median latency and stimulus RT for young-adult (diamond) and old (square) sample groups containing: (a) all units analyzed; (b) units stimulated at 65 dB SPL; and (c) MTn-matched young-adult and old units stimulated at 65 dB SPL and equal SL.

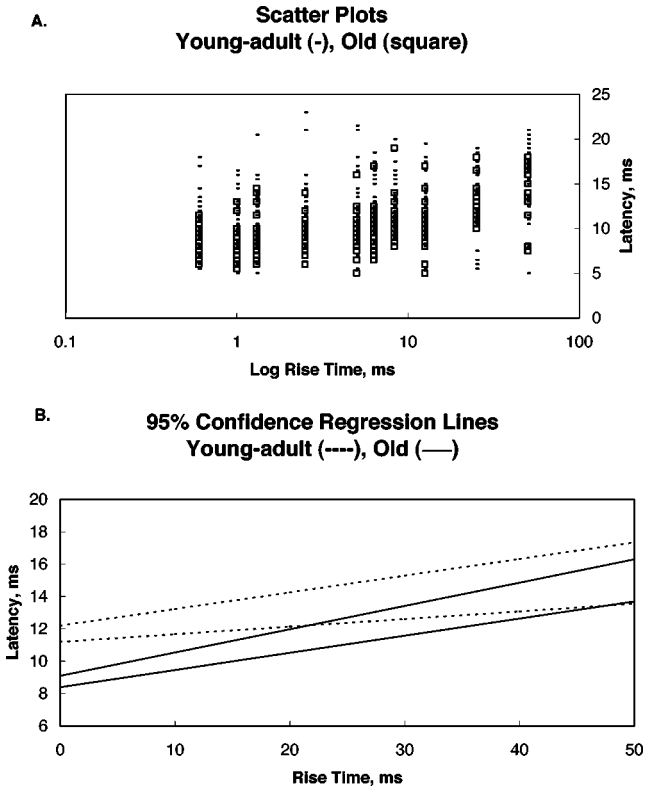

FIG. 3. Scatter plots (a) and 95% confidence linear regression lines (b) showing the relationship between latency and RT for the 27 unit, matched SL, Group 3 units. Linear regressions are presented at minimum intercept, minimum slope and maximum intercept, maximum slope values for young-adult (— — —) and old (——) groups. Nominal intercept and slope linear regression latencies were: 11.7+0.075 (RT) for young-adult; and 8.7 +0.125 (RT). Young-adult and old correlations (r) were 0.31 and 0.63, respectively, with respective explained variations of 0.09 and 0.39.

nificant. The lack of significance at RTs of 25.0 and 50.0 ms may reflect Type II errors resulting from the small sample sizes.

E. Scatter plots and linear regressions for 65 dB SPL, equal SL groups

Although latency–RT scatter plots of young-adult and old equal SL sample groups exhibited considerable overlap [Fig. 3(a)], linear regression analysis of the data showed the relationships to be highly significant ($F<0.001$), and age-related differences in correlation (Rickers and Todd, 1967), intercept, and slope to be significant at the 95% confidence level [Fig. 3(b)]. The regressions were based on 266 young-adult and 270 old data points. Nominal and 95% confidence values for young-adult and old regression parameters were, respectively, correlations of 0.31 and 0.62 (range: 0.25 to 0.45 and 0.55 to 0.75); intercepts of 11.7 and 8.7 ms (range: 11.2 to 12.2 and 8.4 to 9.1); and slopes of 0.075 and 0.125 ms/ms (range: 0.047 to 0.103 and 0.106 to 0.144).

IV. DISCUSSION

A. Influence of IC unit and stimulus characteristics on latency: Comparisons with previously reported AN, IC and AI latencies

In young-adult animals, a number of IC unit and stimulus parameters are known to nonlinearly and interdependently influence IC latency, including unit MTn, BF, BMF, stimulus SPL (or more precisely, peak plateau level), RT, VPP, APP_{max}, and SL. In the present investigation, these stimulus parameters were controlled for to a first approximation, and the findings strongly suggest that the latency differences identified here were age-related.

Langner and coworkers (1987, 1988) reported that average IC latency varied inversely with BF and BMF in cat. Here, all old sample groups had median BFs and BMFs that were equal to or less than those of the corresponding young-adult group. Consequently, to the extent latency findings reported here were influenced by BF or BMF differences, the Langner and coworkers results would predict a relative increase in median latencies of the old sample groups compared to the young-adult.

At a given BF, IC latencies have been shown to vary widely in response to the same stimulus. Langner and Schreiner (1988) reported that 90% of onset latencies to 60 dB SL characteristic frequency (CF) tones ranged from 5 to 15 ms in cat IC. Latencies from 5 to 15 ms were measured for CF's from 0.5 to 15 kHz. Latencies at higher CF's narrowed to a 5 to 10 ms range. Given the effect of SL on IC latency, as discussed below, the 5 to 30 ms latency range reported here is consistent with these findings.

For BF tone stimuli, decreases in latency with increasing SPL, and consequently SL, have been widely reported for AN fibers (Anderson 1971, Phillips *et al.*, 2001), cochlear nucleus (Moller, 1975), IC (Langner and Schreiner, 1988; Phillips *et al.*, 2001), and AI (Heil and Irvine 1996; Heil 1997). The peak latency of acoustic brainstem response (ABR) has also been reported to show a similar dependence on SPL (Boettcher *et al.*, 1993). Such latency dependence is illustrated in the current data by a comparison of 65 dB SPL to 65 dB SPL, equal SL young-adult sample groups, and all stimulus intensity to 65 dB SPL old sample groups (Table I).

The effects of stimulus onset parameters on response latency have been reported at various locations within the auditory system. In anesthetized cat, Heil and Irvine (1997) have shown that the timing of both AN and AI, the mean first spike response to onsets of CF tone bursts with $\cos^2$-gated RT, were invariant, inverse functions of stimulus APP_{max}, a characteristic of the second derivative of the stimulus. For linear RT stimuli, Heil (1997) has also shown, in anesthetized cat, AI latency to be a function of stimulus VPP, a characteristic of the first derivative of the stimulus. Similarly, Phillips *et al.* (2001) have shown in anaesthetized chinchillas, gross near-field AN and IC mean latency responses, to linear rise time noise burst stimuli, to be inverse functions of stimulus VPP. For the 65 dB SPL SAM stimuli used here, RT varied inversely with maximum VPP (VPP_{max}), and inversely with $(APP_{max})^{1/2}$. The range of values for VPP_{max}, in Pascals/second (Pa/s), and APP_{max}, in Pascals/(second)^2 (Pa/s^2), for the 65 dB SPL stimuli used here, are shown in Table II. In their Fig. 6(a), Heil and Irvine (1997) showed AN latency values of approximately 6 to 18 ms at an APP_{max} of 70 Pa/s^2, and 3 to 5 ms at an APP_{max} of 4.5×10^5 Pa/s^2. At these same APP_{max} values, AI latencies to contralateral stimulation [Fig. 6(b)] were approximately 15 and 12.5 ms, respectively. Here, for 65 dB SPL, equal SL sample groups,

TABLE II. 65 dB SPL stimulus ranges—VPP_{max}, APP_{max}, RT

Stimulus	VPP_{max}, Pa/s	APP_{max}, Pa/s^2	RT, ms
Unmodulated[a]	36.0		1.0
10 Hz SAM	1.1	70	50.0
800 Hz SAM	91.2	4.5×10^5	0.625

[a]For linear RT stimuli, VPP and RT are constant, and APP is undefined.

at 70 and 4.5×10^5 Pa/s^2, median latencies were, respectively, 16.5 and 11.5 ms for the young-adult and 14.0 and 8.5 ms for the old sample groups. At all other APP_{max} measurement points, median latencies fell between the corresponding AN and AI data points shown in Heil and Irvine (1997), their Figs. 6(a) and 6(b).

The IC latencies shown in Phillips *et al.* [2001, Fig. 7(b)], are considerably less than those reported here. For linear RT stimuli VPP values of 1 and 100 Pa/s, Phillips *et al.* showed near-field recorded IC potential latencies of 5.5 and 2.5 ms, respectively, as compared with median latency ranges measured here of 17.0 to 14.0 and 10.5 to 8.0 ms at the respective VPP_{max} values of 1.1 and 91.2 Pa/s. Given the extent of these differences, the relationship between the near-field and single unit measurements suggests that the Phillips *et al.* recordings may have been dominated by lateral lemniscus fibers' potentials as they enter the IC.

B. Variables affecting IC response latency

IC response latency can be divided into two types of signal delay, namely, propagation and processing. The propagation time from stimulus onset to IC discharge reflects delays introduced by outer ear to oval window conduction, basilar membrane wave mechanics, inner hair cell synaptic kinetics, and AN-fiber action potential transmission, and multi-nuclei, polysynaptic brainstem processing. Peripheral signal processing delays are dependent on stimulus temporal envelope parameters (Heil and Irvine, 1997) and their effect on basilar membrane/inner hair cell discharge dynamics, a process which is also influenced by efferent feedback through the outer hair cells. Sound reflex feedback to the middle ear tensor tympani and stapedius muscles may also influence processing delays. Given that AN latency sensitivity to stimulus VPP has been established for several RT shapes (Heil and Irvine, 1997; Heil 1997), it is likely that the age-related increase in the IC latency rate of change with stimulus RT reported here was also present in AN latency, and resulted from age-related, peripheral signal processing changes. Within the IC, signal processing delays are mediated by excitatory and inhibitory processes which are dependent on neural interconnection pathways and chemistry, specifically the number, location, strength, and type of excitatory and inhibitory synapses associated with a given IC unit. These may come from interneurons, or from descending pathways from the cortex and thalamus, via the dorsal cortex and external nucleus of the IC.

The significant age-related decrease in latency identified between 65 dB SPL, equal SL sample groups at all RTs $\leqslant$12.5 ms, and the age-related increase in the correlation of latency with RT, are consistent with an age-related reduction in IC inhibition as documented by Caspary and colleagues (Caspary *et al.*, 1990, 1995, 1999), and the decrease in latency demonstrated by blocking the inhibitory neurotransmitter GABA with the application of the $GABA_A$ antagonist bicuculline in the IC of mustache bats (Park and Pollak, 1993). Park and Pollak reported that the degree of bicuculline induced latency reduction varied with unit type, location within the IC and with SL. For all unit locations, at 20 and 30 dB SL, they reported that the mean latency of 113 phasic unit responses to a 0.5 ms RT, CF tone burst stimulus was reversibly decreased by 2 ms (13.5 to 11.5 ms) with a bicuculline application. As mentioned above, IC latency is influenced by a number of auditory processes occurring from eardrum to IC. The Park and Pollak data illustrate that inhibitory processes within the IC can account for at least 2 out of 13.5 ms, or 8% of total latency, consistent with the previous study by LeBeau *et al.* (1996). If inhibition-driven processes declined with age, then the influence of the remaining latency determinants, such as stimulus RT, would be increased. The age-related increase in latency correlation with RT (0.31 to 0.62) and latency variation explained by RT (0.09 to 0.39) are consistent with such a reduction in the influence of inhibition on latency. Additionally, the age-related increase in driven spike activity reported in Walton *et al.* (2002) is consistent with a reduction in IC inhibition during aging.

C. Age-related changes in threshold

Age-related increases in threshold have been documented at various locations in the auditory system peripheral to the IC. Mills *et al.* (1990) reported an age-related increase in auditory thresholds of Mongolian gerbils. Thresholds were estimated from the measurement of evoked potentials originating in the auditory nerve and brainstem. When compared with those of 6 to 8 month old animals, mean auditory thresholds increased by about 10 dB at 22 to 24 months and by 25 to 35 dB at 36 months of age. Similar results were reported by Li (1991) for ABR in CBA mice. When compared with those of 1 and 6 month old animals, mean ABR thresholds (collapsed across frequencies) increased by 10 dB at 18 months and by 30 dB at 24 months of age. Consequently, it is most likely that the 17.0 dB median age-related increase in IC MTn reported here originated peripherally, the result of increased AN thresholds.

Although IC unit MTn has been treated as an independent variable in this study, Heil and Neubauer (2001) argue that in AN fibers, MTn is not a constant but varies as a function of the time integral of sound pressure and, therefore, cannot be treated as an independent property of a neuron. This distinction is not material to the age-related findings reported here for sample groups stimulated at 65 dB SPL since the time integral of the sound pressure at each MF was identical for all units, and consequently, did not influence the reported latency findings.

D. Comparison of latency and mean first spike latency measures

Mean first spike latency, an average over all stimulus presentations of the timing of the first spike elicited in response to a stimulus, is commonly used to quantify stimulus-to-IC-response delay. When assessing mean first spike latency, a stimulus-driven response, as opposed to a background response, is typically identified by visual inspection of recorded spike data in appropriately positioned measurement time windows. In some cases, researchers have chosen to disregard units with spontaneous activity because of the difficulty they pose to accurate latency measurement (Park and Pollak, 1993). The latency parameter used in the present study permitted computer controlled assessment of unit background activity and the application of quantitative criteria for identifying the first response to occur above the background level. Over 97% of all computed latency values were $\leqslant 30$ ms, and were included in the analysis. Furthermore, measurements of phasic IC unit mean first spike latency by Barsz *et al.* (1998), in young-adult CBA mice, were consistent with latency values determined here. Barsz *et al.* found that mean first spike latency to 20 dB SL unmodulated noise carriers, were 10.0 and 14.4 ms with linear rise times of 0.5 and 16.0 ms, respectively.

E. Speech comprehension implications of findings

Given the 17 dB higher median MTn of all old IC units measured here (relative to young-adult MTns), in actual listening situations, old units would be stimulated at lower SL than young-adult units. Consequently, age-related performance comparisons made at SLs that differed by 17 dB would be more representative of actual listening circumstances. It could be argued that the age-related increases in threshold and in the rate of change of latency with RT, represent age-related plasticity intended to increase response latency at typical speech formant RTs, thereby compensating for the age-related decrease in inhibition-driven IC response latency. The effect of such changes can be seen by a comparison of Figs. 2(a) and 2(c). At equal SL [Fig. 2(c)], old median latencies were 2.5–3.0 ms less than those of young-adults at each RT.

An age-related change in IC response latency dependence on RT will cause an age-related alteration in the AI representation of stimulus element onset timing. With speech stimuli, this will introduce a RT dependent variation in AI representation of formant onset timing and, in the case of timing of the second formant transition, degradation of a critical place-of-articulation cue.

ACKNOWLEDGMENTS

We appreciate the critical comments of Dr. Sandra McFadden and Dr. Robert Burkard in the preparation of this article, and the comments of two anonymous reviewers. The computer program for analysis of driven response latency was written by Beth Hickman, and we are grateful for her diligence. This work was supported by National Institute of Health Grants No. P01 AG09524 from the National Institute on Aging, No. P30 DC05409 from the National Institute on Deafness and Communication Disorders, and the International Center for Hearing and Speech Research, Rochester NY, USA.

Anderson, D. J., Rose, J. E., Hind, J. E., and Brugge, J. F. (**1971**). ''Temporal position of discharge in single auditory nerve fibers within the cycle of a sine-wave stimulus: Frequency and intensity within the cycle of a sine-wave stimulus: Frequency and intensity effects,'' J. Acoust. Soc. Am. **49**, 1131–1139.

Barsz, K., Benson, P. K., and Walton, J. P. (**1998**). ''Gap encoding by inferior collicular neurons is altered by minimal changes in signal envelope,'' Hear. Res. **115**, 13–26.

Boettcher, F. A., Mills, J. H., Norton, B. L., and Schmiedt, R. A. (**1993**). ''Age-related changes in auditory evoked potentials of gerbils. II. Response latencies,'' Hear. Res. **71**, 146–156.

Caspary, D. M., Raza, A., Armour, B. A. K., Pippin, J., and Arneric, S. P. (**1990**). ''Immuno-cytochemical and neurochemical evidence for age-related loss of GABA in the inferior colliculus: implications for neural presbycusis,'' J. Neurosci. **10**, 2363–2372.

Caspary, D. M., Milbrandt, J. C., and Helfert, R. H. (**1995**). ''Central auditory aging: GABA changes in the inferior colliculus,'' Exp. Gerontol. **30**, 349–360.

Caspary, D. M., Holder, T. M., Hughes, L. F., Milbrandt, J. C., McKernan, R. M., and Naritoku, D. K. (**1999**). ''Age-related changes in $GABA_A$ receptor subunit composition and function in rat auditory system,'' Neuroscience **93**, 307–312.

Cohen, N. K., Waltzman, S. B., and Fisher, S. G. (**1993**). ''A prospective, randomized study of cochlear implants. The Department of Veterans Affairs Cochlear Implant Study Group,'' N. Engl. J. Med. **328**, 233–237.

Covey, E., and Casseday, J. H. (**1995**). ''The lower brainstem auditory pathways,'' in *Hearing by Bats, Springer Handbook of Auditory Research*, edited by A. Popper and R. Fay (Springer-Verlag, New York), pp. 235–295.

Covey, E., and Casseday, J. H. (**1999**). ''Timing in the auditory system of the bat,'' Annu. Rev. Physiol. **61**, 457–476.

Covey, E. (**2000**). ''Neural population coding and auditory temporal pattern analysis,'' Physiol. Behav. **69**, 211–220.

DeCharms, R. C., and Merzenich, M. M. (**1996**). ''Primary cortical representation of sounds by the coordination of action-potential timing,'' Nature (London) **381**, 610–613.

Eggermont, J. J. (**2001**). ''Between sound and perception: reviewing the search for a neural code,'' Hear. Res. **157**, 1–42.

Finlayson, P. (**2002**). ''Paired-tone stimuli reveal reductions and alterations in temporal processing in the inferior colliculus of aged animals,'' J. Assoc. Res. Otolaryngol. **3**, 321–330.

Fitzgibbons, P. J., and Gordon-Salant, S. (**1996**). ''Auditory temporal processing in elderly listeners,'' J. Am. Acad. Audiol **7**, 183–189.

Frisina, D. R., Frisina, R. D., Snell, K. B., Burkard, R., Walton, J. P., and Ison, J. P. (**2001**). ''Auditory temporal acuity during aging,'' in: *Functional Neurobiology of Aging* (Academic, San Diego), pp. 565–579.

Frisina, R. D., Karcich, K., Tracy, T., Sullivan, D., and Walton, J. P. (**1996**). ''Preservation of amplitude modulation coding in the presence of background noise by chinchilla auditory-nerve fibers,'' J. Acoust. Soc. Am. **99**, 465–490.

Frisina, R. D., O'Neill, W. E., and Zettel, M. L. (**1989**). ''Functional organization of mustached bat inferior colliculus. II. Connections of the FM_2 region,'' J. Comp. Neurol. **284**, 85–107.

Frisina, R. D., Walton, J. P., Lynch-Armour, M. A., and Klotz, D. (**1997**). ''Outputs of a functionally-characterized region of the inferior colliculus of the young adult CBA mouse model of presbycusis,'' J. Acoust. Soc. Am. **101**, 2741–2753.

Frisina, R. D., and Walton, J. P. (**2001**). ''Aging of the mouse central auditory system,'' in *Handbook of Mouse Auditory Res: Behavior to Molecular Biology*, edited by J. P. Willott (CRC Press, New York), Chap. 24, pp. 339–379.

Frisina, R. D., Walton, J. P., Lynch-Armour, M. A., and Byrd, J. D. (**1998**). ''Inputs to a physiologically-characterized region of the inferior colliculus of the young adult CBA mouse,'' Hear. Res. **115**, 61–81.

Gordon-Salant, S., and Fitzgibbons, P. J. (**1993**). ''Temporal factors and speech recognition performance in young and elderly listeners,'' J. Speech Hear. Res. **36**, 1276–1285.

Heil, P., and Irvine, D. R. F. (**1996**). ''On determinants of first-spike latency in auditory cortex,'' NeuroReport **7**, 3073–3076.

Heil, P. (**1997**). ''Auditory cortical onset responses revisited. I. First-spike timing,'' J. Neurophysiol. **77**, 2616–2641.
Heil, P., and Irvine, D. R. F. (**1997**). ''First-spike timing of auditory-nerve fibers and comparison with auditory cortex,'' J. Neurophysiol. **78**, 2438–2454.
Heil, P., and Neubauer, H. (**2001**). ''Temporal integration of sound pressure determines thresholds of auditory-nerve fibers,'' J. Neurosci. **21**, 7404–7415.
Helfert, R. H., Sommer, T. J., Meeks, J., Hofstetter, P., and Hughes, L. F. (**1999**). ''Age-related synaptic changes in the central nucleus of the inferior colliculus of Fisher-344 rats,'' J. Comp. Neurol. **406**, 285–298.
Kiang, N. Y.-S. (**1965**). *Discharge Patterns of Single Fibers in The Cat's Auditory Nerve*, M.I.T. Research Monograph No. 35 (MIT Press, Cambridge).
Langner, C., Schreiner, C., and Merzenich, M. M. (**1987**). ''Covariation of latency and temporal resolution in the inferior colliculus of the cat,'' Hear. Res. **31**, 197–202.
Langner, C., and Schreiner, C. E. (**1988**). ''Periodicity coding in the inferior colliculus of the cat. I. Neuronal mechanisms,'' J. Neurophysiol. **60**, 1799–1822.
Le Beau, F. E., Rees, A., and Malmierca, M. S. (**1996**). ''Contribution of GABA- and glycine-mediated inhibition to the monaural temporal response properties of neurons in the inferior colliculus,'' J. Neurophysiol. **75**, 902–919.
Lesser, H. D., O'Neill, W. E., Frisina, R. D., and Emerson, R. C. (**1990**). ''ON–OFF units in the mustached bat inferior colliculus are selective for transients resembling ''acoustic glint'' from fluttering insect targets,'' Exp. Brain Res. **82**, 137–148.
Li, H.-S., and Borg, E. (**1991**). ''Age-related loss of auditory sensitivity in two mouse genotypes,'' Acta Otolaryngol. (Stockholm) **111**, 827–834.
Mills, J. H., Schmiedt, R. A., and Kulish, L. F. (**1990**). ''Age-related changes in auditory potentials of Mongolian gerbil,'' Hear. Res. **46**, 201–210.
Meininger, V., Pol, D., and Derer, P. (**1986**). ''The inferior colliculus of the mouse. A Nissl and Gorge study,'' Neuroscience **17**, 1159–1179.
Moller, A. R. (**1975**). ''Latency of unit responses in cochlear nucleus determined in two different ways,'' J. Neurophysiol. **38**, 812–821.
Moller, A. (**1999**). ''Review of the roles of temporal and place coding of frequency in speech discrimination,'' Acta Otolaryngol. (Stockholm) **119**, 424–430.
Park, T. J., and Pollak, G. D. (**1993**). ''GABA shapes a topographic organization of response latency in the mustached bat's inferior colliculus,'' J. Neurosci. **13**, 5172–5187.
Phillips, D. P., Hall, S. E., Guo, Y., and Burkard, R. (**2001**). ''Sensitivity of unanaesthetized chinchilla auditory system to noise burst onset, and the effects of carboplatin,'' Hear. Res. **155**, 133–142.
Rickers, A. D., and Todd, H. N. (**1967**). ''Confidence belts for the coefficients of correlation,'' in *Statistics: An Introduction* (McGraw-Hill, New York), p. 570.
Rosen, S. (**1992**). ''Temporal information in speech: Acoustic, auditory and linguistic aspects,'' Philos. Trans. R. Soc. London, Ser. B **336**, 367–373.
Sachs, M. B. (**1984**). ''Neural coding of complex sounds: speech,'' Annu. Rev. Physiol. **46**, 261–273.
Shannon, R. V., Zeng, F. G., Kamath, V., Wygonski, J., and Ekelid, M. (**1995**). ''Speech recognition with primarily temporal cues,'' Science **270**, 303–304.
Snell, K. B. (**1997**). ''Age-related changes in temporal gap detection.'' J. Acoust. Soc. Am. **101** 2214–220.
Snell, K. B., and Frisina, D. R. (**2000**). ''Relations among age-related differences in gap detection and speech perception,'' J. Acoust. Soc. Am. **107**, 1615–1626.
Souza, P. E. (**2000**). ''Older listeners' use of temporal cues altered by compression amplification,'' J. Speech Lang. Hear. Res. **43**, 661–674.
Souza, P. E., and Kitch, V. (**2001**). ''The contribution of amplitude envelope cues to sentence identification in young and aged listeners,'' Ear Hear. **22**, 112–119.
Takahashi, G. A., and Bacon, S. P. (**1992**). ''Modulation detection, modulation masking, and speech understanding in noise in the elderly,'' J. Speech Hear. Res. **35**, 1410–1421.
Walton, J. P., Frisina, R. D., Ison, J. E., and O'Neill, W. E. (**1997**). ''Neural correlates of behavioral gap detection in the inferior colliculus of the young CBA mouse,'' J. Comp. Physiol. [A] **181**, 161–176.
Walton, J. P., Frisina, R. D., and O'Neill, W. E. (**1998**). ''Age-related alteration in neural processing of silent gaps in the central nucleus of the inferior colliculus in the CBA mouse model of presbycusis,'' J. Neurosci. **18**, 2764–2776.
Walton, J. P., Simon, H., and Frisina, R. D. (**2002**). ''Age-related alterations in the neural coding of envelope periodicities,'' J. Neurophysiol. **88**, 565–578.
Warren, R. M. (**1970**). ''Perceptual restoration of missing speech sounds,'' Science **167**, 392–393.

External and internal limitations in amplitude-modulation processing

Stephan D. Ewert[a] and Torsten Dau[b]
Carl von Ossietzky Universität Oldenburg, Medizinische Physik, D-26111 Oldenburg, Germany

(Received 30 August 2002; accepted for publication 15 March 2004)

Three experiments are presented to explore the relative role of ''external'' signal variability and ''internal'' resolution limitations of the auditory system in the detection and discrimination of amplitude modulations (AM). In the first experiment, AM-depth discrimination performance was determined using sinusoidally modulated broadband-noise and pure-tone carriers. The AM index, m, of the standard ranged from -28 to -3 dB (expressed as $20\log m$). AM-depth discrimination thresholds were found to be a fraction of the AM depth of the standard for standards down to -18 dB, in the case of the pure-tone carrier, and down to -8 dB, in the case of the broadband-noise carrier. For smaller standards, AM-depth discrimination required a fixed increase in AM depth, independent of the AM depth of the standard. In the second experiment, AM-detection thresholds were obtained for signal-modulation frequencies of 4, 16, 64, and 256 Hz, applied to either a band-limited random-noise carrier or a deterministic (''frozen'') noise carrier, as a function of carrier bandwidth (8 to 2048 Hz). In general, detection thresholds were higher for the random- than for the frozen-noise carriers. For both carrier types, thresholds followed the pattern expected from frequency-selective processing of the stimulus envelope. The third experiment investigated AM masking at 4, 16, and 64 Hz in the presence of a narrow-band masker modulation. The variability of the masker was changed from entirely frozen to entirely random, while the long-term average envelope power spectrum was held constant. The experiment examined the validity of a long-term average quantity as the decision variable, and the role of memory in experiments with frozen-noise maskers. The empirical results were compared to predictions obtained with two modulation-filterbank models. The predictions revealed that AM-depth discrimination and AM detection are limited by a combination of the external signal variability and an internal ''Weber-fraction'' noise process.
[DOI: 10.1121/1.1737399]

PACS numbers: 43.66.Ba, 43.66.Dc, 43.66.Mk [NFV] Pages: 478–490

I. INTRODUCTION

Intensity discrimination represents one of the basic measures in psychoacoustics. Discrimination functions for stimulus intensity provide information about the fidelity of intensity coding in the auditory system. For pure-tone (deterministic) stimuli, the smallest detectable change in intensity, ΔI, is, to a first approximation, a constant fraction of the intensity, I, of the stimulus (Riesz, 1928; Florentine, 1983; Florentine *et al.*, 1987). Thus Weber's law, stating that $\Delta I/I$ is constant, roughly describes listeners' performance; the quantity $\Delta I/I$ is referred to as the Weber fraction.[1] Empirically obtained intensity differences amount to about 1 dB, corresponding to a Weber fraction of about -6 dB when expressed in terms of $10\log(\Delta I/I)$. For deterministic stimuli, a constant Weber fraction can generally be modeled by the assumption that there is ''internal noise,'' or variability, in the internal (decision) variable reflecting stimulus intensity, proportional to the mean of the variable. This variability is intended to reflect an inherent property of the internal coding mechanism. Alternatively, a constant Weber fraction might also be modeled by combining a logarithmic transformation of the internal variable with a fixed-variance additive internal noise following it. In terms of signal detection theory (Green and Swets, 1966) such assumptions are necessary to account for the discrimination performance of the real observer (subject) in comparison to that of an ideal observer. For deterministic stimuli, such as pure tones, the detection performance of the ideal observer would be determined by the amount of change, ΔI, independent of the stimulus intensity, I, since the stimuli exhibit no ''external'' variability. If stochastic stimuli are used, such as random noise, ''external noise'' comes into play, in addition to the internal variability of the coding process. As soon as the external noise, introduced by the stimulus, significantly adds to the internal noise, it will affect the observer's detection performance. In the case of intensity discrimination, broadly similar results have been obtained for deterministic pure-tone and broadband ''pseudo-random'' as well as for random stimuli (Raab and Goldberg, 1975; Florentine *et al.*, 1987), indicating that the internal noise represents the main determinant.[2]

The present study is concerned with the coding mechanisms and the role of internal and external noise in

[a]Current address: Center for Applied Hearing Research, Acoustic Technology, Ørsted·DTU, Technical University of Denmark. DK-2800 Kgs. Lyngby, Denmark. Electronic mail: se@oersted.dtu.dk
[b]Current address: Center for Applied Hearing Research, Acoustic Technology, Ørsted-DTU, Technical University of Denmark, DK-2800 Kgs. Lyngby, Denmark. Electronic mail: tda@oersted.dtu.dk

amplitude-modulation (AM) processing. Amplitude modulation is a common feature of sounds in our natural surroundings. The temporal structure of the envelope of a stimulus conveys important information, such as in human speech, animal sounds, and environmental sounds. Several studies have investigated the limitations of the auditory system to resolve AM. For example, Fleischer (1980) obtained AM-depth discrimination functions for sinusoidal AM of pure-tone carriers, for standard modulation depths in the range from -14 to 0 dB (in units of $20 \log m$, where m is the modulation index). For a similar limited range of standards (-12 to 0 dB), Ozimek and Sek (1988) measured discrimination thresholds for modulated octave-band noises. Modulation frequencies in the range from 1 to 64 Hz were tested, imposed on carriers with center frequencies in the range from 250 to 2000 Hz. Wakefield and Viemeister (1990) studied AM-depth discrimination for modulation rates of 25, 100, and 400 Hz, using broadband noise carriers. In the comparable range of standard modulation depths, their results were in agreement with the findings of Fleischer (1980) and Ozimek and Sek (1988). More recently, Lee and Bacon (1997) investigated AM-depth discrimination for a sinusoidal carrier as a function of stimulus duration. For the longest signal durations, 400 and 800 ms, their results were also broadly compatible with the findings from the other studies mentioned above: A roughly constant relative AM-depth discrimination threshold, corresponding to a roughly constant Weber fraction, was found in all conditions where the standard AM depth was greater than about -15 dB, i.e., well above detection threshold. On average, the AM-depth discrimination threshold was slightly greater than 1 dB in these conditions, independent of carrier type.

Wakefield and Viemeister (1990) and Fassel (1995) also obtained discrimination thresholds for standard depths near the absolute AM-detection threshold. For small standard depths below -15 dB, Wakefield and Viemeister found a region of roughly constant AM-depth discrimination thresholds ($\Delta m = \text{const}$), using a broadband-noise carrier. Similarly, Fassel (1995) found an essentially constant discrimination threshold, using a sinusoidal carrier. However, he observed a constant discrimination threshold throughout the entire range of standards tested (-40 to -3 dB), in contrast to the studies by Wakefield and Viemeister (1990) and Fleischer (1980). Whether the differences between the studies were due to differences of the carrier type (broadband noise versus pure tone), or due to other factors, has not been clarified yet.

In Wakefield and Viemeister (1990), the leaky-integrator model proposed by Viemeister (1979) was tested in conditions of AM-depth discrimination. The model was originally designed to account for the temporal modulation transfer function (TMTF) obtained with a broadband noise carrier. It consists of a 2-kHz-wide bandpass filter, a half-wave rectifier, and a single-pole low-pass filter with a time constant of 2.5 ms, representing a modulation low-pass filter with a cut-off frequency of about 64 Hz. The detection device is based on the comparison of the rms (root-mean-square) envelope power at the output of the modulation low-pass filter in a simulated two-alternative forced-choice procedure. When this model is applied to two noise stimuli, one modulated at a certain rate and standard modulation depth, the other one modulated at the same rate but higher modulation depth, the model is able to correctly discriminate between the two stimuli if the increase in rms power at the output of the modulation low-pass filter, caused by the increase in AM depth, exceeds the random fluctuations of the rms power due to the stochastic nature of the noise carrier. The model was shown to accurately account for discrimination data when the AM depth of the standard was below -10 dB. However, for greater standard depths of -7.5 and -5 dB, predicted thresholds were considerably lower (better performance) than the data. The reason for this discrepancy between data and model predictions might have been that the discrimination performance within the model is entirely determined by the external variability of the noise carrier. This results in a constant discrimination threshold, independent of the standard AM depth of the noise. The model therefore failed for large standard depths where a constant Weber fraction was observed (corresponding to an increase of the discrimination threshold with increasing standard depth). Moreover, the model would predict infinitely small discrimination thresholds in conditions with deterministic stimuli, such as sinusoidal or frozen-noise carriers, because it does not make any assumptions about the internal limitations inherent in the encoding of AM.

In the present study, three experiments are presented to explore the relative role of internal and external limitations in auditory AM processing. The first experiment examined AM-depth discrimination with a (random) broadband-noise carrier and a (deterministic) pure-tone carrier. Thus, this experiment investigated the influence of external noise (introduced by the random-noise carrier) and the role of internal noise (representing the only limitation in the case of the pure-tone carrier), using the same group of subjects and experimental setup. The second experiment compared AM-detection thresholds obtained for a random-noise and a frozen-noise carrier, as a function of the carrier bandwidth. This experiment addressed the question of to what extent AM detection can be explained in terms of the average envelope power only, or in terms of a combination of the average envelope power and the variability of this value. In the third experiment, AM masking was investigated. The detection of a sinusoidal signal modulation was measured in the presence of a narrow-band-noise masker modulation, centered at the signal-modulation frequency. The degree of variability of the noise masker was changed as a parameter such that conditions ranging from entirely frozen to entirely random were tested. The long-term average envelope power spectrum remained constant across all conditions. This was done in order to examine the validity of a long-term average quantity as the decision variable, and to investigate the role of memory in experiments with frozen stimuli.

The empirical data of the present study were compared to predictions of two models of auditory signal processing in order to quantitatively examine the role of external and internal noise in AM processing. The signal processing model by Dau *et al.* (1997a,b), in the following referred to as the ''perception model'' (PEMO), served as a model incorporat-

ing a fixed-variance internal-noise process. The envelope power spectrum model according to Ewert and Dau (2000), in the following referred to as the EPSM, served as a model that assumes a Weber-fraction-type internal-noise process. Constraints on future models of AM processing are also discussed.

II. MODELS OF AM PROCESSING

In the following, the two processing models used in the present study are briefly described. For a detailed description, the reader is referred to the respective publications.

The first model used in the present study, the envelope power spectrum model (EPSM; Ewert and Dau, 2000), has a structure similar to Viemeister's (1979) leaky-integrator model, but assumes a modulation filterbank instead of the low-pass filter. The model has proven successful in various conditions of AM detection and AM masking. It consists of three stages: Hilbert-envelope extraction of the stimuli, a modulation filterbank, and a decision stage. The modulation-filterbank design was chosen according to Ewert and Dau (2000). Only the filter tuned to the signal modulation was considered. Effects of peripheral bandpass filtering and adaptation were not taken into account. Within EPSM, decisions are based on the long-term mean integrated envelope power and the standard deviation of this value at the output of the modulation filter. As described in Ewert and Dau (2000), the standard deviation was computed by adding up the variances of the individual components in the envelope spectrum passing through the modulation filter. The variances of these components were assumed to equal their squared means, since the components closely follow an exponential distribution (Green *et al.*, 1992). It is assumed that the detection of the signal requires an increase in power that is proportional to three times its standard deviation. This value was determined in Ewert and Dau (2000) where it resulted in the best prediction of performance. It is further assumed that the required increase in power cannot be less than 1 dB relative to the mean power, reflecting the ''classical'' constant Weber fraction. In addition, an absolute lower limit for the increase in mean power corresponding to a modulation depth of -30 dB is assumed. This assumption corresponds to the addition of a fixed-variance internal-noise process. Without this absolute limit, the model would predict infinitely low modulation-detection thresholds for pure-tone carriers. The model parameters were kept constant for all predictions shown here.

The second, more complex, perception model (PEMO; Dau *et al.*, 1997a,b) was designed to account for detection data in various experimental conditions. It has proven successful in predicting data from spectral and spectro-temporal masking (Verhey *et al.*, 1999; Derleth and Dau, 2000; Verhey, 2002), non-simultaneous masking (Dau *et al.*, 1996a,b), and modulation detection and modulation masking (Dau *et al.*, 1997a,b; Dau *et al.*, 1999). The model consists of the following basic stages: Peripheral filtering, envelope extraction, nonlinear adaptation, modulation filtering, and an optimal detector as the decision device. To simulate the bandpass characteristic of the basilar membrane, the gammatone filterbank by Patterson *et al.* (1987) was used. At the output of each peripheral filter, the model includes half-wave rectification and low-pass filtering at 1 kHz, i.e., for high center frequencies, this stage essentially preserves the envelope of the signal. Effects of adaptation were simulated by a nonlinear adaptation circuit (Püschel, 1988; Dau *et al.*, 1996a). For a stationary input stimulus, this stage realizes a compression close to logarithmic. With regard to the transformation of signal envelope fluctuations, the adaptation stage transforms the AM depth of input fluctuations with rates higher than 2 Hz almost linearly. The model can be considered as being linear in AM depth for all modulation frequencies tested here. The stimuli at the output of the adaptation stage for each channel are then processed by a linear modulation filterbank. In the present study, only the output of the modulation filter tuned to the signal-modulation frequency was considered. When considering modulation processing, the most relevant difference from the EPSM was reflected in the decision criterion. Limitations of resolution were simulated by adding a fixed-variance internal noise to the modulation-filter output. The variance of the internal noise was adjusted to account for a lower resolution limit of about -30 to -40 dB for AM detection with frozen-noise carriers. The decision device was realized as an optimal detector. Decisions were based on the cross correlation between the internal representation of the current stimulus and a template, which is a stored representation of a stimulus with a supra-threshold signal modulation. The signal-modulation depth at which the template was derived was fixed for each of the three experiments. It was set to 0 dB in the first experiment and -6 dB in the two other experiments. All other model parameters were the same in all of the predictions presented here. Within the model, the same adaptive procedure as in the experiments was used. The final threshold estimate was taken as the average across three simulation runs in the first two experiments and four runs in the last experiment.

When tested in modulation-detection conditions with noise carriers, the detection performance of PEMO is mainly limited by the statistical properties of the stimulus. So far, the model has not been tested explicitly in conditions of AM-depth discrimination. Even though the model's preprocessing stages and the decision device differ considerably from Viemeister's (1979) leaky-integrator model, described in the Introduction, it can be expected to predict the same constant AM-depth discrimination threshold when applied to broadband noise carriers. However in contrast to the Viemeister model which has so far only been applied to stochastic stimuli, PEMO includes an internal-noise source of constant variance that limits the resolution in conditions without external variability of the stimuli.

III. AM-DEPTH DISCRIMINATION WITH NOISE AND PURE-TONE CARRIERS

A. Method

1. Subjects

Five normal-hearing subjects participated in the experiment. Their ages ranged from 23 to 36 years. Three subjects (MB, TD, and SE) had experience in other psychoacoustic experiments. Subjects SE and TD were the two authors. Two

subjects (FM and CS) had no previous experience in psychoacoustic experiments and received at least 3 h of training before data collection started. Subjects MB, FM, and CS were paid for their participation on an hourly basis.

2. Apparatus and stimuli

The subjects were seated in a double-walled sound attenuating booth and listened diotically via AKG K-501 headphones. Signal generation and presentation during the experiments were computer controlled using the AFC software package for MATLAB, developed at the University of Oldenburg. The stimuli were digitally generated at a sampling rate of 48 kHz and converted to analog signals by a two-channel 24-bit DAC including reconstruction filtering (SEKD ADSP 2496). The transfer function of the headphones was digitally equalized (64 point FIR filter) to match a flat amplitude response between 0.1 and 20 kHz, measured with the artificial ear (B&K 4153). A sinusoidal AM of 16 Hz was applied to a broadband-noise or a pure-tone carrier. The noise carrier had a bandwidth of 2048 Hz and an upper cutoff frequency of 4 kHz. The pure-tone carrier had a frequency of 4 kHz. Modulations were applied during the entire carrier duration of 500 ms. The stimuli were gated with 50-ms $\cos^2$ onset and offset ramps.

The equation describing the stimulus, $s(t)$, is

$$s(t)=[1+m_s\sqrt{1+m_{inc}}\sin(2\pi f_m t)]c(t), \quad (1)$$

where m_s is the standard modulation index, m_{inc} is the relative AM increment, and $c(t)$ represents the carrier waveform. The signal-modulation frequency, f_m, was 16 Hz. In the two reference intervals, m_{inc} was set to zero. The standard modulation depth was varied in 5-dB steps, ranging from -28 to -3 dB. To avoid possible level cues, compensation for the energy increment due to modulation was used. Each stimulus was scaled by a factor of $\sqrt{1+m^2/2}$, where m was the standard or current signal-modulation index. The overall presentation level was 65 dB SPL.

3. Procedure

A three-interval, three-alternative forced-choice paradigm was used to measure AM-depth discrimination functions. A two-down one-up procedure was used to estimate the 70.7% correct point of the psychometric function (Levitt, 1971). Subjects had to identify the one randomly chosen interval containing the increased AM depth of $m_c = m_s\sqrt{1+m_{inc}}$. The standard AM depth in the two reference intervals was m_s. The fractional increment m_{inc}, corresponding to the Weber fraction $(m_c^2-m_s^2)/m_s^2$, was varied in dB ($10\log m_{inc}$). The three observation intervals were separated by 500-ms silent intervals. The threshold run started at $10\log m_{inc}=0$ dB. The initial step size was 2 dB and was divided by 2 after every second reversal until it reached the final stepsize of 0.5 dB. Six reversals were obtained at the final stepsize and the threshold estimate was taken as the mean value of $10\log m_{inc}$ at these reversals. Reported thresholds represent the mean of the estimates from four runs.

As already reported in Wakefield and Viemeister (1990), sequential dependencies among conditions can strongly influence AM-depth discrimination thresholds. Comparable with Wakefield and Viemeister's observations, our own preliminary experiments revealed that, particularly for low standard modulation depths, a much higher increment was required for detection when the task followed a run with a more than 5-dB higher standard modulation depth than when it followed a run with a lower or only slightly higher standard modulation depth. Therefore, following the findings of Wakefield and Viemeister (1990), AM-depth discrimination thresholds were measured in three blocks of two randomly mixed standard modulation depths separated by only 5 dB (-3 and -8, -13 and -18, -23 and -28 dB). For each subject, the three blocks were presented in random order.

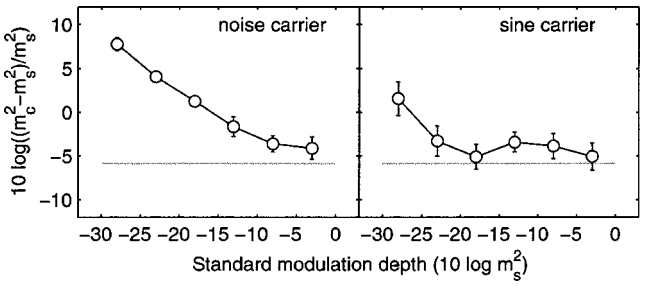

FIG. 1. Weber fractions for AM-depth discrimination as a function of the AM depth of the standard. The left panel shows data for a 2048-Hz-wide random-noise carrier with an upper cutoff frequency of 4 kHz. The right panel shows data for a 4-kHz sinusoidal carrier. The horizontal line indicates the expectation for a 1-dB increase required for discrimination.

B. Results and discussion

The pattern of results was similar for the five subjects, so the mean data and standard deviations (indicated by the errorbars) are shown. Figure 1 shows AM-depth discrimination thresholds, expressed as Weber fractions, as a function of the standard AM depth. The left panel shows results for the broadband-noise carrier, the right panel shows results for the pure-tone carrier. For the highest standard depth (rightmost data point in each panel), the Weber fraction is similar for the two carrier types (-4 dB for the noise, and -5.2 dB for the tone carrier). For standard depths below -8 dB, the Weber fraction rises continuously with decreasing standard depths in the case of the noise carrier. In contrast, in the case of the pure-tone carrier, the Weber fraction tends to stay constant for standard depths down to -18 dB. For smaller standards, the Weber fraction increases at approximately the same rate as in the case of the noise carrier; here the slope of the curves approaches -1, reflecting that the task becomes detection rather than discrimination. For the lowest standard depth (-28 dB), the Weber fraction is 2 dB for the pure-tone carrier, compared to 7.5 dB for the noise carrier. A constant 1-dB increment in AM-depth discrimination (constant (S+N)/N) would correspond to a value of -5.9 dB, if expressed as a Weber fraction. This value is indicated by the horizontal line in Fig. 1. At high standard depths, the obtained Weber fractions in the data would correspond to a just-detectable AM-depth increment of about 1.4 dB for the noise carrier and 1.2 dB for the pure-tone carrier.

In Fig. 2, the data from Fig. 1 are replotted as $10\log(m_c^2-m_s^2)$ (indicated by the circles) and plotted together

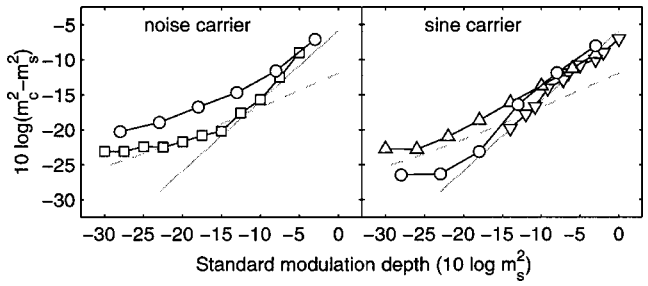

FIG. 2. Comparison of the data from Fig. 1 (circles), replotted as AM-depth discrimination functions, and data from the literature. The left panel (noise carrier) shows data by Wakefield and Viemeister (1990) as squares. In the right panel (sinusoidal carrier) the downward pointing triangles show data by Fleischer (1980) while the upward pointing triangles represent data by Fassel (1995). The solid line indicates the expectation for a constant 1-dB increase (Weber fraction) required for discrimination. The dashed line indicates the slope for a constant increment.

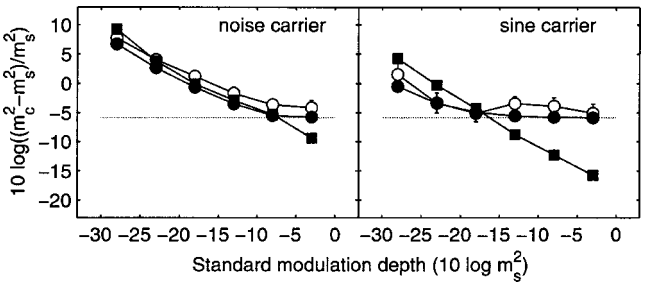

FIG. 3. Model predictions (closed symbols) and empirical data (open symbols, replotted from Fig. 1) for AM-depth discrimination. The closed circles represent predictions obtained for the EPSM, the closed squares represent PEMO predictions.

with data from Wakefield and Viemeister (1990) (left panel, squares) as in Fig. 5 of their study. For sinusoidal carriers (right panel) data by Fassel (1995) and Fleischer (1980) are shown as upward and downwards triangles, respectively. The discrimination function that would correspond to a constant 1-dB increment is indicated by the solid line. The expectation assuming a constant increment is represented by the dashed line. Altering the magnitude of either the relative or the constant increment would result in a (vertical) displacement of the corresponding lines, while maintaining the slope. At high standard depths, the measured threshold function from the present study approaches the 1-dB-increment criterion (solid line) while, at small standard depths, it has about the same slope as the expected curve assuming the constant-increment criterion (dashed line). The transition occurs at standard depths of about -8 dB for the noise carrier and at about -18 dB for the pure-tone carrier. In contrast to the gradual transition between the two slopes for the noise carrier in the present data, the existence of two different characteristic regions seems more distinct in the Wakefield and Viemeister (1990) data. Compared to the current data, they found generally lower (better) discrimination thresholds, except for the highest standard depth of -5 dB. The reason for the differences between both sets of data is not clear, since the experimental paradigm used in the two studies is the same. One explanation might be the larger carrier bandwidth used in their study: The noise carrier had a bandwidth of 10 kHz, compared to a bandwidth of only 2048 Hz in the present study. Another difference is that, in the present study, the Weber fraction m_{inc} was directly adjusted during a threshold run (and was dependent on the standard depth) while Wakefield and Viemeister (1990) used a constant stepsize, independent of the standard modulation depth, resulting in much larger steps for small standards than in the present study.

For the pure-tone carrier (right panel of Fig. 2), the data of the present study are similar to the data of Fleischer (downward triangles): For standards depths above -18 dB, both data sets closely match the 1-dB-increment expectation (solid line). This is also the case for the data by Fassel (upward triangles). However, for standard depths below -15 dB, he obtained considerably higher (worse) discrimination thresholds. In this case, the threshold function by Fassel exhibits about the same slope as the expected function for the constant increment (dashed line). The discrepancy between the data by Fassel (1995) and the other data might be explained by the fact that he applied a Hanning window over the entire duration of the modulation, whereas, for example, in the present study only the first and last 50 ms of the 500-ms modulation were windowed. At small AM depths, this probably resulted in a reduced effective observation interval for the modulated part of the stimulus, since only the central part of the Hanning window contributed to detection. Such an effect might also have caused the increased discrimination thresholds for the smallest standard depths observed in Lee and Bacon (1997).

Figure 3 shows model predictions (closed symbols), obtained with the two AM-processing models described in Sec. II, in comparison to the experimental data (open symbols) replotted from Fig. 1. The closed circles represent predictions obtained with the envelope power spectrum model (EPSM), while the closed squares show results for the perception model (PEMO). For the noise carrier, shown in the left panel, the EPSM predictions follow the empirical data nicely. The prediction shows a constant Weber fraction for standard depths greater than -8 dB, while below -8 dB, the model predicts an increase of the Weber fraction with decreasing standard depth. The maximum deviation between data and prediction is less than 3 dB. The other model, PEMO, predicts a continuously changing Weber fraction throughout the entire range of standard depths. For standard depths below -10 dB, the slope of the predicted curve follows the slope in the data. For standard depths above -8 dB, the model clearly overestimates the experimental performance (i.e., underestimates the measured Weber fractions). The differences between the two models are larger in the right panel of Fig. 3 where the results for the pure-tone carrier are shown. Here, EPSM describes the data well; for standard depths higher than -18 dB, it accounts for the constant Weber fraction observed in the data. In contrast, PEMO predicts a continuously changing Weber fraction throughout the entire range of standard depths. This model thus underestimates listeners' performance for standard depths below -18 dB, while it increasingly overestimates the listeners' performance for increasing standard depths.

In the framework of the models, the two characteristic regions in the data can be explained in terms of two different

resolution limitations. One limitation is related to the external variability of the stimuli. A second limitation is related to the properties of the internal coding process. PEMO is limited by the external fluctuations inherent to the noise carrier or, in the case of the sinusoidal carrier, by the assumption of a fixed-variance internal-noise process. Both limitations are independent of the standard modulation depth. These two limitations can explain the region of decreasing Weber fractions as observed for small standard modulation depths in the data. However, these model characteristics are also responsible for the overestimation of the discrimination performance for large modulation depths of the standard, as is also the case for the leaky-integrator model in Wakefield and Viemeister (1990). EPSM adds the assumption of an internal-noise process with a variance equal to the value of the decision variable. With this assumption, EPSM is able to account for the region of constant Weber fractions observed in the data.

IV. AM DETECTION WITH FROZEN- AND RANDOM-NOISE CARRIERS

A. Rationale

In the previous experiment, AM-depth discrimination was investigated using a random-noise carrier and a deterministic pure-tone carrier. While the random-noise carrier exhibits random envelope fluctuations, the pure-tone carrier has a flat temporal envelope. In the latter case, the auditory system's resolution can only be limited by internal noise. The same is true for frozen-noise carriers that also do not exhibit any variability of stimulus parameters across presentation intervals but have, of course, a different distribution of power in the envelope spectrum than sinusoidal carriers. In this experiment, AM-detection thresholds were obtained for random- and frozen-noise carriers, as a function of the carrier bandwidth. The question was whether the detection performance in these conditions can be explained in terms of the ''long-term'' average distribution of the envelope power only, or whether the statistical variability of the envelope power also must be taken into account.

B. Method

1. Subjects

Four male subjects participated in the experiment. Two subjects (SE and MB) also participated in the first experiment. All subjects had clinically normal hearing and had, with the exception of subject CP, experience in other psychoacoustic experiments. Their age ranged from 27 to 29 years. Subjects MB, JD, and CP were paid for their participation on an hourly basis.

2. Apparatus, stimuli, and procedure

The same apparatus, adaptive procedure, and signal duration as in the first experiment were used. Only the differences are reported here. AM-detection thresholds were measured for modulation frequencies of 4, 16, 64, and 256 Hz, applied to either a random or deterministic (''frozen'') noise carrier. The bandwidth of the carrier ranged from 8 to 2048 Hz, in two-octave steps (8, 32, 128, 512, 2048 Hz). The bandlimited noise carrier was generated in the temporal domain by selecting 2^{17} samples ($\approx$2.7 s) from a Gaussian random variable. Bandlimiting was done in the frequency domain by zeroing the Fourier coefficients outside the passband of the noise representation. In the case of the random-noise carrier, this representation was refreshed prior to each trial and the three presentation intervals were consecutively cut from the 2.7-s representation. In the case of the frozen-noise carrier, a single noise representation was generated once prior to each threshold run and a fixed portion of that representation served as the carrier in all presentation intervals during the entire threshold run. Note that this procedure results in a different frozen-noise realization for each subject and threshold run.

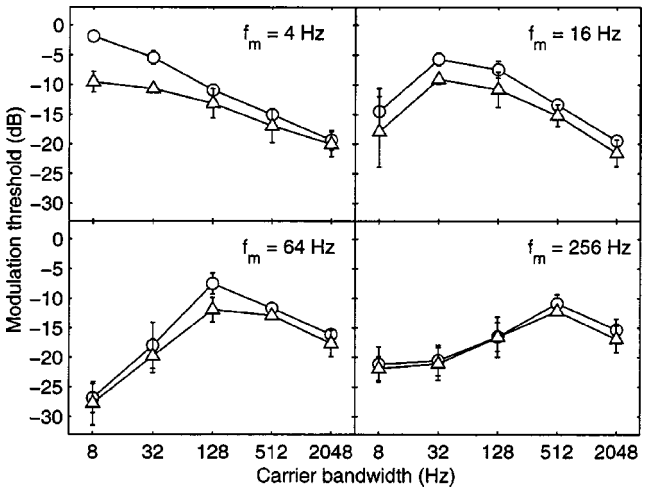

FIG. 4. Modulation-detection thresholds as a function of the bandwidth of a noise carrier. In each of the panels, the circles are for the random-noise carrier and the triangles indicate data for the frozen-noise carrier. The different panels show average data for the modulation frequencies of 4 Hz (upper left), 16 Hz (upper right), 64 Hz (lower left), and 256 Hz (lower right).

The equation describing the stimuli is

$$s(t)=[1+m\sin(2\pi f_m t)]c(t), \tag{2}$$

where m is the modulation index, f_m is the modulation frequency, and $c(t)$ is the carrier waveform. During a threshold run, the modulation index m was varied in logarithmic steps ($20\log(m)$). The initial modulation index was -6 dB. The initial step size was 4 dB and was divided by 2 after every second reversal until it reached the final step size of 1 dB. For each subject and threshold run, the threshold estimate was taken as the mean value of $20\log m$ across eight reversals obtained at the final step size. The thresholds reported are the mean of the estimates from three runs.

C. Results and discussion

Mean data and standard deviations (indicated by the errorbars) across subjects are shown in Fig. 4. The four panels show data for the modulation frequencies 4 Hz (upper left), 16 Hz (upper right), 64 Hz (lower left), and 256 Hz (lower right). In each panel, the data for the random-noise carrier are indicated by the circles while the triangles represent the data for the frozen-noise carrier. Detection thresholds are

plotted as a function of the carrier bandwidth. In all conditions, a threshold maximum is seen at a carrier bandwidth twice the modulation frequency. Except for the 4-Hz signal modulation, where the maximum occurs at the smallest bandwidth tested, thresholds decrease at both sides of the maximum. The thresholds obtained for the frozen-noise carrier are always lower than or equal to those obtained for the random-noise carrier. The data obtained for the frozen-noise carrier show a somewhat higher variability (indicated by the larger errorbars) than the random-noise data. This is probably caused by the relatively small number n of frozen-noise samples presented ($n=12$, three for each of the four subjects). In contrast, for the random-noise carrier, about 150 different random-noise samples were presented in each of the 12 runs. The maximum threshold difference between the two carrier types generally occurs at a carrier bandwidth near the maximum of the threshold pattern. The largest difference between the random- and frozen-noise-carrier results can be observed for the lowest modulation frequency (4 Hz), when applied to the 8-Hz-wide carrier (upper left panel). Overall, the differences between the two carrier types decrease with increasing signal frequency. The maximum threshold differences for 16- and 64-Hz modulation frequency are 4 and 5 dB, respectively, in both cases for a carrier bandwidth of 128 Hz. For the highest modulation frequency (256 Hz), thresholds are very similar for the two carrier-noise types. A two-way repeated-measures analysis of variance (ANOVA) using all conditions (carrier type [2]×carrier bandwidth [5]) showed a highly significant main effect of carrier type for the signal-modulation frequencies 4 and 16 Hz ($p<0.01$), and 64 Hz ($p<0.001$). A significant main effect of carrier type was still found for the 256-Hz signal modulation ($p<0.05$).

AM-detection thresholds with random-noise carriers are mainly determined by the spectral distribution of the envelope fluctuations inherent to the noise carrier, as was already demonstrated in Dau *et al.* (1997a,b). Thresholds for a sinusoidal amplitude modulation, imposed on a bandlimited noise carrier, depend in a characteristic way on the carrier bandwidth. In the conditions considered here, the maximum threshold is observed when the carrier bandwidth equals two times the frequency of the signal modulation. Dau *et al.* (1999) demonstrated that such a threshold pattern can be accounted for if a modulation-bandpass filter rather than a modulation-low-pass filter is assumed.

The data in Fig. 4 demonstrate that the empirical threshold patterns obtained for the frozen-noise carriers are quite similar to those obtained for the random-noise carriers, i.e., the absence of any variability in the envelope waveform in the case of the frozen-noise carrier has little impact on the listener. Thus, detection performance can not only be limited by the stochastic nature of the envelope fluctuations inherent to the random-noise carrier but must also be affected by internal noise in the coding of the envelope in deterministic conditions.

Predictions obtained with the two models, EPSM and PEMO, are shown in Figs. 5 and 6 (closed symbols), respectively. Each figure also replots the corresponding empirical data (open symbols) from Fig. 4. The circles represent thresholds for the random-noise carrier and the triangles show results for the frozen-noise carrier. The EPSM (Fig. 5) captures all main effects apparent in the data. It accounts for the general shape of the threshold patterns as well as for the differences between random and frozen noise. As observed in the data, these differences decrease with increasing signal frequency. Within EPSM, the reason for the diminishing difference is that with increasing signal-modulation frequency (and thus increasing bandwidth of the constant-Q modulation filter), the standard deviation of the integrated envelope power decreases relative to the mean value, as more and more components of the envelope spectrum fall within the passband of the filter. For 256-Hz signal modulation, the mean integrated envelope power becomes the limiting quantity in both cases, the random- and the frozen-noise carriers. For the small signal-modulation frequencies where only a few components of the envelope spectrum pass the filter, the standard deviation of the integrated envelope power is in-

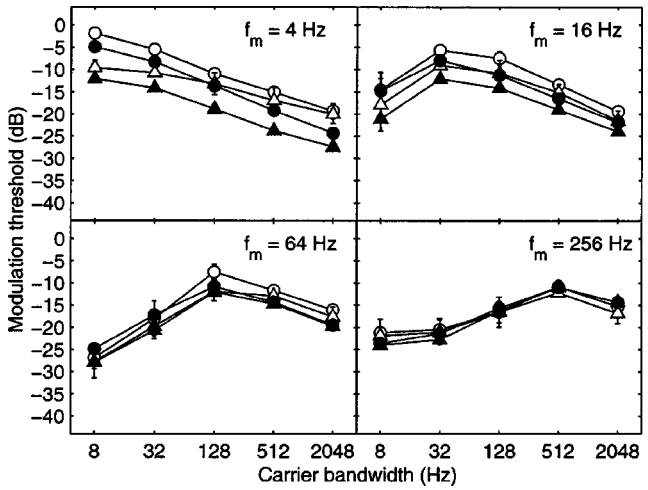

FIG. 5. Predictions obtained with EPSM (closed symbols) together with empirical data (open symbols), replotted from Fig. 4. The four panels show modulation-detection thresholds for signal modulations of 4, 16, 64, and 256 Hz, respectively, as a function of the bandwidth of the carrier. The circles represent thresholds for the random-noise carrier and the triangles show results for the frozen-noise carrier.

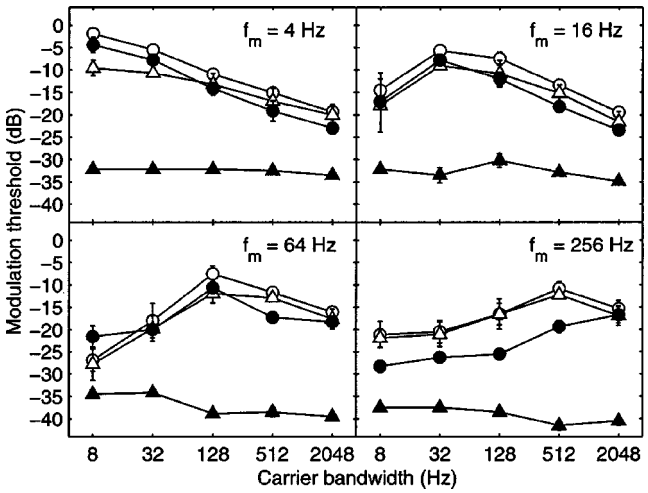

FIG. 6. Predictions obtained with PEMO (closed symbols) together with the empirical data (open symbols) as in Fig. 5.

creased relative to the mean and thus limits performance for the random-noise carrier. In the case of the frozen-noise (deterministic) carrier, only the mean integrated envelope power determines performance. The standard deviation is always zero, independent of the filter bandwidth. The other model, PEMO (Fig. 6), also accounts for the data in the random-noise carrier conditions (circles). Here, the model produces similar predictions as EPSM. However, PEMO completely fails in all frozen-noise carrier conditions (filled triangles) where it predicts a constant threshold of about -35 dB, independent of carrier bandwidth and signal frequency. This is a direct consequence of the fixed-variance internal noise that does not depend on the magnitude of the mean envelope power of the stimulus.

V. AM MASKING AS A FUNCTION OF MASKER VARIABILITY

A. Rationale

In the previous experiment, the detection performance for the signal modulation was limited by the inherent envelope fluctuations of the carrier noise. The current experiment examines modulation masking as a function of the statistical properties of a narrow-band-noise masker modulation, centered at the signal-modulation frequency. The experiment is designed to allow for a more gradual transition between deterministic and stochastic stimuli: Semi-frozen and rms-equalized random-noise maskers are used in addition to frozen- and random-noise maskers. This is done in order to examine the validity of a ''long-term'' average quantity as the decision variable, such as the mean envelope power within the framework of EPSM, and in order to investigate the role of memory in experiments with frozen and semi-frozen stimuli.

B. Method

1. Subjects

Four male subjects participated in the experiment. Three of the subjects (MB, JD, and author SE) also participated in the second experiment. All subjects (except the fourth subject, PE) had experience in psychoacoustic experiments. All subjects had clinically normal hearing. Their ages ranged from 25 to 29 years. Subjects MB and PE were paid on an hourly basis for their services.

2. Apparatus, stimuli, and procedure

The same apparatus, adaptive procedure and signal duration were used as in the previous experiment. Detection thresholds for 4-, 16-, and 64-Hz signal modulation were measured in the presence of a narrow-band-noise masker modulation. Signal and masker modulation were applied to a 4-kHz pure-tone carrier. The masker was geometrically centered at the signal-modulation frequency and had a half-octave bandwidth (1.4, 5.6, and 22.4 Hz). The equation describing the stimuli is

$$s(t)=[1+m\sin(2\pi f_m t)+n_m(t)]c(t), \tag{3}$$

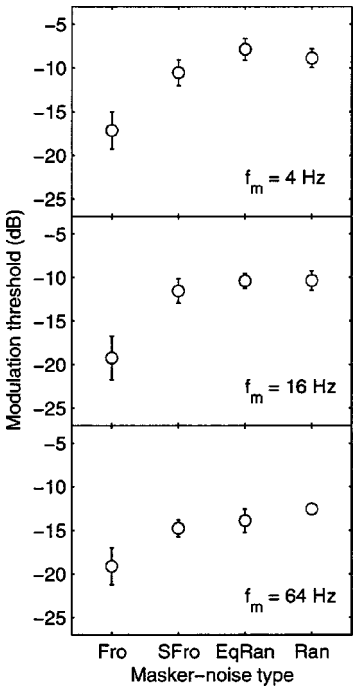

FIG. 7. Masked-modulation-detection thresholds in the presence of different types of narrow-band (half-octave) noise. The panels display the data for the different signal-modulation frequencies 4 Hz (upper panel), 16 Hz (middle panel), and 64 Hz (lower panel). The noise-masker modultion was always centered at the signal-modulation frequency. The abbreviations at the abscissa indicate frozen (Fro), semi-frozen (SFro), equalized random (EqRan), and random (Ran) noise maskers.

where m is the signal-modulation index, f_m is the signal-modulation frequency, and $c(t)$ denotes the carrier waveform. The masker modulation $n_m(t)$ was either frozen noise, semi-frozen noise, rms-equalized random noise, or random noise. All noise-masker modulations were generated in the temporal domain by selecting 2^{17} samples ($\approx$2.7 s) from a Gaussian random variable. The signals were then transformed to the frequency domain, bandlimited by zeroing the Fourier-coefficients outside the desired passband, and transformed to the time domain by inverse Fourier transformation. For the frozen-noise masker, the identical noise realization was used in each interval. The rms value of this masker was set to -15 dB. In the case of the semi-frozen noise, a different frozen-noise realization was used for each trial during a threshold run, i.e., the masker modulation was only frozen throughout the three presentation intervals but not during the entire run. In the case of the two random maskers, the 2.7-s-long representation was refreshed prior to each trial and three different portions were cut out randomly for each presentation interval. For the rms-equalized random noise, the rms value of each masker realization was set to -15 dB while, for the random-noise masker, the rms value of the entire 2.7-s representation was set to -15 dB. In the latter case, only the long-term average across the rms values of the individual masker waveforms was -15 dB.

C. Results and discussion

Figure 7 shows the mean detection thresholds, averaged across the subjects, for the signal-modulation frequencies 4 Hz (upper panel), 16 Hz (middle panel), and 64 Hz (lower

panel). The four different masking-noise conditions are indicated on the abscissa: frozen noise (Fro), semi-frozen noise (SFro), rms-equalized random noise (EqRan), and random noise (Ran). For each signal frequency, the lowest detection threshold is observed for the frozen-noise masker. For the other three masker-noise types, thresholds are increased by about the same amount. The detection threshold decreases with increasing signal-modulation frequency in all masking conditions. The threshold difference between 4 and 64 Hz amounts to 4 dB, averaged across all conditions. The maximum difference is observed for EqRan noise (6 dB), while the minimum difference (2 dB) is observed in the Fro condition.

The effect of masker-noise type was investigated using a one-way repeated-measures analysis of variance (ANOVA). A highly significant main effect of noise type was found for all signal frequencies ($p<0.001$). *Posthoc* comparisons based on Tukey's honestly significant difference (HSD) criterion showed that the threshold in the frozen-noise condition was significantly different from all other conditions ($p<0.001$). For 4 Hz, the threshold for the semi-frozen and the EqRan noise, and for 64 Hz the threshold for the semi-frozen and the Ran noise, were significantly different ($p<0.05$). For all signal frequencies tested, the listener's detection performance clearly improved only in the case of the frozen-noise masker. Although the other three types of maskers differed in their variability, all three resulted in similar masked thresholds except for two cases, where a slight improvement for the semi-frozen noise masker was found. The large threshold difference between the frozen and the semi-frozen masker conditions is somewhat surprising. Decisions seem to be more based on the comparison of an internally formed expectation for the target signal with each of the signals in the intervals of a trial, rather than on the comparison of the three intervals without any history. Thus, memory effects during the threshold run seem to play an important role. Unlike the expectation based on the deterministic nature of each of the trials in the semi-frozen condition, listeners are not able to improve their detection performance relative to the two stochastic conditions (equalized random and random). It is possible that the significantly higher thresholds in the semi-frozen condition compared to the frozen condition were observed because the different masker types were presented in a randomly mixed order. While a frozen-noise run can be easily identified out of the three others, listeners may not be able to identify a semi-frozen run. It can only be speculated whether prior knowledge of the masker type would lead to a better performance in the semi-frozen runs.

Figure 8 shows the predictions of the two models (filled symbols) in these conditions. The experimental data are replotted and indicated as open symbols. As mentioned in Sec. II, the two models do not only differ in their assumptions about the internal variability, inherent in the coding process, but also differ in terms of considering memory effects in their decision devices. Both models account for the thresholds in the rms-equalized and the random-noise conditions. However, neither of the two models is able to capture all aspects of the data. EPSM (closed circles) predicts a threshold difference between the random and frozen conditions.

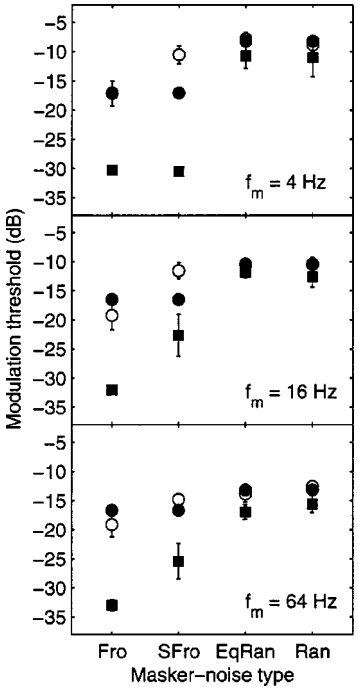

FIG. 8. Comparison of model predictions for EPSM (close circles) and PEMO (closed squares) with the empirical data from Fig. 7 (open symbols). The abbreviations at the bottom represent the different masker types, frozen (Fro), semi-frozen (SFro), equalized random (EqRan), and random (Ran).

However, it cannot, per definition, distinguish between the two random conditions, and between the two frozen conditions. In the two random conditions, the decision variable within EPSM, the long-term average integrated envelope power, is the same. Considering EPSM as a memoryless model, it is clear that it cannot predict any difference between the frozen and semi-frozen condition. Since all stimuli in a trial are deterministic in the frozen and the semi-frozen condition, detection performance within EPSM is purely limited by internal noise. As in the previous experiment, PEMO largely overestimates detection performance in the two frozen-masker conditions. However, except for the 4-Hz condition, this model predicts a threshold difference between the frozen and semi-frozen conditions. The reason for this difference is that PEMO, in contrast to EPSM, includes memory effects in the detection process. The model permanently ''recalls'' specific features of the internal representation of the stimulus (the template), derived by averaging a suprathreshold representation of the signal. The template is ''perfect'' for deterministic stimuli while it is corrupted by the external variability in case of stochastic stimuli. It can be assumed that the template mechanism quite realistically simulates the formation and short-term presence of a ''matched'' feature-selective filter during a threshold run. Despite the fact that the overall deviation from the data in the frozen and semi-frozen conditions is larger for PEMO than for EPSM, PEMO can, in principle, account for a difference in performance between the frozen and the semi-frozen condition. The relatively larger overall deviation is, again, a consequence of the fixed-variance internal noise.

VI. OVERALL DISCUSSION

AM-depth discrimination with broadband noise and pure-tone carriers (first experiment) showed that Weber's law

holds for standard modulation depths well above absolute (modulation) detection threshold. It does not hold for small standard depths where a constantly rising Weber fraction is observed, as has already been shown in Wakefield and Viemeister (1990) for broadband-noise carriers. The present study demonstrates that, in the framework of AM-processing models, the assumption of a ''Weber-fraction''-type internal noise is essential in order to account for the data. The fact that Weber's law does not apply over the entire range of standard depths for the noise carrier can be explained by the external variability inherent to the envelope of the noise carrier. The envelope power spectrum model, EPSM, is able to account for the data by combining internal noise that is proportional to the mean of the decision variable, the integrated envelope power, and external noise as inherent property of the stimuli. The perception model, PEMO, accounts well for the data as long as the stimulus variability limits performance, while it cannot predict Weber's law since a fixed-variance internal noise that is independent of the mean of the decision variable is assumed.

The empirical findings of AM detection with random- and frozen-noise carriers (second experiment) are perfectly in line with the assumption that a Weber-fraction-type internal noise in combination with the external variability of the stimuli limits detection performance. The comparison of the data in the random- and frozen-noise conditions clearly demonstrates that listeners gain only little from the absence of external stimulus variability as given in the frozen-noise conditions. This proves that internal noise plays a dominant role in conditions with frozen-noise carriers. It also demonstrates that the internal noise must be proportional to the envelope power of the stimuli (at the output of an envelope-frequency selective process), since the data for random- and frozen-noise carriers follow the same threshold pattern. A different behavior would be expected from an ''ideal'' observer as reflected by the threshold predictions of PEMO. In the absence of external variability, thresholds are only determined by a constant amount of internal noise, independent of the stimulus. The EPSM behaves more like a ''real'' observer, severely hampered by internal noise that is proportional to the mean of the decision variable.

The role of internal and external limitations in AM detection were further investigated in the third experiment, where thresholds were obtained in the presence of a narrowband-noise masker as a function of the degree of the variability in the masker. The most interesting observation was that masking is considerably reduced in the frozen condition compared to the semi-frozen condition. This result could not have been expected if decisions within the three-alternative forced-choice task were assumed to be based on a comparison of the stimuli within a trial. In this case, there should be no difference between the frozen and semi-frozen conditions. However, the listeners seem to have developed a different strategy in the frozen than in the semi-frozen condition. This result draws some interesting conclusions for the two models of the present study. Within EPSM, decisions are based only on the increase of the decision variable in comparison to the standard intervals. This results in the same predictions for the frozen and the semi-frozen masker noise. The fact that the decision variable is a long-term average quantity leads to the same threshold predictions for the two random-noise conditions. The latter observation is in line with the data. The other model, PEMO, while overestimating detection performance in the two frozen-noise conditions, is in principle able to predict a threshold difference between the frozen and the semi-frozen condition. This can be explained in terms of the larger amount of information reflected in the decision variable within PEMO, in comparison to EPSM, independent of the differences in the internal-noise process described above. PEMO calculates the cross-correlation coefficient (cross-power) between the current stimulus representation and a stored template representation which incorporates internal memory and information about the temporal course of the internal representation. In contrast, EPSM only uses a strongly reduced amount of information: The envelope power spectrum represents the Fourier transform of the autocorrelation of the internal stimulus representation, neglecting memory and temporal information. Thus, the decision variable in PEMO, based on the cross-correlation with a template, might be more realistic than the integrated envelope power in EPSM, since it is in principle suitable to account for effects of memory. This clearly demonstrates a possible limit of applicability of the EPSM. Since, overall, the EPSM accounts better for the data of the present study than PEMO, an incorporation of the template mechanism into the EPSM might seem appealing. However, with such a modification of the decision variable, the EPSM would no longer be a power spectrum model. More generally, a valuable step in the direction of a more realistic decision variable within the EPSM might be a reintroduction of the time axis into the model and the computation of the envelope power spectrum for certain successive temporal windows. The duration of the temporal windows might then be related to the center frequency of the different modulation filters. Such modifications, however, are beyond the scope of the present study.

As pointed out in the Introduction, the most severe difference between the two models in these conditions is reflected in the assumptions about the nature of the internal-noise process. As a consequence, one model (EPSM) accounts for the data in deterministic conditions while the other model (PEMO) fails in these conditions. Both models successfully describe the data when the external variability of the stimuli limits performance in AM-depth discrimination and AM detection. In principle, the two models can be tested with both types of internal-noise processes. Such an analysis would have shown that EPSM fails (like PEMO) in the deterministic conditions if a fixed-variance internal noise was assumed instead of the Weber-fraction-type noise. Likewise, PEMO would lead to more realistic predictions in the deterministic conditions if a Weber-fraction noise was used instead of the fixed-variance noise. Based on the results of the present study, a modification of the original PEMO was explicitly attempted and is described in the following. The modification applies a logarithmic transformation to the rms value of the internal representation at the output of the modulation filter. The rms value of the steady-state portion of the internal representation at the output of the modulation filter tuned to the signal-modulation frequency was calcu-

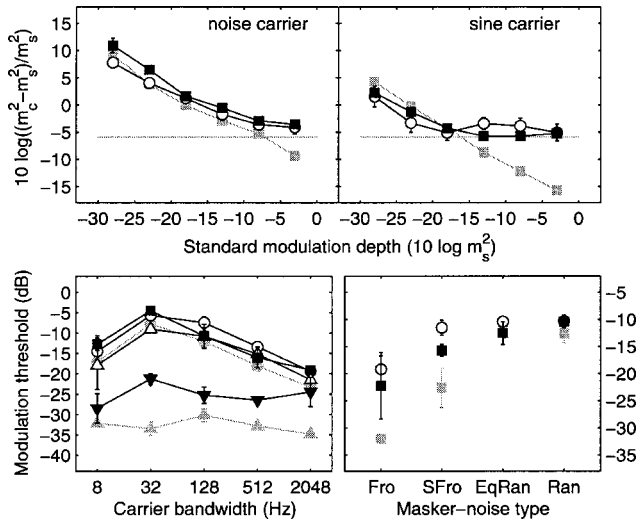

FIG. 9. Model predictions for the modified PEMO version (black closed symbols), the original PEMO (gray closed symbols), and empirical data (open symbols) for selected conditions of the three experiments. The upper two panels are comparable to Fig. 3. The lower left and right panel show the 16-Hz conditions from Figs. 6 and 8, respectively. See text for details.

lated. The internal representation was then normalized to a rms value of one and multiplied by a factor of $s = 2.5(\log \mathrm{rms} + 4)$. The factor s was restricted to positive values and was zero for rms values $\leqslant 0.0001$. All other parameters of the original model remained unchanged. Since the internal noise inherent in the PEMO is now added to the logarithmically transformed internal representation, it acts like a Weber-fraction-type noise. Figure 9 shows predictions for the modified model (black closed symbols) in comparison to the data (open circles) and the original model predictions (gray closed symbols). The upper two panels refer to Fig. 3. In principle, the pattern of results obtained with the modified model version (black closed squares) follows the expectation: The logarithmic transformation of the rms value of the internal representation leads to constant Weber fractions down to −18-dB AM depth of the standard in the case of the pure-tone carrier (right panel). The model also accounts well for the region of rising Weber fractions for standard AM depths smaller than −18 dB for the tonal carrier.[3] The predictions obtained with the modified PEMO also provided a better account of the data in the case of the broadband-noise carrier, as shown in the upper left panel of Fig. 9. However, listeners' performance is underestimated for the two lowest standard AM depths. The modified model also shows improvements in the prediction of data from the second experiment (AM detection of random- and frozen-noise carriers) and the third experiment (AM masking for different masker-noise types). For example, results for the 16-Hz signal-modulation condition from the second experiment are shown in the lower left panel (see also Fig. 6) and results for the 16-Hz condition from the third experiment are indicated in the lower right panel (see also Fig. 8). The results for the other signal-modulation frequencies were similar and are not shown explicitly. In particular, in the case of the frozen-noise carrier (black triangles in the lower left panel) and the frozen masker (two left most filled symbols in the lower right panel), the modified model shows a significant improvement (higher thresholds) of the model predictions. There remain, however, some clear differences in the data.[4]

Thus, a straightforward modification of PEMO leads to a correct prediction of the AM-depth discrimination data, while some discrepancies remain in the detection conditions with the frozen-noise carriers or maskers. Further modeling work is needed here. The generality of such a modified version of the model will, in any case, have to be tested and evaluated in all experimental conditions that have already been described by the original model in earlier publications (e.g., Dau *et al.*, 1997a,b; Verhey *et al.*, 1999; Derleth and Dau, 2000; Verhey, 2002).

VII. SUMMARY AND CONCLUSIONS

This study demonstrated that effects of (external) stimulus envelope variability and effects of internal envelope coding in the auditory system can be separated as two independent limiting factors in AM-depth discrimination and AM-detection experiments. The following conclusions can be drawn from the present study:

(i) AM-depth discrimination thresholds for a modulation frequency of 16 Hz closely follow Weber's law for large standard AM depths, when applied to a broadband-noise or a pure-tone carrier. Discrimination thresholds showed a systematic deviation from Weber's law for standard depths below −8 dB in the case of the broadband-noise carrier and below −18 dB in the case of the pure-tone carrier. In this region, a constant AM-depth increment was required for discrimination rather than a constant relative increment.

(ii) AM-detection thresholds with frozen- and random-noise carriers followed a similar characteristic pattern as a function of the carrier bandwidth. The maximum masked threshold was observed when the carrier bandwidth equals twice the signal-modulation frequency which can be explained as a result of an envelope-frequency selective process. In general, modulation-detection thresholds were lower for the frozen- than for the random-noise carrier. The maximum threshold difference between the frozen and random conditions was observed for signal-modulation frequencies $\leqslant 16$ Hz. Differences diminished with increasing carrier bandwidth and increasing signal-modulation frequency.

(iii) The empirical findings could be accounted for by the envelope power spectrum model (EPSM) that assumes a constant relative detection criterion and takes the stimulus envelope variability into account. The perception model (PEMO) was shown to account for the data as long as the envelope variability limits the detection performance. Since PEMO assumes a constant detection criterion in the envelope domain, the model failed to account for the data in deterministic conditions where internal noise inherent to the internal coding mechanisms limits the detection performance. The different assumptions about the nature of

the inherent noise process in the two models were shown to be responsible for the main differences in the model predictions.

(iv) Masked AM thresholds in the presence of a narrowband-noise masker modulation were considerably lower for a frozen-noise masker than for a semi-frozen or random-noise masker. It was shown that listeners were not able to gain information from identical masker-modulation waveforms within the trials (semi-frozen) 3-AFC run, while the gain was significant when the identical masker waveform was presented during the entire threshold run (frozen). This observation contradicts the assumption that decisions in a 3-AFC task are based on a ''memoryless'' comparison of the three intervals within a single trial. As a consequence, models without memory (like the EPSM) fail to correctly mimic the decision process in human listeners.

(v) Future models of AM detection should probably combine the more realistic internal variability, as assumed in EPSM, with the more realistic decision variable as assumed in PEMO. A first straightforward implementation of a modified PEMO has been described in the present study.

ACKNOWLEDGMENTS

We thank Neal F. Viemeister and two anonymous reviewers for very helpful comments on the manuscript. We also thank Birger Kollmeier and Stefan Uppenkamp for comments on an earlier version of the manuscript. This work was supported by the Deutsche Forschungsgemeinschaft (DFG), Research Project SPP 1046.

[1]For pure tones, Weber's law does not hold strictly. The fraction $\Delta I/I$ slightly decreases as a function of I. This has been termed the ''near miss'' to Weber's law.

[2]When intensity discrimination for a pure tone is measured in the presence of a masker noise, the effect of the masker is negligible when the pedestal is more than 5–10 dB above its threshold (Jesteadt *et al.*, 1977). However, slight changes in performance are observed for pedestals up to 15–20 dB above masked threshold due to the external variability of the masker (Henning and Psotka, 1969). In addition to the strong influence of masking noise in conditions where the pedestal is close to its threshold, broadband masking noise is also known to eliminate the ''near miss'' to Weber's law for pedestal levels well above threshold (Bos and de Boer, 1966; Viemeister, 1972).

[3]Since the model only contains a single source of noise after the logarithmic transform, this should result in a constant Weber fraction. The region of rising Weber fractions as observed in the predictions is a consequence of the dc sensitivity of the modulation filters (see Dau *et al.*, 1997a,b). The small amount of dc passing the filter acts like an additive noise prior to the logarithmic transformation and thus makes the model capable of accounting for realistic AM detection thresholds for deterministic carriers (not shown) and the resulting rising Weber fraction towards small standard AM depths.

[4]In addition to the modified model version presented here, another approach was tested, with similar but generally worse results. Like in the above modification, the rms value of the steady-state portion of the internal representation at the output of the modulation filter tuned to the signal-modulation frequency was calculated. A Gaussian noise was generated and bandpass filtered with the respective modulation filter. The rms value of the filtered noise was set to the rms value of the internal representation and the two waveforms were added. This procedure adds a Weber-fraction-type internal noise to the internal envelope representation for each of the stimuli during a threshold run.

Bos, C. E., and deBoer, E. (**1966**). ''Masking and discrimination,'' J. Acoust. Soc. Am. **82**, 708–715.

Dau, T., Kollmeier, B., and Kohlrausch, A. (**1997a**). ''Modeling auditory processing of amplitude modulation. I. Modulation detection and masking with narrowband carriers,'' J. Acoust. Soc. Am. **102**, 2892–2905.

Dau, T., Kollmeier, B., and Kohlrausch, A. (**1997b**). ''Modeling auditory processing of amplitude modulation. II. Spectral and temporal integration in modulation detection,'' J. Acoust. Soc. Am. **102**, 2906–2919.

Dau, T., Püschel, D., and Kohlrausch, A. (**1996a**). ''A quantitative model of the ''effective'' signal processing in the auditory system. I. Model structure,'' J. Acoust. Soc. Am. **99**, 3615–3622.

Dau, T., Püschel, D., and Kohlrausch, A. (**1996b**). ''A quantitative model of the ''effective'' signal processing in the auditory system. II. Simulations and measurements,'' J. Acoust. Soc. Am. **99**, 3623–3631.

Dau, T., Verhey, J. L., and Kohlrausch, A. (**1999**). ''Intrinsic envelope fluctuations and modulation-detection thresholds for narrowband noise carriers,'' J. Acoust. Soc. Am. **106**, 2752–2760.

Derleth, R. P., and Dau, T. (**2000**). ''On the role of envelope fluctuation processing in spectral masking,'' J. Acoust. Soc. Am. **108**, 285–296.

Ewert, S. D., and Dau, T. (**2000**). ''Characterizing frequency selectivity for envelope fluctuations,'' J. Acoust. Soc. Am. **108**, 1181–1196.

Fassel, R. (**1995**). ''Experimente und Simulationsrechnungen zur Wahrnehmung von Amplitudenmodulationen im menschlichen Gehör,'' doctoral thesis, Universität Göttingen.

Fleischer, H. (**1980**). ''Subjective Größe von Unterschieden im Amplitudenmodulationsgrad von Sinustönen,'' Acustica **46**, 31–37.

Florentine, M. (**1983**). ''Intensity discrimination as a function of level and frequency and its relation to high-frequency hearing,'' J. Acoust. Soc. Am. **74**, 1375–1379.

Florentine, M., Buus, S., and Maason, C. R. (**1987**). ''Level discrimination as a function of level for tones from 0.25 to 16 kHz,'' J. Acoust. Soc. Am. **81**, 1528–1541.

Green, D. M., and Swets, J. A. (**1966**). *Signal Detection Theory and Psychophysics* (Wiley, New York).

Green, D. M., Berg, B. G., Dai, H., Eddins, D. A., Onsan, Z., and Nguyen, Q. (**1992**). ''Spectral discrimination of narrow-band sounds,'' J. Acoust. Soc. Am. **92**, 2586–2597.

Henning, G. B., and Psotka, J. (**1969**). ''Effect of duration on amplitude discrimination in noise,'' J. Acoust. Soc. Am. **45**, 1008–1013.

Jesteadt, W., Wier, C. C., and Green, D. M. (**1977**). ''Intensity discrimination as a function of frequency and sensation level,'' J. Acoust. Soc. Am. **61**, 169–177.

Lawson, J. L., and Uhlenbeck, G. E. (**1950**). *Threshold Signals*, Vol. 24 of *Radiation Laboratory Series* (McGraw–Hill, New York).

Lee, J., and Bacon, S. P. (**1997**). ''Amplitude modulation depth discrimination of a sinusoidal carrier: Effect of stimulus duration,'' J. Acoust. Soc. Am. **101**, 3688–3693.

Levitt, H. (**1971**). ''Transformed up-down procedures in psychoacoustics,'' J. Acoust. Soc. Am. **49**, 467–477.

Ozimek, E., and Sek, A. (**1988**). ''AM difference limens for noise bands,'' Acustica **66**, 153–160.

Patterson, R. D., Nimmo-Smith, I., Holdsworth, J., and Rice, P. (**1987**). ''An efficient auditory filterbank based on the gammatone function,'' paper presented at a meeting of the IOC Speech Group on Auditory Modeling at RSRE, 14–15 December.

Püschel, D. (**1988**). ''Prinzipien der zeitlichen Analyse beim Hören,'' doctoral thesis, Universität Göttingen.

Raab, D. H., and Goldberg, I. A. (**1975**). ''Auditory intensity discrimination with bursts of reproducible noise,'' Phys. Rev. **31**, 867–875.

Riesz, R. R. (**1928**). ''Differential intensity sensitivity of the ear for pure tones,'' J. Acoust. Soc. Am. **57**, 437–447.

Verhey, J. L. (**2002**). ''Modeling the influence of inherent amplitude fluctuation simultaneous masking experiments,'' J. Acoust. Soc. Am. **111**, 1018–1025.

Verhey, J. L., Dau, T., and Kollmeier, B. (**1999**). ''Within-channel cues in comodulation masking release (CMR): Experiments and model predictions using a modulation-filterbank model,'' J. Acoust. Soc. Am. **106**, 2733–2745.
Viemeister, N. F. (**1972**). ''Intensity discrimination of pulsed sinusoids: The effects of filtered noise,'' J. Acoust. Soc. Am. **51**, 1265–1269.
Viemeister, N. F. (**1979**). ''Temporal modulation transfer functions based upon modulation thresholds,'' J. Acoust. Soc. Am. **66**, 1364–1380.
Wakefield, G. H., and Viemeister, N. F. (**1990**). ''Discrimination of modulation depth of sinusoidal amplitude modulation (SAM) noise,'' J. Acoust. Soc. Am. **88**, 1367–1373.

The effects of real and illusory glides on pure-tone frequency discrimination

J. Lyzenga[a] and R. P. Carlyon
MRC Cognition and Brain Sciences Unit, 15 Chaucer Road, Cambridge CB2 2EF, United Kingdom

B. C. J. Moore
Department of Experimental Psychology, University of Cambridge, Downing Street, Cambridge CB2 3EB, United Kingdom

(Received 24 October 2003; revised 3 March 2004; accepted 10 April 2004)

Experiment 1 measured pure-tone frequency difference limens (DLs) at 1 and 4 kHz. The stimuli had two steady-state portions, which differed in frequency for the target. These portions were separated by a middle section of varying length, which consisted of a silent gap, a frequency glide, or a noise burst (conditions: gap, glide, and noise, respectively). The noise burst created an illusion of the tone continuing through the gap. In the first condition, the stimuli had an overall duration of 500 ms. In the second condition, stimuli had a fixed 50-ms middle section, and the overall duration was varied. DLs were lower for the glide than for the gap condition, consistent with the idea that the auditory system contains a mechanism specific for the detection of dynamic changes. DLs were generally lower for the noise than for the gap condition, suggesting that this mechanism extracts information from an illusory glide. In a second experiment, pure-tone frequency *direction*-discrimination thresholds were measured using similar stimuli as for the first experiment. For this task, the type of the middle section hardly affected the thresholds, suggesting that the frequency-change detection mechanism does not facilitate the identification of the direction of frequency changes. [DOI: 10.1121/1.1756616]

PACS numbers: 43.66.Fe, 43.66.Mk, 43.66.Ba [NFV] Pages: 491–501

I. INTRODUCTION

In this paper we address two issues: the mechanisms by which we perceive frequency changes and the possible influence of the continuity illusion on those mechanisms. First, we consider whether there are any mechanisms in the auditory system specifically involved in the perception of dynamic frequency changes (frequency glides or frequency modulations), as opposed to mechanisms taking discrete samples of the (quasi-static) frequency. One successful approach to modeling the detection of periodic frequency modulation (FM) is to assume that the listener takes a series of samples, or ''snapshots'' of the stimulus, and compares the frequencies estimated from each snapshot (Hartmann and Klein, 1980; Demany and Semal, 1989). This approach essentially assumes that the auditory system detects dynamic changes in frequency in the same way as it compares the frequencies of two steady sounds.

Evidence that the auditory system is able to use dynamic changes *per se* was presented by Dooley and Moore (1988). They measured duration discrimination for tones that were either steady, or contained frequency glides of fixed extent. For the latter stimuli, the rate of change of frequency covaried with duration. They found that duration discrimination was better for the gliding tones than for the steady tones. They argued from this that subjects were sensitive to the rate of change of frequency, and used the rate of change as a cue in the duration-discrimination task.

Other evidence supports the idea that specific mechanisms exist for the processing of dynamic changes (Kay and Matthews, 1972; Regan and Tansley, 1979; Carlyon *et al.*, 2004; Cusack and Carlyon, 2003). One source of evidence comes from adaptation studies that showed a selective increase in frequency-modulation detection thresholds following adaptation with FM stimuli (e.g., Kay and Matthews, 1972; Regan and Tansley, 1979). However, the interpretation of these results has been questioned, as the adaptation effects decrease or disappear with training (Moody *et al.*, 1984) and may be partly caused by shifts in criterion (Wakefield and Viemeister, 1984).

The present study extends an approach developed by Sek and Moore (1999). They used pure-tone stimuli with an overall duration of 500 ms. The stimuli had two steady-state portions, which differed in frequency in the target stimulus, and middle sections that could consist of either a very short (5 ms) silent interval, or of linear frequency glides of varying lengths that smoothly connected the steady portions. These two conditions are similar to the ''gap'' and ''glide'' conditions shown in Fig. 1(a). They found that, for some durations of the middle section, thresholds were significantly lower in the glide than in the gap condition. Because this finding would not be predicted by a ''snapshot'' hypothesis, they concluded that there were different mechanisms for the detection of differences in frequency between steady tones and for detecting frequency glides. They were able to fit their data very well using a model based on the assumption that information was combined from two mechanisms: one sensitive to frequency glides and one sensitive to differences in frequency between steady-state portions. Here, we extend the work of Sek and Moore by including extra conditions, which

[a]Electronic mail: johannes.lyzenga@mrc-cbu.cam.ac.uk

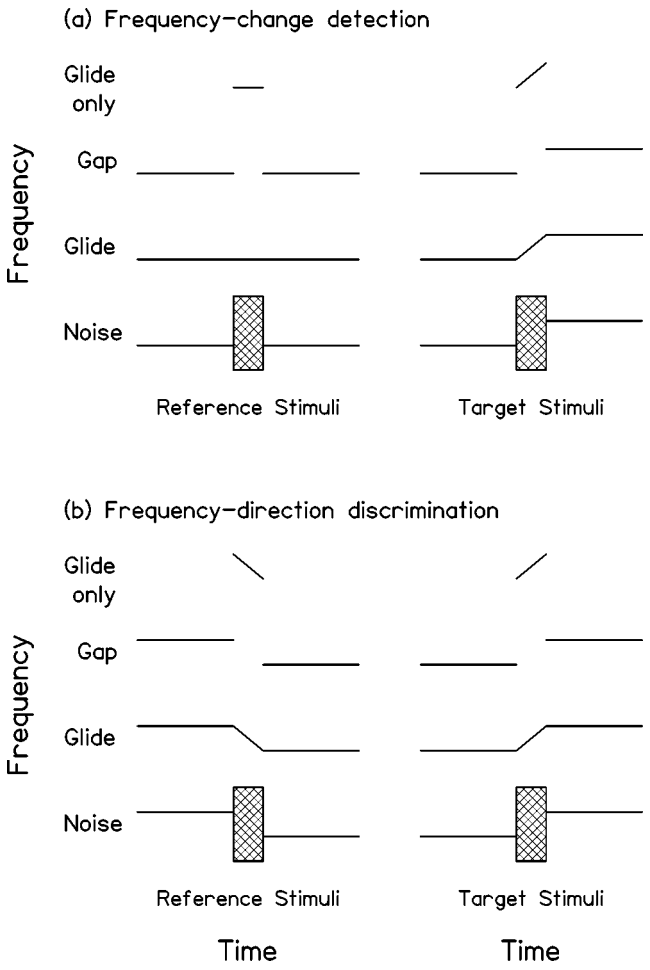

FIG. 1. Schematic spectrograms for the different stimulus conditions. The top panel illustrates the frequency-change detection task, and the bottom panel illustrates the frequency-direction discrimination task. The reference stimuli are shown on the left side, and the target stimuli on the right, of each panel.

allows us to make a direct comparison between thresholds for dynamic and static frequency changes and the combination of the two.

A further topic addressed in the present study concerns the direction sensitivity of the supposed mechanism for the detection of frequency changes. Gardner and Wilson (1979) argued for the existence of direction-specific channels in the perception of frequency sweeps on the basis of the reduction of the sensitivity of these channels produced by preceding sweeps. However, Wakefield and Viemeister (1984) argued that the results of Gardner and Wilson were caused by effects of the measurement procedure and did not provide conclusive proof for the existence of direction-specific channels in the auditory system. For intensity changes (brief increments or decrements), human listeners can detect the changes much better than they can discriminate the direction of the changes (Macmillan, 1971, 1973; Hafter *et al.*, 1996). This suggests that, for intensity changes, there is a mechanism that is sensitive to change *per se*, but not to the direction of change. Returning to frequency changes, Gordon and Poeppel (2002) measured the detection of very rapid upward and downward frequency modulations, and found that listeners were much better at detecting upward than downward changes. They suggested a possible explanation for this asymmetry based on the idea of a single neural change detector in combination with the temporal delays imposed by the traveling wave in the cochlea. In the present study we make a comparison between the detection of frequency changes and discrimination of the direction of frequency changes. This was intended to allow us to assess whether the hypothetical change-detection mechanism for frequency is sensitive to the direction of the frequency change.

The final question addressed in this paper concerns the continuity illusion (Miller, 1947; Thurlow, 1957; Houtgast, 1972; Warren *et al.*, 1972, 1988; Pollack, 1977; Bregman, 1990; Kluender and Jenison, 1992). When a short section of a stimulus is replaced by a noise or other sound, listeners often experience that stimulus as unbroken. Most behavioral studies addressing this continuity illusion provided subjective reports of the phenomenon. However, more recently, a few psychoacoustic studies have used performance measures (Plack and White, 2000; Carlyon *et al.*, 2002). For example, Plack and White (2000) measured fundamental frequency difference limens (DLs) for groups of unresolved harmonics that were either 40-ms long or consisted of two 20-ms portions separated by a brief gap. They found that DLs were higher in the latter condition, but dropped when the silent gap was filled by a noise burst that induced the illusion of continuity. In that condition, each interval consisted of two tones of the same fundamental frequency with the gap within each interval filled by noise. Here, we examine whether the continuity illusion can aid performance when a noise fills the gap between two pure tones with a small frequency difference, leading to the perception of an illusory glide [see Fig. 1(a), noise condition].

II. STIMULI AND METHODS

A. Detection and discrimination of frequency changes

The stimuli were pure tones with nominal frequencies of 1 and 4 kHz. They consisted of two tone bursts surrounding a middle section that could vary in nature. The frequency was kept fixed during the bursts and, in the case of the target stimulus, it was higher in the second than in the first burst. The middle section of the stimulus could contain either a silent period (the ''gap'' condition), a frequency glide that made a smooth connection between the two tone bursts (the ''glide'' condition), or a noise burst (the ''noise'' condition). These were the three main conditions used in the two experiments. In a fourth condition only a gliding middle section was used (the ''glide only'' condition). Figures 1(a) and 1(b) give an overview of the stimulus spectra and types used in the change-detection (experiment 1) and direction-discrimination (experiment 2) conditions. All start and end points of the stimuli had 5-ms ramps, shaped with a half-cycle of a raised-cosine function. In conditions gap and noise, this also applied to the steady portions of the stimulus surrounding the middle portion. In the special case when the middle-section duration was 0 ms (see below for details), the ramps of the signal on either side of the middle portion were separated by 0 ms. Thus, the envelope had a dip lasting 10

ms between the full-amplitude points and 5 ms between the half-amplitude points. In the noise condition, the noise bursts also had 5-ms raised-cosine ramps, which overlapped with the ramps of the sinusoid. Thus, when the middle-section duration was 0 ms, the noise burst consisted only of the ramps, with no steady-state portion.

In one set of conditions, the overall length of the stimuli was kept fixed at 500 ms, including the ramps, while the duration of the middle section was 0, 10, 50, 200, or 500 ms; the last stimulus consisted of just a frequency glide without steady-state portions. In a second set of conditions, the duration of the middle section was fixed at 50 ms, and the duration of the leading and trailing steady-state portions was 0, 20, 50, 100, or 200 ms. For the gap and noise conditions, the durations of the steady portions include 5-ms ramps at both onset and offset of the portions, except for the duration of 0 ms, for which there were no steady portions. For the glide condition, ramps were applied only to the start of the first steady portion, and the end of the last steady portion.

In all conditions, the overall frequency was roved within trials to force subjects to use the change within the target stimulus, rather than, for example, to compare the end frequency of the target with that of the standard. To achieve this, the stimuli were constructed for eleven logarithmically spaced frequencies between 806 and 1239 Hz, or between 3226 and 4960 Hz. The size of the rove was approximately equal to an amount equal to four times the ''normal'' equivalent rectangular bandwidth of an auditory filter centered on the nominal frequency of the standard (Glasberg and Moore, 1990). For each trial, a reference tone and a target were chosen randomly from this set using a rectangular distribution. With the rove, the set of signals used for the determination of one detection or discrimination threshold consisted of a reference sound with one of the eleven roving center frequencies, and 23 targets with an increasing frequency difference between the two steady-state portions (making $11 \times 23 = 253$ stimuli). The frequency difference ranged from 0.0221% to 45.3% in 22 steps of a factor $\sqrt{2}$, giving a large frequency range with a small step size.

The signal levels were set to 50 dB SPL for the 1-kHz tones and to 51 dB SPL for the 4-kHz tones. These corresponded to average sensation levels of 48 and 54 dB for the 1- and 4-kHz stimuli, respectively. Spectral splatter can occur in the transition from a steady frequency to a glide, or *vice versa*. To mask such splatter, a low-level pink background noise was present during all measurements with a spectral level of 10 dB (*re* 20 μPa) at 1 kHz. Detection thresholds in the noise showed the signal levels to correspond to average sensation levels of 34 and 43 dB, respectively. The noise bursts used in the noise condition were band-pass filtered between 500 and 2500 Hz for the 1-kHz stimuli and between 2 and 10 kHz for the 4-kHz stimuli (see below); the overall noise levels were 72 dB SPL and 64 dB SPL, respectively. The choice of noise levels is discussed in the following section.

The stimulus waveforms were computed digitally offline with 16-bit resolution on a PC and stored on disk. 24 exemplars of each noise burst were generated and stored on disk. When needed in the measurements, one of these noise bursts was picked randomly and added to the tonal stimulus parts. In the experiments, the stimulus waveforms were retrieved by a PC and converted to analog signals using a 16-bit DAC (CED 1401 plus) at a sample rate of 44.1 kHz. The waveforms were low-pass filtered at 17.2 kHz (3-dB-down point, Kemo VBF/25.01, slope = 100 dB/oct). Attenuation and mixing were performed by computer-controlled attenuators and mixers (Tucker-Davis Technologies PA4 and SM3). The noise bands were band-pass filtered to the desired bandwidth (Kemo VBF/25.03, slope = 48 dB/oct). All stimuli were presented through Sennheiser HD250 Linear 2 headphones. Stimuli were checked using a Hewlett-Packard 3561A spectrum analyzer.

An adaptive procedure was used to measure change-detection thresholds (experiment 1) and direction-discrimination thresholds (experiment 2). We used a two-interval, two-alternative forced-choice (2I, 2AFC) paradigm and a two-down one-up stepping rule (Levitt, 1971). Each estimation was terminated after 16 reversals of the up–down direction. For the change-detection task, the target stimulus contained an upward frequency change, while the reference stimulus did not change in frequency. For the direction-discrimination task, the target stimulus contained an upward frequency change, and the reference stimulus a downward frequency change of equal magnitude; both were adaptively changed. For each task, Fig. 1 shows examples of stimulus sequences (the second interval is the signal interval). The inter-stimulus interval was 400 ms. Subjects were asked to identify the tone with the upward change in frequency. Immediate feedback was given. Four subjects (including the first author) with copious experience in this type of experiment, and ages ranging from 25 to 41, participated for the 4-kHz stimuli. One of those subjects (age 25) was not available for the 1-kHz conditions and was replaced by two less experienced subjects, aged 34 and 35 years. All subjects listened through their right ear and had normal absolute thresholds (better than 20 dB HL) at the audiometric frequencies in that ear. Depending on their familiarity with such threshold measurements, subjects performed all conditions three or four times in a blocked fashion with reversed stimulus-condition order in consecutive blocks. After these blocks, the scores for each stimulus were checked for consistency and, where the thresholds showed a spread greater than a factor of two, one or more additional estimations were made. A small proportion (98 of 2012) of runs gave estimates that were more than a factor of four away from the other estimates (or a factor of 5.6 for the direction-discrimination task), or ended prematurely (if subjects made three consecutive errors for the largest possible frequency change; this only happened for the shortest stimuli in the glide-only condition), and were discarded. For each subject, the percent correct, $p(c)$, as a function of the frequency difference (ΔF) was estimated by averaging the scores for each target frequency difference for which they produced responses. Under the assumption of proportionality between ΔF and detectability index d' (Hartmann and Klein, 1980; Nelson and Freyman, 1986), the ratio between ΔF and d' can be estimated by finding the least-squares fit of the $p(c)$ versus ΔF data to the theoretical curve of $p(c)$ versus d' [$p(c) = \Phi(d'/\sqrt{2})$, where Φ is the

TABLE I. Thresholds for detecting the presence of glides during the noise bursts in the middle sections of the stimuli for four different lengths of the middle sections. Thresholds have been averaged over five subjects for the 1-kHz condition and over four subjects for the 4-kHz condition. They are given as broadband signal-to-noise ratios (SNR) in dB. The noise was filtered between 0.5 and 2.5 kHz for the 1-kHz center frequency and between 2 and 10 kHz for the 4-kHz center frequency. The SNR used in the main experiments is given in the right-most column.

Middle section:	0 ms	10 ms	50 ms	200 ms	SNR during main exp.
Freq.=1 kHz	19.0	12.2	−0.7	−6.2	−22.0
Freq.=4 kHz	15.4	5.2	−4.7	−5.8	−13.0

cumulative Gaussian probability density]. The resulting ratio between the frequency difference and d' represents a threshold that corresponds to a d' of 1.0. Thresholds estimated by averaging the turn points would correspond to a d' of 0.78, so that method would give slightly lower values than those shown in Figs. 2–8.

B. The continuity illusion

In this section we describe how we selected the levels of the noise bursts to be used in the noise conditions of experiments 1 and 2. Recall that this noise was intended to produce the continuity illusion such that the steady-state start and end sections were heard as ''glued'' together into a continuous tone.

First, we performed a detection experiment in which listeners had to discriminate between tones that had a gap filled with a noise burst and tones having a glide through the noise burst. These thresholds were measured for all subjects participating in the main experiments, using an adaptive two-interval, two-alternative forced-choice paradigm (two-down one-up stepping rule, 1-dB level steps, 16 reversals) in which the level of the tones was varied. The average thresholds, expressed as the ratio of signal level to overall noise level, are given in Table I. They are all above the signal-to-noise ratios used in the experiments, indicating that the subjects would have been unable to hear the difference between a continuous tone with a noise burst superimposed on it and a tone with a gap filled by a noise burst.

As a check, a subjective evaluation of the perceived continuity was made after the experiment proper, by requiring a continuous *versus* noncontinuous judgment using different levels of the noise burst for blocks of stimuli from the noise condition, with a 500-ms overall duration and 0-, 10-, 50-, and 200-ms middle sections. For each noise level, subjects listened to three repetitions of the stimuli (containing six steady-state portions that were spaced evenly in time) including three noise bursts and indicated whether they heard three or six tones in that whole stimulus. These judgments were performed for stimuli with a fixed frequency of either 1 or 4 kHz, and for stimuli with frequency increases that were approximately double the detection thresholds. The signal levels were set to 40 dB SPL for the 1-kHz tones and to 41 dB SPL for the 4-kHz tones. In the first block, the starting level of the noise was high and subsequently decreased in steps of 3 dB to a very low level, after which the noise level was increased back to the starting level using 3-dB steps. After such a block, a subsequent block was run in the opposite direction. This sequence was then repeated to produce a total of eight judgments for each stimulus. Four out of the total number of six subjects participated in these experiments. The number of perceived tones was averaged across subjects for each noise level to give average psychometric functions. The 50-percent points of those curves were taken as the thresholds of continuity. The results of these measurements are given in Table II. They show that the signal-to-noise ratios necessary for a percept of continuity were smaller than those used in the discrimination experiments. So, for the ratios used, these four subjects will have perceived most of the stimuli as continuous, although perceived continuity was somewhat weaker for the 4-kHz stimuli with a 0-ms middle section.

III. RESULTS OF EXPERIMENT 1: FREQUENCY-CHANGE DETECTION

A. Fixed 500-ms overall duration

DLs for the detection of frequency change (experiment 1) are shown in Fig. 2, for the set of conditions where the overall duration was fixed at 500 ms. The abscissa shows the duration of the middle section, and the ordinate gives the DL as a percentage of the center frequency; this was 1 kHz for panel (a) and 4 kHz for panel (b). For both center frequencies, the thresholds for the glide-only condition without the steady-state portions (filled diamonds) rise dramatically with decreasing glide duration, which is consistent with the results of Sergeant and Harris (1962); they found a linear decrease in detection threshold with the logarithm of the glide length. In contrast, the thresholds for the conditions with the steady-state sections rise slightly with increasing middle-section duration, which is consistent with the results of Tsumara *et al.*

TABLE II. Thresholds of subjective continuity derived from the 50% points of the psychometric functions averaged across four subjects. Thresholds are presented as broad-band SNRs, where the noise was band-pass filtered between 0.5 and 2.5 kHz for the 1-kHz center frequency and between 2 and 10 kHz for the 4-kHz center frequency. Results are shown for stimuli with and without an increase in frequency during the middle section. The corresponding SNRs used in the main experiments are given in the third row for the 1-kHz stimuli and in the bottom row for the 4-kHz stimuli.

Middle section:	0 ms	10 ms	50 ms	200 ms
Freq.=1 kHz, steady freq.	−0.2	1.0	−0.3	−3.2
Freq.=1 kHz, gliding freq.	−2.8	1.0	0.0	−2.1
SNR during main exp.	−22.0	−22.0	−22.0	−22.0
Freq.=4 kHz, steady freq.	−11.0	−4.5	−4.8	−7.0
Freq.=4 kHz, gliding freq.	−3.4	−2.8	−0.6	−2.0
SNR during main exp.	−13.0	−13.0	−13.0	−13.0

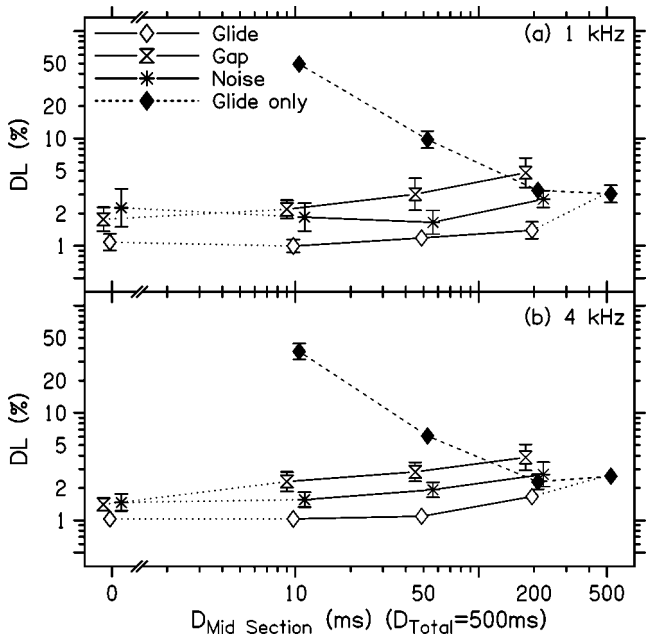

FIG. 2. Frequency-change detection thresholds for the stimuli with an overall duration of 500-ms for the conditions: glide (open diamonds), gap (hour-glass symbols), noise (asterisks), and glide only (filled diamonds). The top and bottom panels show the data for the 1- and the 4-kHz stimuli, respectively. Thresholds are expressed in percent, and they are plotted as a function of the middle-section duration. To prevent symbols from overlapping, the thresholds for the different conditions are plotted with small horizontal offsets. The error bars indicate the across-subject standard errors.

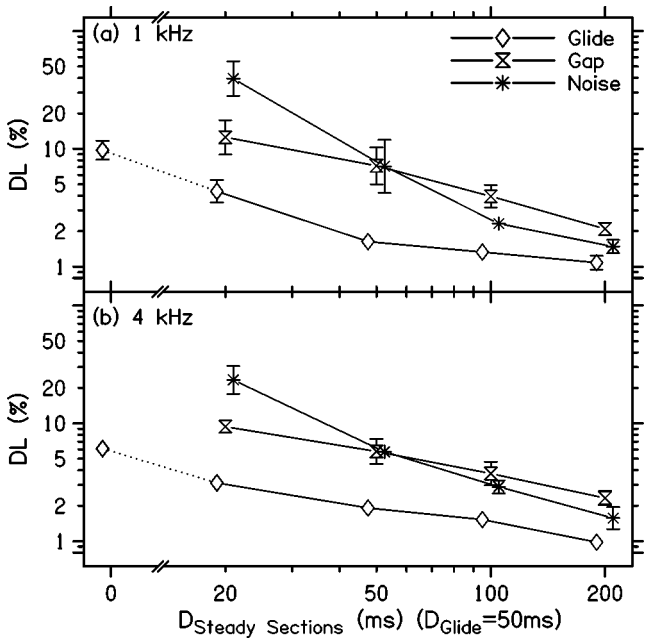

FIG. 3. The same as Fig. 2, but for the stimuli with a fixed middle-section duration of 50 ms. Thresholds are plotted as a function of the steady-state duration. The glide-only condition is represented by the open diamond at the steady-state duration of 0 ms.

(1973); they found a very similar pattern for stimuli with an overall duration of 302 ms, which were split up into a number of different steady-state and glide durations. In our data, even the smallest thresholds for the glide-only condition, observed for the longer glide durations (200 and 500 ms), are consistently larger than those found for stimuli with both a glide and steady-state portions (open diamonds: glide condition, middle-section durations of 10, 50, 200 ms). The thresholds for the gap condition (hour-glass symbols) are also consistently higher than those for the glide condition (open diamonds). These two aspects of the data are consistent with the idea that the auditory system combines information from the glides and the steady-state portions, as suggested by Sek and Moore (1999). For the middle-section durations of 10, 50, and 200 ms, the thresholds are consistently lower for the glide (open diamonds) than for the noise condition (asterisks), which in turn are consistently lower than those for the gap condition (hour-glass symbols). Such a difference is not seen for the discontinuous 0-ms middle-section duration, where the instantaneous frequency jumped abruptly between the first and the second steady-state portions of the stimuli. That thresholds are consistently lower for the noise than for the gap condition indicates an effect of the continuity illusion on the frequency DLs that is similar to, but somewhat smaller in size than, that of the gliding middle sections.

To assess the statistical significance of these effects, a repeated-measures analysis of variance (ANOVA) was conducted with factors condition (gap, glide, and noise) and middle-section duration (10, 50, and 200 ms). For each subject the last four measurements for each condition (using the average of the last twelve turning points as threshold) were used in the ANOVA, with the exception of one subject (first author) for the 1-kHz stimuli for whom only three runs were obtained. This was done separately for the two center frequencies. To make the variance more uniform across conditions, the ANOVAs were performed on the logarithms of the DLs. Both ANOVAs showed strong effects of condition and middle-section duration: for condition at 1 kHz, $F(2,36) = 38.5$, $p < 0.001$; for condition at 4 kHz, $F(2,30) = 21.5$, $p < 0.001$; for duration at 1 kHz, $F(2,36) = 17.8$, $p < 0.001$; for duration at 4 kHz, $F(2,30) = 20.0$, $p < 0.001$. Post-hoc tests showed that the means for all three conditions were significantly different from each other after Bonferroni correction (For gap and glide at 1 kHz and 4 kHz; $p < 0.001$. For gap and noise at 1 and 4 kHz, $p < 0.02$. For noise and glide: at 1 kHz, $p < 0.001$; at 4 kHz, $p < 0.05$.). In summary, the results showed that, relative to the gap condition, performance was significantly improved by the presence of a real or illusory glide, at both 1 and 4 kHz.

B. Fixed 50-ms middle-section duration

Figure 3 shows the thresholds obtained with the middle-section duration fixed at 50 ms, as a function of the duration of the steady-state sections. For both center frequencies, thresholds for all conditions decrease with increasing steady-state duration. In both panels, the thresholds for the glide condition (open diamonds) are highest for the 0-ms steady-state stimuli that contain only the 50-ms frequency glides. Also, the thresholds for the gap condition (hour-glass symbols) are always above the corresponding ones for the glide condition. These findings corroborate our earlier conclusion based on results for the 500-ms stimuli, that subjects can combine information from the frequency glides and the

steady-state portions to reduce thresholds for the combined (glide) condition. The thresholds for the noise condition (asterisks) decrease more steeply with increasing steady-state duration than do those for the gap and the glide condition. The thresholds for the noise condition drop below those for the gap condition for the longer durations of the steady-state sections (100 and 200 ms), confirming the effect of the continuity illusion, as found for the 500-ms stimuli, for these longer steady-state durations. For the short steady-state durations, the noise seems to have no effect (50 ms), or even a detrimental effect (20 ms). This implies that the steady-state sections need to have a minimum length before any positive effect of an illusion of the tone continuing through the noise occurs. This effect may also be partly explained by the noise burst producing backward and forward masking of the first and second steady-state portions, respectively.

To assess the statistical significance of these effects, a repeated-measures ANOVA was conducted on the logarithms of the DLs with factors condition (gap, glide, and noise) and steady-state duration, initially considering only the data for the two longest steady-state durations (100 and 200 ms). This was done separately for the two center frequencies. For each subject, the last four measurements for each condition were used in the ANOVA (the last three for the first author). These ANOVAs showed effects of both condition [at 1 kHz, $F(2,36)=29.4$, $p<0.001$; at 4 kHz, $F(2,28)=20.4$, $p<0.001$] and steady-state duration [at 1 kHz, $F(1,18)=16.5$, $p\leqslant 0.001$; at 4 kHz, $F(1,14)=28.3$, $p<0.001$]. Post-hoc tests showed that the means for the gap, glide, and noise conditions were all significantly different from each other after Bonferroni correction (gap and glide at 1 and 4 kHz, $p<0.001$. Gap and noise at 1 and 4 kHz, $p<0.05$. Noise and glide: at 1 kHz, $p<0.001$; at 4 kHz, $p<0.02$). These outcomes show that both the real and illusory glides led to better performance than for the gap condition, for the two longest steady-state durations.

Separate 2×4 repeated-measures ANOVAs were conducted for the gap and noise conditions, including the steady-state durations of 20, 50, 100, and 200 ms. These showed a highly significant effect of duration [at 1 kHz, $F(3,54)=122.6$, $p<0.001$; at 4 kHz, $F(4,42)=104.0$, $p<0.001$] and significant interactions between condition and steady-state duration [at 1 kHz, $F(3,54)=9.85$, $p<0.001$; at 4 kHz, $F(3,42)=16.4$, $p<0.001$], confirming the steeper slope for the noise than for the gap condition as functions of the steady-state duration. This indicates that the noise bursts are detrimental for short steady-state sections but beneficial when the continuity illusion occurs for the longer steady-state durations.

IV. RESULTS OF EXPERIMENT 2: DIRECTION DISCRIMINATION

The results of the second experiment, for the direction-discrimination task, are shown in Figs. 4 and 5 for both the 1- and the 4-kHz stimuli. The format of these figures is the same as for Figs. 2 and 3.

Figure 4 shows, for both center frequencies, that the thresholds for the glide-only condition rise dramatically with decreasing glide duration. The remaining conditions show

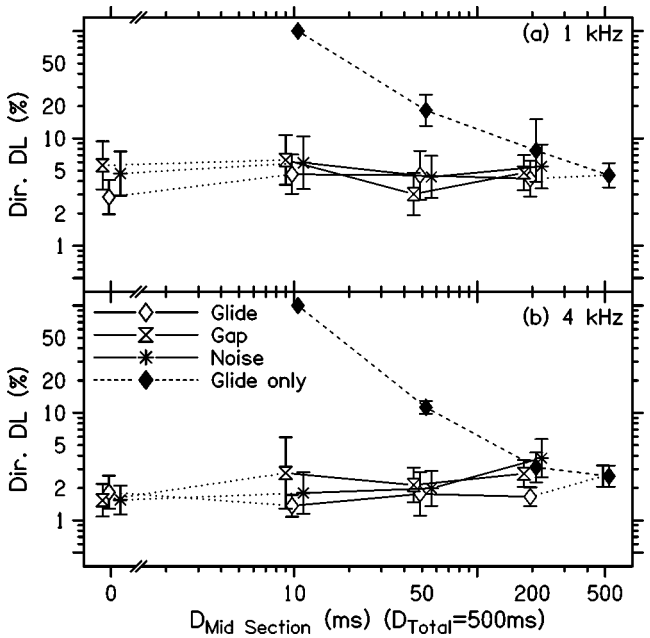

FIG. 4. The same as Fig. 2, but for the frequency-direction discrimination task. These thresholds express the amount of frequency change in the target which was just discriminable from the opposite change in the reference stimuli. The values of these thresholds represent the amount of change in the target stimuli.

almost no effect of glide duration, and do not differ markedly between each other. Similar 3×3 repeated-measures ANOVAs as for the change-detection data were performed. For the center frequency of 1 kHz, neither the effect of the middle-section duration nor that of the condition was significant. At 4 kHz, the effect of the middle-section duration for the 4-kHz stimuli was small, but significant [$F(2,28)=12.7$, $p<0.001$]—presumably because the pattern of results was very consistent across listeners. The mean DLs increased slightly with increasing steady-state duration. In

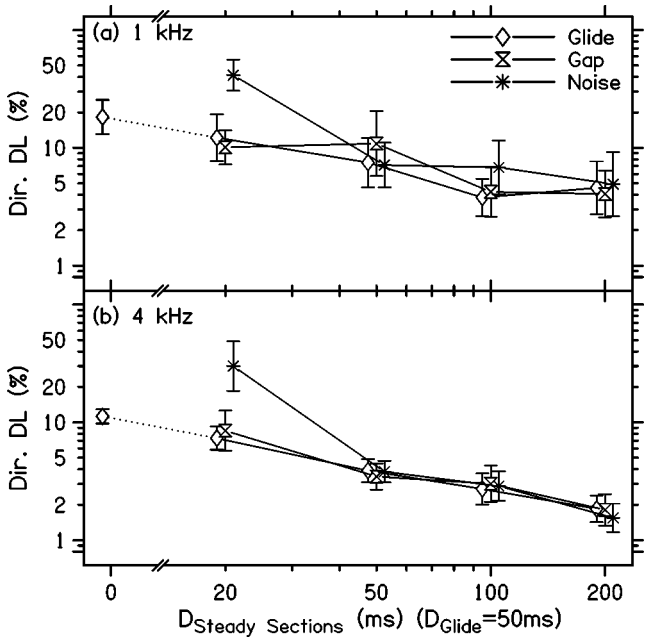

FIG. 5. The same as Fig. 3, but for the frequency-direction discrimination task.

addition, the effect of condition just reached significance at 4 kHz [$F(2,28)=5.28, p<0.05$]. Post-hoc comparisons revealed that thresholds for the glide condition were significantly lower than those for the gap condition ($p<0.05$). However, a comparison with Fig. 2 shows that this effect was much less clear than for the change-detection task of experiment 1.

Figure 5 shows results with the 50-ms middle section. For steady-state durations of 50 ms or more, there are no consistent differences between thresholds for the gap, glide, and noise conditions. However, for the 20-ms steady-state duration, the performance was consistently worse for the noise condition than for the other conditions. ANOVAs were conducted for the two longer steady-state durations, as in the earlier analyses of the change-detection data. The results showed significant effects of steady-state duration [1 kHz, $F(1,18)=5.42$, $p<0.05$; 4 kHz $F(1,14)=23.7$, $p<0.001$], but not of the condition. Overall, the results suggest that real or illusory glides were of little or no benefit in the direction-discrimination task.

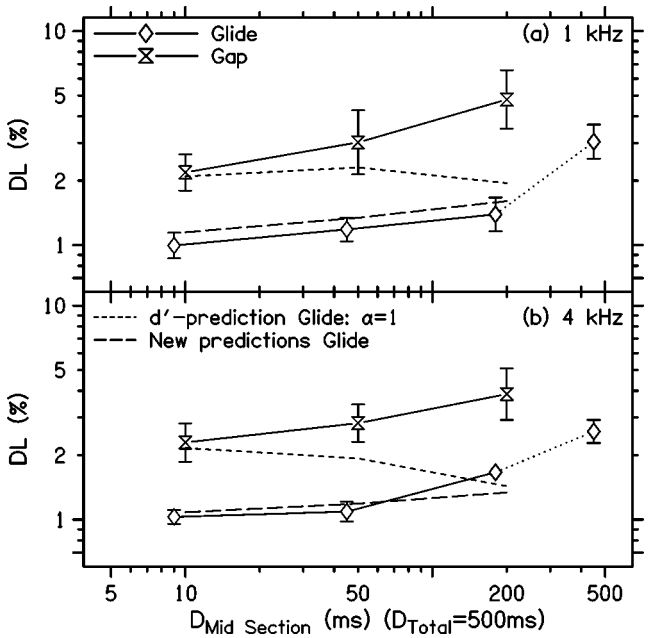

FIG. 6. A comparison of obtained and predicted results for experiment 1, for the stimuli with an overall duration of 500-ms. The top and bottom panels reproduce the frequency-change detection thresholds for the 1- and 4-kHz stimuli, respectively. The short-dashed lines show predictions for the glide condition based on thresholds for the gap and the glide-only conditions. The long-dashed lines show the predictions of a model based on the data for the gap condition, assuming a fixed contribution from the glide.

V. DISCUSSION

A. Predicting thresholds for the change-detection task

The results of experiment 1 showed that, for many conditions, listeners were better at detecting a frequency difference between two steady tones when they were joined by a glide than when they were separated by a silent interval, consistent with the findings of Sek and Moore (1999). This effect occurred for glide durations between 10 and 200 ms (Fig. 2), provided that the steady-state duration was at least 100 ms (Fig. 3). Interestingly, the advantage of introducing the glide occurred even for short glide durations, for which thresholds in the glide-alone condition were very high (Fig. 2). This leads one to suspect that the mechanisms involved in processing the gliding and steady-state portions operate in a synergistic way: the glide is poorly detected on its own, but aids the detection of differences between two steady-state portions. To evaluate this idea, we have used the thresholds for the gap and glide-only conditions to calculate predictions for the thresholds in the glide condition.

The information from the steady and gliding parts of the stimuli can be combined according to

$$(d'_{\text{glide}})^{\alpha}=(d'_{\text{gap}})^{\alpha}+(d'_{\text{glinde only}})^{\alpha}. \quad (1)$$

As Sek and Moore (1999) pointed out, an exponent, α, of two corresponds to the predictions of signal detection theory if performance is limited by two independent sources of noise: one for each mechanism. An exponent of unity represents the prediction if performance is limited by a common internal noise which occurs after the information from the two sources has been combined. Intermediate values of the exponent represent the case where the noise is partly independent and partly common.

Under the assumption that d' for a given source of information is directly proportional to ΔF (Nelson and Freyman, 1986), the d' value for a given value of ΔF is equal to $(\Delta F)/\Delta F_{\text{thr}}$, where ΔF_{thr} is the value of ΔF at threshold, corresponding to $d'=1$. Equation (1) can thus be written as

$$(d'_{\text{glide}})^{\alpha}=((\Delta F_{\text{gap}})/\Delta F_{\text{thr gap}})^{\alpha} + ((\Delta F_{\text{glide only}})/\Delta F_{\text{thr glide only}})^{\alpha}. \quad (2)$$

For the glide condition, ΔF_{gap} is equal to $\Delta F_{\text{glide only}}$, and, when $d'=1$ in the glide condition, both of these are equal to $\Delta F_{\text{thr glide}}$. Using this information, Eq. (2) can be rewritten as

$$(1/\Delta F_{\text{thr glide}})=\{(1/\Delta F_{\text{thr gap}})^{\alpha}+(1/\Delta F_{\text{thr glide only}})^{\alpha}\}^{1/\alpha}. \quad (3)$$

Because we were interested in whether there was any threshold reduction greater than that predicted by this class of model, we calculated thresholds with an α of unity, which leads to substantially lower predicted thresholds than for an α of two. These predictions are shown by the short-dashed lines in Fig. 6, along with the data re-plotted from Fig. 2. For the 10- and 50-ms middle sections, the predicted thresholds are substantially higher than the obtained thresholds (diamonds). This is consistent with a synergistic combination of the steady-state and gliding portions. A similar effect is apparent in Fig. 7, which compares the predictions of the model to the observed effects of varying the steady-state duration, re-plotted from Fig. 3. In addition, it can be seen that, for the glide condition, the steep decrease in thresholds with an increasing steady-state duration from 20 to 50 ms is not reflected in the predictions, which show a more gradual decline. This means that the contribution of the glide is larger for the longer steady-state durations, implying greater perceptual effects when glides are ''assisted'' by bordering

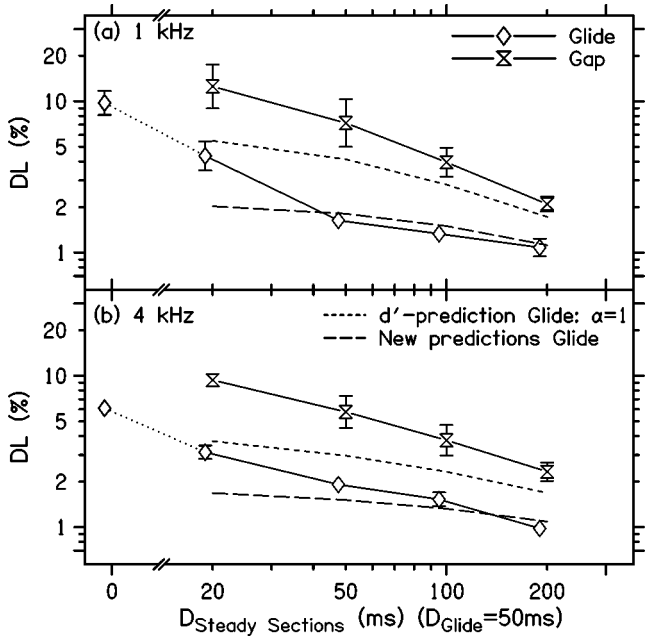

FIG. 7. The same as Fig. 6, but for the stimuli of experiment 1 with a fixed 50-ms steady-state duration.

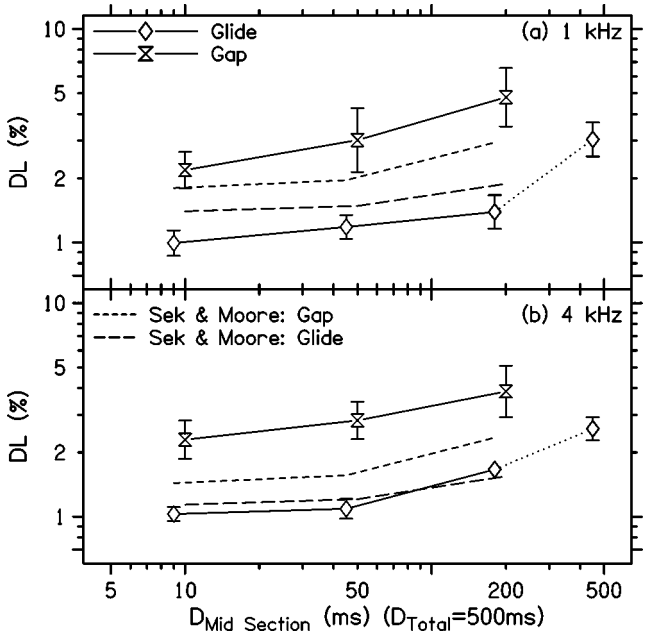

FIG. 8. A comparison of obtained and predicted results for experiment 1, for the 500-ms stimuli. The structure of this figure is the same as for Fig. 6. The long- and short-dashed lines show the predictions of the model of Sek and Moore (1999) for the glide and gap conditions, respectively.

steady-state sections. This is in agreement with the findings of Sergeant and Harris (1962) and with our results for the glide-only condition for the 500-ms stimuli (Fig. 2), where thresholds rose sharply for the shorter glide-only durations, but a corresponding rise did not occur for the glide condition.

An alternative approach to modeling the data was adopted by Sek and Moore (1999), for stimuli with a 500-ms overall duration. In their model, the contribution produced by the glide was assumed to be independent of its duration, and was estimated from the threshold for a 500-ms glide (they did not have data for shorter glide durations in the glide-only condition). Sensitivity to the steady-state differences was estimated from threshold for the 5-ms gap (which they named the 0-ms condition), with a correction for the duration of the steady-state portions using the assumption that thresholds for shorter durations are proportional to the reciprocal of the duration. Using the assumption of a linear relation between d' and frequency difference, they subsequently combined the assumed d'-values for these conditions using Eq. (1) with a value of 1.5 for the exponent α. With this model, they were able to produce a very good fit to almost all their data points. The predictions of that model for our 500-ms stimuli for the gap and glide conditions are shown in Fig. 8 by the short and long dashes, respectively. Their model predicts a difference between thresholds in the gap and glide conditions that is much smaller than that observed.

The predictions of a new model are shown by the long dashed lines in Fig. 6. To generate these predictions, we again assumed a linear relation between d' and ΔF, and we used an α of unity (values smaller than unity would have allowed closer matches, but they would not be plausible). We also assumed that the gliding section made a fixed contribution to performance in the glide condition. However, we assumed that this contribution was actually greater than would be inferred from the threshold measured for the 500-ms glide (without steady portions). This may happen because the hypothetical change detection mechanism benefits from the steady portions on either side of the glide. The d' value for the glide was set to 1.26 times the value inferred from the 500-ms glide threshold, as this gave a good fit to the data (see below). The contribution of the steady-state portions was derived directly from the data for the gap condition. The new model produced a good fit to the data. The model also accounted well for the effects of steady-state duration with a 50-ms glide, provided that the steady-state duration was at least 50 ms. However, the model clearly underestimated thresholds for the 20-ms steady-state duration. This is not unexpected given our assumption that the change-detection mechanism is helped by steady-state portions on either side of the change; if the steady-state portions are made short enough, this benefit would be lost. Disregarding those two data points, the remaining 12 in the glide conditions could be fitted using one parameter, the ratio of 1.26 referred to above. The new model clearly produces a better correspondence between predictions and data then the model of Sek and Moore (1999), which is confirmed by a smaller root-mean-square difference between the predictions for the glide conditions and the data (0.73 for the 12 data points under consideration, as compared to 1.79 for the model of Sek and Moore).

Overall, this analysis is consistent with the idea that, in condition glide, the glides contribute a fixed amount of information, independent of the glide duration used (provided this is longer than 0 ms), except for very short steady-state durations, when the glide appears to contribute less information. In the scope of the present model, the exponent of unity indicates that the information from the glides and the steady-state portions is combined optimally in terms of d', with a

common source of internal noise occurring after the combination.

B. Continuity illusion for the change-detection task

For the change-detection task, the differences between the results for the gap and the noise conditions suggest that an illusory glide is sufficient to trigger the change-detection mechanism. To check that this was due to the continuity illusion and not just to the presence of the noise bursts, we ran a fifth condition for the 500-ms overall duration at 1 kHz, using five subjects (the four subjects from the 4-kHz conditions plus one subject from the 1-kHz conditions). In this fifth condition, a noise burst was added in the stimulus gap, but it was filtered into a remote frequency region (from 2 to 10 kHz), so a perceptual illusion of continuity would not be generated. The results for these five subjects were compared with remeasured thresholds for the original on-frequency noise condition. The latter were significantly lower than the former, implying that the spectral position of the noise bursts affected the thresholds. The significance of this effect was evaluated using a 2×3 repeated-measures ANOVA on the logarithmic transform of the data for the on- and the off-frequency noise for middle-section durations of 20, 50, and 200 ms. For each subject, the last four measurements for each condition were used in the ANOVA. As found earlier, this analysis showed a strong effect of duration [$F(2,38)=49.6$, $p<0.001$]. More importantly, it showed a significant effect of noise frequency region [$F(1,19)=5.33$, $p<0.05$], with the average thresholds for the on-frequency noise being a factor of 1.2 smaller than those for the off-frequency noise. These results support the idea that the relatively low thresholds found in experiment 1 for the noise condition were caused by the on-frequency noise producing perceived continuity of the stimuli. This in turn suggests that the combination of information from the steady portions and from the change detector occurs at a rather late point along the auditory pathway, after the illusion of continuity has been generated.

In the Introduction, we described a study of Plack and White (2000) in which they measured frequency DLs for groups of unresolved harmonics that were either 40-ms long or consisted of two 20-ms portions separated by a brief gap. They found that DLs were higher in the latter condition, but dropped when the silent gap was filled by a noise burst that induced the illusion of continuity. They argued that the perceived continuity influenced the internal, integrating, pitch-estimation process. The noise burst between the two 20-ms tone bursts prevented this integrating process from being reset in the stimulus gap, allowing the integration to carry on longer and produce a more accurate pitch estimate. It is unlikely that a similar process took place in the present study. First, thresholds in the glide condition were lower than in the gap condition by a ratio of roughly 2, which is a larger ratio than would be expected for a doubling of duration (Moore, 1973). Second, in the present experiment only the second stationary section of the target tones had the increased frequency, so a process of integration across both sections would be of no benefit. The most parsimonious explanation of the effect of the noise bands on pure-tone frequency-change detection seems to be the existence of a specific mechanism for the detection of frequency changes that responds to illusory frequency glides as well as to real ones, albeit somewhat less strongly.

C. The direction-discrimination task

The results for the direction-discrimination task did not show any substantial difference between the gap and the glide conditions. This indicates either that the frequency-change detection mechanism does not encode the direction of the change very well, or that the direction is encoded but this information is not combined effectively with the information from the steady parts of the stimulus. A possible alternative explanation is related to the spectral splatter that occurs in the transition from a steady frequency to a glide, or *vice versa*. Such splatter would only be present in the target stimulus for the detection task, but it would be present in both reference and target for the direction-discrimination task. Thus, the detection of spectral splatter could have an effect on the frequency-change detection task but not on the direction-discrimination task. To assess the amount of spectral splatter, we used an 11.6-ms segment of the signal (512 sample points) centered on the transition from the steady-state portion to the glide, or from the glide back to the steady-state portion. The segment was windowed using a Blackmann–Harris window, and a fast Fourier Transform was used to determine the spectrum. For frequency changes corresponding to the largest measured thresholds (experiment 2: 12% for the 20-ms middle-section and 50-ms steady-state duration, and 4.6% for the 10-ms middle section and 500-ms overall duration), the level of the splatter was more than 50 dB below the level of the peak in the spectrum. The relative level of the splatter was somewhat higher for the 0-ms glide condition, for which the frequency jumped abruptly from one value to another. However, the threshold was not smaller for the glide than for the gap condition for the 0-ms middle-section duration. Therefore, we consider it unlikely that the detection of spectral splatter was responsible for the different pattern of results for the change-detection and direction-discrimination tasks, especially given that a pink-noise background was used.

The most plausible explanation of our results is that the change-detection mechanism is not of much help in the task of discriminating the frequency-change direction. However, thresholds for direction-discrimination at 4 kHz were slightly lower for the glide than for the gap condition when the overall duration was fixed at 500 ms. The subjects who were tested using the 4-kHz stimuli were, on average, more experienced in pitch discrimination tasks than the subjects who were tested for the 1-kHz stimuli. Thus, it is possible that extended training may lead to an improved ability to make use of the change-detection mechanism for discriminating a frequency-change direction. However, it seems very unlikely that the improvement produced by the glide would approach that found for frequency-change detection in experiment 1. Thus, the change-detection mechanism appears to be much more effective in the detection of changes than in indicating their direction.

There is some other evidence consistent with the idea that the activation of a change detector can aid performance in a forced-choice experiment. Cusack and Carlyon (2003) measured frequency-modulation (FM) detection performance, using a three-interval two-alternative forced-choice procedure. When two of the (sequentially presented) sounds were steady and the target was modulated, performance was substantially better than when there were two modulated standards and a single, steady, target. They concluded that the dynamic frequency change helped the modulated target to ''pop out'' from the steady distracters. This interpretation was supported by an experiment showing that listeners were better at detecting a FM tone against a background of steady-state distracters, distributed quasi-randomly in frequency and time, than *vice versa*. Change detectors could also help account for the ''transient masking'' phenomenon reported by Bacon and Moore (1987). They showed that the detection of a brief tone presented in the middle of a higher-frequency masker could be disrupted by a brief low-level remote-frequency tone, gated on and off in the intervals in which the signal might occur. In this case, the change detector would be activated in both intervals, rather than just the one in which the signal occurred.

The basic idea of a general change detector is consistent with several aspects of the results presented here. First, the analysis described above indicates that the ''added value'' of the glide was independent of its duration. This would be expected if the detector was activated by *any* change. Second, thresholds in the glide-only condition of experiment 1 increased markedly with decreasing duration. At short durations, the onsets and offsets of the tone would activate change detectors close in time to the portion potentially containing the glide, even when the tone was steady. Hence a mechanism which simply detected any change would not discriminate between the standard and signal. Third, the glide aided performance in experiment 1, even for short middle-section durations, at which thresholds in the glide-only condition were very high. This could have happened because, in the glide condition, the presence of the steady-state sections meant that no ''distracting'' onsets and offsets occurred immediately adjacent to the glide. Finally, there was little or no difference between the gap and glide conditions of experiment 2. This would be expected, because in a frequency-direction discrimination task, the dynamic portion would be present in *both* intervals of each trial, thereby activating a change detector in both intervals. If this interpretation is correct, it has two interesting implications. First, the ''glide specific'' mechanism proposed by Sek and Moore may actually form part of a more general mechanism, that is also sensitive to other kinds of change. Second, as discussed below, the present results indicate that this change detector must operate at a stage after that at which the continuity illusion occurs.

The concept of a change detector that is insensitive to the direction of change has been proposed previously by Macmillan (1971, 1973) for intensity changes. His evidence for such a detector came from comparisons of performance for detecting a change in level of a continuous tone and for recognizing whether the change was an increment or decrement in level. He found that detection performance was generally better than recognition performance, especially for short durations of the increment/decrement. Also, detection performance improved less with increasing duration than recognition performance. Results supporting the idea of a change detector have also been presented by Hafter *et al.* (1996). Thus, it may be the case that change detectors exist for both intensity and frequency, or that there is a more general mechanism which responds to any kind of change, but is relatively insensitive to its direction.

VI. CONCLUSIONS

For stimuli with two portions of steady frequency connected by a frequency glide, the auditory system appears to be able to combine information from the steady parts and from the glide in a synergistic way to produce relatively small frequency-change detection thresholds. When detecting a frequency glide, we appear to use a specific change-detection mechanism, whose operation is facilitated by the steady-state portions on either side of the glide. For stimuli with the glides replaced by gaps, the presentation of noise bursts in the gaps reduced frequency-change detection thresholds, suggesting that an illusory glide can trigger the change-detection mechanism. However, the change-detection mechanism appears to be of little help in discriminating the direction of a frequency change.

ACKNOWLEDGMENTS

This research was supported by Grant No. GR/N64861/01 from the (British) Engineering and Physical Sciences Research Council. The authors would like to thank Chris Plack, Neal Viemeister, and an anonymous reviewer for their helpful comments on the paper.

Bregman, A. S. (**1990**). *Auditory Scene Analysis* (MIT Press, Cambridge, MA).

Bacon, S. P., and Moore, B. C. J. (**1987**). ''Transient masking and the temporal course of simultaneous tone-on-tone masking,'' J. Acoust. Soc. Am. **81**, 1073–1077.

Carlyon, R. P., Micheyl, C., and Deeks, J. (**2004**). ''Coding of FM and the continuity illusion,'' to appear in *Auditory Signal Processing: Physiology, Psychoacoustics, and Models*, edited by D. Pressnitzer, A. de Cheveigné, S McAdams, and L. Collet (Springer-Verlag, New York).

Carlyon, R. P., Deeks, J., Norris, D., and Butterfield, S. (**2002**). ''The continuity illusion and vowel identification,'' Acust. Acta Acust. **88**, 408–415.

Cusack, R., and Carlyon, R. P. (**2003**). ''Perceptual asymmetries in audition,'' J. Exp. Psychol. Hum. Percept. Perform. **26**, 713–725.

Demany, L., and Semal, C. (**1989**). ''Detection thresholds for sinusoidal frequency modulation,'' J. Acoust. Soc. Am. **85**, 1295–1301.

Dooley, G. J., and Moore, B. C. J. (**1988**). ''Duration discrimination of steady and gliding tones: a new method for estimating sensitivity to rate of change,'' J. Acoust. Soc. Am. **84**, 1332–1337.

Gardner, R. B., and Wilson, J. P. (**1979**). ''Evidence for direction-specific channels in the processing of frequency modulation,'' J. Acoust. Soc. Am. **66**, 704–709.

Glasberg, B. R., and Moore, B. C. J. (**1990**). ''Derivation of auditory filter shapes from notched-noise data,'' Hear. Res. **47**, 103–138.

Gordon, M., and Poeppel, D. (**2002**). ''Inequality in identification of direction of frequency change (up vs. down) for rapid frequency modulated sweeps,'' Acoust. Lett. **3**, 29–34.

Hafter, E. R., Bonnel, A. M., and Gallun, E. J. (**1996**). ''Detection of change without regard to its valence,'' J. Acoust. Soc. Am. **99**, 2541.

Hartmann, W. M., and Klein, M. A. (**1980**). ''Theory of frequency modulation detection for low modulation frequencies,'' J. Acoust. Soc. Am. **67**, 935–946.
Houtgast, T. (**1972**). ''Psychophysical evidence for lateral inhibition in hearing,'' J. Acoust. Soc. Am. **51**, 1885–1894.
Kay, R. H., and Matthews, D. R. (**1972**). ''On the existence in human auditory pathways of channels selectively tuned to the modulation present in frequency-modulated tones,'' J. Physiol. (London) **225**, 657–677.
Kluender, K. R., and Jenison, R. L. (**1992**). ''Effects of glide slope, noise intensity, and noise duration on the extrapolation of FM glides through noise,'' Percept. Psychophys. **51**, 231–238.
Levitt, H. (**1971**). ''Transformed up–down procedures in psychoacoustics,'' J. Acoust. Soc. Am. **49**, 467–477.
Macmillan, N. A. (**1971**). ''Detection and recognition of increments and decrements in auditory intensity,'' Percept. Psychophys. **10**, 233–238.
Macmillan, N. A. (**1973**). ''Detection and recognition of intensity changes in tone and noise: the detection-recognition disparity,'' Percept. Psychophys. **13**, 65–75.
Moody, D. B., Cole, D., Davidson, L. M., and Stebbins, W. C. (**1984**). ''Evidence for a reappraisal of the psychophysical selective adaptation paradigm,'' J. Acoust. Soc. Am. **76**, 1076–1079.
Moore, B. C. J. (**1973**). ''Frequency difference limens for short-duration tones,'' J. Acoust. Soc. Am. **54**, 610–619.
Miller, G. A. (**1947**). ''The intelligibility of interrupted speech,'' J. Acoust. Soc. Am. **22**, 167–173.
Nelson, D. A., and Freyman, R. L. (**1986**). ''Psychometric functions for frequency discrimination from listeners with sensorineural hearing loss,'' J. Acoust. Soc. Am. **79**, 799–805.
Plack, C. J., and White, L. J. (**2000**). ''Perceived continuity and pitch perception,'' J. Acoust. Soc. Am. **108**, 1162–1169.
Pollack, I. (**1977**). ''Continuation of auditory frequency gradients across temporal breaks: The auditory Poggendorff,'' Percept. Psychophys. **21**, 563–568.
Regan, D., and Tansley, B. W. (**1979**). ''Selective adaptation to frequency-modulated tones: Evidence for an information-processing channel selectively sensitive to frequency changes,'' J. Acoust. Soc. Am. **65**, 1249–1257.
Sergeant, R. L., and Harris, J. D. (**1962**). ''Sensitivity to unidirectional frequency modulation,'' J. Acoust. Soc. Am. **34**, 1625–1628.
Sek, A., and Moore, B. C. J. (**1999**). ''Discrimination of frequency steps linked by glides of various durations,'' J. Acoust. Soc. Am. **106**, 351–359.
Thurlow, W. R. (**1957**). ''An auditory figure-ground effect,'' Am. J. Psychol. **70**, 653–654.
Tsumara, T., Sone, T., and Nimura, T. (**1973**). ''Auditory detection of frequency transition,'' J. Acoust. Soc. Am. **53**, 17–25.
Wakefield, G. H., and Viemeister, N. F. (**1984**). ''Selective adaptation to linear frequency-modulated sweeps: Evidence for direction-specific FM channels?,'' J. Acoust. Soc. Am. **75**, 1588–1592.
Warren, R. M., Obusec, C. J., and Ackroff, J. M. (**1972**). ''Auditory induction: Perceptual synthesis of absent sounds,'' Science **176**, 1149–1151.
Warren, R. M., Wrightson, J. M., and Puretz, J. (**1988**). ''Illusory continuity of tonal and infratonal periodic sounds,'' J. Acoust. Soc. Am. **84**, 1338–1342.

Limits to the role of a common fundamental frequency in the fusion of two sounds with different spatial cues

C. J. Darwin[a] and R. W. Hukin
Department of Psychology, University of Sussex, Brighton, BN1 9QG, United Kingdom

(Received 17 November 2003; revised 16 April 2004; accepted 18 April 2004)

Two experiments establish constraints on the ability of a common fundamental frequency (F0) to perceptually fuse low-pass filtered and complementary high-pass filtered speech presented to different ears. In experiment 1 the filter cut-off is set at 1 kHz. When the filters are sharp, giving little overlap in frequency between the two sounds, listeners report hearing two sounds even when the sounds at the two ears are on the same F0. Shallower filters give more fusion. In experiment 2, the filters' cut-off frequency is varied together with their slope. Fusion becomes more frequent when the signals at the two ears share low-frequency components. This constraint mirrors the natural filtering by head-shadow of sound sources presented to one side. The mechanisms underlying perceptual fusion may thus be similar to those underlying auditory localization. © *2004 Acoustical Society of America.* [DOI: 10.1121/1.1760794]

PACS numbers: 43.66.Pn, 43.66.Rq [PFA] Pages: 502–506

I. INTRODUCTION

In a well-known paper, Broadbent and Ladefoged (1957) demonstrated the importance of a common fundamental frequency (F0) in the perceptual fusion of sounds with different spectral composition presented to different ears. They played the first formant of a synthetic sentence to one ear of their listeners, the second formant to the other ear, and asked how many voices listeners heard and where they were located. When the two formants were excited by pulses at the same F0, the majority of listeners reported hearing a single voice (13/18) in a single place (15/18), but when the two formants were excited by pulses with different F0s (125 vs 135 Hz), the majority of listeners heard two voices (15/18) in two places (12/18). The ability of a common F0 to fuse sounds with different spectral content across the two ears had previously been noted by Fletcher, following a suggestion by Arnold (Fletcher, 1953 p 216) and by Broadbent (1955). Fletcher describes the fusion that occurred when speech that had been high-pass filtered at 1 kHz was presented to one ear, with the complementary low-pass filtered speech to the other ear (Fletcher also observed that a similar fusion did not occur with polyphonic music). Broadbent produced a more extreme manipulation of speech, with low-pass filtered speech at 450 Hz (-18 dB/oct) to one ear and the same speech high-pass filtered at 2000 Hz to the other ear. Of 18 listeners, 14 reported hearing one voice rather than two. Broadbent comments that the common spectral envelope across the two ears might be responsible for the perceived fusion.

These early observations provided the starting point for a number of papers investigating the effect on the intelligibility of speech of varying the fundamental frequency relations within and between speech sounds (Cutting, 1976; Darwin, 1981; Scheffers, 1983; Assmann and Summerfield, 1989; Assmann and Summerfield, 1990; Culling and Darwin, 1993; Culling and Darwin, 1994; Bird and Darwin, 1998). The Broadbent and Ladefoged original observation on the number of sound sources that listeners hear has received less attention, although it has been confirmed with syllabic sounds where the output of the first-formant filter was led to one ear and that of the second-formant to the other ear (Darwin, 1981).

In setting up demonstrations of the fusion across the ears of bands of speech on a common F0, we had noticed that when there was no spectral overlap between the sounds played to the two ears, fusion was less likely to occur than when there was greater spectral overlap. This observation is interesting, not only because it suggests that there might be limits to the fusion by F0 reported by Broadbent and Ladefoged, but also because it might provide a link between observations on auditory fusion and the extensive literature on auditory localization.

The following experiments explore how fusion depends on spectral overlap between the sounds presented to each ear and demonstrate that sounds are more likely to fuse when they share low-frequency components. This constraint mirrors the diffraction of low-frequency (but not high-frequency) sound around the head.

II. EXPERIMENT 1

The Broadbent and Ladefoged speech sounds were prepared using Walter Lawrence's PAT (Parametric Artifical Talker) synthesizer (Lawrence, 1953). PAT consisted of analogue resonator circuits that filtered a periodic electrical laryngeal signal. Each ear in the Broadbent and Ladefoged experiment thus received the output of a simple resonant filter. Figure 1 shows the transfer function of two such resonators (following Fant, 1970 p. 54 Eq. 1.3-7), one tuned to 800 Hz with a bandwidth of 90 Hz and the other tuned to 1400 Hz with a bandwidth of 150 Hz. Below the axis is shown the negative of the absolute difference between the two functions. It is clear that there is considerable spectral

[a]Correspondence and proofs to C. J. Darwin, Department of Psychology, University of Sussex, Brighton BN1 9QG, England. Electronic mail: cjd@biols.susx.ac.uk

 0001-4966/2004/116(1)/502/5/$20.00

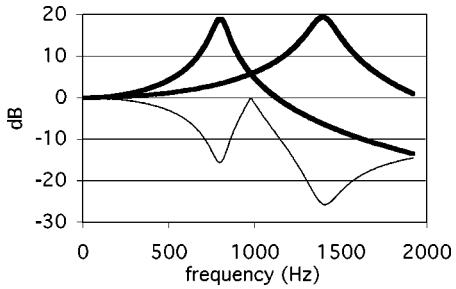

FIG. 1. Transfer functions for two single-formant resonators at 800 Hz and 1400 Hz with bandwidths of 90 and 150 Hz, respectively. The thin line shows the difference in level between the two functions.

overlap between the two. Although the stimuli used by Broadbent (1955) had considerably less spectral overlap than those used by Fletcher or by Broadbent and Ladefoged (see above), the frequency region around 950 Hz would have had the same level in both ears (with an attenuation of about 19 dB) and the high-pass band would have had relatively little energy because of its high lower-frequency limit.

In Experiment 1 we ask how listeners' judgements of the number of sound sources change when the speech to each ear is filtered through complementary high- and low-pass filters whose 6-dB cut-off frequency is fixed at 1 kHz and whose steepness is systematically varied. We also included an additional set of conditions where the high- and low-frequency signals were each sent to both ears, but with complementary interaural time differences (ITDs) in order to investigate whether the basic phenomenon reported by Broadbent and Ladefoged is also obtained using ITDs rather than their dichotic infinite interaural level difference. A number of studies have recently demonstrated the weaker effect of simultaneous auditory grouping by ITD than by infinite ILD (Culling and Summerfield, 1995; Darwin and Hukin, 1997; Drennan *et al.*, 2003).

A. Stimuli and procedure

Two sentences from a speech corpus (Bolia *et al.*, 2000) were used, one spoken by a woman (Talker 4: ''Ready Charlie, go to blue one now''), and one by a man (Talker 5: ''Ready Ringo, go to red six now''). The sentences were first low-pass filtered at 8 kHz. In the simplest condition (dichotic, Same F0), either the male or female sentence was resynthesized with no change to its F0 using the Praat 3.9 (Boersma and Weenink, 1996) implementation of PSOLA (Moulines and Charpentier, 1990). Then a low-pass version was played to one ear of a listener at the same time as a high-pass version was played to the other ear. The filtering was carried out in the frequency domain using Praat's implementation of a Hann filter, which produced (symmetrically around the cut-off frequency) a linear attenuation of the sound on linear frequency and amplitude scales. The cut-off frequency, in this case 1 kHz, is defined as the 6-dB (50% linear) attenuation point of the filter, and is the frequency at which the complementary high- and low-pass filters cross. The total width of the linear attenuation zone varied in 400-Hz steps from 200 Hz to 1800 Hz.

The sounds of two further conditions had different F0s in their low-pass and high-pass parts. The Low–High condition had the lower F0 in its low-pass part and the higher F0 in its high-pass part. The High–Low condition was the opposite. The changes to F0 were made on the intact original sentences again using Praat's PSOLA implementation. For the lower F0 sounds, the F0 was lowered by 4% from its original value, and for the higher F0 it was raised by 4%, giving an overall F0 difference of a little over 8% of the lower value.

In the ''Dichotic'' set of conditions, the low-pass and high-pass parts of a sentence were played to different ears (low-pass always to the left ear). In the ''ITD'' set of conditions, both parts were played to both ears but with an ITD of ± 571 μs applied so that the low-pass part led on the left ear and the high-pass led on the right.

Eight audiometrically normal listeners who had the general experience of taking psychoacoustic experiments, though not of this type, listened to 10 replications of each stimulus in a pseudo-random order in an audiometric booth over Sennheiser 414 headphones. They were asked to indicate on each trial whether they heard one (fused) voice or two. The presentation gain produced a level for the low-pass sound (1000-Hz filter transition width) of 62-dB SPL.

B. Results

The results for the dichotic and ITD presentations are shown in the upper and lower panels of Fig. 2, respectively, as the percentage of trials on which listeners heard a single, fused sound. For both dichotic and ITD presentation, sounds that had a different F0 in their low- and high-pass parts (triangles and squares) were heard as fused on less than 25% of occasions, with the female voice (filled symbols) being heard as less fused than the male (unfilled). There were no systematic changes with the filter transition width.

However, sounds that had the same F0 in both parts (circles) showed a different response pattern. With dichotic presentation (as in the original Broadbent studies) sounds that had been filtered through filters with wide transitions (>500 Hz), were heard as fused, whereas those from filters with narrower transitions were not heard as fused. A repeated-measures ANOVA on the dichotic data (with the scores of the two sub-classes of different F0 averaged) showed a highly significant interaction of ''same vs different F0'' with ''filter transition width'' ($F_{4,28}=44.3, p<0.0001$) which itself interacted only weakly with talker gender ($F_{4,28}=4.0, p<0.05$). These results replicate the Broadbent and Ladefoged result described above, but only for wide filter transitions. For narrow filter transitions, a common F0 is insufficient to give the impression of a single sound source. With ITD presentation, all the sounds with the same F0 were heard as fused more than 75% or so of the time. A repeated-measures ANOVA on the ITD data (with the scores of the two sub-classes of different F0 averaged) showed a highly significant effect of same vs different F0 ($F_{1,7}=53.3, p<0.0002$), but no other main effects or interactions.

C. Discussion

This experiment has confirmed one aspect of the Broadbent and Ladefoged results, namely that when two different

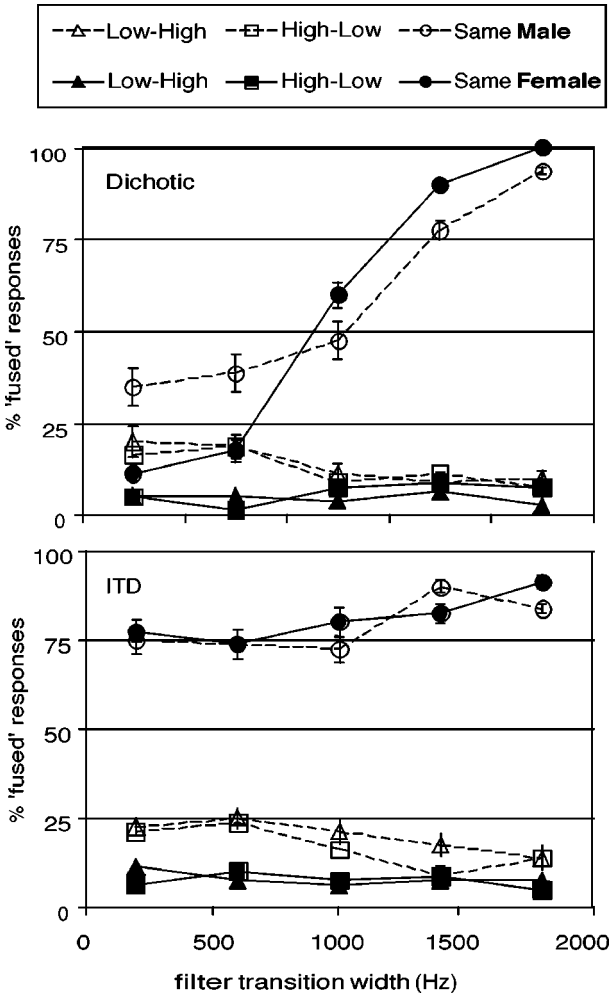

FIG. 2. Percentage of single voice (fused) responses (± 1 s.e.m) in Experiment 1. The upper panel shows data for dichotic presentation of a 1-kHz high-pass and low-pass filtered version of a sentence from a male (open symbols) or female (closed symbols) voice as a function of the width of the linear (in amplitude and frequency) skirts of the filters which crossed at -6 dB. The ''Low–High'' condition had the lower F0 in the low-pass part and the higher F0 in the high-pass part. The ''High–Low'' condition had the opposite assignment. Some error bars fall within their symbols. The lower panel shows data from similar sounds presented with ITDs of ± 571 μs rather than dichotically.

frequency bands are led to opposite ears, fusion is more likely when the sounds are on the same F0 than when they are on different F0s. But the experiment has also qualified this conclusion: such fusion only occurs for frequency bands that have been obtained by passing the original speech through relatively shallow filters. With steeper filters, listeners consistently report two sound sources even when the bands share a common F0.

The need for shallow filters may be because some frequency components must be shared between the two ears for fusion to occur, or it may be due to the need to share specific frequencies (such as the low-frequency region that is dominant for auditory localization). This question is addressed in the second experiment.

The first experiment also examined the fusion of different frequency bands that were played both to each ear but with different interaural time differences. Previous work on auditory grouping has indicated that ITDs provide at best only a weak basis for auditory grouping compared with grouping by ear of presentation (Culling and Summerfield, 1995; Darwin and Hukin, 1997). In the present results we extend this conclusion to judgements of auditory fusion: sounds on the same F0 presented with different ITDs were judged as fused regardless of the width of the filters through which they had been passed. This experiment thus shows that grouping by common F0 overrides potential separation by an ITD of over 500 μs. This result complements previous findings that a difference in F0 is more salient than a difference in ITD at improving the identification of simultaneous pairs of vowels (Shackleton and Meddis, 1992).

III. EXPERIMENT 2

In the second experiment, we vary the cut-off frequency as well as the transition-width of the filters used to generate the low- and high-pass versions of the sentences. The reason for varying both these parameters is to distinguish an explanation in terms simply of filter sharpness from one that requires frequency overlap between the ears in a particular frequency region such as, for example, the dominant region for localization (Raatgever, 1980; Wightman and Kistler, 1992).

A. Stimuli and procedure

The stimuli and procedure were similar to those used in the first experiment, except that there were 5 different cut-off frequencies of the low-/high-pass filter (600, 800, 1200, 1400, 2000 Hz), and presentation was only dichotic. Each cut-off frequency of the filter had the same 5 transition-widths used in the previous experiment. The transition-widths were thus constant on a linear scale, and did not increase in proportion to the filter cut-off frequency.

B. Results

This experiment replicates the dichotic results from the first experiment. For the 800-Hz and 1200-Hz cut-off frequencies (which are the most similar to the 1000-Hz cut-off of the first experiment) there are very few fusion responses when the two pass-bands have different F0s, but when they have the same F0, fusion responses increase as the filter transition width increases.

More generally, as in the first experiment, listeners reported very little fusion for sounds that had a different F0 in the low-pass and high-pass parts: only the male sentence with the highest (2 kHz) cut-off frequency approached 30% fusion responses.

By contrast, the sounds that had the same F0 in both the low- and high-pass parts showed high levels of fusion in some conditions. The percentage of fusion responses for sounds on the same F0 are shown separately for the male and female sentences in Fig. 3.

The data (with the scores of the two sub-classes of different F0 averaged) were subjected to a repeated measures ANOVA which gave a substantial three-way interaction between ''cut-off frequency,'' ''same vs different F0'' and ''filter transition width'' ($F_{16,112}=9.2, p<0.0001$) which weakly interacted with talker gender ($F_{16,112}=3.0, p<0.05$).

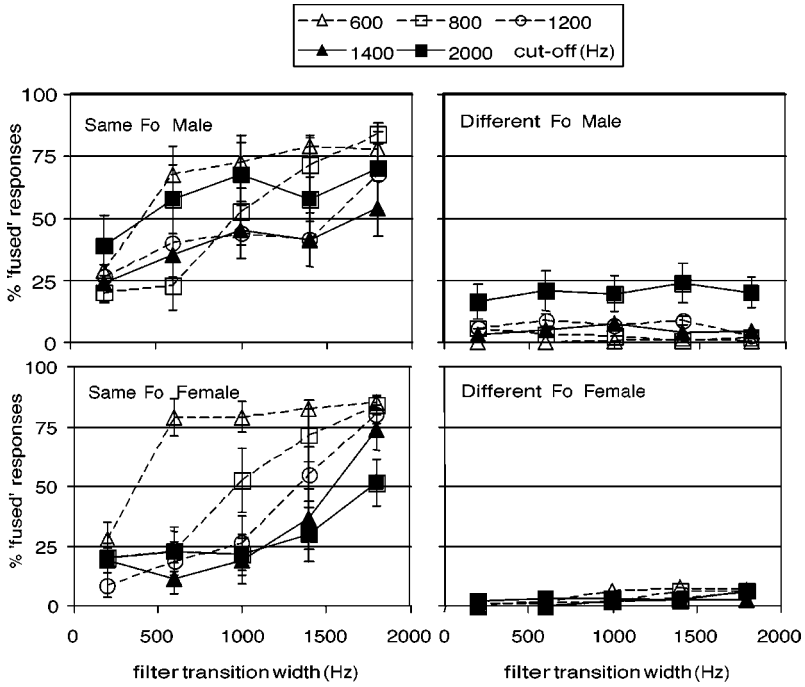

FIG. 3. Percentage of single voice (fused) responses (± 1 s.e.m) in Experiment 2 for sounds on the same F0 as a function of the filter transition width for 5 different filter cut-off frequencies. The upper panels show data from the male talker, the lower from the female; the left column shows data from conditions on the same F0, the right from those on a different F0.

The data from the female talker when the F0s were the same are more orderly than the male and show two trends. First, as in the previous experiment, fusion generally increases with increasing filter transition width. Second, fusion increases as the cut-off frequency of the filter is decreased. So, for example, for a transition width of 500 Hz, fusion responses are less than 25% for filter cut-offs of 1200 to 2000 Hz, but increase to over 75% with a cut-off of 600 Hz. Viewed another way, the higher the cross-over frequency of the filter, the wider must be the filter transition to give fusion.

The male same-F0 data show similar trends to the female, with the exception that the highest filter cross-over frequency 2000 Hz gives substantially more fusion responses than do the female data. The reason for this is not clear, but may reflect weaker pitch information from the high-numbered harmonics of the low-pitched male voice in the region above 2 kHz compared with the lower-numbered harmonics in the same frequency region for the female voice (Houtsma and Smurzynski, 1990). The different phonetic content of the two voices may also have been a factor, giving different distributions of energy between the two pass bands, and this variable needs to be explicitly controlled in future systematic comparisons of different pitched or different gender voices.

C. Discussion

The main result of this experiment is that a broader filter transition region is required for fusion as the cross-over frequency between the low-pass and high-pass sounds is increased. The implication of this result is that successful fusion requires that the high-pass stimulus contain sufficient low-frequency energy. If we consider sounds at around the 50% threshold for fusion responses in the female data in Fig. 3, then the high-pass component of these threshold sounds generally starts to show some energy above about 400 to 600 Hz, and would therefore have substantial energy at slightly higher frequencies—in the dominance region for localization (Raatgever, 1980; Wightman and Kistler, 1992). The level difference between the two ears as a function of frequency is shown in Fig. 4 for filters at these 50% threshold frequencies (for the female voice). With the exception of the highest filter cut-off, all the filters at threshold show overlap of frequencies in the frequency region around 600–700 Hz.

IV. GENERAL DISCUSSION

These two experiments have shown that although a common F0 may be a necessary condition to ensure binaural fusion of two different frequency bands led to opposite ears, it is not a sufficient condition. If the frequencies of a sentence below 1 kHz are played to one ear, and those above 1 kHz to the other, listeners will either report hearing one or two sound sources depending on whether the cross-over filter

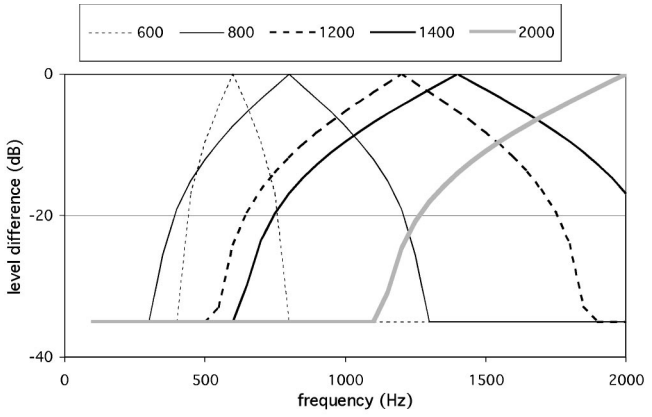

FIG. 4. Level differences between low-pass and high-pass filter transfer functions for female-voice stimulus conditions in Experiment 2 that gave 50% fused responses. The filter widths that corresponded to 50% fused responses were estimated from the average data across listeners at each cut-off frequency, and transfer functions for those filter widths calculated that were linear in frequency and amplitude.

has shallow or steep skirts, respectively. As the cross-over frequency is moved from lower to higher frequencies, shallower skirts to the filters are needed to produce fusion.

A possible explanation for these effects is that for fusion to occur, the high-pass sound must have sufficient energy in the dominance region for lateralization. This constraint may reflect the natural constraint on real sound sources that the head produces a darker acoustic shadow for high frequencies than for low; consequently although it is natural to encounter sounds at one ear from which the high frequencies have been removed (by the head shadow), it is not natural to encounter sounds at one ear from which the low frequencies have been removed. The mechanisms of binaural fusion may be sensitive to this constraint and produce the percept of a separate sound source for a sound that, although likely to be from the same sound source as a low-frequency sound at the other ear by virtue of their sharing a common F0, has too little low-frequency energy. The unity of the resulting percept would then be a trade-off between these two opposing factors.

ACKNOWLEDGMENTS

The research was supported by a grant from the UK Medical Research Council to the first author. This data was initially presented at the Short Papers Meeting of the British Society for Audiology, 2001.

Assmann, P. F., and Summerfield, A. Q. (**1989**). ''Modelling the perception of concurrent vowels: Vowels with the same fundamental frequency,'' J. Acoust. Soc. Am. **85**, 327–338.

Assmann, P. F., and Summerfield, A. Q. (**1990**). ''Modelling the perception of concurrent vowels: Vowels with different fundamental frequencies,'' J. Acoust. Soc. Am. **88**, 680–697.

Bird, J., and Darwin, C. J. (**1998**). ''Effects of a difference in fundamental frequency in separating two sentences,'' in *Psychophysical and Physiological Advances in Hearing* edited by A. R. Palmer, A. Rees, A. Q. Summerfield and R. Meddis (Whurr, London), pp. 263–269.

Boersma, P., and Weenink, D. (**1996**). ''Praat, a system for doing phonetics by computer, version 3.4,'' Institute of Phonetic Sciences, University of Amsterdam, Vol. 132, pp. 1–182, www.praat.org

Bolia, R. S., Nelson, W. T., Ericson, M. A., and Simpson, B. D. (**2000**). ''A speech corpus for multitalker communications research,'' J. Acoust. Soc. Am. **107**, 1065–1066.

Broadbent, D. E. (**1955**). ''A note on binaural fusion,'' Q. J. Exp. Psychol. **7**, 46–47.

Broadbent, D. E., and Ladefoged, P. (**1957**). ''On the fusion of sounds reaching different sense organs,'' J. Acoust. Soc. Am. **29**, 708–710.

Culling, J. F., and Darwin, C. J. (**1993**). ''Perceptual separation of simultaneous vowels: within and across-formant grouping by F0,'' J. Acoust. Soc. Am. **93**, 3454–3467.

Culling, J. F., and Darwin, C. J. (**1994**). ''Perceptual and computational separation of simultaneous vowels: cues arising from low frequency beating,'' J. Acoust. Soc. Am. **95**, 1559–1569.

Culling, J. F., and Summerfield, Q. (**1995**). ''Perceptual separation of concurrent speech sounds: absence of across-frequency grouping by common interaural delay,'' J. Acoust. Soc. Am. **98**, 785–797.

Cutting, J. E. (**1976**). ''Auditory and linguistic processes in speech perception: inferences from six fusions in dichotic listening,'' Psychol. Rev. **83**, 114–140.

Darwin, C. J. (**1981**). ''Perceptual grouping of speech components differing in fundamental frequency and onset-time,'' Q. J. Exp. Psychol. **33A**, 185–208.

Darwin, C. J., and Hukin, R. W. (**1997**). ''Perceptual segregation of a harmonic from a vowel by inter-aural time difference and frequency proximity,'' J. Acoust. Soc. Am. **102**, 2316–2324.

Drennan, W. R., Gatehouse, S., and Lever, C. (**2003**). ''Perceptual segregation of competing speech sounds: the role of spatial location,'' J. Acoust. Soc. Am. **114**, 2178–89.

Fant, G. (**1970**). *Acoustic Theory of Speech Production* (The Hague, Mouton).

Fletcher, H. (**1953**). *Speech and Hearing in Communication* (Van Nostrand, New York).

Houtsma, A. J. M., and Smurzynski, J. (**1990**). ''Pitch identification and discrimination for complex tones with many harmonics,'' J. Acoust. Soc. Am. **87**, 304–310.

Lawrence, W. (**1953**). ''The synthesis of speech from signals which have a low information rate,'' in *Communication Theory*, edited by W. Jackson (Butterworths Scientific, London, England).

Moulines, E., and Charpentier, F. (**1990**). ''Pitch synchronous waveform processing techniques for text-to-speech synthesis using diphones,'' Speech Commun. **9**, 453–467.

Raatgever, J. (**1980**). ''On the binaural processing of stimuli with different phase relations,'' Technische Hogeschool Delft. Doctoral dissertation.

Scheffers, M. T. (**1983**). ''Sifting vowels: Auditory pitch analysis and sound segregation,'' Ph.D. dissertation, Groningen University, The Netherlands.

Shackleton, T. M., and Meddis, R. (**1992**). ''The role of interaural time difference and fundamental frequency difference in the identification of concurrent vowel pairs,'' J. Acoust. Soc. Am. **91**, 3579–3581.

Wightman, F. L., and Kistler, D. J. (**1992**). ''The dominant role of low-frequency interaural time differences in sound localization,'' J. Acoust. Soc. Am. **91**, 1648–1661.

Specification of cross-modal source information in isolated kinematic displays of speech[a)]

Lorin Lachs[b)]
Department of Psychology, 5310 North Campus Drive, California State University, Fresno, California 93740

David B. Pisoni
Speech Research Laboratory, Department of Psychology, Indiana University, Bloomington, Indiana 47405

(Received 15 August 2002; accepted for publication 1 April 2004)

Information about the acoustic properties of a talker's voice is available in optical displays of speech, and vice versa, as evidenced by perceivers' ability to match faces and voices based on vocal identity. The present investigation used point-light displays (PLDs) of visual speech and sinewave replicas of auditory speech in a cross-modal matching task to assess perceivers' ability to match faces and voices under conditions when only isolated kinematic information about vocal tract articulation was available. These stimuli were also used in a word recognition experiment under auditory-alone and audiovisual conditions. The results showed that isolated kinematic displays provide enough information to match the source of an utterance across sensory modalities. Furthermore, isolated kinematic displays can be integrated to yield better word recognition performance under audiovisual conditions than under auditory-alone conditions. The results are discussed in terms of their implications for describing the nature of speech information and current theories of speech perception and spoken word recognition. © *2004 Acoustical Society of America.* [DOI: 10.1121/1.1757454]

PACS numbers: 43.71.Ma, 43.71.Bp [DOS] Pages: 507–518

I. INTRODUCTION

Optical information about vocal articulation has been shown to have substantial effects on speech perception. In the absence of auditory stimulation, visual information is sufficient to support accurate spoken word recognition (Bernstein *et al.*, 2000). Combined with acoustic information, visual stimulation can also enhance speech intelligibility in noise by +15 dB (Sumby and Pollack, 1954; Summerfield, 1987). Conflicting information in the acoustic and optic displays of an audiovisual speech stimulus can also interact to form illusory percepts in speech perception [the ''McGurk'' effect (McGurk and MacDonald, 1976)].

These core phenomena in audiovisual speech perception are robust and reliable (Summerfield, 1987), and provide strong evidence that some components of the speech perception process must also be involved in combining different sources of information across sensory modalities. A great deal of research, especially over the past two decades, has focused on the nature of the perceptual integration process—how sensory stimulation from disparate and seemingly incommensurate modalities can influence the perception of a multimodal stimulus. Theories of this process vary considerably. For example, Braida's (1991) prelabeling model represents audiovisual stimuli in a multidimensional space consisting of acoustic- and optic-specific dimensions. Alternatively, Massaro's (1998) fuzzy logical model of perception represents multimodal perception as the outcome of a decision process that evaluates the degree of support from each modality for unimodal prototypes.

Another class of theory for explaining the process of multimodal integration proposes that auditory and visual inputs are somehow evaluated in terms of a common representational format. According to Schwartz *et al.* (1998), there are two alternatives for common format models. In one, information from one modality is translated or recorded into a format that is compatible with another, more familiar or ''dominant'' modality. Schwartz *et al.* assert that models based on this type of a representation necessarily predict that visual influences on speech perception will only be observed when optical information conflicts with the auditory stimulus, or when the auditory stimulus is degraded. This prediction was disconfirmed by Sumby and Pollack (1954), who found that auditory-alone performance improved as the signal-to-noise ratio increased. After scores in the audiovisual condition were normalized relative to this increasing baseline, Sumby and Pollack discovered that the amount by which performance improved due to audiovisual stimulation remained constant over the entire range of signal-to-noise ratios tested. This important finding indicates that the effect of the additional visual information is not conditional on the degree of ambiguity in the auditory signal. Remarkably, this finding was reconfirmed by Reisberg *et al.* (1987), who showed that concurrently presented visual information facilitated the repetition of foreign-accented speech and semantically complex sentences presented with no background noise at all. These findings demonstrate that visual information about speech is useful and informative, and is not simply compensatory in situations where auditory information is insufficient to support perception.

The currently available evidence therefore indicates that

[a)]This work was previously submitted by Lorin Lachs to Indiana University in partial fulfillment of the requirements for a Ph.D.
[b)]Electronic mail: llachs@csufresno.edu

translation of information into a dominant modality format is not a viable theoretical construct. Instead, Schwartz *et al.*'s alternative ''common format'' model assumes that acoustic and optic information about speech is analyzed with reference to some kind of multimodal, amodal, or modality-neutral representational space. In one theoretical approach of this type, the modality-neutral perceptual space relates to the vocal tract articulation that underlies the production of auditory or visual speech signals (Fowler, 1986; Liberman and Mattingly, 1985; Summerfield, 1987).

Convincing evidence for a modality-neutral form of speech information comes from a study of the McGurk effect using auditory and *tactile* information about speech. Fowler and Dekle (1991) had naive participants listen to spoken syllables synthesized along a /ba/-/pa/ continuum while using their hands to obtain information about the articulation, in much the same way that deaf-blind users of the Tadoma method do (Schultz *et al.*, 1984). The tactile information on every trial was either a /ba/ or a /ga/, articulated by a talker who was unable to hear the auditory syllable. Observers were then asked to categorize the heard stimulus as either a /ba/ or a /ga/ in a forced choice task. Fowler and Dekle found that the auditory perceptual boundary for /ba/ and /ga/ was shifted by the phonetic content of the tactile pattern. Interestingly, this effect was found with subjects who had no training in Tadoma at all, indicating that stored associations between tactile and auditory speech gestures could not be involved in the integration results.

In a second experiment, observers were simultaneously presented with the acoustic syllables and *orthographic* displays of ''BA'' or ''PA.'' Because all of the observers were literate college undergraduates, Fowler and Dekle assumed that they had stored robust associations between the orthographic symbols and their phonetic counterparts in memory. However, the visual orthographic displays (with visual masking designed to bring performance down to a level equitable with performance in the tactile condition) did not affect the position of the category boundary along the continuum at all. Fowler and Dekle interpreted these findings as evidence that the ability to ''integrate'' information about speech is *not* based on matching features to learned representations, but is rather based on the detection of amodal information about speech articulation. Their results also demonstrate that some degree of useful information about speech can be obtained through sensory modalities other than audition and vision.

Further support for the modality-neutral form of speech information comes from a recent series of studies using a novel cross-modal matching task (Lachs and Pisoni, in press). In this cross-modal matching task, participants view a visual-alone, dynamic display of a talker speaking an isolated English word and are then asked to match the pattern with one of two auditory-alone displays. One of the alternative auditory displays is the acoustic specification of the *same articulatory events* that produced the visual-alone pattern. The other alternative is the acoustic specification of a different talker saying the same word that was spoken in the visual-alone pattern. When matching a visual-alone token to one of two auditory-alone tokens, the ''order'' is said to be ''V-A.'' In contrast, when participants hear an auditory-alone display first, and then are asked to match to one of two visual-alone alternatives, this is referred to as the ''A-V'' order.

Lachs and Pisoni (in press) found that participants performed above chance ($M = 0.60$ for A-V; $M = 0.65$ for V-A) when asked to match the same phonetic events across different sensory modalities, regardless of the order in which the modalities were presented. That is, observers could match a speaking face with one of two voices, or match a voice with one of two speaking faces. Lachs and Pisoni argued that the results provided evidence for the existence of ''cross-modal source information,'' that is, modality-neutral, articulatory information about the source or speaker of an utterance that is specified by sensory patterns of both acoustic or optic energy. In a series of further experiments, Lachs and Pisoni extended these findings using a series of manipulations to the acoustic and optical displays that were presented for cross-modal matching. One experiment found that participants were not able to match across sensory modalities when optical and acoustic patterns were played backwards in time, indicating that talker-specific information is sensitive to the normal temporal order of spoken events. Another experiment showed that static visual displays of faces could not be matched to dynamic acoustic displays. This result suggested that talker-specific information is specified in the dynamic, time-varying structure of visual displays, and not in their static features. Finally, an additional experiment showed that noiseband stimuli (Smith *et al.*, 2002) preserved talker-specific information, despite the elimination of a traditional acoustic cue to vocal identity: fundamental frequency (f0). This result was interpreted as evidence that talker-specific information in speech is specified in the pattern of formant resonances as they evolve over time, irrespective of the f0 used to excite them.

In another set of experiments, Lachs and Pisoni (2004) subjected the acoustic speech signal to various acoustic transformations, which were then used as the auditory stimulus in a cross-modal matching task (using fully illuminated faces) and a word identification task. Several of these transformations affected the frequency domain of the recorded words. Lachs and Pisoni found that, in general, transformations that preserved the linear relationship between formant frequencies of a speech utterance also preserved the ability to perform the matching and word identification tasks. However, there were transformations that destroyed this relationship. For example, frequency rotation around a central frequency value (Blesser, 1972) also destroyed participants' ability to perform both tasks, as did a nonlinear scaling transformation of the frequency components of the utterance. Because the formant frequencies associated with speech are, to a rough approximation, markers of the instantaneous configuration of the vocal tract as it evolves over time, Lachs and Pisoni claimed that only acoustic patterns that carry information about the kinematics of articulation are informative for the completion of both word identification and cross-modal matching.

The results of this series of experiments suggest that cross-modal matching can be carried out because of a common articulatory basis for acoustic and optic displays of

speech. Lachs and Pisoni (in press) proposed that, because both visual and auditory displays of speech are lawfully structured by the same underlying articulatory events (Vatikiotis-Bateson *et al.*, 1997), matching is accomplished by comparison to a common, underlying source of information about vocal tract activity.

The proposal that audiovisual integration reflects a common underlying articulatory basis for audiovisual speech integration is also supported by a correlational analysis of the stimuli used in Grant's (2001) recent detection experiments. Grant showed that the rms amplitude of the acoustic signal (especially in the bandpass filtered F2 region) was strongly related to the area of the opening circumscribed by the lips. He proposed that this correlation between an acoustic variable and an optical variable may have been responsible for his finding that auditory speech detection thresholds were reduced under concurrent visual stimulation. It is interesting to note that the relationship reported by Grant between the auditory and visual variables is also related to a common, underlying kinematic variable based on jaw and mouth opening. Further work on the correspondence between auditory and visual speech signals has also been carried out by Vatikiotis-Bateson and colleagues (e.g., Vatikiotis-Bateson *et al.*, 2002; Yehia *et al.*, 1998).

An articulatory foundation for modality-neutral information is also consistent with the observation that the visual correlates of spoken language arise as a direct result of the movements of the vocal tract that are necessary for producing linguistically significant speech sounds (Munhall and Vatikiotis-Bateson, 1998). An articulating vocal tract structures acoustic and optic energy in space and time in highly constrained ways. As a consequence, the auditory and visual sensory information present in those displays is lawfully structured by a common unitary articulatory event. Thus, the seemingly disparate patterns of acoustic and optic energy are necessarily and lawfully related to each other by virtue of their common origin in articulation.

One avenue of investigation, then, is to discover the ways in which optical and acoustical structure specify the informative properties of vocal tract articulation. A growing body of research suggests that both the acoustic or optical properties of speech carry *kinematic* or *dynamic* information about vocal tract articulation (Rosenblum, 1994), and that these sources of information drive the perception of linguistically significant utterances (Fowler, 1986; Summerfield, 1987). Kinematic variables refer to position and its time derivatives: velocity, acceleration, etc.; dynamic variables refer to forces and masses (Bingham, 1995). These variables are necessarily grounded in spoken events: they do not refer to specific properties of visual or auditory stimulation, but rather to the physical events that structure light or sound. As such, these variables are prime theoretical candidates for the modality-neutral, articulatory, properties of events.

The point-light display (PLD) technique developed by Johansson (1973) has been used extensively to investigate the perception of kinematic variables (e.g., Kozlowski and Cutting, 1978; Runeson and Frykholm, 1981). By placing small reflective patches at key positions on a talker's face and darkening everything else in the display, researchers have been able to theoretically isolate the kinematic properties of visual displays of talkers articulating speech (Rosenblum *et al.*, 1996; Rosenblum and Saldaña, 1996). These ''kinematic primitives'' have been shown to behave much like unmodified, fully illuminated visual displays of speech (Rosenblum and Saldaña, 1996), albeit with smaller effect sizes. Indeed, Rosenblum and Saldaña found that the McGurk illusion can be induced by dubbing visual point-light displays onto phonetically discrepant auditory syllables (Rosenblum and Saldaña, 1996). In addition, Roseblum *et al.* (1996) also demonstrated that providing point-light information about articulation in conjunction with auditory speech embedded in noise can result in increased speech intelligibility scores, just as fully illuminated visual displays can improve speech intelligibility (Sumby and Pollack, 1954).

As with optic displays, kinematic information can also be theoretically isolated and examined in acoustic displays of speech. ''Sinewave speech replicas'' (Remez *et al.*, 1981) are time-varying acoustic signals that contain three sinusoidal tones generated at the frequencies traced by the centers of the three lowest formants in a speech signal. Because the formants in speech are resonances of the vocal tract, that is, bands of energy at frequencies specified by the evolving configuration of the vocal tract transfer function, these ''sinewave speech replicas'' can be said to isolate kinematic information in the auditory domain. Pioneering experiments by Remez and his colleagues using sinewave speech replicas have demonstrated that listeners can perceive linguistically significant information from these minimal kinematic displays in many of the same ways that they can from untransformed acoustic displays (Remez *et al.*, 1981).

Two studies using unimodal kinematic primitives have indicated that indexical information in speech signals may be carried in the very same ''kinematic details'' that support phonetic identification (Runeson, 1994). In the visual domain, Rosenblum *et al.* (2002) presented participants with point-light displays of a talker speaking a sentence and then asked them to match the point-light display with one of two fully illuminated faces speaking the same sentence. One of the fully illuminated faces belonged to the same talker who had generated the point-light display. Their results showed that visual point-light displays of a talker articulating speech could be matched accurately to fully illuminated visual displays of the same utterances. This finding suggests that some talker-specific details are contained in the visually isolated kinematics of vocal tract activity. Analogously, in the auditory domain, Remez *et al.* (1997) presented listeners with sinewave replicas of English sentences and asked them to match the token with one of two untransformed auditory tokens. As above, one of the untransformed auditory tokens was spoken by the same talker who had spoken in the sinewave replica. The results showed that sinewave speech replicas carry enough idiosyncratic phonetic variation to support correct matching between untransformed, natural utterances and their sinewave speech replicas.

Several parallel lines of investigation have also investigated spoken word recognition and the *integration* of these minimal, unimodal stimulus displays with untransformed auditory stimuli or fully illuminated visual stimuli. For ex-

ample, in one recent study, Remez *et al.* (1999) demonstrated that the intelligibility of sinewave replicas of sentences was significantly enhanced when presented in conjunction with a full visual display of the talker. In another study Rosenblum *et al.* (1996) showed that point-light displays of a talker speaking sentences could enhance recognition of untransformed auditory displays embedded in noise.

In summary, kinematic information about speech articulation is carried by both acoustic and optic energy, and these sources of information appear to be sufficient to support both speech perception and talker identification in each modality alone. In the present investigation, we extend the seminal work of Rosenblum and Remez in a study investigating talker-identification and speech perception using fully isolated displays of speech, that is, stimuli consisting of both point-light displays and sinewave speech replicas.

For the set of experiments reported here, point-light displays (PLDs) of four talkers speaking isolated English words were recorded, and the accompanying acoustic displays were converted into sinewave speech replicas. In the first experiment, we examined whether theoretically isolated kinematic displays of speech can carry indexical information about a talker. Participants were asked to match point-light displays and sinewave speech replicas of the same talker using a cross-modal matching task. In the second experiment, we investigated whether these minimal, ''skeletonized'' versions of speech could also be integrated across sensory modalities in an open set word recognition task and whether they would display the audiovisual enhancement effects: combined audiovisual stimulation leads to higher speech intelligibility scores than auditory-alone stimulation.

II. EXPERIMENT 1: CROSS-MODAL MATCHING OF KINEMATIC PRIMITIVES

Experiment 1 was designed to test the hypothesis that talker-specific information is specified in the kinematic behavior of the vocal tract. To accomplish this goal, we used a cross-modal matching task and asked participants to match point-light displays with sinewave speech replicas. If the object of perception is modality-neutral and based on the articulation of the vocal tract, we would expect that observers should be able to match faces and voices with only the minimal, theoretically isolated kinematic information about articulation available in point-light displays and sinewave replicas of speech.

A. Method

1. Participants

Participants were 40 undergraduate students enrolled in an introductory psychology course who received partial credit for participation. All of the participants were native speakers of English. None of the participants reported any hearing or speech disorders at the time of testing. In addition, all participants reported having normal or corrected-to-normal vision. None of the participants in this experiment had any previous experience with the audiovisual speech stimuli used in this experiment.

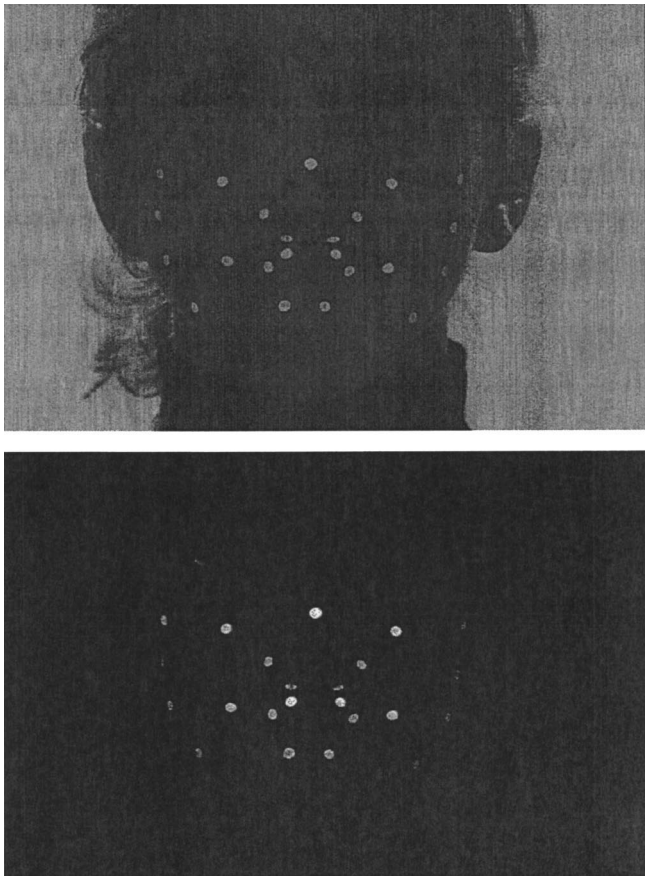

FIG. 1. Dot configuration for point-light displays. All dots were of a uniform diameter. Five dots are not visible due to occlusion by the lips: upper teeth (two dots), lower teeth (two dots), and tongue tip (one dot).

2. Stimulus materials

a. Point-light displays of speech. To capture and record the movement of the articulators, it was necessary to videotape a set of four talkers. Four females between the ages of 23 and 30 volunteered as talkers for the recording session. To create a point-light display, the motion of the points selected must be recorded directly; that is, the motion of the articulators cannot simply be extracted in postproduction from a recording of a fully illuminated display of the talker's face (Runeson, 1994). Before recording, therefore, each talker glued glow-in-the-dark dots, each approximately 3 mm in diameter, to her face in the pattern outlined in Fig. 1. For dots on the outside of the mouth, the adhesive used was a spirit gum commonly used for adhesion of latex masks (Living Nightmare® Spirit Gum). Dots on the lips, teeth, and tongue were affixed with an over-the-counter dental adhesive (Fixodent® Denture Adhesive Cream).

Stimuli were recorded using a digital video camera and microphone (Sony AKGC414) in a sound-attenuated room onto Sony DVCam PDV-124ME digital media tapes. Each talker was seated approximately 56 in. from the camera lens, and the zoom control on the camera was adjusted such that the visual angle subtended by the distance between the talker's ears was equal across talkers. The camera lens and face of the talker were placed at a height of approximately 44 in. Two black lights (15.7 cm long, 15 W each) were secured on permanent fixtures placed 13.5 in. on either side of the cam-

era lens, on an axis perpendicular to the line between the talker's face and the camera lens. The two black lights were the only source of illumination used during videotaping, and did not significantly illuminate the skin of the talker being recorded. However, the glow in the dark dots reflected the black light in the normal visible spectrum. The video track of the recorded movies thus recorded only the movement of the glow-in-the-dark points in isolation of the face to which they were affixed.

During videotaping, talkers read a list of 96 English words off a teleprompter configured with a green font and black background so that it provided no additional ambient illumination in the recording session. There was a 3-s delay between the presentation of successive words on the teleprompter. The digitized stimuli were segmented later such that each word was preceded and followed by ten silent frames (10∗29.97 fps=333.66 ms) with no speech sounds.

b. Sinewave speech replicas. The audio track of each utterance was extracted from the videotape and stored in a digital audio file for transformation into sinewave replicas of speech (Remez *et al.*, 1981). Sinewave speech transformations were created by tracking the frequencies and amplitudes of the first four formants as they varied over time.

These acoustic measurements were obtained in a two-step process. First, each sound file (originally recorded at a sampling rate of 22.050 kHz) was resampled to 10 kHz. The resampled sound file was then broken into windows of 10 ms each. Each window was the subject of an eight-order LPC analysis, and the four coefficients with the highest magnitudes were then converted to frequencies and magnitudes and stored in a data file. Each sound file thus had an associated data file with eight parameters (four frequencies and four magnitudes) per 10-ms window, corresponding to the change in the formants in the original sound file over time.

Sometimes the LPC analysis would output erroneous or spurious noises in the original sound file. To deal with this problem, the automated output file was scrutinized by hand to determine the accuracy of the automated process. Overall, the automated process proved to be an excellent starting point, although some slight adjustments in frequency and amplitude were necessary in several windows for most of the stimuli. The automated process had some difficulty in tracking formants during unvoiced portions of the speech waveform corresponding to periods of aspiration, consonant transitions, and frication. Adjustments in frequency and amplitude were made by hand using home-grown software constructed within MATLAB for this purpose.

The output of the two-stage process was a new data file specifying eight parameters (four frequencies and four associated amplitudes) for each 10-ms window in the original sound file. These data were then submitted to a synthesis routine that produced four sinusoidal tones that varied over time according to the parameter's output by the measurement process.

Figure 2 shows examples of the spectrograms of an original sound file from the stimulus set and its corresponding sinewave speech replica. As shown in the figure, the sinewave replica eliminated all extraneous information from the sound file other than the variation of the formants over time.

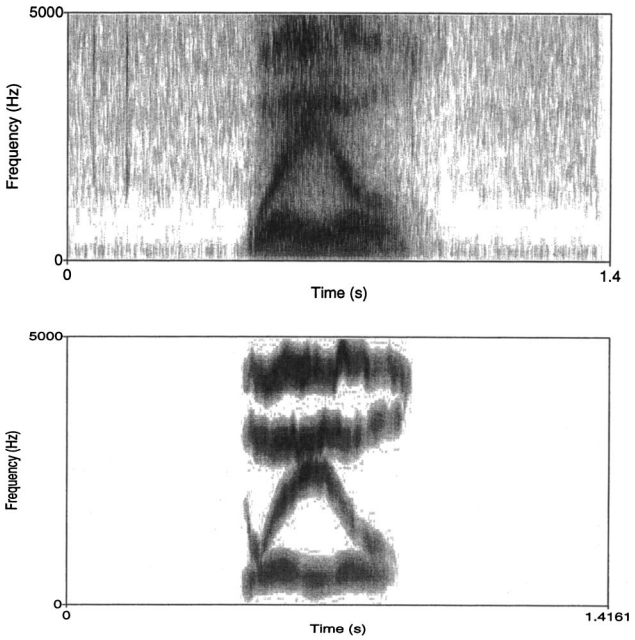

FIG. 2. The top panel shows a spectrogram of talker F1 speaking the word ''WAIL.'' The bottom panel shows a spectrogram of a synthetic sinewave replica of this token.

c. Familiarization phase. There was also a short familiarization phase so that participants could become accustomed to the unnaturalness of the sinewave speech replicas. The stimulus materials used during the familiarization phase were 20 isolated, monosyllabic English words that were not used in the final test list. These 20 words were spoken by a different talker who was not used to create the stimuli used in the point-light display database. The 20 familiarization words were converted into sinewave speech replicas using the same methods outlined earlier.

3. Procedure

During the familiarization phase, participants heard a sinewave speech replica of a spoken word and then the original, untransformed utterance from which that replica was constructed. This sinewave-original pair was presented three times in succession. After the third presentation of the stimulus pair, participants were asked to rate on a three-point scale how closely the sinewave replica matched the natural utterance. No feedback was provided. The familiarization task gave participants some exposure to the unusual nature of sinewave speech replicas without explicitly instructing them on how to identify words from them.

Figure 3 shows a schematic description of the cross-modal matching task. Participants in the ''V-A'' condition were first presented with a visual-alone point-light display video clip of a talker uttering an isolated, English word. Shortly after seeing this video display (500 ms), they were presented with two auditory-alone, *sinewave replicas* of speech. One of the clips was the same talker they had seen in the video (taken from the same utterance), while the other clip was a different talker. Participants were instructed to

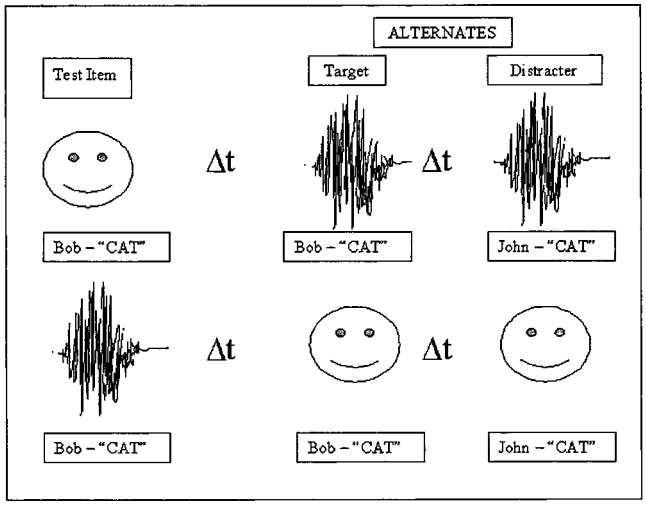

FIG. 3. Schematic of the cross-modal matching task. The top row illustrates the task in the ''V-to-A order.'' The bottom row illustrates the task in the ''A-to V order.'' Faces denote stimuli that are presented visual-alone. Waveforms denote stimuli that are presented auditory-alone. Δt is always 500 ms.

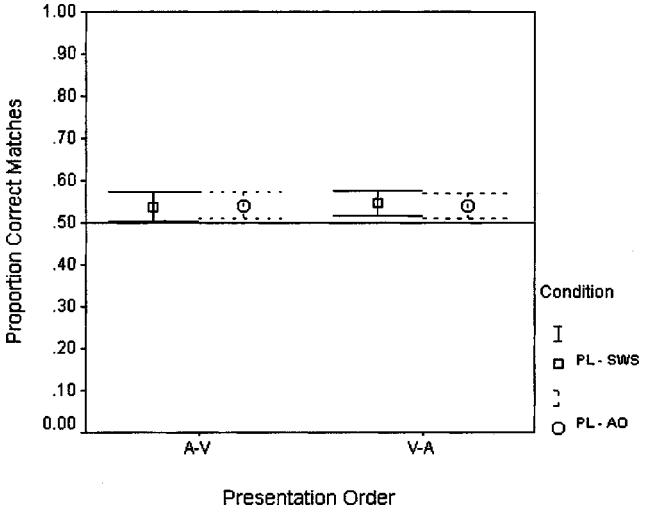

FIG. 4. Average proportion correct in the point-light to sinewave speech (PL+SWS) and point-light to untransformed audio (PL−AO) conditions of experiment 1. Error bars show standard errors.

choose the audio clip that matched the talker they had seen (''first'' or ''second''). Similar instructions were provided for participants in the ''A-V'' condition. These participants heard the audio clip first, and had to make their decision based on two video displays.

On each trial of the experiment, the test stimulus was either the video or audio portion of one movie token. Each movie token displayed an isolated word spoken by a single talker. The order in which the target and distracter choices were presented was randomly determined on each trial. For each participant, talkers were randomly paired with each other, such that each talker was contrasted against one and only one other talker for all trials in the experiment. For example, ''Mary'' was always contrasted with ''Jane,'' regardless of whether ''Mary'' or ''Jane'' was the target alternate on the trial. Responses were entered by pressing one of two buttons on a response box and transferred to a log file for further analysis.

A short training period (eight trials) preceded each participant's test session. During the training period, the participant was presented with a cross-modal matching trial and asked to pick the correct alternate. During training only, the response was followed immediately by feedback. The feedback consisted of playing back the entire audiovisual movie clip of the test word. The talkers and words used in the familiarization phase were different from those used in the testing period.

Half of the participants matched point-light displays with the original, untransformed sound files; the other half of the participants matched point-light displays with sinewave replicas of speech.

B. Results

Figure 4 shows performance on the cross-modal matching task when point-light (PL) displays were matched to untransformed auditory-only (AO) speech tokens (PL−AO) or sinewave speech (SWS) tokens (PL−SWS). The figure shows that cross-modal matching performance with point-light displays was quite poor, although statistically different from chance (0.5). Table I provides a summary of the descriptive statistics for each of the conditions pictured in Fig. 4. As shown in the table, performance in both matching conditions and both orders differed significantly from chance, indicating that cross-modal matching judgments can be carried out using only isolated kinematic displays in both the visual and auditory sensory domains.

The data were submitted to a 2×2 repeated measures ANOVA (order, matching condition). The ANOVA did not reveal any significant main effects or interactions.

C. Discussion

Point-light displays and sinewave speech replicas of isolated spoken words can be matched at above chance levels of performance across sensory modalities in a cross-modal matching task. This finding suggests that theoretically isolated kinematic displays of speech (visual and auditory) contain some information for cross-modal specification. The results are consistent with the proposal that cross-modal matching performance is based on the ability to detect vocal tract movement information from unimodal displays. Furthermore, the results are consistent with the hypothesis that cross-modal comparisons are made using a common, modality-neutral metric based on the kinematics of articulatory activity. Because these extremely simplified stimulus

TABLE I. Descriptive statistics for cross-modal matching performance when visual stimuli were point-light displays (PL) and auditory stimuli were either untransformed, natural utterances (AO) or sinewave speech replicas (SWS).

Matching condition	Order.	Mean	SE	t vs. 0.5
PL−AO	A-V	0.538	0.017	2.17[a]
	V-A	0.547	0.015	3.19[b]
PL−SWS	A-V	0.541	0.016	2.58[a]
	V-A	0.541	0.015	2.78[a]

[a] $p<0.05$.
[b] $p<0.01$.

displays were designed to eliminate all traditional cues to visual identity (e.g., configuration of facial features, shading, shape, etc.) and to auditory vocal identity (e.g., f0, average long-term spectrum, etc.), but preserve only the isolated movement of the vocal articulators, the results suggest that the common talker-specific information is sensory information that is related to articulatory kinematics of vocal tract activity.

It is interesting to note here that, compared to the performance on a similar cross-modal matching task (Lachs and Pisoni, in press) using fully illuminated faces and untransformed speech, performance was low. In those experiments, Lachs and Pisoni found that performance was 0.60 in the A-V condition and 0.65 in the V-A condition. There are two alternative explanations for this decrement in performance. First, it is possible that perceivers use more than just visible kinematics to successfully match identity across modality. However, because static images and dynamic video displays played backward do not allow for cross-modal matching above chance at all, this possibility seems unlikely. A second explanation is that the point-light displays used in experiment 1 failed to capture all of the relevant kinematic activity of the articulators. This seems plausible, as previous work has shown that the number and placement of points on a face during recording of point-light images affects performance on speech reception thresholds in noise (Rosenblum *et al.* 1996).

III. EXPERIMENT 2: WORD IDENTIFICATION WITH KINEMATIC PRIMITIVES

Taken together with the findings of experiment 1, the available evidence about the perception of indexical information from isolated kinematic primitives supports the hypothesis that talker-specific information is carried in parallel with phonetic information in the fine-grained kinematic details of a talker's articulator motions over time. These kinematic details are inherently modality-neutral because they refer to the common articulatory event, not the surface patterns of acoustic or optic energy impinging on the eyes or ears. As discussed above, an articulatory, modality-neutral form for speech information has also been proposed to account for audiovisual speech phenomena (Rosenblum, 1994), like the McGurk effect and audiovisual enhancement to speech intelligibility. Is the kinematic information available in sinewave speech and point-light displays also sufficient to support accurate word recognition?

Experiment 2 was designed to show that multimodal kinematic primitives are also integrated in a classic audiovisual integration task. Participants were asked to identify spoken words under two presentation conditions. In the auditory-alone condition, they were presented with sinewave replicas of isolated English words. In the audiovisual condition, they were presented with *multimodal* kinematic primitives: point-light displays of speech paired with sinewave replicas of the same utterance. Based on the earlier findings reported by Rosenblum *et al.* (1996) and Remez *et al.* (1999), we expected that word identification performance under combined, multimodal stimulation would show enhancement and would be better than performance under unimodal, auditory-alone stimulation. This finding would provide evidence in support of the proposal that auditory and visual displays of speech are ''integrated'' because they both carry information about the underlying kinematics of articulation.

A. Method

1. Experimental design

Experiment 2 used a word recognition task to measure speech intelligibility for isolated words. One within-subjects factor was manipulated. ''Presentation mode'' consisted of two levels: sinewave speech alone (SWS) and point-light display plus sinewave speech (PL+SWS). The levels of this factor were presented in blocks, which were counterbalanced for order of presentation across participants. In addition, an equal number of participants were presented with each word in each presentation mode.

2. Participants

Participants were 32 undergraduate students enrolled in an introductory psychology course who received partial credit for participation. All of the participants were native speakers of English and none of them reported any hearing or speech disorders at the time of testing. In addition, all participants reported having normal or corrected-to-normal vision. None of the participants in this experiment had any previous experience with the audiovisual speech stimuli used in this experiment.

3. Stimulus materials

The stimulus materials used during the familiarization phase were 20 isolated, monosyllabic English words that were not used in the final test list. These 20 words were spoken by a different talker who was not used to create the stimuli used in the point-light display database. The 20 familiarization words were converted into sinewave speech replicas using the same methods outlined in experiment 1.

The stimulus materials used during testing were identical to those used in experiment 1. However, only the sinewave replicas of the spoken words were used as auditory tokens in this experiment.

4. Procedures

Each session began with a short familiarization phase identical to the one outlined earlier in experiment 1 so that participants could become accustomed to the unusual nature of the sinewave speech replicas. It should be emphasized here that the familiarization task only asked for judgments of ''goodness'' and provided no feedback at all.

During the testing phase, each participant heard all 96 words spoken by one of the four point-light talkers. Every participant heard each talker speak on an equal number of trials, and no participant ever heard a word twice over the course of the experiment. The talker who spoke a given word was counterbalanced across participants. For each participant, 48 words were presented under audio-only (AO:SWS) conditions and the other 48 words were presented under audiovisual (AV:PL+SWS) conditions. A separate analysis, using another group of participants, revealed that the visual-

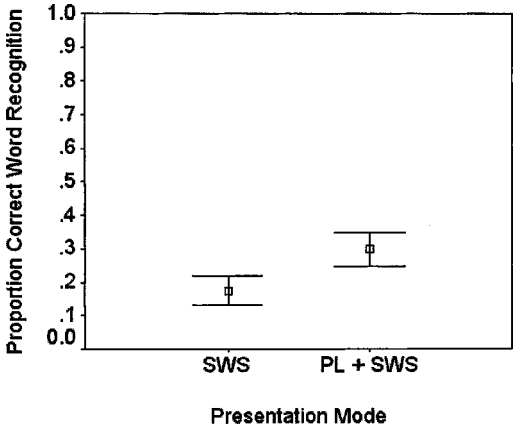

FIG. 5. Average proportion correct in the auditory-alone (SWS) and audiovisual (PL+SWS) conditions of experiment 2. Error bars show standard errors.

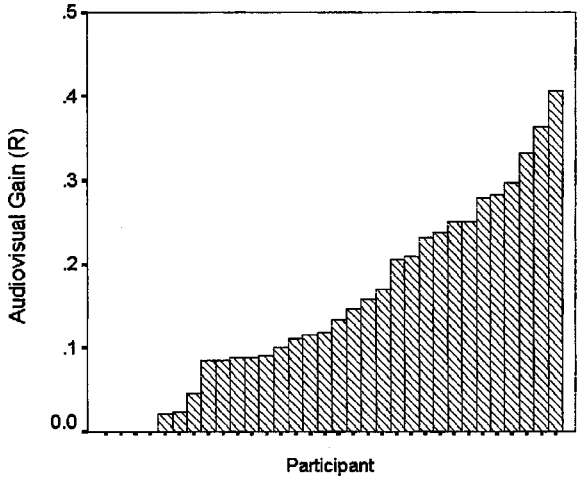

FIG. 6. *R* scores for each participant in experiment 2, sorted by performance. *R* scores represent the gain over auditory-alone performance due to additional visual information. Auditory stimuli were sinewave speech replicas and visual stimuli were point-light displays. The first four participants in the graph did not show any audiovisual gain.

alone intelligibility of the 96 words was 1.6% (Bergeson *et al.*, 2003). The assignment of a presentation context to each list and the order in which presentation contexts were viewed was counterbalanced across participants.

After each stimulus item was presented, the participant simply typed in the word he/she heard on a standard keyboard and clicked the mouse button to advance to the next trial.

B. Results

Each participant's responses were hand-screened for typing and spelling errors by two reviewers who worked independently. A typing error was defined as a substituted letter within one key on a standard keyboard of the target key or an inserted letter within one key of an adjacent letter in the response. Spelling errors were only accepted if the letter string did not form a word in its own right. Using this conservative method of assessment, the two reviewers had a 100% agreement rate on classifying responses as typing and spelling errors. Responses on this task were scored correct if, and only if, they were homophonous with the target word in a standard American English dialect (e.g., "bare" for "bear," but not "pin" for "pen").

A paired-samples *t*-test comparing scores on the SWS and PL+SWS conditions revealed a significant difference between auditory-only and audiovisual performance, $t(31) = 7.69$, $p < 0.05$. Figure 5 shows that performance with the audiovisual (PL+SWS) stimuli was higher than performance with the auditory-only (SWS) stimuli. The mean difference between the SWS and PL+SWS conditions was 12.4% (SE =1.6%).

a. Audiovisual gain (R scores). In order to examine individual differences in the extent to which combined audiovisual stimuli enhanced word intelligibility, the scores in the SWS and PL+SWS conditions were combined into a single metric to obtain the measure *R*, the relative gain in speech perception due to the addition of visual information (Sumby and Pollack, 1954). *R* was computed using the following formula:

$$R_a = \frac{\mathrm{AV} - \mathrm{A}}{100 - \mathrm{A}}$$

where AV and A represent the speech intelligibility scores obtained in the audiovisual and auditory-alone conditions, respectively. From this formula, one can see that *R* measures the gain in accuracy in the AV condition relative to the accuracy in the A condition, normalized relative to the amount by which speech intelligibility could have possibly improved above the auditory-alone scores. The *R* score can be used as an effective measure for comparing audiovisual gain across participants, because it effectively normalizes for the baseline, auditory-alone performance.

Figure 6 shows the *R* scores for all 32 participants in experiment 2 ($M = 0.154$, SE=0.020). A few participants ($N = 4$) showed no gain at all over auditory-alone performance. However, most of the participants showed some advantage in identifying words in the audiovisual condition relative to the auditory-alone condition. One participant showed a gain of 41% due to multimodal presentation. The *R* scores were significantly different from zero [$t(31) = 7.67$, $p < 0.05$] indicating that the point-light displays facilitated the intelligibility of all words, despite the fact that they were virtually unintelligible under visual-alone conditions (Bergeson *et al.*, 2003).

C. Discussion

The present set of results using point-light displays and sinewave replicas of speech demonstrate that some information for the combined perception of visual and auditory speech exists in highly impoverished displays that isolate the kinematics of articulatory activity that underlie the production of speech. Even with limited, minimal information in the two sensory modalities, participants were able to perceive point-light displays and sinewave speech as integrated patterns, and they were able to exploit the two sources of sensory information to aid them recognizing isolated spoken words. On average, additional point-light information in-

creased intelligibility by 12%, almost doubling the intelligibility of the sinewave speech tokens observed in isolation. Furthermore, this performance advantage was well above the reported intelligibility of the PL stimuli in visual-alone conditions, indicating that the two sources of information were indeed integrated, and not simply linearly combined (Grant and Seitz, 1998; Massaro, 1998).

1. Individual differences in perceptual integration

In a recent study, Grant *et al.* (1998) compared observed audiovisual gain scores to the gains predicted by several models of sensory integration. These models predicted optimal AV performance based on observed recognition scores for consonant identification in auditory-alone and visual-alone conditions. Grant *et al.* (1998) found that the models either over- or underpredicted the observed audiovisual data, indicating that not all individuals integrate auditory and visual information optimally. The present results also revealed individual differences in the extent to which sources of auditory and visual information could be combined and integrated together to support spoken word recognition. Audiovisual gain scores in the present experiment ranged from 0% to 41%.

Without question, the informative value of optic and acoustic arrays for specifying linguistic information must be interpreted in terms of a perceiver's sensitivity to relevant phonetic contrasts in the language. It is well known that speechreading performance in hearing-impaired and normal-hearing listeners is subject to wide variation (Bernstein *et al.*, 2000). It is not unreasonable to assume that the speechreading of point-light displays will be subject to at least the same degree of variation, and that such variation might have extensive effects on the ability to integrate auditory and visual displays of speech. Investigations into the role of individual differences in multisensory perception may provide important insights into the perceptual integration of audiovisual speech information and its development (Lewkowicz, 2001).

Despite the individual variation, however, the results of the present study are consistent with the hypothesis that auditory and visual speech information are combined and integrated with reference to the underlying kinematic activity of the vocal tract. With dynamic movement information available from either sensory modality, perceivers appear to have evaluated the two kinds of information together, and exhibited the audiovisual gain finding that has been replicated many times in the literature (see Grant and Seitz, 1998). The present results extend and complement the recent findings of Rosenblum *et al.* (1996) and Remez *et al.* (1999) who found that theoretically isolated kinematic displays could facilitate word identification in conjunction with untransformed displays in the other sensory modality. The present results also provide additional support for the proposal that the evaluation of optical and acoustic information conceptualized along a common, kinematic and articulatory metric underlies classic audiovisual integration phenomena such as audiovisual enhancement (Summerfield, 1987).

IV. GENERAL DISCUSSION

Taken together, the results of these experiments using multimodal kinematic primitives reveal that talker-specific and phonetic information may be specified in the kinematics of a talker's vocal tract activity. A common form of phonetic representation, focusing on the articulatory origin of spoken language, may therefore be needed to account for the robust findings in the audiovisual speech perception literature (Schwartz *et al.*, 1998; Summerfield, 1987), as well as investigations into the indexical properties of spoken language (Remez *et al.*, 1997; Rosenblum *et al.*, 2002).

Our conclusion is drawn based on the unique nature of the stimuli used in the present experiments. We claim that our results do not simply imply that perceivers are sensitive to two impoverished signals in disparate sources of sensory information. The important point here is that the signals in our experiments are impoverished in a principled way that theoretically *isolates* important kinematic information about the underlying articulation. The sinewave speech transformation is a systematic way of removing all information from an acoustic speech signal, while at the same time preserving information about the resonances of the front and back cavities of the vocal tract (Remez *et al.*, 1981). Similarly, point-light displays of speech do not simply make visual displays of speech harder to recognize. Rather, they specifically attempt to isolate the motion of points (or near-points) on the talker's face while eliminating all other sources of visual information (Rosenblum and Saldaña, 1996). The results presented here dovetail with the experiments presented in Lachs and Pisoni (2004), in which it was found that only acoustic transformations that preserve the linear relationship between formant frequencies preserved the ability to match faces and voices cross-modally. In that series of experiments, as in the present studies, the data were consistent with the assertion that preservation of articulatory information about speech is important for specifying the underlying link between the optical and acoustic correlates of speech.

One potential problem with the results from experiment 1 is that performance levels, although statistically above chance, were not very high. However, we point out that our main goal in the present experiment was to demonstrate that it was, in practice, *possible* for participants to perform this extremely difficult cross-modal matching task with minimal feedback, training, or other prior experience. As discussed above, the difficulty of the general cross-modal matching task was demonstrated in the fully illuminated, full bandwidth version of the cross-modal matching task (Lachs and Pisoni, in press), in which performance was only between 60% and 65% accurate (depending on the condition). Whether manipulations such as training, feedback, or other types of experience can raise performance (as we suspect they will) remains an empirical question we have chosen to leave to another series of experiments. Further evidence for the reliability of the basic cross-modal matching results reported here using kinematic primitives has also been established by two independent research groups working with different stimulus materials. Kamachi *et al.* (2003) investigated cross-modal matching ability with sentence-length stimuli. Their results showed that fully illuminated faces could be

matched to sinewave speech with an average accuracy of 61%. In another recent study, Rosenblum *et al.* (under review) also used sentence-length stimuli and showed that point-light faces could be matched to untransformed speech at above chance levels of performance. Rosenblum *et al.* also compared performance in this condition to conditions in which the visual point-light information was either jumbled or staggered. In the jumbled condition, video frames from the original recording were presented out of their originally recorded temporal sequence. In the staggered condition, frames were presented in the correct order, but were presented such that the duration of the frame's presentation was varied. In both of these control conditions, Rosenblum *et al.* found that performance in the cross-modal matching task was inferior to performance with the unaltered point-light stimuli. The authors concluded from this pattern of results that the evolving dynamics of visible articulatory activity are implicated in the ability to perform this task.

One alternative explanation of the present findings could appeal to the use of an abstract (rather than articulatory) modality-neutral representational format. For example, in experiment 2, stimulation from the various sensory modalities could be converted, in isolation, to some kind of amodal, symbolic, phonetic description, and then these two phonetic descriptions could be evaluated and integrated, without recourse to articulatory behavior. However, such a representational format would not account for the results of experiment 1, where no phonetic information could possibly have helped match talkers' faces and voices (because the utterance used for both the target and distracter was identical). To account for these findings, it is necessary to propose a secondary set of abstract representations for talker identity to account for the cross-modal matching findings of experiment 1. We propose that our articulatory account is simpler and more parsimonious than the alternative, abstractionist account.

It is also possible that the results of experiment 1 could be explained by perceptual sensitivity to some kind of cross-correlation between information presented in the auditory and visual domains, without reference to articulation or any sort of articulatory metric. This might be a plausible explanation for the results of experiment 1, given the growing evidence that correlations between surface features of visual and auditory signals can explain reductions in detection thresholds for auditory speech in noise (Grant and Seitz, 2000) and speech band-pass filtered to isolate F1 or F2 (Grant, 2001). Indeed, the results of experiment 1 emphasize the need for models of audiovisual integration to recognize and incorporate sensitivity to cross-modal information. However, it is not clear how an account of cross-modal information based on cross-correlations of surface features in the acoustic and optic signals could account for the findings of experiment 2, in which the combination of isolated kinematics in both sensory modalities was used to enhance word recognition performance. While it seems reasonable to suggest that perceptual sensitivity to correlations between surface features would aid in lowering detection thresholds and in explicitly identifying cross-modal relationships, it is unclear how such sensitivity to multimodal correlations might assist in recognizing the meaningful linguistic content of an utterance.

The results presented here are consistent with direct-realist theories of speech perception (Fowler, 1986; Gibson, 1979). These ''ecological'' theories of perception are based on the findings that patterns in light and sound are structured and lawfully related to the physical events that caused them. For example, the ambient light in a room is reflected off multiple surfaces, like the floor, walls, tables, chairs, etc., before it stimulates the retina. The pattern of light observable from the point-of-view of an active observer, then, is highly *structured* with respect to the relationship between the observer and his or her environment. Furthermore, this structure is lawfully determined by the physical properties of light. In the same way, events in the environment that have acoustic consequences structure patterns in pressure waves by virtue of the physical properties of sound (Gibson, 1979). Direct realists therefore assert that direct and unmediated perceptual access to the causes of ecologically important events is possible simply by virtue of the lawful relations between the patterns of energy observable by a perceiver and the events that caused them.

According to this theoretical perspective, the question for audiovisual speech research is not to determine how auditory and visual signals are translated into a common representational format, but rather to discover the ways in which optical and acoustical signals structure or specify the informative properties of vocal tract articulation. The present results add to the now growing body of research suggesting that both the acoustic and optical properties of speech carry *kinematic* or *dynamic* information about the articulation of the vocal tract (Rosenblum, 1994), and that these sources of information drive the perception of linguistically significant utterances (Summerfield, 1987). As demonstrated in the present investigation, kinematic parameters provide enough detailed information to support spoken word recognition and talker identification. The kinematic description for speech information may then dovetail with attempts to recast computational models of the mental lexicon in terms that incorporate both linguistic and indexical information in memory for spoken words (Goldinger, 1998). Indeed, a modality-neutral basis for lexical knowledge has been implicated in recent investigations of speechreading that show an underlying similarity in the factors relevant to visual-alone and auditory-alone spoken word recognition. For example, Auer (2002) found that phonological neighborhood density (the number of words in the lexicon that are phonologically similar to a target word) influences speechreading for isolated words. Lachs and Pisoni (submitted) also reported similar results, showing that word frequency and phonological neighborhood frequency (i.e., the average frequency of phonological neighbors) also affect speechreading performance.

Such a reconceptualization of the mental lexicon might also help to integrate direct realist theories of speech perception (Fowler, 1986) with research on the traditionally higher-order, ''cognitive'' mechanisms involved in spoken word recognition and language processing (see Luce and Pisoni, 1998). At first glance, these abstract symbol processing approaches seem inherently incompatible with ecologically ori-

ented approaches to psychology. However, some recourse to lexical knowledge must be incorporated into any theory of speech perception, direct-realist or otherwise. By grounding perceptual information about speech in a modality-neutral, ecologically plausible framework, it may be possible to reformulate traditional cognitive architectures in a format that is more amenable to ecological principles (see also Brancazio, 1998).

We should note that the modality-neutral form of talker-specific information suggested here is restricted to sensory patterns that are lawfully structured by articulatory events, and not to static visual features that are commonly implicated in models of face recognition [e.g., configuration of facial features, color, shading, and shape; see Bruce (1988)]. This observation raises an interesting dichotomy: the difference between visual kinematic information about *facial* identity versus visual kinematic information about *vocal* identity. The point-light displays used in the present experiment contained sufficient detail about the idiosyncratic speaking style (or ''voice'') of the talker to specify the auditory form of the utterance. Thus, the kinematic motions that were useful to participants in the present experiment could be called ''visual voice'' or ''visual indexical'' information. In contrast, visual motion information can be useful for identifying the person portrayed in the visual display, *irrespective of* that person's unique vocal qualities or articulatory behaviors.

Bruce and Valentine (1988), for example, showed that participants could identify familiar faces when shown point-light displays of familiar persons making different facial expressions and moving their heads. This kind of dynamic information reflects the identity of the person but is not related to the idiosyncratic speaking style of the talker, because the faces to be identified in their study were not speaking. Moreover, visual identity information can also be obtained from point-light displays of talkers *speaking*, as discussed above (Rosenblum *et al.*, 2002).

Evidence for the dichotomy between visual face and visual indexical information has also been found in neuropsychological investigations of prospopagnosia and aphasia. For example, Campbell *et al.* (1986) reported on two patients: Mrs. ''D.'' had the ability to speechread and was susceptible to the McGurk effect, despite having a profound prosopagnosia that rendered her incapable of discriminating the identity of various faces. In contrast, another patient, Mrs. ''T.,'' showed no ability to lipread, yet she could recognize faces quite well.

It should be emphasized that the present results are only relevant to the ability of optic displays to convey voice information; modality-neutral information for voice perception appears to be conveyed by kinematic movements of the articulators. It remains to be seen whether such information is also useful for discriminating faces in the absence of speech. For example, it is not clear from these results whether training with point-light displays of a person engaged in the act of speaking would facilitate the subsequent recognition of that person's face engaged in *other* types of facial motion (e.g., laughing, smiling, frowning, nodding, etc.). What is clear from the present results, however, is that the idiosyncratic speaking style of a talker is partially conveyed in modality-neutral form and is comparable across visual and auditory sensory modalities as long as the underlying kinematics of the time-varying pattern of articulation is preserved.

The present findings demonstrate that theoretically isolated kinematic information in both the optical and acoustic displays of speech are able to specify talker-specific information that can be successfully combined during the process of speech perception. Future work on audiovisual speech perception may need to formulate more rigorous theoretical descriptions of the nature of audiovisual speech integration effects by recasting speech information in terms of its dynamic, articulatory, and ultimately modality-neutral form.

ACKNOWLEDGMENTS

This research was supported by NIH-NIHCD Training Grant No. DC00012 and NIDCD Research Grant No. DC-00111 to Indiana University. The authors would like to thank Luis R. Hernandez, Ralph Zuzolo, Alan Mauro, Jeff Karpicke, and Jeff Reynolds for invaluable assistance during all phases of this research. In addition, the authors thank Geoffrey Bingham, Robert Port, Thomas Busey, and four anonymous reviewers for their valued input and advice.

Auer, Jr., E. T. (**2002**). ''The influence of the lexicon on speechread word recognition: Contrasting segmental and lexical distinctiveness,'' Psychonom. Bull. Rev. **9**(2), 341–347.

Bergeson, T. R., Pisoni, D. B., Lachs, L., and Reese, L. (**2003**). ''Audiovisual integration of point light displays of speech by deaf adults following cochlear implantation,'' in *Proceedings of the 15th International Conference on Phonetic Sciences* (Causal Productions, Adelaide, Australia), pp. 1469–1472.

Bernstein, L. E., Demorest, M. E., and Tucker, P. E. (**2000**). ''Speech perception without hearing,'' Percept. Psychophys. **62**(2), 233–252.

Bingham, G. P. (**1995**). ''Dynamics and the problem of visual event recognition,'' in *Mind as Motion: Explorations in the dynamics of cognition*, edited by R. F. Port and T. Van Gelder, Cambridge, MA: The (MIT, Cambridge), pp. 403–448.

Blesser, B. (**1972**). ''Speech perception under conditions of spectral transformation: I. Phonetic characteristics,'' J. Speech Hear. Res. **15**(1), 1–41.

Braida, L. D. (**1991**). ''Crossmodal integration in the identification of consonant segments,'' Q. J. Exp. Psychol. **43A**(3), 647–677.

Brancazio, L. (**1998**). ''Contributions of the lexicon to audiovisual speech perception,'' unpublished Ph.D., dissertation, University of Connecticut.

Bruce, V. (**1988**). *Recognising Faces* (Erlbaum, Hove, UK).

Bruce, V., and Valentine, T. (**1988**). ''When a nod's as good as a wink: The role of dynamic information in facial recognition,'' in *Practical Aspects of Memory: Current research and issues: Vol. 1. Memory in everyday life*, edited by M. M. Gruneberg, P. E. Morris, and R. N. Sykes (Wiley, New York), pp. 169–174.

Campbell, R., Landis, T., and Regard, M. (**1986**). ''Face recognition and lipreading: A neurological dissociation,'' Brain **109**, 509–521.

Fowler, C. A. (**1986**). ''An event approach to the study of speech perception from a direct-realist perspective,'' J. Phonetics **14**, 3–28.

Fowler, C. A., and Dekle, D. J. (**1991**). ''Listening with eye and hand: Cross-modal contributions to speech perception,'' J. Exp. Psychol. Hum. Percept. Perform. **17**(3), 816–828.

Gibson, J. J. (**1979**). *The Ecological Approach to Visual Perception* (Houghton-Mifflin, Boston).

Goldinger, S. D. (**1998**). ''Echoes of echoes? An episodic theory of lexical access,'' Psychol. Rev. **105**(2), 251–279.

Grant, K. W. (**2001**). ''The effect of speechreading for masked detection thresholds for filtered speech,'' J. Acoust. Soc. Am. **109**, 2272–2275.

Grant, K. W., and Seitz, P. F. (**1998**). ''Measures of auditory-visual integration in nonsense syllables and sentences,'' J. Acoust. Soc. Am. **104**, 2438–2450.

Grant, K. W., and Seitz, P. F. (**2000**). ''The use of visible speech cues for improving auditory detection of spoken sentences,'' J. Acoust. Soc. Am. **108**(3), 1197–1208.

Grant, K. W., Walden, B. E., and Seitz, P. F. (**1998**). ''Auditory-visual speech recognition by hearing-impaired subjects: Consonant recognition, sentence recognition, and auditory-visual integration,'' J. Acoust. Soc. Am. **103**, 2677–2690.
Johansson, G. (**1973**). ''Visual perception of biological motion and a model for its analysis,'' Percept. Psychophys. **14**, 201–211.
Kamachi, M., Hill, H., Lander, K., and Vatikiotis-Bateson, E. (**2003**). '''Putting the face to the voice': Matching identity across modality,'' Curr. Biol. **13**, 1709–1714.
Kozlowski, L. T., and Cutting, J. E. (**1978**). ''Recognizing the gender of walkers from point-lights moutned on ankles: Some second thoughts,'' Percept. Psychophys. **23**, 459.
Lachs, L., and Pisoni, D. B. (**2004a**). ''Crossmodal source information and spoken word recognition,'' J. Exp. Psychol. Hum. Percept. Perform. **30**(2), 378–396.
Lachs, L., and Pisoni, D. B. (**in press**). ''Crossmodal source identification in speech perception,'' Ecol. Psychol.
Lachs, L., and Pisoni, D. B. (**submitted**). ''Spoken word recognition without audition,'' Percept. Psychophys.
Lewkowicz, D. J. (**2001**). ''Infants' perception of the audible, visible and bimodal attributes of multimodal syllables,'' Child Dev. **71**(5), 1241–1257.
Liberman, A., and Mattingly, I. (**1985**). ''The motor theory revised,'' Cognition **21**, 1–36.
Luce, P. A., and Pisoni, D. B. (**1998**). ''Recognizing spoken words: The neighborhood activation model,'' Ear Hear. **19**, 1–36.
Massaro, D. W. (**1998**). *Perceiving Talking Faces: From speech perception to a behavioral principle* (MIT, Cambridge, MA).
McGurk, H., and MacDonald, J. (**1976**). ''Hearing lips and seeing voices,'' Nature (London) **264**, 746–748.
Munhall, K. G., and Vatikiotis-Bateson, E. (**1998**). ''The moving face during speech communication,'' in *Hearing by Eye II: Advances in the Psychology of Speechreading and Auditory-visual Speech*, edited by R. Campbell, B. Dodd, and D. Burnham (Psychology, East Sussex, UK), pp. 123–139.
Reisberg, D., McLean, J., and Goldfield, A. (**1987**). ''Easy to hear but hard to understand: A lip-reading advantage with intact auditory stimuli,'' in *Hearing by Eye: The psychology of lip reading*, edited by B. Dodd and R. Campbell (Erlbaum, Hillsdale, NJ), pp. 97–114.
Remez, R. E., Fellowes, J. M., and Rubin, P. E. (**1997**). ''Talker identification based on phonetic information,'' J. Exp. Psychol. Hum. Percept. Perform. **23**(5), 651–666.
Remez, R. E., Rubin, P. E., Pisoni, D. B., and Carrell, T. D. (**1981**). ''Speech perception without traditional speech cues,'' Science **212**, 947–950.
Remez, R. E., Fellowes, J. M., Pisoni, D. B., Goh, W. D., and Rubin, P. E. (**1999**). ''Multimodal perceptual organization of speech: Evidence from tone analogs of spoken utterances,'' Speech Commun. **26**(1–2), 65–73.
Rosenblum, L. D. (**1994**). ''How special is audiovisual speech integration?'' Curr. Psychol. Cognition **13**(1), 110–116.
Rosenblum, L. D., and Saldaña, H. M. (**1996**). ''An audiovisual test of kinematic primitives for visual speech perception,'' J. Exp. Psychol. Hum. Percept. Perform. **22**(2), 318–331.
Rosenblum, L. D., Johnson, J. A., and Saldaña, H. M. (**1996**). ''Point-light facial displays enhance comprehension of speech in noise,'' J. Speech Lang. Hear. Res. **39**, 1159–1170.
Rosenblum, L. D., Smith, N. M., Nichols, S. M., Hale, S., and Lee, J. (**under review**). ''Hearing a face: Cross-modal speaker matching using isolated visible speech,'' Percept. Psychophys.
Rosenblum, L. D., Yakel, D. A., Baseer, N., Panchal, A., Nodarse, B. C., and Niehaus, R. P. (**2002**). ''Visual speech information for face recognition,'' Percept. Psychophys. **64**(2), 220–229.
Runeson, S. (**1994**). ''Perception of biological motion: The KSD-principle and the implications of the distal versus optimal approach,'' in *Perceiving Events and Objects*, edited by G. Jansson, S. S. Bergström, and W. Epstein (Erlbaum, Hillsdale, NJ), pp. 383–405.
Runeson, S., and Frykholm, G. (**1981**). ''Visual perception of lifted weight,'' J. Exp. Psychol. Hum. Percept. Perform. **7**, 733–740.
Schultz, M., Norton, S., Conway-Fithian, S., and Reed, C. (**1984**). ''A survey of the use of the Tadoma method in the United States and Canada,'' Volta Rev. **86**, 282–292.
Schwartz, J.-L., Robert-Ribes, J., and Escudier, P. (**1998**). ''Ten years after Summerfield: A taxonomy of models for audio-visual fusion in speech perception,'' in *Hearing by Eye II*, edited by R. Campbell, B. Dodd, and D. Burnham (Psychology, East Sussex, UK), pp. 85–108.
Smith, Z. M., Delgutte, B., and Oxenham, A. J. (**2002**). ''Chimaeric sounds reveal dichotomies in auditory perception,'' Nature (London) **416**, 87–90.
Sumby, W. H., and Pollack, I. (**1954**). ''Visual contribution of speech intelligibility in noise,'' J. Acoust. Soc. Am. **26**, 212–215.
Summerfield, Q. (**1987**). ''Some preliminaries to a comprehensive account of audio-visual speech perception,'' in *Hearing by Eye: The Psychology of Lip-Reading*, edited by B. Dodd and R. Campbell (Erlbaum, Hillsdale, NJ), pp. 3–51.
Vatikiotis-Bateson, E., Hill, H., Kamachi, M., Lander, K., and Munhall, K. (**2002**). ''The stimulus as basis for audiovisual integration,'' paper presented at the International Conference on Spoken Language Processing, Denver, CO.
Vatikiotis-Bateson, E., Munhall, K. G., Hirayama, M., Lee, Y. V., and Terzepoulos, D. (**1997**). ''The dynamics of audiovisual behavior in speech,'' in *Speechreading by Humans and Machines*, edited by D. G. Stork and M. E. Hennecke (Springer-Verlag, Berlin), pp. 221–232.
Yehia, H., Rubin, P. E., and Vatikiotis-Bateson, E. (**1998**). ''Quantitative association of vocal-tract and facial behavior,'' Speech Commun. **26**(1–2), 23–43.

Blind normalization of speech from different channels

David N. Levin[a)]
Department of Radiology, University of Chicago, Chicago, Illinois 60637

(Received 13 April 2003; accepted for publication 5 April 2004)

We show how to construct a channel-independent representation of speech that has propagated through a noisy reverberant channel. This is done by blindly rescaling the cepstral time series by a nonlinear function, with the form of this scale function being determined by previously encountered cepstra from that channel. The rescaled form of the time series is an invariant property of it in the following sense: It is unaffected if the time series is transformed by any time-independent invertible distortion. Because a linear channel with stationary noise and impulse response transforms cepstra in this way, the new technique can be used to remove the channel dependence of a cepstral time series. In experiments, the method achieved greater channel-independence than cepstral mean normalization, and it was comparable to the combination of cepstral mean normalization and spectral subtraction, despite the fact that no measurements of channel noise or reverberations were required (unlike spectral subtraction). © *2004 Acoustical Society of America.*
[DOI: 10.1121/1.1755235]

PACS numbers: 43.72.Ar, 43.72.-p, 43.60.Lq [DO] Pages: 519–529

I. INTRODUCTION

A. The problem

An ideal automatic speech recognition (ASR) system would be speaker-independent and channel-independent. After training during its manufacture, it would work ''out of the box'' to successfully recognize the utterances of different individuals speaking through a variety of channels. However, despite the steady progress of speech recognition technology in recent years, existing systems with large vocabularies are still sensitive to the nature of the acoustic environment and to the identity of the speaker.[1–3] For example, extensive retraining is often required if the acoustic channel is altered because the noise level changes, the speaker's room or position changes, or the signal conduit changes (e.g., telephone versus room speech). This paper considers the problem of designing speaker-dependent systems that are channel-independent. In other words, the objective is to create an ASR system that can accurately recognize a given speaker's utterances after they have propagated through any linear channel, once the system has been trained to recognize that speaker's speech from one linear channel. Ideally, the system would quickly adapt to changing channel conditions (e.g., to the changing noise and impulse response function of a moving speaker and/or microphone). This report describes a nonlinear signal processing method that makes speech signals more channel-independent and that can be used in the ''front end'' of any ASR system.

B. Conventional methods of achieving channel-independent ASR

In most commonly encountered situations, the acoustic environment can be characterized in the time domain by a convolutive impulse response function and additive noise. In this case, the corrupted speech signal is parametrized by the filterbank outputs:

$$P_i = \int |X(f)|^2 |H(f)|^2 M_i(f) df + N_i, \tag{1}$$

where P_i is the power of the corrupted signal from the ith filterbank element, $|X(f)|^2$ is the power density of the channel's input (clean) signal, $|H(f)|^2$ is the power density of the channel's impulse response function, $M_i(f)$ is the profile of the ith filterbank element, and N_i is the noise power from that element. This equation depends on the following approximations, which are commonly made and often work well in practice:[1] (1) the impulse response is small at time delays greater than the length of the spectral window; (2) the noise is not correlated with the speech. Notice that the noise term in Eq. (1) represents the noise power integrated over relatively wide filterbank elements (e.g., elements of a mel frequency filterbank). Therefore, to the extent that the underlying noise distribution is stationary and ''white,'' this term is an average quantity with small frame-to-frame fluctuations.

Now, suppose that an ASR system was trained to recognize speech in one environment (e.g., clean speech) and it is now being used to analyze utterances from another channel (e.g., corrupted speech). If the channel transfer function H is approximately constant over each filterbank element, it can be factored out of the integral in Eq. (1). Then, in the absence of noise, it simply has the effect of a translation in cepstral space, and cepstral mean normalization[4] (CMN) can be used to ''subtract it out'' in order to remove the effects of reverberations. However, if noise is present and/or the transfer function is narrow, there is a nonlinear relationship between the cepstra from the two channels, and CMN is not as effective. Alternatively, reverberations can be compensated by accounting for the form of the impulse response after it has been measured by playing white noise, sine waves, or a chirp through the channel of interest.[5] However, this proce-

a)Electronic mail: d-levin@uchicago.edu

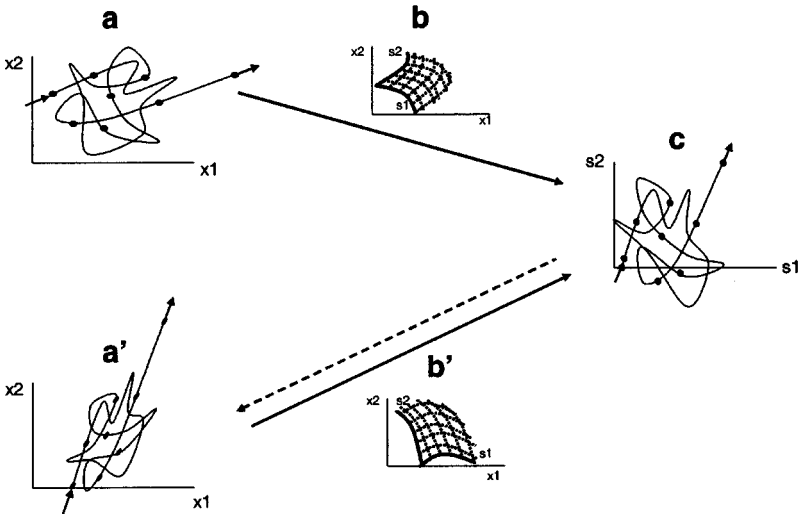

FIG. 1. Schematic outline of the new method. (a) The cepstral trajectory of an utterance from channel 1. (b) The scale function derived from a speech sample from channel 1. (a′) The cepstral trajectory of the channel 2 version of the utterance in *a*. (b′) The scale function derived from a channel 2 speech sample. (c) The trajectory found by using *b* to rescale *a*, which is also equal to the trajectory found by using b' to rescale a'. The dotted arrow shows how the channel 1 cepstra (*a*) can be converted into the channel 2 cepstra (a') by mapping the rescaled values of *a* through the inverse of the channel 2 scale function (b').

dure can be impractical because such measurements may have to be repeated frequently in order to track a changing channel. Reverberations can also be combated with even more elaborate (and more cumbersome) methods involving microphone arrays.[6]

The simplest way of accounting for noise is spectral subtraction, but this requires periodic noise power measurements.[7] Therefore, its implementation requires accurate discrimination between speech and no speech, which may require the help of the recognizer in the system's ''back end.'' Wiener filtering can also be used to suppress noise, but this requires measurements of both the speech and noise power spectra.[8]

Another approach is to modify the system's back end in order to incorporate the expected effects of a channel. For example, in ''multistyle training,'' the recognizer is trained on a database that contains speech samples from a variety of common channels.[9] In principle, this method has the disadvantage of ''blurring'' the statistical distributions of the recognizer, and, of course, it may perform poorly in the presence of an unanticipated channel. Alternatively, a clean speech model can be adapted to the channel of interest by using maximum likelihood linear regression[10] or by a parallel combination of clean speech and noise models.[11] However, this may entail a significant computational expense. Of course, one can attempt to fully retrain the recognizer for the channel of interest after it is first encountered. This is just the ''brute force'' approach that channel normalization techniques seek to avoid because it requires access to a full database of corrupted speech, and this must be measured or it must be synthesized from a database of clean speech after the channel's characteristics have been estimated. The experimental or computational burden is great, particularly if the system is meant to handle large vocabularies.

C. The proposed method of channel normalization

Humans accurately perceive the information content of ordinary speech that has undergone a variety of channel-dependent signal transformations that often confound existing ASR systems. Yet there is no evidence that the speaker and listener exchange calibration data or that they measure the channel's impulse response and noise. Evidently, listeners can blindly extract the same invariant content from multiple acoustic signals that are transformed versions of one another. In earlier reports,[12–17] the author showed how to design sensory devices that have this ability to normalize time-dependent signals differing by unknown transformations (linear or nonlinear). In such devices, the signal is blindly rescaled by a nonlinear function, with the form of this scale function being determined by previously encountered signal levels. The rescaled form of a signal time series is an invariant property of it in the following sense: It is unaffected if the time series is transformed by any time-independent invertible (one to one) distortion. In other words, the original time series and the transformed versions of it have the same rescaled form. This is because a transformation's effect on the signal level at any time is compensated by its effect on the scale function. In earlier publications, this method was illustrated by applying it to analytic examples, simulated signals, acoustic wave forms of human speech, spectral time series of bird songs, and spectral time series of synthetic speech-like sounds.[12,13,15,16]

This approach is relevant to speech recognition for the following reason.[14] After an utterance is passed through two different channels, the cepstral time series of the resulting output signals are related to one another by a nonlinear transformation that characterizes the differences between the two channels. As shown in Sec. II, Eq. (1) implies the invertibility and time-independence of this transformation, as long as each channel's impulse response and noise distribution are stationary. Therefore, the same representation will result when the cepstral time series from either channel is blindly rescaled by the new signal processing method (Fig. 1). Alternatively, the cepstral time series of utterances from channel 1 can be used to estimate the cepstral time series of the same utterances from channel 2 by first finding the invariant representation of the channel 1 signal and then synthesizing the channel 2 signal having the same invariant representation (dotted arrow in Fig. 1). This ''channel conversion'' procedure can be performed as long as one has: (1) samples of the speaker's utterances from the two channels (possibly *different* utterances from each channel); (2) a few reference cep-

stra from each channel, which represent the same input sounds and are used to define the origin and orientation of each channel's scale function. Notice that the new method has the following advantages compared to conventional approaches to channel normalization: (1) It does not require explicit measurements of the channel's impulse response and noise; (2) it is a pure front end technology and avoids the computational demands of modifying or retraining the system's recognizer. Furthermore, the method can be run in an adaptive mode in order to account for changing channel conditions. This is done by using the most recent speech from the changing channel to continually update that channel's scale function.

The mathematical framework of the new method is described in Sec. II. Section III describes experiments in which the technique was used to normalize dimensionally reduced speech data from different channels. The implications of these results and possible extensions of this work are discussed in Sec. IV.

II. THEORY

In this section, we argue that a time-independent invertible transformation must relate the pair of cepstral time series, produced by the same utterance propagating through two time-independent channels. Then, we demonstrate how these two cepstral time series can be blindly rescaled so that they have the same representation. This rescaling process can be used to perform channel conversion, i.e., to modify the cepstral coefficients of an utterance from one channel so that they resemble those of the same utterance from another channel.

We make use of the embedding theorem that is well known in the field of nonlinear dynamics.[18] This theorem states that almost every mapping from a d-dimensional space into a space of more than $2d$ dimensions is invertible (i.e., one-to-one). Essentially, this is because so much ''room'' is provided by the ''extra'' dimensions of the higher dimensional space that the d-dimensional subspace, which is the range of the mapping, is very unlikely to self-intersect. Now, consider a speech signal that forms the input of any channel with stationary impulse response and noise. Because speech has three to five degrees of freedom[19–21] (S. Parthasarathy, AT&T Labs, private communication, 2001), the power spectra of this input signal lie in a three- to five-dimensional subspace within the space of all possible power spectra. For the linear channels described in Sec. I, the cepstral coefficients of the channel's output signal are time-independent functions of the input power spectra [Eq. (1)], and they lie in a three- to five-dimensional subspace within the space of all possible cepstra. The embedding theorem almost guarantees that this mapping is invertible, as long as the cepstra are sensitive to the degrees of freedom of the input power spectra and as long as we are using enough cepstral coefficients (more than six to ten) to avoid self-intersections. Therefore, if the same input signal propagates through two different channels, the pair of output cepstral time series will be related by an invertible mapping, because each of them is invertibly related to the same time series of input power spectra. As is well known,[1] this transformation between cepstra is quite nonlinear if noise is present. Note that if a channel's output power spectra are parametrized by quantities that are *not* invertibly related to the input power spectra, it follows that those parameters are insensitive to the differences between some pairs of input power spectra, i.e., some information may be lost during the propagation and detection of the signal. Essentially, the embedding theorem guarantees that this is exceedingly unlikely to happen as long as we use enough (more than six to ten) spectral parameters.

Let $x(t)\,(x_k, k=1,2,...,N)$ be the time-dependent function that describes the trajectory of N cepstral coefficients of speech from a channel. In the following, we show how the speech normalization problem can be mapped onto the geometric problem of finding an invariant description of nonlinearly related cepstral trajectories, and the latter problem is then solved with the help of differential geometry. Specifically, we show how a special coordinate system (or scale) $s(x)$ is determined by a differential geometry that the speech trajectory imposes on the x manifold. Speech is invariantly represented in this coordinate system in the following sense: if its cepstral trajectory is subjected to any invertible transformation, the representation of the transformed trajectory in *its s* coordinate system is the same as the representation of the untransformed speech in *its s* coordinate system. To see how this comes about, consider a point y in a region of the x manifold that is densely sampled by the speech trajectory. Define g^{kl} to be the average outer product of the time derivatives of the speech trajectory as it passes through a small neighborhood of y:

$$g^{kl}=\left\langle \frac{dx_k}{dt}\frac{dx_l}{dt}\right\rangle_{x(t)\sim y},$$

where the brackets denote the average over time. As long as this neighborhood contains trajectory points at which there are N linearly independent time derivatives, g^{kl} is positive definite, and its inverse g_{kl} is well defined and positive definite. Under any change of coordinate system $x\rightarrow x'=x'(x)$, dx/dt transforms as a contravariant vector. Therefore, g^{kl} and g_{kl} transform as contravariant and covariant tensors, respectively. This means that g_{kl} can be taken to define a metric on the x manifold, and a coordinate-system-independent process for moving (parallel transporting) vectors across the manifold can be derived from this metric by means of the methods of Riemannian geometry.[22] For instance, the parallel transport process can be defined so that, when a vector V at x is moved along line segment δx, it is changed into the vector $V+\delta V$ at $x+\delta x$, where

$$\delta V^k=-\sum_{l,m=1,...,N}\Gamma^k_{lm}V^l\delta x_m \tag{2}$$

and the affine connection Γ^k_{lm} is given by the Christoffel symbol

$$\Gamma^k_{lm}=\frac{1}{2}g^{kn}\left(\frac{\partial g_{mn}}{\partial x_l}+\frac{\partial g_{nl}}{\partial x_m}-\frac{\partial g_{lm}}{\partial x_n}\right). \tag{3}$$

An attractive feature of this choice is that the parallel transport process is independent of the speaking rate. This is because g^{kl} scales as the second power of this rate, g_{kl} scales as

its inverse second power, and the affine connection is unaffected. Now suppose that N linearly independent ''reference'' vectors $h_a\,(a=1,2,...,N)$ can be defined at a special ''reference'' point x_0 on the manifold. For example, in the experiments in Sec. III, we identified all trajectory segments connecting consecutive cepstral points in a small neighborhood of cepstral space, found N linear combinations of their cepstral velocities that were nonvanishing and linearly-independent, and defined those to be the reference vectors. Alternatively, as proposed in Sec. IV, the derivation of this reference information can be made almost completely automatic. In any event, the reference vectors can be parallel transported across the manifold to determine the s coordinates of any point x. Specifically, the point x can be assigned the coordinates $s\,(s_k,k=1,2,...,N)$, if it is reached by starting at x_0, then parallel transporting h_1 along itself s_1 times while simultaneously parallel transporting the other h_a along the same path, then parallel transporting h_2 along itself s_2 times while simultaneously parallel transporting the other h_a along the same path,..., and finally parallel transporting h_N along itself s_N times. In practice, this means that Eqs. (2) and (3) are used to compute this sequence of parallel transport movements for all integer values of s_k leading to points within the speech-traversed part of the cepstral manifold. If the h_a are sufficiently small, this produces a dense array of cepstral points with known values of s. Interpolation can then be used to estimate scale values at other points. In analogy to the problem of navigation, the reference vectors allow one to get one's ''bearings'' by establishing standard increments along ''cardinal'' directions at a certain point on the manifold. Once that is done, the parallel transport process can be used to carry those increments across the manifold in order to describe where other points are located with respect to the reference point. Notice that this parallel transport process is independent of what coordinate system is used on the cepstral (x) manifold.[22] Therefore, as long as the reference point/vectors can be identified in a coordinate-system-independent manner, the s representation of the speech trajectory will also be independent of the choice of coordinate system. Because an invertible transformation of the trajectory is mathematically equivalent to a change of the manifold's coordinate system, this means that speech trajectories related by invertible transformations will have the same s representation. Recall that the embedding theorem implies the existence of an invertible mapping between the pair of cepstral trajectories of an utterance that propagated through two different channels. It follows that these trajectories have identical s representations (Fig. 1). In principle, this representation can be used directly as channel-independent input of a recognizer.

However, in this report, we use this procedure to perform channel conversion: i.e., to modify the cepstral time series of speech from one channel (a corrupted channel) so that it resembles the cepstral time series of the same utterance from another (clean) channel (Fig. 1). Then, the converted cepstral coefficients can be fed into a conventional recognizer that has been trained on clean speech. To see how this is done, let $x(t)$ be the cepstral time series of an utterance from channel 1, and let $s(x)$ be the scale function derived from a speech sample from channel 1. Likewise, let $x'(t)$ be the cepstral trajectory of the same utterance from channel 2, and let $s'(x')$ be the scale function derived from the aforementioned speech sample after propagation through channel 2. In the previous paragraph, we showed that the rescaled representations of these two trajectories are the same, i.e., $s[x(t)]=s'[x'(t)]$. Therefore, the cepstral coefficients of the channel 2 speech can be found by mapping the s representation of the channel 1 speech through the inverse of the scale function of the channel 2 speech: $x'(t)=s'^{-1}[s[x(t)]]$. Now, in the above discussion, it was assumed that the two scale functions were derived from identical speech samples that had propagated through the two channels. However, suppose that different utterances from the same speaker/channel combination always lead to the same metric and scale function. Then, the above channel conversion procedure can be performed even if different speech samples have been observed in the two channels. In other words, one can use the scale functions derived from different clean and corrupted speech samples to predict the cepstral coefficients of the clean versions of corrupted utterances. The success of the experiments in Sec. III suggests that speech scale functions have this property of utterance-independence, i.e., they are stable with respect to speech content. This is not surprising for the following reason. We know that speech is composed of a small number of units (e.g., phonemes) that occur repeatedly with certain frequencies. Therefore, two sufficiently large samples of speech are likely to produce the same distribution of cepstral velocities in each cepstral neighborhood. Because the metric reflects the statistical distribution of those velocities (i.e., the velocity covariance matrix), two speech samples will lead to the same metric and the same scale function.

III. EXPERIMENTAL RESULTS

We performed experiments on data from three speakers of American English, who were part of the Air Travel Information System (ATIS0) corpus of speaker-dependent training data.[23] As shown in Table I, these subjects were from a variety of accent regions and included males and females of different ages. The ATIS0 speech samples were recorded with a Sennheiser microphone at a 16 kHz sampling rate with 16 bits of depth. For each speaker, the clean speech sample was comprised of the unmodified data representing 11 or 12 sentences (approximately 80 s) of this corpus. Non-overlapping sets of sentences were used to define the clean speech samples of different speakers. The acoustic wave form of each sentence was Fourier transformed, after it had been Hamming-windowed in 24 ms time frames at 4 ms intervals. Each frame's power spectrum was used to compute 20 mel frequency cepstral coefficients[24] (MFCC). For each speaker, the set of sentences defined a time series of approximately 2×10^4 cepstra, which formed a trajectory in cepstral space. This trajectory densely traversed and retraversed a compact ''speech domain,'' whose location, size, and shape depended on the speaker and channel characteristics (Fig. 2). The speech trajectory was dimensionally reduced by projecting the cepstral vectors onto the subspace defined by the first two eigenvectors of the covariance matrix of all cepstral

TABLE I. The mean Euclidean distance between clean cepstra and those corrupted by reverberations and noise, after ''normalization'' by CMN, CMN+SS, and the new channel conversion procedure. In each case, the cepstra describe 1068–2860 time points in all words in three typical sentences. The 99% confidence interval of each mean distance is listed.

Speaker	Age/gender/accent	Room/MIC	SNR (dB)	CMN	CMN+SS	Chan Conv
BF	20/M/western	Hard/close	16	35.4±0.9	22.9±0.6	23.4±1.0
		Soft/far	10	35.5±1.1	26.9±0.9	27.9±1.4
B0	40/F/north midland	Soft/far	16	40.1±0.8	28.4±0.7	27.8±1.3
B5	30/F/south midland	Hard/close	20	53.8±0.6	36.7±0.4	35.5±1.1
		Soft/far	14	52.8±1.2	38.9±0.9	34.7±1.5

data. In other words, we retained the first two principal components of cepstral data, which contained approximately 95% of the data's variance. In Sec. IV, we propose to include more of the data's variance by retaining more principal components or by using more efficient nonlinear methods of dimensional reduction.

Each trajectory was covered with a uniform 64×64 array of rectangular neighborhoods within which the clean speech metric was computed by the formula in Sec. II. If more data were available, it would be possible to either: (1) Obtain a 64×64 sampling of the metric that is more statistically stable (i.e., more independent of speech content) or (2) increase the size of the sampling array and thereby achieve higher ''cepstral'' resolution in our estimate of the metric. However, in preliminary experiments of this kind, more input data did not lead to greatly improved speech normalization, at least when just two principal components of the cepstra were retained. After the metric computation, parallel transport was defined in terms of the affine connection given by Eq. (3). For each speaker, we manually defined a small neighborhood in cepstral space (e.g., a neighborhood with dimensions equal to 5%–10% of the size of the whole speech trajectory), and we identified all clean speech trajectory segments in that neighborhood that connected consecutive cepstral points (i.e., points representing consecutive frames separated by 4 ms time intervals). The average position of these points was taken to be the origin (x_0) of the clean speech scale. Next, we computed the cepstral velocities during the above-mentioned time intervals, found two linear combinations of those velocities that were nonvanishing and linearly-independent, and defined those combinations to be the reference vectors (h_a) that determined the orientation of the scale's axes at x_0. Then, the complete scale (Fig. 2) was formed by parallel transporting these reference vectors away from the origin, as described in Sec. II. Scale values in regions immediately outside the traversed speech domain were estimated by extrapolating the scale values found by parallel transport within the speech region.

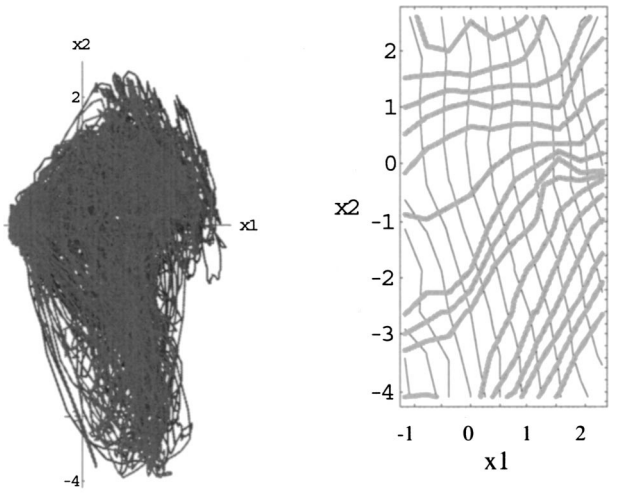

FIG. 2. Left panel: The trajectory of the first two principal components (x_1 and x_2) of the cepstra of 12 clean sentences from speaker BF. This figure has been rescaled along each axis to show detail. Right panel: The scale function derived from the left panel. The thin black (thick gray) lines are $s_2(s_1)$ isoclines corresponding to integer values of $s_2(s_1)$ that differ by $\Delta s_i = 4$.

For each speaker, a corrupted speech sample was created from 11 or 12 *different* sentences by convolving each ATIS0 signal with a channel impulse response function and adding stationary Gaussian white noise in the time domain. Note that different sets of clean and corrupted sentences were used for different speakers. Each speaker's speech was corrupted by one of two impulse responses (Fig. 3), which were synthesized by the ''image source'' method.[25] One of these functions described a relatively ''hard'' or reverberant small room (reflectivity ~0.9), in which the speaker and microphone were ''close'' (25 cm apart). The other impulse response corresponded to a ''softer'' version of the same room (reflectivity ~0.7), in which the speaker and microphone were ''far'' apart (112 cm apart). Each impulse response included all reverberations with echo times less than 64 ms. After addition of noise, the SNR of the corrupted speech was 10–20 dB in each case. As above, the acoustic wave form of the corrupted speech was used to compute an MFCC time series, which was dimensionally reduced by retaining its first two principal components (containing approximately 90% of the data's variance). Notice that the resulting cepstral trajectory (Fig. 4) is somewhat centrally compressed relative to the clean speech trajectory (Fig. 2). These data were used to compute the metric and affine connection of corrupted speech. Corrupted versions of the clean speech reference cepstra were used to determine the corrupted reference information (x_0' and h_a'), and the corrupted speech scale was then defined by parallel transporting the reference vectors away from the origin (Fig. 4). It is important to note that these reference cepstra were the only information that was common to the derivations of the clean and corrupted speech scales, which were otherwise based on entirely different sets of sentences. In Sec. IV, we propose to use the methods of Ref. 12 to automatically derive reference vectors, thereby reducing the shared information to a single reference sound

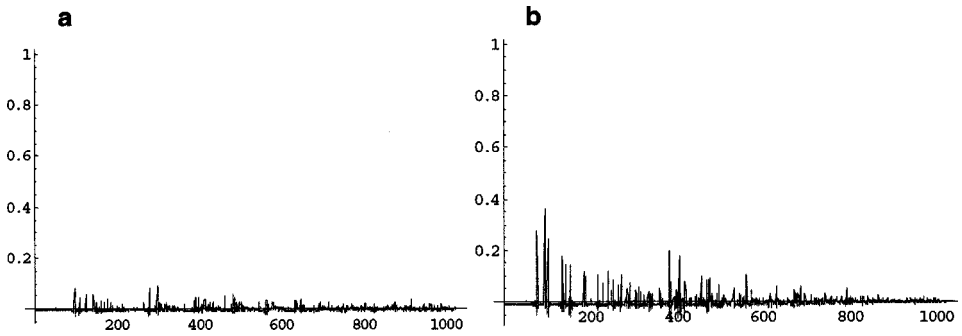

FIG. 3. Impulse response functions of a "hard" room with a close (25 cm) microphone (a) and a "soft" room with a far (112 cm) microphone (b). The time axis is labeled by the number of 16 kHz samples. The impulse response at $t=0$ is unity.

necessary to fix the location of each scale's origin. Notice that the corrupted speech scale (Fig. 4) is compressed centrally relative to the clean speech scale (Fig. 2), reflecting a similar relative compression of the corrupted speech trajectory.

Next, the scales of clean and corrupted speech were used to perform the channel conversion process described in Sec. II (Fig. 1). Specifically, the MFCCs of corrupted sentences were used to predict the MFCCs of clean versions of those sentences. First, the corrupted MFCCs were rescaled with the scale function of corrupted speech. The rescaled values were then mapped through the inverse scale function of clean speech to predict the MFCCs of the clean versions of the corrupted utterances. These were compared to the MFCCs of the actual clean versions of those utterances (i.e., the original ATIS0 versions before corruption by the channel's impulse response and noise). The upper panel of Fig. 5 shows an example of this type of comparison for the words "traveling at," spoken by speaker BF. It is apparent that the channel-converted corrupted MFCCs and the clean MFCCs were much closer to one another than were the corrupted and clean MFCCs after normalization by CMN, where the cepstral mean was computed from all 12 sentences. Notice that this result was produced by a procedure that does not involve the variation of any free parameters in order to best fit the data. The lower panel of Fig. 5 shows the distributions of Euclidean distances between the corrupted and clean MFCCs (after CMN) and between the channel-converted corrupted and clean MFCCs, at 1068 time points during all words in three typical sentences. These histograms (as well as the confidence intervals of their means in Table I) show that the channel conversion process did a much better job than CMN in moving the corrupted MFCCs close to the clean MFCCs. Furthermore, the new channel conversion procedure was comparable to the combination of CMN and spectral subtraction (CMN+SS) in its ability to normalize speech from different channels. Specifically, Fig. 5 and Table I show that the distribution of distances between the corrupted and clean MFCCs after channel conversion was comparable to the distribution of distances between corrupted and clean MFCCs, after "normalization" by CMN+SS. This is true despite the fact that the channel conversion procedure did not involve the measurement of noise levels required by spectral subtraction. Figures 6 and 7 and Table I show that similar results were obtained for the other speakers and channels. The evident success of the channel conversion operation shows that the rescaled version of a corrupted utterance can be used to reconstruct the MFCCs of a clean version of the utterance. Because clean MFCCs can be used to successfully recognize speech, it follows that the rescaling procedure did not lead to the loss of information critical to ASR.

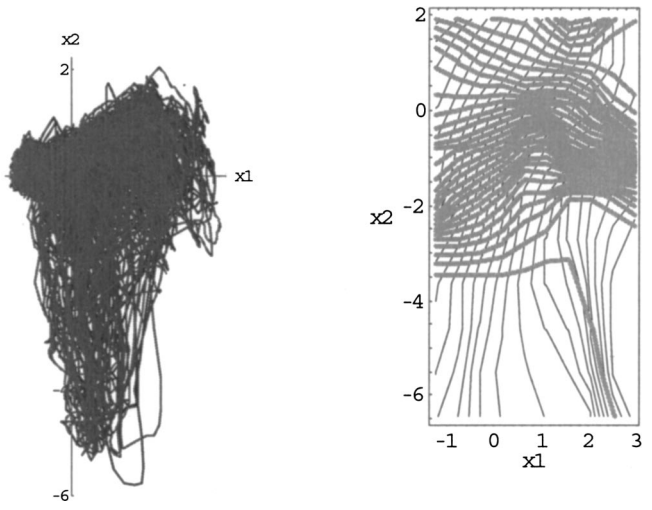

FIG. 4. Left panel: The trajectory of the first two principal components (x_1 and x_2) of the cepstra of 12 sentences from speaker BF, after corruption with reverberations ("soft" room, "far" microphone) and noise (SNR=10 dB). This figure has been rescaled along each axis to show detail. Right panel: The scale function derived from the left panel. The thin black (thick gray) lines are $s_2(s_1)$ isoclines corresponding to integer values of $s_2(s_1)$ that differ by $\Delta s_i=4$.

Two technical comments should be made at this point. First, recall that the scales of clean and corrupted speech were derived from dimensionally reduced data. Therefore, the channel conversion process is only expected to predict the *dimensionally reduced* MFCCs of clean versions of corrupted speech. It is *not* capable of predicting higher principal components of these MFCCs. Therefore, in Figs. 5–7, we compared how well the channel conversion process and conventional normalization methods (CMN alone or CMN+SS) could predict the dimensionally reduced clean MFCCs from dimensionally reduced corrupted MFCCs. However, similar results were obtained when we compared how well each method predicted the fully dimensional clean MFCCs. For example, for speaker BF (hard room, close microphone, SNR=16 dB), the distance between fully dimensional clean MFCCs and the corrupted MFCCs after channel conversion was equal to 29.5 ± 0.9, which is less than the distance between the fully dimensional clean and corrupted MFCCs after CMN, namely 37.4 ± 0.7 (99% confidence intervals). Similar results were found for other speakers.

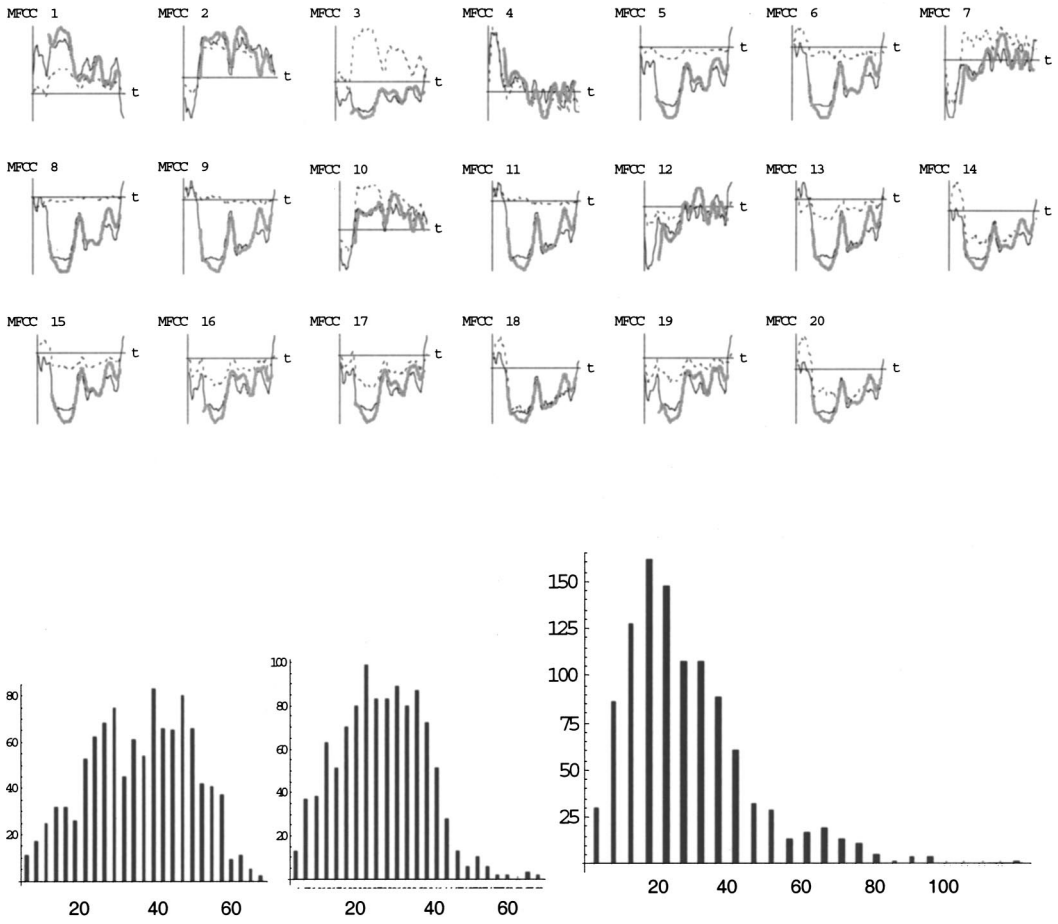

FIG. 5. Speaker BF. Upper panel: The dark solid and dashed lines show the MFCCs of the clean and corrupted (soft room, far microphone, SNR=10 dB) versions of the words ''traveling at,'' respectively, after ''normalization'' by CMN. The solid gray lines show the corrupted MFCCs after the new channel conversion procedure. Lower panel: The distribution of Euclidean distances between the corrupted and clean cepstra after CMN (left), after CMN+SS (center), and after the new channel conversion process (right). These distributions describe cepstra at 1068 time points during all words in three typical sentences.

Another technical issue concerns the ranges of the scale functions derived from the clean and corrupted speech samples. Each of these scale functions sweeps out a range of rescaled cepstra (s values) over the domain of the unrescaled cepstra (x values) of the corresponding speech sample. In principle, these two ranges should be the same, but they differed somewhat in actual practice. Because of this, some cepstra near the edges of the corrupted speech domain (constituting approximately 35% of the total) were rescaled to values outside the range of the clean speech scale function. Therefore, they fell outside the domain of the inverse of the clean speech scale function, and they could not be mapped through that inverse in order to compute their channel-converted values (Fig. 1). In Sec. IV, we propose to solve this problem by improved sampling of the speech data near the edges of the clean and corrupted speech domains.

IV. CONCLUSIONS

Previous publications[12–17] described a new method of representing signal time series that essentially ''filters out'' the effects of unknown distortions. In this paper, the method was used to blindly create relatively channel-independent representations of speech cepstra. Mathematically, this is achieved by finding a measure of distance between an utterance's cepstra that is not changed by channel-dependent transformations of the utterance and by using this distance measure to construct an invariant representation of the utterance. The experimental results suggest that the new technique is more successful than CMN and comparable to CMN+SS in its ability to decrease the signal's channel dependence. Even better results can be expected if more of the data's variance is retained in the dimensional reduction step and if longer speech samples are used to compute the metric and scale. Notice that the new method has the following advantages compared to conventional approaches to channel normalization: (1) it does not require prospective measurements of the channel's impulse response and noise; (2) it is a pure front end technology and avoids the computational demands of modifying or retraining the system's recognizer. In principle, an ASR system with the new front end can be trained in one environment and then used in another without additional measurements or retraining. Of course, this hypothesis must be tested by comparing the word error rates of ASR systems with and without the new front end.

The implementation of these ideas can be improved in several ways.

(a) More accurate dimensional reduction. Others have demonstrated that speech data have three to five underlying

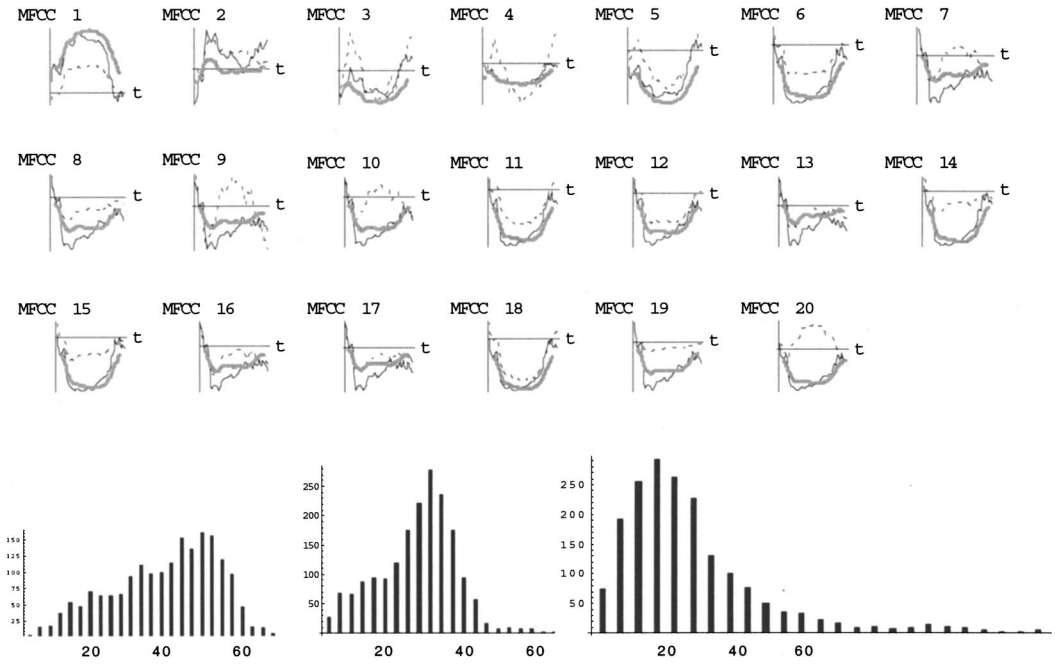

FIG. 6. Speaker B0. Upper panel: The dark solid and dashed lines show the MFCCs of the clean and corrupted (soft room, far microphone, SNR=16 dB) versions of the word ''flight,'' respectively, after ''normalization'' by CMN. The solid gray lines show the corrupted MFCCs after the new channel conversion procedure. Lower panel: The distribution of Euclidean distances between the corrupted and clean cepstra after CMN (left), after CMN+SS (center), and after the new channel conversion process (right). These distributions describe cepstra at 1863 time points during all words in three typical sentences.

degrees of freedom, which presumably correspond to independent ways of moving the tongue, lips, soft palate, and other vocal structures.[19–21] However, for computational simplicity, the experiments in Sec. III were performed on speech signals that were approximated by their first two principal components, which contained 90%–95% of the data's variance. This approximation obviously limited the accuracy of the attempted channel conversion by making it impossible to predict the higher principal components of the clean speech corresponding to observed corrupted speech. In addition, it probably violated the requirement that the rescaling method be applied to clean and corrupted speech data that are invert-

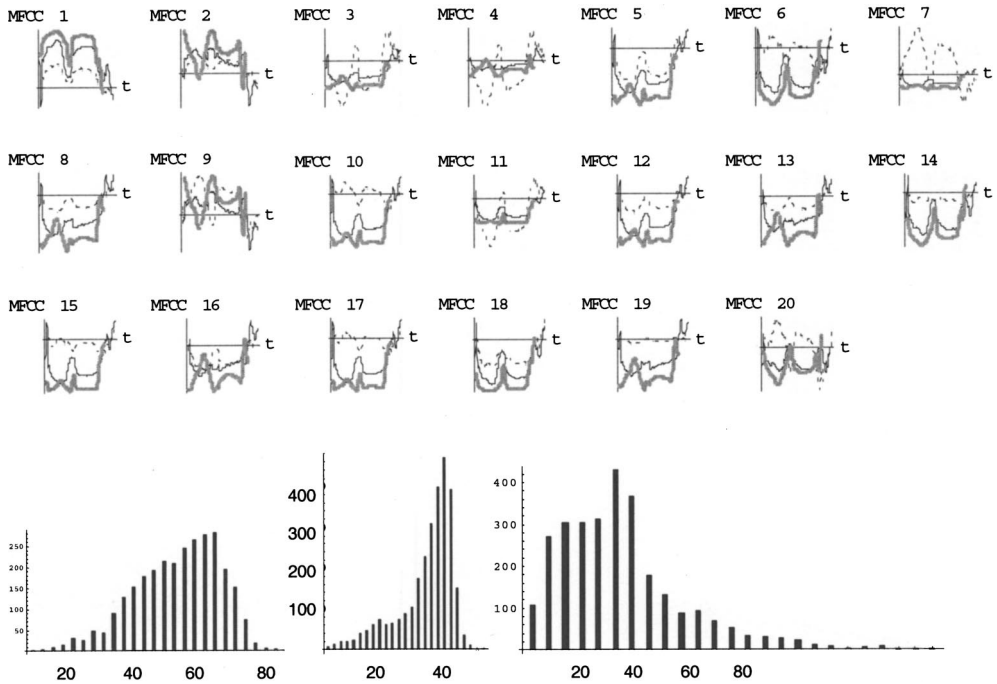

FIG. 7. Speaker B5. Upper panel: The dark solid and dashed lines show the MFCCs of the clean and corrupted (hard room, close microphone, SNR=20 dB) versions of the word ''airlines,'' respectively, after ''normalization'' by CMN. The solid gray lines show the corrupted MFCCs after the new channel conversion procedure. Lower panel: The distribution of Euclidean distances between the corrupted and clean cepstra after CMN (left), after CMN+SS (center), and after the new channel conversion process (right). These distributions describe cepstra at 2860 time points during all words in three typical sentences.

ibly related. This is because the dimensionally reduced cepstra need not have been related by an invertible transformation even though it is very likely that the exact cepstra were so related (Sec. II). These observations suggest that better channel normalization can be expected if more of the data's variance is included in the analysis. This can be done most simply by retaining more principal components of the data. Alternatively, one can use existing methods of nonlinear dimensional reduction,[26,27] which find curved subspaces that optimally contain the data. Because of their greater generality, these techniques can be expected to find subspaces that contain more of the data's variance than linear subspaces of the same dimensionality. If a relatively large number of dimensions (e.g., five) have to be retained, a long sample of corrupted speech (e.g., tens of minutes) may be needed to compute the metric on a dense array of sample points in cepstral space. However, this ''front end training'' can be performed with corrupted speech that we ultimately seek to recognize. Unlike ''back end training,'' it is not necessary to use special training utterances with known content.

(b) More accurate sampling of the cepstral trajectory. As shown in Fig. 2, speech cepstra densely traverse and retraverse a compact domain that has a speaker-dependent and channel-dependent configuration. At the edges of this domain, the velocity of the speech trajectory tends to change its direction and magnitude as the trajectory curves in order to stay within the domain. However, the metric computation in Sec. III assumed constant velocity of the speech trajectory between the cepstral points corresponding to individual frames in the time domain. Therefore, the metric computation was likely to be less reliable at the edges of the traversed domain. This may explain why some rescaled values of cepstra near the edges of the corrupted speech domain fell outside the range of rescaled values of the clean speech sample, making it impossible to estimate the corresponding clean speech cepstra at those time points. This problem can be ameliorated in two ways. First, when a trajectory is near the edge of the cepstral domain of speech, it can be sampled at higher temporal resolution by computing cepstra corresponding to more closely spaced frames. Alternatively, the trajectory's velocity in these regions can be monitored, and those time intervals with rapidly changing velocity can be excluded from the metric computation. These steps are expected to increase the accuracy of the metric computation near the edges of the speech domain and thereby make it possible to channel-convert the signal in these regions.

(c) Automatic computation of most reference information. In Sec. III, channel normalization was achieved by analyzing *different* utterances that propagated from a single speaker though clean and corrupted channels. It was not necessary to know the correspondence between clean and corrupted cepstra except in small neighborhoods of the clean and corrupted cepstral spaces, which contained reference cepstra known to represent the same speech sounds from the two channels. These ''reference'' signals were used to define the locations of the origins of the clean and corrupted speech scales and to derive vectors defining unit increments along each scale's axes at its origin. However, it may be possible to use the method in Ref. 12 to *automatically* derive such vectors from the local directionality of the cepstral velocity distribution at each scale's origin. Once this procedure is in place, channel normalization will only depend on the identification of a single reference cepstrum in each channel, analogous to the reference tone that a choir leader uses to coordinate the musical scales of individual singers prior to a concert.

(d) Adaptive channel normalization. The proposed system can adapt to changing channel conditions by using the most recent sample of corrupted speech in order to periodically update the metric and scale function. The updated scale of corrupted speech, together with the static scale of the clean speech, can be used to estimate the clean speech cepstra corresponding to observed corrupted speech. This adaptive rescaling technique was demonstrated successfully on one-dimensional signals in Ref. 13. Of course, the reference cepstrum of corrupted speech must also be periodically identified in order to update the origin of the corrupted speech scale [see item (*c*) above]. This can be done automatically by having the system continuously track and identify the reference sound as it recurs in the corrupted speech. For example, suppose that the reference point is chosen to be the average cepstrum of a frequently heard vowel-like sound with nearly stationary spectra. If the channel conditions change smoothly, it should be possible to track and identify this reference sound (possibly with the help of the recognizer) in order to update the origin of the corrupted speech scale.

It should be pointed out that the ideas in this paper can be applied in more general circumstances. In Sec. II, the embedding theorem was used to argue that the power spectrum of an acoustic channel's input and the MFCCs of its output are almost certainly related by an invertible transformation, which characterizes the channel. By similar reasoning, the input power spectrum is invertibly related to the values of *any* set of spectral parameters that are used to characterize the output power, as long as those parameters are sensitive to the degrees of freedom of the input power spectra, as long as they are sufficiently numerous (more than six to ten), and as long as they average the power over many frequencies. Therefore, if a channel's output is detected with two different spectral parameter measurements (e.g., MFCCs versus linear frequency cepstral coefficients), the pair of output time series will be invertibly related to one another, because each of them is invertibly related to the same time series of input power spectra. It follows that these output time series will rescale to the same form. This means that two ASR systems will derive the same rescaled representation of a signal, even though they used different spectral parameters to ''detect'' it and even though they received it through two different channels. In Ref. 13, this insensitivity of the rescaled signal to the choice of spectral measurements was demonstrated in experiments on bird songs having one underlying degree of freedom. Furthermore, the embedding theorem virtually guarantees that the power spectrum of the channel's input is a one-to-one function of the three to five parameters that characterize the instantaneous configuration of the speaker's vocal tract. It follows that the measured spectral parameters of the channel's output are also invertibly related to the speaker's vocal tract parameters. There-

fore, the rescaled form of a measured spectral parameter trajectory is the same as the rescaled form of the spatial trajectory of the articulatory apparatus. In other words, although the observed time series of speech spectral parameters may not enable one to recover an absolute description of vocal tract motion in a specific laboratory spatial coordinate system, it does enable one to recover its rescaled form. In this sense, the theoretical framework of this paper is consistent with the ''motor'' theory of speech perception, which asserts that the listener perceives aspects of the articulatory gesture of the speaker.[28] Because an invertible mapping is mathematically equivalent to a change of coordinate systems, the measured spectral parameters can be considered to describe the speaker's vocal tract configuration in a particular coordinate system. Therefore, if two ASR systems are ''listening'' to a given speaker through different channels and/or are measuring different spectral parameters, they are both recording the trajectory of the speaker's vocal tract, although they are describing it in different coordinate systems. Mathematically speaking, the ''inner'' properties of a geometrical figure are those that are independent of the coordinate system used to numerically describe it (or, equivalently, independent of transformations of the figure in a fixed coordinate system). Geometry seeks to find these ''inner'' properties and is less concerned with the figure's ''outer'' properties, i.e., aspects of its description that depend on the choice of a coordinate system. For example, Euclidean geometry studies the properties of a figure that do not depend on how the coordinate system has been rotated or translated, and differential geometry focuses on properties that are invariant under general, nonlinear coordinate transformations. From a geometrical perspective, the trajectory of a particular set of speech spectral parameters (e.g., MFCCs) derived from a particular channel's signal is an ''outer'' property of the articulatory gesture because it depicts the articulatory gesture in a coordinate-dependent manner (in a special coordinate system that depends on the nature of the spectral parameters and the nature of the channel). In contrast, the rescaled form of a speech signal is an ''inner'' property of the vocal tract motion, describing aspects of the motion that are independent of the coordinate system used to depict it (and, therefore, independent of the nature of the spectral parameters and channel).

It is interesting to consider the possibility that rescaling can be used to create *speaker-independent* representations of speech signals. This idea is outlined here, but in other reports this process was experimentally demonstrated with synthetic speech-like sounds having a single degree of freedom.[13] Suppose there is an invertible transformation that consistently maps the instantaneous configuration of one speaker's vocal tract onto the configuration of the other speaker's vocal tract when they utter the same words. This is equivalent to the assumption that the two speakers' articulatory gestures consistently mimic each other when the same words are uttered. In this case, the MFCC trajectories of the two speakers' signals must be invertibly related to one another, because each is invertibly related to the trajectory of the originating vocal tract and the configurations of the two vocal tracts are invertibly related to each other. It follows that the MFCC trajectories of the two signals have the same rescaled form, i.e., a speaker-independent form. This will be true even if their speaking rates differ by a multiplicative constant because the parallel transport process is independent of temporal scaling, as noted in Sec. II. Notice that the spectral parameter trajectories of both speakers' signals can be considered to describe the vocal tract trajectory of one of the speakers in two different coordinate systems. More generally, *all* of the different spectral parameter trajectories of a given utterance (corresponding to different combinations of speakers, channels, and spectral measurements) can be generated by describing the vocal tract trajectory of a single ''standard'' speaker in different coordinate systems. From this perspective, the rescaled form of an utterance's trajectory is expected to be independent of the speaker, channel, and detection process because the rescaled signal is an inner property of the ''standard'' vocal tract trajectory that is being described from multiple ''points of view.''

The rescaling procedure may be useful for addressing the problem of speaker identification, because it cleanly separates speech content from the characteristics of speaker and channel. Specifically, each speaker/channel combination is associated with a nonlinear scale function or coordinate system that covers the patch of cepstral space traversed by the signals from that source (e.g., the warped grid of s isoclines in Figs. 2 and 4). The speaker/channel is characterized by the location and configuration of this scale. The content of an utterance is given by describing its cepstral trajectory in this coordinate system, which can be considered to define a speaker/channel-dependent ''medium'' on which the message is ''written.'' Although the trajectory of a given utterance in MFCC space is nonlinearly transformed by a change of speaker/channel, it has an invariant form in the special s coordinate system associated with each speaker/channel combination, because the s coordinate system is nonlinearly transformed in the same way.

In closing, it is worth mentioning that the ideas described in this paper may be useful in areas other than automatic speech recognition and speaker identification.

(a) The nature of spoken language. The experimental results in this paper indicate that spoken American English is characterized by an utterance-independent metric. Furthermore, it was argued that the metrics derived from different speakers, channels, and spectral measurements can be considered to be the same metric ''viewed'' in different coordinate systems. Such a metric is evidently an intrinsic property of spoken American English. If these ideas are confirmed by further experimentation, it will be interesting to learn whether other spoken languages (and other auditory communication systems such as music) are also characterized by intrinsic metrics and, if so, it will be interesting to compare these quantities. If the same metric characterizes languages with distinct historical origins, it will be tempting to speculate that the metric reflects an innate property of the human brain.

(b) Computer vision and multimodal sensor systems. Earlier reports[12,15–17] described how the above-mentioned approach can also be applied to build computer vision systems that create detector-independent representations, and

these ideas were illustrated by experiments with simulated data in the absence of noise. In principle, it is also straightforward to apply this approach to multimodal sensor systems. As long as a system is equipped with detectors that are sensitive to the stimulus degrees of freedom and there are a sufficient number of them (e.g., a sufficient number of cepstral coefficients and pixels from a sufficient number of microphones and cameras, respectively), the embedding theorem[18] almost guarantees that the detectors' output $x(t)$ is invertibly related to the stimulus configuration. It follows that the same rescaled representation $s(t)$ of an evolving stimulus will be produced by two such sensor systems, even if they are equipped with significantly different detector arrays (e.g., different combinations of detectors from multiple modalities).

(c) Speech-like telecommunications systems. Earlier reports[16,17] also described how the ideas in this paper can be used to create a telecommunications system that is resistant to channel-induced corruption of the transmitted information. In such a system, information is carried by rescaled versions (i.e., the s representation) of the transmitted and received signals. As an example, imagine that the transmitter broadcasts a power spectrum that is an invertible function of two time-dependent variables, and suppose that the rescaled version of the variables' trajectory constitutes the information to be communicated. Suppose that the signal propagates through a linear channel and is detected by a receiver, which computes the outputs of a filterbank with more than four broad elements [Eq. (1)]. The embedding theorem almost guarantees that the filterbank output trajectory is invertibly related to the two transmitter variables. Therefore, the receiver can compute the rescaled version of the filterbank output trajectory in order to recover the rescaled transmitter variables' trajectory, which is the desired information.

[1] X. Huang, A. Acero, and H-W. Hon, *Spoken Language Processing* (Prentice–Hall, Upper Saddle River, NJ, 2001), Chap. 10, pp. 477–544.
[2] S. Young, "A review of large-vocabulary continuous-speech recognition," IEEE Signal Process. Mag. **13**, 45–57 (1996).
[3] R. V. Cox, C. A. Kamm, L. R. Rabiner, J. Schroeter, and J. G. Wilpon, "Speech and language processing for next-millennium communications services," Proc. IEEE **88**, 1314–1337 (2000).
[4] B. S. Atal, "Effectiveness of linear prediction characteristics of the speech wave for automatic speaker identification and verification," J. Acoust. Soc. Am. **55**, 1304–1312 (1974).
[5] Y. Suzuki, "An optimum computer-generated pulse signal suitable for the measurement of very long impulse responses," J. Acoust. Soc. Am. **97**, 1119–1123 (1995).
[6] T. M. Sullivan and R. M. Stern, "Multi-microphone correlation-based processing for robust speech recognition," Proceedings of the International Conference on Acoustics, Speech, and Signal Process., Minneapolis, MN, 1993, pp. 2091–2094.
[7] S. F. Boll, "Suppression of acoustic noise in speech using spectral subtraction," IEEE Trans. Acoust., Speech, Signal Process. **27**, 113–120 (1979).
[8] J. M. Mendel, *Lessons in Estimation Theory for Signal Processing, Communications, and Control* (Prentice–Hall, Upper Saddle River, NJ, 1995).
[9] R. P. Lippmann, E. A. Martin, and D. P. Paul, "Multi-style training for robust isolated-word speech recognition," Proceedings of the International Conference on Acoustics, Speech, and Signal Process., Dallas, TX, 1987, pp. 709–712.
[10] M. Matassoni, M. Omologo, and D. Giuliani, "Hands-free speech recognition using a filtered clean corpus and incremental HMM adaptation," Proceedings of the International Conference on Acoustics, Speech, and Signal Process., Istanbul, Turkey, 2000, pp. 1407–1410.
[11] M. J. F. Gales and S. J. Young, "Robust speech recognition in additive and convolutional noise using parallel model combination," Comput. Speech Lang. **9**, 289–307 (1995).
[12] D. N. Levin, "Sensor-independent stimulus representations," Proc. Natl. Acad. Sci. U.S.A. **99**, 7346–7351 (2002).
[13] D. N. Levin, "Representations of sound that are insensitive to spectral filtering and parameterization procedures," J. Acoust. Soc. Am. **111**, 2257–2271 (2002).
[14] D. N. Levin, "Blind normalization of speech from different channels," on the CD-ROM: *Proceedings of 2003 IEEE Workshop on Automatic Speech Recognition and Understanding*, St. Thomas, U.S. Virgin Islands, 30 November–4 December, 2003 (ISBN 0-7803-7981-0, see http://www.asru2003.org/).
[15] D. N. Levin, "Stimulus representations that are invariant under invertible transformations of sensor data," Proc. SPIE **4322**, 1677–1688 (2001).
[16] See preprints posted at: http://www.geocities.com/dlevin2001/.
[17] D. N. Levin, US patent #6,687,657 B2 ad patents pending.
[18] T. Sauer, J. A. Yorke, and M. Casdagli, "Embedology," J. Stat. Phys. **65**, 579–616 (1991).
[19] N. Tishby, "A dynamical systems approach to speech processing," Proceedings of the 1990 International Conference on Acoustics, Speech, and Signal Process. Vol. 1, pp. 365–368.
[20] B. Townshend, "Nonlinear prediction of speech signals," in *Nonlinear Modeling and Forecasting*, edited by M. Casdagli and S. Eubank (Addison–Wesley, New York, 1992), pp. 433–453.
[21] W. B. Kleijn and K. K. Paliwal, *Speech Coding and Synthesis* (Elsevier, Amsterdam, 1995).
[22] E. Schrodinger, *Space-Time Structure* (Cambridge University Press, Cambridge, UK, 1963), p. 66.
[23] See the web site of the Linguistic Data Consortium: http://www.ldc.upenn.edu.
[24] S. B. Davis and P. Mermelstein, "Comparison of parametric representations for monosyllabic word recognition in continuously spoken sentences," IEEE Trans. Acoust., Speech, Signal Process. **28**, 357–366 (1980).
[25] J. Allen and D. Berkeley, "Image method for efficiently simulating small room acoustics," J. Acoust. Soc. Am. **65**, 943–950 (1979).
[26] J. B. Tenenbaum, V. de Silva, and J. C. Langford, "A global geometric framework for nonlinear dimensionality reduction," Science **290**, 2319–2323 (2000).
[27] S. T. Roweis and L. K. Saul, "Nonlinear dimensionality reduction by locally linear embedding," Science **290**, 2323–2326 (2000).
[28] A. M. Liberman, F. S. Cooper, D. P. Shankweiler, and M. Studdert-Kennedy, "Perception of the speech code," Psychol. Rev. **74**, 431–461 (1967).

The relationship between professional operatic soprano voice and high range spectral energy

Jennifer J. Barnes and Pamela Davis
Sydney Conservatorium of Music, The University of Sydney, Sydney, Australia

Jennifer Oates
School of Human Communication Sciences, La Trobe University, Melbourne, Australia

Janice Chapman
Vocal consultant, London

(Received 13 October 2002; revised 30 January 2004; accepted 1 March 2004)

Operatic sopranos need to be audible over an orchestra yet they are not considered to possess a singer's formant. As in other voice types, some singers are more successful than others at being heard and so this work investigated the frequency range of the singer's formant between 2000 and 4000 Hz to consider the question of extra energy in this range. Such energy would give an advantage over an orchestra, so the aims were to ascertain what levels of excess energy there might be and look at any relationship between extra energy levels and performance level. The voices of six operatic sopranos (national and international standard) were recorded performing vowel and song tasks and subsequently analyzed acoustically. Measures taken from vowel data were compared with song task data to assess the consistency of the approaches. Comparisons were also made with regard to two conditions of intended projection (maximal and comfortable), two song tasks (anthem and aria), two recording environments (studio and anechoic room), and between subjects. Ranking the singers from highest energy result to lowest showed the consistency of the results from both vowel and song methods and correlated reasonably well with the performance level of the subjects. The use of formant tuning is considered and examined.
[DOI: 10.1121/1.1710505]

PACS numbers: 43.75.Rs, 43.70.Fq [SEM] Pages: 530–538

I. INTRODUCTION

Opera singers need to be audible over an orchestra without amplification, often in large theaters, and a singer's formant is considered to be a factor in the singer's ability to be audible or to project the voice. First described by Bartholomew (1934), the singer's formant is defined (Sundberg, 1987) as a pronounced peak of energy located at about 3000 Hz which is formed by the clustering of the third, fourth, and fifth vowel formants (F3, F4, and F5). Orchestral sound decays through the 2- to 4-kHz range, making the singer's formant an important tool in being heard (Sundberg, 1987), and the human ear is at its most sensitive in this range (Yost and Nielson, 1977).

The singer's formant is also associated with vocal quality except in the case of soprano voice, a view supported by Sundberg (1977, 1995, 2001) who found no evidence of formant clustering even in soprano voices of acknowledged quality. There is more energy near 3 kHz in a soprano note at high fundamental frequency (F0) than in the notes of lower voice types and consequently there is less need for the assistance of a singer's formant. The space between partials is greater so the loss of 12 dB per octave (Fant, 1960) has less impact on the perceived loudness. These partials would not consistently coincide with the center frequency of the singer's formant during a vibrato cycle and so a singer's formant would have an inconsistent effect.

Sopranos are thought to gain more energy from formant tuning at high F0 (Sundberg, 1977), when they open the jaw to raise the first formant (F1) of the vowel, usually the loudest partial, so that it is at least as great as F0. This will raise the level of all partials and so it could be assumed that the distribution of energy in the high partials of soprano voice requires little attention, but there have been some interesting results that require further study.

Earlier studies by Rossing *et al.* (1987) and Sundberg (1995) found that the spectra of their international status soprano subjects exhibited much greater energy near 3 kHz than did those of other classically trained sopranos, including an oratorio soloist. The results of these two studies suggest that operatic sopranos may need to produce greater energy near 3 kHz, particularly those performing internationally. Hence the energy at about 3 kHz may be just as important for operatic sopranos as it is for other voice types as they aim to improve. Operatic style, individual technique, and experience probably contribute to the development of this skill.

In this study we set out to add further to the known data about operatic soprano voice, so we investigated the relationship between high range energy and professional operatic soprano singing. All subjects were operatic sopranos performing professionally as soloists. Would their spectra exhibit higher energy levels than generally expected for soprano voice and would there be any link to the level of experience or level of performance? Would the results confirm the few exceptional cases or would they show that the previous results were rare occurrences?

In order to obtain samples most representative of the

TABLE I. Age range, taxonomy level (Bunch and Chapman, 2000), and musical detail of the aria excerpts chosen by each of the soprano subjects.

Subject	Age range (years)	Taxonomy	Aria	Segment
1	40–49	3.4 National/ Big City Recital	Vissi d'arte (Tosca)	''diedi gioielli...'' to the end
2	40–49	3.1a National—Major Principal	Un bel di (Madama Butterfly)	''tutto questo avverra...'' to the end
3	40–49	2.1 International	Un bel di (Madama Butterfly)	''tutto questo avverra...'' to the end
4	20–29	3.1a National—Major Principal	Caro nome (Rigoletto)	''fin l'ultimo sospir'' to the end
5	40–49	2.1 International	Hore ich Zigeunergeigen (Countess Maritza)	''Höre ich Zigeunergeigen''
6	50–59	1.1 Superstar	Entweiter Gotte (Lohengrin)	''Entweiter Gotte...''

singer in performance, the study considered the recording environment and the type of song task, and used two levels of intended projection in order to provoke dynamic performances.

II. METHOD

A. Subjects and recording conditions

In this study, which was approved by the institutional ethics committee, the voices of six professional operatic sopranos were recorded in a studio of approximately 40-m^2 size. A brief curriculum vitae for each subject provided subject classification, from superstar to national/big city, based on experience level using a singing taxonomy (Bunch and Chapman, 2000). Four subjects (3,4,5,6) worked full-time in opera, while two subjects performed regularly as soloists. Subject 2 has since been engaged to perform principal operatic roles and subject 1 is now a permanent chorus member. Five subjects had released commercial recordings and most subjects had long performing careers of at least 10 years.

In addition to the studio recordings, three subjects recorded the protocol a second time in an anechoic chamber to enable comparison of the recording environments. The same equipment was used for all sessions: a Tascam DA-P1 DAT tape recorder and a Bruel and Kjaer (B&K) Falcon 4190 microphone set at 30 cm. Calibration of the recordings was carried out using the B&K coupled tone generator as well as a 1000-Hz tone produced at 30 cm from the microphone, and the sound pressure level (SPL) was noted for several tones using a sound level meter.

To quantify the effect of the recording environment on resulting spectra, we used a software program called MLSSA (Maximum Length Sequence Signal Analyzer) (Stan *et al.*, 2002; Cabrera *et al.*, 2002). MLSSA uses a pseudo-random noise signal with a ''white'' spectral envelope to determine the impulse response of a system by cross-correlating the original signal with the measured signal. A signal of similar SPL to the singers was emitted through a speaker 30 cm from the microphone, identical to the position of the singers. The spectral effect of the room alone was found by measuring the same loudspeaker and microphone in an anechoic room, then using the anechoic transfer function for reference.

B. Recording tasks

Subjects were given time to warm up and become comfortable with the room before beginning the tasks. A piano was available in the studio and a keyboard was used in the anechoic room to assist with warming up and pitch. Recorded accompaniment and open headphones were available and were used by all subjects for the anthem and by subjects 1, 4, and 5 in the aria task. Subjects were also able to take the initial pitch of the arpeggio from the recorded tape. No subject expressed any discomfort while using this equipment; however a problem in the playing speed of the recorded accompaniment resulted in subjects 4 and 5 being recorded at a higher pitch in the arpeggios and anthem than the remaining subjects. The change in pitch was such that some notes were within 50 Hz of the F0 of other subjects and so these were included in the arpeggio analysis. Where the subject did not require the use of a recorded accompaniment, the starting pitch was provided and they were then free to sing at their own tempo.

Each subject was asked to sing arpeggios beginning on the pitch A=440 Hz using the Italian singing vowels /a/,/i/, and /o/ sung loudly so that the vowels produced would be of similar dynamic to the song tasks. The song tasks were the first verse of the Australian national anthem, ''Advance Australia Fair,'' which was familiar to all subjects, and an excerpt of at least 30 s singing time from an aria in their regular repertoire (Table I).

Two conditions of intended projection were used in the song tasks. First, a ''maximal'' level of projection was described to the subjects as being like singing in a very large opera theatre (example New York Metropolitan Opera House, 3800 seats). Second, a ''comfortable'' level of projection was described to the subjects as being like singing in a smaller opera theatre (example Sydney Opera House, 1500 seats). These conditions were previously used by Thorpe

et al. (2001) with the goal of producing voice samples as close as possible to performance level.

C. Acoustic analysis

The recordings were acquired to computer at 16 kHz with a Loughborough Sound Images PC/C32 board and analyzed using Soundswell Version 4.00 and Phog Version 2.0 software (Hitech, Sweden) using A-weighting for SPL measurement. Spectra of individual arpeggio vowels (filter 15 Hz) provided clear information about the partials. LTAS of the song tasks (filter 300 Hz) provided a broader picture of changes in spectral energy for different singers, conditions, and repertoire. After 30–40 s, an LTAS provides stable and reproducible information on averaged voice characteristics over a variety of voiced consonants and vowels (Sundberg, 2001), reducing any sensitivity to the particular song sample. A 300-Hz filter is also less sensitive to movement in the partials at high F0. This is not so with FFT where a single time window measures an instantaneous spectrum dependent on pitch, vowel, and loudness.

Acoustic analyses focused on two frequency ranges: LF (0–2 kHz) and HF (2–4 kHz). For the arpeggio vowels, the level of HF energy (L_{HF}) was found by comparing the observed energy level to the expected energy level using a method taken from Sundberg (2001). This method is limited at high F0 by the difficulty of identifying formants and measuring their levels, so the results were considered as estimates to be compared to the song task results. There is also no mechanism to allow for loudness and this is a weakness, given that HF energy levels increase at a faster rate than LF energy levels as SPL rises.

The expected energy level is read from a nomogram using the first and second vowel formants and F0. Values for the first and second vowel formants were obtained from recordings of subject 2 in the anechoic room, using a method described earlier by Sundberg (1975). Each vowel was sung at low (440 Hz), medium (685 Hz), and high F0 (880 Hz) while the vocal tract was subject to low frequency excitation. An external neck tone generator (an ''artificial larynx,'' Servox set at 70 Hz) was coupled to the skin of the lateral neck region and angled so that its head was towards the back of the tongue. Subject 2 then stopped singing while the tone generator continued, maintaining the same tongue and jaw position for that vowel. As the vibrator produced a constant F0, an FFT (see Fig. 1), 30-Hz filter, was used to provide the formants shown in Table II. These values were also allowed to vary by 100 Hz up and down, reflecting the variation that might occur between singers.

The observed level of energy is the difference between the levels of the first and third formants. These were read from the line spectrum of each individual vowel over two stable cycles of vibrato using a filter of 15 Hz. These spectra provided average levels of energy during the vibrato cycles, thus reducing variability for each vowel (where FFT would be dependent on the part of the vibrato cycle). Where F0 was below the first formant, the level of the first formant was taken from the peak closest to its location. When F0 was higher than the first formant, we assumed that they were colocated and took the level as that of the greatest peak in the LF range.

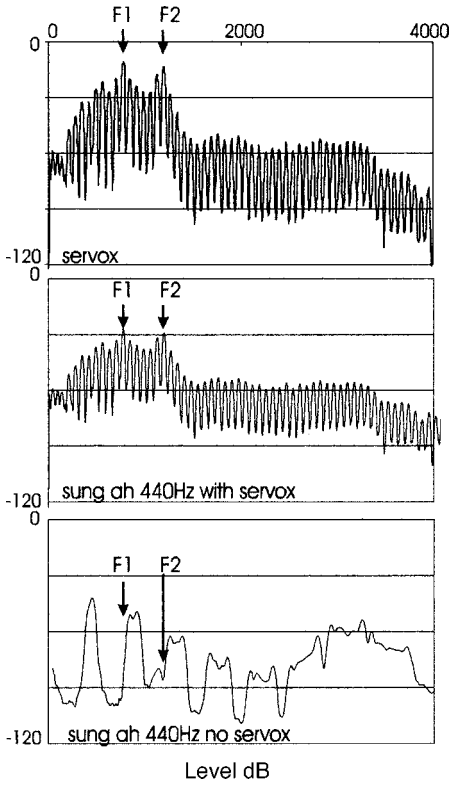

FIG. 1. Three spectra of the /a/ vowel of Subject 2 at 440 Hz, arrows indicate the formants F1 and F2: (*i*) produced by external excitation of the vocal tract (Servox vibrator, F0=70 Hz), (*ii*) voice with external excitation, and (*iii*) voice only.

The difference between the observed and expected energy levels gave the amount of extra energy in the HF range, L_{HF}, which was noted according to subject, note, and vowel. L_{HF} was positive when the vowel had more observed energy than expected and if this value reached 6 dB it was considered to be significant and equivalent to that of a vowel influenced by a singer's formant (Sundberg, 2001). Individual vowel energy ratings for each subject were calculated by averaging the L_{HF} results across the vowel sounds and pitch levels, so measuring the overall HF vowel energy for the arpeggio task. The subjects were then ranked from 1 (highest vowel energy) to 6 (lowest vowel energy).

LTAS were recorded for each subject, song task, projec-

TABLE II. F1 and F2 values of subject 2 for the three Italian vowels /a/, /i/, and /o/. Formants marked (#) lie outside the range used by Sundberg (2001) to calculate energy levels in the high range of the frequency spectrum, L_{HF}.

Vowel	F0	F1	F2
/a/	440	781	1203
	685	562	1203
	880	804	1070
/i/	440	500	2195
	685	562	2109
	880	1148#	1750
/o/	440	703	1203
	685	742	1203
	880	968#	1390

tion condition, and recording room and calibrated using the method described by White (1997), to enable graphing in absolute SPL. The singing power ratio (SPR) (Omori, 1996) and the energy ratio (EnR) (Thorpe *et al.*, 2001) were calculated to measure the HF energy in the LTAS. EnR compares the overall energy between the LF range and the HF range and is calculated by taking the difference between the average energy values for the two frequency ranges. The lower the EnR value the greater the amount of HF energy and the better the balance between LF and HF. A higher EnR means more difference between LF and HF and so less HF energy.

The SPR value compares the maximum energy levels between the LF and HF ranges, located at P1 and P2, respectively, and is a measure of spectral slope. EnR and SPR are useful for relative comparison of HF energy between samples but there is no absolute value to decide if there is more HF energy than expected. Individual mean EnR and mean SPR ratings were calculated for each subject by averaging across song tasks and projection conditions. These measures of overall HF energy in the song tasks were then ranked from 1 (greatest HF energy) to 6 (lowest HF energy). Any correlation between the individual ratings for overall energy in the vowel and song task results would allow more confidence in their interpretation, as the outcomes were derived using different methods from different data. Dmitriev and Kiselev (1979) associated the center frequency of the HF peak with voice type, stating that it was in the range 2500 to 3100 Hz for sopranos and 3100 to 3400 Hz for high sopranos. In this study, the P2 positions for the studio data of each subject were averaged across the song tasks and projection conditions to provide a subject-specific value for center frequency and these were compared with Dmitriev and Kiselev (1979). Peak width was taken from the song task P2 at −3 dB from the maximum level.

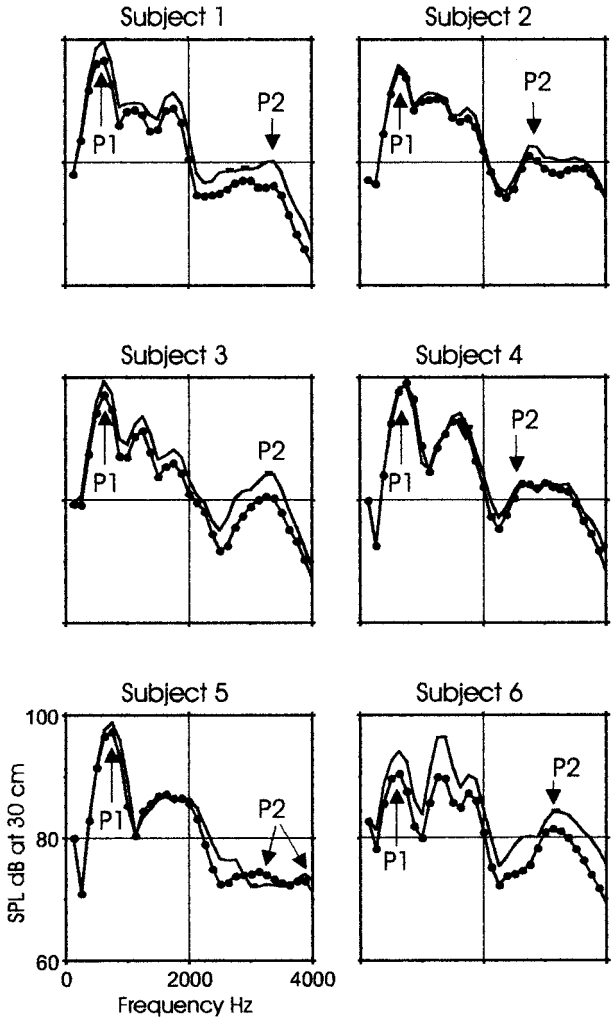

FIG. 2. Long-term average spectrum (LTAS) results for the anthem task recorded in the studio, showing ''maximal'' intended projection (solid lines) and ''comfortable'' intended projected (beaded lines). P1 and P2 indicate maxima for LF and HF, respectively. An arrow for each ''maximal'' and ''comfortable'' condition marks P2 for subject 5.

III. RESULTS

A. Recording environment

The MLSSA software showed that the recording studio exhibited a number of room reflections, the strongest being at 21.5 ms and level −30 dB due to a glass wall 3.4 m in front of the subject. There was negligible effect in the frequency range of interest when plots for the anechoic room and studio were overlaid with less than 1-dB difference in the high range. The studio midfrequency reverberation time was 0.4 s. This confirmed the reliability of the spectra derived from the studio recordings so the anechoic room results are not reported in this paper. Two subjects (1,4) expressed discomfort when recording in the anechoic room and the studio recordings offered a larger subject group for analysis.

B. Properties of the song task spectra

1. Long term average spectral energy distribution

LTAS of the song tasks (Figs. 2 and 3) featured between one and three LF peaks of varying level and the spectral level dropped markedly from LF to HF. The anthem task (Fig. 2) varied less than the aria task (Fig. 3) for the location of P1 (anthem 625–750 Hz; aria 625–1125 Hz), the level of P1 (anthem 90–100 dB; aria 95–110 dB) and the dynamic range (anthem 81–87 dB; aria 84–97 dB). In Fig. 2, P1 was exceeded in level by the second LF partial in the maximal anthem of subject 6.

The shape of the HF spectrum varied from single peak (subjects 1, 3, and 4 anthem tasks) to clear double peaks (subjects 2, 3, and 6 aria task). In both song tasks, P2 was located between 2625 and 3375 Hz while the level of P2 ranged from 75 to 84 dB (anthem) and from 78 to 95 dB (aria). The center frequency of the P2 peak was located between 2750 (subject 2) and 3315 Hz (subject 3) and the peak width ranged from 560 (subject 3) to 1115 Hz (subject 1).

2. Effect of vocal projection

Differences in SPL for the song tasks and two projection conditions are shown in Fig. 4 and were often very small (2,4,5), although maximal projection (darker columns) and the aria task (two right hand columns of each subject) usually resulted in greater SPL. When averaged across all subjects and song tasks, SPL for maximal projection was 1.6 dB greater than for comfortable projection and, when averaged

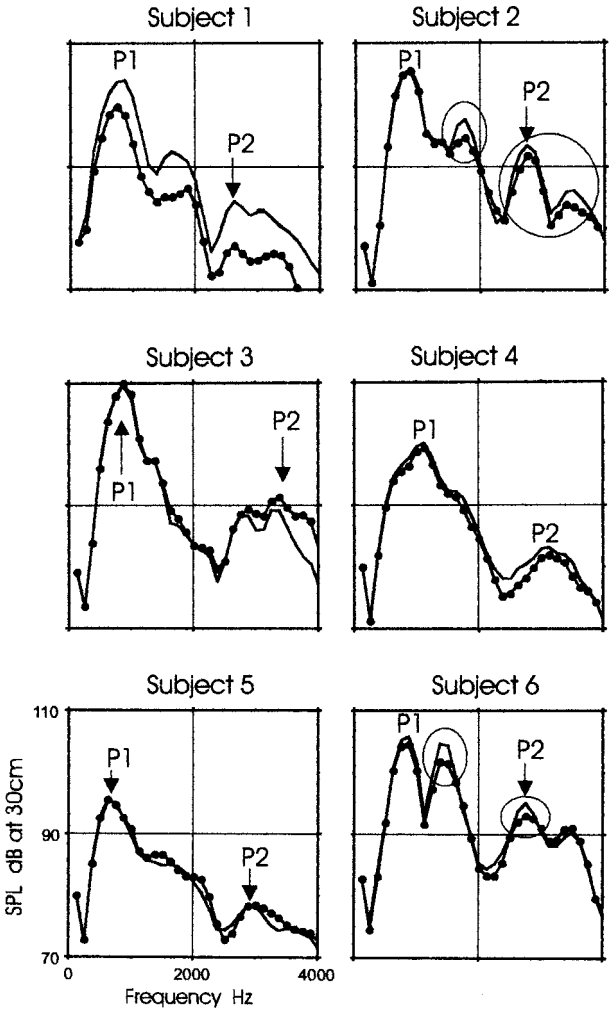

FIG. 3. The long-term average spectrum (LTAS) results for the aria task recorded in the studio. P1 and P2 indicate maxima for LF and HF, respectively. Maximal projection is denoted by solid lines and beaded lines denote comfortable projection. Circles show increased level from comfortable to maximal projection.

across the subject and projection conditions, SPL for the aria task was 7.5 dB greater than for the anthem task.

The difference between the LTAS of maximal and comfortable projection was seen in two ways: a consistently greater energy level across the spectrum, for example, Fig. 2, subject 1, or most noticeable increase in energy at P2, for example, Fig. 2, subject 2. This indicated two different approaches to the task of improving audibility. When averaged across all subjects, the greatest difference in maximal and comfortable projection occurred at 2625 and 4000 Hz for anthem (thin line) and aria (thick line) (see Fig. 5). The peak at 2625 Hz would have more impact on the perceived sound due to the drop in spectral energy once the frequency reaches 4000 Hz.

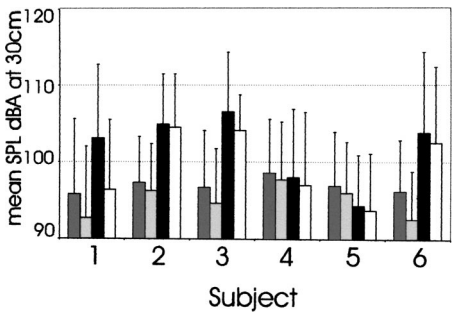

FIG. 4. Mean sound pressure level (SPL)+1 SD shown by subject, song task, and projection condition. Each subject is represented by four columns: maximal projection anthem (dark shading), comfortable projection anthem (light shading), maximal projection aria (black), and comfortable projection aria (white).

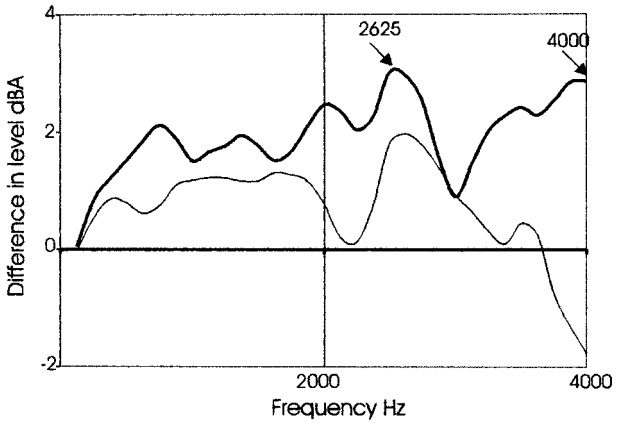

FIG. 5. Difference between maximal projection and comfortable projection up to 4 kHz. The greatest difference is in the aria task (thick line) while the anthem task (thin line) displayed a similar trend up to 3 kHz before it dropped away sharply. The greatest differences in level occur at 2625 Hz (both song tasks) and at 4 kHz (aria), as indicated by the arrows.

C. High range energy in the soprano voice

1. High range spectral energy in the arpeggio vowels

Each recording session yielded 21 arpeggio vowels per subject, being seven notes each of the Italian vowels /a/,/i/, and /o/. This made a total of 126 vowels which was reduced to 68 vowels by limitations on the possible values of the first and second formants (F1,F2) in the procedure described by Sundberg (2001) and no formant values for F0 554 Hz. The formant estimations in this study agree well with those from the work of Sundberg (1977) and Rossing (1990) and so gave confidence in the results for expected HF energy. These estimates of HF energy in the arpeggio vowels, L_{HF}, are shown in Fig. 6. The error bars were arrived at by allowing the values of F1 and F2 to vary by 100 Hz in each direction to indicate possible variation between singers. Twenty-nine vowels (43%) had positive measures of L_{HF}, that is, they exhibited at least as much HF energy as would be expected (see Fig. 7). Seven vowels, all on /a/ and /o/, had L_{HF} between 6 and 12 dB, similar energy to vowels influenced by a singer's formant (see Sec. II).

Every subject produced vowels with positive L_{HF} and four of these produced vowels where L_{HF} was at least 6 dB. The results for subjects 4 and 5 may have been affected by the higher starting pitch of their arpeggios and thus reduced the number of positive results for these two singers. The /a/ vowels of subjects 2, 3, and 6 exhibited the highest L_{HF} values (Fig. 7) and, averaged across subjects, the /a/ vowel exhibited the greatest HF energy, followed by the /o/ vowel. The /i/ vowel always resulted in negative L_{HF}.

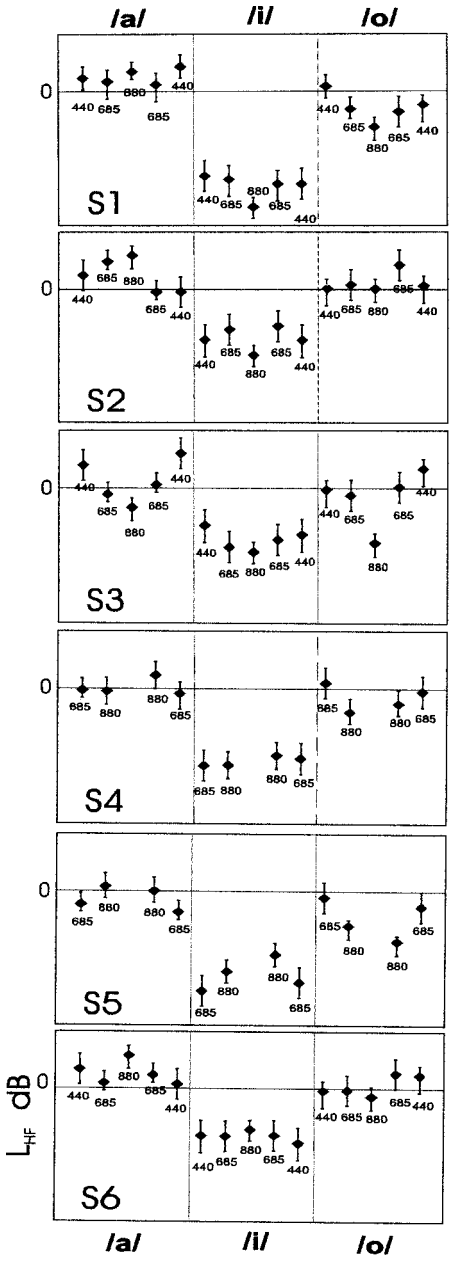

FIG. 6. Level of the high range energy (L_{HF}) is shown by pitch for the three Italian vowels /a/, /i/, and /o/ and subjects (1–6). Error bars indicate the results of allowing F1 and F2 to vary by 100 Hz.

Two vowels with $L_{HF} > 6$ dB were examined to look at the level of the partials within the spectrum (Fig. 8). HF energy increased between 2300 and 4000 Hz as seen in the third, fourth, and fifth partials for subject 2 and the second and third partials for subject 6.

2. Comparison of spectral energy for song tasks, vowels, and taxonomy

In Table III, the individual mean SPR, mean EnR, and vowel energy values followed similar trends. When two subjects were compared, lower mean SPR corresponded to lower mean EnR and higher vowel energy. Maximal and comfortable projection produced almost identical mean SPR and mean EnR values while the song tasks produced a small variation between anthem and aria. Table IV ranks the subject results from greatest HF energy (1) to least HF energy (6), making the consistency of the results clearer. For example, subject 6 records the highest rank for mean SPR, mean EnR, and vowel energy. This means that this subject produced the greatest HF energy in both song tasks and arpeggio vowels. Subject rankings were the same, or differed by one place, implying that the subjects used stable techniques, whether in vowels or songs and that their relative ability to produce HF energy would be evident no matter whether vowel or song methods were used. HF peak width (Table IV) was narrower in subjects with more HF energy while the center frequency ranged from 2845 to 3315 Hz and was not related to the subject rankings of HF energy.

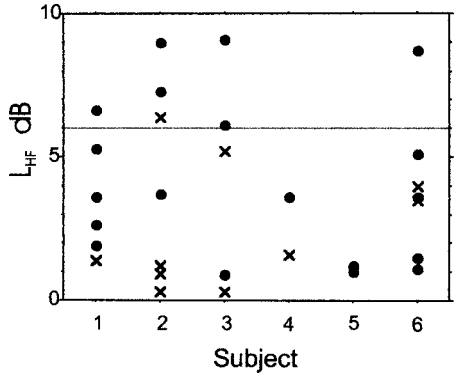

FIG. 7. Vowels with a positive L_{HF} plotted by subject. The horizontal line at 6 dB indicates the equivalent energy level to a vowel influenced by singer's formant. Dots indicate /a/ vowels and crosses indicate /o/ vowels.

The subject rankings of Table IV were supported by the normalized LTAS of the song tasks (Fig. 9). Subjects 2, 3, 4, and 6 were above the mean spectrum for the anthem task and Subjects 2, 4, and 6 were above the mean spectrum for the

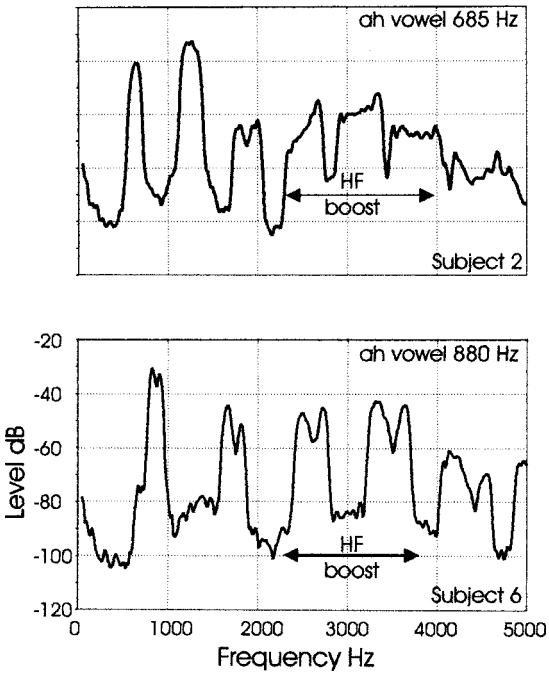

FIG. 8. Two vowels with LHF equivalent to a singer's formant: /a/ at 685 Hz for subject 2 and /a/ at 880 Hz for subject 6. There is a boost in energy in the high (2–4 kHz) range. The second partial in the low range for subject 2 is larger than the fundamental.

TABLE III. Measures of high range energy (singing power ratio, SPR, energy ratio, EnR, and vowel energy) are shown for each subject, the mean maximal and mean comfortable song, and the mean anthem and mean aria. Standard deviation is shown in brackets.

	Mean SPR (dB)	Mean EnR (dB)	Vowel Energy (dB)
Subject 1	20.1 (1.1)	13.9 (0.7)	−7.3 (12.1)
Subject 2	13.3 (0.6)	8.7 (0.7)	−2.4 (7.8)
Subject 3	18.0 (2.2)	9.6 (1.7)	−3.7 (7.7)
Subject 4	16.5 (0.9)	10.8 (1.2)	−5.1 (9.1)
Subject 5	19.7 (3.2)	11.2 (0.8)	−8.7 (10.7)
Subject 6	10.3 (1.1)	8.0 (0.8)	−2.3 (8.0)
Maximal	16.3 (3.9)	10.2 (1.9)	
Comfortable	16.5 (1.0)	10.5 (2.6)	
Anthem	16.1 (4.4)	10.8 (1.7)	
Aria	16.7 (1.0)	9.8 (2.6)	

aria task reflecting the top three ranks for HF energy. The normalized LTAS dropped 17 dB with range 9 to 22.5 dB for the anthem task and 11 to 22 dB for the aria task. The subject with the highest singing taxonomy rating (1.1—international superstar) also recorded the highest rankings of HF energy in both the song tasks and the arpeggio vowels while the lowest rankings of HF energy were recorded by a subject with the lowest taxonomy level (3.4).

IV. DISCUSSION

A. High range spectral energy in the soprano voice

The operatic soprano singers in our study did produce /a/ and /o/ vowels with L_{HF} up to 10 dB in the arpeggio task, i.e., up to 10 dB above expectations. Sundberg (2001) suggested that when L_{HF} reaches 6 dB, the excess energy is sufficient to say that there may be a singer's formant. Hence those /a/ and /o/ vowels with L_{HF} between 6 and 10 dB had HF energy equivalent to vowels with singer's formant, a stark contrast to the Italian /i/ vowels where L_{HF} was always below zero. This meant that no /i/ vowel possessed excess HF energy, implying that the normal articulation for this vowel is probably sufficient for good audibility.

Positive L_{HF} values occurred even at high F0 (Fig. 6, Subjects 1, 2, 3, 4, 6), contrasting with Bloothooft and Plomp (1986) who found that L_{HF} decreased as F0 increased in their study of Dutch vowels and that the /i/ vowel had higher L_{HF} than the /a/ vowel. Our results were more in agreement with those of Sundberg (1995), where L_{HF} was positive on /a/ and /o/ for the international star subjects, but always negative for the /i/ vowel. The operatic Italian vowels used in this study may have given rise to different formants than the Dutch vowels of Bloothooft and Plomp and the methods used here were similar to those of Sundberg, which would make agreement more likely.

TABLE IV. Subject rankings from 1 (greatest high range energy) to 6 (lowest high range energy) for each high range (HF) energy measure against taxonomy level, center frequency, and peak width.

		High range energy rankings			High range peak	
Singer	Taxonomy	Rank mean SPR	Rank mean EnR	Rank vowel energy	Center frequency (Hz)	Mean peak width (Hz)
1	3.4	6	6	5	2875	1115
2	3.1a	2	2	2	2750	600
3	2.1	4	3	3	3315	560
4	3.1a	3	4	4	2970	875
5	2.1	5	5	6	3220	900
6	1.1	1	1	1	2845	770

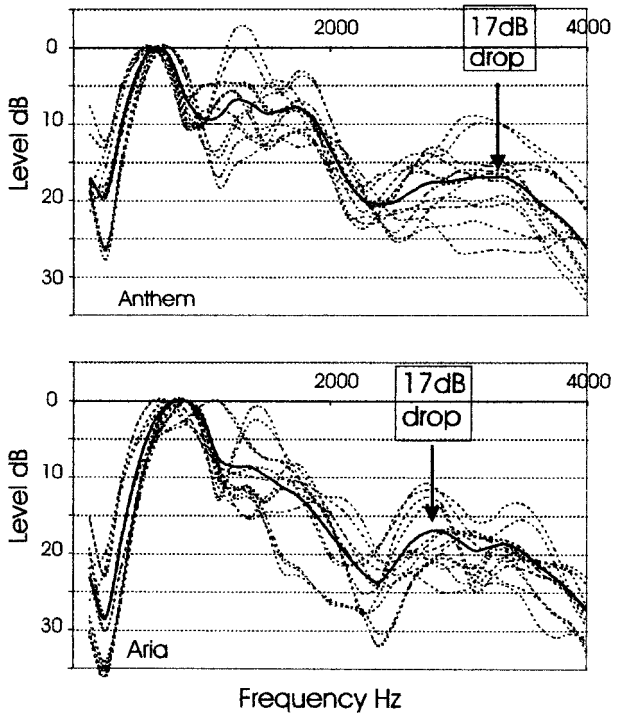

FIG. 9. Normalized long-term average spectra for the anthem and aria tasks. The mean curve (bold line) for both song tasks drops by 17 dB from the normalized peak to the peak in the high range.

The availability of a criterion for excess energy helped in the interpretation of the vowel results but the absence of such a value for LTAS meant that their greatest value was for the comparison of relative HF energy levels. The mean anthem and aria LTAS in this study (Fig. 9, bold line spectra) had SPR of approximately 16 dB, similar to the mean soprano LTAS in Sundberg (2001), SPR 17 dB [estimated from Fig. 7 (Sundberg, 2001)]. The highest SPR results in this study, range 9 to 22 dB (Fig. 9), were considerably higher than the mean and were in accordance with those Thorpe *et al.* (2001), 8 to 12 dB, whose subjects were mostly performers with international experience as principal artists (personal communication with J. Chapman). The broader range of SPR in this study may reflect the inclusion of subjects not experienced or currently working at international level.

B. Low range spectral characteristics

The second LF partial was above the mean spectrum for four subjects (2, 3, 4, and 6). In the case of subject 6 maximal anthem, its amplitude exceeded that of F0 by 3 dB, indicating that this was related to vocal tract modification.

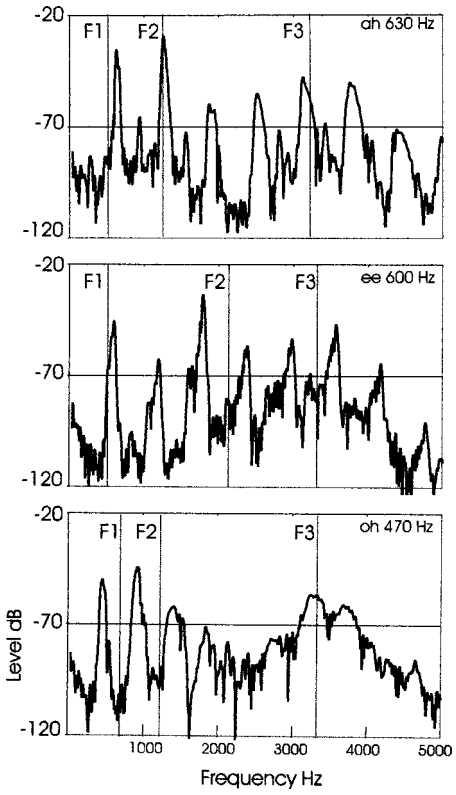

FIG. 10. FFT plots of three vowels taken from the maximal anthem of subject 6 with positions of the first three vowel formants shown according to Rossing (1990). They feature an enhanced low range partial and an energy boost between 2000 and 4000 Hz.

FFT plots were used to identify points in the anthem where this second LF partial was larger than F0 and the resulting spectra are shown in Fig. 10.

The position of this large partial was 1260 Hz for /a/, 1790 Hz for /i/, and 940 Hz for /o/. Since F1 is the loudest partial it is reasonable to assume that this large partial is being enhanced by F1. Using the formants in Table II, it can be seen that the location of F1 is higher than expected and close or coincidental with F2 for all three vowels: F2 for /a/ 1200 Hz, F2 for /i/ 1750–2200 Hz, and F2 for /o/ 1200–1400 Hz. This suggests that F1 has been raised above its expected frequency. Since F1 and F2 are normally associated with jaw and tongue position, respectively, refined skill with jaw and tongue would make this phenomenon possible and would accord well with singing pedagogy.

C. Source of the high range boost

Spectra containing LF partials with above average energy also displayed above average HF energy. The spectra in Fig. 10 all have a broad HF boost centered on 3 kHz. This pattern is also seen in the arpeggio vowel spectrum of Fig. 8, subject 2 (taken over two vibrato cycles) which indicates that the HF spectral shape of the FFT is consistent through the vibrato cycle. Values of F3 taken from Rossing (1990), shown by dotted line, demonstrate that F3 is located in the boosted region. Fant (1960) gives values of F3 and F4 for male speaking voice to be increased by 17% for female voice, making F3 2000 to 4000 Hz, F4 3000 to 5000 Hz. Considering these values, we see that F3 falls within the boosted region but F4 has a moderate probability of falling outside the affected frequency range. The sharp drop in energy at the upper end of the boost implies that F4 is close to F3 and hence that these formants are reinforcing each other to form the HF boost.

Titze and Story (1997) acknowledged that the narrow epilarynx is the configuration of choice in high-pitched operatic singing. They also stated that when there is a narrowing of the epilarynx tube, its characteristic frequency captures F3 (and sometimes F4) and attracts the other vocal tract formants to itself, i.e., F1 and F2 are pulled upwards while F4 and F5 are pulled downwards. It has already emerged that, for subject 6 maximal anthem, F1 has moved upwards in the spectrum towards the expected F2 position and, from Fant's F4 formant values, that F4 has moved towards F3. A narrowed epilarynx can be justified by the link between opera quality and *twang* (Titze and Story, 1997) but the double peak of most song task LTAS shows that there is no consistent clustering of F3, F4, and F5. It may be that subject 6 used a narrowed epilarynx but insufficient pharyngeal width, a high larynx or the type of vocal fold vibratory pattern may be reasons why there was no singer's formant. Sundberg (1974) showed that pharyngeal width and low larynx were favorable conditions for singer's formant and Bartholomew (1934) postulated that a standing wave is set up in the epilarynx tube by the vocal fold action. The reduced closed phase in the vocal fold vibratory pattern at high F0 would reduce the likelihood of any standing wave and consequently the existence of a singer's formant.

D. The importance of subject classification

The subject taxonomy built on earlier studies where subject descriptions appeared to acknowledge that different vocal styles might be reflected in different spectral features. Subjects were described as ''female singers with varying degrees of training and ability,'' ''church soloist,'' ''outstanding professional,'' ''professional opera singer,'' and ''international star'' (Bartholomew, 1934; Sundberg, 1995; Bloothooft and Plomp, 1986; Seidner *et al.*, 1983; Rossing *et al.*, 1986, 1987; Thorpe *et al.*, 2001). The care taken in these subject descriptions enabled better understanding and interpretation of the results, making them more useful to teachers and singers and the taxonomy offers the opportunity to further standardize subject description.

Our results agree well with Sundberg (1995) who used ''international stars'' but differs from Bloothooft and Plomp (1986), who used ''professional singers'' but did not say whether any of the sopranos had an artistic need to use HF energy, that is, if they sang regularly with orchestra or without the assistance of amplification.

In our study, the highest taxonomy level was associated with the highest rank for HF energy for subject 6. The two subjects on the next taxonomy level, subjects 3 and 5, varied in their results. As expected for her international level, subject 3 was above average for HF energy and produced the greatest SPL but the results for subject 5 were unexpectedly low. A comparison of the respective performance histories revealed that subject 3 is constantly performing at international level while subject 5 currently does little work at this

level. So it seems that the frequency of work combined with performance level may have affected this outcome. Further studies using this taxonomy may support this conclusion.

The measures of HF energy produced here agreed well with two other studies (Sundberg 2001; Thorpe *et al.,* 2001) and reinforce the proposal that boosting HF energy is an important skill for operatic sopranos as it is for other voice types.

V. CONCLUDING REMARKS

The link between high performance level and HF energy has been confirmed in this study. The subject with the highest taxonomy ranked first for HF energy and the lowest rank for HF energy corresponded to the subject with lowest taxonomy. The amount of HF energy produced by this set of operatic sopranos reached a level equivalent to a singer's formant on some vowels and the HF energy level in the mean LTAS was similar to that of Sundberg (2001) and Thorpe *et al.* (2001) where the subjects were also internationally experienced principal operatic singers.

Consistent experience at a high level appeared to affect the outcome for one international level subject and suggests that enhanced HF energy is something that develops through both experience and practice. The possibility emerged that epilaryngeal narrowing may play a part in assisting sopranos toward their goal. Further investigation through laryngoscopy would allow the observation of the larynx during sounds with excess HF energy and would help us to understand whether this might be so. While no evidence could be found to support the use of a soprano singer's formant, it was shown that HF energy is important to sopranos who sing opera and requires the attention of teachers and singers.

Across the different tasks the trends in HF energy between singers were similar and indicated that the technique used by professional singers is stable across differing demands. A perceptual study was not carried out here but would provide more information on the way these HF energy levels are perceived by the listener. We assumed that HF energy is used by these singers for audibility or quality. A perceptual evaluation could test the value of this assumption.

The comparison of recording studio and anechoic room environments demonstrated that spectra produced from the studio recordings were as accurate as those from the anechoic room under the same recording conditions. The ability of these operatic sopranos to produce high levels of SPL meant that they could be recorded in surroundings more conducive to the feeling of performance, making the recorded samples more reliably representative of the subject's professional sound.

ACKNOWLEDGMENTS

The authors wish to thank the subjects for their willing participation and interest. We are indebted to Professor Johan Sundberg for his willing advice and suggestions. We also acknowledge the assistance of Associate Professor Fergus Fricke, Dr. Densil Cabrera, Konrad Skirlis and Ken Stewart from the Acoustics Laboratory, Faculty of Architecture, Design Science and Planning, The University of Sydney, for their invaluable acoustic advice, assistance with recording and access to recording facilities and equipment.

Bartholomew, W. (**1934**). ''A physical definition of 'good voice-quality' in the male voice,'' J. Acoust. Soc. Am. **6**, 25–33.

Bloothooft, G., and Plomp, R. (**1986**). ''The sound level of the singer's formant in professional singing,'' J. Acoust. Soc. Am. **79**, 2028–2033.

Bunch, M., and Chapman, J. (**2000**). ''Taxonomy of Singers Used as Subjects in Research,'' J. Voice **14**, 363–369.

Cabrera, D., Davis, P., Barnes, J., Jacobs, M., and Bell, D. (**2002**). ''Recording the operatic voice for acoustic analysis,'' Acoust. Austral. **30**(3), 103–108.

Dmitriev, L., and Kiselev, A. (**1979**). ''Relationship between the formant structure of different types of singing voices and the dimension of supraglottal cavities,'' Folia Phoniatr. **31**, 231–241.

Fant, G. (**1960**). *Acoustic Theory of Speech Production* (Mouton, The Hague).

Omori, K., Kacker, A., Carroll, L. M. *et al.* (**1996**). ''Singing Power Ratio: Quantitative Evaluation of Singing Voice Quality,'' J. Voice **10**, 228–235.

Rossing, T. D. (**1990**). *The Science of Sound* (Addison-Wesley, Reading, MA).

Rossing, T. D., Sundberg, J., and Ternstrom, S. (**1986**). ''Acoustic comparison of voice use in solo and choir singing,'' J. Acoust. Soc. Am. **79**, 1975–1981.

Rossing, T. D., Sundberg, J., and Ternstrom, S. (**1987**). ''Acoustic comparison of soprano solo and choir singing,'' J. Acoust. Soc. Am. **82**, 830–836.

Seidner, W., Schutte, H., Wendler, J., and Rauhut, A. (**1983**). ''Dependence of the high singing formant on pitch and vowel in different voice types,'' Proceedings of the Stockholm Music Acoustics Conference 1983 (SMAC 83) (no. 1), ed. Askenfelt A., Felicetti, S., Jansson, E., and Sundberg, J. pp. 261–268. Royal Swedish Academy of Music, Stockholm.

Stan, G., Embrechts, J., and Archambeau, D. (**2002**). ''Comparison of different impulse response measurement techniques,'' J. Audio Eng. Soc. **50**(4), 249.

Sundberg, J. (**1974**). ''Articulatory interpretation of the 'singing formant','' J. Acoust. Soc. Am. **55**, 838–844.

Sundberg, J. (**1975**). ''Formant Technique in a Female Professional Singer,'' Acustica **32**, 89–96.

Sundberg, J. (**1977**). ''The Acoustics of the Singing Voice,'' Sci. Am. **March**, 82–91.

Sundberg, J. (**1987**). *The Science of the Singing Voice* (Northern Illinois U.P., DesKalb, IL).

Sundberg, J. (**1995**). ''The singer's formant revisited,'' Voice **4**, 106–119.

Sundberg, J. (**2001**). ''Level and center frequency of the singer's formant,'' J. Voice **15**, 176–186.

Thorpe, W. C., Cala, S. J., Chapman, J., and Davis, P. (**2001**). ''Patterns of Breath Support in Projection of the Singing Voice,'' J. Voice **15**, 86–104.

Titze, I. R., and Story, B. H. (**1997**). ''Acoustic interactions of the voice source with the lower vocal tract,'' J. Acoust. Soc. Am. **101**, 2234–2243.

White, P. (**1997**). ''A study of the effects of vocal intensity variation on children's voices using long-term average spectrum (LTAS) analysis,'' TMH-QPSR **1**, 119–131.

Yanigasawa, E., Estill, J., Kmucha, S. T., and Leder, S. B. (**1989**). ''The contribution of aryepiglottic constriction to ''ringing'' voice quality—A videolaryngoscopic study with acoustic analysis,'' J. Voice **3**(4), 342–350.

Yost, W. A., and Nielsen, D. W. (**1977**). *Fundamentals of Hearing: An Introduction* (Holt, Rinehart and Winston, New York).

Frequency dependence of acoustic properties of aqueous glucose solutions in the VHF/UHF range

Naoyuki Akashi[a)]
Ichinoseki National College of Technology, Ichinoseki 021-8511, Japan

Jun-ichi Kushibiki
Department of Electrical Engineering, Tohoku University, Sendai 980-8579, Japan

Floyd Dunn
University of Illinois, Urbana-Champaign, 1406 West Green Street, Urbana, Illinois 61801

(Received 24 December 2003; revised 13 April 2004; accepted 29 April 2004)

The bioultrasonic spectroscopy system was employed for measurements of velocity and attenuation coefficient of glucose solutions in the VHF/UHF range. The relation between the slope of the square of velocity and the relaxation parameters, and the relation between the frequency exponent on attenuation coefficient and the relaxation parameters are investigated. In order to carry out numerical calculations, a model for a single relaxation process is employed, wherein the attenuation coefficient is expressed as $(A/(1+(f/f_\alpha)^2)+B)f^2$ where f_α is the attenuation relaxation frequency, and A and B are constants. The numerical calculations show that the slope of the square of the velocity is determined uniquely by the velocity relaxation frequency f_v and $v_\infty^2-v_0^2$ where v_0 is the zero-frequency velocity and v_∞ is the infinite-frequency velocity, and that the frequency exponent on the attenuation coefficient is determined uniquely by f_α and A/B. For experimental considerations, the velocities and the attenuation coefficients of 5, 15, and 25% concentration aqueous solutions of glucose were measured in the frequency range 20 to 700 MHz. The data for the 5 and 15% aqueous solutions can be explained using the single relaxation model. However, the data for the 25% aqueous solution suggest the existence of multirelaxation processes. [DOI: 10.1121/1.1763955]

PACS numbers: 43.80.Cs, 43.80.Ev, 43.35.Fj [WWL] Pages: 539–544

I. INTRODUCTION

The bioultrasonic spectroscopy system was developed for doing ultrasonic tissue characterization studies of biological specimens in the VHF/UHF range.[1] The acoustic properties, viz., attenuation coefficient, velocity, acoustic impedance, and density, can be determined with high accuracy by an ultrasonic transmission comparison method using pure water as the reference. The frequency dependences of the acoustic properties of bovine tissues, egg yolk and albumen, and aqueous solutions of biomacromolecules such as bovine hemoglobin and sugars measured in the frequency range have been reported.[2–4] We also have developed a measurement method for the acoustic nonlinearity parameters of liquids and biological materials in the VHF/UHF range and have been conducting basic research with the system.[5] Since the frequency characteristics of the attenuation coefficients and the velocities are obtained with high accuracy by the bioultrasonic spectroscopy, they are very useful for the research of frequency dependences of acoustic properties.[1–4] We have proposed using the exponent on the attenuation coefficient as a characterizing parameter.[1]

In this paper, the bioultrasonic spectroscopy system is employed for measurements of velocity and attenuation coefficient of aqueous glucose solutions. The relation between the slope of the square of velocity and the relaxation parameters, and the relation between the frequency exponent on the attenuation coefficient and the relaxation parameters are investigated. In order to carry out numerical calculations, a model for a single relaxation process is employed. For experimental considerations, the velocities and the attenuation coefficients of 5, 15, and 25% concentration aqueous solutions of glucose were measured in the frequency range 20 to 700 MHz and relaxation parameters were obtained.

II. NUMERICAL CALCULATIONS

In this paper, only absorption due to a relaxation phenomenon was taken into consideration as the mechanism of the propagation attenuation of ultrasonic waves. In order to carry out numerical calculations, a model for a single relaxation process is employed. Based on the acoustic relaxation theory,[6] the velocity v and the attenuation coefficient α are expressed, respectively, as

$$v^2=v_0^2+(v_\infty^2-v_0^2)\cdot\frac{(f/f_v)^2}{1+(f/f_v)^2}, \tag{1}$$

$$\alpha/f^2=\frac{A}{1+(f/f_\alpha)^2}+B, \tag{2}$$

where

a)Electronic mail: akashi@ichinoseki.ac.jp

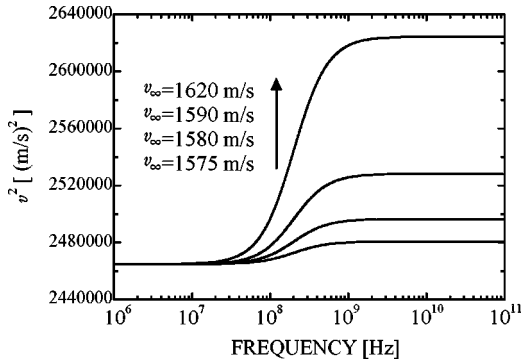

FIG. 1. Frequency dependence of the square of velocities for $v_\infty = 1575$, 1580, 1590, and 1620 m/s.

$$f_v = (v_\infty / v_0)^2 f_\alpha . \tag{3}$$

v_0 is the zero-frequency velocity and v_∞ is the infinite-frequency velocity. f is the frequency, f_v is the velocity relaxation frequency associated with the velocity, and f_α is the attenuation relaxation frequency associated with the attenuation. $A = \pi\varepsilon/(v_0 f_\alpha)$, B represents the absorption due to all other absorption mechanisms, and ε is the relaxation strength given by $\varepsilon = 1 - v_0^2/v_\infty^2$.

Numerical calculations were carried out assuming that the specimens are biological tissues or biopolymer solutions. The zero-frequency velocity v_0 was taken to be 1570 m/s. f_v in Eq. (1) was set to be 200 MHz.

Figure 1 shows the calculated results of the frequency characteristics of the square of the velocity v. In the calculations, v_∞ was taken as 1575, 1580, 1590, and 1620 m/s. v^2 has the value of v_0^2 at the zero frequency, but it gradually increases as the frequency increases. v^2 increases significantly around the velocity relaxation frequency f_v, and it has the value of v_∞^2 at the infinite frequency. It should also be noted that these curves have the inflection point at the velocity relaxation frequency f_v. The slopes of the curves in Fig. 1 are shown in Fig. 2. They are the first derivatives of v^2 with respect to the logarithm of frequency. The slope is zero at the zero frequency, but it increases as the frequency increases, and reaches its maximum value at the velocity relaxation frequency f_v. Then it decreases as the frequency increases, and becomes zero again at the infinite frequency. The maximum value of the slope is determined uniquely by the difference between v_0^2 and v_∞^2, viz., $v_\infty^2 - v_0^2$. The maximum slope increases as $v_\infty^2 - v_0^2$ increases. After all, the slope

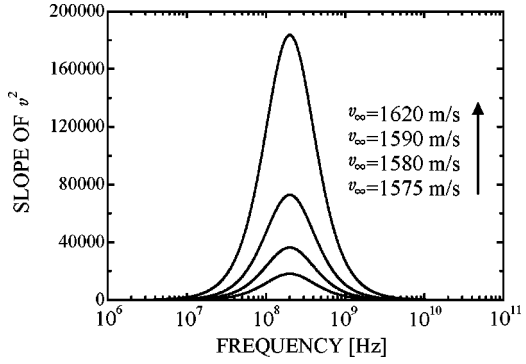

FIG. 2. Slope of the v^2 curves.

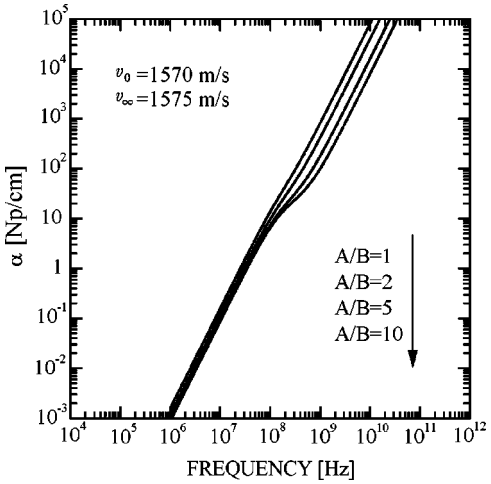

FIG. 3. Frequency dependence of attenuation coefficients for $A/B = 1$, 2, 5, and 10.

curve of the frequency characteristics of the square of the velocity v^2 is determined uniquely by f_v and $v_\infty^2 - v_0^2$. Note that when $v_\infty = 1575$, 1580, 1590, and 1620 m/s, $v_\infty^2 - v_0^2$ is 15 725, 31 500, 63 200, and 159 500 (m/s)^2, respectively.

Figure 3 shows the calculated results of the frequency characteristics of the attenuation coefficient α. In the calculations, $v_0 = 1570$ m/s, $v_\infty = 1575$ m/s, and B was set to satisfy $A/B = 1$, 2, 5, and 10. The attenuation relaxation frequency f_α is calculated to be 198.7 MHz from Eq. (3). For every A/B, the slope of the α curve is 2 at the zero frequency, but it decreases around the attenuation relaxation frequency f_α, and becomes 2 again at the infinite frequency. Figure 4 shows the frequency characteristics of the exponent on the attenuation coefficient α in Fig. 3. The exponent on α is 2 both at the zero and infinite frequencies, but it decreases significantly in the neighborhood of the attenuation relaxation frequency f_α and reaches its minimum value. It is found that the minimum value of the exponent on the attenuation coefficient decreases as A/B increases. It is also observed that the frequency, at which the exponent on the attenuation coefficient reaches its minimum, increases as A/B increases, even though the attenuation relaxation frequency f_α is unchanged.

It is concluded that the frequency characteristics of the exponent on the attenuation coefficient are determined

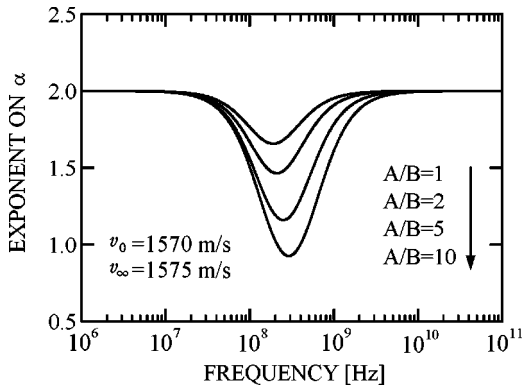

FIG. 4. Frequency dependence of the exponent on attenuation coefficients for $A/B = 1$, 2, 5, and 10.

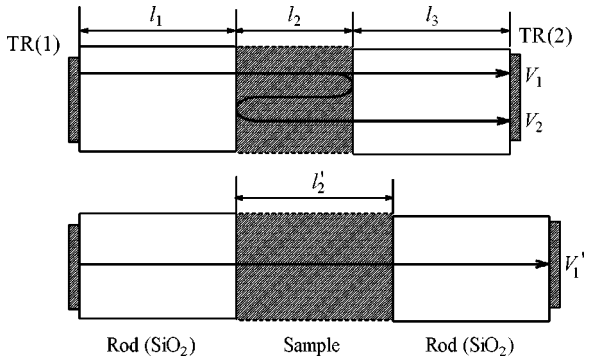

FIG. 5. Definition of transducer outputs V_i for measuring acoustic properties of biological media.

uniquely by the attenuation relaxation frequency f_α and the relaxation parameter ratio A/B. Note that scattering in the media due to structural features may affect the exponent on the attenuation coefficient, for example, in biological media.

III. MEASUREMENT METHOD

Measurements were performed using the bioultrasonic spectroscopy system. The system is capable of measuring acoustic properties, viz., attenuation coefficient, velocity, acoustic impedance and density of liquid, biological tissues, and solids in the VHF/UHF range. The system is described in detail elsewhere.[1] The system has further been improved to measure the amplitude and phase of radio frequency (rf) tone burst signals in the VHF range.[7,8]

The experimental configuration for measurements is illustrated schematically in Fig. 5, in which a specimen is inserted between the parallel surfaces of synthetic silica (SiO_2) buffer rods having ZnO piezoelectric film transducers on their outer ends. The gap length between the two buffer rods is determined by measuring frequency characteristics of the interference output of V_1 and V_2 for pure water of which the velocity is used as the reference.[1]

The velocity is obtained by the complex-mode velocity measurement method,[7,8] in which the phase of the transducer output V_1 and V_2 is measured as a function of frequency. From the measured phase difference ϕ ($0<\phi<2\pi$) between V_1 and V_2, the velocity is obtained as

$$v=-\frac{4\pi f l_2}{(\phi+2\pi n)-\Delta\theta}, \tag{4}$$

where n is the integer number and $\Delta\theta$ is the phase advance effect due to diffraction, which can be corrected numerically. The numerical calculations are performed using the exact integral expression of diffraction by Williams.[9] Since the value of the measured phase difference ϕ is smaller than 2π, the value of n must be determined. If the velocity at a frequency is given, n can be determined by using Eq. (4). The velocity was measured at one frequency using the z-interference method,[1] in which the interference output of V_1 and the reference electrical signal derived from the signal generator of the measurement system is measured as a function of gap length l_2.

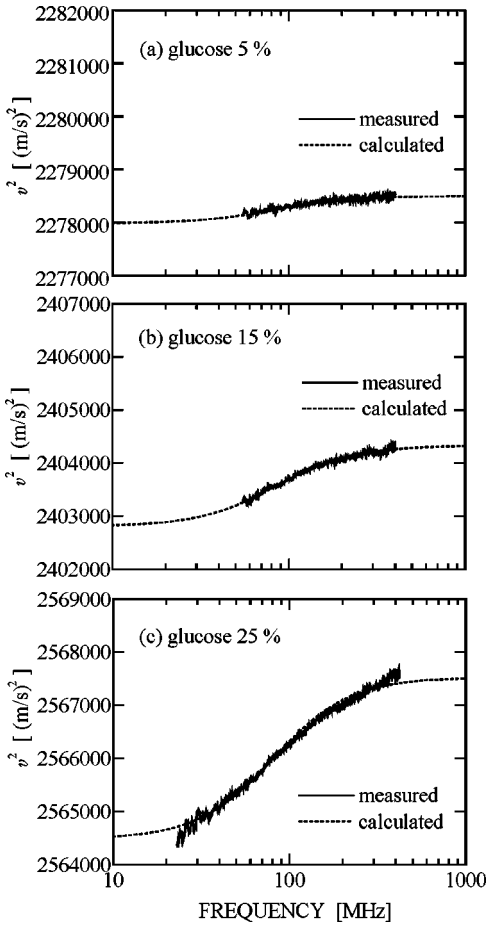

FIG. 6. Measured and calculated frequency dependence of the square of velocities of 5, 15, and 25% aqueous solutions of glucose at 23 °C.

The attenuation coefficient is determined by measuring the amplitude of the transducer outputs V_1 and V_1' for different gap lengths l_2 and l_2' as

$$\alpha=\frac{1}{l_2'-l_2}\ln\frac{|V_1|}{|V_1'|}-\frac{1}{l_2'-l_2}\cdot\ln\frac{|ATT_1|}{|ATT_1'|}, \tag{5}$$

where ATT_1 and ATT_1' are the diffraction loss for the transducer outputs V_1 and V_1', respectively. The diffraction loss can be corrected numerically using the exact integral expression of diffraction by Williams.[9]

IV. EXPERIMENTS AND RESULTS

5, 15, and 25% concentration aqueous solutions of glucose were used. The frequency characteristics of the velocities and the attenuation coefficients were measured using the bioultrasonic spectroscopy system. To cover the frequency range from 20 to 700 MHz, four different ultrasonic devices having operating center frequencies of 70, 150, 420, and 700 MHz, respectively, were employed. The temperature of the specimen was controlled to be 23.00 ± 0.05 °C.

A. Velocity

Figure 6 shows the measured frequency characteristics of the square of the velocity v^2 for 5, 15, and 25% aqueous solutions of glucose in the frequency ranges 55 to 400 MHz, 55 to 400 MHz, and 23 to 420 MHz, respectively. It is seen

TABLE I. Acoustic parameters used for numerical calculations of the velocities and the attenuation coefficients.

		Concentration		
		5%	15%	25%
Velocity measurement	v_0 [m/s]	1509.30	1550.10	1601.40
	v_∞ [m/s]	1509.47	1550.59	1602.35
	f_v [MHz]	85	85	81
	$A[\times 10^{-17}\ \mathrm{s}^2/\mathrm{cm}]$ (determined using v_0, v_∞, and f_v)	5.5	15.1	28.7
Attenuation measurement	$A[\times 10^{-17}\ \mathrm{s}^2/\mathrm{cm}]$	6.0	15.0	29.0
	$B[\times 10^{-17}\ \mathrm{s}^2/\mathrm{cm}]$	23.5	27.0	32.5
	f_α [MHz]	85	85	84

that the velocities increase with frequency for every concentration. The dotted curves in the figures are the calculated results of v^2 with the acoustic parameters of v_0, v_∞, and f_v listed in Table I. Figure 7 shows the determined slopes of the frequency characteristics of v^2 in Fig. 6. The maximum value of the slope increases with concentration. The dotted curves in the figures are the calculated results. The measured curves are in excellent agreement with the calculated curves in both Figs. 6 and 7 for the concentration of 5 and 15%. However, there are differences in shape between the measured and calculated velocity curves for the 25% aqueous solution. By comparing Figs. 6 with 7, it is seen that the velocity relaxation frequency f_v is clearly detected in the frequency characteristics of the slopes of v^2. From the frequency characteristics of the slopes of v^2 shown in Fig. 7, f_v and $v_\infty^2 - v_0^2$ can be determined. $v_\infty^2 - v_0^2$ was determined as 513, 1519, and 3044 $(\mathrm{m/s})^2$ for the concentration of 5, 15, and 25%, respectively.

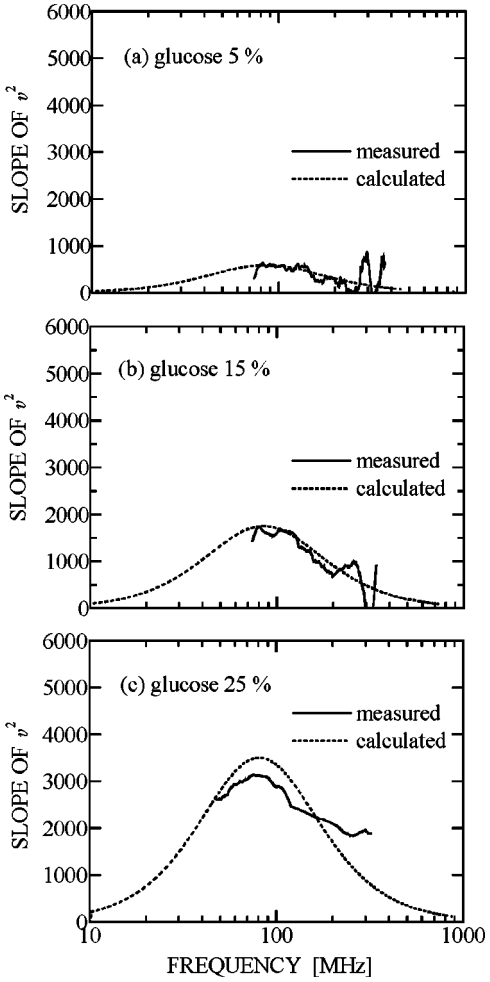

FIG. 7. Measured and calculated frequency dependence of the slope of the square of velocities of 5, 15, and 25% aqueous solutions of glucose at 23 °C.

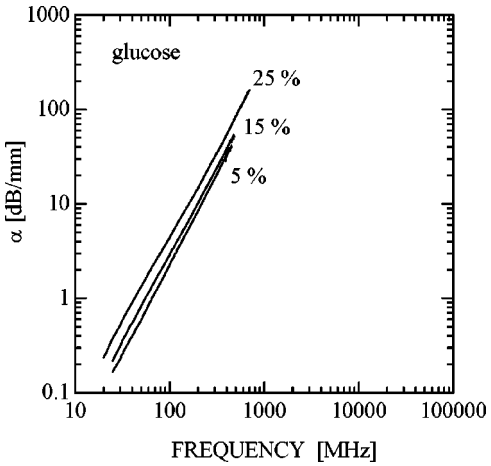

FIG. 8. Measured attenuation coefficients α of 5, 15, and 25% aqueous solutions of glucose at 23 °C.

B. Attenuation coefficient

Figure 8 shows the measured frequency characteristics of the attenuation coefficients α for 5, 15, and 25% aqueous solutions of glucose in the frequency ranges 25 to 450 MHz, 25 to 480 MHz, and 20 to 700 MHz, respectively. Figure 9 shows the attenuation coefficient α divided by the square of frequency f, viz., α/f^2. The solid and dotted curves represent the measured and calculated values, respectively. The calculations were performed using Eq. (2) with the acoustic parameters of A, B, and f_α listed in Table I. Figure 10 shows the determined frequency characteristics of the exponent on α in Fig. 8. The solid and dotted curves in the figure represent the measured and calculated values, respectively. The measured curves are in agreement with the calculated curves in both Figs. 9 and 10. From the exponent on α shown in Fig. 10, f_α and A/B can be determined. A/B was determined as 0.255, 0.556, and 0.892 for the concentration of 5, 15, and 25%, respectively.

C. Discussion

The value of A in Eq. (2) can be determined either by the velocity or the attenuation measurement. According to the relations of $A=\pi\varepsilon/(v_0 f_\alpha)$, $\varepsilon=1-v_0^2/v_\infty^2$, and $f_v=(v_\infty/v_0)^2 f_\alpha$, A is determined using the values of v_0, v_∞, and f_v. Table I shows the values of A determined by the velocity and attenuation measurements, where it is seen that they are in excellent agreement with each other for the concentrations of aqueous solutions of glucose.

For the 5 and 15% aqueous solutions of glucose, the measured curves are in excellent agreement with the calculated curves for both velocity and attenuation coefficient.

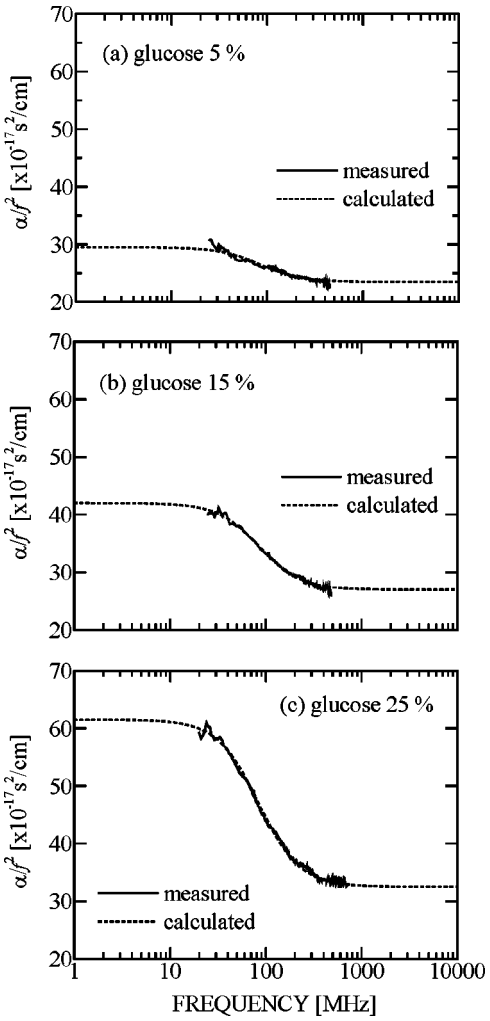

FIG. 9. Measured and calculated α/f^2 of 5, 15, and 25% aqueous solutions of glucose at 23 °C.

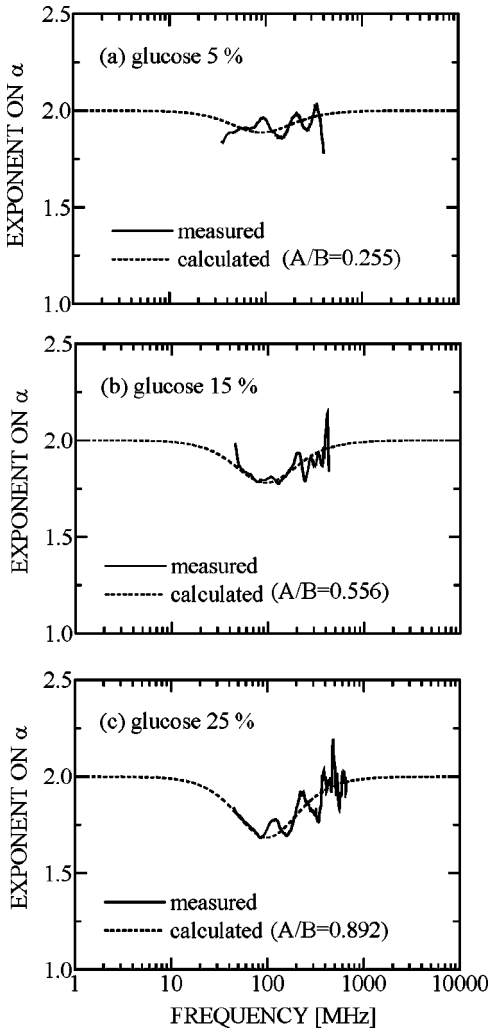

FIG. 10. Measured and calculated frequency dependence of the exponent on attenuation coefficients of 5, 15, and 25% aqueous solutions of glucose at 23 °C.

However, there are differences in shape between the measured and calculated velocity curves for the 25% aqueous solution. Further, $f_v = 81$ MHz was obtained from the velocity, and $f_\alpha = 84$ MHz was obtained from the attenuation coefficient for the 25% aqueous solution. The difference between them is 4%. Since $f_v = 1.0012 f_\alpha$ is obtained by substituting $v_0 = 1601.40$ m/s and $v_\infty = 1602.35$ m/s into Eq. (3), viz., $f_v = (v_\infty / v_0)^2 f_\alpha$, the difference between f_v and f_α which is predicted from the difference between v_0 and v_∞ is 0.12%. The causes of the 4% difference between the measured values of f_v and f_α cannot be explained by this relaxation theory. It is necessary to analyze the data by introducing multirelaxation processes. Since the value of the relaxation frequencies obtained from the 5, 15, and 25% aqueous solutions are nearly equal, a main relaxation process may be due to the same mechanism for all the concentration solutions. A second relaxation process in the 25% aqueous solution may arise from solute–solute interaction processes.

V. SUMMARY

In this paper, the bioultrasonic spectroscopy system has been employed for measurements of velocity and attenuation coefficient of aqueous glucose solutions in the VHF/UHF range. The relation between the slope of the square of velocity and the relaxation parameters, and the relation between the frequency exponent on attenuation coefficient and the relaxation parameters were numerically calculated and presented. It was shown that the slope of the frequency characteristics of the square of the velocities was determined uniquely by the velocity relaxation frequency f_v, and the difference between the square of the velocity at zero frequency v_0^2 and the square of the velocity at infinite frequency v_∞^2, viz., $v_\infty^2 - v_0^2$. Also, the exponent on the attenuation coefficient α was determined uniquely by the attenuation relaxation frequency f_α and the ratio of the parameters A/B, when $\alpha/f^2 = A/(1+(f/f_\alpha)^2) + B$.

To verify the calculated results through experiments, the frequency characteristics of velocities and attenuation coefficients were measured for 5, 15, and 25% concentration aqueous solutions of glucose in the frequency range from 20 to 700 MHz. The measured data for the 5 and 15% aqueous solutions can be explained using the single relaxation model. On the other hand, it is necessary to introduce a model for multirelaxation processes in order to understand the data for the 25% aqueous solution.

[1] J. Kushibiki, N. Akashi, T. Sannomiya, N. Chubachi, and F. Dunn, ''VHF/UHF range bioultrasonic spectroscopy system and method,'' IEEE Trans. Ultrason. Ferroelectr. Freq. Control **42**, 1028–1039 (1995).
[2] N. Akashi, J. Kushibiki, N. Chubachi, and F. Dunn, ''Acoustic properties of selected bovine tissues in the frequency range 20 to 200MHz,'' J. Acoust. Soc. Am. **98**, 3035–3039 (1995).
[3] N. Akashi, J. Kushibiki, and F. Dunn, ''Acoustic properties of egg yolk and albumen in the frequency range 20 to 400 MHz,'' J. Acoust. Soc. Am. **102**, 3774–3778 (1997).
[4] N. Akashi, J. Kushibiki, and F. Dunn, ''Measurements of acoustic properties of aqueous dextran solutions in the VHF/UHF range,'' Ultrasonics **38**, 915–919 (2000).
[5] J. Kushibiki, M. Ishibashi, N. Akashi, T. Sannomiya, N. Chubachi, and F. Dunn, ''Transmission line method for the measurement of the acoustic nonlinearity parameter in biological liquids at very high frequencies,'' J. Acoust. Soc. Am. **102**, 3038–3044 (1997).
[6] A. B. Bhatia, ''Discussion of experimental data in polyatomic liquids,'' in *Ultrasonic Absorption* (Dover, New York, 1967), Chap. 10, pp. 194–263.
[7] J. Kushibiki and M. Arakawa, ''Diffraction effects on bulk-wave ultrasonic velocity and attenuation measurements,'' J. Acoust. Soc. Am. **108**, 564–573 (2000).
[8] J. Kushibiki, R. Okabe, and M. Arakawa, ''Precise measurements of bulk-wave ultrasonic velocity dispersion and attenuation in solid materials in the VHF range,'' J. Acoust. Soc. Am. **113**, 3171–3178 (2003).
[9] A. O. Williams, Jr., ''The piston source at high frequencies,'' J. Acoust. Soc. Am. **23**, 1–6 (1951).

The corono-apically varying ultrasonic velocity in human hard dental tissues

Christoph John[a)]
Biomedical Engineering Laboratory, Department of Conservative Dentistry, University of Tuebingen, Osianderstr. 2-8, D-72076 Tuebingen, Germany

(Received 23 October 2003; revised 15 March 2004; accepted 19 March 2004)

The speed of ultrasound at 20 MHz is measured for hard dental tissues inside human teeth. This includes the cementum, for which no data are available. The spatial distribution, extrema, and means of the longitudinal ultrasound velocity (LUV) are determined with an emphasis on the apical thirds and an extended spectrum. Tissue areas are investigated by optical means and by acoustical scanning, in order to compare apical regions-of-interest with the complete mineralized wet porous tissue that lies beneath the enamel cap. The maximal LUV in a single dentin specimen varies from 3903 m/s to 4226 m/s. The dentin's frequency distribution of LUV at 20 °C exhibits a predominant peak feature comprising several Voigt functions. Introducing standardized relative tooth width portions, the corono-apical decrease in LUV of 21 specimens is approximated by $\mathrm{LUV}=4224-(257*\ln(y))$ along reduced distances in dentin. Abnormal teeth require a higher resolution and an approximate equation of the form $\mathrm{LUV}=(\Sigma(a_i*y^i))/(1+\Sigma(b_{i+1}*y^{(i+1)}))$. It can be used each time the corono-apical variation has to be quantified in each of the three tissues. Ten coefficients are numerically exemplified. An error evaluation is performed, which denotes errors of $0.2\%\pm1.3\%$ (enamel), $-0.1\%\pm1.6\%$ (cementum), and acceptable residual errors for dentin. © *2004 Acoustical Society of America.* [DOI: 10.1121/1.1738454]

PACS numbers: 43.80.Ev, 43.80.Jz, 43.35.Cg, 43.20.Jr [FD] Pages: 545–556

I. INTRODUCTION

Hard dental tissues (HDTs) can be understood as ''natural composites'' made of hydroxyapatite and collagen and they are known to be inhomogeneous materials, which have anisotropic structures and constituents.[1–3] Human teeth comprise locally differing tissue layers, some spatially winding asymmetries, and an irregular porosity.[4] In general, every physical property of interest may be seen with respect to both tooth aspects: anisotropy and inhomogeneity.[5–8] Among the studies of the mechanical characteristics, the determination of a tooth's hardness is most commonly carried out, but not all investigators are focusing on a description that shows the variation as a function of location (e.g., from the inside out, or in the corono-apical direction, i.e., from the crown towards the far-off located root portion, called the apex).[9–12]

Besides the importance of the plastic deformation, there is the range of elasticity within which the deformation of a tooth occurs under normal physiological conditions.[3,13,14] For obtaining the anisotropic elastic properties of crystalline materials in small specimens, ultrasonic wave propagation measurements are considered ideal.[15,16] Ultrasound and laser-based ultrasonics frequently serve as a basis for attempts to analyze the elastic properties of anisotropic materials, including composite systems of organic and apatitic components.[17–19] Conventional ultrasonic techniques are applied to teeth in order to explore their internal structure by using different couplants (water, mercury, aluminum, and glycerine) and the determination of the HDT's acoustic properties is the subject of several investigations, which include the measurement of the speed of sound[20–23] and the detection of carious tissues.[24–27]

II. LIMITATIONS AND DETAILS

In the literature, there are no values for the very thin cementum layer that covers a human tooth (''C'' in Fig. 1). An ultrasonic velocity in dentin of 4000 m/s is stated first by Kossoff and Sharpe in an article with data on the transmission of ultrasonic pulses in hard dental tissues.[28] There are publications that follow in order[21,29] and an average of $3600\ \mathrm{m/s}\pm200\ \mathrm{m/s}$ of five separate previous determinations is estimated for dentin by Lees and Rollins.[1] In their article, one-dimensional plots show some small variations with depth and orientation. However, these values and variations belong to the dentin of bovine incisors, but not to the generally much smaller human dentin (''D'' in Fig. 1).[1] Although the speed of sound in enamel (''E'' in Fig. 1) is described in the literature by including considered aspects, like anisotropy,[1,22] (de-/re-)[25,27,30] mineralization,[31,32] and inhomogeneity,[33–35] there are still some problems and questions. Interesting aspects arise from a recent study with new, relatively high values for control groups of both tissues: enamel and dentin.[23] Another kind of diagnostic study is requiring a ''principally known'' speed of sound in enamel to evaluate the thickness of enamel unless a ''quasi-constant,'' wrong velocity is assumed.[32,36] A variation of density with depth is known and the acoustic impedance is already described.[37,38] Another argument for the variation of the speed of sound as a function of location may be derived from a recent study. This study deals with human dentin and different sound velocities, similarly varying Poisson's ratios

a)Electronic mail: cjohn@ieee.org

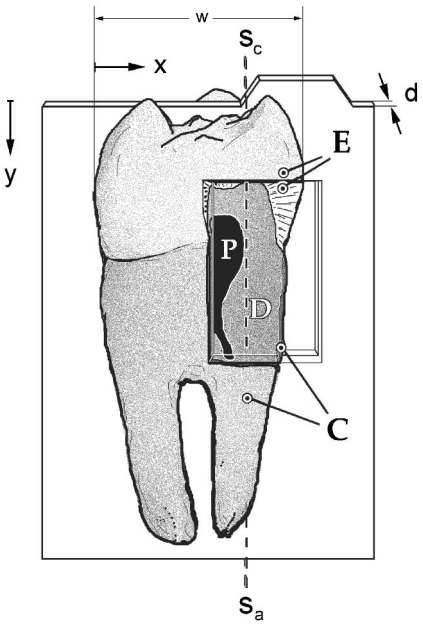

FIG. 1. Sketch of a human tooth and coordinates of a section of thickness *d*. The crown of the tooth and its width (''w'') are shown in the top region of the illustration. The coronal tooth portion is covered by an enamel (''E'') cap. The inserted view illustrates the interior of the tooth in order to locate the pulp chamber (''P'') and the surrounding dentin core (''D''). In the apical portions, the tooth's root is covered by a thin cementum layer (''C''). The dashed line represents a corono-apical scan line on the front surface of a section (partly hidden line between ''s_c'' and ''s_a'').

and densities for unresolved larger areas of two groups: horizontally sectioned dentin specimens and vertically sectioned dentin specimens.[14]

III. MATERIALS AND METHODS

In this paper, the measurement of the locally varying speed of sound at 20 MHz is addressed to describe its variation in human teeth as a function of position in 22 specimens.

A. Specimens

Vital human teeth—caries and restoration free—are extracted for orthodontic or periodontic reasons. After mechanical cleaning, all teeth are stored in PP-jars filled with a 0.9% saline solution. The jars are characterized by a measured diffusion rate that contributes to a loss of water of 0.07 grams per square meter and day.

Nonvital and vital teeth are embedded in PMMA in order to evaluate and control the influences and stresses during the curing and the cutting of the covering material, whereas 17 vital teeth are embedded in another technical resin with a lower temperature excursion during curing (Technovit©; Kulzer, Hamburg, Germany). One ground section from each of 22 teeth is obtained from their central sagittal area (the *xy*-plane in Fig. 1). All ground sections are cut by means of a low-speed saw, equipped with a thin diamond wafering blade of thickness 0.15 mm (Isomet© and 11-4243; Buehler, Lake Bluff, IL). During the cutting process the blade orientation is sometimes re-adjusted by a fixative. Since the central plane within a tooth is crucial, an adjacent ground section is taken in three cases. A careful selection of the cutting parameters reduces or avoids any ripping pattern. The thickness *d* (Fig. 1) of all sections is ranging from 0.55 mm to 1.42 mm with an individual corono-apical variation in section thickness of between ± 0.005 mm and ± 0.05 mm, with one exception being ± 0.13 mm in one test specimen.

Depending on the axial length of the teeth (the *y*-direction in Fig. 1), this corresponds to deviations from an ideally coplanar section by angles that are no greater than 0.3° in all but one exceptional specimen—where the greatest slanting is 0.8°. The relevant axial length, as measured on the section surface, ranges from 19 mm to 26 mm, with a mean axial length of 22.1 mm ± 2.15 mm.

B. Inspected regions

Taking the sections from the center of human teeth, it is assumed to readily achieve the largest inherent region of interest one can simultaneously monitor during ultrasonic measurements in each specific sample. In general, an approximation of the required scan area may utilize an offset and the product of the given axial length and the crown width *w* of the tooth (Fig. 1). In the present study, the width is varying from 5 mm to 10.3 mm, with a mean of 7.3 mm ± 1.67 mm. More precise surface areas are measured for the complete area that covers the dentin and all the regions of the endodontic system. Photographic images are analyzed by means of a computer-based imaging analysis system. Although the resolution of this system allows to depict 0.01 mm * 0.01 mm, the areas obtained are rounded so that four figures less than measured are kept. A second subset area is derived excluding the soft tissues of the pulp chamber and the wavy root canals in order to allow for improved comparisons between optical and acoustical surfaces. This makes the evaluation possible whether the present study is covering significant amounts of the possible areas that could have been investigated.

C. Anamnestic data (age distribution)

Since the influences of mineral density, temperature, moisture content, type of interface, and porosity on the ultrasonic behavior of oral hard dental tissues are still not clearly known, storage conditions, temperature variations during measurements, and data about the age are recorded.[19,25,39,41]

The age of each patient at the time of extraction is $(4.5 \pm 2) * 10^2$ months, with a minimum of 12.5 years and a maximum of 76 years. Accounting for the mean time of permanent dentition as a function of the type of tooth, the mean functional time is defined. The definition is given by an elapsed time span prior to extraction, during which a specimen is present inside the individual oral cavity. In general, a greater functional time increases the probability of stress induced microcracks and is related to age-dependent mineralization, including multiple demineralization processes (food) and remineralization mechanisms (saliva). The mean functional years are given in Table I.

D. Experiments

One ground section is used to perform a linear scan through an exceptionally old sample with exceptional veloci-

TABLE I. The age of the patients from which the teeth are extracted after a specific time period of oral function.

Type of tooth	Mean age of patient (a)	Functional years (a)
Molars (M)	26±19	10±14
Premolars (P)	26±14	14±14
Incisors (I)	40±14	31±14
Canines (C)	60±22	49±22
Total	37±17	26±17

ties and the remaining 21 sections are used for standardized line-scans, two-dimensional scans, and the frequency distribution analysis.

Measurements of the varying speed of sound are determined by means of typical corono-apical line scans along the direction of the long axis of the tooth. A typical scan line ("$s_c \ldots s_a$" in Fig. 1) starts at the enamel crown (E), runs through the dentin (D) and ends at the apical cementum (C). This type of scan is used to build up the two-dimensional distribution of the speed of sound at a perpendicular direction of propagation.

In order to summarize the general corono-apical variation of sound velocity in dentin, the longitudinal ultrasound velocity (LUV) at 20 MHz is recorded for many adjacent equidistant locations in every single specimen (APPENDIX B: INDIVIDUAL INHOMOGENEITY), and also for standardized locations at eight vertical positions (APPENDIX A: GENERAL TENDENCY).

In order to provide adequate descriptions four procedures are utilized, typical locations are described, the quality of the fit is mentioned, errors are computed, and economical aspects are considered in Appendices A and B.

Two functional descriptions are generated: one set of functions [Eq. (1)] with numerous, partly differing coefficients, and another function [Eq. (2)] with rather uniform coefficients. Regardless of which tissue is involved during the fitting of the measured LUV data, it is evaluated here, as long as one single appropriate set of functions [Eq. (1)] exists for all tissues. It is appropriate, provided that

(a) each of its functions makes it possible to quantitatively compare all vertical scan lines by its coefficients;

(b) each of its functions makes it possible to individually describe the corono-apical variation of LUV as a function of location at a high precision;

(c) the set of functions enables to partly substitute shape functions for macro finite elements;

(d) the set of coefficients makes it possible to integrate data with medical element engineering and simulation (MEES);

(e) at least one of its functions makes it possible to convert varying Poisson's ratios into a factor that relates elasticity to the square of LUV (times density); and

(f) presently redundant coefficients can be added at no greater efforts once an upgrade seems to become necessary from the results of velocity excursions of any future work.

The idea is to utilize the various coefficients of the first set of functions [Eq. (1)] for detecting abnormal features, individual distributions, and any pathologic changes of tissues by comparison with the regular results of Eq. (2). It is desired that the second function comprises only two coefficients for all regular teeth and that it is providing acceptable, individual residual differences along vertical scans through central portions of regular dentin. In addition, the locally varying longitudinal ultrasound velocity at 20 MHz is presented by a histogram that shows the frequency distribution of the measurements in the major tissue, the dentin core.

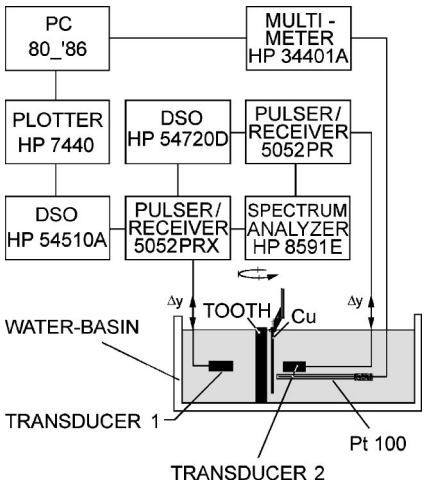

FIG. 2. Measuring setup showing the ultrasonic measuring system. Generated high frequency pressure pulses and received echograms are performed by a pair of spherically focussed 20 MHz-transducers and a pair of pulser/receivers. A removable tooth section and a rotating copper reflector ("Cu") are utilized for the rotatory pulse-echo mode application and optional transmission experiments with and without a specimen in the ultrasonic path. The post-processing of the acquired data is carried out in personal computers.

E. Measurement arrangement

The velocity is measured using a modified pulse-echo method. This is accomplished utilizing a measurement setup shown in Fig. 2.

Ultrasonic pressure pulses are generated by one of two immersion transducers attached to the high-voltage outputs of two pulser/receivers (5052 PRX; Panametrics, Waltham, MA). The transducers used are spherically focused 20 MHz-transducers (V317; Panametrics, Waltham, MA). The arrangement comprising the transducer 1, the tooth section, and the removable ideal reflector (copper) is primarily used for the pulse-echo experiments. However, a second transducer and a rotating reflector that can be re-arranged on the opposite side of the section is found to be helpful. The second transducer provides an interim verification of the ultrasonic path and an optional transmission method signal in cases of higher attenuation. An xyz-table allows for movements at equidistant steps. The Pt-100 sensor and a GPIB-bus-multimeter (HP 34401 A; Hewlett Packard, Colorado Springs) are used to measure the equilibrium temperature excursion of the tooth section and the water. A low capacity, high frequency active probe (HP 85024 A; Hewlett Packard, Colorado Springs) is attached to an optional spectrum analyzer (HP 8591 E: Hewlett Packard, Colorado Springs) in order to adjust the alignment of both transducers prior to the measurements. Additional details about the equipment and the former arrangement can be found elsewhere.[6,11]

TABLE II. The (contour ''minus'' endodontic) areas of the irradiated front sides of the tooth sections. Please note, that in contrast to the mean area values provided, standard deviations and maximal areas cannot be subtracted in a mathematical manner.

Type of area	Mean area (mm^2)	Maximal area (mm^2)
Molars (M)	150-13±32-9	159-27
Premolars (P)	120-10±32-9	151-26
Incisors (I)	93-4±20-4	135-12
Canines (C)	122-12±7-2	127-14
Dentin (Molars)	116±12	124
Dentin (Premolars)	90±20	108
Dentin (Incisors)	74±18	109
Dentin (Canines)	102±8	108
Total (dentin)	84±22	124

F. Measurement principle

When an ultrasonic pressure pulse propagates in a medium, the wave speed, the distance traveled by the pulse, and the time-of-flight are coupled together. If two of them are known, the third can be calculated. However, it is possible to determine the speed of sound without the simultaneous knowledge of the distance traveled by the pulse.[6,11,40] The combination of the reflection and the substitution method is used in the present study to avoid separate measurements of sample thickness.[40] The frequency distribution of the LUV of vital human specimens is calculated from the two-dimensional distribution of LUV using the longitudinal data acquisition model. The frequency distribution of every single specimen is determined as a function of velocity clusters at 100 m/s. For each cluster, the percentage of the measured velocities falling into the corresponding given range is calculated relative to the total number of measured velocities in that specimen. Each relative frequency given in the table corresponds to one cluster, each optical area to the average of two separate measurements, and all ultrasonic velocity data to the average of all specimens measured.

IV. RESULTS

A. Optical measurements

The size and shape of the cross-sectional areas show a great variation due to detailed contours and different types of teeth. The dentin areas exhibit an average value of $84.2\ mm^2 \pm 21.8\ mm^2$ on every plane surface of all longitudinal sections. A detailed description of the distribution of the areas involved is given in Table II.

TABLE III. The mean number of irradiated focal spot regions that represent multiples of a spot area of $0.01\ mm^2$ in dentin and in the apical thirds (approx. 1/3), each. Different type of teeth are represented by M (Molars), P (Premolars), I (Incisors), and C (Canines). Their greatest individual contributions (Max. Spots) came from the greatest ultrasonically detected, cohering area of a specific tooth.

Type of area	Mean spots ($*10^2$)	Max. spots ($*10^2$)
M (ap. 1/3)	4±4	7
P (ap. 1/3)	4±5	10
I (ap. 1/3)	13±11	34
C (ap. 1/3)	15±6	19
Total (approx 1/3 Dentin)	10±10	34
Dentin (M)	118±26	136
Dentin (P)	75±13	94
Dentin (I)	71±20	96
Dentin (C)	100±96	107
Total (dentin)	79±23	136

B. Number of ultrasonic measurements

The mean number of focal spot regions in dentin that are irradiated by ultrasonic energies is 7921±2302. The corresponding mean ± S.D. (and maximal) number of spot regions in the apical third of the dentin in each type of tooth is compared to their complete, ultrasonically detected surfaces (Table III).

C. Longitudinal ultrasound velocity

1. Mean and maxima (dentin)

The LUV's arithmetic mean ± S.D. in dentin of the apical thirds is lowest in the molars and highest in the canines, but although the maximal mean of specimen LUVs is lowest in molars, too, the highest maximal mean of apical specimen LUVs is calculated for an incisor. The corresponding arithmetic mean of the LUV in the whole dentin of sections is lowest in the canines and highest in the premolars. More details about the relevant LUVs in (m/s) for the dentin of vital teeth are given in Tables IV and V. In Table V the maximal values of the measured longitudinal sound velocities are summarized.

TABLE IV. Mean and maximal arithmetic means of all the dentin's longitudinal ultrasound velocities (LUVs) found for every single sample in (m/s) and their variation between specimens as a function of the type of tooth. Mean velocities are rounded to the next full ten m/s. Maximal individual mean LUVs are rounded to the next full hundred m/s. Please note that the asterisk * is indicating a summary for which only two specimens are left.

Type of tissue	Mean velocity (m/s)	Max. Mean speed (m/s)
approx. 1/3 (M)*	3090±210	3200
approx. 1/3 (P)	3440±140	3600
approx. 1/3 (I)	3390±180	3600
approx. 1/3 (C)*	3450±70	3500
Total (aprox. 1/3 Dentin)	3370±190	3600
Dentin (Molars)	3090+470*=3560±20	3200+400*=3600
Dentin (Premolars)	3440+190=3630±60	3600+100=3700
Dentin (Incisors)	3390+190=3580±130	3600+200=3800
Dentin (Canines)	3450+20=3470±10	3500+0*=3500
Total (Dentin)	3580±110	3600+200=3800

TABLE V. Maximal longitudinal ultrasound velocities (LUVs) in dentin found for every single sample in (m/s) and their variation between specimens as a function of the type of tooth.

Type of Tissue	Maximal LUV (m/s)	Range (Max.LUVs) (m/s)
Dentin (Molars)	4100±70	[4044–4144]
Dentin (Premolars)	4050±50	[4003–4132]
Dentin (Incisors)	4000±50	[3903–4056]
Dentin (Canines)	4150±130	[4038–4226]
Total (Dentin)	4040±70	[3900–4230]

TABLE VI. Frequency distribution of the measured LUVs in dentin as a function of the type of tooth and of increasing velocity clusters at 100 m/s. Values with two asterisks result from individual contributions but are excluded from summary due to nonsignificant digits. The variation of the mean cluster contributions at ''All Teeth'' are seen in Fig. 3.

LUV-Cluster (m/s)	All teeth (mean) (%)	Canines (median) (%)	Incisors (median) (%)	Molars (median) (%)	Premolars (median) (%)
2800–2900	4.8	14	4	6	2
2900–3000	3.6	2	4	7	2
3000–3100	2.7	2	3	4	2
3100–3200	3.0	3	3	5	2
3200–3300	4.4	6	4	4	4
3300–3400	6.0	8	6	6	6
3400–3500	7.7	11	7	7	8
3500–3600	11.7	12	11	10	15
3600–3700	15.7	13	17	9	16
3700–3800	15.2	12	19	9	10
3800–3900	12.4	7	13	10	15
3900–4000	9.8	6	8	17	13
4000–4100	2.8	3	1	6	5
4100–4200	0.2	1	0.1**	0.6**	0.2**
4200–4300	0	0.2**	0	0	0
Total**	100	100	100	100	100

2. Frequency distribution (dentin)

The frequency distribution of every single specimen is determined as a function of velocity clusters at 100 m/s. For each cluster, the percentage of the measured velocities falling into the corresponding given range is calculated relative to the total number of measured velocities in that specimen. All specimens that belong to the same type of tooth are summarized by the details given in Table VI. Figure 3 shows the corresponding histograms of ''All Teeth'' and ''Incisors'' using the mean values of the corresponding frequency distributions of LUVs in all specimens. In the lower third of Fig. 3 the standard deviation is shown for all teeth (filled circles)—and changes are indicated by the approximated dashed line,

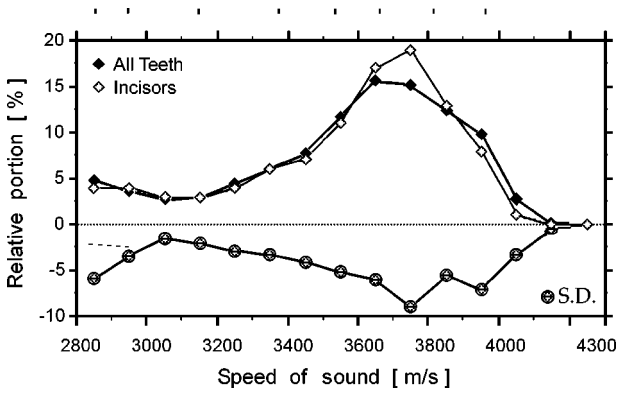

FIG. 3. The longitudinal ultrasound velocity is summarized by two mean histograms that are divided into clusters at 100 m/s. The corresponding data about the variation of velocity within clusters are given in Table VI and by the standard deviation shown in the lower third of the diagram. Two similar frequency distributions of the longitudinal ultrasound velocity are shown: one for 21 vital ground sections taken from the center of vital human teeth and another one for incisors only. Predominant individual peak contributions from corresponding center wave numbers of Voigt distributions (top) can be uniformly allocated in each but one nonvital specimen.

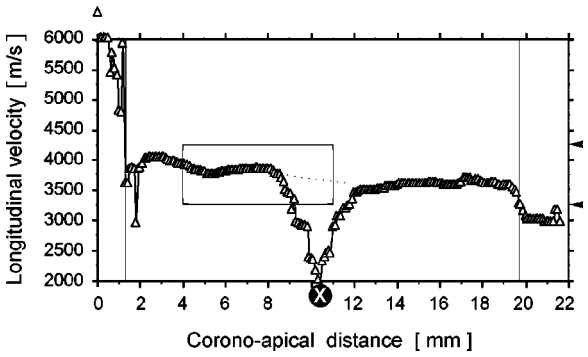

FIG. 4. Diagram showing the corono-apically varying longitudinal ultrasound velocity (LUV) along one individual scan line. The vertical scan involves each of the three different tissues. The highest values correspond to the enamel (0···1.2 mm). Passing the dento-enamel-junction (DEJ, left vertical help-line), the dentin is mainly exhibiting moderate LUV values at distances ranging from 1.30 mm to 19.75 mm. However, very low velocities are also observed (Marked cross), which are even smaller than those of cementum (19.75···21.6 mm). A loosely interconnecting line of dots is indicating a likely distribution of a regular tissue (i.e., with no excessive regional behavior and no pathologic changes). This estimation is based on a special domain of dentin (the inserted rectangle), for which all regular dentin specimens are numerically summarized by Eq. (2) and Fig. 5.

for the case when those specimens that experienced a direct embedding with only the PMMA are removed prior to calculating statistics.

3. Individual spatial distributions (three tissues)

A typical ultrasonic scan performed at a fixed temperature of $20\pm0.4\,^{\circ}\mathrm{C}$ along the vertical tooth axis resulted in 216 (or more) data pairs, depending on the length of the tooth (here, no more than 24.4 mm under a slightly inclined angle). Unexpectedly, extremely low velocities of sound are observed near the center of a corono-apical line scan (the marker in Fig. 4). The scan is performed for an extra specimen extracted from a lady aged over 82 years. This one-dimensional scan starts in the enamel crown of her nonvital canine (at the vertical y-position ''0 mm''), continues in the dentin (the left vertical help-line in Fig. 4) by collinearly following the tooth's long-axis adjacent to the pulp walls where the region of the minimum is tangentially traversed (the end of rectangular box in Fig. 4), and finally ends at the apical root portion (behind 19.75 mm in Fig. 4). Those val-

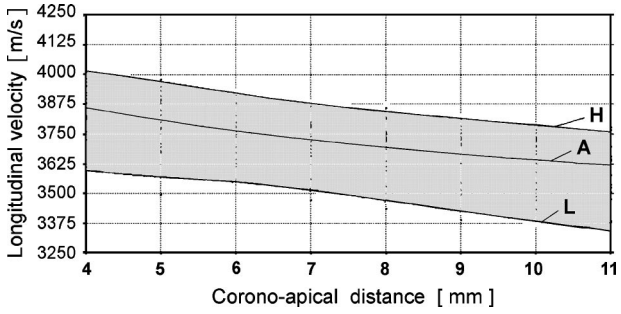

FIG. 5. Diagram of 21 specimens showing the corono-apically decreasing velocity in dentin along a shorter vertical distance. Three graphs are computed from the data of standardized central portions of dentin ($x_j=0.7w$; $\triangle y=1$ mm) using all velocities (''A''), highest velocities (''H''), and lowest (''L'') velocities. The corresponding numerical values of Eq. (2) are given in Table VIII.

TABLE VII. Coefficients of Eq. (1). The spatial distribution of LUVs can be approximated as a function of the y-location. The coefficients are based on 216 measured LUVs in three hard dental tissues: enamel, dentin, and cementum ($n=1$). Two versions of the approximation are provided for the thin cementum layer of the nonvital tooth.

	Enamel $n=1$	Dentin $n=1$	Dentin $n=21$	Cementum (Vers. A) $n=1$	Cementum (Vers. B) $n=1$
Valid y	0.0–1.2	1.3–19.8	4.0–11.0	19.7–21.6	19.7–21.6
Distance	1.2 mm	18.5 mm	8.0 mm	2.0 mm	2.0 mm
Where ?	At start	Central	Fig. 5''L''	Apex	Apex
Fit.Std.Err.	165.2	165.6	122.1	62.2	55.9
R^2	0.98	0.85	0.77	0.66	0.76
Procedure	(A)	(A)	(III)	(A)	(A)
a_0	6010.5	4182.9	4388.6	−250.1	−0.00527
a_1	−30442.55	−2382.55	−739.23	6.65	0
a_2	56046.188	558.199	−26.429	0	0
a_3	−44307.8758	−56.7743	24.7526	0	0
a_4	12764.1259	2.064076	0	0	0
	1	1	1	1	1
b_1	−5.07	−0.57	−0.07	−0.10	−0.24
b_2	9.4006	0.1371	−0.0346	0.0025	0.0235
b_3	−7.57943	−0.01422	0.00883	0	−0.00114
b_4	2.3557864	0.0005267	0	0	27.577 $E-6$
b_5	−0.0885893	0	0	0	−267.16 $E-9$

ues of the speed of sound that correspond to the thin cementum layer are found to be approximately 3 km/s. The values of the speed of sound in enamel are greater than 4807 m/s, with a maximum that does not exceed a value of about 6000 m/s for this individual (Fig. 4). Other samples reveal other maxima.

A fitting according to least squares is performed that provides for all tissues a uniform equation of the form

$$\mathrm{LUV}(y,20\,^\circ\mathrm{C})/(\mathrm{m/s}) = \frac{\Sigma_{i=0}^{4} a_i \cdot y^i}{(1+\Sigma_{j=1}^{5} b_j \cdot y^j)}, \tag{1}$$

with $j=i+1$ and i ranging from 0 to 4, where y is the unitless vertical position (only the decimal number of the mm distance) relative to the top of the crown. For the selected tooth a total of 10 coefficients are considered enough (Procedure (A)). For each of the tissues involved, the corresponding R^2 and the coefficients are listed in Table VII, where $n=1$.

4. Spatial distribution (enamel)

The values of the speed of sound in enamel are greater than ~4.8 km/s, with a maximum that does not exceed an observed value of 6500 m/s for the measured data of one specific tooth within the group of teeth. However, even higher values are estimated to exist in cases where two peaks overlap each other due to the thinness of the samples.

5. Spatial distribution (dentin)

A second fitting is performed with respect to the ease of use. It accounts for all vertical scan lines at the standardized relative tooth width portions. The corresponding corono-apical decrease in the sound velocity of 21 specimens can be approximated by means of

$$\mathrm{LUV}_{n=21}(y,20\,^\circ\mathrm{C})/(\mathrm{m/s}) = a + b \cdot (\ln y), \tag{2}$$

along a reduced distance in dentin (with y ranging from 4.0 mm to 11.0 mm). The application of procedure (I) contributes to $a=4224$ (rounded 4225) and $b=-257$. The variation of the quality of 21 individually fitted spatial distributions of LUV in dentin is given by 75 ± 47 (Fit. Std. Err.).

The third and fourth fittings result from procedures (II) and (III), respectively. The corresponding coefficients of Eq. (2) are given in Table VIII. The spatial distribution of LUV exhibits a corono-apical decrease in the central portion of dentin. Finally, the general corono-apical behavior of the major tissue is alternatively summarized by means of procedure (III) and Eq. (1). All specimens yield a corono-apical decrease in the sound velocity of dentin along a shortened distance, too. For all of the regular dentin portions, the corresponding R^2 and the coefficients of fitted lower LUVs ''L'' are listed in Table VII, where $n=21$ (Procedure (III)).

6. Spatial distribution (cementum)

The corresponding data are incomplete, because the LUV in cementum cannot be determined for every single specimen. The regular values of the measured speed of sound in cementum are similar to those of a lower-to-medium dentin quality, but are much higher than the lowest LUV observed in an exceptional region that exhibits the poorest dentin quality. The number of data is not sufficient to distinguish between general, single, and individual data.

TABLE VIII. Coefficients of Eq. (2), describing the corono-apical decrease in longitudinal ultrasound velocity of dentin (general tendency).

	$\mathrm{LUV}=a+b*\ln y$		
Criteria (Eq. 2)	a	b	Procedure
8*Mean ($n=21$)	4225	−257	(I)
⟪A⟫ in Fig. 5	4190	−238	(II)
⟪H⟫ in Fig. 5	4375	−255	(III)

D. Errors

The error in measured velocity is less than a tenth of a percent and mainly depends on the general possibility to control and maintain a fixed temperature inside the water-bath where the ultrasonic waves are propagating. The speed of sound in water serves for calibration and for testing any changes of the focusing lens of the immersed transducers due to swelling and shrinkage processes. Individually predicted LUVs that vary as a function of the y-location (for Procedure (A), APPENDIX B, and also for Procedure (III), APPENDIX A, using 10 coefficients) deviate from the measured data by a relative residual error of less than $0.2\% \pm 1.3\%$ for enamel. The corresponding deviation for individual dentin is less than 2.4% for all 0.1 mm-increments of y ranging from 2.2 mm to 8.7 mm, and from 12.8 mm to 16.3 mm, as well as from 16.9 mm to 18.0 mm; this corresponds to a residual error at every data point of individual approximation that is always much less than 94 m/s. The corresponding relative residual error of cementum is less than $-0.1\% \pm 1.6\%$. The overall-summary given by Eq. (2) is based on measured values at standardized locations that are assumed to be precise with a spatial error of ± 0.05 mm. The individual residual error in each specimen (Procedure (I), Appendix A) is ranging from a minimum of -112 ± 112 m/s to a maximum of 105 ± 69 m/s.

V. DISCUSSION AND OUTLOOK

A. Region-of-interest

Emphasis is given to completely characterize the whole tissue regions and selected regions-of-interest. For this purpose, it is a prerequisite to independently determine the areas involved by a second method, in both cases. This way, it is possible to relate the resulting data to a precisely known percentage of the chosen tissue. The values obtained for the LUV in the enamel and in almost the complete dentin are in accordance with numerous articles, with the exception of the reported extremely high values of Al-Nawas *et al.*[30]

B. Extended range (dentin)

However, since the residual belongs to four extremely low velocities inside one additionally added nonvital tooth, the control data of the former investigators specify the upper end of the total range observed. The extended range of the LUVs observed may be further discussed with respect to potential drying processes, temperature, and local position. The extended range of the maximal LUV is predominant for the canine group.

C. Type of tooth

It is questionable whether this finding is mainly due to a typical feature of this type of tooth or the greater variation of the group's functional age ($> +50\%$) relative to the corresponding variations of the other groups. However, a separate finding is related to the type of tooth: The ultrasonic representation of molars by multiples of $100*0.01$ mm^2 is erroneously over-estimated by an amount of 1.6%. In general, since there is no magnification for orthogonally directed incident beams, either a small misalignment from being perpendicularly irradiated by ultrasonic waves has to be argued or this effect is probably due to the smaller curvatures of the greater and more compact molars. This amount corresponds to less than 1.9 mm^2, where significant concerns about refraction may be an aspect to discuss for those samples that are not coplanar and show surface deviating angles. The second effect may be considered responsible for a mixed ultrasonic path along the specimen's thickness that allows waves to propagate through a remaining thin resin layer and the main HDT. If this is a true assumption, then the LUV in molars is under-estimated and the actual values in the corresponding frequency distribution may represent some more higher velocities for dentin.

D. Cementum

Finally, since there are no data available that describe the problematic cementum layer, a comparison cannot be made here. However, since the chemical composition of the cementum resembles that of bone and because this HDT exhibits the smallest mineral content (61 wt.% or 33 vol.%) and the greatest amount of water (12 wt.% or 36 vol.%) compared with dentin and enamel, the main organic component (27 wt.% or 31 vol.% of human cementum collagen of type I) plays a greater role regarding HDT's elasticity (largely reduced) and its moderate reduction in mass density. If the influence of crystallites on elasticity is greater than on density then both mentioned parameters explain an overall reduction in the speed of sound, especially when the mineralized tissue may become brittle and exhibits lower Poisson's ratios.

E. Corono-apical portions and locations

To account for the corono-apical variation in the speed of sound as a function of location, the mean and standard deviations of the LUV is calculated twice: for the apical third only and for the complete longitudinal section. An add-on of the coronal two thirds results in an increase in mean velocity and in maximal mean velocity for the same type of tooth by about 200 m/s. The value of ''two thirds'' is arbitrarily chosen and may be changed in future studies, if a statistically significant difference between different portions of the dentin core is an objective.

F. Drying effects and the role of water

Since moisture content affects the mechanical properties of dentin,[9,41] care is taken during our experiments that the dentin is not exposed to any dry condition. Otherwise, it might become dehydrated and the collagen fibers may shrink and then seem to let the crystallites approach each other until a release of energy by acoustic emission is caused by breaking ends of hydroxyapatite crystallites under local stresses.[42] It is the clinical observation of fractured teeth with a reduced dentinal toughness and a lower water content that makes endodontically treated teeth to be considered more susceptible to fracture. Paying attention to this, it is worth noting that completely dried teeth can be broken without any tool by the applied forces of the author's competing fingers.

G. SEM and AFM

A series of corresponding SEM-pictures do indicate broken ends of the nm-sized apatitic crystallites. Since former AFM-results of another research group show some cracks that have to be attributed to stresses induced during the desiccation of samples, this may impact on some areas of fracture mechanics in calcified tissues. Furthermore, dehydrated dentin reveals a tendency towards an increased proportional limit, elastic modulus, and excess strength under compression and tension.[14] Therefore, the sections of the present study are immersed in a water basin and it is necessary that water serves as the couplant during the ultrasonic measurements. However, there may be some arguments against a long-term storage of the specimens in pure water with regards to the physiological situation in the human mouth. For this reason, all teeth are stored in a physiological 0.9% saline solution.

H. Collagen content and minima

Research is already cited that reports a correlation between ultrasonic velocity and the content of collagen in human wall tissue.[43] A variation of 10% in ultrasonic velocity is outlined by suggesting that different concentrations of its constituents may lead to such variations.[44] Although this finding is related to the (soft) artery wall (in which the speed of sound in highly organized calcified lesions can be significantly elevated by some 30% up to between 1900 and 2000 m/s), this may be a hint to explain the newly observed low velocities near the pulp and close to the tooth's center.

I. Temperature

These low ultrasonic velocities are in the same order of magnitude—and do even reach the same value depending on the circumstance and knowledge about which temperature is (or is not) recorded during measurements. Since the speed of sound depends on several factors, further research is necessary to clarify the role of different boundary conditions and the phenomenon of the observed very low velocities. Although present results are based on similar room conditions during measurements, the longitudinal sound velocity in teeth might be investigated at different temperatures.

J. Physical properties

In addition, one may be interested in other physical properties of the mineralized tissues involved, as well as in its mineral densities, the mass density, or its chemical aspects?

Since the mechanical properties of dentin substrate are one of the important factors that determine the stability of a tooth under load and the bond strength of dentin to bonding systems, it is desirable to derive values for the Young's modulus. As previously reported,[14] one may (or may not) assume Poisson's ratios of vertically sectioned dentin specimens that range from 0.099 to 0.327. For a most likely, rounded mean density of 1.95 kg/dm^3 the elastic modulus can be calculated.

1. Elasticity for varying Poisson's ratio (constant density)

This way, those almost isotachographic areas that exhibit velocities ranging from 3700 m/s to 3800 m/s (i.e., which represent the present peak frequencies by a relative area of 19% for incisors, or 15.2% for all teeth) would already correspond to values of the Young's modulus that vary between 18.2 GPa and 27.5 GPa.

2. Elasticity for varying density

Furthermore, if variations in density between 1.74 and 2.16 are valid for physical measurements, a theoretical range based on mathematical permutation including extremes results in a computed span between a minimum of 16.2 GPa and a maximum of 30.5 GPa. This is in accordance with the findings of Miyazaki *et al.*, who reported an elastic modulus that ranged from 13.4 GPa to 25.4 GPa in longitudinal sections of dentin.[14]

3. Elasticity for varying velocity (different portions)

a. Medium class at 100 m/s. In order to discuss the aspect of the class width and the remaining parts of the given histogram, the latter portion at 100 m/s may only be hypothesized as a first case that can be critically summarized by the following:

$$\mathrm{CASE\_1}_{20\,^\circ\mathrm{C}} = \mathrm{POI}[\underline{0.099}\ldots 0.327]\_\mathrm{RHO}[1.74\ldots\underline{2.16}] \times \_\mathrm{LUV}[3700\ldots\underline{3800}]\_\mathrm{E}[16.2\ldots\underline{30.5}]_{0.15}^{0.19}.$$

b. Narrow band at 3 m/s. Since the same span of elasticity can be computed, if neither a variation in medium density nor in highest LUV is assumed, a second case can be considered, where the portion is further reduced:

$$\mathrm{CASE\_2}_{20\,^\circ\mathrm{C}} = \mathrm{POI}[\underline{0.242}\ldots 0.405]\_\mathrm{RHO}[\underline{1.95}]\_\mathrm{LUV} \times [\underline{4300}]\_\mathrm{E}[16.2\ldots\underline{30.5}]_{0.00}^{0.01}.$$

c. Broad band (full range, ~1500 m/s). Furthermore, if no variation in the Poisson's ratio is allowed, but the full range of the LUV in dentin has to be covered, then the same span of Young's modulus can be similarly computed according to:

$$\mathrm{CASE\_3}_{20\,^\circ\mathrm{C}} = \mathrm{POI}[\underline{0.149}]\_\mathrm{RHO}[\underline{1.74}\ldots 2.16]\_\mathrm{LUV} \times [2813\ldots\underline{4300}]\_\mathrm{E}[16.2\ldots\underline{30.5}]_{0.99}^{1.00}.$$

Although this case could already represent relevant parts of the true nature of the dentin and about 100% of the measured results of the histogram, the chosen value of the Poisson's ratio may not be valid.

4. Elasticity using combinations

Any estimated

$$\mathrm{CASE\_4}_{20\,^\circ\mathrm{C}} = \mathrm{POI}[\ ]\_\mathrm{RHO}[\ ]\_\mathrm{LUV}[\ ]\_\mathrm{E}[\ ]^{\mathrm{Rel.Area}}$$

that better accounts for other Poisson's ratios and that is also representing our ultrasonic measurements may be simultaneously created for several classes or the mentioned Voigt distributions. Then, appropriate relative areas listed in Table

VI may represent a set of 15 case(_4)s, by using a generally greater variation in the Poisson's ratio than in CASE_3, a greater variation in the density than in CASE_2, a greater variation in the speed of sound than in CASE_1, no mismatch in combining underlined values and nonmarked values, and by any maximal variations that do not exceed the mentioned ranges. With respect to our measurements, the real distribution of elasticity therefore can be regarded as a likely combination of the mentioned theoretical cases.

K. Corono-apical decrease of LUV in dentin

1. Local means

The corono-apical decrease in sound velocity of 21 specimens can be approximated by a fitting of the local means (LoMe) according to $\mathrm{LUV(LoMe)} = 4224 - (257 * \ln(y))$ and errors of $-112 - 112 = -224$ m/s to $+105 + 69 = +174$ m/s.

2. Local maxima

Other descriptive formulas are given for the fitting of different LUV-parameters, including highest velocities ($R^2 = 0.979$), where a similar slope-factor is listed according to $\mathrm{LUV}(H) = 4373 - (255.3 * \ln(y))$ and the rounded intercept is 4375 (Table VIII).

3. Regular dentin

Cancellation of one percent of the measured data—i.e., the two most extreme velocities—provides an additional fit that alternatively represents the ''more regular'' dentin by: $\mathrm{LUV(All\text{-}2)} = 4193 - (239.8 * \ln(y))$. However, the data provided by the tables do cover a greater range of possible LUVs in dentin. The mean of the two intercepts ''H'' and ''LoMe'' is 4298.5 m/s.

4. Range of input variable (y)

With respect to modeling, the LUV(LoMe)-approximation can be algorithmically used for y-values ranging from 0.74 mm to the apex (tooth length 22...32 mm). However, the approximation is valid only for the range between 4 mm and 11 mm. The underlined values of CASE_2 can now be utilized for new attempts to transform the intercept values of the ''LoMe''- and the ''H''-approximation into other physical properties and technical constants, like the Young's modulus.

5. Interpretation

Please note that the intercept value of the ''LoMe''-approximation is almost the same as the maximal speed of sound that is measured in any specimen. The difference of 2 m/s is not great. Assuming a linear increase in density towards 2.01 kg/dm^3 at 11 mm, and a linear decrease in Poisson's ratio to 0.23 at $y = 11$ mm, the computed Young's modulus may vary between 25 GPa at $y = 4$ mm and 22.57 GPa at $y = 11$ mm.

L. Validation

The mentioned values of our results and the concept are in accordance with the findings of Miyazaki *et al.* In their article one can read an elastic modulus that ranges from 13.4 GPa to 25.4 GPa in longitudinal sections of dentin.[14]

A further validation may be discussed by the following. Using a Poisson's ratio of $0.29 \pm x_1$ and a material density estimated by $1.18 \pm x_2$ kg/dm^3 one can relate the newly observed very low velocities of 1900 m/s$\pm x_3$ to an almost nonmineralized tissue that exhibits a Young's modulus of 3.25 GPa$\pm x_4$. This value is in accordance with the findings of Katz *et al.*, who reported a limit elastic moduli of 1.76 GPa for the collagen alone.[8]

The rational polynomial proposed for the all-tissues-description of the vertical variation in LUV can be also used to convert the Poisson's ratios into a ''quasi-factor'' that relates the product of the square of that LUV and the density to the Young's modulus.

M. Possible reasons for lack of data

The ultrasonic velocity for the covering human cementum layer has still not been reported by any researcher. This may be mainly due to the difficulties in measuring only the relevant tooth portion of that thin cementum layer. Although, a certain control may be theoretically given, if the speed of sound is additionally derived from indirect measurements of the acoustic impedance using reflection coefficients, this tissue causes the total ultrasonic energy to become reflected by different amounts as a function of both, the natural curvature of the cementum layer and the varying surface roughness.

N. Storage medium

Concerning the remaining two mineralized tissues, the corono-apically varying ultrasonic velocity found in the present study helps explain the great standard deviation published by Barber *et al.*[21] These previously reported velocities vary as well. Their means are about 220 m/s (dentin) and 150 m/s (enamel) faster than those of the present study, but the partly porous material of the former study belongs to mineralized, collageneous tissues of teeth that came in contact with a 5% formalin solution. The former article is often cited and it is also recognized by being included in an updated version of an extensive, early compilation of empirical ultrasonic properties of mammalian tissues, where, amongst others, tabular data about the ultrasonic velocity of dentin and enamel from a dog, cows, and human origin are listed.[45]

VI. SUMMARY

The two-dimensional (2D) longitudinal ultrasound velocities (LUV) are measured in longitudinal sections of extracted human teeth. The LUV of the apical thirds is compared to that of the complete mineralized wet porous tissue, that lies beneath the enamel cap and around the pulp. The irradiated dentin area is 79.2 mm$^2 \pm 23.0$ mm^2 out of a total area of 84.2 mm$^2 \pm 21.8$ mm^2.

Corono-apically varying means and maxima of LUV are determined for 21 specimens of intact teeth.

In all but one dentin specimen eight Voigt distributions are observed that build up the individual frequency distributions of LUV at 20 °C. The frequency distribution of the LUV in the specimens investigated resembles a complex mixture of several modified Gaussian and Lorentzian curves. The frequency distribution in all specimens shows a predominant peak feature of about 15.5% per 100 m/s class in favor of velocities ranging from 3600 m/s to 3800 m/s ($31\% \pm 11\%$). This peak feature tends to shift as a function of the tooth type. The range of the highest LUVs in each dentin specimen varies from 3903 m/s to 4226 m/s. To account for specific contributions a deviation of 100 m/s up to 188 m/s is measured as a function of the type of tooth. The complete range of all LUV in hard dental tissues (HDTs) of 21 vital specimens and one nonvital tooth observed at room temperatures covers all values between 1900 m/s and 6500 m/s. Although explanations and literature data of human tissues are provided, the low velocity in dentin is usually typical for shear waves, but is discovered first for longitudinal waves propagating in mineralized HDTs of teeth. Direct measurements for the moderate and low velocities (2900 m/s) in cementum are difficult to perform and data cannot be obtained in all specimens due to their thinness and shape properties.

In this study, the spatial distribution of the LUV follows a fractional polynomial law.

A least-squares error fitting is performed to quantitatively describe all discovered lowest velocities and to illustrate the spatial variation for all HDTs by LUV $= \Sigma(a_i y^i)/(1 + \Sigma(b_{i+1} y^{(i+1)}))$ with the corresponding regression coefficients ($R^2 > 0.976$ enamel, $R^2 > 0.845$ dentin, $R^2 > 0.757$ cementum). This equation can be used each time when the corono-apical variation has to be quantified. Using 10 coefficients for a nonvital tooth, predicted LUV at location y deviate from measured data by acceptable residual errors for dentin and by $0.2\% \pm 1.3\%$ and $-0.1\% \pm 1.6\%$ for enamel and cementum, respectively. Vertical scan lines are compared for standardized relative tooth width portions along a reduced distance in dentin. The corono-apical decrease in sound velocity can be approximated by a fitting of the local means of 21 specimens according to LUV(20 °C) $= 4224 - (257 * \ln(y))$ and with absolute deviations of -224 m/s to $+174$ m/s at y-locations with coordinates ranging from 4.0 mm to 11.0 mm. Greater deviations result for vertical distances ranging from 0.74 mm to 32 mm, where no fitting is evaluated. A variation of the corresponding Young's modulus is discussed.

VII. CONCLUSIONS

(1) The LUV in human teeth reveals an extended and continuous broad spectrum of values, with no regular indication that any value of the enclosed range would be generally missing. Each of the 22 specimens reveals a single, or up to seven missing velocities of bandwidth ± 2.9 m/s (but no missing value of bandwidth ± 3.0 m/s); this leads to a strong assumption that actually a continuous spectrum exists. This means that all velocities of the selected bandwidth can be simultaneously found in each specimen, especially if more than a sliced thick section is taken from a tooth sample as an individual specimen of interest.

(2) The specific range that covers only all of the highest LUVs found within longitudinal dentin specimens, shows an actual lower and upper limit of 3900 m/s and 4230 m/s, respectively. Although there are no significant differences between the complete specific maximum ranges of different type of teeth, future investigations may use the local ranges of maximum LUV as indicators for any drying process and for a specific type of tooth, provided that smaller-sized specific regions-of-interest will be compared to each other and/or a spatial isotachographic voxel accumulation is determined for a bandwidth-of-interest.

(3) Because the completely represented HDT's range of all LUVs observed at room temperatures has to be extended on both sides, it is concluded that longitudinal waves in permanently wet hard dental tissues can propagate at velocities ranging from even 1900 m/s to 6500 m/s within the same group of intact specimens at these temperatures.

(4) From all vertical direction data of perpendicular insonification and several predictions of locally varying LUVs in the most critical tooth sample, it is concluded that the spatial distribution of the longitudinal ultrasound velocity can be analogously described for all the given three mineralized tissues using the same fractional polynomial law.

(5) One can utilize any greater differences between the individual corono-apical variation in LUV (fractional polynomial law) and the first, regular corono-apical estimation:

LUV(20 °C, $x = 0.7w$, $3.9\ \text{mm} < y < 11.1\ \text{mm}) = 4224 - (257 * \ln(y))$ as an indicator for an abnormal behavior. The use of both equations is proposed as an attempt to regionally detect and numerically describe any pathologic changes or any abnormal dentin quality.

(6) A histogram that represents a total of 21 intact specimens shows a characteristic feature. Frequency peaks can help to characterize the native structure of the porous material and its locally varying ''dental quality'' by evaluation of what is likely and what is seldom. A predominant appearance probability that represents about one third of the full dentin area is associated with about 13% of the spectral range of velocities ($3700\ \text{m/s} \pm 100\ \text{m/s}$). From the spectral velocity range of maximum likelihood and statistical data of other physical properties it is thereby concluded that regular dentin reveals a certain, most likely elasticity, which ranges from 18 GPa to 27 GPa.

ACKNOWLEDGMENTS

The author would like to thank Professor Dr. Claus Löst, as the Medical Director of the Department of Conservative Dentistry and Professor Dr.-Ing. U. Faust (Emeritus), as the former Director of the Biomedical Engineering Institute and its Division of Ultrasound. The author is grateful to Dr.-Ing. K.-M. Irion and Dipl.-Ing. Werner Nüssle for enabling the utilization of the earliest measurement setup, and Dr. Birgit Linder-Lais, Dr. Michael Aschenbrenner, and Professor Dr. Michael Brecx for their individual contributions and also for providing numerous samples of the extracted tooth material at no extra costs. Some aspects of the present material are

based on work that was initially supported, in part, by Grant No. Lo328/2-1,2 from the German Science Foundation (DFG).

APPENDIX A: GENERAL TENDENCY

1. Locations

Each of the standardized locations corresponds to distances that are allocated inside the rectangular insight view of Fig. 1 and the rectangular window shown in Fig. 4. The first set of 8* 21 locations is characterized by equidistant increments in the y-direction (1 mm) and identical horizontal tooth width portions with central x-coordinates at $x=0.7w$ for teeth with a single root (majority). A substitute with a relative x-location at $x=0.826w$ is defined in cases where teeth have two (or more) roots, (i.e., where the absolute coordinates of the corresponding relative x-location and the absolute y-location would otherwise represent the soft tissue inside the tooth's pulp chamber).

2. Procedures and details

For an evaluation of the general tendency, all velocity values of every single specimen are processed by mathematical algorithms. A total of over 72 000 different equations are evaluated with respect to best fitting results. Three procedures are used.

(1) Procedure (I): Initial calculation of the mean LUV at a certain location and the next location utilizing data of all specimens; then the mean data are fitted as a function of location.
(2) Procedure (II): Simultaneous fitting of all the individual LUVs as a function of the location.
(3) Procedure (III): Fitting of the data of two sub-sets: (a) highest LUVs at 8 locations; and (b) lowest LUVs at 8 locations.

For all procedures, the best general least squares fitting equation is evaluated for dentin.

3. Individual residual deviation

The individual residual deviation (IRD) at every location in the dentin is calculated from the difference between the actual velocity and the predicted velocity. Two threshold level criteria are defined that makes an evaluated fitting equation incongruous and incompetent for further approval: (a) via regression coefficients and (b) via relative residual errors (RRE). For this purpose the variation of the quality of the fits of all specimens is determined (Fit. Std. Err.). The fitting is accepted for (a) $R>0.84$ if $N>166$ and if (Fit.Std.Err.$<(n-1)*30$), and (b) RRE$<0.22\%+n*0.5\%$). The RRE at each location is calculated from the quotient of the IRD and the corresponding actual velocity at this location. Using N data points per n scans, an arbitrary cut-off level value of 10.7% is resulting for $N/n=8$.

4. Economics

From all of the generally best least squares fitting equations, the best fitting equation that comprises only two adjustable parameters is chosen.

APPENDIX B: INDIVIDUAL INHOMOGENEITY

1. Locations

A set of numerous locations comprises irradiated spots that are characterized by equidistant increments at 0.1 mm in the y-direction.

2. Procedures

In order to allow for direct numerical comparisons of adjacent scans and to uniformly describe each of the vertical scans, a general least squares fitting equation is found to be appropriate, provided that it is guaranteeing a possible description of all of the measured corono-apical scans in every single tissue in the same manner. Two procedures are considered: Procedure (A), a linear fitting of measured data (the LUV and only the y coordinates of all locations are used as the running variable). Procedure (B) represents a scattered-data surface fitting, which requires data triplets. A decision about which procedure is applied depends on economic aspects and the quality of the fit.

3. Quality of the fit

A compromise is made between a smaller number of coefficients and a greater precision of the fit. Regardless of which of the three tissues is involved (!) the corresponding errors of predicted LUV at all locations are not allowed to exceed 2%. The number of coefficients is adopted by iteration until it is provided that the individual inhomogeneity can be sufficiently described for all adjacent locations separated by 0.1 mm. This is a prerequisite regardless of whatever selection is made with respect to the individual tooth.

The way of finding out the coefficients causes different amounts of errors and different numbers of input data points are also contributing to a varying quality of the fit. The way how the most appropriate type of formula is selected depends on the quality of the fits (Fit. Std. Err.), the general ability to upgrade and transform the data by further studies, the compatibility with other technical constants (Poisson's ratio and Young's modulus), and the considered engineering models, for which the data may serve as suitable inputs (finite difference simulations, morphometric boundary elements, and macro element methods, or both medical element engineering and simulation (MEES)).

4. Economics

Since the present measurements are considered for the economic use of a new MEES-approach with macro-elements, the linear fitting is performed by means of a special group of interpolating functions. Considering Padé shape functions, rational polynomials are utilized as interpolating functions in many numerical applications and studies where the macro-element method is used. For a certain rational

polynomial with numerator coefficients and denominator coefficients, it can be shown that a normally obsolescent parameter can be introduced or a redundant rational polynomial of the same category can be used as the replacement denominator. This ''upgrade''-feature may become necessary once it is required to integrate the present (or older) set of MEES-data of vertical scan data in mineralized tooth tissues into a newer set of vertical distribution data.

For economic reasons, the procedure (A) is more suitable and a linear fitting is chosen.

[1] S. Lees and F. R. Rollins, ''Anisotropy in hard dental tissues,'' J. Biomech. **5**, 557–566 (1972).
[2] J. L. Katz and K. Ukraincik, ''On the anisotropic elastic properties of hydroxyapatite,'' J. Biomech. **4**, 221–227 (1971).
[3] I. R. Spears, ''A three-dimensional finite element model of prismatic enamel: a re-appraisal of the data on the Young's modulus of enamel,'' J. Dent. Res. **76**, 1690–1697 (1997).
[4] H. E. Schroeder, *Orale Strukturbiologie* (Thieme-Verlag, Stuttgart, NY, 1987), Chaps. 1.1.6–1.6, pp. 20–186.
[5] C. E. Renson and M. Braden, ''Experimental determination of the rigidity modulus, poisson's ratio and elastic limit in shear of human dentine,'' Arch. Oral Biol. **20**, 43–47 (1975).
[6] C. John, ''Recovering echo signals for *in-vitro* characterization of hard dental tissues,'' in *Nondestructive Characterization of Materials VIII* (Plenum, New York, 1998), pp. 763–768.
[7] V. Lertchirakarn, J. E. A. Palamara, and H. H. Messer, ''Anisotropy of tensile strength of root dentin,'' J. Dent. Res. **80**, 453–456 (2001).
[8] J. L. Katz, P. Spencer, T. Nomura, A. Wagh, and Y. Wang, ''Micromechanical properties of demineralized dentin collagen with and without adhesive infiltration,'' J. Biomed. Mater. Res. **66A**, 120–128 (2003).
[9] V. P. Totah, ''Increase in hardness of dentin on drying,'' J. Dent. Res. **21**, 99–101 (1942).
[10] H. G. Klinger and E. Gabriel, ''Über die räumliche Variation der mechanischen Eigenschaften von Schmelz und Dentin (The spatial variation of the mechanical properties of enamel and dentin),'' Dtsch. Zahnaerztl. Z. **33**, 421–425 (1978). (in German).
[11] C. Löst, K. M. Irion, C. John, and W. Nüssle, ''Two-dimensional distribution of sound velocity in ground sections of dentin,'' Endod. Dent. Traumatol. **8**, 215–218 (1992).
[12] G. Willems, J. P. Celis, P. Lambrechts, M. Braem, and G. Vanherle, ''Hardness and Young's modulus determined by nanoindentation technique of filler particles of dental restorative materials compared with human enamel,'' J. Biomed. Mater. Res. **27**, 747–755 (1993).
[13] C. John, R. Weiger, K. M. Irion, M. Brecx, and C. Löst, ''Ultrasonic velocity measurements of human dentin of sectioned vital teeth,'' J. Dent. Res. **74**, 924–924 (1995).
[14] M. Miyazaki, H. Inage, and H. Onose, ''Use of an ultrasonic device for the determination of elastic modulus of dentin,'' J. Oral Sci. **44**, 19–26 (2002).
[15] J. L. Katz and R. A. Harper, ''Calcium phosphates and apatites'' in *Encyclopaedia of Materials Science and Engineering*, edited by M. B. Bever (Pergamon, Oxford, 1986), pp. 474–481.
[16] A. D. Degtyar and S. I. Rokhlin, ''Comparison of elastic constant determination in anisotropic materials from ultrasonic group and phase velocity data,'' J. Acoust. Soc. Am. **102**, 3458–3466 (1997).
[17] V. Bucur and I. Böhnke, ''Factors affecting ultrasonic measurements in solid wood,'' Ultrasonics **32**, 385–390 (1994).
[18] F. Reverdy and B. Audoin, ''Elastic constants determination of anisotropic materials from phase velocities of acoustic waves generated and detected by lasers,'' J. Acoust. Soc. Am. **109**, 1965–1972 (2001).
[19] D. W. Blodgett, ''Applications of laser-based ultrasonics to the characterization of the internal structure of teeth,'' J. Acoust. Soc. Am. **114**, 542–549 (2003).
[20] G. Baum, I. Greenwood, S. Slawski, and R. Smirnow, ''Observation of internal structures of teeth by ultrasonography,'' Science **139**, 495–496 (1963).
[21] F. E. Barber, S. Lees, and R. R. Lobene, ''Ultrasonic pulse-echo measurements in teeth,'' Arch. Oral Biol. **14**, 745–761 (1969).
[22] S. Y. Ng, P. A. Payne, N. A. Cartledge, and M. W. J. Ferguson, ''Determination of ultrasonic velocity in human enamel and dentine,'' Arch. Oral Biol. **34**, 341–345 (1989).
[23] B. Al-Nawas, K. A. Grötz, E. Rose, H. Duschner, P. Kann, and W. Wagner, ''Using ultrasound transmission velocity to analyse the mechanical properties of teeth after *in vitro*, *in situ*, and *in vivo* irradiation.,'' Clin. Oral Investig. **4**, 168–172 (2000).
[24] S. D. Peck and G. A. D. Briggs, ''The caries lesion under the scanning acoustic microscope,'' Adv. Dent. Res. **1**, 50–63 (1987).
[25] S. Lees, F. B. Gerhard, and F. G. Oppenheim, ''Ultrasonic measurement of dental enamel demineralization,'' Ultrasonics **11**, 269–273 (1973).
[26] F. C. Yanikoglu, F. Öztürk, O. Hayran, M. Analoui, and G. K. Stookey, ''Detection of natural white spot caries lesions by an ultrasonic system,'' Caries Res. **34**, 225–232 (2000).
[27] S. Y. Ng, M. W. J. Ferguson, P. A. Payne, and P. Slater, ''Ultrasonic studies of unblemished and artificially demineralized enamel in extracted human teeth: a new method for detecting early caries,'' J. Dent. **16**, 201–209 (1988).
[28] G. Kossoff and C. J. Sharpe, ''Examination of the contents of the pulp cavity in teeth,'' Ultrasonics **4**, 77–83 (1966).
[29] S. Lees and R. A. Barber, ''Looking into teeth with ultrasound,'' Science **161**, 477–478 (1968).
[30] S. Lees, F. E. Barber, and R. R. Lobene, ''Dental enamel: detection of surface changes by ultrasound,'' Science **169**, 1314–1316 (1970).
[31] S. D. Peck, J. M. Rowe, and G. A. D. Briggs, ''Studies on sound and carious enamel with the quantitative acoustic microscope,'' J. Dent. Res. **68**, 107–112 (1989).
[32] M. C. D. N. J. M. Huysmans and J. M. Thijssen, ''Ultrasonic measurement of enamel thickness: a tool for monitoring dental erosion?,'' J. Dent. **28**, 187–191 (2000).
[33] S. Mezawa, T. Kawato, K. Yoshida, H. Nozaki, T. Saito, K. Tamura, and M. Onozawa, ''Evaluation of human tooth structure with the ultrasonic imaging technique,'' J. Oral Sci. **41**, 191–197 (1999).
[34] C. Dean, M. G. Leakey, D. Reid, F. Schrenk, G. T. Schwartz, C. Stringer, and A. Walker, ''Growth processes in teeth distinguish modern humans from *Homo erectus* and earlier hominins,'' Nature (London) **414**, 619–622 (2001).
[35] R. G. Maev, L. A. Denisova, E. Y. Maeva, and A. A. Denissov, ''New data on histology and physico-mechanical properties of human tooth tissue obtained with acoustic microscopy,'' Ultrasound Med. Biol. **28**, 131–136 (2003).
[36] Z. Yang, ''Tooth enamel thickness measurement by ultrasound imaging method,'' J. Acoust. Soc. Am. **100**, 2710–2710 (1996).
[37] S. M. Weidmann, J. A. Weatherell, and S. M. Hamm, ''Variations of enamel density in sections of human teeth,'' Arch. Oral Biol. **12**, 85–97 (1967).
[38] S. Lees, ''Specific acoustic impedance of enamel and dentine,'' Arch. Oral Biol. **13**, 1491–1500 (1968).
[39] S. Lees and F. E. Barber, ''Looking into teeth and its surfaces with ultrasonics,'' Ultrasonics **9**, 95–100 (1971).
[40] R. H. Eichler, ''Apparatus for measurement of sound velocity in a workpiece,'' U.S. Patent 3 690 155, 1972.
[41] D. J. Haines, ''Physical properties of human tooth enamel and enamel sheath material under load,'' J. Biomech. **1**, 117–125 (1968).
[42] C. John, ''Are teeth crying when they become to be dying? I) Early detection of acoustic emission from extracted human teeth,'' edited by T. Lokajicek and O. Jiricek, *collected papers* ''Ultrasonics and AE (Acoustic Emission)'' of the *35th International Conference on Ultrasonics and Acoustic Emission Conference of the Czech Technical University and Czech Acoustical Society* (ISBN 80-01-02065-7), probably available from the editor, Thomás Lokajícek, Geophysical Institute GFU AV CR, Bocni 2, CZ-14131 Prague 4, Czech Republic, Fax: 00420-2-7176 1549; 1998, Vol. 1, pp. 24–30.
[43] J. A. Rooney, P. M. Gammell, J. D. Hestenes, H. P. Chin, and D. H. Blankenhorn, ''Velocity and attenuation of sound in arterial tissues,'' J. Acoust. Soc. Am. **71**, 462–466 (1982).
[44] S. L. Bridal, P. Fornès, P. Bruneval, and G. Berger, ''Correlation of ultrasonic attenuation (30 to 50 MHz) and constituents of atherosclerotic plaque,'' Ultrasound Med. Biol. **23**, 691–703 (1997).
[45] S. A. Goss, R. L. Johnston, and F. Dunn, ''Compilation of empirical ultrasonic properties of mammalian tissues. II,'' J. Acoust. Soc. Am. **68**, 93–108 (1980).

Sounds produced by Norwegian killer whales, *Orcinus orca*, during capture

Sofie M. Van Parijs[a)]
Norwegian College of Fishery Science, University of Tromsø, 9037 Tromsø, Norway

Teo Leyssen
Rozenlaan 8, 3650 Dilsen-Stokkem, Belgium

Tiu Similä
Institute of Marine Research, P.O. Box 1870 Nordnes, 5817 Bergen, Norway

(Received 3 November 2003; revised 22 April 2004; accepted 29 April 2004)

To date very little is still known about the acoustic behavior of Norwegian killer whales, in particular that of individual whales. In this study a unique opportunity was presented to document the sounds produced by five captured killer whales in the Vestfjord area, northern Norway. Individuals produced 14 discrete and 7 compound calls. Two call types were used both by individuals 16178 and 23365 suggesting that they may belong to the same pod. Comparisons with calls documented in Strager (1993) showed that none of the call types used by the captured individuals were present. The lack of these calls in the available literature suggests that call variability within individuals is likely to be large. This short note adds to our knowledge of the vocal repertoire of this population and demonstrates the need for further studies to provide behavioural context to these sounds. [DOI: 10.1121/1.1763954]

PACS numbers: 43.80.Ka [WWA] Pages: 557–560

I. INTRODUCTION

Cetaceans produce a vast array of underwater sounds for the purpose of communication and foraging (e.g., Herman and Tavolga, 1980). Acoustic communication has been shown to be important in mediating cetacean social interactions (Tyack, 1999). Studies of the acoustic behavior of individual animals have provided insights into the social contexts in which cetaceans use communication (e.g., Caldwell *et al.*, 1990). In particular, studies of individual signal production in cetaceans have increased the understanding of the function of signals in social and group cohesion (e.g., Caldwell and Caldwell, 1968; Caldwell *et al.*, 1990; Janik and Slater, 1998).

Killer whales, *Orcinus orca*, produce a wide range of variable underwater sounds. Most information on the sounds produced by killer whales have been derived from studies carried out around British Columbia, where they have been shown to use a variety of call types, in particular clan specific dialects (e.g., Ford and Fisher 1982; Ford, 1989; Ford, 1991). The sound production of northern Norwegian killer whales is less well known. Two previous studies have described some of the sounds that occur within this population; one study described 23 discrete calls (Moore *et al.*, 1988), while another described a range of calls among which a number that are thought to be pod specific dialects for six out of nine pods (Strager, 1993, 1995). To date no information is available on the sound production of individual killer whales from this region. In this study we aim to increase our knowledge concerning the vocal behavior of individuals during capture. In northern Norwegian waters the presence of killer whales is associated predominantly with the presence of herring (Similä *et al.*, 1996). Five killer whales were captured for the purpose of tagging while in their wintering feeding grounds around the Vestfjord area of northern Norway. Recording calls from individuals is logistically difficult in the wild, especially in cetaceans that travel in close groups composed of several individuals, and is frequently only possible in a captive animal. In this short note we provide a detailed description of the sounds produced by individual killer whales during their brief capture.

II. METHODS

This study was carried out between late November to mid December 2000 and 2001 in the Vestfjord area, northern Norway (68° to 69°N, and 14° to 16°E). Killer whales were captured using a herring net set from a purse-seine vessel. The sex, age class and where possible the identity of the individual was determined with reference to an existing photographic catalog for this region (Similä, 1997). The whales were captured for the purpose of deploying satellite transmitters. During the handling process continuous recordings were made of the sounds of each captured whale. A hydrophone was placed 0.5 m in front of the head of each individual and recordings were made of any sounds that were produced during handling. Recordings of the sounds were made using a HTI SSQ94 hydrophone (sensitivity: −170 db, frequency response: 5 Hz–30 kHz) and a Sennheiser microphone (MD421-II, sensitivity: −170 dB *re*: 2 mV/Pa, frequency response: 30 Hz–17 kHz±3 dB) and a digital audio tape recorder (Sony TCD—D8: frequency response 5 Hz–22 kHz ±1.0 dB) in 2000 and a omni directional Sony microphone

[a)]Address for correspondence: Sofie Van Parijs, Norwegian College of Fisheries Science, University of Tromsø, 9037 Tromsø, Norway. Electronic mail: sofie@npolar.no

TABLE I. Details on the five killer whales and the call types that were made during capture.

Whale ID	Capture Date	Age	Length (m)	Sex	Pod	Recording Time (min)	Discrete	Compound
14976	24/11/01	Adult	6, 10	M	KA1	1′15	N1	
16175	01/12/00	Sub adult	4, 80	F	NC	8′06	N2, N3, N4, N5	N6
16178	22/11/01	Juvenile	4, 30	F	?	21′31	N7i	N7ii, N8i, N8ii
16179	05/12/00	Juvenile	4, 10	F	NY14	43′09	N9i, N9ii, N10i, N10ii, N10iii, N11, N13	N12
23365	30/11/01	Juvenile	3, 20	M	NW	1′19	N14	N8i, N7i

ECM-T145 and minidisk MZR55 (frequency response: 50 Hz–15 kHz) in 2001. The recordings were digitized and displayed as spectrograms (Fast Fourier Transforms, dt: 10 ms, df: 102 Hz, FFT size: 512) using the BatSound analysis PC software program (Pettersson Elektronik A. B., 1996).

Sounds were divided into two broad categories: discrete and compound calls (e.g., Awbrey *et al.*, 1982; Dahlheim and Awbrey, 1982). Discrete calls consisted of a single pulsed call while compound calls were composed of a sequence of pulsed calls. No other call types, such as whistles (Thomsen *et al.* 2001; Thomsen *et al.*, 2002), variable or aberrant (Ford, 1989) were observed. Only high quality records, where all sound contours were distinctly measurable on the spectrograms were used for these analyses. Sounds were categorized into groups based on their spectral contours. Discrete and compound calls were compared, using two independent observers, with those documented in a sound catalog of known pods from northern Norway obtained from Strager (1993) and those documented from unknown killer whales in Iceland and from northern Norway obtained from Moore *et al.* (1988).

III. RESULTS

Five whales were captured during the study period: one adult, one sub adult and three juveniles. Two were males and three were females (Table I). The adult male, 14976, was kept in the water during the capture, which limited the duration of the recordings that were made of this individual. All individuals were thought to belong to separate pods, however, 16178 is not present in the existing photo identification catalog and could not be ascribed a pod number. Each individual produced sounds almost continually during handling (14976=was vocal 89% of the recording period, 16175 =81%, 16178=89%, 16179=78%, 23365=92%). All individuals produced discrete calls: the sub adult and all individuals except for the adult male produced compound calls (Table II). In total, 14 discrete call types were described and seven compound calls (Fig. 1). Two call types, one discrete and one compound, were used both by 16178 and 23365. All discrete and compound calls were compared with those described in the above-mentioned sound catalogs. The Strager (1993) catalog contained the documented sounds for 10 pods of which one was pod NC. Individual 16175 is thought to belong to the NC pod. However, 16175 used none of the sounds produced by the NC pod during capture. All other individuals came from other pods than those described in this catalog. Comparisons were made between spectrograms of 23 discrete calls recorded in northern Norway and 35 discrete call types recorded off Iceland (Moore *et al.*, 1988). From the northern Norwegian calls, N18i and N23i, from Moore *et al.* (1988) resembled N2 from our recordings, while N14i resembled N8 and, N9 resembled N1. From the Icelandic calls no clear resemblances were found with our recordings. However, more detailed comparison was not possible, given the available information.

IV. DISCUSSION

The calls used by individual killer whales during capture were highly variable and most individuals produced more than one call type. Killer whales in British Columbia use distinctive call dialects based on discrete call types (e.g., Ford and Fisher, 1982; Ford 1989, 1991). Discrete calls are used in numerous behavioral contexts including foraging, traveling, group resting and socializing (Ford, 1989). These calls can show variability within an individual particularly during ''excited'' behavioral states as described in Ford (1989). A number of discrete calls have been described for the northern Norwegian killer whale population (Moore *et al.*, 1988; Strager 1993, 1995). Furthermore, Strager (1995) showed that dialects are thought to exist in the northern Norwegian population, at least for six of the nine recorded pods.

TABLE II. The total number of calls recorded for each call type for the five captured individuals (ID).

Call type	ID 14976	ID 16175	ID 16178	ID 16179	ID 23365
N1	7				
N2		9			
N3		18			
N4		1			
N5		1			
N6		2			
N7i			121		12
N7ii			10		
N8i			65		9
N8ii			43		
N9i				77	
N9ii				34	
N10				54	
N10i				154	
N10ii				7	
N11				35	
N12				7	
N13				20	
N14					6

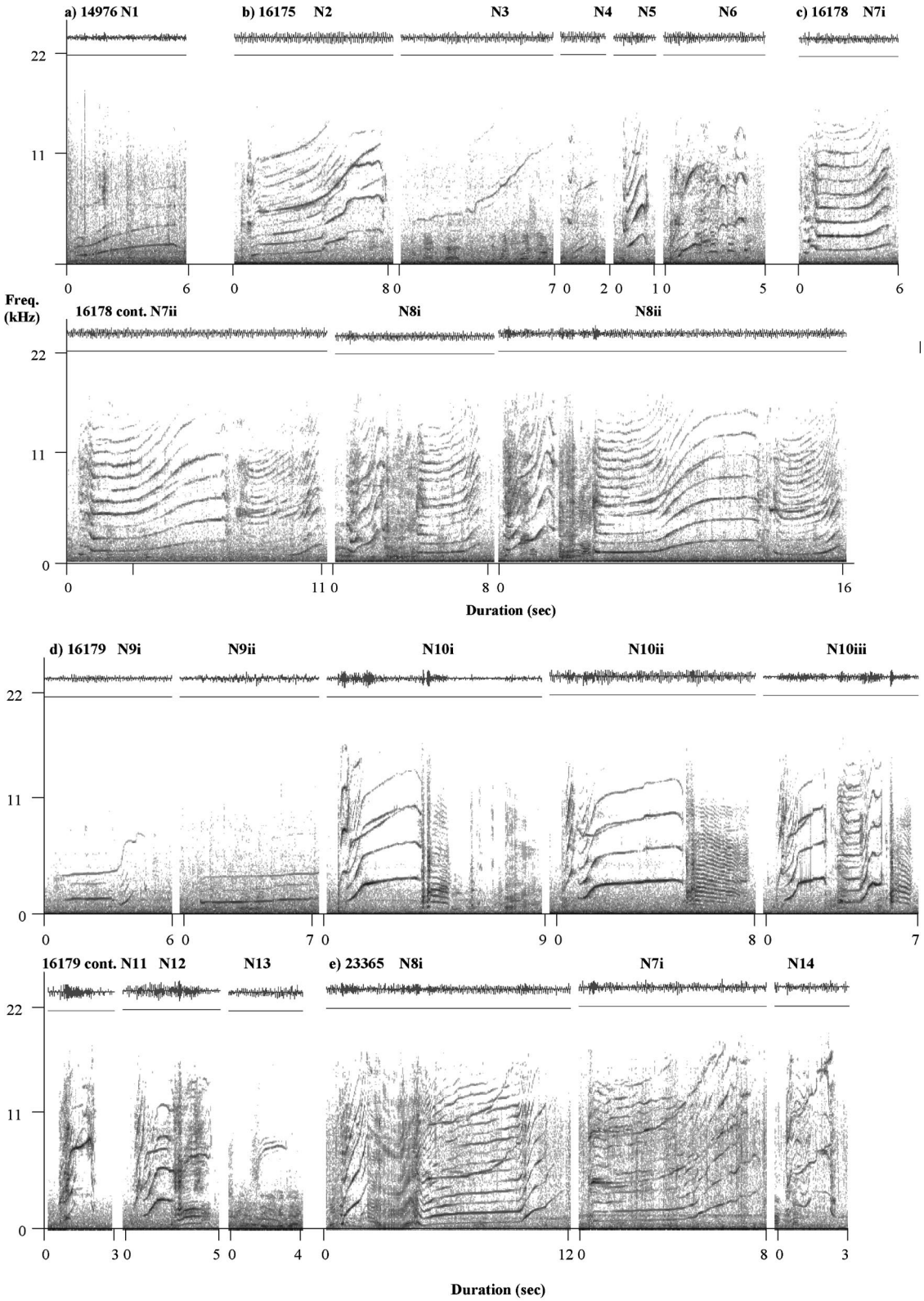

FIG. 1. Spectrograms of sounds produced by the five, (a) 14976, (b) 16175, (c) 16178, (d) 16179, (e) 23365, individual Norwegian killer whales during capture. Different sounds are defined as in Strager (1993) as N for Norway, followed by a number defining the call type.

We thought that it was likely that discrete calls and possibly call dialects would be used in preference to other call types during stressful circumstances. One of the pods that exhibited call dialects was the NC pod, to which captured individual 16175 belonged. None of the calls recorded from 16175 were similar to those recorded from the NC pod. Given that pod dialects can exhibit large variability it is impossible to determine whether individual 16175 was using a variant of its pod's specific dialect or a call related directly to the stress of the capture.

Two call types, one discrete and one compound, were used both by individuals 16178 and 23365. It was not certain which pod individual 16178 belonged too however it might be possible that these two individuals belonged to the same pod based on the sounds that they produced. However, after capture these individuals were not re-sighted together and their movements and area usage very different (http://www.imr.no/orca). Certain call types recorded from individuals during capture resembled four of those reported by Moore *et al.* (1988) obtained from Norwegian killer whales.

It is difficult to draw any definitive conclusions from the call types recorded by individual killer whales during capture, primarily because too little is know about the sound production of the northern Norwegian killer whales. Although restricted, this study documents the sound production of five individuals during capture. It demonstrates that killer whales used a wide variety of call types during capture. Clearly, individual call usage and composition is complex and variable and requires further investigation. Through documenting a number of their sounds in this study we hope to stimulate and help develop a more clear understanding of the sound production of the northern Norwegian killer whale population.

ACKNOWLEDGMENTS

Thanks go to the crew of the purse-seiner ''Inger-Hildur'' and Eythor Thordarsson, Gudlaugur Bjarnasson and Jeff Foster for skilful capture and handling of the killer whales and to Nils Øien for providing comments on the manuscript. Doug Allan from BBC for providing recordings in 2000. The Norwegian Research Council, BBC, Sea World Inc. and NOKIA funded the satellite-tagging project. We would like to thank Brad Hanson and Jens Christian Holst for their help in making the satellite-tagging project happen.

Awbrey, F. T., Thomas, J. A., Evans, W. E., and Leatherwood, S. (**1982**). ''Ross Sea killer whale vocalizations: Preliminary description and comparison with those of some northern hemisphere killer whales,'' Rep. Int. Whal. Comm. **32**, 667–670.

Caldwell, D. K., and Caldwell, M. C. (**1968**). ''Vocalization of naïve captive dolphins in small groups,'' Science **159**, 1121–1123.

Caldwell, M. C., Caldwell, D. K., and Tyack, P. L. (**1990**). ''Review of signature whistles hypothesis for the Atlantic bottlenose dolphin,'' in *The bottlenose Dolphin*, edited by S. Leatherwood and R. R. Reeves (Academic, San Diego, CA), pp. 199–234.

Dahlheim, M. E., and Awbrey, F. T. (**1982**). ''A classification and comparison of vocalizations of captive killer whales (*Orcinus orca*),'' J. Acoust. Soc. Am. **72**, 661–670.

Ford, J. K. B., and Fisher, H. D. (**1982**). ''Killer whale (*Orcinus orca*) dialects as an indicator of stocks in British Columbia,'' Rep. Int. Whal. Comm. **32**, 671–679.

Ford, J. K. B. (**1989**). ''Acoustic behaviour of resident killer whales (*Orcinus orca*) off Vancouver Island, British Columbia,'' Can. J. Zool. **67**, 727–745.

Ford, J. K. B. (**1991**). ''Vocal traditions among resident killer whales (*Orcinus orca*) in coastal waters of British Columbia,'' Can. J. Zool. **69**, 1454–1481.

Herman, L. M., and Tavolga, W. N. (**1980**). ''The communication system of cetaceans,'' in *Cetacean Behavior: Mechanisms and Functions*, edited by L. M. Herman (Wiley, New York), pp. 149–209.

Janik, V. M., and Slater, P. J. B. (**1998**). ''Context-specific use suggests that bottlenose dolphin signature whistles are cohesion calls,'' Anim. Learn Behav. **56**, 829–838.

Moore, S. E., Francine, J. K., Bowles, A. E., and Ford, J. K. B. (**1988**). ''Analysis of calls of killer whales, *Orcinus orca*, from Iceland and Norway,'' Rit Fisk. **11**, 225–250.

Pettersson Elektronik, A. B. (**1996**). ''Batsound,'' Tallbacksvagen 51, S-75645, Uppsala, Sweden.

Strager, H. (**1993**). ''Catalogue of underwater calls from killer whales (*Orcinus orca*) in Northern Norway,'' MSc. thesis, University of Aarhus, Denmark.

Strager, H. (**1995**). ''Pod-specific call repertoires and compound calls of killer whales, *Orcinus orca* Linnaeus, 1758, in the waters of northern Norway,'' Can. J. Zool. **73**, 1037–1047.

Simila, T., Holst, J. C., and Christensen, I. (**1996**). ''Occurrence and diet of killer whales in northern Norway: seasonal patterns relative to the distribution and abundance of Norwegian spring-spawn herring,'' Can. J. Fish. Aquat. Sci. **53**, 769–799.

Simila, T. (**1997**). ''Behavioral ecology of killer whales in northern Norway,'' Ph.D. thesis, University of Tromsø, Norway.

Thomsen, F., Franck, D., and Ford, J. K. B. (**2001**). ''Characteristics of whistles from the acoustic repertoire of resident killer whales (*Orcinus orca*) off Vancouver Ilsand, Bristish Columbia,'' J. Acoust. Soc. Am. **109**, 1240–1246.

Thomsen, F., Franck, D., and Ford, J. K. B. (**2002**). ''On communicative significance of whistles in wild killer whales (*Orcinus orca*),'' Behav. Ecol. Sociobiol. **89**, 404–407.

Tyack (**1999**).

Directionality of dog vocalizations

Karl-Heinz Frommolt[a)]
Humboldt University, Museum für Naturkunde, Invalidenstrasse 43, D-10115 Berlin, Germany

Alban Gebler
Institute of Zoo and Wildlife Research, Alfred-Kowalke-Strasse 17, D-10315 Berlin, Germany

(Received 30 September 2003; revised 16 April 2004; accepted 16 April 2004)

The directionality patterns of sound emission in domestic dogs were measured in an anechoic environment using a microphone array. Mainly long-distance signals from four dogs were investigated. The radiation pattern of the signals differed clearly from an omnidirectional one with average differences in sound-pressure level between the frontal and rear position of 3–7 dB depending from the individual. Frequency dependence of directionality was shown for the range from 250 to 3200 Hz. The results indicate that when studying acoustic communication in mammals, more attention should be paid to the directionality pattern of sound emission. © *2004 Acoustical Society of America.* [DOI: 10.1121/1.1758971]

PACS numbers: 43.80 Ka, 43.64 Tk [WA] Pages: 561–565

I. INTRODUCTION

When studying acoustic communication in animals, we should be aware that the characteristics of a recorded signal are not only influenced by distance and the transmission properties of the habitat, but may also depend on the directionality of the sound emitter. Though many aspects of animal vocalization are studied in detail, our knowledge of their radiation patterns still remains poor. Only a few animal species have been examined for the directionality of their signals. In mammals, sound radiation patterns are best documented for echolocation signals of dolphins and bats. Both groups use ultrasound for sonar where the wavelength of the emitted signal is small in comparison to the size of the head and the body of the animal. The highest directionality of an acoustic signal produced by an animal was observed in dolphins. Au (2000) reported that the bottlenosed dolphin, *Tursiops truncatus*, had a beamwidth, defined as the angle between the 3-dB points, of approximately 10.2° in the vertical plane and 9.7° in the horizontal plane. In bats the directionality of the sonar pulse is much lower. The values of the half-angle-6-dB beamwidth vary between 22° and 55° (Pye, 1980; Hartley and Suthers, 1987). Concerning communicative signals, our knowledge of radiation patterns is based only on few observations. In mammals, detailed measurements are available only for the human voice (Marshall and Meyer, 1985). The human voice is nearly omnidirectional at frequencies below 500 Hz. At higher frequencies complex radiation patterns are observed. To our knowledge, Brown (1989) reported the only data for nonhuman mammals. He measured the radiation pattern for two primate species, *Cercopithecus mitis* and *Cercocebus albigena*, at four points and found that the monkey vocalizations were mostly omnidirectional.

In our paper we present experimental data on directionality of vocalizations of domestic dogs. The aim of our study was to evaluate the range of direction-dependent differences in sound-pressure level. The intent was to examine whether vocalizing mammals could be considered as omnidirectional sound sources or if we need to take account of the directionality patterns. Directionality of the sound-emitting system should have consequences for long-distance communication affecting both transmission range and spectral parameters depending on the position of the receiver relative to the sender.

II. MATERIALS AND METHODS

A. Acoustic measurement

Three adult domestic dogs, a male German shepherd–Husky hybrid (Thorsten), and two female Rhodesian ridgebacks (Amali and Luna) were trained to direct their vocalizations towards the owner. The animals were placed on a small rostrum in the center of an anechoic chamber with a volume of 1850 m^3 ($11\times16\times10.5$ m). Vocalizations of the dogs were elicited by vocal commands from a distance of 5 m before the animal. Six omnidirectional electret microphones (Sennheiser MKE 2P powered by 8-channel microphone preamplifier TASCAM MA-8) were positioned at a distance of 2 m in two semicircles around the dog. The microphone positions were: 0° (straight before the dog's mouth); 30°, 90°, and 180° in the horizontal plane; and additionally at 30° and 90° in the vertical plane. The reference point was the opening of the mouth. The vocalizations were recorded on hard disk with a sample rate of 32 kHz using a 16-bit data acquisition card (National Instruments PCI 6035E) and a custom-designed MATLAB script. Two additional condenser microphones (MK 221, Microtech Gefell, Germany) were positioned at a distance of 5 m at 30° and 180° in the horizontal plane. We refer to the 30° in this measurement as frontal. This position was selected to minimize reflections from the body of the dog's owner standing at the 0° position. The signals from these two microphones were recorded at a sample rate of 48 kHz with the digital acoustic system DAS-P1 (TEAC, Wiesbaden, Germany) consisting of a digital measurement front-end DF-1 and a TASCAM DA-P1 DAT recorder. Prior to recording, these two

a)Electronic mail: karl-heinz.frommolt@rz.hu-berlin.de

microphones were calibrated using the calibrator CEL-284/2. At the end of the measurement session, for calibration purposes all microphones were placed close together. A stepped sinusoidal tone was broadcast via a one-way monitor loudspeaker (MM 201, Klein and Hummel) and recorded simultaneously with the six-channel DAQ system and the TEAC DAS-P1. The calibration procedure revealed that the electret microphones differed for the signals over the relevant frequency range (300 to 5000 kHz) no more than 0.2 dB. The recordings from the DAT recorder were transferred via a soundcard with digital I/O (DIGI96/8 Pro, RME Mittweida, Germany) to the hard disk of the computer. In parallel with the audio data, the movements of the animals were recorded on a VHS videotape. The camera was positioned at the height of the animal at the left side of the animal. The camera controlled for vertical movements of the animal and its position relative to the center of the semicircle. Since the animal gazed towards its owner during the experiment, sideward directions of the head could be minimized.

Additional data were obtained from an adult female German shepherd dog (Lisa) in a prior experiment (Frommolt and Gebler, 2002). In this experiment the radius of the microphone array was 1.5 m. No video control and no additional distant microphones were used.

In this study, a total of 588 vocalizations could be used. During the experiment the animals showed no signs of stress. After 10–20 min a break was taken to allow the animal to move. When the animal exhibited any signs of tiredness the experiment was immediately halted.

B. Signal processing

Signals for analysis were selected by evaluating spectrograms. In total, 588 signals with a high signal level were used for further analysis. Signals with a low amplitude were excluded because of their low dynamic range. Prior to the acoustic analysis the signals were adjusted to the same calibration level by multiplying the signal by the calibration factor using a MATLAB script. Differences in sound-pressure levels and spectrograms were calculated with SASLAB PRO VERSION 4 software (Avisoft, Berlin, Germany). For each vocalization the maximum frequency was obtained from mean power spectra calculated by a 1024-point Fourier analysis (Hamming weighting, 75% overlap) from the frontal microphones recording. Here, we defined the maximum frequency as the frequency with the maximum amplitude of the spectrum. Directionality patterns were estimated as differences in the sound-pressure level (SPL). Sound-pressure level was calculated both as mean and as peak-to-peak values. The mean SPL was based on the root-mean-square-values averaged over the whole sound. Prior to calculation of level differences the position of the distance of the sound source was evaluated using cross-correlation calculation between the signals at neighboring channels. In the case of front–back differences the level difference was corrected by the value $k = 20^* \log_{10}((r-\Delta s/2)/(r+\Delta s/2))$ [dB], with r the radius of the semicircle, Δs the difference in acoustic pathway as estimated by the cross-correlation procedure. We assumed spherical spreading of the signal, which would lead to rather underestimated values for level differences. In the case of the other directions we included only values where the difference in the acoustic pathways was lower than 5 cm. The frequency dependence of directionality patterns was calculated from the data of the 5-m distance measurements on the basis of an averaged power spectrum using MATLAB 6.1 (PSD command, 1024 samples, Hann window, 75%, overlap 786 samples). To avoid artifacts in FFT analysis (sidelobes), for this calculation we used only data from frequency bands with a level no lower than -55 dB in the rear direction. This procedure restricted our analysis to a frequency range from 250 to 3200 Hz.

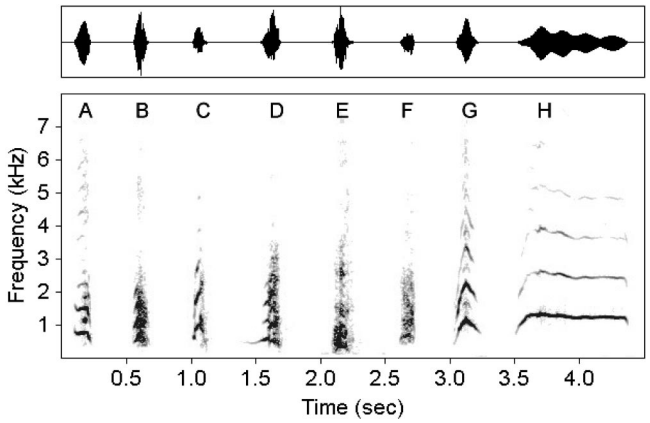

FIG. 1. Spectrograms and waveform (upper part) from typical dog vocalizations: (A) harmonic bark (German shepherd–husky hybrid Thorsten); (B) noisy bark [same dog as (A)], (C) harmonic bark (Rhodesian ridgeback Amalie); (D) predominantly noisy bark [same dog as (C)]; (E) noisy bark (Rhodesian ridgeback Luna); (F) noisy bark (German shepherd Lisa); (G) harmonic bark [same dog as (F)]; (H) yelp [same dog as (F)]. Spectrogram calculated using AVISOFT SASLAB, downsampled to 16 000 Hz, FFT size 512, Hamming window, 75% overlap.

III. RESULTS

A. Structure of the sounds and behavior of the animal while vocalizing

The owners of the dogs stimulated the animals to vocalize. During the observation session the animals directed their gaze towards the person standing. At the beginning of the vocalization the mouth of the animal was typically parallel to the bottom. While vocalizing, the animals raised the head so that at the end of the vocalization the midline between the jaws was at an angle of approximately 45°–70°.

We distinguished three main types of loud vocalizations: harmonic barks, noisy barks, and yelps (Fig. 1). Barks were short, loud sounds with a duration of less then 240 ms. Sounds with predominantly noisy character were classified as noisy barks, whereas sounds with clearly expressed harmonics were classified as harmonic barks. Yelps were sounds with a duration of more then 330 ms. Generally, they had a harmonic structure and were characterized by multiple amplitude modulations. While the dogs Thorsten and Luna produced predominantly barks, Luna and Lisa often yelped. Sometimes they uttered high-frequency squeaks with a fundamental frequency of 4 to 5 kHz. The individuals differed both in the frequency range and the intensity of vocalizations (Table I). In general, the barks of the two German shepherd

TABLE I. Basic characteristics of domestic dog vocalizations. The data were obtained from the measurement in 5-m distance in front of the animal (30° lateral), except the dog Lisa, where the data from the frontal measures at 1.5 m were given. In this analysis, high-frequency whines were excluded.

		Sound-pressure level *re*: 20 μPa (dB)					
		Calculated as root mean square value			Calculated as peak-to-peak value		
Dog	Maximun frequency (Hz) ± s.d.	Mean ± s.d.	Min	Max	Mean ± s.d.	Min	Max
Lisa ($N=104$)	1116 ± 284	99.5 ± 8.4	79.2	112.4	107.1 ± 8.3	87.6	119.1
Thorsten ($N=329$)	830 ± 187	94.7 ± 4.5	69.0	98.9	101.6 ± 5.0	75.5	106
Amali ($N=77$)	603 ± 210	77.4 ± 9.8	57.9	94.3	87.5 ± 9.8	66.3	104.0
Luna ($N=78$)	449 ± 143	67.9 ± 6.9	55.6	82.6	78.4 ± 6.4	64.5	92.2

hybrids had a higher maximum frequency and higher sound-pressure level than the two Rhodesian ridgebacks.

B. Dependence of sound-pressure level on the direction

In all four animals the sound-pressure level at the back position was lower than at the frontal position in the 2-m setup (Fig. 2). Similar results were obtained in the 5-m setup (Thorsten—4.6 dB peak to peak; Amali—3.4 dB; Luna—1.9 dB). For both setups the signals of Luna had the lowest differences in sound-pressure level between front and back, followed by Amali. Differences between the individuals were significant for all measurements (one-way ANOVA, $p < 0.001$). The measurements with the six-channel microphone array revealed a systematic increase of sound-pressure level in dependence from the angle of microphone relative to the medial line of the animal (Fig. 3). The differences in mean and peak sound-pressure level were significant between all directions (one-way ANOVA df = 4, $F = 305.4$, $p < 0.001$ for mean SPL and $F = 342.2$, $p < 0.001$ for peak SPL, respectively).

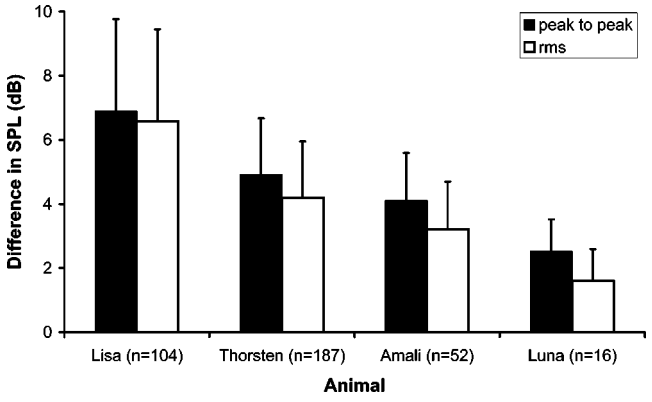

FIG. 2. Mean difference in sound-pressure level between front and back direction calculated as ratio of the root-mean-square values averaged over the whole sound and peak-to-peak values. Distance between microphones and the mouth of the animals was 2 m (in the case of Thorsten, 1.5 m). The difference in rms values of sound-pressure level is calculated as $20^* \log 10(\mathrm{rms}_{180°}/\mathrm{rms}_{0°})$, with $\mathrm{rms}_{180°}$—root-mean-square of back direction and $\mathrm{rms}_{0°}$—root-mean-square in the frontal direction. The peak-to-peak values were calculated in an analogous manner. Error bars indicate the standard deviation. Differences between individuals were significant at $p < 0.001$ (one-way ANOVA, df = 3; $F = 36.8$ for peak SPL; $F = 48.3$ for mean SPL).

C. Changes in frequency components in relation to recording direction

The frequency dependence curve was calculated for the 5-m distance measurements, since here the results were less affected by deviations of the dog's position from the midpoint. We restricted the calculation to the dogs Thorsten and Amali, since the recordings of the lower intensity signals from Luna had a much lower dynamic range. For the same reasons we restricted our calculations to a frequency range up to 3200 Hz. In both animals front–back differences were low at frequencies below 1 kHz (Fig. 4). At higher frequencies the differences increased systematically, reaching a value of nearly 17 dB in Thorsten and 13 dB in Amali. In general, the front–back differences were lower in Amali.

IV. DISCUSSION

Our results have clearly demonstrated that the radiation patterns of domestic dog vocalizations are far from omnidirectional. Our measurements revealed clear front–back differences and systematic changes with frequency. In general, the results are in good agreement with the findings of Marshall and Meyer (1985) for the human singing voice. We found differences in directionality between the individuals. These differences in directionality reflect differences in head

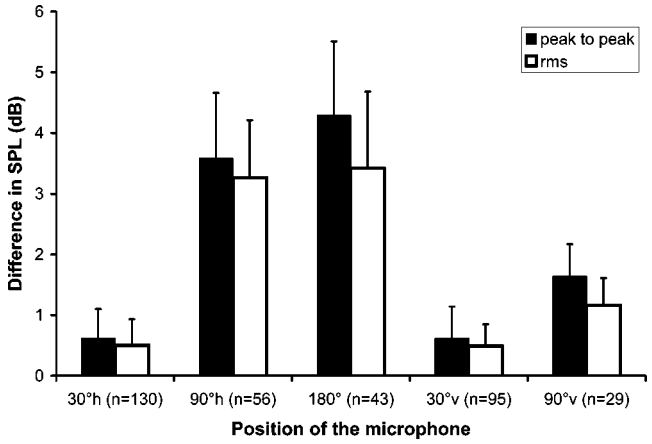

FIG. 3. Decrease in sound-pressure level relative to frontal direction for the German shepherd–husky hybrid (Thorsten). The horizontal plane is indicated by h, the vertical by v. Included are only data where the acoustic pathway between sound source and microphone did not differ more than 5 cm from the acoustic pathway between frontal microphone and sound source. Distance between dog's mouth and animal is 2 m.

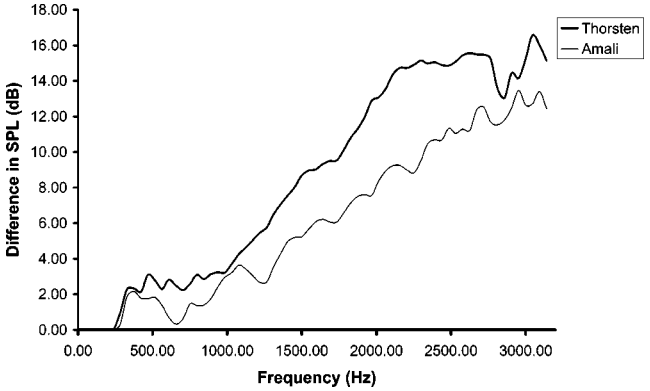

FIG. 4. Frequency dependence of directionality of dog vocalizations. Differences were calculated by power spectral density estimation on the base of 1024-point FFT with a sampling rate of 32 000 Hz. Calculated are only data where the 180° measurement had an acceptable signal/noise ratio. Data calculated for 5-m measurements.

size and the frequency range between the animals. It is obvious that the signals of Luna, the animal with the thinnest head and the lowest maximum frequency, had the lowest directionality. In contrast, the signals of the two German shepherd hybrids with wider heads and much higher maximum frequencies were clearly more directed. Differences in the frequency dependence curves between Thorsten and Amali can be easily explained by their difference in head width.

The relatively high standard deviations of the SPL values lead us to the assumption that the directionality of the emitter is not constant. We assume that the directionality could be affected by the vertical orientation of the head and the angle of mouth opening. We should note that the animals move their head and jaws during vocalization. Rapid movements during short signals, mostly with a duration no longer than 0.1 s, make a quantitative study on the influence of the position of the sound source very difficult.

Although the restriction of our measurements to six points did not allow us to make final conclusions, some considerations concerning the mechanism underlying the directionality are possible. Our data on the domestic dog could be compared with theoretical data for a small piston set in a sphere with 18-cm diameter plotted by Flanagan (1960). The dog vocalizations are much more attenuated in the backward direction than predicted by the piston model. While this model is in good agreement with experimental data of radiation patterns in songbirds (Hunter *et al.*, 1986; Larsen and Dabelsteen, 1990), we expect that for domestic dogs the model of a conical horn as described by Hartley and Suthers (1990) for the mustached bat would be more applicable. However, measurements including more angles are needed to evaluate this model and to investigate the occurrence of sidelobes in directionality plots.

Since our measurements were made on domesticated animals, we should be careful with transfer of the results on wild animals. However, we will expect for vocalizations of the wolf, the ancestor of domestic dogs, a similar sound radiation pattern. Heptner and Naumov (1973) reported a mean skull width of adult European wolves, *Canis lupus*, of 14 cm for males and 13 cm for females. The dogs used in our study had a head width of 12 to 16 cm. This is in good agreement with the head size of a wolf. Also, in their general shape our dogs were wolflike. The investigated frequency range (200 to 3200 Hz) would be relevant for long-distance vocalizations for wild canids (Harrington and Mech 1978; Nikol'skii and Frommolt 1989). We should expect that howls and barks of wolves travel over larger distances in the forward direction than in the backward direction.

The directionality of the vocalizing animal will influence the spectrum of sound depending on the direction. Sounds heard from the side or from behind will lack higher frequencies and will sound muffled. We have indications for Arctic foxes, *Alopex lagopus*, that the spectral cues of barks could be used for individual recognition (Frommolt *et al.*, 2003). Since during counterbarking the animals are facing towards the direction of the other caller, higher frequency components in the vocalizations should be available too for the receiver of the signal.

The above problems indicate that directionality pattern should not be neglected in studies of acoustic communication of mammals.

ACKNOWLEDGMENTS

We wish to acknowledge Michael Möser for the opportunity to provide measurements in the anechoic chamber of the Institute of Technical Acoustics of the Free University of Berlin. Thanks to Joachim Feldmann for technical support. We are much obligated to Hanspeter Herzel (Humboldt-University of Berlin), Gustav Peters (Museum Alexander Koenig Bonn), Jack Bradbury (Cornell University), and two anonymous referees for valuable comments on the manuscript.

Au, W. W. L. (**2000**). "Echolocation in dolphins," in *Hearing by Whales and Dolphins*, edited by W. W. L. Au, A. N. Popper, and R. R. Fay (Springer, New York), pp. 364–408.

Brown, C. H. (**1989**). "The measurement of vocal amplitude and vocal radiation pattern in blue monkeys and grey-cheeked mangabeys," Bioacoustics **1**, 253–271.

Flanagan, J. L. (**1960**). "Analog measurements of sound radiation from the mouth," J. Acoust. Soc. Am. **32**, 1613–1620.

Frommolt, K.-H., and Gebler, A. (**2002**). "Richtcharakteristik der Lautgebung des Haushundes" ("Directivity of domestic dog vocalizations"), Fortschr. Akustik. DAGA **02**, 452–453.

Frommolt, K.-H., Goltsman, M. E., and Macdonald, D. W. (**2003**). "Barking foxes, *Alopex lagopus*: Field experiments in individual recognition in a territorial mammal," Anim. Behav. **65**, 509–518.

Harrington, F. H., and Mech, L. D. (**1978**). "Wolf vocalization," in *Wolf and Man: Evolution in Parallel*, edited by R. L. Hall and H. S. Sharp (Academic, New York), pp. 109–132.

Hartley, D. J., and Suthers, R. A. (**1987**). "The sound emission pattern and the acoustical role of the noseleaf in the echolocating bat, *Carollia perspicillata*," J. Acoust. Soc. Am. **82**, 1892–1900.

Hartley, D. J., and Suthers, R. A. (**1990**). "Sonar pulse radiation and filtering in the mustached bat, *Pteronotus parnellii rubiginosus*," J. Acoust. Soc. Am. **87**, 2756–2772.

Heptner, V. G., and Naumov, N. P. (**1973**). *Die Säugetiere der Sowjetunion. Band II: Seekühe und Raubtiere* (Mammals of the Soviet Union. Vol II: Sirenas and Carnivores) (Gustav Fischer, Jena).

Hunter, M. L. J., Kacelnik, A., Roberts, J., and Vuillermoz, M. (**1986**). "Directionality of avian vocalizations: A laboratory study," Condor **88**, 371–375.

Larsen, O. N., and Dabelsteen, T. (**1990**). ''Directionality of blackbird vocalization. Implications for vocal communication and its further study,'' Ornis Scand. **21**, 37–45.
Marshall, A. H., and Meyer, J. (**1985**). ''The directivity and auditory impressions of singers,'' Acustica **58**, 130–140.
Nikol'skij, A. A., and Frommolt, K.-H. (**1989**). *Sound Activity of the Wolf* (in Russian) (Moscow University Press, Moscow).
Pye, J. D. (**1980**). ''Echolocation signals and echoes in air,'' in *Animal Sonar Systems*, edited by R.-G. Dusbel and J. F. Fish (Plenum, New York), pp. 309–353.

Non-Gaussian statistics and temporal variations of the ultrasound signal backscattered by blood at frequencies between 10 and 58 MHz

Guy Cloutier[a)]
Laboratory of Biorheology and Medical Ultrasonics, Research Center, University of Montreal Hospital and Department of Radiology, University of Montreal, Québec H2W 1R7, Canada

Michel Daronatand David Savéry[b)]
Laboratory of Biorheology and Medical Ultrasonics, Research Center, University of Montreal Hospital, Québec H2W 1R7, Canada

Damien Garcia and Louis-Gilles Durand
Laboratory of Biomedical Engineering, Clinical Research Institute of Montreal, Québec H2W 1R7, Canada

F. Stuart Foster
Department of Medical Biophysics, Sunnybrook and Women's College Health Sciences Centre, University of Toronto, Ontario M4N 3M5, Canada

(Received 21 October 2003; revised 7 April 2004; accepted 22 April 2004)

Very little is known about the blood backscattering behavior and signal statistics following flow stoppage at frequencies higher than 10 MHz. Measurements of the radio frequency (rf) signals backscattered by normal human blood (hematocrit=40%, temperature=37 °C) were performed in a tube flow model at mean frequencies varying between 10 and 58 MHz. The range of increase of the backscattered power during red blood cell (RBC) rouleau formation was close to 15 dB at 10 and 36 MHz, and dropped, for the same blood samples, below 8 dB at 58 MHz. Increasing the frequency from 10 to 58 MHz raised the slope of the power changes at the beginning of the kinetics of aggregation, and could emphasize the non-Gaussian behavior of the rf signals interpreted in terms of the *K* and Nakagami statistical models. At 36 and 58 MHz, significant increases of the kurtosis coefficient, and significant reductions of the Nakagami parameter were noted during the first 30 s of flow stoppage. In conclusion, increasing the transducer frequency reduced the magnitude of the backscattered power changes attributed to the phenomenon of RBC aggregation, but improved the detection of rapid growth in aggregate sizes and non-Gaussian statistical behavior. © *2004 Acoustical Society of America.* [DOI: 10.1121/1.1760791]

PACS numbers: 43.80.n, 43.80.Qf, 43.80.Vj [FD] Pages: 566–577

I. INTRODUCTION

Blood is a heterogeneous suspension of erythrocytes, leukocytes, and platelets in plasma. The scattering of ultrasound by blood is mainly attributed to the erythrocytes, or red blood cells (RBCs), because they are larger and much more numerous than the other blood particles (they constitute around 35%–45% of the blood volume in normal individuals). The phenomenon of RBC aggregation, which is known to have a determinant effect on the ultrasound backscattered signal intensity and spectral slope,[1–3] was described as a blood coagulating and decoagulating event more than 300 years ago.[4] In 1929, Fahraeus studied the sedimentation rate of RBCs in various conditions and depicted aggregation as the binding of erythrocytes to form rouleaux and clusters.[5]

It is known from the contemporary literature that the formation and breakup of aggregates depends on the shearing conditions of the flow, biological factors such as the concentration of certain plasma proteins, and cellular adhesion mechanisms.[6] The rheological impacts of RBC aggregation on blood flow are numerous and affect both the macro- and microcirculation. Among them may be cited its effect on the formation of sludge blood in microvessels,[7] increased blood viscosity,[8] occurrence of vascular thrombosis,[9] increased flow resistance,[10] increased interaction of leukocytes with the endothelium,[11] and hemodynamics.[12] In addition, the ability of blood to perform its main function, i.e., to transport oxygen, carbon dioxide, nutrients, and metabolic products can be affected by RBC aggregation.[13,14]

The main purpose of the present study was to investigate possible changes in the statistics of the ultrasound signal backscattered by blood, at frequencies between 10 and 58 MHz, as a mean to characterize the dynamics of RBC aggregation. Compared to other hemorheological methodologies used in medicine and research, ultrasound penetrates tissues and can provide measurements *in situ*.[15] Mean frequencies between 10 and 58 MHz were selected to cover a wide range of spatial resolutions allowing access to different vessel sizes.

[a)]Director, Laboratory of Biorheology and Medical Ultrasonics, Research Center, Centre hospitalier de l'Université de Montréal, 2099 Alexandre de Sève (room Y-1619), Montréal, Québec, Canada, H2L 2W5. Electronic mail: guy.cloutier@umontreal.ca
[b)]Present address: Philips Research USA, 345 Scarborough Road, Briarcliff Manor, NY 10510, USA.

 0001-4966/2004/116(1)/566/12/$20.00

A. Statistical models and ultrasound tissue characterization

The statistical analysis of the ultrasound radio-frequency (rf) signal and of its envelope (B-mode image) has been used for some years as an approach to differentiate normal and pathological biological tissues. Kuc[16] introduced the coefficient of kurtosis (K_u) as a mean to differentiate Gaussian from non-Gaussian ultrasound signals. The method was applied to characterize the rf signals backscattered by normal livers (Gaussian distribution, $K_u=3$), and by fatty-infiltrated hepatic tissues (uniform distribution, $K_u<3$). It may be noted that a non-Gaussian random variable with a peaking histogram (leptokurtic distribution) results in $K_u>3$. The kurtosis coefficient of a given statistical distribution is defined by the ratio of the fourth central moment to the square of the second central moment of the random variable X

$$K_u=\frac{E[(X-\mu_x)^4]}{E[(X-\mu_x)^2]^2}, \tag{1}$$

where $E[\,]$ represents the ensemble average and $\mu_x=E[X]$.

From here on, let us consider the ultrasound time-domain rf signal as being statistically described by the random variable X. Assuming that the scattering tissue is composed of many independent subscatterers and according to the central limit theorem, the backscattered echo $x(t)$ is Gaussian distributed and the envelope $A(t)$ thus follows a Rayleigh distribution.[17] However, as presented in the present article, the above considerations may not always be valid when $x(t)$ comes from the backscattering of RBCs or RBC aggregates.

To consider the complexity of ultrasound backscattering by biological tissues, and to better characterize the deviation from the Gaussian (for rf signals) and Rayleigh (for B-mode images) distributions, other statistical models were investigated. The K distribution, derived from works in optics, was proposed to study the effect of the concentration of scatterers on the ultrasound speckle statistics of $A(t)$.[18] It was postulated by Weng *et al.*[18] that clustered scattering may result in non-Rayleigh distributions if one considers a small number of scatterers per resolution cell. In their model, the envelope signal $A(t)$ is K distributed, the probability density function (PDF) $P_K(A)$ is being given by

$$P_K(A)=\frac{2b}{\Gamma(M)}\left(\frac{bA}{2}\right)^M J_{M-1}(bA), \tag{2}$$

where the two PDF parameters b and M can be expressed as a function of the moments of the K variable A according to

$$b=\left[\frac{\Gamma(M+1/2)}{\Gamma(M)}\right]\frac{2\Gamma\left(\frac{3}{2}\right)}{\mathrm{E}[A]}$$

and

$$K_u=2\left(1+\frac{1}{M}\right),$$

K_u being the kurtosis of the random variable $A(t)$.
In these equations, Γ is the gamma function, and J_{M-1} is the modified Bessel function of order $M-1$. By considering $A(t)=|x(t)|$, one can derive the following relationship:[19]

$$K_u=3\left(1+\frac{1}{M}\right), \tag{3}$$

where K_u is the kurtosis of the random variable $x(t)$. When M becomes large, the K distribution is equivalent to the Rayleigh distribution, i.e., the envelope signal PDF obtained when $x(t)$ is Gaussian.

Very interestingly, it was shown that the parameter M (effective number density) of the K distribution is physically related to the nonuniformity in scattering cross sections (ν) and to the number of particles in the scattering volume (N), determined by the beam cross section and length of the incident pulse[20]

$$M=N(\nu+1), \quad \nu>-1. \tag{4}$$

It may be worth mentioning that the parameter ν was unfortunately not explicitly defined in the above article. For human blood at a typical hematocrit of 40%, RBC counts are $4.6-6.2\times10^6$ particles per ml for man, and $4.2-5.4\times10^6$ per ml for woman.[1] Thus, because N is very large in a given range cell and because each RBC has a similar acoustic impedance, changes in the number of particles N should play a minor role in affecting the statistics of the backscattered echoes, for the experimental conditions of the present study.

Using simulations, Narayanan *et al.*[21] tested the range of validity of the Rayleigh probability distribution of the B mode signal ($A(t)$). Non-Rayleigh histograms were characterized by the K distribution parameters. As the scattering cross sections became more random ($\nu\rightarrow-1$), the effective number density M was shown to decrease. In the same study, the effect of the scatterer's density (number of scatterers per unit volume) on the departure from the Rayleigh histogram was experimentally verified in a phantom (the K distribution functions were plotted for estimated M values of 0.076, 0.707, and 3.940). *In vivo*, the effective number of scatterers M was used to identify breast tumors,[20] and to study breast and liver tissues.[22,23] Equation (3) of the K distribution model was also considered to characterize *in vitro* non-Gaussian Doppler signals from a suspension of calf RBCs (no aggregation) circulating through a severe stenosis.[24] The clustering of RBCs caused by the acceleration of the flow in the stenotic jet was suggested as a mechanism to explain the non-Gaussian behavior of the backscattered signals ($K_u>3$). A link can thus be made between Eq. (4) and the phenomenon of RBC aggregation, where broad ranges of scatterer's size (parameter ν) may exist depending on the flow conditions.

Other probability distributions were proposed in the field of ultrasound tissue characterization to consider the spatial correlation of complex heterogeneous tissues. These are introduced here because they may complement the information provided by the K distribution. The Rician,[25] homodyned K,[26] gamma,[27] and Nakagami[28] distributions were adapted from the literature in other fields, and used to characterize the envelope of the ultrasound (US) backscattered signal. The Nakagami distribution is relatively simple to characterize and has a PDF given by

$$P_N(A) = \frac{2m^m A^{2m-1}}{\Gamma(m)\Omega^m} e^{-mA^2/\Omega}, \tag{5}$$

where Γ is the gamma function, $\Omega = E[A^2]$ is a scaling factor computed from the envelope $A(t)$, and m, the Nakagami parameter, is given by

$$m = \frac{E[A^2]^2}{E[(A^2 - E[A^2])^2]}. \tag{6}$$

If one considers a large number of scatterers it is, by definition, greater than or equal to $\frac{1}{2}$. As reported in the literature, m is greater than one for a quasiperiodic half-wavelength spacing of particles, whereas for structures showing some level of organization it is between $\frac{1}{2}$ and one.[28] For $m=1$, the Nakagami distribution is equivalent to the Rayleigh distribution, which corresponds to the case of $x(t)$ being a Gaussian signal scattered by randomly located particles. Because some level of spatial correlation among scatterers may be expected for blood with RBC aggregation,[29,30] the Nakagami parameter m may be of interest to study the backscattered signal by blood.

B. Objectives and hypotheses

In the present study, the first objective was the analysis of the non-Gaussian statistical properties of the backscattered echoes by blood by using the coefficient of kurtosis (K_u) of the rf signal $x(t)$, and the Nakagami parameter (m) of the envelope $A(t)$ obtained by the Hilbert transform of $x(t)$. It was hypothesized that the effective number density of scatterers [parameter M of the K distribution model, Eq. (4)] should decrease during the formation of RBC aggregates because of the presence of disparity in aggregate' sizes within the volume of interest ($\nu \to -1$). This should be reflected by an increase of K_u above 3 during the kinetics of aggregation [Eq. (3)] because of the nonhomogeneity of the scattering crosssections induced by the formation of RBC clusters (for simplicity, RBC aggregates are considered as the basic scattering units for this study). Another hypothesis justifying the use of m [Eq. (6)] is the possibility of identifying regularity in the aggregate structures (if $m>1$ or $\frac{1}{2} \leqslant m < 1$). A second objective of this study was to extend, to higher frequencies, experimental measurements related to changes in blood echogenicity during the kinetics of RBC aggregation.[31] In the study by Qin *et al.*, horse blood was used and the frequency was limited to 10 MHz.

II. METHODS

A. Description of the flow model

All experiments were performed in the steady flow phantom of Fig. 1. The flow model was composed of a peristaltic pump that circulated human blood from a bottom reservoir to a hermetically closed top reservoir. The height difference between both reservoirs determined the flow rate in the main conduit (measurement chamber). The pressurization of the top reservoir allowed damping of oscillations produced by the pump. A magnetic stirrer was used to continuously mix blood in the top reservoir, thus eliminating the sedimentation of RBCs and contributing to the disaggregation of rouleaux before entering the descending conduit. The entrance length between the top reservoir and measurement chamber was greater than 22 cm (the distance from the on/off valve was 12 cm). A cannulating type flow probe (Carolina Medical Electronics, model EMPCO 300 AP1 1/16) was inserted into the tubing to measure the flow rate in the measurement chamber with an electromagnetic flowmeter (Cliniflow II, model FM701D, King, N.C.). To control the flow rate in the main vessel, two valves were inserted in the model. The one on the left (see Fig. 1) regulated the flow in the measurement chamber, while the right valve on the main conduit was maintained open. This allowed adjustment of the flow (prereduction flow rate) before totally closing the right valve to promote RBC aggregate formation (flow stoppage). Hot water was circulated within the double walls of the bottom and top reservoirs to regulate the temperature of blood at 37 °C.

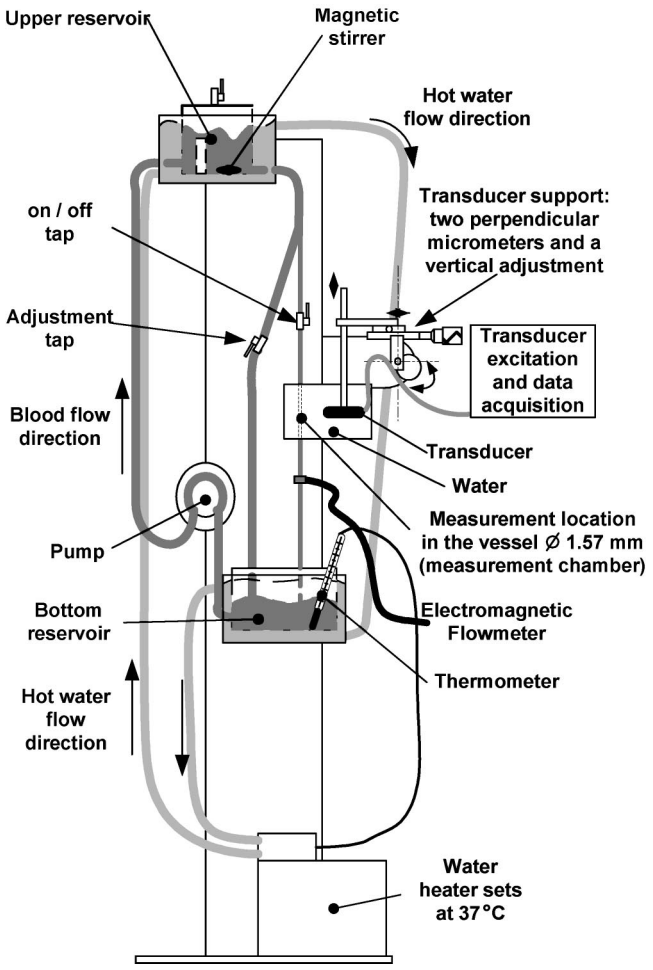

FIG. 1. Schematic representation of the flow loop model used to study the backscattered power and statistics of the ultrasound radio frequency (rf) signals backscattered by blood during the kinetics of red cell aggregate formation.

A closeup view of the measurement chamber is described in Fig. 2. The main wall-less flow conduit, of inner diameter of 1.6 mm, was made by pouring agar gel around a rigid cylinder maintained on both sides by holes made through the walls of an acrylic box. Following the hardening of the gel, the bar was removed to create the lumen. An acoustic window was made in the agar block, in front of the

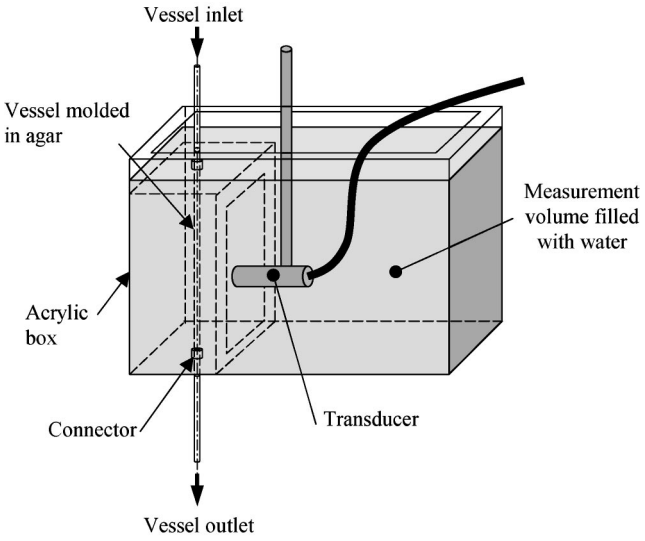

FIG. 2. Closeup schematic description of the measurement chamber.

ultrasound transducer, to adjust the position of the probe. The focused transducer was at 90° with respect to the flow conduit, and the focal point matched the center of the wall-less vessel. The agar gel within an acrylic box and the transducer were immersed in distilled water (room temperature) filling another acrylic container. Connectors allowed the coupling of the measurement chamber with the rest of the flow phantom. The method used to produce the agar gel was described earlier.[32] The gel was made by mixing 3 g of agar powder (Sigma Chemical, high strength agar No. A-6924) with 8 ml of glycerol and 86 ml of distilled water at room temperature. The mixture was then heated at ebullition and progressively cooled to provide hardening. The speed of sound in the solidified gel was close to that of biological tissues (1540 m/s).

B. Blood preparation

Human whole blood and human RBCs, washed and resuspended in saline solution (no aggregation), were used as ultrasound scatterers. The donors were patients suffering from pathologies requiring recurring bleeding of approximately 450 ml. The patients entered into one of these categories: porphyry, hemochromatosis, and polycythemia vera (Vaquez' disease). To our knowledge, these pathologies are not associated to morphological or structural modifications of the RBC membrane, nor to significant changes in the plasma composition. Consequently, it was assumed that the rheology of RBC aggregation was that of normal human blood. Following oral approval by the patient, blood withdrawal was done at the University of Montreal Hospital.

All experiments were done within 24 h of blood collection. For whole blood experiments, the samples anticoagulated with ethylenediamine tetra acetic acid (EDTA) were centrifuged for 20 min at 2300 rpm to separate plasma from blood cells, and the hematocrit was adjusted to 40%. The hematocrit was measured by microcentrifugation at 15 000 rpm for 10 min. For some experiments, the aggregation of RBCs was prevented by using washed erythrocytes. Following the first centrifugation, the plasma was removed and replaced by an isotonic saline solution (Celline II™). After mixing blood, centrifugation was performed again. This procedure was repeated twice to ensure that all plasma proteins responsible for the aggregation were removed. At the end, the washed erythrocytes were mixed with the Celline II solution at a hematocrit of 40%. A volume of approximately 350 ml of blood was necessary to fill the flow model. Before recording any data, the blood sample was introduced in the phantom, and circulated for approximately 1/2 h to eliminate air bubbles and to raise blood temperature to 37 °C.

For each experiment, a blood sample of 1.5 ml was taken from the flow model to measure the aggregation. The erythrocyte aggregation level was determined with a validated erythroaggregameter (Regulest, France) based on a Couette flow configuration.[33] The instrument provides measurements on the aggregation kinetics following flow stoppage, and on the shear rates necessary to partially or totally break RBC rouleaux. A list of aggregation indices measured with this instrument is provided in Sec. III. Blood viscosity measurements were also performed with a cone–plate rheometer (Brookfield, MA, model LVDVIII-CP-42, cone angle$=1.56°$). One ml of blood was withdrawn from the flow model and sheared from 288 to $1\,s^{-1}$ in the rheometer. At each step shear rate, 30 s were allowed to obtain a steady state of viscosity. Measurements were discarded if the torque of the instrument, at a given shear rate, was not high enough to produce repeatable results.

C. Hemodynamic conditions

An analytical biomechanical model was used to determine the velocity profile and thus the shear rate condition before stopping the flow in the phantom. This was required because no measurement of velocity profiles could be performed in the small vessel considered (diameter$=1.6$ mm). For the case of a laminar non-Newtonian steady flow in a rectilinear tube, the velocity profile $V(r)$ of an incompressible fluid can be defined by the following equation:[34]

$$\mu \frac{\partial V}{\partial r} = \frac{1}{2} r \frac{\partial P}{\partial z}, \tag{7}$$

where μ is the dynamic viscosity of the fluid, r is the radial position within the tube, z is the longitudinal distance along the tube, and $\partial P/\partial z$ is the pressure gradient. Since blood is a non-Newtonian fluid, its viscosity μ varies as a function of the shear rate $\partial V/\partial r$. For $\mu = f(\partial V/\partial r)$, one can note that the above equation only depends on $V(r)$. As mentioned earlier, the dynamic viscosity μ was measured for each blood sample by using a cone–plate viscometer.

Knowing the relation $\mu = f(\partial V/\partial r)$ from experimental measurements and the prereduction flow rate that was set to 40 ml/min for all experiments, the numerical solving of Eq. (7) is straightforward. For a given pressure gradient $\partial P/\partial z$, there is only one solution $V(r)$ that corresponds to the limit conditions of the problem. A dichotomic iterative method was used to solve Eq. (7). For a fixed value of $\partial P/\partial z$, $V(r)$ and the related flow rate were calculated. If the flow rate did not match the experimental value of 40 ml/min, $\partial P/\partial z$ was

changed and $V(r)$ was recalculated. When the solution was found, the mean and maximal shear rates were estimated as follows:

$$\overline{\gamma} = \frac{2}{R^2} \int_0^R \frac{\partial V}{\partial r} r \; dr$$

and

$$\gamma_{\max} = \left. \frac{\partial V}{\partial r} \right|_{r=R}, \tag{8}$$

where R is the radius of the tube.

D. Ultrasound transducers

The ultrasound signals were collected with three focused transducers with mean frequencies at 10, 36, and 58 MHz. The descriptions given below were provided by the manufacturers. For all transducers, the frequency response was measured in water, at room temperature, by using a flat reflector positioned at 90° with respect to the probe. The pencil-type piezoelectric (PZT) narrow-band 10 MHz transducer had a diameter of 3 mm, a focal length at 15 mm, and a bandwidth at −6 dB ranging from 7.6 to 12.4 MHz (Etalon Inc., Lebanon, IN). Two wideband polyvinylidene flouride (PVDF) transducers were used to collect data at higher frequencies (Visualsonics, Toronto, Canada). The 36 MHz transducer had a diameter of 3 mm, a focal length at 6 mm, and a bandwidth ranging from 18 to 54 MHz at −6 dB. The probe at 58 MHz had a diameter of 2 mm, a focal length at 4 mm, and a bandwidth of 30–77 MHz (−6 dB).

E. Data acquisition

Two different pulser–receiver instruments were used to collect the rf ultrasound data at a pulse-repetition frequency (PRF) of 1 kHz. A Panametrics system (model 5900 PR, Waltham, MA) was used to transmit negative impulses to the 10 MHz transducer. The echoes backscattered by blood within the vessel lumen were amplified and filtered between 1 and 20 MHz by the Panametrics receiver. An ultrasound biomicroscope (Visualsonics, model UBM VS40) was used to pulse the high-frequency transducers with bipolar square waves (the frequencies available were 19, 25, 40, or 55 MHz). The biomicroscope was operated in rf mode. To facilitate the experiments, the probe was not fixed to the moving scan head during recordings of data. The 36 MHz transducer was fired at 19 MHz and a bandpass filtering between 5 and 40 MHz was applied to the received echoes. The excitation frequency was 55 MHz and the bandpass filter covered the range of 30–80 MHz for the 58 MHz transducer. For experiments performed with the ultrasound biomicroscope, the excitation frequencies and bandpass filtering values were selected to reduce overlap in the frequency response of the backscattered ultrasound signals.

The PRF trigger at 1 kHz of the Panametrics and Visualsonics systems were used to synchronize the acquisition of the backscattered echoes by an 8-bit Gagescope acquisition board (model 8500 CS, Montreal, Canada). The rf signal was digitized at 500 MHz by using the following multiple record acquisition strategy. Ten successive echoes from within the vessel lumen were acquired and stored into the memory of the Gagescope (typically 750 samples or 1.5 μs of data were acquired from a window centered with the tube axis for each excitation pulse separated by a duration of 1 ms). A delay of 3 s was allowed between each record of ten echoes to transfer the data to a microcomputer. This process was repeated for a duration of 1 min before stopping the flow, and for more than 6 min during the process of RBC aggregate formation. For each blood sample studied, measurements were performed with the three transducers. The selection order of the probe frequency was randomly chosen to avoid time effect in the interpretation of the results. For a given blood sample and probe frequency, measurements were repeated five times for averaging purposes. A total of six experiments with different blood samples were performed (three whole blood and three saline suspended RBC experiments).

F. Kurtosis and Nakagami estimates and confidence intervals

Having obtained a finite number N_s of random samples $[X_1,\ldots,X_{Ns}]$ that satisfies the same PDF [computed from the rf signal $x(t)$ or envelope $A(t)$], one wants to assess the kurtosis and Nakagami parameters of the underlying distribution of X. The empirical mean

$$M_1 = \frac{1}{N_s} \sum_{i=1}^{N_s} X_i, \tag{9}$$

and the central empirical moments

$$M_k = \frac{1}{N_s} \sum_{i=1}^{N_s} (X_i - M_1)^k \tag{10}$$

are first defined. They are biased estimators of the kth central moments of X for $k>1$. The two random quantities $\hat{K}_u$ and $\hat{m}$ given by the equations

$$\hat{K}_u = \frac{M_4}{M_2^2} \tag{11}$$

and

$$\hat{m} = \frac{(M_2 + M_1^2)^2}{\frac{1}{N_s} \sum_{i=1}^{N_s} (X_i^2 - M_2 - M_1^2)^2}, \tag{12}$$

are then estimators of the kurtosis and Nakagami parameters that are used from now. Considering that $\hat{K}_u$ and $\hat{m}$ can take random values around the real K_u and m, a convenient method must be used to interpret them and to assess their robustness.

The estimator $\hat{K}_u$ was used to test if the random signal X was effectively Gaussian. Let $H0$ be the hypothesis "X is a Gaussian variable." Under $H0$, $\hat{K}_u$ has a certain PDF, which is independent of the mean and standard deviation of X but dependent on N_s. Using many Monte Carlo simulations of unit centered normal variables (in our case, 10 000 simulations of N_s Gaussian variables), the histogram of $\hat{K}_u$ and the

TABLE I. RBC aggregation indices measured with the erythroaggregameter at 37 °C. The hematocrit was 40% for all measurements.

RBC[a] aggregation indices	Washed human RBCs[a] ($n=3$)	Calf blood[f] ($n=10$)	Human blood ($n=3$)	Normal human blood[f] ($n=19$)
tA (s)[b]	318 ± 108	N/A[g]	3.3 ± 0.5	2.9 ± 0.8
S_{10} (no unit)[c]	10.70 ± 0.04	N/A[g]	19 ± 2	23 ± 3
γD (s^{-1})[d]	18 ± 3	23 ± 13	40 ± 16	49 ± 4
γS (s^{-1})[e]	20 ± 6	27 ± 16	102 ± 39	119 ± 18

[a]Red blood cell.
[b]Aggregation time.
[c]Aggregation index at 10 s.
[d]Partial dissociation shear rate.
[e]Total dissociation shear rate.
[f]Data reproduced from Ref. 35.
[g]Not available.

95% confidence interval $G_1(N_s)$ for the value $|\hat{K}_u-3|$ (the absolute error of estimation) were computed under the hypothesis $H0$:

$$P(|\hat{K}_u-3|\leq G_1(N_s)|H0)=0.95. \quad (13)$$

Using measured data, if the estimated kurtosis $\hat{K}_u$ did not fall inside the interval $[3-G_1(N_s);\ 3+G_1(N_s)]$, then the hypothesis $H0$ of normality of the random samples was rejected.

A similar approach was used to test if a given random positive signal envelope satisfied the Rayleigh distribution by using the Nakagami parameter that is theoretically one in this case. The N_s dependent PDF of $\hat{m}$ was estimated by using many simulations of Rayleigh variables and the hypothesis $H1$: "X is a Rayleigh random signal" was considered. One can then extract a value for $G_2(N_s)$, the 95% confidence interval of the error of estimation $|\hat{m}-1|$

$$P(|\hat{m}-1|\leq G_2(N_s)|H1)=0.95. \quad (14)$$

In the case that $\hat{m}$ differed from 1 by more than $G_2(N_s)$, then the hypothesis $H1$ was rejected.

III. RESULTS

A. Aggregation levels

Table I summarizes the aggregation indices measured with the erythroaggregameter. The third and last columns show results reported in the literature for calf blood (no aggregation), and normal human blood collected from young healthy volunteers.[35] It is well known that bovine blood does not form RBC aggregates. The instrument provided measurements of aggregation indices following flow stoppage (tA in seconds and S_{10} no unit), and shear rate values necessary to break rouleaux (γD and γS in s^{-1}). The parameter tA is the aggregation time, S_{10} is the aggregation index at 10 s, and γD and γS are the partial and total dissociation shear rates, respectively. A complete description of those indices can be found elsewhere.[36] The aggregation kinetics is inversely proportional to tA. In other words, a low value of tA indicates rapid formation of RBC aggregates. On the other hand, low values of S_{10} indicate a slow kinetics, and small γD and γS signify fragile aggregates. As observed in Table I, very little, if any aggregation, was found for the washed human erythrocytes (γD and γS are similar to values measured for calf blood). For the human blood samples, the parameters were close to the data reported earlier by our group for healthy subjects.[35] This indicates that the levels of aggregation measured for the patients with porphyry, hemochromatosis, and polycythemia vera were similar to those of normal human blood.

B. Hemodynamic conditions

As discussed earlier, the solution of Eq. (7) for $V(r)$ provided an estimate of the hemodynamic flow conditions before closing the valve to promote the formation of RBC aggregates. The dynamic viscosities μ, measured for each experiment, were used in this equation. The non-Newtonian property of blood did not affect the velocity profiles for the conditions of the present study. For instance, the estimates of $V(r)$ were very similar for whole blood ($n=3$) and RBC suspension ($n=3$) experiments. The velocity profiles ($n=6$) were parabolic with mean velocities of 34.4 ± 0 cm/s [mean $\pm$ standard deviation, the standard deviation is zero because the mean velocity is computed from the prereduction flow rate that is imposed in the model of Eq. (7)], maximum centerline velocities of 68.6 ± 0.2 cm/s, mean shear rates of $1170\pm0\ s^{-1}$, maximum shear rates at the wall of $1755\pm6\ s^{-1}$, and Reynolds numbers of 182 ± 13 (laminar flow). For the entrance length considered in Fig. 1 (>12 cm), fully developed parabolic flow profiles were expected since the non-Newtonian effects are nonsignificant. According to these shear rate values, it is reasonable to postulate that all RBC aggregates were disrupted before stopping the flow.

C. Power and frequency content of the backscattered signals

Figure 3 presents the rf backscattered power variations following flow stoppage for both RBC suspension and whole blood experiments. The backscattered power was computed from the time domain signal by summing the squared values of the rf signal $x(t)$ over the time window considered (10 ms, ten records of 1.5 μs separated by time intervals of 1 ms). The results are shown for transducer mean frequencies of 10, 36, and 58 MHz. For all measurements, the backscattered power before stopping the flow (at $t=0$) was averaged

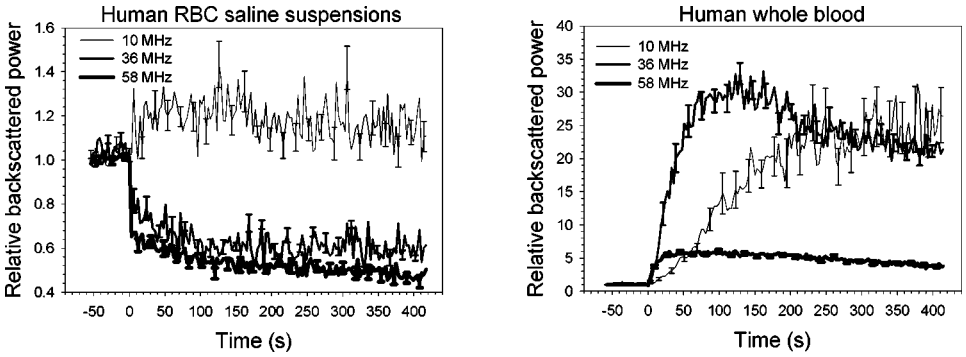

FIG. 3. Relative changes in the ultrasound backscattered power for human RBCs suspended in saline and human whole blood at a hematocrit of 40%, and a temperature of 37 °C. The measurements were performed with three transducers at mean frequencies of 10, 36, and 58 MHz. The standard errors are only displayed for selected times to reduce the density of the graphs ($n = 15$; three blood samples and five measurements per sample).

and set to one to facilitate comparisons. For RBC suspensions, a slight increase of the backscattered power (below 1 dB) was observed at 10 MHz following flow stoppage. At 36 and 58 MHz, the power dropped rapidly after flow stoppage by factors of approximately 1.7 times (-2.2 dB) and 2.2 times (-3.5 dB), respectively, after more than 6 min of flow stoppage. For human whole blood, much larger changes in backscattered power were observed during the kinetics of RBC aggregate formation. At 10 MHz, the power increased 26-fold (14.2 dB) between 0 and 410 s. At 36 MHz, the rate of increase of the backscattered power, between 0 and 70 s, was much faster than at 10 MHz. The maximum reached after 70 s corresponded to changes in backscattered power of more than 15 dB (32 times). A reduction of the power by approximately 2 dB was noted following the maximum. The rate of increase of the power was similar between measurements at 36 and 58 MHz, for the first few seconds following $t=0$. However, at 58 MHz, the plateau was reached earlier and the power increase was below 8 dB (6.3 times).

To allow comparisons of the frequency bandwidths measured in water with the three transducers (as provided by the manufacturers) to those obtained from the flow model, the power spectra of the rf backscattered signals at the end of the kinetics of aggregation were computed. For each transducer, an average spectrum was evaluated from the spectra of 1500 rf lines (10 rf lines$\times$10 records separated by 3 s between 384 and 414 s$\times$5 measurements per sample$\times$3 blood samples). Figure 4 combines the results for the three transducers. The mean frequencies within -20 dB of the main lobe were, respectively, 11, 22, and 42 MHz, which is similar to or lower than the mean values of 10, 36, and 58 MHz measured in water with a flat reflector. The frequency chosen for the transmitted pulses, the bandpass filters selected, the frequency-dependent attenuation of blood, and artifacts produced by the measurement chamber can explain the differences. For RBCs suspended in saline, the mean frequencies were 11, 23, and 47 MHz, respectively (results not shown). The lower frequency-dependent attenuation in the absence of RBC aggregation can explain the higher mean frequencies obtained for RBC suspensions with the two highest frequency transducers. From here on, to avoid ambiguity, the transducers are still designated as the 10, 36, and 58 MHz probes.

D. Coefficient of kurtosis

Figure 5 describes the coefficients of kurtosis as a function of time for both RBC suspension and whole blood experiments at 10, 36, and 58 MHz. Similar results were obtained for both types of blood. To this matter, the formation of RBC aggregates following flow stoppage did not affect significantly the estimates of the coefficients of kurtosis. At 10 and 36 MHz, Gaussian rf signals with $\hat{K}_u$ close to 3.0 were observed for both types of blood (most values were within the confidence interval). Increasing the transducer frequency to 58 MHz raised the values of $\hat{K}_u$ slightly above the Gaussian limit.

Since it was hypothesized that disparity in scatterer sizes within the volume of interest may produce non-Gaussian scattered signals, the coefficients of kurtosis were recomputed by considering four window durations for which different ranges of aggregate sizes would be expected. The same strategy was also applied for the suspensions of RBCs but as expected, changing the window length had no effect on the values of $\hat{K}_u$ (the results are not shown but they were similar to those of Fig. 5—left panel). Window durations of 12, 30, 42, and 60 s were considered. Increasing the window length systematically emphasized the non-Gaussian behavior of the backscattered signals for human whole blood, whatever the frequency ($\hat{K}_u$ progressively increased for larger windows). From here on, only the results for a window du-

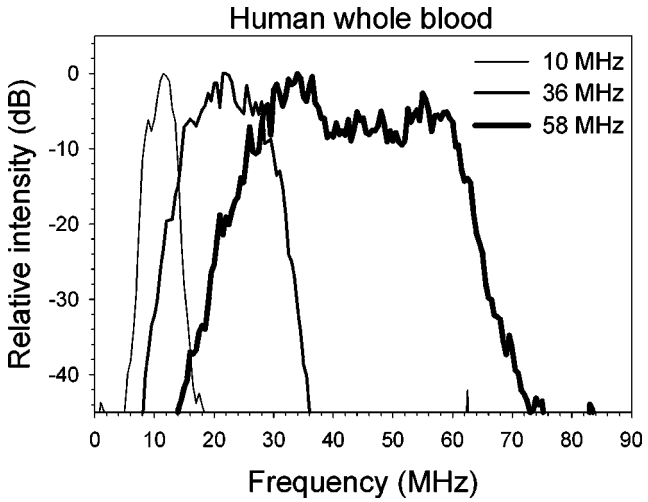

FIG. 4. Normalized power density spectra of the rf signals backscattered by human whole blood at a hematocrit of 40%, and a temperature of 37 °C. The maximum of each mean spectrum was normalized to 0 dB. The measurements were obtained from the flow phantom of Fig. 1, by using three different transducers. The 10 MHz transducer was fired by negative impulses, whereas the 36 and 58 MHz probes were excited by bipolar square pulses at 19 and 55 MHz, respectively.

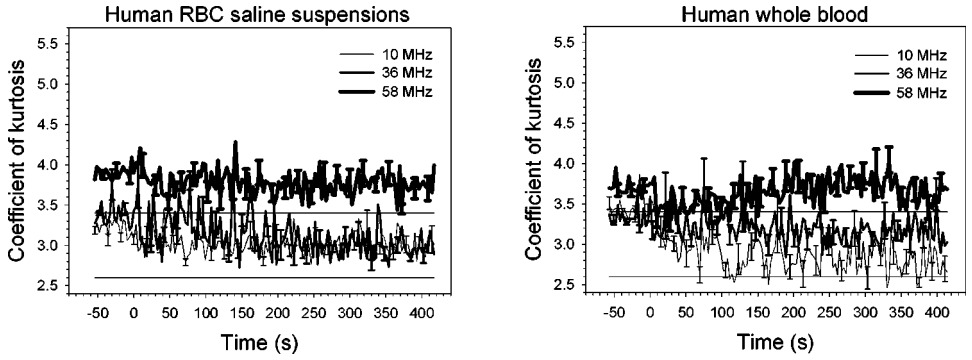

FIG. 5. Coefficient of kurtosis ($\hat{K}_u$) for human RBCs suspended in saline and human whole blood at a hematocrit of 40%, and a temperature of 37 °C. A time window of 10 ms was considered for the computation of $\hat{K}_u$. The measurements were performed with three transducers at mean frequencies of 10, 36, and 58 MHz. The standard errors are only displayed for selected times to reduce the density of the graphs ($n=15$; three blood samples and five measurements per sample). The horizontal lines correspond to the confidence interval of the estimates $[3 \pm G_1(N_s)$, as defined by Eq. (13)].

ration of 42 s are presented. At 10 MHz, as shown in Fig. 6, a significant increase of $\hat{K}_u$ to 3.8 was observed during the first few seconds following flow stoppage. Between 120 and 420 s, $\hat{K}_u$ values were close to the confidence interval. The non-Gaussian effect was largely amplified at higher frequencies. Maximum averaged values of $\hat{K}_u$ close to 5.4 were obtained at 36 and 58 MHz. For the three frequencies considered, the peaks of $\hat{K}_u$ occurred between 18 and 27 s after flow stoppage.

E. Coefficient of Nakagami

According to Fig. 7, the information conveyed by the coefficient of Nakagami seems to be very similar to that provided by the coefficient of kurtosis. For instance, each panel of Fig. 7, obtained from the instantaneous rf signal envelopes, is close to a mirror of that presented in Fig. 5. At a given time instant and frequency, an increase of $\hat{K}_u$ corresponds to a similar reduction of $\hat{m}$, and vice versa. As reviewed in Sec. I, a Gaussian rf signal gives $m=1$. For the human erythrocytes suspended in saline, the rf signals were Gaussian at 10 and 36 MHz. At 58 MHz, the same blood samples resulted in non-Gaussian backscattered signals with $\hat{m}$ close to 0.7. For whole blood, the rf signals were generally Gaussian except for some results at 10 and 58 MHz. Surprisingly, non-Gaussian behavior was found at 10 MHz after approximately 100 s of flow stoppage. Figure 8 summarizes, for human whole blood, the results of the coefficients of Nakagami for a window of 42 s. Increasing the window length emphasized the non-Gaussian property of the rf signals, especially at 36 and 58 MHz. The increase in the size of aggregates during the first few seconds of rouleau formation clearly reduced the values of $\hat{m}$. The minimums reached after 10–25 s following flow stoppage were below 0.4. As reported before for the coefficient of kurtosis, using a window of 42 s (or any others between 12 and 60 s) had very little effect on $\hat{m}$ for the RBC suspension experiments (the results are not shown but they were similar to those of Fig. 7—left panel).

IV. DISCUSSION

A. Ultrasound backscattered power variations

The following discussion intends to provide an explanation for the results of Fig. 3 (left panel). It is known that flow disturbance can increase the echogenicity of RBC suspensions,[37,38] if the number density of scatterers is sufficient to provide variance in their spatial distribution (that variance affects the packing or structure factor). Changes in echogenicity on the order of 3–5 dB were reported at frequencies of 10 MHz and below, for hematocrits higher than 10%, approximately. It is not clear, in Fig. 3 (left panel), why stopping the flow provided a slight increase on the order of 1 dB of the backscattered power at 10 MHz. This increase may not be significant, considering the standard deviations reported. A more robust explanation can be provided for the results at 36 and 58 MHz. As seen on the left panel of Fig. 3, the backscattered power was higher by approximately 2.2 and 3.5 dB at 36 and 58 MHz, respectively, before stopping

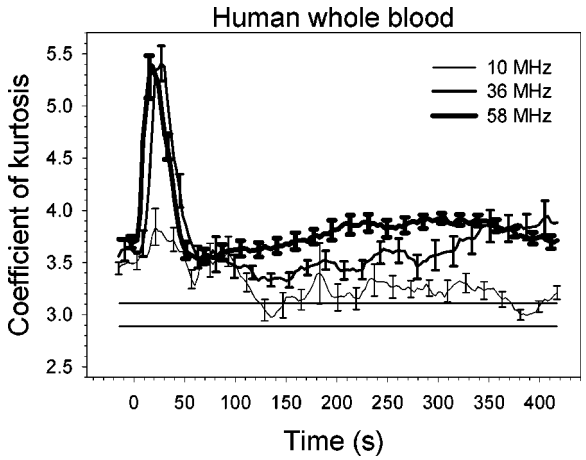

FIG. 6. Coefficient of kurtosis ($\hat{K}_u$) for human whole blood at a hematocrit of 40%, and a temperature of 37 °C. A time window of 42 s was considered for the computation of $\hat{K}_u$. The measurements were performed with three transducers at mean frequencies of 10, 36, and 58 MHz. The standard errors are only displayed for selected times to reduce the density of the graphs ($n=15$; three blood samples and five measurements per sample). The horizontal lines correspond to the confidence interval of the estimates $[3 \pm G_1(N_s)$, as defined by Eq. (13)].

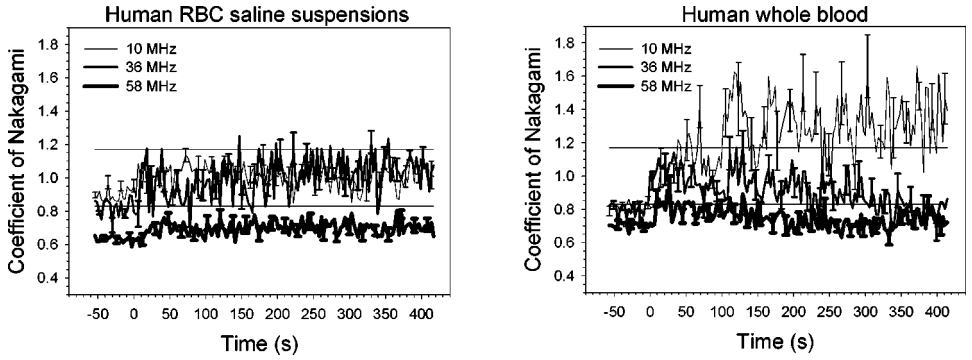

FIG. 7. Coefficient of Nakagami ($\hat{m}$) for human RBCs suspended in saline and human whole blood at a hematocrit of 40%, and a temperature of 37 °C. A time window of 10 ms was considered for the computation of $\hat{m}$. The measurements were performed with three transducers at mean frequencies of 10, 36, and 58 MHz. The standard errors are only displayed for selected times to reduce the density of the graphs ($n=15$; three blood samples and five measurements per sample). The horizontal lines correspond to the confidence interval of the estimates $[1\pm G_2(N_s)$, as defined by Eq. (14)].

the flow. This seems to indicate that a Reynolds number, as low as 182 before flow stoppage, may be sufficient to provide variance in the RBC spatial distribution that is detectable at high frequencies. This suggest that the use of transducers at 36 and 58 MHz may improve the detection of blood flow disturbances with ultrasound, but this still needs to be confirmed. Very interestingly, Lookwood *et al.*[39] reported an increase by 1.6 times of the backscattering coefficient at a mean frequency close to 50 MHz when the flow in a phantom was increased from 18 to 36 cm/s. Flow turbulence was then postulated as a possible mechanism to explain the backscattered power increase (RBC aggregation was prevented in these experiments).

Very little is known about the backscattering of ultrasound by whole blood at high frequencies.[3,40] To our knowledge, the kinetics of RBC aggregation following flow stoppage has never been studied at frequencies higher than 10 MHz.[31,41,42] According to Fig. 3 (right panel), increasing the ultrasound frequency seemed to improve the sensitivity of the method to rapid changes in RBC aggregate sizes by decreasing the time response of the US power. On the other hand, it can be observed in Fig. 3 that the range of variation of the backscattered power during the kinetics of aggregation was much lower at 58 MHz (8 dB) then at 36 MHz (15 dB) or 10 MHz (14.2 dB). Although only one human blood sample was analyzed in their study, Foster *et al.*[3] also noticed a lower sensitivity to the phenomenon of RBC aggregation at high frequency. For instance, by studying the backscattering coefficient as a function of the shear rate and frequency they observed, at 35 MHz, a 14.3 dB variation between 0.1 and 100 s^{-1}, and a variation of only 2.9 dB, for the same range of shear rate, at 70 MHz. Very recent simulation results[29,43] predicted the reduced sensitivity of US backscattering to the phenomenon of RBC aggregation at high frequency. The reduction of the sensitivity was attributed to a decrease of the spectral slope at frequencies above 30 MHz, approximately (the fourth power frequency dependence of US backscattering, which is characteristic of Rayleigh scatterers, is no longer valid in the presence of RBC aggregation at these frequencies; consequently, for a step increase in aggregate sizes, smaller power enhancements are obtained at high frequencies).

According to the results of Fig. 3 (right panel), increasing the frequency from 10 to 36 MHz seemed to be beneficial for the application in hand because the rate of increase of the backscattered power for small changes in aggregate sizes (at the beginning of the kinetics of aggregation) was raised, without significant reduction in sensitivity to large variations in aggregate dimensions during the whole process of RBC rouleau formation. This result is interesting and may deserve more attention. For instance, it would be of interest to determine which frequency between 10 and 36 MHz is optimal to detect dynamic changes in RBC aggregate sizes. The observations of Fig. 3 also may be of interest to interpret the cyclic variations in echogenicity observed at various frequencies under pulsatile flow.[44,45] Finally, this study had a limitation that may deserve discussion. Because three different transducers with different aperture sizes, focal distances, and frequencies were used, the scattering volumes were different. To allow comparison of the results, the mean backscattered power before flow stoppage had to be normalized to one for each transducer, and only relative backscattered

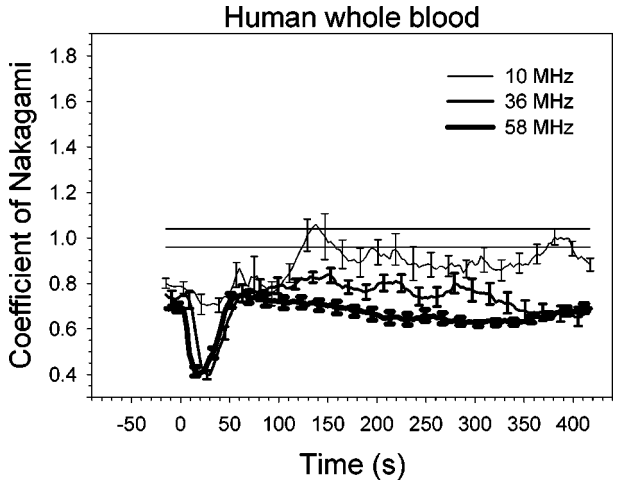

FIG. 8. Coefficient of Nakagami ($\hat{m}$) for human whole blood at a hematocrit of 40%, and a temperature of 37 °C. A time window of 42 s was considered for the computation of $\hat{m}$. The measurements were performed with three transducers at mean frequencies of 10, 36, and 58 MHz. The standard errors are only displayed for selected times to reduce the density of the graphs ($n=15$; three blood samples and five measurements per sample). The horizontal lines correspond to the confidence interval of the estimates $[1\pm G_2(N_s)$, as defined by Eq. (14)].

power changes were investigated. It would have been preferable to measure the absolute backscattering coefficient compensated for the frequency-dependent attenuation, but the experimental setup made this difficult to do.

B. Coefficient of kurtosis

As observed in Fig. 5 for both RBC suspension and whole blood experiments, Gaussian statistics ($\hat{K}_u \approx 3.0$) were obtained at 10 and 36 MHz when the instantaneous rf signals were analyzed. Raising the frequency resulted in an overall significant increase of $\hat{K}_u$ whatever the time instant before or after stopping the flow. For any frequency, the formation of RBC aggregates at $t>0$ did not affect $\hat{K}_u$ when small time windows were considered (the instantaneous analyses of $\hat{K}_u$ were obtained from time windows of 10 ms — i.e., ten records of 1.5 μs at a PRF of 1 kHz). The Gaussian backscattering behavior at 10 and 36 MHz can thus be interpreted from the analysis of Eqs. (3) and (4). For instance, the K-distribution model stipulates that the effective number of scatterers ($M=3/(K_u-3)$) is a function of the actual number of particles (N), and of the lack of uniformity of their cross sections (ν). At a normal hematocrit of 40% (the hematocrit determines the value of N), it can be concluded that the spatial and temporal variations in RBC aggregate sizes (ν) were not sufficient to reduce the value of M for a time window of 10 ms.

A different backscattering behavior was observed for whole blood experiments when longer windows (12–60 s) and the unstationary RBC aggregation process were considered. As seen in Fig. 6 for a time window of 42 s, the non-Gaussian statistics were emphasized at 36 and 58 MHz at the beginning of the kinetics of aggregation. This suggests reductions in the effective number of scatterers ($M=1.25$ for $\hat{K}_u=5.4$) at these frequencies. The lack of uniformity of the backscattering cross sections of scatterers is the mechanism proposed to explain the large increases of $\hat{K}_u$. Similar findings have never been reported in the literature on blood scattering. According to Fig. 6, the 10 MHz probe did not seem to be as sensitive to the presence of a broad range of RBC aggregate sizes within the volume of interest. Because Rayleigh scattering that likely occurs at 10 MHz is theoretically independent of the scatterer shape,[1] this explains why the transitory increases in $\hat{K}_u$ are mainly detected at the highest frequencies.

To our knowledge, Fontaine *et al.*[24] were the only group to study the statistics of the rf signals backscattered by blood. However, their study was based on nonaggregating RBC experiments. In addition, it can be mentioned that few studies investigated the effect of the ultrasound transmitted frequency on non-Gaussian properties of US backscattered signals. All of them were at frequencies below 7.5 MHz. In a study by Chen *et al.*,[19] tissue phantoms were used to demonstrate the effect of the transducer frequency, ultrasound field, and density of scatterers on non-Rayleigh characteristics of the envelope. Deviation from the Rayleigh distribution (reduction of K_u) was observed when the frequency was increased from 3.5 to 5 MHz. These results were explained by the larger ultrasound beam of the 3.5 MHz transducer (the beam incorporated more scatterers). In the present study, the beam profiles were different between the 10, 36, and 58 MHz transducers (the larger beam was at 10 MHz and the smaller one was at 58 MHz; the length of the range cell within the tube was kept close to constant for all transducers). The larger beam may be considered as a confounding factor that could have contributed to the overall tendency toward an increase of $\hat{K}_u$ as a function of frequency. However, the likelihood that this happened is small, considering the large number of RBCs present in the sample volume (at a hematocrit of 40%). Futhermore, it is important to emphasize that changes in the beam width cannot explain the time variations of $\hat{K}_u$ observed in Fig. 6 for a given transducer since the beam characteristics did not change over time.

C. Coefficient of Nakagami

As shown in Figs. 7 and 8, the information conveyed by the coefficient of Nakagami is very similar to that provided by the coefficient of kurtosis. The inverse relation or correlation between both parameters can be appreciated by comparing Eqs. (1) and (6). As introduced earlier, the literature suggests a quasiperiodic half-wavelength spacing of particles for m greater than one, whereas structures showing some level of organization should give values of m between $\frac{1}{2}$ and one.[28] The following explanation is suggested for the results of Figs. 7 and 8. At 10 MHz, since the wavelength is approximately 154 μm, the periodic spacing of RBCs or RBC aggregates may not correspond to half or a larger fraction of the wavelength. Consequently, $\hat{m}$ was close to one, suggesting randomly located particles when *viewed* at such a relatively low spatial resolution. Surprisingly, for a temporal window of 10 ms, $\hat{m}$ reached values close to 1.4 during the kinetics of aggregation (Fig. 7, right panel). Since we observed a lower signal-to-noise ratio at 10 MHz than at the other frequencies, this may reflect a lack of statistical robustness of the Nakagami estimates for the small window of 10 ms. Less variances in the estimates of m were obtained for a window of 42 s (see Fig. 8).

When the frequency was increased to 36 and 58 MHz, the same spacing in the spatial organization of RBCs or RBC aggregates started to be on the order of a fraction of the wavelength, as suggested by the $\hat{m}$ values between $\frac{1}{2}$ and one, for both time windows of 10 ms and 42 s. Interestingly, as shown in Fig. 8, the rapid growth in RBC aggregate sizes between 10 and 25 s following flow stoppage momentarily reduced the Nakagami coefficient at the higher frequencies, which suggest some additional level of spatial organization. It is important to point out here that a thorough analysis of the phase of the rf signals would be required to confirm the existence of spatial coherence among scatterers at a fraction of the wavelength, as suggested in Ref. 46. To our knowledge, the effect of frequencies between 10 and 58 MHz on the Nakagami coefficient has never been addressed. It may be worth mentioning that the values of $\hat{m}<\frac{1}{2}$ observed in Fig. 8 are probably not artifactual. The theoretical lower limit of $\frac{1}{2}$ can be violated for specific conditions (such as a small number of scatterers in the volume of interest), as shown

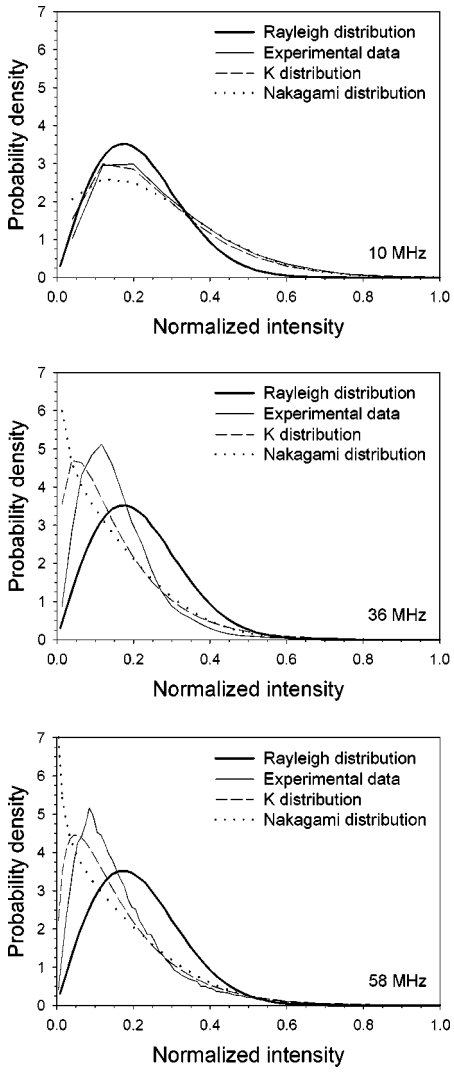

FIG. 9. Normalized probability density distributions of the envelope $A(t)$ of the rf signals backscattered by whole blood for a time window of 42 s, at the peak of $\hat{K}_u$ in Fig. 6 and minimum of $\hat{m}$ in Fig. 8. The data were collected for three transducers at mean frequencies of 10, 36, and 58 MHz. Each panel gives the experimental PDF and those computed from Eq. (2) (K model) and Eq. (5) (Nakagami model). The values of $\hat{K}_u$ (K model) were 3.91, 5.40, and 5.44, and $\hat{m}$ (Nakagami model) were 0.65, 0.39, and 0.38 at 10, 36, and 58 MHz, respectively.

earlier.[28] Finally, one may be cautious with the physical interpretation of $\hat{K}_u$ and $\hat{m}$, because of the inverse correlation between both parameters and the fact that the literature interprets them differently (K_u is affected by the nonuniformity in scattering crosssections, whereas m reflects periodic organization among scatterers; both parameters are influenced by the number of particles in the scattering volume).

D. Validity of the *K* and Nakagami probability density distributions

The validity of the K and Nakagami PDF [Eqs. (2) and (5)] to describe the histogram of $A(t)$ was tested on the data available. For all results in Figs. 5–8 where $\hat{K}_u \approx 3.0$ and $\hat{m} \approx 1.0$, the experimental histogram could adequately be modeled with either the K, Nakagami, or Rayleigh PDF. However, for non-Rayleigh conditions, discrepancies were observed between the experimental histograms and those modeled with Eqs. (2) and (5). For example, Fig. 9 shows probability density distributions of $A(t)$ for whole blood experiments performed with a time window of 42 s, at 10–25 s following flow stoppage (the data corresponding to the maximum of $\hat{K}_u$ in Fig. 6 and minimum of $\hat{m}$ in Fig. 8 were used for this example). At 10 MHz, the K PDF adequately described the experimental histogram of $A(t)$. As the frequency was raised to 36 and 58 MHz, neither the K nor the Nakagami distributions adequately fit the experimental results. This suggest that the physical conclusions extrapolated from these models [effective number density of scatterers, parameter M of Eq. (4); and orderliness in the spatial arrangement of scatterers, Eq. (5)] may not be valid for some of the experimental conditions considered here.

V. CONCLUSION

Experimental measurements of backscattered power changes from human RBC suspensions and whole blood were presented. The most significant power variations were attributed to the phenomenon of RBC aggregation. The backscatter enhancement due to aggregation was shown to decrease with frequency, which agree with recent simulation models.[29,43] It appeared that the time response to rapid changes in scatterer sizes, from individual cells to aggregates of a few RBCs, increased by raising the frequency of the US transducer. Among the three tested frequencies, the best compromise between the echogenicity enhancement and time response was obtained at 36 MHz.

The statistics of the backscattered signals also was investigated by computing the coefficients of kurtosis of the rf signal and the Nakagami parameter on the signal envelope. By computing the statistics over short signal segments (10 ms), Gaussian distributions were obtained at 10 and 36 MHz for both RBC suspension and whole blood experiments ($\hat{K}_u \approx 3.0$ and $\hat{m} \approx 1.0$). Increasing the frequency to 58 MHz modified the statistical nature of the rf backscattered signal to non-Gaussian distributions. By using time windows between 12 and 60 s (only the results for a window of 42 s were presented), a significant non-Gaussian behavior, highly emphasized at the beginning of the kinetics of aggregation, was observed at 36 and 58 MHz. Although attributed to the nonuniformity in backscattering cross sections or to some orderliness in the spatial arrangement of scatterers, it is clear from the results of the current study that the mechanisms of the non-Gaussian backscattering behavior at high frequency may deserve more attention. It was also shown that the K and Nakagami statistical distributions do not always adequately describe the ultrasound signals backscattered by normal human whole blood.

ACKNOWLEDGMENTS

The authors acknowledge Dr. Raymond Beaulieu of the Department of Hematology at the University of Montreal Hospital for providing the human blood samples. This work was supported by operating grants from the Institutes of Health Research of Canada (Grant No. MOP-36467) and the Heart and Stroke Foundation of Quebec, and by an equip-

ment grant from the Foundation of the University of Montreal Hospital (ultrasound biomicroscope). The salary of Dr. Guy Cloutier is partially supported by a National Scientist award of the Fonds de la Recherche en Santé du Québec.

[1] K. K. Shung and G. A. Thieme, *Ultrasonic Scattering in Biological Tissues*, edited by K. K. Shung and G. A. Thieme (CRC, Boca Raton, 1993).
[2] G. Cloutier and Z. Qin, ''Ultrasound backscattering from non-aggregating and aggregating erythrocytes-A review,'' Biorheology **34**, 443–470 (1997).
[3] F. S. Foster, H. Obara, T. Bloomfield, L. K. Ryan, and G. R. Lockwood, ''Ultrasound backscatter from blood in the 30 to 70 MHz frequency range,'' IEEE Ultrasonics Symposium Proceedings, 1994, Vol. 3, Nov. 1–4, Cannes, France, pp. 1599–1602.
[4] A. van Lewenhoek, ''Concerning the circulation and stagnation of the blood in tadpoles,'' Philos. Trans. R. Soc. London **22**, 447 (1702).
[5] R. Fahraeus, ''The suspension stability of the blood,'' Physiol. Rev. **IX**, 241–275 (1929).
[6] H. J. Meiselman, ''Red blood cell role in RBC aggregation: 1963–1993 and beyond,'' Clin. Hemorheol. **13**, 575–592 (1993).
[7] M. H. Knisely, E. H. Bloch, T. S. Eliot, and L. Warner, ''Sludged blood,'' Science **106**, 431–440 (1947).
[8] S. Chien, ''Blood viscosity: Influence of erythrocyte aggregation,'' Science **157**, 829–831 (1967).
[9] A. Chabanel, M. H. Horellou, J. Conard, and M. M. Samama, ''Red blood cell aggregability in patients with a history of leg vein thrombosis: influence of post-thrombotic treatment,'' Br. J. Haematol. **88**, 174–179 (1994).
[10] M. Cabel, H. J. Meiselman, A. S. Popel, and P. C. Johnson, ''Contribution of red blood cell aggregation to venous vascular resistance in skeletal muscle,'' Am. J. Physiol. **272**, H1020–H1032 (1997).
[11] M. J. Pearson and H. H. Lipowsky, ''Influence of erythrocyte aggregation on leukocyte margination in postcapillary venules of rat mesentery,'' Am. J. Physiol. **279**, H1460–H1471 (2000).
[12] J. J. Bishop, P. R. Nance, A. S. Popel, M. Intaglietta, and P. C. Johnson, ''Effect of erythrocyte aggregation on velocity profiles in venules,'' Am. J. Physiol. **280**, H222–H236 (2001).
[13] N. Maeda, ''Erythrocyte rheology in microcirculation,'' Jpn. J. Physiol. **46**, 1–14 (1996).
[14] C. Dupuy-Fons, J. F. Brun, F. Pellerin, J. C. Laborde, L. Bardet, A. Orsetti, and C. Janbon, ''Relationships between blood rheology and transcutaneous oxygen pressure in peripheral occlusive arterial disease,'' Clin. Hemorheol. **15**, 191–199 (1995).
[15] G. Cloutier, X. Weng, G. O. Roederer, L. Allard, F. Tardif, and R. Beaulieu, ''Differences in the erythrocyte aggregation level between veins and arteries of normolipidemic and hyperlipidemic individuals,'' Ultrasound Med. Biol. **23**, 1383–1393 (1997).
[16] R. Kuc, ''Ultrasonic tissue characterization using kurtosis,'' IEEE Trans. Ultrason. Ferroelectr. Freq. Control **UFFC-33**, 273–279 (1986).
[17] M. Evans, N. Hastings, and B. Peacock, Statistical Distributions, 3rd ed. (Wiley, New York, 2000).
[18] L. Weng, J. M. Reid, P. M. Shankar, and K. Soetanto, ''Ultrasound speckle analysis based on the *K* distribution,'' J. Acoust. Soc. Am. **89**, 2992–2995 (1991).
[19] J. F. Chen, J. A. Zagzebski, and E. L. Madsen, ''Non-Gaussian versus non-Rayleigh statistical properties of ultrasound echo signals,'' IEEE Trans. Ultrason. Ferroelectr. Freq. Control **41**, 435–441 (1994).
[20] P. M. Shankar, J. M. Reid, H. Ortega, C. W. Piccoli, and B. B. Goldberg, ''Use of non-Rayleigh statistics for the identification of tumors in ultrasonic B-scans of the breast,'' IEEE Trans. Med. Imaging **12**, 687–692 (1993).
[21] V. M. Narayanan, P. M. Shankar, and J. M. Reid, ''Non-Rayleigh statistics of ultrasonic backscattered signals,'' IEEE Trans. Ultrason. Ferroelectr. Freq. Control **41**, 845–852 (1994).
[22] R. C. Molthen, P. M. Shankar, J. M. Reid, F. Forsberg, E. J. Halpern, C. W. Piccoli, and B. B. Goldberg, ''Comparisons of the Rayleigh and *k*-distribution models using *in vivo* breast and liver tissue,'' Ultrasound Med. Biol. **24**, 93–100 (1998).
[23] P. M. Shankar, R. Molthen, V. M. Narayanan, J. M. Reid, V. Genis, F. Forsberg, C. W. Piccoli, A. E. Lindenmayer, and B. B. Goldberg, ''Studies of the use of non-Raleigh statistics for ultrasonic tissue characterization,'' Ultrasound Med. Biol. **22**, 873–882 (1996).
[24] I. Fontaine, G. Cloutier, and L. Allard, ''Non-Gaussian statistical property of the ultrasonic Doppler signal downstream of a severe stenosis,'' Ultrasound Med. Biol. **23**, 41–45 (1997).
[25] R. F. Wagner, M. F. Insana, and D. G. Brown, ''Unified approach to the detection and classification of speckle texture in diagnostic ultrasound,'' Opt. Eng. (Bellingham) **25**, 738–742 (1986).
[26] V. Dutt and J. F. Greenleaf, ''Ultrasound echo envelope analysis using a homodyned *K* distribution signal model,'' Ultrasonic Imaging **16**, 265–287 (1994).
[27] R. B. Cramblitt and K. J. Parker, ''Generation of Non-Rayleigh speckle distributions using marked regularity models,'' IEEE Trans. Ultrason. Ferroelectr. Freq. Control **46**, 867–874 (1999).
[28] P. M. Shankar, ''A general statistical model for ultrasonic backscattering from tissues,'' IEEE Trans. Ultrason. Ferroelectr. Freq. Control **47**, 727–736 (2000).
[29] D. Savéry and G. Cloutier, ''A point process approach to assess the frequency dependence of ultrasound backscattering by aggregating red blood cells,'' J. Acoust. Soc. Am. **110**, 3252–3262 (2001).
[30] I. Fontaine, D. Savéry, and G. Cloutier, ''Simulation of ultrasound backscattering by red cell aggregates: Effect of shear rate and anisotropy,'' Biophys. J. **82**, 1696–1710 (2002).
[31] Z. Qin, L. G. Durand, L. Allard, and G. Cloutier, ''Effects of a sudden flow reduction on red blood cell rouleau formation and orientation using rf backscattered power,'' Ultrasound Med. Biol. **24**, 503–511 (1998).
[32] D. W. Rickey, P. A. Picot, D. A. Christopher, and A. Fenster, ''A wall-less vessel phantom for Doppler ultrasound studies,'' Ultrasound Med. Biol. **21**, 1163–1176 (1995).
[33] L. L. Houbouyan, M. Delamaire, A. Beauchet, M. Gentil, G. Cauchois, A. Taccoen, J. P. Yvert, N. Montredon, M. F. Roudaut, S. Zhao, A. Goguel, G. Potron, M. Boisseau, and J. F. Stoltz, ''Multicenter study of an erythroaggregometer: quality control and standardization,'' Clin. Hemorheol. Microcirc. **17**, 299–306 (1997).
[34] P. J. Carreau, D. C. R. De Kee, and R. P. Chhabra, *Rheology of Polymeric Systems: Principles and Applications* (Hanser, Munich, 1997).
[35] X. Weng, G. Cloutier, P. Pibarot, and L. G. Durand, ''Comparison and simulation of different levels of erythrocyte aggregation with pig, horse, sheep, calf, and normal human blood,'' Biorheology **33**, 365–377 (1996).
[36] X. Weng, G. Cloutier, R. Beaulieu, and G. O. Roederer, ''Influence of acute-phase proteins on erythrocyte aggregation,'' Am. J. Physiol. **271**, H2346–H2352 (1996).
[37] K. K. Shung, Y. W. Yuan, D. Y. Fei, and J. M. Tarbell, ''Effect of flow disturbance on ultrasonic backscatter from blood,'' J. Acoust. Soc. Am. **75**, 1265–1272 (1984).
[38] K. K. Shung, G. Cloutier, and C. C. Lim, ''The effects of hematocrit, shear rate, and turbulence on ultrasonic Doppler spectrum from blood,'' IEEE Trans. Biomed. Eng. **39**, 462–469 (1992).
[39] G. R. Lockwood, L. K. Ryan, J. W. Hunt, and F. S. Foster, ''Measurement of the ultrasonic properties of vascular tissues and blood from 35–65 MHz,'' Ultrasound Med. Biol. **17**, 653–666 (1991).
[40] M. S. Van Der Heiden, M. G. M. De Kroon, N. Bom, and C. Borst, ''Ultrasound backscatter at 30 MHz from human blood: influence of rouleau size affected by blood modification and shear rate,'' Ultrasound Med. Biol. **21**, 817–826 (1995).
[41] V. Rouffiac, P. Péronneau, A. Hadengue, A. Barbet, P. Delouche, P. Dantan, N. Lassau, and J. Levenson, ''A new ultrasound principle for characterizing erythrocyte aggregation - In vitro reproducibility and validation,'' Invest. Radiol. **37**, 413–420 (2002).
[42] S. Y. Kim, I. F. Miller, B. Sigel, P. M. Consigny, and J. Justin, ''Ultrasonic evaluation of erythrocyte aggregation dynamics,'' Biorheology **26**, 723–736 (1989).
[43] I. Fontaine, and G. Cloutier, ''Modeling the frequency dependence (5–120 MHz) of ultrasound backscattering by red cell aggregates in shear flow at a normal hematocrit,'' J. Acoust. Soc. Am. **113**, 2893–2900 (2003).
[44] G. Cloutier and K. K. Shung, ''Study of red cell aggregation in pulsatile flow from ultrasonic Doppler power measurements,'' Biorheology **30**, 443–461 (1993).
[45] M. G. M. De Kroon, C. J. Slager, W. J. Gussenhoven, P. W. Serruys, J. R. T. C. Roelandt, and N. Bom, ''Cyclic changes of blood echogenicity in high-frequency ultrasound,'' Ultrasound Med. Biol. **17**, 723–728 (1991).
[46] V. M. Narayanan, R. Molthen, P. M. Shankar, L. Vergara, and J. M. Reid, ''Studies on ultrasonic scattering from quasi-periodic structures,'' IEEE Trans. Ultrason. Ferroelectr. Freq. Control **44**, 114–124 (1997).

Scatterer size estimation in pulse-echo ultrasound using focused sources: Theoretical approximations and simulation analysis

Timothy A. Bigelow and William D. O'Brien, Jr.[a)]
Bioacoustics Research Laboratory, Department of Electrical and Computer Engineering, University of Illinois, 405 North Mathews, Urbana, Illinois 61801

(Received 13 June 2003; revised 31 March 2004; accepted 12 April 2004)

The speckle in ultrasound images has long been thought to contain information related to the tissue microstructure. Many different investigators have analyzed the frequency characteristics of the backscattered signals to estimate the scatterer acoustic concentration and size. Previous work has been mostly restricted to unfocused or weakly focused ultrasound sources, thus limiting its implementation with diagnostically relevant fields. Herein, we derive equations capable of estimating the size of a scatterer for any reasonably focused source provided that the velocity potential field in the focal region can be approximated as a three-dimensional Gaussian beam, scatterers are a sufficient distance from the source, and the field is approximately constant across the scatterer. The calculations show that, when estimating the scatterer size, correcting for focusing requires a generalized attenuation-compensation function that includes both attenuation and focusing along the beam axis. The Gaussian approximation is validated by comparing the ideal velocity potential field for three spherically focused sources with *f*-numbers of 1, 2, and 4 to the Gaussian approximation for frequencies from 2 to 14 MHz. The theoretical derivations are evaluated by simulating the backscatter by using spherically focused sources (*f*-numbers of 1, 2, and 4) adjacent to attenuating media (0.05 to 1 dB/cm/MHz) that contain scatterers with Gaussian impedance distributions. The generalized attenuation-compensation function yielded results accurate to 7.2% while the traditional attenuation-compensation functions that neglected focusing had errors as high as 103%. [DOI: 10.1121/1.1757452]

PACS numbers: 43.80.Qf, 43.80.Vj [FD] Pages: 578–593

LIST OF SYMBOLS

a	aperture radius for a spherically focused source.
A_{comp}	generalized attenuation-compensation function including focusing effects along the beam axis.
a_{eff}	effective radius of scatterer.
a_{eff_j}	estimated effective radius of scatterer found from one set (i.e., 25 averaged rf echoes) of simulated backscatter waveforms.
$\overline{a}_{\text{eff}}$	mean value of estimated effective radius from all sets of simulated backscatter waveforms (i.e., $\overline{a}_{\text{eff}}=\Sigma_{\forall j}a_{\text{eff}_j}/\Sigma_{\forall j}j$).
A_{OO}	Oelze–O'Brien attenuation-compensation function.
A_{OM}	O'Donnell–Miller attenuation-compensation function.
A_{PC}	point attenuation-compensation function.
B_γ	correlation function related to field and scatterers.
c	small-signal sound speed of background medium.
F	focal length for a spherically focused source.
f	frequency.
$f\#$	*f*-number for a spherically focused source (i.e., $f\#=F/2a$).
$g(\vec{r}_d,\vec{r}')$	Green's function for the background medium containing the scatterers valid from the detector to the scattering region.
G_o, G_{o_trans}	geometric gain value on receive/transmit for velocity potential field at focus when W_{source} is approximated by a Gaussian (units of m).
G_T	dimensionless aperture gain function that accounts for the focusing of the ultrasound source.
g_{win}	windowing function used to gate the signal.
H	dimensionless filtering characteristics for the ultrasound source.
k	wave number in the scattering region, V' (i.e., $k=2\pi/\lambda$).
$\tilde{k}$	complex wave number of the background about the scatterers (i.e., $\tilde{k}=k+i\alpha$).
k_o	wave number in water.
K_{uV}	conversion constant relating voltage to particle velocity for ultrasound source (units of m/s V^{-1}).
L	total width of rectangular windowing function.
$\overline{n}$	average scatterer number density.
p_{inc}	pressure field incident on the scatterers.
p_s	scattered pressure field.
p_{tot}	total pressure field (i.e., $p_{\text{tot}}=p_s+p_{inc}$).

[a)]Author to whom all correspondence should be addressed. Electronic mail: wdo@uiuc.edu

$\vec{r},\vec{r}',\vec{r}''$ spatial locations in spherical coordinates.
$\Delta\vec{r},\vec{s}$ change of spatial variables [i.e., $\Delta\vec{r}=\vec{r}'-\vec{r}''$ and $\vec{s}=(\vec{r}'+\vec{r}'')/2$].
$\vec{r}_f$ locations on rigid reference plane in spherical coordinates.
$r_{\max}$ upper limit of integration when comparing Gaussian approximation to real source [i.e., $r_{\max}=12.5\cdot 0.51\lambda(f\#)$].
$\vec{r}_T,\vec{r}_d$ locations on aperture plane of transmitter/detector in spherical coordinates.
r_ρ coordinate distance away from beam axis (i.e., $r_\rho=\sqrt{x^2+y^2}$).
$R_{\gamma\gamma}$ autocorrelation function for the scatterer (i.e., $R_{\gamma\gamma}(\Delta\vec{r})=\mathrm{E}[\gamma(\vec{s}+\Delta\vec{r}/2)\gamma(\vec{s}-\Delta\vec{r}/2)]$).
$\Re_{\gamma\gamma}$ power spectral density function for the scatterer.
S_f rigid plane near focal plane used to acquire reference waveform.
S_T aperture area of ultrasound transmitter.
T_{win} total width of rectangular windowing function applied to time-domain waveform (i.e., $T_{win}=2L/c$).
u_z particle velocity perpendicular to aperture plane of ultrasound transmitter/detector.
V' volume containing scatterers contributing to the scattered signal.
V_{inc} voltage applied to the ultrasound source during transmit.
V_{plane} voltage from ultrasound source due to the backscatter from rigid plane near focus.
V_{refl} voltage from ultrasound source due to the backscatter from scatterers.
V_s average scatterer volume.
W_{source} geometric falloff of field intensity in focal region (units of m^2).
w_x,w_y,w_z equivalent Gaussian dimensions on receive of velocity potential field in focal region.
$w_{x\_trans},w_{y\_trans},$ w_{z_trans} equivalent Gaussian dimensions on transmit of velocity potential field in focal region.
z_f distance of rigid plane used to acquire reference waveform to the focal plane.
z_o the shift of the focus away from the theoretical location at a particular frequency.
z_T,z_d distance of aperture plane of the ultrasound transmitter/detector to the focal plane.
z_{trans} distance from transmit focus to receive focus.
α attenuation in the scattering region, V'.
α_{eff} effective attenuation for all tissue between focal plane and aperture plane (i.e., total attenuation along beam axis $=\alpha_{\mathrm{eff}}z_T$).
γ combined perturbation of density and compressibility [i.e., $\gamma(\vec{r})=\gamma_\kappa(\vec{r})-\gamma_\rho(\vec{r})$].
γ_o mean squared variation in acoustic impedance per scatterer.
γ_κ local perturbation in the compressibility due to the scatterers [i.e., $\gamma_\kappa(\vec{r})=[\kappa_s(\vec{r})-\kappa]/\kappa$].
γ_ρ local perturbation in the density due to the scatterers [i.e., $\gamma_\rho(\vec{r})=\rho_s(\vec{r})-\rho/\rho_s(\vec{r})$].
κ compressibility of background medium surrounding scatterers.
κ_s compressibility of scatterers.
ϕ_{real} velocity potential field for real source (i.e., not approximate three-dimensional Gaussian distribution).
λ wavelength.
λ_o the wavelength corresponding to the spectral peak from the reference spectrum (i.e., V_{plane}) used to calculate the depth of focus for the transducer.
ρ density of background medium surrounding scatterers.
ρ_o density of water.
ρ_s density of scatterers.
σ_{lower} percent deviation in values of scatterer size for sizes smaller than the mean size (i.e., $a_{\mathrm{eff}_j}<\overline{a_{\mathrm{eff}}}$).
σ_{upper} percent deviation in values of scatterer size for sizes larger than the mean size (i.e., $a_{\mathrm{eff}_j}>\overline{a_{\mathrm{eff}}}$).
ω radian frequency.

I. INTRODUCTION

One of the distinguishing features of backscattered waveforms returned from biological tissue is the scattering observed within homogeneous tissues between the tissue boundaries. These signals have long been thought to contain information related to the tissue microstructure.[1–6] In order to extract microstructure information, models have been developed to elucidate scattering details. By fitting the measured backscattered data to the model, structural characteristics of the tissue, such as mean scatterer size and acoustic concentration (acoustical impedance of the scatterer multiplied by the number of density scatterers in the region), can be estimated.[4–7] Determining either of these quantities accurately and precisely is hypothesized to improve the diagnostic potential of medical ultrasound by allowing for quantitative measurements to be made of the underlying scattering structure of the tissue that could then be correlated with tumor morphology.[7]

Most of the previous models have assumed plane waves incident on the scattering region (i.e., inside focal zone of weakly focused source) while only considering diffraction effects in the transverse plane.[3–5] Diffraction effects along the beam axis have been neglected. Other authors included a complete Green's function description of the source when determining the scattered field.[8–12] In their calculations, they assumed that the excitation across the entire surface of the source was known or could be accurately determined. They also assumed that the scatterers were a sufficient distance from the source, and the field was approximately constant across the scatterer. Unfortunately, the resulting equations were cumbersome, requiring a precise knowledge of the source's excitation in order to solve for the required fields. As a result, it is difficult to use their results when experimentally calibrating a focused source for the purpose of estimat-

ing scatterer size. Furthermore, their analysis still does not provide analytical insight into the effects of beam diffraction. Recently, Gerig *et al.*[13] proposed using a reference phantom to obtain a reference spectrum that could potentially account for focusing. However, the ability of the reference phantom technique to correct for focusing has not been fully evaluated, and the reference phantom technique still does not provide any analytical insight.

Due to these limitations most investigators only use large *f*-number transducers in their backscatter analyses where diffraction effects along the beam axis can be neglected over the size of the region of interest (i.e., time-gated region). Reducing the length of the time gate to allow for smaller *f*-number transducers is not feasible because both the accuracy and precision of the scatterer size estimates degrade when the window length is too small. This is potentially restrictive in diagnostic imaging systems where smaller *f*-numbers may be desirable to improve the spatial resolution of the parametric image. Hence, the purpose of our work is to allow for the use of focused sources when quantifying the backscattered ultrasound waveforms regardless of the size of the gated region.

In this paper, we re-derive the expected backscattered signal from a region of randomly positioned identical scatterers without the plane wave approximation. Instead, we assume that the velocity potential field near the focus can be accurately modeled as a three-dimensional Gaussian beam while continuing to assume that the scatterers are a sufficient distance from the source, and the field is approximately constant across the scatterer. Then, the validity of the Gaussian approximation of the field is assessed by comparing the approximation to calculations of the velocity potential field from ideal spherically focused sources. Based on our theoretical approximations, we then generate computer simulations to aid in the understanding of the impact of diffraction along the beam axis. Specifically, the computer simulations quantify the effect of varying tissue attenuation as well as assess the accuracy and precision of the scatterer size estimator for a focused source. Simulations are also performed to validate the three-dimensional Gaussian beam approximation for spherically focused sources. Finally, we discuss some of the implications of our results.

II. THEORETICAL DEVELOPMENTS

In this section of the paper, we re-derive the expected backscattered voltage spectrum from a region of randomly positioned uniform scatterers (i.e., same size and shape) and from a rigid plane (a reference) upon being exposed to a focused ultrasound field assuming linear acoustics. The goal of our analysis is to provide insight into the effects of focusing along the beam axis as well as provide useful equations that are easily implemented by future investigators. The coordinate system for our derivations has the origin at the focus of the ultrasound field with the beam axis lying along the z axis and the source positioned at $z_T>0$ (Fig. 1). Although the initial equations can be found in the previously published literature, we have elected to include them in this work because the notation used to denote the variables varies between publications.[4,8,14] In addition, it is critical to the understanding of the derived equations that all of the assumptions made during the derivation be clearly known. Otherwise, the derived equations may not be appropriately applied in the future.

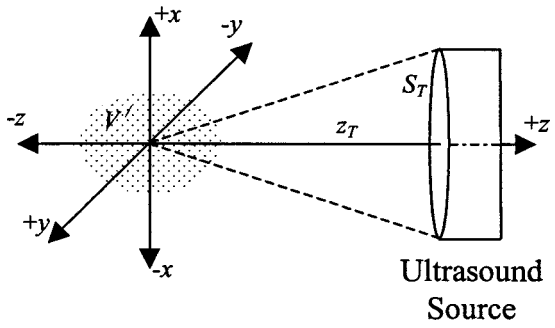

FIG. 1. Coordinate system for theoretical derivations.

A. Derivation of backscattered voltage from scatterers

From a Green's function analysis, it can be shown that the scattered field from the particles at some detector location should be given by[14]

$$p_s(\vec{r}_d)=\int\int_{V'}\int \{\tilde{k}^2\gamma_\kappa(\vec{r}')p_{\text{tot}}(\vec{r}')g(\vec{r}_d,\vec{r}') + \gamma_\rho(\vec{r}')\nabla' p_{\text{tot}}(\vec{r}')\cdot\nabla' g(\vec{r}_d,\vec{r}')\}\,d\vec{r}'. \tag{1}$$

If we assume that the fluctuations in κ and ρ are small throughout the background region, then $g(\vec{r}_d,\vec{r}')$ is approximated by the homogeneous Green's function given by

$$g(\vec{r}_d,\vec{r}')\cong\frac{1}{4\pi}\frac{e^{i\tilde{k}|\vec{r}_d-\vec{r}'|}}{|\vec{r}_d-\vec{r}'|}. \tag{2}$$

To simplify Eq. (1), we assume that the scatterers satisfy the Born approximation,[3,4] so that p_{tot} can be replaced by only the incident field on the scatterers given by[14]

$$p_{inc}(\vec{r}')=-2i\omega\rho\int\int_{S_T} u_z(\vec{r}_T)g(\vec{r}',\vec{r}_T)\,d\vec{r}_T. \tag{3}$$

Substituting Eqs. (2) and (3) into Eq. (1) then yields

$$p_s(\vec{r}_d)=-2i\omega\rho\int\int_{S_T}d\vec{r}_T\int\int_{V'}\int\left\{\begin{matrix}\tilde{k}^2\gamma_\kappa(\vec{r}')u_z(\vec{r}_T)g(\vec{r}',\vec{r}_T)g(\vec{r}_d,\vec{r}')\\ +\gamma_\rho(\vec{r}')u_z(\vec{r}_T)\nabla' g(\vec{r}',\vec{r}_T)\cdot\nabla' g(\vec{r}_d,\vec{r}')\end{matrix}\right\}d\vec{r}'. \tag{4}$$

Equation (4) can be further simplified assuming that the dimensions of the scattering region are small compared to its distance from the source and detector. This can be expressed mathematically as[14]

$$|\vec{r}_T-\vec{r}'|\cong r_T-\frac{\vec{r}_T}{r_T}\cdot\vec{r}',$$
$$|\vec{r}_d-\vec{r}'|\cong r_d-\frac{\vec{r}_d}{r_d}\cdot\vec{r}'. \tag{5}$$

The validity of this approximation increases with decreasing window length used to gate the signal in the time domain (i.e., artificial decrease in the size of the scattering region), with increasing focusing (i.e., decreasing *f*-number), and with increasing focal length. If we also assume that the source and detector are in approximately the same direction (i.e., different elements on the same source so that angle dependence of the backscatter can be neglected), then

$$\left(\frac{\vec{r}_d\cdot\vec{r}_T}{r_d r_T}\right)\approx 1. \tag{6}$$

Similar approximations to those given in Eqs. (5) and (6) were also made by Madsen *et al.*[8] Using these approximations and solving for the gradient of the Green's function results in the scattered pressure field being approximately given by

$$p_s(\vec{r}_d)=(-2i\omega\rho)\left(\frac{\tilde{k}}{4\pi}\right)^2\frac{e^{i\tilde{k}r_d}}{r_d}\int\int_{S_T}d\vec{r}_T \times\left(u_z(\vec{r}_T)\frac{e^{i\tilde{k}r_T}}{r_T}\int\int\int_{V'}d\vec{r}'\,\gamma(\vec{r}')\times e^{-i\tilde{k}\vec{r}'\cdot(\vec{r}_d/r_d\vec{r}_T/r_T)}\right). \tag{7}$$

Now that we know the scattered field within the bounds of our assumptions at some detector location, we need to translate it into the voltage output by the transducer. Hence, we assume that the voltage across the transducer is directly related to the normal particle velocity at the aperture plane according to the relations

$$u_z(\vec{r}_T,\omega)=K_{uV}(\omega)V_{inc}(\omega)G_T(\vec{r}_T,\omega)H(\omega),$$
$$V_{refl}(\omega)=\frac{H(\omega)}{S_T K_{uV}(\omega)}\int\int_{S_T}d\vec{r}_d u_z(\vec{r}_d,\omega)G_T(\vec{r}_d,\omega). \tag{8}$$

The focusing ability of the source (i.e., concavity of the aperture) is captured by the spatially varying complex gain term, $G_T(\vec{r}_T,\omega)$, defined at the aperture plane. Combining Eqs. (7) and (8), while assuming that $z_d\cong r_d$ for amplitude terms, yields

$$V_{refl}(\omega)=\frac{H(\omega)}{i\omega\rho S_T K_{uV}(\omega)}\int\int_{S_T}d\vec{r}_d G_T(\vec{r}_d,\omega)\frac{\partial p_s(\vec{r}_d)}{\partial z_d}$$
$$\cong\frac{V_{inc}(\omega)H^2(\omega)(-2i\tilde{k})(\tilde{k}/4\pi)^2}{S_T}\times\int\int\int_{V'}d\vec{r}'[\gamma(\vec{r}')W_{source}(\tilde{k},\vec{r}')], \tag{9}$$

where

$$W_{source}(\tilde{k},\vec{r}')=\left(\int\int_{S_T}d\vec{r}_T G_T(\vec{r}_T,\omega)\frac{e^{i\tilde{k}r_T-i\tilde{k}\vec{r}'\cdot\vec{r}_T/r_T}}{r_T}\right)^2. \tag{10}$$

Equations (9) and (10) are valid for any source provided that the scattering region is a reasonable distance from the source [i.e., Eqs. (5) and (6) valid]. We can simplify our analysis by assuming that the ultrasound source produces a velocity potential field with a three-dimensional Gaussian distribution. As a result, Eq. (10) can be rewritten as

$$W_{source}(\tilde{k},\vec{r}')\cong(G_o e^{-((x'/w_x(\lambda))^2+(y'/w_y(\lambda))^2+(z'/w_z(\lambda))^2)})^2\times e^{i2\tilde{k}(z_T-z')}. \tag{11}$$

Now that the scattered field at the detector location has been found given a known arrangement of scatterers, $\gamma(\vec{r}')$, the analysis needs to be extended for multiple randomly oriented scatterers. Consider the second moment of the received voltage given by

$$E[V_{refl}(\omega)V^*_{refl}(\omega)]=4\left|\frac{\tilde{k}}{S_T}\right|^2\left|\frac{\tilde{k}}{4\pi}\right|^4|H(\omega)|^4|V_{inc}(\omega)|^2\int\int\int_{V'}d\vec{r}'\left(\int\int\int_{V'}d\vec{r}''\begin{pmatrix}W_{source}(\tilde{k},\vec{r}')W^*_{source}(\tilde{k},\vec{r}'')\\ E[\gamma(\vec{r}')\gamma(\vec{r}'')]\end{pmatrix}\right)$$
$$=4G_o^4\left|\frac{\tilde{k}}{S_T}\right|^2\left|\frac{\tilde{k}}{4\pi}\right|^4|H(\omega)|^4|V_{inc}(\omega)|^2e^{-4\alpha_{\text{eff}}z_T}\int\int\int_{V'}d\vec{r}' \times\left(\int\int\int_{V'}d\vec{r}''\begin{pmatrix}e^{-2(((x'^2+x''^2)/w_x^2)+((y'^2+y''^2)/w_y^2)+((z'^2+z''^2)/w_z^2))}\\ E[\gamma(\vec{r}')\gamma(\vec{r}'')]e^{-2ik(z'-z'')+2\alpha(z'+z'')}\end{pmatrix}\right), \tag{12}$$

where "*" is the complex conjugate and E[~] denotes expected value.[15] If we then perform the change of variables letting $\Delta\vec{r}=\vec{r}'-\vec{r}''$ and $\vec{s}=(\vec{r}'+\vec{r}'')/2$ as was done by Insana *et al.*,[4] Eq. (12) becomes

$$\mathrm{E}[|V_{refl}(\omega)|^2]=4G_o^4\left|\frac{\tilde{k}}{S_T}\right|^2\left|\frac{\tilde{k}}{4\pi}\right|^4|H(\omega)|^4|V_{inc}(\omega)|^2 \times \mathrm{e}^{-4\alpha_{\mathrm{eff}}z_T}\int\int_{V'}\int d\Delta\vec{r} \times(\mathrm{e}^{-((\Delta r_x^2/w_x^2)+(\Delta r_y^2/w_y^2)+(\Delta r_z^2/w_z^2))} \times \mathrm{e}^{-2ik\Delta r_z}B_\gamma(\Delta\vec{r})), \quad (13)$$

where

$$B_\gamma(\Delta\vec{r})=\int\int_{V'}\int d\vec{s}\left(\mathrm{E}\left[\gamma\left(\vec{s}+\frac{\Delta\vec{r}}{2}\right)\gamma\left(\vec{s}-\frac{\Delta\vec{r}}{2}\right)\right] \times \mathrm{e}^{-4((s_x^2/w_x^2)+(s_y^2/w_y^2)+(s_z^2/w_z^2))}e^{4\alpha s_z}\right). \quad (14)$$

Equation (14) can be further simplified by making some reasonable assumptions about the scatterers. If γ is weakly stationary within the scattering volume, then the autocorrelation function $E[\gamma(\vec{s}+\Delta\vec{r}/2)\gamma(\vec{s}-\Delta\vec{r}/2)]$ depends only on the separation between the points being correlated, $\Delta\vec{r}$, and is negligible for $\Delta\vec{r}$ larger than the size of the scatterers.[4] Furthermore, because the scatterers are typically much smaller than the focal dimensions, we can make the approximation that the amplitude of the field is constant across each individual scatterer, or $\mathrm{e}^{-((\Delta r_x^2/w_x^2)+(\Delta r_y^2/w_y^2)+(\Delta r_z^2/w_z^2))}\approx 1$, an approximation also made by Madsen *et al.*[8] This approximation restricts our theory to subresolution scatterers. Lastly, if we assume that the beam width in the focal plane (i.e., w_x and w_y) is much smaller than the width of the scattering region so that the integration in the focal plane can be extended to infinity, then Eq. (13) becomes

$$E[|V_{refl}(\omega)|^2]=4G_o^4\left|\frac{\tilde{k}}{S_T}\right|^2\left|\frac{\tilde{k}}{4\pi}\right|^4|H(\omega)|^4|V_{inc}(\omega)|^2\mathrm{e}^{-4\alpha_{\mathrm{eff}}z_T}\left(\begin{array}{l}\int\int_{V'}\int d\Delta\vec{r}(\mathrm{e}^{-2ik\Delta r_z}R_{\gamma\gamma}(\Delta\vec{r}))\\ \int\int_{V'}\int d\vec{s}(\mathrm{e}^{-4((s_x^2/w_x^2)+(s_y^2/w_y^2)+(s_z^2/w_z^2))}\mathrm{e}^{4\alpha s_z})\end{array}\right)$$

$$=4G_o^4\left|\frac{\tilde{k}}{S_T}\right|^2\left|\frac{\tilde{k}}{4\pi}\right|^4|H(\omega)|^4|V_{inc}(\omega)|^2\mathrm{e}^{-4\alpha_{\mathrm{eff}}z_T}\Re_{\gamma\gamma}(2k\hat{z})\left(\frac{w_xw_y\pi}{4}\right)\left(\int_{V'}ds_z\mathrm{e}^{-4(s_z^2/w_z^2)}\mathrm{e}^{4\alpha s_z}\right), \quad (15)$$

where, for Gaussian spheres and spherical shells, $\Re_{\gamma\gamma}$ is given by[4]

$$\Re_{\gamma\gamma}(2k\hat{z})=\begin{cases}\overline{n}V_s^2\gamma_o^2\left[\dfrac{\sin(2ka_{\mathrm{eff}})}{2ka_{\mathrm{eff}}}\right]^2 & (Shell),\\ \overline{n}V_s^2\gamma_o^2\mathrm{e}^{-0.827k^2a_{\mathrm{eff}}^2} & (Gaussian).\end{cases} \quad (16)$$

At this point, we can consider the effects of windowing in the time domain. Windowing, to a first-order approximation, causes a blurring (i.e., convolution) of the spectrum in the frequency domain and eliminates the contribution of scatterers a distance from the focus greater than the window length along the beam axis (i.e., the s_z integration). The impact of the convolution on the estimate of scatterer size is only significant at small window lengths as has been addressed by previous authors.[16] As a result, we will only consider the elimination of scatterers by the window. Hence, Eq. (15) becomes

$$\mathrm{E}[|V_{refl}(\omega)|^2]=\frac{4G_o^4|\tilde{k}|^6|H(\omega)|^4|V_{inc}(\omega)|^2}{(4\pi)^4S_T^2A_{comp}(\omega)}\left(\frac{w_xw_y\pi}{4}\right) \times\Re_{\gamma\gamma}(2k\hat{z}), \quad (17)$$

where

$$A_{comp}(\omega)=\frac{\mathrm{e}^{4\alpha_{\mathrm{eff}}z_T}}{(\int_{-L/2}^{L/2}ds_z\,g_{win}(s_z)\mathrm{e}^{-4(s_z^2/w_z^2)}\mathrm{e}^{4\alpha s_z})}. \quad (18)$$

Equations (17) and (18) are applicable for any type of windowing function, g_{win}, and Eq. (18) is a generalized attenuation-compensation function that includes attenuation, windowing, and focusing. If, for example, we let $w_z\to\infty$ (i.e., remove focusing along the beam axis) and use a rectangular windowing function, then Eq. (18) becomes

$$A_{OM}(\omega)=\frac{4\alpha\mathrm{e}^{4\alpha_{\mathrm{eff}}z_T}}{\mathrm{e}^{4\alpha L/2}-\mathrm{e}^{-4\alpha L/2}}, \quad (19)$$

which is the O'Donnell–Miller attenuation-compensation

function.[17] Hence, the O'Donnell–Miller attenuation-compensation function neglects the natural falloff of the field, increasing the evaluation of the integral in Eq. (18) and subsequently undercompensating for the attenuation. As a result, O'Donnell–Miller compensation should result in an overestimate of the scatterer size because the values at higher frequencies are smaller than they should be due to the uncompensated attenuation. Likewise, if we neglect all field variations in the scattering region, Eq. (18) becomes

$$A_{PC}(\omega)=\frac{e^{4\alpha_{\text{eff}}z_T}}{L}, \tag{20}$$

which is the point compensation.[18] Point compensation will either under- or overestimate the scatterer size depending upon the relative importance of diffraction (w_z term) and attenuation (α term) due to the sign difference in the integrand of Eq. (18).

In our derivation of Eqs. (17) and (18), we assumed that the transmit and receive foci were at the same location. In diagnostically relevant fields, however, the two foci often occur at different locations due to the smaller number of foci used on transmit. When the two foci are at different locations, Eq. (11) becomes

$$W_{source}(\tilde{k},\vec{r}\,')\cong(G_o e^{-((x'/w_x)^2+(y'/w_y)^2+(z'/w_z)^2)})(G_{o\_trans}e^{-((x'/w_{x\_trans})^2+(y'/w_{y\_trans})^2+(z'-z_{trans})/w_{z\_trans})^2})e^{i2\tilde{k}(z_T-z')}. \tag{21}$$

As a result, Eqs. (17) and (18) become

$$\mathrm{E}[|V_{refl}(\omega)|^2]=\frac{2G_{o\_trans}^2G_o^2|\tilde{k}|^6|H(\omega)|^4|V_{inc}(\omega)|^2}{(4\pi)^4S_T^2A_{comp}(\omega)}\times\left(\frac{\pi w_x w_{x\_trnas}w_y w_{y\_trans}}{\sqrt{(w_{x\_trans}^2+w_x^2)(w_{y\_trans}^2+w_y^2)}}\right)\times\Re_{\gamma\gamma}(2k\hat{z}) \tag{22}$$

and

$$A_{comp}(\omega)=\frac{e^{4\alpha_{\text{eff}}z_T}}{(\int_{-L/2}^{L/2}ds_z g_{win}(s_z)e^{-2(s_z^2/w_z^2+(s_z-z_{trans})^2/w_{z\_trans}^2)+4\alpha s_z})}. \tag{23}$$

Hence, our analysis can be easily extended to diagnostically relevant fields even though we restrict our attention to sources with a single transmit and receive focus in the remainder of this paper.

B. Derivation of backscattered voltage from rigid plane near focus

In this section, we derive the received voltage for scattering sound off of a rigid plane located near the focal plane due to its popularity as a method for obtaining a reference.[3,4,6,8] We can solve for the received voltage by treating the reflected field at the rigid plane as a virtual source. Hence, the reflected field at the aperture of the transducer is given by

$$p_{plane}(\vec{r}_d,\omega)=-2i\omega\rho_o\int\int_{S_f}d\vec{r}_f u_z(\vec{r}_f)\frac{e^{ik_o r_d}}{4\pi r_d}e^{-ik_o(\vec{r}_d/r_d)\vec{r}_f}, \tag{24}$$

where

$$u_z(\vec{r}_f)=\frac{-2ik_oK_{uV}(\omega)V_{inc}(\omega)H(\omega)}{4\pi}\int\int_{S_T}d\vec{r}_T G_T(\vec{r}_T,\omega)\times\frac{e^{ik_o r_T-ik_o\vec{r}_f\cdot(\vec{r}_T/r_T)}}{r_T}. \tag{25}$$

As a result, the received voltage detected by the source is given by

$$V_{plane}(\omega)=\frac{-4k_o^2V_{inc}(\omega)H^2(\omega)}{S_T(4\pi)^2}\int\int_{S_f}d\vec{r}_f\times\left(\int\int_{S_T}d\vec{r}_d G_T(\vec{r}_d,\omega)\frac{e^{ik_o r_d-ik_o\vec{r}_f\vec{r}_d/r_d}}{r_d}\right)^2. \tag{26}$$

Likewise, if we again assume the velocity potential field near the focus has a three-dimensional Gaussian distribution, then Eq. (26) becomes

$$\begin{aligned}V_{plane}(\omega)&=\frac{-4k_o^2V_{inc}(\omega)H^2(\omega)}{S_T(4\pi)^2}e^{i2k_o(z_T-z_f)}e^{-2(z_f/w_z)^2}\times\int\int_{S_f}d\vec{r}_f(G_o e^{-(x_f/w_x)^2-(y_f/w_y)^2})^2\\&=\frac{-2\pi w_x w_y k_o^2G_o^2V_{inc}(\omega)H^2(\omega)}{S_T(4\pi)^2}\times e^{i2k_o(z_T-z_f)}e^{-2(z_f/w_z)^2}.\end{aligned} \tag{27}$$

Based on Eq. (27), the expected normalized backscatter is then given by

$$\frac{\mathrm{E}[|V_{refl}(\omega)|^2]}{|V_{plane}(\omega)|^2} = \frac{|\tilde{k}|^6 \mathrm{e}^{4(z_f/w_z)^2}}{4\pi w_x w_y k_o^4} \frac{\Re_{\gamma\gamma}(2k\hat{z})}{A_{comp}(\omega)}$$

$$\propto k_o^4 \mathrm{e}^{4(z_f/w_z)^2} \frac{\Re_{\gamma\gamma}(2k\hat{z})}{A_{comp}(\omega)}, \tag{28}$$

where the k_o^4 dependence results from both w_x and w_y being proportional to λ. Equation (28) can then be solved to yield the scatterer size, given that the form of $\Re_{\gamma\gamma}$ is known, using standard techniques that minimize the squared error in the log domain assuming that both the sound speed and the attenuation of the medium are known.[4] Notice that focusing along the beam axis introduces the error term $\mathrm{e}^{4z_f^2/w_z^2}$ whenever the plane is not placed exactly at the focus. However, the experimental error in positioning the plane also scales with w_z, so there is no calibration advantage in using larger *f*-number transducers.

III. VALIDATION OF GAUSSIAN APPROXIMATION

The theoretical derivations in the previous section were simplified by assuming that the velocity potential field for a focused source could be accurately approximated by a three-dimensional Gaussian in the focal region. However, the validity of this approximation needs to be addressed before the derived generalized attenuation-compensation function can be applied. In this section of the paper, the Gaussian approximation is compared to a complete velocity potential field (i.e., complete field) as computed from an established code.[19] The complete field was calculated for spherically focused transducers with *f*-numbers of 1, 2, and 4 and diameters of 5, 2.5, and 1.25 cm, respectively, at frequencies from 2 to 14 MHz in steps of 1 MHz. For each source at each frequency, the field was calculated on a rectangular grid corresponding to a single slice through the cylindrically symmetric field extending from 4 to 6 cm from the aperture plane of the source along the beam axis (theoretical focal length for all sources was 5 cm) and radially 2 cm off of the beam axis using a grid spacing of 10 μm. The medium in which the field was calculated was lossless and had a sound speed of 1540 m/s.

After calculating the complete field for each source at each frequency, the Gaussian approximation was compared to the complete field by calculating the percent difference as given by

$$\%Difference = 100 \cdot \frac{\int_{-L/2}^{L/2}\int_0^{r_{\max}}((\phi_{real}(\lambda)/\max(\phi_{real}(\lambda_o)))^2 - e^{-2((r'_\rho/w_x(\lambda))^2+(z'/w_z(\lambda))^2)})^2 r'_\rho\, dr'_\rho\, dz'}{\int_{-L/2}^{L/2}\int_0^{r_{\max}}(\phi_{real}(\lambda)/\max(\phi_{real}(\lambda_o)))^4 r'_\rho\, dr'_\rho\, dz'}, \tag{29}$$
V' V'

where the limits of integration were set by using a window length of $L=13$ mm and $r_{\max}=12.5\cdot 0.51\lambda(f\#)$ for each source and frequency. Also, λ_o was the wavelength corresponding to 8 MHz, and the "focus" at which the Gaussian approximation was centered (i.e., $x'=y'=z'=0$) was defined to be location at which $\phi_{real}(\lambda_o)$ was maximum for each source. Notice that $r_{\max}$ is 12.5 times the -3 dB radius of the beam intensity in the focal plane[20] for each frequency. The values of w_x (same as w_y for cylindrically symmetric sources) and w_z used in Eq. (29) for the Gaussian approximation were given by

$$w_x = w_y = 0.87\lambda f\#, \tag{30}$$

$$w_z = 6.01\lambda(f\#)^2.$$

Equations (30) result from matching the -3 dB transmit beamwidth as given by Kino [20] (i.e., $1.02\lambda f\#$ and $7.08\lambda f\#^2$) to the corresponding Gaussian beamwidth as was done for $w_{x,y}$ by Barber.[21]

The double integral in Eq. (29) was evaluated using the double integration function in MATLAB based on the adaptive-recursive Newton-Cotes eight-panel rule where ϕ_{real} values away from the grid points were linearly extrapolated from the closest grid values. In addition to calculating the percent differences according to Eq. (29), the percent differences were also calculated from

$$\%Difference = 100 \cdot \frac{\int_{-L/2}^{L/2}((\phi_{real}(\lambda)/\max(\phi_{real}(\lambda_o)))^2 - e^{-2(z'/w_z(\lambda))^2})^2\, dz'}{\int_{-L/2}^{L/2}(\phi_{real}(\lambda)/\max(\phi_{real}(\lambda_o)))^4\, dz'}, \tag{31}$$
V' V'

also using an L of 13 mm due to the importance of Gaussian approximation of the field along the beam axis in the equation for the generalized attenuation-compensation function.

The percent differences from Eqs. (29) and (31) for all three sources at each frequency are given in Fig. 2. The percent differences calculated over the entire field [i.e., from Eq. (29)] are always less than 18.75%, indicating that assuming the velocity potential field is a three-dimensional Gauss-

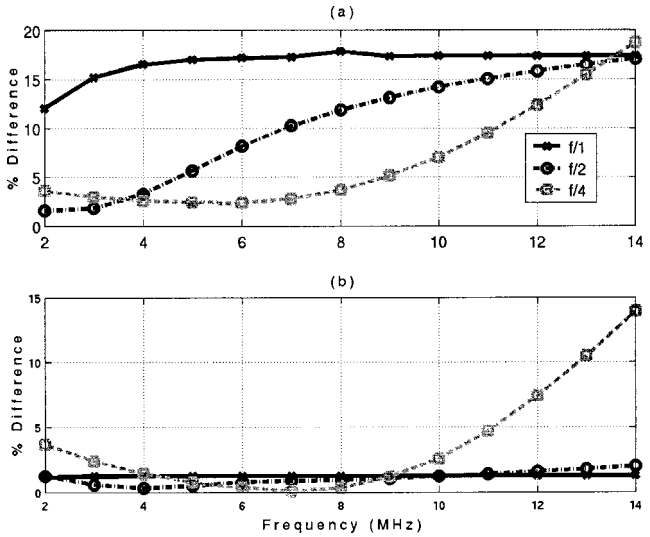

FIG. 2. The percent differences between the complete field and the Gaussian approximation for spherically focused transducers with *f*-numbers of 1, 2, and 4 for frequencies from 2 to 14 MHz calculated using (a) Eq. (29) and (b) Eq. (31).

ian distribution is a reasonable approximation. However, before concluding, the differences between the real and Gaussian fields were explored in greater detail. The percent differences calculated from Eqs. (29) and (31) both exhibit a large increase after a frequency of 8 MHz for the $f/4$ transducer. However, the percent differences from both equations for the $f/1$ transducer are relatively constant with frequency with the results from Eq. (29) plateauing at ~18%. Likewise, the percent differences for the $f/2$ transducer as given by Eq. (29) also seem to approach a plateau of ~18% while the percent differences from Eq. (31) are relatively constant with frequency. Hence, the percent differences for the $f/4$ transducer are probably related to errors in the approximation along the beam axis, z axis, whereas the differences for the $f/1$ and $f/2$ transducers are probably more related to other errors in the approximation (i.e., possibly side lobes).

In order to investigate the errors in the approximation in greater detail, the normalized complete field intensity [i.e., $(\phi_{real}(\lambda)/\max_{V'}(\phi_{real}(\lambda_o)))^2$] and the accompanying Gaussian approximation were plotted for the beam axis (i.e., z axis) and the beamwidth axis (i.e., r_ρ axis) for each of the transducers for frequencies of 4, 8, and 12 MHz as shown in Figs. 3, 4, and 5. For all three transducers and all three frequencies, the Gaussian approximation is in good agreement with the complete field intensity along the beamwidth axis with only a slight discrepancy in the peak value for the $f/4$ transducer at 4 and 12 MHz. Likewise, the agreement is good along the beam axis for the $f/2$ and $f/1$ transducers for all three frequencies as well as for the $f/4$ transducer at 8 MHz. However, the Gaussian approximation differs significantly from the complete field for the $f/4$ transducer at frequencies of 4 and 12 MHz. The discrepancy for the $f/4$ transducer is due to the location of the maximum field intensity (i.e., focus) changing with transmitted frequency whereas the basic Gaussian approximation assumes that the location is independent of frequency. The effects of the shift of the focus are more pronounced at the higher frequency [i.e., Fig. 5(c)] due to the smaller depth of focus. In addition, the shift of the focus is also responsible for the change in the maximum value of field intensity (i.e., G_o^2) with frequency because matching the peak intensities for the real and Gaussian approximation results in an ideal G_o given by

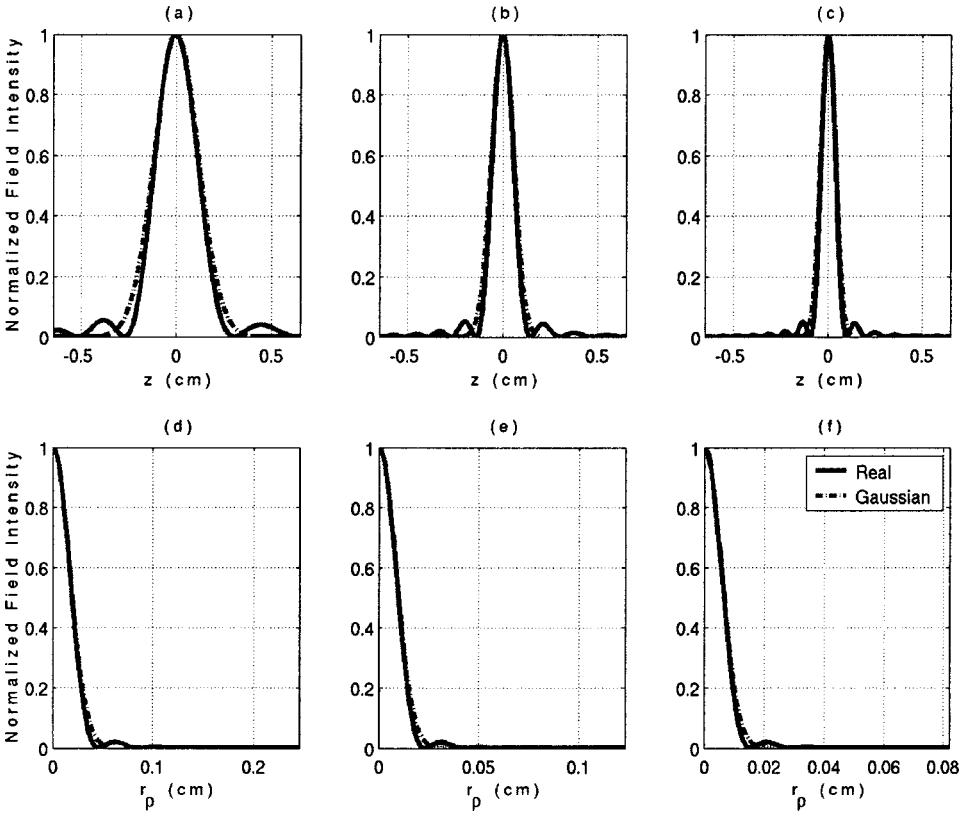

FIG. 3. Plots showing the normalized complete field intensity with the accompanying Gaussian approximation for the z axis at frequencies of (a) 4 MHz, (b) 8 MHz, and (c) 12 MHz as well as the r_ρ axis at frequencies of (d) 4 MHz, (e) 8 MHz, and (f) 12 MHz for an $f/1$ spherically focused transducer.

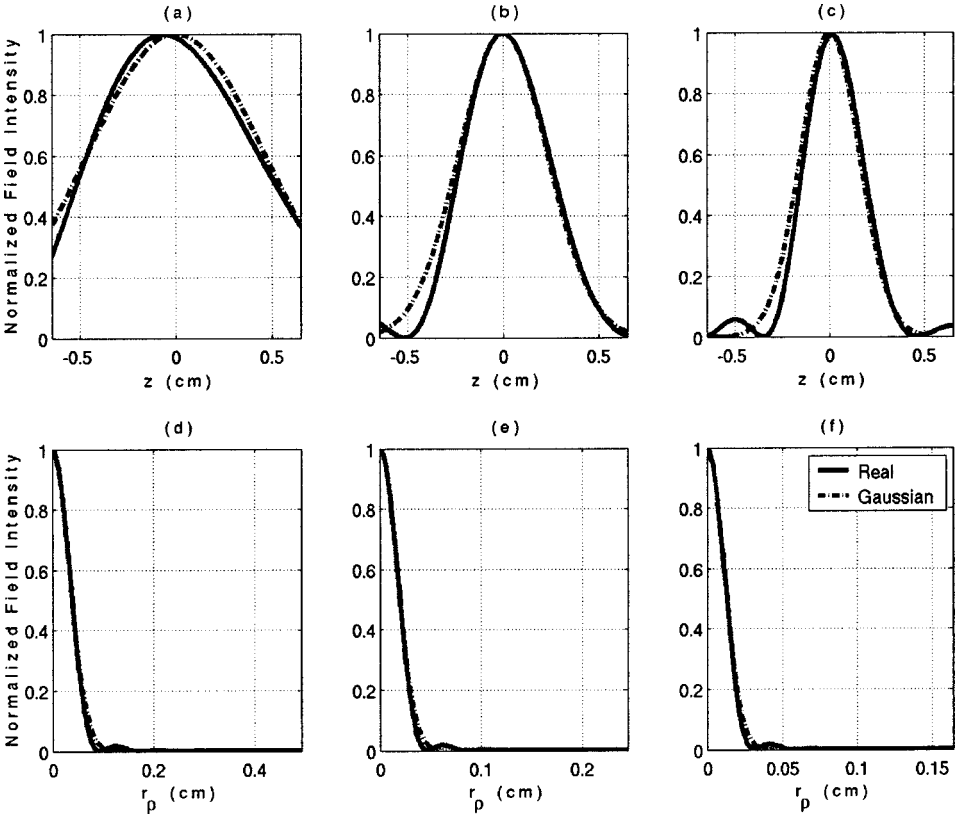

FIG. 4. Plots showing the normalized complete field intensity with the accompanying Gaussian approximation for the z axis at frequencies of (a) 4 MHz, (b) 8 MHz, and (c) 12 MHz as well as the r_ρ axis at frequencies of (d) 4 MHz, (e) 8 MHz, and (f) 12 MHz for an $f/2$ spherically focused transducer.

$$G_o = \frac{a^2}{2F}. \tag{32}$$

Having identified the shifts of the focus with frequency for the weakly focused source, the next step is to determine if the Gaussian approximation could be improved by properly accounting for the shift. Because the shift is always along the beam axis, the integral along ds_z in Eq. (15) could be modified to yield

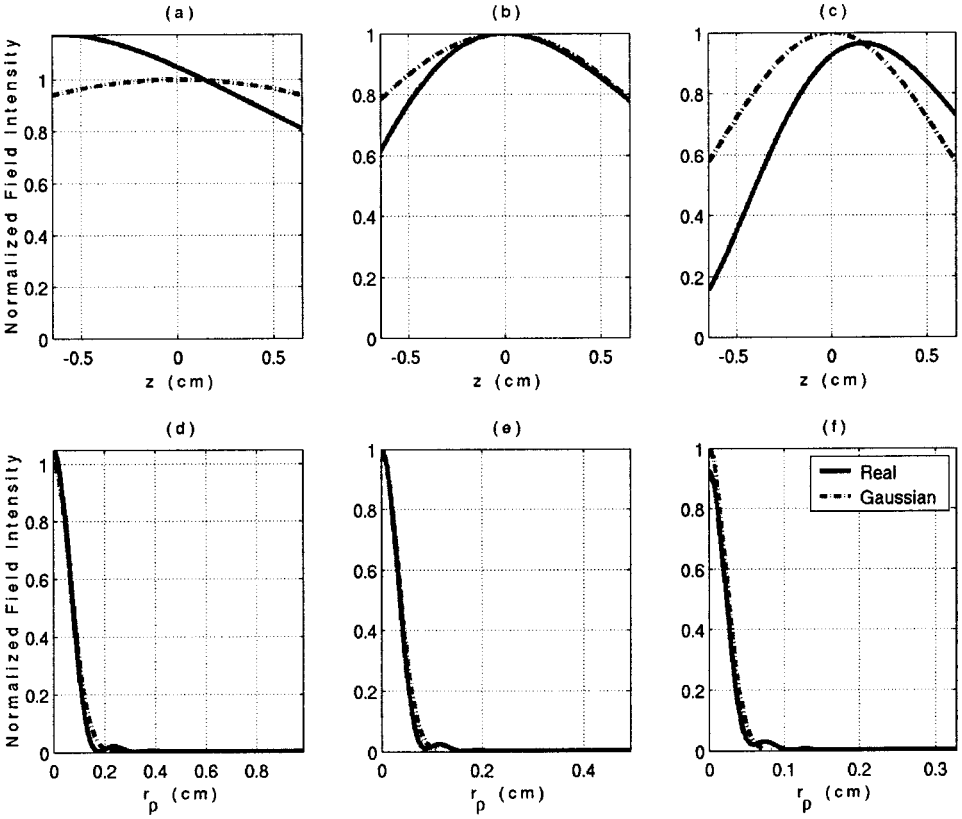

FIG. 5. Plots showing the normalized complete field intensity with the accompanying Gaussian approximation for the z axis at frequencies of (a) 4 MHz, (b) 8 MHz, and (c) 12 MHz as well as the r_ρ axis at frequencies of (d) 4 MHz, (e) 8 MHz, and (f) 12 MHz for an $f/4$ spherically focused transducer.

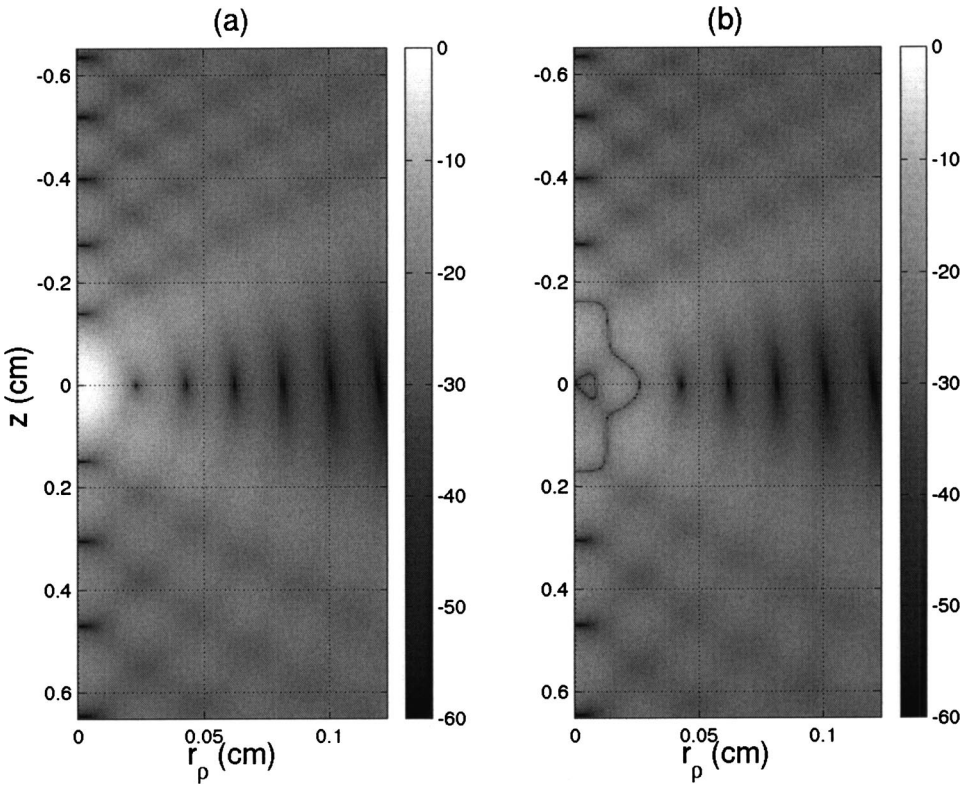

FIG. 6. Images showing (a) the calculated field intensities in dB and (b) the difference term from the integrand in Eq. (29) also in dB for the real $f/1$ source at a frequency of 8 MHz over the integration region.

$$\int_{-L/2}^{L/2} ds_z (g_{win}(s_z) e^{-4(s_z - z_o(f))^2/w_z^2} e^{4\alpha s_z})$$

$$= \int_{-L/2}^{L/2} ds_z (g_{win}(s_z) e^{-4s_z^2/w_z^2 + 8s_z z_o(f)/w_z^2 - 4z_o^2(f)/w_z^2} e^{4\alpha s_z})$$

$$= e^{-4z_o^2(f)/w_z^2} \int_{-L/2}^{L/2} ds_z (g_{win}(s_z) e^{-4s_z^2/w_z^2} \times e^{(4\alpha + 8z_o(f)/w_z^2)s_z}), \quad (33)$$

where z_o is the shift of the focus at a particular frequency. However, the shift of the focus is typically much smaller than w_z. Hence, the terms involving z_o can be ignored, resulting in the same generalized attenuation-compensation function given in Eq. (18). Therefore, the Gaussian approximation could be improved for weakly focused sources provided the equivalent Gaussian depth of focus is found by an independent fit to a Gaussian distribution for every frequency of interest while allowing the peak of the Gaussian to occur at different spatial locations for each frequency.

Now that the percent differences for the weakly focused $f/4$ source have been analyzed, the percent differences for the $f/1$ and $f/2$ sources can be explored in greater detail. The calculated field intensities in dB [i.e., $10 \cdot \log_{10}((\phi_{real}(\lambda)/\max_{V'}(\phi_{real}(\lambda_o)))^2)$] for the real $f/1$ source at a frequency of 8 MHz is shown with the difference term from the integrand in Eq. (29) [i.e., $10 \cdot \log_{10}(|(\phi_{real}(\lambda)/\max_{V'}(\phi_{real}(\lambda_o)))^2 - e^{-2((r'_\rho/w_x(\lambda))^2 + (z'/w_z(\lambda))^2)}|)$] also in dB over the integration region in Fig. 6. Likewise, the calculated field intensities and difference term for the $f/2$ source at frequency of 4 MHz are shown in Fig. 7. Notice that the largest differences between the complete fields and Gaussian approximations in Fig. 6 [i.e., (b) image] result from the "V" shaped side lobe structure before and after the focal plane. When very little of this side lobe structure is included in the integration region (Fig. 7), the corresponding percent difference in Fig. 2(a) is 3.3%. However, when all of the "V" is included in the integration region (Fig. 6), the corresponding percent difference in Fig. 2(a) is close to 18%. Hence, the side lobe structure reduces the accuracy of the Gaussian approximation for focused sources up to a percent difference of ~18%. One way to improve the agreement between the complete fields and Gaussian approximation for focused sources is to use smaller window lengths to gate the time domain signal so that not all of the "V" shaped side lobe structure would influence the backscattered power spectrum.

Before concluding, we need to take another look at the equivalent Gaussian dimensions given in Eq. (30). Although Barber showed that $w_{x,y}$ in Eq. (30) is a good approximation to the real beamwidth for the ideal transducer,[21] the expression for w_z has not been validated. Hence, we tested the equation for w_z by fitting a Gaussian distribution to the calculated complete field intensities along the beam axis for the $f/1$, $f/2$, and $f/4$ sources at each frequency independently (i.e., location of focus along beam axis was allowed to change for the different frequencies). The Gaussian fit was done for a window length of 13 mm about the location of maximum field intensity as measured at a frequency of 8 MHz for all of the frequencies from 2 to 14 MHz except for the $f/4$ source where the Gaussian fit was only done from 4 to 14 MHz due to the real focus shifting outside of the 13 mm window. The difference for the w_z from the fit and the w_z from Eq. (30) was always less than 11.5% for the $f/1$, 6.5% for the $f/2$, and 21.1% for the $f/4$. Also, the w_z values from the Gaussian fit at each frequency could be fit by line

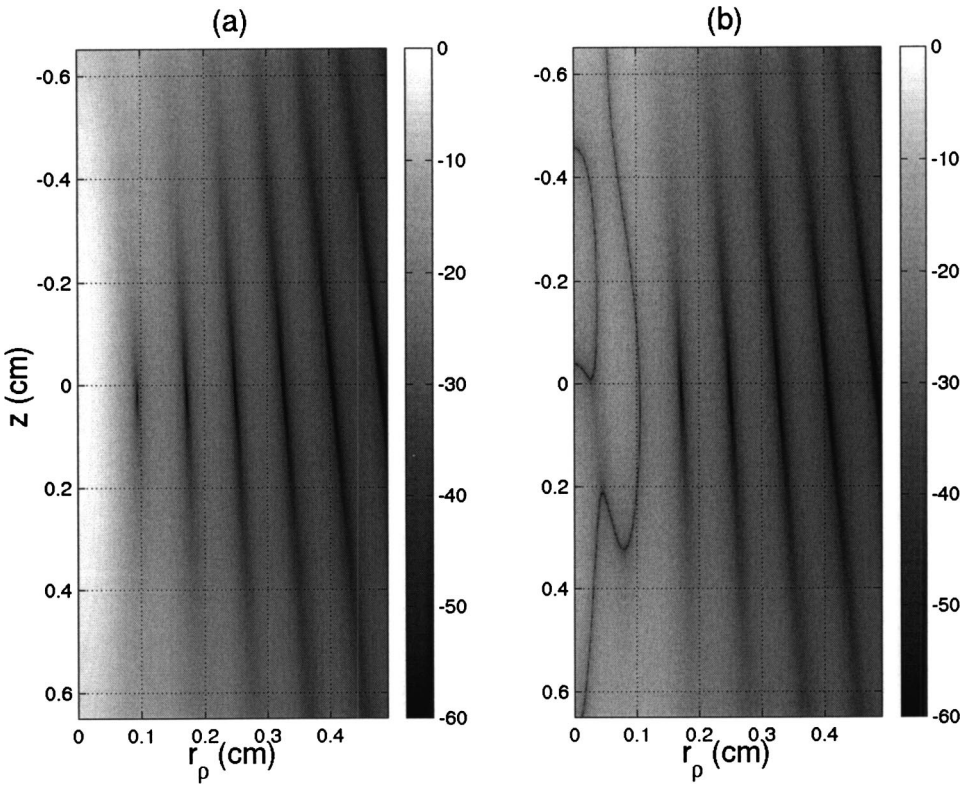

FIG. 7. Images showing (a) the calculated field intensities in dB and (b) the difference term from the integrand in Eq. (29) also in dB for the real $f/2$ source at a frequency of 4 MHz over the integration region.

for each transducer, yielding a wavelength dependence of $5.43\lambda + 15.5\ \mu$m for the $f/1$ [Eq. (30) predicts 6.01λ], $23.1\lambda - 37.2\ \mu$m for the $f/2$ [Eq. (30) predicts 24.0λ], and $84.1\lambda - 503\ \mu$m for the $f/4$ [Eq. (30) predicts 96.2λ]. Hence, the equivalent Gaussian dimensions in Eq. (30) are reasonable first-order approximations for the real ideal focused source.

IV. SIMULATION ANALYSIS

In Sec. II of this paper, we re-derived the backscattered voltage from a region of homogeneous scatterers and from a rigid plane placed near the focus. Based on these equations, we were able to conclude that focusing along the beam axis can be corrected by using a generalized attenuation-compensation function. We also concluded that for focused sources, O'Donnell–Miller compensation should result in an overestimate of the scatterer size, and point compensation may either over- or underestimate the scatterer size depending on the degree of focusing and amount of attenuation. However, the overall estimation performance has not been quantified. Therefore, a series of simulations was performed to quantify the performance of the different attenuation-compensation functions similar to the study done by Oelze and O'Brien.[18] In their work, they introduced a new attenuation-compensation function given by

$$A_{OO}(\omega) = \frac{e^{4\alpha_{\text{eff}} z_T} e^{-4\alpha L/2}}{L} \left(\frac{2\alpha L}{1 - e^{-2\alpha L}} \right)^2, \tag{34}$$

which they found underestimated the scatterer size for the unfocused source. Therefore, their attenuation-compensation function was also considered in our analysis. A_{OO} cannot be derived from Eq. (18) because our derivation dealt with the $E[|V_{refl}(\omega)|^2]$ whereas A_{OO} was originally derived for $(E[|V_{refl}(\omega)|])^2$.

In the simulations, the sources were spherically focused transducers with their apertures placed in contact with an attenuating infinite half-space (infinite region bounded by aperture plane of source) containing scatterers. The transducers were excited by an impulse spike, and the dimensionless filtering characteristics for the ultrasound source, $H(f)$, from Eq. (8) were given by

$$H(f) = \frac{f \cdot \exp(-((f - 8\ \text{MHz})/6\ \text{MHz})^2)}{\max_{\forall f}(f \cdot \exp(-((f - 8\ \text{MHz})/6\ \text{MHZ})^2))}, \tag{35}$$

which was comparable to a single element transducer in our lab. A Rayleigh distribution was selected over a Gaussian distribution so that nothing would be transmitted at zero frequency similar to the filtering characteristics of a real source. Also, the sources had a focal length of 5 cm and *f*-numbers of 1, 2, and 4. The velocity potential field at the focus in the simulations followed a three-dimensional Gaussian distribution (i.e., only approximation of field for focused source) with G_o, w_x, w_y, and w_z given by Eqs. (32) and (30), respectively.

The backscattered voltage for the simulations was generated by solving Eq. (9) analytically for a single Gaussian scatterer at an arbitrary location in the Gaussian field of the focal region. The backscatter for many scatterers in the half-space was then obtained by adding together the backscatter from many different randomly distributed scatterers. In the simulations, the scatterers were positioned according to a uniform probability distribution throughout the focal region

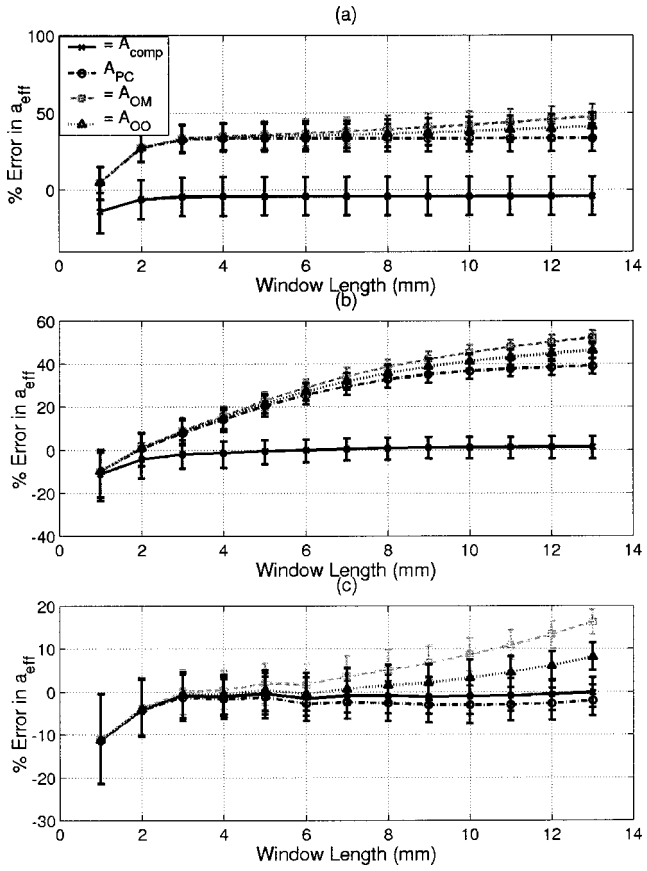

FIG. 8. The % error versus rectangular window length when compared to known a_{eff} at $\alpha=0.5$ dB/cm/MHz for simulated fields from (a) $f/1$, (b) $f/2$, and (c) $f/4$ transducers for each of the attenuation-compensation functions (A_{comp}, A_{PC}, A_{OM}, and A_{OO}).

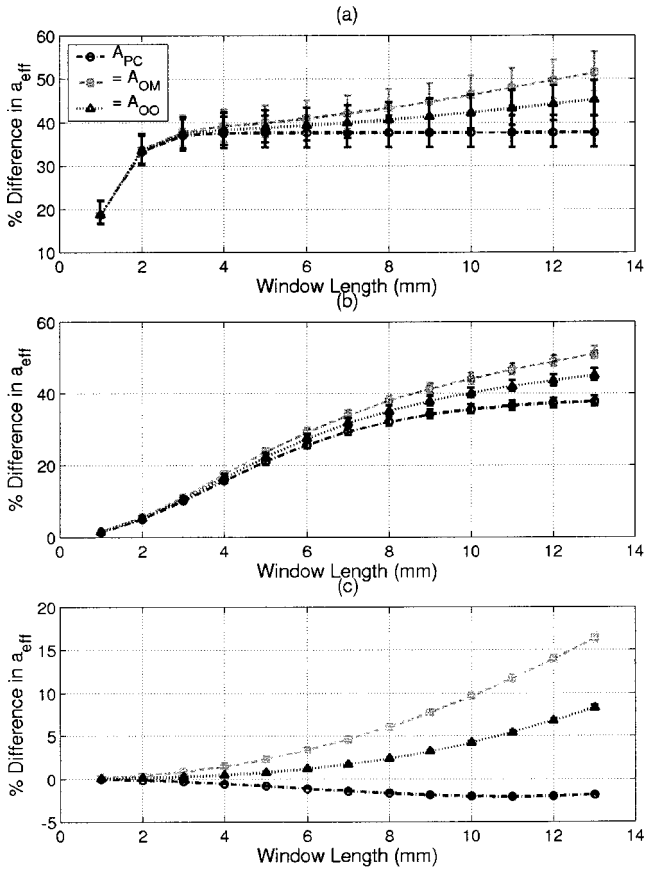

FIG. 9. The % difference between a_{eff} found using the traditional attenuation-compensation functions (A_{PC}, A_{OM}, and A_{OO}) when compared to a_{eff} found using A_{comp} in Eq. (26) versus rectangular window length at $\alpha=0.5$ dB/cm/MHz for simulated fields from (a) $f/1$, (b) $f/2$, and (c) $f/4$ transducers.

at a density of 35/mm^3 and each had an effective radius, a_{eff}, of 25 μm.

A density of 35/mm^3, given that the approximate length of the transmitted pulse was 0.286 mm, translates to 4.8, 1.2, and 0.3 scatterers per resolution cell in the B-mode image for the $f/4$, $f/2$, and $f/1$, respectively. Hence, the speckle would not be fully developed in a B-mode image from the $f/1$ and $f/2$ transducers. This is of little concern because we are not analyzing the speckle, but rather the frequency spectrum of the backscattered signal. As a result, we do not need fully developed speckle to perform our analysis. To verify this assertion, we varied the number density of the scatterers from 35/mm^3 to 3500/mm^3 for the $f/1$ transducer. The accuracy of the scatterer size estimates was the same for all of the number densities ($\sim$1%). The precision of the estimates was improved for larger number densities (from $\sim$26% to $\sim$15%), but the amount of improvement did not warrant an increase in the number density for the simulations.

The sound speed for the half-space was 1532 m/s, which is the sound speed for liver (characteristic of tissue). The attenuation was uniform throughout the half-space for each simulation and was varied from 0.05 to 1 dB/cm/MHz for different simulations. The reflection off of the rigid plane at the focus in a water bath was also simulated according to Eq. (27) using a constant sound speed of 1540 m/s and setting $z_f=0$. The code used a sampling rate of 53 MHz when "digitizing" the signal significantly oversampling the waveform, and no electronic noise was added to the simulated waveforms.

For each value of attenuation, the backscattered voltage (i.e., rf echo) from 1000 independent random scatter distributions was generated. The waveforms were then separated into 40 independent sets with 25 waveforms per set and windowed in the time domain using a rectangular gating function centered at the focus. The width of the rectangular window was varied from 1 to 13 mm in steps of 1 mm with corresponding time gates found from $T_{win}=2L/c$. Then, $\mathrm{E}[|V_{refl}(\omega)|^2]$ was calculated by averaging the magnitude squared of the frequency spectrum of the 25 signals. Equation (28) was then solved by minimizing the squared error using standard techniques[4] in the log domain yielding 40 independent estimates of the effective scatterer radius, a_{eff_j}. In all cases, the bandwidth selected for the minimization was the set of frequencies for which

$$\frac{k_o^4 \mathrm{e}^{-4\alpha z_T}|V_{plane}(\omega)|^2}{\max\limits_{\forall\omega}(k_o^4 \mathrm{e}^{-4\alpha z_T}|V_{plane}(\omega)|^2)} > 0.05. \tag{36}$$

The results for an attenuation of 0.5 dB/cm/MHz for all three transducers (i.e., $f/1$, $f/2$, and $f/4$) and all window lengths are shown in Figs. 8, 9, and 10. In Fig. 8, the percent error in the scatterer size is compared to the known size for the three transducers for each of the different attenuation-

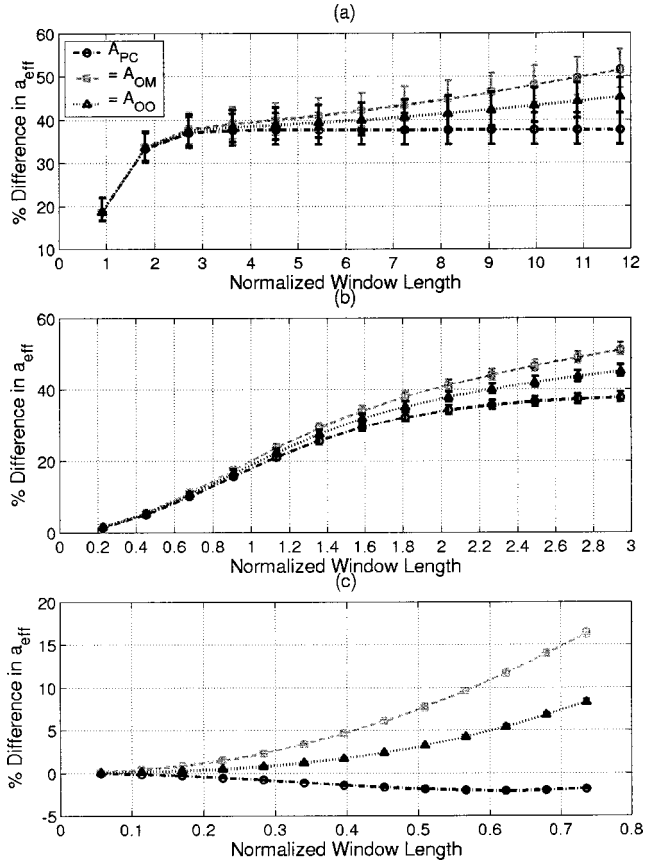

FIG. 10. The % difference between a_{eff} found using the traditional attenuation-compensation functions (A_{PC}, A_{OM}, and A_{OO}) when compared to a_{eff} found using A_{comp} in Eq. (26) versus window length normalized to the depth of focus (i.e., $7.08\lambda_o f\#^2$) at $\alpha = 0.5$ dB/cm/MHz for simulated fields from (a) $f/1$, (b) $f/2$, and (c) $f/4$ transducers.

compensation functions. The upper and lower error bars were found from

$$\sigma_{upper} = \frac{100}{a_{\text{eff}}|_{Theory}} \sqrt{\frac{\sum_{\forall a_{\text{eff}_j} > \overline{a}_{\text{eff}}} (a_{\text{eff}_j} - \overline{a}_{\text{eff}})^2}{\sum_{\forall a_{\text{eff}_j} > \overline{a}_{\text{eff}}} j}},$$
$$\sigma_{lower} = \frac{100}{a_{\text{eff}}|_{Theory}} \sqrt{\frac{\sum_{\forall a_{\text{eff}_j} < \overline{a}_{\text{eff}}} (a_{\text{eff}_j} - \overline{a}_{\text{eff}})^2}{\sum_{\forall a_{\text{eff}_j} < \overline{a}_{\text{eff}}}}}. \tag{37}$$

The accuracy of all estimates drops off significantly at smaller window lengths for all of the attenuation-compensation functions as a result of the convolution in the frequency domain associated with the windowing. In Fig. 9, the percent difference between the scatterer size given by the generalized attenuation-compensation function, A_{comp}, and the scatter size from the other attenuation-compensation functions are compared for the three transducers. It is clear that the error bars are reduced when the difference between the attenuation-compensation functions are found (Fig. 9) as compared to plotting the straight error values (Fig. 8). Hence, the differences between the different attenuation-compensation functions should be relatively constant between different scatterer distributions even though the absolute errors vary. Figure 10 shows the percent differences again but here the window length has been normalized with respect to the calculated depth of field for the transducer (i.e., $7.08\lambda_o f\#^2$)[20] where λ_o was the wavelength of the dominate frequency from the reference spectrum (i.e., V_{plane}).

The errors (Fig. 8) and differences (Fig. 9) in A_{OM}, A_{OO}, and A_{PC} are larger for the smaller *f*-number transducers (i.e., $f/1$ and $f/2$) and increase for longer window lengths. This makes sense because the importance of diffraction along the beam axis increases with increasing window length. Likewise, all four attenuation-compensation functions converge to the same result for decreasing window lengths. Oelze and O'Brien[18] also observed this when diffraction along the beam axis was neglected. Furthermore, A_{comp} yields excellent results regardless of window length or *f*-number and even provides improved estimates for the scatter size for long window lengths when the beam is relatively unfocused (i.e., $f/4$). Also, when the results for the $f/1$ and the $f/2$ transducers are compared, we see that the errors/differences plateau with increasing window length, so that the differences are greater for the $f/1$ transducer for smaller window lengths and then are approximately the same for large window lengths.

The plateau can be better illustrated by the results for the normalized window lengths (Fig. 10). The plateau is reached once the window length is several times the calculated depth of field (i.e., $7.08\lambda_o f\#^2$), hence, the contributing scatters are being limited by the focusing of the field and not by the windowing. Also, when comparing the differences between the $f/1$ and the $f/2$ transducers at the same normalized window length, the $f/2$ transducer has a larger difference for both the A_{OM} and A_{OO} estimates, and the A_{PC} estimate values converge to the same difference of 37.6% for normalized window lengths greater than approximately 2.5. Likewise, when comparing the differences between the $f/2$ and $f/4$ transducers at the same normalized window length, the $f/4$ transducer has a larger difference for the A_{OM} estimate. Also, for the $f/4$ transducer, the concavity of the A_{PC} estimate changed direction at a normalized window length of 0.65. Hence, A_{PC} may overestimate the scatterer size for large enough window lengths. Therefore, the error in using A_{OM} is greater for transducers with larger *f*-number when comparing across the same normalized window length, and the error in A_{PC} appears to plateau at sufficiently large normalized window length at approximately 37.6%. However, the performance of the attenuation-compensation functions cannot be generalized for small normalized window lengths for the different focused transducers.

The improvement in the estimates using the new generalized attenuation-compensation function can be illustrated further by considering the error in $\overline{a}_{\text{eff}}$ for different values of attenuation at set rectangular window lengths of 6 and 13 mm (Figs. 11 and 12, respectively). Notice that for the $f/1$ and $f/2$ transducers, A_{OM}, A_{OO}, and A_{PC} consistently overestimate the scatterer size on the order of 20% to 100% while A_{comp} gives almost exactly the right answer with errors typically less than 2%, with the largest error being 7.2%. However, for the $f/4$ transducer, although A_{OM} consistently overestimates the scatterer size, both A_{OO} and A_{PC} overestimate the scatterer size for small values of attenuation and then underestimate the scatterer size as the attenuation is in-

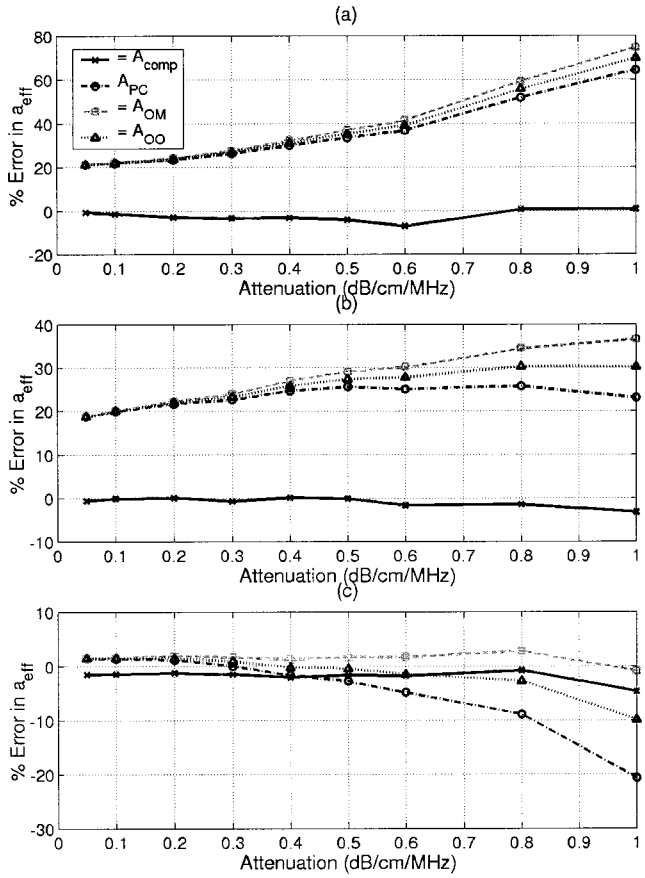

FIG. 11. The % error in $\overline{a}_{\text{eff}}$ when compared to known value of a_{eff} for $L=6$ mm for simulated fields from (a) $f/1$, (b) $f/2$, and (c) $f/4$ transducers for each of the attenuation-compensation functions (A_{comp}, A_{PC}, A_{OM}, and A_{OO}).

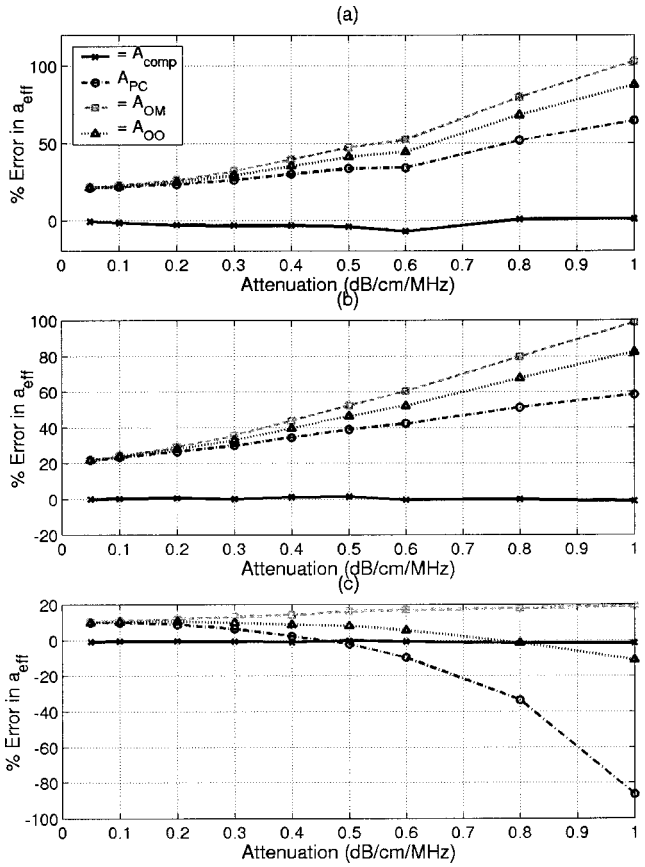

FIG. 12. The % error in $\overline{a}_{\text{eff}}$ compared to known value of a_{eff} for $L=13$ mm for simulated fields from (a) $f/1$, (b) $f/2$, and (c) $f/4$ transducers for each of the attenuation-compensation functions (A_{comp}, A_{PC}, A_{OM}, and A_{OO}).

creased. This is in agreement with Oelze and O'Brien[18] who also observed that A_{OM} should overestimate the scatterer size and both A_{OO} and A_{PC} should underestimate the scatterer size for long window lengths when diffraction along the beam axis can be neglected. The results for A_{PC} also agree with our predictions that A_{PC} will under/overestimate the scatterer size based on the relative importance of α and w_z. Once again, A_{comp} gives consistently good results for all attenuation values for the $f/4$ transducer with errors less than 5%. Hence, including diffraction along the beam axis with the generalized attenuation-compensation function improves the accuracy of the scatterer size estimate and allows for more strongly focused sources (i.e., $f/1$ and $f/2$) to be used in the data acquisition.

Although the accuracy of the scatterer size estimate is an important measure of the performance of the estimator, the precision of the estimate is also of great importance when performing tissue characterization. Figure 13 shows the deviations in the scatterer size calculated from Eq. (35) for each of the attenuation-compensation functions at a window length of 6 mm for all three of the transducers. Results at other window lengths are typically comparable to within a few percent. Notice that there is a slight degradation in the precision of the algorithms with increasing attenuation (i.e., change on the order of 8% from 0.05 to 1 dB/cm/MHz) and with decreasing *f*-number (i.e., change on the order of 8% from $f/1$ to $f/4$). These losses in precision may be a result of having fewer scatterers contributing to the backscattered signal as well as having the ka_{eff} values shift out of the optimal range[7] of $ka_{\text{eff}}=0.5\rightarrow1.2$ due to the increased attenuation (i.e., from $ka_{\text{eff}}=0.67\rightarrow1.6$ to $ka_{\text{eff}}=0.26\rightarrow0.96$). Also, although the precision of the different attenuation-compensation functions are comparable, A_{comp} is slightly less precise than the other algorithms for the $f/1$ and $f/2$ transducers (i.e., change on the order of 1% to 7%). This loss in precision, however, is insignificant compared to the simultaneous gain in accuracy.

V. DISCUSSION

In this paper, we considered the effects of focusing on estimating the size of scatterers in random media. Our development did not address estimating acoustic concentration although the derived equations would still be applicable. In our analysis, we assumed that the velocity potential field near the focus can be modeled as a three-dimensional Gaussian beam, the scatterers are a sufficient distance from the source, and the field is approximately constant across the scatterer. Our derivations demonstrated that correcting for focusing along the beam axis when obtaining estimates of scatterer size requires a generalized attenuation-compensation function that includes attenuation, windowing, and diffraction. Furthermore, our results provided insight into the applicability and

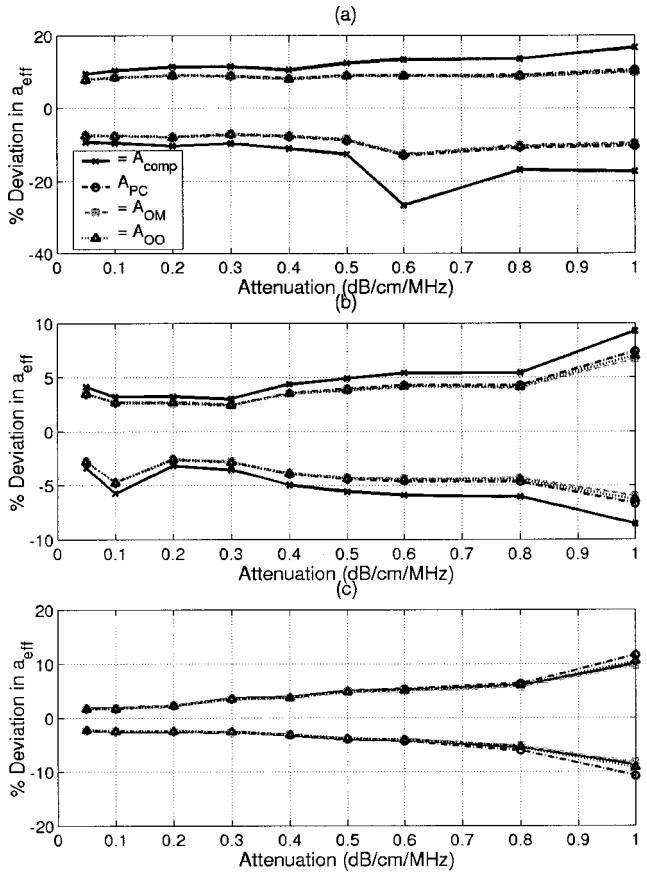

FIG. 13. The % deviations in the a_{eff} for a window length of 6 mm for each of the attenuation-compensation functions (A_{comp}, A_{PC}, A_{OM}, and A_{OO}) for simulated fields from (a) $f/1$, (b) $f/2$, and (c) $f/4$ transducers. The upper curves in each plot are the values of σ_{upper} and the lower curves in each plot are σ_{lower}.

robustness of previous attenuation-compensation functions in light of diffraction along the beam axis. Our theoretical work was also extended to diagnostically relevant fields where the transmit and receive foci are not necessarily at the same depths.

Also, an analysis of A_{comp} in Eq. (18) can also provide insight into the reference phantom methods proposed[13] that could also potentially correct for focusing. Using a reference phantom would be equivalent to applying Eq. (18) provided that the attenuation of the reference phantom was the same as the attenuation of the tissue. When the two values of attenuation are different, the value of the integrand [i.e., $g_{win}(s_z)\exp(-4(s_z^2/w_z^2))\exp(4\alpha s_z)$] would be different because the value of α would not be the same. The significance of this difference may be minor, but should be investigated before the reference phantom technique is generally accepted.

The Gaussian approximation of the velocity potential field in the focal region was also validated by comparing the approximation to complete calculated fields for a focused source. The approximation was found to be sufficiently accurate for all of the frequencies and degrees of focusing tested. In addition, the validity of the approximation was the same regardless of the degree of focusing (i.e., compare results for $f/1$ and $f/2$). Hence, our theoretical analysis should be valid for all of the sources encountered in clinical practice. However, the Gaussian approximation would be improved if the ultrasound system were engineered to reduce the side lobe structure observed for the ideal focused sources.

In our simulation analysis, we demonstrated that including the effects of diffraction along the beam axis improves the accuracy of the scatterer size estimator even for a weakly focused $f/4$ transducer when the pressure fields at the focus had a three-dimensional Gaussian distribution. The improvement in accuracy for the more strongly focused $f/1$ and $f/2$ transducers was on the order of 20% to 100% depending on the length of the window and the amount of attenuation without a significant loss in precision. Hence, using the generalized attenuation-compensation function allows for the use of focused sources when estimating scatterer properties that otherwise would not give usable results. Therefore, the new generalized attenuation-compensation function gives extensive improvement over the traditional methods.

ACKNOWLEDGMENTS

This work was supported by the University of Illinois Research Board, by a NDSEG Fellowship awarded to T. A. Bigelow, and by a Beckman Institute Graduate Fellowship awarded to T. A. Bigelow.

[1] R. C. Chivers and C. R. Hill, "A spectral approach to ultrasonic scattering from human tissue: methods, objectives, and backscattering measurements," Phys. Med. Biol. **20**(5), 799–815 (1975).
[2] J. C. Gore and S. Leeman, "Ultrasonic backscattering from human tissue: a realistic model," Phys. Med. Biol. **22**(2), 317–326 (1977).
[3] F. L. Lizzi, M. Greenebaum, E. J. Feleppa, and M. Elbaum, "Theoretical framework for spectrum analysis in ultrasonic tissue characterization," J. Acoust. Soc. Am. **73**, 1366–1373 (1983).
[4] M. F. Insana, R. F. Wagner, D. G. Brown, and T. J. Hall, "Describing small-scale structure in random media using pulse-echo ultrasound," J. Acoust. Soc. Am. **87**(1), 179–192 (1990).
[5] F. L. Lizzi, M. Astor, T. Liu, C. Deng, D. J. Coleman, and R. H. Silverman, "Ultrasonic spectrum analysis for tissue assays and therapy evaluation," Int. J. Imaging Syst. Technol. **8**, 3–10 (1997).
[6] M. L. Oelze, J. F. Zachary, and W. D. O'Brien, Jr., "Characterization of tissue microstructure using ultrasonic backscatter: theory and technique optimization using a Gaussian form factor," J. Acoust. Soc. Am. **112**, 1202–1211 (2002).
[7] M. F. Insana and T. J. Hall, "Parametric ultrasound imaging from backscatter coefficient measurements: image formation and interpretation," Ultrason. Imaging **12**, 245–267 (1990).
[8] E. L. Madsen, M. F. Insana, and J. A. Zagzebski, "Method of data reduction for accurate determination of acoustic backscatter coefficients," J. Acoust. Soc. Am. **76**(3), 913–923 (1984).
[9] M. F. Insana, E. L. Madsen, T. J. Hall, and J. A. Zagzebski, "Tests of the accuracy of a data reduction method for determination of acoustic backscatter coefficients," J. Acoust. Soc. Am. **79**, 1230–1236 (1986).
[10] K. A. Wear, M. R. Milunski, S. A. Wickline, J. E. Perez, B. E. Sobel, and J. G. Miller, "Differentiation between acutely ischemic myocardium and zones of completed infarction in dogs on the basis of frequency-dependent backscatter," J. Acoust. Soc. Am. **85**, 2634–2641 (1989).
[11] J. F. Chen, J. A. Zagzebski, and E. L. Madsen, "Tests of backscatter coefficient measurement using broadband pulses," IEEE Trans. Ultrason. Ferroelectr. Freq. Control **40**(5), 603–607 (1993).
[12] T. J. Hall, E. L. Madsen, J. A. Zagzebski, and E. J. Boote, "Accurate depth-independent determination of acoustic backscatter coefficients with focused transducers," J. Acoust. Soc. Am. **85**, 2410–2416 (1989).
[13] A. Gerig, J. Zagzebski, and T. Varghese, "Statistics of ultrasonic scatterer size estimation with a reference phantom," J. Acoust. Soc. Am. **113**, 3430–3437 (2003).
[14] P. M. Morse and K. U. Ingard, *Theoretical Acoustics* (McGraw–Hill, New York, 1968).

[15] P. Z. Peebles, *Probability, Random Variables, and Random Signal Principles*, 3rd ed. (McGraw–Hill, New York, 1993).
[16] K. A. Wear, ''A Gaussian framework for modeling effects of frequency-dependent attenuation, frequency-dependent scattering, and gating,'' IEEE Trans. Ultrason. Ferroelectr. Freq. Control **49**(11), 1572–1582 (2002).
[17] M. O'Donnell and J. G. Miller, ''Quantitative broadband ultrasonic backscatter: an approach to nondestructive evaluation in acoustically inhomogeneous materials,'' J. Appl. Phys. **52**(2), 1056–1064 (1981).
[18] M. L. Oelze and W. D. O'Brien, Jr., ''Frequency-dependent attenuation-compensation functions for ultrasonic signals backscattered from random media,'' J. Acoust. Soc. Am. **111**, 2308–2319 (2002).
[19] D. S. Ellis and W. D. O'Brien, Jr., ''The monopole-source solution for estimating tissue temperature increases for focused diagnostic ultrasound,'' IEEE Trans. Ultrason. Ferroelectr. Freq. Control **43**(1), 88–97 (1996).
[20] G. S. Kino, *Acoustic Waves: Devices, Imaging, and Analog Signal Processing* (Prentice–Hall, Englewood Cliffs, NJ, 1987).
[21] F. E. Barber, ''The scanning acoustic microprobe: I. Analysis and synthesis of a spherically symmetric point spread function,'' J. Acoust. Soc. Am. **90**, 1–10 (1991).

Scatterer size estimation in pulse-echo ultrasound using focused sources: Calibration measurements and phantom experiments

Timothy A. Bigelow and William D. O'Brien, Jr.[a)]
Bioacoustics Research Laboratory, Department of Electrical and Computer Engineering, University of Illinois, 405 North Mathews, Urbana, Illinois 61801

(Received 13 June 2003; revised 31 March 2004; accepted 12 April 2004)

In a companion paper [T. A. Bigelow and W. D. O'Brien Jr., J. Acoust. Soc. Am. **116**, 578 (2004)], theory, supported by simulations, showed that accurate scatterer size estimates could be obtained using highly focused sources provided that the derived generalized attenuation-compensation function was used and the velocity potential field near the focus could be approximated as a three-dimensional Gaussian. Herein, the theory is further evaluated via experimental studies. A calibration technique is developed to find the necessary equivalent Gaussian dimensions for a focused source using reflections obtained from a rigid plane scanned through the focus. Then, the theoretical analysis of focused sources is validated experimentally using three spherically focused ultrasound transducers to estimate the radius of glass beads imbedded in tissue mimicking phantoms. Both the impact of focusing ($f/1$, $f/2$, and $f/4$) and the effect of scatterer type (comparing glass bead results to simulation results that used scatterers with Gaussian impedance distributions) were tested. The simulated differences agree with the measured differences to within 2.5% provided that the comparison is made between the same scatterer type and sources with the same equivalent Gaussian dimensions. The improvement provided by the generalized attenuation-compensation function is greatly influenced by the type of scatterer whose size is being estimated and decreases as the wavelength dependence of the Gaussian depth of focus is reduced. [DOI: 10.1121/1.1757453]

PACS numbers: 43.80.Qf, 43.80.Vj [FD] Pages: 594–602

Pages: 594–602 Pages: 594–602602

LIST OF SYMBOLS

$A_{current}$	attenuation-compensation function currently being used by the estimator (i.e., A_{comp}, A_{OO}, A_{OM}, or A_{PC}).
A_{comp}	complete attenuation-compensation function including focusing effects along the beam axis [i.e., $A_{comp}(\omega)=e^{4\alpha_{eff}z_T}/(\int_{-L/2}^{L/2}ds_z g_{win}(s_z)e^{-4(s_z^2/w_z^2)}e^{4\alpha s_z})$].
a_{eff}	estimated radius of glass beads.
A_{OO}	Oelze–O'Brien attenuation-compensation function [i.e., $A_{OO}(\omega)=(e^{4\alpha_{eff}z_T}e^{-4\alpha L/2}/L)(2\alpha L/(1-e^{-2\alpha L}))^2$].
A_{OM}	O'Donnell–Miller attenuation-compensation function [i.e., $A_{OM}(\omega)=4\alpha e^{4\alpha_{eff}z_T}/(e^{4\alpha L/2}-e^{-4\alpha L/2})$].
A_{PC}	point attenuation-compensation function [i.e., $A_{PC}(\omega)=e^{4\alpha_{eff}z_T}/L$].
ASD	average squared difference term minimized when estimating scatterer size.
c	small-signal sound speed of phantom.
c_o	small-signal sound speed of water.
F	form factor describing power spectral density function for scatterer.
$f\#$	f-number for a spherically focused source.
f_R	principle frequency of Rayleigh distribution [i.e., $f\cdot\exp(-((f-f_R)/\sigma_R)^2)$].
G_o	geometric gain value for pressure field at focus when W_{source} is approximated by a Gaussian (units of m).
H	dimensionless filtering characteristics for the ultrasound source.
k_o	wave number in water.
L	total width of rectangular windowing function.
PII	pulse intensity integral.
S_T	aperture area of ultrasound transmitter.
T_{win}	total width of rectangular windowing function applied to time-domain waveform (i.e., $T_{win}=2L/c$).
V'	volume containing glass beads contributing to the scattered signal.
V_{inc}	voltage applied to the ultrasound source during transmit.
V_{plane}	voltage from ultrasound source due to the backscatter from rigid plane near focus.
V_{refl}	voltage from ultrasound source due to the backscatter from glass beads.
w_x, w_y, w_z	equivalent Gaussian dimensions of velocity potential field in focal region.
w_{zb}	intercept term for equivalent Gaussian depth of focus as a function of wavelength (i.e., $w_z=w_{zm}\cdot\lambda+w_{zb}$).
w_{zm}	slope term for equivalent Gaussian depth of focus as a function of wavelength (i.e., $w_z=w_{zm}\cdot\lambda+w_{zb}$).

[a)]Author to whom all correspondence should be addressed. Electronic mail: wdo@uiuc.edu

X log difference between calibrated scattered spectrum and form factor used in minimization.

$\overline{X}$ mean value of X over bandwidth of minimization.

z_f distance of rigid plane used to acquire reference waveform to the focal plane.

z_T distance of aperture plane of the ultrasound transmitter/detector to the focal plane.

α attenuation in the scattering region, V'.

α_{eff} effective attenuation for all tissue between focal plane and aperture plane (i.e., total attenuation along beam axis$=\alpha_{eff} z_T$).

α_o slope of attenuation in the scattering region assuming strict linear frequency dependent attenuation (i.e., $\alpha=\alpha_o \cdot f$).

λ wavelength.

λ_0 the wavelength corresponding to the spectral peak from the reference spectrum (i.e., V_{plane}) used when calculating the depth of field (i.e., $7.08\lambda_0 f\#^2$) to normalize the window length.

σ_R bandwidth of Rayleigh distribution [i.e., $f \cdot \exp(-((f-f_R)/\sigma_R)^2)$].

I. INTRODUCTION

Quantifying the ultrasonic backscatter returned from a medium of interest has been important in many different applications of acoustics ranging from nondestructive testing[1] to tissue imaging.[2] Regardless of the application, the goal remains the same: use the statistics of the frequency envelope of the backscattered signal to estimate the size of the scatterer in the medium. This involves first developing an impedance distribution to describe the scattering (model), and then fitting the measured backscattered data to the model to determine the mean scatterer size.[2–5]

Most of the models developed previously have assumed that large *f*-numbers are required to accurately extract information on the microstructure of the medium.[3,5,6] However, in our companion paper,[7] we have shown that smaller *f*-numbers can be used provided that the velocity potential field is modeled as a three-dimensional Gaussian beam in the focal region, and the correct generalized attenuation-compensation function is used. The companion paper restricted its attention to computer simulations of ideal sources where the impedance of the scatterers varied according to a Gaussian distribution. Hence, the impact of different scatterer types and nonideal beams was not addressed. A Gaussian impedance distribution is commonly assumed when analyzing the backscatter from biological tissues,[8] but the exact impedance distribution for tissue scatterers remains to be determined. Therefore, any relationship between the type of scatterer and the accuracy of the estimates of scatterer size for focused sources should be investigated.

In this paper, we build upon our previous work[7] by using real rather than ideal sources and by considering glass bead scatterers instead of scatterers with a Gaussian impedance distribution (Gaussian scatterer). The power spectral density functions (or form factors) for these two types of scatterers are very different,[5] and are given by

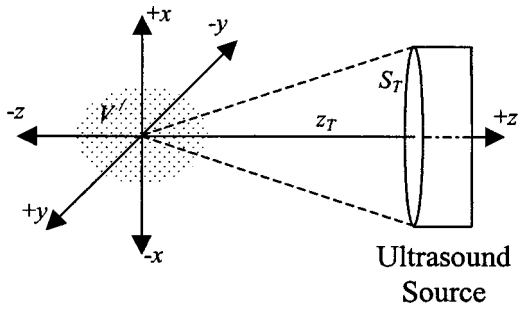

FIG. 1. Coordinate system selected for experiment.

$$F(k)=\begin{cases}\left[\dfrac{\sin(2ka_{eff})}{2ka_{eff}}\right]^2 & (Bead),\\ e^{-0.827k^2a_{eff}^2} & (Gaussian).\end{cases} \quad (1)$$

The form factor approximating the glass bead falls off much faster with increasing scatterer radius than does the Gaussian scatterer.[5]

Because the sources are real, the first challenge is to measure the equivalent frequency-dependent Gaussian beamwidths, w_x and w_y, and Gaussian depth of focus, w_z, of the field in the focal region. Two different methods are examined using a spherically focused transducer, and the results from the two methods are compared. One of the methods is then used to find the equivalent Gaussian depth of focus for three spherically focused transducers ($f/1$, $f/2$, and $f/4$). These three transducers are then used experimentally to obtain scatterer size estimates for an ultrasound phantom containing glass beads. Then, the effect of scatterer type is assessed by repeating the simulations using glass bead scatterers and comparing the bead simulation and phantom results to our earlier simulation results[7] that used scatterers with Gaussian impedance distributions. Likewise, the influence of the wavelength dependence of w_z of the sources is investigated through more computer simulations and analytical calculations. In the last section of the paper, some conclusions based on the experimental results are provided with the hope of guiding future investigators.

II. GAUSSIAN DIMENSION MEASUREMENTS

There are many possible methods for determining the equivalent Gaussian dimensions (beamwidth and depth of focus) of an ultrasound source, two of which were compared experimentally in our investigation. The evaluation was done using a spherically focused $f/2$ transducer (Valpey Fisher Instruments, Inc., Hopkinton, MA) with a diameter of 2.1 cm, a center frequency of 8.7 MHz, and a -3 dB bandwidth of 1.6 MHz as measured from a wire reflection.[9] The transducer was placed in a water bath and shock excited using a Panametrics 5900 pulser/receiver (Waltham, MA) operating in pulse-echo mode, and the returned waveforms were recorded using a digital oscilloscope at a sampling frequency of 100 MHz (Lecroy 9354 TM, Chestnut Ridge, NY). The coordinate system for the experiment is shown in Fig. 1. Although a spherically focused transducer was selected for the evaluation, the experimental techniques can be applied to any focused source including dynamically focused arrays.

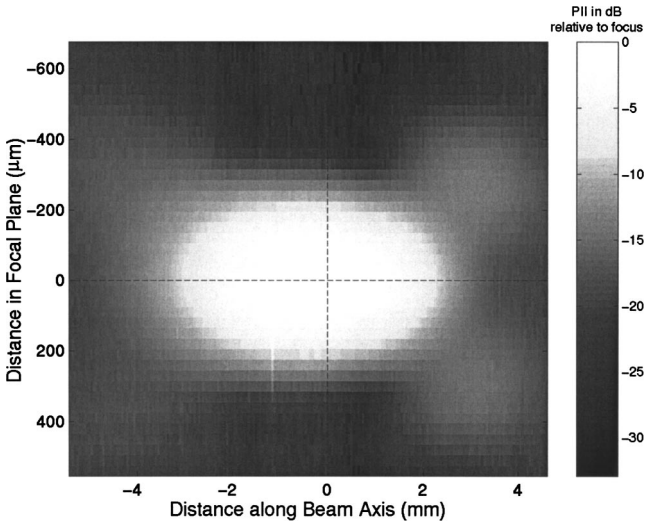

FIG. 2. Image of *PII* in dB showing location of field axes (dotted line) for the Gaussian dimension measurement from the wire reflections.

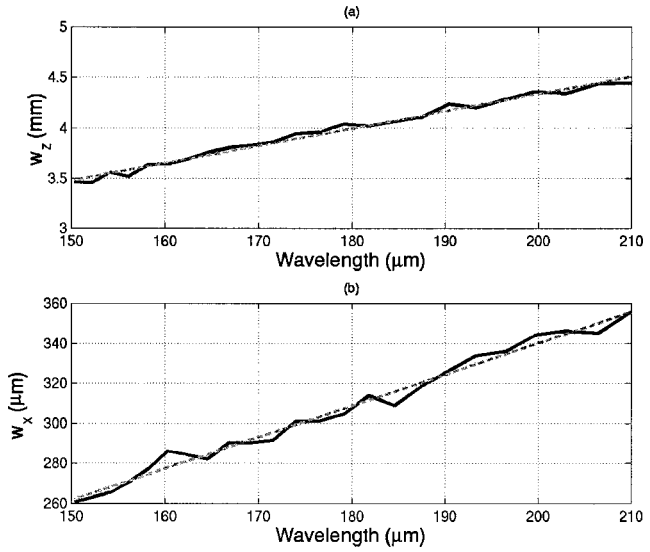

FIG. 3. Measured Gaussian dimensions and the resulting linear fits for the beam axis (a) and the focal plane axis (b) from the wire reflections.

A. Gaussian dimensions from wire

The first method considered for determining the Gaussian dimensions was the traditional technique of passing a wire target systematically through the entire ultrasound beam in a water bath and recording the pulse/echo waveform for each field location.[9] The wire target is then assumed to approximate a point target (i.e., neglect integration of wire across beam). In order to insure that the correct dimensions were measured, the wire needs to be moved throughout the entire field because it is difficult to align the beam axis with the scan axis when using a wire. In our experiment, the 38-μm-diam tungsten wire (California Fine Wire Company, Grover City, CA) was moved in a rectangular grid of dimension 10 mm by 1.2 mm in steps of 50 and 30 μm, respectively, using a Daedal microprecision positioning system (Daedal Inc., Harrison City, PA). The pulse intensity integral (PII) was then calculated for the return echo from every wire location yielding a map of the beam pattern. From the PII beam pattern, the beam axis (z axis) and focal plane axis (x axis) were determined. An image showing the log-compressed PII beam pattern along with the field axes is shown in Fig. 2. For arrays or other beams lacking circular symmetry in the focal plane, the experiment would need to be repeated with the wire target rotated so that the field intensity at each frequency along the y axis could also be obtained.

Once the field axes were determined, the magnitude of the Fourier transform for each waveform at each location along the axes was calculated yielding the field intensity at each frequency and axial position. The field intensities for frequencies between 7 and 10 MHz versus the location on the field axes were then normalized and fit by a Gaussian distribution yielding the appropriate frequency-dependent Gaussian dimensions. Also, the location of the focus was allowed to change for the different frequencies because this has been shown to improve the accuracy of the Gaussian approximation.[7] Working with the normalized field intensity at each frequency was equivalent to working with the square of the velocity potential when finding the Gaussian dimensions. Finally, a linear fit was performed on the measured dimensions versus the acoustic wavelength yielding frequency-dependent Gaussian dimensions of $w_z = 17.1\lambda + 924 \cdot 10^{-6}$ m and $w_x = 1.57\lambda + 27.0 \cdot 10^{-6}$ m. Plots showing the measured dimensions and the resulting linear fits are shown in Fig. 3. When λ goes to zero, the beamwidths and depth of focus do not go to zero due to the intercept term. This intercept term is ~25 times larger than the intercept term found for the ideal focused source.[7] Hence, the large intercept results from the sources not being ideally diffraction limited.

The determination of the frequency-dependent Gaussian dimensions of a source using the wire technique is robust. However, it is very time consuming due to the need to map out most of the acoustic field, a problem that is only compounded by diagnostically relevant fields. Furthermore, it provides more information than is required (i.e., w_x). In the companion paper,[7] we demonstrated that in order to correct for focusing along the beam axis when determining the scatterer size we only need to know w_z. Hence, in the next section we explore a faster measurement technique that only yields w_z and is also a simple extension to the calibration methods currently used to obtain a reference in scatterer size estimates.[2,3,5,10]

B. Gaussian dimensions from rigid plane

The second method used to obtain the equivalent frequency-dependent Gaussian dimensions is based on the theoretical backscattered signal from a rigid plane positioned near the focal plane given by[7]

$$V_{plane}(\omega) = \frac{-2\pi w_x w_y k_o^2 G_o^2 V_{inc}(\omega) H^2(\omega)}{S_T (4\pi)^2} \times e^{i2k_o(z_T - z_f)} e^{-2(z_f/w_z)^2}. \quad (2)$$

A measurement for w_z can be obtained from Eq. (2) by varying the location of the plane in the focal region, z_f. Equation (2) includes a complete description of the reflection from the

TABLE I. Relevant properties of transducers used in the phantom experiments.

f#	Center frequency (MHz)	−3 dB bandwidth (MHz)	Transducer diameter (cm)	Scan length (step size) to find w_z	w_z	Depth into phantom (mm)
1	8.7	1.5	2.1	−2 mm→2 mm (50 μm)	$3.22\lambda + 1285$ μm	6
2	8.7	1.6	2.1	−2 mm→2 mm (150 μm)	$16.1\lambda + 802$ μm	12.5
4	9.4	3.8	1.4	−8 mm→8 mm (200 μm)	$76.8\lambda + 4207$ μm	15

plate, unlike the wire technique that neglected the field integration along its length, provided that the velocity potential field from the source obeys a Gaussian distribution. Therefore, the measurement should only be made in the focal region where the Gaussian approximation is valid and secondary field properties (i.e., side lobes and waveform curvature) can be neglected.

Hence, a smooth Plexiglas surface was initially positioned 2 mm past the focal plane for the transducer in a water bath ($z_f = -2$ mm). The Plexiglas was then moved along the beam axis passing through the focus in steps of 150 μm until it was 2 mm in front of the focus ($z_f = 2$ mm) using the Daedal microprecision positioning system, and the echo waveforms were recorded for each Plexiglas location. The magnitude of the Fourier transform was then calculated for each of the acquired waveforms. The resulting magnitude spectra were then divided by the spectrum obtained for the Plexiglas located at the focal plane ($z_f = 0$) for frequencies between 7 and 10 MHz (i.e., normalized for each frequency) and fit by a Gaussian distribution yielding the equivalent Gaussian depth of focus, w_z. Then, a linear fit was performed on the measured depth of focus versus wavelength yielding a frequency-dependent Gaussian depth of focus of $w_z = 16.1\lambda + 802 \cdot 10^{-6}$ m which differed by less than 7.6% from depth of focus found using the wire technique. Therefore, the two methods for measuring the frequency-dependent Gaussian depth of focus along the beam axis, w_z, are equivalent. Due to the reduced measurement time, the measurement of the depth of focus using the rigid plane was also used to determine the w_z values for the other sources used in the phantom experiments. These values are provided in Table I along with the scan length the planar reflector was moved when acquiring the reflections. Variations in the scan length about 4 mm did not significantly change the resulting w_z values, indicating secondary field properties did not dramatically affect the measured Gaussian depth of focus for this scan length.

III. PHANTOM EXPERIMENTS

The phantom experiments were designed to validate the use of focused sources in predicting scatterer size as well as investigate the effects of focusing along the beam axis in greater detail. Hence, the three transducers described in Table I were used to estimate the radius of glass beads in a tissue mimicking phantom. The reported center frequencies and −3 dB bandwidths had been previously measured by a wire reflection technique.[9]

A. Experimental procedure and initial results

The agar phantom used in the experiment was produced at the University of Wisconsin and was part of an interlaboratory comparison of ultrasonic backscatter, attenuation, and sound speed measurements.[11] The phantom consisted of degassed water, agar, *n*-proponal, finely powdered graphite, and glass beads whose radii varied between 22.5 and 26.5 μm with an average concentration of 20.454/mm^3. The attenuation of the phantom (0.55 ± 0.08 dB/cm/MHz) was measured by both insertion loss techniques as well as by observing the change in backscatter with propagation depth into the phantom at room temperature. The sound speed of the phantom was reported by Madsen *et al.*[11] to have a mean value of 1534.4 m/s at 22 °C with a temperature dependence of 1.7 m/s/°C.

The experiments were performed by first positioning a rigid plane at the focus of the transducer in a degassed water bath. The transducers were shock excited using a Panametrics 5900 pulser/receiver operating in pulse-echo mode, and the echo waveforms were captured using a Lecroy 9354 TM digital oscilloscope with a sampling frequency of 100 MHz. The focus was defined as the plane location that resulted in the largest peak–peak voltage for the returned echo waveform. This echo waveform was then recorded as the reference waveform, V_{plane}. The rigid plane used to obtain the reference waveform was made of either Plexiglas or polished metal. The plane was then moved along the beam axis so that the values of w_z could be determined as described previously.

The phantom was then placed such that the reflection from the front surface of the phantom corresponded in time with the previously acquired reference waveform, thereby positioning the front surface of the phantom in the focal plane of the transducer. The focus was then moved into the phantom a known distance by using the Daedal microprecision positioning system. Care was taken so that secondary reflections between the surface of the transducer and the surface of the phantom did not interfere with the speckle from the glass beads. The distance the focus was moved into the phantom for each transducer is also given in Table I. After positioning the focus, 25 independent rf echoes were acquired by moving the phantom along a square grid parallel to the focal plane using the Daedal microprecision positioning system. The grid consisted of five columns and five rows each separated by a distance of 450 μm, 450 μm, and 1 mm for the $f/1$, $f/2$, and $f/4$ transducers, respectively. For each grid position, the echo waveform was averaged between

1000 and 2200 times to remove as much electronic noise as possible.

During processing, each rf echo was windowed by a rectangular gating function centered at the focus, the location of which was known from the reference signal. A rectangular gating function was selected because the traditional attenuation-compensation functions (A_{OO} and A_{OM}) are defined for a rectangular gate. The positioning was done by measuring the water temperature, calculating the sound speed of the water/phantom medium (c_o and c) from the temperature, and then using these sound speeds to position the window at the correct location in time. The length of the gating functions varied from 1 to 13 mm in steps of 0.5 mm with corresponding time gates given by $T_{win}=2L/c$. After windowing, the magnitudes of the Fourier transforms for each rf echo were averaged together yielding an estimate for $E[|V_{refl}(\omega)|^2]$. An estimate for the radius of the glass beads was then obtained by finding the value of a_{eff} that minimized the average squared difference (*ASD*) given,[5]

$$ASD=\underset{\omega}{\text{mean}}[(X(\omega,a_{eff})-\overline{X}(a_{eff}))^2], \tag{3}$$

where

$$\begin{aligned} X(\omega,a_{eff}) &= \ln\left(\frac{E[|V_{refl}(\omega)|^2]}{|V_{plane}(\omega)|^2 k_o^4}\right)+\ln(A_{current}(\omega)) \\ &\quad -\ln\left(\left[\frac{\sin(2ka_{eff})}{2ka_{eff}}\right]^2\right), \\ \overline{X}(a_{eff}) &= \underset{\omega}{\text{mean}}[X(\omega,a_{eff})]. \end{aligned} \tag{4}$$

For the purpose of comparison, the minimization was done for frequencies in the range of 6.5 to 10.5 MHz for all three of the transducers.

The average values of the glass bead radius for window lengths between 3 and 8 mm found using the generalized attenuation-compensation function were 26.1, 22.8, and 22.9 μm for the $f/1$, $f/2$, and $f/4$ transducers, respectively. Hence, the estimated bead radius was well within the range of bead radii known to be in the phantom (i.e., 22.5 to 26.5 μm). In the companion paper,[7] it was shown that the differences between the different attenuation-compensation functions should be relatively constant between different scatterer distributions even though the absolute errors would vary. Hence, the percent difference between the traditional attenuation-compensation functions and the generalized attenuation-compensation function relative to the mean glass bead radius of 24.5 μm was used in the remainder of our evaluation.

The percent difference versus window length for each of the transducers is shown in Fig. 4. λ_0 was the wavelength corresponding to the spectral peak from the reference spectrum (i.e., V_{plane}). The traditional attenuation-compensation functions, A_{PC}, A_{OM}, and A_{OO}, all predict larger bead sizes than the generalized attenuation-compensation function for the $f/1$ and $f/2$ transducers. Also, for the $f/4$ transducer, A_{PC} gives a smaller estimate while A_{OM} and A_{OO} continue to give larger estimates. This same qualitative behavior was

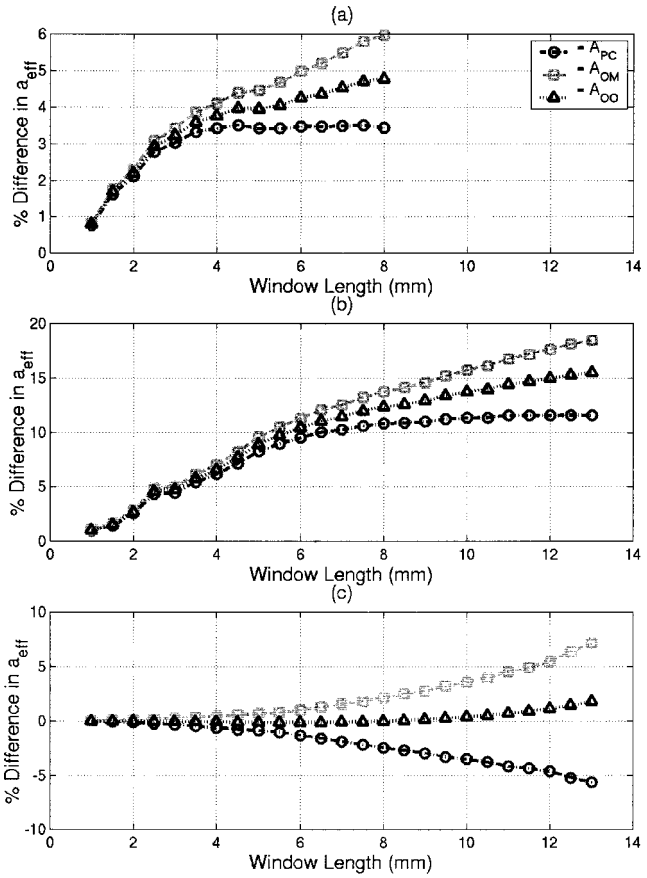

FIG. 4. Experimental results for % differences in a_{eff} versus window length found using traditional attenuation-compensation functions (A_{PC}, A_{OM}, and A_{OO}) as compared to a_{eff} found using A_{comp} for a glass bead phantom with an attenuation of 0.55 ± 0.08 dB/cm/MHz, a concentration of 20.454 beads/mm^3, and a mean bead radius of 24.5 μm from spherically focused transducers with *f*-numbers of (a) $f/1$, (b) $f/2$, and (c) $f/4$.

also observed in our earlier simulation study reported in the companion paper.[7] However, there was not quantitative agreement in the amount of improvement provided by the new generalized attenuation-compensation function.

In the companion paper,[7] the generalized attenuation-compensation function gave an improvement in the scatterer size estimate of 40% to 50% over the traditional attenuation-compensation functions for the $f/2$ transducer with a window length of 13 mm and an attenuation of 0.5 dB/cm/MHz. In the experiment, the $f/2$ transducer only gave an improvement of 12% to 18%. Likewise, the improvement in the experiment for the $f/1$ transducer was only about 3.5% to 6% when our previous simulation study[7] predicted an improvement of 35% to 55%. Also, the $f/1$ transducer yielded improvements in the scatterer size estimate much smaller than the $f/2$ transducer when our previous simulation study[7] indicated that the amount of improvement should plateau at approximately the same values as the window length is increased for both transducers. Even the $f/4$ transducer had less improvement in the experiment (i.e., 7.1% for A_{comp} compared to A_{OM} at 13 mm) as compared to our earlier simulation study[7] (i.e., 17% for A_{comp} compared to A_{OM} at 13 mm). Clearly, these differences in the improvements in the scatterer size estimate when using A_{comp} in the experiment as compared to our earlier simulations[7] need to be understood.

B. Effect of scatterer type

The most obvious difference between our previous simulation study[7] and the phantom experiments is the type of scatterer. Our earlier simulation study[7] used scatterers with Gaussian impedance distributions (i.e., assumed impedance distribution for tissue) whereas the experimental study used glass beads. The form factor for glass beads has a stronger dependence on the scatterer size than does the form factor for Gaussian scatterers. As a result, errors in the minimization routine due to errors in the attenuation-compensation function are less significant when estimating the size of the glass beads. This would result in a decrease in the improvement provided by the new generalized attenuation-compensation function.

In order to test whether the use of glass beads instead of scatterers with Gaussian impedance distributions was responsible for the loss in improvement between our earlier simulation study[7] and the current experimental study, simulations were run using glass beads for the scatterers. However, the sources were still assumed to be diffraction limited whose velocity potential fields had a three-dimensional Gaussian distribution at the focus. Hence, w_z was given by $6.01\lambda f\#^2$, and $w_{x,y}$ was given by $w_x = w_y = 0.87\lambda f\#$. In the new simulations, the attenuation, sound speed, and scatterer concentration were set to the values determined for the phantom. Likewise, the radius of the shells was set at 24.5 μm. One thousand independent scatterer distributions were generated yielding 1000 independent backscattered waveforms. The waveforms were then separated into 40 independent sets with 25 waveforms per set. Each set was then processed to yield 40 independent estimates for the scatterer size.

The simulated sources were also excited by an impulse spike (to model the Panametrics pulse) and had Rayleigh frequency responses found by fitting a Rayleigh distribution [i.e., $f \cdot \exp(-((f-f_R)/\sigma_R)^2)$] to the measured frequency spectrum from the reflection off of the rigid plane at the focus. This was done so that the resulting spectrum of the simulated sources would be as close as possible to the real sources. The bandwidth used in the estimate, however, consisted of the frequencies in the range between 6.5 and 10.5 MHz as was done for the experimental results. Other source parameters, including the depth at which the focus was placed in the simulated phantom, were identical to those provided in Table I.

A plot showing the simulated phantom results is given in Fig. 5. The differences between the different attenuation-compensation functions are greatly reduced. For the $f/4$ transducer at a window length of 13 mm, the difference between the size estimate given by A_{OM} and A_{comp} is 6.4% compared to 7.1% for the experimental results. Likewise, A_{OO} and A_{PC} gave simulated differences from A_{comp} of 2.9% and -1.75%, respectively, comparable to the experimental differences of 1.8% and -5.6%. Similarly, the $f/2$ transducer at a window length of 13 mm gave simulated differences from A_{comp} of 18% for A_{OM}, 15.6% for A_{OO}, and 12.4% for A_{PC} that were very close to the differences of 18.4%, 15.5%, and 11.5%, respectively, that were found experimentally. Therefore, the decrease in improvement discussed previously (i.e., % difference of 12% to 18% instead of 40% to 50% for the $f/2$) can be directly attributed to the type of scatterer being measured. This is of great importance for estimating scatterer sizes of biological tissue because the fundamental scatterer geometry (type) in tissue has not been determined. Hence, the improvement of the new generalized attenuation-compensation function compared to the traditional attenuation-compensation functions may be even more significant in a clinical setting because the correct scatterer geometry may exhibit an even stronger dependence on the attenuation-compensation function.

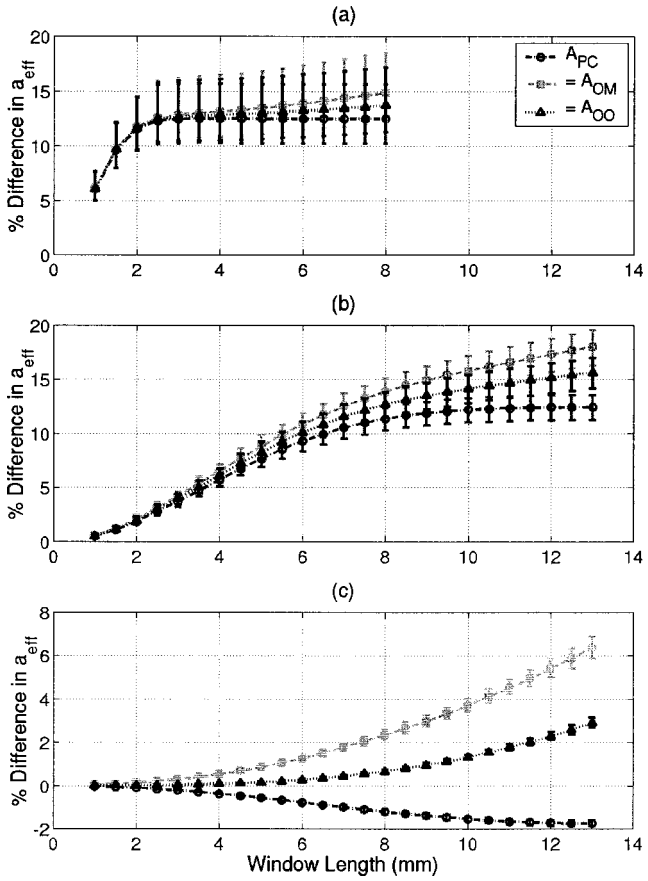

FIG. 5. Simulation results for % difference in a_{eff} found using traditional attenuation-compensation functions (A_{PC}, A_{OM}, and A_{OO}) as compared to a_{eff} found using A_{comp} for a glass bead phantom with an attenuation of 0.55 ± 0.08 dB/cm/MHz, a concentration of 20.454 beads/mm^3, and bead radius of 24.5 μm from spherically focused transducers with *f*-numbers of (a) $f/1$, (b) $f/2$, and (c) $f/4$, and $w_z = 6.01\lambda f\#^2$.

C. Effect of wavelength dependence of focusing

Although the type of scatterer and the subsequent dependence on the attenuation-compensation function explains the reduction in the improvement provided by the new attenuation compensation function, it does not explain why the plateau of the $f/1$ transducer (i.e., difference from A_{comp} for A_{PC} of 3.4%) was different than the plateau for the $f/2$ transducer (i.e., difference from A_{comp} for A_{PC} of 11.5%). The previous simulation study (Sec. III B) showed them converging to the same value whereas, in the experiment, they converged to different amounts of improvement. In order to understand this behavior, we explore another difference between the previous simulation studies and the experimen-

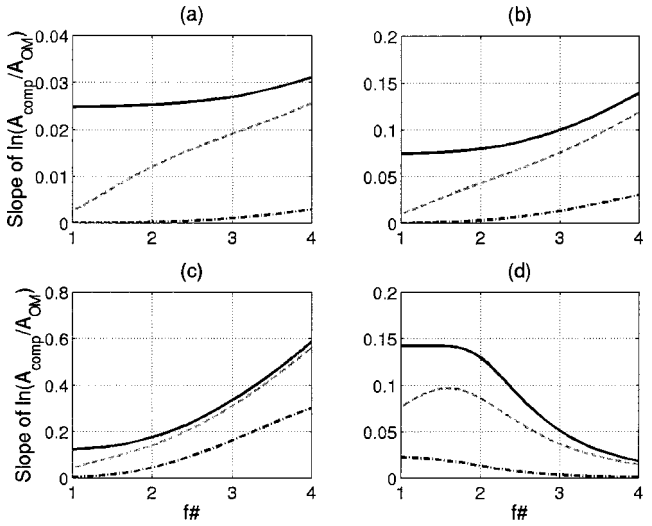

FIG. 6. Calculated slope of $\ln(A_{comp}/A_{OM})$ versus frequency for transducers with varying degrees of focusing (i.e., $f\#$). The three curves in the plots correspond to w_z values with three different dependencies on wavelength; ——— for $w_z = 6.01(f\#)^2 \cdot \lambda$, – – – for $w_z = 6.01(f\#)^2 \cdot \lambda + 1285\ \mu$m, and -·- for $w_z = 6.01(f\#)^2 \cdot (181\ \mu\text{m})$. The plots had (a) window length normalized to the depth of focus (i.e., $7.08\lambda_0 f\#^2$) of 0.5, (b) window length normalized to the depth of focus (i.e., $7.08\lambda_0 f\#^2$) of 1, (c) window length normalized to the depth of focus (i.e., $7.08\lambda_0 f\#^2$) of 2.5, and (d) window length of 8 mm.

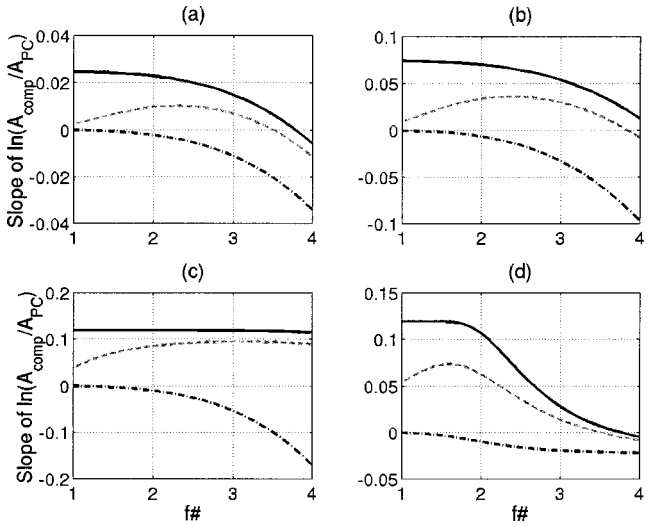

FIG. 7. Calculated slope of $\ln(A_{comp}/A_{PC})$ versus frequency for transducers with varying degrees of focusing (i.e., $f\#$). The three curves in the plots correspond to w_z values with three different dependencies on wavelength; ——— for $w_z = 6.01(f\#)^2 \cdot \lambda$, – – – for $w_z = 6.01(f\#)^2 \cdot \lambda + 1285\ \mu$m, and -·- for $w_z = 6.01(f\#)^2 \cdot (181\ \mu\text{m})$. The plots had (a) window length normalized to the depth of focus (i.e., $7.08\lambda_0 f\#^2$) of 0.5, (b) window length normalized to the depth of focus (i.e., $7.08\lambda_0 f\#^2$) of 1, (c) window length normalized to the depth of focus (i.e., $7.08\lambda_0 f\#^2$) of 2.5, and (d) window length of 8 mm.

tal study: the wavelength dependence of the effective Gaussian depth of focus along the beam, axis, w_z. In the earlier simulations, w_z was directly proportional to the wavelength [i.e., $w_z = 6.01(f\#)^2 \cdot \lambda$], but, in the experiment, w_z had the form

$$w_z = w_{zm} \cdot \lambda + w_{zb}, \tag{5}$$

where w_{zb} was a constant independent of wavelength (Table I).

In order to understand the impact of the wavelength dependence of w_z, the curves of $\ln(A_{comp}/A_{OM})$ and $\ln(A_{comp}/A_{PC})$ versus frequency were fit by a line. The slope of this line could then be used to predict how the scatterer size estimate from A_{comp} would compare to the estimate from A_{OM} and A_{PC}. A positive slope means that the estimate from $A_{PC/OM}$ is larger than the estimate obtained from A_{comp}. Likewise, a negative slope means that the estimate from $A_{PC/OM}$ is smaller than the estimate from A_{comp}. The wavelength dependence of w_z was evaluated for three different w_z values: (a) $6.01(f\#)^2 \cdot \lambda$, as was used in the previous simulation study,[7] (b) $6.01(f\#)^2 \cdot \lambda + 1285\ \mu$m, similar to the wavelength dependence found for the measured transducers, and (c) $6.01(f\#)^2 \cdot (181\ \mu\text{m})$. The calculations were performed for window lengths normalized to the traditional depth of focus (i.e., $7.08\lambda_0 f\#^2$) of 0.5, 1, and 2.5 as well as for a window length of 8 mm. The resulting slopes are shown in Figs. 6 and 7.

Consider first the w_z values of $6.01(f\#)^2 \cdot \lambda$ shown by the solid curves. For any given normalized window length, the A_{OM} estimate is larger than the A_{comp} estimate and increases with increasing *f*-number. Likewise, the A_{PC} estimate is larger than the A_{comp} estimate for smaller *f*-numbers and then decreases with increasing *f*-number for smaller normalized window lengths resulting in the A_{PC} estimate being smaller than the A_{comp} estimate. For larger normalized window lengths, the A_{PC} estimate is always larger than the A_{comp} estimate and there is no longer any dependency on *f*-number corresponding to the plateau observed earlier.

Now consider the w_z values illustrated by the remaining curves. The sizes of the $A_{PC/OM}$ estimates relative to the size of the A_{comp} estimate are reduced as the wavelength dependency of w_z is reduced as is illustrated by the dash-dot-dash curve $[6.01(f\#)^2 \cdot \lambda + 1285\ \mu\text{m}]$ being lower than the dashed curve $[6.01(f\#)^2 \cdot (181\ \mu\text{m})]$. Also, for w_z given by $6.01(f\#)^2 \cdot \lambda + 1285\ \mu$m, the estimates approach the $6.01(f\#)^2 \cdot \lambda$ curve for larger *f*-number and approach the $6.01(f\#)^2 \cdot (181\ \mu\text{m})$ curve for smaller *f*-number. As a result, the A_{PC} estimates no longer plateau independent of *f*-number. Therefore, the $f/1$ transducer used in the experiment should have yielded a smaller difference between the A_{PC} and A_{comp} estimates than the $f/2$ transducer, just as was observed, due to its weaker dependence on wavelength.

The results for A_{PC} as compared to A_{comp} at large normalized window lengths can also be shown mathematically. For sufficiently large window lengths, the integral along the beam axis in A_{comp} can be evaluated in closed form, yielding

$$A_{comp}(\omega) = \frac{2}{w_z\sqrt{\pi}} e^{4\alpha_{\text{eff}} z_T} e^{-\alpha^2 w_z^2}. \tag{6}$$

Hence, the derivative of $\ln(A_{comp}/A_{PC})$ versus frequency is given by

$$\frac{\partial}{\partial f}\left\{\ln\left(\frac{A_{comp}}{A_{PC}}\right)\right\} = -\frac{1}{w_z}\frac{\partial w_z}{\partial f} - 2(\alpha w_z) \times\left[w_z\frac{\partial \alpha}{\partial f} + \alpha\frac{\partial w_z}{\partial f}\right], \tag{7}$$

which can be simplified to

$$\frac{\partial}{\partial f}\left\{\ln\left(\frac{A_{comp}}{A_{PC}}\right)\right\} = \frac{w_{zm}c(f^{-2})}{w_{zm}\cdot\lambda + w_{zb}} + \left[2\alpha^2[w_{zm}\cdot\lambda + w_{zb}]w_{zm}c(f^{-2}) - 2\alpha[w_{zm}\cdot\lambda + w_{zb}]^2\frac{\partial\alpha}{\partial f}\right] \tag{8}$$

if w_z has the form given in Eq. (5). Hence, the significance of the wavelength dependence of w_z is also affected by the magnitude and frequency dependence of the attenuation. For the purpose of comparison, we will assume that the attenuation has a strict linear frequency dependence (i.e., $\alpha = \alpha_o \cdot f$), allowing Eq. (8) to be rewritten as

$$\frac{\partial}{\partial f}\left\{\ln\left(\frac{A_{comp}}{A_{PC}}\right)\right\} = \frac{1}{f}\left(\frac{w_{zm}\cdot\lambda}{w_{zm}\cdot\lambda + w_{zb}}\right) - 2\alpha_o^2 f w_{zb}[w_{zm}\cdot\lambda + w_{zb}]. \tag{9}$$

Hence, if $w_{zb}=0$, then the slope of $\ln(A_{comp}/A_{PC})$ versus frequency is equal to $1/f$ and is independent of the value of w_{zm}. Likewise, if $w_{zm}=0$, then the slope of $\ln(A_{comp}/A_{PC})$ versus frequency decreases approximately parabolically with increasing values of w_{zb}. Both of these effects are evident in Fig. 7(c).

In order to further test the impact of the wavelength dependence of w_z on the different attenuation-compensation functions, the simulation of the glass bead phantoms was repeated using the w_z values found experimentally. Once again, the attenuation, sound speed, and scatterer concentration were set to the values determined for the phantom, and the radius of the shells was set at 24.5 μm. Also, 40 independent estimates were obtained for 1000 independent scatterer distributions that were generated and then processed in groups of 25 using frequencies in the range between 6.5 and 10.5 MHz. The simulated sources were also modeled to have the same Rayleigh frequency response as was found experimentally and were excited by an impulse spike. The resulting differences between the different attenuation-compensation functions are shown in Fig. 8.

Once the measured values for w_z were used in the simulations, the differences between A_{comp} and the other attenuation-compensation functions for the $f/1$ transducer at 8 mm were 7.4%, 5.9%, and 4.3% whereas the differences for the $f/2$ transducer at 13 mm were 16%, 13.4%, and 10% for A_{OM}, A_{OO}, and A_{PC}, respectively. Hence, A_{PC} for the $f/1$ transducer and the $f/2$ transducer now plateau at different levels in agreement with the observed experimental results. Therefore, the wavelength dependence of w_z was responsible for their earlier discrepancy. Furthermore, the differences found experimentally and the mean differences found in the simulations using the correct value for w_z were consistently within 2.5% of each other, validating the theoretical analysis provided in the companion paper.[7]

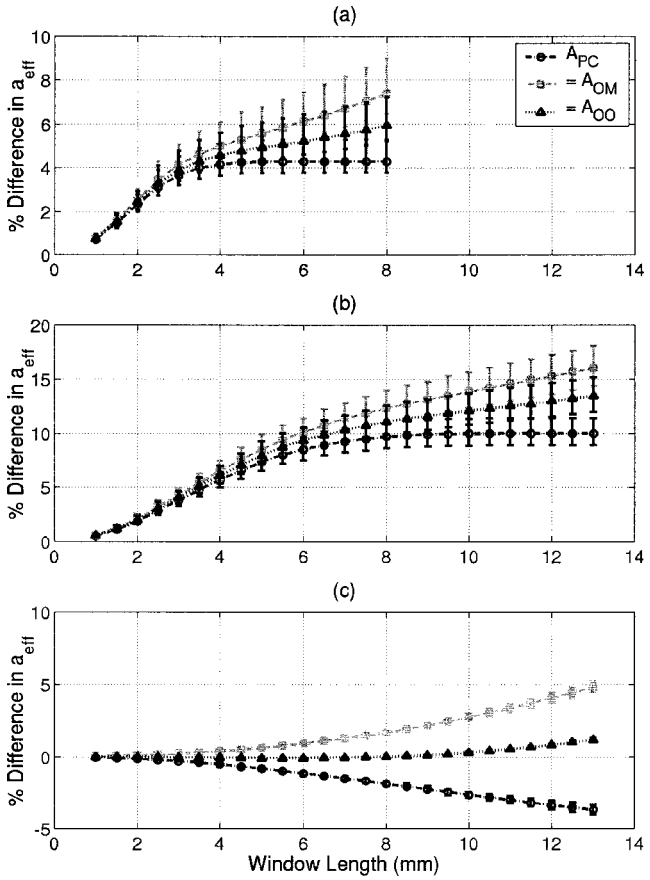

FIG. 8. Simulation results for % difference in a_{eff} found using the traditional attenuation-compensation functions (A_{PC}, A_{OM}, and A_{OO}) as compared to a_{eff} found using A_{comp} for a glass bead phantom with an attenuation of 0.55 ± 0.08 dB/cm/MHz, a concentration of 20.454 beads/mm^3, and bead radius of 24.5 μm from spherically focused transducers with *f*-numbers of (a) $f/1$, (b) $f/2$, and (c) $f/4$, and w_z as given in Table I.

IV. CONCLUSIONS

In this paper, we further explored the use of focused sources for estimating scatterer sizes. First, we compared two different methods to calibrate a focused source, and found that simply recording/processing the echoes from a rigid plane moved along the beam axis could yield sufficient calibration information. This calibration routine is a straightforward extension to the current calibration techniques used to obtain a reference in scatterer size estimates.[2,3,5,10] Then, we attempted to validate our previous theoretical work by using real focused transducers to estimate the size of glass beads in a tissue mimicking phantom. We found agreement better than 2.5% provided that the same type of scatterers and sources were being compared. Errors in the attenuation-compensation function when estimating the radius of the glass beads were much less significant than the same errors when estimating the radius of a Gaussian scatterer, indicating a strong dependence on the type of scatterer when assessing the accuracy of any attenuation-compensation function. Lastly, we explored the effects of focusing in greater detail

and found that the improvement provided by the new generalized attenuation-compensation function decreases as the wavelength dependence of w_z was reduced.

The dependence of the performance of the attenuation-compensation function on the scatterer type is very important in light of the reference phantom technique that has recently been proposed to correct for focusing when estimating the characteristic size of the tissue microstructure.[12] Namely, tissue mimicking phantoms with glass beads should not be used to test the validity of the reference phantom technique as an attenuation-compensation method because the estimation of glass bead radius has a very weak dependence on the attenuation-compensation function. Hence, if the reference phantom technique introduces large errors into the compensation for attenuation and focusing, these errors will not be detected in phantom experiments using glass beads. Ideally, the assessment should be done using real tissue. However, the real size of scatterers in tissue is not known, so simulation studies similar to those presented in this paper may have to suffice. Another possibility would be to use tissue while using our generalized attenuation-compensation function as a standard to which the reference phantom results could be compared.

From these results, it is clear that weakly focused sources are not required when estimating the scatterer size even for window lengths much greater than the depth of focus for the source. Because increased focusing provides for increased signal-to-noise ratios and better lateral resolution, focused sources may perform better when quantifying the size of the tissue microstructure. However, the exact effect of focusing on signal-to-noise ratios as it applies to scatterer size estimation remains to be quantified.

ACKNOWLEDGMENTS

A special thanks to Deepti Narla for her help in acquiring the wire reflection data. This work was supported by the University of Illinois Research Board, by a NDSEG Fellowship awarded to T. A. Bigelow, and by a Beckman Institute Graduate Fellowship awarded to T. A. Bigelow.

[1] T. Wang, J. Saniie, and X. Jin, ''Analysis of low-order autoregressive models for ultrasonic grain signal characterization,'' IEEE Trans. Ultrason. Ferroelectr. Freq. Control **38**(2), 116–124 (1991).
[2] M. L. Oelze, J. F. Zachary, and W. D. O'Brien, Jr., ''Characterization of tissue microstructure using ultrasonic backscatter: theory and technique optimization using a Gaussian form factor,'' J. Acoust. Soc. Am. **112**, 1202–1211 (2002).
[3] F. L. Lizzi, M. Greenebaum, E. J. Feleppa, and M. Elbaum, ''Theoretical framework for spectrum analysis in ultrasonic tissue characterization,'' J. Acoust. Soc. Am. **73**, 1366–1373 (1983).
[4] M. F. Insana and T. J. Hall, ''Parametric ultrasound imaging from backscatter coefficient measurements: image formation and interpretation,'' Ultrason. Imaging **12**, 245–267 (1990).
[5] M. F. Insana, R. F. Wagner, D. G. Brown, and T. J. Hall, ''Describing small-scale structure in random media using pulse-echo ultrasound,'' J. Acoust. Soc. Am. **87**, 179–192 (1990).
[6] F. L. Lizzi, M. Astor, T. Liu, C. Deng, D. J. Coleman, and R. H. Silverman, ''Ultrasonic spectrum analysis for tissue assays and therapy evaluation,'' Int. J. Imaging Syst. Technol. **8**, 3–10 (1997).
[7] T. A. Bigelow and W. D. O'Brien, Jr., ''Scatterer size estimation in pulse-echo ultrasound using focused sources: Theoretical approximations and simulation analysis,'' J. Acoust. Soc. Am. **116**, 578–593 (2004).
[8] P. Chaturvedi and M. F. Insana, ''Error bounds on ultrasonic scatterer size estimates,'' J. Acoust. Soc. Am. **100**, 392–399 (1996).
[9] K. Raum and W. D. O'Brien, Jr., ''Pulse-echo field distribution measurement technique for high-frequency ultrasound sources,'' IEEE Trans. Ultrason. Ferroelectr. Freq. Control **44**(4), 810–815 (1997).
[10] E. L. Madsen, M. F. Insana, and J. A. Zagzebski, ''Method of data reduction for accurate determination of acoustic backscatter coefficients,'' J. Acoust. Soc. Am. **76**, 913–923 (1984).
[11] E. L. Madsen, F. Dong, G. R. Frank, B. S. Garra, K. A. Wear, T. Wilson, J. A. Zagzebski, H. L. Miller, K. Kirk Shung, S. H. Wang, E. J. Feleppa, T. Liu, W. D. O'Brien, Jr., K. A. Topp, N. T. Sanghvi, A. V. Zaitsev, T. J. Hall, J. B. Fowlkes, O. D. Kripfgans, J. G. Miller, ''Interlaboratory comparison of ultrasonic backscatter, attenuation, and speed measurements,'' J. Ultrasound Med. **18**, 615–631 (1999).
[12] A. Gerig, J. Zagzebski, and T. Varghese, ''Statistics of ultrasonic scatterer size estimation with a reference phantom,'' J. Acoust. Soc. Am. **113**, 3430–3437 (2003).

Erratum: "The acoustical Klein-Gordon equation: The wave-mechanical step and barrier potential functions" [J. Acoust. Soc. Am. 114(3), 1291–1302 (2003)]

Barbara J. Forbes[a)]
Phonologica, PO Box 43925, London NW2 1DJ, UK

E. Roy Pike
Department of Physics, King's College London, Strand, London, WC2R 2LS, UK

David B. Sharp
Department of Environmental and Mechanical Engineering, The Open University, Walton Hall, Milton Keynes, MK7 6AA, UK

(Received 26 April 2004; revised 28 April 2004; accepted 29 April 2004)

[DOI: 10.1121/1.1763951]

PACS numbers: 43.20.Ks, 43.20.Mv, 43.70.Bk, 43.10.Vx [ADP]

Equations (46) and (82) should read

$$F_n \approx \frac{c}{2\pi}\left\{\frac{-\arctan(\gamma_n^{-1})+\left(n+\frac{1}{2}\right)\pi}{l}\right\}, \quad n=0,1,2...,$$

and

$$\arg R = -(2ak+\theta),$$

respectively.

The second sentence below Fig. 13 on p. 1301 should read: ''Further, they were found to be identical, up to a scaling factor of $[S(L)]^{-1/2}$, with those of the equivalence set.''

[a)]Electronic mail: forbes@phonologica.com

 0001-4966/2004/116(1)/603/1/$20.00